CAS IHEP

LINAC18

29th Linear Accelerator Conference
September 16-21, 2018, Friendship Hotel, Beijing, China

https://indico.ihep.ac.cn/e/linac18
Email:linac18@ihep.ac.cn

Main Topics

Electron Accelerators and Applications
Proton and Ion Accelerators and Applications
Linear Accelerator Technology
Beam Dynamics, Extreme Beams, Sources and Beam Related Technology

Important Dates

Abstract Submission Deadline: April 15, 2018
Early Registration Deadline: June 11, 2018

LINAC18 IOC Members

Guoxi Pei (IOC Chair)	**IHEP, China**
John Barnard	LLNL, USA
Winfried Barth	GSI, Germany
Dan Berkovits	Soreq, Israel
Enrica Chiadroni	INFN, Italy
Hakan Danared	ESS, Sweden
Jean Delayen	ODU, USA
Alberto Facco	FRIB/INFN, USA/Italy
Robert W. Garnett	LANL, USA
Roland Garoby	ESS, Sweden
Terence Garvey	PSI, Switzerland
Kazuo Hasegawa	JAEA, Japan
Hitoshi Hayano	KEK, Japan
Yoshihisa Iwashita	Kyoto U., Japan
Kevin W. Jones	SNS, USA
Heung-Sik Kang	PAL, Korea
Dinakar Kanjilal	IUAC, India
Leonid Kravchuk	INR, Russia
Robert E. Laxdal	Triumf, Canada
L.K. Len	DOE, USA
Peter McIntosh	STFC, UK
Alban Mosnier	CEA, France
Peter Ostroumov	ANL/FRIB, USA
Fulvia Pilat	JLAB, USA
Milorad Popovic	FNAL, USA
Deepak Raparia	BNL, USA
Ulrich Ratzinger	U. Frankfurt, Germany
Stanley Schriber	Ldaho, USA
John Seeman	SLAC, USA
Alessandro Variola	LAL, France
Maurizio Vretenar	CERN
Hans Weise	DESY, Germany
Marion White	ANL, USA
Yoshishige Yamazaki	FRIB, USA




LINAC18
29th Linear Accelerator Conference
September 16-21, 2018, Friendship Hotel, Beijing China
FRIENDSHIP PALACE

International Organization Committee

Name	Institute
Guoxi Pei (IOC Chair)	IHEP, China
John Barnard	LLNL, USA
Winfried Barth	GSI, Germany
Dan Berkovits	Soreq, Israel
Enrica Chiadroni	INFN, Italy
Hakan Danared	ESS, Sweden
Jean Delayen	ODU, USA
Alberto Facco	FRIB/INFN, USA/Italy
Robert W. Garnett	LANL, USA
Roland Garoby	ESS, Sweden
Terence Garvey	PSI, Switzerland
Kazuo Hasegawa	JAEA, Japan
Hitoshi Hayano	KEK, Japan
Yoshihisa Iwashita	Kyoto U., Japan
Kevin W. Jones	SNS, USA
Heung-Sik Kang	PAL, Korea
Dinakar Kanjilal	IUAC, India
Leonid Kravchuk	INR, Russia
Robert E. Laxdal	Triumf, Canada
L.K. Len	DOE, USA
Peter McIntosh	STFC, UK
Olivier Napoly	CEA, France
Peter Ostroumov	ANL/FRIB, USA
Fulvia Pilat	JLAB, USA
Milorad Popovic	FNAL, USA
Deepak Raparia	BNL, USA
Ulrich Ratzinger	U. Frankfurt, Germany
Stanley Schriber	Retired, Idaho, USA
John Seeman	SLAC, USA
Alessandro Variola	LAL, France
Maurizio Vretenar	CERN, Switzerland

Hans Weise	DESY, Germany
Marion White	ANL, USA
Yoshishige Yamazaki	FRIB, USA

Scientific Program Committee

Name	Institute
Alexander Aleksandrov	ORNL, USA
Dan Berkovits	Soreq, Israel
Kip Bishofberger	LANL, USA
Graeme Burt	Cockcroft Institute, UK
Alok Chakrabarti	VECC, India
Enrica Chiadroni	INFN/LASA, Italy
Yong Ho Chin (SPC Co-Chair)	KEK, Japan
Yong-Sub Cho	KAERI, Korea
Stefan Choroba	DESY, Germany
Eric Colby	OHEP/DOE, USA
Jean Delayen	ODU, USA
Alberto Facco	INFN/LNL, Italy
Robin Ferdinand	GANIL, France
Shinian Fu (SPC Co-Chair)	IHEP, China
Terence Garvey	PSI, Switzerland
Cameron Geddes	LBNL, USA
Frank Gerigk	CERN, Switzerland
Lars Groening	GSI, Germany
Kazuo Hasegawa	JEAE, Japan
Dong-O Jeon	IBS, Korea
Walid Kaabi	LAL, France
Osamu Kamigaito	RIKEN, Japan
Shigeru Kashiwagi	Tohoku Univ., Japan
Sang-Ho Kim	ORNL, USA
Geoffrey Krafft	JLab, USA
Timur Kulevoy	ITEP, Russia
Robert Laxdal	TRIUMF, Canada
Matthias Liepe	Cornell, USA
Oliver Napoly	CEA/DSM/IRFU, France
Subrata Nath	LANL, USA

Peter Ostroumov	MSU, USA
Yuji Otake	Spring-8, Japan
Valentin Paramonov	RAS/INR, Russia
Milorad Popovic	FNAL, USA
Jürgen Pozimski	Imperial College London, UK
Deepak Raparia	BNL, USA
Tor Raubemheimer	SLAC, USA
Alwin Schempp	IAP, Germany
Daniel Schulte	CERN, Switzerland
Nikolay Solyak	FNAL, USA
Chuanxiang Tang	TUB, China
Sami Tantawi	SLAC, USA
Alexey Tribendis	NSTU, Russia
Dong Wang	SINAP, China
Hans Weise	DESY, Germany
Guan Xialing	CIAE, China
Vyacheslav Yakovlev	FNAL, USA
Yoshishige Yamazaki	MSU, USA
Hongwei Zhao	IMP/CAS, China
Shu-xin Zheng	TUB, China

Local Organization Committee

Name	Institute
Yunlong Chi (LOC chair)	IHEP, China
Xueying Hou	IHEP, China
Ning Zhao	IHEP, China
Qian Pan	IHEP, China
Lin Bian	IHEP, China
Jie Zhou	IHEP, China
Jiyuan Zhai	IHEP, China
Xing Liu	IHEP, China

Contents

Preface i
Committees . . . iii
Contents . . . vi

Papers 1
MO1A01 – CSNS Front End and Linac Commissioning . . . 1
MO1A02 – An Overview of Recent Developments in SRF Technology . . . 6
MO2A03 – Technology Developments for ELI-NP Gamma Beam System . . . 13
MO2A04 – Compact SRF Linac for High Brilliance Inverse Compton Scattering Light Source . . . 19
MO1P01 – Status of the SNS Proton Power Upgrade Project . . . 24
MO1P02 – Approaches to High Power Operation of J-PARC Accelerator . . . 29
MO1P03 – Status of the ESS Linac . . . 35
MOPO004 – Commissioning of the SRF Booster Cavity for LEReC . . . 40
MOPO005 – Commissioning of the Normal Conducting Cavities for LEReC Project . . . 44
MOPO006 – Crosstalk Effect in the LEReC Booster Cavity . . . 47
MOPO007 – The Developing of the Beam Injection Section with Laser Source and S-Band Electron RF Gun for SuperKEKB Project . . . 50
MOPO008 – The RF Gun Adopting the Dielectric Assist Accelerating Structure . . . 54
MOPO009 – ELI-NP Gamma Beam System - Current Project Status . . . 59
MOPO010 – JINR Photocathode Research: Status and Plans . . . 62
MOPO016 – Narrow-Band Terahertz Generation from Beam Pipe with Helix Wires . . . 65
MOPO018 – Development of an Improved Capture Section for the S-DALINAC Injector* . . . 68
MOPO019 – Study on Cleaning of Copper Plated Bellows for LCLS-II . . . 71
MOPO020 – Beam Dynamics Studies and Instrumentation Tests for Bunch Length Measurements at CLEAR . 74
MOPO024 – Development of High Power Coherent Terahertz Wave Sources at Lebra 125 MeV Linac in Nihon University . . . 78
MOPO026 – The Resonance Frequency Shift After Applying the Cooling System for a Side Coupled Standing Wave Linac . . . 81
MOPO027 – Photocathode Laser Pulse Shaping for Improved Emittance . . . 84
MOPO028 – Survey and Alignment System of 100 MeV/100 kW Electron Linear Accelerator . . . 87
MOPO029 – Physics design and dynamic simulation of a C-band photocathode electron gun for UEM . . . 90
MOPO034 – Dielectric Waveguide-Based THz Radiator Study for SwissFEL . . . 94
MOPO035 – Status of CLARA Front End Commissioning . . . 98
MOPO036 – Status of the 10 MW MBKs during Commissioning of the European XFEL in DESY . . . 102
MOPO037 – SRF Gun Development at DESY . . . 105
MOPO038 – RF Operation Experience at the European XFEL . . . 109
MOPO039 – Status Update of the Fast Energy Corrector Cavity at FLASH . . . 112
MOPO040 – Coherent Synchrotron Radiation Monitor for Microbunching Instability in XFEL . . . 115
MOPO041 – Performance Test Results of Magnet Power Supply . . . 118
MOPO042 – Evolutionary Many-objective Optimization Algorithm for Large-bandwidth Free-Electron-Laser Generation . . . 121
MOPO058 – Industrial Electron Linear Accelerator R&D in CIAE . . . 124
MOPO059 – Choke-Type Resonator for a Compact Storage Ring . . . 126
MOPO060 – Linacs for Industry, Cargo Inspection and Medicine Designed by Moscow University . . . 130
MOPO061 – Beam Parameters Measurement of C-band 6 MeV Linear Electron Accelerator . . . 133
MOPO062 – Linear Electron Accelerator for Radiation Technologies with Beam Parameters Varied in a Wide Range 136
MOPO063 – Development of Side-coupled X-band Medical Linear Accelerator for Radiotherapy . . . 139
MOPO064 – O-Arm Mounted X-Band Linear Accelerator System for Radiotherapy . . . 142
MOPO066 – Simulation of the Transitional Process in Accelerating Sections by Equivalent Circuit Method . . . 145
MOPO069 – Nuclear and Mechanical Basic Design of Target for Mo-99 Production Using High Power Electron Linac . . . 148
MOPO070 – Construction of the Side-coupled Standing-wave e-Linac . . . 151
MOPO073 – Coherent Edge Radiation Sources in Linac-Based Infrared Free-Electron Laser Facilities . . . 154
MOPO076 – Study on Generation of Variable Polarized Coherent THz Radiation Using a Crossed Undulator . . 157
MOPO077 – Design of the High Gradient Negative Harmonic Structure for Compact Ion Therapy Linac . . . 160

MOPO079 – Cavity Design of a 7 MeV 325 MHz Proton APF IH-DTL for a Compact Injector . . . 163
MOPO080 – The Manufacturing of the CSNS DTL Tank . . . 167
MOPO081 – Light Proton Therapy Linac LLRF System Development . . . 171
MOPO082 – Commissioning Status of the Linac for the iBNCT Project . . . 174
MOPO084 – The Simulation and Manufacture of the Room Temperature CH-DTL . . . 177
MOPO085 – Prototype of an Inter-digital H-mode Drift-tube Linac for Muon Linac . . . 180
MOPO087 – Cold Test of Hybrid RFQ Prototype . . . 184
MOPO088 – Study on a 325 MHz HOM Drift Tube Linac . . . 187
MOPO089 – Design Details of the European Spallation Source Drift Tube LINAC . . . 190
MOPO090 – Measurements of the First Room Temperature CH Cavity for MYRRHA at IAP Frankfurt . . . 193
MOPO092 – A 3-gap Booster Cavity to Match Ion Source Potential to RFQ Acceptance . . . 196
MOPO093 – A Study of a Cooling Configuration for an OFHC Copper Rebuncher . . . 200
MOPO094 – RF Stability Test of RFQ Cavity with Prototype Low-level Radio Frequency in RAON . . . 204
MOPO095 – A Risk Based Approach to Improving Beam Availability at an Accelerator Facility . . . 207
MOPO096 – Realistic Modeling of MEBT for the New LANSCE RFQ Injector . . . 211
MOPO100 – Doubly Stripped Proton Causing Vacuum Leak at Brookhaven 200 MeV H^- linac Complex . . . 214
MOPO101 – LINAC-multitool - an Open Source Java-toolkit . . . 217
MOPO102 – Progress of MicroTCA.4 based LLRF System of TARLA . . . 220
MOPO104 – LLRF R&D Towards CW Operation of the European XFEL . . . 223
MOPO106 – New Digital LLRF System for HIT . . . 227
MOPO107 – Performance Evaluation of the RF Reference Phase Stabilization System on Fiber-optical Link for KEK e^-/e^+ Injector LINAC . . . 230
MOPO111 – Development of New LLRF System at the J-PARC Linac . . . 233
MOPO115 – CEBAF Photo Gun RF System . . . 236
MOPO116 – Study on the Control Technology of Large-load Time Constant Accelerator Magnet Power Supply 239
MOPO118 – Optimized Design for a Compact Linac with Collinear Absorbing Loads at the Hust FEL-THz . . . 242
MOPO119 – Design of a Fully Automated Test Bench for Measuring the Field Distribution in Standing Wave Cavity 246
MOPO120 – Improvement of the Linear Part in the Tuner System of ADS 25 MeV Linac . . . 250
MOPO121 – Large-Scale Optical Synchronization System of the European XFEL . . . 253
MOPO122 – European XFEL Cooling and Ventilation Systems . . . 257
MOPO124 – Details of the Manufacturing Processes of the ESS-DTL Components . . . 260
MOPO125 – Steering Magnets with Permanent Magnets . . . 264
MOPO127 – Recent Results from MICE on Multiple Coulomb Scattering and Energy Loss . . . 267
MOPO129 – Recent Results from the Study of Emittance Evolution at MICE . . . 270
MOPO130 – Magnetic Flux Generated by Thermal Current in CEBAF 5-Cell Cavity System . . . 273
MOPO132 – The 7 MeV APF DTL for Proton Therapy . . . 277
TU1A01 – Challenges in Superconducting Accelerating Module Design and Construction for High Power Proton Accelerators . . . 280
TU1A03 – Status and Issues (Microphonics, LFD, MPS) with TRIUMF ARIEL e-Linac Commissioning . . . 286
TU1A05 – Seamless Quarter Wave Resonators for HIE ISOLDE . . . 292
TU2A01 – First Acceleration of Heavy Ion Beams with a Superconducting Continuous Wave HIM/GSI CW-linac 297
TU2A03 – Layout of the New FAIR Post-stripper DTL for Intense Heavy Ion Beams . . . 303
TU2A04 – Progress Report on LIPAC . . . 308
TU1P01 – Extreme High Brightness Electron Beam Generation in a Space Charge Regime . . . 314
TUPO001 – About the Limits for the Accelerated Beam Current in the LUE-200 Linac of the IREN Facility . . . 320
TUPO002 – Electron Gun for 100 MeV / 100 kW Linear Accelerator of Electrons as the Driver of Nuclear Subcritical Assembly Neutron Source . . . 323
TUPO003 – Development of CW Heavy Ion Linac at IMP . . . 326
TUPO004 – RF Design and Cold Model Measurement of an IH-DTL for HIMM Injector . . . 329
TUPO005 – Initial Beam Commissioning of LEAF at IMP . . . 332
TUPO007 – FRIB Fast Machine Protection System: Chopper Monitor System Design . . . 336
TUPO009 – Heat Treatment for a Prototype Half-Wave Resonator Cavity . . . 339
TUPO010 – Muon Acceleration Test with the RFQ Towards the Development of the Muon Linac . . . 342
TUPO011 – Upgrade of Heavy Ion Injector I-3 at ITEP . . . 346
TUPO012 – Compact Multipurpors Facility - BELA . . . 349
TUPO013 – Commissioning Status of the LIGHT Development Machine . . . 352

TUPO014 – TRIUMF ISAC LINAC Developments and Upgrades . . . 355
TUPO016 – High Frequency RFQ Design and LEBT Matching for the CERN TwinEBIS Ion Source . . . 358
TUPO017 – The New Light Ion Injector for NICA . . . 362
TUPO019 – SPIRAL2 Cryogenic System Thermodynamic Behavior Prediction Through Dynamic Modeling . . . 366
TUPO020 – Microphonics Investigation of ARIEL e-Linac Cryomodules . . . 370
TUPO022 – Manufacturing of X-band Accelerating Structures: Metrology Analysis and Process Capability . . . 374
TUPO023 – Preserving Micron Tolerances Through the Assembly Process of an X-band Accelerating Structure 377
TUPO027 – Series Production of the Specific Waveguide Distribution for the European XFEL at DESY . . . 380
TUPO028 – Retreatment of European XFEL Series Cavities at DESY as Part of the Repair of European XFEL Accelerating Modules . . . 384
TUPO029 – Highlights of the XM-3 Cryomodule Tests at DESY . . . 388
TUPO030 – Precise Evaluation of Characteristic of the Multi-layer Thin-film Superconductor Consisting of NbN and Insulator on Pure Nb Substrate . . . 391
TUPO031 – Investigation of the Surface Resistance of Niobium Between 325 MHz and 1300 MHz Using a Coaxial Half-wave Cavity . . . 395
TUPO032 – First Test Results of Superconducting Twin Axis Cavity for ERL Applications . . . 398
TUPO033 – Cryogenic Test Results of the SPS Prototype RF-dipole Crabbing Cavity with Higher Order Mode Couplers . . . 402
TUPO035 – Determination of the Field-dependence of the Surface Resistance of Superconductors from Cavity Tests . . . 405
TUPO036 – Vertical Test Results of Plasma In-situ Cleaning on Low Beta HWR Cavity . . . 408
TUPO038 – Several Experimental Phenomena of Sn Nucleation on Nb Surface Observed at IMP . . . 412
TUPO039 – Tests of the Balloon Single Spoke Resonator . . . 417
TUPO040 – Tests of Multi-frequency Coaxial Resonators . . . 420
TUPO041 – LCLS-II Cavity Higher Order Modes Coupler Tuning Optimization and Challenges at Jefferson Lab 423
TUPO042 – RF Results of Nb Coated SRF Accelerator Cavities via HiPIMS . . . 427
TUPO043 – New Progress with HF-free Chemical Finishing for Nb SRF Cavities . . . 431
TUPO045 – Optimization of Dual Axis Asymmetric Cavity for Energy Recovery Linac . . . 435
TUPO048 – Study Progress of Pulse Laser Annealing for Niobium Film on Copper . . . 438
TUPO049 – Nitrogen Doping Study With 1.3 GHz Single Cell Superconducting Cavities . . . 442
TUPO050 – Construction of Thin-film Coating System Toward the Realization of Superconducting Multilayered Structure . . . 445
TUPO051 – Design Considerations of a Balloon-shaped SSR Superconducting Cavity . . . 448
TUPO052 – Design Study of a Prototype 325MHz RF Power Coupler for Superconducting Cavity . . . 451
TUPO053 – Fabrication of Nb Mushroom Shaped Cavity for Evaluation of Multi-layer Thin-film Superconductor 454
TUPO054 – Fundamental Studies of Impurity Doping in 1.3 GHz and Higher Frequency SRF Cavities . . . 458
TUPO055 – Next Generation Nb3Sn SRF Cavities for Linear Accelerators . . . 462
TUPO057 – Low-temperature Baking and Infusion Studies for High-gradient ILC SRF Cavities . . . 466
TUPO058 – Cool Down Studies for the LCLS-II Project . . . 470
TUPO059 – Latest Results of Salt Based Bipolar Electro-polishing R&D at Cornell . . . 473
TUPO064 – Pre-study of CEPC SRF Cavity . . . 476
TUPO065 – Improvement of Cavity Performance by Nitrogen Doping at KEK . . . 480
TUPO066 – Lower Critical Field Measurement of Thin Film Superconductor . . . 484
TUPO067 – Study on New Removal Thickness Distribution Improvement Methods for Niobium 9-cell Cavity Vertical Electropolishing with Ninja Cathode . . . 488
TUPO068 – Vertical Electropolishing of 1.3 GHz Niobium Nine-cell SRF Cavity: Bulk Removal and RF Performance 491
TUPO069 – Development of Vertical Electropolishing Facility for Nb 9-cell Cavity (2) . . . 494
TUPO070 – Design and Commissioning of KEK New Vacuum Furnace for SRF Cavity Development . . . 496
TUPO071 – Study on Nitrogen Infusion for 1.3 GHz SRF Cavities Using J-PARC Furnace . . . 499
TUPO072 – First Trial of the In-situ Nitrogen Infusion at KEK . . . 503
TUPO073 – Niobium Sample Analysis for Nitrogen Infusion and Doping . . . 506
TUPO074 – Design and Fabrication of KEK Superconducting RF Gun #2 . . . 510
TUPO076 – An Innovative Nb3Sn Film Approach and Its Potential for SRF Applications . . . 513
TUPO078 – Extension of Busch's Theorem to Particle Beams . . . 516
TUPO079 – Numerical and Experimental Study of H^- Beam Dynamics in J-PARC LEBT . . . 519
TUPO083 – Beam Dynamics for the FAIR p-Linac Ladder RFQ . . . 522

TUPO084 – Beam Dynamics Simulations for the New Superconducting CW Heavy Ion LINAC at GSI 525
TUPO085 – Modelling of Beam Parameters of RF Linac for GBS-ELI-NP 528
TUPO088 – Measurement of Diagnostics Response by RF Parameters for Hard X-ray Line in PAL-XFEL* . . . 531
TUPO090 – Electron-beam Matching to Solenoid Magnetic Field in a Klystron 534
TUPO091 – Beam Break Up Instability Analysis for Cavities, Linacs and Energy Recovery Linacs 537
TUPO092 – Beam Dynamics and Collimation Following MAGIX at MESA* 540
TUPO093 – Excitation of Millimeter Wavelength Cavity Structure 543
TUPO095 – Beam Loading with the First Rebuncher of Spiral2, First Measurements 546
TUPO097 – Design of C-band Electron Linear Accelerator for a Complex of Radiation Therapy 550
TUPO098 – Proof-of-Principle Tests for Slit-scan-based Slice Emittance Measurements at PITZ 553
TUPO101 – Design of Practical HSC Type Injector for Cancer Therapy 557
TUPO106 – Mathematical Principle and Numerical Reconstruction in Real Space Measurement with a Rotating BPM 560
TUPO109 – Electron Cloud Estimates for the Jefferson Lab EIC 563
TUPO112 – Calculation of Electron Beam Dynamics in Four Accelerating Stations for JINR Linear Electron Accelerator LINAC-200 566
TUPO113 – Beam Dynamics Studies Through Dielectric THz Accelerating Structures 569
TUPO114 – Beam Dynamics Studies for the CSNS DTL Due to a Quadrupole Fault 573
TUPO115 – Beam Parameters Measurement and Correction in CSNS Linac 576
TUPO116 – Particle Dynamics Optimization in DTL 579
TUPO119 – A Diagnostics Box for the Linear Accelerator of Institute for Research in Fundamental Science (IPM) 581
TUPO120 – The Study of the Length and Shape of Beam in a High Power Electron Accelerator 584
TUPO127 – Activities at the Linac4 Test Stand 587
TUPO130 – The Design of HEPS Magnet Database and Applications 591
TUPO132 – Implementation of the Beam Loading Compensation Algorithm in the LLRF System of the European XFEL 594
WE1A03 – Latest Results of CW 100 mA Electron RF Gun for Novosibirsk ERL Based FEL 598
WE1A04 – The High Power RF System for the European XFEL 601
WE1A05 – SwissFEL Linac Commissioning Status, Current Performance and Future Plans 605
WE1A06 – Pulse-to-pulse Beam Modulation for 4 Storage Rings with 64 Pulsed Magnets 609
WE2A01 – First Acceleration at FRIB 615
WE2A03 – Construction Status of the Superconducting Linac at RIKEN RIBF 620
WE2A04 – Commissioning of New SARAF RFQ and Design of New Linac 626
TH1A01 – First Ever Ionization Cooling Demonstration in MICE 632
TH1A03 – High Brightness Electron Beams from Plasma-based Acceleration 637
TH1A04 – The Proton Driven Advanced Wake Field Acceleration Experiment (AWAKE) at CERN 642
TH1A05 – Jitter Study for the APS Linac Photo-injector Beam 647
TH2A01 – Nitrogen Infusion R&D for CW Operation at DESY 652
TH1P01 – Commissioning of CERN LINAC4 658
TH1P02 – Injection Complex Development for the NICA-project at JINR 663
TH1P03 – New Trends in Proton and Carbon Therapy Linacs 666
THPO001 – Design Study on CEPC Positron Damping Ring System 672
THPO002 – Investigation of SRF Elliptical Cavities Made by New Nb Materials in KEK 676
THPO003 – L-band Resonant Ring for Testing RF Windows for ILC 679
THPO004 – Pulsed Operation of CEBAF for JLEIC Injection 682
THPO005 – High Aspect Ratio Beam Generation with the Phase-space Rotation Technique for Linear Colliders 685
THPO006 – Status of 650 MHz SRF Cavity for eRHIC SRF Linac 688
THPO007 – MESA - Status of the Implementation of the MicroTCA.4-based LLRF Control System 691
THPO008 – Long-term 0peration with Beam and Cavity Performance Degradation in Compact-ERL Main Linac at KEK 695
THPO009 – Evaluation of 60pC Beam Performance at cERL Injector for ERL Based EUV-FEL 699
THPO010 – Novel Straight Merger for Energy Recovery Linacs 702
THPO011 – First Energy Recovery Operation at the S-DALINAC: RF Control Stability Measurements 706
THPO012 – Once Recirculating Energy Recovery Linac Operation of S-DALINAC* 710
THPO016 – Investigation of 2D PBG Waveguides for THz Driven Acceleration 714
THPO017 – Progress of the Novel Three-dimensional Spiral Injection Scheme Test Experiment 717

THPO018 – Building a 12GHz Traveling Wave Accelerating Structure Brazed Through Irises . . . 721
THPO020 – Dynamic Behavior of Electron Beam under Rf Field and Static Magnetic Field in Cyclotron Autoresonance Accelerator . . . 725
THPO021 – Research on X Ray Characteristics Produced by Highenergy Picosecond Electron Beam Shooting 729
THPO022 – Development Progress of the H^+/H^- Linear Accelerators at Tsinghua University . . . 732
THPO026 – The Multi-physics Analysis of Dual-beam Drift Tube Linac . . . 735
THPO028 – Magnetic Field Measurement and Analysis for Drift Tube Linac of CSNS . . . 738
THPO029 – Quality Factor and Power Loss of the CSNS DTL . . . 741
THPO030 – Operation Experience of the CSNS DTL . . . 744
THPO031 – RF Conditioning and Beam Commissioning Status of CSNS DTL . . . 747
THPO032 – CSNS Linac Beam Commissioning Tools and Experience . . . 750
THPO033 – The Development of Permanent Magnet Quadrupoles for Xipaf DTL . . . 753
THPO034 – Experimental Study of Tuning Method on a Model Alvarez DTL Cavity for CPHS Project . . . 756
THPO035 – Tuning and Low Power Test of the 325 MHz IH-DTL at Tsinghua University . . . 759
THPO036 – Error Study of CPHS DTL after Assembly . . . 763
THPO038 – Status of the Power Couplers for the CSNS DTL . . . 767
THPO039 – The Status of CSNS Front End . . . 771
THPO040 – Operation Experiences of the J-PARC Linac . . . 774
THPO042 – An Optimization Method of the Nose-cone Buncher Cavity . . . 778
THPO043 – ESS Normal Conducting Linac Status and Plans . . . 781
THPO045 – Tuning Esperience on the ESS DTL Cold Model . . . 784
THPO046 – Status of the FAIR Proton Linac . . . 787
THPO047 – SPIRAL2 Injector Commissioning . . . 790
THPO048 – Low Power Measurement of a 1300-MHz RFQ Cold Model . . . 794
THPO049 – Field Tuning of a Radio-frequency Quadrupole Using Full 3D Modeling . . . 798
THPO050 – Research on the New Cavity Structure of RFQ Accelerator With Bent Vanes at IMP . . . 802
THPO051 – The Multi-physics Analysis of LEAF RFQ . . . 805
THPO052 – High Power Test of the LEAF-RFQ . . . 808
THPO053 – Status of the China Material Irradiation Facility RFQ . . . 811
THPO054 – Recent Progress of a CW 4-rod RFQ for the SSC-LINAC . . . 814
THPO057 – Redesign of CERN Linac3 RFQ for Lead 29+ . . . 818
THPO058 – RF Design of a High-frequency RFQ Linac for PIXE Analysis . . . 822
THPO060 – First RF Measurements of the 325 MHz Ladder RFQ . . . 826
THPO061 – Beam Characterization of the MYRRHA-RFQ . . . 830
THPO062 – IFMIF/EVEDA RFQ Preliminary Beam Characterization . . . 834
THPO064 – Tuning of a Four-vane RFQ for Xi'an 200 MeV Proton Application Facility . . . 838
THPO066 – First High Power Test of the ESS High Beta Elliptical Cavity . . . 841
THPO067 – Control System and Experiment for RAON HWR Cryomodules . . . 845
THPO068 – AN Effect of Field Emission on Low Beta Superconducting Cavities . . . 849
THPO069 – The Electromagnetic Optimization of TE-sample Host Cavity at IMP . . . 852
THPO072 – Cryogenic Tests of the Superconducting β=0.069 CH-cavities for the HELIAC-project . . . 855
THPO073 – RF Commissioning of the Superconducting 217 MHz CH Cavity for Heavy Ions and First Beam Operation . . . 859
THPO076 – Multiphysics Design Studies of a Superconducting Quarter-wave Resonator at Peking University . 863
THPO079 – RF Test of Standing Wave Deflecting Cavity with Minimized Level of Aberrations . . . 866
THPO080 – Design Validation of a Chopping and Deflecting System for the High Current Injector at IUAC . . . 869
THPO082 – Physical Design of a Rectangular RF Deflector for Ultrashort Bunch Length Measurement . . . 872
THPO083 – Transverse Deflecting Cavity for Longitudinal Beam Diagnostics at B*ERL*inPro . . . 875
THPO084 – BPM Time of Flight Measurements for Setting-up the RF Cavities of the CERN Linac4 . . . 879
THPO086 – Beam Loss and Average Beam Current Measurements Using a CWCT . . . 882
THPO090 – The Analysis of Module Failure in High Solid-state Amplifier for High Current RFQ . . . 886
THPO091 – 90 kW Solid-state RF Amplifier with a TE011-mode Cavity Power-combiner at 476 MHz . . . 889
THPO092 – LCLSII Fundamental Power Coupler Manufacturing Status and Lesson Learned . . . 893
THPO093 – Status and Results Obtained on a RF Conditioning Test Bench for 704 MHz Couplers in the Frame of ESS Project . . . 895

THPO095 – Present Status of Capacitor-charging Power Supplies for Klystron Modulators in SuperKEKB Injector Linac . . . 898
THPO096 – Design Study of a High Efficiency Klystron for SuperKEKB Linac . . . 901
THPO097 – Recent Results for Study of Ceramic and Copper Plating for Power Couplers . . . 905
THPO100 – Development of a 1.5 GHz High-power CW Magnetron for SRF Accelerator . . . 908
THPO102 – Design Studies of Output Window for CEPC Klystron . . . 911
THPO103 – Application of Solid State Amplifiers in ADS Project at IHEP . . . 914
THPO104 – Development of 150.4MHz Continuous Wave Solid-state Amplifier . . . 917
THPO107 – High Power Coupler R&D for Superconducting CH-cavities . . . 920
THPO108 – Development of an High Gradient Side Coupled Cavity for PROBE . . . 924
THPO109 – A New Spherical Pulse Compressor Working with Degenerated "Whispering Gallery" Mode . . . 928
THPO111 – The Test of RF Breakdowns of CPHS RFQ . . . 931
THPO113 – Design of 4 Ampere S-Band Linac Using Slotted Iris Structure for Hom Damping . . . 934
THPO115 – Consolidation and Extension of the High-gradient LINAC RF Technology at PSI . . . 937
THPO116 – Space-Charge Dominated Photoemission in High Gradient Photocathode RF Guns . . . 941
THPO118 – Beam Transverse Coupling and 4D Emittance Measurement Simulation Studies for PITZ . . . 945
THPO124 – Design of Pulsed HV and RF Combined Gun System Using Gridded Thermionic-Cathode . . . 949
THPO125 – Runing Status of SRF Gun II at the ELBE Radiation Center . . . 952
THPO126 – Compact H^+ ECR Ion Source with Pulse Gas Valve . . . 955
THPO127 – The Effect of Energy Fluctuation on the Multi-bunch Acceleration in E-driven ILC Positron Source . . . 958
THPO132 – Study of the Electron Beam Transfer Line for the AWAKE RUN II Experiment at CERN . . . 962
FR1A01 – Results From the 6D Diagnostics Test Bench at SNS . . . 966
FR1A02 – Bunch Length Measurements using Transverse Deflecting Systems . . . 972
FR1A03 – Frontiers of Beam Diagnostics in Plasma Accelerators . . . 977
FR1A05 – Development of Pulsed Gas Strippers for Intense Beams of Heavy and Intermediate Mass Ions . . . 982
FR1A06 – Pulse-by-Pulse Beam Parameter Switching of High-Quality Beams for Multi-Beamline Operation at SACLA . . . 988
FR2A02 – Commissioning of the European XFEL . . . 994

Appendices **1001**
List of Authors . . . 1001
Institutes List . . . 1019
Participants List . . . 1039

ISBN: 978-3-95450-194-6 ISSN: 2226-0366 doi:10.18429/JACoW-LINAC2018-MO1A01

CSNS FRONT END AND LINAC COMMISSIONING

S.N.Fu[1,2†], H.F.Ouyang[1], H.C.Liu[1], J.Li[1], J. Peng[1], S.Wang[1]
[1] Dongguan Campus, Institute of High Energy Physics, 523803 Dongguan China
[2]University of Chinese Academy of Science, 100049 Beijing China

Abstract

The China Spallation Neutron Source (CSNS) accelerator systems is designed to deliver a 1.6GeV, 100kW proton beam to a solid metal target for neutron scattering research. The accelerator consists of a front end, an 80MeV DTL linac, and a 1.6GeV Rapid Cycling Synchrotron (RCS). In August 2017 the first 1.6GeV proton beam hit on the tungsten target and production neutrons were monitored. This paper will report the major steps and results of the machine commissioning and beam commissioning of the CSNS front end and linac. In the first section, a brief introduction of the CSNS accelerator design and present status will be presented. Then, we will share our commissioning experience in the front end and the DTL linac in the following sections. Finally, a brief introduction to the linac energy upgrade design options are presented.

INTRODUCTION

After 6.5 years construction [1], the CSNS completed its project construction in March 2018. The bird view of the CSNS campus is shown in Fig. 1. In this photo, from right to left we can see the buildings of klystron gallery for the linac, target station and synchrotron hall.



Figure 1: CSNS site bird view.

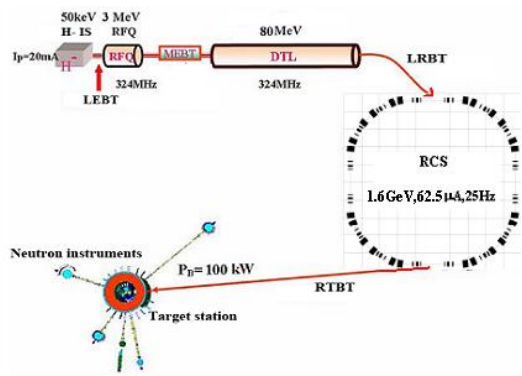


Figure 2: CSNS facility layout.

CSNS accelerator is designed with a beam power of 100kW in the phase-1 and reserved capability to upgrade the beam power to 500kW in Phase-2. The accelerator complex consists of an 80MeV H^- linac and a rapid cycling synchrotron of 1.6GeV at 25Hz repetition rate. CSNS facility layout is schematically plotted in Figure 2. Whole machine complex has been commissioned in the second half of 2017, with the first beam on the target in August 2017. Now the facility has been put into user operation at 20kW beam power. We are going to raise the power to 100kW within two years. This means the beam commissioning work will continue along with some user time about 7000 hours during the two years. As soon as we hit this target, phase-2 program for accelerator power upgrade to 500kW will be hopefully launched. For injecting 5-times more beam current into the RCS, it is necessary to raise linac beam energy to compensate for the space charge tune shift in the ring. The CSNS linac tunnel reserve a space of 80m long in the LRBT beam line for installing additional linac cavities for up to 300MeV output beam. Both RT and SC cavity are our present options for the linac section from 80MeV to 300MeV.

The present 80MeV linac consists of a Penning H^- ion source, a LEBT, a 3MeV RFQ powered by two tetrodes at 324MHz, a MEBT and a DTL linac with 4 tanks driven by 4 klystrons at 324MHz, as shown in Fig. 3.

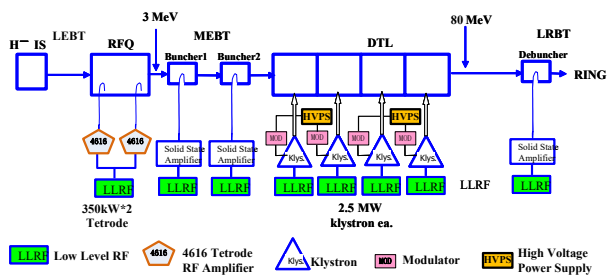


Figure3: Schematics of CSNS linac.

Beam chop at 50%-70% rate is performed by an electrostatic chopper at the end of the LEBT with space charge neutralization. There is no further chopping in the MEBT.

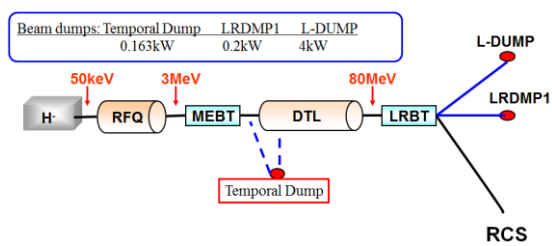


Figure 4: Linac beam dumps for beam commissioning.

† email address: fusn@ihep.ac.cn

Content from this work may be used under the terms of the CC BY 3.0 licence (© 2018). Any distribution of this work must maintain attribution to the author(s), title of the work, publisher, and DOI.

ISBN: 978-3-95450-194-6 ISSN: 2226-0366 doi:10.18429/JACoW-LINAC2018-MO1A01

Content from this work may be used under the terms of the CC BY 3.0 licence (© 2018). Any distribution of this work must maintain attribution to the author(s), title of the work, publisher, and DOI.

A series of beam diagnostics are arranged in the MEBT and LRBT for beam commissioning of the front end and the DTL tanks. A temporal diagnostic plate (D-plate) with a beam dump was used for the beam commissioning of the front end and the DTL tank-1, and two fixed beam dumps (LRDMP1 and L-DUMP) are used for DTL tank-2 to tank-4, as shown in Fig. 4.

FRONT END COMMISSIONING [2]

The CSNS front end started beam commissioning first and finished step by step. Finally we achieved design specification, as listed in Table 1.

Table 1: Front End Beam Commissioning Results

	Design	Measured
Ion source current [mA]	20	31
MEBT peak current [mA]	15	17
RFQ beam energy [MeV]	3.0258	3.02±0.01
Chopping rat e [%]	50	50
Chopper rise time [ns]	20	10
Pulse width [μs]	420	500
Pulse repetition rate [Hz]	25	25
Emittance (π mm mrad)	0.22	0.27

Ion Source and LEBT

Thanks to the nice cooperation with ISIS, we developed an H^- Penning source. In Oct. 2014 the ion source, as the first CSNS facility, was moved into the linac tunnel after long-term beam commissioning in laboratory. It initially run at lower duty of 50μs at 1Hz and then gradually increase the duty to the design value of 500μs at 25Hz. The extracted H^- beam current can reach more than 30mA at the exit of LEBT, which is sufficient for our phase-1 operation. The real challenge is long-term stability, especially at low duty operation. Tightly controlling Cesium deposition on the extractor helps a lot for better stability. In addition to some other improvements including power supply, extractor and penning magnet, now the beam interruption duration becomes very short: about tens of ms for each spark, and the spark numbers are several times a day, satisfying user operation, as shown in Fig. 5.

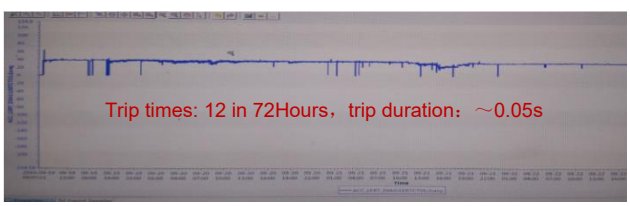


Figure 5: Record of the ion source trip rate in 72 Hours after improvement.

LEBT is a space-charge neutralized beam line for controlling beam emittance growth. Three solenoids focus the beam in two transversal directions to match the beam with the RFQ acceptance. And also a larger emittance (0.75-0.9πmm.mrad) from ion source is collimated to 0.2πmm.mrad for matching with RFQ acceptance. At the downstream end of the LEBT, there is a pair of electrostatic deflecting plates as a beam chopper. The chopper does not disturb the space-charge neutralization in the LEBT owing to the screening plate with a small beam hole. We require it must have fast rise time because there is no further chopping in the MEBT. The achieved rise time of the beam is about 10ns, as we can see from Figure 6. In this figure, one can see the rise time is about 3-4 periods of 324MHz and one period last about 3ns. The chopped beam is dumped on the entrance plate of RFQ and partially into RFQ cavity.

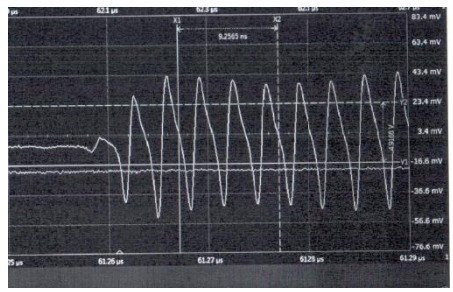


Figure 6: Measured beam rise time about 10ns after LEBT chopper.

RFQ and MEBT

RFQ cavity is a four-vane structure at 324MHz RF frequency. Two tetrodes powered the cavity through two power couplers with total power of 450kW pulse power. Due to the trouble of water leakage of the linac tunnel RFQ tunnel installation was delayed about one year. For catching up the schedule, we installed the RFQ and its RF power supply, as well as water cooling system in our laboratory and conducted high power conditioning. After 11 days conditioning with RF pulse length of 700μs at 25Hz, the RF power reached 480kW and the cavity gradually became almost no spark, as shown in Fig.7. Before this high power conditioning, the four sections of the RFQ cavity had been aligned and bead-pulling measurement had been conducted for field tuning. Two MEBT buncher cavities together with their solid-state power sources were also conducted high power conditioning.

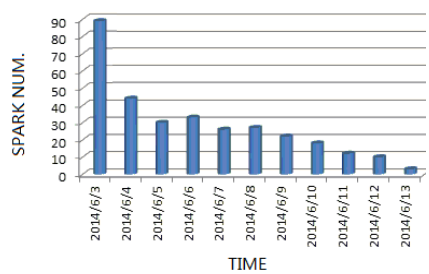


Figure 7: Spark number of RFQ cavity declined during high-power conditioning of 11 days.

ISBN: 978-3-95450-194-6 ISSN: 2226-0366 doi:10.18429/JACoW-LINAC2018-MO1A01

The RFQ was reinstalled in the linac tunnel in Feb. 2015. RFQ high-power conditioning was conducted again. This time it took only 5 days owing to the previous work. The first beam came then from the RFQ in April 2015 at low duty factor of 50μs pulse length at 1Hz for initial beam commissioning of the RFQ. Pulse length was doubled for beam chopping experiment. Then we returned to RFQ beam commissioning at high duty factor up to 500μs at 25Hz. Beam transmission rate was measured with a pair of CTs at the entrance and exit of the RFQ. Initially, the transmission rate was not so high as our expectation, around 75% - 85%. The reason is the beam emittance from the ion source is much larger than the acceptance of the RFQ. To deal with this issue, a collimator was added into LEBT and then the best transmission rate can reach up to 94%, as shown in Fig. 8. As a result the LEBT transmission rate becomes low.

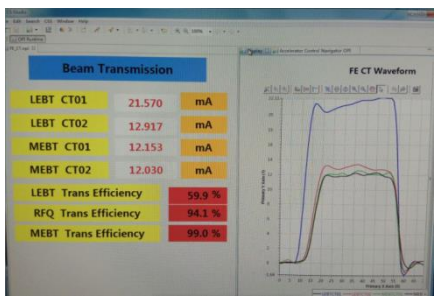


Figure 8: The best beam transmission rate of the RFQ.

After the initial independent beam commissioning, RFQ run a long period for beam commissioning of the following DTL tanks, RCS, as well as target and neutron spectrometers. It also serves for user operation since this year. After more than two years' operation, its performance gradually becomes worse in term of the stability, especially during the user operation with beam power of 20kW. Serious spark happened frequently and we had to conduct high power conditioning again and again. It seriously interrupted user operation. After excluding the vacuum problem, we realized that the chopped beam dumped onto the RFQ vane may be most susceptive issue. Even though the thermal damage is neglect according to calculation, the sputtering effect may make the roughness of the vane tip getting worse. Two measures have been taken: (1) turn the chopper 45 degree around beam axis so that the deflected beam can go through the gap between the vanes and then hit on the cavity wall surface, instead of the vane surface; (2) Add a smaller aperture in the entrance hole to limit beam into the cavity. After implement of these measures and improvement of high power conditioning strategy, the RFQ runs much more stable in recent.

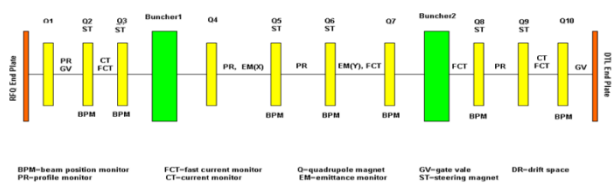


Figure 9: MEBT major elements.

The MEBT consist of 10 quadrupoles for transversal matching of the beam with DTL, two bunchers for longitudinal direction matching, 6 steering magnets for orbit correction and some beam diagnostics, such as BPM, PR, CT, FCT, EM and WS, as shown in Figure 9.

Four wire scanners are located along the MEBT to measure the Twiss parameters of the RFQ output beam. Table 2 shows the comparison of the design values (with PARMTEQM[3]) and the measured values. The Twiss parameters in the horizontal plane are agreed well with the simulated values, while those in the vertical plane are somewhat deviated from the simulated values. The emittance also agrees well in both directions. To confirm the measured results, we use PARMILA[4] code and the measured data in y-direction as input to simulate beam transmission to the location of the double-slit emittance monitor, as shown on the left of Fig.10. The measure emittance on the right of Fig.10 indicates a good agreement with the simulation.

Table 2: RFQ Output Twiss Parameters (I=10mA)

	α	β [mm/mrad]	Emittance rms, normalized [π mm mrad]
Horizontal			
Measured	*-1.716*	0.256	0.215
Simulated	*-1.773*	0.233	0.215
Vertical			
Measured	*1.944*	0.173	0.211
Simulated	*0.639*	0.074	0.212

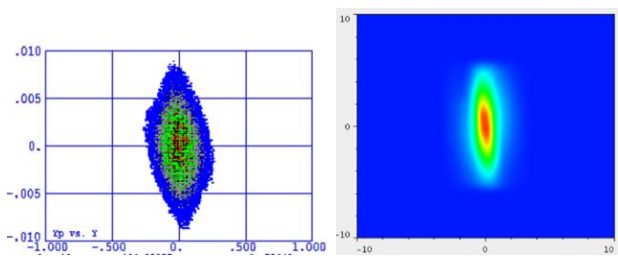


Figure 10: Simulated and measured emittance in y-direction in MEBT.

As the beam phase space in two directions is almost the same as the design values, we set all 10 quadrupoles in MEBT according to the design. The resulted beam transmission rate of the MEBT can easily reach 100% and a nice matching with the following DTL. During DTL beam commissioning, we majorly tune the orbit correctors and the two bunchers in the MEBT. The phase scan method is used for finding the RF set points of two bunchers. The beam phase is provided by Fast Current Transforms (FCTs) which are located at the downstream of the measured cavity. For three different RF amplitudes, three sets of measured phase differences vs. cavity phase were recorded, as shown in Fig. 11 with experimental data in solid curve and simulation results in circles. The red curve was taken at nominal RF amplitude, the blue one at 25% below nominal, and the black one at 25%

Content from this work may be used under the terms of the CC BY 3.0 licence (© 2018). Any distribution of this work must maintain attribution to the author(s), title of the work, publisher, and DOI.

ISBN: 978-3-95450-194-6 ISSN: 2226-0366 doi:10.18429/JACoW-LINAC2018-MO1A01

above nominal. The buncher setting phase is located at the intersection of the three curves. At this point, the amplitude of the FCTs' signal was observed maximum.

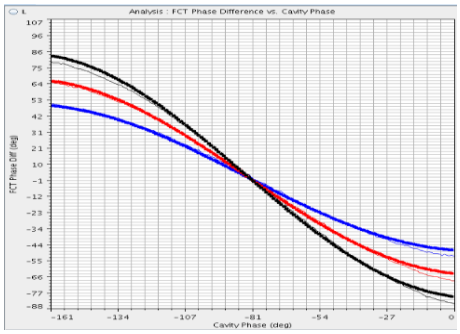


Figure 11: Measured phase differences (degrees) between two FCTs as functions of the buncher01 cavity phase.

DTL LINAC

The DTL consists of four tanks, and each tank is fed by a klystron power source. Beam commissioning of the 80MeV DTL majorly took three steps. Firstly, when the first tank had been installed together with its RF power source, the following three tanks were not ready for installation. So the first tank conducted beam commissioning with our reformed D-plate ever used for the front end. Secondly after we installed the rest three tanks beam commissioning was performed for the second and the third tanks. Through LRBT, the beam was initially sent to LRDMP1 for low duty factor beam and beam was measured with LRBT beam diagnostics. To catch up our schedule, we initiated RCS beam commissioning with 61MeV beam output from the third DTL tank and successfully obtained the first neutron beam from the target with 61MeV injection to the RCS. At this time, the fourth tank was only powered for quadrupoles in drift tubes, but no RF power at all, due to lack of klystron which was sent back to manufacture for repair. Finally in January 2018 we could start tank-4 beam commissioning and thus whole linac beam commissioning at 80MeV output beam energy.

The DTL transverse focusing was arranged in a FFDD lattice utilizing electromagnetic quadrupoles. Because no drift tube is empty, diagnostics have to be imbedded between tanks. After each tank, a FCT and a CT were installed to monitor beam phase and current. Between DTL 3 and DTL 4, a Beam Position Monitor (BPM) was added for monitoring beam orbit. A pair of FCTs were used for each tank, as shown in Fig.12, for phase difference measurement in RF phase scan.

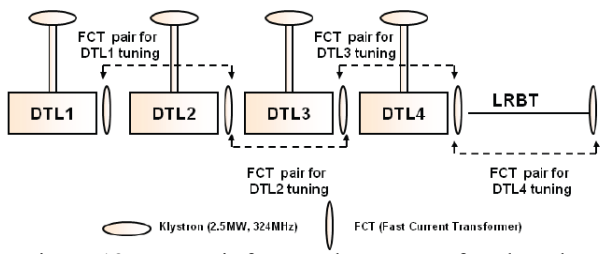


Figure 12: FCT pair for RF phase scan of each tank.

For DTL tanks, it is essential to find the correct tank RF field amplitude and phase to minimize energy spread and mismatch, which are highly required by the following RCS. A method called "phase scan signature matching" was adopted for determining the RF set points of DTL tanks [5]. The method involves varying an RF cavity amplitude and phase settings over a fairly large range and comparing the measured downstream beam phase response "signatures" to model predictions. A software application called PASTA was applied for phase scan and analysis [6]. The RF amplitude, relative phase of beam and the input energy were used as variables in model fitting.

Time of flight measurement was also performed. For each tank, three FCTs were used to form two short pairs and a long pair. The two short pairs were used to determine the number of integer periods and the long pair was used to calculate beam energy. The beam energy calculated with TOF and phase scan are summarized in Table 3. The deviation of measured beam energy from the design value is less than 1%.

Table 3: Beam Energy From Two Methods

	TOF [MeV]	Phase scan [MeV]	Design [MeV]
DTL1	21.73±0.01	21.67	21.67
DTL2	41.54±0.01	41.45	41.41
DTL3	61.36±0.02	61.05	61.07
DTL4	80.34±0.01	80.17	80.09

During DTL commissioning a great challenge came from water leakage of the quadrupole coil in a drift tube into the cavity of the first tank. A new drift tube was manufactured for replacing the failure one, however we realized it would be very difficult to do so with both time risk and quality risk. The commissioning schedule as well as the project schedule would certainly be affected seriously. Another way is to cut-off magnet power supply and the coil cooling water, and seal the inlet of the coil cooling water. In this way the focusing lattice is seriously perturbed and beam simulations indicated an obvious beam loss. To deal with this issue, we modified the focusing lattice so as to compensate for the lost function of the quadrupole. More details can be found in this proceedings [7]. After the change of the cable connections, a new lattice is formed. Linac beam commissioning resumed and beam transmission rate keeps nearly 100%, confirming the new lattice can fully compensate for the cut-off quadrupole, the same as the simulation expectation.

LINAC UPGRADE OPTIONS

In the linac physics design we leave the possibility for increase of the beam average current 5-times, and the linac tunnel also leaves a space of 85m long for installation of more cavities for beam energy up 300MeV in future. Under this space limitation, we find both room temperature cavity and superconducting cavity can accelerate beam to 300MeV from the present 80MeV.

Content from this work may be used under the terms of the CC BY 3.0 licence (© 2018). Any distribution of this work must maintain attribution to the author(s), title of the work, publisher, and DOI.

ISBN: 978-3-95450-194-6 ISSN: 2226-0366 doi:10.18429/JACoW-LINAC2018-MO1A01

In our present design, room temperature cavity will use PI-mode structure which has successfully operated in LINAC-4 of LHC upgrade program [8]. PIMS cavity keeps the same RF frequency as the DTL.

Spoke cavity is a candidate for superconducting structure. Double spoke with geometrical beta 0.5 at 324MHz is designed. A similar cavity at 325MHz has been developed for ADS project at IHEP [9]. The vertical test has been conducted with promising performance. Table 4 lists the major design parameters for RT and SC structures respectively for CSNS linac energy upgrade.

Table 4: Major Design Parameters of RT Structure and SC Structure for CSNS Linac Energy Upgrade

Parameters	**RT PIMS**	**SC Spoke**
Frequency/MHz	324	324
Energy range/MeV	80-306	80-306
Length/m	83	82.9
Cavity number	40	57
Module number	20	19
Cells per cavity	7	3
Energy gain /cavity/MeV	4.3~6.65	3.7
Quad. number	42	41
Lattice structure	FD	R^3FD
Aperture/mm	40	60
Cavity length/mm	1273~2119	710
Fill factor	0.8	0.5
Cavity diameter/mm	610	512
E0/MV/m	3.7 – 4.0 (<1.8Kilp)	5.2
Voltage/MV (E_{peak}=30MV/m)		3.9
B_{peak} /mT (E_{peak}=30MV/m)		73

CONCLUSION

The CSNS front end and DTL linac have been successfully commissioned. The peak current and beam energy have achieved the design goal. The rise time of the LEBT chopper is about 10ns. Beam transmission rate of the RFQ is around 92%. DTL has a higher beam transmission rate about 98%. Linac beam was sent to RCS ring for RCS, target, neutron spectrometer commissioning. Now the CSNS construction project has been completed. Machine is put into user operation at beam power of more than 20kW. Meanwhile, we will raise beam power to 100kW, the design specification of the first phase of CSNS project. For the second phase, beam power will rise to 500kW. For this target, CSNS linac will increase its beam energy up to 300MeV. Now we designed both RT and SC structure for linac upgrade.

ACKNOWLEDGEMENT

Thanks to the great efforts of all the members of CSNS Accelerator Division the beam commissioning of CSNS front end and DTL has achieved a full success.

REFERENCES

[1] Shinian Fu, Hesheng Chen, et al., Status of CSNS Project, IPAC2013, Shanghai, 2013.

[2] H. Li, H.F.Ouyang, et al., "The Status of CSNS Front End", presented at the 29th Linear Accelerator Conf. (LINAC'18), Beijing, China, Sep. 2018, paper THPO039, this conference.

[3] K.R.Crandall et al., "RFQ Design Codes", LA-UR-96-1836.

[4] T. Harunori, PARMILA, LA-UR-98-4478, 1998.

[5] T.L Owens et al., "Phase Scan Signature Matching for Linac Tuning", *Particle Accelerators*, 1994, Vol98, p.169.

[6] J.Galambos et al., "PASTA-An RF Phase Scan and Tuning Application", *Proceedings of PAC2005*, Knoxville, Tennessee.

[7] J. Peng, H.C Liu, et.al, "Beam dynamics studies for the CSNS Linac due to a quadrupole fault", presented at the 29th Linear Accelerator Conf. (LINAC'18), Beijing, China, Sep. 2018, paper. TUPO114.

[8] A.M.Lombardi, Linac4: from initial design to final commissioning, *Proceedings of IPAC2017*, Copenhagen, Denmark, 2017.

[9] Zhongquan Li,Weimin Pan, Yunlong Chi et.al, Development of spoke cavity for main Linac of China ADS, in *Proceedings of SRF2017*, Lanzhou, China, 2017.

Content from this work may be used under the terms of the CC BY 3.0 licence (© 2018). Any distribution of this work must maintain attribution to the author(s), title of the work, publisher, and DOI.

ISBN: 978-3-95450-194-6 ISSN: 2226-0366 doi:10.18429/JACoW-LINAC2018-MO1A02

AN OVERVIEW OF RECENT DEVELOPMENTS IN SRF TECHNOLOGY

R.E. Laxdal, TRIUMF, Vancouver, Canada, V6T 2A3

Abstract

Superconducting Radio-Frequency (SRF) is now the technology of choice for both large and small linac projects. Several challenging projects are in progress or planned that are pushing SRF technology and/or are enabled by SRF technology. This paper gives an overview of the present status of the field.

INTRODUCTION

Present research has been focussed on the key projects of the day, namely LCLS-II, FRIB, ESS as well as preparing for near term future projects ERLs, RISP, EIC and ILC. As LCLS-II represents a cw electron project, much of the elliptical cavity research focus has been on achieving, and maintaining, high Q in a cryomodule environment. The holy grail of projects is still the ILC. Here research is focussed on reliably increasing gradient and quality factor in an effort to reduce costs. Researchers are also pursuing thin films and new materials in order to either reduce the cost of Nb or increase the performance or operating temperature.

SRF BASICS

A characteristic of superconductors is that below some critical temperature, T_c, the DC resistance vanishes, allowing lossless transmission of electrical current. The rf surface resistance does not drop to zero, but still decreases dramatically. SRF technology offers a reduction of ~5 orders of magnitude in rf surface resistance compared to room temperature Cu that, after considering Carnot efficiency of cryogen production, still improves electrical efficiency by more than a factor of 100.

SRF Surface Resistance

The SRF surface resistance is typically described as the sum of a strongly temperature dependent component called the BCS resistance, and a second term called the 'residual resistance' (Fig. 1a).

$$R_s = R_{BCS}(\omega,T) + R_0 \quad \text{with} \quad R_{BCS} = \frac{A(\ell)}{T}\omega^2 e^{-\Delta/kT} \qquad (1)$$

The operating temperature is chosen so that R_{BCS} is reduced to an economically tolerable value for cryogenic losses with higher frequency cavities requiring colder operating temperatures. The A term depends on material parameters of the superconductor: the London penetration depth (λ_L), the coherence length (ξ_0) and the electron mean free path (ℓ). For a given temperature and rf frequency R_{BCS} can be optimized by modifications of the mean free path within the first 100nm of the surface and finds an optimum between shorter (dirty) and longer (clean) mean free paths (Fig. 1b).

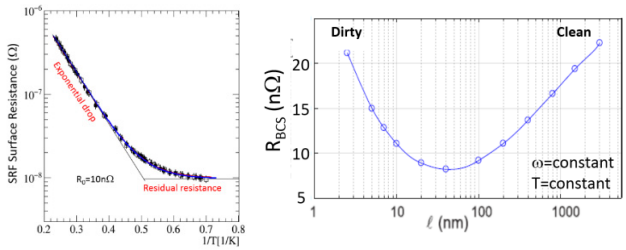


Figure 1: (a) RF surface resistance vs. temperature, and (b) BCS surface resistance as a function of mean free path for constant rf frequency and temperature.

The two most important features of an rf cavity are the accelerating gradient and the quality factor; the first impacts linac length (infrastructure cost) and the second impacts the cryogenic load (operating costs). Note that since the cavity quality factor is roughly proportional to the inverse of the average surface resistance

$$Q_0 = \frac{G}{R_s} = \frac{\omega_0 U}{P_c} \quad \text{and} \quad P_c = \frac{(E_a L)^2}{\frac{R_{sh}}{Q_0}Q_0} \qquad (2)$$

then a reduction of surface resistance by four can allow a doubling of the gradient for the same cryogenic load.

Meissner Effect

Niobium is a weak Type-II superconductor. Raising the applied field past a critical value H_{c1} leads to a mixed state (also known as the vortex state) in which an increasing amount of magnetic flux penetrates the material in quantized flux vortices. At a second critical field strength, H_{c2}, superconductivity is destroyed. However, above H_{c1} a metastable state persists up to the superheating field H_{sh} allowed by a surface energy barrier that inhibits vortex nucleation. As rf fields increase in amplitude magnetic vortices with normal cores can nucleate in the near surface and rf losses, hence surface heating occurs. For high gradient performance we need a material that can withstand vortex penetration up to a high peak magnetic field.

Present Performance

SRF research and development [1] have targeted limitations on cavity performance. Extrinsic sources include multi-pacting, field emission, surface residues, trapped magnetic flux, and surface defects. Multipacting is combated with new cavity shapes, better simulation codes and pre-test bake. Field emission has largely been controlled by high pressure water rinse (HPWR) and clean assembly techniques to eliminate particulate contamination. Defects that could cause quench (local heating) are reduced by choosing pure material with high thermal conductivity (RRR>250) and maintaining the purity through fabrication with EB welding and care. A final material removal by electro-polish (EP) or buffered chemical polish (BCP) of

Content from this work may be used under the terms of the CC BY 3.0 licence (© 2018). Any distribution of this work must maintain attribution to the author(s), title of the work, publisher, and DOI.

ISBN: 978-3-95450-194-6 ISSN: 2226-0366 doi:10.18429/JACoW-LINAC2018-MO1A02

120-150 microns is found to remove the surface layer damaged during manufacture. Magnetic flux from remnant fields that can be trapped during cooldown and cause loss are controlled with magnetic shielding material.

The intrinsic performance of SRF cavities is determined by the first 100 nm of the inner cavity surface, where rf currents flow within the London Penetration Depth. A main technology driver has been the global effort towards the realization of XFEL (and the ILC) where significant gains have been made in establishing industrially qualified techniques in producing high performing cavities for pulsed operation. Of the 815 cavities delivered for XFEL the average useable gradient in vertical test was an impressive 28.3 MV/m with a reduction to only 27.5 MV/m when tested in the cryomodule [2]. These values can be compared to the goal specification of 23.6 MV/m. Many of the techniques developed for XFEL are being applied successfully in both elliptical and non-elliptical cavities.

Two significant developments impacting the field were the development of high temperature degassing and the 120°C bake. Typically the cavity is heated to 800°C (650°C) in a vacuum furnace for 3 (10) hours to degas hydrogen from the surface. The hydrogen produces lossy hydrides on the surface during cooldown (Q-disease) that reduces the quality factor [3]. After degassing, a final light chemistry is applied to remove any contamination deposited on the surface during the heat treatment.

A 120°C bake under vacuum for 48 hours eliminates the high field Q slope (HFQS) in 1.3 GHz elliptical cavities at 2 K (Fig. 2) [4]. Studies suggest that the 120°C bake promotes the diffusion of oxygen in the bulk from the oxide surface layer. This produces a dirty layer of 20-50 nm with a mean free path of ~10 nm and a reduction in BCS resistance (Fig. 1b). Other studies show that the 120°C bake introduces vacancies in the near-surface layer, which bind hydrogen and prevent its precipitation in nano-hydrides that are responsible for the HFQS (Fig. 2) [5].

ELLIPTICAL CAVITY PERFORMANCE

A main thrust of recent SRF developments is to push the performance of elliptical cavities. New surface treatments, nitrogen doping [6] and nitrogen infusion [7] have been developed to change (in a systematic way) the near-surface nanostructure – impurity, dislocation and vacancy content, in the first hundreds (or less) nanometers of the niobium surface to improve Q or gradient or both.

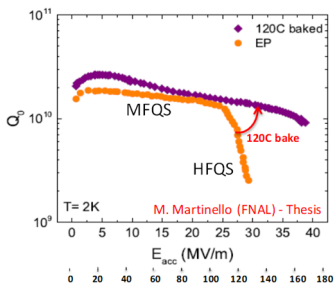


Figure 2: EP'ed cavity before and after 120°C bake.

High Q and LCLS-II

LCLS-II consists of 35 cryomodules each with 8 cavities in an XFEL-like cryomodule for a total of 280 cavities operating at 1.3 GHz. Unlike X-FEL LCLS-II operates CW. LCLS-II, and other cw high beta projects, have concentrated efforts on achieving high Q at modest gradients compatible with cw operation in the range 15-20 MV/m (E_{peak}=30-40 MV/m, B_{peak}=65-85 mT). LCLS-II (boldly) chose N-doping as the baseline recipe with a cavity performance specification of 2.7 x 10^{10} at 16 MV/m and 2 K.

In large part the research effort has focused on perfecting Nitrogen doping as an industrial process (1) to reproducibly reduce R_{BCS}, and (2) to understand and mitigate the main sources of R_0 either enhanced by the doping or exposed due to the reduced value of R_{BCS}.

Nitrogen Doping at 1.3 GHz

Nitrogen doping is a relatively new process that is performed as part of the degassing treatment. After the cavity is baked 3 hours at 800°C the temperature in the furnace is typically maintained constant and nitrogen is introduced at a constant pressure of 25 mTorr. Nitrogen is then left in the furnace for a certain amount of time (minutes) followed by a non-Nitrogen anneal of some minutes more before cooling. After the thermal treatment, the cavity is electro-polished to remove the first 5-10 µm of material from the inner surface in order to get rid of lossy niobium nitride phases. Substantial Q_0 enhancements of 1.3 GHz cavities have been demonstrated. Q_0 values between 3–4×10^{10} at 2 K and 8×10^{10} at 1.8 K can be obtained at gradients of 15-20 MV/m. The N-doping treatment also shows a remarkable behavior in that the Q_0 increases with field from 5–15 MV/m, counter to the general trend of the MFQS using standard recipes (example Fig. 3).

The presence of nitrogen as an interstitial impurity decreases the temperature dependent part of the surface impedance through manipulation of the MFP (Fig. 1b) [8]. The main drawbacks of the N-doping is a reduction in the quench field and an increased sensitivity to flux trapping [9]. Despite success in prototyping studies first articles from the vendors for LCLS-II did not perform as well as the qualifying cavities (Fig. 4a) [10].

To understand the ensuing development, it is useful to look separately at the contribution of the trapped flux to the residual resistance by defining the term R_{fl} – the residual resistance due to flux trapping [11]. The residual resistance

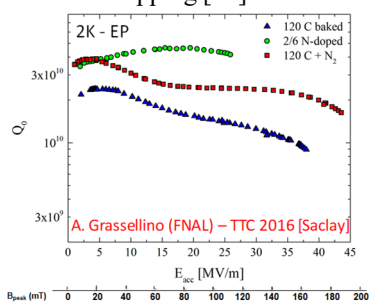


Figure 3: 1.3 GHz elliptical performance for: [blue] standard ILC recipe (120°C bake), [green] N-doped recipe, and [red] nitrogen infusion recipe.

Content from this work may be used under the terms of the CC BY 3.0 licence (© 2018). Any distribution of this work must maintain attribution to the author(s), title of the work, publisher, and DOI.

ISBN: 978-3-95450-194-6 ISSN: 2226-0366 doi:10.18429/JACoW-LINAC2018-MO1A02

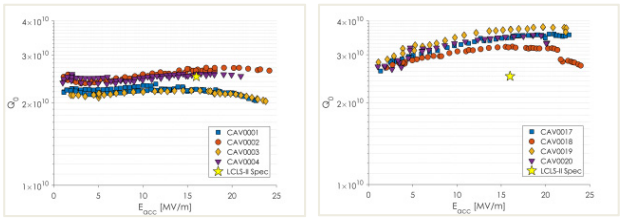


Figure 4: Q vs E of LCLS-II cavities with (a) the original recipe, and (b) the updated recipe.

is a combined product of the background flux, B_{res}, the fraction of the flux trapped, η, and the sensitivity of the residual resistance to the trapped flux, S, with

$$R_S = R_{BCS} + R_0 + R_{fl} \text{ where } R_{fl} = S * \eta * B_{res} \quad (3).$$

It is found that the sensitivity of the trapped flux is dependent on the mean free path with an N-doped cavity having a higher S than an un-doped cavity by 3-4 times (Fig. 5a) [12]. Secondly it is found that trapping percentage is impacted by the speed of cooldown – a higher temperature gradient across the cavity at Tc is favoured [13]. Thirdly trapping percentage is impacted by material – heat treatments >800°C helps mitigate poorer expelling material by reducing pinning (Fig. 5b) [14]. Achieving high Q0 through N-doping in industry has now been consistently demonstrated after early teething pains. The gains made in the new process are illustrated in Fig. 4b where LCLS-II cavities from later series comfortably meet the specification [10]. The new understanding is also demonstrated in the performance of completed cryomodules. An initial assembly using first series cavities had an average Q at 16 MV/m and 2 K of 2.1e10 while a later series, FNAL CM-3, was measured with an average Q at 3.5e10 [15]. The SRF community is engaged with vendors to better understand the material production process in terms of flux trapping characteristics [16].

Frequency Dependence of N-Doping

The field dependence of the BCS resistance of N-doped cavities changes as a function of rf frequency. Various cavity frequencies ranging from 650 MHz to 3.9 GHz were tested at FNAL. The conclusion is that the characteristic medium field Q rise due to doping is steeper in higher frequency cavities with a flattening of the slope near 1 GHz [17].

Another interesting result comes from Cornell where a 500 MHz single cell cavity was treated with N-doping and tested at 4.2 K where the BCS resistance is high. Here the Q improved by a factor of two over an undoped case [18].

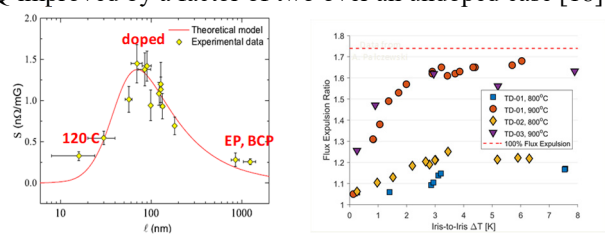


Figure 5: a) Sensitivity to trapped flux as a function of mean free path, and b) Flux expulsion comparing baseline (800°C) treatment and modified (900°C) treatment as a function of temperature gradient across the iris.

High Gradient Studies

New processes that push high gradient with improved Q offer the promise to cut the total cost and operating cost for high energy linear machines like the ILC.

N Infusion

A recent development is the so-called Nitrogen Infusion recipe from FNAL [7]. The process is analogous to the 120°C bake but instead of baking under vacuum the bake is done under low pressure Nitrogen. After the standard 800°C bake, the temperature in the furnace is lowered between 120-160°C without breaking the vacuum. Nitrogen is then introduced at a pressure of 25 mTorr for 48 hours or more. No chemistry is required after treatment. Cavities prepared with this new surface treatment show high accelerating gradients and Q-factors about two times larger than standard 120°C baked cavities (Fig. 3). This thermal treatment (like the 120°C baking) creates an enriched interstitial N layer just below the oxide layer at the near surface [19].

The recipe has proven challenging and not every lab has had the success of FNAL [20]. The treatment is very dependent on the quality of the vacuum in the furnace. At KEK the recipe has succeeded but only 20% of the time [21] with a small gain in both Q and gradient over the baseline. At JLab and Cornell recipes have not increased gradient over the baseline but interestingly some infusion recipes give results that replicate N-doping, with strong anti-Q-slope, suggesting that N-Infusion could replace N-doping as a chemistry free high Q process [22]. Cornell is also looking at other dopants like C and O [23]. Recently FNAL has succeeded in applying N-infusion to a BCP'ed cavity [24].

Low Temperature (Magic) Recipe

A new recipe has now been reported by FNAL (Fig. 6). While performing a standard 120°C bake the cavity was initially rested at 75°C for 4 hours followed by 48 hours at 120°C. In this case no nitrogen and no chemistry were involved. Nevertheless, a gradient of 49 MV/m was achieved (210 mT) with a Q above 1e10 at 2 K [25].

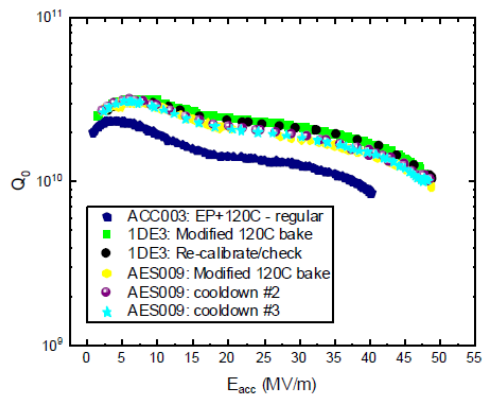


Figure 6: Low temperature bake treatment (FNAL) [25].

Content from this work may be used under the terms of the CC BY 3.0 licence (© 2018). Any distribution of this work must maintain attribution to the author(s), title of the work, publisher, and DOI.

ISBN: 978-3-95450-194-6 ISSN: 2226-0366 doi:10.18429/JACoW-LINAC2018-MO1A02

Material Development

Large Grain Niobium

While most elliptical cavities are made with fine grain RRR material several labs are also pursuing large grain material. The large grain Nb is sliced directly from ingot simplifying the sheet production sequence and reducing material costs [26]. The process has the potential to reduce embedded defects during sheet manufacturing and to reduce the variability in flux trapping characteristics seen in the LCLS-II cavity production. The large grain material is more difficult to form than fine grain and demonstrating industrial production is part of a future development path. DESY (nine cell) and KEK (single cell) have reported impressive high field performance - near 50 MV/m and Q=1e10 (Fig. 7) [27]. Large grain nine cell cavities from PKU prepared by BCP pushed nicely out to ~30 MV/m [28] while RRR=100 material used by KEK achieved >35 MV/m and Q=2e10 in a cold test at JLab [27].

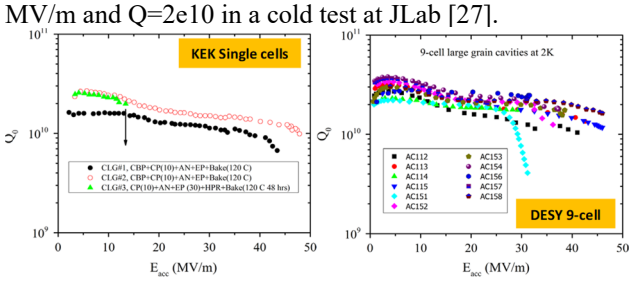


Figure 7: Large grain cavity test results from KEK and DESY.

Nb3Sn Development

Nb3Sn coating via vapor deposition still remains the only new material process that has produced a cavity suitable for acceleration. To date Cornell has achieved a gradient of 18 MV/m at 4.2 K with a single cell 1.3 GHz cavity, with a Q of 2e10, 20x higher than that for Nb (Fig. 8a) [29]. Pulsed performance has reached 26 MV/m. Performance at FNAL is also limited to the 18 MV/m gradient (Fig. 8b) [30]. Research continues globally to optimize the coating with a focus on understanding limitations in the film including defects and tin depleted regions. The question

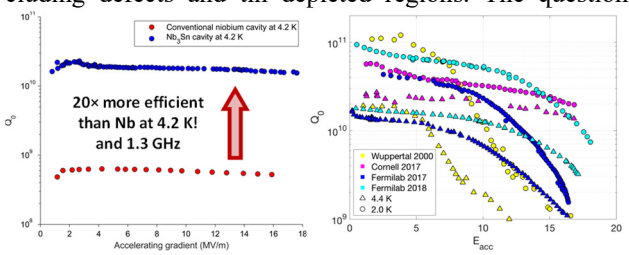


Figure 8: (a) Test results for Nb3Sn from Cornell (left), and (b) FNAL (right).

remains whether 18 MV/m is a fundamental or merely a technical limit. JLab has recently upgraded their coating furnace to be able to coat CEBAF 5-cell cavities with end-groups. At FNAL, a large coating furnace capable of coating 9-cell ILC cavities or 650 MHz 5-cell PIP-II cavities is prepared. At CERN, work has begun on producing Nb3Sn on a copper substrate.

NON-ELLIPTICAL CAVITIES

FRIB

The largest ever SRF hadron accelerator is being built at FRIB. The cavity fabrication is almost complete (340 cavities received) and 50% of the cryomodules are assembled with tunnel installation of the first linear segment complete [31]. Cryomodule qualification is proceeding well with installed cavity performance matching vertical test. A recent beam test with the front end and the first three cryomodules was very successful [32]. FRIB offers a rich data set due to the high cavity numbers. It is noted that the high field Q-slope (HFQS) (without X-rays) is observed in each cavity family with the average onset field coincident at a B_p ~ 85 mT [33]. Interestingly, this corresponds to E_{acc}=20 MV/m for an ILC cavity – similar to the onset field of HFQS with BCP'ed cavities. It begs the question whether high field performance could be improved with EP.

High Performance in TEM Mode Cavities

TEM mode cavities continue to make performance gains. Two examples of state of the art performance are the HWRs fabricated by ANL for PIP-II and processed with EP [34] and a QWR cavity by RISP and tested by TRIUMF using a BCP process [35] - both reached a peak magnetic field of 143 mT. The ANL HWR is particularly noteworthy in that a peak electric field of 135 MV/m was reached. IPN-Orsay is pursuing novel heat treatments with 352 MHz spoke resonator for ESS and Myrte. Here also the cavities reach Bp=140 mT. It is found that the use of Nb caps during the degassing cycle at 650°C can eliminate the need for a final chemical etch even with a Ti jacket yielding a higher Q with a very low residual resistance of R0=1.3 nΩ! [36]. They are also studying flux expulsion as a function of geometry in QWR vs SSR vs DSR [37].

New Cavity Variants

While SSR cavities report excellent results, the adverse impact of strong multipacting (MP) in SSR cavities is also noted by recent test reports, consistent with 3D simulations. TRIUMF has recently designed, fabricated and tested a new variant of SSR termed the balloon cavity [38], that by design reduces multipacting probability and restricts the multipacting regime to low field levels. While traditional SSRs are built like a drum with two end plates and a central spool, the balloon cavity is more like an elliptical cavity with two end shells and no central spool. The cavity is inherently more mechanically stable than the traditional SSR with less ribs required, simplifying fabrication. The design recalls the evolution of the elliptical cavity from the initial pillbox shape to mitigate MP. A cavity at 352 MHz and β=0.3 has been built and tested. The cavity performance matches design with MP limited from 0.2 to 1.8 MV/m well away from the operational gradient at 9 MV/m (Fig. 9) [39].

ODU has fabricated and tested a coaxial HWR for fundamental SRF studies. The goal is to study frequency dependent surface resistance using the fundamental and

Content from this work may be used under the terms of the CC BY 3.0 licence (© 2018). Any distribution of this work must maintain attribution to the author(s), title of the work, publisher, and DOI.

ISBN: 978-3-95450-194-6 ISSN: 2226-0366 doi:10.18429/JACoW-LINAC2018-MO1A02

Content from this work may be used under the terms of the CC BY 3.0 licence (© 2018). Any distribution of this work must maintain attribution to the author(s), title of the work, publisher, and DOI.

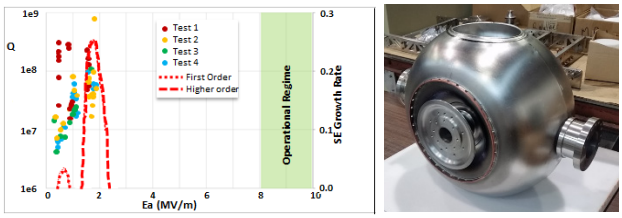


Figure 9: Balloon cavity variant and MP test results.

higher harmonics in the same cold test [40]. TRIUMF has made two cavities, a QWR and an HWR for the same purpose. A collaboration between GSI, IAP Frankfurt and HIM Mainz has successfully produced, installed and beam tested a 217 MHz CH cavity at GSI [41].

Technological Developments

Nb on Cu

The HIE-Isolde project recently installed 20 QWR cavities utilising Nb sputtered on a Cu substrate using DC bias sputtering. Each cavity can work at 6 MV/m, 101 MHz with < 10 W dissipation, at 4.5 K. After early developments they evolved to a seamless substrate, machined from bulk, to achieve the specified performance. After cooldown, partially screened with compensation coils, QSS2 reached unprecedented peak fields for Nb/Cu film technology (Fig. 10) [42]. While still lagging behind bulk niobium in ultimate gradient and Q reach Nb/Cu may be suitable for certain niche applications. CERN, JLab and others are continuing to develop the technology. IMP is also pursuing Nb/Cu as a development towards CiADS.

Hi-Lumi Beam Test

CERN has recently completed the fabrication of two Double Quarter Wave (DQW) deflecting mode cavities, first developed by BNL. The cavities were assembled into a cryomodule and installed in SPS for a proof of principle crabbing demonstration [43].

Low Cost Fabrication of Deflecting Cavity

TRIUMF has succeeded in fabricating and testing a new deflecting cavity variant to be used as an rf splitter [44]. The cavity was fabricated using low cost methods with production via bulk machining of low cost reactor grade Niobium and parts joining via TIG welding.

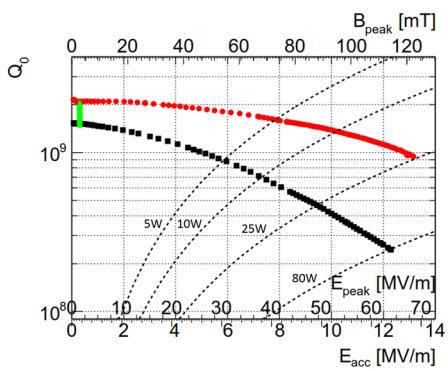


Figure 10: HIE ISOLDE two seamless cavities performance at 4.5 K.

Plasma Cleaning of TEM Cavities

Both IMP and FNAL are developing plasma cleaning for TEM mode cavities. IMP has successfully applied cleaning to a HWR in a vertical test after first depositing pollution on a cavity and then successfully cleaning the surface [45]. FNAL has initiated a program of plasma cleaning on a SSR cavity [46].

FUTURE PATHS

The 120°C bake is known to manipulate the mean free path at the near surface to create a dirty layer of ~50 nm [47]. Interestingly the dirty layer seems beneficial in order to increase the quench field beyond Bc1. Theoretical models are being developed that show that a high κ coating on clean Nb can enhance the field of first flux penetration [48][49]. N infusion and the low temperature bake variations provide additional means to manipulate the dirty layer.

MuSR findings from TRIUMF show that baking at 120°C enhances the field of first flux entry in ellipsoid samples while a layer of high κ and T_c material on niobium enhances the field of first entry by ~40% to a value near H_{sh} consistent with the `dirty layer' hypothesis [50].

ILC and other projects are looking for reproducible robust recipes that can be replicated in industry. We know that variations in the dirty layer produce significant variations in performance from N-Infusion results. The strategy moving forward will be to engineer a surface layer on bulk Nb to reproducibly optimize the performance beyond pure Nb. Thin film research and theory are continuing in parallel with work on Nb3Sn, MgB2 and SIS layers. Alternatively, it is suggested that vortex nucleation time presents a `time barrier' that may be more important than the surface barrier (H_{sh}) in governing flux penetration. Such a barrier would favour higher frequencies and influence thin coating choice towards slower materials. [51].

Stay tuned!

ACKNOWLEDGMENTS

Many thanks to the following for supplying material: P. Dhakal (Jlab), S. Posen (FNAL), M. Liepe (Cornell), D. Longuevergne (IPN-Orsay), C. Madec (Saclay), W. Venturini Delsolaro (CERN), K Umemori (KEK), H. Sakai (KEK), H. Podlech (IAP), K. Liu (PKU).

I also acknowledge contributions from the following by liberally stealing from their fine work: A. Grassellino (FNAL), D. Gonnella (SLAC), M. Martinella (FNAL), M. Checchin (FNAL), A. Romanenko (FNAL), F. Dziuba (IAP), T. Kubo (KEK,ODU), J. Delayen (ODU).

REFERENCES

[1] H. Padamsee, "50 years of success for SRF accelerators – a review", Supercond. Sci. Technol. 30, 053003 (2017) p. 23.

[2] N. Walker *et al.*, "Performance Analysis of the European XFEL SRF Cavities, from Vertical Test to Operation in Modules", presented at the 27th Linear Accelerator Conf. (LINAC'16) Lansing, Michigan, Sep. 2016, p. 657. doi:10.18429/JACoW-LINAC2016-WE1A04

ISBN: 978-3-95450-194-6 ISSN: 2226-0366 doi:10.18429/JACoW-LINAC2018-MO1A02

[3] B. Bonin and R. Roth, "Q-Degradation of Niobium Cavities due to Hydrogen Contamination" in *Proc. 5th Workshop on RF Superconductivity (SRF'91),* Hamburg, Germany, Oct. 1991, p 210.

[4] L. Lilje *et al*., Nucl. Instrum. Methods Phys. Res. **A516** (2004) p. 213.

[5] A. Romanenko *et al*., Appl. Phys. Lett. 102, 232601 (2013).

[6] A.Grassellino *et al*., Supercond. Sci. Technol. 26, 102001 (2013).

[7] A. Grassellino *et al*., Supercond. Sci. Technol. 30, 094004 (2017).

[8] M. Martinello *et al.*, "Effect of interstitial impurities on the field dependent microwave surface resistance of niobium", Appl. Phys. Lett. **109** (2016) p. 062601.

[9] D. Gonnella, J. Kaufman and M. Liepe, "Impact of nitrogen doping of niobium superconducting cavities on the sensitivity of surface resistance to trapped magnetic flux", J. Appl. Phys 119 (2016), p. 073904.

[10] D. Gonnella, "Achieving High Q_0 is LCLS-II Cavity Production" TTC Milano (Feb. 2018).

[11] M. Martinello, PhD thesis, IIT (Dec. 2016) p. 5.

[12] M. Checchin *et al*., Supercond. Sci. Technol. 30, 034004 (2017).

[13] T. Kubo, "Flux trapping in superconducting accelerating cavities during cooling down with a spatial temperature gradient", Prog. Theor. Exp. Phys. (2016) p. 053G01.

[14] S. Posen *et al*., "Efficient expulsion of magnetic flux in superconducting radiofrequency cavities for high Q0 applications", J. Appl. Phys 119 (2016) p. 213903.

[15] S. Posen *et al*., "Magnetic Flux Expulsion Studies on Niobium", presented at the 18th Int. Conf. RF Superconductivity (SRF'17), Lanzhou, China, Jul. 2017.

[16] S. Posen, C. Antoine, and A. Yamamoto, "Summary of WG2", TTC Riken (Jun. 2018).

[17] M. Martinello *et al*.,"Advancement in the Understanding of the Field and Frequency Dependent Microwave Surface Resistance of Niobium" Lanzhou, China, Jul. 2017, p. 364. doi:10.18429/JACoW-SRF2017-TUYAA02

[18] F. Furuta *et al*., "RF Test Result of a BNL N-Doped 500 MHz B-Cell Cavity at Cornell", in *Proc. IPAC'18*, Vancouver, Canada, Apr.-May 2018, p. 2440. doi:10.18429/JACoW-IPAC2018-WEPMF036

[19] M. Checchin *et al*., "New Insight on Nitrogen Infusion Revealed by Successive Nanometric Material Removal", in *Proc. 9th Int. Particle Accelerator Conf. (IPAC'18),* Vancouver, Canada, Apr.-May 2018, p. 2665. doi:10.18429/JACoW-IPAC2018-WEPMK016

[20] M. Wenscat, "Infusion R&D at DESY", TTC Riken (Jun. 2018).

[21] K. Umemori, "Recent results of N-infusion at KEK/J-PARC", TTC Riken (Jun. 2018).

[22] P. Dhakal, "Update on infusion studies at JLab", TTC Riken (Jun. 2018).

[23] P. Koufalis, "Update on infusion studies at Cornell", TTC Riken (Jun. 2018).

[24] A. Grassellino, "Update on high Q/high G R&D @ FNAL", TTC Riken (Jun. 2018).

[25] A. Grassellino *et al*., "Accelerating fields up to 49 MV/m in TESLA-shape superconducting RF niobium cavities via 75°C vacuum bake", arXiv:1806.09824.

[26] P. Kneissel *et al.*, "Review of ingot niobium as a material for superconducting radiofrequency accelerating cavities", NIM **A774** (2015), pp. 133-150.

[27] P. Dhakal, "Ingot Niobium for Efficient and Potentially Low Cost SRF Cavities", TTC Riken (Jun. 2018).

[28] Jiankui Hao *et al*., "Fabrication, Treatment and Test of Large Grain Cavities", in *Proc. 18th Int. Conf. RF Superconductivity (SRF'17)*, Lanzhou, Jul. 2017, p. 700. doi:10.18429/JACoW-SRF2017-THXA04

[29] M. Liepe, private communication.

[30] S. Posen, "Nb_3Sn Results from FNAL", TTC Riken (Jun. 2018).

[31] C. Compton, "FRIB Cavities and Cryomodule Production", TU1A04, this conference.

[32] E. Pozdeyev, "First Acceleration at FRIB", WE2A01, this conference.

[33] K. Saito, "Cavity Performance from FRIB".

[34] Z. Conway, "Optimizing TEM Mode Cavity Performance", TTC Riken (Jun. 2018).

[35] R. Laxdal, "HWR/QWR Test Data", TTC Riken (Jun. 2018).

[36] D. Longuevergne, private communication.

[37] D. Longuevergne, "Flux trapping studies on low beta cavities", TTC Milano (Feb. 2018).

[38] Z. Yao *et al*., "Design and Fabrication of a β=0.3 SSR1 for RISP", in *Proc. 28th Linear Accelerator Conf. (LINAC'16)*, East Lansing, MI, USA, Sep. 2016, p. 226. doi:10.18429/JACoW-LINAC2016-MOPLR041

[39] Z. Yao *et al*., "Fabrication and Test of a β=0.3 325 MHz Balloon Single Spoke Resonator", in *Proc. 9th Int. Particle Accelerator Conf. (IPAC'18)*, Vancouver, Canada, Apr.-May 2018, p. 3934. doi: 10.18429/JACoW-IPAC2018-THPAL123

[40] H.K. Park *et al.*, "Investigation of Low Temperature Baking on the Surface Resistance of Niobium Between 325 MHz and 1300 MHz Using a Coaxial Half Wave Cavity", TUPO031, this conference.

[41] W. Barth *et al*., "First Acceleration of Heavy Ion Beams with a Superconducting Continuous Wave HIM/GSI CW-linac", TU2A01, this conference.

[42] W. Venturini Delsolaro, "Seamless Quarter Wave Resonators for HIE-ISOLDE", TU1A05, this conference.

[43] R. Calaga, "HL-LHC WP4 Crab Cavities & RF", TTC Riken (Jun. 2018).

[44] D. Storey *et al*., "Fabrication of a SRF Deflecting Cavity for the ARIEL-Linac", in *Proc. 18th Int. Conf. RF Superconductivity (SRF'17)*, Lanzhou, China, July 2017, p. 524. doi: 10.18429/JACoW-SRF2017-TUPB063

[45] Y. He *et al*., "HWR performance and performance recovery in IMP", TTC Riken (Jun. 2018).

[46] P. Berutti, "Plasma Cleaning R&D at FNAL", TTC Riken (Jun. 2018).

[47] A. Romanenko *et al*., Appl. Phys. Lett. **104**, 072601 (2014).

Content from this work may be used under the terms of the CC BY 3.0 licence (© 2018). Any distribution of this work must maintain attribution to the author(s), title of the work, publisher, and DOI.

ISBN: 978-3-95450-194-6 ISSN: 2226-0366 doi:10.18429/JACoW-LINAC2018-MO1A02

[48] T. Kubo and A. Gurevich, "A unified theory of surface resistance and the residual resistance of SRF cavities at low temperatures", presented at the *18th Int. Conf. RF Superconductivity (SRF'17)*, Lanzhou, China, July 2017 (slides only).

[49] Mattia Checchin *et al*., "Ultimate gradient limitation in niobium superconducting accelerating cavities", in *Proc. 7th Int. Particle Accelerator Conf. (IPAC'16),* Busan, Korea, May 2016, pp. 2254-2257. doi:10.18429/JACoW-IPAC2016-WEPMR002

[50] T. Junginger, W. Wasserman and R.E. Laxdal, "Superheating in coated niobium", Supercond. Sci. Technol. 30, No. 12, published 7 Nov. 2017.

[51] A. Romaneko, "Pathway to High Gradients in Superconducting rf Cavities by Avoiding Flux Dissipation", presented at *9th Int. Particle Accelerator Conf. (IPAC'18)*, Vancouver, Canada, Apr.-May 2018 (slides only).

Content from this work may be used under the terms of the CC BY 3.0 licence (© 2018). Any distribution of this work must maintain attribution to the author(s), title of the work, publisher, and DOI.

ISBN: 978-3-95450-194-6 ISSN: 2226-0366 doi:10.18429/JACoW-LINAC2018-MO2A03

TECHNOLOGY DEVELOPMENTS OF ELI-NP GAMMA BEAM SYSTEM

L. Piersanti*, D. Alesini, A. Battisti, M. Bellaveglia, S. Bini, F. Cardelli, R. Di Raddo, A. Falone, A. Gallo, V. Lollo, L. Pellegrino, S. Pioli, S. Tomassini, A. Variola INFN-LNF, Frascati, Italy
L. Ficcadenti, M. Migliorati[1], A. Mostacci[1], L. Palumbo[1], V. Pettinacci INFN-Roma, Rome, Italy
D. T. Palmer, L. Serafini INFN-Sezione di Milano
K. Cassou, D. Douillet, K. Dupraz, T. Le Barillec, A. Martens, C. F. Ndiaye, Y. Peinaud, F. Zomer LAL, CNRS/IN2P3 Université Paris Sud - France
N. Beaugerard, B. Lacrampe, H. Rocipon, ALSYOM/SEIV-ALCEN, France
[1]also at Sapienza University of Rome, SBAI Department Rome, Italy

Abstract

The ELI-NP gamma beam system (GBS) is a linac based gamma-source in construction in Magurele (RO) by the European consortium EuroGammaS led by INFN. Photons with tunable energy, from 0.2 to 19.5 MeV, and with intensity and brilliance beyond the state of the art, will be produced by Compton back-scattering between a high quality electron beam (up to 740 MeV) and an intense laser pulse at 100 Hz repetition rate. Production of very intense photon flux with narrow bandwidth requires multi-bunch operation and laser recirculation at the interaction point. In this paper, the main technological developments carried out by the EuroGammaS consortium for the generation of the ELI-NP gamma beam will be described with a special emphasis on the electron linac technology, such as: RF-gun and C-band accelerating structures design fabrication and tests; low level RF (LLRF) and synchronization systems specifications and development. Finally, the laser recirculation apparatus design is briefly described and first results reported.

INTRODUCTION

An advanced source of gamma-ray photons will be built in Magurele in the framework of the ELI-NP project [1, 2] by the EuroGammaS consortium. The gamma-rays will be generated by a high quality electron beam colliding with a high power laser pulse (200 mJ, 3.5 ps, 515 nm) recirculated 32 times at the interaction point. The machine is expected to produce photons with tunable energy between 0.2 and 19.5 MeV with a narrow bandwidth (< 0.5 %) and a high spectral density ($0.8\text{-}4 \times 10^4$ ph/s eV) [3].

The accelerator layout is based on a C-band (5712 MHz) RF linac, with a S-band (2856 MHz) photo-injector similar to that of SPARC_LAB at LNF-INFN (Frascati, Italy) [4], able to deliver a high phase space density electron beam in the 300-740 MeV energy range. The repetition rate is 100 Hz and, in order to reach the required photon flux, the machine is foreseen to work in multi-bunch mode (fitting 32 electron bunches spaced by 16 ns in each RF pulse), thus with an effective repetition rate of 3.2 kHz. The main electron beam parameters of the ELI-NP-GBS, together with the description of the complete RF system have been reported in [2, 5].

* luca.piersanti@lnf.infn.it

LINAC OVERVIEW

ELI-NP-GBS photo-injector comprises a 1.6 cell S-band RF-gun, which has been manufactured with a new fabrication technique which does not require copper brazing [6–9], and two S-band 3 m long SLAC-type TW constant gradient accelerating structures. The S-band system comprises also two deflecting cavities used for longitudinal beam diagnostics. The linac booster is made of 12 travelling wave (TW) C-band disk loaded accelerating structures. Moreover, a waveguide high order mode (HOM) damping system that employs 4 SiC RF absorbers for each cell [10–13] has been included in the design, to avoid beam break up instabilities that may arise due to multi-bunch operation.

In order to reduce bunch-by-bunch energy spread due to structure beam loading (BL), a tailored pulse shaping compensation has to be provided to the klystrons by the LLRF systems [5]. Moreover, since the use of pulse compressors would make the pulse shaping even more critical, each accelerating section is individually driven by a dedicated power station (with the exception of the last 4 TW sections that are fed by 2 klystrons). A sketch of the linac has been reported in Figure 1.

S-BAND RF-GUN DESIGN, LOW AND HIGH POWER TESTS

RF photo-guns find several type of applications including high brightness electron sources for free-electron lasers, energy recovery linacs, Compton/Thomson photon sources. Being the achievable beam brightness proportional to the peak field at the cathode, in the last generation of RF guns a great effort has been put to increase the field amplitude while reducing, at the same time, the breakdown phenomena. Moreover, modern RF guns must be able to withstand high repetition rate operation (of the order of 100 Hz) with a reasonable realization cost. Currently the standard fabrication process relies on copper brazing. However, this technique requires large vacuum furnaces, it is expensive and has a non-negligible risk of failure. Furthermore, studies carried out on X-band prototypes indicated that it is possible to reduce the breakdown probability if copper thermal stress is avoided [14]. For all these reasons, a new brazing-free fabrication method based on the use of special RF-vacuum gaskets has been recently developed at LNF-INFN [7], and

Content from this work may be used under the terms of the CC BY 3.0 licence (© 2018). Any distribution of this work must maintain attribution to the author(s), title of the work, publisher, and DOI.

ISBN: 978-3-95450-194-6 ISSN: 2226-0366 doi:10.18429/JACoW-LINAC2018-MO2A03

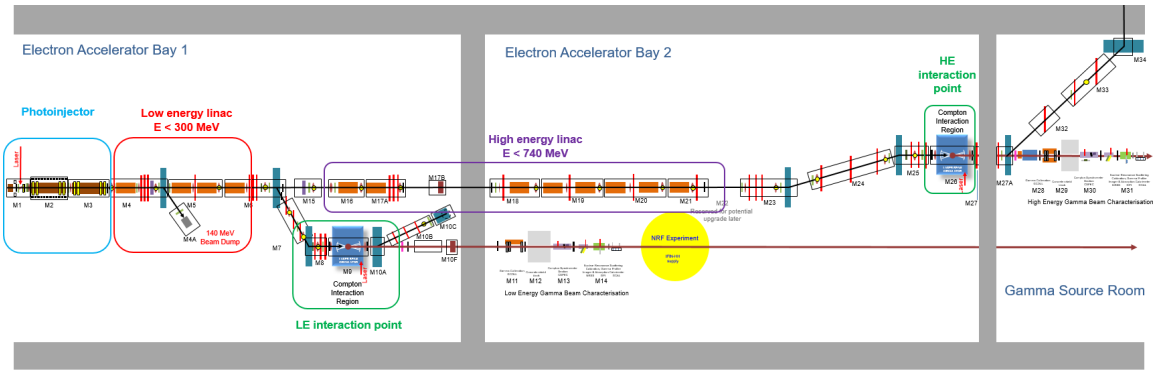


Figure 1: ELI-NP GBS linac overview.

successfully applied to the realization of a first RF gun prototype [6, 15–17]. The same technique has also been adopted for the realization of the 1.6 cell S-band ELI-NP-GBS RF gun.

Electromagnetic Design

The electromagnetic design of the gun has been performed using 2D and 3D codes (Poisson Superfish [18] and ANSYS Electronics [19]). The iris profile, with an elliptical shape and a large aperture, simultaneously reduces the peak surface electric field, increases the frequency separation between the two resonant modes and improves the pumping efficiency on the half-cell. The coupling window between the rectangular waveguide and the full cell has been strongly rounded to reduce the peak surface magnetic field and, consequently, the pulsed heating [6, 20]. To compensate the dipole field component, induced by the presence of the coupling hole in the full cell, a symmetric port (connected to a circular pipe below cut off) has been included in the gun [21–23] and is used as vacuum pumping port. The RF-gun main parameters have been reported in Table 1.

Table 1: ELI-NP-GBS RF-gun Design Parameters

Parameter	Value
Resonant frequency (f_{res})	2856 MHz
Cathode peak field (E_{cath})	120 MVm
Filling time (τ)	410 ns
Quality factor (Q_0)	14 600
Coupling coefficient (β)	3
Total RF pulse length	1.5 µs
Shunt impedance (R)	1.64 MΩ
Frequency separation $0/\pi$ mode	41.5 MHz
Pulsed heating	< 36 °C
Average dissipated power	1.3 kW

The operation at 100 Hz with 1.5 µs RF pulses results in an average dissipated power into the structure larger than 1 kW. To avoid detuning during operation, a careful design of the cooling system has been performed. The gun has 6 cooling channels: three for the full cell, one for the iris, one for the half cell and one for the cathode. The fully coupled thermal, structural and electromagnetic analysis, has been carried out by means of ANSYS Workbench [19]. The final temperature distribution at regime has been calculated and corresponds to a deformation of few microns. As far as the electromagnetic design is concerned, the expected frequency detuning of the gun during operation is lower than 100 kHz and the field flatness perturbation is completely negligible. Such detuning can be compensated changing the water inlet temperature of about 2 °C .

RF-Gun Manufacturing

The body of the gun has been fabricated from a single piece of OFHC copper using diamond tools. The rounded coupler geometry and the overall gun body have been realized with a 5 axis milling machine. The full cell has then been sealed clamping the body with the pipe by means of the special gasket [7, 9], that simultaneously guarantees the RF contact and the vacuum seal, avoiding sharp edges and gaps. The RF gun has been manufactured by COMEB [24] with a precision on the internal dimensions of ≈10 µm and surface roughness lower than 150 nm. The cathode has been realized from a single piece of copper and has been clamped to the structure. The RF contact between the cathode and the gun body is guaranteed by pressure, while the vacuum seal by a special aluminum gasket not exposed to RF. The cathode dissipates around 200 W, thus it has to be cooled independently. Before the final clamping, the gun has been cleaned with ALMECO-19 detergent in an ultra-sound bath.

Low and High Power Tests

Low power RF test and tuning of the gun have been performed with the bead drop technique [25], measuring the reflection coefficient with a Network Analyzer. The tuning has been done by means of deformation tuners placed in the full cell. The resulting measured coupling coefficient was $\beta = 2.64$ in fair agreement with the design value, while all other parameters were in very good agreement with the ones reported in Table 1.

High power RF tests have been performed at Bonn University in collaboration with Research Instruments [26]. The power source employed was the ELI-NP-GBS Scandinova RF unit based on a solid state modulator (K2-3) and 60 MW

Content from this work may be used under the terms of the CC BY 3.0 licence (© 2018). Any distribution of this work must maintain attribution to the author(s), title of the work, publisher, and DOI.

ISBN: 978-3-95450-194-6 ISSN: 2226-0366 doi:10.18429/JACoW-LINAC2018-MO2A03

S-band Toshiba klystron. The aim of the test was to achieve 120 MV/m at the cathode (corresponding to 14 MW input power) at the nominal repetition rate and RF pulse duration. The klystron power, repetition rate and pulse length were progressively increased, while breakdown phenomena were detected looking at the ion pumps current absorption and RF signals from pickups. The modulator HV interlock conditions were: (a) ion pumps current absorption exceeding a pressure of 5×10^{-8} mbar; (b) high reflected power towards the klystron; (c) distortions of the reflected signal due to breakdown phenomena. The RF conditioning lasted about 160 hours and the gun reached the nominal parameters with a breakdown rate (BDR) of few 1×10^{-5} bpp. Since the BDR trend was constantly decreasing, and considering the test stand limited time availability, the test has been considered successful. At the end of conditioning and without power the vacuum pressure in the gun was lower than 5×10^{-10} mbar.

C-BAND STRUCTURES DESIGN, TUNING AND HIGH POWER TESTS

ELI-NP-GBS booster linac consists of 12 TW C-Band disk loaded accelerating sections. Each section is 1.8 m long, quasi-constant gradient with a $2\pi/3$ field phase advance per cell and will operate at an average accelerating gradient of 33 MV/m. Since the linac operation is multi-bunch, the structures have been designed with an effective damping of the cell dipole HOM based on waveguide coupled to SiC absorbers. The design criteria together with the main structure parameters have been thoroughly illustrated in [13]. The HOM damping system is similar to the one adopted for the CLIC X-band structures [27], but the mechanical design has been strongly simplified in order to reduce the cost and to ease the manufacturing. Each cell has four waveguides that allow the excited HOMs to propagate and dissipate into RF absorbers. A dedicated study performed on a single 12-cell module to assess the effectiveness of the SiC absorbers can be found in [13]. The input and output couplers have two symmetric ports and race track cell geometries to minimize the dipole and quadrupole field components introduced by the coupling holes. The input coupler integrates also a splitter that allows a symmetric RF feeding of the structure, while the output one has two symmetric ports connected to two RF loads.

Structure Fabrication

In order to have a better control of the brazing process, each structure has been conceived in 10 separate modules, which have been individually realized, brazed and vacuum tested: the input and output couplers (including two adjacent cells) plus eight 12-cell modules. The manufacturing of the cells required several steps. After a rough machining, the cells underwent a stress relieving treatment in a vacuum furnace. Then, they have been milled, while the final machining of the irises has been performed by means of the ultra-precise lathe Schaublin 225 TM-CNC that guarantees a precision ±5 µm and a surface roughness lower than 50 nm. Each cell includes also four deformation tuners and eight cooling pipes, needed to withstand the 100 Hz operation. The manufacturing of the input and output couplers followed a similar procedure. All components have been then cleaned in several steps in an ultrasound bath. After brazing a vacuum test with a sensitivity lower than 5×10^{-10} mbar/l/s has been carried out. The SiC (Ekasic-P) absorbers tiles (pre-machined) have then been inserted in the modules and the whole structure was assembled together and brazed. After the final brazing, performed at INFN Legnaro National Laboratories, and a moderate bake-out at 100 °C, a leak test has been performed with a sensitivity lower than 5×10^{-10} mbar/l/s. A pressure of few 1×10^{-9} mbar has been reached with just one ion pump connected on one side.

Low and High Power Tests

Eight structures have been tuned at LNF so far, measuring the scattering parameters at the input and output ports with a network analyzer. The magnitude of the accelerating field and the phase advance per cell have been evaluated with the bead pull technique, using a metallic sphere as perturbing object. The tuning has been done acting on the four deformation tuners of each cell, using the same procedure illustrated in [28–30]. The field flatness, the phase advance and the cumulative phase advance after the tuning procedure were the nominal ones for all the fabricated structures. As example, the calculated field flatness of structure number 6 is below 1%, the phase advance per cell is within ±2 deg, while the cumulative phase advance error is limited within ±5 deg. At the resonant frequency the reflection coefficient at the input port is lower than −25 dB, while the transmission coefficient between input and output port is ≈−8.5 dB, i.e. in good agreement with the designed total attenuation.

The first prototype structure has also been tested at high power at the Bonn University under the responsibility of Research Instruments. The power source was one of the ELI-NP-GBS C-band station, i.e. a Scandinova RF unit based on K2-2 solid state modulator adapted for 50 MW C-band Toshiba klystron (E37212). The aim of the RF conditioning was to reach the nominal power at the input coupler (40 MW), repetition rate (100 Hz) and pulse length (820 ns). The klystron power, repetition rate and pulse length were progressively increased following the same procedure reported in the previous section for the RF-gun. The RF conditioning was successfully completed after 190 hours. The vacuum pressure, measured both at the beginning and at the end of the structure, was of the order of 1×10^{-8} mbar. The BDR at the end of the conditioning was of the order of few 1×10^{-6} bpp/m.

LLRF AND SYNCHRONIZATION SYSTEMS

LLRF System

The LLRF system for the ELI-NP-GBS (Libera LLRF) has been developed by Instrumentation Technologies [31]

Content from this work may be used under the terms of the CC BY 3.0 licence (© 2018). Any distribution of this work must maintain attribution to the author(s), title of the work, publisher, and DOI.

ISBN: 978-3-95450-194-6 ISSN: 2226-0366 doi:10.18429/JACoW-LINAC2018-MO2A03

Content from this work may be used under the terms of the CC BY 3.0 licence (© 2018). Any distribution of this work must maintain attribution to the author(s), title of the work, publisher, and DOI.

and consists of 13 temperature stabilized boards (one dedicated to each power unit): 3 S-band and 10 C-band. This choice has been made in order to guarantee the maximum flexibility in terms of pulse shaping and machine operation stability. One of the main features of Libera LLRF platform is, in fact, the possibility to perform a pulse-by-pulse feedback. Moreover, the pulse shape can be arbitrarily set (e.g. for BL compensation) simply loading a user defined mask to Libera FPGA. The request for thermal stabilization has been introduced to compensate the long-term effect of temperature drifts, that must not exceed 100 fs for normal operation: (24 ± 2) °C. Overall Libera LLRF modules have to guarantee an amplitude resolution of 0.1 % RMS and a phase added jitter lower than 10 fs. Each board contains four main elements: (i) the temperature stabilized analog front-end,(ii) the analog back-end (with 1 RF vector modulator), (iii) the main CPU (which hosts the sampling cards, the FPGA and the EPICS control system server), and (iv) the LO generator and timing unit. The main parameters of Libera LLRF together with some preliminary measurements performed at LNF have been reported in [32].

Synchronization System

The general ELI-NP-GBS synchronization requirement is that the relative arrival time jitter of the electron bunches and laser pulses has to be lower than 500 fs rms at the interaction point (IP). For this reason, the synchronization system has been designed to provide to all clients an ultra-stable reference with a relative jitter < 70 fs. Given the significant link lengths, the reference will be distributed with optic fibers (very low attenuation over hundreds of meters, larger sensitivity obtainable by optical based timing detection). The ELI-NP-GBS synchronization system has been manufactured by Menlo Systems [33] and it consists of two main parts: reference generation and distribution, client synchronization. The reference signal is provided by a Reference Master Oscillator (RMO) which is a μ-wave crystal oscillator (MO-2856-V3 produced by Laurin A.G.) with ultra-low phase noise (10 Hz-10 MHz measured absolute jitter < 60 fs). The RMO provides a stable reference tone to Menlo Optical Master Oscillator (OMO), which is a Er-doped mode-locked laser oscillator, that encodes the reference timing information in the repetition rate of short optical pulses at 1560 nm. Using such configuration, the RMO guarantees the long term stability of the OMO, and imprints its low-frequency noise figure to the whole facility timing.

Once the laser pulses are generated, they are amplified and distributed to all the clients. One of the channels is further amplified and converted by a second harmonic generator to a 780 nm free space output, used as direct seed for the photocathode laser system. Four main clients have been identified in the ELI-NP-GBS machine: two interaction lasers and two RF extractors (one at 2856 MHz and one at 5712 MHz) that provide the RF reference to the LLRF systems and power units. Depending on the nature of the clients, the PLL can be either “fully optical” (employing optical cross-correlators), or “electro-optical” locking the RF-extractor to a μ-wave VCO. The clients will be reached by means of four dispersion compensated fiber links with active length stabilization, in order to deliver short (< 200 fs) synchronous pulses to the end users. The active length stabilization is achieved sending back a fraction of pulse from the link-end and comparing it to a reference pulse near the oscillator. A full description of the synchronization system has been reported in [32].

LASER BEAM CIRCULATOR

The IP laser architecture is based on a chirped-pulse amplification scheme, composed of an Yb oscillator (20 nJ, 62 MHz, 200 fs, 1030 nm), a stretcher, several amplifier stages (regenerative + cryo-cooled 350 mJ, 100 Hz), and a compressor. Finally the pulses are frequency doubled in a second harmonic conversion stage to reach the IP specifications (200 mJ, 100 Hz, 3.5 ps, 515 nm).

To optimize the γ-ray beam quality, the optical system at the IP must preserve laser spectral bandwidth while maximizing its flux. The effective increase of the laser beam power at the Compton IP can be obtained with two types of optical systems, namely a Fabry-Perot resonator [34] or an optical recirculator [35–37]. Since the ELI-NP-GBS linac operates in multi-bunch at 100 Hz, a passive optical device able to recirculate and focus several times a single laser pulse at the IP is the optimal solution to maximize the γ flux. As already mentioned, this system must assure a minimal variation of the γ-ray central spectral line. This can be obtained by keeping a constant collision angle (Φ) between laser and electron beam. Furthermore, it is also important to preserve polarization and quality of the wave front. The working principle of the proposed laser beam circulator (LBC) is illustrated in Figure 2: two confocal concave mirrors reflect a circulating Gaussian beam [8] back and forth by forcing it to cross the electron beam axis (i.e., the z axis) at the focus point (the IP). The sequence of lenses equivalent to a "round-trip" is also shown in Figure 2. With a proper choice of the mirror radii of curvature it is possible to alternate beam focusing and collimation.

The final geometry chosen is the so-called "dragon-shape" recirculator depicted in Figure 3. The LBC is made of two big confocal parabolic reflectors, to preserve the quality of the wave front after each pass. Since the crossing angle must be kept constant, the laser-electron beams interaction plane must rotate if more than two recirculations are foreseen. Therefore, a series of two parallel flat mirrors are used to switch from one interaction plane to the next one, while keeping the optical axis parallel to the z axis. Such a pair of parallel mirrors forms an optical invariant providing an emerging beam parallel to the entrance independently of its orientation. Then, the recirculating laser beam axis is always parallel to the symmetry axis z when impinging the parabolic reflectors. By construction, as shown in Figure 3, the mirror-pairs systems are located on a circular helix. It is important to remark that the IP positions is fixed for all laser passes.

ISBN: 978-3-95450-194-6 ISSN: 2226-0366 doi:10.18429/JACoW-LINAC2018-MO2A03

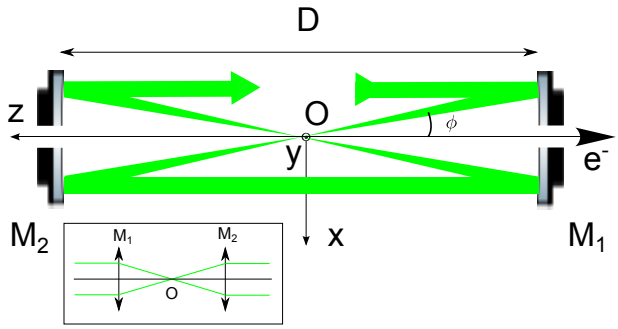


Figure 2: Illustration of the planar confocal recirculator working principle and its equivalent sequence of lenses.

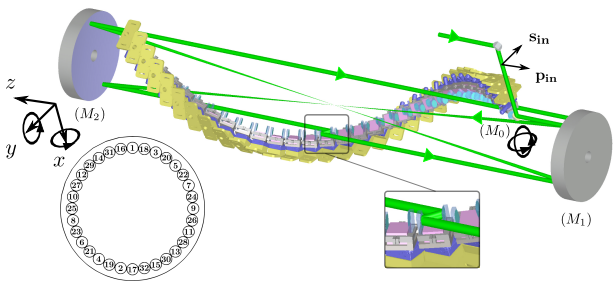


Figure 3: Schematic view of ELI-NP-GBS LBC. The mirror M0 is used to inject the incident laser beam. The 7 degrees of freedom for the mirror motions are sketched: two tilts for M0; two tilts and three translations for M2. Finally the bottom left scheme shows the optical pass ordering.

The time structure of the electron bunch train is strongly related to the RF frequency of the accelerating cavities. Thus, the laser pulse round-trip period must be tightly matched to the bunch repetition frequency. However, since the LBC round-trip lengths are fixed by the parabolic mirrors radius of curvature, the only way to adjust the round-trip path is to rotate the mirror pair system around its own axis. The rotation, in fact, changes the incident angle on the mirrors and consequently the laser optical path length. Moreover, this change is made without modifying the laser beam direction, as it is independent of the mirror pair orientation. Therefore, in order to adjust the timing of each optical recirculation independently, a mirror pair must be placed before each IP crossing. In order to asses the optical alignment of the LBC, a robust optical estimator must be defined. The simplest solution is the intersection point $\{x_n; y_n\}$ of the nth optical pass with the plane $z = 0$ (i.e., the IP). Measurements of $\{x_n; y_n\}$ can be performed inserting a thin pellicle at the LBC center and using an ultrafast CCD. Since the exact position of the electron beam axis with respect to $\{x_n; y_n\}$ cannot be known in advance, the Transverse Distance between the n-th intersection point and the Barycenter (TDB) of all 32 intersection points can be defined instead:

$$TDB_n = \left[\left(x_n - \frac{1}{32} \sum_{i=1}^{32} x_i \right)^2 + \left(y_n - \frac{1}{32} \sum_{i=1}^{32} y_i \right)^2 \right]^{1/2}$$

The alignment system will also be used for the synchronization: adding a second laser pulse train, whose repetition frequency is the same of the electron bunch train, with the same pellicle it is possible to generate an interference pattern which provides information on the relative delay between the two pulses. From previous simulations, the insertion of the pellicle induces a cumulative time delay below 90 fs. This method has the great advantage that only a single pellicle for alignment and synchronization is used, moreover, such solution can monitor online the performance of the LBC, since it is a non-intercepting beam diagnostic element. A detailed description of the LBC design, tolerance and error studies, simulations and some preliminary test results can be found in [38, 39]. The commissioning of the first LBC started in November 2017 in the clean assembly area (PUPS) of ALSYOM [40] (Bordeaux), and it has been carried out by a joint effort of LAL/CNRS and ALSYOM people. A low power circulating laser pulse has been focalized 32 times at the IP with a laser spot waist of (27 ± 2) µm over 32 passes, a TDB lower than 10 µm and synchronized to an external optical reference with time precision of less than 160 fs in air with a transmission of (84 ± 3) % (theoretical 87.5 %). The enhancement factor obtained is 25.6 times the input laser power. The measured values are fully compliant to ELI-NP-GBS specifications.

CONCLUSIONS

In this paper, some of the most relevant technology developments carried out for the ELI-NP-GBS project have been introduced. In particular, an optimization of a 1.6 cell BNL/SLAC/UCLA SW RF gun realized with a brazing-free fabrication technique, the design and realization of HOM damped TW C-band structures and the IP laser recirculation system have been presented. The discussion is also integrated with a brief overview of the LLRF and synchronization systems. All the presented devices have been successfully tested and their installation and commissioning is foreseen in the next future in Magurele.

REFERENCES

[1] O. Adriani *et al.*, "Technical Design Report EuroGammaS proposal for the ELI-NP Gamma beam System", arXiv:1407.3669, 2014.

[2] A. Giribono *et al.*, "ELI-NP GBS Status", in *Proc. IPAC'17*, Copenhagen, Denmark, 2017, pp. 880–883. doi:10.18429/JACoW-IPAC2017-MOPVA016

[3] C. Vaccarezza *et al.*, "Optimization studies for the Beam Dynamics in the RF linac of the ELI-NP Gamma Beam System", in *Proc. IPAC'16*, Busan, Korea, 2016, pp. 1850–1853. doi:10.18429/JACoW-IPAC2016-TUPOW041

[4] M. Ferrario *et al.*, "Experimental Demonstration of Emittance Compensation with Velocity Bunching", *Phy. Rev. Lett.*, vol. 104, no. 5, p. 054801, 2010.

[5] L. Piersanti *et al.*, "The RF system of the ELI-NP gamma beam source", in *Proc. 7th Int. Particle Accelerator Conf. (IPAC'16)*, Busan, Korea, 2016, pp. 407–410. doi:10.18429/JACoW-IPAC2016-MOPMW006

Content from this work may be used under the terms of the CC BY 3.0 licence (© 2018). Any distribution of this work must maintain attribution to the author(s), title of the work, publisher, and DOI.

ISBN: 978-3-95450-194-6 ISSN: 2226-0366 doi:10.18429/JACoW-LINAC2018-MO2A03

Content from this work may be used under the terms of the CC BY 3.0 licence (© 2018). Any distribution of this work must maintain attribution to the author(s), title of the work, publisher, and DOI.

[6] D. Alesini *et al.*, "New technology based on clamping for high gradient radio frequency photogun", *Phys. Rev. ST Accel. Beams*, vol. 18, no. 9, p.092001, 2015.

[7] D. Alesini *et al.*, "Process for manufacturing a vacuum and radio-frequency metal gasket and structure incorporating it", International patent application PCT/IB2016/051464.

[8] F. Cardelli *et al.*, "Design of linac with the new gasket-clamping fabrication technique", in *Proc. 7th Int. Particle Accelerator Conf. (IPAC'16)*, Busan, Korea, 2016, pp. 403–406. doi:10.18429/JACoW-IPAC2016-MOPMW005

[9] D. Alesini *et al.*, "High power test results of the ELI-NP S-band gun fabricated with the new clamping technology without brazing", in *Proc. IPAC'17*, Copenhagen, Denmark, 2017, pp. 3662–3665. doi:10.18429/JACoW-IPAC2017-THOBB1

[10] D. Alesini *et al.*, "The damped C-band RF structures for the European ELI-NP proposal", in *Proc. 4th Int. Particle Accelerator Conf. (IPAC'13)*, Shanghai, China, 2013, pp. 2726–2728.

[11] D. Alesini *et al.*, "Design and RF test of damped C-band accelerating structures for the ELI-NP linac", in *Proc. IPAC'14*, Dresden, Germany, 2014, pp. 3856–3859. doi:10.18429/JACoW-IPAC2014-THPRI042

[12] D. Alesini *et al.*, "Realization and high power tests of damped C-band accelerating structures for the ELI-NP linac", in *Proc. IPAC'16*, Busan, Korea, 2016, pp. 399–402. doi:10.18429/JACoW-IPAC2016-MOPMW004

[13] D. Alesini *et al.*, "Design of high gradient, high repetition rate damped C-band rf structures", *Phys. Rev. Accel. Beams*, vol. 20, no. 3, p. 032004, 2017. doi:10.1103/PhysRevAccelBeams.20.032004

[14] V. Dolgashev *et al.*, "Status of high power tests of normal conducting single-cell standing wave structures", in *Proc. 1st Int. Particle Accelerator Conf. (IPAC'10)*, Kyoto, Japan, 2010, pp. 3810–3812.

[15] D. Cesar *et al.*, "Demonstration of single-shot picosecond time-resolved MeV ilectron imaging using a compact permanent magnet quadrupole based lens", *Phys. Rev. Lett.*, vol. 117, no. 2, p. 024801, 2016. doi:10.1103/PhysRevLett.117.024801

[16] J. Maxson *et al.*, "Direct measurement of sub-10 fs relativistic electron beams with ultralow emittance", *Phys. Rev. Lett.*, vol. 118, no. 15, p. 154802, 2017. doi:10.1103/PhysRevLett.118.154802

[17] D. Cesar *et al.*, "Ultrafast gating of a mid-infrared laser pulse by a sub-pC relativistic electron beam", *J. Appl. Phys.*, vol. 118, p. 234506, 2015. doi:10.1063/1.4937401

[18] Poisson Superfish, http://laacg.lanl.gov/laacg/services/download_sf.phtml

[19] Ansys, http://www.ansys.com

[20] V. Dolgashev, "High Magnetic Fields in Couplers of X-Band Accelerating Structures", in *Proc. Particle Accelerator Conf. (PAC'03)*, Portland, Oregon, USA, 2003, pp. 1267–1269.

[21] D. T. Palmer *et al.*, "Microwave Measurements of the BNL/SLAC/UCLA 1.6 Cell Photocathode RF Gun", in *Proc. Particle Accelerator Conf. (PAC'95)*, Dallas, Texas, USA, 1995, pp. 982–984.

[22] X. Guan *et al.*, "Study of RF-asymmetry in photo-injector", *Nucl. Instrum. Methods Phys. Res. Sect. A*, vol. 574, no. 1, p. 17, 2007. doi:10.1016/j.nima.2007.01.088

[23] M. S. Chae *et al.*, "Emittance growth due to multipole transverse magnetic modes in an rf gun", *Phys. Rev. ST Accel. Beams*, vol. 14, no. 10, p. 104203, 2011. doi:10.1103/PhysRevSTAB.14.104203

[24] COMEB, http://www.comeb.it

[25] L. C. Maier *et al.*, "Field strength measurement in resonant cavities", *J. Appl. Phys.*, vol. 23, no. 1, pp. 68–77, 1952. doi:10.1063/1.1701980

[26] Research Instruments, http://research-instruments.de

[27] A. Grudiev *et al.*, "Design of an X-Band Accelerating Structure for the CLIC Main Linac", in *Proc. 24th Linear Accelerator Conf. (LINAC'08)*, Victoria, BC, Canada, 2008, paper THP062, pp. 933–935.

[28] D. Alesini *et al.*, "The C-Band accelerating structures for SPARC photoinjector energy upgrade", *J. Inst.*, vol. 8, no. 5, p. P05004, 2013. doi:10.1088/1748-0221/8/05/P05004

[29] D. Alesini *et al.*, "Tuning procedure for traveling wave structures and its application to the C-Band cavities for SPARC photo injector energy upgrade", *J. Inst.*, vol. 8, no. 10, p. P10010, 2013. doi:10.1088/1748-0221/8/10/P10010

[30] D. Alesini *et al.*, "Design, realization and test of C-band accelerating structures for the SPARC_LAB linac energy upgrade", *Nucl. Instrum. Methods Phys. Res. Sect. A*, vol. 837, pp. 161–170, 2016. doi:10.1016/j.nima.2016.09.010

[31] Instrumentation Technologies, http://www.i-tech.si

[32] L. Piersanti *et al.* "Review of the ELI-NP-GBS Low Level RF and Synchronization Systems", in *Proc. 9th Int. Particle Accelerator Conf. (IPAC'18)*, Vancouver, BC, Canada, Apr-May 2018, pp. 2162–2165. doi:10.18429/JACoW-IPAC2018-WEPAL010

[33] Menlo Systems, http://www.menlosystems.com

[34] H. Kogelnick *et al.*, *Appl. Opt.*, vol. 5, p. 1550, 1966.

[35] T. Omori *et al.*, *Nucl. Instrum. Methods Phys. Res., Sect. A*, vol. 500, pp. 232–252, 2003. doi:10.1016/S0168-9002(02)01985-X

[36] A. J. Rollason *et al.*, *Nucl. Instrum. Methods Phys. Res., Sect. A*, vol. 526, pp. 560–571, 2004. doi:10.1016/j.nima.2004.02.017

[37] I. Yamane *et al.*, in *Proc. 1st Int. Particle Accelerator Conf. (IPAC10)*, Kyoto, Japan, 2010, pp. 1402–1404.

[38] K. Dupraz *et al.*, "Design of a polarized positron source for linear colliders", emphPhys. Rev. ST Accel. Beams, vol. 17, p. 033501, 2014. doi:10.1103/PhysRevSTAB.17.033501

[39] K. Cassou *et al.*, "Laser Beam Circulator for the Generation of a High Brilliance Gamma Beam at ELI-NP", in *Proc. High Intensity Lasers and High Field Phenomena 2018*, Strasbourg, France, 2018. doi:10.1364/HILAS.2018.HW4A.7

[40] Alsyom Alcen, https://www.alsyom-alcen.com

ISBN: 978-3-95450-194-6 ISSN: 2226-0366 doi:10.18429/JACoW-LINAC2018-MO2A04

COMPACT SRF LINAC FOR HIGH BRILLIANCE INVERSE COMPTON SCATTERING LIGHT SOURCE

K. E. Deitrick*, G. A. Krafft[1], B. Terzić, J. R. Delayen[1],
Center for Accelerator Science, Old Dominion University, Norfolk, VA, 23529, USA
[1]also at Thomas Jefferson National Accelerator Facility, Newport News, VA 23606, USA

Abstract

New designs for compact SRF linacs can produce micron-size electron beams. These can be used for inverse Compton scattering light sources of exceptional flux and brilliance.

INTRODUCTION

Currently, there exist many x-ray techniques which are used in several different fields, including material science, cultural heritage, medicine, national security, and basic research in biology, chemistry, and physics. While a number of light source facilities around the world produce very high quality X-ray beams, there is a significant gap between this performance and the one most X-ray users experience from their laboratory-scale sources.

Increasing research over recent years has been aimed at bridging this gap through compact inverse Compton light sources (ICLSs). One of the significant benefits of this type of source is their production of narrow bandwidth x-ray beams, which is not a feature of most typical small-scale sources, but is required for a number of techniques. In the most general description, the target specifications for these compact ICLS designs has been for high average flux, high average brilliance x-rays - while keeping the requisite electron accelerator compact in size and cost. The design presented here, shown in Fig. 1, has the highest anticipated performance to date among compact Inverse Compton Light Source (ICLS) designs.

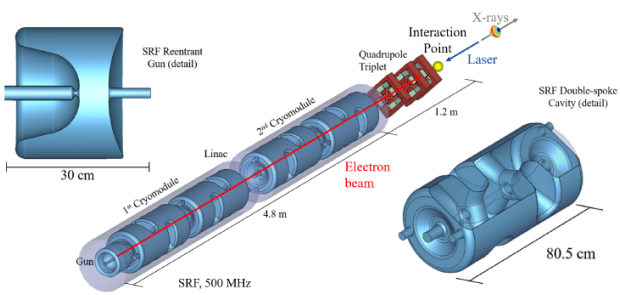


Figure 1: A schematic of the entire design. The first cryomodule contains the gun and two double-spoke cavities, the second contains the last two double-spoke cavities. Three quadrupole magnets follow the linac, before the interaction point. Detailed images of the gun and the double-spoke cavity are shown in the top left and bottom right, respectively.

* kdeit001@odu.edu; deitrick@jlab.org

INVERSE COMPTON SCATTERING

Compton scattering is the process of scattering a photon off of an electron at rest. Inverse Compton scattering (ICS) is the process of scattering a photon off a moving electron, leading the electron losing energy in the process. This collision between electron beam and incident laser occurs at the interaction point (IP).

For this compact ICLS design, we operate in a regime where the Thomson formula is a good approximation - the energy of the incident laser in the beam frame is significantly less than the rest mass of the electron. Consequently, the energy of the x-rays produced in the collision are given by

$$E_x(\Phi,\theta) \approx E_{\text{laser}} \frac{1-\beta\cos\Phi}{1-\beta\cos\theta}, \tag{1}$$

where Φ is the angle between the electron beam and scattering laser, θ is the angle between the electron beam and generated x-rays, E_{laser} is the energy of the incident scattering laser, and β is the relativistic factor v_z/c of the electron beam. For a head-on collision, the highest energy x-rays are those scattered in the same direction as the electron beam is traveling; this is the case shown in Fig. 1. The energy of these x-rays is given by $E_x(\Phi=\pi,\theta=0) \approx \gamma^2(1+\beta)^2 E_{\text{laser}} \approx 4\gamma^2 E_{\text{laser}}$, where γ is the typical relativistic factor for the electron beam and is significantly greater than 1.

The number of scattered x-rays from this collision is given by

$$N_x = \sigma_T \frac{N_e N_{\text{laser}}}{2\pi(\sigma_e^2+\sigma_{\text{laser}}^2)}, \tag{2}$$

where σ_T is the Thomson cross section, N_e is the number of electrons in the bunch, N_{laser} is the number of photons in the scattering laser, σ_e is the *rms* size of the electron beam, and σ_{laser} is the *rms* size of the laser. The assumption behind this formula and those following is that the distribution of both the electron and laser beams are Gaussian. The number of x-rays within a 0.1% bandwidth at the highest possible x-ray energy is $N_{0.1\%} = 1.5\times10^{-3}N_x$, so it follows that the flux into this bandwidth is $\mathcal{F}_{0.1\%} = 1.5\times10^{-3}\dot{N}_x$. For high frequency repetitive sources, $\dot{N}_x = fN_x$, where f is the repetition rate.

The spectral brightness or brilliance of an x-ray beam is the density of x-rays in the six-dimensional phase space containing the beam. The general formula for the brilliance of an x-ray beam into a 0.1% bandwidth is

$$\mathcal{B} = \frac{\mathcal{F}_{0.1\%}}{4\pi^2\sigma_{\gamma,x}\sigma_{\gamma,x'}\sigma_{\gamma,y}\sigma_{\gamma,y'}} \tag{3}$$

Content from this work may be used under the terms of the CC BY 3.0 licence (© 2018). Any distribution of this work must maintain attribution to the author(s), title of the work, publisher, and DOI.

ISBN: 978-3-95450-194-6 ISSN: 2226-0366 doi:10.18429/JACoW-LINAC2018-MO2A04

Content from this work may be used under the terms of the CC BY 3.0 licence (© 2018). Any distribution of this work must maintain attribution to the author(s), title of the work, publisher, and DOI.

where $\sigma_{\gamma,x}$ and $\sigma_{\gamma,y}$ are the *rms* transverse sizes of the x-ray beam and $\sigma_{\gamma,x'}$ and $\sigma_{\gamma,y'}$ are the *rms* transverse angular sizes of the x-ray beam. However, by taking advantage of the analogy to undulator radiation, it is possible to approximate the brilliance of the scattered photons using the parameters of the electron beam at the collision. The standard approximation for a non-diffraction limited beam is $\sigma_{\gamma,x'} \approx \sqrt{\epsilon_x/\beta_x}$, where ϵ_x and β_x are parameters of the electron beam. Taking this approximation into account, Eq. (3) becomes

$$\mathcal{B} = \frac{\mathcal{F}_{0.1\%}}{4\pi^2 \sigma_{\gamma,x}\sqrt{\epsilon_x/\beta_x}\sigma_{\gamma,y}\sqrt{\epsilon_y/\beta_y}}. \quad (4)$$

The approximation that the x-ray source size is the size of the electron is typical in the characterization of compact sources. In this approach, $\sigma_{\gamma,x} = \sigma_x = \sqrt{\beta_x \epsilon_x}$, so Eq. (4) becomes

$$\mathcal{B} \approx \frac{\gamma^2 \mathcal{F}_{0.1\%}}{4\pi^2 \epsilon^N_{x,rms}\epsilon^N_{y,rms}}. \quad (5)$$

If instead we take the position that the source size is a convolution of the electron and laser beam sizes, such that

$$\frac{1}{\sigma_\gamma^2} = \frac{1}{\sigma_{laser}^2} + \frac{1}{\sigma_x \sigma_y}. \quad (6)$$

Using this, Eq. (4) becomes

$$\mathcal{B} \approx \frac{\gamma \mathcal{F}_{0.1\%}}{4\pi^2 \sigma_\gamma^2 \sqrt{\epsilon^N_{x,rms}\epsilon^N_{y,rms}/\beta_x\beta_y}}. \quad (7)$$

As the laser spot size becomes increasingly greater than the electron beam spot size, the difference between Eq. (5) and Eq. (7) becomes negligible. However, for the compact source presented here, the spot sizes are roughly equivalent, making Eq. (7) more appropriate. From either brilliance formula, it becomes clear that to maximize brilliance requires maximizing the photon flux, maximizing the electron beam energy, or minimizing the electron beam normalized *rms* transverse emittances [1].

DESIGN CONSIDERATIONS

There are two pieces in an ICLS - a relativistic electron beam and an incident laser. In recent years, laser technology has made significant progress in producing suitable lasers - the details of this advancement are largely out of the scope of this paper. Instead, we assume an ideal scattering laser and focus on the development of a compact linac for a high-flux, high-brilliance ICLS that is compact, relatively affordable, and feasible for non-expert operation.

The desire for a high average flux x-ray beam leads to cw operation and an SRF linac, while cost concerns and operation ease suggest a cryogenics system of atmospheric helium at 4.2 K or above. This temperature necessitates a low-frequency system, in the range of 300 to 500 MHz. In this frequency range, TM_{010} cavities are too large, leading towards the use of spoke cavities in the linac. While a 325 MHz single-spoke cavity has been developed, it was also deemed too large, leading to the decision of using 500 MHz double-spoke cavities. However, further advancements in SRF technology could lead to reconsidering the geometry and/or frequency choice.

Table 1: Desired Electron Beam Parameters at Interaction Point

Parameter	Quantity	Units
Kinetic energy	25	MeV
Bunch charge	10	pC
Repetition rate	100	MHz
Average current	1	mA
Transverse *rms* normalized emittance	0.1	mm mrad
$\beta^*_{x,y}$	5	mm
$\sigma_{x,y}$	3.2	μm
FWHM bunch length	3 (0.9)	psec (mm)
rms energy spread	7.5	keV

The goal for high flux also leads to a high repetition rate of 100 MHz and a small spot size of 3.2 μm at the IP. This small spot size is made possible by a low bunch charge of 10 pC, which allows for a low transverse normalized *rms* emittance of 0.1 mm mrad and results in an increased brilliance of the x-ray beam. While this emittance is smaller than other reentrant gun designs, the bunch charge makes it attainable. Additionally, this low emittance and low bunch charge is comparable to current high performance normal temperature guns.

An electron beam kinetic energy of 25 MeV and an incident scattering laser energy of 1.24 eV were chosen, leading to the production of x-rays with energies of up to 12 keV. To control energy smearing of the forward flux, the relative beam energy spread needs to be less than 0.03%. At the energy of 25 MeV, this leads to *rms* energy spread of no more than 7.5 keV. To limit the flux reduction due to the hourglass effect, the bunch length at the IP needs to be less than 1 mm. All of the desired electron beam properties at IP are summarized in Table 1.

To evaluate the performance of this electron beam as an x-ray source, we assumed a high-quality, high-power laser. This ideal laser would have a circulating power of 1 MW, a wavelength of 1 μm (1.24 keV), rep rate of 100 MHz, *rms* pulse duration of 2/3 ps, and a spot size of 3.2 μm. Due to the difficulties associated with achieving a 3.2 μm laser spot, we also consider the case of a 12 μm spot laser, while keeping the electron spot size at 3.2 μ. These properties are summarized in Table 2.

Using the properties in Tables 1 and 2 with the formulae presented in the previous section, we can calculate the anticipated properties of the resulting x-ray beam. However, the extremely short Rayleigh range of the laser spot size requires that a reduction factor must be applied. Using the formulae given in [2], we anticipate a reduction of 85% and 26% for the 3.2 and 12 μm laser spot sizes, respectively.

ISBN: 978-3-95450-194-6 ISSN: 2226-0366 doi:10.18429/JACoW-LINAC2018-MO2A04

Table 2: Laser Parameters at Interaction Point

Parameter	Quantity	Units
Wavelength	1 (1.24)	μm (eV)
Circulating power	1	MW
N_γ, Number of photons/bunch	5×10^{16}	
Spot size (*rms*)	3.2, 12	μm
Repetition rate	100	MHz
rms pulse duration	2/3	ps

The anticipated x-ray performance is given in Table 3; for both laser spot sizes, the top energy is 12 keV, the flux is on the order of 10^{13} ph/s, and the average brilliance is on the order of 10^{14} ph/(s mm^2 mrad^2 0.1%BW). The use of a non-diffracting laser beam, such as an Airy or Bessel beam, should lead to a smaller reduction, though it is currently unclear if the use of such a beam would negate or only ameliorate the reduction effect.

ACCELERATING SECTION

SRF Reentrant Gun and Emittance Compensation

We chose to use an SRF reentrant gun, a concept originally proposed in the early 1990s. A few other SRF reentrant guns do exist, none which operate near a 10 pC bunch charge - consequently, none match the emittance goals of this accelerator. However, there do exist high performing normal temperature guns which closely match our desired performance, particularly the Cornell DC gun [3] and the normal conducting rf gun at APEX [4]. Our final gun geometry design is shown at the top left in Fig. 1. The bunch exits the gun with a kinetic energy of 1.5 MeV and a transverse normalized *rms* emittance, $\epsilon^N_{(x,y),\mathrm{rms}}$, of 0.2 mm mrad. While larger than our desired emittance at IP, $\epsilon^N_{(x,y),\mathrm{rms}}$ decreases before exiting the linac due to emittance compensation - the manipulation of a beam's transverse phase space to decrease the projected emittance.

The most critical and challenging electron beam parameter is the $\epsilon^N_{(x,y),\mathrm{rms}}$ at the IP, which must be achieved by emittance compensation. Frequently, emittance compensation is achieved by placing a solenoid following the gun. In this concept, emittance compensation is performed through rf focusing, altering the geometry of the reentrant gun to produce the necessary fields to compensate for the space charge fields of the bunch.

To refine the gun geometry appropriately, the shape was parameterized, shown in Fig. 2, the electromagnetic (EM) fields were calculated using Superfish [5] for the gun and CST Microwave Studio [6] for the double-spoke cavity, and the initial distribution was tracked to the exit of the linac using IMPACT-T [7]. The initial distribution was assumed to be a radially uniform distribution of 1 mm radius, a plateau longitudinal distribution of 4.5 ps, and no initial emittance or energy spread. The main focus was on parameters closest to the cathode, where the energy of the bunch is lowest and the effect of space charge most significant.

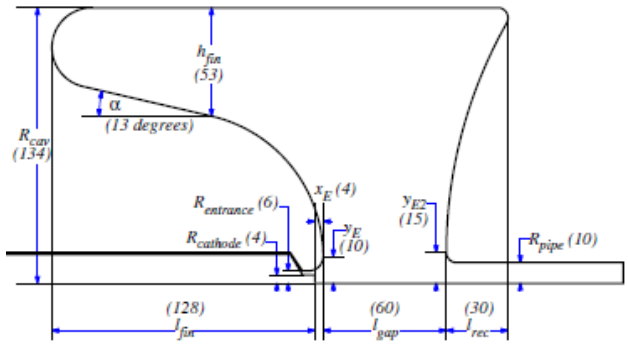


Figure 2: Diagram of gun geometry with parameters and quantities. Quantities are rounded to the nearest millimeter and given in millimeters, except where explicitly indicated.

To demonstrate the effectiveness of this emittance compensation, two horizontal normalized phase spaces are shown in Fig. 3. The normalized phase spaces are shown at the exit of the gun on the left and the exit of the linac on the right, with the particles color-coded according to their longitudinal position within the bunch. Exiting the gun, it is clear to see that the emittance slices along the bunch length are not well-aligned. However, when the bunch exits the linac, these longitudinal slices are better aligned, leading to a significant reduction in projected normalized *rms* emittance.

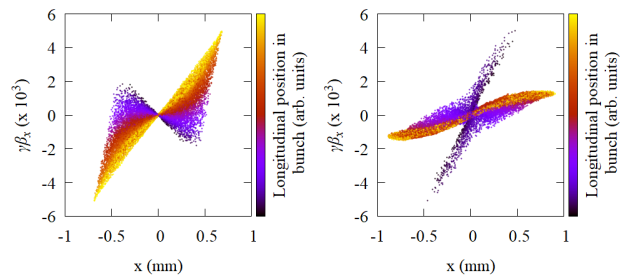


Figure 3: Normalized transverse phase spaces exiting the gun (left) and the linac (right), with the longitudinal position of the particle within the bunch indicated by color. The emittance slices along the bunch length rotate to align better, for a decrease in projected normalized *rms* emittance.

Linac

The linac consists of four double-spoke cavities, shown in detail at the bottom right of Fig. 1, designed by Christopher Hopper during his ODU PhD research [8]. For the emittance compensation to be most effective, the gun and first linac cavity must be placed within the same cryomodule. The double-spoke cavities have a "quadrupole-like" focusing effect on the beam. Consequently, to achieve a relatively round beam at exiting the linac, the center two cavities are rotated so that the beam is focused in both transverse planes.

Content from this work may be used under the terms of the CC BY 3.0 licence (© 2018). Any distribution of this work must maintain attribution to the author(s), title of the work, publisher, and DOI.

ISBN: 978-3-95450-194-6 ISSN: 2226-0366 doi:10.18429/JACoW-LINAC2018-MO2A04

Content from this work may be used under the terms of the CC BY 3.0 licence (© 2018). Any distribution of this work must maintain attribution to the author(s), title of the work, publisher, and DOI.

Table 3: Desired Light Source Parameters. Flux and brilliance reported for top x-ray energy, reduced for lower energies

Parameter	Laser spot (μm)		Units
	3.2	12	
X-ray energy	1.2 - 12	1.2 - 12	keV
Photons/bunch	2.4×10^5	1.6×10^5	
Flux	2.4×10^{13}	1.6×10^{13}	ph/s
Average brilliance	4.4×10^{14}	1.6×10^{14}	ph/(s mm^2 mrad^2 0.1%BW)

Table 4: Select Properties of the Electron Beam Parameters, both Desired and Achieved, at the IP.

Parameter	Desired	Achieved	Units
β_x^*	5	5.4	mm
β_y^*	5	5.4	mm
$\epsilon_{rms,x}^N$	0.1	0.1	mm mrad
$\epsilon_{rms,y}^N$	0.1	0.13	mm mrad
σ_x	3.2	3.4	μm
σ_y	3.2	3.8	μm
> 76% longitudinal distribution	3	3	ps
rms energy spread	7.5	3.4	keV

At the end of the linac, the bunch exits with a kinetic energy of 25 MeV, *rms* transverse sizes less than 0.4 mm, transverse normalized *rms* emittances of 0.1 mm mrad (horizontal) and 0.13 mm mrad, a bunch length of 0.67 mm, and and *rms* energy spread of 3.4 keV.

FINAL FOCUSING

Final focusing is achieved using a quadrupole triplet; simulations were performed using `elegant` [9]. Table 4 compares the target goals of the electron beam and the simulated beam parameters, which are quite close in all parameters. The longitudinal length of the beam containing more than 76% of the beam is quoted instead of the *rms* bunch length because the beam does not have a Gaussian distribution. The beam spot and transverse phase spaces at the IP are shown in Fig. 4. The transverse distributions of the beam at IP is shown in Fig. 5, compared with the distribution of a Gaussian distribution with the same *rms* value. It is clear that the transverse beam distribution is significantly non-Gaussian.

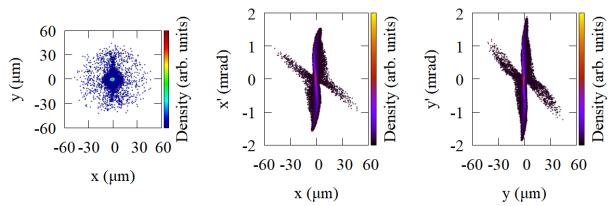


Figure 4: Beam spot (top left), longitudinal phase space (top right), horizontal phase space (bottom left), and vertical phase space (bottom right) of the electron bunch at the IP.

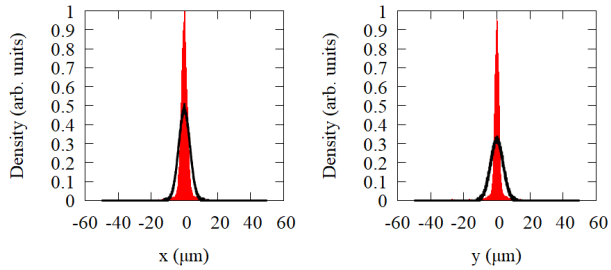


Figure 5: The horizontal (left) and vertical (right) distribution of the start-to-end simulated beam at the IP (red) and a Gaussian distribution with the same *rms* values (black).

X-RAY PERFORMANCE

To evaluate the success of this design, it is not enough to simply compare the electron beam parameters; the anticipated x-ray parameters must be determined. However, Fig. 5 has clearly demonstrated the non-Gaussian distribution of the beam, calling into question the validity of using the formulae presented previously. Improved codes for Compton simulation (ICCS) [10] allows for the calculation of x-ray spectra for an arbitrary electron distribution. Using ICCS, the spectra of the x-ray beam was calculated for both 3.2 and 12 μm, shown in Fig. 6. Using the pin-hole brilliance formula

$$\mathcal{B}_p = \lim_{\theta_a \to 0} \frac{\mathcal{S}_{0.1\%}}{2\pi^2 \sigma_e^2 \theta_a^2}, \tag{8}$$

where θ_a is the aperture, it is possible to calculate the anticipated brilliance, given in Table 5. Also listed are the average flux and average brilliance, both anticipated and desired. Taken together, several things become clear. First, anticipated flux and brilliance using the Gaussian model for both spot sizes is comparable with the original goals. Second, the anticipated average brilliance is almost the same whether calculated using the Gaussian model or ICCS for the 12 μm case. Finally, the fact that ICCS calculates a much higher brilliance than using the Gaussian model is reasonable, but not physical - the model used in ICCS assumes that every electron sees the same scattering potential. While this is a valid assumption for laser spots much larger than the electron beam szie, it loses validity and leads to overestimation as the sizes become comparable. Overall, however, the anticipated x-ray properties are quite close to the high-flux, high-brilliance source that was the original goal.

ISBN: 978-3-95450-194-6 ISSN: 2226-0366 doi:10.18429/JACoW-LINAC2018-MO2A04

Table 5: X-ray performance of the designs attained by numerical simulation with an aperture of 1/40γ (top) and by formulae from Gaussian model (middle), compared to original design goals (bottom). Suggested aperture for brilliance calculation only.

Parameter	Laser Spot (μm)		Units
	3.2	12	
X-ray energy	12.3	12.3	keV
$N_{0.1\%}$	1230	92.4	ph/0.1%BW
$\mathcal{S}_{0.1\%}$	1.23×10^{11}	9.24×10^{9}	ph/(s 0.1%BW)
Average brilliance, from ICCS	$^{*}7.2 \times 10^{14}$	1.18×10^{14}	ph/(s mm^2 mrad^2 0.1%BW)
Average flux, Gaussian model	2.2×10^{13}	1.6×10^{13}	ph/s
Average brilliance, Gaussian model	3.4×10^{14}	1.2×10^{14}	ph/(s mm^2 mrad^2 0.1%BW)
Desired average flux	2.4×10^{13}	1.6×10^{13}	ph/s
Desired average brilliance	4.4×10^{14}	1.6×10^{14}	ph/(s mm^2 mrad^2 0.1%BW)

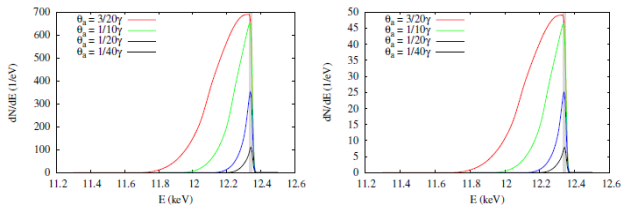


Figure 6: Number spectra for different apertures generated using 4,000 particles for a 3.2 μm laser spot size (left) and a 12 μm laser spot size (right). Grey box indicates 0.1% bandwidth. Suggested apertures for brilliance calculation only.

CONCLUSION

The design concept presented is the highest average brilliance x-ray beam currently proposed by any compact Compton source. While the current parameters are for 12 keV x-rays, placing additional cryomodules after the existing linac can increase the energy of the electron beam, resulting in x-rays with higher energies and a wider range of applications. The high brilliance of this source is achieved through a number of factors, particularly a superconducting drive linac operating cw at 4 K and an electron beam with a low emittance and small spot size at the IP, made possible by a low bunch charge and emittance compensation through rf focusing, instead of the more typical solenoid. With the proper R&D, this promises an exceptional x-ray source; further details are available in [1].

ACKNOWLEDGEMENTS

This material is based on work supported by the U.S. Department of Energy, Office of Science, Office of Nuclear Physics, Office of High Energy Physics, and Office of Basic Energy Science; and by the National Science Foundation. K. E. D. would like to thank LINAC'18 for conference support. K. E. D and J. R. D. were supported at ODU by DOE Office of Nuclear Physics Award No. DE-SC00004094, DOE Office of High Energy Physics Award No. DE-SC0010081, and NSF Award No. 1416051. B. T. was supported at ODU by NSF Award No. 1535641. G. A. K was supported at Jefferson Lab by Contract No. DE-AC05-06OR23177; additional support was provided by DOE Office of Nuclear Physics Award No. DE-SC004094 and Basic Energy Sciences Award No. JLAB-BES11-01. This research used resources of the National Energy Research Scientific Computing Center (NERSC), a U.S. Department of Energy Office of Science User Facility operated under Contract No. DE-AC02-05CH11231.

REFERENCES

[1] K. E. Deitrick, G. A. Krafft, B. Terzić, and J. R. Delayen, *Phys. Rev. Accel. Beams*, vol. 21, p. 080703, 2018.

[2] M. A. Furman, in *Proc. PAC'91*, San Francisco, CA, USA, May 1991, pp. 422-424.

[3] C. Gulliford *et al.*, *Phys. Rev. ST Accel. Beams*, vol. 16, p. 073401, 2013.

[4] F. Sannibale *et al.*, *Phys. Rev. ST Accel. Beams*, vol. 15, p. 103501, 2012.

[5] "Poisson Superfish," `http://laacg.lanl.gov/laacg/services/download_sf.phtml`, 2012.

[6] "Computer simulation technology website," `http://www.cst.com`.

[7] J. Qiang, S. Lidia, R. D. Ryne, and C. Limborg-Deprey, *Phys. Rev. ST Accel. Beams*, vol. 9, p. 044204, 2006.

[8] C. S. Hopper, Ph.D. thesis, Old Dominion University, 2015.

[9] M. Borland, Advanced Photon Source LS-287, 2000.

[10] N. Ranjan, B. Terzić, G. A. Krafft, V. Petrillo, I. Drebot, and L. Serafini, *Phys. Rev. Accel. Beams*, vol. 21, p. 030701, 2018.

Content from this work may be used under the terms of the CC BY 3.0 licence (© 2018). Any distribution of this work must maintain attribution to the author(s), title of the work, publisher, and DOI.

ISBN: 978-3-95450-194-6 ISSN: 2226-0366 doi:10.18429/JACoW-LINAC2018-MO1P01

STATUS OF THE SNS PROTON POWER UPGRADE PROJECT *

J. Galambos†, M. Champion, M. Connell, M. Howell, S. Kim, J. Moss, M. Plum, B. Riemer, W. Steffey, K. White, Oak Ridge National Laboratory, 37831 Oak Ridge TN, USA

Abstract

The Proton Power Upgrade (PPU) project [1,2,3] will double the accelerator power capability at Spallation Neutron Source (SNS) [4], from 1.4 to 2.8 MW. This project received initial funding in 2018, and plans have been formulated to complete equipment installation and begin beam commissioning in 2024. The project plans and status, with an emphasis on recent progress, are summarized for the different sub-systems.

INTRODUCTION

The SNS is a short pulse neutron scattering facility with a 1.4 MW capable accelerator powering the neutron source. The SNS accelerator complex includes a linear accelerator, an accumulator ring and transport lines. This accelerator complex was constructed with built-in upgrade provisions, and these are being exploited to double the power capability to 2.8 MW. High level parameters are shown in Table 1, indicating the strategy to double the power by increasing the beam energy by 30% and the linac beam current by ~ 50%. The higher power will allow new science capabilities and will also increase capacity by increasing beamline throughput [5].

The PPU project is organized into primary subsystems of Superconducting RF cryomodules, RF equipment, Ring systems, Conventional Facilities, and Target systems. Controls efforts are distributed throughout these systems. Much of the project upgrade is focused in the SNS linac and consists of providing additional equipment similar to presently operating equipment (for example, RF equipment and superconducting cryomodules). This aspect reduces project risks and permits early movement on the design and procurement of some linac associated equipment. The sections below describe the upgrade approaches in the PPU sub-systems, and recent progress.

PPU SUB-SYSTEMS

Superconducting Linac (SCL)

The increased beam energy will be provided by the addition of 7 new cryo-modules in existing empty slots at the high energy end of the linac [6]. These cryo-modules will be similar to a spare cryomodule built at SNS, installed and operated since 2012, and has demonstrated the required PPU gradient level [7]. This cryomodule is shown in Fig. 1. The cryomodules will be fabricated by Thomas Jefferson Accelerator Facility, through a partnership. SNS will oversee the cavity fabrication, and this is part of a recently initiated Long Lead Procurement strategy to minimize schedule risk. The cryomodules will be installed in seven of the nine available empty slots.

Table 1: PPU High Level Parameters

Parameter	Present operation	PPU
Beam power (MW)	1.4	2.8
Beam energy (GeV)	1.0	1.3
Average linac current (mA)	1.6	2.3
Linac macropulse current (mA)	25	39
Beam repetition rate (Hz)	60	60
Linac pulse length (ms)	1	1
Medium beta cryomodules	11	11
High beta cryomodules	12	19
High beta cavities	48	76

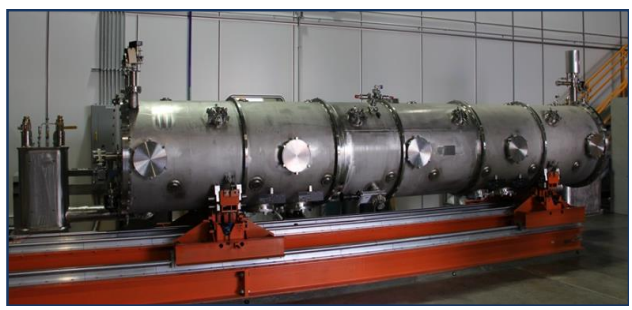


Figure 1. The spare SNS cryomodule, in operation since 2012 and demonstrating PPU gradient.

Key changes in the PPU cryomodules from the operational high beta cryomodules already installed in the SNS linac are: improved Nb material quality for the cavity end groups, higher power capability for the RF couplers, and elimination of the Higher Order Mode couplers. A prototype cavity with high quality end groups and no HOM coupler was recently fabricated and tested, and successfully demonstrated gradients required for PPU (see Fig. 2.)

* ORNL is managed by UT-Battelle, LLC, under contract DE-AC05-00OR22725 for the U.S. Department of Energy. This research was supported by the DOE Office of Science, Basic Energy Science, Scientific User Facilities.
† jdg@ornl.gov

Content from this work may be used under the terms of the CC BY 3.0 licence (© 2018). Any distribution of this work must maintain attribution to the author(s), title of the work, publisher, and DOI.

ISBN: 978-3-95450-194-6 ISSN: 2226-0366 doi:10.18429/JACoW-LINAC2018-MO1P01



Figure 2: An SNS cavity with PPU modifications.

RF Systems

The RF systems includes scope for upgrading existing systems to accommodate the increased beam loading (higher beam current) and adding new equipment to power the new cryomodules. Additionally, the low-level RF is being upgraded to accommodate handling 2 types of beam pulses headed to either the existing present First Target Station (FTS), or to a future Second Target Station (STS) [8].

Over the past year a task force has performed equipment measurements to better understand the installed equipment power capability, and to understand the PPU needs. These also include tests with beam at the PPU beam current levels (albeit at reduced duty factor). Results have helped refine the existing RF systems PPU will need to upgrade. Fig. 3 shows a test setup for a Drift Tube Linac (DTL) RF station. The tests show that three of six DTL systems will require increased power capability (from 2.5 to 3.0 MW.) The Coupled Cavity Linac (CCL) systems and the existing Superconducting RF systems are adequate for PPU.



Figure 3: Test setup for the SNS warm linac high power RF.

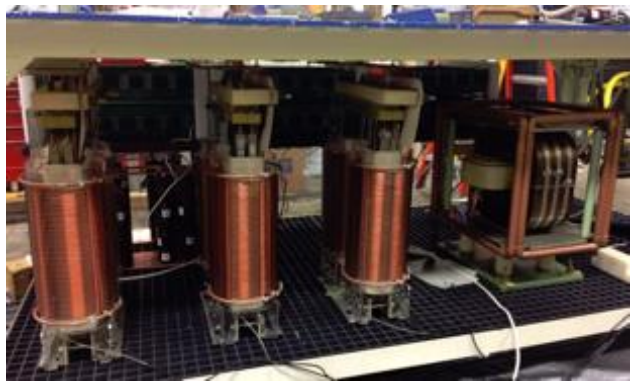


Figure 4: Alternate topology HVCM prototype.

The klystrons powering the new SRF cavities will be 700 kW klystrons, identical to ones presently in operation, so there is minimal risk here. The high voltage pulse modulation will be provided by a High Voltage Convertor Modulator (HVCM) that is a new design, an “alternate topology” HVCM [9]. A prototype (see Fig. 4) has been built and initial testing is promising.

Ring Systems

About 96% of the transport line and ring magnets and power supplies are capable of supporting 1.3 GeV operation and were successfully tested at this level during the summer of 2018. Three magnets in the ring injection area (see Fig. 5) and their vacuum chambers will be replaced for 1.3 GeV operation, to accommodate handling the excited state H^0 transport at higher beam energy [10]. PPU is partnering with Fermi National Accelerator Laboratory (FNAL) for the design and manufacturing oversight of these magnets. The baseline plan for the extraction region is to add 2 additional extraction kicker magnets (see Fig. 6). An alternative and simpler approach is being investigated to upgrade the existing extraction kicker power supplies. Initial testing of a prototype power supplies indicated adequate voltage and rise time, and system reliability is now being addressed.



Figure 5: The SNS Ring injection region.

Content from this work may be used under the terms of the CC BY 3.0 licence (© 2018). Any distribution of this work must maintain attribution to the author(s), title of the work, publisher, and DOI.

ISBN: 978-3-95450-194-6 ISSN: 2226-0366 doi:10.18429/JACoW-LINAC2018-MO1P01

Content from this work may be used under the terms of the CC BY 3.0 licence (© 2018). Any distribution of this work must maintain attribution to the author(s), title of the work, publisher, and DOI.



Figure 6: One of 2 extraction kicker magnet sets, with space indicated (red) for an extra magnet placement.

Another area of concern in the ring upgrades is the injection dump, which is presently rated for 150 kW. This represents ~5.3% of 2.8 MW which is adequate, but more headroom in the allowable dump power will provide operational margin. A thermal analysis and the measurements of the operational injection dump system are being conducted to assess whether the dump power limit can be increased. Also, a new diagnostic to image the waste beam position on the injection dump is included in PPU, to provide better confidence in proper handling of this high-power waste beam.

Target Systems

Beyond providing for 2.8 MW accelerator power capability, PPU also provides a 2.0 MW capable target (the remaining power is planned to be delivered to a new Second Target Station [8]). The PPU 2.0 MW target design is influenced by operational lessons from the present 1.4 MW target design. The key issues addressed are reduction of the large pressure pulse from the short pulse proton beam, and mitigation of cavitation induced erosion on the inner surfaces of the upstream target vessel. Fig. 7 shows the PPU 2 MW target design, which has a tapered nose feature that provides more effective flow in the nose corners (an area of erosion concern.) Other features include elimination of a center baffle, inclusion of a gas wall curtain in the nose region, and swirl bubblers to provide increased gas bubble dispersion in the bulk mercury flow. The gas curtain provides erosion mitigation and the gas bubble injection is aimed at pressure pulse and erosion mitigation [11].

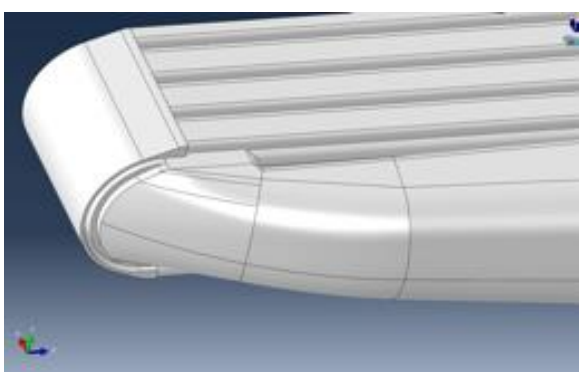


Figure 7: The PPU 2 MW target.

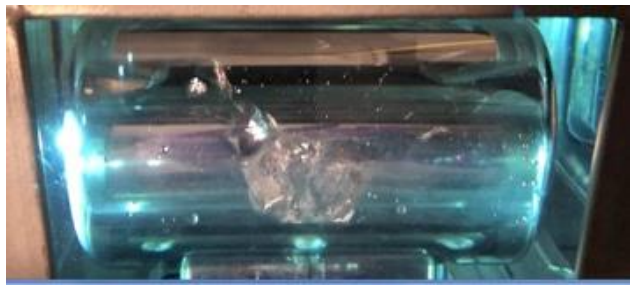


Figure 8: A test loop for the gas-curtain concept, with gas bubbles visible in the nose center region.

Target R&D is primarily aimed at understanding the gas wall and bubble injection. Tests are being performed on a full scale mercury loop and on visible water flow setups to measure the bubble coverage based on gas injection orifice geometry, gas flow, mercury flow etc. Fig. 8 shows a test of the gas wall concept in a mercury flow test loop, designed to measure gas coverage on the inner target wall surface.

A key element of the target development is learning from the operational experience of the SNS high power target. There is a systematic Target Management Plan [12] that implements changes to the targets, the beam power and the injected gas level. Over the past year key lessons have been learned from the operational targets. In particular, two key observations from gas injection implementation are PPU relevant: 1) reduced strain on the target vessel that contains the mercury with the presence of injected gas [13,14] and 2) reduced cavitation induced pitting on the front inner wall of the target vessel. SNS plans to increase the gas flow in targets and these results will factor into PPU design considerations.

Conventional Facilities

The conventional facilities scope includes finishing out the high energy section of the linac klystron gallery and adding a “stub” to the Ring Target Beamline Transport (RTBT) line tunnel. This stub will accommodate a seamless tie into the future Second Target Station [8]. The high energy end of the klystron gallery has been cleaned out (it had been used for storage), and the passages to the linac tunnel (“chases”) have been fitted with inserts that house waveguide and conduit for cabling. This work was done during a maintenance outage in the Spring of 2018 and included moving magnet cables that had been routed in incorrect chases. Fig. 9 shows the klystron gallery after this preparation activity. The site-preparation of the klystron gallery permits handover of the building design and finishing work to an outside A-E construction management firm. This contracted work will include the coordinated design of conventional systems (e.g. utilities and HVAC) with the layout of co-located technical items (e.g. RF wave-guide, technical cooling systems, circulators, etc.) using a Building Information Model (BIM) approach. Cannon Design has been chosen as the A-E partner to perform the klystron gallery design.

ISBN: 978-3-95450-194-6 ISSN: 2226-0366 doi:10.18429/JACoW-LINAC2018-MO1P01



Figure 9: Klystron gallery after the completion of the chase insert activity.

The stub in the RTBT is shown in Fig. 10. Construction of this stub will allow construction and connection of a new proton beamline transport line to a future Second Target Station (STS) [8] to proceed while SNS is operating, thus minimizing user support interruption. The stub will be constructed while the SNS needs to be shut down for other PPU activities, as discussed below.

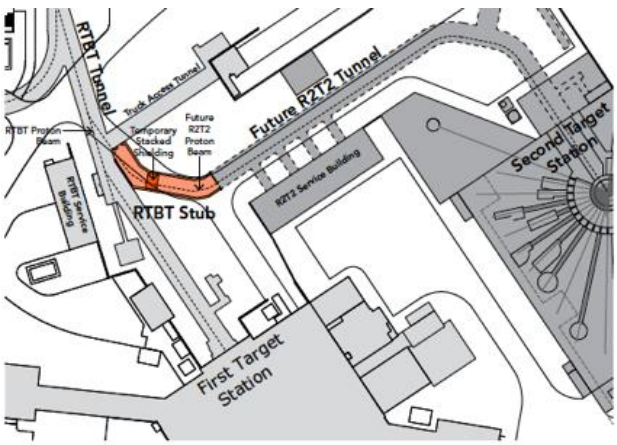


Figure 10: Layout of the RTBT tunnel stub (red) for connection to the STS.

PROJECT STATUS

Funding and Approval

PPU received Critical Decisison-1 approval April 4, 2018, which permits moving towards the baselining of the project and initiating the preliminary design process. A review for the approval of Long Lead Procurement of the superconducting RF cavities and associated equipment was held in August 2018, and approval is expected in Oct. 2018. Funding for FY 2018 was approved at $36M, and this represents the first year PPU has line-item funding approval. The next project approval step is Critical Decision 2/3b, which will permit movement towards final design for systems (CD-2 part) and approval of final design for many systems (CD-3b part). Final design will be sought for systems already in place, or prototyped and tested, such as much of the RF systems, and the superconducting RF cryomodules. Since PPU leverages existing equipment design and experiences, this should allow a faster approach to equipment procurement.

Cost and Schedule

PPU is in the process of baselining the cost and schedule for CD-2. The schedule presently calls for procurement and assembly of much of the superconducting cryomodules and RF equipment in 2020-2021. We plan to install RF equipment in the klystron gallery during normal machine operation, but cryomodule installation in the tunnel will begin during normal maintenance outages beginning in 2022. The normal operations schedule will remain unaffected through this period. PPU is however planning a 6-month long outage beginning in late 2023 to perform installation that requires a longer than usual machine-outage: cryomodule installation, target systems upgrades, ring injection system upgrade, and the RTBT tunnel stub. This approach minimizes the longest concurrent “dark-time” imposed by the PPU upgrade to only 6 months, and also is being planned to avoid having the SNS down during a planned upgrade for the ORNL reactor neutron source HFIR. Beam commissioning following equipment installation completion is scheduled to start in 2024. The Total Project Cost (TPC) point estimate is ~ $240M.

CONCLUSION

The PPU is aimed at doubling the SNS accelerator power capability to 2.8 MW and received initial line-item funding this year. The project leverages existing designs, equipment and experience to reduce risk. The project schedule minimizes operational disruption, and initial beam commissioning following final equipment installation is anticipated in 2024.

REFERENCES

[1] J. Galambos *et al*., “Proton Power Upgrade Project Conceptual Design Report”, ORNL-TM-2016/672, Feb.2018, https://info.ornl.gov/sites/publications/Files/Pub71531.pdf

[2] M. Champion *et al*., “Progress on the Proton Power Upgrade of the Spallation Neutron Source”, pp 2445-2448 in *Proceedings of the 8th International Particle Accelerator Conference (IPAC2018)*, Copenhagen, 2017.

[3 M. Plum, et al., “SNS Proton Power Upgrade Status”, pp 1120-1122 in *Proceedings of the 9th International Particle Accelerator Conference (IPAC2018)*, Vancouver, 2018.

[4] S. Henderson *et al.*,“The Spallation Neutron Source Accelerator System Design,” *Nucl Instrum Meth A*, vol. 763, pp. 610-673, 2014, doi: 10.1016/j.nima.2014.03.067.

[5] “The Science Case for a Proton Power Upgrade”, Spallation Neutron Source report, January 2018, https://neutrons.ornl.gov/sites/default/files/Proton%20Power%20Upgrade%20Science%20Case.pdf

[6] S-H. Kim, et al., “Superconducting Linac Upgrade Plan for the Second Target Station Project at SNS”, in *Proceedings of the SRF Conference 2015*, Whistler, BC, Canada, Sep. 2015, pp. 268-271.

Content from this work may be used under the terms of the CC BY 3.0 licence (© 2018). Any distribution of this work must maintain attribution to the author(s), title of the work, publisher, and DOI.

ISBN: 978-3-95450-194-6 ISSN: 2226-0366 doi:10.18429/JACoW-LINAC2018-MO1P01

Content from this work may be used under the terms of the CC BY 3.0 licence (© 2018). Any distribution of this work must maintain attribution to the author(s), title of the work, publisher, and DOI.

[7] M. Howell, et al., "The First ASME Code stamped cryomodule at SNS," pp. 2465–2467 in *Proceedings of the 3rd International Particle Accelerator Conference (IPAC2012)*, New Orleans, May 20–25, 2012.

[8] J. Galambos et al., "Technical Design Report Second Target Station", ORNL TM-2015/24, January 2015, https://www.osti.gov/biblio/1185891

[9] D.J. Solley, D.E. Anderson, and M.W. Wezensky, "Development and Testing of the Alternate Topology HVCM Modulator to Support the Proton Power Upgrade (PPU) at SNS," to be presented at the 21st IEEE International Pulsed Power Conference (PPC2017), Brighton, U.K., Jun. 2017.

[10] M. Plum, T. Gorlov, J. Holmes, T. Hunter, T. Roseberry, and J. G. Wang, "Challenges for the SNS ring energy upgrade," *Proceedings of the International Particle Accelerator Conference (IPAC12)*, New Orleans, LA, May 20–25, 2012. http://accelconf.web.cern.ch/AccelConf/IPAC2012/papers/moppd069.pdf

[11] B. Riemer, PPU FTS Systems 2 MW Target Development Plan, PPU-P05-PN0001, R00, Oak Ridge National Laboratory, April 2017.

[12] Target Management Plan, ORNL report 106010000-PN0005, R04, Oak Ridge National Laboratory, July 2018.

[13] W. Blokland, Y. Liu, M. Wendel, and D. Winder, "Measurements of the effects of gas injection into SNS target T18," *SNS Technical Report*, 106010101- TR0043, 2018.

[14] Y. Liu *et al*., "Strain Measurement of Recent SNS Mercury Target with Gas Injection", pp. 1117-1119 in *Proceedings of the 9th International Particle Accelerator Conference (IPAC2018)*, Vancouver, 2018.

ISBN: 978-3-95450-194-6 ISSN: 2226-0366 doi:10.18429/JACoW-LINAC2018-MO1P02

APPROACHES TO HIGH POWER OPERATION OF J-PARC ACCELERATOR

Hidetomo Oguri, JAEA/J-PARC, 319-1195 Tokai-mura, Japan

Abstract

The J-PARC linac started beam operation with an energy of 181 MeV in 2006. To realize the nominal performance of 1 MW at a 3 GeV Rapid Cycling Synchrotron (RCS) and 0.75 MW at a Main Ring synchrotron (MR), the linac beam energy was increased to 400 MeV and the beam current was also increased from 30 to 50 mA. After the upgrade, the RCS demonstrated 1 MW equivalent beam operation and currently operates 500 kW for the Material and Life Science Facility. The MR beam power is also increasing and it recently achieved the beam operation of 490 kW for the Neutrino experiment and 51 kW for the Hadron experiment, respectively. At present, we are considering two further upgrade plans increasing the RCS beam power to 1.5 MW and duplation the linac repetition rate to 50 Hz for the planned Transmutation Experimental Facility. To achieve 1.5 MW from the RCS, it is necessary to increase both the beam current and the pulse length about 20% at the linac.

INTRODUCTION

A layout of the J-PARC facilities is shown in Fig. 1. The J-PARC facilities consist of the linac, the 3-GeV Rapid Cycling Synchrotron (RCS), the Main ring Synchrotron (MR) and three experimental facilities of the Material and Life Science Facility (MLF), the Hadron Experimental Facility (HD) and the Neutrino Facility (NU). Construction of a Transmutation Experimental Facility (TEF) is planned in phase-II in the near future. The goal of the J-PARC project in phase-I is to achieve a 1-MW beam power at the RCS and a 0.75-MW beam power at the MR [1].

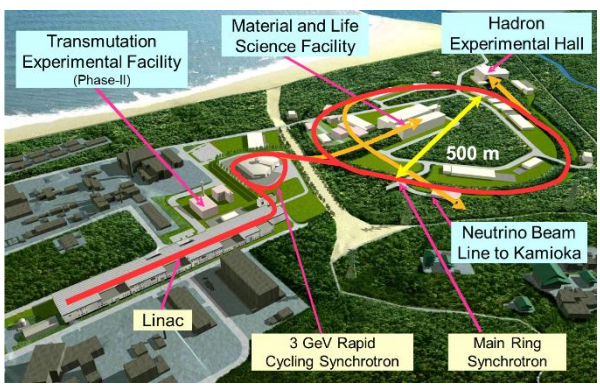


Figure 1: A layout of J-PARC facilities.

In 2006, the J-PARC linac started beam operation with an output energy of 181 MeV and a designed peak current of 30 mA. Thereby, we could reach an RCS output beam power of 600 kW in principle. The space charge effect in the RCS injection is increased with the beam intensity upgrade, and it limits the obtainable beam power. To suppress the space-charge effect to a tolerable level, it was necessary to increase the injection energy. Therefore, we conducted both the energy and the intensity upgrade of the linac. For the intensity upgrade, we replaced a front-end system, which consists of an ion source, a radio frequency quadrupole linac (RFQ) and a beam chopper system to deliver a peak current of 50 mA. For the energy upgrade, the linac output energy was increased to 400 MeV by adding an annular-ring coupled structure linac (ACS) after the separated drift tube linac (SDTL). A layout of the linac before and after upgraded is shown in Fig. 2.

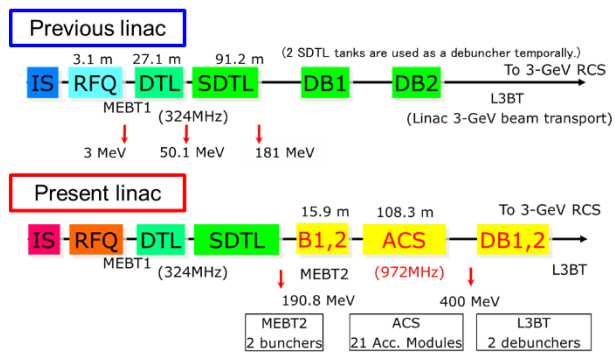


Figure 2: A layout of previous and present linac.

Two further upgrade plans of 1.5-MW beam power at the RCS and construction of the TEF are now in consideration. To achieve the 1.5-MW beam, it is necessary to increase both the peak beam current and the beam pulse length about 20% at the linac. For the TEF, duplation the linac repetition rate to 50 Hz is necessary. The detail process in the past upgrade and the possibility for further upgrade at the linac are presented in this paper.

BEAM INTENSITY UPGRADE

High Intensity Negative Hydrogen Ion Source

A cesium-free negative hydrogen ion source driven with a lanthanum hexaboride (LaB_6) filament was used since linac operation started in 2006 [2]. Although it satisfied the J-PARC's initial stage requirements of 30 mA, it was confirmed that the current level did not increase by cesiation and the life time of the filament of approximately 500 h was insufficient for the desired life of 2000 h at least. In order to satisfy linac upgrade requirements, a cesiated RF-driven negative hydrogen ion source has been developed. A schematic of the RF-driven ion source is shown in Fig. 3. An internal antenna that was developed at Spallation Neutron Source at Oak Ridge National Laboratory [3] is used for the source of plasma. The RF-driven ion source was tested on an off-line test stand for about five years, and it was found to satisfy the requirements. The RF-driven ion source was installed in the summer of 2014.

Content from this work may be used under the terms of the CC BY 3.0 licence (© 2018). Any distribution of this work must maintain attribution to the author(s), title of the work, publisher, and DOI.

ISBN: 978-3-95450-194-6 ISSN: 2226-0366 doi:10.18429/JACoW-LINAC2018-MO1P02

Content from this work may be used under the terms of the CC BY 3.0 licence (© 2018). Any distribution of this work must maintain attribution to the author(s), title of the work, publisher, and DOI.

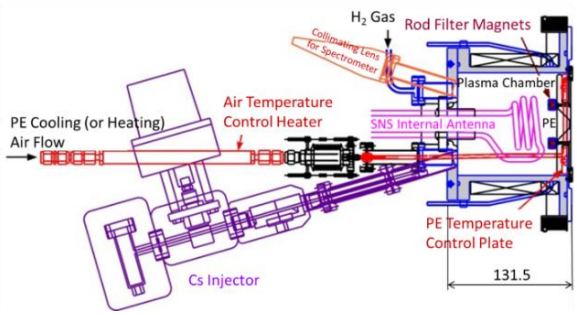


Figure 3: A schematic of the RF-driven ion source.

The operation history of the ion source from October 2014 is shown in Fig. 4. The user operation was started with the beam current of 33 mA from the ion source. The RF source has been successfully providing the required beam to the accelerator with almost no serious problem except for the RF antenna failure caused by the excess cesium due to a misoperation in October, 2014 [4]. From January, 2016, the ion source beam current increased to approximately 45 mA. We gradually increased continuous operation times of the ion source. In spring, 2018, approximately 2,200 hours continuous operation was achieved with the typical beam current, pulse length and repetition rate of 47 mA, 300 μs and 25 Hz, respectively [5]. Based on the result, we decided to change the operation duration of a single RUN cycle from 1.5 to 3 months.

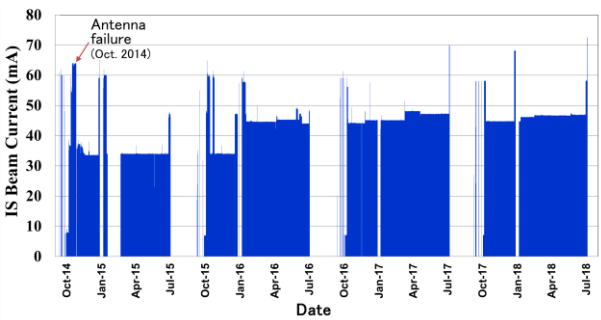


Figure 4: Operation history of the RF-driven ion source.

High Intensity RFQ

At the beginning of the J-PARC linac operation, the RFQ which was fabricated for the Japan Hadron Facility project (we call it "RFQ-I") was used. The design peak beam current of the RFQ-I was 30 mA. To achieve 1 MW, an RFQ with a design current of 50 mA (we call it "RFQ-III") was newly developed and replaced. In the design, we adopted a modified conventional design, that is both the average-bore radius and intervane voltage are constant along the RFQ. The beam is also held equipartitioned through the gentle buncher section. As the result of the simuration, the beam transmission, transverse and longitudinal emittance of 98.5%, 0.21 πmm.mrad and 0.11 πMeV.deg are obtained for the input beam condition of 60 mA and the transverse emittance of 0.20 π mm.mrad [6]. This result satisfies the requirement for the upgraded RFQ.

In designing RFQ-III, fabrication methods were changed from the RFQ-I to increase the resistance to discharge [7] which was the main issue of J-PARC linac at the beginning of the operation. The major engineering change is in the design of the RF cavity structure. The RF cavity of the RFQ-I was installed in a large vacuum vessel. Because the surface area of this type is very large, it is difficult to obtain good vacuum quality. Therefore, a vacuum-tight cavity structure is adopted for the RFQ-III. For this purpose, we adopted brazing for the assembly method. Many vacuum pumps of three 2700-L/s cryopumps, four 400-L/s ion pumps and two 1000-L/s non-evaporable getter (NEG) pumps are equipped. A B-A gauge and a residual gas analyzer are also installed for monitoring the vacuum. The longitudinal distribution of these devices is shown in Fig. 5. The fabrication of the RFQ-III was completed in March 2013. After the off-line beam test, the RFQ was installed in the summer of 2014 as the same time of the ion source.

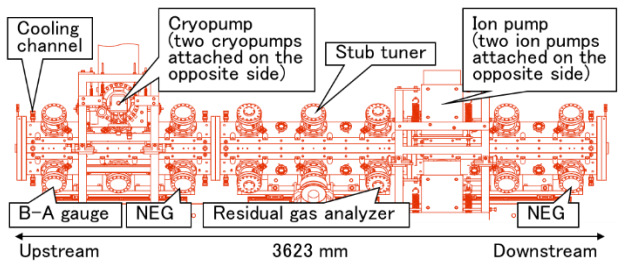


Figure 5: View of the RFQ vacuum devices.

The RFQ has been successfully operated without any serious trouble. Figure 6 shows the operation time variation of number of the RFQ RF-trip. The trip at the beginning of the operation was typically about 20 times per day. The number of trip decreased gradually and almost saturated at about 15 times a day. These trip events reduce the beam availability by approximetaly 1%. We supposed the origin of the trip is the sparking between vane tips, which had been contaminated by the carbon-related contaminants [8]. Inprovement of the evacuation performance and performing the high power conditionign are planned to clean up the inner surface of the RFQ.

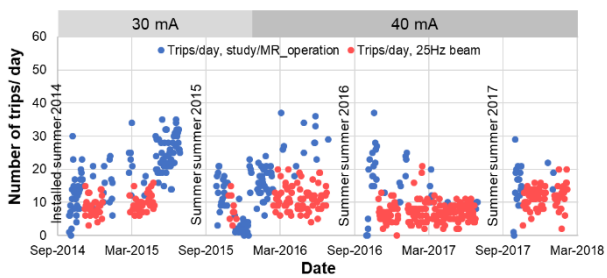


Figure 6: Time variation of number of RFQ RF-trip.

Beam Chopper System

In order to form the intermediate-pulse structure, a beam chopper system is used. The chopper system consists of an RF chopper cavity and a scraper. Both of the components are installed in the beam line between the RFQ and the

ISBN: 978-3-95450-194-6 ISSN: 2226-0366 doi:10.18429/JACoW-LINAC2018-MO1P02

DTL. The RF chopper cavity is an RF deflector with a TE_{111}-like mode with the same RF frequency as the RFQ. While the RF chopper cavity is on, the beam is deflected horizontally to be absorbed by a scraper. The scraper is made of carbon fiber composition (CFC).

The original chopper system, which was designed with a beam current of 30 mA, worked well. For the intensity updrade, the chopper cavity was replaced with a newly fabricated one, which has a larger aperture and longer gap length between electrodes to decrease beam loss in the cavity in 2014 [9]. Until 2016 summer, the cavities were connected in series with a coaxial line and powered by one RF power system. The large ringing on the RF falling of the intermediate-pulse appeared due to the reflected wave from the downstream cavity, and it caused beam loss at the RCS. The ringing problem was solved by supplying the RF power to the two cavities independently by installing an additional RF power system, as shown in Fig. 7.

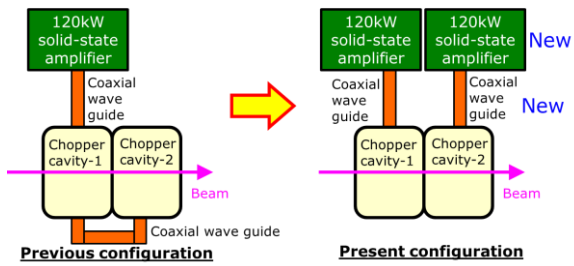


Figure 7: Beam chopper cavity configuration.

Recently, the 300-400 kW user operation with single-bunch was conducted at the RCS. In the 400 kW and single-bunch operation, the scraper received the heat flux approximately 1.3 times larger than that at the 1 MW double-bunch operation (our goal). The measured surface temperature of the scraper is shown in Fig. 8 as the function of the operation time. At 400 kW and single-bunch operation, the temperature reaches and saturates about 1800 °C, which is sufficiently lower than the tolerable temperature of 2900 °C [10].

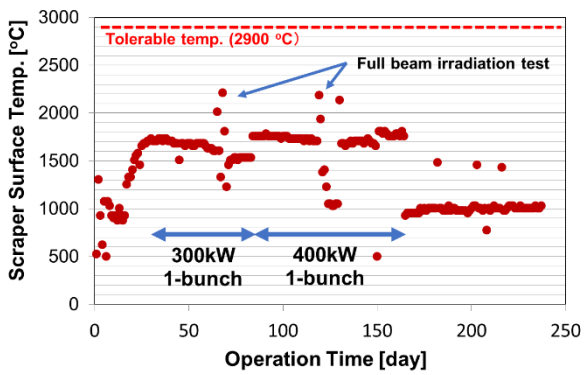


Figure 8: Time variation of the temperature on the scraper on the scraper surface.

After 237-hours operation, we removed the used scraper from the beam line and measured the depth of damaeged part using the laser microscope. Shallow crater of approximately 0.7 mm in depth was observed [10]. In case of 1-MW operation, the depth of damaged part is estimated to be approximetaly 1 mm. The damage level is sufficiently permissible because the beam axial thickness of the scraper material is 40 mm. These results shows the present scaper is saticfied with our requirement.

BEAM ENERGY UPGRADE

As the space charge effect in the RCS injection is increased with the beam intensity, it limits the obtainable beam power. To suppress the space-charge effect to a tolerable level, the beam energy was increased from 181 MeV to 400 MeV, which is the original design energy, by adding ACS cavities after the SDTL [11].

ACS Cavity

Figure 9 shows the configuration of the ACS accelerating module. One ACS module consists of two accelerating tanks and one bridge tank. Twenty-one ACS modules in total are installed for the beam acceleration. In addition, two ACS bunchers are installed between the SDTL and the ACS for longitudinal matching. After the acceleration cavities (before the RCS injection), two ACS debunchers are installed to reduce the energy spread, since the energy acceptance of the RCS is relatively limited compared with the accumulator ring.

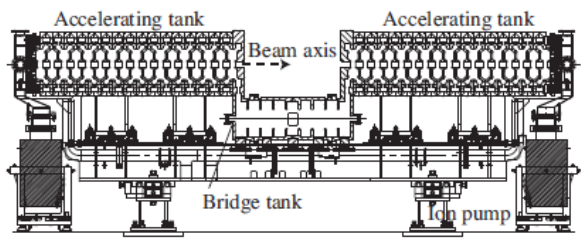


Figure 9: Configuration of ACS accelerating module.

In the end of 2010, the first mass-produced ACS module was completed and its high-power test was performed [12]. In the original plan, the high power test would have been conducted for all the ACS modules before installation at the beam line. However, the test was suspended because the test area was broken by the earthquake in 2011. The test was resumed in May, 2013, however only five modules could be tested before the installation because of time constraints. In the middle of August 2013, we started to install the ACS modules to the beam line. It took one day to complete the transportation and the alignment for one ACS cavity [13]. After completing the installation work in the middle of November, we performed the high-power conditioning of all the ACS cavities. The modules were conditioned more than 2 MW with a short pulse length of 50 μs, and then they were powered to 2 MW with a long pulse length of 600 μs, which is the design pulse length of the ACS. An average conditioning time is 149 hours for all the modules. The beam commissioning of the linac was started in the middle of December, then the designed beam energy of 400 MeV was achieved in January 2014 [14-17].

Content from this work may be used under the terms of the CC BY 3.0 licence (© 2018). Any distribution of this work must maintain attribution to the author(s), title of the work, publisher, and DOI.

ISBN: 978-3-95450-194-6 ISSN: 2226-0366 doi:10.18429/JACoW-LINAC2018-MO1P02

Content from this work may be used under the terms of the CC BY 3.0 licence (© 2018). Any distribution of this work must maintain attribution to the author(s), title of the work, publisher, and DOI.

The ACS cavities have been successfully operated without any serious troubles. The operation time variation of the RF trip rate per day for all ACS cavities is shown in Fig. 10. The trip rate decreases with the time to an acceptable value of approximately 0.3 times per day.

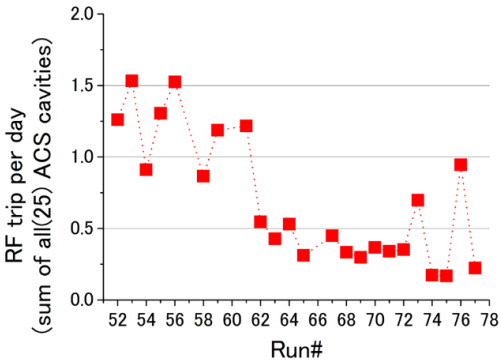


Figure 10: Time variation of number of ACS RF-trip.

972-MHz RF System

The 972-MHz klystron for the ACS cavity was evaluated using an own test-stand in 2001. The prototype of the klystron had strong oscillations due to a drift tube oscillation. Therefore, we improved the RF structure with an asymmetric cavity, a short gap length and a reduced Q value [18]. After the evaluation of the prototypes, mass production of the klystron was started. Four 972-MHz klystrons are driven by a High Voltage DC power supply (HVDC), which is the same system of the 324-MHz one [19]. Figure 11 shows the 972-MHz klystron station. After the ACS conditioning started in November 2013, we had discharge problems at ten circulators due to the malfunction of an RF contact between a body and a post. Because we replaced the RF contact with improved one after the conditioning completed promptly, this trouble did not affect the beam operation schedule.



Figure 11: 972-MHz klystron station.

The LLRF control systems for both the 324-MHz and 972-MHz stations are basically the same. However, many improvements of the 972-MHz-LLRF control systems have been carried out [20-22]. The reference 12-MHz signal delay settings for the feed-back control systems have been optimized using 12-MHz delay modules. The stability performances of the 972-MHz RF&Clock and the Mixer & IQ-modulator) boards have been improved using temperature-compensation techniques. Owing to the improvement, very good stability of the accelerating fields for beam operation was achieved about ±0.2% in amplitude and ±0.2° in phase, which is much better than the requirements of ±1% and ±1°, respectively [23]. However, it has become difficult to keep such a good stability with increasing the beam current. Therefore, we started to use the new beam loading compensation method which the feed-forward (FF) system is operated by assuming the shape of the intermediate pulse [24].

OPERATION STATUS AFTER URGRADES

At present, the linac is being operated successfully with high availability of approximately 90% [25]. After the beam current upgrade work, the linac was started to operate with the beam current of 30 mA. From January, 2016, the beam current was increased to 40 mA. At present, the RCS operates 500 kW for the MLF user operation. The MR beam power is gradually increasing and becomes 490 kW at the NU and 51 kW at the HD, respectively. Beam studies have been conducted at the interval of the user operation. In January, 2015, the RCS successfully demonstrated the beam acceleration and extraction of 1MW-equivalent with a single-shot operation mode [26]. At that time, the ion source kept the peak beam current of 60 mA because the peak beam current of 50 mA is necessary at the end of the linac. We have already demonstrated this condition in a few days duration and up to 2.5 Hz repetition rate. Further beam loss is studied to reduce residual radioactivity for long time user operation.

FUTURE UPGRADE PLAN

We are considering two upgrade plans that increasing the RCS beam power from 1 MW to 1.5 MW and duplation the linac repetition rate to 50 Hz for the TEF which is planned in the near future. In order to reach 1.5 MW at the RCS, the beam current and the beam pulse length are needed to increase to 60 mA and 600 μs respectively, it corresponds to increase by 20% than the present design values.

60-mA Operation Plan

The ion source is the key component to realize the 1.5 MW upgrade plan. We have been performed the R&D work of the ion source at an off-line test-stand. Figure 12 shows the waveforms of the ion source output current (cyan) and input RF power (blue) without (a) and with (b) impurities ventilation system [27]. The beam current of 66 mA had previously been demonstrated. However, we observed the approximately 10% current droop. Recent R&D has shown that the constant current without droop, a 10 % smaller emittance and the reduction of the required RF power from 40.6 kW to only 24.6 kW are achieved by removing N_2 & Ar impurities in the plasma [27].

ISBN: 978-3-95450-194-6 ISSN: 2226-0366 doi:10.18429/JACoW-LINAC2018-MO1P02

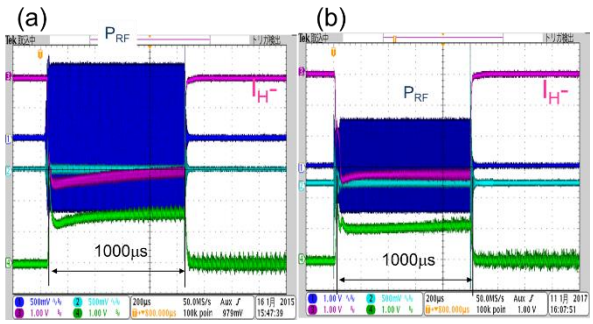


Figure 12: Waveforms of the H- beam current (cyan) and input RF power (blue) without (a) and with (b) impurities ventilation system.

Trial beam study with 60 mA was started in July 2017 just before the longer accelerator shutdown. The first 400-MeV and 56-mA beam at the linac exit was demonstrated in December, 2017, as shown in Fig.13 [28].

We were concerning that a significant beam loss occurs at the DTL1 section, because the alignment of DTs in DTL1 was deformed by the huge earthquake in 2011 so that the actual aperture was reduced. However, no significant beam loss was observed during the beam study. Therefore, the shift of the DT alignment is not probably fatal to the 60-mA operation.

The beam study showed that issues of the linac are the transmission in the RFQ and the MEBT1 scraper. The RFQ transmission is about 6 % lower than that of nominal 40 mA. On the other hand, a drop of the transmission of MEBT-1 happened for 60 mA by the scraper. In order to avoid the decrease of the beam transmission, we have the plan for increasing the RFQ tank level, re-optimization of the MEBT1 lattice and adjustment of the scraper gap at the next trail study. As the result of the beam simulation, reduction of the beam halo from the ion source is effective to improve the beam transmission at the RFQ. We will continue the R&D work of the ion source in the future.

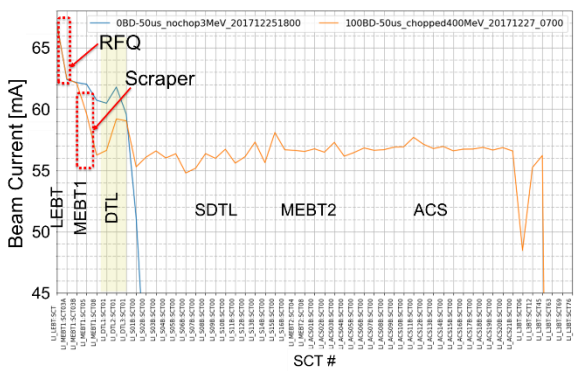


Figure 13: Transmission measured 60-mA trial beam study in December 2017.

600-μs Operation Plan

To obtain a 600-μs pulsed beam, approximately 750-μs RF pulse from the klystrons is necessary. Figure 14 shows the simulation result in case of 800-μs operation. The result shows the cathode voltage drops from 110 kV to 103 kV, corresponding to the output power from 2.47 MW to 2.22 MW across the pulse due to the capacitor bank droop. The reduction is not fatal because the maximum power required from a klystron at 60 mA beam current is 1.89 MW [29].

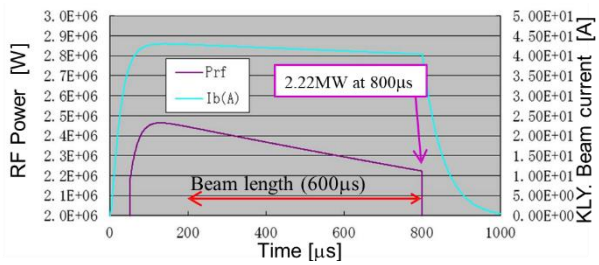


Figure 14: Simulation result of klystron power in case of 800 μs operation.

50-Hz Operation Plan

Because the TEF will use 400 MeV beam with 25 Hz from the linac, alternating 50 Hz pulses from the linac are sent to both RCS and TEF using a separator [30]. The main issues for the 50 Hz operation are insufficiency of the klystron AC power, that of the water-cooling system capacity and the increase of the beam loss. The klystron high voltage transformer is rated at 1000 kVA but 1154 kVA is necessary for 50-Hz and 600-μs operation. Therefore, it is planned to add auxiliary power supplies. For the 50-Hz and 600-μs operation, increase the cooling water system is also necessary because the capacity of the present system has little redundancy. Although some hardware upgrades are required to fix the issues described above, the issues are not so serious except for beam loss. For the mitigation of beam loss, the beam simulation and experiment are ongoing.

CONCLUSION

In 2006, the J-PARC linac started beam operation with the energy of 181 MeV and the design peak beam current of 30 mA. To realize the nominal performance of 1 MW at RCS and 0.75 MW at a MR, the beam intensity and energy upgrade were performed. The upgrades were completed in 2014. At present, the linac is operated with the beam current of 40 mA and high availability of approximately 90%. The beam current will be increased to 50 mA after 2018 summer shutdown. We are considering two upgrade plans that increasing the RCS beam power 1.5 MW and duplation the linac repetition rate to 50 Hz for construction of the TEF. We started trial beam studies with 60 mA in July 2017. 400 MeV and 56 mA beam at the linac exit was demonstrated in December, 2017. Further trial beam studies are planned to demonstrate 1.5 MW-equivalent beam at the RCS.

REFERENCES

[1] Y. Yamazaki ed., “Accelerator Technical Design Report for High-Intensity Proton Accelerator Project, J-PARC”, KEK Report 2002-13 and JAERI-Tech 2003-44.

Content from this work may be used under the terms of the CC BY 3.0 licence (© 2018). Any distribution of this work must maintain attribution to the author(s), title of the work, publisher, and DOI.

ISBN: 978-3-95450-194-6 ISSN: 2226-0366 doi:10.18429/JACoW-LINAC2018-MO1P02

Content from this work may be used under the terms of the CC BY 3.0 licence (© 2018). Any distribution of this work must maintain attribution to the author(s), title of the work, publisher, and DOI.

[2] H. Oguri, A. Ueno, K. Ikegami, Y. Namekawa, and K. Ohkoshi, "Status of the Japan Proton Accelerator Research Complex H- ion source", Phys. Rev. ST Accel. Beams 12, p. 010401, 2009.

[3] M. P. Stockli *et al.,* "Ramping up the Spallation Neutron Source beam power with the H- source using 0 mg Cs/day", Rev. Sci. Instrum. 81, p. 02A729, 2010.

[4] H. Oguri *et al.*, "Status of the RF-driven H- ion source for J-PARC linac", Rev. Sci. Instrum. 87, p. 02B138, 2016.

[5] K. Shinto, *et al.,* "Progress of the J-PARC Cesiated RF-driven Negative Hydrogen Ion Source", presented at NIBS2018, Novosibirsk, Russian, Sep. 2018, paper TueO1.

[6] Y. Kondo, K. Hasegawa, T. Morishita, and R. A. Jameson, "Beam dynamics design of a new radio frequency quadrupole for beam-current upgrade of the Japan Proton Accelerator Research Complex linac", Phys. Rev. ST Accel. Beams 15, p. 080101,2012.

[7] K. Hasegawa *et al.*, "Status of the J-PARC RFQ", in *Proc. IPAC'10,* Kyoto, Japan, May, 2010, pp. 621-623.

[8] T. Morishita, Y. Kondo, H. Oguri, and K. Hasegawa, "Vacuum properties and operation stability of the radio-frequency quadrupole accelerator in Japan Proton Accelerator Research Complex linac", Journal of Vacuum Science & Technology A 35, p. 041602, 2017.

[9] K. Hirano *et al.*, "Development of RF Chopper System at J-PARC Linac", *in Procs. of 10th Annual Meeting of Particle Accelerator Society of Japan*, p. 858, 2013.

[10] K. Hirano, T. Sugimura, and T. Kurihara, "Status of 3MeV Beam Scrapers for the J-PARC Linac", presented at 15th Annual Meeting of Particle Accelerator Society of Japan, Nagaoka, Japan, Aug. 2018, paper WEP016.

[11] K. Hasegawa, "Commissioning of Energy Upgrade Linac of J-PARC", in Proc. LINAC'14, Geneva Switzerland, Aug. 2014, pp. 417-422

[12] H. Ao *et al.*, "Annular-Ring Coupled Structure for the Energy Upgrade of the J-PARC Linac", in *Proc. LINAC12*, Tel-Aviv, Israel, Sep., 2012, pp. 888-890.

[13] J. Tamura, H. Ao, Y. Nemoto, and H. Oguri, "ACS Installation for Beam Energy Upgrade in J-PARC Linac", JPS Conf. Proc. 8, p. 011011, 2015.

[14] T. Maruta *et al.*, "Recent Progress of Beam Commissioning at J-PARC Linac", in *Proc. LINAC14*, Geneva, Switzerland, Aug. 2014, pp. 646-648.

[15] T. Maruta, Y. Liu, and A. Miura., "Longitudinal Measurement of Annular-type Coupled Structure Linac", in *Proc. LINAC14*, Geneva, Switzerland, Aug. 2014, pp. 1056-1058.

[16] Y. Liu, K. Futatsukawa, T. Maruta, and A. Miura., "Studies on Wake Field in Annular Coupled Structure", in *Proc. LINAC14*, Geneva, Switzerland, Aug. 2014, pp. 593-595.

[17] M. Ikegami *et al.*, "Commissioning Plan for Energy Upgrade of J-PARC Linac", in *Proc. IPAC13*, Shanghai, China, May 2013, pp. 3821-3823.

[18] E. Chishiro *et al.*, "Recent Status of RF Source in J-PARC Linac", in *Proc. 2005 Particle Accelerator Conference*, Knoxville, Tennessee, USA, May 2005, pp. 1123-1125.

[19] M. Kawamura *et al.*, "Power Supply System for Klystron in J-PARC Linac", in *Proc. LINAC10*, Tsukuba, Japan, Sep. 2010, pp. 887-889.

[20] Z. Fang *et al.*, "Present Status of J-PARC Linac LLRF System", in *Proc. LINAC14*, Geneva, Switzerland, Aug. 2014, pp. 224-226.

[21] T. Kobayashi, "Stability Evaluation for Long FB Loop Delay in the ACS Cavity Field Control for the J-PARC Linac 400-MeV Upgrade", in *Proc. LINAC10*, Tsukuba, Japan, Sep. 2010, pp. 253-255.

[22] K. Futatsukawa *et al.*, "Upgrade of the RF Reference Distribution System for 400 MeV Linac at J-PARC", in *Proc. IPAC'12*, New Orleans, Louisiana, USA, May, 2012, pp. 2630-2632.

[23] Z. Fang *et al.*, "Improvements of Low Level RF Control Systems for J-PARC LINAC 400-MeV Upgrade", JPS Conf. Proc. 8, p. 011001, 2015.

[24] K. Futatsukawa, *et al*., "Study of Beam Loading Compensation with Comb-like Structure at J-PARC Linac", in Procs. of 13th Annual Meeting of Particle Accelerator Society of Japan, p. 327, 2016.

[25] K. Hasegawa, "Operation Experiences of the J-PARC Linac", presented at LINAC18, Beijing, China, Sep. 2018, paper THP0040, this conference.

[26] H. Hotchi, "Recent Progress of J-PARC RCS Beam Commissioning toward Realizing the 1-MW Output Beam Power", in *Proc. IPAC'15,* Richmond, VA, USA, May, 2015, pp. 1346-1348.

[27] A. Ueno, "Cesiated surface H⁻ ion source: optimization studies", New J. Phys.19, p. 015004, 2017.

[28] Y. Liu, M. Otani, T. Miyao, T. Shibata, and A. Miura, "60 mA Beam Study in J-PARC Linac", in *Proc. HB2018*, Daejeon, Korea, Jun. 2018, pp. 60-63.

[29] E. Chishiro, private communication, 2017.

[30] M. Yoshimoto, K. Okabe, and M. Kinsho, "Conceptual Design of Beam Dividing System for J-PARC Transmutation Experimental Facility", JPS Conf. Proc. 8, p. 041003, 2015.

ISBN: 978-3-95450-194-6 ISSN: 2226-0366 doi:10.18429/JACoW-LINAC2018-MO1P03

STATUS OF THE ESS LINAC

A. Sunesson†, R. Garoby, M. Lindroos, M. Jensen, C. Martins, T. Shea, J. Weisend,
P. Arnold, A. Nordt, S. Birch, European Spallation Source ERIC, 22100, Lund, Sweden

Abstract

The European Spallation Source (ESS) under construction in Lund (Sweden) uses a 2 GeV-5 MW pulsed superconducting linac as proton driver. Normal conducting accelerating structures are used up to 90 MeV and superconducting structures up to 2 GeV. Most linac components are designed and procured as in-kind contributions by institutes/laboratories in the partner countries in Europe. Installation of the Ion source delivered by INFN-Catania started January 2018. Installation of more components and infrastructure progresses at a high pace. Commissioning of the normal conducting linac section will take place in parallel with installation of the superconducting section. Beam commissioning of the superconducting section will start in 2021, interlaced with the installation of additional high beta cryomodules. Beam will be sent to the target in 2022, initially at an energy of 1.3 GeV. Start of the User Program is scheduled in 2023, when some neutron instruments will be ready and end of construction is in 2025, with the full set of instruments operational. This paper reports the status of linac components construction, the progress with installation on site, and the overall project schedule.

INTRODUCTION

ESS will be a long pulse neutron source of the next generation with performance exceeding all similar existing and planned facilities world-wide [1]. The ESS superconducting proton linac is a key ingredient for that purpose, with a beam power of 5 MW at 2 GeV delivered in 2.86 ms pulses at a 14 Hz rate. ESS is being built north of the University town of Lund in the south of Sweden. The site layout can be seen in Fig. 1. The facility is presently (2018) under construction, with the start of user operations planned to late 2023. At the end of construction, in 2025, ESS will operate 15 instruments for neutron users.

A facility of ESS size and scope is a major undertaking both cost and scope-wise, and even more when starting from a green field. The project in general and the accelerator in particular are therefore extensively relying on knowledge and competences throughout Europe, provided as in-kind contributions. For the accelerator project, partners and contributions are listed in [1].

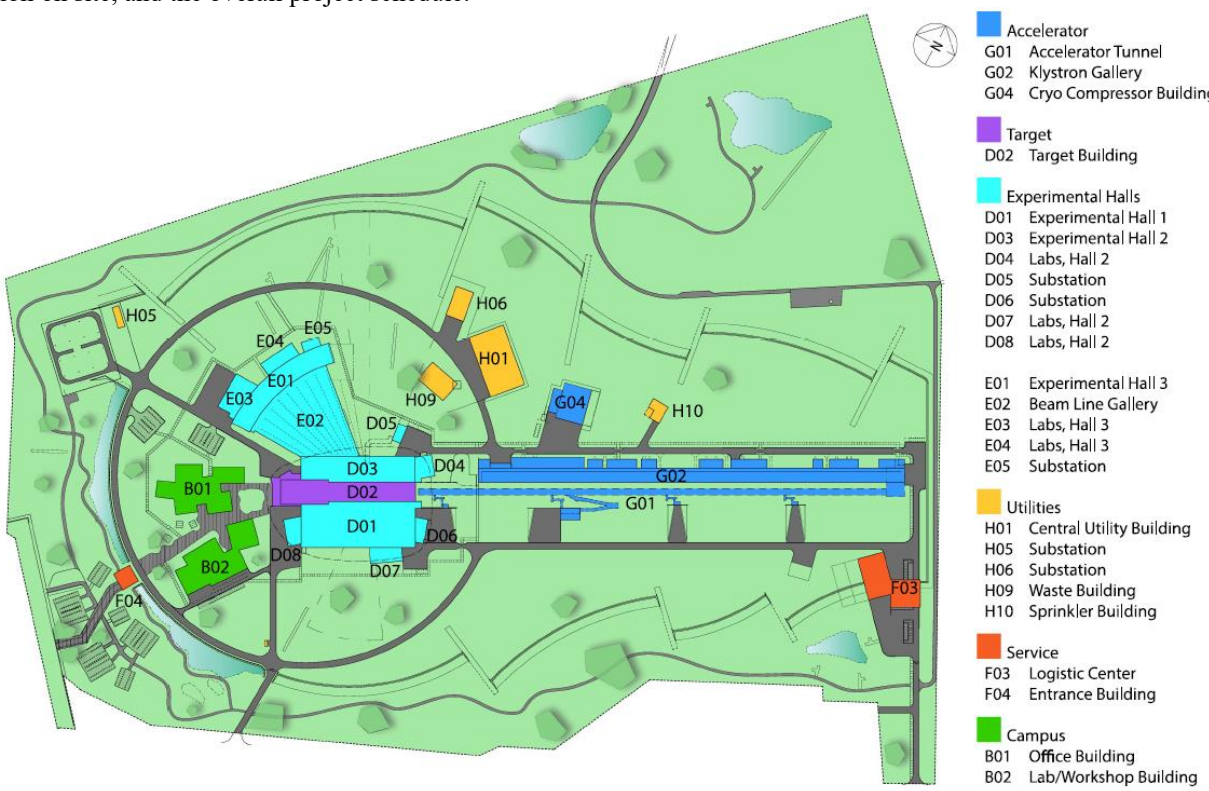


Figure 1: ESS site layout.

† anders.sunesson@esss.se

Content from this work may be used under the terms of the CC BY 3.0 licence (© 2018). Any distribution of this work must maintain attribution to the author(s), title of the work, publisher, and DOI.

ISBN: 978-3-95450-194-6 ISSN: 2226-0366 doi:10.18429/JACoW-LINAC2018-MO1P03

Content from this work may be used under the terms of the CC BY 3.0 licence (© 2018). Any distribution of this work must maintain attribution to the author(s), title of the work, publisher, and DOI.

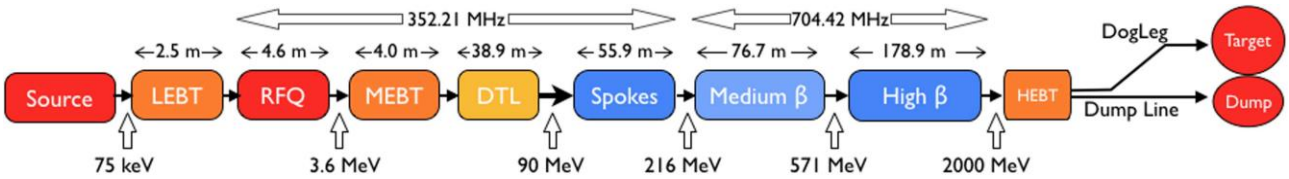


Figure 2: ESS Linac lattice overview.

ESS LINAC DESIGN

Lattice and Linac Design

The linac is approximately 450 m long. A 100 m long High Energy Beam Transport (HEBT) section at its end provides the possibility to add accelerating structures in the future. Table 1 shows the main characteristics of the linac.

Table 1: Linac General Parameters

Parameter	Unit	Value
Energy	GeV	2.0
Current	mA	62.5
Pulse length	ms	2.86
Pulse repetition rate	Hz	14
Average beam power	MW	5
Power during pulse	MW	125
Beam emittance at target, ϵ_x	π mm mrad	0.34
Beam emittance at target ϵ_y	π mm mrad	0.36

The lattice is shown in Fig. 2. It starts with the Ion source and Low Energy Beam Transport, followed by the RFQ, three bunchers in the Medium Energy Beam Transfer (MEBT) section, and five DTL tanks. This part of the linac is normal conducting. The DTL tanks are succeeded by the Spoke section, consisting of 26 Superconducting double spoke superconducting cavities in 13 cryomodules. Next come 36 six-cell superconducting medium-beta elliptical cavities in 9 cryomodules. The final section of the linac makes use of 84 five-cell high-beta elliptical cavities in 21 cryomodules. It is worth noting that 95% of the final beam energy is due to superconducting cavities, an unusually high portion. After the linac the beam drifts through the HEBT section until is it diverted towards the target using dipole magnets. Just before hitting the target the beam is swept using a magnet raster system, to illuminate the target more uniformly.

Parameters of the linac cavities and their RF sources are listed in Table 2. Up till the end of the Spoke linac section, the RF frequency is 352.21 MHz. The 4 vane RFQ accelerates protons to 3.6 MeV. After the bunchers, the five DTL tanks bring the energy to 90 MeV. The Spoke cavities section increases the energy up to 216 MeV. The medium beta and high beta sections both operate at 704.42 MHz. Beam energy is 570 MeV after the medium beta section, and 2 GeV at the end of the high beta section.

The Ion source and LEBT are designed and built by INFN Catania (Italy). They are presently at Lund and installation will be complete by Q3 2018. The RFQ is designed and built by CEA-Saclay (France), and delivery is planned during Q4 2018. MEBT bunchers are designed and constructed by ESS Bilbao (Spain), and delivery is planned during Q1 2019. INFN Legnaro (Italy) will successively deliver all DTL tanks between Q1 2019 and Q1 2020. For more details on the normal conducting linac, see [2]. Spoke cavities and cryomodules are under the responsibility of IPNO (France). They will be tested at FREIA lab in Uppsala (Sweden) before delivery at Lund. Design is finished, fabrication has started and delivery is planned between June 2019 and December 2020. Elliptical cavities come from INFN Milano (Italy) for medium beta and STFC Daresbury (UK) for high beta. CEA Saclay will take care of assembling all elliptical cavity cryomodules. The first four cryomodules will be fully tested at CEA Saclay before shipment. All the others will be tested at high RF power on the surface at Lund before installation in the tunnel. Design and prototyping of medium beta section is finalized (Fig. 3). Delivery is planned between October 2019 and August 2020 for medium beta cryomodules and between October 2020 and end 2021 for high beta cryomodules.

Table 2: Parameters for the Linac Cavities and RF Sources

Linac section	Energy (MeV)	Frequency (MHz)	Number of cavities	Temp (K)	RF power required (kW)	RF source	RF power specified (kW)
Source	0.075	-	-	300	-0		
LEBT	0.075	-	-	300	-		
RFQ	3.6	352.21	1	300	1600	Klystron	3000
MEBT	3.6	352.21	3	300	20	SSPA	35
DTL	90	352.21	5	300	2200	Klystron	3000
Spoke	220	352.21	26	2	330	Tetrode	450
Medium beta	570	704.42	36	2	870	Klystron	1500
High beta	2000	704.42	84	2	1100	Klystron/IOT	1500/1200

ISBN: 978-3-95450-194-6 ISSN: 2226-0366 doi:10.18429/JACoW-LINAC2018-MO1P03

RF Systems

The RF systems located in the RF gallery are providing the power necessary for getting the required accelerating fields in the accelerating structures. Their inventory is given in Table 2. RF systems are grouped in cells, each cell in the SC sections of the linac typically powering 8 cavities. A view of a medium beta cell can be seen in Fig. 4.

The 352 MHz sources chosen for the RFQ and DTL are klystrons that two major suppliers have already developed. A dual-tetrode RF transmitter powers the spoke section. Elettra (Italy) delivers these power stations.

The need for 120 amplifiers to drive the 704 MHz elliptical cavities triggered an ESS/CERN/industry collaborative project for the development of high power 704 MHz Multi-beam IOTs as high efficiency alternatives to klystrons. Two prototypes were funded by the ESS project and CERN provided a test facility. Both prototypes successfully reached nominal performance and 1200 kW power [3].

These new devices are however not mature enough for series production according to the ESS schedule and klystrons have therefore been selected for the medium and the first part of the high beta linac sections. Prototype klystrons have been ordered from 3 manufacturers. To improve the efficiency of the klystrons which will operate well below saturation power in the medium beta section, a mismatch is created in the output cavity. In the high beta section, klystrons are being ordered for the first batch of 44 cavities. The RF amplifiers for the last 40 cavities will be ordered at a later date and MB-IOTs may be the best choice at that time.



Figure 3: Cryomodule for installation tests at ESS.

The LLRF system is based on the MTCA-4 platform, and FPGA units from Struck. Overall system has been designed by Lund University. Polish Electronic Group designs, constructs, and delivers vital subsystems to the LLRF system. The phase reference distribution system has been designed and installed by Warsaw university of Technology. It is based on a coaxial line transporting both 352.21 and 704.42 MHz references to RF and beam diagnostics systems along the linac.

RF interlock systems are built by Atomki (Hungary) using an ESS design based on PLCs and dedicated fast FPGA processing for fast interlock, see controls.

IFJ PAN from Krakow (Poland) contributes to the installation of RF equipment with manpower.

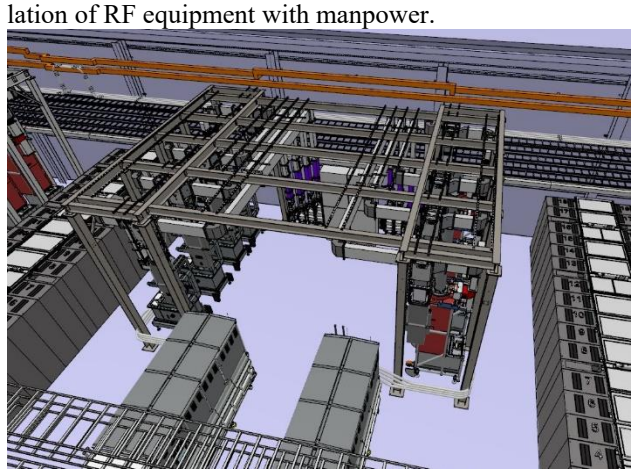


Figure 4: Medium beta cell view. Modulators are to the bottom, klystrons and waveguide systems are in the center, and the waveguides transmit RF power to the tunnel.

Cryogenic Systems

ESS uses cryogenics in three principal applications: The cryomodules require 2 K, 4.5 K, and 40 K cooling. The target moderator requires 16.5 K cooling, and many of the instruments also require cooling. Liquid helium (LHe) is used in most cases. The helium is produced by three cryoplants and an extensive distribution system [4]. The cryoplants have been built by Linde Kryotechnik (Switzerland) and Air Liquide (France). The cryogenic transfer lines are contributions from CNRS (France) and Wroclaw University of Science and Technology (Poland) for spoke linac and Medium/high beta linac/test stand, respectively.

The status Q3 2018 is that the cryoplant for the cryomodule test stand and neutron instruments and the accelerator cryoplant are both being commissioned and production of LHe has commenced. The transfer line between the cryoplant and the test stand is under installation.

Power Converters and Magnets

Power converters for the magnets in the Linac Warm Units (LWU) are contributed by INFN (Italy).

A novel modulator topology called stacked multi-level (SML) [5] is used to power the klystrons. It meets stringent requirements and provides long pulse (3.5 ms), high pulse power (11.5 MWpk) and high average power (660 kVA) while minimizing disturbance to the electrical grid. Its development was made at ESS in collaboration with Lund University. Due to its modularity and extensive utilization of standard off the shelf components, the topology brings considerable advantages in terms of compactness, cost efficiency and maintainability. A prototype was successfully built and tested in the ESS test labs.

Content from this work may be used under the terms of the CC BY 3.0 licence (© 2018). Any distribution of this work must maintain attribution to the author(s), title of the work, publisher, and DOI.

ISBN: 978-3-95450-194-6 ISSN: 2226-0366 doi:10.18429/JACoW-LINAC2018-MO1P03

Content from this work may be used under the terms of the CC BY 3.0 licence (© 2018). Any distribution of this work must maintain attribution to the author(s), title of the work, publisher, and DOI.

The SML topology is used for the three modulators of the normal conducting linac ordered by ESS Bilbao (Spain) and for the nine modulators of the medium beta section procured by ESS.

In the A2T area the raster magnets are powered by a system from our partner Aarhus University. This system scans the beam across the target in a raster, so that the target is more uniformly illuminated. See Fig. 5.

LEBT magnets are part of the Ion source/LEBT contribution from INFN Catania (Italy). MEBT magnets come from ESS Bilbao (Spain). All magnets in the Spoke section and onwards is a contribution from Elettra (Italy), manufactured by Danfysik (Denmark) and SigmaPhi (France). The rastering magnets come from Aarhus University (Denmark). STFC (UK) assembles the Linac Warm Units (LWUs) and puts the magnets into them.

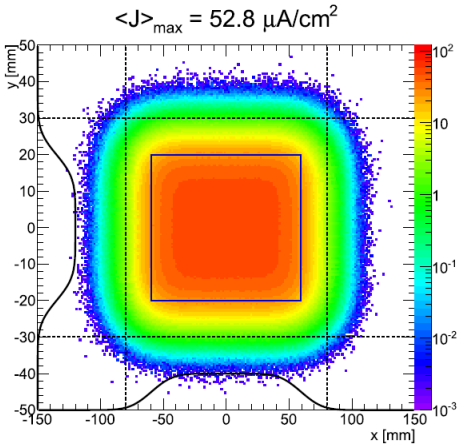


Figure 5: The intensity profile across the target after raster scanning. Note 3:1 aspect ratio on scales.

Beam diagnostics

An overview of the beam diagnostic efforts can be found in [6]. The diagnostic suite contains more than 20 system types, produced by a global collaboration of more than 20 institutes. Table 3 shows the main measurement categories and system types. The total number of diagnostic stations exceeds 450. All systems deliver measurement data via the EPICS-based control system, while a large subset also use FPGA-based processing to provide protection functions with microsecond latency.

Controls, MPS, and PSS

ESS integrated control system is based on EPICS. Information about ESS controls can be found in [7]. The Integrated Control Systems (ICS) division will provide software integration, control room, Machine Protection System, Personnel Safety System, process control, timing, and other services. ICS has adopted for data collection three hardware platforms:

- MicroTCA-4 for fast applications like LLRF and beam diagnostics with MHz and higher data rate
- EtherCAT for slower applications, up to 100 kHz
- PLC for industrial type process control

These platforms are standardized so that as few device families as possible is achieved.

Table 3: Beam Diagnostics

Category	System
Beam accounting	Doppler System
	Beam Current Monitors
	Faraday Cups
	Beam Loss Monitors (ionization, neutron)
	Aperture Monitors
Centroid	Beam Position Monitors
Distribution	Emittance measurements
	Bunch Shape Monitors
	Wire Scanners
	Beam Induced Fluorescence
	Ionization Profile
	Imaging

The purpose of ESS machine protection is to support the operational availability of ESS by preventing equipment damage. A dedicated machine protection concept [ESS-0035197] has been developed and is being implemented to mitigate the risks and achieve the high operational availability [ESS-0057245]. Several machine protection systems (MPSs) are used to implement the relevant protection functions and are connected to the Fast Beam Interlock System (FBIS) [ESS-0275481], which can stop beam within 2-4 µs through a set of dedicated actuators [ESS-0231457], like the Ion Source, LEBT chopper, MEBT chopper and timing system. The Beam Current Monitoring System (BCMs) is connected to the FBIS to ensure that pulse length, repetition rate, and beam current are not being exceeded [ESS-0178171]. The fastest reaction time of BCMs is 1-2 µs.

The primary role of the Personnel safety Systems (PSS) at ESS is to protect workers from being harmed by exposure to ionising prompt radiation generated by the proton beam and high power RF systems, during all operating modes and lifecycle phases. This will be achieved by preventing the access of personnel to the PSS controlled areas when a hazard is present and controlling access under safe conditions. All hazards within the PSS controlled areas will be identified, assessed, and analysed during the hazard identification process.

Typical hazards that shall be considered are ionising prompt radiation from the proton beam; ionising radiation (X-ray) from high power radio frequency (RF) devices; electrical hazards; high powered radio frequency hazards; magnetic field; motion/mechanical hazards; laser hazards; oxygen deficiency hazards. The PSS systems are developed and comply with IEC-61508/IEC-61511: Functional safety of electrical/electronic/programmable electronic safety-related systems. All PSS systems will be designed, manufactured, commissioned and validated to IEC61508, using proven commercial of the shelf technology.

ISBN: 978-3-95450-194-6 ISSN: 2226-0366 doi:10.18429/JACoW-LINAC2018-MO1P03

SCHEDULE

The schedule of the ESS project has recently been re-baselined mostly because of delays in the construction of the target station building. That is due to revised requirements related to earthquakes in the aftermath of the Fukushima incident and concerns about antagonistic threats. The start of the user program, when scientific users make use of neutrons from the source in experiments, is at the end of 2023. For this to be achieved, the accelerator is scheduled to achieve beam on target (BOT) in the middle of 2022. Accelerator readiness for beam on target is scheduled to mid 2021 (Accelerator RBOT). At this stage, 570 MeV beam shall be available, so all the needed hardware (cavities, RF, BI, etc.) need to be installed and commissioned. Fig. 6 depicts the startup steps for the accelerator.

Currently the subsystems are being delivered and installed. The Ion source and LEBT are finalized during Q3 2018, and the plan is to start running the Ion source during September 2018. In the RF Gallery, racks and structures to support waveguides, circulators, and loads are being delivered and installed. To accommodate the schedule in Fig. 6, the beam commissioning of Ion source, LEBT, RFQ, Bunchers, MEBT, and DTL 1-4 will be done in parallel with the installation of the superconducting cavities. This will be achieved installing a shield wall in the tunnel where DTL 5 will ultimately be located.

To test cryomodules and HV/RF equipment the gallery holds a test stand area. Klystrons/HV modulator for these tests are in place and the assembly of the bunker will proceed in October 2018.

The licensing process is complex and progresses thanks to tight interactions and transparent exchanges between ESS and the Swedish nuclear safety authorities for which this is a new type of facility. It is staged and takes place in parallel with testing activities. Permits for running klystrons in the test stand area as well as the Ion Source and LEBT are obtained. The next step is to get permits for operating the test stand bunker and the normal conducting linac.

SUMMARY

The ESS linac will at completion be the world's most powerful proton linac with a proton energy of 2 GeV and a beam power of 5 MW. The linac employs an unusually high portion of superconducting cavities for the acceleration, 95% of the final proton energy. Among the achievements are development of the new SML modulator topology and the MB-IOT tube amplifiers, both of which have been verified experimentally. The next step during Q3 2018 is to start commissioning of the Ion Source and LEBT, in parallel with installation of infrastructure in the RF gallery. Start of the neutron production is scheduled by mid-2022, user scientific program at the end of 2023, and end of construction in December 2025.

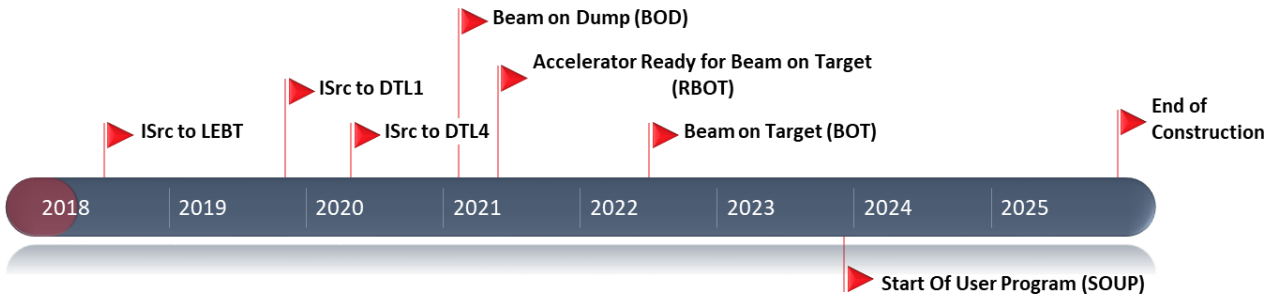


Figure 6: Overall schedule of ESS linac milestones.

ACKNOWLEDGEMENTS

The authors wish to thank all of the institutes providing in-kind contributions to the ESS project.

REFERENCES

[1] R. Garoby *et al*, "The European Spallation Source Design", *Physica Scripta*, vol. 93, p. 014001, Dec 2017, doi.org/10.1088/1402-4896/aa9bff

[2] E. Sargsyan *et al.*, "ESS Normal Conducting Linac Status and Plans", presented at 29th Linear Accelerator Conf. (LINAC2018), Beijing, China, Sep. 2018, paper THPO043, this conference.

[3] M. Jensen *et al.*, "Testing of the ESS MB-IOT Prototypes", in*Proc. of 9th International Particle Accelerator Conference (IPAC2018),* Vancouver, BC, Canada, pp. 1759-1764, 2018, doi:10.18429/JACoW-IPAC2018-WEXGBF1

[4] J. G. Weisend II, P. Arnold. J. Frydrych, W. Hees, J. M. Jurns, and X. L. Wang, "Cryogenics at the European Spallation Source", *Physics Procedia*, vol. 67, p.27, 2015, doi:10.1016/j.phpro.2015.06.006

[5] M. Collins, C. A. Martins, "A Modular and Compact Long Pulse Modulator based on the SML Topology for the ESS Linac", *IEEE Transactions on Dielectrics and Electrical Insulation,* vol. 24, Issue 4, pp. 2259 – 2267, 2017, doi:10.1109/TDEI.2017.006284

[6] T. Shea *et al.*, "Overview and Status of Diagnostics for the ESS Project," in *Proc. of International Beam Instrumentation Conference (IBIC'17)*, Grand Rapids, MI, USA, 20-24 August 2017, no. 6 in International Beam Instrumentation Conference, (Geneva, Switzerland), pp. 8–15, JACoW, Mar. 2018. doi.org/10.18429/JACoW-IBIC2017-MO2AB2

[7] T. Friedrich *et al*, "Overview of the Integrated Control System", ESS report ESS-0297798, 2018.

Content from this work may be used under the terms of the CC BY 3.0 licence (© 2018). Any distribution of this work must maintain attribution to the author(s), title of the work, publisher, and DOI.

ISBN: 978-3-95450-194-6 ISSN: 2226-0366 doi:10.18429/JACoW-LINAC2018-MOPO004

COMMISSIONING OF SRF BOOSTER CAVITY FOR LEReC*

Wencan Xu†, A. Fedotov, T. Hayes, D. Holmes, G. McIntyre, K. Mernick, S. Seberg, K. Smith, F. Severino, R. Than, Q. Wu, B. Xiao, T. Xin, A. Zaltsman
Collider-Accelerator Department, Brookhaven National Laboratory, Upton, NY 11790, USA

Abstract

One important component for LEReC project is a 704 MHz booster cavity, which was modified from the BNL ERL 704 MHz SRF gun cavity. Within one and half year, the modification completed. The booster cavity cryomodule was successfully commissioned in mid-October 2017, and it was moved to LEReC location at RHIC tunnel 2 O'clock, where it has been serving routine operation since March 2018. This paper will report the configuration of the new cryomodule and its commissioning results.

INTRODUCTION

Low Energy RHIC Electron Cooling (LEReC) [1] aims to improve luminosity lifetime by counteracting Intra-Beam Scattering (IBS). The Energy scan of interest are 7.7, 9.1, 11.5, 14.6, 19.6 GeV, which requires corresponding kinetic energy of electron beam to be 1.6 – 2.6 MV. The energy gain is provided by SRF booster and a 400 kV DC gun. The 704 MHz SRF booster cavity introduces an energy chirp that causes ballistic stretching of the bunch as it drifts down the beam line. Additional RF systems (2.1 GHz, 704 MHz warm RF cavity, 9 MHz warm cavity) are employed to remove the energy chirp, longitudianl bunch curvature and bunch-by-bunch energy variation. Figure 1 shows the beamline layout LEReC.

The 704 MHz SRF booster cavity was converted from ERL SRF gun cavity [1]. The major conversion includes 1) convertion of the choke-joint cathode support to a beampipe, 2) retracting FPC for optimum coupling, 3) improvement of cryogenic plumbing for microphonics suppression, 4) change of beampipe HOM damper to coaxial line HOM damper, etc. This paper will describe the convertion of booster cavity and cryomodule, vertical test, commissioning results, and operation status of the booster cavity.

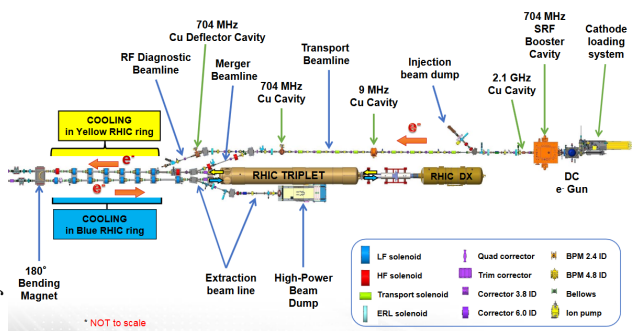


Figure 1: LEReC layout.

704 MHz SRF GUN CAVITY REVIEW

Before describing the modification, it is necessary to review the performance of the booster cavity as a gun cavity. Figure 2 shows the high current SRF gun cavity configuration. Two high power fundamental power coupler were used to deliver up to 1 MW RF power to the cavity. A choke-joint structure was used for photocathode support. Beam commissioning with this gun was carried out during end of 2014 to mid. 2015, which one can find more detail about the commission in reference [2]. One important point about the commission is that the cavity without cathode was able to reach CW 2.3 MV (although a lot of radiation), as shown in Figure 3. However, it kept quenching at around 1.6 MV after commissioning with cathode stalk a few month, which we believe that is due to cavity (near the cathode area) contamination by the either cathode stalk (Cu) or cathode (K_2CsSb). Due to tight schedule of LEReC and as the cavity reached 2.3 MV (shown in Figure 3), which is higher than the requirement of LEReC, we had sufficient confidence to convert the gun to LEReC booster.

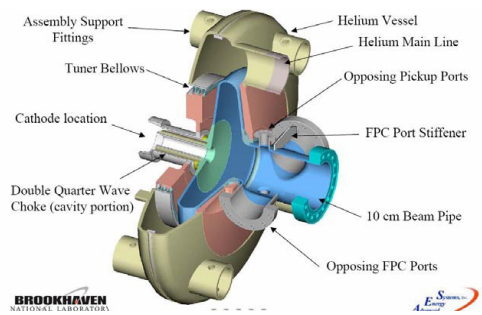


Figure 2: 704 MHz SRF gun cavity.

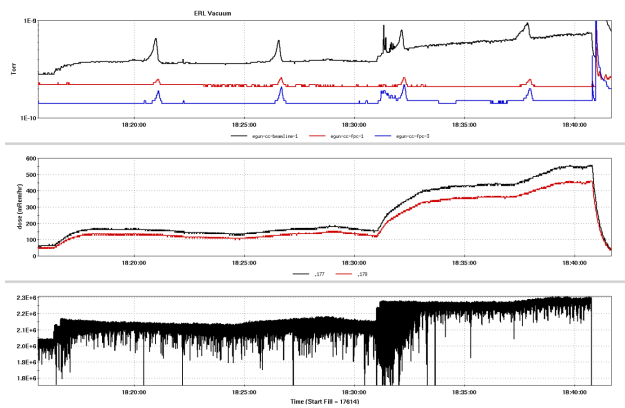


Figure 3: 704 MHz SRF gun cavity reached 2.3 MV prior to cathode commissioning.

* Work supported by LDRD program of Brookhaven Science Associates, LLC under Contract No. DE-AC02-98CH10886 with the U.S. DOE.
† email: wxu@bnl.gov

Content from this work may be used under the terms of the CC BY 3.0 licence (© 2018). Any distribution of this work must maintain attribution to the author(s), title of the work, publisher, and DOI.

ISBN: 978-3-95450-194-6 ISSN: 2226-0366 doi:10.18429/JACoW-LINAC2018-MOPO004

CONVERSION TO BOOSTER

Beamline Conversion

Figure 4 (top) shows conversion from choke-joint cathode support to a beam pipe. This is done by cut off the outer second ring of the choke joint, and weld a "dome' around the first ring of the choke joint or the beampipe of the booster cavity. Eighteen 0.375 inch holes are drilled to connect between the new dome with helium vessel. A conical beampipe transits the cavity to a beampipe with RF shield and particular trapping function.

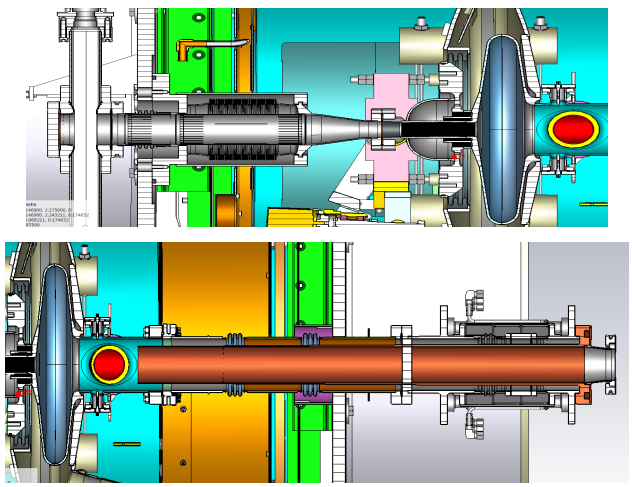


Figure 4: Booster cavity beamline configuration. Top: upstream, Bottom: downstream.

The downstream conversion involves the modification of HOM damper design [3]. In SRF gun, the HOM damper is a warm beampipe Ferrite HOM absorber, which is not sufficient to damp the trapped TM011 mode. Damping TM011 mode is very critical for LEReC because the energy spread for LEReC should be better than 5E-4 at the cooling area. So, an idea with coupling the HOM out of the cavity through a coaxial line and damp the HOM with ferrite at room temperature was developed and worked out. In Figure 4 (bottom) shows the downstream beamline of the booster cavity.

FPC Modification

The FPC coupling factor was 5.5E4 in the gun, which is optimized for 1 MW beam loading. However, the maximum beam power for LEReC is 120 kW, so the RF power source for LEReC is two 65 kW IOT tubes. The coupling factor of booster cavity was optimized to be 1.7E5. This coupling factor assumed the Q_0 at maximum voltage should be better than 7E8, and peak-to-peak microphonics should be smaller than 200 Hz. Based on simulation, each coupler has to retract 5 mm from the original position, which is realized by a thicker gasket spacer. The maximum RF field on the pringle increases about 20%, but still way below the break down level.

Cryomodule Modification

Comparing with SRF gun cavity, the majority additional heat load may come from two sources. The first one is heating by the beam loss or beam halo on the upstream beam pipe area. The worst scenario is all 20 kW beam power hitting on the upstream beampipe transition area for 20 μs, which will cause cavity quench. To avoid damage caused by beam loss, it is relied on cryogenic temperature sensors on the beampipe and He pressure sensor beam interlock. In Figure 5, it shows the cryogenic temperature sensor location, where three sensors were installed to the upstream transition area. The second one is the RF loss on the inner surface of the beam pipe and gasket, and radiation heat from the 300 K HOM inner conductor. To reduce the thermal radiation, the Cu surface was polished such that emissivity of the radiation is as low as 0.1. A 5 K cold anchor was added between cavity downstream flange and the first bellow. Eventually, the total heat load is reduced to 7.9 W, which is close to 7 W static heat load of the SRF gun cavity.

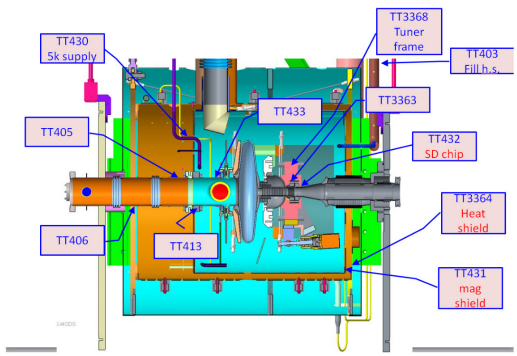


Figure 5: Temperature sensors on the booster cavity.

CRYOMODULE ASSEMBLY

Vertical Test of the Booster Cavity

The cavity was light BCP by ANL, and shipped to Jlab for vertical test. Two tests were carried out and HPR in between. The result of the last test is shown in Figure 6. The cavity reached 2.4 MV, and a field emitter lit up, somehow. After that the field emission onset is low at 1.6 MV. Due to tight schedule, and mainly because we are confident that we can condition through the field emission, the cavity was shipped to BNL for cryomodule installation.

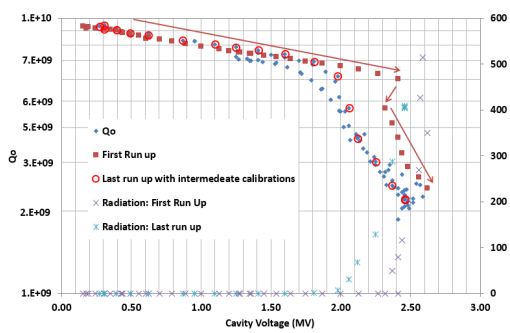


Figure 6: Vertical test results of booster cavity.

Content from this work may be used under the terms of the CC BY 3.0 licence (© 2018). Any distribution of this work must maintain attribution to the author(s), title of the work, publisher, and DOI.

ISBN: 978-3-95450-194-6 ISSN: 2226-0366 doi:10.18429/JACoW-LINAC2018-MOPO004

Content from this work may be used under the terms of the CC BY 3.0 licence (© 2018). Any distribution of this work must maintain attribution to the author(s), title of the work, publisher, and DOI.

Reconditioning of FPC

Two FPCs were taken apart, inspected and determined to be re-conditioned without any wet processing. The conditioning setup and procedure was similar to the original one used in 2012. As shown Figure 7, the FPCs were re-conditioned up to 120 kW in standing wave, which is double of the required maximum power.

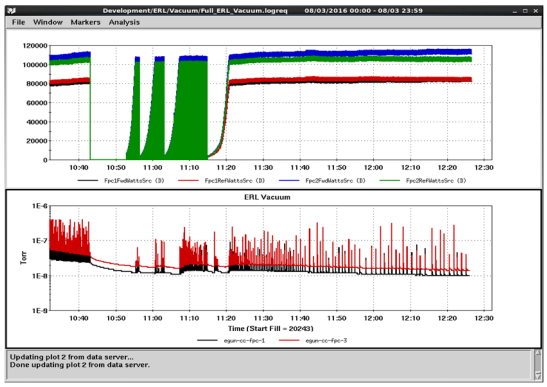


Figure 7: Reconditoning FPCs for LEReC.

Reinstallation of the Cryomodule

The cryomodule was assembled at BNL and moved to ERL blockhouse for high power RF test in summer 2017. Figure 8 shows the cavity in the clean room and cryomodule for high power test.



Figure 8: SRF booster cryomodule in ERL blockhouse.

COMMISSIONING RESULTS

Firstly, the booster cavity was commissioned in ERL Blockhase without HOM damper. Benefitting from the well-conditioned FPC before cryomodule installation, the cavity reached 2.2 MV smoothly, without much vacuum activity, arcing or tripping. Figure 9 shows the cavity commissioning results prior HOM injection. There was very small level the field emission at 2.2 MV. The static heat loss is about 6 W, and the dynamic loss at 2.2 MV is about 15 Watt, which corresponds to cavity quality of 4E9.

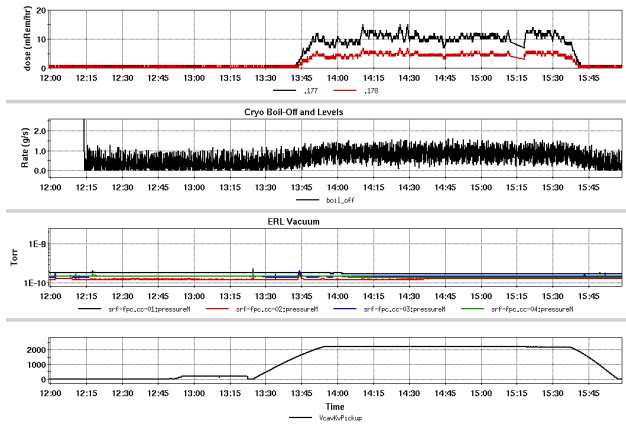


Figure 9: Booster cavity commissioning result before HOM insertion.

The HOM damper, shown in Figure 4 (bottom) was inserted in situ with a portable cleanroom. And the full-dressed booster cavity's test results are shown in Figure 10. The insertion was very successfully, the cavity ramped up the voltage very smoothly, and it only took two days to get to 2.2 MV. The field emission at 2.2 MV only increased slightly, comparing with the no HOM insertion case.

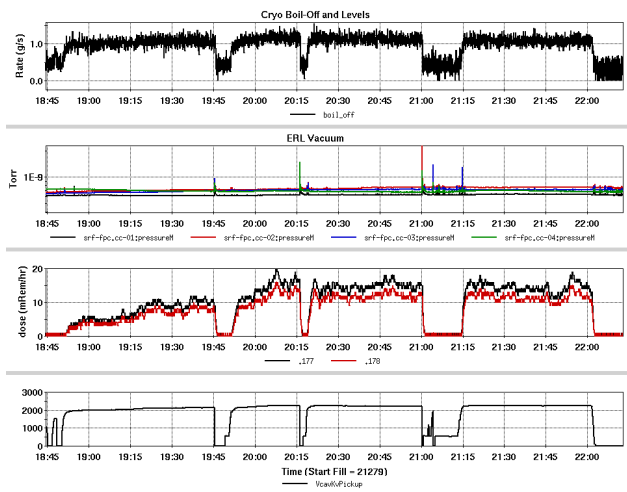


Figure 10. Booster cavity commissioning result after HOM insertion.

SUMMARY

LEReC booster cavity was successful converted from ERL SRF gun cavity. This paper reviewed the ERL SRF gun cavity tested results, discussed the conversion from SRF gun cavity to booster for LEReC, and presented the commissioning results. The booster cavity has been routine operating since it was installed in LEReC beam line.

REFERENCES

[1] A. Fedotov, M. Blaskiewicz, W. Fischer, *et al.*, "Accelerator physics design requirements and challenges of RF based electron cooler LEReC", in *Proc. 2016 North American Particle Accelerator Conf. (NA-PAC'16)*, Chicago, IL, USA, Oct. 2016. doi:10.18429/JACoW-NAPAC2016-WEA4CO05

ISBN: 978-3-95450-194-6 ISSN: 2226-0366 doi:10.18429/JACoW-LINAC2018-MOPO004

[2] Wencan Xu *et al.*, ``SRF Gun at BNL: First Beam and Other commissioning Results'', in *Proc. 17th Int. Conf. on RF Superconductivity (SRF'15)*, Whistler, BC, Canada, 13-18, 2015, pp. 1001-1005. doi:10.18429/JACoW-SRF2015-THAA03

[3] Wencan Xu *et al.*, "Design, simulation, and conditioning of 500 kW fundamental power couplers for a superconducting rf gun", *Phys Rev ST Accel. Beams*, vol. 15, p. 072001, 2012. doi:10.1103/PhysRevSTAB.15.072001

Content from this work may be used under the terms of the CC BY 3.0 licence (© 2018). Any distribution of this work must maintain attribution to the author(s), title of the work, publisher, and DOI.

ISBN: 978-3-95450-194-6 ISSN: 2226-0366 doi:10.18429/JACoW-LINAC2018-MOPO005

COMMISSIONING OF THE NORMAL CONDUCTING CAVITIES FOR LEReC PROJECT*

Binping Xiao†, K. Mernick, F. Severino, K. Smith, Tianmu Xin, A. Zaltsman
Brookhaven National Laboratory, Upton, New York 11973-5000, USA

Abstract

To improve RHIC luminosity for heavy ion beam energies below 10 GeV/nucleon, the Low Energy RHIC electron Cooler (LEReC) is designed and is currently under commissioning at BNL. The linac of LEReC consists of a DC photoemission gun, a 704 MHz superconducting radio frequency (SRF) booster cavity, a three-cell 2.1 GHz third harmonic cavity for RF curvature correction, a single-cell 704 MHz cavity for energy de-chirping and a 704 MHz deflecting cavity for diagnostic line. In this paper, we present the commissioning of three normal conducting cavities mentioned above.

INTRODUCTION

A bunched beam electron cooler called LEReC [1] has been designed and is under construction at the Relativistic Heavy Ion Collider (RHIC) to significantly improve the collider luminosity at energies below 10 GeV/nucleon to map the QCD phase diagram, especially to search the QCD critical point.

The electron linac of LEReC consists of a DC photoemission gun, one 704 MHz SRF booster cavity [2], and four normal conducting cavities: a 2.1 GHz third harmonic cavity, a 704 MHz cavity [3-5], a 9 MHz cavity, and a 704 MHz deflecting cavity on the beam diagnose line for longitudinal energy spread measurement. The 704 MHz SRF booster cavity accelerates 400 keV bunches from the DC gun near the top of the RF wave, with an accelerating voltage up to 2.2 MV. The booster also introduces an energy chirp for ballistic stretching of the bunches in a beam transport section. The remaining curvature of the bunch in longitudinal phase space is then corrected by decelerating the beam in the 2.1 GHz third harmonic cavity, so that the bunch is nearly linear in phase space. After the 30-meter long transport section, the bunch is still short enough so that the energy chirp can be removed with the normal conducting 704 MHz cavity.[6]

The 2.1 GHz cavity is a three-cell cavity operating at 2.112 GHz. It delivers an accelerating voltage up to 250 kV, at 9 kW power dissipation in the cavity walls, and 21.2 kW maximum power from the beam (decelerating). The 704 MHz cavity is a single-cell structure operating at 704.0 MHz that delivers a voltage up to 251 kV, at 9.5 kW power dissipation in the cavity walls, and 13.4 kW maximum power to the beam (accelerating). The 704 MHz deflecting cavity is a single-cell structure operating at 704.0 MHz that delivers a voltage up to 50 kV, at 150 W power dissipation in the cavity walls, and the power goes to the beam can be ignored since it works at zero phase and only limited number of electron bunches go into the diagnose line per second. In this paper, we describe the commissioning of these three normal conducting cavities.

CAVITY COMMISSIONING

The 2.1 GHz cavity was measured using network analyzer. At 2.1127 GHz, cavity unloaded Q was at 2.0e4, FPC Q_{ext} was at 2.0e4, critically coupled to the cavity. Pickup coupler 1 Q_{ext} was at 1.25e8 and pickup coupler 2 Q_{ext} was at 2.71e7. Cavity R/Q was calculated to be 175.1 Ω in circuit definition.

The RF window was first tested at JLab using 12.1 kW amplifier at 1.5 GHz. An IR camera was used to monitor the temperature on the ceramic, and 8 thermal sensors were attached outside the RF window to monitor the temperature on the stainless-steel frame. The highest temperature on the ceramic was 161.6 °C, and on the stainless-steel was 109.6 °C. The RF window was installed on a JLab530 to WR430 transition piece with two knobs so that it can be tuned to match the new working frequency at 2.112 GHz. The S-parameter results with optimized knob locations are shown in Figure 1.

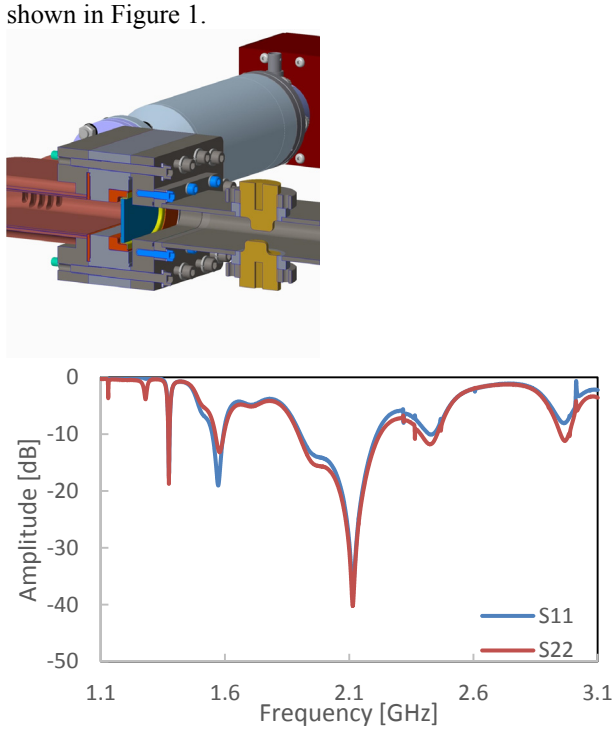


Figure 1: (top) RF window with two tuning knobs (yellow) to tune the frequency from 1.5 GHz to 2.1 GHz; (bottom) S-parameter of the JLab530 RF window with tuning knobs.

* Work is supported by Brookhaven Science Associates, LLC under contract No. DE-AC02-98CH10886 with the US DOE.
†binping@bnl.gov

Content from this work may be used under the terms of the CC BY 3.0 licence (© 2018). Any distribution of this work must maintain attribution to the author(s), title of the work, publisher, and DOI.

ISBN: 978-3-95450-194-6 ISSN: 2226-0366 doi:10.18429/JACoW-LINAC2018-MOPO005

During the conditioning of the 2.1 GHz cavity, the valve between 704 MHz superconducting radiofrequency (SRF) booster cavity and the 2.1 GHz cavity was closed to prevent possible contamination to the SRF booster cavity by vacuum spikes produced by the conditioning of the 2.1 GHz cavity.

The cavity resonant frequency was scanned by changing the tuner position, with nominal frequency at 2.112 GHz, the tuner shifts the frequency in a -0.7 MHz to +1.3 MHz range. Due to the design issue of the 2.1 GHz amplifier, only half of the power was used. With 6 kW out of the amplifier modules, 5 kW power was introduced into the cavity. The 2.1 GHz cavity was conditioned to 180 kV, with RF window stainless-steel frame temperature at 52.1 °C, the connection between beam port and cavity body at 36.8 °C, and tuner port blending area at 33.5 °C.

During the conditioning of the 2.1 GHz cavity, there were some vacuum activities that cannot be conditioned away. Further conditioning was done by ramping the amplifier's output power up and down, thus cavity voltage can be scanned. During this procedure, Inphase-Quadrature (IQ) loop was used to automatically adjust the tuner location to keep the cavity frequency constantly at 2.112 GHz. The condition showed that the cavity voltage cannot be maintained while ramping down the amplifier's output power, and vacuum activities appeared with this effect, as shown in Figure 2 top and middle. The vacuum activity appeared at around 150 to 160 kV, however it was not associated with this certain field level since during the power ramping up it did not appear. The only difference between power ramping up and power ramping down is that the tuner movement was in opposite direction in these two cases. An independent measurement was done by using Phase Lock Loop (PLL) without IQ, and then scan the tuner position up and down while monitoring the cavity resonant frequency at low field level (around 0.5 kV). Result is shown in Figure 2 (bottom). In this plot we found there is a backlash, which get corrected after tightening the motor belt. While moving the tuner out of the cavity, cavity resonant frequency decreased monotonically, and while moving the tuner into the cavity, a few "dead bands" appeared. Further investigation on the tuner actuator showed that there was a mechanical "dead band" while moving the tuner into the cavity, due to the distortion of the guiding rods and threads. To repair it, it was suggested by the vendor that the cavity should not be kept under vacuum (back fill with clean nitrogen), thus decision was made that the actuator will be fixed after this LEReC run. And a temporary fix was made by applying a "dead band" on the PLL phase error so that even the cavity resonant frequency gets detuned by a certain amount, the tuner is not going to move. Instead, amplifier is forced to provide more power to maintain the cavity accelerating voltage.

For the 704 MHz warm cavity, at 703.75MHz, cavity unloaded Q was at 3.38e4, FPC Q_{ext} was at 1.43e4, pickup coupler 1 Q_{ext} was at 1.12e8 and pickup coupler 2 Q_{ext} was at 9.08e7. Cavity R/Q was calculated to be 126.7 Ω in circuit definition.

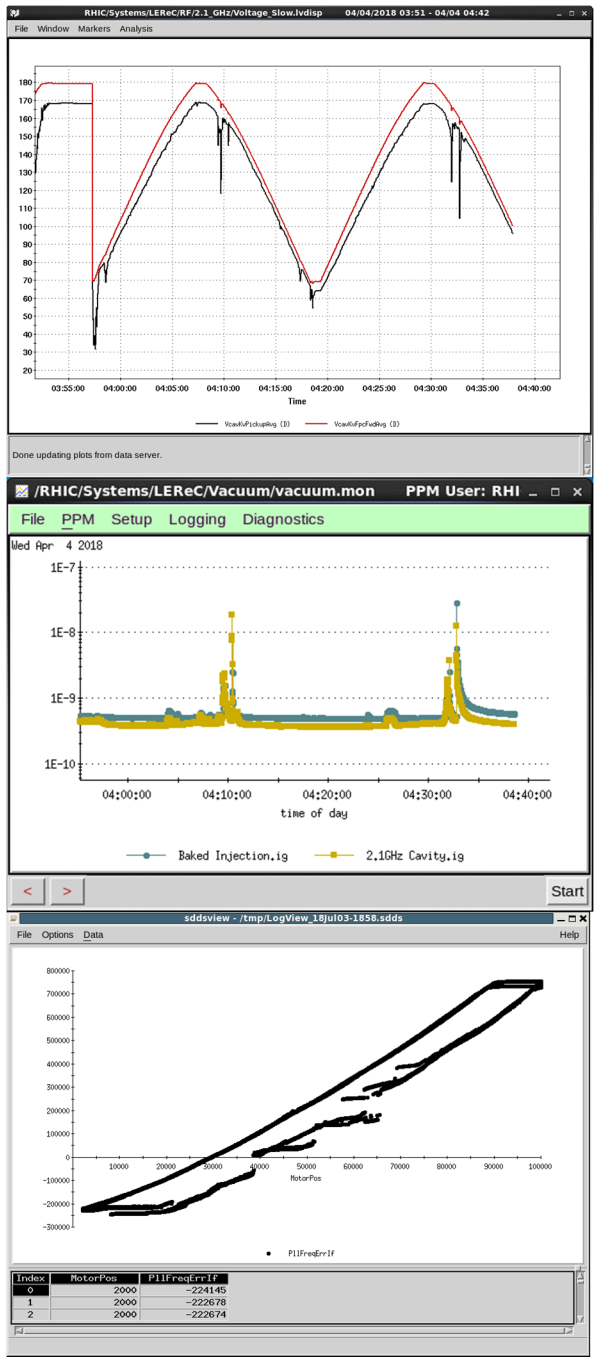


Figure 2: 2.1 GHz cavity conditioning, from top to bottom: (a) ramping amplifier output power up and down; (b) vacuum change during this procedure; (c) tuner position versus cavity resonant frequency.

The 704 MHz warm cavity was conditioned to 262 kV using 9.1 kW power with 1.35 kW reflected, with FPC port blending area at 41.2 °C, tuner port blending area at 35.3 °C, the connection between beam port and cavity body at 31.5 °C, cavity body temperature at 30.3 °C, and RF window at 30.6 °C. The FPC port blending area shows the highest temperature since it is the highest magnetic field region. The 704 MHz warm cavity uses an actuator similar to the one for 2.1 GHz cavity, measurement similar to Figure 2(c) was done for this cavity, and no backlash or

Content from this work may be used under the terms of the CC BY 3.0 licence (© 2018). Any distribution of this work must maintain attribution to the author(s), title of the work, publisher, and DOI.

ISBN: 978-3-95450-194-6 ISSN: 2226-0366 doi:10.18429/JACoW-LINAC2018-MOPO005

Content from this work may be used under the terms of the CC BY 3.0 licence (© 2018). Any distribution of this work must maintain attribution to the author(s), title of the work, publisher, and DOI.

"dead band" was found. Visual inspection was also done to the actuator while the tuner was moving, this system worked fine without any issue.

For the 704 MHz deflecting cavity, unloaded Q was at 1.24e4, FPC Q_{ext} was at 1.22e4, critically coupled to the cavity. There is only one pickup coupler on the cavity, with Q_{ext} at 1.86e5. Cavity R/Q was calculated to be 750 Ω in circuit definition.

The 704 MHz deflecting cavity was first measured on an optical table using wire-stretching technique to find the electric center, and to measure the deflecting field uniformity with possible beam trajectories that are parallel to the electric center [7, 8]. The cavity was then installed in the RHIC tunnel and was conditioned to 90 kV using 490 W power.

CONCLUSIONS

In this paper, the commissioning of three normal conducting RF cavities were presented: the 2.1 GHz cavity, the 704 MHz normal conducting cavity and the 704 MHz deflecting cavity.

For the 2.1 GHz cavity, the RF window was first high power tested at JLab using a 12.1 kW 1.5 GHz klystron amplifier, and then it was installed on a JLab530 to WR430 transition piece and was tuned to work at 2.1 GHz. The cavity was conditioned to 180 kV using 6 kW out of the amplifier modules, with highest measured temperature on the RF window stainless-steel frame at 52.1 °C.

For the 704 MHz cavity, it was conditioned to 262 kV using 9.1 kW power with 1.35 kW reflected, with highest measured temperature on the FPC port blending area at 41.2 °C.

The 704 MHz deflecting cavity was first measured using wire-stretching technique, and it was then conditioned to 90 kV using 490 W power.

ACKNOWLEDGEMENT

The authors would like to thank M. Brennan, J.C. Brutus, J. Butler, N. Laloudakis, G. Narayan, S. Polizzo, and Wencan Xu for the help during the installation and operation of these cavities.

REFERENCES

[1] A. Fedotov, M. Blaskiewicz, W. Fischer, *et al.*, "Accelerator physics design requirements and challenges of RF based electron cooler LEReC", in *Proc. NAPAC'16,* Chicago, IL, USA, 2016. doi:10.18429/JACoW-NAPAC2016-WEA4CO05

[2] B. Xiao, M. Blaskiewicz, J. M. Brennan, *et al.*, "Higher Order Mode Damper for Low Energy RHIC Electron Cooler Superconducting Radiofrequency Booster Cavity", To be published.

[3] B. P. Xiao, S. Belomestnykh, I. Ben-Zvi, *et al.*, "HOM consideration of 704 MHz and 2.1 GHz Cavities for LEReC Linac", in *Proc. IPAC'16,* Busan, Korea, 2016. doi:10.18429/JACoW-IPAC2016-MOPMY009

[4] B. P. Xiao, S. Belomestnykh, I. Ben-Zvi, *et al.*, "Design of Normal Conducting 704 MHz and 2.1 GHz Cavities for LEReC Linac", in *Proc. IPAC'15,* Richmond, VA 23219 USA, 2015. doi:10.18429/JACoW-IPAC2015-WEPWI061

[5] J. C. Brutus, S. Belomestnykh, I. Ben-Zvi, *et al.*, "Mechanical Design and 3-D Coupled RF, Thermal-Structural Analysis of Normal Conducting 704 MHz and 2.1 GHz Cavities for LEReC Linac", in *Proc. IPAC'16,* Busan, Korea, 2016. doi:10.18429/JACoW-IPAC2016-MOPMY007

[6] J. Kewisch, A. Fedotov, D. Kayran, *et al.*, "Beam Optics for the RHIC Low Energy Electron Cooler (LEReC)", in *Proc. NAPAC'16,* Chicago, IL, USA, 2016. doi:10.18429/JACoW-NAPAC2016-WEPOB56

[7] H. Wang, "Wire stretching technique for measuring RF crabbing/deflecting cavity electrical center and a demonstration experiment on its accuracy", in *Proc. NAPAC'16,* Chicago, IL, USA, 2016. doi:10.18429/JACoW-NAPAC2016-MOPOB69.pdf

[8] T. Xin, B. Xiao, J. M. Brennan, *et al.*, "Measuring the electrical center and field flatness of 704 MHz deflecting cavity for LEReC with wire stretching system", in *Proc. IPAC'18,* Vancouver, BC, Canada, 2018. doi:10.18429/JACoW-IPAC2018-tupmf034.pdf

ISBN: 978-3-95450-194-6 ISSN: 2226-0366 doi:10.18429/JACoW-LINAC2018-MOPO006

CROSSTALK EFFECT IN THE LEREC BOOSTER CAVITY*

Binping Xiao†, K. Mernick, F. Severino, K. Smith, Tianmu Xin, Wencan Xu, A. Zaltsman
Brookhaven National Laboratory, Upton, New York 11973-5000, USA

Abstract

The Linac of the Low Energy RHIC electron Cooler (LEReC) is designed to deliver a 1.6 MeV to 2.6 MeV electron beam, with peak-to-peak *dp/p* less than ±7e-4. The booster cavity is the major accelerating component in LEReC, which is a 0.4 cell cavity operating at 2 K, with a maximum energy gain of 2.2 MeV. It is modified from the Energy Recovery Linac (ERL) photocathode gun, with fundamental power couplers (FPCs), pickup (PU) couplers and HOM coupler located close to each other. Crosstalk effects in this cavity are simulated and measured. A correction method is proposed to meet the energy spread requirement.

INTRODUCTION

The LEReC design is a non-magnetized cooling scheme that uses electron bunches at kinetic energies between 1.6 MeV and 2.6 MeV that match the ion beam velocity, with peak-to-peak *dp/p* less than ±7e-4, to cool RHIC ion bunches [1]. The electron linac of LEReC consists of a DC photoemission gun, a 704 MHz SRF booster cavity, and three normal conducting cavities [2, 3]. The 704 MHz SRF booster cavity accelerates 400 keV bunches from the DC gun, near crest with an accelerating voltage up to 2.2 MV. It is modified from the ERL photocathode gun [4]. It has two FPCs, two PUs, and one HOM coupler, with a PU (HOMPU) on the HOM coupler. All couplers are on the same side of the cavity, shown in Figure 1. Please note the second PU is located opposite to the one shown in the figure.

Typically, the FPC and the PU are positioned on different sides of the cavity, and thus isolated by the cavity with no direct coupling (normally capacitive) between them. In an SRF gun, however, one side of the cavity is reserved for photocathode with its stalk, thus the FPC and PU are installed on the same side of the cavity that is opposite to the photocathode. The only exception so far is the 112 MHz SRF gun for the Coherent electron Cooler (CeC) experiment at BNL, in which the PU is on the same side of the photocathode, and the FPC is on the other side of the cavity. In that design the coupling strength (Q_{ext}) of the PU in the 112 MHz gun varies with the insertion depth of the photocathode, thus calibration is required every time after cathode installation.

With FPC and PU on the same side of the cavity, the direct coupling between FPC and PU causes distortion of the RF response, the so-called crosstalk effect. This effect was first studied by Zhao at BNL using an equivalent circuit model of the cavity with couplers, by applying an additional capacitor between FPC and PU [5]. Later He at PKU proposed a simple method to extract the resonance frequency and loaded quality factor Q from the RF response with crosstalk [6]. As pointed out by both Zhao and He, the crosstalk effect severely distorts the RF response (S-parameter) between FPC and PU when the cavity is at room temperature, and makes it difficult to measure the resonance frequency and Q. While in the superconducting state, the distortion of the RF response is insignificant.

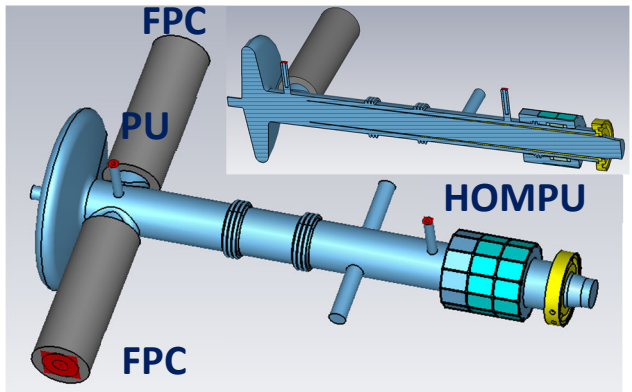


Figure 1. LEReC booster cavity with cross-section view (top-left).

In the LEReC booster cavity, however, the crosstalk effect is important, and its effect needs to be corrected. During operation, due to the limited life time of the main tuner, a "dead band" is applied to limit total tuner motion. Within this dead band, the cavity resonant frequency is allowed to vary, and LLRF feedback loops must stabilize the cavity voltage and phase (V_{pu}) using available RF power. It is found that there is a ±1000 Hz slow frequency drift, and a ±100 Hz frequency shift due to microphonics, with its source yet to be identified during operation. These frequency shifts cause a deviation between amplifier's output frequency and cavity's resonance frequency. Since the S-parameter is slightly distorted by the crosstalk effect in superconducting state, it is no longer in Lorentz form. With V_{pu} fixed, the cavity accelerating voltage V_{acc} deviates from the reference accelerating voltage without crosstalk effect, $V_{acc\text{-}ref}$. With the tight *dp/p* requirement, at 1.6 MeV, the voltage fluctuation should be within ±1.12 kV for the whole LEReC system, the fluctuation from V_{acc} should be a small portion of this number. Even though the crosstalk effect insignificantly distorts resonance frequency and Q, the voltage fluctuation caused by it might not be tolerable. In this paper the crosstalk effect in the LEReC booster cavity is analyzed. A method of correction is proposed so that the design specification can be met.

* Work is supported by Brookhaven Science Associates, LLC under contract No. DE-AC02-98CH10886 with the US DOE.
† binping@bnl.gov

Content from this work may be used under the terms of the CC BY 3.0 licence (© 2018). Any distribution of this work must maintain attribution to the author(s), title of the work, publisher, and DOI.

ISBN: 978-3-95450-194-6 ISSN: 2226-0366 doi:10.18429/JACoW-LINAC2018-MOPO006

Content from this work may be used under the terms of the CC BY 3.0 licence (© 2018). Any distribution of this work must maintain attribution to the author(s), title of the work, publisher, and DOI.

CROSSTALK EFFECT IN BOOSTER CAVITY

The crosstalk effect gives a distortion in S_{21}, with a valley adjacent to the resonance peak (In some special cases the valley might not appear though). In a polar plot, it is a translation of the Lorentz curve. It can be expressed as a standing wave in the cavity (Lorentz curve) with an additional travelling wave between FPC and PU (translation), as shown in [6]:

$$Signal_{whole} = \frac{K}{\left(f_0^2 - f^2\right) + i\frac{f_0 f}{Q_L}} + Md \times e^{iPd}$$

In the RF simulation, two FPC ports are connected to form a new 25 Ω FPC port (port 1), one of the PU is used (port 3), and the HOMPU is assigned as port 4. Field monitors are assigned to the on-resonance frequency and ±1 kHz, ±2 kHz, ±3 kHz off-resonance frequencies. Please note in the simulation the power source's frequency is changing, and cavity's resonant frequency is fixed, while during operation, amplifier's frequency is fixed, and cavity's resonant frequency is vibrating. For comparison, similar simulation is done with port 3 (PU) move to the other side of the cavity, in which the crosstalk is insignificant. The S_{31} in dB (amplitude), and in polar plot are shown in Figure 2. The S_{41} results are similar to those for S_{31}, with differences in the amplitude (Md) and phase (Pd) of the crosstalk effect.

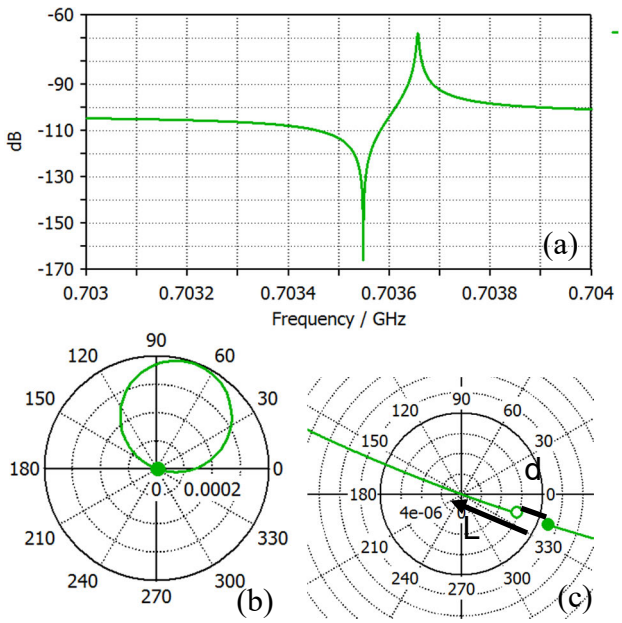


Figure 2. S_{31} in (a) dB (amplitude), and in (b) polar plot with (c) a zoom in near the original point.

In the field monitor which is normalized to 0.5 W input power, one can extract the power coming out of each port, as well as V_{acc}. The results are then normalized to the same PU power. Using the on-resonance results as references, with fixed PU power, the V_{acc} changes linearly with frequency deviation, with -0.94%/kHz, the HOMPU power also changes linearly with frequency deviation, with 5.56%/kHz. For comparison, the V_{acc} change with frequency deviation for the case without crosstalk is -1.5e-4/kHz, by using a reference PU on the other side of the cavity to suppress the crosstalk effect. This result implies that the simulation accuracy is better, or at least not worse, than this number.

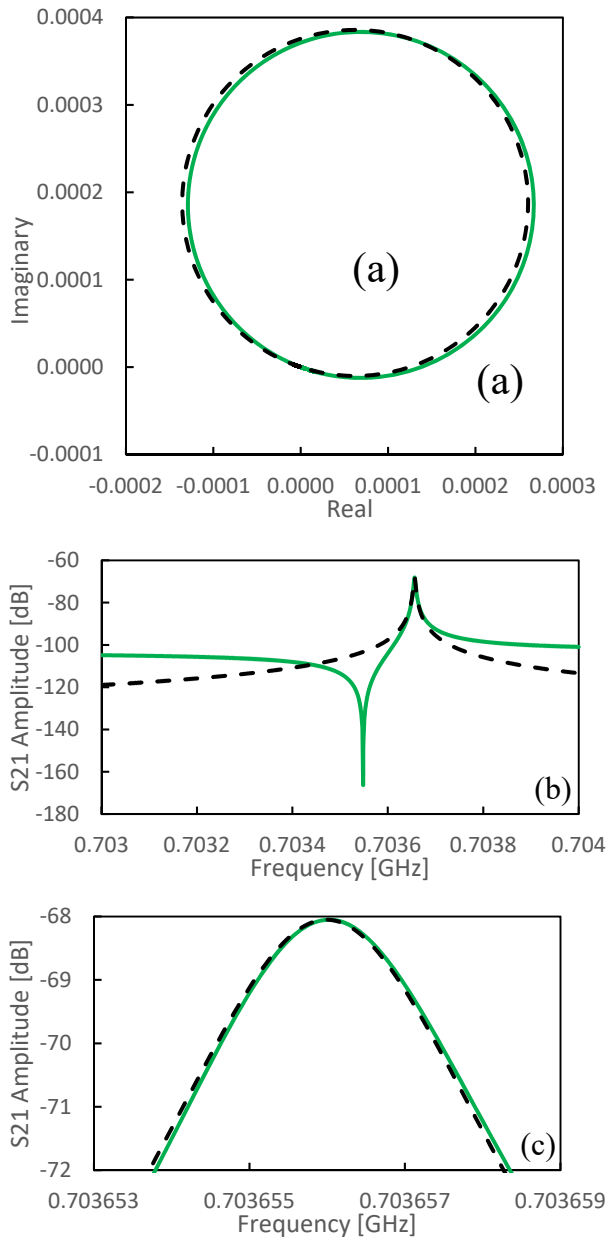


Figure 3. Correction of S-parameter to separate the crosstalk effect from Lorentz curve, with green curves with crosstalk, and black dash curves without. (a) polar plot, (b) in dB amplitude, (c) zoom in of (b) near the resonance.

The above results can also be understood from the S-parameter. To separate the crosstalk effect from the Lorentz curve, one needs to translate the S-parameter in the polar plot so that the point between highest frequency and lowest frequency (with the same distance from the resonant frequency, the middle point of d shown in Figure 2(c)) to the original point, shown as the arrow line (vector L) in

ISBN: 978-3-95450-194-6 ISSN: 2226-0366 doi:10.18429/JACoW-LINAC2018-MOPO006

Figure 2(c). The results are shown in Figure 3. Based on Figure 3 (c), with 1 kHz deviation, there is a 0.08 dB difference between the curve with crosstalk and the one without, corresponding to 0.93% difference in voltage. With 2 kHz deviation, it is 0.17 dB, 2.03% in voltage, and with 3 kHz, it is 0.26 dB, 3.08% in voltage. It is roughly -0.99%/kHz, close to the result based on field monitor analysis.

Based on the above simulations, with a ±1000 Hz slow frequency shift, the V_{acc} deviates ±0.99%, and even though this slow frequency shift can be suppressed, a ±100 Hz frequency shift due to microphonics, the V_{acc} still deviates ±0.1%, beyond the design specification.

An additional simulation was done by cutting the PU probe by 5mm, with 3kHz away from resonance, there is still a ~0.26 dB deviation between the curves with and without crosstalk, corresponding to 3% in voltage, thus changing the PU probe length is not helping. The reason is that cutting the PU probe shorter not only changes *Md*, but it also changes *K*, it changes the Lorentz term and the crosstalk term simultaneously, and in a proportional way.

There is another effect that needs to be investigated. During operation, the two FPCs are driven by two LLRF systems and two amplifiers. Efforts are made to keep the amplitude and phase of the signals from two amplifiers the same by controlling the LLRF, however they are still slightly different, estimated to be within 5% in the amplitude, and within 10 degrees in the phase. It is not easy to model this effect in CST. In this case the S-parameter of the booster cavity with 2 FPCs, 1 PU and 1 reference PU on the other side of the cavity, similar to the above simulation without crosstalk, are modeled. With this set of S-parameter, signals with different amplitude and phase can be assigned to 2 FPCs. Please note using the loss in the cavity to get V_{acc} is difficult since most of the power is reflected back, and only a tiny fraction of power is dissipated on Nb cavity wall, so the power coming out of the reference PU port (without crosstalk) is used to monitor the V_{acc}. This method was proved to be accurate previously. This method is further crosschecked with the on-resonance and ± 1, 2, 3 kHz off-resonance cases with crosstalk effect that analysed above by assigning identical amplitude and phase to 2 FPCs. Results from this analysis showed that for the signals on 2 FPCs, with difference within 5% in the amplitude, and within 10 degrees in the phase, and with frequencies ranges within ±3 kHz of the resonant frequency, the V_{acc} deviation from the case with crosstalk and with the same frequency deviation is better than 10^{-4}, thus the crosstalk effect is not sensitive to the slight input difference between 2 FPCs.

CORRECTION OF CROSSTALK EFFECT

During the correction of S-parameter shown in Figure 3, a method was proposed to correct the fluctuation in V_{acc} induced by the crosstalk effect. First the S-parameter should be measured to get the resonant frequency f_0. Then the complex S-parameter at two frequency points $f_0 \pm \Delta f$, or frequency bands near these two points, should be measured, with the selection of Δf big enough so that the amplitude of L is much larger than the amplitude of d, shown in Figure 2 (c). During this measurement fine IF bandwidth should be used to resolve the small signals. Vector L can be calculated using the above measurement results. The S-parameter can then be corrected by applying vector L into LLRF system to get the Lorentz curve without crosstalk.

CONCLUSIONS

During operation, a dead band is assigned to the main tuner, and LLRF system is adjusting the amplitude and phase of two amplifiers to get a fixed voltage on the PU. Due to the resonant frequency drifting in the LEReC booster cavity during operation, the crosstalk effect caused by direct coupling between FPC and PU brought fluctuation in V_{acc}. This fluctuation is analyzed to be larger than the longitudinal momentum spread specification, and thus needs to be corrected. The effect of slight imbalance between two FPC input signals is also studied, conclusion is made that crosstalk effect is not sensitive to this imbalance. A method to correct the crosstalk effect is proposed.

ACKNOWLEDGEMENT

The authors would like to thank M. Blaskiewicz, Tom Hayes, G. Narayan, S. Seletskiy and V. Schoefer for the useful discussion, and for the help on measuring this effect.

REFERENCES

[1] A. Fedotov, M. Blaskiewicz, W. Fischer, *et al.*, "Accelerator physics design requirements and challenges of RF based electron cooler LEReC", in *Proc. of the North American Particle Accelerator Conf. 2016,* Chicago, IL, USA, 2016. doi:10.18429/JACoW-NAPAC2016-WEA4CO05

[2] B. P. Xiao, S. Belomestnykh, I. Ben-Zvi, *et al.*, "RF Design of Normal Conducting 704 MHz and 2.1 GHz Cavities for LEReC Linac", in *Proc. of the 7th Int. Particle Accelerator Conf. (IPAC'16),* Busan, Korea, 2016. doi:10.18429/JACoW-IPAC2016-MOPMY010

[3] B. P. Xiao, S. Belomestnykh, I. Ben-Zvi, *et al.*, "HOM consideration of 704 MHz and 2.1 GHz Cavities for LEReC Linac", in *Proc. of the 7th Int. Particle Accelerator Conf. (IPAC'16),* Busan, Korea, 2016. doi:10.18429/JACoW-IPAC2016-MOPMY009

[4] W. Xu, Z. Altinbas, S. Belomestnykh, *et al.*, "Multipacting-free Quarter-wavelength Choke Joint Design for BNL SRF", in *Proc. of the 6th Int. Particle Accelerator Conf. (IPAC'15)*, Richmond, VA, USA, 2015. doi:10.18429/JACoW-IPAC2015-TUPMA047

[5] Y. Zhao, "Analysis and Measurement of Cross-talk in a Superconducting Cavity", BNL, NY, USA, 2002. https://www.bnl.gov/isd/documents/79902.pdf

[6] F. He, B. Zhang, W. Xu, *et al.*, "Analytical and Experimental Study of Crosstalk in the Superconducting Cavity", in *Proc. of Particle Accelerator Conf. 2009 (PAC'09)*, Vancouver, Canada, 2009, pp. 2098 http://jacow.org/PAC2009/papers/we5pfp045.pdf

Content from this work may be used under the terms of the CC BY 3.0 licence (© 2018). Any distribution of this work must maintain attribution to the author(s), title of the work, publisher, and DOI.

ISBN: 978-3-95450-194-6 ISSN: 2226-0366 doi:10.18429/JACoW-LINAC2018-MOPO007

THE DEVELOPING OF THE BEAM INJECTION SECTION WITH LASER SOURCE AND S-BAND ELECTRON RF GUN FOR SUPERKEKB PROJECT

Xiangyu Zhou†, Mitsuhiro Yoshida, Rui Zhang, Yujiro Ogawa, High Energy Accelerator Research Organization (KEK/SOKENDAI), 305-0801, Tsukuba, Ibaraki, Japan

Abstract

For the beam injection at Linac accelerator of the SuperKEKB project, the s-band RF gun needs to provide low-emittance high-charge electron bunches. A photocathode RF gun system with an advanced RF cavity structure (quasi-travelling side-coupled structure, cut disk structure), a new photocathode material (Ir_5Ce cathode) and a hybrid laser system (Yb fiber and Nd:YAG hybrid system) have been developing in the SuperKEKB injector Linac. Furthermore, many monitors and remote controls program were built to increase the stability of operation. By the injection system, the required charge and emittance for Phase-II commissioning were achieved.

INTRODUCTION

KEK injector Linac has delivered electrons and positrons source for high energy accelerator research, particle physics and photon science experiments for more than 30 years. Then, KEKB is being upgraded towards the SuperKEKB which is an asymmetric energy of 7-GeV electron and 4-GeV positron double-ring collider [1]. Full-energy, high-charge and low-emittance beams are necessary in order to achieve a design luminosity of 8×10^{35} $cm^{-2}s^{-1}$ for the study of the flavour physics of elementary particles. The injector continues to deliver various beams to SuperKEKB and light source rings such as PF and PF-AR.

In the positron beam, new Flux Concentrator (FC) and capture section was developed for efficient positron generation. Since generated positron beam has large emittance, new damping ring (DR) has been constructed to reduce beam emittance. Therefore, the thermionic electron gun was reinstalled for positron beam generation with the charge of 10 nC [2].

For the injector upgrade, the electron beams with a charge of several nC and a normalized emittance of less than 10 μm are expected to be generated in the electron gun. A thermal cathode DC gun had been used for KEKB. Because the DC gun could not make low-emittance beam, a quasi-traveling wave side couple (QTWSC) RF gun which has two side coupled standing wave field was developed [3]. This gun has a strong focusing field at the cathode and the acceleration field distribution also has a focusing effect. In addition another cut disk structure (CDS) RF gun was installed to 90 degree injection line. These guns have been used for electron beam study.

A multi-crystalline iridium cerium (Ir_5Ce) compound is used as a photoemitter of a high charge and low emittance RF gun [4]. The quantum efficiency (QE) is approximately 9.1×10^{-4} with 219 nm laser source at room temperature, which has the long lifetime (>LaB_6).

For the laser source, an Ytterbium-doped (Yb-doped) fiber and Ytterbium-doped YAG (Yb:YAG) hybrid laser system was development. 30 ps, mJ-class, 257 nm ultraviolet (UV) pulse was provided and injected to the photocathode [5].

The Phase I beam commissioning successfully ended in the June of 2016. The electron beam and positron beam with the bunch charge of around 0.7 nC is successfully delivered to the end of beam transport line.

Table 1: Requirements for Linac in SuperKEKB Phase II

	Electron HER 7 GeV	Positron LER 4 GeV
Normalized emittance $\gamma\beta\varepsilon_x$ / $\gamma\beta\varepsilon_y$	150 / 150 [μm]	200 / 40 [μm] with damping ring
Energy spread σ_δ	0.10 [%]	0.16 [%]
Bunch charge at injection point	1.0 [nC]	0.5 [nC]

Towards Phase-II beam commissioning, the high-charge and low-emittance beam development is going on for the higher requirement (Table. 1). The mainly improvement is the laser source. An Ytterbium/Neodymium (Yb/Nd) hybrid laser system was developed. With the synthetic crystalline material Neodymium-doped YAG (Nd:YAG), high reliability of the laser source is realized. The layout of the electron guns and laser system is shown in Fig.1. The transport line between the laser and RF gun was restored with the backup line and remote control system.

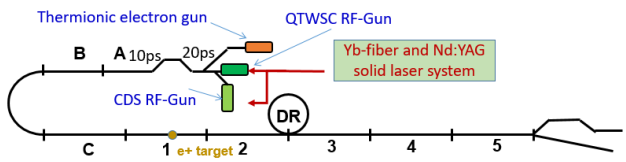


Figure 1: Layout of Linac.

Yb/Nd DOPED HIBRID LASER SYSTEM OF RF GUN

Based phase-I commissioning, the laser system for RF gun consisted Yb-doped fiber oscillator, Yb-doped fiber amplifiers and Yb:YAG thin-disk laser amplifiers. Yb:YAG crystal has large absorption bandwidth to reduce thermal management requirements for diode lasers, a

† email address : xiangyu.zhou@kek.jp

Content from this work may be used under the terms of the CC BY 3.0 licence (© 2018). Any distribution of this work must maintain attribution to the author(s), title of the work, publisher, and DOI.

ISBN: 978-3-95450-194-6 ISSN: 2226-0366 doi:10.18429/JACoW-LINAC2018-MOPO007

longer upper-state lifetime, three to four times lower thermal loading per unit pump power, which is more suitable for diode-pumping for high power diode-pumped lasers. Yb:YAG Thin-disk regenerative amplifier system was employed in phase-I commissioning. Compared with the Yb:YAG crystal, commonly used Nd:YAG rods with high optical homogeneity, high damage threshold, consistent performance and high processing accuracy. Although the pulse shaping of Nd:YAG is difficult to be adjusted because of the narrow spectrum gain, the structure of the Nd:YAG is simple, that means reliable convenience and less maintenance. The Emission wavelength of Yb:YAG and Nd:YAG are around 1030 nm and 1064 nm with the bandwidth of ~3.0 ns and ~0.5 ns, which contained in the spectrum of Yb-doped fiber oscillator. Therefore, the Yb-doped oscillator and Yb-doped fiber amplifier also can be used with Nd:YAG amplification. For higher reliability requirement of the Phase-II commissioning, Nd:YAG are appropriate candidate for laser amplifier system [6].

Therefore, the laser system upgraded, consists Yb-doped fiber oscillator, Yb-doped fiber amplifiers and Nd:YAG rod laser amplifiers. The detail of laser part that shows in Fig. 2.

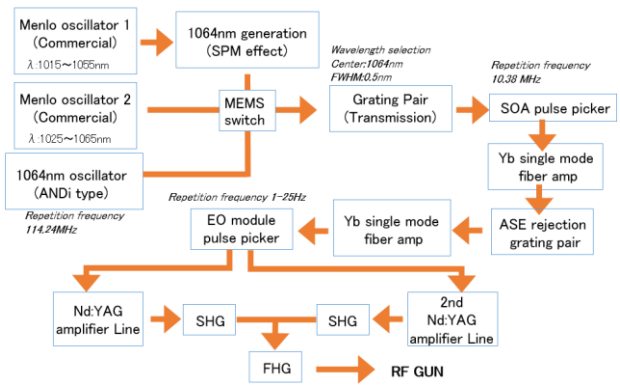


Figure 2: Layout of laser system.

Yb-doped Fiber Part

The laser system starts with three 114 MHz mode lock Yb-doped fiber oscillators. Two of them are commercial products (Menlo system), the other one is homemade cavity with the all normal dispersion (ANDi) structure. One MEMS optics switch is adopted to select oscillator for the following amplifier stages. A transmission grating pair stretcher was employed to expend pulse to ~10 ps and select the spectrum width of 0.5 nm with the centre wavelength of 1064 nm. The weak pulses reduced repetition rate to 10.38 MHz by a semiconductor optical amplifier (SOA) pulse picker, which was driven by a ~5 ns 100 mV electrical pulse at 10.38 MHz amplified through a high power RF amplifier. To compensate the energy loss of the gratings and SOA, two stages Yb-doped single mode fiber amplifier was employed. Because the amplified spontaneous emission (ASE) easy to be amplified with the weak seed pulse by strong pump power, an additional transmission grating was used to separate and cut the noise by a slit. After fiber amplifier, an Electro-optic module (E.O.) adopted as a pulse picker is used to pick out the 1-25 Hz signal from a sequence of pulses of 10.38 MHz [7].

Nd:YAG Amplifier Part

In order to guarantee the injection and commissioning reliably, two beam lines were prepared. At the end of the fiber part, the signal was separate to two equal parts (first beam line and second beam line) by a polarizer.

The first line which has 4 stages Nd:YAG rod amplifiers is proposed to provide the stable laser pulses with high quality. 2×79 mm Nd:YAG rod crystal are used in the first and second stages for high amplification efficiency. A Pockels cell pulse picker is insert to switch the single/double bunch mode. After the Pockels cell, the third and fourth stages amplify the pulse energy up to the 4.0 mJ by using of 4×93 mm Nd:YAG rod crystal. Then the green pulses of 532 nm were generated by using a frequency-doubling stage with 5 mm thickness beta barium borate (BBO) crystal. As the Fig. 3, more than 1.8 mJ second harmonic generation (SHG) pulses was obtained with the good beam profile and 17 ps pulse width that measured by the streak camera.

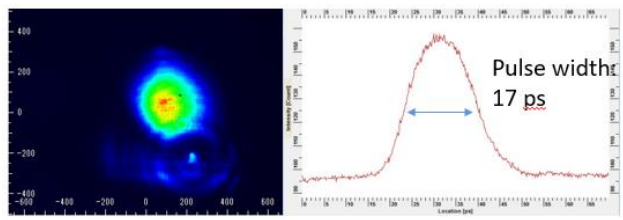


Figure 3: Beam profile and beam width of laser source.

Different from the first line, an additional fifth Nd:YAG amplifier stage (Φ8 mm) is built in the second line to pursue higher pulse energy. The amplified pulse energy is up to 8.0 mJ. And more than 3.8 mJ pulse energy of SHG beam is obtained during the frequency-doubling stage.

TRANSPORTING LINE

There is about 12 m distance from the laser clean room to the underground RF gun. The transport line is focus to reduce the energy loss and jitter in the air. Therefore, vacuum tube was built to isolate the air turbulence between the laser room and RF box. Two laser beams are converged by a polarizer and transported to RF gun box by one transporting line. Inside the RF gun box, the laser beams are separated again by another polarizer. The transport rate can be up to 80%. UV pulses were generated by BBO frequency-doubling stages. 450 μJ and 800 μJ are achieved by the first and second laser line to RF gun. The optics system is shown in Fig. 4. The total efficiency of the ω-4ω is more than 10%.

Content from this work may be used under the terms of the CC BY 3.0 licence (© 2018). Any distribution of this work must maintain attribution to the author(s), title of the work, publisher, and DOI.

ISBN: 978-3-95450-194-6 ISSN: 2226-0366 doi:10.18429/JACoW-LINAC2018-MOPO007

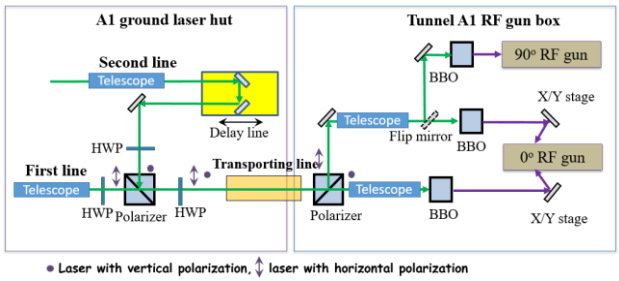


Figure 4: Transporting line.

The QTWSC RF gun could be irradiated by each laser sources with 60 degree, and another laser source works with the backup line. Furthermore, it is optional to select two laser injection with both sides. A delay line is inserted into the second laser line to adjust the optical path for realizing two laser synchronous injection into RF gun.

Also, a flip mirror is placed in the first laser line for changing the transmission direction to the 90 degree CDS RF gun.

MONITORING AND REMOTE CONTROL SYSTEM

Since the electron beam with high stability and quality are required in Phase-II commissioning, the status of laser system and RF cavity are monitored and recoded.

In oscillator, the stepping motor and piezo that adjust the frequency in the cavity is controlled to synchronize RF frequency signal. Status monitors and I/Q monitor are employed for detect the mode-lock and synchronization. When the RF frequency is drift, the laser frequency can be auto-adjusted immediately.

The temperature of the laser room and RF gun cavity and all the current of the power supply are monitored and recorded. Furthermore, the pulse output power of the every stages and the pulse shaping of the every pulse pickers are also monitored by photo diode detectors. The long term reliability of laser are recorded, and any unusual changes will be alarmed by monitoring system.

The optics system inside RF gun box is set near the electron gun. A beam profile monitor and laser energy meter are set in the first laser line to oversee the laser status. The real-time data can be confirmed on internet anytime. For optimize the laser source in the commissioning study, lots of adjustment unit were insert, such as telescope lenses distance, BBO crystal angle, X/Y stage and rotation stage. All of these units are adjusted by fully remote control. Thus, we can get the best condition to generate highest electron charge during beam study.



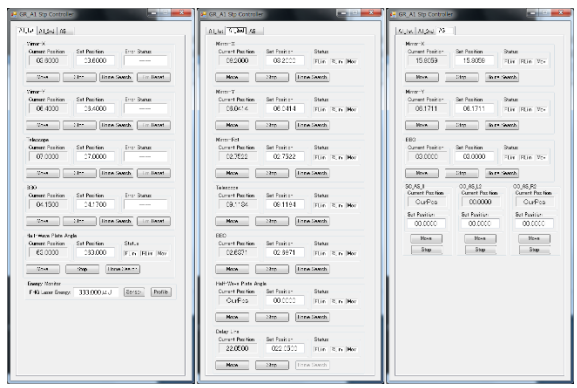


Figure 5: monitoring and remote control panel.

Figure 5 shows the monitoring and remote control system panel by windows-PC. Thanks to the monitoring and remote control system, the all beam injection section is continuously working during the Phase-II commissioning.

RF GUN STUDY FOR PHASE-II COMMISSIONING

SuperKEKB phase II commissioning has been performed since March to July 2018. The injection sector beam study has also performed. By use of first line laser source, 1.4 nC electron beam is generated, and the 1.1 nC electron charge is remained at end of the Linac. The beam orbit, energy were carried out without any significant issues. In contrast, 2.4 nC is obtained at end of the Linac by use of the second beam line. By the both side lasers irradiation, 3.3 nC electron beam is delivered successfully. Accordingly, about 2.3 nC electron charge is prepared for injection to High energy ring (HER) of the ring accelerator. The orbit and electron charge records are shown in Fig.6.

Content from this work may be used under the terms of the CC BY 3.0 licence (© 2018). Any distribution of this work must maintain attribution to the author(s), title of the work, publisher, and DOI.

ISBN: 978-3-95450-194-6 ISSN: 2226-0366 doi:10.18429/JACoW-LINAC2018-MOPO007



Figure 6: Orbit and electron charge by laser source.

The emittance of electron beam generated by RF gun is also measured by wire scan method. At Linac sector B, the end of the RF gun, the horizontal and vertical emittance $\gamma\varepsilon_x$=24.958, $\gamma\varepsilon_y$=18.640 was obtained respectively. Then the high bunch low emittance electron beams are transporting the Linac include the J-arc section. The horizontal and vertical emittance are less than 50 μm at the sector 5 (Fig. 7). Low emittance and high charge achieved, and its performance is enough for the Phase-II commissioning.

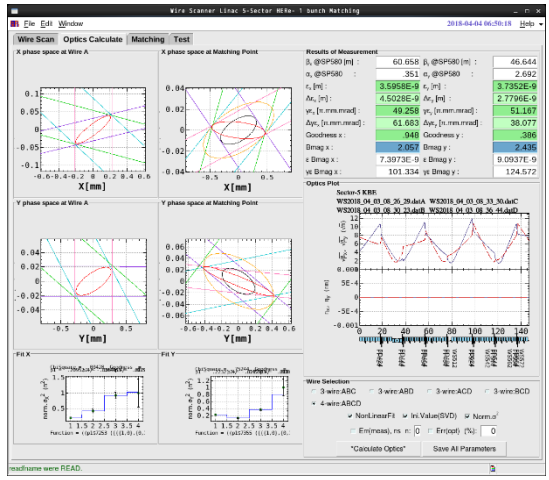


Figure 7: Wire scan measurement of 5 sector.

CONCLUSION

An Yb/Nd hybrid laser source is upgrade to deliver qualified electron beam by QTWSC RF gun and Ir5Ce cathode for SuperKEKB phase-II commissioning. Three laser oscillators and two beam lines were created. A lot of improvements of the monitoring and remote control system have been done to increase the reliability of the injection department. Electron charge of 2.4 nC and emittance of 50 μm fulfilled the phase-II requirements.

REFERENCES

[1] Y. Ohnishi et al., "Accelerator design at SuperKEKB", Prog. Theor. Exp. Phys., **2013**, 03A011.

[2] M. Satoh et al., "Commissioning Status of SuperKEKB Injector Linac", in *Proc. IPAC'18*, Vancouver, Canada, Apr.-May 2018, paper MOPMF075.

[3] T. Natsui et al., "Injector Linac Upgrade and New RF Gun Development for SuperKEKB", in *Proc.eeFACT'16*, Daresbury, UK, Oct.2016, paper TUT2H2, pp.74-78.

[4] D. Satoh et al., "Development of Better Quantum Efficiency and Long Lifetime IrCe Photocathode for High Charge electron RF Gun", in *Proc.* IPAC'13, Shanghai, China, May 2013, paper MOPFI023.

[5] X. Zhou et al., "25 Hz, Sub-mJ Ytterbium Laser Source of RF Gun for SuperKEKB Linac", in *Proc. IPAC'15*, Richmond, USA, May 2015, paper WEPMA044.

[6] X. Zhou et al., "Developing an Yb/Nd Doped Hybrid Solid Laser of RF Gun for SuperKEKB Phase II Commissioning", in *Proc. IPAC'17*, Copenhagen, Denmark, May 2017, paper THPVA047.

[7] X. Zhou et al., "Neodymium and Ytterbium Hybrid Solid Laser of RF Gun for SuperKEKB", in *Proc. IPAC'16*, Busan, Korea, May 2016, paper THPMY041.

Content from this work may be used under the terms of the CC BY 3.0 licence (© 2018). Any distribution of this work must maintain attribution to the author(s), title of the work, publisher, and DOI.

ISBN: 978-3-95450-194-6 ISSN: 2226-0366 doi:10.18429/JACoW-LINAC2018-MOPO008

THE RF GUN ADOPTING THE DIELECTRIC ASSIST ACCELERATING STRUCTURE

Shingo Mori*, Mitsuhiro Yoshida†, KEK, Tsukuba, Japan
Daisuke Satoh‡, National Institute of Advanced Industrial Science and Technology, Tsukuba, Japan

Abstract

We apply the dielectric assist accelerating (DAA) structure to the RF gun, which is a candidate for a high average current and high brightness electron source. The DAA structure consists of ultralow-loss dielectric cylinders and disks which are periodically arranged in a metallic enclosure. Due to the high quality factor and the high shunt impedance of the DAA cavity, the RF gun adopting the DAA cavity can be a high-duty electron beam source at room temperature. We provide design work for RF gun adopting the DAA structure.

INTRODUCTION

The RF photoinjectors have been widely used as a source of high-quality beam. The electron beam of low emittance and high beam current are now considered as the electron sources for the x-ray free electron laser (FEL) which requires lower emittance to obtain shorter wavelengths and high peak current to obtain good gain, and linear colliders to meet the requirement of a complex pulse structure and to provide small emittance flat beam [1].

The first use of the RF photoinjector was done by Fraser et al. [2] in 1985 at LANL for the application to the FEL. The idea to combine a photocathode and a laser system with an RF cavity that supports a standing-wave field has many advantages. First, the electron bunch length is determined by the laser pulse without the following buncher section and provides narrow energy spread. Second, the electron beam is immediately accelerated up to relativistic energy by high RF field on the cathode within the first cell, which can decrease the space-charge growth of the emittance when the electrons are non-relativistic. Third, the quite low emittance beams can be produced by decreasing the laser spot size at the photocathode [3] which can reach as small emittance as 0.1 mm · mrad with relatively small bunch charge $>$ 0.1 nC. The electron beam dynamics after generation from the cathode is well understood analytically [4, 5] and numerically. The emittance of the beam produced by the RF electron gun is determined by three contributions: the emittance as the bunch emerges from the cathode; the electromagnetic interaction among the non-relativistic electrons called as the space charge effect; nonlinear radial dependence of the transverse components of RF.

In most cases, the RF photoinjector operates at a low duty factor and have relatively low average current. The first photoinjector with a duty factor of 25% was designed by Boeing in 1992 [6]. Currently, a collaboration between LANL and AES is developing a normal conducting photoinjector, which works in the CW mode. In the CW mode operation of a normal conducting photoinjector, the large amount of RF power loss causes cooling problems and bounds the gradient, e.g. 7 MV/m in ref. [6], which becomes drawbacks in the emittance. While superconducting RF photoinjectors also provides CW mode operation with high average current, with low emittance $O(1)$ mm · mrad due to the moderate gradient 20-50 MV/m.

A dielectric assist accelerating (DAA) structure [7, 8] is promising in power efficiency and could be a new candidate of photoinjector with CW mode operation, because it provides high efficiency $Q \sim O(10^5)$ at room temperature. Due to the structures of the dielectrics and the use of the ultra-low-loss dielectric material [8], the five cell DAA cavity provides the Q-value, $Q = O(10^5)$, and the shunt impedance $Z_{sh} \simeq 650$ MΩ/m. We have constructed the test stand for the DAA test cavity whose design frequency is 5712 MHz. In the tentative high voltage test, we found the gradient can reach up to multi-MV/m. This test cavity is planned to examine the main cavity to accelerate a relativistic electron beam which is generated from the RF photoinjector. In order to examine the possibility of the high-duty operation of the DAA main cavity, it is reasonable to construct the RF photoinjector which applies the DAA structure as well.

In order to investigate the possibility of the DAA structure as an RF photoinjector, we carry out the numerical calculation of the electromagnetic field in the cavity and the coupler, and the dynamics of an electron bunch generated by the photocathode.

This paper is organized as follows. In Sec.2, the dielectric cell of the DAA structure is introduced and we discuss the boundary problem which appear when the beam hole opens. In Sec.3, we introduce the novel structure of the end cell to avoid the boundary problem. In Sec.4, we will show the numerical result of the RF photoinjector based on the DAA structure. In Sec.5, we will summarize our result.

THE DAA STRUCTURE AND THE BOUNDARY PROBLEM

In this section, we will review the concept of the DAA structure and its boundary effect.

The basic structure of the DAA cavity is periodic, which is composed of the cylindrical waveguide made of metal and a cell called regular cell. Figure 1 shows the distribution of the electric force line calculated using *SUPERFISH* in the pillbox cavity which contains a regular cell. We call the

* smori@post.kek.jp
† mitsuhiro.yoshida@kek.jp
‡ dai-satou@aist.go.jp

Content from this work may be used under the terms of the CC BY 3.0 licence (© 2018). Any distribution of this work must maintain attribution to the author(s), title of the work, publisher, and DOI.

ISBN: 978-3-95450-194-6 ISSN: 2226-0366 doi:10.18429/JACoW-LINAC2018-MOPO008

horizontal axis and vertical axis as z and r direction, which describe the beam axis and radial direction of the dielectric cell. The dielectric cell is the combination of the disk-like structure and the coaxial structure, which are shown as the rectangular region around $z \in (1, 1.5)$ cm and the horizontal region around $r \sim 2.5$ cm, respectively. *SUPERFISH* provides us the electromagnetic field distribution in the frequency domain in (z, r) coordinates assuming the rotational symmetry about the beam axis. The red lines denote the real part of the electric force line and the green lines shows the imaginary part of them, which describe the magnitude of the accelerating field $E_z(z, r)$ has maximum value at the beam axis.

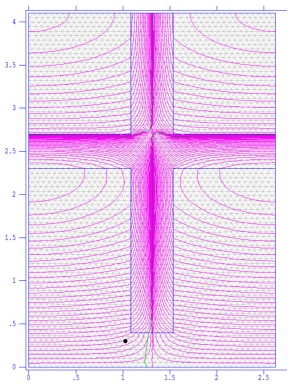


Figure 1: The electric field configuration in the frequency domain calculated by *SUPERFISH*. The ticks denote the dimension in cm unit. This figure describes the field configuration of the design frequency of the test cavity, i.e. 5712 MHz. The red curves denotes the electric force line.

In Fig. 1, the electric field is the standing wave along the z-direction and has periodic structure due to the metal walls on the left and the right side. The whole field configuration inside the DAA cavity is similar to the TM_{02n} mode in the pillbox cavity, whose difference appears from the dielectric cells. The dimensions of the dielectric structure are determined so that the peaks of the electric field is confined within the ceramics which has relatively high permittivity, $\epsilon_r \sim 10$ and can hold many electric force lines.

The structure of the DAA cavity has advantage of the high Q-value and the high shunt impedance as described below. As for the Q-value, the coaxial dielectric layer partially confines the electromagnetic field in the cavity so that the surface magnetic field at the copper surface becomes relatively small compared to one of the pillbox cavity. As for the shunt impedance, it is known that the waveguides with dielectric disks have a higher shunt impedance than all-metal waveguides [9]. Naively, this is because the dielectric disks make the electric force line concentrated around the beam axis, which is also applied in the DAA structure.

Due to the efficient structure to keep the RF energy and concentrate them to the beam axis, the result of the simulation shown in Fig. 1 is $Q = 1.4 \times 10^5$ and $Z_{sh} \simeq 900\ \mathrm{M\Omega/m}$. However, once the beam hole opens, the figures of merit significantly decrease by around 80%.

In the large number of cells limits, the effect of the beam hole to the cavity parameters is negligible. If the cavity contains N_{cell} regular cells, the boundary cells of the both ends effect by $2/N_{cell}$ in the figure of merit of the whole cavity. However, in the test DAA cavity shown in Fig. 2, we apply $N_{cell} = 6$ and boundary effect is huge. In order to avoid the reduction from the boundary effect, we apply additional cylinder in the end cell, which is shown in $r \in [0.5, 1]$ and $z \in [0.5, 2]$ in Fig. 2, so that most of the electric force lines hit above the beam hole and electric field around beam hole becomes smaller. Applying the end-cell structure, we obtained $Q = 1.2 \times 10^5$ and $Z_{sh} \sim 600\ \mathrm{M\Omega/m}$.

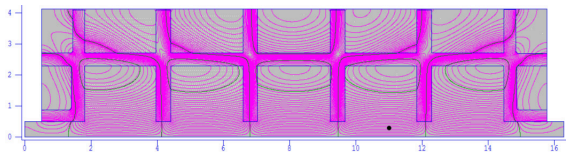


Figure 2: The electric field configuration in the frequency domain calculated by *SUPERFISH*. The ticks denotes the dimension in cm unit. This figure describes the field configuration of the design frequency of the test cavity, i.e. 5712 MHz. The red curves denotes the electric force line.

The above naive solution still causes a new problem that the symmetry of the field in terms of each disk is broken by the boundary effect. Moreover, the peaks of the field across the surface of the dielectric cells which would cause the discharge in the high voltage test.

THE NOVEL END CELL STRUCTURE OF THE DAA CAVITY

We found a configuration shown in Fig. 3 which can confine the field in the dielectric cells approximately restoring the symmetry even the neighboring cell of the end cell, which can also optimize the figures of merit.

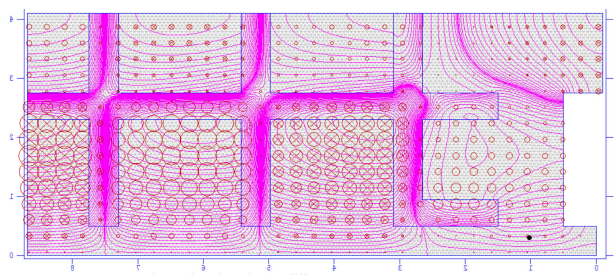


Figure 3: The electric field configuration in the frequency domain calculated by *SUPERFISH*. The ticks denotes the dimension in cm unit. This figure describes the field configuration of the design frequency of the optimized end cell, i.e. 5712 MHz. The red curves denotes the electric force line.

The class of field configurations like Fig. 3 can be reproduced by considering the interference condition along z di-

Content from this work may be used under the terms of the CC BY 3.0 licence (© 2018). Any distribution of this work must maintain attribution to the author(s), title of the work, publisher, and DOI.

ISBN: 978-3-95450-194-6 ISSN: 2226-0366 doi:10.18429/JACoW-LINAC2018-MOPO008

Content from this work may be used under the terms of the CC BY 3.0 licence (© 2018). Any distribution of this work must maintain attribution to the author(s), title of the work, publisher, and DOI.

rection. In Fig. 4, we show a schematic figure to explain the concept of the end cell structure. The gray region denotes the dielectrics and the white region denotes the vacuum. The parameters a, b, c, δ, d, and D are numerically determined so that the field configuration in the regular cell is optimized in terms of the Q-value and the shunt impedance. Other three parameters, l_1, l_2, and l_3 are determined as below. Compared with the regular cell shown in Fig. 1, here we introduce an additional dielectric cylinder near the beam hole with a length of l_1 and a vacuum region with a length of l_2. Considering the optical path length of the path1 and the path2 which are shown in Fig. 4 as L_1 and L_2, since the refractive index n of the dielectric cell is greater than one, apparently they should satisfy $L_1 < L_2$. As the length of a regular cell corresponds to a half wavelength, it is natural to consider the interference conditions, $L_1 = \lambda$, $L_2 = 3\lambda/2$, which determine two parameters, l_1 and l_2. We found the field configuration calculated with the dimensions l_1 and l_2 obtained as above can improve both Q and Z_{sh}. Then, we tune the third parameter l_3 in order to confine the electric force lines in the dielectrics and optimize the Q-value and the shunt impedance, further.

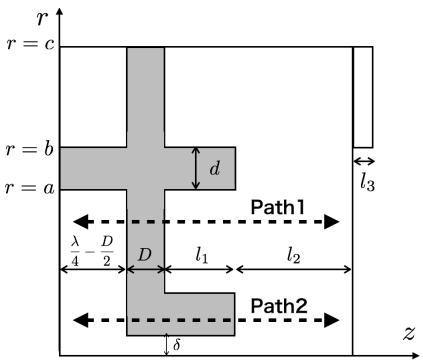


Figure 4: The schematic picture of the new end cell structure.

THE APPLICATION OF THE DAA CELL TO THE RF PHOTO INJECTOR

In this section, we show the numerical result of the particle-in-cell simulation using *CST MICROWAVE STUDIO* (CST) in the RF photoinjector applying the DAA structure. In the following calculation, we adopt the end cell shown in Fig. 3. Since the high power test of the DAA cavity has not been completed and tens of MV/m region has not been established yet, we assume the moderate value for the accelerating gradient, i.e. 20 MV/m. Although the DAA test cavity is designed to work with the frequency of 5712 MHz, the RF frequency of 5712 MHz is too high, in the gradient assumed here, to accelerate non-relativistic electrons bunches generated at the cathode up to relativistic energy within the first half cell. Thus, we adopt a frequency of 2856 MHz as the design frequency, which enlarges all the dimensions of the cavity in Fig. 3 by a factor of two.

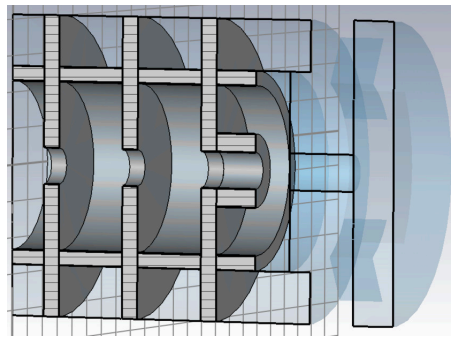


Figure 5: The RF photoinjector and the coupler used in our simulation.

Figure 5 shows the picture of the DAA applied RF photoinjector. We introduce a coupler between the waveguide and the cavity as four coaxial holes which are on the periphery of the cavity, so that the iris of the beam hole can be minimized keeping the coupling large. Due to the parity symmetry of the system in terms of the x-z plane and the y-z plane, we apply the symmetry condition to reduce the calculation cost as $H_t = 0$ on the both planes.

In Fig. 6, we show the distribution of the electric field in unit of V/m in the (z, r) plane calculated by CST. In Fig. 7, we show the magnetic field in unit of A/m in the (z, r) plane calculated by CST.

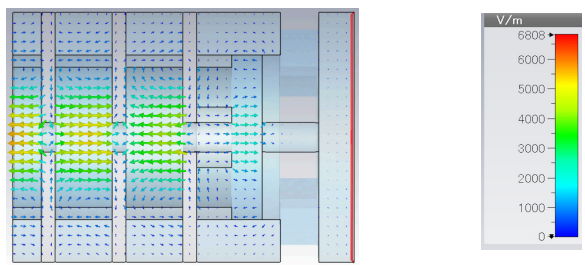


Figure 6: The contour plot of the tangential component of the electric field calculated using CST.

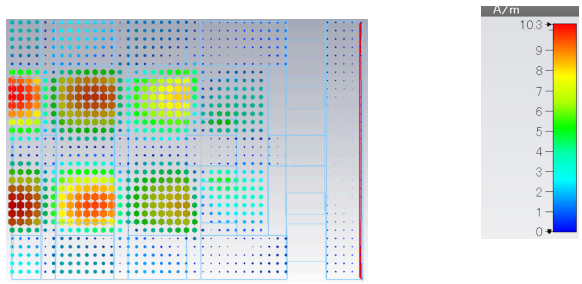


Figure 7: The contour plot of the normal component of the magnetic field calculated using CST.

In Fig. 8, we show the distribution of the gradient on the beam axis normalized by the maximum magnitude of it, $E_z(z, r = 0)/E_z(z = 0, r = 0)$, and the phase, $\mathrm{Arg}(E_z(z, r =$

ISBN: 978-3-95450-194-6 ISSN: 2226-0366 doi:10.18429/JACoW-LINAC2018-MOPO008

0)), calculated by CST as blue dots and orange dots, respectively. The plot shows the field configuration when the amplitude of the electric field is maximum. As expected from the coupler structure, the gradient outside the cavity is suppressed well.

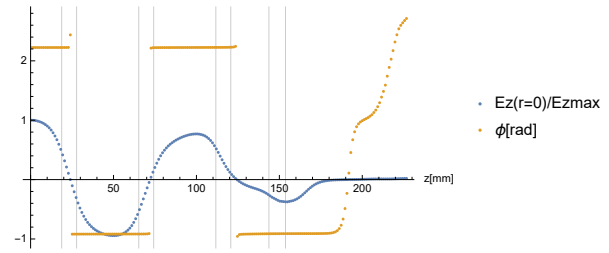


Figure 8: The accelerating field $E_z(z, r = 0)$ calculated by numerical simulation.

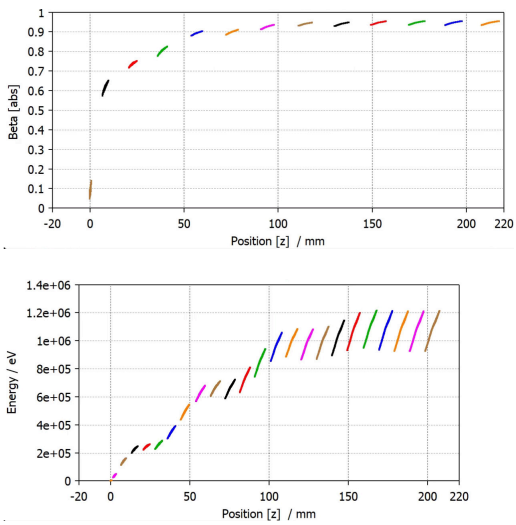


Figure 9: The z dependence, namely time dependence, of the β distribution and the energy distribution of a bunch calculated by CST.

The upper and lower figures in Fig. 9 show the β-z distribution and the Energy-z distribution in a bunch for each time step with a step size of 52 ps, respectively. Apparently, the electrons become relativistic at the exit of the RF cavity.

In Table 1, we show the parameters used in our calculation and beam parameters measured at the outside of the cavity. In our analysis, we synchronize the laser pulse and the RF phase so that emitted electron bunches are maximally accelerated in the first half cell. We numerically estimate the thermal loss in the cavity to support the gradient of 20 MV/m, which is about 290 kW in our simulation. At present, the water cooling can remove the power deposited as the surface temperature, whose typical capacity is 100 kW, which corresponds to the duty factor about 34 %. In contrast, if we want to operate the system with the duty factor of 1 %, the cooling power required is about 2.9 kW.

Table 1: The Parameters Related to the RF and the Emittance

RF frequency [MHz]	2856
field on cathode [MV/m]	20
RF phase at cathode for laser pulse	$3\pi/2$
thermal loss [kW]	290
laser spot [σ in mm]	2.0
laser pulse width [σ in ps]	10
charge in bunch [nC]	0.1
ϵ_z at exit [mm · mrad]	1.5
ϵ_T at exit [mm · mrad]	1.3
beam energy spread at exit [%]	4.0
bunch length at exit [σ in mm]	1.5
bunch radius at exit [σ in mm]	1.5

The thermal loss contains two contributions from the surface of the cavity and the dielectric loss, whose power dissipation is 245 kW and 45 kW, respectively. The thermal conductivity of the ceramics we adopt is about ten times smaller than one of the pure copper, while the heating power generated at the dielectrics is around ten times smaller than one of the pure copper. Then, the difference of the thermal conductivity is canceled by the difference of the power loss.

CONCLUSION

The DAA structure is a candidate for the highly efficient accelerator which could realize the continuous-wave-mode operation at room temperature with a relatively larger current. We investigate the application of the DAA structure to the RF electron gun, which could provide the high-quality beam with high peak current.

In our analysis, the structure of the end cell appears to be important since the RF photoinjector is constructed from a small number of cells. First, we try to optimize the effect of opening the beam hole by introducing the vacuum region between the end cell and the wall, which weakens the strength of the field at the beam hole satisfying the interference conditions along z direction.

We apply the optimized structure to the DAA applied RF photoinjector and numerically investigate the behavior of a electron bunch generated at the cathode, which shows that a bunch with the normalized emittance of $O(1)$mm · mrad can be generated by the DAA adopted photoinjector. The duty factor of 1 % is possible with the cooling power of 2.9 kW. Considering the water cooling capacity of 100 kW the possible duty factor is 34 %.

ACKNOWLEDGEMENTS

This work is supported by JSPS KAKENHI Grant No. 16H02134. The authors would like to thank N. Shigeoka from the Mitsubishi Heavy Industries Mechatronics Systems Ltd. for their continued support of the development of DAA structures.

Content from this work may be used under the terms of the CC BY 3.0 licence (© 2018). Any distribution of this work must maintain attribution to the author(s), title of the work, publisher, and DOI.

ISBN: 978-3-95450-194-6 ISSN: 2226-0366 doi:10.18429/JACoW-LINAC2018-MOPO008

Content from this work may be used under the terms of the CC BY 3.0 licence (© 2018). Any distribution of this work must maintain attribution to the author(s), title of the work, publisher, and DOI.

REFERENCES

[1] R Brinkmann, Ya Derbenev, and K Flöttmann. A low emittance, flat-beam electron source for linear colliders. *Physical Review Special Topics-Accelerators and Beams*, 4(5):053501, 2001.

[2] JS Fraser, RL Sheffield, ER Gray, PM Giles, RW Springer, and VA Loebs. Photocathodes in accelerator application, ieee particle accelerator conf., washington, dc. In *IEEE Cat*, number 87CH2387-9, pages 1705–1709, 1987.

[3] Y Kim, A Andersson, M Dach, R Ganter, T Garvey, C Gough, CH Hauri, R Ischebeck, F Le Pimpec, M Paraliev, et al. Low thermal emittance measurements at the psi-xfel low emittance gun test facility. In *Proceeding of FEL*, volume 8, 2008.

[4] Kwang-Je Kim. Rf and space-charge effects in laser-driven rf electron guns. *Nuclear Instruments and Methods in Physics Research Section A: Accelerators, Spectrometers, Detectors and Associated Equipment*, 275(2):201–218, 1989.

[5] Bruce E Carlsten. New photoelectric injector design for the los alamos national laboratory xuv fel accelerator. *Nuclear Instruments and Methods in Physics Research Section A: Accelerators, Spectrometers, Detectors and Associated Equipment*, 285(1-2):313–319, 1989.

[6] DH Dowell, KJ Davis, KD Friddell, EL Tyson, CA Lancaster, L Milliman, RE Rodenburg, T Aas, M Bemes, SZ Bethel, et al. First operation of a photocathode radio frequency gun injector at high duty factor. *Applied physics letters*, 63(15):2035–2037, 1993.

[7] D Satoh, M Yoshida, and N Hayashizaki. Dielectric assist accelerating structure. *Physical Review Accelerators and Beams*, 19(1):011302, 2016.

[8] D Satoh, M Yoshida, and N Hayashizaki. Fabrication and cold test of dielectric assist accelerating structure. *Physical Review Accelerators and Beams*, 20(9):091302, 2017.

[9] LB Mullett, W Walkinshaw, JS Bell, BG Loach, et al. A theoretical and experimental investigation of anisotropic-dielectric-loaded linear electron accelerators. *Proceedings of the IEE-Part B: Radio and Electronic Engineering*, 104(15):273–290, 1957.

ISBN: 978-3-95450-194-6 ISSN: 2226-0366 doi:10.18429/JACoW-LINAC2018-MOPO009

ELI-NP GAMMA BEAM SYSTEM – CURRENT PROJECT STATUS

Piotr Tracz†#
ELI-NP/IFIN-HH, RO-077125, Bucharest-Magurele, Romania

Abstract

The Gamma Beam System at the ELI-NP (Extreme Light Infrastructure – Nuclear Physics) under construction in Bucharest-Magurele, Romania, aims at producing high brilliance gamma-rays, based on the laser Compton backscattering, up to 3.5 and 19.5 MeV out of two interaction chambers. The design of a warm radio frequency linac is optimized to meet a unique source specification i.e. high brilliance, small relative bandwidth, tunable energy, and high spectral density. Together with the technological development in the field of high energy/high quality lasers it will open new opportunities for nuclear physics research in fields like nuclear photonics, nuclear astrophysics, photofission, and production of exotic nuclei, applications in industry, medicine, and space science. The S-band laser driven RF gun and two accelerating sections constitute the injector. Then the beam is accelerated by C-band linac up to 350 and 720 MeV. The GBS was designed and is being constructed by the EuroGammaS Association – a consortium of European academic and research institutions and industrial partners.

This paper gives an overview of the facility, describes the linac system and summarizes the project status.

INTRODUCTION

The Gamma Beam System (GBS) at ELI-NP was designed to provide gamma beam with unprecedented features: continuous tunable γ-ray energy over a broad range from 0.2 to 19.5MeV, high spectral density about 10^4photons/sec/eV, small relative bandwidth $< 0.5\%$, high degree of polarization $> 95\%$, and high peak brilliance $10^{20} \div 10^{23}$ N_{ph}/sec mm^2 mrad^2 0.1% [1].

The high brightness electron beam will be provided by a warm multi-bunch RF linear accelerator, operating with repetition rate 100 Hz. Electrons will be formed in trains of 32 micro-bunches of 250pC each, separated at 16ns from each other, repeating every 10ms. To achieve small emittance with low energy spread a particular care was paid to a damping of higher-order modes to reduce the beam break-up effects and beam loading effects of the cavities due to the short-time separation between the electron micro-bunches [2, 3]. The expected parameters of the electron beam at the high energy interaction point are given in the Table 1 [1].

The experimental activities with gamma beams at ELI-NP are evolving on three main lines of research: fundamental research, applied physics and gamma beam diagnostic tools development. In Fig. 1 the location of the GBS in the ELI-NP building is illustrated. The main experimental halls dedicated to measurements with gamma beams are indicated on the figure.

Table 1: Electron Beam Parameters at High Energy Interaction Point [1]

Energy	720MeV
Bunch charge	250 pC
Bunch length	1 ps
Norm. transverse emittance	0.4 mm·mrad
Bunch energy spread	0.04÷0.1 %
Energy variation along macro-bunch	0.1%
Energy jitter shot to shot	0.1%
Time arrival jitter	< 0.5 ps
Pointing jitter	1 μm
Focal spot size	~ 15 μm
Number of bunches per RF pulse	32
Bunch-to-bunch distance	16 ns
RF pulse repetition rate	100 Hz

The ELI-NP facility covers an area of approx. 33 000m^2. It will be a user facility. The civil construction comprised office building, a guest house and a canteen. ELI-NP is hosted by the Horia Hulubei National Institute of Physics and Nuclear Engineering (IFIN-HH) [4].

GBS DESCRIPTION

A schematic view of the GBS layout is shown in Fig. 2. The electron source is a 1.6 cell gun BNL/SLAC/UCLA type. Nevertheless it was fabricated with a new technique developed at LNF-INFN that does not involve brazing and, consequently, avoiding a thermal stress on copper. Several other improvements were implemented to increase the peak field at the cathode but reducing the break down rate probability [5]. The gun is equipped with a copper photocathode and there is a focusing solenoid at the exit of the gun for emittance compensation due to the space charge effects. The accelerating field at the cathode is 120MV/m and energy gain is 5.7MeV. The S-band TW accelerating sections will act as a bunch compressor decreasing the bunch length from 10 to 1ps in the velocity bunching process. There are twelve independent coils mounted on the first S-band section. The S-band sections will be driven by independent klystrons. A separate klystron will feed the RF gun and two S-band transverse deflecting structures, for the measurement of the longitudinal charge profile, located after injector and at the entrance of the high energy linac.

The C-band linac is divided into two segments – the low energy linac (LEL) and the high energy linac (HEL)

†piotr.tracz@eli-np.ro
#For the ELI-NP team

Content from this work may be used under the terms of the CC BY 3.0 licence (© 2018). Any distribution of this work must maintain attribution to the author(s), title of the work, publisher, and DOI.

ISBN: 978-3-95450-194-6 ISSN: 2226-0366 doi:10.18429/JACoW-LINAC2018-MOPO009

Content from this work may be used under the terms of the CC BY 3.0 licence (© 2018). Any distribution of this work must maintain attribution to the author(s), title of the work, publisher, and DOI.

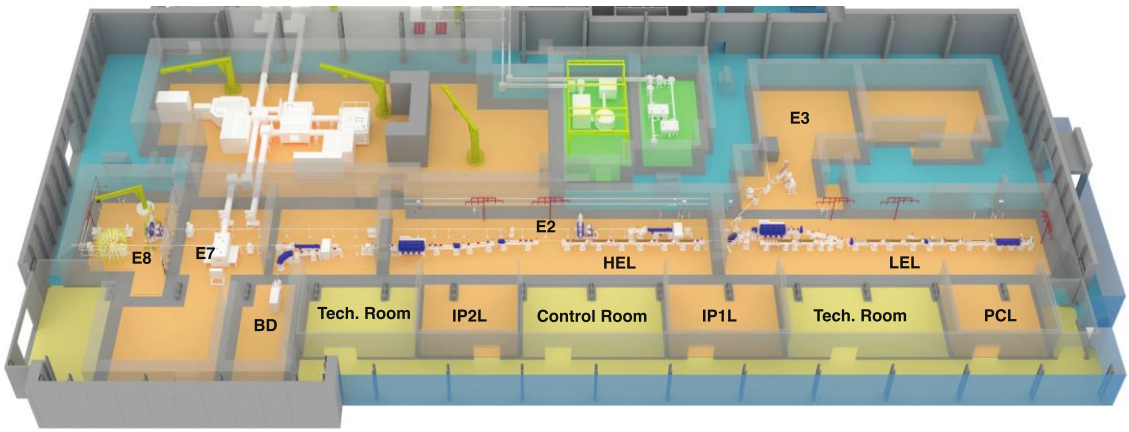


Figure 1: Partial layout of the ELI-NP experimental building showing the Gamma Beam System and the experimental halls where measurements with gamma beams will be performed. On the figure: LEL = Low energy linac, HEL = High energy linac, BD = beam dump, PCL = Photo-cathode laser, IP1L = Low energy interaction laser, IP2L = High energy interaction laser, E2, E8 = nuclear physics experiments hall, E3 = hall for experiments with positrons, E7 = hall for combined laser-gamma beam experiments.

(see Fig. 1). The beam is transported by dogleg type transfer lines to the low energy interaction point (IP1) and to the high energy interaction point (IP2).

The eight C-band sections are fed by individual klystrons, and the last four are grouped into two sections per klystron. All RF Units use ScandiNova K2 solid state modulators as the power source to drive Toshiba klystrons. The microwave source for the C-band sections is the 5.712GHz, 50MW klystron Toshiba E37212, and for S-band sections – 2.856GHz, 60MW, Toshiba E37314.

A network of rectangular waveguides distributes the power to the RF structures. There are several major diagnostic sections – after the injector, at the end of LEL and HEL, and before IP1 and IP2.

The cryo-cooled Ti:sapphire ~10ps laser in UV range (266nm), 150μJ/pulse will produce a train of 32 pulses at photocathode at repetition rate of 100Hz. Two identical lasers, Yb:YAG J-class type, will be used at the interaction points (IP lasers), each emitting sequences of single pulses of 3.5ps duration, 0.2J energy, and 515nm wavelength [1]. An optical system, the multi-pass recirculator, will allow circulating 32 times each IP laser pulse within a time window less than 600ns, and with no significant degradation of the pulse quality. It will lock the laser pulses to the RF clock. The recirculator system provides a fixed electron-laser beam crossing angle. This is one of the most advanced conceptual developments and most challenging technological device to be implemented in the GBS [6].

Appropriate collimators to filter out the energy spectrum and the gamma beam characterization system will be used. The gamma beam characterization system consists of a beam position imager, a Compton spectrometer, a sampling calorimeter, and a resonant scattering spectrometer. Two similar systems will be used for the low and the high energy branches, optimized for the different energy regimes [1].

PROJECT PROGRESS

The GBS building is available since September 2016. Figure 3 shows one of the accelerator bays in the ELI-NP building ready to host the GBS.

The implementation of the GBS is scheduled to be performed in several stages. The first stage consisting in the delivery of the components compatible with a system able to deliver 1 MeV gamma rays was successfully accomplished in 2015. Stages II and III imply the delivery, installation, testing, and commissioning of the low energy gamma beam system while Stage IV corresponds to the full system installation and commissioning.

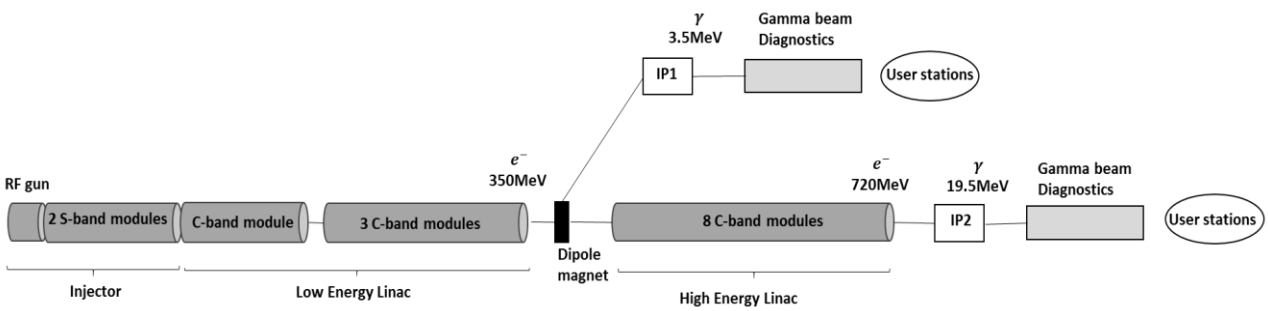


Figure 2: Schematic layout of the Gamma Beam System.

ISBN: 978-3-95450-194-6 ISSN: 2226-0366 doi:10.18429/JACoW-LINAC2018-MOPO009

The Stage I system comprises the photoinjector, one C-band structure, one interaction laser, and the auxiliary components.



Figure 3: Accelerator Bay in the ELI-NP building to host the components of the Gamma Beam System.

The accelerating structures, magnets, and beam diagnostic components were assembled on the girders and tested at INFN Frascati and STFC Daresbury. The completed modules were back-filled with dry nitrogen and transported to ELI-NP where they are waiting to be installed in the GBS tunnel. A network of reference points in accelerator tunnel was completed for the alignment of the system. In Fig. 4 the picture of one of the linac module with C-band section assembled on the girder stored at ELI-NP is shown.



Figure 4: Picture of one linac module at ELI-NP.

One C-band structure was conditioned at full RF power by Research Instrument at the Bonn University. Conditioning of the rest of C-band sections will be done at ELI-NP after the installation of the linac.

The S-band RF gun and sections were all tested at low power and conditioned at full power in Bonn.

The RF Units were successfully tested at the factory and transported to warehouse at ELI-NP. Conditioning of all klystrons at full RF power will take place after installation in klystron gallery at ELI-NP. One S-band and one C-band RF Unit were used for conditioning of the RF gun and accelerating sections in Bonn, Germany.

Waveguide components as well as mechanical supports for waveguides are transported and stored at ELI-NP.

The diagnostic devices for electron beam are manufactured, tested at factory and ready for installation. All magnets, vacuum pumps were tested at factory and nowadays are delivered to ELI-NP. Tests of the power supplies for magnets were done in factory.

The hardware for control system is delivered to ELI-NP. Clean rooms for the lasers are installed.

CONCLUSION

In the paper an overview of the Gamma Beam System was presented. The design of the GBS RF linac was optimized to guarantee the required level of performance for the high brilliance Compton gamma ray source. For this purpose, the manufacturer of the GBS has made several developments: the RF gun was fabricated using a new technique with several improvements from the electromagnetic point of view, C-band technology for the linac was chosen as a good compromise between acceleration gradient and compactness. The electromagnetic and mechanical design was optimized to control beam loading and beam breakup issues in multi-bunch operation. It was developed a new optical recirculator for the laser pulses at the interaction point and assuring a constant crossing angle between laser and electron beam, and optimizing its flux. The Stage I components are delivered to ELI-NP, and are ready for the installation. All of them were tested at factories. The performance of Stages II and III of the GBS installation is in delay.

The full Gamma Beam System is planned to be completed by July 2019.

ACKNOWLEDGEMENTS

The GBS-ELI-NP project is co-funded by the European Union through the European Regional Development Fund.

REFERENCES

[1] O. Adriani *et al.*, "Technical Design Report; EuroGammaS proposal for the ELI-NP Gamma Beam System", arXiv: 1407.3669v1 [physics.acc-ph].

[2] D. Alesini *et al.*, "Design and RF test of damped C-band accelerating structures for the ELI-NP linac", in *Proc. IPAC'14*, Dresden, Germany, June 2014, pp. 3856-3859.

[3] D. Alesini *et al.*, "The damped C-band RF structures for the European ELI-NP proposal", in *Proc. IPAC'13*, Shanghai, China, May 2013, pp. 2726-2728.

[4] http://www.nipne.ro/ and http://www.eli-np.ro/.

[5] D. Alesini *et al.*, "New technology based on clamping for high gradient radio frequency photogun", *Phys. Rev. ST Accel. Beams*, vol. 18, p. 092001, 2015.

[6] K. Dupraz *et al.*, "Design and optimization of a high efficient optical multipass system for γ-ray beam production from electron laser beam Compton scattering", *Phys. Rev. ST Accel. Beams*, vol. 17, p. 033501, 2014.

Content from this work may be used under the terms of the CC BY 3.0 licence (© 2018). Any distribution of this work must maintain attribution to the author(s), title of the work, publisher, and DOI.

ISBN: 978-3-95450-194-6 ISSN: 2226-0366 doi:10.18429/JACoW-LINAC2018-MOPO010

JINR PHOTOCATHODE RESEARCH: STATUS AND PLANS

M. A. Nozdrin*, N. I. Balalykin, V. F. Minashkin, G. D. Shirkov, JINR, Dubna, Russia
E. I. Gacheva, A.K. Potemkin, V. V. Zelenogorskii, IAP RAS, Nizhny Novgorod, Russia
J. Huran[1], IEE SAS, Bratislava, Slovakia
[1]also at JINR, Dubna, Russia

Abstract

Photocathode research in the frame of the "transmission" photocathode conception (backside illuminated cathode based on a quartz/sapphire plate or a metal mesh which is a substrate for thin film made of a photomaterial) is being conducted in the Veksler and Baldin Laboratory of High Energy physics (LHEP) of the Joint Institute for Nuclear Research (JINR). Status of the 30-kev DC Photogun test bench and recent results of the extremely thin carbon film based cathodes research are described. Progress in the full-scale photoinjector prototype (max electron energy of 400 keV) is given. Startup of the photoinjector was performed, 70 keV electrons were extracted (650 pC).

INTRODUCTION

Initial beam quality is of high importance for contemporary and future electron accelerators. Photoinjector sources provide beams of unexcelled quality.

Two main material types for photocathodes are metals and semiconductors. Latter have high quantum efficiency (>10% for CsTe at UV [1]), but have relatively small operational lifetimes and are sensitive to environment [2]. Metals are robust but have low quantum efficiency [3]. Also, GaAs should be mentioned for its ability to produce polarized electrons [4].

Diamond films are considered as promising photo emission cathodes because of their low threshold field as well as high thermal conductivity, high breakdown field and chemical inertness.

Quantum efficiency of diamond films can be additionally increased (up to 14% [5] or even up to 47% [6]) by hydrogenation and usage of the vacuum ultraviolet laser (140 nm).

A new concept of photocathode design was proposed at JINR [7]: a backside-illuminated "transmission" photocathode — an optically polished quartz/sapphire plate or a metal mesh (copper or stainless steel, 40×40 µm cell size, 30 µm wire diameter). This plate or mesh is a substrate for thin film made of a photomaterial. The metal mesh can also work as a photocathode without any coating. Such cathode geometry permits an increase in quantum efficiency due to the vectorial photoeffect. Furthermore, intrinsic emittance reduction is expected for the transmission mode operation [8].

EQUIPMENT

Photocathode research at JINR is being conducted at two benches: Photogun and Photoinjector.

* nozdrin@jinr.ru

Photogun Bench

Photogun bench is the main research instrument so far. It consists of the DC photogun (max anode voltage 30 kV), industrial single-pulse driver laser by LOTIS TII, focusing magnet with correction windings and various diagnostics (Faraday cup, laser energy meter, CCD camera for beam imaging). Main laser model is LS-2134 (wavelength 266 nm, pulse length 15 ns, pulse energy 15 mJ). This year second beamline was assembled (Fig. 1). It is based at LS-2132UTF laser (wavelength 266 nm, pulse length 8 ns, pulse energy 45 mJ) with a fifth harmonic external assembly which allows 213-nm laser beam generation.



Figure 1: 213-nm photogun bench setup.

Photoinjector Bench

Photoinjector bench is the photogun bench development. It features the full scale accelerating structure (triode type gun with forced resistive potential distribution which can provide electron beam with an energy of up to 400 keV) and the unique laser driver by IAP RAS (Table 1).

Table 1: Photoinjector Laser Driver Parameters

Parameter	Value
Wavelength	262 nm
Bunch train repetition rate	10 Hz
Bunch train duration	800 µs
Bunches in the train	8000
Bunch duration	10 ps
Bunch energy	1.5 µJ

First electron beam at the bench was obtained in April 2017. Bunch trains with 650 pC total charge were registered, what corresponds to current of 8 mA in the bunch, 0.8 µA in the bunch train and 6.5 nA average current(10 Hz repetition rate). Copper mesh photocathode (40×40 µm cell size,

Content from this work may be used under the terms of the CC BY 3.0 licence (© 2018). Any distribution of this work must maintain attribution to the author(s), title of the work, publisher, and DOI.

ISBN: 978-3-95450-194-6 ISSN: 2226-0366 doi:10.18429/JACoW-LINAC2018-MOPO010

30 µm wire diameter) was used. Electron bunch charge was measured by the Faraday cup grounded through 1 nF measuring capacitor. Faraday cup self-capacitance was negligibly small and was ignored in calculations. Capacitor voltage was registered by the oscilloscope, whereupon charge calculation was made according to a formula $Q = C \cdot U$, where C is the measurement capacitor capacitance and U is voltage on it. Bench setup during the startup is shown at the Fig. 2.

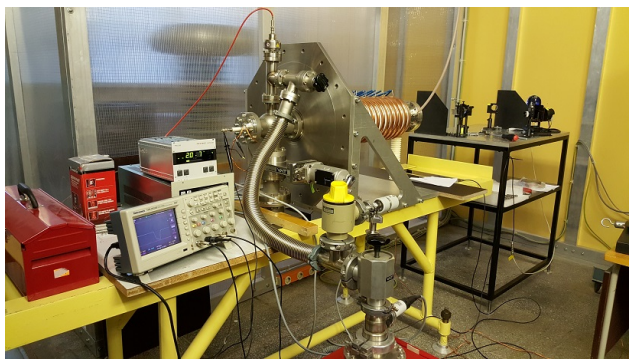


Figure 2: Photoinjector bench setup during the startup.

EXTREMELY THIN CARBON FILM BASED CATHODES

Of particlular interest is a study of the cathodes based on extremely thin films. Characterization of the photocathodes based on N-doped carbon-based films is given below.

Cathodes Preparation

Films were deposited on double side polished quartz glass by radio-frequency (RF) reactive magnetron sputtering using a carbon target and gas mixtures Ar, N_2 and H_2 or D_2. The magnetron carbon target was a high-purity graphite disk three inches in diameter. Prior to deposition, the quartz glass was cleaned in the ultrasonic bath containing acetone for 30 minutes and then rinsed in deionized water and dried in nitrogen ambient. Carbon films were deposited at the working pressure of 0.7 Pa and the magnetron input RF power of 150 W at 13.56 MHz. For all samples argon and nitrogen flows were 25 sccm and 6 sccm, respectively. Flows of hydrogen were: 1 sccm for sample QT2, 3 sccm for QT3 and 6 sccm for QT4. Flow of deuterium for sample QT5 was 3 sccm. Substrate holder temperature during magnetron sputtering was 900 °C. Carbon film thicknesses on quartz glasses were in the range 18–25 nm. Concentration of elements in the films was determined by RBS (Rutherford backscattering spectrometry) and ERD (elastic recoil detection) methods simultaneously. Scanning Electron Microscopy (SEM) was used to investigate the structural morphology of carbon thin films. Raman spectroscopy using a Thermo Fisher Scientific DXR Raman microscope with 532 nm laser was used for determination of the I(D)/I(G) intensity ratios of D and G peaks of carbon films. The G and D peaks were fitted with Gaussians and the intensity was calculated as the peak's area. Electron beam evaporation was used for Ti contact frame preparation on carbon/quartz structures.

Films Properties

Concentration of elements in the carbon fims was calculated from RBS and ERD experimental spectra using program SIMNRA. Concentration data are given in Table 2.

Table 2: Films Elemental Composition [in. at. %]

Sample	C	N	H	D	O
QT1	83	13	2	0	2
QT2	83	12	4	0	1
QT3	82	12	5	0	1
QT4	82	12	5	0	1
QT5	83	12	2	2	1

Results show that concentrations of hydrogen or deuterium in the carbon films are very small due to high substrate temperature i.e. hydrogen or deuterium escapes from growing carbon films at 900 °C. Hydrogen or deuterium and oxygen can be incorporated to the films after magnetron sputtering from the vacuum chamber atmosphere during decreasing of substrate temperature and can be absorbed from air atmosphere after deposition.

Figure 3 shows SEM images of QT1, QT3 and QT5 sample surfaces. Fully amorphous structure was observed for sample QT1 while samples QT2 and QT3 show amorphous structure with nanoscale thickness flakes of random arrangement. Surface images of QT3 and QT5 samples showed no significant difference between its surface morphology, i.e. adding of hydrogen or deuterium to the gas mixture has practically the same influence on carbon very thin films growth conditions.

Figure 4a shows Raman spectra of samples QT1–QT5. Peak intensities that occur at 1350 cm^{-1}, 1580 cm^{-1}, and 2700 cm^{-1} are called the D band, G band, and G' or 2D band, respectively. The G band is a primary an in-plane vibrational mode, and the 2D band is a second-order overtone of a different in-plane vibration. The D band around 1350 cm^{-1} is a breathing mode of A_1g symmetry involving phonons near the K zone boundary, which is activated due to defects and disorder of sp^2 carbon, and the D+G band (2940 cm^{-1}) is a combination scattering peak [9].

Results showed a change in the shape of broad asymmetric Raman scattering bands in the range from 900 to 1800 cm^{-1} due to change of deposition conditions.

Raman bands shape for sample QT1 is owned for GNDC (graphite-like nanocrystalline diamond) and activated carbon. Adding hydrogen or deuterium, Raman bands shapes were changed and can be compared with Raman spectra of mixture of GNCD [10] and small amount of graphene-like carbon. The asymmetric Raman peaks can be fitted with two peaks: the G-peak around 1580 cm^{-1} and the D-peak around 1350 cm^{-1}. In our case, for better deconvolution, we used tree peaks fitting. 1270 cm^{-1} can be assigned to ta-C. Figure 4b shows tree peaks fitting of Raman band from

Content from this work may be used under the terms of the CC BY 3.0 licence (© 2018). Any distribution of this work must maintain attribution to the author(s), title of the work, publisher, and DOI.

ISBN: 978-3-95450-194-6 ISSN: 2226-0366 doi:10.18429/JACoW-LINAC2018-MOPO010

Content from this work may be used under the terms of the CC BY 3.0 licence (© 2018). Any distribution of this work must maintain attribution to the author(s), title of the work, publisher, and DOI.

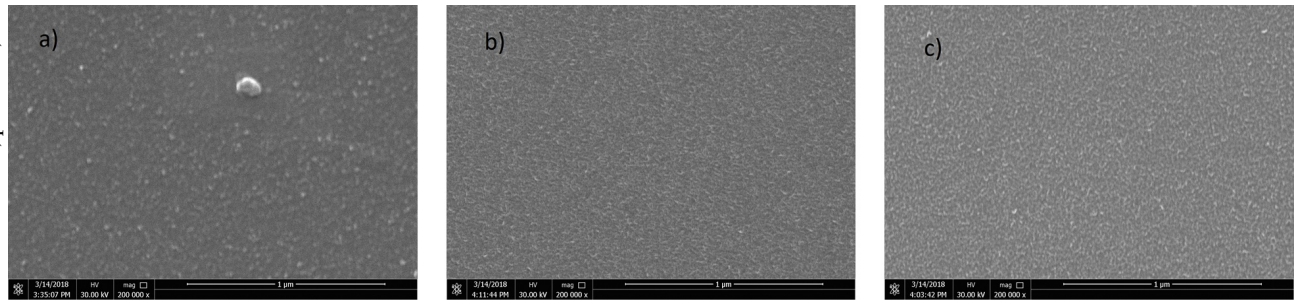


Figure 3: SEM images pf QT1 (a), QT3 (b) and QT5 (c) sample surfaces.

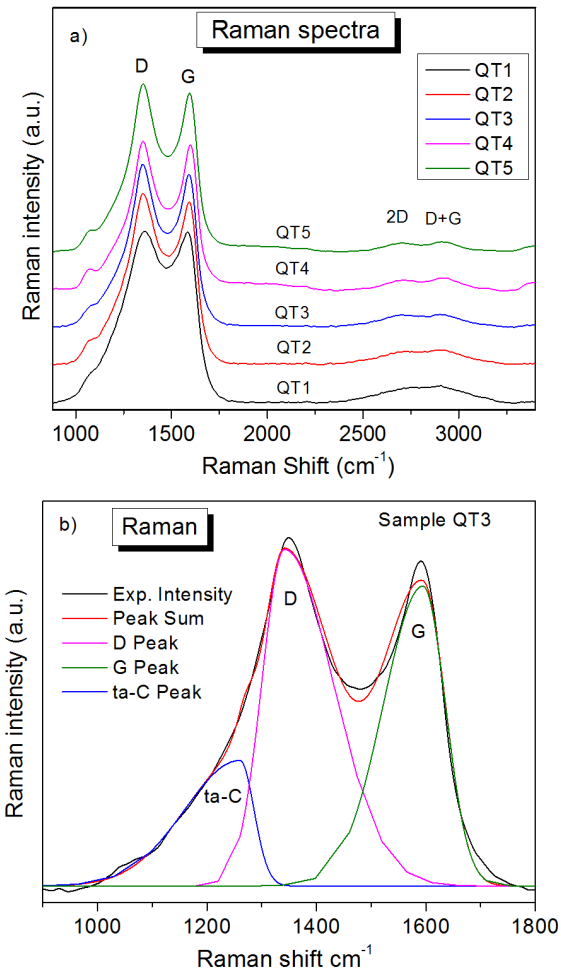


Figure 4: Raman spectra for samples QT1–QT5 in the range from 900 to 3400 cm^{-1} (a) and deconvoluted Raman spectrum in the range from 900 to 1800 cm^{-1} for QT3 (b).

900 to 1800 cm^{-1} for sample QT3. Calculated I(D)/I(G) of all samples are given in Table 3. The decreasing value of I(D)/I(G) ratio in the case of samples QT2–QT5 can be used to estimate the transition of disordered to ordered structure.

Emission Properties

Measured bunch charges, calculated quantum efficiencies (QE) and I(D)/I(G) ratios are given in Table 3.

Table 3: Cathodes Emission Properties and I(D)/I(G) Ratio

Sample	Q, pC	QE (% $\times 10^{-4}$	I(D)/I(G)
QT1	930	4.9	1.14
QT2	1140	6.1	1.39
QT3	1590	8.4	1.29
QT4	840	4.5	1.34
QT5	1470	7.8	1.17

CONCLUSION

Photocathode research infrastracture in JINR is being developed: new beamline with 213-nm laser driver was added to the Photogun bench, startup of the Photoijnector bench was performed, 70 keV electrons were extracted (650 pC). Study of the transmissive photocathodes based on extremely N-doped carbon-based films was conducted. Maximum bunch charge and QE were 1.59 nC and $8{,}4\times10^{-4}$ respectively.

REFERENCES

[1] R. Xiang and J. Teichert, *Physics Procedia*, vol. 77, pp. 58–65, 2015

[2] R. A. Loch, "Cesium-Telluride and Magnesium for high quality photocathodes," *Master thesis*, 2005

[3] A. Lorusso *et al.*, *Phys. Rev. AB* vol. 14.9, 2011

[4] D. H. Dowell *et al.*, *Nucl. Instrum. Methods Phys. Res. A*, vol. 622, pp. 685–697, 2010

[5] Sh. Michaelson *et al.*, *Diam. Relat. Mater.*, vol. 14, pp. 546–551, 2005

[6] L. Velardi, A. Valentini, and G. Cicala, *Diam. Relat. Mater.*, vol. 76, pp. 1–8, 2017

[7] N. I. Balalykin *et al.*, *Physics–Uspekhi*, vol. 60 (10), pp. 1051–1058, 2017

[8] H. Lee, L. Cultrera, and I. Bazarov. in *Proc. IPAC2016*, doi:10.18429/JACoW-IPAC2016-THPOW023

[9] P-T. Tseng, P-H. Tsai, A. Lu, J-L. Hou, and H-Y. Tsai, *Diam. Relat. Mater.*, vol. 73, pp. 121–131, 2017.

[10] M. A. Nitti *et al.*, *Nucl. Instrum. Methods Phys. Res. A*, vol. 595, pp. 131-13, 2008.

ISBN: 978-3-95450-194-6 ISSN: 2226-0366 doi:10.18429/JACoW-LINAC2018-MOPO016

NARROWBAND-FREQUENCY TERAHERTZ GENERATION FROM BEAM PIPE WITH HELIX WIRES

D. Wang†, Y. Liang, Q. Tian, Y. Du, L. Yan‡, W. Huang, C. Tang
Department of Engineering Physics, Tsinghua University, Beijing, China

Abstract

We studied through analysis and numerical simulations the use of a relativistic electron bunch to drive a metallic beam pipe with helix wire inside, for the purpose of generating narrowband-frequency terahertz radiation. We have shown that the frequency is related to the radius of the pipe and that of the wire, thus one can generate a narrow-band radiation pulse with frequency tunable through this scheme with different pipes and wires. The total energy of a few milli-Joules. The pulse length tends to be on the order of hundreds of picoseconds. We have also shown that, if the pipe radius is tapered along its length, the generated pulse will end up with a frequency chirp.

INTRODUCTION

The development of an accelerator-based Terahertz (THz) source could represent a real advancement for the scientific community [1], with important perspectives in different areas of fundamental research and applied physics, including applications in medical imaging, spectroscopy of solids and liquids, and chemical and security identification [2].

To generate THz radiation, the electron beam has to pass through a slow-wave structure, such as a corrugated metallic waveguide and a dielectric-loaded waveguide. The relativistic electron bunch generates radiation that follows the beam, which is also referred to as wakefield. The electron beam excites only modes with phase velocity equal to the velocity of beam, i.e., close to the speed of light c. With a sufficiently short (rms bunch length σ_z less than a radiation wavelength λ) driving beam, the radiation from the electron bunch is coherent [3].

In a recent experiment at FACET, a metallic beam pipe with round bore and small, rectangular corrugations is used to generate narrow-band radiation at 0.4 THz, with depth of corrugation $\delta = 60\mu$m and pipe radius $a = 1$mm the corrugated structure is 50 mm long, a 50 pC electron beam with $\sigma_z = 50\ \mu m$ has passed through the structure and transferred 1.2 uJ energy into the THz radiation [4]. Another example is a W-band flat metallic corrugated structure at around 0.1 THz driven by AWA bunch train, few millijoules of pulse energy with MW peak power was generated with 3 sub-bunches of 75 MeV, 500 μm long, 2 nC electron beam passing through a 12-cm long structure [5].

In this report, we design a simpler layout of a THz wakefield structure, which we call it as helix-wire pipe structure (HWP). This structure can be taken as a corrugated structure, with the wire diameter $2r$ is equivalent to the peak to peak depth of corrugation δ. Therefore, similar analytical estimates in corrugated structure can be applied for the HWP [6]. For the simulations, we employ electromagnetic design and analysis program CST, which computes the fields generated by an ultra-relativistic bunch in a structure in the time domain [7]. Simulations agree well with the theoretical analysis, which show that a 50-mm long HWP structure is able to generate mJ energy at THz freqeuncy when driven by 1nC electron beam, the gradient is in order of 100MV/m, and THz power is 10 MW The frequency from HWP is narrow-band frequency is tunable with wire diameter and pipe diameter We have also shown that, if the pipe radius is tapered along its length, the generated pulse will end up with a frequency chirp.

BASIC DESIGN OF THE STRUCTURE

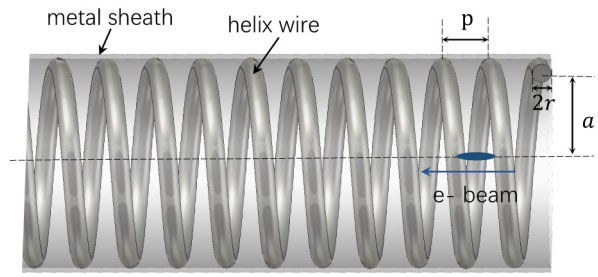


Figure 1: Basic design of the helix-wire pipe (HWP) structure, which is a helix wire inserted into a metal round pipe, the whole serves as a high impedance THz wakefield structure, parameters of the structure is listed in Table 1.

In our study, a metal round pipe with helix wire inside serves as the THz wakefield structure, the parameters are helix period p, wire diameter $2r$, pipe radius a and total length of the structure L_s, which are list in Table 1.

Table 1: Parameters of HWP Structure

parameter	DLW No.1
a	1.0 mm
r	0.1 mm
p	0.5 mm
L_s	50 mm

The wire diameter $2r$ in HWP is equivalent to the peak to peak depth of corrugation δ. Similar analytical estimates is applicable. Analytical formulas as following: the frequency $f = \frac{c}{\pi\sqrt{2ar}}$=0.2 [THz] only depends on the wire diameter and the pipe radius, while the group velocity v_g is also highly depend on the helix wire period parameter p,

†wangdan16@mail.tsinghua.edu.cn
‡ yanlx@mail.tsinghua.edu.cn

Content from this work may be used under the terms of the CC BY 3.0 licence (© 2018). Any distribution of this work must maintain attribution to the author(s), title of the work, publisher, and DOI.

ISBN: 978-3-95450-194-6 ISSN: 2226-0366 doi:10.18429/JACoW-LINAC2018-MOPO016

Content from this work may be used under the terms of the CC BY 3.0 licence (© 2018). Any distribution of this work must maintain attribution to the author(s), title of the work, publisher, and DOI.

for structure in Table 1, $\beta_g = v_g/c = 0.54$, which predicted that the generated THz wakefield pulse duration $\tau_s = \frac{L_s}{v_g}(1-\beta_g)$=0.14 ns from the 5 cm long structure.

When excited by electron beam of 1nC Gaussian beam with rms bunch length 0.1 mm, the form factor of the beam $F(f) = e^{-(k^2\sigma_z^2/2)} = 0.9$, and the loss factor $\kappa = \frac{Z_0 c}{2\pi a^2} e^{-(k^2\sigma_z^2)} = 1.47 \times 10^{16}$ V/m/C. The THz wakefield gradient $E_s = 2\kappa q/1-\beta_g = 64$ MV/m and total power $U = q^2\kappa L_{s/1-\beta_g} = 1.6$ mJ, THz power $P = U/\tau_s = 11.3$ MW, the theoretical wake function is:

$$w(s) = 2\kappa q L_s \left(1 - \frac{s}{\tau_s c}\right)(s < \tau_s c) \cdot \cos(ks) \qquad (1)$$

Note that we have considered the group velocity enhancement effect, i.e., factor $1/(1-\beta_g)$, when calculate the wakefield gradient and the THz power, which comes from the compression of the travelling wave inside the structure [8].

SIMULATION RESULTS

THz Wakefield Generation

CST particle tracking studio is used to get the electric field and the spectrum from the Fast Fourier Transform (FFT) algorithm, results are shown in Fig. 2. A drive beam of 1 nC with 0.1mm rms. bunch length is used to go through the structure, and the monitor is posited at Z=52 mm.

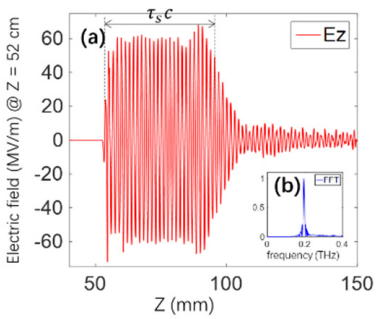


Figure 2: (a) Simulated THz electric field at monitor (position Z=52 mm); (b) FFT of the electric field.

As Fig. 1 (a) shows, the generated Terahertz is about 64 MV/m, and radiation pulse length is about 42.6 mm which equal to $\tau_s c$ as theory results. The FFT results in Fig. 1 (b) shows the frequency of the wakefield is 0.2 THz, which also agree with the formula above.

We also applied wakefield studio in CST to get the wake function and the wake impedance of the HWP driven by electron beam of 1 nC with 0.1 mm rms bunch length. Results are shown in Fig. 3, in Fig. 3 (a) we have also compared the simulation (red curve) with theoretical analysis of wake function envelope from equation (1) (blue curve), they agree well with each other. The wake impedance in Fig. 3 (b) is FFT of the wake function in Fig. 3 (a), which centred at 0.2 THz with a high quality, which also demonstrated the narrow band of the THz wakefield radiation.

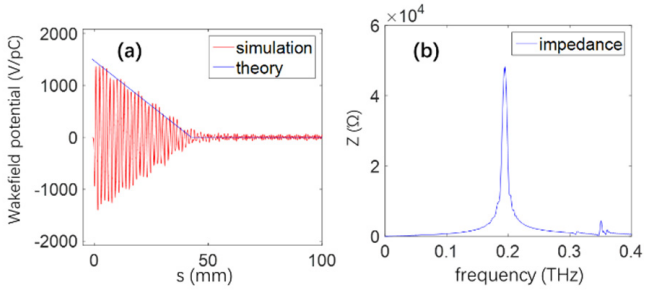


Figure 3: (a) Simulated wake function from CST (red curve) and the theoretical envelope of wake function (green curve); (b) simulated wake impedance from CST.

Frequency Tenability

As the theory predicted that the frequency of HWP structure follows formula of $f = c/\pi\sqrt{2ar}$. We do parameter scan to build different models and use CST to compute the centroid frequency, results are shown in Fig. 4.

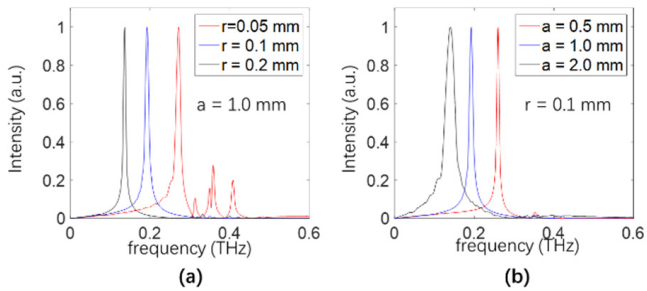


Figure 4: Simulated frequency with different parameters of the HWP structure. (a) different helix wire radius r with same pipe radius a=1 mm (b) different pipe radius a with same helix wire radius r=0.1mm.

Simulations demonstrate that the frequency is related to the root mean square of both pipe radius and helix wire radius. Thus, provided a new method to process THz wakefield structures with different frequency.

Figure 5 shows preliminary results on frequency spectrum of tapered HWPs with parameter a uniformly varies along the tubes, one is from 0.1 mm to 0.5 mm (red curve) and one is from 0.1mm to 0.2 mm (blue curve). The length of the structure is 50 mm. Results shown a relatively broad band frequency compared to the uniform pipe, which implies that the frequencies are chirped, and should be compressed this is followed by a properly designed dispersive device—analogous to what is done in chirped pulse amplification (CPA) in high power lasers—the pulse can then be compressed. This chirped THz generation based on taper HPW is simpler to process compared to that based on normal round corrugated structures, in which the depth of corrugation is varied along the pipe as designed in Ref. [6].

ISBN: 978-3-95450-194-6 ISSN: 2226-0366 doi:10.18429/JACoW-LINAC2018-MOPO016

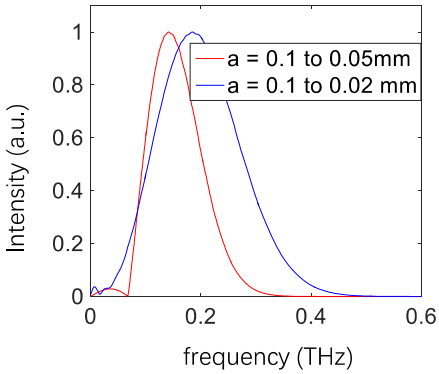


Figure 5: Preliminary results on frequency spectrum of HWPs with parameter a uniformly varies along the tubes, one is from 0.1 mm to 0.5 mm (red curve) and one is from 0.1mm to 0.2 mm (blue curve).

SUMMARY

We designed a HPW structure for THz wakefield/radiation generation, which is a metallic beam pipe with helix wire inside. Theoretical analysis and simulations show the frequency is related to the radius of the pipe and that of the wire, the frequency is narrow-band and tunable with structure parameters. The total energy is a few milli-Joules, and gradient is 100 MV/m when driven by 1nC electron beam. Primary results also shown that the HPW is suitable for chirped THz generation.

ACKNOWLEDGEMENTS

The author would like to thank K. Bane from SLAC and D. Xiang from Shanghai Jiao Tong University. Work supported by the General Financial Grant from the China Postdoctoral Science Foundation (Grant No.2017M620036) and Special Financial Grant from the China Postdoctoral Science Foundation (Grant No.2018T110107).

REFERENCES

[1] G. L. Carr *et al.*, "High-power terahertz radiation from relativistic electrons". *Nature*, vol. 420, pp. 153-156, 2002.

[2] S.S. Dhillon *et al.*, "The 2017 terahertz science and technology roadmap", *Journal of Physics D: Applied Physics*, vol. 50, p. 043001, 2017.

[3] B.D. O'Shea *et al.*, "Observation of acceleration and deceleration in gigaelectron-volt-per-metre gradient dielectricwakefield accelerators", *Nature Communications*, vol. 7, p. 12763, 2016.

[4] K.L.F. Bane *et al.*, "Measurements of Terahertz generation in a metallic, corrugated beam pipe", SLAC-PUB-16536, 2016.

[5] D. Wang *et al.*, "Interaction of an ultrarelativistic electron bunch train with a W-band accelerating structure: high power and high gradient", *Phy. Rev. Lett.*, vol. 116, no. 5, p. 054801, 2016.

[6] K.L.F. Bane and G. Stupakov, "Terahertz radiation from a pipe with small corrugations", *Nucl. Instr. Meth.*, vol. 667, pp. 67-73, 2012.

[7] CST, https://www.cst.com/products/csts2

[8] D. Wang *et al.*, "High power RF generation from a W-band corrugated structure excited by a train of electron bunches", in *Proc. 7th Int. Particle Accelerator Conf. (IPAC'16)*, Busan, Korea, May 2016, pp. 3040-3043.

Content from this work may be used under the terms of the CC BY 3.0 licence (© 2018). Any distribution of this work must maintain attribution to the author(s), title of the work, publisher, and DOI.

ISBN: 978-3-95450-194-6 ISSN: 2226-0366 doi:10.18429/JACoW-LINAC2018-MOPO018

DEVELOPMENT OF AN IMPROVED CAPTURE SECTION FOR THE S-DALINAC INJECTOR*

S. Weih#, M. Arnold, J. Enders, N. Pietralla,
Institut für Kernphysik, TU Darmstadt, Germany
D. Bazyl, W.F.O. Müller, H. De Gersem,
Institut für Theorie Elektromagnetischer Felder, TU Darmstadt, Germany

Abstract

For the injector of the superconducting Darmstadt electron linear accelerator S-DALINAC, the design of a new capture cavity was recently completed. This beta-reduced structure will optimize the capture of low-energy electron bunches from the gun section and therefore improve the longitudinal beam quality of the injector beam, as simulations have shown. The existing cryomodule of the injector has to be modified for the installation of the new cavity. These modifications include adaptions of the tuner frame as well as modifications of other surrounding parts. To improve the diagnostics in the low-energy section, an energy-spread measurement setup is currently also under development. In this contribution the cryomodule modifications as well as simulation results for the longitudinal beam dynamics are presented.

INTRODUCTION

The injector of the superconducting Darmstadt linear accelerator S-DALINAC [1] provides electrons with a kinetic energy of up to 10 MeV. It consists of a normal conducting section where the beam is prepared for RF acceleration and two cryomodules containing superconducting elliptical Nb accelerator structures (Fig. 1). The injector is driven by a 250 keV thermionic gun, the also existing spin-polarized gun [2] is currently being prepared for an upgrade to 200 keV [3]. In its present state, the superconducting part of the injector features a five-cell capture cavity and two 20-cell cavities similar to the structures used in the main LINAC. All cavities are operated at 3 GHz and designed for a β of 1. However, the 250 keV beam from the thermionic gun corresponds to a relativistic β of only 0.74, introducing significant phase slippage effects as the low-energy bunch travels through the current five-cell cavity. In order to increase the efficiency of the electron capture and the longitudinal beam quality of the beam after injection it is therefore intended to replace the five-cell structure with a new dedicated capture cavity. The design of the new capture structure, a 6-cell cavity with a reduced β of 0.86, has been recently completed [4,5] and its construction will start in the near future.

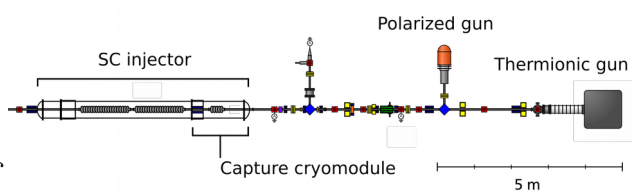


Figure 1: Overview of the S-DALINAC injector. Main subject of this project is the capture cryomodule which is part of the superconducting (SC) injector. It currently houses a 5-cell β=1 cavity.

MECHANICAL MODIFICATIONS

Inside the liquid helium vessel of the cryostat, the cavity is surrounded by its input and output RF coupler as well as the tuner system. It was already decided in the early stage of the project to keep the overall cavity length fixed, enabling the re-use of the couplers and the cryostat. However, the tuner frame has to be adapted. First CAD models of the tuner system were created in order to apply the necessary modifications. Figure 2 shows the finished tuner frame model. The tuner frame is fixed at the cavity cutoff tubes with aluminum plates (grey), which can be re-used from the existing 5-cell frame. Since the overall length of the cavity cell region will be increased by 8 mm, the tuner frame length has to be adapted. A shorter cutoff-tube at the output coupler side will compensate this additional length. However, due to the longer cell region, the titanium fixation rods (yellow), which stabilize the frame and guide the cavity, have to be modified. The piezo tuner system for microphonics compensation is

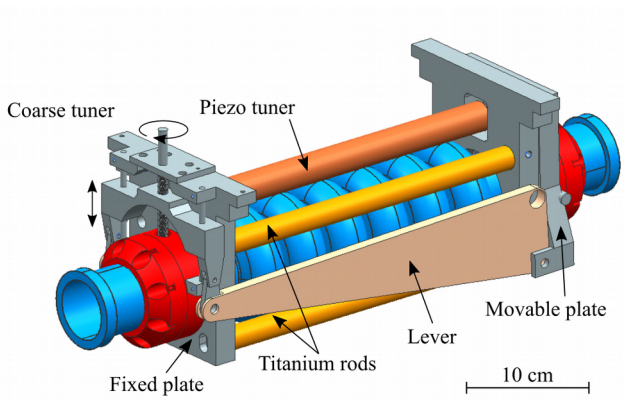


Figure 2: Trimetric view of the tuner frame CAD model with the applied modifications for the new capture cavity. The grey parts will be re-used from the existing setup, the piezo tuner and the support rods (orange and yellow) as well as the lever (pink) have to be adapted according to the increased length of the cell region. The cavity fixation rings shown in red have to be increased in diameter to adapt to the larger wall thickness of the cavity.

* Work supported by DFG (GRK 2128).
# sweih@ikp.tu-darmstadt.de

Content from this work may be used under the terms of the CC BY 3.0 licence (© 2018). Any distribution of this work must maintain attribution to the author(s), title of the work, publisher, and DOI.

ISBN: 978-3-95450-194-6 ISSN: 2226-0366 doi:10.18429/JACoW-LINAC2018-MOPO018

contained in a titanium tube which also has to be adjusted. Due to the increased cavity wall thickness (to protect the cavity from deformations during installation and handling), the fixation rings which attach the cavity to the frame (shown in red) have to be increased in diameter to match the new outer cutoff tube radius. Due to the increased wall thickness of the cavity compared to the current 5-cell setup, the stiffness also increases [5]. It was therefore verified that the tuner strength of one piezo actuator is sufficient for tuning. Two actuators will be used for redundancy in the final tuner system. With the CAD model of the modified tuner frame prepared, manufacturing of the adapted parts can be carried out in the in-house workshop of the institute in parallel to cavity production.

BEAM DYNAMICS

In order to obtain first estimates of the beam quality improvement introduced by the new capture section, the longitudinal phase space downstream the superconducting injector was simulated with ASTRA [6]. The input bunch length and energy spread for the 250 keV thermionic gun beam were estimated to 5 ps and 3 keV, respectively using the properties of the chopper/prebuncher section within the normal conducting part of the injector. In a first set of simulations, the phase of the three injector cavities (the capture cavity followed by the two 20-cell cavities) was set according to the maximum energy gain, the peak electric field on axis was 10 MV/m. Figure 3 shows the phase space at injection exit for the current 5-cell setup (left) and for the new capture structure (right) for an input bunch energy of 250 keV (top) and 200 keV (bottom), corresponding to the two electron guns. A large low-energy tail is generated by the phase slippage in the 5-cell cavity, producing halo and beam loss as the bunch travels towards the main LINAC. This tail gets significantly decreased in the case of the new 6-cell structure. A similar simulation was run for the 200 keV beam delivered by the spin-polarized gun after the planned upgrade. For 200 keV, the β-mismatch of the 5-cell gets too large to maintain a compact bunch structure, while the 6-cell is able to maintain a stable bunch throughout the injector. Furthermore, a phase setting of the capture structure leading to a minimum energy spread at injection exit was found through simulations. For this operation mode, the energy gain of the capture section is still close to the maximum while leading to a significant energy spread reduction at the end of the injector. Overall, the benefit of the new capture structure for beam dynamics could be validated. The structure is expected to yield an efficient electron capture for both the 250 keV and 200 keV beam. However, the beam quality at the end of the injector highly depends on the input bunch shape, which was seen in a third set of simulations where the input bunch energy spread and length was varied for the new setup (6-cell cavity). For the lowest longitudinal emittance, the bunch has to be as short as possible when it enters the first cell of the capture structure (Fig. 4). As expected, a small energy spread of the input bunch also contributes to a good beam quality after the injector. However, there are no diagnostics at the end of the normal conducting injection section so far to measure this properties of the input bunch. Therefore, a dipole spectrometer setup for energy spread measurement is currently being planned.

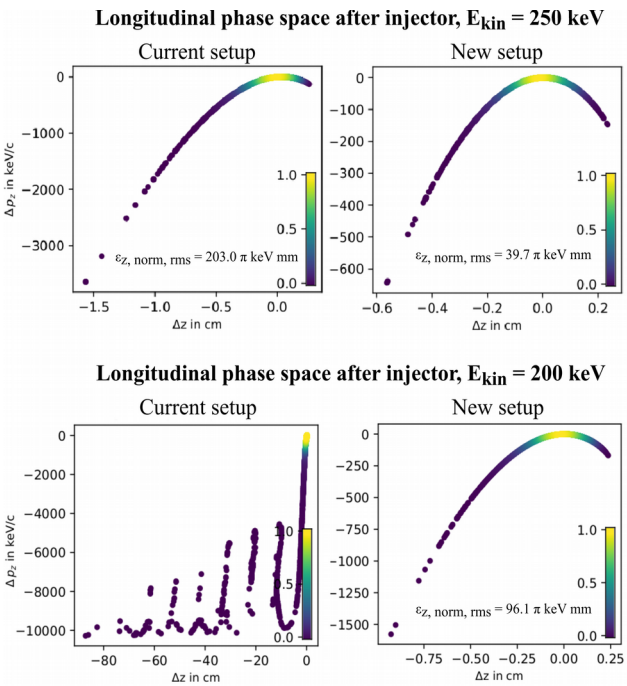


Figure 3: Simulated longitudinal phase space for the 250 keV input bunch (top) at injector exit for the existing 5-cell setup (left) and the new 6-cell capture structure (right). The phases were set according to the maximum energy gain of the beam. Relative phase space density is indicated by the colormap. The bottom figures show a similar simulation for the 200 keV input bunch. With the current capture structure it is not possible to maintain a stable bunch structure along the injector for this input energy, while the 6-cell cavity shows an efficient capture also in this case.

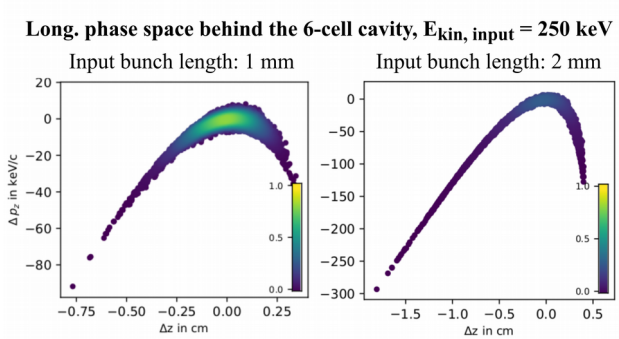


Figure 4: Simulated longitudinal phase space behind the new 6-cell capture structure for different input bunch parameters. The quality of the beam after the capture highly relies on proper prebuncher settings, which determine the input bunch length. A diagnostics setup is needed in front of the SC injector entry to verify this parameter.

Content from this work may be used under the terms of the CC BY 3.0 licence (© 2018). Any distribution of this work must maintain attribution to the author(s), title of the work, publisher, and DOI.

ISBN: 978-3-95450-194-6 ISSN: 2226-0366 doi:10.18429/JACoW-LINAC2018-MOPO018

Content from this work may be used under the terms of the CC BY 3.0 licence (© 2018). Any distribution of this work must maintain attribution to the author(s), title of the work, publisher, and DOI.

An existing vertical diagnostic beam line located behind the prebuncher could be used for this setup.

CONCLUSION AND OUTLOOK

For an efficient electron capture in the first cavity of the superconducting injector of the S-DALINAC, a new beta-reduced structure will replace the current 5-cell cavity. CAD models of the relevant tuner frame parts within the cryostat were created and modifications were applied according to the geometry of the new cavity to prepare the installation. Longitudinal beam dynamics simulations were carried out in order to validate the expected improvement in beam quality introduced by the new structure. They can be also used as a guideline for the phase settings of the injector during commissioning of the new capture section. In order to get a better understanding of the real bunch properties after the normal-conducting injection, a measurement setup is needed close to the SC injector entrance. Measurements of longitudinal beam parameters of the normal conducting injection could then be performed to support the commissioning. Furthermore, upgrade options of the normal conducting injection can be investigated.

REFERENCES

[1] N. Pietralla, "The Institute of Nuclear Physics at the TU Darmstadt", in *Nuclear Physics News*, vol. 28, no. 2, pp. 4-11, 2018.

[2] Y. Poltoratska *et al.*, "Status and recent developments at the polarized-electron injector of the superconducting Darmstadt electron linear accelerator S-DALINAC", in *J. Phys: Conf. Ser.,* vol. 298, no. 1, p. 012002, 2011.

[3] M. Herbert *et al.*, "Inverted Geometry Photo-Electron Gun Research and Development at TU Darmstadt", in *Proc. IPAC'18*, Vancouver, BC, Canada, May 2018, pp. 4545-4547. doi:10.18429/JACoW-IPAC2018-THMPMK101

[4] D. Bazyl *et al.*, "Upgrade of the Capture Section of the S-DALINAC Injector", in *Proc. IPAC'17*, Copenhagen, Denmark, May 2017, pp. 993–995. doi:10.18429/JACoW-IPAC2017-MOPVA055

[5] D. Bazyl *et al.*, "A 3 GHz SRF Reduced-beta Cavity for the S-DALINAC", in *Proc. IPAC'18*, Vancouver, BC, Canada, May 2018, paper THPAL08, pp. 3838-3840.

[6] A Space Charge Tracking Algorithm (ASTRA), http://www.desy.de/~mpyflo/

ISBN: 978-3-95450-194-6 ISSN: 2226-0366 doi:10.18429/JACoW-LINAC2018-MOPO019

STUDY ON CLEANING OF COPPER PLATED BELLOWS FOR LCLS-II*

L. Zhao†, E. Daly, K. Davis, G. Eremeev, T. Reilly, A-M. Valente-Feliciano, K. Wilson
Thomas Jefferson National Accelerator Facility, Newport News, Virginia, USA

Abstract

Inter-cavity copper plated bellows are part of the LCLS-II cryomodule beamline components. Since the bellows are close to superconducting radio frequency (SRF) cavities during accelerator operation, it is desirable that these bellows have similar cleanliness as SRF cavities. Studies have been done to help evaluate bellows interior cleanliness after the standard bellows cleaning procedure at Jefferson Lab.

BACKGROUND

LCLS-II cryomodule design includes copper plated bellows between each cavity, similar to that of the European XFEL [1, 2]. During string assembly at JLab, bellows are assembled to the cavity vertically as part of the cavity sub-assembly. Connections made on the rail were done horizontally [3]. Bellows are cleaned in a manner similar to the standard hardware cleaning processes except that lower solution temperature and expedited drying are applied. Bellows present some challenges for cleaning, for example, the convoluted shape is more difficult to clean and dry, the adhesion quality of the plating added concerns during processing [4]. To help confirm our horizontal assembly practice as well as understanding bellows cleanliness, three cavities were tested with a bellows assembled to the top of each cavity. Particle samples were collected from one of the three cavity-bellows assembly after vertical testing for further study.

EXPERIMENTS

Processing of Cavities and Bellows

Bellows were cleaned in an ultrasonic tank with ultrapure water and Citranox®, thoroughly rinsed with ultrapure water, dipped in acetone, and blown dry with nitrogen. Previously field-emission-free cavities were selected for this experiment. CAV0116: cleaned bellows were assembled horizontally onto cavity; cavity was pumped down, and then attached to the test stand with bellows on the top. After vertical test, the bellows were stretched and squeezed 0.5 inch while staying on top of the cavity before the next vertical test. CAV0278 and CAV0286: Bellows were assembled vertically onto the cavity; the cavity was flipped and received the final HPR with the bellows on the top; after final assembly (the bellows were still wet), the cavity was pumped down and attached to the test stand with bellows on the top.

Vertical RF Test

The three cavities were tested vertically at 2.0 K to see if there was any early field emission onset. The cavity configuration during vertical testing is shown in Fig. 1.

Sampling of Bellows and Cavity

After vertical test, the interior of CAV0278 and bellows 2068 were sampled to help understand the source of field emitters. Sampling was performed by two operators using two types of tooling, to allow comparison of findings from the two sampling process. Particles found in both sampling processes are likely from the surface of interest, while those found in only one sampling process could be introduced by the sampling process. In the first method (L series), a cleaned Gore-Tex (Teflon, or PTFE) piece was used to sample the surface of interest and transfer any particles onto a carbon tape, and the carbon tape was preserved carefully until SEM analysis. Two samples were collected at each of three locations: the flat region and inside of one convolution of the bellows (L1, L2), the cavity beam tube next to the bellows (L3, L4), and the cavity beam tube on the other end (L5, L6). In the second method (S series), a piece of isopropanol soaked cleanroom wipe (TX®1082 QuanSat, polyester) was used to sample the surface of interest and transfer the sample to a carbon tape, which was preserved inside a commercially available standard SEM sample case [5]. Sample locations are shown in Figure 1. One sample was collected at each of eight locations: bellows top flat region (S0456), inside top first convolution (S0457), several iris (S0458), inside bottom first convolution (S0459), bottom flat region (S0460), shaking of bellows (S0461), cavity top beam tube (S0462), and cavity bottom beam tube (S0463).

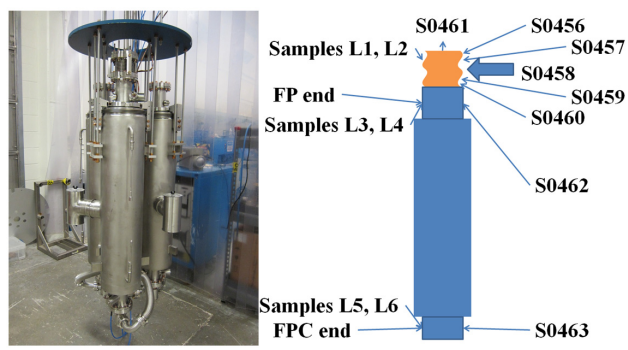


Figure 1: Bellows attached cavity on a test stand waiting to be loaded into the Dewar (left). Sampling locations on CAV0278-Bellows 2068 (right).

* Authored by Jefferson Science Associates, LLC under U.S. DOE Contracts DE-AC05-06OR23177 and DE-AC02-76SF00515 for the LCLS-II Project.
† lzhao@jlab.org

Content from this work may be used under the terms of the CC BY 3.0 licence (© 2018). Any distribution of this work must maintain attribution to the author(s), title of the work, publisher, and DOI.

ISBN: 978-3-95450-194-6 ISSN: 2226-0366 doi:10.18429/JACoW-LINAC2018-MOPO019

Content from this work may be used under the terms of the CC BY 3.0 licence (© 2018). Any distribution of this work must maintain attribution to the author(s), title of the work, publisher, and DOI.

Analysis Process

SEM/EDS analysis: The topography and elemental analysis of the particles are performed on TESCAN Vega3 SEM equipped with TEAMTM EDS System.

Interpretation and sizing: Based on the elemental ratio from EDS analysis, each particle is assigned as a compound or a mixture of several species. The sizes of particles are decided manually from the SEM image.

Categorize: Particles are categorized according to the interpretation of SEM/EDS data.

Count: The number of particles is counted in each category for each sample.

Separate distractions from suspects: Particles which are likely to be introduced from elsewhere rather than the sampled surface are considered distractions.

RESULTS AND DISCUSSION

VTA performance of each cavity is shown in Fig. 2. CAV0116 showed no early field emission onset during all three tests, indicating that the standard cleaning process and horizontal assembly procedure is providing satisfactory cleanliness. Exercising bellows mildly in-situ did not degrade the cavity performance. On the other hand, early onset of field emission was observed for both CAV0278 and CAV0286 after rinsing with bellows on top of the cavity, indicating that particulates were likely introduced into the cavities from the bellows during the HPR.

After sampling, 14 carbon tape samples were generated and a total of 219 particles were characterized in this study, as shown in Fig. 3. Particles from sampling media (Teflon and polyester) were not included. The number of particles on each sample varies between a few and 30. The number of particles in each category on each sample gives the distribution of particle categories inside the cavity and bellows.

A total of 24 categories were identified. A few categories of particles are described below, and their typical SEM images shown in Fig. 4. The average particle size in each category is shown in Fig. 5.

- Cu plating: From bellows inner surface, has a unique porous texture, possibly CuO, $Cu(OH)_2$, or $CuCO_3$ according to the atomic ratio;
- Precipitates, Ca: Mostly Ca and O, possibly CaO, $Ca(OH)_2$, or $CaCO_3$ according to the atomic ratio;
- Precipitates, mixed: Contains elements such as P, S, Cl, together with Na, Mg, K, Ca, and sometimes Fe, possibly metal and/or mineral particles that have been through chemical or cleaning process where they are mixed with salt or residue in the solution;
- Mixed metal clusters: Contains several metal elements such as Fe, Cu, Ti, Mn, Si, Cr, but no anions, likely resulted from cross contamination between different metal parts during handling;
- Mineral: Usually contains Si, Al, Mg, Ca, Na, K, and O, such as Talc, Kaolinite, and Dolomite); SiO_2 and Al_2O_3 are not included in mineral category, they are listed separately instead.

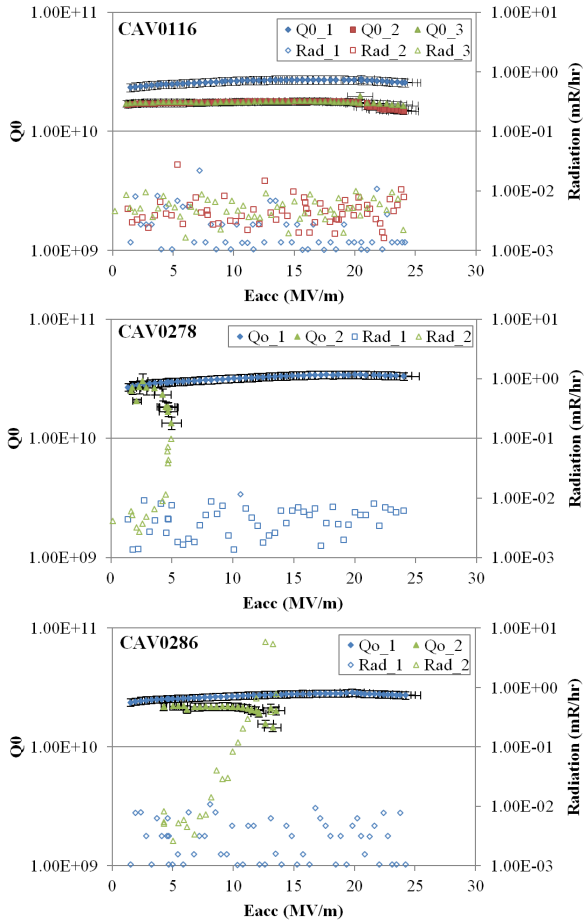


Figure 2: Vertical testing results of CAV0116 (without bellows, with bellows before exercising, with bellows after exercising), CAV0278 (without bellows and with bellows), and CAV0286 (without bellows and with bellows).

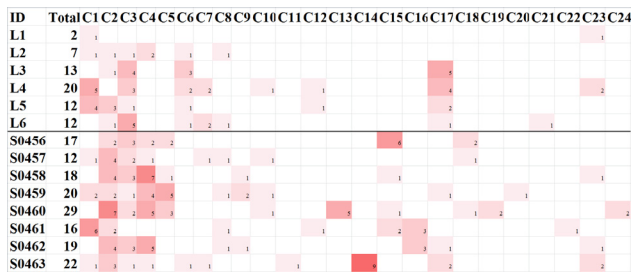


Figure 3: The number of particles in each category (C1-C24) on each sample. The color of each cell is scaled based on the number of particles in the cell (0~9). Darker color means more particles.

Several types of particles are decided to be distractions, due to their apparent source, distribution, or very low count: Particles introduced by tooling and sampling process, such as polymer material from the wipe (C-F, C-O), metal from scissors and tweezers (stainless steel, other types of steel, and Al-Mg), protein from operators (C-N-O-S), particles existing in the cleanroom from other processes (Sn, SnO, Ag, AgO, Al, Fe, Cu (non-plated copper)), and other stray particles (Zn-Al-O, Na_2SO4, NaCl,

ISBN: 978-3-95450-194-6 ISSN: 2226-0366 doi:10.18429/JACoW-LINAC2018-MOPO019

Cr). Species such as mixed metals, Fe oxide, and Talc were considered distractions because they appear only in one sampling process.

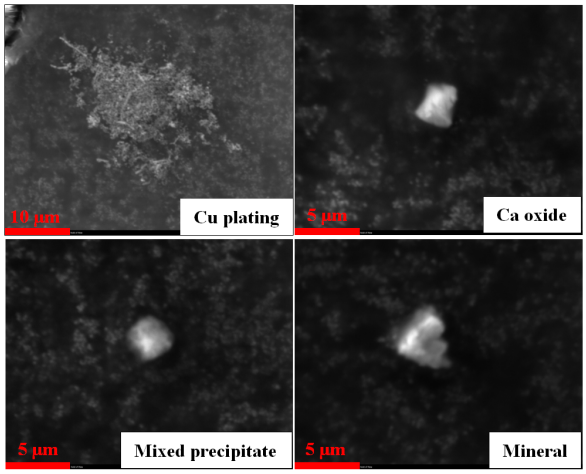


Figure 4: Typical particles of several main categories: Cu plating, Ca oxide, mixed precipitate, mineral.

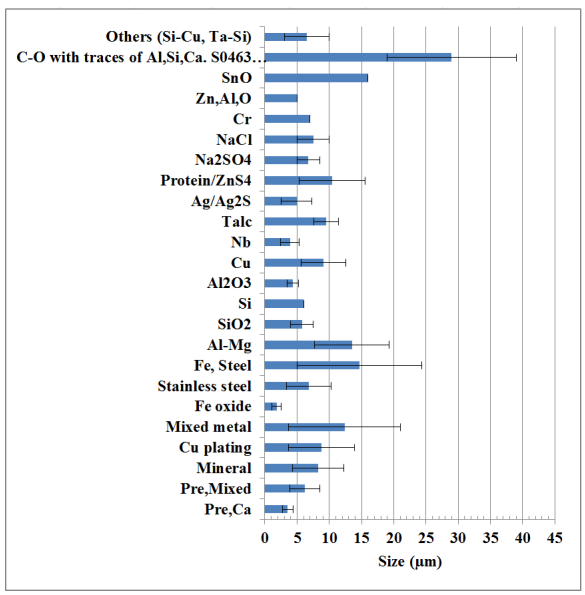


Figure 5: Size of different categories of particles, average and standard deviation.

Cu plating particles (C4) are seen in both sampling process, more on bellows than on cavities. Sample S0458 was from wiping several iris regions of the bellows, and it showed the most Cu plating particles, indicating that the plating particles tend to dislodge more easily on a surface under stretch. Interestingly, sample S0461 was from shaking bellows above a clean wipe then sampling the wipe; it showed no Cu plating particles, which could indicate that Cu plating does not come off bellows surface without strong force such as wiping.

Mineral particles (C3) also showed wide appearance. Many of precipitates (C1, C2) were observed in both the bellows and the cavity, even on the shaking sample (S0461). This indicates the precipitation particles dislodged easily from the bellows surfaces.

Figure 5 shows the size of particles in each category from both sampling methods. It should be noted that particles collected with two different methods showed slightly different characteristics. Even though assigned to the same category based on element presence, they can vary in sizing and topography.

CONCLUSION

Based on particle analysis, copper plating, mineral, and precipitates are likely related to the early onset of field emission in CAV0278. Extra cleaning steps have been added to reduce the chance of surface residue in bellows. Also, any changes to bellows cleaning need to be carefully assessed since aggressive methods can remove Cu from the plating.

As for the analysis process, it is noticed that a few factors could introduce bias. Since it is not practical to sample the entire inner surface of the cavity and bellows, therefore limited coverage of the interested surface during sampling could limit the information obtained from the surface. Not necessarily all particle collected is characterized in the SEM, although efforts were made to cover most of the particles on each carbon tape. Categorizing is subjective due to complication of particle history; particles with the same element may present in different forms (big particle vs. powder), which also affects size determination.

Despite the limitations, this study provided a procedure to analysis contamination and added knowledge to the understanding of particle species in our processing environment. Collecting more data to build up a database of particles would be beneficial in long term.

ACKNOWLEDGEMENTS

Authored by Jefferson Science Associates, LLC under U.S. DOE Contracts DE-AC05-06OR23177 and DE-AC02-76SF00515 for the LCLS-II Project. We thank Josh Spradlin and Olga Trofimova for helping with SEM/EDS analysis, Chris Dreyfuss for assisting with sampling process.

REFERENCES

[1] E. Vogel *et al.*, "Integration of the European XFEL Accelerating Modules", in *Proc. LINAC'12*, Tel-Aviv, Israel, MOPB017, pp. 207-209.

[2] S. Berry *et al.*, "Clean Room Integration of the European XFEL Cavity Strings", in *Proc. IPAC'14*, Dresden, Germany, WEPRI001, pp. 2474-2476.

[3] L. Zhao *et al.*, "Cavity Processing and Testing Activities at Jefferson Lab for LCLS-II Production", in *Proc. SRF'17*, Lanzhou, China, MOPB050, pp. 173-176.

[4] K. Wilson *et al.*, "Production of Copper-Plated Beamline Bellows and Spools for LCLS-II", in *Proc. IPAC'17*, Copenhagen, Denmark, MOPVA132, pp. 1167-1169.

[5] C. Reece, "Developing and Using Particulate Assays to Manage Cryomodule Contamination", Operating SRF systems reliably in a "dirty" accelerator, https://www.helmholtz-berlin.de/events/operating-srf/index_en.html

Content from this work may be used under the terms of the CC BY 3.0 licence (© 2018). Any distribution of this work must maintain attribution to the author(s), title of the work, publisher, and DOI.

ISBN: 978-3-95450-194-6 ISSN: 2226-0366 doi:10.18429/JACoW-LINAC2018-MOPO020

BEAM DYNAMICS STUDIES AND INSTRUMENTATION TESTS FOR BUNCH LENGTH MEASUREMENTS AT CLEAR

L. Garolfi*, S.Doebert, M. Bergamaschi, R. Corsini, A. Curcio,
W. Farabolini[1], D. Gamba, I. Gorgysian, CERN, Geneva, Switzerland
C. Bruni, P. Lepercq, H. Purwar, C. Vallerand, LAL, Orsay, France
[1]also at CEA/DSM/IRFU, Saclay, France

Abstract

A new CERN Linear Electron Accelerator for Research (named CLEAR) has been installed as a general-purpose user facility to study novel accelerating techniques, high-gradient structures, instrumentation and irradiation experiments. CLEAR is a flexible accelerator that can provide high quality bunched electron beams with a wide range of beam parameters up to an energy of 220 MeV, offering several testing capabilities. Among all the potential applications, novel accelerating techniques, such as plasma acceleration and THz generation are considered. These applications require shorter bunches, down to the 100 fs level. This paper reports on beam dynamics studies and instrumentation tests to establish a bunch length of this order in CLEAR. The short bunches are generated using adiabatic bunching in the first accelerating structure. For bunch length diagnostic, CLEAR is equipped with a streak camera and a transverse deflecting cavity. Alternatively, a phase-scan of the last accelerating structure could be used as well to estimate the bunch length. The experimental results with respect to these different techniques are presented and compared with simulations.

INTRODUCTION

CALIFES (Concept d'Accélérateur LInéaire pour Faisceau d'Electron Sonde) [1] represented the electron probe beam injector for the CLIC Test Facility 3 (CTF3) [2] at CERN. Recently, this accelerator has been refurbished as a new general-purpose user facility for accelerator R&D and components tests for existing and future accelerator applications. CLEAR [3, 4] can provide high quality bunched electron beams from 60 to 220 MeV in single or multi-bunch configuration with a bunch spacing of 1.5 GHz. The test accelerator exhibits a broad range of capabilities, such as prototyping and validation of accelerator components (for the Large Hadron Collider upgrade and its injector), high-gradient acceleration studies (normal-conducting X-band structures), irradiation of electronic components and medical applications. Furthermore, novel concepts as plasma acceleration and THz generation [5] could profit from the CLEAR beam line optimized for short bunches and low emittance beyond the current performances achieved by the CALIFES photo-injector, in the past. The improvement of the electron bunches quality in terms of length and emittance would also be beneficial to AWAKE (Advanced WAKEfield Experiment) [6], which will need a new short-pulse electron source in view of the "Run 2" phase. Therefore, beam dynamics studies and instrumentation tests have been performed for both determining an accelerator injection configuration that allows bunch lengths less than 1 ps and its subsequent experimental measure.

CLEAR LAYOUT AND DIAGNOSTICS

The accelerator is composed of the CALIFES injector (around 25 meters-long), which provides the electron beam to a subsequent 16 meters-long diagnostics and test lines. The electron photo-injector is composed of a 2.5-cell S-band RF gun [7] where the electrons are extracted and accelerated from a Cs_2Te cathode when illuminated by laser pulses. Two solenoids surround the gun for space charge emittance compensation. The RF gun is able to provide electron bunches with an energy of around 6 MeV, then three S-band LIL (LEP Injector Linac) [8] accelerating sections allow to boost the beam energy up to 220 MeV. An Integrated Current Transformer (ICT) [9] and a ceramic screen are installed right after the RF gun, for beam diagnostics. The first structure can be used to compress the bunch by using the velocity bunching technique. A matching section with a quadrupole triplet and a spectrometer line complete the accelerator. An S-band RF deflecting cavity is also installed along the beam line (Fig. 1). Bunch length measurements are possible by streak camera measurements [10] of Optical Transition Radiation (OTR) or by using an S-band RF deflecting cavity [11]. A transverse beam profile monitor [12] equipped with a Yttrium Aluminium Garnet (YAG) scintillator and an OTR screen is installed before the spectrometer. An additional ICT and YAG screen in the spectrometer line complete the longitudinal beam diagnostic capabilities. The beam-line ends about 20 cm after the spectrometer dipole with a 100 μm-thickness aluminium window, leaving about 1 meter-long in-air test stand. This area hosts the main THz radiation diagnostics [13].

BEAM DYNAMICS MODEL

A train of laser pulses, each one a few ps length spacing, impinges the photocathode. The number of pulses that constitutes the train can be controlled remotely. The number of pulses in the train was set to two, for most of the measurements. The RF gun is surrounded by two solenoids, the focusing and bucking coils. Three dimensional simulations have been performed using the Opera-3D FEA software. The latter allows to obtain the on-axis longitudinal magnetic field profile along the beam axis. The right current values

* luca.garolfi@cern.ch

Content from this work may be used under the terms of the CC BY 3.0 licence (© 2018). Any distribution of this work must maintain attribution to the author(s), title of the work, publisher, and DOI.

ISBN: 978-3-95450-194-6 ISSN: 2226-0366 doi:10.18429/JACoW-LINAC2018-MOPO020

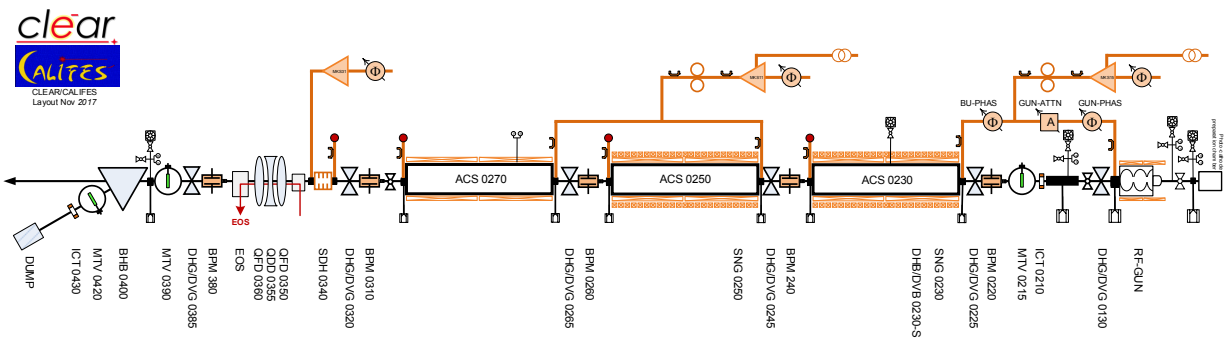


Figure 1: CLEAR accelerator layout.

of the coils is set in order to cancel the induced magnetic field (B = 0 T) at the photocathode location (z = 0 m). This allows to prevent beam transverse emittance degradation due to the residual angular momentum increase. The maximum current through the focusing coil can be set to 340 A. Also, the on-axis longitudinal electric field amplitude has been extracted from 2D Superfish simulation. These two field profiles are used as inputs for the tracking of electrons in the linac by ASTRA (A Space Charge Tracking Algorithm) [14] in order to have a close match between simulations and experimental data. Table 1 indicates the most relevant parameters that have been used for simulations.

Table 1: Simulation Parameters

Parameter	Value
Photocathode	Cs_2Te
Laser spot size $\sigma_{x,y}$	0.4 mm - Gaussian
Laser pulse duration σ_t	4 ps - Gaussian
Steerer position	0.305 m
ICT position	1.63 m
MTV position	1.825 m

We performed beam charge measurement using the ICT (see Fig. 2) as a function of the gun RF-phase. This so-called "phase scan" is usually used to characterize the electric field interacting with the photo-cathode triggering the charge extraction phenomenon. These experimental data are compared with the ASTRA beam dynamics model considering a gun peak accelerating fields of 90 MV/m and a suitable Schottky value. As we can see from Fig. 2 the ASTRA model is in good agreement with the experimental data for this set of parameters. Figure 3 shows the comparison between the experimental transverse beam size measured on the MTV screen at around 1.8 m after the cathode with ASTRA simulations. In this case, the trend of the simulated values looks in agreement with the experimental values. Some of the simulated values are within the experimental error bars. Even if the simulated position of the beam waist fits the experimental one, these values seem to underestimate the experimental values at the minimum.

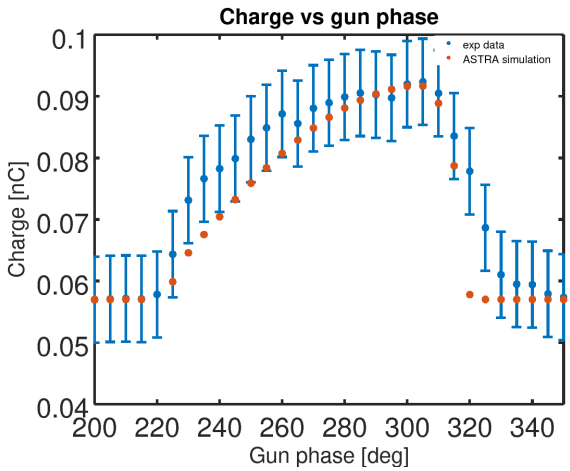


Figure 2: Comparison between the experimental extracted charge at ICT vs gun phase (blue line) and ASTRA simulation (orange line).

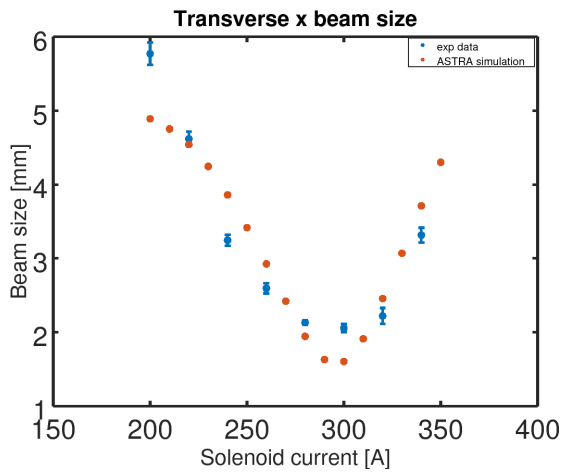


Figure 3: Comparison between the transverse beam size at ICT vs focusing solenoid current (blue line) and ASTRA simulation (orange line).

The discrepancy between the experimental data and simulations, especially at the minimum value, will be further investigated by improving the accuracy of the ASTRA model.

Content from this work may be used under the terms of the CC BY 3.0 licence (© 2018). Any distribution of this work must maintain attribution to the author(s), title of the work, publisher, and DOI.

ISBN: 978-3-95450-194-6 ISSN: 2226-0366 doi:10.18429/JACoW-LINAC2018-MOPO020

Content from this work may be used under the terms of the CC BY 3.0 licence (© 2018). Any distribution of this work must maintain attribution to the author(s), title of the work, publisher, and DOI.

BUNCH LENGTH MEASUREMENTS

The bunch length has been measured by different techniques aiming at testing the CLEAR instrumentation and potential for short bunches. First measurement has been performed by using an RF deflecting cavity, after the three accelerating sections. In Fig. 4, the data have been recorded for different gun-phases (blue) and compared with simulations (red). We considered a good match between measured and simulated charge as a reference for the gun-phases.

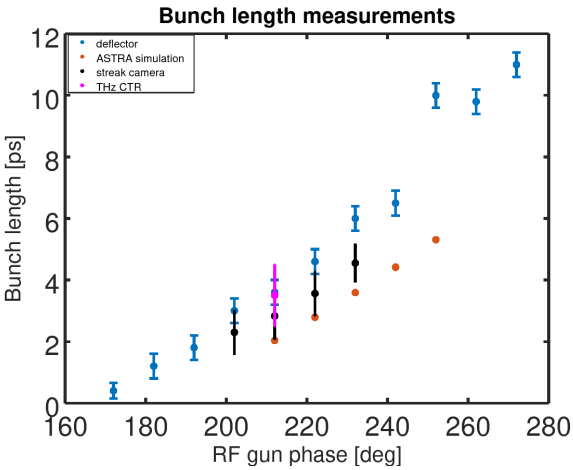


Figure 4: Bunch length experimental measurements with RF deflector, simulations, streak camera and THz radiation.

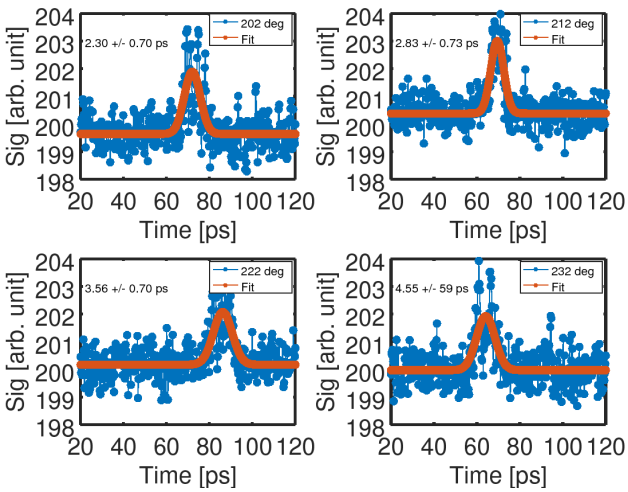


Figure 5: Bunch experimental temporal profiles recorded by the streak camera, for different RF gun phases.

Figure 5 shows the profiles recorded by the streak camera for measuring the bunch duration. By means of the Gaussian fit we can extrapolate the bunch length taking into account also the slit aperture contribution. As we can see from the Fig. 4, the bunch length values are in agreement with those obtained by the deflector measurements for the same gun phases. We point out that all measurements with the streak camera have been taken with band-pass filter (centered at 450 nm, 35 nm bandwidth) and that experimental errors have been evaluated doing statistics over tens of pictures for each gun phase. Moreover, the bunch length measurements have been performed with Coherent Transition Radiation (CTR) in the region of mm-waves (see Fig. 6). The data has been recorded wit a set of four zero-biased Schottky diodes each one coupled to a waveguide band–pass filter. The frequencies studied have been 36, 60, 72 and 84 GHz, respectively. A model has been used for fitting the data, taking into account the finiteness of the radiator (Aluminium disk, 10 cm diameter), the angular distribution of the CTR at the plane of the detectors and assuming that the bunch has a gaussian longitudinal shape. The bandwidth of the CTR spectrum is inversely proportional to the bunch length. Experimental errors come from shot-to-shot statistical fluctuations (measurements recorded with a train of twenty bunches), depending in turn on charge fluctuations and background noise from other metallic parts located on the table around the detectors. From Figure 5 the bunch length is 3.5 ± 1 ps in agreement with the value obtained by the RF deflector (3.6 ± 0.4 ps) for the same gun-phase (212 deg).

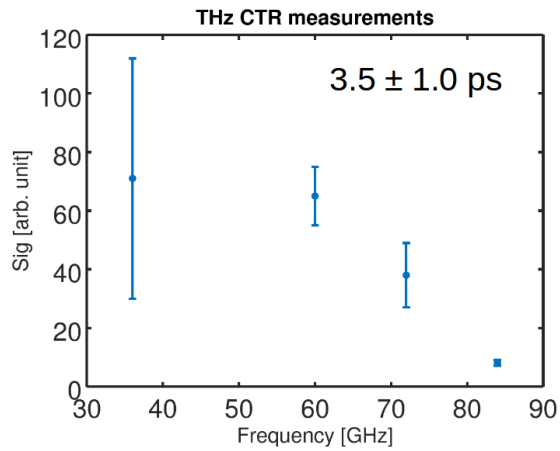


Figure 6: Bunch length experimental measurements from coherent transition radiation (CTR) recorded by zero-biased Schottky diodes.

CONCLUSION

The CLEAR user facility is devoted to R&D for accelerators and instrumentation in a broad range of applications. Beam dynamics studies, bunch length measurements and instrumentation tests have been carried out. The ASTRA code has been used to perform simulations and their comparison with the experimental data demonstrated a promising starting point toward a solid tool for predicting the best configuration for very short electron bunches. Bunch length measures have been performed with three different techniques: RF deflecting cavity, streak camera and THz coherent transition radiation. Although the experimental data exhibit good agreement for different techniques, in order to produce electron bunches of length of 100 fs further improvements are needed.

ISBN: 978-3-95450-194-6 ISSN: 2226-0366 doi:10.18429/JACoW-LINAC2018-MOPO020

REFERENCES

[1] A. Mosnier *et al.*, "The probe beam linac in CTF3", in *Proc. 10th European Particle Accelerator Conf. (EPAC'06)*, Edinburgh, UK, Jun. 2006, paper MOPLS059, pp. 679–681.

[2] R. Bossart *et al.*, "CTF3 Design Report", Eds. G. Geschonke and A. Ghigo, Apr. 2002, CERN Rep. CERN/PS-2002-008 (RF).

[3] CALIFES Workshop 2016, Geneva, Switzerland, 2016. http;//indico.cern.ch/event/533052

[4] R. Corsini *et al.*, "First Experiments at the CLEAR User Facility', in *Proc. 9th Int. Particle Accelerator Conf. (IPAC'18)*, Vancouver, BC, Canada, Apr.-May 2018, pp. 4066–4069, doi:10.18429/JACoW-IPAC2018-THPMF014

[5] A. Curcio *et al.*, "Resonant plasma excitation by single-cycle THz pulses", *Sci. Rep.*, vol 8., no. 1 p. 1052, 2018. doi:10.1038/s41598-017-18312-y

[6] A. Caldwell, "AWAKE design report", CERN, Geneva, Switzerland, CERN Technical Design Rep. CERN-SPSC-2013-013, 2013.

[7] J. Brossard *et al.*, "Construction of the Probe Beam Photoinjector of CTF3", in *Proc. 10th European Particle Accelerator Conf. (EPAC'06)*, Edinburgh, UK, Jun. 2006, paper MOPLS114, pp. 828-830.

[8] G. Bienvenu *et al.*, "Accelerating structure developments for the LEP injector linacs (LIL)", in *Proc. 1984 Linear Accelerator Conf. (LINAC'84)*, Seeheim, Germany, May 1984, pp. 463-465.

[9] Bergoz Instrumentation, http://www.bergoz.com

[10] C. P. Welsch *et al.*, "Longitudinal beam profile measurements at CTF3 using a streak camera", *J. Inst.*, vol. 1, no. 9, p. P09002, 2006. doi:10.1088/1748-0221/1/09/P09002

[11] W. Farabolini, "Califes probe beam status", International Workshop on Linear Colliders 2010, ECFA-CLIC-ILC Joint Meeting, Geneva, 2010.

[12] W. Farabolini *et al.*, "Video profile monitors development for the CTF3 probe beam linac", in *Proc. 11th European Particle Accelerator Conf. (EPAC'08)*, Genoa, Italy, Jun. 2008, paper TUPC024, pp. 1101-1103.

[13] A. Curcio *et al.*, "THz at CLEAR: source and diagnostics for the electron acceleration", presented at CLIC Workshop 2018, http://.cern.ch/event/656356

[14] ASTRA, http://www.desy.de/~mpyflo/

Content from this work may be used under the terms of the CC BY 3.0 licence (© 2018). Any distribution of this work must maintain attribution to the author(s), title of the work, publisher, and DOI.

ISBN: 978-3-95450-194-6 ISSN: 2226-0366 doi:10.18429/JACoW-LINAC2018-MOPO024

DEVELOPMENT OF HIGH POWER COHERENT TERAHERTZ WAVE SOURCES AT LEBRA 125MeV LINAC IN NIHON UNIVERSITY*

T. Sakai†, T. Tanaka, Y. Hayakawa, Y. Sumitomo, K. Hayakawa, Y. Takahashi, K. Nogami,
LEBRA, Nihon University, Funabashi, Japan
N. Sei, H. Ogawa, AIST, Tsukuba, Japan

Abstract

Development of a high performance electron linac for the generation of FEL, Parametric X-ray Radiation (PXR) and THz waves has been continued at the Laboratory for Electron Beam Research and Application (LEBRA) of Nihon University as a joint research with KEK and National Institute of Advanced Industrial Science and Technology. The transport systems of the THz wave were installed in the vacuum chamber on the downstream side of the bending magnet of the PXR and FEL beam-line. The CER and the CSR are generated by the bending magnet each of the beam line. In addition, the CTR using thin metal foil is also generated. The average power of the CTR wave was measured approximately 1 mJ/macro-pulse (pulse width 4.5 μs) near the CTR wave beam source point in the frequency range of 0.1 - 2.5 THz. In addition, the energy of the CER as high as 0.5 mJ/macro-pulse were achieved with the experimental room. Furthermore, CER of the generated the FEL beam line can also be guided from the bending magnet on the downstream side of the undulator without disturbing the FEL oscillations. THz transport beam-lines and the characteristics of the THz waves are discussed in this report.

INTRODUCTION

Research and development of a high performance electron linac for the generation of the infrared Free Electron Laser (FEL), Parametric X-ray Radiation (PXR) and THz waves has been continued at the Laboratory for Electron Beam Research and Application (LEBRA) of Nihon University as a joint research with the High Energy Accelerator Research Organization (KEK) and National Institute of Advanced Industrial Science and Technology (AIST) [1-3].

The LEBRA linac consists mainly of the -100 kV DC electron gun, the pre-buncher, the buncher and the three 4 m long traveling wave accelerating tubes. The electron-beam energy is freely adjustable from 40 to 100 MeV according to the purpose of use. The RF power sources has been powered by two S-band klystrons (Mitsubishi Electric Corporation, PV-3030A1, the peak output power of 20 MW, the repetition rate of 2 ~ 12.5 Hz and the pulse duration of 5 ~ 20 μs).

The saturated FEL lasing has been obtained in the wavelength region of 0.4 ~ 6 μm [4]. The PXR generator covers the X-ray energies from 4 to 34 keV by using Si(111) and Si(220) planes as the target and the second crystals [5]. CSR-THz wave source development in the FEL Beam line has been carried out since 2011 [6]. Based on the results of the CSR-THz wave source development in the FEL line, higher power CTR-THz and CER-THz wave sources line has been constructed in the PXR line since 2016. In addition to these, the new high power CER-THz wave transportation line have been constructed between the downstream bending magnet in the FEL undulator section and the downstream optical cavity mirror since 2017.

CER-THZ WAVE SOURCE OF FEL BEAM LINE

Measurements of the spectrum of coherent radiation generated by the electron bunch are well suited for monitoring the condition of the electron beam. Therefore, based on the results of the CSR-THz wave source

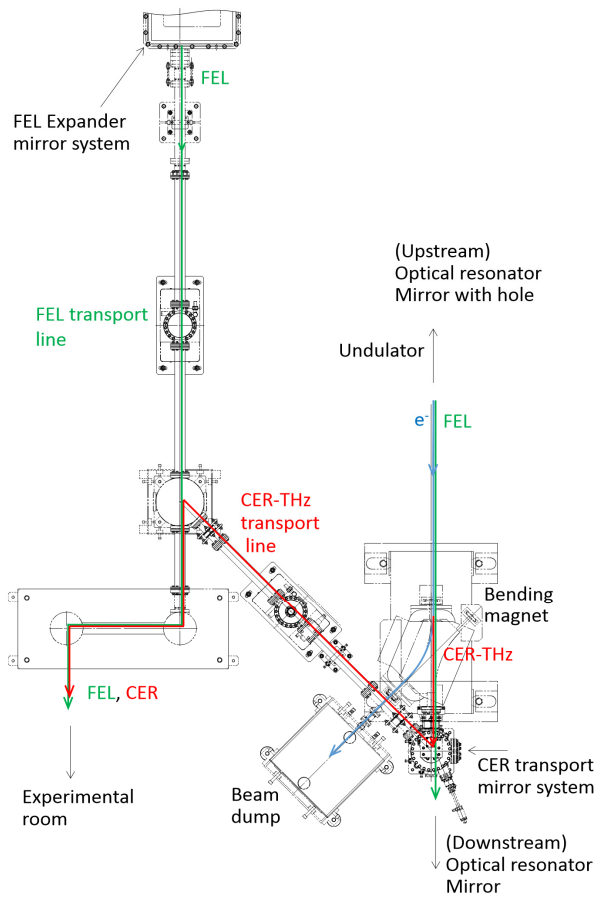


Figure 1: FEL beam line, CER-THz transport line and CER-THz wave transport concave mirrors system.

* This work was supported by JSPS KAKENHI (Grant-in-Aid for Young Scientists (B)) Grant Number JP16K17539.
† sakai@lebra.nihon-u.ac.jp

Content from this work may be used under the terms of the CC BY 3.0 licence (© 2018). Any distribution of this work must maintain attribution to the author(s), title of the work, publisher, and DOI.

ISBN: 978-3-95450-194-6 ISSN: 2226-0366 doi:10.18429/JACoW-LINAC2018-MOPO024

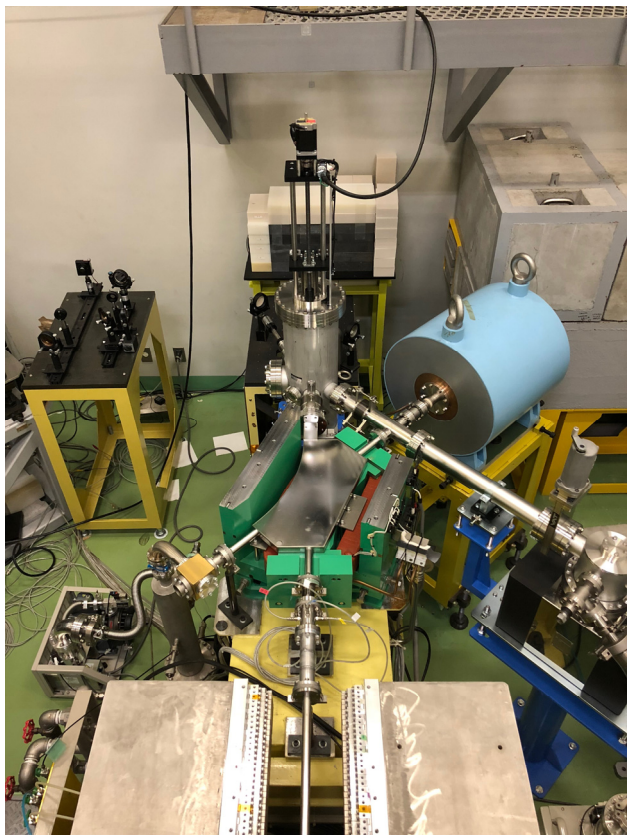


Figure 2: CER-THz transportation line as viewed from the upstream side after installation of the mirror system.

development in the FEL line, the new high power CER-THz wave transportation line have been constructed between the downstream bending magnet in the FEL undulator section and the downstream optical cavity mirror (see Figs. 1 and 2). The opening diameter of the vacuum chamber in the bending magnet can correspond to a horizontal surface of 30 mrad.

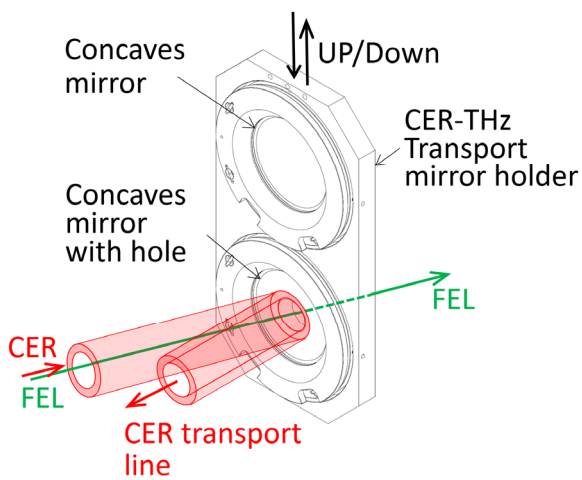


Figure 3: Transport mirrors system consists of the total reflection concave mirror and the concave mirror with a hole.

The main purpose of this mirror system is the monitoring of the electron beam bunch length and the control of FEL lasing. The edge radiation from the bending magnet has an annular shape distribution. In this case, by using a hole-coupled concave mirror, the CER-THz can be reflected and focused from the optical cavity of the FEL without a diffraction loss of the FEL beam (see Fig. 3). The diameter of the mirrors were 74 mm (effective diameter: about 68 mm) and the inner diameter of the hole was 25 mm. As a result, the simultaneous measurement of the FEL and the CER-THz wave are achieved. In addition, this mirror system can switch total reflection mirror and hole-coupled mirror in tens of seconds by remote control.

MEASUREMENTS OF CER-THz

Figure 4 shows the spectrum of the CER-THz wave at the accelerator room. The electron beam states were the electron-beam energy of 57 MeV, the macropulse duration of about 18 us and the macropulse repetition of 2 Hz. The wavelength of the FEL was 5.4 μm. The following instruments were used for the measuring. The energy measurement of the CTR-THz was carried out using a power sensor (Ophir 3A-P-THz [7]) with calibration for terahertz wavelengths. In addition, the spectrum was carried out using an interferometer (pyroelectric detector: THZ10 [8]). The average power of the CER-THz wave was measured approximately 0.5 mJ/macro-pulse (by the total reflection mirror) at the accelerator room the frequency range of 0.1 - 2.5 THz. Additionally, inserting the hole-coupled concave mirror, the reflection efficiency was about 70% as compared with the total reflection mirror. Confirmation of operation of the CER-THz transport system was achieved. Furthermore, simultaneous measurement of the CER-THz and the FEL oscillation succeeded.

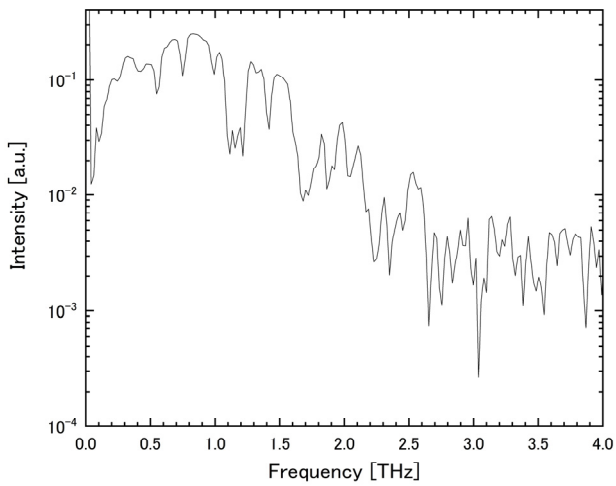


Figure 4: Spectrum of CER-THz measured using an interferometer.

Content from this work may be used under the terms of the CC BY 3.0 licence (© 2018). Any distribution of this work must maintain attribution to the author(s), title of the work, publisher, and DOI.

ISBN: 978-3-95450-194-6 ISSN: 2226-0366 doi:10.18429/JACoW-LINAC2018-MOPO024

Content from this work may be used under the terms of the CC BY 3.0 licence (© 2018). Any distribution of this work must maintain attribution to the author(s), title of the work, publisher, and DOI.

SUMMARY

On the basis of the CSR-THz wave source development in the FEL line, the CER-THz wave transportation line have been constructed between the downstream bending magnet in the FEL undulator section and the downstream optical cavity mirror.

Simultaneous measurement of the CER-THz and the FEL oscillation succeeded beam by using the hole-coupled concave mirror without a diffraction loss of the FEL. The average power of the CER-THz wave was measured approximately 0.5 mJ/macro-pulse (by the total reflection mirror) the frequency range of 0.1 - 2.5 THz. The reflection efficiency was about 70% as compared with the total reflection mirror.

The monitoring of the electron beam bunch length and the control of FEL lasing are possible from the use of this CER-THz transport system.

REFERENCES

[1] K. Hayakawa *et al*., "Operation of Near-infrared FEL at Nihon University", in *Proc. FEL'07*, Novosibirsk, Russia, Aug. 2017, pp. 114-117.

[2] Y. Hayakawa *et al*., "Dependence of PXR beam performance on the operation of the pulsed electron linac", *Nucl. Instr. Method. B*, vol.. 266, no.17, pp. 3758-3769, 2008.

[3] N. Sei *et al*., "Observation of intense terahertz-wave coherent synchrotron radiation at LEBRA", *J. Phys. D*, vol. 46, p. 045104, 2013.

[4] Y. Hayakawa *et al*., "First lasing of LEBRA FEL at Nihon University at a wavelength of 1.5 μm", *Nucl. Instr.. Meth. Phys. Res. Sec. A,* vol. 483, pp. 29-33, 2002.

[5] Y. Hayakawa *et al*., "X-ray imaging using a tunable coherent X-ray source based on parametric X-ray radiation", *JINST*, vol. 8, p. C08001,Aug. 2013. doi:10.1088/1748-0221/8/08/C08001.

[6] N. Sei *et al*., "Characteristics of Transported Terahertz-wave Coherent Synchrotron Radiation at LEBRA", in *Proc. FEL'14*, Basel, Switzerland, Aug. 2014, pp. 541-544.

[7] Ophir Optronics Solutions Ltd., http://www.ophiropt.com/laser--measurement/laser-power-energy-meters/products/Laser-Thermal-Power-Sensors/High-Sensitivity-Thermal-Laser-Sensors/3A-P-THz

[8] https://www.pyrosensor.de/Standard-924644.html

ISBN: 978-3-95450-194-6 ISSN: 2226-0366 doi:10.18429/JACoW-LINAC2018-MOPO026

THE RESONANCE FREQUENCY SHIFT AFTER APPLYING THE COOLING SYSTEM FOR A SIDE COUPLED STANDING WAVE LINAC

Masoud Mohseni Kejani†, Fereydoon Abbasi Davani, Shahid Beheshti University, Tehran, Iran
Sasan Ahmadiannamin, Iranian Light Source Facility (ILSF), Tehran, Iran
Farshad Ghasemi, Sara Zarei, Nuclear Science and Technology Research (NSTRI), Tehran, Iran

Abstract

A radio frequency accelerator tube used in linear medical accelerators includes three main sections of the radio frequency cavity, an electron gun and the X-ray target, which is vacuumed by a pump inside it. The electromagnetic energy loss in the structure of the cavity can increase the temperature of the tube, resulting in changes in the geometric dimensions and then changes in some of the cavity characteristics, such as the resonance frequency. A cooling system is required to prevent excessive change in the resonant frequency due to thermal loss. Also, it is necessary to perform some computer simulations to stabilize the cavity's performance in the presence of electromagnetic energy thermal dissipation and the cooling system. In this paper, the simulation results of resonant frequency shifts after applying the cooling system have been reported.

INTRODUCTION

As we know, in terms of the accelerating structure, essentially electron linear accelerators are divided into traveling wave and standing wave structures. The design and construction of standing wave cavities are more complicated than standing wave cavities. On the other hand, the stability of the cavity's performance plays an important role in the characteristics of the outlet beam. In medical applications, the stability of cavities is more important [1]. By changing the nominal frequency of the cavity, the impedance matching of the transmission line and the accelerating cavity are changed and a large part of the power is reflected. Due to the high quality factor of standing wave cavities (about 17000), and 1.23 coupling constant, the cavity bandwidth (FWHM) will be about 400 kHz. It means that, by varying the frequency of 200 kHz, the input power to the cavity will halved and the output energy will be 4.28 MeV instead of 6MeV. The acceptable frequency shift of the cavity applied by using the cooling system, depends on the ability of the automatic frequency control system (AFC) [2]. The operation of the automatic frequency control system is determined by the two factors of the linear behavior and the response rate of the system relative to the radiofrequency pulse repetition rate [3, 4]. In the conventional analog frequency regulator system used in medical linear accelerators, the frequency correcting range in about 0.9 MHz with 300 pulse per second repetition rate. Therefore, the maximum frequency shift of the cavity after applying the water cooling system should not exceed 450 kHz. That can be easily stabilized by the automatic frequency control system [3].

GEOMETRY AND COOLING SYSTEM DESIGN

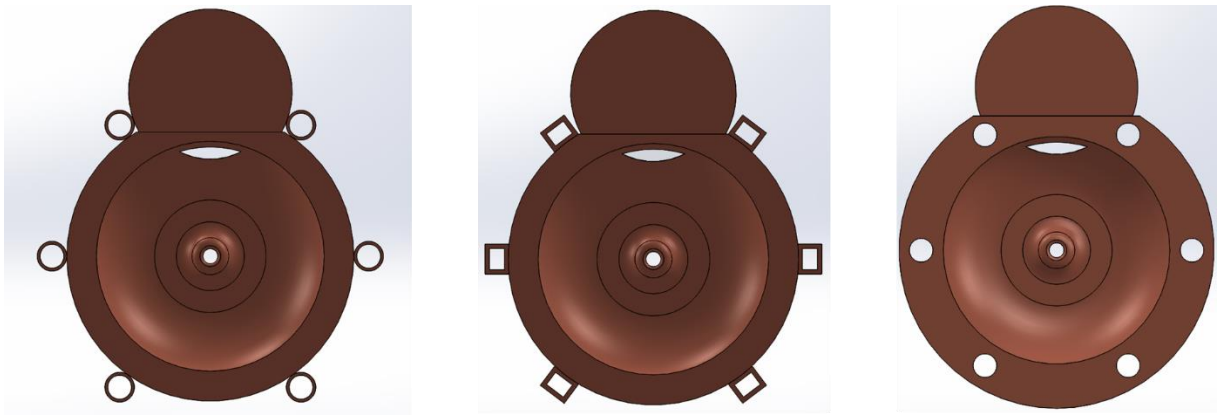
The geometrical parameters of RF cavity were optimized for operation in 2998.5 MHz in coupled cells configuration. The cavity will be operated with 2.6 MW input power with 5 μs beam length and 150, 200 and 300 Hz repetition rate. The loss of each accelerating cell will be calculated for mentioned repetition rate equal to 250, 350 and 500 watts for each accelerating cell for beam current of 100 mA by dividing to number of accelerating cells respectively. For this cavity, three types of cooling systems were investigated. The first type is the cooling system with tangential circular cross section, the second type is the cooling system with tangential rectangular cross section, and the third type is internal cooling system with circular cross-section. The inner diameter of the circular cross-section pipes is 8mm and the internal dimensions for the rectangular cross-section is 7mm*5mm. The inlet water velocity and temperature for all three types is 2m/s and 20, 22, 25°C respectively. The thermal calculations and total deformation of the cavities after applying of the cooling system have been reported in another paper [5]. Figure 1 illustrates the cooling system designs and Table 1 shows the temperature comparison for them.

† Masoud.mohseni.kejani@gmail.com

Content from this work may be used under the terms of the CC BY 3.0 licence (© 2018). Any distribution of this work must maintain attribution to the author(s), title of the work, publisher, and DOI.

ISBN: 978-3-95450-194-6 ISSN: 2226-0366 doi:10.18429/JACoW-LINAC2018-MOPO026

Content from this work may be used under the terms of the CC BY 3.0 licence (© 2018). Any distribution of this work must maintain attribution to the author(s), title of the work, publisher, and DOI.



(a) (b) (c)

Figure 1: Cooling System Designs.
a) Tangential Pipe. b) Tangential Duct. c) Internal Pipe.

Table 1: Comparison of Cooling Systems for 250, 350 and 500W Power Loss

Power Loss (W)	Cooling Water Temp. (°C)	Pipe		Duct		Internal Pipe	
		Temperature (°C)		Temperature (°C)		Temperature (°C)	
		Min.	Max.	Min.	Max.	Min.	Max.
500	20	25.603	55.208	27.66	49.592	28.628	45.86
	22	27.6	57.2	29.656	51.586	30.622	47.855
	25	30.595	60.187	32.65	54.576	33.614	50.849
350	20	23.923	44.648	25.363	40.716	26.041	38.103
	22	25.92	46.64	27.359	42.71	28.036	40.099
	25	28.915	49.627	30.353	45.701	31.028	43.093
250	20	22.803	37.608	23.832	34.799	24.317	32.932
	22	24.8	39.6	25.828	36.793	26.311	34.928
	25	27.795	42.587	28.822	39.783	29.303	37.922

FREQUENCY SHIFT

To obtain the resonant frequency shift after the deformation caused by the stresses introduced into the cavity, HFSS coupling with Steady-State Thermal and Static Structural were used in Ansys workbench[6]. After obtaining the initial resonance frequency and the power loss, the geometry was transferred to the Steady-State Thermal with its power loss. After thermal analysis and transferring the temperature distribution to the Static Structural as a load, the geometry of the deformed cavity was obtained. By resetting the deformed geometry to HFSS, the resonant frequency of the deformed cavity was obtained. The configuration of this multi-physics analysis at the ansys workbench in shown in Figure 2. The frequency shift for all three types of cooling system is shown in Table 2 for comparison.

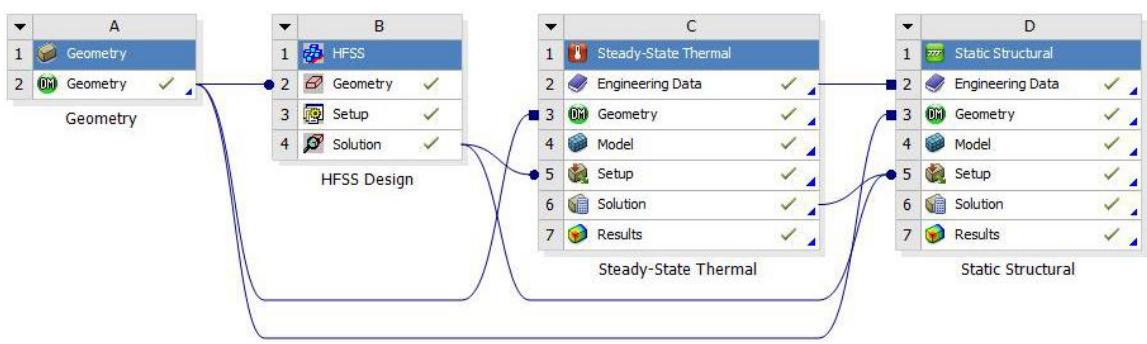


Figure 2: RF-Thermal-Structural-RF Coupling analysis in Ansys Workbench.

ISBN: 978-3-95450-194-6 ISSN: 2226-0366 doi:10.18429/JACoW-LINAC2018-MOPO026

Table 2: The Obtained Frequency Shift for the Different Conditions of Cooling Systems

Power Loss (W)	Cooling Water Temp. (℃)	Pipe	Duct	Internal Pipe
		Frequency (MHz)	Frequency (MHz)	Frequency (MHz)
500	20	0.35	0.30	0.19
	22	0.39	0.34	0.21
	25	0.45	0.39	0.24
350	20	0.16	0.19	0.13
	22	0.19	0.22	0.15
	25	0.25	0.28	0.18
250	20	0.15	0.13	0.08
	22	0.17	0.17	0.10
	25	0.21	0.22	0.13

CONCLUSION

The lowest frequency variation for the internal cooling system with circular cross section with a dissipation power of 250W and an inlet water temperature of 20 ℃ was 0.08 MHz and the highest frequency variation for a tangential cooling system with circular cross section with a power loss of 500 W and an input water temperature 25 ℃ was 0.45 MHz Due to the automatic frequency control (AFC) used in linear medical accelerators, and their frequency range (about 0.9 MHz), designed cooling systems have a good performance.

REFERENCES

[1] S. Zarei *et al.*, "Design of a side coupled standing wave accelerating tube for NSTRI e-Linac'', *Journal of Instrumentation,* Volume 12, (2017).

[2] Kamino Y1 *et al.*, "Development of a new concept automatic frequency controller for an ultrasmall C-band linear accelerator guide", *Med Phys,* (2007);34(8):3243-8.

[3] S. S. Cha *et al.*, "Advanced automatic frequency control system for a dual energy s-band RF electron linear accelerator", in *Proc. IPAC2014,* Dresden, Germany.

[4] Sungsu Cha *et al.*, "Development of an automatic frequency control system for an X-band (=9300 MHz) RF electron linear accelerator", *Nuclear Instruments and Methods in Physics Research Section A,* Volume 855, 21 May (2017), Pages 102-108.

[5] M. Mohseni Kejani *et al.*, "Thermal and Mechanical Analysis of 3 GHz Side Coupled RF Cavity for Medical Linacs", in *Proc. 8th Int. Particle Accelerator Conf. (IPAC'17)*, Copenhagen, Denmark, May 2017, paper THPVA087, pp. 4660-4663, ISBN: 978-3-95450-182-3, https://doi.org/10.18429/JACoW-IPAC2017-THPVA087, http://jacow.org/ipac2017/papers/thpva087.pdf

[6] www.ansys.com/products

Content from this work may be used under the terms of the CC BY 3.0 licence (© 2018). Any distribution of this work must maintain attribution to the author(s), title of the work, publisher, and DOI.

ISBN: 978-3-95450-194-6 ISSN: 2226-0366 doi:10.18429/JACoW-LINAC2018-MOPO027

PHOTOCATHODE LASER PULSE SHAPING FOR IMPROVED EMITTANCE

M. Kotur*, J. Andersson, M. Brandin, J. Björklund Svensson, F. Curbis, F. Lindau, R. Lindvall, E. Mansten, L. Isaksson, R. Svärd, S. Thorin, S. Werin
MAX IV Laboratory, Lund University, Lund, Sweden

Abstract

We present a setup for producing and characterizing picosecond ultraviolet laser pulses for use in the MAX IV photocathode electron gun preinjector. Frequency-tripled laser pulses from a commercial laser system are shaped directly in the ultraviolet domain using a Fourier-domain pulse shaper. The pulses were characterized using a transient grating FROG. We discuss a proposed upgrade of the pulse shaper, as well as its limitations.

INTRODUCTION AND MOTIVATION

The MAX IV Laboratory is a synchrotron radiation facility. Its two storage rings reach electron energies of 1.5 and 3 GeV. In addition to the rings, the lab operates a short pulse facility [1], while a design study for a soft X-ray free electron laser (FEL) at 1-5nm is currently in progress. Both rings are injected by a full energy linac at 3 GeV [2]. The linac can use either a thermionic or a photocathode gun as a source of electrons, but only the photocathode gun can deliver the short electron bunches required for the short pulse facility and the possible future FEL. Our 1.6-cell, normal-conducting, BNL/SLAC-type photocathode gun [3] is operated at 2.9985 GHz. We make use of a polished copper cathode. An emittance-compensating solenoid is installed directly following the gun. The emittance requirement for the short pulse facility of 10 μm has already been met. The more stringent requirement for the free electron laser, of 0.4 μm, at a charge of 40 pC is likely to necessitate developments of both the gun laser and the electron gun itself. Preliminary simulations conducted in Astra [4] indicate that the emittance of a spatially relatively uniform electron bunch is dependent on the shape of the photocathode laser pulse. In the case of a flat-top pulse shape with a finite rise-time, decreasing the rise time was predicted to reduce the emittance by up to 25%.

Our laser pulses are produced by a commercial laser system, which is capable of outputting 9 mJ infrared pulses at 790 nm, with a bandwidth of 25 nm. The laser system specifications have been summarized in Table 1. The infrared pulses are frequency tripled in a pair of β-BBO crystals, yielding ultraviolet pulses at 262 nm, with a photon energy of 4.7 eV, and a spectral bandwidth of 1.6 nm. Table 2 lists the UV pulse properties. These pulses are normally stretched to a duration of about 1.4 ps using a prism stretcher, and subsequently stacked to a final pulse duration of either 3ps or 6ps using birefringent α-BBO crystals [5]. The pulse energy is about 100 µJ on cathode. The laser setup is described in more detail in [6].

Table 1: IR Pulse Specifications

Parameter	Value
Central wavelength	790 nm
Bandwidth	25 nm
Pulse energy	9 mJ
Repetition rate	100 Hz

Table 2: UV Pulse Specifications

Parameter	Value
Central wavelength	262 nm
Bandwidth	1.6 nm
Pulse energy	1 mJ
Repetition rate	20 Hz

The stacked pulses are characterized using two-color cross-correlation, where the picosecond UV pulses are gated using the IR pulses that are left over from the tripling, whose duration is about 100 fs. The IR pulses thenselves are independently characterized in a second harmonic generation frequency resolved optical gating (SHG FROG). The pulses have a double Gaussian longitudinal profile, with a rise time of about 1 ps.

In order to produce picosecond pulses with a closer to a flat-top shape, we direct our pulses through a 4-f pulse shaper (Fig. 1). The pulse is first spectrally dispersed using a diffraction grating. A lens is placed a focal f length away from the grating (g=3846 mm^{-1}), collimating the dispersed beam, and focusing it in the Fourier plane a distance f away. A double knife edge in the Fourier plane can be used to cut out some of the spectral components, and acts as a simple amplitude mask. After the Fourier plane the setup is reversed, so the beam is first collimated by another lens and finally the spectral components are overlapped again using another

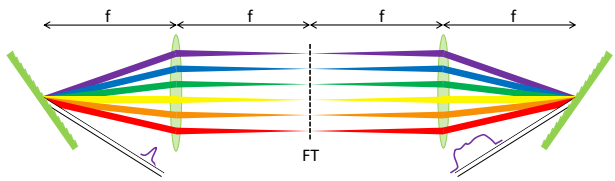


Figure 1: The principle of Fourier domain pulse shaping.

* marija.kotur@maxiv.lu.se

Content from this work may be used under the terms of the CC BY 3.0 licence (© 2018). Any distribution of this work must maintain attribution to the author(s), title of the work, publisher, and DOI.

ISBN: 978-3-95450-194-6 ISSN: 2226-0366 doi:10.18429/JACoW-LINAC2018-MOPO027

grating. Manipulating the different spectral components in the Fourier plane, e.g. by introducing either transparent or absorptive elements will modify the phase and/or the amplitude of the pulse, changing the temporal shape of the pulse at the output of the shaper. A deviation from the 4-f geometry would also lead to temporal reshaping the pulse. We make use of a commonly explored feature of imaging optical stretchers, where a translation of one of the gratings in the direction of the beam propagation leads to a quadratic phase being imparted on the pulse. This phase corresponds to a linear frequency chirp, which can be either positive or negative, depending on the direction in which the grating is moved.

The pulse shaper output is characterized using transient-grating frequency resolved optical gating (TG-FROG) [7]. The characterization setup is described in [6]. Directly after the frequency-tripling crystals, the UV pulses are close to transform limited with a pulse duration of about 80 fs, and an approximately Gaussian longitudinal profile.

RESULTS

Figure 2 demonstrates the possibilities for pulse shaping by adding quadratic phase through a modification in the pulse shaper geometry, in combination with simply cutting out the spectral components in the tails of the spectral intensity distribution. The added phase stretches the pulse, while the cutting the frequencies in the tails reduces the rise time of the final shape. Here we show the predicted and measured 3ps pulse.

The top panel shows the pulse in the spectral domain. A Gaussian with the FWHM of 1.6 nm is a good approximation for the measured spectrum, while a pure quadratic phase is assumed. The amplitude mask that was applied to the pulse is also shown. The middle panel shows the calculated temporal intensity and phase of the pulse. Here we also compare the resulting pulses with and without an amplitude mask applied. The effect of the mask is two-fold. While it does decrease the rise time of the pulse, it also introduces ringing in the amplitude, due to its sharp edges. The bottom panel shows the measured temporal shape of the pulse, which is in very good agreement with the calculated temporal shape. The temporal profile of a pulse produced through pulse stacking is plotted for comparison, and to highlight the improvement in the rise time.

In order to achieve a greater degree of control over the temporal shape of the pulse, we propose using a programmable device in the Fourier plane of the pulse shaper. A number of devices capable of shaping the electric field of a laser have been demostrated, however only an acousto-optic modulator (AOM) can be used for the short wavelengths needed to photoionize a copper cathode [8, 9]. An AOM is essentially a programmable transmissive grating, consisting of a crystal and a piezo-electric transducer attached to it. Fused silica is commonly used at UV wavelengths. An RF wave sent to the piezo forms an acoustic wave in the crystal, resulting in a density and refractive index modulation. The device

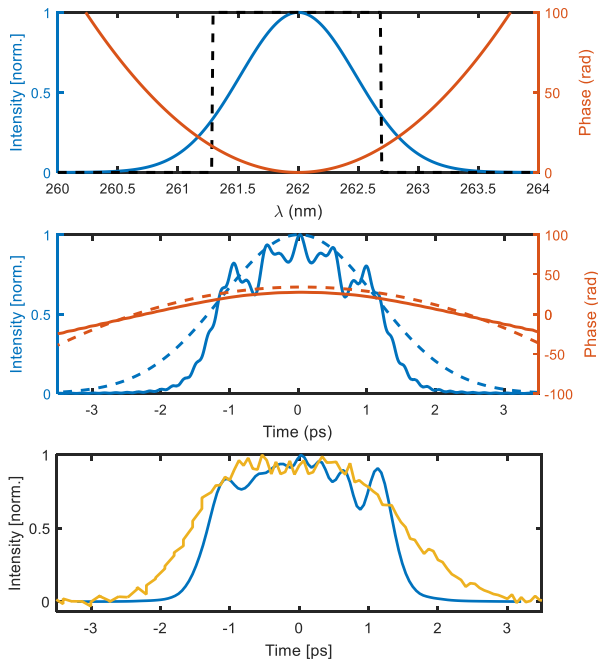


Figure 2: [Top panel] shaped laser pulse in the spectral domain: spectral intensity (sold blue), spectral phase (solid red), amplitude mask (dashed black). [Middle panel] shaped laser pulse in the temporal domain: temporal intensity with the amplitude mask applied (solid blue), and without the amplitude mask (dashed blue), temporal phase with the amplitude mask applied (solid red), and without the amplitude mask (dashed red). [Bottom panel] measured pulses, at the output of the pulse shaper (blue), stacked pulses (yellow).

allows for independent modification of the spectral phase and amplitude. It is worth noting that amplitude modification results in losses, while a smooth phase modification in principle does not.

The limitation in the phase variation rate an AOM can achieve is set by the pulse dispersion in the Furier plane, as well as by the response of the AOM crystal itself. Commercially available AOM devices are typically operated at frequencies in the 100-200 Mhz range. At the commercially available 3dB bandwidth of 100 MHz, the rise time is limited to 10ns. In our case, at f=450 mm, the spatial spread in the Fourier plane is 1.9 mm/nm and thus the slope of the phase variation rate is limited to about 100 rad/nm. This also limits the pulse duration that can be reached by applying only a quadratic phase to about 2 ps given our current optics and an input bandwidth of 1.6 nm. For this reason, we propose the use of a combined method. If the desired pulse shape is significantly longer than the input pulse, then the phase needed to achieve that pulse will have a large quadratic component. This component can be imparted on the pulse geometrically, i.e. by departing from the 4-f configuration. The pulse shaper is then only used for smaller adjustments in the pulse duration, as well as to shorten the rise time of the pulse.

Content from this work may be used under the terms of the CC BY 3.0 licence (© 2018). Any distribution of this work must maintain attribution to the author(s), title of the work, publisher, and DOI.

ISBN: 978-3-95450-194-6 ISSN: 2226-0366 doi:10.18429/JACoW-LINAC2018-MOPO027

Content from this work may be used under the terms of the CC BY 3.0 licence (© 2018). Any distribution of this work must maintain attribution to the author(s), title of the work, publisher, and DOI.

Figure 3, top panel, shows a pulse shaped to produce a nearly flat-top distribution in the temporal domain. The phase need to achieve this is a sum of quadratic and a generalized Gaussian component, which are shown separately. The parameters of the generalized Gaussian were optimized in order to obtain the desired pulse shape. In addition, a smooth amplitude mask (a Tukey window) can be applied to the pulses. The bottom panel shows the same pulse in the temporal domain, including a comparison beteen the shapes obtained with (solid blue) and without (dashed blue) the phase mask. It is evident that applying a phase mask results in a reduction in the rise time, from about 0.7ps to 0.3ps. Using a smooth amplitude mask also reduces the ringing significantly. This highlights the clear advantages of using a fully controllable amplitude filter over a simple knife-edge

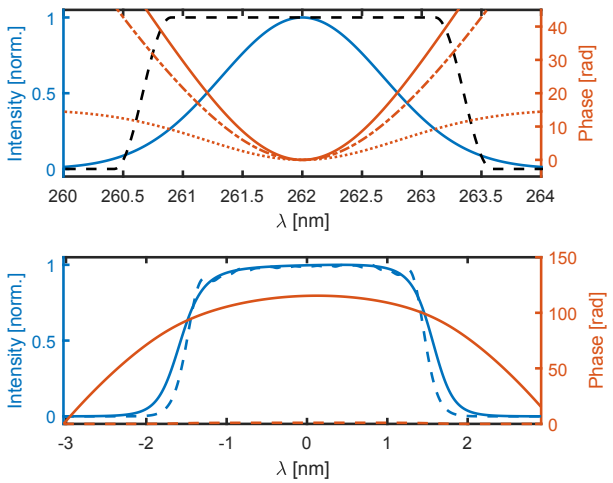


Figure 3: Top panel: a shaped laser pulse in the spectral domain. Here we show the spectral intensity (solid red) and the spectral phase (solid red). In addition, a the phase is decomposed into two components, a quadratic one (red dash-dotted line) and the remaining quasi-Gaussian (dotted red). A phase mask is shown (dashed black). Bottom panel: the same pulse in the temporal domain. We plot the temporal intensity corresponding to the pulse with a Gaussian spectram (solid blue), and a temporal intensity corresponding to truncated Gaussian spectrum (dashed blue). The temporal phase is also shown (solid red).

CONCLUSION

We briefly present the laser setup used to produce femtosecond ultraviolet pulses. We discuss the different approaches to stretching and shaping these pulses. An existing setup consisting of a prism stretcher and birefringent crystals is compared with a newly built Fourier domain shaper. In addition, the use of a AOM device to improve the temporal shape is discussed, and simulated pulse shapes are presented.

REFERENCES

[1] S. Werin *et al.*, "Short pulse facility for MAX-lab", *Nucl. Instr. Meth. A*, vol. 601, pp. 98–107, 2009.

[2] S. Thorin *et al.*, "The MAX IV Lina", in *Proc. 27th Linear Accelerator Conf. (LINAC'14)*, Geneva, Switzerland, Aug.-Sep. 2014, paper TUIOA03, pp. 400–403.

[3] M. Trovo *et al.*, "Status of the FERMI@ELETTRA photoinjector", in *Proc. 11th European Particle Accelerator Conf. (EPAC'08)*, Genoa, Italy, Jun. 2008, pp. 247–249.

[4] K. Floettmann, "ASTRA - A space charge tracking algorithm - DESY", DESY, Hamburg, Germany, 2011.

[5] J. G. Power *et al.*, "Temporal Laser Pulse Shaping for RF Photocathode Guns: The Cheap and Easy way using UV Birefringent Crystals", in *Advanced Accelerator Concepts: Proc. 13th Advanced Accelerator Concepts Workshop*, Santa Cruz, CA, USA, Jul.-Aug. 2018, *AIP Conference Proceedings*, vol. 1086, pp. 689–694, 2009. doi:10.1063/1.3080991

[6] F. Lindau, *et al.*, "MAXIV Photocathode Gun Laser System Specification and Diagnostics", in *Proc. 8th Int. Particle Accelerator Conf. (IPAC'17)*, Copenhagen, Denmark, May 2017, pp. 1544–1546. doi:10.18429/JACoW-IPAC2017-TUPAB097

[7] D. J. Kane *et al.*, "Characterization of arbitrary femtosecond pulses using frequency-resolved optical gating", *IEEE J. Quant. Electron*, vol. 29, no. 2, p. 571, 1993.

[8] A. M. Weiner *et al.*, "Femtosecond optical pulse shaping and processing", in *Prog. Quantum Electron.*, vol. 19, pp. 161-–237, 1995.

[9] B. J. Pearson and T. C. Weinacht, "Shaped ultrafast laser pulses in the deep ultraviolet", in *Opt. Express*, vol. 15, no .7, pp. 4385–4388, 2007.

ISBN: 978-3-95450-194-6 ISSN: 2226-0366 doi:10.18429/JACoW-LINAC2018-MOPO028

SURVEY AND ALIGNMENT SYSTEM OF 100 MeV/100 kW ELECTRON LINEAR ACCELERATOR

O. Bezditko, A. Zelinsky, I. Karnaukhov, M. Moisieienko, A. Mytsykov,
NSC KIPT, Kharkov, Ukraine

Abstract

For successful operation and working of electron linear accelerator of "NEUTRON SOURCE" driver it is necessary that all the acceleration sections, the quadrupole triplets, the quadrupole lenses, the dipole magnets, the scanning magnets and the chicane should be installed in design position according design parameters. Accuracies of all electromagnetic elements installation are 150 mkm for all three rotation freedom. The whole process, fiducialization and developing of survey net, alignment is controlled by laser tracker Leica AT 401.

INTRODUCTION

According to the design, to provide required electron beam parameters at the target, accuracies of NSC KIPT 100 MeV/100 kW electron linear accelerator electromagnetic element installations are 150 mkm in the transverse coordinate, 200 mkm in the longitudinal coordinate and 200 mrad for all three rotation freedom. The whole installation and alignment process is controlled by Leica Absolute Tracker AT401 [1]. The electromagnetic system of the linear accelerator consists of quadrupole lenses, quadrupole triplets, bending magnets and scanning magnets.

Leica Absolute Tracker AT401 is a portable coordinate measuring machine (CMM) that allows extreme precision over ultra large distances. The Leica Absolute Tracker AT401 are shown in Fig. 1.

All accuracies are specified with Leica Geosystems precision 1.5" Red Ring Reflectors and a measurement mode of 2 seconds per point under stable environmental conditions.

Full range is specified as 1.5 to 80 meters away from the laser tracker within a vertical range of +/- 45˚. All accuracies are stated in maximum permissible error (MPE).

Absolute Angular Performance:

Resolution: 0.07 arc Seconds

1. Accuracy (MPE): +/- 15 μm + 6 μm/m (+/- 0.0006" + 0.00007″/ft);
2. Repeatability (MPE): +/- 7.5 μm + 3 μm/m (+/- 0.0003″ + 0.00004″/ft);
3. Inclination Setting Accuracy (2σ): +/- 1 arc second.

Absolute Distance Performance:

1. Resolution: 0.1 μm;
2. Accuracy (MPE): +/- 10 μm (+/- 0.00039″).



Figure 1: The Leica Absolute Tracker AT401.

ACCELERATOR COORDINATE NET

For linear accelerator electromagnetic element installations a survey coordinate net was developed. The coordinate net was formed by 23 survey targets, that were installed on the walls and in the floor of accelerator tunnel and 4 survey targets were installed in the experimental hall. 23 survey target design is like nest with magnet for the red ring reflector installation. To develop the coordinate net it is necessary to identify and fix the coordinates of all survey targets along the accelerator tunnel in vertical plane considering the electron beam reference orbit as a longitudinal horizontal coordinate axis. The vertical coordinate axis is axis of the electron beam and the neutron-generating target interaction.The process of the survey targets coordinate measurements and fixations was carried out by the laser tracker with move station method. The move station method was used between every two neighbouring sections consist of at least 3 (or more) survey targets. Measuring coordinates of 3 survey targets in the previous group is necessary and sufficient for the transition to the measurement of the positions of the targets in the new group. Taking into account the number of survey targets (23) NSC KIPT 100 MeV/100 kW has 7 sets of target for the move station method. The process of coordinate determinations is shown Fig. 2.

Content from this work may be used under the terms of the CC BY 3.0 licence (© 2018). Any distribution of this work must maintain attribution to the author(s), title of the work, publisher, and DOI.

ISBN: 978-3-95450-194-6 ISSN: 2226-0366 doi:10.18429/JACoW-LINAC2018-MOPO028

Content from this work may be used under the terms of the CC BY 3.0 licence (© 2018). Any distribution of this work must maintain attribution to the author(s), title of the work, publisher, and DOI.

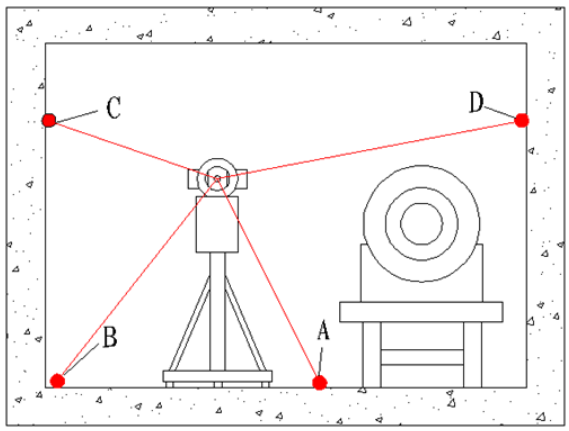


Figure 2: The process of survey target coordinate determinations.

Using this method, the cloud of all survey target point coordinates for all 7 groups of survey targets was obtained in the neutron-generating target coordinate system, where the coordinate X is longitudinal coordinate of the accelerator axis, Y is transverse coordinate that perpendicular to the longitudinal one, Z is vertical coordinate of the neutron generating target axis interaction with electron beam.

The longitudinal coordinate axis X was set with installation of basic survey target nests at the back wall of accelerating tunnel and opposite wall of the experimental hall of the NSC KIPT Neutron Source Facility.

Initial transverse coordinate Y was set with installation of basic survey target nests at the both left and right sides walls of NSC KIPT Neutron Source experimental hall before final installation of the top moveable biological shielding.

The vertical coordinate system axis at real facility realization was determined as the central axis of rotation of rotating top part of biological shielding. Using the coordinates of two support rollers of top rotating part of biological shielding and radius of the rotating plate that is 1365.65 mm the coordinate of the vertical axis was determined and set as the basic in the Leica coordinate system for further measurements. At 2016 all electromagnetic elements were installed. At 2017 and 2018 positions of the electromagnetic elements were checked.

FIDUCIALIZATION OF THE ACCELERATOR ELECTROMAGNETIC ELEMENTS

The basic elements of the NSC KIPT 100 MeV/100 kW linear accelerator are electron gun, prebuncher, buncher, injection section, 4 chicane magnets, 9 regular accelerating sections, 5 focusing triplets, 6 quadrupole lenses of the transportation channel, 2 of 45 degree bending magnets of the transportation channel, 2 neutron generating target scanning magnets [2].

The basic elements of the NSC KIPT 100 MeV/100 kW linear accelerator are electron gun, prebuncher, buncher, injection section, 4 chicane magnets, 9 regular accelerating sections, 5 focusing triplets, 6 quadrupole lenses of the transportation channel, 2 of 45 degree bending magnets of the transportation channel, 2 neutron generating target scanning magnets [2].

All elements, mentioned above were design and manufactured by IHEP, Beijing, China. After manufacturing all elements were tested with electromagnetic and mechanical tests but fiducialization and alignment of the individual units has been done in NSC KIPT.

Quadrupole Lenses

Quadrupole lenses of the transportation channel of the electron beam are used for focusing of the electron beam to obtain the required beam geometric dimensions at the neutron generating target (see Fig. 3).

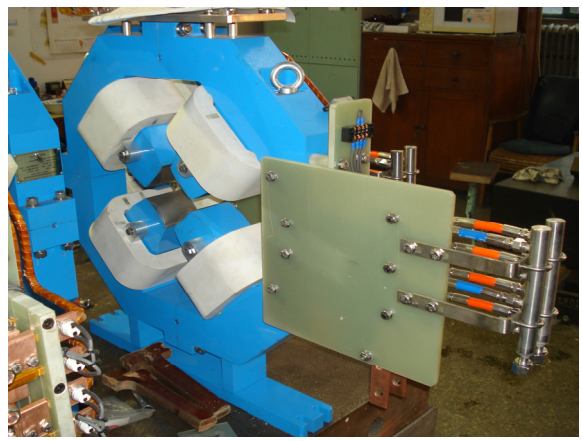


Figure 3: NSC KIP 100 MeV/100 kW linear accelerator quadrupole lens.

The quadrupole lenses, the quadrupole triplets, the bending magnets and the scanning magnets manufactured on high-precision machines. Manufacturing accuracies of yoke and poles of the electromagnetic elements are equal to 50 mkm. It gives the possibility to use the yoke and pole surfaces as a basic planes and points for the mechanical element center axis determination and set of the local element coordinate system for the element fiducialization. At first, the front and back yoke planes were measured with laser tracker. After constructing of two vertical planes and averaging the position of the vertical center element plane was determined. Second, the coordinate of quadrupole poles were measured and four points were projected onto the median vertical plane. Then two vectors were constructed between the projected points, the intersection of the vectors determines the absolute center of the lens, where the coordinate system was placed. The accuracy of the quadrupole lenses fiducialization is about 70 mkm. Accuracy of alignment of quadrupole lenses is shown in Table. 1.

ISBN: 978-3-95450-194-6 ISSN: 2226-0366 doi:10.18429/JACoW-LINAC2018-MOPO028

Table 1: Accuracy of Alignment of Quadrupole Lenses

Y(mm)	Z (mm)	Name
0.02	0.01	Q9_F1
0.01	0.03	Q9_F2
0.04	0.01	Q9_F3
0.02	0.03	Q10_F1
0.03	0.02	Q10_F2
0	0.06	Q10_F3
0.01	0.07	Q10_F4

Fiducialization of Accelerator Dipole Magnets

NSC KIPT 100 MeV/ 100 kW linear accelerator first chicane bending magnet, 45 degree transportation channel bending magnet and vertical scanning magnet are shown in Fig. 4. As one can see the nest for the survey targets installed at the top of rectangular yokes of the chicane and scanning magnets and at special vertical support of the sector transportation channel magnet.

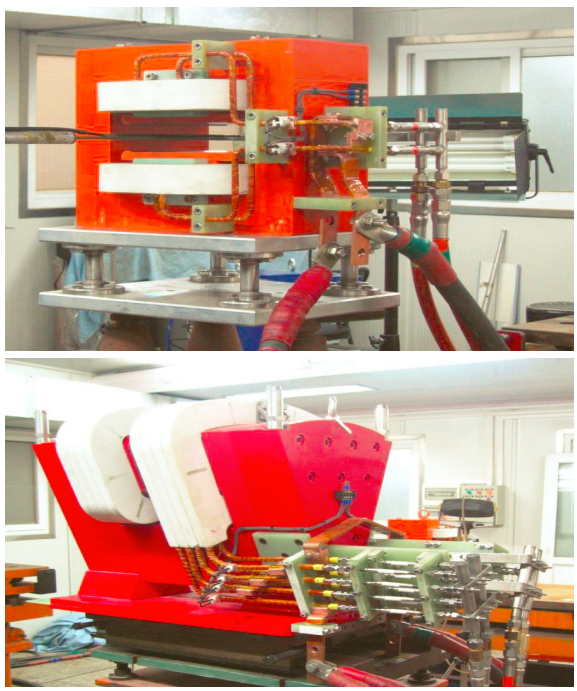


Figure 4: NSC KIPT 100 MeV/100 kW linear accelerator first chicane magnet, 45 degree bending magnet.

The procedure of the elements fiducialization was similar to the procedure of the quadrupole fiducialization with difference of dipole poles number and shape. The accuracies of the fiducialization for all dipole magnets were better than 70 mkm.

Fiducialization of Quadrupole Triplets

Quadrupole triplet is shown in Fig. 5.

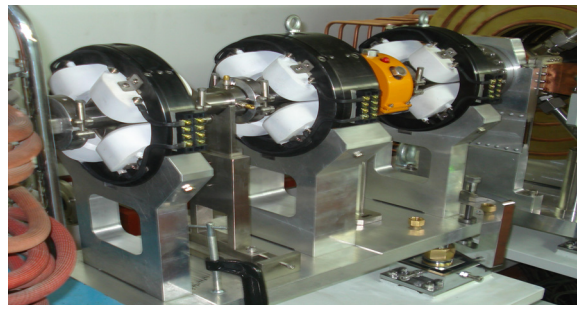


Figure 5: NSC KIPT 100 MeV/100 kW linear accelerator quadrupole triplet.

Due to mechanical design of the quadrupole triplets of the linear electron accelerator, the access to the apertures of the lenses is blocked. Since it is impossible to use the fiducialization method described above, it was decided to determine the magnetic center of the quadrupole triplet determining the centers of the circle yokes of the lenses. Thus, the center of the circles of all 3 lenses of one triplet were measured and the value of the displacement of the centers of circles relative to each other was estimated. If the displacement value did not exceed 50 μm, the coordinate system was set into one of the centers of the circle. Accuracy of alignment of quadrupole triplets according the procedure of the fiducialization is shown in Table. 2.

Table 2: Accuracy of Alignment of Quadrupole Triplets

Y(mm)	Z (mm)	Name
0.2	0.02	TRIPLET1_1
0.09	0	TRIPLET1_2
0.14	0.01	TRIPLET1_4
0.09	0.1	TRIPLET2_1
0.16	0.06	TRIPLET2_2
0.03	0.04	TRIPLET2_4

CONCLUSION

NSC KIPT Neutron source facility coordinate system was designed and developed. The procedure of fiducialization of dipole and quadrupole magnets, quadrupole triplets, scanning magnets with use of the laser tracker Leica AT 401 was done. The process was optimized and magnetic elements error budget of 150 mkm in the vertical and in the horizontal planes has been provided.

REFERENCES

[1] http://www.leica.com/
[2] A. Zelinsky, “Test and Commissioning Results of NSC KIPT 100 MeV/ 100 kW Electron Linear Accelerator, Subcritical Neutron Source Driver”, in *Proc. 8th Int. Particle Accelerator Conf. (IPAC’17)*, Copenhagen, Denmark, May 2017, paper TUPIK033.

Content from this work may be used under the terms of the CC BY 3.0 licence (© 2018). Any distribution of this work must maintain attribution to the author(s), title of the work, publisher, and DOI.

ISBN: 978-3-95450-194-6 ISSN: 2226-0366 doi:10.18429/JACoW-LINAC2018-MOPO029

PHYSICS DESIGN AND DYNAMIC SIMULATION OF A C-BAND PHOTOCATHODE ELECTRON GUN FOR UEM*

T.J. Chen, Y.J. Pei#, Z.X. Tang, W.M. Li
NSRL, University of Science and Technology of China, Hefei, China

Abstract

For discovering structure at atomic scale and getting more details of chemical material and biological tissue, an ultrafast electron microscopy (UEM) has been developed and applied in plenty of subjects and studies. This paper described a C-band photocathode electron gun which will be working at 5712 MHz to produce ultrashort electron beams with better dynamic parameters. The RF gun is using coaxial coupler to decrease the size of the gun and keep better symmetry of the field in the photocathode gun so that the beam emittance and energy spread can be reduce a lot. The photocathode rf gun will be an important part of the ultrafast electron microscopy (UEM). Using CST MWS and superfish code to simulate design the gun. After dynamic simulation, the beam parameters as the following: Energy is of 3MeV, Normal emittance of 0.12mm-mrad in both direction, energy spread is of 5.8×10^{-4}, which are better enough for an UEM.

INTRODUCTION

The electron microscope is a kind of useful experimental instrument for observing structure of chemical material and biological tissue and studying the composition of them at small length scale. The electron gun, which provides electron beams with high energy to probe materials, is the most important part in electron microscope and also determines the quality of projective images [1, 2]. Photocathode gun, field-emission gun and thermal emission gun are the most common kinds used in electron microscopes as the electron source. Photocathode gun, which could provide electron beams with much higher energy and better dynamic properties, is suitable for ultrafast electron microscope (UEM).

The UEM, which differs from the traditional electron microscope, uses ultrafast electron beams with higher energy from hundreds of keV to several MeV level as a probe to discover molecule structure. Besides, the ultrafast electron beams with short pulse of femtosecond level, could also be used to observe the dynamic process with high temporal resolution.

Due to breakdown limit, electron gun using direct current could only accelerate electrons to hundreds of keV, which would cause the expansion of dimension due to space charge effect [3-5]. Thus, radio frequency gun (RF gun) is chosen to be used to get electron beams with higher energy of MeV. With RF gun, the electron beams will be accelerated rapidly to near realistic speed, which will decrease space charge effect.

A solenoid magnet is used at the downstream of accelerating cavity to focus the electron beams and compensate the emittance of the electron beams so that the dynamic parameters of the exit beam of the photocathode gun will be improving. With emittance compensation, the emittance of both x and y plane would be decreased to the desired value [6].

In this research, CST Microwave Studio is used to simulate the 1.6-cell C-band gun cavity and optimize the structure of coaxial coupler. With smaller radius due to coaxial coupling, the solenoid could produce stronger magnetic field and will compensate the emittance much better. The magnetic field of solenoid is simulated and optimized to keep the dimension of electron beams and compensate emittance by using Parmela code. The dynamic parameters after optimization are calculated at the exit of the photocathode gun.

PHYSICS DESIGN OF THE PHOTOCATHODE

The photocathode gun consists of two parts: 1.6-cell accelerating cavity and waveguide coupler. The 1.6-cell cavity is designed and simulated by superfish code and CST MWS. Radius and shape of iris and length of cells are mainly optimized to get higher shunt impedance and cavity radius of half-cell and full-cell is adjusted to tune the frequency to working frequency of 5712 MHz. The result of 2D pi-mode field is calculated in superfish and the electric field along z-axis is showed in Fig. 1, which is used to accelerate electron beams.

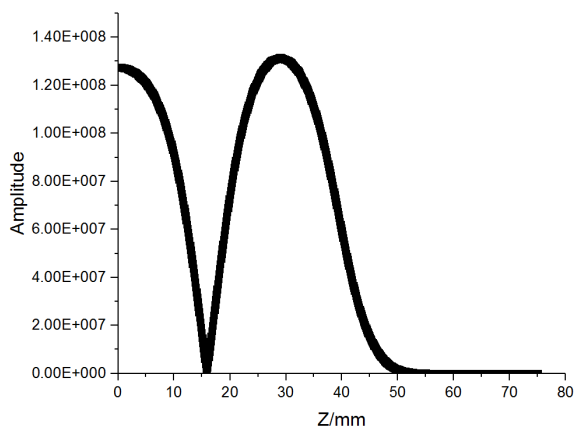


Figure 1: Ez of pi-mode along axis.

The coaxial coupler is adopted in this C-band gun to keep symmetry of field and decrease the radius of gun cavity to save space for solenoid in order to compensate emittance better. The coaxial coupler connects two rectangular waveguides and a coaxial transmission line.

* Supported by National High-tech R&D Program (No.na8211009b).
# Corresponding author (email: yjpei@ustc.edu.cn)

Content from this work may be used under the terms of the CC BY 3.0 licence (© 2018). Any distribution of this work must maintain attribution to the author(s), title of the work, publisher, and DOI.

ISBN: 978-3-95450-194-6 ISSN: 2226-0366 doi:10.18429/JACoW-LINAC2018-MOPO029

Main microwave parameters are listed in Table 1. The shape design uses LCLS gun as reference [7]. The full model is built and simulated using time domain solver in CST. The pi-mode electric field has been simulated and S11 curve is calculated and showed in Fig. 2. This curve has two resonance peaks at 5700 MHz and 5712 MHz, which represents the 0-mode and the pi-mode.

Table 1: Main Microwave Parameters

Pi-mode frequency	5712.02MHz
0-mode frequency	5699.82MHz
Mode separation	12.22MHz
Shunt impedance per meter	143.879 MΩ/m
Q factor	12084.4

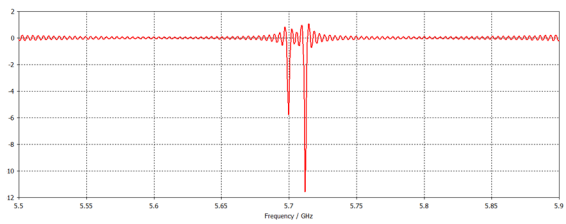


Figure 2: S11 curve of full model.

SIMULATION IN DYNAMIC PROCESS

Solenoid Design

A solenoid magnet is designed to prevent the expansion of beam size and emittance due to space charge effect [6]. The length of coaxial line needs to be extended by a wavelength of 52.48 mm in order to leave space for installing the solenoid. The pattern of the electric field in 2D model calculated in superfish is showed in Fig. 3.

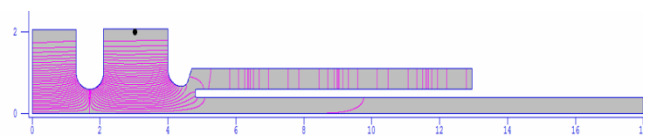


Figure 3: the electric field in 2D model after coaxial length extended.

In this paper, shape and magnetic field strength of the solenoid are mainly optimized. The initial shape of the solenoid and the magnetic field strength is presented in Fig. 4, from which we could find out that the length of magnet is too long and the maximum of the magnetic field is not high enough. To improve the maximum of the magnetic field and shorten the effective field length, the new solenoid shape is designed and simulated, the results of which are in Fig. 5. The maximum has been promoted by about 50% with the same ampere turns in simulation and the effective field length decrease, which could offers stronger focus strength.

Different values of maximum magnetic field have been simulated to determine the most suitable value of the magnet and the results are showed in Fig. 6. The range of scanning is from 2100 G to 3500 G, and from the results the value of 3100 G is enough to prevent the electron bunches from expansion.

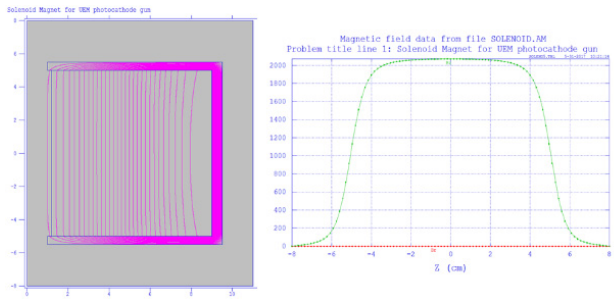


Figure 4: Initial solenoid shape and magnetic field.

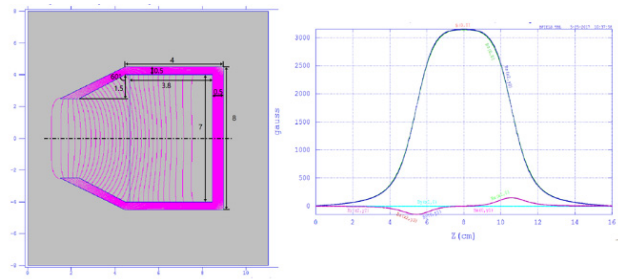


Figure 5: Optimized solenoid shape and magnetic field.

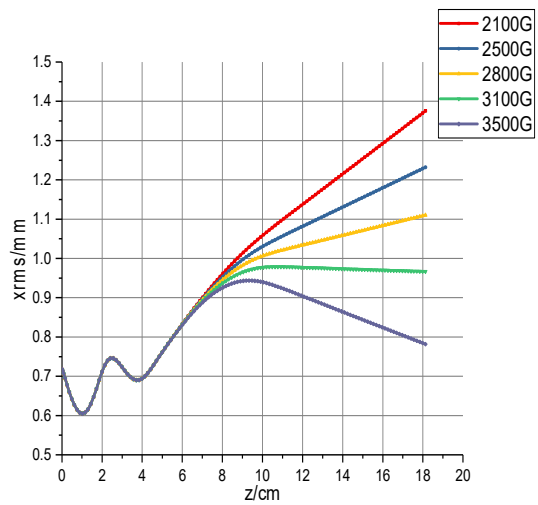


Figure 6: rms size in x-plane of the electron bunches in scanning different values of maximum of magnetic field.

Initial Phase Scan

To find out the range of initial phase of captured electron bunches, dynamic process of electron bunches emitting from the photocathode is simulated and different values of initial phase are scanned. The result that electron bunches with initial phase from 165 degree to 200 degree could be captured and accelerated in the C-band photocathode gun is presented in Fig. 7-9.

Content from this work may be used under the terms of the CC BY 3.0 licence (© 2018). Any distribution of this work must maintain attribution to the author(s), title of the work, publisher, and DOI.

ISBN: 978-3-95450-194-6 ISSN: 2226-0366 doi:10.18429/JACoW-LINAC2018-MOPO029

Content from this work may be used under the terms of the CC BY 3.0 licence (© 2018). Any distribution of this work must maintain attribution to the author(s), title of the work, publisher, and DOI.

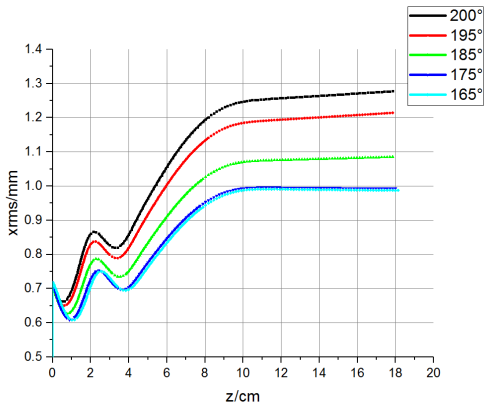


Figure 7: The change of rms size in x-plane.

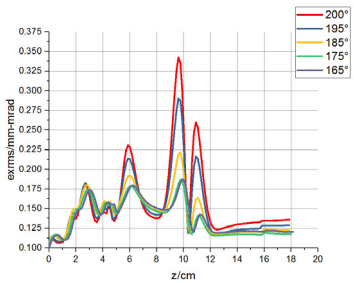


Figure 8: The change of rms emittance in x-plane.

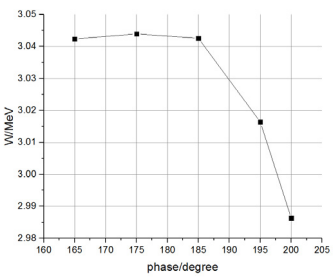


Figure 9: Energy of electron bunches at exit of electron gun with different initial phase.

Figure 7 shows the change of rms size and Fig. 8 shows the change of rms emittance in x-plane of electron bunches during dynamic process, which suggests that the initial phase from 165 degree to 175 degree are with best rms size and smallest emittance of 0.1 mm-mrad. Figure 9 suggests that electron bunches with initial phase from 165 degree to 185 degree gain energy of 3 MeV. Due to the results, the initial phase should be limited in the range of 165 degree to 175 degree to gain better properties of beams.

Simulation of Dynamic Parameters

Electron emitting from cathode would have external thermal emittance, which could not ignored in dynamic simulation [7]. Thermal emittance of electron bunches could be calculated using the relationship for uniform emission from a thermionic cathode of radius r_c and effective temperature T_e:

$$\varepsilon_{th} = \frac{r_c}{2}\sqrt{\frac{kT_e}{m_0c^2}}$$

Table 2: Main Dynamic Parameters at the Exit of Gun

Rms size in x-plane	0.9874mm
Rms size in y-plane	0.9897mm
Emittance size in x-plane	0.1205mm-mrad
Emittance size in y-plane	0.1203mm-mrad
Energy gain	3.0423MeV
Energy spread	5.84e-04

In this condition, the thermal emittance is about 0.1 mm-mrad when r_c =0.1mm and T_e =300 K. The dynamic simulation results with thermal emittance are presented in Fig. 10, which shows the change of rms size and rms emittance of electron bunches.

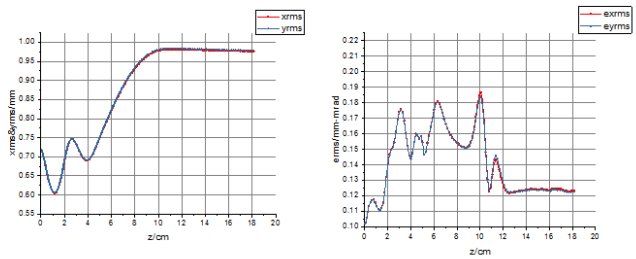


Figure 10: Rms size and emittance in x-plane and y-plane of electron bunches.

The main dynamic parameters of electron bunches at the downstream of the coaxial photocathode gun are listed in the Table 2. The final rms emittance in both x-plane and y-plane are 0.12 mm-mrad, which has been satisfied the gun requirement, and magnetic field produced by solenoid maintains the size of electron bunches bleow 1mm in both x-plane and y-plane. The electron bunches finally gain energy of 3 MeV with energy spread of 5.84e-04.

CONCLUSION

In this paper, we design a 1.6-cell C-band photocathode electron gun with coaxial coupler. After finishing the physical design, the solenoid magnet has been designed and dynamic process has been simulated using Parmela and dynamic parameters are calculated. Furthermore, after fabricating the model of gun, the electric field and shunt impedance would be measured.

REFERENCES

[1] F R. Egerton, *Physical Principles of Electron Microscopy: An Introduction to TEM, SEM, and AEM*, 2005: Springer Science+ Business Media, doi:10.1007/b136495

[2] P J,Goodhew, J. Humphreys, R. Beanland, *Electron microscopy and analysis,* CRC Press, 2000.

[3] J. B. Hastings, F. M. Rudakov, D. H. Dowell, *et al.,* "Ultrafast time-resolved electron diffraction with megavolt electron beams," *Applied Physics Letters*, vol. 89(18), pp. 184109, 2006.

ISBN: 978-3-95450-194-6 ISSN: 2226-0366 doi:10.18429/JACoW-LINAC2018-MOPO029

[4] P. Musumeci, J. T. Moody, C. M. Scoby, *et al.*, "Laser-induced melting of a single crystal gold sample by time-resolved ultrafast relativistic electron diffraction," *Applied Physics Letters*, vol. 97(6), pp. 063502, 2010.

[5] F. Fu, S. Liu, P. Zhu, *et al.,* „High quality single shot ultrafast MeV electron diffraction from a photocathode radio-frequency gun". *Review of Scientific Instruments*, vol. 85(8), pp. 083701, 2014.

[6] J. Schmerge, "LCLS gun solenoid design considerations," SLAC National Accelerator Lab., Menlo Park, CA, USA, 2010.

[7] J. Arthur, W. Graves, M. Renner, *et al.,* "Linac coherent light source (LCLS) conceptual design report," SLAC National Accelerator Lab., Menlo Park, CA, USA, 2002.

Content from this work may be used under the terms of the CC BY 3.0 licence (© 2018). Any distribution of this work must maintain attribution to the author(s), title of the work, publisher, and DOI.

ISBN: 978-3-95450-194-6 ISSN: 2226-0366 doi:10.18429/JACoW-LINAC2018-MOPO034

DIELECTRIC WAVEGUIDE BASED THz RADIATOR STUDY FOR SwissFEL*

L. Shi†, F. Marcellini, S. Reiche, R. Ischebeck, A. Mittelbach,
S. Bettoni, V. Thominet, B. Hermann, E. Ferrari, M. Dehler
Paul Scherrer Institut, 5232 Villigen PSI, Switzerland

Abstract

THz pulses have many unique properties in terms of radiation matter interaction. In particular, their non-ionizing excitation of phonons in matter makes them a preferred pump for pump-probe studies at free-electron laser facilities. Among many THz generation techniques, the one based on dielectric lined waveguide and electron beam is emerging as a compact and powerful means for the THz generation. We will investigate the feasibility of this technique to produce narrowband pulses of 1-20 THz with above 100 µJ per pulse for SwissFEL. As a first step, we focus on the proof of principle experiments. This paper overviews the project with a focus on the numerical study of the dielectric lined waveguide, in terms of mode structure, energy, pulse length etc, which are essential parameters for the pump-probe experiments. These waveguides will be fabricated and tested in the near future at SwissFEL.

INTRODUCTION

THz radiations, which lie between approximately 1 and 20 THz, have multiple properties in terms of radiation matter interaction due to the unique spectroscopic signatures for a wide range of phenomena. In particular, their non-ionizing excitation of phonons in matter, which is important to understand the physiochemical as well as biological processes of condensed matter [1]. The dynamics of the excited states can be probed by the high brightness, ultrashort X-ray pulses available at free electron laser facilities [2].

Due to the appealing characteristics and the great potential applications of the THz radiation, there are ever-increasing efforts in generating THz [3], including but not limited to the methods based on the solid state oscillators, the quantum cascaded laser, the laser pumped solid state devices and accelerators etc. In this paper, we report on a THz radiator study based on a relativistic electron beam and a dielectric lined waveguide (DLW) [4]. Many experiments have been performed in the field in order to show the validity of this means of high power generation but they are normally limited to a few tens or hundreds GHz due to the quality and the length of the electron beam. We aim to demonstrate the generation of narrowband pulses in the range of 1-20 THz, which will require a rather small vacuum aperture for the electron beam to traverse. If demonstrated successfully, this narrowband THz source can be a strong candidate for the pump-probe setup aforementioned. Especially, the high power of these THz pulses would open new possibilities of experiments for the photon beamline users at SwissFEL (Swiss Free Electron Laser) [5].

SwissFEL is a less than one kilometer long free electron laser facility based on normal conducting RF technique as schematically shown in Fig. 1. It is able to generate ultrashort and ultra-bright soft and hard X-ray pulses simultaneously in the two undulator lines Athos and Aramis, respectively [5]. These are driven by the electron bunches from an RF injector followed by S and C-band RF accelerating structures.

To demonstrate the plausibility of the THz generation based on this method, the proof of principle beam test of the DLW will be carried out in the ACHIP vacuum chamber [6] in the switchyard of the Athos beamline. If this DLW based THz source can provide above 100 µJ per pulse, less than 10% bandwidth in the frequency range of 1-20 THz, we then plan to investigate further to propose a possible design implementation of such a DLW based device for the THz generation. By exploiting the electron bunches after the Aramis undulator right before the electron beam dump as indicated in Fig. 1 , the THz could be generated together with a DLW device without too much complication. This is essentially due to the insensitivity to the energy spread of the otherwise still bright blow-up electron beam. The THz could be transported to the ATHOS station before the soft X-ray pulse to form a pump-probe experiment setup.

THE DLW BASED THZ RADIATOR

An electromagnetic field is excited when a relativistic electron bunch traverses a DLW. The electromagnetic fields can be decomposed in multipole expansion into orthogonal modes. Among these modes, the monopole transverse magnetic modes, showing azimuthal symmetry, are of particular interest due to the strong coupling between the electron beam and its longitudinal field. By tailoring the geometry size of the DLW, radiation in the THz can be obtained. The mode can be guided out of the DLW and is the principal source of the THz radiation.

A sample DLW is shown in Fig. 2 and it consists of a vacuum channel ($0 < r < a$) for the electron bunch passage, and a dielectric layer ($a < r < b$), characterized by the relative permitivity ε_r, for slowing down the phase velocity of the mode to match it with the velocity of the electron bunch. The outer side of the DLW is coated with metallic material to enclose the radiation and to form a set of discrete electromagnetic modes. The total length L of the DLW governs the bandwidth and power of the THz pulses. In

* Work supported by Marie Curie Action H2020
† liangliang.shi@psi.ch

Content from this work may be used under the terms of the CC BY 3.0 licence (© 2018). Any distribution of this work must maintain attribution to the author(s), title of the work, publisher, and DOI.

ISBN: 978-3-95450-194-6 ISSN: 2226-0366 doi:10.18429/JACoW-LINAC2018-MOPO034

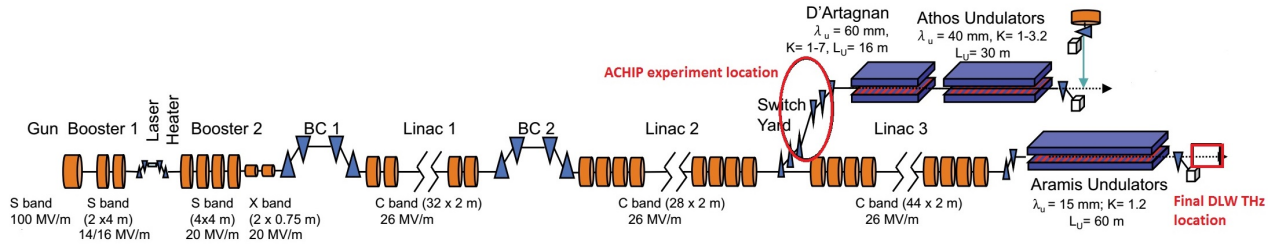


Figure 1: Layout of SwissFEL.

this paper, we only consider the DLW with a circular cross section due to its robustness and simplicity.

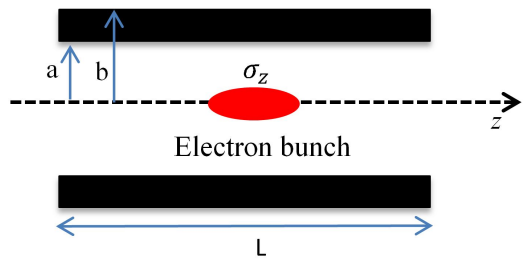


Figure 2: Schematic of a DLW structure with its inner and outer radius a and b respectively.

The mode frequencies and the field distributions can be solved analytically as shown in [7] and [8]. These are functions of a, b and ε_r. The longitudinal field component of TM_{0n} is shown in Fig. 3. In the vacuum passage the field strength is almost constant, which indicates that the interaction between electron bunch and the field is independent of the bunch transverse position. The oscillatory behavior of the field is only in the dielectric layer.

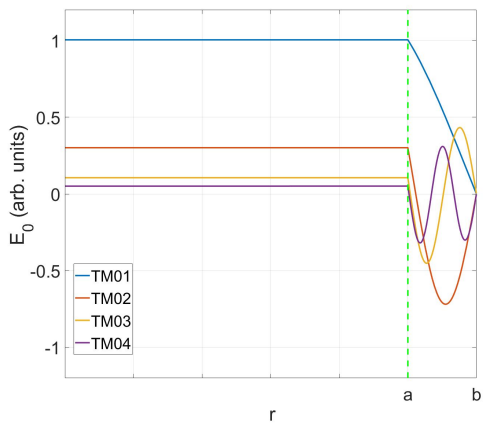


Figure 3: Transverse profile of the longitudinal field strength of the TM mode.

Figure 4 shows the mode frequencies for a parametric scan of a and b, with $\varepsilon_r = 3.8$. To get the TM_{01} above 1 THz, a and b should be approximately in the range of one hundred micrometers.

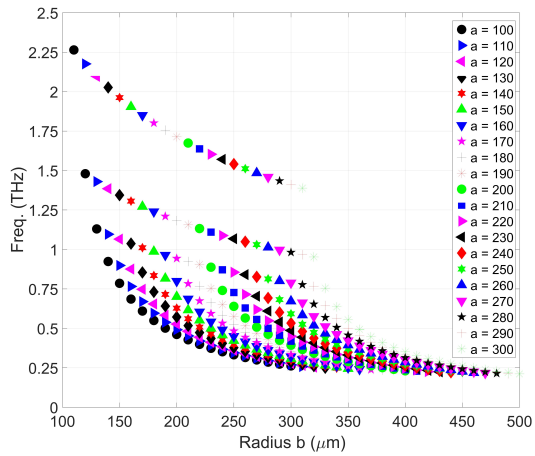


Figure 4: TM_{01} mode frequency versus radius b at different a.

Our design aims to cover the frequency range between 1-3 THz with the fundamental mode TM_{01}, and the remaining 3-20 THz with its harmonics. The pulse length, group velocity, energy per pulse can be obtained as described in [8]. A case study with $a = 100\,\mu m$, $b = 120\,\mu m$, and $\varepsilon_r = 3.8$ is summarized in Table 1. The following estimates the associated parameters for a point charge of 1 pC traveling through a 1 cm long DLW.

Table 1: THz Pulse Parameter Estimation for a Point Charge of 1 pC

TM_{0n} n	Freq. (THz)	Vg (c)	E (μJ)	T_{pulse} (ps)	E0 (MV/m)	BW (%)
1	1.48	0.53	0.0113	30	2.26	2.2
2	5.06	0.75	0.0034	11	0.68	1.8
3	9.29	0.78	0.0012	9.6	0.24	1.1
4	13.66	0.78	0.0006	9.2	0.11	0.8
5	18.09	0.79	0.0003	9.2	0.07	0.6

The energy per pulse scales with the charge q, DLW inner radius a and length L as $E \propto q^2 \times L/a^2$. One will obtain approximately 100 μJ with 100 pC charge for the DLW parameters in the case study. Increasing the length L or

Content from this work may be used under the terms of the CC BY 3.0 licence (© 2018). Any distribution of this work must maintain attribution to the author(s), title of the work, publisher, and DOI.

ISBN: 978-3-95450-194-6 ISSN: 2226-0366 doi:10.18429/JACoW-LINAC2018-MOPO034

Content from this work may be used under the terms of the CC BY 3.0 licence (© 2018). Any distribution of this work must maintain attribution to the author(s), title of the work, publisher, and DOI.

decreasing the inner radius a can increase pulse energy. At the same time, this also increases the head-tail kick to the bunch and imposes severe beam transmission issue if the bunch is not well centered. However, this is mitigated in our case by using external focusing magnets as we discuss the experiment setup in the next section. One can observe from the table that the relative bandwidth due to the finite length of the DLW is well below 10% requested as a user pump, however there are other processes which degrade the bandwidth in any real experimental setup. This will be reported in another paper.

After the generation of THz pulse, it can be guided out of the DLW structure with an opening end, which is essentially converting the waveguide mode into a Gaussian Hermite mode of the free space propagation [11]. Due to the impedance mismatch, part of the THz will be reflected back to the DLW. The power transmission versus the inner and outer radius ratio is calculated by the electromagnetic field solver HFSS [10] and is shown in Fig. 5 for $\varepsilon_r = 3.8$.

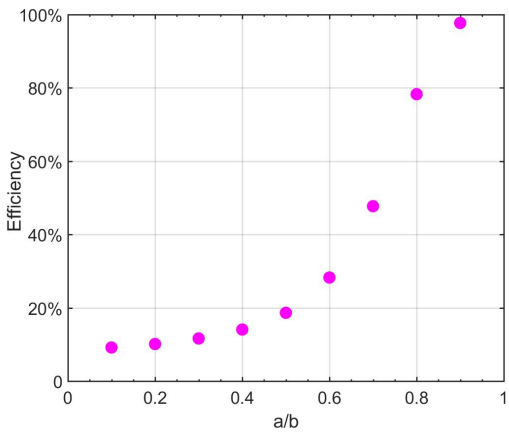


Figure 5: Radiation extraction efficiency with a vertical cut end.

It can be concluded that higher transmission can be obtained with relatively thinner dielectric layer. The opening can form certain angle with respect to the beam axis as described in [11] and the angle can also affect the radiation efficiency. The optimal angle will be studied in the future. This method has the advantage of separating the exiting electron bunch from the radiation and therefore it reduces the background radiation.

The fundamental mode frequencies can be varied by changing the parameter a (though there is complicated nonlinear dependence on other parameters as well). For example, if b is fixed at 120 µm, 90 um in a gives 1.1 THz as fundamental mode and 3.5 THz as its second harmonic mode. On the other hand, 110 µm in a gives 2.2 THz, while the second harmonic is 9.5 THz. A parametric scan of dielectric thickness $(b - a)$ and ε_r at fixed inner radius $a = 100$ µm is show in Fig. 6. To get the mode above 1 THz at $\varepsilon_r = 3.8$, the dielectric thickness should be less than 35 µm. One can choose relatively small ε_r to relieve the requirements on the thickness. Though dielectric material can provide continuous ε_r up to hundred, the multiphysics effects such as vacuum compatibility, heat conduction, mechanical rigidity should be taken into account.

So far, we have considered the eigenmode of the DLW and the excitation with a single point charge. In reality not all modes supported by a DLW can be excited due to the finite length of the electron bunch. For example, to excite 1 THz, an electron bunch which is approximately 1 ps long will be required for the coherent excitation. Thanks to the ultrashort electron bunches (~ 25 fs) available at SwissFEL, the frequency range of 3-20 THz can be covered via harmonic excitation.

One disadvantage with the circular cross section DLW is that the mode in the different set of frequencies will require a different DLW, which might be inconvenient for some experiments involving frequency scan. If the requested pulse frequency falls out of the mode family of a certain structure, then a different DLW is requested, which could be also easily loaded into the experimental environment. As an alternative, a variable gap may be introduced into the DLW as an additional degree of freedom for frequency control. However, this is reserved for future research and is beyond the scope of the current paper.

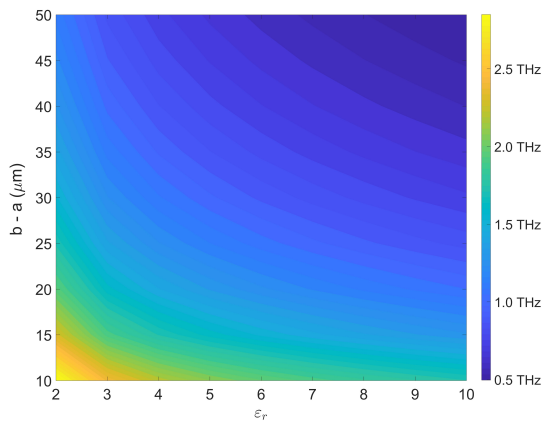


Figure 6: TM_{01} frequency versus ε_r with different thickness $b - a$.

EXPERIMENTS AT SWISSFEL

To test the numerical model, we have several DLW with different sizes (a, b and L) available in the lab. These DLWs are normally with 10% nominal tolerance in their radii. They will be tested in the switchyard of the ATHOS beamline in the ACHIP chamber [6] as depicted in Fig. 1. A schematic of the experimental setup is shown in Fig. 7. The beam optics study in [12] shows the promise of the electron transmission as outlined for the dielectric laser acceleration structure for the ACHIP experiment. In that numerical study, the electron beam could be focused strongly down to sub µm size with a quadrupole triplet made of permanent magnet before the DLW location in the chamber and another quadrupole triplet

ISBN: 978-3-95450-194-6 ISSN: 2226-0366 doi:10.18429/JACoW-LINAC2018-MOPO034

was designed to rematch the beam optics to the following beam line. Though the study in [12] was for 1 pC charge, 100 pC would only bring the transverse size approximately twice larger if one assumes that the emittance scales roughly with the charge Q as $Q^{1/3}$ when generated in the RF gun and optimized for the minimal emittance. This is not an issue for the present hundred μm aperture of the DLW.

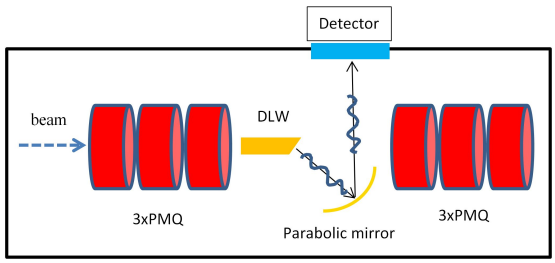


Figure 7: Experimental setup for THz generation and detection.

Subject to the success of the proof of principle experiment in the ACHIP chamber, the final THz setup could be located at the end of the ARAMIS beamline. We could then transport the generated THz to the photon end station in combination with the soft X-ray pulses from ATHOS for pump-probe experiments. The THz pulse due to its high power and peak field can certainly serve as an independent THz source as well. Although the DLW can be used for the experiments if the mode frequencies matches with what requested by users, a different tunable structure might be needed in case a continuous scanning of the spectrum is desired. We therefore will also investigate other tunable dielectric structures after the first demonstration experiment.

CONCLUSION & OUTLOOK

We presented the numerical study of the DLW based THz radiator. It can provide high power, narrowband pulses with certain tunability operating in the range of 1-20 THz. The DLWs will be characterized both in the lab and at SwissFEL.

The transmission, attenuation and heat load will need to be quantified for the DLW in 1-20 THz. We also ignored the nonlinear effect of the dielectric material, which should be investigated in the future. To achieve continuous tunability of the mode frequency, a more advanced dielectric structure with a tunable gap will have to be investigated in the future.

ACKNOWLEDGEMENTS

We would like to thank Sergey Antipov from EUCLID TECHLABS for the discussion and proofreading.

This project has received funding from the European Union's Horizon 2020 research and innovation programme under the Marie Skłodowska-Curie grant agreement No 701647.

REFERENCES

[1] J. M. Manceau, P. A. Loukakos, and S. Tzortzakis, "Direct acoustic phonon excitation by intense and ultrashort terahertz pulses," *Appl. Phys. Lett.*, vol. 97, no. 25, p. 251904, 2010. https://doi.org/10.1063/1.3529466

[2] S. Kovalev, *et al.*, "Probing ultra-fast processes with high dynamic range at 4th-generation light sources: Arrival time and intensity binning at unprecedented repetition rates," *Struct. Dyn.*, vol. 4, no. 2, p. 024301, 2017. https://doi.org/10.1063/1.4978042

[3] R. A. Lewis, "A review of terahertz sources," *J. Phys. D. Appl. Phys.*, vol. 47, no. 37, p. 374001, 2014.

[4] S. Antipov *et al.*, "High power terahertz radiation source based on electron beam wakefields," *Rev. Sci. Instrum.*, vol. 84, no. 2, p. 022706, 2013. https://doi.org/10.1063/1.4790432

[5] C. Milne *et al.*, "SwissFEL: The Swiss X-ray Free Electron Laser," *Appl. Sciences-Basel*, vol. 7, no. 7, p. 720, 2017. https://doi.org/110.3390/app7070720

[6] E. Ferrari *et al.*, "The ACHIP experimental chambers at the Paul Scherrer Institute," *Nucl. Inst. Meth. Phys. Res. A*, 2018. https://doi.org/10.1016/j.nima.2018.02.112

[7] S. Y. Park and J. L. Hirshfield, "Theory of wakefields in a dielectric-lined waveguide," *Phys. Rev. E - Stat. Physics, Plasmas, Fluids, Relat. Interdiscip. Top.*, vol. 62, no. 1 B, pp. 1266–1283, 2000. https://doi.org/10.1103/PhysRevE.62.1266

[8] A. M. Cook *et al.*, "Dielectric wakefield accelerating structure as a source of terahertz coherent Cerenkov radiation," in *AIP Conf. Proc.*, vol. 877, pp. 831–836, 2006. https://doi.org/10.1063/1.2409222

[9] A. M. Cook, "Generation of narrow-band terahertz coherent Cherenkov radiation in a dielectric wakefield structure," PhD thesis, University of California, Los Angeles, USA, 2009. ISBN:9781109470550.

[10] HFSS, http://www.ansys.com

[11] S. Antipov *et al.*, "Efficient extraction of high power THz radiation generated by an ultra-relativistic electron beam in a dielectric loaded waveguide," *Appl. Phys. Lett.*, vol. 109, no. 14, p. 142901, 2016. https://doi.org/10.1063/1.4963762

[12] E. Prat *et al.*, "Outline of a dielectric laser acceleration experiment at SwissFEL," *Nucl. Instr. Meth. Phys. Res. Sec. A*, vol. 865, pp. 87–90, 2017. https://doi.org/10.1016/j.nima.2017.01.016

Content from this work may be used under the terms of the CC BY 3.0 licence (© 2018). Any distribution of this work must maintain attribution to the author(s), title of the work, publisher, and DOI.

ISBN: 978-3-95450-194-6 ISSN: 2226-0366 doi:10.18429/JACoW-LINAC2018-MOPO035

STATUS OF CLARA FRONT END COMMISSIONING

D. Angal-Kalinin[1†], A. D. Brynes[1], S. Buckley[1], R. Cash, R. F. Clarke, P. Corlett[1], L. S. Cowie[1], G. Cox, K. Dumbell[1], D. J. Dunning[1], C. Hodgkinson, P. Hornickel[1], F. Jackson[1], J. K. Jones[1], J. W. McKenzie[1], B. L. Militsyn[1], A. J. Moss[1], J. Murphy[1], T. C. Q. Noakes[1], M. D. Roper[1], D. J. Scott[1], B. J. A. Shepherd[1], R. J. Smith[1], E. Snedden[1], N. R. Thompson[1], C. Tollervey[1], D. A. Walsh[1], T. Weston[1], A. E. Wheelhouse[1], J. T. G. Wilson
STFC, Sci-Tech Daresbury, UK, also at [1]Cockcroft Institute, Sci-Tech Daresbury, Warrington, UK

Abstract

CLARA (Compact Linear Accelerator for Research and Applications) is a Free Electron Laser (FEL) test facility under development at Daresbury Laboratory. The progress in commissioning of the CLARA front end focussing on recent investigations into photoinjector (PI) drive laser transport and development/commissioning of high level software scripts are presented.

INTRODUCTION

CLARA is a proposed 250 MeV FEL test facility [1] based at Daresbury Laboratory. The test facility has been designed to test advanced FEL concepts and capabilities for next generation X-ray FELs as well as to provide high brightness beam to academic and industrial users. CLARA is intimately linked to the VELA facility based on the RF photocathode gun, which was commissioned in 2013 and successfully delivered beam to academic and industrial users from 2013-2015 [2]. During 2016-2017, the Front End of CLARA has been installed in the accelerator hall. This consists of a 10 Hz S-band RF gun [3] and a S-band Linear accelerator Linac1. An S-bend incorporating the spectrometer dipole, a quadrupole triplet and a Lozenge dipole transports high energy beam from CLARA FE to the existing VELA beam line. The 10 Hz RF gun, earlier used on VELA is now installed on the CLARA beam line. First results of CLARA Front End commissioning were reported at IPAC18 [4]. This paper gives an update since May 2018 on investigations into PI laser transport and future plans as well as problems in linac wave guide and the remedial actions taken. The progress in commissioning of high level software scripts with beam is presented.

PHOTOINJECTOR LASER TRANSPORT INVESTIGATIONS AND PLANS

Systematic investigation of the laser system (10 mJ Ti:Sapphire, 80 fs @ 10 Hz; frequency tripling from 800 to 266 nm through harmonic generation in consecutive BBO crystals) and transport have been performed with three primary goals: 1) to increase the total UV pulse energy reaching the photocathode and facilitate >100 pC charge extraction from the Cu photocathode; 2) understand and mitigate factors responsible for deterioration of the laser transverse profile (nominally Gaussian); and 3) replace a number of contaminated and damaged optics along the UV transport line.

After optimisation the third harmonic generator at saturation now yields 850 μJ pulse energy at 266 nm. An additional 20% gain in transport efficiency has been obtained by moving the pulse energy control from the UV directly (previously performed using a UV half-wave plate and pair of Brewster polarisers for rejection) to the near infrared (NIR) by exploiting the polarisation sensitivity of the sum-frequency generation process.

Visible contamination of exit face of the sum frequency crystal and first four mirrors in the UV transport line is responsible for a significant decrease in transport efficiency (as much as 40%). The mirror contamination is largely reversible through standard cleaning procedures which must be performed weekly to maintain reasonable transport efficiency. Surface analysis of the contamination reveals primarily hydrocarbon components, likely formed through UV-induced breakdown.

Laser transport consists of relay imaging of a truncated Gaussian beam from an aperture in the Photoinjector Laser Laboratory to the cathode. Investigations have revealed damage to optics in the transport plane due to hot spots in the UV beam profile. These hot spots are generated at source and are not a function of the transport optics. We believe these hot spots originate due to variation in the NIR profile following single-pass amplification (as a result of damage to the Ti:Sapphire crystal), which is then effectively amplified through harmonic generation.

To mitigate damage due to hot spots and improve the transverse profile, a UV-based vacuum spatial filter has been designed with a view to implementation early 2019. With the hot spots removed, an aspheric lens beam shaper will be used to generate a flat-top transverse profile as required for CLARA beam physics.

ISSUES WITH LINAC WAVEGUIDE

Linac1 is a two meter S-band travelling wave linac, and has been in operation on CLARA since November 2017. The waveguide system is operated with 3 bar of SF6 and has a circulator after the klystron. The waveguide is sealed with CPR flat and grooved flanges which seal on a rubber gasket. The klystron power for the system is 35 MW, giving 45 MeV/c of measured momentum gain from the linac. In June 2018 the beam momentum jitter measured on CLARA increased dramatically, and the forward power pulse measured just before the linac was discov-

† deepa.angal-kalinin@stfc.ac.uk

Content from this work may be used under the terms of the CC BY 3.0 licence (© 2018). Any distribution of this work must maintain attribution to the author(s), title of the work, publisher, and DOI.

ISBN: 978-3-95450-194-6 ISSN: 2226-0366 doi:10.18429/JACoW-LINAC2018-MOPO035

ered to be dropping off towards the end of the pulse. Breakdown in the waveguide was suspected.

Analysis of the SF_6 gas and inspection of the waveguide showed breakdown products on the inside of the waveguide, plus burn marks on the flanges as well as damage to some of the waveguide o-ring gaskets. The circulator had suffered catastrophic damage to the ferrite and one ceramic dielectric component was detached completely.

The complete waveguide system was removed and cleaned. A survey of the waveguide flanges was completed and found that the flatness was generally poor, between 50 - 100 µm. This could lead to poor RF contact and arcing. However the flanges with the worst flatness did not correlate with breakdown location. The worst burn marks were on a waveguide twist. Work is underway to understand the breakdown locations, including analysing previous mechanical simulations of the effect of temperature changes, and calculations to assess the likelihood of standing wave build-up between bends or twists.

After cleaning, damaged or warped flanges were re-machined and the waveguide was replaced without the circulator. For the short term CLARA will run with this system at a limited forward power of 20 MW. The measured acceleration from the linac is 35 MeV/c at this power. In the longer term the system will be replaced with waveguide with a vacuum flange such as DESY or LIL flange. As these use a soft copper gasket to form a crush seal the RF contact is guaranteed, and gives the option of running under UHV conditions.

HIGH LEVEL SOFTWARE COMMISSIONING WITH BEAM

A software development framework has been built that sits above the EPICS control system. For each main hardware type (magnets, BPMs, LLRF, cameras, etc.) there is a C++ interface to EPICS, These interfaces are extensible and configurable via plaintext configuration files parsed at run-time. Working in concert the C++ modules can be used to perform any reasonable commissioning or machine characterisation experiment. To streamline all high level software is developed in Python, using the C++ interface to EPICS. The first phase of application development aims to provide robust, repeatable daily machine set-ups, basic online data analysis and characterisation of crucial diagnostics such as BPMs.

Charge Scans and RF/Solenoid Centring

A routine to automatically centre the PI laser/beam source on the cathode with respect to the gun RF field and its solenoid has been developed. This uses the final laser mirror and the virtual cathode image to control the position of the spot on the cathode. This routine also enables variations in bunch charge (measured at the first wall current monitor (WCM) as a function of cathode position, to be mapped. Significant variations in bunch charge are observed within the ±3 mm (and even within ±1 mm) around the nominal RF centre, although it is not established with certainty the exact contributions of laser transport, cathode quantum efficiency, and transport to the WCM to this effect.

Respective centres of the RF field and the main solenoid are found, referenced to the virtual cathode x/y position, by measuring the amount of deflection of the beam on a downstream screen or BPM caused by RF phase changes and solenoid strength changes. For example, Fig. 1 illustrates the data gathered to determine the RF centre.

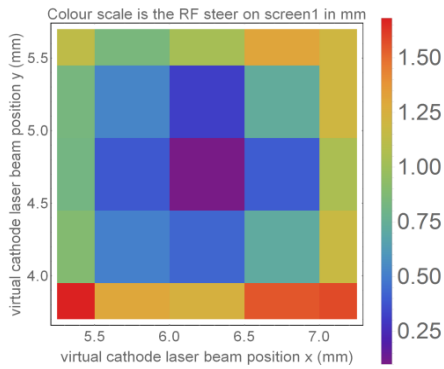


Figure 1: Illustration of position of PI laser on virtual cathode for determining the RF centre.

Image Acquisition and Online Analysis

The CLARA image acquisition system has an image processing module running in EPICS. The data from each image is cropped to a user-defined region-of-interest (ROI), chosen to include the beam spot, the weighted means and covariance matrix of this region are computed giving the beam centroid and RMS (first and second moments) and the x-y correlation (beam tilt). For smooth changes in these properties the ROI can be updated using simple feedback algorithms to give an online diagnostic of beam position, size and intensity. This system currently works at 10 Hz and is being developed to be more robust and operate at higher repetition rates. The system will be used in many procedures, particularly those that require the beam covariance and cross-checking beam position with BPMs. Figure 2 shows online analysis of the laser beam spot.

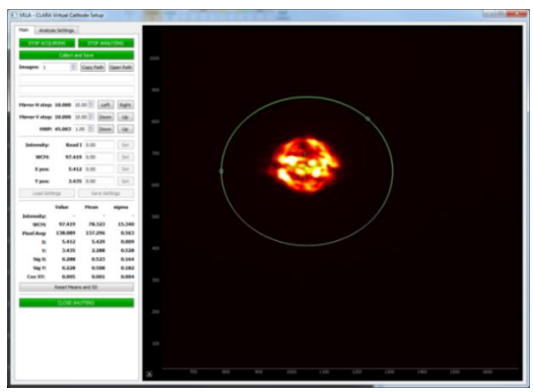


Figure 2: Online analysis of the laser beam spot. The ellipse is an ROI, with cross hairs indicating the beam centroid and widths; the analysis results are also in a table in the left hand panel.

Content from this work may be used under the terms of the CC BY 3.0 licence (© 2018). Any distribution of this work must maintain attribution to the author(s), title of the work, publisher, and DOI.

ISBN: 978-3-95450-194-6 ISSN: 2226-0366 doi:10.18429/JACoW-LINAC2018-MOPO035

Content from this work may be used under the terms of the CC BY 3.0 licence (© 2018). Any distribution of this work must maintain attribution to the author(s), title of the work, publisher, and DOI.

Diagnostic Characterisation

Characterisation of the BPMs requires accurate calibration at various bunch charges and then cross-checking the BPM response with a downstream screen. During commissioning of the auto-phase application it was noticed that severe mis-steering of the beam into the vessel walls upstream of a BPM can generate spurious 'false-positive' signals in the BPMs. This effect is being further investigated to with the aim of including 'false-positive' tags to all BPM data.

Auto-Phasing RF Structures

Accurate phasing of the gun and linac cavities is required to find the phase of maximum energy gain (crest). This is achieved through an automated procedure that can start from any starting phase. An initial estimate of the gun crest is found by scanning the gun phase and finding the centre of the emission range as measured on a Wall Current Monitor directly after the gun. The beam is transported to the spectrometer line where a BPM and screen are used to fine crest the gun. Figure 3 shows the Auto-crester panel for the gun and linac.

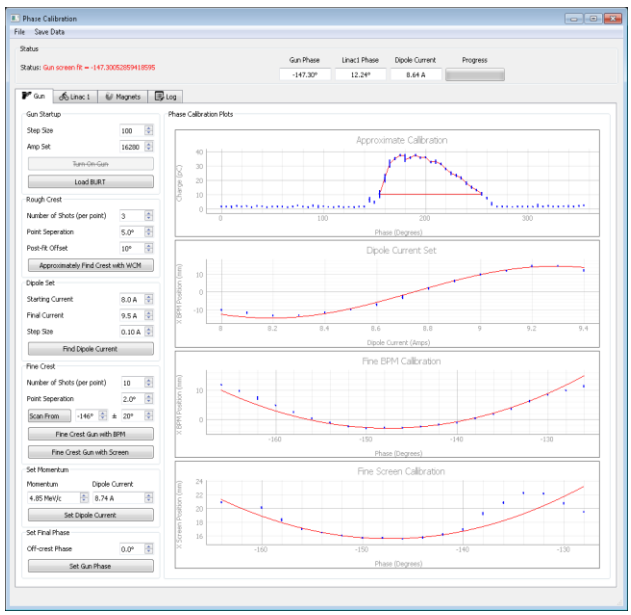


Figure 3: Auto-crester panel for RF structures.

Beam Orbit and Steering

Before more sophisticated beam steering and orbit correction algorithms are developed a simple point-to-point steering app that minimises positions on BPMs using the first upstream corrector has been developed (see Fig. 4). This automated procedure allows for a quick initial steering set-up to be found, saved and re-applied. The sum signal from BPMs is used to infer charge transport through the beamline.

Measurement of Momentum

Measuring the momentum combines many aspects of the above applications, as well as overlapping with the auto-cresting. BPMs and online image analysis is used to accurately steer the beam into the spectrometer dipole and then use the dipole field, known bend angle, position on the spectrometer BPM to measure the beam momentum.



Figure 4: Beam orbit and steering through the beam line, with charge transport.

Steering Through the Linac

Automatic scanning of parameters is easy to accomplish with the different Python modules. Figure 5 shows the app developed for steering through the linac using set of steering magnets located before the linac. A broad 'valley' of different steering gives optimal steering through the linac. This is being investigated further, for example including the steering through downstream quadruples, thereby finding an optimum orbit through both RF and magnetic elements.

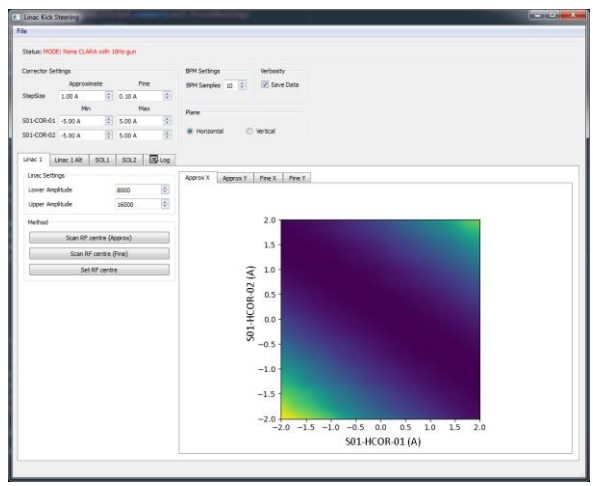


Figure 5: Beam position on screen located downstream of linac as a function of steering through linac.

SUMMARY

The Front End of the CLARA test facility at Daresbury Laboratory has been recently commissioned. Investigations into the photoinjector laser and transport line, and linac waveguide system, have demonstrated the areas which require improvements during the shutdown in 2019. A number of high-level software applications have been developed and tested with beam, this will help reliable beam delivery during beam exploitation period scheduled for the remainder of 2018.

ISBN: 978-3-95450-194-6 ISSN: 2226-0366 doi:10.18429/JACoW-LINAC2018-MOPO035

REFERENCES

[1] J. A. Clarke *et al.*, "CLARA Conceptual Design Report", JINST, 9:T05001, 2014.

[2] D. J. Scott *et al.*, "VELA machine development and beam characterisation", in *Proc. 6th Int. Particle Accelerator Conf. (IPAC'15),* Richmond, USA, 2015, paper TUPJE056, pp. 1752-1755.

[3] J. Rodier *et al.*, "Construction of the ALPHA-X Photoinjector Cavity", in *Proc. European Particle Accelerator Conf. (EPAC'06),* Edinburgh, Scotland, 2006, paper TUPCH113, pp. 1277-1279.

[4] D. Angal-Kalinin *et al.*, "Commissioning of Front End of CLARA Facility at Daresbury Laboratory", in *Proc. Int. Particle Accelerator Conf. (IPAC'18),* Vancouver, Canada, 2018, paper THPMK059.

Content from this work may be used under the terms of the CC BY 3.0 licence (© 2018). Any distribution of this work must maintain attribution to the author(s), title of the work, publisher, and DOI.

ISBN: 978-3-95450-194-6 ISSN: 2226-0366 doi:10.18429/JACoW-LINAC2018-MOPO036

STATUS OF THE 10MW MBKS DURING COMMISSIONING OF THE EUROPEAN XFEL IN DESY

Vladimir Vogel, Lukasz Butkowski, Stefan Choroba, Andrey Cherepenko and Jens Hartung
DESY, 22607 Hamburg, Germany

Abstract

At present 26 RF stations for European XFEL are in operation. Each RF station consists of a HV modulator located in a separate building on the DESY campus, up to 1600 m long 10 kV HV cables that connect the modulator and the HV pulse transformer located in the underground tunnel, 120kV, 3 m long HV cable connecting the HV pulse transformer and the connection module (CM) of the horizontal multi-beam klystron (MBK). The klystron can produce RF power up to 10 MW, at a RF frequency of 1.3 GHz, 1.5 ms pulse length and 10 Hz repetition rate. Two RF stations of the injector have already got about 24000 hours of operation, RF stations of the XFEL bunch compressor area have operated up to 13000 hours and the klystrons in the XFEL main linac already have about 11000 hours of operation (Status August 2018). To increase the lifetime of the klystrons, we use a fast protection system (KLM) that is based on the comparison of the actual RF shape and the expected RF shape. In the case of a difference exceeding a certain margin, for example, in the case of RF breakdown in a klystron or RF breakdown in a waveguide system (WGS), the KLM quickly, shorter than 800 ns, switches off the input RF signal. Thus, it does prevent the vacuum level in the klystron worsen too much or it minimizes the RF overvoltage time at the output windows of the klystron in case of breakdown in WGS. In this article we will give a summary of the present klystron status including the numbers of HV klystron gun and RF arcs in the klystrons.

INTRODUCTION

The European X-ray Free-Electron Laser (XFEL) [1] can be operated up to energy of 17.5 GeV (July 2018). Currently up to 300 coherent laser pulses per second with duration of less than 100 fs and with photon energy up to 19.1keV are delivered to the experiments. In future the number of pulses will increase to the design value of 27000 per second. For the production of these laser pulses, electrons have to be accelerated using a 2 km long accelerator based on superconducting radio frequency (RF) technology. For the XFEL project for a source of RF power of 26 RF stations were chosen the series horizontal MBKs made by two companies: MBK TH1802 from "Thales" [2 and 3] and MBK E3736H from "Toshiba" [4 and 5]. Both types of MBKs were equipped with CMs [6 and 7] and 3 meter long HV cables, and then they were tested on DESY MBK test stands [8]. The test was done with full RF power of 10 MW, full RF pulse length of 1.5 mS and with repetition rate of 10 Hz. Two types of HV cables and HV connectors were tested. Big advantages of using CM and HV cable connection between MBK and HV transformer are that we don't have to work with the open transformer oil during MBK installation in the tunnel and that MBK and WGS can be easy connected together. CM has monitors for the measurement of klystron voltage and cathode current. Figure 1 shows the one of 24 RF stations in the XFEL tunnel.



Figure 1: XFEL tunnel view.

Since 2013 the commissioning of the first RF station for XFEL injector has been started. In 2015 the second RF station started operation for the first cold AC module and since 2016 the commissioning of the main part of linac has been started.

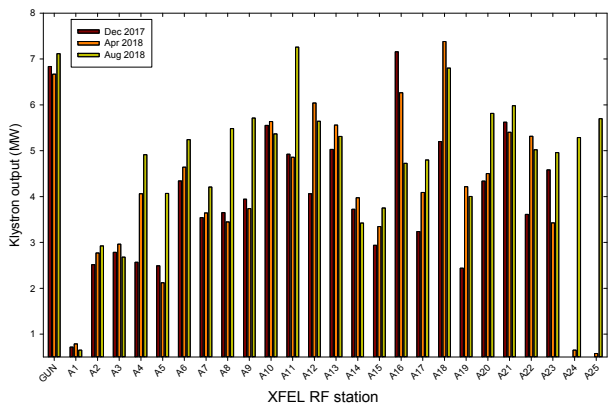


Figure 2: Output power for each of MBK.

In beginning of 2018 the commissioning of last two RF stations was done and in July 2018 the XFEL reached the design energy of 17.5 GeV. Figure 2 shows the output RF power for each of RF station. The average power from one MBK is 4.87 MW, but for several of RF stations the level of output power are more than 7 MW. Figure 3 shows the high voltage level for each of RF stations. In average the high voltage is 104.5 kV. For the moment we don't have any limitation for XFEL operation from RF

Content from this work may be used under the terms of the CC BY 3.0 licence (© 2018). Any distribution of this work must maintain attribution to the author(s), title of the work, publisher, and DOI.

ISBN: 978-3-95450-194-6 ISSN: 2226-0366 doi:10.18429/JACoW-LINAC2018-MOPO036

stations, the level of RF power from each of RF stations are determinates by XFEL longitudinal beam dynamics and bunch compression system.

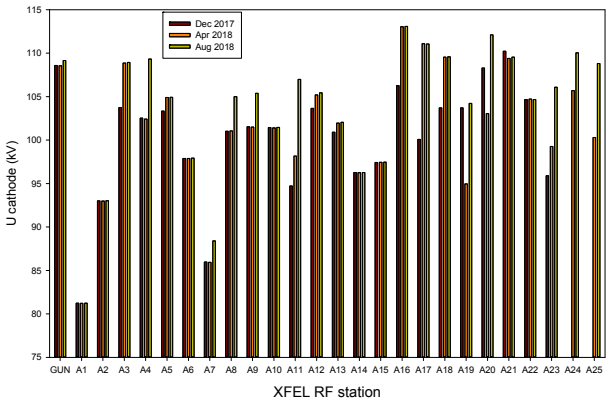


Figure 3: Cathode voltage for each of RF stations.

PROTECTION SYSTEM AND OPERATING STATISTICS

To make the operation of XFEL more reliable and increase the lifetime of the MBKs, in additional to the common interlock system since middle of 2018 we have started to use a fast protection system (KLM) [9 and 10] that was developed and tested during MBKs initial tests. The fast protection system is based on the comparison of the actual RF shape and the expected RF shape. In the case of a difference exceeding a certain margin, for example, in the case of RF breakdown in a klystron or RF breakdown in a waveguide system (WGS), the KLM faster than 800 ns, switches off the input RF signal.

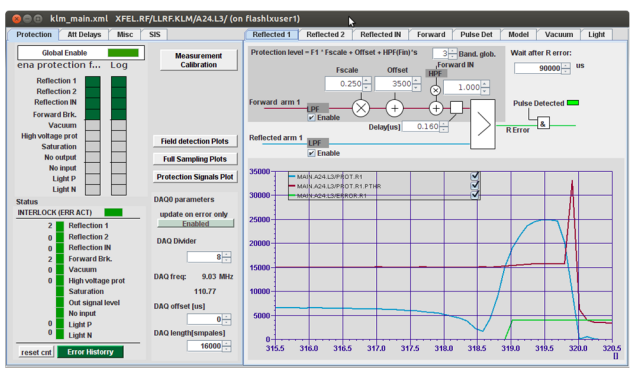


Figure 4: Detection of WG breakdown, A24.L3.

Thus, it does prevent the vacuum level in the klystron to worsen too much or it minimizes the RF overvoltage time at the output windows of the klystron in case of breakdown in WGS. Figure 4 shows the shapes of RF signals in case of RF breakdown in one arm of WGS of RF station A24.L3. The KLM system includes the partial discharge measurement in all of HV parts of RF station. Especially we were worry about life time of enough new HV components which were developed during MBKs test that are the CM that was produced by BINP Novosibirsk and is a new device never before used in accelerator, the PFISTERAR 3S type HV connector with 3 meter long NEXANS type 79470576, 54 kV AC HV cable. To be sure that we don't have any degradation in HV system one of HV cable from RF station A19.L3 after 11000 hours of operation on HV level of 104,5 kV, was sent back to factory. The factory test has confirmed the good state of this cable and HV connectors; the level of partial discharge was the same as just after initial cable test. The test of HV quality of CM will be possible to make only after one of MBK will be for some reason removed from XFEL tunnel because CM and MBK can't be separated without working with open transformer oil in the tunnel. At the end of this year it is planned to make the tests of oil quality in several CM. Figure 5 shows the number of events that have happened inside of MBKs since beginning of 2017. The most parts of events are the high voltage breakdowns in the gun area of klystrons, usually this type of breakdowns doesn't show the big increasing of vacuum level in the tubes, in contrast with RF breakdown inside of tube, where the vacuum level in the klystron greatly increases and it can provoke the arc in the gun area or, if vacuum level becomes very big, the main interlock system can be switched off the filament for this tube. For the filament recovery procedure for our type of MBKs it needs at least one hour. It is very important to switch off very fast the drive signal in case of RF breakdown inside the tube. Since the KLM system for MBKs has been implemented as routine for XFEL operation, the number of cases of filament recovery was reduced noticeably.

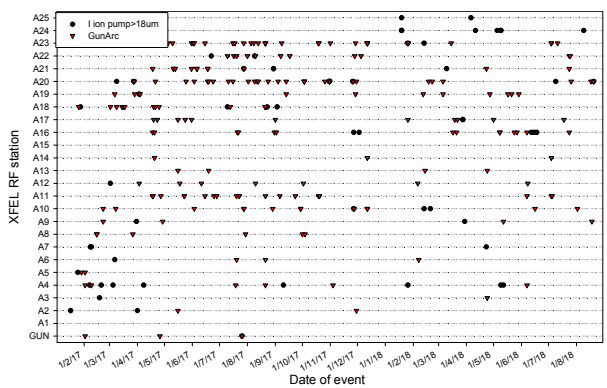


Figure 5: Gun HV arcing and RF breakdowns in XFEL MBKs.

Figure 6 shows the number of events that happened inside MBKs for full 2017 year and in comparison the events number for 8 months of 2018, one can see that in the beginning of XFEL operation during the conditioning period the number of events are greater than we have in this year. This is in the good agreement with what was expected; exclude the station A16.L3, but for this station the HV setting was increased at 6 kV in 2018.

Content from this work may be used under the terms of the CC BY 3.0 licence (© 2018). Any distribution of this work must maintain attribution to the author(s), title of the work, publisher, and DOI.

ISBN: 978-3-95450-194-6 ISSN: 2226-0366 doi:10.18429/JACoW-LINAC2018-MOPO036

Content from this work may be used under the terms of the CC BY 3.0 licence (© 2018). Any distribution of this work must maintain attribution to the author(s), title of the work, publisher, and DOI.

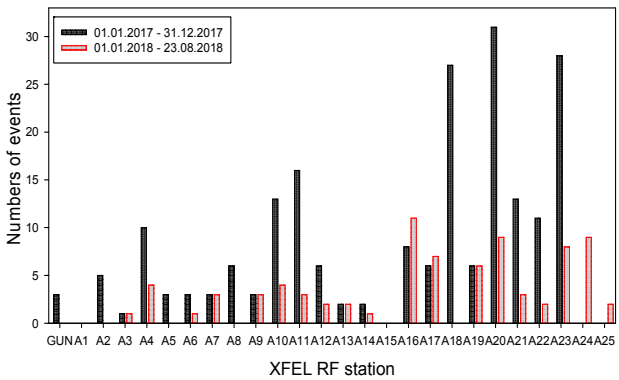


Figure 6: Number of events inside MBKs in year 2017 and for 8 months of 2018.

But we also expect that in future the number of events in the klystrons will increase. The good way to reduce the number of events in the future is the reducing the cathode voltage and klystron output power and this is possible using developed in 2010 in DESY the phase modulation procedure [11]. It is the method of changing of the klystron output phase which allows decreasing the required klystron peak power by reducing the reflected power during cavity filling time.

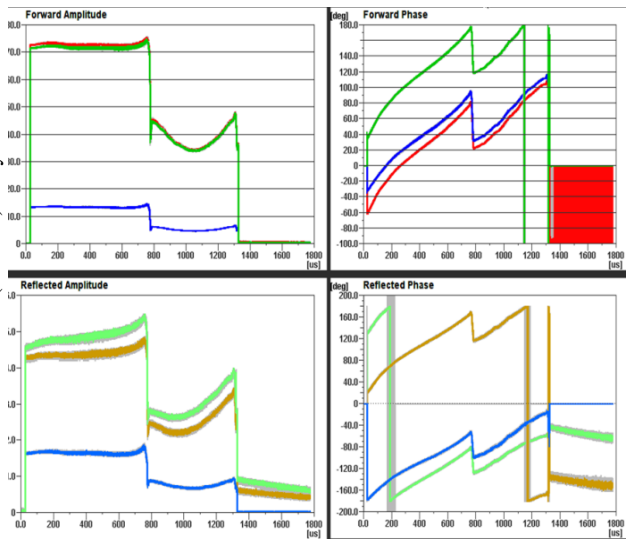


Figure 7: The output RF shapes of MBK in case of using phase modulation.

In case of phase modulation we can get the same gradient in the accelerate cavity but using up to 20% less RF power. Figure 7 shows RF shapes for amplitude and phase on the klystrons output. For the moment the phase modulation procedure is implemented only for several of RF stations, to use it for all XFEL RF stations we need make more investigations.

CONCLUSION

In February 2008 the first prototypes of MBK for XFEL had been installed on the MBK test stand DESY. Since August 2012 we have started a test and conditioning of the first one from 27 series MBKs for XFEL. The klystrons were tested together with connection modules (CM) and with different types of HV cables. To increase the lifetime of klystron a special fast protection system (KLM) was designed and tested. In March 2015 we started the installation of MBK to the XFEL tunnel. In July 2018 XFEL reached the design energy of 17.5 GeV. For the moment 26 XFEL RF stations produce in total 124.6 MW impulse power, 4.87 MW in average, the average cathode voltage is 104.5 kV, RF and HV breakdown rate for the MBK during last 8 months is 0.443 breakdowns per day for all of XFEL klystrons. For the moment the XFEL operators can get as much RF power from MBKs as it is necessary for current mode of XFEL operation without any limitation.

REFERENCES

[1] M. Atarelli *et al.* (Eds.), "XFEL: The European X-Ray "Free-Electron Laser: Technical Design report", *Proc. Report DESY 2006-097,* July 2006.

[2] A. Beunas, G. Faillon, "10MW/1.5ms,L band multi beam klystron", *Proc. Conf. Displays and Vacuum Electronics,* Garmisch-Paterkirchen, Germany, April 29-30, 1998.

[3] V. Vogel *et al.*, "Testing of 10MW Multibeam Klystrons for the European X-Ray FEL at DESY", *Proc. of PAC07*, Albuquerque, New Mexico, USA, 2007.

[4] A. Yano *et al.*, "The Toshiba E3736 Multi-Beam-Klystron", *Proc. of LINAC'04,* Lubeck, Germany.

[5] V. Vogel and S. Choroba, "Status of Horizontal MBK for XFEL". http://www.xfel.eu/project/meetings/project_meetings/2009

[6] V. Vogel *et al.*, "Connection Module for the European X-ray FEL 10MW Horizontal Multibeam Klystron", *Proc. of IPAC10,* Kyoto, Japan, THPEB043, 2010.

[7] P. Bak, V. Zabrodin, A. Korepanov and V. Vogel, "Klystron Cathode Heater Power Supply System Based on the High-Voltage Gap Transformer", *Proc. of PAC09,* Vancouver, BC, Canada, TU6RFP016, 2009.

[8] V. Vogel and S. Choroba, "Status of Multi-Beam Klystrons", *Proc. of 51th ILC DESY General Project Meeting".* http://ilcagenda.cern.ch/categoryDisplay.py?categId=16

[9] V. Vogel "MBK protection" LLRF seminar, 2008. http://ttfinfo.desy.de/LLRFelog/index.jsp

[10] V. Vogel *et al.*, "Summary of the test and installation of 10 MW MBKS for the XFEL project", *Proc.* of *LINAC16,* East Lansing, MI, USA, TUPLR017, 2016.

[11] V. Ayvazyan *et al.*, "Optimization of felling procedure for TESLA-type cavities for klystron RF power minimization for European XFEL", *Proc. of IPAC10,* Kyoto, Japan, TUPEA039, 2010.

ISBN: 978-3-95450-194-6 ISSN: 2226-0366 doi:10.18429/JACoW-LINAC2018-MOPO037

SRF GUN DEVELOPMENT AT DESY

Elmar Vogel, Jacek Sekutowicz, Serena Barbanotti, Ingmar Hartl, Kay Jensch, Daniel Klinke, Denis Kostin, Wolf-Dietrich Moeller, Manuela Schmoekel, Sven Sievers, Nicolai Steinhau-Kuehl, Alexey Sulimov, Jan-Hendrik Thie, Birte van der Horst, Hans Weise, Lutz Winkelmann, DESY, Hamburg, Germany
John Smedley, BNL, Upton, Long Island, NY, USA
Jochen Teichert, HZDR, Dresden, Germany
Mateusz Wiencek, IFJ-PAN, Kraków, Poland
Jerzy Andrzej Lorkiewicz, Robert Nietubyc, NCBJ, Świerk/Otwock, Poland

Abstract

A future upgrade of the European XFEL (E-XFEL) foresees an additional CW operation mode, which will increase the flexibility in the photon beam time structure [1–3]. One of the challenges of this operational mode is the need for a CW operating photo injector. We believe that using an SRF gun is the preferred approach as the beam parameters of normal conducting pulsed guns can be potentially met by SRF guns operating CW. For more than a decade DESY, in collaboration with TJNAF, NCBJ, BNL, HZB and HZDR, has performed R&D to develop an all superconducting RF gun with a lead cathode. In the frame of E-XFEL CW upgrade feasibility studies, the SRF-gun R&D program gained more attention and support. Within the next few years we would like to demonstrate the performance of the all superconducting injector required for the E-XFEL upgrade. The selected approach offers advantages w.r.t. the cleanliness of the superconducting surface, but requires a complete disassembly of a cryostat and stripping the gun cavity in a clean room to exchange the cathode. Thus it is practical only when the life time of the cathode is at least several months. In this paper we present the actual status of the R&D program, next steps and the longer term plans.

INTRODUCTION

At present, the high brightness beams required for the E-XFEL are reliably generated by normal conducting (NC) pulsed RF gun technology [4]. The NC CW gun technology developed by LBNL has been chosen as baseline for LCLS-II, operating CW, because SRF guns have not yet demonstrated reliable operation [5]. In contrast to LCLS-II the schedule of the future upgrade of the E-XFEL permits some development time to demonstrate reliable operation of SRF guns. Table 1 contains a comparison of the basic parameters of the three technologies.

ALL SUPERCONDUCTING GUN

RF guns are commonly first installed and aligned to the subsequent accelerator components before inserting cathodes via cathode insertion systems. This approach permits a quick exchange of cathodes but faces challenges at ultra-clean superconducting (SC) cavities w.r.t. cathode heating, cathode lifetime, field emission and multipacting. R&D is still required and ongoing, e.g. performed at HZDR [6–8] and HZB [9–11]. Work on SRF guns performed elsewhere can be found in [12].

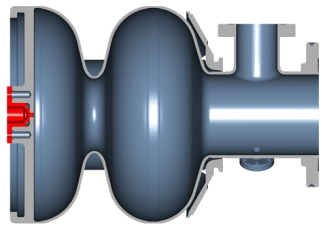


Figure 1: All superconducting gun with a plug (red) with lead cathode screwed into a hole on the cavity backside.

Since more than a decade DESY in collaboration with TJNAF, NCBJ, BNL, HZB and HZDR performs R&D to develop an all superconducting RF gun, e.g. see [13–17]. The recent design foresees a plug with a lead cathode screwed in a clean room into a hole on the cavity backside and sealed with indium, Fig. 1. Doing so, the cavity can be cleaned after the cathode insertion, and possibly lost cathode particles should not heat and quench the cavity, as they are all superconducting. In contrast to setups with cathode insertion systems, exchanging cathodes requires a complete disassembly of the cryostat and bringing the gun cavity back into the clean room. Consequently, this approach requires reasonable long cathode lifetimes above 100 days.

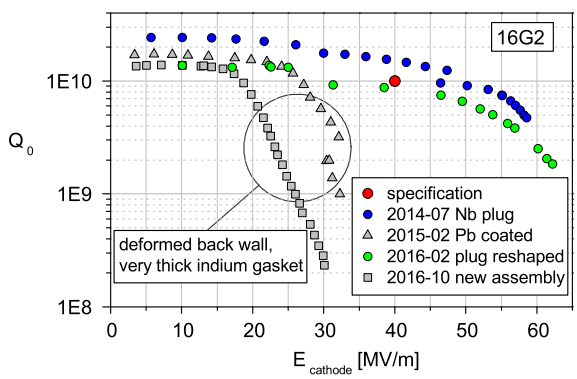


Figure 2: Promising vertical test results of the first prototypes of an all superconducting gun.

Content from this work may be used under the terms of the CC BY 3.0 licence (© 2018). Any distribution of this work must maintain attribution to the author(s), title of the work, publisher, and DOI.

ISBN: 978-3-95450-194-6 ISSN: 2226-0366 doi:10.18429/JACoW-LINAC2018-MOPO037

Content from this work may be used under the terms of the CC BY 3.0 licence (© 2018). Any distribution of this work must maintain attribution to the author(s), title of the work, publisher, and DOI.

Table 1: Photocathode Gun Technology Providing High Brightness Beams

Design beam parameters	**Unit**	**CW SRF Gun for European XFEL**	**APEX CW Gun (NC) for LCLS-II**	**Pulsed NC Gun at European XFEL**
bunch train duty cycle	[%]	100	100	0.6
beam current	[μA]	up to 25	up to 60	up to 27
bunch repetition rate	[kHz]	1000 to 100	620 to 100	up to 4500
bunch charge	[pC]	20 to 250	10 to 300	20 to 1000
transverse emittance	[μm]	0.4 to 0.8	0.2 to 0.6	0.2 to 1.0
beam energy at gun exit	[MeV]	3	0.75	5.1
RF parameters				
operation frequency		3 GHz	186 MHz	1.3 GHz
accelerating gradient	[MV/m]	21	19.5	31
electric peak (cathode) field	[MV/m]	40	19.5	60
RF inout power		750 W	about 100 kW	about 42 kW

Vertical tests of the first prototype SRF Gun cavities with cathode plugs called 16G1 and 16G2 performed at DESY [18] showed promising results with world record gradients of up to 60 MV/m at the cathode, Fig. 2. This was achieved with buffered chemical polishing (BCP) surface treatment of 16G2 performed at JLAB. The mechanical instability of the back wall required very thick indium gaskets and degraded the performance of this prototype.

At BNL we measured the quantum efficiency (QE) of lead cathodes, Fig. 3 and [15, 19], and at HZDR we examined the lifetime by irradiating a lead cathode over 550 hours [20]: The QE is sufficient for the specified bunch charge using an industry built laser. So far, we didn't observe a degradation of the QE over time.

TEST WITH BEAM

The tests performed so far indicate this type of SRF gun may work as needed. Nevertheless, the next required step is the demonstration of a sufficiently long lifetime of the cathode irradiated with a laser in a cavity operating at the design gradient and generating electron bunches with charge up to 250 pC. We choose this as our goal for the next years, after finalizing the construction and commissioning of the E-XFEL.

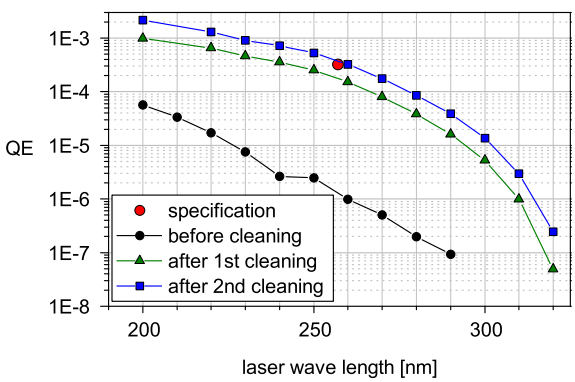


Figure 3: At BNL measured QE of DESY lead cathodes: before laser cleaning at 248 nm, after 1st cleaning applying 1000 shots with 0.06 mJ/mm^2 each, after and 2nd cleaning applying 10000 shots the QE specification of 3.2 10^{-4} at 257 nm was met.

This system test will be performed in one of tests stands used for series module testing during the E-XFEL construction phase. New SRF gun cavities with improved design where built. In addition, some other components need to be developed, constructed and purchased. These are a cryomodule, housing the SRF cavity and a cold beamline with solenoid magnet together with the cryogenic supply of such a module. Power couplers and a power rf source for CW operation need to be adapted. A cathode laser, a laser beam line and a mirror chamber for bringing the laser beam into the beam line is required, plus some beam diagnostics and a small beam dump.

COMPONENTS AND DEVELOPMENTS

In spring 2017 we built together with industry two **new SRF gun cavities** (16G3 and 16G4) with improved mechanical design of the back wall and cathode plugs. It was first validated by a mechanical model and includes stiffening ribs and titanium thread inserts. New auxiliaries like handling frames for the clean room and the chemical surface treatments were designed and built.

At DESY we have well-established procedures for the **surface treatment** of single- and nine-cell SRF cavities where acid and water flows through two big holes of the beam pipes at both ends. In contrast, the SRF gun cavities have one beam pipe and opposite the tiny hole for the cathode plug which in addition needs to be protected from the acid for keeping the design value of the diameter. R&D for the SRF gun recipe and treatment has been performed and is still ongoing. This includes the adaptation of the electropolishing (EP) apparatus and the design of new EP cathodes. A new high pressure rinse (HPR) nozzle for optimal cleaning

ISBN: 978-3-95450-194-6 ISSN: 2226-0366 doi:10.18429/JACoW-LINAC2018-MOPO037

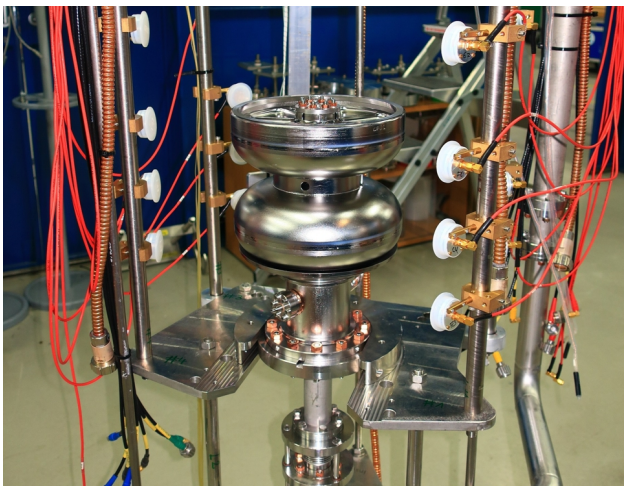


Figure 4: The new SRF gun cavity 16G3 in the insert ready for a first vertical test.

of the half-cell and avoiding impacting the cathode area is under construction. Acrylic glass models are ordered to study the HPR. In autumn 2017 EP and HPR was applied to the new SRF gun cavities and lead coated niobium cathode plugs were installed.

End 2017 and beginning 2018 we performed vertical tests of 16G3 and 16G4 at temperatures of 2 K, 1.8 K and 1.6 K applying normal cool down and slow cool down (from 13 K with ap. −0.1 K/min) for flux expulsion. In all cases the maximum gradients were below specification. There was no field emission. Second sound data was taken and first analysis performed. Obviously the surface treatment was not optimal. There are rough areas at the cavity surfaces visible.

Surface removal by buffered chemical polishing (BCP) may be less sensitive on the cavity geometry and was successful applied at the first two cavities, see above. Therefore, BCP (removal of 110 to 140 µm) at industry followed by a so-called flash EP (removal of 10 to 40 µm) at DESY will be applied next. The subsequent vertical tests are panned before End 2018.

We investigate different types of **cathodes and cathode plugs**. These are lead coated niobium plugs, bulk lead disks on niobium plugs and bulk lead plugs. The focus of the R&D is on the preparation of the niobium plugs before the coating, the lead coating performed at NCBJ and the clean room compatibility. First bulk lead plugs have been assembled to the mechanical model of the cavity back wall and leak tests performed at 2 K.

A **cryo-module** surrounding the SRF gun cavity and a cold beamline with solenoid magnet and other cold components is under development and construction. For future flexibility we decided HZDR and HZB cavities with their cathode exchange systems should also fit in. Special features are the ability to align the gun cavity and beam line when the module is cold, likewise the (cold) solenoid. There is a common interest on such a flexible platform for testing different SRF gun designs from HZDR, HZB and DESY. We coordinate design items at regular meetings with the relevant colleagues of all three laboratories.

We purchased an industry built laser similar to the ones already used at DESY as **cathode laser**, e.g. [21]. It consists of an infrared laser (1030 nm) whose light (average 20 W) is converted by a exchangeable conversion unit to the ultraviolet at 257 nm with a tunable pulse length from 300 fs to 15 ps and 2 W average power. One conversion unit is optimized for beam operation at a repetition rate up to 1.13 MHz, the other one for 100 kHz for laser cleaning of the cathode. The laser will next be installed in the laser laboratory adding a mirror chamber, a dummy beamline and a model of the SRF gun cavity back wall. We foresee QE measurements of the lead cathodes and studies for scanning the cavity backside to locate the cathode.

Other components required for the system test with beam are either already available and may need to be integrated into the setup and test stand, like the RF power source, or still need to be developed, constructed and purchased. Just started beam dynamic examinations are needed for the design, e.g. before deciding on a solenoid magnet.

SUMMARY AND OUTLOOK

First component tests of an all superconducting RF gun showed promising results. SRF gun cavities surpassed the required gradients in vertical tests, the QE is sufficient for the specified bunch charge and did not degrade within 550 hours of irradiation. The next step is the demonstration of a sufficiently long lifetime of the cathode irradiated with a laser in a cavity operating at the design gradient and generating electron bunches. We stated working on this goal which we plan to achieve within the next few years. In the successful case the setup of an injector operating CW in the second injector tunnel of the E-XFEL will follow. It will consist of the gun, L-band and third harmonic SRF modules and all the other beam line components and used for testing accelerator components operating CW.

ACKNOWLEDGEMENTS

The authors acknowledge the significant contributions from numerous colleagues at all institutes joining the effort for an all superconducting RF gun. Many people from industry contribute to this effort as well.

REFERENCES

[1] J. Sekutowicz *et al.*, *PRST AB* 8, 010701 (2005)

[2] J. Sekutowicz *et al.*, in *Proc. FEL2013*, paper TUOCNO04

[3] R. Brinkmann *et al.*, in *Proc. FEL2014*, paper MOP067

[4] F. Stephan *et al.*, *PRST AB* 13, 020704 (2010)

[5] J. F. Schmerge *et al.*, in *Proc. FEL2014*, paper THP042

[6] A. Arnold *et al.*, *NIM* A 577 (2007) 440–454

[7] A. Arnold and J. Teichert, *PRST AB* 14, 024801 (2011)

[8] J. Teichert *et al.*, *NIM* A 743 (2014) pp.114–120

Content from this work may be used under the terms of the CC BY 3.0 licence (© 2018). Any distribution of this work must maintain attribution to the author(s), title of the work, publisher, and DOI.

ISBN: 978-3-95450-194-6 ISSN: 2226-0366 doi:10.18429/JACoW-LINAC2018-MOPO037

[9] A. Burrill *et al.*, in *Proc. IPAC2014*, paper WEPRI005
[10] A. Burrill *et al.*, in *Proc. IPAC2015*, paper WEPMA011
[11] A. Neumann *et al.*, in *Proc. SRF2015*, paper THPB026
[12] J. Sekutowicz, SRF2015, paper THAA02
[13] A. Neumann *et al.*, in *Proc. IPAC2011*, paper MOODA03
[14] M. Schmeißer *et al.*, in *Proc. IPAC2013*, paper MOPFI002
[15] R. Barday *et al.*, *PRST AB* 16, 123402 (2013)
[16] J. Lorkiewicz *et al.*, *Proc. SPIE*[0] Vol. 9662 (2015) 966233
[17] R. Nietubyc *et al.*, *NIM* A 891 (2018) 78–86
[18] D. Kostin *et al.*, in *Proc. SRF2015*, paper THPB056
[19] J. Smedley, T. Rao, and J. Sekutowicz, *PRST AB* vol. 11, pp. 013502, 2008
[20] J. Teichert *et al.*, EuCARD-2 report 12.9, 2016
[21] B. Marchetti *et al.*, in *Proc. IPAC2017*, paper TUPAB040

Content from this work may be used under the terms of the CC BY 3.0 licence (© 2018). Any distribution of this work must maintain attribution to the author(s), title of the work, publisher, and DOI.

ISBN: 978-3-95450-194-6 ISSN: 2226-0366 doi:10.18429/JACoW-LINAC2018-MOPO038

RF OPERATION EXPERIENCE AT THE EUROPEAN XFEL

J. Branlard†, V. Ayvazyan, Ł. Butkowski, M. Grecki, M. Hierholzer, Mar. Hoffmann, Mat. Hoffmann, M. Killenberg, D. Kostin, T. Lamb, L. Lilje, U. Mavrič, M. Omet, S. Pfeiffer, R. Rybaniec, H. Schlarb, C. Schmidt, N. Shehzad, V. Vogel, N. Walker, DESY, Hamburg, Germany

Abstract

After its successful commissioning during the first half of 2017, the European X-ray free electron laser is now in regular operation delivering photons to users since September 2017.

This contribution presents an overview on the experience gathered during the first couple of years of operation. In particular, the focus is set on RF operation, advanced commissioning and RF related machine studies.

INTRODUCTION

The European X-ray free electron laser (XFEL) is a user facility delivering ultra-short hard and soft X-ray flashes with the highest brilliance worldwide, through 3 undulator lines and serving up to 6 experiments. It is based on a 10 Hz pulsed 17.5 GeV superconducting linac, commissioned since 2017. The first self-amplified spontaneous emission (SASE) light was demonstrated in May 2017, the first user run took place in September 2017 delivering photons at a wavelength of 1.3 Å. After a month shutdown in April 2018, the last 2 RF stations were commissioned. In May 2018, lasing was demonstrated simultaneously in all 3 beam lines (SASE 1, 2 and 3). A total of 1600 hours are devoted to user programs in 2018; this number should increase to 4800 hours in 2019. A summary on the machine commissioning and its highlights is given in [1, 2]. In this contribution, the focus is set on the experience gathered during the first operation years of the XFEL, in particular the commissioning of the LLRF system beyond its basic functionality, reported in the following section and an insight on a couple of dedicated machine studies is given in the subsequent section.

LLRF ADVANCED COMMISSIONING

The LLRF commissioning procedure was first presented in [3], and the accelerator operation and performance was reported in [4]. These commissioning steps guaranteed the proper operation of all RF stations, controlling the RF field inside the superconducting cavities and accelerating the beam to the desired energy. The advanced LLRF commissioning covers taking into operation LLRF subsystems related to performance optimization such as the drift compensation module [4], or modules related to more advanced exception handling mechanism such as the klystron lifetime management system (KLM) [5]. Figure 1 gives an example of this protection mechanism where a sudden increase in reflected power (P_{REFL}) was observed on one arm of the 10 MW klystron. This anomaly was detected within 200 nsec and resulted in switching off the drive 600 nsec later, preventing a high reflected waveform potentially harmful for the klystron. The increase in P_{REFL} is likely due to waveguide sparking, which started appearing when operating the klystron above 7 MW.

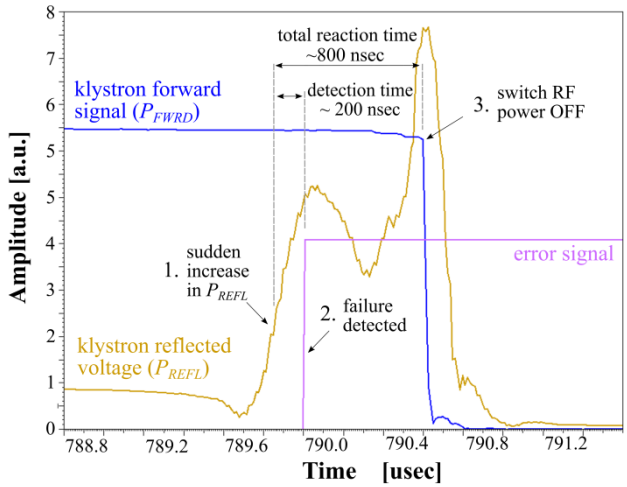


Figure 1: Event observed on August 29th 2018 at station A6. A sudden increase of the reflected power (1) triggered the klystron management system (2) to stop the klystron drive (3).

During this advanced commissioning phase, servers to monitor and service LLRF auxiliary modules were also deployed and commissioned (modules responsible for the local oscillator and clock generation, for the power supplies, for the remote controllable fuse and relay submodules or for the piezo driver for example). During this phase, firmware and server updates were deployed to improve the performance of the LLRF system. One can cite the toroid-based beam loading compensation algorithm as an example [6]. The optical RF synchronization (REFM-OPT) module was also taken into operation. This module synchronizes the 1.3 GHz RF reference distributed along the accelerator with respect to sub-fs stabilised optical links. Based on a Mach-Zender modulator, the REFM-OPT compares the phases of the optical link and RF signals and corrects for any drifts taking place in the RF distribution chain [7]. The re-synchronized RF is distributed locally to the nearest RF stations. The plot in Fig. 2 shows the temperature drift measured in the Linacs 1, 2 and 3 and the corresponding phase corrections applied by the different REFM-OPT units along the accelerator. Although there were no temperature data available for the injector, the tighter ambient temperature regulation in the injector directly translates into smaller reference phase corrections required from the injector REFM-OPT.

† julien.branlard@desy.de

Content from this work may be used under the terms of the CC BY 3.0 licence (© 2018). Any distribution of this work must maintain attribution to the author(s), title of the work, publisher, and DOI.

ISBN: 978-3-95450-194-6 ISSN: 2226-0366 doi:10.18429/JACoW-LINAC2018-MOPO038

Content from this work may be used under the terms of the CC BY 3.0 licence (© 2018). Any distribution of this work must maintain attribution to the author(s), title of the work, publisher, and DOI.

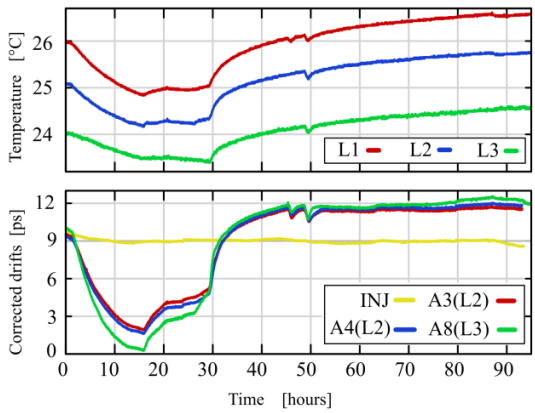


Figure 2: Temperature drifts measured in the different sections of the main accelerator, and the reference phase corrections applied by the REFM-OPTs.

RF SPECIFIC OPERATION STUDIES

Energy Reach and Radiation Related Studies

Since last year, weekly studies are devoted to assess the maximum reachable gradient for individual RF stations [4]: the possible limiting factors being (1) cavity quench, (2) field emission or (3) limitations coming from the high power chain (modulator voltage, waveguide sparks…). The RF station is time shifted off beam so that the investigation can take place parasitically along normal machine operation and beam delivery. Special care is taken to fine tune the cavity coupling, to verify the calibration of forward and reflected power with respect to probe signals, and to tune all cavities for all investigated gradient set points. Gradient limiters and quench reaction algorithms are disabled; finally, the beam block mechanism triggered by the machine protection system is masked for this station. This measure guarantees that quenching the station under investigation does not inhibit beam transport. The gradient is then carefully increased in open loop until one the 3 limitations mentioned above is encountered.

Although sometimes operating in full saturation, insufficient klystron power is most often not the limiting factor; a waveguide spark, quench or field emission is. Quenches are detected by the quench detection system, while field emission is measured by the online radiation monitor, the dark current monitor and periodic runs of the radiation measurement robot [8]. In the example of Fig. 3, the gradient of station A12 was increased, triggering a field emitter in one of the cavities. The resulting increase in radiation scattered to the nearest stations upstream (A11) and downstream (A13) was measured with thermoluminescent dosimeters (TLDs) placed underneath the cryomodules. The control electronics is protected by a concrete shielding, damping the radiation by a factor of 20-30. Nevertheless, the higher rate of 60 mGy/day observed outside the shielding of A12 was evaluated to be too high for the acceptable threshold of 1 Gy per year for the electronics underneath the concrete shielding. The operating gradient of A12 was subsequently reduced. For the weekly scans performed by the radiation monitor robot, an administrative limit of 500 µSv/h was set, which was reached on a couple of stations so far (A9 and A12).

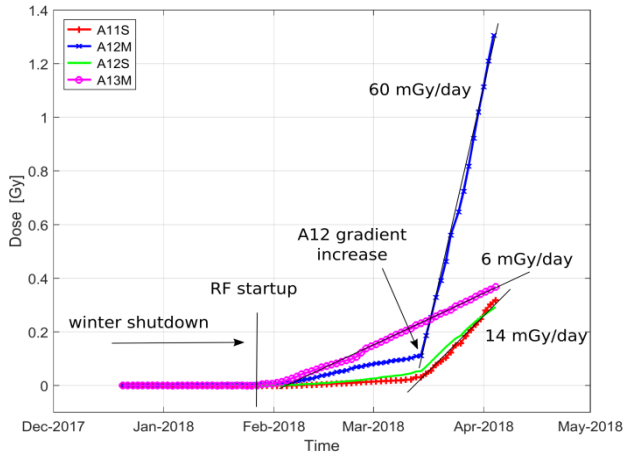


Figure 3: Accumulated radiation dose measured by TLDs placed underneath the cryomodules and outside the electronic shielding (M and S are the master and slave LLRF).

In the case where the limiting factor is a quench, the limiting cavity is detuned and the energy set point ramp up is repeated. In some cases, detuning the limiting cavity(-ies) might still result in a higher overall energy gain for the RF station. This can be mostly explained by the fact that the tailoring of the waveguide distribution according to each cavity performance has inherent limitations and limited precision. Removing the weakest cavity (by detuning it) can at times facilitate achieving maximum performance out of other cavities, yielding a net energy gain. 16 cavities (2%) fell in that category and were detuned as a consequence.

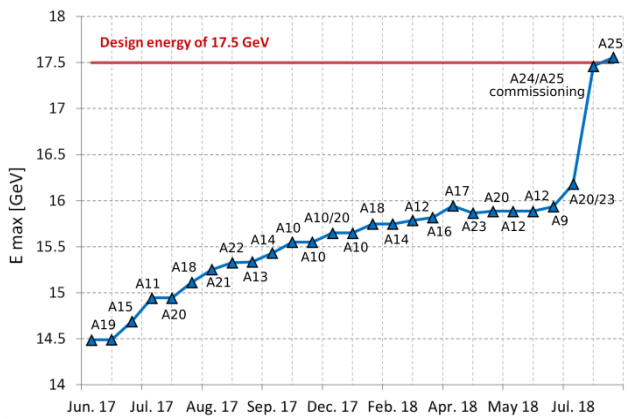


Figure 4: incremental energy gain resulting from the maximum gradient investigations (delta markers).

The outcome of each investigation is a report summarizing the findings and possibly proposing an optimization scenario. The energy gain observed since the beginning of this energy reach campaign is illustrated in Fig. 4. The steady raise comes from investigation of individual RF stations. The large step in July 2018 corresponds to the

ISBN: 978-3-95450-194-6 ISSN: 2226-0366 doi:10.18429/JACoW-LINAC2018-MOPO038

commissioning of the last 2 RF stations (A24 and A25) for which the installation was finalized during the April shutdown. The milestone of reaching the XFEL design energy of 17.5 GeV was then achieved mid of July 2018.

Cryogenic Pressure versus Detuning Study

Another study was carried out to evaluate the dependency of cavity detuning on fluctuations of the cryogenic helium (He) pressure (see Fig. 5). In this study, the He pressure was purposefully changed by ±3 mBar from its nominal 30 mBar set point over a total of 8 hours, while measuring the detuning for all 1.3 and 3.9 GHz cavities in the accelerator. The RF was kept constant for all RF stations, operating in open loop at a reduced gradient (typ. 10 MV/m per cavity) to minimize the impact of Lorentz force detuning and reduce the risk of high-power related RF trips. The outcome is a detuning sensitivity of 39.6 ±3 Hz/mBar for the 1.3 GHz cavities and 62.4 ±2 Hz/mBar for the 3.9 GHz cavities, in good agreement with the partial measurement reported in [9].

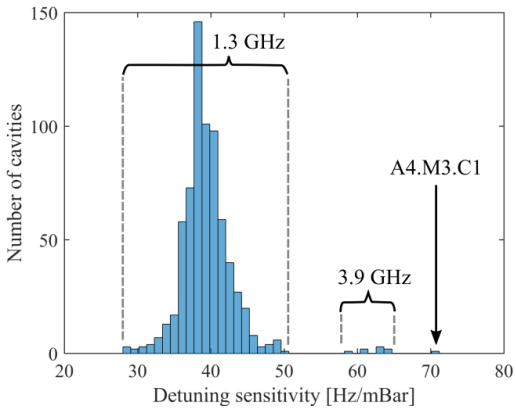


Figure 5: Histogram of the detuning sensitivity to He pressure fluctuations for XFEL superconducting cavities.

In the absence of piezo resonance control and for the XFEL cavity half bandwidth of 140 Hz, the typical 20% RF power overhead reserved for controls would be consumed compensating for a detuning of ±130 Hz. This corresponds to ±3.28 mBar He pressure fluctuation for the measured 1.3 GHz sensitivity. A ±3 mBar safety threshold was then set on the He pressure, beyond which RF operation is not allowed. The typical He pressure stability is better than 0.1 mBar rms, so this interlock system would prevent operation, should an uncontrolled drift of the He pressure occur. Although the sensitivity of the third harmonic cavities is higher, the situation there is relaxed due to their broader bandwidth. It is worth mentioning the special case of the first cavity, in the third cryomodule of the fourth RF station (A4.M3.C1) whose sensitivity is almost twice as high as the average 1.3 GHz cavities. This peculiarity had been caught during the cryomodule horizontal tests, but does not hinder regular operation. As a final remark, we have also observed some hysteresis effect accounting for ~50 Hz on 8 cavities (~1%). These cavities did not return to their initial tuning and required retuning although the initial He pressure had been restored. In almost all cases, this was observed on the first cavity of a cryomodule. This hysteresis effect is not yet fully understood. One explanation could be linked to the fact that the first half cell of the first cavity in a cryomodule is not included in the He vessel and therefore exhibits a slightly different cooling profile.

CONCLUSION

This contribution gives an overview on the continued RF commissioning and RF related studies performed at the European XFEL. In particular, some aspects of the advanced LLRF commissioning such as klystron lifetime management and optical reference synchronization were described. An insight on some RF operation related studies was also presented to illustrate the continuing work to better understand and characterize this new accelerator. Two examples were given, one illustrating the effort to assess the maximum gradient the European XFEL can reach and the limiting factors; another to assess the dependency of cavity detuning on the stability of the cryogenic He pressure. While the focus will shift in the coming years towards more user operation and less machine study time, the XFEL operation team is building up the effort to increase machine availability and reliability. This includes developing tools to catch, analyze and document any RF trips, their root cause and recovery time. More sophisticated tools to help operators monitor the health of the LLRF systems and the machine in general or tools to automate system start up, calibration procedures and optimize performance are also under development.

REFERENCES

[1] M. Scholz *et al.*, "FEL performance achieved at European XFEL", *Proc. of IPAC'18*, Vancouver, Canada, May 2018.

[2] D. Noelle *et al.*, "Commissioning of the European XFEL", Presented at LINAC'18, Beijing, China, Sept. 2018.

[3] J. Branlard *et al.*, "Installation and first commissioning of the LLRF system for the European XFEL", *Proc. of IPAC'17*, Copenhagen, Denmark, May 2017.

[4] M. Omet *et al.*, "LLRF operation and performance at the European XFEL", *Proc. of IPAC'18*, Vancouver, Canada, May 2018.

[5] Ł. Butkowski *et al.*, "A Model-Based Fast Protection System for High-Power RF Tube Amplifiers Used at the European XFEL Accelerator", *IEEE Trans. on Nuclear Science*, vol. 64, no. 6, Jun. 2017.

[6] Ł. Butkowski *et al.*, "Implementation of the Beam Loading Compensation Algorithm in the LLRF System of the European XFEL ", presented at LINAC18, Beijing, China, Sept. 2018.

[7] T. Lamb, *et al.* "Laser-to-RF synchronization with femtosecond precision", *Proc. of FEL'17*, Santa Fe, NM, USA, Aug. 2017.

[8] A. Dehne *et al.*, "MARWIN: a mobile autonomous robot for maintenance and inspection", *Proc. of ICALEPCS'17*, Barcelona, Spain, Oct. 2017.

[9] R. Paparella *et al.* "Operational Experience of the European-XFEL 3.9 GHz Coaxial Tuners", *Proc. of SRF'17*, Lanzhou, China, Aug. 2017.

Content from this work may be used under the terms of the CC BY 3.0 licence (© 2018). Any distribution of this work must maintain attribution to the author(s), title of the work, publisher, and DOI.

ISBN: 978-3-95450-194-6 ISSN: 2226-0366 doi:10.18429/JACoW-LINAC2018-MOPO039

STATUS UPDATE OF THE FAST ENERGY CORRECTOR CAVITY AT FLASH*

S. Pfeiffer†, J. Branlard, Ł. Butkowski, M. Hierholzer, M. Hoffmann, K. Honkavaara, H. Schlarb, C. Schmidt, S. Schreiber, M. Vogt, J. Zemella, DESY, 22607 Hamburg, Germany
M. Fakhari, Department of Physics, Universität Hamburg, 20355 Hamburg Germany

Abstract

Linear accelerator facilities driving a free-electron laser require femtosecond precision synchronization between external laser systems and the electron beam. Such high precision is required for pump-probe experiments and also for example for the electron bunch injection into a plasma bubble for laser plasma acceleration. An upgrade of the fast intra-train beam-based feedback system is planned at the Free-Electron Laser FLASH in Hamburg, Germany. This linear accelerator is based on superconducting (SRF) technology operating with pulse trains of maximum 1 MHz bunch repetition rate. Arrival time fluctuations of the electron beam are correctable by introducing small energy modulations prior to the magnetic bunch compressor. This contribution focuses on the design and the characterization of a normal-conducting RF (NRF) cavity with large bandwidth, mandatory to correct fast arrival time fluctuations. The cavity has recently been installed in the FLASH beamline. First measurements with the new cavity will be presented.

INTRODUCTION

The Free Electron LASer at Hamburg (FLASH) is a facility for research with tunable laser light in the X-ray range [1]. It delivers to its users a pulsed light with tunable wavelength down to 4.2 nm generated by SASE processes. Electron bunch trains of variable length and frequency with a repetition rate of 10 Hz are accelerated to a maximum energy of 1.2 GeV. Each pulse is enabled for about 1.4 ms while up to 800 bunches with a repetition rate of 1 MHz are injected. Providing stable and reproducible photon pulses needs a precise acceleration field control. During the last years additional control strategies were developed and included in the LLRF controller. This includes RF-field control and its superposition with beam-based information using the bunch arrival time and bunch compression information, [2–4]. By this the stability of the bunch arrival time at the end of the main accelerator could be improved, highly important e.g. for the precise synchronization between an external laser system and the electron beam [5]. To further improve the arrival time a fast energy corrector cavity prior to the bunch compressor is needed. This corrector cavity should be operated in the upper kHz bandwidth. The technical design and specifications for the fast corrector cavity named BACCA (Bunch Arrival Corrector CAvity) are given in [6].

DESIGN OF THE CAVITY

The basis for the design was the buncher cavity at the *Relativistic Electron Gun for Atomic Exploration* (REGAE) accelerator facility [7]. The main difference is the power coupling to the cavity. Due to longitudinal space constraints for the installation at FLASH this is realized by magnetic coupling, i.e. coupling loop instead of coaxial coupler. Figure 1 shows the first 3D drawing of the cavity with the beamline connection and the feedthroughs hosting the loops for magnetic coupling.

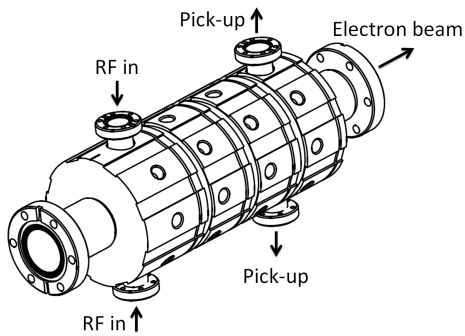


Figure 1: Technical design of the 4-cell fast corrector cavity with the 2 beamline flanges and the 4 feedthroughs for RF input and output loops/pickup.

The main design requirements are given as maximum energy correction of about 50 keV, a maximum feedback loop latency of 700 ns and a corrector cavity half bandwidth of 500 kHz. Furthermore, longitudinal and transverse wakefields as well as orbit changes for multi bunch operation should not occur during operation.

There is a trade-off between the accelerating voltage and the bandwidth of the corrector cavity as a function of the coupling constant [8]. The thermal stress to the input loop has been simulated justifying the power distribution with 2 input loops, [9]. Two output loops, i.e. the probe pickups, are used for symmetry reasons. The NRF cavity cells were produced at the Hansa Press- und Maschinenbau GmbH in Hamburg, Germany. Its assembly and the soldering of all parts were done at DESY. The assembled corrector cavity is shown in Fig. 2 with its 4 feedthroughs; 2 for in-coupling and 2 for the pick-up antennas.

CHARACTERIZATION OF THE CAVITY

The corrector cavity has been characterized and tuned for resonance after production. First we were driving the cavity with a test signal from the network analyzer via the input loop

* The work is part of EuCARD-2, partly funded by the European Commission, GA 312453.
† sven.pfeiffer@desy.de

Content from this work may be used under the terms of the CC BY 3.0 licence (© 2018). Any distribution of this work must maintain attribution to the author(s), title of the work, publisher, and DOI.

ISBN: 978-3-95450-194-6 ISSN: 2226-0366 doi:10.18429/JACoW-LINAC2018-MOPO039

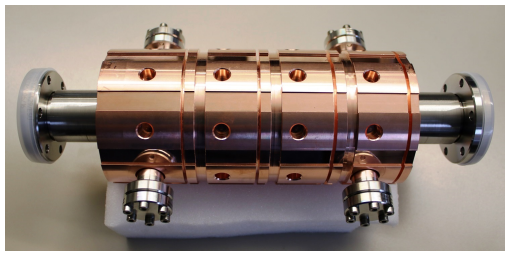


Figure 2: Assembled cavity after cell production, complete soldering and initial cleaning. The input and output loops are not connected.

of the cavity. For our set-up we used the S_{11} measurement of the network analyzer, i.e. the frequency dependent reflection coefficient. The frequencies where the S_{11} magnitude significantly reduces represent the resonance frequencies of the cavity. A change of the resonance frequency was observed while adjusting the magnetic coupling by rotating the input loop to the cavity [10]. Here 0 deg. means full magnetic coupling and 90 deg. no magnetic coupling of the cavity. Finally, both input loops were adjusted to a loop angle of 50 deg. which has been measured with half bandwidth of 500 kHz and a coupling factor of about 2.5. Each input loop has been adjusted to a half bandwidth of about 250 kHz and a coupling factor of about 1, i.e. critical coupling. In total 4 resonant peaks are visible, i.e., the operating π-mode frequency of about 2.998 GHz and the 3 remaining modes which are natural for a 4-cell cavity. The other modes are separated in the technical design and also in the measurements by more than 8 MHz from the operating mode. The electrical field flatness for the cavity was measured and corrected using the bead-pull method [11]. The cavity and all attached components like input loops were cleaned after the characterization of the cavity at air. This cleaning is required for installation into the FLASH beamline and its operation under vacuum. The input loops and pickup antennas were mounted and remeasured in a clean-room at DESY.

INSTALLATION

The tunnel installation took place in January 2018. The section after the third harmonic module ACC39 and before the first bunch compressor BC2 was renewed completely. During the removal of all components a damage of the first bunch compressor magnet was observed. The damaged magnet has been exchanged delaying the originally installation schedule by 2 days. Finally, the new cavity, 3 new quadrupoles and a new bunch arrival time monitor (BAM) body were installed together with the old horizontal and vertical steerer, strip-line bunch position monitor (BPM), charge monitor and vacuum pump, see Fig. 3. The picture was taken before end of installation, but before placement of the shielding wall.

At the end of the shutdown all main components, like vacuum pump, steerer, diagnostic and the three new quadrupoles were operable again. The installation of the power amplifier for the cavity together with the MicroTCA.4 system for LLRF regulation and the cable installation has been completed. The common forward and reflected signal as well as both probe signals were initially calibrated. The frequency generation module, converting the main 1.3 GHz frequency to the cavity operating and intermediate frequencies for signal detection (in-phase and quadrature) has been installed and commissioned, [6]. A commercially available cooler from TermoTek GmbH [12], in our case a modified version allowing heating, has been installed to bring the cavity to its resonance which is at about 40 deg. Celsius. Three temperature sensors for cavity body and cavity input loop supervision were installed.

FIRST BACCA MEASUREMENTS

The first measurements were done without RF and with beam loading only. Hereby the cavity can be used as charge detector by analyzing bunch transients. Figure 4 shows the peak amplitude of the beam transient measured with one probe antenna of the cavity and the charge monitor information. The cavity probe signals were finally calibrated using the bunch arrival time monitor (BAM) behind BC2. The calibrated gradient of the first accelerating module ACC1 has been used as reference. The gradient of ACC1 has been varied leading to a change in beam energy and arrival time behind the bunch compressor BC2. This resulting calibration factor was used to calibrate the BACCA probes. The BACCA energy gain was switched from maximum deceleration to maximum acceleration by imposing a 180 deg. RF phase change. The common forward and reflected signals were finally calibrated using a resonant circle scan with variation in drive frequency. First energy modulations with maximum possible energy change lead to no orbit variations. Furthermore, multi bunch effect were not observed for the maximum bunch repetition rate of 1 MHz at FLASH.

CONCLUSION AND FUTURE WORK

The cavity and the main components in the FLASH BC2 section were changed during the winter shutdown in 2018. The cavity together with additional modules providing e.g. the operating frequency and the MicroTCA.4 based LLRF system has been installed and commissioned. First RF measurements without and with beam were performed. The first measurements in multi bunch operation look promising. The next step is the interconnection with the BAM such that bunch arrival information can be used within a train of electron bunches for fast arrival time feedback.

ACKNOWLEDGEMENTS

The authors would like to thank all the technical groups at DESY helping with the production and the installation of the new corrector cavity upstream of the UBC2 section at FLASH. I would like to express my very great appreciation to Moein Fakhari for the NRF cavity simulations, measurements and tuning, and to Sven Lederer for the technical drawing and organization of the cavity fabrication. Advice

Content from this work may be used under the terms of the CC BY 3.0 licence (© 2018). Any distribution of this work must maintain attribution to the author(s), title of the work, publisher, and DOI.

ISBN: 978-3-95450-194-6 ISSN: 2226-0366 doi:10.18429/JACoW-LINAC2018-MOPO039

Content from this work may be used under the terms of the CC BY 3.0 licence (© 2018). Any distribution of this work must maintain attribution to the author(s), title of the work, publisher, and DOI.

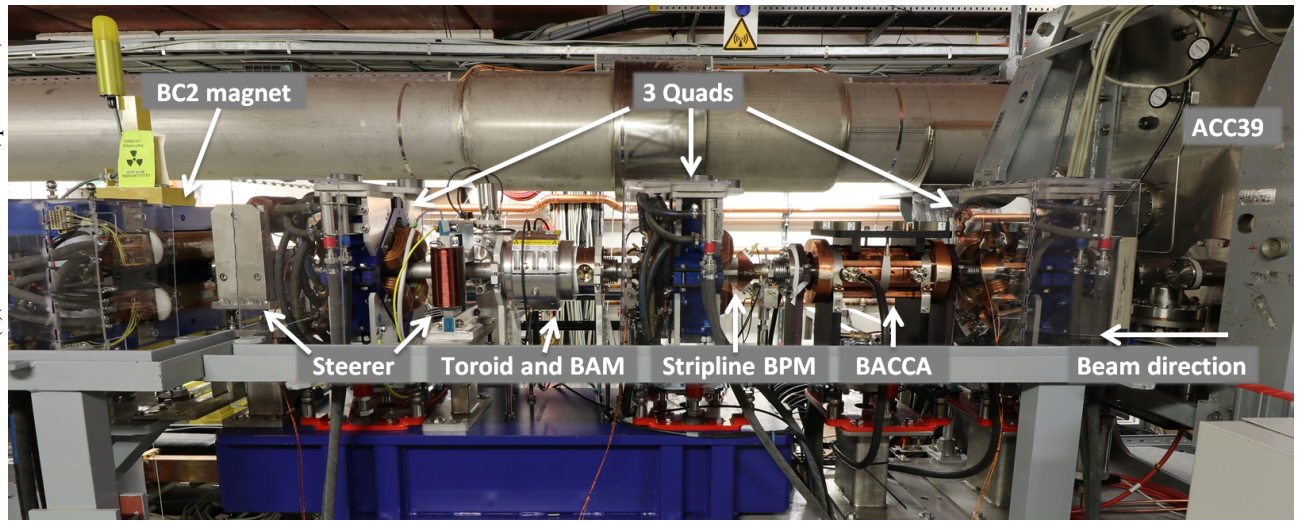


Figure 3: Picture from the installation during shutdown in January 2018. Beam direction is from right to left, with third harmonic RF module (ACC39) to the right and the entrance of the first bunch compressor (BC2) to the left.

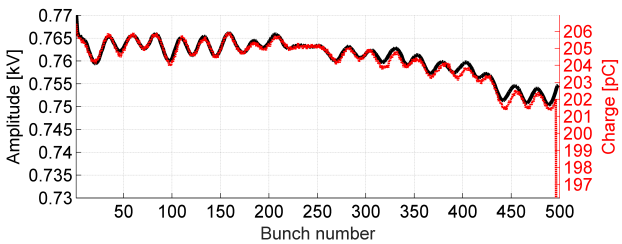


Figure 4: Maximum bunch transient amplitude in comparison to the charge measurement in the BC2 section. The black curve shows the maximum peak voltage and the red dashed line the charge readout for each bunch.

given by Klaus Flöttmann and Markus Hüning has been a great help in designing and tuning of the NRF cavity. Special thanks to Katja Honkavaara and Siegfried Schreiber for their driving support for this work at a time of other dominant projects such as the European XFEL. Furthermore, I would like to thank the following groups at DESY for their assistance and support: D3, MCS, MDI, MEA, MIN, MKK, MPS, MPY, MSK, MSL, MVS and ZM1. Without their help it wouldn't be possible to redesign the BC2 section at FLASH for the later installation of the NRF cavity.

REFERENCES

[1] FLASH, "Free-electron laser FLASH," 2016, [Online]. Available: http://flash.desy.de/

[2] M. Viti *et al.*, "Recent Upgrades of the Bunch Arrival Time Monitors at FLASH and European XFEL,", in *8th Int. Particle Accelerator Conf. (IPAC'17)*, Copenhagen, Denmark, May 2017, pp. 695–698. https://doi.org/10.18429/JACoW-IPAC2017-MOPIK072

[3] C. Behrens *et al.*, "Upgrade and Evaluation of the Bunch Compression Monitor at the Free-Electron Laser in Hamburg (FLASH)," in *1st Int. Particle Accelerator Conf. (IPAC'10)*, Kyoto, Japan, May 2010, pp. 912–914.

[4] S. Pfeiffer, "Symmetric Grey Box Identification and Distributed Beam-Based Controller Design for Free-Electron Lasers," PhD thesis, Hamburg University of Technology, Germany, 2014.

[5] S. Schulz *et al.*, "Femtosecond all-optical synchronization of an X-ray free-electron laser," in *Nature Communications*, vol. 6, pp. 5938–5949, 2015. https://doi.org/10.1038/ncomms6938

[6] S. Pfeiffer, "Technical design report on ultra-fast longitudinal feedback for FLASH," EuCARD2, Deliverable 13.1, 2014, [Online]. Available: http://eucard2.web.cern.ch/science/deliverables

[7] REGAE, "Relativistic Electron Gun for Atomic Exploration," 2016, [Online]. Available: https://regae.desy.de/

[8] M. Fakhari, "Design of Radio-Frequency Cavities and Tera-Hertz Electron Injectors for Advanced Applications," PhD thesis, Universität Hamburg, Germany, 2016.

[9] M. Fakhari *et al.*, "Thermal Simulation of an Energy Feedback Normal Conducting RF Cavity," in *7th Int. Particle Accelerator Conf. (IPAC'16)*, Busan, Korea, May 2016, pp. 396–398. https://doi.org/10.18429/JACoW-IPAC2016-MOPMW003

[10] S. Pfeiffer, "FLASH NRF cavity and FB system," EuCARD2, Deliverable 13.5, 2017, [Online]. Available: http://eucard2.web.cern.ch/science/deliverables

[11] L. C. Maier Jr. and J. C. Slater, "Field Strength Measurements in Resonant Cavities," in *Journal of Applied Physics*, vol. 23, pp. 68-77, 1952. http://dx.doi.org/10.1063/1.1701980

[12] Termotek GmbH, [Online]. Available: http://www.termotek-ag.com/de/

ISBN: 978-3-95450-194-6 ISSN: 2226-0366 doi:10.18429/JACoW-LINAC2018-MOPO040

COHERENT SYNCHROTRON RADIATION MONITOR FOR MICROBUNCHING INSTABILITY IN XFEL

J. H. Ko, I. S. Ko, POSTECH, Pohang, Korea
G. J. Kim, C. Kim, H. -S. Kang, Pohang Accelerator Laboratory, Pohang, Korea

Abstract

The microbunching instability is an important issue in an X-ray Free Electron Laser (XFEL) [1-4]. In Pohang Accelerator Laboratory X-ray Free Electron Laser (PAL-XFEL), the CCD camera installed in the accelerator tunnel at Coherent Radiation Monitor. The CCD camera measured the Coherent Synchrotron Radiation which made from the electron bunch compressor. This facility is called the Coherent Synchrotron Radiation (CSR) monitor. The CSR monitor measured the CSR and used for the microbunching instability measurement tool.

INTRODUCTION

The X-ray Free Electron Laser of the Pohang Accelerator Laboratory (PAL-XFEL) can produce a 0.1 nm wavelength XFEL [5]. The electron beam of the 150 pC charge is generated in the photo-cathode RF gun with an ultraviolet (UV) laser pulse. The generated electron bunch is accelerated by the 4 accelerating columns, and the electron bunch accelerated to 10 GeV energy. Moreover, four magnetic bunch compressor installed next to the accelerating column 1, 2, and 3 and soft x-ray part. Each electron bunch compressor has the coherent radiation monitor (CRM). The coherent radiation generated by the dipole magnet of the bunch compressor. They are synchrotron radiation and edge radiation. Also, another coherent radiation produced by a mirror with a hole in the middle which is called the diffraction radiation [6,7]. The PAL-XFEL structure is shown in Fig. 1. In the CRM, the pyro-electric detector is installed to detect the THz range coherent radiation. Using the pyro-electric detector, we can measure the THz range of coherent radiation, and it related with the electron bunch length. However, the measurement result of the pyro-electric detector in the very short electron bunch length range shows the saturation result. So, we need shorter electron bunch length range measurement tool. For this purpose, we installed the CCD camera in the CRM. In the CRM, we installed the moving stage then we can choose the CCD camera and pyro-electric detector. The CRM structure is shown in Fig. 2.

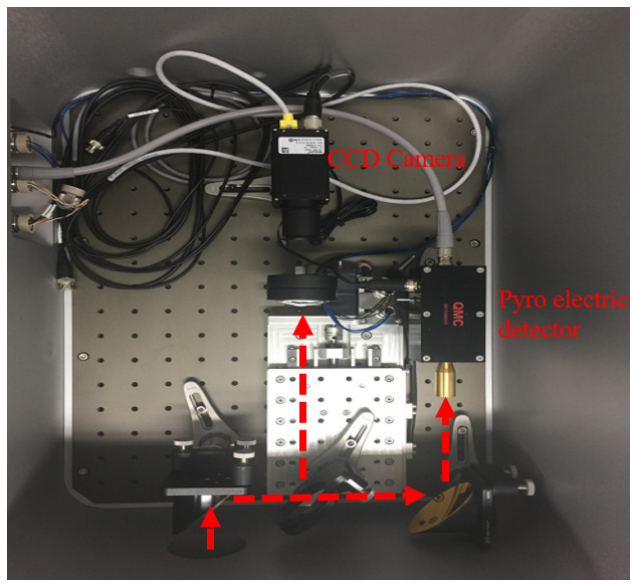


Figure 2: CRM structure.

The CCD camera is called the coherent synchrotron radiation (CSR) monitor, and it is detected the visible range radiation. The detecting radiation image is shown in Fig. 3. The visible range radiation made from the shorter longitudinal structure than the longitudinal structure of the THz radiation range. So, we can conclude that the visible radiation is related to small longitudinal structure such as the microbunching state.

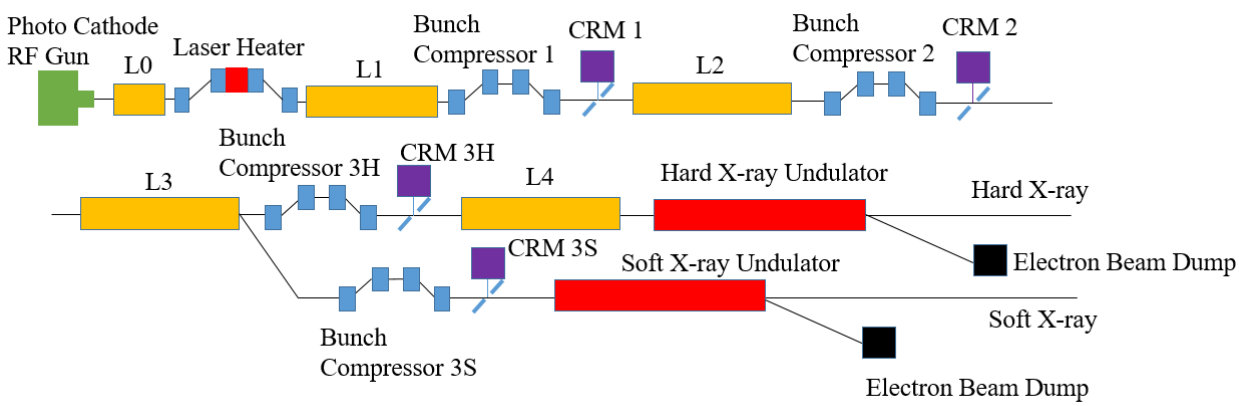


Figure 1: Schematic structure of PAL X-FEL.

Content from this work may be used under the terms of the CC BY 3.0 licence (© 2018). Any distribution of this work must maintain attribution to the author(s), title of the work, publisher, and DOI.

ISBN: 978-3-95450-194-6 ISSN: 2226-0366 doi:10.18429/JACoW-LINAC2018-MOPO040

Content from this work may be used under the terms of the CC BY 3.0 licence (© 2018). Any distribution of this work must maintain attribution to the author(s), title of the work, publisher, and DOI.

In Fig. 3, we can see the partial circle. The partial ring shows the diffraction radiation from the mirror with a hole in the middle. To explain the physical property of the CSR monitor's detecting result, we compare the detecting result of the pyro-electric detector and the CSR monitor. We use the laser heater to show the relation of the coherent radiation result and a laser heater condition. And, we concluded that the CSR monitor is a measurement tool for the microbunching instability. These results are shown in the next chapter.

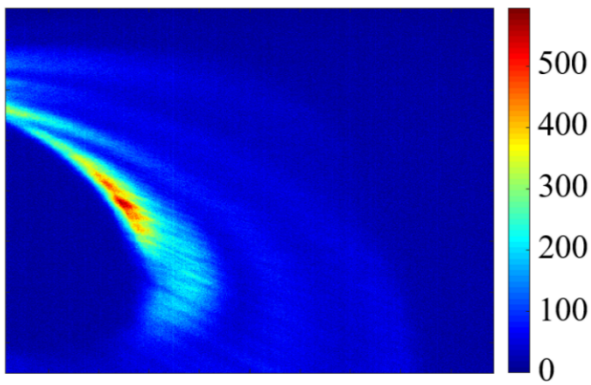


Figure 3: Detecting image in the CCD camera.

EXPERIMENT RESULT

In our experiment, we use the electron bunch compressor 1, 2 and we do not use the bunch compressor 3, and we use the CRM 3H. The RF phases fixed in the L0, L1, L3, L4 and the bunch compressor 1 is fixed. We control the L2 RF phase and the bunch compressor 2 and laser heater.

In the PAL-XFEL, the laser heater is installed to reduce the microbunching instability [8]. If the CSR monitor is the detecting tool of the microbunching instability, the CSR monitor and pyro-electric detector showed the different measurement result. We measure the radiation intensity of the CSR monitor and pyro-electric detector with the different laser heater condition. These results are shown in Figs. 4 and 5.

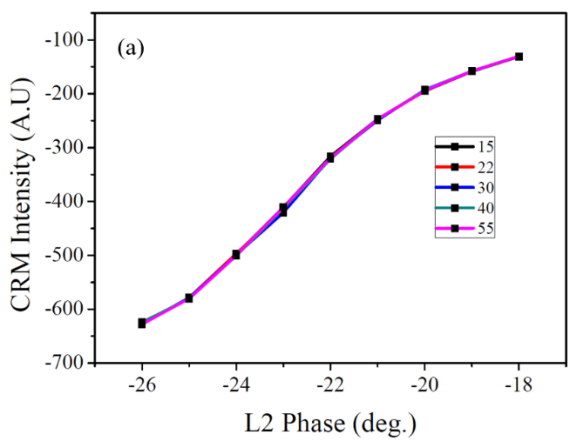


Figure 4: Pyro-electric detector intensity in different half wave plate angle.

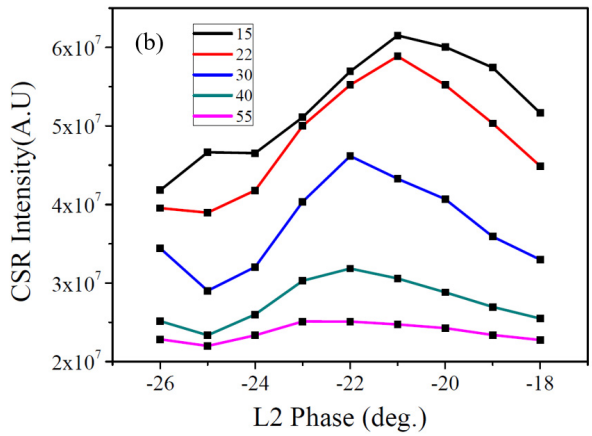


Figure 5: CSR monitor intensity in different half wave plate angle.

Figures 4 and 5 show the radiation intensity of the pyro-electric detector and CSR monitor. The CRM means the radiation intensity of the pyro-electric detector. The CSR implies the radiation intensity of the CCD camera. The radiation intensities measured in the different laser heater condition that is called the half wave plate angle. The IR laser energy of the laser heater is controlled by the half wave plate angle. The number 15, 22, 30, 40, 55 of Figs. 4 and 5 mean the different half wave plate angle. In Figs. 4 and 5, the different half wave plate angle does not relate with the radiation intensity but in Fig. 5, the radiation intensity is changed by the changes of half wave plate angle value. It means the measurement results of the pyro-electric detector do not relate with the laser heater. Because the pyro-electric detector detects the THz range radiation, and it did not associate with the microbunching instability. However, the CCD camera detects the visible radiation, so the measurement result of the CCD camera is related to the microbunching instability. The L2 RF phase related to the electron bunch length and the laser heater condition associated with the microbunching instability. Using this result, we can conclude the pyro-electric detector is the measurement tool of the electron bunch length, and the CCD camera is the measurement tool of the microbunching instability.

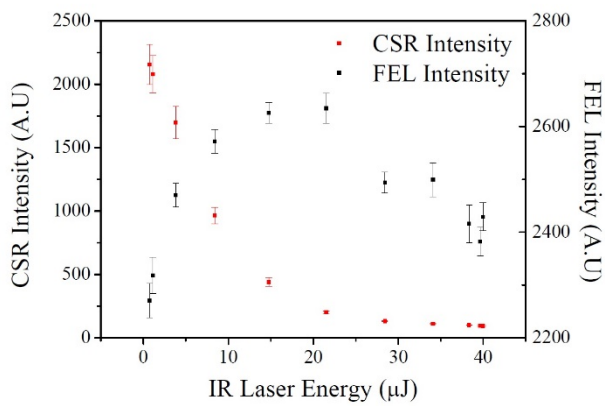


Figure 6: CSR intensity and FEL intensity as a function of IR laser heater energy.

ISBN: 978-3-95450-194-6 ISSN: 2226-0366 doi:10.18429/JACoW-LINAC2018-MOPO040

We compare the CSR intensity which is detected by the CCD camera and the FEL intensity in different laser heater condition [9]. The result is shown in Fig. 6.

In Fig. 6, the CSR intensity decreases as the IR laser energy increases. It means the microbunching instability is reduced by the IR laser energy increasing. The CSR intensity decreased until the IR laser energy is 20 μJ and over the 20 μJ, the CSR intensity has nearly zero intensity. The FEL intensity increased to the 20 μJ, and over the 20 μJ, the FEL intensity decreased. It means the decreasing microbunching instability has a good effect on the FEL intensity but over the 20 μJ, IR laser Energy the effect of the laser heater is worse than under 20 μJ IR laser energy.

Using this result, we can control the IR laser Energy of the laser heater. So we can find the optimization of IR laser energy value.

CONCLUSION

In the PAL-XFEL, the CCD camera is installed to measure the visible radiation which is related to the microbunching instability. The CCD camera is called the coherent synchrotron radiation (CSR) monitor, and it installed in the coherent radiation monitor (CRM) which is the next part of the electron bunch compressor. Using the detection data of the pyro-electric detector and the CSR monitor, we can conclude the CSR monitor is the detecting tool of the microbunching instability, and we show the CSR monitor can use the laser heater optimization. In the future, we can conduct the particular experiment of the microbunching with the CSR monitor in the BC2, BC3 H, and BC 3 S.

ACKNOWLEDGEMENTS

This research has been supported by the Ministry of Science and ICT of Korea and partly by Basic Science Research Program [Grant No. 2017R1A2B4007274] through the National Research Foundation of Korea (NRF) funded by the Ministry of Science and ICT of Korea.

REFERENCES

[1] S. Heifets, G. Stupakov, and S. Krinsky, "Coherent synchrotron radiation instability in a bunch compressor", *Phys. Rev. ST Accel. Beams*, vol. 5, p. 064401, June 2002. doi:10.1103/physreva.44.1316

[2] Z. Huang and K.-J. Kim, "Formulas for coherent synchrotron radiation microbunching in a bunch compressor chicane", *Phys. Rev. ST Accel. Beams*, vol. 5, p. 074401, July 2002. doi:10.1103/physrevstab.5.074401

[3] T. Limberg, P. Piot, and E. A. Schneidmiller, "An analysis of longitudinal phase space fragmentation at the TESLA test facility", *Nucl. Instr. Meth.*, *Phys. Res., Sect. A*, vol. 475, p. 353-356, Dec. 2001. doi:10.1016/s0168-9002(01)01538-8

[4] M. Borland et al., "Start-to-end simulation of self-amplified spontaneous emission free electron lasers from the gun through the undulator", *Nucl. Instr. Meth.*, *Phys. Res., Sect. A*, vol. 483, p.268-272, May 2002. doi:10.1016/s0168-9002(02)00325-x

[5] H.-S. Kang *et al.*, "Hard X-ray free-electron laser with femtosecond-scale timing jitter", *Nat. Phot.*, vol. 11, p. 708–713, Oct. 2017. doi:10.1038/s41566-017-0029-8

[6] H. Loos, T. Borden et al., "Relative bunch length monitor for the linac coherent light source (LCLS) using coherent edge radiation", in *Proc. 22nd Particle Accelerator Conf, (PAC'07),* Albuquerque, NM, USA, Jun. 2007, pp. 4189-4191.

[7] J. Wu, P. Emma, "Linac coherent light source (LCLS) bunch-length monitor using coherent radiation", in *Proc. 23rd Linear Accelerator Conf. (LINAC' 06)*, Oak Ridge, Tennessee, USA, 2006, pp. 277-279.

[8] J. H. Lee *et al.*, "PAL-XFEL laser heater commissioning", *Nucl. Instr. Meth.*, *Phys. Res., Sect. A*, vol. 843, p. 39- 43, Jan. 2017. doi:10.1016/j.nima.2016.11.001

[9] J. H. Ko *et al.*, "Coherent synchrotron radiation monitor for microbunching instability in XFEL", *Rev. of Sci. Inst.*, vol. 89, p. 063302, June 2018. doi: 10.1063/1.5023848

Content from this work may be used under the terms of the CC BY 3.0 licence (© 2018). Any distribution of this work must maintain attribution to the author(s), title of the work, publisher, and DOI.

ISBN: 978-3-95450-194-6 ISSN: 2226-0366 doi:10.18429/JACoW-LINAC2018-MOPO041

PERFORMANCE TEST RESULTS OF MAGNET POWER SUPPLY*

K. H. Park†, S. H. Jeong, Y. G. Jung, D. E. Kim, H. S. Suh, H. G. Lee, S. B. Lee, B.G. Oh, M. J. Kim and J. H. Han, PAL, POSTECH, Pohang, Korea

Abstract

A high stable magnet power supply (MPS) was developed, which was a bipolar type with 200 A of the output current at the 36 V of output voltage. The MPS has been implemented by the digital signal processing technology using the DSP, FPGA, ADCs and so on. The output current stability of the MPS showed about 6 ppm peak-to-peak in a short term experiment at its full 200 A output current. The long term stability was shown in 15 ppm peak-to-peak for 10 hours at 200 A. And the others experimental results about the MPS were shown in this paper.

INTRODUCTION

The particle accelerator needs a highly stable magnet power supply (MPS) to assure the stable beam dynamics. A MPS must provide high-stability output current, fast response, high reliability, etc. It should also be easy to maintain. The stability and accuracy of the MPS are very important specifications because they directly affect the beam dynamics of the accelerator operation. Nowadays the MPS is developed by switching mode type using FET or IGBT devices that are controlled by a digital signal processor (DSP). This design is efficient, small, light-weight, and has good dynamic response but switching-mode MPS generates electrical noises whenever switching devices are turning on or turning off because of their generally high switching voltage and current. The short-term stability of the MPS is affected by the several causes which come from the control loop responses, surrounding switching noise, analog signal processing including ADC circuits, and so on [1]. Ripple components of the input rectifier are also one of the sources which make MPS stability worse [2]. The one of the cause of the long-term stability of the MPS comes from the temperature drift of components in MPS. Improper ground configurations can provide the path on which noise can propagate from its source point to all over the system. These components are very small but can degrade the performances of an analog-to-digital converter (ADC) circuits with the fine voltage fluctuation.

This paper describes the design schemes of the MPS. The results of the various experiments such as short term stability, long term stability, repeatability and step responses were showed.

SYSTEM CONFIGURATION

The developed MPS was divided into three parts as shown in the Fig. 1. The first is a rectifier to make DC link voltage. The second is the two power stacks which has the current driving capacity of 100 A, respectively. Thus two power stacks are operated in parallel to increase the current driving capability. The last is digital controller configured with DSP TMS320F28335 from TI [3].

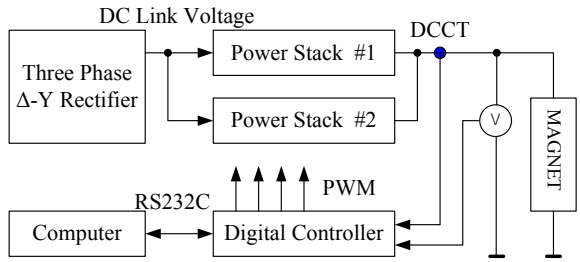


Figure 1: The block diagram of the developed MPS.

The rectifier to make DC link voltage with low ripple components was assembled. The primary winding of the transformer was configured with three phase in Wye configuration for AC 380 V. The secondary winding is consisted of two configurations of the Wye and Delta. The output voltage of the each winding on the secondary side is 33 V, respectively. They are fully rectified by the twelve diodes and connected in series to make DC link voltage of 66 V. Two diode modules of SEMIX341D16s from SEMICRON Co. were assembled on the water cooled aluminium plate. The input rectifier has an inductor of 1 mH to compose the input filter with the capacitor bank, 12000 μF x 4, in two power converter modules, respectively.

The performances of the ADC were very important part for the high stable MPS. The circuits of around ADCs for the MPS should have a good signal to noise ratio. The major specifications when the ADC was chosen were the throughput, resolution, input range, interface, DC accuracy, and so on [4]. Two different types of ADCs were tested to confirm their performances under the same conditions. The first one is the AD7690 from Analog Devices that is 18-bit resolution. The tested effective resolution of this ADC showed only 10-bit. The 8-bit in 18-bit was meaningless. The last one is the AD977 from also Analog Devices showed the effective resolution of 12-bit in spite of the 16-bit resolution in the given specification. These test results showed sometimes worse resolution than that of the datasheets. It might be depended on design scheme of the ADC and the conditions around circuits such as reference voltage source type, supply voltage and ground conditions, etc. The higher resolution than 16-bit in ADC may be meaningless because the ground thickness was about 1mV in general analog and digital mixed circuits. It was corresponding to nearly 1-bit at 10 V reference voltage.

Two types of ADC daughter boards for the MPS were developed as in the Fig. 2. The type 1 ADC board was to

*Work supported by Ministry of Science and ICT
†pkh@postech.ac.kr

Content from this work may be used under the terms of the CC BY 3.0 licence (© 2018). Any distribution of this work must maintain attribution to the author(s), title of the work, publisher, and DOI.

ISBN: 978-3-95450-194-6 ISSN: 2226-0366 doi:10.18429/JACoW-LINAC2018-MOPO041

digitize the load current or voltage for the feedback control loop. This type was designed by combining two ADCs that sampled the input signal simultaneously, which increased the SNR by the over-sampling technology. The type 2 ADC board for other purposes such as heat sink temperature, link voltage, etc. was assembled with one ADC and analog multiplexer as the bottom side at the Fig. 2. The interface signals between FPGA and ADC were isolated using the digital isolators ISO7241 from TI. And the DC power supply for the each ADC daughter board was also isolated to minimize the noise coupling through the ground or power plane in the PCB.



Figure 2: ADC daughter boards for current and voltage for feedback control (upper) and general purpose (lower).

The interfaces among the devices of the MPS were shown in the Fig. 3. The ADCs up to seven and a DAC were interfaced by the SPI to the FPGA. The DSP and FPGA were assembled in a board. The interface between them uses a Multichannel Buffered Serial Port of the DSP peripheral. The ADC data were transferred to the DSP whenever the DSP sends the designated signal to the corresponding ADC channel. The MMI was composed by the Labview and communicated by the RS232C. The Easy-DSP which is the tool for downloading program and monitoring the variables in real time was also connected by another RS232C.

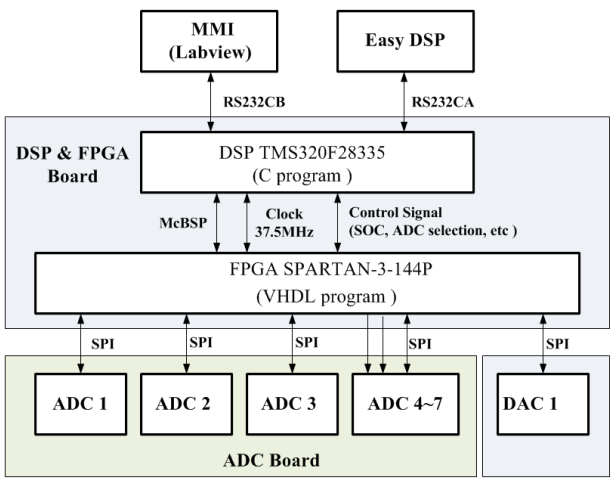


Figure 3: Interface signals between devices in the MPS.

The feedback control signals, load current and voltage, were sampled every 200 kHz by the FPGA. These data were moving-averaged out with the stored data in the FIFO buffer at the FPGA SPARTAN-3 from Xilinx [5]. The functions in VHDL program were written by modular type, so it was easy to modify. And the functions in FPGA were processed in parallel, so program execution time was not issue here. The data were always ready to send to the DSP whenever requested. The DSP program was divided into two parts. The one is interrupt routine which is generated at every PWM frequency, 15 kHz, to calculate the duty ratio for the IGBT control. The other is the base routine that scans the interlock signals and RX buffer of the RS232C for the MMI as shown in the Fig. 4. The interlock signals like the IGBT failure directly make the PWM signals disable by the hardware which is programed in the CPLD XCR3064 from Xilinx.

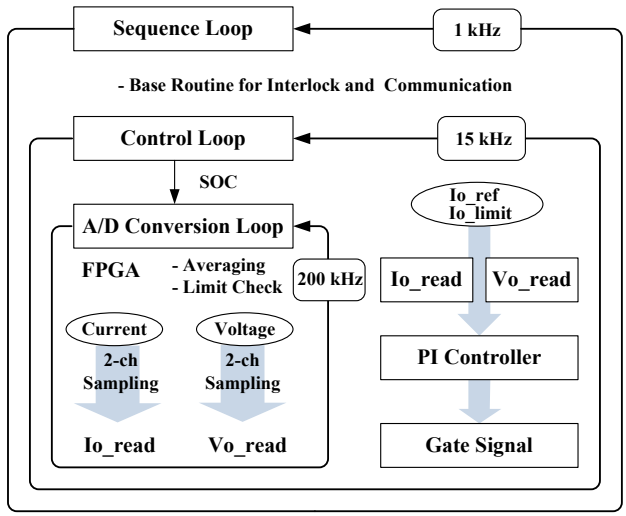


Figure 4: DSP and FPGA program timing assignment.

EXPERIMENTAL RESULTS

The DC link voltage is sixty-six volt which supplies two power stacks in parallel connection. The Fig. 5 shows the load voltage developed on the magnet when output current is 200 A. It is about 36 V with very small ripple voltage which can seem to be ignored.

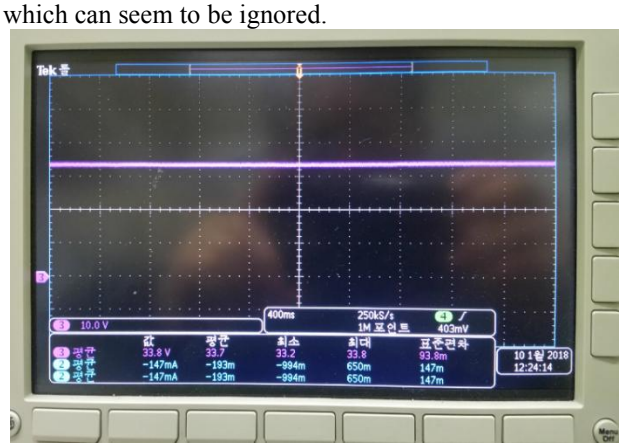


Figure 5: Load voltage developed at the magnet at 200 A.

Content from this work may be used under the terms of the CC BY 3.0 licence (© 2018). Any distribution of this work must maintain attribution to the author(s), title of the work, publisher, and DOI.

ISBN: 978-3-95450-194-6 ISSN: 2226-0366 doi:10.18429/JACoW-LINAC2018-MOPO041

Content from this work may be used under the terms of the CC BY 3.0 licence (© 2018). Any distribution of this work must maintain attribution to the author(s), title of the work, publisher, and DOI.

The short term stability of the MPS was measured for 60 minutes. The Fig. 6 shows the output current stability of the developed MPS. It showed the 6 ppm-pp at its full output current of 200 A.

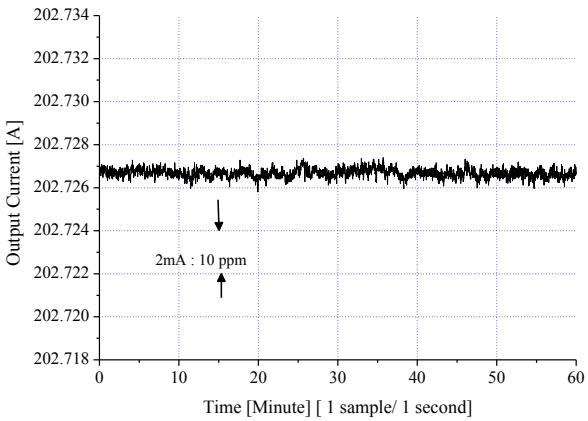


Figure 6: Short term output current stability.

The long term stability for ten hours was also measured. It showed less than 15 ppm-pp as shown in the Fig. 7. If temperature variation was considered, the stability could be reduced to 10 ppm-pp.

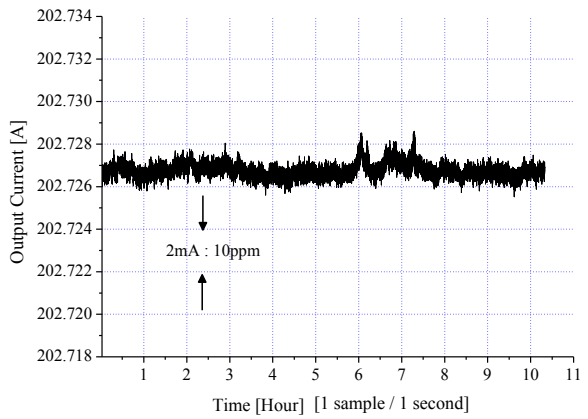


Figure 7: Long term output current stability.

The step responses was tested by the 10 ppm step command at the output current of 180 A as shown in the Fig. 8. It shows less than 5 ppm while repeats several times.

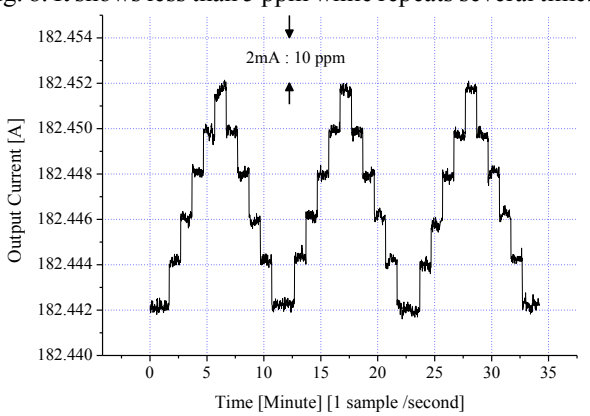


Figure 8: Step responses shows about 5 ppm at output current of 180 A.

Repeatability responses were tested by changing the set current from 170 A to 180A and vice versa several times. It shows about 4 ppm pp as shown in the Fig. 9. The other side of 170 A also shows the same as this value.

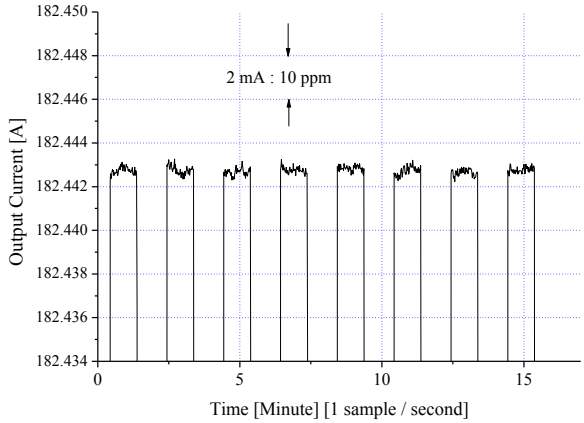


Figure 9: Repeatability test results. This shows about 4 ppm-pp.

CONCLUSIONS

The performance tests of the two ADCs with different resolution were carried out. The ADC which resolution was 16-bit was showed better than that of 18-bit at the same test conditions. It means that the higher resolution of the ADC is not always the best design. It might be depended on the given surrounding circumstances.

The MPS which has output current capability of 200 A was assembled and finished important performance tests. The short term stability for one hour was showed the less than 6 ppm-pp at the output current of 200 A. The long term stability also was very good, which was less than 15 ppm-pp for ten hours at 200 A output current. The step responses showed about 5 ppm-pp with set current command of 10 ppm around 180 A output current. The repeatability test showed within 4 ppm from 170 A to 180 A output current for eight times. The various tests have been going on the developed MPS.

REFERENCES

[1] W. S. Choi, M. J. Kim, I. W. Jeong, D. E. Kim, H. C. Park, and K. H. Park, "Development of high-stability magnet power supply", *Nucl. Instr. Meth.*, vol. 822, pp. 15-24, 2016.

[2] K. Koseki and Y. Kurimoto. "Development of a magnet power supply with sub-ppm ripple performance for J-PARC with a novel common-mode rejection method with an NPC inverter", *Nucl. Instr. Meth.*, vol. 747, pp. 24-29, 2014.

[3] Texas Instruments Co., www.ti.com

[4] Analog Devices Co., www.analog.com

[5] Xilinx Co., www.xilinx.com

ISBN: 978-3-95450-194-6 ISSN: 2226-0366 doi:10.18429/JACoW-LINAC2018-MOPO042

EVOLUTIONARY MANY-OBJECTIVE OPTIMIZATION ALGORITHM FOR LARGE-BANDWIDTH FREE-ELECTRON-LASER GENERATION

J. W. Yan[1,2], H. X. Deng[1*],
[1]Shanghai Institute of Applied Physics, Chinese Academy of Sciences, Shanghai 201800, China
[2]University of Chinese Academy of Sciences, Beijing 100049, China

Abstract

X-ray free-electron lasers (XFELs) are leading-edge instruments in a wide range of research fields. Besides pursuing narrow bandwidth FEL pulses, the large-bandwidth XFEL pulses are very useful in various spectroscopy experiments, multi-wavelength anomalous diffraction, and X-ray crystallography. Overcompression operation scheme can be utilized to generate electron beams with large energy chirp which is benefit for bandwidth broadening. Recently, an evolutionary many-objective (having four or more objectives) algorithm, NSGA-III, was used to optimize the electron beam parameters in the overcompression including energy chirp, energy spread, current profile, peak current, and projected emittance. In this paper, combining with the Xie's semianalytical estimate formula, the NSGA-III is utilized to find an optimal working point of linac by optimizing the XFEL pulse properties directly. Start-to-end numerical simulations based on the Shanghai soft X-ray Free-Electron Laser user facility parameters demonstrate that a full bandwidth of 4.75% can be generated.

INTRODUCTION

X-ray free electron lasers (XFEL) are capable of providing x-ray pulses with high peak brightness, narrow bandwidth spectrum and ultra-fast time structure. Besides pursuing narrow bandwidth XFEL pulses, large-bandwidth XFEL pulses are demanded for several certain types experiments such as X-ray absorption spectroscopy, multi-wavelength anomalous diffraction and X-ray crystallography.

The FEL wavelength is decided by the resonance condition [1]:

$$\lambda = \frac{\lambda_u}{2\gamma^2}(1 + \frac{K^2}{2}), \quad (1)$$

where λ_u is the undulator period length, γ is the mean Lorentz factor of the electrons, and K is the undulator field parameter. Therefore, the XFEL bandwidth is related to the electron beam energy chirp and the undulator field parameters. In principle, making different parts of a transverse tilted electron beam experience different magnetic fields [2, 3] or utilizing an energy-chirped electron beam can broaden the XFEL bandwidth. While the beam tilt always needs additional hardware elements like the transverse deflecting structure or de-chirper device. The beam energy chirp can be achieved by just changing operation parameters of the acceleration sections. One natural way to obtain energy chirp is to let the electron bunch be accelerated at the off-crest phase, however, it at the cost of the beam energy. Overcompression [4–7] is a promising scheme to increase correlated energy spread of electron beams. In this scheme, electron bunches are overcompressed in one bunch compressor and the sign of the energy chirp of the electron bunches are changed. Therefore, the wakefields of the subsequent rf structures will increase the beam energy chirp. One of the crucial problem for the overcompression scheme is how to find an optimal working point of the linac where electron beams can generate XFEL pulses with large bandwidth while other properties like pulse energy and power profile can be maintain. The recent paper [7] utilized an evolutionary many-objective algorithm, NSGA-III [8], to optimization electron beam parameters and analyze the dependencies between these parameters. However, the optimization of the electron beam is difficult to analyze the relations between radiation pulse properties, which is also important for exploring the limitations of an operation scheme. As an extended work, in the following sections, based on the Shanghai soft x-ray free-electron laser (SXFEL) user facility [9] parameters, the NSGA-III is used to optimize the XFEL pulse properties directly.

OPTIMIZATION STRATEGY

The SXFEL user facility is under construction at Shanghai, which is the first X-ray FEL in China. The SXFEL user facility consists of a two-stage seeded FEL line and a SASE line. This optimization is to design the large-bandwidth mode for the SASE line. The layout of the SXFEL user facility linac and the SASE line are presented in Fig. 1. 0.5 nC electron beams are generted and accelerated to 130 MeV in the injector. Downstream of the injector are the main linac including one S-band (L1), one X-band (LX), and two C-band (L2, L3) accelerating sections. And there are two magnetic chicanes between these accelerating sections to further compress the electron bunches. To let the overcompressed electron beam be accelerated in more rf structures, turning off the second bunch compressor and utilizing single bunch compressor are considered in this optimization. To produce high qualities XFEL pulses, angle of the first bunch compressor, phases and voltage of the L1 and LX are selected as optimization variables. The corresponding optimization objectives are pulse energy, bandwidth, and power distribution.

In this optimization, the ASTRA and ELEGANT are used to tracking electron beams in the injector and main linac separately. The calculation of the objectives are based on the ELEGANT simulations where one hundred thousand

* denghaixiao@sinap.ac.cn

Content from this work may be used under the terms of the CC BY 3.0 licence (© 2018). Any distribution of this work must maintain attribution to the author(s), title of the work, publisher, and DOI.

ISBN: 978-3-95450-194-6 ISSN: 2226-0366 doi:10.18429/JACoW-LINAC2018-MOPO042

Content from this work may be used under the terms of the CC BY 3.0 licence (© 2018). Any distribution of this work must maintain attribution to the author(s), title of the work, publisher, and DOI.

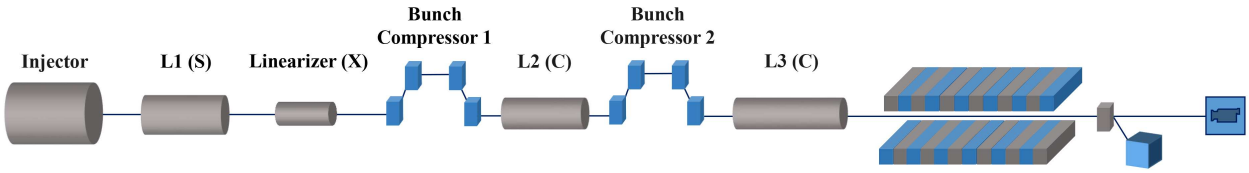


Figure 1: Layout of the SXFEL user facility linac including the injector section, S-band sections (L1), one X-band linearizer (LX), C-band sections (L2, L3) and two bunch compressor chicanes (BC1, BC2).

macroparticles are used. One electron bunch from the simulation results will be divided into 100 slices. The saturation power of the radiation generated by one electron slice is calculated by the semianalytical estimate formula [10]:

$$P_{sat} \approx \frac{1.6}{(1+\Lambda)^2}\rho P_{beam}, \tag{2}$$

where the Λ can be calculated by the Xie's fitting formula [11]. Therefore, the radiation energy generated by each electron slice can be obtained. The pulse energy is defined as the sum of the slice energy. The XFEL wavelength generated by each slice is calculated by the Eq. (1). Treating 2% of the peak slice energy as a cut-off value. The bandwidth is defined as the relative wavelength between the two cut-off slice on the two sides of an electron bunch. In this optimization, the sum of the radiation energy of the middle 50 slices divided by the whole pulse energy is treated as the FEL power profile factor. The lager power profile factor means the lasing part are more concentrate on the central part of the electron beam. In addition, the coherent synchrotron radiation (CSR) effect is strong in the overcompression. The slice misalignment caused by the CSR will reduce the pulse energy and this effect cannot be expressed by Eq. (2). Therefore, the horizontal projected emittance of the electron beam is treated as the fourth objective and the two quadrupoles in the first bunch compressor are added to the optimization variables to eliminate the CSR effect. To analysis the relations between these objectives and find the optimal solution, the NSGA-III is used to optimize the four objectives simultaneously. The population and iteration in the algorithm are set 300 and 100 to ensure the convergence of the solutions.

OPTIMIZATION RESULTS

The Pareto-optimal front and its projection at several two-dimensional surfaces in the last generation are shown in Fig. 2. The pareto front (Fig. 2 (top left)) shows that the horizontal projected emittance of most solutions are well optimized and does not correlate with other three objectives. As shown in the Fig. 2 (top right), the bandwidth and pulse energy are two conflicting objectives. The pulse energy is quite low when the bandwidth is larger than 5%. The Fig. 2 (bottom left) the Fig. 2 (bottom right) present the dependencies between the power profile and pulse energy, bandwidth which show that the larger profile factor corresponds to larger

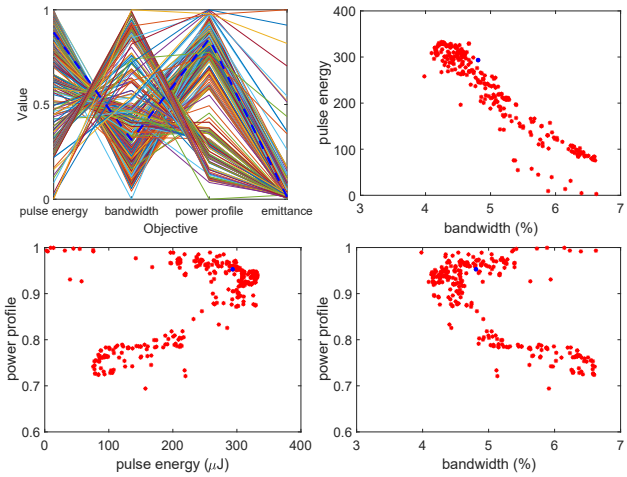


Figure 2: Parallel coordinate plots of the Pareto-optimal front and its two-dimensional projection on several planes.

pulse energy and narrower bandwidth for most cases. The optimization results of the electron parameters presented in [7] can be used to further understand this optimization results. Those electron beams with poorer current profile always lead to poorer power profile of the XFEL pulses and larger energy chirp, i.e., larger XFEL bandwidth, which finally cause the bandwidth and pulse energy are two conflicting objectives.

After weighing the four objectives, as the blue dashed line shown in the pareto front (blude points in other two-dimensional surfaces), a solution with a pulse energy of 293 μJ and a bandwidth of 4.8% is selected for the large bandwidth operation mode of the SXFEL user facility. Based on the parameters of the selected solution, ELEGANT simulation with one million macroparticles and the time-dependent GENESIS simulation are performed to verify the electron beam and the XFEL pulse generation. As shown in the Fig. 3 (top left and right), the selected electron bunch with a 1175 A peak current and an energy chirp of 2.5%. The FEL simulation results show that the corresponding pulse energy is 386 μJ and the bandwidth is 4.75% (including a 2% cut).

CONCLUSION

In this paper, the NSGA-III is used to optimize pulse properties for large bandwidth XFEL pulses generation. The optimization results show that pulse energy and bandwidth are two contradictory objectives. In addition, the power

ISBN: 978-3-95450-194-6 ISSN: 2226-0366 doi:10.18429/JACoW-LINAC2018-MOPO042

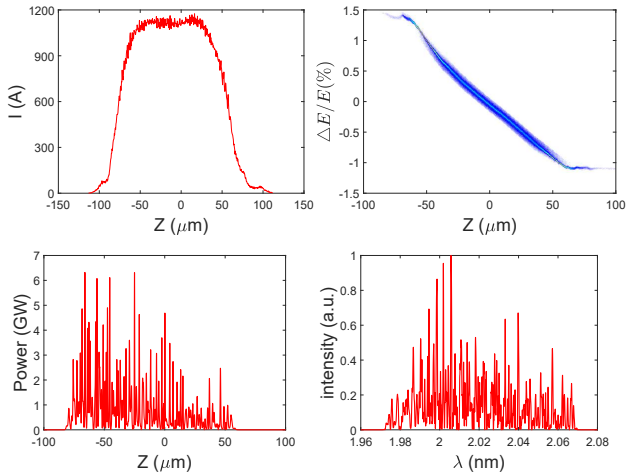


Figure 3: Current profile (top left), longitudinal phase space (top right) of the chosen electron beam and the power distribution (bottom left), spectrum (bottom right) of the XFEL pulse.

profile has a strong correlation with the pulse energy and bandwidth. Considering the broad bandwidth XFEL demands including the larger pulse energy, bandwidth and profile factor, a solution that generates XFEL pulse with 386 μJ and 4.75% full bandwidth is selected for the SXFEL user facility. Comparing with the electron beam optimization [7], this optimization can be used to further explore the dependencies between different pulse properties in the overcompression mode and makes it much easier to choose suitable solutions for the large bandwidth operation mode. At the same time, this optimization results can be further understood by the electron beam optimization results.

ACKNOWLEDGEMENTS

The author would like to thank Z. Wang, M. Zhang, B. Liu, D. Wang and Z. Zhao for helpful discussions on beam dynamics and SXFEL projects. This work was partially supported by the National Natural Science Foundation of China (11775293), the National Key Research and Development Program of China (2016YFA0401900), the Young Elite Scientist Sponsorship Program by CAST (2015QNRC001) and Ten Thousand Talent Program.

REFERENCES

[1] C. Pellegrini, A. Marinelli, and S. Reiche, "The physics of x-ray free-electron lasers", *Reviews of Modern Physics*, vol. 88(1), pp. 015006, 2016

[2] E. Prat, M. Calvi, and S. Reiche, "Generation of ultra-large-bandwidth X-ray free-electron-laser pulses with a transverse-gradient undulator", *Journal of synchrotron radiation*, vol. 23(4), pp. 874-879, 2016

[3] M. Song, J. Yan, K. Li, *et al.*, "Bandwidth broadening of X-ray free electron laser pulses with the natural gradient of planar undulator", *Nuclear Instruments and Methods in Physics Research Section* A: Accelerators, Spectrometers, Detectors and Associated Equipment, vol. 88, pp. 11-17, 2018

[4] P. Emma, "Chirping the LCLS electron beam", Stanford Linear Accelerator Center (SLAC), Menlo Park, CA, 2005

[5] A. S. Hernandez, E. Prat, S. Bettoni, *et al.*, "Generation of large-bandwidth X-ray free-electron-laser pulses", *Physical Review Accelerators and Beams*, vol. 19(9), pp. 090702, 2016

[6] J. L. Turner, F. Decker, Y. Ding, Z. Huang, R. Iverson, J. Krzywinski, H. Loos, A. Marinelli, T. Maxwell, H. Nuhn, *et al.*, in *Proceedings of the 36th International Free Electron Laser Conference (FEL'14)*, Basel, Switzerland, p. 337, 2014

[7] J. Yan and H. Deng, "Generation of large-bandwidth x-ray free electron laser with Evolutionary Many-Objective Optimization Algorithm", arXiv preprint arXiv:1806.04993, 2018

[8] K. Deb and H. Jain, "An evolutionary many-objective optimization algorithm using reference-point-based nondominated sorting approach, part I: Solving problems with box constraints", *IEEE Trans. Evolutionary Computation*, vol. 18(4), pp. 577-601, 2014

[9] Z. Zhao, D. Wang, Q. Gu, *et al.*, "Status of the SXFEL Facility", *Applied Sciences*, vol 7(6), pp. 607, 2017

[10] M. Xie, "Design Optimization for an X-Ray Free Electron Laser Driven by SLAC Linac", in *Proceedings of the 1995 Particle Accelerator Conference (PAC'95)*, Dallas, TX, USA, pp. 183–185, 1995

[11] M. Xie, "Exact and variational solutions of 3D eigenmodes in high gain FELs", *Nuclear Instruments and Methods in Physics Research Section* A: Accelerators, Spectrometers, Detectors and Associated Equipment, vol. 445(1-3), pp. 59-66, 2000

Content from this work may be used under the terms of the CC BY 3.0 licence (© 2018). Any distribution of this work must maintain attribution to the author(s), title of the work, publisher, and DOI.

ISBN: 978-3-95450-194-6 ISSN: 2226-0366 doi:10.18429/JACoW-LINAC2018-MOPO058

INDUSTRIAL ELECTRON LINEAR ACCELERATOR R&D IN CIAE

Jinghe Yang †, Guolong Yu, Zhibin Zhu, Ziqiang Zeng,China Institute of Atomic Energy, Beijing, China

Abstract

Electron linear accelerator(E-LINAC) is a vital accelerator type for accelerator applications, which widely applied in industry, agriculture and medical industry. The paper introduces R&D of industrial E-LINAC in China Institute of Atomic Energy (CIAE), including electron gun, modulator, accelerating tube, assembling and testing. Based on these R&D results, the GT series for non-destructive test (NDT) and FZ series for radiation processing are developed successfully. At present these E-LINACs play important roles in pressure vessel inspection, food preservation, sterilization and material modification, promoting the E-LINACs application as well as economic development in China.

INTRODUCTION

Accelerator-based high energy X-ray source and accelerator-based high energy electron source are two kinds of important instruments for NDT and electron beam (EB) radiation processing. Both the first NDT accelerator and the first 10MeV/20kW EB processing accelerator in China were developed successfully by CIAE about 20 years ago and 10 years ago respectively [1]. After a long-term development and improvement, the NDT accelerators form a series of accelerator, so called GT series, which can generate X ray with energy ranging from 1 MeV to 12MeV. 10MeV/20kW EB accelerator for radiation processing has been widely applied in China.

NDT ACCELERATOR

The GT series is used for NDT. See Table 1.

Table 1: The GT Series Accelerator for NDT

Model No.	X-ray energy	X-ray dose rate
GT-2/200	2MeV	200cGy/min.m
GT-2D/200	1MeV/2MeV	200cGy/min.m
GT-4/500	4MeV	500cGy/min.m
GT-4D/500	2MeV/4MeV	500cGy/min.m
GT-6/1000	6MeV	1000cGy/min.m
GT-6D/1000	4MeV/6MeV	1000cGy/min.m
GT-9/3000	9MeV	3000cGy/min.m
GT-9D/3000	6MeV/9MeV	3000cGy/min.m
GT-12/5000	12MeV	5000cGy/min.m
GT-12D/5000	9MeV/12MeV	5000cGy/min.m

The letter “D” in the model No. stands for Dual-energy type.

NDT accelerator consist of modulator [2]., X-ray head, cooling unit and control system [3]. This parts are connected by cables including electric power cable, Ethernet cable, signal cable and so on. See Fig. 1.

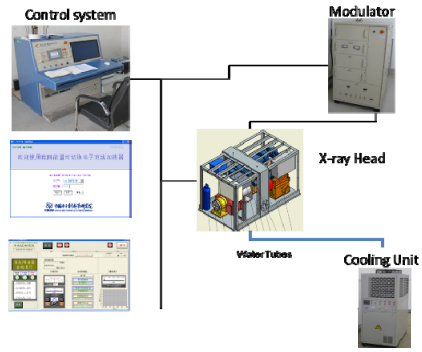


Figure 1: NDT accelerator sketch.

NDT accelerator can be used as a high energy X ray source for film imaging (see Fig. 2) and industrial CT.

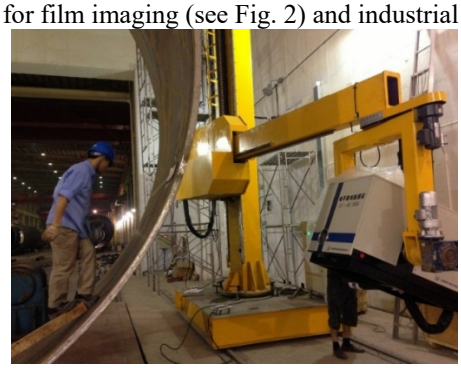


Figure 2: NDT accelerator on duty.

RADIATION PROCESSING ACCELERATOR

The FZ series is used for radiation processing. See Table 2.

Table 2: The FZ Series Accelerator

Model No.	EB energy	Avg. beam power
FZ-10/20	10MeV	20kW
FZ-2/1	2MeV	1kW

10MeV/20kW accelerator is applied in EB radiation processing including sterilization, material modification and so on. 2MeV/1kW accelerator is applied in mail sterilization, radiation curing because of short penetration depth.

High Voltage Pulse Modulator

The line-type modulator is used for 10MeV/20kW to generate 130kV/90A pulse to drive the klystron. The IGBT is used for charging unit and hydrogen thyratron is used for discharging unit. The pulse forming net (PFN) generate 16 μs pulse width. The duty factor is 9‰.

† 13811486349@163.com

Content from this work may be used under the terms of the CC BY 3.0 licence (© 2018). Any distribution of this work must maintain attribution to the author(s), title of the work, publisher, and DOI.

ISBN: 978-3-95450-194-6 ISSN: 2226-0366 doi:10.18429/JACoW-LINAC2018-MOPO058

Electron Gun

The electron gun power supply is integrated with the high voltage pulse modulator. The electron gun power supply is a pulsed power supply too. It generates 50kV pulse voltage.

Normally, we use a thermal cathode electron gun for a 10MeV/20kW accelerator. While we use a grid-control electron gun, showed in Fig. 3, for a multi-energy accelerator because the beam current can be adjusted and controlled precisely.

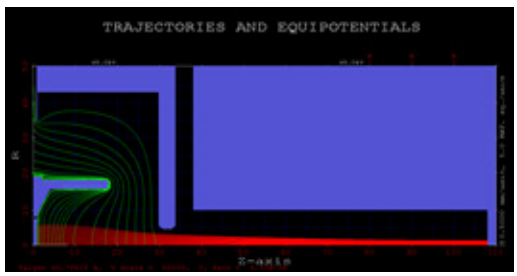


Figure 3: design of a grid-control electron gun.

Travelling Wave Accelerating Tube

The travelling wave accelerating tube [4-5] is used for 10MeV/20kW to accelerate electron beam to 10MeV. The pulse current is 300mA. The microwave power source is 5MW/45kW klystron.

Based on the disk-loaded structrue, the travelling wave accelerating tube consists 58 cells, 6 of which are bunching cells. The total length is 1.97m. The tube works at 2π/3 mode

SUPERFISH and PARMELA are used to calculate the electromagnetic field and beam dynamics.

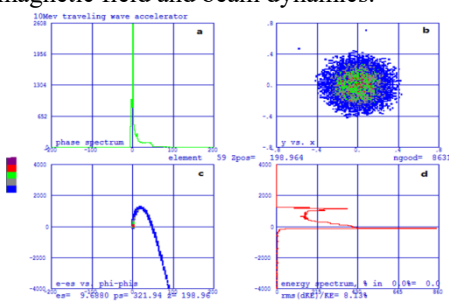


Figure 4: beam dynamic simulation with PARMELA.

As we can see in Fig. 4, most electrons within a microwave period are bunched into a relative narrow width of phase. Beam spot is about 8 mm and energy spread is less than 10% at output of the tube. The tube is showed in Fig. 5.

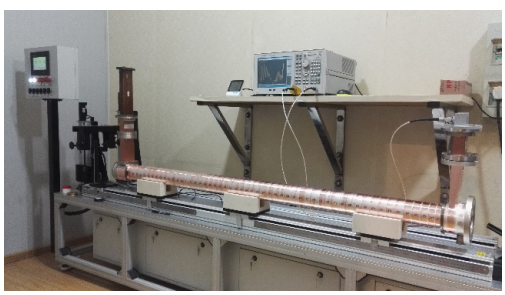


Figure 5: Travelling wave accelerating tube tuning.

DISTRIBUTION OF INDUSTRIAL ACCELERATOR APPLICATIONS

The industrial electron linear accelerator developed by CIAE has been applied widely in China showed in Fig. 6. These accelerators have good reliabilty, stability and maitanability.

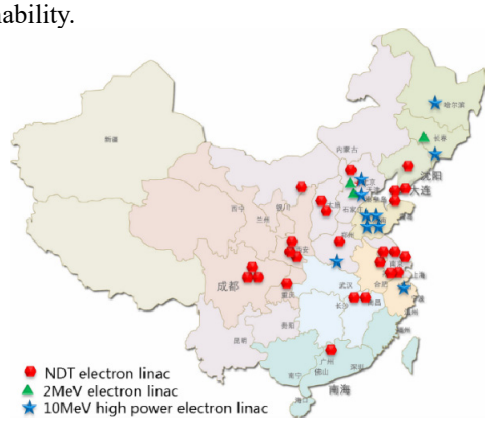


Figure 6: Distribution of industrial accelerator developed by CIAE.

CONCLUSION

CIAE has been absorbed in development of industrial electron linear accelerator for more than 20 years. These accelerators has widely used in scienctifc research and industrial application. Most key devices and components have been developed successfully. As the rapid development of the economy and science, the requirement for the accelerator become more strict. CIAE has been studying on R&D of the new accelerator to meet the new requirement.

REFERENCES

[1] ZENG Zi-qiang *et al.* "Control System for 10 MeV Irradiation Electron Linac", *Atomic Energy Science and Technology*, vol. 39, no. 2, p.114-117. Feb. 2005.

[2] YANG Jing-he *et al.* "Design and Application of Series Resonant Charging Power Supply for Electron Linear Accelerator", *Atomic Energy Science and Technology*, vol. 48, no. 7, p. 1296-1299. Jul. 2014.

[3] LV Wei-xing *et al.* "The Development of Control System for Electron Linear Accelerator Based on Computer", *Atomic Energy Science and Technology*, vol. 36, no. 2, p.134-136. Feb. 2002.

[4] YANG Jing-he *et al.* "Tuning and Matching of 10 MeV Travelling Wave Electron Linear Accelerating Tube", *Atomic Energy Science and Technology*, vol. 51, no. 5, p.930-933. Jul. 2017.

[5] Jinghe Yang and Yu Yang *et al.* "Development of disk-loaded travelling wave accelerating structure for a 10MeV E-LINAC", *in Proc. 9th Int. Particle Accelerator Conf. (IPAC'18),* Vancouver, Canada, Apr. 2018, pp.443-444.

Content from this work may be used under the terms of the CC BY 3.0 licence (© 2018). Any distribution of this work must maintain attribution to the author(s), title of the work, publisher, and DOI.

ISBN: 978-3-95450-194-6 ISSN: 2226-0366 doi:10.18429/JACoW-LINAC2018-MOPO059

CHOKE-TYPE RESONATOR FOR A COMPACT STORAGE RING

L. Ovchinnikova*[1], V.I. Shvedunov[1], Skobeltsyn Institute of Nuclear Physics,
Lomonosov Moscow State University (SINP MSU), 119991 Moscow, Russia
A.D. Ryabov, Institute for High Energy Physics (IHEP), 142281 Protvino, Russia
[1]also at Laboratory of Electron Accelerators MSU Ltd (LEA MSU), 119234 Moscow, Russia

Abstract

We present the results of calculations and measurements of the electrodynamic characteristics of the operating and high order modes of a choke-type resonator, intended for a 35–50 MeV storage ring, which is part of the Thomson X-ray generator.

INTRODUCTION

In [1] a variant of a normally conducting choke type RF resonator [2] was proposed (Fig. 1) for a compact storage ring X-ray source [3]. The resonator operates continuously at a frequency of 2856 MHz, has an effective shunt impedance of 3.8 MΩ, and quality factor of 14,000. The nominal voltage at the gap of the resonator is 300 kV while the level of RF power losses in the walls is 24 kW. With the use of the choke structure, the field of the operating mode is effectively isolated from the outer area of the resonator, where the energy of the higher order modes is absorbed.

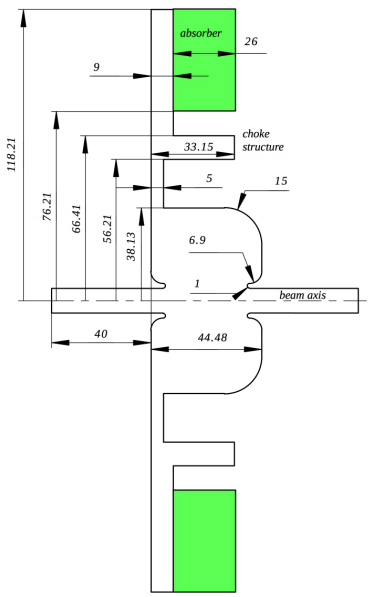


Figure 1: Geometry of the RF resonator.

In this paper we describe the design of a two cavities resonator fed through a 3-dB coupler, which allows to significantly reduce the RF power consumption and get rid of the ferrite isolator in the RF power supply system. The results of calculation of the RF coupler and of cavities thermal conditions with CST [4] and ANSYS [5] codes, as well as the results of measurements of characteristics of higher order modes performed for an aluminum prototype of the RF cavity are presented.

TWO CAVITIES RESONATOR

The presence of sufficient free space in the orbit of our Thomson generator storage ring [3] allows, with the aim of reducing the RF power consumption, to install resonator comprising two RF cavities fed from a single RF source.

The supply of the two cavities from a single RF source can be realized in several ways. For example, a structure comprising two cavities coupled by a magnetic field, which operates at π-mode, or uncoupled cavities fed through a 3-dB coupler [6] can be used. We chose the second solution, since it allows to get rid of the ferrite isolator in high power RF system, and, as it follows from our calculations, requires less RF power to achieve a given effective voltage at the accelerating gap. The design of the two cavities resonator fed through a 3-dB coupler is shown in Fig. 2.

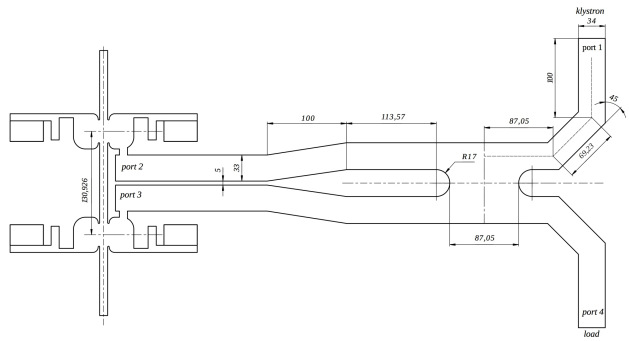


Figure 2: The design of the two cavities resonator fed through a 3-dB coupler.

The two cavities resonator operates as follows. An RF signal from the klystron is fed to port 1 of the 3-dB coupler, this signal is divided equally with the phase difference of 90° between ports 2 and 3, to which the cavities are connected. The signals reflected from the cavities enter port 4 with a phase difference of 180° compensating each other, due to which the klystron is protected from the reflected RF power.

In the chosen design, the RF power is transferred to the cavity via a coupling window cut at the side wall. The cavity coupling window dimensions were tuned to provide coupling factor 1 by adjusting the angle of the window (Fig. 3, parameter a_{sh}); the quality factor of the cavity decreased by 14% due to cutting window, which resulted in a corresponding increase in the RF power consumption. The total RF power consumption for generating effective voltage of

* lub.ovch@yandex.ru

Content from this work may be used under the terms of the CC BY 3.0 licence (© 2018). Any distribution of this work must maintain attribution to the author(s), title of the work, publisher, and DOI.

ISBN: 978-3-95450-194-6 ISSN: 2226-0366 doi:10.18429/JACoW-LINAC2018-MOPO059

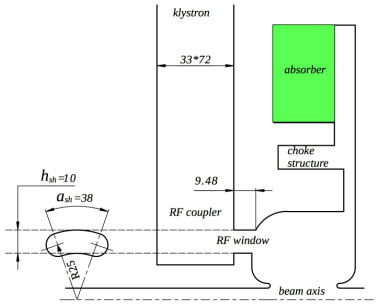


Figure 3: Arrangement of RF energy input.

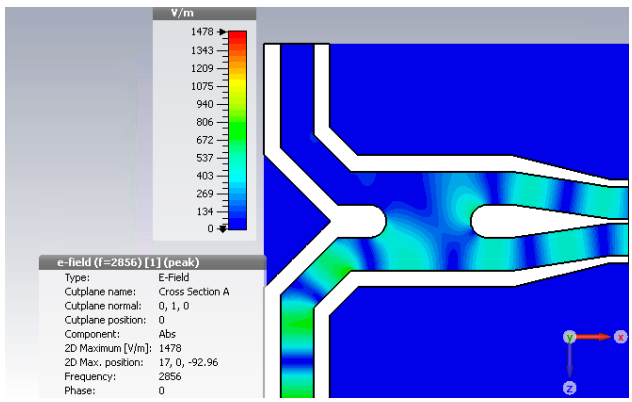


Figure 4: Distribution of the electric field component in the cross section of the 3-dB coupler.

300 kV when using two cavities is 14 kW. The distribution of the electric field in the waveguide for the tuned 3-dB coupler is shown in Fig. 4.

It should be noted that in the alternative case of a resonator comprising two coupled cavities, the decrease in the quality factor due to the coupling slot between the cavities is 21%.

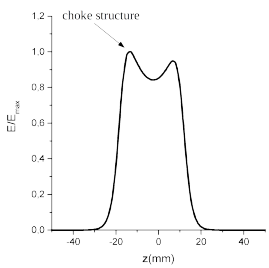
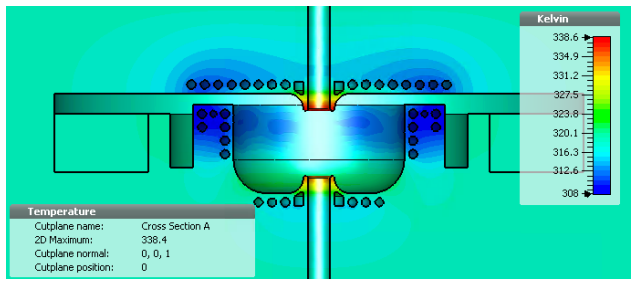


Figure 5: Distribution of the electric field of the operating mode along the axis of the cavity.

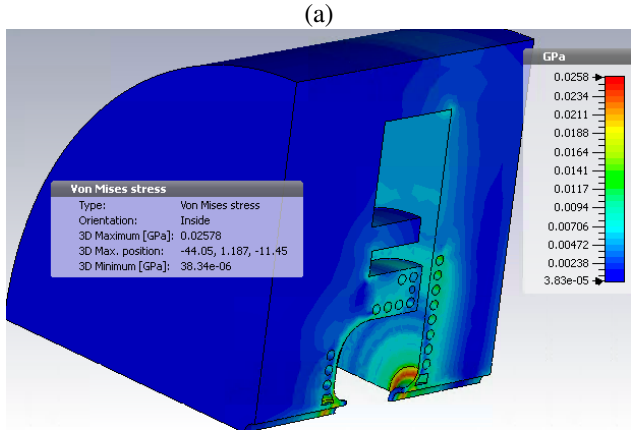
When choosing the optimum distance between the centers of the cavity gaps, which ensures the maximum change in the energy of the relativistic particle for a given RF source power, it is necessary to take into account both the phase shift between ports 2 and 3, and the asymmetry of the distribution of the field of the operating mode along the axis (Fig. 5). Given these two circumstances, the optimal distance between the centers of the gaps is 130.93 mm.

CALCULATION OF THERMAL CONDITIONS

The high average level of RF power losses in the walls, amounting to 7 kW per cavity, leads to the resonance frequency shift due to walls heating and their deformations due to nonuniform temperature distribution. To reduce the frequency shift, optimization of the cooling channels position was carried out (Fig. 6(a)). Maximum temperature gradient and, accordingly, maximum stresses take place near the cavity noses, which requires the channels to be placed as close to them as possible.



(a)



(b)

Figure 6: (a) Temperature distribution in the walls of the RF cavity for the voltage at the gap of 150 kV. (b) Distribution of mechanical stresses.

The temperature distribution in the cavity walls for the optimized channels arrangement and for the heat transfer coefficient of 1.5×10^4 W/m^2/°K calculated using CST code [4] is shown in Fig. 6(a); the distribution of mechanical stresses is shown in Fig. 6(b).

The shift of the frequency of the operating mode at the nominal RF power is about −700 kHz. The maximum stress is 25.8 MPa, which is below the elastic strain limit for copper.

A relatively small decrease in the cavity resonance frequency can be compensated by a decrease in the coolant fluid temperature by approximately 15.5 °C. This makes it possible to dispense with a tuning plunger, stabilizing the frequency of the cavity operating mode frequency by changing the coolant fluid temperature.

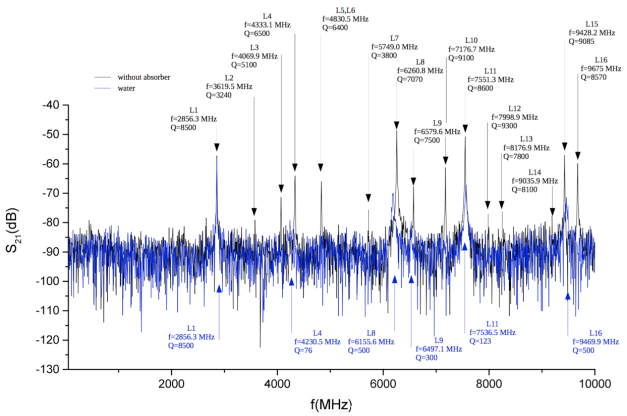
Content from this work may be used under the terms of the CC BY 3.0 licence (© 2018). Any distribution of this work must maintain attribution to the author(s), title of the work, publisher, and DOI.

ISBN: 978-3-95450-194-6 ISSN: 2226-0366 doi:10.18429/JACoW-LINAC2018-MOPO059

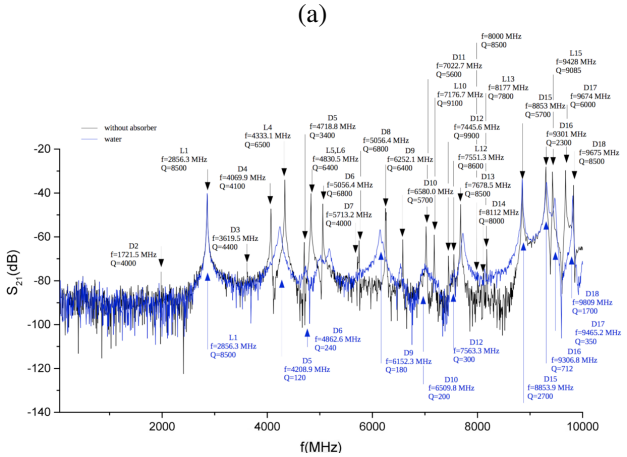
Content from this work may be used under the terms of the CC BY 3.0 licence (© 2018). Any distribution of this work must maintain attribution to the author(s), title of the work, publisher, and DOI.

MEASUREMENT OF THE HIGH-ORDER MODES CHARACTERISTICS

To test the operability of the method for lowering the quality factor of high-order modes, we made an aluminum prototype of the RF cavity. Identification of longitudinal modes was carried out based on the measured field distribution on the axis; identification of dipole modes was done by measuring the number of angular field variations. After identification, the electrodynamic characteristics of each mode with and without the absorber were measured. Water was used as an absorber. Figure 7 shows the spectra of (a) longitudinal modes, (b) transverse modes; the black curve reflects measurements without an absorber, the blue curve — with an absorber.



(a)



(b)

Figure 7: Measured spectra of (a) longitudinal modes, (b) dipole modes. Black curve — measurements without an absorber, blue curve — with an absorber.

An important indicator of the operability of the cavity is the influence of the absorber on the characteristics of the operating mode. For the tested aluminum prototype, the calculated values of the frequency and quality factor of the operating mode without an absorber and with water as an absorber are 2856 MHz, 8482 and 2855.9 MHz, 8482. Measured values, respectively, are 2856.3 MHz, 7630 ± 100 and 2856.3 MHz, 8500 ± 100.

Table 1: Change in the Characteristics of Higher Order Modes Due to the Absorber

Type	W/o absorber		With absorber	
	f, MHz	Q_0	f, MHz	Q_0
L_4	4333.1	6500	4230.5	76
L_8	6260.8	7070	6155.6	500
L_9	6679.6	7500	6497.1	300
L_{11}	7551.3	8600	7536.5	123
L_{16}	9675.0	8570	9469.9	500
D_5	4718.8	3400	4208.9	120
D_6	5056.4	6800	4862.6	240
D_9	6252.1	6400	6152.3	180
D_{10}	6580.0	5700	6509.8	200
D_{12}	7445.6	9900	7563.3	300

The measured frequencies and quality factors of a number of higher order modes, which are potentially dangerous in terms of beam dynamics in the storage ring, without an absorber and with an absorber, are summarized in Table 1. As can be seen the ratio of quality factors with the absorber and without absorber for different modes is in the range 0.01–0.1.

CONCLUSION

In this paper we propose the design of a RF resonator for a storage ring, which consists of two cavities fed through a 3-dB coupler, and makes it possible to use a single RF source without a ferrite isolator. The results of optimization of a 3-dB coupler and of RF energy input are presented as well as the results of thermal condition calculations, which showed the possibility of adjusting the operating mode frequency by means of the coolant fluid temperature, which makes it possible not to complicate the design by the presence of a tuning plunger. The results of measurements of characteristics of higher order modes are given. It is shown that the chosen design of the RF cavity provides an effective reduction in the quality factor of the potentially dangerous modes.

ACKNOWLEDGEMENTS

The authors express their gratitude to N.V. Shvedunov for developing the design and issuing the drawings of the prototype.

REFERENCES

[1] L. Ovchinnikova, A. Ryabov, V.I. Shvedunov, "S-Band Choke Mode Cavity for Low Energy Storage Ring", in *Proc. 25th Russian Particle Accelerator Conf. (RuPAC'16)*, St. Petersburg, Russia, Nov. 2016, pp. 300–302, 2017. doi:10.18429/JACoW-RuPAC2016-TUPSA040

[2] T. Shintake, "The Choke Mode Cavity", *Japanese Journal of Applied Physics*, v. 31, no. 11A, pp. L1567, 1992. doi:10.1143/JJAP.31.L1567

ISBN: 978-3-95450-194-6 ISSN: 2226-0366 doi:10.18429/JACoW-LINAC2018-MOPO059

[3] L. Ovchinnikova, V. Shvedunov K. Ivanov, "Compact Storage Ring for an X-Ray Source", *Journal of Physics: Conference Series*, vol. 941, no. 1, pp. 012096, 2017. doi:10.1088/1742-6596/941/1/012096

[4] Computer Simulation Technology, https://www.cst.com

[5] ANSYS, https://www.ansys.com

[6] V.F. Vikulov, A.A. Zavadtsev, B.V. Zverev, V.E. Kalyuzhny, V.I. Kaminsky, N.N. Nechaev, V.V. Ruzin, N.P. Sobenin, V.V. Stepov, "A Compact Standing-Wave Electron Linac with RF Drive System Using 3 dB Hybrid Junction", *IEEE Transactions on Nuclear Science*, vol. 26, no. 3, pp. 4292–4293, 1979. doi:10.1109/TNS.1979.4330772

Content from this work may be used under the terms of the CC BY 3.0 licence (© 2018). Any distribution of this work must maintain attribution to the author(s), title of the work, publisher, and DOI.

ISBN: 978-3-95450-194-6 ISSN: 2226-0366 doi:10.18429/JACoW-LINAC2018-MOPO060

LINACS FOR INDUSTRY, CARGO INSPECTION AND MEDICINE DESIGNED BY MOSCOW UNIVERSITY*

A.N. Ermakov†[1], A.S. Alimov[1], L.Yu. Ovchinnikova[1], A.N. Kamanin[1], V.V. Khankin[1], N.I. Pakhomov[1], N.V. Shvedunov[1], V.I. Shvedunov[1], D.S. Yurov[1], Skobeltsyn Institute of Nuclear Physics Lomonosov Moscow State University, 119991, Moscow, Russia
[1]also at Laboratory of Electron Accelerators MSU Ltd., 119992, Moscow, Russia
I.V. Shvedunov, A.S. Simonov, Laboratory of Electron Accelerators MSU Ltd., 119992, Moscow, Russia

Abstract

The report presents the results of development of applied linear electron accelerators with an energy of up to 10 MeV, performed by the Laboratory of Electron Accelerators MSU. We describe linear accelerators for mobile, stationary and train cargo inspection systems with interlaced energies and pulse repetition rate up to 2 kHz, accelerators for radiography, a sterilization accelerator with beam parameters that are adjustable over a wide range, and an accelerator for a radiotherapy complex.

INTRODUCTION

Laboratory of Electron Accelerators MSU Ltd. (LEA MSU) was established on the base of Skobeltsyn Institute of Nuclear Physics Lomonosov Moscow State University (SINP MSU) in 2013. Within five years we have designed six different types of linear accelerators for security, industry and medicine and supplied customers with more than 20 units. The customer of accelerators for security systems is the co-founder of the LEA MSU - Scantronic Systems LLC, which developed a number of cargo inspection systems, including stationary, train and mobile [1]. LEA MSU closely cooperates with the JSC "SPE" Toriy" [2] - enterprise that produces the powerful vacuum RF devices. We use in our accelerators the multi-beam klystrons, accelerating structures and electron guns manufactured by "Toriy" and carry out joint deliveries of accelerators. Our accelerators operate in S-band (2856 MHz) and C-band (5712 MHz). Examples of klystrons and sealed accelerating systems are shown in Figs. 1-2.

The accelerators designed by LEA MSU are equipped with a control system based on specialized controllers - each controller is responsible for a separate accelerator system [3]. The control system allows remote monitoring of the accelerator operation while saving the accelerator regime and beam parameters on the server. The control system allows changing the parameters of the accelerated beam within wide limits in accordance with the requirements of the technological process.

An important part of the RF system of our accelerators is a fast digital AFC system, permitting to reach stable beam energy and dose rate for a time of less than 1 s after start.

* Work supported in part by Ministry of Education and Science of Russia Grant # RFMEFI58217X0011
† email address a_ermak1978@mail.ru.

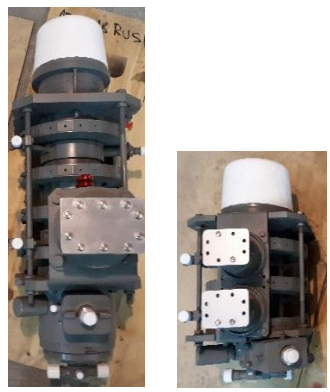


Figure 1: S-band (left) KIU-168 and C-band KIU-271 klystrons [2].

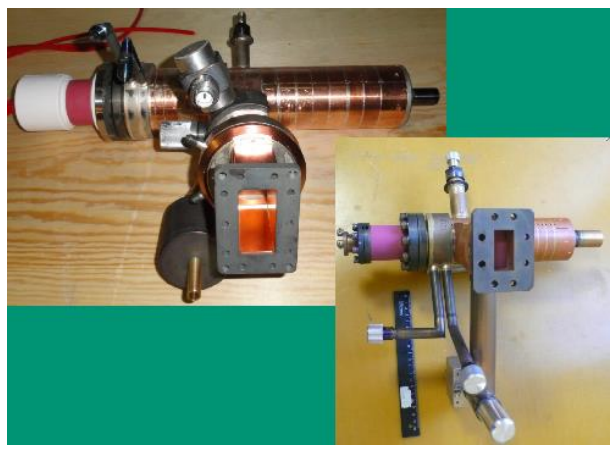


Figure 2: S-band (upper) and C-band accelerating systems.

Preliminary information about LEA MSU accelerators was given in [4-5].

CARGO INSPECTION

We have designed and manufacture accelerators for three types of cargo inspection systems: stationary, train and mobile. All these accelerators operate in interlaced energies mode with beam energy switching between 3.5 and 6 MeV. The beam spot size at the placed in vacuum, liquid cooled bremsstrahlung target is less than 1.5 mm for low energy and less than 1 mm for high. Accelerators are equipped with a local radiation shielding with a narrow gap collimator. Pulse to pulse beam energy stability is about 0.6 % rms. Some additional parameters are given in Table 1, accelerators photo are in Fig. 3. High repetition rate

Content from this work may be used under the terms of the CC BY 3.0 licence (© 2018). Any distribution of this work must maintain attribution to the author(s), title of the work, publisher, and DOI.

ISBN: 978-3-95450-194-6 ISSN: 2226-0366 doi:10.18429/JACoW-LINAC2018-MOPO060

of train system accelerator permits to inspect trains at velocity 70 km/h.

Table 1: Parameters of Accelerators for Cargo Inspection

Parameter	Stationary	Train	Mobile
Rep. rate, Hz	2×200	2×1000	2×200
Dose rate, Gy/min	4	6	0.2
Radiation leakage	2×10^{-5}	2×10^{-5}	10^{-6}
Frequency, MHz	2856	2856	5712

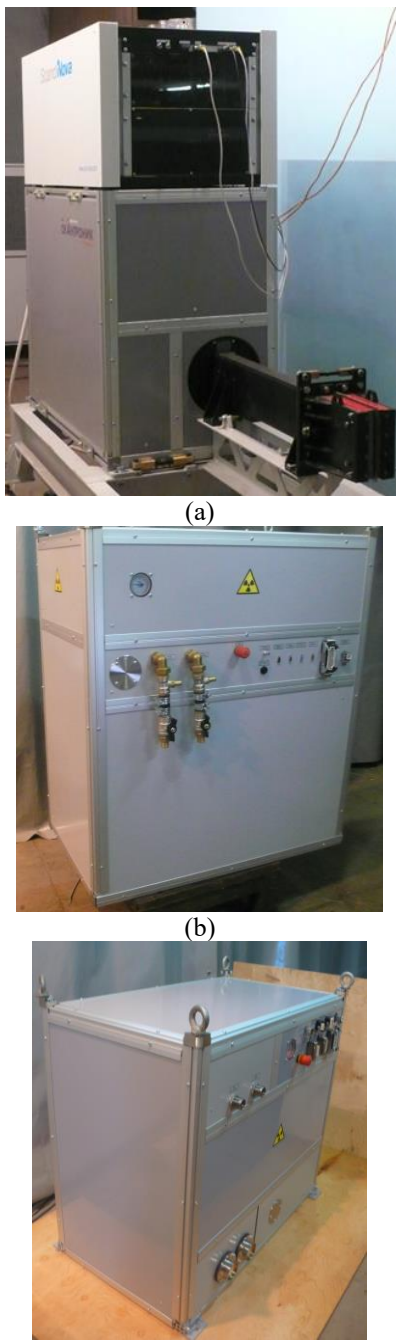


Figure 3: Accelerators for cargo inspection systems, (a) stationary (with modulator), (b) train and (c) mobile.

RADIOGRAPHY

Accelerators for radiography are simplified versions of the accelerator for a stationary cargo inspection system, they are produced with three maximum beam energies: 6 MeV, 8 MeV and 10 MeV. The maximum dose rate at energy of 10 MeV is 40 Gy/min. The energy of the accelerated beam for each version of the accelerator can be reduced in wide range, down to 50% of the nominal value to ensure the best image quality depending on the thickness of the object under inspection. Accelerator for radiography in operation is shown in Fig. 4.



Figure 4: Accelerators for radiography in operation.

STERILIZATION

The first accelerator for sterilization produced by the LEA MSU and JSC "SPE" Toriy" was installed in the pilot complex of antimicrobial product processing [6] in the Kaluga region (Russia) – Fig. 5. Its main parameters are given in Table 2. An important feature of the accelerator is the possibility of adjusting the parameters of accelerated beam and scanning system according to parameter of the product to be treated [7].

Table 2: Parameters of Accelerator for Sterilization

Parameter	Value
Beam energy, regulated, MeV	5 - 10
Pulsed beam current, mA	400
Average beam power, regulated, kW	5-15
Klystron pulsed power, max, MW	6
Klystron average power, max, kW	25
Operating frequency, MHz	2856
Wall plug efficiency	20%
Beam scanning width, regulated, cm	40-60

Content from this work may be used under the terms of the CC BY 3.0 licence (© 2018). Any distribution of this work must maintain attribution to the author(s), title of the work, publisher, and DOI.

ISBN: 978-3-95450-194-6 ISSN: 2226-0366 doi:10.18429/JACoW-LINAC2018-MOPO060

Content from this work may be used under the terms of the CC BY 3.0 licence (© 2018). Any distribution of this work must maintain attribution to the author(s), title of the work, publisher, and DOI.



Figure 5: Accelerators for sterilization.

MEDICINE

LEA MSU is developing an electron accelerator for the radiotherapy complex, which is designed by JSC "Scientific Research Institute of Technical Physics and Automation", Moscow, Russia [8]. The accelerator provides a beam energy of 6 MeV at a dose rate of 10 Gy/min in the therapeutic mode and 2.5 MeV energy in the portal image acquisition mode. To have a compact design the accelerator is operating at 5712 MHz. The results of the beam dynamics calculations are presented in [9], experiments on measuring electron beam parameters are described in [10]. At present, the design of the accelerator is being completed-its design is shown in Fig. 6. Tests of the accelerator and its transfer for installation in gantry are planned for December 2018.

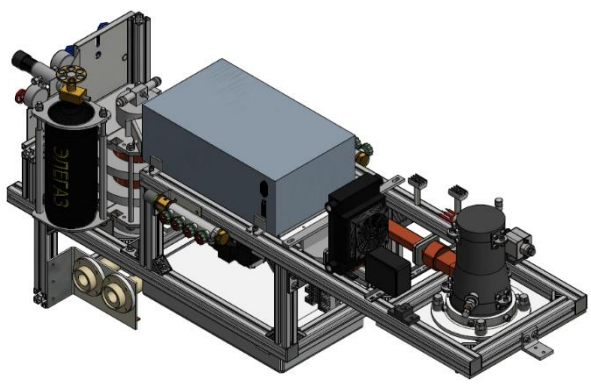


Figure 6: Accelerators for medicine.

CONCLUSION

During last 5 years the LEA MSU has designed and supplied to customers 25 accelerators, including 5 for radiography, 19 for X-ray inspection systems, 1 for sterilization. Accelerator for medicine is under construction. Contracts for ten more machines have been signed. Design of accelerators is based on the results of fundamental research conducted in previous years at Skobeltsyn Institute of Nuclear Physics Lomonosov Moscow State University.

ACKNOWLEDGEMENTS

The authors are grateful to professor B.S. Ishkhanov, academician of the RAS V.P. Smirnov, A.V. Nalivaev and Dr. S.A. Ogorodnikov for supporting this work.

REFERENCES

[1] http://www.scantronicsystems.com

[2] http://www.toriy.ru

[3] A.N. Ermakov, A.N. Kamanin, V.G. Sayapin, I.V. Shvedunov, V.I. Shvedunov and D.S. Yurov,, "Control Systems for Radiography and Cargo Inspection RF Accelerators", in *Proc. of RuPAC2014*, Obninsk, Kaluga Region, Russia, pp. 410-412.

[4] A.N. Ermakov, A.S. Alimov, B.S. Ishkhanov et al, "Main Parameters and Operational Experience with New Generation of Electron Accelerators for Radiography and Cargo Inspection", *in Proc. of RuPAC2014*, Obninsk, Kaluga Region, Russia, pp. 143-145.

[5] A.N. Ermakov, V.V. Khankin, A.S. Alimov et al, "Commissioning of High Efficiency Standing Wave Linac for Industrial Applications", in *Proceedings of RuPAC2016*, St. Petersburg, Russia, pp. 99-101

[6] http://www.tecleor.com

[7] V.V. Khankin, A.S. Alimov, A.N. Ermakov, A.N. Kamanin, A.S. Kurilik, N.I. Pakhomov, N.V. Shvedunov, V.I. Shvedunov, D.S. Yurov, I.V. Shvedunov, A.S. Simonov, "Linear Electron Accelerator for Radiation Technologies with Beam Parameters Varied in a Wide Range", presented at the 29th Linear Accelerator Conference, LINC18, Beijing, China on 16-21 September 2018, paper MOPO62, this conference.

[8] http://www.niitfa.ru

[9] L.Yu. Ovchinnikova, V.I. Shvedunov, "Design of C-Band Electron Linear Accelerator for a Complex of Radiation Therapy", presented at the 29th Linear Accelerator Conference, LINC18, Beijing, China on 16-21 September 2018, paper MOPO59, this conference.

[10] D.S. Yurov, L.Yu. Ovchinnikova, A.S. Alimov, A.N. Ermakov, V.V. Khankin, N.V. Shvedunov, V.I. Shvedunov, A.S. Simonov "Beam parameters measurement of C-band 6 MeV linear electron accelerator", presented at the 29th Linear Accelerator Conference, LINC18, Beijing, China on 16-21 September 2018, paper MOPO61, this conference.

ISBN: 978-3-95450-194-6 ISSN: 2226-0366 doi:10.18429/JACoW-LINAC2018-MOPO061

BEAM PARAMETERS MEASUREMENT OF C-BAND 6 MeV LINEAR ELECTRON ACCELERATOR*

D. S. Yurov[1], A. S. Alimov[1], A. N. Ermakov[1], V. V. Khankin[1], L. Yu. Ovchinnikova[1], N. V. Shvedunov[1], V. I. Shvedunov[1], A. S. Simonov, Laboratory of Electron Accelerators MSU Ltd., Moscow, Russia
[1]also at Skobeltsyn Institute of Nuclear Physics, Lomonosov Moscow State University, Moscow, Russia

Abstract

The new linear electron accelerator with beam energy varied in the range of 2-6 MeV with dual-energy option has been designed by Laboratory of Electron Accelerators MSU Ltd. Linac is based on compact high gradient standing wave C-band accelerating structure fed by multi-beam klystron and is used in the cargo inspection and cancer therapy complexes. In the report, we present the results of electron beam parameters measurements at special stand.

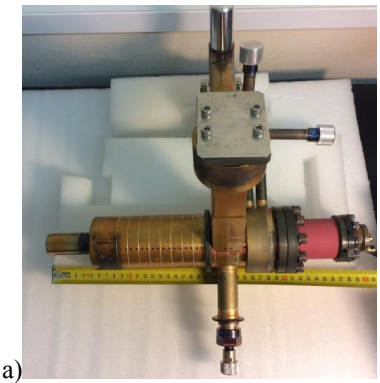
INTRODUCTION

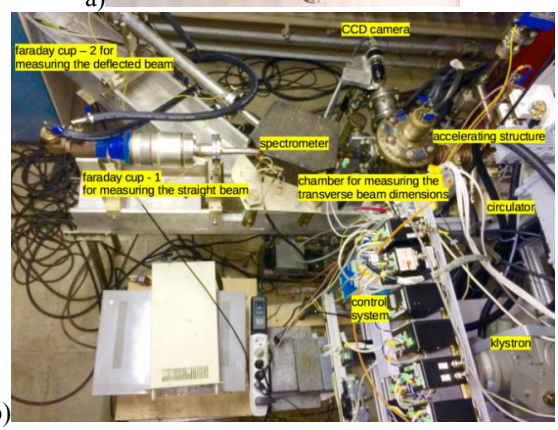
We have developed an accelerating system based on C-band on-axis coupled bi-periodic standing wave accelerating structure (AS) connected to a three-electrodes electron gun [1] for electron accelerators designed for cargo inspection and radiation therapy systems. The above application areas require narrow energy spectrum of the beam and ability to control its energy in the range of 2-6 MeV. In order to measure beam parameters and select an optimal operating mode, a prototype of the accelerating system without the bremsstrahlung target has been built and installed on a special stand. The paper provides a description of the stand and gives the measurement results.

EXPERIMENTAL SETUP

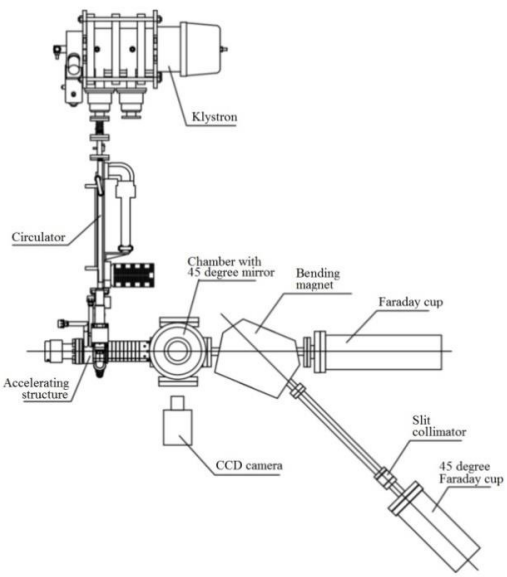
Photo and layout of the stand are given in Fig. 1.

The accelerating system that includes an AS, electron gun, feeding waveguide with vacuum RF window and antenna installed in the coupler cell is connected to a vacuum chamber with a viewing window and a movable screen made of titanium foil mounted at 45^0-angle to the beam axis. The screen is intended to measure transverse charge distribution of accelerated beam by registering generated at foil transition radiation by the CCD camera. A spectrometer based on 45^0 magnet with Faraday cups (FC) located at 0^0 and 45^0 is installed at the output of the vacuum chamber. A slit collimator with the slit width of 3 mm is placed at the 45^0 FC input. 0^0 FC signal comes to an oscilloscope for measuring amplitude of pulsed current of accelerated beam, and 45^0 FC signal is measured with ADC through an integrating chain or sent to an oscilloscope as well. Power supply of the AS is provided by multi-beam klystron KIU-273 with operating frequency of 5712 MHz and maximum pulsed RF power of 3.5 MW [2].


a)



b)



c)

Figure 1: Photo of a) the accelerating system and b) the stand. c) Stand layout.

* Work supported in part by Grant of the Ministry of Education and Science of the Russian Federation #RFMEFI58217X0011

Content from this work may be used under the terms of the CC BY 3.0 licence (© 2018). Any distribution of this work must maintain attribution to the author(s), title of the work, publisher, and DOI.

ISBN: 978-3-95450-194-6 ISSN: 2226-0366 doi:10.18429/JACoW-LINAC2018-MOPO061

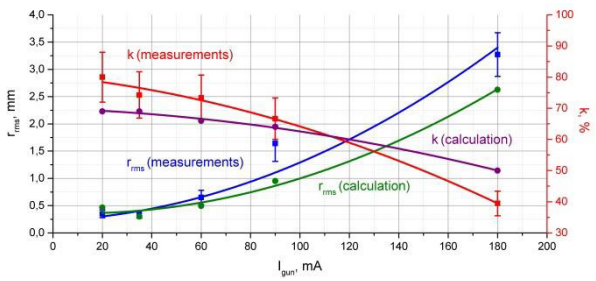
Content from this work may be used under the terms of the CC BY 3.0 licence (© 2018). Any distribution of this work must maintain attribution to the author(s), title of the work, publisher, and DOI.

DC high voltage controlled in the range of -10 ÷ -27 kV is applied to the cathode of the gun, the control electrode is fed by pulses with the amplitude set in the range of 0 ÷ +3 kV with respect to the cathode with controlled duration and delay relative to the RF field envelope pulse. Maximum pulsed gun current is 180 mA.

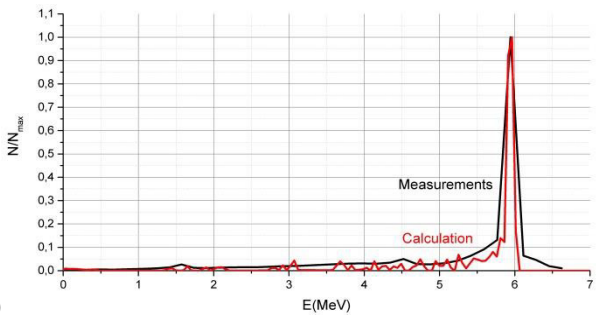
Average RF power loss in the AS walls is measured by the difference between input and output temperatures of the coolant and its flow rate with calorimeter Calec ST II. Pulsed RF power loss is calculated through duty cycle. Accelerating field level is additionally controlled with a RF detector, which receives signal from the antenna.

MEASUREMENT RESULTS

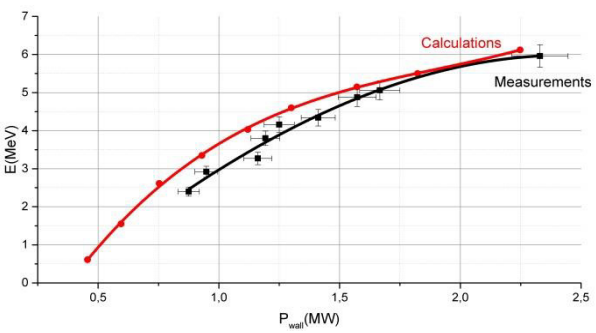
There were several series of beam parameter measurements conducted at the stand. Electron beam spectra, capture coefficient, RF power dissipated in the walls of the AS, as well as transverse charge distribution in the beam were measured as part of the first series.



a)



b)



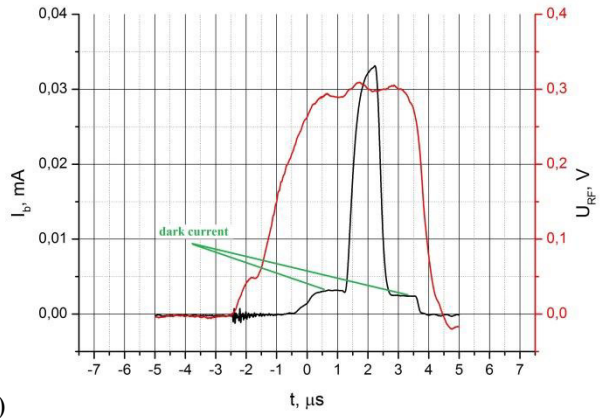
c)

Figure 2: a) Measured and calculated dependencies of rms beam radius (blue and green) and capture coefficient (red and purple) on gun current at the accelerated beam energy of 6 MeV. Measured (black) and calculated (red) b) beam spectra at gun current of 20 mA and accelerated beam energy of 6 MeV, c) dependencies of beam energy on pulsed RF power loss in the AS walls.

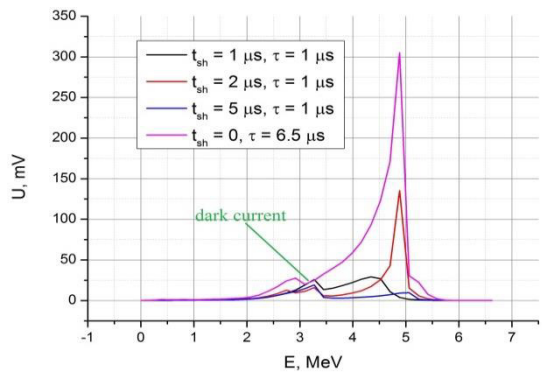
The measurements were conducted for various gun currents and different accelerating field levels that correspond to the maximum electron energy from 2 to 6 MeV. At that, width of the accelerating field envelope was 4.4 μs, and the pulse of the gun current completely overlapped the pulse of the envelope of the accelerating field.

Figure 2 shows dependencies of rms beam radius and capture coefficient on gun current at the accelerated beam energy of 6 MeV (a), beam spectrum at gun current of 20 mA and pulsed RF power loss in the walls of 2.5 MW (b), as well as dependence of beam energy on pulsed RF power loss in the AS walls as compared to calculated data (c). As one can see, calculated results agree rather well with measurement results.

In the second series of experiments, measurements were conducted for a fixed level of klystron pulsed power and for different duration of electron gun pulse and its delay relative to pulse of accelerating field envelope (Fig. 3). The graphs clearly show the dark current contribution.



a)



b)

Figure 3: a) Pulse of accelerating field envelope (red) and accelerated beam current pulse at 0^0 FC (black) at gun current pulse duration of 1 μs and its delay with regard to the front edge of RF pulse of 3 μs. b) Measured spectra for different duration of the gun current pulse τ and its different delays with regard to the front edge of RF pulse t_{sh}.

ISBN: 978-3-95450-194-6 ISSN: 2226-0366 doi:10.18429/JACoW-LINAC2018-MOPO061

MEASURING SPECTRA AT SHORT TIME INTERVALS

The shape of measured accelerated beam spectra (Figs. 2, 3), besides the specific characteristics of beam dynamics in the AS and energy resolution of the spectrometer, is also determined by the following factors. At short width and amplitude of the gun current pulse one can notice contribution of dark currents: faint spectral peaks seen at Figs. 3b and 2b, as well as the base of dark current at a pulse at the 0^0 FC shown in Fig. 3a. For the pulse of gun current that fully overlaps with the pulse of accelerating field envelope, contribution from the electrons accelerated at the pulse front to the spectral width becomes noticeable.

To minimize these factors we have used a method that allows one to obtain beam spectrum at a specific moment of the pulse of accelerating field envelope averaged over the time interval of 50-100 ns. For that purpose, oscillograms of beam current from 45^0 FC for various values of spectrometer magnet current were measured. An example of such pulse is shown in Fig. 4 (blue curve) for magnet current corresponding to the energy of 4.93 MeV.

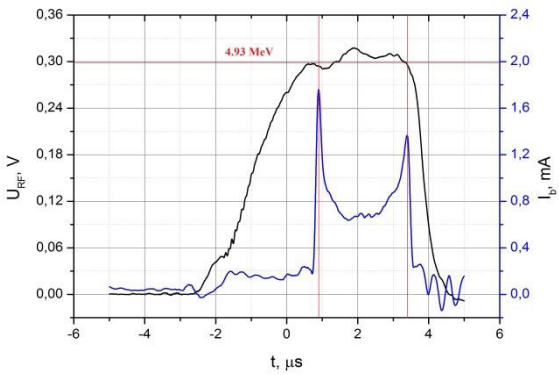


Figure 4: Pulse of accelerating field envelope (black) and current pulse at the 45^0 FC at the spectrometer magnet current corresponding to the beam energy of 4.93 MeV.

When magnet coils current approaches the value corresponding to the maximum beam energy, "rabbit ears" of the current pulse in Fig. 4 converge and ultimately merge into one peak. By measuring 45^0 FC current pulse amplitude depending on magnet coils current for a given time t_0, one can obtain beam spectrum for the point on the accelerating field envelope corresponding to the moment t_0. The spectrum obtained in this way for the moment of time t_0 = 2 μs (in Fig. 4) is shown in Fig. 5 by the black curve as compared to the calculated data (red curve) and as compared to the spectrum (blue curve) measured in a conventional way, with the gun current pulse that fully overlaps with the accelerating field envelope pulse. Width of the spectrum measured in accordance with the method described turns out to be much closer to the calculated spectrum width.

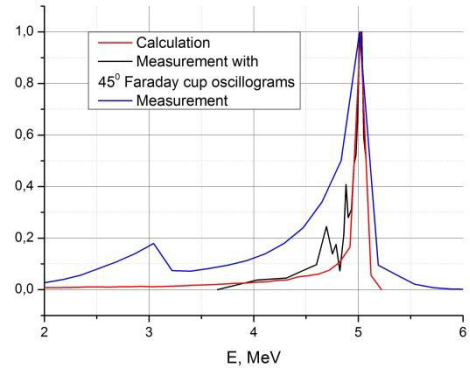


Figure 5: Accelerated beam spectra: red line – calculated, black line – measured with the help of the method described in this section, blue line – measured in a conventional way.

CONCLUSION

We have carried out beam parameter measurements for the newly developed electron accelerator based on C-band AS at a stand specifically built for this purpose. Electron beam with energy controlled in the range of 2-6 MeV and characteristics that are well correlated with calculated results has been obtained. Study of various accelerator operating modes has shown that dark currents and fronts of accelerating field envelope pulse have great influence on spectrum shape. To minimize contribution of these factors it is necessary that the electron gun current pulse would span the top of the accelerating field envelop to the maximum extent possible not capturing the edges. In addition, we have developed a new spectrum measurement method that allows one to take measurements for the selected moment of the accelerating field envelope in the short time interval of 50-100 ns.

REFERENCES

[1] L. Yu. Ovchinnikova, V. I. Shvedunov, "Design of C-band electron linear accelerator for a complex of radiation therapy", presented at the 29th Linear Accelerator Conf. (LINAC'18), Beijing, China, Sep. 2018, paper MOPO059, this conference.

[2] www.toriy.ru

Content from this work may be used under the terms of the CC BY 3.0 licence (© 2018). Any distribution of this work must maintain attribution to the author(s), title of the work, publisher, and DOI.

ISBN: 978-3-95450-194-6 ISSN: 2226-0366 doi:10.18429/JACoW-LINAC2018-MOPO062

LINEAR ELECTRON ACCELERATOR FOR RADIATION TECHNOLOGIES WITH BEAM PARAMETERS VARIED IN WIDE RANGE

V.V. Khankin†, A.S. Alimov, A.N. Ermakov, A.N. Kamanin, A.S. Kurilik, N.I. Pakhomov, N.V. Shvedunov, V.I. Shvedunov, D.S. Yurov, Skobeltsyn Institute of Nuclear Physics, MSU, Moscow, Russia and Laboratory of Electron Accelerators MSU, Ltd., Moscow, Russia.
I.V. Shvedunov, A.S. Simonov, Laboratory of Electron Accelerators MSU, Ltd., Moscow, Russia.

Abstract

We present the overview and beam parameters measurements results as well as the operational experience with the S-band pulsed linear electron accelerator with beam energy in the range of 5-10 MeV and maximum beam power of up to 15 kW. The possibility of adjusting the beam parameters in a wide range, provided by the design and control system of the accelerator, allows to use the accelerator in a wide variety of radiation technologies.

INTRODUCTION

Linear electron accelerators with the energy up to 10 MeV and beam power up to 50 kW are widely used in various radiation technologies. In the cases, when the specifications of the products being processed making use of the same installation are significantly changed, in order to optimize the radiation process it is necessary to have the possibility of on-line adjustment of the accelerated beam parameters. For example, during the radiation processing of the food products the mass-per-unit-area thickness of the products and the required dose can vary multi-fold; this requires for the several-fold change of beam power and value of dose for one beam pulse. The adjustment of the accelerated beam power with respect to the mass-per-unit-area thickness of the products enables not only to ensure the required uniformity of the dose distribution by the depth, but also to save the electric power to the considerable extent with proper design of the accelerator RF power supply system. The adjustment of dose being delivered to the products per one beam pulse enables to change the dose from hundreds of Grays to tens of kilo Grays with ensuring the uniformity of dose distribution along the surface and with high efficiency of the process.

ACCELERATOR DESCRIPTION

The linear accelerator described earlier in [1] has been installed in the centre for antimicrobial processing of products of vegetable and animal origin by the stream of accelerated electrons [2]. The photo and schematic view of the accelerator are given in Fig. 1, main parameters are presented in table 1.

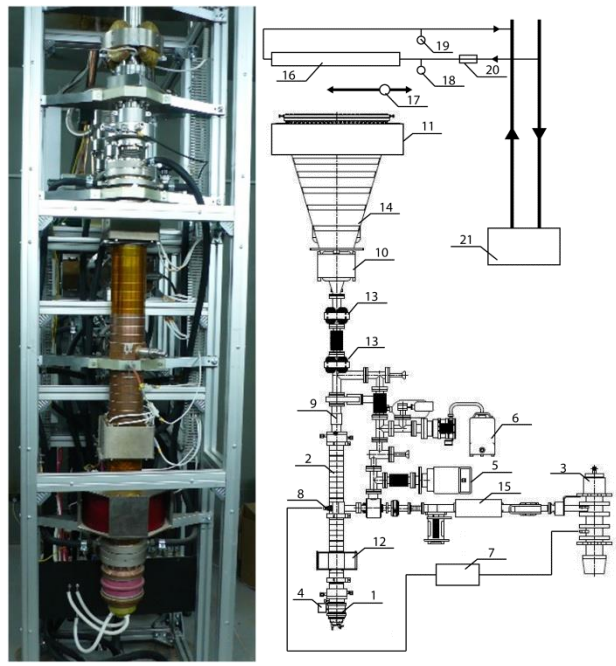


Figure 1: Photo and schematic view of the accelerator. 1 – electron gun, 2 – accelerating structure, 3 – klystron, 4, 5, 6 – vacuum pumps, 7 – low power RF unit, 8 – RF antenna, 9 – beam current monitor, 10 – scanning magnet, 11 – correcting magnet, 12 – solenoid, 13 – quadrupole lenses, 14 – scanning chamber, 15 – circulator, 16 – beam absorber 1, 17 – beam absorber 2, 18, 19 – temperature sensors, 20 – flow meter, 21 – chiller.

Table 1: Accelerator Parameters

Range of beam energy regulation	5-10 MeV
Pulsed beam current	400 mA
Range of beam power regulation	1-15 kV
Range of pulse duration regulation	4-12 μs
Range of pulse repetition rate regulation	50-400 Hz
Range of beam scanning width regulation	40-60 cm
Range of scanning frequency regulation	1-30 Hz
Operating frequency	2856 MHz
Maximum power of klyastron, pulse/average	6 MW/25 kW
Wall plug efficiency	>20%

† v-k32@yandex.ru

Content from this work may be used under the terms of the CC BY 3.0 licence (© 2018). Any distribution of this work must maintain attribution to the author(s), title of the work, publisher, and DOI.

ISBN: 978-3-95450-194-6 ISSN: 2226-0366 doi:10.18429/JACoW-LINAC2018-MOPO062

In order to implement the accelerator operation modes with different energies of the accelerated electrons it is necessary to have the possibility of smooth adjustment of the power being supplied from the klystron to the accelerating structure. The most energy-efficient adjustment of the output power of the klystron is achieved by means of changing its cathode voltage with maintaining the input RF signal at the optimal level. Matching of the accelerating structure with feeding waveguide is performed by means of choosing of the optimal beam current with the help of voltage adjustment on the control electrode of the three-electrode electron gun.

During commissioning period we did measurements of the accelerated beam parameters, for the purpose of calibration. The following auxiliary elements shown in Fig. 1 were used: beam absorber 15 in the form of isolated thick-wall copper tube of rectangular section cooled by water, and beam absorber 16 – isolated steel cylinder of small diameter that is moved along the output deflecting flange remotely.

METHODS

The average beam power, $\bar{P}$, released in the absorber 15 (Fig. 1), is measured by means of precise calorimeter CALEC ST II, with the temperature sensors PLH 100/105 CE M and flow meters AMFLO MAG Smart DN15. In order to measure the beam pulse current I oscilloscope is used, to which the signal is sent from the precise 50 Ohm resistor that connects absorber with ground.

When determining the average beam power it is taken into account that during the interaction of accelerated electrons with the absorber wall the bremsstrahlung radiation is generated, main part of which leaves the absorber. Also the significant part of the beam energy is taken away by the electrons reflected from the absorber. The latter process contributes also to the measured beam current. In order to take into account these factors the process of beam interaction with absorber was modeled making use of GEANT4 library. Calculated dependence of the beam power and charge leakage on the electron energy is shown on Fig. 2.

Average beam energy is calculated as per formula $\bar{E} = \bar{P}_{corr}/\bar{I}$, where $\bar{I} = I_{corr} \times \tau \times f$ is average current, $\bar{P}_{corr}$ and I_{corr} are average beam power and pulsed beam current corrected with the use of data from Fig. 2, τ is the pulse duration and f is pulse repetition rate.

Also the efficient energy of the accelerated electrons is estimated by standard method based on measurements of depth-dose distribution curves in Al according to [3]. For this purpose the multi-layer target made of Al and radiochromic film DEX B3 with operating range of the measured doses 10-50 kGy was used.

Finally, the third method of evaluation of the beam energy and energy spectra is the use of scanning magnet as a spectrometer. In order to implement this possibility the precision measurement of the magnetic field map was done and, the relation of coils current, deflection angle and electron energy was determined. The spectrum measurement is carried out with the fixed coils current by means of measurements of the beam current distribution beyond the exit window with the help of movable absorber 16 (Fig. 1) or radiochromic film.

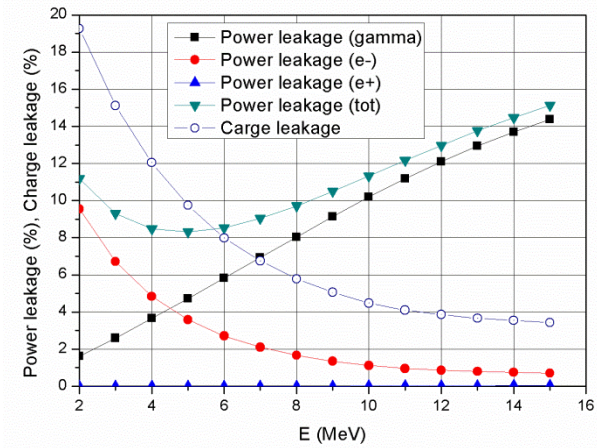


Figure 2: The dependence of the beam power and charge leakage on the electron energy due to the bremsstrahlung, secondary electrons and positrons.

RESULTS

As it was noticed above, the main parameters that determine the accelerator operation mode are voltages on klystron cathode and on control electrode of electron gun. For the solid-state modulator from ScandiNova used in our accelerator, the amplitude of high-voltage pulse coming to the klystron cathode is determined by the charge voltage of primary circuit U_{HVPS}. The dependence of pulse power $P = \bar{P}_{corr}/\tau \times f$ and beam energy $\bar{E}$ on the selected operation mode of the accelerator is shown on Fig. 4, where $U_{C.E.}$ is gun control electrode voltage. From the figure it can be seen that maximum power of 4.25 MW is achieved with the energy of 8.5 MeV. For the maximum possible duty factor of our equipment equal to 0.4%, the average power in this mode achieves 17 kW.

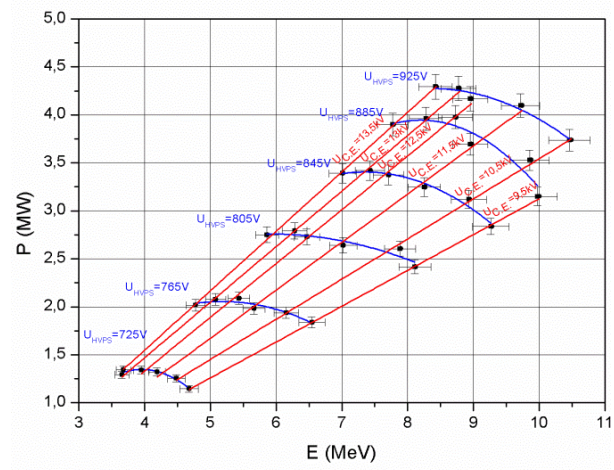


Figure 3: The relation of pulsed beam power and beam energy for the selected operation mode of the accelerator. U_{HVPS} is the charging voltage of modulator, $U_{C.E.}$ is the electron gun control electrode voltage.

Content from this work may be used under the terms of the CC BY 3.0 licence (© 2018). Any distribution of this work must maintain attribution to the author(s), title of the work, publisher, and DOI.

ISBN: 978-3-95450-194-6 ISSN: 2226-0366 doi:10.18429/JACoW-LINAC2018-MOPO062

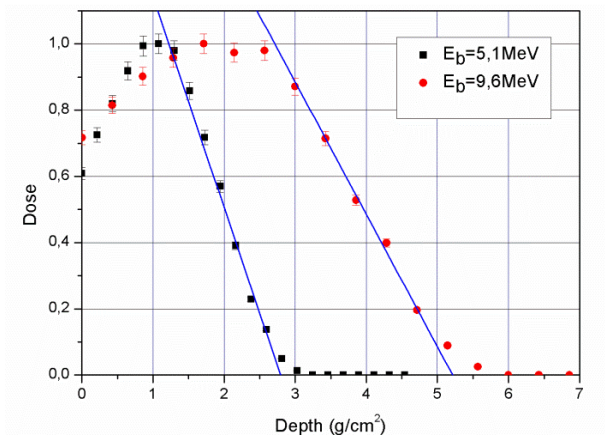


Figure 4: Measured dose - depth distribution in Al. Set energies are 5 MeV and 10 MeV.

The results of the absorbed dose - depth distribution in the Al measurements with radiochromic film are given in Fig. 4. The beam energies were set to 5 MeV and 10 MeV according to calibration based on average beam power and pulsed current measurements described above. Results of two types of beam energy measurements are in rather good agreement.

The spectra measured with the scanning magnet for several modes of the accelerator operation are shown in Fig. 5. For the mode with maximum energy the spectrum is measured both with the movable absorber and with the radiochromic film. The spectrum width is determined mainly with energy resolution of the "spectrometer". The vertical line mark the result of energy measurement with two methods described above. It is seen that the results are in good agreement.

The beam energy measurement results were used to calibrate signal of RF detector, to which the signal from the RF antenna installed in the accelerating structure comes. The signal from RF detector is used for continuous monitoring of the beam energy during the accelerator operation.

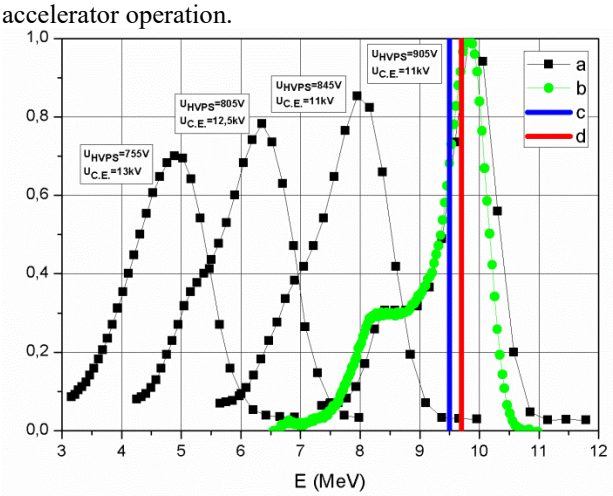


Figure 5: The beam spectra measured by the absorber 16 (Fig. 1) (a), by radiochromic film (b), beam energy from dose-depth distribution measurement (c) and from average power and pulsed current measurements (d).

PRACTICAL USE

In order to ensure the convenient and efficient operation of the accelerator on the basis of the above-described measurements of the accelerated beam parameters, we have developed the algorithm enabling on the basis of the parameters of the products being irradiated (i.e. required dose, dimensions and weight of the box) to determine the accelerator operation mode parameters, ensuring the maximum capacity of the complex with the minimum energy consumption. Besides, the remote control of the accelerator operation via Internet and continuous record of beam main parameters and mode parameters to a server are ensured.

CONCLUSION

The presented results demonstrate wide capabilities for flexible adjustment of energy and power of accelerated beam. In combination with the beam scanning system and conveyor that is a part of the complex, the accelerator enables processing of the products with effective thickness from 0.1 g/cm^2 up to 8.1 g/cm^2 with maximum efficiency, delivering the dose starting from 0.8 kGy.

REFERENCES

[1] Ermakov A.N. *et al.*, "Commissioning of High Efficiency Standing Wave Linac for Industrial Applications", in *Proc. RUPAC16*, p.99-101.

[2] https://www.tecleor.com

[3] ISO/ASTM 51649:2005(E) "Practice for dosimetry in an electron beam facility for radiation processing at energies between 300 keV and 25 MeV".

Content from this work may be used under the terms of the CC BY 3.0 licence (© 2018). Any distribution of this work must maintain attribution to the author(s), title of the work, publisher, and DOI.

ISBN: 978-3-95450-194-6 ISSN: 2226-0366 doi:10.18429/JACoW-LINAC2018-MOPO063

DEVELOPMENT OF SIDE COUPLED X-BAND MEDICAL LINEAR ACCELERATOR FOR RADIOTHERAPY*

Y. S. Lee†, G. J. Kim, S. H. Kim, J. H. Lee, I. S. Kim, Y. W. Choi, J. I. Kim††,
Medical Device Research Center, Korea Electrotechnology Research Institute, Ansan 15588, Republic of Korea
J. H. Hwang[1,2], A.R Kim[1,2], J. N. Kim[1,2], J. S. Shin[1,2], Y. J. Seol[1,2], T. G. Oh[1,2], Y. A. Oh[2], Y. N. Kang[2,3]
[1]Department of Biomedicine & Health Sciences, The Catholic University of Korea, Seoul 06591, Republic of Korea
[2]Advanced Institute for Radiation Fusion Medical Technology, College of Medicine, The Catholic University of Korea, Seoul 06591, Republic of Korea
[3]Department of Radiation Oncology, Seoul St. Mary's Hospital, College of Medicine, The Catholic University of Korea, Seoul 06591, Republic of Korea

Abstract

Recently, LINAC-based radiotherapy equipment are being developed by combining with imaging devices such as CT or MRI, so that it is possible to precisely focus high dose radiation on tumor tissues while minimizing the normal tissue damage. In order to place the diagnostic and treatment devices simultaneously in a confined space, constraints related to interference and volume between the subsystems must be considered. To meet these requirements, the size and weight of the LINAC system need to be reduced, which can be achieved by applying X-band technology. For the purpose of use in IMRT based on image guided radiotherapy, we developed a 9.3 GHz X-band medical LINAC using side-coupled structure. The LINAC is designed to have the accelerating field strength of 16.8 MV/m, and the beam current transmission efficiency of 26 % at the end of accelerating cell when the supplied RF power is at 1.7 MW. Therefore, it can accelerate the electron beam up to 6.2 MeV with having about 90 mA beam current. We plan to carry out the performance test using beam diagnostics system and X-ray measurement system, and the details of design and experimental results of LINAC will be described in this paper.

DESIGN OF X-BAND LINAC

RF Cavity Structure

The developed 9.3 GHz X-band LINAC system accelerates electron beam and finally produce high energy X-rays and, the specifications are shown in Table 1. The RF cavity include 4 bunching cells, 20 accelerating cells, coupler port and vacuum port (see Fig. 1). The side coupling method is applied to distribute RF energy supplied from magnetron, which is an external RF source, to each cell inside cavity. The advantage of the side coupling method is higher acceleration efficiency per unit length, so it is possible to make the LINAC length shorter. In addition, since the cavity operate with π/2 mode which has the largest mode spacing comparing with other mode, it has advantage related to the performance and stability [1].



Figure 1: X-band RF cavity.

The total length of the RF cavity is 42 cm, which includes the flange for assembly. When 1.7 MW of RF power is supplied from the magnetron to the LINAC system, the RF loss is occurred in the coupler port and the RF module such as 4-port circulator and directional coupler, so the 1.58 MW of RF power is actually transmitted to the RF cavity. In this RF condition, the LINAC system is designed to generate the 90 mA electron beam 6.2 MeV.

Electron Gun Type

For the radiation therapy, the triode e-gun is mainly used, because it is essential to precisely control the beam current

* This research was supported by the KERI Primary Research Program of MSIT/NST (No. 18-12-N0101-42)
†yongseok@keri.re.kr
††sky@keri.re.kr

Content from this work may be used under the terms of the CC BY 3.0 licence (© 2018). Any distribution of this work must maintain attribution to the author(s), title of the work, publisher, and DOI.

ISBN: 978-3-95450-194-6 ISSN: 2226-0366 doi:10.18429/JACoW-LINAC2018-MOPO063

Content from this work may be used under the terms of the CC BY 3.0 licence (© 2018). Any distribution of this work must maintain attribution to the author(s), title of the work, publisher, and DOI.

generated by LINAC. The triode e-gun has a grid electrode in addition to the cathode and the anode. Therefore, it can regulate the amount of current emitted from the cathode by means of applying current across the heater. This means that the beam current produced from LINAC system is also regulated by grid control. The specification of the e-gun is shown in Table 1.

Table 1: Specifications of X-band LINAC

System	Parameter	Value
Cavity	Frequency	9.3 GHz
	Coupling	Side coupled
	Operating Mode	π/2
	Length	38 cm
	Material	OFHC
	Effective Shunt Impedance	116 MΩ/m
	No. of Cells	24
RF Source	Type	Magnetron
	Power Output (Peak).	1.7 MW
	Pulse Width	4 us
	Duty Cycle	0.0008
E-Gun	Type	Triode e-gun
	Cathode Voltage	18 kV
	Emission Current	350 mA

LINAC SYSTEM DEVELOPMENT

RF Cavity Manufacturing

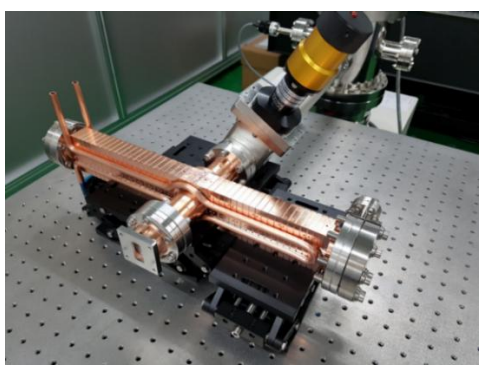


Figure 2: Fabricated RF cavity module.

To improve the accelerating efficiency inside the RF cavity, the shunt impedance should be increased. The shunt impedance is influenced by the cavity material and its geometry. Another important characteristic associated with the RF cavity is the quality factor, which is the ratio between stored energy and dissipated power in the cavity [2]. Because the quality factor also depends on the cavity material, both the choice of material for cavity fabrication and the precision of the machining is important. Therefore, we fabricated RF cavity using Oxygen free High Conductivity copper (OFHC) (see Fig. 2), which has high electrical conductivity, high thermal conductivity and relatively low secondary emission yield [3]. The surface roughness maintain less than 30 nm to reduce the RF loss and the break down inside cavity.

X-ray Target

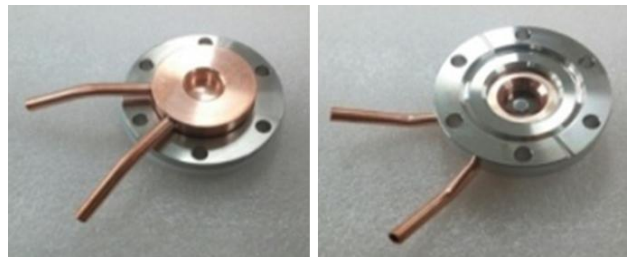


Figure 3: X-ray target for the 6 MV X-ray beam.

When a high energy electron beam bombards a metallic X-ray target, high energy X-ray is produced by the process of bremsstrahlung. The efficiency of the generation of the X-ray is determined by the geometry and the target material. The X-ray target is manufactured by tungsten which has high atomic number, high melting point and good thermal conductivity [3]. The dose rate from X-ray target depends on thickness of both the tungsten and the copper used for electron filtering. The X-ray target with a thickness of 0.87 mm for tungsten and 1.61 mm for copper is fabricated to generate the efficient 6 MV X-ray beam (see Fig. 3). The maximum dose rate that can be achieved using the manufactured X-ray target is measured to be 5 Gy. (Beam energy: 6 MeV, Beam current: 90 mA, PRF: 200 Hz, RF pulse width: 4 us, The distance from target to ion chamber: 100 cm)

Electron Beam Diagnostic System

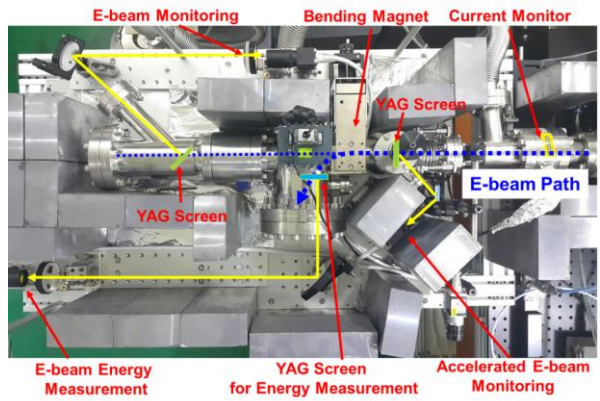


Figure 4: Beam diagnostic system.

Figure 4 shows the configuration of the developed electron beam diagnostic system. The system can measure the electron beam energy by orbit change under externally applied magnetic field from permanent magnet and measure the accelerating electron beam current by using beam current monitor. In addition, the electron beam diameter of the electron beam can be measured using a CCD camera by the visible light generated by the acceleration electron beam colliding with the YAG screen.

ISBN: 978-3-95450-194-6 ISSN: 2226-0366 doi:10.18429/JACoW-LINAC2018-MOPO063

PERFORMANCE TEST

RF Cold Test

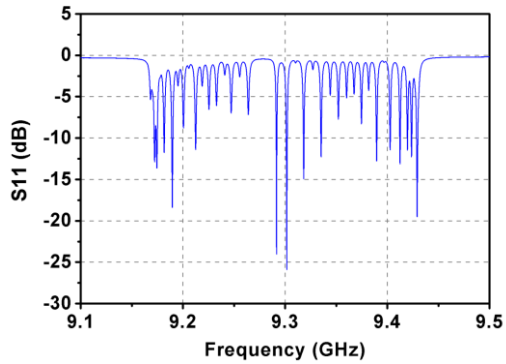


Figure 5: RF spectrum of the cavity.

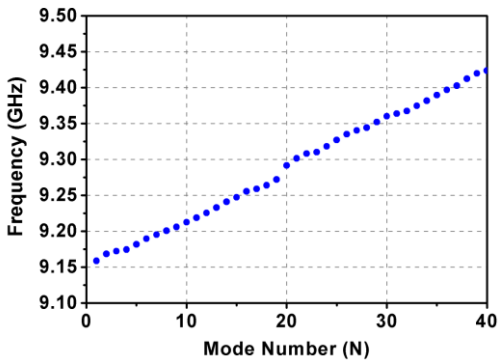


Figure 6: Dispersion curve of the cavity.

As shown in Fig. 5, the S11 parameters were measured to analyze RF resonance characteristics of the fabricated cavity after brazing process. We analyzed the existence of the stop band in the dispersion curve plot and it was confirmed that the fabricated cavity operates with the desired π/2 mode properties (see Fig. 6).

RF High Power Conditioning

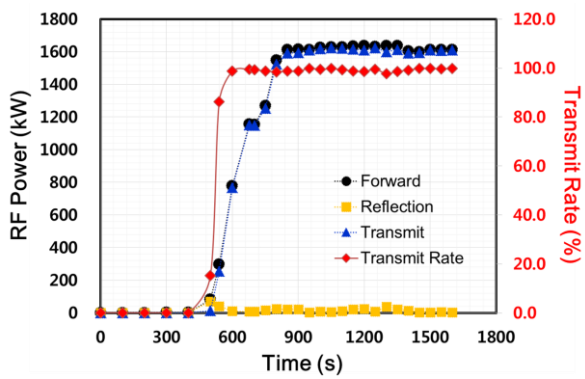


Figure 7: RF power and transmission ratio.

A newly fabricated RF cavity frequently undergoes arcing or breakdown in the high accelerating field due to the scratches or the impurities inside cavity. Therefore, it is necessary to provide RF input strength gradually from low power before supplying full RF power to LINAC. The field strength can be controlled by adjusting the pulse repetition frequency (PRF) and the pulse width. This process allows LINAC to maintain a stable state without arcing even when full RF power required for operating is supplied. The fabricated RF cavity is able to maintain the RF transmission ratio at about 95% or more (see Fig. 7).

Electron Gun Activation

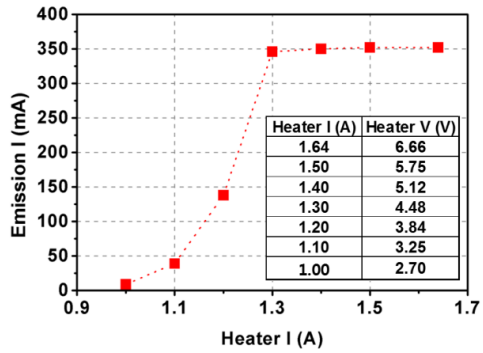


Figure 8: E-gun activation result.

The e-gun activation is the stabilization process for e-gun with emitting a steady electron flow. A fully activated e-gun has a constant emission region as shown in Fig. 8. Operating in this region after activation will allow current emit to be stable even with cathode temperature variation.

FUTURE WORKS

The recent trend related to the development of radiotherapy devices is fusion with imaging devices, so there are needs for miniaturization and weight reduction of LINAC system. Therefore, we developed 9.3 GHz X-band side coupled standing wave LINAC, and have finished the fundamental performance test. We have plan to measure the diameter, energy and beam current of the accelerated electron beam using the electron beam diagnostic system. After this process, we will perform QA processes to measure the X-ray energy, beam profile (flatness, symmetry, and penumbra) and dose rate based on the AAPM TG51, 142 Protocol.

REFERENCES

[1] U. Amaldi, S. Braccini, P. Puggioni," High Frequency Linacs for Hadrontherapy", *Rev. Accel. Sci. Technol,* vol. 2, pp. 111–131, 2009.

[2] J. Shao *et al.*, "Development of a C-band 6 MeV standing wave linear accelerator", *Phys. Rev. ST Accel. Beams*, vol. 16, p. 090102, 2013.

[3] S. Hanna, *RF Linear Accelerators for Medical and Industrial Applications*. Norwood, MA, USA: Artech House, 2012.

Content from this work may be used under the terms of the CC BY 3.0 licence (© 2018). Any distribution of this work must maintain attribution to the author(s), title of the work, publisher, and DOI.

ISBN: 978-3-95450-194-6 ISSN: 2226-0366 doi:10.18429/JACoW-LINAC2018-MOPO064

O-ARM MOUNTED X-BAND LINEAR ACCELERATOR SYSTEM FOR RADIOTHERAPY*

S. Kim†, G. J. Kim, Y. S. Lee, J. H. Lee, I. S. Kim, Y. W. Choi, and J. I. Kim‡
Medical Device Research Center, Korea Electrotechnology Research Institute, Ansan 15588, Republic of Korea
J. Hwang[1,2], A. Kim[1,2], J. Kim[1,2], J. S. Shin[1,2], Y. Seol[1,2], T. Oh[1,2], Y. Oh[2], Y. N. Kang[2,3]
[1]Department of Biomedicine & Health Sciences, The Catholic University of Korea, Seoul 06591, Republic of Korea
[2]Advanced Institute for Radiation Fusion Medical Technology, College of Medicine, The Catholic University of Korea, Seoul 06591, Republic of Korea
[3]Department of Radiation Oncology, Seoul St. Mary's Hospital, College of Medicine, The Catholic University of Korea, Seoul 06591, Republic of Korea

Abstract

Current advances in radiotherapy are based on the precise imaging techniques, and there is a pressing need for the development of techniques capable of visualizing cancer tissues in real time in conjunction with radiotherapy. Indeed, the image-guided radiotherapy systems in which conventional diagnostic tools such as CT and MRI are combined with the linear accelerator (LINAC)-based radiotherapy have been extensively studied. In this work, we mounted 9.3 GHz X-band LINAC system designed by KERI on the 360 degree-rotatable O-arm system, which allows efficient integration of a diagnostic tool with the radiotherapy equipment. After mounting, the X-ray profile and percentage depth dose were measured by following the quality assurance using the AAPM TG-51, 142 protocol. The beam profile symmetry was estimated to be 102.44% with ± 3% tolerance. The X-ray dose was also measured by rotating the O-arm gantry system to confirm the stable operation of the mounted X-band LINAC. As a result, the standard deviation of the X-ray dose was 0.016 while rotating. Therefore, we demonstrate the operational stability of our O-arm mounted X-band LINAC system for use in highly effective radiotherapy combined with simultaneous Computerized Tomography image guidance.

INTRODUCTION

Radiotherapy is preferred as a common choice in the management of patients with cancers as treatment outcomes (i.e. patients' survival or quality of life) are importantly considered. It is moving towards image-guided radiotherapy (or combined radiotherapy) that allows delivering highly precise radiotherapy with periodic image guidance before and/or during each treatment. A core technology in such radiotherapy lies with LINAC devices that generate high energy radiation required for both imaging and treatment. Although the S-band LINAC is widely used, it is not suitable for the compact radiotherapy system. On the other hand the X-band LINAC is fits into small space, thereby reducing the costs of the system [1]. The X-band LINAC system recently developed by Korea Electrotechnology Research Institute (KERI) could reduce the overall device size by about 2/3 compared to the current S-band LINAC system [2]. In this study, we developed a compact X-band LINAC system and integrated into the O-arm computed tomography (CT) diagnostic system for image guided radiotherapy. We confirmed the normal operation of the developed O-arm CT-LINAC by mechanical analysis and ensured its stability and maintainability with the optimized quality assurance (QA) tests.

O-ARM BASED X-BAND LINAC

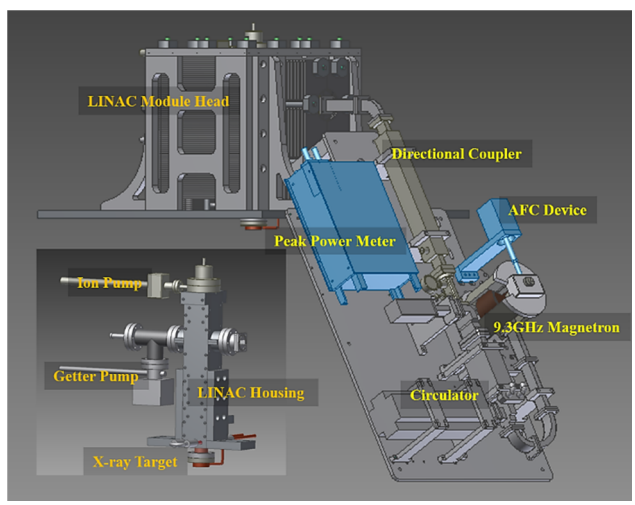


Figure 1: Compact X-band LINAC system.

Miniaturization and reduction in the weight of the LINAC are highly required for combined radiotherapy. In comparison with the 3.0 GHz S-band LINAC system, the 9.3 GHz X-band LINAC produces the same level of X-ray output while reducing the size and weight of the system. Therefore, we designed a compact LINAC system (LINAC module & RF Module) by mounting the X-band LINAC on the O-arm gantry (see Fig. 1). LINAC module consists of a triode type of the electron gun, a side-coupled structure

* Work supported by MSIT/NST (No. 16-11-N0101-06, 18-12-N0101-42)
† skim428@keri.re.kr
‡ sky@keri.re.kr

Content from this work may be used under the terms of the CC BY 3.0 licence (© 2018). Any distribution of this work must maintain attribution to the author(s), title of the work, publisher, and DOI.

ISBN: 978-3-95450-194-6 ISSN: 2226-0366 doi:10.18429/JACoW-LINAC2018-MOPO064

based X-band LINAC with 445 mm long, and a tungsten X-ray target. An ion pump and getter pump were used to maintain a high-degree vacuum when the LINAC is operated. Water cooling was used to maintain the temperature of the LINAC and X-ray target, respectively. The RF module is mainly composed of a 9.3 GHz magnetron with 1.7 MW output for stable RF supply, an AFC device to maximize the RF signal into the LINAC, a 4-port circulator for the protection of the reflected RF power, a directional coupler for the detection of the forward and backward RF signal, and a peak power meter for RF power measurement. Both the waveguide connecting the RF module and the connected components were filled with SF6 gas. Flexible and band waveguides were used to connect LINAC module and RF module in the O-arm gantry structure. All the components mentioned above are mounted in the limited space of the gantry. The LINAC housing, and RF module fixture jigs and frames were designed and fabricated to keep the position of the gantry fixed during a full 360 degree rotation. For radiation shielding, the LINAC head was constructed by filling the outside part of the housing with lead.

O-ARM CT-LINAC SYSTEM

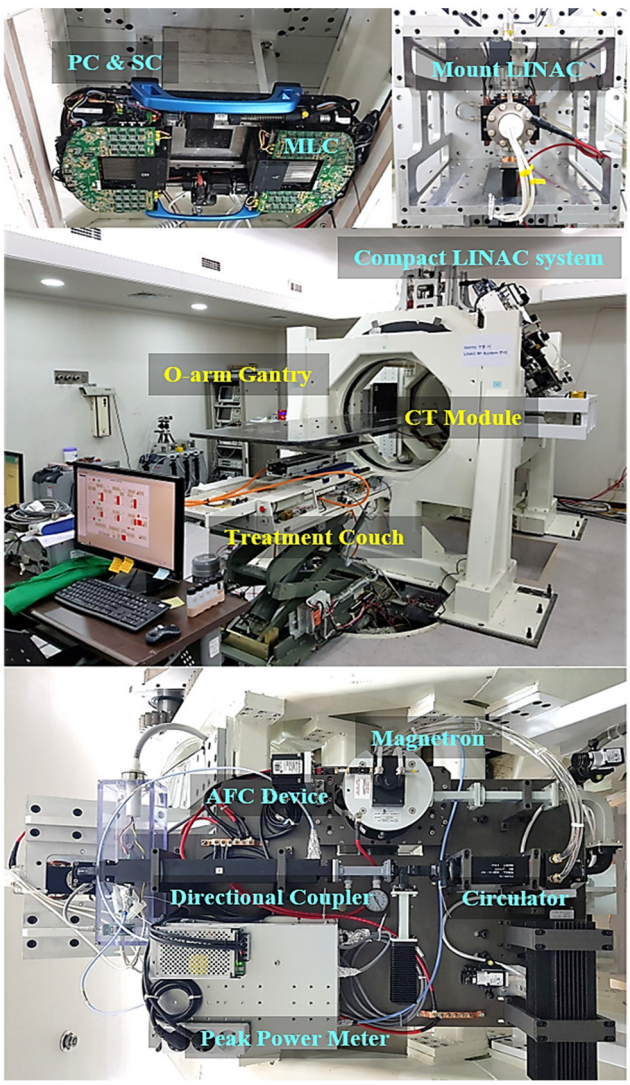


Figure 2: Combined radiotherapy with O-arm CT.

Image guidance in radiotherapy enables real-time tracking of the tumor of interest that may move out of the radiotherapy field, thereby offering potential for accurate and improved radiation treatment of cancers. The new combined radiotherapy machine that integrates compact X-band LINAC system into a medical O-arm CT system are developed [3]. Figure 2 shows the constructed compact O-arm CT-LINAC equipment. The compact LINAC module and CT imaging module are installed in the O-arm structured gantry. It is operated by the therapy integrated control system along with the treatment planning system. The X-band LINAC was mounted onto the gantry, and three collimators, including primary collimator (PC), secondary collimator (SC), and multi-leaf collimator (MLC), were installed under the X-ray target for intensity modulated radiation therapy (IMRT). The X-ray generation and MLC operation were then confirmed by exposing the MLC pattern to a Gafchromic EBT3 dosimetry film under radiation (see Fig. 3).

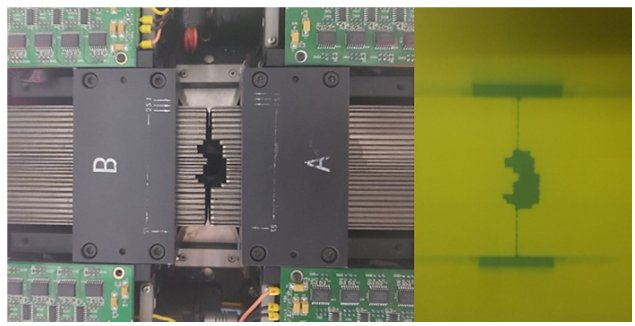


Figure 3: Image of X-ray irradiation controlled by MLC operation in the O-arm CT-LINAC system.

It is important to note that X-ray should be uniformly irradiated onto the selected area along the tumour site of patients over a 360-degree rotation of the gantry. To evaluate this, we measured the generated X-ray dose amounts at different gantry angles. Figure 4 shows relatively constant dose amounts during a full rotation with the standard deviation of the normalized doserate of 0.016.

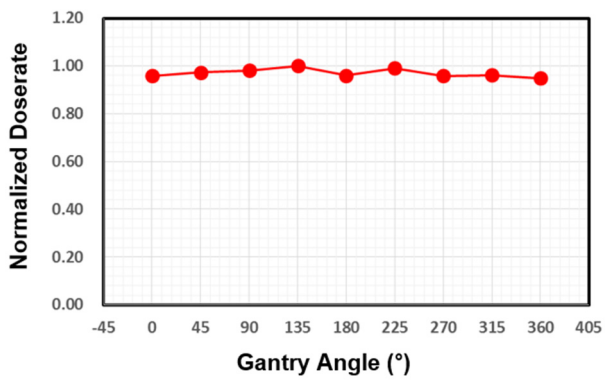


Figure 4: Dose measurement during a full rotation.

QUALITY ASSURANCE TESTS

Medical LINAC as a radiotherapy device should be carefully evaluated based on international standard protocols. In our study, we performed mechanical and dosimetry QA

Content from this work may be used under the terms of the CC BY 3.0 licence (© 2018). Any distribution of this work must maintain attribution to the author(s), title of the work, publisher, and DOI.

ISBN: 978-3-95450-194-6 ISSN: 2226-0366 doi:10.18429/JACoW-LINAC2018-MOPO064

Content from this work may be used under the terms of the CC BY 3.0 licence (© 2018). Any distribution of this work must maintain attribution to the author(s), title of the work, publisher, and DOI.

tests of our X-band LINAC using the optimized QA, based on the international standard protocol AAPM TG-51, 142, at Seoul St. Mary's Hospital. For the QA tests, we equipped the gantry with radiation measurement devices, including a 3D water phantom, an electrometer, and an ionization chamber. As shown in Fig. 5, the beam profiles along the x-axis were measured by normalizing the charge amounts at each depth to that in the center when the source-surface distance is 80 cm, and the field size is 10 cm × 10 cm. The results of the beam profile were also reported in Table. 1. We confirmed the beam profile symmetry using the standard protocols and found the tolerance was within ± 3%.

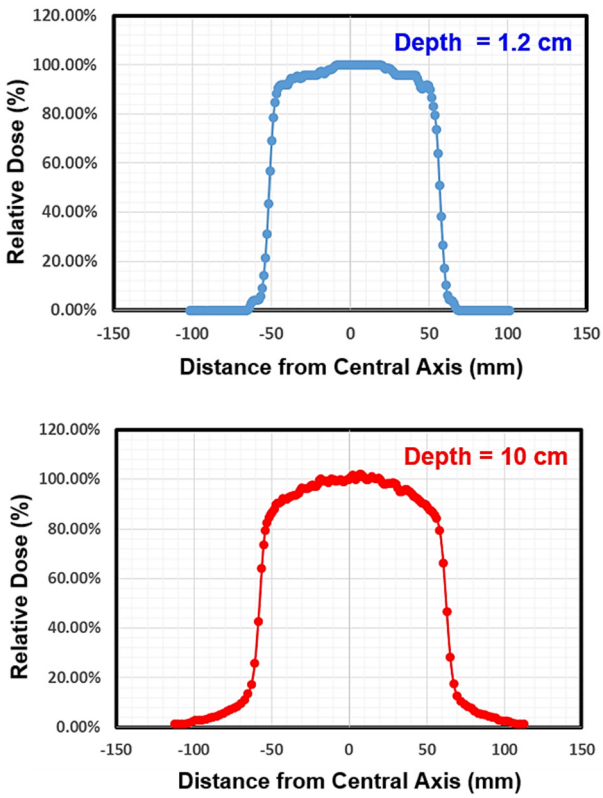


Figure 5: Beam profiles of the O-arm CT-LINAC system at different depths (1.2 and 10 cm).

Table 1: Beam Profile Results

Depth	Penumbra ^{L}	Penumbra ^{R}	Symmetry
1.2 cm	0.55 cm	0.59 cm	2.4%
10.0 cm	0.89 cm	0.93 cm	3.5%

CONCLUSIONS

O-arm mounted X-band LINAC system has been developed and tested for a compact advanced radiotherapy system. To construct this, we integrated a compact X-band LINAC into the actual O-arm CT system and ensured its stable operation. We further assessed the possible use of our system in medical radiotherapy using the optimized standard QA tests. Thus, our system allows optimal diagnosis with CT imaging and concurrent treatment with X-Band LINAC-based radiotherapy. Therefore, we envisage that this system would be utilized in the development of integrated systems for image-guided radiotherapy such as MR-LINAC, Tomotherapy, and Cyberknife [4, 5].

ACKNOWLEDGEMENTS

This research was supported by Korea Electrotechnology Research Institute (KERI) Primary research program through the National Research Council of Science & Technology (NST) funded by the Ministry of Science and ICT (MSIT) (No. 16-11-N0101-06, 18-12-N0101-42).

REFERENCES

[1] M. El-Ashmawy, "Overall quality comparison of C-band and X-band medical linacs", in *Proc. 14th Symposium on Accelerator Science and Technology*, Tsukuba, Japan, Nov 2003.

[2] D. Shin and S. G. Jeon, "Design study of X-band Linear accelerator", in *Proc. IVEC'15*, Beijing, China, Apr 2015. doi:10.1109/IVEC.2015.7223809

[3] NDSL, http://www.ndsl.kr/ndsl/commons/util/ndslOriginalView.do?dbt=TRKO&cn=TRKO201800037882&rn=&url=&pageCode=PG06

[4] Blom, J. Gerrit *et al.*, "Improving radiotherapy planning for large volume lung cancer: a dosimetric comparison between hybrid-IMRT and RapidArc", *Acta Oncol.*, vol. 54, issue. 3, p. 427, Jul. 2015. doi:10.3109/0284186X.2014.963888

[5] Adler JR Jr *et al.*, "The CyberKnife: a frameless robotic system for radiosurgery", *Stereo. Funct. Neurosurg.*, vol. 69, no. 1-4, p. 124, Jul. 1998. doi:10.1159/000099863

ISBN: 978-3-95450-194-6 ISSN: 2226-0366 doi:10.18429/JACoW-LINAC2018-MOPO066

SIMULATION OF THE TRANSITIONAL PROCESS IN ACCELERATING SECTIONS BY EQUIVALENT CIRCUIT METHOD

S. V. Matsievskiy*, V. I. Kaminskiy, Ya. V. Shashkov
National Research Nuclear University MEPhI , Moscow, Russia

Abstract

Nowadays linac accelerating RF systems design is usually done by the finite difference method. It provides high accuracy of calculations and freedom in topology choosing, but may draw considerable amounts of computer resources with long calculation times. Alternative to this method, equivalent circuit method exists. The basic idea of this method is to build a lumped element circuit, which with certain approximation acts as an original accelerating cell. It drastically reduces the number of equations to solve. This method is long known but usually only used for the particular accelerating structures when speed of calculation is a key-factor. Present paper describes a way to numerically simulate transition processes in arbitrary coupled accelerating cells using the equivalent circuit method. This approach allows simulating transitional processes in accelerating structures significantly faster and allows doing so for structures with high quality factor and many cells – a hard task for conventional transient solvers based on the finite difference method.

CALCULATION MODEL

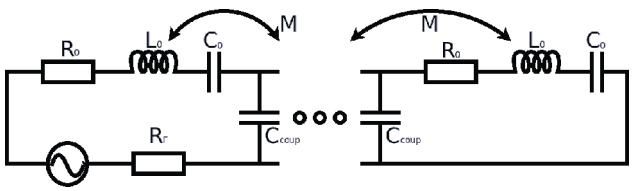


Figure 1: Equivalent circuit of the accelerating structure.

Equivalent Circuit

In Fig. 1 the equivalent circuit of the accelerating structure is presented. In it distributed parameters of the accelerating structure are substituted with the lumped elements. This circuit may be used to simulate accelerating RF structures with electric and magnetic coupling between cells. It appropriately represents structures operating on TM_{01} and TM_{11} wave modes, which covers most types of accelerating cells for the electron accelerators [1, 2]. Depending on the generator and load positions, standing and travelling wave structures may be simulated.

Usually accelerating cells are connected in serial manner but it's possible to simulate more complex connection topologies by introducing additional C_{coup} and M components between non-adjacent cells to the circuit 1.

Equations

Each circuit contour is described by the Kirchhoff Equation (1).

$$L\frac{di}{dt} + \frac{1}{C}\int idt + (R + R_G + R_L)i + \\ + \sum_{n=1}^{N} \frac{1}{C_n^{coup}} \int (i - i_n)dt + \sum_{n=1}^{N} M_n \frac{di_n}{dt} = e_n \quad (1)$$

It has been shown that for serial connected cells analytical solution of the system of Equations (1) may be presented in a recurrent form [3]. However, for the cases with more complex coupling topologies, in which the matrix of the Laplacian transformations is not tridiagonal, obtaining analytical solution may become problematic.

Solution of the system of Equations (1) may be obtained using classical or operator methods. For the operator method, numerical solution of the algebraic system of Laplacian transformations is straightforward. Several algorithms are available for the numeric calculation of the inverse Laplace transformation. In this paper the classical method of direct solution of the system of DAE equations will be described.

After substituting lumped element parameters with electrodynamic parameters and getting rid of second derivatives, equation takes the form 2.

$$\begin{cases} \frac{dx}{dt} = \hat{x} \\ \frac{d\hat{x}}{dt} + \sum_{n=1}^{N} -\frac{K_n^H}{2}\frac{f}{f_n}\frac{d\hat{x}_n}{dt} = \sum_{n=1}^{N} 2\pi^2 f^2 K_n^E x_n - \\ -(1 + \chi_G + \chi_L)\frac{2\pi f}{Q}\hat{x} + 4\pi f^2 x + \\ + \sqrt{\frac{4\chi_G P_g}{\pi f_G Q}} \cos(2\pi f_G t + \varphi) \end{cases} \quad (2)$$

Which, written in matrix form, looks like this:

$$\begin{cases} |\dot{X}| = |\hat{X}| \\ |K^H||\dot{\hat{X}}| = |K^e||g(t, \hat{x}, x)| \end{cases} \quad (3)$$

Here, $|\dot{X}|$, $|\hat{X}|$ and $|\dot{\hat{X}}|$ are the vectors of normalised amplitudes of electric field and its derivatives. $|g(t, \hat{x}, x)|$ is the vector of functions, independent of the adjacent cells parameters. $|K^H|$ and $|K^E|$ are the matrices of magnetic and electrical connection between cells respectively.

Finally, for numerical solution of the system, only derivative vectors should remain on the left part of equations.

$$\begin{cases} |\dot{X}| = |\hat{X}| \\ |\dot{\hat{X}}| = |K^H|^{-1}|K^e||g(t, \hat{x}, x)| \end{cases} \quad (4)$$

* MatsievsliySV@gmail.com

Content from this work may be used under the terms of the CC BY 3.0 licence (© 2018). Any distribution of this work must maintain attribution to the author(s), title of the work, publisher, and DOI.

ISBN: 978-3-95450-194-6 ISSN: 2226-0366 doi:10.18429/JACoW-LINAC2018-MOPO066

Content from this work may be used under the terms of the CC BY 3.0 licence (© 2018). Any distribution of this work must maintain attribution to the author(s), title of the work, publisher, and DOI.

Amplitudes of the electrical field in cells may be obtained from the normalised amplitude vector using equation:

$$U = \sqrt{\frac{\pi r_{sh} f}{2Q}} X \tag{5}$$

Implementation

Transitional solver, capable of solving systems of differential Eqs. (4) has been developed in R programming language; interface for it was implemented in form of the wab application. Base equations set is defined for the electrically and magnetically coupled cells, however, new cell types can be added.

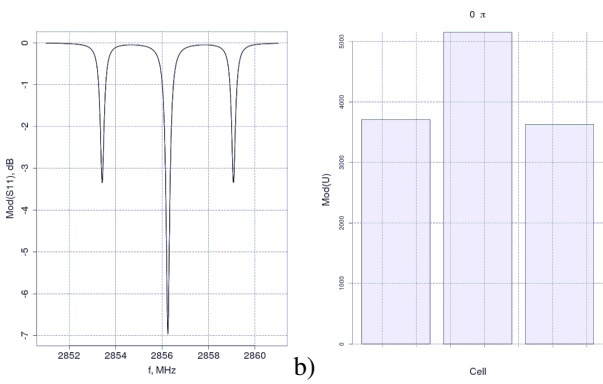
Numerical calculation of the DAE system is done using the deSolve library [4]. Its functions are implemented in Fortran, C and C++ which provides great performance even when used in context of the R language. Default method LSODA automatically switches between stiff and non-stiff systems, making solver very robust.

MODELLING

In order to test transitional solver, two sections were modelled: 3-cell standing and travelling wave structures.

Standing Wave Section

In Fig. 2 a) reflection of the 3-cell standing wave section is presented.



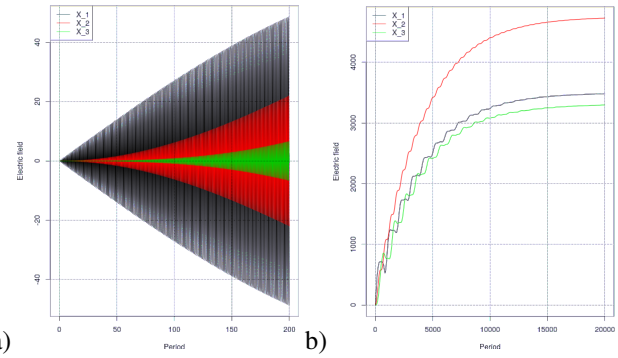
a) b)

Figure 2: Standing wave section reflection (a), mode 0 field distribution (b).

First peak in Fig. 2 a) corresponds to mode 0, static field distribution for which is shown in Fig. 2 b).

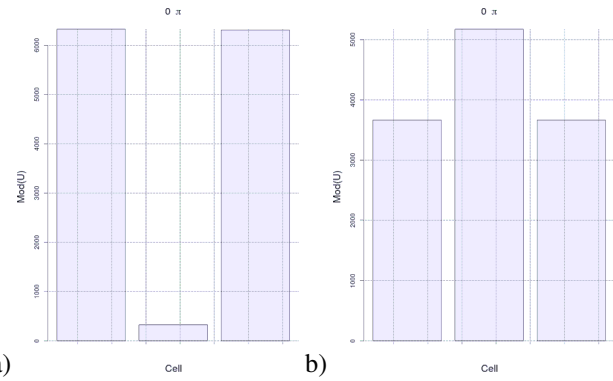
In Fig. 3 transitional process in the structure operating in mode 0 is shown. In Fig. 3 a) oscillations for the first 200 oscillation periods are shown; Fig. 3 b) only shows oscillation envelope. After the 20000 periods of oscillations it appears, that relative amplitudes in the cells are close to those, obtained by the static solver.

For the $\pi/2$ (Fig. 4 a) and π (Fig. 4 b) modes of operation transitional processes are shown in Fig. 5 a) and 5 b) respectively. Again, relative field amplitudes after the end of the transitional process appear to match those, obtained by the static solver.



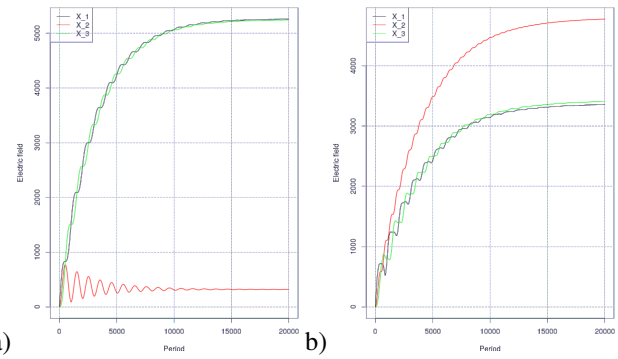
a) b)

Figure 3: Transitional process in standing wave section for 0 mode of operation.



a) b)

Figure 4: Standing wave mode $\pi/2$ (a) and π (b) field distributions.



a) b)

Figure 5: Standing wave mode $\pi/2$ (a) and π (b) transitional processes.

Table 1: Standing Wave Relative Field Amplitudes in Cells

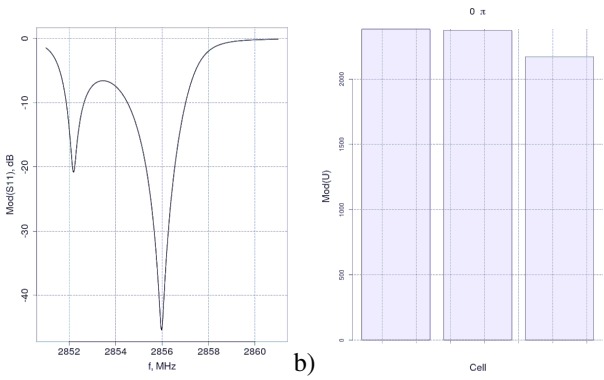
Mode	Static solver	Transitional solver
0	1.02/1.42/1	1.06/1.43/1
$\pi/2$	19.65/1/19.6	20.27/1/20.2
π	1/1.41/1	1/1.42/1.01

Relative field amplitude comparison for the standing wave section is shown in the Table 1. For the mode 0 maximum field difference is 4%, for the mode $\pi/2$ – 3% and for the mode π – 2%.

ISBN: 978-3-95450-194-6 ISSN: 2226-0366 doi:10.18429/JACoW-LINAC2018-MOPO066

Travelling Wave

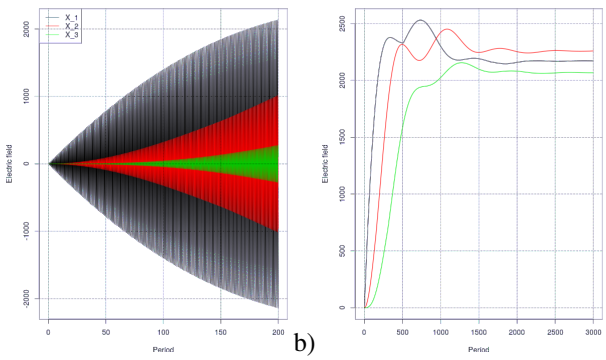
In Fig. 6 a) reflection of the 3-cell travelling wave section is presented.



a) b)

Figure 6: Travelling wave section reflection (a), mode $2\pi/3$ field distribution (b).

Second peak in Fig. 6 a) corresponds to mode $2\pi/3$. Static field distribution for this mode is shown in Fig. 6 b). In Fig. 7 the transitional process for this mode is shown.



a) b)

Figure 7: Travelling wave section reflection (a), mode $2\pi/3$ field distribution (b).

Table 2: Travelling Wave Relative Field Amplitudes in Cells

Mode	Static solver	Transitional solver
$2\pi/3$	1.1/1.09/1	1.05/1.09/1

Relative field amplitude comparison for the travelling wave section is shown in the Table 2. For the mode $2\pi/3$ maximum field difference is 5%.

CONCLUSION

Calculation of the transitional processes using the equivalent circuit method was discussed in this paper. One of the possible approaches to this problem – direct solution of the system of DAE – was described. Calculations of the standing wave and travelling wave sections were presented. Maximum field difference between static and transitional solvers is 4% for the standing wave section and 5% for the travelling wave section.

ACKNOWLEDGEMENTS

The collective of authors would like to thank N.P. Sobenin for the useful discussion of the work and its results.

REFERENCES

[1] V. Kaluzny, O. Kaluzny, A. Y. Smirnov, and O. A. Adonev, "Linear accelerator and deflector rf section analysis and optimization with the equivalent cirquit scheme," *Journal of Technical Physics*, vol. 87, no. 7, pp. 101–109, 2014, ISSN: 0044-4642.

[2] V. Kaluzny, "Analysis of dlw accelerating structures with equivalent scheme," *Engineering physics*, no. 3, pp. 27–37, 2006.

[3] V. Kaluzny and O. Kaluzny, "Transitional process analisys in multicell cavities with electrical and magnetic coupling," *Engineering physics*, no. 3, pp. 46–59, 2008.

[4] K. Soetaert, T. Petzoldt, and R. W. Setzer, "Solving differential equations in R: Package deSolve," *Journal of Statistical Software*, vol. 33, no. 9, pp. 1–25, 2010, ISSN: 1548-7660. DOI: 10.18637/jss.v033.i09. http://www.jstatsoft.org/v33/i09

Content from this work may be used under the terms of the CC BY 3.0 licence (© 2018). Any distribution of this work must maintain attribution to the author(s), title of the work, publisher, and DOI.

ISBN: 978-3-95450-194-6 ISSN: 2226-0366 doi:10.18429/JACoW-LINAC2018-MOPO069

NUCLEAR AND MECHANICAL BASIC DESIGN OF TARGET FOR Mo-99 PRODUCTION USING HIGH POWER ELECTRON LINAC

H. Khalafi, Atomic Energy Organization of Iran (AEOI), Thran, Iran
A. T. Khotbeh-Sara†, F. Rahmani, Department of Physics, K. N. Toosi University of Technology, Thran, Iran
M. M. Kejani, F. Ghasemi, Nuclear Science and Technology Research Institute (NSTRI), Thran, Iran

Abstract

Today providing enough supplies of ^{99m}Tc / ^{99}Mo as a most applicable radioisotope in diagnostic nuclear medicine for the world demand is an important challenge. One of the proofed ways to access reliable source of this radioisotopes is the production using e-Linac [1]. In this investigation it has been tried to find the simple and the optimized design of ^{99}Mo production target based on photoneutron reaction using e- Linac. Based on the Monte-Carlo calculation for radiation transport and finite element thermal analysis, 9 thin plates of enriched ^{100}Mo has been suggested. Equal distance between plates has been considered for cooling to prevent target melting. The main target includes only ^{100}Mo in one-stage approach method to increase production rate in comparison with two-stage approach [2]. Applying 2.5 m/s for inlet velocity of cooling water provides suitable cooling process with maximum temperature of target about 900 ˚C.

INTRODUCTION

The most widely used diagnostic radioisotope in clinical practice of nuclear medicine is ^{99m}Tc, which covering 35 million diagnostic imaging process annually [3]. Its short half-life limits the distribution process to long distances, so suppliers generally try to produce ^{99}Mo, which transforms into ^{99m}Tc nucleus in β decay mode ($t_{1/2}$= 66 h).

Production of ^{99}Mo using e-Linac is a common method with two main approaches. Two-stage approach is a general method (W target as a photon converter and ^{100}Mo as a photoneutron target). In one-stage approach, the Mo target is electron-photon converter as well as the photoneutron target simultaneously, so self-absorption of photons in electron-photon converter will be prevented and produced photons participate directly in photoneutron reactions. In this study, the one-stage approach has been selected.

The maximum cross section of ^{99}Mo production reaction is on 14 MeV and by considering of logarithmic bremsstrahlung spectrum, the beam with energies between 30 to 45 MeV is desired. So 30 MeV e-beam has been selected for irradiation the target. It should be mentioned that this energy is edge of commercial high power e-Linacs abilities [4].

The different geometries for target has been investigated that reported in ref. [5]. According to it, the hemispherical target is efficient than other geometries. But due to the thermal and mechanical challenges in construction, it is decided to use simplest geometry. To achieve better results of cooling, the scanning e-beam on long ^{100}Mo plates has been considered.

NUCLEAR SIMULATION

Molybdenum is a dense metal that can be used as an electron-photon converter. Of course the photon flux of molybdenum is not as high as the produced photon flux in tungsten, but in two-stage approach, some portion of photons are absorbed in tungsten before they can be able to participate in photoneutron reaction in ^{100}Mo target. So using ^{100}Mo target as an electron-photon converter and an isotope production target simultaneously, resolves this problem.

The peak forward direction of bremsstrahlung photons are in the limited conical shape area [2], but since these photons creation happen rarely in the angles of 0, 90 and 180 degrees (relative to e-beam direction), photons population is minimum in these areas. Figure 1 shows the distribution of particles in volume of massive cylindrical target.

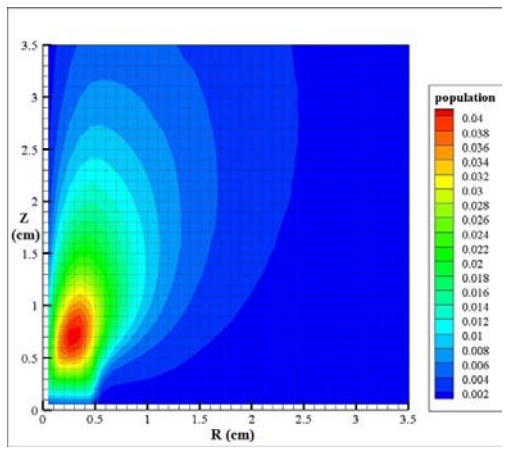


Figure 1: Distribution of photons population in volume unit of each mesh, per one incident electron.

In ^{100}Mo(γ,n)^{99}Mo reaction, the created photoneutrons during this reaction, is corresponded with produced ^{99}Mo. So the photoneutron production rate is equal to ^{99}Mo production rate. The distribution of neutrons population is shown in Fig. 2.

† khotbesara@email.kntu.ac.ir

Content from this work may be used under the terms of the CC BY 3.0 licence (© 2018). Any distribution of this work must maintain attribution to the author(s), title of the work, publisher, and DOI.

ISBN: 978-3-95450-194-6 ISSN: 2226-0366 doi:10.18429/JACoW-LINAC2018-MOPO069

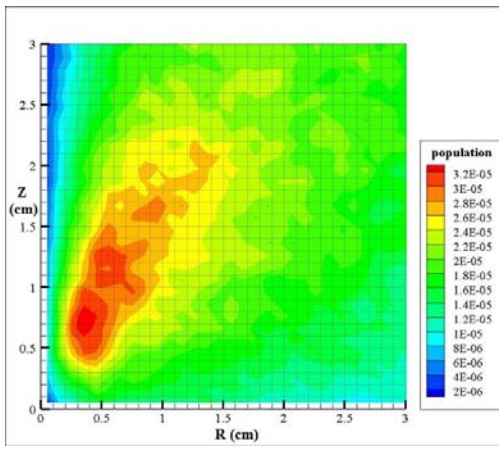


Figure 2: Distribution of photoneutrons population in volume unit of each mesh, per one incident electron.

From Fig. 2, the optimized dimension has been obtained about 1.5 cm in radius and 1.8 cm in thickness. But to decreasing heat flux, it has been decided to apply beam scan system on the long metal target (Fig. 3). The target has been divided to 9 plates (gray sections in Fig. 3) by thickness of 0.2 cm, and 0.2 cm free space between each plate. Also to avoid contacting of water and plates (because of corrosion), the copper clamps (brown sections in Fig. 3) has been considered as water cooling pipes.

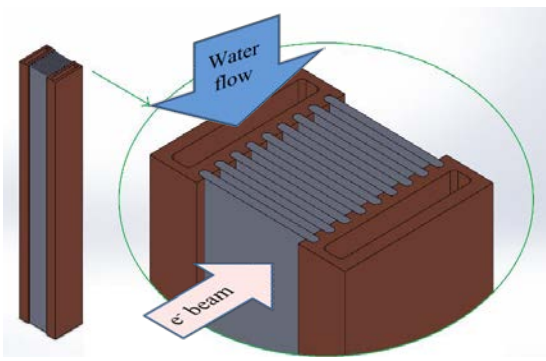


Figure 3 : Schematic view of target and cooling ducts.

THERMAL CALCULATION AND COOLING SYSTEM DESIGN

Based on Newton's law of cooling, Eq. 1, the heat transfer coefficient is related to heat transfer rate [6].

$$Q=h.A.(T_w-T_\infty) \quad (1)$$

where Q is the heat transfer rate (W), A is the cross-sectional area (m^2), h is the heat transfer coefficient ($W/m^2.K$), T_w is the object's surface temperature and T_∞ is the fluid temperature (K). According to heat transfer coefficient changes in corresponding by flow regime, the turbulent flow is a desired regime [6]. Therefore the Reynolds number (Eq. 2), has been considered more than 10000 to be sure about the regime type (turbulent) [7].

$$Re = \rho v D_H/\mu \quad (2)$$

where ρ is the fluid density (kg/m^3), μ is the dynamic viscosity of the fluid (kg/m.s), D_H is the hydraulic diameter (m) and v is the velocity of the fluid (m/s).

Finite Element Analysis

Melting point of molybdenum and copper is 2623 and 1085 ˚C, respectively. It should be noted the temperature must keep low enough to avoid recrystallization of target [8]. During recrystallization, cracks, surface roughening, and swelling may occur and affect the mechanical and thermal properties of the material. Recrystallization happens at 50-70% of the melting point temperature [9]. So the assurance temperature of target has been considered 1300 ˚C.

First, a target with 5 cm height has been simulated by Fluent software. The deposited energy of the target plates is shown in table 1 (for 1mA current at 30 MeV of continues e-beam). The related temperature distribution is shown in Fig. 4.

Table 1: The Deposited Energy in Target

^{100}Mo plates	Energy (MeV)
Plate 1	2.867
Plate 2	3.619
Plate 3	4.013
Plate 4	3.598
Plate 5	2.752
Plate 6	1.637
Plate 7	0.856
Plate 8	0.508
Plate 9	0.369

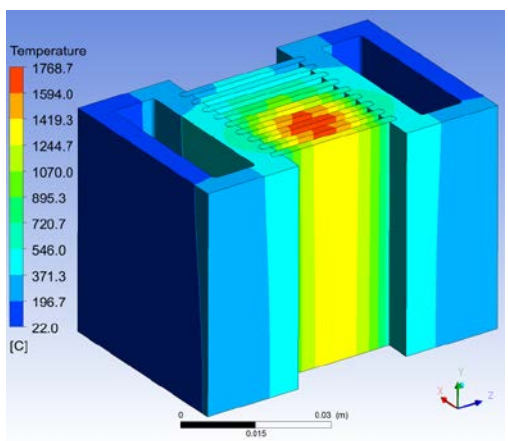


Figure 4: The temperature distribution in target with 5 cm in height ($D_H = 15.65 \times 10^{-3}$ m, v = 2.5 m/s).

In this case, the maximum temperature of target is more than 1700 ° C that clearly exceeds the assurance temperature. For the next step, a target with 10 cm in height has been tested. Figure 5 shows the related temperature distribution as well as Fig. 6 shows the water temperature profile.

Content from this work may be used under the terms of the CC BY 3.0 licence (© 2018). Any distribution of this work must maintain attribution to the author(s), title of the work, publisher, and DOI.

ISBN: 978-3-95450-194-6 ISSN: 2226-0366 doi:10.18429/JACoW-LINAC2018-MOPO069

Content from this work may be used under the terms of the CC BY 3.0 licence (© 2018). Any distribution of this work must maintain attribution to the author(s), title of the work, publisher, and DOI.

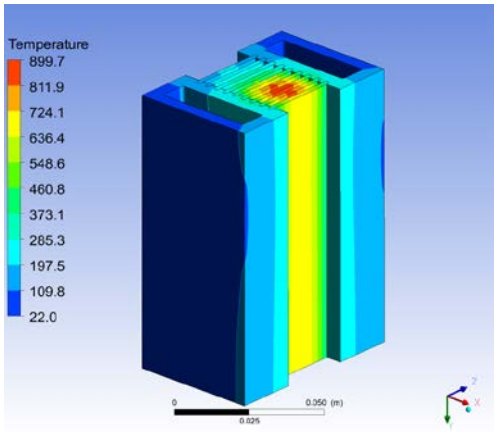


Figure 5: The temperature distribution in target with 10 cm in height ($D_H = 15.65 \times 10^{-3}$ m, v = 2.5 m/s).

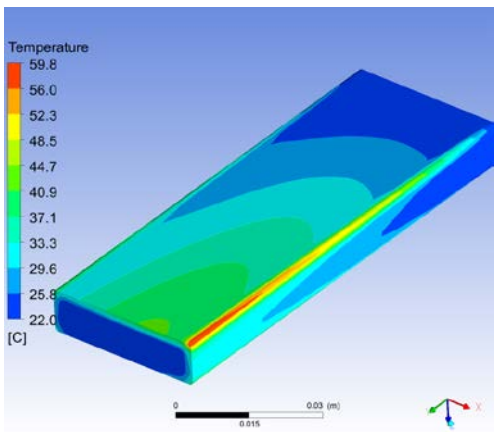


Figure 6: The water temperature profile in target with 10 cm in height.

As shown in Fig. 5, the maximum temperature is about 900 ˚C, which is below than assurance temperature. Also Fig. 6 illustrates that the maximum temperate of water does not exceed 60 ˚C.

CONCLUSION

In this investigation, simulation of ^{99}Mo production target based on using e-Linac has been performed, also the appropriate cooling system has been designed as well.

Molybdenum-99 production system including 9 ^{100}Mo plates with 3 cm in width, 10 cm in height and 0.2 cm in thickness has been designed. The reaction rate for such target is about 1.24×10^{13} event per second (for 1mA current at 30 MeV of continues e-beam). Also two copper ducts with internal cross section of 3.6 cm × 1 cm have been considered for cooling tube and target clamps. By applying 2.5 m/s of inlet velocity for cooling water, the maximum temperature will be about 900 ˚C. Therefore, the designed cooling system performance is acceptable.

REFERENCES

[1] Bennett, R.G *et al.*, "A System of 99mTc Production Based on Distributed Electron Accelerators and Thermal Separation" *Nuclear Technology*, 1999. 126(1): p. 102-121.

[2] A. Tsechanski *et al.*, "Electron accelerator-based production of molybdenum-99: Bremsstrahlung and photoneutron generation from molybdenum vs. tungsten", *Nuclear Instruments and Methods in Physics Research Section B*: Beam Interactions with Materials and Atoms, 366: p. 124-139, 2016.

[3] Report on the 1st Research Coordination Meeting on "New Ways of Producing ^{99m}Tc and ^{99m}Tc Generators", coordinated by the IAEA.

[4] "High power linacs for isotope production", MEVEX Company Brochure.
http://www.testmevex.com/wp-content/uploads

[5] A. T. Khotbeh-Sara *et al.*, "Optimization Study on Production of Mo-99 Using High Power Electron Accelerator Linac", in *Proc. 8th Int. Particle Accelerator Conf. (IPAC'17)*, Copenhagen, Denmark, May 2017, pp. 4667-4668, ISBN: 978-3-95450-182-3. doi:10.18429/JACoW-IPAC2017-THPVA089

[6] Bergman ,T.L. and F.P. Incropera, *Fundamentals of heat and mass transfer*. 2011: John Wiley & Sons.

[7] Robert W. Fox, Alan T. McDonald, Philip J. Pritchard, *Introduction to Fluid Mechanics*, John Wiley & Sons Inc.

[8] R. D. Doherty *et al*., "Current issues in recrystallization: a review," *Mater. Sci. Eng.* 238, 219-274 (1997)

[9] Stefania Trovati *et al*., "Thermal limits on MV x-ray production by bremsstrahlung targets in the context of novel linear accelerators", *American Association of Physicists in Medicine.* (2017)

ISBN: 978-3-95450-194-6 ISSN: 2226-0366 doi:10.18429/JACoW-LINAC2018-MOPO070

CONSTRUCTION OF THE SIDE-COUPLED STANDING-WAVE e-LINAC

S. Zarei, F. Ghasemi†, Nuclear Science and Technology Research Institute (NSTRI), Tehran, Iran
M. Lamehi Rachti, M. Bahrami, Iranian Light Source Facility (IPM), Tehran, Iran
F. Abbasi Davani, Shahid Beheshti University, Tehran, Iran

Abstract

Due to Iran's growing need for accelerators in various applications, NSTRI electron linear accelerator project has been defined for medical and inspection applications. This accelerator is a 6 MeV side-coupled standing-wave that operate is π /2 mode in the frequency of 2998.5 MHz.

In this paper the construction and measurement results of the tube of this accelerator are presented. The prototype tube was constructed from aluminum and was clamped with bolts. By using a network analyzer, electric and magnetic probes and a side-coupled cavity tuning method and a bead-pull measurement technique, RF measurements were carried out. The resonant frequency and quality factor have been achieved 2998.5 MHz and 7940 respectively

INTRODUCTION

In Iran, a project has been started in Nuclear Science and Technology Research Institute to build an electron linear accelerator for medical and inspection applications.

For this accelerator, a side-coupled standing-wave accelerating tube was selected that the main specifications of it are given in Table 1 and also a layout of it is given in Fig. 1.

Table 1: The Desirable Tube Specifications

Parameters	Value
RF frequency	2998.5 MHz
Input beam energy	30 keV
Output beam energy	6 MeV
Operating mode	π/2
Maximum RF power	2.6 MW

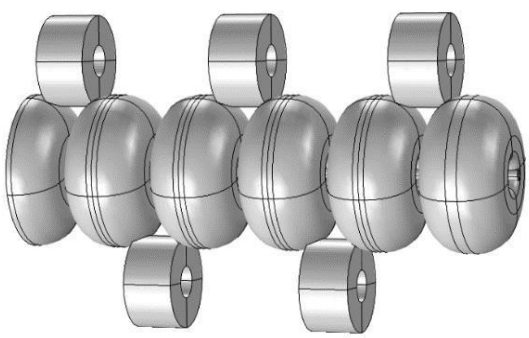


Figure 1: The layout of the entire accelerating tube.

Electromagnetic design, beam dynamics studies and thermal and mechanical simulations of the tube have been carried out by using COMSOL [1], ASTRA [2] and ANSYS [3] respectively [4-6]. After the design was completed, construction and RF measurement of the porotype aluminum tube carried out that the results of them are presented in this paper.

CONSTRUCTION

The design of the tube has been carried out and the mechanical drawings of the tube have been prepared, then each cavity of the tube was machined and polished. The exploded view drawing of the prototype tube is shown in Fig. 2.

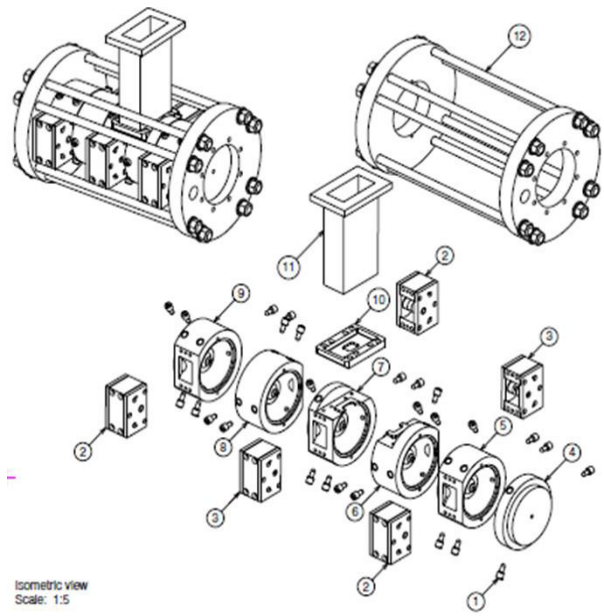


Figure 2: The exploded view drawing of the entire tube.

The first prototype tube was built from aluminium. The cavities were machined and polished and the bolts clamp the cavities in place. We have created six holes on the accelerating cavities wall and one hole on the coupling cavities wall for frequency tuning. The constructed tube is shown in Fig. 3.

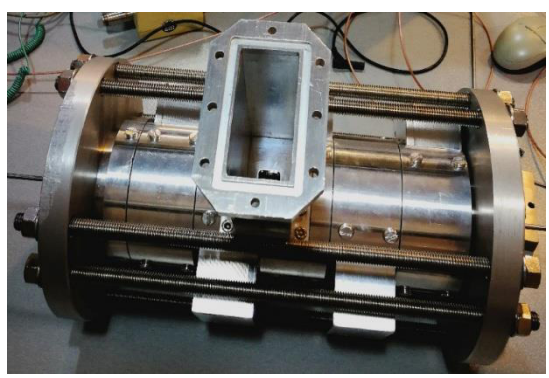


Figure 3: The constructed tube.

Content from this work may be used under the terms of the CC BY 3.0 licence (© 2018). Any distribution of this work must maintain attribution to the author(s), title of the work, publisher, and DOI.

ISBN: 978-3-95450-194-6 ISSN: 2226-0366 doi:10.18429/JACoW-LINAC2018-MOPO070

Content from this work may be used under the terms of the CC BY 3.0 licence (© 2018). Any distribution of this work must maintain attribution to the author(s), title of the work, publisher, and DOI.

MEASURMENT

After frequency tuning of the tube, the resonant frequency and quality factor of the constructed tube were measured by using a network analyzer (VNA). To tune the frequency of the cavities and measure the RF properties of the tube, methods discussed in reference [7] have been applied. The resonant frequency of the accelerating and coupling cavities after the frequency tuning is shown in Table 2. As shown each accelerating and side cavity individually resonating at 2998.5±0.1 MHz.

The resonant frequency and quality factor of the tube are represented in Table 3. As shown in Table 3 the measured resonant frequency is equal to the predicted value from simulation, but the measured quality factor is about 62 % of the predicted values from simulation.

Table 2: The Accelerating and Coupling Cavities Frequency (MHz)

accelerating	frequency	coupling	frequency
AC1	2998.6	**SC1**	2998.4
AC2	2998.4	**SC2**	2998.5
AC3	2998.4	**SC3**	2998.4
AC4	2998.6	**SC4**	2998.5
AC5	2998.4	**SC5**	2998.5
AC6	2998.5		

Table 3: RF Properties by Measurement and Simulation

Parameters	simulation	measurement
Frequency	2998.5 MHz	2998.5 MHz
Quality factor	12930	7940

In RF test, S11 reflection spectrum results of VNA for the entire tube for two frequency ranges were obtained that are shown in Fig. 4.

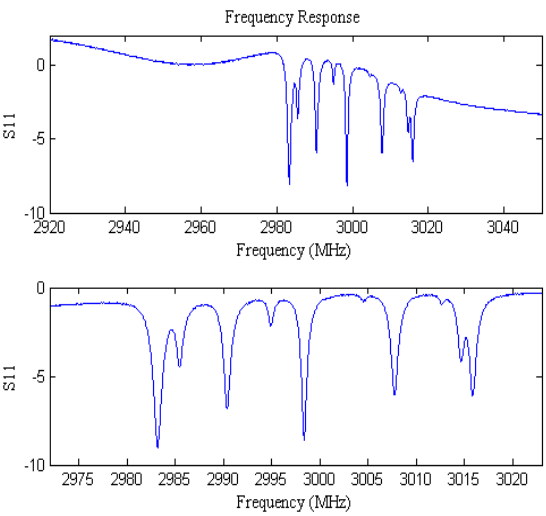


Figure 4: S11 reflection spectrum of the tube.

The bead-pull measurement system is a device that determining the relative amplitude of the electric field generated inside the tube by measuring the magnitude of change in the resonant frequency while a small bead moves through the tube [8].

The axial field profile by bead pull measurement results of VNA before and after frequency tuning and the simulated electric field profile along the tube axis are represented in Fig. 5, Fig. 6 and Fig. 7 respectively. As shown in Fig. 6 and Fig. 7, the RF field peak in the first half accelerating cavity (buncher cavity) is smaller than in the other accelerating cavities and we obtain a good agreement between the simulated and the measured electric field. But as shown in Fig. 5 axial electric field before tuning is not suitable and frequency tuning is required.

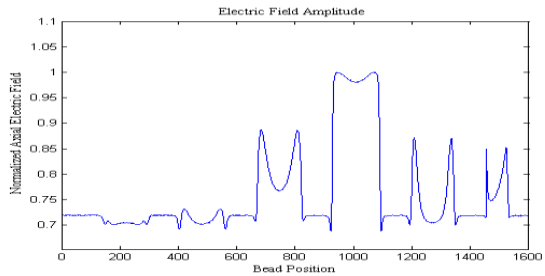


Figure 5: The measured axial electric field profile before frequency tuning.

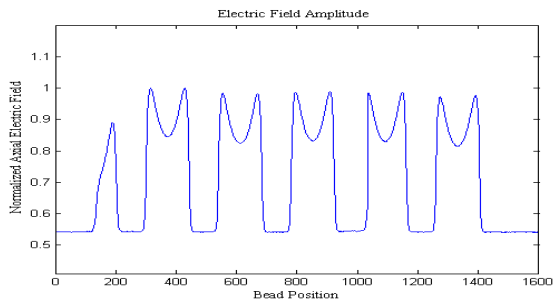


Figure 6: The measured axial electric field profile after frequency tuning.

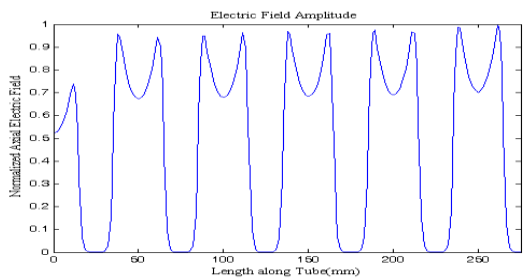


Figure 7: The simulated axial electric field profile.

The resonant frequencies plotted against the phase shifts per cavity produce a dispersion curve (Fig. 9) that was compared to the simulated curve from COMSOL (Fig. 8). Although the center frequency of both curves is equal to 2998.5 MHz, but Fig. 8 shows 11 frequencies against the phase shifts per cavity and Fig. 9 shows 10 frequencies against the phase shifts per cavity. This difference is due to that "0" mode has great loss and the

ISBN: 978-3-95450-194-6 ISSN: 2226-0366 doi:10.18429/JACoW-LINAC2018-MOPO070

peak of this mode disappears in the measurement reflection spectrum.

Because the "0" mode is not the designed operation mode of the tube, this imperfection does not affect the π/2 mode operation.

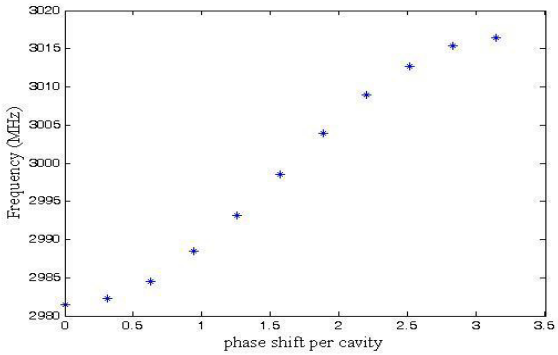


Figure 8: The simulated dispersion curves.

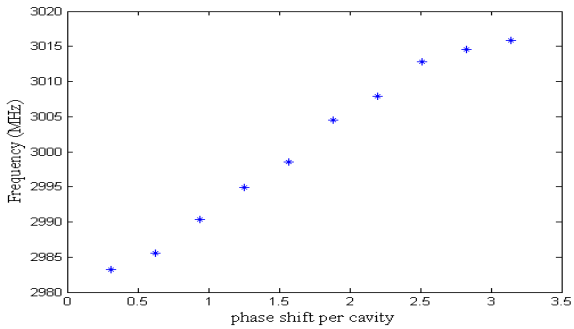


Figure 9: The measured dispersion curves.

CONCLUSION

Because of Iran's need to develop the application of accelerators in medicine, environment, cargo inspection, physics researches and industries, the design and construction of low and medium energy accelerators was started. In this regard, the project of design and construction of the 6 MeV e-linac for medical and cargo inspection application was defined. For the desired accelerator, a side coupled standing wave tube was selected to resonate at the frequency of 2998.5 MHz in π/2 mode.

The design stage of the accelerating tube was done and the prototype tube was constructed from aluminium and RF measurement was carried out. The constructed tube resonated at the frequency of 2998.5 MHz in π/2 mode and a good agreement between the measured and the predicted field distribution (by simulation) was obtained.

ACKNOWLEDGEMENTS

The authors wish to acknowledge the guidance and support of IPM researchers for providing many helpful comments during measurements.

REFERENCES

[1] COMSOL, https://www.comsol.com

[2] ASTRA, http://www.desy.de/mpyflo

[3] ANSYS, http:// www.ansys.com/Products

[4] S. Zarei *et al.*, "Design of a side coupled standing wave accelerating tube for NSTRI e-Linac", *JINST*, vol. 12, p. 09026, Sep. 2017, doi: 10.1088/1748-0221/12/09/P09026

[5] S. Zarei, S. Ahmadidannamin, M. Lamehi, F. Ghasemi and F. Abbasi, "Beam dynamics studies of an accelerating tube for 6 MeV electron Linac", in *Proc. IPAC'17*, Copenhagen, Denmark, May 2017, pp. 4657-4659. doi:10.18429/JACoW-IPAC2017-THPVA086

[6] M. Mohseni Kejani, F. Abbasi, S. Ahmadidannamin, F. Ghasemi and S. Zarei, "Thermal and Mechanical Analysis of 3 GHz Side Coupled RF Cavity for Medical Linacs", in *Proc. IPAC'17*, Copenhagen, Denmark, May 2017, pp. 4660-4663. doi:10.18429/JACoW-IPAC2017-THPVA087

[7] G. Benguang, CH. Xiuqi, Y. Junqi and F. Jianian, "A Tuning Method for Side coupled standing Wave Accelerating Tubes", *Nucl. Instr. Meth.*, vol. 261, pp. 339-342, 1987.

[8] P. Schmuser., "Tuning of multi-cell cavities using Bead Pull Measurements", SRF920925-10, 1992,

Content from this work may be used under the terms of the CC BY 3.0 licence (© 2018). Any distribution of this work must maintain attribution to the author(s), title of the work, publisher, and DOI.

ISBN: 978-3-95450-194-6 ISSN: 2226-0366 doi:10.18429/JACoW-LINAC2018-MOPO073

COHERENT EDGE RADIATION SOURCES IN LINAC-BASED INFRARED FREE-ELECTRON LASER FACILITIES

N. Sei†, H. Ogawa, Research Institute for Measurement and Analytical Instrumentation, National Institute of Advanced Industrial Science and Technology, 1-1-1 Umezono, Tsukuba, Ibaraki 305-8568, Japan
T. Tanaka, Y. Hayakawa, T. Sakai, Y. Sumitomo, K. Hayakawa, K. Nogami, Laboratory for Electron Beam Research and Application, Nihon University, 7-24-1 Narashinodai, Funabashi, 274-8501, Japan.
H. Ohgaki, H. Zen, Institute of Advanced Energy, Kyoto University, Gokasho, Uji, Kyoto 611-0011, Japan

Abstract

National Institute of Advanced Industrial Science and Technology has been studied far-infrared coherent radiation at Linac-based infrared free-electron laser (FEL) facilities in collabo-ration with Nihon University and Kyoto University. Generally, it is possible to extract information about the electron bunch by observing the coherent radiation. To clarify the relationship between the FEL interaction and the coherent radiation, we developed coherent edge radiation, from which the bunch length could be evaluated, in FEL straight sections.

INTRODUCTION

In order to oscillate an FEL, it is necessary to estimate characteristics of an electron beam in a straight section in which an undulator is installed. The bunch length of the electron beam related to the electron density is a significant parameter which characterizes behavior of the FEL. The bunch length influences not only the gain but also the pulse width of the FEL and the cavity-length detuning curve [1]. Observing the behavior of the bunch length in the straight section with the undulator is useful for understanding the FEL physics.

Observations of spectra of coherent radiation generated by the electron bunch are suitable for monitoring the bunch length of a short-pulse electron beam. However, FEL pulses exist on the electron-beam orbit in the straight section with the undulator. A target for transition radiation cannot be inserted into the straight section. Hence, the transition radiation cannot be used to generate coherent radiation. The usage of synchrotron radiation is unlikely because the radiation power becomes week away from the axis of the electron-beam orbit. Diffraction radiation can be extracted for the spectral measurement without losing the FEL oscillations. However, the spectrum of the diffraction radiation depends on the aperture diameter of the diffraction element. Because it is necessary to enlarge the aperture for long-wavelength FELs, conditions in which the diffraction radiation can be applied for a bunch length measurement are limited. Therefore, we used the coherent edge radiation (CER) generated by the downstream bending magnet in the FEL straight section. Because edge radiation has an annular shape distribution as the asymmetric first-order Laguerre-Gaussian (LG_{01}) mode [2], the CER can be extracted from the optical cavity without a diffraction loss of the FEL beam. In the terahertz (THz) region, where the edge radiation becomes coherent, the intensity of the edge radiation is much higher than that of the synchrotron radiation. In this paper, CER sources at Kyoto University Free Electron Laser (KU-FEL) [3] and at Laboratory for Electron Beam Research and Application (LEBRA) in Nihon University [4] are discussed.

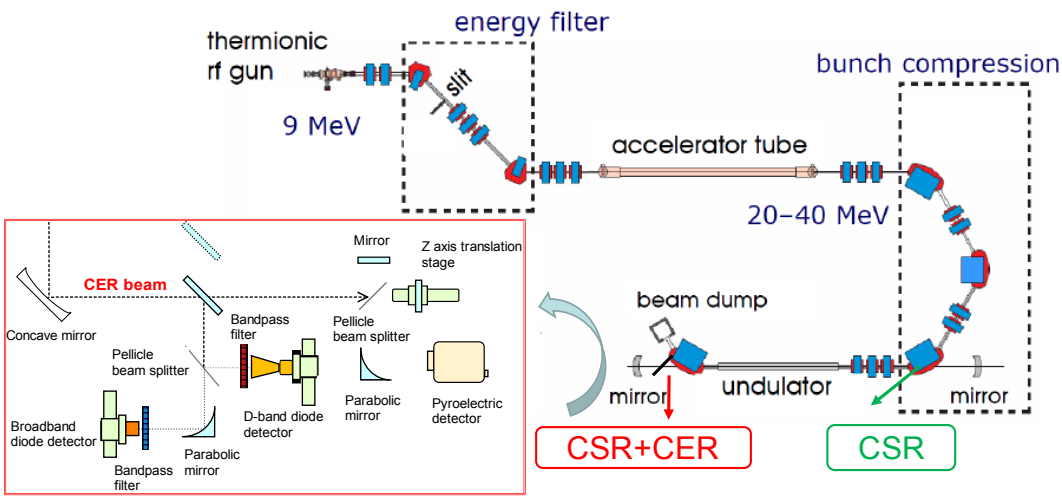


Figure 1: Schematic layout of the CER source and the measurement system at KU-FEL.

Content from this work may be used under the terms of the CC BY 3.0 licence (© 2018). Any distribution of this work must maintain attribution to the author(s), title of the work, publisher, and DOI.

ISBN: 978-3-95450-194-6 ISSN: 2226-0366 doi:10.18429/JACoW-LINAC2018-MOPO073

COHERENT EDGE RADIATION SOURCE AT KU-FEL

KU-FEL consists of an S-band 4.5-cell thermionic RF gun, an energy filtering dog-leg section, a 3 m accelerator tube, a 180° arc section, and a 1.8-m hybrid planner undulator with the number of periods of 52. The maximum energy of the electron is 40 MeV and the maximum duration of the electron-beam macropulse is approximately 8 μs. The charge of the micropulse increases from 20 to 50 pC due to back-bombardment effects on the thermionic RF gun [3]. The root-mean-square (RMS) bunch length of the electron beam was designed to be 1 ps or less in the FEL straight section using the magnetic compression of the 180° arc section. The tunable range of the FEL wavelength is from 3.5 to 23 μm.

Coherent synchrotron radiation (CSR) was observed at the upstream bending magnet in the straight section [5]. The angle between the CSR beam and the straight section was 30°. Because the solid angle to pass CSR without impinging a vacuum pipe was as large as 0.10 rad, the measured CSR energy was 55 μJ per macropulse of the electron beam. The RMS bunch length evaluated from the measured CSR spectrum was approximately 1.4 ps. The electron bunch was not sufficiently compressed, so that it was necessary to measure the bunch length in the straight section.

We, therefore, observed the CER at the downstream bending magnet in the straight section. Figure 1 shows a schematic layout of the CER source at KU-FEL. The CER beam was extracted from the optical cavity by inserting a deflection mirror tilted by 45° to the optical axis in the horizontal plane. The effective area of the deflection mirror that was projected onto the plane perpendicular to the optical axis was 20 mm square. The distance from the light source of the downstream bending magnet to the deflection mirror was 0.56 m. The electron beam generated the intense CER at the upstream and downstream bending magnets. However, because the inner sizes of the rectangular undulator vacuum duct were only 11 mm in horizontal and 56 mm in vertical direction, the CER generated at the upstream bending magnet in the THz region did not directly arrive at the deflection mirror. Generally, the electron beam also generated the CER at both ends of an undulator. However, regarding the undulator at KU-FEL, the magnetic field was designed to gradually disappear at the ends of the undulator in order to avoid a walkoff of the electron-beam trajectory. The magnetic field at the end of the undulator was much lower than that at the bending magnet. Then, it was expected that only the CER generated at the downstream bending magnet was observed as a THz-wave beam.

The profile of the THz beam was observed by a pyroelectric THz camera in air. The electron-beam energy was 28 MeV and the macropulse duration was 7μs. The profile measured with a polytetrafluoroethylene lens had a hollow structure resembling the LG_{01} mode with the asymmetric intensity in horizontal direction, and it roughly agreed with the calculated CER profile at the deflection mirror. Then, it was confirmed that the observed THz beam was the CER beam generated at the downstream bending magnet. The power of the THz-wave beam was evaluated to be 0.10 mW considering the sensitivity of the THz camera.

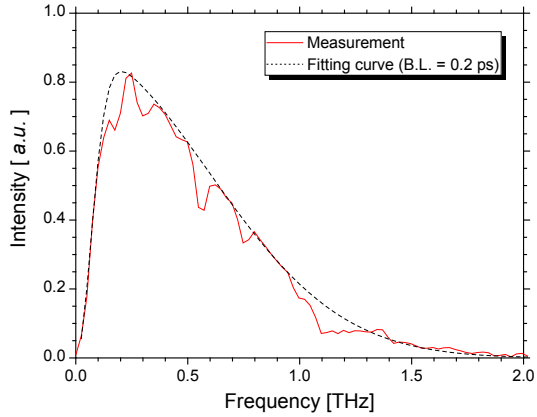


Figure 2: Spectrum of the CER beam at KU-FEL.

CER spectra were measured by using a Michelson-type interferometer. Figure 2 shows the CER spectrum in the operation condition that the FEL output power was maximized. The RMS bunch length evaluated from the measured CER spectrum was approximately 0.2 ps, so that it was clarified that the electron bunch was sufficiently compressed. Because a rectangular mirror was used to extract the CER beam from the optical cavity as the deflection mirror, the measurement of RMS bunch length was impossible on FEL oscillations. A mirror having a hole-coupled structure can solve this problem. We planned to use a hollow mirror at LEBRA.

COHERENT EDGE RADIATION SOURCE AT LEBRA

The S-band linac at LEBRA consists of a 100 keV DC electron gun, prebuncher, buncher, and three 4 m long traveling wave accelerator tubes [4]. The electron-beam energy can be adjusted from 30 to 125 MeV, and the charge in a micropulse is approximately 30 pC in full-bunch mode, where the electron beam is bunched in 350-

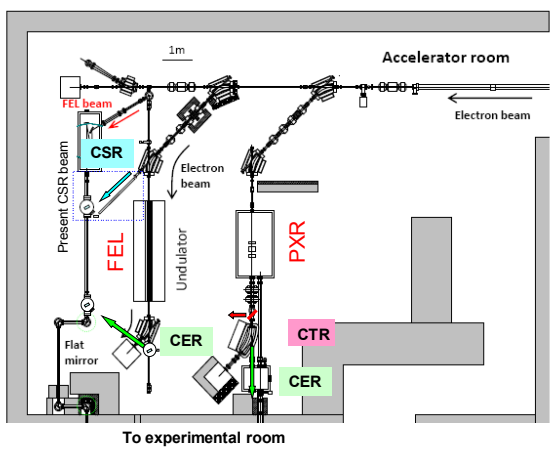


Figure 3: Coherent radiation sources at LEBRA.

Content from this work may be used under the terms of the CC BY 3.0 licence (© 2018). Any distribution of this work must maintain attribution to the author(s), title of the work, publisher, and DOI.

ISBN: 978-3-95450-194-6 ISSN: 2226-0366 doi:10.18429/JACoW-LINAC2018-MOPO073

Content from this work may be used under the terms of the CC BY 3.0 licence (© 2018). Any distribution of this work must maintain attribution to the author(s), title of the work, publisher, and DOI.

ps intervals. The accelerated electron beam is allocated to two straight sections by bending magnets. Each straight section is used for the infrared FEL and parametric X-ray radiation (PXR). The schematic layout of LEBRA is shown in Fig. 3. The electron beam is guided to an FEL straight section by two 45° bending magnets. The insertion device is a 2.4-m planar undulator with a maximum K value of 1.9. The length of the undulator period and number of the periods are 48 mm and 50, respectively. Mirror chambers, each containing a metal mirror, are set at the ends of the FEL straight section. The mirrors are 6.72 m apart. Fundamental FELs oscillate at wavelengths of 1–6 μm.

A few coherent radiation sources have been developed at LEBRA. In the FEL straight section, CSR generated at the entrance of the second 45° bending magnet was observed [6], and it was transported to the experimental room using the FEL beamline [7]. Because the electron bunch was not sufficiently compressed, the measured CSR energy was as low as 1 μJ per macropulse of the electron beam. Then, a thin titanium screen was installed instead of an alumina fluorescent plate used for the profile monitor in the PXR straight section, and coherent transition radiation (CTR) source was developed. The measured CTR energy was as high as 1 mJ per macropulse [8]. Moreover, the CTR beam was transported to the experimental room using the PXR beamline and was applied to imaging experiments on biological samples in the THz region. A CER beam generated at the downstream bending magnet was observed in the PXR straight section. The RMS bunch length evaluated from the CER spectrum was approximately 0.2 ps, and it was expected that the electron bunch was also compressed to the same length even in the FEL straight section.

To investigate effects of the FEL interaction on the electron bunch in the FEL straight section, a deflection mirror system was inserted between the downstream bending magnet and the downstream optical cavity mirror. This mirror system can switch with a hole-coupled concave mirror or a normal concave mirror and without the mirrors under remote control. The effective diameter of the mirrors was 60 mm and the inner diameter of the hole was 25 mm. Considering the inner shape of the downstream bending magnet chamber, the extraction efficiency for the CER was approximately 30% for the hole-coupled concave mirror and 60% for the normal concave mirror in the electron-beam energy of 57 MeV. By using the hole-coupled concave mirror, we succeeded in observing the CER on FEL oscillations for the first time. Figure 4 shows the CER power extracted to the air with the hole-coupled concave mirror at the electron-beam energy of 57 MeV. The measured power was 0.35 mW at the macropulse duration of 18 μs and the macropulse repetition of 2 Hz. The wavelength of the FEL was 5.4 μm and the FEL macropulse energy measured was 1.5 mJ in the experimental room. The RMS bunch length evaluated from the measured CER spectrum was 0.2 ps or less. It was confirmed that the FEL energy was higher as the bunch length was shorter even if the bunch length was shorter than the slippage length under the perfect synchronism of the optical cavity. We plan to measure the correlation between the CER spectrum and the evolution of the FEL macropulse.

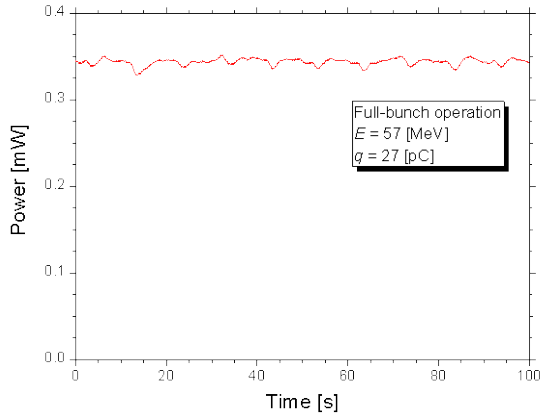


Figure 4: Measured CER power on FEL oscillations.

CONCLUSION

Intense CER sources have been developed at the FEL facilities KU-FEL and LEBRA. Despite using the small mirror to extract the CER beam from the optical cavity at KU-FEL, the output power of the CER beam was 0.10 mW in air. The RMS bunch length evaluated from the measured CER spectrum was approximately 0.2 ps, so that it was clarified that the electron bunch was sufficiently compressed. At LEBRA, the hole-coupled mirror was used to extract the CER beam from the optical cavity. The CER was observed on FEL oscillations for the first time. We will study influence of FEL oscillations on the electron bunch by measuring the CER with the constructed observation system in addition to a new development of coherent Cherenkov radiation [9].

APPENDIX

This work has been supported under the ZE Research Program ZE30B-12, the Visiting Researchers Program of Kyoto University Research Reactor Institute 30025, and JSPS KAKENHI Grant Number JP16H03912.

REFERENCES

[1] G. Dattoli *et al.*, *Nucl. Instrum. Methods Phys. Res., A*, 285 (1989) 108.
[2] O. Grimm, *TESLA-FEL Report*, 2008-05 (2008).
[3] H. Ohgaki, *Jpn J. Appl. Phys.*, 47 (2008) 8091.
[4] T. Tanaka *et al.*, *Nucl. Instrum. Methods Phys. Res., A*, 528 (2004) 486.
[5] N. Sei *et al.*, *Nucl. Instrum. Methods Phys. Res., A*, 832 (2016) 206.
[6] N. Sei *et al.*, *J. Phys. D: Appl. Phys.*, 46 (2013) 045104.
[7] N. Sei *et al.*, *J. Opt Soc. Am B*, 31 (2014) 2150.
[8] N. Sei *et al.*, *Jpn J. Appl. Phys.*, 56 (2017) 032401.
[9] N. Sei *et al.*, *Sci. Rep.*, 7 (2017) 17440.

ISBN: 978-3-95450-194-6 ISSN: 2226-0366 doi:10.18429/JACoW-LINAC2018-MOPO076

STUDY ON GENERATION OF VARIABLE POLARIZED COHERENT THz RADIATION USING A CROSSED UNDULATOR

Hirotoshi Saito†, Hiroyuki Hama, Fujio Hinode, Ken Kanomata, Shigeru Kashiwagi, Sadao Miura, Toshiya Muto, Ikurou Nagasawa, Ken-ichi Nanbu, Shingo Ninomiya, Ken Takahashi, Research Center for Electron Photon Science, Tohoku University, Sendai, Japan

Abstract

A variable polarized THz radiation source using a crossed undulator system has been developed at Tohoku University. In this scheme, two coherent undulator radiations from an extremely short electron bunch are used to control the polarization. They are linearly polarized radiations orthogonal to each other. Polarization of superimposed radiation is controlled by adjusting a relative phase between them. A compact planar undulator with seven periods has been designed for an experiment at our facility. The radiation frequency is 2.06 THz for electron beam energy of 22 MeV. The opening angle of the crossed undulator radiation was estimated to be 34 mrad (FWHM). Since the polarization state of the crossed undulator depends on observation angle, its angular dependence was evaluated. It was found that ideal polarization control is realized only in the angle range of 2.5 mrad, which is quite smaller than that of the radiation itself.

INTRODUCTION

Coherent THz light sources based on an accelerator have been developed at Research Center for Electron Photon Science, Tohoku University. A test accelerator called t-ACTS (test Accelerator as Coherent THz Source) has been constructed for generating coherent THz radiation from an extremely short electron bunch. It consists of a thermionic rf gun, an alpha magnet with an energy filter and 3 m long accelerating structure. An electron bunch is compressed down to shorter than 100 fs by means of a velocity bunching scheme in the traveling wave accelerating structure. Coherent transition radiation of a frequency range up to about 4 THz and coherent undulator radiation from 2.6 to 3.6 THz have been successfully observed [1].

At present, we are considering a variable polarized THz light source using a crossed undulator system. In order to carry out a demonstration experiment of its polarization control at t-ACTS, design consideration of the crossed undulator system and an investigation of its polarization properties are underway.

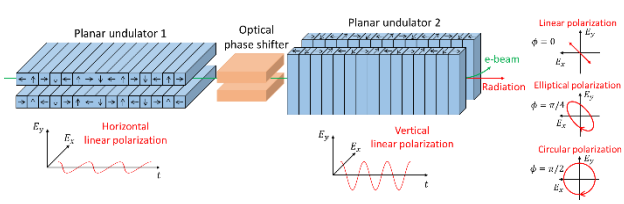


Figure 1: Concept of a crossed undulator.

† hsaito@lns.tohoku.ac.jp

CONCEPT OF A CROSSED UNDULATOR

Concept of the crossed undulator system is shown in Fig. 1. It consists of two planar undulators and an optical phase shifter between them. The undulators are arranged so that polarization direction of each radiation is orthogonal. Two linearly polarized coherent radiations are generated from an extremely short electron bunch passing through the undulators. They are superimposed both spatially and temporally by delaying the first radiation in the optical phase shifter using mirrors. Polarization is controlled by changing the optical path length in the phase shifter and adjusting phase difference between the two radiations.

PLANAR UNDULATOR

In order to carry out a demonstration experiment, the crossed undulator system must be designed considering some constrains and beam conditions at t-ACTS. Total length of each planar undulator must be shorter than 1 m because of a constraint of the experimental space. Radiation frequency must be lower than 3 THz because of beam conditions of the bunch compression mode of t-ACTS, namely, the electron energy of 22 MeV and the bunch length of approximately 80 fs. A planar undulator was designed taking these requirements into account. The undulator parameters are shown in Table 1. Block dimensions 60 mm, 30 mm and 20 mm are width, height and thickness, respectively.

Electric field radiated from an electric charge q is calculated from the Lienard-Wiechert potential. Its radiation field term is expressed as [2]

$$\vec{E}(\vec{r},t) = \frac{q}{4\pi\varepsilon_0}\left[\frac{\vec{n}\times\left\{(\vec{n}-\vec{\beta})\times\dot{\vec{\beta}}\right\}}{Rc\left(1-\vec{n}\cdot\vec{\beta}\right)^3}\right]_{\mathrm{ret}}, \qquad (1)$$

where ε_0 is the dielectric constant of vacuum, R the observation distance, c the speed of light, $\vec{\beta}$ the velocity vector normalized by c and $\vec{n}$ the unit vector in the observation direction. The bracket $[\ ]_{\mathrm{ret}}$ denotes that values inside it are evaluated at the retarded time. A frequency spectrum of the radiation field can be calculated by the Fourier transformation.

Angular distribution of the undulator radiation can be derived by changing observation point and calculating radiation field Eq. (1) emitted from an electron passing through the magnetic field in the undulator. The angular spread is 34 mrad in the x direction (the electron oscillation direction) and 96 mrad in the y direction in FWHM.

Content from this work may be used under the terms of the CC BY 3.0 licence (© 2018). Any distribution of this work must maintain attribution to the author(s), title of the work, publisher, and DOI.

ISBN: 978-3-95450-194-6 ISSN: 2226-0366 doi:10.18429/JACoW-LINAC2018-MOPO076

Content from this work may be used under the terms of the CC BY 3.0 licence (© 2018). Any distribution of this work must maintain attribution to the author(s), title of the work, publisher, and DOI.

Table 1: Undulator Parameters

Magnet material	Sm_2Co_{17}
Residual magnetic field	1.09 T
Magnet array type	Halbach array
Block dimension	60 mm, 30 mm, 20 mm
Period length	80 mm
Number of periods	7
Gap	33 mm
Peak magnetic field	0.454 T
K value	3.39
Fundamental frequency	2.06 THz (E=22 MeV)

It should be considered that the angular spread of the crossed undulator radiation is the narrower one, 34 mrad because two undulators are arranged orthogonally.

POLARIZATION

Consideration on Angular Dependence

Phase difference of the two undulator radiations is determined by difference between path lengths from each undulator to an observation point. However, the path length difference depends on observation angle. In addition, wavelength of undulator radiation also depends on observation angle. Therefore polarization of crossed undulator radiation has dependence on observation angle.

Consider a simple layout of the crossed undulator (Fig. 2). L_1 is a distance between the center of each undulator and L_2 is a distance from the center of the second undulator to an observation plane. θ_1 and θ_2 are observation angles from undulator U_1 and U_2, respectively. R_1 and R_2 are observation distances from each undulator. Path length difference at an observation angle θ is expressed as

$$R_1 - R_2 = \frac{L_1 + L_2}{\cos\theta_1} - \frac{L_2}{\cos\theta_2}. \tag{2}$$

Subtracting the path length difference at $\theta = 0$, namely, L_1, the difference $L_\delta(\theta)$ can be given by

$$L_\delta(\theta) = \frac{L_1(1-\cos\theta_1)}{\cos\theta_1} + L_2\left(\frac{1}{\cos\theta_1} - \frac{1}{\cos\theta_2}\right). \tag{3}$$

Note that θ_1 and θ_2 are functions of θ. Path length difference becomes larger by this L_δ at an observation angle θ than that on the axis ($\theta = 0$). On the other hand, angular dependence of wavelength of undulator radiation is

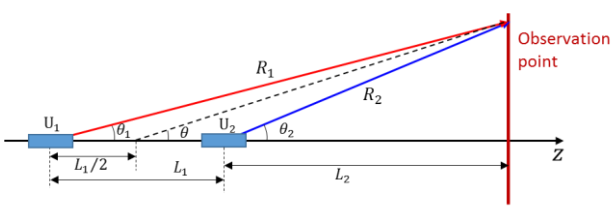


Figure 2: Schematic layout of two undulators and observation plane.

known to be expressed as

$$\lambda(\theta) = \frac{\lambda_u}{2\gamma^2}\left(1 + \frac{K^2}{2} + \gamma^2\theta^2\right), \tag{4}$$

where λ_u is period length of an undulator, γ the Lorentz factor of an electron, θ observation angle and K a deflecting parameter of the undulator.

Figure 3 shows calculation results of Eqs. (3) and (4) when L_1 = 2.59 m and L_2 = 4.0 m. The range of the horizontal axis corresponds to the angular spread of the crossed undulator radiation.

Since the wavelength shift is about 8 % ($\lambda(0)$ = 146 μm and λ(17 mrad) = 157 μm), the phase difference in the front of light doesn't change largely even if θ changes. However, the phase difference differs by about $0.6\lambda_r$ (λ_r denotes wavelength on the axis) between the front and rear of the seven cycle light because $|\lambda(\theta_1) - \lambda(\theta_2)|$ = 13 μm. Therefore polarization change caused by this wavelength shift cannot be ignored. On the other hand, L_δ becomes nearly λ_r at 11 mrad and $2\lambda_r$ at 15 mrad, so that the influence on polarization is about three to four times larger than that of wavelength shift. Therefore the polarization largely changes in the range of the radiation angle mainly because of the shift L_δ.

Evaluation of Angular Dependence

Employing Stokes parameters (see APPENDIX), the polarization of the crossed undulator radiation was evaluated. Undulator radiations were assumed to be monochromatic and linearly polarized seven cycle lights, whose electric fields were sinusoidal as follows,

$$\begin{aligned} E_x(t) &= E_{0x}(t)e^{i(k_x(\theta)z - \omega_x(\theta)t)}, \\ E_y(t) &= E_{0y}(t)e^{i\left(k_y(\theta)z - \omega_y(\theta)t + \delta(\theta)\right)}, \end{aligned} \tag{5}$$

where E_x (horizontal polarization) denotes the first undulator radiation and E_y (vertical polarization) the second one. k and ω are wave number and angular frequency, respectively, which were calculated taking the angular dependence into account. E_{0x} and E_{0y} were set to zero in the external time range of seven cycles. δ is phase difference between two radiations. It was evaluated as follows assuming the angular dependence $L_\delta(\theta)$ (Eq. (3)) and $\lambda(\theta)$ (Eq. (4)):

$$\begin{aligned} \delta(\theta) &= \delta_0 + \delta_1(\theta), \\ \delta_1(\theta) &\equiv -\frac{2\pi L_\delta(\theta)}{\lambda_y(\theta)}, \end{aligned} \tag{6}$$

where δ_0 denotes a phase difference on the axis. Radiation intensity I_0, I_1, I_2 and I_3 can be calculated by integrating the square of each polarization component of the electric field Eq. (5). Stokes parameters can be derived from the values of intensity.

Figure 4 shows a calculated angular dependence of degree of circular polarization P_C (defined as S_3/S_0). Conditions were as follows: L_1 = 2.59 m, L_2 = 4 m, $\delta_0 = \pi/2$ and

ISBN: 978-3-95450-194-6 ISSN: 2226-0366 doi:10.18429/JACoW-LINAC2018-MOPO076

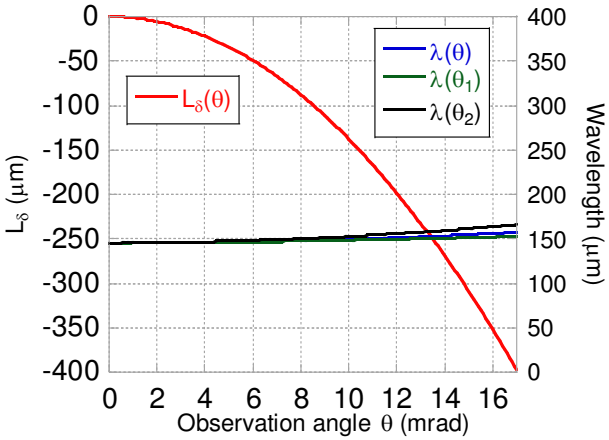


Figure 3: Angular dependence of L_δ and λ.

$E_{0x} = E_{0y}$. Wavelength of undulator radiation was calculated assuming parameters of Table 1. The red line and the green line denote P_C and intensity distribution of the single undulator radiation in the x direction, respectively. As the observation angle becomes larger, the phase difference changes in the positive direction and take the value of $+2\pi$ at approximately 11 mrad. Radiation with P_C larger than 0.9 is obtained in the angular range narrower than approximately 2.5 mrad, which is about 15% of the angular spread of the radiation. It was found from the result that ideal polarization control of the crossed undulator radiation can be realized only in the narrower angle range than its angular spread.

CONCLUSION

A vaiable polarized THz light source using a crossed undulator system has been developed at Tohoku University. A compact planar undulator was designed forthe demonstration experiment : the period length is 80 mm, the number of periods seven, the K value 3.39 and the fundamental freqency 2.06 THz (for the enectron energy of 22 MeV). The angular spread of the crossed undulator radiation is 34 mrad in FWHM. Polarization of the crossed undulator radiation depends on observation angle mainly because of angular dependence of path length of each undulator radiation. The angular dependence of degree of polarization was evaluated assuming sinusoidal radiation fields. It was found from the result that ideal polarization control can be realized only in the angle range of smaller than 2.5 mrad, which is narrower than that of the radiation itself.

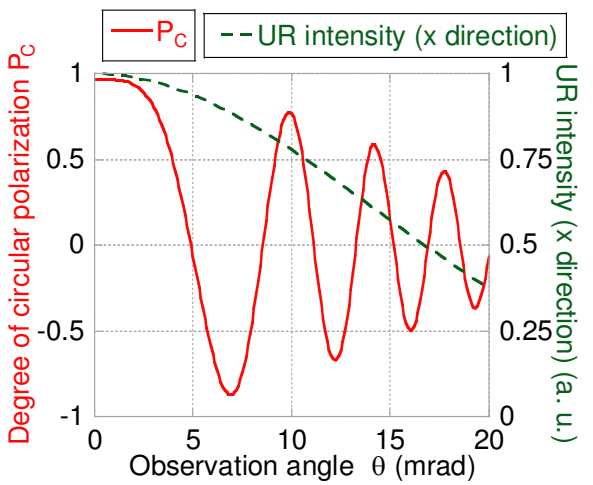


Figure 4: Angular dependence of degree of circular polarization.

ACKNOWLEDGEMENTS

This work was supported by JSPS KAKENHI Grant Number JP17H01070 and JP15K13401.

APPENDIX

The Stokes Parameters [3, 4]

The Stokes parameters are four observable quantities introduced by Stokes in 1852, which have dimensions of intensity of an electric wave. The polarization state of radiation can be practically described by these quantities. They are operationally defined by using a set of four filters F_1, F_2, F_3 and F_4. Each has a transmittance of 0.5 for incident unpolarised light. Suppose that F_1 is isotropic irrespective of the polarization. F_2 and F_3 are linear polarizers whose transmission axes are horizontal and at +45°, respectively. F_4 is a circular polarizer opaque to left polarization. Supposing that I_1, I_2, I_3 and I_4 are intensity of the transmitted light passing through only one filter F_1, F_2, F_3 and F_4, respectively, Stokes parameters are defined as

$$\begin{aligned} S_0 &= 2I_0, \\ S_1 &= 2I_1 - 2I_0, \\ S_2 &= 2I_2 - 2I_0, \\ S_3 &= 2I_3 - 2I_0. \end{aligned} \tag{7}$$

S_0 is the total intensity of the incident light. S_1 reflects a tendency for the polarization to resemble either horizontal linear one ($S_1 > 0$), vertical linear one ($S_1 < 0$) or neither ($S_1 = 0$). Similarly, S_2 reflects a tendency for the light to resemble +45° linear polarization ($S_2 > 0$), -45° linear one ($S_2 < 0$) or neither ($S_2 = 0$). S_3 indicates a tendency for the polarization toward right-handedness ($S_3 > 0$), left-handedness ($S_3 < 0$) or neither ($S_3 = 0$).

REFFERENCES

[1] T. Abe, "Study of the coherent radiation in THz region generated by an extremely short electron beam", Master's thesis, Phys. Dept., Tohoku University, Japan, 2017.

[2] J. D. Jackson, *Classical Electrodynamics*. Third Edition, John Wiley & Sons, Inc., 1998.

[3] W. A. Shurcliff, *Polarization Light: Production and Use*. Cambridge, MA, USA: Harvard University Press, 1962.

[4] E. Hecht, Optics. Fourth Edition, Addison-Wesley, 2001.

Content from this work may be used under the terms of the CC BY 3.0 licence (© 2018). Any distribution of this work must maintain attribution to the author(s), title of the work, publisher, and DOI.

ISBN: 978-3-95450-194-6 ISSN: 2226-0366 doi:10.18429/JACoW-LINAC2018-MOPO077

DESIGN OF THE HIGH GRADIENT NEGATIVE HARMONIC STRUCTURE FOR COMPACT ION THERAPY LINAC*

S.V. Kutsaev[1], R. Agustsson[1], A. Barcikowski[2], R. Fischer[2],
B. Mustapha[2], A.Yu. Smirnov[1], A. Verma[1],
[1]RadiaBeam Systems, LLC, Santa Monica, CA, 90404, USA
[2]Argonne National Laboratory, Lemont, IL, 60439, USA

Abstract

A novel concept for an Advanced Compact Carbon Ion Linac (ACCIL) that will deliver up to 1 pnA of carbon ions with variable energy from 45 MeV/u to 450 MeV/u in a 45m footprint, has been developed by Argonne National Laboratory (ANL) in collaboration with RadiaBeam. The ACCIL will have a 35 MV/m real-estate accelerating gradients that became possible to achieve with the development of novel S-band high-gradient structures, capable of providing 50 MV/m accelerating gradients for particles with β>0.3. In particular, a β=0.3 structure based on the novel approach of operation at the first negative spatial harmonic with the increased distance between the accelerating gaps will be presented. This is the first attempt to reach such high gradients at such small velocities. RadiaBeam and ANL have demonstrated the feasibility of building this structure for accelerating carbon ions by means of advanced computer simulations and are currently working towards the fabrication of this structure for high power tests.

INTRODUCTION

A usable device for cancer therapy needs to produce up to 200-250 MeV protons or/and up to 400-450 MeV/u carbon ions [1]. Both cyclotrons and synchrotrons that are currently used for these purposes are expensive and bulky constructions with large magnets and have significant limitations with rapid and efficient energy adjustment [2].

Within hadron therapy, proton therapy is the most common [3], although studies indicate that carbon ion therapy offers additional advantages [4], and combined proton and carbon therapy could achieve the most precise dose confinement to the tumor volume [5], while sparing healthy tissues.

Argonne National Laboratory and RadiaBeam are seriously considering the development of an ultra-high gradient linear accelerator, named ACCIL, for the full energy range from ion source to 450 MeV/u for $^{12}C^{6+}$ and 250 MeV for protons [6], which includes the following main sections: a radiofrequency quadrupole (RFQ) accelerator operating at a sub-harmonic of the S-band frequency, a conventional DTL section followed by a CCDTL section up to 45 MeV/u, and a high-energy section made of high-gradient structures for the energy range from ~45 MeV/u to ~450 MeV/u.

The compact footprint of ACCIL (8x45m) can be achieved by the development of accelerating structures capable of providing 50 MV/m for the particles with beta from 0.3 to 0.7. Such a high accelerating gradient for the ACCIL linac is possible due to the operation at high frequency, 2856 MHz, at very low duty cycle <0.06% and very short <0.5 μs beam pulses.

There are several ongoing projects worldwide [7,8] pursuing the development of S-band high gradient structures. Among the proposed structures only TULIP's backward-traveling wave structure (BTW) provides parameters close to ACCIL requirement. However, the direct scaling of BTW cells design from β=0.38 to β=0.3 beam velocities lead to unacceptably high peak fields (>220 MV/m) or dramatically lower power efficiencies.

ACCELERATING STRUCURE

To work around this issue, we have designed a cavity where the beam is synchronous with the higher spatial harmonic (NHS) [9]. The structure was designed to operate at the -1st harmonic, capable of producing 50 MV/m gradient at peak field levels of <160 MV/m with 50% higher shunt impedance than the β=0.3 structure scaled from TULIP's fundamental harmonic BTW. However, the NHS design had mechanical stresses of ~60 MPa as shown in Fig.1, left, which is slightly above the yield stress of the annealed copper.

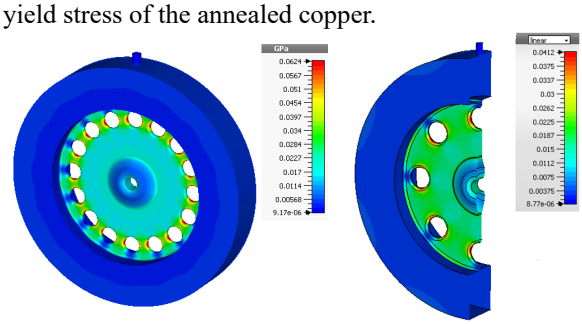


Figure 1: Mechanical stress maps in NHS with 16 (left) and 8 (right) coupling holes.

To reduce peak stresses, we investigated several approaches. Since the location of these stresses is the coupling hole, the strategy to reduce them is by reinforcing the iris part between the holes. The first obvious approach was to reduce the number of coupling holes, and thus increase the distance between them. The simulation results, shown in Fig.1, right, demonstrate that lesser number of holes makes the structure more rigid and improves thermal conductance at the cost of the group velocity, which can be compensated by increasing the hole diameter. The optimal number of holes is eight since

* This work was supported by the U.S. Department of Energy, Office of High Energy Physics, under Accelerator Stewardship Grant, Proposal No. 0000219678 and STTR grant DE-SC0015717

Content from this work may be used under the terms of the CC BY 3.0 licence (© 2018). Any distribution of this work must maintain attribution to the author(s), title of the work, publisher, and DOI.

ISBN: 978-3-95450-194-6 ISSN: 2226-0366 doi:10.18429/JACoW-LINAC2018-MOPO077

the four-holes option has a much higher (~40%) Poynting vector value while the stresses are only 10% lower.

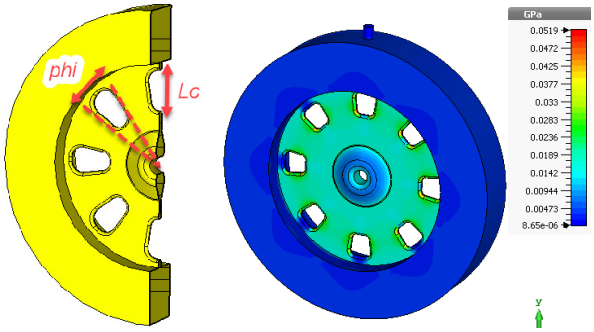


Figure 2: The cell with sector-shaped geometry (left) and the stress distribution map (right).

Since the stresses are still located in the coupling holes, we have attempted to apply a sector-shaped geometry to make holes' edges parallel and reduce peak stresses, as shown in Fig.2. In this case, the cell's group velocity doesn't depend on the hole length but only on the opening angle. However, this approach hasn't solved the problem, since stresses are still on the hole roundings and their peak values remain the same. We have also tried to reduce blending radius of the holes, but this has increased the stresses.

The other way to reinforce the iris is to increase its thickness. Thicker irises have higher thermal conductivity, and thus lower thermal gradient can develop, which results in lower stresses. However, since the EM field are concentrated in a smaller volume (around the beam axis), the modified Poynting vector becomes larger, which increases the risks of voltage breakdown. The simulation results suggest that increasing the iris thickness by 0.5mm is an acceptable solution leading to the reduction of the stresses by ~20%.

Another option is to increase the cell blend radius to improve the thermal conductivity further. However, in this case, the thermal conductivity is only increased outside the coupling holes, while the thermal gradient across the cell is even higher. Also, the Poynting vector becomes dramatically higher, which makes the idea of increasing the blending radius risky and unreasonable.

Table 1: Optimized NHS Parameters for Different Group Velocities

Group velocity, %c	0.45	0.30	0.15
Peak E-field, MV/m	155.2	155.5	155.6
Pulsed heating, K	24.7	21.5	17.54
Shunt impedance, MΩ/m	32.3	33.1	34.2
Mod. Poynt. vect., MW/mm^2	1.68	1.39	1.02
Temperature gradient, K	11.9	10.7	9.5
Mechanical stresses, MPa	37.0	32.8	29.0

Finally, by implementing 8 round holes, 3 mm thick iris, and 1 mm blending radius we were able to reduce the peak stresses by almost a factor of two: from 62.4 MPa to 33.8 MPa (as simulated in CST Studio for the individual cells) for the cell with 0.33%c group velocity, which is a great result in conjunction with 5MW peak power reduction, achieved by the increase of filling time from 350 ns to 500 ns due to the smaller group veloicty. We have also checked that the parameters stay within the required limits within the broad range of group velocities as shown in Table 1.

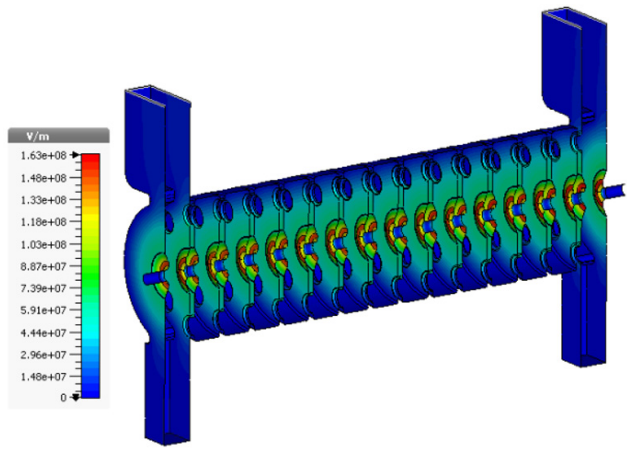


Figure 3: Surface electric field distribution in full 15-cells NHS section.

The input and output couplers were tuned by adjusting coupler cell diameter and coupling window width individually for both couplers so that there are no reflections from the couplers, which yields to two criteria: high field flatness inside the structure, which should be <2%, and low reflection from input port 1 at operation frequency <-30 dB. The actual achieved field flatness is 1.36% and S_{11}=-31.5 dB. From figure 3 it is possible to calculate VSWR=1.069, which refers to the internal reflection coefficient of -29.5 dB. The phase advance spread is less than 0.6° while the cumulative phase advance error is 0.25°. The tuned 15-cells model is shown in Fig. 3.

ENGINEERING DESIGN

We have performed static thermal, fluid dynamic and structural analysis in ANSYS Multiphysics. The designed cooling blocks geometry is shown in Fig.4. These blocks have a flat bottom and are easier to machine. CFD Conjugate Heat Transfer simulations with flow velocity ~ 1.5 m/s demonstrate the average heat transfer coefficient of 8300 W/m^2-C and maximum temperature of the whole structure 18.2 C above the ambient level as shown in Fig.5, with cooling water temperature increase of only ~0.5 C. Ansys Mechanical Transient Heat Transfer analysis for one cycle at 1.0 ms heating time was also performed and demonstrated peak heating of 19.8 C, similar to analytical calculations.

Loading for the structural analysis consisted of vacuum, physical constraints, and temperatures from the thermal analyses. All material data used in the structural analysis was taken in the annealed state. This included Young's modulus, yield strength, the stress-strain curve used for

Content from this work may be used under the terms of the CC BY 3.0 licence (© 2018). Any distribution of this work must maintain attribution to the author(s), title of the work, publisher, and DOI.

ISBN: 978-3-95450-194-6 ISSN: 2226-0366 doi:10.18429/JACoW-LINAC2018-MOPO077

Content from this work may be used under the terms of the CC BY 3.0 licence (© 2018). Any distribution of this work must maintain attribution to the author(s), title of the work, publisher, and DOI.

the BISO material model, and the low and high cycle fatigue data taken from [10, 11]. The physical constraints were chosen to approximate a stress-free state. The heat load consisted of the temperature distribution from the steady-state analysis, with temperatures from the transient analysis superimposed on the whole structure. Two load cases consisting of the temperature at the end of the last pulse, and the temperature at the end of the last cycle were run to determine the mean and alternating stresses.

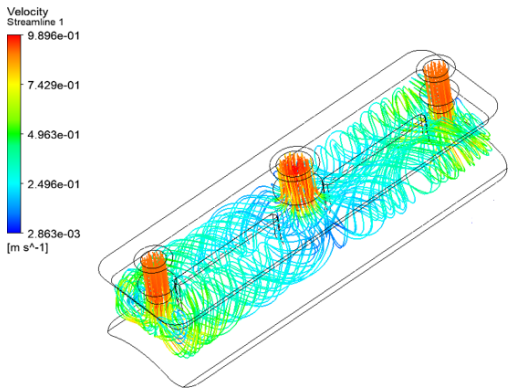


Figure 4: Water flow in the structure cooling blocks.

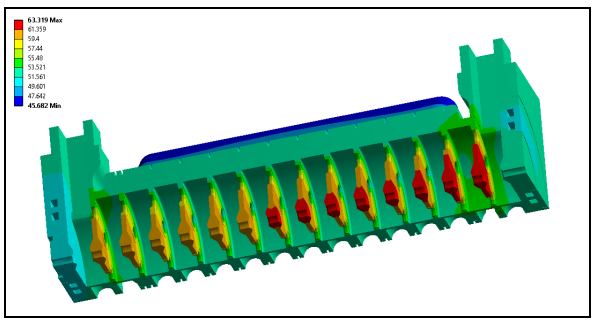


Figure 5: Stationary temperature distribution in the 15-cell NHS section.

At 70°C, copper yield occurs at about 52 MPa. The calculated von Mises stress at end of RF pulse during the stationary regime is 46.4 MPa. Therefore, no yielding or plastic strain is expected.

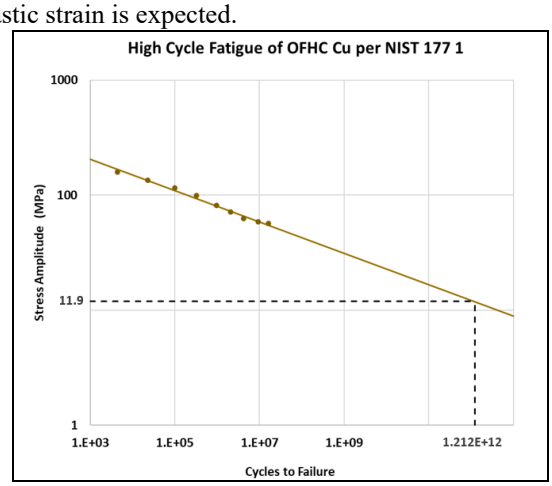


Figure 6: High Cycle Fatigue of copper calculated with different models. The actual amplitude is 11.9 MPa.

Fatigue does not appear to be an issue. The calculated maximum fatigue stress is 11.9 MPa. Fig. 6 shows the total strain range and stress amplitude are well below the allowable values. The low cycle fatigue data is taken at 56.7°C, so using that data is conservative. The high cycle fatigue was generated at room temperature. Estimated maximum cycle count of the structure is about 10^7 cycles, and the projected life is ~10^{12} cycles, which corresponds to 320 years of operation.

SUMMARY

The proposed acceleration with higher spatial harmonics has enabled the development of a novel high-gradient accelerating structure design for protons and carbon ions with low β. The prototype structure being developed will become the enabling technology for compact hadron therapy linacs. We have performed electromagnetic optimization of 50 MV/m β=0.3 NHS cell to achieve mechanical stresses below the annealed yield stresses of 52 MPa. The design of a robust cooling system and the careful structural analysis helped to ensure the stable operation at high gradients in long-term applications. The NHS section is currently being built and is planned to be tested in 2019.

REFERENCES

[1] K. Yamanouchi *et al.*, "Progress in Ultrafast Intense Laser Science XII", Springer International Publishing (Switzerland), 2015.

[2] K. Peach *et al.*, "Accelerator science in medical physics", Br J Radiol. 2011 Dec; 84(Spec Iss 1): S004–S010.

[3] Hadron Therapy Patient Statistics: Particle Therapy Co-Operative Group, 2013.

[4] U. Amaldi and G. Kraft, "Radiotherapy with beams of carbon ions" in Rep. Progr. Physics 68, 2005.

[5] A.J. Lomax, "Charged particle therapy: the physics of interaction", Cancer J. 2009, 15(4):285-91.

[6] P. Ostroumov *et al.*, "Compact Carbon Ion Linac", NAPAC'16, Chicago, IL, 2016, MOA4CO04.

[7] S. Benedetti *et al.*, "High gradient linac for proton therapy", Phys. Rev. Accel. Beams 20, 040101 (2017).

[8] U. Amaldi et al., "LIBO a linac-booster for proton therapy: construction and test of a prototype", NIM A, 521:512–529, 2004.

[9] S.V. Kutsaev *et al.*, "High-gradient low-β accelerating structure using the first negative spatial harmonic of the fundamental mode", Phys. Rev. Accel. Beams 20, 120401 (2017).

[10] J. Esposito, R. Zabora, "Thrust Chamber Life Prediction", Volume I, Mechanical and Physical Properties of High Performance Rocket Nozzle Materials, NASA CR 124806, Boeing Aerospace Co, Seattle WA, March 1975.

[11] J.E. Jensen *et al.*, "Selected Cryogenic Data Notebook", Volume I, BNL 10200-R, Brookhaven National Laboratory, Upton NY, August, 1980.

ISBN: 978-3-95450-194-6 ISSN: 2226-0366 doi:10.18429/JACoW-LINAC2018-MOPO079

CAVITY DESIGN OF A 7MeV 325MHz PROTON APF IH-DTL FOR A COMPACT INJECTOR*

X. Li[1], Y.H. Pu†, X.C. Xie, M.H. Zhao, Shanghai Institute of Applied Physics, Chinese Academy of Sciences, Shanghai, China
F. Yang, Shanghai APACTRON Particle Equipment Co., Ltd, Shanghai, China
[1]also at University of Chinese Academy of Sciences, Beijing, China

Abstract

An Interdigit H-mode Drift-Tube-Linac (IH-DTL) with Alternating-Phase-Focusing (APF) method working at 325 MHz was designed. With the RF field established properly in the cavity, protons can be accelerated from 3 MeV to 7 MeV successfully. In this paper, the process of designing such an APF IH-DTL cavity is going to be presented. Also, the characteristics of the cavity and parameters studying of RF are going to be demonstrated.

INTRODUCTION

Over the recent decades, with the development of particle accelerator physics and related technologies, using energetic particles such as protons, electrons provided from them to treat cancers is more and more efficient and practical. Because of protons' unique Bragg peak, proton accelerators attract a lot of attention.

As a key member, Shanghai Institute of Applied Physics (SINAP) work together with other two members to establish a joint company named Shanghai APACTRON Particle Equipment Co., Ltd to manufacture the Advance Proton Therapy Facilities. To be competitive, we are going to improve the facility in many aspects. A 7 MeV injector is one of main components which are being improved by us now.

Usually, this typical injector consists of a compact Electron-Cyclotron-Resonance Ion Source (ECRIS), a Radio-Frequency-quadrupole (RFQ) and a Drift-Tube-Linac (DTL), the RFQ and DTL accelerates protons from 40keV to 3 MeV and then to 7 MeV respectively. Traditional DTL is quite bulky, heavy, high-cost and difficult-to-maintain which limits its popularization as an injector for medical facility.

IH-DTL working with APF have the advantages of compact, cost-efficient and easy-to-maintain, so we adopt it as a candidate for our compact injector. Interdigit H-mode as an idea was first proposed in the 1950s by J. P. Blewett [1]. High shunt impedance is one of its main features, so this type of structure's RF power consumption is much lower than that of a conventional Alvarez-type DTL with energy lower than 10 MeV. Unfortunately, due to the slow development of three-dimensional(3D) electromagnetic (EM) field solver and rather complicated cavity structure, this advanced structure didn't have a good development over the past decades.

Entering the 21st century, well-developed 3D EM solvers like CST, HFSS, etc. make it practical to get the precise field distribution and optimize the cavity dimensions and RF characteristics [2]. Also, we exported the 3D RF field from CST microwave studio and got rather good results using a third-part code TraceWin [3].

In the following sections, a latest design of the APF IH-DTL for a compact injector is going to be presented. It concludes considerations of the cavity, the RF characteristics and geometric dimensions, the comparison between the calculated-voltages and required-voltages from beam dynamics.

APF IH-DTL

There are several linear accelerators adopting APF IH-DTL cavities [4-6]. Regarding to the principle of APF, A sequence of negative and positive phases alternatively appear between adjacent two electrodes(tubes). When the particles go through these different gaps and the tubes along the longitudinal axis, the negative phases they meet will focus the particle bunches longitudinally but defocus them radially. Conversely, the positive phases will focus the particles bunches radially but defocus them longitudinally. After several sinusoidal like periods of the phase sequence, we can get the particles focused successfully both in longitudinally and radially. Figure 1 shows the principle of APF [7]. Then the additional focusing elements in the case of conventional DTL can be saved in the APF LINACs. These features can significantly reduce the construction and maintenance cost of the radio therapy facilities adopting APF IH-DTL as its injector.

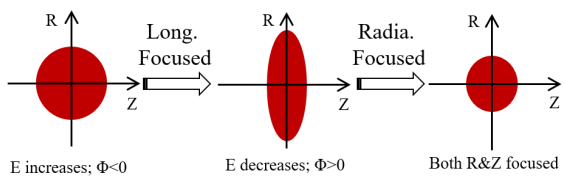


Figure 1: Demonstration of focusing principle of APF.

Unlike TM_{010} mode in the conventional DTL, TE_{111} mode is excited in an IH-DTL cavity. Alternatively introducing tubes supported by the stem connecting to the opposite wall, we can get the longitudinal accelerating E-field at π mode in Fig. 2.

† corresponding author: Tel: +86 130 6260 1189
E-mail address: puyuehu@sinap.ac.cn

Content from this work may be used under the terms of the CC BY 3.0 licence (© 2018). Any distribution of this work must maintain attribution to the author(s), title of the work, publisher, and DOI.

ISBN: 978-3-95450-194-6 ISSN: 2226-0366 doi:10.18429/JACoW-LINAC2018-MOPO079

Content from this work may be used under the terms of the CC BY 3.0 licence (© 2018). Any distribution of this work must maintain attribution to the author(s), title of the work, publisher, and DOI.

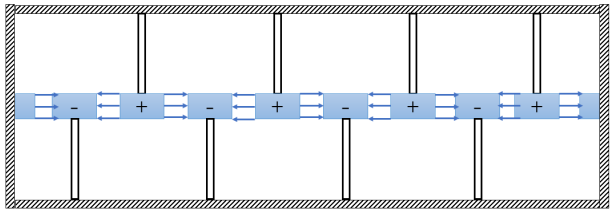


Figure 2: A drawing for principle of IH-DTL.

DESIGN OF APF IH-DTL CAVITY

The job of RF design of a cavity is to get the voltages distribution between adjacent tubes along longitudinal axis required by beam dynamics. Based on principle of IH-DTL cavity, E-field directly excited by the structure like in Figure 2 can't be suitable to accelerate particles efficiently. Besides, there is no any additional elements can be employed to focus particles, the motion inside the cavity is strongly determined by the electromagnetic (EM) field distribution in the cavity. And as mentioned previously [8], the EM-field distribution would depend strongly on the whole structure of the cavity, including the diameters of the cavity, the widths of the ridge, the shapes of the End-Ridge-Cut, the shapes of the stem, the diameters of the drift tubes, tuners, vacuum pipes, RF power feed coupler, etc. Dimensional changes occur on anyone of those structures can change the distribution of EM-field. So, looking for an efficient designing procedure among above variables is a challenge. We choose CST MWS as the 3D EM solver to establish model, calculate and optimize the cavity [5].

The frequency of the cavity depends on the capacitance and inductance of the whole IH-DTL structure. The following Eq. (1) shows the relation among them. Capacitance mainly comes from gaps of the tubes and that of the two ridges; correspondently, inductance mainly depends on the cross-section area enclosed by the cavity wall, tubes' outer radii, two ridges' height.

$$f \propto \frac{1}{\sqrt{L_e C_e}} . \qquad (1)$$

Because the velocity at the exit is 1.52 times of that at the entrance, it causes the length of the unit cells and the gap increasing, then it makes the capacitance decreasing from the entrance to the exit, the results is the E-field would peak near the entrance of the cavity. In order to get the maximum shunt impedance, a uniform E-field distribution is the goal we are working for. It is easy to reach this by reducing the radius at the entrance or increase the radius at the exit.

Even then, the first and last few cells can't establish the same E-field as it at the middle of the cavity, this is ascribed to the characteristic of TE111 mode. Here we can use End-Ridge-Cuts (ERC) to enhance the E-field by increasing magnetic flux. Figure 3 shows the End-Ridge-Cuts, now the mode looks like TE11(0).

To get larger beam transmission, the inner radii of the drift tubes are determined to be 6mm. In our cavity, the maximum E-field should be no more than 1.6 times of E_{Kilpat}, which comes from the Kilpatric criterion. Regarding to the frequency 325 Mhz, the maximum E-field is about 29 MV/m, namely the bravery factor is 1.6. The most probably area where RF breakdown happens easily is around the outer edge of the tubes. So, we chamfer the outer edge of the tube with the radius of 4 mm, and the outer radius of the tube is 13 mm. To get optimum value of quality factor, the inner edge of the tube is chamfered with radius of 1 mm.

When designing the support stems, the main concern is the structural maximum E-field on the tube, the vertical component of E-field, the quality value and the heat transmission efficiency. So, we adopt tapered stems which has large base and small top to meet the above four requirements, as shown in Figure 3.

The following procedure is the designing procedure we developed for an APF IH-DTL cavity:

1. Construct a structure model based on the cell table, which determines the cell length, namely the synchronous phases sequence.
2. Segmentally adjust the diameters of the cavity to make the axial longitudinal E-field uniform.
3. Adjust the width of the End-Ridge-Cut to refine the E-filed near the both ends of the cavity.
4. Tune the resonant frequency of the cavity to 325 MHz by adjusting the diameter of the cavity.
5. Iterate the step 2- 4 to refine the uniformity of axial longitudinal E-field and frequency of the cavity.
6. Refine chamfering radius of the outer edge of the drift tubes to make sure the maximum E-field is less than 29 MV/m (1.6times E_{Kilpat})
7. Export the 3D EM distribution to re-calculate the beam dynamics with a third-part code like TraceWin. Optimize the geometry and dynamics by doing co-iteration with each other.
8. Add the tuners, Couplers, Vacuum pipes. Iterate the step 2-4 if necessary. Redo the step 7 to make a check.
9. After the mechanical design of the cavity, re-construct the model in CST MWS. Make sure the E-field distribution and voltage distribution meet the requirement of dynamics.

Table 1: The Main Parameters of the APF IH-DTL

Parameters items	Value	Unit
Frequency	325	MHz
Length	1514.6	mm
Input energy	3	MeV
Output energy	7	MeV
Unit cells number	32	-
Inner radius of the cavity	95.6-116	mm
Outer radius of the tube	13	mm
Inner radius of the tube	6	mm
Bravery factor of the cavity	1.53	-
Quality factor (0.8)	8900	-
Establishing field power (0.8Q)	195	kW
Woking mode	TE11(0)	-

ISBN: 978-3-95450-194-6 ISSN: 2226-0366 doi:10.18429/JACoW-LINAC2018-MOPO079

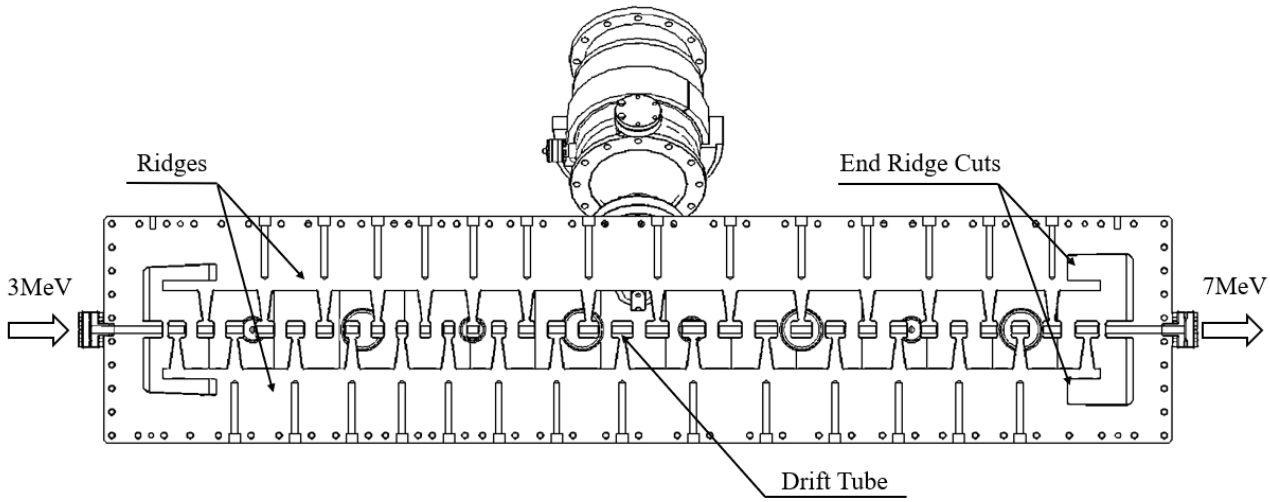


Figure 3: Cross-section drawing of the APF IH-DTL cavity.

Based on the above study of the cavity designing, we successfully get the cavity structure of APF IH-DTL working at 325 MHz as shown in Figure 3.

Results of the Design

After co-iteration between cavity optimization and beam dynamics tracking, some key RF characteristics parameters can be calculated with post-processing templates. Some of these main parameters of are summarized in Table 1.

Draw a line along the Z axis from the beginning to the end of the cavity, longitudinal component of E-field distribution can be plotted by the post-processing template too. Figure 4 shows uniformity of the E_Z. we can see the uniformity is rather good, which keep a good coincidence with the quality factor.

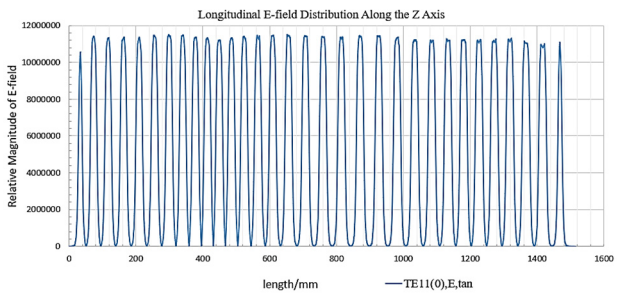


Figure 4: Longitudinal E-field distribution along the Z axis.

Integrating voltage is visual and useful way to see if the cavity meets requirements from the dynamics or not. According to the definition of the integral voltage, we get the gap voltages cell by cell orderly and plot them as the function of the gap number. A comparison between the calculated and dynamics is shown in Figure 5.

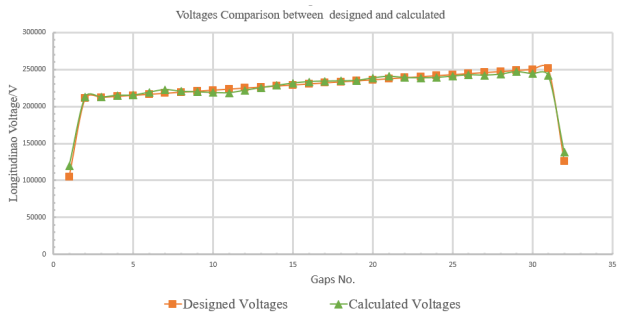


Figure 5: A comparison of voltage between the designed from dynamics and calculated by CST MWS. The triangle and square show the calculated and designed respectively.

CONCLUSION

We developed a useful way to design an APF IH-DTL cavity, according to this procedure, we designed a cavity working at 325 MHz, its corresponding E-field and integral voltage distribution were plotted by post-processing template of CST. Meanwhile, exported 3D EM field was used to track the protons with a third-part code TraceWin, the results met the expectations from the dynamics very well. According to the plan, we are going to do the machining work soon and the cold test and tuning of the cavity.

ACKNOWLEDGEMENTS

This work was supported by the National Key Research and Development Program of China (grant number 2016YFC0105408).

REFERENCES

[1] J.P. Blewett, CERN Symposium 159 (1956).

[2] CST, https://www.cst.com/

[3] D. Uriot and N. Pichoff, "Status of TraceWin Code", in *Proc. 6th Int. Particle Accelerator Conf. (IPAC'15)*, Richmond, VA, USA, May 2015, pp. 92-94.

Content from this work may be used under the terms of the CC BY 3.0 licence (© 2018). Any distribution of this work must maintain attribution to the author(s), title of the work, publisher, and DOI.

ISBN: 978-3-95450-194-6 ISSN: 2226-0366 doi:10.18429/JACoW-LINAC2018-MOPO079

[4] R.A. Jameson, "Practical design of alternating-phase-focused", in *Proc. RuPAC'12*, St. Petersburg, Russia, September 2012, paper MOACH02, p. 12.

[5] Y. Iwata *et al.*, "Alternating-phase-focused IH-DTL for an injector of heavy-ion medical accelerators", *Nucl. Instr. Meth.*, A vol. 569, pp. 658-696, 2006.

[6] K. Yamamoto *et al.*, "Experimental verification of an APF linac for a proton therapy facility", *Nucl. Instr. Meth.*, B vol. 269, pp. 2875-2878, 2011.

[7] S. Ogata, "Design and Analysis of APF-Linac with 'PiMLOC'", private communication, Shanghai, China, Sep. 2014.

[8] U. Ratzinger, "H-Type Linac Structures", CERN Accelerator School, Lufthansa Training Center, Seeheim, Germany, May, 2000, pp. 351-380, 2005.

Content from this work may be used under the terms of the CC BY 3.0 licence (© 2018). Any distribution of this work must maintain attribution to the author(s), title of the work, publisher, and DOI.

ISBN: 978-3-95450-194-6 ISSN: 2226-0366 doi:10.18429/JACoW-LINAC2018-MOPO080

THE MANUFACTURING OF THE CSNS DTL TANK

X. L. Wu[1,†], H. C. Liu[1], K. Y. Gong, H. Song, S. M. Liu[1], L. Dong, T. Luo[1], Institute of High Energy Physics, Chinese Academy of Sciences (CAS), 100049 Beijing, China
[1]also at Dongguan Neutron Science Center, 523803 Dongguan, China

Abstract

The DTL tank is a crucial component of the China Spallation Neutron Source (CSNS) linear accelerator (LINAC), which mainly use the technology of oxygen-free copper (OFC) electroplating on the inner surface of the 20# carbon steel tube. It is the first time to perform OFC electroplating with high electrical conductivity in the high intensity beam accelerator in China. In the process of cavity manufacturing, problems such as machining deformation, plating surface nodule and plating peeling are encountered. In this project, based on pre-research and information from literature, the formula of acid solution was improved to construct a stable pickling process protocol. The manufacturing process of DTL tank and the measurement details are introduced in this paper.

INTRODUCTION

The CSNS DTL tank is approximately 36m long and contains 4 RF cavities. A total of 153 drift tubes are installed on the top of the cavities. Each RF cavity is equipped with 12 fixed tuners evenly distributed at the bottom of cavity, these tuners are used to compensate for the frequency shift caused by machining errors. 2 movable tuners are also used to modulate local frequency disturbances caused by high frequency heating. The high frequency power is fed by an iris waveguide coupler mounted in the middle of the cavity. There are 12 water cooling channels embedded into the tank out-wall. The tank will operate in a sufficiently high vacuum for RF environment by using 3 turbo molecular pumps and 9 ion pumps per RF cavity [1].

For ease of manufacturing, transportation and installation, each RF cavity is divided into 3 unit sections which can be bolted together [2]. The inner diameter of the unit section is about 566mm, and the length ranges from 2760mm to 3100mm. The manufacturing precision is high, and the key technical indicators are shown in Table 1.

The cavity manufacturing mainly include machining, electroplating, pickling and measuring. The machining factory that cooperated during the pre-research period is replaced by two new manufacturers. The electroplating process is also changed, which must be re-explored. The manufacturing and test details are presented in this paper.

Table 1: Key Technical Indicators of DTL Tank

Indicators	Tolerance
Length (before plating)	-0.30~-0.10 (mm)
Inner diameter (before plating)	± 0.10 mm
Side holes position (before plating)	± 0.10 mm
Plating thickness	0.15 ± 0.05 (mm)
Surface roughness	0.8 um
Plating adhesion	No peeling after baking
Vacuum	≤ 1.0 E-5 Pa

MACHINING

The cavity has a large size, a large number of side holes, and requires high precision. There are 15 key processes in machining, including turning, welding, benching, heat treatment, milling, boring, grinding, measuring, etc. The cylindricity of the cavity 1# machined by manufacturer A is out of tolerance (0.50mm>0.10mm). The precision of milling machine in the manufacturer B is low (the worktable moves 3000mm, its displacement deviation is -0.36mm; the reset deviation is -0.22mm, after the worktable moves 3000mm)，which results in difficulty in fine boring of the side holes on the cavity 2#.

It's analyzed that the reason for the deviation of the cavity 1# is because the process has been reversed between turning the inner surface of the cavity and milling cooling sink around the out-wall. In order to solve the problem, we strengthened communication with manufacturers, reconfirmed the process route, and required manufacturers to strictly implement the process. Offset value is offered by the laser tracker before the fine boring of the side holes on the cavity 2#. Our colleagues were stationed in factories to track the quality of machining at the critical stage of the processing. Finally, we successfully completed the machining of all cavities. The key indicators are shown in Fig.1.

The length precision is partially out of tolerance (Max ΔX=0.13mm), which can meet the design requirements (after plating) by controlling the plating thickness on the end plate. The inner diameter precision of all cavities meets the requirements. The position of all 153 drift tube holes is measured and only 3 out of tolerance (Max ΔX=0.02mm), which we considered to meet the installation requirements.

† wuxiaolei@ihep.ac.cn

Content from this work may be used under the terms of the CC BY 3.0 licence (© 2018). Any distribution of this work must maintain attribution to the author(s), title of the work, publisher, and DOI.

ISBN: 978-3-95450-194-6 ISSN: 2226-0366 doi:10.18429/JACoW-LINAC2018-MOPO080

Content from this work may be used under the terms of the CC BY 3.0 licence (© 2018). Any distribution of this work must maintain attribution to the author(s), title of the work, publisher, and DOI.

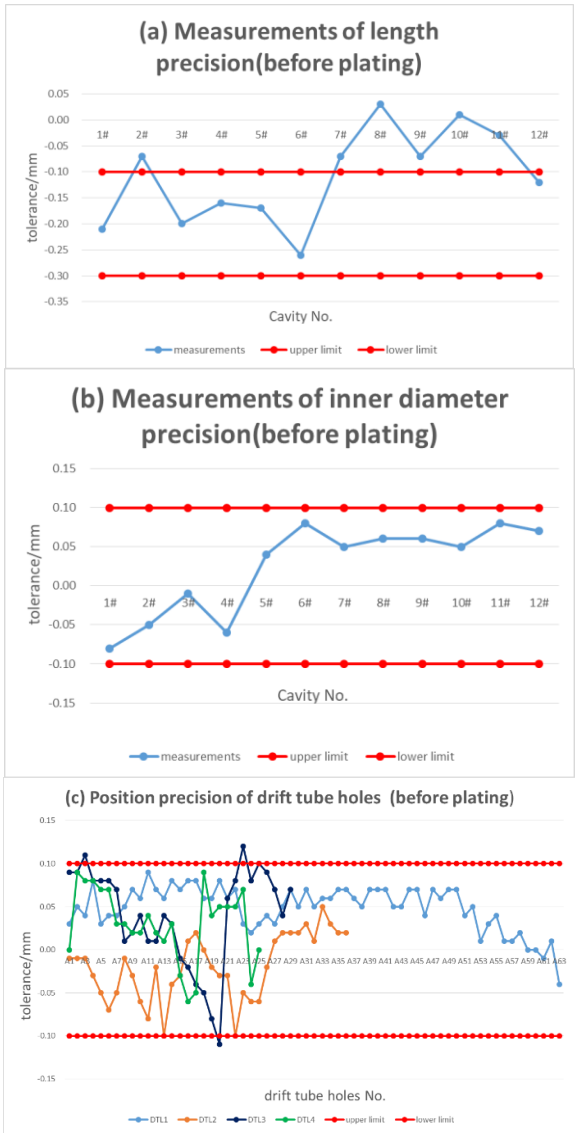


Figure 1: Measurements of the machining: (a) length precision, (b) inner diameter precision, (c) position precision.

ELECTROPLATING

Electroplating is the most critical technic in manufacturing of the cavity. The electroplating process has been changed compared to the pre-research process, which must be re-explored. The new process has led to two difficulties, plating surface nodule and peeling.

Plating Surface and Nodule

All side holes of the cavity 1# are nodulated (Fig. 2) after electroplating. The nodules are in the same direction of each side hole (downward by gravity), and the closer to the bottom of the plating bath, the more severe the nodule.

The main reason for the nodule are as follows: 1) the surface isn't completely degreased before plating; 2) the dirty things flow out of the screw holes to contaminate the plating solution; 3) the anode current density of the side holes is high.



Figure 2: Electroplating of the first three cavities.

We improved the process when plating the cavity 2#, including: 1) the plating solution is equipped with circulating filtration equipment; 2) all the screw holes are blocked with clean rubber; 3) all side holes are installed with flushing pipes; 4) filter bags are installed on all side anodes; 5) reduce anode current. The nodules of the cavity 2# are significantly reduced (Fig. 2).

The process was further improved when plating the cavity 3#: 1) we use a cleaning agent to scrub the oil instead of the electrolytic degreasing; 2) cleaning the anode mud and the filter bag; 3) reduce the copper plating time of the side holes by half. There is no nodule on the inner wall of all side holes after the improvement (Fig. 2).

Plating Peeling

After electroplating, the cavity 2# was cleaned and baked at a high temperature (100℃ for 72 hours), followed by a large amount of peeling phenomenon (Fig. 3), that is ,the plating layer and the substrate were detached.



Figure 3: Plating peeling.

We performed ultrasonic testing on the material to eliminate the possibility of defects in the substrate. It's judged that the factors causing peeling mainly include: 1) machining defects on the surface, such as gear mark, scratches, etc. 2) there are still uncleaned areas on the surface. The following improvements are made: 1) strengthened the surface quality acceptance of machining; 2) strengthened the intensity of degreasing and eliminated the blind spot (Fig.4). The standard of degreasing is that the water film does not crack 30s while washing.

ISBN: 978-3-95450-194-6 ISSN: 2226-0366 doi:10.18429/JACoW-LINAC2018-MOPO080



Figure 4: Surface acceptance and degreasing.

Each cavity was baked and pumped to ensure that the plating and the substrate are tightly bonded. Polishing, brush plating and re-baking are needed in case of some peeling occurred on the inner surface of the cavity after baking and vacuum test. Finally，we solved the problem of plating peeling after improving the process.

Measuring

The plating thickness is controlled from 0.05mm to 0.21mm, and the surface roughness is about 0.5 um<0.8um (Fig. 5).

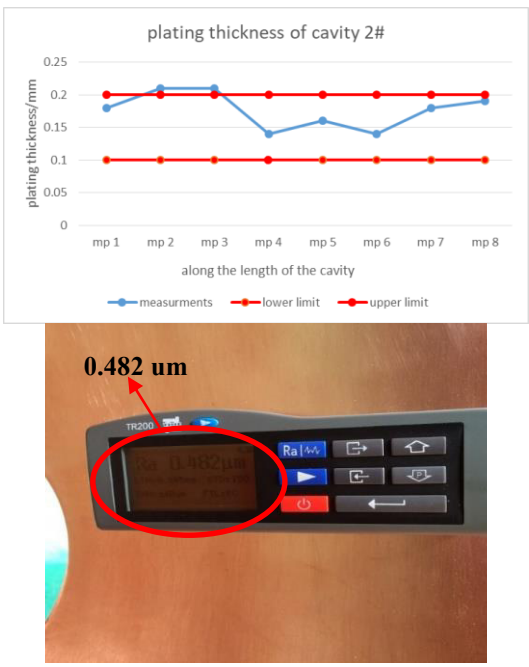


Figure 5: Plating thickness measurements and surface roughness measuring.

The RF properties of cavity 1# and 3# are measured by using network analyser. All holes are covered with copper-plated plugs and RF springs are added for measurement. The results are shown in Table 2, which meet the requirements.

Table 2: RF Parameter Measurements

No.	Measurements (Q_0)	Q	Q_0/Q	Freq. (MHz)
1#	70.099	78.023	90%	405.030
3#	73.126	77.983	94%	404.983

PICKLING

The purpose of pickling is to remove the oxide film on the plating and reduce the possibility of vacuum venting. We improve the acid ratio based on pre-research and form the final formula by carrying out small sample pickling test. The pickling process is also improved. The actual operation proves that the acid ratio is simple, no toxic gas is generated, the operation is simple, the cost is low, the oxide film can be effectively removed and the surface can be passivated.

The main process (Fig, 6) of pickling is as follows: degreasing, water washing (cold, hot) and drying, pickling, wash (tap-water, pure water) and dry, vacuum baking and seal.



Figure 6: Pickling.

We performed vacuum leak detection on all the cavities after pickling, and the leak rate satisfy the requirements. The ultimate vacuum test and residual gas analysis (RGA) were performed on the cavity 2#. The result was that the lowest pressure reached 3.3E-6 Pa, and the RGA spectrum (Fig. 7) showed no macromolecules such as oil. The vacuum test results meet the requirements.

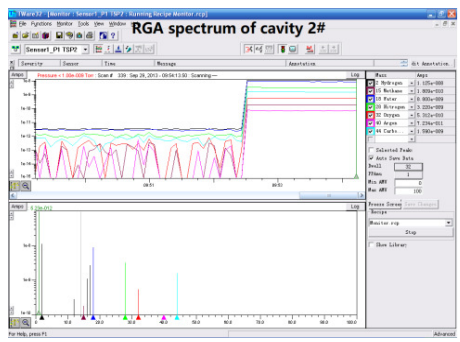


Figure 7: RGA spectrum of cavity 2#.

CONCLUSION

The DTL tank has a large size, a complicated structure, and high precision. Electroplating requires high-precision surface roughness, high uniformity, high electrical conductivity, strong adhesion, complicated process and great difficulty. The manufacturing of the DTL tank lasted 2 years, and the measurement results showed that the final product meet the physical design. In January 2015, the manufacturing of 12 cavities was completed and they were delivered to the CSNS site.

Content from this work may be used under the terms of the CC BY 3.0 licence (© 2018). Any distribution of this work must maintain attribution to the author(s), title of the work, publisher, and DOI.

ISBN: 978-3-95450-194-6 ISSN: 2226-0366 doi:10.18429/JACoW-LINAC2018-MOPO080

Content from this work may be used under the terms of the CC BY 3.0 licence (© 2018). Any distribution of this work must maintain attribution to the author(s), title of the work, publisher, and DOI.

REFERENCES

[1] X. Yin, K. Gong, J. Peng, H. song, Y. Xiao, L. Liu, S. Fu, "Development of a 324 MHz drift tube Linac for CSNS", in *Proc. LINAC'10*, Tsukuba, Japan, 2010,TUP061, pp. 548-550.

[2] H.C. Liu, S.N. Fu, J. Peng, S. Wang, "DTL construction status of CSNS project", in *Proc. LINAC'14*, Geneva, Switzerland, 2014, TUIOB04, pp. 423-425.

ISBN: 978-3-95450-194-6 ISSN: 2226-0366 doi:10.18429/JACoW-LINAC2018-MOPO081

LIGHT PROTON THERAPY LINAC LLRF SYSTEM DEVELOPMENT

B. Baricevic, A. Bardorfer, R. Cerne, Instrumentation Technologies, Solkan, Slovenia
G. De Michele, Y. Ivanisenko, AVO-ADAM, Meyrin, Switzerland

Abstract

Proton cancer therapy is a state-of-the-art medical treatment technique based on an accelerator beam production facility. The LIGHT linear accelerator design by AVO-ADAM offers a modular compact solution for precise control of the treatment dose delivery, both position and energy wise. Proton energy can be modulated at up to 200 Hz in a range from 70 to 230 MeV by varying the gradient of the accelerating structures. The normal conducting LINAC RF system is based on a 750 MHz RFQ and 12 S-band stations individually controlled. A customized LLRF system is being developed on the Libera LLRF platform for the LIGHT project. The paper is describing the required cavity field control functionality and the other subsystems such as master oscillator reference, cavity tuning, real-time control, data acquisition, control system and synchronization interfaces.

INTRODUCTION

The LIGHT (Linac for Image Guided Hadron Therapy) proton cancer therapy LINAC, designed by AVO-ADAM, is based on 13 normal conducting RF station modular design, conceived to modulate independently the RF power at 200 Hz, at the level of each high-power station. Together with low emittance it allows accurate dose delivery within the tumour volume and longitudinal layer switching on pulse-to-pulse basis. Moreover this feature opens up the highly desirable possibility to implement image-guided adaptive radiation therapy with protons, which is a unique property of the LIGHT system [1].

The compact LIGHT LINAC design consists of:

- a proton source at 40 keV providing currents up to 300 uA with pulses up to 20 us at 200 Hz repetition rate.
- an RFQ (Radio Frequency Quadrupole) at 749.48 MHz accelerating the protons up to 5 MeV, operated at the forth sub-harmonic of the 2997.92 MHz LINAC frequency. The RFQ RF system provides to the LLRF system, 4 cavity probe signals and 4 pairs of directional coupler forward and reflected signals.
- Two SCDTL (Side Coupled Drift Tube LINAC) high power RF units at 2997.92 MHz, delivering the beam at 37.5 MeV. Each SCDTL RF station provides 4 cavity probe signals and 3 pairs of directional coupler forward and reflected signals, as the klystron amplifier output is split between two accelerating structures.
- Ten CCL (Coupled Cavity LINAC) high power RF units at 2997.92 MHz accelerating beam up to 230 MeV. Five CCL units provide 2 RF probe signals and 2 pairs of directional coupler forward and reflected signals. In the other five CCL RF stations, 4 probes and 3 pairs of directional coupler signals are provided as the high-power drive is split among two accelerating structures.

In Figure 1 a scheme of the LIGHT proton accelerator compact design is presented. The total peak RF power required by the structures would therefore be 400 kW, 8 MW and 45 MW, respectively for the RFQ, SCDTL and CCL structures [2,3].

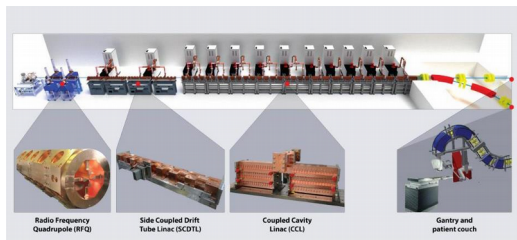


Figure 1: A scheme of the LIGHT proton accelerator.

THE LLRF SYSTEM REQUIREMENTS

To control the proton acceleration, it's required that all the 13 RF stations are tightly synchronized to the Master Oscillator (MO) and the LLRF system provides field control at the level of individual RF stations. Moreover, the LLRF system must apply the RF pulses of specific shape at nominal RF pulse length 20 μs and 7μs for the RFQ and the S-band structures respectively. Parameters defining RF pulse shape, it's amplitude and phase, must be provided to the LLRF system in real-time at 200 Hz rate in order modulate the proton energy according to the programmed treatment plan.

For cavity conditioning purpose, it's further required that the LLRF system has the ability to drive the cavity in a frequency range of 749.38 ± 1 MHz and 2997.92 ± 4 MHz. The LLRF system is also designed to automatically track the cavity resonant frequency within the range.

For the purpose of proton energy modulation, it is required that the LLRF system is operated in a 20 dB dynamic range, where also amplitude and phase stability requirements are specified (Table 1) [4].

To avoid the transmission of the reference MO signal over distance, it's required that the LLRF units controlling the RF stations are tightly synchronized to a common MO source to be installed at the same location of the LLRF units. The required stability for the MO signal distribution shall be within ±0.1°.

Content from this work may be used under the terms of the CC BY 3.0 licence (© 2018). Any distribution of this work must maintain attribution to the author(s), title of the work, publisher, and DOI.

ISBN: 978-3-95450-194-6 ISSN: 2226-0366 doi:10.18429/JACoW-LINAC2018-MOPO081

Content from this work may be used under the terms of the CC BY 3.0 licence (© 2018). Any distribution of this work must maintain attribution to the author(s), title of the work, publisher, and DOI.

Table 1: Required Amplitude and Phase Stability

Parameter	Requirement	Signal level
RMS amplitude stability	< 0.05 %	0 dB_{FS}
RMS phase stability	< 0.05 °	0 dB_{FS}
RMS amplitude stability	< 0.1 %	> -20 dB_{FS}
RMS phase stability	< 0.1 °	> -20 dB_{FS}

Additional Requirements

For the purpose of cavity tuning, the LLRF system must continuously measure the cavity resonant frequency and report the results through a dedicated Modbus interface to an external cavity temperature controller, acting on the water cooling system.

The LLRF system must tolerate certain kind of RF system failure before triggering an interlock event. An archiving system shall be in place to record the evolution of all RF signals during the applied treatment, which implies the LLRF system shall have a dedicated data streaming interface.

The triggering scheme involves two separate trigger events per LLRF unit generated by the LIGHT control system. An RF pulse shape will be set depending on the trigger event: either a pulse pre-configured over the real-time interface or a pre-loaded on the LLRF unit start-up. This implementation grants flexibility to differentiate treatment run with beam from stand-by states without beam to keep the accelerator thermalized for the operation. The trigger events have to be synchronized with the MO reference to achieve the required phase and amplitude stability.

STATUS OF THE LLRF DEVELOPMENT

The LIGHT LLRF system is being developed on the Libera LLRF platform. The Libera LLRF system for LIGHT will be provided in two 19” 2U chassis. At the bottom of Figure 2, a 14-channel temperature stabilized RF front end is presented, to be used together with an AMC based Libera LLRF processing system (on the top of Figure 2). In the case of the RFQ LLRF system, the RF front end will integrated within the processing 19” 2U unit [5-7].

For the LIGHT LLRF application, the Libera LLRF system will be controlling the amplitude and phase of a probe signal through pulse-by-pulse feedback. Two separate amplitude and phase controllers will be in place in order to simplify the process of closing the loop. The pulse shape of the drive signal will be modulated by acting on the amplitude and phase envelopes by means of 2nd order spline polynomial sections, to be configured in real-time. For this purpose, an additional SER-RJ1 AMC module has been developed to enable the Control System (CS) to talk directly to FPGA. The CS, with enough time margin with respect to the applied trigger, will be sending a command over an RS-485 interface implemented on the SER-RJ1 module in order to define the pulse amplitude and phase shapes. For this purpose a specific protocol has been developed together by ADAM and Instrumentation Technologies teams, according to the requirements, to fulfil different LIGHT operation scenarios including the cases of real-time interface failure or RF system failure. In these specific cases, the LLRF system applies predefined RF pulse settings depending from the specific failure. The real-time LLRF control is entirely implemented in FPGA, while the slower settings are handled by the computing module in processing unit also connected to the Control System through an interface based on SCPI-like TCP/IP protocol.



Figure 2: The LIGHT LLRF system implemented in the Libera LLRF platform.

The same SER-RJ1 AMC module features also a Modbus interface used by the LLRF system to talk to the external cavity tuning controller: cavity decay analysis is performed at the tail of the pulses and the cavity detune information is calculated, averaged among pulses and delivered at 1 Hz rate.

An RMO (Reference Master Oscillator) temperature stabilized RF source and distribution amplifier units are used to provide stable, low jitter MO signals to all 12 LLRF units at 2997.92 MHz and a sub-harmonic RFQ MO frequency at 749.38 MHz (Figure 3).



Figure 3: Instrumentation Technologies RMO and distribution amplifier temperature stabilized units.

According to LIGHT requirements the Libera LLRF systems has been upgraded to process two different trigger signals named as *idle* and *beam* triggers. The type of the trigger signal defines from which pulse parameters the RF is fired each trigger. A Trigger Synchronization Unit (TSU) has been developed for the purpose of aligning the provided Control System trigger signals to the MO reference with the ability to program arbitrary delays on individual trigger lines. The TSU is a 19” 1U unit and has the capability of processing 26 input trigger lines, provides 26 outputs and additional 13 outputs that can be further delayed for the purposed of triggering the

ISBN: 978-3-95450-194-6 ISSN: 2226-0366 doi:10.18429/JACoW-LINAC2018-MOPO081

RF system modulators. All the TSU settings can be updated through the Control System.

The second Libera LLRF Ethernet interface is used for the archiving purposes. Demodulated 512 sample RF signal traces, from 7 to 13 channels (depending on the station configuration), are streamed at 200 Hz pulse rate within UDP packets over a dedicated network and collected by archiving servers during duration of the treatment.

The classical Libera LLRF threshold-based interlock triggering is upgraded to report failures detected on individual sources. The failures are detected on directional coupler reflected signals when the reflection exceeds a specified fraction of the forward signal. The failures locally detected by the new relative detection concept are locally counted for diagnostic purposes. When the number of counted failures in a preconfigured time window exceeds a certain threshold the interlock is triggered and the RF output is disabled, while individual failures would still enable to operate the RF system at lower power.

CONCLUSION

The LIGHT LLRF has been designed in most of its subsystems and the units are being produced, assembled and tested in order to be delivered to AVO-ADAM within the first half of 2019. It became possible as a result of a strong collaboration between AVO-ADAM and Instrumentation Technologies teams, as both companies are building up their positions in industrial accelerator applications. The innovative LLRF solution for LIGHT, based on the versatile Libera platform, ensures the performance for a successful accomplishment of this challenging medical accelerator project.

REFERENCES

[1] ADAM/AVO website, https://www.avoplc.com

[2] A. Degiovanni *et al.*, "Status of the commissioning of the LIGHT prototype", in *Proc. IPAC'18*, Vancouver, BC, Canada, Apr. 2018, pp. 425-428, doi:10.18429/JACoW-IPAC2018-MOPML014

[3] G. De Michele *et al.*, "Commissioning status of the LIGHT development machine", presented at LINAC'18, Beijing, China, Sep. 2018, paper TUPO013, this conference.

[4] ADAM/AVO, private communication.

[5] L. Piersanti *et al.*, "Review of the ELI-NP-GBS Low Level RF and synchronization systems", in *Proc. IPAC'18*, Vancouver, BC, Canada, Apr. 2018, pp. 2162-2165, doi:10.18429/JACoW-IPAC2018-WEPAL010

[6] D. Angal-Kalinin *et al.*, "Commissioning of front end of CLARA facility at Daresbury Laboratory", in P*roc. IPAC'18*, Vancouver, BC, Canada, Apr. 2018, pp. 4426-4429. doi:10.18429/JACoW-IPAC2018-THPMK059

[7] R. Cerne *et al.*, "Temperature stabilized LLRF control for new generation linear accelerators", presented at LLRF'17, Barcelona, Spain, Oct. 2017, poster P-19.

Content from this work may be used under the terms of the CC BY 3.0 licence (© 2018). Any distribution of this work must maintain attribution to the author(s), title of the work, publisher, and DOI.

ISBN: 978-3-95450-194-6 ISSN: 2226-0366 doi:10.18429/JACoW-LINAC2018-MOPO082

COMMISSIONIG STATUS OF THE LINAC FOR THE iBNCT PROJECT

M. Sato†, Z. Fang, M. Fukuda, Y. Fukui, K. Futatsukawa, Y. Honda, K. Ikegami, H. Kobayashi, C. Kubota, T. Kurihara, T. Miura, T. Miyajima, F. Naito, K. Nanmo, T. Obina, T. Shibata, T. Sugimura, A. Takagi, E. Takasaki, High Energy Accelerator Research Organization (KEK), 305-0801 Tsukuba, Japan
H. Kumada, Y. Matsumoto, T. Ohnishi, S. Tanaka, University of Tsukuba, 305-8577 Tsukuba, Japan
N. Nagura, T. Ohba, Nippon Advanced Technology 319-1112 Tokai, Japan
T. Ouchi, H. Sakuryama, ATOX Co., Ltd., 319-1112 Tokai, Japan
K. Hasegawa, Japan Atomic Energy Agency, 319-1195 Tokai, Japan

Abstract

For a new type of cancer therapy, the accelerator-based boron neutron capture therapy (BNCT) has been attracted renewed interest. The basic concept of BNCT is to utilize secondary products from a neutron capture reaction on boron medicaments locally-implanted into cancer cells. It has been originally studied with neutrons from nuclear reactors for a long time, meanwhile many activities have been recently projected with accelerator-based neutron generation techniques. In the iBNCT (Ibaraki BNCT) project, the accelerator is consisted with RFQ and Alvarez DTL. We have started the beam commissioning of the accelerator from the end of 2016, and an acceptably-stable operation was achieved with beam repetition of 50 Hz, which is equivalent of the average current of 1.4 mA at the target. This current makes the project possible to proceed to non-clinical bench test toward a first-phase clinical trial study. Further beam commissioning will be performed toward higher beam current. In this paper, a present status of the iBNCT linac and its future prospect will be reported.

INTRODUCTION

An academic-industrial collaborative project for BNCT, Ibaraki-Boron Neutron Capture Therapy (iBNCT) project, has been started in the year of 2010. It is a collaboration with High Energy Accelerator Research Organization (KEK) for an accelerator part, Tsukuba University for a medical part and supportive works by neighbouring companies and Ibaraki prefecture in Japan [1].

BNCT has been originally studied with neutrons generated from a nuclear reactor, but the recently many activities have been started with accelerator-based neutron generation methods. In the iBNCT project, the accelerator is consisted of an RFQ and Alvarez DTL, whose configuration was based on that in J-PARC linac. Primary 50-keV protons extracted from an ECR ion source are accelerated by RFQ and DTL up to 3 MeV and 8 MeV, respectively, and bombarded onto a beryllium target to generate neutrons by the ^{9}Be(p, n) reaction. The most significant difference from J-PARC one is the higher duty factor, more than 5 %, is necessary to have a sufficiently-strong epithermal neutron flux for BNCT. Detailed parameters of RFQ and DTL are found in Ref. [2]. One of the features of the iBNCT project is to take aim for BNCT to become a popular cancer therapy not to need specific irradiation facilities. Thus, iBNCT makes compact the whole size of the components to be enable to install inside hospitals.

We have confirmed the first 8-MeV proton beam and neutron generation from the target in 2014 and 2015, respectively. The beam commissioning for higher beam current has been started since 2016. After that, the iBNCT accelerator has been officially certificated as a radiation generator facility since Jan. 2017. In this paper, recent commissioning status will be reported

INSTABILITY OF RFQ AND ITS IMPROVEMENTS

In the former half of 2017, instability of the beam operation caused by an RF interlock followed by a failure in its recovery made difficult to keep the operation for 1 hour which is required for a typical medical-treatment time of BNCT. A discharge inside RFQ frequently occurred and it stopped the RF pulse for the machine protection system of the cavity. In a normal situation, we can quickly re-input RF after the stop (Quick-Recovery) within 1 second. However, a success rate of this Quick-Recovery functionality is not so high due to a problem on RFQ cooling water system described later. Another problem is a pressure in RFQ. A hydrogen gas flow from the ion source increases the pressure in RFQ during the beam operation. It was obviously shortage of the pumping power for the 1-hour operation. Therefore, we first tried to improve these two issues, and details are described in the following sections.

Reinforcement of the Vacuum System

In the beam operation with 50 Hz repetition, due to the hydrogen gas flow from the ion source, the pressure in RFQ gradually increased and sometimes came up to the interlock level. For the beam operation longer than 1 hour, it is necessary that the reinforcement of the vacuum system of RFQ. Originally, 2 cryo-pumps, 10 ion pumps and 2 NEG pumps were equipped to RFQ. We newly installed turbo molecular pumps (TMP). To have enough compulsivity to hydrogen, two TMPs with evacuation

† email address masaharu.sato@kek.jp

Content from this work may be used under the terms of the CC BY 3.0 licence (© 2018). Any distribution of this work must maintain attribution to the author(s), title of the work, publisher, and DOI.

ISBN: 978-3-95450-194-6 ISSN: 2226-0366 doi:10.18429/JACoW-LINAC2018-MOPO082

speed of 800 L/s were installed in tandem configuration. Besides that, fixed tuner ports of RFQ were connected to manifolds to have higher conductance for TMP and cryo pump lines because the top of tuners have slits for the evacuation of RFQ. Furthermore, after the beam parameter tuning, amount of the hydrogen gas flow rate into the ion source was reduced from 6.5 to 3.1 SCCM (Standard cc per minute), and to reduce hydrogen gas flowed into RFQ, TMP at the LEBT was replaced from 300 L/s to 800 L/s. With these improvements, the pressure in RFQ during the beam operation was reduced to 1×10^{-4} Pa, which is about 1/3 of the value before the improvements

Improvement of the Cooling Water System

In the original plan of a cooling water system for the accelerator cavity, a large temperature increase after RF input was allowed up to 10 ˚C by keeping the average of inlet and outlet temperatures constant. This was based on the concept that the iBNCT accelerator should be compact as possible to install whole equipment inside a hospital including cooling water system. However, if RF is suspended by the interlock, temperature immediately decreases and the resonance frequency is largely deviated, and that situation causes a failure to re-input RF quickly. In such a case, we must restart RF from low power level and it takes several minutes to reach the operation power. For BNCT, a stable beam operation is required because an effective time of the boron medicament in cancer is limited. To avoid such a beam suspension, it is essential to minimize the temperature difference (ΔT) between inlet and outlet of the cavity. Due to a limitation of time and cost for the improvement, extensive replacements of the cooling water system were impossible. Thus, we took two measures: One is to increase RFQ cooling water flow by dividing a part of cooling water for DTL (Measure 1). The other is to replace a water-circulation pump (Measure 2). For the former case, this is because the RF interlock is mainly caused by discharges in RFQ. In original, water flow of RFQ and DTL are 100 L/m for each, but we changed them to 160 L/min for RFQ and 40 L/min for DTL, respectively. In this measure, the temperature difference in RFQ was reduced from 1.5 ˚C to 1.2 ˚C with RF repetition of 50 Hz. Meanwhile, that in DTL was increased from 1.5 ˚C to 5.3 ˚C. We accepted this temperature difference because the rate of RF interlock in DTL is extremely low and DTL equips with a variable tuner. In the second measure, we replaced a water-circulation pump to one having twice higher power from 5.5 kW to 11.0 kW. With this replacement, both flows of RFQ and DTL were increased to 220 L/min, respectively. Due to the pressure loss of the cooling pipes just before and after RFQ, the maximum water flow rate for RFQ was limited to be about 260 L/min. We will tune the flow rate between RFQ and DTL after replace and simplify those pipes in the summer maintenance in 2018. We already confirmed that water flow for RFQ was improved to be 330 L/min. Further adjustment of the flow rate will be done in Sept. 2018 after resuming the beam operation. Table 1 is a summary of the measures for cooling water system for cavities. As a result, we can decrease temperature differences about 2/3 of the original values.

Furthermore, the stability of the inlet temperature was improved by changing the PID algorism of the cooling water temperature control. Originally, each PID device was controlled by thier built-in PID. In the new algorism, control of several PID devices were unified in a program. Fine temperature tuning is only done by a local in-line heater attached just before the cavity. Here, the detailed explanation is omitted because of limitation of space.

Table 1: Cavity Temperature Increases and Water Flow

	Original	Measure 1	Measure 2
		RFQ	
ΔT	1.5 ˚C	1.2 ˚C	1.0 ˚C
Flow rate	100 L/min	160 L/m	220 L/m
		DTL	
ΔT	1.5 ˚C	5.3 ˚C	1.0 ˚C
Flow rate	100 L/min	40 L/min	220 L/min

COMMISSIONIG STATUS

Stability of the Beam Operation

After the improvements done for RFQ as mentioned above, the beam operation with 50 Hz repetition and width of 920 μs became very stable to keep more than 1 hour. Since typical medical-treatment time for BNCT is about 1 hour, the iBNCT project aims to start first-phase clinical trial study for melanoma patients by considering the beam stability as a first priority. At the beginning of the commissioning, average beam current was 1 mA at the target. As a result of tuning for the hydrogen gas flow rate, the current of a solenoid magnet of the ion source, an electrostatic lens after an extraction electrode, the beam current was increased up to 1.3 mA. After the retuning of the hydrogen gas flow, the current was increased up to 1.4 mA with the gas flow of 3.1 SCCM. This current is equivalent with an epi-thermal neutron flux to complete clinical treatment to melanoma patients within 1 hour

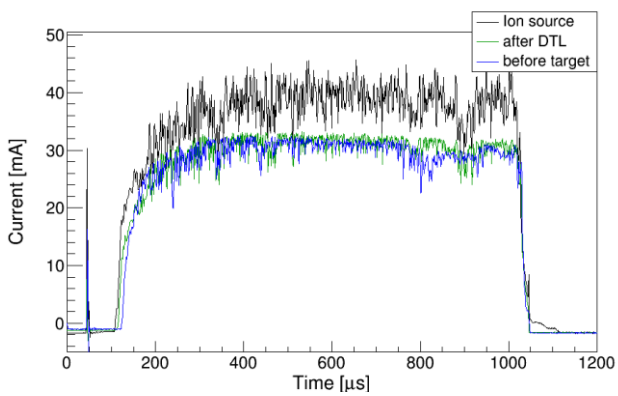


Figure 1: Waveforms taken with CTs installed at the ion source (black), after DTL (green) and before the target (blue), respectively.

Content from this work may be used under the terms of the CC BY 3.0 licence (© 2018). Any distribution of this work must maintain attribution to the author(s), title of the work, publisher, and DOI.

ISBN: 978-3-95450-194-6 ISSN: 2226-0366 doi:10.18429/JACoW-LINAC2018-MOPO082

Content from this work may be used under the terms of the CC BY 3.0 licence (© 2018). Any distribution of this work must maintain attribution to the author(s), title of the work, publisher, and DOI.

which is issued a guideline by IAEA [3]. Figure 1 shows the waveform taken with current transformers (CTs) installed at the ion source, after DTL, and before the target, respectively. The peak currents at the ion source and the target are about 40 and 30 mA, respectively. We consider that further optimization is enable by the increase of the diameter of extraction hole which is presently rather small one of 6 mm in diameter.

With this beam condition, we have finished data taking for basic information on neutron beam, such as intensity and spatial distributions of epi-thermal neutrons. Furthermore, irradiation tests with cells with boron medicaments were performed 3 times in the fiscal year of 2017. An irradiation test with mice was performed in Jan. 2018, which was the first animal irradiation test for iBNCT.

Integrated Charge

Figure 2 shows the integrated charge of the beam commissioning by the end of Jul. 2018. Blue and green lines indicate the charges just after the ion source and at the beam transport line before the beryllium target, respectively. We optimized the solenoid magnet for the ion source at Apr. 2017 to have higher plasma density, and we were keeping beam operation with a fixed repetition rate of 50 Hz since Sept. 2017. At Jul. 2018, the integrated charges are 2500 C at the ion source, and 2000 C before the target. A typical BNCT medical treatment to a melanoma patient needs about 4 C, thus current operational result is equivalent to 500-times medical treatments. Although this remarkably-large charged was irradiated to the target, no deterioration of the neutron yield was observed. Red triangle plots in Fig. 2 show the thermal neutron flux (right scale) measured with a gold-activation method in a water phantom. Values are normalized with a proton average current of 1 mA. Each point has systematic error of 8 % as shown in the leftmost point, and all points are consistent within the systematic error. The irradiation result definitely shows that the stability and usefulness of our beryllium target [4]. We still have an enough margin

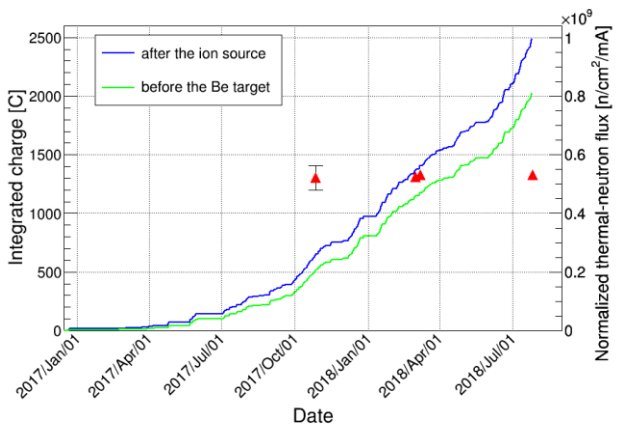


Figure 2: History of the amount of integrated charges after the ion source (blue) and the beam transport line before the target (green), respectively. Triangle plots indicate the thermal-neutron flux normalized the current.

to an estimated lifetime of the target, however, the accurate estimation is fairly difficult. Thus, it is important to check the soundness of the target by an online monitor of the neutron flux with LiCAF ($LiCaAlF_6$ doped rare-earth ion) scintillators and periodical observations of the surface of the beryllium target.

Toward Higher Beam Current

Since the stability of the operation with an average beam current of 1.4 mA was already confirmed, the iBNCT project will start non-clinical bench tests as soon as possible toward the first-stage clinical trial study aiming the realization in the fiscal year of 2019. To achieve higher beam current makes it possible to enlarge the applicable range of cancer and to shorten medical treatment time. A present goal is to achieve the current of 5 mA, and it is necessary to increase the repetition rate up to 150 Hz. We have been ready to start high repetition test from this June. We increase the repetition rate to be 66.7 Hz, and already achieved the average beam current of 1.9 mA with a considerable stability. Toward realization of 5 mA, we keep the beam commissioning with increasing the beam repetition rate up to 150 Hz by a stepwise tuning.

CONCLUSION

In the iBNCT project, instability of RFQ was serious problem for the stable operation at beginning of 2017 after the certification of the radiation generator facility. With improvements of the vacuum and cooling water system of RFQ, we have achieved stable beam operation with an average beam current of 1.4 mA at the repetition of 50 Hz. This beam current enables the iBNCT project to start non-clinical tests necessary for a first-phase clinical trial study aiming at the realization in the fiscal year of 2019. We keep the beam commissioning to achieve more than 5 mA for future extension of the iBNCT project.

ACKNOWLEDGEMENTS

Authors appreciate supports and encouragements from doctors in the hospital attached to Tsukuba University. We are grateful to the J-PARC accelerator group for fruitful discussions, freed-backs from their experiences and continuous supports. We would like to acknowledge Prof. Masanori Yamauchi (Director General, KEK) for financial supports to our project.

REFERENCES

[1] H. Kumada *et al.*, "Project for the development of the linac based BNCT facility in University of Tsukuba", *Applied Radiation and Isotopes*, pp. 88, 211-215, 2014.

[2] F. Naito *et al.*, "BEAM COMMISSIONING OF THE i-BNCT LINAC", *Proceedings of LINAC16*, (2016), pp. 760-762.

[3] International Atomic Energy Agency, "Current status of neutron capture therapy", IAEA-TECDOC-1223, 2001.

[4] T. Kurihara *et al.*, "Neutron target research and development for BNCT: direct observation of proton induced blistering using light-polarization and reflectivity changes", *Journal of Radioanalytical and Nuclear Chemistry* (2015), pp. 305, 935-942.

ISBN: 978-3-95450-194-6 ISSN: 2226-0366 doi:10.18429/JACoW-LINAC2018-MOPO084

THE SIMULATION AND MANUFACTURE OF THE ROOM TEMPERATURE CH-DTL*

Jinhai Li†, Chunguang Li, Guangwen Han, China Institute of Atomic Energy, Beijing,China
Zhihui Li, Institute of Nuclear Science and Technology, Sichuan University, Chengdu,China

Abstract

The room temperature Cross-bar H Type Drift Tube Linac (CH-DTL) is one of the candidate acceleration structures working in CW mode. In order to optimize the parameters, the 3 dimensional electromagnetic field of the CH-DTL cavity is simulated. The method of parameter sweeping with constraint variable is better than the method of parameter sweeping with only one variable during the optimization. In order to simplify the manufacture, the drift tube surface can be designed as spherical shape. The CH-DTL cavity has been manufactured and tested.

INTRODUCTION

An Accelerator Driven transmutation System (ADS) [1, 2], currently under development in China, will be used to reduce both the toxicity and half-life of the long-lived radioactive nuclear waste created in light-water reactors to a controllable level [3]. An industrial scale ADS will require an average beam current of≥10 mA. In 2010, the Institute of High Energy Physics (IHEP) and the Institute of Modern Physics (IMP) are both developing superconducting accelerating structures which would follow an RFQ [4].

Although low power consumption and a large aperture favor superconducting structures following a 2-3.5MeV RFQ, normal-conducting accelerating structures have some advantages [5, 6]. Normal-conducting structures in the energy range from 2 to a few tens of MeV are more compcter and can obtain high acceleration gradient than the superconducting ones and, when located downstream of the RFQ, they can serve as a beam filter to reduce the potential for beam loss at higher energies. The CH structure, initially proposed by IAP [7, 8], belongs to the π-mode family of accelerating structures and is typically characterized by high shunt impedance, low stored energy and stable geometry that is relatively easy to cool. This structure is evaluated as a potential candidate for CW operation. In this paper it is presented the results of geometry optimization of the CH structure using the method of parameter sweeping with constraint variable (PSCV) [9].

THE METHOD OF PARAMETER SWEEPING WITH CONSTRAINT VARIABLE

The parameters of a single cell are shown in Fig. 1. The outer drift tube radius (TR) and the radius of the drift tube aperture (HR) are fixed during the optimization. Typically a single parameter was swept while monitoring the cavity's RF properties. However, by changing the length of the drift tube, the resonant frequency changes. Our objective is to optimize the cavity geometry at a fixed frequency (325 MHz). If the frequency changes during the optimization, the optimized value of the swept parameter will differ from the value corresponding to the correct frequency as shown in Fig.2 and Table1. In Fig. 2 the radius of the drift-tube stem base (R2) was swept while fixing the cavity radius (CR). It can be seen that the effective shunt impedance decreases with increasing R2 while the resonant frequency increases from 321.7 to 333.5 MHz. It is convenient to use the cavity radius (CR) as a "constraint variable" to fix the resonant frequency to 325 MHz as shown in Table1. By doing so, it can be found that the maximum effective shunt impedance at the correct frequency occurs at R2=22. This method can be named after "parameter sweeping with constraint variables" (PSCV). Other parameters can be selected as constraint variables, but it is found that the resonant frequency is more sensitive to cavity radius than it is to other geometrical parameters.

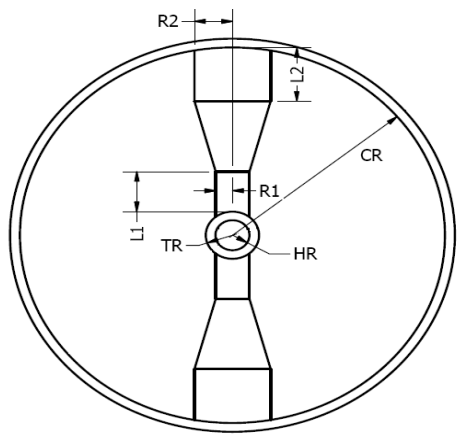


Figure 1: Geometry of a CH single cell.

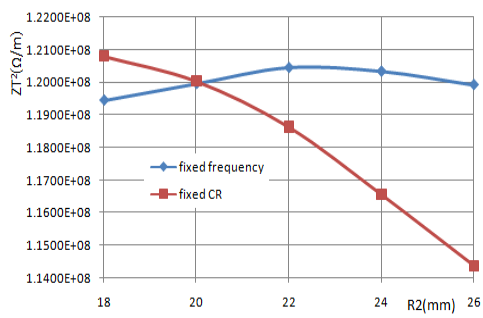


Figure 2: Shunt impedance as a function of outer stem radius using two methods of parameter sweeping.

* Work supported by the National Natural Science Foundation of China (NSFC)
† email address:13661338455@163.com

Content from this work may be used under the terms of the CC BY 3.0 licence (© 2018). Any distribution of this work must maintain attribution to the author(s), title of the work, publisher, and DOI.

ISBN: 978-3-95450-194-6 ISSN: 2226-0366 doi:10.18429/JACoW-LINAC2018-MOPO084

Content from this work may be used under the terms of the CC BY 3.0 licence (© 2018). Any distribution of this work must maintain attribution to the author(s), title of the work, publisher, and DOI.

Table 1: Comparison of Parameter Sweeping with and without a Constraint Variable

Fixed frequency			
R2(mm)	**CR(mm)**	**f(MHz)**	**ZT^2(Ω/m)**
18	140.9	324.69	1.1945E+08
20	142	324.9	1.1996E+08
22	143.1	324.52	1.2045E+08
24	144.2	324.18	1.2033E+08
26	145.2	324.06	1.1992E+08
Fixed cavity radius			
R2(mm)	**CR(mm)**	**f(MHz)**	**ZT^2(Ω/m)**
18	142	321.7	1.2080E+08
20	142	324.9	1.2004E+08
22	142	327.9	1.1864E+08
24	142	330.8	1.1656E+08
26	142	333.5	1.1438E+08

SPHERICAL DRIFT TUBE

The drift tube in CH-DTL is typically much smaller than drift tubes in a conventional DTL, and the small drift tubes have much smaller capacitance resulting in a higher shunt impedance, but they are so small they are difficult to manufacture with integral cooling channels. Traditional drift tubes are nominally cylindrical as shown in Fig. 3. By modifying the design to have a spherically shaped drift tube, the stem and drift tube can be manufactured (turned) in one step without welding or brazing. In Fig. 4 it can be seen that axis of revolution for the stem is coaxial with that of the drift tube. The effective shunt impedance of the spherical drift tube is only slightly lower than that of the cylindrical drift tube (<1%) as shown in Fig. 5.

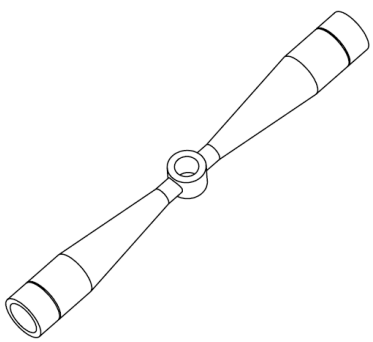


Figure 3: Cylindrical drift tube.

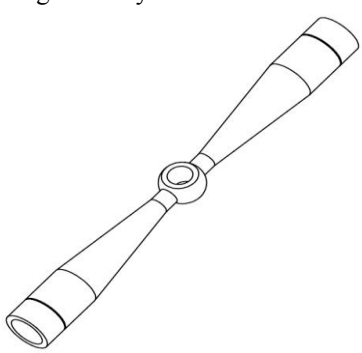


Figure 4: Spherical drift tube.

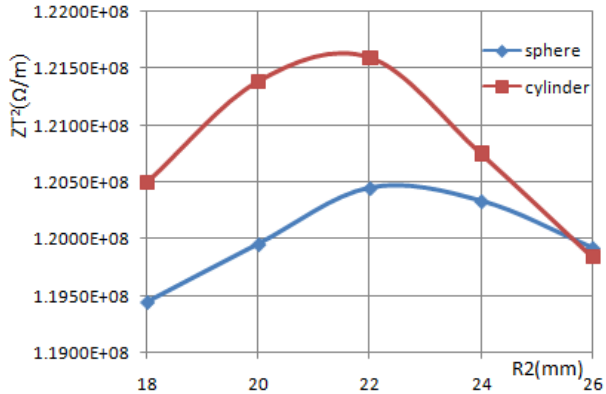


Figure 5: Shunt impedance for two different drift tube shapes as a function of the stem-base radius.

OPTIMIZING THE MULTI-CELL CAVITY

The multi-cell CH-DTL cavity model includes four drift tubes and five gaps as shown in Fig.6. In addition to the parameters optimized above, the multi-cell cavity contains two additional geometrical features requiring optimization. These include the length and radius of the end cups (EL and ER). ER is first swept to find that the effective shunt impedance is inversely proportional to ER as shown in Fig. 7.

As the end cup length (EL) increase, it can be seen that the effective shunt impedance decreases rapidly due to the power dissipated in the end regions where no acceleration occurs as shown in Fig. 8.

CAVITY MANUFACTURE AND LOW POWER RF MEASUREMENT

The stem, the cavity wall and drift tube is made of the oxygen free copper, and the flange is made of the stainless steel with copperized inside as shown in Fig. 9. The network analyzers is used for the low power RF measurement, and the Q value is about 7194.

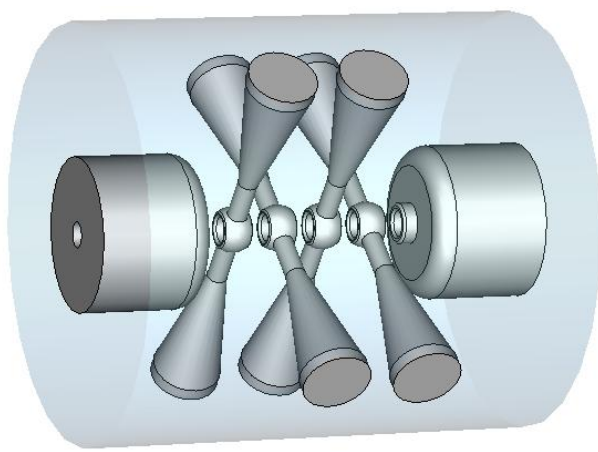


Figure 6: 3-D geometry of the 5-cell CH-DTL cavity model.

ISBN: 978-3-95450-194-6 ISSN: 2226-0366 doi:10.18429/JACoW-LINAC2018-MOPO084

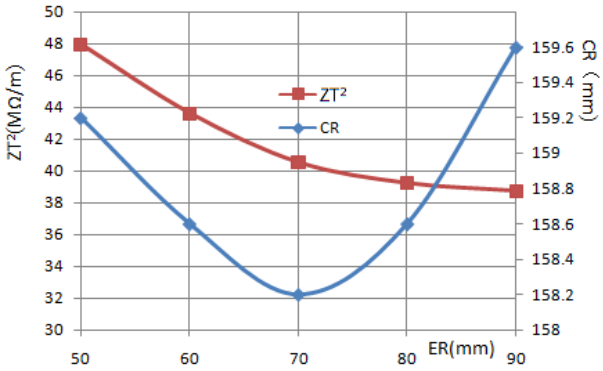


Figure 7: Shunt impedance and cavity radius at a fixed frequency as a function of ER for a 5-cell cavity without end cups.

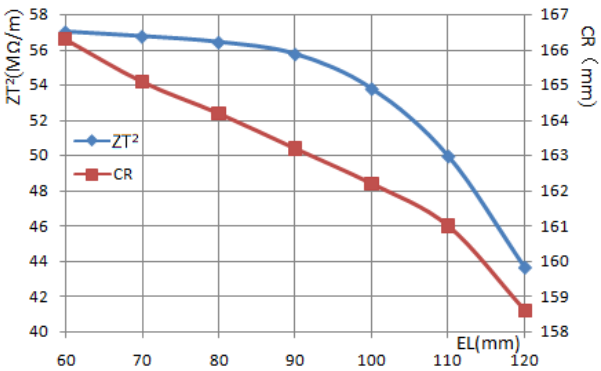


Figure 8: Shunt impedance and cavity radius at a fixed frequency as a function of EL for a 5-cell cavity with end cups.



Figure 9: The inside view of the manufactured cavity.

ACKNOWLEDGMENT

This work is supported by the National Natural Science Foundation of China (NSFC). I would show my best thanks to James Edward Stovall for his kind help.

REFERENCES

[1] Pramod Kumar Nema, "Application of Accelerators for Nuclear Systems Accelerator Driven System (ADS)", *Energy Procedia*, vol 7, pp. 597–608, 2011.

[2] Rubbia, C., J. A. Rubio, S. Buono *et al.*, "Conceptual design of a fast-neutron operated high power energy amplifier", CERN/AT/95-44 (ET), European Organisation for Nuclear Research, 1995.

[3] Jean Pierre Revol, "An Accelerator-Driven System for the Destruction of Nuclear Waste", *Progress in Nuclear Energy*, vol. 38, no. 1-2, pp. 153-166, 2001.

[4] WeimingYue, X. L. Guo, S. He *et al.*, "R&D of IMP Superconducting HWR for China ADS", in *Proceedings of LINAC2012*, 2012, paper TUPB055, pp. 600-602.

[5] L. Ristori, G Apollinari, I. Gonin *et al.*, "Design of normal conducting 325 MHz crossbar H-type Resonators at fermilab", in *Proceedings of LINAC2006*, 2006, paper THP057, pp. 710-712.

[6] L. Ristori, G. Apollinari, I. Gonin *et al.*, "fabrication and test of the first normal-conducting crossbar H-type accelerating cavity at fermilab for HINS", in *Proceedings of PAC07*, New Mexico, 2007, pp. 2292–2294.

[7] U. Ratzinger, "The new high current ion accelerator at GSI and perspectives for Linac design based on H-mode cavitys", in *Proceedings of the European Particle Accelerator Conference*, Vienna, 2000, (EPS, Geneva, 2000), pp. 98–102.

[8] R. M. Brodhage, U. Ratzinger, G. Clenente, W. Vinzenz, "First coupled CH power cavity for the FAIR proton injector", in *Proc. 4th Int. Particle Accelerator Conf. (IPAC'13)*, Shanghai, China, May 2013, paper THPWO015, pp. 3791-3793.

[9] J. Li, Z. Li, "The simulation and optimization of a room-temperature Cross-Bar H-Type Drift- Tube Linac", *Journal of Instrumentation*, vol. 10, pp. 1-10, 2015.

Content from this work may be used under the terms of the CC BY 3.0 licence (© 2018). Any distribution of this work must maintain attribution to the author(s), title of the work, publisher, and DOI.

ISBN: 978-3-95450-194-6 ISSN: 2226-0366 doi:10.18429/JACoW-LINAC2018-MOPO085

PROTOTYPE OF AN INTER-DIGITAL H-MODE DRIFT-TUBE LINAC FOR MUON LINAC

Y. Nakazawa*, H. Iinuma, Ibaraki University, Mito, Ibaraki, Japan
Y. Iwata, National Institute of Radiological Sciences, Chiba, Japan
Y. Iwashita, Kyoto University, Kyoto, Japan
M. Otani, N. Kawamura, T. Mibe, T. Yamazaki, M Yoshida, KEK ,Tsukuba, Ibaraki, Japan
R. Kitamura, H. Yasuda, University of Tokyo, Hongo, Tokyo, Japan
Y. Kondo, K. Hasegawa, T. Morishita, JAEA, Tokai, Naka, Ibaraki, Japan
N. Saito, J-PARC center, Tokai, Naka, Ibaraki, Japan
Y. Sue, Nagoya University, Nagoya, Japan
N. Hayashizaki, Tokyo Institute of Technology, Tokyo, Japan

Abstract

An inter-digital H-mode (IH) drift-tube linac (DTL) is developed for a low velocity part in a muon linac at the J-PARC E34 experiment. It will accelerate muons from $\beta = 0.08$ to 0.28 at an operational frequency of 324 MHz. In order to achieve higher acceleration efficiency and make cost lower, an alternative phase focusing (APF) scheme is adopted. A prototype with 6 cells of 0.45 m length was manufactured. The prototype accelerates muons from $\beta = 0.08$ to 0.15 stage. We conducted frequency measurement and bead-pull measurement as a low-power measurement, in order to evaluate the prototype product. In this paper, the results of the low-power measurement for prototype cavity will be presented.

INTRODUCTION

The muon anomalous magnetic moment (g-2) is the one of the promising signals of beyond the Standard Model. The E821 experiment at Brookhaven National Laboratory found the 3.7σ discrepancy between the SM theoretical calculation and the measurement of the muon g-2 [1, 2]. The muon beam in the E821 experiment was produced by in-flight pion decay with large emittance, which requires electric quadrupoles to keep the muon beam inside of the beam pipe. In order to avoid muon precession in the electric field, the muon beam should be well adjusted to the fixed value (magic momentum).

In the case of J-PARC experiment (J-PARC E34), we plan to measure muon g-2 and EDM (Electric Dipole Moment) with new technique [3]. We will provide a low emittance muon beam for high precision measurement from the stopping pion decay and their reacceleration steps [4]. In this method, electric field is not needed in storage ring, and the systematic error is reduced.

Figure 1 shows the schematic image of muon linac. μ^+ with a kinetic energy of 30meV called ultra slow muon (USM) is accelerated by muon linac. The muon linac is composed of a radio frequency quadrupole (RFQ) linac, the IH-DTL, a disc and washer coupled cavity linac (DAW-CCL), and a disc loaded structure (DLS). The USM is accelerated to 212 MeV. The IH-DTL is employed during the particle velocity $\beta = 0.08$ to 0.28 stage with an operational frequency of 324 MHz.

In this paper, we describe the result of the low-power measurement of the prototype cavity. The paper is structured as follows. First the prototype design is described. Next, the results and discussion of frequency measurement and bead-pull measurement is presented. Finally, the summary is presented.

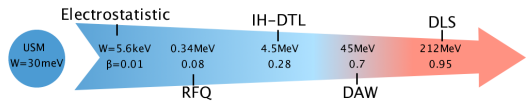


Figure 1: Schematic image of muon linac.

APF IH-DTL

H-mode DTL is installed hollow conducting drift tube along the beam axis. The drift tube is supported by stems attached to the outer wall. In time variation, the magnetic fields at the surface of the stems induce current. The structure of IH-DTL prototype is shown in Fig. 2. The IH cavity consists of two ridges arranged on both the top and bottom sides of the cavity. Five drift tubes are arranged alternately on the top and bottom via stems on the ridges, in order to excite TE_{11}-mode. The beams are accelerated by the longitudinal electric field with the gap.

The focusing section is necessary for linac to suppress the beam dispersion. The usual focusing method is provided by a quadrupole magnet and a permanent magnet. However, our IH-DTL employs the alternating phase focusing (APF) method [5, 6]. In APF method, the focusing or divergence of beam is controlled with the RF field only by optimizing synchronous phase of gap. Thus, the IH structure is simplification and is able to be fabricated at lower cost.

The motion equation of the longitudinal and transverse focusing in RF field are expressed as

$$z'' - \frac{\pi e E_0 T \sin\phi}{2 m_0 c^2 \beta^3 \gamma^3 \lambda} z = 0 \qquad (1)$$

* 18nm021f@vc.ibaraki.ac.jp

Content from this work may be used under the terms of the CC BY 3.0 licence (© 2018). Any distribution of this work must maintain attribution to the author(s), title of the work, publisher, and DOI.

ISBN: 978-3-95450-194-6 ISSN: 2226-0366 doi:10.18429/JACoW-LINAC2018-MOPO085

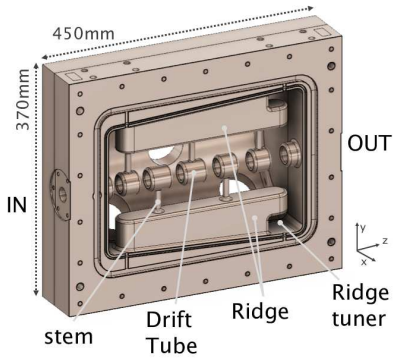


Figure 2: Sectional view of IH-DTL prototype in 3D model.

$$r'' + \frac{\pi e E_0 T \sin\phi}{2m_0 c^2 \beta^3 \gamma^3 \lambda} r = 0 \qquad (2)$$

where E_0 is the unperturbed electric field, T Transit time factor, γ Lorentz factor, λ RF wave length, and ϕ is the synchronous phase [7, 8]. Equations (1) and (2) show that negative synchronous phase provides longitudinal focusing and transverse defocusing, and positive synchronous phase provides longitudinal defocusing and transverse focusing. Hence, we are able to control the longitudinal and transverse focusing by optimizing the gap-to-gap synchronous phases.

For APF method, an acceleration and the focusing are achieved with the RF field only. In order to optimize the cavity structure, synchronous phase array optimization, cavity optimization, and particle tracking are required. The prototype design is determined by the actual cavity optimization. The actual cavity is calculated [9] and has 16 cells and the cavity length is approximately 1.3 m to correspond to approximately 4 MeV. The 1–6 cells of the actual cavity are in the prototype cavity [10]. We calculated the electromagnetic field in the prototype cavity by using the CST Micro Wave (MW) Studio [11]. Table 1 shows the cell parameters of the prototype cavity optimization. The prototype cavity is employed during the particle velocity $\beta = 0.08$ to 0.28 stage.

Moreover, the beam particle trajectory was calculated by using general particle tracer (GPT) [12]. The most precise evaluation of the output beam can be obtained using realistic input beam distributions. The input beam was used muon beam that the normalized root mean square (rms) emittances of the input beam were evaluated as ε_x=0.297π mm mrad in the x-direction, ε_y=0.168π mm mrad in the y-direction. This beam was simulated from the surface muon beam line, the USM system, and the RFQ acceleration [13]. The output beam of the normalized emittance (and emittance growth) was calculated to be ε_x=0.312π mm mrad (+5.1%) and ε_y=0.182π mm mrad (+8.2%) in the x-direction and y-directions, respectively.

FREQUENCY MEASUREMENT

Prior to bead-pull measurement, we estimated the resonant frequency and an unloaded Q (Q_0) in prototype cavity by measuring the scattering parameters. First, the cavity frequency and coupling constant β were measured in reflection (S_{11} and S_{22}). This was done with a vector network analyzer (VNA) coupled to two RF pick-up loops as cavity probes. Next, the resonant frequency and a loaded Q (Q_L) were measured in transmission measurement (S_{21}). Then, the Q_0 was calculated by the measured β and the Q_L. Table 2 shows a comparison of the designed value with the measured value by VNA.

Table 1: Cell Parameters for Optimized Phase Array

Cell	W [MeV]	β	ϕ [degree]
1	0.34	0.08	-35.9
2	0.43	0.09	-14.9
3	0.57	0.10	12.9
4	0.74	0.12	32.9
5	0.92	0.13	15.4
6	1.14	0.15	-13.8
exit	1.3		

Table 2: Frequency Measurement

	Simulation	Measurement
Resonant frequency [MHz]	321.53	321.21
Q_L (loaded Q)	-	6125.8
β_1	-	0.075
β_2	-	0.1814
Q_0 (unloaded Q)	8700	7695.2

BEAD-PULL MEASUREMENT

Slater Perturbation Theorem

According to the slater perturbation theorem for electromagnetic field in cavity, the resonant frequency is shifted, when a small volume like a bead is removed from the cavity volume [14]. The shift of the resonant frequency depends on the relative strengths of the electric field and the magnetic field. For a spherical perfectly conducting bead of radius r, the shift given as a function of the unperturbed field amplitudes E_0 and H_0, by

$$\frac{f_p - f_0}{f_0} = -\frac{\pi r^3}{U}\left[\varepsilon_0 E_0^2 - \frac{\mu_0 H_0^2}{2}\right] \qquad (3)$$

where f_p is the perturbed frequency, f_0 is the unperturbed frequency U is the stored energy in cavity, ε_0 is the permittivity of vacuum, and μ_0 is the permeability of vacuum [15].

Instead of measuring the shift of frequency, the shift of the phase has been measured and then translated it into frequency-shift by

$$\frac{f_p - f_0}{f_0} = \frac{\tan(\Delta\phi)}{2Q_L} \qquad (4)$$

Content from this work may be used under the terms of the CC BY 3.0 licence (© 2018). Any distribution of this work must maintain attribution to the author(s), title of the work, publisher, and DOI.

ISBN: 978-3-95450-194-6 ISSN: 2226-0366 doi:10.18429/JACoW-LINAC2018-MOPO085

Content from this work may be used under the terms of the CC BY 3.0 licence (© 2018). Any distribution of this work must maintain attribution to the author(s), title of the work, publisher, and DOI.

where $\Delta\phi(= \phi_p - \phi_0)$ is the phase-shift derived from the unperturbed phase and the perturbed phase.

Experimental Setup

Figure 3 shows the experimental setup for bead-pull measurement. In the experiments, we used the aluminum bead with a 1.5 mm radius assumed the spherical perfectly conducting bead. The bead is attached to a non-conducting wire (fishing line) that is driven through the IH cavity.

The stepping motor was controlled by stored program controller and was used to move the bead and the wire on the beam axis. In this time, the position of bead is in beam axis with an uncertainty of 2 mm.

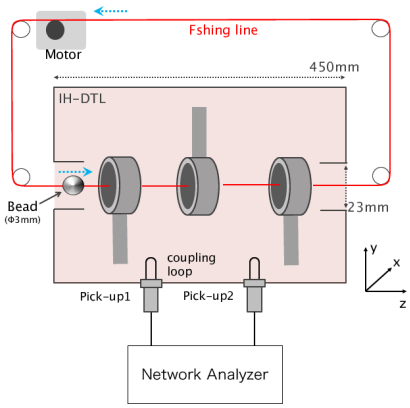


Figure 3: Experimental setup for bead measurement.

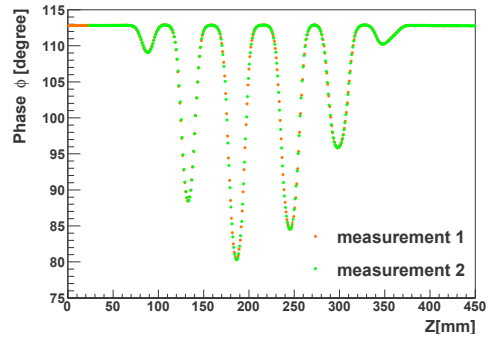
Result & Discussion

The phase of S_{21} at the unperturbed frequency was measured by the VNA. Figure 4(a) shows the plot of phase in cavity versus bead position, when the bead traveled between incident port and outgoing port as measurement 1 and measurement 2, respectively. The measurement 1 was consistent with the measurement 2 with an uncertainty of 1%. The baseline of unperturbed phase is 113 degrees. The six phase-shifts derived from the perturbation was measured in IH cavity.

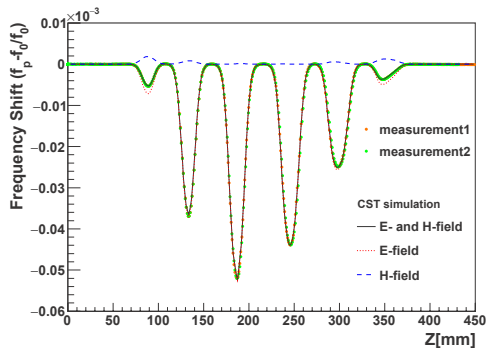
Figure 4(b) shows the dependence of frequency-shift converted by using the measured phase shift and Eq. (4) on the bead position with overwriting of the electromagnetic field (right side of Eq. (3)), E field (the first term on the right side of Eq. (3)), and H field (the first second on the right side of Eq. (3)) by CST.

For IH cavity, there is the magnetic field on the beam axis. In order to confirm whether to be excited the designed accelerating electric field, it is necessary to consider the electromagnetic field in bead-pull measurement. As a result of Fig. 4(b), the measured value is consistent with the simulated value of the field with an uncertainty of 3%.

The cause of the uncertainty is systematic error by mismatching beam axis of bead. We estimated the variation of electric field distribution by CST, when the bead deviated from beam axis in the transverse directions. The variation of



(a)



(b)

Figure 4: (a) Phase shift ($\Delta\phi$) measurement 1 (or 2) as a function z-axis, when bead is moved from incident (outgoing) port to outgoing (incident) port. (b) A comparison between frequency shift by measurement and E and H field (Solid line), E field and H field (dotted line) as a function z.

accelerating electric field is approximately 2–3% at the position located in transverse direction of 3 mm from the beam axis. The bead is located in beam axis with an uncertainty of 2 mm. Therefore, we verified that the electromagnetic field of prototype cavity is consistent with the simulated field within the systematic error.

SUMMARY

In this paper, the prototype cavity was evaluated for studying the actual cavity of IH-DTL in J-PARC g-2/EDM experiment. The resonant frequency and Q_0 in cavity were estimated by measuring the scattering parameters. Moreover, the electric and magnetic field of prototype cavity was measured by bead-pull measurement. As a result, we confirmed the electromagnetic field distribution of prototype cavity is consistent with the simulated field by CST. The prototype cavity was manufactured as intended.

ACKNOWLEDGMENT

This work is supported by JSPS KAKENHI Grant Numbers JP15H03666, JP18H03707, JP16H03987, and JP16J07784.

ISBN: 978-3-95450-194-6 ISSN: 2226-0366 doi:10.18429/JACoW-LINAC2018-MOPO085

REFERENCES

[1] G. W. Bennett *et al*., *Phys. Rev.*, vol. D73, pp. 072003, 2006.

[2] A. Keshavarzi *et al*., *Phys. Rev*. vol. D 97, pp. 114025, 2018.

[3] T. Mibe *et al*. edit., *J-PARC E34 Conceptual Design Report, Technical Design Report*, 2011.

[4] Y. Kondo *et al*., "Re-Acceleration of Ultra Cold Muon in JPARC Muon Facility", in *Proc. IPAC'18*, Vancouver, BC, Canada, Apr./May 2018, pp. 5041–5046. doi:10.18429/JACoW-IPAC2018-FRXGBF1

[5] S. Minaev, U. Ratzinger, and B. Schlitt, "APF or KONUS drift tube structures for medical synchrotron injectors – A comparison", in *Proc. PAC'99*, New York, NY, USA, pp. 3555–3557, 1999.

[6] Y. Iwata *et al*., "Alternating-phase-focused IH-DTL for an injector of heavy-ion medical accelerators", *Nucl. Instrum. Methods Phys. Res.*, Sect. A, vol. 569, pp. 685, 2006.

[7] T. Hata *et al.*, in *Proc. of the 26th Linear Accelerator Meeting in Japan*, pp. 186-188, 2001.

[8] J. Pang, L. Zhao, X. He, and Z. Ying, "Progress of An Interdigital H-mode Drift-Tube-Linac with low injection energy", *PACS* 29.20.Ej; 41.75.-i, 2010.

[9] M. Otani *et al.*, "Interdigital H-mode drift-tube linac design with alternative phase focusing for muon linac", *Phys. Rev. Accel. Beams.* vol. 19, pp. 040101, 2016.

[10] N. Hayashizaki and M. Yoshida, "Development of low energy muon linac", in *Proc. of the 11th Annual Meetings of Particle Accelerator Society of Japan* Particle Accelerator Society in Japan, Tokyo, Japan, paper SUP043, Aug. 2014.

[11] CST Studio Suite, Computer Simulation Technology (CST), https://www.cst.com/products/CSTMWS

[12] General Particle Tracer, Pulsar Physics, http://www.pulsar.nl/gpt/

[13] Y. Kondo *et al*., "Simulation study of muon acceleration using RFQ for a new muon g-2 experiment at J-PARC", in *Proc. IPAC'15*, Richmond, VA, USA, May 2015, pp. 3801–3803. doi:10.18429/JACoW-IPAC2015-THPF045

[14] Sumit Som *et al*., "Bead-Pull Measurement Using Phase-Shift Technique In Multi-Cell Elliptical Cavity"; in *Proc. IPAC'11*, San Sebastian, Spain, Sep. 2011, paper MOPC088, pp. 280–282.

[15] Thomas P. Wangler, *RF Linear Accelerators*, 2008, Wiley-VCH Verlag GmbH&Co.

Content from this work may be used under the terms of the CC BY 3.0 licence (© 2018). Any distribution of this work must maintain attribution to the author(s), title of the work, publisher, and DOI.

ISBN: 978-3-95450-194-6 ISSN: 2226-0366 doi:10.18429/JACoW-LINAC2018-MOPO087

COLD TEST OF HYBRID RFQ PROTOTYPE

P.Y. Yu †, B. Zhang, C.X. Li, F.F. Wang, Z.J. Wang, Y. He
Institute of Modern Physics, Chinese Academy of Sciences, Lan Zhou 730000, China

Abstract

Hybrid RFQ is proposed as a potential good choice at the low-energy range of linear accelerator, which is combined by four-vane RFQ structure and CH-DTL structure. It has higher energy gain rate compared to conventional RFQ, and it is more compact than traditional DTL. In order to research on the RF performance and process exploration of this structure, an aluminium prototype is developed. The cold test of Hybrid RFQ prototype is completed. This paper will present the results and analysis of the test.

INTRODUCTION

Hybrid RFQ is a spatially periodic structure with RF quadrupoles [1, 2], which is combined by alternating CH-DTL sections and four-vane RFQ sections. It has higher accelerating efficiency than traditional RFQ, and shows stronger focusing strength than magnetic focusing DTL, especially when accelerating low r/q ions [3]. The results of beam dynamics and RF simulation of the Hybrid RFQ operated at 81.25 MHz show that the structure has a good performance to accelerate $^{238}U^{34+}$ from 0.38 MeV/u to 1.33 MeV/u [4].

In order to verify the RF performance and the mechanical structure (see Fig. 1) of Hybrid RFQ, as well as to explore the machine processing, an aluminium prototype is developed. The frequency is chosen as 325 MHz to reduce the size of cavity. The length is 1m, and the diameter is approximately 0.3m. The mechanical structure of Hybrid RFQ is complicated. Thus on the one hand, it requires high precision for machining. On the other hand, it is difficult to assemble [5]. The manufacture and cold test of Hybrid RFQ are completed; the results and analysis will be presented.

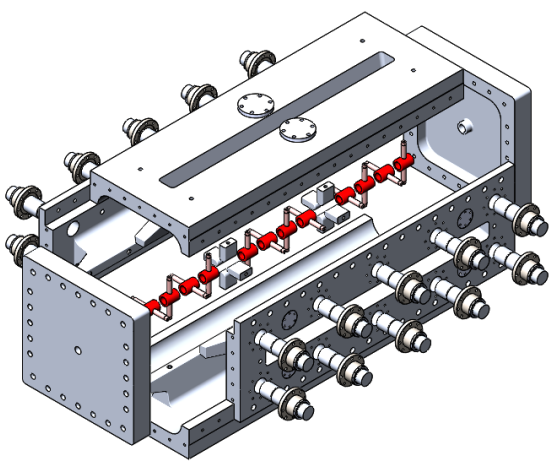


Figure 1: The overall mechanical model of Hybrid RFQ.

† email address: peiyanyu@impcas.ac.cn

RF MEASUREMENT

Measurement Instrument

According to the resonator perturbation theory, the cold test of Hybrid RFQ is conducted using the bead-pull measurement system. During the progress of the C-ADS project, a motion control and data acquisition system for bead-pull measurement has been fabricated [6]. The system including equipment is shown in Fig. 2. The computer controls the motor to drive the wire to move the bead through the cavity, and records the motion steps of the motor. The Vector Network Analyzer transports the frequency or phase signal to the computer.



Figure 2: Bead-pull measurement system.

Measurement of Frequency and Q Value

The frequency and Q value are measured at first after processing. The measured frequency is 326.72 MHz with each penetration depth of 20 tuners is 20 mm. It's 1.72 MHz higher than designed frequency, which is in the adjustable range of tuners. In consideration of the measured size of the parts of cavity, it shows that the main reason of this frequency deviation is the lack of constant temperature condition while processing. The ambient temperature is high when machining, while the measurement is conducted in low temperature. The shrinkage of size leads to the increase of frequency. Furthermore, this point needs verification by simulation. The measured unloaded Q value is 7198. Compared with the calculated value 9083, the measurement value reaches 79.2% of it. Considering there is no RF sealing in the aluminium cavity, this result is acceptable.

The RF measurement of Hybrid RFQ is performed to verify the accuracy of processing and assembly. It includes two parts, one is the measurement of the accelerating field of central axis, and the other is the measurement of the quadrupole field at the RFQ section. The measurement results are compared with the theoretical results which are simulated using CST software. The perturbation body is chosen as a plastic sphere bead with a diame-

Content from this work may be used under the terms of the CC BY 3.0 licence (© 2018). Any distribution of this work must maintain attribution to the author(s), title of the work, publisher, and DOI.

ISBN: 978-3-95450-194-6 ISSN: 2226-0366 doi:10.18429/JACoW-LINAC2018-MOPO087

ter of 6 mm, and the largest frequency perturbation arisen by this bead is about 6 kHz.

Measurement of Field of Central Axis

Fig. 3 shows the measured Ez of central axis. In the graph, the electric field intensity is normalized for more intuitive, and the largest electric field intensity is normalized to 1. At the both ends of the cavity, the field intensity at the gap reaches 0.58 as designed. It can be seen that the measured result has nearly consistent tendency with the simulation except for the quadrupole section.

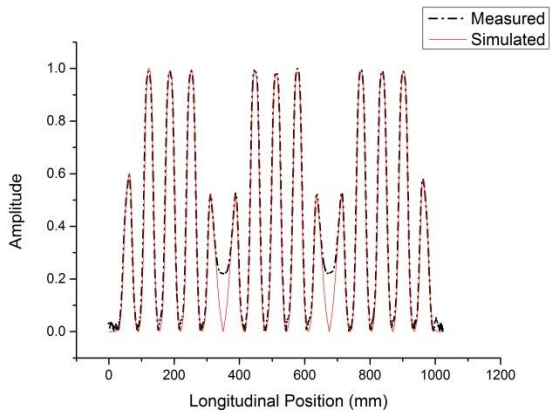


Figure 3: Ez distribution along Z direction.

According to the simulation, the electric field intensity at the longitudinal center of the quadrupole is 0, however it is measured to be 0.2. That is because the perturbation bead is 6 mm, not ideal as a particle. The electric field distribution along the angle bisector of quadrant at the longitudinal center of the RFQ section is presented in Fig.4. It can be seen the electric field intensity at center is 0, and it gets larger as the location is farther away from center. When the 6 mm bead goes through the RFQ section, the bead covers the area where high electric field distributes. Fig. 5 shows the peak value of each gap between drift tubes. The unevenness is below 1.3%.

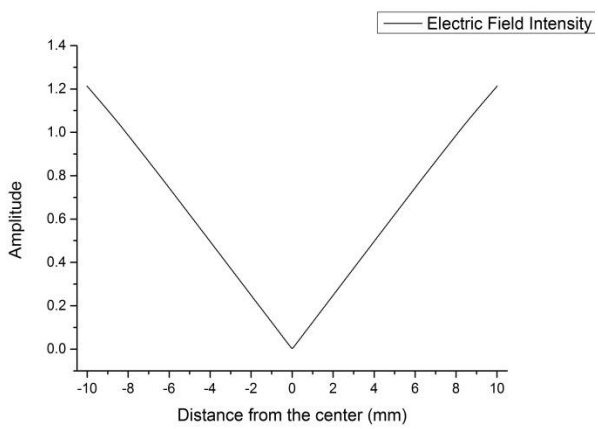


Figure 4: Electric field distribution along the angle bisector of quadrant at the RFQ section.

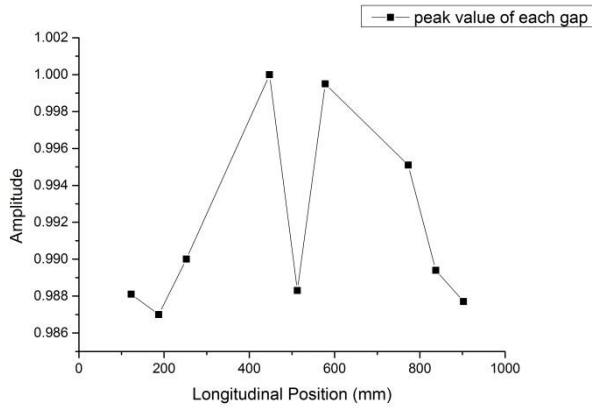


Figure 5: The peak value of 9 drift tube gaps.

Measurement of Quadrupole Field

The inner diameter of drift tube is 20 mm, so the location to measure quadrupole field is chosen as the point 5 mm away from the center along the angle bisector of quadrant. The results are shown in Fig. 6. The measurement is through the whole cavity, but the figure only shows the RFQ sections. The normalization method is the same as above. The field intensity of the longitudinal center of quadrupoles reaches 0.6 as designed. There are two sets of RFQ sections in this prototype. In the first set of quadrupole, the maximum deviation between four quadrants is 5.6%, while it's 6.9% in the second set of quadrupole. We think there are two main reasons caused this unsatisfactory result. One is the positioning accuracy is not high enough, another is the gravity affection of the bead.

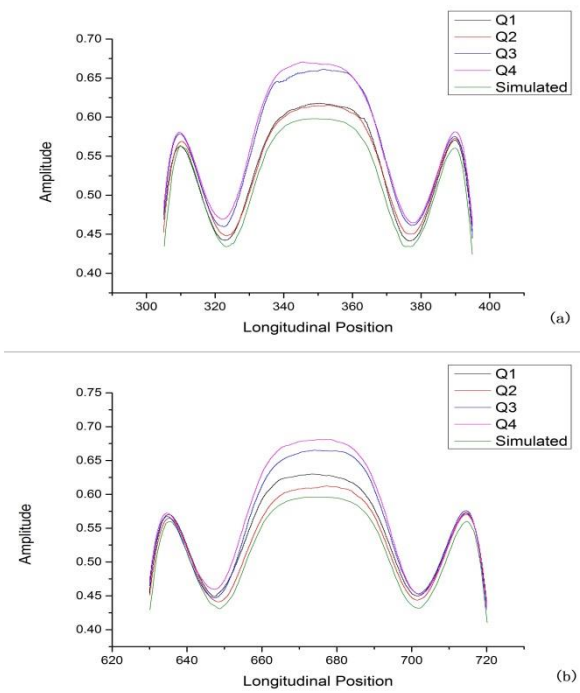


Figure 6: Quadrupole field distribution. (a) shows the first set of quadrupole. (b) shows the second set of quadrupole.

Content from this work may be used under the terms of the CC BY 3.0 licence (© 2018). Any distribution of this work must maintain attribution to the author(s), title of the work, publisher, and DOI.

ISBN: 978-3-95450-194-6 ISSN: 2226-0366 doi:10.18429/JACoW-LINAC2018-MOPO087

Content from this work may be used under the terms of the CC BY 3.0 licence (© 2018). Any distribution of this work must maintain attribution to the author(s), title of the work, publisher, and DOI.

CONCLUSION

The cold test of Hybrid RFQ prototype is performed. The frequency is 1.72 MHz higher than designed value. The reason needs to be analysed by simulation. Unloaded Q value reaches 79.2% of the calculated value. The filed distribution of accelerating field of central axis and the quadrupole filed are measured. The unevenness of accelerating field is below 1.3%. The deviation between four quadrants of first set of quadrupole is 5.6%, while that of second set of quadrupole is 6.9%.

There is still some problems need to be solved, like improving the positioning accuracy and diminishing the gravity affection of the bead. The tuning and further research on the RF parameters of Hybrid RFQ will be performed soon.

REFERENCES

[1] D.A. Swenson, "An RF Focused Interdigital Linac Structure", in *Proc. LINAC2002*, Gyeongju, Korea, 2002, pp. 225-227.

[2] Yu.A. Budanov et al. "RFQ Drift-tube Proton Linacs in IHEP", in *Proc. LINAC2004*, Lubeck, Germany, 2004, pp.285-287.

[3] P.N. Ostroumov, A.A. Kolomiets, et al. "An Innovative Concept for Acceleration of Low-Energy Low-Charge-State Heavy-Ion Beams" Nuclear Instruments and Methods in Physics Research A, 2005, 547: 259-269.

[4] Wang Zhi-Jun, et al. "A New Compact Structure for A High Intensity Low-Energy Heavy-Ion Accelerator" Chinese Physics C Vol. 37, No. 12 (2013) 127001.

[5] P.Y. Yu, et al. "Design and Fabrication of Hybrid RFQ Prototype", in *Proc. IPAC'18*, Vancouver, Canada, 2018, pp. 1032-1034.

[6] Chenxing Li, et al. "Radio Frequency Measurements and Tuning of The China Material Irradiation Facility RFQ", *Nuclear Instruments and Methods in Physics Research* A, 2018, 890: 43-50.

ISBN: 978-3-95450-194-6 ISSN: 2226-0366 doi:10.18429/JACoW-LINAC2018-MOPO088

STUDY ON A 325MHz HOM DRIFT TUBE LINAC*

L. Lu†, C. C. Xing[1], T. He[1], L. Yang[1], X. B. Xu, L. B. Shi, L. P. Sun, J. Li[1], Q. X. Xia[1], Z. C. Gao
Institute of Modern Physics (IMP), CAS, 730000 Lanzhou, China
[1] also at University of Chinese Academy of Sciences, 100049 Beijing, China

Abstract

Normally, drift tube linacs (DTL) are used following RFQ linacs for beam acceleration in middle and high beam energy region. but acceleration efficiency of DTLs is decreasing with beam energy increasing. Using resonated higher order mode (HOM) of cavity, DTL can get higher effective shunt impedance. we proposed a 325MHz DTL with TE_{115} mode. In this paper, the dynamics calculation and electromagnetic design of the HOM-DTL will be reported.

INTRODUCTION

Shown in Fig. 1, in the low energy region, because the Interdigital-H (IH) type drift tube linacs (DTLs) have a higher shunt impedance and suitable accelerating structure for heavy ion acceleration, the DTLs operated in TE111 mode are normal used following the RFQ type linac [1-3]. However, in the medium and high energy region, the Alvarez type DTLs operated in TM010 mode are normally used although its shunt impedance reduces rapidly [4-5], shown in Fig. 2, because its higher shunt impedance is higher than the IH-DTLs in those energy regions.

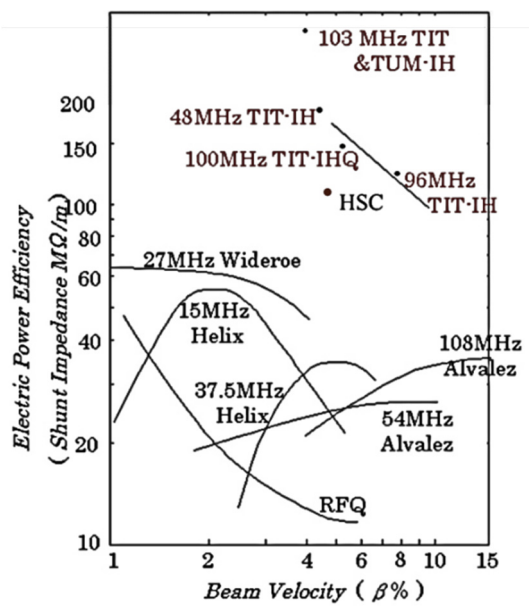


Figure 1: The shunt impedance of the low beta linacs.

Since the DTLs operated in TE11n mode of the higher order mode have a property which is suitable to accelerate ions in medium and high energy region [6], we proposed a 325MHz DTL operated in TE115 mode. Our proposed HOM-DTL is designed as a prototype buncher and its structure is shown in Fig. 3.

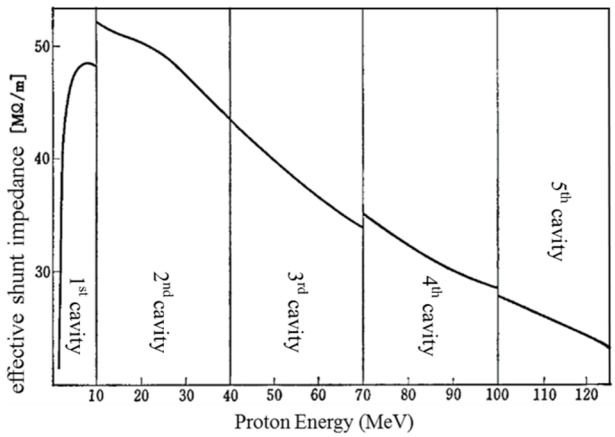


Figure 2: The shunt impedance changing of the Alvarez type DTLs.

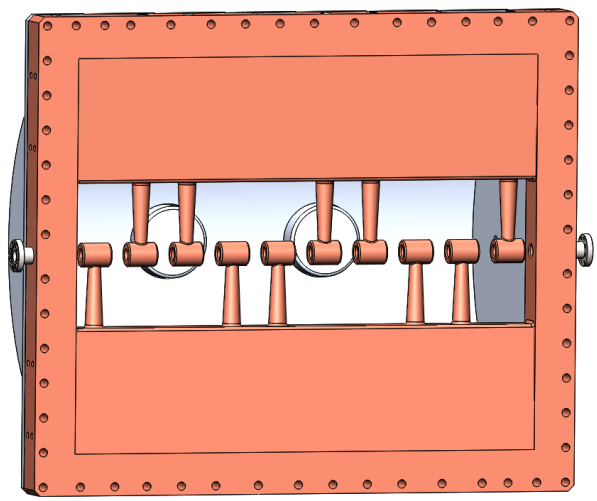


Figure 3: The inner structure of proposed HOM-DTL.

ELECTROMAGNETIC DESIGN

The frequency of proposed HOM-DTL is 325MHz which is 4th harmonic of the frequency of 81.25MHz. This HOM-DTL is a prototype research for future heavy ion buncher. The estimated peak voltage is rather high as several mega-voltages (MV). The Microwave Studio (MWS) code and ANSYS code are used to calculate the cavity electromagnetic simulation and mechanical simulation [7-8].

*Work supported by NSFC under Grant No. 11427904, No. 11475232 and No. 11535016
† luliang@impcas.ac.cn

Content from this work may be used under the terms of the CC BY 3.0 licence (© 2018). Any distribution of this work must maintain attribution to the author(s), title of the work, publisher, and DOI.

ISBN: 978-3-95450-194-6 ISSN: 2226-0366 doi:10.18429/JACoW-LINAC2018-MOPO088

Content from this work may be used under the terms of the CC BY 3.0 licence (© 2018). Any distribution of this work must maintain attribution to the author(s), title of the work, publisher, and DOI.

As shown in Fig. 3, the HOM-DTL has drift tubes and ridges that is same to the normal type IH-DTLs with TE111 mode, however, the resonated frequency of cavity can be tuned to TE115 mode by configuring directions of the stems. Shown in Fig. 4 and Fig. 5, the biggest feature of the HOM-DTL is that the axial accelerating e fields of every gaps are quiet flat, even in the two end gaps. The flat e field distribution makes the field tuning of cavity very easy. The proposed HOM-DTL adopts 10 stems and 11 gaps, and the total length is 1m. Shown in the Table 1, when the Kilpatrick factor adopts 1.5, the simulated total voltage of the HOM-DTL is 1.93MV, and the shunt impedance of the HOM-DTL is calculated as 91.8 MΩ /m that is higher than other structure linacs in same beam beta region shown in Fig. 1 and normal DTLs shown in Fig. 2. That indicates the proposed 325MHz HOM-DTLs have a better power efficiency in the medium energy region.

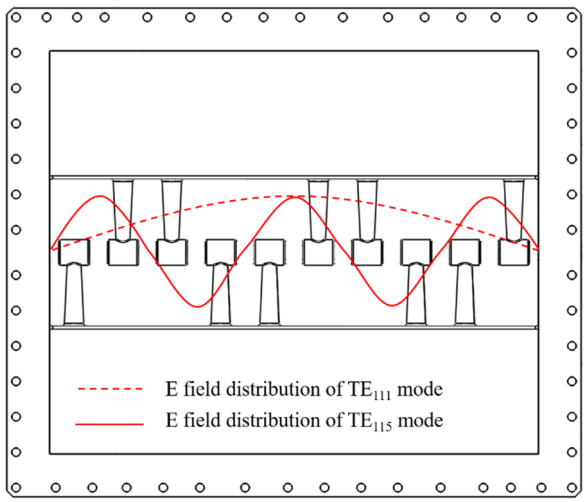


Figure 4: RF property of TE_{115} mode (solid line) in the HOM-DTL. Dot line shows a RF property in IH-DTLs.

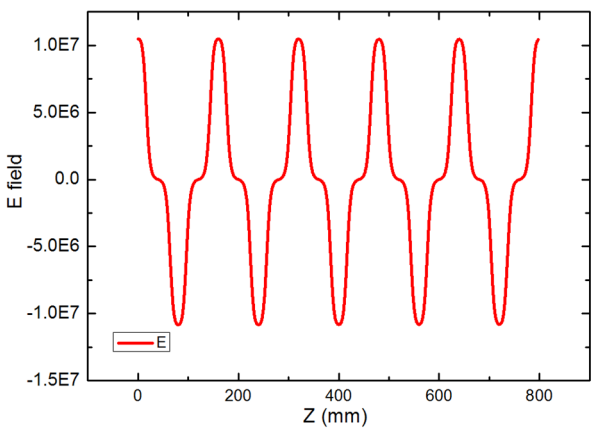


Figure 5: A flat e field distribution of TE_{115} mode in the HOM-DTL.

Table 1: The Simulated Parameters of the HOM-DTL

Items	Value
Frequency / MHz	325.008
Gap No.	11
DT No.	10
Cavity diameter / mm	660
Beam bore / mm	20
DT diameter / mm	40
β (particle energy)	0.173
Inner length / mm	800
Total voltage / MV	1.93 @ 1.5 Kp.
Dissipated power / kW	50.6 @ 1.5 Kp.
Q value	9167
Shunt impedance / MΩ /m	91.8

Because an existing mail coppery frame (copper-colored part shown in the Fig. 3) was adopted for simulations and fabrications of the 325MHz HOM-DTL, the optimization of the RF structure design is limited. In our opinion, the shunt impedance could be increased 1.5 times of the calculated 91.8 MΩ/m.

The RF properties of proposed HOM-DTL is confirmed by MWS, shown in Fig. 6, according to the resonated TE11n order, the frequency shows an uptrend and the Q value shows a downtrend. The downward Q indicates that the RF mode is much higher, the higher RF power is needed. Based on our calculations, the ridges have a big effect to the cavity RF property. The height of the ridges is much higher, meanwhile the stems are more longer, the Q value is more higher. The TE114 is 308.223MHz, the desired resonated RF mode is 325MHz which is totally separated from the neighbor mode.

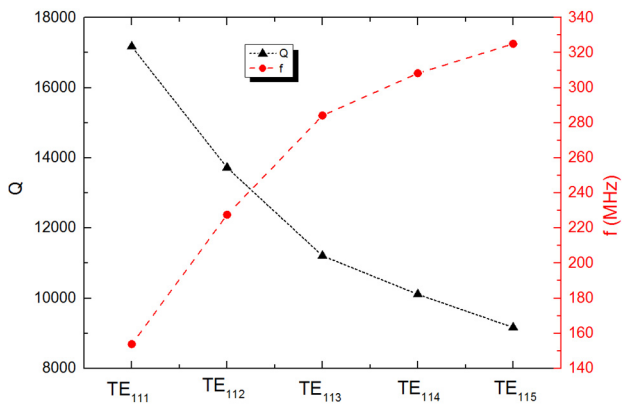


Figure 6: Resonated RF mode and Q values of calculated HOM-DTL. According to the TE_{11n} order, the Q shows a downtrend and the frequency shows uptrend.

And same to the normal IH-DTLs, the hottest part of the HOM-DTL is the stem [9]. Shown in Fig. 7, the surface current is concentrate in the stems. Though we are limited by budgets, and the HOM-DTL will be carried out low power test and aimed to test the shaping method without alignment. However, the cooling designs of stems

ISBN: 978-3-95450-194-6 ISSN: 2226-0366 doi:10.18429/JACoW-LINAC2018-MOPO088

must be considered for possibilities of future use. According to the ANSYS calculations, with 10 water routes for stem cooling and 10% duty, the maximum deformation is occurred in the cavity (between two tuners) and the maximum temperature is about 400C and is located in the first tube.

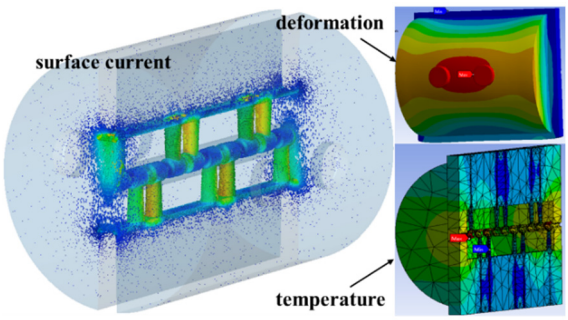


Figure 7: Images of surface current (left part) and multi-physics analysis. The intensity increases as the color changes from blue to yellow and to red.

The frequency tuning is being designed using four tuners. Both side of the main frame has two tuners, and the tuners are uniform distribution in the beam direction. The diameter of tuners is 60mm, and the preset inserting length of the tuners is 35mm. According to our simulations, the adjustment region of frequency is ±1.56MHz which is enough for frequency tuning.

FABRICATION

The HOM-DTL is being fabricated in manufacturing company, shown in Fig. 8. However, this research is limited by budget. Although the main frame is being shaped from a block copper by using a numerical-controlled machine tool, the cavity wall is being bent from an aluminum sheet. The stand supports the main frame directly by using two stainless holders. And two tuner-supports fixes the four tuners. The tuners are also made from aluminum material.

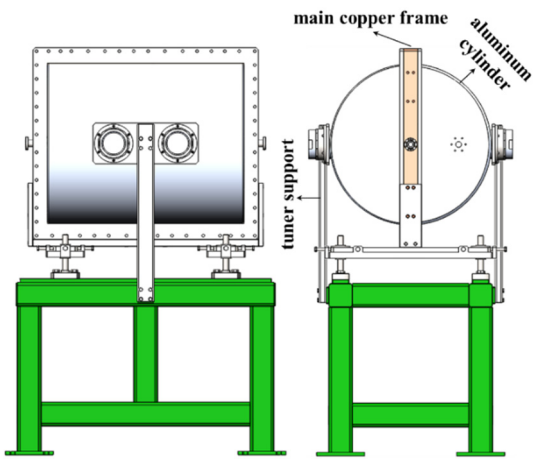


Figure 8: Assembly image of the HOM-DTL. The main frame is made from copper material, the other cavity parts (walls and the tuners) are being made from aluminium material.

SUMMARY AND FUTURE PLAN

A HOM structure cavity driven by TE115 RF mode was calculated and simulated for high energy beam bunching. Its shunt impedance is higher than IH-DTLs and Alvarez type DTLs in medium energy acceleration. Along the 800mm axis, the designed 325MHz HOM-DTL buncher could induce 1.93MV with flat e field distribution on the axis. Its shunt impedance is 91.8 MΩ/m in a safe Kp factor. The core part of the HOM-DTL is being shaped from a copper block, and other parts is being fabricated from aluminium material.

The fabrication and assembly will be finished in the end of this October. Our team will carry out a low power test for measuring the RF properties such as resonated frequency and e field distribution. Also, we are applying a national natural science foundation of China for future copper fabrication of the cavity wall.

ACKNOWLEDGEMENTS

Return to our researcher, the authors would like to convey thanks to Prof. Dacheng ZHANG for fruitful discussions and comments on the cavity designs.

REFERENCES

[1] T. Ito, N. Hayashizaki *et al.*, "Research of hybrid single cavity linac", *Nucl. Instrum. Methods Phys. Res. B*, Vol. 261, p. 17-20, Aug. 2007.

[2] L. Lu, T. Hattori *et al.*, "Design and simulation of C6+ hybrid single cavity linac for cancer therapy with direct plasma injection scheme", *Nucl. Instrum. Methods Phys. Res. A,* Vol. 688, p. 11-21, Oct. 2012.

[3] L. Lu, T. Hattori, H.Y. Zhao *et al.,* "High Power Test of an Injector Linac for Cancer Therapy Facilities", *Phys. Rev. ST Accel. Beams*, vol. 18, p. 111002, Nov. 2015.

[4] L.W. Alvarez; *Phys. Rev.*, vol. 70, p. 799, 1946.

[5] M. Heilmann, X. Du, P. Gerhard, L. Groening, M. Kaiser *et al.*, "Design Study for A Prototype Alvarez-Cavity for the Upgraded Unilac", in *Proc. IPAC'17*, Copenhagen, Denmark, May 2017, pp. 2205-2207

[6] N. Hayashizaki, T. Hattori, "IH Linac with Higher Order Modes", in *Proc. EPAC'08*, Genoa, Italy, June 23-27, pp. 3419-3421

[7] CST Microwave Studio, http://www.cst.com

[8] ANSYS, https://www.ansys.com/

[9] L. Lu, L. P. Sun, T. He, L. Yang, W. Ma *et al.*, "Research on A Two-Beam Type Drift Tube Linac", in *Proc. LINAC'16*, East Lansing, MI, USA, Sep. 2016, pp. 989-991.

Content from this work may be used under the terms of the CC BY 3.0 licence (© 2018). Any distribution of this work must maintain attribution to the author(s), title of the work, publisher, and DOI.

ISBN: 978-3-95450-194-6 ISSN: 2226-0366 doi:10.18429/JACoW-LINAC2018-MOPO089

DESIGN DETAILS OF THE EUROPEAN SPALLATION SOURCE DRIFT TUBE LINAC

P. Mereu*, M. Mezzano, C. Mingioni, M. Nenni, INFN-TO, Torino, Italy
F. Grespan, A. Pisent, INFN-LNL, Legnaro, Italy
G. Cibinetto, INFN-FE, Ferrara, Italy

Abstract

The Drift Tube Linac (DTL) of the European Spallation Source (ESS) is designed to operate at 352.2 MHz with a duty cycle of 4% (3 ms pulse length, 14 Hz repetition period) and will accelerate a proton beam of 62.5 mA pulse peak current from 3.62 to 90 MeV. This paper gives a detailed overview of the ESS-DTL current mechanical design, and the related driving criteria. It presents also an outlook of the main aspects of the assembly and installation, with related equipments, tooling and procedures.

DTL GENERAL DESIGN

In the ESS accelerator the initial warm linac section is composed by the Ion Source, Low Energy Beam Transport line (LEBT), Radio Frequency Quadrupole (RFQ), Medium Energy Beam Transport line (MEBT) and DTL [1].

The DTL has a partially similar design to the CERN LINAC4: it is a 38.8 m long system, divided in five cylindrical RF cavities (Tanks) [2]. Each tank is a standalone structure composed by four 2 m long modules, made of AISI 304L stainless steel with copper plating on internal surfaces. The Drift Tubes are positioned in the girder, a precisely machined aluminium alloy structure housed in the upper part of each module [3].

The tank is closed at both ends by a closing cover with a half DT on the inner side. Each tank is individually supported by an isostatic mechanical support, which provide also the fine alignment of the tank on the beam line. The space between two consecutive tanks, Inter-Tank (IT), is taken up by a vacuum valve and a stain-less steel vacuum chamber, which houses diagnostic instrumentation such as Faraday Cup (FC), Wire Scanner (WS) and non-invasive Profile Monitor (PM).

COVER DESIGN

The tank covers are composed mainly by an AISI 304L circular plate and a half DT on the inner wall. Depending on the position along the beam line, the cover houses a Permanent Magnet Quadrupole (PMQ) or a Beam Current Monitor (BCM).

The steel plate is 30 mm thick and is copper plated on the inner surface facing the RF cavity. It houses 8 V-shaped cooling channels, 10 mm offset from the inner wall, each one obtained by intersecting two ⌀6 mm holes deep-drilled in the thickness of the material. Two additional ⌀8 mm channels provide the inlet and outlet for the DT cooling circuit.

The half DT is made by an external copper profile and an internal steel sleeve, both vacuum brazed on the steel plate. The DT cooling circuit is obtained by machining a circumferential channel on the sleeve, in a single or double loop depending on the DT length.

In the cover with PMQ (Fig. 1) the magnets assembly is housed inside the sleeve, while in the BCM version a current transformer is placed in a seat on the outer wall of the cover; in both cases the components are fixed by a flange on the outer side.

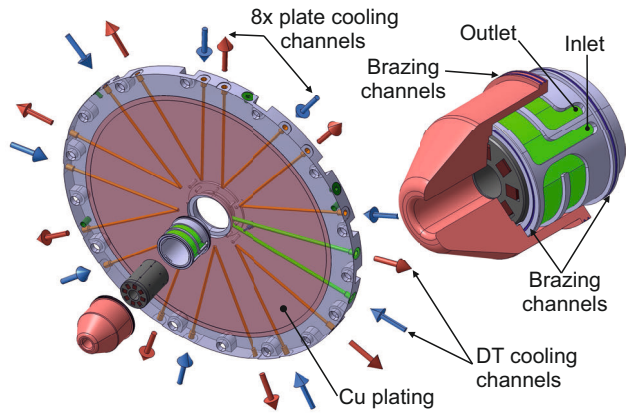


Figure 1: Layout of the cover with PMQ. Plate cooling channels coloured in orange, DT cooling circuit in green, brazing channels in blue.

Table 1: Boundary conditions and results of CFD simulation: inlet mass flow rate ($\dot{m}$) and temperature (T_{in}), average convective heat-flux coefficient (h) and pressure drop (Δp)

Circuit	$\dot{m}$ [kg/s]	T_{in} [°C]	h [W/m^{2}K]	Δp [bar]
DT channel	0.11	30	7350	0.41
Plate channel	0.05	30	6500	0.12

Computational Fluid Dynamics (CFD) and Finite Element Method (FEM) simulations were carried out to validate the design of the cover. For those analysis the maximum thermal load, corresponding to the last cover in tank 5, was set at 3869 W/m^2 on the cover wall facing the RF, and spanning from 154 W/m^2 and 23 520 W/m^2 on the DT (depending on the position). First a CFD simulation was performed in Ansys Fluent on a simplified geometry, in order to evaluate the convective heat-flux coefficient and pressure loss on both DT and plate channels (see Table 1) [4]. On this bases, a FEM thermo-structural analysis was performed in Ansys Mechanical. Figure 2 shows the results obtained from the

* paolo.mereu@to.infn.it

Content from this work may be used under the terms of the CC BY 3.0 licence (© 2018). Any distribution of this work must maintain attribution to the author(s), title of the work, publisher, and DOI.

ISBN: 978-3-95450-194-6 ISSN: 2226-0366 doi:10.18429/JACoW-LINAC2018-MOPO089

latter: the simulations show a peak temperature of 41.8 °C on the steel plate and 47.9 °C on the DT. The deformation along the beam axis is 49 µm on the DT.

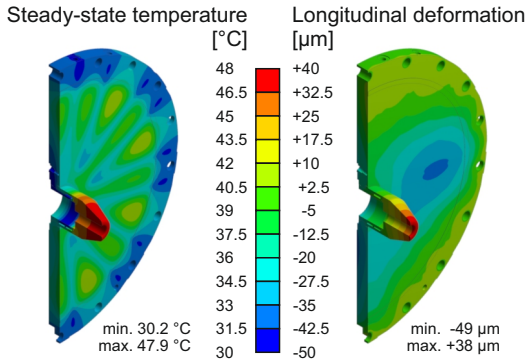


Figure 2: Temperature and longitudinal deformation maps resulting from FEM analysis on the cover with PMQ.

INTER-TANK DESIGN

Along the DTL there are two types of Inter-Tank: IT 1, which is entirely under vacuum and contains only the diagnostic instrumentation, due to the limited space available, and IT 2-3-4, which contain a vacuum valve and a vacuum chamber for instrumentation. Table 2 reports the space available for the ITs, while Figure 3 shows the layout of both IT types.

Table 2: Longitudinal Space Available in Each Inter-Tank Between the Corresponding Covers

Inter-Tank	Between tanks	l [mm]
IT 1	1-2	118.301
IT 2	2-3	178.368
IT 3	3-4	223.482
IT 4	4-5	259.125

The beam box in each Inter-Tank has interfaces for the FC, WS, two PM and three vacuum feed-through.

The beam box is sealed by a FPM elastomer O-ring, on the cover side, and is connected to the valve through a bellow, on the opposite side. Since the O-ring requires a replacement every five years, the Inter-Tanks are designed to be assembled and disassembled directly in the accelerator tunnel without moving the tanks from the beam line. During those operations, the bellow is compressed using a threaded tie-rod, and the beam box is extracted (or inserted) from the side of the DTL. A similar procedure is used for the bellow in IT1.

INSTALLATION PROCEDURE AND EQUIPMENT

Assembly operations are carried out in the DTL Workshop (DTLW) at the ESS site in Lund, with a defined tank sequence. First, each module is assembled independently, with corresponding girder, drift tubes and ancillaries; the four modules are then aligned and coupled together on an assembly table; finally, are installed the tank covers, cooling water manifolds, hydraulic connections and the upper section of the mechanical supports.

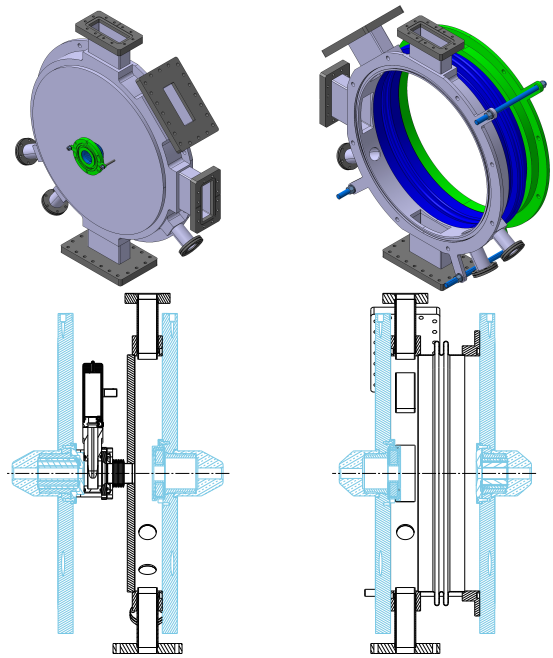


Figure 3: Isometric view (on top) and longitudinal section view (on bottom) of IT 1 (right) and IT 2 (left). Tank covers in section views are coloured in light blue.

A series of tests is performed on each tank in the DTLW after the assembly. These include position measurements, hydraulic tests, vacuum leak tests and bead-pulling measurements.

Installation of the Tanks on the Beam Line

After the tests, the tank is lifted with a crane in the DTLW and positioned on the Tank Handling Trolley (THT), showed in Figure 4. The tank is positioned on the four cradles of the THT (coloured in light blue in Figure 4) and fastened with straps; the THT is adaptable to the different length of the tanks by replacing special sections of beams (coloured in green in Figure 4), so that the cradles interface each tank across the junction of modules 1-2 and 3-4, avoiding any interference with the flanges.

The tank, positioned on the THT, is loaded on a truck and transported up to a loading bay next to the accelerator tunnel, where is unloaded again to the floor. The tank is then moved up to the tunnel by pulling the THT with a manual operated tractor.

Whenever a change in trajectory is needed, the four screw jacks on the sides of the THT are lowered down, freeing the load from the main wheels (coloured in purple in Figure 4). The wheels are pivoted by a proper angle and the load is charged again by retracting the screw jacks, so the movement can start again. A manual winch is used for minor movements during these adjustments. Reached the tunnel,

Content from this work may be used under the terms of the CC BY 3.0 licence (© 2018). Any distribution of this work must maintain attribution to the author(s), title of the work, publisher, and DOI.

ISBN: 978-3-95450-194-6 ISSN: 2226-0366 doi:10.18429/JACoW-LINAC2018-MOPO089

Content from this work may be used under the terms of the CC BY 3.0 licence (© 2018). Any distribution of this work must maintain attribution to the author(s), title of the work, publisher, and DOI.

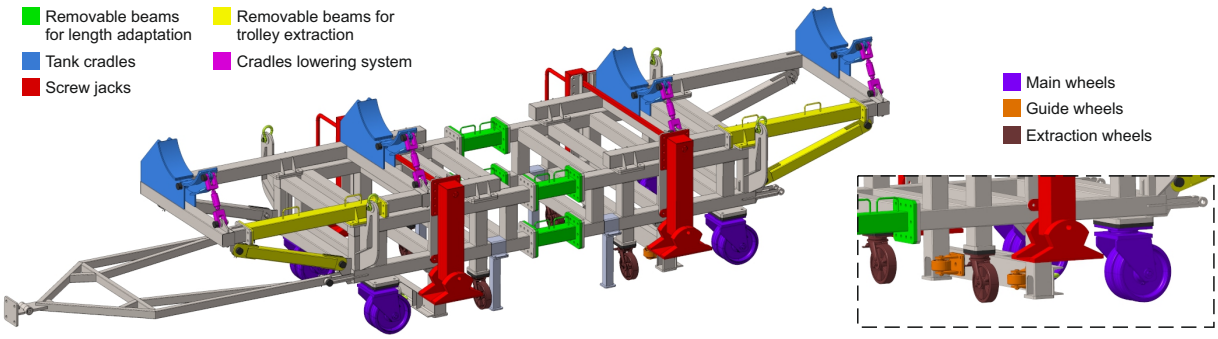


Figure 4: Design of the Tank Handling Trolley (THT).

the tank is moved along the installation corridor, parallel to the beam line, up to the nominal longitudinal position.

The insertion of the tank on the beam line is done by pivoting the wheels by 90°, with the same procedure already mentioned, and pulling transversally the THT using a manual winch. During this operation, the horizontal wheels at the base of the THT (see detail in Figure 4, wheels in orange) engage with a couple of temporary linear guide installed on the floor, which avoid deviations from the right trajectory.

At this stage the tank axis is 50 mm higher than the nominal position. The screw jacks are lowered again, discharging the load from the wheels, which are removed. The screw jacks are retracted until the upper section of the mechanical support, installed on the tank, engages with the lower section of the support, already installed on the floor. In this way, the load of the tank is transferred to the supports and the THT can be removed. The screw jacks are further retracted until the extraction wheels reach the floor (see Figure 4, wheels coloured in brown). Finally, a portion of the THT beam is removed (see Figure 4, yellow coloured beams), and the cradles are opened, allowing the extraction of the THT from the side of the tank.

MECHANICAL SUPPORT DESIGN

Each tank is independently supported by an isostatic support, composed by 2 columns, which interfaces the tank under modules 1 and 4. The column under module 1 has a spherical joint between support and tank, while the other one has a ball-plane and a ball-groove contact. The ensemble of the two column forms a Kelvin isostatic coupling.

Every column is divided in upper and lower section (see Figure 5). The upper section is mounted under the tank during the assembly operation in the DTLW, and is transported in the tunnel together with the tank. From bottom to top, it is composed by: a screw jack, a cylindrical guide, the kinematic coupling mechanism and a plate-plate interface. In case of the double coupling column, the upper section has 2 screw jacks cylindrical guides, one for the ball plane and one for the ball-groove coupling. The screw jacks and the Kelvin coupling provide a fine regulation of the vertical position and yaw-pitch-roll angles, while the plate-plate interface, and a set of driving screws on it, allow the translation on the plane. Vertical and in-plane regulation are decoupled.

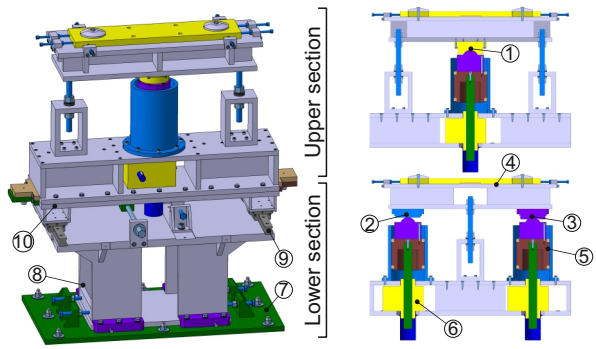


Figure 5: Isometric view of the single joint column (on left), section view of the upper section of single (top-right) and double (bottom-right) joint column. The numbers identify: 1) sphere joint, 2) ball-plane joint, 3) ball-groove joint, 4) plate-plate interface, 5) cylindrical guide, 6) screw jack, 7) floor plate, 8) H-beam, 9) linear guide, 10) interface block.

The lower section is composed by a floor plate, a couple of H-beams and an interface block. The floor plate allows a translation of the support parallel to the floor, by means of screws acting on the H-beams. The interface block provides the coupling with the upper section; moreover, is equipped with 2 linear guides which provide a coarse longitudinal regulation and allow the thermal expansion of the tank.

REFERENCES

[1] W. Wittmer *et al.*, "European Spallation Source (ESS) Normal Conducting Front End Status Report," in *Proc. of LINAC'16, 25-30 Sept., 2016*, (East Lansing, MI, USA), pp. 274–276. DOI: 10.18429/JACoW-LINAC2016-MOPLR062.

[2] F. Grespan *et al.*, "ESS DTL Design and Drift Tube Prototypes," in *Proc. of LINAC'14, 31 Aug.-5 Sept., 2014*, (Geneve, Switzerland), pp. 1050–1052.

[3] P. Mereu *et al.*, "ESS DTL Mechanical Design and Prototyping," in *Proc. of IPAC'16, 8-13 May, 2016*, (Busan, Korea), pp. 2131–2133. DOI: 10.18429/JACoW-IPAC2016-WEPMB008.

[4] P. Mereu *et al.*, "Thermo Mechanical Study of the ESS DTL," in *Proc. of IPAC'17, 14-19 May, 2017*, (Copenhagen, Denmark), pp. 4537–4539. DOI: 10.18429/JACoW-IPAC2017-THPVA046.

ISBN: 978-3-95450-194-6 ISSN: 2226-0366 doi:10.18429/JACoW-LINAC2018-MOPO090

STATUS OF THE MYRRHA CH CAVITIES

K. Kümpel, S. Lamprecht, P Müller, N. F. Petry, H. Podlech, S. Zimmermann
IAP, Goethe Universität Frankfurt, Germany

Abstract

The MYRRHA (Multi-purpose hYbrid Research Reactor for High-tech Applications) project is a planned accelerator driven system (ADS) for the transmutation of long-living radioactive waste [1]. A critical passage for the beam quality and especially for the emittance is the injector, which for the MYRRHA project consists of a 4-rod RFQ, two Quarter Wave Rebunchers (QWR) and a total of 16 normal conducting CH-DTL cavities [2]. The first installment of the MYRRHA injector in Louvein-La-Neuve (Belgium) will include an ion source, a RFQ, the QWRs and the first seven CH cavities.

This paper will report on the status of the first tests of CH 1 and 2 as well as on further developments on CH 8 to 15.

THE CH SECTION OF THE MYRRHA INJECTOR

The CH section of the MYRRHA injector (see Figure 1) consists of 15 room temperature CH cavities and accelerates the proton beam from 1.5 MeV up to 16.6 MeV while using a constant phase configuration.

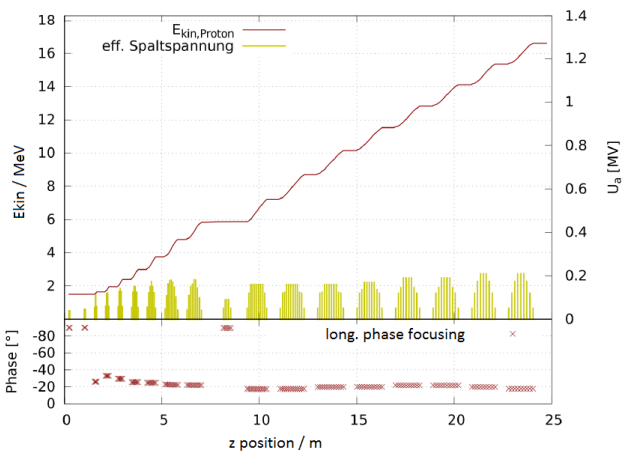


Figure 1: The estimated proton energy after the RFQ is 1.5 MeV [3] and increases up to 16.6 MeV at the end of CH 15 (upper graph in red). The effective voltages of the gaps are plotted in yellow. The lower graph shows the constant phase configuration of the CH cavities. An additional 5-gap CH Rebuncher (CHR) can be seen between CH 7 and CH 8.

Table 1: The Number of Gaps and Shunt Impedances of the CH Structures. The shunt impedances have been simulated with CST Microwave Studio [4].

Cavity	Number of Gaps	Shunt impedance [MΩ/m]
CH 1	3	22.18
CH 2	4	36.18
CH 3	5	48.38
CH 4	6	56.91
CH 5	7	61.50
CH 6	9	65.06
CH 7	9	61.06
CH 8	11	56.6
CH 9	12	53.3
CH 10	12	49.4
CH 11	11	47.8
CH 12	10	43.1
CH 13	10	41.5
CH 14	9	40.1
CH 15	9	38.8

STATUS OF CH 1

The CH 1 has been manufactured by NTG (Gelnhausen, Germany), it was copper plated at Galvano-T (Windeck, Germany) and is now in the experimental hall of the IAP (see Figure 2).

Both after production and after copper plating, measurements of the resonance frequency could be carried out and compared with the simulation result of the STEP model of the cavity (without copper plating) made with CST Microwave Studio (see Table 2).

Table 2: The Resonance Frequency f_0 of the CH 1 Simulated with CST (left), Measured Before (Middle) and After Copper Plating (right).

f_0 (simulation model) [MHz]	f_0 (before copper plating) [MHz]	f_0 (after copper plating) [MHz]
177.296	177.251	176.536

Content from this work may be used under the terms of the CC BY 3.0 licence (© 2018). Any distribution of this work must maintain attribution to the author(s), title of the work, publisher, and DOI.

ISBN: 978-3-95450-194-6 ISSN: 2226-0366 doi:10.18429/JACoW-LINAC2018-MOPO090

Content from this work may be used under the terms of the CC BY 3.0 licence (© 2018). Any distribution of this work must maintain attribution to the author(s), title of the work, publisher, and DOI.

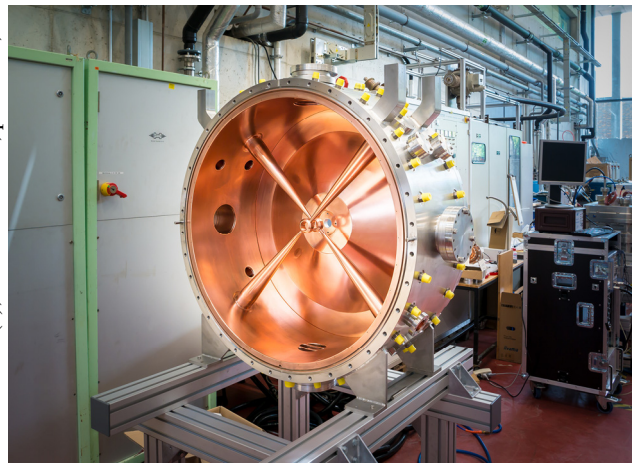


Figure 2: Copper plated CH 1 at the IAP experimental hall with open front lid.

The desired resonance frequency of 176.1 MHz will be achieved with the use of two tuning plungers, one of which is static and one dynamic to regulate the frequency during operation.

For the comparison of the gap voltage ratios, the distribution from the beam dynamics simulation could also be used (see Figure 3).

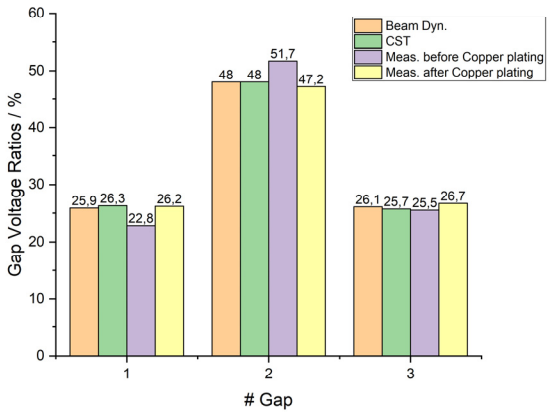


Figure 3: Comparison of the gap voltage ratios for CH 1.

In the next steps, the tuner, coupling loop and vacuum system will be installed before the CH can be conditioned with full power at IAP Frankfurt.

STATUS OF CH 2

The CH 2 cavity has been manufactured by PINK (Wertheim, Germany) and is currently being prepared for copper plating.

A comparison of the resonance frequencies between the simulation and the measurement of the CH 2 before copper plating is shown in Table 3 and the comparison of the gap voltage ratios is shown in Figure 4.

Table 3: The resonance frequency f_0 of the CH 2 simulated with CST (left) and measured before copper plating (right).

f_0 (simulation model) [MHz]	f_0 (before copper plating) [MHz]
177.006	176.711

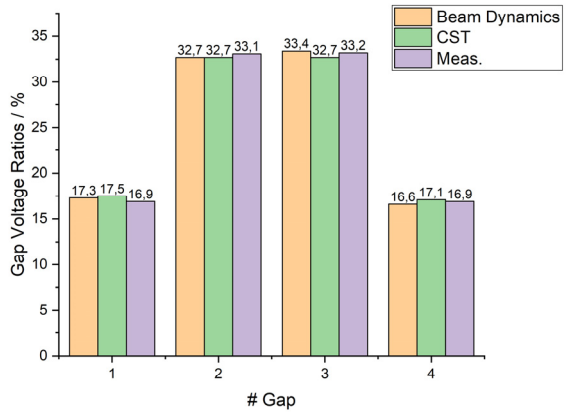


Figure 4: Comparison of the gap voltage ratios for CH 2.

DEVELOPMENTS OF THE COOLING SYSTEM

Due to the cw operation of the MYRRHA LINAC, the design of the cooling channels is very important to ensure a high reliability of the CH cavities. Therefore it was necessary to develop a new cooling channel design for the tank of CH 8 to 15, while the CH 1 to 7 and the CHR can be manufactured with the old design which is already used in the CHs 1 and 2.

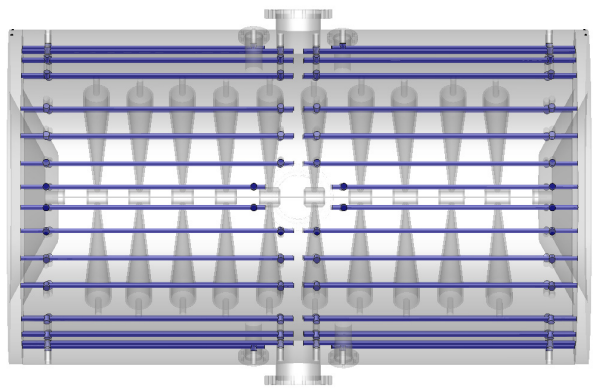


Figure 5: Cooling system of CH 8 tank (side view).

The cooling layout for the structures of CH 8 to 15 has been adjusted because of total length increase and higher power losses of the cavities [5]. Their total length exceeds one meter each and led to the decision to split each of the tank cooling channels into two separate channels (see Figure 5).

ISBN: 978-3-95450-194-6 ISSN: 2226-0366 doi:10.18429/JACoW-LINAC2018-MOPO090

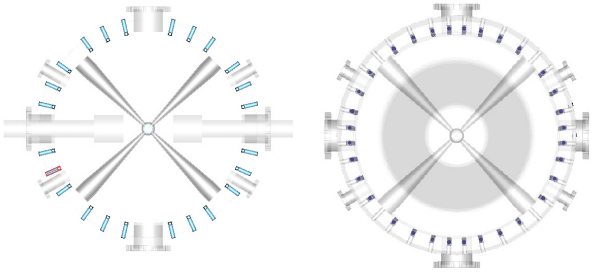


Figure 6: Comparison of the cooling channels inside the tank of CH 7 (left side) and CH 8 (right side) with additional cooling channels.

In addition, the former layout showed for the CH 8 to 15 insufficient cooling in the area of the flanges intended for the tuners, the vacuum system and the coupling. This is solved by inserting additional channels at the angle position of the flanges shown in Figures 5 and 6.

SUMMARY AND OUTLOOK

The tests on the first two CH cavities of the MYRRHA injector have started and show satisfactory results. It is planned to complete tests and the conditioning of these two by the end of the year, while at the same time the tender for CH 3 to 7 has already started. In addition, the thermal simulations for the remaining CH 8 to 15 were completed.

ACKNOWLEDGMENT

This work has been supported by the BMBF, project number 05P15RFBA and by MYRTE which is funded by the European Commission under Project-ID 662186.

REFERENCES

[1] D. Vandeplassche, J.-L. Biarrotte, H. Klein, H. Podlech, "The MYRRHA Linear Accelerator", in *Proc. 2nd International Particle Accelerator Conf. (IPAC11),* San Sebastian, Spain, Sep. 2011, paper WEPS090, pp. 2718-2720.

[2] K. Kümpel, D. Mäder, P. Müller, N. F. Petry, H. Podlech, "The New Injector Design for MYRRHA", in *Proc. 5th International Particle Accelerator Conf. (IPAC17),* Copenhagen, Denmark, May 2017, paper TUPVA068, pp. 2234-2236.

[3] C. Zhang, H. Podlech, "New Reference Design of the European ADS RFQ Accelerator for MYRRHA", in *Proc. 5th International Particle Accelerator Conf. (IPAC14),* Dresden, Germany, June 2014, paper THPME008, pp. 3223-3225.

[4] https://www.cst.com

[5] P. Müller, M. Busch, K. Kümpel, D. Mäder, N. F. Petry, H. Podlech, "RF Simulations of the Injector Section from CH8 to CH15 for MYRRHA", in *Proc. 9th International Particle Accelerator Conf. (IPAC18)*, Vancouver, BC, Canada, May 2018, pp. 2790-2792. doi: 10.18429/JACoW-IPAC2018-WEPML043

Content from this work may be used under the terms of the CC BY 3.0 licence (© 2018). Any distribution of this work must maintain attribution to the author(s), title of the work, publisher, and DOI.

ISBN: 978-3-95450-194-6 ISSN: 2226-0366 doi:10.18429/JACoW-LINAC2018-MOPO092

A 3-GAP BOOSTER CAVITY TO MATCH ION SOURCE POTENTIAL TO RFQ ACCEPTANCE

R.E. Laxdal†, ZT Ang, T. Au, S. Kiy, S. Rädel, O. Shelbaya, V. Zvyagintsev TRIUMF, Vancouver, Canada

Abstract

The ISAC RFQ can accelerate ions with A/Q ration from 1 to 30 and requires an input energy of 2.04keV/u. The harsh environment of the ISAC on-line ISOL target facility is challenged to meet the energy for the heaviest masses. For these cases we have designed and installed a short three gap device that accelerates the beams produced at source potential to match the required energy for RFQ acceptance. The booster cavity operates at 11.7MHz the RF frequency of the pre-buncher and delivers up to 9.8kV to the beam. The device can also be used as a second buncher to augment the acceptance in the RFQ or to improve the acceptance of higher space charge beams.

INTRODUCTION

The Isotope Separator and ACcelerator (ISAC) at TRIUMF produces rare-isotope beams (RIB) for studies in astrophysics, nuclear structure and reactions, electroweak interactions and material science [1]. A variety of radioisotope beams, below the space charge regime, can be generated and accelerated to a high energy area in ISAC-I or to the superconducting linac (SCL) in ISAC-II. In both cases the first accelerator in ISAC-I is a 35.4MHz split ring, four vane Radio Frequency Quadrupole (RFQ), designed without a gentle buncher or buncher section. The RFQ focusses and accelerates RIB from 2.04 keV/u (β= 0.0021) to 153 keV/u with a mass-to-charge ratio of $1 \leq A/Q \leq 30$ [2]. The source must extract ions with a bias voltage of up to about ~60 kV, depending on A/Q. Current ISAC target modules have issues holding biases beyond V_s = 52 kV. Thus for charge to mass ratios of $A/Q \geq 25$ a boost in energy is required for successful RFQ injection.

The pre-bunching of the beam allows the use of an RF device to match the beam energy to the RFQ acceptance. An RF Booster was designed, providing a voltage kick of up to10 kV to compensate for the target module issues to achieve matching to the RFQ energy acceptance of 2.04 keV/u. The booster has been designed as a three gap RF device, with an aperture large enough to avoid interference with the existing beam envelop. Fig. 1 depicts a schematic of the booster and its position in ISAC-I located between the RFQ and the three harmonic 11.8MHz pre-buncher. The required booster voltage V_b is determined by the ion's mass-to-charge ratio A/Q and the target module's extraction voltage V_s:

$$V_b[\mathrm{kV}] = 2.04[\mathrm{keV/u}]\frac{A}{Q} - V_s \quad . \qquad (1)$$

In this paper we present test results of the booster cavity as an energy compensation device and as a supplemental buncher. The relationship between bunch current and space charge is investigated for the bunching case.

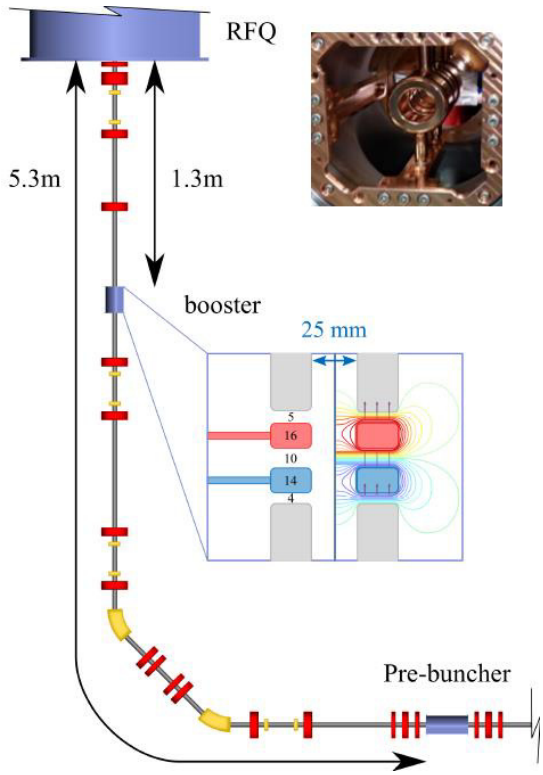


Figure 1: Pre-buncher, booster (inlay photo) and RFQ location at ISAC-I.

BOOSTER DESIGN FEATURES

An efficient design for the booster is a three gap RF device driven by an external lumped circuit. The booster drift tubes operate in a π-mode at 11.8MHz, the pre-buncher's fundamental frequency. An initial variant was described in [3]. The initial device was tested to V_{eff}=7kV and then modified to allow a power increase. The Macor used to support the drift tubes was found to be too lossy and was replaced with a small Teflon brace to support the HV feedlines to the two central drift tubes (Fig. 2).

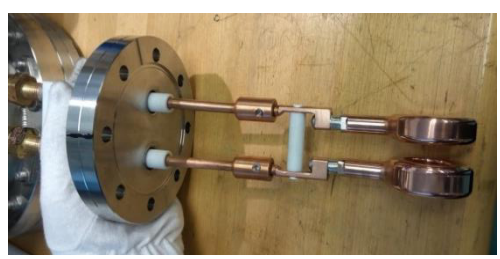


Figure 2: Booster central drift tubes and voltage feed.

Content from this work may be used under the terms of the CC BY 3.0 licence (© 2018). Any distribution of this work must maintain attribution to the author(s), title of the work, publisher, and DOI.

ISBN: 978-3-95450-194-6 ISSN: 2226-0366 doi:10.18429/JACoW-LINAC2018-MOPO092

The present design achieves an effective voltage of 9.8 kV, while keeping the peak voltage at the two feed-throughs to reasonable values, ~4.7 kV. A lumped circuit Q of 1500 is attained. The gap spacing is optimized to efficiently accelerate over the velocity range of interest [4].

The booster has to fit within the existing space just upstream of the final matching optics to the RFQ. The booster electrode aperture is necessarily much larger than the booster gaps, to prevent the limitation of beamline aperture in the existing beamline. This configuration is characterized by significant field penetration inside the drift tubes, as shown in Fig. 1. The drift tube geometry causes an inherent coupling between radial position and longitudinal fields, as depicted in Fig. 3. Thus, off axis particles receive more energy gain than on-axis particles [4], and results in debunching of the beam at the RFQ for typical beam emittances. The radial longitudinal coupling limits RFQ transmission dependent on the relative voltage gain supplied by the RF booster and the transverse size or mis-steering of the beam through the booster.

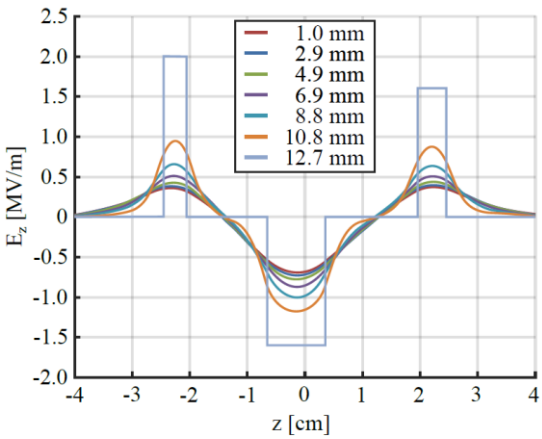


Figure 3: Accelerating field amplitude as a function of beam radius through the booster.

BOOSTER ENERGY KICK

It is found [3] that the expected energy gain through the 3 gap structure is a slowly varying function of the initial velocity and for the A=30 design case is approximately given by:

$$\Delta W(r) \approx 2.1 \frac{Q}{A} V_0 I_0 (k_s r) \cos\varphi_0 \qquad (2)$$

where V_0 is the drift tube voltage, $k_s = 2\pi/(\beta_s \lambda) = 141\text{m}^{-1}$ and $\beta_s = 0.00175$. A simulation of the expected transmission of the booster cavity is done by integrating a well aligned beam of a given beam size through the booster cavity and comparing the phase spread of the beam at the RFQ against the RFQ acceptance as a function of booster relative voltage. Beam test results have been done to confirm the actual performance. Figure 4 displays the effect of the installed RF booster providing energy $^{16}O^{1+}$ with a required terminal voltage of 32.62kV. The booster is powered such that the RFQ injection energy is always optimal as shown in Eq. 1. The reduction in RFQ transmission with increasing relative booster voltage demonstrates the coupling/debunching effects. Beam measurements compare well with simulations shown by the dashed line in Fig. 4 [4] where a beam size of σ=2.5mm is assumed.

BUNCHING MODE

The booster may also be operated at 90 degree phasing, enabling its use as a supplemental bunching device. This mode can be used to augment beam manipulation from the pre-buncher alone to improve the RFQ capture or for stable beam high intensity beam delivery can be used to reduce the impact of longitudinal space charge.

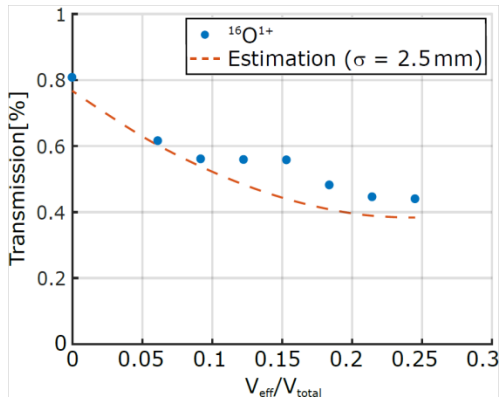


Figure 4: Measured RFQ transmission versus relative booster voltage, compared against simulation for a beam of σ_t = 2.5mm.

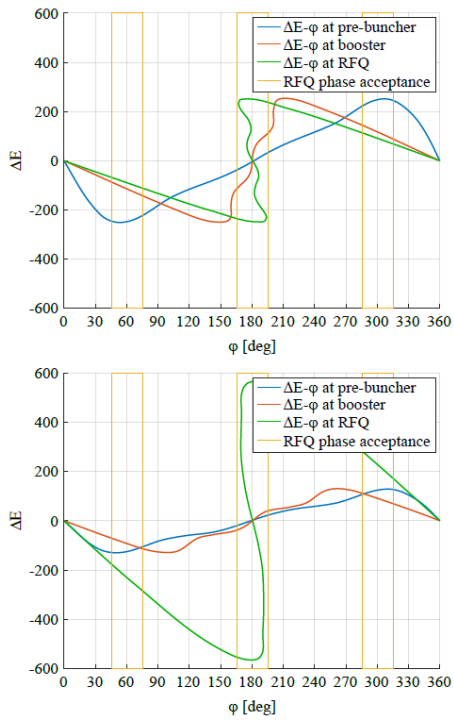


Figure 5: On top is the longitudinal phase space development for the multi-harmonic pre-buncher and at the bottom the longitudinal phase space development for tandem operation (pre-buncher and booster) is depicted for a 16O1+ ion beam at different positions in ISAC-I.

Content from this work may be used under the terms of the CC BY 3.0 licence (© 2018). Any distribution of this work must maintain attribution to the author(s), title of the work, publisher, and DOI.

ISBN: 978-3-95450-194-6 ISSN: 2226-0366 doi:10.18429/JACoW-LINAC2018-MOPO092

Content from this work may be used under the terms of the CC BY 3.0 licence (© 2018). Any distribution of this work must maintain attribution to the author(s), title of the work, publisher, and DOI.

Standard Bunching

Fig. 5 (top) shows the effects of bunching the beam with the multi-harmonic pre-buncher only, highlighting the evolution of the time focus from pre-buncher to RFQ entrance. The booster can be used to provide further bunching (with increased energy spread), as evidenced in the bottom of Fig. 5. This extra bunching is particularly useful for lighter beams, where solo pre-buncher operation typically has a lower capture efficiency in the RFQ thought to be due to insufficient stability of low voltage optics or the pre-buncher RF systems.

Bunching in Space Charge Regime

Typically the ISAC linear accelerators boost the energy of low intensity RIB beams but there are cases where high intensity stable beams are required. Longitudinal space charge at high current tends to debunch the beam at the RFQ entrance, reducing the RFQ transmission. A simulation of the space charge effect is illustrated in Fig. 6 [5]. Given the booster's position 1.3m upstream of the RFQ, it can be operated in tandem with the pre-buncher as a double bunching system to counteract space charge effects, thereby increasing the amount of beam within the RFQ acceptance.

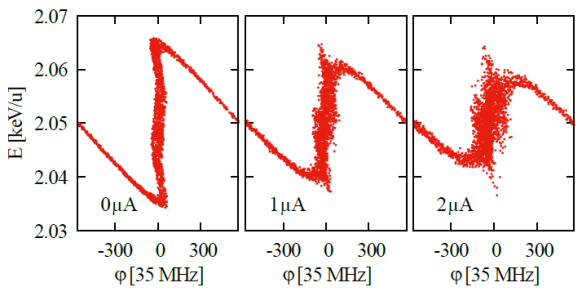


Figure 6: PARMELA simulated particle distribution including space charge effects for three different bunch charges and an A/Q = 30 for 2000 particles. [5]

Beam test results were performed with a 20Ne1+ beam and are presented in Fig. 7. A combination of different collimators and attenuators near the source were used to adjust different beam intensities from 0 to 13μA. RFQ capture data was taken for different combinations of bunching with the prebuncher and the booster. The source energy was constant for all measurements. A transmission of 25% is expected in the RFQ during acceleration of an unbunched beam, as presented in Fig. 7, in blue.

Establishing a time focus, either with the pre-buncher, booster or both, causes an increase in RFQ transmission, as expected. For example, at low intensity, up to 80% transmission is observed for pre-buncher alone (yellow line) and 85% for the tandem of prebuncher and booster (purple line). As the beam current increases space charge reduces the RFQ transmission for the prebunched beam eventually to a transmission equivalent to the unbunched case. Solo booster bunching operation is represented by the red line in Fig. 7. An RFQ transmission of 60% was achieved with the booster in single mode operation, in line with expectations. The sensitivity to space charge is significantly reduced since the debunching distance is considerably shorter than when using the pre-buncher. An increase in the space charge on-set by a factor of ~10 is demonstrated. Tandem operation with the pre-buncher is depicted as the purple line in Fig. 7. It gives higher low current values that reduce to booster only values at high space charge. The pre-buncher's sawtooth RF is better suited to produce a time focus, compared to the booster's purely sinusoidal RF for non-space-charge regimes.

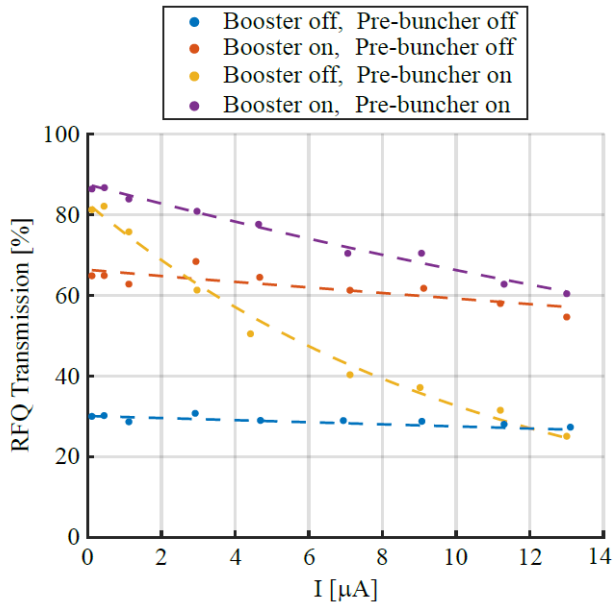


Figure 7: Booster operating as a buncher in different modes, as single or tandem with the pre-buncher, for 20Ne1+.

CONCLUSION

A three gap rf device of very low beta has been designed, built and tested to supply up to 10kV to match an ion beam to the velocity acceptance of the ISAC RFQ. Two operation modes have been demonstrated with beam measurements. In acceleration mode, the booster has been used to augment the source potential by up to 25% for reasonable RFQ transmission. Higher relative voltages are less efficient due to strong radial longitudinal coupling. When operated as a buncher, the booster can be used in tandem with the pre-buncher (or solo) to improve the RFQ transmission and provides a ~10-fold increase of the onset of space charge effects, by mitigating those effects on the time focus at the RFQ entrance.

REFERENCES

[1] Dilling J., Krücken R., Ball G. (2013), *ISAC overview*, In:Dilling J., Krücken R., Merminga L. (eds) ISAC and ARIEL:The TRIUMF Radioactive Beam Facilities and the Scientific Program, Springer, Dordrecht. https://doi.org/10.1007/978-94-007-7963-1_1

[2] R. E. Laxdal, R. A. Baartman and L. Root, "Beam test results with the ISAC 35-MHz RFQ", in *Proceedings, 1999 Particle Accelerator Conference (PAC'99)*, New York, New York, March 29-April 2, 1999.

ISBN: 978-3-95450-194-6 ISSN: 2226-0366 doi:10.18429/JACoW-LINAC2018-MOPO092

[3] V. Zvyagintsev, et al., "Novel RF Structure for Energy Matching into an RFQ", in *Proceedings of IPAC2017*, Copenhagen, Denmark, May 2017, THPIK003.

[4] R. E. Laxdal, V. Zvyagintsev, "Design of the ISAC RF Booster", TRIUMF, TRI-DN-17-23, 2017.

[5] O. Shelbaya, O.Kester, "Toward an end-to-end model for ISACI accelerators,", in *Proc. 9th Int. Particle Accelerator Conf. (IPAC'18)*, Vancouver, Canada, May 2018, paper THPAK112.

Content from this work may be used under the terms of the CC BY 3.0 licence (© 2018). Any distribution of this work must maintain attribution to the author(s), title of the work, publisher, and DOI.

ISBN: 978-3-95450-194-6 ISSN: 2226-0366 doi:10.18429/JACoW-LINAC2018-MOPO093

A STUDY OF A COOLING CONFIGURATION FOR AN OFHC COPPER REBUNCHER

O. Mazor, M. Bukai, D. Nusbaum, J. Rodnizki†, Soreq NRC, Yavne, Israel
G. Ziskind, Ben-Gurion University in the Negev, Beer Sheva, Israel
E. Dyunin, Ariel University, Ariel, Israel

Abstract

A four gap OFHC copper rebuncher is developed at SNRC as a research study and a risk reduction for the MEBT of SARAF Phase II proton/ deuteron linac. The rebuncher is designed to bunch a 5 mA CW beam at 176 MHz. The required cavity voltage according to beam dynamics evaluation is 150 kV with a beam aperture diameter of 40 mm, beam energy of 1.3 MeV/u with a Q value of 8000. Considering utilizing this cavity for enhancing the beam energy, the cooling configuration is explored for a cavity voltage of 300 kV, consuming 20 kW dissipated power, at a peak electric field of 14 MV/m, equivalent to the Kilpatrick limit. The electromagnetic study conducted with the CST MW Studio was reproduced at ANSYS HFSS. The simulated dissipated power was assigned to the ANSYS Fluent model to explore the resulted temperature map. Several evolved cooling configurations were studied, including cooling of the drift tubes. In this configuration the temperature rise along the cavity is in the range of 30 K. A detailed design of the four gap rebuncher is following this study.

INTRODUCTION

An Oxygen Free High Conductivity (OFHC) copper 4 gap rebuncher is developed for the proton/ deuteron 5 mA Continues Wave (CW) SARAF linac at 176 MHz. The rebuncher beam energy is 1.3 MeV/u (beam $\beta = 0.053$) [1-3]. The required cavity voltage according to beam dynamics simulation is 150 kV with an aperture diameter of 40 mm with a Q value of 8000 [4]. We consider applying this cavity for enhancing the beam energy in order to reduce the ion velocity mismatch upstream the RFQ. In this case the peak electric field on the cavity surface is 14 MV/m (1 Kilpatrick Criterion) and the expected cavity voltage and dissipated power are 300 kV and 20 kW respectively. For normal functioning as a rebuncher the maximum field is 50% and, thus, the dissipated power is 25%. The rebuncher cooling configuration for 20 kW dissipated power is explored in this study.

MODEL ANALYSIS

The rebuncher configuration is shown in Fig. 1. The main components are: the RF cavity chamber, the upper fork with two drift tubes and the base cone with a drift tube. All these elements are made from OFHC copper. The electro-magnetic properties were simulated with CST MW Studio using the eigenmode solver (Fig. 2).

The next stage of the research was to simulate the 20 kW injected power regime. The coupler (Port 1) and the pickup antenna (Port 2) were introduced into the CST MW Studio and HFSS designs. The driven modal HFSS solver (Fig. 3) reproduced the similar results pattern that was generated by the CST eigenmode and driven modal solvers.

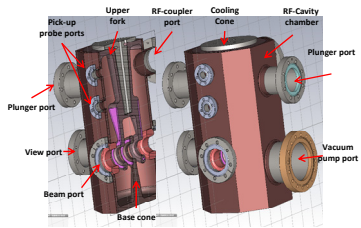


Figure 1: The rebuncher design.

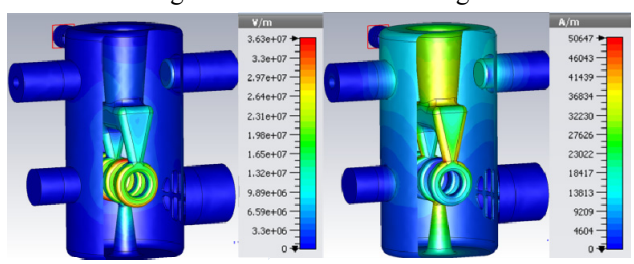


Figure 2: The induced eigenmode surface electric field (left) and magnetic field (right) at 176 MHz normalized for a 1 Joule rebuncher stored energy received from CST MW studio.

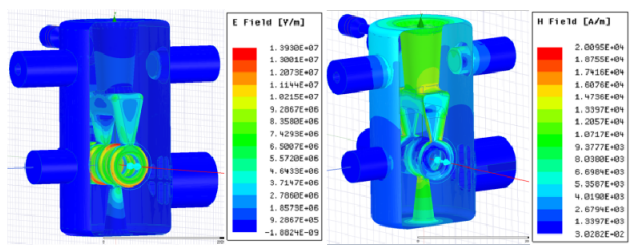


Figure 3: The induced surface electric field (left) and magnetic field (right) for 20 kW input power received with the driven modal HFSS solver.

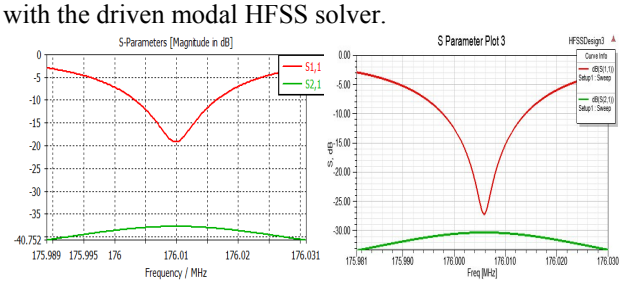


Figure 4: S-parameters of the rebuncher results from driven modal solvers of CST (left plot) and HFSS (right plot) - S11 (red curve) and S21 (green curve). The frequency range is the FWHM value (S21 -3dB level).

† jacob@soreq.gov.il

Content from this work may be used under the terms of the CC BY 3.0 licence (© 2018). Any distribution of this work must maintain attribution to the author(s), title of the work, publisher, and DOI.

ISBN: 978-3-95450-194-6 ISSN: 2226-0366 doi:10.18429/JACoW-LINAC2018-MOPO093

Results of HFSS and CST driven mode solvers are shown in Fig. 4. The resonance frequency/Q-factor are 176.05MHz/3667 in HFSS simulation and 176.01MHz/4193 in CST. Small differences between the resonance frequencies and the Q-factor are well fitted into the tuning range of the system. The external coupling will be matched by the coupler antenna rotation; the resonance frequency will be tuned by two plungers.

The temperature mapping and the heating power flow were received by the rebuncher ANSYS Fluent solver and the HFSS driven solver co-simulations. Several evolved cooling configurations were studied. The basic cooling configuration is shown in Fig. 5. It includes cooling of the upper fork, base cone and the surrounding RF-cavity chamber.

The surrounding body temperature and the inlet water temperature are taken as 300 K. The water velocity at the entrance to each pipe was defined as 5 m/s. The temperature rise for the basic cooling geometry at 5 kW dissipated power is 46 K above the surrounding temperature (Fig. 6). Review of the obtained temperature map shows that the drift tubes are overheated and the outer wall is overcooled. The main goal of the future improvements of the cooling system design is to reduce the maximal temperature on inner surface of the rebuncher and reduce the temperature gradient along the rebuncher due to uniform of the thermal deformation of the structure.

The basic configuration was updated as follow: the cooling channels were included in the top drift tubes; four pipes in the central upper stem were replaced with two-pipe configuration (to reduce the manufacturing effort); the central drift tube was cooled by the long coaxial cone channel which penetrates the drift tube body up to the center of the ring wall (Fig. 7).

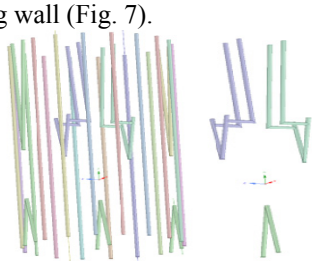


Figure 5: Basic cooling geometry: main chamber + central bodies (left) central bodies only (right).

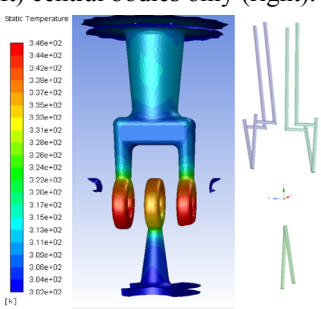


Figure 6: Temperature map on inner surface of the rebuncher due to 5 kW dissipated power (left) utilizing central cooling configuration basic model (right). All surfaces with a temperature increment less than 2 K are filtered out.

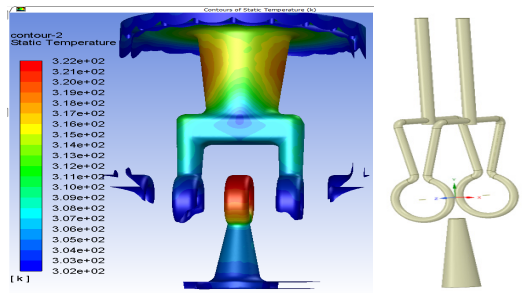


Figure 7: Rebuncher temperature map with two cooling pipes in the central stem and cooling lines in the top drift tubes due to 5kW dissipated power.

The improved configuration demonstrated a significant cooling increment of the drift tubes related to the basic configuration: 4 K compare with 46 K for the top rings and 22 K compare with 38 K for the central ring. On the other hand, the cooling abilities of the upper stem were reduced. As a result of this, the stem temperature increment and the azimuthal temperature deviation were increased from 14 K to 20 K and from 1 K to 8 K respectively.

Based on the previous stages, the derived configuration for the central elements of the rebuncher was introduced. Four cooling pipes configuration with the coaxial cooling channel was adopted for the upper fork. The central drift tube was cooled by an internal cooling line similar to the cooling lines configuration of an upper drift tube.

The 20 kW forward power regime was examined (Fig. 8). The maximal temperature increment 35 K was achieved on the upper fork. The drift tube temperature increment in the area of the peak surface electric field is 12 K. The temperature profile of the central elements is well balanced.

The peripheral elements of the rebuncher were taken into account on the next stage of the study. The coupler and pick-ups, two plungers, vacuum pump and viewport were located on their positions. This caused to the space separation of the cooling pipes located in the external wall of the cavity (Fig. 9). The 20 kW coupler loop and the plungers were cooled by additional water cooling channels. The neutral-convection boundary condition was defined on the external surfaces of the plungers and the pick-ups ports.

The temperature increment for the finalized rebuncher engineering assembly design is 38 K (Fig. 10) for 20 kW dissipated power and 300 kV cavity voltage. The stress analysis, point out that the maximum Von-Mises stress is 7 MPa (Fig. 11). This value is well below the yield strength of OFHC copper (69 MPa). The integrated thermal displacement of the drift tubes is defined as:

$$\Delta L = \alpha_L \Delta T^* L$$

where α_L is the linear thermal expansion coefficient, ΔT is the temperature increment, L is the original body length. Under a uniform 38 K temperature increment assumption, the OFHC copper body (α_L = 16*10^{-6} K^{-1}) with the designed length 250 mm (the upper fork length), the integrated thermal displacement is equal to 0.15 mm. The mechanical displacement due to the atmospheric-vacuum

Content from this work may be used under the terms of the CC BY 3.0 licence (© 2018). Any distribution of this work must maintain attribution to the author(s), title of the work, publisher, and DOI.

ISBN: 978-3-95450-194-6 ISSN: 2226-0366 doi:10.18429/JACoW-LINAC2018-MOPO093

Content from this work may be used under the terms of the CC BY 3.0 licence (© 2018). Any distribution of this work must maintain attribution to the author(s), title of the work, publisher, and DOI.

pressure and the gravity results in the 5 µm displacement of the drift tube (Fig. 11), which may be neglected compare with the thermal one. The maximum off-axis transverse displacement limit, defined by the beam dynamics error study [1], is 1 mm.

Our cooling design presents higher cooling capability comparing to the CADS Injector2 recent two gap rebuncher, designed for a similar frequency (162.5 MHz) 40 mm beam aperture with a copper electroplated stainless steel chamber wall for a 10 mA, 2.1 MeV CW proton beam revealed – 10 kW dissipated power at 135 kV cavity voltage, 22 K temperature rise generated at a location between the stem and the drift tube with 0.1 mm drift tube thermal displacement, utilizing 2.5 m/s water cooled OFHC copper stem and drift tube [5].

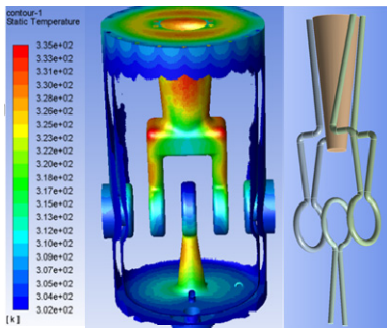


Figure 8: The Rebuncher temperature map for the derived cooling configuration with 4 cooling lines and a coaxial cooing cone at the top fork top cone and a cooling line for the central drift tube due to 20 kW dissipated power.

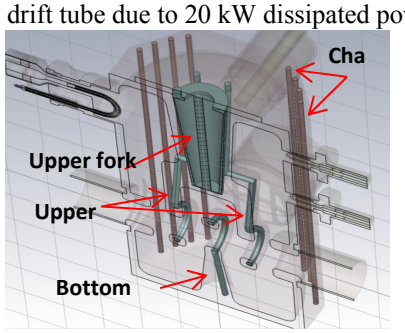


Figure 9: The rebuncher finalized engineering design with the integrated derived cooling configuration.

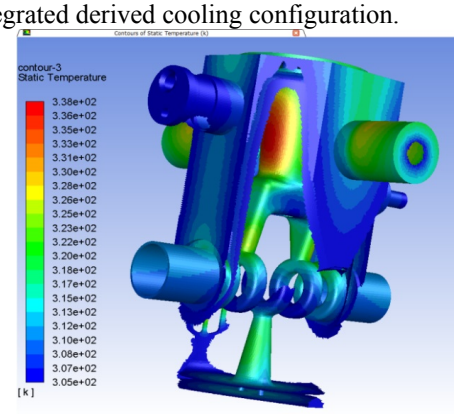


Figure 10: The rebuncher temperature ANSYS Fluent map for 20 kW dissipated power assuming reasonable distilled cooling water velocity of 5 m/s demonstrate modest temperature rise of 38 K.

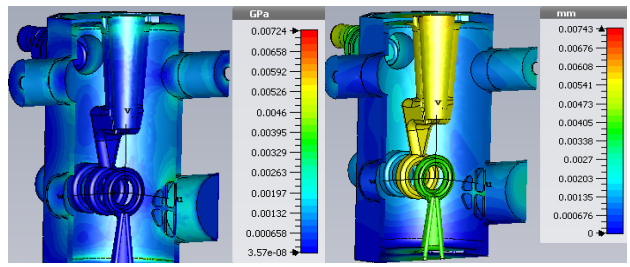


Figure 11: Von Mises Stress and displacement due to 1 bar pressure on the rebuncher external wall (internal vacuum) and self-weight assuming the auxiliary system will be supported independently neglecting the residual moment on the rebunc her- supported around the surrounding of the chamber bottom wall.

VERIFICATION ANALYSIS

The standard K-epsilon model was selected to simulate the fluent flow and heat transfer along the cooling paths. This is a robust model for a turbulent flow with a moderate pressure drop [6]. The inlet fluent velocity was studied in the range of 3-7 m/s for the 20 kW dissipated power.

The temperature profile was examined for the inlet flow velocity of 5 m/s and for cell mesh length of 3 and 4 mm. Comparison of the results for different mesh size does not show any significant deviation (less than 1 K). Due to this fact, all future simulations were run with 4mm cell mesh-length.

A 3D velocity distribution in a cooling channel corner is shown in Fig. 12. It was found that the temperature rise reduces from 38 K to 33 K for coolant inlet flow velocity variates in between 5-7 m/s. At the same time, the simulated pressure drop along the cooling lines increases above 1bar. Based on these simulations, the recommended distilled water flow inlet velocity is 5 m/s.

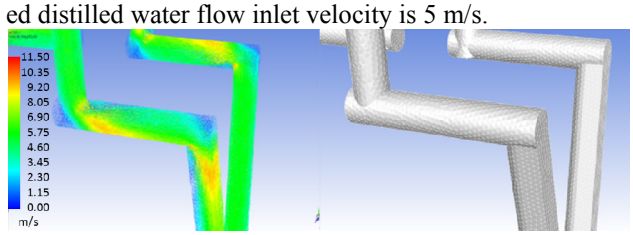


Figure 12: The fluent velocity path (left) for the derived 4 mm cell mesh-length (right)

CONCLUSIONS

An effective cooling configuration was derived in this study for the 4 gap rebuncher. A surface temperature increment of 38 K for 20 kW dissipated power for a reasonable distilled water inlet flow of 5 m/s was achieved. The total water pressure drop in the cooling system is less than 1 bar. The next step is to manufacture the rebuncher and to condition it for 5-20 kW dissipated power.

ACKNOWLEDGEMENT

This work is partially funded by Pazy Foundation. We would like to acknowledge Mr. E. Sayag, Mr. L. Danon and Mr. M. Alefe from SNRC Engineering Department for their support during the design phase.

ISBN: 978-3-95450-194-6 ISSN: 2226-0366 doi:10.18429/JACoW-LINAC2018-MOPO093

REFERENCES

[1] N.Pichoff *et al.*, "The SARAF-Linac project 2018 status", in *Proc. IPAC'18,* Vancouver, BC, Canada, Apr.-May 2018, paper TUPAK015.

[2] A. Perry *et al.*, "Commissioning of the new SARAF RFQ and design of the new linac", presented at the 29th Linear Accelerator Conf. (LINAC'18), Shanghai, China, Sep. 2018, paper WE2A04, this conference.

[3] L. Weissman *et al.*, "Installation, high-power conditioning and beam commissioning of the upgraded SARAF 4-rods RFQ", JINST Technical Report, May 8, 2018, https://doi.org/10.1088/1748-0221/13/05/T05004

[4] B.Kaizer, J.Rodnizki, E.Farber, A.Perry, L.Danon *et al.*, "Study and development of CW room temperature rebuncher for SARAF accelerator", *Nucl. Instr. Meth.*, vol. 871, pp. 161-168, 2017.

[5] N. Haihua, L.Youtang, H.Yuan, Z.Bin, H.Shichun, Y.Chenzhang, J.Huan, and Z.Shenghu, "The mechanical design and fabrication of 162.5 MHz buncher for China accelerator driven sub-critical system injector II", *Nuclear Engineering and Technology,* vol. 49, pp. 1071-1078, 2017.

[6] Modeling Turbulent Flows - University of Southampton. www.southampton.ac.uk/~nwb/lectures/.../Turbulence_Notes_Fluent-v6.3.06.pdf

Content from this work may be used under the terms of the CC BY 3.0 licence (© 2018). Any distribution of this work must maintain attribution to the author(s), title of the work, publisher, and DOI.

ISBN: 978-3-95450-194-6 ISSN: 2226-0366 doi:10.18429/JACoW-LINAC2018-MOPO094

RF STABILITY TEST OF RFQ CAVITY WITH PROTOTYPE LOW-LEVEL RADIO FREQUENCY IN RAON

Doyoon Lee†, Bonghyuk Choi, Ohryong Choi, Kitaek Son, Hyojae Jang and Hoechun Jung
Rare Isotope Science Project, Institude for Basic Science, Daejeon 34047, Republic of Korea

Abstract

RAON is a heavy ion accelerator of the Institute for Basic Sciences (IBS) in Korea. The prototype Low-Level Radio Frequency (LLRF) operated at 81.25 MHz has been designed and fabricated for a prototype Radio Frequency Quadrupole (RFQ) cavity in RAON. Stabilities of ±1 % in amplitude and ±1 degree in phase are required for specifications of the RFQ system. The prototype LLRF controls the RF amplitude and phase in the cavity by PID feedback loop. The prototype LLRF has been tested with one RFQ cavity and stabilities have been measured. In this paper, we present the design and results of stability test.

INTRODUCTION

Prototype LLRF for RFQ cavity is designed to maintain the stability of amplitude and phase of RF power in the cavity at 81.25 MHz frequency within ±1 % and ±1 degree through PID feedback control. Table 1 shows parameter of 81.25 MHz LLRF. The prototype LLRF has one reference clock, two RF input channels and one output channel. The reference clock input channel operates with a reference signal of -15 to 0 dBm and the sampling frequency is generated by using a clock signal down-converted to 4/5 times. The operating frequency range is 81.25 ±1 MHz. The RFQ pick-up signal is put into the RF input channel and feedback control is performed. The RF power from the output channel is used as the input drive power for the SSPA (solid state power amplifier). The LLRF controller based on EPICS OPI (operator interface) communicates with the LLRF module via ethernet. It is responsible for controlling the RF field of the RFQ cavity, interlocking, monitoring and data archiving. Feedback on-off is applied independently to amplitude and phase. User can set the target values of amplitude and phase and the PID coefficients. The RF output power limiter is equipped for SSPA protection. The LLRF module consists of RF module and FPGA board as shown in Fig. 1.

Table 1: Parameter of 81.25 MHz LLRF

Parameter	Value
Frequency Range	81.25 ± 1 MHz
Amplitude Stability	< ± 1 %
Phase Stability	< ± 1 degree
Operating Mode	CW, Pulse
RF Input	Ref. : -15 ~ 0 dBm Ch 1, 2 : -40 ~ 0 dBm
RF Output	-40 ~ 0 dBm
I/O Impedance	50 ohm

† dylee@ibs.re.kr

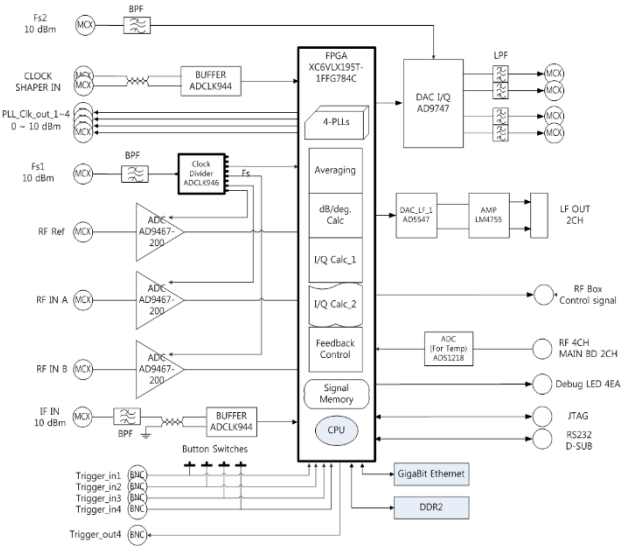


Figure 1: Block diagram of 81.25 MHz LLRF module.

STABILITY TEST

We set up the test bench with 81.25 MHz LLRF, 15 kW SSPA and RFQ cavity as shown in Fig. 2. The block diagram of the test bench for stability test is shown in Fig. 3.

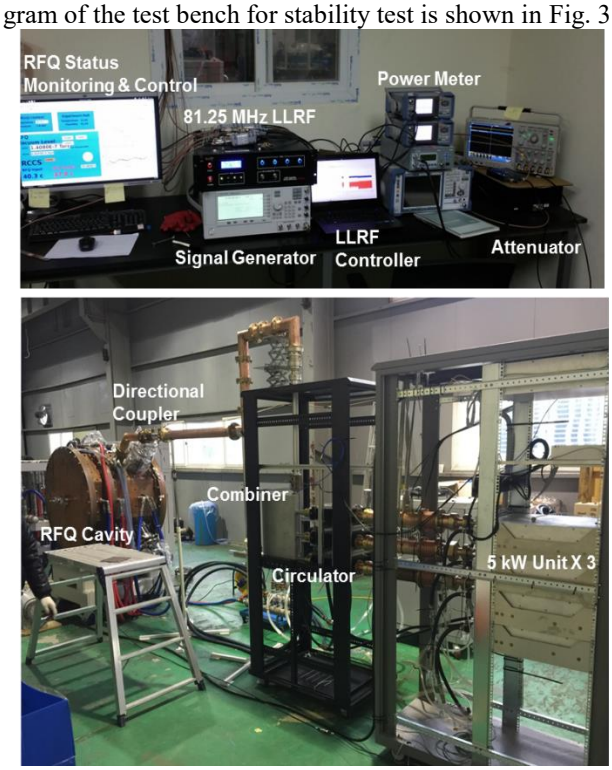


Figure 2: Test setup with 81.25 MHz LLRF,15 kW SSPA and RFQ cavity.

Content from this work may be used under the terms of the CC BY 3.0 licence (© 2018). Any distribution of this work must maintain attribution to the author(s), title of the work, publisher, and DOI.

ISBN: 978-3-95450-194-6 ISSN: 2226-0366 doi:10.18429/JACoW-LINAC2018-MOPO094

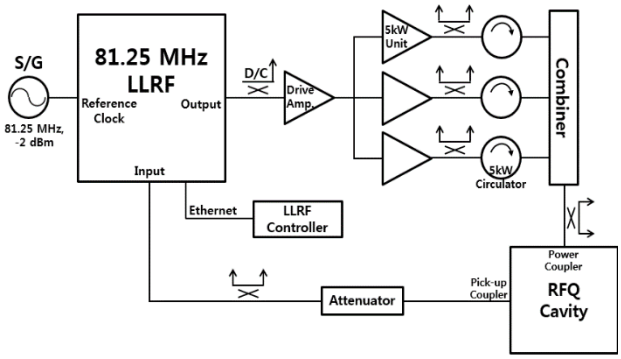


Figure 3: Block diagram of test bench for stability test

Operating frequency for RFQ system is 81.25 MHz. The reference clock signal of the prototype LLRF is –2 dBm of 81.25 MHz RF signal generated by the signal generator. The output RF power of the prototype LLRF is amplified by the SSPA and then put into the cavity from the RF power coupler. The RF field of the RFQ through the pick-up coupler is sent to prototype LLRF to constitute the amplitude and phase loop. The SSPA output power is 15 kW by combining three 5 kW amplifier units. The 3-1/8" coaxial type rigid transmission lines are designed to deliver the RF power to RFQ up to 15 kW (CW). Because handling power of 3-1/8" 50 Ohm coaxial line is approximately 50 kW at 81.25 MHz, no additional cooling is needed [1]. The Dual Directional Coupler is used to monitor the forward and reflected power. Directivity is more than 20 dB for correct power measurements because of minimizing the effects of coupling signals. The circulator is used to protect the SSPA from over-reflected RF power from RFQ. The isolation is higher than 20 dB and insertion loss is less than 0.3 dB. The RFQ adopts the RCCS (Resonance Control Cooling System), which supplies cooling water to each vane and quadrant, to control the temperature and adjust the resonance frequency. Experiment conditions are $1\sim2\times10^{-7}$ torr, 29.4~36 ˚C of RCCS temperature, 10~45 Hz of pump speed, 1~50 % of heater level and 13~15 ˚C of SSPA cooling water temperature. To control the resonance frequency of the RFQ, the target values for RCCS temperature, pump speed, and heater level are set manually.

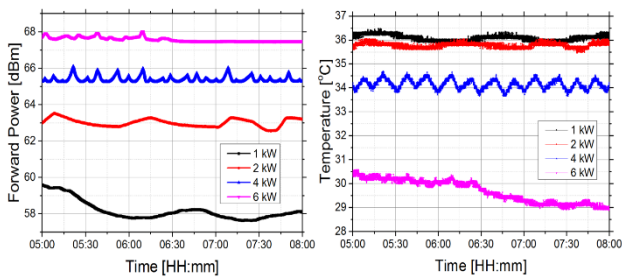


Figure 4: Forward power and temperature of RCCS during the stability test.

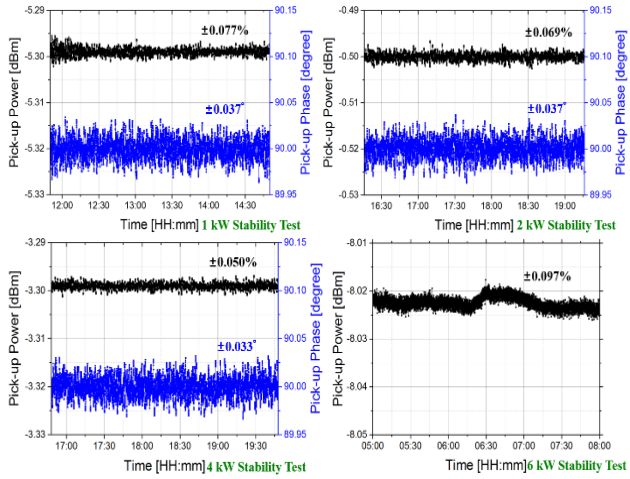


Figure 5: RF amplitude and phase stability.

Figure 4 shows the forward power and temperature of RCCS during the stability test. Figure 5 shows the RF amplitude and phase stability for each test and the measurement time is 3 hours.

We control the RCCS temperature and pump speed to avoid over-reflected power of the interlock during the experiments. Each attenuator used in the stability test is 40, 40, 46 and 53 dB. The fluctuation of forward power is respectively 2.00, 0.96, 0.85 and 0.56 dB and 335, 446, 724 and 769 W based on power of watt. The period of RCCS temperature is getting shorter as the power is higher and can not know at the 6 kW stability test. The reflected power changes according to the temperature change of RCCS. Stabilities of ±1 % in amplitude and ±1 degree in phase are required for specifications of the RFQ system. The amplitude stability is less than ±0.097 % and the phase stability is less than ±0.037 degree, so the measurement values satisfied specifications during the stability tests. In the 6 kW stability experiment, the phase stability was satisfied but the data was not stored. Stability may vary depending on the PID coefficient. Table 2 shows the experimental conditions and results for each stability test.

Table 2: Experimental Conditions and Results for Each Stability Test

Parameter	1 kW	2 kW	4 kW	6 kW
Amplitude Stability [%]	±0.077	±0.069	±0.050	±0.097
Phase Stability [degree]	±0.037	±0.037	±0.033	-
Forward Power Fluctuation [dB]	2.00	0.96	0.85	0.56
RCCS Temperature [˚C]	36	36	34.5 ~ 35.0	29.4 ~ 31.0
Pump Speed [Hz]	10~15	26~30	25~30	37~45
Heater Level [%]	50	50	50	1
Attenuator [dB]	40	40	46	53

Content from this work may be used under the terms of the CC BY 3.0 licence (© 2018). Any distribution of this work must maintain attribution to the author(s), title of the work, publisher, and DOI.

ISBN: 978-3-95450-194-6 ISSN: 2226-0366 doi:10.18429/JACoW-LINAC2018-MOPO094

Content from this work may be used under the terms of the CC BY 3.0 licence (© 2018). Any distribution of this work must maintain attribution to the author(s), title of the work, publisher, and DOI.

Figure 6 shows the correlation between pick-up power and temperature of prototype LLRF module. The pick-up power values measured by the power meter was different from the LLRF module at the beginning of the experiment, while the actual power is the same as the temperature trend of the LLRF module. Therefore, all subsequent experiments are conducted by using the temperature control rack with a temperature setting of 22 degrees. This problem disappeared after using the temperature control rack.

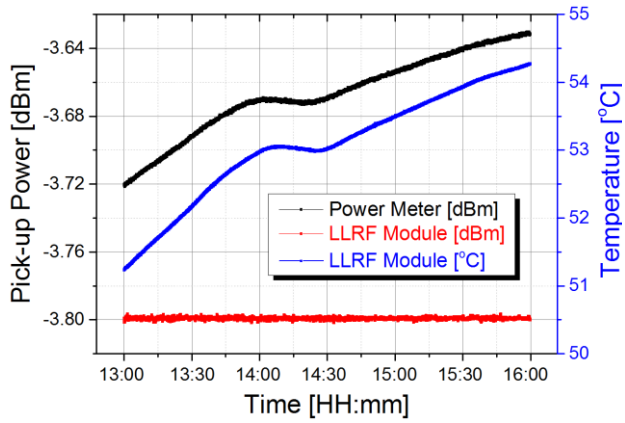


Figure 6: Correlation between pick-up power and temperature of LLRF module.

RF CONDITIONING

We set up the 2ea × 40 kW SSPAs and coaxial type rigid transmission lines from SSPA to RFQ cavity for RF conditioning as shown in Fig. 7. In order to synthesize 20 kW power, 4ea × 5 kW final amplifiers are combined with 4-way Gysel method [2, 3]. Two 20 kW racks are synthesized by using the hybrid combiner, and the two RFQ couplers are supplied with up to 40 kW power respectively.

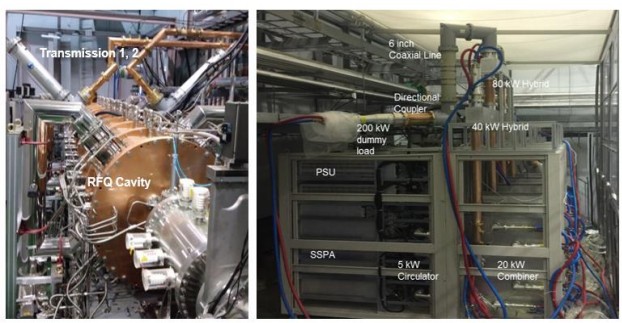


Figure 7: RFQ cavity, transmission lines and SSPAs for RFQ RF conditioning.

After approximately 6 weeks of scan conditioning for RFQ cavity, its multipacting region has been improved. The applied power is up to 40 kW in pulsed and CW mode.

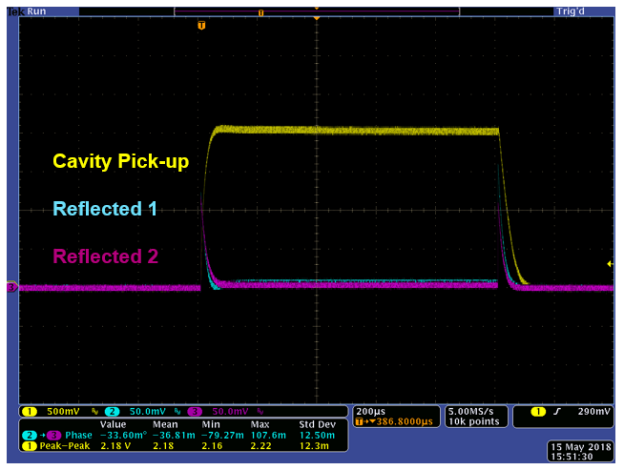


Figure 8: Measured RFQ field and reflected power in pulsed mode.

Figure 8 shows the measured RFQ field and reflected power in pulsed mode. The conditions of pulse operation are 30 kW, 1 ms, 20 Hz by combining two power couplers. The reflected waveform shows almost critical coupling and the vacuum level is also maintained steadily with no significant change.

CONCLUSION

A prototype LLRF is developed and successfully tested for RFQ cavity and showed promising results, for the RAON specifications. The amplitude stability is less than ±0.097 % and the phase stability is less than ±0.037 degree, so the measurement values satisfies with specifications during the stability tests. RFQ RF conditioning is performed up to 40 kW through two couplers to improve the multipacting and maintain the vacuum level.

In the future, RF Conditioning for RFQ cavity will be performed more than 40 kW of RF power and stability test will be conducted for beam acceleration. We will improve the reliability of LLRF and optimize the PID coefficients.

ACKNOWLEDGEMENTS

This work was supported by the Rare Isotope Science Project of Institute for Basic Science funded by Ministry of Science, ICT and Future Planning and National Research Foundation of Korea (2013M7A1A1075764).

REFERENCES

[1] http://www.megaind.com/assets/files/mega-data/coaxial-Line-Power-Handling.pdf

[2] O.R. Choi et al., "Development of 81.25 MHz 20 kW SSPA for RAON accelerator", *Proceeding of SRF2017*, Lanzhou, China, pp. 210-212.

[3] K.T. Son et al., "Development of 4-Way 81.25 MHz 20 kW High Power Combiner Using Parallel Plate Structure", *Proceeding of SRF2017*, Lanzhou, China, pp. 213-215.

ISBN: 978-3-95450-194-6 ISSN: 2226-0366 doi:10.18429/JACoW-LINAC2018-MOPO095

A RISK BASED APPROACH TO IMPROVING BEAM AVAILABILITY AT AN ACCELERATOR FACILITY*

W. C. Barkley†, M. J. Borden, R. W. Garnett, M. S. Gulley, E. L. Kerstiens, M. Pieck, D. E. Rees, F. E. Shelley, B. G. Smith, Los Alamos National Laboratory, Los Alamos, NM 87545, USA

Abstract

This paper describes a risk-based approach to improving beam availability at an accelerator facility. Los Alamos Neutron Science Center (LANSCE), like many other accelerator facilities, was built many years ago and has been repurposed when new missions were adopted. Many of the upgrades to the accelerator and beamlines allowed partial improvements but large-scale, system-wide improvements were never accomplished. Because of this, the facility operates with a mix of old and new equipment of varying conditions. Limited budgets have constrained spending for spare part procurement making it vital to prioritize those items predicted to have the highest impact to availability, should they fail. A systematic approach is described where equipment is inventoried, condition assessed, rated for potential failure and finally compiled into a risk-based priority list.

Introduction

The LANSCE facility operates a proton accelerator originally built in the late 60s and early 70s to deliver beam to five experimental areas. The facility has done very well over the years delivering beam at an overall 80-85% availability [1] even as the original mission has changed and expanded by several other Experimental Areas (EAs). Accelerator availability is a measure of uptime divided by total time so the Mean-Time-To-Repair (MTTR) metric lowers available beam time to each of the EAs. The Availability metric is calculated weekly during production runs to each EA and then combined into an overall total for the accelerator.

It is the objective of Accelerator Operations and Technology (AOT) Division management, the organization operating and maintaining LANSCE, to improve the availability metric to 90% or greater using a risk-based approach for identifying and purchasing adequate operational spares to lower the unscheduled down time (MTTR). To achieve this goal, risks of failure shall be identified and prioritized from the top level down, from systems to structures to components (SSCs). Downtime (MTTR) data for the past history of failures along with the trends associated with particular equipment has already been captured for the availability metric. By mining this data, performing equipment assessments and assigning risk by subject matter experts, the most appropriate spares procurement list can be created.

* Work supported by the United States Department of Energy, National Nuclear Security Agency, under contract DE-AC52-06NA25396
† barkley@lanl.gov

Unscheduled Down Time

An intricate set of systems operate in unison to produce and deliver particle beam to EAs at LANSCE. In fact, AOT division is organized such that key disciplines are grouped according to areas of specialty. Each of these AOT groups is populated with Subject Matter Experts (SMEs) that are intimately familiar with the details of their respective systems and can troubleshoot and repair issues arising that cause unscheduled downtime. The key to dealing with the unscheduled downtime lies in the recognition that the systems have single point failures that will turn off all or part of the entire machine if not functional. These single point failures are partially depicted, at a high level, in Fig. 1:

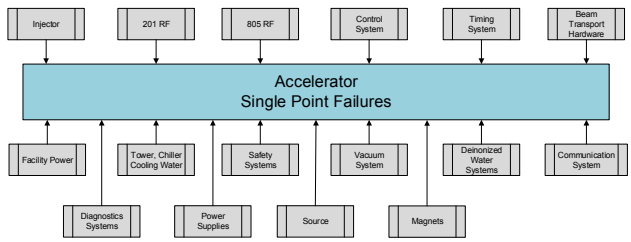


Figure 1: Single point failure diagram of the LANSCE accelerator.

As a 24 hour, 7 day a week operation, the LANSCE accelerator is attended by an excellent Operations staff that resolves many of the unscheduled downtime issues themselves with only small impacts to MTTR. For issues beyond their expertise or knowledge base, staff rotate on-call schedules to address the more difficult or complex issues that arise. The use of on-call staff affects the availability metric in terms of wait time for personnel to arrive on site, of proper diagnosis of the problem and whether the right person or persons have been called. These times contribute to the MTTR metric.

Maintainability

The maintainability for LANSCE is measured as the Mean Time to Repair [2]:

$$MTTR_i = RT + AD + LD \quad (1)$$

where RT is the repair time, AD is the administrative delay and LD is the logistical delay or lead time waiting for parts and/or people. Repair times for unscheduled events have been mined from the Operator Logs and categorized into specific SSCs that caused the failure. The

Content from this work may be used under the terms of the CC BY 3.0 licence (© 2018). Any distribution of this work must maintain attribution to the author(s), title of the work, publisher, and DOI.

ISBN: 978-3-95450-194-6 ISSN: 2226-0366 doi:10.18429/JACoW-LINAC2018-MOPO095

Content from this work may be used under the terms of the CC BY 3.0 licence (© 2018). Any distribution of this work must maintain attribution to the author(s), title of the work, publisher, and DOI.

logistical delay will typically dominate this expression if the parts to be replaced are not readily available but need to be procured, designed and/or fabricated.

It is the logistical delay that is of particular interest to AOT Management. From the limited budget used to operate the accelerator, it is not possible to procure a spare for every SSC. And it is not necessary since many of the SSCs will probably last the lifetime of the LANSCE facility. Therefore, the knowledge and experience of SMEs along with historical data, guides the selection of SSCs that are more prone to or at risk for failure, thus causing unscheduled downtime.

Availability

The system availability for LANSCE is a known quantity that has been tracked and recorded for many years. Availability is a measure of the accelerator's ability to deliver beam to the experimental areas and is usually expressed as a percentage. It does not necessarily mean the accelerator is delivering beam but is available to do so.

$$A = \frac{MTBF}{(MTBF + MTTR)} = \frac{Uptime}{Total\ Time\ (Uptime + Downtime)} \tag{2}$$

where $MTBF$ is the Mean-Time-Between-Failure and $MTTR$ is as before. For a system made up of many single point failures, the system availability is defined as:

$$A_{sys} = \left(\frac{MTBF_{sys}}{MTBF_{sys} + MTTR_{sys}}\right) \tag{3}$$

where

$$MTBF_{sys} = \left(\frac{1}{MTBF_1} + \frac{1}{MTBF_2} + \cdots + \frac{1}{MTBF_n}\right)^{-1} \tag{4}$$

and

$$MTTR_{sys} = \sum_{i=1}^{m} MTTR_i \tag{5}$$

A_{sys} is the system availability, $MTBF_{sys}$ is the system $MTBF$ and $MTTR_{sys}$ is the system $MTTR$. $MTTR_i$ are the subsystem $MTTRs$. The future $MTBF$ is obtained from SME predictions, which can be derived from data trends, manufacturer data and/or comparable accelerator facilities. This data provides a baseline and trend for specific issues but does not predict future availability and performance. It is these predictions that help to determine the prioritized list for spares procurement.

Interrelationships

Each Experimental Area (EA) at LANSCE is dependent on the upstream status of the systems that precede it (Fig. 2). For example, if the H+ source is down, the Isotope Production Facility (IPF) will be down. If the H- Source is down, all other EAs will be down except IPF. As one imagines, the SSCs that are integrated into each upstream section affect the Availability of the downstream EAs. Therefore, the $MTBF_i$ and $MTTR_i$ of Eqs. (4) and (5) are those particular SSCs that are upstream of the EA. Obviously, if these upstream SSCs are down, the EA is down.

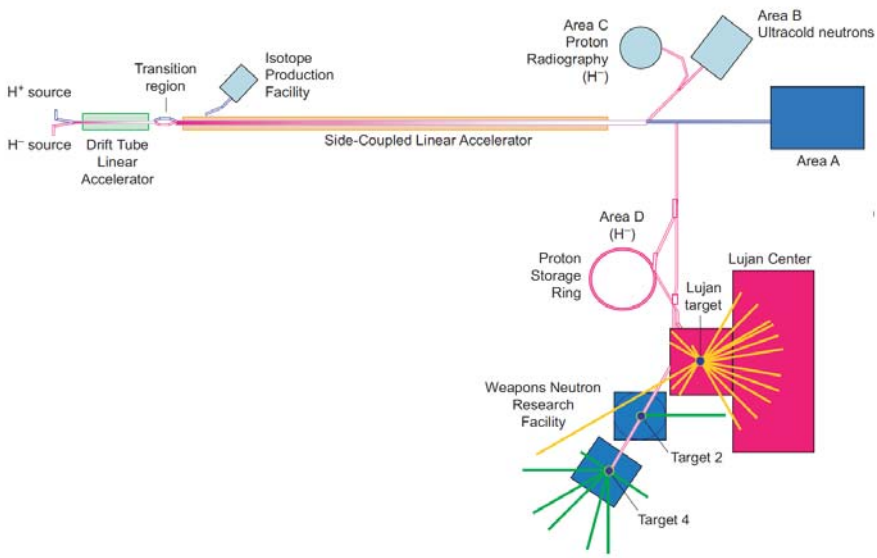


Figure 2: Graphical representation of the LANSCE accelerator.

ISBN: 978-3-95450-194-6 ISSN: 2226-0366 doi:10.18429/JACoW-LINAC2018-MOPO095

Table 1: Equipment Assessment Criteria

	Safety	Environment	Security	Reliability	Availability	Maintainability	System Physical Condition	Aging Degradation	Equipment Obsolescence	Spares	Mission Opportunity
3	Imminent Safety Issue	Severe environmental risk	Compromise of security	Greater than 20 failures during a ~5000 h Run Cycle; incl. machine turn on & beam tune	Overall downtime of more than 1 week in a run cycle	Greater than 1 days of Mean Time To Repair	System provides frequent evidence of not performing to its design requirements	System shows significant evidence of ageing	System is past End-Of-Life. Spare Parts are Unavailable for purchase	No spares in stock	Strong business case for upgrade
2	Code issue, Engineered Controls Issues, Potential for Adverse Safety from Failure Modes	Minor environmental risk, of compliance issues	Security incident	Greater than 5 but less than 20 failures during a ~5000 h Run Cycle, incl. machine turn on & beam tune	Overall downtime of less than 1 week but more than 1 day in a run cycle	More than 2 hour but less than 1 days of Mean Time To Repair	System provides occasional evidence of not performing to its design requirements	System shows evidence of ageing that will increasingly affect performance	System is approaching end of life and it is difficult to obtain Spare Parts	Limited spares in stock	Moderate business case for upgrade
1	No Safety Issue	Negligible environmental impact	Inconsequential impact to security	Less than 5 failures during a ~5000 h Run Cycle, incl. machine turn on & beam tune	Overall downtime of less than 1 day in a run cycle	Less than 2 hours of Mean Time To Repair	System provides no evidence of performance degradation	System shows no evidence of ageing	System is available for purchase - No End-Of-Life date	No spares issue	No business case for upgrade

Equipment Assessment

Each operational group at LANSCE tasked SMEs in their individual organizations to generate an SSC equipment list, rolled up to an appropriate replacement level, and assess each of these with a set of criteria as agreed to by the AOT management team. Table 1 lists the criteria with accompanying boundaries for scoring such that a number (1, 2 or 3) could be assigned to each individual criteria.

The equipment assessment includes categories that affect safety, security, the environment and mission. By including these factors, the intent of the LANL guiding document "Conduct of Research and Development" is addressed [3]. This policy document provides the architecture for structuring approaches to engineering endeavors, such as this one, in an R&D environment. Note that the equipment assessment is somewhat qualitative since it is partially objective.

The broad category of mission in the assessment criteria does take into account the metrics for a production facility such as reliability, availability and maintainability (RAM). Such categories are carefully considered when proposing upgrades to the accelerator [4].

Furthermore, the equipment assessment is augmented with categories that include performance degradation, signs of ageing and the subject of spare parts. Because spares are not kept in stock for every SSC, the vulnerability to increased MTTR is obvious. For those SSCs that are not readily available as Commercial off the Shelf (COTS) parts, the Logistical Delay can be quite long in duration, especially for long-lead items such as klystrons or magnets. For this reason, a weighting system was devised to put more emphasis on the two categories of whether the SSCs are COTS and whether or not spares are available and/or serviceable.

As seen from Table 1, the rating of 1, 2 or 3 with its weighting factor is assigned to each SSC for each category listed based on the descriptions in the columns. This rating task results in a cumulative total score for each SSC by adding the scores in each column of the table. Although thousands of SSCs were rated during this undertaking, a definite breaking point or gap could be identified in each discipline's equipment assessment. This gap produced a Top 10-15 SSCs in the list that showed the most vulnerability to generating unscheduled downtime.

Risk Register

As explained earlier, AOT Management's goal is to reduce the risks leading to unscheduled downtime and to optimize risk mitigation strategies to lower the highest risks. Starting with the equipment assessment, the Top 10-15 for the four disciplines compiled into a list of ~50 which became the basis for the risk register.

As was originally proposed, the risk register is a list of risks that lead to exceptional unscheduled downtime should they occur, thereby substantially affecting the availability metric. Each risk is evaluated for probability and consequence with availability (or schedule) as one of the major factors in the risk consequence (Table 2).

Table 2: Consequence Criteria

Rating	Mission	Schedule	Safety/Environment/Security
Low	Production beam (Criteria) to all areas not affected	Overall downtime of less than 1 day in a run cycle	No safety impact / Negligible environmental impact / Inconsequential impact to security
Moderate	Production beam to one or more areas affected	Overall downtime of less than 1 week but more than 1 day in a run cycle	Code issue, Engineered Controls Issues, Potential for Adverse Safety from Failure Modes / Minor environmental risk, of compliance issues / An IMI 3 or 4 security incident
High	Production beam to all areas affected	Overall downtime of more than 1 week in a run cycle	Imminent Safety Issue / Severe environmental risk / Compromise of national security due to the release of classified information. Compromise of Personally Identifiable Information (PII). A security incident having an Impact Measurement Index (IMI) of 1 or 2.

Risk Analysis

Modern and well tested methods of risk-based analysis and planning are regularly applied to complex systems in industry to ensure maximized performance within imposed constraints. Such methodologies, strategic maintenance planning, can also be applied to a large and complex expert-based scientific infrastructure such as the LANSCE proton accelerator system. AOT SMEs assign probability and consequence to the SSCs on the risk register, prioritize the results, and then optimize the overall list. The resulting list would then allow AOT division to strategically fine tune its operational, maintenance, and improvement priorities based on the risks and the available resources. The goal of this endeavor has been to generate a pilot program that can be carried forward, refined, and fully-implemented in future years.

Content from this work may be used under the terms of the CC BY 3.0 licence (© 2018). Any distribution of this work must maintain attribution to the author(s), title of the work, publisher, and DOI.

ISBN: 978-3-95450-194-6 ISSN: 2226-0366 doi:10.18429/JACoW-LINAC2018-MOPO095

Content from this work may be used under the terms of the CC BY 3.0 licence (© 2018). Any distribution of this work must maintain attribution to the author(s), title of the work, publisher, and DOI.

REFERENCES

[1] M. Eriksson, "Reliability Assessment of the LANSCE Accelerator System", M.Sc. thesis, Stockholm, Sweden, 1998.

[2] DOD Guide for Achieving Reliability, Availability and Maintainability, *Systems Engineering for Mission Success*, August 2005.

[3] Conduct of Research and Development (R&D), LANL Policy Publication SD601, July 2016.

[4] K. A. Young, G. Bolme, M. Lynch, E. Partridge, and D. Rees, "LANSCE 201 MHz and 805 MHz RF System Experience", in *Proc. PAC'07*, Albuquerque, NM, USA, Jun. 2007, pp. 2412-2414. doi:10.1109/PAC.2007.4441267/JACoW-PAC07-WEPMS033.

ISBN: 978-3-95450-194-6 ISSN: 2226-0366 doi:10.18429/JACoW-LINAC2018-MOPO096

REALISTIC MODELING OF MEBT FOR THE NEW LANSCE RFQ INJECTOR

S.S. Kurennoy, LANL, Los Alamos, NM 87545, USA

Abstract

The new RFQ-based proton injector at LANSCE requires a specialized medium-energy beam transfer (MEBT) after the RFQ at 750 keV due to a following long (~3 m) existing common transfer line that also transports H^- beams to the DTL entrance. The horizontal space for MEBT elements is limited because two beam lines merge at 18-degree angle. The MEBT includes two compact quarter-wave RF bunchers and four short quadrupoles with steerers, all within the length of about 1 m. The beam size in the MEBT is large, comparable to the beam-pipe aperture, hence non-linear 3D fields at large radii and field-overlap effects become important. With CST Studio codes, we calculate buncher RF fields and quadrupole and steerer magnetic fields, and use them for particle-in-cell beam dynamics modeling of MEBT with realistic beam distributions from the RFQ. Our results indicate a significant emittance growth in MEBT not predicted by the standard beam dynamics codes. Its origin is traced mainly to the quadrupole edge fields; the buncher RF fields also contribute noticeably. Proposed design modifications improve the MEBT performance.

INTRODUCTION

A modern front end for the LANSCE linac is under development: the aging Cockcroft-Walton based injectors will be replaced by modern RFQ-based ones [1]. Now two lines, one for H^+ (proton) and the other for H^- ions, produce 750-keV beams that merge into a common transport, which goes to the entrance of the first DTL tank. The proton injector will be upgraded first, but the existing common transport line for different beam species creates significant constrains for the injector line design. The first challenge is a very long distance from the proton RFQ exit to the DTL entrance, almost 4 m. Second, because the two beam lines merge at 18-degree angle, the horizontal space for proton-line elements is limited by the existing hardware near the merging area. Therefore, a specialized medium-energy beam transfer (MEBT) after the new proton RFQ at 750 keV was developed [2] with envelope codes, and the beam dynamics in MEBT was modeled using Parmila [3]. The MEBT shapes the RFQ output beam to transfer it through the long existing common transport to the DTL with minimal losses. The MEBT includes four electromagnetic (EM) quadrupole magnets and two buncher cavities [2], all within about 0.9 m along the beam line, followed by a 0.5-m long drift to the merging point of the common transport line, which continues for ~2.6 m to the DTL entrance. The beam pipe in the injector line has inner diameter (ID) 1.875" (aperture radius $a \approx 2.381$ cm) and outer diameter 2"; the pipe wall thickness is 1/16" (≈ 0.159 cm).

The proton beam size in the MEBT is large, comparable to the beam-pipe aperture; therefore, non-linear 3D field effects at large radii become important, both in bunchers and quadrupoles. We calculated buncher RF fields and quadrupole and steerer magnetic fields with CST Studio codes [4], and applied them in particle-in-cell (PIC) beam dynamics modeling of MEBT [5]. The beam transverse emittances increase after MEBT significantly more than predicted by design [2]. Here we study the effects of MEBT element modifications and the beam transport to DTL using PIC simulations with CST Particle Studio (PS).

MEBT AND TRANSPORT TO DTL

The main MEBT elements are two compact quarter-wave (QW, $\lambda/4$) 201.25-MHz RF cavity bunchers and four short EM quadrupole magnets with additional windings for beam steering. Both elements have a small footprint on the beamline, shorter than 8 cm. The QW buncher is a coaxial resonator with two gaps separated by distance $\beta\lambda/2 = 2.98$ cm for $\beta = 0.04$ [5, 6]. The bunchers (B) and quadrupoles (Q) are arranged in the MEBT in the following order: Q_1, B_1, Q_2, Q_3, Q_4, and B_2. The buncher and quadrupole EM parameters and fields were calculated in CST MicroWave and EM Studios, see details in [6]. The maximal effective voltage of QW buncher in the design [2] is $V_{\text{eff}} = 25$ kV (12.5 kV per gap). The quad effective length is 7.6 cm with gradients G from 7.1 to 10.8 T/m.

The beam envelopes in the MEBT and transport to DTL corresponding to the design [2] are shown in Fig. 1. The MEBT includes elements 1-12 in Fig. 1. The proton and H^- beams merge in the bending dipole (elements 14-16), then pass through the main buncher (20) and a long drift (21-36) with 4 tuning quadrupoles to the DTL entrance. The main buncher (MB) is a single-gap reentrant 201.25-MHz cavity with a narrow aperture of 1-cm radius.

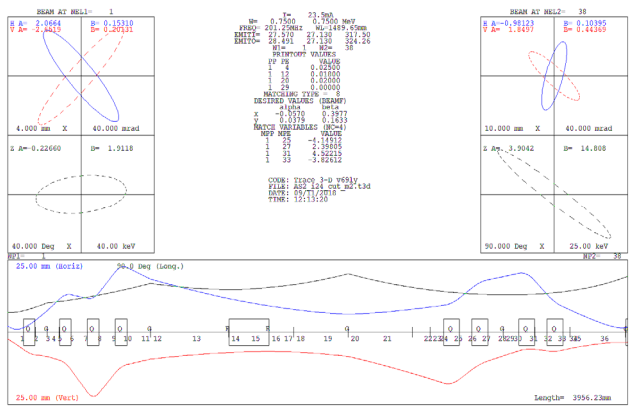


Figure 1: Trace 3D beam envelopes in the proton RFQ MEBT and common transport line to DTL.

Content from this work may be used under the terms of the CC BY 3.0 licence (© 2018). Any distribution of this work must maintain attribution to the author(s), title of the work, publisher, and DOI.

ISBN: 978-3-95450-194-6 ISSN: 2226-0366 doi:10.18429/JACoW-LINAC2018-MOPO096

Content from this work may be used under the terms of the CC BY 3.0 licence (© 2018). Any distribution of this work must maintain attribution to the author(s), title of the work, publisher, and DOI.

BEAM DYNAMICS

Initial Beam Distributions

For initial beam distributions in PIC modeling of MEBT and following beam line we use two realistic distributions for the proton beam at the RFQ exit from previous macro-particle simulations, the same as in [5, 6]. In both cases, a 24-mA current beam was simulated with 10K macro-particles at the RFQ entrance. The first output distribution (A) is from ParmteqM runs (L. Rybarcyk), converted into PS input format. The second (B) is from our PS simulations of the RFQ [7] that used MWS-calculated 3D RFQ fields. Some parameters of these initial beam distributions are summarized in Table 1, cf. [5, 6] for more details.

Table 1: Initial Beam Distribution Parameters

Parameter, units	**A**	**B**
Proton beam current, mA	23.5	22.6
Number of macro-particles *N*	9788	9397
Average particle energy, keV	750	754
Norm. rms emittance $\varepsilon_{x,}$ π μm	0.22	0.25
Norm. rms emittance $\varepsilon_{y,}$ π μm	0.22	0.25
Rms longit. emittance $\varepsilon_{z,}$ π μm	0.28	0.35

MEBT PIC Simulation Results

The MEBT models use scaled CST-calculated buncher RF fields and quad magnet fields. The effective voltages are 25 kV in B_1 and 18 kV in B_2 [2], with RF phases properly set for bunching as the bunch center arrives at the cavity center [6]: 180° in B_1 and 152° in B_2 for input A. For input B, the beam energy is corrected (-4 keV) in B_1, so the RF phase is 167° in B_1 and 152° in B_2.

The beam dynamics has been modeled with the CST PS PIC solver by running the initial beam through the MEBT fields. The particle parameters are recorded using 2D plane particle monitors in the exit plane, at 15 cm from the B2 center. The beam steering was added as necessary using CST-calculated steerer fields to minimize the beam-center displacements along the MEBT [6]. We considered various MEBT configurations in [5, 6], e.g., substituting CST-computed quad fields (EM) by ideal quadrupole fields (HE), turning bunchers on and off, etc. Some important simulation results from [5, 6] are listed in Table 2.

Table 2: Parameter Changes vs. MEBT Configuration

#	D	Q	N/N_0	$\varepsilon_x/\varepsilon_{x0}$	$\varepsilon_y/\varepsilon_{y0}$	$\varepsilon_z/\varepsilon_{z0}$
1	A	EM	0.979	3.14	1.77	1.36
2	A	HE	0.991	1.68	1.14	1.18
3	B	EM	0.968	3.08	2.32	1.37
4	B	HE	0.979	1.92	1.24	1.26

The notations in Table 2 are D for initial distribution, Q for quads; the ratios in the last four columns are for final / initial values. The beam transverse emittances increase significantly: the horizontal ε_x by a factor of ~3, the vertical ε_y by a factor of <2, for the realistic MEBT with EM quads (#1). For the PS input (B), the emittance behavior is similar (#3). Such large emittance increases are unexpected and much higher than ~30% predicted by design [2] for transverse emittances. On the other hand, the longitudinal emittance increases by ~35% for both distributions, mainly in the second buncher, B_2, while the design [2] predicts much larger increase, by 128%.

We explored possible reasons for such a large transverse emittance growth and how it can be mitigated. Some can be attributed to the differences between Trace/Parmila and CST models: (i) Parmila uses ideal hard-edge quadrupole fields, and (ii) the bunchers in Parmila are modeled as zero-length single gaps, with longitudinal and transverse kicks to the passing particles that depend on the particle radial position. With ParmteqM input (A), we compared various MEBT configurations: realistic quad fields (EM) vs. ideal ones (HE), turning bunchers on and off, etc. [5, 6]. With HE-quad fields the emittance growth is noticeably smaller, cf. #2 vs. #1 and #4 vs. #3 in Table 2. It was found that steerer effects are small. QW bunchers work slightly better than 1-gap ones for the same wide apertures [6]. The buncher fields mostly affect the horizontal emittance, increasing it by a factor of 1.5 on top of the space charge increase. With bunchers off, the EM quad fields increase the horizontal emittance by a factor of ~1.75 above the space charge. Finally, the combined effect of the buncher RF fields and realistic quadrupole magnetic fields on the transverse emittances was approximately multiplicative.

Some MEBT elements modifications were necessary to mitigate the emittance growth. First, quadrupole design modifications were introduced to reduce the field non-linearities at large radii and edge fields: increasing the quad aperture and/or length; replacing EM (some or all) with permanent-magnet quadrupoles (PMQ); or adjusting pole-tip shapes [6, 5]. Two possible options are shown in Fig. 2.

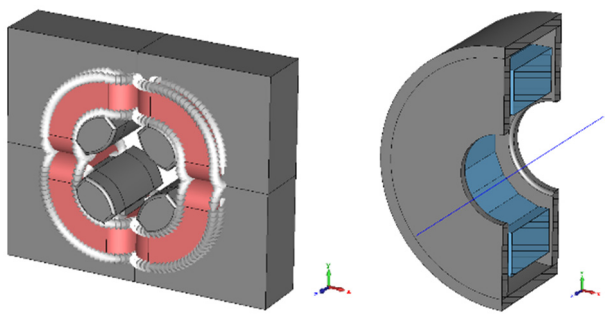


Figure 2: Quad modifications: EM quad with extended core (left) and 16-segment PMQ with outer shield (right).

The EM quadrupole with extended inner core (Fig. 2, left) increases the region of good field without increasing the quad footprint. The PMQ with an outer shield for clamping edge fields (Fig. 2, right) allows small adjustments of *GL* by changing the shield dimensions.

ISBN: 978-3-95450-194-6 ISSN: 2226-0366 doi:10.18429/JACoW-LINAC2018-MOPO096

Obviously, with PMQs additional steerers are still needed. Some PIC simulation results for modified MEBT with B input were given in [6, 5]. Additional results for a few MEBT configurations are presented in Table 3, for comparison with Table 2.

Table 3: Parameter Changes vs. MEBT Configuration

#	D	Q	N/N_0	$\varepsilon_x/\varepsilon_{x0}$	$\varepsilon_y/\varepsilon_{y0}$	$\varepsilon_z/\varepsilon_{z0}$
5	A	PMQ	0.988	2.64	2.18	1.21
6	A	PMQL	0.988	2.41	1.73	1.21
7	A	E/PM	0.988	2.64	1.77	1.25

The cases in Table 3 are: #5 – short PMQs; #6 – longer PMQs with shielding; #7 – combined EM ($Q_{1,4}$) and long shielded PM ($Q_{2,3}$) quadrupoles. The last configuration allows steering with EM quads. Compared to Table 2 (#1), one can see some improvements, though the emittance growth is still quite large.

PIC Simulations of Transport to DTL and DTL

To evaluate how the beam after MEBT is transported to and captured in the DTL, we followed it along the transport line and in the first tank (T1) of DTL. Two distributions after MEBT were chosen for these PIC simulations – cases #2 and #3 in Table 2, as the best (the closest to design [2]) and the worst (though more realistic) case. The magnetic field of the merging dipole and RF fields of the main buncher (MB) were calculated with CST. The MB voltage was set at 20 kV [2]. We used hard-edge magnet fields for the large-aperture (3"-diameter) quadrupoles in the drift from MB to DTL. Finally, beam dynamics in the DTL T1 was studied using a CST model developed earlier [8].

As one can expect, the results for two cases are quite different. In case #2, the beam losses in the transport are relatively small (1.8% in MB, 4.6% in the drift). The emittances at the DTL entrance are $\varepsilon_{x,y,z}$ = 0.29, 0.25, 0.45 π μm, close to the design values [2] and those used as input in [8]. Comparing with values in Tables 1-2, we see that an exchange between transverse and longitudinal emittances occurs. However, the beam fraction captured into a bunch and accelerated to 5.4 MeV in T1 is only 86.4%, compared to 95% for a similar beam after RFQ [8]. This difference is due to a beam mismatch at the DTL entrance. For case #3, the transport beam losses are significant: 22% is scraped by the narrow aperture of MB, and 5.7% more is lost in the drift. Clearly, the MEBT should be tuned differently in this case to provide a waist at MB. The beam emittances at the DTL entrance are $\varepsilon_{x,y,z}$ = 0.50, 0.41, 0.68 π μm, and the capture in T1 is only 82.2%, again due to an even larger beam mismatch at the linac entrance. We conclude that the beam transmission to and its capture in DTL are very sensitive to the MEBT setup. The MEBT should be tuned for a particular beam distribution coming out of the RFQ, taking into account the realistic 3D fields of MEBT elements, to optimize the transmission through the common transport line and match the beam to the DTL.

CONCLUSION

We explored beam dynamics in the MEBT for the new RFQ-based proton injector at LANSCE and the following beam transport line to the DTL with CST Particle Studio particle-in-cell (PIC) 3D simulations to take into account effects of the large beam size and field overlaps. The CST-calculated fields of quarter-wave RF buncher cavities and of quadrupole magnets with steerers in MEBT [5, 6] were used. For the transport line PIC simulations we calculated RF fields of the main buncher and the magnetic field of the merging dipole. We found that the transverse emittances increase significantly more than was predicted in the original MEBT design [2], which was based on the standard approach using envelope codes and Parmila simulations. One the other hand, the longitudinal emittance growth is lower than predicted [2]. The differences are due to a very large beam size in MEBT, which is required to further transfer the beam through a long transfer line to DTL. 3D effects and field overlaps of adjacent elements become essential but cannot be taken into account by traditional beam dynamics codes. From this viewpoint, it is one more example where simulations with standard codes are insufficient to predict beam dynamics correctly.

The emittance growth is caused mainly by the magnetic fields of short EM quadrupoles. The buncher RF fields also contribute. We considered some modifications of the MEBT quads and demonstrated their positive effects. However, further MEBT optimization is still required. Our results show that the beam transmission through the common transport and its capture in the DTL are rather sensitive to the MEBT setup, which should be adjusted with account of 3D effects.

ACKNOWLEDGMENT

The author would like to thank Y. Batygin and L. Rybarcyk (LANL) for useful information and discussions.

REFERENCES

[1] R.W. Garnett *et al.*, "Status of the LANSCE front-end upgrade," in *Proc. NA-PAC13*, Pasadena, CA, 2013, p. 327.

[2] C.M. Fortgang *et al.*, "A specialized MEBT design for the LANSCE H^+ RFQ upgrade project," in *Proc. NA-PAC13*, Pasadena, CA, USA, Sep.-Oct. 2013, TUPSM17, p. 670.

[3] Los Alamos Accelerator Code Group, laacg.lanl.gov

[4] CST Studio Suite, CST, www.cst.com

[5] S.S. Kurennoy, "3D beam dynamics modeling of MEBT for the new LANSCE RFQ injector," in *Proc. IPAC18*, Vancouver, BC, Canada, Apr.-May. 2018. doi:10.18429/JACoW-IPAC2018-TUPAL035

[6] S.S. Kurennoy, Tech notes AOT-AE: 17-009, 18-005; "Beam dynamics modeling of the proton RFQ MEBT with CST PS," LA-UR-18-23434, Los Alamos, 2018.

[7] S.S. Kurennoy, "3D effects in RFQ accelerators," in *Proc. Linac14*, Geneva, Switzerland, 2014, THPP097, p. 1077.

[8] S.S. Kurennoy, "Beam dynamics modeling of drift-tube linacs with CST Particle Studio," in *Proc. IPAC16*, Busan, Korea, p. 689. DOI:10.18429/JACoW-IPAC2016-MOPOR042

Content from this work may be used under the terms of the CC BY 3.0 licence (© 2018). Any distribution of this work must maintain attribution to the author(s), title of the work, publisher, and DOI.

ISBN: 978-3-95450-194-6 ISSN: 2226-0366 doi:10.18429/JACoW-LINAC2018-MOPO100

DOUBLY STRIPPED PROTON CAUSING VACUUM LEAK AT BROOKHAVEN 200 MeV LINAC COMPLEX*

D. Raparia†, G. Atoian, T. Lehn, V. Lodestro, M. Mapes, A. McNerney, J. Ritter, A. Zelenski
Brookhaven National Laboratory, P. O. Box 5000, Upton, NY 11973, USA

Abstract

Doubly stripped protons in the low energy transport are captured at 180 degree apart in RF of RFQ and accelerated to the full energies. These protons are bend in the opposite direction of the H^- after 200 MeV drift tube linac and caused a vacuum leak. A new beam dump and a faraday cup for these stripped protons are planned.

INTRODUCTION

The Brookhaven National Laboratory (BNL) 200 MeV drift tube linac (DTL) provides H^- beam at 6.67 Hz, 200 MeV for the polarized proton program of Relativistic Heavy Ion Collider (RHIC) and 66-200 MeV for Brookhaven Linac Isotope Production (BLIP) [1-5]. The RHIC polarized proton program needs 2 pulses every super cycle (~4 sec), one for injection into booster and other for polarization measurement at 200 MeV-polarimeter located in the high-energy transport line (HEBT). The rest of the pulses go to BLIP. BNL 200 MeV H^- linac consists of a 35 keV high intensity (magnetron) ion source [6], polarized source (optically pumped polarized H^- ion source, OPPIS) [7], low energy beam transport (LEBT), a 750 keV radio frequency quadrupole accelerator (RFQ), medium energy beam transport (MEBT) and 200 MeV drift tube linac. Space charge effects are most severe at low energy i.e. in the LEBT where the H^- energy is 35 keV and current excess of 100 mA. To overcome space charge effects in the LEBT, different gases are used to charge neutralize the H^- beam.

LOW ENERGY BEAM TRSPORT (LEBT)

LEBT connects RFQ to two ion sources, namely high intensity magnetron ion source (source-1) and OPPIS. Figure 1 shows layout of LEBT. A 45-degrees pulse dipole magnet connects these two ion sources to RFQ. High intensity part of LEBT consists of two solenoids, two quadrupoles, and two set of steering magnets in each horizontal and vertical plane, a beam chopper, a beam stop, a cryopump, and two gate valves. First gate valve is located just after the first solenoid and second gate valve is located just before the RFQ. Base pressure in LEBT is about $2x10^{-7}$ Torr with ion source gate valve closed and with ion source gate valve open, pressure is about $1x10^{-6}$ Torr.

*Work performed under Contract Number DE-AC02-98CH10886 with the auspices of the US Department of Energy
†raparia@bnl.gov

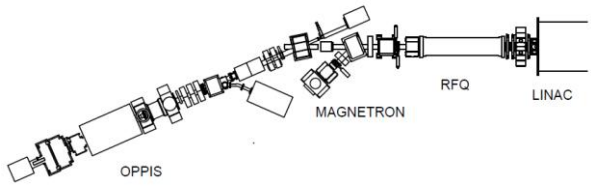


Figure 1: LEBT layout showing OPPIS and Magnetron source.

Cryopump is located under chopper box and equipped with two gate valves, one pneumatic and other hand operated gate valve. There is a provision to inlet various gas via needle valves at two places, first in ion source gate valve and second in chopper box.

Last year (Run 2018), no polarized protons were needed for RHIC program; a second magnetron source (source-2), a solenoid and two steering magnets were installed by replacing spin-solenoid and diagnostic box in OPPIS line before the 45-degree dipole magnet. Second source was installed for source development and as back-up source for BLIP. Source-2 is at 0 degrees with RFQ. Source-2 is bit different than source-1; it has smaller vacuum chamber and smaller turbo pump. It operates at little higher pressure ($8x10^{-6}$ Torr) than source-1; it has better gas injection pulse valve, ion source body temperature control, better electric connection etc.

DOUBLY STRIPPED H^-

H^- can be can be converted to protons via two channels, (1) stripping two electrons $H^- \Rightarrow P$ and (2) two step process (a) $H^- \Rightarrow H^0$ (b) $H^0 \Rightarrow P$. Cross-sections for these processes at 35 keV and Hydrogen & Nitrogen as background gases are given in Table 1 [8, 9].

Table 1: Summary of 35 keV H- Cross Sections Used in Calculations.

Gas	σ_{-10} (10^{-16} cm^2)	σ_{-11} (10^{-16} cm^2)	σ_{01} (10^{-16} cm^2)
Hydrogen	7.3	0.43	*2.4
Nitrogen	13.2	1.7	*4.4

* Scaled

For source-1, doubly stripped protons generated between 45-degree dipole and RFQ are captured and accelerated by RFQ. For source-2, doubly stripped protons generated between source-2 and RFQ are captured and accelerated by RFQ. Nitrogen gas was injected at the chopper camber, which is located after the 45-degree dipole magnet in LEBT, to optimize the average beam current at the BLIP target. For both sources, optimized pressure in LEBT was about $3x10^{-6}$ Torr. Transmissions

Content from this work may be used under the terms of the CC BY 3.0 licence (© 2018). Any distribution of this work must maintain attribution to the author(s), title of the work, publisher, and DOI.

ISBN: 978-3-95450-194-6 ISSN: 2226-0366 doi:10.18429/JACoW-LINAC2018-MOPO100

and average currents at BLIP were same for the both sources. At the first dipole magnet (BM1) after linac, radiations were about five times higher for source-2 compared to source-1 for the same H^- average current.

Estimates for Stripped Protons

In magnetron source hydrogen gas is injected through a pulsed valve at linac repetition rate, which causes relatively higher pressure (~$1.0x10^{-4}$ Torr) at source exit (5-10 cm) during the beam pulse. Source-1 housing has bigger volume than source-2, and it consumes about half hydrogen gas than source-2. Source-1 also has high capacity vacuum pump. Estimated pressures at exit of source (5 cm) are about $1x10^{-4}$ and $3x10^{-4}$ Torr for source-1 and source-2 respectively. Estimated fractions of the H^-, which stripped at source exit to protons via both stripping channels are $0.7x10^{-3}$ and $21x10^{-3}$ for source-1 and source -2 respectively.

For source-1, proton generated before 45-degree dipole magnet will bend in the opposite direction of the H^- and protons generated between 45-degree dipole magnet and RFQ will reach to the RFQ. In this part of the LEBT, background gas mainly is Nitrogen at $3x10^{-6}$ Torr. Estimated protons fraction at RFQ is about 0.17%. For source-2, estimated protons fraction at RFQ is about 0.81%.

These protons will be capture in the RFQ at 180 degree apart from H^- and accelerated to the final energy of RFQ, which is 750 keV. Protons and H^- enter MEBT in the same orientation of the transverse phase space but at 180 degree apart in the longitudinal phase. Transmission efficiencies through MEBT and linac for protons are only about 1% (PAMILA simulation). Fractions of H^- as protons, which reach at BM1, are $1.7x10^{-5}$ and $8.1x10^{-5}$ for source-1 and source-2 respectively.

It is counter intuitive that fraction of proton increases approximately as x^2, where x is pressure. Figure 2 depicts protons and neutrals as fraction of H^- generated by different stripping channels.

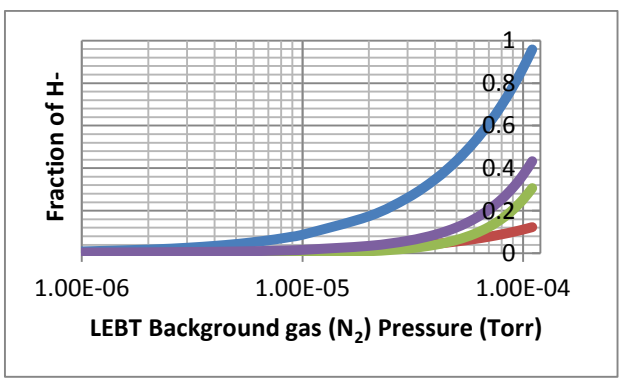


Figure 2: Fractions of H^- as a function of background gas (Nitrogen) pressure. Blue: Neutrals (σ_{-10}), Red: Protons, channel-1 (σ_{-11}), Green: Protons, channel-2 ($\sigma_{-10} * \sigma_{01}$), Violet: Proton, sum of channel 1 and 2 ($\sigma_{-11} + \sigma_{-10} * \sigma_{01}$).

At higher pressure ($5x10^{-5}$ Torr) number of protons produce by channel 2 are higher than channel 1. At pressure $1.1x10^{-4}$ Torr, H^- beam is fully stripped and about 30% of protons are generated.

HIGHER PRESUURE IN LEBT CACUSED VACUUM LEAK

During Run 18, ion source-1 was shorted and source-2 was brought on line to provide beam to BLIP. In the process of optimising beam current, a higher amount of gas (Nitrogen) was injected (human error) into LEBT through a pulse valve and within seconds stripped protons caused the leak in the bellow after the first dipole BM1. Figure 3 shows the pressure at LEBT, linac tanks and high-energy beam transport (HEBT) as a function of time. Pressure rise in LEBT causing pressure increase in HEBT but linac vacuum remains unaffected. Figure 4 depicts beam current at RFQ, at linac and after linac during the LEBT tuning with gas. Figure 5 shows radiation at BM1 and average current at BLIP. Source-1 was shorted at 17:45 HRS and source-2 came on line at 20:00 HRS. Radiation label for source-2 is about 10 times. Figure 6 shows bellow and the Y chamber after BM1. Figure 7 shows leaked bellow.

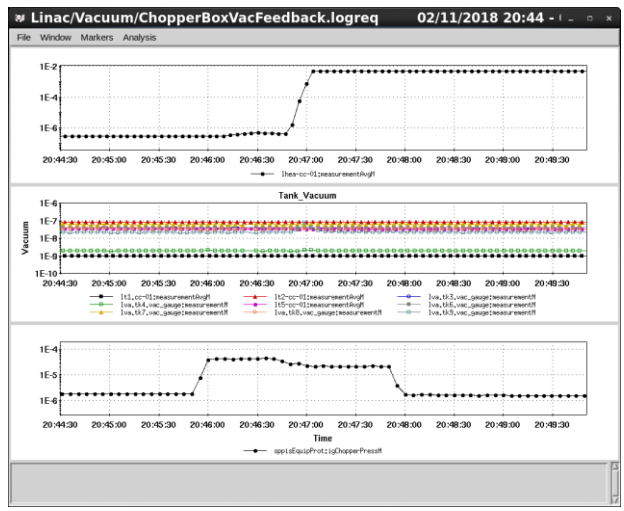


Figure 3: Vacuum at LEBT, Linac Tanks and HEBT in Torr as function of time in HRS.

Beam size at bellow is approximately 0.1x1 cm^2. Stain steel bellow is 0.020 cm thick. For normal running protons deposit about 1.4 mW and 6 mW for source-1 and source-2 respectively. Calculations show that displacement per atom (DPA) is only 0.1 for integrated intensity for last 20 years. For last about 20 years, protons are going through at same spot.

Content from this work may be used under the terms of the CC BY 3.0 licence (© 2018). Any distribution of this work must maintain attribution to the author(s), title of the work, publisher, and DOI.

ISBN: 978-3-95450-194-6 ISSN: 2226-0366 doi:10.18429/JACoW-LINAC2018-MOPO100

Content from this work may be used under the terms of the CC BY 3.0 licence (© 2018). Any distribution of this work must maintain attribution to the author(s), title of the work, publisher, and DOI.

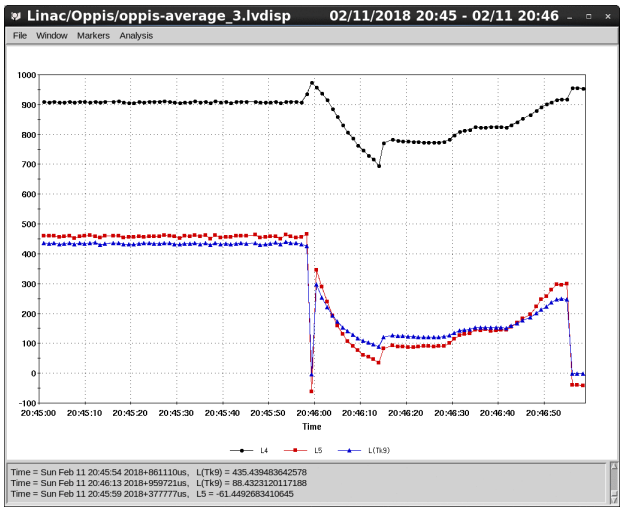


Figure 4: Beam current in unit of 0.1 mA at RFQ entrance (Black, L4), at linac entrance (Red L5), and after linac (Blue, T9) as function of time in HRS.

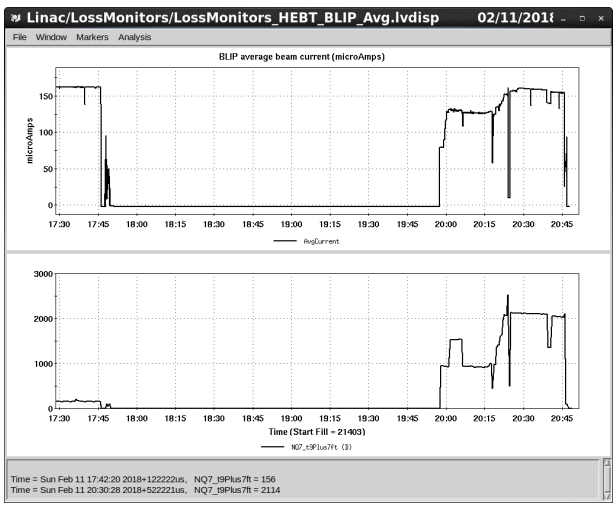


Figure 5: Average beam current and count on beam loss monitor as a function of time in HRS. Source-1 shorted at 17:45 and source-2 came on line at 20:00. Radiation for source-2 is about 10 times than source-1 for the similar average current.

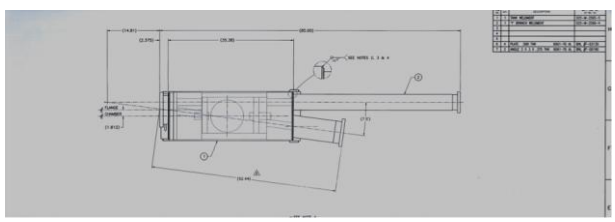


Figure 6: Bellow and Y chamber after the first dipole (BM1) after the linac.

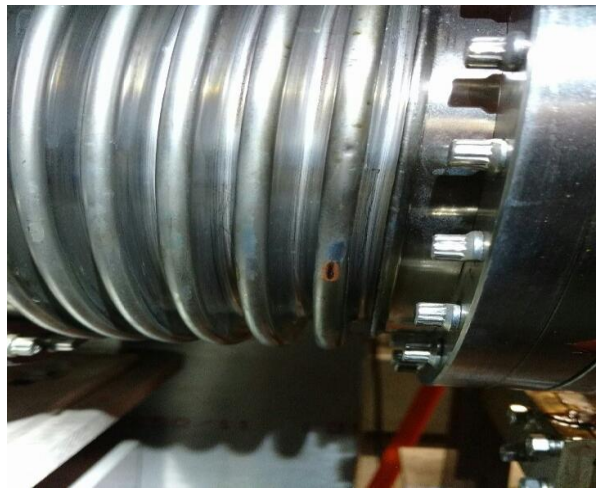


Figure 7: Hole in the bellow after BM1 chamber consistent with proton trajectory.

OUTLOOK

After Run 18, polarity of dipole in the LEBT was reverse to measure protons by Faraday cup in front of Linac for source-1 and source-2. The measured values were 0.09% and 0.27 % for source- 1 and 2 respectively. It is planed (a) to move source-2 at -45 degree by installing a new dipole magnet; (b) modify BM1 vacuum chamber to accommodate proton beam dump and (c) faraday cup to measure proton current.

REFERENCES

[1] G. W. Wheeler *et al.*, "The Brookhaven 200 MeV proton linear accelerator", *Particle Accelerator*, vol. 9, pp. 1-156, 1979.

[2] D. Raparia, *et at.*, "Results of LEBT/MEBT reconfiguration at BNL 200 MeV Linac", in *Proc. 23rd Particle Accelerator Conf. (PAC'09)*, Vancouver, Canada, May 2009, pp. 441.

[3] D. Raparia, *et at.,* "Reliability and Intensity Upgrade for Brookhaven 200 MeV Linac", in *Proc. 27th Linear Accelerator Conf. (LINAC'14)*, Geneva, Switzerland, Aug.-Sep. 2014, pp. 67.

[4] D. Raparia, *et al.,* "Charged neutralized low energy Beam transport at Brookhaven 200 MeV Linac", Review of Scientific Instruments, 2015, vol. 87, paper 02B935.

[5] D. Raparia, *et al.*, "200 MeV H- Linac upgrade at Brookhaven", in *Proc. IPAC'16*, Busan, Korea, May 2016, pp. 968.

[6] J. Alessi, "Performance of the Magnetron H- Source on the BNL 200 MeV Linac", in *AIP Conference Proceedings*, vol. 642, pp. 279-281, 2002.

[7] A. Zelenski, *et at.,* "Optically Pumped Polarized H- Ion Source for RHIC Spin Physics", *Rev. Sci. Ins.* vol. 73, pp. 888, 2002.

[8] J. Sherman, E. Pitcher, R. Stevens, P. Allison, Production and neutralization od neutralization of negative Ion and Beam", Upton, NY USA, 9-13 Nov, 1992.

[9] G. H. Gillespie, *Phys. Rev. ST Accel. Beams*, vol. 15, p. 563, 1977.

ISBN: 978-3-95450-194-6 ISSN: 2226-0366 doi:10.18429/JACoW-LINAC2018-MOPO101

LINAC-MULTITOOL – AN OPEN SOURCE JAVA-TOOLKIT*

M. Schwarz†, D. Bade, J. Corbet, H. Podlech
IAP, Goethe University, Frankfurt am Main, Germany

Abstract

Dedicating more precious time to advanced research instead of spending it towards time-consuming routine tasks is a desirable goal in particle accelerator simulation and development. Requirements engineering was started at IAP in order to identify routine processes at our institute's R&D that can be automated or simplified. Results indicated that there were several areas to consider: Bead pull measurements, data processing and visualization for the beam dynamics code LORASR, CST field map processing for the use with TraceWin, conversion between different particle distribution data formats and more. Subsequently development of the LINAC-Multitool started to rationalize these processes and replace preexisting scripts also to ensure consistency of results and increase transparency and reliability of computation. In order to guarantee maintainability, expandability and platform independence, LINAC-Multitool is programmed using Java and will be open source. This contribution presents the current state of development.

SOFTWARE ARCHITECTURE

In preparation of choosing an appropriate platform (programming language, GUI toolkit, other libraries) three key factors emerged: Ease of use, maintainability and expandability. In conclusion Java, the probably most widely used programming language for the development of desktop applications, was chosen. It offers a convenient GUI toolkit (JavaFX [1]), which is bound to be supported for a long time by Oracle but still enables us to integrate all the features one would expect from a modern UI. The same goes for Java as a programming language and has been proven in the past as code that was written years ago can still be used. Other languages which sparked our interest however have undergone design changes in their past which broke source code compatibility and therefore were not as suitable as Java. In addition, we profited from the availability of a competent plotting framework – JFreeChart [2], which allowed us to introduce advanced features like data selection into our graphs and proved to be a stable base. As a team of two students and one supervisor kicked off this project, we chose to part the program along the lines of frontend and backend. The backend part includes all the parsing of files and most of the computational aspects for bead–pull measurements while the frontend part focuses on GUI, handling 3d field maps as well as particle distributions and better visualizations for LORASR-computations [3] in order to minimize friction and overall improve efficiency of implementation. In order to maximize our throughput we chose to minimize our reliance on expensive computational libraries wherever we could come up with more resource-conservative ideas. Figure 1 depicts an excerpt of the program architecture whose classes and functions can be categorized on the whole as *read*, *parse*, *analyze* and *visualize*.

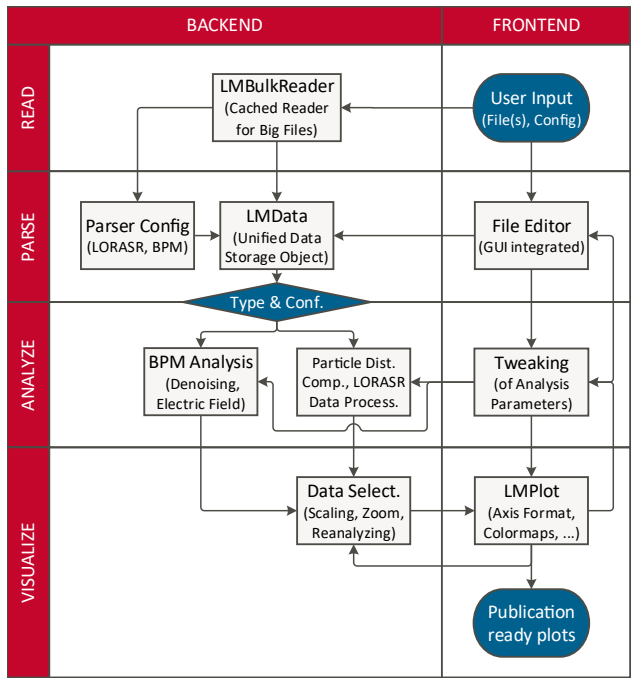


Figure 1: Schematic layout of the program architecture.

RANGE OF FUNCTIONS

An overview of the planned features for the LINAC-Multitool is given in Fig. 2. Up to now they can be divided into four parts: *LORASR*, *Bead Pull Measurement*, *Particle Distributions* and *CST Field Maps*. Finally, they will be documented in detail both in the source code and the user manual. The initial features are given in the following:

LORASR LORASR is a multi-particle tracking code for the beam dynamics design for all kind of DTLs, optimized for the "Combined Zero Degree Structure (KONUS)" lattices [4–8]. The code has been used for the beam dynamics design of many linacs in operation or under construction like GSI-HLI, -HSI and -pLINAC, CERN Linac 3, TRIUMF ISAC-I, HIT, MedAustron, HILac/NICA and MYRRHA. As its first code version was already developed in the late 80s, the possibilities for graphical user interactions were and are still not very wide-ranging. Nevertheless, the code has been significantly improved in the past decades with better gap field representation, a PIC space charge routine, error study

* Work supported by BMBF contr. No. 05P15RFRBA and HIC for FAIR.
† schwarz@iap.uni-frankfurt.de

Content from this work may be used under the terms of the CC BY 3.0 licence (© 2018). Any distribution of this work must maintain attribution to the author(s), title of the work, publisher, and DOI.

ISBN: 978-3-95450-194-6 ISSN: 2226-0366 doi:10.18429/JACoW-LINAC2018-MOPO101

Content from this work may be used under the terms of the CC BY 3.0 licence (© 2018). Any distribution of this work must maintain attribution to the author(s), title of the work, publisher, and DOI.

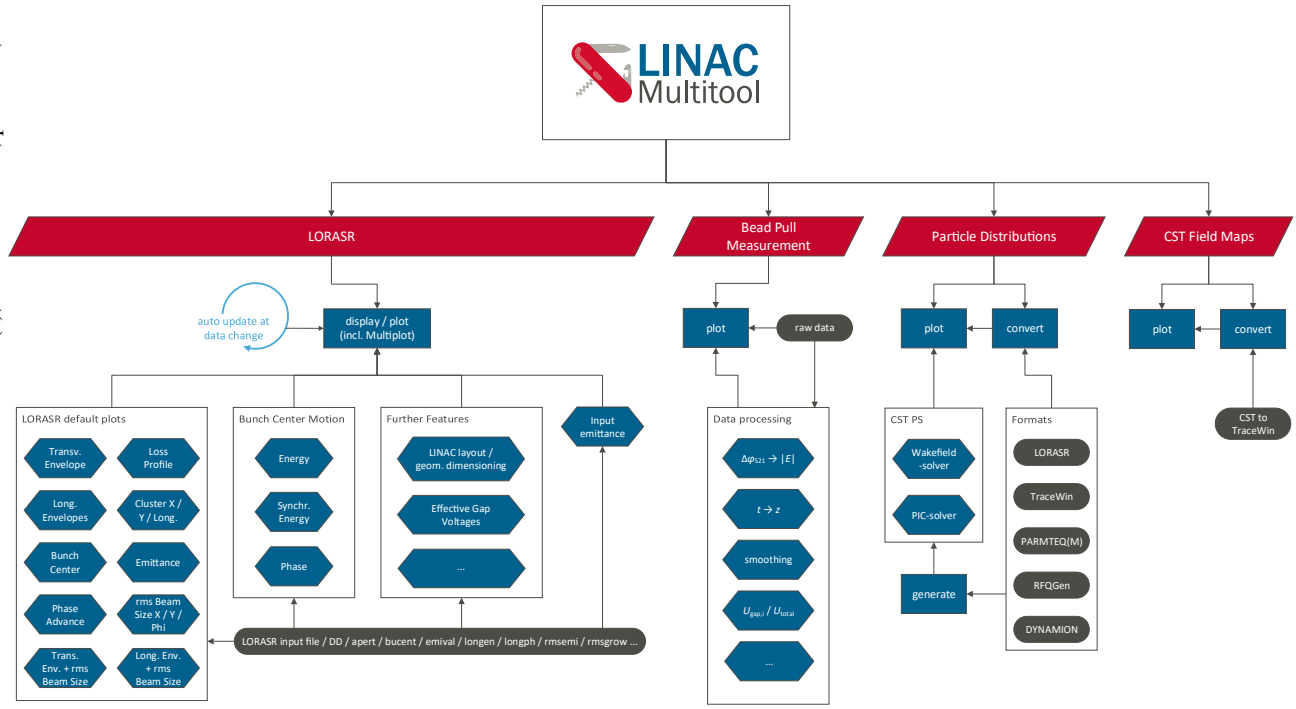


Figure 2: Feature diagram of the LINAC-Multitool giving an overview of the so far planned subprograms.

tools and more so it is still an important and powerful design tool. To optimize the workflow in daily work routines, LINAC-Multitool offers users not only the same plotting functionalities as already given by LORASR, but extends it by features like export of vector graphics, color-coded plots of phase space distributions (see Fig. 3), a schematic of the designed linac layout geometry, stacked plots and additional plots like energy and gap voltages as function of z-position.

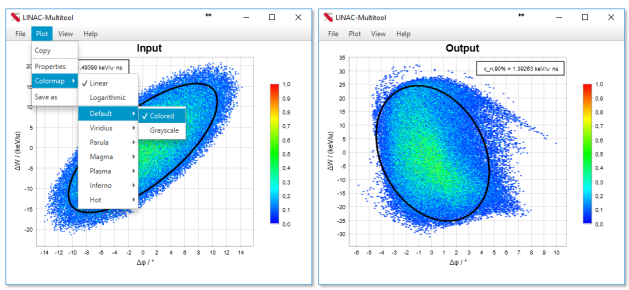


Figure 3: Longitudinal phase space input/output distribution of a LORASR-simulation, plotted with color-coded density. Beside the standard rainbow-colormap, perceptually-uniform colormaps will be implemented to ensure printability in color and grayscale as well as for being viewed by persons with a color vision deficiency, too.

Bead-pull measurement A bead-pull measurement is usually done after cavity manufacturing by placing a small dielectric or metallic bead inside the cavity. By pulling it with a non-conducting wire (e.g. made of a polyamide or rather nylon fishing line) through the cavity, one can measure the electromagnetic fields distribution on resonance inside. To speed up the analysis of bead-pull measurements, usual data processing steps can be manually and automatically done with the LINAC-Multitool (see Fig. 4). These involve:

- Plotting the absolute value of the relative E-field distribution $|E(z)|$ (obtained by calculation from the measured phase shift $\Delta\varphi_{S21}$) as function of the position on beam axis z (obtained by the acquisition time t),
- smoothing the measurement by a weighted moving average with adjustable window size,
- classification of noise at the beginning and end points,
- identification of individual gaps and calculation of the relative voltage distribution,
- comparison between multiple measurements and/or imported simulation data,
- extensive data and graphic export functionalities,
- potentially further calculations like R/Q and more.

Particle Distributions The data format of particle distributions of most beam dynamics codes like LORASR, TraceWin [9], DYNAMION [10] and PARMTEQ [11] differ from each other. While converting is basically quite simple, LINAC-Multitool makes programming of separate converting scripts redundant. However, additional data formats can be defined straightforward and saved by the user for future use.

ISBN: 978-3-95450-194-6 ISSN: 2226-0366 doi:10.18429/JACoW-LINAC2018-MOPO101

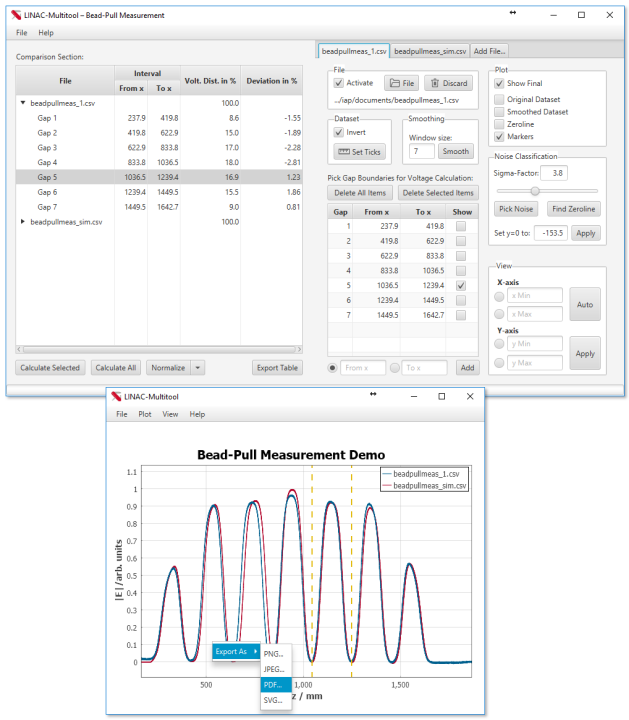


Figure 4: Screenshot of the bead-pull measurement GUI.

3D Field Maps Electric and magnetic field data gained by simulations of CST EM STUDIO and CST MICROWAVE STUDIO [12] can be used in TraceWin after data format conversion. With LINAC-Multitool this conversion can easily be done, providing 3D field maps for TraceWin as an alternative to the use of elements with "hard edge"-approximation.

Outlook

Code development for the LINAC-Multitool has started successfully and first nightly build versions will be tested soon. An extensive feature list will tackle several routine tasks in R&D of linear accelerators and thus simplify workflows.

ACKNOWLEDGMENT

We thank our colleagues at IAP for fruitful discussions and their valuable suggestions.

REFERENCES

[1] JavaFX, http://docs.oracle.com/javase/8/javafx/get-started-tutorial/jfx-overview.htm

[2] JFreeChart, http://www.jfree.org/jfreechart

[3] R. Tiede *et al.*, "LORASR Code Development", in *Proc. 10th Europ. Particle Accelerator Conf. (EPAC'06)*, Edinburgh, Scotland, UK, Jun. 2006, paper WEPCH118, pp. 2194–2196.

[4] R. Tiede *et al.*, "Improvements of the LORASR Code and their Impact on Current Beam Dynamics Designs", in *Proc. 27th Linear Accelerator Conf. (LINAC'14)*, Geneva, Switzerland, Aug.-Sep. 2014, paper TUPP063, pp. 569–571.

[5] R. Tiede *et al.*, "KONUS Beam Dynamics Designs Using H-mode Cavities", in *Proc. 42nd ICFA Advanced Beam Dynamics Workshop on High-Intensity and High-Brightness Hadron Beams (HB'08)*, Nashville, TN, USA, 2008, paper WGB11, pp. 223–230.

[6] U. Ratzinger, "The New High Current Ion Accelerator at GSI and Perspectives for Linac Design Based on H-Mode Cavities", in *Proc. 7th European Particle Accelerator Conf. (EPAC'00)*, Vienna, Austria, Jun. 2000, paper TUZF204, pp. 98–102.

[7] C. Kitegi, U. Ratzinger, and S. Minaev, "The IH Cavity for HITRAP", in *Proc. 22nd Linear Accelerator Conf. (LINAC'04)*, Lübeck, Germany, 2004, paper MOP10, pp. 54–56.

[8] J.H. Hähnel, "Development of an IH-type linac for the acceleration of high current heavy ion beams", PhD. thesis, IAP, Goethe University, Frankfurt, Germany, 2017.

[9] S. Yaramyshev *et al.*, "Development of the versatile multiparticle code DYNAMION", *Nucl. Instr. Meth. Phys. Res. Sect. A*, vol. 558, pp. 90–94, 2006. https://doi.org/10.1016/j.nima.2005.11.018

[10] D. Uriot and N. Pichoff, "Status of TraceWin Code", in *Proc. 6th Int. Particle Accelerator Conf. (IPAC'15)*, Richmond, VA, USA, May 2015, pp. 92–94. https://doi.org/10.18429/JACoW-IPAC2015-MOPWA008

[11] K. Crandall and T. Wangler, "PARMTEQ – A beam-dynamics code for the RFQ linear accelerator", *AIP Conf. Proc.*, vol. 177, pp. 22–28, 1988. https://doi.org/10.1063/1.37798

[12] CST STUDIO SUITE, http://www.cst.com

Content from this work may be used under the terms of the CC BY 3.0 licence (© 2018). Any distribution of this work must maintain attribution to the author(s), title of the work, publisher, and DOI.

ISBN: 978-3-95450-194-6 ISSN: 2226-0366 doi:10.18429/JACoW-LINAC2018-MOPO102

PROGRESS OF MicroTCA.4 BASED LLRF SYSTEM OF TARLA

C. Gumus*, M. Hierholzer, H. Schlarb, C. Schmidt, DESY, Hamburg, Germany
O. F. Elcim, A. Aksoy, A. Aydin, C. Kaya, Ankara University, Ankara, Turkey

Abstract

The Turkish Accelerator and Radiation Laboratory in Ankara (TARLA) is constructing a 40 MeV Free Electron Laser with continuous wave (CW) RF operation. In order to control and monitor the RF field inside four superconducting (SC) 9-cell TESLA type cavities as well as the two normal conducting (NC) buncher cavities, a MicroTCA.4 based LLRF system is foreseen. This highly modular system is also used in resonance control of the cavities via piezo actuators and mechanical motor tuners. This paper gives brief overview on hardware and software components of LLRF control of TARLA, as well as updates of the ongoing integration tests at DESY.

PROJECT OVERVIEW

TARLA facility, located in Ankara, will be the first particle accelerator of Turkey with the Free Electron Laser (FEL) of operating at 3–250 μm wavelength. Other usages will be the Bremsstrahlung radiation and the fixed target experiments [1]. The MicroTCA Technology Lab (A Helmholtz Innovation Lab) of DESY is responsible for delivering a turn-key system for Low Level Radio Frequency (LLRF) control to TARLA. There are six cavities that need to be controlled by LLRF system. Four of these cavities are TESLA type 1.3 GHz superconducting whereas others are normal conducting buncher cavities operating with 1.3 GHz and 260 MHz respectively. The RF operation will be continuous wave (CW) with the expected maximum total beam energy of 40 MeV. Main parameters of the accelerator are shown in Table 1.

Main design of the accelerator is quite similar to Electron linac for beams with high brilliance and low emittance (ELBE) in HZDR-Dresden / Germany where difference is that TARLA uses additional piezos for resonance control. Since ELBE is also in the process of switching their control system to MicroTCA.4 standard, parallel development is ongoing [2]. The main construction on TARLA facility has been finished and accelerator modules have been delivered.

Apart from the hardware delivery and the commissioning of the complete system, DESY is also cooperating with TARLA to train personnel in order to make sure that know-how is transferred.

Table 1: Machine and Beam Parameters

Parameter	Unit	Base Value	Upgraded Value
Beam Energy	MeV	0 - 40	0 - 40
Max. Bunch Charge	pC	77	115
Max. Average Beam Current	mA	1	1.5
Horizantal Emittance	mm mrad	<15	<15
Vertical Emittance	mm mrad	<12	<12
Longitudinal Emittance	keV ps	<85	<85
Bunch Length	ps	0.4 – 6	0.3 - 6
Bunch Repetition	MHz	13	0.001 – 52
Macro Pulse Duration	μs	10 – CW	10 – CW
Macro Pulse Repetition	Hz	1 – CW	1 - CW

LLRF DESIGN

MicroTCA.4 Standard Overview

Using the MicroTCA.4 technology standard, each cavity's RF regulation is controlled by a pair of Advanced Mezzanine Card (AMC) in which FPGA holds the controller and digital signal processing and Rear Transition Module (RTM) card which has the analog RF circuitry to provide the down converted cavity signals over the Z3 connection. On the same crate CPU-AMC board communicates with digitizer AMCs with PCIe lanes using the backplane. Remote access is established through Ethernet via MicroTCA Carrier Hub where crate management takes place [3].

LLRF System Architecture

The LLRF system for TARLA consists of 6 RF station controls and the corresponding resonance control components. In additional to RF and mechanical tuning of the cavities, additional drift compensation modules (DCM) will be installed to the rack in order to compensate the slow drifts on RF signal paths caused by humidity and temperature.

The RF amplification of the drive signal on LLRF system is realized by Solid State Power Amplifiers (SSPA). As for the control system environment, EPICS will be used on the LLRF system.

* cagil.guemues@desy.de

Content from this work may be used under the terms of the CC BY 3.0 licence (© 2018). Any distribution of this work must maintain attribution to the author(s), title of the work, publisher, and DOI.

ISBN: 978-3-95450-194-6 ISSN: 2226-0366 doi:10.18429/JACoW-LINAC2018-MOPO102

Master Oscillator (MO) provides the 1.3GHz and 260 MHz reference to MTCA crate where Local Oscillator Generation Module (LOGM) then produces the LO signal at 1354 MHz and distributes it to the downconverting RTMs.

Mechanical tuning of the cavities is done via stepper motors attached the the cavities. These motors will be controled via FMC carrier AMC (DFMC-FMC25) where MD22 FMC card will drive the motors. In order to compensate microphonic effects on super conducting cavities, piezos will be driven by PZT4 RTM. [4]

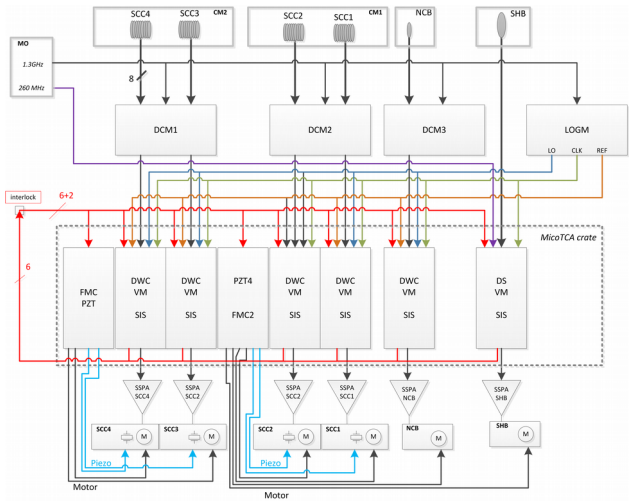


Figure 1: Overview on TARLA LLRF system.

Figure 1 shows the block diagram for complete LLRF system for TARLA. All the LLRF components and their spare parts will be housed in one single rack with inter rack cabling and custom top patch panel for connecting RF signals, motor cabling, interlock connections etc.

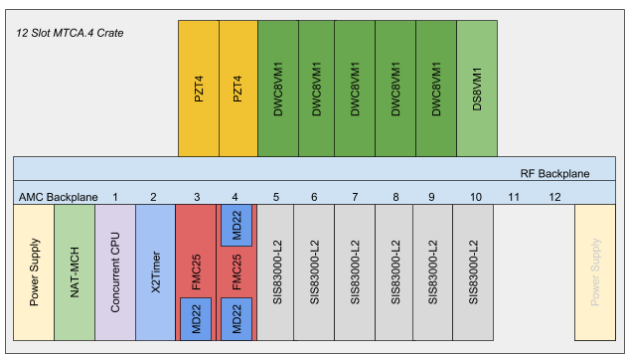


Figure 2: Main MTCA crate layout.

Complete LLRF system also has spare MTCA Crate with bare minimum components to run the each of 6 cavities. This option will be also used as research and development crate where new features can be tested before it gets deployed to the main crate.

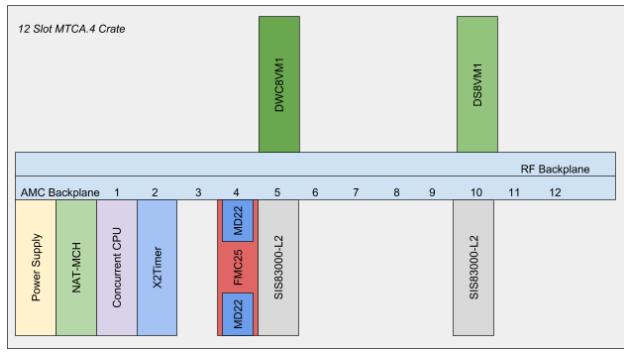


Figure 3: Spare MTCA crate layout.

Current Schedule

All the hardware components of LLRF system delivered to DESY site for tests. After the system integration, one rack containing all the hardware with the cabling will be shipped to TARLA around Q3 of 2019. In order to commission the cavities and first tests, spare crate and LOGM module have been shipped to TARLA site. Currently, system integration for hardware firmware and software is being finalized. After this step, inner rack cabling will begin to take place.

During the system integration, additional proof of concept setups are constructed at Cryo Module TestBench (CMTB) facility at DESY in order to test the hardware, firmware and servers. These setups are mostly for LLRF field regulation stability using setup similar to European XFEL and single cavity regulation like TARLA [5].

Once the hardware is shipped next stage will be functionality and performance demonstration on site. Acceptance is done for a set of default machine operation parameters. Finally, several upgrades to the system like beam position monitors, beam based feedbacks are foreseen.

USER INTERFACE IMPROVEMENTS

TARLA is using EPICS Control System for their major subsystems. This requires that all the servers that are running on the MTCA crate must be interfaced to EPICS in order to have common ground. This interfacing is possible with the ChimeraTK framework.

ChimeraTK Framework

In order to access the data from the MicroTCA.4 crate bidirectionally over PCIe bus, the ChimeraTK framework was developed in DESY. The scope of this framework focuses on abstracting specifics of underlying system as well as giving user the ability to create portable user applications across different control system choices [6].

Content from this work may be used under the terms of the CC BY 3.0 licence (© 2018). Any distribution of this work must maintain attribution to the author(s), title of the work, publisher, and DOI.

ISBN: 978-3-95450-194-6 ISSN: 2226-0366 doi:10.18429/JACoW-LINAC2018-MOPO102

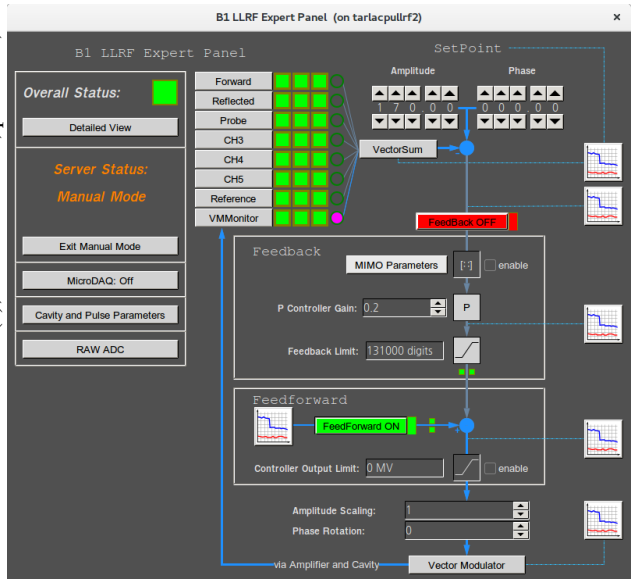


Figure 4: LLRF Expert panels on CSS.

The ChimeraTK toolkit comes with Control System Adapter which makes application to be interfaced to different control systems such as EPICS, DOOCS, OPC-UA etc. This gives ability to re-use the LLRF server written for one facility at another facility with completely different control system. Same LLRF server written for TARLA is currently used in ELBE.

All the LLRF servers (LLRF server, timing server, watchdog server piezo server and motor server), are developed using ChimeraTK framework. Currently these servers are being tested at the DESY site. First successful close loop LLRF operation on dummy load using the MicroTCA.4 crate with the LLRF server written on ChimeraTK framework has been demonstrated.

The graphical user interface for control panels are developed using Control System Studio (CSS). Figure 3. shows the latest LLRF expert panels designed with CSS. These panels went through a significant improvement regarding usability and performance. Remote access to Process Variables (PVs) have been tested along with the logging functionality of the Input Output Controllers (IOCs) output.

CONCLUSION

The Technology Lab of DESY will be delivering a turnkey LLRF system to TARLA to monitor and control 4 SC cavities and 2 NC buncher cavities. Resonance control for the 6 cavities will be also a part of the LLRF system which will be achieved via stepper motors and piezos on the cavities.

Currently, complete system integration is taking place at DESY site. This includes hardware test, software and firmware design and complete system integration. Spare crate which is foreseen for research and development has been already shipped to TARLA. This crate will be used for first RF operation on normal conducting cavities. The LLRF expert panels which was designed using CSS is improved and successfully interfaced to LLRF servers. All electronics housed in a single rack, will be shipped to TARLA around Q3 of 2019.

REFERENCES

[1] A. Aksoy *et al.*, "TARLA: The First Facility of Turkish Accelerator Center", in *Proc. 8th Int. Particle Accelerator Conf. (IPAC'17)*, Copenhagen, Denmark, May 2017, pp. 2776-2778. doi:10.18429/JACoW-IPAC2017-WEPAB087

[2] M. Kuntzsch *et al.*, "MicroTCA.4-Based LLRF for the Superconducting CW LINAC ELBE – Status And Outlook", in *Proc. LLRF Workshop 2017*, Barcelona, Spain, Oct. 2017, p. 4.

[3] PICMG Micro Telecommunications Computing Architecture Short Form Specification, http://www.picmg.org/

[4] K. Przygoda *et al.*, "MicroTCA.4 Based Single Cavity Regulation Including Piezo Controls", in *Proc. 7th Int. Particle Accelerator Conf. (IPAC'16)*, Busan, Korea, May 2016, pp. 3512-3514. doi:10.18429/JACoW-IPAC2016-THOAA03

[5] A. Bellandi *et al.*, "LLRF R&D towards CW operation of the European XFEL", presented at 29th Linear Accelerator Conf. (LINAC'18), Beijing, China, Sep. 2018, paper MOPO104.

[6] G. Varghese *et al.*, "CHIMERATK – A Software Tool Kit for Control Applications", in *Proc. 8th Int. Particle Accelerator Conf. (IPAC'17)*, Copenhagen, Denmark, May 2017, pp. 1798-1801. doi:10.18429/JACoW-IPAC2017-TUPIK049

Content from this work may be used under the terms of the CC BY 3.0 licence (© 2018). Any distribution of this work must maintain attribution to the author(s), title of the work, publisher, and DOI.

ISBN: 978-3-95450-194-6 ISSN: 2226-0366 doi:10.18429/JACoW-LINAC2018-MOPO104

LLRF R&D TOWARDS CW OPERATION OF THE EUROPEAN XFEL

A. Bellandi*, V. Ayvazyan, J. Branlard, C. Gümüs, S. Pfeiffer, K. Przygoda, R. Rybaniec, H. Schlarb, C. Schmidt, J. Sekutowicz, DESY, Hamburg, 22607 Hamburg, Germany
W. Cichalewski, TUL-DMCS, Łódź, Poland

Abstract

The ever growing request for machines with a higher average beam pulse rate and also with a relaxed (< 1 MHz) pulse separation calls for superconducting linacs that operate in Long Pulse (LP) or Continuous Wave (CW) mode. For this purpose the European X-ray Free Electron Laser (European XFEL) could be upgraded to add the ability to run in CW/LP mode. Cryo Module Test Bench (CMTB) is a facility used to perform tests on superconducting cavity cryomodules. Because of the interest [1] in upgrading European XFEL to a CW machine, CMTB is now used to perform studies on XM-3 [2], a 1.3 GHz European XFEL-like cryomodule with modified coupling that is able to run with very high quality factor ($Q_L = 10^7 ... 10^8$) values. The RF power source allows running the cavities at gradients larger than 16 MV/m. Because of the Q_L and gradient values involved in these tests, detuning effects like mechanical resonances and microphonics became more challenging to regulate. The goal is then to determine the appropriate set of parameters for the LLRF control system to keep the error to be less than 0.01° in phase and 0.01% in amplitude.

A POSSIBLE CW UPGRADE AT EUROPEAN XFEL

XFELs are important tools of discovery that allow unprecedented brightness and spectral purity. In 2017 the European XFEL came into operation, producing the brightest and hardest X-ray FEL light in the world. At the moment European XFEL can produce a maximum of 2700 pulses with a temporal distance of 220 ns and a repetition rate of 10 Hz. Because of the advantage (from the experimental point of view) of having a bigger temporal separation between the pulses and simultaneously increasing the average number of pulses per seconds, a CW upgrade of European XFEL could be made. For such upgrade the duty cycle would change from the actual value of 1.4% at 17.5 GeV for Short Pulse (SP) to a maximum value of 100% at 8.6 GeV, for CW, or 10% to 50% at 12.8 GeV for LP [1]. For CW/LP operations, IOT amplifiers, along with the existing klystrons, will be installed in European XFEL tunnel to allow both SP (high gradient) and CW/LP (reduced gradient) with minimum downtime between the switch of the two modes. To limit the required RF power, the Q_L could be increased to values higher than 10^7. To meet the field quality requirements inside the cavities with an increased Q_L and to decide the optimal set of parameters of the Low Level RF (LLRF) controller, further studies have to be done both on European XFEL and dedicated test facilities.

* andrea.bellandi@desy.de

CHALLENGES OF CW OPERATION

Increasing the Q_L from the current European XFEL value of $4.6 \cdot 10^6$ to values bigger than 10^7 results in a full bandwidth less than 100 Hz that will make the cavities more susceptible to detuning effects. In order to keep the cavities on resonance with the required field stability but, at the same time, to limit the required peak RF power, these effects must be canceled out using a LLRF control system that acts on the fast piezoelectric tuners.

Lorentz Force Detuning

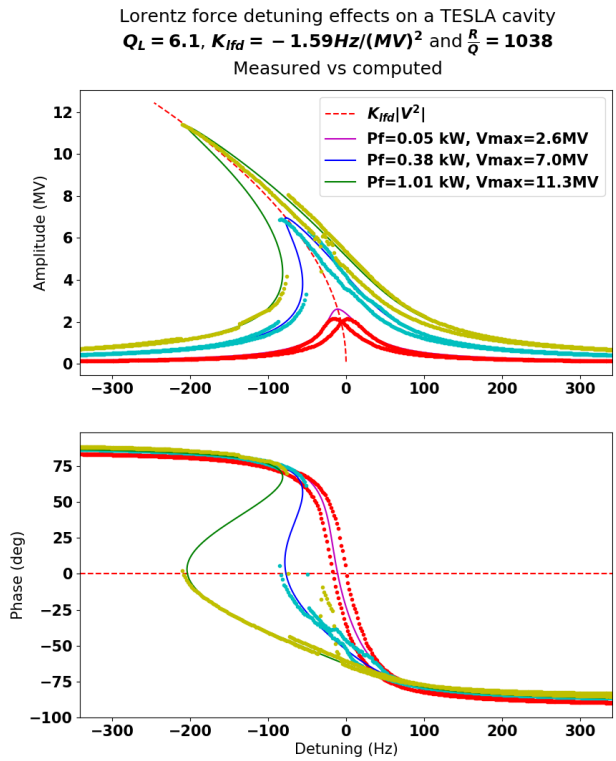


Figure 1: Resonance scan of a TESLA-like superconducting cavity at different values of the forward power using piezoelectric actuators. Computed (lines) vs. measured (points) values are shown. Tests were taken on cavity 2 of XM-3 module.

Lorentz Force Detuning (LFD) is a detuning effect that arises from the electromagnetic pressure that the accelerating field exerts on cavity walls. The detuning produced by LFD is proportional to the square value of the field.

$$\Delta f_{lfd} = K_{lfd} \cdot (\Delta V)^2$$

Content from this work may be used under the terms of the CC BY 3.0 licence (© 2018). Any distribution of this work must maintain attribution to the author(s), title of the work, publisher, and DOI.

ISBN: 978-3-95450-194-6 ISSN: 2226-0366 doi:10.18429/JACoW-LINAC2018-MOPO104

Content from this work may be used under the terms of the CC BY 3.0 licence (© 2018). Any distribution of this work must maintain attribution to the author(s), title of the work, publisher, and DOI.

Because for European XFEL TESLA-like cavities $K_{lfd} \approx -1\text{Hz/(MV)}^2$ [3], when driving the cavities at accelerating fields higher than 10 MV, the resulting detuning becomes comparable to a full bandwidth of 130 Hz, equivalent to a $Q_L = 10^7$.

With even higher fields and Q_Ls (eg. in Fig. 1) the resonance curve becomes metastable and shows a strong hysteretic behaviour [4] Fig. 1. When driving cavities near resonance with such conditions, a transient effect, like cavity oscillations driven by microphonics, or forward RF power oscillations, can trigger a jump of the field to low gradients. The LLRF controller should then be able to prevent static drops and automatically adjust the tune correction to be applied when the accelerating gradient is changed or the forward power is switched on.

Microphonics and Mechanical Properties of Fast Tuners

External disturbances, commonly referred to microphonic noise, produce a detuning that can be periodic (the noise produced by turbopumps, air conditioning, 50 Hz electric hum) or temporary (vehicle passing near the facility, routine activation other acceleration devices). Also long time drifts of the spectral properties of the noise have to be taken in account. This is particularly important because our current LLRF control system for CW uses an Active Noise Compensation unit (ANC) [5] to compensate the microphonic noise detuning. This unit, using the detuning information as input signal, locks on a particular microphonic frequency and produces a signal to actuate the fast tuner. The result of such operation is the cancellation of the locked noise component. Because the capture bandwidth is limited and has to be set up with a fixed central frequency, the stability of time-dependent spectral properties of the noise has to be measured. Additionally, the mechanical properties of the fast piezoelectric tuners has to be modeled . This is particularly important because the control algorithms that use these tuners have to take into account mechanical resonances in order to work in a correct way.

MEASUREMENTS AT EUROPEAN XFEL

Microphonic and mechanical studies during shutdown periods were conducted even if European XFEL is not operated in CW mode. These measurements were done only using the installed piezoelectric sensors/tuners. Because of the limitations of the system during the measurements, the length of the acquired signals was only 100 ms, thus producing a separation between the recorded frequency components of 10 Hz. The measurements on the first module of European XFEL station 15 are shown in Fig. 2. The main noise component frequency is at 160 Hz with a possible second and third harmonic components at 320 Hz and 470 Hz. The origin of this signal is at the moment still unknown. Also a 50 Hz signal was detected.

Mechanical resonances were also measured exciting the cavities with the fast piezoelectric tuner and reading back

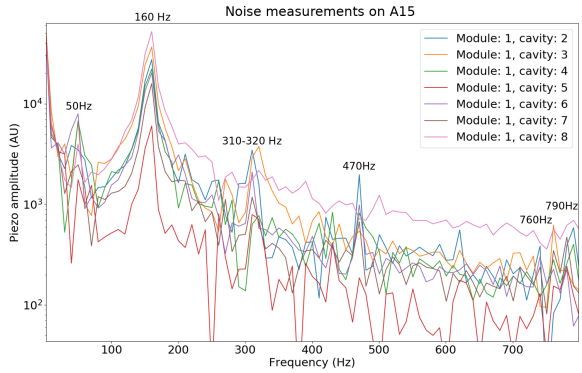


Figure 2: Microphonics recorded at European XFEL RF station A15 cryomodule 1 with piezoelectric sensor. Cavity 1 is not shown.

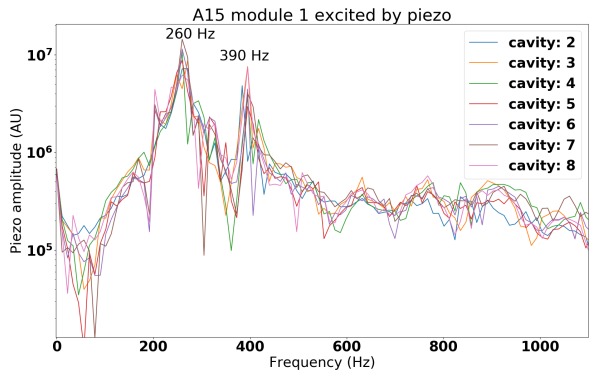


Figure 3: Transfer function between excitation produced by the fast tuner and piezo sensor.

the produced signals with the piezoelectric sensor. In Fig. 3 such measurements were displayed for RF station A15 for a periodic excitation of 10 Hz. For each cavity resonance peaks were observed at 260 Hz and 390 Hz.

MEASUREMENTS AT CMTB

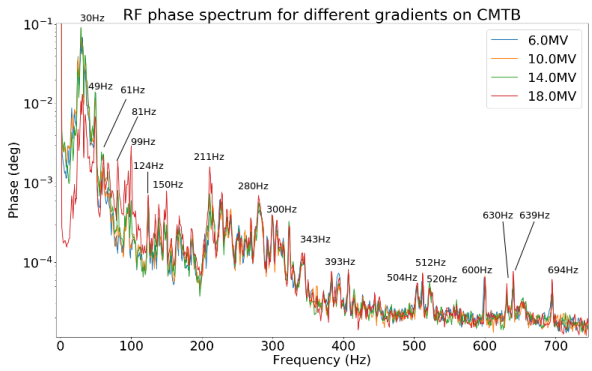


Figure 4: Microphonic noise recorded on the probe signal of cavity 1 at different accelerating voltages. $Q_L = 5 \cdot 10^7$.

ISBN: 978-3-95450-194-6 ISSN: 2226-0366 doi:10.18429/JACoW-LINAC2018-MOPO104

Measurements on microphonics and on the fast tuner transfer function with CW fields were made on XM-3. Noise measurements were done recording the spectrum of the RF signal in open loop. Results are displayed in Fig. 4 for different gradients. As it was already found in previous measurements [5], the two main noise components are at 30 Hz and 49 Hz and are produced by the vacuum pumps installed in the facility.

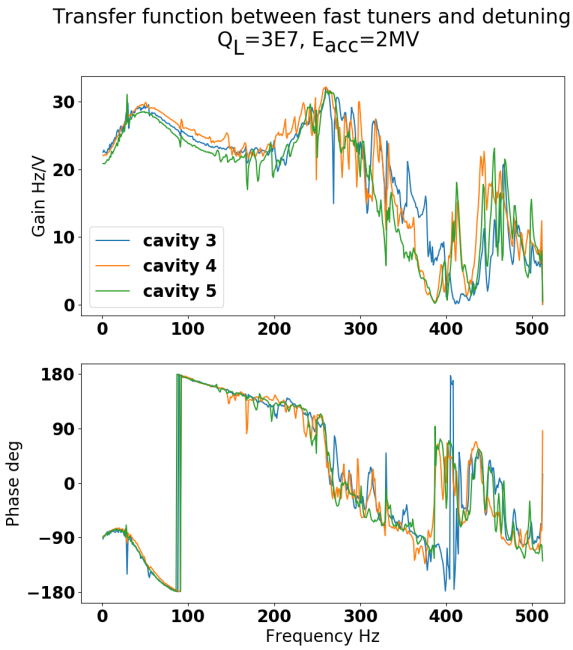


Figure 5: Mechanical transfer function between piezoelectric actuators of cavity 3,4,5 XM-3 and probe signals. The Y axis is the amount of detuning produced by a sinusoidal excitation from the piezoelectric actuators.

The mechanical transfer function between the fast tuners and the accelerating field was also measured (Fig. 5) using the piezoelectric actuators excited with a varying frequency sinusoidal signal. A central component of 260 Hz matches the measurement at European XFEL, whereas the 390 Hz component was not found.

To observe the long time stability of the microphonics, a 24 hours-long test acquisition of piezoelectric sensor signal (Fig. 6) was recorded. The spectrogram shows the stability of the microphonic specrum over the entire measurement time.

CONCLUSION AND OUTLOOK

Previously done measurements [6, 7] demonstrated that it is possible to achieve high CW RF fields (>15 MV/m) while meeting the required stability (less than 0.01° in phase and 0.01% in amplitude). However a simple, automatic and reproducible way to achieve these results has to be developed. Furthermore the knowledge acquired at CMTB has to be adapted to large scale working facilities like European XFEL. Then some additional development should be done:

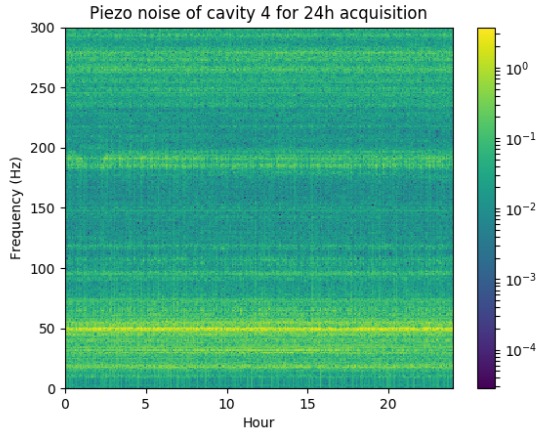


Figure 6: Noise spectrogram taken during a 24h data recording. The signal is recorded from a piezoelectric sensor.

- Develop a reliable detuning estimation.
- Simulate how beam loading affects the system.
- Estimate an RF plant model of a module driven by an IOT. Optimize the MIMO feedback controller parameters with the model.
- Develop algorithms that counteracts LFD related issues. A simple and reproducible way to achieve these results has to be found.
- Find a way to optimally and automatically setup ANC.
- Develop diagnostic routines to find out important information (Q_L, detuning, quench detection, etc.) about the system while minimizing the downtime.
- Find automated procedures to automatically raise CW gradient to a desired level while meeting European XFEL specifications. This should be proven with multiple long term studies.
- Update hardware/firmware/software stack to industrial quality level. The increased performance possibilities of new hardware has to be exploited to improve the LLRF system regulation ability.

The measurements done at European XFEL and CMTB will then be used to enhance the model used in our LLRF control system.

REFERENCES

[1] J. Sekutowicz *et al.*, "Feasibility of CW and LP Operation of the XFEL Linac", in *Proc. FEL'13*, New York, USA, Aug. 2013, paper TUOCNO04, pp. 189–192.

[2] J. Branlard *et al.*, "Highlights of the XM-3 Cryomodule Tests at DESY", presented at the 29th Linear Accelerator Conf. (LINAC'18), Shanghai, China, Sep. 2018, paper TUPO029, this conference.

Content from this work may be used under the terms of the CC BY 3.0 licence (© 2018). Any distribution of this work must maintain attribution to the author(s), title of the work, publisher, and DOI.

ISBN: 978-3-95450-194-6 ISSN: 2226-0366 doi:10.18429/JACoW-LINAC2018-MOPO104

[3] V. Ayvazyan and S. Simrock, "Dynamic Lorentz force detuning studies in Tesla cavities", in *Proc. EPAC'04*, Lucerne, Switzerland, Jul. 2004, paper TUPKF016, pp 994–996.

[4] J. R. Delayen, "Ponderomotive instabilities and microphonics - a tutorial", in *Proc. 12th Int. Workshop on RF Superconductivity (SRF'05)*, Ithaca, NY, USA, Jul. 2005, *Physica C: Superconductivity*, vol. 441, no. 1–2, pp. 1–6, 2006. https://doi.org/10.1016/j.physc.2006.03.050

[5] R. Rybaniec *et al.*, *IEEE Transactions on Nuclear Science*, vol. 64, no. 6, pp. 1382–1388, 2017. https://doi.org/10.1109/TNS.2017.2687981

[6] W. Cichalewski *et al.*, "High loaded quality factor superconducting cavities accelerating field parameters regulation during continuous wave operation", *IEEE Transactions on Nuclear Science*, to be published.

[7] K. Przygoda *et al.*, 'MicroTCA. 4 based Single Cavity Regulation including Piezo Controls", in *Proc. IPAC'16*, Busan, Korea, May 2016, pp. 3152-3154. https://doi.org/10.18429/JACoW-IPAC2016-THOAA03

Content from this work may be used under the terms of the CC BY 3.0 licence (© 2018). Any distribution of this work must maintain attribution to the author(s), title of the work, publisher, and DOI.

ISBN: 978-3-95450-194-6 ISSN: 2226-0366 doi:10.18429/JACoW-LINAC2018-MOPO106

NEW DIGITAL LLRF SYSTEM FOR HIT

E. Feldmeier, Th. Haberer, A. Peters, HIT, Heidelberg, Germany

Abstract

The Heidelberg Ion Therapy Center HIT is in clinical operation since 2009. The accelerator complex consists of a linear accelerator and a synchrotron to provide carbon ions and protons for clinical use as well as helium and oxygen ions. The analog LLRF system for the linac should be replaced after more than 10 years of continuous operation. In its life-time the LLRF caused no interruption of the clinical operation with a downtime of more than 15 minutes. In order to keep the reliability in the next 10 years at least as high, a new digital LLRF system is planned. Further difficulties for the installation of a new system are due to the clinical full time usage of the accelerator and the short maintenance slots of only two days in series.

INTRODUCTION

The layout of the accelerator of the Heidelberg Ion Therapy Center HIT [1] includes three ECR ion sources, a 7 MeV/u injector linac, a 6.5 Tm synchrotron and a high energy beam transport line to deliver beam for the four target places: Two treatment rooms with a horizontally fixed beam-line, the worlds first heavy ion gantry and an experimental area.



Figure 1: The accelerator of the Heidelberg Ion-Beam Therapy Center (HIT) with three ion sources, the LINAC (7 MeV/u) consisting of a 4-rod-RFQ and a IH-DTL, the synchrotron (48-430 MeV/u), the beam lines to the treatment rooms and the experimental area and the heavy ion gantry [2].

The ECR ion sources produce proton, helium, carbon and oxygen beam, of which the protons and the carbon ions are used for the medical treatment of localized tumors.

In the injector linac, beams with an AoQ of 1-3 can be accelerated to 7 MeV/u. The synchrotron accelerates the beam to an energy of up to 430 MeV/u for carbon ions.

LINAC AND RF SYSTEMS

The LINAC RF system shown in Fig. 2 supplies three RF cavities in front of the Synchrotron to accelerate and form the beam from the ion sources. A 4-rod-RFQ is used to accelerate the beam to 400 keV/u, focus the beam and form bunches. The following IH-DTL accelerates the beam to 7 MeV/u and the Debuncher spreads the bunches longitudinal to match the acceptance of the synchrotron. The cavities are operated at 216.816 MHz. For a beam with an $AoQ = 3$ a power for the RFQ of 200 kW, for the IH-DTL of 900 kW and for the Debuncher of 1.2 kW is needed.

The RF system (Fig. 2) consists of a common master oscillator providing the frequency. A amplifier and splitter is used to distribute the RF signal to the three power amplifiers. The RFQ has a 8 kW transistor preamplifier and a 250 kW tube final stage. The IH-DTL has a 4 kW transistor preamplifier, a 120 kW tube stage and a 1.4 MW tube final stage. The RF system for the Debuncher only uses a 4 kW transistor amplifier.

The analog PI-controller for each system corrects the amplitude and the phase of the decoupled cavity signal.

The RF system was designed by GSI in Darmstadt, Germany and build by Bertronix in Munich, Germany and Ampegon in Turgi, Switzerland.

LLRF SYSTEM

The requirements for the new digital LLRF system are based on the current analog LLRF system. Even there are new advantages with digital systems the great useability of the given system with its various possibilities for fault diagnostics and well-thought-out features must not be reduced. The preferred solution is a ready to use system with a lot of flexibility and free to program. Whether projects like microTCA [3] [4] or Libera [5] [6] can be used has to be proven. Otherwise a complete new system has to be developed.

In the following section the most important features will be discussed.

Master Oscillator

The HIT Linac works at 216.816 MHz and needs a frequency stability of better than 10^{-6}. The master oscillator can be set up separately and needs 4 or more output ports for the 3 rf systems and for the diagnostics. The phase stability of $< 0.1°$ is required.

Content from this work may be used under the terms of the CC BY 3.0 licence (© 2018). Any distribution of this work must maintain attribution to the author(s), title of the work, publisher, and DOI.

ISBN: 978-3-95450-194-6 ISSN: 2226-0366 doi:10.18429/JACoW-LINAC2018-MOPO106

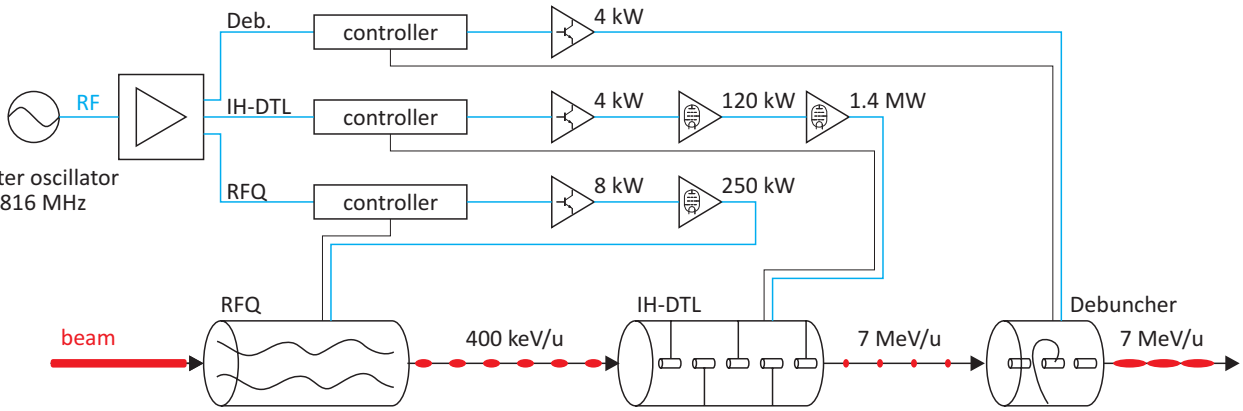


Figure 2: Schema of the LINAC RF System: One Master oscillator at 216.816 MHz, amplifier and divider distributes the RF to the three amplifiers, amplifier for the RFQ (8 kW transistor, 250 kW tube amplifier), amplifier for the IH-DTL (4 kW transistor, 120 kW tube amplifier, 1.4 MW tube amplifier), amplifier for the Debuncher (4 kW transistor). The control loop corrects amplitude and phase of the decoupled signal of the accelerator cavities.

Amplitude and Phase Control Loop

The amplitude and phase control loop has to provide a amplitude stability of better than 0.5% and a phase stability of better then 0.2°. The rf system operates in puled mode with a duty cycle of 0.5% and a pulse length of 500 μs. The repetition frequency is 10 Hz.

Since the beam current with a maximum of 10^{11} proton particles 10^8 carbon particles per pulse are small, beam-loading does not has to be considered.

The regulation parameters of the amplitude and phase control loop are different, since the phase control loop is much slower than the amplitude control loop. In addition to the feedback loop, a feed-forward loop with a non-linear calibration curve is foreseen.

In normal operation, the reference value for the feedback loop is taken from a decoupling loop of the rf cavity (cavity signal). Where the cavity is out our resonance for some reason and only less rf power is accepted, the decoupled cavity signal is very low. Then the feedback controller will operate on the reflected rf power with a fixed small set value (f.e. 10%), since the cavity gets in resonance and the cavity signal reaches the reflected power. The reference value is now switched back to the cavity signal and the normal set value. This leads to a smooth start up of the cavity and gives the ω_0 controller enough signal to work. A very simple block diagram of the foreseen controller is shown in Fig. 3.

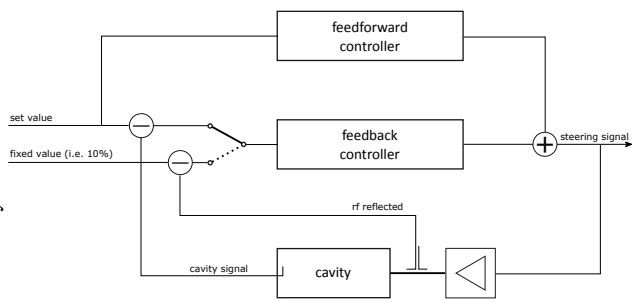


Figure 3: Basic block diagram of the foreseen controller with the feedforward controller and the feedback controller. When the cavity is out of resonance i.e. during startup phases, the reflected rf power is used as the reference value.

The controller has to handle fast interlocks from the analog measurements in less than a few micro seconds like over ref power, over fwd power, vacuum interlock, et cetera with reducing the rf output and restarting after the interlock has gone within on rf pulse.

ω_0 Control Loop

The ω_0 controller steers the eigenfrequency of the cavity by adjusting the position of one ore more plungers per cavity. Since we are using pulsed rf with a low duty cycle, the feedback controller has to take account of this fact. The reference value can only be measured during a rf pulse but the pulse is to short measure an effect of the steering. When no new pulses are generated by the central control system, the controller has to stop the steering and move the plunger to an inital position. Ideally the controller has a model of the heating and cooling of the cavity and can adjust this position in response to the thermal history of the cavity.

As reference value for the feedback controller the phase difference between forward rf power and reflected rf power is used.

Timing

The timing is delivered by the central accelerator control system (ACS) and is synchronous to the 50 Hz mains supply. In times where no timing is delivered for example during maintenance or in case of a failure in the ACS the LLRF generates its own timing signals. This leads to a more stable operation of the cavities without restarting the rf system after an ACS breakdown. It is also very useful to be independent to other systems which may be down during maintenance.

Content from this work may be used under the terms of the CC BY 3.0 licence (© 2018). Any distribution of this work must maintain attribution to the author(s), title of the work, publisher, and DOI.

ISBN: 978-3-95450-194-6 ISSN: 2226-0366 doi:10.18429/JACoW-LINAC2018-MOPO106

Operation Elements and Test Terminals

During operation, maintainance and service of the HIT linac rf system over the past 12 years some operating elements and test terminals were used quite often and improved the workflow. In case of an failure the right test terminals and service friendly systems can be repaired much faster and improves therefor the up-time. Even if they might seem to be obsolete in modern systems, they are foreseen in the new digital LLRF.

The system will have a potentiometer for the local set value of the amplitude and phase and a switch to select feedback mode or feed-forward mode.

Measuring terminals will be preset for pulsed amplitude and phase signal, DC set value for amplitude and phase, steering signal, controller deviation and two free configurable measurement ports for any other signal.

CONCEPT OF THE NEW DIGITAL LLRF

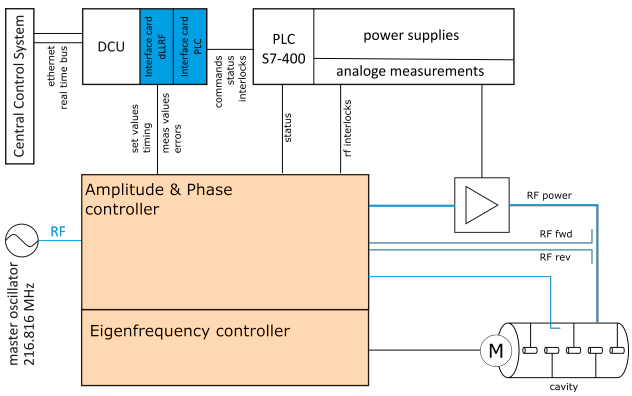


Figure 4: The block diagram of the new digital LLRF system for HIT. Central Control System, DCU, PLC, power supplies, amplifier and cavity are the given parts (white background). The amplitude & phase controller and the ω_0-controller will be renewed. A custom made solution as well as a industrial or scientific system are useful (orange background). While the *Interface card dLLRF* and the *Interface card PLC* has to be custom solutions. A new master oscillator can be taken from the stock.

The basic block diagram of the new dLLRF system is shown in Fig. 4. The central control system with the *Digital Device Unit* (DCU), as well as the power supplies, the amplifier and the cavity is given (white background).

Next to the DCU a new *Interface card dLLRF* and a new *Interface card PLC* has to be developed. They communicate with the DCU by a proprietary back-plane bus and translate signals from the ACS to the connected subsystems, such as set values, timing, interlocks, measurement values, et cetera. These two cards will be custom-made products, since they are only usable for the HIT system.

For the amplitude and phase controller as the centerpiece of the new dLLRF system, an open hardware and open software project with a widespread community is desirable. The advantages of an existing project with an active community leads to a reduced effort in development tasks, the availability of hardware in short term, the possibility to adjust it to the HIT system and program it with the needed features, outweigh a complete new development. Even when a custom made system would fit all the requirements best and could be the slimmest solution with maybe the highest reliability and availability, the effort in building such a system by their own is to much for a small team like HIT.

One boundary condition which cannot be changed is the small amount of space of only 6 rack units for the amplitude and phase controller as well as the ω_0-controller.

The system specifications are listed in Table 1.

Table 1: LLRF System Specifications

Requirements	Value
frequency	216.816 Mhz
frequency stability	$< 10^{-6}$
phase stability of the master oscillator	$< 0.1°$
duty cycle	0.5%
rf pulse length	500 μs
repetition rate	10 Hz
amplitude error	$< 0.5\%$
phase stability	$< 0.2°$
output rf power	+10 dBm

REFERENCES

[1] Th. Haberer, J. Debus, H. Eickhoff, O. Jäkel, D. Schulz-Ertner, and U. Weber, "The Heidelberg Ion Therapy Center", in *Radiotherapy and Oncology*, vol. 73 (Supplement 2), pp. S186-190, 2004.

[2] D. Ondreka and U. Weinrich, "The Heidelberg Ion Therapy (HIT) Accelerator Coming into Operation", in *Proc. EPAC'08*, Genoa, Italy, Jun. 2008, p. 979.

[3] J. Branlard *et al.*, "The European XFEL LLRF system", in *Proc. IPAC'12*, New Orleans, LA, USA, May 2012, p. 55.

[4] MicroTCA® is a trademark of PICMG, MTCA.4 specifications: `http://www.picmg.org`

[5] B. Baricevic *et al.*, "Evaluation of the Analog and Digital Receiver Section in the Libera LLRF System", in *Proc. PAC'09*, Vancouver, BC, Canada, May 2009, p. 2210.

[6] G. Jug and A. Kosicek "Libera LLRF – Development and Tests", in *Proc. IPAC'10*, Kyoto, Japan, May 2010, p. 1455.

Content from this work may be used under the terms of the CC BY 3.0 licence (© 2018). Any distribution of this work must maintain attribution to the author(s), title of the work, publisher, and DOI.

ISBN: 978-3-95450-194-6 ISSN: 2226-0366 doi:10.18429/JACoW-LINAC2018-MOPO107

PERFORMANCE EVALUATION OF THE RF REFERENCE PHASE STABILIZATION SYSTEM ON FIBER-OPTICAL LINK FOR KEK e-/e+ INJECTOR LINAC

N. Liu†,1, T. Miura1,2, T. Matsumoto1,2, F. Qiu1,2, D. Arakawa2, H. Katagiri2, Y. Yano2, S. Michizono1,2, B.T. Du1, 1SOKENDAI, Kanagawa 240-0193, Japan, 2KEK, Ibaraki 305-0801, Japan

Abstract

The KEK e-/e+ injector is the 600 m J-shaped LINAC, which has 8 RF sectors. Stabilization of the RF phase reference for long distance transmission is necessary for stable RF operation. In the present system, single-mode fiber-optical links without feedback control are used from sector 2 to 5. The long-term phase drift of the reference phase at sector 5 was observed for more than 10° over 7 days. For SuperKEKB injector LINAC, the phase stability requirement is estimated to be 0.2° rms corresponding to 195 fs at 2856 MHz including short-term jitter and long-term phase drift. A more stable RF phase reference is necessary for the improvement of the phase stability. An RF reference phase stabilization system using a pair of wavelength division multiplexing (WDM) devices and a variable optical delay line (VODL) is constructed for the evaluation of the system's performance. The temperature and humidity characteristics of the electric and optical components, in addition to the phase stabilized optical fiber (PSOF) with different wavelengths are measured. In this paper, the performance of the proposed phase stabilization system will be evaluated.

INTRODUCTION

The KEK e-/e+ injector LINAC comprises of 124.8 m long and 488.3 m long straight beam lines, which consist of 8 sectors (sector A-C and 1-5) [1]. The Master Oscillator (MO, 571 MHz) system generates a 2856 MHz reference signal, which is delivered to sector A-C, 1 by coaxial cables and to sector 2 to 5 by optical links. During the long-distance transmission, the RF reference phase drifts due to the effect of temperature and humidity fluctuations on the propagation medium (coaxial cables and optical fiber) and the electric/optical components, especially for the S-band signal. The phase stability of the RF reference will contribute to the beam arrival jitter and influence the beam quality accordingly. In this paper, we focus on the phase stabilization system of the optical fiber link.

The phase stability of the RF reference depends on the short-term RF jitter and the long-term phase drift. The RMS jitter of the RF reference transmitted signal was found to be 100-200 fs for each sector [2]. In addition, the long-term phase drift of the reference phase at sector 5 was observed to be more than 10° for 7 days by the phase monitoring system, as shown in Fig. 1.

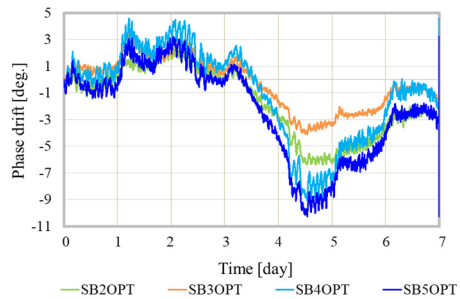


Figure 1: Phase drift of the optical link from sector 2-5 at injector LINAC.

In order to stabilize the RF reference phase, a phase stabilization system using a pair of wavelength division multiplexing (WDM) device and variable optical delay line (VODL) is implemented in the laboratory in order to evaluate the system's performance. In this paper, the temperature and humidity characteristics of the phase stabilized optical fiber (PSOF) are measured with different wavelengths (1310 nm, 1550 nm) and the performance of the phase stabilization system is evaluated.

OVERVIEW OF RF REFERENCE PHASE STABILIZATION SYSTEM

A similar feedback system to [3-5] is considered according to the current status of the injector LINAC. Figure 2 shows a schematic diagram of the proposed phase stabilization system for performance evaluation in the laboratory. The 2856 MHz electric RF signal is generated by a signal generator (SG) as the reference signal (REF). This signal is subsequently converted into an optical signal with a wavelength of 1310 nm (λ_1) using an optical transmitter (E/O). The optical signal is then transmitted by the single-mode phase-stabilized optical fiber (PSOF) and converted into an electrical signal (transmitted signal) by an optical receiver (O/E). In order to stabilize the transmitted signal, it is sent back using the same PSOF but at a different wavelength 1550 nm (λ_2) with a pair of WDM devices and another pair of E/O and O/E. All the S-band signals (REF, transmitted signal and returned signal) are down-converted to the intermediate frequency (IF, 14.28 MHz) by a local oscillator (LO, 2870 MHz). The phase difference (feedback phase) between the returned signal and REF is used for the feedback control. The transmitted signal is monitored in order to evaluate the performance of the feedback system.

† liuna@post.kek.jp

Content from this work may be used under the terms of the CC BY 3.0 licence (© 2018). Any distribution of this work must maintain attribution to the author(s), title of the work, publisher, and DOI.

ISBN: 978-3-95450-194-6 ISSN: 2226-0366 doi:10.18429/JACoW-LINAC2018-MOPO107

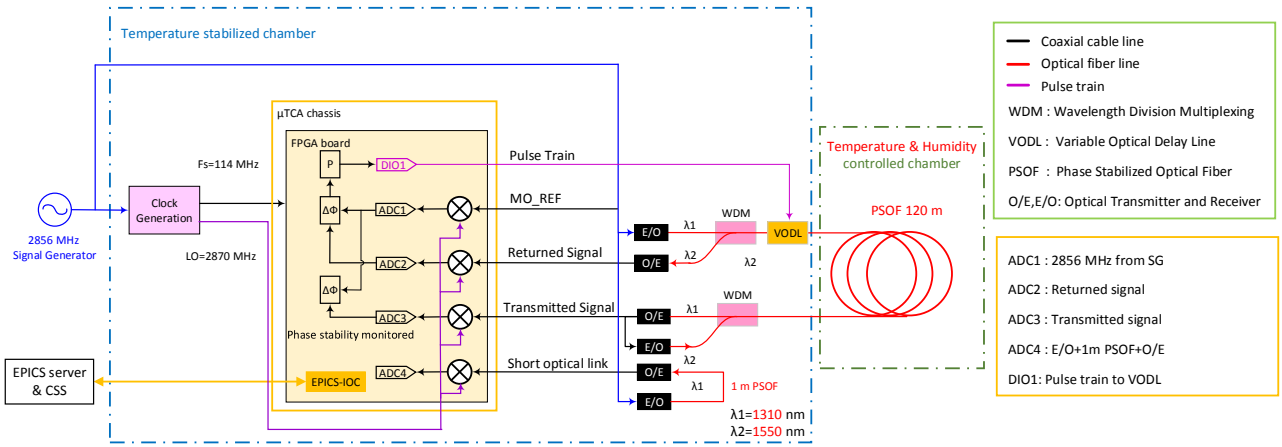


Figure 2: Schematic diagram of the phase stabilization system on the optical fiber for the performance evaluation.

Optical Transmitter and Receiver

The E/O (EOC-144) and O/E (OEC-1041), which operate at a wavelength of 1310 nm provided by TAMAGAWA Inc. are installed in sector 2-5 and the integral RMS jitter of a pair of E/O and O/E is 90 fs from 10 Hz to 10 MHz [6]. The specifications are also shown in Table 1. The same type of TAMAGAWA E/O and O/E with different wavelengths 1310 nm and 1550 nm are used in the test system. The electrical and optical components are necessary to keep inside the temperature-stabilized chamber.

Table 1: The Specification of EOC-144/OEC-1041

Items	EOC-144/OEC-1041
RF Input range	10 ~ 3000 MHz
Temperature range	+10 ~ +40 ºC
Temperature coefficient	-0.6154 ps/ºC
Humidity coefficient	-0.0382 ps/%RH

Variable Optical Delay Line

In order to compensate for the phase drift of the PSOF due to temperature and humidity fluctuations, a mechanical variable optical delay line (VODL) driven by a stepping motor is used. Figure 3 shows the feedback phase as a function of the pulse of the stepping motor. The feedback phase resolution of the VODL module is 2.15 mdeg/pulse and the phase range of the VODL module is more than 90°.

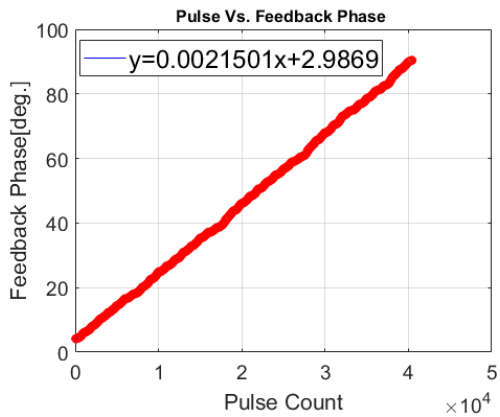


Figure 3: Measurement of the coefficient between the stepping motor pulse and the feedback phase.

PHASE-STABILIZED OPTICAL FIBER

The phase stabilized optical fiber is used to distribute the reference signal in the gallery of the injector LINAC. In the linac gallery, the temperature is stabilized to within ± 1 □ over a range of 24□ ~ 27□ and the humidity usually fluctuates between 10% RH and 50% RH from Sep. 2017 to Sep. 2018. The temperature and humidity characteristics of the PSOF will directly influence the phase stability. The PSOF was provided by Furukawa Inc. and the propagation delay temperature coefficient is 5 ps/km/□ as provided in the specifications. It is important to note that, for the phase stabilization system, the wavelength of the transmitted signal and the returned signal should be different due to inherent requirements of the WDM technology. In order to study the effect of the wavelength difference on the feedback system, the temperature coefficient and humidity coefficient of both wavelengths (λ_1=1310 nm, λ_2=1550 nm) are measured using a network analyzer. The measurement system is explained in [6]. In order to guarantee the free extension of the PSOF, the fiber should be unbound. The fiber length is 120 m and this fiber will be used for the evaluation system.

Figure 4 shows the propagation delay temperature coefficient of the PSOF for different wavelengths. The temperature coefficient difference is 0.2 ps/km/□. The distance from the MO station to sector 5 is 240 m long. Assuming the humidity is stable, the phase difference between the forward line (1310 nm) and the backward line (1550 nm) is less than 0.1 ps in the case of a temperature fluctuation of ±1 □. We started the humidity coefficient measurement from 30% RH at a stable temperature taking into consideration the control range of the humidity chamber. Figure 5 shows the transmission time delay difference of the PSOF from 30% RH to 50% RH, with the reference transmission time delay at 30% RH. The time delay difference between the two wavelengths depends on the different relative humidity values. Therefore, the humidity coefficient is difficult to estimate. The maximum difference is 5.38 ps/km at approximately 45% RH. If the humidity fluctuation is from 35% RH to 50% RH, careful attention should be paid to the wavelength difference. The performance of the phase sta-

Content from this work may be used under the terms of the CC BY 3.0 licence (© 2018). Any distribution of this work must maintain attribution to the author(s), title of the work, publisher, and DOI.

ISBN: 978-3-95450-194-6 ISSN: 2226-0366 doi:10.18429/JACoW-LINAC2018-MOPO107

Content from this work may be used under the terms of the CC BY 3.0 licence (© 2018). Any distribution of this work must maintain attribution to the author(s), title of the work, publisher, and DOI.

bilization system is limited due to the wavelength difference of the forward and backward line in the phase stabilization system.

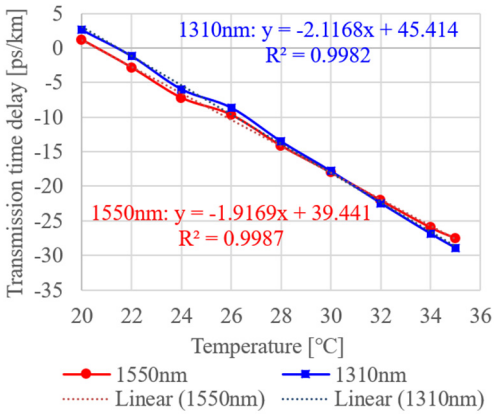


Figure 4: Transmission time delay temperature coefficient of PSOF.

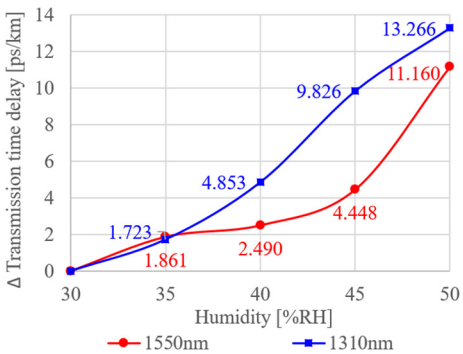


Figure 5: Transmission time delay difference of the PSOF from 30% RH to 50% RH.

FEEDBACK PERFORMANCE

In order to evaluate the performance of the phase stabilization system, a feedback test was performed in the laboratory. The same 120 m PSOF used for experimental measurement is used as the simulated transmission line. This PSOF is placed inside the temperature and humidity-controlled chamber (THC). All the feedback system including the VODL, WDM, E/O, and O/E are temperature stabilized in the chamber (TC). The temperature inside the THC was then decreased from 30 □ to 20 □ in 4 hours and the humidity was stabilized at 40% RH. The phase drift of the transmitted and returned signals depend on the temperature in the THC. Without feedback, the phase difference (feedback phase) between the returned signal and REF is 5.5°. Figure 6 shows the long-term phase stability of the returned signal with feedback control. It is observed that the feedback phase is compressed from 5.6° to 0.05° in the red solid box. However, some noise (in red dashed circle) appeared. To date, the origin of this noise in unknown and further study is necessary. Figure 7 shows the phase stability of the transmitted signal with feedback control. Although the feedback phase is controlled within 50 fs at 2856 MHz, the transmitted phase still depends on the temperature in the THC. Part of the residual phase drift of 0.25° might be caused by the wavelength difference of the PSOF.

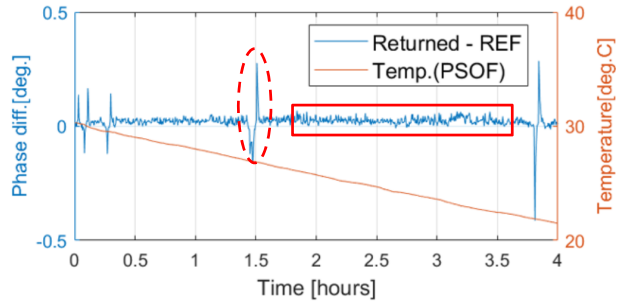


Figure 6: Long-term phase stability of the feedback phase with feedback.

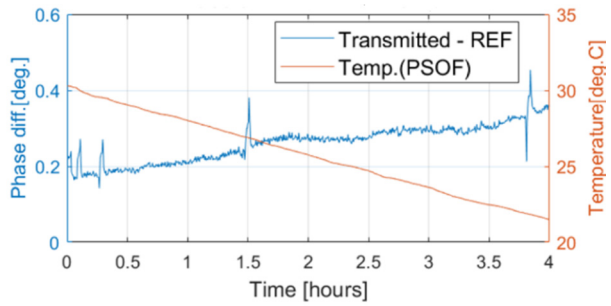


Figure 7: Phase stability of the transmitted signal.

CONCLUSION

The performance of the RF reference phase stabilization system was evaluated. The feedback phase was controlled within 50 fs for 120 m PSOF transmission. The phase drift of the transmitted signal depends on the temperature near the PSOF. This might be caused by the wavelength difference of the PSOF. A smaller wavelength difference between the forward line and backward line will be considered. The source of the noise in the feedback system will be investigated in the future in order to improve the phase stability.

REFERENCES

[1] M. Akemoto *et al.*, "The KEKB injector linac", *Prog. Theor. Exp. Phys.*, 03A002, 2013.

[2] N. Liu *et al.*, "Measurement of the RF Reference Phase Stability in the SuperKEKB Injector LINAC", in *Proc. 9th Int. Particle Accelerator Conf. (IPAC'18)*, Vancouver, BC, Canada, May 2018, paper THPML072, pp. 4815-4818, doi:10.18429/JACoW-IPAC2018-THPML073.

[3] T. Kobayashi *et al.*, "RF reference distribution system for J-PARC linac", *Nucl. Instr. Meth.*, vol. 585, pp. 12-19, 2008, doi:10.1016/j.nima.2007.11.006.

[4] T. Kobayashi *et al.*, "RF reference distribution system for the 400-MeV proton linac of the KEK/JAERI joint project", in *Proc. LINAC'02*, Gyeongju, Korea, Aug. 2002, paper MO463, pp. 187-189.

[5] T. Naito *et al.*, "Development of timing distribution system with femto-second stability", in *Proc. IPAC 2011*, San Sebastian, Spain, Sep. 2011, paper MOPC146, pp. 421-423.

[6] N. Liu *et al.*, "The consideration of RF phase reference distribution system for the injector LINAC of SuperKEKB", in *Proc. 14th Annual Meeting of the Japanese Society of accelerator (PASJ'17)*, Hokkaido, Japan, Aug. 2017, paper WEP065, pp. 1015-1018.

ISBN: 978-3-95450-194-6 ISSN: 2226-0366 doi:10.18429/JACoW-LINAC2018-MOPO111

DEVELOPMENT OF NEW LLRF SYSTEM AT THE J-PARC LINAC

K. Futatsukawa*, Z. Fang, Y. Fukui, KEK, Ibaraki, Japan
S. Shinozaki, JAEA, Ibaraki, Japan
Y .Sato Nippon Advanced Technology Co.,Ltd., Ibaraki, Japan

Abstract

In the Low-Level RF (LLRF) system of the J-PARC linac, the digital feedback (DFB) and the digital feedforward (DFF) were adopted to meet the requirement of amplitude and phase stabilities. Almost all modules of the LLRF system were operated without serious problems. However, those for the 324 MHz LLRF system have been used since the beginning of the J-PARC linac and it is concerned about increasing the failure rates. It is difficult to maintain the exact same system because some boards of the present one were discontinued. In addition, the OS and the software to develop FPGA, DSP and the server of this system are too old to be purchased. Therefore, we are starting to study the new LLRF system of the next generation. The digital board of the LLRF system with the Zynq FPGA on the µTCA.4 platform was produced and its basic performance meets the requirement.

INTRODUCTION

In the J-PARC linac, the energy of the beam injected to RCS was upgraded and the front-end was improved to achieve the design power of 1 MW [1, 2].

The twenty-four 324 MHz LLRF systems were installed to accelerate the H^- beam to 191 MeV using RFQ, DTL, and SDTL. The twenty-five 972 MHz LLRF ones were used to drive the ACS cavities of the normal-conducting and the beam is accelerated to 400 MeV for the injection to RCS. These two types of th LLRF system have the functions of DFB and DFF using the Vertex-II FPGA to satisfy the requirement of amplitude and phase stabilities (less than ±1%, less than ±1 deg. at peak-to-peak) [3–5]. However, almost all modules of the 324 MHz LLRF system, which were developed more than ten years ago, have been used since the beginning of the J-PARC linac. Therefore it is concerned about increasing the failure rates.

In the present system of DFB and DFF, the cPCI platform have been adopted and the five modules of cPCI have been used. The three digital modules consist of a FPGA/DSP board, an IO, and a CPU. The two analog ones correspond to a RF&CLK board and a Mixer&IQ-modulator. However, some of the digital boards are already discontinued and the software and the OS to develop FPGA and DSP for this system are too old to be purchased. Table 1 shows the discontinued boards and too old development environment on the LLRF system of the J-PARC linac.

Therefore, we are starting to study the new LLRF system of the next generation.

Table 1: Agenda of the Problems and Too Old Development Environment on the J-PARC LLRF System

FPGA module	discontinued
DSP module	discontinued
CPU module	discontinued, but fungible
FPGA	Xilinx ISE Ver 6.2i
DSP	TI Code Composer Studio Ver 2.1
Host program	Redhat 8.0 gcc compiler Ver 3.2
Application	python2.4, wxPython 2.6

PROTOTYPE BOARD

In the first step, a new digitizer instead of the present three digital modules of cPCI are being developed. The µTCA.4 AMC and RTM is adopted as the platform in the consideration of the future. The feature of this prototype board in Table 2.

Table 2: Feature of the New Prototype Board

platform	µTCA.4 AMC, µTCA.4 RTM
FPGA	Zynq XC7Z045-1FFG900C, QSPI FLASH-ROM 16MB, SD-card Remote Update
RAM	DDR3-SDRAM 1GB×2 (PL, PS)
OS	Xilinx Linux (EPICS-IOC)
ADC	8 ch, 16 bit, 370 MSPS (max.), BW: 800 MHz
DAC	2 ch, 16 bit, 500 MSPS
SFP	2 ports

The AMC board having Zynq FPGA, 16bit-370MSPS ADC, and 16bit-370MSPS DAC is specialized to use the bus of the µTCA.4 standard. The number of ADC becomes eight channels from four of the present system. In addition, two SFPs are mounted for the future expansions and we will be planning to be applied to acquire the all macro-pulse data and to take the J-PARC event-tag.

The RTM board has the PLL and the multiplicity of the clock using VCO. The frequency of the input TTL signal is 48 MHz and the 96 MHz clock to use in FPGA, ADC, and DAC is generated. Whether the clock is inputted from the front panel of the RTM module or from the RF-backplane of µTCA.4 can be selected by the jumper pin. The eight input channels just go through to the µTCA.4 AMC ADCs.

The shelf of µTCA.4 with the bus and the RF-backplane is not used in the first step and the µTCA.4 AMC and RTM are installed to a box with a power supply. The ARM on the Zynq FPGA with linux installed is used as the communication tools instead of a CPU board. Figure 1 shows the block

* kenta.futatsukawa@kek.jp

Content from this work may be used under the terms of the CC BY 3.0 licence (© 2018). Any distribution of this work must maintain attribution to the author(s), title of the work, publisher, and DOI.

ISBN: 978-3-95450-194-6 ISSN: 2226-0366 doi:10.18429/JACoW-LINAC2018-MOPO111

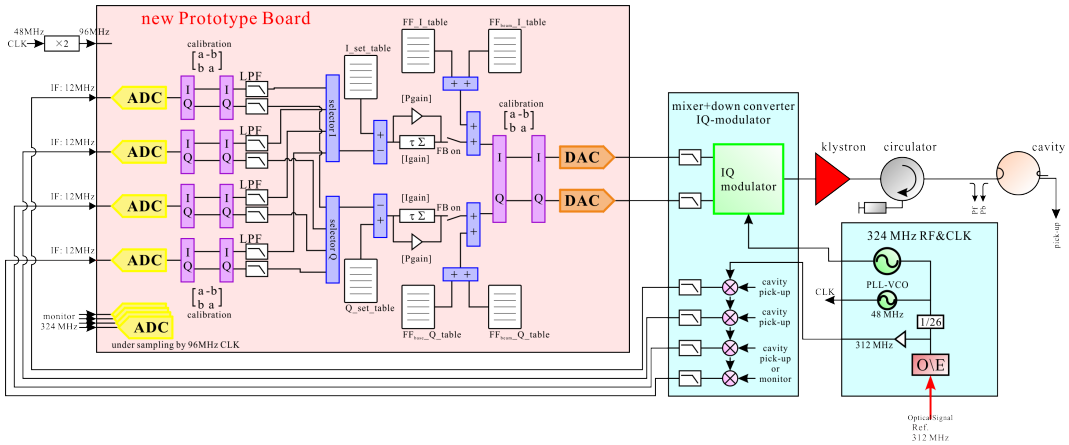


Figure 1: Block diagram of the new prototype board. The red hatching region is the new prototype board, and the modules of the sky blue region, RF&CLK board and mixer&IQ-modulator, of the present cPCI are used in the first step.

diagram of this prototype system. The algorithm of FPGA is almost same as that of the present cPCI system. The IF signals using the present mixer and downconverter are measured by ADC1 to 4 and the 324 MHz RF are monitored using ADC5 to 8 by the direct-sampling.

In the next stage, we would like to develop an analog board of a μTCA.4 RTM.

CROSS-TALK

When the signal was inputted to a certain ADC channel, the separation level of the other channels (cross-talk) was measured as shown in Fig. 2. If a channel of ADC1 to 4 have the 12 MHz RF input signal, the cross-talk was estimated to less than −80 dB in the every channels. On the other hand, the 324 MHz RF signal is inputted to ADC5, 6, and 7[1] which channel is used by direct-sampling method, the −50 dB cross-talk level was obtained in the worst case. It is seen as the cause of the RF characteristic of the zone3 connector between the AMC board and the RTM. However, even in this case, this cross-talk level against ADC1 to 4 using in DFB was less than −80 dB and it is not serious problem.

AMPLITUDE AND PHASE STABILITIES

The stabilities of amplitude and phase in a macro-pulse were measured in the condition using DFB for only ADC1 as shown in Fig. 3. The ADC1 and ADC2 channels using a down-converter and measuring an IF signal were used in the DFB and those stabilities are highly significant. The peak-to-peak values of amplitude and phase in Fig. 3(a) and (b) were archived to ±0.14% and ±0.07 deg., respectively. These results are less than those of the present system and enough to meet our requirement (less than ±1%, less than ±1 deg. at peak-to-peak). In the case of (c) ADC5 using the direct-sampling method and utilized just as a monitor, those were obtained to ±0.37% and ±0.45 deg., respectively.

[1] Since the ADC8 channel was broken, the cross-talk level could not be investigated.

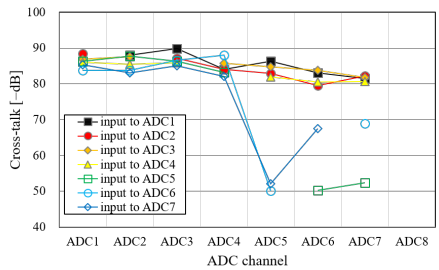


Figure 2: Cross-talk level in the new board. The −50 dB cross-talk level was obtained in the case of the 324 MHz RF signal inputted to ADC5 to 7. However, the ADC1 to 4 channels for the use of DFB were estimated to have the insignificant effect.

Figure 4 shows the frequency components of the ADC amplitudes calculated by fast Fourier transform, FFT. The color lines means the difference of the ADC sampling. There is not an especial spurious and it is a positive result.

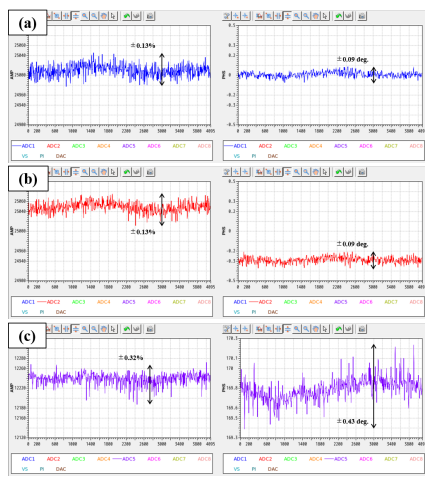


Figure 3: Stabilities of amplitude and phase for (a) ADC1 channel, (b) ADC2, and (c) ADC5 with the condition of DFB using ADC1.

Content from this work may be used under the terms of the CC BY 3.0 licence (© 2018). Any distribution of this work must maintain attribution to the author(s), title of the work, publisher, and DOI.

ISBN: 978-3-95450-194-6 ISSN: 2226-0366 doi:10.18429/JACoW-LINAC2018-MOPO111

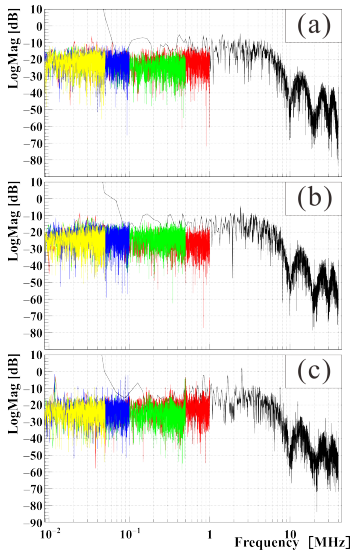


Figure 4: FFT results of (a) ADC1 channel, (b) ADC2, and (c) ADC5 with the condition of DFB using ADC1.

PHASE NOISE

The new RTM board plays a role of the frequency multiplier and generates the 96 MHz clock. Figure 5 shows the phase noises of the 48 MHz input signal and the generated 96 MHz clock measured using the signal source analyzer, Agilent Technologies E5052B. The jitter values of each RF, which are the integral calculation from 10 Hz to 1 MHz, were obtained to 19.4 mdeg. and 26.8 mdeg., respectively. These values were sufficiently smaller than the requirement of the RF clock system (<0.3 deg.).

FUTURE PLAN

The latency of this prototype board was estimated to 1.385 µs. It comes from the high-speed serial communication between ADC and FPGA (JESD204B), which is 1.1875 µs (114 clk at 96 MHz) already after adjusting the elastic buffer. This latency will be causes the increment of the FB-loop delay and decrement of the stability margin. Therefore, the sampling clock will be improved to be 240 MHz from 96 MHz and the latency of the communication process will be reduced to about 0.718 µs.

The beam current of 60 mA will be planned [2] and the beam-loading will be increased. Therefore, we are preparing for the flexible DFF and exploring the possibilities of adaptive DFF [6].

CONCLUSION

In the J-PARC linac, Almost all modules of the LLRF system were operated without serious problems. However, those for the 324 MHz LLRF system have been used since the beginning of the J-PARC linac and it is concerned about increasing the failure rates. We are starting the development of the new digitizer.

The prototype digitizer having the µTCA.4 platform was produced and its performance was estimated. The cross-talk

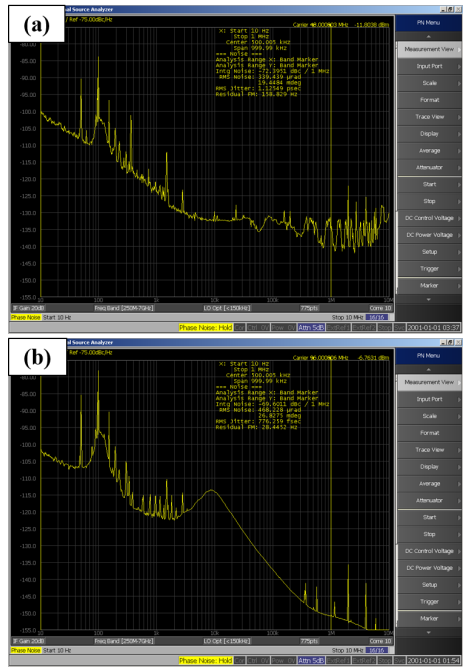


Figure 5: Phase noise of (a) the 48 MHz input signal and (b) the 96 MHz generated clock. The jitter values of the input signal and the clock were obtained to 19.4 mdeg. and 26.8 mdeg., respectively.

level is obtained to less than −80 dB for ADC1 to 4 using for DFB. The peak-to-peak values of amplitude and phase in ADC1 to 4 were archived to ±0.14% and ±0.07 deg., respectively. The phase noises for the 48 MHz input signal and the generated 96 MHz clock were measured and the calculated jitter values were obtained to 19.4 mdeg. and 26.8 mdeg., respectively. These results satisfy our requirement of the LLRF system.

REFERENCES

[1] Y. Yamazaki for J-PARC accelerator design team, Accelerator technical design report for J-PARC KEK Report 2002-13 and JAERI-Tech 2003-44; http//www.j-parc.jp

[2] H. Oguri *et al.*, "Approaching to High Power Operation of J-PARC Accelerator", in *Proc. LINAC'18*, Beijing, China, Sep 2018. doi:10.18429/JACoW-LINAC2018-MO1P02

[3] S. Michizono *et al.*, "Digital Feedback System for J-PARC Linac RF Source", in *Proc. LINAC'04*, Lübeck, Germany, Aug 2004, pp. 742–744.

[4] S. Anami *et al.*, "Control of the Low Level RF System for the J-PARC Linac", in *Proc. LINAC'04*, Lübeck, Germany, Aug 2004, pp. 739–741.

[5] Z. Fang *et al.*, "Auto-tuning systems for J-PARC LINAC RF cavities", *Nucl. Instr. Meth*, A, vol. 767, p. 135-145, 2014.

[6] S. Li *et al.*, "Adaptive feedforwad control design based on simulink for J-PARC linac LLRF system", in *Proc. IPAC'18*, Vancouver, BC, Canada, Apr-May 2018, pp. 2187–2189, 2018. doi:10.18429/JACoW-IPAC2018-WEPAL017

Content from this work may be used under the terms of the CC BY 3.0 licence (© 2018). Any distribution of this work must maintain attribution to the author(s), title of the work, publisher, and DOI.

ISBN: 978-3-95450-194-6 ISSN: 2226-0366 doi:10.18429/JACoW-LINAC2018-MOPO115

CEBAF PHOTO GUN RF SYSTEM*

T. Plawski†, R. Bachimanchi, M. Diaz, S. Higgins, C. Hovater, C. Mounts, D. Seidman,
Jefferson Lab, Newport News 23606, VA, USA

Abstract

During the CEBAF 12 GeV Upgrade at Jefferson Lab, a fourth experimental hall, "D", was added to the existing three halls. To produce four beams and deliver them to all halls concurrently requires new frequencies and a new timing pattern of the electron bunches. Since a photo-gun is used to produce electron bunches, the gun's drive laser pulses need to be synchronized with the required bunch rate frequencies of 499 MHz or 249.5 MHz. To meet these new operational requirements, a new RF system has been proposed.

Very specific requirement of dual frequency operation prohibited us from using a typical LLRF system. Limited budget and time forced us to use commercial off-the-shelf digital platforms. The commercial boards we chose include, the Texas Instruments FPGA board, the high-speed 8-Channel, 14-Bit ADC board, and a 4-Channel, 16-Bit DAC board. The DAC board includes the clock generator for clocking ADCs, DACs and the FPGA. A custom designed RF transceiver section provides the RF to the digitizer and vice versa for the DACs. The Gun Laser RF system has been designed, built, and recently commissioned in the CEBAF Injector. This paper will detail the design and report on commissioning activities.

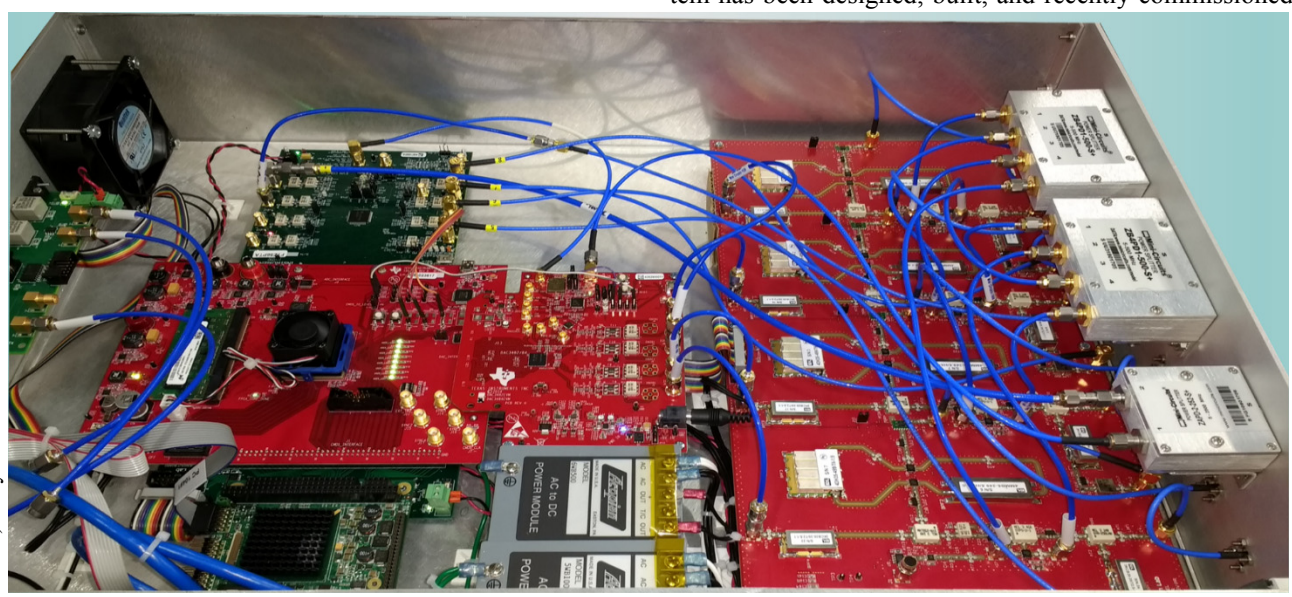


Figure 1: LLRF Chassis.

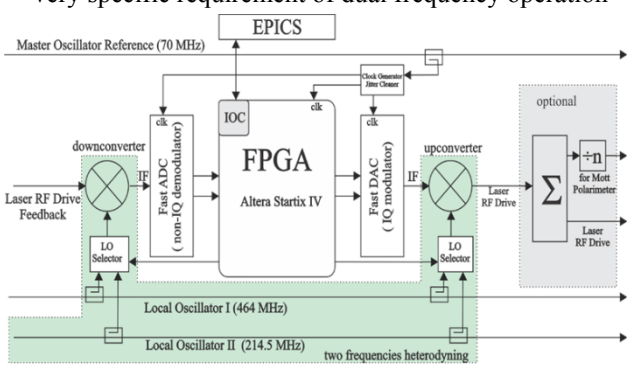


Figure 2: One channel of the Laser LLRF.

SYSTEM DESCRIPTION

Laser RF System consists of four RF receivers and four RF transmitters (see Fig. 1) allowing independent operation of four RF driven lasers [1]. The RF front-end section uses heterodyning in order to obtain 35 MHz IF signal (see Fig. 2). Depending on the required frequency of operation (499 MHz or 249.5 MHz), one of the two local oscillator (LO) frequencies (464 MHz or 214.5 MHz) can be selected. The digital section of the system contains an Altera Stratix IV FPGA, 1 GB memory and support up to 1.5 GSPS LVDS I/O rates for both ADCs and DACs (see Fig. 3). This board was built by Texas Instrument as a pattern generator/data capture system, and is compatible with multiple ADC and DAC boards from this manufacturer.

The ADS5294EVM board is an eight-channel, 14-bit serial LVDS interface, analog-to-digital converter with sampling speeds up to 80 MSPSs. that can be connected directly to the FPGA board. The DAC3484EVM is a DAC board that allows a user to operate a four-channel, ultra-

*Authored by JSA, LLC under U.S. DOE Contract DE-AC05- 06OR23177 and DE-SC0005264
† email: plawski@jlab.org

Content from this work may be used under the terms of the CC BY 3.0 licence (© 2018). Any distribution of this work must maintain attribution to the author(s), title of the work, publisher, and DOI.

ISBN: 978-3-95450-194-6 ISSN: 2226-0366 doi:10.18429/JACoW-LINAC2018-MOPO115

low power, 16-bit, 1.25 GSPS DAC3484 digital-to-analog converter with 16-bit or 8-bit wide DDR LVDS data input, integrated 2x/4x/8x/16x interpolation filters, 32-bit NCO and PLL. We are using the DAC board's CDCE62005 based PLL system to generate clock signals for ADC and FPGA boards as well. For both boards, data and clock are sent through HSMC (High Speed Mezzanine Card) connectors.

The purpose of the digital section of RF is to regulate the magnitude and phase of the measured RF signal to a controlled set point. The input to the digital section is from an analog-to-digital converter that is driven by the down converted IF signal (35 MHz) which is clocked at 56 MHz (IQ sampling). The digital controller then compares this to the set points and processes the error signal such that a correction can be applied to the concerned signals. The correction signal from the FPGA drives a single digital to analog converter running at 140 MHz and then is up-converted to the required frequency. Although the presented RF system has a bandwidth of several MHz, feedback bandwidth will be limited down to a few kHz by digital filtering.

System is connected to the accelerator network via a PC104 operating as an EPICS input-output computer (IOC).

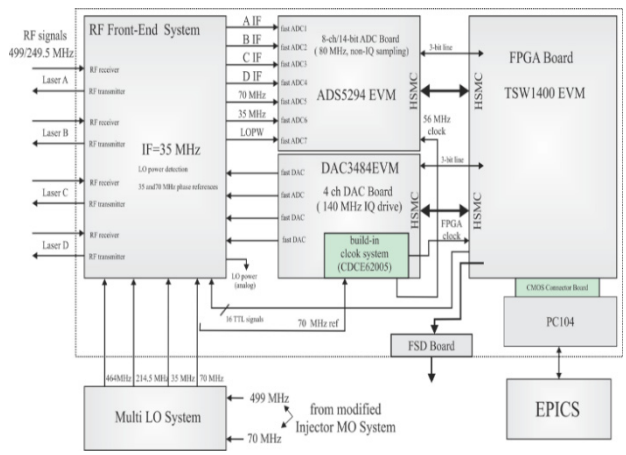


Figure 3: Block diagram of the system.

ADC/DAC BOARD CONFIGURATION

In order to send the register configuration to ADC and DAC boards without using the PC-USB interface (as expected by manufacturer), the TSW1400EVM board was modified in order to add six signal lines. Three of these lines are used to configure the ADC board and another three for the PLL clock configuration.

As it was already mentioned, for clock generation we use a CDCE62005 Clock Generator, Jitter Cleaner with Integrated Dual VCOs installed on the DAC board. RMS noise of this generator is typically below 1ps. We did consider to add alternative ultralow noise PLL system but bench testing of the existing one shows adequate noise performance.

PLL settings provides configuration of the on-chip PLL and is stored in EEPROM. This allows system to resume appropriate operation after power cycle.

BEAM FAST SHUTDOWN

Two out of eight ADC channels (ADS5294EVM) are used for continuous phase monitoring of two external reference signals: 70 and 35 MHz. In the case of a phase disturbances larger than 5°, the system interrupts beam delivery via the fast shutdown (FSD) system. The reason we monitor these signals is possibility of phase ambiguity produced by frequency divider used in Local Oscillator System (shown in Fig. 3).

OPERATIONAL EXPERIENCE

Figure 4 shows the four [2] gun operation screen. Operators can set amplitude, phase and one of the two possible beam frequencies for laser RF drive signal. Changing the frequency requires the RF signal to be off. EPICS expert level screens with detailed diagnostic and configuration tools can be launched from the operator screen. Selected signals are stored in the accelerator archiver and can be used off-line for system troubleshooting.

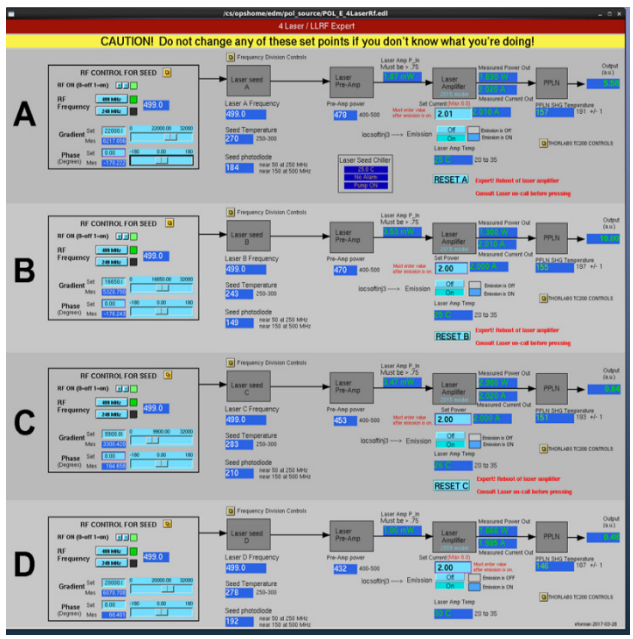


Figure 4: Operation screen.

In situ performance measurements were made during system commissioning. There was no measureable phase drift between beams over the course of several days. All RF signal spurs remained below -50 dBc, well below requested -40 dBc. Figure 5 shows chopper cavity viewers with four beams running at 249.5 MHz. By using one beam and sweeping the phase setpoint from -180 to +180 deg, the beam makes two successive circuits on the 499 MHz (2ns) chopper view screen.

Content from this work may be used under the terms of the CC BY 3.0 licence (© 2018). Any distribution of this work must maintain attribution to the author(s), title of the work, publisher, and DOI.

ISBN: 978-3-95450-194-6 ISSN: 2226-0366 doi:10.18429/JACoW-LINAC2018-MOPO115

Content from this work may be used under the terms of the CC BY 3.0 licence (© 2018). Any distribution of this work must maintain attribution to the author(s), title of the work, publisher, and DOI.



Figure 5: Four beams visible on the chopper viewer.

SUMMARY

This project is a good use of single unit production based on "off-the shelf" available evaluation modules rather than in-house design. The only custom design part remains the RF transceiver. By following this strategy we achieved significant reduction in the design effort, the cost of materials (e.g. cost of FPGA EVAL board is smaller than FPGA itself) and the delivery time.

There is no guarantee of future availability of evaluation modules, therefore purchasing additional spares is critical. There is always the possibility in the future of changing the system requirements, but by using modular product evaluation boards we have the flexibility to make future changes.

REFERENCES

[1] M. Poelker et al., "Experience with fiber based drive laser at CEBAF-Jefferson Lab and high current lifetime", *in Proc. ERL'07*, Daresbury, UK, May 2007, paper 27, pp.119

[2] R. Kazimi et al., "Source and extraction for simultaneous four-hall beam delivery system at CEBAF", in *Proc. IPAC'13*, Shanghai, China, May 2013, paper WEPF1085, pp.2896

ISBN: 978-3-95450-194-6 ISSN: 2226-0366 doi:10.18429/JACoW-LINAC2018-MOPO116

STUDY ON THE CONTROL TECHNOLOGY OF LARGE–LOAD TIME CONSTANT ACCELERATOR MAGNET POWER SUPPLY*

X. Wang†, F. L. Long, Institute of High Energy Physics, CAS, Beijing, China

Abstract

With the increasing application of power supply to industrial system, digital control system has become the mainstream of modern industrial control system. The wide application of digital control system has also led to the rapid development of digital controller. In the field of accelerator magnet power supply, the adoption of digital closed-loop control has become a trend in recent years. Due to the system's tracking and regulation characteristics, the output current will slowly track the change of the given value in the course of the given current gradually rising. When the system reaches steady state, the disturbance of the system requires the regulator to adjust at a faster rate to correct the impact of the disturbance on the system. Today's digital power supply control method mainly reflected in when load time constant is large, interference or load change, the power output is prone to overshoot or adjust the time is long, so the tracking and adjustment features cannot be met simultaneously. Therefore, this paper will study the power supply digital control technology for large - load time constant and the independent control method of tracking and regulating.

INTRODUCTION

The control algorithm of digital controller is one of the key factors that affect the performance of digital power supply. Compared to the traditional analogy power and digital power supply has the short design cycle, flexible control method, is easy to realize the modular management, to eliminate instability caused by discrete components and the characteristics of electronic jamming, so digital power source is a development trend of accelerator magnet power supply. Digital power supply control module has a great influence on the performance of the digital power supply, if digital control technology want to get further development in the digital power supply, depends on whether can achieve what we need in accelerator magnet power supply control algorithm.

Due to the tracking and regulation characteristics of the system, the output current will slowly track the change of a given value in the course of a given current. When the system reaches steady state, the disturbance of the system requires the regulator to be adjusted at a faster rate to correct the influence of the disturbance on the system. Today's digital power supply control method generally uses the traditional digital PID control algorithm [1], but poor dynamic performance of traditional PID algorithm, mainly reflected in when load time constant is large, there is interference or load change, the power output is prone to overshoot, or adjust the time is long, the tracking and adjusting performance cannot be consideration. This topic makes it possible to obtain the desired tracking behaviour (following the reference) independent of the desired regulation behaviour (rejection of a disturbance).

LOAD TIME CONSTANT

For any accelerator magnet power supply, its load characteristics are the basis of power closed-loop control. For the normal temperature magnetic we generally adopt, for example, digital proportional integral differential (PID) control as a closed loop control algorithm, and the design of the core of current loop integral time constant will be set mainly depends on the load time constant. This research institute is aimed at the load of a special kind of accelerator magnet power supply, namely the superconducting magnet load with very large time constant.

High energy particle accelerator technology has led the rapid development of superconducting technology in the past 30 years. The Fermi national accelerator laboratory (Fermi lab) in the 1980s of the construction of the TEVATRON collider particles, using the 774 for the first time in the world based on the technology of titanium niobium NbTi superconducting accelerator dipole magnets, applying NbTi superconducting technology from the laboratory into the industrialization level, to promote this technology in the civilian fields such as medical nuclear magnetic spectrometer (MRI) and so on a wide range of applications. Compared with the normal temperature magnet, the superconducting magnet can achieve the super high field strength that ordinary magnet cannot reach with a smaller volume. At the same time, due to the superconductivity of the load, its resistance is almost zero, which can greatly reduce the output voltage demand of the excitation power supply and reduce the operating cost of the accelerator excitation power system.

For example, BEPCII quadrupole magnet power supply (normal temperature magnet) and the LHC's diode of superconducting magnet power supply load [2], the time constant of the different types of load ratio on the following: time constant has the difference of several orders of magnitude. For different loads, the bandwidth and algorithm of the current closed-loop of digital controller will be different.

BEPCII quadrupole power supply load: Resistance =0.266Ω, Inductance=0.14H and Time constant τ =L/R=0.14/0.266 = 525ms.

LHC diode load: Resistance=0.8mΩ, Inductance=18H and Time constant τ=L/R=18/0.0008=22500=6.25 h.

Taking the future circular collider CEPC-SPPC project as an example, In order to deflect and focus on high-energy proton beams, the SPPC needs to install thousands of high field strong diodes and quadrupole magnets in a 100-kilometer circular tunnel in order to deflect and focus

* Work supported by IHEP
† wangxu@ihep.ac.cn

Content from this work may be used under the terms of the CC BY 3.0 licence (© 2018). Any distribution of this work must maintain attribution to the author(s), title of the work, publisher, and DOI.

ISBN: 978-3-95450-194-6 ISSN: 2226-0366 doi:10.18429/JACoW-LINAC2018-MOPO116

Content from this work may be used under the terms of the CC BY 3.0 licence (© 2018). Any distribution of this work must maintain attribution to the author(s), title of the work, publisher, and DOI.

on high-energy proton beams. The effective aperture of these magnets is 40~50mm, the field intensity of the dipole magnet is as high as 12~24 T, and the field uniformity needs to be 10 to the minus fourth magnitude within 2/3 of the aperture. Such high field strength and performance demand make high field accelerator magnet technology one of the most challenging technical requirements in SPPC design. Therefore, the research on the power digital control technology of this type of load is one of the key technologies in the future research of accelerator power system based on superconducting magnet load.

THE CLOSED LOOP ALGORITHM

Authors are requested to go over the following checklist for electronic publication: At present, the accelerator of using digital control power source such as Swiss light source (SLS) adopts PID control scheme (see Fig. 1). In recent years, the newly built accelerator in China, its magnet power supply basically adopts the digital PID method to complete the closed-loop control [3], as shown in Eq. (1).

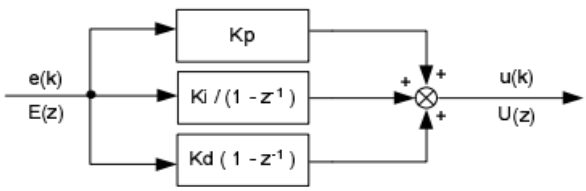


Figure 1: PID algorithm block diagram.

$$u_p(k)=K_p e(k)$$
$$u_i(k)=K_i \sum_{j=0}^{k} e(j) \quad (1)$$
$$u_i(k)=K_d[e(k)-e(k-1)]$$

PID control has been widely applied because of its simple structure, parameters, easy setting, characteristics such as good robustness as well as the development of mature, the right to adjust the three parameters of PID control can obtain good control effect. Because of when no-load model of the power supply similar to a second order critical link of oscillation, the existence of the integral term makes the phase lag. On the premise of guarantee the system stability, must limit proportion coefficient, namely reduces the dynamic performance of the control system. The disadvantage of PID control technology is that it can't effectively suppress the disturbance caused by nonlinear load, and the system's stability is limited, so it can't be tracked without directional tracking. In accelerator magnet power supply closed loop control, because the PID parameters is easy to adjust and mainly static power, and the dynamic response of the power supply without strict requirements, so for ordinary magnet load digital power supply usually use PID control algorithm.

In the large hadron collider (LHC) high-power superconducting magnet power supply [4], due to the strict requirements for beam damage, the current of each power supply in the process of rising can accurate control, and can quickly response to the disturbance. An independent control algorithm with closed-loop tracking and adjusting characteristics is adopted to overcome the shortcomings of PID controller which cannot be tracked and adjusted simultaneously (see Fig. 2 and Fig. 3).

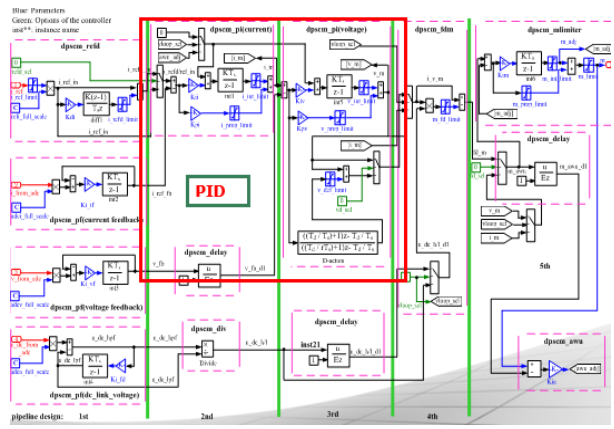


Figure 2: Flow chart of DPSCM closed-loop algorithm.

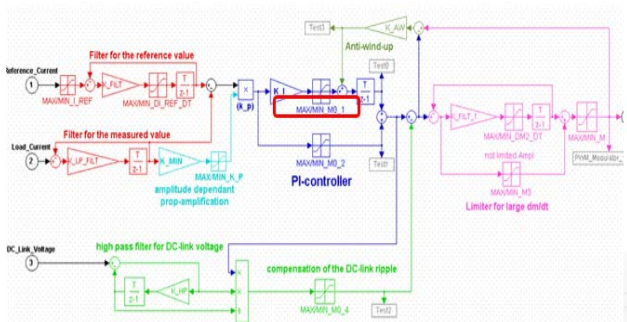


Figure 3: The closed-loop control block diagram of digital controller DPC of Swiss light source.

RST CONTROLLER DESIGN

The general structure of RST regulation is divided into three parts: forward control polynomial module S(z-1), feedback polynomial module R(z-1) and precompensation polynomial module T(z-1) (see Fig. 4).

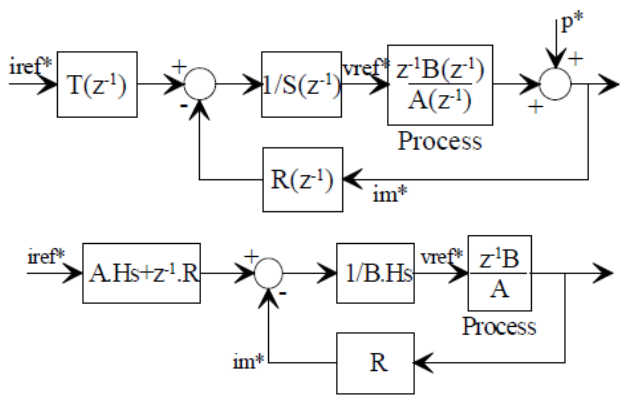


Figure 4: RST controller block diagram.

The tracking transfer function is shown in Eq. (2):

$$\frac{r(k)}{y(k)}=\frac{z^{-d}\cdot B\cdot T}{A\cdot S+R\cdot B\cdot z^{-d}} \quad (2)$$

ISBN: 978-3-95450-194-6 ISSN: 2226-0366 doi:10.18429/JACoW-LINAC2018-MOPO116

And the regulation transfer function is shown in Eq. (3):

$$\frac{y(k)}{P}=\frac{A\cdot S}{A\cdot S+R\cdot B\cdot z^{-d}} \quad (3)$$

The RST controller makes it possible to obtain the desired tracking behaviour (following the reference) independent of the desired regulation behaviour (rejection of a disturbance) [5]. The RST control can be evaluated by the "Tracking and Regulation with Independent Objectives" method (R and S give the regulation behaviour and T gives the tracking behaviour) (see Fig. 5).

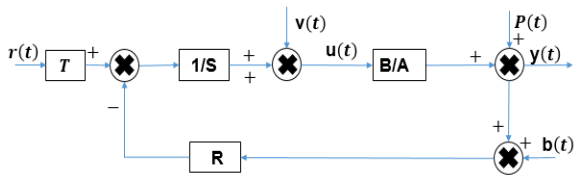


Figure 5: Tracking and regulation with independent objec-tives.

Interference and output ($\mathbf{p} \rightarrow \boldsymbol{y}$) transfer function is shown in Eq. (4):

$$S_{yp}(z^{-1})=\frac{A(z^{-1})S(z^{-1})}{A(z^{-1})S(z^{-1})+B(z^{-1})R(z^{-1})} \quad (4)$$

Interference and input ($\mathbf{p} \rightarrow \boldsymbol{u}$) transfer function is shown in Eq. (5):

$$S_{up}(z^{-1})=\frac{-A(z^{-1})R(z^{-1})}{A(z^{-1})S(z^{-1})+B(z^{-1})R(z^{-1})} \quad (5)$$

Noise and output ($\boldsymbol{b} \rightarrow \boldsymbol{y}$) transfer function is shown in Eq. (6):

$$S_{yb}(z^{-1})=\frac{-B(z^{-1})R(z^{-1})}{A(z^{-1})S(z^{-1})+B(z^{-1})R(z^{-1})} \quad (6)$$

Input interference and output ($\mathbf{v} \rightarrow \boldsymbol{y}$) transfer function is shown in Eq. (7):

$$S_{yv}(z^{-1})=\frac{B(z^{-1})S(z^{-1})}{A(z^{-1})S(z^{-1})+B(z^{-1})R(z^{-1})} \quad (7)$$

SIMULATION

The accelerator, which requires very strict beam damage, is also more stringent for accurate current control. Taking the large hadron collider as an example, the superconducting diode magnet is 27 km, working at a low temperature environment of 1.9 K, and the excitation current is strong to 13 kA, resulting in a curved magnetic field of 8.4 T. These thousands of magnet currents must be precisely controlled to reduce the beam loss. Because even a very small beam loss can generate enough energy to cause a superconducting coil to lose its superposition. Therefore, the precise control of the dynamic process is the basic requirement of the LHC superconducting magnet power supply [6]. To evaluate the synthesis and the performance of the RST controller, a digital simulation has been performed using MATLAB software (see Fig. 6 and Fig. 7).

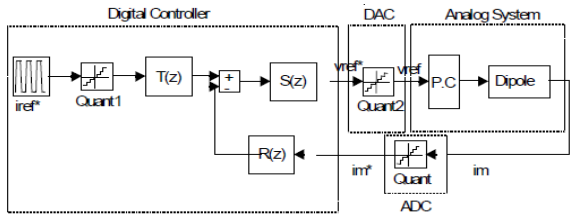


Figure 6: The MATLAB simulation diagram.

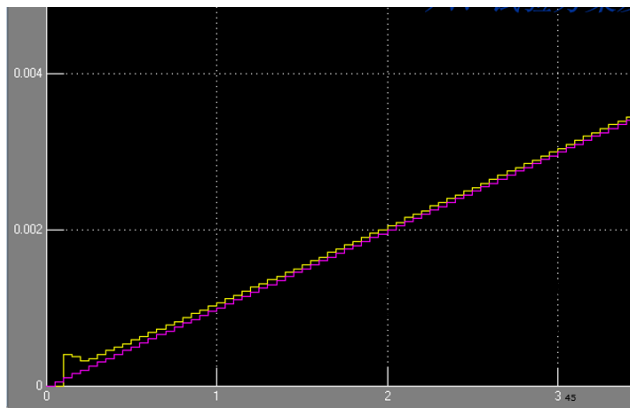


Figure 7: The simulation results.

CONCLUSION

As a result of the tests completed to date, the digital loop using RST controller seems to fulfil all the performance requirements of the LHC (no overshoot, static or lagging error below 1ppm). The robustness of the algorithm avoids the use of more complex adaptive control. The following research mainly focuses on the parameter calculation of RST algorithm.

ACKNOWLEDGEMENT

The authors thank the Accelerator Centre of Institute of High Energy Physics for financial support. Also thanks to the experimental conditions and experimental guidance provided by the power supply group of IHEP.

REFERENCES

[1]. I. Landau, "System Identification and Control Design", Prentice-Hall International, 1990.

[2]. RDL. Calle *et al.*, "All-Digital Control and Regulation System for SCR Converters with Active Filter", EP2 Forum98, Power Technology in European Physics Research, Oct. 1998, CERN-PS-98-056-PO.

[3]. I. Barnett *et al.*, "A Strategy for Controlling the LHC Magnet Currents", in *Proc. EPAC'96*, Jun. 1996, paper MOP020G, p. 2317.

[4]. I. Barnett *et al.*, "Developments in the high precision control of magnet currents for LHC", in *Proc. PAC'99*, New York, USA, p. 3743.

[5]. P. Proud lock, "Electrical Powering Strategy of LHC", in *Proc. EPAC'96*, Jun. 1996, paper MOP021G.

[6]. Q. King *et al.*, "The All-digital Approach to LHC Power Converter Current Control", in *Proc. ICALEPCS'01*, San Jose, CA, USA, paper THBT004, pp. 453-455.

Content from this work may be used under the terms of the CC BY 3.0 licence (© 2018). Any distribution of this work must maintain attribution to the author(s), title of the work, publisher, and DOI.

ISBN: 978-3-95450-194-6 ISSN: 2226-0366 doi:10.18429/JACoW-LINAC2018-MOPO118

OPTIMIZED DESIGN FOR A COMPACT LINAC WITH COLLINEAR ABSORBING LOADS AT THE HUST FEL-THz

J. Jiang, T. N. Hu*, G.Y. Feng, Y. Lu, X. D. Tu, Y. Q. Xiong,
Huazhong University of Science & Technology, 430074 Wuhan, China
Y. J. Pei, National Synchrotron Radiation Laboratory, USTC, Hefei, China

Abstract

To meet the requirement of miniaturization for high power THz radiation in the field of commercial and civil use, RF Linacs have been applied widely as beam injectors, and the Linac with collinear absorbing loads reveals the potential to achieve a tradeoff between performance and compactness. Under overall consideration of systematic conflicts, optimization choices for such Linacs involving power absorbing ability, accelerating efficiency, as well as beamline length were described in this context. Meanwhile, cold testing has been conducted to verify design parameters for the collinear absorbing loads. Furthermore, elaborated calculation of thermal power loss and integrated helical water channel cooling has been performed for the 14MeV Linac with collinear absorbing loads installed on the HUST FEL-THz, and online experiments demonstrated that both the accelerating efficiency and the water cooling performance fulfilled operation demands.

INTRODUCTION

In recent decades, a lot of attention has been paid on compact high-power free-electron laser (FEL)-based terahertz (THz) radiation sources, which can be applied to the fields of security, communications and other scientific fields [1,2]. Since Linac-based FEL can provide above megawatt (MW) peak power radiation with the spectrum covering entire THz band [3,4], efforts have been made to reduce the facility scale and simplify peripheral systems.

Huazhong University of Science and Technology has built a porotype of compact FEL-THz facility [5], which has chosen a room-temperature accelerator to provide high-quality electron beams. Similar as typical beam injectors, the HUST-FEL-THz injector consists of a RF gun and a Linac, and the latter is set to boost the beam extracted by the RF gun to an energy of 14MeV. In order to absorb remnant RF power, an output coupler is commonly installed at the termination of the Linac. Since collinear load instead of traditional waveguide load is advanced for Linac miniaturization [6] and field symmetry, design of the beam injector based on the acceleration section with collinear loads, which aim at implementing layout compactness and high performance, will be introduced in this context.

DESIGN FOR THE LINAC WITH COLLINEAR LOAD

The HUST-FEL-THz Injector

At the HUST-FEL-THz, the booster Linac, which aims at accelerating the beams and driving them out of space-charge-dominated range, has been designed around disk-loaded constant gradient travelling-wave structures. According to the design demands of THz radiation [5], the driving beams should have the energy of about 14 MeV, so that a normal SLAC-like Linac has been adopted to provide adequate acceleration fields. Furthermore, since the beams extracted by the RF gun is still subject to space-charge effects before and in the Linac, as a common solution for emittance compensation, magnetic coils have wrapped around the Linac to provide focusing fields. According to the beam dynamic simulation in physical design of the HUST-FEL-THz injector [7], to obtain sufficient magnetic field strength and adjustment flexibility, a short lens has been placed downstream of the RF gun, and seven pancake-like solenoids cast with epoxy resin have surrounded the Linac. As suggested by Ref. 6, the collinear load based on FeSiAl material has been applied at the Linac to absorb the remnant RF power, so that the sizes of the focusing coils can be reduced. Moreover, comparing with traditional output coupler and waveguide absorbing load, the collinear load is perfectly symmetric which avoids transverse excitation of the beam and intrinsically does not contribute to any emittance growth.

According to the required THz radiation power of the HUST-FEL-THz, the injector must have the ability to work under the beam energy of 14 MeV, the repetition frequency of 50 Hz and the macro-pulse width of 4 μs. In order to accelerate the beam to 14 MeV within a distance as short as possible, a 19-cell Linac with the constant gradient of about 20.77 MV/m in each cell has been adopted, and a 4-cell collinear load has been set subsequently. Thus, the peak value of input RF power should be 16 MW. For a single load cavity, the input power (P_{in}) and transmitted power (P_{out}) is related by the following relation

$$P_{out} = P_{in} \cdot e^{-2\alpha D} \tag{1}$$

where α is attenuation constant, D is cavity length.

Since the calculated remnant power at the termination of the 14 MeV Linac is 12.10 MW and 5.54 MW with the beam turned-off and turned-on respectively. According to the principle of distribution of average power, to make the

*Corresponding author.
E-mail addresses: TongningHu@hust.edu.cn (T.N. Hu)

Content from this work may be used under the terms of the CC BY 3.0 licence (© 2018). Any distribution of this work must maintain attribution to the author(s), title of the work, publisher, and DOI.

ISBN: 978-3-95450-194-6 ISSN: 2226-0366 doi:10.18429/JACoW-LINAC2018-MOPO118

remnant RF power be dissipated in the last 4 cells, the collinear load must be designed to have a one-way attenuation of -20 dB. Corresponding power allocations for each cell of the total 24-cell Linac are illustrated in Fig. 1(a), while magnetic field distribution along the Linac is shown in Fig. 1(b).

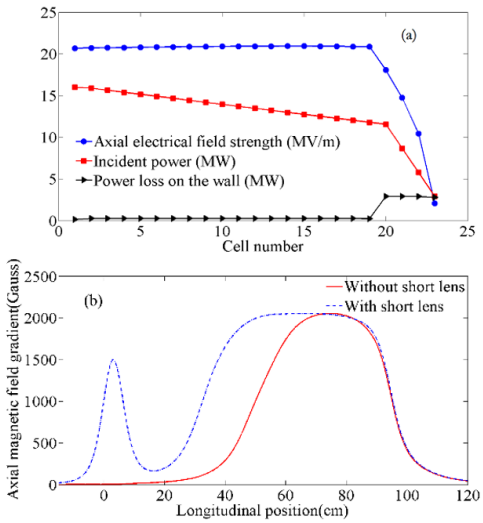


Figure 1: (a) Power and acceleration field distributions along Cell number in the Linac; (b) magnetic field distributions of the focusing coils.

Design of Collinear Load Section

Previous researches [6] show that FeSiAl alloy, the electromagnetic parameters of which are measured to be ε=114.15-16.96i, μ=1.21-1.90i, is suitable for the case of high remnant power. Moreover, when the Q-factor of the load cavity is small, the FeSiAl alloy only needs to be coated on the cavity ring.

From Eq. (1) the attenuation factor α is obtained, and the Q-factor of the load cells can be further calculated by the following formula,

$$Q = \frac{\omega}{2V_g\alpha} \tag{2}$$

where V_g is group velocity and is calculated by

$$V_g = \frac{\mathrm{d}\omega}{\mathrm{d}\beta} = 2\pi D \cdot \frac{\mathrm{d}f}{\mathrm{d}\phi} \cdot \tag{3}$$

The upper df is the change of the working frequency of the cavity, and the dΦ is the phase shift of the adjacent accelerating cavity. The performance parameters of the collinear absorbing load under the equal loss power allocation principle obtained by the above steps are shown in Table 1. After determining the Q-factor, thickness and width of the coating material in each cell are determined according to the inverse proportional relationship between Q-factor and the coating volume of FeSiAl alloy material. Then, according to the negative linear relationship between resonant frequency and cavity diameter b, the resonant frequency of the modified cavity is simulated by HFSS Eigen-mode solution to ensure that the resonant frequency is kept at 2856 MHz.

Table 1: Parameters of Load Cavities under the Principle of Distribution of Average Power

Cavity No.	P_{loss}(kW)	α	Q
1	274.29	4.063	622.07
2	274.29	5.699	443.49
3	274.29	9.624	262.62
4	274.29	46.40	54.473

Corrections Considering Thermal Load

Since most of the heat is absorbed by the FeSiAl material on the copper substrate of the cavity, a water cooling system is needed to solve the temperature rise problem to ensure that the accelerator works at about 30□. The fluid-solid coupling thermal characteristics of the integrated water-cooling system with accelerating tube and collinear load are analyzed by ANSYS. It is found that the temperature field distribution of each cell of the collinear load is not uniform under the principle of distribution of average power and the thermal deformation is also different. That is, the power distribution scheme needs to be optimized. The final simulation results for the optimized power distribution show that the temperature distribution of the four cavities is between 30~32□ and the frequency offset of the cavities is within 30 kHz (Table 2), under the condition that the accelerator working around 30±0.5□. The actual one-way attenuation of the collinear load is about -23.55dB.

Table 2: Temperature Distribution and Frequency Offset of Load Cavities

Cavity No.	Temperature Range(□)	Δb_{avg}(μm)	Freq Pre(MHz)	Freq After(MHz)	Δf(kHz)
1	30.064~31.931	0.16	2856.042	2856.013	-29
2	30.523~32.003	0.29	2856.027	2856.003	-24
3	30.710~32.014	0.36	2856.014	2855.996	-18
4	30.427~32.015	0.22	2856.023	2856.011	-12

Content from this work may be used under the terms of the CC BY 3.0 licence (© 2018). Any distribution of this work must maintain attribution to the author(s), title of the work, publisher, and DOI.

ISBN: 978-3-95450-194-6 ISSN: 2226-0366 doi:10.18429/JACoW-LINAC2018-MOPO118

Table 3: Corrected Collinear Load Parameters after considering Machining Accuracy Error

Cavity No.	b(mm)	m_l(mm)	m_t(mm)	Q	α	P_{loss}(kW)
1	40.834	3.5	0.12	702.99	3.595	246.52
2	40.833	6.0	0.12	418.8	6.035	296.85
3	40.828	10.5	0.12	242.39	10.43	292.58
4	40.810	14.0	0.47	44.218	57.16	267.32

In addition, due to the measurement error and machining accuracy limitations, especially the thickness of FeSiAl alloy coating is about 0.1 mm, so it cannot reach the design value. The actual structure of the load cavity needs to be adjusted on the premise that the microwave physical parameters (such as attenuation coefficient α, Q-factor and resonant frequency f) meet the requirements. The final test cavity parameters after adjustment are shown in Table 3.

EXPERIMENTAL RESULTS

We have used a 2π/3 mode standing wave resonant assembly, as illustrated in Fig. 2(a), to conduct microwave parameter measurements for the collinear load as shown in the Fig. 2(b). Obviously, four TM01 modes, 0, π/3, 2π/3 and π, can be driven in this structure. The third mode has the same field pattern and characteristics as those in the 2π/3 mode traveling-wave Linac, in which the resonant frequency is 2.856 GHz. In actual experiments, a load cavity would be chosen to replace one of the normal cavities in the resonant assembly.

In order to measure the resonant frequency f and Q-factor of the resonant assembly at 2π/3 mode, a coaxial probe connected to the Network Analyzer is used to transmit and receive signals. The resonant frequency f can be obtained by sweeping the S parameter response curve, and the corresponding frequency at the curve trough is the resonant frequency. To measure the Q-factor, the Critical-Points Method (CPM) [8] is applied to calculate the Q-factor of the resonant assembly through the Smith chart on the Network Analyzer. centred, as far as is possible:

$$Q_0 = \frac{\omega_1 + \omega_2}{2|\omega_1 - \omega_2|} \cdot |x| \approx \frac{f_1 + f_2}{2|f_1 - f|}, \text{for} |x| \approx 1 \quad (4)$$

where f_1 and f_2 are the corresponding frequencies of the reactance extreme points of the impedance circle on the Smith chart.

Because the assembly is simulated in vacuum and the actual measurement is in the atmosphere, it is necessary to correct the measurement error. The resonant frequency f is affected by the relative dielectric constant of air in atmospheric environment as well as the difference between the measuring temperature and the operating temperature of the cavity. The relationship between the frequency f_r in the atmosphere and the frequency f_0 in vacuum is mainly depend on Eq. (5),

$$f_r = \frac{f_0 + \Delta f_T}{\sqrt{\varepsilon_r}} = \frac{f_0 + \partial f / \partial T \cdot \Delta T}{\sqrt{\varepsilon_r}} \quad (5)$$

where Δf_T is the frequency offset caused by the temperature difference between the measuring and the working temperature, $\partial f/\partial T$ is the rate of change of resonant frequency with cavity temperature, generally taken as -48 kHz/□. ΔT is the difference between the working temperature of the cavity and the testing temperature. ε_r is the relative permittivity of air under test conditions, and its empirical formula is as follows:

$$\varepsilon_r = 1 + 210\times10^{-6} \cdot \frac{P_d}{T} + 180\times10^{-6} \cdot (1 + \frac{3580}{T}) \cdot \frac{P_w}{T} \quad (6)$$

In the above formula, P_d and P_w are the partial pressure of dry gas and water vapor (in torr units) at a certain temperature T respectively, and T is the Kelvin temperature. Finally, the measured value after error correction is shown in Table 4.

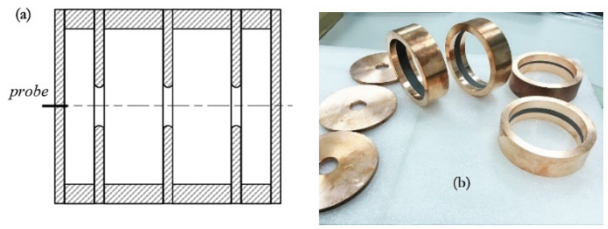


Figure 2: (a) Schematic of a 3-cavity assembly with a feed-in probe; (b) collinear load cavities.

Table 4: The Frequency and Q-factor of the Resonant Assembly Cavities

Cavity No.	Simulation		Measurement	
	Freq(MHz)	Q	Freq(MHz)	Q
1	2854.130	456.395	2854.766	—
2	2854.272	291.685	2854.866	—
3	2854.550	168.144	2856.242	—
4	2855.761	50.079	2856.317	49.901

Finally, it can be seen from the measured data that the processing thickness of the absorbing coating at the first three cavities is thicker than the design value, which makes the volume of FeSiAl material too large, causing that the attenuation of signal is more than expected which leads too much error. Only the Q-factor of the last collinear cavity can be calculated as Q = 49.901, which matches the result well. In this case, in order to reduce the deviation between the results and the design values, achieving the desired

Content from this work may be used under the terms of the CC BY 3.0 licence (© 2018). Any distribution of this work must maintain attribution to the author(s), title of the work, publisher, and DOI.

ISBN: 978-3-95450-194-6 ISSN: 2226-0366 doi:10.18429/JACoW-LINAC2018-MOPO118

function of the collinear load, it is very important to re-process the thickness of the coating material and the inner diameter of the cavity ring copper base.

The HUST-FEL-THz injector has been constructed since autumn of 2014 [5]. The Linac typically operate at about 20 MV/m, corresponding equipment on-site photo is shown in Fig. 3. After adequate parameter adjustment, the injector can generate high-performance electron beams with the energy of 13.7 MeV, the energy spread of 0.41%, the bunch length of 3.05 ps, and the Nor. Emittance of 8.8 mm mrad, which is more than sufficient to drive the FEL-THz radiation as designed.



Figure 3: The HUST-FEL-THz injector equipment.

As illustrated in Fig.3, the beamline length of the traveling-wave structure with collinear load is only 0.805 m, and the gap between the Linac and the surrounding coils is less than 1 mm.

CONCLUSION

In this context, a SLAC-like traveling wave acceleration tube with collinear load has been described in detail. A design strategy of simulation combined experiment is proposed. Both theoretic and testing results demonstrates that the final design can achieve a tradeoff between performance and compactness, and involved entire injector can be confined within a very compact scale with facility performance improved by avoiding asymmetric fields.

REFERENCES

[1] S. Krishnagopal *et al.*, “Free-electron lasers”, *Radiation Physics & Chemistry*, vol. 70, pp. 559-569, 2004.

[2] S. G. Biedron *et al.*, "Compact High-Power Electron Beam Based Terahertz Sources", *Proceedings of the IEEE*, vol. 95, pp. 1666-1678, 2007.

[3] G. P. Gallerano *et al.*, "Overview of terahertz radiation sources", in *Proc. of the 2004 FEL Conference*, Trieste, Italy, Aug.-Sep. 2004, paper FRBIS02, pp. 216-221.

[4] H. Hama *et al.*, “Intense coherent terahertz generation from accelerator-based sources”, *Nuclear Instruments & Methods in Physics Research A,* vol. 637, pp. 57-61, 2011.

[5] T. N. Hu *et al.*, “Development of a novel thermionic RF electron gun applied on a compact THz-FEL facility”, *Nuclear Instruments & Methods in Physics Research A*, vol. 887, pp. 1-6, 2018.

[6] Y. Sun *et al.*, “Numerical analysis and design of collinear load for s-band linac based on fesial material”, *Nuclear Inst & Methods in Physics Research A,* vol. 623, pp. 883-887, 2010.

[7] T. N. Hu *et al.*, "Study of beam transverse properties of a thermionic electron gun for application to a compact THz free electron laser", *Review of Scientific Instruments*, vol. 85, pp. 559-569, 2014.

[8] P. Wang *et al.*, “Accurate characterization of Low-Q microwave resonator using critical-points method”, *IEEE Transactions on Microwave Theory & Techniques*, vol. 53, pp. 349-353, 2005.

Content from this work may be used under the terms of the CC BY 3.0 licence (© 2018). Any distribution of this work must maintain attribution to the author(s), title of the work, publisher, and DOI.

ISBN: 978-3-95450-194-6 ISSN: 2226-0366 doi:10.18429/JACoW-LINAC2018-MOPO119

Content from this work may be used under the terms of the CC BY 3.0 licence (© 2018). Any distribution of this work must maintain attribution to the author(s), title of the work, publisher, and DOI.

DESIGN OF A FULLY AUTOMATED TEST BENCH FOR MESURING THE FIELD DISTRIBUTION OF STANDING WAVE CAVITY*

Y. Lu, T. N. Hu, G. Y. Feng, J. Jiang, X. D. Tu, Y. Q. Xiong
School of Electrical and Electronic Engineering,
Huazhong University of Science and Technology, Wuhan, China

Abstract

The resonant cavity plays a great role in the linear accelerator. An accurate measurement of the cavity field distribution is very important to design linear accelerators. A fully computer controlled bench for the electric field distribution has been developed in this context. Based on the perturbation theory, the acquisition of the resonant frequency shift is proportional to the square of E (electric field). In order to verify the reliability of the test bench, a standard cylindrical cavity has been tested in this measurement system. The simulation by HFSS (High Frequency Structure Simulator) and the practice will be both presented in this paper. And the result demonstrates that, because of its high concentricity, the automated test bench achieves high precision in measuring the distribution of electric field.

INTRODUCTION

RF cavities can support various electromagnetic fields. When designing a cavity to accelerate electrons, the field distribution should be calculated analytically. Bead pulling method based on perturbation theory is the most common technique to measure the field distribution in the cavity. This paper describes that a fully automated test bench that has been applied to detect the electric field distribution. The test bench has a compact structure, but realizes an accurate measurement and costs a little time to complete measurement due to automated measurement system.

BASIC PERTURBATION THEORY

The perturbation theory describes that the presence of a small volume of dielectric sample in the resonant cavity can make a slight change in resonant frequency and perturb the electromagnetic field [1]. The frequency shift is related to the intensity of electric field and magnetic field where the dielectric sample exists. According to Maxwell equations, the equation between frequency shift and electromagnetic parameters can be given as

$$\frac{\omega-\omega_0}{\omega_0} \approx -\frac{\int_{\Delta V}(\Delta\varepsilon|\boldsymbol{E_0}|^2+\Delta\mu|\boldsymbol{H_0}|^2)\mathrm{d}\Delta V}{\int_V(\varepsilon|\boldsymbol{E_0}|^2+\mu|\boldsymbol{H_0}|^2)\mathrm{d}V} \quad (1)$$

The volume of resonant cavity is V. In the unperturbed state, let the relative permittivity and the magnetic permeability be ε and μ. The electric field and magnetic field are $\boldsymbol{E_0}$ and $\boldsymbol{H_0}$, and the resonant frequency is ω_0. After placing a conductor sample whose volume is ΔV in the cavity, the electric field, the magnetic field and the resonant frequency become $\boldsymbol{E}$, $\boldsymbol{H}$ and ω. Let the relative permittivity and the magnetic permeability of the bead be $(\varepsilon+\Delta\varepsilon)$ and $(\mu+\Delta\mu)$.

For cylindrical accelerating cavities work at the TM010 mode, the magnetic field on the central axis is zero, namely $\boldsymbol{H}=0$ at $r=0$, where r is the radial position in the cavities. So if the dielectric sample is placed on the central axis, in the region of the sample, the equation (1) can be simplified as

$$\frac{\omega-\omega_0}{\omega_0} \approx -\frac{\int_{\Delta V}(\Delta\varepsilon|\boldsymbol{E_0}|^2)\mathrm{d}\Delta V}{\int_V(\varepsilon|\boldsymbol{E_0}|^2+\mu|\boldsymbol{H_0}|^2)\mathrm{d}V} \quad (2)$$

Hence,

$$E_z(r=0,z) \propto \sqrt{\Delta f(z)} \quad (3)$$

Therefore, it's feasible to get the distribution of axial electric field by moving the dielectric sample along the central axis and measuring the resonant frequency point by point.

MEASUREMENT PROCEDURE OF THE TEST BENCH

According to the perturbation theory, the axial electric field is acquired by measuring the resonant frequency when a metallic conductor sample is displaced through the cavity. In the design of automated test bench, a small bead is used as a small conductor sample and it is moved by the bead displacement system which consists of a wire, a stepper motor and several pulleys. The bead gets accurate position along the central axis by a stepper motor, which is controlled by a computer over a LAN(Local Area Network). Besides the resonant frequency of cavity could be measured by the VNA(Vector Network Analyzer) with the same control method. An agilent E5061B VNA measures the S11 transmission coefficient through the cavity and find the resonant frequency [2, 3]. And it offers an excellent stability and accuracy, and an easy control via LAN.

Thus, the data collection and processing are achieved automatically. The design of automated measurement system, shown in Figure 1, could obtain the distribution of the axial electric field by perturbation method. The components of the measurement system: a computer, a VNA, a cylindrical cavity excited by a probe, a stepper motor and several pulleys.

ISBN: 978-3-95450-194-6 ISSN: 2226-0366 doi:10.18429/JACoW-LINAC2018-MOPO119

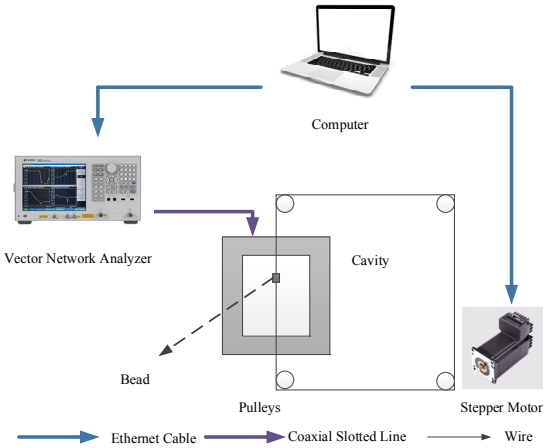


Figure 1: The scheme of automated measurement system.

Based on LabVIEW, the system program consists of program module for main control, communication module for stepper motor and VNA, data processing and online display module. Figure 2 presents the block diagram of the main program.

The automated measurement system prevents the measurement error from manual operation and avoids the measurement error which is caused by the jitter of the bead. Therefore, it's convenient and efficient to measure the axial electric field of microwave cavity with high precision.

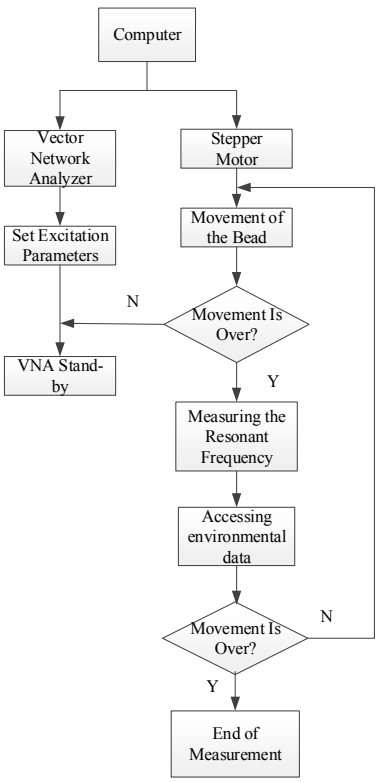


Figure 2: The block diagram of the main program.

SIMULATION AND MEASUREMENT

After establishing the test bench, in order to verify the reliability of the test bench, a standard cylindrical cavity has been used for detecting the axial electric field by this measurement system. The results of the measured electric field will be compared with the simulation results.

An S-band cavity has been designed in ANSYS HFSS software as shown in Figure 3 [4]. The radius of the cavity is 40.2mm, the length is 50.2mm, and the wall thickness is 10mm.The material of the cavity is aluminum. There are two holes on the cross section. And they will allow the bead to move through the central axis of the cavity to complete the measurement of the electric field and they are also used as beam holes in linear accelerator. The radius of the hole is 2.5mm. The cavity is excited via an external coupling probe whose material is copper. And the coupling probe is formed by extending the feeding coaxial cable.

According to probe coupling theory, the current in the probe is small, but the voltage creates an electric field between the probe and the adjacent wall of the resonator. The filed radiates energy into the resonator like a small monopole antenna. The mode in the cavity and the strength of the electromagnetic field are related to the position and the length of the probe [5]. Considering the size of the N to SMA adapter, the section radius of the coupling probe is 0.5mm.

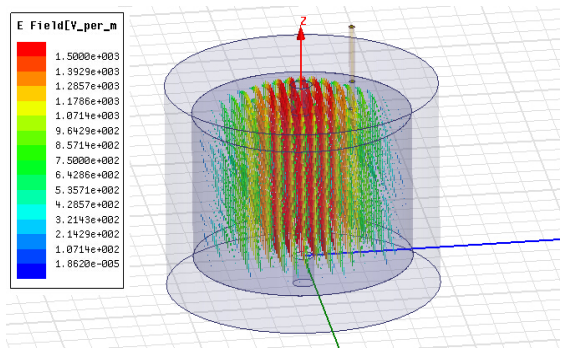


Figure 3: Design of an S-band resonant cavity and the electric field inside cavity.

Since TM010 is the mode that we need, the probe should locate at the top place of the cavity and unwanted modes can be avoided. And the electromagnetic field should be as large as possible so that the resonant frequency shift could be measured. After several simulations, the length of the coupling probe might better be 4mm. Figure 3 also shows the simulation of the electric field inside the TM010 mode resonant cavity.

The automated measurement system is shown in Figure 4. The bead displacement system consists of 6 pulleys so that the bead could realize movements on both horizontal and vertical directions. Therefore, different kinds of cavities could be measured by this system.

In the practice, the parameters of the resonant cavity are the same with parameters of simulation. The radius of the bead is 1mm and its material is stainless steel. The motor step size is 1mm.

Before operating the system, it's necessary to adjust the position of pulleys which are collinear with the bead, so that the moving trail of the bead coincides with the central

Content from this work may be used under the terms of the CC BY 3.0 licence (© 2018). Any distribution of this work must maintain attribution to the author(s), title of the work, publisher, and DOI.

ISBN: 978-3-95450-194-6 ISSN: 2226-0366 doi:10.18429/JACoW-LINAC2018-MOPO119

Content from this work may be used under the terms of the CC BY 3.0 licence (© 2018). Any distribution of this work must maintain attribution to the author(s), title of the work, publisher, and DOI.

axis of the cavity. And the basis of the coincidence between the bead and the axis is that the guiding wire is collinear with the axis. The direction of guiding wire is the horizontal tangent line of the bottom of pulleys on both sides of the bead. If the geometric center of the bead coincides with the center of the beam hole in the entrance and exit of the cavity, then it satisfies that the bead moves along the central axis of the cavity.

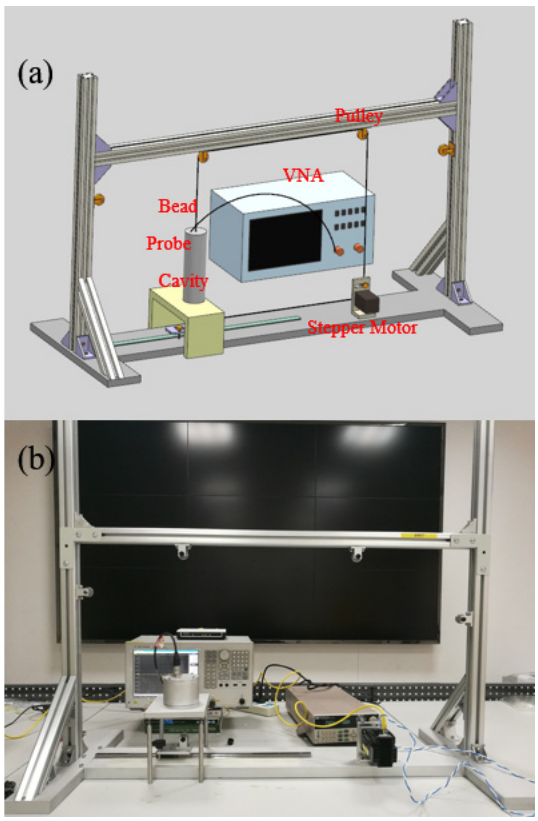


Figure 4: The automated measurement system. (a) design drawing (b) photograph of the system.

From the S11 data of VNA, the resonant frequency without perturbation is 2848.497MHz and in the perturbed state, the maximum value of frequency shift is 2MHz. The reasons why the resonant frequency is smaller than 2856MHz are machining error and the influence of air. The relationship between frequency in air and frequency in vacuum could be given as

$$f_r \approx \frac{f_0}{\sqrt{\varepsilon_r}} \tag{4}$$

f_r is the resonant frequency in the air, f_0 is resonant frequency in the vacuum and ε_r is relative permittivity of the air. ε_r could be figured out by the following equation.

$$\varepsilon_r = 1 + 210\times10^{-6}\frac{P_d}{T} + 180\times10^{-6}\left(1+\frac{3580}{T}\right)\frac{P_w}{T} \tag{5}$$

The T is the environment temperature. P_w and P_d are the water vapor pressure and the dry air pressure respectively, which could be given by the air humidity. When the temperature is 18□ and the humidity is 75%, the resonant frequency in the air is 2855MHz. It implies that the machining error has a greater impact on the resonant frequency than the environment.

After data processing, Figure 5 shows normalized electric field curves about simulation and measurement. The electric field intensity of measurement is smaller than that of simulation at the entrance and exit of the cavity. Maybe it's because that the bead makes a large perturbation at the entrance and exit and results in the distortion of measurement result [6]. But if the size of the bead is too small, the bead won't perturb the cavity so that the resonant frequency shift is impossible to be measured. In the cavity, the distribution curve of the electric field intensity is in good agreement with that of simulation. Compared with the traditional manual measurement, the automated measurement system has an excellent accuracy of position and a good repeatability of measurement. The measurement error has been reduced as much as possible. It's a highly efficient measurement and it takes no more than 5 minutes to complete the measurement after choosing a reasonable step size of the stepper motor.

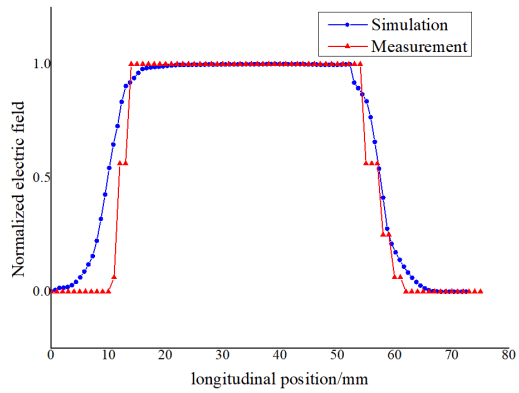


Figure 5: Electric field curves of simulation and measurement.

CONCLUSION

The fully automated test bench has turned out to be efficient by measuring the electric field distribution of an S-band cylindrical cavity. The automation and high sensitivity of the bead displacement system is very important to the measurement system.

Compared to traditional measurement, the measurement system has a high accuracy and saves time, furthermore the complete system has a compact structure and is easily transportable.

The system program is based on LabVIEW. Due to its convenient operation and easily extending function, the measurement system can be easily adapted to measure other parameters such as Q factor and R/Q. In the future, and it will be used for measurement in other normal conducting cavities.

ISBN: 978-3-95450-194-6 ISSN: 2226-0366 doi:10.18429/JACoW-LINAC2018-MOPO119

REFERENCES

[1] David M. Pozar. “Microwave Engineering”, 2011.

[2] Agilent Technologies, Inc., Fundamentals of RF and microwave noise figure measurements, *Agilent Application Note* 57-1, 2010.

[3] F. Caspers, “RF engineering basic concepts: S-parameters”, *CAS Proc. CERN Accelerator School,* Ebeltoft, Denmark Jun. 2010*,* CERN Yellow Report 2011-007, pp. 67-93.

[4] ANSYS HFSS (High Frequency Structure Simulator) Manual[M], *Ansoft Corporation*, 2008.

[5] Ebbe G. Nyfors, “Cylindrical microwave resonator sensors for measuring materials under flow”. *Finland: Helsinki University of Technology*, (2000).

[6] K. Sarabandi et al., “Technique for measuring the dielectric constant of thin materials” *IEEE Trans. Instrum. Meas.*,1988, 37:31–636.

Content from this work may be used under the terms of the CC BY 3.0 licence (© 2018). Any distribution of this work must maintain attribution to the author(s), title of the work, publisher, and DOI.

ISBN: 978-3-95450-194-6 ISSN: 2226-0366 doi:10.18429/JACoW-LINAC2018-MOPO120

IMPROVEMENT OF THE LINEAR PART IN THE TUNER SYSTEM OF ADS 25 MeV LINAC

L. Zhang†, F.F. Wang, L.B. Liu, Z. Gao, B. Zhang
Institute of Modern Physics, Chinese Academy of Science, Lanzhou, China

Abstract

Tuner system is the indispensable part of ADS high current proton superconducting linac. It influences the working frequency of superconducting cavity of particle accelerator. To completely understand the working situation of the tuner system and analyses the problems existing in it, experiments of linear part were fully conducted.

INTRODUCTION

The tuner system of ADS 25 MeV Linac (Fig. 1) built in CM1, CM2 and CM3 consists of 17 tuners[1], and every tuner consists of two parts – linear part and tuning implement unit. Linear part is mainly composed of step motor, reduction box, screw-nut and coupler (Fig. 2). To learn about the working conditions and structure characteristics, the linear parts of 17 tuners were tested and the CM1-2, CM2-3 and CM3-1 were chosen as representatives to give a brief introduction of test procedure and results. Through the analysis of the problem, the linear part was improved and tested again, and the effect was remarkable.

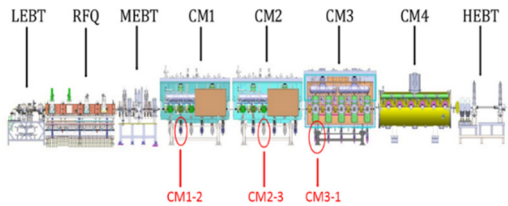


Figure 1: The layout of ADS 25MeV linac.

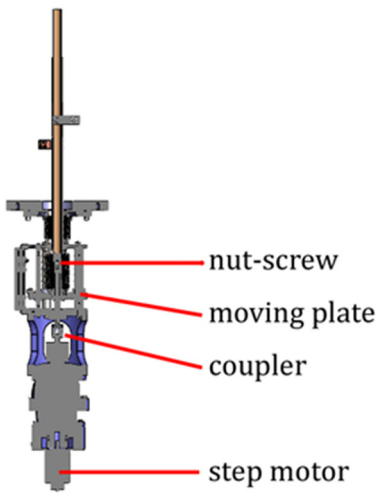


Figure 2: The sectional view of the tuner linear part.

THE TEST OF LINEAR PART

The linear part of tuners was tested at 300 K as shown in Fig. 3. The moving plate was adjusted to a suitable position to ensure enough space to move up and down. Then the dial indicator was fixed on the bracket and was properly set at an indication that later we took as the center. With 200 steps at a time, the step motor was made to move 25 times in the direction where the moving plate rose and fell respectively. Positions of every movement were recorded by the dial indicator.

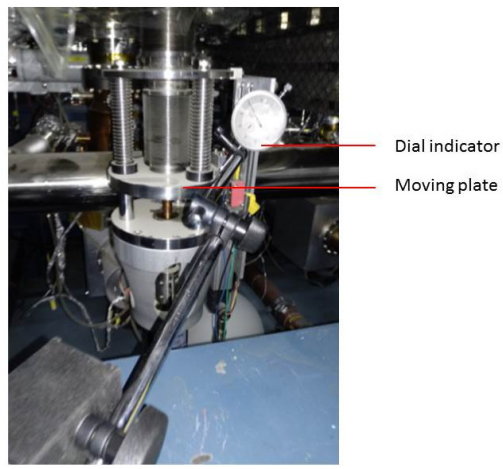


Figure 3: The test of the linear part.

The result of CM1-2 tuner linear driving part (Fig. 4) test shows that the plate tends to move linearly and is barely influenced by hysteresis, which shows the linear drive part works well and meets the requirement of tuners.

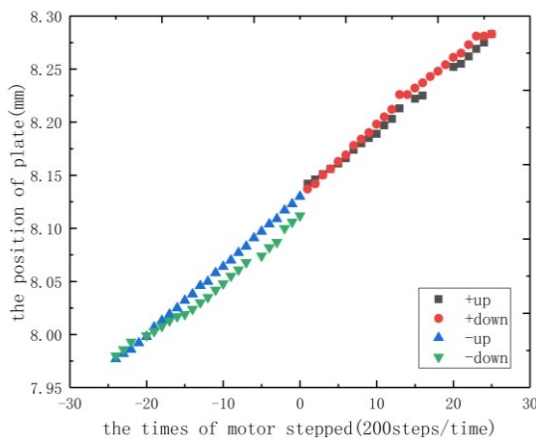


Figure 4: The curve of the line part test in CM1-2.

† zhanglei@impcas.ac.cn

Content from this work may be used under the terms of the CC BY 3.0 licence (© 2018). Any distribution of this work must maintain attribution to the author(s), title of the work, publisher, and DOI.

ISBN: 978-3-95450-194-6 ISSN: 2226-0366 doi:10.18429/JACoW-LINAC2018-MOPO120

From the curve of CM2-3 (Fig. 5), five times (1000 steps) of delay of moving plate can be seen. This could be caused by worn screw-nut and fatigue damage of coupler.

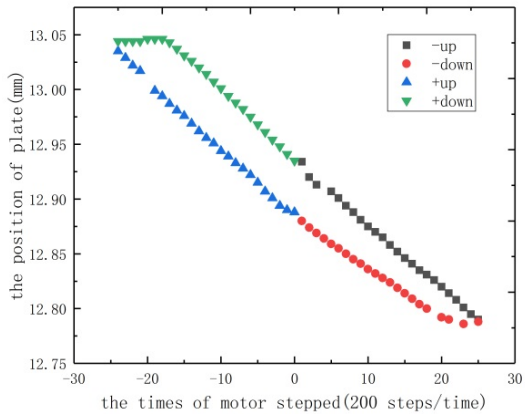


Figure 5: The curve of line part test in CM2-3.

The curve in Fig. 6 shows much of delays in linear part of CM3-1. 3800 steps of returns occurred throughout all 5000 steps of processes. The rate is up to 76%. This may also result from worn screw-nut and fatigue damage of coupler. Moreover, the positon of the return processes in positive direction slightly lifts before it descends. As for this phenomenon, further experimental analysis is needed.

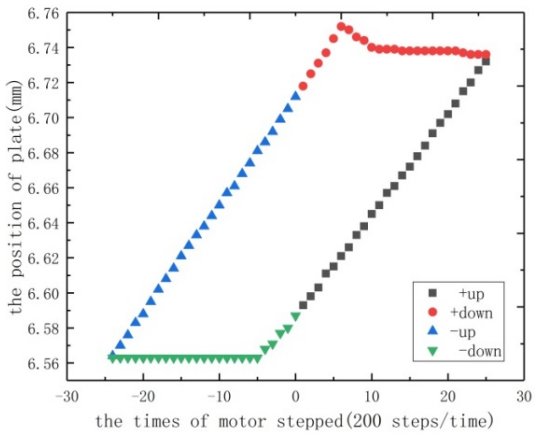


Figure 6: The curve of linear part test in CM3-1.

THE IMPROVEMENT IN LINEAR PART

Tests in the linear part helped find the main reasons, the gap formed when the reduction box is moving and the wear of the nut-screw, for hysteresis. Therefore, we substituted the trapezoidal screw with ball screw that is more precise and the precision can reach 30 um level. Then we accurately computed the tuning force and torque according to the tuning requirement of HWR cavity, and selected a step motor which is 4.2 Nm in torque and removed the reduction box.

The mechanical structure of tuner was modified as well. The top of the screw was fixed on the third flange, the third flange and the first flange were fixed on the support of motor. So the situation of the screw deviation from axis when it works is avoided. Nut was fixed on the second flange, second flange and the forth flange was install together. Three linear bearings are evenly distributed on the second flange and forth flange. It increases the flexibility and linearity of the second and forth flanges linear motion. The rotational motion of screw was converted to the linear motion of second flange and forth flange. Guide rod fixed on forth flange, so it can motion with forth flange. Figure 7 shows the structure of the improved tuner linear part.

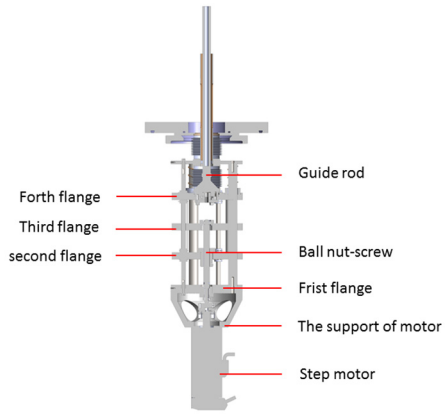


Figure 7: The sectional view of improved linear part.

The improved linear part was tested. Figure 8 shows the relationships between motor stepped and positions of the forth flange. As is shown above, the motion of forth flange almost linear. The coincidence degree of the three lines is high, and when the motor rotate reversed, there is no delay. After 800 steps of the motor stepped, there are 25 μm return. The 25 μm return main come from the precision of ball nut-screw.

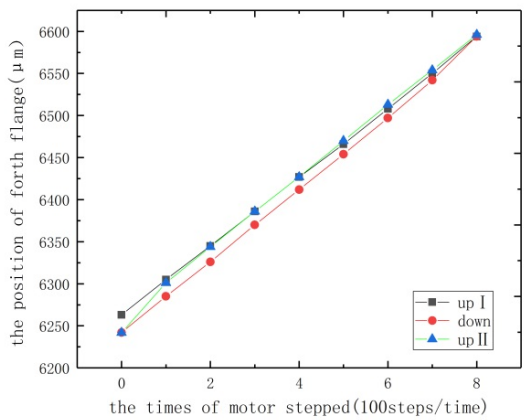


Figure 8: The curve of improved linear part.

CONCLUSION

The experiment found the delays of the tuner linear part in ADS 25 MeV Linac. After analysised the problem and found the cause of the problem, and proposed improvements. The improved linear part solves the cause of delays well, but there is still a little return. The reason for this phenomenon comes from the difference in the return stroke that the mechanical structure itself cannot be excluded, and the accuracy of the ball screw nut. This phenomenon can be greatly improved if a higher precision ball screw is used.

Content from this work may be used under the terms of the CC BY 3.0 licence (© 2018). Any distribution of this work must maintain attribution to the author(s), title of the work, publisher, and DOI.

ISBN: 978-3-95450-194-6 ISSN: 2226-0366 doi:10.18429/JACoW-LINAC2018-MOPO120

REFERENCES

[1] Q. Wu , H. Jia, H.Y. Ma, et al. Research of emittance matching on the low energy beam transport line for ADS proton LINAC. Nuclear Physics Review, 2015, (32): 5-9

Content from this work may be used under the terms of the CC BY 3.0 licence (© 2018). Any distribution of this work must maintain attribution to the author(s), title of the work, publisher, and DOI.

ISBN: 978-3-95450-194-6 ISSN: 2226-0366 doi:10.18429/JACoW-LINAC2018-MOPO121

LARGE-SCALE OPTICAL SYNCHRONIZATION SYSTEM OF THE EUROPEAN XFEL

J. Müller*, M. Felber, T. Kozak, T. Lamb, S. Schulz, C. Sydlo,
M. Titberidze, F. Zummack, and H. Schlarb
Deutsches Elektronen-Synchrotron (DESY), Notkestraße 85, 22607 Hamburg, Germany

Abstract

At the European XFEL, a facility-wide optical synchronization system providing a femtosecond-stable timing reference at more than 40 end-stations had been developed and installed. The system is based on an ultra-stable, low-noise laser oscillator, whose signals are distributed via actively length-stabilized optical fibers to the different locations across the accelerator and experimental areas. There, it is used to locally re-synchronize radio frequency signals, to precisely measure the arrival time of the electron beam for fast beam-based feedbacks, and to phase-lock optical laser systems for electron bunch generation, beam diagnostics and user pump-probe experiments with femtosecond temporal resolution. In this paper, we present the system's architecture and discuss design choices to realize an extensible, large-scale synchronization infrastructure for accelerators that meets reliability, maintainability as well as the performance requirements. Furthermore, the latest performance result of an all-optically synchronized laser oscillator is shown.

INTRODUCTION

The European X-ray Free-Electron Laser (XFEL) is a fourth-generation linac-based light source being capable of producing X-ray pulses with a duration of only a few to tens of femtoseconds. In particular for time-resolved pump-probe experiments it is crucial to achieve a synchronization between the FEL and the pump-probe laser systems with an accuracy on the same timescale. Accordingly, the synchronization system for the European XFEL was designed and built [1] to achieve a point-to-point timing jitter of 10 fs.

The foundation of the system is a low-noise laser oscillator synchronized to the master radio-frequency (RF) oscillator (MO) of the facility to provide a long- and short-term stable timing reference to critical subsystems using optical fiber links (see Fig. 1). For this, an active fiber length stabilization scheme [2] is employed to compensate optical path length changes, and by this keeping the laser pulse arrival time at the fiber link end stable with a jitter of less than 1 fs (rms) [3]. Since in a large-scale accelerator like the European XFEL the radio-frequency signals, which are the reference signals for the accelerating modules, are distributed over kilometers of cables and amplified several times, phase drift and jitter contributions can add up significantly. To achieve low-drift and low-timing jitter FEL performance, optical reference modules ("REFM-OPT") are installed along the accelerator to re-synchronize the degraded LLRF signals. These modules provide a femtosecond-precise, low-drift and amplitude-insensitive laser-to-RF phase detection based on an integrated Mach-Zehnder interferometer [4]. Another end-station type is the electron bunch arrival-time monitor [5] which, with it's femtosecond temporal resolution, is used for diagnostic purposes as well as within a fast feedback loop on the electron arrival time. In addition to a well stabilized accelerator and thus low-timing jitter X-ray pulses, external laser systems are required to be synchronized with femtosecond precision for time-resolved pump-probe user experiments. Therefore, an all-optical scheme based on two-color balanced optical cross-correlation [6] is applied to precisely measure the timing error between two pulsed laser sources and keep their relative timing jitter at a minimum.

Key requirement for all subsystems relevant for operation of the European XFEL as a facility with over 8000 hours yearly for user experiments is reliability and high availability to ensure minimum amount of downtime. Therefore, strong focus had been laid on development of mechanically, electronically and optically robust systems with large amount of automation, monitoring and redundancy [7, 8].

OPTICAL REFERENCE DISTRIBUTION

Master Laser Oscillator

A commercial, passively mode-locked SESAM-based master laser oscillator (MLO) with a repetition rate of 216.7 MHz (one-sixth of the main RF cavity resonance frequency of 1.3 GHz) provides the main optical reference pulse train. The laser is synchronized to the MO at the 7th harmonic of its repetition rate (1516.7 MHz) in a PLL-type scheme, such that the phase detection is realized at an intermediate frequency. This kind of down-conversion instead of applying a conventional DC phase detection scheme bypasses problems like DC offsets, electromagnetic interference at low-frequencies as well as $1/f$ noise related jitter contributions. Furthermore, this scheme allows for choosing an arbitrary phase set point and thus enabling the possibility to electronically shift the timing of the laser pulses. To achieve the highest level of availability a second, redundant laser oscillator of the same type is installed while an automatized and fast switching procedure ensures the possibility of an uninterrupted switching in case of a failure. At the same time the MLOs, together with the complete optical synchronization infrastructure and the MO, are connected to an uninterruptible power supply for maximum uptime.

* jost.mueller@desy.de

Content from this work may be used under the terms of the CC BY 3.0 licence (© 2018). Any distribution of this work must maintain attribution to the author(s), title of the work, publisher, and DOI.

ISBN: 978-3-95450-194-6 ISSN: 2226-0366 doi:10.18429/JACoW-LINAC2018-MOPO121

Content from this work may be used under the terms of the CC BY 3.0 licence (© 2018). Any distribution of this work must maintain attribution to the author(s), title of the work, publisher, and DOI.

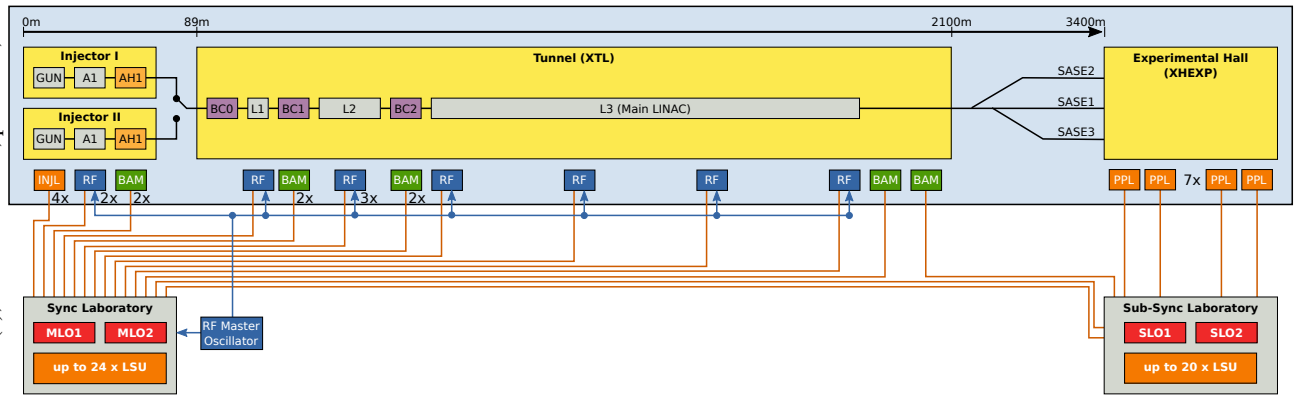


Figure 1: Schematic overview of the optical synchronization system at the European XFEL.

Free-Space Distribution

The beam of the MLO is split up in a free-space distribution system based on half-wave plates and polarizing beam splitters to serve for a total of 24 end stations. To minimize drifts caused by a change of the optical beam path a custom optical table with both sides made from SuperInvar and by this eliminating bi-metallic effects was chosen, and, moreover, the path length between laser source and LSUs is identical for all 24 end stations resulting in identical beam parameters. Taking into account the beam path length between the MLO and the link stabilization units (LSU, see below), the thermal expansion coefficient of SuperInvar (1 fs/K/m) and the temperature stability of the laboaratory ($\ll 0.1$ K) the residual drift due to thermal expansion of the optical table can be estimated as less than 300 as [1]. Another drift source on the non-stabilized beam path to the LSUs is the change of the refractive index of air with temperature, relative humidity and air pressure. This problem can be solved by synchronizing the MLO to a reference point with a distance equal to the LSU beam path length. As a result, all residual drifts are common mode and do not degrade the overall stability.

Sub-Distribution System

The main synchronization laboratory at the European XFEL is located in the injector building between the MO room and the photocathode laser laboratory. Additionally, a secondary synchronization system (see Fig. 1, "sub-sync") was located close to the scientific instruments in the so-called experimental hall to provide the optical reference signals to a further 20 end stations. This sub-distribution system is operated with another laser oscillator (of the same type as the MLO) in a master-slave configuration, where the slave laser oscillator is tightly synchronized to the optical reference pulse train provided by a stabilized fiber link from the MLO. In fact, two stabilized fiber links connect the secondary synchronization system to the main optical reference, while also a second SLO is installed for redundancy reasons.

FIBER LINK STABILIZATION UNITS

The basic principle of the LSUs is an all-optical measurement of arrival time changes between a laser pulse which had traveled forth and back through the optical fiber to the end station and fresh ones from the MLO. This measurement is based on a twofold non-linear optical frequency conversion process (sum-frequency generation, SFG) in a balanced configuration to eliminate deterioration of the timing error detection due to amplitude fluctuations [3]. For the LSUs installed at the European XFEL a type-II phase-matched PPKTP[1] crystal was chosen for maximum conversion efficiency at low optical power levels. Additionally, the required back reflection for the balanced operation is realized by coating the crystal with a dichroic layer at its back surface. The two SFG signals are detected using a low-noise balanced photo detector, digitized and fed into a feedback loop to keep the optical path length to the end station constant utilizing two actuators as part of the overall link path. A piezo-based fiber stretcher is used for compensation of fast timing errors while a 4 ns (single-pass) optical delay line is used to cover larger drifts once the fiber stretcher reaches it's limit. Under realistic conditions, drift compensation of up to 200 ps/km had been required. All fiber links at the European XFEL, being up to 3.6 km long, are based on polarization maintaining fiber to mitigate the effect of polarization mode dispersion which would in particular for longer links degenerate timing detection.

LASER SYNCHRONIZATION

An essential feature of the optical synchronization system based on the distribution of pulsed laser radiation is the ability of synchronizing external laser systems to the optical reference by a direct all-optical technique. Similar to the scheme for fiber link stabilization, it is based on a two-color balanced optical cross correlation (see Fig. 2 and [6]), which provides high-resolution measurement of the timing error between the reference and the external laser. Again, a twofold sum-frequency generation process in a nonlinear crystal re-

[1] periodically-poled potassium titanyl phosphate

ISBN: 978-3-95450-194-6 ISSN: 2226-0366 doi:10.18429/JACoW-LINAC2018-MOPO121

sults in a pure timing-sensitive error signal not affected by amplitude fluctuations of the two input signals. To lock the

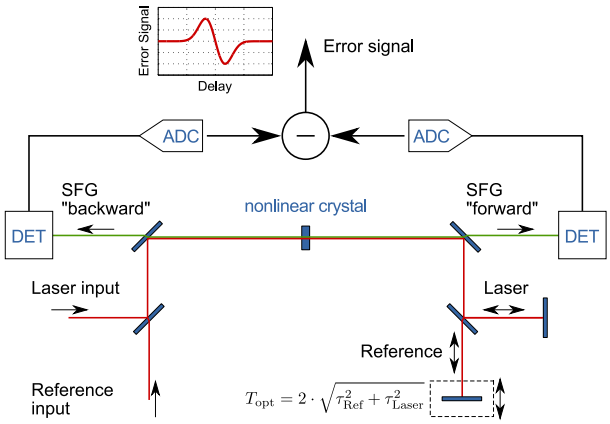


Figure 2: Balanced optical cross-correlation - principle.

laser repetition rate to the one of the reference, the error signal is fed back within an electronic control loop based on the MTCA.4 computing architecture that tunes the laser cavity length. The fast FPGA-based control system firmware allows for establishing of this optical synchronization loop even without prior locking to RF-based loops. At the European XFEL, different types of laser oscillator configurations need to be covered and supported by the synchronization system, in terms of parameters as wavelength, pulse duration or repetition rate as well as the type of cavity tuning. Therefore, the MTCA.4-based electronics provides drivers for multiple piezo actuators, stepper motors, piezo-based motors as well as temperature tuning.

Measurement Results

In case of the synchronization of the slave laser oscillator to the reference laser pulse train two-color optical cross-correlation can not be applied, since both lasers operate at the same wavelength. Therefore, polarizing optics are used instead of dichroic mirrors for the combination of the two input beams, while the same type-II non-linear process in a PPKTP crystal as in the fiber link stabilization is employed and in fact realized on a only slightly modified mechanically engineered LSU optomechanical base plate. Figure 3 (upper panel) shows the result of the phase noise measurement while the SLO is optically locked to the reference pulse train with power levels of 20 mW and 11.3 mW, respectively. The in-loop differential signal was recorded from the balanced photo detector and evaluated using a baseband analyzer[2]. Integrating the phase noise in the lower panel of Fig. 3 in the measurement bandwidth (10 Hz - 10 MHz) yields a total rms jitter of 1.25 fs. The two main contributions can be identified at around 400 Hz as well as the superelevation between 1 kHz and 20 kHz. While the prominent distortion around 400 Hz is caused by acoustic coupling from rack cooling fans, the main contribution of approximately 1 fs) to the total jitter is caused by the waterbed-related peak, which, however, strongly suppresses low-frequency contributions to the phase noise.

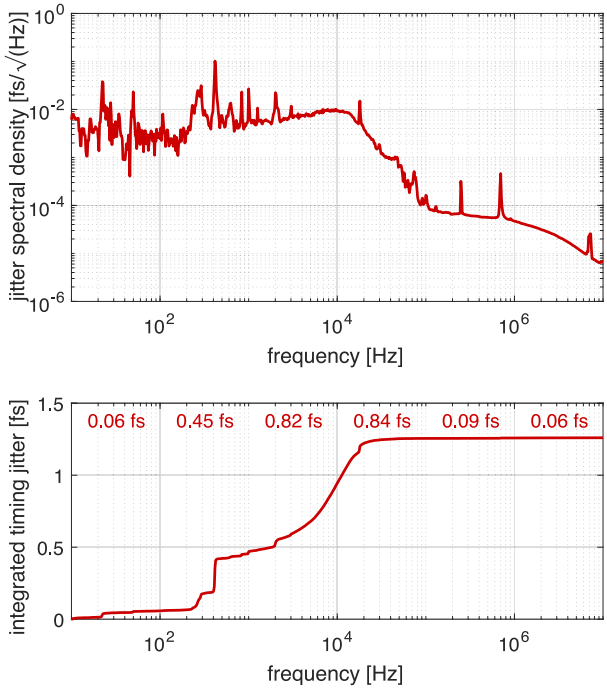


Figure 3: SLO phase noise and integrated rms timing jitter.

CURRENT STATUS AND SUMMARY

The European XFEL started operation in 2016 and pump-probe experiments at the first beamline (SASE1) have been performed in September 2017 using the pump-probe laser phase-locked to the optical synchronization system. However, installation and commissioning of several further subsystems is still ongoing. This mainly concerns fiber links in the experimental hall as well as the corresponding laser synchronization systems for the upcoming scientific instruments at the beamlines SASE2 and SASE3, where just recently X-ray radiation had been produced. The total number of 8 fiber links within the sub-distribution system and 7 laser synchronization systems in the experimental hall will be in operation until early 2019, with 3 fiber links and 1 laser synchronization system already running. In the main synchronization laboratory all installations are finished and all required 18 length-stabilized optical fiber links are in operation. For the present status of the accelerator and in particular the experimental facilities, the optical synchronization system has practically reached its final state, but is at the same time prepared for future upgrades. In summary, an overview of the laser-based synchronization system at the European XFEL was presented, as well the current status of the latest installations. Recent performance studies of an all-optical laser-to-laser synchronization scheme with an integrated rms jitter below 1.3 fs have been shown.

[2] Agilent E5052B

Content from this work may be used under the terms of the CC BY 3.0 licence (© 2018). Any distribution of this work must maintain attribution to the author(s), title of the work, publisher, and DOI.

ISBN: 978-3-95450-194-6 ISSN: 2226-0366 doi:10.18429/JACoW-LINAC2018-MOPO121

Content from this work may be used under the terms of the CC BY 3.0 licence (© 2018). Any distribution of this work must maintain attribution to the author(s), title of the work, publisher, and DOI.

REFERENCES

[1] C. Sydlo *et al.*, "Femtosecond optical synchronization system for the European XFEL", in *Proc. IPAC2017*, Copenhagen, Denmark, May 2017, pp. 3969–3971. doi:10.18429/JACoW-IPAC2017-THPAB108

[2] J. Kim *et al.*, "Drift-free femtosecond timing synchronization of remote optical and microwave sources", *Nature Photonics*, vol. 2, pp. 733–736, 2008

[3] J. Kim *et al.*, "Long-term femtosecond timing link stabilization using a single-crystal balanced cross correlator", *Opt. Lett.*, vol. 32, pp. 1044–1046, 2007

[4] T. Lamb *et al.*, "Laser-to-RF synchronization with femtosecond precision", in *Proc. FEL2017*, Santa Fe, NM, USA, Aug. 2017, pp. 399-402. doi:10.18429/JACoW-FEL2017-WEB04

[5] M. K. Czwalinna *et al.*, "New design of the 40 GHz bunch arrival time monitor using MTCA.4 electronics at FLASH and for the European XFEL", Proc. IBIC2013, paper WEPC31, pp. 749–752, 2013.

[6] T. R. Schibli *et al.*, "Attosecond active synchronization of passively mode-locked lasers by balanced cross correlation", *Opt. Lett.*, vol. 28, pp. 947–949, 2003

[7] J. M. Müller *et al.*, "All-Optical Synchronization of Pulsed Laser Systems at FLASH and XFEL", in *Proc. IPAC'15*, Richmond, VA, USA, May 2015, pp. 854–856, doi:10.18429/JACoW-IPAC2015-MOPHA032

[8] F. Zummack *et al.*, "Custom optomechanics for the optical synchronization system at the European XFEL", in *Proc. IPAC2017*, Copenhagen, Denmark, May 2017, pp. 3976–3978. doi:10.18429/JACoW-IPAC2017-THPAB110

ISBN: 978-3-95450-194-6 ISSN: 2226-0366 doi:10.18429/JACoW-LINAC2018-MOPO122

EUROPEAN XFEL COOLING AND VENTILATION SYSTEMS

Jens-Peter Jensen, Andreas Block, Sylke Feuker; DESY, D 22607 Hamburg, Germany

Abstract

The European Xray Free Electron Laser EuXFEL is operating since 2016. The technical systems for cooling and ventilation CV were designed, built and commissioned by the DESY work package WP34. The water cooling systems consists of 3 cooling systems: 30/45°C low conductivity water LCW for klystron, power converter and magnet cooling; 20/30°C LCW for tunnel rack cooling and 8/14°C for air conditioning and for air-drying. The ventilations of the tunnels are connected to a serial ventilation system. The air flow starts from the experimental hall in opposite direction of the beams until to the injector. The series ventilation system of the tunnels saves costs for air treatment like cooling, heating and air-drying. The tunnel walls are a good heat storage that increases the air temperature stability by a factor of ten. The advantages of this concept will be described.

INTRODUCTION

The European XFEL starts on the DESY premises and ends after 3.4 km at the experimental hall in Schenefeld. The beam direction is from east to west. Figure 1 shows the site map of the facility.



Figure 1: Map of the Eu-XFEL in Hamburg.

WATER COOLING SYSTEM OF XFEL

The water cooling system is divided in 2 sections since the tunnels are about 3.5 km long from the gun to the experimental hall XHEXP1.

- XHM Pump House:

The XHM pump house (Fig. 2) is located on the DESY premises and serves the injector in DESY-Bahrenfeld and the 2 km long XTL tunnel until the first separation shaft XS1 in Osdorfer Born. That is why the main cooling demands are in the linac tunnel XTL for the RF stations, the electronic racks and the normal conducting magnets.

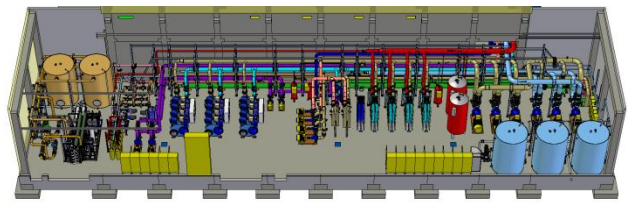


Figure 2: XHM pump house DESY Bahrenfeld, 3D model.

Figure 2 shows the 3D model of the pump house with its piping, pumps, chillers, water storage tanks and control cabinets. Figure 3 is a photo of the final installation.



Figure 3: XHM pump house installation.



Figure 4: XHM cooling towers for dry and wet cooling.

Figure 4 shows the hybrid cooling towers. Each tower has a rated power of 2 MW. The water temperature is controlled by variable speed fans. If the air temperature

Content from this work may be used under the terms of the CC BY 3.0 licence (© 2018). Any distribution of this work must maintain attribution to the author(s), title of the work, publisher, and DOI.

ISBN: 978-3-95450-194-6 ISSN: 2226-0366 doi:10.18429/JACoW-LINAC2018-MOPO122

Content from this work may be used under the terms of the CC BY 3.0 licence (© 2018). Any distribution of this work must maintain attribution to the author(s), title of the work, publisher, and DOI.

exceeds 25°C, the coolants air sprayed with deionized water to apply the evaporation cooling.

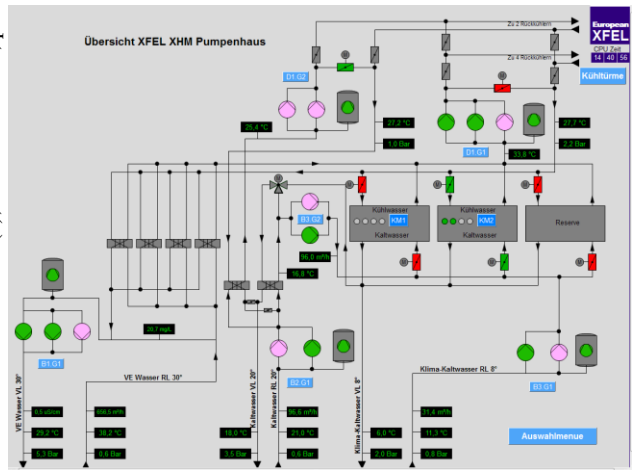


Figure 5: Display of XHM cooling system.

Figure 5 is a screen shot of the cooling system. The control system is EPICS, which supervises the temperatures and pressures of the cooling loops. It stores the data and generates alarms as well. The regulation of the temperatures and the protection of the machines are done by PLCs.

-XHPSC pump house on Schenefeld premises:

It supplies the distribution and photon tunnels, named as XTD1 to XTD10, the experimental hall XHEXP1 and their hutches, the laboratory and the office building XHQ as well.

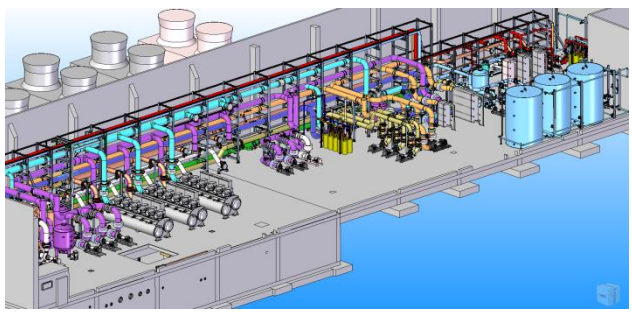


Figure 6: XHPSC pump house Schenefeld, 3D model.

Figure 6 shows the 3D model of the XHPSC pump house for the Schenefeld premises. It is similar to the XHM pump house on the DESY site. There are 3 chillers installed. Each chiller has a nominal power of 2 MW of cold water. For further buildings and laboratories there is a spare place for another chiller. There are 5 cooling tower behind the building with 2 MW each.

Figure 7 is a photo of the final pump house installation.



Figure 7: XHPSC pump house installation.

TUNNEL VENTILATION SYSTEM

The tunnel ventilation system was an important issue for the success of the SASE lasing of the undulator lines. There is only access to the tunnel through the shafts for the tunnel air. This is absolute different to the access of the existing undulator line installations.

In the undulator lines the tunnel air temperature should be constant over the time but may vary along the tunnel. The time variation should not exceed +/- 0.1°C. The dew point of the tunnel air should be above 14°C. This corresponds to 21°C and 65% humidity. This avoids corrosion of the equipment, special of the printed circuit boards. The water temperatures in the tunnels are all above 18°C. This avoids condensation on pipes and coolants as well.

Figure 8 shows the air flow in the tunnels. The air volumes of the tunnels were chosen for the linac tunnel XTL to 60,000m³/h, the XTD tunnels, equipped with undulators and dumps, to 30,000m³/h and the pure XTD photon tunnels to 20,000m³/h. In the first design each tunnel has its own ventilation system. That means one has to condition 270,000m³/h outside air. The most impact has the day and night temperature slope. She slope is typically 10°C. You can find a slope of 0.3°C in the tunnel supply air after cooling and heating the outside air.

The temperature stability is significant better if one uses the tunnel exhaust air instead of the outside air. But recirculation is not feasible because of the length of the return channel. The idea was to use the tunnel walls as a thermal storage. This is for free. The photon installations are less sensitive to temperature drifts. Therefore the treated air flows first over 360 m to 660 m through the photon tunnels XTD6,8,9 before the exhaust air is retreated and send to the XTD7,10 tunnels. See Fig. 8. The photon tunnels XTD6,8,9 have simple plate radiators with heat thermostats to replace the heat losses of the tunnel walls.

The shafts XS2,3,4 are bypassed by the tunnel air. The tunnel exhaust air is retreated before it flows into the next

ISBN: 978-3-95450-194-6 ISSN: 2226-0366 doi:10.18429/JACoW-LINAC2018-MOPO122

tunnel. Therefore the air temperature treatment is minimal. An air-drying is not required.

The undulator line requires tight temperature constancy. Therefore the undulator sections in XTD1,2,4 have their own high precision ventilation compartment. The high precision air conditioning for the undulator line uses the tunnel air as supply air.

The temperature monitoring is ongoing and will be evaluated in the next winter shut down.

The next benefit of the series ventilation is that the air stays long in the tunnel before the air is released to the outside. The dumps produce isotopes, mostly with short decay time. The dump caverns (Fig. 8) are part of a tunnel and the air should stay in the tunnel as long as possible. Therefore the tunnels are put in series from the dump to the entrance shaft XSE.

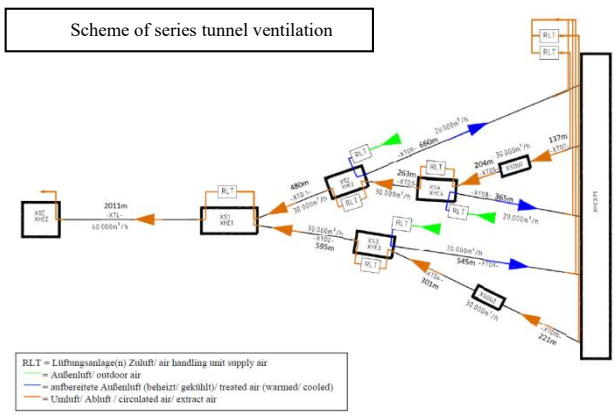


Figure 8: Scheme of the Series Tunnel Ventilation.



Figure 9: Tunnel Air Handling Unit.

Figure 9 shows an air handling unit AHU with air cooler (pipe with black insulation in the back) und air heater (pipe with white insulation in the front). Each tunnel has its own AHU.

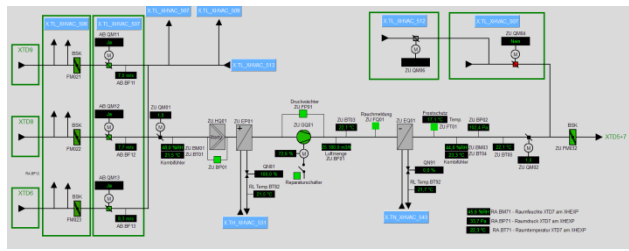


Figure 10: Control Display of tunnel air handling unit AHU.

Figure 10 shows the control display of a tunnel AHU. This figure shows for example that the exhaust airs of the 3 photon tunnels are collected and retreated by the AHU before the supply air flows into the next tunnel with a dump.

SUMMARY

The water cooling systems run since beginning reliable. The temperature levels are 8/14°C for the air conditioning, the 20/30°C for electronic rack cooling and 30/45°C for the high power cooling. The cooling towers are hybrid types. They run most of the year dry without water evaporation. On hot days the coolants are sprayed to apply the evaporation cooling. The temperature regulation is done by variable speed fans.

The ventilation of the tunnels was a challenge because of the requirements from the accelerator installations and the undulator lines in the tunnels. The temperature constancy over long distances depends on the air volume flow and the load balances along the tunnels. The access is only through the tunnel ends possible. In the first design every tunnel has its own ventilation system. This was changed to series tunnel ventilation against the electron beam direction.

The benefits for series ventilation are

- Increased temperature stability below 0.1 °C by using tunnel air as supply air.
- Lower operation costs for air treatment, because only 60,000m³/h outside air instead of 270,000m³/h is heated, cooled and dried.
- Isotopes from the beam dumps stay longer in the tunnels before they are released to the outside.

Content from this work may be used under the terms of the CC BY 3.0 licence (© 2018). Any distribution of this work must maintain attribution to the author(s), title of the work, publisher, and DOI.

ISBN: 978-3-95450-194-6 ISSN: 2226-0366 doi:10.18429/JACoW-LINAC2018-MOPO124

DETAILS OF THE MANUFACTURING PROCESSES OF THE ESS-DTL COMPONENTS

P. Mereu*, F. Borotto Dalla Vecchia, C. Mingioni, M. Nenni, R. Panero, INFN, Torino, Italy
A. Battistello, P. Bottin, D. Conventi, L. Ferrari, A. Colombo, F. Grespan, A. Pisent, INFN-LNL, Italy

Abstract

The Drift Tube Linac (DTL) of the European Spallation Source (ESS) is designed to operate at 352.2 MHz with a duty cycle of 4% (3 ms pulse length,14 Hz repetition period) and will accelerate a proton beam of 62.5 mA pulse peak current from 3.62 to 90 MeV. This paper presents the details of the manufacturing processes with quality control reports reports of the components of the DTL.

DTL DESIGN

In the ESS accelerator the initial warm linac section is composed by Ion Source, Low Energy Beam Transport line (LEBT), Radio Frequency Quadrupole (RFQ), Medium Energy Beam Transport line (MEBT) and DTL [1]. The ESS-DTL is a 38.8 m long system, divided in five tanks [2]; each tank is a stand-alone structure, composed of four 2 m long modules made of AISI 304L stainless steel with internal copper electro-deposition. The nominal position of the 168 DTs is demanded to the girder, a precisely machined aluminium alloy structure, which is housed in the upper part of each module. The DTL comprises 4 types of DTs, depending on the beam components integrated in the body: Permanent Magnet Quadrupole (PMQ), Beam Position Monitor (BPM), Electro-Magnetic Dipole (EMD) and Empty body [3]. Figure 1 indicates the main components of a typical DT. The DTs are made by a Cu-OFE body and an AISI 304L Cu-plated stem; internally there are machined steel components which provide the proper cooling water flow around the DT body. DTs are assembled by Vacuum Brazing (VB) and Electro Beam Welding (EBW).

DRIFT TUBES MANUFACTURING

The DT production and assembly, apart the EBW and all DTs-BPM, is made internally at INFN, in Torino (Tanks 1, 2) and in Legnaro (Tanks 3, 4, 5). The production of one typical DT is made of different phases, summarized as follows:

1) Machining of Body, Cover, Stem and internal steel components.
2) Copper plating of stem surfaces, housed in the RF cavity of the DTL.
3) VB of body with stem and relative internal components.
4) For the DT-BPM and DT-EMD, inner-pipe welding on the sleeve (see Brazing section in the following).
5) Machining of the coupling references in the stem for the integration in the girder and laser tracker housing.
6) For DT-PMQ, machining of the references surfaces of the PMQ housing.
7) Integration of the internal beam components (PMQ, EMD, BPM).
8) Sealing of the DT cover with EBW. For BPM and EMD, EBW of the Beam-Pipe on both ends of the DT.
9) Machining to the definitive external profile, by removing the EBW allowance at the Beam-Pipe interfaces with the DT.

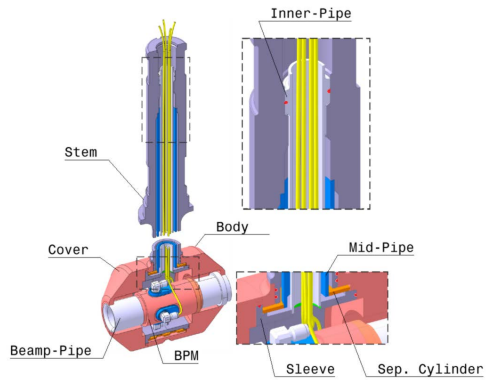


Figure 1: Main components of a DT-BPM. Details show the brazing channels (in red) and press-fit interfaces.

PART PRODUCTION

Mechanical production of bodies and cover is made of different phases, (each one involving different machines and thus different alignment). Referring to Figure 2:

1) Initial rough milling.
2) Lathing of the internal profile. The part is fixed with a classic bracket claw with no pre-alignment.
3) Milling of 90 mm external cylinder. Pre-alignment is made measuring the internal datum plane B and consequently compensating the machine.
4) Milling of 28 mm cylinder for stem integration. Pre-alignment is made with a dedicated alignment block.
5) Lathing of external profile of the angular cone, along with the "nose" plane. The part is fixed on the inner profile with a dedicated alignment as in second picture.

The procedure was continuously improved, in term of production rate, also using feedback from metrology results.

QUALITY CONTROL AND METROLOGY

INFN has developed a quality system in which every single part is designed, producing an executive drawing for each one, then machined and finally measured. This work-flow

* paolo.mereu@to.infn.it

Content from this work may be used under the terms of the CC BY 3.0 licence (© 2018). Any distribution of this work must maintain attribution to the author(s), title of the work, publisher, and DOI.

ISBN: 978-3-95450-194-6 ISSN: 2226-0366 doi:10.18429/JACoW-LINAC2018-MOPO124

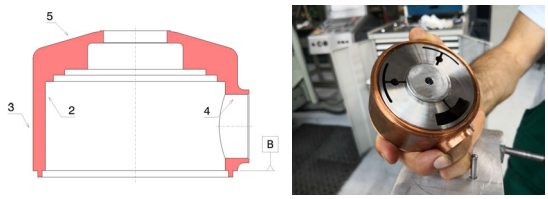


Figure 2: Recap of the different body production phases (left), INFN Alignment blocks for cone profile lathing (right).

allows to highlight immediately anomalies in components or procedures. Both INFN-LNL and INFN-Torino has a Coordinate Measuring Machine (CMM), so parts and assemblies can be measured in parallel in the two workshops. Quality system in DTs production involves the following steps:

1) Marking during production all DTs components.
2) Part metrology with CMM. For every part a summary report is saved.
3) Metrology of the pre-brazing assembly.
4) Metrology of the post-brazing assembly with CMM.
5) Vacuum test, performed at INFN-LNL, of the hydraulic seals in the post-brazing assembly.
6) Test of hydraulic seals at INFN-LNL with He, pressurized N2 or water.
7) Metrology with CMM.
8) Before the integration of the PMQs, each PMQ is characterized by company supplier (Elytt Energy) with rotating probe in order to identify his magnetic axis. After that each PMQ is coupled to the DT with corresponding reference surfaces.
9) Coupling each cover with the corresponding DT.
10) Vacuum packing on each DT for EBW.
11) New test for vacuum seals, performed at INFN-LNL, after welding.
12) Metrology after machining with CMM.

CMM accuracy, according to EN ISO 10360-2 over a temperature band of 18–22 °C, is:

$$MPE_E[\mu m] = 3.00 + 4.00 \cdot L[mm]/1000 \qquad (1)$$

Where MPE_E is the CMM maximum permissible error of indication for size measurement and L is the measurement length. Both bodies and covers were measured in the external and then in the internal side, for the VB coupling, in two separate routines. The dedicated clamping system, shown in Figure 3 (left and centre), was developed internally at INFN for a fast and accurate part alignment. Histograms in Figure 4 shows the measured deviation from the nominal value. Dotted lines corresponds to the prescribed dimensional tolerances. Most results are within the machining tolerances. Concerning the DT length graph, there are 10 Drift Tube out of tolerance about 20 µm; those parts was not rejected since they correspond to non-consecutive DT and thus the RF profile along the cavity is not affected by the cell geometry.



Figure 3: Setup for a DT body metrology at INFN.

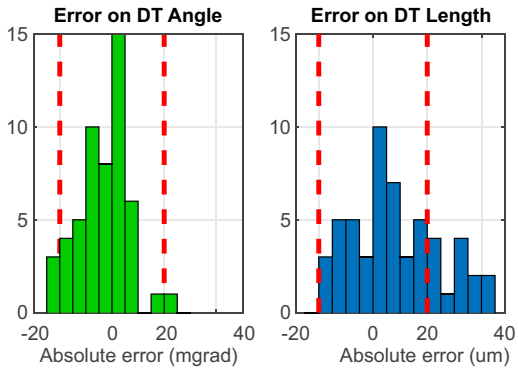


Figure 4: Absolute error histograms for DT bodies.

DRIFT TUBES BRAZING

The SS sleeve is brazed in both ends to the body as it must provide sealing of different interfaces. The Separation Cylinder is inserted in the sleeve's pad with a *H7/g6* coupling [4]. The Mid-pipe is inserted in the stem with interference coupling $\varnothing 20H7/r6$ for a press-fit coupling between stem and pipe in 4 mm length.

The inner pipe has 11 mm internal diameter, used to route the BPM and EMD cables outside the RF cavity to the controller. The inner pipe is integrated in the DT with a VB joint with the stem in his upper end, and with a GTAW joint in the sleeve in the lower end (Figure 1).

The VB phase has been prototyped at INFN-LNL along the project in order to optimize positioning, tooling and thermal cycle and demonstrate the possibility of brazing after Cu-plating of the stems. All prorotypes were succesfully brazed. For the production phase DTs are brazed inserted in 8 elements batches in order to optimize spacing and thermal distributions (left picture in Figure 5). The Oven thermal cycle (right picture in Figure 5) allows a proper thermalization of the DT main components and the complete removal of chrome oxides from all steel surfaces. The temperature of different components is monitored by dedicated thermosensors. First 8 DTs batch has been brazed at end of July 2018: 7 DTs, more precisely 3 DT-PMQ, 2 DT-EMD and 2 DT-Empty, has been successfully brazed and passed vacuum (10^{-9} mbar l/s) and pressure test (1 hour test with water at 8 bar). One DT-Empty presents a leak on the internal sleeve brazing joint. It will be repaired with a dedicated oven cycle after a small machining.

Content from this work may be used under the terms of the CC BY 3.0 licence (© 2018). Any distribution of this work must maintain attribution to the author(s), title of the work, publisher, and DOI.

ISBN: 978-3-95450-194-6 ISSN: 2226-0366 doi:10.18429/JACoW-LINAC2018-MOPO124

Content from this work may be used under the terms of the CC BY 3.0 licence (© 2018). Any distribution of this work must maintain attribution to the author(s), title of the work, publisher, and DOI.

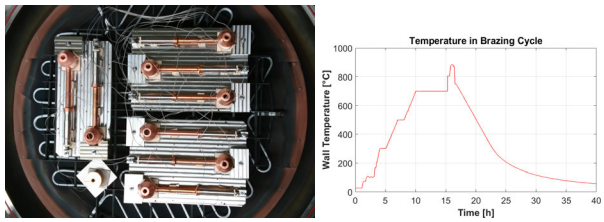
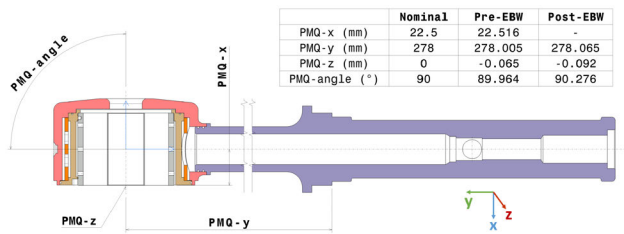


Figure 5: 8 DTs batch inside INFN-LNL brazing furnace (left) and his thermal cycle (right).

DT PROTOTYPE METROLOGY

After brazing each DT has to be machined for nominal positioning and alignment, using the same coupling references of the stem with the girder. For DTs-PMQ, also sleeve pads must be machined at PMQ nominal diameter, assuring that the PMQ magnetic axis is close to the theoretical value with allowable deviations around 5 µm.

In order to study the EBW induced deformation observed in a previous prototype, a second DT-PMQ prototype, was brazed and machined 2018, machined in July and then qualified with CMM. The measuring routine identifies the key housing position in the stem, dimensions and position of sleeve pads for PMQ coupling. After this first routine, a 45 mm prototype PMQ was inserted in the Drift Tube. The measuring routine was performed a second time, with a carbon fiber non-magnetic stylus, measuring the PMQ internal cylinder of the PMQ. A third routine was performed on the welded prototype, in order to detect deviations in the PMQ position due to the EBW: the magnetic axis position was thus qualified (Figure 6).



	Nominal	Pre-EBW	Post-EBW
PMQ-x (mm)	22.5	22.516	-
PMQ-y (mm)	278	278.005	278.065
PMQ-z (mm)	0	-0.065	-0.092
PMQ-angle (°)	90	89.964	90.276

Figure 6: Measured PMQ axis position.

BPM AND EMD INSERTION, EBW

BPM and EMD have power and control cable, housed in the central part of the DT body, in air. The vacuum tightness is guaranteed by a Copper Beam-pipe, with EBW at both DT ends. The welding area is then finished by milling at nominal geometry (right details in Figure 7). For BPMs the beam pipe is EBW on the BPM body before the integration in the DTs. The prescribed tolerances during the BPM production, assembly and welding to the two pipe ends guarantee a correct positioning in the DT.

The proper EMD angular reference is given by a slot in the magnet coil, coupled with a corresponding reference in the sleeve (green in Figure 7); the sleeve longitudinal reference is shown in cyan in Figure 7. Beam-pipe in inserted independently before EMD.

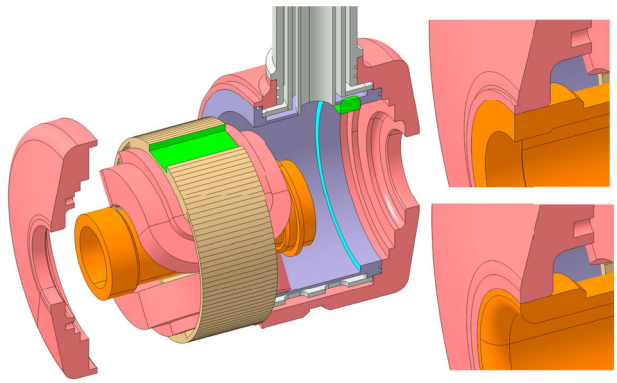


Figure 7: EMD insertion in corresponding DT assembly.

DTL PRODUCTION STATUS

At September 2018, the status of production of the various parts of ESS DTL cavity is the following.

- All the 4 modules of Tank 4 and Tank 1 module 1 and relative girders are delivered to INFN by CINEL (Figure 8);
- Tank 4-Module 1 has been Cu-plated at GSI;
- The other modules are under production by Cinel Strumenti Scientifici;
- DT Bodies and Covers were produced and measured for Tank 1 and 4;
- DT internals were produced for Tank 4, outsourced to 3rd party supplier for Tank 1;
- All the stem production were outsourced to UMAS. 50 Stems have been delivered to INFN;
- All 30 EMDs have been designed, produced and delivered to INFN by DANFYSIK;
- 15 DTs-BPM were outsourced to 3rd party supplier (CINEL);
- The PMQs supply for Tanks 1, 3 and 4 is already delivered to INFN by Elytt Energy. PMQs of Tank 2 and 5 are under production;
- VB for DTs in Tank 4 is started in July. First batch of 8 DTs have been brazed (see Section Drift Tubes brazing);
- All EBW is outsourced to Zanon SPA.

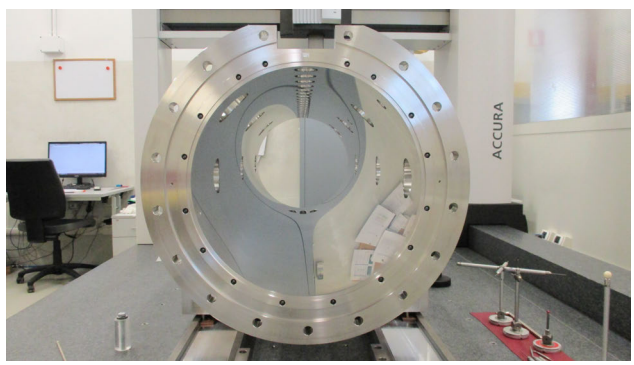


Figure 8: T1-M1 under CMM qualification.

ISBN: 978-3-95450-194-6 ISSN: 2226-0366 doi:10.18429/JACoW-LINAC2018-MOPO124

REFERENCES

[1] W. Wittmer *et al.*, "European Spallation Source (ESS) Normal Conducting Front End Status Report," in *Proc. of LINAC'16, Sep. 2016*, (East Lansing, MI, USA), pp. 274–276. DOI: 10.18429/JACoW-LINAC2016-MOPLR062.

[2] F. Grespan *et al.*, "ESS DTL Design and Drift Tube Prototypes," in *Proc. of LINAC'14, Aug.-Sep. 2014*, (Geneve, Switzerland), pp. 1050–1052.

[3] P. Mereu *et al.*, "ESS DTL Mechanical Design and Prototyping," in *Proc. of IPAC'16, May 2016*, (Busan, Korea), pp. 2131–2133. DOI: 10.18429/JACoW-IPAC2016-WEPMB008.

[4] P. Mereu *et al.*, "Thermo Mechanical Study of the ESS DTL," in *Proc. of IPAC'17, May 2017*, (Copenhagen, Denmark), pp. 4537–4539. DOI: 10.18429/JACoW-IPAC2017-THPVA046.

Content from this work may be used under the terms of the CC BY 3.0 licence (© 2018). Any distribution of this work must maintain attribution to the author(s), title of the work, publisher, and DOI.

ISBN: 978-3-95450-194-6 ISSN: 2226-0366 doi:10.18429/JACoW-LINAC2018-MOPO125

STEERING MAGNETS WITH PERMANENT MAGNETS

Y. Iwashita†, M. Abe, T. Yako, ICR, Kyoto Univ., 611-0011, Uji, Kyoto, Japan
Y. Fuwa, KURNS, Kyoto Univ., 590-0494, Osaka, Japan
N. Terunuma, KEK, 305-0801, Tsukuba, Japan

Abstract

Steering magnets with permanent magnets are investigated. They need to generate both polarities of magnetic fields, which can be realized by rotating permanent magnet rods. Such a magnet system will reduce not only electricity but also maintenance cost. The structure and the field adjustment scheme of a trial conceptual design will be discussed.

INTRODUCTION

Electromagnets, which are widely used as optics elements for beam handling, may be replaced by permanent magnets. In addition to reductions of the electricity for coil excitation and cooling, thick electric cabling and water piping, power supply and their maintenance cost-down are also expected. Among optics elements, steering magnets need to generate bipolar magnetic fields, which can be realized by rotating permanent magnet rods [1].

One demand for such a device comes from Ring To Main Linac (RTML) beam lines, whose lengths are more than that of the main linac. Another demand comes from ILC Damping Ring (DR), where more than 300 steering magnets will be installed for orbit correction [2]. With permanent magnets, there is no DC power supplies, no cooling water, and then these failures will never happen. Water leaks have been annoying events among maintenance activities, which would also be dramatically reduced if permanent magnets were applied. These items offer cost reductions for both construction and operations.

While many advantages are expected, we need some investigations in applying permanent magnets. At least three subjects have to be considered: temperature dependence of remnant field (Br), adjustability and demagnetization caused by radiation. The temperature coefficient can be compensated by magnetic shunts made of magnetic materials with low Curie temperature, which have large temperature coefficient around their operating temperatures [3]. Although the strength adjustment of magnets made of permanent magnets are not easy compared with electromagnets, there are some methods that can be incorporated. In order to change the magnetic flux density generated in a gap, we rotate permanent magnets in the structure, which enables a bipolar operation and is suitable for correction magnets. The rotating mechanism may also have troubles like a failure of power supply for electromagnet. The permanent magnet system, however, will not lose the deflecting strength but just the adjustability from the current position, which will not prevent the machine operation immediately, since the adjustment is not expected to be so often in a daily operation.

† iwashita@kyticr.kuicr.kyoto-u.ac.jp

CORRECTION MAGNET

Assumed magnet length and beam pipe diameter are about 32 cm and 6 cm, respectively. Eight ferrite permanent magnet rods with about ø50mm diameter can generate enough strength. We assume to use Y30H, whose remnant field Br is about 0.4T. The magnet diameter is chosen from an available magnet ingot size (25.4×100×150 mm). The octagon shaped magnet rod has a slightly larger volume than a cylindrical rod that can be machined from the ingot with the same size. Figure 1 shows a possible bipolar correction magnet, where the magnet rods are rotated by a stepping motor to vary the magnetic field strength (see Fig. 2). The adjacent rods rotate with opposite directions each other so that the mag-

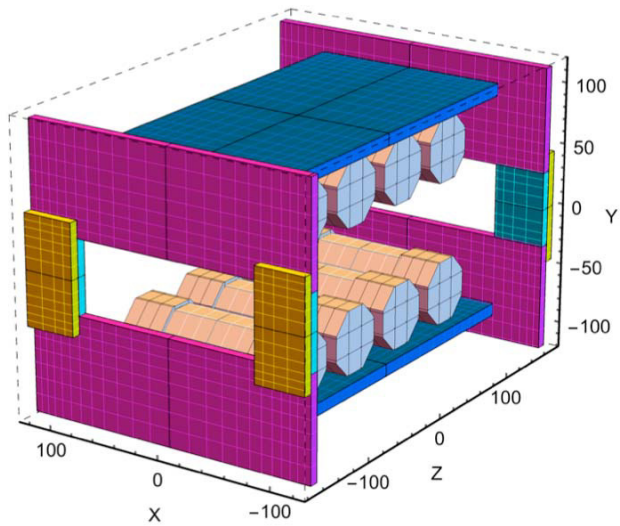


Figure 1: Outline of the permanent steering magnet.

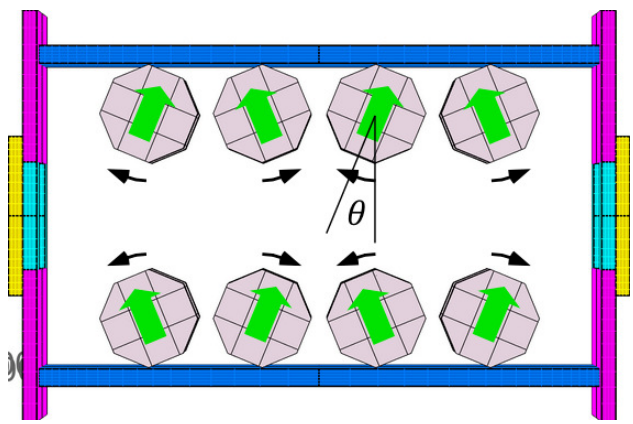


Figure 2: Cut view of the permanent steering magnet. The magnet rods rotate oppositely each other.

Content from this work may be used under the terms of the CC BY 3.0 licence (© 2018). Any distribution of this work must maintain attribution to the author(s), title of the work, publisher, and DOI.

ISBN: 978-3-95450-194-6 ISSN: 2226-0366 doi:10.18429/JACoW-LINAC2018-MOPO125

netic field is perpendicular to the median plane and the integrated magnetic field along the axis (so called BL product) can be cancelled out in a short period, which minimizes a beam shift. Figure 3 shows the schematic flux plot for three rotation angles calculated by PANDIRA. When the rotation angle is zero, easy axes of the rods are aligned. The rod rotation makes the part of the magnetic field on the axis cancel each other.

For realistic analysis, 3D calculations with RADIA 4.31 4 were carried out based on the geometry as shown in Fig. 1. In order to achieve a better flatness of the magnetic field, the center part of the magnet rod is modified. The width and the radius at the center are adjusted so that the multipole components other than the dipole component around the beam axis become small. Figure 4 shows two lines where the sextupole or decapole component becomes zero when the width and the radius of the middle part of the magnet rods are changed. The crossing point of these two lines satisfies the condition that both the multipole components become zero in this configuration.

The resulted magnetic field map on the median plane is shown in Fig. 5 at the rotation angle of zero. Figure 6 shows the calculated By distributions along the beam lines of X=0, 10 and 20 mm at the rotation angle of zero in this geometry. Because the field flatness is well optimized, all there lines are overlapped in this figure. Owing to the Maxwell equation, vertical variation should show the similar magnitude.

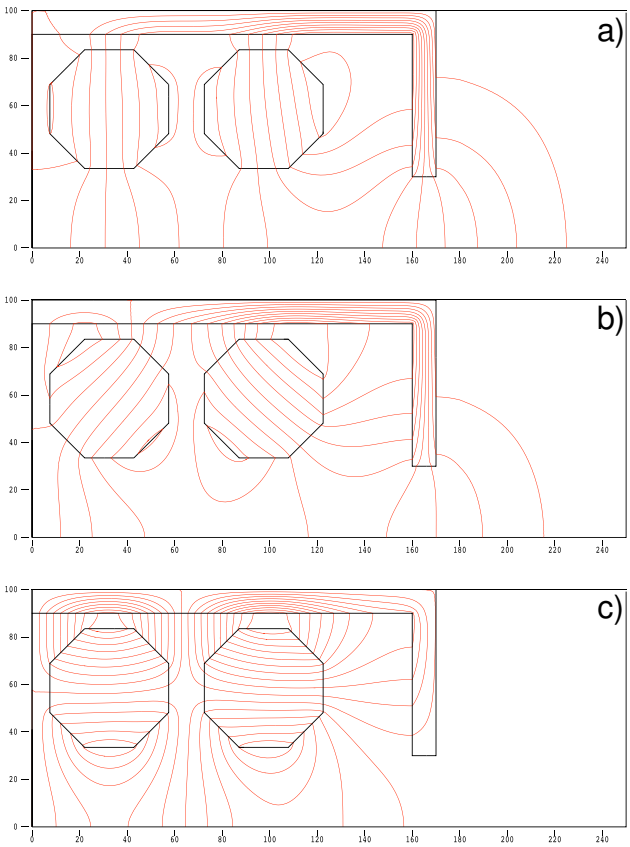


Figure 3: Schematic flux plots for three rotation angles. a) θ=0°, b) θ=45°, c) θ=90°.

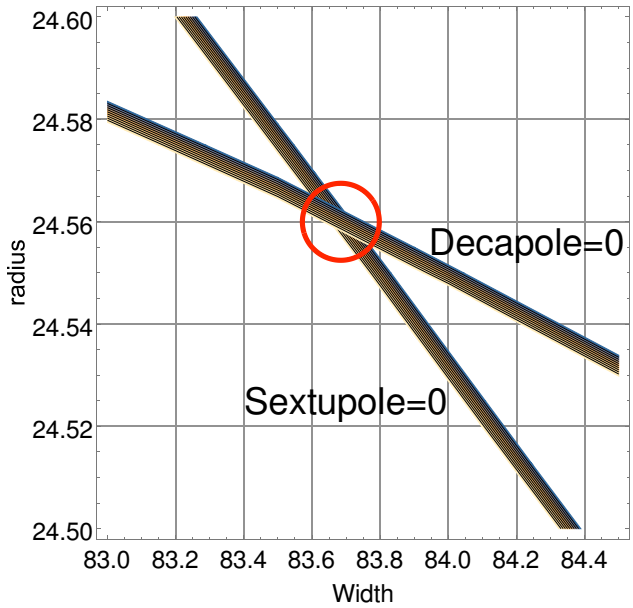


Figure 4: The lines where the sextupole or decapole components becomes zero when the width and the radius of the middle part of the magnet rods are changed. The radius refers to facing corner to corner distance in here. The crossing point of these two lines satisfies the condition that both the multipole components become zero.

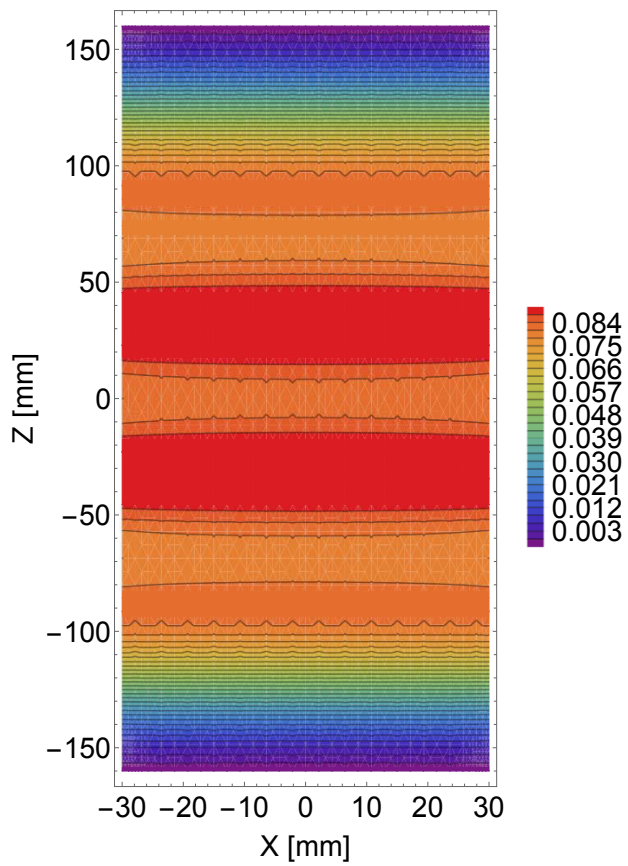


Figure 5: Magnetic field (By [T]) map on the median plane along the full span in Z direction. Fairly flat magnetic field distribution is achieved.

Content from this work may be used under the terms of the CC BY 3.0 licence (© 2018). Any distribution of this work must maintain attribution to the author(s), title of the work, publisher, and DOI.

ISBN: 978-3-95450-194-6 ISSN: 2226-0366 doi:10.18429/JACoW-LINAC2018-MOPO125

Content from this work may be used under the terms of the CC BY 3.0 licence (© 2018). Any distribution of this work must maintain attribution to the author(s), title of the work, publisher, and DOI.

Figure 7 also shows the calculated By distributions along the beam line at X=0, but for the rotation angles of 0º, 45º, 90º, 135º and 180º. The reflection symmetry of the field distributions at 0º and 180º should show the consistency in the calculation. The distribution changes with the rotation angle and then the BL product changes. The BL product value based on this calculation is shown in Fig. 7. As can be seen, the BL product changes sinusoidally with the rotation angle. Because the field flatness is well achieved, the higher multipole components are fairly small and the extracted values may not be precise. This may be the reason why some calculated points in Fig. 8 show discontinuities on their curves. In spite of the possible numerical errors in the multipole components, they grow when the permanent magnet rods are rotated, while the values at zero angle is well suppressed. These components tend to become large when the main dipole component becomes small, which results large relative error. If these values are not acceptable for beam dynamics, compensation techniques would be needed such as putting tiny correction magnets on the rods.

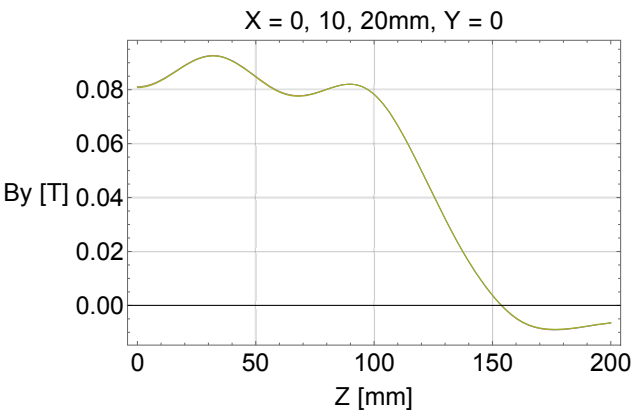


Figure 6: Magnetic field (By [T]) distribution along beam at X=0, 10 and 20 mm positions. Because of the well-optimized geometry, all three lines are overlapped in this figure.

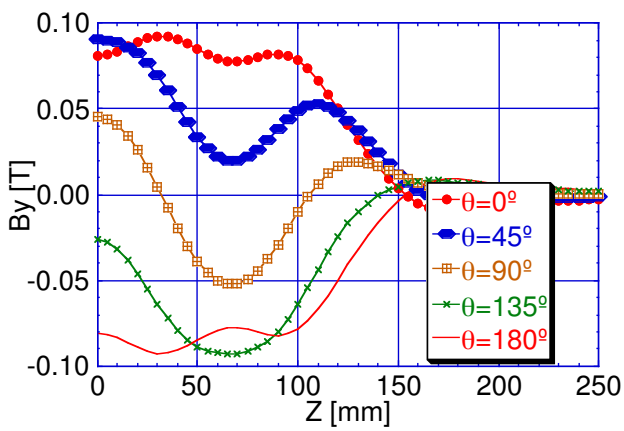


Figure 7: Magnetic field (By [T]) along beam line. The distribution changes with the rotation angle.

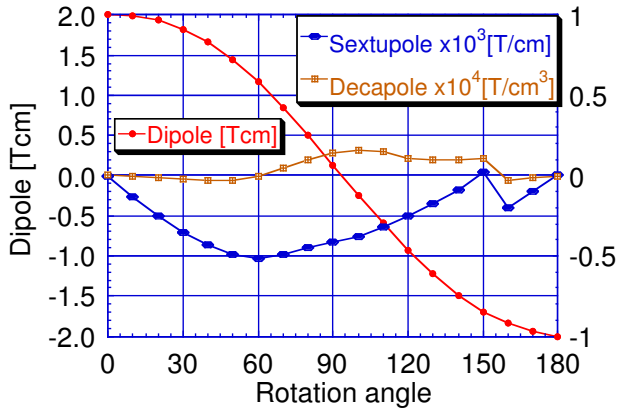


Figure 8: BL product as a function of rotor angle. Multipole components are also shown.

CONCLUSION

While some studies on PM dipoles as unipolar dipoles have been reported [5, 6], a permanent magnet system with bipolar adjustability is under investigation. Permanent magnets have a possibility to reduce the fabrication cost in addition to the operation and maintenance cost. A conceptual design of the magnet is proposed using less expensive ferrite magnet compared with strong rare earth magnets. Magnetic field adjustability for the correction magnet can be realized by rotation of magnet rods, which vary the magnetic field distribution. Reduction of the higher multipole components during rotation has to be investigated. Temperature dependence of the magnet material can be cancelled by shunt circuits with special magnetic material and/or the adjustability function. The study on the demagnetization caused by radiation of ferrite magnets is planned.

REFERENCES

[1] Y. Iwashita and N. Terunuma, "Design study of pm dipole for ilc damping ring", in Proc. 9th International Particle Accelerator Conference (IPAC'18), Vancouver, BC, Canada, April 29-May 4, 2018, pp. 505-507.

[2] ILC Technical Design Report (TDR). https://www.linearcollider.org/ILC/Publications/Technical-Design-Report

[3] T. Mihara, Y. Iwashita, M. Kumada, C. M. Spencer, "Variable Permanent Magnet Quadrupole", *IEEE Trans. Appl. Supercond*, vol. 16, pp. 224-227, 2006.

[4] RADIA. http://www.esrf.eu/Accelerators/Groups/InsertionDevices/Software/Radia

[5] J. Citadini, P. P. Sanchez, R. Basilio, M. Rocha, E.W. de Siqueira, M. Potye, and G. Tosin, "Sirius—a 3 GeV electron storage ring based on permanent magnets", *IEEE Trans. Appl. Supercond*, vol. 22, p. 4004404, 2012.

[6] T. Watanabe *et al.*, "Permanent magnet based dipole magnets for next generation light sources", *Phys. Rev. Accel. Beams*, vol. 20, p. 072401, 2017.

ISBN: 978-3-95450-194-6 ISSN: 2226-0366 doi:10.18429/JACoW-LINAC2018-MOPO127

RECENT RESULTS FROM MICE ON MULTIPLE COULOMB SCATTERING AND ENERGY LOSS*

Jingyu. Tang†, Institute of High Energy Physics, CAS, P. R. China
J. Nugent, University of Glasgow, UK

Abstract

Multiple Coulomb scattering and energy loss are well known phenomena experienced by charged particles as they traverse a material. However, from recent measurements by the MuScat collaboration, available simulation codes (GEANT4, for example) are known to overestimate the scattering of muons in low Z materials. This is of particular interest to the Muon Ionization Cooling Experiment (MICE) collaboration that has the goal of measuring the reduction of the emittance of a muon beam induced by energy loss in low Z absorbers. MICE took data without magnetic field suitable for multiple scattering measurements in the fall of 2015 with the absorber vessel filled with xenon and in the spring of 2016 using a lithium hydride absorber. In the fall of 2016, MICE took data with magnetic fields on and measured the energy loss of muons in a lithium hydride absorber. These data are all compared with the Bethe formula and with the predictions of various models, including the default GEANT4 model.

INTRODUCTION

Muon colliders and neutrino factories will require stored muons with high intensity and low emittance [1]. Muons are produced as tertiary particles ($p + N \rightarrow \pi + X$, $\pi \rightarrow \mu + \nu$) inheriting a large emittance (volume of the beam in the position and momentum phase space). For efficient acceleration, the phase-space volume of these beams must be reduced significantly ("cooled"), in order to be accepted by traditional accelerators. Due to the short muon lifetime, ionization cooling is the only practical and efficient technique to cool muon beams [2]. In ionization cooling, the muon beam loses momentum in all dimensions by ionization energy loss when passing through an absorbing material, reducing the RMS emittance (ε_{RMS}) and increasing its phase space density. Subsequent acceleration by radio-frequency cavities restores longitudinal energy, resulting in a beam with reduced transverse emittance. A factor of 10^5 in reduced 6D emittance has been achieved in simulation with a 970 m long channel [3].

The rate of change of the normalized transverse RMS emittance ε_T is given by the ionization cooling equation [4]:

$$\frac{d\varepsilon_T}{dz} \cong -\frac{\varepsilon_T}{E_\mu \beta^2}\frac{dE_\mu}{dz} + \frac{\beta_\perp}{2mc^2\beta^3}\frac{(13.6\ \text{MeV/c})^2}{E_\mu X_0}, \qquad (1)$$

where E_μ is the muon energy, β the muon velocity, dE_μ/dz the magnitude of the ionization energy loss, m the muon mass, X_0 the radiation length, and $\beta_\perp$ the transverse beta function at the absorber. The first term on the right can be referred as the "cooling" term given by the "Bethe equation", while the second term is the "heating term" that uses the PDG approximation [5] for the multiple Coulomb scattering.

MICE is instrumented with a range of detectors used for particle identification and position-momentum measurements. This includes a scintillating fiber tracker upstream and downstream of the absorber placed in a strong solenoid field to measure the position and the momentum (with a spatial resolution around 0.3 mm). MICE is also equipped with a series of particle identification detectors, including three time-of-flight hodoscopes (ToF0/1/2, with a time resolution around 60 ps), two threshold Cherenkov counters, a pre-shower calorimeter and a fully active scintillator calorimeter. A schematic drawing of MICE Step IV is shown in Fig. 1.

MICE data taking was concluded in December 2017 (in the Step IV configuration) in order to make detailed measurements of multiple Coulomb scattering and energy loss of muon beams at different momenta and channel configurations, with lithium hydride (LiH) and liquid hydrogen (LH_2) absorbers. The collaboration also sought to measure the reduction in normalized transverse emittance [6], comparing the emittance of a sample of muons selected in the upstream tracker with the emittance of the same sample measured in the downstream one, after passing through the absorber.

MEASUREMENTS OF SCATTERING DISTRIBUTIONS

Though multiple Coulomb scattering is a well understood phenomenon, results from MuScat [7-8] indicate that the effect in low Z materials is not well modelled in simulations such as GEANT4 [8]. MICE therefore measured the multiple Coulomb scattering distribution to validate the scattering model and understand the heating term in Eq. (1), in order to make more realistic predictions of the emittance reduction.As MICE was designed to measure the emittance change to 0.1% level, precise measurements on multiple Coulomb scattering are required. Both data with field off and field on in the scintillating fiber tracker are available for MICE. While the field on data is still being analysed, the field off analysis is presented here.

MICE has collected data for muon beams at three different momenta, 172 MeV/c (in order to compare with MuScat), 200 MeV/c and 240 MeV/c with and without the LiH absorber in place (thickness 65 mm, X_0 = 79.62 g/cm^2) and with a full and an empty liquid hydrogen absorber vessel (~22 litre). Here the LiH analysis is presented.

*on behalf of the MICE Collaboration
†tangjy@ihep.ac.cn

Content from this work may be used under the terms of the CC BY 3.0 licence (© 2018). Any distribution of this work must maintain attribution to the author(s), title of the work, publisher, and DOI.

ISBN: 978-3-95450-194-6 ISSN: 2226-0366 doi:10.18429/JACoW-LINAC2018-MOPO127

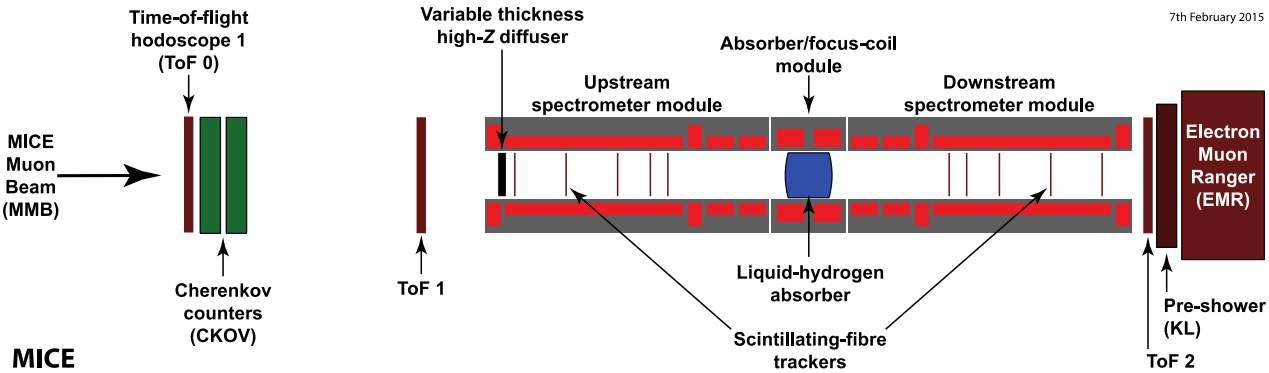


Figure 1: Schematic diagram of MICE in its final configuration (Step IV).

The position and momentum of each muon is measured by the trackers along with the time-of-flight, the latter also provides particle identification. Selection criteria were imposed on each track to select a well-understood sample. Bayesian deconvolution was applied to the selected data in order to extract the scattering distribution within the absorber material and comparisons have been made to GEANT4 [9], to the Molière model [10] as well as to a stand-alone scattering model developed by Carlisle and Cobb [11]. Data taken with LiH on a full range of beams, deconvolved using the GEANT model, are shown in Fig. 2. Different contributions to the systematic uncertainty have been considered: sensitivity to the thickness of the absorber, time of flight cuts used for momentum selection, alignment of the detectors and choice of the fiducial cuts. The time of flight systematics dominate. The scattering width taken from the scattering distributions projected in the X-Z and Y-Z planes are $\Theta = 23.3 \pm 0.9 \pm 0.2$ mrad at 172 MeV/c, $\Theta = 17.9 \pm 0.4 \pm 0.5$ mrad at 200 MeV/c and $\Theta = 14.2 \pm 0.1 \pm 0.5$ mrad at 240 MeV/c in LiH. The preliminary analysis indicates that the PDG model overestimates [12]. The PDG recommended formula is:

$$\theta_0 = \frac{13.6\,\text{MeV}}{p_\mu c \beta_{\text{rel}}} Z \sqrt{\frac{\Delta z}{X_0}} \left[1 + 0.038 \ln \frac{Z^2 \Delta z}{\beta_{\text{rel}}^2 X_0} \right]. \quad (2)$$

Data were collected over a wide range of momenta. The data were then binned in momentum and the analysis repeated for each bin with the scattering width determined in each case. The angular distribution has been fitted with an expression with a $1/p\beta$ dependence of a similar form to the Rossi and Greisen expression for the RMS scattering recommended by the PDG [13] (Fig. 3).

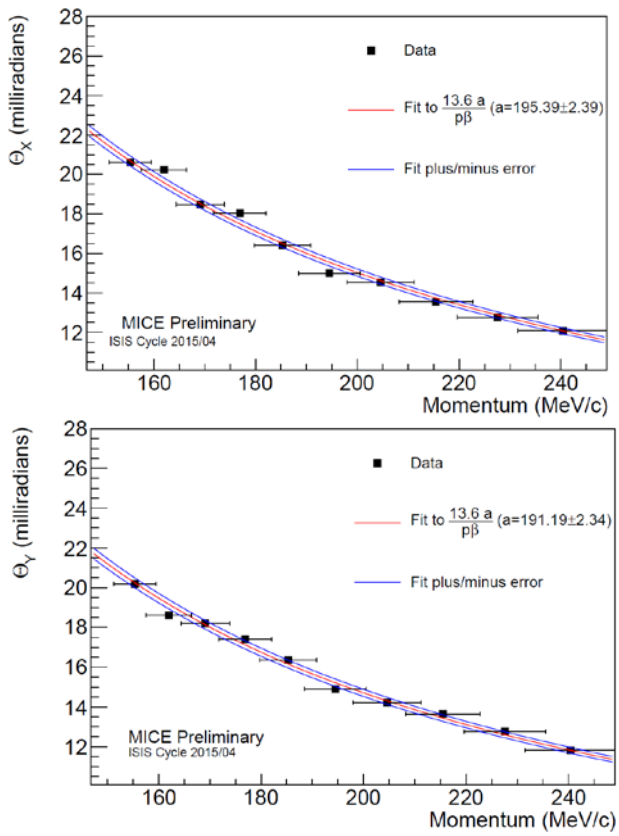


Figure 2: Results of the scattering analysis using data from all three nominal beam settings. Scattering widths are reported after application of deconvolution. Projected in the X-Z (top) and Y-Z (bottom) planes.

Content from this work may be used under the terms of the CC BY 3.0 licence (© 2018). Any distribution of this work must maintain attribution to the author(s), title of the work, publisher, and DOI.

ISBN: 978-3-95450-194-6 ISSN: 2226-0366 doi:10.18429/JACoW-LINAC2018-MOPO127

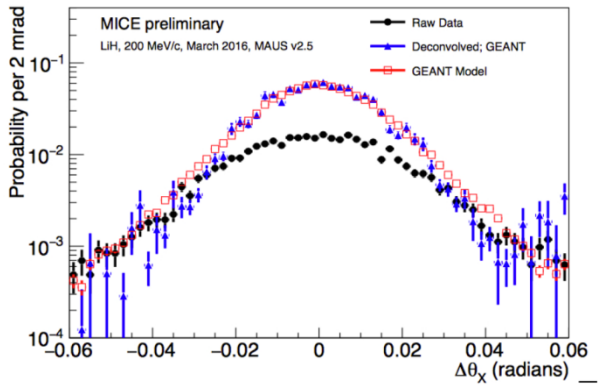


Figure 3: Scattering angular distributions in the X-Z plane, raw data and deconvolved data.

MEASUREMENT OF ENERGY LOSS

The mean rate of energy loss for relativistic charged heavy particles traversing matter is given by the "Bethe formula" [14]:

$$-\left\langle \frac{dE}{dX} \right\rangle = Kz^2 \frac{Z}{A}\frac{1}{\beta^2}\left[\frac{1}{2}\ln\frac{2m_e c^2\beta^2\gamma^2 W_{\max}}{I^2} - \beta^2 - \frac{\delta(\beta\gamma)}{2}\right], \quad (3)$$

where the mean excitation energy, I, in hydrogen is known at the 5% level. Small differences are expected between the energy loss in LH_2 and in LiH.

MICE measured the momentum upstream and downstream of the absorber using information from the trackers combined with measurements of the time of flight. Data has been analyzed using central muon-beam momenta of 140, 170, 200 and 240 MeV/c in the presence of 3 T magnetic fields, with the LiH absorber (Fig. 4). Preliminary results for 200 MeV/c muons in magnetic field traversing the LiH absorber show that the mean momentum loss is $\Delta p = 12.8 \pm 5.3$ MeV/c. Further studies are planned to deconvolve the energy loss measured without absorber from the measurement with the absorber in order to obtain the energy loss in the absorber. The final goal will be to determine the correlation between energy loss and multiple Coulomb scattering.

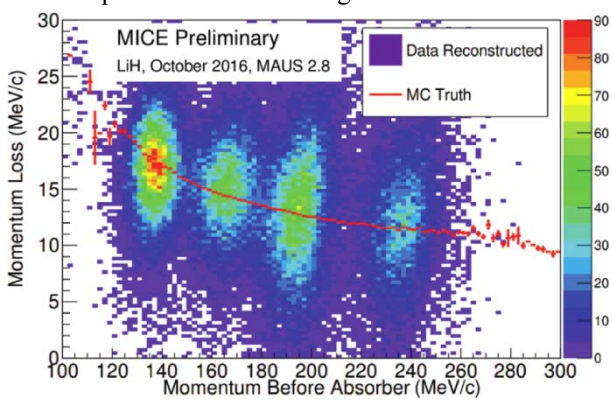


Figure 4: Distribution of the reconstructed momentum loss across the absorber compared with the MC truth.

CONCLUSION

MICE, at Step IV, has successfully collected all the required data in order to measure the properties of liquid hydrogen and lithium hydride that affect the performance of an ionization cooling channel. Step IV data taking commenced in 2015 and concluded at the end of 2017: scattering and energy loss measurements on LiH and LH_2 have been performed. The Step IV configuration will also be used to study the effect of channel optics and of the input beam momentum and emittance on the ionization cooling. Several studies are in progress and results are in preparation for publication.

ACKNOWLEDGEMENTS

MICE has been made possible by grants from funding agencies from ten participating countries. We acknowledge the support of the staff of the STFC Rutherford Appleton and Daresbury Laboratories, and the use of Grid computing resources deployed and operated by GridPP in the U.K., http://www.gridpp.ac.uk/. The author acknowledges the support from China-US collaboration fund on High-Energy Physics jointly by CAS and IHEP.

REFERENCES

[1] S. Geer, "Neutrino beams from muon storage rings: Characteristics and physics potential". *Phys. Rev. D*, vol. 57, p. 6989, 1998.

[2] D. Neuffer, "Principles and applications of muon cooling", *Part. Accel.*, vol. 14, p. 75, 1983.

[3] D. Stratakis and R. Palmer, *Phy. Rev. ST Accel. Beams*, vol. 18, p. 031003, 2015.

[4] R. C. Fernow and J. C. Gallardo. "Muon transverse ionization cooling: Stochastic approach". *Phys. Rev. E*, vol. 52, p.1039, 1995.

[5] C. Patrignani *et al.*, (Particle Data Group), *Chin. Phys. C*, vol. 40, p. 100001, (2016, 2017 update).

[6] V. Blackmore, "Recent results from the study of emittance evolution in MICE", presented at IPAC'18, paper TUPML067.

[7] MuScat Collaboration, W. J. Murray, "Comparison of MuScat data with GEANT4", *Nucl. Phys. Proc. Suppl.*, vol. 149, p. 99-103, 2005.

[8] D. Attwood *et al.*, "The scattering of muons in low Z materials", *Nucl. Instrum. Meth.*, B251 (2006) 41.

[9] GEANT4 Collaboration, S. Agostinelli *et al.*, "GEANT4: A Simulation toolkit", *Nucl. Instrum. Meth. A*, vol. 506, p. 250-303, 2003.

[10] G. Moliere. Theory of the scattering of fast charged particles. 2. Repeated and multiple scattering. Z. Naturforsch., A3:78–97, 1948.

[11] T. Carlisle, "Step IV of the Muon Ionization Cooling Experiment (MICE) and the multiple scattering of muons". PhD thesis, Oxford U., 2013.

[12] R. Bayes, "Measurements of the Multiple Coulomb Scattering of Muons by MICE", NuFact16, 2016.

[13] B. Rossi, K. Greisen, "Cosmic-Ray Theory", *Rev. Mod. Phys.*, vol. 13, p. 240, 1941.

[14] S. Peter, "Particle penetration and radiation effects". Springer Series in Solid State Sciences, 151. Berlin Heidelberg: Springer-Verlag.

Content from this work may be used under the terms of the CC BY 3.0 licence (© 2018). Any distribution of this work must maintain attribution to the author(s), title of the work, publisher, and DOI.

ISBN: 978-3-95450-194-6 ISSN: 2226-0366 doi:10.18429/JACoW-LINAC2018-MOPO129

RECENT RESULTS FROM THE STUDY OF EMITTANCE EVOLUTION AT MICE

V. Blackmore, C. Hunt*, Imperial College London, London, UK
W. B. Liu, Institute of High Energy Physics, CAS, Beijing, China
on behalf of the MICE Collaboration

Abstract

The Muon Ionization Cooling Experiment (MICE) has measured the evolution of emittance due to ionization energy loss. Muons were focused onto an absorber using a large aperture solenoid. Lithium-hydride and liquid hydrogen-absorbers have been studied. Diagnostic devices were placed upstream and downstream of the focus, enabling the phase-space coordinates of individual muons to be reconstructed. By observing the properties of ensembles of muons, the change in beam emittance was measured. Data taken during 2016 and 2017 are currently under study to evaluate the change in emittance due to the absorber for muon beams with various initial emittance, momenta, and settings of the magnetic lattice. The current status and the most recent results of these analyses will be presented.

INTRODUCTION

Low emittance stored muon beams have been proposed as the source of neutrinos at a neutrino factory [1, 2] or as the means to deliver multi-TeV lepton-antilepton collisions at a muon collider [3]. The muons at such a facility originate from the decay of pions and occupy a large volume in phase space (emittance). This must be reduced (cooled) to fit within the acceptance of a storage ring or accelerating structure. The short muon lifetime prohibits existing cooling techniques such as synchrotron or stochastic cooling. Ionisation cooling is the only viable method that can act within the short muon lifetime to reduce phase space volume of a muon beam.

Ionisation cooling occurs when a muon beam passes through an absorber material and ionises atomic electrons, losing both transverse and longitudinal momentum. This reduces the volume in phase space occupied by the beam, and thus reduces the beam emittance. Concurrently, multiple Coulomb scattering within the absorber increases the angular divergence of the beam, increasing the emittance. The interplay of emittance reduction, due to energy loss by ionisation, and emittance growth, through multiple Coulomb scattering, results in a change in normalised RMS emittance, $\varepsilon_\perp$, over a distance, dz, given by [4],

$$\frac{d\varepsilon_\perp}{dz} \approx -\frac{\varepsilon_\perp}{\beta^2 E_\mu}\left\langle\frac{dE}{dz}\right\rangle + \frac{\beta_\perp (13.6MeV/c)^2}{2\beta^3 E_\mu m_\mu X_0} \quad (1)$$

where $\beta_\perp$ is the transverse optical Twiss function, βc, E_μ, and m_μ are a particle's velocity, energy, and mass respectively, and X_0 is radiation length of the absorber material. Maximum emittance reduction is achieved by using absorbers with large radiation lengths such as liquid hydrogen or lithium hydride.

THE MUON IONISATION COOLING EXPERIMENT

The Muon Ionisation Cooling Experiment (MICE) [5] consists of a transfer line that transports particles from the ISIS synchrotron at the Rutherford Appleton Laboratory, UK, to a segment of a cooling lattice. The beam is transported through PID detectors using conventional quadrupole magnets, then by large-aperture superconducting solenoids through the cooling channel operated at up to 3 T. At the centre of the cooling lattice is an absorber material. The beam is measured before and after the absorber in the constant 3 T field of the up- and down- stream spectrometer solenoid modules using scintillating fibre trackers. A schematic drawing of MICE is shown in Fig. 1.

MICE has measured the passage of individual muons through an empty channel, 21 litres of liquid hydrogen contained within an aluminium vessel, and a 65 mm solid lithium hydride disc. These measurements were made with the same magnetic optical configuration to evaluate phase space evolution across a cooling cell and compare the cooling performance of liquid hydrogen and lithium hydride. Individual particle trajectories are measured as they cross the experiment and are assembled offline into analysable particle ensembles. These ensembles consist of particles with: 1) an upstream Time-of-Flight consistent with a muon, 2) a measured total momentum, p, in the range 135–145 MeV/c, 3) a single, good quality track in the upstream tracking detector, and 4) a measured momentum in the upstream tracking detector consistent with the Time-of-Flight. The current status of the analysis of the measured ensembles is presented here.

EMITTANCE EVOLUTION

The measured components of transverse phase space, x, y, p_x, p_y are compared to those of a Monte Carlo simulation, that includes the response of instrumentation, in Fig. 2. The reconstructed data (black, circles) and the reconstructed simulation (filled histogram) show good agreement. Distributions of x, y, p_x, p_y are shown (left) up- and (right) downstream of the liquid hydrogen absorber.

The ensemble's covariance matrix, $\Sigma_\perp$, is calculated from the measured transverse quantities as,

* Christopher.hunt08@imperial.ac.uk

Content from this work may be used under the terms of the CC BY 3.0 licence (© 2018). Any distribution of this work must maintain attribution to the author(s), title of the work, publisher, and DOI.

ISBN: 978-3-95450-194-6 ISSN: 2226-0366 doi:10.18429/JACoW-LINAC2018-MOPO129

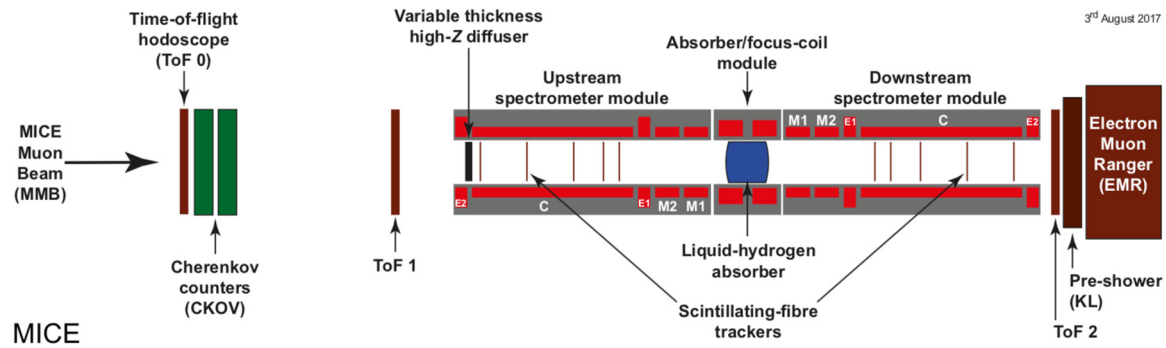


Figure 1: The instrumentation of MICE. Single muons cross two Time-of-Flight detectors and Cherenkov detectors, then enter the solenoidal field of the MICE magnetic lattice. The muon's position and momentum is measured in the upstream solenoid module using a scintillating fibre tracker. The muon then crosses an absorber, losing momentum, and is re-measured in the downstream solenoid module with a scintillating fibre tracker. The muon is instrumented on its exit with Time-of-Flight, Kloe-lite and Electron-Muon Ranger detectors.

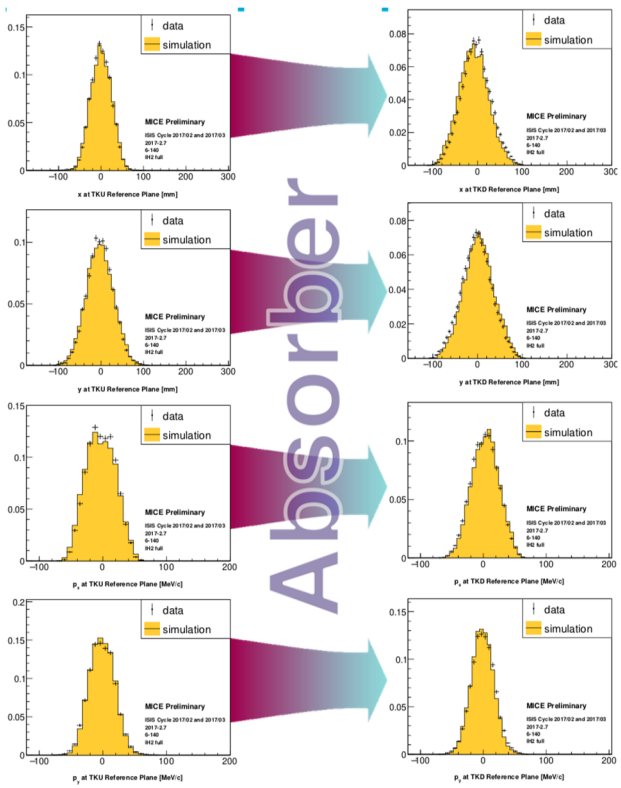


Figure 2: The position and momentum components of individual muons are measured before and after crossing an absorber (LiH or Liquid Hydrogen) by a scintillating fibre tracker immersed in a 3T uniform field. Reconstructed data (black, circles) compare well with reconstructed Monte Carlo simulations (filled histogram).

$$\Sigma_{4D} = \begin{pmatrix} \sigma_{x,x} & \sigma_{x,p_x} & \sigma_{x,y} & \sigma_{x,p_y} \\ \sigma_{x,p_x} & \sigma_{p_x,p_x} & \sigma_{y,p_x} & \sigma_{p_x,p_y} \\ \sigma_{x,y} & \sigma_{y,p_x} & \sigma_{y,y} & \sigma_{y,p_y} \\ \sigma_{x,p_y} & \sigma_{p_x,p_y} & \sigma_{y,p_y} & \sigma_{p_y,p_y} \end{pmatrix}, \quad (2)$$

and the transverse RMS emittance is,

$$\varepsilon_N = \frac{1}{m_\mu}\sqrt[4]{det|\Sigma_{4D}|}. \quad (3)$$

The transverse amplitude, $A_\perp$, of a particle with respect to the ensemble is,

$$A_\perp = \varepsilon_N(\mathrm{v}-\mu)^T\Sigma_{4D}^{-1}(\mathrm{v}-\mu), \quad (4)$$

where $\mathbf{v}$ is the phase space vector of the particle, $\mathbf{v} = (x, p_x, y, p_y)$, and $\mu = (\langle x\rangle, \langle p_x\rangle, \langle y\rangle, \langle p_y\rangle)$ is the beam centroid. An ensemble of muons with large emittance, consists of a large spread of particle amplitudes, whereas an ensemble with small emittance has a more particles occupying lower amplitudes.

Data were taken with the same magnetic configuration and beamline settings, with $\beta_\perp \approx 660$ mm at the absorber. Measurements were made of the particles that crossed the experiment up- and down-stream of the absorbers. As the magnetic field was the same in each data set the empty channel measurements enable observation of optical aberrations and will be used to cross-check for other systematic effects. Additionally in the case where Liouville's theorem holds true, such as for an empty channel, emittance should be conserved between the up- and downstream reference surfaces of the tracking detectors.

The amplitude of particles measured up- and down-stream in each case (empty channel, liquid hydrogen, lithium hydride) were calculated according to Eq. 4. These amplitudes were binned in 5 mm increments, from $0 \le A_\perp \le 60$ mm. In order to prevent sensitivity to tail effects, the covariance matrix is recalculated excluding all higher-amplitude particles for each amplitude bin. The number of muons within each amplitude bin in the up-stream and downstream samples was calculated. An increase in the number of low-amplitude particles down-stream implies an increase in density of the beam core, or a lower emittance.

The cumulative transverse amplitude was calculated for each use case (empty channel, liquid hydrogen, lithium hydride) and the ratio of the number of muons in the down-stream to up-stream samples was taken as

Content from this work may be used under the terms of the CC BY 3.0 licence (© 2018). Any distribution of this work must maintain attribution to the author(s), title of the work, publisher, and DOI.

ISBN: 978-3-95450-194-6 ISSN: 2226-0366 doi:10.18429/JACoW-LINAC2018-MOPO129

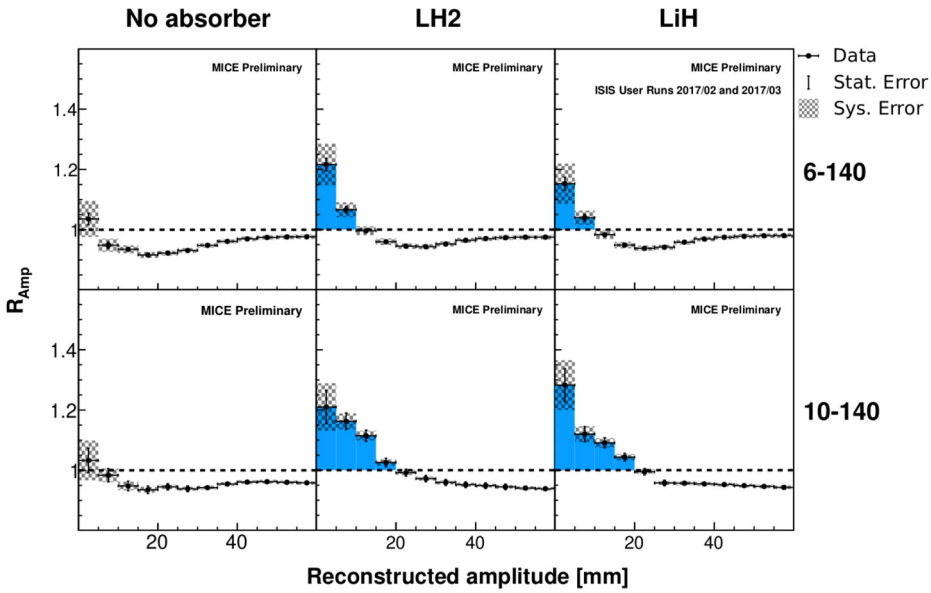


Figure 3: The ratio, R_{Amp}, of the downstream and upstream samples for (left) an empty channel, (middle) liquid hydrogen, and (right) lithium hydride. The ratios are shown for two input beam line settings, with a nominal momentum of p = 140 MeV/c and nominal emittance of 6 (top), and 10 mm (bottom). Cooling is seen where $R_{\mathrm{Amp}} > 1$. Statistical uncertainties are given as bars, systematic uncertainties (grey) are under study.

$$R_{Amp} = \frac{N_{downstream}}{N_{upstream}}, \quad (5)$$

where N is the number of muons with amplitude equal to or less the amplitude under consideration. Figure 3 shows the variation of this ratio with increasing amplitude, encompassing increasing amounts of the ensemble, for the empty channel, liquid hydrogen, and lithium hydride absorbers. Two different input beams are also shown, with a nominal $\varepsilon_{\perp,\mathrm{upstream}} \approx 6$ and 10 mm. If the ensemble is cooled, the ratio $R_{\mathrm{Amp}} > 1$ in the lowest amplitude bins, as is seen in both liquid hydrogen and lithium hydride absorbers. No cooling is seen in the empty channel ensemble.

CONCLUSION

MICE has measured a reduction in the transverse amplitude of muons crossing liquid hydrogen and lithium hydride absorbers. Particles observed with large transverse amplitude upstream of the absorber material migrate to lower amplitude areas after crossing the absorber. No emittance reduction is seen with the same optical field configuration but without an absorber in place. The Monte Carlo simulation is representative of the transverse distributions of the ensemble. Further analysis is in progress, including a robust estimate of systematic uncertainties due to field non-uniformity and other sources. Additional analyses are underway to study the equilibrium emittance of each absorber material, and the dependence of Eq. 1 on momentum and the value of $\beta_\perp$ at the absorber.

ACKNOWLEDGEMENTS

MICE has been made possible by grants from funding agencies from ten participating countries. We acknowledge the support of the staff of the STFC Rutherford Appleton and Daresbury Laboratories, and the use of Grid computing resources deployed and operated by GridPP in the U.K., *http://www.gridpp.ac.uk/*. The author acknowledges the support from China-US collaboration fund on High-Energy Physics jointly by CAS and IHEP.

REFERENCES

[1] S. Choubeyetal *et al.*, "International Design Study for the Neutrino Factory", *Interim Design Report*, http://arxiv.org/abs/arXiv: 1112.2853

[2] S. Geer *et al.*, "Neutrino beams from muon storage rings: Characteristics and physics potiential", *Phys. Rev. D*, vol. 57, pp. 6989-6997, 1998, doi:10.1103/PhysRevD.57.6989

[3] R. B. Palmer *et al.*, "Muon Colliders", *Rev. Accel. Sci. Tech.*, vol. 7, pp. 137–159, 2014.

[4] R. C. Fernow and J. C. Gallardo, "Muon transverse ionization cooling: Stochastic approach", *Phys. Rev. E*, vol. 52, p. 1039, 1995.

[5] MICE Collaboration, MICE: *An International Muon Ionization Cooling Experiment*, http://mice.iit.edu/micenotes/public/pdf/MICE002 1/MICE0021.pdf

Content from this work may be used under the terms of the CC BY 3.0 licence (© 2018). Any distribution of this work must maintain attribution to the author(s), title of the work, publisher, and DOI.

ISBN: 978-3-95450-194-6 ISSN: 2226-0366 doi:10.18429/JACoW-LINAC2018-MOPO130

MAGNETIC FLUX GENERATED BY THERMAL CURRENT IN CEBAF 5-CELL CAVITY SYSTEM*

R. L. Geng†, S. C. Huang[1], Jefferson Lab, Newport News, VA 23693, USA

Abstract

The unloaded quality factor Q_0 of many 5-cell CEBAF cavities was lowered by a factor of ~2 from their vertical qualification testing to their beam operation in CEBAF tunnels. Causes of this Q_0 degradation were studied previously, including a more recent one addressing static flux arising from magnetic components near these cavities. This paper reports on a preliminary study of the dynamic flux generated by a thermal current, arising from the Seebeck effect and flowing in closed-loops formed by a niobium cavity and its surrounding tuner rods and liquid helium vessel made of stainless-steel. Flux generation in response to various thermal profiles in a 5-cell CEBAF cavity with integrated tuner rods were studied through varied cool-down cycles in a vertical dewar at JLAB. One outcome of this study is a proposed cool-down procedure for eliminating the thermal current generated magnetic flux around 5-cell cavities placed in CEBAF tunnels. This procedure may be useful for improving cavity Q_0 in a cost-effective manner, which in turn saves cryogenic expenditures for more efficient CEBAF operation.

INTRODUCTION

The unloaded quality factor of an RF cavity Q_0 can be described by $Q_0 = {}^{G}/_{R_s}$, where G is the geometry factor determined solely by the cavity geometry and resonating mode, R_s is the RF surface resistance which consists of the BCS term R_{BCS} and residual term R_{res}. The Q_0 values of many original 5-cell cavities placed in the CEBAF tunnels were degraded by a factor of ~2 as compared to that measured during their vertical qualification testing. The origin of this Q_0 degradation is attributed to an increase of R_{res}. Magnetic flux trapped in the RF penetration layer of an SRF cavity during its cool-down crossing Tc contribute to R_{res}, as it has been well established. Sources of magnetic flux include *static* ones, such as the remaining earth magnetic field inside the magnetic shielding, magnetized components enclosed in the inner magnetic shield, and *dynamic* ones such as thermal current generated magnetic flux. A recent prior work revealed large remnant magnetic fields in various magnetic components being near a cavity yet enclosed inside the inner magnetic shield [1]. That work led to a change in CEBAF cryomodule refurbishing practice. Non-magnetic strut springs made of 316L stainless-steel (SS) replaced their magnetic counterparts starting at the 11th rework module C50-11, eliminating one source of static magnetic flux that was enclosed in the inner magnetic shield. In the best case for C50-11, the cavity Q_0 at 5 MV/m measured in cryomodule was preserved at 88% of the value measured during its vertical qualification. However in the worst case, the preservation was still poor, at 40% level, begging additional effort.

More recently, systematic measurements of an original CEBAF cavity in a vertical cryostat with progressively added cryomodule components were carried out with an effort of degaussing the remaining magnetic components enclosed in the inner magnetic shield [2]. That work led to a new change in refurbishment practice starting at C50-12. The tuner components and helium vessel were all degaussed with a surface demagnetizer. In the best case for C50-12, the cavity Q_0 at 5 MV/m measured in cryomodule was preserved at 100% of the value measured during its vertical qualification. However in the worst case, the preservation was still ~ 60%, despite the static magnetic flux having fallen into the specification of ±10 mG for that cavity when measured in the tunnel.

Aiming for CEBAF operation with improved energy efficiency, the effort is continuing at JLAB, in pursuit of origin and remediation of the low Q_0 observed in original and refurbished 5-cell cavity cryomodules placed in linac tunnels. In this contribution, we report on preliminary studies of a *dynamic* source for magnetic flux, arising from the thermal-electric effect. Similar effects were observed in 9-cell cavities jacketed with titanium helium vessels [3]. Through these elementary studies, we seek ways for thermal-current elimination and raising Q_0 [4].

5-CELL CAVITY SYSTEM

As completed in 1994, the original CEBAF accelerator was consisted of 338 L-band (1497 MHz) 5-cell SRF niobium cavities hosted in 42 8-cavity cryomodules plus an additional 2-cavity cryomodule. The basic building block is a cryo-unit as shown in Fig. 1. Two 5-cell cavities are connected back-to-back, which in turn are enclosed in a 610 mm diameter liquid helium vessel made of SS. Each end of the unit is isolated by a gate valve (not shown in Fig. 1). The overall length of this unit is about 1778 mm.

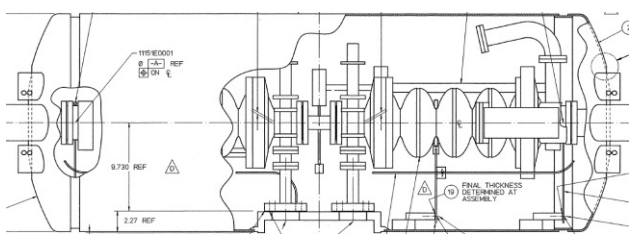


Figure 1: CEBAF Cryo-unit. Each cryomodule consists of four of such cryo-units.

* Authored by Jefferson Science Associates, LLC under U.S. DOE Contract No. DE-AC05-06OR23177.
†geng@jlab.org.
[1] former graduate student, presently at IMP, CAS.

Content from this work may be used under the terms of the CC BY 3.0 licence (© 2018). Any distribution of this work must maintain attribution to the author(s), title of the work, publisher, and DOI.

ISBN: 978-3-95450-194-6 ISSN: 2226-0366 doi:10.18429/JACoW-LINAC2018-MOPO130

Content from this work may be used under the terms of the CC BY 3.0 licence (© 2018). Any distribution of this work must maintain attribution to the author(s), title of the work, publisher, and DOI.

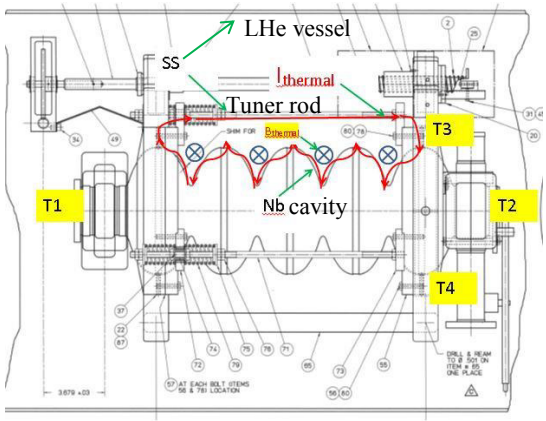


Figure 2: CEBAF 5-cell niobium cavity system with mounted SS tuner components.

Figure 2 illustrates the CEBAF 5-cell cavity system consisting of a 5-cell niobium cavity and its tuner components, including three SS supporting rods. A closed-loop is formed by the niobium cavity and SS tuner rods. During cryomodule cooldown process, the initial temperature equilibrium over the cavity length is broken until equilibrium is restored when the cavity is fully immersed in liquid helium bath. During this cool-down period, two cavity ends are at different temperatures, T_1 and T_2. A thermal current, $I_{thermal}$, is resulted due to Seebeck effect and it flows in the closed-loop mentioned above, as depicted in Fig. 2. Dynamic magnetic flux generated by this transient thermal current, $B_{thermal}$, may be trapped in the RF penetration layer of the cavity when it is cooled across the transition temperature of niobium. Like trapped *static* flux, the trapped *dynamic* flux will contribute to surface resistance as well, lowering the cavity Q_0.

EXPERIMENTAL APPARATUS

We carried out measurements of magnetic flux of a simplified 5-cell cavity model system subjected to various thermal profiles by cool-down and warm up the measurement apparatus. The 5-cell cavity was vertically oriented with one SS tuner rod mounted, forming a close loop including aluminium blocks between cavity end cells and the rod. A sketch and a photo are shown in Fig. 3.

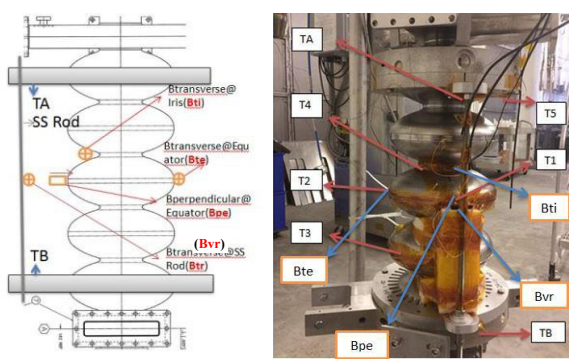


Figure 3: Instrumented experimental apparatus modelling one closed loop in the 5-cell cavity system.

Four Bartington single-axis fluxgate magnetometers were mounted at locations indicated in Fig. 3. Three of them were oriented for the maximum sensitivity to azimuthal flux (Bte at middle-cell equator, Bti at iris above middle-cell, Bvr at center of rod). One was oriented for the maximum sensitivity to the flux normal to the outer surface of the middle-cell equator (Bpe). Each magnetometer was accompanied by a temperature sensor. Additional temperature sensors were placed at the aluminium blocks holding the end cells. A key control parameter was the temperature difference DeltaT between the upper block (TA) and lower block (TB).

The experimental apparatus was suspended in a vertical testing dewar in JLAB VTA area. Cold helium gas was injected from the bottom of the dewar. The dewar space was shielded from earth magnetic fields as usual. Residual background magnetic flux were recorded initially and subtracted later on in data analysis for obtaining the flux entirely originated from the thermal-electric currents. Warming up was realized by turning on a resistive heater placed at the bottom of the dewar.

A natural consequence of our experimental arrangement is that a superconducting phase front appears first at the lower cavity flange. That front then moves upward as the cooling continues, ultimately sweeps through the entire cavity length. This arrangement leads also to a temperature profile in which TA > TB, thus a positive DeltaT at any instant during cool-down. Such a profile is desirable for creating needed control in DeltaT.

EXPERIMENTAL RESULTS

A series of measurements were carried out in the spring of 2015. Of interest to us are data taken after the appearance of a superconducting phase front, hence only data for TB < 10 K will be presented. A typical result is shown in Fig. 4, illustrating the dependence of Bte, Bvr and Bti with DeltaT for two sequential cooldown cycles. Thermal current generated magnetic flux is evident from Bte, Bvr, and Bti during the 1st cool-down cycle, which started at room temperature, resulted in a DeltaT of 30 - 90 K for TB < 10 K. In contrast, negligibly small flux is detected during 2nd cool-down cycle where DeltaT < 10 K.

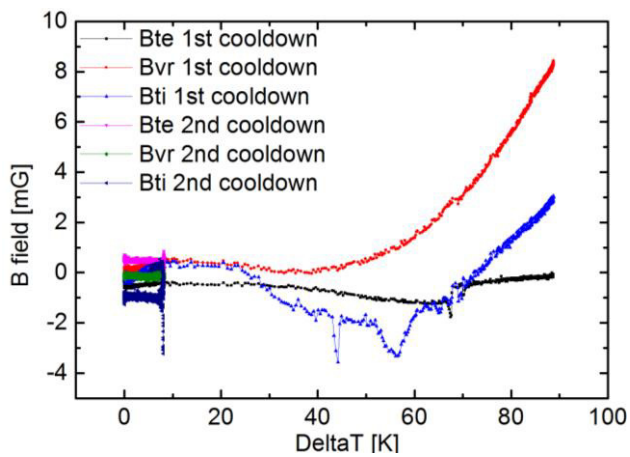


Figure 4: Test results for two sequential cooldown cycles.

ISBN: 978-3-95450-194-6 ISSN: 2226-0366 doi:10.18429/JACoW-LINAC2018-MOPO130

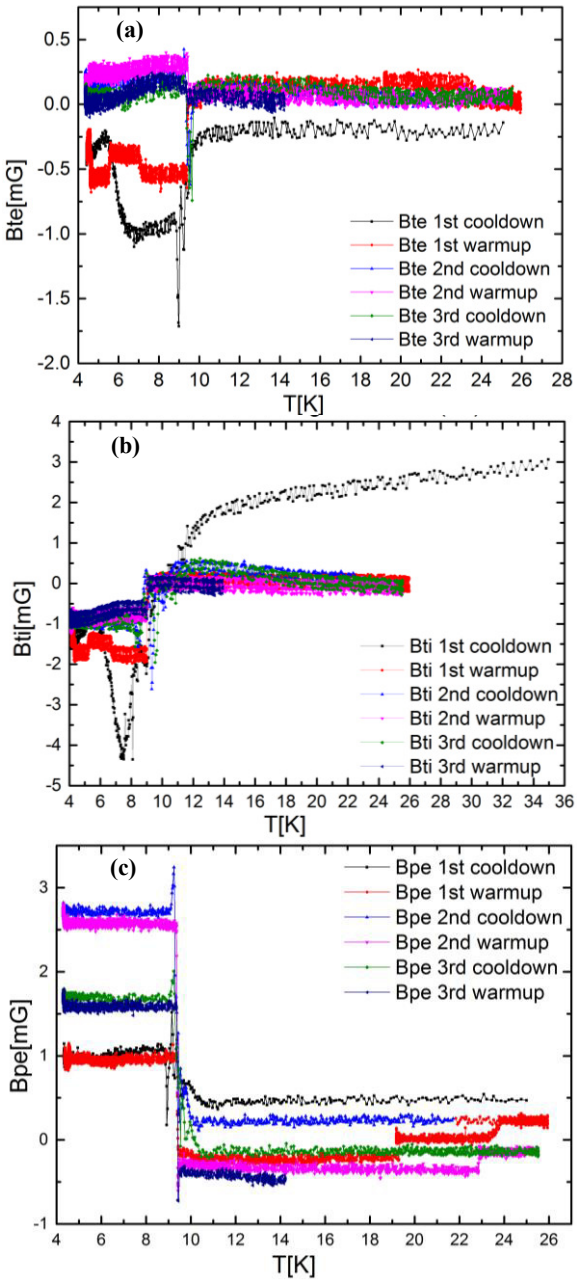


Figure 5: Dependence of flux densities on local temperatures for three sequential cooldown cycles. (a)Bte, (b)Bti, and (c)Bpe.

In Fig. 5, Bte, Bti, and Bpe are plotted against their local temperatures for three consecutive cool-down cycles on March 9, 2015. A step transition in the flux density near the cavity wall (Bte, Bti, and Bpe) at Tc crossing is consistent with the well-established picture of flux expulsion from that wall upon its phase transition from normal state into Meissner state. In contrast, no such step transition is apparent in Bvr (not shown), despite a large value being detected during the 1st cool-down cycle. Absence of step transition in Bvr seems to be reasonable as a result of its sensor being remote to cavity surface.

Once again, the generated magnetic flux during the 1st cycle (large DeltaT) is highly distinguishable as compared to subsequent 2nd and 3rd cycles (small DeltaT by warming up to 40 K followed by re-cooldown).

DISCUSSIONS

It is worth noting that Bpe (Fig. 5(c)) exhibits well-defined step transitions as well. This is a surprise as the sensor is oriented normal to the local cavity surface, hence insensitive to generated flux. Presently, this observed behaviour is not understood, but we speculate that it is connected with the dynamical process of fluxoid formation and movement. A possible explanation is flux tube re-orientation preferentially in the normal direction.

Additional tests were carried out with three SS rods attached to the same 5-cell cavity, resulted in similar observations. An apparent deviation lies in a much larger Bte and Bti as compared to 1-rod. This can be understood as a result of additive effect of currents as the number of rod increases. The SS helium vessel hosting the cavity pair in cryomodules can be regarded as a limiting case with many rods (see Fig. 1). Its presence may give rise to a significant magnetic flux generation. It should be mentioned that testing of a 5-cell cavity with tuner components was done in [2] and no significant change in Q_0 was observed between fast and slow cool down. This suggests that the thermal current from tuner rods alone maybe not significant. Further tests are required for assessment the effect of the SS helium vessel, including the effect of its deviation from the axisymmetric configuration [5]. Studies may be extended to new 7-cell cavities for their helium vessels, albeit compact, are made of SS as well.

We should point out that this study is not intended to be systematic. Rather it addressed two limiting cases, practically large and small DeltaT. These controls resulted in two outcomes: (1) Direct observation of magnetic flux generated by thermal currents in CEBAF cavity systems; (2) A proposed cool-down procedure for eliminating the thermal current generated magnetic flux:

- Standard initial cool-down to 4 K.
- Warm up to 40 K.
- Re-cool-down to 4 K, keep DeltaT < 10 K.
- Pump to 2K.

CONCLUSION

We carried out a series of experimental measurements with a 5-cell CEBAF niobium cavity system with integrated SS tuner rod, instrumented with thermometers and magnetometers, with which the *dynamic magnetic flux* generated by a thermal current was established. A surprising result is the observation of a large transient step in the flux density detected at the outer surface, in normal direction, of the cavity equator region. This puzzling phenomenon deserves further studies. This work resulted in a proposed cool-down procedure for eliminating the thermal-electric current generated magnetic flux around 5-cell cavities placed in CEBAF tunnels. This procedure may be useful for improving cavity Q_0 in a cost-effective manner, which in turn saves cryogenic expenditures for more efficient CEBAF operation.

Content from this work may be used under the terms of the CC BY 3.0 licence (© 2018). Any distribution of this work must maintain attribution to the author(s), title of the work, publisher, and DOI.

ISBN: 978-3-95450-194-6 ISSN: 2226-0366 doi:10.18429/JACoW-LINAC2018-MOPO130

REFERENCES

[1] R. L. Geng et al., in *Proc.* IPAC2014, Dresden, Germany, 2014, pp. 2828-2830.

[2] G. Ciovati et al., *IEEE Trans. Appl. Supercond.*, vol. 27, no. 4, p. 3500106, 2017.

[3] J. -M. Vogt, O. Kugeler, and J. Knobloch, Phys. Rev. Spec. Topics – Accel. and Beams, 18, 042001, 2015.

[4] S. C. Huang, R. L. Geng, JLAB Internal Tech Note, JLAB-TN-18-003, 2018.

[5] Anthony C. Crawford, arXiv: 1403.7996, 2014.

Content from this work may be used under the terms of the CC BY 3.0 licence (© 2018). Any distribution of this work must maintain attribution to the author(s), title of the work, publisher, and DOI.

ISBN: 978-3-95450-194-6 ISSN: 2226-0366 doi:10.18429/JACoW-LINAC2018-MOPO132

THE 7 MeV APF DTL FOR PROTON THERAPY

Xiucui Xie, Yuehu Pu[1], Jian Qiao, Fan Yang[1], Xuan Li, Deming Li, Minghua Zhao, Zhentang Zhao
Shanghai Institute of Applied Physics, Chinese Academy of Sciences, Shanghai 201800, China
[1] also at Shanghai APACTRON Particle Equipment Co.Ltd, Shanghai, China

Abstract

A 7 MeV alternating phase focused (APF) drift tube linear (DTL) for proton therapy has been designed, and a design code has been developed based on a sinusoidal synchronous phase formula and a linearly increasing electrode voltage assumption. The design procedure includes the radio frequency quadrupole (RFQ) to drift tube linac (DTL) matching, and end-to-end simulation that conducted by Trace Win. Moreover, a cutting method has been performed to correct the integral electric field deviation of RF gaps.

INTRODUCTION

The Advance Proton Therapy Facility APTRON is a dedicated proton therapy facility located in Shanghai, China. The facility made up by a linac injector and a synchrotron of 24.6 m circumference, providing proton beam from 70 MeV to 250 MeV. Two fixed beam treatment rooms and one rotating gantry room is located downstream of the accelerator. A schematic layout of the facility is shown in Figure 1.

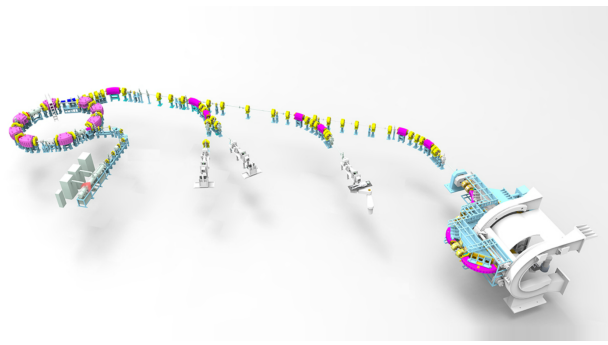


Figure 1: The bird's eye schematic view of the APTRON facility.

The alternating phase focused (APF) drift tube linac (DTL), together with a radio frequency quadrupole (RFQ), has been developed as the injector of the synchrotron ring. With its advantages of dimensions compactness and cost effectiveness, the APF DTL is an ideal choice for proton therapy facilities.

THE APF DESIGN CODE

The beam dynamics of the APF is solely depends on the electromagnetic field of the RF gaps, which determined by the synchronous phase sequence. In the past decades, several APF schemes has been proposed and developed. According to solid theoretical considerations as well as empirical rules, we choose the phase variation scheme that proposed by Yoshiyuki Iwata. In this scheme, the synchronous phase sequence is described by the following Equation (1) [1]:

$$\phi_s(n) = \phi_0 e^{-a \cdot n} sin\left(\frac{n - n_0}{b \cdot e^{c \cdot n}}\right), \quad (1)$$

where n is the number of the acceleration gaps; ϕ_0, a, b, c, and n_0 are free parameters.

Moreover, we add two hypotheses to our design strategy:

1. The potential of the electrodes are increasing monotonically and linearly.
2. The average electric field of the accelerating gaps is maintained.

Therefore, two extra parameter VE_0 and ΔVE, which stands for the voltage of the first electrode and the voltage growth of the successive electrode, together with the five Iwata formula parameters, could determine the structure of the APF.

Therefore, we developed the design code with the Iwata formula and the hypothesis to optimize the APF parameters automatically. The beam dynamics code is based on the BEAMPATH [2], and the parameters optimization algorithm is based on the nonlinear correlated stacking optimization method:

1. Estimate a set of initial parameters, generate the structure of the accelerator by the matrix transport method, feed the structure data into the BEAMPATH code, calculate the beam dynamics and evaluate the obtained results by a cost function.
2. Change two of the seven structural parameters described above to generate a new structure, feed the new structure data into the BEAMPATH and simulate the acceleration process. Compare the new results to the preceding results until all the possible parameter combinations have been considered and the best combination will be found.

THE APF DTL

The injection beam parameters for designing the APF DTL are obtained from the simulation results of a four-vane RFQ which serves as a pre-accelerator. Because the beam that extract from RFQ diverges horizontally but converges vertically while the horizontal and vertical focusing forces of the APF structure is totally identical, therefore a matching section is typically required to convert the injection beam from the RFQ into a symmetric one with symmetric properties in both the X and Y directions.

The injection and extraction energy of the APF is 3 MeV and 7 MeV, respectively. The cell number is 32 and the working frequency is 325 MHz; the on-axis acceleration field is 8.9 MV/m, corresponding to 0.5 times the Kilpatric limit.

Content from this work may be used under the terms of the CC BY 3.0 licence (© 2018). Any distribution of this work must maintain attribution to the author(s), title of the work, publisher, and DOI.

ISBN: 978-3-95450-194-6 ISSN: 2226-0366 doi:10.18429/JACoW-LINAC2018-MOPO132

Content from this work may be used under the terms of the CC BY 3.0 licence (© 2018). Any distribution of this work must maintain attribution to the author(s), title of the work, publisher, and DOI.

With the basic parameters described above, the APF DTL structure is determined automatically by executing our APF optimization code. The seven optimized parameters are $\phi_0 = 74$, $a = 0.007375$, $b = 1.925$, $c = 0.006625$, $n_0 = -8.25$, $VE_0 = 0.0805$, and $\Delta VE = 0.00165$.

Using these optimized parameters, the synchronous phases as a function of the gap number are shown in Figure 2.

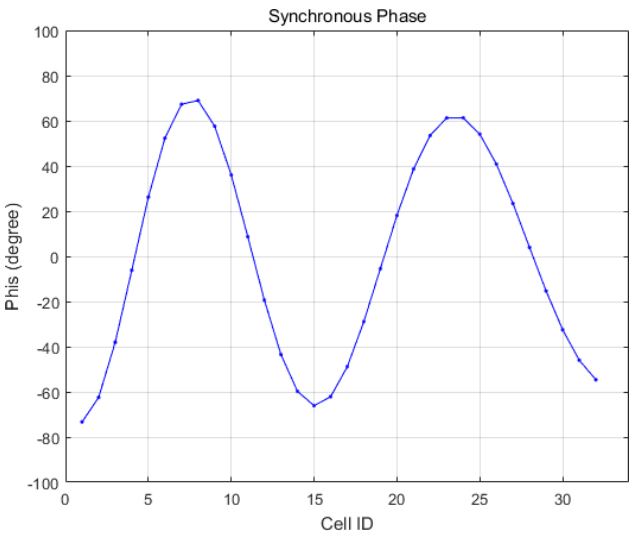


Figure 2: The synchronous phase sequence of the APF structure.

The physical parameters are summarized in the Table 1.

Table 1: The Basic Parameters of the APF DTL

Parameter	Value
Extraction structural energy	7.0000 MeV
Extraction beam energy	7.0428 MeV
Total length	1.5056 m
Total transmission	97.55 %
Effective transmission	67.90 %
Normalized RMS emittance X	0.2777 π mm mrad
Normalized RMS emittance Y	0.2660 π mm mrad
Total bunch length (2 RMS)	26.1476 mm
Momentum spread (2 RMS)	±2.835 %
Maximum surface field	26.0739 MV/m

ELECTROMAGNETIC DESIGN AND END-TO-END SIMULATION

With the APF structure above, the CST Microwave Studio code was used to compute the three-dimensional (3D) electromagnetic fields [3].

A comparison between the BEAMPATH analytical field and the CST numerical field is shown in Figure 3.

The difference between the analytical field that is used by the BEAMPATH and the simulation field calculated by CST is shown. As the integral electric field is our primary

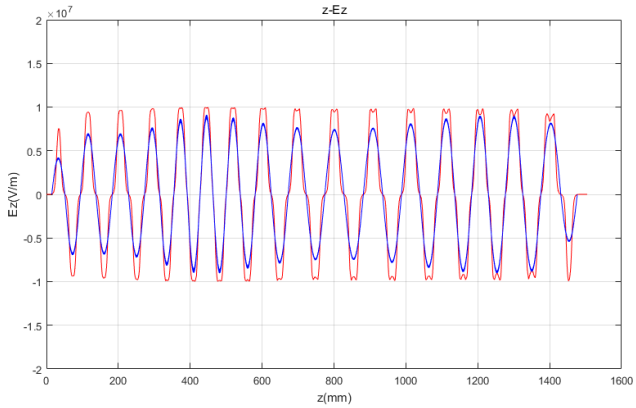


Figure 3: A comparison between the analytical fields used in BEAMPATH (blue) and the accurate 3D field generated by CST Microwave Studio (red).

focus, the ratio between the BEAMPATH integral field and the CST integral field was compared. The coherency of the middle cells (cell 2 to cell 31) are less than 2 %, but the first and the last cell has about 10 % deviation from the design value. As showing in Figure 4.

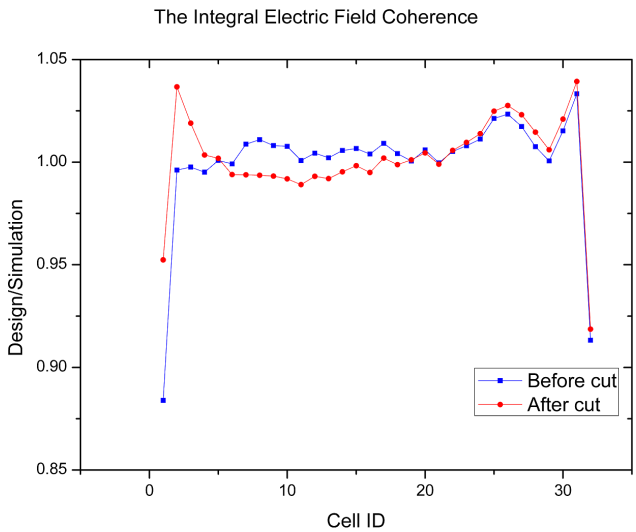


Figure 4: The integral field deviation between BEAMPATH and CST.

This deviation is cause by the half gap effect of the end cells, where the outer wall of the DTL cavity is electrical grounded. To correct this deviation, we keep the center of the first gap fixed ,and simultaneously cut the left side of the first tube and the right side of the second tube by 1.75 mm, as showing in the Figure 5. There we have the new integral electric field deviation showing in Figure 4.

The comparison shows this cutting method is an effective way to correct the integral electric field deviation, cutting the cells one by one, we had the integral electric field deviation of all cells below 2 %, and the effective transmission that calculated by Trace Win rise from 57.8 % to 66.8 % [4].

ISBN: 978-3-95450-194-6 ISSN: 2226-0366 doi:10.18429/JACoW-LINAC2018-MOPO132

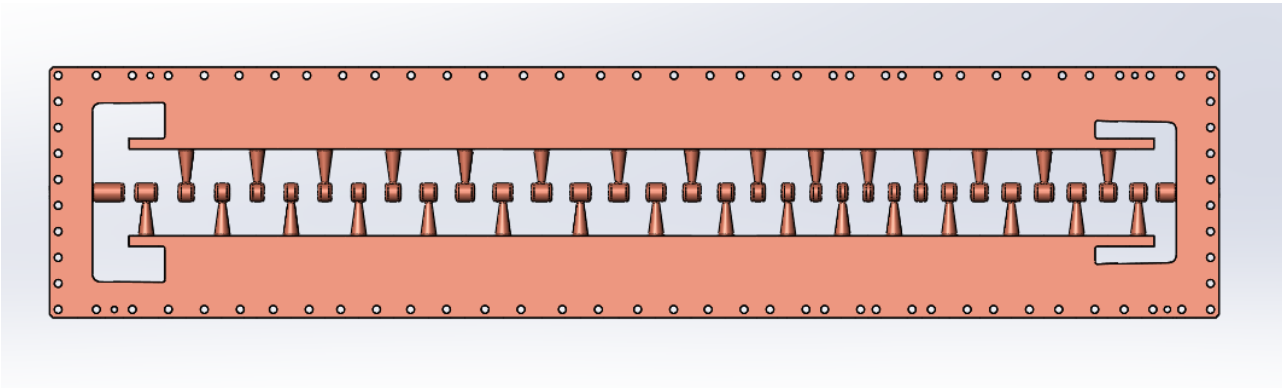


Figure 5: The tube and gap structure of the APF.

CONCLUSIONS

An effective APF DTL design and optimization code was successfully developed based on the Iwata synchronous phase formula and linearly electrode voltage assumption. Moreover, an APF DTL for proton therapy facility has been designed with consideration about various independent errors and joint error. Finally , an integral electric field deviation correction method was founded to rise the effective transmission from 57.8 % to 66.8 %.

REFERENCES

[1] T. P. Wangler, *RF Linear Accelerators*, 2nd ed., Wiley-VCH, Weinheim, 2008.

[2] Y. Batygin, *BEAMPATH User Manual*, Los Alamos National Laboratory, Los Alamos, New Mexico, 2012.

[3] CST – Computer Simulation Technology AG, CST STUDIO SUITE, Darmstadt, 2008.

[4] D. Uriot and N. Pichoff, "Trace Win Documentation", French Alternative Energies and Atomic Energy Commission, 2011.

Content from this work may be used under the terms of the CC BY 3.0 licence (© 2018). Any distribution of this work must maintain attribution to the author(s), title of the work, publisher, and DOI.

ISBN: 978-3-95450-194-6 ISSN: 2226-0366 doi:10.18429/JACoW-LINAC2018-TU1A01

CHALLENGES IN SUPERCONDUCTING ACCELERATING MODULE DESIGN AND CONSTRUCTION FOR HIGH POWER PROTON ACCELERATORS

C. Madec†, CEA, Saclay, France

Abstract

CEA is engaged in the construction of the Linear IFMIF-Prototype Accelerator (LIPAc), SARAF and ESS superconducting linacs and in particular in the design and production of their accelerating cryomodules: 1 for LIPAc composed of low-beta half-wave 175 MHz resonators, 4 half-wave 176 MHz resonators for SARAF and 32 medium and high-beta elliptical cavity resonators for ESS. The developments of these RF cryomodules, although at various stages, are led in parallel by the cryomodule team at CEA-Saclay, including all RF, mechanical, thermal, cryogenic, integration and QA-QC aspects in a global approach which attempts to optimise synergies and lessons learnt between these projects. A status report will be presented describing the common approaches and methods, and the systemic particularities of each project.

INTRODUCTION

CEA is designing, building, testing, installing and commissioning accelerator (or part of them) for others labs since 20 years : 352MHz cryomodule for SOLEIL, 88 MHz QWR cryomodules for SPIRAL2, 1.3 GHz cryomodules for XFEL, 175 MHz cryomodule for LIPAC [1] and SARAF [2], 704MHz cryomodules for ESS [3]. Among those cryomodules, SOLEIL and XFEL are operating; SPIRAL2 is under commissioning; LIPAC is under construction; ESS is under prototyping, SARAF is finishing its design. The development of last three cryomodules (CM) are led in parallel by the cryomodule CEA team. This talk will highlight the challenges faced and fruitfully used for the other next projects.

The LIPAC, SARAF and ESS will serve various applications (material study for fusion, nuclear science, production of radiopharmaceuticals, neutrons production for physics studies) and their overview is presented below.

PROJECTS OVERVIEW

The International Fusion Materials Irradiation Facility (LIPAC) aims at producing intense neutron fluxes so as to characterize materials envisioned for future fusion reactors. To this end, two identical Linacs, each accelerating a continuous-wave 125-mA deuteron beam at the final energy of 40 MeV, would be necessary to produce by break-up interactions of the D+ beam with the Li target the required 10^{17} neutrons per seconds with the appropriate energy. Because the accelerators have to reach unprecedented performances, the feasibility is being tested through the design, manufacturing, installation, commissioning and testing activities of a 1:1-scale prototype accelerator from the injector to the first cryomodule [4]. The cryomodule (Figure 1) is one of CEA Saclay's contribution, the others being the injector, the cryoplant and some beam diagnostics.

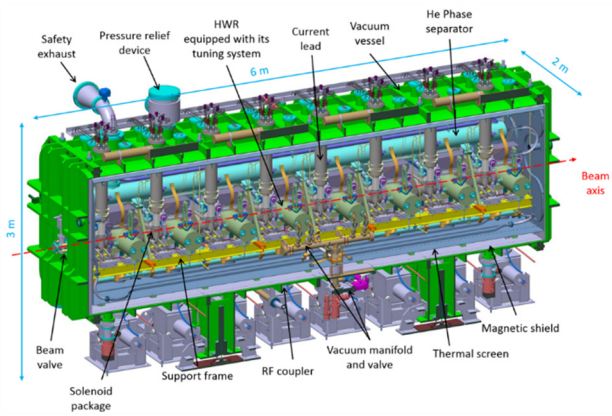


Figure 1 : LIPAC/IFMIF cryomodule.

The European Spallation Source (ESS) will bring new insights to the grand challenges of science and innovation in fields as diverse as material and life sciences, energy, environmental technology, cultural heritage, solid-state and fundamental physics. A 2GeV, long pulse proton accelerator is used to reach this goal. The pulsed length is 2.86 ms and the repetition frequency is 14 Hz (4 % duty cycle). The protons beam is accelerated in a superconducting linac [5] composed of one section of spoke cavity cryomodules and two sections of elliptical cavity cryomodules (Figure 2). These cryomodules, under CEA responsibility, contain elliptical cavities operating at 2 K.

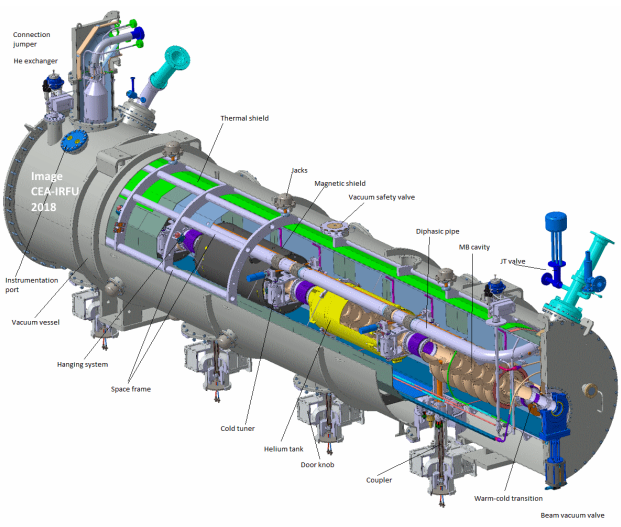


Figure 2 : ESS cryomodule.

Content from this work may be used under the terms of the CC BY 3.0 licence (© 2018). Any distribution of this work must maintain attribution to the author(s), title of the work, publisher, and DOI.

ISBN: 978-3-95450-194-6 ISSN: 2226-0366 doi:10.18429/JACoW-LINAC2018-TU1A01

ESS is a collaboration project of 17 European countries and is under construction in Lund, Sweden.

Soreq Applied Research Accelerator Facility (SARAF) will be a multi-user and versatile particle accelerator facility. It is based on a proton/deuteron RF superconducting linear accelerator, with variable energy (5-40 MeV) and a continuous wave (CW) high ion current (0.04-5 mA). The high ion current generates an unprecedented amount of fast neutrons and radioactive nuclei, that may be used to explore rare nuclear reactions, produce new types of radiopharmaceuticals and more. Moderated neutrons can be used for non-destructive tests with similar resolution and contrast as performed in reactors. SNRC and CEA collaborate to upgrade the SARAF accelerator to 5 mA CW 40 MeV deuteron and proton beams by means of a four-vane 176 MHz RFQ, a MEBT and a superconducting linac [6] made of four five-meter cryomodules housing superconducting Half Waves Resonators (HWR), superconducting solenoids and Beam Position Monitor (BPM) (Figure 3).

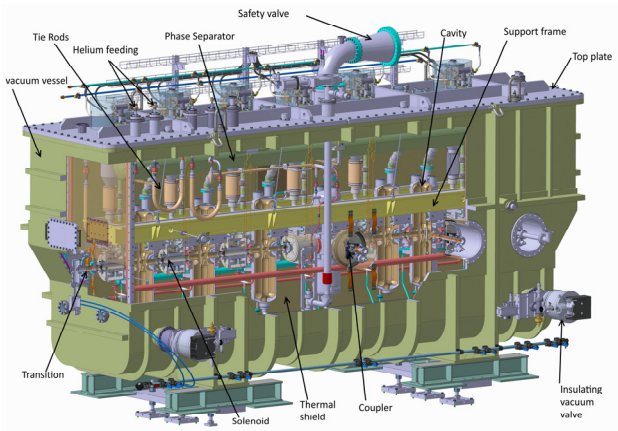


Figure 3 : SARAF Low beta cryomodule.

DEVELOPMENT PLAN

For each cryomodule, CEA cryomodule team is following a development plan including the definition of the requirements, the design of the components (cavities with tuning system, couplers, solenoids and cryomodules), the review of the design by a panel of international experts, the risk analysis and the implementation of a mitigation plan which mostly led to design optimization and critical components prototype manufacturing and validation, the tooling development, the mock-ups tests, the integration and validation with tests. For SARAF and LIPAc, CEA will participate in the installation of the cryomodules and the commissioning of the SRF Linac.

This generic description of the development is adapted for each project and detailed in Table 1. The "x" means that the study and work was not fully under CEA responsibility. As examples, the LIPAC solenoids are a contribution from Spain; ESS transport study output led to secure the cryomodule and the cold mass but the damping frame development and manufacturing is the responsibility of ESS; ESS components manufacturing refers to the manufacturing and qualification of the components but the cavities which are procured by INFN and STFC.

Table 1: Development Plan Steps for Each CEA Project

	SARAF	LIPAC	ESS
Requirements definition	X	X	X
Design	X	X	X
Review	X	X	X
Risk analysis and mitigation plan	X	X	X
Prototypes	X	X	X
Tooling design and Mock-up tests	X	x	X
Transport studies and tests	X	x	x
Manufacturing	X	x	x
Assembly	X		X
CM test at CEA	X		X
Transport	X		

As another example, from the table, one can read that LIPAc CM will not be assembled at CEA. It will be assembled under the responsibility of F4E, with the assistance of CEA. To insure the process, CEA has developed mock-ups and cavity-to-coupler tooling. LIPAc transport study examines whether the shipment would be by plane or sea.

THE REQUIREMENTS

CEA is implementing standard engineering method for the requirements which are defined with the collaborators. Table 2 is a summary of the requirements on the cavities.

Table 2: Cavities Parameters

	ESS	SARAF	LIPAc
Particules	P+	P+/D+	D+
Energy [MeV]	2000	40/35	5 à 9
Frequency [MHz]	704	176	175
Operating temp.	2K	4.45K	4.45K
Beta value	0.67/0.86	0.09/0.18	0.094
Eacc [MV/m]	16.7/19.9	7	4.5
Epk [MV/m]	45/45	34.6/35.9	21.6
Bpk [mT]	80/85.6	65.6/65.3	49.5
Beam pipe ID (mm)	94/120	40	40

The performance required for SARAF are 32% higher than for LIPAC and ESS is the most demanding one with 85.6mT at 2K compare to the 140mT Hc1 limit.

THE DESIGN

LIPAC first design consisted in a cryomodule to be as short as possible along the beam axis so as to meet the beam dynamics requirements. The cryomodule is made up with a rectangular section vacuum vessel, room temperature magnetic shield, MLI, thermal shield cooled down by GHe, and cold-mass wrapped in MLI. This is similar for SARAF [7]. ESS CM includes the same functionalities though the magnetic shield is around the cavity on top of the MLI, the CM section is round and the Helium circuit has to provide 2K to the cavities.

Content from this work may be used under the terms of the CC BY 3.0 licence (© 2018). Any distribution of this work must maintain attribution to the author(s), title of the work, publisher, and DOI.

ISBN: 978-3-95450-194-6 ISSN: 2226-0366 doi:10.18429/JACoW-LINAC2018-TU1A01

Content from this work may be used under the terms of the CC BY 3.0 licence (© 2018). Any distribution of this work must maintain attribution to the author(s), title of the work, publisher, and DOI.

LIPAC and SARAF cold mass is made up of the phase separator, cryogenic circuit, titanium cavity support frame, hanging from the top of the vacuum vessel thanks to TA6V rods plus rods ensuring lateral and horizontal positioning. Similarities are on the tie rods which are used in the 3 projects (antagonist tie rods for ESS). The number and type of cavities are 4 elliptical cavities for ESS, 6 or 7 HWR for SARAF and 8 HWR for LIPAC. The material of the space and support frame are different between the three projects. SARAF and LIPAC support frame are at temperatures between 70K and 4K and shall have low permeability since they are located close to the cavity torus. Therefore, Titanium, has been chosen. ESS space frame is at room temperature, it should hold the weight and cope with alignment constrains : aluminium meets those specifications and has been chosen for ESS. ESS tie rods are also able to take the shipping loads and maintain the cavities aligned during the transport between CEA and ESS (about 1300kms).

Both support and space frame allow easy access to the cavity string and permits intermediate alignment verification before insertion in the vacuum vessel and additional clamping for transportation.

Due to their size and weight, the ESS [8] and LIPAC [9] couplers are mounted vertically. The ESS coupler to cavity assembly tooling has been derived from LIPAC lessons learned on the mock-up test. On SARAF CM, the cavities are vertical thus the coupler is horizontal.

The support or space frame allow assembling the cold mass and adjusting the component for alignment outside the vacuum tank. The cryomodule is for that reason designed in two main sub-assemblies : the cold mass and a vacuum vessel fitted with magnetic and thermal shields. The vacuum tanks are also outfitted with traps and doors to allow the access to the cold mass and to carry out the necessary controls and possible maintenance after installation in the tunnels.

The SARAF tunnel width and the beam axis position are set by the already existing infrastructures. During installation and maintenance, two cryomodules should be rolled side by side. Therefore the cryomodule width can not exceed 1850 mmm. The cavity RF design has set its dimension to 1018 mm. Taking into account the vacuum vessel wall thickness, the magnetic and thermal shield thickness and the short coupler cavities have to stand vertically. Unlike the IFMIF cryomodule, a top loading solution have been chosen for the insertion of the cold mass in the vacuum vessel

LIPAC and SARAF CM are connected to a valve box thanks to transfer lines and operate at 4.45K. ESS cryomodule will operate at 2K. Each ESS cryomodule is linked to an individual valve box by a jumper connexion which provides the 4.5 K – 3 bars liquid helium (LHe) supply and return for the cavities and couplers cooling, as well as the 40 K – 19.5 bara helium cooling circuit of the thermal shield. The 2 K superfluid helium is produced inside the cryomodule by a Joule-Thomson valve.

In ESS CM, the spacing and location of the coupler port are the same on both type of cryomodules allowing capability to interchange modules in the tunnel. Thus most of the components are identical between 2 types of cryomodules but the number of cells per cavities and the intermediate beam line bellows. This standardisation has been implemented also on SARAF where a 7th cavity will assemble in the 2nd cryomodule. Instead of designing three different support frame, we have only 2, one for the low beta, one for the high beta. SARAF CM have been designed to use the same tie-rods, couplers and interfaces.

THE REVIEW AND MITIGATION PLAN

Cryomodule designs, including detailed technical analysis, are submitted to a panel of international experts (Detailed Design Review for LIPAC cryomodule, EDR for SARAF and CDR for ESS). The risks are addressed in a mitigation plan to prevent their occurrence. Mitigation plans have been implemented and led to the design optimization. For the three projects, it was decided to perform early testing on dedicated test bench and mock-ups to check critical components and operations before the beginning of the cryomodule assembly. To detect potential issues during operation of such complete set of components, SaTHoRI test stand [10] has been built and was used to test LIPAC jacketed cavity with coupler and tuner. SARAF is building a similar test. A Medium beta Elliptical Cavity Cryomodule Technical Demonstrator (MECCTD) ESS has been built [11].

For LIPAC, the risk of not meeting the Japanese regulatory requirements with regard to High Pressure Gas Safety Law (HPGSL) had been identified as a potential definite show-stopper for the cryomodule project. To meet the Japanese regulatory requirements with regard to HPGSL, it has been agreed in the collaboration to design, fabricate and test according to ASME standards all components containing helium gas or liquid during operation of the LIPAc. The cavity was the most complicated part to be licensed due to the use of non-referenced materials (Nb, NbTi) and the complicated geometry. It went through validating process with KHK, a Japanese Safety Institute. The first discussion took place in December 2011 at KHK in Tokyo. The application form of the cavity licensing was finally approved in March 2016. For ESS and SARAF, European Pressure Equipment Device regulation could be applied and pressure levels allow to comply with the state-of-the art follow-up.

PROTOTYPES

Meanwhile the cryomodule design is going on, the critical components namely solenoid, coupler, tuner and cavity are built in order to test and validate their design. The LIPAC superconducting HWR prototype, which was first equipped with a plunger for frequency tuning, was finally qualified after removing the plunger and associated flanges, and replacing these with a more conservative mechanical tuner including a disengagement system [12]. Such a solution based on the cavity wall led to a lengthening of the cryomodule in order to accommodate the tuner. The flange to flange length of the HWR was increased by

ISBN: 978-3-95450-194-6 ISSN: 2226-0366 doi:10.18429/JACoW-LINAC2018-TU1A01

100 mm. As a consequence, SARAF implemented a standard mechanical tuner. The cleaning of the LIPAC cavity through the 18mm HPR port, the orientation of the HPR ports with respect to the central stem and the oscillation of the HPR stem when under 100bars of water pressure were lessons learned [13] which led SARAF to increase as much as possible the HPR ports diameter and turn them by 30° so that the HPR water scanning could go over the beam axis and scan more thoughtfully the surface. Still, the cavity will have to be flipped to clean all areas.

Five ESS medium beta cavities were manufactured and vertically tested. The challenging specifications were met on the cavities [14]. As the INFN cavity was successfully tested and ready [15], it was integrated inside the prototype CM named M-ECCTD (Medium beta Elliptical Cavity Cryomodule Technical Demonstrator). 6 pairs of couplers have been manufactured and successfully conditioned up to 1.1MW. Among those, 4 couplers are assembled on the MECCTD.

TOOLING DESIGN AND MOCK-UP TESTS

The tooling designs were done in house. To lower the occurrence of critical events during cavity string assembly and to optimize and validate the assembly procedure and associated tools, test bench and mock-ups are built. LIPAC has developed mock-ups to test the assembly of the cavity-to-solenoid and coupler-to-cavity. This last assembly was validated during SATHORI assembly. The LIPAC mock-ups are now used by the company in charge of the cryomodule assembly at Rokkasho. ESS has used tooling principles from XFEL (clean room rails and vacuum groups). ESS built mock-ups for all the assembly steps to control the alignment preservation after integration in the cryomodule. During ESS mock-up assembly, the procedure were written and tests template drafted.

The LIPAC support frame enables to hold together all the cold mass components from the first assembly steps in clean room to the final assembly inside the vacuum tank. It aims to minimize the handling of a heavy cold mass (around 2.5 tons) and to avoid as much as possible to damage the components. The parts shall undergo a cleaning and the tooling shall hold the support frame at a working height with a good stability making the access to the beam port connection less practical. For SARAF, the cold mass is assembled on a clean room tooling, transferred outside and equipped with tuner, MLI. Then the support frame, hooked on the top plate, is lowered and the cold mass is attached.

PROTOTYPING

MECCTD has been built and prototyping was performed to validate all the assembly steps and toolings. After the qualifications of the cavities and couplers and the manufacturing of all the components and toolings, the MECCTD was assembled in the ISO4 clean room on a movable cart which was initially designed to be used in the ISO5 clean room. The procedure inherited from E-XFEL cryomodule such as venting procedure or pre-alignment in the clean room were implemented for the string assembly. The string composed 4 cavities with coupler, 4 bellows and 2 warm-to-cold transition has been leak tested and backfilled to atmospheric pressure with filtered dry nitrogen in the clean room. A carefull pre-alignment of the cavities occurs in the clean room and is checked with calipers. The string is then rolled outside of the clean room. The cavities are aligned to +/-1.5mm from the theoretical axis with a laser tracker. The string was equipped with tuners, MLI, magnetic shield and rolled in the space frame. The tie rods are mounted between the cavity titanium half rings and the space in order to transfer the cold mass from the cavity vertical clean room tooling to the space frame. The axial position of the cavities is fixed by transverse bars until the axial blocking of the couplers. Those bars used also for the cryomodule transportation are removed for pump down and operation. The alignment is checked again. The space frame was inserted in the vacuum vessel by means of wheels and in-situ rails. The jumper and doors were mounted and the cryomodule transferred to the test area where the doorknob assembly took place. All the steps were successfully passed. It led to tooling refurbishment.

TRANSPORT STUDIES AND TESTS

What makes CEA design unique is that the cryomodules are assembled at CEA and then transported to the accelerator site in Sweden or Israel. This led to transport study and development of structure that can handle the road transport and maintain the alignment over more than one thousand kilometer or airplane transport. ESS transport studies led to the clamping of the thermal shield and cavities on the space frame and the reinforcement of the feet of the cryomodule. SARAF transport studies are underway and benefit from ESS experiences. The mitigation of the transport risk for LIPAC has been to assemble the cryomodule on site at Rokkasho.

MANUFACTURING

For the manufacturing follow-up, the cryomodule team is supported by a dedicated group of engineers experienced in manufacturing. The dedicated group is writing the technical specifications using the cryomodule team expertise on specific themes, following the call for tender process. Once the contract are signed, they are following the contractual aspects, registering the non-conformities and validated them, traveling to the subcontractors for intermediate meetings and participating to factory acceptance tests. This support is off great value. To follow regulations (pressure equipment or seismic), the call for tender and contract follow-up could be tedious.

The ESS construction schedule imposed to anticipate the procurement of the long lead components and be prepared for the one month throughput. It has been agreed with ESS to launch the procurement before the qualification of the MECCTD. This excludes major redesign though hold points have been set to allow feedbacks and minor changes.

Content from this work may be used under the terms of the CC BY 3.0 licence (© 2018). Any distribution of this work must maintain attribution to the author(s), title of the work, publisher, and DOI.

ISBN: 978-3-95450-194-6 ISSN: 2226-0366 doi:10.18429/JACoW-LINAC2018-TU1A01

Content from this work may be used under the terms of the CC BY 3.0 licence (© 2018). Any distribution of this work must maintain attribution to the author(s), title of the work, publisher, and DOI.

The number of contracts to be signed is unpreceded for CEA.

ASSEMBLY

CEA has gained experience over the years in cryomodule assembly [16, 17]. It has developed an assembly "factory" in which an industrial operator assembled 100 cryomodules for 3 years for the E-XFEL project. The factory includes three assembly halls comprising a dedicated ISO-4 clean room 14 m long with two parallel integration rails (the clean room complex is 200m2 with the ISO4-5-7) and a 50m2 ISO5 clean room used for the individual components (cavities, couplers, solenoids). For ESS, the 30 cryomodules will assembled in the "cryomodule" factory by an industrial operator wheras the SARAF cryomodule will be assembled by a CEA team which was involved on SPIRAL2, E-XFEL and ESS prototyping phase. CEA ensures a close follow-up of the industrial operator with a CEA team always in the factory.

CM TEST AT CEA

A dedicated cryomodule test stand has been built for the different projects. It is fed with cryogenic fluid from the CEA facilities and RF power equipments are connected accordingly. The command control and test equipment are developed according to the projects needs and standardized allowing easy exchange of components.

The test conditions are different from the operation conditions. As a matter of fact, one out 4 1.1MW klystrons is installed in Saclay for ESS. The 4.5 K – 3 bars superfluid helium (SHe) supply is replaced by 4.64K -1.2 bara Gas helium supply and the 40 K – 19.5 bara helium cooling circuit of the thermal shield is fed with liquid nitrogen at 77K.

For SARAF, the thermal shield will be supplied by liquid nitrogen at 77K instead of 14.5Bar, 60K GHe.

TRANSPORT

CEA has transported cryomodule from CEA to GANIL (200kms) by road on a damping frame maintaining the alignment of the cavities [18]. The one hundred cryomodules assembled at CEA have been transported to DESY on a damping frame [19] under DESY responsibility. More recently, ESS cryomodule transport test of the vacuum vessel have been conducted.

CONCLUSION

CEA is working on three projects and uses lessons learned from one project to the other ones. Methods are shared and singularities are individually treated. The cryomodules will be assembled in a close future : LIPAc CM assembly will start at the end of year and the CM will be operating by the end of 2019. ESS cryomodules assembly production will start by January 2019 and should last 1.5 years. SARAF CM assembly will start January 2020. ESS and SARAF will start operating by 2022.

REFERENCE

[1] M. Sugimoto *et al*., "Progress Report on LIPAC", presented at Linac'18, Beijing, China, Sep. 2018, paper TU2A04, this conference.

[2] N. Pichoff *et al*., "The SARAF-LINAC Project for SARAF-Phase 2", in P*roc. 6th Int. Particle Accelerator Conf.* (*IPAC2015*), Richmond, VA, USA, May 2015, pp. 3683-3685.

[3] A. Sunesson *et al.,* "Status of the ESS Linac", presented at Linac'18, Beijing, China, Sep. 2018, paper MO1P03, this conference.

[4] H. Dzitko, *et al.,* "Technical and Logistical Challenges for IFMIF-LIPAC Cryomodule Construction", in Proc. 17th Int. Conf. on RF Superconductivity (SRF'15), Whistler, Canada, September 2015, pp. 1453-1459.

[5] P. Bosland *et al.,* "Status of the Elliptical Cavities Cryomodule at CEA Saclay", in *P*roc. *8th Int. Particle Accelerator Conf.* (*IPAC'17*), Copenhagen, Denmark, May 2017, pp. 945-947.

[6] C. Madec *et al.,* "Design of the Superconducting LINAC for SARAF", in *Proc. 17th Int. Conf. on RF Superconductivity (SRF'15)*, Whistler, Canada, Jul. 2015, pp. 250-254.

[7] R. Cubizolles *et al.,* "Preliminary Design of the Cryomodules for the SCL for SARAF phase 2", in *P*roc. *8th Int. Particle Accelerator Conf.* (*IPAC'17*), Copenhagen, Denmark, May 2017, pp. 994-996.

[8] C. Arcambal *et al*., "Conditioning of the RF Power Couplers for the ESS Elliptical Cavity Prototypes", in P*roc. 8th Int. Particles Accelerator Conf. (*IPAC'17*)*, Copenhagen, Denmark, May 2017, pp. 957-959.

[9] H. Jenhani *et al.,* "Manufacturing of the IFMIF Series Power Couplers", in P*roc. 7th Int. Particle Accelerator Conf. (*IPAC'16*)*, Busan, Korea, May 2016, pp. 1122-1124.

[10] O. Piquet, et al., "First Results of the IFMIF/EVEDA SaTHoRI Tests, in *P*roc. *18th Int. Conf. on RF Superconductivity (SRF'17)*, Lanzhou, China, Jul. 2017, pp. 262-265.

[11] F. Peauger et al., "Progress in the elliptical cavities and cryomodule demonstrators for the ESS LINAC", in P*roc. 18th Int. Conf. on RF Superconductivity (SRF'17)*, Lanzhou, China, Jul. 2017, pp. 729-735.

[12] N. Bazin, et al., "Cavity Development for the Linear IFMIF Prototype Accelerator", in *Proc. 16th Int. Conf. on RF Superconductivity (SRF2013)*, Paris, France, Sep. 2013, pp. 878-883.

[13] G. Devanz et al, "Progress in IFMIF Half Wave Resonators Manufacturing And Test Preparation", in *Proc. 17th Int. Conf. on RF Superconductivity (SRF'15),* Whistler, Canada, Sep. 2015, pp. 1193-1195.

[14] E. Cenni et al., "Vertical test results on ESS medium and high beta elliptical cavity prototypes equipped with helium tank", *Proc. 8th Int. Particles Accelerator Conf. (IPAC2017)*, Copenhagen, Denmark, May 2017, pp.948-950.

[15] P. Michelato et al., "Vertical tests of ESS Medium Beta Prototype Cavities at LASA", *Proc. 8th Int. Particles Accelerator Conf. (IPAC2017)*, Copenhagen, Denmark, May 2017, pp. 1015-1018.

[16] S. Berry, O. Napoly, "Assembly of XFEL Cryomodules : Lessons and Results", *Proc. 28th LINEAR Accelerator Conf. (LINAC2016)*, East Lansing, MI, USA, pp.646-650

ISBN: 978-3-95450-194-6 ISSN: 2226-0366 doi:10.18429/JACoW-LINAC2018-TU1A01

[17] C. Marchand, et al., "Performances of SPIRAL2 Low and High Beta Cryomodules", in *Proc. 17th Int. Conf. on RF Superconductivity (SRF2015)*, Whistler, Canada, September 2015, pp. 967-972,

[18] P-E Bernaudin et al., « Assembling, Testing and installing the SPIRAL2 Superconducting LINAC, *Proc. 4th Int. Particles Accelerator Conf. (IPAC2013)*, Shanghain China, pp. 3752-3754

[19] S. Barbanotti et al., "XFEL Cryomodule Transport : From the Assembly laboratory in CEA-Saclay (France) to the Test-Hall in DESY-Hamburg (Germany)", *Proc. 27th LINEAR Accelerator Conf. (LINAC2014)*, Geneva, Switzerland, pp. 98-100,

Content from this work may be used under the terms of the CC BY 3.0 licence (© 2018). Any distribution of this work must maintain attribution to the author(s), title of the work, publisher, and DOI.

ISBN: 978-3-95450-194-6 ISSN: 2226-0366 doi:10.18429/JACoW-LINAC2018-TU1A03

STATUS AND ISSUES (MICROPHONICS, LFD, MPS) WITH TRIUMF ARIEL e-LINAC COMMISSIONING

S. R. Koscielniak†, T. Planche, S. Radel, Y. Ma, M. Alcorta, B. Humphries, F. Ames, E. Chapman, K. Fong, O. Kester, D. Kishi, R. Laxdal, M. Rowe, V. Verzilov, Z. Yao
TRIUMF, V6T 2A3, Vancouver, B.C., Canada

Abstract

The ARIEL electron linac (e-linac) is designed to generate cw beams of up to 30 MeV and 10 mA for delivery to a photo-convertor. Bremsstrahlung induced fission of a production target yields neutron-rich rare isotope beams to be supplied to the ISAC experimental facilities. The beam power will eventually reach 300 kW, and a machine protection system (MPS) with 10 μs rapidity is essential. The e-linac, which adopts 1.3 GHz, 2K SRF technology, is composed of a 10 MeV single-cavity injector cryomodule (EINJ) and a 20 MeV two-cavity accelerator cryomodule (EACA). The latter has vector-sum control of two cavities driven from a single klystron. Beam commissioning of these systems is ongoing since 2016. The magnetic optics and MPS commissioning to 10 MeV is reported herein. Beam has been accelerated up to 25 MeV, and threaded to the high energy dump (EHD). A campaign to investigate microphonics driving terms, LN2 disturbances, and a ponderomotive instability in the EACA, is underway.

INTRODUCTION

The ARIEL* facility for rare isotope nuclear science was proposed in 2008 [1]. The facility and science program are described in [2, 3]. ARIEL-I Funding emerged in 2010, plans solidified in 2011 [4], leading to a mature linac design 2012 [5], construction of the EINJ in collaboration with VECC, Kolkota [6], and installation of EACA, with a single 9-cell cavity, was completed 2014.

Figure 1 shows the main sections of the e-linac and their naming. TRANSOPTR is adopted as the online beamline modeling and optimization tool [7] in the control room, and is used throughout the e-linac from source to beam dump.

Commissioning of the 300 keV low energy beam transport (ELBT/D) up to 1 kW beam power is reported in Refs. [7, 8]. Rudimentary beam tests on EINJ at 10 MeV and on EACA at 23 MeV each equipped with a single RF cavity were reported in 2014 [9] and 2015 [8], respectively. Preparation of the EACA for two-cavity operation is reported in [10, 11, 12, 13].

Throughout 2016 and 2017, attempts to commission the injector and medium energy transport were compromised by RF phase and amplitude jitter. Therefore, the 2018 campaign includes two objectives: commission magnetic optics, and identify (and abate) RF jitter sources. Further, by mutual agreement with the regulatory authority, e-linac operations at ≥ 10 MeV are not permitted above 100 W beam power until the machine protection is commissioned.

ELECTRON GUN

Operation of the thermionic electron gun (EGUN) is reported in Ref. [14]. Performance of the gun itself has been excellent. After overhaul of the high-voltage power supply by Glassman in 2016, the HVPS has also proven reliable.

For >10 MeV commissioning it is critical that the EGUN supports a duty factor ranging from 0.01% to cw so that beamline components are subjected to low average power during beam threading if there is accidental beam loss.

Stable Duty Factor Parameters

The HVPS is nominally a DC supply, but we pulse it. Stable combinations of repetition rate and pulse length have been measured. At 100 μA peak, the combinations of 50 Hz to 10 kHz and 5-200 μs are stable. At 10 mA, the combinations 100 Hz to 2 kHz and 5-50 μs are verified stable duty factors [15].

Measured Beam Energy Stability

Results from ELBD with high-dispersion optics confirm the energy stability of the HVPS at 0.01%. Contrastingly, the sum signal from the first beam position monitor (BPM) after the gun show a 60 Hz phase jitter ~ 0.2° at 650 MHz.

OPTICS COMMISSIONING

Polarity Check

Prior to beam tests, the polarity of every magnetic element was checked using a Hall probe. This proved to be a worthwhile time saver as the polarity of several steerers and quadrupoles was found to be incorrect.

Optics Commissioning with Beam

Beam commissioning began at very low average power (< 10 W). All magnetic elements were tested individually:

- Steerers by their effect at downstream beam position monitors (BPM).
- Quadrupoles by searching for the setting which achieves minimum beam size on a fluorescent screen, and by comparing this setting with our optics model.

All magnetic elements performed precisely as expected.

RF Commissioning with Beam

The injector optics design is given in Ref. [16]. The gun emits 650 MHz bunches; these are energy modulated, head-to-tail, by a 1.3 GHz buncher cavity [6] to prepare them for the EINJ 9-cell cavity acceptance at 300 keV.

* ARIEL is funded by the Canada Foundation for Innovation, the Provinces AB, BC, MA, ON, QC, and TRIUMF. TRIUMF receives funding via a contribution agreement with the National Research Council of Canada.
† shane@triumf.ca.

Content from this work may be used under the terms of the CC BY 3.0 licence (© 2018). Any distribution of this work must maintain attribution to the author(s), title of the work, publisher, and DOI.

ISBN: 978-3-95450-194-6 ISSN: 2226-0366 doi:10.18429/JACoW-LINAC2018-TU1A03

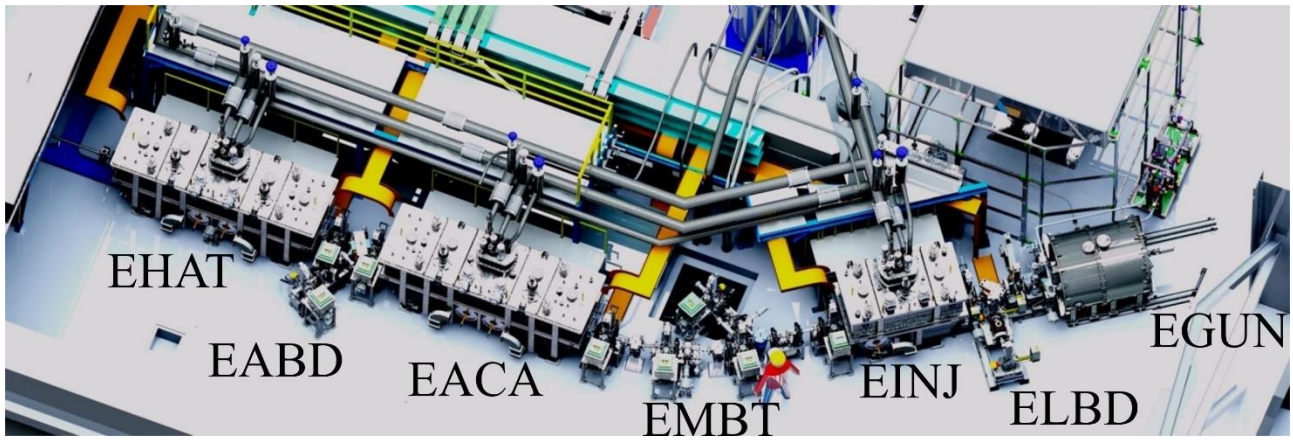


Figure 1: Rendering of the e-linac. The future, cryomodule EACB is presently replaced by the EHAT beam transport.

The three SRF cavities were initially commissioned without bunching. The accelerated beam energy was measured at an analyzer dipole magnet, and the cavity phase set to achieve maximum energy gain.

The RF buncher was then phased to minimize the energy spread downstream of EINJ as inferred from the beam profile on a fluorescent screen at a dispersive location. The buncher amplitude was determined by minimizing the beam loss monitors readings. Transmission down all beamline sections was, within the few percent accuracy of our Faraday cups, 100%. Note, when properly set, variation of the buncher phase and amplitude has little impact on the beam position, although it alters the horizontal beam size, as a consequence of energy spread.

Tune Development

Steerers were adjusted such that each quadrupole would not steer. This was verified by varying each quadrupole while looking at downstream BPMs. The doubly achromatic EMBT bend section was tested by varying together dipoles at both ends, while making sure that the beam does not move on any of the downstream BPMs.

Medium Energy Beam Transport

The EMBT optics design (magnets & diagnostics) is given in Ref. [17]. Our overall understanding of the optics was tested by measuring the RMS size of the beam along the beamline, and comparing it to our linear optics model (see Fig. 2). The actual settings for quadrupoles differ from theoretical values by less than 0.5%.

EABT/D & EHAT Beamlines

The accelerated beam optics design, EACA to EABT to EHAT, is described in Ref. [17]. Nominally, the EACA output is 30 MeV, but is limited by the Ponderomotive instability to 25 MeV. Failure of one of the three sub-atmospheric pumps further reduced the output beam to 22 MeV. EABT consists of three weak quadrupoles (like those upstream), two steerers, three BPMs and view screen (VS). Between the first two quadrupoles a dipole can bend the beam into the EABD section with two weak quadrupoles,

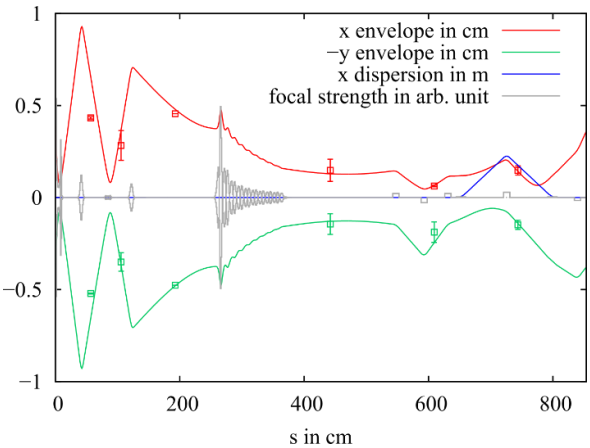


Figure 2: Beam envelope along ELBT and EMBT calculated by TRANSOPTR (solid lines) compared to measured 2 r.m.s beam sizes (square dots). The error bars reflect the sensitivity of the r.m.s value to the background cut.

two steerers and one screen in front of the dump, a Faraday cup. The EABD quadrupoles were used to increase the dispersion in x to observe the beam energy instability from EACA on the view screen.

The EHAT beamline consists mainly of a long drift where the future cryomodule EACB is placed, four medium quadrupoles (with stronger focussing strength), three steerers and three beam position monitors.

The functionality of all quadrupoles was verified, as well as all steerers. All optic elements in EABT/D and EHAT work as expected. For the commissioning all quadrupoles in EABT and EHAT were turned off. Thus, these beamlines acted as a very long drift as depicted in Fig. 3.

EHDT Beamline & Dump

Beam transport (magnets & diagnostics) to the dump is specified in Ref. [18]. The EHDT beamline is not commissioned. A 3 W beam was sent to the EHD dump. The fact that we can form a sharp beam image, Fig. 4, of the cathode and that it is free of distortions illustrates that overall the transverse optics is very linear.

Content from this work may be used under the terms of the CC BY 3.0 licence (© 2018). Any distribution of this work must maintain attribution to the author(s), title of the work, publisher, and DOI.

ISBN: 978-3-95450-194-6 ISSN: 2226-0366 doi:10.18429/JACoW-LINAC2018-TU1A03

Content from this work may be used under the terms of the CC BY 3.0 licence (© 2018). Any distribution of this work must maintain attribution to the author(s), title of the work, publisher, and DOI.

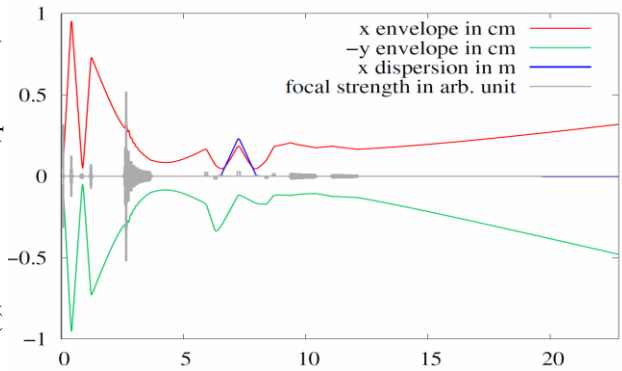


Figure 3: Beam envelope along ELBT, EMBT, EACA, EABT and EHAT calculated by TRANSOPTR.

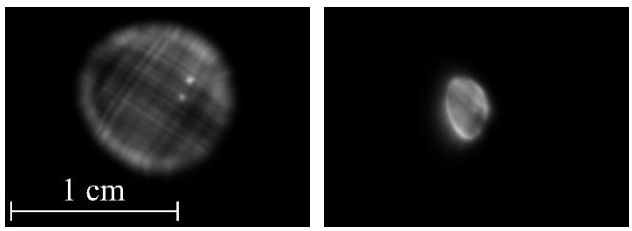


Figure 4: Left: beam spot object on ELBT:VS2. Right: beam spot image at EHDT:VS4.

The core of the EHD tuning dump [19, 20] is an inclined plane of Al alloy with water cooling on the back surface. The dump is rated for 100 kW with beam spot scanning and 10 kW without. Cooling circuits, temperature sensors and interlocks, including FSD interface, are all functional.

CONTROLS

In the interest of control systems reliability, several incremental improvements were made: modifications to view-screen IOCs, updating support packages for the beam positions monitors, and expanding Beam Modes (allowed combinations of beam path and beam power) logic to include paths beyond EACA to EHD.

When a beam mode is granted, the magnetic benders on that beam path are restricted to ±1% about the excitation current calculated from beam energy.

An extensive package has been written to interface the TRIUMF-designed beam loss monitor data acquisition boards to the EPICS support of the overall MPS.

Optics Lock

The most recent and significant advance is the introduction of the Optics Lock (OL) as part of the Beam Modes. OL facilitates the transition from tuning to operation. The changing of magnetic optics and RF cavity set points is only permitted below 100 W beam power. With the exception of the duty factor, the equipment set points must be locked before the power can be raised above 100 W.

MACHINE PROTECTION SYSTEM (MPS)

The MPS must have rapidity (trip < 10 μs) to respond to full beam loss and large dynamic range (> 10^4) to detect the onset of beam loss. System has three layers of protection: (1) interlocks, (2) trip on beam position, (3) trip on beam loss. All trips are implemented by the Fast Shut Down (FSD). Commissioning of the ELBT/D MPS which uses photo-multiplier tubes (PMTs) and a JLab-supplied electronics board was reported in Ref. [7]. The downstream beamlines use long ionization chambers (LICs) as the backbone BLMs, supplemented by PMTs in shadowed locations. Since 2016, TRIUMF has developed its own more versatile integration and threshold electronics board [21, 22] and deployed in EMBT/D and beyond.

Beam Position & Loss Monitors (BPM & BLM)

Each BPM consists of 4 buttons, and measures horizontal and vertical beam offset for display in the control room. Firmware on the 100 MHz data acquisition boards monitors the beam position; if it exceeds prescribed limits then a beam trip request is send to the FSD on an optical fibre link. The BPM MPS layer is complete to the EHDT dump.

Two types of loss monitor are used: scintillators, consisting of a small BGO crystal coupled to a PMT; and LICs filled with a flow of Argon gas for prompt charge collection. Both BLM types have proven a range of 10^6, from 100 pA to 100 mA.

BLM Electronics Board (TBLM)

The BLMs are connected directly to the TRIUMF electronics boards (TBLM) which integrates incoming signals, and sends a trip via fibre-optic to the FSD upon exceeding a pre-determined threshold. The hardware integration time is set to 100 ms with a total charge of 1 nC. An ADC samples the output of the integrator at 1 MHz, so that a continuous difference calculation is available every 1 μs.

The trip is defined by either of two conditions: a "delta" trip (for large/fast losses) and a "100 ms" trip (for lower/slower losses) each with a configurable threshold. The "delta" trip occurs when a single difference value is above a configurable threshold. The "100ms" trip uses a sliding window integration: 10^5 consecutive readings summed.

EMBT/D and EABT/D & EHAT

The BLM aspect of the EMBT/D MPS has recently been commissioned up to 100 W and 10 MeV. Four BLMs are used to ensure total coverage of this section: three LICs and one PMT. The LICs are positioned to include redundancy in most areas of the beamline, while the PMT is placed at the dipole magnet leading to EMBD to detect spills inside the magnet. Commissioning took place over two weeks and consisted of first performing beam spills to determine optimal numbers of BLMs and their locations, and then a final step which included purposeful beam spills above threshold to ensure a trip of the e-gun takes place within the specifications. The controlled spills were performed at low duty factors using a combination of quadrupoles and steerers to mimic point losses in both planes (H & V) of the beamline.

Commissioning the beamlines immediately downstream of EACA is ongoing. The total number and type of BLM has not yet been finalized, but it is likely to include six LICs and at least two PMTs (placed to detect losses inside dipole magnets).

ISBN: 978-3-95450-194-6 ISSN: 2226-0366 doi:10.18429/JACoW-LINAC2018-TU1A03

Dark Current Effects

Above a gradient ≈ 9 MV/m per cavity, the EINJ and EACA cavities both produce dark currents significant enough to compromise the BLMs. The currents are seen on view screens upstream and downstream of the cavities and found to extend up to 4.5 MeV.

MPS Outlook & Future Developments

The TBLM board stores up to 1 s of data in memory. All data is frozen at the trip condition, and can be interrogated via the EPICS interface. This will allow the beam operators to visualize the post mortem waveform for each BLM, synchronized in time, to determine where a loss took place and troubleshoot the cause of the spill.

RF REGULATION & INSTABILITY

Synchronization of the radio frequency (RF) with the electron beam is critical to acceleration. The combination of narrow electrical bandwith of SRF cavities and the high oscillation frequency (1.3 GHz) makes acceleration very sensitive to phase and amplitude jitter. The possible causes of jitter are: RF source master oscillator, external disturbances, microphonics, ponderomotive instability, and the inability of the RF control loops to supress the effect of these disturbances; all have been observed in the e-linac.

The best probe of jitter effects is the electron beam itself, particularly downstream of bending magnets – whose effect is sensitive to momentum. Some RF measurement devices perform averaging due to their inherent time constants, and so fail to report meaningful values for phase and/or amplitude noise. Contrarily, r.m.s and peak-to-peak variations are easily seen on beam diagnostic devices such as BPMs or view screens [23]. However, stroboscopic effects can mask the underlying frequencies.

Microphonic versus Ponderomotive

Cavity mechanical modes can respond both to external acoustic noise and to internal electro-magnetic pressure; respectively called the microphonic and ponderomotive effects. Both can lead to changes in the cavity electrical resonance frequency. They differ in that above a threshold accelerating gradient, the ponderomotive effect [24, 25] can be self-enhancing leading to an exponential and/or oscillatory instability of all system signals. A microphonic detuning can act as the seed for instability.

Master Oscillator (MO)

Significant phase drift and jitter between the EGUN, buncher and EINJ were witnessed in 2016, and a program of upgrades to the MO and LLRF were performed in 2017. Originally four MOs were used, 1 for each RF device, and synchronized by a 10 MHz clock. Now, there is a single MO signal split between the devices; stability is excellent.

Injector & Accelerator Cryomodules

Design and construction of EINJ is described in Ref. [26]. EINJ is a top-loading cryomodule. 2 K liquid helium is produced on board via a Joule-Thomson (JT) expansion of externally supplied 4 K LHe. The assembly is enclosed in a LN2-cooled thermal shield. The cold mass comprises a strong back, cavity and scissor-type tuner. The tuner is actuated by a stepper motor at room temperature via rods that pass through the lid and shield. The cavity is driven via two Cornell-type coaxial couplers; each is rated at 50 kW and cooled by compressed air.

At the outset of the 2018 commissioning, momentum jitter of ~ 0.5% was observed at the exit of EINJ. Adjustments in phase set points and tuning of LLRF control loop parameters has reduced this to $\Delta p/p \sim 0.1\%$.

The 0.1% level $\Delta p/p$ is tolerable, but not conducive to easy/fast tuning of correction bends in EMBT/D. Therefore, a campaign to investigate underlying causes was begun; starting with a frequency analysis of the cavity pick-up signal versus the master oscillator. A strong and persistent 40 Hz sideband, among other frequencies, gave cause to initiate a campaign of diagnosing microphonic sources and effects in EINJ and EACA.

Design and construction of EACA, which adopts features from the EINJ, is described in [26]. EACA operated with a single cavity in 2014 and 2016. The second EACA cavity was installed in 2017 but not operated. The two cavities are driven from a single klystron through a power divider. In addition to microphonic effects similar to those in EINJ, operation of EACA in 2018 revealed an oscillatory ponderomotive instability occurring at positive detuning and threshold gradient of ~ 6 MV/m per cavity. This discovery initiated measurements of the Lorentz Force Detuning (LFD) characteristics of the cavities, theoretical analysis and simulation of LFD instability.

MICROPHONICS INVESTIGATION

If a peak in the acoustic noise spectrum lies within the bandwidth of a mechanical mode of the cavity, then oscillations will alter the cavity electrical resonance frequency.

Cavity Mechanical Normal Modes

The low order transverse and longitudinal mechanical modes of the 9-cell cavities have been computed [27] with 3D modelling software. The presence of the coupler ports splits the transverse modes. The 3D model has limitations. An attempt to verify the mode frequencies has been made with a swept-frequency external shaker. The shaker does not couple equally well to all modes, but confirms the fundamental and first three harmonic transverse oscillations.

Acoustic Noise Sources

Comprehensive measurements of noise sources, including turning equipment on/off or throttling, have been made leading to the identification of sources, locations, frequency spectra, and transmission through ground, plumbing, waveguides, RF input couplers, etc. The main sources:

- Water cooling systems for klystrons & waveguides: multiples of 60 Hz up to 420 Hz; and sum/diff 30 Hz satellites. The 60 and 300 Hz lines are very strong.
- On-board Joule-Thomson valves (act like blown pipe), particularly for EINJ. Strong components at 40, 80 Hz

Content from this work may be used under the terms of the CC BY 3.0 licence (© 2018). Any distribution of this work must maintain attribution to the author(s), title of the work, publisher, and DOI.

ISBN: 978-3-95450-194-6 ISSN: 2226-0366 doi:10.18429/JACoW-LINAC2018-TU1A03

Content from this work may be used under the terms of the CC BY 3.0 licence (© 2018). Any distribution of this work must maintain attribution to the author(s), title of the work, publisher, and DOI.

- Air cooling for RF input couplers; line around 200 Hz and strong noise above 300 Hz.
- Cryomodule roughing pump vacuum lines: transmit 30, 60, 120, 180, 220 Hz.

Example measurements are shown Ref. [27] Fig. 3. The GHe and LHe plant and trunk seem not to be noise sources.

Response of Cavities to Microphonics

The response to microphonics has been measured using cavity pick-up signals and phase error within the LLRF, and with a variety of instruments. The most successful has been the Phase Analyzer on loan from Rhode & Schwarz. This has requisite resolution and sensitivity, and automatically orders spectral lines according to impact. A 1:1 correspondence between noise sources and RF phase modulations based on their frequency spectra. E.G. the EINJ spectra and noise source identification is given in Ref. [27] Fig. 2. The spectra show also a non-acoustic source: lines at multiples of 60 Hz from 480 to 900 Hz emanate from the klystron DC high voltage switch-mode power supply; these lines are inconsequential.

Liquid Nitrogen Disturbances

The cryomodule LN2 supply valve is controlled by exhaust temperature, and poorly regulated. This leads to LN2 & temperature bursts & RF power fluctuations all with period 500 secs. Moreover refilling the LN2 reservoir/phase-separator leads to transients twice/hour. Both effects can exceed the microphonic sources. See Ref. [27] Figs. 8-10.

Proposed Mitigations

Water cooling pumps and piping system will be acoustically damped, as will be the RF waveguides. The acoustic property of the 4K/2K LHe insert including JT valves will be examined. A non-intermittent regulation of the LN2 supply will be implemented.

PONDEROMOTIVE INVESTIGATION

The e-linac SRF cavities are operated in self-excited (SE) loop. The EINJ has been operated in four years, and never displayed an instability. The EACA was operated for the first time with two cavities regulated in vector sum, in June 2018. An instability emerges when the combined accelerating gradient of EACA cavities exceeds 12 MV/m. Properties of the instability include the following:

- Thresholding
- Modulation of cavity amplitudes in-antiphase
- Frequency around 160 Hz, but varies with parameters
- Slow growth: over minutes at 12 MeV, secs at 17 MeV
- Final amplitude limited by klystron forward power
- Growth rate rises with accelerating gradient
- Sensitive to individual cavity detunings.
- In-phase AM if the cavities are grossly mis-phased.

See Ref. [27] Fig.1. Investigation and explanation of the instability is progressing on three fronts. [Previous analysis [28] of vector sum control revealed sensitivity, but not instability.]

Lorentz Force Detuning Measurements

LFD changes the response of cavity mechanical modes to acoustic noise, and is the foundation for understanding how the ponderomotive instability arises and is influenced by RF distribution and control loops. Dynamic LFD is used as an input to ponderomotive simulations.

Steady State or Static LFD: the cavity fundamental resonance frequency falls proportional to gradient squared.

In the dynamic LFD measurement, the carrier is amplitude modulated (AM) at a certain frequency. Cavity mechanical modes near that frequency respond, leading to detuning. The phase difference between drive and pickup is used as proxy for the frequency detuning. LFD measurements on EINJ and EACA single cavities have been performed at frequencies (20 – 300 Hz) found to be important with the R&S phase analyzer; an example is given Fig. 5-left for 5% AM at 60 Hz and carrier 8.5 MV/m gradient.

LFD Instability Analysis & Simulations

Two explanations are being considered. (1) The power divider does not isolate CAV#1 from reverse power from CAV#2, and visa versa. This unintended feedback, along with the quasi-static tuning response and LLRF control loops may, alone, be sufficient cause. (2) LFD Coupling of the cavities to mechanical modes. Preliminary Routh-Hurwitz analysis [29] of (1) indicates stability in the absence of the power divider F/B path. Preliminary time domain simulation [30] of (2) in the absence of the PD F/B shows thresholding and sensitivity to the cavity static detuning. In the simulation, the microphonic frequency is taken as a given (e.g. 120 Hz), and the cavity detunings varied. As gradient is raised, the working area of shrinks to zero indicating the threshold (Fig. 5-right).

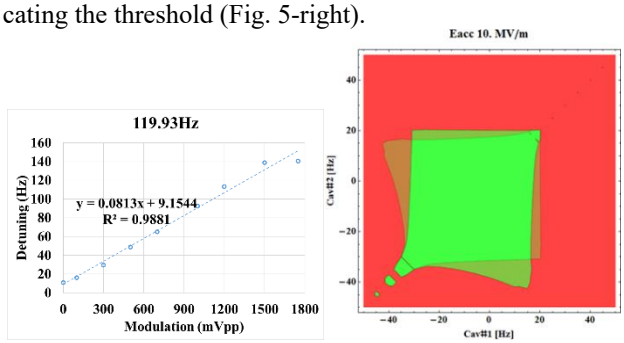


Figure 5: Left: Dynamic LFD measurement at 120 Hz. Right: Simulation output for 4 mechanical modes/cavity. Working area shrinks to 10 Hz×10 Hz at 20 MV/m.

CONCLUSION

The magnetic optics is commissioned to 10 MeV and in excellent agreement with the theoretical model. Following the development of a new data acquisition, integration and thresholding electronic board for the BLMs, the MPS is also commissioned to 10 MeV. Troublesome microphonics effects are understood and mitigations proposed. Resolution of the ponderomotive instability through analysis, simulation and experiment will be ongoing in the spring of 2019 – when e-linac operations resume. A key will be to increase data acquisition rates from 10s to 100s of Hz.

ISBN: 978-3-95450-194-6 ISSN: 2226-0366 doi:10.18429/JACoW-LINAC2018-TU1A03

REFERENCES

[1] S. Koscielniak, *et al*., "Proposal for a ½ MW Electron Linac for Rare Isotope and Materials Science", in *Proc. 11th European Particle Accelerator Conf. (EPAC'08)*, Genoa, Italy, Jun. 2008, paper TUOCG03, p. 985.

[2] Dilling, *et al*., "ISAC and ARIEL: The TRIUMF Radioactive Beam Facilities and the Scientific Program", Hyperfine Interactions, January 2014, Volume 225, Issue 1.

[3] J. Bagger, *et al*., "TRIUMF IN THE ARIEL ERA", in *Proc. IPAC'18*, Vancouver, Canada, Apr-May 2018, p. 6. doi:10.18429/JACoW-IPAC2018-PAMOXGB2

[4] L. Merminga, *et al*., "ARIEL: TRIUMF's Advanced Rare Isotope Laboratory", in *Proc. IPAC'11*, San Sebastian, Spain, Sep. 2011, paper WEOBA0, p. 1917.

[5] S. Koscielniak, *et al*., "ARIEL Superconducting Electron Linac", in *Proc. 26th Linear Accelerator Conf. (LINAC'12)*, Tel Aviv, Israel, Sep. 2012, paper WE1A04, p. 729.

[6] R. Laxdal, *et al*., "TRIUMF/VECC E-linac Injector Beam Test", in *Proc. 26th Linear Accelerator Conf. (LINAC'12)*, Tel Aviv, Israel, Sep. 2012, paper MOPB026, p. 231.

[7] T. Planche, *et al*., "Commissioning and Early Operation of the ARIEL E-linac", in *Proc. LINAC'16*, East Lansing, MI, USA, Sep. 2016, pp. 12-16. doi:10.18429/JACoW-LINAC16-MO2A03

[8] M. Marchetto, *et al*., "Commissioning and Operation of the ARIEL Electron Linac at TRIUMF", in *Proc. IPAC'15*, Richmond, USA, May 2015, paper WEYC3, p. 2444.

[9] R. Laxdal, *et al*., "Status of Superconducting Electron Linac Driver for Rare Ion Beam Production at TRIUMF", in *Proc. LINAC'14*, Geneva, Switzerland, Aug.-Sep. 2014, paper MOIOC01, pp. 31-35.

[10] S. Koscielniak, *et al*., "TRIUMF ARIEL e-Linac Ready for 30 MeV", in *Proc. 8th Int. Particle Accelerator Conf. (IPAC'17)*, Copenhagen, Denmark, May 2017, pp. 1361-1364. doi:10.18429/JACoW-IPAC2017-TUPAB022

[11] R. Laxdal, *et al*., "The 30 MeV stage of the ARIEL E-linac", in *Proc. 18th Int. Conf. RF Superconductivity (SRF'17)*, Lanzhou, China, Jul. 2017, pp. 6-12. doi:10.18429/JACoW-SRF2017-MOXA03

[12] Y. Ma, *et al*., "First RF Test Results of Two-Cavity Accelerator Cryomodule for ARIEL E-Linac at TRIUMF", in *Proc. IPAC'18*, Vancouver, Canada, Apr-May 2018, p. 4512-4515. doi:10.18429/JACoW-IPAC2018-THPMK090

[13] K. Fong, *et al*., "Tuners Alignment on Two 9-cell Cavities with Single Amplifier Under Self-Excited Loop", in *Proc. IPAC'18*, Vancouver, Canada, Apr-May 2018, p. 4527-4529. doi:10.18429/JACoW-IPAC2018-THPMK096

[14] F. Ames, *et al*., "Operation of an RF Modulated Thermionic Electron Source at TRIUMF", in *Proc. IPAC'18*, Vancouver, Canada, Apr-May 2018, p. 4705-4707. doi:10.18429/JACoW-IPAC2018-THPML025.

[15] F. Ames, "Commissioning Report for the TRIUMF ARIEL 300 keV electron source", TRIUMF Document -144733

[16] Y.C. Chao, "E-Linac Major Components and Layout up to Exit of Injector Cryomodule" TRIUMF internal report TRI-DN-10-08.

[17] Y.C. Chao, "E Linac EMBT-EABT-EHAT Phase One Major Components and Layout", TRIUMF report TRI-DN-12-03.

[18] Y.N. Rao, "Electron High Energy Dump Transport (EHDT) Optics Design", TRIUMF internal report TRI-DN-12-11.

[19] S. Koscielniak, "Preliminary Design of Target/Cooling Plate and Raster Pattern for a 100kW Electron Beam Dump (EBP) at 25-75 MeV", TRIUMF internal report TRI-DN-13-03.

[20] I. Earle, "E-Linac 100kW Beam Dump Insert Design Review", TRIUMF internal report DR.P0104-24.

[21] M. Alcorta, *et al*., "Status of the Machine Protection System for ARIEL E-linac", in *Proc. IPAC'18*, Vancouver, Canada, Apr-May 2018, p. 4829-4831. doi:10.18429/JACoW-IPAC2018-THPML077

[22] H. Hui, *et al*., "The TRIUMF Beam Loss Monitor Board for ARIEL", in preparation, 2018.

[23] D. Storey, *et al*., "Performance of OTR and Scintillator View Screens for the ARIEL Electron Linac", in *Proc. 8th Int. Particle Accelerator Conf. (IPAC'17)*, Copenhagen, Denmark, May 2017, pp. 117-119. doi:10.18429/JACoW-IPAC2017-MOPAB021

[24] D. Schulz, "Ponderomotive Stability of RF Resonators and Resonator Control Systems", ANL internal report, ANL-TRANS-944.

[25] J. Delayen, "Phase and Amplitude Stabilization of Superconducting Resonators", California Institute of Technology Thesis, 1978.

[26] N. Muller, *et al*., "TRIUMF's Injector and Accelerator Cryomodules", in *Proc. 17th Int. Conf. RF Superconductivity (SRF'15)*, Whistler, Canada, Sep. 2015, paper THPB115, pp. 1409-1412.

[27] Y. Ma, *et al*., "Microphonics Investigation of ARIEL E-Linac Cryomodules", the presented at the 29th Linear Accelerator Conf. (LINAC'18), Beijing, China, Sep. 2018, paper TUPO020, this conference.

[28] C. Schmidt, "Concept of Vector-Sum Control for cw-Operation", in Proc. ERL07, Daresbury UK, p. 80-84.

[29] Shane Koscielniak, personal communication.

[30] Zhongyuan Yao, personal communication.

Content from this work may be used under the terms of the CC BY 3.0 licence (© 2018). Any distribution of this work must maintain attribution to the author(s), title of the work, publisher, and DOI.

ISBN: 978-3-95450-194-6 ISSN: 2226-0366 doi:10.18429/JACoW-LINAC2018-TU1A05

SEAMLESS QUARTER WAVE RESONATORS FOR HIE ISOLDE

W. Venturini Delsolaro†, A. Miyazaki[1]
CERN, 1211 Geneva, Switzerland
[1]also at Manchester University, M13 9SPL, Manchester, United Kingdom

Abstract

The HIE-ISOLDE post accelerator consists of 4 cryomodules with 5 niobium-coated Quarter Wave Resonators (QWR) each. The standard manufacturing technique was to machine the inner and outer conductor separately, to shrink-fit the 2 pieces and to apply an electron beam welding at the interface. Due to micro cracks, observed on some of the cavities around the welds, we took the decision to explore the possibility of a seamless design. First cavities became available in late 2017 and were then cold-tested in the vertical cryostat. These seamless coated quarter wave resonators have shown some of the highest Q-values of all HIE-ISOLDE cavities in the acceptance tests. Furthermore, we studied the cavity performance with different compensations of the earth magnetic field and different temperature gradients upon cool down. These tests have demonstrated record-breaking RF surface fields for the Nb/Cu technology. This paper reviews the design and fabrication, and reports on the cold tests results of seamless quarter wave resonators. Possible future applications are briefly illustrated.

INTRODUCTION

The HIE-ISOLDE post accelerator is in operation at CERN since 2015, delivering a rich physics program to the community of users. The project was staged, and the high beta section of the machine was completed in spring 2018 with the addition of the fourth cryomodule. The backbone of the accelerator are the niobium sputter coated QWR,realized at CERN using copper cavity substrates done in industry. The early cavity development is documented in [1]. During the production phase, we faced performance degradations, which could be traced back to defects on the copper substrates, in proximity of the electron beam weld. In response to this issue, a seamless design was developed, as reported in [2]. In this paper we report more results, including the performance with beam. Cavities of the new design are labelled QSS, as opposed to the old QS type.

SEAMLESS QWR DESIGN

The main rationale for a seamless design was in our case to remove the possible source of defects in the copper substrates, represented by the electron beam weld, which was located close to the peak magnetic field. Small cracks on the copper substrate can trap fluids during the chemical polishing phases, which then contaminate the niobium layer. However, there are more advantages: the fabrication is simpler and cost effective with respect to the old design. Also, removing the weld allowed to greatly increasing the cross section for the heat path between the lower portion of the resonator and the heat sink in the inner conductor, with beneficial effects on the cooling, both during coating and in operation. This is because in the old design an annular gap remains above the weld, as the required mechanical tolerances for the mating pieces are more easily achieved over a short length. In Fig. 1 the seamless QWR is compared to the welded design.

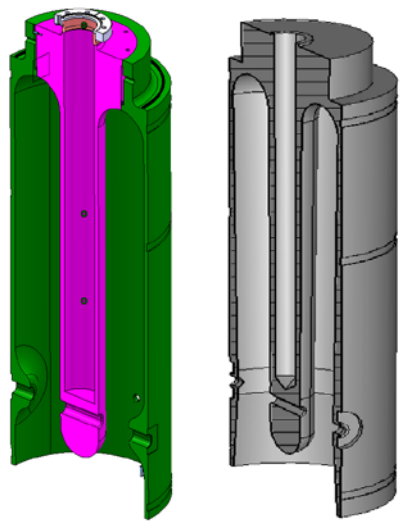


Figure 1: Welded and seamless HIE-ISOLDE QWRs.

In order to make possible the use of a lathe, and avoid milling, the cavity had to be axially symmetric. However, the removal of the cavity “noses” posed a difficulty as it severely decreased the R/Q and thinned the cavity wall, with consequent potential risk of RF leakage. We adopted a double conical shape mainly to recover R/Q.

RF leakage was suppressed by changing the beam port aperture from a racetrack to a circle with a diameter reduction of 2 mm, and by extending the cut-off length in a matching piece, which is made to support the cavity in the cryomodule, as shown in Fig. 2.

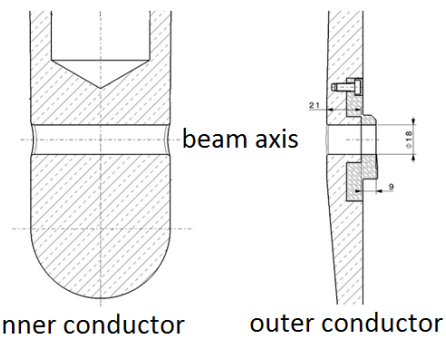


Figure 2: Beam port of the seamless HIE-ISOLDE QWR.

† walter.venturini@cern.ch

Content from this work may be used under the terms of the CC BY 3.0 licence (© 2018). Any distribution of this work must maintain attribution to the author(s), title of the work, publisher, and DOI.

ISBN: 978-3-95450-194-6 ISSN: 2226-0366 doi:10.18429/JACoW-LINAC2018-TU1A05

RF simulations with two different codes, and laboratory measurements, demonstrated that RF leakage was under control. Beam simulations had shown that the aperture restriction was tolerable. All this has found finally confirmation in July 2018 when the first ion beam was accelerated through the full linac. Changing the shape of the beam aperture from a racetrack to a circle also had the consequence of giving up the compensation for the vertical steering. This was not expected to be a problem, as the cavity was to be installed in the high-energy section in the linac. However, the absence of compensation for the vertical beam steering limits the use of these cavities as spare units to the cryomodules after the first one on line, where steering compensation is not necessary. In addition, the optimum beta of the seamless cavities is higher than in the welded version, making the use of this cavity more favourable in the higher energy end of the linac. Table 1 shows the optimized RF parameters, compared with the welded design.

Table 1: Figures of Merit of Welded and Seamless QWR

Parameters	QS	QSS
β_{opt} [%]	10.9	12.2
R/Q [Ω]	520	502
E_{peak}/E_{acc}	5.4	5.2
B_{peak}/E_{acc} [Gauss/(MV/m)]	96	93
G= R_s.Q [Ω]	30.34	30.71
U/E_{acc}^2 [J/(MV/m)^2]	0.207	0.214
P_c at 6 MV/m [W]*	7.7	7.9

* calculated assuming R_s = 50 n[Ω]

Peak fields are comparable, and the loss of R/Q was maintained well below 5%.

VERTICAL TESTS

The first two seamless cavities were acceptance-tested at 4.5 K in the CERN vertical test facility and scored above all the other cavities in the series production (Fig. 3).

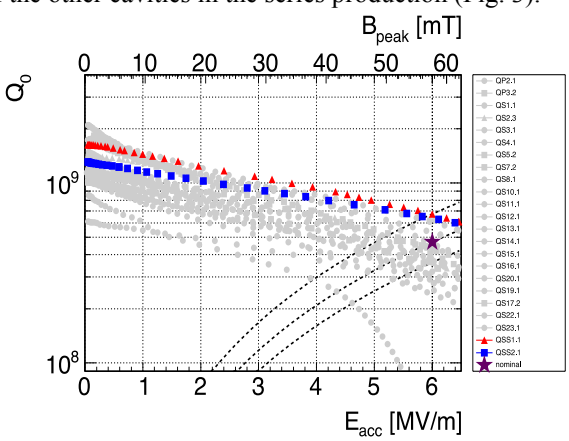


Figure 3: RF performances of welded and seamless HIE-ISOLDE QWRs in the vertical tests at 4.5 K.

The first cavity was qualified in time for installation in the fourth cryomodule, while, in order to respect the project schedule, the second had to be kept as a spare. On this second cavity, we carried out a dedicated test campaign, to understand the origin of the good performance. Full scans of Q values between 2.4 K and 4.6 K were done at several values of the RF field, as shown in Fig. 4, for different amounts of trapped flux (obtained by means of compensation coils placed outside the cryostat), and for different cool down speeds, resulting in different temperature gradients across the cavity at the superconducting transition.

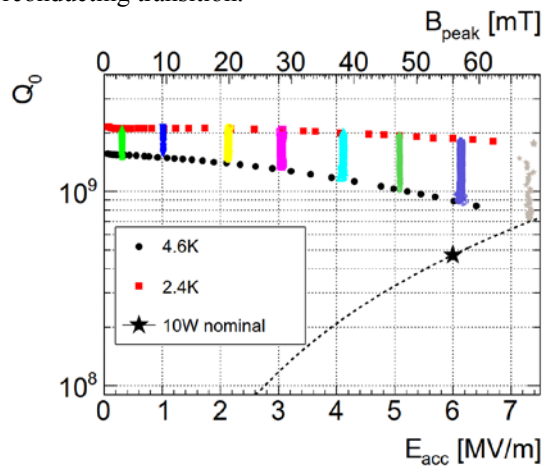


Figure 4: Q versus E and Q versus T curves of a seamless HIE-ISOLDE QWRs.

The seamless cavities were found to behave in a very different way with respect to the normal cavities. A first difference is the higher sensitivity to trapped magnetic flux. Nb/Cu cavities were known to be insensitive to flux trapping, and in all accelerators where they have been employed they operate without magnetic shielding. In contrast, this cavity shows a significantly higher sensitivity, as shown in figures 5 and 6. Still, these values are lower than in typical bulk niobium cavities by about a factor of ten.

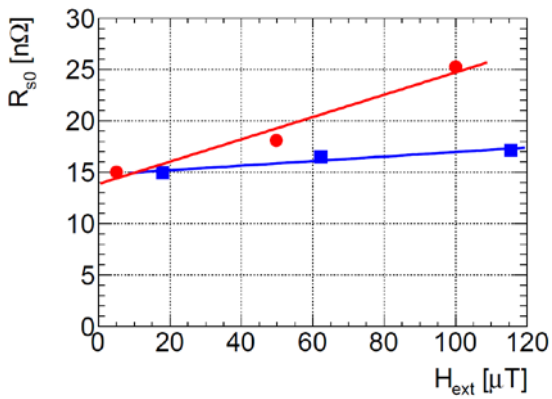


Figure 5: Dependence of the zero-field surface resistance on trapped flux (circles: QSS; squares: QS).

Content from this work may be used under the terms of the CC BY 3.0 licence (© 2018). Any distribution of this work must maintain attribution to the author(s), title of the work, publisher, and DOI.

ISBN: 978-3-95450-194-6 ISSN: 2226-0366 doi:10.18429/JACoW-LINAC2018-TU1A05

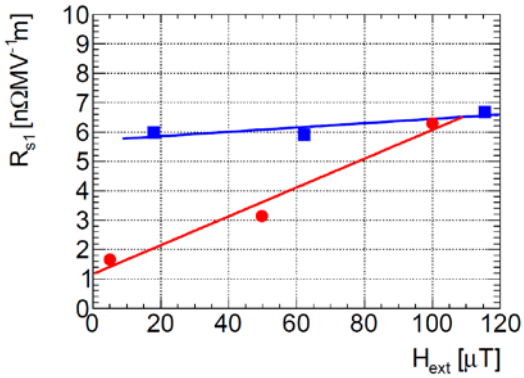


Figure 6: Dependence of the surface resistance slope on trapped flux (circles: QSS, squares: QS).

A second striking difference is that, contrary to their welded counterparts [3], these cavities show the same Q values, irrespective of the thermal gradient measured on the cavity when crossing Tc during cool down. It is possible that, due to the much higher cooling efficiency, the actual temperature gradient on the RF surface is always very small, no matter how fast the cooling is. Therefore, it is not possible to conclude that the cavity is less sensitive to the thermal gradient, as it would seem from the raw data. As a fact, the cavity performance does not depend on the modalities of cool down, and it is uncorrelated to the thermal gradient measured on the outer surface. These findings also suggest a possible interpretation for the spread in sensitivity to the thermal gradient, observed in the QS population. The weld penetration was at the beginning of the production only specified as a minimum value (2 mm), and in a second time the company was instructed to reduce it, in an attempt to mitigate the damages around the welds. This may have resulted in a variability of effective cooling cross sections at the weld in the series production, determining the actual temperature gradients on the RF surfaces. On the other hand, the insensitivity to cool down, together with a higher sensitivity to trapped flux would cast a doubt on the usual interpretation of the dependence on thermal gradient of the residual resistance, in terms of trapped thermoelectric currents.

Having realized that the cavity was sensitive to ambient magnetic fields, we have tried to test it as close as possible to zero field-cooling conditions, by making use of compensation coils placed outside the cryostat. The results were spectacular, as shown in Fig. 7. The cavity reached a peak magnetic field of 120 mT, which is the highest ever achieved with the Nb/Cu technology. At 120 mT, we observed a reversible Q switch, without quench, and decided not to push the cavity any further. The most interesting feature of this result lies in the fact that the infamous Q-slope, which has-so far-prevented the use of sputtered cavities in high gradient machines, was almost absent at low temperature. Actually, this cavity behaves as bulk niobium, as far as the Q- slope is concerned, while the residual resistance is still higher than in state of the art bulk niobium cavities in this frequency range.

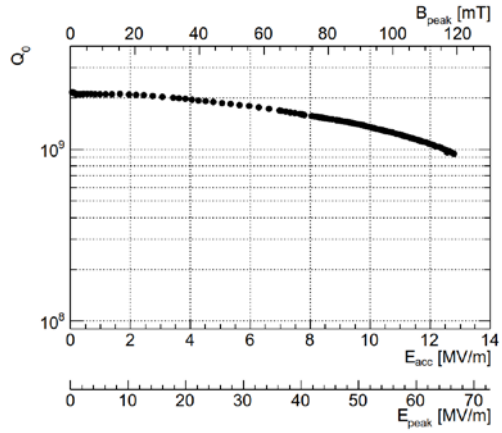


Figure 7: RF performance of a seamless QWR in reduced magnetic field at 2.5 K.

We realised that, once the linear Q slope due to magnetic flux trapping was eliminated, there remained a temperature dependent slope (non-quadratic losses), which behaved exponentially with respect to the RF field, and which can be empirically fitted by assuming a reduced superconducting gap, the reduction being proportional to the RF field. From a literature survey, it appeared that this component is common to both bulk Nb and Nb/Cu technologies, and is not usually visible in bulk niobium data just because it is strongly temperature dependent and prominent at 4.5 K, while most published bulk niobium data are at superfluid temperatures. This topic will be the subject of a dedicated paper.

PERFORMANCE IN HIE-ISOLDE LINAC

All HIE-ISOLDE cavities of the QS type, once installed in the linac, have shown a remarkable improvement in performance with respect to the vertical tests (see Table 2). Although the reason for this performance gain is not completely clear, we believe it is due to more homogenous cooling conditions: indeed the Q values in the linac are close to a zero gradient extrapolation from the vertical tests carried out at different temperature gradients.

The insensitivity to the cool down conditions of the seamless cavity made us expect no performance improvement from the vertical tests to the cryomodule. This was confirmed in the 2018 campaign. The QS cavities had their Q values changed due to slightly different cooling conditions, while the QSS cavity displayed the same results as in the vertical test, within the calibration uncertainty.

The absence of magnetic shielding in the HIE-ISOLDE cryomodules also favours the insensitive welded cavities in the comparison with the QSS. In spite of that, the seamless cavity is still well above specification in the linac and it has the advantage of a reproducible performance after thermal cycles, which might be caused by outages of the cryoplant, or by the normal annual operation schedule.

In Fig. 8, we show the RF performance of the HIE-ISOLDE cavities on line during the 2018 commissioning campaign. One of the cavities developed

Content from this work may be used under the terms of the CC BY 3.0 licence (© 2018). Any distribution of this work must maintain attribution to the author(s), title of the work, publisher, and DOI.

ISBN: 978-3-95450-194-6 ISSN: 2226-0366 doi:10.18429/JACoW-LINAC2018-TU1A05

an RF connection fault and we decided not to use it for this year.

In Table 2, we report the Q values at nominal field for each cavity, at the vertical test and in the linac over the years. The suffixes in the legend refer to the substrate serial number and the coating number, respectively. QP are prototype cavities of the welded type.

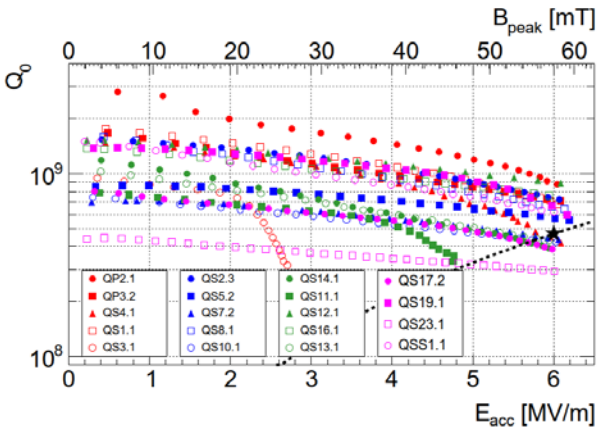


Figure 8: RF performance in 2018 of HIE ISOLDE linac cavities.

Table 2: $Q/10^8$ values of the HIE ISOLDE cavities at 6 MV/m in vertical tests (VT) and before each physics run. The HIE-ISOLDE specification is 4.7 (10 W at 4.5 K). Where field emission limited the operational gradient, the onset field is indicated.

Cavity	VT	L2015	L2016	L2017	L2018
QP2.1	6.3	8.2	3.5MV/m	11.0	8.7
QP3.2	4.3	5.4	7.9	7.7	7.3
QS4.1	4.3	5.9	6.6	7.1	4.4
QS1.1	3.7	6.6	7.1	7.9	6.9
QS3.1	3.6	4.4	4.5MV/m	4.5MV/m	2MV/m
QS2.3	3.6	-	6.4	8.4	7.4
QS5.2	3.5	-	4.2	6.2	5.7
QS7.2	4.0	-	4.3	5.3	4.4
QS8.1	3.7	-	4.9	7.2	6.5
QS10.1	3.1	-	4.0	5.7	4.2
QS14.1	2.4	-	-	4.1	3.9
QS11.1	2.8	-	-	3.5MV/m	4MV/m
QS12.1	3.0	-	-	9.0	9.0
QS16.1	5.3	-	-	9.4	7.6
QS13.1	2.8	-	-	4.1	4.3
QS17.2	4.3	-	-	-	3.9
QS19.1	4.6	-	-	-	6.6
QS22.2	3.7	-	-	-	-
QS23.1	3.2	-	-	-	2.9
QSS1.1	6.7	-	-	-	6.2

DESIGN EVOLUTIONS AND POSSIBLE FUTURE APPLICATIONS

The first obvious extension of this design is to reintroduce a mechanism for the correction of the vertical beam steering, which is inherent to the QWR geometry [4]. This would allow having a universal spare for the HIE-ISOLDE machine. Due to the tight space constraints in the existing cryomodules, tilting of the beam ports is the favoured option to achieve this result.

A more ambitious goal is to develop seamless QWRs for higher beta acceleration, having in mind applications for high current proton machines. The production of a large series of such cavities would be quite cost effective, when compared with alternatives like for instance half wave resonators made of bulk niobium. We made some explorative steps in this direction: Fig. 9 shows the RF design of a QWR with optimum beta of 0.36. The usual figures of merit are listed in Table 3. This shape would be easy to machine out of a copper billet, and the same coating recipe used for HIE-ISOLDE would be applicable.

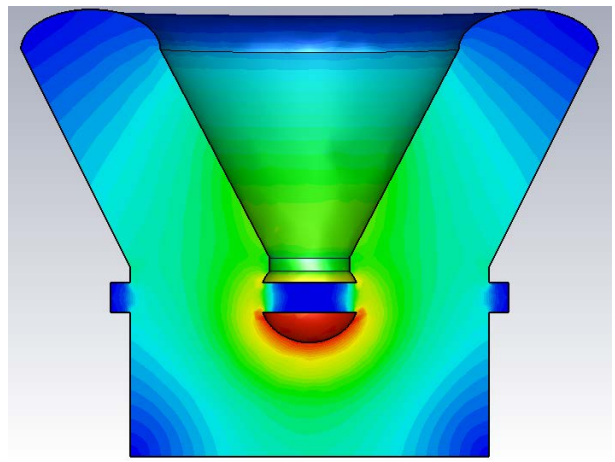


Figure 9: RF design of a seamless QWR for high beta.

Table 3: Figures of Merit of a beta=0.36 Seamless QWR

Figure of merit	Value
f [MHz]	229
Γ [Ω]	183
E_{pk}/E_0	5.6
B_{pk}/E_0 [mT/(MV/m)]	6.4
L_{cav} [mm]	360
β_{opt}	0.36
TTF(β_{opt})	0.77
R/Q(β_{opt}) [Ω]	309

Due to the large velocity acceptance, about 50 cavities of this type would be sufficient to accelerate protons between 100 MeV and 220 MeV. The total cryogenics power would be of the order of 2-3 kW at 4.5 K. The mechanical aperture for the beam was 30 mm in this simulation. If necessary, beam steering correction could be achieved by using a racetrack shaped beam aperture, and offsetting the beam. Microphonics would be utterly suppressed by the rigid copper substrate.

For a large accelerator, this solution could represent non-negligible savings on capital costs.

Content from this work may be used under the terms of the CC BY 3.0 licence (© 2018). Any distribution of this work must maintain attribution to the author(s), title of the work, publisher, and DOI.

ISBN: 978-3-95450-194-6 ISSN: 2226-0366 doi:10.18429/JACoW-LINAC2018-TU1A05

Content from this work may be used under the terms of the CC BY 3.0 licence (© 2018). Any distribution of this work must maintain attribution to the author(s), title of the work, publisher, and DOI.

CONCLUSION

Seamless Quarter Wave Resonators for the HIE-ISOLDE post accelerator were designed at CERN with optimized RF parameters, fitting the existing cryomodules. The cavity substrates have been obtained in industry by machining single OFE copper billets, and then coated with niobium and tested at CERN. Two cavities have completed this process so far, while a third is about to be coated. The RF performances of these cavities were the best of the whole series production in the acceptance tests in a vertical cryostat. Moreover, the second cavity, which was extensively studied in various conditions of shielding, showed unprecedented peak fields for the Nb/Cu technology. Peculiar features of the seamless cavities are the higher sensitivity to magnetic flux trapping, and the lack of sensitivity to the cool down conditions.

This technique, while removing at the source the risk of defects around the electron beam welds, is also cost effective and provides a much better cooling of the resonator.

The validation of the QSS design was complete in summer 2018, with the first ion beam acceleration. Since then, the first seamless cavity is operating and delivering accelerated beam to the users.

Stimulated by this success, we plan to improve the design, incorporating a correction of the vertical beam steering, which would allow to install these cavities also in the low energy section of the linac.

As a possible future application, we sketched a seamless QWR, which could be apt to accelerate protons in the energy range of 100-200 MeV, with the known advantages of the Nb/Cu technology.

ACKNOWLEDGEMENTS

We warmly acknowledge the essential contribution of all technical teams at CERN and in industry.

S. Teixeira Lopez and T. Mikkola carried out most of the design work of the QSS cavity, M. Garlasche followed up the manufacturing in industry, and A. Sublet performed the niobium coatings at CERN.

We thank the CERN management for the steady support.

REFERENCES

[1] W. Venturini Delsolaro, S. Calatroni, B. Delaup, A. D'Elia, N. M. Jecklin, Y. Kadi, G. Keppel, D. Lespinasse, P. Maesen, I. Mondino, V. Palmieri, S. Stark, A. R. M. Sublet, M. Therasse, "Nb Sputtered Quarter Wave Resonators for HIE-ISOLDE", in *Proc. SRF'13*, Paris, France, Sep. 2013, paper WEIOA03, pp. 767.

[2] S. Teixeira López, M. A. Fraser, M. Garlasché, T. Mikkola, A. Miyazaki, A. Sublet, W. Venturini Delsolaro, "A seamless Quarter Wave Resonator for HIE-ISOLDE", in *Proc. SRF'17*, Lanzhou, China, Jul. 2017, pp. 686, https://doi.org/10.18429/JACoW-SRF2017-WEYA03

[3] P. Zhang, G. Rosaz, A. Sublet, M. Therasse, W. Venturini Delsolaro, "The influence of cooldown conditions at transition temperature on the quality factor of niobium sputtered quarter wave resonators for HIE-ISOLDE", in *Proc. SRF'15*, Whistler, Canada, Sep. 2015, paper TUPB077, p. 765.

[4] A. Facco and V. Zvyaginsev, "Beam steering in superconducting quarter-wave resonators: an analytical approach", Phys. Rev. ST Accle. Beams 14, 070101, July 2011

ISBN: 978-3-95450-194-6 ISSN: 2226-0366 doi:10.18429/JACoW-LINAC2018-TU2A01

FIRST ACCELERATION OF HEAVY ION BEAMS WITH A SUPERCONDUCTING CONTINOUS WAVE HIM/GSI CW-LINAC

W. Barth†,1,2, K. Aulenbacher1,3, M. Basten4, M. Busch4, F. Dziuba1, V. Gettmann1, M. Heilmann2, T. Kürzeder1, M. Miski-Oglu1, H. Podlech4, A. Rubin2, A. Schnase2, M. Schwarz4, S. Yaramyshev2
[1] Helmholtz Institute Mainz, Germany
[2] GSI Helmholtzzentrum für Schwerionenforschung, Darmstadt, Germany
[3] Johannes Gutenberg-Universität Mainz, Mainz, Germany
[4] IAP Goethe-Universität Frankfurt, Frankfurt, Germany

Abstract

First acceleration of heavy ion beams with a superconducting continuous wave HIM/GSI cw-Linac. After successful RF-testing of a new superconducting Linac RF-cavity at GSI Helmholtzzentrum für Schwerionenforschung and a short commissioning and ramp up time of some days, this 15-gaps Crossbar H-cavity accelerated first time heavy ion beams with full transmission up to the design beam energy. The design acceleration gain of 3.5 MV inside a length of less than 70 cm has been verified with heavy ion beam of up to 1.5 pμA. The measured beam parameters show a nice beam quality. The machine commissioning with beam is a milestone of the R&D work of Helmholtz Institute Mainz (HIM) and GSI in collaboration with IAP Goethe-University Frankfurt in development of the superconducting heavy ion continuous wave linear accelerator cw-Linac.

INTRODUCTION

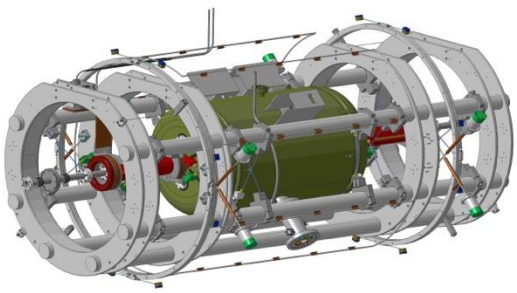


Figure 1: Demonstrator CH-cavity (CH0) with two sc-solenoids inside the support frame.

The design and construction of cw high intensity Linacs is a crucial goal of worldwide accelerator technology development [1]. Above all, compactness of a particle accelerator is a beneficial demand for the development of high intensity cw proton and ion Linacs [2]. In the low- and medium-energy range cw-Linacs can be used for several applications, as boron-neutron capture therapy, high productivity isotope generation and material science. A high-energy Linac is an integrated and essential part of several large scale research facilities, as spallation neutron sources or accelerator driven systems. Thus the study and investigation of the design, operation and optimization of a cw-Linac, as well as progress in elaboration of the superconducting technology [3] is of high relevance.

For the HIM/GSI cw-Linac HELIAC (HElmholtz LInear ACcelerator) several superconducting CH cavities operated at 217 MHz should provide for ion acceleration to beam energies between 3.5 MeV/u and 7.3 MeV/u, while the energy spread should be kept smaller than ±3 keV/u. The cw-Linac allows the acceleration of highly charged ions with a mass to charge ratio of up to 6. For proper beam focusing superconducting solenoids have to be mounted between the CH cavities. The general parameters are listed in Table 1 [4]. R&D and prototyping (demonstrator project) [5] in preparation of the proposed HELIAC is assigned to a collaboration of GSI, HIM and GUF. The demonstrator setup is located in straightforward direction of the GSI–High Charge State Injector (HLI).

Table 1: Design Parameters of the cw-Linac

Mass/charge		6
Frequency	MHz	216.816
Max. beam current	mA	1
Injection energy	MeV/u	1.4
Output energy	MeV/u	3.5 – 7.3
Output energy spread	keV/u	±3
Length of acceleration	m	12.7
Sc CH-cavities	#	9
Sc solenoids	#	7

The demonstrator comprises a 15 gap sc CH-cavity (CH0) embedded by two superconducting solenoids; all three components are mounted on a common support frame (see Fig. 1) [6]. The beam focusing solenoids provide maximum fields of 9.3 T, the free beam aperture is 30 mm. A configuration of one main Nb_3Sn-coil and two compensation coils made from NbTi shields the maximum magnetic field of 9.3 T within a longitudinal distance of 10 cm down to 30 mT. The solenoids are connected to LHe ports inside the cryostat by copper tapes allowing dry cooling. The sc CH structure CH0 is the key component and offers a variety of research and development [7].

*Work supported by the BMBF, project number 05P15RFBA, MYRTE which is funded by the European Commission under Project-ID 662186 and Helmholtz International Center for FAIR.
†w.barth@gsi.de

Content from this work may be used under the terms of the CC BY 3.0 licence (© 2018). Any distribution of this work must maintain attribution to the author(s), title of the work, publisher, and DOI.

ISBN: 978-3-95450-194-6 ISSN: 2226-0366 doi:10.18429/JACoW-LINAC2018-TU2A01

Content from this work may be used under the terms of the CC BY 3.0 licence (© 2018). Any distribution of this work must maintain attribution to the author(s), title of the work, publisher, and DOI.

PREPARATION OF RF-CAVITY AND SUPPLY SYSTEM

The sc 15 gap CH-cavity is directly cooled with liquid helium, supported by a helium jacket made by titanium. The vendor Research Instruments GmbH (RI) provided for sufficient cavity preparation. After high pressure rinsing (HPR) a performance test in a vertical cryostat at low RF power was performed at IAP, reaching gradients up to 7 MV/m. After the final assembly of the helium vessel and further HPR preparation at RI, the cavity was tested again, but in a horizontal cryostat. As shown in Fig. 2, the cavity showed improved performance due to an additional HPR treatment, the initial design quality factor Q_0 has been exceeded by a factor of four, a maximum accelerating gradient of E_{acc} = 9.6 MV/m at $Q_0 = 8.14\times10^8$ has been achieved [8-10]. Prior beam commissioning of the cavity, the RF power couplers [11-12] were tested and conditioned with a dedicated test resonator [13].

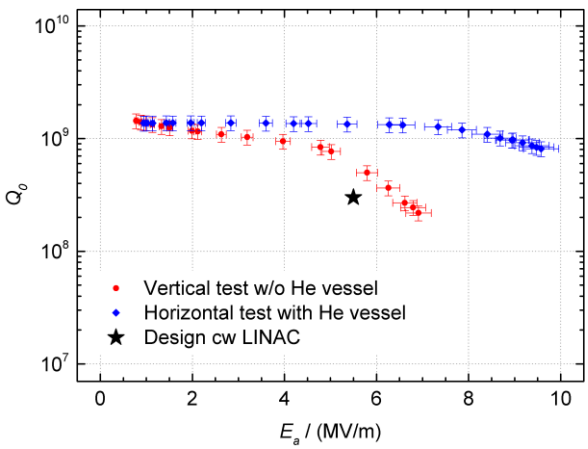


Figure 2: RF-testing of CH-demonstrator cavity - improved performance (add. HPR), low field emission rate, high field gradient, therm. quenching beyond 9.6 MV/m.

The couplers are equipped with sensors to control the temperature of the ceramic windows and Langmuir probes to detect the multipacting current. A first conditioning [14] has been performed with pulsed RF (up to 5 kW) and finally in cw-mode (up to 2 kW). Further increase of the forward cw-RF power leads to a temperatures rise of more than 80°C at the ceramic window, potentially sufficient to damage the coupler. During the operation, the "cold" coupler window has been anchored to the liquid nitrogen supply tube by copper ribbons. In a clean room of class ISO4 the power couplers were integrated in the RF-cavity, as well as three frequency tuners, developed at IAP [15] and manufactured at GSI for the control of resonance frequency. Furthermore, the CH-cavity and both solenoids were assembled on a string. After leak testing of the accelerating string the complete cold mass was integrated [16] into the cryostat outside of the clean room.

DEMONSTRATOR-BEAM DYNAMICS

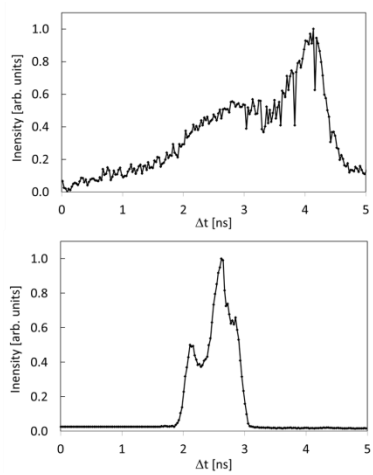


Figure 3: Bunch shape measurement for HLI beam at 1.366 MeV/u (top) and at same energy for matched case with rebuncher R1 and R2 (down).

The beam dynamics layout behind the HLI at 1.4 MeV/u has been simulated in advance. In a preparing beam test run, it could be confirmed, that the room temperature focusing quadrupoles (triplet and two duplets) and two rebuncher cavities are sufficient to provide for full 6D-matching to the demonstrator [17]. At the same time, the input beam is axially symmetric for further solenoid focusing due to especially chosen gradients, while bunch length (see Fig. 3) and momentum spread are matched as well.

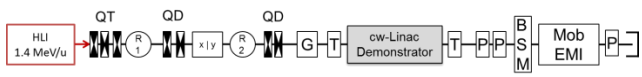


Figure 4: Layout of matching line to the Demonstrator and beam diagnostics test bench; QT/QD = quadrupole triplet/duplet, R = rebuncher, X/Y = beam steerer, G = SEM-grid, T = current transformer, P = phase probe, BSM = bunch shape monitor, EMI = emittance meter.

The transport line (see Fig. 4) provides also for beam instrumentation. Moreover, beam transformers, Faraday cups, SEM-profile grids, a dedicated emittance meter, a bunch structure monitor and phase probe pickups (beam energy measurements applying time of flight) provide for proper beam characterization behind the demonstrator.

The beam dynamics layout of the sc cw-Linac is based on the EQUUS (EQUidistant mUltigap Structure) concept, as proposed in [18]. It features high acceleration efficiency with longitudinal and transversal stability, as well as a straightforward energy variation. Energy variation can easily be achieved by varying the applied RF-voltage or the RF-phase of the amplifier. Highly charged ions with a mass-to-charge ratio of maximum 6 will be accelerated from 1.4 MeV/u up to 3.5 - 7.3 MeV/u. Energy variation while maintaining a high beam quality is the core issue with respect to beam dynamics, simulated using advanced software [19-20] and previously developed algorithms [21-24]. The cell length inside an EQUUS designed cavity is

ISBN: 978-3-95450-194-6 ISSN: 2226-0366 doi:10.18429/JACoW-LINAC2018-TU2A01

kept constant and is fixed with a higher (geometrical) β compared to the injection beam energy (constant-β structure). As a consequence the constant-β structure leads to a sliding movement in longitudinal phase space. Trajectory and energy gain depend strongly on the initial phase at the first gap centre and the difference between particle energy and design energy. The corresponding transversal emittance evolution has been measured in a broad range with small emittance growth.

Beam dynamics behind the HLI has been carried out with the LORASR code (see Fig. 5) [25]. The quadrupole triplet and duplets provide for an axially symmetric input beam for further solenoid focusing. The beam is matched to the demonstrator in the 6d phase space.

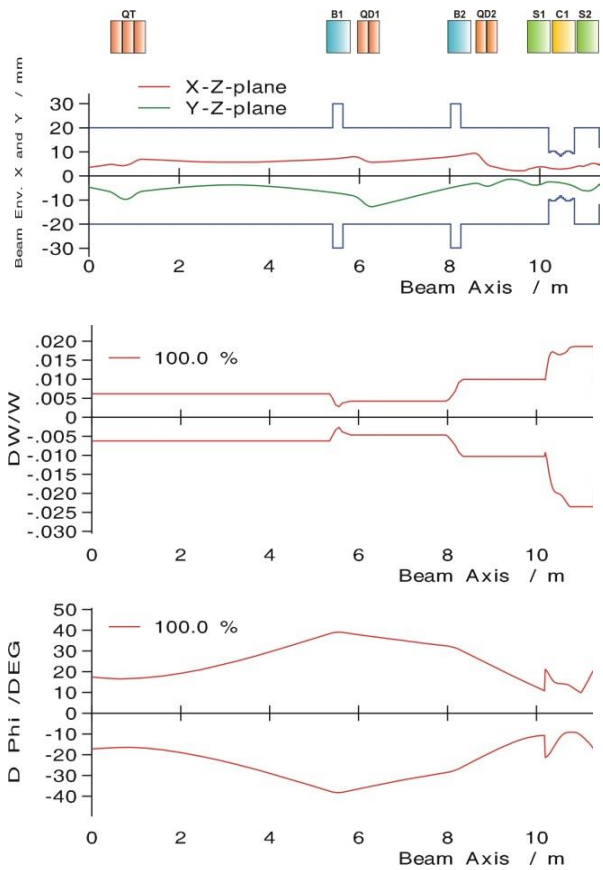


Figure 5: Beam envelopes (matching the demonstrator).

FIRST BEAM ACCELERATION

At June 2017, after successful RF-testing of the sc RF-cavity in 2016, set up of the matching line to the demonstrator and a short commissioning and ramp up time of some days, the CH0-cavity first time accelerated heavy ion beams (Ar^{11+}) with full transmission up to the design beam energy of 1.866 MeV/u (ΔW_{kin} = 0.5 MeV/u) [26], as shown in Fig. 6. For the first beam test the sc cavity was powered with 10 Watt of net RF power, providing an accelerating voltage of more than 1.6 MV inside a length of 69 cm. Further on the design acceleration gain of 3.5 MV has been verified and even exceeded by acceleration of beam with high rigidity (A/q = 6.7). As summarized in Table 2, argon and helium ion beams with different charge state from an ECR ion source ($^4He^{2+}$, $^{40}Ar^{11+}$, $^{40}Ar^{9+}$, $^{40}Ar^{6+}$) were accelerated at HLI with the demonstrator. For longitudinal beam matching the rebuncher settings were adapted according to the mass of charge ratio A/q, as well as the acceleration voltage.

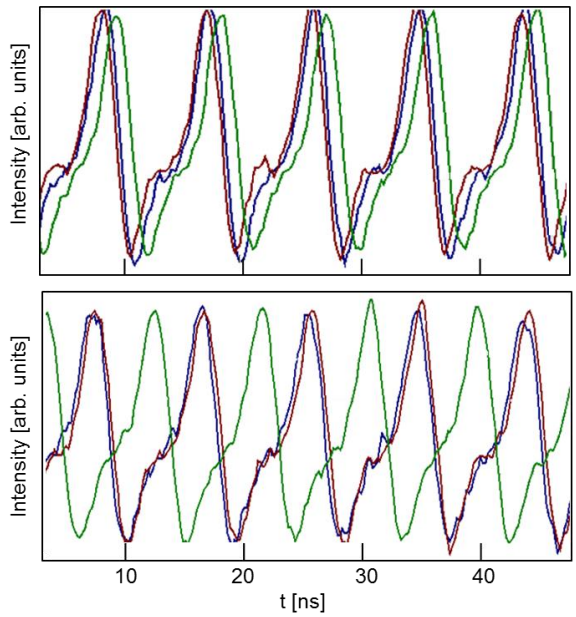


Figure 6: First RF-acceleration with the 216.816 MHz-CH-cavity; measured Ar^{11+}-phase probe signals from HLI beam at 1.366 MeV/u (top), HLI-RF-frequency is 108.408 MHz (T = 9.224 ns). By acceleration up to the nominal beam energy (down), the coarse time of flight between blue and red signal is slightly reduced. The time of flight for the fine measurement between red and green signal is significantly shifted, according to the beam energy of 1.866 MeV/u.

Table 2: RF- Parameters for Matched Case

	He^{2+}	Ar^{11+}	Ar^{9+}	Ar^{6+}
A/q	*2.0*	*3.6*	*4.4*	*6.7*
$U_{Reb1,eff.}$ [kV]	8.3	15.0	18.3	27.9
$U_{Reb2,eff.}$ [kV]	22.7	40.8	49.9	75.9
$E_{acc,CH}$*[MV/m]	1.8	3.2	3.9	5.9
U_0 [MV]	1.2	2.2	2.7	4.0

*E_{acc} = *transit time factor* × *total accelerating voltage*/(*n*×0.5×*βλ*)

A maximum average beam intensity of 1.5 pμA has been achieved, limited only by the beam intensity of the ion source and maximum duty factor (25%) of the HLI, while the CH-cavity was operated in cw-mode. All presented measurements were accomplished with high duty factor beam and maximum beam intensity from the HLI.

Content from this work may be used under the terms of the CC BY 3.0 licence (© 2018). Any distribution of this work must maintain attribution to the author(s), title of the work, publisher, and DOI.

ISBN: 978-3-95450-194-6 ISSN: 2226-0366 doi:10.18429/JACoW-LINAC2018-TU2A01

Content from this work may be used under the terms of the CC BY 3.0 licence (© 2018). Any distribution of this work must maintain attribution to the author(s), title of the work, publisher, and DOI.

SYSTEMATIC BEAM INVESTIGATIONS

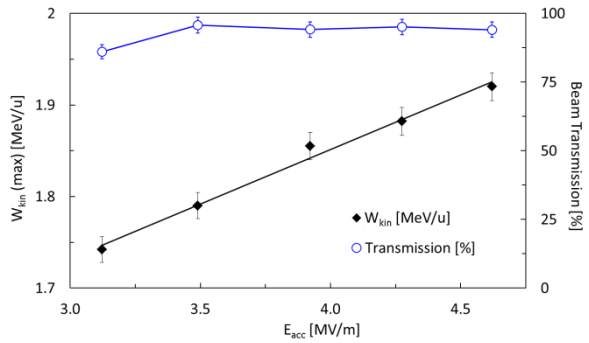


Figure 7: Acceleration of an Ar^{9+}-beam; maximum achieved beam energy and transmission as function of the (eff.) accelerating gradient [26].

A full measured 2D-scan of beam energy and beam transmission for a wide area of different accelerating fields and RF-phases has been performed. The linear increase of beam energy with ramped accelerating gradient (as shown in Fig. 7) could be observed for different RF-phase settings, while the beam transmission is kept above 90 %. In general these measurements confirm impressively the EQUUS beam dynamics, featuring effectively beam acceleration up to different beam energies without particle loss and significant beam quality degradation. As measured with helium beam, for lighter ions a maximum beam energy of up to 2.2 MeV/u could be reached with the demonstrator cavity, but with reduced beam quality.

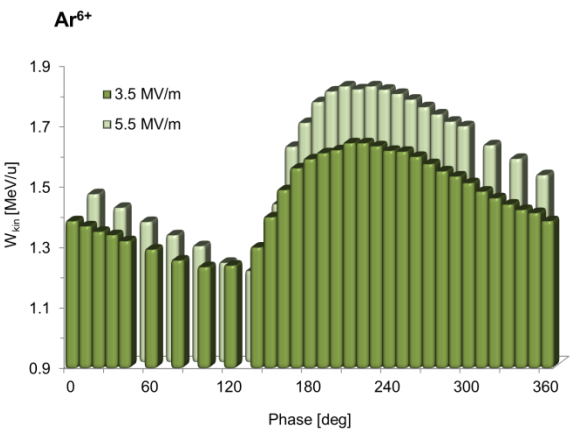


Figure 8: Phase-scan of Ar^{6+}-beam energy for 3.5 MV/m and 5.5 MV/m [26].

With Ar^{6+}-beam (A/q = 6.7), an energy gain above 0.5 MeV/u could be reached with an accelerating gradient of 6 MV/m. As an example, Fig. 8 shows a fully measured 360° phase scan for two different accelerating gradients (3.5 MV/m and 5.5 MV/m). All individual data as well as the characteristic shapes of the phase scans are in good agreement according to the accelerating gradient. For an increased gradient the maximum beam energy at an RF-phase of 210° boosts as well, while the minimum beam energy at 130° could be decreased down to 1.2 MeV/u. The bunch length detected with a bunch shape monitor (BSM) [27-28] was measured as very sensitive to RF-phase changes. A change of RF-phase by 30° only, leads to a significant change of bunch length (by more than a factor of 4), while the beam transmission is not affected. For further matching to another CH-cavity, the adjustment of the beam energy setting by changing the RF-amplitude is more favourable - compared to changing the RF-phase - as no significant bunch shape change could be observed.

PHASE SPACE MEASUREMENTS

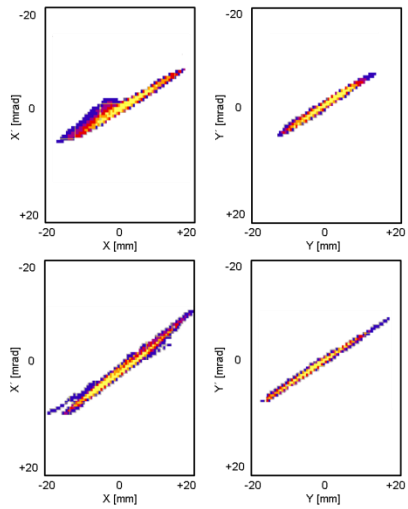


Figure 9: Ar^{9+}-beam emittance at 1.366 MeV/u (top) and at 1.85 MeV/u (down); normalized (horizontal) emittance growth is measured for 15% [26].

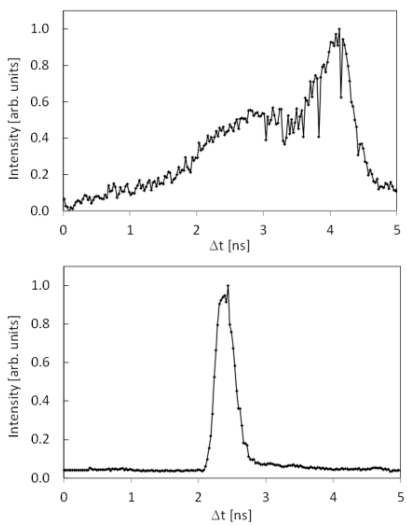


Figure 10: Bunch shape of Ar^{9+}-beam at 1.366 MeVu (top) and fully matched after acceleration to 1.85 MeV/u (down) [26].

The beam quality has been characterized by measuring the phase space distribution, as shown in Fig. 9. The measured emittance of the argon beam, delivered by the ECR and HLI, shows an adequate beam quality: the total 90% horizontal beam emittance is measured for 0.74 µm, while

ISBN: 978-3-95450-194-6 ISSN: 2226-0366 doi:10.18429/JACoW-LINAC2018-TU2A01

in the vertical plane the total 90% emittance is 0.47 µm only. All measurements have been performed without solenoidal field, therewith any additional emittance degradation effects by different beam focusing could be avoided. The measured (normalized) beam emittance growth at full beam transmission is sufficiently low: 15 % (horizontal plane) and 10% (vertical plane). Selective measurements at other RF-amplitudes and -phases, as well as for other beam rigidities confirmed the high (transversal) beam performance in a wide range of different parameters. Besides beam energy measurements the bunch shape was measured after successful matching (see Fig. 10) with the Feschenko monitor [28]. As shown, an impressive small minimum bunch length of about 300 ps (FWHM) and 500 ps (base width) could be detected, sufficient for further matching to and acceleration in future RF-cavities

ADVANCED R&D

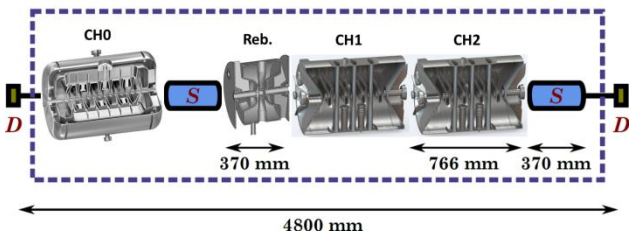


Figure 11: Advanced cryo module layout containing demonstrator CH0 cavity, two short CH cavities, a rebuncher and two solenoids.

Up to now, the reference design for the cw-Linac dates back to [4]. Meanwhile many experiences have been gained in design, fabrication and operation of sc CH-cavities and the associated components. In this context, a revision of the Linac layout was recommended. Optimized cavity layouts [29] resulted in modified voltage distributions. Furthermore, the layout - now with three CH-cavities and a rebuncher (see Fig. 11) [30] per cryo module - has been specified with more details. It features high acceleration efficiency with longitudinal and transversal stability, as well as a straightforward energy variation. Energy variation can easily be achieved by varying the applied RF-voltage or the RF-phase of the amplifier. Highly charged ions with a mass-to-charge ratio of maximum 6 will be accelerated from 1.4 MeV/u up to 3.5- 7.3 MeV/u. Energy variation while maintaining a high beam quality is the core issue with respect to beam dynamics, simulated using advanced software [19-20] and previously developed algorithms [21, 24, 31-33].

Promising power and beam tests with the 15-gap CH0 showed successfully, that higher accelerating gradients can be achieved, thus leading to a more efficient design with four cryo modules (CM1-CM4). Consequently an advanced beam dynamics layout [34] is carried out with respect to the ambitious beam-, RF- and mechanical requirements. Fig.12 shows phase space portraits based on the recent advanced layout applying a max. accelerating gradient of 7.1 MeV/u. Applying the advanced beam dynamics layout for lower mass to charge ratios, significant higher beam energies could be achieved (e.g. up to 14.6 MeV for a p^+-beam).

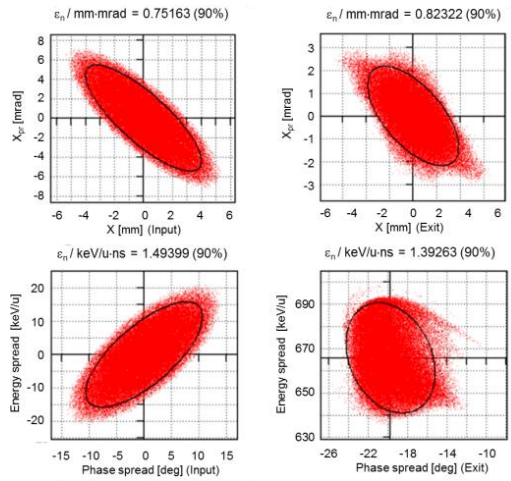


Figure 12: Phase space portraits applying an advanced Linac layout; top: x - x', bottom: $\Delta\varphi$ - ΔW, left: CM1-Input (emittance size as at HLI), right: Output of CM4 [35].

SUMMARY

An advanced cw-Linac approach, based on a standard cryomodule equipped with three CH-cavities and a sc-rebuncher, demonstrates the high capabilities due to energy variation preserving the beam quality, as shown in the first beam test. The design acceleration gain of the first sc CH-cavity was achieved with heavy ion beams even above the design mass to charge ratio at full transmission and maximum available beam intensity [35]. The beam quality was measured as excellent in a wide range of different beam energies, This new design could provide beam acceleration for a wide range of different ions (protons to uranium) above the design beam energy, featuring the ambitious GSI-user program [36], while the GSI-UNILAC is upgraded for short pulse high current FAIR-operation. [37]. The achieved demonstrator beam commissioning confirms the capabilities of the applied EQUUS beam dynamics design and is a major milestone paving the way to the cw-Linac HELIAC.

ACKNOWLEDGEMENTS

Successful beam testing could not be accomplished without strong support of highly committed people from different GSI-departments. The beam test is a milestone of the R&D work of HIM and GSI in collaboration with GUF in preparation of a superconducting heavy ion continuous wave linear accelerator.

Content from this work may be used under the terms of the CC BY 3.0 licence (© 2018). Any distribution of this work must maintain attribution to the author(s), title of the work, publisher, and DOI.

ISBN: 978-3-95450-194-6 ISSN: 2226-0366 doi:10.18429/JACoW-LINAC2018-TU2A01

Content from this work may be used under the terms of the CC BY 3.0 licence (© 2018). Any distribution of this work must maintain attribution to the author(s), title of the work, publisher, and DOI.

REFERENCES

[1] C. Prior, Overview of High Intensity Accelerator Projects, Proceedings of HB'10, Morschach, Switzerland, pp. 6-10 (2010).

[2] S.M. Polozov *et al.*, Beam dynamics study and electrodynamics simulations for the cw RFQ, Proceedings of IPAC2017, Copenhagen, Denmark, pp. 1333-1336 (2017).

[3] R. Laxdal, Physica C-Superconductivity and its Applications, Volume: 441, Issue: 1-2, Pages: 13-20, (2006), doi: 10.1016/j.physc.2006.03.096

[4] S. Minaev *et al.*, "Superconducting, energy variable heavy ion linac with constant β, multicell cavities of CH-type", Phys. Rev. ST Accel. Beams 12, 120101, (2009). doi: 10.1103/PhysRevSTAB.12.120101

[5] W. Barth *et al.*, "A superconducting CW-LINAC for heavy ion acceleration at GSI", EPJ Web of Conferences, vol. 138, article number 01026, (2017). doi: 10.1051/epjconf/201713801026

[6] F. Dziuba *et al.*, "First Cold Tests of the Superconducting cw Demonstrator at GSI", in *Proc. of RuPAC'16*, St. Petersburg, Russia, Oct. 2016, paper WECBMH0, pp. 83-85.

[7] T. Kürzeder *et al.,* Infrastructure for Superconducting CH-Cavity Preparation at HIM *Proc. IPAC'18* (Vancouver, Canada) Preprint

[8] F. Dziuba *et al.*, First Performance Test on the Superconducting 217 MHz CH Cavity at 4.2 K, Proceedings of LINAC'16, East Lansing, MI, USA, pp. 953-955 (2016).

[9] F. Dziuba *et al.*, First Cold Tests of the Superconducting cw Demonstrator at GSI, Proceedings of RuPAC'16, St. Petersburg, Russia, p. 83-85 (2016).

[10] F. Dziuba *et al*.," RF Commissioning of the Superconducting 217 MHz CH Cavity for Heavy Ions and First Beam Operation", Proc. of LINAC2018, paper THPO073, this conference.

[11] M. Heilmann *et al.*, High power RF coupler for the cw-linac demonstrator at GSI, in proceedings of IPAC'17, Copenhagen, Denmark, pp. 990–992 (2017).

[12] J. List *et al.*, "High Power Coupler R&D for Superconducting CH-cavities", Proc. of LINAC2018, paper THPO107, this conference

[13] M. Busch *et al.*, Update on the sc 325 MHz CH-cavity and power coupler processing, proceedings of LINAC'16, East Lansing, MI, USA, pp. 913–915 (2017).

[14] F. Dziuba *et al.*, "Performance tests of the superconducting 217 MHz CH cavity", in *Proc of SRF'17*, Lanzhou, China, 2017, paper TUPB024.

[15] M. Amberg *et al.*, The fast Piezo-based frequency tuner for sc CH-cavities, Proceedings of LINAC'14, Geneva, Switzerland, pp. 214-216 (2014).

[16] V. Gettmann *et al.*, "Commissioning of a superconducting cw heavy ion Linac@GSI", in *Proc of SRF'17*, Lanzhou, China, 2017, paper MOPB094.

[17] M. Schwarz *et al.*, "Beam Dynamics for the sc cw heavy ion Linac at GSI", in *Proc of IPAC'15*, Richmond, VA, USA, 2015, p. 3742-3744.

18] M. Miski-Oglu *et al.*, „Steps towards superconducting cw-Linac for heavy ions at GSI", in *Proc of SRF'17*, Lanzhou, China, 2017, paper MOPB024.

[19] R. Tiede *et al.*, "LORASR Code Development", in *Proc of EPAC'06*, Edinburgh, Scotland, 2006, pp. 2194-2196.

[20] S. Yaramyshev *et al.*, Nucl. Instr. Meth. Phys. Res., Sect. A, vol. 558/1 (2006), pp. 90-94. doi: 10.1016/j.nima.2005.11.018

[21] S. Yaramyshev *et al.*, "An advanced procedure for longitudinal beam matching for sc cw heavy ion linacs", *in Proc of HB'16*, Malmö, Sweden, 2016, pp. 571-574.

[22] M. Schwarz *et al.*, "Beam Dynamics Simulations for the New Superconducting CW Heavy Ion Linac at GSI", in *Proc of SRF'17*, Lanzhou, China, 2017, paper MOPB005.

[23] S.M. Polozov *et al.*, "Beam Dynamics Simulations and Code Comparison for a New CW RFQ Design", in *Proc of HB'16*, Malmö, Sweden, 2016, pp. 188-191.

[24] S. Yaramyshev *et al.*, "Virtual charge state separator as an advanced tool coupling measurements and simulations", Phys. Rev. ST Accel. Beams 18, 050103, (2015). doi: 10.1103/PhysRevSTAB.18.050103

[25] W. Barth *et al.*, "Advanced superconducting cw heavy ion linac R&D", in *Proc of IPAC'13*, Shanghai, China, 2013, pp. 3770-3772.

[26] W. Barth *et al.*, "First heavy Ion Beam Test with a superconducting multi gap CH-cavity", Phys. Rev. ST Accel. Beams 21, 020102, (2018). doi: 10.1103/PhysRevAccelBeams.21.020102

[27] T. Sieber *et al* 2018 Bunch Shape Measurements at the GSI cw-Linac Prototype *Proc. J. Phys.: Conf. Ser.* (*Preprint IPAC'18 WEPAK006*)

[28] A.V. Feschenko, "Technique and instrumentation for bunch shape measurements", in *Proc of RuPAC'12*, St. Petersburg, Russia, Oct. 2016, pp. 181-185, paper FRXOR01.

[29] M. Basten *et al.*, "Cryogenic tests of the superconducting beta=0.069 CH-cavities for the HELIAC-project", Proc. of LINAC2018, THPO072

[30] M. Gusarova *et al*., Multipactor discharge in superconducting accelerating CH cavities *Proc. J. Phys.: Conf. Ser.* (*Preprint IPAC'18 TUPAK002*)

[31] S. Yaramyshev *et al* 2018 Advanced approach for beam matching along the multi-cavity sc cw Linac at GSI *Proc. J. Phys.: Conf. Ser.* (*Preprint IPAC'18 TUPAK002*)

[32] M. Schwarz *et al.*, "Further steps towards the superconducting CW-linac for heavy ions at GSI", in *Proc. of IPAC'16,* Busan, South Korea, May 2016, paper MOPOY023, p. 896-898.

[33] S. M. Polozov *et al.*, "Beam dynamics study and electrodynamics simulations for the cw RFQ", in *Proc. of IPAC'17*, Copenhagen, Denmark, May 2017, paper TUPAB013, pp. 1333–1336.

[34] M. Schwarz *et al*.," Beam Dynamics Simulations for the New Superconducting CW Heavy Ion LINAC at GSI", Proc. of LINAC2018, paper TUPO084, this conference

[35] W. Barth *et al*., Superconducting CH-Cavity heavy ion beam testing at GSI *Proc. J. Phys.: Conf. Ser.* (*Preprint IPAC'18 TUPAK004)*

[36] M. Block *et al.*, "Direct mass measurements above uranium bridge the gap to the island of stability", Nature, vol. 463, (2010), pp. 785–788, doi:10.1038/nature08774

[37] W. Barth *et al.*, "High brilliance uranium beams for the GSI FAIR", Phys. Rev. ST Accel. Beams 20, 050101, (2017). doi: 10.1103/PhysRevAccelBeams.20.050101

ISBN: 978-3-95450-194-6 ISSN: 2226-0366 doi:10.18429/JACoW-LINAC2018-TU2A03

THE NEW FAIR POST-STRIPPER DTL - ALVAREZ 2.0

Sascha Mickat, Norbert Bönsch, Xiaonan Du, Peter Gerhard, Jens Holluba, Lars Groening, Manuel Heilmann, Stefan Jagsch, Michael Kaiser, Eberhard Merz, Carsten Mühle, Markus Romig, Marcel Rosan, Anna Rubin, Vaishnavi Srinivasan, Wilfried Sturm, Stephan Teich

GSI Helmholtzzentrum für Schwerionenforschung GmbH, Planckstraße 1, 64291 Darmstadt, GER

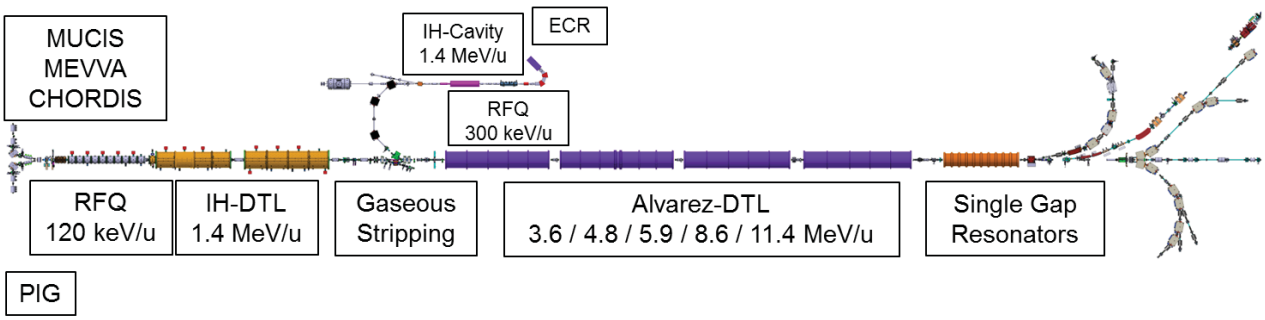
Abstract

The existing GSI accelerator facility, comprising both the UNILAC and the SIS18, is assigned to be the dedicated injector chain for FAIR. Two aspects require the substitution of the existing post-stripper section of the UNILAC, which is an Alvarez type drift tube linac (DTL).

- With respect to its beam dynamic design the existing Alvarez DTL does not cover high current applications for heavy ions as required for FAIR. This will limit the performance of FAIR from the middle 2020's on.
- The existing Alvarez DTL is in regular operation since 1978. An increase in failures due to material fatigue is observable and can be avoided in parts just by an out of scale maintenance effort. A new Alvarez DTL will minimize the operational risk for FAIR commissioning from the middle 2020's.

THE UNILAC POST-STRIPPER DTL

Since the commissioning of the original UNILAC in 1978 the facility was adapted to the demands of its users and to its present expansion (Fig. 1). A complex technical system has grown comprising technologies of different decades. Within this context next to the performance upgrades for reaching the FAIR design parameters, the upgrades aiming at operation reliability have to be considered also. Sections like the existing Alvarez (DTL), the section behind the gaseous stripper (post-stripper), are over 40 years in operation, which is far beyond of its expected lifetime of about 20 years.



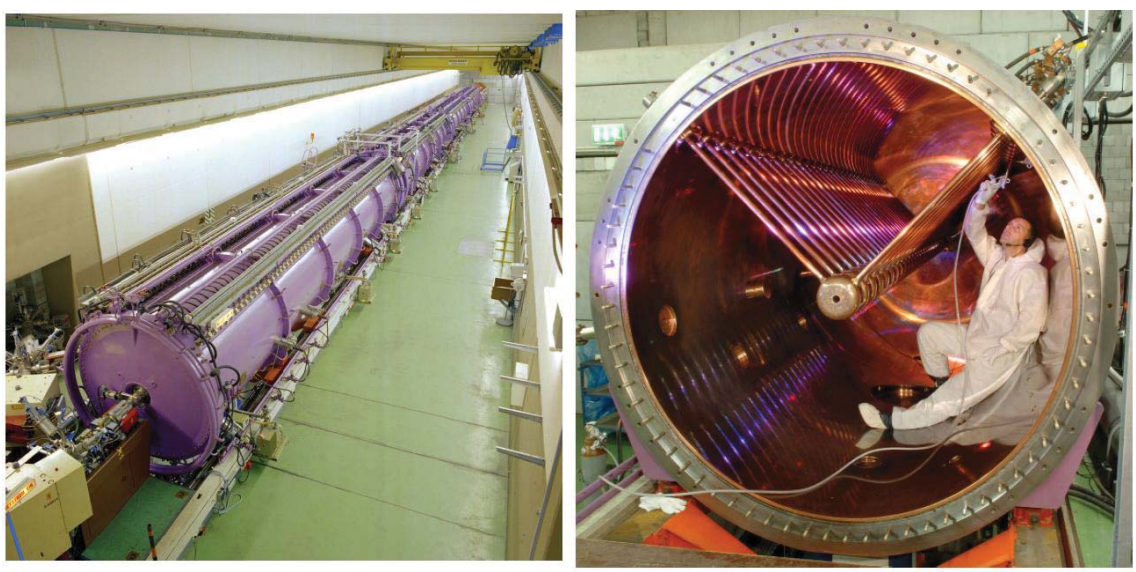


Figure 1: Top: Overview of the existing UNILAC. Left: View into the UNILAC tunnel along the 55 metres long post-stripper. Right: View into the Alvarez DTL cavity during maintenance.

Content from this work may be used under the terms of the CC BY 3.0 licence (© 2018). Any distribution of this work must maintain attribution to the author(s), title of the work, publisher, and DOI.

ISBN: 978-3-95450-194-6 ISSN: 2226-0366 doi:10.18429/JACoW-LINAC2018-TU2A03

Content from this work may be used under the terms of the CC BY 3.0 licence (© 2018). Any distribution of this work must maintain attribution to the author(s), title of the work, publisher, and DOI.

Operational Risk

As weak points of the existing Alvarez DTL the cooling concept of the drift tubes itself and its internal quadrupole magnets were recognised. Corrosion products clogged the filigree cooling channels in the past. The aged electric insulation of the internal quadrupoles' windings triggers short cuts increasingly. Next to the failures of the drift tubes a failure of the RF tanks themselves becomes probable. Taking the refurbishment of the existing Alvarez DTL into consideration the consequence is its substitution by its one-to-one copy. This makes no sense for economic reasons as well as for full-filling the FAIR beam intensity requirements.

FAIR Requirements

Regarding the UNILAC the space charge limit of the upgraded SIS18 defines its target parameters. The existing Alvarez DTL is not designed for high current heavy ion beam applications as required (16.5 emA, $^{238}U^{28+}$). Despite this it copes with intermediate mass ion beams of considerable space charge forces. For instance a $^{40}Ar^{10+}$ beam of 7.1 emA, which is equivalent to a $^{238}U^{28+}$ beam of 15 emA concerning its space charge characteristics, was provided successfully [1].

RF-LAYOUT

The RF layout of the new Alvarez follows the existing boundary conditions on the campus. The input energy is 1.4 MeV/u and the output energy is 11.4 MeV/u. The total installation length must fit into 55 meters. According to five cavities for the future RF supply five amplifiers each with 1.8 MW in total ($P_{cavity} + P_{beam} + P_{margin}$) are assumed.

Within the RF layout an algorithm was developed, which provides a homogeneous surface field distribution at the drift tube's front sides [2]. The peaks of the E-field at both radii of the existing Alvarez drift tubes, the radius at the beam pipe and the drift tube's outer radius, have been smoothened (Fig. 2).

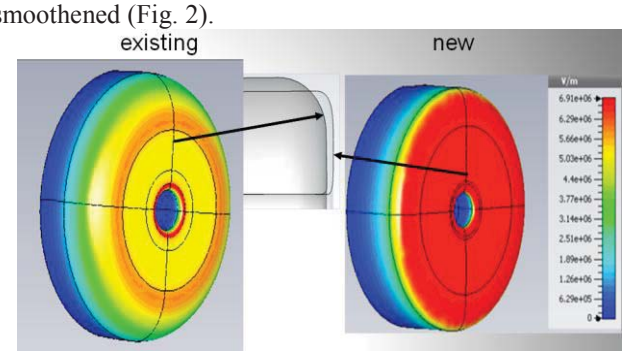


Figure 2: The new drift tube design realises a homogenous surface E-field on the drift tubes' front side.

There are two options to benefit from the new drift tube shape. Keeping the maximum surface field smaller than 1.0 Kilpatrick the shunt impedance as a measure of RF efficiency is increased by nearly 13% in comparison to the existing Alvarez DTL. This option is preferred. The other option is to lower the peak surface field by about 17% while keeping the shunt impedance of the existing design (Fig. 3). The need of reducing herewith the break down probability is not seen.

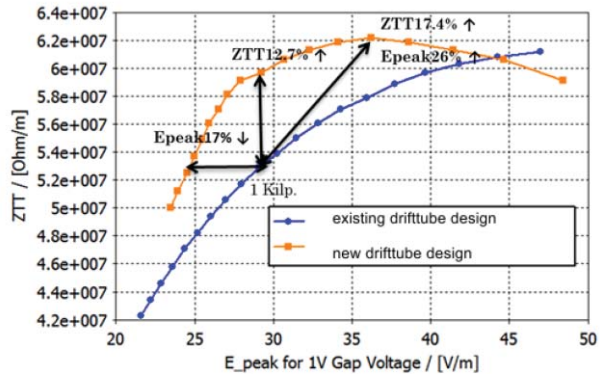


Figure 3: Shunt impedances for the original and the new drift tube design as functions of the peak field per gap voltage. The field is varied with the gap length while the voltage is normalised to 1 Volt. At surface fields about 1.0 Kilpatrick the RF-efficiency is increased by nearly 13%. The option to lower the peak surface field is marked as well.

BEAM DYNAMICS

To overcome the limitation of the existing Alvarez DTL in heavy ion beam intensity as well as quality the new Alvarez design follows the strategy of a strict focussing periodicity. The design of the existing inter-tank section breaks this strict periodicity, whereas the new design takes it into account (Fig. 4).

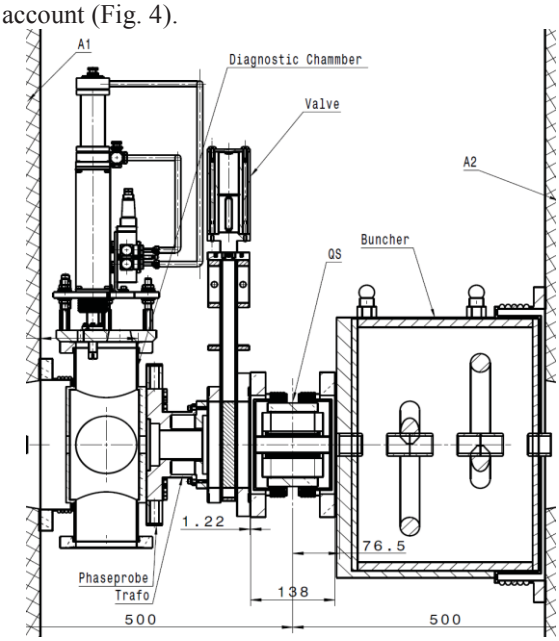


Figure 4: Cross section of the planned A1-A2 inter tank section. The quadrupole configuration (focusing periodicity) leaves tight installation length for beam diagnostics, a valve, and a re-buncher.

In addition, the new Alvarez DTL is designed to avoid the space charge driven emittance growth resonances (Fig. 5).

ISBN: 978-3-95450-194-6 ISSN: 2226-0366 doi:10.18429/JACoW-LINAC2018-TU2A03

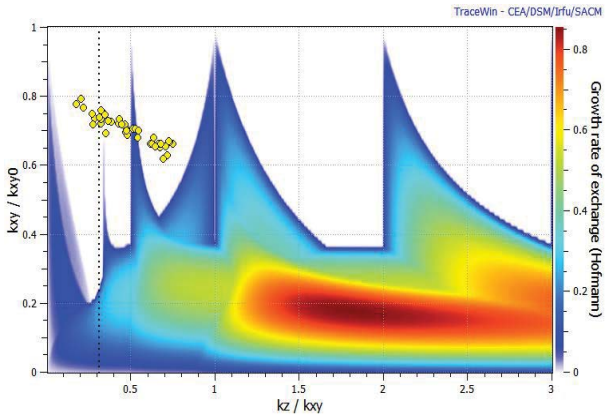


Figure 5: Hofmann's stability chart for the new DTL. The tune depression at the beginning of each tank is lower than 0.7, i.e. there is considerable space charge. The yellow dots mark the variation of the working point during acceleration along the Alvarez DTL.

The DTL's working point for the phase advances is shifted away from those resonances by setting the internal quadrupoles to higher gradients. The existing DC quadrupoles are limited to phase advances of up to 55°, while values between 65° and 70° are desirable. The synchronous rf-phases along the five cavities are -30°, -30°, -30°, -25°, and -25°.

The beam dynamic layout was done using the TraceWin code for $^{238}U^{28+}$ at currents of 16.5 emA, beam intensity requirement at the post-stripper DTL entrance. Input distributions are assumed as Gaussian truncated at 3σ. Input rms emittances were chosen as Ex=Ey=0.175 mm mrad (norm.) and Ez=70 deg keV/u. These parameters were deduced from various simulations and measurements [1, 3, 4, 5]. Corresponding transverse enevelopes assigned to the nominal FAIR case are shown in Fig. 6.

The beam dynamic design was benchmarked by means of six operational scenarios in total against three different DTL concepts successfully. Prioritised is the scenario as a FAIR high current injector. Further two scenarios taking into account that the UNILAC also serves established GSI experiments requiring lower currents and beam energies, i.e. it should provide energies in the range from 3.0 MeV/u up to 11.7 MeV/u. For low energy operation the RF-power of some tanks is switched off from the back end starting with A5, A4, A3, and A2 if requested. The gradients of the drift tubes quadrupoles are scaled down in such an operational mode with the corresponding beam rigidity. The benchmarking is completed by taking care about three further possible operational scenarios like twice larger or twice smaller input longitudinal emittances as well as a transverse flat input beam [6]. The results of beam dynamics simulations for the six different scenarios are presented in Tab. 1. For all scenarios 100% transmission and small emittance growth is reached.

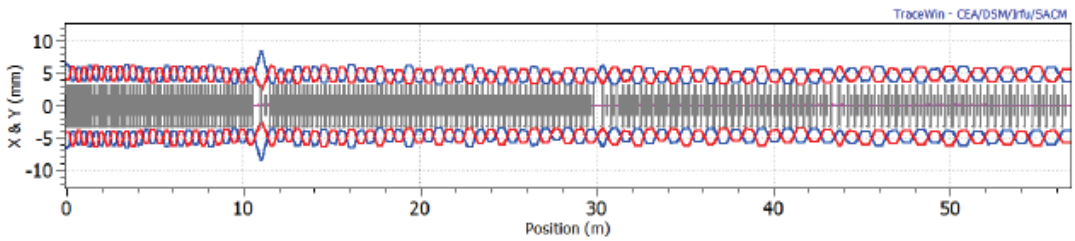


Figure 6: Transverse envelopes along the complete DTL for the nominal FAIR case (16.5 emA, $^{238}U^{28+}$) at an initial transverse zero current phase advance of 65°.

Table 1: Results of Beam Dynamic Simulations for the Six Operational Scenarios of the UNILAC

	FAIR	Zero current	Low energy	Larger long. emit.	Smaller long. emit.	Transvers. flat beam
Current, mA	16.5	**0**	**0**	16.5	16.5	16.5
Input ε_x (rms), mm mrad	0.175	0.175	0.175	0.175	0.175	**0.0875**
Input ε_y (rms), mm mrad	0.175	0.175	0.175	0.175	0.175	**0.35**
Input ε_z (rms), mm mrad	0.07	0.07	0.07	**0.14**	**0.035**	0.07
Output energy, MeV/u	11.4	11.4	**3.3**	11.4	11.4	11.4
Transmission, %	100	100	100	100	100	100
Δ ε_x (tot, 95%), %	7	0	0	7	8	16
Δ ε_y (tot, 95%), %	7	0	0	10	7	3
Δ ε_z (tot, 95%), %	10	0.7	1.7	5	11	4

Content from this work may be used under the terms of the CC BY 3.0 licence (© 2018). Any distribution of this work must maintain attribution to the author(s), title of the work, publisher, and DOI.

ISBN: 978-3-95450-194-6 ISSN: 2226-0366 doi:10.18429/JACoW-LINAC2018-TU2A03

Content from this work may be used under the terms of the CC BY 3.0 licence (© 2018). Any distribution of this work must maintain attribution to the author(s), title of the work, publisher, and DOI.

MATCHING FAIR REQUIREMENTS

The above introduced beam dynamic design was checked towards the beam requirements in front of the SIS18 by tracking the beam behind the DTL through the SIS18 transfer channel (TK) (Fig. 7). Pessimistic tolerances for alignment and machining of the accelerator components as well as for beam parameter fluctuations within the intervals were assumed (Table 2).

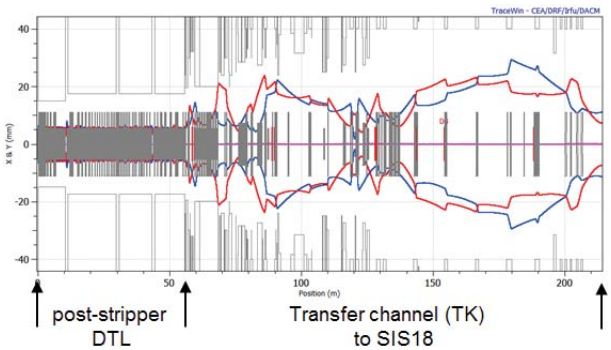


Figure 7: Transverse envelope along the post-stripper DTL and transfer channel to the SIS18 (TK).

Table 2: Tolerances for Error Studies

Quadrupole x,y displacement	± 0.15mm
Quadrupole x,y rotation	± 1°
Quadrupole z rotation	± 0.1°-0,4°
Gap voltage	± 1%
Gap phase	± 1°
Initial energy	± 0.5%
Input rms emittance (x,y,z)	± 15%
Input beam mismatches (x,y,z)	± 10%
Input Current	± 15%

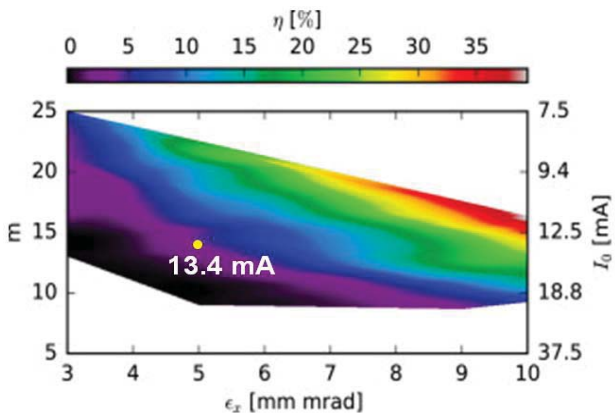


Figure 8: SIS18 multi-turn injection performance chart, where the dependency between multiplication factor, losses, and emittance as well as beam current is illustrated. Black and purple regions are preferable.

The results are classified with help of the SIS18 multi-turn performance chart, where the dependency between losses (η), multiplication factor (m), and emittance as well as beam current is illustrated [7]. Black and purple regions are preferable. Losses below 5% for the multi-turn injection into the SIS18 are accepted. The simulations result in beam currents of 13.4 mA within an emittance of 5 mm mrad in front of the SIS18, which is within the preferable region (Fig. 8).

FIRST OF SERIES (FOS)

The FoS (First of Series) is the realisation of the first cavity section of the Alvarez 2.0 DTL. Innovations in design and fabrication will be tested intensively with respect to their feasibility and reliability in future operation until 2021 (Table 3).

Table 3: FoS Milestones

Feb 2017	System decision: Alvarez type DTL
Jul/Aug 2017	FoS funded with 1.5 M€ until 2021
2018-2020	• R&D • Test stand assembly • Delivery • Process development (fabrication, handling, Cu-plating, etc.)
2021	Full performance tests

The FoS comprises the first tank section equipped with eleven drift tubes and two cooled endplates each with integrated half drift tubes (Fig. 9).

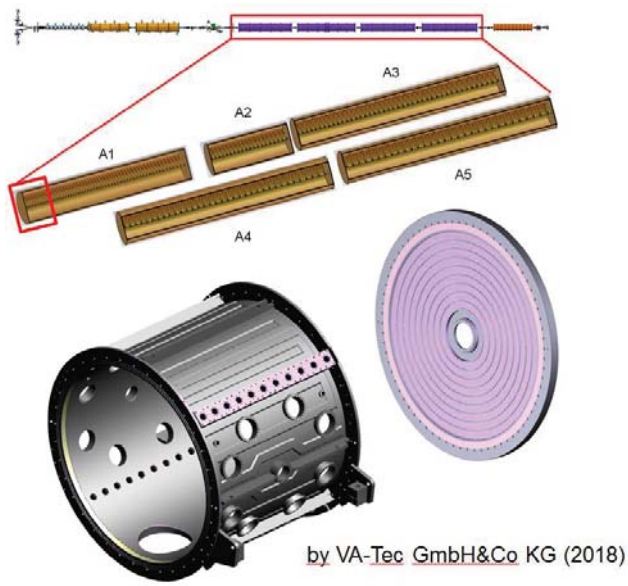


Figure 9: The FoS as the 1st section of cavity *A1*.

The aim of the FoS is testing at nominal operational parameters. The expected RF-properties of the new drift tube geometry shall be confirmed, the superposition of the accelerating fields with the pulsed quadrupole fields shall be investigated, and the performance of the cooling system at high power operation shall be checked for instance. Next to the technical innovations the FoS allows to optimise the processing of the next Alvarez DTL generation starting

ISBN: 978-3-95450-194-6 ISSN: 2226-0366 doi:10.18429/JACoW-LINAC2018-TU2A03

from ordering, fabrication, Cu-plating, and installation in the tunnel.

SCHEDULE

Table 4 gives the major milestones of the post-stripper DTL project under assumption of successful FoS tests in 2021. If pursued with priority and according scheduling of future beam times, the new DTL could be finished with commissioning at full performance at the end of 2025.

Table 4: Alvarez 2.0 Milestones

Q2/2021	Successful FoS project, TDR & funding available
Q2/2022	Delivery of components/cavities starts
Q2/2024	All components in-house
Q2/2024 + X	De-installation of existing post-stripper DTL
Q4/2024 + X	Cavity-wise installation and commissioning
Q4/2025 + X	DTL commissioning w/o and with beam

The focus on the substitution is to minimise the UNILAC downtime. The existing post-stripper shall not be de-installed as there are any uncertainties with the new DTL. Since from first principles there is no urgency to install the components as soon as they are ready for doing so, a planned delay X can be allowed for until de-/ installation starts. At that time an appropriate slot for the replacement shall be defined in view of the overall advance of the FAIR project.

STATUS

Dummy Cavity

A dummy cavity, which has been delivered in September 2018, serves two purposes (Fig.10). i) Finding the balance between effort for fabrication and acceptable tolerances. ii) Cu-plating w.r.t. handling, alternative Cu-plating process, sufficient surface quality ex factory.



Figure 10: Dummy cavity (L=2.5m, D_{out}=2.4m) at the factory acceptance test (FAT).

Drift Tube Prototyping and Quadrupole Design

The new rf-design leads to a new drift tube geometry, which leaves in comparison to the 1970's design less installation space for the internal quadrupole. Simultaneously, the conditions are tightened by the requirements of higher quadrupole gradients (Tab.5).

Table 5: Quadrupole Parameters

Gradient	51 T/m
Effective length	99.5 mm
Integral field	5.07 T
Current	1109.6 A
Yoke material	VACOFLUX50
Conductor	5.5mm x 1 mm
No. of windings	5

A 1st drift tube prototype with a dummy quadrupole has been fabricated for checking its feasibility w.r.t. single part production, welding, fitting the quadrupole into the drift tube, etc. (Fig.11).



Figure 11: Drift tube prototyping.

REFERENCES

[1] L. Groening *et al.*, Experimental evidence of the 90° stop band in the GSI UNILAC, *Phys. Rev. Lett.* 102 234801 (2009).

[2] X. Du *et al.*, "Alvarez DTL Cavity Design for the UNILAC Upgrade", in *Proceedings of IPAC2015*, Richmond, VA, USA, May 2015, paper WEPMA017.

[3] U. Ratzinger, "The New GSI Pre-stripper Linac for High Current Heavy Ion eams", in *Proceedings of LINAC1996*, Geneva, Switzerland, August 1996, paper TU202.

[4] W. Barth *et al.*, "High Current Transport and Acceleration at the Upgraded UNILAC", in *Proceedings of LINAC1998* Chicago, IL, USA, August 1998, paper TU027.

[5] M. Bei, U. Weinrich, Beam input parameter for UNILAC post stripper, internal report (2017)

[6] L. Groening *et al.*, "Demonstration of flat ion beam-creation and injection into a synchrotron", in Proceedings, *ofIPAC2015*, Richmond, VA, USA, May 2015 paper MOPWA026.

[7] S. Appel *et al.*, Injection optimization in a heavy-ion synchrotron using genetic algorithms, *Nucl. Instr. and Meth.* A 852 73–79 (2017).

Content from this work may be used under the terms of the CC BY 3.0 licence (© 2018). Any distribution of this work must maintain attribution to the author(s), title of the work, publisher, and DOI.

ISBN: 978-3-95450-194-6 ISSN: 2226-0366 doi:10.18429/JACoW-LINAC2018-TU2A04

PROGRESS REPORT ON LIPAC*

M. Sugimoto†, T. Akagi, T. Ebisawa, Y. Hirata, R. Ichimiya, A. Kasugai, K. Kondo, S. Maebara, K. Sakamoto, T. Shinya, QST, 039-3212 Rokkasho, Japan
P. Abbon, N. Bazin, B. Bolzon, N. Chauvin, S. Chel, R. Gobin, J. Marroncle, B. Renard, CEA/IRFU, 91191 Gif-sur-Yvette, France
D. Jimenez-Rey, D. Gavela, I. Kirpitchev, P. Méndez, J. Molla, C. de la Morena, I. Podadera, D. Regidor, R. Varela, M. Weber, CIEMAT, 28040 Madrid, Spain
G. Pruneri, Consorzio RFX, 35127 Padova, Italy
J. Knaster, Fusion for Energy, 13067 Saint Paul lez Durance Cedex, France
P.-Y. Beauvais, H. Dzitko, D. Gex, R. Heidinger, A. Jokinen, A. Marqueta, I. Moya, G. Phillips, Fusion for Energy, Garching, D-85748 Germany
P. Cara, IFMIF/EVEDA, 039-3212 Rokkasho, Japan
L. Antoniazzi, L. Bellan, D. Bortolato, M. Comunian, E. Fagotti, F. Grespan, M. Montis, A. Palmieri, A. Pisent, F. Scantamburlo, INFN/LNL, 35020 Legnaro (PD), Italy

Abstract

LIPAc (Linear IFMIF Prototype Accelerator) for challenging the technical validation of the low energy section up to 9 MeV of the IFMIF accelerator, consisting of 2 units of 40 MeV, 125 mA CW deuteron accelerator, is under construction and staged commissioning is ongoing in QST Rokkasho, Japan. The injector commissioning was completed in summer 2017 and the latest results of the beam characteristics showed good emittance acceptable for RFQ injection. The installation and checkout of 5 MeV deuteron RFQ, beam transport & instrumentation, temporary beam dump and RF power system were finished in early 2018 including the RF conditioning of RFQ in low duty pulsed mode. At the initial beam commissioning of RFQ in June 2018, the 50 keV proton beam with <30 mA and 0.3 ms pulse was used for simulating the 100 keV deuteron beam acceleration in RFQ and transport up to beam dump, without a risk of activation. The good transmission around 93% was observed for input beam current of 8–30 mA. The installation work for the final configuration of LIPAc with a superconducting RF linac is continuing and ready to start by end of 2018.

INTRODUCTION

The Engineering Validation and Engineering Design Activities for the International Fusion Materials Irradiation Facility (IFMIF/EVEDA) project is underway as one of three projects of the Broader Approach (BA) agreement between the Japanese government and EURATOM [1]. The concept of the IFMIF was matured through the activities under the IEA's Fusion Materials Technology Collaboration Program over 10 years since 1994 [2]. The mission of IFMIF is to provide an accelerator-based, D-Li neutron source to produce high energy neutrons at sufficient intensity and irradiation volume to test samples of candidate materials up to about a full lifetime of anticipated use in fusion energy reactors. IFMIF would also provide calibration and validation of data from fission reactor and other accelerator-based irradiation tests. It would generate an engineering base of material-specific activation and radiological property data, and support the analysis of materials for use in safety, maintenance, recycling, decommissioning, and waste disposal systems.

The mission of the IFMIF/EVEDA project is to provide the detailed engineering design of the IFMIF and to validate the technological challenges on the major components. One of the major technological challenges is the demonstration of the low energy section of one of two accelerators of the IFMIF called as LIPAc (Linear IFMIF Prototype Accelerator) to accelerate the 125 mA CW D+ beam up to 9 MeV, while the IFMIF accelerator is a 40 MeV linac (see Fig. 1 for full IFMIF linac design in 2013 [3]).

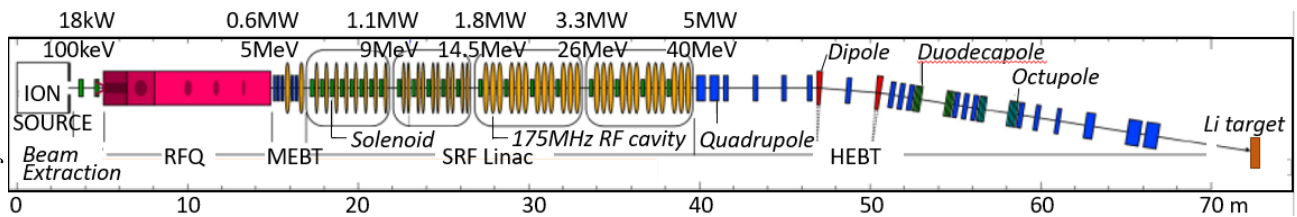


Figure 1: Schematic representation of IFMIF linac. LIPAc is a prototype up to 9 MeV including the first SRF linac.

As show in in Fig. 2, the LIPAc plant consists of the following subsystems:

* Work undertaken under the Broader Approach Agreement between the European Atomic Energy Community and the Government of Japan. The views and opinions expressed herein do not necessarily state or reflect those of the Parties to this Agreement.
† email address sugimoto.masayoshi@qst.go.p

Content from this work may be used under the terms of the CC BY 3.0 licence (© 2018). Any distribution of this work must maintain attribution to the author(s), title of the work, publisher, and DOI.

ISBN: 978-3-95450-194-6 ISSN: 2226-0366 doi:10.18429/JACoW-LINAC2018-TU2A04

1. Injector (2.45 GHz ECR ion source and Low Energy Beam Transport (LEBT) line using dual solenoid focusing system);
2. RFQ (175 MHz, 9.8 m-long, 4-vane, 5 MeV/125 mA output) with the associated RF power system (8 x 175 MHz, 200 kW CW chains of tetrode system);
3. Medium Energy Beam Transport (MEBT) line consisting of a sequence of a triplet quad – first re-buncher – a doublet quad – second re-buncher with the associated RF power system for 5-gaps, IH type re-bunchers (2 x 175 MHz, 16 kW CW solid-state amplifiers);
4. Superconducting RF linac (SRF linac, 175 MHz, 9 MeV/125 mA output) containing 8 pairs of Half-Wave Resonator (HWR) and superconducting solenoid magnet coil;
5. High Energy Beam Transport (HEBT) line and final Beam Dump (BD);
6. Diagnostic plate (D-Plate) dedicated for the beam diagnostics (moved after MEBT for RFQ commissioning);
7. Low Power Beam Dump (LPBD) for low duty operation of RFQ commissioning (not shown in Fig. 2);
8. Control System/Timing System and safety management systems (Personnel Protection System and Machine Protection System);
9. Cryoplant for supplying liquid helium and
10. Other ancillaries providing electricity, cooling water, pressurized air, nitrogen gas and HVAC.

The specification/target of major parameters in 2 step validation of LIPAc are shown in Table 1, interim target for confirming the beam characteristics at the entrance of SRF linac, and final target for qualifying the output beam from SRF linac.

Table 1: Main Targets of LIPAc Validation

Items	Interim Target*	Final Target
Particles	D^+ (H^+)**	
Output energy (MeV)	0.1 @ RFQ in / 5.0 @ RFQ out	8.0-9.0 @ BD
Output current (mA)	140 @ RFQ in / 125 @ RFQ out	125 @ BD
rms emittance (π mm mrad)	<0.25 @ RFQ in <0.30 @ RFQ out	<0.36 @ SRF linac out***
(MeV deg)	<0.2 @ RFQ out	<0.2 @ SRF linac out
Pulse mode	0.3 ms/1Hz (typ.) using chopper + source magnetron pulsing	
Linacs	175 MHz 4-vane RFQ	same and 8 x 175 MHz HWR
Re-bunchers	to provide the proper matched beam at the end of the MEBT both in transverse and longitudinal phase space to the SRF LINAC input	
Max. RF power (kW)	1.2 @ injector 1600 @ RFQ 32 @ re-bunchers	840 @ SRF linac
Total length (m)	20	36

* Interim target is set for validating the beam characteristics before entering the SRF linac.

** H^+ beam with half-energy/half-current is used for machine tuning to simulate the beam acceleration/transport with the perveance equivalent to that for D^+.

*** Assuming 0.2π mm mrad at RFQ exit. About 3/4 of emittance growth will be produced in MEBT.

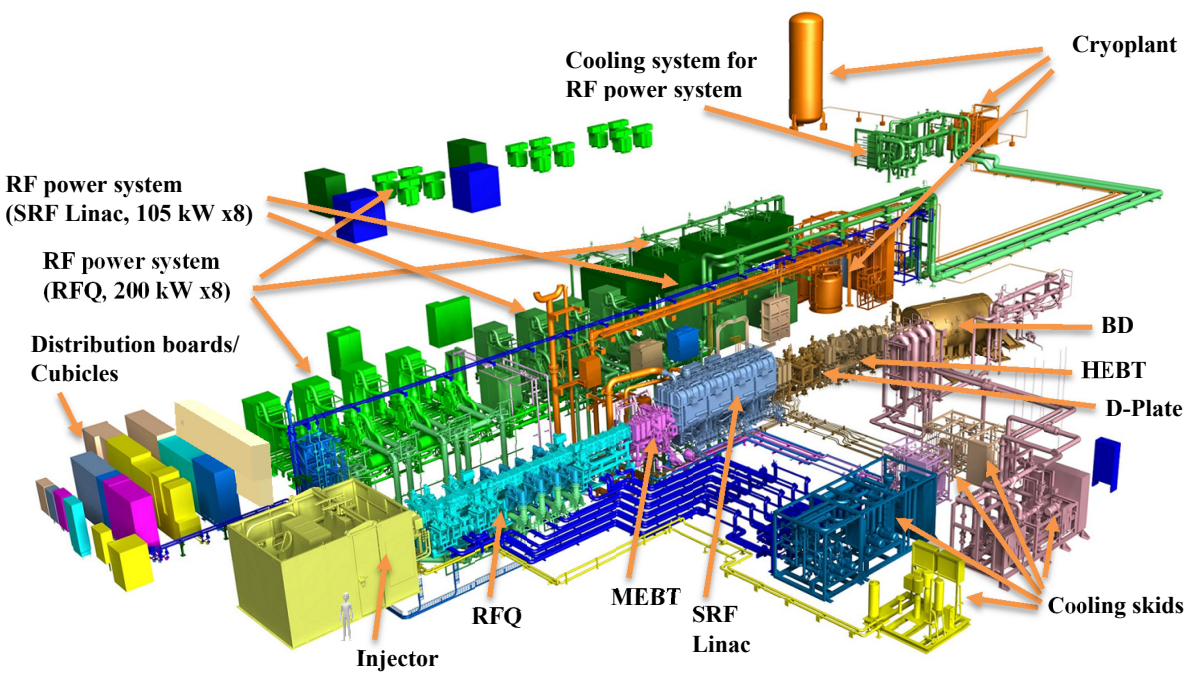


Figure 2: Layout of main components of LIPAc at the final stage. For the RFQ beam commissioning, the D-Plate and LPBD are temporarily installed immediately after the MEBT.

Content from this work may be used under the terms of the CC BY 3.0 licence (© 2018). Any distribution of this work must maintain attribution to the author(s), title of the work, publisher, and DOI.

ISBN: 978-3-95450-194-6 ISSN: 2226-0366 doi:10.18429/JACoW-LINAC2018-TU2A04

Content from this work may be used under the terms of the CC BY 3.0 licence (© 2018). Any distribution of this work must maintain attribution to the author(s), title of the work, publisher, and DOI.

The paper provides a general view on the progress of the IFMIF/EVEDA project and the phased approach employed for the installation, checkout and commissioning of the LIPAc. Next, we summarize the present status of each subsystems and major outcomes obtained in the latest beam commissioning performed in June – August 2018.

PROJECT PLAN AND LIPAC PHASES

From the project management view, the BA activities are authorized by the steering committee through Project Plan and Work Programme for annual schedule, and the components necessary to achieve the project mission are delivered through Procurement Arrangements dedicated to each system. In LIPAc project case, all the accelerator equipment and the infrastructure on site are shared by Japan and Europe, and agreed by the Implementing Agencies responsible to procure them. Such organizations, QST in Japan and F4E in Europe, jointly work together to provide the components to assemble and to commission at Rokkasho. The IFMIF/EVEDA Project Leader in Rokkasho takes leadership to coordinate all the work as a chief project manager. In Europe the actual work is contributed from the Voluntary Contributors, France, Italy, Spain and Belgium, and institutions designated by these countries. A deep collaboration among many contributing organizations is an essential key to reach the final objectives. In the Project Plan a top-level project schedule is given with the achieved milestones. The validation using LIPAc is the latest mandate on the project.

The validation of the LIPAc is scheduled in 3 phases (A: injector only, B: up to RFQ and MEBT, and final C: whole system up to BD through SRF linac and HEBT). The first phase A was started in February 2014 and its commissioning was conducted in several steps, which were completed in August 2017. In parallel with these commissioning campaigns, the installation of the components for the phase B (RFQ, MEBT, D-Plate, LPBD and RF power system) and the installation and commissioning of Cryoplant (phase C) were conducted and completed in June and April 2017, respectively (Fig. 3).

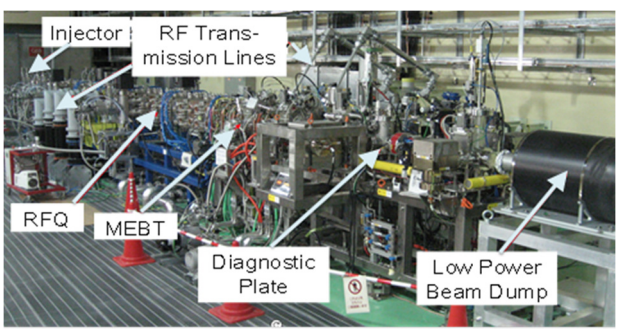


Figure 3: Components of LIPAc installed in the accelerator vault for RFQ beam commissioning.

After completion of the fundamental check of the integrated behavior of RFQ cavity and RF power system, the RF conditioning of RFQ cavity was started and succeeded to reach the power level equivalent to 132 kV of maximum vane voltage, to accelerate D+ beam in February 2018 [4]. At the beginning of the beam commissioning in phase B, low duty cycle ~0.1% and low current 50 keV H+ beam was proposed to check the proper behavior of all the systems and to avoid the risk of errant beam which could induce activation and mechanical damage. In the first beam commissioning stage, June – August 2018, 50 keV H+ with various injection currents (8 ~ 30 mA) were succeeded [5] and functional tests of the equipment of MEBT and beam diagnostic elements were performed.

STATUS OF SUBSYSTEMS

Injector

The injector developed by CEA/Saclay [6] has a 2.45 GHz ECR type ion source driven by a 1200 W CW magnetron with a capability of pulsing, fast blanking (beam reset to zero (BRTZ) within 50 μs in a pule at low duty cycle mode) and conventional type fast (10 μs)/slow beam inhibition interlocks [7]. To produce a high density and stable D_2/H_2 plasma, 4-stub automatic tuning unit is incorporated to control the RF reflection from plasma and 2 coils are used to adjust magnetic field pattern along the axis of 100 mm-long and 90 mm-diam. cylindrical copper plasma chamber, for keeping the value near 0.0875 T at both BN disks placed at end sides of the chamber. The resultant axial magnetic field inside the chamber is well approximated by the simple parabolic shape.

The 5 electrodes extraction system (named as plasma – PE, puller/intermediate – IE, first ground – GE1, repeller – RE and second ground – GE2) was employed to satisfy lower divergence and less sparking compared with 3- or 4-electrodes systems [6]. From the beam optics point of view, the gap distances among PE, IE and GE1 and the concentricity of apertures are critical. In the recent beam campaign, we paid attention on this point to reproduce the specification values, which were optimized for 155 mA beam extraction from the PE with 12mm-diam. aperture.

Through the several campaigns to improve the beam characteristics predicted by design simulation, a good emittance (< 0.15 π mm mrad, rms norm.) was achieved in December 2017 for D+ 140 ~ 160 mA at 5% duty cycle [8].

As low beam current with a good stability and emittance was requested for the initial RFQ beam commissioning, PE with appropriate aperture size should be used for each current level. An intensive characterization of the extracted beam was performed in advance until May 2018 [9].

As mentioned in the section of First Beam Commissioning of RFQ, a misalignment of beam axis of injector is suspected and to be remedied. The characterization of CW beam, which is not completed yet, should be planned in the coming campaigns.

RFQ with RF Power System for RFQ

The RFQ developed by INFN/LNL is a 175 MHz, 4-vane 9.8 m-long cavity with a ramping vane voltage rule from 79 to 132 kV at the middle region of cavity, 3 – 7.4 m [4]. The RF power system for all the cavities (except the

ISBN: 978-3-95450-194-6 ISSN: 2226-0366 doi:10.18429/JACoW-LINAC2018-TU2A04

injector magnetron) were procured by CIEMAT, CEA/Saclay and SCK-CEN, and installed (Fig. 4).

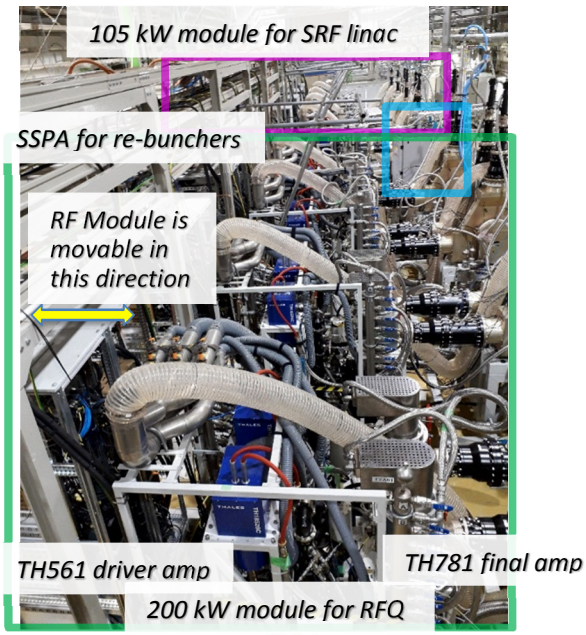


Figure 4: Components of RF power system in RF room.

Through the RF condition of RFQ cavity using 8 RF chains with a precise phase synchronization 132 kV with 5% margin was achieved with short pulse mode (20 μs). Further conditioning is ongoing to extend the pulse width to reach CW mode, however, for starting the beam commissioning of H+ 50 keV at half cavity voltage, this trial was concentrated on the condition with a half cavity voltage. For stable operation of anode HVPS in pulsed mode, it was effective to apply the pulsed RF power (1 ms) superimposed over a portion of CW power. The control of power balance of 8 RF chains is a critical to establish the stability. Particularly, we encountered a failure of anode HVPS or a 6.6 kV breaker, and we were obliged to use 7 RF chains instead of 8. The unused RF chain received the reflection power from RFQ cavity through the coupling of coupler and it should be kept within a limit acceptable by circulator dummy load.

In the last beam commissioning, it was unnecessary to apply the frequency feedback control loop based on the cooling water temperature (mixing of hot and cold flows) control, due to very low heat generation rate by RF power. To use this function, we must refurbish the RFQ cooling skid, of which piping is planned to be repaired in autumn 2018. The secondary cooling system to supply the chilled water to the primary loop was designed without a control of intermediate level of heat load, which causes a serious problem when the low to medium level power is dissipated in RFQ cavity. These points will be tackled in the period of maintenance until next beam commissioning.

MEBT with RF Power System for Re-bunchers

The MEBT developed by CIEMAT has a sequence of elements, Q-triplet, fist rebuncher, Q-doublet and second rebuncher [10]. Since magnets were properly characterized in a test bench prior to installation, during the RFQ beam commissioning, all the magnetic parameters were set to the recommend values given by beam dynamics simulation. About the rebunchers, the reconditioning of cavities using SSPA RF power system tests up to 11.8 kW (E_0LT>350kV) were successfully carried out in January 2018.

SRF Linac and Cryoplant

After the manufacturing studies needed for the licensing of the cavities [11] and the validation of the application form by KHK in March 2016, the manufacturing of the pre-series cavity and the 8 series HWRs is ongoing. All the bare cavities have been tested in vertical cryostat and are over the requirements (Q_0=5·10^8 @ E_{acc_nom}=4.5 MV/m). Seven cavities have been through the final qualification process: heat treatment, tank welding and controls needed for the licensing at the manufacturer, fine chemical etching, clean room preparation and vertical qualification test at CEA Saclay. The tank integration process of the last series-cavity is close to completion. Operational equivalent tests -in a dedicated test stand named SaTHoRi - were performed on two different accelerating units (i.e. HWR cavity equipped with its tuning system and power coupler). The nominal accelerating field of 4.5 MV/m was achieved with an injected power of 14 kW and the tuning range exceeds the requirement of 50 kHz [12].

The manufacturing of the power couplers ended in April 2017. Three pairs have been successfully conditioned up to 100 kW. The conditioning of the fourth pair is ongoing. The superconducting solenoids are under manufacturing and shall be ready by end of 2018 for the assembly of the cryomodule. This assembly will take place at Rokkasho Fusion institute where a clean room is built.

Cryoplant procured by CEA/Saclay is needed for cryogenic cooling of the SRF linac and consists of cryogenic power equipment providing helium refrigeration (He refrigerator, He compressor, oil removal system etc.) and cryogenic transfer lines (including liquid He Dewar, gas He buffer tank, etc.), in addition to the Cryomodule fluid supplying equipment [13]. The plant was installed and commissioned in April 2017.

Beam Diagnostics

The beam diagnostics of LIPAc developed by CEA/Saclay, CIEMAT and INFN/LNL, consist of (1) non-interceptive devices and (2) interceptive devices. As for category (1), Current Transformers, 3 ACCTs in LEBT, MEBT and D-Plate for RFQ beam commissioning (FCT worked properly, and DCCT was not used); 7 BPMs (4 in MEBT, 3 in D-Plate); 2 profile monitors, fluorescence-type (FPM) and ionization-type (IPM), were installed in D-Plate, where the signal intensity of IPM was too small to detect profile, while FPM detected some patterns varying with the beam transport condition. The residual gas bunch length monitor is also available in D-Plate, to be used in the next step. In LEBT, Doppler shift spectrometer for ion species fraction measurement and four grid analyzer for space charge compensation measurement are available. About

Content from this work may be used under the terms of the CC BY 3.0 licence (© 2018). Any distribution of this work must maintain attribution to the author(s), title of the work, publisher, and DOI.

ISBN: 978-3-95450-194-6 ISSN: 2226-0366 doi:10.18429/JACoW-LINAC2018-TU2A04

Content from this work may be used under the terms of the CC BY 3.0 licence (© 2018). Any distribution of this work must maintain attribution to the author(s), title of the work, publisher, and DOI.

category (2), secondary electron emission (SEM) grid profiler+slits+steerers were installed for measuring emittance at very low duty cycle, however it is necessary further tuning to complete the commissioning of the diagnostics and to have them fully operational to allow a full characterization of the beam.

Control System

The EPICS-based central control, timing system, safety protection (personnel and machine) systems, developed by QST in collaboration with F4E for the central control, are already running daily. However, the integration work considering the interfacing with the individual local control systems provided by EU Home Team is not obvious and required a proper coordination within the LIPAc Unit. For preparing the licensing requirement in RFQ beam commissioning, new function in personnel protection system to count up the amount of beam particles entering into RFQ was successfully tested, including the careful calibration to avoid underestimating the amount of particles from a safety point of view.

FIRST BEAM COMMISSIONING OF RFQ

The detail of the preliminary result of beam experiment is presented elsewhere [5], however the essential outcomes are summarized below.

At the very beginning of the beam commissioning with 50 keV H+, the beam current extracted from ion source (I_{ext}) was set to 13 mA to inject a minimal current <10 mA achievable by PE with 6 mm diam. aperture, and also duty cycle was set with 0.3 ms pulse per 1s repetition, for reducing the possible beam induced damage to the interceptive diagnostic devices. The proton fraction in this case was small and actual injection current was 6.6 mA. However, its emittance was so small 0.09π mm mrad rms norm that the transmission was 95%. On the other hand, total transmission to LPBD was 87%.In this campaign, a large amount of steering for beam injection was required, which means re-alignment of injector is mandatory.

When I_{ext} is increased systematically (20, 30, 35 and 40 mA), the proton faction was improved (>70%) and the emittance was kept <0.2π mm mrad rms norm. The transmission down to LPBD was >90% for all cases except for 40 mA case (89%). As a result, in this first campaign, the RFQ output current of 26 mA at maximum was observed.

The output energy was measured using time-of-flight method for comparing the 175 MHz bunch signals detected by 3 BPMs installed in D-Plate with fixed drift lengths (0.16 and 1.27 m). The results, 2.5±0.02 MeV, showed a good agreement with the design value.

CONCLUSION

Many activities were carried out in 2017 – 2018, to focus primarily on the kick off of the RFQ beam commissioning achieved in June 2018. It was a true integration work to solve the interface problems not experienced in the individual tests on each subsystem. Firstly, a good indication of validity of RFQ design was achieved at beam transmission, >90%, and output energy, 2.5 MeV, under the condition of current, 35 mA, which is about half of required value. The other important characteristics, like beam size, emittance and bunch length, were tried to examine, however it was unfinished. The injector beams with current up to 70 mA for 50 keV H+ and 140 mA for 100 keV D+ satisfying required emittance have been already established and will be tested in the next beam commission time. In parallel, further RF conditioning of RFQ is required to conduct the high current beam injection in D+. The assembly work of SRF linac is waiting for the completion of delivery of the last components in Rokkasho.

ACKNOWLEDGEMENT

The present work was performed in the framework of the Broader Approach Agreement. The authors thank all the members in the home institutions and research founders, especially those who have involved or supported the LIPAc project, the former IFMIF/EVEDA project leaders, P. Garin, H. Matsumoto and J. Knaster, the home team/ILIC unit leaders, R. Heidinger, Y. Okumura, T. Nishitani, S, O'hira and A. Mosnier. Views and opinions expressed herein do not necessary reflect those of QST, Fusion for Energy, or of the authors' home institutions or research founders.

REFERENCES

[1] T. Tsunematsu, "Broader Approach to Fusion Energy", *Fus. Eng. Design*, vol. 84, p. 122, 2009, doi:10.1016/j.fusengdes.2009.02.029

[2] IEA Technology Collaboration Programmes, Fusion Materials, https://www.iaea.org/tcp/fusionpower/fm

[3] J. Knaster *et al.*, "The accomplishment of the Engineering Design Activities of IFMIF/EVEDA: The European-Japanese project towards a Li(d,xn) fusion relevant neutron source", *Nucl. Fusion*, vol. 55, 086003 (30pp), 2015, doi:10.1088/0021-5515/086003

[4] E. Fagotti *et al.*, "Beam commissioning of the IFMIF EVEDA very high power RFQ", in *Proc. 9th Int. Particle Accelerator Conf. (IPAC'18)*, Vancouver, Canada, April 2018, pp. 2902-2907, doi:10.18429/JACoW-IPAC2018-THXGBF2

[5] E. Fagotti *et al.*, "IFMIF EVEDA RFQ preliminary beam characterization", in *Proc. 29th Linear Accelerator Conf. (LINAC'18)*, Beijing, China, September 2018.

[6] R. Gobin *et al.*, "Final design of the IFMIF injector at CEA/Saclay", in *Proc. 4th Int. Particle Accelerator Conf. (IPAC'13)*, Shanghai, China, May 2018, pp. 3758-3760, doi:10.18429/JACoW-IPAC2013-THPWO003

[7] A. Marqueta *et al.*, "Machine protection and safe operation of LIPAc accelerator", in *Proc. 7th Int. Particle Accelerator Conf. (IPAC'16)*, Busan, Korea, May 2016, pp. 4178-4181, doi:10.18429/JACoW-IPAC2016-THPOY035

[8] A. Kasugai *et al.*, "Commissioning status of Linear IFNIF Prototype Accelerator (LIPAc)", in *Proc. 61st ICFA Advanced Beam Dynamics Workshop on High-Intensity-Brightness Hadron Beams (HB'18)*, Daejeon, Korea, June 2016, pp. 4178-4181, doi:10.18429/JACoW-HB2018-THP1WB01

ISBN: 978-3-95450-194-6 ISSN: 2226-0366 doi:10.18429/JACoW-LINAC2018-TU2A04

[9] T. Akagi *et al.*, "Characterization of the input beam to RFQ of the Linear IFMIF Prototype Accelerator (LIPAc)", in *Proc. 30th Symp. on Fusion Technology (SOFT'18)*, Sicily, Italy, September 2018.

[10] I. Podadera *et al.*, "Manufacturing, assembly and tests of the LIPAc Medium Energy Beam Transport line (MEBT)", in *Proc. 28th Linear Accelerator Conf. (LINAC'16)*, East Lansing, USA, September 2016, pp.554-557, doi:10.18429/JACoW-LINAC2016-TUPLR041

[11] H. Dzitko *et al.*, "Technical and logistical challenges for IFMIF-LIPAc cryomodule construction", in *Proc. 17th Int. Conf. on RF Superconductivity (SRF'15)*, BC, Canada, September 2015, pp.1453-1459, doi:10.18429/JACoW-SRF2015-FRBA01

[12] O. Piquet *et al.*, "First results of the IFMIF/EVEDA SaTHoRI tests", in *Proc. 18th Int. Conf. on RF Superconductivity (SRF'17)*, Lanzhou, China, pp.262-265, doi:10.18429/JACoW-SRF2015-MOPB086

[13] B. Renard *et al.*, "Design and preliminary performance tests of the IFMIF-LIPAc Cryoplant", in *Proc.2 7th Int. Cryogenic Engineering Conf. and Int. Cryogenic Materials Conf. (ICEC27-ICMC 2018)*, Oxford, England, September 2018.

Content from this work may be used under the terms of the CC BY 3.0 licence (© 2018). Any distribution of this work must maintain attribution to the author(s), title of the work, publisher, and DOI.

ISBN: 978-3-95450-194-6 ISSN: 2226-0366 doi:10.18429/JACoW-LINAC2018-TU1P01

EXTREME HIGH BRIGHTNESS ELECTRON BEAM GENERATION IN A SPACE CHARGE REGIME

A. Bacci, L. Faillace, M. Rossetti Conti* INFN-Mi, 20133 Milano, Italy
*also at Università degli Studi di Milano, 20133 Milano, Italy

Abstract

The generation of ultra-short, low emittance and low energy spread electron bunches is nowadays a critical requirement for accelerators in plasma wave or for femtosecond light sources. A new longitudinal compression scheme, based on velocity and ballistic bunching techniques in presence of space charge forces, allows to enter in a peculiar regime, so-called laminar bunching (LB). In this regime, the bunch is longitudinally compressed, at the expense of its transverse size, and the over-bunching is forbidden by the laminarity: going to the minimal longitudinal dimension the bunch is adiabatically frozen and transversally refocused. Furthermore, this technique heats slightly the uncorrelated energy spread resulting in electron distributions that, in case of bending paths, does not require Laser Heater devices.

INTRODUCTION

In the last decade the production of ultra-short electron bunches has become a major item in many fields that are related to accelerating machines. One of the main application interested in such kind of beams is the Free Electron Lasers (FELs) with the aim to produce ultra-short light pulses, femtosecond orders, to explore ultra-fast phenomena like chemical reactions or phase transitions. A typical example is the study of the water splitting in the photosynthesis that ranges from 1 up to 100 fs [1]. Other technologies pursuing ultra-short electron bunches are the plasma wave acceleration [2-5], the femtosecond electron diffraction FED [6] and the coherent THz transition radiation [7].

There are many techniques to longitudinally compress electron bunches. Basically all these techniques are based on a linearly correlated energy spread (linear chirp) given along the distribution and accordingly on the velocity differences of the particles which return in to the compression effect. The compression is performed along a drift in terms of time of flight (ballistic bunching [8, 9]) or along a dispersive line, in terms of different paths length (magnetic chicanes) [10]. An alternative compression technique, named Velocity Bunching (VB) [11], occurs inside a traveling wave (TW) accelerating cavity, where the beam is accelerated and chirped at the same time. The VB technique operates at low energies, typically electron guns exit energies which are lower than 7 MeV. In order to prevent the emittance degradation, the laminarity of the beam, which permits to damp the emittance oscillations during the compression, has to be preserved. This laminarity beam condition is kept propagating the beam as close as possible to an equilibrium invariant envelope, representing an exact solution of the envelope equation, that is obtained by the following conditions: inject in to the compressor with a laminar envelope waist ($\sigma' = 0$), a compression factor that scale linearly with the acceleration $I = \frac{\gamma}{\gamma_0} I_0$ where I stands for the current, γ for the relativistic factor and the index 0 for values before the compression.

The VB is a technique used, or tested, worldwide in different labs and nowadays it is a reference technique to compress electron beams at low energy. Typical VB performances, easily reached, are peak beam currents approaching, or overcoming, 1 kA and emittance values lower than 1 mm-mrad for bunch charge of few hundreds of pico-coulombs and final energies of 80-100 MeV [12]. These high brightness bunches generated by VB show the common characteristics to have a spike current on the bunch head, where most of the charge is stacked and a long low charge tail. The beam quality of the tail is usually poor, shown a very high energy spread, which is a peculiarity of the VB itself where the compression is obtained at the expense of the energy spread, then damped by the acceleration.

In this work is presented a new compression technique that permits to compress an electron bunch in an almost uniform way, if compared to the VB and, at the same time, to quasi fully compensate the bunch energy spread. This method takes advantage from a space-charge dominated regime and because most of the compression happens along a drift, where the bunch is laminar, under the effect of its only field, it has been named laminar bunching LB. In the following paragraph is presented an ideal machine layout to perform the LB and discussed it beam dynamics, considering the longitudinal and the transversal envelop equations. At the end of the proceeding is presented a comparison between the VB and the LB from simulations point of view and from the different evolutions of the envelope equation self-fields terms.

LAMINAR BUNCHING

The LB machine layout presented in this work is as follows (Fig. 1): 1.6 cells s-band photoinjector coupled to a solenoid for the emittance compensation; a drift of about 1.3 meters; a x-band TW 9 cells accelerating cavity, which is used in decelerating mode; a s-band 3 m long, SLAC type, accelerating cavity embedded into a solenoids array; a quite long drift, about 3 m long, where the electron bunch enters into the LB; a couple of equal TW c-band accelerating cavities, 114 cells, 2 meters long, that boost the beam.

For sake of a better LB beam dynamics understanding let us start analyzing transverse and longitudinal envelope equation, respectively Equations (1) and (2):

Content from this work may be used under the terms of the CC BY 3.0 licence (© 2018). Any distribution of this work must maintain attribution to the author(s), title of the work, publisher, and DOI.

ISBN: 978-3-95450-194-6 ISSN: 2226-0366 doi:10.18429/JACoW-LINAC2018-TU1P01

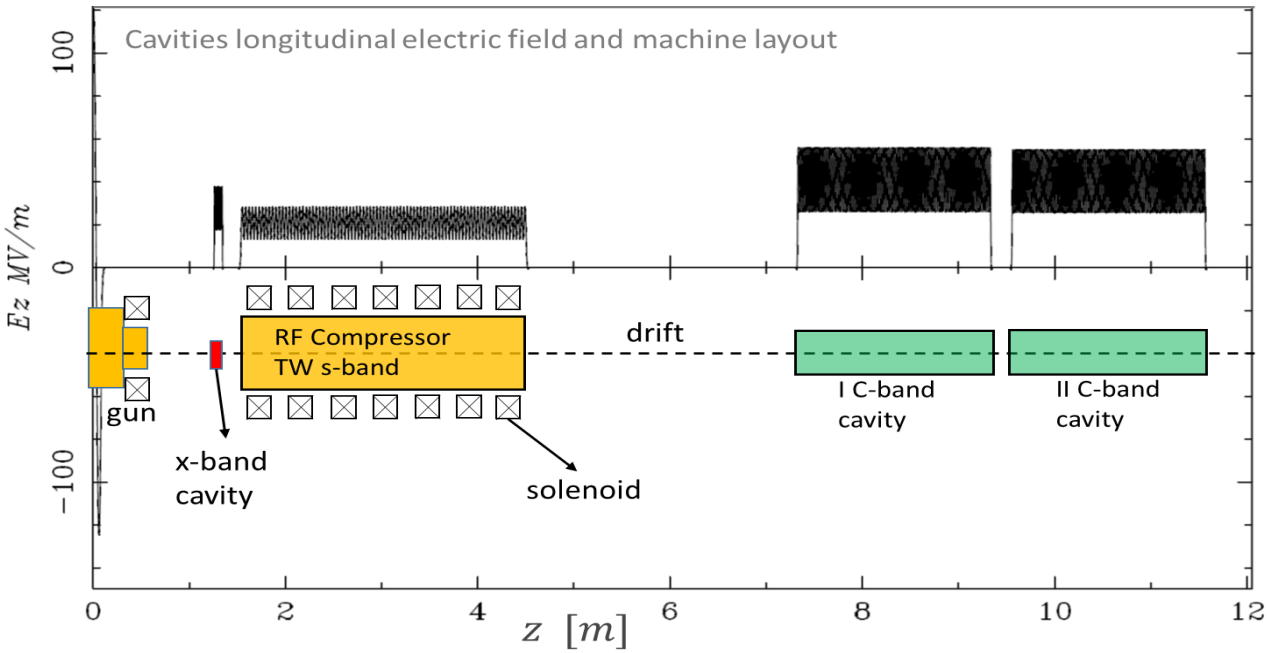


Figure 1: The machine layout used for the laminar bunching simulations and the longitudinal fields intensity of the different cavity involved in the new compression method. The gun is a standing wave accelerating cavity, the other cavities work in traveling wave.

$$\sigma'' + \frac{\gamma'}{\gamma}\sigma' + \left(\frac{k}{\gamma}\right)^2 \sigma = \frac{Qc}{2I_A\gamma^3\sigma_z\sigma} + \frac{\varepsilon_n^2}{\gamma^2\sigma} \quad (1)$$

where σ is the rms beam envelope, γ the Lorentz factor, $\gamma' \approx 2E_{acc}$, $E_{acc}\ [MV/m]$ being the accelerating field, $k = \frac{eB_{SOL}}{mc}$ the solenoid focusing strength, considering negligible the rf ponderomotive focusing force, B_{SOL} the field intensity of the solenoids around s-band TW structure, $I_A = 17kA$ the Alfvén current and ε_n the normalized rms transverse emittance.

The longitudinal envelope equation can be written as follows:

$$\sigma_z'' + K_z\sigma_z + \frac{\gamma'\sigma_z'}{\beta^2\gamma} = \frac{I}{I_A\beta^2\gamma^4\sigma} + \frac{\varepsilon_z^2}{\beta^2\gamma^6\sigma_z^3} \quad (2)$$

with σ_z the rms bunch length, β the normalize velocity, ε_z the normalize rms longitudinal emittance, σ the rms bunch transversal dimension $\sigma=\sigma_x=\sigma_y$ (which couples the two envelope equations Eq. (1) and Eq. (2)), $\gamma_0' = \frac{eE_{acc}}{m_0c^2}$ the normalized acceleration gradient and K_z the RF longitudinal strength:

$$K_z = \frac{4\pi\gamma_0'\sin|\varphi_0(z)|}{\lambda_{RF}(\beta\gamma)^3} \quad (3)$$

with $\varphi_0(z) = \frac{z}{c}\left(1 - \frac{\gamma}{\sqrt{\gamma^2-1}}\right)$ (maximum acceleration at $\varphi_0 = 0$).

The third term on the left of Eq. (2) is a velocity damping term, always in contrast with focusing or defocusing. The last two terms, on the right hand of the same equation, represent internal forces and are respectively the space charge and the emittance longitudinal pressure, from which is possible to define the longitudinal laminar parameter ρ_z:

$$\rho_z = \frac{Qc(\gamma\sigma_z)^2}{I_0\sigma_x\varepsilon_z^2} \quad (4)\ .$$

This parameter provides a value of the bunch laminarity and also of the bunch stiffness with respect to the compression. The laminarity is guarantee for values greater the one ($\rho_z > 1$), which is a typical condition during compressions at low energy (VB or LB), differently for over-compression regimes, where the laminarity is lost (next paragraph). The stiffness of the bunch versus the compression decreased for ρ_z approaching the unity, favoring a more effective compression process.

A description of the LB beam dynamics, following the Fig. 1 layout and showing in advance some results of the simulations paragraph, is as follows:

- The bunch exiting from the gun, with an energy of 5.9 MeV, under the effect of the gun-solenoid and being space charge dominated, undergoes the emittance compensation process along a drift [13]. So far the dynamics is known, equal to many other low emittance injectors.
- Downstream the drift the bunch enters into a short, high frequency (x-band) accelerating cavity (see the paragraph: RF SYSTEM), that decelerate the bunch of 2.3 MeV. This deceleration that bring the bunch at the low energy of 3.6 MeV has many important effects: 1) it strengthens the long. space charge effects, also if

Content from this work may be used under the terms of the CC BY 3.0 licence (© 2018). Any distribution of this work must maintain attribution to the author(s), title of the work, publisher, and DOI.

ISBN: 978-3-95450-194-6 ISSN: 2226-0366 doi:10.18429/JACoW-LINAC2018-TU1P01

Content from this work may be used under the terms of the CC BY 3.0 licence (© 2018). Any distribution of this work must maintain attribution to the author(s), title of the work, publisher, and DOI.

the long. laminarity decreases, favouring a faster compression; 2) moves the bunch spike current on the bunch tail pre-compensating the symmetric VB effects (Fig. 2 and 3), resulting in a much more uniform charge distribution at the compression end; 3) provides a pre-compression; 4) it enlarges the envelope relaxing transversal space charge effects; 5) applies a pre-correction of the radio rf curvature (Fig. 3, upper plot); 6) the energy decreasing results in an larger bunch vs. rf-phase slippage, a key effect for the VB technique.

- After the high harmonic cavity, the bunch is injected into a typical cavity for the VB where it is chirped (in the longitudinal phase-space), compressed and accelerated.
- Downstream the VB cavity there is a long drift where the bunch enters at about 20 MeV and the full effectiveness of the LB takes place, region highlighted in Fig. 4. The beam propagates under the effects of its own fields and of the momentum distribution at the VB cavity exit. The resulting beam dynamic is peculiar: an envelope that grows linearly (in first approximation) and a bunch length σ_z that decreases following a hyperbolic trend (Fig. 4, zoomed box). This behaviour shows to be in balance and the compression can be pushed at very high values, at the expense of the envelope enlargement. The peculiar equilibrium of the LB, compression versus enlargement, going forward in the drift at some point is lost. The beam parameters to check are the energy spread σ_E and the transverse normalized emittance ε_n, the first is wonderfully damped by the longitudinal space charge effect (Fig. 4, lower plot), while the second, i.e. the ε_n, ends a long chromatic oscillation, closing the bow tie distribution of the transverse phase space (Fig. 4, lower plot). The bunching can be frozen by boosting the beam, when the emittance and energy spread are fully damped. The final result is impressive as reported in the next paragraph, where it is shown a longitudinal phase space of a bunch almost homogeneous in charge, with a spike current close to the central position and with an energy spread comparable to the one at the gun exit (below 100keV for the whole bunch, below 20 keV for the spike current). The energy spread, initially responsible of the compression, is quasi completely cancelled by the space charge effect. Furthermore, the space charge dominated regime heats the uncorrelated energy spread, which can be an important advantage for applications needed laser-heater devices (typically FEL).

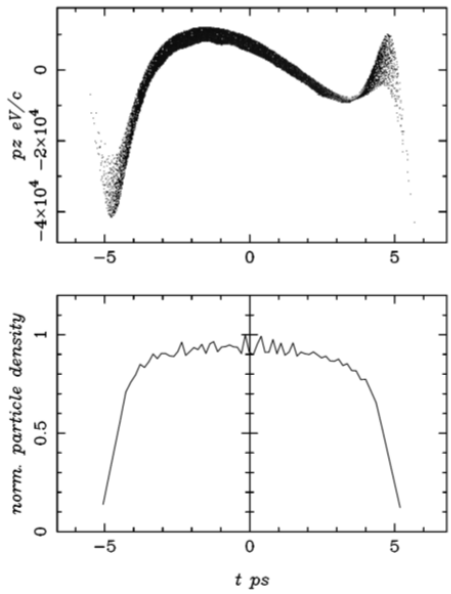


Figure 2: The upper plot is the beam Longitudinal phase space, at 1 m from the cathode, i.e. before entering in the high harmonic cavity. It is visible the rf curvature inherited from the gun. The lower image is the particle density along the bunch.

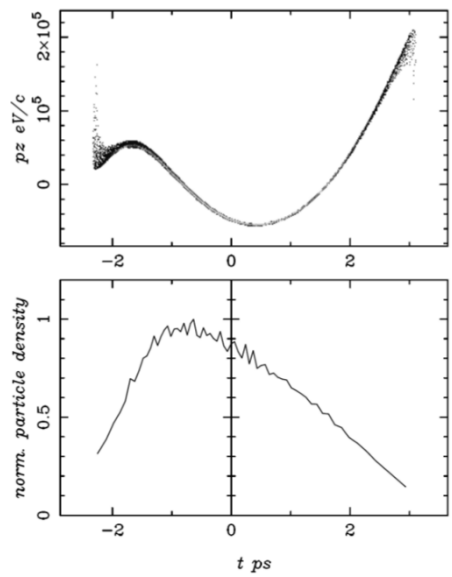


Figure 3: The upper plot is the beam Longitudinal phase space, at 2 m from the cathode, i.e. after the high harmonic cavity. It is visible the rf curvature correction (and pre-correction). The lower image is the particle density along the bunch; It is well shown the effect of the decelerating x-banc cavity, which pre-correct the current distribution by moving charge on the bunch tail.

ISBN: 978-3-95450-194-6 ISSN: 2226-0366 doi:10.18429/JACoW-LINAC2018-TU1P01

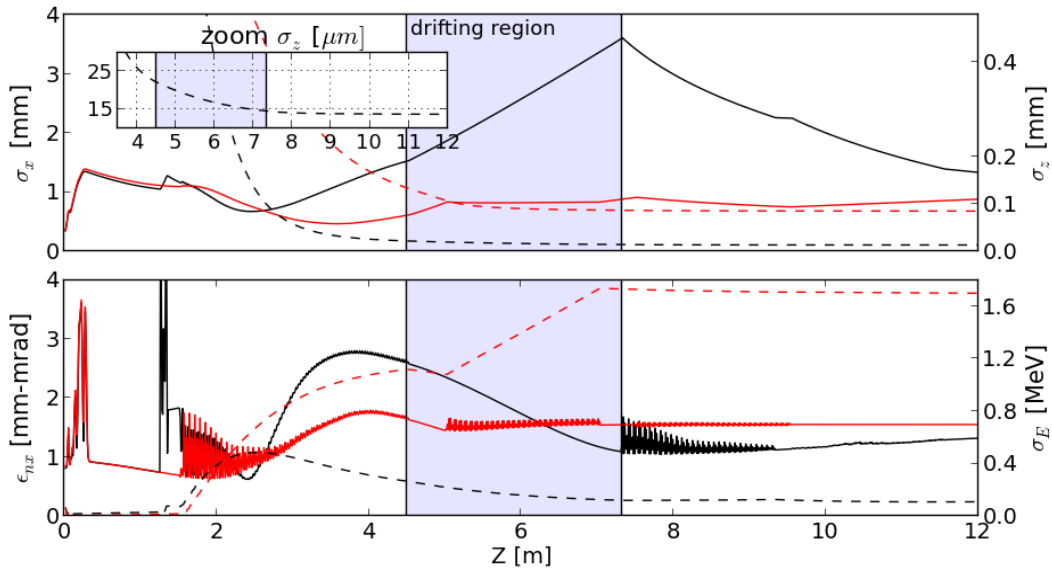


Figure 4: VB and LB comparison for simulations that aim to maximize the bunch brightness. In red are reported the VB results, in black the LB ones. The upper plot reports the envelopes (solid lines) and the bunch lengths (dashed lines), in the box is zoomed the bunch length for the LB case, to highlight the hyperbolic trend along the drift. The lower plot reports the emittances (solid lines) and the bunch energy spreads (dashed lines).

SIMULATIONS

In this paragraph is presented a comparison between two different compression methods, the VB and the LB. The both have been optimized, on the bunch brightness, by using the genetic algorithm GIOTTO [14,15], and the particles track have been done by using the code ASTRA [16]. The aim is not that to show what compression technique is better, but to outline the peculiarities of the LB (a new technique here proposed), versus a known technique, that as the VB, bunches linearly and works in the same energy range. Indeed, the two methods are relatives, but their final results are quite different. As we pointed out above, the VB, pushed at high compression values, favors a single spike compression, on the bunch head, differently the LB works almost on all the bunch charge, therefore also if the spikes current, at maximum compression, for both VB and LB can be equal (or quasi), the rms computed values can be very different, e.g. the compression factor ($\sigma_{z,i}/\sigma_{z,f}$) into Fig. 5.

The layout used for the LB is shown and described in the previous paragraph (Fig. 1). The VB layout is very close to the LB one, however with the following differences: the x-band cavity is missing; the long drift is missing and soon after the s-band cavity the bunch is frozen in terms of compression and emittance compensation (a c-band booster in place of the LB drift).

Figure 4, the upper plot, reports the invariant envelopes (red curve) typical of the VB technique. For sake of completeness the Fig. 5 reports also a VB case where, after the s-band cavity, the booster is removed and the bunch enters into a LB drift like. Along this drift the bunch goes straight into the over compression regime (Fig. 5 upper plot, cyan curve), and, here not reported, the emittance compensation is completely lost. It is interesting to note the ρ_z parameter that, because the VB beam conditions are different than for the LB case, the laminarity is lost (Fig. 5, lower plot, cyan curve: $\rho_z < 1$), giving the over compression and beam qualities degradation. The ρ_z is also a measure of the beam reaction to the compression and in the lower plot of the Fig. 5, the black curve shows the benefit of the high harmonic cavity, that drops down the beam laminarity, keeping it $\rho_z > 1$, with favors the compression, compensate the energy spread and prevent bunch slices overlapping.

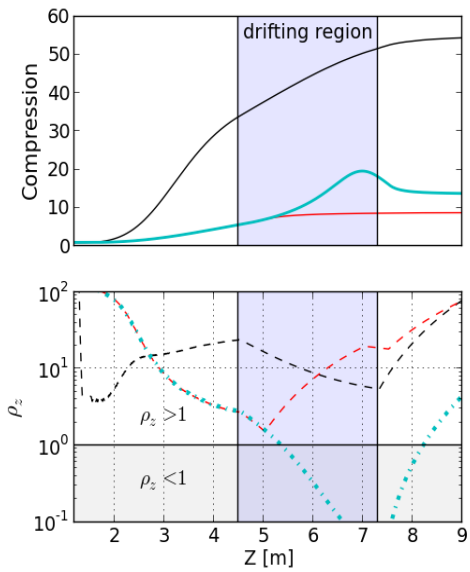


Figure 5: The upper plot reports the compression factor for the LB case (in black), the VB case in red and a VB test case (in cyan) where, after the s-band cavity, the bunch travels a drift, rather than being boosted. The lower plot reports the relative laminar parameters (Eq. (4)).

Content from this work may be used under the terms of the CC BY 3.0 licence (© 2018). Any distribution of this work must maintain attribution to the author(s), title of the work, publisher, and DOI.

ISBN: 978-3-95450-194-6 ISSN: 2226-0366 doi:10.18429/JACoW-LINAC2018-TU1P01

Content from this work may be used under the terms of the CC BY 3.0 licence (© 2018). Any distribution of this work must maintain attribution to the author(s), title of the work, publisher, and DOI.

Figures 6 and 7 show the longitudinal phase spaces and the slices bunch current, respectively for the VB and LB simulations.

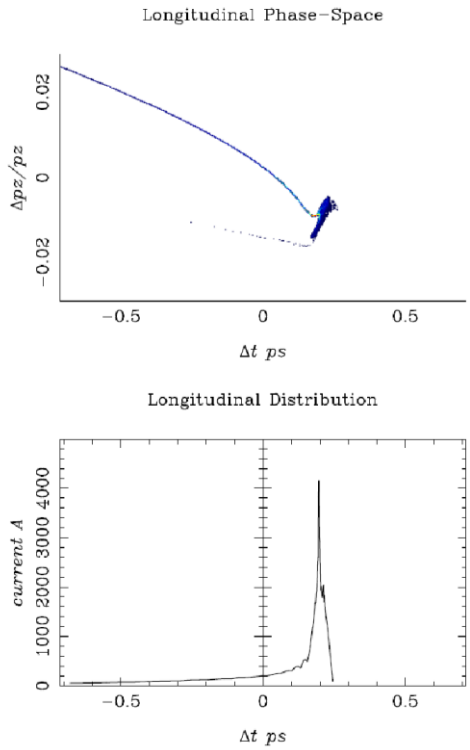


Figure 6: Bunch long. phase space (upper plot) and slices beam current (lower plot) at the end of the linac optimized by the VB technique.

The log. phase space obtained by using the VB, as well reported in Fig. 6, shows a long tail and a very high bunch density on the head, which is its typical charge distribution. The bunch head shows a space charge dominated shape that reshapes the head distribution but the final effect is not under control. The VB final performances, considering the bunch spike, are very good: a slice emittance of 2.5 mm-mrad, a slice current of 4 kA and a slice spread of 350 keV. What is new and peculiar in the LB is the capability to work with a much more uniform bunch distribution, which is clearly shown by the current binning of the Fig. 7. Here, differently from the VB, the capability to control the space charge effect to quasi completely compensate the energy spread, result in a very cold bunch, with the following slice performances: slice emittance below 1 mm-mrad, maximum current of 4kA and a really low energy spread of only 20 keV.

RF SYSTEM

The RF power for the system in Fig. 1 will be provided high-power klystrons driven by solid-state modulators. The 1.6 cell S-Band RF photoinjector is fed by about 10MW of RF power.

The C-band and X-band represent the most crucial components in the proposed LB scheme, therefore particular designs will be carried. Such ad-hoc structures will be powered by two different high-power klystrons at 5.712 GHz and 11.424 GHz, respectively.

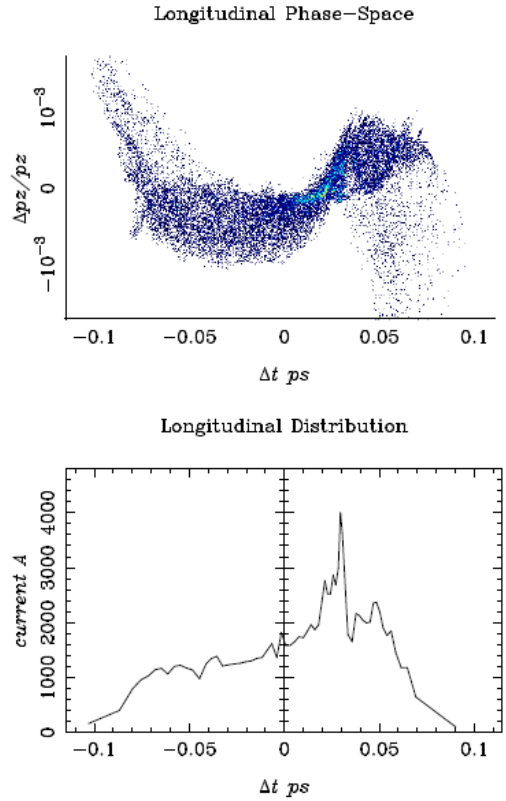


Figure 7: Bunch longitudinal phase space (upper plot) and slices beam current (lower plot) at the end of the linac optimized by the LB technique.

The C-band and X-band devices represent the most crucial components in the proposed LB scheme, therefore particular designs will be carried out. Such ad-hoc structures will be powered by two different high-power klystrons at 5.712 GHz and 11.424 GHz, respectively.

In our simulations, we employed a TW-type *"decelerating"* X-band structure but the standing-wave (SW) option will be also considered, as well as a C-band short cavity, more details are reported into the Ref. [17].

The booster first C-band accelerating structure will be optimized in future studies in order to maximize also the beam focusing. We foresee, for example, the use of cells with modular lengths and fed by separate RF power sources for maximum beam matching.

CONCLUSION

The LB represents another electron beam manipulation method that takes advantage form the space charge nonlinear effects tuning, which is already used for the gun emittance correction; i.e. the great advantage to be able to use non-linear phenomena. The LB performances, as discussed in the paper, are really impressive. It can be considered the only method that besides compressing and preserving the emittance, makes it possible to quasi fully correct the energy spread, opening the horizon to a new type of electron beams: extremely high average current, ultra-cold beams.

ISBN: 978-3-95450-194-6 ISSN: 2226-0366 doi:10.18429/JACoW-LINAC2018-TU1P01

REFERENCES

[1] Christopher Kupitz *et al.*, "Serial time-resolved crystallography of photosystem II using a femtosecond X-ray laser", *Nature*, vol. 513, pp. 261–265, Sep. 2014.

[2] T. Tajima, J.M. Dawson, Phy. Rev. Lett., vol. 43, p. 267, 1979.

[3] E. Esarey, Phillip Sprangle, Jonathan Krall, Antonio Ting, *IEEE Transactions on Plasma Science*, vol. 24, 1996.

[4] P. Muggli, Mark J. Hogan, *Comptes Rendus Physique*, vol. 10, p. 116, 2009.

[5] J.B. Rosenzweig, N. Barov, M.C. Thompson, R.B. Yoder, *Phys. Rev. ST Accel. Beams*, vol. 7, p. 061302, 2004.

[6] R. J. Dwayne Miller," Femtosecond Crystallography with Ultrabright Electrons and X-rays: Capturing Chemistry in Action*" Science*, vol. 343, pp. 1108-1116, 2014, doi:10.1126/science.1248488.

[7] E. Chiadroni *et al.*, "Characterization of the THz radiation source at the Frascati linear accelerator", *Review of Scientific Instruments*, vol. 84, p. 022703, 2013, doi.org/10.1063/1.4790429

[8] B. Zeitler, K. Floettmann, and F. Grüner, "Linearization of the longitudinal phase space without higher harmonic field", *Phys. Rev. ST Accel. Beams*, vol. 18, p. 120102, 2015.

[9] k. Floettmann, "Generation of sub-fs electron beams at few-MeV energies", *Nucl. Instr. Meth.*, vol. 740, pp. 34-38, 2014.

[10] C. R. Prokop, P. Piot, B. E. Carlsten, and M. Church, "Beam dynamics performances and applications of a low-energy electron-beam magnetic bunch compressor", *Nucl. Instr.-Meth., Sect. A*, vol. 719, pp. 17-28, 2013.

[11] M. Ferrario *et al.*, "Experimental Demonstration of Emittance Compensation with Velocity Bunching", *Phy. Rev. Lett.*, vol. 104, p. 054801, 2010.

[12] A. Giribono *et al.*, "EuPRAXIA@SPARC_LAB: The high-brightness RF photo-injector layout proposal", *Nucl. Instr. Meth., A*, in press. https://doi.org/10.1016/j.nima.2018.03.009

[13] M. Ferrario *et al.*, "Direct Measurement of the Double Emittance Minimum in the Beam Dynamics of the Sparc High-Brightness Photoinjector", *Phy. Rev. Lett.,* vol. 99, p. 234801, 2007.

[14] A. Bacci *et al.*, "GIOTTO: A Genetic Code for Demanding Beam-dynamics Optimizations", in *Proc. 7th Int. Particle Accelerator Conf. (IPAC'16)*, Busan, Korea, May 2016, pp. 3073-3076, doi:10.18429/JACoW-IPAC2016-WEPOY03

[15] A.Bacci *et al.*, "Wide-Ranging Genetic Research of Matching Line Design for Plasma Accelerated Beams with Giotto", in *Proc. 9th Int. Particle Accelerator Conf. (IPAC'18)*, Vancouver, BC, Canada, May 2018, pp. 3561-3564, doi:10.18429/JACoW-IPAC2018-THPAK136

[16] K. Floettmann, ASTRA—A space charge tracking algorithm, http://www.desy.de/~mpyflo/.

[17] D. Alesini *et al.*, "Study of A C-Band Harmonic RF System to Optimize the RF Bunch Compression Process of the Sparc Beam", in *Proc. 6th Int. Particle Accelerator Conf. (IPAC'15)*, Richmond, VA, USA, May 2015, pp. 1552-1555, doi:10.18429/JACoW-IPAC2015-TUPW058

Content from this work may be used under the terms of the CC BY 3.0 licence (© 2018). Any distribution of this work must maintain attribution to the author(s), title of the work, publisher, and DOI.

ISBN: 978-3-95450-194-6 ISSN: 2226-0366 doi:10.18429/JACoW-LINAC2018-TUPO001

ABOUT THE LIMITS FOR THE ACCELERATED BEAM CURRENT IN THE LUE-200 LINAC OF THE IREN FACILITY

A.P. Sumbaev †, JINR, 141980, Dubna, Russia
A. Barnyakov, A. Levichev, Budker INP, 630090, Novosibirsk, Russia

Abstract

The beam current loading of the accelerating fields is discussed for the linear accelerator LUE-200 of the IREN facility (a neutron source at Frank Laboratory of Neutron Physics JINR). The LUE-200 electron linac consists of two disk loaded travelling wave accelerating structure with the operating frequency of 2856 MHz and power compression SLED-type system. The limits by the accelerated beam current are defined for different pulse durations of the beam current and RF power. The calculated results are discussed and compared with the measurements.

INTRODUCTION

The IREN facility [1, 2] of the Joint Institute for Nuclear Research (JINR) is the ADS neutron source (**a**ccelerator **d**riving **s**ystem). It is known that for electron beams with energy more than 20-25 MeV the integral photoneutron yield from a target is directly proportional to energy of electrons. The beam energy is limited by the beam current loading effect. Therefore, analysis of the properties of the accelerating structure and search of the optimum parameters of the acceleration is very actual problem for LUE-200 linac.

In the current work calculations for a beam accelerated in one accelerating section, powered by klystrons of three types have been carried out: 5045 SLAC (the maximum pulse power 63 MW), E3730A Toshiba (the maximum pulse power 50 MW) and TH2129 Thomson (the maximum pulse power 20 MW) taking into account the use of SLED - system.

BEAM LOADING EFFECT FOR THE CZ ACCELERATING STRUCTURE

In a stationary regime the accelerating field of the wave travelling along the z axis of the constant impedance (CZ) structure can be described by the superposition of two equations [3]:

$$E_z(z) = E_0 e^{-\alpha z} - I_0 R_{sh}(1 - e^{-\alpha z}) \quad (1)$$

The first term of the right side of equation is caused by an external generator field: $E_0 = \sqrt{2\alpha R_{sh} P_0}$, where P_0 - power of the generator, R_{sh} - shunt impedance of structure, α - loss factor in the structure. The second term defines the field induced by an electron beam with an average current of I_0. It is supposed that the beam consists of dot bunches with length of much less than that of a wave which follow with frequency of own working mode of structure $f_0 = \omega_0/2\,\pi$.

† sumbaev@nf.jinr.ru

By means of (1) it is possible to receive additional beam potential which the beam will obtain at the acceleration:

$$U(z) = \int_0^z E_z(z)dz = (E_0 + I_0 R_{sh})\frac{1-e^{-\alpha z}}{\alpha} - I_0 R_{sh} z. \quad (2)$$

From (2) it is visible that there is a beam current I_{cr} at which the average growth of energy in CZ structure of L length will be equal to zero:

$$I_{cr} = \sqrt{\frac{2\alpha P_0}{R_{sh}}}\frac{1-e^{-\alpha L}}{\alpha L-(1-e^{-\alpha L})}. \quad (3)$$

In a nonstationary regime, changing of the beam potential will be defined by changing of the generator power $P_0(t)$ and of the beam induced field by the following equation [4]:

$$\Delta U_b(\tau) = -R_{sh} L I_0 \left\{\left(1 - \frac{\tau_{0A}}{T_f}\right)\left[1 - e^{-\tau/\tau_{a0}}\right] + \frac{\tau}{T_f} e^{-\tau/\tau_{a0}}\right\}. \quad (4)$$

Here τ - time from the injection start in accelerating structure of the first bunch ($0 \le \tau \le \tau_b$, where τ_b – beam current duration), $\tau_{a0} = 2Q_{a0}/\omega_0$ –time constant of the accelerating structure, Q_{a0} – quality factor of structure, $T_f = L/V_{gr}$ – filling time of structure, V_{gr} – wave group velocity of an accelerating field. The beam full potential will compose of the potential obtained from the external generator field without a beam and from the field, induced by a beam (4). For a case when the beam flies in the accelerating structure already completely filled with the RF power at $\tau \ge T_f$, it is possible to write down:

$$U(\tau) = U_m + \Delta U_b(\tau), \quad (5)$$

where $U_m = E_0(1\text{-}e^{-\alpha z})/\alpha$. Thus, the beam particles energy spread-out is defined by a beam current and its duration.

In case of using of SLED system [4] RF power gained from the generator is nonstationary in time. Let normalized pulse amplitude of an input signal is defined by the dependence shown in Fig. 1. The condition normalizing is expression for power $P(t) = P_o E^2(t)$, where P_0 - power of the generator.

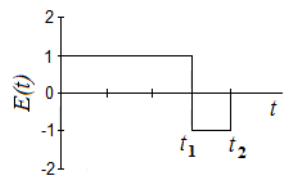


Figure 1: The RF power signal coming at the input of SLED system.

The phase inversion is carried out at the moment of time t_1 and lasts till time t_2. In this case, the wave amplitude

Content from this work may be used under the terms of the CC BY 3.0 licence (© 2018). Any distribution of this work must maintain attribution to the author(s), title of the work, publisher, and DOI.

ISBN: 978-3-95450-194-6 ISSN: 2226-0366 doi:10.18429/JACoW-LINAC2018-TUPO001

E_{in} coming in load and normalised on amplitude of the wave of the generator, it is possible [5] to write down in the following form:

$$E_{in}(t) = \begin{cases} \frac{E_{1in}(t)}{E_g}, 0 \le t < t_1 \\ \frac{E_{2in}(t)}{E_g}, t_1 \le t \le t_2 \\ \frac{E_{3in}(t)}{E_g}, t_2 < t \end{cases}, \quad (6)$$

$$\frac{E_{1in}(t)}{E_g} = \sqrt{\frac{P_{1in}(t)}{P_0}} = \frac{\beta_{sl}-1}{\beta_{sl}+1} - \frac{2\beta_{sl}}{\beta_{sl}+1} e^{-t/\tau_{slL}},$$

$$\frac{E_{2in}(t)}{E_g} = \sqrt{\frac{P_{2in}(t)}{P_0}} = -\frac{\beta_{sl}-1}{\beta_{sl}+1} + \frac{2\beta_{sl}}{\beta_{sl}+1} e^{-t/\tau_{slL}}\left(2e^{t_1/\tau_{slL}} - 1\right),$$

$$\frac{E_{3in}(t)}{E_g} = \sqrt{\frac{P_{3in}(t)}{P_0}} = \frac{2\beta_{sl}}{\beta_{sl}+1} e^{-t/\tau_{slL}}\left(2e^{t_1/\tau_{slL}} - 2e^{t_2/\tau_{slL}} - 1\right),$$

where P_{in} – the power coming in load, β_{sl} - resonator cavity coupling factor of SLED system, $\tau_{slL} = 2Q_{slL}/\omega_0$ – loaded time constant ω_0 – resonant operating frequency, $Q_{slL} = Q_{sl0}/(1+\beta_{sl})$ – loaded Q factor, Q_{sl0} – own Q factor of the resonator. The index "sl" indicates that parameter concerns the resonator of SLED system. The power which arrives at accelerating structure, will be defined by the following expression:

$$P_{in}(t) = P_0 \cdot E_{in}(t)^2. \quad (7)$$

In accelerating structure the RF power defined by expression (7) will travel:

$$P_{str}(z,t) = P_{in}\left(t - \frac{z}{V_{gr}}\right) \cdot e^{-2\alpha z}, \quad (8)$$

with an accelerating field

$$E_{str}(z,t) = \sqrt{2\alpha R_{sh} P_{str}(z,t)}. \quad (9)$$

Let's consider the period of time from the generator phase inversion t_1 till filling of accelerating structure of the RF power: $t_1 \le t \le t_1 + T_f$, i.e. we will choose for a reference mark $t = t_1$. Then the potential which a beam will receive from the external generator field, in view of (9) will be as follows

$$U_{str}(t) = \int_0^L E_{str}(z,t)dz. \quad (10)$$

The potential received by a beam after flight of the accelerating structure at $\tau < T_f$ is

$$U(t) = U_{str}(t + \Delta t) + \Delta U_b(t). \quad (11)$$

Here it is meant that RF power impulse can be shifted on time respectively the beam injection on Δt.

For the accelerating structure of LUE-200 (Table 1) in a stationary regime the critical currents received from expression (3), are presented on Fig. 2. Apparently from Fig. 2, there is a strong dependence of a critical current on power of generator P.

Let's consider the excitation of accelerating structure with the parameters presented in Table 1, powered by a klystron with the SLED system with characteristics, specified in Table 2.

Table 1: Parameters of the LUE-200 Accelerating Section

Operational frequency f_0	2855.5 MHz
Internal cell diameter $2b$	83.75 mm
Iris diameter $2a$	25.9 mm
Iris thickness t	6 mm
Period D	34.99 mm
Operational mode of oscillation θ	$2\pi/3$
Relative phase velocity β_p	1
Relative group velocity β_g	0.021
Section length L	2.93 m
Total number of cells (incl. 2 WTT)	85
Unloaded quality factor Q_0	13200
Shunt impedance R_{sh}	51 MOhm/m
Time constant $\tau_{0a}=2Q_0/\omega_0$	1.471 μs
Attenuation (by field) $\alpha=1/(\tau_{0a}v_{gr})$	0.108 m^{-1}
Filling time $T_f=L/v_{gr}$	0.465 μs

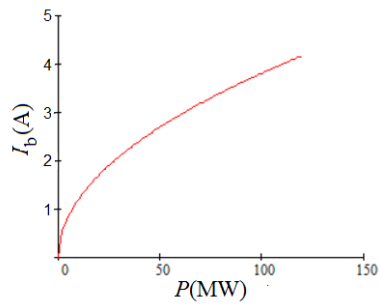


Figure 2: Critical beam current which can pass through structure at a zero gradient of a field in a stationary regime.

Table 2: Resonator Cavity Parameters of SLED System

Operational frequency	2855.5 MHz
Quality factor Q_{sl0}	86000
Coupling factor β_{sl}	5

Let's choose time of phase inversion $t_1 > \tau_{slL}$, for example, $t_1 = 3.1$ mks, time $t_2 - t_1 \sim T_f$ or 3.6 mks. Taking into account (6) and (7), the power coming from resonators of SLED system will look like in Fig. 3.

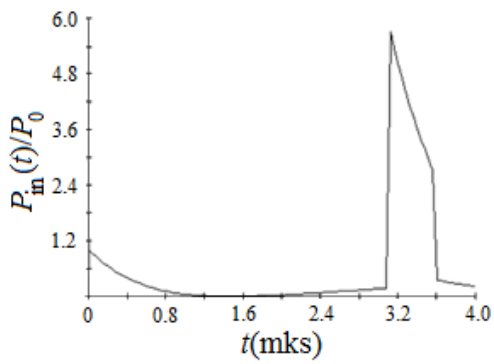


Figure 3: The envelope of RF power coming to input of the accelerating structure after the SLED system.

Content from this work may be used under the terms of the CC BY 3.0 licence (© 2018). Any distribution of this work must maintain attribution to the author(s), title of the work, publisher, and DOI.

ISBN: 978-3-95450-194-6 ISSN: 2226-0366 doi:10.18429/JACoW-LINAC2018-TUPO001

Content from this work may be used under the terms of the CC BY 3.0 licence (© 2018). Any distribution of this work must maintain attribution to the author(s), title of the work, publisher, and DOI.

Let's consider a beam with a duration of τ_b = 0.1 mks and with a squared shape envelope curve of the beam current. In Fig. 4 the losses of beam energy $\Delta W_b = e\Delta U_b$ for different beam currents are calculated according to (4).

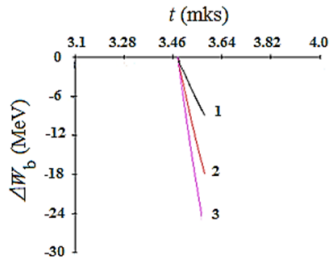


Figure 4: Losses of beam energy for different beam currents: 1 - I_b=1 A, 2 - I_b=2 A, 3 - I_b=3 A.

The full energy $W_b = eU_b$ received by a beam (11) after flight through the accelerating section, calculated depending on beam duration is presented in Fig. 5 for different beam currents and different klystrons. Diagrams are constructed on a condition that in the accelerating section all RF power comes after multiplication in the SLED system, and the time of the beam injection is equal to $t_0 = t_1 + T_f - \tau_b$.

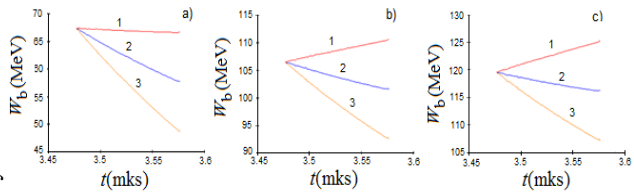


Figure 5: Full energies received by a beam in the accelerating structure for different RF power of the generator and different beam currents: a - TH2129 + SLED, b - E3730A + SLED, c - 5045 SLAC + SLED,
1 – I_b = 1 A, 2 – I_b = 2 A, 3 – I_b = 3 A.

From Fig. 5 it follows that for TH2129 klystron + SLED (Fig. 5,a) and for beam currents 1 A, 2 A, and 3 A the average energy and the energy spread are equal to 67 MeV, 62 MeV, 57 MeV and 1.2 %, 16 %, 33 % accordingly. For E3730A klystron + SLED (Fig. 5b) the same values for currents 1 A, 2 A and 3 A are equal to 108 MeV, 104 MeV, 99 MeV and 4%, 5%, 14% correspondingly. And for 5045 klystrons + SLED (Fig. 5c) - 122 MeV, 117 MeV, 112 MeV and 5 %, 3 %, 11 % accordingly for beam currents 1 A, 2 A and 3 A.

From these estimations follows that the beam with duration of 0.1 mks loads the accelerating field so, that even at relatively high average energy the beam particles possess substantial energy spread. In Fig. 6 the results of measurements of a beam energy spectra of LUE-200 accelerator after the first accelerating section are presented [2]. On the vertical axis the position of maxima of the energy spectrum, on the abscissa axis - the current of the beam which has passed accelerating section are specified. The results have been obtained using TH2129 Thomson klystron at pulse power of 17 MW with SLED system.

It should also be stated that the current results will only qualitatively be co-ordinated with the results of calculations. Most likely, for the complete analysis of results of measurements it is necessary to consider as well the efficiency of beam bunching in real buncher which is used on the accelerator. Such calculations are carried out in work [6] and confirm justice of the current assumption.

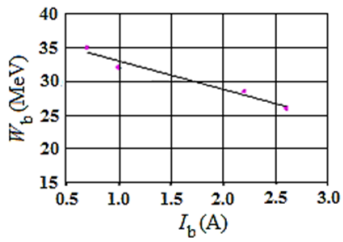


Figure 6: Position of the maximum of the energy spectrum depending on the current of the beam accelerated in one accelerating section of LUE-200 linac. Duration of the beam current is τ_b = 0.1 mks.

CONCLUSION

From the presented modelling calculations it is possible to formulate following short conclusions:

- At decrease of the RF power reaching accelerating sections, there is not simply energy spectrum "shift" of beam particles to smaller energies, but also the spectrum expansion that can result both in disproportionate decrease in the power content of the bunch in a separate cycle, and to disproportionate decrease in the beam average power.
- Analytical estimations show that values of critical currents of an electron beam for the accelerating section of LUE-200 linac are in the range of 3.0 - 3.5 A which is necessary to consider in search of optimal regimes of acceleration.
- For optimisation of acceleration regimes on the LUE-200 linac it is necessary to test the properties of the SLED system and the efficiency of the operating buncher of the accelerating system.

REFERENCES

[1] A.V. Novokhatski *et al.,* "Linear accelerator for Intense Resonance Neutron source (IREN)". Proc. of the 2nd Workshop on JINR Tau-Charm Factory, JINR, D1,9,13-93-459, p. 197, Dubna, 1994.

[2] A.V. Belozerov, Yu. Becher, Yu. Bulycheva, *et al.*, "Physical Startup of the IREN Facility". *Particles and Atomic Nuclei, Letters*, V. 7, N 7(163), JINR, Dubna, p. 923 – 932, 2010.

[3] T. Wangler, *Principles of RF Linear Accelerators*, New York: John Wiley & Sons, pp. 62–72, 1998.

[4] Z. D. Farkas, H. A. Hogg, G. A. Loew, and P. B. Wilson, "SLED: A Method of Doubling SLAC's Energy", in *Proc. of the 9th Int. Conf. on High Energy Accelerators*, SLAC, Stanford, CA, May, 1974, pp. 576-586, SLAC-PUB-1453.

[5] J. Wang, "RF Properties of Periodic Accelerating Structures for Linear Colliders", SLACReport-339, July 1989.

[6] T. V. Bondarenko, S. M. Polozov, and A. P. Sumbaev, "Numerical simulation of the beam loading effect at the LUE-200 accelerator", *Particles and Nuclei, Letters*, JINR, Dubna, vol. 13, no.7 (205), pp. 1432-1437, 2016.

ISBN: 978-3-95450-194-6 ISSN: 2226-0366 doi:10.18429/JACoW-LINAC2018-TUPO002

ELECTRON GUN FOR 100 MeV / 100 kW LINEAR ACCELERATOR OF ELECTRONS AS THE DRIVER OF NUCLEAR SUBCRITICAL ASSEMBLY NEUTRONS SOURSE

M. Moisieienko, O. Bezditko, I. Karnaukhov, A. Mytsykov, A. Zelinsky

NSC KIPT, Kharkov, Ukraine

Abstract

100 MeV / 100 kW linear electron accelerator of The NSC KIPT "Neutron Source" nuclear subcritical assembly uses the 120 kV triode electron gun as the primary source of electrons. The gun was designed, manufactured and tested at IHEP, Beijing, China. At present, the gun was installed and are under testing. The maximum pulse current of the gun is equal to 2 A. In design operation, the pulse current of the gun should be equal to 0.55 A. The report describes the design of the 120 kV triode electron gun, the results of testing and test operation.

INTRODUCTION

100 MeV/100 kW electron linear accelerator that is a driver of the ADS NSC KIPT Neutron Source was design and manufactured in IHEP, Beijing, China and assembled in NSC KIPT, Kharkov, Ukraine during 2010-2014 [1] .

In 2015 and 2016 the accelerator technological systems commissioning and beam commissioning were started in Spring 2017 the design value of pulse electron beam current was obtained in the end of the accelerator horizontal part. During the last year the main task of the accelerator commissioning was to optimize the technological system parameters and improve the accelerator performance in accordance with basic design parameters listed in Tab. 1 [2].

Table 1: Main KIPT Linac Parameters

Parameter	Value
RF frequency	2856 MHz
Beam energy	100 MeV
Pulse beam current	0-0.6 A
Average beam power	0.005 – 100 kW
Energy spread (1)	2 %
Emittance (1)	$5x10^{-7}$ m-rad
Beam pulse length	2.7 μs
RF pulse duration	3 μs
Pulse repetition rate	2 - 625 Hz
Gun voltage	~120 kV

The electron gun is a triode-type gun, which consists of an anode, cathode, and grid. The electron gun system consists of an electron gun body, a high voltage power supply, a high voltage deck, a pulser and a control unit. The gun should be able to operate in long beam pulse mode to generate the electron beam. The electron gun includes the following systems:

- electron gun cathode manufactured by EIMAC Y824;
- high-voltage power supply unit of the electron gun manufactured by GLASSMAN LT150N10;
- high-voltage station of GloryMV Electronics Limited, China;
- control system of the electron gun;
- Switching power supply of the electrode gun control grid developed at IHEP Institute of High Energy Physics, Beijing, China;
- electron gun protection and interlock system;
- vacuum system of the electron gun.

The main parameters of the electron gun are shown in Tab. 2.

Table 2: Main Electron Gun Parameters

Items	Value
Type	Triode
Beam Current （max） A	2
Anode Voltage kV	~120
Filament Voltage V	6.4
Filament Current A	5.5
Grid Bias V	50~ 500
Bunch length μs	3.0
Repetition Rate (max) Hz	625

GUN BODY

A planar triode electron gun, the EIMAC Y824 shown in Fig 1 with 150 kV (maximum) GLASSMAN high-voltage deck, is used with a fast pulser cathode driver. The acceleration voltage is 120 kV, the maximum extraction current is 2 A (normal operation is about 0.6 A) with minimum pulse width of less than 3.0 μs. The gun pulser system contains a driving circuit. A 3.0 μs FWHM pulser is used to drive the cathode for long pulse operation. The gun structure and the gun beam pulse form are shown in Fig. 2, 3.

Content from this work may be used under the terms of the CC BY 3.0 licence (© 2018). Any distribution of this work must maintain attribution to the author(s), title of the work, publisher, and DOI.

ISBN: 978-3-95450-194-6 ISSN: 2226-0366 doi:10.18429/JACoW-LINAC2018-TUPO002

Content from this work may be used under the terms of the CC BY 3.0 licence (© 2018). Any distribution of this work must maintain attribution to the author(s), title of the work, publisher, and DOI.



Figure 1: The EIMAC Y824 Cathode grid assembly.

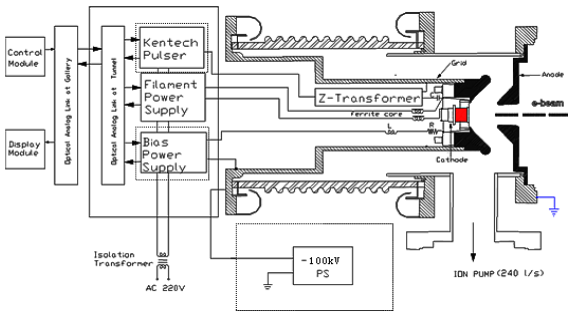


Figure 2: The gun structure.

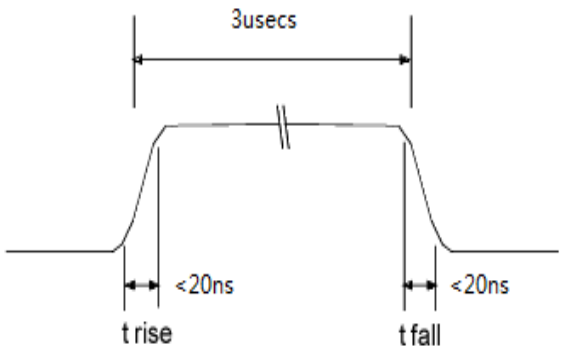


Figure 3: The gun beam pulse form.

BEAM TRANSPORT AND ELEMENTS

Two magnetic lenses and two sets of steering coils are adopted in the design to focus and adjust the beam between the gun and the bunching system. A few beam instrumentation elements, such as beam position monitors and beam profile monitor, are placed between the gun and the prebuncher. With such instruments, one can tune the beam flexibly and reliably. By some compromise between simulation and real mechanical layout, the element distribution is shown in Figure 4.

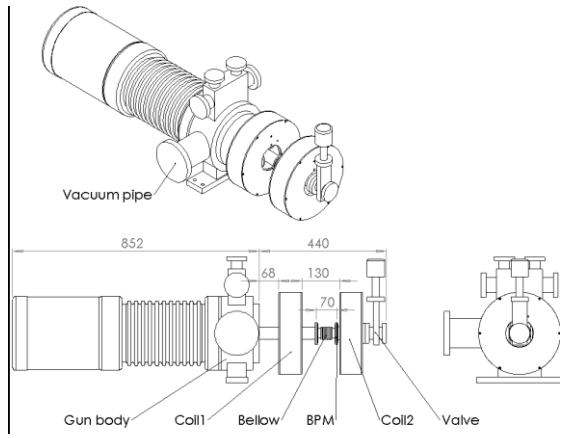


Figure 4: The process of survey target coordinate determinations.

THE ELECTRON GUN TESTING

When testing the gun at IHEP (Beijing, China), an electron beam current of 3.5 A was obtained at a voltage of -120 kV at the cathode of the gun and a pulse repetition rate of 1÷10 Hz. The pulse duration was 3.5 μs

Typical dependences of the gun current on the value of the voltage on the cathode (current-voltage characteristics) obtained during testing are shown in Fig. 5. The data were obtained with a fixed bias voltage on a grid of -100 V and an amplitude of a control pulse of 200 V.

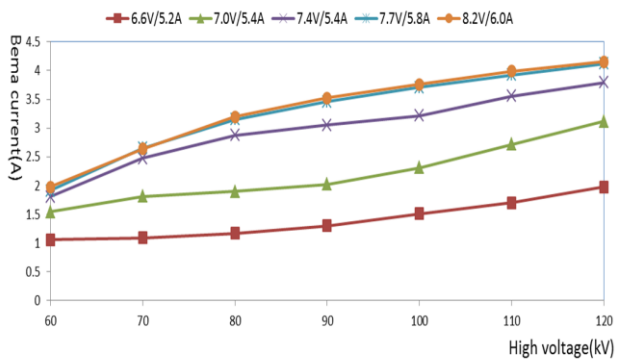


Figure 5: Current of the electron beam of the gun as a function of the voltage at the cathode for several values of the cathode heating current.

Figure 6 shows the dependence of the gun beam current on the bias voltage on the grid at a voltage and cathode filament current of about 7.4 V and 5.8 A respectively, the voltage at the cathode is -120 kV, the amplitude of the control pulse is 200 V.

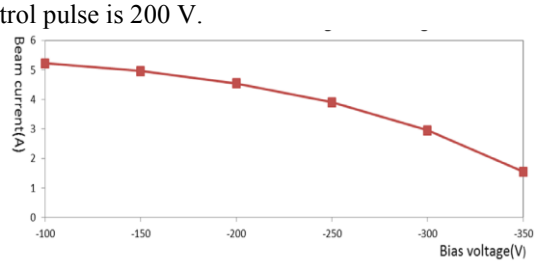


Figure 6: The current of the gun beam as a function of the bias voltage on the grid.

ISBN: 978-3-95450-194-6 ISSN: 2226-0366 doi:10.18429/JACoW-LINAC2018-TUPO002

ELECTRON GUN PERFORMANCE

During beam commissioning the gun showed the stable performance in pulse current range of 0.5 – 1 A (green line in Fig. 7) .

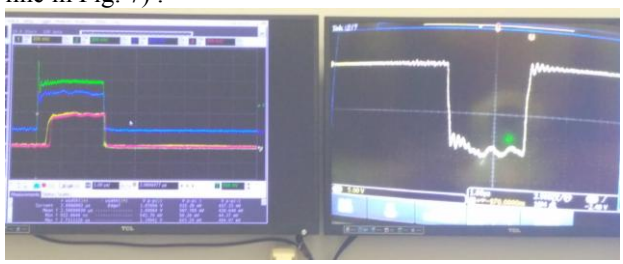


Figure 7: The electron beam current along accelerator (left photo, green line is FCT 1 pulse, blue line FCT 2, yellow is FCT 4, purple is FCT 5) and at the Faraday cup at the Neutron generating target (right photo).

In the same time, for observing of the beam IHEP and KIPT staff used a profile monitor detectors (PR) (see Fig. 8)

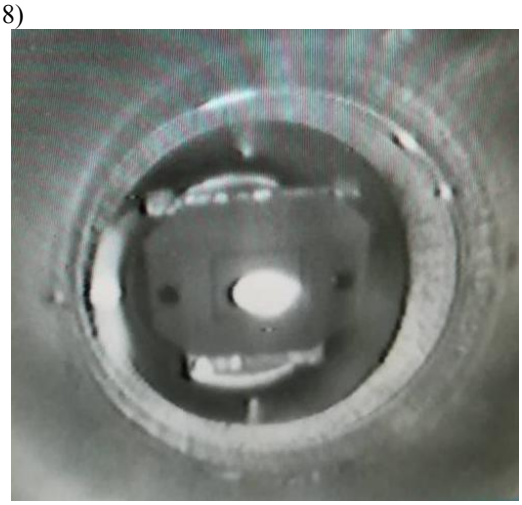


Figure 8: Signal from the PR monitor.

During the NSC KIPT Neutron Source commissioning, facility tests, neutron flux measurement system calibration and official State accepting tests and to avoid unnecessary equipment irradiation it is necessary to operate electron gun at low pulse beam current (10-100 μA). To test the performance of the gun in low current mode the gun current-voltage characteristic was measured. Figure 9 shows the anode electron gun current measured with FCT1 beam current monitor in dependence on gun grid pulser voltage. 50 V bias voltage was installed during the measurements. The pulser grid voltage can be controlled in the range of 0-200 V. As one can see from the figure the minimal electron gun at 0 V grid pulser voltage is about 225 mA. To have possibility to decrease beam current to zero it is necessary to have possibility to put negative voltage to the grid pulser [3]. According to the foregoing parameters, the pulser was modified and tested. The test results are shown on Figure 10.

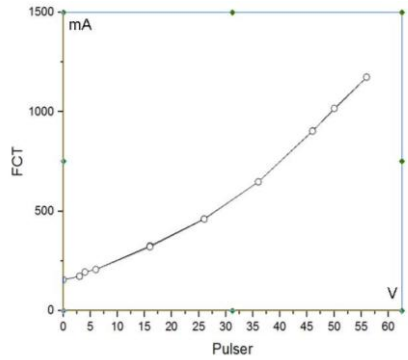


Figure 9: Triode electron gun current vs grid pulser voltage. Bias voltage is 50 V.

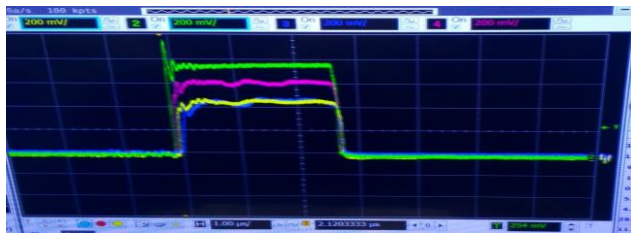


Figure 10: Result of testing of the gun after the replacement of the pulser.

CONCLUSION

Now the gun has passed all the tests shows a stable performance and provides design parameters necessary for regular and stable operation 100 MeV / 100 kW Linear Accelerator of Electrons as the Driver of Nuclear Subcritical Assembly Neutrons Source

REFERENCES

[1] O. Bezditko *et al.*, NSC KIPT Neutron Source on the base of Subcritical Assembly Driven with Electron Linear Accelerator, *Proc. Of IPAC'2013*, 12-17 May, 2013, Shanghai, China, THPFI080, pp. 3481-3483, http://www.JACoW.org

[2] A. Zelinsky *et al.*, NSC KIPT Neutron Source on the Base of Subcritical Assembly with Electron Linear Accelerator Driver, *Proc. Of IPAC'2017*, 14-19 May, 2017, Copenhagen, Denmark, TUPIK034, pp. 1754-1756, http://www.JACoW.org

[3] A. Zelinsky *et al.*, Status of the NSC KIPT Neutron Source, *Proc. Of ICALEPCS'2017*, 8-13, October, 2017, Barcelona, Spain, TUPHA061, pp. 537-539, http://www.JACoW.org

Content from this work may be used under the terms of the CC BY 3.0 licence (© 2018). Any distribution of this work must maintain attribution to the author(s), title of the work, publisher, and DOI.

ISBN: 978-3-95450-194-6 ISSN: 2226-0366 doi:10.18429/JACoW-LINAC2018-TUPO003

DEVELOPMENT OF CW HEAVY ION LINAC AT IMP*

X. J. Yin†, Y. J. Yuan, J.W. Xia, Y. He, H.W. Zhao, H. Du, Z. S. Li, X. N. Li, K. D. Wang, Q. Y. Kong, Y. Q. Yang, P. Jin, C. Qian, L.Z. Ma, J. X. Wu, Z. Xu, L.T. Sun, W. Zhang, X. Z. Zhang, J. Meng, W. J. Xie, Z. Z. Zhou, Q.G. Yao, S. M. Wang, X. W. Xu, H. N. Wang, Y. Zhang,
Institute of Modern Physics, Chinese Academy of Sciences, Lanzhou, China
Y. R. Lu, K. Zhu, G. Liu, X. Q. Yan, S. L. Gao, Z. Wang, and J. E. Chen,
State Key Laboratory of Nuclear Physics and Technology, Peking University, Beijing, China

Abstract

A new heavy ion linac as the injector for the Separated Sector Cyclotron (SSC), named SSC-Linac [1], is being under constructed at the national laboratory Heavy Ion Research Facility in Lanzhou (HIRFL). The SSC-Linac mainly consists of a 4-rod RFQ and three IH-DTL cavities which can accelerate ion of $A/q \leq 7$ from 3.73 keV/u to 1.025 MeV/u. Both of them operating at 53.667MHz had been developed. In the commissioning, ions were successfully accelerated to 0.295 MeV/u by IH-DTL1. The beam commissioning of the IH-DTL2 which can accelerate the ion to 0.586 MeV/u will come soon. In this paper, the recent R&D progress of the SSC-Linac including the development of key components and the beam commissioning results are presented.

INTRODUCTION

As the main part of the upgrade project of Heavy Ion Research Facility in Lanzhou (HIRFL), a new heavy-ion linac which operated at Continuous Wave (CW) mode was designed and constructed as the injector for the separated-sector cyclotron (SSC).The design parameters of SSC-Linac were listed in Table 1.There are two stages for the energy upgrade project. In the first stage, the ion particles will be accelerated to 0.586 MeV/u using two IH-DTL cavities. And then they will be further injected and accelerated to 6 MeV/u by the SSC facility. In the second stage, the particle will be accelerated to 1.025 MeV/u by adding the DTL3.

Table 1: Design Parameters of SSC-Linac

Parameters	Values
Design ion	$^{238}U^{34+}$
ECR ion source	
Extraction voltage	25 kV
Max. axial injection field	2.3 T
Frequency	18 GHz
RFQ Type	4-rod
Input /Output energy	3.73/143 keV /u
Inter-electrode voltage	70 kV
Max.current	200.0 eμA
IH-DTLs	
Input /Output energy	0.143/1.025 MeV/u

*Work supported by National Natural Science Foundation of China (10635090, 11375243)
†yinxj@impcas.ac.cn

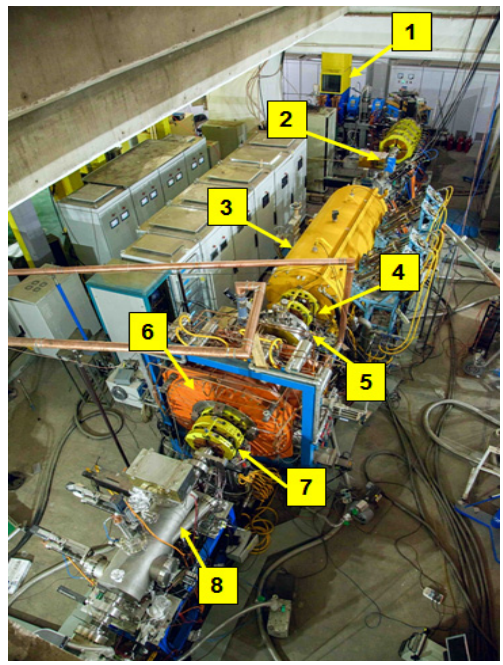


Figure 1: General view of the SSC-Linac. 1-ECR ion source; 2-LEBT section; 3-RFQ; 4-MEBT section; 5- Rebuncher cavity; 6- IH-DTL1; 7-Foucsing triplets; 8-Beam diagnostics system.

Finally, the particles will be accelerated to 10.7 MeV/u also by the SSC facility. Figure 1 shows the layout of the front end section of the SSC-Linac.

ION SOURCE&LEBT

The high charge state room temperature ECR ion source had been successfully constructed. This source magnet coils were cooled through evaporative cooling technology. The maximum mirror field was 2.3 T (with iron plug) and the effective plasma chamber volume was Ø76 mm×260 mm. The commissioning test of ECR ion source had been performed continually from 2014. Various specie ion beams had been successfully delivered for the linac commissioning.

With 0.1 kW RF injection power and 11.92 kV extraction voltage, 200 eμA of $^{16}O^{5+}$ was produced. The transverse emittances were measured by the emittance scanners located at the downstream of the analysing magnet. As shown in the Fig. 2, the measured normalized rms emittances at 200 eμA beam current for $^{16}O^{5+}$ were 0.22π mm.mrad and 0.15π mm.mrad in horizontal and vertical plane, respectively.

Content from this work may be used under the terms of the CC BY 3.0 licence (© 2018). Any distribution of this work must maintain attribution to the author(s), title of the work, publisher, and DOI.

ISBN: 978-3-95450-194-6 ISSN: 2226-0366 doi:10.18429/JACoW-LINAC2018-TUPO003

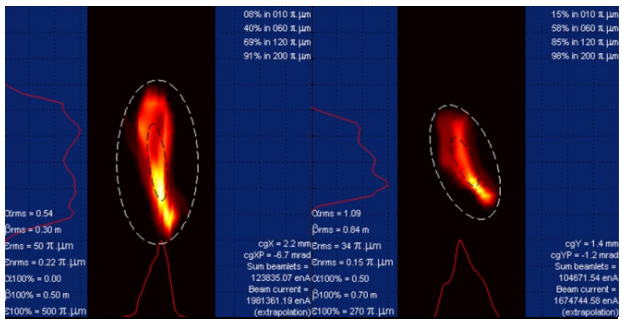


Figure 2: Measured transverse emittances after analysing dipole magnet.

CW 4-ROD RFQ

The CW 4-rod RFQ had been developed under the successful cooperation between Peking University and IMP. Low level RF measurement of RFQ was carried out. The frequency of the cavity without tuning was 53.607 MHz, which was not far from the operation frequency of 53.667 MHz and can be easily tuned by the tuners. On the critical coupling state, the Q_0 value of the cavity was 6440, which was 97% of the design value. The electric field distribution along the bam line was measured adopting the conventional perturbation method. The error of the results had been analysed in details [2].

The high power conditioning took a few days from pulse mode to CW. After about 30 hours conditioning, 35 kW with 30% duty factor was fed into the cavity. After then, 35 kW in CW mode had been successfully carried out almost no feedback. The temperature of the cooling water increased from 15.1 °C to 20.4 °C while the RF power increased from 0 to 32 kW. And the maximum temperature occurred at the RF power coupler.

The first beam commissioning ($^{16}O^{5+}$, 149.5 eμA) was successfully performed and ion was accelerated to 141.9 keV/u measured by the TOF method. After carefully RF conditioning, $^{40}Ar^{8+}$ ion beam was successfully accelerated, the measured energy and current were 142.8 keV/u and 198 eμA, respectively. The transmission efficiency was 94%. The more detail had been reported in [3].

MEBT RE-BUNCHER

In the MEBT section of SSC-Linac, a spiral re-buncher with four gaps structure had been developed to implement the longitudinal matching between the RFQ and the DTL operating, as shown in Fig. 3. The design β and the shunt impedance were 0.0175 and 5812 kΩ, respectively. Due to the limited space, the cavity was designed as Ø600 mm and 197 mm in length. The designed total power was 1.8 kW for the design ion and the corresponding gap voltage amplitude was 35 kV. The measured Q_0 was 3628 which was the 86.5% of the design value.

A fixed tuner and a movable tuner were employed for frequency compensated during the operation. It meant that the cavity was tuned to the working frequency by fixed tuner. After then the movable tuner was devoted into the normal operation.

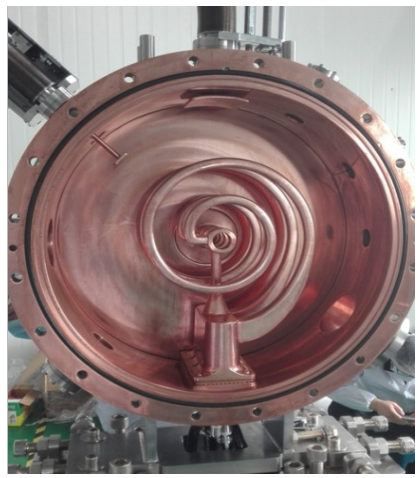


Figure 3: Spiral re-buncher cavity.

The RF power was generated and feed into the bunch cavity by a commercial solid state RF power amplifier system including the LLRF system. The conditioning process was smooth without any interruption. It took about 40 hours from low RF power in the pulse mode shift to the full RF power in CW mode.

Figure 4 shows the bunch efficiency when the buncher turns on comparing it turns off. It can be found that the bunch efficiency is very efficient. The measured energy spread of bunched beam was $|\Delta W/W| \leq \pm 2\%$.

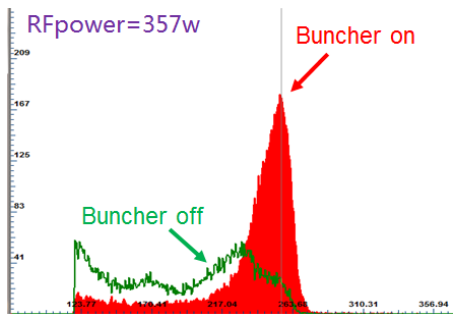


Figure 4: Measured bunch efficiency.

IH-DTLS

In the original design, the particle will be accelerated to 1.025 MeV/u by four IH-DTL cavities. However in the optimized design, the high energy section of the SSC-Linac adopted three IH-DTL cavities obtaining the same energy as origin design value. The first cavity DTL1(295 keV/u) had been installed and beam commissioning was successfully performed.

The second DTL had been finished in manufacture and is under the preparation of the RF measurement as shown in Fig. 5. The cavity body was made of steel ion with copper plated on the inner surface. The T-type stems and drift tubes were made of OFC. Water cooling channels were designed in the T-type stems which were housed in the tank wall.

The preliminary low level RF measurement for the DTL2 had been carried out using a network analyser in this May. The frequency response as a function of tuner

Content from this work may be used under the terms of the CC BY 3.0 licence (© 2018). Any distribution of this work must maintain attribution to the author(s), title of the work, publisher, and DOI.

ISBN: 978-3-95450-194-6 ISSN: 2226-0366 doi:10.18429/JACoW-LINAC2018-TUPO003

Content from this work may be used under the terms of the CC BY 3.0 licence (© 2018). Any distribution of this work must maintain attribution to the author(s), title of the work, publisher, and DOI.

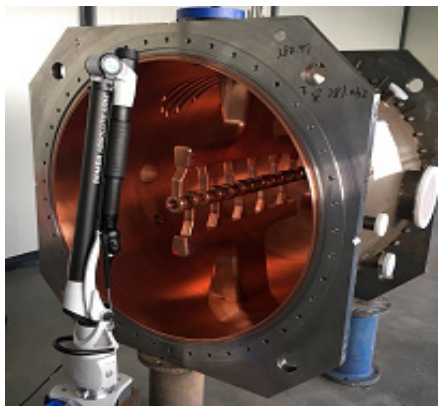


Figure 5: The second IH-DTL cavity.

position is plotted in Fig. 6. As shown in this figure, the adjustable range of the frequency change was up to 1.44MHz using the fixed tuner with Ø230 mm. As also indicated in the Fig. 6, the working frequency of 53.667 MHz can be obtained at the fixed tuner position of 82 mm from beam axis.

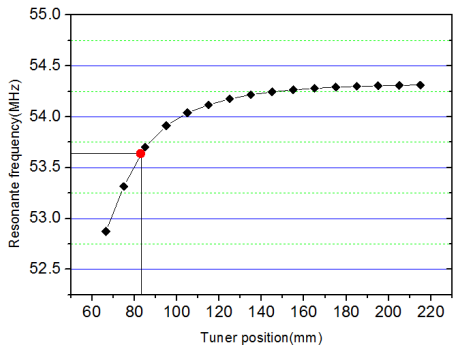


Figure 6: Frequency range of the DTL2 as a function of tuner position.

The electric field distribution along the beam axis had also been measured using the conventional bead perturbation method. Figure 7 shows the measurement result. Comparing with the simulation by CST-MWS code, the measured field distribution was consistent with the design value. The further measurement with fine RF coupler and tuners will be carried out as soon.

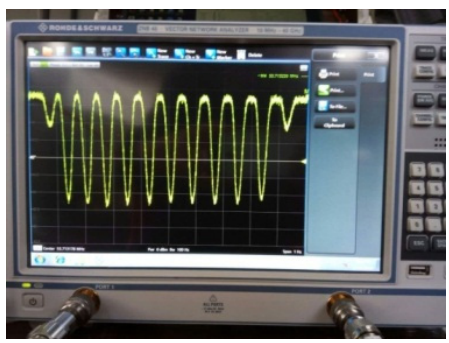


Figure 7: The field measurement results of the DTL2.

BEAM COMMISSIONING

The first beam commissioning had been performed using $^{16}O^{5+}$ ion. Beam current 100 eμA was extracted from ion source and accelerated by RFQ and IH-DTL1 in sequences. The commissioning results were listed in the Table 2. As can be seen, the transmission efficiency was only 70%. The main reason was that the match conditions were not implemented perfectly both at LEBT and MEBT section. Due to the lack of the diagnostic instrument, the matching condition between RFQ and DTL would be carefully tuned especially in the future experiment. The emittances at the DTL1 exit were also measured as shown in Fig. 8. Transverse normalized rms emittances both in horizontal and vertical plane were in good agreement with the simulation results. After this experiment, more beam experiments were carried out using some other specie ions such as $^{12}C^{4+}$, $^{40}Ar^{8+}$, $^{209}Bi^{30+}$. The higher transmission 82% was obtained in the experiment within $^{12}C^{4+}$ ion beam. Investigations of transmission are still under continuing.

Table 2: Beam Commissioning Results of SSC-Linac

Parameters	Values
Ion	$^{16}O^{5+}$
Measured beam current	70 eμA
Input/ Output energy	3.73/295.6 keV/u
$\varepsilon_{x/y\ nrms}$	0.18/0.14 π·mm·mrad

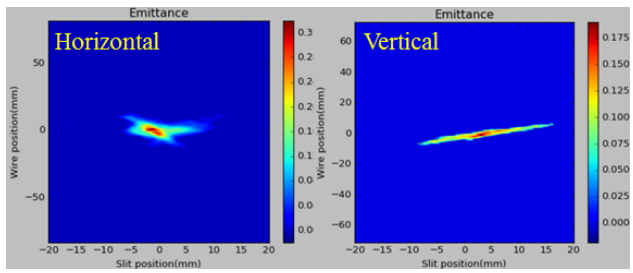


Figure 8: Measured transverse emittances at DTL1 exit.

SUMMARY AND OUTLOOK

The front end section of the SSC-Linac has been fabricated and commissioned at IMP. Beam commissioning with various specie ions had also been carried out successfully. The measured particle energy was in good agreement with design value. However the beam transmission has some optimize rooms. So the match input would be studied carefully for improving the beam transmission efficiency. Furthermore, the low level RF measurement and higher power conditioning of IH-DTL2 will be carried out in the near future. The beam commissioning will also be performed in the sequence.

REFERENCES

[1] XIAO Chen *et al.*, "A particle-in-cell mode beam dynamics simulation of medium energy beam transport for the SSC-Linac", *Chinese Physics C* (HEP&NP), vol. 36(1), pp. 84-90, 2012.

[2] LIU Ge *et al.*, "RF and field measurements of the SSC-LINAC RFQ", *Sciencechina Physics, Mechanics & Astronomy,* vol. 57(7), pp. 1311-1317, 2014.

[3] X.J.Yin *et al.*, "Design, fabrication, and beam commissioning of a continuous-wave for-rod rf quadrupole", *Phys. Rev. ST Accel. Beams*, vol. 19, Jan. 2016.

ISBN: 978-3-95450-194-6 ISSN: 2226-0366 doi:10.18429/JACoW-LINAC2018-TUPO004

RF DESIGN AND COLD MODEL MEASUREMENT OF AN IH-DTL FOR HIMM INJECTOR*

H. Du†,1, X. J. Yin1, Z. S. Li1, K. D. Wang, Q. Y. Kong,Institute of Modern Physics, Chinese Academy of Sciences, 730000 Lanzhou, China
1also at Huizhou Research Center of Ion Sciences, 516003 Huizhou, Guangdong, China

Abstract

An interdigital H-mode drift tube linac (IH-DTL) will be constructed as a postinjector linac for the Heavy Ion Medical Machine (HIMM). Its resonant frequency, injection and final energies are determined from beam dynamics and hardware parameters considerations of the entire machine to be 162.5MHz, 600keV/u and 4MeV/u, respectively. The beam duty cycle of the injector linac is less than 0.1% based on the injection requirements of the synchrotron. Beam dynamics and RF structure design and optimize of the IH-DTL has been finished. The maximum surface electric field is less than 2.0-times the Kilpatric limit for accelerating C^{4+} beam. This IH-DTL contains 41 accelerating gaps and two focusing quadrupole triplets. In order to examine the field distribution of the IH-DTL which reaches the length of 3.17m, an aluminium alloy 1:1 cold model cavity with 4 moveable tuners and 2 empty focusing magnet shell was constructed. The relative intertube-distance errors are less than ±0.05mm. The measurements show that the gap voltage values can match the CST-MWS simulating results within relative difference of ±3% by adjusting the 4 moveable tuners.

INTRODUCTION

To improve the performance and reduce the cost of the Heavy Ion Medical Machine (HIMM), Institute of Modern Physics designed a compact C^{4+} linac injector to replace the C^{5+} cyclotron injector [1,2]. This linac injector mainly contains an ECR ion source, a RFQ, an IH-DTL, two buncher cavity and several beam lines. KONUS beam dynamics design of the IH-DTL has been reported in the previous paper [3]. This IH-DTL cavity with a resonant frequency of 162.5MHz and a length of 3.17m will be constructed as the main accelerating section for the HIMM linac injector. Its total integral gap voltage on the beam axis is above than 10MV, which is fairly high as a normal conducting cavity. In general, it is difficult to design fabricate a long IH-DTL which contains several focusing quadrupole triplets. In the cavity design process, on-axis electric field distribution is tuned carefully by adjusting the cavity structure. On the other hand, nearest mode problem of a long IH-DTL cavity must be considered. In order to examine the on- axis electric field distribution and the nearest mode of such a long IH-DTL cavity, a cold model cavity of the IH-DTL has been constructed. The measurement results of this cold model will be discussed in this proceeding.

* Work supported by National Natural Science Foundation of China (11375243, 11405237) and Guangdong Innovative and Entrepreneurial Research Team Program (2016ZT06G373).
† duheng@impcas.ac.cn

RF STRUCTURE DESIGN OF IH-DTL

CST-MWS code [4] has been used to make the RF structure design and simulation. The optimized 3D RF structure is shown in Fig. 1. To make the on-axis electric field match with the dynamics requirement, end cut tuner, lens coupling tuner and local volume tuner are used and fine adjusted. Four movable plunger tuners are installed in the IH-DTL cavity, which has totally 0.9 MHz frequency tuning range. Remove the 4 plunger tuners, the H_{110} mode (operation mode) resonance frequency, Q0 value and RF power loss for C^{4+} is 163.0MHz, 14200 and 332kW respective. For the H_{111} mode (nearest mode), the resonance frequency and Q0 value is 165.4MHz and 12400. The on-axis electric field distribution compare between the H_{110} and H_{111} mode is shown in Fig. 2.

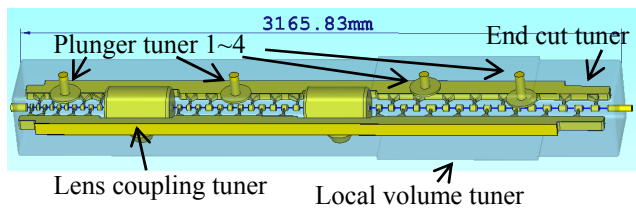


Figure 1: CST-MWS 3D model.

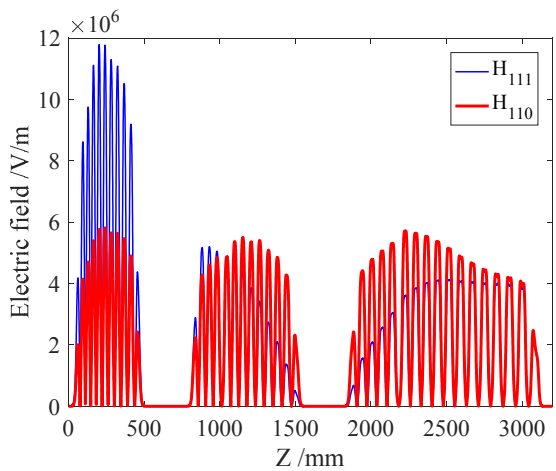


Figure 2: The on-axis electric field distribution compare between the H_{110} and H_{111} mode.

To avoid stimulating the H_{111} mode, the magnetic field distributions of both the operation and nearest mode are studied. As shown in Fig. 3, the magnetic field distributions are different between these two modes at the second focusing lens, so we can locate the power coupler here. When the coupler is tuned to the critical coupling for the H_{110}

Content from this work may be used under the terms of the CC BY 3.0 licence (© 2018). Any distribution of this work must maintain attribution to the author(s), title of the work, publisher, and DOI.

ISBN: 978-3-95450-194-6 ISSN: 2226-0366 doi:10.18429/JACoW-LINAC2018-TUPO004

Content from this work may be used under the terms of the CC BY 3.0 licence (© 2018). Any distribution of this work must maintain attribution to the author(s), title of the work, publisher, and DOI.

mode, the coupling coefficient for the H_{111} mode is near zero.

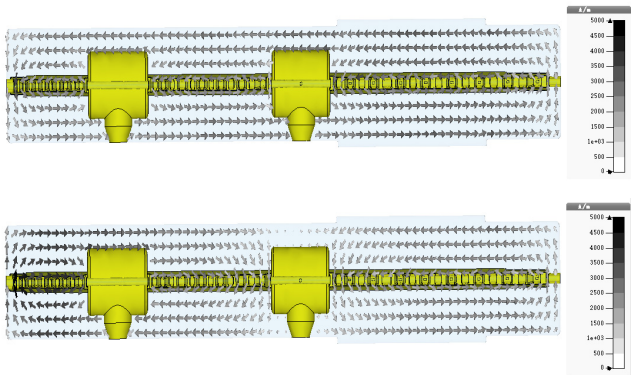


Figure 3: Compare of magnetic field distributions between the operation (up) and nearest mode (down).

BEAM DYNAMICS CHECK USE 3D EM-FIELD

The actual electromagnetic field in the IH-DTL can hardly be in full accord with the dynamics designed values. In order to check the 3D field generated by CST-MWS, a PIC (Particle in Cell) particle tracking code Beampath [5] is employed to simulate the transmission and acceleration situation of the beam in the IH-DTL. Because the 3D electromagnetic field from the CST-MWS corresponds with 1Joule stored energy, the field value must be scaled to the dynamic design value before imported to the Beampath code. This scale coefficient can be obtained by one particle tracking which with 0 emittance and 0 current.

Table 1: Phase Space Parameters at the Entrance of IH-DTL

Parameter	Value
$\varepsilon_{x/y,n,rms}$	0.24 πmm·mrad
$\alpha_{x/y}$	0.7
$\beta_{x/y}$	0.5 mm/mrad
$\varepsilon_{z,n,rms}$	30 πkeV/u·Deg
α_z	-1.0
β_z	1.76 Deg/(keV/u)

After the RF phase and scale coefficient of the 3D field are ascertained, multiparticle tracking can be launched. At the starting point of the simulation, 10000 macro particles with 500eμA beam current, the phase space parameters in table 1 and Water Bag distribution are generated. Beam transverse envelope (90% particles) is matched by tuning the focusing parameters of quadrupole triplets inside the cavity which shown in Fig. 4. The Fig. 5 shows the evolution of beam bunch length and energy spread in the IH-DTL. For the structure asymmetry of the IH-DTL in X direction, electric field in the drift tube is also unsymmetry in this direction. It will diverge the beam centre from the cavity axis, as shown in Fig. 6. This deviation of 0.5mm is acceptable in the operation. At the exit of the IH-DTL (including a quadrupole triplet subsequent), beam phase space distribution is shown in Fig. 7. Beam transfer efficiency of the IH-DTL is 100%. PIC particle tracking proves the validity of the RF design.

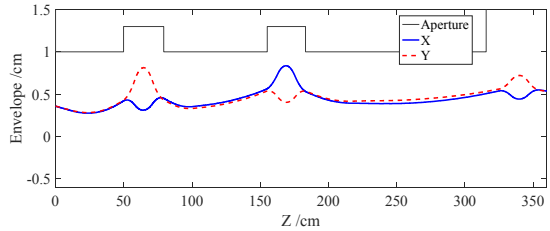


Figure 4: Beam transverse envelope in the IH-DTL.

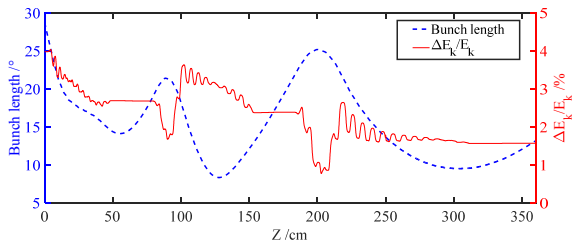


Figure 5: Beam bunch length and energy spread in the IH-DTL.

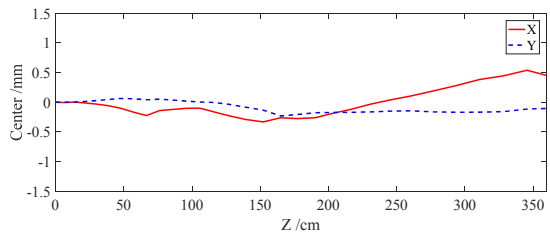


Figure 6: Beam centre deviation in the IH-DTL.

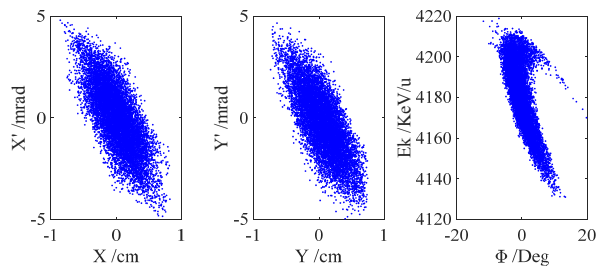


Figure 7: Beam phase space distribution at the exit of the IH-DTL.

COLD MODEL RF MEASUREMENT

A cold model cavity of the IH-DTL, as Fig. 8, has been constructed which machining precision of all the components is less than ±0.02mm. 4 plunger tuners and 2 shells of the quadrupole triplet are mounted on the upper and bottom cover. 40 drift tubes are installed on the middle frame by the stems and two girders. The final 3D installation accuracy of the drift tubes reaches ±0.05mm by using the FARO arm which one point accuracy reaches ±0.025mm, a high precision cylindrical rod which outer diameter

ISBN: 978-3-95450-194-6 ISSN: 2226-0366 doi:10.18429/JACoW-LINAC2018-TUPO004

equals to the inner diameter of the drift tube and some hollow cylinder which height equals to the each gap length respectively.

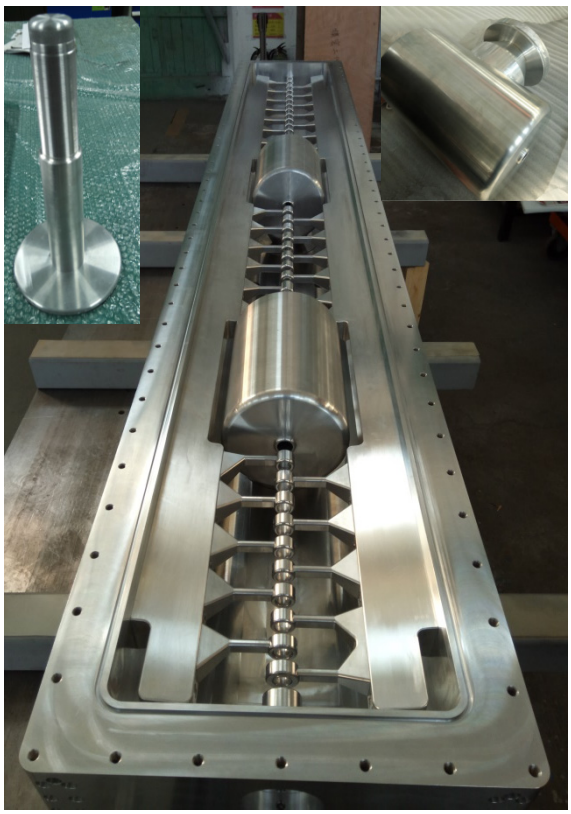


Figure 8: The assembled aluminium alloy cavity of the IH-DTL.

Before the low level RF measurement, a power coupler of test case has been adjusted to critical coupling state. And the resonance frequency without 4 plunger tuner is 162.86MHz which is 14kHz lower than the CST-MWS simulation result. The measured frequency adjustable volume of the 4 plunger tuners is about 0.9MHz, which is big enough to resist the frequency detuning during the high power operation of the formal cavity in future. The measured Q0 value is about 5100 which is much lower than the simulation value of 9000 with the conductivity of 2.0e7 S/m. It is mainly because the surface of the components has not been polished carefully. Because after local manual polishing of one girder, the measured Q0 value is enhanced slightly.

Frequency tuning ability of each plunger is slightly different which can be seen in Fig. 9. The most important is that the electric field distribution is effect by the plunger tuner severity. The perturbation method is used as usually in the low level RF measurement of the IH-DTL. By adjusting the 4 plunger tuner combined with each other, the resonance frequency reaches to 162.5MHz, and the on-axis electric field distribution, as shown in Fig. 10 matches with the beam dynamics design situation at the same time. Comparing the measured value and the simulation value of the integral voltage of each cell, the maximum error is less than 3%. In principle, above-mentioned error can be tuned smaller by more elaborate adjusting on the 4 plunger tuner. On the other hand, the field distributions corresponding to the different position (in 5mm step) of each plunger tuner are measured which will help the future beam commissioning.

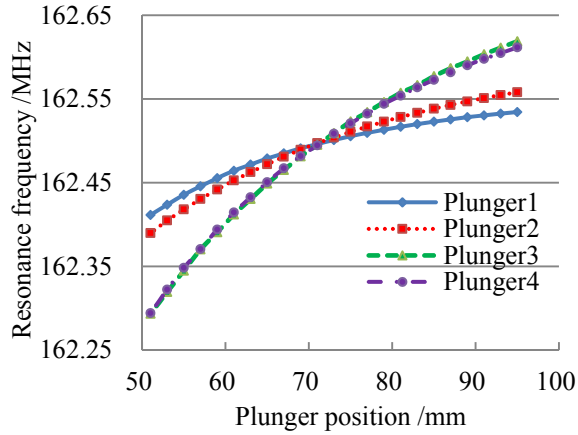


Figure 9: Frequency tuning ability of each plunger tuner vs. the distance between the plunger and the axis of the cavity.

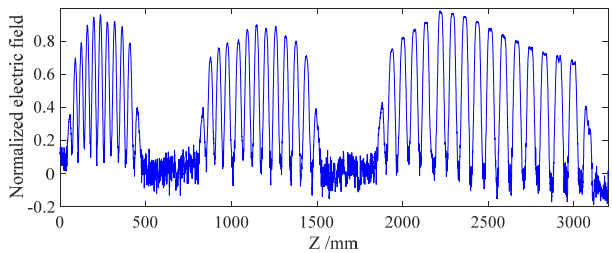


Figure 10: The measured on-axis electric field distribution.

CONCLUSION

RF structure design of the IH-DTL for the HIMM linac injector have been finished and proved to be effective to the beam dynamics design. The cold model of this IH-DTL is also constructed and tested. The LLRF measurement results can meet the design expectations. Power cavity and the internal quadrupole triplet of this IH-DTL are during the optimization process and will be completed in 2019.

ACKNOWLEDGMENTS

We are grateful to Y.R. Lu at PKU for his suggestions and would like to thank J. X. Wu and Z. Xu at IMP for their help.

REFERENCES

[1] J. C. Yang *et al.*, *Nucl. Instr. Meth.* A, 2014, 756: 19.

[2] B. Wang *et al.*, *Physics of Particles and Nuclei Letters*, 2012, 9 (3): 288.

[3] H. Du *et al.*, *Nuclear Physics Review*, 2018, 35(2): 140-146.

[4] Computer Simulation Technology (CST)-Micro Wave Studio (MWS), https://www.cst.com/

[5] Y. K. Batygin, *Nucl. Instr. Meth.* A, 2005, 539: 455.

Content from this work may be used under the terms of the CC BY 3.0 licence (© 2018). Any distribution of this work must maintain attribution to the author(s), title of the work, publisher, and DOI.

ISBN: 978-3-95450-194-6 ISSN: 2226-0366 doi:10.18429/JACoW-LINAC2018-TUPO005

INITIAL BEAM COMMISSIONING OF LEAF AT IMP*

Y. Yang†, Y. H. Zhai, L. T. Sun, L. Lu, H. Jia, W. P. Dou, X. Fang, L. Jing, Y. Wei, W. Ma, L. P. Sun, W. Lu, Y. H. Guo, X. J. Liu, H. W. Zhao, IMP/CAS, Lanzhou, China

Abstract

A Low Energy intense-highly-charged ion Accelerator Facility (LEAF), which mainly includes an ECR ion source, LEBT and an 81.25 MHz RFQ, was designed to produce and accelerate heavy ions, from helium to uranium with A/Q between 2 and 7, to the energy of 0.5 MeV/u. The typical beam intensity is designed up to 2 emA CW for the uranium beam. The facility has been successfully commissioned with He^+ (A/Q=4) and N^{2+} (A/Q=7) beams and accelerated the beams in the CW regime to the designed energy of 0.5 MeV/u. Beam properties and transmission efficiencies were measured, indicating a good consistency with simulated data. After having briefly recalled the project scope and parameters, this paper describes the beam commissioning strategy and detailed commissioning results.

INTRODUCTION

A Low Energy intense-highly-charged ion Accelerator Facility (LEAF) was launched at IMP in 2015 for researches of irradiation material, highly charged atomic physics, low energy nuclear astrophysics, *et. al*. Meanwhile, this facility can be a prototype of the frontend of HIAF project [1] which is a new national project proposed by IMP and officially approved for heavy ion related researches. LEAF is mainly composed of a superconducting ECR ion source, a LEBT line and a RFQ. The ion source, a so-called 4th generation ECR ion source with 45 GHz microwave hearting, FECR, is expected to be able to provide 2 emA U^{34+} beam. The RFQ, operating at 81.25 MHz, is a 4-vane structure cavity designed to accelerate various heavy ion beams from 14 keV/u to 0.5 MeV/u, in CW mode. The layout of LEAF is shown in Fig. 1. DC beam produced by the ECR ion sources is bunched and matched to the RFQ acceptance by an external Multi-Harmonic Buncher (MHB) located in the LEBT upstream of the RFQ. The MHB helps to produce a smaller longitudinal output emittance and reduce the length of the RFQ since the starting synchronous phase of the RFQ is set to -45 degree and therefore the RFQ should only accept the well-bunched central part of the distribution containing more than 80% of the particles. Table 1 shows the main RFQ parameters.

The RFQ was assembled in Dec. 2017 and the cavity RF conditioning finished in Feb. 2018. The conditioning in CW mode up to 75 kW (1.1 times the required maximum RF power) went smoothly, consuming only 44 hours. The whole complex installation was finished in May 2018, and the beam commissioning started soon after that. However, the 45 GHz superconducting ECR source and MHB are still under development. In the initial beam commissioning, we use a 14.5 GHz room-temperature ECR source as a proxy and DC beam injection into RFQ. The facility has been successfully commissioned with A/Q=4 ion He^+ and A/Q=7 ion N^{2+}. This paper will present the beam commissioning details and characteristics.

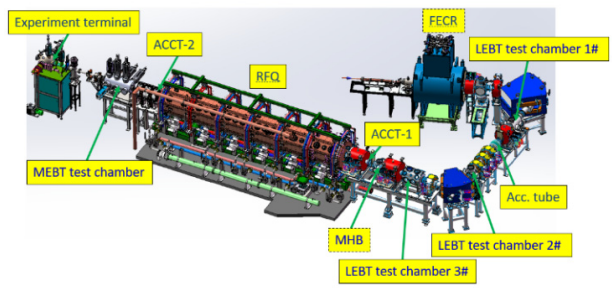


Figure 1: Layout of LEAF.

Table 1. Basic Design Specifications of LEAF-RFQ

Duty cycle	100%
Operating frequency	81.25 MHz
Resonant cavity	4-vane
Input particle energy	14 keV/u
Output particle energy	500 keV/u
Max. Vane voltage	70 kV (U^{34+})
CW RF power	67 kW (U^{34+})
Peak field at electrode surface	1.67 Kilpatrick units
Length of the RFQ vane	~596.4 cm

BEAM COMMISSIONING

Diagnostics

Diagnostic devices were installed in both LEBT and MEBT lines to validate the facility performances and measure the following beam characteristics:

- ✧ LEBT Test Chamber 1# (LTC 1#):
  - ➢ Intensity with Faraday cup (FC).
  - ➢ Transverse emittance with Allison scanners.
  - ➢ Beam transverse profile with fluorescent target.
- ✧ LEBT Test Chamber 2# (LTC 2#):
  - ➢ Intensity with Faraday cup.
  - ➢ Beam transverse profile with fluorescent target.
- ✧ LEBT Test Chamber 3# (LTC 3#):
  - ➢ Intensity with FC.
  - ➢ Transverse emittance with Allison scanners.
  - ➢ Beam transverse profile with fluorescent target.

* This work is supported by the National Nature Science Foundation of China (contract No. 11427904 and 11575265).

† yangyao@impcas.ac.cn.

Content from this work may be used under the terms of the CC BY 3.0 licence (© 2018). Any distribution of this work must maintain attribution to the author(s), title of the work, publisher, and DOI.

ISBN: 978-3-95450-194-6 ISSN: 2226-0366 doi:10.18429/JACoW-LINAC2018-TUPO005

- ✧ Beam intensity with ACCT-1 and ACCT-2 before and after RFQ respectively.
- ✧ MEBT Test Chamber (MTC):
  - ➢ Intensity with FC.
  - ➢ X and Y transverse emittance with slit+slit+FC.
  - ➢ Beam transverse profile with slit+FC.
  - ➢ Longitudinal profile with a Fast Faraday Cup (FFC) whose time resolution can be 80 ps due to bandwidth limitation (12.5 GHz).
  - ➢ Energy with a Time of Flight (TOF) monitor based on two Beam Position Monitors (BPM) with a distance of 1068.9 mm between them.
  - ➢ Energy spread with a scattered particle monitor (unavailable) [2].

Source Results

Since 45 GHz FECR is still under development a 14.5 GHz room-temperature permanent magnetic ECR ion source LAPECR1U was employed for the commissioning of LEAF. Up to 5 emA He^{+}, 1.5 emA He^{2+}, 1.7 emA N^{2+} and 0.16 emA N^{5+} have been extracted from the source. In the initial commissioning the slits at the end of charge selection were throttled to confine the beam emittance. Figure 2 shows the measured beam emittance in the LTC 1# for a 90 eμA He^{+} beam at energy of 20 keV/q. The rms emittances in both directions are 0.05 π.mm.mrad.

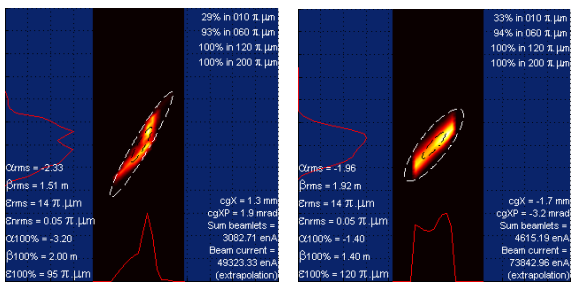
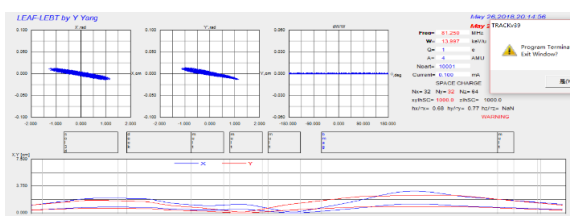


Figure 2: LEBT test chamber 1# emittance measurement for 90 eμA He^{+} beam, throttled slits.

Beam Transmission in LEBT Line

By having the beam parameters after charge selection, beam transmission simulation in the LEBT line was performed. Figure 3 gives the simulated result from LTC 1# to 3#. By adjusting the field gradients of the quadrupoles an approximately axisymmetric beam was obtained. We set the currents of the quadrupoles according to the simulation and measured the emittance in LTC 3#. The results are shown in Fig. 4. Beam current measurement indicates a 100% transmission in LEBT.


Figure 3: Beam transmission simulation in the LEBT line.

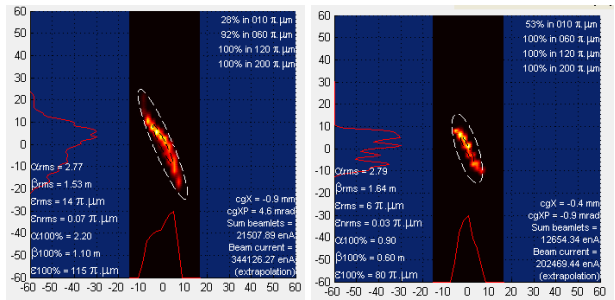


Figure 4: LTC 3# emittance measurement.

RFQ Commissioning and Beam Characteristics

Before entering the RFQ the beam was chopped by an electrostatic chopper that is installed in LTC 3#, so that the transmission efficiency of RFQ could be measured by two ACCTs situated on both sides of the RFQ. According to the current readings of ACCTs, as shown in Fig. 5, the measured transmission efficiency was ~98.5%. The accelerated particles could pass through the MEBT quadrupole triplet channel and be detected by the FC in MEBT test chamber while the non-accelerated ones would be lost in the focusing channel due to the widely different rigidity from the synchronous particles. The measured acceleration efficiency was ~46.5%. The low acceleration efficiency can be due to the factor that the MHB was not operational.

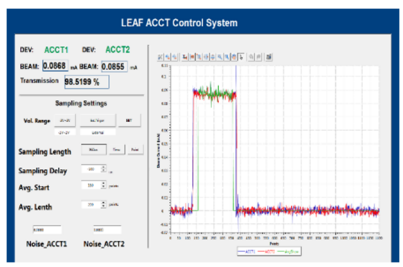


Figure 5: Current readings of two ACCTs.

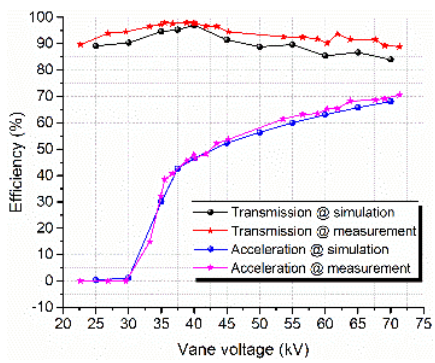


Figure 6: Measured and simulated RFQ transmission and acceleration efficiencies as a function of the vane voltage.

The RFQ transmission and acceleration efficiencies were measured as a function of the RFQ vane voltage (RF power). Figure 6 shows the measured results and the results simulated by TRACK for He^{+} beam. The figure demonstrates good agreement between the measurements and simulations. For the nominal voltage of 40 kV the transmission efficiency reaches maximum, while the

Content from this work may be used under the terms of the CC BY 3.0 licence (© 2018). Any distribution of this work must maintain attribution to the author(s), title of the work, publisher, and DOI.

ISBN: 978-3-95450-194-6 ISSN: 2226-0366 doi:10.18429/JACoW-LINAC2018-TUPO005

Content from this work may be used under the terms of the CC BY 3.0 licence (© 2018). Any distribution of this work must maintain attribution to the author(s), title of the work, publisher, and DOI.

acceleration efficency increases with the voltage. That's because the longitudinal acceptance of the RFQ is enlarged while increasing the vane voltage. However, the output longditudinal emittance is minimal with the designed voltage of 40 kV, as shown in Fig. 7.

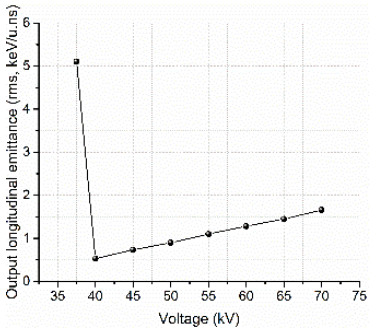


Figure 7: Simulated RFQ output longitudinal emittance as a function of the vane voltage.

The beam energy measured with TOF monitor was ~0.5 MeV/u. Figure 8 illustrates the signals detected by two BPMs. The bunch length was measured by the FFC. Figure 9 shows the measured (FFC signal) and simulated bunch length. The measured Full Width at Half Maximum (FWHM) was ~0.83 ns which is similar to the simulated number. Transverse emittances were measured based on slit+slit+FC in MEBT test chamber. Figure 10 demonstrates the measured and simulated particle distributions in the phase spaces. The measured rms emittances were 0.08 π.mm.mrad in horizontal and 0.078 π.mm.mrad in vertical, respectively. The simulated values were slightly smaller, with 0.074 π.mm.mrad in horizontal and 0.062 π.mm.mrad in vertical, since we used an idealized 4-D water-bag model in the simulation.

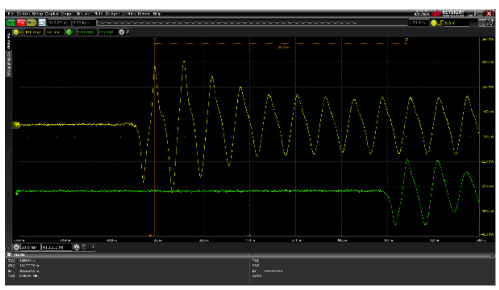


Figure 8: BPM signals (yellow: BMP-1, green: BPM-2).

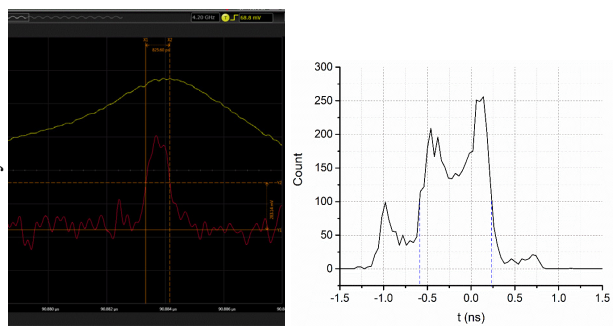


Figure 9: FFC signal (left, red line) and simulated (right) bunch length.

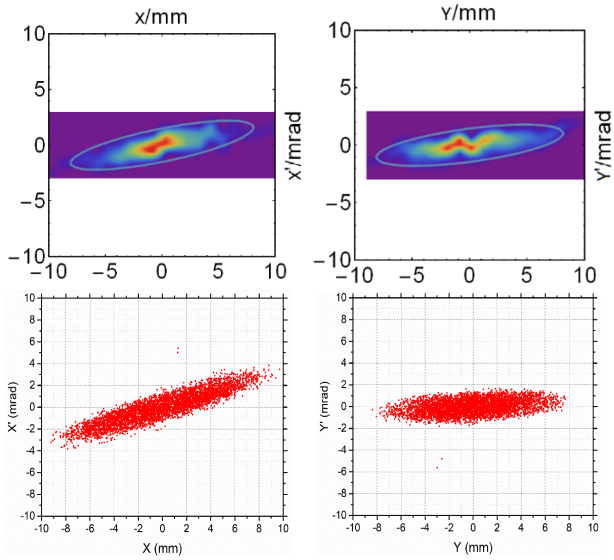


Figure 10: Measured (up) and simulated (down) beam emittance in MEBT test chamber after triplet focusing.

The RFQ transmission and acceleration efficiencies versus input beam energy were also measured and simulated. The results were plotted in Figure 11. Both measurements and simulations show the acceleration efficiency is maximal with input energy of 14.75 keV/u. The reason can be explained with the RFQ londitudinal acceptance as shown in Figure 12. More particles can be accepted by the RFQ for input energy of 14.75 keV/u than that for 14 keV/u.

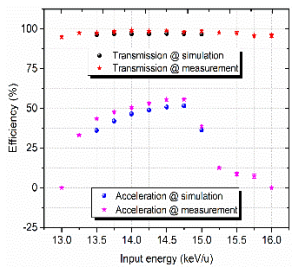


Figure 11: Measured and simulated RFQ transmission and acceleration efficiency versus the input beam energy.

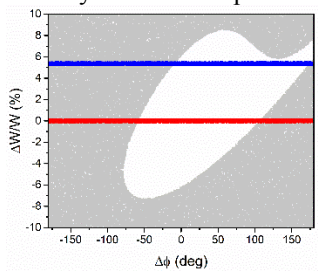


Figure 12: Simulated RFQ longitudinal acceptance and DC beam longitudinal distributions with input energy of 14 keV/u (red) and 14.75 keV/u (blue).

CONCLUSIONS

LEAF has been successfully commissioned with He^+ and N^{2+} beams. Key performance parameters demonstrated, satisfying the dynamics design. The facility has been operated at CW mode for more than one month, providing stable He^+ beam for the terminal experiments.

ISBN: 978-3-95450-194-6 ISSN: 2226-0366 doi:10.18429/JACoW-LINAC2018-TUPO005

REFERENCES

[1] J.C. Yang *et. al*, *Nucl. Instr. Meth. B*, vol. 317 (2013) 263-265.

[2] V. A. Verzilov *et. al*., in *Proc. DIPAC 2007*, Venice, Italy, paper WEPB07.

Content from this work may be used under the terms of the CC BY 3.0 licence (© 2018). Any distribution of this work must maintain attribution to the author(s), title of the work, publisher, and DOI.

ISBN: 978-3-95450-194-6 ISSN: 2226-0366 doi:10.18429/JACoW-LINAC2018-TUPO007

FRIB FAST MACHINE PROTECTION SYSTEM: CHOPPER MONITOR SYSTEM DESIGN *

ZhiYong Li†, D. Chabot, R. C. Webber, S.M. Lidia, S. Cogan,
Facility for Rare Isotope Beams, East Lansing, Michigan, USA

Abstract

The Facility for Rare Isotope Beams tunes the beam power from 0 to 400KW by chopping the beam current with a beam chopper in the Low Energy Beam Transport. A chopper monitoring system is employed to verify proper chopper operation to avoid delivery of undesired high-powered beam and to inhibit beam for machine protection purposes. The system monitors the incoming beam gate time structure, the chopper switch high voltage pulses, the chopper electrode charge/discharge currents, and the status of machine protection system. It is designed to switch off the beam within tens of nanoseconds of a detected fault. Challenges include a dynamic beam gate pulse structure with pulse lengths as short as 0.6 μs and high voltage power supply current pulses of ~25 ns. A high speed "integrate and hold circuit with reset", Field Programmable Gate Array based digital control circuit and high speed ADC circuit were developed to fulfil the required functions. Design approach, simulation, and test results with the beam are the focus of this paper.

INTRODUCTION

The average beam power in Facility for Rare Isotope Beams (FRIB) [1-3] is determined by the instantaneous beam current and the duty factor. When beam is requested, the duty factor is determined solely by the beam chopper in the Low Energy Beam Transport (LEBT). Therefore, chopper is actually a fast-acting, 0-400 kW control knob on the beam power. The FRIB chopper control devices, displayed in Fig. 1, include an Event Receiver (EVR) providing the beam gate signal, positive and negative high voltage (HV) power supplies providing 0-4kV and -4kV-0V respectively, and positive and negative HV switches to drive the chopper electrodes in the beam line. The chopper monitor system serves the ultimate purposes of preventing delivery of undesired high-powered beam and inhibiting beam for machine protection purposes [4]. The system is designed to receive the beam gate signal from the EVR, verify its acceptability for the current beam mode, drive the HV switch inputs, monitor the high voltage output pulses, monitor the chopper charge/discharge current, monitor the status of Fast machine Protection System (FPS) [4], and to inhibit the beam within tens of nanoseconds of a fault. The beam gate can exhibit a dynamic structure to ramp up beam power in a few seconds and the pulse lengths can range from 0.6 μs to nearly 10 ms. It is an engineering challenge to monitor every pulse of this ramp up process with a set of configurable parameters. The high voltage pulses exhibit rise and fall times ≤25 ns which poses difficulty for accurately measuring the charge and discharge currents. A Field Programmable Gate Array (FPGA) based digital control circuit, high speed "integrate and hold circuit with reset", and high speed ADC are employed to fulfil the required functions. Design approach, architecture, simulation, test results to meet these challenges are discussed in the following sections.

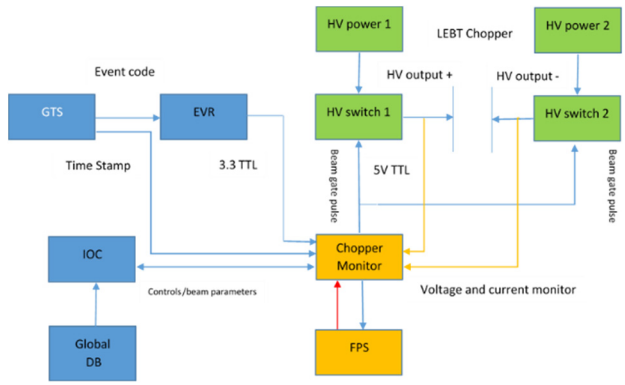


Figure 1: FRIB Chopper Control and Monitor System block diagram.

DESIGN

The chopper monitor system consists of chopper monitor chassis, Input Output Controller (IOC), and Operator Interface (OPI). The IOC/OPI serves to establish the chopper operational state, configure the chopper monitor for checking the beam pulse pattern for various beam modes, and provide the threshold values necessary for checking the amplitudes of each HV pulse and charge/discharge current. The chopper monitor system hardware consists of an FRIB General Purpose Digital Board (FGPDB) [4], the chopper monitor ADC board, and required power supplies. The chopper monitor ADC board interfaces to the MPS, the beam gate signal from the EVR, the control inputs to the HV switches, and the HV switch output voltage and current monitor signals (V_{mon} and I_{mon}). The I_{mon} signal is integrated by a high speed integrator circuit. A 14 bit, 125 Msps low power quad ADC, the LTC2175, is used to digitize the V_{mon} and integrated I_{mon} signals. The ADC board also contains a high speed DAC circuit to calibrate the ADC circuit and a circuit to monitor the board power. The FGPDB controls the DAC circuits, resets the integrator, initializes the ADC, and reads ADC outputs. The core of the FGPDB is a Spartan-6 XC6SLX150T-2FGG900C FPGA [4].

The FPGA firmware architecture includes a Micro-Blaze System to manage the circular buffers of ADC waveform data, EPICS communication and other management functions. It also includes a chopper monitor logic which consists of an embedded EVR, MPS-related logic, pulse

*Work supported the U.S. Dept. of Energy Office of Science under Cooperative Agreement DE-SC0000661.
†liz@fnib.msu.edu

Content from this work may be used under the terms of the CC BY 3.0 licence (© 2018). Any distribution of this work must maintain attribution to the author(s), title of the work, publisher, and DOI.

ISBN: 978-3-95450-194-6 ISSN: 2226-0366 doi:10.18429/JACoW-LINAC2018-TUPO007

checkers, ADC and DAC logic, and board power monitor logic.

PULSE CHECKER

The pulse checker verifies the beam gate pulse structure from EVR and the HV pulse applied to the chopper. FRIB beam modes require various beam gate time structures, where those of the beam power ramp up processes are the most dynamic and complicated. Each ramp up process consists of N_{RP} number of ramp up phases where pulse width or cycle time will be linearly ramped up to a target value at each phase through numbers of steps. Following parameters are used to define these steps: S_w, the step size to increase pulse width; N_{sw}, the total number of steps to increase pulse width; S_c, the step size to increase the pulse rate; N_{sc}, the total number of steps to increase the pulse rate; N_R, the numbers of repeated machine cycles at each step. Each machine cycle starts with a gap time of T_G (usually 50 µs) and repeats the machine cycle time T_{MC} (usually 10 ms). The pulse will be repeated with the numbers of N_p at each machine cycle and the pulse width T_w and the pulse period of T_c. The pulse checker is configurable with all the parameters described above to check various beam mode pulse structures. The pulse check is designed with a clock rate of 80.5MHz and time resolution of ~12.5 ns to check the pulse width and cycle time.

VOLTAGE AND CURRENT MONITOR

The voltage monitor circuit includes Vmon analog output from HV switch, attenuator, ADC and FPGA. A sample of Vmon is displayed in channel 4 of Fig. 2. Both the low and high of the Vmon will be measured and registered in FPGA. The current monitor circuit includes Imon analog output from HV switch, the 'integrate and hold circuit with reset', attenuator, ADC, and FPGA. The Imon signal of each HV switch is integrated for 25-50 ns during the electrode voltage transition time. The integrator output is held until it is readout by the ADC, and then reset before the next electrode voltage transition. The integrator must be fast enough to separately capture the current at both the rise and falling edge of a 0.6 µs pulse. Current monitor signals are displayed in Fig. 2 with a 3.5 kV pulse is applied to a capacitive load equivalent to real case. Channel 4 is the voltage monitor output from the positive HV switch showing 3.5 kV switched off for 600 ns and then back on. Channel 3 is the current monitor output from HV switch, showing the discharge current (with some ringing) when HV is removed from positive plate of chopper and then the charging current when HV is re-applied. Channel 2 is the integrator output, which represents the total charge applied to or removed from the chopper plate and associated cables. Channel 1 is the charge reset signal (active high) which resets the integrator capacitor. This capacitor is reset just before the charge and discharge current arrives to minimize signal offsets. The delay apparent between the reset signal and the integrator output resetting to zero is caused by switch-on time of the analog switch used in the reset circuit.

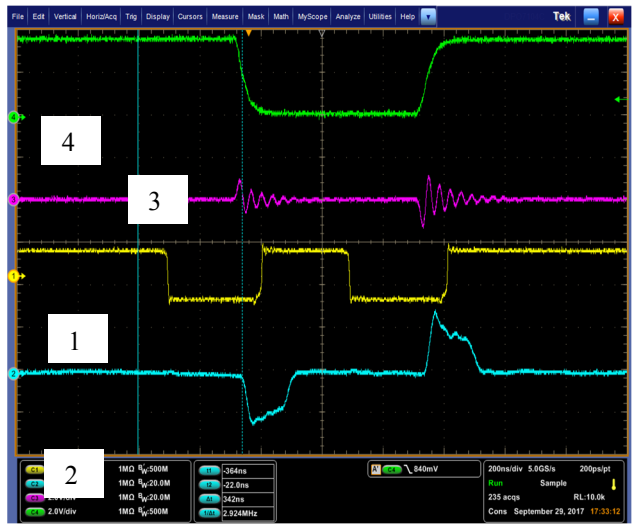


Figure 2: Signals of integrate and hold circuit. Channel 1 is the charge reset signal (active high), channel 2 is integrator output, channel 3 is the current monitor output from HC switch, and channel 4 is the voltage monitor output.

The sensitivity of the charging current measurement to faults in the HV electode and associated cabling is as follows. Let the load capacitance of the HV switch be C_{load}, which is the sum of C_{sw} (the HV switch internal capacitance), C_{cable} (the HV cable capacitance), and C_{chop} (the chopper electrode capacitance). Let V_H be the HV switch output voltage, Q_{chop} be the charge required to achieve V_H at the electode, R_{int} and C_{int} be the integrator parameters, V_{in} and V_{int} respectively be the integrator input and output voltages, and k be a constant.
The following equations apply:

$$Q_{chop} = V_H \times C_{load}$$

$$V_{int} = \int_0^T \frac{V_{in}}{R_{int}C_{int}}\,dt = \frac{kQ_{chop}}{R_{int}C_{int}}$$

$$C_{load} = C_{sw} + C_{cable} + C_{chop}$$

R_{int}=50 Ω, C_{int} =1nF, C_{sw} = 120 pF, C_{cable} = 129 pF.

This shows that V_{int} measured is proportional to Q_{chop}. Measured V_{int} versus V_H is shown in Fig. 3. Find V_{int} is 2530 when V_H is 3.5 kV with chopper electrode connected

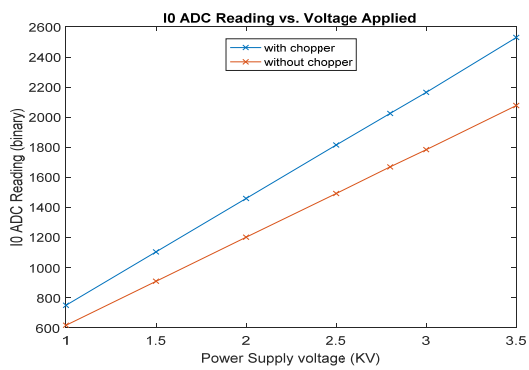


Figure 3: ADC reading of integrated charge/discharge current versus high voltage applied to the capacitor load of HV switch, with and without chopper (with C_{cable} and C_{sw} only).

Content from this work may be used under the terms of the CC BY 3.0 licence (© 2018). Any distribution of this work must maintain attribution to the author(s), title of the work, publisher, and DOI.

ISBN: 978-3-95450-194-6 ISSN: 2226-0366 doi:10.18429/JACoW-LINAC2018-TUPO007

Content from this work may be used under the terms of the CC BY 3.0 licence (© 2018). Any distribution of this work must maintain attribution to the author(s), title of the work, publisher, and DOI.

and 2080 with the same set up but chopper electrode disconnected. The above equations then give C_{chop} = 53.9 pF, which is very close to actual value of chopper capacitance. A disconnected electrode is thus easily detected.

$$I0_{ADC} = 710 * Vout + 39$$

TEST IN THE BEAM LINE

The chopper monitor chassis is installed in a rack directly beneath the chopper in the LEBT beam line. Starting from the bottom, the negative HV switch, positive HV switch, chopper monitor chassis and EVR chassis are mounted in the rack. The chopper monitor function of pulse checker, voltage and current monitoring and machine protection have been verified under conditions to limit total average beam power for FRIB beta=0.041 cryomodule commissioning. An example of a pulse check verification test is given below.

To validate the response to changes in pulse duration, beam events are configured for 100 µs duration pulses at 100 Hz. Chopper monitor is configured to check the same pulse width with error range of 1.2 µs. Beam is delivered and monitored at a Faraday Cup (FC) immediately downstream of the chopper. To validate the MPS response, a change to the pulse duration is requested that lies outside the allowed limits of 1.2 µs. Once 100 µs operation is established, a change to 120 µs pulse duration is requested without chopper monitor reconfiguration.

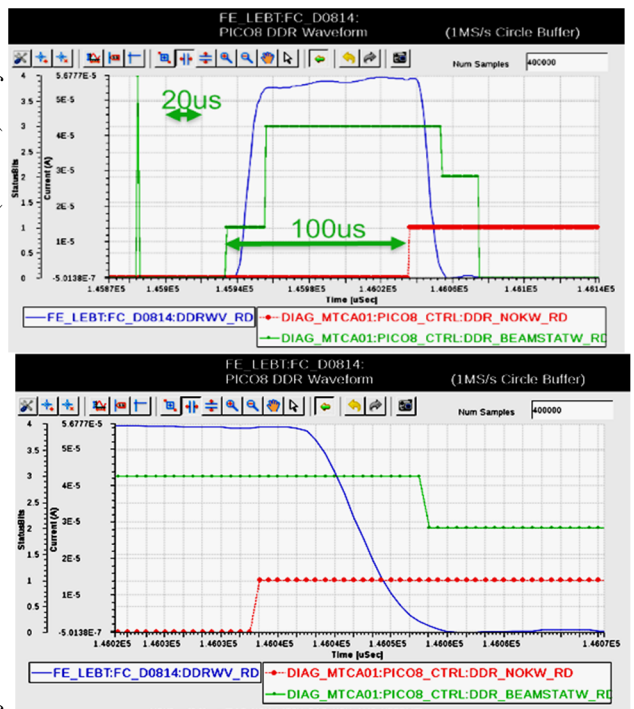


Figure 4: State transitions immediately following the request for 120 us pulse duration. Top display: the chopper monitor detects a beam-on condition (green) persisting longer than authorized, initiating the MPS NPERMIT response (red). Bottom display: expanded view of Faraday cup beam current signal.

Figure 4 displays the beam state transitions immediately following the 120 µs pulse duration request. It shows detection of beam-on condition persisting longer than authorized, initiation of the MPS NPERMIT response, and the resulting beam shutdown. The blue pulse is the beam current, the green line is the beam state detected at FC, where value 1 is beam start and 3 is beam on. The total pulse width applied is 120 µs. The red line is the MPS NPERMIT asserted high when a fault. When chopper monitor detects the pulse width exceeded 101.2 µs, it applies HV to chopper to cut off beam within tens of ns, meanwhile sends fault to MPS, MPS is tripped and sends NPERMIT high to FC, this period of time is about 3 µs. The blue pulse current in Fig. 4 cuts off 5 µs after NPERMIT high because of display delay of FC. The real beam actually is cut off before NPERMIT high. This test demonstrated that chopper monitor and MPS behave as expected [4].

CONCLUSION

The FRIB chopper monitor system is designed and deployed in the front end area of the high power heavy ion accelerator. The system checks every pulse width and cycle time, monitors the chopper high voltage pulses and the charge and discharge currents of the chopper electrodes, and forces a beam shutdown if any of these parameters are out of configured range. Chopper monitor functions have been tested for commissioning the FRIB beta=0.041 cryomodule and diagnostic beamline, and all results meet MPS requirements [4]. Implementation of the FPGA logic to check the dynamic beam power ramp-up processes will be the next level development for the chopper monitor.

REFERENCES

[1] J. Wei, *et al.*, "The FRIB Project – Accelerator Challenges and Progress", in *Proc. HIAT 2012*, Chicago, USA, June 18-21, 2012, paper MOB01, p. 8.

[2] R.York, *et al.*, "Technical Challenges in Design and Construction of FRIB", in *Proc. Particle Accelerator Conf. (PAC'11)*, New York, NY, USA, Mar.-Apr. 2011, paper FROBN2, p. 256.

[3] G. Kiupel, S. Assadi, *et al.*, "Fast and Critical Detection Devices Planned for the Machine Protection System at the Facility for Rare Isotope Beams in *Proc. 10th European Workshop on Beam Diagnostics and Instrumentation for Particle Accelerators (DIPAC'11)*, Hamburg, Germany, May 2011, paper TUPD96, p. 53

[4] ZhiYong Li, *et al.*, "FRIB fast machine protection system: engineering for distributed fault monitoring system and light speed response", in *Proc. 28th Linear Accelerator Conf. (LINAC'16)*, East Lansing, MI, USA, Sep. 2016, p. 956 doi:10.18429/JACoW-LINAC16-THPLR046.

ISBN: 978-3-95450-194-6 ISSN: 2226-0366 doi:10.18429/JACoW-LINAC2018-TUPO009

HEAT TREATMENT FOR A PROTOTYPE HALF-WAVE RESONATOR CAVITY*

Yoochul Jung† Junwoo Lee, Sangbeen Lee, Juwan Kim, Bonghyuk Choi,
Heetae Kim, Jongdae Joo, Youngkwon Kim, Hoechun Jung
RISP, IBS, Daejeon, South Korea

Abstract

Performance of a superconducting cavity, which is made of niobium, tends to be degraded easily depending on the surface resistance. Surface residual resistance of the cavity can be increased during the cavity fabrication process such as pressing, cutting and welding, because these multiple steps can lower the crystallinity of the cavity surface not only by disordering the lattice atoms but also by supplying lattice atoms with impurity atoms. Among the impurity atoms, hydrogen is a well-known impurity that lowers the cavity performance in the form of Q-disease. High temperature heat treatment was performed to remove impurity gas (mainly hydrogen) from the surface of a cavity, and to anneal the cavity to increase the crystllinity. Optical images of the heat treated niobium sample were investigated. Crystallinity was improved after the heat treatment by investigating X-ray diffraction (XRD), thus it confirmed that the annealing was successfully carried out. The residual gas analysis (RGA) was investigated and it confirmed that hydrogen was removed successfully during the heat treatment.

INTRODUCTION

For a LINAC, called "RAON" adopts four types of superconducting cavities: quarter-wave (81.25 MHz), half-wave (162.5 MHz), and two different single-spoke resonators. All the superconducting cavities operate with an alternating current of high frequency; thus, the surface resistance must be extremely low to maintain the superconductivity. Superconductivity will vanish easily if the temperature of any part in the cavity reaches a critical temperature (Nb_{T_c} is around 9.2K).

The temperature-dependent BCS resistance decreases as the temperature goes down but the residual resistance is independent of the temperature [1]. The residual resistance due to the imperfection of a raw superconducting material is almost fixed during the production. However, multiple steps for fabricating cavities can inevitably increase the residual resistance additionally by creating other sources such as a dislocation, a vacancy and a grain boundary. Therefore, the cavity fabrication must be carefully processed not to have additional surface resistance [2, 3].

One of the surface treatments to improve the surface resistance, the high temperature baking is well known for both annealing the cavity and removing hydrogen from the surface of the cavity. In case of annealing, it is for recovering the crystallinity of the cavity by moving disordered atoms to their original lattice points. In case of removing hydrogen, it is for outgassing impurity gas, which acts as a potential scattering center as a form of hydride at low temperatures.

From the earlier studies, hydrogen, which is easily introduced into the cavity surface during the chemical etching, is well known for deteriorating cavity performance in the form of Q-disease [4]. The residual gas analysis (RGA) and the X-ray analysis were performed after the heat treatment to check the baking effect. In this study, we report how the heat treatment process was carried out. Furthermore, we discuss the results along with the cavity performance in terms of the residual gas and X-ray analyses.

FURNACE SETUP & EXPERIMENTAL

Specifications of a vacuum furnace for the heat treatment are listed Table 1. Figure 1 shows the vacuum furnace.

Table 1: Specifications of Vacuum Furnace

Items	Specification	Unit
Dimension	1 × 1 × 3 (W×L× H)	Meter
Vacuum	10^{-6}@650°C, 10^{-8}@25°C	Torr
Temperature	Max. 1400°C,	Celsius
Heating element	Molybdenum	Mo



Figure 1: Vacuum furnace for heat treatment:cavity is loaded horizontally.

And Fig. 2 shows the horizontally loaded half-wave resonator cavity (HWR) with a titanium box in the furnace. HWR cavity is in contact with the titanium box through alumina (Al_2O_3) frame in order to avoid the chemical reaction between the cavity and the titanium box, as shown in Fig. 2. Two thermocouple wires are connected to titanium box, and two additional thermocouple wires are connected to cavity flanges, which are made of SUS316L.

* This work was supported by the Rare Isotope Science Project of Institute for Basic Science funded by the Ministry of Science, ICT and Future Planning (MSIP) and the National Research Foundation (NRF) of the Republic of Korea under Contract 2013M7A1A1075764
† sulsiin@ibs.re.kr

Content from this work may be used under the terms of the CC BY 3.0 licence (© 2018). Any distribution of this work must maintain attribution to the author(s), title of the work, publisher, and DOI.

ISBN: 978-3-95450-194-6 ISSN: 2226-0366 doi:10.18429/JACoW-LINAC2018-TUPO009

Content from this work may be used under the terms of the CC BY 3.0 licence (© 2018). Any distribution of this work must maintain attribution to the author(s), title of the work, publisher, and DOI.

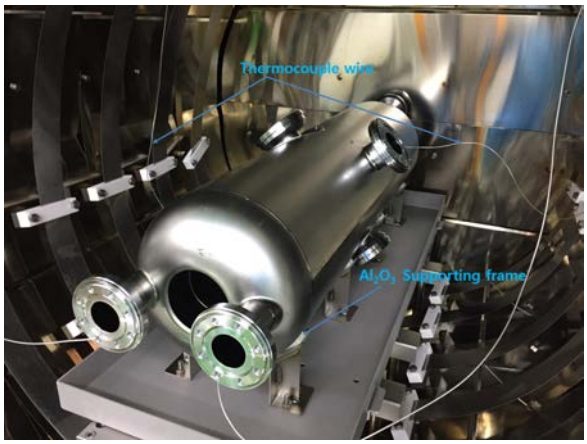


Figure 2: Loaded HWR cavity in the furnace: two thermocouples are connected to the cavtiy's flanges, two additional thermocouples are connected to titanium box, cavity is contact to the titanium box through alumina frame.

The titanium box is shown in Fig. 3, it is useful for removing hydrogen during the heat treatment since titanium has a relatively low vapor pressure compared to the niobium at a temperature of 650°C. The temperature for heating cavity is 650°C, and the ramping-up speed is 10°C per minute. Once the temperature reaches to 650°C, heating lasts for 10 h under the vacuum of about 10^{-6} Torr. The vacuum furnace is cooled naturally once the heat treatment is over. Two days are required for the cavity to cool down to 50°C naturally. For measuring the outgassed gases from the cavity, we monitored the partial pressures during the entire heat treatment by using a RGA analyzer (QME220, Pfeiffer Vacuum Co.). For investigating the effect of the heat treatment on the microstructure of the cavity, we prepared niobium samples having sizes of around 1×1 cm^2. All samples were cut from the beam port cup part by using the electrical discharge method (EDM). Samples were put on an alumina plate having the size of 10×10 cm^2 so as to avoid the chemical bond between the samples and the titanium carrier.



Figure 3: Titanium box: body, top, and bottom part.

Figure 4 shows the Nb samples in the furnace for XRD analysis. Optical images were taken after heat treatment by using an optical microscope (Xi-Cam, VesticVison Co.). The grain sizes of the samples were also measured by using an optical microscope. X-ray diffraction analysis was performed to investigate the effect of the heat treatment on the sample's crystallinity.

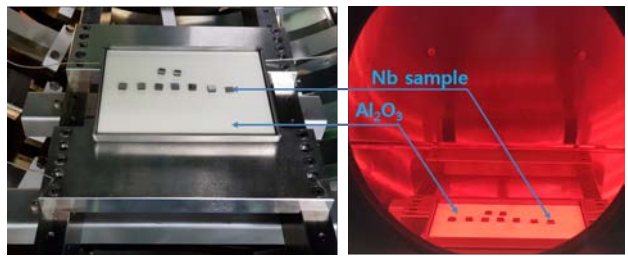


Figure 4: Niobium sample setup for XRD analysis: samples are mounted on the alumina plate (left), samples are heated in the furnace (right).

XRD AND RGA

Crystallinity means how much atoms are ordered in the microstructure, thus, the more the atoms are ordered, the more the crystallinity increased. High crytallinity also means that low resistance because carriers can travel long distance without colliding with scattering centers. Thermodynamically, heat energy lowers an activation energy of disordered atoms to return to their lattice points. However, at the same time, a grain growth must be suppressed. which means grains must not be grown to a great extent during the heat treatment. A mechanical strength strongly depends on the microstructure. The microstructure of fine grains have a high yield strength than that of the large grains. Therefore, annealing cavity must be carefully performed to satisfy two purposes simultaneously, one is to increase crystallinity (decrease residual resistance), the other is to suppress the grain growth of the cavity. It is known that hydrogens in the cavity can easily form hydrides on the cavity surface unless the cavity is cooled down quickly, these hydrides increase surface resistance only to deteriorate cavity performance. This is reported as Q-disease. Thus, removing hydrogen from the surface of niobium cavity must be performed in order to avoid the Q-disease phenomenon.

Niobium sample after the 10-h heat treatment was investigated by using an optical microscope, and the Fig. 5 shows the optical images. Also, XRD analysis is also shown in Fig. 6. The average grain sizes in Fig. 5 lie in the range of between 30 ~70 µm. Since the average grain size of the niobium was less than 50 µm from the certificate supplied by niobium company (ATI, USA), Thus, it was confirmed that the heat treatment was successfully carried out in terms of microstructure because grains did not grow to a great extent during the heat treatment.

The X-ray diffraction analysis was performed to confirm the effect of the heat treatment on the crystallinity of the niobium. The measured XRD patterns of the sample before

ISBN: 978-3-95450-194-6 ISSN: 2226-0366 doi:10.18429/JACoW-LINAC2018-TUPO009

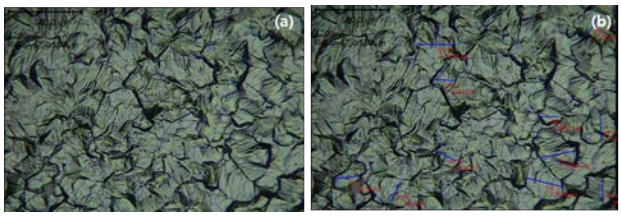


Figure 5: (a) Optical images of the surface of the heat treated sample and (b) grain sizes are drawn in the figure (a) with optical microscope's software. The optical resolution is X1200.

and after heat treatment are shown in Fig. 6. It shows that intensity counts from all 2θ angles were increased after heat treatment, which means that the degree of the crystallinity increased. Also, the FWHM decreased after heat treatment, which means the XRD peak was sharpened. In addition, the relative intensity of the 55° planes increased more than those of the other planes did.

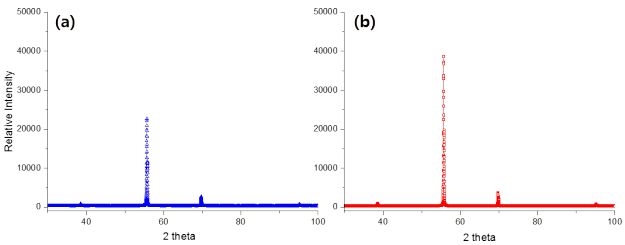


Figure 6: X-ray diffraction analysis: (a) XRD results with no heat treatment and (b) XRD results with a 650°C for 10 hours.

Partial pressures of a few typical gases in the furnace were monitored during the heat treatment by using a residual gas detector. Figure 7 shows the RGA results. Hydrogen showed the highest partial pressure peak about 10^{-4} Torr, consequently, the hydrogen determined the total pressure of the furnace. RGA result shows qualitatively that large amounts of hydrogen were outgassed during the heat treatment.

SUMMARY

Heat treatment of the prototype half-wave resonator cavity was carried out for 10 hrs at 650°C. Nb samples were prepared to investigate the effect of the heat treatment on the niobium material. XRD and RGA analyses confirmed that the heat treatment was successfully carried out in a way

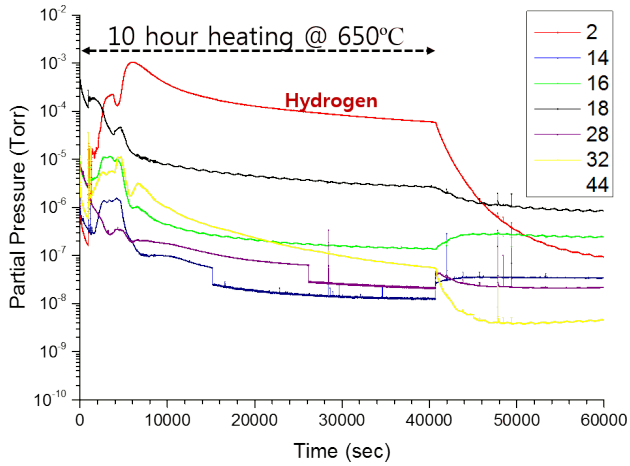


Figure 7: Residual gas analysis: partial pressures of the typical gases. A red graph shows the partial pressure of the outgassed hydrogen from the cavity.

that the cavity was well-annealed and hydrogen impurity was removed from the surface of the niobium cavity. The quality factor of the HWR cavity has been ready to tested in SRF test facility. The effect of the heat treatment on the dimension change of the cavity and the performance of the cavity will be reported.

ACKNOWLEDGMENTS

This work was supported by the Rare Isotope Science Project, which is funded by the Ministry of Science, ICT and Future Planning (MSIP) and the National Research Foundation (NRF) of the Republic of Korea, under Contract 2011-0032011.

REFERENCES

[1] C. Kittel, *Introduction to Solid State Physics*, New York, NY, USA: John Wiley & Son, Inc. 1996.

[2] A. Romanen, *et al*, "SRF Cavity Fabrication and Materials", AIP Conference Proceedings, vol. 671, 2011.

[3] Y. Jung *et al*, "Analysis of BCP Characteristics for SRF Cavities", in *Proc. IPAC'14*, Dresden, Germany, June 2014, doi:10.18429/JACoW-IPAC2014-WEPRI034

[4] B. Bonin and R.W Roeth, "Q Degradation of Niobium Cavities due to Hydrogen Contamination", in *Proc. SRF'91*, Hamburg, Germany, paper SRF91D01.

Content from this work may be used under the terms of the CC BY 3.0 licence (© 2018). Any distribution of this work must maintain attribution to the author(s), title of the work, publisher, and DOI.

ISBN: 978-3-95450-194-6 ISSN: 2226-0366 doi:10.18429/JACoW-LINAC2018-TUPO010

MUON ACCELERATION TEST WITH THE RFQ TOWARDS THE DEVELOPMENT OF THE MUON LINAC

R. Kitamura*, S. Li, University of Tokyo, Hongo, Tokyo, Japan
M. Otani, Y. Fukao, K. Futatsukawa, N. Kawamura, T. Mibe, Y. Miyake, T. Yamazaki, KEK, Tsukuba, Ibaraki, Japan
Y. Kondo, K. Hasegawa, T. Morishita, JAEA, Tokai, Naka, Ibaraki, Japan
S. Bae, B. Kim, S. Choi, SNU, Seoul, Korea
T. Iijima, Y. Sue, Nagoya Univ., Chikusa-ku, Nagoya, Japan
H. Iinuma, Y. Nakazawa, Ibaraki Univ., Mito, Ibaraki, Japan
K. Ishida, RIKEN, Wako, Saitama, Japan
G. Razuvaev, BINP SB RAS, Novosibirsk, Novosibirsk State Univ., Novosibirsk 630090 and Pulkovo Observatory, St. Petersburg, 196140, Russia
N. Saito, J-PARC center, Tokai, Naka, Ibaraki, Japan

Abstract

The muon linac is planned at the Japan Proton Accelerator Research Complex (J-PARC) for the precision measurement of the muon dipole moments. However, the muon acceleration with an radio-frequency (RF) accelerator was not carried out yet. Then, the first muon RF acceleration experiment using an radio-frequency quadrupole (RFQ) linac was carried out in the J-PARC. The incident positive muon was cooled using the production of the negative muonium ion (Mu^-) before the accelaration. Subsequently, the Mu^- was accelerated to 89 keV with the RFQ. Thanks to the pulsed muon beam in the J-PARC, the accelerated Mu^- was clearly identified with the Time-Of-Flight measurement after the momentum selection with the bending magnet. The measured event rate of the accelerated Mu^- was consistent with the expectation using the simulation and the result of the Mu^- production experiment as the preparatory experiment of the acceleration experiment. The first muon RF acceleration was successful.

INTRODUCTION

A muon anomalous magnetic moment $(g-2)_\mu$ is one of the quantities theoretically predicted with the high precision. The E821 experiment at the Brookhaven National Laboratory (BNL) measured $(g-2)_\mu$ with the precision of the 0.54 ppm and reported a discrepancy of more than three standard deviations between the experimental value and the prediction with the standard model (SM) of the particle physics [1]. Since the $(g-2)_\mu$ includes contributions from the physics beyond the SM via quantum loop effects, this discrepancy may imply the evidence of the new physics (NP). As one possibility, the non-zero small muon electric dipole moment (EDM) may contribute the discrepancy of the $(g-2)_\mu$ [2] [3]. Therefore, a more precise and independent measurement of the $(g-2)_\mu$ and the muon EDM than the BNL E821 has been desired to search the NP.

The new precision measurement of the $(g-2)_\mu$ and the muon EDM, the E34 experiment is proposed at the Japan Proton Accelerator Research Complex (J-PARC) using the low-emittance muon beam [4]. Final goals of the J-PARC E34 are 0.1 ppm for the $(g-2)_\mu$ and 10^{-21} e·cm for the muon EDM, respectively. One of the key components is the low-emittance muon beam produced using the low-energy muon source and the muon linac [5]. However, the muon acceleration with the radio-frequency (RF) accelerator was not carried out yet. Therefore, the demonstration of the muon RF acceleration should be carried out to develop the method of the measurement for the accelerated muon beam towards the construction of the muon linac. The first muon RF acceleration using an radio-frequency quadrupole (RFQ) linac was demonstrated at the J-PARC Material and Life science experimental Facility (MLF) [6] [7]. This paper reports the result of the first muon RF acceleration in the world.

PRODUCTION OF THE NEGATIVE MUONIUM ION

To accelerate muons using the RFQ, the muons should be cooled to match the input energy of 5.6 keV for the RFQ, because the kinetic energy of the high-intensity muon beam supplied at the J-PARC MLF is about 4 MeV. When the positive muon penetrates through a thin aluminum foil target (Al target), the negative muonium ion (Mu^-) is produced [8] [9]. The Mu^- is in the bound state of a positive muon and two electrons. Since the mean initial kinetic energy of the Mu^- is in vicinity of 0.2 keV, the Mu^- production can be used as the cooling method for the muon RF acceleration.

The Mu^- production was carried out to estimate the event rate of the accelerated Mu^- in the muon acceleration experiment. Figure 1 shows the experimental setup of the Mu^- production experiment as the preparatory experiment of the muon acceleration experiment [10].

Both of this Mu^- production experiment and the muon acceleration experiment were carried out at the Muon D-

* rkita@post.kek.jp

Content from this work may be used under the terms of the CC BY 3.0 licence (© 2018). Any distribution of this work must maintain attribution to the author(s), title of the work, publisher, and DOI.

ISBN: 978-3-95450-194-6 ISSN: 2226-0366 doi:10.18429/JACoW-LINAC2018-TUPO010

line in the J-PARC MLF [11] [12]. The proton beam power was about 150 in the Mu^- production experiment and about 300 kW in the muon acceleration experiment, respectively. The repetition rate and the pulse mode of the proton beam were 25 Hz and single-bunch mode, respectively, for both experiments.

Incident positive muons with 3 MeV energy were decelerated with a SUS foil window, a Kapton degrader and the Al target. Then, the Mu^- is produced at the Al target. The produced Mu^- was extracted with an electrostatic accelerator, which is referred to as a "Soa lens" [13] and transported to the detector through the diagnostic beam line.

The diagnostic beam line consists of the an electrostatic deflector, a bending magnet and several electric quadrupoles. Since the Mu^- beam includes the backgrounds such as incident positive muons, decay positrons and low-energy electrons produced by the field emission at the Soa lens, the backgrounds can be suppressed by kinetic-energy and momentum selections using the electrostatic deflector and the bending magnet.

The Mu^- was detected with a micro-channel plate (MCP) detector [14] located at the end of the diagnostic beam line. The time difference between the collision time of the incident muons at the Al target and the detection time at the MCP is defined as a Time-Of-Flight (TOF). Thanks to the pulsed muon beam supplied from the J-PARC, the measurement of the TOF can be used to identify the Mu^-. Figure 2 shows the measured TOF distribution using the MCP. The clear signal of the Mu^- was observed with the TOF measurement. Since the measured TOF was consistent with the expectation in the simulation, the Mu^- source for the muon acceleration experiment was developed.

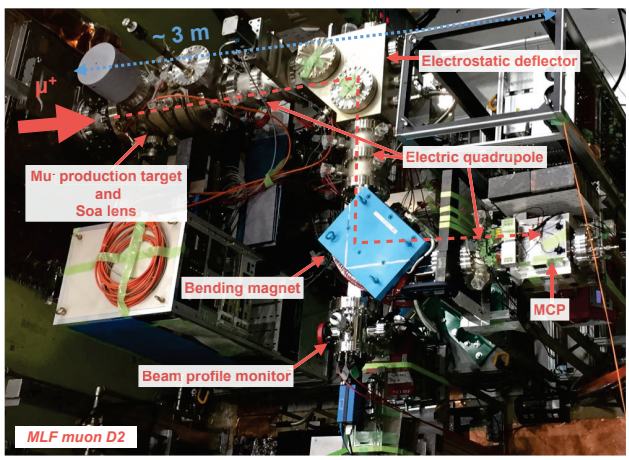


Figure 1: Experimental setup of the Mu^- production experiment.

MUON ACCELERATION EXPERIMENT

Using the developed Mu^- source, the muon acceleration experiment with the RFQ [15] was carried out [16]. Figure 3 shows the experimental setup of the muon acceleration

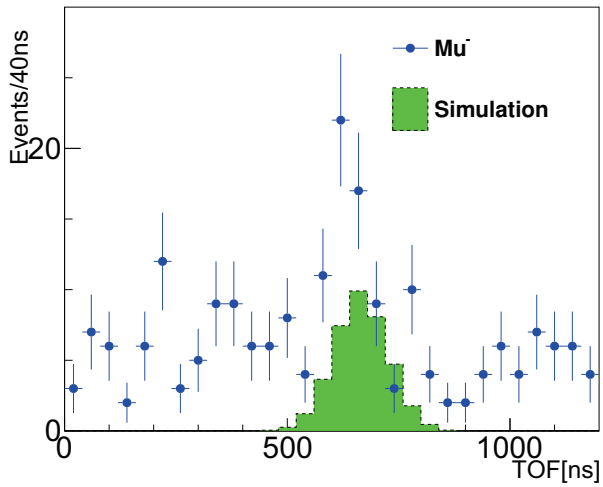


Figure 2: Measured TOF distribution in the Mu^- production experiment.

experiment. The produced Mu^- was extracted with the Soa lens and transported into the entrance of the RFQ. Then, the Mu^- was accelerated to 89 keV with the RFQ.

The accelerated Mu^- was transported to the MCP through the diagnostic beam line. This diagnostic beam line is composed of two magnetic quadrupoles (QM) and a bending magnet (BM). The accelerated Mu^- beam contains the backgrounds such as positive muons penetrating through the Al target and decay positrons from incident muons. Therefore, the accelerated Mu^- was identified with the TOF measurement as well as the momentum selection using the BM to suppress the backgrounds. The definition of the TOF is same as that in the Mu^- production experiment. The Soa lens and the diagnostic beam line were tested using a H^- beam before the acceleration experiment [17].

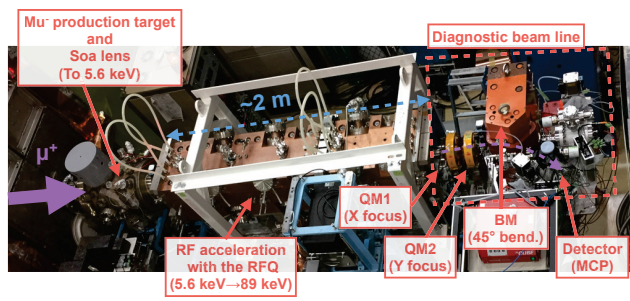


Figure 3: Experimental setup of the muon acceleration experiment.

SIMULATION

The beam transport in the muon acceleration experiment was simulated using some simulation software. The in-

Content from this work may be used under the terms of the CC BY 3.0 licence (© 2018). Any distribution of this work must maintain attribution to the author(s), title of the work, publisher, and DOI.

ISBN: 978-3-95450-194-6 ISSN: 2226-0366 doi:10.18429/JACoW-LINAC2018-TUPO010

Content from this work may be used under the terms of the CC BY 3.0 licence (© 2018). Any distribution of this work must maintain attribution to the author(s), title of the work, publisher, and DOI.

cident muon beam was simulated using G4beamline [18]. At the Mu^- production, the initial kinetic-energy distribution of the Mu^- was generated using the data of the deceleration for the low-energy proton [19]. The electrostatic acceleration with the Soa lens was simulated using musrSim [20]. The muon acceleration in the RFQ was simulated with PARMTEQM [21] and GPT [22]. Finally, the beam transport in the diagnostic beam line was simulated using TRACE3D [23] and PARMILA [24]. Figure 4 shows simulated phase space distributions of the accelerated Mu^- at the MCP. The accelerated Mu^- beam was transported into the effective area of the MCP as shown in Fig. 4. The expected TOF of the accelerated Mu^- in the muon acceleration experiment was evaluated using the simulation. The expected TOF's in the electrostatic acceleration, the RFQ and the diagnostic beam line are 289.3 ns, 460.6 ns and 63.2 ns, respectively. Therefore, the total TOF is 813.1 ns. The expected event rate was calculated from the transport efficiency estimated using the simulation and the result of the Mu^- production experiment. The expected event rate of the accelerated Mu^- is $(6.8 \pm 1.2) \times 10^{-4}$ /s.

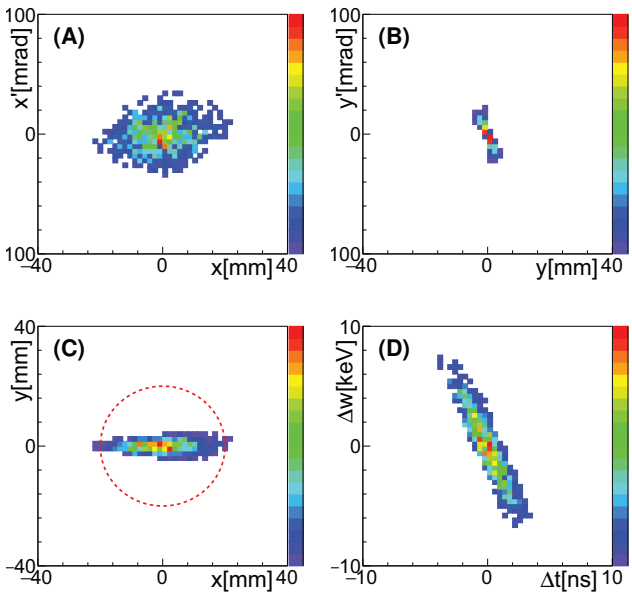


Figure 4: Simulated phase space distributions at the MCP. (A) the horizontal divergence angle x' vs the horizontal position x, (B) the vertical divergence angle y' vs vertical position y, (C) y vs x, and (D) the displacement from the mean kinetic energy ΔW vs the displacement from the mean kinetic energy Δw vs the displacement from the mean TOF Δt. Red dotted line shows the effective area of the MCP.

RESULT

The clear signal of the accelerated Mu^- was observed with the TOF measurement. Figure 5 shows the TOF distributions for the RF-on and RF-off data, and the simulation. When the RF power of the RFQ was tuned on, the signal peak of the accelerated Mu^- was observed. The measured TOF was 827.8±8.8 ns and corresponded to the expectation in the simulation. On the other hand, no significant signal was observed when the RF power was tuned off.

The measured event rate of the accelerated Mu^- was evaluated with the fitting in the TOF distribution and was $(5.1 \pm 0.8) \times 10^{-4}$ /s. Therefore, the measured event rate was consistent with the expectation. We concluded that the muon (Mu^-) was exactly accelerated with the RFQ.

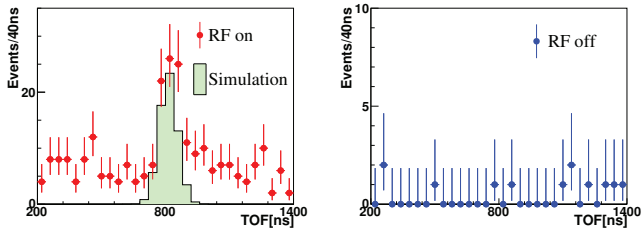


Figure 5: Measured TOF distributions between the RF-on and RF-off data, and simulation in the muon acceleration experiment. The numbers of triggers for RF-on and RF-off data are 4×10^6 and 4×10^5, respectively.

SUMMARY

The J-PARC E34 experiment aims to measure the $(g-2)_\mu$ and the muon EDM precisely using the low-emittance muon beam. Although the muon linac is one of the key components to obtained the low-emittance muon beam, the muon RF acceleration was not demonstrated yet.

The Mu^- source for the muon cooling before the acceleration was developed to demonstrate the muon RF acceleration using the RFQ. Then, using the developed Mu^- source, the muon acceleration experiment was carried out. Thanks to the TOF measurement and the momentum selection, the clear signal of the accelerated Mu^- was observed. This result is the first muon RF acceleration in the world and the important milestone to construct the muon linac.

ACKNOWLEDGEMENT

We would like to deeply thank the RIKEN Advanced Meson Science Laboratory and the KEKB group for their significant supports. This work is supported by JSPS KAKENHI Grant Numbers JP25800164, JP15H03666, JP16H03987, JP15H05742, JP16J07784 and JP18H03707. This work is also supported by the Korean National Research Foundation grants NRF-2015H1A2A1030275, NRF- 2015K2A2A4000092, and NRF-2017R1A2B3007018; the Russian Foundation for Basic Research grant RFBR 17- 52-50064; and the Russian Science Foundation grant RNF 17-12-01036. The muon experiment at the Materials and Life Science Experimental Facility of the J-PARC was performed under user programs (Proposal No. 2017A0263).

REFERENCES

[1] G.W. Bennett *et al.*, Phys. Rev. D **73**, 072003 (2006).

ISBN: 978-3-95450-194-6 ISSN: 2226-0366 doi:10.18429/JACoW-LINAC2018-TUPO010

[2] G.W. Bennett *et al.*, Phys. Rev. D **80**, 052008 (2009).

[3] B. L. Roberts, J. Phys. Soc. Jpn. **76**, 111009 (2007).

[4] T. Mibe *et al.* edit., J-PARC E34 Conceptual Design Report, Technical Design Report (2011).

[5] Y. Kondo *et al.*, "Re-acceleration of ultra cold muons in J-PARC muon facility", Proc. of IPAC'18, Vancouver, Canada, FRXGBF1, pp. 5041–5046 (2018).

[6] S.Bae *et al.*, Phys. Rev. Accel. Beams, **21** 050101 (2018).

[7] R. Kitamura, Ph.D. thesis, Univ. of Tokyo (2018).

[8] Y. Kuang *et al.*, Phys. Rev., A **35**, 3172 (1987).

[9] Y. Kuang, Ph.D. thesis, College of William and Mary (1989).

[10] R. Kitamura *et al.*, in Proc. of IPAC'17, Copenhagen, Denmark, pp. 2311–2313, (2017).

[11] P. Strasser *et al.*, J. Phys.: Conf. Ser. **225** 012050 (2010).

[12] W. Higemoto *et al.*, "Materials and Life Science Experimental Facility at the Japan Proton Accelerator Research Complex IV: The Muon Facility", Quantum Beam Sci. **2017**, 1, 11.

[13] K. F. Canter, P. H. Lippel, W. S. Crane, and A. P. Mills Jr., "Positron studies of solids, surfaces and atoms" (World Scientific, Singapore, 1986) p.199.

[14] MCP assembly F9892-21/-22 data sheet, TMCP1037E01, HAMAMATSU Photonics Co (2009).

[15] Y. Kondo, K. Hasegawa, and A. Ueno, in Proc. of LINAC'06, Knoxville, Tennessee, pp. 749–751 (2006).

[16] R. Kitamura *et al.*, "Result of the first muon acceleration with radio frequency quadrupole", in Proc. IPAC'18, Vancouver, Canada, TUPAL076, pp. 1190–1193 (2018).

[17] Y. Nakazawa *et al.*, "Commissioning of the diagnostic beam line for the muon RF acceleration with H- ion beam derived from the ultraviolet light", in Proc. IPAC'18, Vancouver, Canada, TUPAK016, pp. 997–1000 (2018).

[18] G4beamline, http://public.muonsinc.com/Projects/G4beamline.aspx

[19] M. Gonin, R. Kallenbach and P. Bochsler, Rev. Sci. Instrum. **65** 648(1994).

[20] musrSim, https://www.psi.ch/lmu/geant4-simulations

[21] K. R. Crandall *et al.*, "RFQ design codes", LA-UR-96-1836 (1996).

[22] General Particle Tracer, Pulsar Physics, http://www.pulsar.nl/gpt/

[23] K. R. Crandall and D. P. Rusthoi, "Trace 3-D Documentation", LA-UR-97-886 (1997).

[24] H. Takeda, "*Parmila*", LA-UR-98-4478 (1998).

Content from this work may be used under the terms of the CC BY 3.0 licence (© 2018). Any distribution of this work must maintain attribution to the author(s), title of the work, publisher, and DOI.

ISBN: 978-3-95450-194-6 ISSN: 2226-0366 doi:10.18429/JACoW-LINAC2018-TUPO011

UPGRADE OF HEAVY ION INJECTOR I-3 AT ITEP

N. N. Alexeev, P. N. Alekseev, V. A. Andreev, T. V. Kulevoy, A. D. Milyachenko, V. I. Nikolaev, Yu. A. Satov, A. V. Shumshurov, A. B. Zarubin
ITEP, B. Cheremushkinskaya 25, 117218 Moscow, Russia

Abstract

Heavy ion injector I-3 represents two-gap 2.5 MHz resonator with accelerating voltage 2x2 MV. It's used with laser ion source (LIS) for acceleration of ions in wide range of charge to mass ratio. As a result of modernization, injector structure will be supplemented by the second two-gap resonator, RF voltage will be increased to 3x4 MV and accelerated beam structure has to be improved by increasing accelerating frequency to 5 MHz. Design features of upgraded linac I-3M and peculiarity of beam dynamics for different types of ions are presented.

INTRODUCTION

Linac I-3 with laser ion source LIS100, constructed on the base of 100 J CO_2 laser, had been used many years as the ion injector for booster synchrotron UK of proton-ion accelerator-accumulator facility ITEP-TWAC [1, 2]. Generated at the output of injector I-3 ion, such as C^{4+}, Al^{11+}, Si^{10+}, Fe^{16+}, Cu^{17+}, Ag^{19+} etc., with energy of 4Z MeV had been accelerated in UK ring up to the energy of several hundred MeV per nucleon with intensity limited by high charge density of 2 MHz bunch structure of injected beam. Upgraded structure of I-3M is optimized for acceleration of heavy ions with A/Z in the range from 3 to 10. For acceleration of protons and light ions, injectors I-2 [3, 4] and I-4 [5] are used. The energy of accelerated in I-3M ions increased by factor of three at some improvement of beam density uniformity will allow to raise the intensity of accelerated in booster ring beam by more than an order of magnitude.

Increasing of accelerating voltage in I-3M is achieved by optimizing the configuration of accelerating electrodes, which will reduce the maximum electric field strength on the surfaces of electrodes that will allow to raise by half the amplitude of operating voltage on the accelerating gaps to 3 MV. The structure of two two-gap phased resonators allows having an accelerated voltage close to maximum of up to 12 MV for ions with variable charge-to-mass ratio.

OPTIMIZATION OF ACCELERATING ELECTRODES CONFIGURATION

Maximum amplitude of voltage 2 MV on the accelerating gaps in existing construction of resonator is limited by electric field strength on the localized areas of the electrode surfaces. Maximum electric field strength on the surface of electrodes as the function of relevant parameters shown in Figure 1 allows optimizing the shape of electrodes providing to reduce electric field strength on the surface of electrodes at a given voltage value at the accelerating gap. The optimum shape of the electrodes, providing extreme voltage value on the accelerating gap, is characterized by a minimum radius of surface curvature of 60 mm at the electrode diameter value of 600 mm.

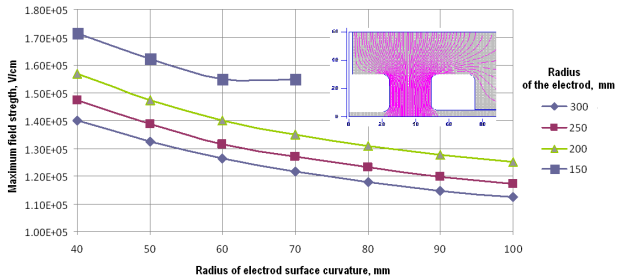


Figure 1: Maximum electric field strength on the surface of electrodes as the function of relevant parameters.

ACCELERATING STRUCTURE

Layout of the injector I-3M accelerating structure is shown in Figure 2, comparison parameters of both I-3 and I-3M injectors are given in Table 1. The length of drift tubes 0.5 m and 1.4 m in resonators is optimized for acceleration of heavy ions with A/Z=6.

The initial beam is formed at the output of the 50 kV gap that breaks the laser plasma generated in the target chamber of LIS100. In the matching channel of I-3M, the beam is focused by three electrostatic lenses and bunched at the input of the first accelerating resonator using the 10x2 kV, 5 MHz, two-gap buncher. Additional transverse focusing of the bunched beam of high charge density is provided in the first accelerating gap by optimized configuration of axially symmetric nonlinear RF field.

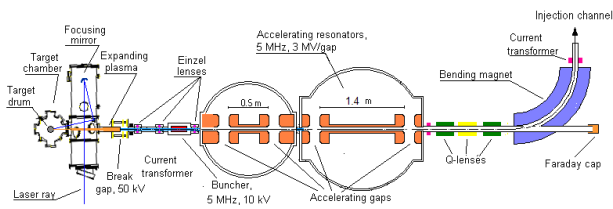


Figure 2: Acceleration structure of I-3M.

Table 1: Comparison Parameters of I-3 and I-3M

Injector	I-3	I-3M
Accelerating frequency, MHz	2.5	5.0
Number of resonators	1	2
Accelerating gaps	2	4
Accelerating voltage, MV	4	12
Bunching voltage, kV	10x2	
Accelerating ions. A/Z	2÷5	3÷10
Injection energy, kV	50	
Trans. acceptance, π mm mrad	>1000	
Momentum spread, Δp/p, %	up to ±2.5	
Transmission factor, %	~50	

Content from this work may be used under the terms of the CC BY 3.0 licence (© 2018). Any distribution of this work must maintain attribution to the author(s), title of the work, publisher, and DOI.

ISBN: 978-3-95450-194-6 ISSN: 2226-0366 doi:10.18429/JACoW-LINAC2018-TUPO011

MODEL OF THE FIRST RESONATOR

The resonator is a circuit with concentrated in the solenoid inductance and capacity distributed inside of the resonator volume. The 3D model of the first resonator with drift tube length of 0.5 m is shown in Figure 3. Main modes of resonant frequency are given in Table 2. The resonant frequency tuner (Figure 4), which is moved inside the solenoid in the displacement range up to 100 mm, allows to adjust the resonant frequency according to the frequency signal of the second resonator within 100 kHz.

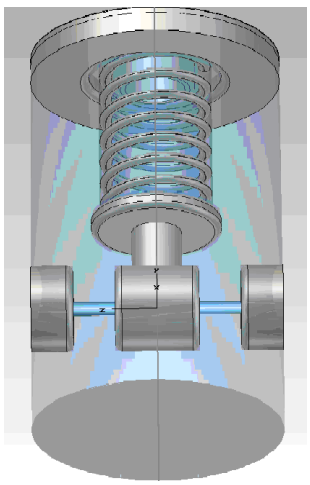


Figure 3: The 3D model of the first resonator.

Table 2: Resonant Mode of the First Resonator

Mode	1	2	3
Frequency, MHz	4.940	19.471	30.364

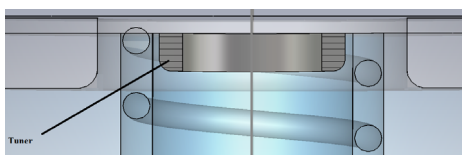


Figure 4: Frequency adjuster tuner core.

The calculated quality factor of the resonator is estimated by the value of Q=5500.

Distribution of power dissipated in the resonator at the maximum amplitude of the accelerating voltage of 3 MV per gap is given in Table 3. The largest amount of dissipated power (78.5%) is concentrated in the water-cooled spiral.

Table 3: RF Power Losses in the First Resonator

Component	Loss/W(peak)	Loss/%
Enclosure	336	2.83
Spiral	9328	78.5
Top	631	5.31
Drift tube	7	0.08
Spiralbott	623	5.24
Solid7	11	0.1
Spiraltopcyl	943	7.94
Sum	11879	100%

MODEL OF THE SECOND RESONATOR

The existing construction of the I-3 resonator is used in I-3M as the second resonator in which the spiral and the accelerating structure are modified. The 3D model of the second resonator with drift tube length of 1.4 m is shown in Figure 5. Main modes of resonant frequency for this resonator are given in Table 4. The second resonator operates in the autogenerator mode. The calculated quality factor of the second resonator is estimated by the value of Q=5520, distribution of power dissipated in the resonator by the components of its construction at the maximum amplitude of the accelerating voltage of 3 MV per gap is similar to that shown in Table 3 for the first resonator.

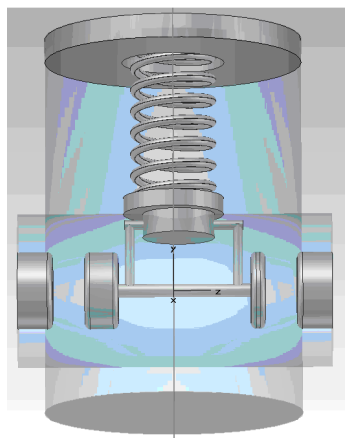


Figure 5: The 3D model of the second resonator.

Table 4: Resonant Mode of the Second Resonator

Mode	1	2	3
Frequency, MHz	4.971	20.974	32.250

BEAM DYNAMICS IN THE ACCELERATING STRUCTURE OF I-3M

Transmission of the beam in the accelerating structure of I-3M is determined by both: limited range of RF phase providing particle acceleration in the first acceleration gap, and Coulomb forces of particles repulsion in the high density beam bunch at the input of the first accelerating gap. Accelerating structure of I-3M has been optimized for acceleration of beam in the range of A/Z from 3 to 10 with current of several tens of mA at transmission of ~50%. The maximum total transmission of the beam with input current of 50 mA at A/Z=6 is estimated as ~58%, herewith the energy spread of accelerated beam is ±5%. The decrease in the energy spread of the beam up to ±2% reduces the transmission of the beam to~53%.

Longitudinal acceptance of I-3M for particles with variable value of A/Z is shown in Figure 6. The diagrams in the same figure show dependences of transmission factors for the beam with input current of ~50 mA on the amplitude of bunching voltage. It can be seen that optimum bunching voltage is sufficiently high and creates a large energy spread of the beam which reaches ±40%.

Content from this work may be used under the terms of the CC BY 3.0 licence (© 2018). Any distribution of this work must maintain attribution to the author(s), title of the work, publisher, and DOI.

ISBN: 978-3-95450-194-6 ISSN: 2226-0366 doi:10.18429/JACoW-LINAC2018-TUPO011

Content from this work may be used under the terms of the CC BY 3.0 licence (© 2018). Any distribution of this work must maintain attribution to the author(s), title of the work, publisher, and DOI.

The nonlinear field in the buncher can significantly increase the transverse emittance of the beam.

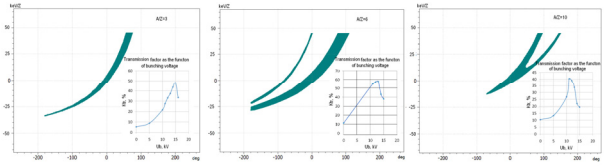


Figure 6: Longitudinal acceptance of I-3M for particles with A/Z=3, 6, 10.

Transverse acceptance of the I-3M accelerating structure at low beam current and optimal phases of accelerated voltage in both resonators is so great as ~8000 π mm mrad. Coulomb forces in bunched beam cardinally increases the transverse emittance of the beam and actually make the effective acceptance of the channel highly dependent on the beam current.

The envelope of the beam in the accelerating structure is limited by the effective aperture of beam line ∅90 mm, as shown in Figure 7. The maximum transmission of the beam is achieved by its sharp focusing at low energy on the input of the first accelerating gap, the optimal focusing properties of which are formed by the position of the grid in the inside of the resonator input electrode.

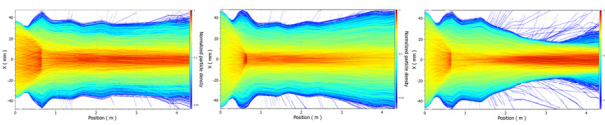


Figure 7: Envelope of 50 mA beam for A/Z=3, 6, 10.

Phase portraits of the accelerated beam at A/Z=6 and the input beam current 50 mA is shown in Figure 8. The energy spread of particles ±2% fits into the beam transverse emittance of 140 π mm mrad. The bunch length of accelerated beam is estimated by the value of 15^0 or 8 ns, duty factor of pulses is more than 20, herewith the amplitude of bunch current reaches 5÷6 A.

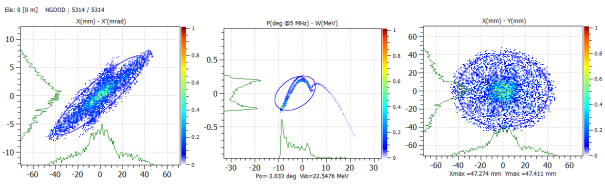


Figure 8: Phase portraits and cross-section of accelerated beam at A/Z=6 and beam current 50 mA.

If the input beam current increases to 100 mA, Coulomb forces don't allow to form an optimal beam configuration at the input to the first accelerating gap, that leads to decrease in transmission to ~40% and increase in emittance of accelerated beam to ~180 π mm mrad. Emittance of the beam can be reduced by factor of 1.5 at a slight decrease in beam transmission (2÷3%) by adjusting the phase difference between the bunching and accelerating voltage. The radical reduction of the accelerated beam emittance can be achieved by eliminating the transverse nonlinearity of the field in the accelerating gaps of the buncher.

CONCLUSION

The upgraded injector I-3M with the laser ion source LIS100 allows to extend a set of ions accelerated in synchrotron up to uranium. Table 5 shows the parameters of some types of heavy ions generated in LIS100 with different A/Z ratio and ionization potential up to ~1 kV after acceleration in I-3M. As can be seen from the table, the effective accelerating voltage of the I-3M structure is reduced at the edges of A/Z operating range by ~10%. The intensity of the accelerated beam given in the Table 5 corresponds to the findings of the ion source LIS100 taking into account the beam transmission factor in I-3M.

Table 5: Parameters of Heavy Ions at the Output of I-3M

A/Z	10(U^{24+})	9(U^{28+})	8(Au^{25+})	7(Ta^{26+})	6(Ag^{19+})	5(Ag^{22+})	4(Fe^{16+})	3(Ni^{18+})
U_{ion}, eV	600	836	763	789	512	974	506	624
m/Z, MeV	9315	8392	7452	6520	5589	4657	3726	2794
Δφ, rad	1.1	1.3	1.9	2.3	2.8	3.2	3.5	3.8
p/Z, MeV/c	440	426	411	390	357	323	283	240
V/Z, MV	10.4	10.8	11.3	11.6	11.4	11.2	10.7	10.3
E, MeV/u	1.0	1.2	1.4	1.6	1.9	2.2	2.6	3.4
β	0.046	0.051	0.055	0.059	0.064	0.069	0.075	0.085
N, p/p	1.3x10^{10}	1.1x10^{10}	1.2x10^{10}	1.2x10^{10}	1.6x10^{10}	1.4x10^{10}	1.9x10^{10}	1.7x10^{10}

Upgraded heavy ion injector I-3M is included in the project of Multipurpose Hadrons Facility (MHF) proposed at ITEP [6]. The key objectives of the MHF mission are the following: effective using and further development of accelerator technologies mastered in ITEP [7]; maintenance, improvement and expanding of the ITEP accelerator facility infrastructure as the basis of scientific and technological developments; fundamental and applied research with proton and ion beams at energy to 10 GeV for protons and to 5 GeV/u for ions; fundamental and applied research, technological development and industrial application with proton and ion beams at energy to 1 GeV/u; technological research and development in the field of generation, acceleration, accumulation, cooling, compression, extraction and sharp focusing of high intensity hadrons beams; expansion of scientific and educational activity in the areas of nuclear technologies. In particular, MHF will allow performing full-scale tests of radiation resistance of modern electronic components intended for use in the space environment. Beams of upgraded linac I-3M will be used also to expand research in the field of materials science and technology in the application to nuclear power and semiconductor industries.

REFERENCES

[1] N.Alexeev *et al.*, Let. of JETP, vol.77-3, p.149.
[2] N.Alexeev, *et al.*, in *Proc. RuPAC'12*, pp.112-116.
[3] I.M.Kapchinsky *et al.*, Preprint IHEP, pp. 67-38, 1967.
[4] V.I.Bobylev, *et al.*, in *Proc LINAC'72,* pp. 275-278.
[5] V. Andreev, *et al.*, in *Proc. IPAC'10*, pp. 801-803.
[6] N.Alexeev *et al.*, in *Proc. RuPAC'16*, pp. 73-77.
[7] N.Alexeev *et al.*, in *Proc. RuPAC'14*, pp. 34-38.

ISBN: 978-3-95450-194-6 ISSN: 2226-0366 doi:10.18429/JACoW-LINAC2018-TUPO012

COMPACT MULTIPURPOSE FACILITY - BELA

T. Kulevoy[1,2,§], R. Fatkullin[2], A. Kozlov, G. Kropachev, D. Seleznev, A. Semennikov, A. Sitnikov
NRC Kurchatov institute - ITEP, 117218, Moscow, Russia
[1]also at NRC Kurchatov institute , 123182, Moscow, Russia
[2]also at NRNU MEPhI, 115409, Moscow, Russia

Abstract

In ITEP the project of multidiscipline facility Based on ECR ion source and Linear Accelerator (BELA) is started. The injector part of facility is based on combinations of ECR ion source and dc H^+ and He^+ source will provide the multi beams irradiation of the reactor materials for modeling experiments. The cw RFQ and following DTL will enable the set of experimental activity both for fundamental physics and for practical applications.

INTRODUCTION

After long time the mega science project NICA (Nucotron-based ion Collider fAcility) based on the modern accelerator technologies is under development in Russia [1]. In framework of this project national research center "Kurchatov institute" – Institute for Theoretical and Experimental Physics (ITEP) developed the new RFQ for polarized ion program which is inder operation for more than two years [2]. Several other mega-science projects are under discussion in Russia. In Dubna that is the DERICA project (Dubna Electron-Radioactive Ion Collider fAcility). DERICA is proposed as the next step rare isotope beam facility. From the accelerator point of view DERICA will include the driver LINAC-100 (energy up to 100 MeV/u) with the operating mode close to CW, the fragment separator, the re-accelerator LINAC-30 (energy up to 30 MeV/u), the fast ramping ring (energy <300 AMeV), the collector ring and the electron storage ring with an injector. DERICA general concept and first results of LINAC-100 and LINAC-30 general layout is presented in [3]. Another project which is under discussion now is a Spallation Source for neutron generation. The need for a next-generation neutron source is evidenced by the analysis of a specially established ESFRI Physical Sciences and Engineering Strategy Working Group [4]. Several neutron generator is either under operation (IPNS [5], Los Alamos Neutron Science Center [6], ISIS [7], SNS [8] and JPARC [9]) or under construction (ESS [10]).

The NEPTUN project where the high intensity linac and the target from neptunium are used for neutron beam generation is under discussion as a Russian Spallation Source [11].

The main trend of the ion linac are the development of (i) cw RFQ and DTL up to 3-10 MeV/n, (ii) different types of superconducting RF cavities (SCRF) and solid state RF amplifiers (SSA).

§kulevoy@itep.ru

Development of cw RFQ and DTL enables the construction of compact devices both for physical researches and industrial application. Today several projects based on compact linacs are under development. First of all it is the IFMIF-EVEDA neutron generator for fission reactor material investigation. The facility is under commissioning in Rokkasho (Japan) [12]. As well it can be mentioned SARAF in Israel [13] , FRANZ [14] in Germany, MUNES in Italy [15] and others.

The project of multidiscipline facility **B**ased on **E**CR ion source and **L**inear **A**ccelerator (BELA) is under development in ITEP. Taking into account the current research activity the facility will provide the experiments for fission and fusion reactor materials investigation, β-nuclear magnetic resonance and semiconductor device modification by ion beams. The technologies developed in framework of this project will be used for serial production of compact facilities based on cw linac for PET, as well as compact neutron generators for BNCT and activation analysis. The further development of the project will lead to construction of Spallation Source and RIB complexes in Russia.

GENERAL LAY-OUT

The general layout of the BELA project is shown in Fig. 1. It consists of injector complex (pos. 1 and 2), proton RFQ, several bunchers and 3-gap DTLs. Such structure enables the material science with ion beams from hydrogen to uranium at injector complex and the semiconductor irradiation by proton beams with variable energy. After the output energy of linac reach the 3 Mev level the neutron generation from lithium target will be started for BNCT and neutron experiments.

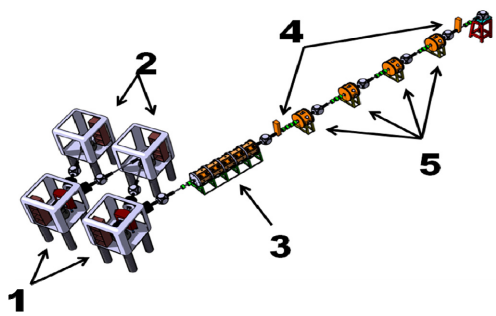


Figure 1: General layout of BELA.

INJECTORS COMPLEX

Injector complex includes several high voltage platforms (HVP) and beam lines connecting them. At HVPs two ECR ion sources are located (pos 1, Fig. 1) and targets (pos. 2, Fig. 1). Ion sources are located at the HVP

Content from this work may be used under the terms of the CC BY 3.0 licence (© 2018). Any distribution of this work must maintain attribution to the author(s), title of the work, publisher, and DOI.

ISBN: 978-3-95450-194-6 ISSN: 2226-0366 doi:10.18429/JACoW-LINAC2018-TUPO012

Content from this work may be used under the terms of the CC BY 3.0 licence (© 2018). Any distribution of this work must maintain attribution to the author(s), title of the work, publisher, and DOI.

with positive potential meanwhile targets are located at HVP with negative one. For simulation experiments of material radiation resistance, the heavy ion ECR as well as a proton one are used. Now the imitation experiments are carried out at heavy ion RFQ HIPr-1 [16]. HIPr-1 operates in pulse mode that limits the beam intensity by the irradiated sample temperature instability. To generate the required dpa (displacement per atom) the dc iron Fe^{10+} ion beam generated by ECR will be used with intensity at least 10 eμA and energy up to3-4 MeV. According to estimation it would be possible to provide 100 dpa for three days operation. Simultaneously either the hydrogen or helium ions will be implanted in the sample of the investigation from another ion source located at the second HVP. The ECRs developed in JINR are planned to be used for heavy ion beam generation both for heavy and light ion generation [17]. To minimize the price of the development, the compact ECR will be used at the beginning till the RFQ is manufactures [18] (see Fig. 2). The compact ECR can provide the proton and helium beam with intensity up to 300 μA.

The target used for the experiment has the heating system providing the irradiated sample temperature stability better than 0.2°C in range from room temperature till 700°C during the experiment.

The second target HVP is used for semiconductor implantation experiments.

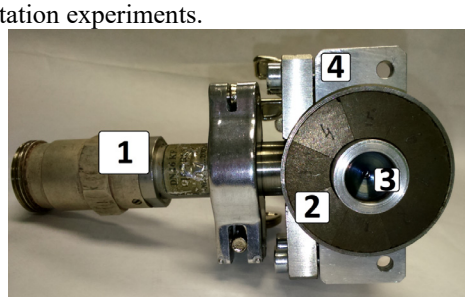


Figure 2: Compact ECR ion source for hydrogen and helium ion beams generation. 1 – RF power input, 2 – ECR magnet, 3 – ion source puller, 4 – support.

RFQ

As an RFQ structure we will use the «shifted coupling window» structure for over than twenty ears [19]. The main advantages of the structure are a high coupling between the RFQ quadrants and the fact that the quadruple mode of fields has the lowest frequency. It provides the high stability of the structure during the operation. That structure was used for single in the world superconducting RFQ in LNL-INFN [20] as well as for RIB RFQ in ANL [21]. The 3D view of the RFQ structure is shown in Fig. 3. The output energy for proton beam at the output of RFQ is 3 MeV. Such energy provides the experiments with neutron beam generation immediately after RFQ start. However the variant with 1.5 MeV RFQ is under discussion now as well. It is the lowest energy required for experiments with semiconductor diods and triods. Providing the radiation damages in the p-n junction it is possible to improve the RF parameters of the semiconductors.

To provide 6D beam matching with RFQ the input buncher is used. As it was shown in [22] the buncher can provide the minimal beam emittance growth along the RFQ as well as the 100% beam transport throughout the RFQ channel with accelerating up to 99% of beam.

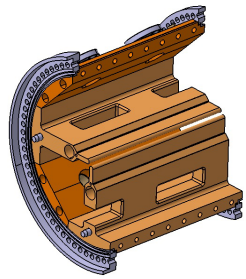


Figure 3: 3D layout for one section of the structure with shifted coupling windows.

DTL

Since the facility have to provide the wide range of proton beam energy the set of short DTL sections with focusing quadruples are used. It enables the beam energy variation at the output of the linac. Some of the section can be switched off so the beam will drift throughout them when the proper magnetic field distribution is set along the linac. Several cavity types were investigated to find the best one for BELA linac. The normal conducting QWR and HWR take too high level of power. The five gap CH and IH resonators have too long focusing period. It results the large diameter of drift tube aperture. As a compromise the three gap IH cavity was chosen (see Fig. 4)

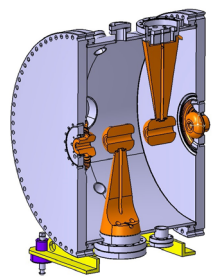


Figure 4: IH three gap resonator for BELA linac.

The preliminary design of linac is shown in Figure 5. The linac parameters are given in Table 1.

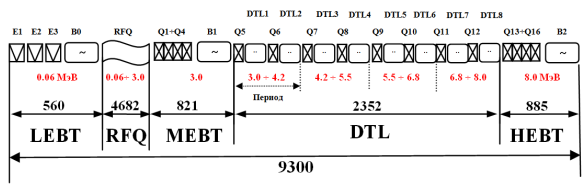


Figure 5: Layout of BELA linac.

ISBN: 978-3-95450-194-6 ISSN: 2226-0366 doi:10.18429/JACoW-LINAC2018-TUPO012

Table 1: Main Parameters for Linac, H^+ Beam of 10 mA

	RFQ	DTL
Frequency, MHz	148.5	
Energy, MeV	0.06÷3	3÷8.0
Beam emittance, π mm mrad	1	
Acceptance, π mm mrad	10	
Max field, Kp	1.6	1.6
Average radius, mm	9	15
Length, mm	4682	2440
Number of sections	1	8
Length of cavity, mm	4682	200
Gap length, mm		40
Phase, ºC	-90÷-35	-30
Max focusing gradient, T/m		27
Accelerating rate, MeV/m	0.7	2.1

TIME SCHEDULE

The project has two milestones. At the end of first one with length of 5 year the injector complex as well as RFQ will be under operation. At the end of second stage with length of 2 - 3 years the normal conducting linac with energy up to 8 - 10 MeV will be manufactured, assembled and put under operation. As the following upgrade the superconducting RF cavities will be developed to increase the accelerated ion beam energy. ITEP participates in the common activity for SC RF cavity development in collaboration with JINR, NRNU MEPhI and several Institutes and University from Belorussia [23].

CONCLUSION

In ITEP the project of multidiscipline facility Based on ECR ion source and Linear Accelerator (BELA) is under development. The technologies developed in framework of this project will be used for serial production of compact facilities based on cw linac for PET, as well as compact neutron generators for BNCT and activation analysis. The further development of the project will lead to construction of Spallation Source and RIB complexes in Russia

REFERENCES

[1] G. Trubnikov *et al.*, "The NICA project at JINR", in *Proc. Int. Particle Accelerator Conf. IPAC2016*, Busan, Korea, May 2016, pp. 2061-2065. doi:10.18429/JACoW-IPAC2016- WEZA02

[2] V. Aleksandrov *et al.*, "Commissioning of New Proton and Light Ion Injector for Nuclotron-Nica": In *Proc. Int. Particle Accelerator Conf. IPAC2016*, Busan, Korea, May 2016, pp. 941-943. doi:10.18429/JACoW-IPAC2016-MOPOY041

[3] L.V. Grigorenko *et al.*, "Design of LINAC-100 and LINAC-30 for new rare isotope facility project DERICA at JINR", in *Proc. Advanced Beam Dynamics Workshop on High-Intensity and High-Brightness Hadron Beams HB2018*, Daejeon, Korea, to be published.

[4] ESFRI Report, "Neutron scattering facilities in Europe, Present status and future perspectives", ESFRI SCRIPTA Vol.1 Published by Dipartimento di Fisica - Universita degli Studi di Milano, September 2016.

[5] IPSN: www.aai.anl.gov/history/project_pages/ipns.html

[6] LANSCE: http://lansce.lanl.gov/

[7] ISIS: http://www.isis.stfc.ac.uk/

[8] SNS: http://neutrons.ornl.gov/sns

[9] JPARC: http://j-parc.jp/index-e.html

[10] ESS: http://europeanspallationsource.se/

[11] V.L. Aksenov, V.D. Ananiev, G.G. Komyshev, A.D. Rogov, and E.P.Shabalin, "On the limit of neutron fluxes in the fission-based pulsed neutron sources", *Phys. Particles and Nuclei Letter*, v. 14, N 5, 2017, pp. 788-797.

[12] E. Fagotti *et al.*, "Beam commissioning of the IFMIF EVEDA very high power RFQ", in *Proc. Int. Particle Accelerator Conf. IPAC2018*, Vancouver, Canada, Apr.-May 2018, pp.2902-2907. doi:10.18429/JACoW-IPAC2018-THXGBF2

[13] N. Pichoff *et al.*, "The SARAF-LINAC project 2018 status", in *Proc. Int. Particle Accelerator Conf. IPAC2018*, Vancouver, BC, Canada, Apr.-May 2018, pp.994-996. doi:10.18429/JACoW-IPAC2018-TUPAK015

[14] C. Wiesner *et al.*, "FRANZ and small-scale accelarator-driven neutron sources", in *Proc. Int. Particle Accelerator Conf. IPAC2015*, Richmond, VA, USA, May 2015, pp.1276-1280. doi:10.18429/JACoW-IPAC2015-TUXB1

[15] A. Pisent, E. Fagotti, and P. Colautti, "MUNES a compact neutron source for BNCT and radioactive wastes characterization", in *Proc. Linear Accelerator Conf. LINAC2014*, Geneva, Switzerland, Aug.-Sep.2014, pp.261-263. doi:10.18429/JACoW-LINAC2014-MOPP088

[16] S.V. Rogozhkin *et al.*, "Effect of irradiation by heavy ions on the nanostructure of perspective materials for nuclear power plants", *The Physics of Metals and Metallography*, Vol. 113, No. 2, 2012, pp. 200–211.

[17] S. Bogomolov *et al.*, "Recent development in ECR ion sources at FLNR JINR", in *Proc. Russian Particle Accelerator Conf. RUPAC2012*, St-Petersburg, Russia, Sep. 2012, pp.203-207, doi:10.18429/JACoW-RUPAC2012-FRYOR01

[18] R. Fatkullin, S. Bogomolov, K. Kuzmenkov, and A. Efremov,"Compact 2.45 GHz ECR Ion Source for generation of singly-charged ions", *EPJ Web of Conferences* 177, 2018, 08003.

[19] V.A Andreev and G. Parisi, "90º-apart-stem RFQ Structure for Wide Range of Frequencies", in *Proc. Particle Acc. Conf.*, Washington DC, May 1993, pp.3124-3126,

[20] A. Pisent *et al.*, "Beam commissioning of the superconducting RFQS of the new LNL injector PIAVE", in *Proc. Particle Acc. Conf. PAC2005*, Knoxville, Tennessee, May 2005, pp.2696-2698.

[21] P.N. Ostroumov *et al.*, "Development and beam test of a continuous wave radio-frequency quadrupole accelerator", *Phys. Rev.* ST–AB 15, Nov. 2012, 110101.

[22] A.I. Balabin and G.N. Kropachev, "6D-High Current Beam Matching at RFQ Entrance", in *Proceedings European Particle Accelerator Conf. EPAC1994*, London, England, Jun.-Jul. 1994, pp.1180-1182.

[23] A.V. Butenko *et al.*, "Status of R&D on new superconducting injector linac for Nuclotron-NICA", in *Proc. Advanced Beam Dynamics Workshop on High-Intensity and High- Brightness Hadron Beams HB2018*, Daejeon, Korea, to be published.

Content from this work may be used under the terms of the CC BY 3.0 licence (© 2018). Any distribution of this work must maintain attribution to the author(s), title of the work, publisher, and DOI.

ISBN: 978-3-95450-194-6 ISSN: 2226-0366 doi:10.18429/JACoW-LINAC2018-TUPO013

COMMISSIONING STATUS OF THE LIGHT DEVELOPMENT MACHINE

G. De Michele†, J. Adam, D. Aguilera Murciano, A. Benot-Morell, R. Bonomi, M. Breitenfeldt, F. Cabaleiro Magallanes, M. Caldara, S. Candolfi, G. Castorina, M. Cerv, G. D'Auria[1], A. Degiovanni, V. A. Dimov, M. Esposito, S. Fanella, D. Fazio, D. A. Fink, Y. Fusco, S. Gibson, M. Gonzalez, P. Gradassi, Y. Ivanisenko, A. Jeff, V. Khan, L. Kobzeva, G. Levy, S. Magnoni, G. Magrin, A. Marraffa, A. Milla, R. Moser, P. Nadig, L. Navarro Quirante, G. Nuessle, A. Patino-Revuelta, H. Pavetits, P. Paz Neira, T. Rutter, F. Salveter, A. Samochkine, A. Sanchez Gonzalez, D. Guillen Soriano, P. Stabile, K. Stachyra, M. Torreira Gallas, A. Valloni, L. Wallet, C. Zannini
ADAM, Meyrin, Switzerland,
[1]also at Elettra-Sincrotrone Trieste S.C.p.A., Trieste, Italy

Abstract

ADAM (Application of Detectors and Accelerators to Medicine) is a CERN spin-off company currently working on the construction and testing of the LIGHT (Linac for Image-Guided Hadron Therapy) machine. LIGHT is an innovative high-frequency linac based proton therapy system designed to accelerate protons up to 230 MeV: it consists of three different linac sections i.e. a 750 MHz Radio Frequency Quadrupole (RFQ) accelerating the beam up to 5 MeV; a 3 GHz Side Coupled Drift Tube Linac (SCDTL) up to 37.5 MeV; and a 3 GHz Coupled Cavity Linac (CCL) section up to 230 MeV. The compact and modular design is based on cutting edge technologies developed for particle colliders and adapted to the needs of hadron therapy beams. The LIGHT development machine is currently being built at CERN and this paper describes its design aspects and its different stages of installation and commissioning.

INTRODUCTION

The LIGHT solution is a unique technology based on years of research at ADAM. There are several advantages of such machine w.r.t. accelerators currently used in proton therapy such as cyclotrons and synchrotrons: among others the fast beam energy change, a smaller beam emittance, reduced losses allowing for less shielding, and modularity that allows an easy installation and fit in already built infrastructures.

This paper is a continuation of the previous report [1].

THE LIGHT DEVELOPMENT MACHINE

The LIGHT development machine is being built and commissioned by ADAM at CERN. It consists of a proton injector assembly (PIA), a high frequency RFQ [2], a four modules SCDTL structure and a four modules CCL structure, designed to deliver a proton beam at 70 MeV. The latter proton energy will suffice to prove the LIGHT technology and that all sub-components (PIA, RFQ, SCDTL, CCL) will work as an embedded system.

General Layout

The details of the lattice of the LIGHT development machine to reach up to 7.5 MeV protons are described in [1]. Figure 1 shows the current status of the installation with all four SCDTL modules on beam line. Another substantial difference w.r.t. the previous commissioning stage [1] is the introduction of the new movable diagnostic test-bench, described in [3], that replaces the spectrometer dipole with a combination of Time-of-Flight (ToF) and multi-layer Faraday cup measurements.

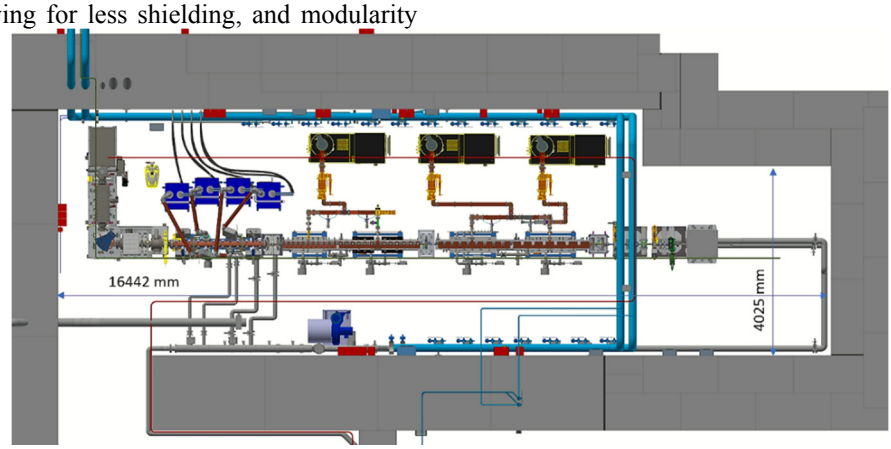


Figure 1: Top view of the current LIGHT development machine. From left to right: the L-shape PIA, the RFQ, four SCDTL modules and the medium energy diagnostic test bench without spectrometer.

† giovanni.demichele@avo-adam.com

Content from this work may be used under the terms of the CC BY 3.0 licence (© 2018). Any distribution of this work must maintain attribution to the author(s), title of the work, publisher, and DOI.

ISBN: 978-3-95450-194-6 ISSN: 2226-0366 doi:10.18429/JACoW-LINAC2018-TUPO013

On the left of Fig. 1, the L-shape PIA delivers 40 keV protons that are injected into the RFQ powered by four Inductive Output Tubes (IOTs). The 5 MeV protons are then injected into the SCDTL modules powered by klystrons in order to get an acceleration up to 37.5 MeV. Table 1 and Table 2 show the main parameters of the RFQ and SCDTL structures.

Table 1: RFQ Parameters

Number of modules	4
Length [m]	1.96
Minimum aperture radius [mm]	1
Input/output energy [MeV]	0.040 / 5
RF power [MW]	0.350
RF frequency [GHz]	0.750

Table 2 : SCDTL Parameters

SCDTL modules	M1	M2	M3	M4
Number of tanks	11	13	9	7
Bore hole [mm]	4	4	4	5
Length [m]	1.12	1.70	1.52	1.60
Output energy [MeV]	7.5	16.0	26.5	37.5
RF power [MW]	0.83	2.59	2.46	2.48
RF frequency [GHz]	3	3	3	3

The Medium Energy Test Bench

As described in [3], increasing beam energy requires to change the beam diagnostic test benches configuration. Up to 16 MeV the medium energy test bench, without spectrometer, was used; among other devices it includes Time-of-Flight system, Beam Position Monitors (BPM), an emittance meter based on the double slit plus Faraday Cup method and a spectrometer sector so to measure energy and energy spread of the beam (Fig. 2). In the present commissioning phase of 26-37 MeV the test bench has been made more compact and it is equipped with an instrumented beam dump, capable to verify the beam energy, and a novel beam profiler for high energies. This test bench can be seen at the right-hand side of Fig. 1 and Fig. 3.

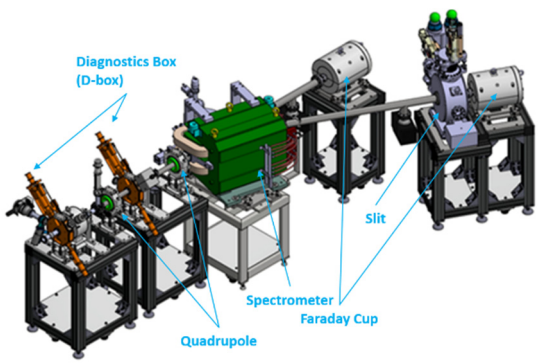


Figure 2: Layout of the medium energy test bench up to 16 MeV.

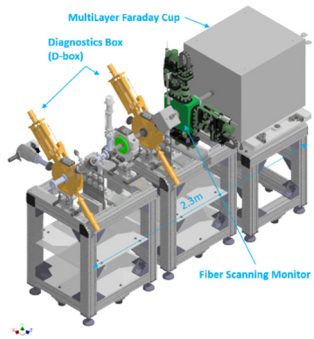


Figure 3: Layout of the test bench above 16 MeV.

COMMISSIONING STAGES

The commissioning of the LIGHT development machine started at the end of summer 2016 with the installation and tests of the PIA [4] followed by the commissioning of the high frequency RFQ at 5 MeV in 2017 [5] and by the commissioning of the low energy part up to 7.5 MeV in the first half of 2018 [1]. Measurements and results at medium energy up to 26.5 MeV are shown in this paper.

BEAM COMMISSIONING RESULTS

The beam commissioning of the LIGHT development machine has been finalized up to 26.5 MeV. The RF cavity phase and amplitude set points were characterized by varying the phase of the cavities at different amplitude levels and measuring the transmission (acceptance scans) and energy with the ToF system (ToF scans) (see Figs. 4 and 5). After operational RF parameters were set, the beam properties were characterized using the diagnostics in the test bench shown in Fig. 2.

Acceptance and ToF Scans

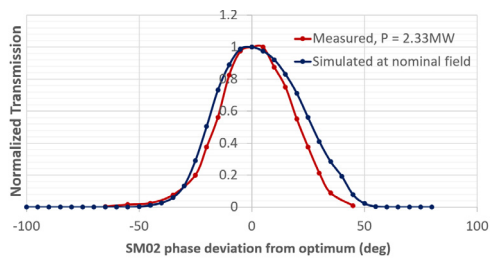


Figure 4: Comparison of measured and simulated curves from acceptance scans at nominal field level in SCDTL Module 02 (SM02).

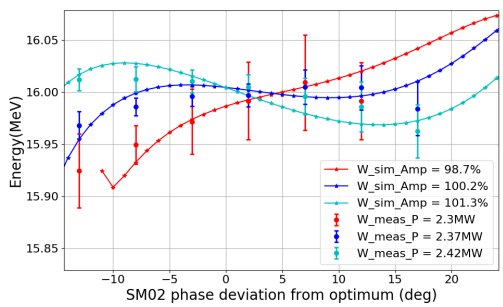


Figure 5: Comparison (best fit) of measured and simulated curves from ToF scans.

Content from this work may be used under the terms of the CC BY 3.0 licence (© 2018). Any distribution of this work must maintain attribution to the author(s), title of the work, publisher, and DOI.

ISBN: 978-3-95450-194-6 ISSN: 2226-0366 doi:10.18429/JACoW-LINAC2018-TUPO013

Content from this work may be used under the terms of the CC BY 3.0 licence (© 2018). Any distribution of this work must maintain attribution to the author(s), title of the work, publisher, and DOI.

Cavity RF power set point was determined to be 2.33 MW and 2.35 MW from acceptance and ToF scans, respectively. These numbers are consistent with those in Table 2 where a power margin of 30% w.r.t. the RF design has been used to take into account the manufacturing process. In the particular case of SM02 the beam measurements have shown that 20% margin is enough.

Beam Emittance

Figure 6 shows the comparison of measured and expected phase space plots of the beam measured at 16 MeV after second SCDTL module. Expected beam is obtained by tracking the beam from RFQ simulations until the emittance measurement location.

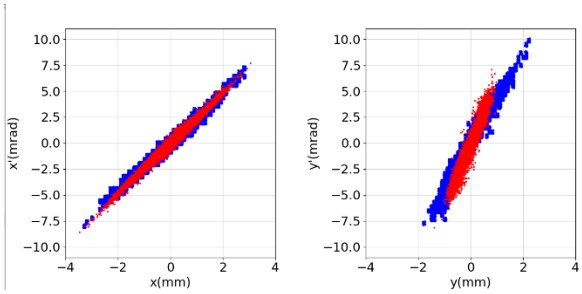


Figure 6: Comparison of measured (blue) and expected (red) transverse phase space plots of the beam at 16 MeV.

Beam at 26.5 MeV

For this energy the spectrometer dipole branch was removed and thus ToF system is acting as the reference for beam energy validation. Figure 7 represents a preliminary measurement of 2 uA beam in the present test bench (Fig. 3) with beam accelerated at 26.5 MeV, transported along SCDTL Module 04, which was not powered.

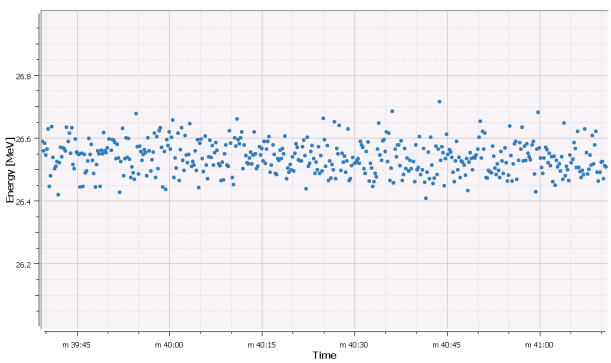


Figure 7: Beam energy of about 450 consecutive beam pulses. Each dot represents the average energy of 1.5 us beam pulse.

CONCLUSION

The LIGHT development machine has been commissioned up to 16 MeV. The validation of two out of three types of accelerating structures operated with beam has been completed. Table 3 summarizes the beam measurements at different sections along the linac.

Currently the LIGHT development machine is under commissioning at 26-37 MeV beam energy range. Installation works for the next commissioning stage (Fig. 8), bringing the energy up to 52 MeV, will start soon.

Table 3: Summary of Beam Measurements

	RFQ input	MEBT1	SM02 output
Beam energy [MeV]	0.04	5.03	16
Beam current [μA]	250	50	20
Hor emittance (norm, rms) [π mm mrad]	0.032	0.032	0.11
Ver emittance (norm, rms) [π mm mrad]	0.025	0.025	0.11

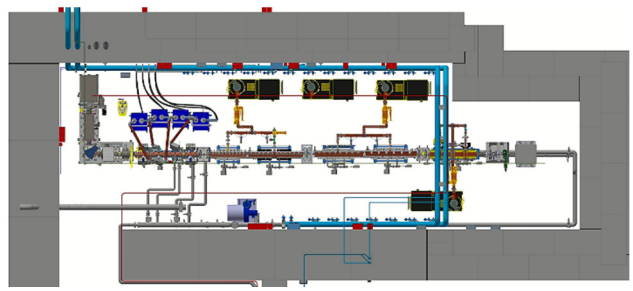


Figure 8: Integration drawing of the next commissioning phase of the LIGHT development machine. Two Coupled Cavity Linac modules will be added to the current configuration.

ACKNOWLEDGEMENTS

The authors would like to acknowledge the support of CERN colleagues and in particular the BE department, the HSE unit and KT group.

REFERENCES

[1] A. Degiovanni *et al.*, "Status of the Commissioning of the LIGHT Prototype", in *Proc. IPAC'18*, Vancouver, BC, Canada, Apr-May 2018, pp. 425-428, doi:10.18429/JACoW-IPAC2018-MOPML014

[2] M. Vretenar *et al.*, "A Compact High-Frequency RFQ for Medical Applications", in *Proc. LINAC'14*, Geneva, Switzerland, Sept 2014, pp. 935-938, paper THPP040

[3] A. Jeff, A. Benot Morell, M. Caldara, P. Nadig, "A Diagnostic Test Bench for the LIGHT Accelerator", in *Proc. IPAC'18*, Vancouver, BC, Canada, Apr-May 2018, pp. 1808-1811, doi:10.18429/JACoW-IPAC2018-WEPAF001

[4] D. Ungaro *et al.*, "LIGHT: a Linear Accelerator for ProtonTherapy", in *Proc. NAPAC'16*, Chicago, IL, USA, Oct. 2016, paper FRB1IO02, pp. 1282-1286

[5] V. Dimov, *et al.*, "Beam Commissioning of the 750 MHz Proton RFQ for the LIGHT Prototype", in *Proc. IPAC'18*, Vancouver, BC, Canada, Apr-May 2018, pp. 658-660, doi:10.18429/JACoW-IPAC2018-TUPAF002

ISBN: 978-3-95450-194-6 ISSN: 2226-0366 doi:10.18429/JACoW-LINAC2018-TUPO014

TRIUMF ISAC LINAC DEVELOPMENTS and UPGRADES

Z. T. Ang†, T. Au, Y. Bylinski, K. Fong, J. Keir, D. Lang, R. Laxdal, R. Leewe, B. Waraich, Z. Yao, Q. Zheng, V. Zvyagintsev

TRIUMF, 4004 Wesbrook Mall, Vancouver V6T 2A3, BC, Canada

Abstract

TRIUMF ISAC accelerator complex is in consists of ISAC-I room temperature linac and ISAC-II superconducting linac structure [1]. ISAC-I linac has seventeen RF systems in operation for about twenty years, and ISAC-II linac has forty superconducting QWR. The SRF cavities in operation for some about ten years. To match beam energy to RFQ, a small booster 3-gap structure at 11.78 MHz has been designed and installed in upstream of RFQ. A sliding mode extremum seeking control for LLRF control was developed and implemented in operation. Test results demonstrated very stable and reliable performs. Six of DTL systems have been working in the control mode. RFQ, two more DTL systems, HEBT and DSB bunchers, Rotator systems will be upgraded in the sliding mode control soon. The amplifiers for twenty ISAC-II QWR superconducting cavity SCB were developed and upgraded from YV-229 triode tube amplifier into a solid-state amplifier (SSA). The prototype and other four SSAs have been commissioned in 2017 and in operation over one year faithfully. The rest of 16 SSAs has been tested on bench at beginning of 2018. All twenty are in operation this year.

INTRODUCTION

The ISAC Linac of radioactive ions beams facility at TRIUMF have been in successfully operation for experiments many years. RFQ at 35.36 MHz to accelerate ions beam with A/Q≤30 from 2.03 keV/u to 153 keV/u and variable energy draft tube linac (DTL) at 106 MHz to accelerate the stripped ions beam of A/Q≤7 between 153 keV/u and 1.53 MeV/u. The designed capacity of beams energy for DTL to accelerate ions from 153 keV/u to 1.5 MeV/u with A/Q≤6. To meet the experiment requirements, some upgrades were done in DTL Tank number 3, number 4 and 5 in the RF power transmission line and final RF power amplifiers. The Tank 3 power amplifier outputs was increased to 20 kW from 16 kW after changing HCA 158-50 J coaxial semi-rigid transmission line to SPX communication technology 3-1/8'' copper rigid transmission line. Tank 5 amplifier's high voltage transformer has been upgraded to 51 KVA from 36.6 KVA, which output power increased from 20.5 kW to 28 kW. Tank 4 amplifier's specified power level increased to 22 kW from 19 kW after retuning amplifiers setup limit trip points. The temperatures of the tuners and RF coupler windows are monitored, and the coarse tuners were setup to meet fine tuner working distances for all power levels. Table 1 shows the DTL amplifiers upgrading results:

†Email address: zang@triumf.ca

Table 1: DTL Amplifiers Output Power

System	Before	After upgrading
Tank 3	16 (KW)	19 (KW)
Tank 4	19 (KW)	22 (KW)
Tank 5	20.5 (KW)	28 (KW)

After the above upgrading for DTL RF systems there are more variable ions beams and beam energies could be delivered for experiments at TRIUMF.

RF BOOSTER

The 35.36 MHz RFQ is designed to accelerate beams with A/Q≤30 in CW. A three harmonic pre-buncher, located 5m upstream of the RFQ, operates with a fundamental frequency of 11.78 MHz so that one of every three RFQ buckets is filled with beams. The RFQ requires a beam injection energy at 2.03 keV/u for about 60% beam transmission. The injection energy acceptance of the RFQ requires that the ions beam must be extracted from a source at an electric potential up to about 60 kV. The ISOL target modules operate in a grim environment that can limit the source bias. Presently the ISAC target modules cannot hold higher than 54 kV and this value can degrade with time so that to schedule experiments for ions with A>25 has a risk.

In order to accelerate high mass beams and to mitigate against further source bias degradation a small 3-gap RF structure cavity has been installed at upstream of RFQ. The effective voltage for the booster was specified 16 KV. A 7 KV effective voltage has been achieved for beam experiments. 2 KV, 4 KV and 6 KV effective voltage for ions beams of Carbon and Nitrogen have been tuned through RFQ at the designed transmissions respectively. Table 2 shows the effective voltages with RF power feeding to the primary coil in the RF circuit box. A stable operation could not be approached while effective voltages applied to beams higher than 8 KV.

Before we installed the RF structure and RF circuitry box in beam line, we powered the system to 150 W RF power through primary coils in RF Lab driven from a 300 watts CW amplifier. The forward and reflected RF powers were monitored. A stable RF performs off line tests gave us a confident to install it for beam test. Instead of real RF structure and feedthrough, we used two capacitors with equal capacitances to the feedthrough and draft tubes for the test and tuning resonance frequency. However, when we installed the structure in beam line to test with beams in vacuum, the effective voltage to beam is much lower from simulations and bench tests.

Content from this work may be used under the terms of the CC BY 3.0 licence (© 2018). Any distribution of this work must maintain attribution to the author(s), title of the work, publisher, and DOI.

ISBN: 978-3-95450-194-6 ISSN: 2226-0366 doi:10.18429/JACoW-LINAC2018-TUPO014

Content from this work may be used under the terms of the CC BY 3.0 licence (© 2018). Any distribution of this work must maintain attribution to the author(s), title of the work, publisher, and DOI.

Table 2: Beams Test with RF Power

Ions	Effective V	RF Power
C/N	2 (KV)	4 (W)
C/N	4 (KV)	7.5 (W)
C/N	6 (KV)	26.5 (W)
C/N	7 (KV)	60 (W)

At 8 KV effective voltage, RF amplifier was driven from 150 W to 200 W in closed loop control. The system could not be in stable operation due to thermal RF dissipation in the system. Further tests and diagnostic tell the strong thermal existing in RF structure and RF circuitry box. The VSWR and the quality factor vary significantly comparison to the higher and lower RF power applied in the system. In Table 2, we could see that the 7 KV effective voltage to beams, much higher RF power dissipated in system.

To reduce the heat impacts in the system, the RF circuitry in box has been modified shown in Fig. 1 (left). The primary coils, tuning capacitors and matching capacitors in Fig. 1 (right) are eliminated; instead, a coupler loop is adopted. Water cooling are applied to coils and through RF feedthrough. It is much simpler for tuning system of the matching and the frequency:

- The matching capacitors in box (in primary circuitry) warm up at high power level, which affects the operation stability.
- The secondary coil and feedthrough capacitors values are fixed. Therefore, the VSWR less than 2 could not be achieved in the previous circuitry.
- The RF structure support and isolation Marco was replaced by a Teflon bar as the Marco RF character is poor than later one. There is a discoloured spot in the Marco bar which shown strong RF power dissipations during RF power tests.
- The new coils supported via two Teflon bars. They are amounted on both side of aluminium box connect with screw nut, which could squeeze or stretch the coils to tune frequency easily. The two bars also tighten the coils from any vibrations.
- The new coils have water cooling. The 1/8" copper tube is inserted inside of the half-inch copper tube. The cooling water through feedthrough and the 1/4" copper leads which joint with the bolted sleeves [2].

After the modification, the system was tested with water-cooling. Two resonant frequencies were measured. The Push-pull mode frequency is 11.78 MHz, and Push-push mode 19.5 MHz. About 10 kV effective voltage achieved for the structure in RF Lab. Beyond the voltage, the system could not be stable operation. Tracing the problem, we realized that a lower rating voltage capability of the feedthrough were being employed, which could not hand higher than 10 kV. A larger diameter feedthrough likes ISAC-I chopper 11 [3] will be procured later. A transition between RF structure and circuitry box will be amended when the new feedthrough arriving.

A new LLRF control board has been developed for ISAC booster based on existing LLRF control configurations. In addition, a new digital LLRF control system is being developed at TRIUMF. It will carry out in this booster system next year. EPICS control panel for the beam operation is under way.

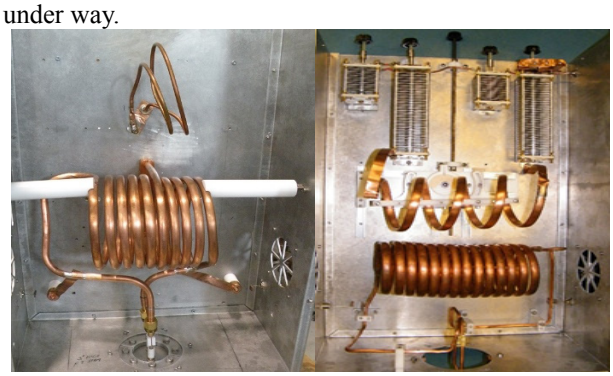


Figure 1: New RF circuitry box replacing the previous one.

SLIDING MODE RF CONTROL

A sliding mode extremum seeking control have been developed at TRIUMF [4]. The idea of the sliding mode control induced into LLRF control for the room temperature resonant is to minimize reflected power and minimize the driven RF power as well. The original LLRF control for ISAC-I DTL system, are based on frequency and phase control, which need to have a stable loop phases within certain range for system control stability. The operational RF cavities are frequency tuned through a phase comparison technique, which is sensitive to temperature variations if the facility or longer signal transportation cables are not temperature controlled. Temperature induced phase errors render this technique labour and time intensive. The temperature variations in ISAC-I linac building can be as high as over twenty degrees between summer and winter. This big temperature divergence could cause burden of the system stability. Figure 2 shows the measuring results of the forward, reflected powers and tuner positions vary with environment temperature during 12 hours without prosecuting the sliding mode control. The Fig. 3 shows the same measurements in another RF system that the sliding mode control has been implemented. It is distinctly shown that much smaller of the forward power and reflected power variations achieved in the new control mode.

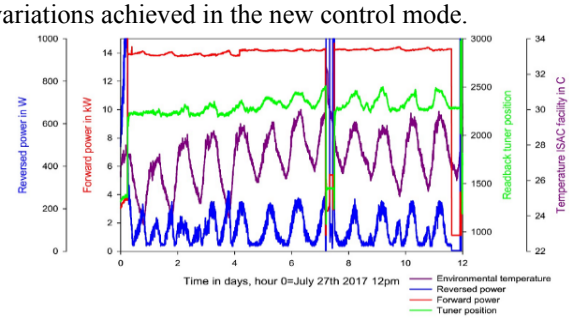


Figure 2: The forward, reflected powers vs. temperature.

The different RF characters among ISAC-I linac room temperature cavities, the control parameters for each system have to be carefully setup to achieve a reliable operation. A stability analysis provides conditions on how to

ISBN: 978-3-95450-194-6 ISSN: 2226-0366 doi:10.18429/JACoW-LINAC2018-TUPO014

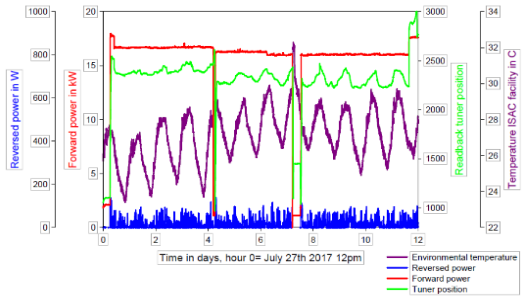


Figure 3: The forward, reflected powers vs. temperature while the sliding mode control implemented.

choose the controller parameters to guarantee stable system operation up to twice the cavity bandwidth, which is a controllable bandwidth improvement of a factor of two. The system first was carried on two of ISAC-I DTL Tank4 and 5 room temperature cavities and long-term measurements show that the system effectively counteracts the RF heating e□ect as well as diurnal temperature variations. Figure 4 shows how stable of Tank 5 at higher power level while sliding mode control applied.

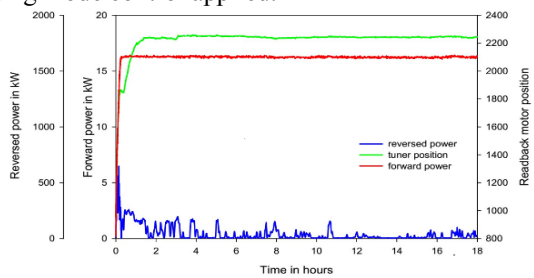


Figure 4: Forward, reflected power Vs. Temperature.

Except for above six DTL RF systems have been working in the sliding mode control, there are another six RF systems in ISAC-I linac will be upgraded in the sliding mode control soon.

ISAC-II SCB AMPLIFIERS

ISAC-II linac are consisting of 40 QWR superconducting cavities, 20 SCB cavities working at 106 MHz and 20 SCC at 141 MHz. SCC system is employing 20 solid-state amplifiers to power cavities. Twenty 600 W tube amplifiers power the SCB. The cavities operate in over coupled regimes with RF forward power up to 250 W CW; seven W is dissipating in the superconducting cavity and the rest of RF power reflected back to the amplifier. The amplifier output is connected with cavity via a 1000 W circulator, and all the reflected RF power is dissipated in a dummy load of the circulator.

The 600 W amplifier have two stage amplifiers. The 50 W pre-amplifier amounted on a heat sink with fan separated from the main amplifier in a chassis. It used a Motorola MRF-141G FET capable 150 watts output maximum. Main amplifier adopted YC-229 ceramic triode tube and employed a grounded grid circuit for the final amplifier. The performance of the amplifiers are not identical. Some of the amplifiers degraded fast, could not last one year, which affects routing operational efficiency a lot.

After last 10-year operation of the tube amplifiers in ISAC-II SCB, the disadvantages of the tube amplifiers are obviously comparison with SCC amplifiers. There are about 100 tubes being used since the SCB commissioned. Each tube costs more than 2000 US dollars. The major handicaps of the amplifier are as following:

- The degradation of the tube amplifiers is very fast.
- Tunings for matching and phases are often to make system operation ineffective.
- Costs to replace the failure/aged tubes are big for long term operations.
- Investigate failures of system is intricate.
- Time of replacing failed amplifier, pre-amplifier or DC power supply is not negligible for operation efficiency.

A 550 W solid-state amplifier for the replacement of the SCB tube amplifiers was developed in TRIUMF. The new amplifier performs met the operational requirements. So complete replacement of the tube amplifiers had been brought forward.

Based on the experience of homemade solid-state amplifier, BBEF produced a prototype amplifier for test and operation for experiments at TRIUMF, which was met our specifications and operation requirements. Then four amplifiers arrived TRIUMF for operation and commissioned in year 2016. The last seventeen amplifiers from BBEF shipped to TRIUMF at the end of 2017. All 20 SCB tube amplifiers were moved out from operations. The new SSAs have all been installed and commissioned for routine operation this year. Instead of individual DC power supply, pre-amplifier and final power amplifier, the new SSA is integrated power supply, pre-amplifier, final amplifier and control board all in one chassis. To replace a fail SSA is only a few minutes. Spare modules for SSA are swappable and easy to access.

CONCLUSIONS

ISAC-I linac RF system upgrading allow experiments having more choices of ions beams and beam energies. The developments and upgrades in ISAC linac RF system have increased the machine operational reliability and reduced beam down times.

REFERENCES

[1] R.E. Laxdal, "ISAC-I and ISAC-II at TRIUMF: Achieved Performance and New Construction," in *Proc.* LINAC2002, Gyeongju, Korea, August 2002, paper TU302, pp. 294.

[2] V. Zvyagintsev, "Novel RF structure for energy matching into an RFQ," in *Proc. 8th Int. Particle Accelerator Conf. (IPAC2017)*, Copenhagen, Denmark, May 2017, pp. 4111, doi:10 https://doi.org/10.18429/JACoW-IPAC2017-THPIK003

[3] A.K. Mitra, "RF Test and Commissioning of Low and High Beta Bunchers for the TRIUMF ISAC Facility" *in Proc.* EPAC, 2002, Paris, France, June 2002, pp. 2178.

[4] R. Leewe, "Novel Scheme to Tune RF Cavities using Reflected Power," in *Proc.* LINAC2016, East Lansing, MI, USA, September 2016, paper THOP06, pp. 757, doi: https://doi.org/10.1829/JACoW-LINAC2016-THOP06

Content from this work may be used under the terms of the CC BY 3.0 licence (© 2018). Any distribution of this work must maintain attribution to the author(s), title of the work, publisher, and DOI.

ISBN: 978-3-95450-194-6 ISSN: 2226-0366 doi:10.18429/JACoW-LINAC2018-TUPO016

HIGH FREQUENCY RFQ DESIGN AND LEBT MATCHING FOR THE CERN TWINEBIS ION SOURCE

V. Bencini*, M. Breitenfeldt, J.B. Lallement, A.M. Lombardi, H. Pahl, J. Pitters, A. Pikin, F. Wenander
CERN, Geneva, Switzerland

Abstract

An Electron Beam Ion Source (EBIS) is being developed at CERN [1] for production of highly charged ions, for instance fully stripped ^{12}C. The focus has so far been on the electron gun design, aiming for a high current compression, which results in a rapid ionisation process and thereby high repetition rate. Initial commissioning tests of such an electron gun, the so-called MEDeGUN [2], have already been performed and we are now in the process of designing a multi-purpose ion extraction and diagnostics line. The Low Energy Beam Transport (LEBT) line will transport the ions into the downstream Radio Frequency Quadrupole (RFQ) with a nominal energy of 15 keV/u. The 750 MHz RFQ is designed to accelerate ions from 15 keV/u up to the final energy of 2.5 MeV/u. After the RFQ design was finalized and its acceptance calculated, the beam matching to the RFQ was studied, finding a set of parameters for the LEBT that maximize the transmission through the RFQ. Details of the RFQ design, of the LEBT matching procedure and its final results are illustrated in this paper.

INTRODUCTION

After the design, construction and successful commissioning of a 750 MHz Radio Frequency Quadrupole for the acceleration of protons from 40 keV to 5 MeV in the space of 2 meters, we have studied a potential extension of the beam dynamics concept from protons to ions. In the framework of the strategy paper for medical applications [3] the layout of a linac-based carbon ion accelerator for medicine is a key ingredient of a potential future study involving other partners. Besides, the availability of a fully stripped carbon ion beam at the energy of 15keV/u in the framework of MEDeGUN allowed for a perfect synergy between the endeavors on the LEBT and the RFQ design. The result of this study is two-fold. First, we have detailed an RFQ designed for fully stripped carbon and tailored to the beam characteristics of the source and LEBT of MEDeGUN that could be used as such as a pre-injector of a linac-based medical facility. Second, we have studied the variation of critical parameters, exploring the trade-off between length, RF power needs, beam throughput and machinability for a standalone RFQ that could accelerate carbon ions as well as alpha particles and could be used for other purposes.

LEBT MATCHING

The LEBT has been designed to transport the ion beam from the TwinEBIS source, set at 30 kV, to the RFQ (at the matching plane). The ion distribution used for the matching is the result of simulations that reproduce the physics of the ion production in the source [4]. The resulting beam is extracted by a 17 kV extractor electrode and accelerated up to 6.5 keV/u. It then travels into a set of nine accelerating rings set between 27 kV and ground voltage that boost the energy up to 15 keV/u. Between the extractor and the accelerating gaps an additional 'adaptor' electrode was added to keep the beam focused. The particles at their final energy are then focused and matched to the RFQ by two gridded lenses and one Einzel lens. The aim of the matching is to maximise the number of particles that fall into the RFQ acceptance, defined as the biggest ellipse in the transverse phase space that can be accelerated and transported through the RFQ with nominal transmission. The matching technique is explained in [4] and consists of finding the optimal set of voltages applied to the focusing elements (the adaptor, the two gridded lenses and the Einzel lens).

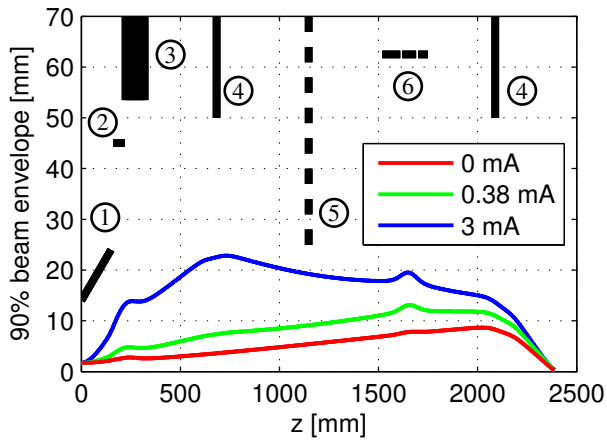


Figure 1: Plot showing the envelope of the matched beam for a current of 0 mA, 1 mA and 3 mA. The apertures of the relevant optical components are indicated: (1) Extractor, (2) adaptor, (3) accelerating gaps, (4) gridded lenses, (5) horizontal collimator, (6) Einzel lens.

The matching was performed for three input currents. 3 mA, corresponding to the maximum theoretical current that can be generated by the TwinEBIS, 0 mA, representing the case without space charge, and 0.38 mA (corresponding to $1{\cdot}10^9$ $^{12}C^{6+}$ ions in a 5 µs pulse), the current that could be extracted by the EBIS source in the present configuration. All the extracted beams are composed of 50% of $^{12}C^{6+}$ and of 50% of other charge states.

In Figure 1 a sketch of the main elements of the LEBT, together with the 90% beam envelopes are showed. The

* vittorio.bencini@cern.ch

Content from this work may be used under the terms of the CC BY 3.0 licence (© 2018). Any distribution of this work must maintain attribution to the author(s), title of the work, publisher, and DOI.

ISBN: 978-3-95450-194-6 ISSN: 2226-0366 doi:10.18429/JACoW-LINAC2018-TUPO016

maximum number of particles falling into the acceptance for a 3 mA beam is 88%. By decreasing the beam current, the space charge effects are reduced and, as a consequence, on one hand the beam size is kept smaller, avoiding aberrations due to the non linear part of the electric field in the focusing elements, and on the other hand the emittance growth due to space charge is reduced. The transmission resulting from the re-matching at different currents is then 96% for the 0.38 mA beam and 99% for the zero space charge case respectively. These values refer to the particles that fall into the acceptance in both transverse planes at the same time.

RFQ DESIGN

Input Parameters

The choice of the characteristic parameters used for the design of the RFQ was driven by different constraints. The $^{12}C^{6+}$ ion beam energy is defined by the maximum accelerating voltage that the LEBT can hold, in this case 30 kV, that leads to an input energy of 15 keV/u at the entrance of the RFQ. Regarding the output energy, two different solutions at 2.5 MeV/u and 5 MeV/u are proposed. The choice of having two alternatives allows to widen the range of options in the selection of the accelerating structure following the RFQ. The minimum vane aperture (minimum distance between two opposite vanes) and the inter-vane voltage are strictly bound to the maximum surface field that can be hold by the vanes without breakdown. In order to define the maximum surface field, Kilpatrick's criterion [5] was used and the maximum surface field was chosen to be $E_{s,max} = 2 \cdot E_k$, E_k being the Kilpatrick field at 750 MHz. The constraints on the minimum required transmission of the RFQ, in the case of a medical machine for carbon therapy, comes from treatment requirements. The dose required for treatment translates to an average current of 0.8 nA [6], corresponding to $8 \cdot 10^8$ ions/s. The TwinEBIS could be able to provide $1 \cdot 10^9$ $^{12}C^{6+}$ ions in a pulse of 5 µs length, at a repetition rate of 200 Hz, resulting in an ion current of $2 \cdot 10^{11}$ ions/s. If one considers that just the 2/3 of the RF pulse are going to be conserved in the following acceleration stage (the pulse length in foreseen to be around 3 µs in the linac), a $^{12}C^{6+}$ current of $1.3 \cdot 10^{11}$ ions/s should be available, which is two order of magnitudes larger than the requirements. Therefore the transmission is not considered as a critical constraint for the design.

Design Procedure

A parametric scan of the maximum surface field as a function of the aperture and the vane voltage was performed in order to define a set of combinations that guarantees a maximum surface field below the defined limit $E_{s,t}$=50.6 MV/m (a variation within 5% is accepted considering that Kilpatrick criterion is highly conservative).

Figure 2 shows the maximum surface field as a function of the initial aperture of the RFQ for different inter-vane voltages. Although an increase in aperture results in a growth of the RFQ acceptance, it leads to a much higher power consumption ($P \propto V^2$) due to the higher vane voltage needed to keep the beam focused. Therefore a good compromise between these two aspects has to be found depending on the specific design requirements. The selected values of aperture and voltage, together with the other parameters, (summarized in Table 1) were used as input for the RFQ codes Curli, RFQuick, Pari and Parmteq [7].

Table 1: RFQ Characteristic Parameters

Parameter	Value
RF frequency [MHz]	750
Ion species	$^{12}C^{6+}$
Input energy [keV/u]	15
Design input current [mA]	0
Output energy [MeV/u]	2.5 / 5
Input transv. emittance 90% norm [π mm mrad]	0.08
Repetition frequency [Hz]	200
Vane voltage [kV]	50
Average aperture r_0 [mm]	1.4
ρ/r_0	0.9

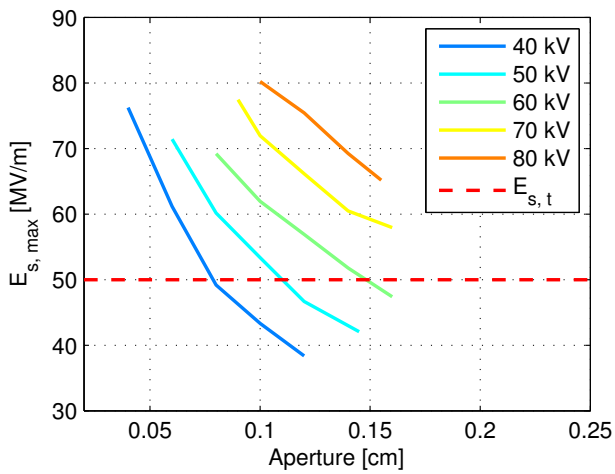


Figure 2: Parametric scan of the inter-vane voltage as a function of the input minimum aperture between the vane and the resulting maximum surface field in the RFQ.

The initial designs have been modified to make it more suitable for this specific application. The first modification was to increase the final modulation of the RFQ. Together with a proper redesign of the modulation profile along the RFQ, it leads to a considerable reduction in the structure length (25%), keeping the transmission (99%) unchanged.

A strong constraint on the RFQ design is given by the longitudinal and transverse acceptance of the structure coming downstream in the accelerator. Two possible accelerating structures are considered. For the 2.5 MeV/u RFQ, the most suitable solution would be a 750 MHz IH-structure [8]. In the case of the 5 MeV/u the output energy would be high enough to inject directly into a 3 GHz structure.

Content from this work may be used under the terms of the CC BY 3.0 licence (© 2018). Any distribution of this work must maintain attribution to the author(s), title of the work, publisher, and DOI.

ISBN: 978-3-95450-194-6 ISSN: 2226-0366 doi:10.18429/JACoW-LINAC2018-TUPO016

Content from this work may be used under the terms of the CC BY 3.0 licence (© 2018). Any distribution of this work must maintain attribution to the author(s), title of the work, publisher, and DOI.

In both cases the longitudinal acceptance is small compared to the initial design output beam. The RFQ was hence re-designed following the procedure illustrated in [9]. The initial phase, that is usually set to −90 deg to capture the continuous beam coming from the source, was set to −50 deg in order to capture only the particles that could fit in the longitudinal bucket of the structure following the RFQ. In this particular design solution, all the losses occur at low energy, avoiding activation of the cavities.

Final Layout

The parameters of the final layout for both the 2.5 MeV/u and the 5 MeV/u RFQ are summarized in Table 2

Table 2: RFQ final layout parameters

Parameter	2.5 MeV/u	5 MeV/u
Output energy [MeV/u]	2.5	5
Length [m]	2.7	5.8
Nominal transmission [%]	54.6	54.6
Max. Surface field [MV/m]	51.6	52.3
Input phase [deg]	-50	
Output phase [deg]	-20	
Power consumption [kW]	280	600
Vane voltage [kV]	50	
Modulation (max.)	2.8	
Average aperture r_0 (const.) [mm]	1.4	
Acceptance 100% norm. [π mm mrad]	1.7	

The nominal transmission refers to a perfectly matched beam with a normalized RMS emittance of 0.02 π mm mrad.

Figure 3 shows the evolution of the main parameters of the 2.5 MeV/u RFQ along the beam axis. The curves for the 5 MeV/u are identical, with the difference that the accelerating section is longer to achieve the required higher energy.

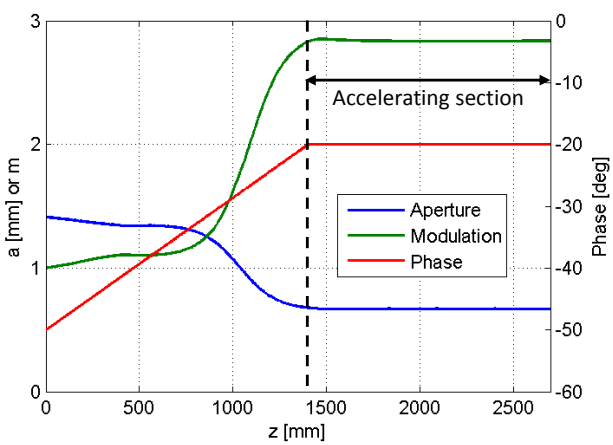


Figure 3: Phase, aperture and modulation along the RFQ.

TRACKING

The beams resulting from the LEBT matching were tracked through the RFQ to evaluate the transmission. The tracking was performed for the zero space charge, the 0.38 mA and the 3 mA input beam through both the 2.5 MeV/u and the 5 MeV/u RFQs. Table 3 summarizes the main parameters of the output beam for the different currents and final energies.

Table 3: Results of Tracking 10000 Particles into the RFQ

I=0 mA	2.5 MeV/u	5 MeV/u
Transmission [%]	57.6	50.3
Transv. input emittance 90% norm. [π mm mrad]	0.09	
Transv. output emittance 90% norm. [π mm mrad]	0.09	0.09
Long. output emittance 90% norm. [π deg MeV]	0.42	0.45
I=0.4 mA		
Transmission [%]	56.6	49 .8
Transv. input emittance 90% norm. [π mm mrad]	0.11	
Transv. output emittance 90% norm. [π mm mrad]	0.11	0.11
Long. output emittance 90% norm. [π deg MeV]	0.46	0.46
I=3 mA		
Transmission [%]	52.3	45.3
Transv. input emittance 90% norm. [π mm mrad]	0.14	
Transv. output emittance 90% norm. [π mm mrad]	0.11	0.11
Long. output emittance 90% norm. [π deg MeV]	0.52	0.51

CONCLUSIONS AND NEXT STEPS

The matching of the LEBT was performed at different currents with the aim of validating its flexibility. The LEBT will be installed and tested during the next year, providing the opportunity to verify the validity of the simulations and to adapt the design of the RFQ to the measured distribution. Tracking through the RFQ shows the capability of the system to provide an ion current that exceeds significantly the clinical requirements. Moreover, this study showed that the LEBT and the RFQ can transport and accelerate relatively high currents (compared with clinical ones), making the present design suitable for different ions with the same charge over mass ratio and for different applications.

ACKNOWLEDGEMENTS

The author acknowledges the CERN Knowledge Transfer Fund and the CERN Budget for Knowledge Transfer to Medical Applications.

ISBN: 978-3-95450-194-6 ISSN: 2226-0366 doi:10.18429/JACoW-LINAC2018-TUPO016

REFERENCES

[1] Breitenfeldt, M., et al. "The TwinEBIS setup: machine description." Nucl Instrum Methods Phys Res A 856 (2017): 139-146.

[2] Mertzig, R. et al. "A high-compression electron gun for C6+ production: concept, simulations and mechanical design." Nucl Instrum Methods Phys Res A 859 (2017): 102-111.

[3] Strategy and Framework Applicable to Knowledge Transfer by CERN for the Benefit of Medical Applications. 304th Meeting of Scientific Policy Committee", CERN/SPC/1091; CERN/FC/6125; CERN/3311, Jun 2017.

[4] Pahl, H. et al, "A Low Ion Energy LEBT for TwinEBIS ", JINST 13.08 (2018): P08012.

[5] Boyd Jr, T. J. "Kilpatrick's criterion." Los Alamos Group AT-1 report AT-1 82 (1982): 28.

[6] Peggs, S., T. Satogata, and J. Flanz. "A survey of hadron therapy accelerator technologies." Particle Accelerator Conference, 2007: MOZAC02

[7] Crandall, K. R., and Wangler, T. P. "PARMTEQ—A beam-dynamics code for the RFQ linear accelerator." AIP Conference Proceedings. Vol. 177. No. 1. AIP, 1988.

[8] Benedetti, S. "High-gradient and high-efficiency linear accelerators for hadron therapy.", Doctoral thesis No. THESIS LIB.EPFL 2018.

[9] Lombardi, A.M, et al. "Beam dynamics in a high frequency RFQ.", International Particle Accelerator Conference, 2015: WEYB2.

Content from this work may be used under the terms of the CC BY 3.0 licence (© 2018). Any distribution of this work must maintain attribution to the author(s), title of the work, publisher, and DOI.

ISBN: 978-3-95450-194-6 ISSN: 2226-0366 doi:10.18429/JACoW-LINAC2018-TUPO017

THE NEW LIGHT ION INJECTOR FOR NICA

B. Koubek*, M. Basten, H. Höltermann, H. Podlech, U. Ratzinger,
A. Schempp, R. Tiede, Bevatech GmbH, Frankfurt am Main, Germany
A. Butenko, A. Govorov, B. Golovenskiy, D. Donets, K. Levterov, D. Lyuosev, A. Martynov,
V. Monchinskiy, D. Ponkin, K. Shevchenko, I. Shirikov, E. Syresin, JINR, Dubna, Russia
C. Kampmeyer, H. Schlarb, DESY, Hamburg, Germany

Abstract

Within the upgrade scheme of the injection complex of the NICA project and after a successful beam commissioning of a heavy ion linac, Bevatech GmbH will build a first part of a new light ion linac as an injector for the Nuclotron ring. The linac will provide a beam of polarised protons and light ions with a mass to charge ratio up to 3 and an energy of 7 MeV/u. The mandate of the Linac does not only include the hardware for the accelerating structures, focusing magnets and beam diagnostic devices, but also the LLRF control soft- and hardware based on the MicroTCA.4 standard in collaboration with the MicroTCA Technology Lab at DESY. An overview of the Linac is presented in this paper.

INTRODUCTION

In the frame of the NICA ion collider upgrade [1] a new light ion frontend Linac (LILac) for polarised particles, protons and ions with a mass to charge ration of up to 3 will be built. Behind the ion source and LEBT, LILac will consist of 3 parts:

1. a normal conducting Linac up to 7 MeV/u
2. a normal conducting energy upgrade up to 13 MeV/u
3. a superconducting section from 13 MeV/u up to a final energy to be determined

In this paper only the Part 1 of LILac up to 7 MeV/u is discussed. This normal conducting Linac will be built in collaboration between JINR and Bevatech GmbH.

The Linac will be located in LU20 hall at JINR and provides a beam energy of 7 MeV/u to be injected into the Nuclotron ring for further acceleration as a first stage of the project. Protons and light ions up to a mass to charge ratio of up to 3 will be used for either fixed target experiments to study baryonic matter or will be injected into the NICA collider ring for hadron matter and its phase transition experiments and to study spin physics on polarised particles.

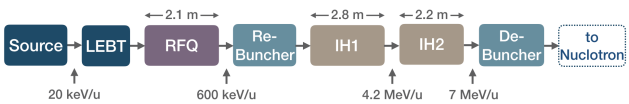


Figure 1: Scheme of the LILac cavities.

The Linac consists of 5 cavities, an RFQ followed by a re-buncher, 2 IH-DTL structures and a de-buncher as shown in Fig. 1. It is operating at 162.5 MHz with a beam repetition rate of 5 Hz and a duty cycle of 0.15 % [2]. The main parameters of the LILac are summarised in Table 1. The length of the Linac comprising the cavities, the beam diagnostic devices and focusing magnets but excluding the de-buncher will be realised within a length of 9 m. A scheme of the LILac cavities is shown in Table1.

Table 1: LILac Main Parameters

Parameter	Protons	C^{4+}
Mass to Charge Ratio	1	3
Injection Energy	20 keV	60 keV
Exit Energy	7 MeV	21 MeV
Beam Current	5 mA	15 mA
Repetition Rate Limit	≤5 Hz	
Current Pulse Duration	30 μs	
RF Pulse Length	200 μs	
RF Frequency	162.5 MHz	
Transmission	≥80 %	
Full Length of the Linac	<9 m	

Each cavity will be fed by a dedicated high power solid state amplifier to provide the corresponding power for the accelerating fields in the cavities. The LLRF control soft- and hardware based on the MicroTCA.4 standard will be developed together with Bevatech and the MicroTCA Technology Lab at DESY.

ARCHITECTURE

Ion Source and LEBT

At the LILac two different ion sources, a laser ion source (LIS) and a source of polarised ions (SPI), will be used. From the LIS it is planned to receive light ions, while the SPI will generate polarised and non-polarised protons [3]. The ion sources are placed on a high-voltage terminal (up to 150 kV) [4]. The LEBT channel with a length of about 1.8 m is split into two main parts. The first part is an electrostatic section with ion optics and an electrostatic tube, and the second part uses two magnetic solenoids with a maximum magnetic field of 1.2 T. This channel will be similar to the existing which works at the LU-20 pre-injector.

* benjamin.koubek@bevatech.com

Content from this work may be used under the terms of the CC BY 3.0 licence (© 2018). Any distribution of this work must maintain attribution to the author(s), title of the work, publisher, and DOI.

ISBN: 978-3-95450-194-6 ISSN: 2226-0366 doi:10.18429/JACoW-LINAC2018-TUPO017

RFQ

A 4-rod type RFQ is the first RF accelerating structure of the Linac. It accelerates, focuses and bunches the continuous 20 keV/u DC beam from the LEBT to 600 keV/u within a length of about 2 m. The cavity will be made of copper plated stainless steel, while the inner structure - the electrodes (rods), the stems and tuning plates - will be machined from solid copper. To ensure a stable operation in terms of field and frequency the RFQ will be equipped with one passive and one active piston tuner.

MEBT

The medium energy beam transport section provides a proper beam matching from the RFQ into the first IH-DTL structure. A standard concept was applied, consisting of two short quadrupole doublet magnets for the transverse beam matching and a two gap re-buncher cavity in the centre. It resulted in a rather compact layout - only about 0.8 m in total - but with enough space reserved for steerers and diagnostic elements. For the latter a BPM as well as an ACCT are foreseen to determine the beam position, current and bunch signal.

IH-DTL

A compact DTL section of the LILac has been designed by using the beam dynamics simulation code LORASR. A beam energy gain from 0.6 MeV/u to 7.0 MeV/u for the design particle with a mass over charge ratio $A/q = 3$ is obtained within a Linac length of about 5.5 m.

This is due to the use of the KONUS beam dynamics, which allows for multi gap cavities and a small number of transverse focusing elements. These are powerful magnetic quadrupole lenses (doublets or triplets), which can be integrated into the cavities or placed as external elements in between the resonators.

The DTL consists of two IH cavities. The first IH tank (IH1) has two internal quadrupole triplet lenses and achieves an energy gain from 0.6 to 4.1 MeV/u, the second one (IH2) is without internal lenses and provides an end energy of 7.0 MeV/u. The transition energy of 4.1 MeV/u has resulted from beam dynamic constraints, but has also been chosen due to RF power considerations - the power demand should be balanced between IH1 and IH2.

BEAM DYNAMICS

The RFQ beam dynamics and electrode design was simulated using Parmteq. The simulations resulted in a compact RFQ with a focus on high transmission, small emittance growth and stable output emittances against changes of the input distribution from the source and LEBT.

For the MEBT and IH-DTL simulations the RFQ output distributions as provided from the RFQ beam dynamics simulations were used. The design current is 15 mA, $A/q = 3$, i.e. 5 mA for protons. Figures 2 and 3 show the results of the beam dynamics simulations with corresponding beam envelopes using the code LORASR. As for the transverse beam envelopes shown in Fig. 2, a major design issue was to provide enough safety margin between beam and aperture, with the goal to minimize beam losses.

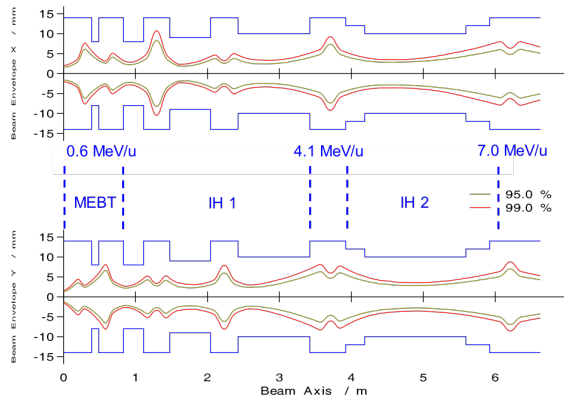


Figure 2: Transverse beam envelopes of the LILac DTL section, 15 mA, $A/q = 3$.

With increasing beam energy, the period lengths are increasing significantly and therefore also the overall section or tank lengths, respectively the distances between the triplets. This is why the beam envelopes tend to get larger towards the high-energy end of the Linac. Taking this into account, the drift tube apertures diameters were gradually increased in IH1 (from 16 to 20 mm), as well as at the tank ends of IH2 (from 20 to 24 mm). The lens aperture diameters were kept constant at 28 mm, which helps to simplify the lens mechanical design.

In Fig. 3 the energy and phase width envelopes along the Linac are shown, with the typical pathway for lattices based on the KONUS beam dynamics: The "jumps" in phase and energy are attributed to the redefinition of the synchronous particle energy and phase at the transitions between re-bunching and zero degree main acceleration sections.

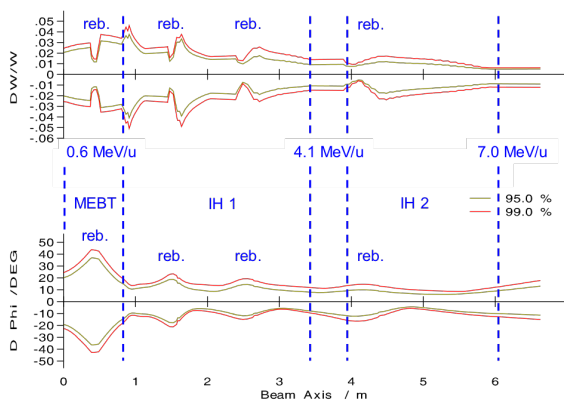


Figure 3: Longitudinal beam envelopes related to the bunch centroid, 15 mA, $A/q = 3$.

Content from this work may be used under the terms of the CC BY 3.0 licence (© 2018). Any distribution of this work must maintain attribution to the author(s), title of the work, publisher, and DOI.

ISBN: 978-3-95450-194-6 ISSN: 2226-0366 doi:10.18429/JACoW-LINAC2018-TUPO017

Content from this work may be used under the terms of the CC BY 3.0 licence (© 2018). Any distribution of this work must maintain attribution to the author(s), title of the work, publisher, and DOI.

RF AND BEAM DIAGNOSTICS

LLRF

The Low Level Radio Frequency (LLRF) system, to control the RF fields of the accelerating cavities, is based on MicroTCA.4 standard.

The system is generator driven, thus, the RF reference adjusted in amplitude and phase with a baseband vector modulator provides the input signal to the high power solid state amplifier (SSAM).

The output power of the SSAM is measured by determining the RF signals from directional waveguide coupler. The accelerating field in the cavity is measured by the RF signals from the cavity pickups. These RF signals are directly sampled with high speed low-noise ADCs. Raw values of the ADCs are converted to I (In-Phase) and Q (Quadrature) values and decimated. Only the probe signal is used for feedback control.

For accelerator operation, the cavity field gradients and phases can be user defined where the stability of the fields is ensured through digital real-time fast feedbacks programmed in Field Programmable Gate Arrays (FPGAs).

The cavities frequency is measured and readjusted on demand through motor tuners with a LLRF system for each cavity.

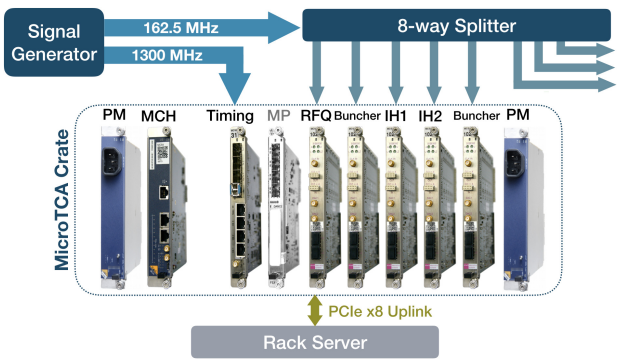


Figure 4: Layout of the LLRF system including RF master oscillator, LLRF controller channels and CPU processing unit.

The configuration of the LLRF system is shown in Fig. 4. The core components of the LLRF controller are based on the MicroTCA.4 standard. Each LLRF regulation consists of an Advanced Mezzanine Card - Rear Transition Module (AMC-RTM) pair. The RTM is an analogue RF preprocessing unit for signal filtering and signal level adjustment and includes the vector modulator, the RF interlock gate and a low-noise clock generator phase locked loop. The AMC performs the sampling of the RF signals and computes the RF field controller on the FPGA. Triggers for data acquisition are generated by a timer module (X2TIMER). The X2TIMER is connected to a 1.3 GHz reference input derived from the 162.5 MHz.

Trigger and clocks are distributed inside the MicroTCA crate over the standard AMC backplane. The CPU is an external 19" mounted rack server that is connected to the AMC modules via 8 PCIexpress Gen 3 uplink in the MicroTCA Carrier Hub (MCH). A dedicated LLRF control server is running on the CPU which allows to control and monitor the controller on the FPGA.

The crate shelf has redundant fan trays and redundant power supplies. The system is fully managed through an Intelligent Platform Management Interface (IPMI). It provides various diagnostic capabilities, remote access to the AMC-RTM modules, remote firmware upgrade and selected power cycling capabilities.

High Power Amplifier

Due to modularity, reliability and decreasing costs, also underpinned by the experience with the HILAC project [5,6], it was decided to use solid state high power amplifier for the 5 cavities. The power budget was planned considering the cavity RF losses, beam loading and a 30 % power margin. It was estimated to use 10 kW amplifier for the buncher cavities, 250 kW and 550 kW for the RFQ and the two IH cavities, respectively. These values may still vary in the future since final RF calculations are still in progress.

Beam Diagnostics

A set of online beam diagnostic tools is positioned along the Linac in order to provide a continuous and stable beam operation, minimising beam losses and allow to protocol beam parameters of long time operation. Since space between the accelerating devices is very limited due to beam dynamics optimisation a sufficient but minimal setup of beam diagnostic devices has been chosen.

A set of 2 current transformers (ACCTs) and 3 beam position monitors (BPMs) are foreseen for the LILac. The location of the devices is shown in Fig. 5. An ACCT as

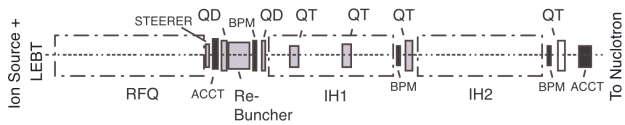


Figure 5: Location of the online beam diagnostic devices.

well as a BPM are located within the MEBT, a second BPM behind IH1 and a BPM and the second ACCT are positioned behind IH2. During commissioning a diagnostic bench is planned to be used in order to tune and optimise the injector but also to calibrate the on-line beam diagnostic elements.

REFERENCES

[1] A. V. Butenko *et al.*, "Development of NICA Injection Complex", in *Proc. IPAC'14*, Dresden, Germany, Jun. 2014, pp. 2103-2105. doi:10.18429/JACoW-IPAC2014-WEPRO067

[2] *Technical Design Document, Light Ion Linear Accelerator up to* 7 MeV/u, Bevatech GmbH, Frankfurt am Main, Germany, 2018.

[3] A. D. Kovalenko *et al.*, "Polarized Deuterons and Protons at NICA@JINR", in *Proc. IPAC'14*, Dresden, Germany, Jun. 2014, pp. 1000-1002, doi:10.18429/JACoW-IPAC2014-TUPRO004

ISBN: 978-3-95450-194-6 ISSN: 2226-0366 doi:10.18429/JACoW-LINAC2018-TUPO017

[4] A. M. Bazanov *et al.*, "Commissioning of new Light Ion RFQ LINAC and first Nuclotron Run with new Injector", in *Proc. RuPAC'16*, St. Petersburg, Russia, Nov. 2016, pp. 153-155. doi:10.18429/JACoW-RuPAC2016-FRCAMH02

[5] A. M. Bazanov *et al.*, "Commissioning of new Heavy Ion LINAC at the NICA Project", in *Proc. IPAC'17*, Copenhagen, Denmark, May 2017, pp. 2362-2365. doi:10.18429/JACoW-IPAC2017-TUPVA116

[6] S. C. Dillon *et al.*, "Development of a Range of High Peak Power Solid-State Amplifiers for use in the Heavy Ion LINAC at JINR, Dubna", in *Proc. IPAC'17*, Copenhagen, Denmark, May 2017,pp. 4108-4110. doi:10.18429/JACoW-IPAC2017-THPIK002

Content from this work may be used under the terms of the CC BY 3.0 licence (© 2018). Any distribution of this work must maintain attribution to the author(s), title of the work, publisher, and DOI.

ISBN: 978-3-95450-194-6 ISSN: 2226-0366 doi:10.18429/JACoW-LINAC2018-TUPO019

SPIRAL2 CRYOGENIC SYSTEM THERMODYNAMIC BEHAVIOUR PREDICTION THROUGH DYNAMIC MODELING

A. Vassal*, P.E. Bernaudin, A. Ghribi, GANIL, 14000 Caen, France
P. Bonnay, F. Bonne, F. Millet, CEA/INAC/SBT, 38000 Grenoble, France

Abstract

SPIRAL 2 (Caen, France) is a state of the art superconducting linear accelerator composed of 26 quarter wave accelerating cavities. Each cavity is plunged in a liquid helium bath at 4.4 K itself surrounded by a thermal shield at 70 K. In this paper, a dynamic model of the cryogenic system of the LINAC is proposed. This model simulates the dynamic behaviour of the 19 cryomodules and their respective valves box connected through the cryodistribution. Model accuracy is evaluated through a comparison between simulation and experimental data. Using the model we should be able to predict the behaviour of the cryogenic system for different beam operating conditions of the accelerator. The model also highlights the link between the cryogenic system and the cavity RF losses through a dynamic estimator of those RF losses in the cavity walls. The latter could be used as a rough estimator of the quality factor of a cavity.

INTRODUCTION

SPIRAL2 accelerator aims at delivering high intensity beams for research in the nuclear fields [1]. It is built around a LINAC (LINear ACcelerator) composed of 26 quarter wave accelerating cavities. Because they are made of bulk niobium, each cavity is plunged in a liquid helium bath. The whole formed by the cavity and its helium bath is called a cryomodule. Liquid helium production and routing is ensured by a complex cryogenic system [2]. To provide the best operating condition for the LINAC it is necessary to understand the behaviour of this cryogenic system. To do so we model the overall SPIRAL2 cryogenic system. Model accuracy is evaluated through experimental comparison. A dynamic estimator of the radio frequency (RF) losses is also proposed as a direct use of the model.

MATERIALS AND METHOD

The oveall cryogenic system of SPIRAL2 is modeled using the Simcryogenics [3] library on MATLAB/SIMSCAPE environment. The model is designed to be control oriented and to allow fast simulation. It means that only the macroscopic physical behaviour (e.g., pressure variation) are considered and not the microscopic ones (e.g., flow distribution in piping). Only two sub-systems of the cryogenic system are considered in this paper: the cryomodules and the cryodistribution. An RF losses estimator is also presented as a direct use of the model.

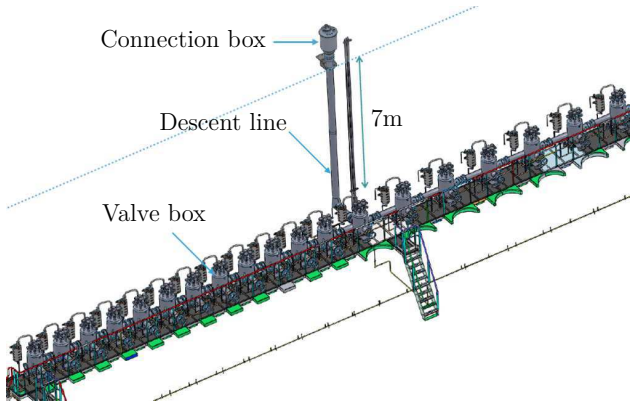


Figure 1: View of the SPIRAL2 cryodistribution without the cryomodules.

The Cryodistribution

The cryodistribution represents the link between the cryoplant and the cryomodules (see Fig. 1). It is composed of four lines: two for the cryomodule bath (supply and return) and two others for the cryomodule shield (also supply and return). The cryodistribution can be seen as multiple pipes connected together as shown in Fig. 2

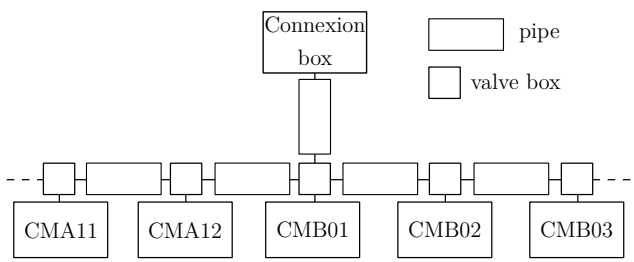


Figure 2: Decomposition of the cryodistribution in multiple pipes - *CMAi represents type A cryomodule whereas CMBi represents type B cryomodule*

To model the flow of helium in those pipes, three physical phenomena are considered:

- Friction: when a fluid is flowing in a pipe, it generates friction between the fluid and the pipe. This friction results in a pressure drop calculated through the Darcy-Weisbach equation: $\Delta P = f_D \frac{L}{D_h} \rho \frac{V^2}{2}$ with ΔP the pressure drop due to pipe friction, f_D the friction factor calculated with the Haaland approximation, L

* adrien.vassal@ganil.fr

Content from this work may be used under the terms of the CC BY 3.0 licence (© 2018). Any distribution of this work must maintain attribution to the author(s), title of the work, publisher, and DOI.

ISBN: 978-3-95450-194-6 ISSN: 2226-0366 doi:10.18429/JACoW-LINAC2018-TUPO019

the length of the pipe, D_h the hydraulic diameter, ρ the fluid density and V the fluid velocity.

- Heat load: the fluid in the pipes is at low temperature (between 80 K to 4.5 K depending on the line) whereas the external environment is at room temperature. So the fluid undergoes a thermal heat load which is modeled through an enthalpy balance equation: $h_{out} \cdot \dot{m}_{out} = h_{in} \cdot \dot{m}_{in} + Q$, where h_{out} and h_{in} respectively represents pipe outlet and inlet specific enthapy, $\dot{m}_{out}$ and $\dot{m}_{in}$ respectively represents pipe outlet and inlet mass flow and Q is the external heat load.

- Gravity: as shown in Fig.1, the LINAC is 7 m underground. Consequently, there is a pressure difference between the bottom and the top of the descent line. This phenomena called hydrostatic pressure is defined by $\Delta P = \rho \cdot g \cdot h$, where ΔP is the pressure difference, ρ is the fluid density, $g = 9.81$ is the gravitational acceleration and h the height.

Once the model of the cryodistribution is established, we use it to define the boundary conditions of the cryomodule model.

The Cryomodule

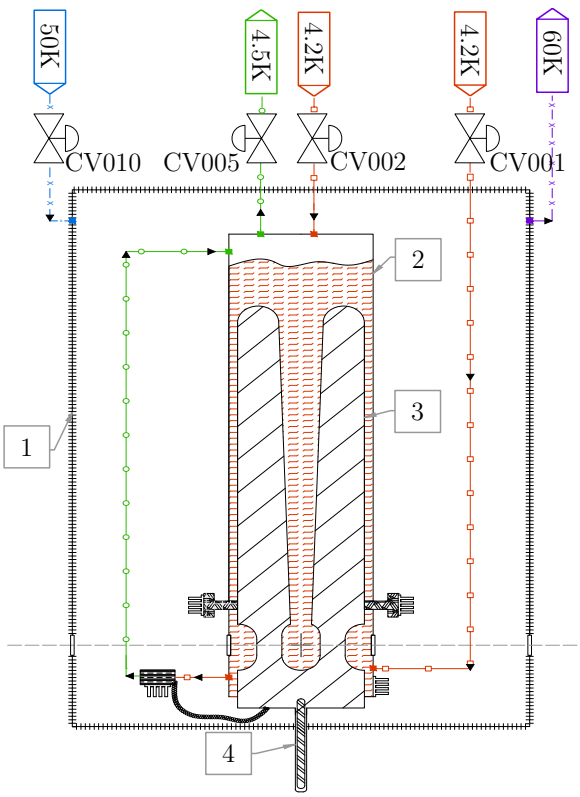


Figure 3: PI& D of type-A cryomodule and its associated valves - *1. The thermal shield, 2. The liquid helium bath, 3. The accelerating cavity, 4. The RF antenna.*

In the case of SPIRAL2 facility, there are two types of cryomodule: a type-A (see Fig. refCryomoduleCMA) and a type-B which respectively contains one and two accelerating cavities. The helium bath is controled through three valves. The valve CV_{001} is used to fill the cryomodule by the bottom during the cooldown whereas CV_{002} and CV_{005} ensure respectively level and pressure regulation in the bath. CV_{010} ensures shiled outlet temperature regulation around 70 K. For more information about the cryomodules please refer to [4] [5].

In terms of thermodynamic behaviour, cryomodule type-A and type-B are similar. The distinctions are the volume of the bath and the heat load extracted by the helium bath as shown in Table 1. The heat load can be decomposed in two parts: the static heat load which represents the influence of the outside environment on the bath and the dynamic heat load due to RF losses in the cavity walls which generate heat according to Joule effect.

Table 1: Comparison of Type-A and Type-B Cryomodule - *The static load is given in measured mean/standard deviation, the dynamic load is the maximum expected.*

Characteristics	Type-A	Type-B
Static load [W]	3.5/1.4	12.5/1.8
Dynamic load [W]	10	20
Helium bath volume [L]	20.5	91.2

The thermodynamic behaviour of a cryomodule is similar to the one of a phase separator: gravity ensures phase separation between liquid and gaseous helium whereas external heat load causes liquid evaporation. From this consideration, we use the equations of previous phase separator model [6] to describe the cryomodule thermodynamic behaviour. An alternative model is also proposed in [7]. Adaptation of this model is necessary to take into account the shape of the helium bath. Using a 3D scheme of the cryomodule, we create a function which takes the volume of liquid in the bath as an argument and outputs the corresponding height of liquid.

The cryomodule model can be used in many ways such as synthesizing controllers for the cryomodule valves, run experiences on simulation or even dynamically estimate the heat load induce by RF losses in the cavity wall as proposed in the next section.

RF Losses Estimator

The measurement of the RF losses (e.g., dynamic heat load) in cavity wall is an indicator of the cavity state. Nevertheless, in the case of SPIRAL2, it is impossible to have a dynamic measurement of those losses while the accelerator is in nominal operating mode. To solve this problem, we design a Luenberger state observer to dynamically estimate this load. This observer (see Fig. 4) is based on a linear version of the proposed cryomodule model and requires the measurement of the valves opening, bath pressure and liq-

Content from this work may be used under the terms of the CC BY 3.0 licence (© 2018). Any distribution of this work must maintain attribution to the author(s), title of the work, publisher, and DOI.

ISBN: 978-3-95450-194-6 ISSN: 2226-0366 doi:10.18429/JACoW-LINAC2018-TUPO019

Content from this work may be used under the terms of the CC BY 3.0 licence (© 2018). Any distribution of this work must maintain attribution to the author(s), title of the work, publisher, and DOI.

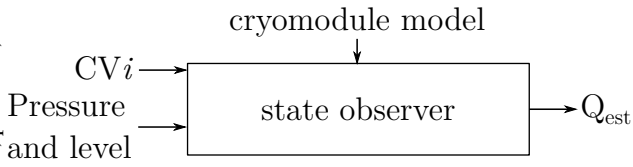


Figure 4: description of the observer - *CVi represents the valves opening whereas Q_{est} is the estimation of the dynamic heat load.*

uide helium level to work in real time. A similar work is proposed in [8] in the case of a refrigerator phase separator.

EXPERIMENTAL RESULTS AND DISCUSSION

Cryomodule Dynamic Model Validation

Cryomodule model accuracy is estimated through a comparison between experimental and simulated data. Do to so, valves CV_{002} and CV_{005} are manually controlled to induce pressure and level variations in the helium bath. Then the same valves variations are applied on the model and both simulated and measured data (i.e., level and pressure) are plotted in the same graphic in Fig. 5.

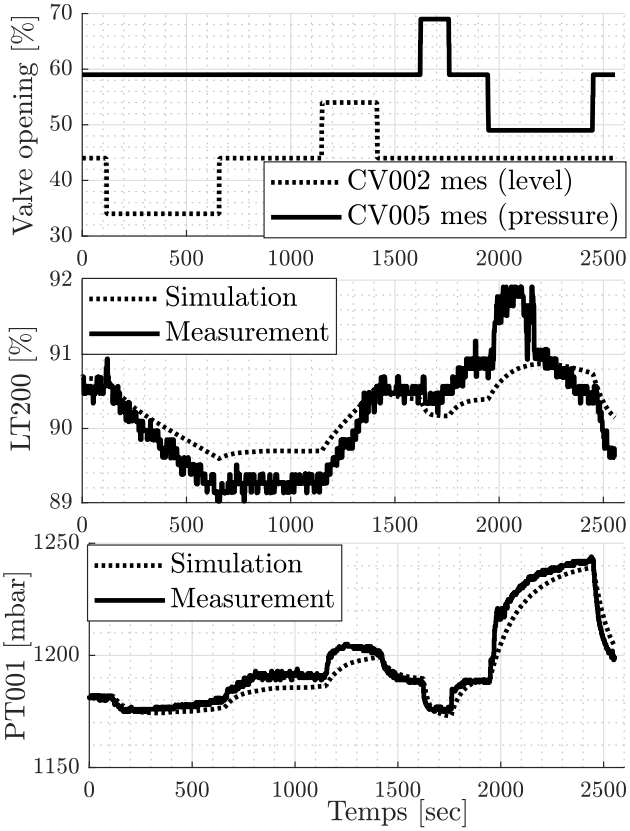


Figure 5: Comparison between experimental and simulated data for type-A cryomodule n°10.

As one can see the model globally reproduces the dynamics of the level and the pressure. The rising pike at time $t = 2000$ s on the level is most certainly due to a sensor deviation as it decreases at time $t = 2200$ s while no valves are moving. Even if it could be improved, we consider that the model is accurate enough to be used for different purposes like the design of an RF losses estimator as described in the next section.

RF Losses Estimator

The goal of the estimator (also called observer in this article) is to estimate the heat load induced by RF losses. As RF system is not fully operational, we mimic the effect of the RF losses with an electrical heater placed at the bottom of the helium bath. To estimate the accuracy of our observer, we generate a heat load step with the electrical heater while the cryomodule is in nominal operating mode. The comparison between estimated and injected heat load is plotted in Fig. 6. At time $t = 25$ s, the electrical heater is risen to its maximum at 43 W.

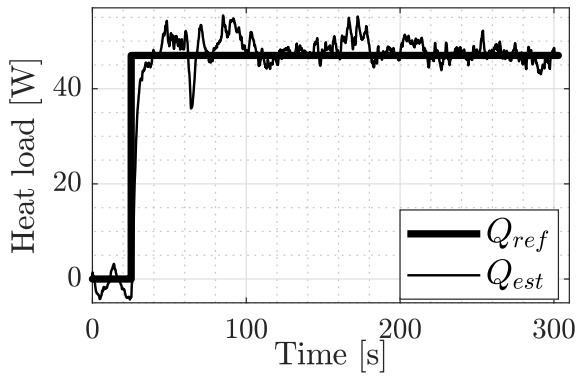


Figure 6: Comparison between injected (ref) and calculated (obs) power.

Despite the oscillations of the estimated heat load around the real value, the observer gives a correct approximation of the heat load injected through the electrical heater. It takes 10 s for the observer to react to the heat load step. The next goals are to reduce this time as much as possible as well as reducing the observer oscillations.

Knowing the RF losses in the cavity, and using equations of the BCS (Bradeen, Cooper, Schriffer) [9] theory, it is possible to have a dynamical estimation of the quality factor of the cavity.

CONCLUSION

SPIRAL2 is a superconducting linear accelerator composed of 19 cryomodules. A model of the cryomodules has been validated through a comparison between simulation and experimental data. As a direct use of the model, an estimator of the RF losses in the cavity walls has also been realized and validated experimentally. Currently, other developments involving the proposed models are in progress,

ISBN: 978-3-95450-194-6 ISSN: 2226-0366 doi:10.18429/JACoW-LINAC2018-TUPO019

especially the design of control algorithm for the cryomodule valves which will be tested during the next cooldown in the late August 2018.

REFERENCES

[1] M. Lewitowicz *et al.*, "The Scientific Objectives of the SPIRAL2 project," GANIL, Research Report, 2006.

[2] A. Ghribi, P.-E. Bernaudin, A. Vassal, and F. Bonne, "Status of the SPIRAL 2 LINAC cryogenic system," *Cryogenics*, vol. 85, no. Supplement C, pp. 44–50, 2017. [Online]. Available: http://www.sciencedirect.com/science/article/pii/S0011227517300553

[3] F. Bonne, P. Bonnay, C. Hoa, G. Mahoudeau, and B. Rousset, "Modelling and Model-Based-Designed PID Control of the JT-60SA Cryogenic System Using the Simcryogenics Library," *IOP Conference Series: Materials Science and Engineering*, vol. 171, no. 1, p. 12028, 2017.

[4] G. Olry, D. Longuevergne, H. Saugnac, P. Bosland, and Y. Gómez-Martínez, "SPIRAL2 cryomodules: status and first tests results," in *14th International Conference on RF Superconductivity (SRF 2009)*. Berlin, Germany: Joint Accelerator Conferences Website, 2009, pp. 495–501. [Online]. Available: http://hal.in2p3.fr/in2p3-00455293

[5] C. Marchand, P. Bosland, G. Devanz, O. Piquet, D. Longuevergne, G. Olry, Y. G. Martínez, P. Bernaudin, and R. Ferdinand, "Performances of SPIRAL2 Low And High Beta Cryomodules," in *SRF Conference*, Sept. 2015, paper WEBA04, pp. 967–972.

[6] B. Bradu, P. Gayet, and S.-I. Niculescu, "A process and control simulator for large scale cryogenic plants," *Control Engineering Practice*, vol. 17, no. 12, pp. 1388–1397, 2009.

[7] C. Regier, J. Pieper, and E. Matias, "Dynamic modeling of a liquid helium cryostat at the Canadian Light Source," *Cryogenics*, vol. 50, no. 2, pp. 118–125, 2010. [Online]. Available: http://www.sciencedirect.com/science/article/pii/S0011227509002197

[8] F. Bonne, M. Alamir, and P. Bonnay, "Nonlinear observer of the thermal loads applied on the heliumbath of a cryogenic refrigerator. Observer design and experimental validation," *Proceedings 5th IFAC Symposium on System Structure and Control*, vol. 46, no. 2, pp. 713–718, 2013. [Online]. Available: https://www.sciencedirect.com/journal/ifac-proceedings-volumes/vol/46/issue/2

[9] J. Bardeen, L. N. Cooper, and J. R. Schrieffer, "Theory of Superconductivity," *Phys. Rev.*, vol. 108, no. 5, pp. 1175–1204, 1957. [Online]. Available: https://link.aps.org/doi/10.1103/PhysRev.108.1175

Content from this work may be used under the terms of the CC BY 3.0 licence (© 2018). Any distribution of this work must maintain attribution to the author(s), title of the work, publisher, and DOI.

ISBN: 978-3-95450-194-6 ISSN: 2226-0366 doi:10.18429/JACoW-LINAC2018-TUPO020

MICROPHONICS INVESTIGATION OF ARIEL e-LINAC CRYOMODULES

Yanyun Ma†, K. Fong, M. Keikha, J. Keir, D. Kishi, S.R. Koscielniak, D. Lang, R.E. Laxdal, R. Nagimov, Z.Y. Yao, Q.W. Zheng, V. Zvyagintsev
TRIUMF, 4004 Wesbrook Mall, Vancouver, BC, Canada
Lutz Lilje, DESY, Notkestrasse 85, D-22607 Hamburg, Germany

Abstract

Now the stage of the 30 MeV portion of ARIEL (The Advanced Rare Isotope Laboratory) e-Linac is under commissioning which includes an injector cryomodule (ICM) and the 1st accelerator cryomodule (ACM1) with two cavities configuration. In this paper, the progress of the microphonics investigation and suppression of ICM and ACM1 is presented.

INTRODUCTION

ARIEL e-Linac is a continuous-wave (CW) electron linear accelerator utilizing superconducting bulk niobium technology at 1.3 GHz. The accelerator is divided into three cryomodules [1, 2]: a single cavity injector cryomodule (ICM) and two accelerating cryomodules (ACM) with two cavities each. The 'Demonstrator' phase of ARIEL was installed for initial technical and beam tests [3]. Then ACM1 cryomodule, high-power RF distribution system and LLRF system were updated for 2 cavities [4]. During commissioning, acoustic noise from the environment vibration generated by cooling water pumps, cryogenic system and vacuum system affect the ACM1 RF performance and final beam energy stability.

PONDERMOTIVE EFFECT

Both ICM and ACM1 are working in phase-locked loop (PLL) self-excited loop (SEL) in CW mode. Unlike the ICM with one cavity and one SEL loop, the two ACM1 cavities are driven by a single klystron with vector-sum control of the two cavity SEL PLL. As such there is no gradient regulation for each individual cavity in the ACM1 [5]. Individual tuner loops are established to maintain the cavity frequency with respect to the established reference phase. Microphonics can excite mechanical resonances in one cavity, perturbing the RF resonant frequency, which can couple to the other cavity via vector-sum regulation. The modulations of the RF field between the two cavities can drive a ponderomotive instability through Lorentz force detuning. The threshold for excitation of this instability is impacted both by ambient microphonic noise that can seed the instability and the precise settings of the two cavity phase loops. The coupled oscillation can deteriorate the e-Linac final energy stability outside specification and needs to be controlled.

During the commissioning, the ACM1 cavities gradients were limited by the ponderomotive effect when the summed voltage was higher than 17 MV. The ACM1 cavities pickup signals showed oscillation in counterphase (Fig. 1) while under vector-sum regulations impacting the energy stability and ultimately the loop stability.

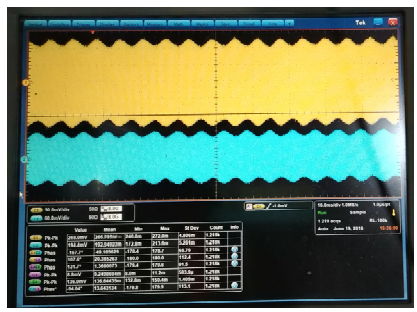


Figure 1: The ponderomotive oscillation of ACM1 pickup signals. The yellow waveform is 1st cavity pickup signal and the green waveform is 2nd cavity pickup signal.

NOISE OF PICKUP SIGNALS

To identify the noise peak for each cavity, the ACM1 was switched from vector-sum mode to single cavity mode and the pickup signals were analysed by phase noise analyser (R&S®FSWP26). Figure 2 shows that there is a noise hump from 10Hz to 400Hz in each pickup signal and indicates the noise sources are universal for all three cavities.

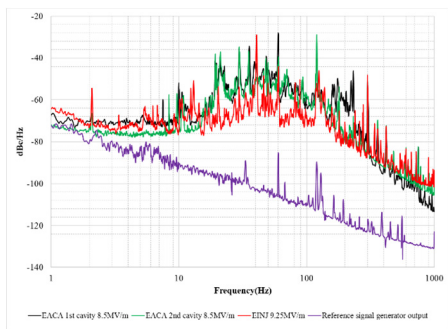


Figure 2: pickup signals noise analyses. During the test the ACM1 was setup in single cavity mode with closed amplitude and phase loop with low proportional gain; the ICM was under operational mode.

The coupling between microphonic noise disturbances and Lorentz force has been measured on ACM1 cavities. Amplitude modulations of various frequencies were added onto the amplitude loop driver while keep the amplitude loop and phase loop closed and fixed tuners position. Both cavities were measured at the similar e-field level. The parameters of the first 5 strongest microphonic disturbances coupling to Lorentz force are listed in Table.1.

† mayanyun@triumf.ca

Content from this work may be used under the terms of the CC BY 3.0 licence (© 2018). Any distribution of this work must maintain attribution to the author(s), title of the work, publisher, and DOI.

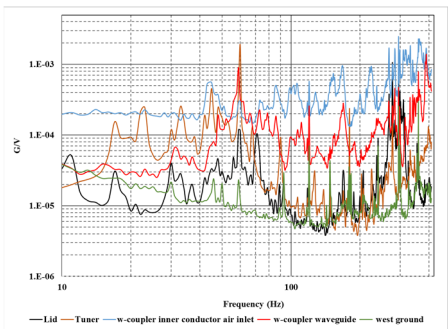
ISBN: 978-3-95450-194-6 ISSN: 2226-0366 doi:10.18429/JACoW-LINAC2018-TUPO020

Table 1. Noise Peaks of ICM and ACM1 Pickup Signals

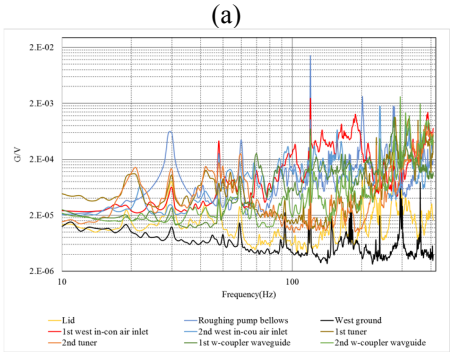
	Frequency (Hz)	Power (dBc/Hz)	Q	K (Hz/(MV/m)^2)
ICM	40.70	-31.60	68.7	
	124.66	-43.57	53.7	
	60.01	-48.38	85.7	
	300.09	-49.76	241.6	
	46.08	-51.26	36.5	
ACM1 1st cavity	59.96	-30.20	96.7	0.2294
	119.96	-36.33	66.6	0.1601
	35.57	-36.66	57.4	0.2359
	48.30	-42.19	60.4	0.3694
	29.66	-42.28	84.7	0.1575
	232.18	-43.11	114.9	0.0727
ACM1 2nd cavity	120.04	-28.87	135.3	0.1386
	35.27	-42.08	93.7	0.1664
	60.02	-44.77	199.9	0.0937
	29.60	-45.15	59.2	0.1597
	47.90	-45.77	159.7	0.0712

MECHANICAL VIBRATION SOURCE

The external vibrations couple to the mechanical system constituted of the cavity and auxiliary components and excite mechanical modes at resonance. An accelerometer (Dytran 3100D24T) was attached to different positions around both cryomodules to measure the mechanical vibrations with Agilent 35670A under different conditions. The results are shown in Fig. 3.



(a)



(b)

Figure 3: ICM and ACM1 vibration signals under operational condition: (a) ICM; (b)ACM1

The water pumps for Klystrons cooling, the roughing vacuum pumping bellows and the couplers air cooling flow have been identified as external vibration sources. Most of the noise peaks in Fig. 3 can be found associated with an external source except 40 Hz signal in ICM and 35 Hz signal in both ACM1 cavities. Cryogenic test result reveals the ICM 40 Hz noise is related with JT valve status as shown in Fig. 4. The 40 Hz noise is also found in ACM1 1st cavity with much less amplitude.

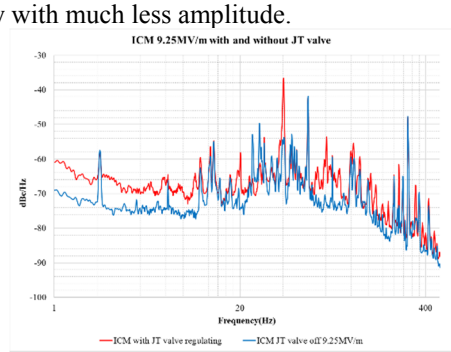


Figure 4: ICM 40 Hz noise and JT valve status. After turning off JT valve the 40 Hz noise peak value decreased about -17 dB.

The 35 Hz is a mechanical mode of cavity as shown in Fig. 5. The external vibration source has not been identified. But it shows correlation with couplers cooling air flow rate and the cooling fans status which was attached on the coupler warm section of the outer conductor.

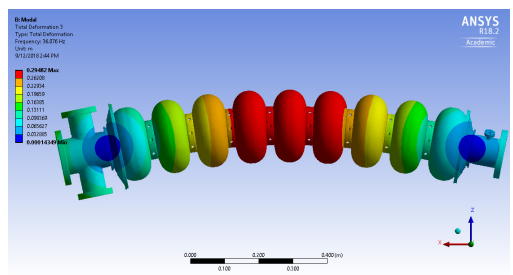


Figure 5: the simulation of 35Hz mode of cavity.

REDUCE EXTERNAL VIBRATION

To improve the beam energy stability, some vibration damping improvements are implemented on both ICM and ACM1 based on the former test results. ACM1 was switched back to vector-sum mode for beam delivery and the vibration damping improvement was implemented step by step with the results shown in Fig. 6.

The ACM1 waveguide damping is temporary proof-of-principle made by wood and rubber inserted between the waveguides and the upper stainless-steel floor near the ACM1. A permanent and optimized damping will be implemented on both ICM and ACM1 waveguide systems in the future.

The ICM vacuum roughing bellows are now fixed and coupler cooling fans are turned off. The most of noise peaks have been reduced as shown in Fig. 7. The coupler cooling air flow optimization and the waveguide vibration absorber installation will be done soon.

DISTURBANCE CAUSED BY LN SYSTEM

The cryomodules use LN_2 for thermal shielding and coupler cooling. The LN_2 supply valve is regulated by the

Content from this work may be used under the terms of the CC BY 3.0 licence (© 2018). Any distribution of this work must maintain attribution to the author(s), title of the work, publisher, and DOI.

ISBN: 978-3-95450-194-6 ISSN: 2226-0366 doi:10.18429/JACoW-LINAC2018-TUPO020

Content from this work may be used under the terms of the CC BY 3.0 licence (© 2018). Any distribution of this work must maintain attribution to the author(s), title of the work, publisher, and DOI.

cryomodule LN_2 exhaust temperature. The ACM1 RF power shows a correlated fluctuation with the LN_2 supply valve status as shown in Fig. 8.

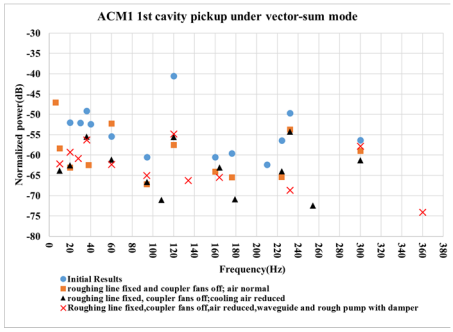


Figure 6: Noise spectra from the phase signal as a function of ACM1 vibration damping. After fixing the roughing bellows and turn off cooling fans most noise peaks are reduced especially the 120 Hz peak; After the cooling air flow is reduced, the noise peaks continue to be reduced with only 3 noise peaks higher than -60 dB; Further damping of the waveguide and the addition of a roughing pump damping pad, the 232 Hz noise peak reduced about -10 dB.

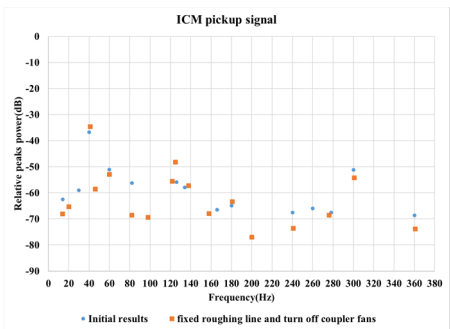


Figure 7: ICM vibration damping.

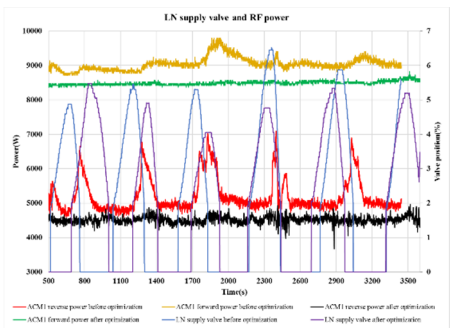


Figure 8: The RF power fluctuation with LN_2 supply valve. The initial regulated temperature was 130K and the reverse power showed 2 kW fluctuation (forward power in yellow and reverse power in red). Then the ACM1 LN_2 regulated temperature decreased to 120 K and the LLRF parameters were optimized, the RF power fluctuation has been reduced (forward power in green and reverse power in black).

After the improvements in Fig. 6, Fig. 7 and Fig. 8 had been implemented, the electron beam was delivered to the final beam dump with 22 MeV (8+7+7) final energy, and the beam energy stability was measured by the BPM which is shown in Fig. 9. The 1mm beam fluctuating translates into about 0.12% of energy fluctuation.

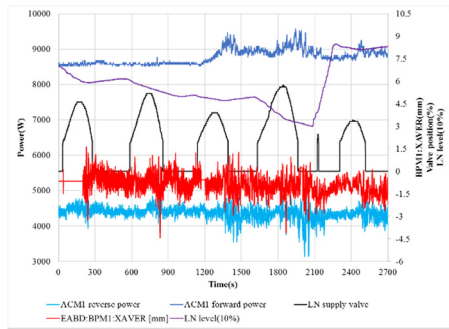


Figure 9: The beam test results with LN_2 supply valve regulated at 120 K. There was still some fluctuation on RF power (forward power in blue and reverse power in green) which became more significant after few LN_2 supply valve opening period (LN_2 level in violet and LN_2 supply valve position in black). The beam energy (red line) had disturbance which correlated with LN valve status.

Then the LN_2 supply valve was switched to constant open mode as shown in Fig. 10.

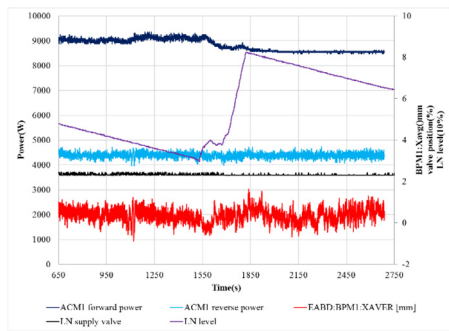


Figure 10: The beam test results with LN_2 supply valve constant open. The fluctuation on beam energy and RF power caused by LN_2 valve has been reduced (in red) and the overall beam energy stability is about ±0.1%. As the LN_2 supply valve (in black) is under constant open mode, the LN_2 tank refilling process (LN_2 level in violet) will affect beam energy (in red) and RF power (forward power in blue and reverse power in green). More optimization need to do on LN_2 system.

DISCUSSION

The stability of ICM and ACM1 cryomodule has been improved and the final beam energy stability is about ±0.1%. In the next step the optimized waveguide damping, coupler cooling air flow rate, water system vibration damping and LN_2 system upgrade will be done. The JT valve mechanical installation and supporter need to be investigated to eliminate the 40 Hz noise. The pickup signals phase monitoring regarding to the reference signal will be set up on EPICS. The effect of the LFD driving ponderomotive instabilities needs further investigation with the threshold presently at a vector sum of 18 MeV.

ISBN: 978-3-95450-194-6 ISSN: 2226-0366 doi:10.18429/JACoW-LINAC2018-TUPO020

ACKNOWLEDGEMENT

ARIEL is funded by the Canada Foundation for Innovation, the Provinces AB, BC, MA, ON, QC, and TRIUMF. TRIUMF receives funding via a contribution agreement with the National Research Council of Canada. The authors would like to thank Tom Powers from JLAB for his inspiring discussion.

REFERENCES

[1] S.R. Koscielniak, *et al.,* "e-Linac photo-fission driver for the Rare Isotope Program at TRIUMF", in Presented at *PAC'11*, New York, USA, April 2011.

[2] R.E. Laxdal, *et al.*, "The Injector Cryomodule for e-Linac at TRIUMF", in *Proc. AIP Conf*, vol. 1434, p. 969, 2012. doi.org/10.1063/1.4707014

[3] M. Marchetto *et al*., "Commissioning and operation of the ARIEL electron LINAC at TRIUMF", in *Proc. IPAC'15*, Richmond, VA, USA, paper WEYC3, pp. 2444–2449.

[4] Yanyun Ma *et al*., "First RF test results of two-cavities accelerating cryomodule for ARIEL e-LINAC at TRIUMF", in *Proc. IPAC'18*, Vancouver, BC, Canada, pp. 4512-4515.. doi:10.18429/JACoW-IPAC2018- THPMK090

[5] Ken Fong *et al*., "Tuners alignment on two 9-cell cavities with single amplifier under self-excited loop", in *Proc. IPAC'18*, Vancouver, BC, Canada, pp.4527-4529 doi:10.18429/JACoW-IPAC2018- THPMK096

Content from this work may be used under the terms of the CC BY 3.0 licence (© 2018). Any distribution of this work must maintain attribution to the author(s), title of the work, publisher, and DOI.

ISBN: 978-3-95450-194-6 ISSN: 2226-0366 doi:10.18429/JACoW-LINAC2018-TUPO022

MANUFACTURING OF X-BAND ACCELERATING STRUCTURES: METROLOGY ANALYSIS AND PROCESS CAPABILITY

J. Sauza Bedolla, S. Atieh, N. Catalan Lasheras, CERN, Geneva, Switzerland

Abstract

The fabrication tolerances of RF components are essential for CLIC X-band accelerating structures to perform efficiently. On one hand, the capability of high power accelerating structures depends on the shape accuracy and the asperity of the inner surfaces, when microwaves pass through the cavity. On the other hand, surface flatness and dimensional tolerances are necessary to guarantee a correct assembly process. Hence, the discs that build up the structure require sub-micrometre specifications and, in order to meet all the needs, ultra-precision machining using single crystal diamond tools is mandatory. This paper shows the analysis of the metrology results of the fabrication of 118 discs (4 accelerating structures). Dimensional and form tolerances are studied following the production order to find drifts in the production and to predict the impact on the assembly process. Finally, process capability is evaluated.

INTRODUCTION

The Compact Linear Collider (CLIC) is an international study for a future high-gradient, multi TeV electron-positron linear collider. In order to test CLIC's main parameters, 72 Accelerating Structures (AS) prototypes, of 22 different designs, have been built during the last ten years. Six principal suppliers of five different countries have participated in the production of CLIC components. This paper evaluates the performance of one of these suppliers in the production of four accelerating structures.

The AS baseline design represents a diffusion bonded stack of cylindrical Oxygen Free Electronic copper discs, which are machined to form a cavity of the RF cells. The discs (or cell) geometry and high order modes damping loads had been extensively optimized in order to maximize the RF-to-beam efficiency, and to meet the beam dynamics and high gradient RF constraints [1]. A regular cell disc is described by about ten different parameters that define its geometry. The internal shape and alignment of the cells are crucial for efficient collider operation. The mechanical tolerances of the cells have been defined according to the RF requirements [2] and they are defined in the CLIC Design Report [3]. Sub-micrometre tolerances are needed to reach the accelerating gradient goal of 100 Mv/m if no tuning is applied and if no temperature correction is allowed to the AS [4].

CLIC TD26R1CC PROTOTYPE

In 2015, there was a re-design of the 3 TeV CLIC main linac AS at 12 GHz [5]. This new prototype is a tapered, damped, 26 regular cells with integrated compact couplers. Main changes include a modification on the "nose" of the waveguide from an elliptical geometry to a 4-th order polynomial function. Moreover, the radius at the bottom of the RF waveguide was increased from 0.5 mm to 1 mm to allow the use of bigger milling cutter, and therefore, to reduce the machining cost. Finally, the disc diameter was increased from 74 mm to 83 mm in order to have a more rigid interface between waveguides and the disc stack. This is the biggest disc diameter design in CLIC production history. The most important tolerances were maintained with respect to the previous design.

- Diameter of the disc Ø83 mm: ±1 µm
- Concentricity of iris with respect to the disc diameter: 2 µm
- Cell iris shape accuracy (zone A): 5 µm
- Cell waveguide shape accuracy: 20 µm
- Flatness accuracy: 1 µm
- Cell iris roughness (zone A) Ra 0.025 µm
- Cell waveguide roughness Ra 0.1 µm

MANUFACTURING

The total fabrication included four structures: 98 standard cells plus 20 compact coupler cells (total 118 discs). This quantity represents the biggest amount of discs ever produced in a single order. The contract was adjudicated to one qualified, CERN's member state company. The production of the whole supply took four months. The parts were produced by a combination of Ultra-Precision diamond fly cutting, milling and turning. All discs were manufactured in batches of four in the milling step, while they were individually machined in the fly cutting and turning steps. The parts were measured at the factory with a customized CMM machine (accuracy better than 0.6 µm) for dimensional control and a white light interferometer (non-contact) for roughness measurements. Results were validated at CERN, where no significant differences were found. Furthermore, visual inspection was also performed before accepting the batch (Figure 1).

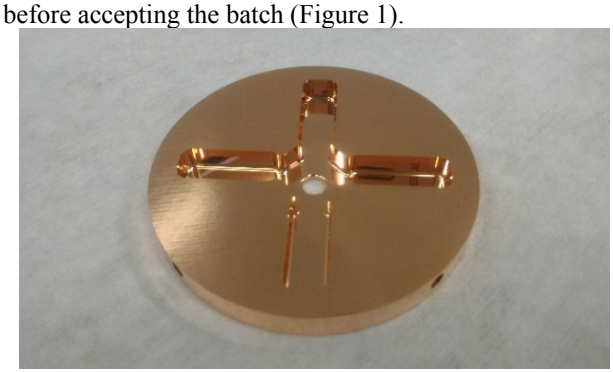


Figure 1: Visual inspection of a standard cell.

Content from this work may be used under the terms of the CC BY 3.0 licence (© 2018). Any distribution of this work must maintain attribution to the author(s), title of the work, publisher, and DOI.

ISBN: 978-3-95450-194-6 ISSN: 2226-0366 doi:10.18429/JACoW-LINAC2018-TUPO022

DIMENSIONAL CONTROL

For each disc, a dimensional report, roughness measurements and form measurements were delivered. Two analyses were performed: production order, to find drifts in the production; the assembly order, to predict the impact on the assembly process. The performed analysis has covered all the tolerances; however, for the sake of brevity, only representative graphs are shown in the following.

The discs were identified according to its position on the AS and to the structure number they belong to. G02-1 represents cell number two of the structure number one. The production order started with regular cell disc number G25 (smallest iris) to G02 (biggest iris); compact coupler cells (G01, G26, G00, G27, G28), that have a different geometry with respect to regular cells, were produced last.

Production Order

Given that, this was the first big production series, the production order analysis allow us to look for signs of non-in statistical control process and to learn if significant changes have been applied during the production. Figure 2 shows the control chart order of the diameter Ø83 mm. Normal variability can be observed along with 14 parts out of tolerance. The non-conform parts were accepted since the maximum deviation was 0.5 µm.

Iris diameter is one important feature since it affects the cell to cell coupling and a variation will cause internal reflections and standing wave pattern [6]. Furthermore, the iris cannot be tuned. Figure 3 shows the difference between the measured iris diameters compared to the nominal. Except from five discs, the process systematically created slightly bigger iris diameter (in average 0.5 µm). The discs that did not follow the trend were originally rejected and manufactured, in a second batch, at the end of the production. Even if the parts do not follow the general trend, they are still within the 5 µm tolerance.

Assembly Order

The objective is to identify the variability, in a single graph, of the 29 discs that builds up one structure. Figure 4 shows the structure number one where two discs, cells G00 and G21, are out of the 1 µm tolerance, while G25 is at the upper limit. The G00 disc geometry is different with respect to the normal cells. It presents a non-continuous surface and, for this reason, when discs are unclamped the flatness increases. The G00 is located at the bottom of the structure and it is assumed that the non-perfect surface will be flattened by the weight of the rest of the structure.

In Figure 5, the four structures are arranged in a boxplot. The bigger the box (and the whiskers), the bigger the variability of the measurements. The graph shows that first and third structure have less variability compare to second and fourth structures. Moreover, outliers, measurements distant from the rest of the observations, are present in the four structures. These outliers correspond to the already cited coupler cells (G00) and to regular cells out of tolerance at the beginning of the production. From the first twenty produced discs, there were six parts out of the tolerances. The firm identified the root-cause and introduced a second intermediate fly-cutting operation that greatly improve the flatness of the rest of the discs.

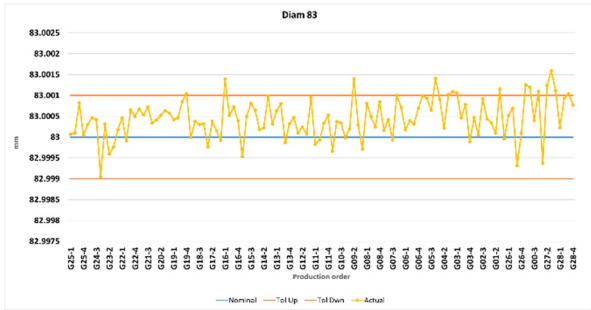


Figure 2: Control chart of Ø83 mm.

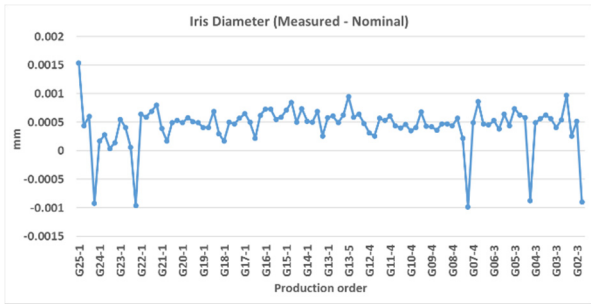


Figure 3: Control chart Iris diameter.

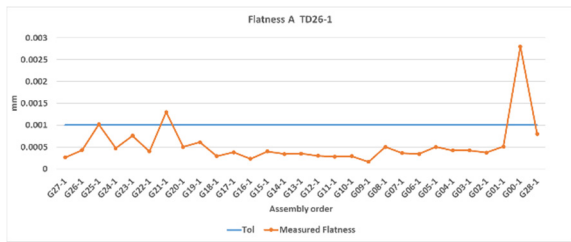


Figure 4: Control chart flatness A structure TD26-1.

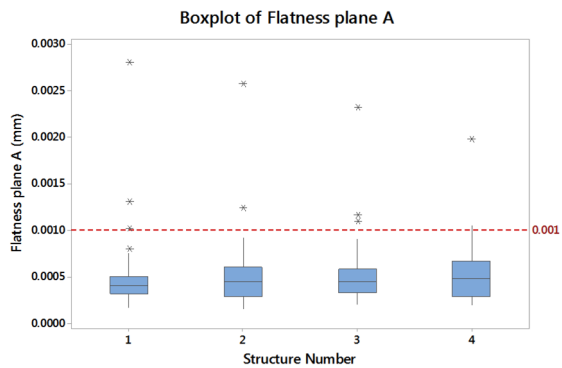


Figure 5: Box plot of flatness plane A.

Roughness and Shape Accuracy.

Scratches, machining marks or sharp features on the cavity surface of the AS can greatly affect its performance. For this reason, roughness was evaluated at six different positions: bottom of the waveguide, turning milling step (two zones), reference plane A, iris (two zones). The roughness measurements were largely conform to the specification. Figure 6 shows the most delicate step for the turning milling zone. In this transition zone, a step of 1 µm is allowed.

Content from this work may be used under the terms of the CC BY 3.0 licence (© 2018). Any distribution of this work must maintain attribution to the author(s), title of the work, publisher, and DOI.

ISBN: 978-3-95450-194-6 ISSN: 2226-0366 doi:10.18429/JACoW-LINAC2018-TUPO022

Content from this work may be used under the terms of the CC BY 3.0 licence (© 2018). Any distribution of this work must maintain attribution to the author(s), title of the work, publisher, and DOI.

Moreover, shape tolerances of the iris and waveguides were also controlled. Figure 7 presents two different shape measurements on one cell: one section of the iris and the nose of the waveguide. All discs were largely in tolerance.

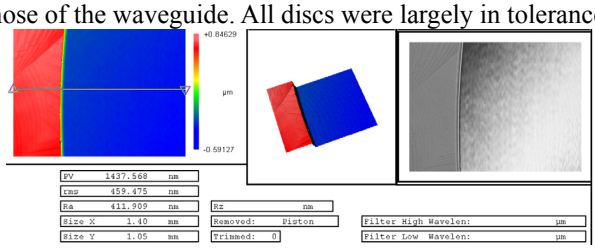


Figure 6: Roughness measurement.

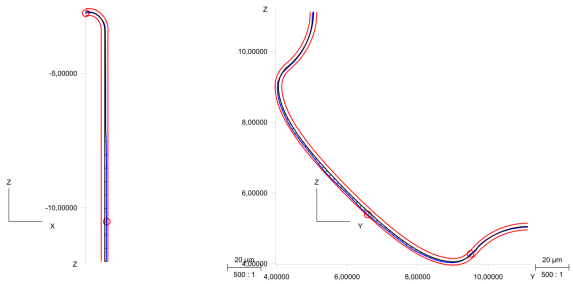


Figure 7: Shape analysis.

PROCESS CAPABILITY

Process evaluation is important for a successful industrialisation. Among several techniques, process capability is considered the most effective method in selecting quality products or parts [7]. Process capability compares the output of an in-control process to the specification limits by using capability indices [8]. Cpk is an index (a unitless number) which measures how close a process is running to its specification limits. The greater the Cpk index, the lesser is the process natural variation.

Figure 8 shows the process capability of Ø83 mm fabrication tolerance. The process has a Cpk = 0.42 which can be translated into 106244 defectives Parts Per Million (PPM). However, at the beginning of the fabrication the tolerance was relaxed from ±1 µm to ±2 µm. Considering this enlarged specification, the production reaches a Cpk = 1.1 thus 14 PPM. The tolerance relaxation was agreed after a technical discussion, capability analysis and commercial settlement. A similar analysis was performed on the concentricity of the iris and external diameter. The Cpk shows an impressive 2.24 hence 0 PPM (Figure 9).

CONCLUSIONS

The production analysis allowed us to identify changes in the manufacturing of the parts: a second fly cutting operation was added in order to improve the flatness. Moreover, the assembly analysis allow us to identify variability among the different structures. Besides some specific problems (i.e. flatness at the beginning of the production), the processes are under statistical control with few parts out of the specifications. The concentricity of the iris w.r.t. external diameter has even a large Cpk. Shape accuracy and roughness of the different features are largely conform. Considering the tight tolerances and the large production, results are positive. An important benefit for CLIC is the correct evaluation of supplier performance by identifying the technically and economically correct tolerances.

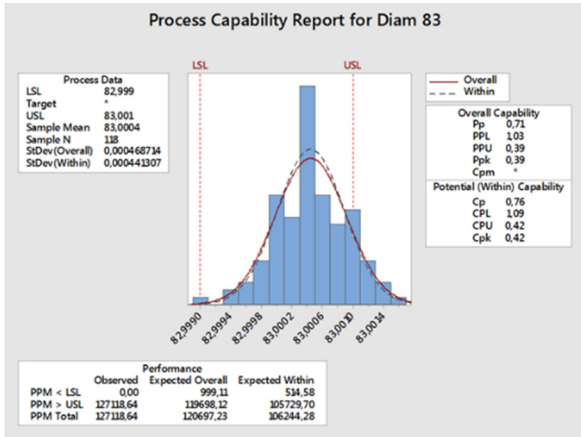


Figure 8: Process capability of Ø83mm.

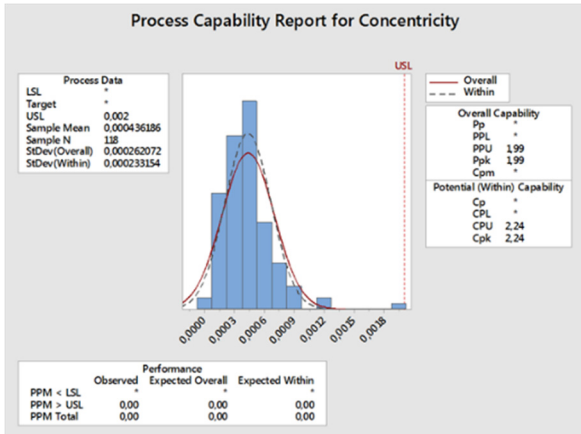


Figure 9: Process Capability of concentricity.

REFERENCES

[1] A. Grudiev and W. Wuensch, "Design of the CLIC main linac accelerating structure for CLIC Conceptual Design Report", in *Proc. of LINAC 2010*, Tsukuba, Japan, 2010, paper MOP068.

[2] V. Soldatov and A. Samoshkin, "Engineering design and fabrication of X-Band damped detuned structure for the CLIC study", in *Proc. of IPAC2011*, San Sebastian, Spain, 2011, paper MOPC037.

[3] CERN, "A Multi-TeV Linear Collider based on CLIC Technology: CLIC conceptual design report", CERN, Geneva, Switzerland, 2012, DOI 10.5170/CERN-2012-007.

[4] R. Zennaro, "Study of the machining and assembly tolerances for the CLIC accelerating structures", EUROTeV, 2008, EUROTeV-Report-2008-081.

[5] H. Zha and A. Grudiev, "New CLIC-G Structure Design", CERN, Geneva, Switzerland, 2016, CLIC-Note-1066.

[6] A. Grudiev, "Tolerances coming from RF", Internal presentation CERN, 2014, unpublished.

[7] R. J. Linn, F. Tsung, L. Ellis and W. Choi, "Supplier Selection Based on Process Capability and Price Analysis", vol. 18, 2006, DOI 10.1080/08982110600567475.

[8] NIST/SEMATECH, e-Handbook of Statistical Methods, NIST, 2012, http://www.itl.nist.gov/div898/handbook.

ISBN: 978-3-95450-194-6 ISSN: 2226-0366 doi:10.18429/JACoW-LINAC2018-TUPO023

PRESERVING MICROMETRE TOLERANCES THROUGH THE ASSEMBLY PROCESS OF AN X-BAND ACCELERATING STRUCTURE

N. Catalan Lasheras, A. Grudiev, J. Sauza Bedolla, H. Bursali, A. Solodko, K. T. Szypula, S. Lebet, E. Rodriguez Castro, P. Sobrino Mompean, CERN, Geneva, Switzerland

Abstract

The CLIC structures are designed for operating at X-Band, 2π/3 traveling wave mode with a loaded 100 MV/m gradient. Mechanical tolerances, at the submicron level, are required to satisfy the RF design constraints and beam dynamics and are reachable using ultra-precision diamond machining. However, inherent to the manufacturing process, there is a deviation from the nominal specifications and as a result; incorrect cavity dimensions produce a less efficient linac. Moreover, the assembly process increase the difference from the original geometry. As part of a cost and manufacturability optimization of the structures for mass production, this study aims to identify a correlation between frequency deviations and geometrical errors of the individual discs of the accelerating structures caused by the production process. A sensitivity analysis has been carried out to determine the most critical parameters. Cell frequency deviations have been monitored by bead pull measurements before and after bonding. Several accelerating structure prototypes have been tested to determine our assumptions and to assess if the assembly process preserves the tight tolerances achieved by machining.

INTRODUCTION

CLIC baseline accelerating structure (AS) stack is composed by a variable quantity of discs of the prototype being produced. The cavity formed by the disc represents the RF zone. The geometry of the disc depends on different parameters and each of these parameters contributes differently to satisfy the RF design. Sub-micrometre tolerances are needed to reach the accelerating gradient goal of 100 MV/m if no tuning is applied and if no temperature correction is allowed to the AS [1]. However, the normal variability of the manufacturing processes makes that the disc presents discrepancies with respect to the nominal design. This paper aims at identifying the most critical design parameters through the means of a sensitivity analysis of the geometrical effects on the AS regular cells. For this purpose, six AS of two different prototypes are analysed: T24 N4 and N5 (Figure 1.a) and TD26 N1 to N4 (Figure 1.b).

GEOMETRICAL PARAMETERS

RF designs of both T24 and TD26 discs has been completed by ANSYS High Frequency Structure Simulator (HFSS) software. The T24 prototype consists of 24 undamped cells with a weak tapering of the irises [2]. The geometry of the standard cell is illustrated in Figure 2.a: ***b*** represents the inner radius; ***a*** is the iris aperture and ***h*** the height of the cell. The TD26 prototype also consists of 26 tapered cells with integrated coupling cells [3]. The TD26 cells have more complicated RF design compare to T24 cells because they include damping waveguides as illustrated in Figure 2.b (design with symmetry plane) where ***a***, ***b***, ***L***, ***w*** and ***HW*** represents iris aperture, inner radius, height, width and length of the damping part of the cell.

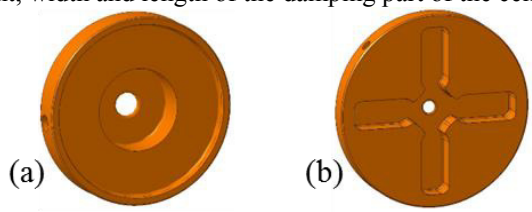


Figure 1: (a) T24 and (b) TD26 regular disc.

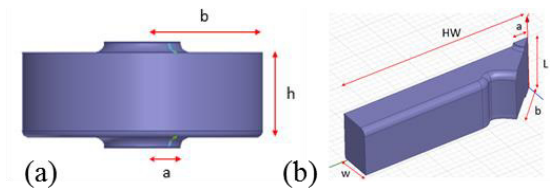


Figure 2: Geometrical parameters of (a) T24 and (b) symmetry plane of TD26.

SENSITIVITY ANALYSIS

In a sensitivity analysis, each geometric parameter is varied slightly around the design value to determine the sensitivity of the return loss to that parameter. The analysis was performed using ANSYS HFSS. The results for both T24 and TD26 included the first, middle and last cells (only first cell is shown) with ±10 µm interval around the nominal design value. According to the simulation results, the most sensitive geometrical parameter to the frequency change is the inner radius ***b*** for T24 cells, followed by the iris diameter **a** (Figure 3).

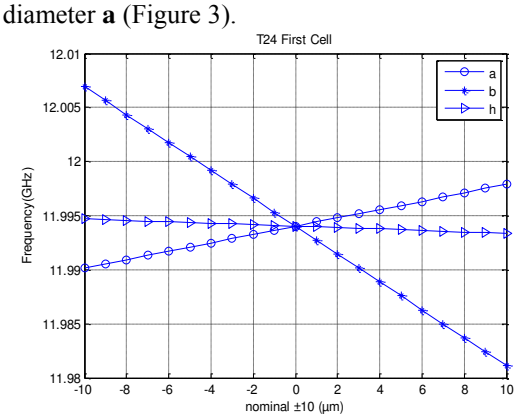


Figure 3: Frequency sensitivity of T24 cell.

The same behaviour of the cell parameters to frequency change is still valid for TD26 cells. The most sensitive geometrical parameter to frequency change is the inner radius ***b*** as T24, followed by the iris diameter (Figure 4).

Content from this work may be used under the terms of the CC BY 3.0 licence (© 2018). Any distribution of this work must maintain attribution to the author(s), title of the work, publisher, and DOI.

ISBN: 978-3-95450-194-6 ISSN: 2226-0366 doi:10.18429/JACoW-LINAC2018-TUPO023

Content from this work may be used under the terms of the CC BY 3.0 licence (© 2018). Any distribution of this work must maintain attribution to the author(s), title of the work, publisher, and DOI.

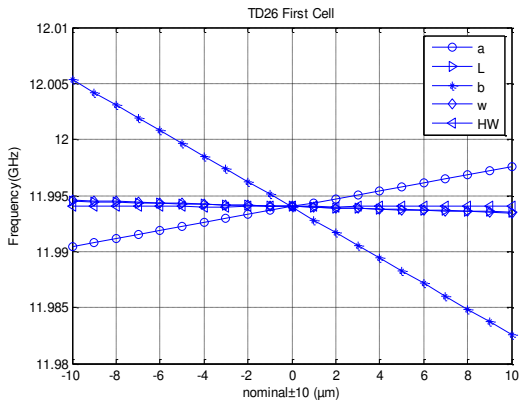


Figure 4: Frequency sensitivity of TD26 cell.

PRODUCTION AND METROLOGY

All discs of both prototypes were produced by ultra-precision diamond machining. In the case of the T24 by turning while TD26 by a mix of turning and milling. They were produced by two different companies. All discs were re-measured at CERN with an optical (non-contact) microscope (accuracy 4 μm).

In general, the ***b*** parameter was always smaller for all discs of both prototypes. The quality of all discs is homogeneous with maximum variability between discs of the same structure up to 5 μm (see Table 1). This range is smaller than the ±10 μm used for the simulation. Figure 5 and Figure 6 presents the b measurements of T24 and T26 structures respectively.

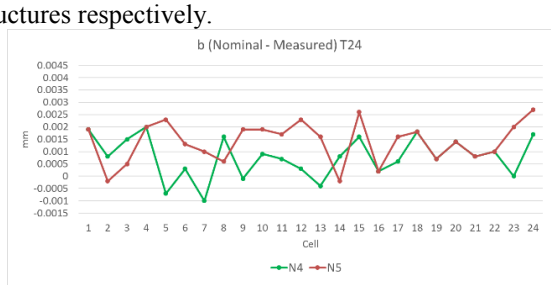


Figure 5: T24 structures (b measurement).

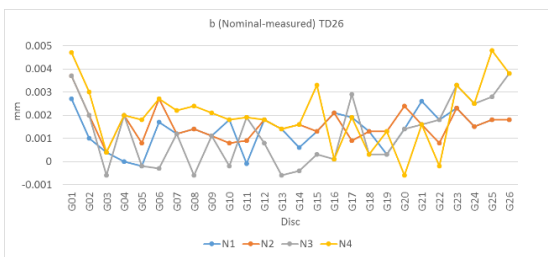


Figure 6: TD26 structures (b measurement).

BEAD PULL MEASUREMENTS

The individual frequency deviations of the accelerating discs were obtained by bead pull measurement and analysed by tuning software [4]. The bead-pull method measures in a single bead passage the amplitude and phase advance of the accelerating mode and allows determining the frequency error of each individual cell. The bead pull measurements were done for all T24 and TD26 disc stacks before bonding (Figure 7 and Figure 8) and T24 structures after bonding (Figure 11). Frequency deviation are uniform with reduced variability.

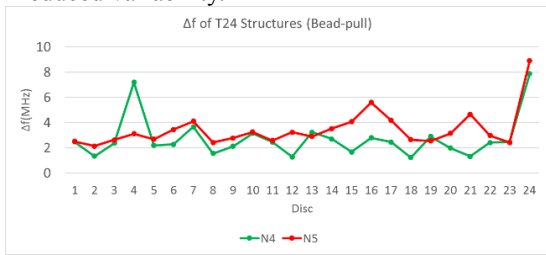


Figure 7: Bead pull measurement T24 before bonding.

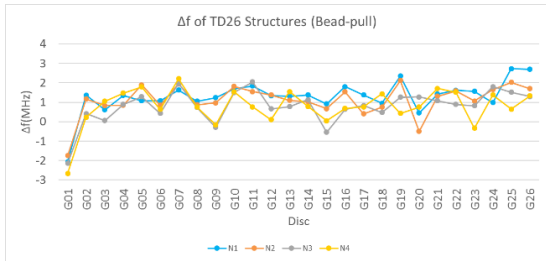


Figure 8: Bead pull measurement TD26 before bonding.

Table 1. Range and Correlation of ***b*** Parameter Before Bonding.

Structure	Min value (mm)	Max value (mm)	Range (mm)	Correlation coefficient (*r*)
T24 N4	-0.001	0.003	0.004	-0.038
T24 N5	-0.001	0.002	0.003	-0.069
TD26 N1	0	0.002	0.002	-0.193
TD26 N2	0	0.003	0.003	-0.59
TD26 N3	0	0.004	0.004	-0.09
TD26 N4	0	0.005	0.005	-0.4

CORRELATION RESULTS

The linear correlation represents the strength of relationship between two different datasets and identified by a coefficient *r*. The coefficient value ranges from +1.0 (strong positive correlation) to -1.0 (strong negative correlation), being 0 no correlation at all. According to the inverse proportion between frequency change and inner radius dimension, a negative correlation is expected.

Before Bonding

The correlation coefficients between imperfections in inner radius and frequency deviations of individual cells is presented in Table 1. There is no visible correlation for both T24 structures (only N4 is shown on Figure 9). For TD 26, on one hand, N1 and N3 structures have no visible correlation. On the other hand, N2 and N4 show negative moderate correlation (only N2 is shown on Figure 10).

After Bonding

After bonding, the straightness of the structure and the disc diameter were measured in a CMM. Since the discs are bonded, neither optical nor mechanical measurements can be done at the interior of the RF cavity. The disc diameter is the only accessible surface. It has been observed in

ISBN: 978-3-95450-194-6 ISSN: 2226-0366 doi:10.18429/JACoW-LINAC2018-TUPO023

several structures that after bonding the external disc diameter reduces in average 8 µm. The only way to assess ***b*** modification after bonding is to cut the structure immediately after with the consequent loss of the structure. Moreover, it is necessary to keep in mind that cutting means also measurement references losses. Therefore, the established hypothesis is that copper sublimation creates a smaller disc and a bigger ***b*** and therefore a reduction on the frequency.

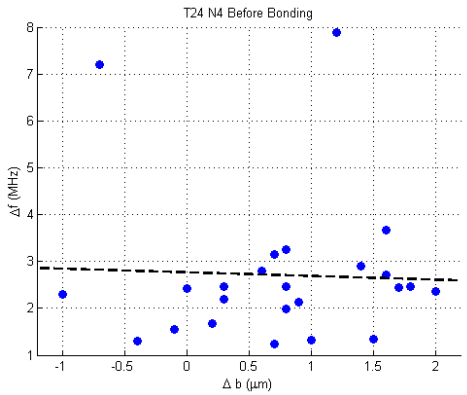


Figure 9: Scatterplot for T24 N4 before bonding.

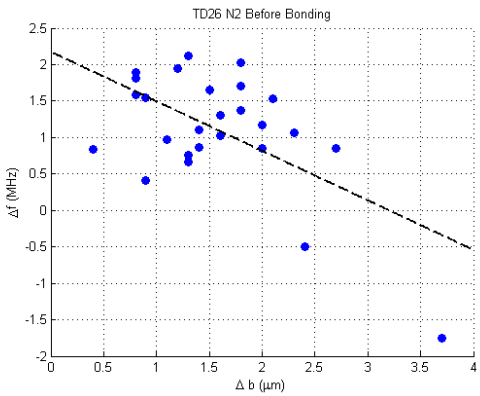


Figure 10: Scatterplot for TD26 N2 before bonding.

Unfortunately, for T24 N4, the diameter after bonding was not measured. The straightness of the structure after bonding was 15 µm. For the N5, there was a diameter reduction of 7 µm on average and a straightness of 30 µm. Frequency deviations of the cells before and after bonding obtained for T24 N4 and N5 have a similar general trend (Figure 11). On both structure there is a reduction of the frequency deviation. It is then clear that there has been a change on the geometry of the cells as expected confirming the hypothesis. The assembly method and bonding temperature curves were almost identical for both structures though two different suppliers perform the heat treatment. Moreover, another source of variation could be that other parameters of the disc were also affected (i.e. iris) and, as a result, they have also impact on the frequency reduction.

At the moment of writing this paper, TD26 structures were not yet bonded, and for this reason, the analysis could not be extended to those structures.

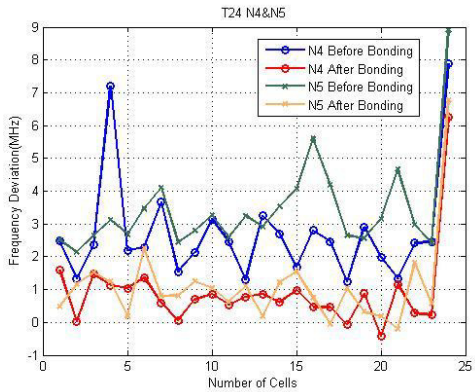


Figure 11: Frequency deviation before and after bonding.

CONCLUSION

The sensitivity analysis found that, among several parameters, the inner radius ***b*** contributes the most to the frequency change for both prototypes. According to the same analysis, a negative correlation between the two factors was expected. Parameter ***b*** measurements of all the discs for both prototypes are homogenous with reduced variability (maximum data range 5µm). As seen from the correlation analysis, before bonding there is no visible linear correlation except of TD26 N2 and N4: both structures show negative moderate correlation. The lack of correlation may be the effect of the low accuracy of the measurements processes: the accuracy of the microscope is worse than the tolerances at stake; frequency deviations before bonding are affected by the mechanical contact of the disc stack. Consequently, both measurement processes have to be greatly improved in order to get reliable data. The ***b*** parameter measurement is now an important requirement for suppliers. Another possibility is that the data follows another type of correlation or the combined effect of more than one parameter.

Finally, there is evidence of a geometry change in the cells after bonding since there is a reduction of frequency deviation. Nevertheless, it is not possible to numerically assess the change due to the inaccessibility of the RF cavity. Other possible causes need to be further investigated.

REFERENCES

[1] R. Zennaro, "Study of the machining and assembly tolerances for the CLIC accelerating structures" EUROTeV, 2008.

[2] A. Grudiev, "T24 vg1.8 disk 12WNSDVG18 CLIC_G undamped 12 GHz" EDMS 1068314, 2011.

[3] H. Zha and A. Grudiev, "RF design and parameters of 2015 re-baselined 3TeV CLIC main linac AS at 12 GHz with compact couplers" EDMS 1524527, 2015.

[4] J. Shi, A. Grudiev and W. Wuensch, "Tuning of X-band traveling wave accelerating structures" *Nucl.Instrum.Meth. A704,* 14-18, March 2013.

Content from this work may be used under the terms of the CC BY 3.0 licence (© 2018). Any distribution of this work must maintain attribution to the author(s), title of the work, publisher, and DOI.

ISBN: 978-3-95450-194-6 ISSN: 2226-0366 doi:10.18429/JACoW-LINAC2018-TUPO027

SERIES PRODUCTION OF THE SPECIFIC WAVEGUIDE DISTRIBUTION FOR THE EUROPEAN XFEL AT DESY

B.Yildirim[1], S.Choroba[1], V.Katalev[1], P.Morozov[1], Y.Nachtigal[1], E.Apostolov[2]
[1]DESY, Hamburg, Germany
[2]Technical University of Sofia, Bulgaria

Abstract

The European XFEL uses 100 accelerating cryomodules. One RF station with 10 MW klystron supplies, through a waveguide distribution, four cryomodules with eight cavities each. The RF station operates at 1.3 GHz, 1.37 ms pulse width and 10 Hz repetition rate. The results of the cryomodule test have shown however different maximum gradients for each cavity. The maximum gradient has been measured between 11 MV/m and 31 MV/m, which requires cavity power of 29 kW to 230 kW. To operate with the maximum energy for every cryomodule, it is necessary to supply individual power to the cavity. In this case the weakest cavity problem can be avoided. For this goal, a specific waveguide distribution has been developed. 100 waveguide distributions have been successfully tailored, produced, and tested at the Waveguide Assembly Test Facility (WATF) at DESY and finally assembled to the cryomodules.

We present the series production of the specific waveguide distributions at the WATF.

REQUIREMENTS FOR WAVEGUIDE DISTRIBUTION PRODUCTION

To meet the requirements for measuring such complex waveguide distribution, basically three different test stands have been created for special procedures of measurements at the Waveguide Assembly Test Facility (WATF), binary cell test stand, LLRF test stand and HPRF test. The installation of all test stands had taken a lot of time due to the mechanical control and RF control. In addition, the custom-built test stands needed special equipment to avoid mistakes during measurements.

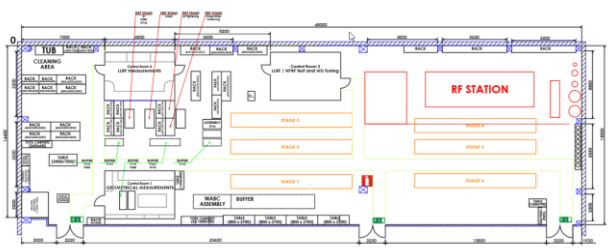


Figure 1: Layout of the WATF.

Fig. 1 shows the 670 m^2 area of the WATF. The WATF includes two RF laboraty for LLRF and HPRF tests of the waveguide distributions. In addition the WATF area has a laboraty for the waveguide components referring to the geometric parameter control. An assembly area with five movable platforms for installation of the waveguide distributions is also part of the WATF. Many auxiliarities systems such as waveguide distribution support hangers, water cooling systems and cable trays are available at the WATF. Furthermore there is a test area for reliability position tests of the movable phase shifters and for pneumatic components. The WATF includes test areas for cooling water leakage, for pressure hydraulic tests and for checking of isolators cooling water flow sensors. In addition there is an area for cleaning, drying and dust hermetically covering of the waveguide components. To avoid problems with logistic time from main store, there is a small area for storing six waveguide distributions.

The working process at the WATF provides a parallel installation of different systems such as waveguide distribution supporting structures, water cooling systems, and flexibility in the assembly activities organization.

More than 150 complex mounting, adjustment, measurement and control operations are performed at the WATF for each waveguide distribution.

The waveguide distribution is based on the tunable binary cells and the tunable asymmetric shunt tees [1]. It consists of several specific waveguide components, which were created precisely to operate with the maximum energy for every cryomodule. On the one hand, the waveguide distribution should have a compact size, on the other hand it should supply high pulse RF power to the individual cryomodule cavities with high flexibility by only one power klystron.

Each RF station of the test facility consists of a 5 MW RF station, with a waveguide distribution. Each waveguide distribution supplies RF power to eight cavities, four pair of cavities as shown in Fig. 2.

In order to satisfy these conditions, specific waveguide components have been developed and integrated in the waveguide distribution for the series production of the specific waveguide distribution.

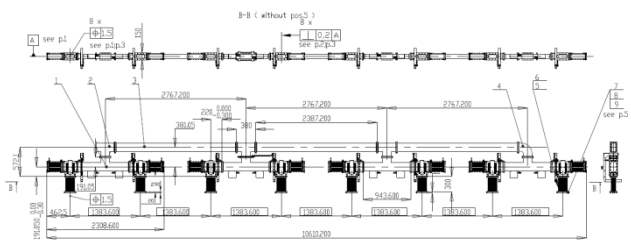


Figure 2: Layout of the XFEL waveguide distribution.

Content from this work may be used under the terms of the CC BY 3.0 licence (© 2018). Any distribution of this work must maintain attribution to the author(s), title of the work, publisher, and DOI.

ISBN: 978-3-95450-194-6 ISSN: 2226-0366 doi:10.18429/JACoW-LINAC2018-TUPO027

FROM SHUNT TEE TO BINARY CELL

In order for the XFEL to work with the maximum energy for every cryomodule, each cavity has to be fed with power individually. Therefore the power distribution for each cavity has to be calculated. The first step is to define the long shunt tee for a pair of cavities. To obtain specific components from standard components, eight types of long shunt tees have been developed. Four each for right waveguide distribution and four each for left waveguide distribution. All waveguide distributions are based exactly on the tunable binary cells. The main reason for these eight types of binary cells is the acceleration of the production rate for the waveguide distributions. The schematic below shows the dynamic range of a right type binary cell (see Fig. 3).

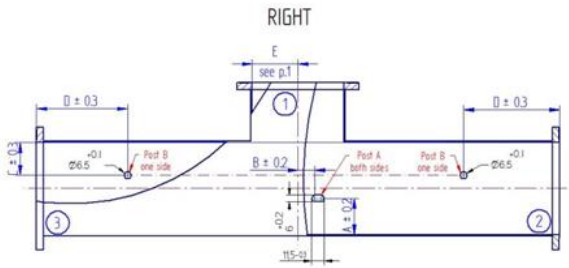


Figure 3: Layout of a right type shunt tee.

Each output port is supplied through the shunt tee which divides the RF power individually to the two cavities. The dimension of B is changing from 0 mm to 15 mm depending on the type of the binary cell [1]. Furthermore, two phase shifters as shown in Fig. 4 are integrated into the shunt tee to compensate the phase difference during tuning. Depending on the phase shifter position, the RF power is distributed between the two output ports. A piston is driven by a linear positioning system with stepping motors. The linear positional accuracy is better than 0.1 mm. By moving the phase shifter up to 25 mm the phase is changing up to 90 degrees. To achieve maximum energy efficiency, the phase has to be 0 degrees between both outputs of the shunt tee. Due to the positions of the phase shifters the coupling ratio and the standing wave ratio (SWR) can be tuned in a very reliable way. This delivers an error rate of only ±0.1 dB coupling ratio and a SWR of maximum 1.20 related to the binary cells [1]. In addition, two isolators are assembled to the two arms of the shunt tee as shown in Fig 4. The isolators consist of a circulator with ferrites and a dummy load, which is used directly after the power source to protect it from high reflected power.

400 binary cells with completely different coupler ratios and SWR have been produced, tuned and tested for the European XFEL at the WATF.



Figure 4: Measuring of a binary cell with all components at the binary cell test stand.

FROM BINARY CELL TO WAVEGUIDE DISTRIBUTION

After the tuning of each waveguide component, the binary cells have been combined with three asymmetric shunt tees, three fixed phase shifters, and one H-bend. One asymmetric shunt tee is shown in Fig. 5. The waveguide distribution enables a flexible division of the power for each cavity to ensure that the cavities can work with their maximal individual power. 300 fixed phase shifters, 100 H-bends and 300 completely individual asymmetric shunt tees with the dynamic range of 0.89 dB to 7.27 dB have been produced, tested and assembled to the waveguide distributions as shown in Fig. 6.

The installation of the 10.6 m long system has completed with a special setup, which provides an accuracy level of ±1 mm and ±0.15 degrees. This allows for the installation of the waveguide distribution to the cryomodule without any stress on the main coupler of the cryomodule.



Figure 5: Asymmetric shunt tee of a waveguide distribution.

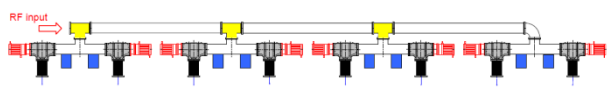


Figure 6: Waveguide distribution for the European XFEL.

Content from this work may be used under the terms of the CC BY 3.0 licence (© 2018). Any distribution of this work must maintain attribution to the author(s), title of the work, publisher, and DOI.

ISBN: 978-3-95450-194-6 ISSN: 2226-0366 doi:10.18429/JACoW-LINAC2018-TUPO027

Content from this work may be used under the terms of the CC BY 3.0 licence (© 2018). Any distribution of this work must maintain attribution to the author(s), title of the work, publisher, and DOI.

LLRF MEASUREMENTS AND HPRF TEST OF WAVEGUIDE DISTRIBUTION

For LLRF measurements SWR, the coupling ratio and the phase of each output and the forward and reflected pickups have been measured by using a special measurement setup. In addition the waveguide distribution has been measured with open and short planes for each output. After fine-tuning at LLRF test stand, final measurements at HPRF test stand have been done as shown in Fig. 7. By using special software, as demonstrated in Fig. 8, the waveguide distribution has been measured under high power. The special software allows for a dramatic decrease of nearly ten times the tuning and test times. To increase the reliability of the waveguide distribution and avoid problems in the XFEL tunnel, a stress test has been done with 20 to 30 percent more power than the specification of the cryomodule allows. Figure 9 shows the temperature for each isolator at HPRF test stand.



Figure 7: Measuring a waveguide distribution at HPRF.



Figure 8: Measuring results of coupling ratio and phase for each output at HPRF test stand.

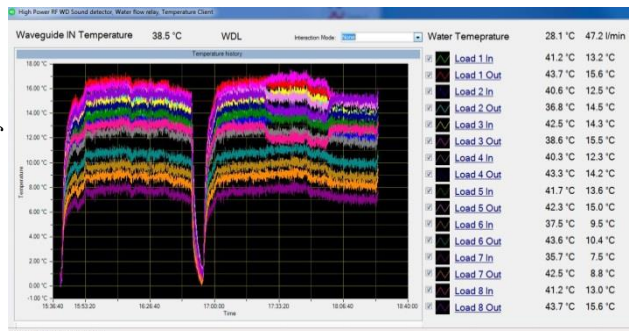


Figure 9: Measuring results of temperature for each isolator at HPRF test stand.

From the Accelerator Module Test Facility measurements (AMTF measurements) cavity accelerating gradient measurement error for the pulsed RF power measurement on the module test stand is evaluated as 8.9 %. For example, measured Eacc of 25.0 MV/m must be treated as Eacc = (25.0 ± 2.2) MV/m.

The WATF production error rate for all one hundred measured waveguide distributions is not more than ±0.2 dB. In this way, all waveguide distributions meet the AMTF requirements.

INSTALLATION OF WAVEGUIDE DISTRIBUTION TO THE CRYOMODULE

In order to save a lot of time and increase reliability, the waveguide distributions have been produced, tuned and tested at the WATF, and finally installed to the cryomodule at the AMTF (see Fig.10). The installation in the XFEL tunnel would have taken much more time. The first waveguide distributions have taken more time for completion (approximately three weeks for one and a half system.) But due to quality management, improvements of measurement and installation procedures, the time for completion has been reduced by one week.



Figure 10: Transportation of the waveguide distribution from WATF to AMTF for installation to the cryomodule.

SUMMARY

25 RF stations, which consist of 5304 waveguide components, have been successfully installed at AMTF and finally in the XFEL tunnel. The waveguide distributions for each station have been tuned and tested up to full power.

ACKNOWLEDGEMENTS

The authors are grateful to all the members of the DESY MHF-p teams for the successful tailoring, producing, tuning and testing of the WATF waveguide distributions.

ISBN: 978-3-95450-194-6 ISSN: 2226-0366 doi:10.18429/JACoW-LINAC2018-TUPO027

REFERENCES

[1] V. Katalev, S. Choroba, "Compact waveguide distribution with asymmetric shunt tees for the European XFEL", in *Proc. PAC'07*, Albuquerque, NM, USA, Jun. 2007, paper MOPAN015, pp. 176-178.

Content from this work may be used under the terms of the CC BY 3.0 licence (© 2018). Any distribution of this work must maintain attribution to the author(s), title of the work, publisher, and DOI.

ISBN: 978-3-95450-194-6 ISSN: 2226-0366 doi:10.18429/JACoW-LINAC2018-TUPO028

RETREATMENT OF EUROPEAN XFEL SERIES CAVITIES AT DESY AS PART OF THE REPAIR OF EUROPEAN XFEL ACCELERATING MODULES

S. Sievers†, N. Krupka, D. Reschke, S. Saegebarth, J. Schaffran, M. Schalwat, P. Schilling, M. Schmoekel, N. Steinhau-Kuehl, B. v. d. Horst, E. Vogel, H. Weise,
Deutsches Elektronen-Synchrotron DESY, 22607 Hamburg, Germany
M. Wiencek, Instytut Fizyki Jądrowej PAN, 31-342 Kraków, Poland

Abstract

For the European XFEL 102 accelerating modules were built and tested. Several accelerating modules had to be reworked due to different kinds of non-conformities. The extent of this rework varied greatly. At the end of production four accelerating modules could not be qualified in time before the tunnel installation was to be finished in September 2016. Meanwhile the cavity strings of two of these accelerating modules have been disassembled in the DESY clean room. The cavities have been retreated at DESY either by additional high pressure water rinsing or BCP flash chemical treatment. All cavities were vertically tested and 15 out of 16 were qualified for the reassembly of the cavity strings. One accelerating module will be reassembled completely and tested until the end of 2018; the other will follow in the first half of 2019. We report on retreatment procedures and performance of these cavities.

INTRODUCTION

The European XFEL was built in a European Collaboration [1] and is located at DESY in Hamburg. The superconducting cavities have been built in industry in Italy [2] and Germany [3] and tested at DESY. From there the cavities were brought to CEA Saclay, France for accelerating module assembly [4,5]. After assembly the accelerating modules were shipped back to DESY for test and tunnel installation.

On 61 of the 102 accelerating modules for the European XFEL, repair actions of different extent have been performed to qualify them for tunnel installation. Four of these accelerating modules did not qualify for tunnel installation in time and had to be further investigated. These accelerating modules (XM8, XM46, XM50 and XM99) are being reworked at DESY in Hamburg [6].

Already during the production phase of the European XFEL, cavities that did not match the acceptance criteria were retreated mostly at DESY [7]. In the same way the cavities of the XFEL accelerating modules XM46 and XM50 have been treated.

RETREATMENT PASSES

For the retreatment of superconducting European XFEL series cavities that did not achieve the approval for string installation, different retreatment passes were specified [8]. During the repair of the accelerating modules XM46 and XM50 only the retreatment passes RP1 and RP2 were applied. The retreatment pass RP1 is mainly an additional high pressure rinsing (HPR), while RP2 is an additional chemical polishing (BCP). The complete retreatment cycles are described in Table 1 and Table 2.

After the retreatment all cavities are vertically tested to determine their usable gradient in the vertical cryostats at the Accelerator Module Test Facility AMTF [9] at DESY.

Table 1: Retreatment Pass - RP1

Cleaning by ultrasonic cleaning and ultra-pure water rinsing to enter ISO 4 cleanroom
Venting to normal pressure with 3 l/min Nitrogen gas flow rate
Dismounting of beam tube flange short side
Six times high pressure rinsing and drying for 12 hours in ISO 4 cleanroom area
Assembly of beam tube flange
Pump down, leak check with standard turbo molecular pumping unit

Table 2: Retreatment Pass – RP2

Cleaning by ultrasonic cleaning and ultra-pure water rinsing to enter ISO 4 cleanroom
Venting to normal pressure with 3 l/min Nitrogen gas flow rate
Dismounting of all cavity accessories
Chemical treatment of maximum removal of 10 µm by BCP, ultra-pure water rinsing and one time HPR.
Drying for 12 hours in ISO 4 cleanroom area
Assembly of accessories and beam tube flanges to cavity, leak check
Dismounting of beam tube flange short side
Six times high pressure rinsing and drying for 12 hours in ISO 4 cleanroom area
Assembly of beam tube flange
Pump down, leak check and residual gas analysis (RGA) with standard standard turbo molecular pumping unit
120°C baking

REWORKED MODULES

On seven accelerating modules beam vacuum leaks were found after the assembly or appeared during the module tests at AMTF. These leaks may affect the cavities directly.

† sven.sievers@desy.de

Content from this work may be used under the terms of the CC BY 3.0 licence (© 2018). Any distribution of this work must maintain attribution to the author(s), title of the work, publisher, and DOI.

ISBN: 978-3-95450-194-6 ISSN: 2226-0366 doi:10.18429/JACoW-LINAC2018-TUPO028

Four leaks could be sealed using a local cleanroom environment either at CEA Saclay for accelerating module XM54 [10] or at DESY for the accelerating modules XM22, XM24 and XM91 [11]. The accelerating modules XM46, XM50 and XM99 are still being reworked at DESY. XM8 had a vacuum leak in the 2K area, which could not be verified in an intensive investigation in 2018. The accelerating module was reassembled without touching the cavity string.

XM46

The accelerating module XM46 was equipped with well performing cavities with usable gradients of approximately 30 MV/m in vertical test. The accelerating module had a first beam vacuum leak already detected after string assembly inside the cleanroom at CEA Saclay. It was sealed by re-tightening the leaky connection. A second beam vacuum leak was discovered at the end of the accelerating module assembly. Tightening of the cold coupler connection at cavity #4 sealed the leak.

XM46 had strong degradation of the cavities between vertical test and module test. It failed the module acceptance test due to the low average usable gradient of 19.7 MV/m and strong dark current. One explanation for the degradation could be beam vacuum leaks; another explanation could be that the cleanroom at CEA Saclay, where the accelerating modules were assembled, had still not fully recovered from a power break that occurred during the previous module assembly.

In February 2018 the cavity string of XM46 was disassembled in the DESY cleanroom and all eight cavities were retreated by six times HPR according to the retreatment pass RP1. The usable gradient of six of the eight cavities was recovered or even enhanced by this retreatment. Only CAV00831 and CAV00869 achieved usable gradients of only about 20 MV/m after RP1, so that an additional RP2 was decided. After 10 µm BCP flash chemical treatment, CAV00869 recovered and its usable gradient surpassed even the value from the vertical test before accelerating module assembly. It was accepted for accelerating module assembly again. CAV00831 is still limited to a usable gradient of 19 MV/m and is not qualified so far. It will be retreated again or replaced for the cavity string assembly of XM46.1 in February 2019.

The usable gradients in MV/m of the cavities from XM46 in the vertical test before accelerating module assembly (UGV1), in the module test (UGM) and after the retreatment (UGV2) together with the retreatment procedure are given in Table 3. The constraint which limits the usable gradient of the cavities is given in brackets. UGV2 for the cavities CAV00831 and CAV00869 were measured after the BCP treatment.

XM50

The accelerating module XM50 was equipped with very well performing cavities with usable gradients in the range from 36 up to 41 MV/m in vertical test.

Already during string assembly at CEA Saclay a leak at the angle valve caused a delay in the assembly of this accelerating module. The final leak check after complete assembly showed a beam vacuum leak again. The accelerating module was disassembled to uncover the cold mass with the cavity string and a detailed leak check took place. At that time no leak could be detected and the accelerating module was reassembled again. At the module tests in AMTF the cavities showed strong degradation and a huge dark current. No other explanation than the beam vacuum leaks could be found to explain the degradation. During warm up after AMTF test a new beam vacuum leak appeared. The accelerating module was not accepted for tunnel installation.

In October 2017 the cavity string of XM50 was disassembled in the DESY cleanroom and the cavities were retreated by six times HPR according to the Retreatment Pass RP1. In vertical test all the cavities met the acceptance criteria of European XFEL serial production phase and qualified for the reassembly of the cavity string.

The string was reassembled as XM50.1 with all the cavities in the same position as in XM50 in May and June 2018. Table 4 lists the usable gradients of the cavities from XM50 according to the description given for XM46.

Table 3: Usable Gradients of the Cavities from Accelerating Module XM46 before and after Retreatment *CAV00831 is not qualified for accelerating module assembly yet. **Sum of the 7 qualified cavities

Position	Cavity-No	UGV1 in MV/m (limitation)	UGM in MV/m (limitation)	Retreatment Procedure	UGV2 in MV/m (limitation)
C1	CAV00831	30 (Q_0)	17,4 (Xray)	BCP	19 (BD)*
C2	CAV00869	30 (Q_0)	17,6 (BD)	BCP	32 (Q_0)
C3	CAV00051	30 (Q_0)	20,7 (BD)	HPR	31 (BD)
C4	CAV00860	30 (Q_0)	24,5 (Xray)	HPR	30 (Q_0)
C5	CAV00279	30 (Xray)	24,9 (Xray)	HPR	36 (BD)
C6	CAV00261	29 (Q_0)	19,8 (Xray)	HPR	27 (Xray)
C7	CAV00850	29 (Q_0)	17,1 (Xray)	HPR	34 (BD)
C8	CAV00818	30 (Emax)	15,3 (Xray)	HPR	33 (BD)
Sum		238	157,3		223**

Content from this work may be used under the terms of the CC BY 3.0 licence (© 2018). Any distribution of this work must maintain attribution to the author(s), title of the work, publisher, and DOI.

ISBN: 978-3-95450-194-6 ISSN: 2226-0366 doi:10.18429/JACoW-LINAC2018-TUPO028

Content from this work may be used under the terms of the CC BY 3.0 licence (© 2018). Any distribution of this work must maintain attribution to the author(s), title of the work, publisher, and DOI.

Table 4: Usable Gradients of the Cavities from Accelerating Module XM50 before and after Retreatment

Position	Cavity-No	UGV1 in MV/m (limitation)	UGM in MV/m (limitation)	Retreatment Procedure	UGV2 in MV/m (limitation)
C1	CAV00207	36 (Emax)	20 (Xrays)	HPR	31 (Q_0)
C2	CAV00789	38 (Q_0)	16.4 (Xrays)	HPR	36 (Q_0)
C3	CAV00253	41 (Emax)	29.1 (BD)	HPR	30 (Q_0)
C4	CAV00256	38 (Emax)	31 (PWR)	HPR	34 (Emax)
C5	CAV00257	40 (Emax)	31 (Xrays)	HPR	33 (Emax)
C6	CAV00260	40 (Emax)	25.6 (Xrays)	HPR	39 (FE)
C7	CAV00265	36 (FE)	23.1 (Xrays)	HPR	37 (Q_0)
C8	CAV00267	37 (Q_0)	20.3 (BD)	HPR	32 (FE)
Sum		306	196,5		272

XM99

During the cool-down of the accelerating module XM99 at AMTF a beam vacuum leak appeared. The accelerating module could still be tested and the cavities kept their performance with regard to the vertical test result. The average usable gradient was 17.9 MV/m. The vacuum leak investigations indicate the leak in the area between cavity #1 and cavity #2. The disassembly of the accelerating module is scheduled for late 2019 and the reassembly will take place after the retreatment of the cavities according to the retreatment passes RP1 and if necessary RP2 in 2020.

RESULTS

15 of 16 cavities retreated during the repair actions of the accelerating modules XM46 and XM50 met the acceptance criteria of European XFEL serial production phase and qualified for the reassembly of the cavity string. Nevertheless some cavities did not recover their original performance. The difference between the usable gradient in vertical test before accelerating module assembly and after the retreatment in the framework of the accelerating module repair efforts are compiled in Fig.1.

Due to the typical uncertainties of cold rf measurements, a variation of ±10 % of the previous performance is marked as “unchanged”.

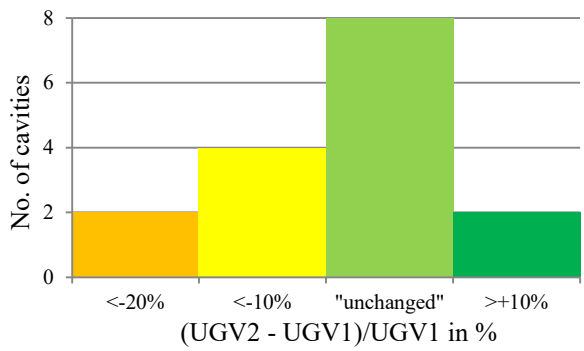


Figure 1: Difference in usable gradient in vertical tests before accelerating module assembly and after retreatment.

SUMMARY AND OUTLOOK

For the repair of the European XFEL accelerating modules XM46 and XM50, 16 SRF cavities have been retreated by DESY according to the retreatment passes already used during the cavity production phase.

All of the cavities passed RP1 and underwent six times HPR. This increased the usable gradient of all the cavities compared to the module test. 14 of them were accepted for accelerating module assembly afterwards. For two cavities an additional BCP flash chemical treatment according to retreatment pass RP2 was performed. One of these cavities achieved a higher usable gradient after this process than in the vertical test prior the accelerating module assembly. One cavity is still not qualified for accelerating module assembly and will be retreated again or replaced.

XM46.1 will be reassembled completely by summer 2019 and tested afterwards.

XM50.1 is being reassembled at the moment and will be tested until the end of 2018.

The repair of XM99 will start late 2019.

REFERENCES

[1] H. Weise *et al.*, "How to Produce 100 Superconducting Modules for the European XFEL in Collaboration and with Industry", in *Proc. IPAC2014*, paper WEIB03.

[2] A. Matheisen *et al.*, "Industrialization of European XFEL Preparation CYCLE "BCP FLASH" at Ettore Zanon Company", in *Proc. SRF2013*, paper TUP056.

[3] A. Matheisen *et al.*, "Industrialization of European XFEL Preparation CYCLE "Final EP" at Research Instruments Company", in *Proc. SRF2013*, paper MOP040.

[4] C. Madec, "Status of E-XFEL String and Cryomodule Assembly at CEA-Saclay", in *Proc. LINAC2012*, paper THPB083.

[5] E. Vogel *et al.*, "Integration of the European XFEL Accelerating Modules", in *Proc. LINAC2012*, paper MOPB017.

[6] E. Vogel *et al.*, "Accelerator Module Repair for the European XFEL Installation", in *Proc. SRF2017*, paper MOPB015.

ISBN: 978-3-95450-194-6 ISSN: 2226-0366 doi:10.18429/JACoW-LINAC2018-TUPO028

[7] D. Reschke *et al.*, "Performance in vertical test of the 832 nine-cell 1.3 GHz cavities for the European X-ray Free Electron Laser", *Phys. Rev. ST Accel. Beams,* vol. 20, p. 042004 (2017).

[8] A. Matheisen *et al.*, "Experience on Retreatment of EU-XFEL Series Cavities at DESY", in *Proc. SRF2015*, paper MOPB075.

[9] K. Kasprzak *et al.*, "First Cryomodule Test at AMTF Hall for the European X-Ray Free Electron Laser (XFEL)", in *Proc. IPAC2014*, paper WEPRI032.

[10] S. Berry and O. Napoly, "Assembly of XFEL Cryomodules: Lessons and Results", in *Proc. LINAC2016*, paper WE1A02.

[11] M. Schmoekel *et al.*, "Experience on In-Situ Module Repair and Set Up of Non XFEL Cavity Strings at DESY", in *Proc. SRF2017*, paper MOPB088.

Content from this work may be used under the terms of the CC BY 3.0 licence (© 2018). Any distribution of this work must maintain attribution to the author(s), title of the work, publisher, and DOI.

ISBN: 978-3-95450-194-6 ISSN: 2226-0366 doi:10.18429/JACoW-LINAC2018-TUPO029

HIGHLIGHTS OF THE XM-3 CRYOMODULE TESTS AT DESY

J. Branlard†, V. Ayvazyan, A. Bellandi, J. Eschke, Ç. Gümüş, D. Kostin, K. Przygoda,
H. Schlarb, J. Sekutowicz, DESY, Hamburg, Germany
W. Cichalewski, DMCS, Łódź, Poland

Abstract

To investigate the feasibility of the continuous wave (CW) upgrade [1] of the European X-ray free electron laser (XFEL), on-going tests are performed on XFEL prototype and production cryomodules since 2011. For these studies, DESY's cryomodule test bench (CMTB) has been equipped with a 105 kW CW capable inductive output tube (IOT) in addition to the 10 MW pulsed klystron, making CMTB a very flexible test stand, enabling both CW and pulsed operation. XFEL-like low level radio frequency (LLRF) electronics is used for these tests to stabilize amplitude and phase of the voltage vector sum (VS) of all 8 cavities of the cryomodule under test. The cryomodule most often tested is the pre-series XM-3, unique since it is housing one fine grain niobium and seven large grain niobium cavities. Modified flanges were installed in autumn 2017 on all 8 input couplers to increase the maximum reachable loaded quality factor (Q_L) beyond 2E7. With higher Q_L, up to 6E7 for 6 cavities and 3E7 for 2 cavities, we have investigated the VS stability and SRF-performance of this cryomodule under various conditions of cooling down rate and operation temperature 1.65K, 1.8K and 2K, at gradients up to 21.5 MV/m. The results of these tests are presented in this paper.

INTRODUCTION

The cryomodule test bench at CMTB offers versatile test conditions to investigate superconducting radio frequency (SRF) cryomodules under various conditions. It is equipped with a 10 MW klystron used for pulsed operations and a 105 kW inductive output tube used for continuous wave (CW) or long pulse (LP) operations. Two independent LLRF systems can be used to perform single cavity or vector sum field regulation. The LLRF system includes RF field feedback and resonance control using stepper motors and fast piezo feedback looped around individual cavities [2]. The waveguide distribution system can be adjusted to distribute power according to the different cavity performance. The cryogenic plant, supporting both the free electron laser in Hamburg (FLASH) and CMTB has a cooling capacity of 6.8 kW at 4.3K making it robust to heat load intensive experiments. Since 2011, several test runs have been carried out at CMTB to investigate the challenges associated with CW operation of XFEL-like cryomodules. The dynamic heat load and in particular the impact of end-cell heating was investigated as a function of RF pulse duty factor and gradient in [3].

More recently RF stability measurements for Q_L as high as 1.5E7 were reported in vector sum [4] and for single cavity operation [5]. To investigate issues related to narrow bandwidth and high gradient operations the input power couplers have been modified to reach higher Q_L, as described in section I. The dynamic heat load of individual cavities was measured to estimate the cavity unloaded quality factor (Q_0) as a function of gradient for different cryogenic temperatures. These results are reported in section II. Section III reports on the RF field stability performance demonstrated in CW for various gradient as high as 21.5 MV/m and various Q_L up to 8.2E7. A short summary and perspectives are given in the conclusion.

COUPLER MODIFICATIONS

The eight couplers of the XFEL pre-series cryomodule XM-3 were modified to move the Q_L range towards higher values. This was achieved by inserting a modified iso-vac flange, shown in blue in the figure below, moving the warm part of the coupler 10 mm further away from the 70K window. The motorized coupler allows for an additional 5mm displacement.

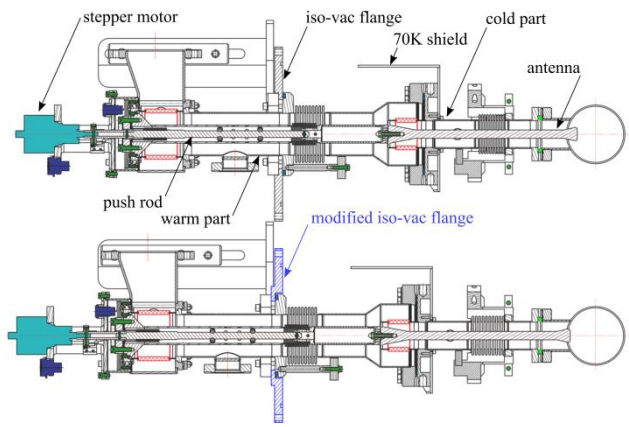


Figure 1: Unmodified XFEL power coupler (top) and with the modified iso-vac flange (bottom), shifting outwards the warm part of the coupler.

The achievable Q_L ranges before and after modification are listed in Table 1. Simulation predicts that a 5 mm displacement induces a Q_L increase from 2E7 to 8E7 which would suffice. In practice this increase in Q_L value was achieved by a 10 mm displacement, due to the fact that the coupling antenna also moved sideways. The improved Q_L range was limited in the case of cavity 7 and 8. This is due to a collision between the coupler 70K shield and the cryomodule 70K shielding cut out appearing after cool down for larger coupler movements on the last cavities (C7 and C8).

† julien.branlard@desy.de

Content from this work may be used under the terms of the CC BY 3.0 licence (© 2018). Any distribution of this work must maintain attribution to the author(s), title of the work, publisher, and DOI.

ISBN: 978-3-95450-194-6 ISSN: 2226-0366 doi:10.18429/JACoW-LINAC2018-TUPO029

Table 1: Coupler Range Before and After Modifications

Cavity	Q_L max (before)	Q_L min (after)	Q_L max (after)
C1	2.8E7	0.6E7	8.4E7
C2	1.9E7	0.5E7	6.8E7
C3	2.2E7	0.8E7	11.0E7
C4	2.0E7	0.6E7	9.1E7
C5	2.0E7	0.5E7	7.5E7
C6	1.9E7	0.4E7	6.6E7
C7	1.8E7	0.5E7	**3.0E7**
C8	2.0E7	0.5E7	**3.0E7**

Another two XFEL cryomodules, not yet installed in the XFEL tunnel are being modified in a similar way: XM46 and XM50 and will be tested in CW mode this year. The shielding cut outs will be adjusted to avoid the misalignment observed on XM-3.

HEAT LOAD MEASUREMENTS

Dynamic heat load studies have been conducted at various temperatures, both for individual cavities and for the whole cryomodule. The goal was to investigate the potential benefit to operate large grain cavities at temperatures lower than 2K. In these measurements Q_0 is computed by measuring the difference in helium mass flow when one (or several) cavities are in operation. Results are summarized in Fig. 2 for the whole cryomodule and Fig. 3 for individual cavities.

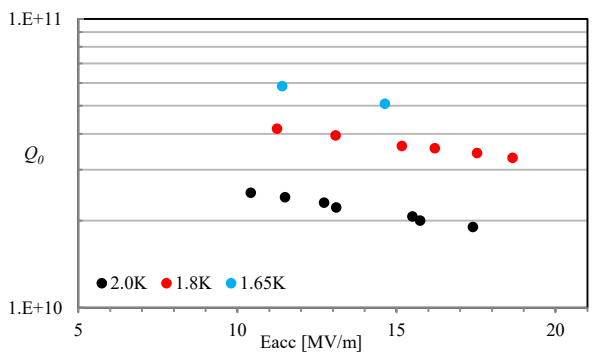


Figure 2: Q_0 vs Eacc for the whole cryomodule at 2K, 1.8K and 1.65K.

The first conclusion is that the Q_0 mean values measured for individual cavities at 1.8K (red dots in both figures) and 2K (black dots in both figures) agree very well with values measured for the whole cryomodule at these temperatures. This validates the accuracy of the dynamic heat load measurement using helium mass flow in the range from 1W (single cavity at 7.0 MV/m, 1.8K) to 140W (whole cryomodule at 17.4 MV/m, 2K). The gain in Q_0 for 1.8K operation compared to 2K operation is about 80%. Further investigation is required to find out if operation at 1.8K will be more efficient for the first 136 cavities (17 cryomodules in the injector section of the European XFEL accelerator). The main linac, extended from 84 to 96 cryomodules, could operate in CW around 8 MV/m. The dynamic heat load at this lower gradient is very low and operation at 1.8K would not be beneficial due to the static heat load.

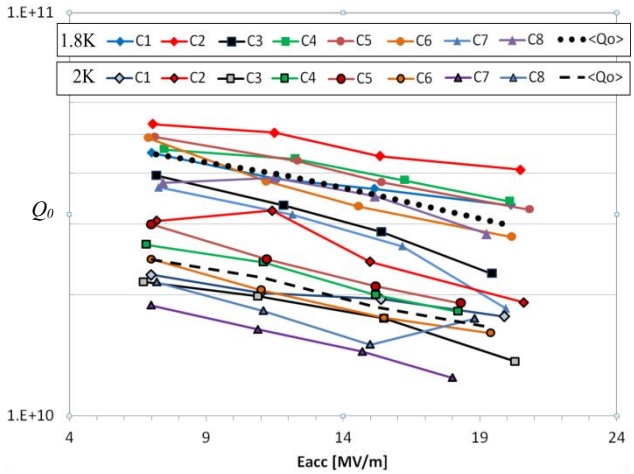


Figure 3: Single cavity tests at 1.8K and 2K.

RF STABILITY MEASUREMENTS

Before proceeding to any RF stability measurement, Q_L is measured for individual cavities. This is performed in pulsed mode where the amplitude decay is used by the diagnostic server to compute Q_L for every cavity. The expected cavity voltage $V_{CAV} = \sqrt{4Q_L R/Q P_{FWR}}$ is estimated based on the forward power P_{FWR} measured by power meters (R/Q = 1012 Ω is the cavity shunt impedance). This estimated voltage assumes perfect tuning of the cavity. In practice a first tuning is performed with the stepper motor, and fine tuning is completed applying piezo DC bias. Due to the narrow cavity bandwidth (~ 20 Hz for Q_L = 6E7) and the presence of microphonics, keeping the cavity on resonance requires piezo feedback. Several piezo feedback operation modes are implemented in the LLRF system; the one typically used is a purely integral feedback using the phase difference between forward and probe signals as input. An active noise cancellation (ANC) algorithm [6] is also applied to notch out the dominant microphonics frequencies (typ. ~30 Hz and 49 Hz), further helping the feedback controller. While the center frequency of the ANC notch filter can be identified by looking at the FFT of the probe and picking out the dominant frequencies, the other ANC parameters (learning rate and delay) are still optimized based on experience. Further work and understanding is required to automate this step. When all cavities are set on resonance, RF feedback can be applied around the vector sum (or around a single cavity field), typically with proportional gain only.

Content from this work may be used under the terms of the CC BY 3.0 licence (© 2018). Any distribution of this work must maintain attribution to the author(s), title of the work, publisher, and DOI.

ISBN: 978-3-95450-194-6 ISSN: 2226-0366 doi:10.18429/JACoW-LINAC2018-TUPO029

Content from this work may be used under the terms of the CC BY 3.0 licence (© 2018). Any distribution of this work must maintain attribution to the author(s), title of the work, publisher, and DOI.

Vector Sum Operation

Due to several boundary conditions (limitation in Q_L range for C7 and C8 and high radiation level at high gradient operation for C3), the operating parameters and corresponding bandwidth (BW) listed in Table 2 were chosen.

Table 2: Individual Cavity Settings for the VS Test

Parameter	C1	C2	C3	C4	C5	C6	C7	C8
E_{ACC} [MV/m]	16	16	8	16	16	16	11	11
Q_L [x10^7]	6	6	**1.4**	6	6	6	**2.5**	**2.5**
BW [Hz]	22	22	93	22	22	22	52	52

The amplitude and phase regulation level achieved during this study met the XFEL specifications of 0.01% and 0.01°. Figure 4 shows the RMS amplitude stability (dA/A) over one and half hour during which the XFEL amplitude regulation was achieved. On average the phase stability is still a factor of 2 above specifications (i.e. 0.02° RMS) but can be controlled for short periods of time (i.e. minutes) as low as 0.009°. This work is ongoing.

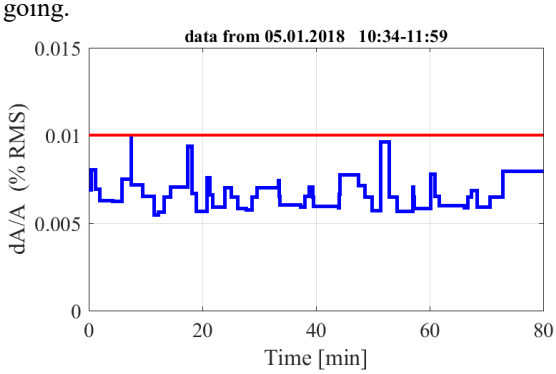


Figure 4: VS signal amplitude regulation dA/A (RMS). XFEL specifications are shown in red.

The vector sum field stability was guaranteed by the RF feedback, while the resonance control of individual cavities was achieved using an integral feedback together with ANC filters acting on the cavity piezos (set to suppress 31 Hz oscillations).

Single Cavity Operation

Single cavity studies were pursuing two objectives. The first goal was to push towards higher gradients (above 20 MV/m) for a constant Q_L. The second goal was to push towards higher Q_L for a gradient set point of 16 MV/m. Due to its high gradient capability (above 40 MV/m), cavity 3 in XM-3 was used for the first goal. An amplitude and phase regulation of dA/A = 0.019% and dP = 0.014° respectively was achieved for a maximum gradient of 23.5 MV/m in CW, still a factor of 2 away from the target specifications. RF and piezo feedback along with ANC set to suppress 31 Hz and 49 Hz were used. For the second goal, cavity 4 was chosen due to its high Q_L tuning range. In this study, Q_L was set to 8.2E7 (corresponding to a half bandwidth ~8 Hz). The achieved RMS performance was dA/A = 0.015% and dP = 0.017°.

CONCLUSION

Some very encouraging results have been obtained at CMTB during CW tests of XFEL prototype cryomodules. The high Q_0 observed on large grain cavities might be an indication to pursue this approach when upgrading the front end cryomodules in the XFEL CW upgrade scenario. Furthermore, RF stability compliant with the XFEL specifications could be achieved in amplitude and phase at a Q_L =1.5E7 and partially in amplitude and phase at Q_L above 6E7. For a given RF power source, increasing Q_L for the cryomodules of the main linac directly translates into higher final beam energy. Since the XFEL cryomodules are equipped with remote tunable couplers, it is interesting to see how high Q_L can be set, while still meeting the RF field stability and heat load specifications. With the next 2 cryomodules to be investigated in CW (XM46 and XM50), we will see how these results translate to series XFEL cryomodules. More work is required on the LLRF system, to improve the robustness of the piezo feedback and automate the optimization of ANC parameters (frequency detection, learning rate…). A better understanding of the cavity mechanical modes and their dependency on gradient and Q_L is currently under investigation as part of the R&D effort towards CW operation of the XFEL [7]. More work is also required to understand the current limitation of the RF feedback preventing to reach the XFEL specifications. In particular, a more sophisticated controller (MIMO-based) is in preparation, and should help run at higher gain by increasing the decoupling between the in-loop and quadrature components of the feedback control signal, providing better amplitude and phase stability.

REFERENCES

[1] J. Sekutowicz *et al.,* "Feasibility of CW and LP operation of the XFEL linac", *Proc. of FEL'13*, New York, USA, Aug. 2013, paper TUOCNO04.

[2] J. Branlard *et al.,* "LLRF system design and performance for XFEL cryomodules continuous wave operation", *Proc. of SRF'13*, Paris, France, Sept. 2013, paper THP086.

[3] J. Sekutowicz *et al.,* "Research and development towards duty factor upgrade of the European X-ray Free Electron Laser linac", *Phys. Rev. ST Accel. Beams*, vol. 18, p.050701, 2015.

[4] W. Cichalewski *et al.*, "High loaded quality factor superconducting cavities accelerating field parameters regulation during continuous wave operation", *Proc. of 21st IEEE real time conference*, Williamsburg VA, USA, Jun. 2018.

[5] K. Przygoda *et al.*, "High Q_L and high gradient CW operation of TESLA SCRF 9-cell cavity", *Proc. of IPAC'18*, Vancouver, BC, Canada, May 2018, paper WEPAF052.

[6] R. Rybaniec *et al.,* "FPGA based RF and piezo controllers for SRF cavities in CW mode", *Proc. of 20th IEEE real time conference*, Padova, Italy, Jun. 2016.

[7] A. Bellandi *et al.*, "LLRF R&D towards CW operation of the European XFEL", presented at LINAC'18, Beijing, China, Sept. 2018, paper MOPO104, this conference.

ISBN: 978-3-95450-194-6 ISSN: 2226-0366 doi:10.18429/JACoW-LINAC2018-TUPO030

PRECISE EVALUATION OF CHARACTERISTIC OF THE MULTILAYER THIN-FILM SUPERCONDUCTOR CONSISTING OF NbN AND INSULATOR ON PURE Nb SUBSTRATE

R. Katayama*, Y. Iwashita, H. Tongu, Kyoto ICR, Uji, Kyoto
A. Four, CEA/DRF/IRFU, Gif-sur-Yvette, C. Z. Antoine, CEA/IRFU, Gif-sur-Yvette
H. Hayano, T. Kubo, T. Saeki, KEK, Ibaraki, Hayato Ito, Sokendai, Ibaraki
R. Ito, T. Nagata, ULVAC, Inc, Chiba
H. Oikawa, Utsunomiya University, Tochigi

Abstract

In recent years, it has been pointed out that the maximum accelerating gradient of a superconducting RF cavity can be pushed up by coating the inner surface of the cavity with a multilayer thin-film structure that consists of alternating insulating and superconducting layers. In this structure, the principal parameter that limits the performance of the cavity is the critical magnetic field or effective H_{C1} at which vortices start penetrating into the superconductor layer, and it is predicted to depend on the combination of the film thickness. We made samples that have NbN/SiO_2 thin-film structure on pure Nb substrate with several thicknesses of NbN film deposited using DC magnetron sputtering method. Here, we report the measurement results of effective H_{C1} of the NbN sample with a thickness of 200 nm by using the third-harmonic voltage method. In addition, we report the preliminary results to evaluate the dependence of the effective H_{C1} on the thickness of the NbN film in the range 50 nm–200 nm.

INTRODUCTION

Recently, it has been pointed out that the effective H_{C1} of a superconducting RF cavity might be pushed up by coating the inner surface of the cavity with a multilayer thin-film structure that consists of alternate insulating and superconducting layers [1–3]. Hereafter, such multilayer structures on pure bulk Nb in superconducting state is referred to as S-I-S (Superconductor-Insulator-Superconductor) structure. Generally, the effective H_{C1} of a superconducting material can be evaluated by applying a sine-wave magnetic field to the material with a small coil and detecting the third-harmonic signal of the coil voltage because the third-harmonic signal occurs when the phase transition from the full Meissner state to the vortex-penetrating state happens. Hereafter, this method is called third harmonic voltage method. C. Antoine already showed that a multilayer structure on a Nb substrate has higher effective H_{C1} than that of the Nb substrate by the third-harmonic voltage method [4]. We also verified that the effective H_{C1} is enhanced for a sample that consists of NbN (200 nm) and SiO_2 (30 nm) formed on pure Nb substrate that has an RRR of >250 [5]. Our measurement result on the third harmonic measurement using AC magnetic fields less than 13 mT are reported in IPAC18 proceedings. This article describes details of the new result to evaluate effective H_{C1} of the NbN(200 nm)/SiO_2(30 nm)/Nb sample using the AC magnetic field of the amplitude up to 44 mT. In addition, in order to evaluate the dependence of effective H_{C1} on the film thickness, this article presents the preliminary result of the measurement of effective H_{C1} of the NbN(50 nm)/SiO_2(30 nm)/Nb sample using the AC magnetic field of the amplitude up to 29 mT.

* katayama@kyticr.kuicr.kyoto-u.ac.jp

THIRD HARMONIC MEASUREMENT

For the third harmonic voltage method, an AC magnetic field at the frequency of 5 kHz is generated by a coil close to the superconducting sample and the third harmonic voltage $v_3(t) = V_3 \sin(3\omega t)$ induced in the coil is simultaneously measured [6]; ω is the frequency of a sinusoidal drive current, $I_0 \sin(\omega t)$ represents the current flowing in the coil, and V_3 is the amplitude of $v_3(t)$. If the temperature of a sample in superconducting state is being raised while amplitude of AC magnetic field H_0 is fixed, V_3 suddenly rises when H_0 exceeds the effective H_{C1} of the sample at a certain temperature. In the measurement performed at Kyoto University, H_0 is controlled by drive current I_0, and the temperature dependence of the effective H_{C1} is estimated from the temperatures at moments when V_3/I_0 suddenly rises. Refer to [5] for details of the measurement setup and flow.

In this study, the coil magnetic field is calibrated with the third harmonic measurement result of pure bulk Nb assuming that the following function $F(T)$ represents the temperature dependence of the effective H_{C1} of pure bulk Nb.

$$F(T) = \begin{cases} 0.18 \times \left(1 - (T/9.2)^2\right) & (T < 9.2\mathrm{K}) \\ 0 & (T > 9.2\mathrm{K}) \end{cases} \quad (1)$$

The calibration curve obtained from this measurement is shown in Fig. 1. The vertical axis is the coil magnetic field, and the horizontal axis is the drive current amplitude I_d derived from the digitized data recorded by our measurement system.

DETAILS OF MEASUREMENT RESULT

We have tested two multilayer samples that consist of NbN and SiO_2 coated on pure bulk Nb. The pure bulk Nb

Content from this work may be used under the terms of the CC BY 3.0 licence (© 2018). Any distribution of this work must maintain attribution to the author(s), title of the work, publisher, and DOI.

ISBN: 978-3-95450-194-6 ISSN: 2226-0366 doi:10.18429/JACoW-LINAC2018-TUPO030

Content from this work may be used under the terms of the CC BY 3.0 licence (© 2018). Any distribution of this work must maintain attribution to the author(s), title of the work, publisher, and DOI.

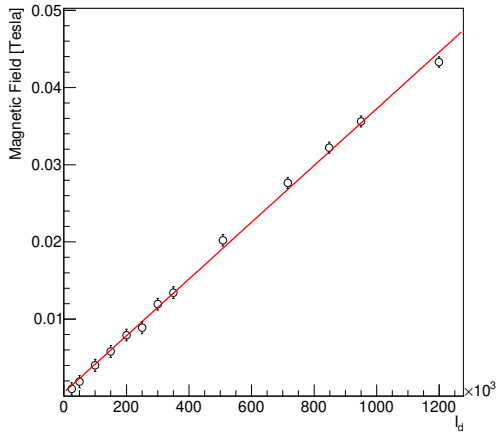


Figure 1: Calibration line of the applied magnetic field vs. the fundamental component of the coil current read I_d (arbitrary unit).

substrate of the sample is pretreated with the standard electropolishing recipe for bulk Nb cavity. Both the multilayer samples are prepared using DC magnetron sputtering technique (ULVAC, Inc.). One of the samples is a thin-film structure of 200-nm-thick NbN and 30-nm-thick SiO_2; the details of thin-film preparation are given elsewhere [7]. This sample is named as 180409-1-B. The other one is a thin-film structure of 50-nm-thick NbN and 30-nm-thick SiO_2; details of thin-film preparation are given elsewhere [8]. This sample is named as 180814-1-B. In the third harmonic measurements, the temperature ramping rates were kept at about 0.01 K/min. The systematic error is estimated to be 0.02 K in the measured temperature due to a thermal nonuniformity. It is noted that the systematic error used in this study is higher than that described in IPAC18 proceedings [5].

In our third harmonic measurements of sample No.180409-1-B, the amplitude of AC magnetic field applied to the sample was chosen to be 1.2 mT, 1.8 mT, 3.7 mT, 5.5 mT, 9.2 mT, 12.9 mT, 36.1 mT, and 44.1 mT. In this measurement, the applied magnetic field is increased by about 3 times than the measurement condition reported at IPAC18. The temperature dependence of the effective H_{C1} of the sample 180409-1-B is depicted in Fig. 2. The horizontal and vertical axes represent the temperature and the measured effective H_{C1}, respectively. The measured values of H_{C1} of pure bulk Nb sample and the effective H_{C1} of NbN(200 nm)/SiO_2(30 nm)/Nb sample are represented by the open circles and black triangles, respectively. The red curve is the theoretical curve obtained from equation (1), which is used for calibration. The green dashed curve is obtained by fitting data points of the sample of 180409-1-B in the region T <9.2 K to the function (2). On the other hand, the blue one dot chain line is obtained by fitting data points of the sample of 180409-1-B in the region T >9.2 K to the function (2). In this fitting, T_C' was fixed at 13.8 K, a value obtained from the measurement result of the critical temperature of NbN film at KEK [9]. At temperatures below around 9.2 K, S-I-S structure is formed because both pure bulk Nb and NbN film are in superconducting state. Thus, the effective H_{C1} of the whole NbN/SiO_2/Nb structure in the superconducting state is expressed by the green dashed curve. On the other hand, for temperatures greater than around 9.2 K, S-I-S structure does not hold. Thus, the blue one dot chain line corresponds to the effective H_{C1} of only NbN film. As a result of fitting, $f(0)$ and T_C', parameters of the function (2), are estimated as $(210 \pm 7) \times 10^{-3}$ and 9.21±0.02 K, respectively for the green dashed curve, whereas $f(0)$ is determined as $(3.3 \pm 0.5) \times 10^{-3}$ for the blue one dot chain line. It is thus confirmed that $f(0)$ of NbN(200 nm)/SiO_2(30 nm)/Nb in the region of T <9.2 K is improved by 17 % compared to that of pure bulk Nb.

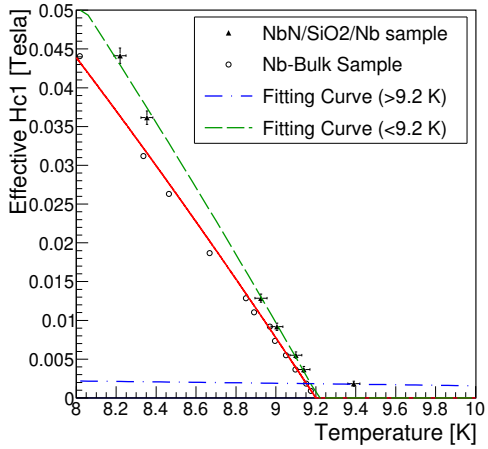


Figure 2: Comparison of measured effective H_{C1} between NbN(200 nm)/SiO_2(30 nm)/Nb and pure bulk Nb samples. The red curve represents the equation (1), which is used for calibration. The green broken line and the blue chain line are obtained by fitting data points of sample No.180409-1-B.

In our third harmonic measurements of sample No. 180814-1-B, the amplitude of AC magnetic field applied to the sample was chosen to be 14.8 mT, 22.6 mT, and 29.3 mT. The preliminary result of the temperature dependence of the effective H_{C1} of NbN(50 nm)/SiO_2(30 nm)/Nb and pure bulk Nb is shown in Fig. 3. The horizontal and vertical axes represent the temperature and the measured effective H_{C1}, respectively. The measurement result of H_{C1} of pure bulk Nb sample and the measurement result of effective H_{C1} of NbN/SiO_2/Nb sample are represented by open circles and black triangles, respectively. The red curve represents the equation (1), which is used for calibration. The green dashed curve is obtained by fitting data points of the sample of 180814-1-B in the region of T <9.2 K, to the function of (2). As a result of fitting, $f(0)$ and T_C', parameters of the function (2), are determined as $(176 \pm 16) \times 10^{-3}$ and 9.21±0.06 K, respectively. The theoretical calculation of the dependence of effective H_{C1} on the film thickness is shown

ISBN: 978-3-95450-194-6 ISSN: 2226-0366 doi:10.18429/JACoW-LINAC2018-TUPO030

in Fig. 4. It is found that the result obtained in this study is qualitatively consistent with the prediction of theory.

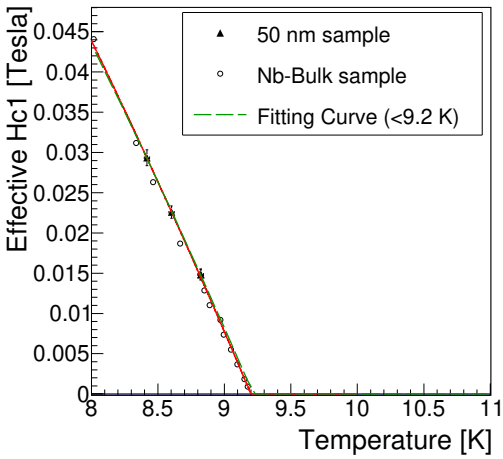


Figure 3: Comparison of measured effective H_{C1} of NbN(50 nm)/SiO_2(30 nm)/Nb and pure bulk Nb samples. The red curve represents the equation (1) used for calibration. The green broken line is obtained by fitting the data points of sample No.180814-1-B.

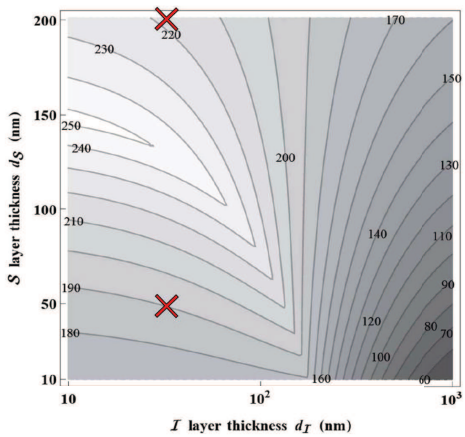


Figure 4: Theoretical calculation of the effective H_{C1} for NbN-I-Nb at T = 2 K (the image is cited from [3] and partially changed). The horizontal and vertical axes represent the thickness of the insulating layer and that of the superconducting layer, respectively. Each value shown in the contour plot denotes the effective H_{C1} that depends on the film thickness, and each cross in the figure corresponds to the test point in this study.

SUMMARY AND FUTURE PROSPECT

We evaluated the temperature dependence of effective H_{C1} of a sample having S-I-S structure that consists of NbN superconducting layer and SiO_2 insulating layer (30 nm) formed on pure bulk Nb. The measurement result clearly showed that the effective H_{C1} of pure bulk Nb improved after NbN/SiO_2 film coating, whereas effective H_{C1} changed depending on the film thickness. As a future prospect, in order to ensure the reproducibility, we plan to test the samples, which were fabricated in the same sputtering method, by other experimental setups at KEK [10] and Saclay [4]. In addition, by using the NbN samples with film thickness of 100 nm, 150 nm, 250 nm, 300 nm, and 400 nm that we have already prepared [8], we would like to clarify the dependence of effective H_{C1} on the film thickness.

ACKNOWLEDGMENTS

This work is supported by JSPS KAKENHI Grant Number JP17H04839, JSPS KAKENHI Grant Number JP26600142, Photon and Quantum Basic Research Coordinated Development Program of MEXT, Japan, Center of Innovation (COI) Program, Japan-US Research Collaboration Program, and the Collaborative Research Program of Institute for Chemical Research, Kyoto University (2016-8).

APPENDIX

In this paper, the following function is used in Fig. 2 and Fig. 3:

$$f(T) = f(0) \times \left(1 - (T/T_C')^2\right) \quad (2)$$

REFERENCES

[1] A. Gurevich, "Enhancement of rf breakdown field of superconductors by multilayer coating", *Appl. Phys. Lett.* 88, 012511 (2006).

[2] T. Kubo, *et al.*, "Radio-frequency electromagnetic field and vortex penetration in multilayered superconductors", *Appl. Phys. Lett.* 104, 032603 (2014).

[3] T. Kubo, "Multilayer coating for higher accelerating fields in superconducting radio-frequency cavities: a review of theoretical aspects", *Supercond. Sci. Technol.* 30, 023001 (2017).

[4] C. Z. Antoine, M. Aburas, A. Four, *et al.*, "Progress on characterization and optimization of multilayers", in *Proc. SRF'17*, Lanzhou, China, Jul. 2017. doi:10.18429/JACoW-SRF2017-TUYBA01

[5] R. Katayama, *et al.*, "Evaluation of superconducting characteristics on the thin-film structure by NbN and Insulator coatings on pure Nb substrate", in *Proc. IPAC'18*, Vancouver, Canada, Apr. 2018. doi:10.18429/JACoW-IPAC2018-THPAL015

[6] Y. Mawatari, *et al.*, "Critical current density and third-harmonic voltage in superconducting films", *Appl. Phys. Lett.* 81, 2424 (2002).

[7] R. Ito, T. Nagata, *et al.*, "Development of Coating Technique for Superconducting Multilayered Structure", in *Proc. IPAC'18*, Vancouver, Canada, Apr. 2018. doi:10.18429/JACoW-IPAC2018-THPML120

[8] R. Ito, T. Nagata, *et al.*, "Construction of Thin-film Coating System Toward the Realization of Superconducting Multilayered Structure", presented at LINAC'18, Beijing, China, Sept. 2018, paper TUPO050, this conference.

Content from this work may be used under the terms of the CC BY 3.0 licence (© 2018). Any distribution of this work must maintain attribution to the author(s), title of the work, publisher, and DOI.

ISBN: 978-3-95450-194-6 ISSN: 2226-0366 doi:10.18429/JACoW-LINAC2018-TUPO030

[9] H. Ito, *et al.*, "Lower Critical Field Measurement System of Thin Film Superconductor", in *Proc. IPAC'18*, Vancouver, Canada, Apr. 2018. doi:10.18429/JACoW-IPAC2018-THPAL105

[10] H. Ito, *et al.*, "Lower Critical Field Measurement of Thin Film Superconductor", presented at LINAC'18, Beijing, China, Sept. 2018, paper TUPO66, this conference.

Content from this work may be used under the terms of the CC BY 3.0 licence (© 2018). Any distribution of this work must maintain attribution to the author(s), title of the work, publisher, and DOI.

ISBN: 978-3-95450-194-6 ISSN: 2226-0366 doi:10.18429/JACoW-LINAC2018-TUPO031

INVESTIGATION OF THE SURFACE RESISTANCE OF NIOBIUM BETWEEN 325 MHz AND 1300 MHz USING A COAXIAL HALF-WAVE CAVITY*

H. Park[1†], J. R. Delayen[1], S. U. De Silva
Center for Accelerator Science, Old Dominion University, Norfolk, VA 23529
[1]also at Jefferson Lab, Newport News, VA 23606, USA

Abstract

The surface resistance of superconductors depends on frequency, temperature, rf field strength, and surface preparation. In particular, a low temperature bake around 100 C has been shown to modify the high-field behavior of the surface resistance. Using a coaxial half-wave resonator operating at 325, 650, 975 and 1300 MHz [1, 2] we have initiated a research program to better understand the role of low temperature heat treatment on the surface resistance of niobium.

INTRODUCTION

The well-known expressions for the surface resistance of superconductors in electromagnetic fields, and its dependence on frequency, temperature, and a few materials parameters, were obtained as a perturbation theory under the assumption that the magnitude of the electromagnetic field is much smaller than the critical field. This resulted in a surface resistance independent of the magnitude of the electromagnetic field.

There have been several attempts at developing theories of the surface resistance at high rf field, up to the critical field [3-5], but, at present, there is no universally accepted consensus on the correct fully self-consistent theory.

So far, the origin of residual resistance is believed to be a result of extrinsic mechanisms such as trapped vortices, metallic suboxide layers at the surface, non-superconducting precipitates (hydrides, etc). The full theory should include residual resistance. Extracting frequency, temperature, rf field dependence will provide significant insight to a better understanding. Because of the statistical nature of multiple materials defect, technological contributions to surface resistance and the lack of reproducibility, it is difficult to extract accurate frequency dependence of the surface resistance when different cavities of different frequencies are tested.

Coaxial half wave resonator provides the frequencies reasonably separated and the same location where the high surface magnetic field is distributed.

FREQUENCY DEPENDENCE

In the low-field limit the BCS surface resistance of superconductors is given by

$$R_{BCS} \cong \frac{\mu_0^2 \omega^2 \lambda^3 \sigma_n \Delta}{k_B T} \ln\left[\frac{C_1 k_B T}{\hbar\omega}\right] \exp\left[-\frac{\Delta}{k_B T}\right] \qquad (1)$$

In real materials, however, the non-isotropy of the gap and the Fermi surface, and the smearing of the gap can produce deviations from Eq. (1).

In the past the frequency dependence of the surface resistance was usually obtained by measurements in different frequencies and, over the range of interest for particle accelerators was of the form $\omega^{1.7\to2}$.

Not included in Eq. (1) also is the so-called residual surface resistance which includes all the sources of power dissipation that do not vanish as $T \to 0$.

Figure 1 shows the temperature dependence of the low-field surface resistance measured in the four lowest TEM modes of the half-wave cavity.

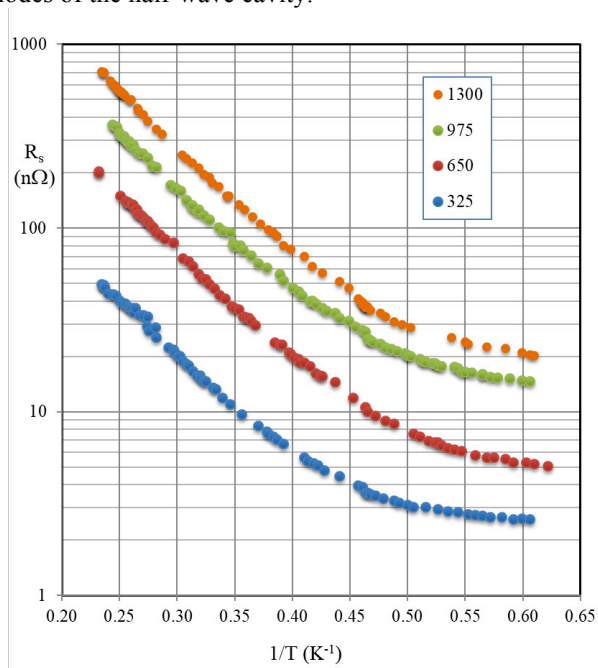


Figure 1: Temperature dependence of the low-field surface resistance of the four lowest TEM modes.

The results of Fig. 1 were obtained after the following surface preparation and treatments.

1. Post fabrication cleaning. Cleaning followed typical UHV cleaning procedure. The cavity was cleaned in a heated ultrasonic tank and triple rinsed with deionized ultra pure water.
2. Bulk BCP. Damaged niobium layer was removed by the chemical composition of HF (48%):HNO_3 (60%):H_3PO_4 (85%) = 1:1:2 inside the clean room. It was aimed to remove 150 microns but the thickness

* Work supported by NSF Award No. PHY-1416051
† hkpark@jlab.org

Content from this work may be used under the terms of the CC BY 3.0 licence (© 2018). Any distribution of this work must maintain attribution to the author(s), title of the work, publisher, and DOI.

ISBN: 978-3-95450-194-6 ISSN: 2226-0366 doi:10.18429/JACoW-LINAC2018-TUPO031

Content from this work may be used under the terms of the CC BY 3.0 licence (© 2018). Any distribution of this work must maintain attribution to the author(s), title of the work, publisher, and DOI.

measurement showed the actual removal 125 micron on average. After the first test additional 50 microns were removed. Figure 2 is showing how it was set up.



Figure 2: BCP set up in the clean room.

3. Heat treatment. High temperature heat treatment was performed at 800 deg C for 2 hours. During the heat treatment elements (especially hydrogen) were monitored.
4. Light BCP. Ten micron removal performed following same set up of bulk BCP.
5. High pressure rinse.
6. Clean room assembly. Rinsed cavity was dried overnight and it was assembled with ancillary parts. The additional parts were input and pick up couplers, vacuum valve and burst disc for safety. Other ports were blanked off as shown in Fig. 3.



Figure 3: Assembled cavity taken out from clean room.

7. Cool down. The cavity was loaded in a dewar of 28 inch diameter. The initial volume of 4.3 K helium liquid was 590 liters.

The data of Fig. 1 can be fitted to the formula

$$R_s(T) = \frac{A(\omega)}{T}\exp\left[-\frac{\Delta}{kT}\right] + R_{res} \qquad (2)$$

where $A(\omega), \Delta/k,$ and R_{res} are fitting parameters.

The frequency dependence of the three fitting parameters are shown in Figs. 4, 5, and 6.

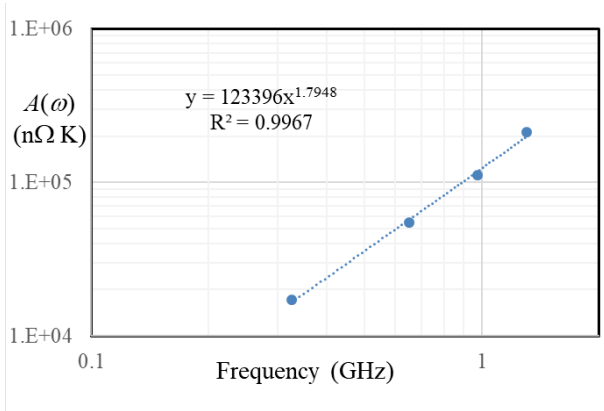


Figure 4: Fitting parameter $A(\omega)$.

In this frequency range and after the surface preparation described above the surface resistance shows a power frequency dependence ~1.8. This is different from the quadratic frequency dependence often assumed but consistent with numerical calculations.

As expected the fitting parameter Δ/k is frequency independent.

The component of the surface resistance that remains finite at T=0 displays a power frequency dependence ~1.5. This is quite different from what would be expected from trapped flux or a normal inclusion (~0.5).

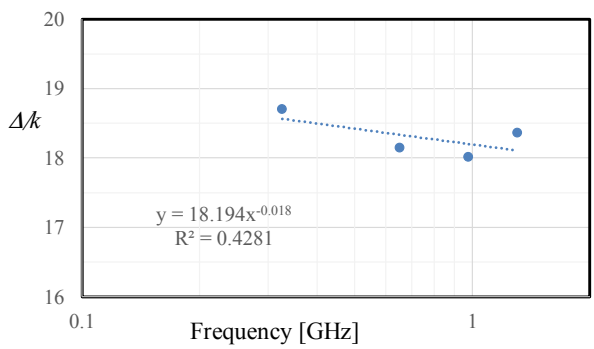


Figure 5: Fitting parameter Δ/k.

ISBN: 978-3-95450-194-6 ISSN: 2226-0366 doi:10.18429/JACoW-LINAC2018-TUPO031

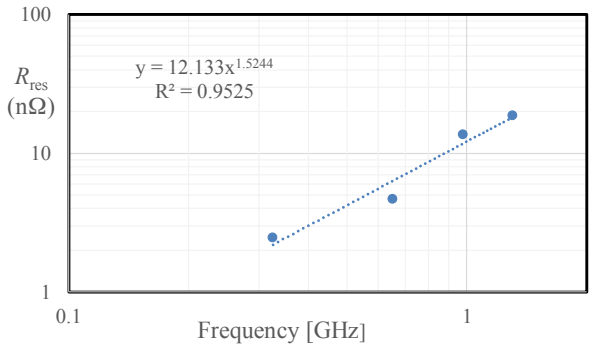


Figure 6: Fitting parameter R_{res}.

FIELD DEPENDENCE

Figure 7 shows a Q-curve as function of the peak surface magnetic field obtained at 4.35 K in the 325 MHz mode.

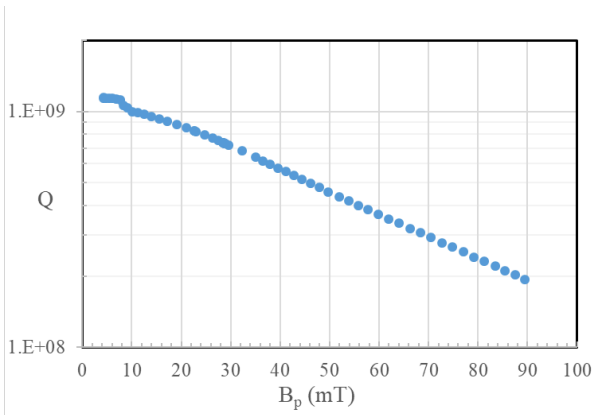


Figure 7: Q-curve at 325 MHz and 4.35 K.

From the Q-curve and the geometrical factor of 59 Ω, an average surface resistance can be obtained and shown as the blue dots in Fig. 8. Following the method described in [6], the actual field-dependent surface resistance $R_s(B)$ can be derived and is shown as the red curve.

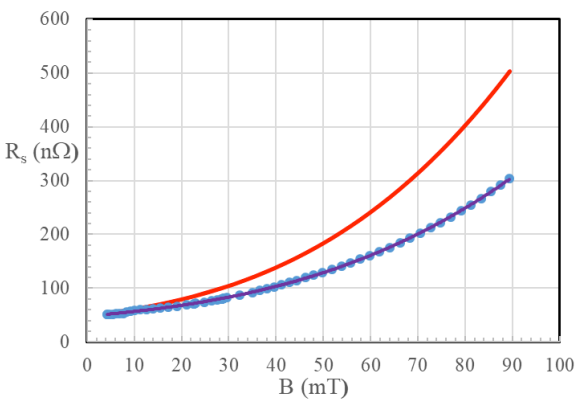


Figure 8: Average surface resistance from Fig. 5 (blue dots and purple curve) and actual surface resistance (red curve).

ON-GOING WORK AND PLANS

The results presented here are part of an investigation of the low-temperature baking (~120 C) of niobium cavities that has shown that it could reduce the high-field surface, at least at high frequency. The underlying physics is still poorly understood and by looking at the frequency dependence one may be able to shed some light on the underlying processes. The complete program involves looking at the evolution of the frequency dependence of the three fitting parameters and the field-dependence of the surface resistance after a low-temperature baking schedule of: no baking, 6 hours, 6+6 hours, 6+6+12 hours, and if warranted 6+6+12+24 hours.

After the completion of this series of tests, our plans are to repeat them following nitrogen infusion in the niobium cavity.

REFERENCES

[1] H. Park, S. U. De Silva, and J. R. Delayen, "Superconducting cavity for the measurements of frequency, temperature, rf field dependence of the surface resistance", *in Proc. SRF2015*, Whistler, Canada, September 2015, pp. 70-73, doi:10.18429/JACoW-SRF2015-MOPB003

[2] H. Park, S. U. De Silva, and J. R. Delayen, "Measurement of frequency, temperature, rf field dependent surface resistance using superconducting half-wave cavity", *in Proc. SRF2017*, Lanzhou, China, July 2017, pp. 925-927, doi:10.18429/JACoW-SRF2017-THPB080

[3] B.Xiao, C. Reece, and M. Kelly, Physica C: Superconductivity 490, 26 (2013).

[4] A. Gurevich, Phys. Rev. Lett. 113, 087001 (2014).

[5] A. Gurevich, Superconductor Science and Technology 30, 034004 (2017).

[6] J. R. Delayen, H. Park, S. U. De Silva, "Determination of the field dependence of the surface resistance of superconductors from cavity tests", presented at LINAC2018, Beijing, China, September 2018 Paper TUPO035, this conference.

Content from this work may be used under the terms of the CC BY 3.0 licence (© 2018). Any distribution of this work must maintain attribution to the author(s), title of the work, publisher, and DOI.

ISBN: 978-3-95450-194-6 ISSN: 2226-0366 doi:10.18429/JACoW-LINAC2018-TUPO032

FIRST TEST RESULTS OF SUPERCONDUCTING TWIN AXIS CAVITY FOR ERL APPLICATIONS *

H. Park[1,2#], S. U. De Silva[1], J. R. Delayen[1], F. Marhauser[2], A. Hutton[2]
[1]Center for Accelerator Science, Old Dominion University, Norfolk, VA 23529, USA
[2]Thomas Jefferson National Accelerator Facility, Newport News, VA 23606, USA

Abstract

RF superconducting (SRF) cavities with two beam pipes have been proposed in the past for energy recovery linac applications. The relatively complex geometry of those cavities presented a serious challenge for fabrication and surface processing. The main concerns have now been overcome with the fabrication and successful RF testing of a new elliptical twin-axis cavity proposed by Jefferson Lab (JLab) and optimized by the Center for Accelerator Science (CAS) at Old Dominion University (ODU) in the framework of a DoE accelerator stewardship program. The cavity design provides uniform accelerating or decelerating fields for both beams. This paper describes the cavity design, fabrication experience, and the first cold RF test results and explores potential applications especially for JLab's EIC (JLEIC).

INTRODUCTION

SRF accelerating structures with two beam pipes ('twin axis' cavity) intended for Energy Recovery Linacs (ERLs) applications were proposed a decade ago [1-3]. A seemingly complicated cavity was fabricated by KEK [1] but such a cavity has never been tested and therefore the feasibility has not been proved. ODU CAS designed the new geometry focusing on ease of fabrication and post-processing utilizing today's well-controlled procedures. The design was optimized to minimize the peak RF surface fields, to provide the same longitudinal electric field profile in both beam tubes, and eliminate multipacting [4]. The cavity design also provides a relatively strong cell-to-cell coupling so that several cells can be joined together for a multiple cell cavity design. The fabrication and post-processing followed typical methods used for conventional single beam pipe elliptical SRF cavities [5]. Room temperature measurements and a vertical cold test have been completed. The results prove the feasibility of the twin axis cavity that could be useful for applications such as in the JLEIC cooler ERL [6] or an asymmetric dual axis ERL [7].

DESIGN

The design went through a couple of evolutions to arrive at an optimized RF design, which provides good RF electromagnetic performance properties [4]. The final design is shown in Fig. 1 and its RF properties are summarized in Table 1 [4].

*Work supported by DOE Office of Science via Accelerator Stewardship Test Facility Pilot Program (Proposal No. 0000219731). This work used resources of the NERSC center, which is supported by DOE Office of Science Contract No. DE-AC02-05CH11231.
#hkpark@jlab.org

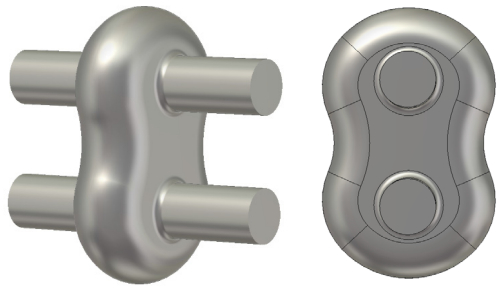


Figure 1: Elliptical-shaped twin axis cavity.

Table 1: Cavity Parameters and rf Properties of the 1497 MHz Single Cell Twin Axis Cavity as Fabricated

Parameter	Value as designed	Unit
Cavity height	202.5	mm
Cavity width	300.0	mm
Cavity length	100.13	mm
Cell length	81.13	mm
Iris curvature	8.0	mm
Beam aperture	60.0	mm
Beam axis separation	136.5	mm
E_p/E_{acc}^*	2.68	-
B_p/E_{acc}^*	5.5	mT/(MV/m)
$[R/Q]$	60.1	Ω
G	320.8	Ω
R_tR_s	1.93×10^4	Ω^2
LOM	1103	MHz
Nearest HOM	1806	MHz

The cavity uses the second TM110 mode as the operating mode. The transverse field components of the operating mode were minimized at the beam pipe centers, and the beam pipes are slightly shifted from the center to cancel the dipole effect [4].

FABRICATION

The fabrication process was comparable to that of typical single beam pipe elliptical cavities. The stamping die set consists of half-cell male and female dies, beam pipe opening punches, and a coining ring with one female

Content from this work may be used under the terms of the CC BY 3.0 licence (© 2018). Any distribution of this work must maintain attribution to the author(s), title of the work, publisher, and DOI.

ISBN: 978-3-95450-194-6 ISSN: 2226-0366 doi:10.18429/JACoW-LINAC2018-TUPO032

die used for all three stamping operations (i.e. forming of the main half-cell, forming of the beam pipe opening, and Coining of the beam pipe leading radius). The forming process was verified successfully with copper blanks, before stamping Nb sheets. The die set and the stamping operations are shown in Fig. 2.

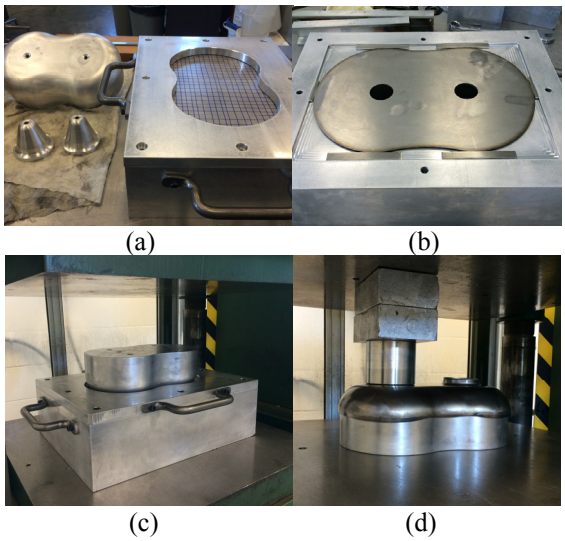


Figure 2: Half cell forming processes. Die set (a), niobium blank (b), first stamping for half cell body (c), and coining after second stamping of beam pipe opening (d).

After stamping, an uneven material thickness around the figure eight shaped equator was observed. It was predicted since the equator is not axisymmetric. The main challenge for this cavity was the electron-beam welding at the cavity equator. The equator seams were prepared for a butt weld. However, the half-cells exhibited a variation in the material thickness along the equator due to uneven spring-back effects. Therefore, the weld preparation machining did not provide a uniform thickness of the weld seam. This resulted in a less than optimal weld quality. Problems with the welding machine also created weld defects. In fact, two prototype cavities were built in the same period and both cavities had weld issues on the equator. One of the defect areas is shown in Fig. 3. For the second cavity, lessons learned were applied and a much better material thickness uniformity was achieved after additional CNC machining around the equators. This resulted in an improved weld joint with less defects.

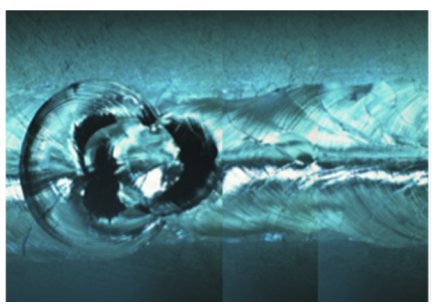


Figure 3: Inside view of equator weld defect.

POST FABRICATION PROCESSING

Standard bulk niobium cavity post-processing procedures were applied for the cavities after UHV cleaning.

- Heavy BCP: The damaged layer removal target was 200 microns. Thickness measurement before and after the process showed an actual removal of 180 micron on average.
- Heat treatment: High temperature heat treatment was performed at 800 deg. C for 3 hours. Residual gas in the furnace was monitored during the process. As temperature increases the hydrogen partial pressure peaked at 2×10^{-7} mbar and was less than 10^{-9} mbar after the heat cycle.
- Light BCP: An additional 25 microns was removed from the interior surface after the heat treatment.
- High pressure rinse: High pressure rinse was performed using JLab's automated system. The water wand went through 3 passes through the cavity cell (up and down) for each beam pipe.
- Clean room assembly: After overnight drying, the cavity was assembled with ancillary parts for testing including an input and pick-up coupler, a vacuum valve, and a safety burst disc. The cavity ready for the vertical test is shown in Fig. 4.
- Low temperature bake: The cavity was baked in the bake box at 120 deg. C for 12 hours for the second cavity (cavity #2) built. The first cavity built (cavity #1) was baked 24 hours at the same temperature.



Figure 4: Cavity ready for test.

Cavity #1 was treated with centrifugal barrel polishing to smooth out the more prevalent weld defects. This provided a mirror finish, but could not fully remove the weld defects.

TEST RESULTS

Cavity #2 was processed and tested first and cavity #1 followed after the centrifugal barrel polish.

Content from this work may be used under the terms of the CC BY 3.0 licence (© 2018). Any distribution of this work must maintain attribution to the author(s), title of the work, publisher, and DOI.

ISBN: 978-3-95450-194-6 ISSN: 2226-0366 doi:10.18429/JACoW-LINAC2018-TUPO032

Content from this work may be used under the terms of the CC BY 3.0 licence (© 2018). Any distribution of this work must maintain attribution to the author(s), title of the work, publisher, and DOI.

Room Temperature HOM Measurement

Figure 5 shows the room temperature HOM spectrum. The line is a S21 transmission measurement and the markers indicate the R/Q-value of each LOM and HOM. Due to the low spectral resolution, some HOMs were not detected.

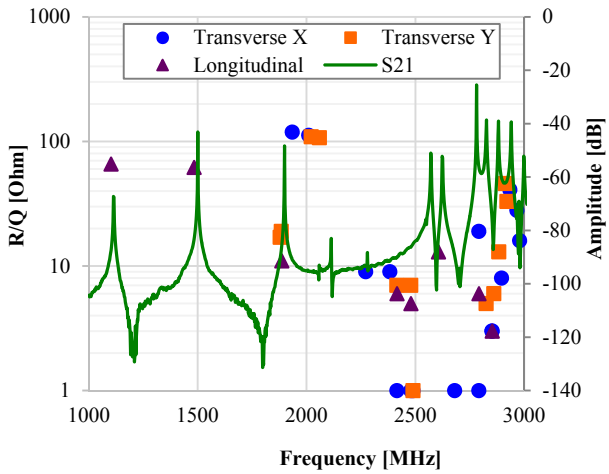


Figure 5: HOM measurement and simulated R/Q.

Cold Test

The main results of the vertical RF tests are plotted in Fig. 6 for both cavities. Cavity #2 reached an accelerating/decelerating field of 23 MV/m with a maximum quality factor of 1.2×10^{10} in the low field regime. As predicted by simulations using Track3P as part of SLAC's ACE3P suite of codes [4], multipacting was not observed.

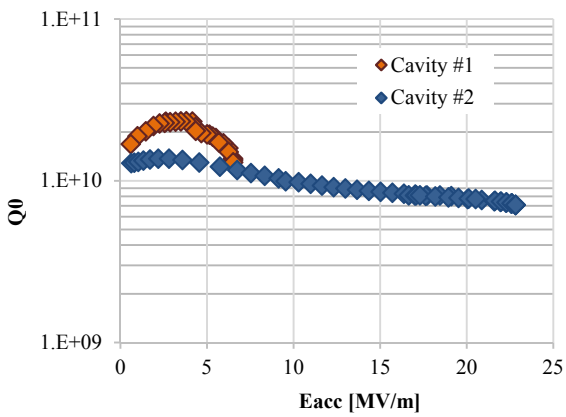


Figure 6: Cold test Q curve.

Four Cernox sensors were mounted on the cavities and the temperatures were monitored during the cold RF test. For both cavities, sensor #1 was installed at the peak magnetic field area, which is located between the beam pipes. All other sensors were placed on the equator weld defect area. The temperature profile of cavity #2 (Fig. 7) shows that the weld quality on the equators did not limit the cavity performance for cavity #2.

Cavity #1 quenched at around 7 MV/m. The test indicates however that the main weld defect could be responsible for the quench. We observed a fast rise of the temperature at the weld defect spot (Fig. 8). This resulted in a strong roll-off of the Q curve at the time of quench. A second-sound quench detection system also pointed to the weld defect as the origin of the quench.

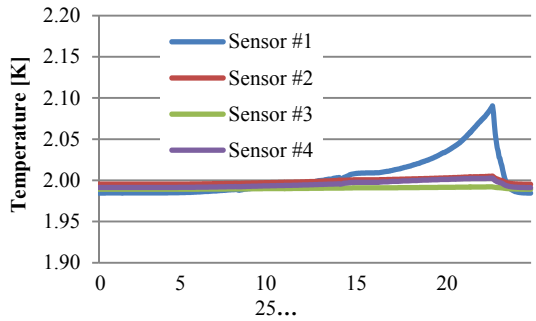


Figure 7: Temperature profile of cavity #2 during rf test.

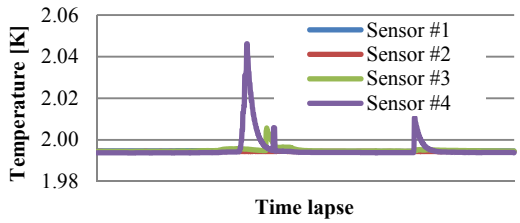


Figure 8: Temperature profile of cavity #1 during rf test.

CONCLUSION

Two proof-of-principle twin axis elliptical cavities were designed, built, and tested. The combined test results of both cavities prove they can be used in ERL applications. The experience shows that the performance can be improved when the processes are custom-fitted to this design, specifically to provide better electron beam welds at the equators. Even though cavity #1 showed a premature quench, the quality factor is very respectable for a BCP'd cavity, although this cavity had a mirror-finish after CBP. The cause of the early quench of cavity #1 is well understood (weld defect) and corrective actions are available. Concerns related to the cavity post-processing due to the relatively complex design are now resolved through this successful test. More studies, for instance HOM damping and implementation, are encouraged to further develop such cavities for actual applications.

REFERENCES

[1] S. Noguchi and E. Kako, "Multi-beam accelerating structures," in *Proc. SRF'03*, Luebeck, Germany, Sep. 2003, paper TUP16, pp. 317-319.

[2] C.-X. Wang, J. Noonan and J. W. Lewellen, "Duel-axis energy-recovery linac," in *Proc. ERL'07*, Daresbury, UK, May 2007, paper 18, pp. 122-125.

ISBN: 978-3-95450-194-6 ISSN: 2226-0366 doi:10.18429/JACoW-LINAC2018-TUPO032

[3] C.-X. Wang, "Conceptual design considerations of a 5-cell duel-axis SRF cavity for ERLs," in *Proc. SRF'07*, Beijing, China, May 2007, paper WEP59, pp. 641-645.

[4] S. U. De Silva et. al., "Electromagnetic design of a superconducting twin axis cavity," in *Proc. LINAC'16*, East Lansing, MI, USA, Sep. 2016, pp. 203-205. doi:10.18429/JACoW-LINAC2016-MOPLR030

[5] H. Park, "Superconducting twin-axis cavity for ERL applications," presented at *SRF'17*, Lanzhou, China, Jul. 2017, WEYA06, unpublished (slides only).

[6] F. Marhauser, "Twin axis elliptical cavity," presented at. *ERL'17*, Geneva, Switzerland, Jun. 2017, TUICCC002, unpublished (slides only).

[7] R. Ainsworth et. al., *Phys. Rev. Accel. Beams* vol. 19, p. 083502, 2016.

Content from this work may be used under the terms of the CC BY 3.0 licence (© 2018). Any distribution of this work must maintain attribution to the author(s), title of the work, publisher, and DOI.

ISBN: 978-3-95450-194-6 ISSN: 2226-0366 doi:10.18429/JACoW-LINAC2018-TUPO033

CRYOGENIC TEST RESULTS OF THE SPS PROTOTYPE RF-DIPOLE CRABBING CAVITY WITH HIGHER ORDER MODE COUPLERS*

S. U. De Silva[1, †], H. Park[2], J. R. Delayen[1], Z. Li[3]
[1]Old Dominion University, Norfolk, VA, USA
[2]Thomas Jefferson National Accelerator Facility, Newport News, VA 23606, USA
[3]Stanford Linear Accelerator National Laboratory, Menlo Park, CA 94025, USA

Abstract

The rf-dipole crabbing cavity planned for the LHC High Luminosity Upgrade is designed to deliver a transverse kick of 3.34 MV; crabbing the proton beam in the horizontal plane. The proton beams of the LHC machine operating at 7 TeV each sets high impedance thresholds on the crabbing cavity systems. The rf-dipole crabbing cavity is designed with a two higher order mode couplers to suppress those HOMs. The first prototype of the HOM couplers are fabricated at Jefferson Lab. This paper reports the cryogenic test results of the HOM couplers with the SPS prototype rf-dipole cavity.

INTRODUCTION

Crabbing cavity systems are an essential component in the LHC High Luminosity Upgrade in recovering the loss of luminosity due to the crossing angle of the colliding bunches [1]. These crabbing systems allow head-on collision of bunches compensating the loss of luminosity. Novel compact crabbing cavities have been designed to meet the tight dimensional constraints in LHC [2]. The SPS prototype rf-dipole crabbing cavity shown in Fig. 1 is one of the cavities that is being designed and fabricated with all the ancillary components including the fundamental power coupler, higher order mode (HOM) couplers, and tuning and He vessel interfaces.

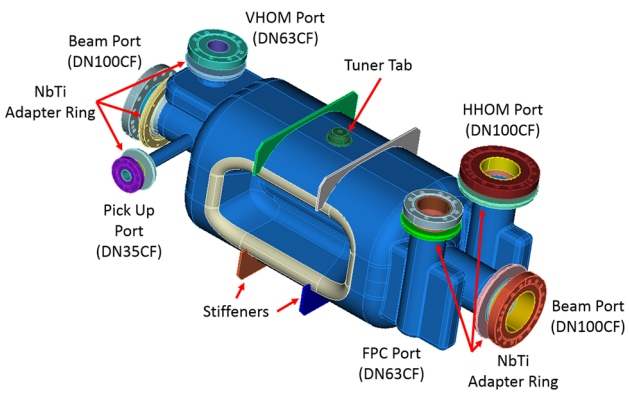


Figure 1: 400 MHz SPS prototype rf-dipole cavity.

The rf-dipole cavity has been designed to operate in a TE_{11}-like mode where the primary contribution to the kick is given by the transverse electric field between the poles [3]. The poles and outer body are optimized to minimize the peak surface field ratios for given transverse kick.

*Work supported by DOE via US LARP Program and by the High Luminosity LHC Project. Work was also supported by DOE Contract No. DE-AC02-76SF00515
†sdesilva@jlab.org

SPS PROTOTYPE RF-DIPOLE CRABBING CAVITY

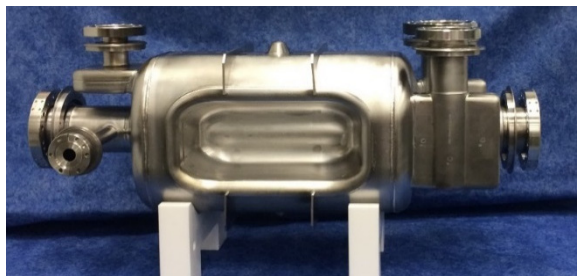


Figure 2: Fabricated Nb rf-dipole cavity.

Two prototype cavities were fabricated by Niowave Inc. and completed at Jefferson Lab under US-LARP. Figure 2 shows the fabricated full prototype rf-dipole crabbing cavity. The cavities were bulk BCPed followed by heat treatment at 600 C for 10 hours. Then the cavities were light BCPed, high pressure rinsed and assembled for rf testing. Prior to rf test the cavity was baked at low temperature of 120 C. The details of the fabrication and cavity processing are given in Ref. [4].

Bare Cavity Test Results

The two cavities were rf tested at Jefferson Lab with performance exceeding the design specifications [5]. Figure 3 shows the measured Q curves of the RFD-CAV-002. The same cavity was rf tested with the HOM couplers following the bare cavity test.

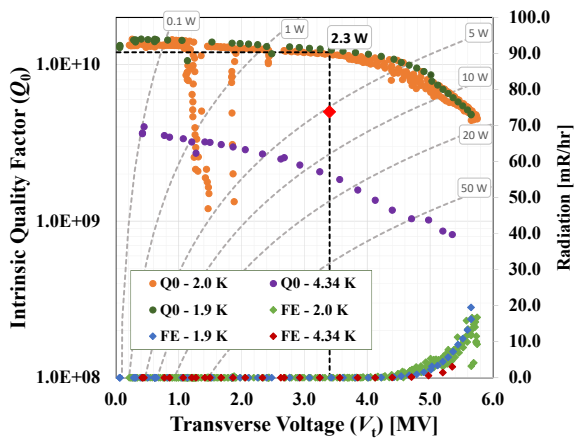


Figure 3: Q curves of the bare RFD-CAV-002.

The cavity achieved a maximum transverse kick of 5.8 MV with peak surface fields of E_p = 56 MV/m and B_p = 96 mT and low field Q_0 is greater than 1.3×10^{10}. The

Content from this work may be used under the terms of the CC BY 3.0 licence (© 2018). Any distribution of this work must maintain attribution to the author(s), title of the work, publisher, and DOI.

ISBN: 978-3-95450-194-6 ISSN: 2226-0366 doi:10.18429/JACoW-LINAC2018-TUPO033

cavity had no field emission below 4.5 MV. Low field multipacting was processed completely and didn't reappear. The cavity Q_0 at operating voltage of 3.4 MV is 1.24×10^{10} with a power dissipation of 2.3 W.

HIGHER ORDER MODE COUPLERS

The rf-dipole cavity is designed with two HOM couplers named Horizontal-HOM (HHOM) coupler and Vertical-HOM (VHOM) coupler as shown in Fig. 4 [6]. These couplers are placed at the ends of the cavity in the low field region and are designed to damp the HOMs up to 2 GHz. The HHOM coupler is a high pass filter designed to cut off the fundamental mode and to damp the horizontal dipole modes where the VHOM coupler damps the vertical dipole modes. The VHOM coupler is designed as a coax-antenna with an asymmetric probe head to strongly damp few modes at higher frequencies.

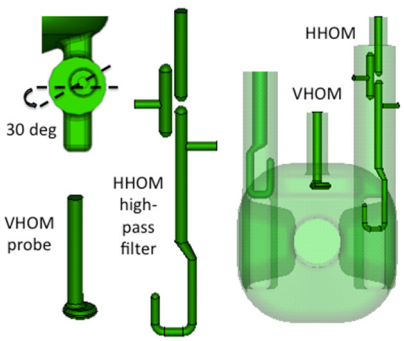


Figure 4: HHOM and VHOM couplers for the rf-dipole crabbing cavity.

Two sets of HOM couplers for the rf-dipole cavity have been fabricated at Jefferson Lab as shown in Fig. 5. The HHOM coupler is a demountable Nb coupler where the probe and VHOM coupler antenna is made out of Cu.



Figure 5: Nb HHOM high pass filter with hook and T (top), HHOM coupler probe (bottom left) and VHOM coupler (bottom right).

The HHOM high pass filter is designed with a separate stainless steel He jacket. However, the HHOM coupler used for the tests doesn't have the He jacket welded. The HOM coupler set, which was used for the cryogenic rf tests with the RFD-CAV-002 was processed and rf tested as follows.

- Light BCP of 24 microns
- Low temperature bake at 120 C for 12 hours after cavity assembly
- First RF test (Test 1) at 2 K
- Additional light BCP of 13 microns
- Low temperature bake at 120 C for 12 hours again after cavity assembly

RF TESTS WITH HOM COUPLERS

A series of rf tests have been performed on the RFD-CAV-002 with HOM couplers. The RF Test 1 of the rf-dipole cavity with HOM couplers were tested with both the HHOM and VHOM couplers and the Q curve is shown in Fig. 6.

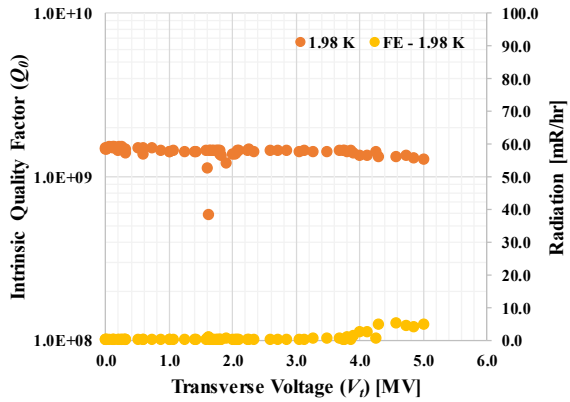


Figure 6: Q curve of the RFD-CAV-002 with both HHOM and VHOM couplers (Test 1).

The cavity reached a transverse kick of 5 MV where cavity had no quench issues and was rf power limited. No new multipacting levels were observed at the cavity or at the couplers and the cavity showed very low field emission similar to that of the bare cavity test.

The cavity showed a low Q_0 compared to that of the bare cavity test. Also, a strong coupling with $Q_{ext} = 2\times10^9$ with equivalent transmitted power of ~13 W was measured at the fundamental mode through the VHOM coupler. It was determined that fabrication imperfections of the waveguide stub of the VHOM port reference to cavity poles results in this strong coupling to the fundamental mode. This also limits the available rf power during the rf test and also increases the error in the measured Q_0.

Additional light BCP was done on the HHOM coupler with the assumption that the reduced Q_0 was due to inadequate removal of the damaged Nb layer at the coupler. In the second RF test (Test 2) the cavity was tested with only the HHOM coupler and the Q curve is shown in Fig. 7. The multipacting and field emission levels are similar to that in RF Test 1 with both HOM couplers. However, the cavity Q_0 was lower than that in RF Test 1.

Content from this work may be used under the terms of the CC BY 3.0 licence (© 2018). Any distribution of this work must maintain attribution to the author(s), title of the work, publisher, and DOI.

ISBN: 978-3-95450-194-6 ISSN: 2226-0366 doi:10.18429/JACoW-LINAC2018-TUPO033

Content from this work may be used under the terms of the CC BY 3.0 licence (© 2018). Any distribution of this work must maintain attribution to the author(s), title of the work, publisher, and DOI.

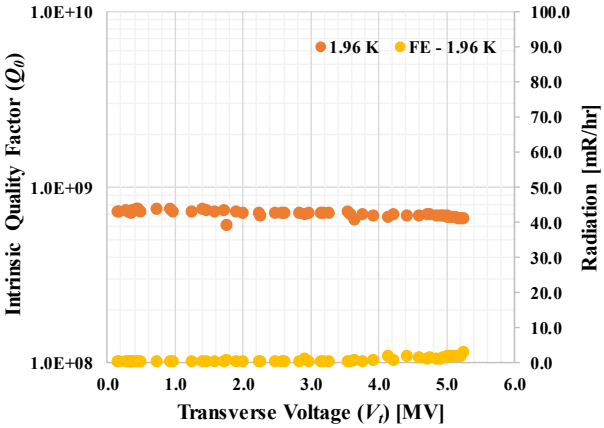


Figure 7: Q curve of the RFD-CAV-002 with only HHOM coupler (Test 2).

A set of Cernox sensors were placed at the HHOM coupler and temperature was recorded during the test. The various locations of the Cernox sensors on the HHOM coupler are shown in Fig. 8.

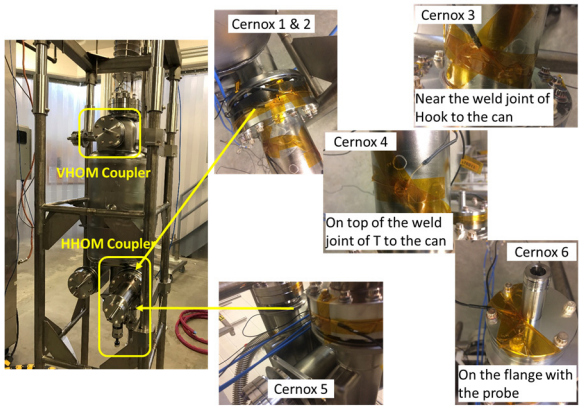


Figure 8: Locations of the Cernox sensors on the HHOM coupler.

The Cernox sensors 4, 5, and 6 show no significant change in the temperature. However, Cernox sensors 1, 2, and 3 show an increase in temperature as shown in Fig. 9.

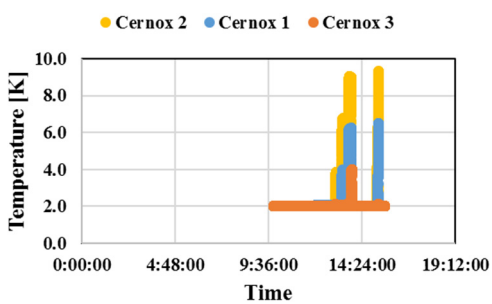


Figure 9: Measured temperature change in Cernox sensors.

The heating (Cernox sensors 1&2) is at stainless steel flanges of both the cavity and couplers facing the cavity body with no heating shown on the stainless steel flange facing the cavity beam pipe (Cernox sensor 5). Also there is heating at the weld joint of Nb hook to the outer can (Cernox sensor 3). This clearly indicates that there is a constant loss present at the HHOM coupler due to rf losses that degrades cavity Q_0 yet doesn't cause cavity to quench. Detailed analysis done with the rf simulation estimated a low Q_0 of 7×10^8 due to the incorrectly sized Cu gasket, which exposed the stainless steel surfaces at both cavity and coupler to rf currents generated by the presence of the hook. Figure 10 shows the Cu gasket location and the corresponding rf losses at the stainless steel flange. In order to recover the cavity Q_0 and to eliminate the rf loses at the exposed stainless steel surfaces; an rf gasket will be used in the future rf tests.

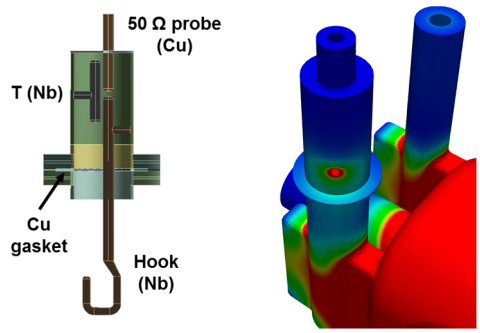


Figure 10: Cu gasket location at the HHOM coupler (left) and rf losses at the stainless steel flange (right).

CONCLUSIONS

Cryogenic tests have been carried out on RFD-CAV-002 to validate the performance of the RFD cavity with HOM couplers. Initial tests (Test 1) were carried out with both the HOM couplers and Test 2 was done only with the HHOM coupler. The cavity achieved a transverse kick of 5 MV and didn't quench in both the rf tests. No new multipacting levels or field emission levels were observed. The cavity Q_0 was low in all the rf tests with the HOM couplers. The reduced Q_0 was caused by the rf losses at the exposed stainless steel surfaces due to incorrectly sized Cu gasket. Next the cavity will be re-tested with only the HHOM coupler and with an rf gaskets to recover the cavity Q_0. Currently new RF gaskets for the HHOM coupler are under fabrication.

REFERENCES

[1] G. Apollinari, *et al.*, "High Luminosity Large Hadron Collider HL-LHC", CERN Yellow Report, p. 19, May, 2017.

[2] P. Baudrenghien, *et al.*, "Functional Specifications of the LHC Prototype Crab Cavity System", Tech. Rep. CERN-ACC-NOTE-2013-003, 2013.

[3] S. U. De Silva and J. R. Delayen, Phys. Rev. Accel. Beams **16**, 012004 (2013).

[4] H. Park, "LARP Cavity Results", International Review of the Crab Cavity Performance for HiLumi, CERN, April, 2017.

[5] S. De Silva, H. Park, J. R. Delayen, Z. Li, in *Proc. of SRF'15*, Whistler, BC, Canada, p. 1222.

[6] Z. Li, J. R. Delayen, S. U. De Silva, H. Park, R, Olave, in *Proc. of IPAC'15*, Richmond, VA, USA (2015), p. 3492.

ISBN: 978-3-95450-194-6 ISSN: 2226-0366 doi:10.18429/JACoW-LINAC2018-TUPO035

DETERMINATION OF THE FIELD DEPENDENCE OF THE SURFACE RESISTANCE OF SUPERCONDUCTORS FROM CAVITY TESTS*

J. R. Delayen†1, H. Park[1], S. U. De Silva,
Center for Accelerator Science, Old Dominion University, Norfolk, VA 23529
[1]also at Jefferson Lab, Newport News, VA 23606, USA

Abstract

Cryogenic tests of superconducting cavities yield an average surface resistance as a function of the peak surface magnetic field. An analytical formalism has been developed to extract the actual field dependence of the surface resistance from cavity tests and is applied to coaxial cavities and cavities of more complex geometries.

INTRODUCTION

The well-known expressions for the surface resistance of superconductors in electromagnetic fields, and its dependence on frequency, temperature, and a few materials parameters, were obtained as a perturbation theory under the assumption that the magnitude of the electromagnetic field is much smaller than the critical field. This resulted in a surface resistance independent of the magnitude of the electromagnetic field.

There have been several attempts at developing theories of the surface resistance at high rf field, up to the critical field, but, at present, there is no universally accepted consensus on the correct fully self-consistent theory.

Experimentally, cryogenic tests of superconducting cavities developed for particle accelerators have shown that superconductors can display a strong dependence of their surface resistance on the rf field. Furthermore, the field dependence can vary greatly depending on the history of the cavities: chemical treatment, high temperature and low heat treatment, impurity, ambient magnetic field during transition, cooling rate during, and so on.

Traditionally superconductors have shown an increase of their surface resistance with rf field which puts a limit to the accelerating gradients achievable for high-energy accelerators. More recently, processes have been developed that yield a decrease of the surface resistance with medium fields, a great benefit for accelerators operating in cw mode.

A strong dependence of the surface resistance on magnetic field is also often observed in cavities made by sputtering of Nb on Cu or in cavities made of Nb_3Sn on Nb

Developing a full understanding and theory of the rf field dependence of the surface resistance of superconductors will require accurate knowledge of that surface resistance as a function of the rf field, and its dependence on preparation and processing parameters.

Experimentally it has proven difficult to develop techniques where a superconductor was exposed to a uniform electromagnetic field. Until now, in all measurements, either the superconducting sample was exposed to a non-uniform field in a test cavity or, more often, an entire cavity was made of superconducting material that was exposed to a field that ranged from 0 to a maximum value.

In this paper we present a method and formulae that allow determination of the actual dependence of the surface resistance from experiments where an "average" surface resistance is derived from tests of superconducting resonators. An underlying assumption is still that, while the surface resistance has a magnetic field dependence, it does not have a dependence on location. This is not always true as it is known that superconducting cavities can have "hot spots" where the surface resistance is higher and with a stronger field dependence than in the rest of the cavity

ANALYTICAL METHOD

The geometrical factor G of a cavity is defined as

$$G = \omega\mu_0 \frac{\int_V |\mathbf{H}|^2 \, \mathrm{d}V}{\int_S |\mathbf{H}|^2 \, \mathrm{d}S}. \quad (1)$$

If the surface resistance is constant, then $G=QR_s$. If it is not, then $G/Q(H) = \bar{R}_s(H)$ where $\bar{R}_s(H)$ is an "average" surface resistance. It is related to the actual one by

$$\bar{R}_s(H_p)\int_S |\mathbf{H}(\vec{r})|^2 \, \mathrm{d}S = \int_S R_s\left(H(\vec{r})\right)|\mathbf{H}(\vec{r})|^2 \, \mathrm{d}S. \quad (2)$$

We define the function $a(h)$ as the fraction of the total cavity surface where $|H| \le hH_p$. The function $a(h)$ is continuous, monotonically increasing, with $a(0)=0$ and $a(1)=1$. It could also be interpreted as the probability distribution for the surface magnetic field, and its derivative $\mathrm{d}a/\mathrm{d}h$ as the probability density. For normal cavity geometries we also have $\mathrm{d}a/\mathrm{d}h\big|_{a=1} = \infty$.

Because of the continuity and monotonicity of $a(h)$ we can make a change of variable in Eq. (2) and integrate over the magnetic field instead of the area.

$$\bar{R}_s(H) = \int_0^1 (hH)^2 \frac{\mathrm{d}a}{\mathrm{d}h}\mathrm{d}h = \int_0^1 R_s(hH)(hH)^2 \frac{\mathrm{d}a}{\mathrm{d}h}\mathrm{d}h. \quad (3)$$

We assume that the experimentally measured average surface resistance can be modelled by a sum of powers of the magnetic field:

$$\bar{R}_s\left(\frac{H}{H_0}\right) = \bar{R}_0 \sum_{\alpha_i} r_{\alpha_i}\left(\frac{H}{H_0}\right)^{\alpha_i}. \quad (4)$$

* Work supported by NSF Award No. PHY-1416051
† jdelayen@odu.edu

Content from this work may be used under the terms of the CC BY 3.0 licence (© 2018). Any distribution of this work must maintain attribution to the author(s), title of the work, publisher, and DOI.

ISBN: 978-3-95450-194-6 ISSN: 2226-0366 doi:10.18429/JACoW-LINAC2018-TUPO035

Content from this work may be used under the terms of the CC BY 3.0 licence (© 2018). Any distribution of this work must maintain attribution to the author(s), title of the work, publisher, and DOI.

The sum can be of any size and the coefficients α_i are not restricted to integers, they can be any non-negative real numbers. $\bar{R}_0$ is the zero-field surface resistance and H_0 is arbitrary; it is introduced to make the coefficients r_{α_i} dimensionless. We assume the same power expansion for the real surface resistance but with modified coefficients:

$$R_s\left(\frac{H}{H_0}\right) = R_0 \sum_{\alpha_i} \beta(\alpha_i) r_{\alpha_i} \left(\frac{H}{H_0}\right)^{\alpha_i} . \quad (5)$$

Replacing $\bar{R}_s(H/H_0)$ and $R_s(H/H_0)$ by their power expansions in Eq. (3) and equating identical powers we obtain the coefficients $\beta(\alpha_i)$ relating the average and actual surface resistance.

$$\beta(\alpha) = \frac{\int_0^1 h^2 \frac{\mathrm{d}a}{\mathrm{d}h}\mathrm{d}h}{\int_0^1 h^{2+\alpha} \frac{\mathrm{d}a}{\mathrm{d}h}\mathrm{d}h} . \quad (6)$$

The function $\beta(\alpha)$ is continuous and, since $\mathrm{d}a/\mathrm{d}h > 0$ and $0 < h < 1$, it is monotonically increasing with $\beta(0) = 1$.

Equation (6) is more appropriate when the function $a(h)$ can be obtained analytically. For most cavities, it can only be obtained numerically; in that case it is more convenient to use an equivalent relationship derived from Eq.(6) by integration by parts.

$$\beta(\alpha) = \frac{2\int_0^1 h[1-a(h)]\mathrm{d}h}{(2+\alpha)\int_0^1 h^{1+\alpha}[1-a(h)]\mathrm{d}h} . \quad (7)$$

In Eq. (7), $[1-a(h)]$ now represents the fraction of the cavity surface where $|H| > H_p$.

APPLICATION TO HALF-WAVE COAXIAL CAVITY

The results of the previous section will now be applied to a coaxial half-wave cavity specifically designed for the measurement of the field dependence of the surface resistance on niobium over a wide range of frequencies [1, 2]. Its length is L (459 mm), the radius of the center conductor is a (20 mm), and the radius of the outer conductor is b (101 mm). We also define the dimensionless parameters $\rho = a/b$ and $\delta = b/L$.

For such a cavity $a(h)$ and its derivative can be obtained analytically. The un-normalized contributions from the cavity components are:

Center conductor:

$$A_1(h) = 4\rho\delta L^2 \arcsin(h) , \qquad \frac{dA_1}{dh} = \frac{4\rho\delta L^2}{\sqrt{1-h^2}} . \quad (8)$$

Outer conductor:

$$A_2(h) = \begin{cases} 4\delta L^2 \arcsin(h/\rho) & 0 \le h < \rho \\ 2\pi\delta L^2 & \rho \le h \le 1 \end{cases}$$
$$\frac{dA_2}{dh} = \begin{cases} \dfrac{4\delta L^2}{\rho\sqrt{1-(h/\rho)^2}} & 0 \le h < \rho \\ 0 & \rho \le h \le 1 \end{cases} . \quad (9)$$

End Plates:

$$A_3(h) = \begin{cases} 0 & 0 \le h < \rho \\ 2\pi\delta^2 L^2\left(1-\dfrac{\rho^2}{h^2}\right) & \rho \le h \le 1 \end{cases}$$
$$\frac{dA_3}{dh} = \begin{cases} 0 & 0 \le h < \rho \\ \dfrac{4\pi\rho^2\delta^2 L^2}{h^3} & \rho \le h \le 1 . \end{cases} \quad (10)$$

The function $a(h)$ for the half-wave cavity and its components from the center conductor, the outer conductor, and the two end plates is shown in Fig. 1. Its derivative is shown in Fig. 2.

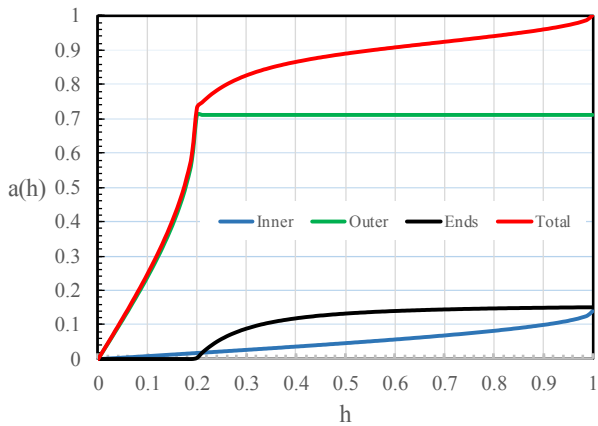


Figure 1: Fraction $a(h)$ of the cavity area where the surface magnetic field is $< hH_p$.

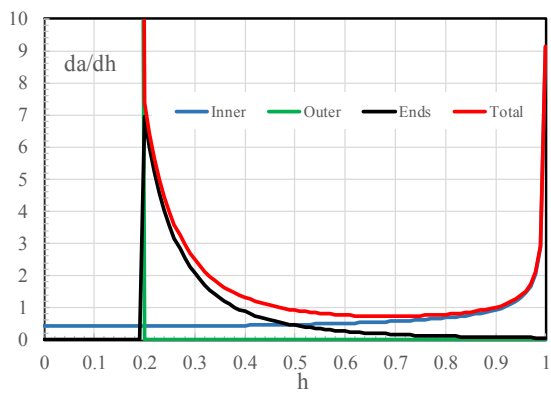


Figure 2: $\mathrm{d}a/\mathrm{d}h$ for the coaxial half-wave cavity.

ISBN: 978-3-95450-194-6 ISSN: 2226-0366 doi:10.18429/JACoW-LINAC2018-TUPO035

The correction function $\beta(\alpha)$ can be ontained analytically and is:

$$\beta(\alpha)=\frac{(1+\rho)/4+\rho\delta\ln(1/\rho)}{\frac{1+\rho^{1+\alpha}}{2\sqrt{\pi}}\frac{\Gamma(\alpha/2+3/2)}{\Gamma(\alpha/2+2)}+\frac{\rho\delta}{\alpha}(1-\rho^{\alpha})} \quad . \quad (11)$$

The correction function $\beta(\alpha)$ is shown in Fig. 3 for various ratio of inner to outer conductor radii. The curve $\rho=0$ is equivalent to assuming that the observed field-dependence of the surface resistance is dominated by the center conductor.

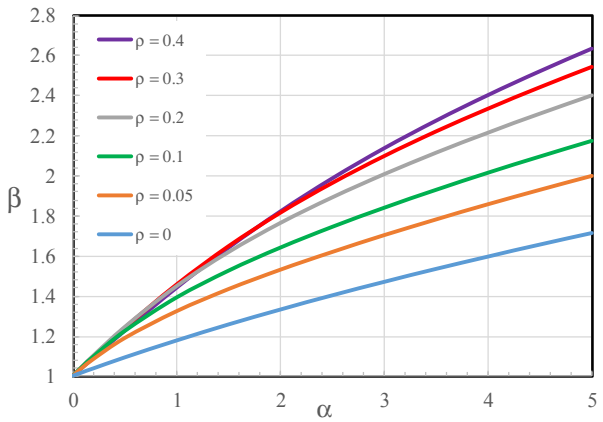


Figure 3: Correction function $\beta(\alpha)$ for different ratio of inner to outer conductor radii.

Figure 3 shows an example of a Q-curve for the half-wave cavity operating in the fundamental TEM mode at 325 MHz and at 4.35 K.

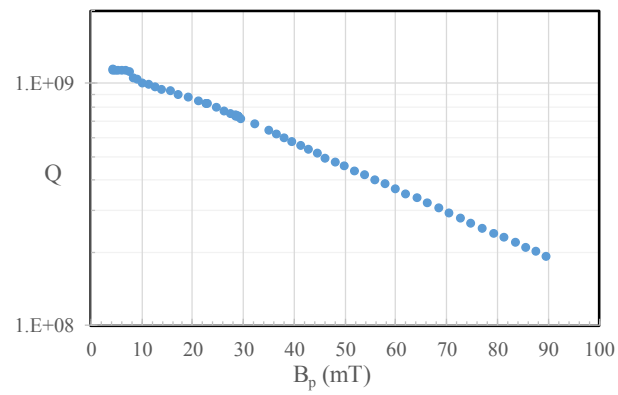


Figure 4: Q-curve for the half-wave cavity at 4.35 K in the fundamental 325 MHz mode.

From the Q-curve and the geometrical factor (59 Ω) the average resistance is calculated and shown as blue dots in Fig. 5. In this example the experimental data is fitted by a third-degree polynomial, shown as the purple line. The surface resistance is in nΩ and the normalizing field is $B_0=100$ mT.

$$\bar{R}_s\left(\tfrac{B}{B_0}\right)=48.2\left[1+1.54\left(\tfrac{B}{B_0}\right)+2.03\left(\tfrac{B}{B_0}\right)^2+3.20\left(\tfrac{B}{B_0}\right)^3\right]$$

From Eq. (11) the correction coefficients re calculated:

$$\beta_0=1,\ \beta_1=1.46,\ \beta_2=1.79,\ \beta_3=2.04$$

This leads directly to an expression to the actual surface resistance as a function of magnetic field shown as the red curve in Fig. 5:

$$R_s\left(\tfrac{B}{B_0}\right)=48.2\left[1+2.24\left(\tfrac{B}{B_0}\right)+3.63\left(\tfrac{B}{B_0}\right)^2+6.52\left(\tfrac{B}{B_0}\right)^3\right]$$

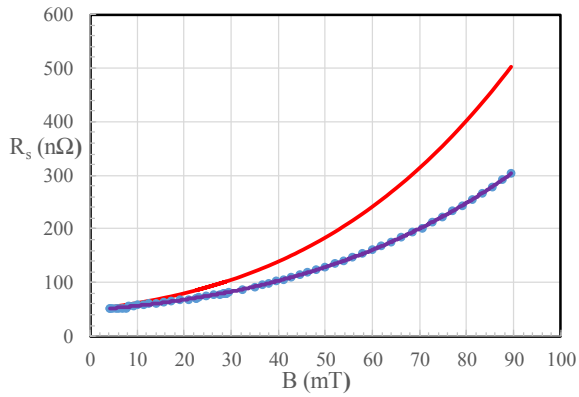


Figure 5: Average surface resistance (blue dots), polynomial fit (purple curve) and derived actual surface resistance (red curve) from the Q-curve of Fig. 4.

CAVITIES OF MORE COMPLICATED GEOMETRY

In most cases the function $a(h)$ and its derivative cannot be obtained analytically. For cavities that still display axial symmetry (e.g. quarter-wave or TM "elliptical" cavities), $a(h)$ can be obtained by a line integration of the magnetic field over the profile. For cavities with full 3-D geometry, $a(h)$ must be obtained by sampling the magnetic field over the whole surface and building the "probability" distribution and density. In both cases $\beta(\alpha)$ is more easily calculated from Eq. (7). As a check on the accuracy of the determination of $a(h)$, for any cavity it should satisfy $\mathrm{d}a/\mathrm{d}h\big|_{a=1}=\infty$.

REFERENCES

[1] H. Park, S. U. De Silva, and J. R. Delayen, "Superconducting cavity for the measurements of frequency, temperature, rf field dependence of the surface resistance", in *Proc. SRF2015*, Whistler, Canada, September 2015, https://doi.org/10.18429/JACoW-SRF2015-MOPB003.

[2] H. Park, S. U. De Silva, and J. R. Delayen, "Measurement of frequency, temperature, rf-field dependent surface resistance using superconducting half-wave cavity", in *Proc. SRF2017*, Lanzhou, China, July 2017, https://doi.org/10.18429/JACoW-SRF2017-THPB080.

Content from this work may be used under the terms of the CC BY 3.0 licence (© 2018). Any distribution of this work must maintain attribution to the author(s), title of the work, publisher, and DOI.

ISBN: 978-3-95450-194-6 ISSN: 2226-0366 doi:10.18429/JACoW-LINAC2018-TUPO036

VERTICAL TEST RESULTS OF PLASMA IN-SITU CLEANING ON LOW BETA HWR CAVITY*

A.D. Wu†, S.C. Huang, C.F. Hu, C. L. Li, Y. M. Li, L. Yang, F. Pan, X. M. Liu, H. Guo
Y. K. Song, P. R. Xiong, W. M. Yue, C. Zhang, Y. He, S. H. Zhang, H.W. Zhao
Institute of Modern Physics, Chinese Academy of Sciences, Lanzhou, China

Abstract

Field emission occurred in SRF cavity is the major limitation to operate at high gradient with stability. The plasma in-situ cleaning for the low beta HWR cavity was carried out to remove the hydrocarbons contaminants on the inner cavity surface. And the vertical test results indicated that the field emission effect was relieved with the increasing of the quench point and emission set-on point. Thus, oxygen active plasma processing can be an effective method to solve the field emission issues for the low beta HWR cavity.

INTRODUCTION

The Chinese-Accelerator Driven System (C-ADS) has been developing for the treatment of the nuclear wastes at Institute of Modern Physics, Chinese Academy of Sciences. A 25 MeV superconducting proton linac injector has been constructed, and it had been commissioned successfully for the continuous wave proton beams with the current of 170 μA. However, the operation stability of this linac was limited by the trips of the HWR cavities caused by field emission. In order to mitigate the field emission issues in the HWR cavities, the in-situ plasma cleaning technique was proposed at IMP.

For removing the hydrocarbon contaminants covered on the inner surface of the cavity, the inert gas argon was used for the plasma ignition and a few percentage of oxygen gas was mixed as oxidant [1-6].To understand the plasma interaction with niobium surface during the plasma cleaning progress, the characteristics of electron temperature, free electron number density and the vertical test results of HWR cavity by plasma cleaning are presented in this paper.

PLASMA EGNITION IN HWR CAVITY

RF plasma discharge experimental platform for the in-situ plasma cleaning is shown in Fig. 1. It consists of RF system, vacuum system and the optical emission spectrum (OES) system and mass spectrometer.

An HWR015 was used for the plasma discharge experimental study offline. HWR15 was optimized for accelerating protons with a relative speed of light at 0.15, and the fundamental eigen frequency is 162.5 MHz. In order to obtain the similar conditions in cryomodule for HWR015 cavity, the fundamental power coupler (FPC) with dual ceramic windows structure was installed for the cavity, as shown in the Fig. 1.

The Argon and oxygen mixed plasma was ignited in the HWR015, and the glow brightness in three directions at different pressures and oxygen volume ratios is illustrated in Fig. 2. The lower gas pressure and the smaller oxygen volume ratio has the stronger luminance of the plasma light and more uniform distribution of discharge will be achieved in the cavity.

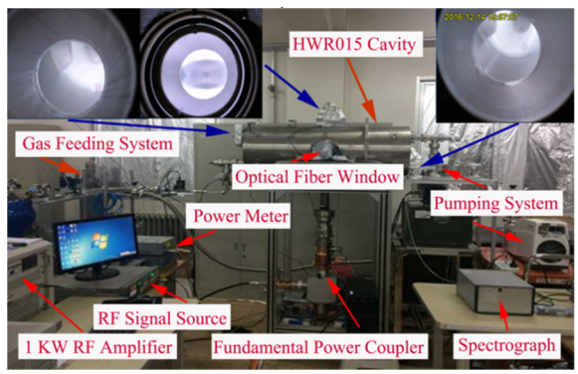


Figure 1: The experimental platform of RF plasma discharge for HWR015 cavity.

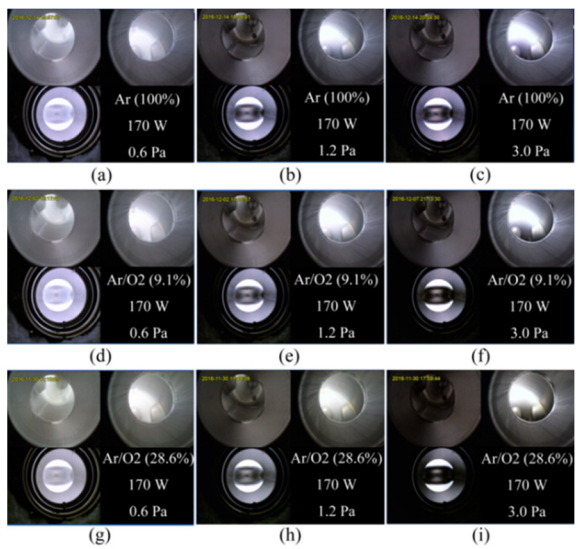


Figure 2: Brightness of the plasma discharge in the HWR015 cavity, at different gas pressures and oxygen volume ratios. The top two cameras were fixed at the two ends of the cavity and the bottom left one was installed at the middle of the cavity.

* Work supported by Major Research Plan of National Natural Science Foundation of China (Grant NO. 91426303) and National Natural Science Foundation for Young Scientists of China (Grant NO. 1150555))
# Email address: antonwoo@outlook.com / antonwoo@impcas.ac.cn

Content from this work may be used under the terms of the CC BY 3.0 licence (© 2018). Any distribution of this work must maintain attribution to the author(s), title of the work, publisher, and DOI.

ISBN: 978-3-95450-194-6 ISSN: 2226-0366 doi:10.18429/JACoW-LINAC2018-TUPO036

Figure 2 indicated that the plasma was concentrated in the middle of cavity, but thin in the both end sides of cavity. This because that the standing wave in the HWR cavity is in the transverse electric and magnetic field mode, which divides the EM field into a strong electric field region at the middle of the cavity and two strong magnetic field regions at the both ends of the cavity [7-8]. This non-uniform electric field distribution leads to the plasma concentrated at the middle of the cavity, because the electric field heats the plasma in this region, from where the seed electrons are mainly produced. Then the above seed electrons are transferred to the both ends of the cavity by drift and diffusion to ignite the plasma discharge in this region.

PLASMA PARAMETERS FROM OES

The optical emission spectroscopy (OES) based technique is a non-invasive method for diagnosing free electron number density, electron temperature and active species in the plasma region by measuring the relative intensity of the emission lines [9-11]. Based on the LET model and the corona model, eleven spectral lines of the argon atom were chosen at the wavelength of 687.1, 693.8, 696.5, 703.0, 706.7, 714.7, 720.7, 731.2, 750.4, 751.5 and 763.5 nm to evaluate the electron temperature, as shown in Fig. 3. The electron temperature decreases between 1.2 eV and 2.2 eV as the increasing of the gas pressure, this matches well from literature with an average 2eV for gas plasma discharges [12].

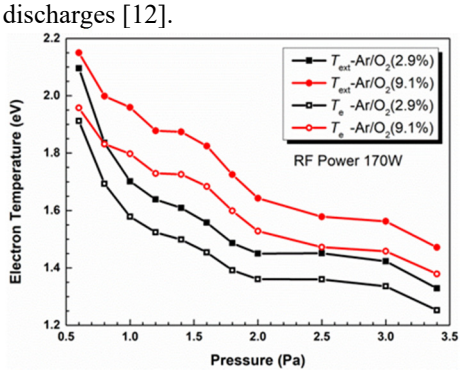


Figure 3: The dependence of the electron temperature on the gas pressure.

The Saha-Boltzmann equation was used to estimate the electron density by using the optical intensity ratio of the argon atomic and ionic lines [13-14]. In this study, the emission lines of the atom at 451.1nm and the ion at 476.5 nm were used to calculate the electron density.

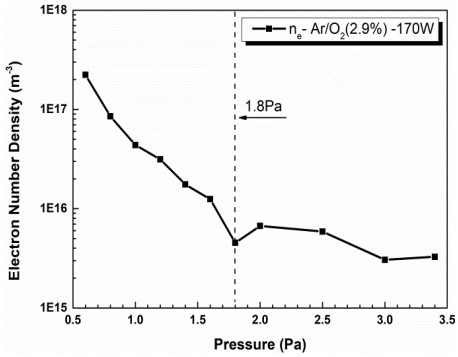


Figure 4: Electron number density as function of the gas pressure.

Figure 4 depicts the electron number density as a function of the gas pressure on the condition of the oxygen volume ratio at 2.9% and RF power at 170 W. As one can see, when the gas pressure is varied from 0.5 Pa to 1.8 Pa, the n_e decreases rapidly from 2.2×10^{17} to 4.5×10^{15} m^{-3}. For gas pressure above 2.0 Pa, the n_e is stable at about 5.0×10^{15} m^{-3}.

PLASMA IN-SITU CLEANING AND CRYOGENIC TEST OF THE HWR CAVITY

Experiment Procedure for Plasma Cleaning on Vertical Test Stand

Following the above experiments of the plasma ignition and characterization, the inner surface of the HWR015 cavity was etched by a light buffered chemical polishing (BCP) with about 21 um material removal, to remove the possible oxidation layers coated on the niobium surface, which caused by the long-time plasma discharge inside the cavity. In order to meet the requirements of the cryogenic test at 4 K and plasma ignition at room temperature, an adjustable coupler (AC) was designed and assembled instead of the FPC. The Qext of AC can be adjusted from 1.0×10^4 to 5.0×10^9. And the experimental setup is identical with the one in Fig. 2 but without the FPC. The procedure is as follows:

(1) Test the cavity at 4 K as baseline after the standard surface treatments, including the BCP, the high pressure rinsing (HPR) by deionized water and the vacuum baking at 120 centigrade for 48 hours.

(2) Process the cavity with reactive oxygen plasma at room temperature to remove the hydrocarbon contaminants.

(3) Test the cavity at 4 K again to verify the effect of the plasma cleaning.

Chemical Reaction and Byproducts During Plasma Cleaning

During the process of in-situ plasma cleaning of the HWR015 cavity, the Q_{ext} of the coupler was set at 1.1×10^4. The oxygen volume ratio was set in the range from 3% to 10%, the gas pressure was between 0.6 Pa and 1.2 Pa, and the RF forward power between 80 and 120 W was used. To avoid the significant heat depositing on the

Content from this work may be used under the terms of the CC BY 3.0 licence (© 2018). Any distribution of this work must maintain attribution to the author(s), title of the work, publisher, and DOI.

ISBN: 978-3-95450-194-6 ISSN: 2226-0366 doi:10.18429/JACoW-LINAC2018-TUPO036

Content from this work may be used under the terms of the CC BY 3.0 licence (© 2018). Any distribution of this work must maintain attribution to the author(s), title of the work, publisher, and DOI.

inner surface of the cavity during the plasma cleaning process, a short plasma pulse was used, which has a width between 5 and 15 seconds, the interval time of each pulse was set between 1 and 3 minutes. The total active plasma processing time was about 95 minutes over 28 hours.

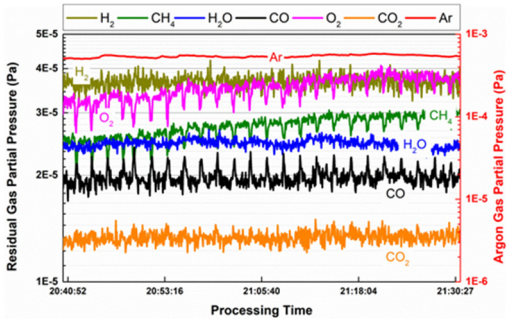


Figure 5: Parts of the RGA data obtained during the plasma processing of the HWR015 cavity.

A quadrupole mass spectrometer (QMS) was used as the residual gas analyser (RGA) to monitor the gas pumped out from the cavity during the plasma in-situ cleaning process. Parts of the RGA data for some selected gas are shown in Fig. 5. The distinctive peaks of each curve correspond to each short plasma pulse. The downward peaks of the oxygen indicate that the oxygen was consumed as the oxidant for the chemical reaction during the plasma cleaning process. The methane, which is one type of the hydrocarbon contaminants of the SRF cavity [1-5], was degraded. Meanwhile, the gas of H_2O, CO and CO_2 were also measured, which are the volatile byproducts of the chemical sputtering of hydrocarbons by the oxygen reactive plasma. Particularly, the obvious peaks of CO indicate that CO is the major component of the volatile byproducts.

Performance of the HWR Cavity Improved by Plasma In-situ Cleaning

The cryogenic test results of the HWR015 cavity are shown in Fig. 6, it indicates that the performance of the cavity can be significantly improved by plasma in-situ cleaning. The maximal peak surface electric field E_{peak}, which relates to the maximal available accelerating gradient, was increased from 54.8 MV/m to 70.3 MV/m. The onset of the X- ray radiation that caused by the bremsstrahlung of the field emitted electrons was raised from 32.1 MV/m to 59.5 M/m, and its maximal dose was decreased from 250.8 μSv/h to 4.5μSv/h. Before the plasma cleaning, the performance of the cavity was limited by the field emission, which induced the Q_0-slope between 43.1 MV/m and 54.8 MV/m, and the cavity finally quenched at 54.8 MV/m by the overheating. After the plasma cleaning, the field emission effect was removed completely until the E_{peak} approaching 59.5 MV/m. Therefore, the oxygen reactive plasma in-situ cleaning is an effective method to improve the performance of the HWR cavity by mitigating the field emission effect.

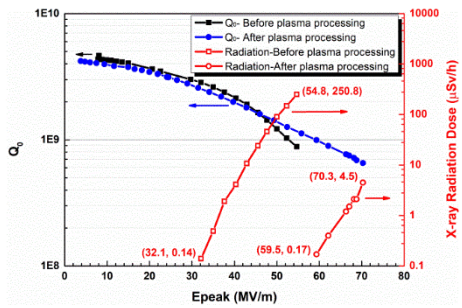


Figure 6: Vertical test results of an HWR015 cavity processed by the standard surface treatments and plasma.

CONCLUSION

The reactive oxygen plasma can be ignited in the HWR cavity. The plasma parameters were diagnosed by the optical emission spectra method. The electron number density and free electron temperature decreases as the increase of the total gas pressure, and the dissociated oxygen atom intensity decreases as the increase of the gas pressure but increases with the increasing oxygen volume ratio. In light of the knowledge learned from the studies of the plasma ignition and characterization, the in-situ plasma cleaning was applied to an HWR cavity with an adjustable coupler for vertical test at 4 K. The RGA data taken from the cavity during the plasma cleaning process revealed that the hydrocarbon contaminants were removed from the inner surface of the cavity. And the vertical test results indicate that the plasma in-situ cleaning is an effective technique to mitigate the field emission effect of the HWR cavity, therefore improve the accelerating gradient significantly. The plasma in-situ cleaning of the cavity in the horizontal test cryomodule will be implemented in our next work.

ACKNOWLEDGEMENT

The authors would like to express his gratitude towards the SRF group and cryogenic group of IMP for their valuable supports in success of these experiments.

REFERENCES

[1] P. V. Tyagi *et al.*, Improving the work function of the niobium surface of SRF cavities by plasma processing, *Applied Surface Science*, 369 (2016) 29-35.

[2] J. Graber *et al.*, Reduction of field emission in superconducting cavities with high power pulsed RF, *Nuclear Instruments and Methods in Physics Research Section A*, 350 (1994) 572-581.

[3] C.E. Reece *et al.*, Improvement of the operational performance of SRF cavities via in situ helium processing and waveguide vacuum processing, in *Proc. PAC'97*, Vancouver, BC, Canada, May. 1997.

[4] S. Ahmed, J. D. Mammosser, Microwave induced plasma discharge in multi-cell superconducting radio-frequency cavity, *Review of Scientific Instruments*, 86 (2015) 073303.

ISBN: 978-3-95450-194-6 ISSN: 2226-0366 doi:10.18429/JACoW-LINAC2018-TUPO036

[5] M. Doleans *et al.*, In-situ plasma processing to increase the accelerating gradients of superconducting radio-frequency cavities, *Nuclear Instruments and Methods in Physics Research Section A*, 812 (2016) 50-59.

[6] P. Berrutti *et al.*, Update on plasma processing R&D for LCLS-II, in: *Proc. IPAC2018*, Vancouver, BC, Canada, Oct. 2018, WEPMK012.

[7] A. Facco, Low- to medium-β cavities for heavy ion acceleration, *Superconductor Science and Technology*, 30 (2017) 023002.

[8] An-Dong Wu *et al.*, Design study on medium beta superconducting half-wave resonator at IMP, *Nuclear Science and Techniques*, 27 (2016) 80.

[9] T. Y. Niu *et al.*, A comparison among optical emission spectroscopic methods of determining electron temperature in low pressure argon plasmas, *Chinese Physics*, 16 (2007) 2757-2763.

[10] S. Iordanova, I. Koleva, Optical emission spectroscopy diagnostics of inductively-driven plasmas in argon gas at low pressures, *Spectrochimica Acta Part B:Atomic Spectroscopy*, 62 (2007) 344-356.

[11] C. Foissac, C. Dupret, P. Supiot, Electrical and spectroscopic characterizations of a low pressure argon discharge created by a broad-band helical coupling device, *Journal of Physics D: Applied Physics*, 42 (2009) 015206.

[12] M. A. Lieberman, A. J. Licbtenberg, Principle of plasma discharge and materials processing, 2th ed., John Wiley & Sons, Hoboken, 2005.

[13] V. K. Unnikrishnan *et al.*, Measurements of plasma temperature and electron density in laser-induced copper plasma by time-resolved spectroscopy of neutral atom and ion emissions, *Pramana-Journal of Physics*, 74 (2010) 983-993.

[14] J. M. Gomba *et al.*, Spectroscopic characterization of laser induced breakdown in aluminium-lithium alloy samples for quantitative determination of traces, *Spectrochimica Acta Part B-Atomic Spectroscopy*, 56 (2001) 695-705.

Content from this work may be used under the terms of the CC BY 3.0 licence (© 2018). Any distribution of this work must maintain attribution to the author(s), title of the work, publisher, and DOI.

ISBN: 978-3-95450-194-6 ISSN: 2226-0366 doi:10.18429/JACoW-LINAC2018-TUPO038

SEVERAL EXPERIMENTAL PHENOMENA OF Sn NUCLEATION ON Nb SURFACE OBSERVED AT IMP*

Z. Q. Yang, Y. He and F. Pan
Institute of Modern Physics, Chinese Academy of Science, Lanzhou 730000, China

Abstract

Nucleation process is an important step that affects the quality of Nb_3Sn films coated by vapour diffusion method. A uniform distribution of nucleation centres is essential to the uniformity of Nb_3Sn films. In this paper we report several experimental phenomena on the Sn nucleation on Nb surface. Better nucleation in the downstream of the pumping direction was observed. Influence of $SnCl_2$ partial pressure inhomogeneity was studied. Samples with higher $SnCl_2$ partial pressure have denser nucleation, which means homogeneous $SnCl_2$ pressure is a critical factor to the uniform nucleation. Less-nuclear zones, mainly distributed at cracks, grain boundaries and even some whole grain surfaces, were found on the surfaces of all samples. The less-nuclear zones may result in the low tin regions of the Nb_3Sn cavities. The specific solution to the less-nuclear problem was proposed. These studies help to better understanding of the mechanism underlying the nucleation process and will be useful foundation for the follow-up Nb_3Sn/Nb project at IMP.

INTRODUCTION

After many years of worldwide exploration and improvement of the post treatment process, niobium cavities are now approaching their fundamental limits both in terms of maximum accelerating field as well as in terms of surface resistance at typical operating temperatures. To continue to keep up with continually increasing demands of future SRF facilities, there exists urgent demand for the development of new technologies for RF superconductivity.

The A15 superconductor Nb_3Sn is one of the most promising alternative materials to standard niobium for SRF applications not only for its material parameters with obvious advantages [1] but also for the breakthrough performance levels achieved for the vapour diffusion coated 1.3 GHz single cell cavity at Cornell University [2].

One key factor limiting the RF performance of the vapor diffusion coated Nb_3Sn thin film cavities is the heterogeneity of film composition and distribution. An important manifestation of inhomogeneity is the existence of areas with low tin content [2-3]. Presently, the main efforts to further improve the RF performance of the vapour diffusion coated Nb_3Sn thin film cavities is through the optimization of the coating parameters at high temperature, however [2, 4], its effects is not obvious. In the past three years, the RF performance of the Nb_3Sn thin film cavities has not been substantially improved [2, 3, 5].

Whether it is from the growth mechanism of vapour diffusion coated Nb3Sn film, or from the research experience of Siemens AG researchers [6], a uniform distribution of nucleation centres is essential to the uniformity of Nb_3Sn films. Without uniform nucleation, it is difficult to avoid the heterogeneity of Nb_3Sn film composition and distribution even with the optimization of the coating parameters at high temperature. Compared to the optimization of the coating parameters at high temperature, the importance of the nucleation process to break through the limitations of the RF performance of Nb_3Sn cavities has not been paid sufficient attention, and research on nucleation [7] is relatively less.

Under such a background, a thorough study of Sn nucleation on Nb surface was carried out at IMP, which will be useful foundation for the follow-up Nb_3Sn/Nb project at IMP. In this paper, several experimental phenomenon of Sn nucleation on Nb surface will be reported.

EXPERIMENTAL

Sample Preparation

The Nb samples were cut by wire electro-discharge machining (EDM) from the same plate. The samples' treatments were attempted to replicate that of the cavities, which includes polishing smoothly on 1000-grit sandpaper, 150μm heavy BCP (HF: HNO_3: H_3PO_4 =1:1:2), 8000C degas for 3 hours and 20μm light BCP.

Nucleation Experiment

The nucleation experiment of the niobium samples was carried out in a furnace using a high purity quartz tube, taking the advantage of high purity quartz's good thermal and chemical stability at high temperature. The furnace's background pressure is better than 5×10^{-5} Pa, which can meet the requirement of nucleation experiment. The nucleation was accomplished by using the nucleation agent $SnCl_2$. After 24 hours of degasing at 200^0C in high vacuum, the temperature was raised up to 500^0C at a rate of 3.50C/min. Then the samples were kept at 500^0C for 4 hours for nucleation. After which, the furnace was turned off to cool down naturally.

RESULTS

Influence of Pumping Direction

The nucleation was accomplished taking the advantage of $SnCl_2$'s high vapour pressure at relatively low temperature. According to common sense, the $SnCl_2$ molecule moves downstream along the pumping direction. This will possibly cause that the partial pressure of $SnCl_2$ in the downstream of the pumping direction is larger than that of the upstream of the pumping direction, resulting in the difference in the nucleation distribution on the surfac-

Content from this work may be used under the terms of the CC BY 3.0 licence (© 2018). Any distribution of this work must maintain attribution to the author(s), title of the work, publisher, and DOI.

ISBN: 978-3-95450-194-6 ISSN: 2226-0366 doi:10.18429/JACoW-LINAC2018-TUPO038

es of the Nb samples in the upstream and downstream direction. To verify this conjecture, an experiment was designed with the size of pipe quartz plug placed both in the upstream and downstream of the pumping direction. The detailed experimental setup was shown in Fig. 1.

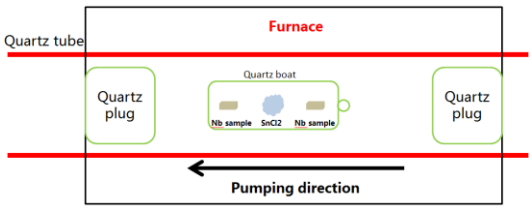
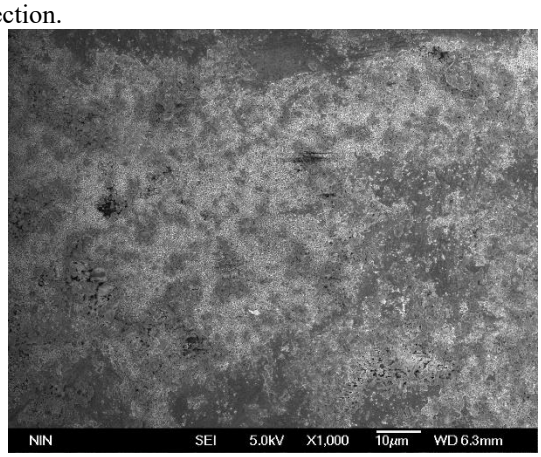
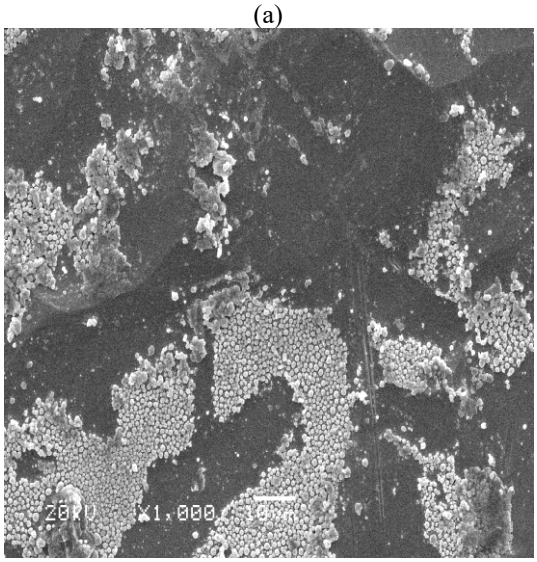


Figure 1: Detailed setup of the experiment to verify the effects of pumping direction.

The SEM images in Fig. 2 directly show that there is denser and better nucleation in the downstream pumping direction.



(a)



(b)

Figure 2: Nucleation of Nb samples in the downstream (a) and upstream pumping direction to study the influence of pumping direction.

Influence of Aeration Condition

To further investigate the effect of $SnCl_2$ partial pressure uniformity on nucleation, another series of experiments were designed with the detailed conditions shown in Fig. 3. A larger pipe quartz plug was placed in the downstream of the pumping direction. In this case, although the $SnCl_2$ molecule still has the desire to move downstream along the pumping direction, due to the blocking of the larger pipe quartz plug in the downstream, the difference of the partial pressure of $SnCl_2$ between the upstream and downstream of the pumping direction will be effectively reduced, and even the partial pressure of $SnCl_2$ in the upstream direction of the pumping direction may be larger.

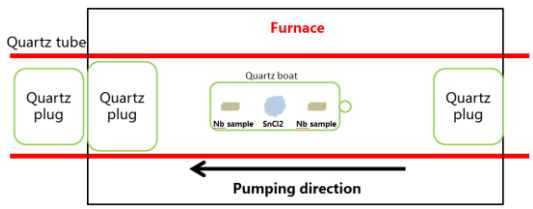
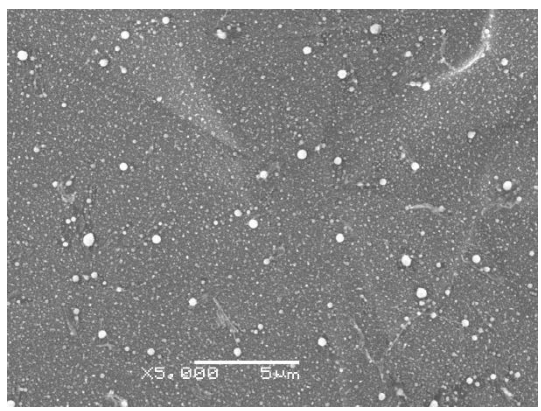
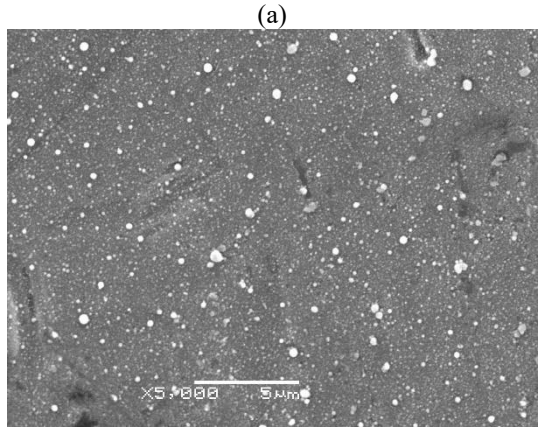


Figure 3: Detailed setup of the experiment to verify the effects of aeration condition.

SEM images of the nucleation Nb samples in the downstream and upstream pumping direction with the $SnCl_2$ dosage of 100mg were shown in Fig. 4 for reference. From the naked eye observation, different from the nucleation in "Influence of pumping direction" part, the Nb sample in the upstream pumping direction seems to have denser nucleation centres.



(a)



(b)

Figure 4: Nucleation of Nb samples in the downstream (a) and upstream (b) pumping direction to study the effect of aeration condition.

Content from this work may be used under the terms of the CC BY 3.0 licence (© 2018). Any distribution of this work must maintain attribution to the author(s), title of the work, publisher, and DOI.

ISBN: 978-3-95450-194-6 ISSN: 2226-0366 doi:10.18429/JACoW-LINAC2018-TUPO038

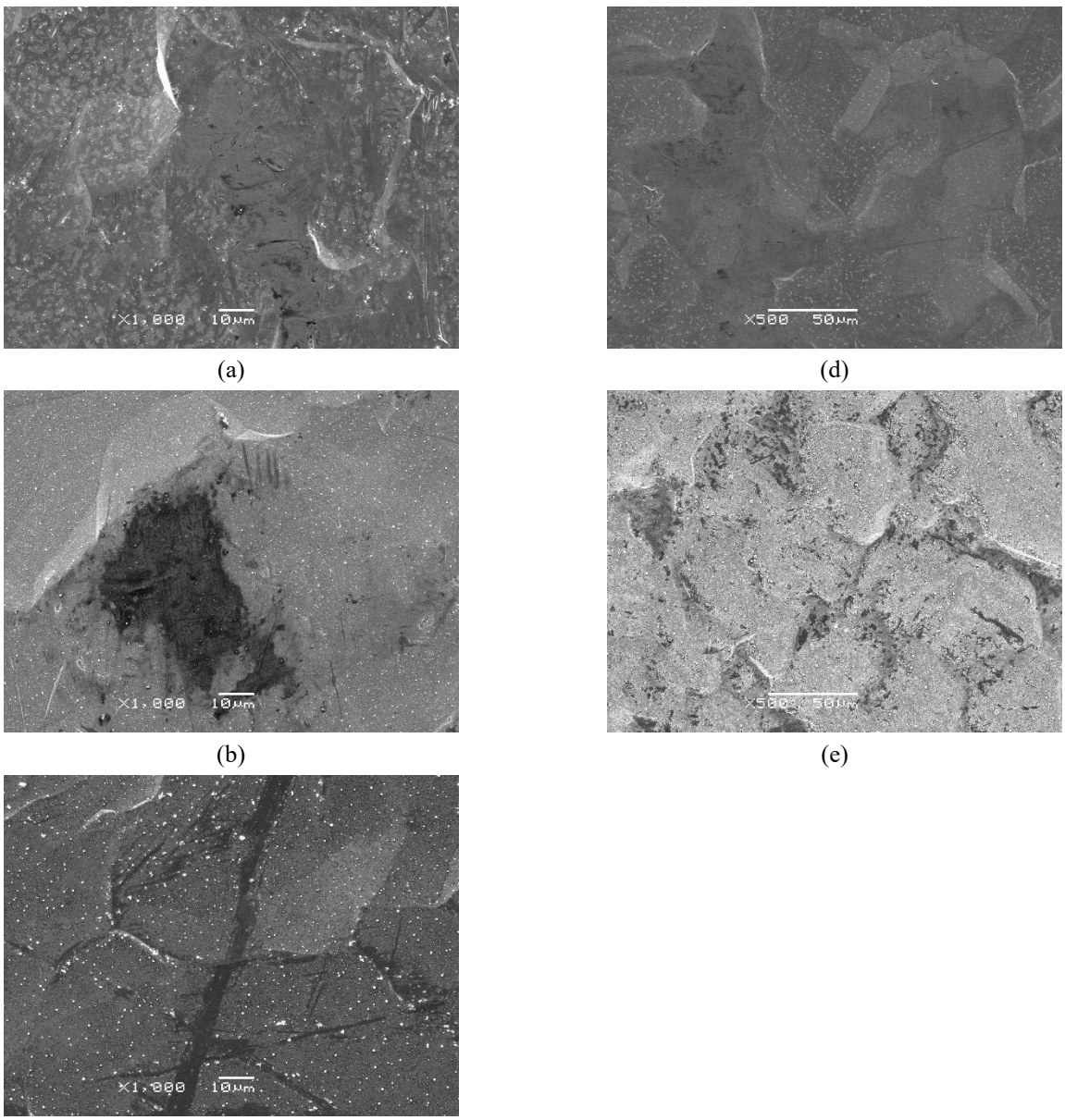
Content from this work may be used under the terms of the CC BY 3.0 licence (© 2018). Any distribution of this work must maintain attribution to the author(s), title of the work, publisher, and DOI.

EDS results of Nb samples both in the downstream and upstream pumping direction with various amounts of $SnCl_2$ dosage was listed in Table 1.

Table 1: EDS Results of Nucleation Nb Samples

Experiment	Sn At %-downstream	Sn At %-upstream
400mg $SnCl_2$+Sn	6.86	9.61
100mg $SnCl_2$	3.03	4.11
400mg $SnCl_2$+Sn	2.31	2.81
11.9mg $SnCl_2$	1.31	1.64
11.8mg $SnCl_2$+Sn	1.27	1.27

The EDS results showed that in the case of the larger pipe quartz plug placed in the downstream pumping direction, all the Nb samples in the upstream pumping direction have higher concentration of Sn on the surfaces. This means the samples in the upstream pumping direction have denser nucleation centres, which implies the higher partial $SnCl_2$ in the upstream pumping direction. This agrees with the tentative presumption.



(a) (d) (b) (e) (c)

Figure 5: Less-nuclear zones in Nb nucleation samples with $SnCl_2$ dosage of 11.9mg (a) and 100mg (b). Less-nuclear zones at scratches (c), grain boundaries (e) and even some whole grain surfaces (d).

ISBN: 978-3-95450-194-6 ISSN: 2226-0366 doi:10.18429/JACoW-LINAC2018-TUPO038

Table 2: EDS Results of Both the Less-nuclear Zones and the Zones with Uniform Nucleation Centres

Experiment	Sn At % of left-uniform nucleaton	Sn At % of left-less-nuclear	Sn At % of right-uniform nucleaton	Sn At % of right-less-nuclear
400mg $SnCl_2$+Sn	6.86	4.94	9.61	2.10
100mg $SnCl_2$	3.03	1.04	4.11	1.34
400mg $SnCl_2$+Sn	2.31	1.25	2.81	1.21
11.9mg $SnCl_2$	1.31	0.86	1.64	1.16
11.8mg $SnCl_2$+Sn	1.27	1.52[1]	1.27	0[2]

[1, 2] Proximity of EDS limit of detection accuracy

Observation of Less-nuclear Zones

As stated in the introduction part, the existence of areas with low tin content is an important factor limiting the RF performance of the vapour diffusion coated Nb_3Sn thin film cavities. The reason and mechanism of the occurrence of the less-tin areas remain unclear, neither the way to restrain it.

During the study of Sn nucleation on Nb surface at IMP, unexpected areas of less nucleation centres were observed at the surfaces of all nucleation Nb samples. The specific distribution of the less-nuclear zones is shown in Fig. 5.

SEM images showed that the less-nuclear zones mainly distributed at scratches, grain boundaries and even some whole grain surfaces. It implies that a smoother surface is beneficial to a uniform nucleation and defects such as pits and scratches should be avoided as much as possible. In addition, the most important information reflected in the observed less-nuclear phenomenon is that the less-nuclear zones even cover some whole grain surfaces, which means that nucleation by $SnCl_2$ agent seems to have crystal direction selectivity.

In order to prove that the observed less-nuclear zones in the SEM images really has less nucleation centres, EDS was performed to measure the exact Sn content both in the less-nuclear zones and the zones with uniform nucleation centres. The results were listed in Table 2. Recently, the presence of less-nuclear zones has also been observed on the surface of the latest batch of nucleation Nb samples. The location of the less-nuclear zones is still the scratches, the grain boundaries and even some whole grain surfaces.

CONCLUSION

From the research status of the past few years, the importance of the nucleation process to break through the limitations of the RF performance of Nb_3Sn cavities has not been paid sufficient attention, and research on nucleation is relatively less. The specific structural design of the furnace for the coating of the Nb_3Sn thin film cavities by the vapour diffusion method also lacks corresponding specifications. The observed influence of pumping direction and aeration condition on the Sn nucleation on Nb surfaces by using the $SnCl_2$ agent clearly showed that a homogeneous SnCl2 pressure is a critical factor to the uniform nucleation. The observed influence of pumping direction and the aeration conditions provides normative guidance for the design and improvement of the furnace, the location of $SnCl_2$ agent and the optimization of nucleation conditions.

Less-nuclear zones were observed on all the nucleation Nb samples. The observed less-nuclear zones mainly distributed at the scratches, the grain boundaries and even some whole grain surfaces. The occurrence of less-nuclear zones at the scratches and the grain boundaries implies that a smoother surface is beneficial to a uniform nucleation. The defects on the inner surface of the substrate Nb cavity such as pits and mechanical scratches must be avoided as much as possible. The information revealed by the presence of less-zones at some whole grain surfaces is more important. It seems that nucleation by $SnCl_2$ agent have crystal direction selectivity. The occurrence of less-nuclear zones at some whole grain surfaces seems to be ineluctable. From the growth mechanism of vapour diffusion coated Nb_3Sn film, the occurrence of the less-nuclear zones will result in the locally too thin Nb_3Sn film or localized Sn deficiency, both of which lead to increased losses. What's more, the size of the less-nuclear zones at the whole grain surface is comparable to that of the less-tin zones reported by Cornell University. The less-nuclear zones may be an important source of the reported less-tin zones. However, in any case, suppressing the occurrence of less nuclear regions will reduce the heterogeneity of the vapour diffusion coated Nb_3Sn films and may be a possible way to break through the RF performance limitation of the Nb_3Sn cavities.

ACKNOWLEDGEMENTS

This work is supported by National Postdoctoral Program for Innovative Talents (BX201700257) and Major Research Plan of National Natural Science Foundation of China (91426303).

REFERENCES

[1] A Godeke. "A review of the properties of Nb3Sn and their variation with A15 composition, morphology and strain state. Superconductor Science and Technology", 19(8):R68—-R80, August 2006.

[2] D.L. Hall, T. Gruber, J.J. Kaufman, M. Liepe, J.T. Maniscalco, S. Posen, et al., "Nb3Sn Cavities: Material Characterization and Coating Process Optimization", in Proc. 17th International Conference on RF Superconductivity, Whistler,

Content from this work may be used under the terms of the CC BY 3.0 licence (© 2018). Any distribution of this work must maintain attribution to the author(s), title of the work, publisher, and DOI.

ISBN: 978-3-95450-194-6 ISSN: 2226-0366 doi:10.18429/JACoW-LINAC2018-TUPO038

BC, Canada, 13-18, 2015, paper TUBA04, pp. 501-504. doi:10.18429/JACoW-SRF2015-TUBA04

[3] D.L. Hall et al., "High Performance Nb3Sn Cavities", in Proc. 18th Int. Conf. on RF Superconductivity (SRF'17), Lanzhou, China, July 2017, paper WEXA01, pp. 667-673, doi:10.18429/JACoW-SRF2017-WEXA01

[4] R. D. Porter et al., "Update on Nb3Sn progress at Cornell University", WEPMF050, Proceedings of IPAC, Canada, 2018.

[5] U. Pudasaini et al., "Nb3Sn Multicell Cavity Coating at JLab", in Proc. 9th Int. Particle Accelerator Conf. (IPAC'18), Vancouver, BC, Canada, Apr. - May 2018, pp. 1798-1803. doi:10.18429/JACoW-IPAC2018-WEYGBF3

[6] B Hillenbrand. The Preparation of Superconducting Nb3Sn Surfaces for RF applications. In Proceedings of the First Workshop on RF Superconductivity, Karlsruhe, 1980.

[7] U. Pudasaini, G.V. Eremeev, M.J. Kelley, C.E. Reece, and J. Tuggle, "Investigation of Structural Development in the Two-Step Diffusion Coating of Nb3Sn on Niobium", in Proc. North American Particle Accelerator Conf. (NA-PAC'16), Chicago, IL, USA, Oct. 2016, paper WEB1CO02, pp. 659-662. doi:10.18429/JACoW-NAPAC2016-WEB1CO02

Content from this work may be used under the terms of the CC BY 3.0 licence (© 2018). Any distribution of this work must maintain attribution to the author(s), title of the work, publisher, and DOI.

ISBN: 978-3-95450-194-6 ISSN: 2226-0366 doi:10.18429/JACoW-LINAC2018-TUPO039

TESTS OF THE BALLOON SINGLE SPOKE RESONATOR*

Z. Yao†, J. Keir, D. Kishi, D. Lang, R.E. Laxdal, H. Liu, Y. Ma, B. Matheson, B.S. Waraich, Q. Zheng, V. Zvyagintsev, TRIUMF, V6T2A3 Vancouver, Canada

Abstract

A novel balloon variant of the single spoke resonator (SSR) has been designed, fabricated and tested at TRIUMF. The cavity is the β=0.3 325 MHz SSR1 prototype for the Rare Isotope Science Project (RISP) in Korea. The balloon variant is specifically designed to reduce the likelihood of multipacting barriers near the operating point. A systematic multipacting study led to a novel geometry, a spherical cavity with re-entrant irises plus a spoke. The balloon cavity provides competitive RF parameters and a robust mechanical structure. Cold tests demonstrated the principle of the balloon concept. The cold test results will be reported in this paper.

INTRODUCTION

RISP has been proposed as a multi-purpose accelerator facility at the Institute for Basic Science (IBS), Korea, for research in atomic and nuclear physics, material science, bio and medical science, etc. At the heart of RISP is a powerful heavy ion linac [1]. The linac consists of three independently phased superconducting sections. The high energy section SCL2 of the driver linac uses two types of 325 MHz single spoke resonators with geometry β at 0.30 and 0.51 corresponding to SSR1 and SSR2 respectively. TRIUMF has been contracted to design, fabricate and test two of the SSR1 variants.



Figure 1: Bare cavity (left) and jacketed cavity (right) of SSR1 prototype.

The prototype cavity of SSR1 β=0.30 designed by TRIUMF is shown in Fig. 1. The cavity is termed the balloon variant due to the conformal shape of the outer conductor that obviates the need for a central spool. The balloon geometry is proposed to suppress multipacting in the accelerating gradient range of several MV/m [2]. It also provides a more inherently robust mechanical structure. The cavity is designed [3] to operate in continuous wave (CW) mode at 2 K with 35 MV/m peak electric field. The design parameters are listed in Table 1. The SSR1 prototype is fabricated with 3 mm RRR niobium for cavity, and 3 mm 316L stainless steel for flanges and the helium jacket. The details were reported in Ref. [4].

Table 1: Design Parameters of SSR1

Parameters	Value
Frequency	325 MHz
Geometry β	0.30
Geometry factor	93 Ω
R/Q	233 Ω
E_{peak}/E_{acc}	3.84
B_{peak}/E_{acc}	6.07 mT/(Mv/m)
df/dp	-1.6/+1.5 Hz/mbar
Lorentz force detuning	-8.7/-1.4 Hz/$(MV/m)^2$
Tuning sensitivity	467 kHz/mm
Spring constant	14 kN/mm

CAVITY PROCESSING

Cavity was inspected, and leak checked after fabrication. 200 μm surface layer was re-moved by buffer chemical polishing (BCP) in several steps with flipping cavity orientation. The BCP solution is mixed with HNO_3, HF, H_3PO_4 in the volume ratio of 1:1:2. The cavity is fixed on a support frame via stiffener rings on both end shells. The RF ports are positioned up and down during etching. RF ports are used as acid inlet and outlet. The acid temperature was monitored during etching and controlled below 15 ˚C.

High pressure rinsing (HPR) is done through beam ports on the horizontal rinsing stand and each RF port on the vertical rinsing stand. A dedicated nozzle is designed for this cavity. There are two water jets on each direction from 30˚ to 150˚ off the rinsing wand axis with an increment of 30˚. Two additional water jets are 10˚ off the axis on the top. For each cavity assembly, the cavity was rinsed 3.5 hours on the horizontal stand at 80 bar pressure, and 2 hours on vertical stand via each RF port with 45 bar pressure.

The cavity was degassed after an integrated 200 μm BCP. There were obvious signs of hydrogen Q-disease in the pre-degassing tests. Due to concerns about the copper brazing between niobium and stainless-steel flanges, 600 ˚C for 10 hours degassing recipe was selected. The hydrogen partial pressure was monitored with residual gas analyser (RGA) and reduced by 3 orders of magnitude. Additional 20 μm BCP followed by HPR was completed prior to cold test.

Low temperature baking was applied as the last treatment for the hermitic seal cavity before cold test. Two recipes, 50 ˚C for 2 hours and 120 ˚C for 48 hours, were tested to evaluate the effects on BCS resistance and multipacting conditioning. The cavity was actively pumped during the baking procedure. The cavity vacuum was improved by 2 orders of magnitude during the 120 ˚C bake.

* Work supported by RISP – TRIUMF Collaboration
† zyyao@triumf.ca

Content from this work may be used under the terms of the CC BY 3.0 licence (© 2018). Any distribution of this work must maintain attribution to the author(s), title of the work, publisher, and DOI.

ISBN: 978-3-95450-194-6 ISSN: 2226-0366 doi:10.18429/JACoW-LINAC2018-TUPO039

Content from this work may be used under the terms of the CC BY 3.0 licence (© 2018). Any distribution of this work must maintain attribution to the author(s), title of the work, publisher, and DOI.

CRYOGENIC TESTS

Cavity Performance

The bare cavity was tested after each BCP step and hydrogen degassing. The helium jacket was welded after Test #4. Additional 20 μm light BCP was employed to remove the surface contamination in the jacketing procedure. The processing steps and cold test sequence are listed in Table 2. Each cold test was completed at both 4 K and 2 K in bath mode, except Test #6 in jacketed mode. The Q-E_{acc} curves are shown in Fig. 2.

Table 2: Processing and Tests of Bare Prototype Cavity

Test #	BCP	Integrated BCP	Heat treatment
1	60 μm	60 μm	N/A
2	80 μm	140 μm	N/A
3	60 μm	200 μm	50 ˚C
4	20 μm	220 μm	600 ˚C + 120 ˚C
5	20 μm	240 μm	N/A
6	-	240 μm	120 ˚C

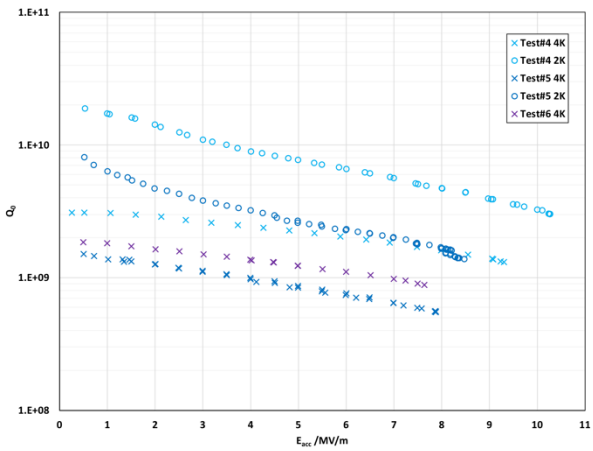


Figure 2: 4K and 2K Q-E_{acc} curves of the prototype SSR1.

The initial Q_0 of bare cavity is 1.9×10^{10} at 2 K. As the BCS resistance is negligible at 2 K for 325 MHz, the residual resistance is 4.9 nΩ. The ambient magnetic field in the cryostat is 35 mG in the vertical direction. Assuming all magnetic flux is trapped in the superconducting transition, the calculated flux sensitivity [5, 6] of SSR1 is 0.12 nΩ/mG. The contribution of trapped flux to residual is estimated at 4.2 nΩ. The 2 K curve has more pronounced Q-slope in the medium field range, which is dominated by the residual resistance. Surface defects in form of either geometry or foreign material are suspected. At the nominal operating gradient, Q_0 is 4.0×10^9 and cavity power dissipation is 6.7 W. Cavity quench limits accelerating gradient at 10.3 MV/m, corresponding to the peak magnetic field of 63 mT, without detectable X-rays.

The jacketed cavity gives declined performance. The BCP after jacketing opened up one or more defects is suspected. The low field Q_0 of unbaked cavity is 8.1×10^9 at 2K. Detectable field emission onset is 7 MV/m. There is Q-switch in the gradient range of above 8.1 MV/m with X-ray dose over 30 μSv/hr at the cavity elevation. Due to TRIUMF's multi-purpose cryostat is not designed for 2K tests in jacketed mode, the 2K curve of Test #6 is missed. However, the 4K results demonstrated baking improves 4K Q.

Cavity inner surface was inspected with high resolution cameras via RF ports. The evidence of bubble trace on cavity shell near RF ports, the small geometry defects on shell, and the imperfect welds at the spoke collar were observed as shown in Fig. 3. It supports the hypothesis of Q-slope, early quench and reduced performance after jacketing.

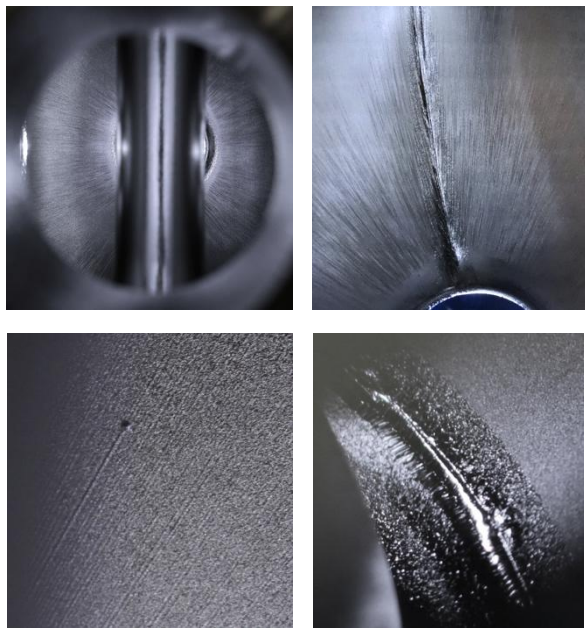


Figure 3: Uneven finish and defects on the RF surface.

The BCS resistance of each test is extracted by measuring Q rise from 4 K to 2 K, shown in Fig. 4. It demonstrates 120 ˚C bake decreases BCS component by a factor of 50% in the low field regime at 325 MHz and mitigates the field dependence of BCS resistance. 120 ˚C baked cavity provides higher Q and less Q-slope at 4 K.

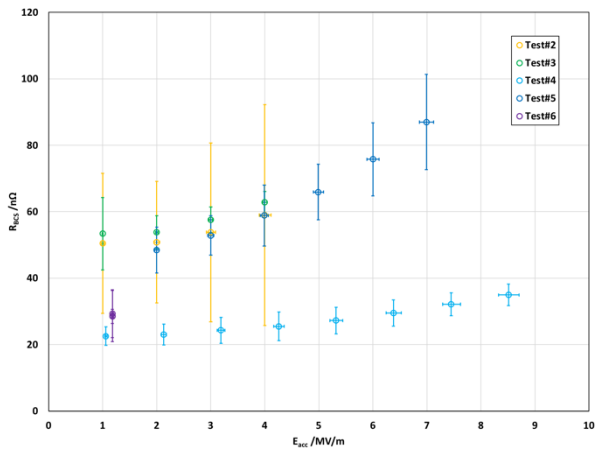


Figure 4: Extracted BCS component of the surface resistance of each cold test at 4K as a function of E_{acc}.

ISBN: 978-3-95450-194-6 ISSN: 2226-0366 doi:10.18429/JACoW-LINAC2018-TUPO039

The cavity resonant frequency at 2 K is 324.995 MHz measured at 1 MV/m in jacketed mode test. Frequency tuning by plastic deformation after fabrication is not needed. The mechanical parameters of the prototype cavity are listed in Table 3. Because of the uneven thinning of the cavity shells in spinning process [4], the cavity rigidity is reduced, and the helium pressure sensitivity is higher than the design specification as expected. As a sequence, the cavity spring constant is also decreased.

Table 3: The Mechanical Parameters of SSR1 Prototype

Parameters	Measured Data
Pressure Sensitivity	-15 Hz/mbar
Lorentz Force Detuning	-7.8 Hz/(MV/m)^2
Tuning Sensitivity	465 kHz/mm
Spring constant	10 kN/mm

Multipacting

The motivation of proposing the balloon variant is to reduce the likelihood of multipacting barriers near the operating gradient. This principle is proved through the prototype cavity cold tests. The comparison of measurement and simulation results is summarized in Fig. 5. The points in the figure represent cavity quality factor with multipacting loading. The lines are the simulated growth rates of the secondary electrons. It indicates multipacting barriers existing if the growth rate is a positive value. The dashed line represents the first order barrier, while the solid line represents the higher order ones (order > 1).

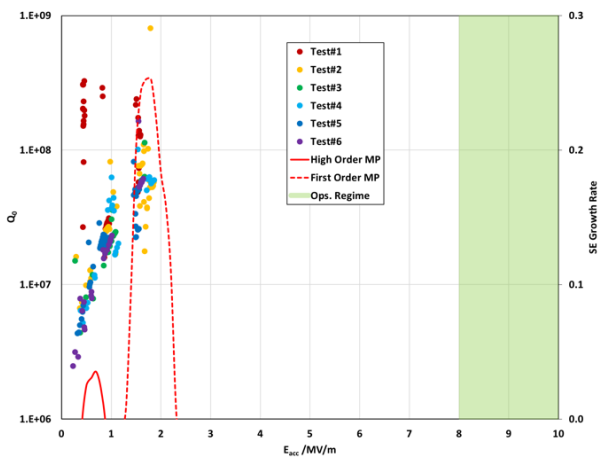


Figure 5: Comparison of measured (Q_0) and predicted (secondary electron growth rate) multipacting barriers of SSR1 prototype.

Some conclusions are obtained as follows. There are no multipacting barriers either around the operational gradient or below 0.1 MV/m. The barriers only exist between 0.2 MV/m and 1.8 MV/m. The measurement results are consistent between tests and they are well predicted by 3D simulation codes, CST MWS and PS [7]. The simulation slightly over estimated the first order barrier in the higher gradient range (1.9 to 2.4 MV/m), while under estimated the higher orders ones (0.2 to 0.4 MV/m and 0.9 to 1.1 MV/m).

Multipacting conditionings were completed at 4 K with a variable RF coupler. Different manners were applied, such as pulse conditioning, amplitude modulation and frequency modulation. Pulse or step function drive provides a chance to jump over multipacting barriers and plunge into the higher gradient range. CW conditioning in self-exited loop was demonstrated as the best setting to clean up barriers. It is found that multipacting is unlikely to reappear after a completed conditioning.

The low temperature baking is verified to mitigate the intensity of multipacting. The baking procedures were performed at 50 ˚C for 2 hours and at 120 ˚C for 48 hours. Both recipes are effective to reduce the conditioning time by about 50 %. Removing the absorbed moisture and residual gas from the RF surface weakens the barriers. Consequently, bake at a lower temperature with a shorter period is more time-efficient for multipacting mitigation purpose.

CONCLUSION

The balloon variant of the single spoke resonator was proposed to mitigate multipacting around operational gradient. The first balloon cavity was designed, fabricated and tested by TRIUMF as the prototype of RISP SSR1. Cold tests demonstrated the principle of the balloon concept. There is no multipacting barrier around the operational gradient. Few barriers exist in the low field regime and are consistent with simulation prediction. Low temperature baking mitigates multipacting intensity. The prototype cavity is processed with BCP, HPR, hydrogen degassing, and low temperature baking. The bare cavity meets the design specifications. Jacketed cavity shows declined performance. Defects in various forms are observed on RF surface. The cavity resonant frequency is 5 kHz off the operating frequency without post-fabrication frequency tuning. Mechanical parameters are also consistent with the design within expected allowance. Further study of eliminating the strong medium field Q-slope and early quench is in progress.

REFERENCES

[1] H.J. Kim, H.C. Jung, W.K. Kim, "Progress on Superconducting Linac for the RAON Heavy Ion Accelerator," in *Proc. 7th Int. Particle Accelerator Conf. (IPAC'16)*, Busan, Korea, May 2016, paper MOPOY039, pp. 935-937.

[2] Z. Yao, R.E. Laxdal, V, Zvyagintsev, "Balloon Variant of Single Spoke Resonator," in *Proceedings of SRF2015*, Whistler, Canada, 2015, paper THPB021, pp. 1110-1114.

[3] Z. Yao, R.E. Laxdal *et al.*, "Design and Fabrication of β=0.3 SSR1 for RISP," in *Proceedings of LINAC2016*, East Lansing, USA, 2016, paper MOPLR041, pp. 226-228.

[4] Z. Yao, R.E. Laxdal *et al.*, "Design and Fabrication of Balloon Single Spoke Resonator," in *Proceedings of SRF2017*, Lanzhou, China, 2017, talk THXA01, unpublished.

[5] D. Longuevergne, P. Duchesne, "Flux Trapping Studies on Low Beta Cavities at IPNO," INFN Milano, Milan, Italy, Feb. 2018.

[6] H. Padamsee *et al.*, *RF Superconductivity for Accelerators.* John Wiley & Sons, New York, 1998.

[7] CST Studio Suite, http://www.cst.com/.

Content from this work may be used under the terms of the CC BY 3.0 licence (© 2018). Any distribution of this work must maintain attribution to the author(s), title of the work, publisher, and DOI.

ISBN: 978-3-95450-194-6 ISSN: 2226-0366 doi:10.18429/JACoW-LINAC2018-TUPO040

TEST OF MULTI-FREQUENCY COAXIAL RESONATORS*

Z. Yao†, J. Keir, P. Kolb, A. Kong, R.E. Laxdal, B. Matheson, E. Thoeng, B.S. Waraich, Q. Zheng, V. Zvyagintsev, TRIUMF, V6T2A3 Vancouver, Canada

Abstract

A significant issue in low β resonators is the 4K medium field Q-slope (MFQS). To systemically study the field dependence of surface resistance in TEM mode resonators, a quarter-wave resonator (QWR) and a half-wave resonator (HWR) were designed to resonant at integer harmonic frequencies of 200 MHz, and up to 1.6 GHz. A series of cavity treatments were proposed to these cavities. It provides opportunity to investigate the field dependent surface resistance as a function of frequency, temperature, and treatment, including heat treatments and doping. The preparation for the baseline cold test and the preliminary test result will be reported in this paper.

COAXIAL RESONATORS

The resonant frequency of low β cavities, operating in TEM mode, of proton or heavy ions linac applications are normally in the range of 80 MHz to 350 MHz. These frequencies provide opportunity of 4 K operation to reduce the cost of cryogenics system. However, strong Q-slope in the medium field regime reduces cavity performance at the operational field level. To developing systemic study tools for MFQS in low β resonators, two delegated QWR and HWR cavities are designed and fabricated, shown in Fig. 1. The coaxial structure is chosen to represent the common geometry of low β resonators. The RF performances can be measured at different harmonic frequencies in the same cold test cycle. The consistent surface field distributions between various TEM modes mitigate the geometry effect on surface resistance. The role of RF frequency on the field dependent resistance and the optimum treatments for low β resonators can be investigated with these coaxial resonators.



Figure 1: HWR (left) and QWR (right).

The resonators are designed as the 'single cell' for the fundamental R&D programs. To be distinct from acceleration purpose SRF cavities, some common features, such as beam ports and helium jacket, are eliminated to simplify the cavity geometries. In accordance to research proposal, the cavities are required to fit TRIUMF RF induction furnace. The lowest resonant frequency is limited by the cavity length. In addition, four cleaning ports are set at the same end of each cavity. A uniform cylinder inner conductor is chosen to employ a common mobile T-map insert to characterize the local RF heating in addition to the global Q measurement. The detail design of these resonators can be found in [1].

The cavities are fabricated with RRR grade and reactor grade niobium. Reactor grade niobium is used for flanges and the cavity parts at the low magnetic field region, such as bottom plate and port tubes of QWR. Indium seal is required on niobium flange for the hermitic unit assembly. There was not frequency tuning step during manufacture as the absolute resonant frequencies are not critical. The harmonic frequencies at room temperature and atmosphere pressure were measured after received from manufacturer and are shown in Table 1. The To-Be-Tested modes are highlighted in bold and italic. The measurement results are well conformed to the design. The closest TE mode is separated by 37 MHz and its transmission signal is more than 10 dB lower with the same RF couplers. A bandpass filter is required in LLRF for each test mode to eliminates the undesired resonances in cold test.

Table 1: Resonant Frequencies of Coaxial Resonators

QWR	Simu. /MHz	Meas. /MHz
TEM	***217***	***217.4***
TEM	***647***	***647.3***
TE111	892	–
TEM	1055	1054.2
TE112	1103	1100.8/1103.5
HWR	**Simu. /MHz**	**Meas. /MHz**
TEM	***389***	***388.6***
TEM	***778***	***777.4***
TE111	905	901.9/906.6
TE112	1128	1125.4/1129.1
TEM	***1166***	***1166.1***
TE113	1424	1421.9/1424.8
TEM	***1555***	***1554.8***
TE211	1602	1600.7

RF AND CONTROLS

Coaxial resonators are to be tested at the harmonic frequencies of 200 MHz and up to 1.6 GHz. Two wide band

* Work supported by NSERC
† zyyao@triumf.ca

Content from this work may be used under the terms of the CC BY 3.0 licence (© 2018). Any distribution of this work must maintain attribution to the author(s), title of the work, publisher, and DOI.

ISBN: 978-3-95450-194-6 ISSN: 2226-0366 doi:10.18429/JACoW-LINAC2018-TUPO040

RF power amplifiers are required to cover the full frequency range of all tested modes. The in-situ 500 W solid states RF amplifier operates in the frequency range from 69 MHz to 651 MHz. Another 250 W RF amplifier covering 650 MHz to 2 GHz is going to be ordered.

Self-excited loop (SEL) is utilized in LLRF control of cryostat cold tests at TRIUMF. The SEL frequency tracks the resonant frequency of the cavity. The resonance is stable in either open or closed amplitude loop and free of ponderomotive instability. SEL in absence of phase loop feedback is ideal for cavity performance characteristics, multipacting conditioning and high-power pulse conditioning. LLRF developed for ISC-II and ARIEL e-Linac projects [2] controls at 140 MHz. An intermedium frequency is employed to down convert RF frequency to 140 MHz for input, and to up convert the output signal to cavity resonant frequency for driving RF amplifier. The essential part of the frequency convertor is the high-performance bandpass filter. Discrete filters with < -20 dBc at ±30 MHz were chosen for 200 MHz and 400 MHz, while cavity filters with < -30 dBc in the same range for higher frequencies. The intermedium frequency and the RF filter should be switched when changing test modes.

The variable capacitance RF coupler developed at TRIUMF for general purpose tests < 650 MHz is to be used for the QWR tests. The external Q varies 5 orders of magnitude with 30 mm stroke. The coupler mechanism allows more than 40 mm travelling range and provides sufficient margin of coupling adjustment for various purposes during cold test. A variable induction RF coupler was designed and fabricated for HWR tests. The coupler mechanical housing is same as capacitance coupler. A set of 50 Ω concentric copper wire and tube connects coupling loop and RF feedthrough. Major RF power is delivered within the copper tube. An impedance matching section with a 2 mm alumina spacer between feedthrough and 50 Ω part is optimized to maintain SWR < 1.2 for all tested modes. 4 orders of magnitude of coupling factor can be adjusted in 30 mm travelling range.

CAVITY PROCESSINGS

A series of cavity treatments, including chemical polishing, heat treatments and doping, were proposed to these coaxial resonates. For the baseline cold tests, ultrasound degreasing, 120 μm buffer chemical polishing (BCP) and high-pressure rinsing (HPR) were applied.

As all opening ports locating on the same end of cavity, a delegated etching fixture is designed to fill and pump acid from top. The fixture assembly with HWR is shown in Figure 2. A water tank contains and circulates cooling water around cavity walls during the whole procedure. Four tubes connected to acid circulation system penetrate through cleaning ports to the bottom. One is the filling pipe, and the opposite one is the pumping pipe. The remaining two tubes are circulating acid in the cavity during the etching process. They are added to prevent trapping gases at the upper flat face or accumulating niobium concentration on the closed end plate which causes gravitational etching discrepancies.

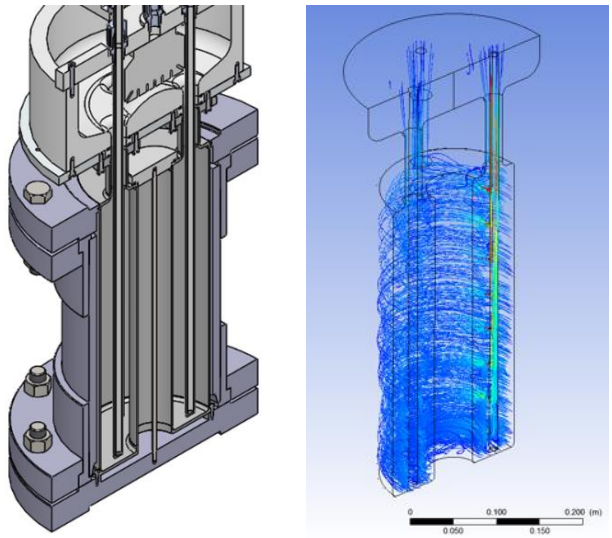


Figure 2: The chemical etching fixture of HWR (left) and the simulated velocity distribution of the acid circulation during BCP process (right).

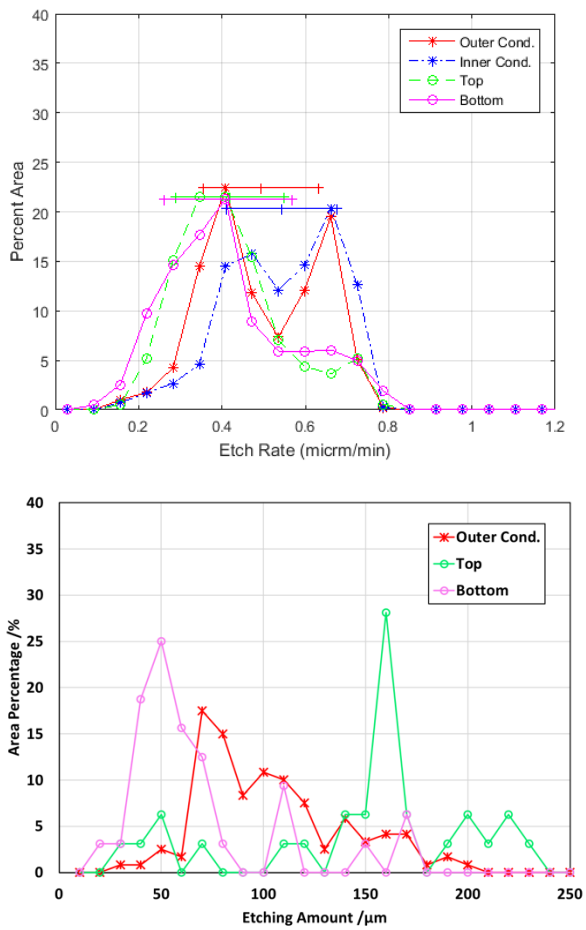


Figure 3: The histogram of the simulated etching rate (top) and the measured etching amount after 120 μm BCP (bottom) of HWR. Various colours represent different parts of cavity.

The number, position, and jet angle of acid diffusion and suction holes on tubes were optimized to achieve an even

Content from this work may be used under the terms of the CC BY 3.0 licence (© 2018). Any distribution of this work must maintain attribution to the author(s), title of the work, publisher, and DOI.

ISBN: 978-3-95450-194-6 ISSN: 2226-0366 doi:10.18429/JACoW-LINAC2018-TUPO040

Content from this work may be used under the terms of the CC BY 3.0 licence (© 2018). Any distribution of this work must maintain attribution to the author(s), title of the work, publisher, and DOI.

etching on the RF surface by using ANSYS Fluent [3]. The velocity dependent etching rate is calculated with turbulent kinetic energy [4]. The optimized average etching rate of HWR is 0.49 μm/min. The deviations of each part from the whole cavity is within ±20 %. The histogram of the simulated etching rate of HWR is shown in the top plot of Figure 3. To further obtain a uniform etching, the 120 μm BCP was divided into 60 μm plus 60 μm. The acid circulation tubes were rotated by 90° after the first 60 μm BCP. Cavity wall thickness was measured with ultrasound prior and after BCP. 120 spots were mapped on the outer conductor, while 32 points on the top plate and bottom plate. The measured etching amount is shown in the bottom plot of Figure 3. The average etching amount on the outer conductor is 104 μm, and the distribution profile is consistent with the simulation. The top plate with opening ports is over etched, while the bottom plate is under etched comparing to the desired amount. The hypothesis is the non-straight acid circulation tubes cause the diffusion holes slightly facing up and introduce stronger turbulence on the top than the bottom. The acid circulation tubes are required to be aligned for future BCP to achieve better result.

HWR was high pressure rinsed through all cleaning ports on the vertical rinsing stand, shown in Figure 4. Because of the limited diameter of opening ports, a Teflon spacer was added to the being rinsed port flange to prevent the wand vibration and touching down the cavity inner surface. The cavity was dried, assembled and leak checked in Class 10 cleanroom. The hermetic unit of HWR which is ready for test is shown in Figure 4.



Figure 4: HPR of HWR on the vertical rinsing stand (left) and the hermetic assembly of HWR (right).

PRELIMINARY COLD TEST

The baseline test of HWR is completed after 120 μm BCP. The cavity coaxial axis is in the horizontal direction. Only the fundamental mode is tested at the moment due to the limitation of the frequency range of the RF amplifier. The resonant frequency is 389.15 MHz at 4 K. Few low level multipacting barriers were easily conditioned away.

The 4 K and 2 K $Q_0 - B_p$ (surface peak magnetic field) curves are shown in Figure 5. The initial Q_0 is 7.9×10^8 at 4 K and 2.2×10^9 at 2 K. The residual resistance extracted from the Q – T data is 47 nΩ at 10 mT. Cavity has obvious and similar Q-slope in the measured field range at both temperatures. The pronounced residual resistance and strong Q-slope in the field range of below 20 mT indicate hydrogen Q-disease.

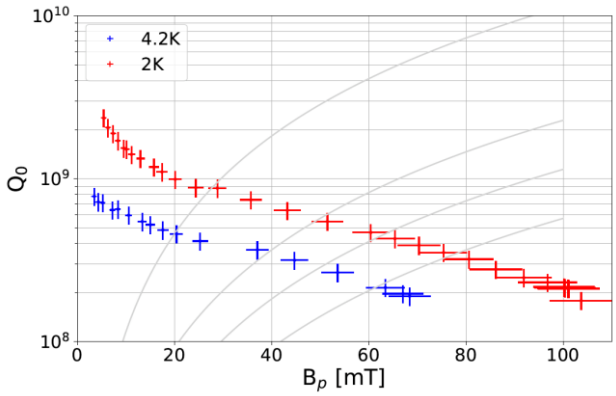


Figure 5: 4 K and 2 K $Q_0 - B_p$ curves of the fundamental mode of HWR baseline test with the constant power lines at 1 W, 5 W, 10 W, and 20 W.

4 K test is limited by cavity quench at 70 mT. But this quench barrier dose not present in 2 K test. Measurable X-ray starts from 80 mT. B_p exceeds 100 mT at 2 K without quench, corresponding to 25 MV/m in a 1.3 GHz elliptical cavity. The RF loss at the last measurement point is around 60 W. The 2 K performance is limited by low Q, which causes high RF loss and reaches the regulation capacity of the 2 K system.

CONCLUSIONS

To systemically study the MFQS and the field dependent surface resistance of low β resonators, a QWR and an HWR are designed and fabricated as the coaxial style 'single cell' cavities. The fundamental mode and its higher harmonic modes will be tested in one cold cycle. To accommodate TRIUMF's SEL LLRF to all required frequencies, the frequency convertor is modified. The existing general-purpose antennas adapts QWR requirements, while a new set of loop coupler and pickup are designed for HWR. A delegated etching fixture was designed to achieve an even etching. The baseline test of HWR is completed after 120 μm BCP. The peak surface magnetic field exceeds 100 mT without quench. The 2K performance is limited by low Q. The high residual resistance and the strong Q-slope in the low field regime indicate Q-disease. Hydrogen degassing will be applied as the next step.

REFERENCES

[1] Z. Yao *et al.*, "Design of Multi-Frequency Coaxial Test Resonators," in *Proc. SRF'17*, Lanzhou, China, Jul. 2017, paper TUPB065, pp. 531-534.

[2] M. Laverty *et al.*, "TRIUMF e-Linac RF Control System Design," in *Proc. PAC'09*, Vancouver, BC, Canada, May 2009, paper WE5PFP099, pp. 2246-2248.

[3] ANSYS, https://www.ansys.com/

[4] T. Jones *et al.*, "Determining BCP Etch Rate and Uniformity in High Luminosity LHC Crab Cavities," in *Proc. SRF'17*, Lanzhou, China, Jul. 2017, paper TUPB100, pp. 635-639.

ISBN: 978-3-95450-194-6 ISSN: 2226-0366 doi:10.18429/JACoW-LINAC2018-TUPO041

LCLS-II CAVITY HIGHER ORDER MODES COUPLER TUNING OPTIMIZATION AND CHALLENGES AT JEFFERSON LAB*

A. Solopova†, D. Forehand, A. Palczewski, Jefferson Lab, 23608, Newport News, VA, USA
T. Khabiboulline, FNAL, 60510, Batavia, IL, USA

Abstract

The Thomas Jefferson National Accelerator Facility is currently engaged, along with several other Department of Energy (DOE) national laboratories, in the Linac Coherent Light Source II project (LCLS II) - a new XFEL linac based on the 1.3 GHz superconducting linear accelerator. Half of the LCLS-II cryomodules are being produced at Jefferson Lab, other half is made at Fermilab. Each cryomodule contains eight 9-cell cavities with two Higher Order Modes (HOM) loop couplers operating at 1.3 GHz. This paper summarizes the HOM filter tuning challenges at Jefferson Lab and describes optimization of the procedure for a 9-cell Tesla type cavity and its integration into a cryomodule production line.

INTRODUCTION

If HOMs are close to the operating mode frequency, they might be excited as well and can disturb the operating mode. HOMs excited in SRF structures by passing beam may deteriorate beam quality and affect beam stability. It is extremely important to properly tune HOM filters, i.e. to minimize RF transmission on the operating mode, to prevent beam breakup and excessive heating of the cavity end group. Capacitive tuning is first done on a single cavity before the vertical test, then checked and adjusted before the cavity string is inserted in the cryomodule vacuum vessel.

CHALLENGES EXPERIENCED

The first production cryomodule (CM02) HOM filters were tuned using the procedure for the Jefferson Lab C100 style cryomodules [1]. CM02 was at the Cryomodule Test Facility in July 2017.

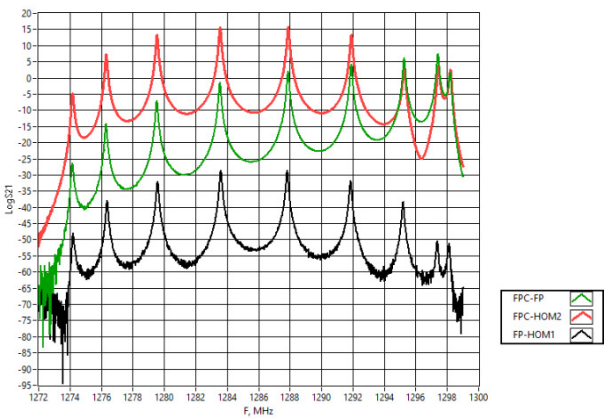


Figure 1: Fundamental mode spectrum of an LCLS-II cavity.

Over a half of the HOMs had a measured quality factor below specification. A plan was developed to asses CM02 and CM03 HOM tuning and HOM heat station connections. Fourteen out of sixteen HOMs accessible through the tuner ports on the CM03 were tuned to the partner laboratory standard notch frequency for a cavity under vacuum, 1297.0 MHz [2].

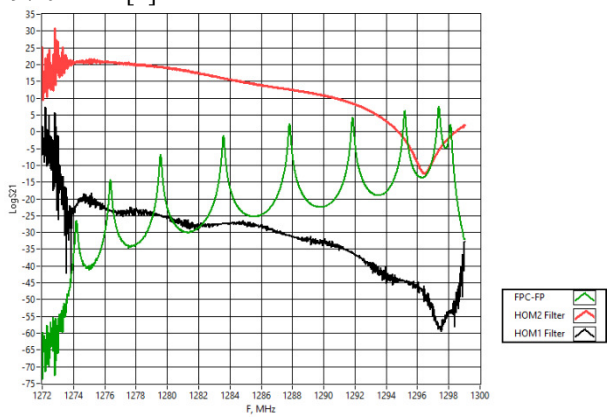


Figure 2: Notch filter view of an LCLS-II cavity spectrum.

We independently discovered that tuning is extremely sensitive to any external manipulation such as tightening cables, assembling magnetic shield covers, tightening of the heat stations. Notch positions were measured multiple times during the process and under several different vacuum conditions, including cavity under vacuum and insulating vacuum at atmosphere, both cavity and insulating vacuum established. Figures 1 and 2 show a typical LCLS-II cavity spectrum and a calculated notch position.

Table 1: Notch Frequency Shift for HOM1

HOM 1 notch atm-vac, MHz	HOM 1 notch vac-vac, MHz	Frequency shift, MHz
1296.7	1297.2	0.5
1297.4	1298.3	0.9
1297.3	1298.0	0.7
1297.3	1298.1	0.8
1297.2	1298.5	1.3
1296.8	1297.4	0.6
1297.4	1297.9	0.5
1296.8	1297.8	1.0

Notch filter position was expected to shift by +0.4MHz [2], observed frequency shift at Jefferson Lab was 0.8MHz for HOM 2, 1 MHz for HOM 1 (Tables 1 and 2). Target notch frequency was lowered to 1296.6 MHz for HOM 1 and to 1296.3 MHz for HOM 2 (Fig. 3 and 4).

*This work was supported by the LCLS-II Project and the U.S. Department of Energy, Contract DE-AC02-76SF00515.
†shabalin@jlab.org

Content from this work may be used under the terms of the CC BY 3.0 licence (© 2018). Any distribution of this work must maintain attribution to the author(s), title of the work, publisher, and DOI.

ISBN: 978-3-95450-194-6 ISSN: 2226-0366 doi:10.18429/JACoW-LINAC2018-TUPO041

Content from this work may be used under the terms of the CC BY 3.0 licence (© 2018). Any distribution of this work must maintain attribution to the author(s), title of the work, publisher, and DOI.

Table 2: Notch Frequency Shift for HOM 2

HOM 2 notch atm-vac, MHz	HOM 2 notch vac-vac, MHz	Frequency shift, MHz
1296.7	1297.1	0.4
1296.8	1297.8	1.0
1297.0	1298.1	1.1
1297.0	1298.1	1.1
1298.6	1300.4	1.8
1297.8	1298.8	1.0
1297.3	1297.9	0.6
1297.1	1297.7	0.6

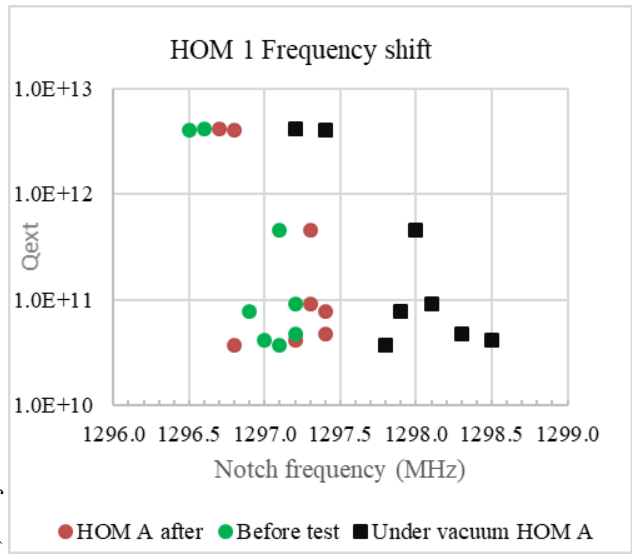


Figure 3: HOM 1 new notch frequency target 1296.5MHz.

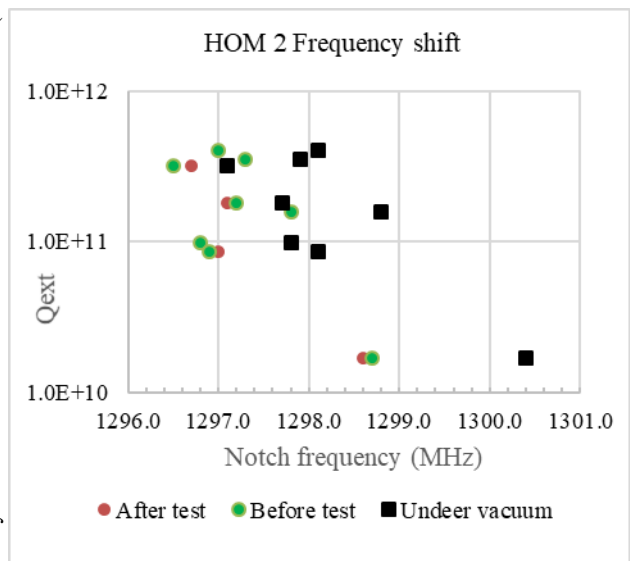


Figure 4: HOM 2 new notch frequency target 1296.3 MHz.

Test results showed inconsistency between the tuned notch frequency and the measured cold external quality factor. Cavities with close notch frequency showed a big difference in Qext and vice versa (Table 3).

Table 3: Notch Frequency *vs* Qext

Cavity	HOM 1 notch, MHz	HOM 1 Qext	HOM2 notch, MHz	HOM 2 Qext
CM03-1	1296.6	4.12E+12	1296.5	3.21E+11
CM03-2	1297.2	4.80E+10	1296.8	9.74E+10
CM03-3	1298.9	4.50E+11	1297.0	4.04E+11
CM03-4	1297.2	9.10E+10	1296.9	8.54E+10
CM03-5	1297.0	4.20E+10	1298.7	1.70E+10
CM03-6	1296.5	4.00E+12	1297.8	1.56E+11
CM03-7	1296.9	7.70E+10	1296.9	3.50E+11
CM03-8	1296.6	3.70E+10	1296.9	1.80E+11

After examining the process used at DESY and consulting with experts at DESY and Fermilab, we implemented an iterative tuning procedure to improve the stability of tuning by reduction of the local stresses and hardening of the material of the HOM coupler (Fig. 5), and improved our notch calculation technique [3, 4, 5]. We think this iterative tuning become even more important after CM02 because the cavity's recipe changed from the baseline 800°C annealing to a 900/950/975°C annealing, which in turn softens the HOM can material even further [6].

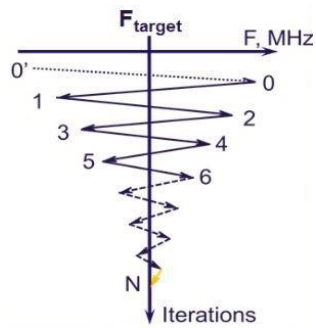


Figure 5: Iterative tuning pattern.

After the second cold test, CM03 results were better, but still inconsistent: notch frequency measured at 2K showed a random shift, more so on the coupler side HOM can, Table 5. Discrepancy led us to believe that some external forces were changing the tune during the cool down. After a meticulous investigation, we have found a mechanical interference between the magnetic shields of the HOM can and the helium vessel (Fig. 6).

For the next cryomoduls, magnetic shielding was modified and mechanical interference was removed, which proved to be effective (Table 4).

ISBN: 978-3-95450-194-6 ISSN: 2226-0366 doi:10.18429/JACoW-LINAC2018-TUPO041

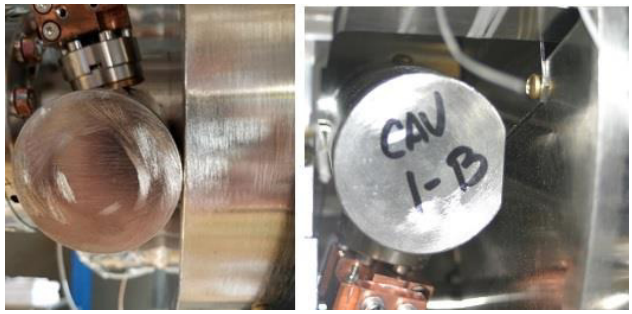


Figure 6: HOM magnetic shield mechanical interference (left) and correction (right).

Table 4: Cryomodule 4 Test Results

Cavity	HOM 1 notch, MHz	HOM 1 Qext	HOM2 notch, MHz	HOM 2 Qext
CM04-1	1296.4	3.6E+13	1296.2	1.5E+13
CM04-2	1296.6	6.8E+12	1296.3	3.5E+13
CM04-3	1296.8	3.0E+16	1296.4	4.0E+13
CM04-4	1296.6	1.7E+14	1297.4	3.8E+11
CM04-5	1296.6	4.2E+13	1296.6	1.1E+13
CM04-6	1296.6	1.5E+14	1296.4	1.6E+12
CM04-7	1296.6	3.2E+13	1296.3	7.7E+12
CM04-8	1297.1	3.2E+12	1296.3	4.1E+12

PROCEDURE OPTIMIZATION

Iterative tuning to the specific notch frequency is a time-consuming procedure: each cryomodule required about 16 hours of work. As a result, iterative tuning was moved to the cavity incoming inspection stage, when all received cavities fundamental modes are measured and recorded. Required tuning time was now reduced by a couple of hours. Different tuning techniques were studied on individual cavities tested at the Vertical Test Area to develop a procedure most consistent with the process at the partner laboratory. As we acquired more data, a pattern became obvious: cavities tuned such that $\frac{7\pi}{9}$, $\frac{8\pi}{9}$ and π modes amplitudes were within 2dB from each other and 12-15dB lower than $\frac{5\pi}{9}$ mode and there is a local minimum between $\frac{7\pi}{9}$ and $\frac{8\pi}{9}$ modes, show the lowest measured power out of the HOM coupler, Figure 7. This visual method is consistent with the previously set target notch frequency, provides good HOM power damping and reduces the time required for tuning. In addition to these improvements, a new LabVIEW software package was developed to help automate data taking and analysis.

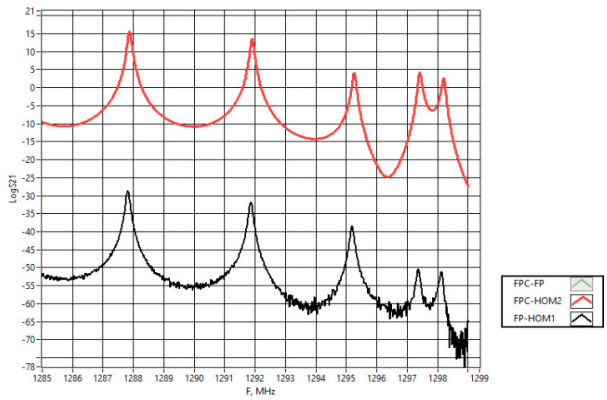


Figure 7: Examples of HOM spectrum: top – properly tuned; bottom – not tuned.

SUMMARY

The HOM notch frequency adjustment must converge iteratively to remove mechanical stress in the end plate. Tuning procedure should be done after all other adjustments and checks have been completed. Small differences in dimensions of the helium vessel and HOM can's magnetic shields caused mechanical interference at 2K. Modified HOM covers corrected the issue. Optimized tuning procedure and updated software allowed to halve the while still providing results well within specification.

Table 5: CM03 Notch Position and Qext Measured at 2K After the Final Tune

Cavity	HOM 1 notch, MHz	HOM 2 notch, MHz	Notch 1 shift, MHz	Notch 2 shift, MHz	HOM 1 Qext	HOM 2 Qext
CM03-1	1299.5	1300.5	2.7	4.2	4.90E+12	3.50E+11
CM03-2	1304.8	1300.8	8.3	4.4	7.50E+10	4.70E+11
CM03-3	1300.9	1300.2	4.4	4	1.70E+12	5.30E+12
CM03-4	1303.3	1301.3	6.9	5.1	1.90E+11	1.50E+11
CM03-5	1304.8	1300.9	8.4	4.8	1.50E+11	4.70E+11
CM03-6	1300.0	1300.4	3.2	4.0	8.00E+12	1.50E+12
CM03-7	1300.9	1300.6	4.5	4.3	1.30E+11	1.84E+11
CM03-8	1300.9	1300.9	4.2	4.5	1.70E+11	5.10E+11

Content from this work may be used under the terms of the CC BY 3.0 licence (© 2018). Any distribution of this work must maintain attribution to the author(s), title of the work, publisher, and DOI.

ISBN: 978-3-95450-194-6 ISSN: 2226-0366 doi:10.18429/JACoW-LINAC2018-TUPO041

Content from this work may be used under the terms of the CC BY 3.0 licence (© 2018). Any distribution of this work must maintain attribution to the author(s), title of the work, publisher, and DOI.

REFERENCES

[1] J. Guo, H. Wang, M. Stirbet, S. Wang, "High Order Modes Survey and Mitigation of the CEBAF C100 Cryomodules", presented at 5th International Particle Accelerator Conference (IPAC2014), Dresden, Germany. doi: 10.18429/JACoW-IPAC2014-WEPRI073

[2] T. Khabiboulline, "LCLS II cavity HOM coupler tuning and measurements during cold test," presented at TESLA Technology Collaboration (TTC'17), Milano, Italy, February 2018, unpublished.

[3] A. Sulimov, "HOM coupler notch filter tuning for the European XFEL cavities in *Proc. 17th Int. Conf. RF Superconductivity (SRF'15)*, Whistler, Canada, Sep. 2015, paper THPB067, p. 1274.

[4] T. Khabiboulline, private communication, September 2017.

[5] J. Sekutowics, private communication, September 2011.

[6] D. Gonnella, *et al*., "RF Performance of Nitrogen-Doped Production SRF Cavities for LCLS-II." ", in *Proc. 8th Int. Particle Accelerator Conf. (IPAC'17)*, Copenhagen, Denmark, May 2017, p. 1156, doi:10.18429/JACoW - IPAC2017-MOPVA128

.

ISBN: 978-3-95450-194-6 ISSN: 2226-0366 doi:10.18429/JACoW-LINAC2018-TUPO042

RF RESULTS OF Nb COATED SRF ACCELERATOR CAVITIES VIA HIPIMS*

M. Burton, A. Palczewski, L. Phillips, A.M. Valente-Feliciano†, and C. E. Reece
Thomas Jefferson National Accelerator Facility, Newport News, VA, USA
R. A. Lukaszew, The College of William & Mary, Williamsburg, VA, USA

Abstract

Bulk Niobium (Nb) SRF (superconducting radio frequency) cavities are currently the preferred method for acceleration of charged particles at accelerator facilities around the world. However, bulk Nb cavities have poor thermal conductance and impose material and design restrictions on other components of a particle accelerator. Since the SRF phenomena occurs within a shallow depth of 40 nm (for Nb), a proposed solution to this problem has been to deposit a superconducting Nb thin film on the interior of a cavity made of a suitable alternative material such as copper or aluminum. While this approach has been attempted in the past using DC magnetron sputtering (DCMS), such cavities have never performed at the bulk Nb level. However, new energetic condensation techniques for film deposition offer the opportunity to create suitably thick Nb films with improved density, microstructure and adhesion compared to traditional DCMS. One such technique that has been developed somewhat recently is "High Power Impulse Magnetron Sputtering" (HiPIMS). Here we report early results from various thin film coatings carried out on 1.3 GHz Cu cavities, a 1.5 GHz Nb cavity, and small Cu coupon samples coated at Jefferson Lab using HiPIMS.

INTRODUCTION

Superconducting radio frequency (SRF) cavities based on bulk Nb have been used for decades in particle accelerators [1]. In order to truly engineer the active SRF surface, one can take advantage of the shallow RF penetration depth by using an alternative material for the resonant cavity structure with more favorable bulk properties, such as Cu, and coating a ~1 μm Nb thin film as the active SRF surface. One can then optimize the RF response by tuning the various coating parameters available during film growth.

Thin film SRF cavities were first implemented in the 1980's at CERN for LEP II [2], with Nb/Cu thin film cavities deposited with DC magnetron sputtering (DCMS). While these films had good low field Q-values, they exhibited a strong decreasing dependence of the Q-value on RF field, known as the "Q-slope", limiting their applications. To this day, the cause of the Q-slope has not been fully understood and has yet to be overcome.

Many causes proposed for the Q-slope [3-5] can be associated with the low energy film deposition method utilized. DCMS has been shown to yield superconducting films with properties below the bulk material. Energetic condensation methods, such as high-power impulse magnetron sputtering (HiPIMS) promise to create films with enhanced SRF properties [6]. HiPIMS is easily adaptable to coating tri-dimensional shapes and can be implemented on existing DCMS cavity coating systems.

In HiPIMS, the magnetron is pulsed to extremely high-power densities thereby increasing the plasma density by several orders of magnitude and resulting in ionization of a significantly higher fraction of the metal atoms [7, 8], allowing control of the deposition energy by applying a substrate bias. HiPIMS has been shown to yield films with much improved microstructure, density, surface roughness, adhesion and overall quality compared to the low energy DC methods [9-12]. This opens the possibility to produce higher quality films for SRF application.

In order to explore HiPIMS for SRF, a cavity deposition system was designed, built and commissioned at Thomas Jefferson National Accelerator Facility (JLab) [13]. This system offers many benefits such as the ability to mount and unmount cavities while leaving the larger system under vacuum, allowing a higher turn-around cycle and reduced risk of contamination; it also allows deposition of small coupon samples under the same pump down cycle as the cavity through a load-lock and enables conditioning of the magnetron before deposition. A custom built HiPIMS pulser, powering a cylindrical Nb cathode in a Kr atmosphere, is used to deposit Nb films. Here we present early HiPIMS coated cavity results and data from small samples carried out in the same system.

EXPERIMENT

A small sample study of Nb films on Cu substrates was performed in order to investigate the effect of peak pulse power and applied voltage bias on the resulting film properties. The Cu substrates used were polished polycrystalline OFE Cu ultrasonically cleaned in successive acetone and methanol baths. After growth, the structural and surface properties of the samples (lattice parameter, grain size, orientation, roughness…etc.) were determined via X-Ray diffraction (XRD) and Electron Backscatter Diffraction (EBSD), and atomic force microscopy (AFM).

While the ultimate goal is to deposit Nb thin films on Cu cavities, it is important to first understand the film deposition process itself, thus, a known good RF Nb cavity surface was used as first substrate. Prior to the initial baseline RF test, the 1.5 GHz C100 end cell low loss (LL) Nb cavity was exposed to a buffered chemical polish (BCP) etch followed by a high-pressure rinse (HPR). While the 1.3 GHz low surface field (LSF) Cu

* Authored by Jefferson Science Associates, LLC under U.S. DOE Contract No. DE-AC05-06OR23177.
† valente@jlab.org

Content from this work may be used under the terms of the CC BY 3.0 licence (© 2018). Any distribution of this work must maintain attribution to the author(s), title of the work, publisher, and DOI.

ISBN: 978-3-95450-194-6 ISSN: 2226-0366 doi:10.18429/JACoW-LINAC2018-TUPO042

Content from this work may be used under the terms of the CC BY 3.0 licence (© 2018). Any distribution of this work must maintain attribution to the author(s), title of the work, publisher, and DOI.

cavities were acid etched via SUBU [14] and rinsed. For all the assembly stages, for coating or RF testing, the cavities were assembled in an ISO-4 cleanroom following stringent quality procedures. Cavities were also mounted under a portable clean hood that creates an ISO-5 quality environment in order to keep particulate contamination within the deposition system and on the deposition surface minimal. The coated cavities were RF tested in JLab's Vertical Test Area (VTA). After RF testing, the Nb film was stripped from the interior cavity surface by BCP for the next coating cycle.

RESULTS

Small Samples

A peak power and bias series of small samples was deposited with a fixed target to substrate distance of 10 cm, the same approximate distance as to the equator region of a 1.3 GHz LSF cavity. The power series samples were deposited at a constant Kr pressure of 3.9 mTorr, substrate temperature of 350°C, bias of -100 V and constant pulse parameters, 83 Hz frequency and 110 µs pulse width, while the peak power (voltage) varied between samples. Power values were varied between 69 and 391 kW. The bias series samples were held at the same deposition parameters, except for the pressure at 4.2 mTorr and peak power around 220 kW. The bias voltage was varied between 0 and -300 V.

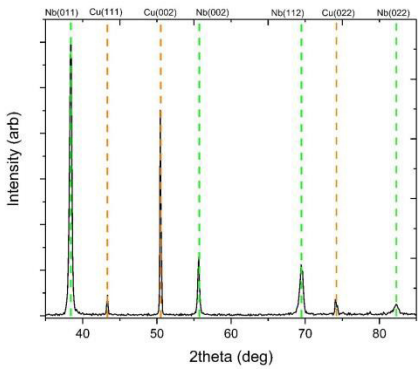


Figure 1: Representative XRD scan of Nb/Cu samples in power series

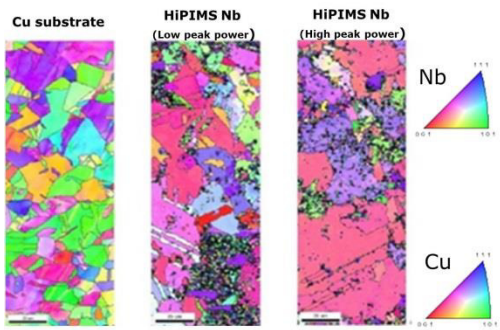


Figure 2: EBSD scans performed on Cu and Nb/Cu samples. From left to right: (a) an uncoated Cu substrate, (b) low peak-power Nb/Cu sample, and (c) high peak-power Nb/Cu sample. OIM color maps included on right for reference of crystal phases.

After deposition, the samples were analyzed using XRD to determine the resulting out-of-plane lattice parameter, grain size and mosaicity. The XRD scan in Fig. 1, shows a polycrystalline texture dominated by the Nb (011) phase. Average grain sizes were obtained using the Scherrer equation and the FWHM of the Nb (011) peak. Figure 2 shows an example of EBSD for the bare Cu substrate and two power series samples showing hetero-epitaxial growth of the film on the polycrystalline Cu. It is also noteworthy that no sharp features, detrimental to the RF performance, were observed on the surface.

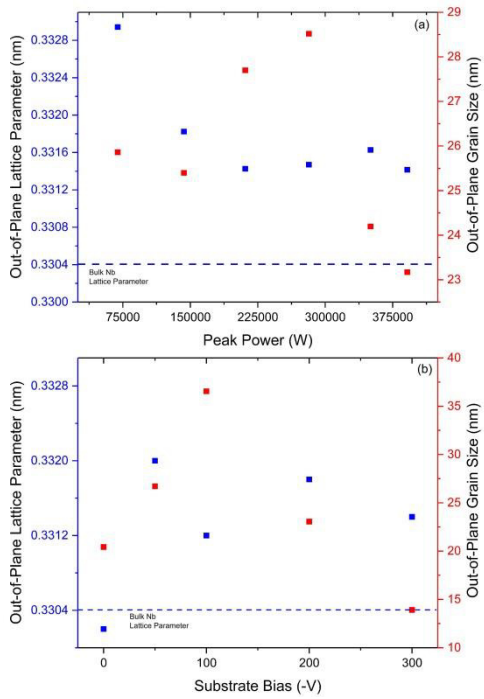


Figure 3: Plot of lattice parameter and grain size vs. (a) peak power in Nb/Cu power series and (b) applied bias in Nb/Cu bias series.

Figure 4 shows the surface roughness measured by AFM. The samples exhibited very low roughness for lower peak power and sample bias, on the order of the underlying Cu substrates. However, both show a strong increasing trend with peak power and bias, with bias much more strongly scaled, hinting at possible roughness limitation of applied bias near RF layer.

Cavity RF Results

Two Nb coatings were performed on the same Nb LL cavity. In between these two cycles, the coating system underwent a major vacuum system upgrade while keeping the overall deposition design fundamentally unchanged.

Figure 5 shows RF results for both coatings done on the LL Nb cavity with their respective baseline RF test results. Both cavities were tested without high pressure water rinsing. The first Nb coating showed a low-field Q equivalent to the underlying bulk Nb and maintained a reasonably flat Q up to 10 MV/m. The performance was limited by field emission beyond 10 MV/m. The second

ISBN: 978-3-95450-194-6 ISSN: 2226-0366 doi:10.18429/JACoW-LINAC2018-TUPO042

coating showed a good low-field Q but exhibited a thermal switch.

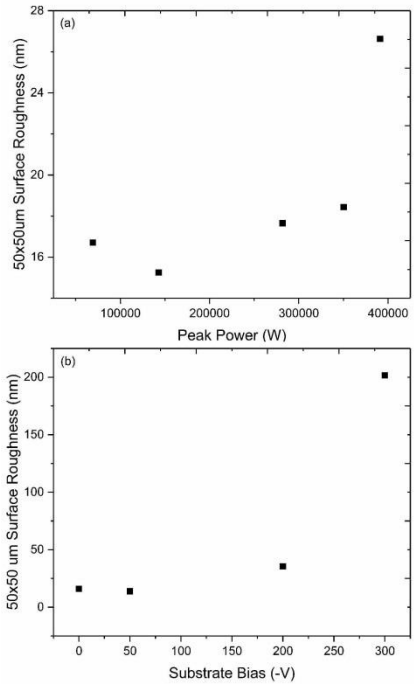


Figure 4: Plot of RMS roughness, on 50×50 µm scale, vs (a) peak power for Nb/Cu power series samples, and (b) applied bias for Nb/Cu bias series samples. Note the roughness scale difference compared to the power series results above.

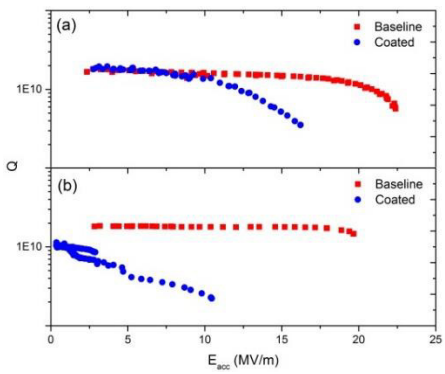


Figure 5: Quality Factor of Nb/Nb coatings (B_{peak}/E_{acc}=4.19) before (red) and after (blue) coating for (a) the first and (b) the second coating done at JLab.

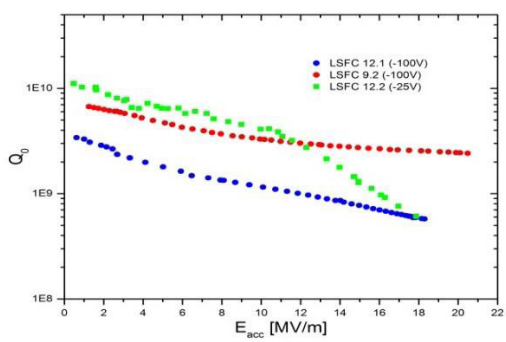


Figure 6: Quality Factor of HiPIMS Nb/Cu LSF cavities (B_{peak}/E_{acc}=3.68). No field emission was detected.

Nb/Cu RF results are shown in Fig. 6, where the cavities exhibit low field Q values in the mid to high 10^9 range and performing up to ~21 MV/m. After high pressure water rinsing, the Nb/Cu cavities had no detectable field emission. The first Nb/Cu coating (LSFC12.1) was hindered by a misalignment of the Nb cathode during coating, i.e. a non-uniformity in coating thickness. After cathode alignment corrections, the same coating parameters were applied to LSFC9.2 which showed a net improvement. However the film had a T_c of 9.5 K suggesting significant intrinsic stress in the film. In an effort to reduce the stress in the film, the next coating was performed at a lower bias (-25 V). The cavity (LSFC12.2) exhibited a slight improvement at low field but had a mid-range Q-slope that seems to be substrate related. These results show a gradual increase in performance of films deposited in this system and hold promise for future film manipulation for RF performance improvement.

CONCLUSION

The results presented here have shown that HiPIMS has great promise for high quality SRF thin films. Small coupon samples were produced with bulk-like lattice parameters and low roughness with implications for future surface engineering. The preliminary results on cavities have also shown great promise. We have achieved a Nb thin film cavity with a Q value equal to that of its bulk Nb counterpart at low field and remaining relatively flat up to 10 MV/m. Also, we have deposited Nb/Cu cavities that exhibit performance in line or better than previously reported results at similar deposition parameters. These give a starting point to begin pursuing control over the flaws observed in the technology over the last 40 years.

ACKNOWLEDGEMENTS

We would like to thank Jefferson Lab and the staff, especially Grigory Eremeev for performing some of the cavity RF tests and Kurt Macha, for their support. The College of William & Mary and its Applied Research Center, in particular Olga Trofimova.

REFERENCES

[1] H. Padamsee, J. Knobloch and T. Hays, "RF Superconductivity for Accelerators," in *RF Superconductivity for Accelerators*, New York, John Wiley & Sons, Inc., 1998, pp. 6-8.

[2] S. Calatroni, "20 Years of Experience with the Nb/Cu Technology for Superconducting Cavities and Perspectives for Future Developments," *Physics C: Superconductivity*, vol. 441, no. 1-2, p. 95-101, 2005.

[3] B. Visentin, "Review on Q-DROP Mechanisms," in 2nd *International Workshop on Thin Films and New Ideas for Pushing the Limits of RF Superconductivity*, Padova, Italy, Oct. 2006.

[4] V. Palmieri and R. Vaglio, "Thermal Contact Resistance at the Nb-Cu Interface," in *Proceedings of the SRF2015*,

Content from this work may be used under the terms of the CC BY 3.0 licence (© 2018). Any distribution of this work must maintain attribution to the author(s), title of the work, publisher, and DOI.

ISBN: 978-3-95450-194-6 ISSN: 2226-0366 doi:10.18429/JACoW-LINAC2018-TUPO042

Content from this work may be used under the terms of the CC BY 3.0 licence (© 2018). Any distribution of this work must maintain attribution to the author(s), title of the work, publisher, and DOI.

Whistler, BC, CA, Sep. 2015, paper TUBA02.

[5] C. Benvenuti, S. Calatroni, P. Darriulat, M. A. Peck, A. -M. Valente and C. A. Van't Hof, "Study of the Residual Resistance of Superconducting Niobium Films at 1.5GHz," in *Proceedings of the 1999 Workshop on RF Superconductivity*, Santa Fe, NM, USA, Nov. 1999, paper THA004.

[6] U. Helmersson, M. Lattemann, J. Bohlmark, A. P. Ethiasarian and J. T. Gudmundsson, "Ionized Physical Vapor Deposition (IPVD): A Review of Technology and Applications," *Thin Solid Films,* vol. 513, no. 1, pp. 1-24, 2006.

[7] A. Anders, J. Andersson , D. Horwat and A. Ethiasarian, "Physics of High Power Impulse Magnetron Sputtering," in *The Ninth Inernational Symposium on Sputtering & Plasma Processes-ISSP*, Kanazawa, Japan, June, 2007.

[8] J. Bohlmark, "Fundamentals of High Power Impulse Magnetron Sputtering," thesis, Phys. Dept., Linkoping University, Linkoping, Sweden, 2006.

[9] M. Samuelsson, D. Lundin, J. Jensen, M. A. Raadu, J. T. Gudmundsson and U. Helmersson, "On the Film Density Using High Power Impulse Magnetron Sputtering," *Surface and Coatings Technology,* vol. 205, no. 2, pp. 591-596, 2010.

[10] K. Macak, V. Kouznetsov, J. Schneider and U. Helmersson, "Ionized Sputter Deposition Using an Extremely High Plasma Density Pulsed Magnetron Discharge," *Journal of Vacuum Science and Technology A,* vol. 18, no. 4, pp. 1533-1537, 2000.

[11] M. Lattemann, U. Helmersson and J. E. Greene, "Fully Dense, Non-Faceted 111-Textured High Power Impulse Magnetron Sputtering TiN Films Grown in the Absence of Substrate Heating and Bias," *Thin Solid Films,* vol. 518, no. 21, pp. 5978-5980, 2010.

[12] A. Anders, R. J. Mendelsberg, S. Lim, M. Mentink, J. L. Slack, J. G. Wallig, A. V. Nollau and G. Y. Yushkov, "Deposition of Niobium and Other Superconducting Materials with High Power Impulse Magnetron Sputtering: Concep and First Results," in *Proceedings of SRF 2011*, Chigaco, IL USA, July, 2011, paper TUIOA06.

[13] L. Phillips, K. Macha and A. -M. Valente-Feliciano, "Design and Commissioning Status of New Cylindrical HiPIMS Nb Coating System for SRF Cavities," in *Proceedings of SRF2013*, Paris, France, Sept. 2013, paper TUP075.

[14] M. Peck, Structural And Superconducting Properties Of Sputter-Deposited Niobium Films For Applications In RF Accelerating Cavities, *PhD thesis*, Dept. Tech. Sciences, Atominstitut der Österreichischen Universitäten, Vienna, Austria, 1999.

ISBN: 978-3-95450-194-6 ISSN: 2226-0366 doi:10.18429/JACoW-LINAC2018-TUPO043

NEW PROGRESS WITH HF-FREE CHEMICAL FINISHING FOR Nb SRF CAVITIES

H. Tian†, B. Straka, J. Carroll, and C. E. Reece, Jefferson Lab, Newport News, VA, USA
T. Hall, R. Radhakrishna, M. Inman, E. J. Taylor, Faraday Technology, Inc., Englewood, OH, USA

Abstract

Jefferson Lab has implemented a bipolar pulsed electropolishing system for final chemical processing of niobium SRF cavities. This FARADAYIC bi-polar electropolishing (BPEP) has been applied to single cells, a 7-cell CEBAF C100 cavity, and to 9-cell TESLA-style cavities [1]. As a mechanistic characterization of the process emerges, the critical role played by the local current density during each cathodic pulse is becoming clear. This influences system and operational parameter refinement. We present current process parameters, removal characterization, and rf performance of the processed cavities. This is the fruit of collaborative work between Jefferson Lab and Faraday Technology, Inc. directed toward the routine commercialization and industrialization of niobium cavity processing. We also present supporting data from controlled-parameter coupon studies.

INTRODUCTION

Bi-polar pulsed electropolishing (BPEP), as an alternative method to treat Nb surfaces, uses anodic pulses to anodize the Nb surface with an HF-free electrolyte and intervening cathodic pulses to erode the oxide via mechanical action of the hydrogen gas bubbles formed at the niobium surface by electrolysis, resulting in a surface leveling polishing [1-3]. This process eliminates the need for HF and/or fluoride salts to remove the Nb surface oxides and is being studied as a safer, greener and more economic method to prepare Nb SRF cavities [4].

BPEP has been used as final chemical processing of niobium SRF cavity recently by Faraday Technology Inc. and Jefferson Lab. Similar work is also being investigated in partnership with KEK and Nomura Plating. The studies demonstrated that bi-polar pulsed electropolishing could effectively polish Nb SRF cavities, and produce a high-quality surface comparable with conventional EP which uses concentrated HF and H_2SO_4 as electrolyte, and provides comparable cavity performance [5-7]. However, optimization of parameters of the BPEP process for improving the removal rate and uniformity, and achieving highly reproducible high RF performance cavities, and utility processing nitrogen "doped" Nb cavities needs further systematic studies.

Jefferson Lab has developed a low cost BPEP control technique and implemented it in a vertical EP processing system. In this study, the systematic mechanistic and surface studies for guiding the design of the BPEP and the optimization of BPEP process for single cells are reported.

EXPERIMENTAL

Cavity processing at JLab by BPEP was performed inside of a closed chemical cabinet where the cavity is mounted on a vertical stand. The mixed metal oxide (MMO)-coated Ti-clad copper rod serving as a counter electrode was inserted coaxially through the cavity. Hydrogen and oxygen generated during BPEP flow back to the solution reservoir where they are diluted and exhausted. The cavity is set as the ground potential; the counter electrode is driven by a custom-designed pulse generator. Figure. 1 is the wiring diagram for the Jefferson Lab pulse generator and controller system, which is under a patent application [8]. Ultrasonic thickness gauges are used to monitor surface removal at different locations of single cell and multi-cell SRF cavities.

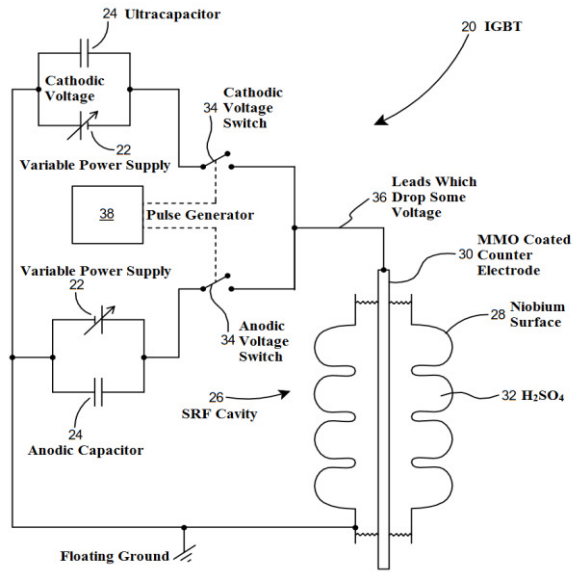


Figure 1: Schematic of the JLab BPEP equipment. [8]

Many standard samples made of high purity niobium with reactive surface of 3.14 cm^2 were fabricated for use exploring process parameters. The counter electrode for such bench-top tests was Ti-clad Cu plate with MMO coating and having reactive surface area of 30 cm^2. The distance between Nb sample and counter electrode was set as 9.8 cm. All the samples underwent 60 µm BCP etching before use. AFM measurements were done on 50 µm × 50 µm areas at three different locations, and the average of root-mean-square roughness (R_q) was calculated for each sample. The surface removal for samples was calculated through loss of mass.

* Authored by Jefferson Science Associates, LLC under U.S. DOE Contract No. DE-AC05-06OR23177.
† huit02@jlab.org

Content from this work may be used under the terms of the CC BY 3.0 licence (© 2018). Any distribution of this work must maintain attribution to the author(s), title of the work, publisher, and DOI.

ISBN: 978-3-95450-194-6 ISSN: 2226-0366 doi:10.18429/JACoW-LINAC2018-TUPO043

Content from this work may be used under the terms of the CC BY 3.0 licence (© 2018). Any distribution of this work must maintain attribution to the author(s), title of the work, publisher, and DOI.

RESULTS AND DISCUSSION

Mechanistic Studies for Optimization of BPEP

The waveform of BPEP could be designed at certain repetition frequency and structure. In this sample study, the waveform consisted of 3 ms cathodic pulse, then 2 ms off time, the 3 ms anodic pulse, and another 2 ms off time, which results in 100 Hz repetition frequency. A set of 20 samples were treated by BPEP with 15% and 37% sulfuric acid with 4 V anodic voltages, varying cathodic voltage from 4 to 13 volts. A consistent 20 µm was removed from all samples. Our studies revealed that cathodic current density on Nb surface increases with the cathodic voltage, which results in the increase removal rate see Fig. 1 and 2. Each cathodic pulse only partially removes the oxide formed during the anodic pulse. The average surface removal by each pulse is less than 0.1 nm, which suggests that the hydrogen formed may strip off the porous oxide layer only at relatively sparse locations each cycle. See Fig. 3. These results also revealed that the net removal rate strongly depends on the cathodic current density and repetition frequency.

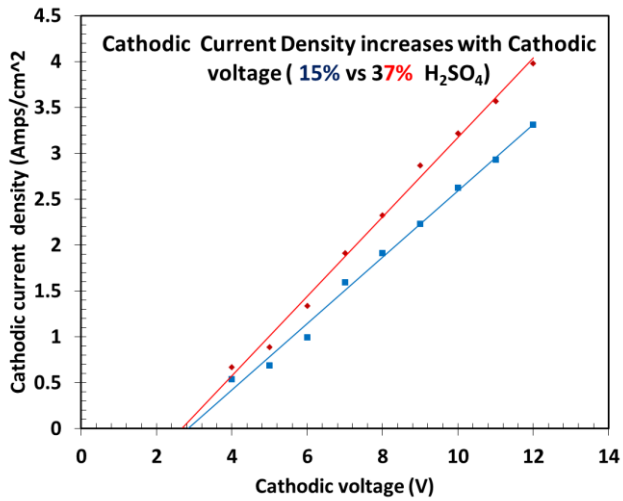


Figure 2: The cathodic current density increases with cathodic voltage for 15% and 37% H_2SO_4.

The surface roughness has been systematically studied for all the samples under different cathodic voltages with 15% and 37% sulfuric acid. See Fig. 4. The lower concentration H_2SO_4 (15%) resulted in a smoother surface than that of high concentrated H_2SO_4 (37%) at lower cathodic voltage.

Using a standard 10 V cathodic pulse with different anodic voltages of 4, 5, 6 and 7 V, our results show no dependence of removal rate or surface finish on anodic voltage.

Optimizing BPEP for Single Cell Cavities

Applying the understanding emerging from sample studies to single/multi cell SRF cavities to improve the removal rate for BPEP processing of cavities indicates that an optimization of repetition frequency and increase of cathodic current density is needed.

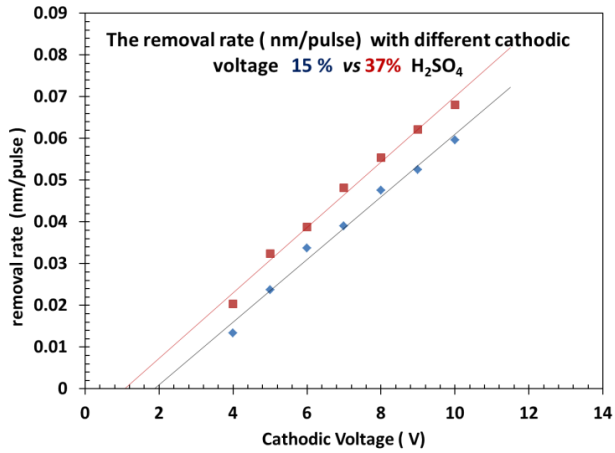


Figure 3: The average removal per pulse increases with cathodic voltage for 15% and 37% H_2SO_4.

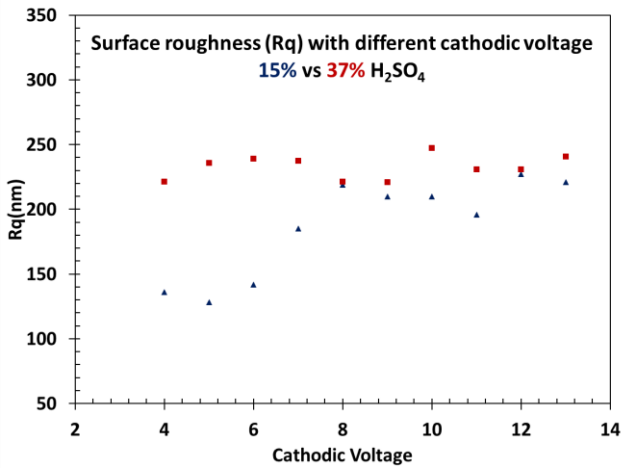


Figure 4: The surface roughness of samples processed by different cathodic voltage for 15% and 37% H_2SO_4.

A systematic study with different cathodic pulse length and voltage in 10% and 37% sulfuric acid was conducted to design an optimized parameter set a for single cell Nb SRF cavity. Figure 5 shows the BPEP current in 10% and 37% sulfuric acid with 4, 7 and 10 V cathodic voltages, with 4 V anodic voltages. The cathodic current density increased linearly with cathodic voltage, as with sample studies. Compared with 10% H_2SO_4, 37% H_2SO_4 not only increased the anodic peak, but also decreased cavity anodization process as a "shrinking" of the current anodic shoulder was observed. Besides, 37% H_2SO_4, which has near maximum electrical conductivity, yields a higher cathodic current at same cathodic voltage, yielding a higher removal rate.

Figure 6 compares the pulse current generated for different cathodic pulse lengths with 37% sulfuric acid. We observed that as the anodic current shoulder shrinks when cathodic pulses decreases to 20 ms and 15 ms there seems no effect on anodic current when comparing with 25 ms and 30 ms cathodic pulse, suggesting that cathodic pulse duration may affect the efficiency of oxide removal at each pulse.

ISBN: 978-3-95450-194-6 ISSN: 2226-0366 doi:10.18429/JACoW-LINAC2018-TUPO043

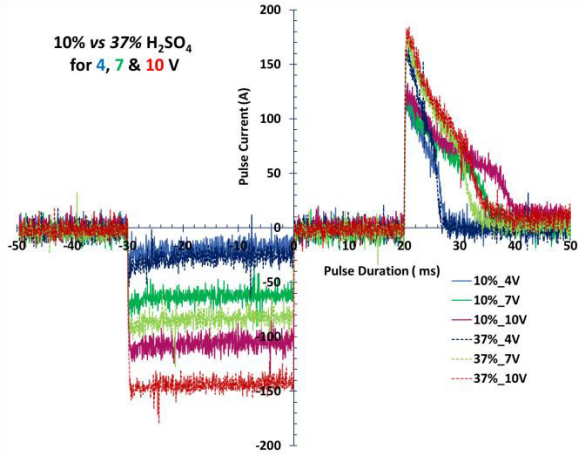


Figure 5: BPEP current with single cell cavity.

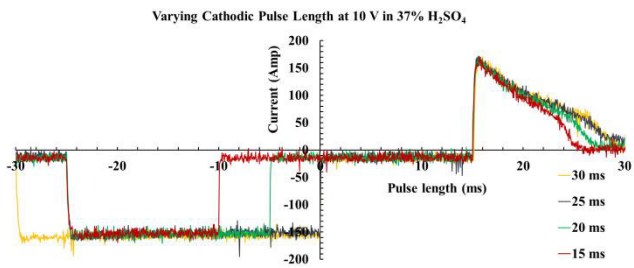


Figure 6: BPEP current with variation of cathodic pulse length.

Therefore, to maximize the removal rate and uniformity of removal for Nb SRF cavities with BPEP, the optimum repetition frequency will be influenced by cavity shape and the reactive surface area of the counter electrode.

Our previous studies noted that beam tube removal is higher than equator when using an unmasked counter electrode, and masking counter electrode at all the beam tubes improves the removal uniformity removal but decreases the removal rate [3].

In this study, a 1.3 GHz nitrogen-doped Nb single-cell was processed with 4 V anodic voltage and 10 V cathodic voltages provided by power supplies, and the counter electrode was masked at the beam tube. For BPEP process for polishing of cavities the voltage was set to a specific value by power supply, but due to voltage drop in the insulated-gate bipolar transistor (IGBT) and the leads, about 2~3 V is lost for cathodic pulse and about 1 V for anodic pulse. The cavity was polished with two parameters in 37% sulfuric acid, one with a 15 ms cathodic pulse and another with a 25 ms cathodic pulse while maintaining 11 Hz repetition frequency. The 15 ms pulse polished at the equator with removal rate of 0.6 µm/hr and 0.4 µm/hr at the beam tubes. The 25 ms pulse polished at the equator with the removal rate of 0.8 µm/hr, and polished the top beam tube with the removal rate of 0.2 µm/hr, and the bottom beam tube with the removal rate 0.6 µm/ hr.

A CEBAF C100 shape 7-cell was polished with 10% sulfuric acid at 6 Hz with a cathodic pulse of 8 V. These parameters were designed to test the capability of our pulse control system for multicell. Further optimization is underway for 7 cells. With masked counter electrode, this 7 cell was polished at a removal rate of 0.1 µm/ hr. The subsequent RF test was complicated by accidental electrode scratching of the cavity; hence RF test result is inconclusive and is not reported here.

The RF Performance of Nb 9 Cell Cavity Processed by BPEP Process

Both JLab and Faraday Tech seek to build experience with multicell cavities, but access has been limited. Under our CRADA, JLab sent Faraday the LCLS-II 9-cell cavity CAV238. Faraday BPEP processed the cavity using 10% H_2SO_4, removing an average of 13.5 µm by weight reduction then shipped it back to JLab for testing, see Fig. 7. The gradient was initially administratively limited by radiation production at 25 MV/m. (3 R/hr + neutron production) Operation in the 8/7/6/π modes to quench were consistent with ~32 MV/m quench field limited in an end cell. After a second HPR and 120°C bake, performance improved nicely. This result suggests that BEPE has no fundamental limit in obtaining a gradient in multi-cell cavities up to 32 MV/m.

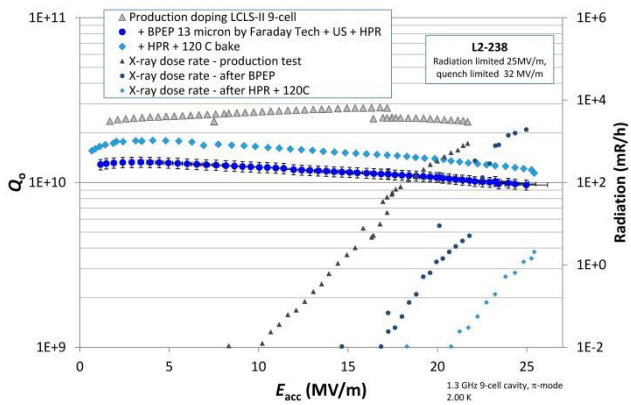


Figure 7: RF test of 9-cell cavity BPEP processed by Faraday.

NEXT

In the near future, we will continue to work with multi-cell cavities to refine process parameters, electrode geometry, and upgrade our pulse control system. We are also planning to start systematic studies of BPEP for N_2 doped samples and single cells.

ACKNOWLEDGMENTS

We acknowledge the support of Josh Spradlin, John Musson, Mark Lester and our colleagues at Jefferson Lab from the SRF Operations group, and we thank the Department of Energy SULI program for supporting Straka and Carroll participation in this work. We remain grateful for the contributions of our late colleague Larry Phillips.

REFERENCES

[1] E. J. Taylor, M. E. Inman, T. D. Hall "Electrochemical system and method for electropolishing superconductive radio frequency cavities," U.S. Pat No. 9 006 147, April 14,

Content from this work may be used under the terms of the CC BY 3.0 licence (© 2018). Any distribution of this work must maintain attribution to the author(s), title of the work, publisher, and DOI.

ISBN: 978-3-95450-194-6 ISSN: 2226-0366 doi:10.18429/JACoW-LINAC2018-TUPO043

Content from this work may be used under the terms of the CC BY 3.0 licence (© 2018). Any distribution of this work must maintain attribution to the author(s), title of the work, publisher, and DOI.

2015; Japanese Pat No. 6 023 323, October 14, 2016; European Pat No. 2 849 908, February 15, 2017.

[2] H. Tian, B. Straka, C. McCord, L. Phillips, C. Reece, "Analysis of pulse/pulse reversed electropolishing parameters for Nb," presented at SRF2017, Lanzhou, Gansu, China, July 2017, paper TUPB107, unpublished.

[3] H. Tian, L. Phillips, J. Musson, C. Seaton, M. Lester C. E. Reece, "Commissioning of JLab vertical cavity processing system for SRF Nb single cell and multicell cavity with HF-free pulse reversed electropolishing". IPAC 2018, Vancouver, British Columbia, Canada, THPAL143.

[4] E. J. Taylor, M. E. Inman, T. D. Hall, S. Snyder "Economics of electropolishing niobium SRF cavities in eco-friendly aqueous electrolytes without hydrofluoric acid," in *Proc. SRF2015*, Whistler, BC, Canada, Sept. 2015, MOPB092, p. 359 (2015).

[5] F. Furuta, M. Ge, T. Gruber, J. Kaufman, J. Sears, M. Liepe, T. Hall, M. Inman, E. J. Taylor, R. Radhakrishnan, S. Snyder, "RF performance of Multi-cell scale Niobium SRF cavities prepared with HF Free bipolar eletro-polishing at Faraday" in *Proc. SRF2017*, Lanzhou, Gansu, China, July 2017,paper TUPB074.

[6] M. Inman, *et al.*, "Electropolishing of Passive Materials in F-Free Low Viscosity Aqueous Electrolytes," *Journal of the Electrochemical Society*, 160 (9), E94-E98 (2013).

[7] A. Rowe *et al.*, "Bipolar EP: electropolishing without fluorine in a water based electrolyte", in *Proc. SRF2013*, Paris, France, Sept. 2013, paper TUIOC02, p. 404 (2013).

[8] J. Musson, L. Philips, H. Tian, C. Reece, "High current bi-polar pulse system for use in electrochemical metal surface finishing", US patent in application.

ISBN: 978-3-95450-194-6 ISSN: 2226-0366 doi:10.18429/JACoW-LINAC2018-TUPO045

OPTIMIZATION OF DUAL AXIS ASYMMETRIC CAVITY FOR ENERGY RECOVERY LINAC

Ya. Shashkov†, A. Bulygin, M. A. Gusarova, National Research Nuclear University MEPhI, 115409, Moscow, Russia
I. V. Konoplev, JAI, Department of Physics, University of Oxford, Oxford, OX1 3RH, UK
F. Marhauser, A. Seryi, Thomas Jefferson National Accelerator Facility, Newport News, VA 23606, USA

Abstract

Optimization of the dual axis asymmetric cavity was performed to minimize the ratio of the peak magnetic and electric fields values to the accelerating voltage, to increase the distance between operating and neighbouring modes as well as to reduce the manufacturing cost of the cavity. To reach the goals several solutions have been suggested bringing the ratios to the acceptable values and leading to simplification of the manufacturing of the structure.

INTRODUCTION

Conceptual design and preliminary RF studies of dual-axis asymmetric RF cavities for energy recovery LINAC has been recently carried out at Oxford and JLab [1-5]. The concept of using two different axes for acceleration and deceleration was known [6,7] but it is only recently the use of asymmetric configuration for acceleration and deceleration of the beam to isolate higher order modes (HOMs) excited in different sections has been suggested [4,8,9]. The objectives were to confine HOMs excited at each pass to either of the axis reducing the feedback between accelerating and decelerating beams and thus increasing BBU start current aiming at creating ERL capable of driving electron beam with an average current above 1 Ampere. The preliminary RF studies at JLab of a single cell dual axis SCRF cavity [1-3] demonstrated very promising results while at Oxford the theoretical and preliminary experimental studies of dual-axis 7 cell cavity had been carried out [4,5].

In this paper we present the results of the theoretical studies carried out to optimise the cavity design and improve the understanding of the cavity parameters on its performance. The overall aim of these studies is to move from the conceptual design to technical drawings enabling the next step – manufacturing and test of SCRF cavity.

ORIGINAL DESIGN OF THE CAVITY AND CHALLENGES

In Fig. 1 the schematic of the original structure made from tesla-type (TT) cells on both axis is presented. The cells on one axis are slightly different than on another. We denote this structure as TT&TT. Recently it was recognised that one of the issues is high picks of the electric (E_p) and magnetic (B_p) fields on the surface (subscript p) of the resonant cell (see Fig. 1), frequency proximity of operating f_0 and nearest parasitic f_p mode with $\Delta f = 0.505$ MHz (Table 1) in pass band and high probability of multipacting discharges due to flat surfaces of the coupling cell.

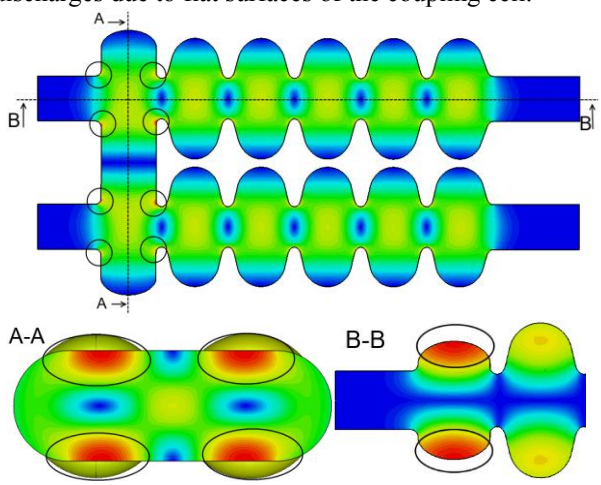


Figure 1: Contour plots of electric (top figure) and magnetic (bottom figure) fields showing the high intensity fields on the surface of the bridge cell.

First we looked at alternative to tesla type (TT) cells. It was suggested that low-loss (LL) cells [10-11] might be a good alternative as they were originally designed to allow high current transportation [11-12] and complete substitution of TT cells with the low-loss cells has been carried out. The substitution led to increase of the field on the surface of the bridge, the distance between modes did not change and the operating field amplitude along the axes became lower. As a result the overall field ratios i.e. field on the surface to the accelerating field on the axis (E_a) have increased $E_p/E_a = 3.22$ and $B_p/E_a = 7.12$ by nearly 20% reaching very high values. Taking this into account the use of solely LL-cells was not persuaded further.

In order to simplify the manufacturing of the structure by reducing the number of forms that are necessary for the machining it was proposed to use a combination of different types of cells (Fig. 2): TT-cells along one axis and LL-cells along second axis (TT&LL). Availability of the forms to stamp the parts, gained experience of making such cells assures relative easiness and quick manufacturing and testing the cells. These features allow minimisation of the cost and research/application risks.

The reported study was funded by RFBR according to the research project № 18-302-00990
† yvshashkov@mephi.ru

Content from this work may be used under the terms of the CC BY 3.0 licence (© 2018). Any distribution of this work must maintain attribution to the author(s), title of the work, publisher, and DOI.

ISBN: 978-3-95450-194-6 ISSN: 2226-0366 doi:10.18429/JACoW-LINAC2018-TUPO045

Content from this work may be used under the terms of the CC BY 3.0 licence (© 2018). Any distribution of this work must maintain attribution to the author(s), title of the work, publisher, and DOI.

The field structure of the operating mode along the axes (Fig. 2) are shown. We note that the frequency of the operating mode (Table 1) as well as its structure did not change while the distance between the modes increased by 0.1MHz to 0.6MHz i.e. by 20%. The fields ratios were also improved as compared with the original design to E_p/E_a =2.77 and B_p/E_a =6.1 (Table 1).

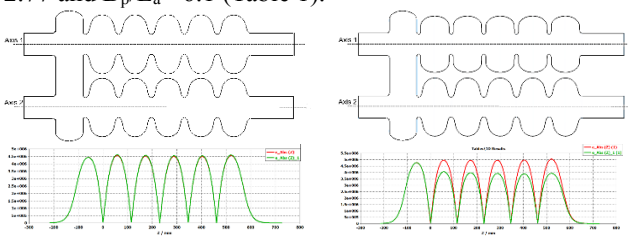


Figure 2: Schematic of TT&TT (left) and TT&LL (right) structures (top) and E_z field distribution along both axis (bottom).

Form Fig. 2 it can be seen that though the operating modes field amplitudes are flat along both axes, the field amplitudes on each axis is now different. This feature can be beneficial for energy recovery. For example, the injected beam is accelerated along the axis with LL-cells. In this case the beam dynamic is less sensitive to beam trajectory deviation from the centre meaning that for the same transvers displacement the transverse kick received by the beam due to HOMs generated will be smaller, while decelerating the beam along the section combined from TT-cells and applying high amplitude field allows improving the efficiency of the energy recuperation. This may also bring the energy of the beam at the dump to below the energy of the injected beam significantly reducing the load on the beam collector.

Table 1: Electordynamic Characteristics for Different Sets of Asymmetric Dual Axis Structures

	TT&TT	TT&LL	TT&LL (TT)	LL&TT (LL)
f_0, GHz	1.3	1.3	1.3	1.3
f_n, GHz	1.2995	1.2994	1.2994	1.2993
E_p/E_a	2.85	2.77	2.78	2.85
B_p/E_a, mT/MV/m	6.23	6.1	6.13	6.35
R/Q_1, Ohm	330	395	380	381
R/Q_2, Ohm	335	277	289	291
V_{z1}, MV*	1.63	1.79	1.76	1.76
V_{z2}, MV*	1.65	1.50	1.53	1.54
R/Q_1, Ohm	249	188	203	211
R/Q_2, Ohm	241	305	281	296

*at 1J stored energy

Table 1 compares the parameters of the cavities discussed i.e. original (made only from TT cells) and combined (LL&TT) cavities. The achievements were not as dramatic as expected however the partial improvements of some of the EM parameters stimulated new design studies to improve further the parameters.

In the attempt to increase the separation of the nearest modes and to reduce the number of stamping forms he last cell on one of the axis has been substituted with the cell from the second axis. In Fig. 3 the cavity with such substitutions are shown and the modified cavities indicated as TT& LL(TT) and LL&TT(LL) and their operating modes electric fields distributions along the axes are show (Fig. 3). With such a substitution it is clear that in spite the fact that the fields in the last cells are now matched the amplitudes along the cavity axis are different allowing application of different fields for acceleration and deceleration.

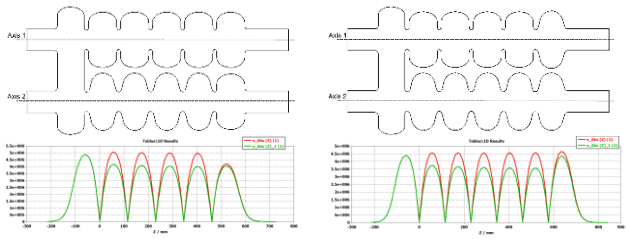


Figure 3: Schematic of TT&LL(LL) (left) and TT&LL(TT) (right) structures (top) and E_z field distribution along both axis (bottom).

The parameters for these structures are shown in the Table 2. One notes that the best field ratios and R/Q observed for the TT&LL(TT) structure. However one may point out that these improvements of the fields ratios are still relatively modest and the fields on the surface are still high E_p/E_a =2.78 and B_p/E_a =6.1 mT/(MV/m) promoting multipacting and further reduction of these ratios is important to assure the cavity reliable operation. To reduce it the optimisation of the geometry of the coupling bridge cell similar to one carried out at JLab [1-3] has been conducted.

OPTIMISATION OF THE BRIDGE CAVITY

To couple both accelerating and decelerating sections the racetrack-like resonant cell (bridge) has been proposed. The cavity design was to simplify the manufacturing of the cavity, to demonstrate the validity of the original concept while the detailed studies of the system needed to make technical design and drawing to construct the operating SCRF cavity were outside the original scope. As soon as the initial task was successfully completed and new comprehensive studies including the field strength on the surfaces of the bridge cell and the uniformity of the transverse field on both axis (to avoid the possible kicks due to field gradient) were initiated. The work strongly benefited from studies carried out at JLab [1-3].

The bridge cell optimisation goals were to: decrease the transverse field components on beam axis; reduce amplitude of magnetic and electric fields on the surface of the cell and further separate the operating mode from its neighbours. To achieve these the following steps to change the original cavity coupling cell (Fig. 4) were taken: the parameters which define the geometry of the structure have been varied and in particular the radii of the cell; the waist in the middle of the bridge has been made to push the magnetic field out while allowing to maintain the frequency position of the cavity operating mode unchanged; the “flat”

ISBN: 978-3-95450-194-6 ISSN: 2226-0366 doi:10.18429/JACoW-LINAC2018-TUPO045

parts of the original bridge cell which are difficult to manufacture from niobium using conventional technology and would potentially promote and increase the probability of the development of the multipacting discharges were removed from the final design and substituted with the curved surfaces. After the optimisations carried out the bridge cell design is similar to that of JLab cavity design [1-3]. In Fig. 4 final view of the bridge cell and iteration steps from initial bridge to the final design are shown.

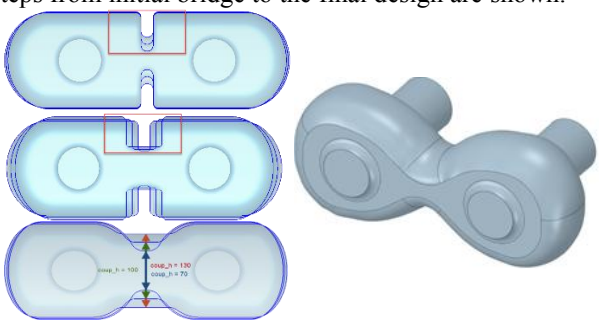


Figure 4: Iteration steps from initial bridge to the final design (left) and final design (right).

The carried out optimisations were significant and led to remarkable improvements of the cavity performance (Table 2) and resulted overall in the reduction of the fields on the surface electric field by 20% and magnetic field by 30% bringing them to conventional and "safe" values which are accepted for the conventional accelerators.

Table 2: RF Characteristics for Different Sets of Asymmetric Dual Axis Structures With New Bridge

	TT&TT	TT&LL (TT)	LL&TT (LL)
f_0, GHz	1.3	1.3	1.3
f_n, GHz	1.29954	1.29942	1.29938
E_p/E_a	2.33	2.28	2.57
B_p/E_a ,mT/MV/m	4.54	4.47	4.63
R/Q_1, Ohm	328	406	385
R/Q_2, Ohm	332	273	287
V_{z1}, MV*	1.65	1.82	1.78
V_{z2}, MV*	1.66	1.49	1.54
R/Q_{1n}, Ohm	263	196	222
R/Q_{2n}, Ohm	254	338	325

*at 1J stored energy

We note that the distance between the operating and the neighbouring modes as well as the difference between (R/Q)s of the modes on the first and second axis are defined by the cells on each axis and namely this underlines the importance of optimisation both the bridge cell and the cell along accelerating and decelerating sections.

CONCLUSION

In this paper we discuss the steps taken to optimise the cavity presenting and discussing the cavity design and performance before and after optimisation. The mode structures were analysed and their R/Q parameters were compared. The final design of the cavity is shown and preparation of the technical drawings to manufacture the SCRF cavity is under development.

REFERENCES

[1] S. U. De Silva, H. Park, J. R. Delayen, F. Marhauser, A. Hutton, "Electromagnetic Design of a Superconducting Twin Axis Cavity", in *Proc. LINAC'16*, East Lansing, MI, USA, Sep. 2016, pp. 203-205, doi:10.18429/JACoW-LINAC16-MOPLR030

[2] H. Park, F. Marhauser, A. Hutton, S. U. De Silva, J. R. Delayen, "Development of a Superconducting Twin Axis Cavity", in *Proc. LINAC'16*, East Lansing, MI, USA, Sep. 2016, pp. 932-935, doi:10.18429/JACoW-LINAC16-THPLR037

[3] A Hutton, H Areti, "Accelerator Stewardship Test Facility Program - Elliptical Twin Cavity for Accelerator Applications" JLab report JLAB-HEP15-03, 2015, https://www.osti.gov/biblio/1209532

[4] R. Ainsworth, G. Burt, I. V. Konoplev and A. Seryi, "Asymmetric dual axis energy recovery linac for ultrahigh flux sources of coherent x-ray and THz radiation: Investigations towards its ultimate performance", *Physical Review Accelerators and Beams* 19, 083502 (2016).

[5] I. V. Konoplev, A. J. Lancaster, K. Metodiev, A. Seryi," Experimental Studies of Asymmetric Dual Axis Cavity for Energy Recovery Linac", in *Proc. IPAC'17*, Copenhagen, Denmark, May 2017, pp. 1105-1107, doi:10.18429/JACoW-IPAC2017- MOPVA106

[6] Chun-xi Wang, "Conceptual design considerations of a 5-cell dual-axis SRF cavity for ERLs", in *Proc. SRF'07*, Beijing, China, Oct. 2007, paper WEP59, pp. 641-645.

[7] S. Noguchi and E. Kako, "Multi-beam accelerating structures", in *Proc. SRF'03*, Lübeck, Germany, Sep. 2003, paper TUP16, pp. 317-319.

[8] A. Seryi, Ultrahigh flux compact x-ray source, Patent PCT Application No. PCT/GB2012/052632 (24 Oct 2012); R. Ainsworth, G. Burt, I. V. Konoplev, and A. Seryi, "Asymmetric superconducting rf structure", Patent PCT Application No. PCT/GB2015/053565 (24 Nov 2015).

[9] M. Topp-Mugglestone, I. V. Konoplev, A. Seryi, "Experimental studies of eigenmodes of dual-axis RF cavity: demonstration of assymetricity of high order modes", submitted for publication in APL, 2018.

[10] H. Padamsee, J. Knobloch, and T. Hays, "RF Superconductivity for Accelerators", Wiley Series in Beam Physics and Accelerator Technology (Wiley, New York, 1998).

[11] J. Sekutowicz *et al.*, "Cavities for JLab's 12 GeV upgrade," in *Proc. PAC'03*, Portland, OR, USA, May 2003, paper TPAB085, pp. 1395-1397.

[12] V. Shemelin," Low Loss and High Gradient SC Cavities with Different Wall Slope Angles", in *Proc. PAC'07*, Albuquerque, NM, USA, Jun. 2007, paper WEPMS012, pp. 2352-2354.

Content from this work may be used under the terms of the CC BY 3.0 licence (© 2018). Any distribution of this work must maintain attribution to the author(s), title of the work, publisher, and DOI.

ISBN: 978-3-95450-194-6 ISSN: 2226-0366 doi:10.18429/JACoW-LINAC2018-TUPO048

STUDY PROGRESS OF PULSE LASER ANNEALING FOR NIOBIUM FILM ON COPPER*

Y. J. Yang†, X. Y. Lu, D. T. Xie, W. W. Tan, L. Xiao, D. Y. Yang, B. T. Li
Peking University, Beijing, China

Abstract

The recent studies of laser annealing on niobium films on copper are reported. Annealing is normally used to deal with the surface, reducing defects and even changing the microstructure of the coating film. Short pulse laser can produce a sharp step temperature field on the film thickness scale (μm), which anneals the surface without substrate heated. The laser annealing experiments of niobium thin film sample have been carried out, and according to SEM and FIB results, Nb films melted and recrystallization occurred. Grains growing up can be observed while the power density of laser pulse increased.

INTRODUCTION

Thin film coated copper cavities are a promising alternative for RF superconducting accelerators with better thermal stability, better mechanical stability and low cost compared with bulk niobium cavities, and have been used in many accelerators. Most of Nb sputter-coated copper cavities suffer from obvious Q-slope with increasing accelerating field. There are many factors contributing to Q-slope, such as surface defect, film granularity, film-substrate binding force and roughness. The microstructure of Nb film on copper behaves like a network of superconducting grains coupled by Josephson junctions (the grain boundaries) [1][2], which gives rise to a RF dependent term in the surface resistance. Reducing the number of defects and grain boundaries per unit area should result in the decrease of surface resistance.

The films qualities seriously affect their superconducting performance, and the ultimate goal is to fabricate the bulk-like thin film, which we try to realize both in better fabrication methods and post-treatment.

The common PVD coating method for superconducting cavities including evaporation coating, magnetron sputtering coating, etc. According to the extended SZD (structure zone diagram) proposed by Andre Anders [3] (Fig. 1), the structure of the film is determined by deposition homologous temperature and the pressure. However, for the thin film deposited on copper, the temperature is limited to copper melting point (1083℃), which means it cannot be annealed with traditional heating. To solve this challenge, we are studying the benefits of short pulse laser annealing for niobium films on copper deposited by magnetron sputtering.

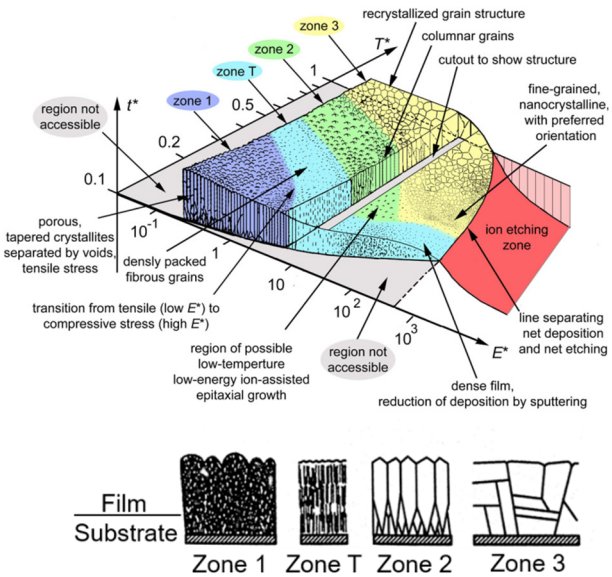


Figure 1: A possible presentation of such extended SZD [3] the figure of different zone. With the increasing temperature and pressure, the film structure changes from zone 1 to zone 3, and the formation of holes and protrusions in grain growth decreases which should make it more similar to bulk material.

EXPERIMENT SET UP AND PROCEDURE

Laser and Sample Preparation

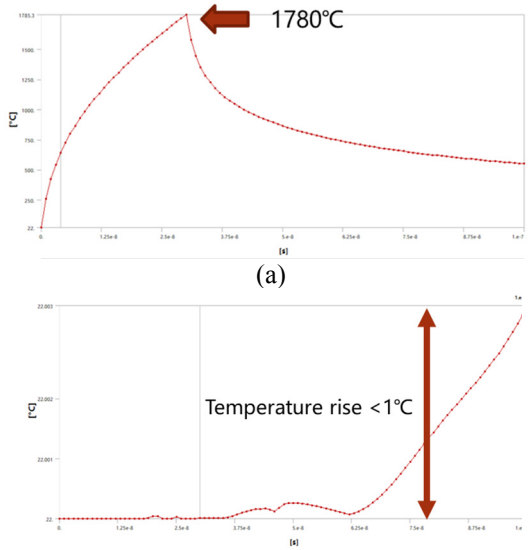
The diffusion of heat generated by laser incident on the film surface satisfies the heat conduction equation, which was simulated by ANSYS first and showed that the pulse width of the incident laser could determine the depth of temperature field distribution. In order to make the heat limited in the film thickness scale, we selected the UV laser pulse of 30ns and changed the voltage and exposure times to explore the proper pulse energy. The simulation results by ANSYS are showed in Fig. 2.

Figure 3 shows the samples we used which were respectively deposited on copper by dcMS (DC magnetron Sputtering) and HIPIMS (High Power Impulse Magnetron Sputtering), both of them have smooth surface and good superconducting performance. The film thickness of the samples is about a few hundred nanometres, while the film of HIPIMS has higher density and compactness, which may benefit the annealing results.

* Work supported by Major Research Plan of National Natural Science Foundation of China (No. 91026001).
† Email address: yangyujia@pku.edu.cn

Content from this work may be used under the terms of the CC BY 3.0 licence (© 2018). Any distribution of this work must maintain attribution to the author(s), title of the work, publisher, and DOI.

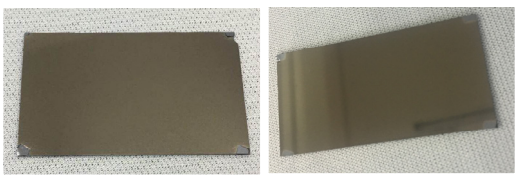
ISBN: 978-3-95450-194-6 ISSN: 2226-0366 doi:10.18429/JACoW-LINAC2018-TUPO048



(a)

(b)

Figure 2: The ANSYS simulation of temperature rise over time (surface(a) and Nb/Cu interface (b)) caused by 30ns, $10^7 W/cm^2$ laser pulse. The top temperature of surface can reach 1780ºC while the interface temperature of film/substrate rises less than 1ºC, which can realize the film annealing without affecting the substrate. The power density used in the experiment will be larger, and the top temperature obtained on the surface will be larger too, but the pulse width remains 30ns, thus the depth of temperature field distribution will not be significantly affected.



(a) (b)

Figure 3: Nb/Cu film deposited by dcMS (a) and HIPIMS (b). The film thickness of is about a few hundred nanometres, both of them have smooth surface and good superconducting performance.

Annealing Process

So far, we only experimented with single point irradiation and plan to add laser scanning system in the future.

The laser repetition frequency is typically 1hz. The duration of the effects caused by laser pulse is about 10 pulse widths, far less than the pulse repetition time, thus multiple pulses can be considered as multiple irradiation. We studied the effects of different energies and different exposures times on the surface.

Samples were cut into small pieces and irradiated by 30ns UV laser pulse. Figure 4 shows the simplified laser path into samples. The exposure area of sample is about $0.7 \times 0.35 cm^2$, and the annealing atmosphere was air.

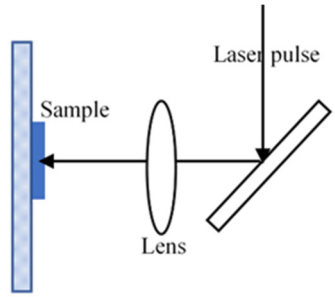


Figure 4: Simplified laser path into samples. The niobium film absorbs laser energy and then produces recrystallization. Such annealing process makes film grain size increase, and reduces impurities effect.

RESULTS AND DISCUSSION

We used the ultraviolet laser pulse (30ns) to anneal the dcMS Nb film first, and there are lots of cracks unfortunately. Figure 5 shows the FIB results and Figure 6 shows the SEM results. As the number of laser pulses increased, niobium films were melted gradually, and recrystallization occurred which made the grain size become larger. FIB images display that the film with smooth surface still have many holes and defects in the grains scale. After laser annealing, the regional compactness was improved and defects were repaired to some degree.

What disappointed us is the cracks also increase with the exposure times. Some samples had vaporization events on their surfaces, even exposing copper substrate. It may relate to the bonding force and the photon energy of UV. Actually, the wavelength of the laser has little effect on the reflectivity of the metal. Infrared to ultraviolet laser could be selected as the annealing heat source[4], while the longer wavelength laser may be selected to avoid the influence of high energy photons onto the surface in the future. Besides, one of the possible contributing factors of cracks is the increase of local area density, and original grains become larger and result in cracks.

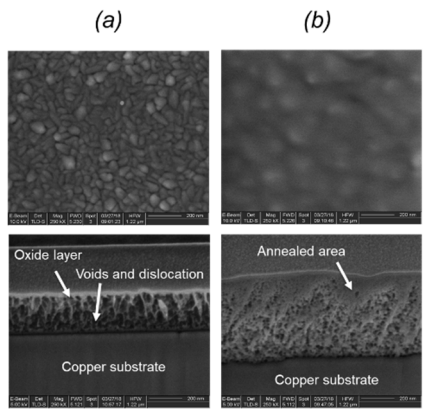


Figure 5: The FIB results of dcMS samples before(a) and after(b) annealed. It can be observed that defects decrease a lot, but the annealing is not very uniform.

Content from this work may be used under the terms of the CC BY 3.0 licence (© 2018). Any distribution of this work must maintain attribution to the author(s), title of the work, publisher, and DOI.

ISBN: 978-3-95450-194-6 ISSN: 2226-0366 doi:10.18429/JACoW-LINAC2018-TUPO048

Content from this work may be used under the terms of the CC BY 3.0 licence (© 2018). Any distribution of this work must maintain attribution to the author(s), title of the work, publisher, and DOI.

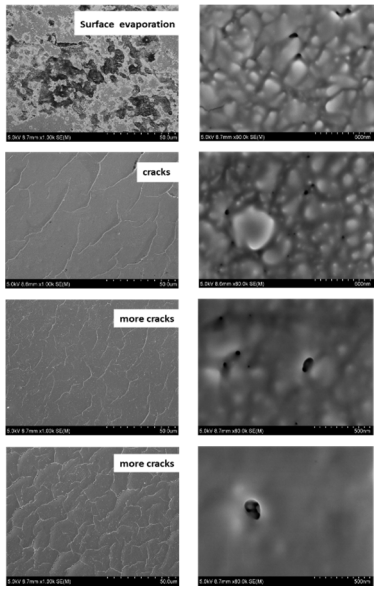


Figure 6: SEM results of annealed samples of dcMS. The voltage of the laser (reflect the power density) is 14kV. Different columns represent different magnification (× 1k and × 80k). With the laser exposure times increased (5s/1Hz, 1~2s/5Hz, 10s/1Hz, 20s/1Hz), the cracks increase too. The film grains melt, and grain boundaries fade away.

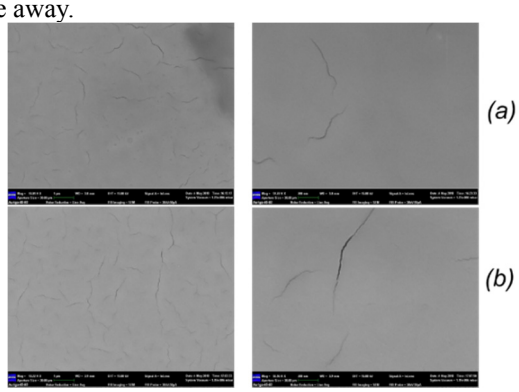


Figure 7: SEM images of HIPIMS samples. (a)~(b) the voltage of the laser (power density) is from 14kV to 16kV (exposure time is 30s). Different columns represent different magnification (× 1k and × 50k).

To reduce the cracks which may be caused by the increase of local area density, we also annealed the Nb/Cu samples deposited by HIPIMS. Figure 7 and Figure 8 showed the surface appearance after annealing. Compared with dcMS samples, the HIPIMS Nb films have better surface performance and what most benefit the annealing process are the compactness and higher film density. With the increase of exposure times or power density, the grain boundaries were gradually blurred and some samples (such as Fig. 8 (b)(c)) obtained very smooth surfaces both on the macro level and microstructure. It is clear that Nb films melted gradually and recrystallized well with HIPIMS samples. When the power density is over high or the exposure too much, cracks still appear, but the vaporization didn't occur which may due to good binding force of HIPIMS films.

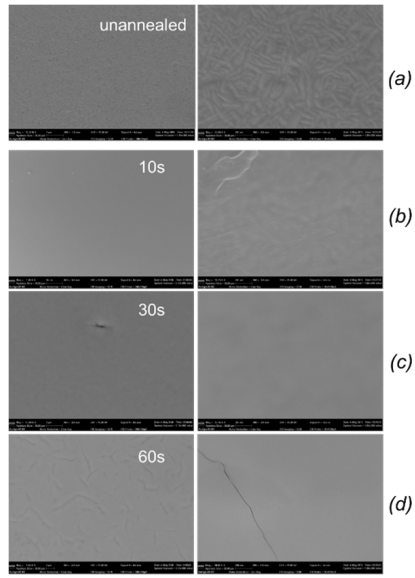


Figure 8: SEM images of HIPIMS samples before and after annealed. There are few cracks and the length of a crack decreases to several hundred nm. (a) Unannealed Nb/Cu film; (b)~(d) The exposure time increased from 10s to 30s, 60s (voltage is 13.5kV). Different columns represent different magnification (× 1k and × 50k).

There are several disadvantages in this experiment, such as the laser power density is not stable enough to repeat the irradiation, and the air annealing atmosphere prevents the further superconducting tests of these samples. The following experiment is preparing and new laser device, laser scanning system and vacuum chamber will be used in annealing system.

CONCLUSION

Niobium thin film coated copper cavities are a promising alternative to bulk niobium cavities for RF superconducting accelerators. As for the thin films, the challenges are improving the surface superconducting performance and reducing defects of the coating film, which can be greatly solved by laser annealing. Our recent studies of laser annealing on niobium films on copper are reported here, including the theorical simulation and primary experiments. Surface appearance measured by SEM and FIB of dcMS and HiPIMS samples are compared after annealing. The laser both wavelength and power density we chose may not very proper to anneal our samples. But it still can be observed that Nb films melted and recrystallization occurred. And because of the higher density and compactness of HiPIMS samples, cracks decreased a lot and better recrystallization happened according to the results. Further experiments will change the annealing environment and exposure method, and superconducting performance tests will be carried out too.

ACKNOWLEDGEMENT

This work has been supported by Major Research Plan of National Natural Science Foundation of China (No. 91026001).

ISBN: 978-3-95450-194-6 ISSN: 2226-0366 doi:10.18429/JACoW-LINAC2018-TUPO048

REFERENCES

[1] C. Benvenuti, S. Calatroni, G. Orlandi, *Physica B* 197(1994)72.

[2] Radicioni E *et al*., Laser annealing of Nb coatings for superconducting RF accelerating cavities, *Nuclear Instruments & Methods in Physics Research*, 1995, 365(1):28-35.

[3] Andr A. A Structure Zone Diagram Including Plasma-based Deposition and Ion Etching, *Thin Solid Films*, 2010, 518(15):4087-4090.

[4] WR Frisken, GH Chapman *et al*., Laser Annealing Experiments with Niobium, 2005.

Content from this work may be used under the terms of the CC BY 3.0 licence (© 2018). Any distribution of this work must maintain attribution to the author(s), title of the work, publisher, and DOI.

ISBN: 978-3-95450-194-6 ISSN: 2226-0366 doi:10.18429/JACoW-LINAC2018-TUPO049

NITROGEN DOPING STUDY WITH 1.3 GHz SINGLE CELL SUPERCONDUCTING CAVITIES *

Shu Chen, Jiankui Hao#, Shengwen Quan, Feng Zhu, Lin Lin, Liwen Feng, Fang Wang, Meng Chen, Kexin Liu
State Key Laboratory of Nuclear Physics and Technology & Institute of Heavy Ion Physics, Peking University, Beijing 100871, China

Abstract

Nitrogen doping studies were carried out at Peking University. A series of 1.3 GHz single cell cavities fabricated with OTIC large grain niobium material were annealed and doped in the furnace of Peking University, and electropolished by a simple EP device. Light doping recipe and heavy doping recipe are both adopted for comparison. The results and analysis are presented in this paper.

INTRODUCTION

Impurity doping has been a hot topic in recent years to increase quality factor Q_0 of superconducting cavity. Especially for nitrogen doping, the effect is much more obviously. Nitrogen doping was discovered by FNAL in 2013 [1], and developed by FNAL, Jlab and Cornell University in the next few years [2]. There are two kinds of doping recipes, light doping and heavy doping. For light doping, the cavity is exposed in nitrogen for 2 minutes and annealed in vacuum for 6 minutes. While for heavy doping, the cavity is exposed in nitrogen for 20 minutes and annealed in vacuum for 30 minutes. Nitrogen doping studies were carried out at Peking University in recent years with 1.3 GHz single cell cavities. The cavities were fabricated with Ningxia OTIC large grain material. After mechanical fabrication, the cavities were eched 250 μm by buffered chemical polishing (BCP) to remove the surface mechanical damage layer. After high pressure rinsing (HPR), the cavities are annealed at 800 °C for 3 hours and nitrogen doping in the high temperature furnace. Following by slightly EP and HPR, the cavities were assembled in clean room and tested in vertical test system.

EXPERIMENTAL SETUP

Nitrogen Doping Furnace

After BCP and HPR, the cavities were annealed and doped in the furnace of Peking University, see Figure 1. The ultimate vacuum of the furnace is 1×10^{-5} Pa. Several 1.3 GHz single cell cavities can be annealed at the same time in the chamber. The cavities were supported by niobium holders and laid on the niobium plate.



Figure 1: High temperature furnace for cavities annealing and three single cell cavities in the chamber before annealing.

The chamber of the furnace is evacuated by cryopump and forepump, including roots pump and screw pump. In operation, the vacuum is reached to 2×10^{-4} Pa from atmospheric pressure in 1 hour. In nitrogen doping procedure, the nitrogen gas was evaporated from liquid nitrogen tank.

Surface Treatment



Figure 2a: Simple EP device.

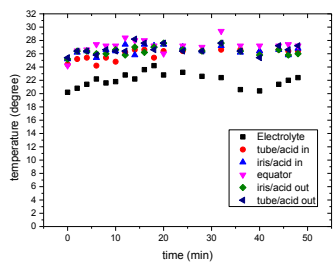


Figure 2b: The temperature in different places of the cavity during the process of EP.

After nitrogen doping, the cavity surface was electropolished with a simple EP device, see Figure 2a. The temperature of electrolyte was controlled under 25 °C. The temperature of the cavity was around 27 °C. Figure 2b shows the temperature in different places of the cavity. The rotation speed was about 1 rpm, and the acid flow rate was about 3 l/min. After EP, high pressure rinsing was used to clean the residual acid at the cavity surface.

*Work supported by National Key Programme for S&T Research and Development (Grant No. 2016YFA0400400) and National Natural Science Foundation of China (Grant No. 11575012)
#E-mail: jkhao@pku.edu.cn

Content from this work may be used under the terms of the CC BY 3.0 licence (© 2018). Any distribution of this work must maintain attribution to the author(s), title of the work, publisher, and DOI.

ISBN: 978-3-95450-194-6 ISSN: 2226-0366 doi:10.18429/JACoW-LINAC2018-TUPO049

Vertical Test System

Vertical tests were carried out at the vertical test system at Peking University. Two single cell cavities were assembled together and tested at the same time, see Figure 3a and Figure 3b. The two cavities were connected by bellows and evacuated in slow rate by molecular pump to avoid turbulence. The antenna can be adjusted by stepping motor to achieve optimum coupling. Since nitrogen doped cavities are sensitive to trapping magnetic flux, fast cooling should be adopted to reduce the influence of magnetic flux [3]. The cavities were cooled down as fast as possible through critical temperature Tc. The temperature variation at the cavity equator during the cooling down is shown in Figure 4. The speed of cooling down is about 18.3 mK/s through transition temperature.

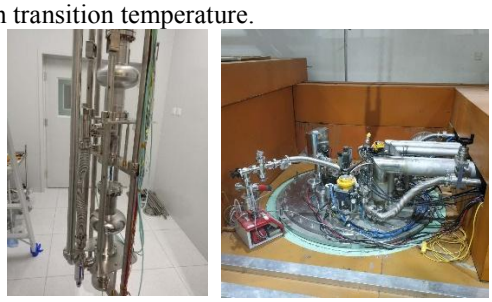


Figure 3a: Two single cell cavities were assembled together. 3b: Vertical test system at Peking University.

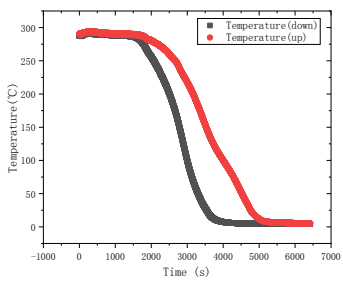


Figure 4: The temperature variation during the cooling down. Red and black curves are the temperatures at the equators of the top and bottom cavity, respectively.

NITROGEN DOPING AND VERTICAL TEST

Heavy Doping Recipe

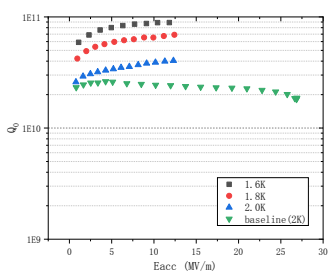


Figure 5: Q_0 vs Eacc for the large grain cavity LG1 after nitrogen doping.

The 1.3 GHz single cell large grain cavity LG1 was nitrogen doped with heavy doping recipe. Nitrogen was injected for 20 minutes and annealing in vacuum for 30 minutes, followed by EP of 15 μm. The details of treatment and results of vertical test are presented in [4]. The Q_0 reaches 4×10^{10} at 2.0K, 7×10^{10} at 1.8K and 9×10^{10} at 1.6K respectively when Eacc is around 12 MV/m, see figure 5. The Q_0 improvement and anti-Q-slope are obvious. However, the maximum Eacc is lower than 13MV/m. The main reason is probably that the surface of the cavity was contaminated during EP process with the simple EP device.

Light Doping Recipe

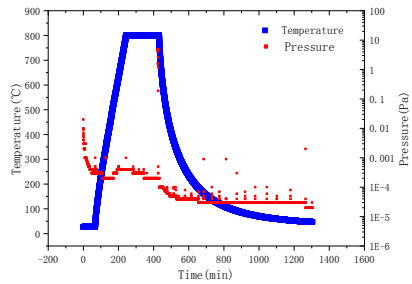


Figure 6a: Variation of temperature and pressure during high temperature treatment.

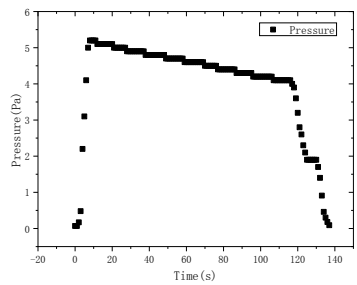


Figure 6b: Nitrogen pressure fluctuation during light N-doping process.

The Eacc is not high for heavy doping recipe. For comparison, we carried out light doping study in order to achieve high Q at higher accelerating gradient. Two 1.3 GHz single cell large grain cavities LG2 and LG3 were prepared. LG2 was light nitrogen doped and LG3 serves as the baseline cavity. Cavity LG2 was nitrogen doped for 2 minutes and annealed in vacuum for 6 minutes. The variations of temperature and pressure during doping and annealing are shown in Figure 6. Nitrogen gas was injected in the furnace chamber after 3 hours annealing. The pressure of nitrogen was about 4.5 Pa. After doping, the cavity was polished 6 μm by EP. As for baseline cavity, LG3 was treated nearly the same with LG2, except for nitrogen injection. LG3 was annealed for 3 hours and cooled down in vacuum, then followed by 6 μm EP and HPR. After treatment, two cavities were assembled together and tested at the same time. The results of vertical test are shown in Figure 7.

Content from this work may be used under the terms of the CC BY 3.0 licence (© 2018). Any distribution of this work must maintain attribution to the author(s), title of the work, publisher, and DOI.

ISBN: 978-3-95450-194-6 ISSN: 2226-0366 doi:10.18429/JACoW-LINAC2018-TUPO049

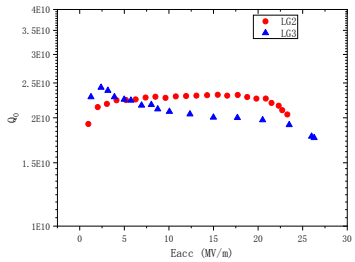


Figure 7: Q_0 vs Eacc at 2.0K for the large grain cavity LG2 and LG3.

After standard treatment, cavity LG3 behaved normally. The Eacc is 26 MV/m and the quality factor Q_0 is more than 2×10^{10} below 20 MV/m at 2 K temperature. For nitrogen doped cavity LG2, the Eacc is 24 MV/m and the quality factor Q_0 is 2.3×10^{10} at 20 MV/m. The Q_0 of light doping cavity LG2 is improved in comparison with cavity LG3. The anti-Q-slope performance is not as good as heavy doping cavity LG1. This might be due to too much trapped magnetic flux in LG2, which increases the residual resistance. Although the BCS resistance decreases with accelerating field because of nitrogen doping, the anti-Q-slope performance is not dramatically. More researches will be carried out for the next step.

SUMMARY

Studies of nitrogen doping with 1.3 GHz single cell cavities have been carried out at Peking University. Light doping recipe and heavy doping recipe are both adopted for comparison. For heavy doping recipe, the Q_0 improvement and anti-Q-slope are obvious in contrast to baseline. But the accelerating gradient is not high. For light doping recipe, accelerating gradient is as much as baseline cavity, reaching 24MV/m. However, the anti-Q-slope performance is not as good as heavy doping recipe. The main reason is probably that too much magnetic flux is trapped and residual resistance of nitrogen doping cavity is much higher. More experiments will be carried out and high Q_0 at high field is expected.

ACKNOWLEDGMENT

The authors would like to thank Ningxia Orient Superconductor Technology Co., Ltd. (OSTEC) for the processing of cavity and great help.

REFERENCES

[1] Grassellino A, Romanenko A, Sergatskov D et al 2013 Supercon. Sci. and Tech. 26(10) 102001

[2] Grassellino A, Romanenko A, Posen S et al N Doping: Progress in Development and Understanding, in *Proc. 17th Int. Conf. RF Superconductivity (SRF'15)*, Whistler, Canada, Sep. 2015, paper MOBA06, pp.48.

[3] Romanenko A, Grassellino A, Melnychuk O *et al.*, 2014 *Journal of Applied Physics* 115(18) 184903

[4] Chen S, Hao J K, Lin L, *et al.*, Successful Nitrogen Doping of 1.3 GHz Single Cell Superconducting Radio-Frequency Cavities[J]. *Chinese Physics Letter*s, 2018, 35(3): 037401.

Content from this work may be used under the terms of the CC BY 3.0 licence (© 2018). Any distribution of this work must maintain attribution to the author(s), title of the work, publisher, and DOI.

ISBN: 978-3-95450-194-6 ISSN: 2226-0366 doi:10.18429/JACoW-LINAC2018-TUPO050

CONSTRUCTION OF THIN-FILM COATING SYSTEM TOWARD THE REALIZATION OF SUPERCONDUCTING MULTILAYERED STRUCTURE

R. Ito†, T. Nagata, ULVAC, Inc, 286-0225 Chiba, Japan
H. Hayano, T. Kubo, T. Saeki, KEK, 305-0851 Tsukuba, Ibaraki, Japan
Y. Iwashita, R. Katayama, Kyoto ICR, Kyoto University, 611-0011 Uji, Kyoto, Japan
H. Ito, SOKENDAI, 305-0801 Tsukuba, Ibaraki, Japan
H. Oikawa, Utsunomiya University, 321-8585 Utsunomiya, Tochigi, Japan

Abstract

Although S-I-S (superconductor-insulator-superconductor) multilayered structure is expected to increase the maximum acceleration gradient of SRF cavities, in order for it to function in reality, it is necessary to develop a coating processing that can realize high purity and quality superconducting thin-films. In this study, we prepared several NbN-SiO_2-Nb multilayered samples which have different NbN film thickness to investigate the film thickness dependence of effective H_{c1} of S-I-S multilayered samples. In addition, we launched the co-sputtering system to get Nb_3Sn thin-film samples. The deposition rates of Nb and Sn cathodes were measured, and then the two cathodes were simultaneously sputtered aiming at appropriate composition ratio. Furthermore, we developed another experimental apparatus for coating on the inner surface of the 3 GHz TESLA type small cavities. A cylindrical Nb cathode was fabricated, and glow discharge was confirmed. This paper reports the specification of the two sputtering apparatuses and future experiment plans for demonstration and realizing of S-I-S multilayered cavities.

INTRODUCTION

S-I-S thin-film multilayered structure theory has been proposed to increase vortex penetration field of SRF cavities [1, 2]. According to this theory, the vortex penetration field of multilayered thin-film structures can reach approximately 250 mT when NbN is used for the superconducting layer and approximately 480 mT when Nb_3Sn is used. However, it is not clear whether this calculated value in this theory can really be achieved, in fact, multilayered thin-film cavities which exceed the maximum acceleration gradient of Nb cavities have not been realized. Thus, it is necessary to demonstrate the multilayered thin-film theory and to establish coating techniques for fabricating S-I-S thin-film multilayered cavities.

In order to demonstrate the theory, we firstly aimed to evaluate the effective H_{c1} of S-I-S samples [3, 4]. In previous studies, we have already established the reactive sputtering conditions for obtaining high quality NbN thin-films. Moreover, we have succeeded in preparing S-I-S samples which consist of 200 nm NbN layer, 30 nm SiO_2 layer, and pure Nb substrate. The XRD patterns of these S-I-S samples showed sharp Nb and NbN peaks [5]. In this study, we prepared several NbN-SiO_2-Nb multilayered sample which have different NbN film thickness to investigate the film thickness dependence of effective H_{c1}. Furthermore, we launched an experimental apparatus for co-sputtering of Nb_3Sn. Co-sputtering is a coating method for obtaining alloy thin-films by simultaneously sputtering two or more cathodes. In this method, it is possible to coat Nb_3Sn thin-films which have composition ratio of 3:1 by adjusting the input power ratio of Nb and Sn cathodes.

Table 1: Details of NbN-SiO_2-Nb Multilayered Thin-film Samples

Sample Name	NbN Layer Thickness [nm]	SiO_2 Layer Thickness [nm]
180814-1-A, B	50	30
180814-2-A, B	100	30
180814-3-A, B	150	30
180814-4-A, B	250	30
180814-5-A, B	300	30
180814-6-A, B	400	30

In order to realize S-I-S multilayered cavities, we also launched another experimental apparatus for basic test of the inner sputtering on TESLA type cavities. We will use this apparatus to deposit Nb or NbN on the inner surface of the 3 GHz cavities and evaluate film thickness distribution and the thin-film characteristics such as crystalline orientation.

MULTILAYERED SAMPLE PREPARING

NbN-SiO_2-Nb multilayered thin-film samples were prepared by using in-house sputtering apparatus. The Nb substrates (RRR > 300) were electro polished before NbN-SiO_2 coating. Our sputtering experimental apparatus adopts inter-back system, and a substrate carrier passes in front of Nb cathode (RRR > 300) and two Si cathodes at a regular speed. Therefore, the sputtered elements are uniformly deposited on substrate. The sizes of both Nb and Si cathodes are 5 inches by 18 inches. The base pressure of the sputtering chamber was about 2×10^{-4} Pa. Ar and N_2 (or O_2) gasses were introduced in the sputtering chamber, NbN or SiO_2 thin-films were reactively sputtered. The Nb cathode was powered by DC supply, and the two Si cathodes were powered by AC supply. In NbN coating, DC input power was set constant at 3.0 kW, and Ar partial pressure was 0.3 Pa. On the other hand, in SiO_2 coating, AC input power was set constant at 6.0 kW, and Ar partial pressure

† ryouhei_itou@ulvac.com

Content from this work may be used under the terms of the CC BY 3.0 licence (© 2018). Any distribution of this work must maintain attribution to the author(s), title of the work, publisher, and DOI.

ISBN: 978-3-95450-194-6 ISSN: 2226-0366 doi:10.18429/JACoW-LINAC2018-TUPO050

Content from this work may be used under the terms of the CC BY 3.0 licence (© 2018). Any distribution of this work must maintain attribution to the author(s), title of the work, publisher, and DOI.

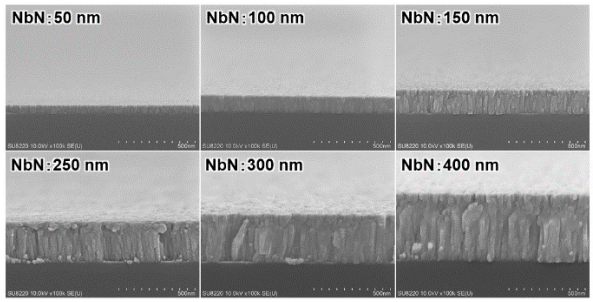


Figure 1: SEM cross-section images of NbN-SiO_2 thin-films.

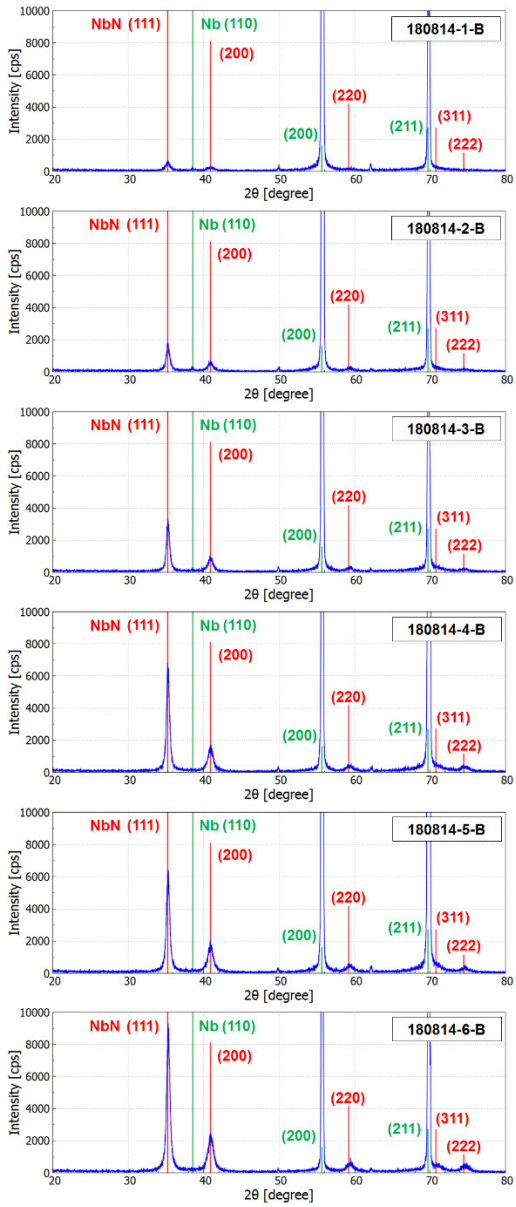


Figure 2: XRD patterns of NbN-SiO_2-Nb samples.

was 0.3 Pa. Table 1 shows the details of the samples prepared this time. The notation "-A" or "-B" attached to the end of the sample names mean that the films were coated with the same deposition lot. Figure 1 shows the SEM cross-section images of NbN-SiO_2 thin-films coated on Si

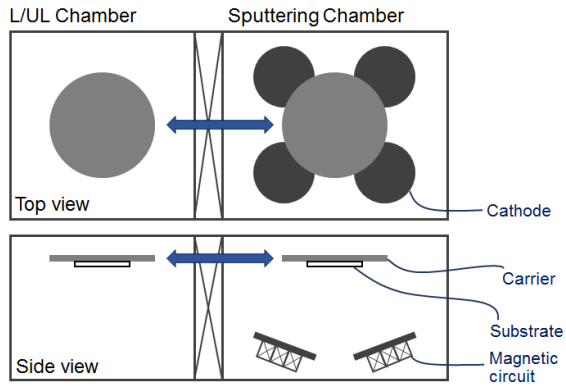


Figure 3: Schematic diagram of our co-sputtering system.

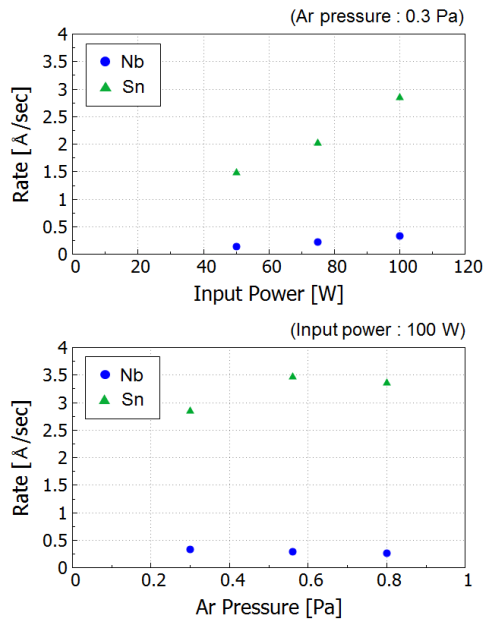


Figure 4: Deposition rates of Nb and Sn for varying input power (top) and Ar pressure (bottom).

wafer with the same deposition lot as the NbN-SiO_2-Nb samples. Figure 2 shows the XRD patterns of the NbN-SiO_2-Nb samples measured by out-of-plane method.

CO-SPUTTERING APPARATUS

Our co-sputtering apparatus can mount four disk cathodes, which are 2 inches in diameters, in one chamber. Pure Nb (RRR > 300) and pure Sn cathodes were prepared and attached for obtaining Nb_3Sn thin-films. Figure 3 shows a schematic diagram of this apparatus. The base pressure of the sputtering chamber was about 3 x 10^{-6} Pa. The substrate can be heated up to approximately 800 degrees. Firstly we measured the deposition rates of Nb and Sn cathodes while changing the input power applied to Nb and Sn cathodes or Ar gas pressure. Figure 4 shows the measured deposition rates of Nb and Sn. We confirmed that the rates of both Nb and Sn change linearly with input power. Secondly, we coated Nb-Sn alloy thin-films on 2 inches Si wafer. Since the deposition rate of Sn was about 10 times the rate of Nb, the input power ratio of Nb and Sn was set to be around

ISBN: 978-3-95450-194-6 ISSN: 2226-0366 doi:10.18429/JACoW-LINAC2018-TUPO050

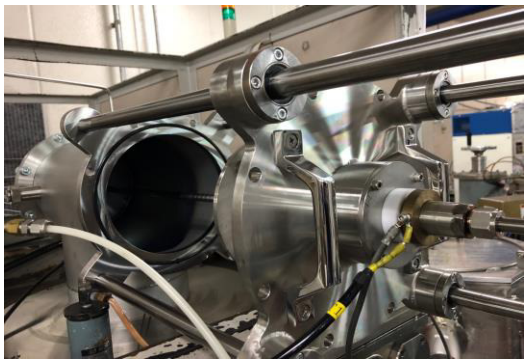
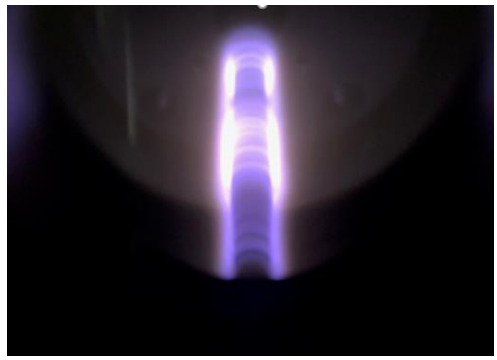

Figure 5: Experimental apparatus for inner sputtering.


Figure 6: Cylindrical pure Nb cathode.

30:1 in order to obtain Nb_3Sn thin-films having appropriate composition ratio. We plan to evaluate the actual composition ratio and the superconducting characteristics of the Nb_3Sn alloy thin-films in the future.

INNER SPUTTERING APPARATUS

We conducted a discharge confirmation experiment using a newly launched inner sputtering apparatus. Figure 5 shows the appearance of the apparatus. The base pressure of the sputtering chamber was about 1 x 10^{-3} Pa. Ar and N_2 gases can be introduced in the chamber. A pure Nb (RRR >300) cylindrical cathode which has a diameter of 12 mm and a length of 800 mm was fabricated and used (Figure 6). As several stick-shaped permanent magnets were inserted into the Nb cathode in a row so as to arrange the N pole and S pole of the adjacent magnets alternately in opposite directions, by the magnetic field lines generated between the adjacent magnets, several ring-shaped glow discharge can be made on the circumference of the Nb cathode. The length of the discharge area is 200 mm because the permanent magnets is inserted in the same area. The DC power source is connected to the both ends of the Nb cathode protruding outside the sputtering chamber. The cooling water was flowed inside the Nb cathode. Figure 7 shows the glow discharge state of the Nb cathode when Ar gas was introduced at 0.3 Pa and 200 W power was applied. After checking the apparatus work normally, we deposited pure Nb on glass substrate for 300 seconds under the same sputtering conditions as above. The distance between cathode surface and substrate was 11.5 mm, and the thickness of the deposited Nb thin-film was 510 nm with a deposition time of 300 seconds. We designed this apparatus so that a 3 GHz small cavity can be mounted in a jig attached to the door of the chamber. We will coat Nb thin-film on the inner surface of a 3 GHz small Cu cavity in the future experiment. The distribution information of the thin-film thickness will be obtained by measurement of cavity cut. Thus, we will be able


Figure 7: Glow discharge of cylindrical Nb cathode.

to decide the optimum coating method and apparatus design for depositing a uniform thin-film thickness on the inner surface of the cavity based on that information.

CONCLUSION

We prepared several NbN-SiO_2-Nb multilayered samples which have different NbN film thicknesses. All the crystalline orientations of these samples were good. From now on, we will measure the effective H_{c1} of these samples and clarify the film thickness dependence of superconducting characteristics of S-I-S multilayered structure.

Furthermore, we launched two more experimental apparatus. One is for preparing Nb_3Sn thin-film multilayered samples and the other is for carrying out basic inner sputtering tests. For both apparatuses, glow discharge was confirmed normally, and first coating tests were completed. We plan to evaluate the co-sputtered Nb_3Sn thin-films and the inner-sputtered Nb or NbN thin-films in the future.

ACKNOWLEDGEMENT

This work was supported by JSPS KAKENHI Grant Number JP17H04839.

REFFERENCES

[1] A. Gurevich, "Enhancement of rf breakdown field of superconductors by multilayer coating", *Appl. Phys. Lett.*, vol. 104, p. 032603, Jan. 2006, doi:10.1063/ApplPhysLett.88.012511

[2] T. Kubo *et al.*, "Radio-frequency electromagnetic field and vortex penetration in multilayered superconductors", *Appl. Phys. Lett.*, vol. 104, p. 032603, Jan. 2014, doi:10.1063/ApplPhysLett.104.032603

[3] C. Z. Antoine *et al.*, "Progress on Characterization and Optimization of Multilayers", in *Proc. 18th Int. on RF Superconductivity Conf. (SRF'17)*, Lanzhou, China, July 2017, pp. 368-373, doi.org/10.18429/JACoW-SRF2017-TUYBA01

[4] R. Katayama *et al.*, "Evaluation of superconducting characteristics on the thin-film structure by NbN and Insulator coatings on pure Nb substrate", in *Proc. 9th Int. Particle Accelerator Conf. (IPAC'18)*, Vancouver, BC, Canada, Apr. 4,, pp. 3653-3655, doi:10.18429/JACoW-IPAC2018-THPAL015

[5] R. Ito *et al.*, "Development of Coating Technique for Superconducting Multilayered Structure", in *Proc. 9th Int. Particle Accelerator Conf. (IPAC'18)*, Vancouver, BC, Canada, Apr. 4,, pp. 4954-4956, doi:10.18429/JACoW-IPAC2018-THPML120

Content from this work may be used under the terms of the CC BY 3.0 licence (© 2018). Any distribution of this work must maintain attribution to the author(s), title of the work, publisher, and DOI.

ISBN: 978-3-95450-194-6 ISSN: 2226-0366 doi:10.18429/JACoW-LINAC2018-TUPO051

DESIGN CONSIDERATIONS OF A BALLOON-SHAPED SSR SUPERCONDUCTING CAVITY

H. J. Cha†, J. Y. Yoon, S. W. Jang, K.-R. Kim[1], S. H. Park and E.-S. Kim
Department of Accelerator Science, Korea University Sejong Campus, Sejong, South Korea
[1]also at Pohang Accelerator Laboratory, POSTECH, Gyeongbuk, South Korea

Abstract

We introduce a balloon-shaped SSR superconducting cavity for multipacting mitigation. The electromagnetic modeling of the SSR was made based on the RF parameter optimization. The simulation results show much narrower multipacting bandwidth, compared to those for the traditional spoke cavity. Mechanical analyses with stiffening structure indicate acceptable stresses at the cavity wall.

INTRODUCTION

A single spoke resonator (SSR) having flat or round end walls has broad multipacting (MP) ranges in acceleration gradient, sometimes including operation region. In order to overcome such MP barriers, quite long radio frequency (RF) conditioning is required, which is not cost-effective and disadvantageous for mass production of the superconducting cavities. An alternative cavity with a resonant frequency f of 325 MHz and an optimum beta β_o of 0.3 has been being developed at TRIUMF [1, 2].

An SSR with f = 325 MHz and β_o = 0.51 has been studied at Korea University. Especially, this spoke cavity may be applied to the high-energy superconducting linac sections for a heavy ion accelerator such as RAON [3]. In this study, we introduce a balloon variant of the superconducting SSR which makes the MP mitigation possible due to its structural simplicity, based on its electromagnetic (EM), MP, and mechanical analyses.

ELECTROMAGNETIC SIMULATIONS

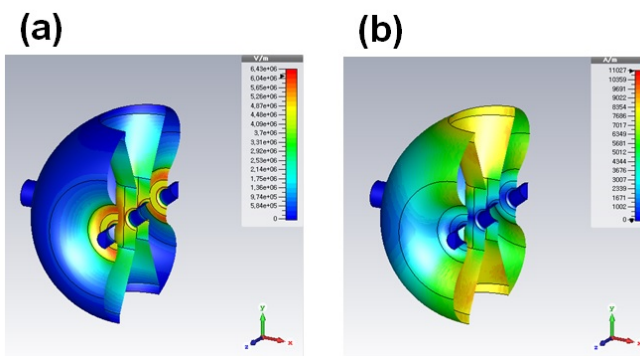


Figure 1: (a) Electric and (b) magnetic field distributions of the balloon-shaped SSR.

Figure 1 shows EM field distributions of the balloon-shaped SSR. The electric fields are mostly distributed at near a beam tunnel and the magnetic fields at loft and base parts of the spoke for the cavity with a transverse electromagnetic (TEM) mode. The horizontal geometric parameters of an EM modeling for the balloon-shaped SSR are based on the definitions from beam dynamics and transit time factor (TTF) studies that an iris-to-iris length L_{iris} is $(2/3)\beta_g\lambda$ and a gap-to-gap length L_{gap} is $\beta_g\lambda/2$, where β_g is a geometric beta ($\approx \beta_o$ of 0.51) and λ a wavelength (~923 mm for 325 MHz). Two (upper and lower) ellipses in a y-z plane were adopted for the balloon-shaped modeling. A view of the balloon-shaped SSR in a x-y plane is nearly circular.

It is well-known that a superconducting cavity should be designed to lower the peak electric field E_{peak} and the peak magnetic field B_{peak} as possible with keeping good RF properties because their increases can limit the acceleration performance by field emission and quench, respectively. In the EM design of the balloon-shaped SSR, we aim the B_{peak} under 80 mT when the E_{peak} is 35 MV/m. The resultant RF parameters are also normalized by 35 MV/m. As the geometric parameters change, we focus on the decrease of E_{peak}/E_{acc} and B_{peak}/E_{acc} and the increase of $G{\cdot}R_{sh}/Q_0$, where E_{acc} is the acceleration gradient, G the geometry factor, R_{sh} the shunt impedance, and Q_0 the unloaded quality factor of the cavity. The surface resistance R_s used for calculating the G (= Q_0R_{sh}) is ~10.64 nΩ from BCS resistance R_{BCS} of 0.64 nΩ at a frequency of 325 MHz and a temperature of 2 K with an assumption of the residual resistance R_{res} of 10 nΩ ($R_s = R_{res} + R_{BCS}$). From proper compromises among simulation results with the geometric parameter sweeps, the final geometry of the balloon-shaped SSR were determined and its RF parameters are summarized in Table 1.

Table 1: EM Simulation Results for the Balloon-shaped SSR.

RF Parameter	Value
Q_0 ($\times 10^9$)	10.7
R_{sh}/Q_0 (Ω)	296
G (Ω)	118
E_{peak} (MV/m)	35
B_{peak} (mT)	75
V_{acc} (MV)	4.2
E_{acc} (MV/m)	9
E_{peak}/E_{acc}	3.9
B_{peak}/E_{acc} (mT/MV/m)	8.4
Stored energy (J)	29.6
Dissipated power (W)	5.6

MULTIPACTING SIMULATIONS

A main advantage of the balloon-shaped SSR is MP suppression due to its simple structure. A traditional spoke

† chahj@korea.ac.kr

Content from this work may be used under the terms of the CC BY 3.0 licence (© 2018). Any distribution of this work must maintain attribution to the author(s), title of the work, publisher, and DOI.

ISBN: 978-3-95450-194-6 ISSN: 2226-0366 doi:10.18429/JACoW-LINAC2018-TUPO051

cavity has an end wall structure, where blending parts exist for convenient e-beam welding with a main cylindrical body. The larger the blending area, the smaller the higher-order MP [4]. The balloon-shaped SSR is an assembly of two half bodies with a spoke and has no end walls. The balloon shape corresponding to maximization of the blending areas gives an effect to eliminate the secondary-electron emission areas. Furthermore, the blending parts at the spoke bases which are the origins of the first order MP [4] were removed in the balloon-shaped SSR.

Figure 2 shows an example of the MP simulation results for the balloon-shaped SSR, where the numbers of secondary electrons vary with time as the E_{acc} increases. The two-point MP shown in the electron trajectories of Fig. 2 is mostly caused by the cyclotronic electron motion by magnetic fields near the spoke base. Figure 3 shows a growth rate α vs. E_{acc} curve calculated for the balloon-shaped SSR. The MP for the balloon-shaped SSR occurs at a very narrow acceleration zone from ~0.8 MV/m to 1.8 MV/m, which is far from the operating E_{acc} of 9 MV/m.

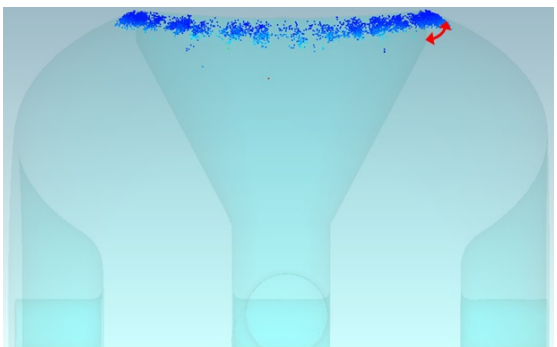


Figure 2: A simulation result on electron trajectories near a spoke base of the balloon-shaped SSR. The red arrow indicates two-point MP.

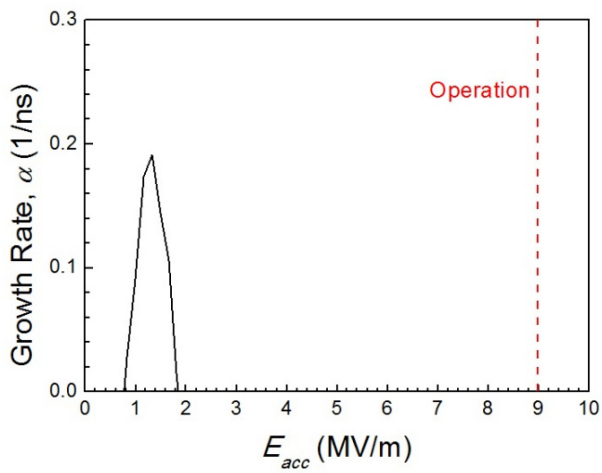


Figure 3: Simulation results on variation of the growth rate with respect to the acceleration gradient for the balloon-shaped SSR.

MECHANICAL SIMULATIONS

After analyzing the mechanical stresses of the balloon-shaped SSR, which is uniformly composed of 3-mm-thick Nb sheets, with an external atmospheric pressure, two kinds of stiffening structures were added to the cavity. We consider two boundary conditions that both beam pipes are fixed and free, respectively. For the former case, most of mechanical stresses are distributed near the beam port surroundings, where the electric field is dominant and the frequency sensitivity by the deformation is very critical. Thus, we adopted two Nb bulks at the beam port surroundings for structural rigidity with avoiding the complicated daisy ribs [5]. With the latter boundary condition, most of stresses are distributed near the equators of the cavity, which can cause the frequency shift by deformation at the magnetic field dominant region. For this reason, we added two ring stiffeners at both equators.

Figure 4 shows a plane view of the balloon-shaped SSR with the stiffening structure. We aim the mechanical stresses less than the maximum allowable stress of 32 MPa at 300 K and 171 MPa at 2 K in the following environments:

Case-1 (Leak check): External pressure of 1 bar, room temperature (293 K), free beam pipes.

Case-2 (Cool-down): External pressure of 5 bar, cryogenic temperature (5 K), fixed beam pipes.

A simulation result on the Case-1 is shown in Fig. 5. The leak-check state means that the cavity inside is maintained with vacuum and the outside with atmospheric pressure. Under such conditions, the mechanical stresses around the equators transfer to the ring stiffeners. The Von Mises stresses in the cavity were around or under 32 MPa. The maximum stresses of ~48 MPa are discretely distributed at the joint parts between the cavity and the ring stiffeners, but it is tolerable compared to the yield strength of 70 MPa. In the Case-2, the maximum allowable working pressure (MAWP) of 5 bar is supposed at 5 K. The corresponding simulation result is shown in Fig. 6. The mechanical stresses uniformly distributed in the cavity are under 100 MPa at cryogenic temperature. The maximum stresses at the beam-port cross-sections are negligible because the areas were used for the fixed boundary condition.

Content from this work may be used under the terms of the CC BY 3.0 licence (© 2018). Any distribution of this work must maintain attribution to the author(s), title of the work, publisher, and DOI.

ISBN: 978-3-95450-194-6 ISSN: 2226-0366 doi:10.18429/JACoW-LINAC2018-TUPO051

Content from this work may be used under the terms of the CC BY 3.0 licence (© 2018). Any distribution of this work must maintain attribution to the author(s), title of the work, publisher, and DOI.

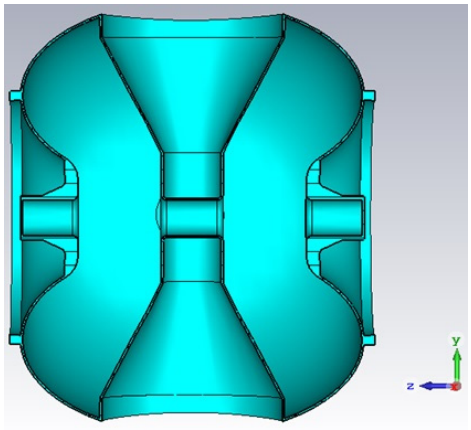


Figure 4: A balloon-shaped SSR and its stiffening structure.

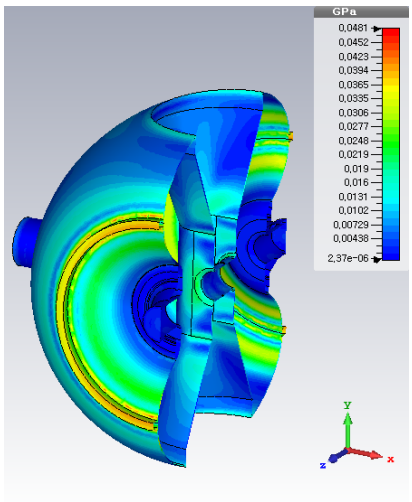


Figure 5: Mechanical simulation results on Case-1 of 1 bar, 293 K, and free beam pipes.

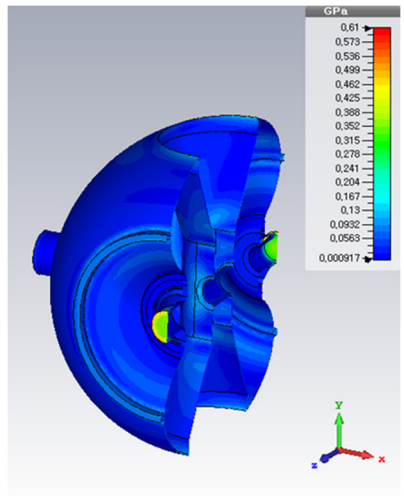


Figure 6: Mechanical simulation results on Case-2 of 5 bar, 5 K, and fixed beam pipes.

CONCLUSION

We proposed a 325 MHz and β_o = 0.51 balloon-shaped SSR for a proton/heavy-ion superconducting linac. The simulation results showed that its structural simplicity made it possible to effectively suppress the MP phenomena, compared to traditional spoke cavities. The balloon-shaped SSR also has a minimal number of stiffeners for mitigating the mechanical stresses at various environments. Pressure vessel studies with a liquid helium jacket design will be followed.

REFERENCES

[1] Z. Y. Yao *et al*., "Study of Balloon Spoke Cavities" in *Proc. SRF'13*, Paris, France, Sep. 2013, paper THP033, pp. 972-974.

[2] Z. Yao *et al*., "Design and Fabrication of Beta=0.3 SSR1 for RISP" in *Proc. LINAC'16*, East Lansing, MI, USA, Sep. 2016, paper MOPLR041, pp. 226-228.

[3] D. Jeon *et al*., "Design of the RAON Accelerator Systems", *J. Korean Phys. Soc.*, vol. 65, no. 7, p.1010, Oct. 2014.

[4] Z. Yao *et al*., "Balloon Variant of Single Spoke Resonator" in *Proc. SRF 2015*, Whistler, BC, Canada, Sep. 2015, paper THPB021, pp. 1110-1114.

[5] G. Apollinari *et al*., "Development of 325 MHz Single Spoke Resonators at Fermilab", *IEEE T. Appl. Supercon.*, vol. 19, pp. 1436-1439, 2009.

ISBN: 978-3-95450-194-6 ISSN: 2226-0366 doi:10.18429/JACoW-LINAC2018-TUPO052

DESIGN STUDY OF A PROTOTYPE 325MHz RF POWER COUPLER FOR SUPERCONDUCTING CAVITY*

Junyoung Yoon, JungBae Bhang, Chong Shik Park, Hyuk Jin Cha, Si-Won Jang, Kyung-Ryul Kim[1], Seong Hee Park, Eun-San Kim† ,Korea University, Sejong, South Korea
Ilkyoung Shin, Institute for Basic Science, Daejeon, South Korea
Jonghwa Lee, Do Yoon Kim, Vitzrotech, Ansan, South Korea
Eiji Kako, KEK, Tsukuba, Japan
[1]also at Pohang Accelerator Laboratory, Pohang,South Korea

Abstract

We present design studies of a prototype RF input Power Coupler, which provides RF powers to 325MHz cavities up to 18.5kW in CW mode. The prototype power coupler is a coaxial capacitive type with single ceramic window. In order to optimize the RF coupler design, we performed multi-physics simulations, including electromagnetic, thermal, and mechanical analyses.

INTRODUCTION

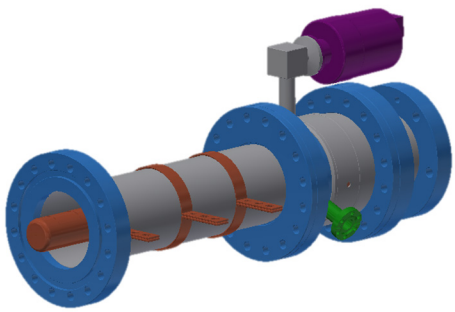


Figure 1: General view of power coupler.

The power coupler is based on conventional 50Ω coaxial transmission line. The prototype coupler has three diagnostic ports for vacuum, arc, and electron pick-ups to prevent RF breakdowns and three thermal interceptors for 4.5K, 40K, and 77K. Figure 1 shows a preliminary design of power coupler and the design requirements are listed in Ta ble 1 [1].

Table 1: Design Requirements of the Input Coupler

Parameters	Values	Unit
Operating frequency	325	MHz
Pass band ($S_{11} < 0.1$)	3	MHz
S_{11} at 325MHz	≤-30	dB
Operating Power	18.5	kW
Q_{ext}	4×10^6	-

SIMULATION

The CST Microwave Studio (MWS) Frequency Domain solver [2] is used for electromagnetic simulations and Ansys Theramal, Structural, Modal solvers were used for the Thermal/Mechanical simulations. [3]

Electromagnetic Simulation

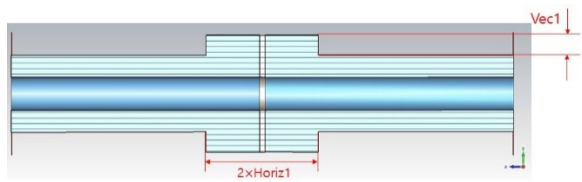


Figure 2: Geometric change of ceramic part.

Figure 2 shows variations of both diameter (Vec1) and length (Horiz1) of the outer conductor at the RF window to minimize reflected powers at 325MHz. We performed simulations to check effects of the diameter change from 8 mm to 10 mm. The optimal values of vertical length were between 8.6 mm to 9 mm shown in Figure 3. Considering engineering and manufacturing errors, we chose the 9 mm variation of the outer diameter at ceramic window.

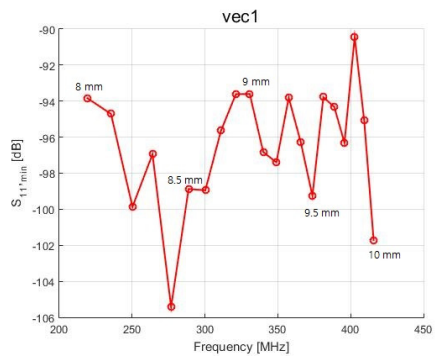


Figure 3: Effect of vertical length change.

The horizontal length change make a small frequency distribution in reflected powers (S_11) at 325MHz. Therefore, we performed the simulation in the narrow range to minimize reflected powers at 325MHz. Figure 4 shows that the optimal horizontal length is 117.2 mm.

† eskim1@korea.ac.kr

Content from this work may be used under the terms of the CC BY 3.0 licence (© 2018). Any distribution of this work must maintain attribution to the author(s), title of the work, publisher, and DOI.

ISBN: 978-3-95450-194-6 ISSN: 2226-0366 doi:10.18429/JACoW-LINAC2018-TUPO052

Content from this work may be used under the terms of the CC BY 3.0 licence (© 2018). Any distribution of this work must maintain attribution to the author(s), title of the work, publisher, and DOI.

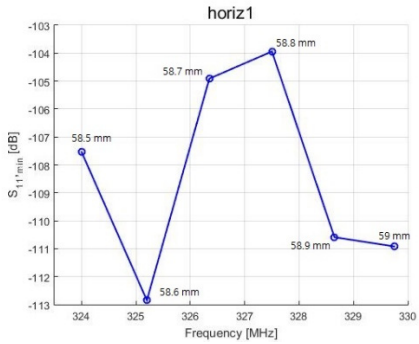


Figure 4: Effect of horizontal length change.

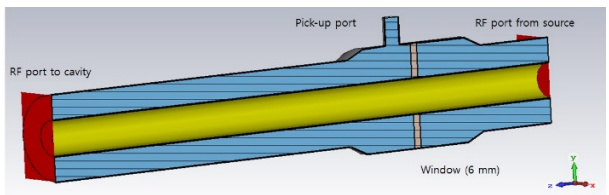


Figure 5: Electromagnetic model of the power coupler.

Figure 5 shows the prototype power coupler modelling in CST MWS. The outer conductor is composed of 0.8-mm-thick stainless steel and the inner conductor is made of 1.5-mm-thick OFHC. We constructed 60-degree angles to the edges of the outer conductor around the ceramic window because the sharp edges make the wake fields and increase the multipacting effect in the coupler [4].

While the changes of the pick-up port length does not significantly affect to the power transmission in the coupler, those of the pick-up port diameter had significant effects to the reflected power. Figure 6 shows the effect of pick-up port diameter change. We chose the 0.5 inch for the least deformation of the RF power transmission as well as consideration of connection with diagnostic devices.

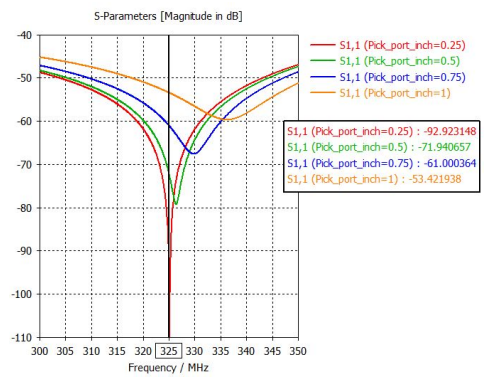


Figure 6: Reflected power (S_{11}) change due to diameter change of pick-up port.

The RF characteristics of the coupler prototype are shown in Figure 7. The point 1 is the minimum point of the reflected power, while and the point 2 is the operating frequency.

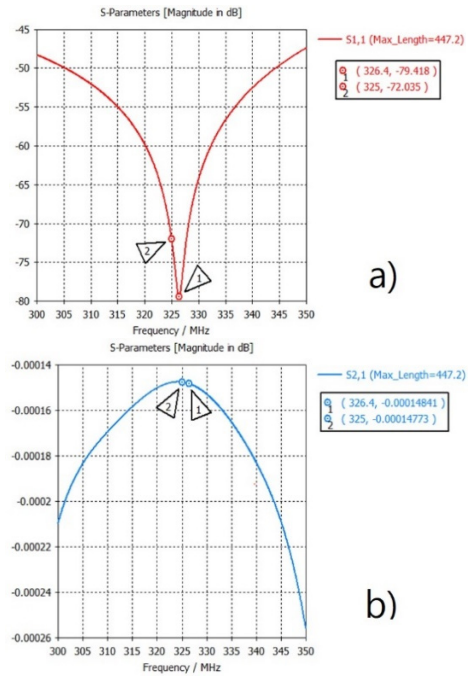


Figure 7: a) Reflected power (S_{11}) b) Transmitted power (S_{21}) of the power coupler.

Thermal Analyses and Simulation

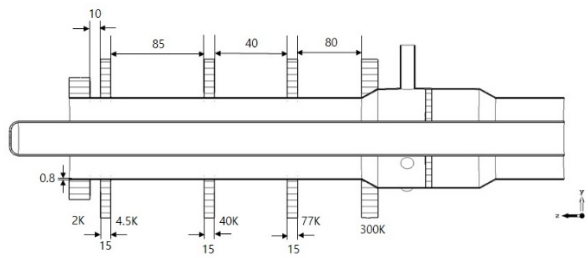


Figure 8: Scheme of a prototype power coupler for thermal analyses.

The power coupler bridged between room temperature (300K) to cryogenic temperature (2K) and acts as a continuous heat source for the superconducting cavities. Therefore, we optimize the thermal interceptor locations of the outer conductor to minimize the static heat loads. Figure 8 shows the locations of 3 interceptors and Table 2 presents analytical thermal loads on each interceptor location.

Table 2: Static Heat Load to Thermal Interceptors

Interceptor Temp. (K)	Values (W)
2K	0.0156
4.5K	0.1679
40K	0.0624
77K	0.1617

The temperature distribution and the heat flux of the coupler are shown in Figure 9.

ISBN: 978-3-95450-194-6 ISSN: 2226-0366 doi:10.18429/JACoW-LINAC2018-TUPO052

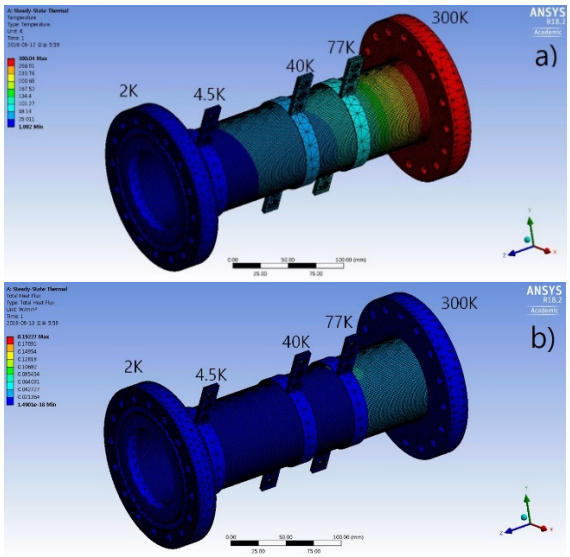


Figure 9: a) Temperature distribution and b) Heat flux result of static thermal load.

Mechanical Simulation

Figure 10 shows the stresses, strains and deformations at the ceramic window when a force of three times of gravity acts on the antenna tip in the opposite y direction..

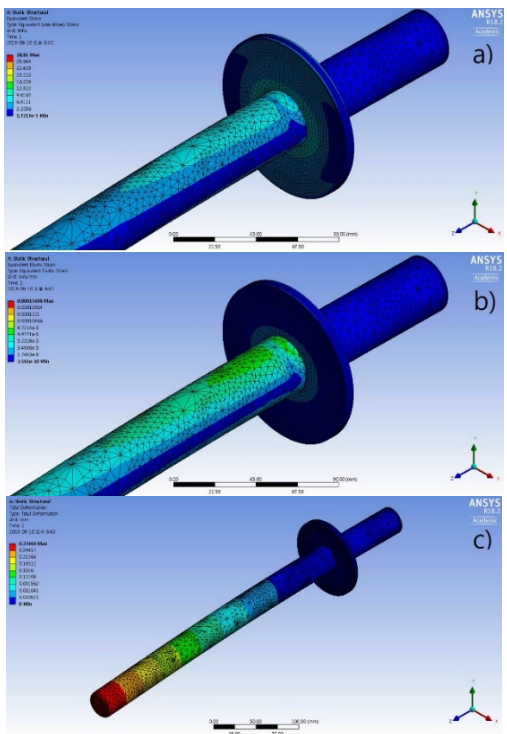


Figure 10: a) Stress, b) Strain, and c) Deformation of inner conductor and ceramic window.

The estimated stresses on the antenna (OFHC, $\sigma_{yield} = 33.3MPa$) and the window (99.7%-alumina, t = 6 mm, $\sigma_{yield} = 2350MPa$) are under than yield strength of the materials. [5]

The modal analysis was performed to avoid the vibration modes due to ground vibrations and harmonics of the AC electric power frequency. The fixed point is same as previous analyses. Figure 11 shows the four vibrational modes of the inner conductor connected with the ceramic window. The resonance frequency modes of the power coupler antenna are listed in table 3. [6]

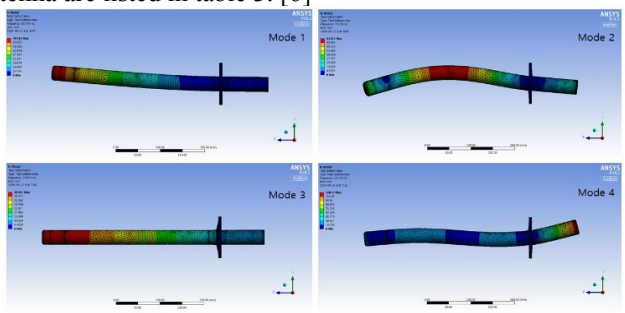


Figure 11: Four resonance modes of antenna.

Table 3: Resonance Mode Frequency of the Antenna

Mode	Frequency [Hz]
Mode 1	80.8
Mode 2	713.6
Mode 3	1349.9
Mode 4	1515.9

The modes 2 and 4 are close to the harmonics of 60Hz, so we need to avoid those frequencies by changing the geometry of antenna inner part.

CONCLUSION

We studied preliminary designs of the 325-MHz input coupler prototype for proton/heavy-ion superconducting cavities. The prototype will be fabricated and low-power tested in near future. Through such experiences, an upgraded version including a cooling scheme will be designed and fabricated.

REFERENCES

[1] Chang Kyu Sung *et al.,* "Development on RF Conditioning System of RF Coupler for Heavy Ion Accelerator, Masters Dissertation, Dept. of Accelerator Science, Korea University, Sejong, Korea. 2016

[2] CST, http://www.CST.com

[3] Ansys, http://www.ansys.com

[4] S.V. Kutsaev *et al*, "Design of RF power coupler for superconducting cavities", *Journal of Instrumentation,* vol. 7, p.11004, Nov. 2012, doi:10.1088/JINST/7/11/P11004

[5] Material properties, http://www.matweb.com

[6] Ilkyoung Shin *et al*, "Design of QWR Power Coupler for the Rare Isotope Science Project in Korea", in *proc. SRF2015,* Whistler, Canada, Sep. 2015, paper THPB082, pp. 1326-1329

Content from this work may be used under the terms of the CC BY 3.0 licence (© 2018). Any distribution of this work must maintain attribution to the author(s), title of the work, publisher, and DOI.

ISBN: 978-3-95450-194-6 ISSN: 2226-0366 doi:10.18429/JACoW-LINAC2018-TUPO053

FABICATION OF Nb MUSHROOM SHAPED CAVITY FOR EVALUATION OF MULTI-LAYER THIN FILM SUPERCONDUCTOR

H. Oikawa†, Utsunomiya University, Utsunomiya Tochigi, Japan
T. Higashiguchi, Center for Optical Research and Education, Utsunomiya, Japan
H. Hayano, H. Inoue, K. Enami, KEK, Tsukuba Ibaraki, Japan

Abstract

The accelerating gradient of the Nb superconducting RF cavity seems to reach the limit due to the RF critical magnetic field of the Nb material. To obtain higher gradient, there has been proposed a method of increasing an RF critical magnetic field of the cavity inner surface by coating of multi-layer thin-film superconductor. It is needed to demonstrate improvement critical magnetic field of the RF cavity coated with multi-layer thin-film superconductor. To optimize thin-film superconductor, sample tests are required. A cavity for sample test is necessary to produce a strong RF magnetic field parallel to the surface of the sample for evaluating RF critical magnetic field. For such a cavity, we designed a mushroom shaped cavity made of Nb which is operated in cryogenic temperature. Input and pick up antenna coupler are also designed electrically and mechanically. The connection design of sample plate and cavity bottom plate in superconducting state is also designed. The Nb mushroom shaped cavity is under fabrication. Fabrication method and status are reported in this paper.

INTRODUCTION

A technique of improving the Q value and acceleration electric field of the cavity by adding a small amount of nitrogen at the time of annealing and by using a method of improving the critical magnetic field leading to a high acceleration electric field by stacking superconducting layers are developing for high performance of the superconducting cavity made of Niobium (Nb) [1, 2]. Those methods improve greatly RF loss and acceleration electric field. In order to optimize each parameter and thin film of the surface treatment, it is necessary to evaluate them repeatedly for manufacturing a cavity having such high performance. However, many cavity evaluations are large-scaled, so that a device for evaluating a test piece subjected to the same treatment is required. Particularly, in the technique using a multilayer thin film structure, it is difficult to form a uniform film from the complicated shape of the cavity and its size. Further, in order to optimize the film forming process, it is necessary to perform film formation many times. Therefore, evaluation with a test piece is desired so that it is smaller than the cavity and easy to form a film, and it is easy to form many times. In this report, in order to evaluate the performance of test piece of multilayer thin film superconductors for superconducting cavity, we report on the design and fabrication of cavities for measuring critical magnetic field at cryogenic temperature.

† oikawah@post.kek.jp

DESIGN, FABRICATION AND EVALUATION OF TEST AL CAVITY

Design and Fabrication of Al Mushroom Shaped Cavity

In evaluating the multi-layer thin-film superconductor for the superconducting cavity, we considered that the following physical quantity evaluation is necessary.

- Superconducting transition temperature (Tc).
- RF surface resistance (Rs).
- critical magnetic field (Hc).

As a device for evaluating these physical quantities, we considered to use a cavity resonator that can replace the test piece repeatedly. This is because excitation of a strong electromagnetic field is possible, the above physical quantity can be measured all at once and it is thought that evaluation of many test pieces becomes easy.

First we started the design with SLAC's 11.4 GHz cavity [3]. The resonance frequency was chosen to 5.2 GHz

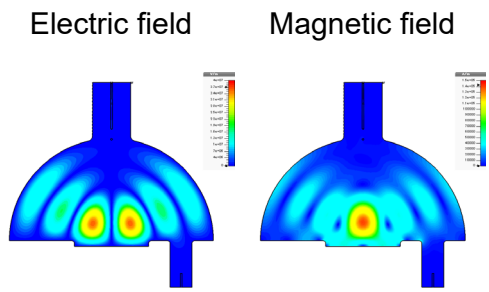


Figure 1: Calculated electromagnetic field in the mushroom-shaped cavity.

and the resonance mode was also chosen to TE_{013}.

Figure 1 shows the electromagnetic field excited in the designed cavity calculated by CST MW STUDIO [4]. As an initial step toward the fabrication of a Nb superconducting cavity, an Al-based cavity was proposed to evaluate the target resonant frequency, the separations of neighboring modes, and the electromagnetic field distribution of the target mode. Figure 2 shows the cross sectional drawing of the aluminum test cavity.

Evaluation of Al Mushroom Shaped Cavity

Figure 3 shows the frequency displacement during bead-pull measurement when a small metal cylinder is inserted into the test cavity and swept. Frequency shift calculated by CST MW STUDIO using perfect conductor cylinder is also inserted. Although there is a difference in frequency deviation along the sweep direction due to the cavity loss and the coupling of the antennas. Since the

Content from this work may be used under the terms of the CC BY 3.0 licence (© 2018). Any distribution of this work must maintain attribution to the author(s), title of the work, publisher, and DOI.

ISBN: 978-3-95450-194-6 ISSN: 2226-0366 doi:10.18429/JACoW-LINAC2018-TUPO053

frequency deviation shapes are similar, it can be evaluated that the excited electromagnetic field distribution is similar the calculated electromagnetic field distribution. Based on these results, we fixed the design of the inner space and the mechanical design of the Nb based cavity was started.

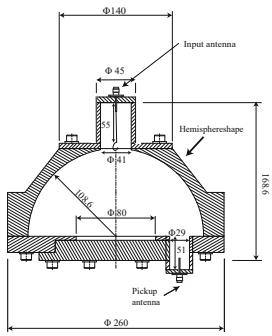


Figure 2: Cross-sectional drawing and picture of the Al test mushroom-shaped cavity.

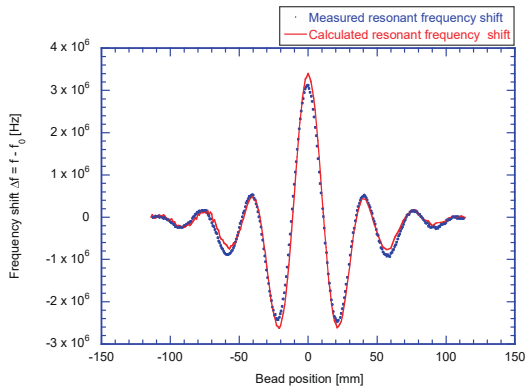


Figure 3: Comparison of bead-pull frequency shift between bead-pull measurement (orange) and CST calculation (blue), at 5.261GHz mode.

DESIGN OF NB BASED MUSHROOM SHAPED CAVITY

Mechanical Design of Cavity

Figure 4 is a design drawing of the mushroom shaped cavity made of Nb. In order to achieve a high Q value, the entire cavity needs to transition to a superconducting state. Therefore, the cavity is made of Nb and the connection flange is made of NbTi. Since the hemispherical part of the cavity is manufactured by press method, it was designed to be 2.8 mm thick like the TESLA type superconducting cavity. The sample part of the bottom plate is planned to be vacuum sealed with Nb gasket or indium seal. Aluminum metal seal is used for the antenna port flange and the vacuum evacuation port flange like the TESLA type superconducting cavity. The input antenna for cavity excitation was shaped like a hook and designed to couple with the internal magnetic field. We designed a pickup antenna inside bottom pickup port so that axial symmetry of the internal electromagnetic field is not disturbed as much as possible and 2 port measurement is possible.

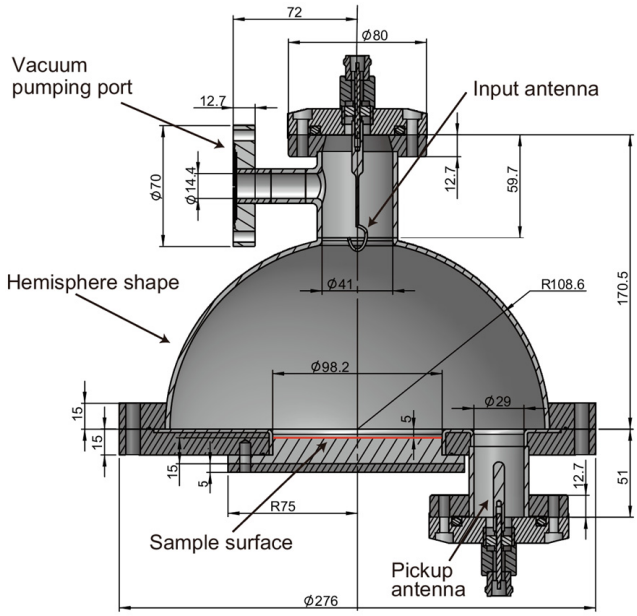


Figure 4: Cross sectional drawing of Nb-based mushroom-shaped cavity.

Vacuum Leak Test of Nb Gasket

The flange is used for exchanging the test piece. If the RF loss at the flange and the seal material is large, it causes a quench of the whole cavity. Therefore, Nb gasket or indium seal is to be used for the seal material of the flange connecting the test piece and the cavity. In order to evaluate Nb gasket, we fabricated a Nb gasket for ICF 70 flange and a vacuum flange with surface without touching edge, and conducted a vacuum sealing test.

Figure 5 shows the outline of the test. The test was conducted in the following two ways.

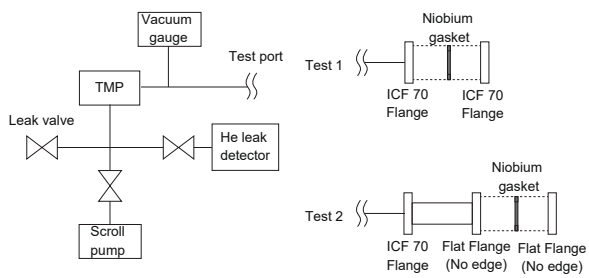


Figure 5: Leak test setup of Nb gasket and flat flange.

- Test 1: Leak test using helium leak detector after immersion in liquid nitrogen Nb gasket for ICF 70 flange with overall baking.
- Test 2: Leak test using helium leak detector after liquid nitrogen immersion face touch flange and Nb gasket with overall baking.

Content from this work may be used under the terms of the CC BY 3.0 licence (© 2018). Any distribution of this work must maintain attribution to the author(s), title of the work, publisher, and DOI.

ISBN: 978-3-95450-194-6 ISSN: 2226-0366 doi:10.18429/JACoW-LINAC2018-TUPO053

Content from this work may be used under the terms of the CC BY 3.0 licence (© 2018). Any distribution of this work must maintain attribution to the author(s), title of the work, publisher, and DOI.

In Test 1, there was no leak in the test at room temperature, but a leak occurred after immersion in liquid nitrogen. In Test 2, a leak at room temperature was occurred. For this reason, we plan to retest by using a vacuum annealed Nb gasket using the same flanges.

Press Fabrication Test of Half-Size Hemisphere Cell

Before manufacturing the actual cavity, the hemispherical part, which is not easy to shape in the press forming, was manufactured in half size. An oxygen free copper plate with a thickness of 3 mm was used as the material to be pressed, and an aluminum alloy was used for the press die. The shape of the pressed hemispherical part was compared between the design and the pressed one using a three-dimensional measurement system. Figure 6 shows the hemispherical part pressed and the result of shape measurement. The dashed line in red is the design value, and the solid line in black is the shape after press.

Evaluated region was set to the lower z region less than circle (X – X'), because the neck region is difficult to form in the miniature hemisphere cell. The maximum error of the hemisphere shapes along the dashed lines in Fig. 6 of a – a', b – b', c – c', and d – d' was measured to be 1 mm, as obtained from a comparison between the measurements (solid, black) and the designs (dashed, red) in Fig. 6. In addition, we measured the circle profiles at an equator (A – A') in Fig. 6. The maximum error was 30 μm. The required accuracy in the case of half-size hemisphere is within 1 mm, to keep the magnetic field ratio between sample surface and hemispherical surface larger than 2.

PLAN OF PERFORMANCE TEST OF NB MUSHROOM SHAPED CAVITY AT CRYOGENIC TEMPERATURE

Cavity Installation Method to Vertical Test Stand

In the KEK Superconducting RF Test Facility (STF), vertical cryostat was placed for superconducting cavity evaluation at 2 K cooled with liquid helium. In this existing measurement system, Nb made mushroom cavity for evaluation of multi-layer thin-film superconductor is placed and cryogenic test is planned. Figure 7 shows the outline. The measurement cavity is suspended from the cryostat top plate and immersed in liquid helium at the bottom of the cryostat. In addition, it is evacuated with an ion pump placed on the top plate, and a high vacuum of about 10 - 8 Pa is maintained during measurement.

Power Test

In order to evaluate the RF characteristics of the cavity cooled to 2 K, RF power of about 1 W is input using a network analyzer. The Q value of the cavity and the coupling of each antenna are evaluated and compared with the design value.

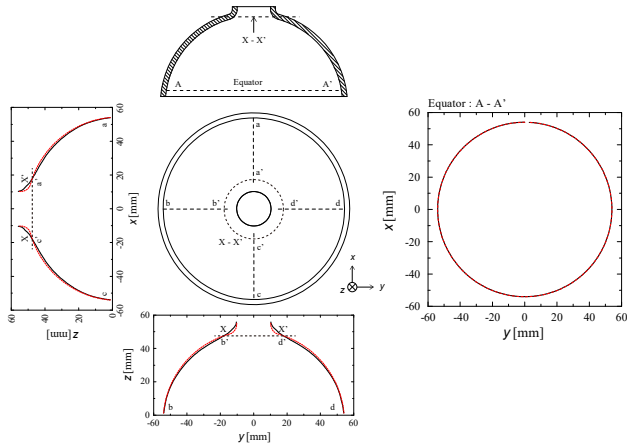


Figure 6: Comparison of press forming shape between design and 3D measurement. Red line is designed line, black line is 3D measurement.

Moreover, in order to realize superconducting quench or magnetic flux penetration of multi-layer thin-film superconductor, we plan to input electric power of about 50 W at maximum.

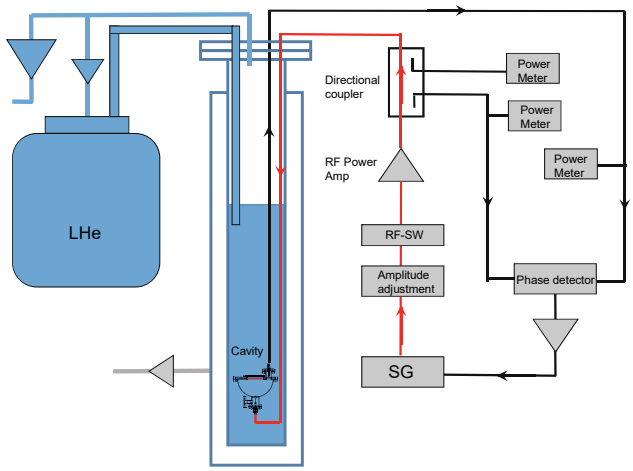


Figure 7: Vertical test setup of mushroom-shaped cavity.

CONCLUSION

We construct and evaluate test cavity for critical magnetic field evaluation of multi-layer thin-film superconductor. We fabricated Al test cavity and confirmed electromagnetic field distribution by bead-pull perturbation measurement with disturbed by antenna shape and insertion length.

We design Nb based cavity based on Al test cavity design. Press test of half size hemisphere cell was performed and confirmed error within design value.

We also test Nb gasket for sample flange sealing. Leak was occurred. Further study is necessary.

ACKNOWLEDGEMENTS

Part of this work was performed under the support of a JSPS KAKENHI (Grants-in-Aid for Scientific Research) Grant-in-Aid for JSPS Fellows, Grant Number 17J09072, Japan.

ISBN: 978-3-95450-194-6 ISSN: 2226-0366 doi:10.18429/JACoW-LINAC2018-TUPO053

REFERENCES

[1] A. Gurevich, *Appl. Phys. Lett.* **88**, 012511 (2006).

[2] A. Grassellino *et al.*, *Supercond. Sci. Technol.* vol. 26, pp. 102001, 2013.

[3] S. G. Tantawi *et al.,* "Superconducting Materials Testing with a High-Q Copper RF Cavity", http://www.slac.stanford.edu/cgiwrap/getdoc/slac-pub-12957.pdf

[4] https://www.cst.com/Products/CSTMWS

Content from this work may be used under the terms of the CC BY 3.0 licence (© 2018). Any distribution of this work must maintain attribution to the author(s), title of the work, publisher, and DOI.

ISBN: 978-3-95450-194-6 ISSN: 2226-0366 doi:10.18429/JACoW-LINAC2018-TUPO054

FUNDAMENTAL STUDIES OF IMPURITY DOPING IN 1.3 GHz AND HIGHER FREQUENCY SRF CAVITIES*

J. T. Maniscalco†, P. N. Koufalis, and M. Liepe
CLASSE, Cornell University, Ithaca, NY 14853, USA

Abstract

As the demand for more powerful, more efficient, and smaller superconducting RF accelerators continues to increase, both impurity doping and high-frequency cavities (>1.3 GHz) have become hot topics for fundamental research because of their potential to significantly decrease surface losses and cost respectively. In this report, we present recent experimental and theoretical results on undoped and nitrogen-doped high-frequency cavities and on alternative doping agents in traditional 1.3 GHz cavities, with a focus on understanding the fundamental science of impurity doping.

"2/6 DOPING" AT 2.6 GHz

Impurity doping is a technique for preparing niobium superconducting radio-frequency (SRF) cavities that can increase the quality factor Q by a factor of two or more at low field and cause an "anti-Q-slope" in which Q rises as the cavity field increases [1–3]. This Q rise has been shown to increase in strength with increasing frequency [4]. At IPAC'18, we presented Cornell's first results of an impurity-doped 2.6 GHz niobium cavity [5, 6]. This ILC/TESLA-shape cavity [7] (B_{pk}/E_{acc} = 4.28 mT/(MV/m)) was treated with the so-called "2/6 doping": a degas step in vacuum for 5 hours, followed by an injection of 40 mTorr (6 Pa) of continuously flowing N_2 gas for 2 minutes, followed by a vacuum anneal step for 6 minutes, all at 800 °C. This is followed by 6 µm of surface removal by vertical electropolish (VEP). In the initial test, the cavity showed a strong field-dependent reduction in the temperature-dependent "BCS" portion of the surface resistance.

In this paper, we present the results of additional study of this cavity, investigating the sensitivity of the temperature-independent "residual" surface resistance R_0 to trapped magnetic flux. This sensitivity has been studied extensively in 1.3 GHz nitrogen-doped cavities, where strongly doped cavities (electron mean free path $\ell < 100$ nm) exhibit up to 5 nΩ of residual resistance per mG of magnetic flux trapped during cooldown [3, 8]. To determine this sensitivity, we record R_0 as a function of field for several different amounts of trapped flux $B_{trapped}$ and subtract the non-flux-dependent R_0 present in a cooldown with no flux trapped (typically a "fast" cooldown with a cross-cavity temperature gradient $\nabla T > 200$ K/m). We then take $R_0/B_{trapped}$ and perform a linear fit over the RF field strength to yield an overall offset sensitivity as well as a field-dependent sensitivity. Previous analyses of 1.3 GHz N-doped cavities largely considered only the offset parameter, *e.g.* the 5 nΩ/mG figure above; analyses of 1.3 GHz Nb_3Sn cavities have included similar two-parameter linear fits [9].

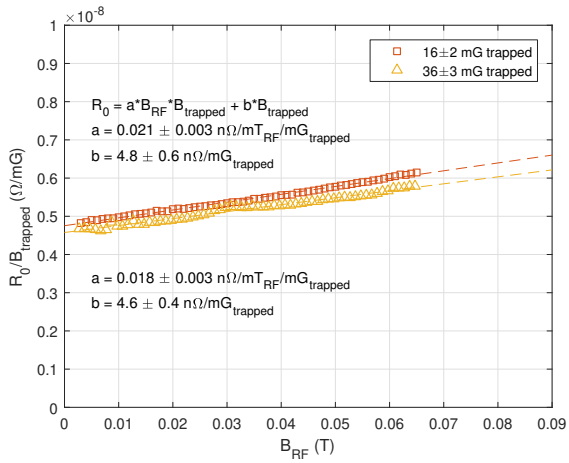


Figure 1: Sensitivity of the residual resistance due to trapped magnetic flux for two cooldowns of a single 2/6-doped 2.6 GHz niobium cavity.

Figure 1 shows these results for two cooldowns of the 2/6-doped 2.6 GHz cavity, which had an $\ell = 46$ nm. The linear fit parameters for both tests (with 16 ± 2 mG and 36 ± 3 mG trapped, respectively) were consistent within uncertainty. Averaging the results yields a sensitivity of $R_0 = aB_{RF}B_{trapped} + bB_{trapped}$ with $a = 0.020 \pm 0.003$ nΩ/mT$_{RF}$/mG$_{trapped}$ and $b = 4.7 \pm 0.5$ nΩ/mG$_{trapped}$.

The offset sensitivity b here is approximately two times larger than the sensitivity we reported at 1.3 GHz for cavities with similar ℓ; in the previously reported model [8], a 1.3 GHz cavity with $\ell = 46$ nm would have sensitivity $b = 2.4$ nΩ/mG$_{trapped}$. This indicates a linear scaling of this effect in 2/6-doped cavities with frequency $b \propto \omega$; other doping protocols may give different scaling. See also [10] for discussion of possible scaling mechanisms.

160 °C "N-INFUSION" AT 2.6 GHz

We also prepared a 2.6 GHz ILC-shape cavity with the "low-temperature dope" or "nitrogen-infusion" procedure, which consists of an 800 °C degas step followed by a ramp down to 160 °C and a 48-hour doping step with 40 mTorr (6 Pa) of continuously flowing N_2 gas. The cavity received no chemical treatment after doping. At 1.3 GHz, this treat-

* This work was supported in part by the U.S. National Science Foundation under Award PHY-1549132, the Center for Bright Beams, and under Award PHY-1734189. This work was also supported by the U.S. Department of Energy and the LCLS-II HE Project.
† jtm288@cornell.edu

Content from this work may be used under the terms of the CC BY 3.0 licence (© 2018). Any distribution of this work must maintain attribution to the author(s), title of the work, publisher, and DOI.

ISBN: 978-3-95450-194-6 ISSN: 2226-0366 doi:10.18429/JACoW-LINAC2018-TUPO054

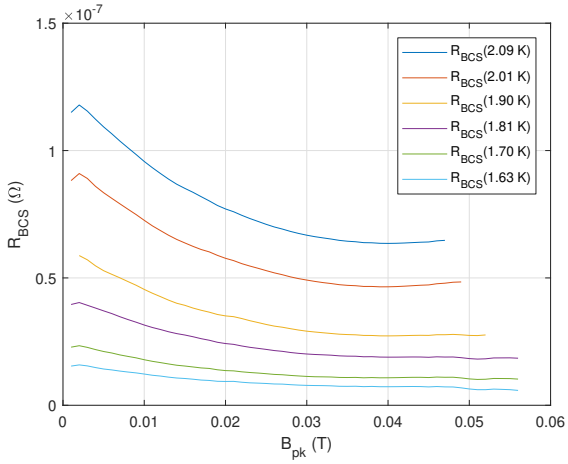


Figure 2: BCS surface resistance of the 2.6 GHz 160 °C-doped cavity.

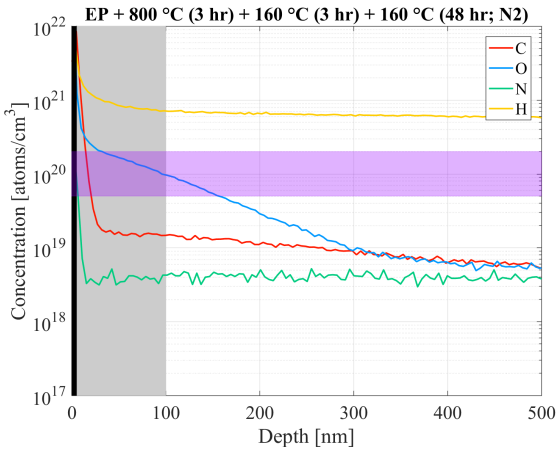


Figure 3: Results of SIMS analysis for a witness sample baked with the 1.3 GHz and 2.6 GHz cavities treated with the 48 hr 160 °C dope. The black line indicates the 5 nm oxide layer at the surface, the gray bar indicates the approximate RF penetration region of 100 nm, and the purple bar indicates the typical nitrogen concentration of a 2/6-doped cavity.

ment has been shown to give results similar to the 800 °C N-dope [11, 12].

Under RF testing, this cavity performed with a strong anti-Q-slope at all temperatures below 2.17 K. Analysis yielded an electron mean free path ℓ of 2.8 nm and a critical temperature of 9.2 K. There was also a high R_0, with a low-field minimum of 18 nΩ rising to 32 nΩ at B_{pk} = 55 mT, possibly due to a furnace contamination issue. Figure 2 shows the field-dependent BCS surface resistance for the cavity, which exhibits a drop of approximately 50% from low field to a minimum near 40 mT. This drop is similar in magnitude to our previous observations for 160 °C-doped 1.3 GHz cavities, both with N_2 gas [12, 13] and with a CO_2 gas mixture in an Ar carrier [5, 14], but more dramatic in slope; tests at 1.3 GHz showed the minimum in BCS resistance to be at 60 mT or higher field.

As with the 2/6-doped 2.6 GHz cavity [5], this slope is steeper than can be predicted by the Gurevich theory of the anti-Q-slope which has produced successful fits for many high- and low-T doped cavities at 1.3 GHz [3, 5, 15]. Moreover, the slope is steeper than that of the 2/6-doped 2.6 GHz cavity; qualitatively, this stronger slope in resistance for this cavity compared with the high-temperature-doped cavity with longer ℓ is consistent with observations at 1.3 GHz, serving as further evidence that cavities with shorter ℓ show stronger anti-Q-slope.

This test result also provides insight into the continuing discussion of the significance of impurity species in the low-T bakes [14]. Figure 3 shows the result of secondary ion mass spectrometry (SIMS) measurements of atomic concentration of impurities in a witness sample baked alongside the 2.6 GHz cavity during the 48-hour 160 °C bake. Similar to our previous report, there is very little N in the material, except for a low concentration < 10^{20} at/cc in the first 10 nm; on the other hand, there is a significant amount of C and O through the RF penetration layer, possibly from impurities in the N_2 gas supply. As in our previous report, this indicates that the C and O impurities are responsible for the short ℓ of the cavity. Further, because the short ℓ correlates with stronger anti-Q-slope, this serves as more evidence for the suggestion that C and O impurities, rather than N, are responsible for the anti-Q-slope in the 160 °C-doped cavities.

160 °C "N-INFUSION" AT 1.3 GHz

In research efforts for the LCLS-II HE upgrade, we have tested several 1.3 GHz cavities with variations of the 160 °C doping treatment. Here we report on three recent tests: a 2-day doping (baked alongside the 2.6 GHz cavity discussed above), a 4-day doping, and the 4-day doping followed by approximately 5 nm surface removal by hydrofluoric acid (HF) rinse.

Figure 4 shows the BCS surface resistance of the 1.3 GHz cavity doped at 160 °C for 48 hours; Fig. 5 shows the same for the 96-hour dope. For both these cavities, unlike in the case of the 2.6 GHz cavity, RF test results did not show a strong anti-Q-slope. Instead, the BCS resistance showed a general field-dependent rise with a small region of decreasing resistance approximately 20 mT < B_{pk} < 40 mT. These cavities also showed high residual resistance, $R_0 \sim 15$ nΩ, which may indicate titanium contamination from the NbTi flanges of these cavities or other furnace contamination, as in the 2.6 GHz 160 °C-doped cavity above.

Fortunately, the third cavity test discussed in this study yielded more positive results, shown in Fig. 6 along with theoretical fits (discussed below). After a ~ 5 nm removal by HF rinse, the cavity performed with a strong anti-Q-slope, reaching a minimum resistance near B_{pk} = 60 mT. The low-field peak in BCS resistance was slightly lower, by ~ 10%, and the residual resistance was lower than in the test before the HF rinse by a factor of 2.

Content from this work may be used under the terms of the CC BY 3.0 licence (© 2018). Any distribution of this work must maintain attribution to the author(s), title of the work, publisher, and DOI.

ISBN: 978-3-95450-194-6 ISSN: 2226-0366 doi:10.18429/JACoW-LINAC2018-TUPO054

Content from this work may be used under the terms of the CC BY 3.0 licence (© 2018). Any distribution of this work must maintain attribution to the author(s), title of the work, publisher, and DOI.

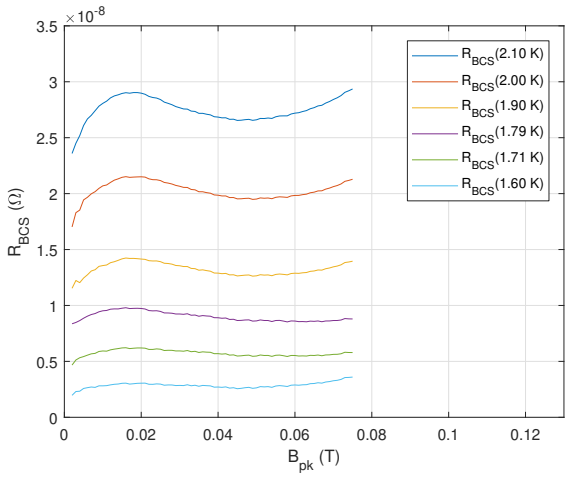


Figure 4: BCS surface resistance of the 1.3 GHz 48-hr 160 °C-doped cavity, with ℓ = 5.3 nm.

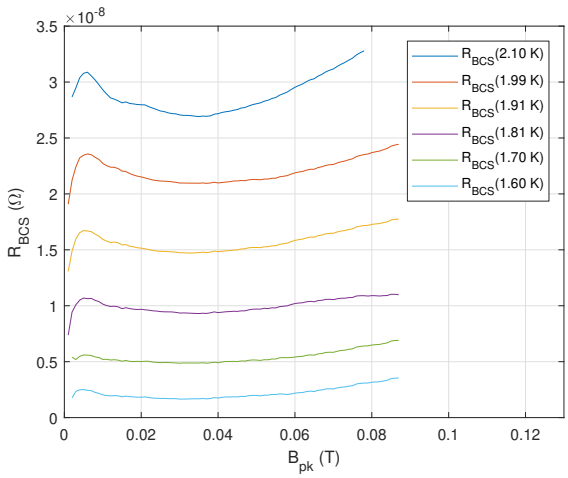


Figure 5: BCS surface resistance of the 1.3 GHz 96-hr 160 °C-doped cavity, with ℓ = 1.9 nm.

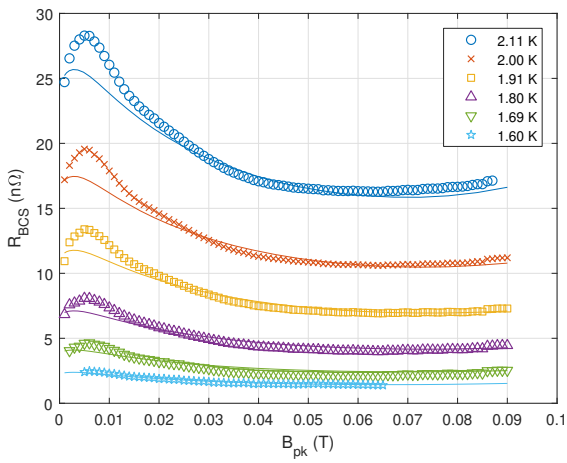


Figure 6: BCS surface resistance of the 1.3 GHz 96-hr 160 °C-doped cavity followed by ~ 5 nm HF rinse, as well as theoretical fit results, with ℓ = 1.7 nm.

Using a recently improved version of our model [3] implementing the Gurevich anti-Q-slope theory [15], which now considers depth-dependent material properties, includes a model of heat transport away from the RF surface and into the liquid helium bath, and treats the quasiparticles as in thermal equilibrium through the RF layer, we have fitted these cavity test data. These fits are shown in Fig. 6. In general, the fit shows good agreement with experiment, except for a "bump" of higher resistance with peak at $B_{\mathrm{pk}} \sim 5$ mT. This bump is also present in the test before the HF rinse.

Because of the thermal equilibrium in the updated model, the fit parameter is not directly comparable to the parameters from previous fits, but the very low level of quasiparticle overheating and strong anti-Q-slope are consistent with previous tests and fits of 160 °C-doped cavities and 800 – 1000 °C-doped cavities with mean free path < 10 nm [3, 5].

These initial results show promise for the 160 °C doping treatment. Though it appears that the treatment is susceptible to surface contamination from the furnace or otherwise, HF rinsing seems to alleviate the high residual resistance and restore the anti-Q-slope in cases of mild contamination. This bodes well for the treatment's potential for future accelerators such as the LCLS-II HE upgrade, especially in terms of re-treatment of cavities: the gentle baking recipe and simple electrolyte-free chemistry can be performed on cavities without removing the welded helium jacket, greatly simplifying re-treatment procedures.

This still leaves the question of what specifically causes the difference in performance between the results in Figs. 5 and 6. The fact that the HF rinse removes only the first several nm suggests that it indeed is a light surface contamination, either present in the ~ 5 nm oxide layer or the first few nm of the Nb surface. For these two cavities, it is possible that the contamination comes from titanium from the NbTi flanges, as mentioned above. In this case, production accelerator cavities using the popular NbTi flanges with diamond-profile aluminum gaskets may suffer from similar contamination in the case of flanges which outgas Ti significantly. Thankfully, HF rinsing may offer a "cure" for such contamination, as indicated by our initial results here. Further study will be required to understand the source and nature of this occasional reduced performance for 160 °C-doped cavities.

CONCLUSIONS

We have studied flux trapping sensitivity in a 2.6 GHz 2/6-doped cavity, finding a sensitivity twice that of 1.3 GHz cavities with the same electron mean free path. We have studied the 160 °C doping at 2.6 GHz, finding a drop in resistance of comparable magnitude and steeper slope than that at 1.3 GHz. SIMS analysis indicates that C and O impurities caused the anti-Q-slope in this cavity. We also studied 160 °C doping at 1.3 GHz, finding poor performance from possible surface contamination, and finding that HF rinsing "cured" the poor performance of one cavity and restored a strong anti-Q-slope.

ISBN: 978-3-95450-194-6 ISSN: 2226-0366 doi:10.18429/JACoW-LINAC2018-TUPO054

REFERENCES

[1] A. Grassellino, A. Romanenko, D. Sergatskov, O. Melnychuk, Y. Trenikhina, A. Crawford, A. Rowe, M. Wong, T. Khabiboulline, and F. Barkov. Nitrogen and argon doping of niobium for superconducting radio frequency cavities: a pathway to highly efficient accelerating structures. *Superconductor Science and Technology*, 26(10):102001, 2013.

[2] P. Dhakal, G. Ciovati, G. R. Myneni, K. E. Gray, N. Groll, P. Maheshwari, D. M. McRae, R. Pike, T. Proslier, F. Stevie, R. P. Walsh, Q. Yang, and J. Zasadzinzki. Effect of high temperature heat treatments on the quality factor of a large-grain superconducting radio-frequency niobium cavity. *Phys. Rev. ST Accel. Beams*, 16:042001, Apr 2013.

[3] J. T. Maniscalco, D. Gonnella, and M. Liepe. The importance of the electron mean free path for superconducting radio-frequency cavities. *Journal of Applied Physics*, 121(4):043910, 2017.

[4] M. Martinello, S. Aderhold, S.K. Chandrasekaran, M. Checchin, A. Grassellino, O. Melnychuk, S. Posen, A. Romanenko, and D.A. Sergatskov. Advancement in the understanding of the field and frequency dependent microwave surface resistance of niobium. In *Proceedings of SRF2017, Lanzhou, China*, pages 364–267, 2017.

[5] J. T. Maniscalco, P. N. Koufalis, and M. Liepe. Modeling of the frequency and field dependence of the surface resistance of impurity-doped niobium. In *Proceedings of IPAC2018, Vancouver, Canada*, pages 2471–2474, 2018.

[6] P. N Koufalis, M. Liepe, J. T. Maniscalco, and T. Oseroff. Experimental results on the field and frequency dependence of the surface resistance of niobium cavities. In *Proceedings of IPAC2018, Vancouver, Canada*, pages 2451–2454, 2018.

[7] B. Aune, R. Bandelmann, D. Bloess, B. Bonin, A. Bosotti, M. Champion, C. Crawford, G. Deppe, B. Dwersteg, D. A. Edwards, H. T. Edwards, M. Ferrario, M. Fouaidy, P.-D. Gall, A. Gamp, A. Gössel, J. Graber, D. Hubert, M. Hüning, M. Juillard, T. Junquera, H. Kaiser, G. Kreps, M. Kuchnir, R. Lange, M. Leenen, M. Liepe, L. Lilje, A. Matheisen, W.-D. Möller, A. Mosnier, H. Padamsee, C. Pagani, M. Pekeler, H.-B. Peters, O. Peters, D. Proch, K. Rehlich, D. Reschke, H. Safa, T. Schilcher, P. Schmüser, J. Sekutowicz, S. Simrock, W. Singer, M. Tigner, D. Trines, K. Twarowski, G. Weichert, J. Weisend, J. Wojtkiewicz, S. Wolff, and K. Zapfe. Superconducting TESLA cavities. *Phys. Rev. ST Accel. Beams*, 3:092001, Sep 2000.

[8] D. Gonnella, J. Kaufman, and M. Liepe. Impact of nitrogen doping of niobium superconducting cavities on the sensitivity of surface resistance to trapped magnetic flux. *Journal of Applied Physics*, 119(7), 2016.

[9] D.L. Hall, M. Liepe, and R. Porter. Field-dependence of the sensitivity to trapped flux in Nb_3Sn. In *Proceedings of SRF2017, Lanzhou, China*, pages 844–847, 2017.

[10] M. Checchin, M. Martinello, A. Grassellino, S. Aderhold, S. K. Chandrasekaran, O. S. Melnychuk, S. E. Posen, A. Romanenko, and D. A. Sergatskov. Frequency dependence of trapped flux sensitivity in SRF cavities. *Applied Physics Letters*, 2017.

[11] A. Grassellino, A. Romanenko, Y. Trenikhina, M. Checchin, M. Martinello, O. S. Melnychuk, S. K. Chandrasekaran, D. A. Sergatskov, S. E. Posen, and A. C. Crawford. Unprecedented quality factors at accelerating gradients up to 45 MVm^{-1} in niobium superconducting resonators via low temperature nitrogen infusion. *Superconductor Science and Technology*, 2017.

[12] P. N. Koufalis, J. T. Maniscalco, and M. Liepe. Low temperature doping of niobium cavities: What is really going on? In *Proceedings of SRF2017, Lanzhou, China*, pages 353–358, 2017.

[13] P.N. Koufalis, F. Furuta, J.J. Kaufman, and M. Liepe. Impact of the duration of low temperature doping on superconducting cavity performance. In *Proceedings of SRF2017, Lanzhou, China*, pages 750–753, 2017.

[14] P.N. Koufalis and M. Liepe. Insights into the role of C, N, and O introduced by low temperature baking on niobium cavity performance. In *Proceedings of IPAC2018, Vancouver, Canada*, pages 2455–2457, 2018.

[15] A. Gurevich. Reduction of dissipative nonlinear conductivity of superconductors by static and microwave magnetic fields. *Phys. Rev. Lett.*, 113:087001, Aug 2014.

Content from this work may be used under the terms of the CC BY 3.0 licence (© 2018). Any distribution of this work must maintain attribution to the author(s), title of the work, publisher, and DOI.

ISBN: 978-3-95450-194-6 ISSN: 2226-0366 doi:10.18429/JACoW-LINAC2018-TUPO055

NEXT GENERATION Nb_3Sn CAVITIES FOR LINEAR ACCELERATORS*

R. D. Porter†, T. Arias, P. Cueva, D. L. Hall, M. Liepe, J. T. Maniscalco, D. A. Muller, N. Sitaraman
Cornell University, Ithaca, NY 14853, USA

Abstract

Niobium-3 Tin (Nb_3Sn) is a very promising alternative material for SRF accelerator cavities. The material can achieve higher quality factors, higher temperature operation and potentially higher accelerating gradients ($E_{acc} \approx 96\,MV/m$) compared to conventional niobium. This material is formed by vaporizing Sn in a high temperature vacuum furnace and letting the Sn absorb into a Nb substrate to form a 2-3 µm Nb_3Sn layer. Current Nb_3Sn cavities produced at Cornell achieve $Q \approx 2 \cdot 10^{10}$ at 4.2 K and $E_{acc} = 17\,MV/m$. Here we present a summary of the current performance of Nb_3Sn cavities at Cornell and recent progress in improving E_{acc}.

INTRODUCTION

Nb_3Sn possesses a high critical temperature (18 K [1]) and superheating field (425 mT [2]) giving it the potential for higher quality factors than Nb, 4.2 K operation, and for accelerating gradients of $\approx 96\,MV/m$. Cornell has a leading program in developing Nb_3Sn accelerator cavities [3–7]. Here we present the current status of the material and review recent progress. In particular we discuss the cause of the low (relative to the maximum possible for this material) quench fields and progress towards raising them.

Nb_3Sn GROWTH PROCESS

Nb_3Sn accelerator cavities cannot be pressed out of a Nb_3Sn sheet as can conventional Nb cavities due to the difficulty of making Nb_3Sn and its brittle nature. Instead, current Nb_3Sn cavity programs use Sn vapor deposition to grow Nb_3Sn on a Nb substrate that is already in the shape of a cavity [8]. In this process an Nb cavity is placed in a high temperature vacuum furnace with a crucible full of Sn and bowl of $SnCl_2$. After a $24 - 48$ hr degas step at 180 °C, the temperature is ramped to 530 °C, and held for 5 hrs while the nucleation agent, $SnCl_2$ vaporizes and decomposes on the Nb leaving behind Sn. The temperature is then raised to ≈ 1150 °C for coating where there is an appreciable Sn vapor pressure. Sn vapor lands on the surface of the cavity where it forms Nb_3Sn. To further increase the Sn vapor pressure the Sn crucible is heated to an even higher temperature. After 1.5 hrs at this temperature the crucible heating is turned off and the surface is allowed to anneal for 1 hr. This process forms a $2-3$ µm Nb_3Sn layer. Figure 1 shows the temperature profile for a Nb_3Sn coating run.

* This work is supported in part by the U.S. National Science Foundation under Award PHY-1549132, the Center for Bright Beams. This work is supported in part by U.S. DOE award DE-SC0008431. This work made use of the Cornell Center for Materials Research Shared Facilities which are supported through the NSF MRSEC program (DMR-1120296).
† rdp98@cornell.edu

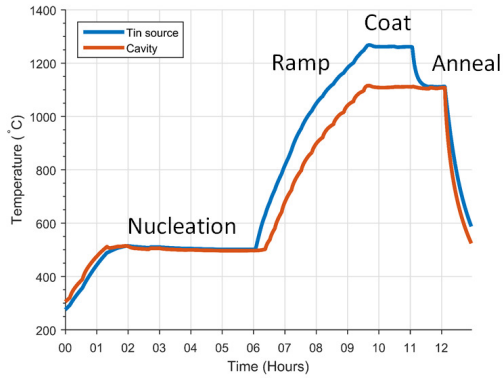


Figure 1: Temperature during Nb_3Sn coating showing both the cavity and the tin source temperatures.

CURRENT PERFORMANCE

Current performance offers transformational quality factors of $2 \cdot 10^{10}$ at 4.2 K and 1.3 GHz (see Fig. 2). This is more than a 20 times improvement in Q over Nb at 4.2 K, allowing 4.2 K operation. In CW operation our Nb_3Sn cavities currently quench around 17 MV/m, capable of meeting accelerator gradient requirement of some current CW LINACs. Pulsed operation (see Fig. 3) sees greater accelerating gradients of up to 26 MV/m [9]. These are usable accelerating gradients, but far below the theoretical maximum of 96 MV/m, giving Nb_3Sn a lot of room for improvement.

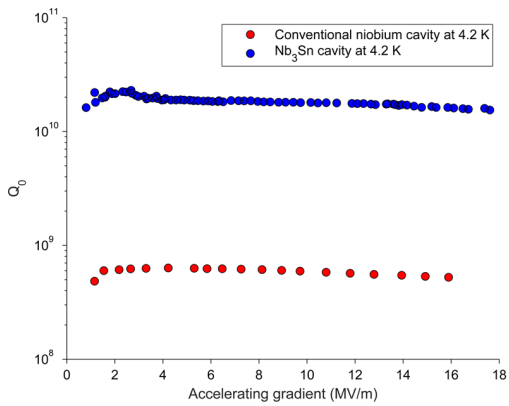


Figure 2: Q versus E performance of a Nb_3Sn cavity versus a Nb cavity at 4.2 K and 1.3 GHz.

THERMOMETRY OF DEFECT

Thermometry (temperature maps) reveal that quench are being caused by heating at some localized defect [10]. The key to raising the quench fields is removing the defect. This requires a firm understanding of what the defect is. To that end Cornell used time resolved thermometry of the quench

Content from this work may be used under the terms of the CC BY 3.0 licence (© 2018). Any distribution of this work must maintain attribution to the author(s), title of the work, publisher, and DOI.

ISBN: 978-3-95450-194-6 ISSN: 2226-0366 doi:10.18429/JACoW-LINAC2018-TUPO055

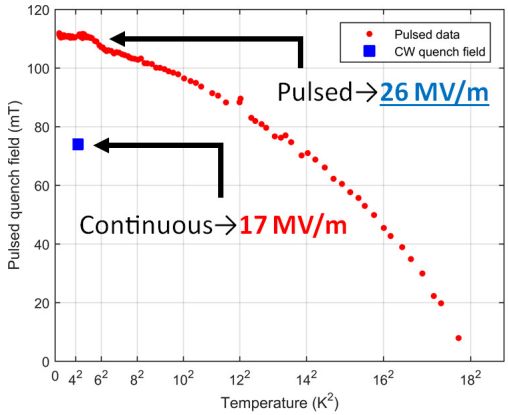


Figure 3: Pulsed quench field versus temperature squared with CW quench field at 4.2 K also shown. At 4.2 K the pulsed quench field reaches 26 MV/m.

site [11]. This revealed an interesting feature of the defect (see Fig. 4): at first when raising the electromagnetic field strength in the cavity the temperature increases with the field squared, as expected from Ohmic heating, but near the quench field there appear sudden jumps in temperature. These jumps appear to be quantized (multiples of the smallest jump). When the field is lowered again there are jumps back down but they occur at a lower field.

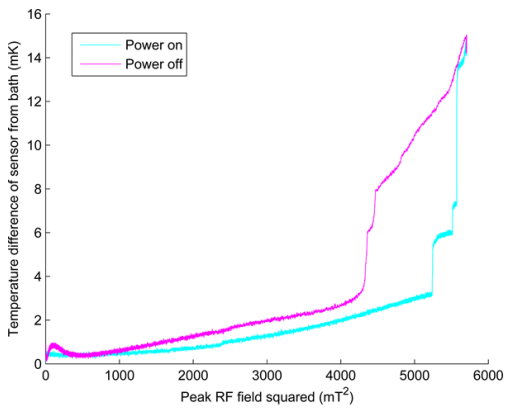


Figure 4: A plot showing the temperature rise of the defect (on the outside of the cavity) while the RF power is cycled and the maximum field is close to, but below, the quench field. Note the sudden jumps in temperature and the hysteresis between the rise and fall of the RF power.

The quantization, hysteresis, and some additional observations discussed in [4, 11] lead us to believe this is magnetic flux entry at a defect. A potential was proposed by Ahmad Sheikhzada and Alex Gurevich [12]. In this model a bad grain boundary could act like a Josephson junction and at critical fields permit quantized flux entry. It replicates many of the observed phenomena and we will be conducting further studies into the thermal properties of the defect to determine if it matches the theory.

SURFACE DEFECTS

In addition to thermal studies we have been using microscopy to look for surface defects that degrade performance or could cause quench. Two discovered defects are Sn depleted regions [10] and thin film regions [13].

Sn depleted Nb_3Sn has the correct crystal structure but with a lower atomic percentage of Sn (see Fig. 5). Sn depletion can heavily lower the critical temperature and possibly the superheating field (maximum possible quench field). These Sn depleted regions occur both on the surface and in the layer and seem to have different formation mechanisms. The surface Sn depleted regions seem to form when Nb_3Sn is annealed for too long. After all the free surface Sn is gone the layer will continue growing by stealing Sn from already formed Nb_3Sn, creating Sn depleted sites on the surface. So far, no surface sufficiently Sn depleted regions on the surface have been observed that could explain the current quench fields, but this may be because we can only look at a small fraction of the cavity surface and may not have seen particularly bad regions in the small sample. Sn depleted regions within the layer tend to have worse Sn depletion, but so far none have been observed near enough to the surface to impact performance. However, some may be closer to the surface and any chemical treatments to remove surface defects may expose this defect, necessitating removal/prevention. In the next section we will discuss a proposed method to prevent this defect.

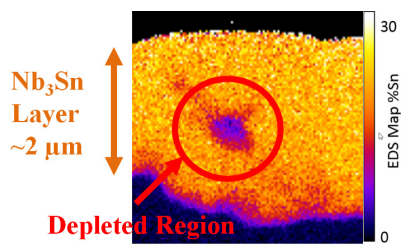


Figure 5: An EDS cross-section of a Nb_3Sn layer showing a tin depleted region within the Nb_3Sn layer.

In addition to Sn depletion, thin regions have been observed in the Nb_3Sn layer. These regions are a single crystal grain only a few hundred nm thick and large compared to the standard grain size. Figure 6 shows an EDS map of an Nb_3Sn surface where the thin regions are shown in red. This may not be thick enough to fully shield the RF field from the possibly highly lossy Nb-Nb_3Sn interface, decreasing Q. Great progress has been made on preventing this type of defect. It was found that growing a thick oxide on the surface (anodization) of the Nb substrate before coating could completely suppress this defect [13]. Studies into why anodization is effective are still on going.

LAYER GROWTH STUDIES AND GROWTH DYNAMICS

Once a defect is identified it must be removed or we must find a way to prevent the defect from forming to be-

Content from this work may be used under the terms of the CC BY 3.0 licence (© 2018). Any distribution of this work must maintain attribution to the author(s), title of the work, publisher, and DOI.

ISBN: 978-3-95450-194-6 ISSN: 2226-0366 doi:10.18429/JACoW-LINAC2018-TUPO055

Content from this work may be used under the terms of the CC BY 3.0 licence (© 2018). Any distribution of this work must maintain attribution to the author(s), title of the work, publisher, and DOI.

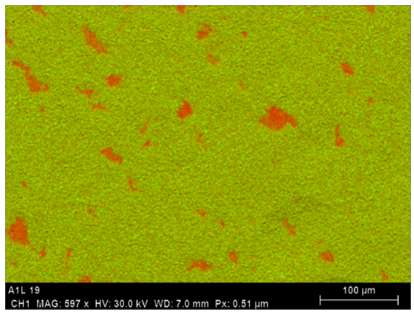


Figure 6: An EDS map of a Nb_3Sn surface. The regions in red are where the Nb_3Sn layer is thin and unable to shield the Nb from the RF field.

gin with. To prevent defects from forming we need a good understanding of how the Nb_3Sn grows. To accomplish this we have been conducting layer growth studies where the coating process is stopped at different points in the process (primarily while ramping up to the coating temperature of 1150 °C) [13]. These samples are then analyzed with microscopy.

False colored SEM scans are shown in Fig. 7 for various stopping temperatures and for substrates that were both anodized and with only the native oxide layer. After nucleation we can already see the difference between the two preparations, with the anodized surface having large droplets of Sn (red). At 800 °C we can see chunks of a Sn rich Nb-Sn compound of the surface (purple) surrounded by a thin layer of Nb_3Sn (green). These large Nb-Sn compounds undergo a phase transition to Nb_3Sn at 875 °C where purple is thick Nb_3Sn and green is thinner Nb_3Sn. Finally by 1120 °C we see more uniform Nb_3Sn, but the native oxide sample has formed a thin region highlighted in green.

The layer growth studies inform theoretical models based on Density Functional Theory that are being developed in collaboration with the Center for Bright Beams (CBB). Recently these models suggested a way to modify the growth process to prevent Sn depleted regions from forming in the layer [14]. In this model the Sn depleted regions form during a Sn-starved phase of the process when all the free Sn from nucleation is used before Sn the crucible gets hot enough to supply more (during the temperature ramp to the coating temperature). These sites can then get buried beneath enough Nb_3Sn that they can't get filled in once more Sn is available (Sn diffusion though Nb_3Sn is slow though bulk but fast through grain boundaries). A change was suggested of adding more $SnCl_2$ to prevent this from happening and is in the process of being tested.

CONCLUSION

Nb_3Sn is a promising material for future LINACs due to the high Q, 4.2 K operation, and high accelerating gradient limit. It currently offers high Q at 4.2 K and usable gradients. Great progress has been made in identifying and removing defects that limit E_{acc}. Many defect types have been identified such as thin film regions and Sn depleted

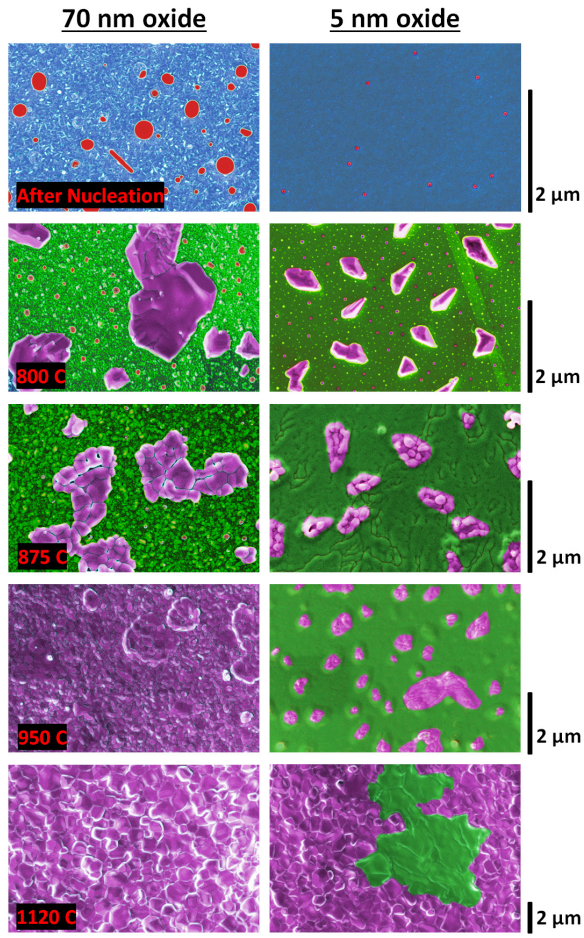


Figure 7: False colored SEM images of layer growth samples of Nb_3Sn terminated at various temperatures in the growth process (see Fig. 1). Two different preparations are shown: one with a 70 nm oxide (anodized) and one with the native oxide layer. The images have been false colored to highlight regions with different morphology. Not false colored SEM images published in [13].

regions. Collaboration in the Center for Bright Beams with microscopists and theorists, combined with layer growth samples has led to an increased understanding of our growth process and has already led to suggestions on how to prevent Sn depleted regions. Flux entry at grain boundaries has been identified as a key quench mechanism. Further work will be conducted to understand this defect and mitigate its effects on performance.

REFERENCES

[1] A. Godeke, "A review of the properties of Nb3Sn and their variation with A15 composition, morphology and strain state," *Superconductor Science and Technology*, vol. 19, no. 8, p. R68, Aug. 2006.

[2] G. Cetelani and J. P. Sethna, "Temperature Dependence of the Superheating Field for Superconductors in the high-kappa London Limit," *Phys. Rev. B*, vol. 78, 224509, 2008.

ISBN: 978-3-95450-194-6 ISSN: 2226-0366 doi:10.18429/JACoW-LINAC2018-TUPO055

[3] S. Posen, "Understanding and Overcoming Limitation Mechanisms in Nb3Sn Superconducting RF Cavities," Ph.D. dissertation, Cornell University, 2014.

[4] D. L. Hall, "New Insights into the Limitations on the Efficiency and Achievable Gradients in Nb3Sn SRF Cavities," Ph.D. dissertation, Cornell University, 2017.

[5] D. L. Hall, J. J. Kaufman, M. Liepe, R. D. Porter, and J. Sears, "First Results From New Single-Cell Nb3Sn Cavities Coated at Cornell University," in *Proc. of IPAC 2017*, Copenhagen, 2017.

[6] S. Posen and M. Liepe, "Advances in development of Nb3Sn superconducting radio-frequency cavities," *Phys. Rev. ST Accel. Beams*, vol. 15, 112001, 2014.

[7] S. Posen and D. L. Hall, "Nb3Sn Supercondcution Radiofrequency Cavities: Fabrication, Results, Properties, and Prospects," *Superconductor Science and Technology*, vol. 30, no. 3, p. 33004, 2017.

[8] S. Posen and D. L. Hall, "Nb3Sn Supercondcution Radiofrequency Cavities: Fabrication, Results, Properties, and Prospects," *Superconductor Science and Technology*, vol. 30, no. 3, p. 33004, 2017.

[9] D. L. Hall, M. Liepe, and J. Maniscalco, "RF Measurements on High Performance Nb3Sn Cavities," in *Proc. of IPAC 2016*, Busan, May 2017.

[10] D. L. Hall, J. J. Kaufman, M. Liepe, J. T. Maniscalvo, and R. Porter, "High Performance Next-Generation Nb3Sn Cavities for Future High Efficiency SRF LINACs," in *Proc. of LINAC 2016*, East Lansing, Michigan, Sept 2016.

[11] D. L. Hall *et. al.*, "Cavity Quench Studies in Nb3Sn using Temperature Mapping and surface Analysis of Cavity Cut-Outs," in *Proc. of SRF 2017*, Lanzhou, China, July 2017.

[12] A/ Sheikhzada and A. Gurevich, "Dynamic transition of vortices into phase slips and generation of vortex-antivortex pairs in thin film Josephson junctions under dc and ac currents," in *Phys. Rev. B*, vol. 95, 214507, 2017.

[13] D. L. Hall *et. al.*, "High Performance Nb3Sn Cavities," in *Proc. of SRF 2017*, Lanzhou, China, July 2017.

[14] R. Porter *et. al.*, "Update on Nb3Sn Progress at Cornell University," in *Proc. of IPAC 2018*, Vancouver, Canada, 2018.

Content from this work may be used under the terms of the CC BY 3.0 licence (© 2018). Any distribution of this work must maintain attribution to the author(s), title of the work, publisher, and DOI.

ISBN: 978-3-95450-194-6 ISSN: 2226-0366 doi:10.18429/JACoW-LINAC2018-TUPO057

LOW-TEMPERATURE BAKING AND INFUSION STUDIES FOR HIGH-GRADIENT ILC SRF CAVITIES*

M. Ge†, P. Koufalis, G. Kulina, M. Liepe, J. Maniscalco,
CLASSE, Cornell University, Ithaca, New York, USA

Abstract

Low-temperature infusion has become a hot-topic in SRF researches recently. Past results show that low-temperature infusion can produce high quality factor at medium accelerating fields. Also, 75ºC baking recently has been shown to improve accelerating gradients of SRF cavities. Hence these treatments are very promising for reducing cost of the ILC. In this work, we present latest results of low temperature infusion and baking, showing that these treatments can improve SRF cavities performance.

INTRODUCTION

The proposed International Linear Collider (ILC) is a proposed 200-500GeV linear electron-positron collider, based on 1.3GHz superconducting radio-frequency (SRF) technology [1]. The total cost of the ILC is an important constraint, determining whether the project is feasible or not. As the main part of the linear collider consist of SRF cryomodules, the performances, e.g. quality factor Q_0 and accelerating gradients (E_{acc}), of the SRF cavities are critical to control the cost of the ILC; because high-Q_0 cavities can reduce cryogenic loads, and high-gradient cavities will decrease the total length of the ILC.

The baseline technology of ILC to produce SRF cavities is electropolishing and 120°C baking which can produce a cavity with E_{acc} ~35 MV/m with $Q_0 \sim 8\times10^9$. However, recently new discoveries in SRF field, e.g. low-temperature infusion [2, 3] and 75°C baking [4], could have large potentials to improve quality factor and gradient, and thereby to reduce cost.

CAVITY PREPERATION

We use two 1.3 GHz ILC-type single-cell SRF cavity (LTE1-14 and LTE1-15) for this work. As the baseline treatment, the two cavities had been treated by the ILC baseline recipe [5], i.e. 100 um surface removal by electropolishing (EP), and 900ºC baking for 3 hours, and then 120ºC baking for 48 hours. After the baseline treatment, both cavities have been vertically tested on the Cornell wave-guide insert allowing regular CW and high-power pulse measurement in same cryogenic cycle, as is shown in Fig. 1 [6]. After that, the cavity LET1-14 was baked at 800 ºC for 3 hours then baked at 120ºC under ~40mTorr N_2 for 48 hours. During the baseline treatment and 120ºC infusion, witness samples were baked with the cavities. SIMS data of the samples showed the 120ºC infusion increases the level of nitrogen and carbon, as is shown in Fig. 2. LET1-14 has been tested after the infusion; then the cavity was 75°C baked for 6 hours on the insert and tested again.

LTE1-15 received the 1st 75°C baking for 6 hours on the insert after the baseline test; then the cavity was tested again. After that we did HF rinsing of the cavity, followed by another test. At last, the 2nd 75°C baking was carried out for the cavity on the insert and followed by a final vertical test.

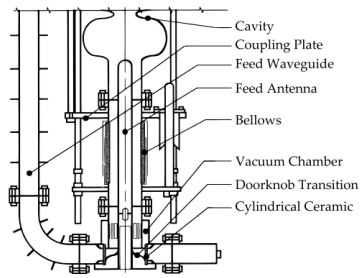
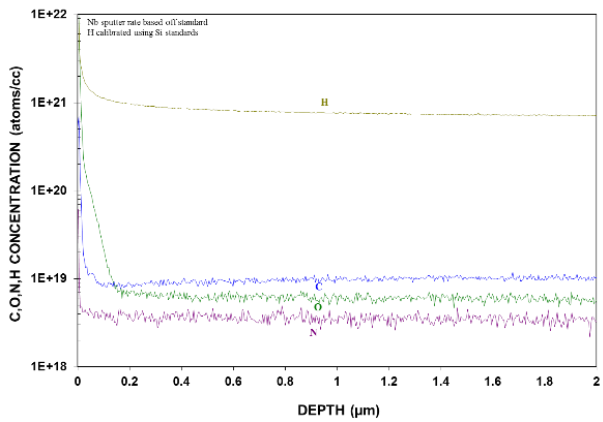
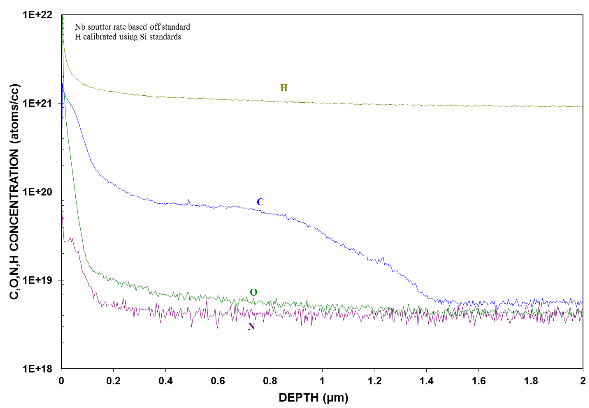


Figure 1: Schematic of wave-guide insert allowing regular CW and high-power pulse measurement in same cryogenic cycle.



(a) SIMS data of samples baked at 120°C under vacuum.



(b) SIMS data of samples baked at 120°C under N_2.

Figure 2: SIMS data comparison between 120°C baking under vacuum and under N_2.

* Work supported by the Department of Energy.
† mg574@cornell.edu.

Content from this work may be used under the terms of the CC BY 3.0 licence (© 2018). Any distribution of this work must maintain attribution to the author(s), title of the work, publisher, and DOI.

ISBN: 978-3-95450-194-6 ISSN: 2226-0366 doi:10.18429/JACoW-LINAC2018-TUPO057

The set-up used during the 75°C baking on the wave-guide insert is shown in Fig. 3. The reason for baking on the insert is to minimize chances of contamination from cavity disassembly. During the baking, a heat gun blows hot air to keep cavity at the temperature of 75 ± 3°C.

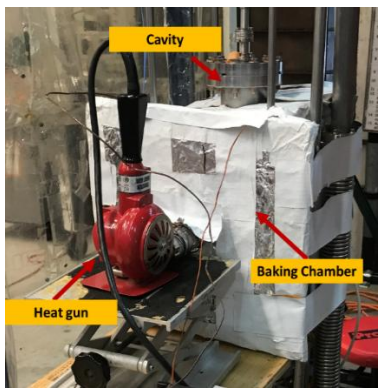


Figure 3: Set-up of 75C baking on the wave-guide insert.

TEST RESULTS AND ANALYSIS

The Q_0 versus E_{acc} results from cavity LTE1-14 are summarized in Fig. 4. The baseline test showed that the cavity quenched around 23MV/m, the average Q_0 is ~1.4×10^{10}. After the 120°C infusion, the quench field was increased to 26 MV/m with average Q_0 ~ 2×10^{10} in CW measurement. The cavity achieved 40MV/m in high-power pulse (HPP) tests in which 300kW 250 us high-power pulses were applied to the cavity, as is shown in Fig. 5. The 75°C baking decreased the cavity Q_0 to 1.2×10^{10}, but the max field was improved to 30 MV/m. In the three test, there is no medium-field Q-slope. The maximum gradients in CW and HPP operation are summarized in Table 1.

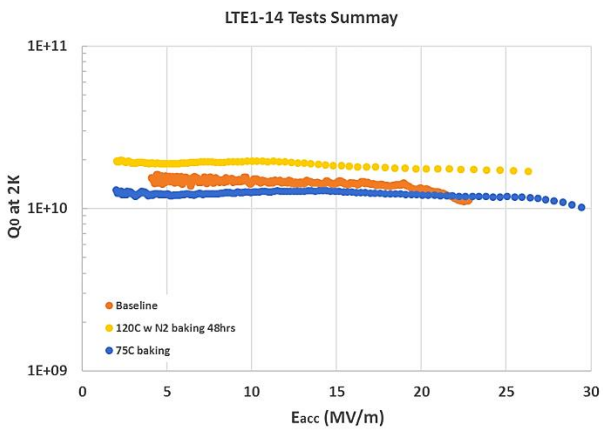


Figure 4: LTE1-14 Q_0 vs. E_{acc} curves.

Figure 6 shows the Q_0 versus E_{acc} measurements for cavity LTE1-15. The baseline test showed a quench around 24 MV/m. After the 1st 75°C baking, the cavity gradient increased to 35 MV/m, but the cavity showed heavy field emission (FE) and low low-field Q_0. The cavity was disassembled for HF rinsing and re-HPR to reduce residual resistance and eliminate the FE. Afterwards, Q_0 had improved, but the quench field decreased to 26 MV/m. Likely, the HF rinsing removed the 75°C baking effect. We then carried out the 2nd 75°C baking of the cavity, but the performance had not charged in the following test. The quench fields of LTE1-15 in CW and HPP measurements are summarized in Table 2.

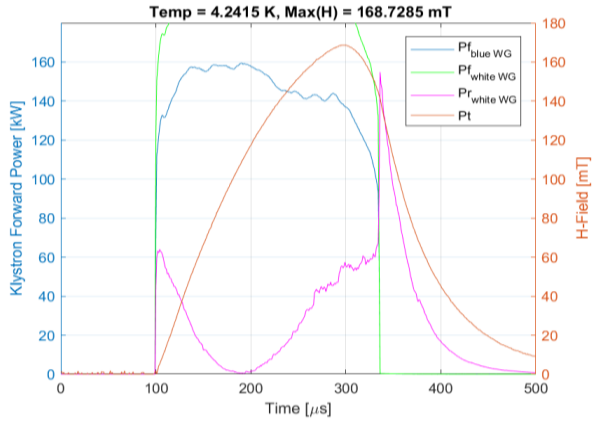


Figure 5: HPP test results after 120°C infusion showing the maximum B-field achieved was 169 mT, i.e. E_{acc} ~ 40 MV/m.

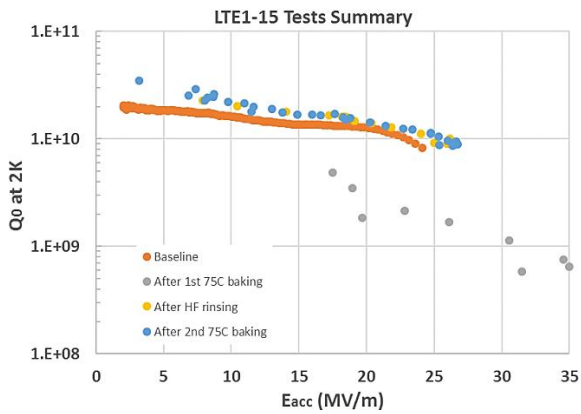


Figure 6: LTE1-15 Q_0 vs. E_{acc} curves.

Table 1: LTE1-14 Quench Field Summary

Treatment	CW (MV/m)	HPP (MV/m)
Baseline	23	NA
120°C baking with N2	26	40.2
75°C baking	30	NA

Table 2: LTE1-15 Quench Field Summary

Treatment	CW (MV/m)	HPP (MV/m)
Baseline	24	34.3
1st 75°C baking	36	NA
HF rinsing	26	NA
2nd 75°C baking	26	NA

Content from this work may be used under the terms of the CC BY 3.0 licence (© 2018). Any distribution of this work must maintain attribution to the author(s), title of the work, publisher, and DOI.

ISBN: 978-3-95450-194-6 ISSN: 2226-0366 doi:10.18429/JACoW-LINAC2018-TUPO057

Content from this work may be used under the terms of the CC BY 3.0 licence (© 2018). Any distribution of this work must maintain attribution to the author(s), title of the work, publisher, and DOI.

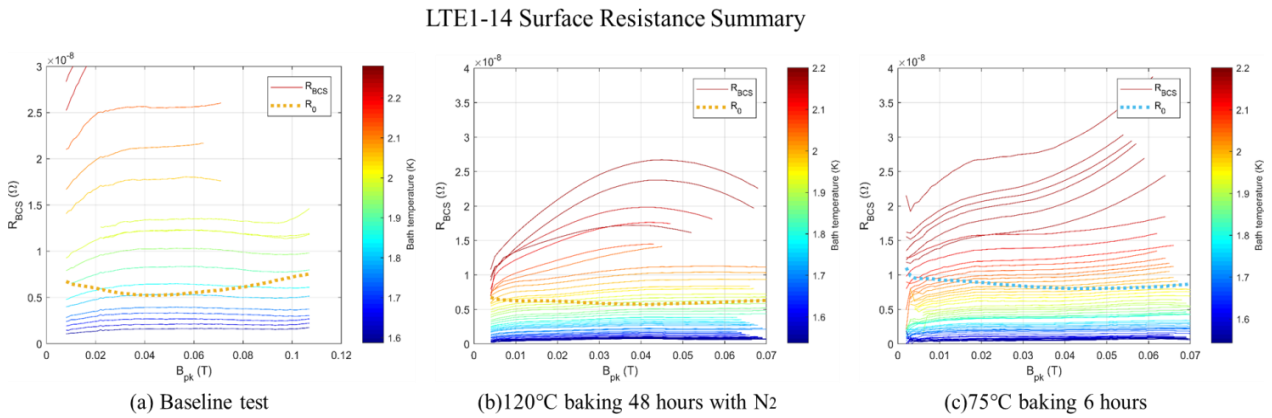


Figure 7: LTE1-14 surface resistance summary.

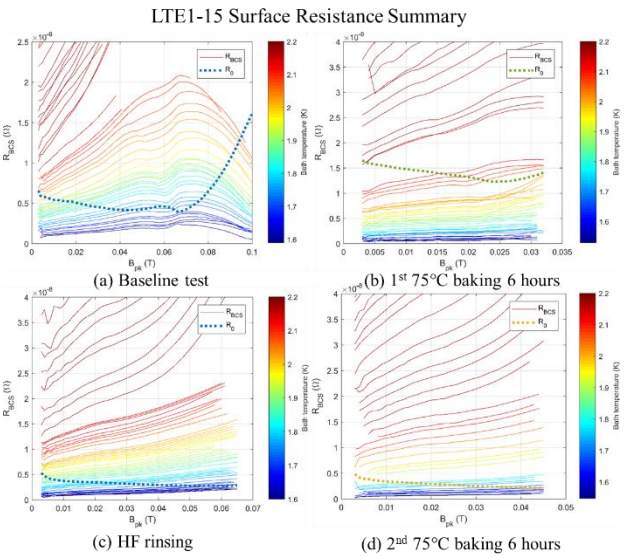


Figure 8: LTE1-15 surface resistance summary.

The LTE1-14 and LTE1-15 surface resistance results are summarized in Fig. 7 and Fig. 8 respectively. Frequency versus temperature data was taken during cavity warm-up. The mean-free-path of each treatment was extract from these, and are listed in Table 3 and Table 4 for LTE1-14 and LTE1-15 respectively.

Table 3: LTE1-14 Mean-free-path Summary

Treatment	**Mean free path** (nm)
Baseline	~260
120C baking with N2	2.4
75C baking	47

Table 4: LTE1-15 Mean-free-path Summary

Treatment	**Mean free path** (nm)
Baseline	~260
1st 75°C baking	83
HF rinsing	71
2nd 75°C baking	62

CONCLUSION

A series of surface preparation recipes have been studied via two 1.3 GHz ILC-type SRF cavities (LTE1-14 and LTE1-15). SIMS data showed that the 120ºC N2-infusion increases the level of nitrogen and carbon in the RF penetration layer. The test results after the infusion showed that the residual resistance was at the same level as during the baseline test, but the BCS resistance had been reduced to below 10 nΩ. Hence the Q_0 has improved to ~2×10^{10}. We applied 75ºC baking after 120ºC baking. The 75ºC baking increased residual resistance in both tests. But it did not dramatically change the BCS resistance.

The cavities achieved much higher E_{acc} in the HPP tests in which ~300kW 250 us high-power pulses were applied to the cavities. We observed that the max field of cavities E_{acc} had been significantly improved after 75ºC baking. HF rinsing can remove the extra residual resistance added by 75ºC baking, but it also removed the gradient improvements from the 75ºC baking.

Frequency versus temperature fitting shows that the mean free path became extreme short ~2.4nm after 120ºC infusion; but the mean-free path level was 47-83 nm after 75ºC baking.

REFERENCES

[1] The International Linear Collider Technical Design Report. Volume 1: Executive Summary, http://www.linearcollider.org/ILC/Publications/Technical-Design-Report

[2] A. Grassellino *et al.*, "Nitrogen and Argon Doping of Niobium for Superconducting Radio Frequency Cavities: a Pathway to Highly Efficient Accelerating Structures," *Superconductor Science and Technology*, Vol. 26, no. 10, Aug. 2013.

ISBN: 978-3-95450-194-6 ISSN: 2226-0366 doi:10.18429/JACoW-LINAC2018-TUPO057

http://iopscience.iop.org/0953-2048/26/10/102001/metrics

[3] P.N. Koufalis *et al.*, "Insights into the role of C, N, and O introduced by low temperature baking on niobium cavity performance", in *Proceeding of IPAC2018*, Vancouver, BC, Canada, 2018, paper WEPMF041.

[4] A. Grassellino *et al.*, "Accelerating fields up to 49MV/m in TESLA-shape superconducting RF niobium cavities via 75C vacuum bake", arXiv: 1806.09824.

[5] H. Hayano, "Review of SRF cavities for ILC, XFEL, and ERL applications", in *Proceeding of IPAC10*, Kyoto Japan, 2010, paper THXRA02.

[6] V. Nicholas, "Pushing the frontiers of superconducting radio frequency science: Form the temperature dependence of the superheating field of niobium to higher-order mode damping in very high quality factor accelerating structures," Ph.D. thesis, Phys. Dept., Cornell University, USA, 2014.

Content from this work may be used under the terms of the CC BY 3.0 licence (© 2018). Any distribution of this work must maintain attribution to the author(s), title of the work, publisher, and DOI.

ISBN: 978-3-95450-194-6 ISSN: 2226-0366 doi:10.18429/JACoW-LINAC2018-TUPO058

COOL DOWN STUDIES FOR THE LCLS-II PROJECT*

M. Ge†, M. Liepe, J. Sears, CLASSE, Cornell University, Ithaca, New York, USA
D. Gonnella, SLAC National Accelerator Laboratory, Menlo Park, California, USA

Abstract

The quality factor of the nitrogen-doped SRF cavities for the LCLS-II project are strongly impacted by cool down speed. A sufficiently fast cool down speed can produce large thermal gradient across a cavity and sufficiently expel magnetic flux when the cavity wall passes from the normal-conducting to the superconducting state. However, instrumentation in LCLS-II production cryomodules has been kept at a minimum, and additional information during the cool down of the modules is therefore desirable. In this work, we study if and how RF data can be used during cavity cool-down to determine the transition speeds of the individual cavities in the LCLS-II linac.

INTRODUCTION

The LCLS-II project requires an average unloaded quality factory Q_0 for the 1.3 GHz SRF cavities of 2.7×10^{10} at an operating temperature of 2K and accelerating gradient of 16 MV/m [1]. The 2N/6 nitrogen doping recipe (2 min N-doping at 800C followed by a 6 min anneal at 800C) [2, 3] has been chosen for the surface preparation of the LCLS-II SRF cavities, However, the quality factor of nitrogen doped SRF cavities are strongly impacted by cool down speed [4] due to their high sensitivity to losses from trapped magnetic flux [5].

New cool down studies on a single-cell cavity were conducted with the goal of developing a means of measuring cool down rate of SRF cavities using RF methods when temperature sensors are not available, such as in the LCLS-II cryomodules. A single-cell cavity was provided by LCLS-II for these studies. This cavity was reset using EP at Cornell, and then given the standard 2/6 nitrogen-doping that LCLS-II production cavities receive. The cavity was tested at Cornell on a test insert fitted with a variable coupler that could reach Q_{ext} close to 4×10^7, the Q_{ext} required by the LCLS-II project for cavities assembled in cryomodules.

32 cool downs of the cavity were completed in total. The goal of these cool downs was to determine

1. If it is possible to identify cool down rate and/or gradient by means of the transition time of the cavity as measured on a network analyzer
2. If 1. is affirmative, define a model which from a given transition time predicts the cool down rate and/or gradient of a cavity in the cryomodules during linac cooling.

METHOD

A single-cell cavity was cooled in a vertical test Dewar multiple times, with different cool down rates and gradients. A picture of the cavity on the test stand is shown in Figure 1. Temperature sensors were placed on the cavity, two on the equator, and two on each of the irises. The Q_{ext} of the input coupler was set to $\sim4\times10^7$. A network analyzer was connected to the forward and transmitted power connections on the cavity and an S_{21} measurement was taken during cool down. The parameters for the network analyzer measurement are given in Table 1.



Figure 1: Test insert with single-cell cavity and instrumentation.

Table 1: Network Analyzer Parameters

Parameter	Value
Center	Resonance f_0 at starting temp, re-centered after each scan
Span	100 kHz
IF Bandwidth	100 Hz
Forward Power	~10 W

From an S_{21} measurement, the loaded quality factor Q_L of the cavity can be calculated,

$$Q_L = \frac{f_0}{\Delta f}, \quad (1)$$

where f_0 is the resonance frequency of the cavity (peak on the network analyzer) and Δf is the width of the resonance

* Work supported by the US DOE and the LCLS-II project.
† mg574@cornell.edu.

Content from this work may be used under the terms of the CC BY 3.0 licence (© 2018). Any distribution of this work must maintain attribution to the author(s), title of the work, publisher, and DOI.

ISBN: 978-3-95450-194-6 ISSN: 2226-0366 doi:10.18429/JACoW-LINAC2018-TUPO058

curve at the points 3 dB below the maximum. Q_L is related to the intrinsic cavity Q, Q_0 by

$$\frac{1}{Q_L} = \frac{1}{Q_{ext}} + \frac{1}{Q_0}. \quad (2)$$

When the cavity is normal conducting, Q_0 is ~1×10^4-5×10^4, heavily dominating Q_L, resulting in a direct measurement of normal conducting Q_0 with the network analyzer. When the cavity is superconducting, Q_0 is significantly higher than Q_{ext} and Q_L is very close to Q_{ext}. In reality, due to cavity microphonics, the network analyzer measurement could not resolve Q's above 10^7, so some saturation occurred when the cavity transitioned. An example S_{21} measurement comparing normal and superconducting states is given in Figure 2.

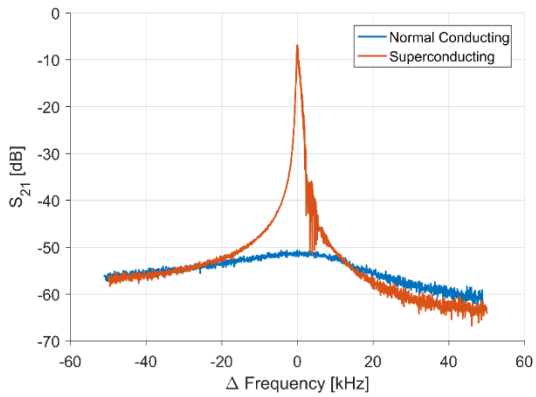


Figure 2: Example of normal and superconducting states on the network analyzer.

From the network analyzer traces, Q_L can be determined. For a given cool down, many traces are taken. Figure 3 shows two measurements of Q_L vs time, first for a fast cool down, and second for a slow cool down. The beginning of the superconducting transition is clearly visible. We then define a transition time as the time it takes for the cavity to go from Q_L of 1×10^5 to 2×10^6 (corresponding to ~50% and ~97% of the cavity being superconducting, respectively). It is clear from Figure 3 that this transition time is quite different in the two cases.

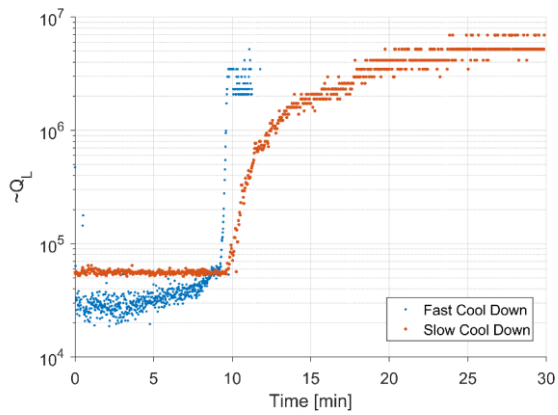


Figure 3: Example Q measurement for two cool downs.

RESULTS

A total of 32 cool downs were completed with different cool down rates and spatial temperature gradients at T_c. These parameters were controlled by varying the starting temperature of the cool down, helium flow rate, and heat applied to the incoming helium gas through the use of a "slow cool down helium transfer line" affixed with resistive heaters in the helium path. For each cool down, transition time, cool down rate, and cool down gradient were measured via the temperature sensors located on the cavity and S_{21} measurements.

The transition time of the cavity versus cool down rate is shown in Figure 4. The data has been colored according to "fast" (temperature gradient $\Delta T > 3K$ across the cavity) or "slow" ($\Delta T < 3K$) cool downs for ease of discussion. For cool downs with small spatial temperature gradients (shown in orange) we can see that there is a clear exponential decrease of transition time as the cool down rate is increased i.e. with faster cool down, the cavity transitions faster. However, at large spatial temperature gradients ($\Delta T > 3K$), the results show no clear trend.

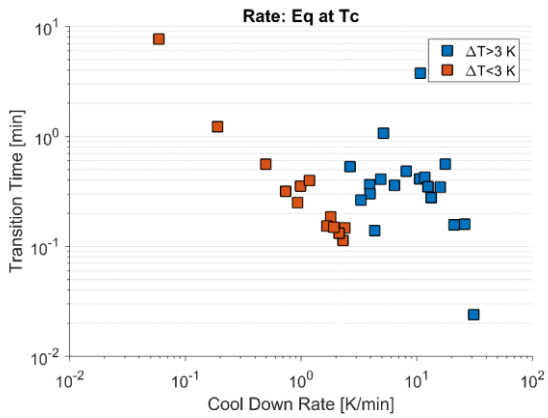


Figure 4: Transition time vs cool down rate.

Looking at the cool down gradient however sheds light on the high gradient region. The transition time of the cavity versus cool down gradient at T_c is shown in Figure 5. We can identify three important regions:

- At very small cool down gradients, the transition time decreases as the gradient is increased. This is in line with the results shown in Figure 4, where faster cool downs (usually accompanied by large spatial temperature gradients) led to shorter transition times.
- At very large gradients, as the gradient is increased, transition time also increases. This suggests that when a cavity begins transitioning with a large spatial gradient, the time it takes for the top of the cavity to become superconducting slows down the overall transition, even though the rate of cool down is quite high.
- Between these two regions there is an intermediate region, where the transition time is relatively constant with increasing cool down gradient. This is due to partial compensating impacts of the increasing

Content from this work may be used under the terms of the CC BY 3.0 licence (© 2018). Any distribution of this work must maintain attribution to the author(s), title of the work, publisher, and DOI.

ISBN: 978-3-95450-194-6 ISSN: 2226-0366 doi:10.18429/JACoW-LINAC2018-TUPO058

temperature gradient and increasing cool down speed on the transition time.

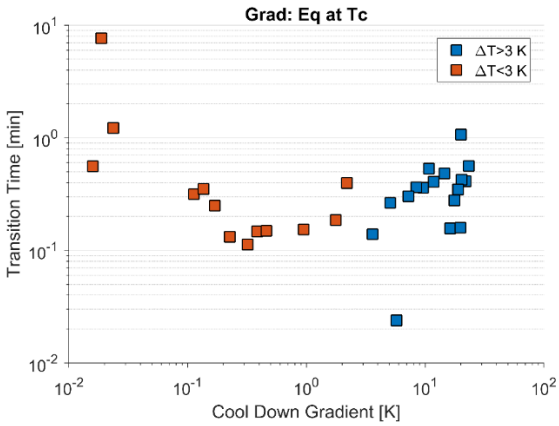


Figure 5: Transition time vs spatial cool down gradient across the cavity cell.

DISCUSSION

What we can see from these results is that two effects play a role in the time it takes for the cavity to transition from normal to superconducting. First, faster cool down results in shorter transition times. This was expected prior to the experiment. However, as the cool down gets faster, typically the spatial temperature gradient at T_c also gets larger. This results in the transition time getting longer again at very fast cool downs, since when the bottom of the cavity begins transition, the top is at a significantly warmer temperature, ultimately increasing the transition time.

This initial analysis suggest that it is not straightforward to use RF measurements to characterize a cavity's cool down gradient in the linac, though further analysis of the experimental data is planned for the future and might result in additional insights. LCLS-II cool downs will be in the large gradient regime, thus likely in the region on the right side of Figure 4, where there is not a clear trend in the data. Moreover, using the transition time analysis, it impossible to distinguish between cavity cool downs with very large and very small gradients as shown in Figure 5.

Work is still underway to completely understand the mechanics behind counteracting effects of the temperature gradient and the cool down speed. Ideally, a model could be developed and fit to the data, however this has not yet been completed. Additional analysis could also lead to a better separation of the cool down rate and gradient. Conducting fast cool downs with very small spatial temperature gradients, or vice-versa could be useful in the future to better understand cool down dynamics.

REFERENCES

[1] LCLS-II Final Design Report, https://portal.slac.stanford.edu/sites/ad_public/people/galayda/Shared_Documents/FDR.pdf

[2] A. Grassellino, A. Romanenko, D. Sergatskov, O. Melnychuk, Y. Trenikhina, A. Crawford, A. Rowe, M. Wong, T. Khabiboulline, and F. Barkov, "Nitrogen and argon doping of niobium for superconducting radio frequency cavities: a pathway to highly efficient accelerating structures", *Superconductor Science and Technology*, vol. 26, no. 10, p. 102001, 2013.

[3] D. Gonnella, S. Aderhold, A. Burrill, E. Daly, K. Davis, A. Grassellino, C. Grimm, T. Khabiboulline, F. Marhauser, O.Melnychuk, A. Palczewski, S. Posen, M. Ross, D.Sergatskov, A. Sukhanov, Y. Trenikhina, K.M. Wilson, "Industrialization of the nitrogen-doping preparation for SRF cavities for LCLS-II", *Nucl. Instr. Meth.*, vol. 883, pp. 143-150, 2018.

[4] A. Romanenko, A. Grassellino, O. Melnychuk, D.A. Sergatskov, "Dependence of the residual surface resistance of SRF cavities on the cooling rate through Tc", *J. Appl. Phys.*, vol. 115, p. 184903, 2014.

[5] D. Gonnella, J. Kaufman, M. Liepe, "Impact of nitrogen doping of niobium superconducting cavities on the sensitivity of surface resistance to trapped magnetic flux", *J. Appl. Phys.*, vol. 119, p. 073904, 2016.

Content from this work may be used under the terms of the CC BY 3.0 licence (© 2018). Any distribution of this work must maintain attribution to the author(s), title of the work, publisher, and DOI.

ISBN: 978-3-95450-194-6 ISSN: 2226-0366 doi:10.18429/JACoW-LINAC2018-TUPO059

LATEST RESULTS OF SALT BASED BIPOLAR ELECTRO-POLISHING R&D AT CORNELL*

M. Ge†, F. Furuta, T. Gruber, J. Kaufman, M. Liepe, R. D. Porter
CLASSE, Cornell University, Ithaca, New York, USA
T. Hall, R. Radhakrishnan, S. Snyder, E. J. Taylor, Faraday Technology, Inc., Clayton, Ohio, USA

Abstract

Acid free electropolishing would be safer to use and friendlier to the environment. A collaboration, supported by the DOE SBIR Phase-II program, between Faraday Technology Inc. and Cornell University focused on salt-based bipolar electropolishing (BEP). In this paper, we present the latest salt-based BEP results. The superconducting performance of a single-cell 1.3GHz cavity has been carefully analyzed, showing that salt-based BEP is promising, but still has large room for improvement.

INTRODUCTION

As superconducting radio-frequency (SRF) technology is increasingly widely used in modern accelerators, the search for an eco-friendly niobium surface process has become an important topic. The objective of this work is finding an alternative to hydrofluoric (HF) and other acids used in the conventional electropolishing process. Acid free electropolishing (EP) uses a near-neutral aqueous salt solution, e.g. $NaNO_3$ or NaCl solution, as electrolyte in bipolar electropolishing [1].

It has been previously reported by Faraday Technology Inc. (Faraday) [1] that the surface roughness of niobium coupons treated with salt-based EP can achieve values as low as 0.05 um, with a material removal rate of ~42 um/hr. The transition from flat coupons to a single-cell cavity requires a more complex set-up, which is based on the bipolar electropolishing system at Faraday. In collaboration with Faraday [2], Cornell tested a 1.3GHz single-cell SRF cavity (LTE1-15) that had been treated by the salt-based bipolar EP at the Faraday EP facility. In the following, we summarize these activities and present results from the single-cell cavity test.

BIPOLAR ELECTROPOLISHING

Bipolar Electropolishing (BEP) applies forward and reverse voltage pulse waveforms on the electrodes, i.e. a cavity and cathode, alternatively, as is shown in Fig. 1. The forward pulse which is positive voltage applied on the cavity enhances mass transport in the EP processing. The reverse pulse is to depassivate the internal surface of the cavity. The off-times are generally inserted between the anodic and catholic pulses to facilitate replenishment of reacting species and removal of by-products and heat. The cathodic pulse eliminates the need for hydrofluoric acid to remove the surface oxide [1]. The bipolar system at Faraday is shown in Fig. 2 [3].

* Work supported by DOE award DE-SC0011235 (1002).
† mg574@cornell.edu

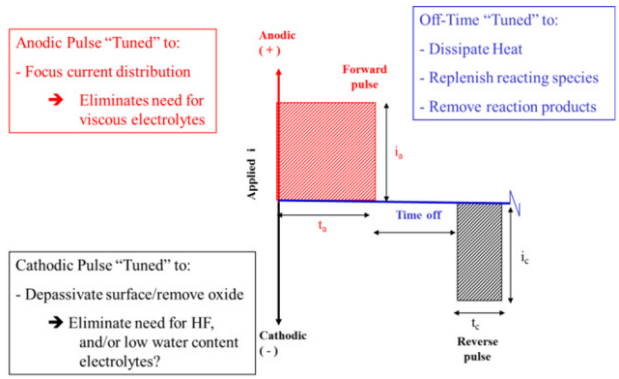


Figure 1: Illustration of the principle of Bipolar EP.



Figure 2: Bipolar EP system at Faraday [3].

SALT ELECTROPOLISHING AND TEST RESULTS

A 1.3GHz ILC-type cavity had been sent to Faraday for the salt-based EP, which was processed in 200 g/L $NaNO_3$ + 19.5 g/L Tris Acid + 1g/L Tris Base mixture. The total removal was ~30um with the polishing rate ~1.6um/hr.

Optical Inspection

After the salt electropolishing, we did optical inspection of the cavity at Cornell [4]. The inner surface of the equator region, shown in Fig. 3, is shiny and looks similar to a surface after conventional EP. However, we observed discoloration on other regions of the cavity wall, as is shown in Fig. 4. These stains are likely thick oxide layers generated in the salt EP processing.

Content from this work may be used under the terms of the CC BY 3.0 licence (© 2018). Any distribution of this work must maintain attribution to the author(s), title of the work, publisher, and DOI.

ISBN: 978-3-95450-194-6 ISSN: 2226-0366 doi:10.18429/JACoW-LINAC2018-TUPO059

Content from this work may be used under the terms of the CC BY 3.0 licence (© 2018). Any distribution of this work must maintain attribution to the author(s), title of the work, publisher, and DOI.

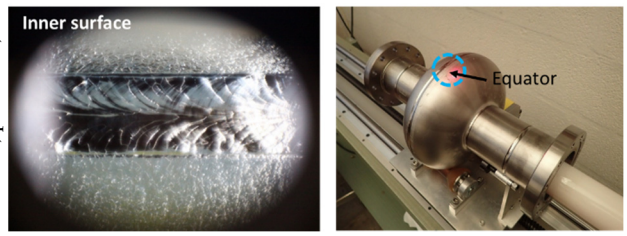


Figure 3: Optical inspection image of equator region indicating the salt EP surface looks similar to a surface after conventional electropolishing.

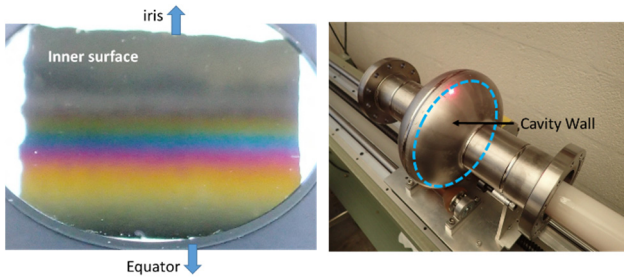


Figure 4: Optical inspection image of cavity wall showing discoloration generated during the salt EP.

Vertical Test

The cavity then was high-pressure water rinsed and cleanly assembled in class 10 clean room. The RF test showed that the cavity had a high residual-resistance R_0 of ~50 nΩ, as is shown in Fig. 5. The cavity quality factor Q_0 at 2K was low, and Q_0 versus gradient (E_{acc}) measurements at 2K were limited by RF power. Hence the Q versus E was measured again at 1.6K; see Fig. 6. The cavity quenched around 40MV/m, with a strong medium Q-slope.

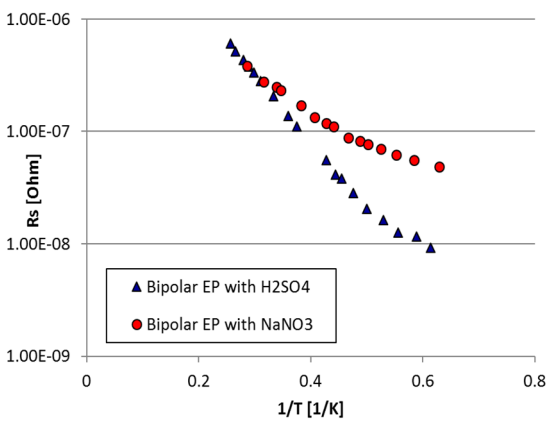


Figure 5: R_s vs. 1/T curves of salt EP compared to regular BEP.

Post Surface Processing

Following the first RF test, the cavity was baked at 120°C for 48 hours in a UHV furnace [5] to reduce surface resistance and improve cavity Q_0. After the baking, the 2K Q_0 at low-field had been dramatically increased from 3.6×10^9 to 6.2×10^9, as is shown in Fig. 7. The gradient was limited by a low helium level in the test dewar, and no cavity quench was observed.

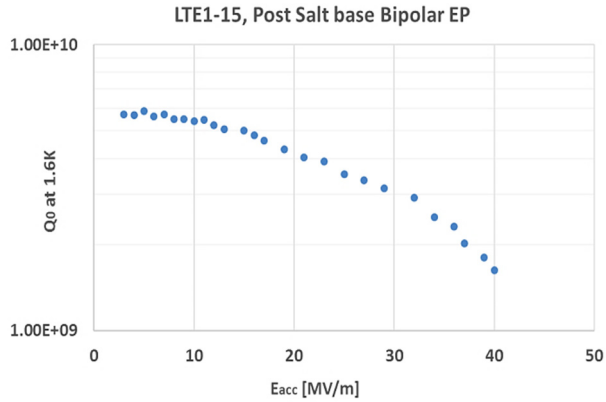


Figure 6: 1.6K Q_0 vs. E_{acc} curve after salt-based EP.

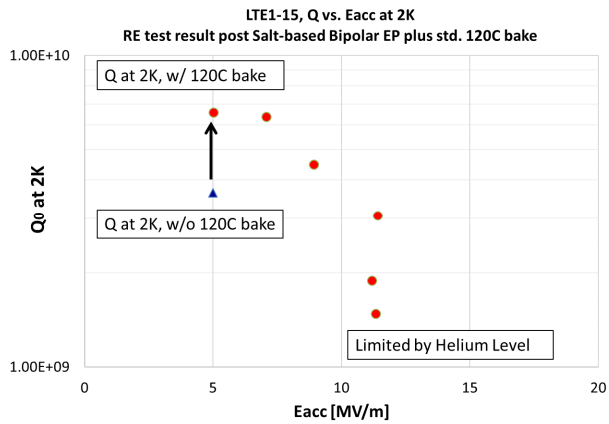


Figure 7: 2K Q_0 vs. E_{acc} curves after 120°C baking showing that Q_0 at low field was improved.

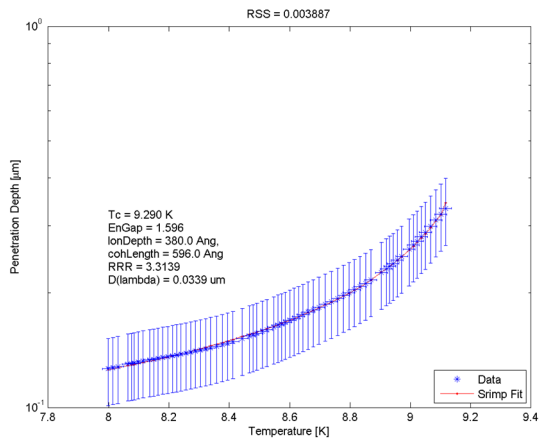


Figure 8: Frequency versus temperature curve fitting indicating that the mean-free-path of the cavity is around 18nm.

The frequency versus temperature data was taken during the cavity warm-up. From the curve shown in Fig. 8, the mean-free-path of the cavity after 120°C baking was determined to be ~18 nm.

CONCLUSION

A salt-based electropolished single-cell cavity was measured at Cornell University. The results showed that

ISBN: 978-3-95450-194-6 ISSN: 2226-0366 doi:10.18429/JACoW-LINAC2018-TUPO059

the cavity had high residual resistance of ~50nΩ, which is likely due to the discoloration found on the cavity wall indicating a thick oxide layer. The cavity quenched around 40MV/m at 1.6K. This results manifest that salt-based EP can produce high-gradient performance, which is close to the theoretical limits of niobium. A subsequent 120ºC bake reduced the surface resistance and improved the low-field Q_0 from 3.6×10^9 to 6.2×10^9 at 2K. Frequency versus temperature measurements indicates that the mean free path of the cavity was ~18 nm, which is shorter than a conventionally electropolished cavity.

The test result suggests that salt-based EP with post surface treatment, e.g. 120 ºC baking and HF rinsing, has the potential of producing a high-gradient cavity. The mean-free-path of the surface after salt-based EP is short, indicating that some impurities are present in the RF penetration layer. The salt-based EP parameters need to be optimized further, which will be the focus of future work.

REFERENCES

[1] M. Inman, *et al.*, "Electropolishing of niobium SRF cavities in eco-friendly aqueous electrolytes without hydrofluoric acid", in *Proc. of SRF2015*, Whistler, BC, Canada, paper MOPB101.

[2] F. Furuta, *et al*., "HF free bipolar electropolishing studies on niobium SRF cavities at Cornell with Faraday Technology", in *Proceedings of IPAC2018*, Vancouver, BC, Canada, paper WEPMF037.

[3] E. Taylor, "Electroplishing of niobium SRF cavties in low viscosity electrolytes without hydrofluoric acid", in Proceedings SRF 2013, Paris, France, paper TUP054.

[4] M. Ge, *et al.*, "Surface topography techniques at Cornell University: Optical inspection and Surface replica", in Proceedings of IPAC2016, Busan, Korea, paper WEPMR015.

[5] F. Furuta, el al., "TM-Furnace qualification at Cornell", in *Proceeding of SRF2013*, Paris, France, paper TUP059.

Content from this work may be used under the terms of the CC BY 3.0 licence (© 2018). Any distribution of this work must maintain attribution to the author(s), title of the work, publisher, and DOI.

ISBN: 978-3-95450-194-6 ISSN: 2226-0366 doi:10.18429/JACoW-LINAC2018-TUPO064

PRE-STUDY OF CEPC SRF CAVITY*

P. Sha†, J. Dai, C. Dong, F. S. He, S. Jin, Z. Q. Li, B. Q. Liu, Z. H. Mi,
J. Y. Zhai, X. Y. Zhang, H. J. Zheng,
Key Laboratory of Particle Acceleration Physics and Technology,
Institute of High Energy Physics, CAS, Beijing, China
J. K. Hao, F. Wang, Peking University, Beijing, China

Abstract

CEPC will use 650 MHz cavities for the collider and 1.3 GHz cavities for the Booster. Each booster cryomodule contains eight 1.3 GHz 9-cell cavities, which is similar as LCLS-II, E-XFEL and ILC. Each collider cryomodule contains six 650 MHz 2-cell cavities, which is totally new. Therefore, the pre-study mainly focuses on the 650 MHz 2-cell cavity. N-doping and vertical tests of 650 MHz 1-cell and 2-cell cavities have been carried out at IHEP, which have achieved good results. A test cryomodule, which consists of two 650 MHz 2-cell cavities, has also begun as the first step to the full-scale cryomodule.

INTRODUCTION

Baseline layout and parameters for CEPC Ring SRF system have been public [1]. There're two SRF sections in total, and each one has two SRF stations. There're 10 cryomodules per station, which consist of six 650 MHz 2-cell cavities each. Hence, there're 240 650 MHz 2-cell cavities in total. RF and Mechanical design of these cavities have been completed. And fabrication of prototype cavities has also been finished. The vertical test goal is 4E10@22MV/m, while the horizontal one is2E10@22MV/m. Both these targets are extremely high to reach, so N-doping would be adopted. In recent years, it has been proposed and proven to increase Q of superconducting cavity obviously, which lowers the BCS surface resistance. N-doping research had begun at IHEP since 2015. There've been initial progress, which mainly focused on Nb samples and 650 MHz 1-cell cavities. After N-doping, the Q values of both 650 MHz 1-cell cavities increased at low fields obviously. Besides, prototypes of 650 MHz 2-cell cavities have finished vertical test and the results are quite good.

N-DOPING RESEARCH OF NIOBIUM SAMPLES

Niobium samples were nitrogen doped at OTIC, as Fig. 1 [2, 3]. The furnace in Fig. 1 is equipped with two cryo-pumps in order to keep ultra-clean, which is key for N-doping. Different methods were tried to achieve the best effects. To verify that, experiments of secondary ion mass spectrometry (SIMS), scanning electron microscope (SEM), transmission electron microscope (TEM) and other experiments were carried out.



Figure 1: Furnace for N-doping at OTIC.

Results of SIMS is shown as Fig. 2 and Fig. 3. After N-doping (3Pa@800C for 2 min), intensity of N atom increased obviously, as well as NbN.

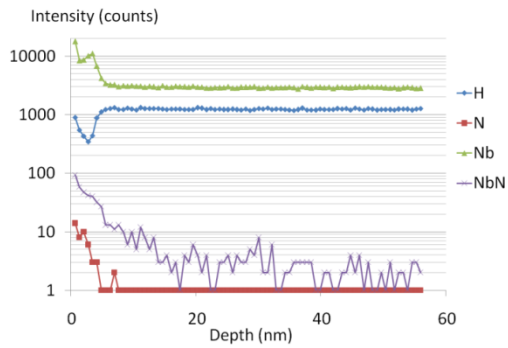


Figure 2: SIMS results before N-doping.

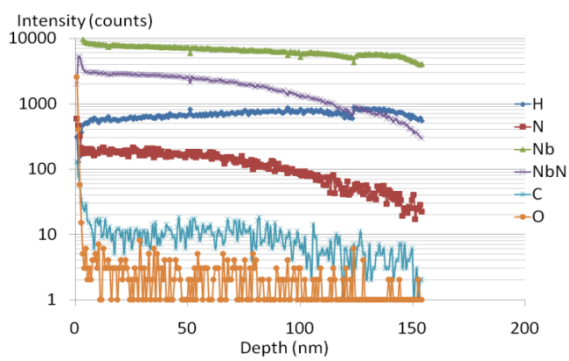


Figure 3: SIMS results after N-doping.

SEM images also show formation of nitride precipitates clearly, as Fig. 4.

*This study was supported by National Key Programme for S&T Research and Development (Grant NO.: 2016YFA0400400)and National Natural Science Foundation of China(Grant NO.:11505197).
#shapeng@ihep.ac.cn

Content from this work may be used under the terms of the CC BY 3.0 licence (© 2018). Any distribution of this work must maintain attribution to the author(s), title of the work, publisher, and DOI.

ISBN: 978-3-95450-194-6 ISSN: 2226-0366 doi:10.18429/JACoW-LINAC2018-TUPO064

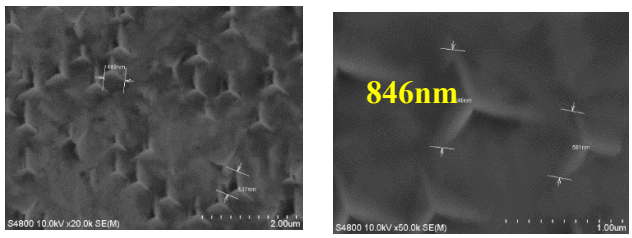


Figure 4: SEM images of Nb sample.

Diffraction patterns of TEM is shown as Fig. 5. The left picture of pure Nb shows only clean niobium with no impurities. The right of Nb N-doped shows poor nitride phases. It is similar as FNAL [4].

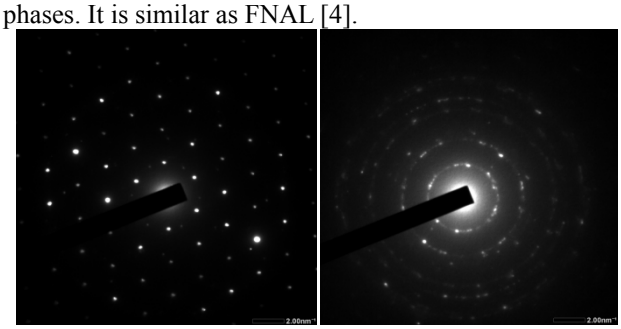


Figure 5: Diffraction patterns of TEM (left: pure Nb; right: Nb N-doped).

650 MHZ 1-CELL CAVITIES

Several 650 MHz 1-cell cavities have been fabricated for N-doping research. Because the EP facility is still under construction, these cavities were all processed with BCP. Before N-doping, baseline vertical tests of these cavities have been held as Fig. 6 and the results are shown in Fig 7. Helmholtz coils and flux gates are used for magnetic flux expulsion research. Meissner effect of superconductor has been observed during cavity cool-down.

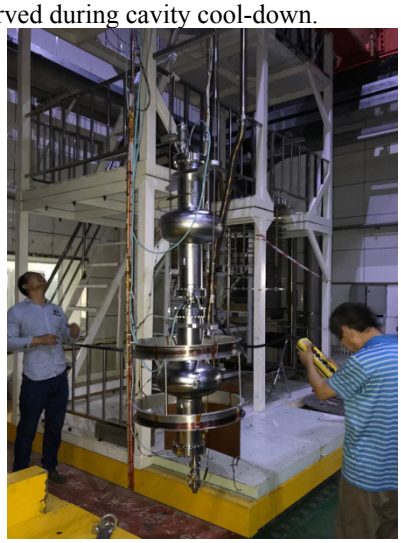


Figure 6: Vertical test of 650 MHz 1-cell cavities.

There're two vertical tests of 650S4# cavity. Before the 1st test, the HPR was done with two times. During the test, field emission began with Q-slope at low field (~10 MV/m). So we did the HPR with four times before the 2nd test. Then field emission was much weaker and the gradient reached 36 MV/m with no quench.

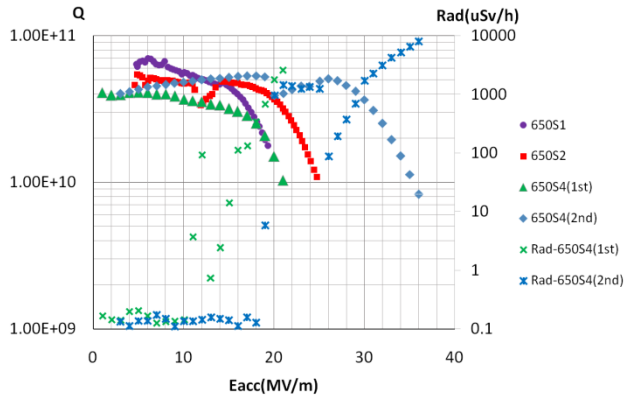


Figure 7: Vertical test results of 650 MHz 1-cell cavities.

N-doping of 650 MHz 1-cell cavities has also been carried out and initial results have been got. Q values of two cavities both increased at low fields (<10MV/m) [5].

650 MHZ 2-CELL CAVITIES

RF design of 650 MHz 2-cell cavities have been introduced in SRF2017 [3]. Cell shape and main parameters are shown as Fig. 8 and Table 1.

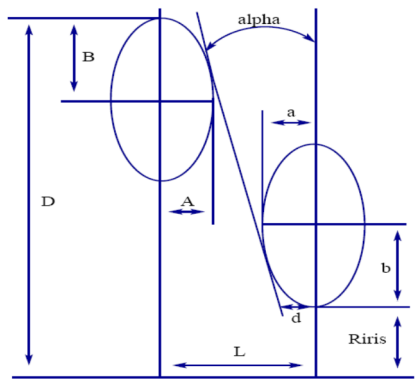


Figure 8: Profile of cell shape.

Table 1: Main Parameters of 650 MHz 2-cell cavity

Parameters	Value	Units
D	204.95	mm
Riris	78	mm
b/a	1.1	
alpha	3.2	degree
R/Q	105.5	Ω
G	284	Ω
E_{peak}/E_{acc}	2.38	
B_{peak}/E_{acc}	4.17	mT/(MV/m)
k	3.05	%

Content from this work may be used under the terms of the CC BY 3.0 licence (© 2018). Any distribution of this work must maintain attribution to the author(s), title of the work, publisher, and DOI.

ISBN: 978-3-95450-194-6 ISSN: 2226-0366 doi:10.18429/JACoW-LINAC2018-TUPO064

Content from this work may be used under the terms of the CC BY 3.0 licence (© 2018). Any distribution of this work must maintain attribution to the author(s), title of the work, publisher, and DOI.

Fabrication of three cavities were completed in late 2017. All these cavities had received post processing for vertical test, which include bulk BCP, annealing, light BCP and HPR. Vertical test of 1# 650 MHz 2-cell cavity was held at Peking University on 11st May, 2018, as Fig. 9 [6]. And the 2# was held at IHEP on 13rd Jul, 2018. Both results are shown as Fig. 10.



Figure 9: Vertical test of 650 MHz 2-cell cavity.

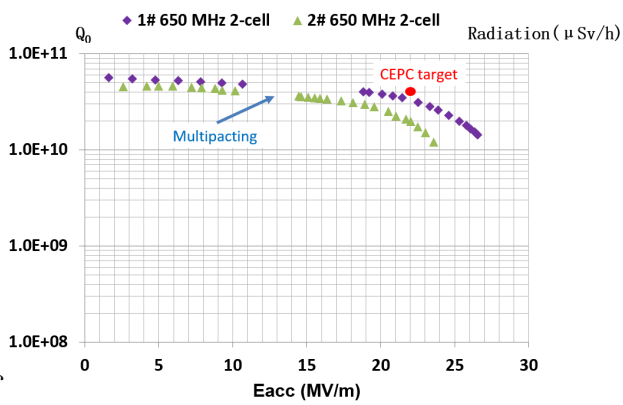


Figure 10: Vertical test results of 650 MHz 2-cell cavities.

The results of two cavities shown in Fig. 10 are both good, especially the 1# cavity. It reached 4E10@19.2MV/m, which is close to the CEPC target (4E10@20MV/m).

DRESSED CAVITIES FOR CRYOMODULE

The 650 MHz 2-cell cavity with Helium vessel and tuner has also finished design work, as Fig. 11. The mechanical performance has been optimized to minimize the Lorentz forcedetuning (LFD), df/dp and the peak stress. Thickness of cavity wall is adopted as 4 mm, and stiff rib 3 mm [7]. Novel design is adopted for Helium vessel. After optimization, mechanical design has reached the requirements finally.

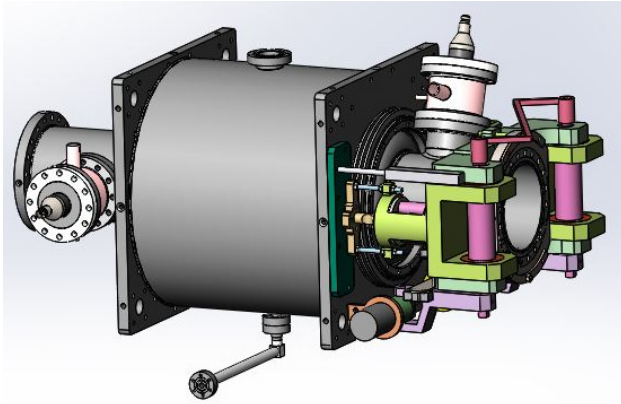


Figure 11: 650 MHz 2-cell cavity with Helium vessel and tuner.

CONCLUSION

The Pre-study of CEPC SRF cavity have begun, which mainly focus on 650 MHz 2-cell cavity. A test cryomodule with two cavities is underway and may be completed in 2019 [8]. The high Q and gradient are expected to achieve during horizontal test, which is the first step to the full-scale cryomodule of six cavities.

ACKNOWLEDGEMENT

Colleagues of IHEP, Peking University, KEK also contribute to this paper. Thanks for them!

REFERENCES

[1] J.Y. Zhai, "CEPC Ring RF System", Workshop on the Circular Electron-Positron Collider, Rome, Italy, 24-26 May, 2018.

[2] P. Sha, *et al.*, "Research of Nitrogen Doping in IHEP", in *Proc. 7th Int. Particle Accelerator Conf. (IPAC'16)*, Busan, Korea, May 2016, p. 2186, doi:10.18429/JACoW-IPAC2016-WEPMB029

[3] P. Sha, *et al.*, "R&D of CEPC Cavity", in *Proc. 18th Int. Conf. RF Superconductivity (SRF'17)*, Lanzhou, China, Jul. 2017, p. 463, doi:10.18429/JACoW-SRF2017-TUPB3036

[4] A. Grassellino, *et al.*, "N-Doping: Progress in Development and Understanding", in *Proc. 17th Int. Conf. RF Superconductivity (SRF'15)*, Whistler, Canada, Sep. 2015, paper MOBA06, p. 48.

[5] P. Sha, "N-doping Research at IHEP", FCC WEEK 2018, Amsterdam, The Netherlands, 9-13 April 2018.

[6] P. Sha, CEPC SRF CAVITY, Workshop on the Circular Electron-Positron Collider, Rome, Italy, 24-26 May, 2018.

ISBN: 978-3-95450-194-6 ISSN: 2226-0366 doi:10.18429/JACoW-LINAC2018-TUPO064

[7] X. Y. Zhang, *et al.,* "Mechanical Design of a 650 MHz Superconducting RF Cavity for CEPC", SRF 2017, Lanzhou, China,17-21Jul, 2017.

[8] J. Y. Zhai, *et al*., CEPC SRF System Design and Challenges, SRF 2017, Lanzhou, China,17-21Jul, 2017.

Content from this work may be used under the terms of the CC BY 3.0 licence (© 2018). Any distribution of this work must maintain attribution to the author(s), title of the work, publisher, and DOI.

ISBN: 978-3-95450-194-6 ISSN: 2226-0366 doi:10.18429/JACoW-LINAC2018-TUPO065

IMPROVEMENT OF CAVITY PERFORMANCE BY NITROGEN DOPING AT KEK

T. Okada*[1], Y. Hori[1, 2], E. Kako[1, 2], T. Konomi[1, 2], H. Sakai[1, 2], T. Saeki[1, 2],
K. Umemori[1, 2], Y. Yamamoto[1, 2], T. Dohmae[2], M. Egi[2] J. Kamiya[3], S. Kurosawa[3], K. Takaishi[3],
[1]SOKENDAI, Oho, Tsukuba, Ibarkai, 305-0801, Japan
[2]KEK, Oho, Tsukuba, 305-0801, Japan, [3]JAEA, Tokai, naka, Ibaraki, 319-1195, Japan

Abstract

Reducing loss at the surface of a superconducting cavity is important for reducing the cost of accelerator operation. Nitrogen doping is an effective breakthrough for direct applicaton in High-Q superconducting cavities. At KEK, the nitrogen doping technique is applied to single and three-cell niobium TESLA-like cavities. A J-PARC furnace has a cryopump and three turbopumps, in addition to scroll-pumps, to achieve an oil-free environment. The quality factor of nitrogen doped cavities was improved in comparison with the standard treatment. The temperature dependent resistance decreased with an increase of the accelerating gradients. The nitrogen doping recipe was applied to the single-cell and three-cell cavities applied, and the results of the vertical test are described.

INTRODUCTION

Nitrogen doping is an effective breakthrough in the field of High-Q superconducting cavities [1]. The quality factor Q_0 is represented by $Q = G/R_s$ without field emission. The geometrical factor G is defined by only the shape of the cavity, while R_s represents its surface resistance. The geometrical factor of the TESLA-like cavity is approximately about 280 Ω. The nitrogen doping technique had been investigated at KEK using the large and small furnaces in the mechanical engineering center at KEK. However, this has resulted in the deterioration in the quality factor of the treated cavities [2]. The likely cause of the unsatisfactory results is related to the vacuum system of the furnace. Nitrogen doping and nitrogen infusion were successfully tested using the other furnace at J-PARC which has an oil-free pump system [3].

DOPING PROCEDURE

The oil-free furnace at J-PARC annealed vacuum components as usual. The cryopump was operated at 10000 L/sec. The three turbopumps and scrollpumps have pumping speeds of 3000 L/sec ×3, 500 L/min ×3, respectively. During the introducing of high purity nitrogen gas, the pumps were stopped and the portable pump was used for a deep doping recipe in the single-cell cavity. Durring this process for a light doping, the pumping speed of the turbpumps and scrollpumps were decreased by 50 %. Both the heavy doped and light doped nitrogen doping recipes were applied to the two cavities as shown in Table 1.

Table 1: Nitrogen Doping Applied to the Two Cavities

Cavity	Recipe
Single-cell	800 °C 3 hour + 800 °C for 20 min 2.7 Pa nitrogen + 800 °C for 30 min w/o nitrogen + EP 15 *m*
Three-cell	800 °C 3 hour + 800 °C, 2 min w/3.0 Pa nitrogen, + 800 °C, 6 min w/o nitrogen + EP 5 *m*

The single cavity is the TESLA-like shape and is made of fine grain niobium from Tokyo Denki, with an RRR is approximately about 300. The three-cell cavity is also a TESLA-like shape and is made of fine grain high tantalum niobium from CBMM that was melted twice to yeild an RRR of less than 300 [4]. Figure 1 shows the set-up of the nitrogen dope treatment at J-PARC furnace. Both recipes begin with 3 hours of annealing at 800 degrees after high-pressure rinsing and packing. Figure 2 shows the temperature and pressure data for the nitrogen dope treatment. The pressure was 4.8 Pa during the period when the nitrogen was introduced to the three-cell, and was steadied 3 Pa state then. After treatment, the cavity was packed into a plastic bag and transported to KEK.



Figure 1: The set-up of nitrogen doping using oil-free furnace at J-PARC.

EXPERIMENTAL SET-UP

The cavities were measured at the vertical test stand in KEK [5]. The ambient magnetic field was maintained to less than a few mG using the solenoid coil for the single-cell

* okadat@post.kek.jp

Content from this work may be used under the terms of the CC BY 3.0 licence (© 2018). Any distribution of this work must maintain attribution to the author(s), title of the work, publisher, and DOI.

ISBN: 978-3-95450-194-6 ISSN: 2226-0366 doi:10.18429/JACoW-LINAC2018-TUPO065

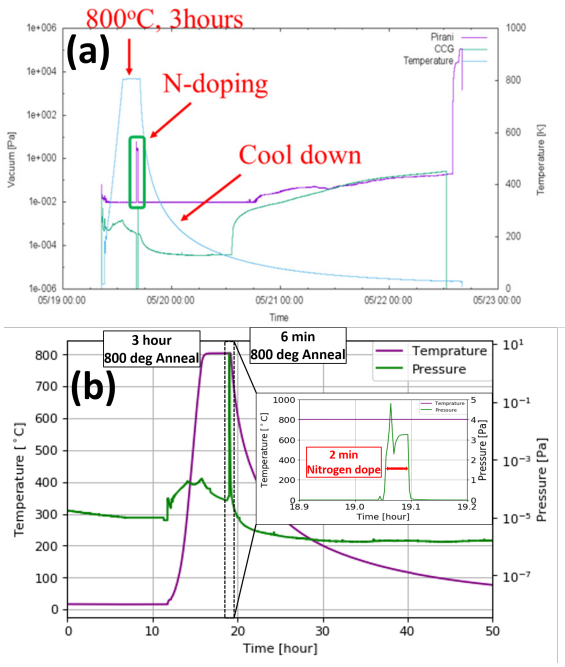


Figure 2: The temperature and pressure data in the nitrogen doping for a) single-cell applied heavy dope [3] and b) three-cell applied light dope.

cavity. The solenoid jig did not fit in the case of the three-cell cavity. The ambient magnetic field is about 6 mG. Figure 3 shows the set-up of the vertical test for the superconducting cavity with fluxgate sensors and silicon thermometers at the equator of cavities. To identify the location of a quench region, the mapping system consists of carbon resisters every 15 degrees, and silicon PIN photodiodes were mounted to each iris area. A heater was used to achieve an temperature gradient [3].

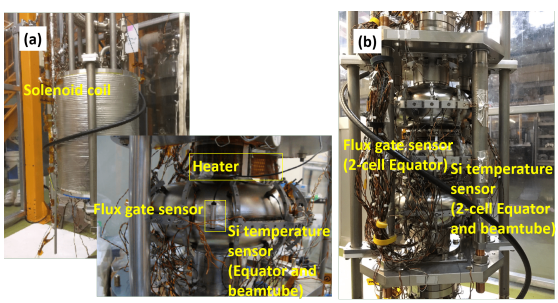


Figure 3: The picture of the set-up for vertical test. a) Solenoid coil, Si sensers and flux gate senser for single-cell cavity applied heavy dope. Using solemoid coil for cancel ambient magnetic field. b) For three-cell cavity applied light dope without solenoid coil.

EXPERIMENTAL RESULTS AND ANALYSIS

The surface resistance is expressed by

$$R_s(T) = R_{BCS}(T) + R_{res}, \quad (1)$$

where $R_{BCS}(T)$ is a temperature depended term and R_{res} is a temperature independent term. Using an approximation, the surface resistance is fitted by as follows:

$$R_s(T) = \frac{A}{T} \exp^{\frac{-\Delta}{k_B T}} + const, \quad (2)$$

the $R_{BCS}(T) = \frac{A}{T} \exp^{\frac{-\Delta}{k_B T}}$ is defined and R_{res} is defined as a constant term. The fitting constant A, exponent related to Δ, and the constant term is determined by a least-squares method in this study.

Single-cell Cavity

The quality factor of the cavity was measured at temperature of 2.0 K, 1.8 K, 1.6 K, and 1.5 K. The upper left of Figure 4 shows the relationship between the quality factor and the accelerating gradient. The reference is the result of the standard recipe that 800 °C annealing and a few EP and 120 °C baking, applied the same cavity. The quench field decrease from 40 MV/m to 14 MV/m and the quench location was changed. The quality factor increased to 3.1×10^{10} from 1.9×10^{10} at 14 MV/m and a temperature of 2.0 K.

The measurement was stoped at 10 MV/m for value of 1.8K, 1.6K, and 1.5K. The surface resistance is separated into the BCS resistance and the residual resistance from the fitting method using data at each temperature. The upper center nad right of Figure 4 shows the result of the BCS and residual resistance as a function of the accelerating gradient. The nitrogen doped cavities exhibitted a distinct anti-Q slope with an increase of accelerating gradient. This result of the BCS resistance exhibits anti-Q slope. The residual resistance decreased to under 2 nΩ. These results show that the nitrogen dope study was successful using the J-PARC furnace.

Three-cell Cavity

Other nitrogen doping recipes light dope was applied to the three-cell cavity. The cavity was measured in the π mode.

The lowerr left of Figure 4 shows the result for measurement of the quality factor as a function of the accelerating gradient at each temperature. The quench field decrease from 35 MV/m to 20 MV/m after nitrogen light doping. The quality factor increase from 1.1×10^{10} to 1.6×10^{10} at 2.0 K. However, at other temperature, the quality factor did not change. Figure 4 lower center and right shows the result of analyzing the surface resistance. The result of the BCS resistance is obtained by fitting of 2 MV/m to 10 MV/m. The BCS resistance decrease with increase accelerating gradient for nitrogen light doped cavity. The analysis of the result includes the quality factor measurement at 4.2 K. The light doping method for three-cell cavity succeeded by anti-Q slope achievement. The residual resistance not changed.

Content from this work may be used under the terms of the CC BY 3.0 licence (© 2018). Any distribution of this work must maintain attribution to the author(s), title of the work, publisher, and DOI.

ISBN: 978-3-95450-194-6 ISSN: 2226-0366 doi:10.18429/JACoW-LINAC2018-TUPO065

Content from this work may be used under the terms of the CC BY 3.0 licence (© 2018). Any distribution of this work must maintain attribution to the author(s), title of the work, publisher, and DOI.

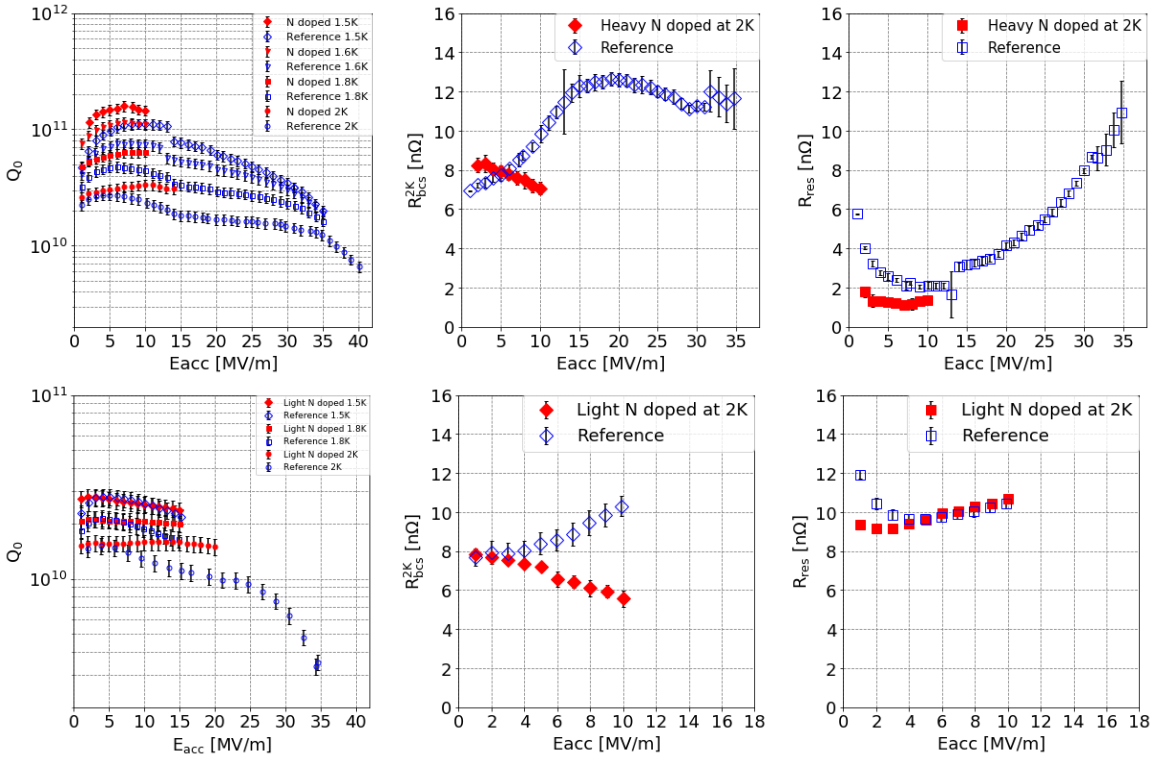


Figure 4: Upper figure shows the result of the heavy doped single-cell cavity. Lower figure shows the result of the light doped three-cell cavity.

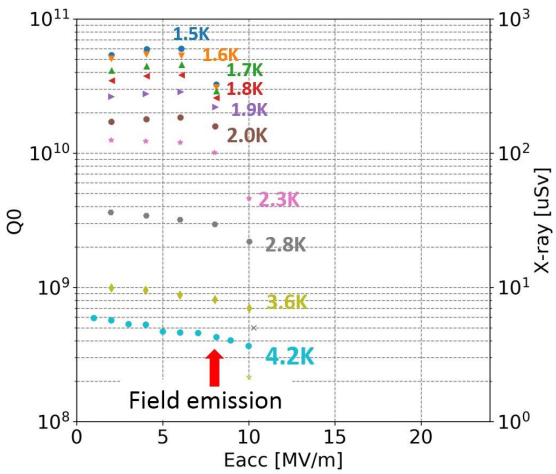


Figure 5: The quality factor measurement retried at each temperature from 1.5 K to 4.2 K.

The test of the three-cell cavity in order to measure the temperature dependence of the nitrogen dope effect was tested. Figure 5 shows the result of measurement at each temperature.

Unfortunately, this measurement occurs the field emission at low gradient about 8 MV/m. Increasing Q starts from about 2.3 K. The re-measurement of the quality factor without field emission is planed.

SUMMARY AND DISCUSSION

Two nitrogen doping recipes were applied in the single-cell cavity and three-cell cavity, respectively. The quality factor at 2.0 K has increased. The BCS resistance exhibit an anti-Q slope in both experiments. The study of nitrogen doping using J-PARC furnace was succeeded. Because the result of the light doped the three cell cavity is not measured with magnetic field cancellation, it is necessary to use the solenoid coil to improve the ambient magnetic field. It is anticipated that the temperature independent term is decreased, result in the quality factor increase. However, the nitrogen doping effect of three-cell over 2.0K temperatures was not outstanding. In particular, an anti-Q slope has not exhibited at 4.2 K.

Overall, the nitrogen doping was successful and the study of nitrogen doping and nitrogen infusion has been initiated at KEK [6, 7].

REFERENCES

[1] A. Grassellino *et al.*, "Nitrogen and argon doping of niobium for superconducting radio frequency cavities:a pathway to highly efficient accelerating structures", *Supercond. Sci. Technol*, vol. 26, no. 10, p. 102001, 2013. doi:10.1088/0953-2048/26/10/102001

[2] K. Umemori *et al.*, "Vertical Test Results of Nitrogen Doped SRF Cavities at KEK", in *Proc. IPAC'16*, Busan, Korea, May 2016, pp. 2154-2157. doi:10.18429/JACoW-IPAC2016-WEPMB016

ISBN: 978-3-95450-194-6 ISSN: 2226-0366 doi:10.18429/JACoW-LINAC2018-TUPO065

[3] T. Konomi *et al.*, "Trial of Nitrogen Infusion and Nitrogen Doping by Using J-PARC Furnace", in *Proc. SRF'17*, Lanzhou, China, July 2017, pp. 775-778. doi:10.18429/JACoW-SRF2017-THPB021

[4] T. Dohmae *et al.*, "Investigation of SRF Elliptical Cavities Made by New Nb Materials in KEK", presented at LINAC'18, Beijing, China, Sep. 2018, paper THPO002, this conference.

[5] K. Umemori *et al.*, "Improvement of Magnetic Condition for KEK-STF Vertical Test Facility toward High-Q study", in *Proc. SRF'17*, Lanzhou, China, July 2017, pp. 444-447. doi:10.18429/JACoW-SRF2017-TUPB028

[6] T. Konomi *et al.*, "Niobium Sample Analysis for Nitrogen Infusion and Doping", presented at LINAC'18, Beijing, China, Sep. 2018, paper TUPO073, this conference.

[7] K. Umemori *et al.*, "Study on Nitrogen Infusion for 1.3 GHz SRF Cavities Using J-PARC Furnace", presented at LINAC'18, Beijing, China, Sep. 2018, paper TUPO071, this conference.

Content from this work may be used under the terms of the CC BY 3.0 licence (© 2018). Any distribution of this work must maintain attribution to the author(s), title of the work, publisher, and DOI.

ISBN: 978-3-95450-194-6 ISSN: 2226-0366 doi:10.18429/JACoW-LINAC2018-TUPO066

LOWER CRITICAL FIELD MEASUREMENT OF THIN FILM SUPERCONDUCTOR

H. Ito†, SOKENDAI, 305-0801 Tsukuba, Ibaraki, Japan
H. Hayano, T. Kubo, T. Saeki, KEK, 305-0801 Tsukuba, Ibaraki, Japan
Y. Iwashita, R. Katayama, H. Tongu, Kyoto ICR, Kyoto University, 611-0011 Uji, Kyoto, Japan
R. Ito, T. Nagata, ULVAC Inc., 286-0225 Chiba, Japan
H. Oikawa, Utsunomiya University, 321-8585, Utsunomiya, Tochigi, Japan
C. Z. Antoine, A. Four, CEA Irfu, F-91191 Gif-sur-Yvette, France

Abstract

The superconducting thin film is the promising technology to increase the performance of SRF cavities. The lower critical field H_{c1}, which is one of the important physical parameters characterizing a superconducting material, will be enhanced by coating Nb with thin film superconductor such as NbN. To measure the H_{c1}, we developed the measurement system using the third harmonic response of applied AC magnetic field from solenoid coil. In order to control the temperature of the sample, we installed heaters and thermal anchors which could be moved by the motor. By this temperature control the sample state can be easily transited from the Meissner state to the mixed state. By raising the temperature of the sample with applying AC magnetic field, H_{c1} and transition temperature, which is point of transition from the Meissner state to the mixed state, can be determined at when the third harmonic response appears in the voltage of solenoid coil. By repeating the measurement for various applied AC magnetic field, the H_{c1} vs temperature can be plotted. In this report, measurement result of the bulk Nb sample and NbN-SiO_2 multilayer thin film sample are presented.

INTRODUCTION

S-I-S (Superconductor-Insulator-Superconductor) thin film multilayer structure has been proposed by Gurevich to enhance the effective H_{c1}, and Kubo made advanced theoretical study [1, 2]. Antoine has measured effective H_{c1} with third harmonic voltage method and shows the possibility of H_{c1} increase [3]. The third harmonic measurement system was also constructed by Iwashita, Katayama, and Tongu in Kyoto University, and improvement of effective H_{c1} has been confirmed by the measurement of NbN-SiO_2 multilayer thin film sample which has been produced by ULVAC, inc. [4-6]. In order to increase H_{c1} measurement capability in our research group and to measure a large number of samples, KEK also set up the third harmonic measurement system. In this report, development status of the measurement system and the measurement result of bulk Nb sample and NbN-SiO_2 multilayer thin film sample are reported.

MEASUREMENT SYSTEM

This experiment is carried out by cooling the sample with liquid helium (LHe) stored in the bottom of cryostat, and LHe is supplied from Helium dewar using transfer tube. The 1kHz AC magnetic field is applied to the superconducting sample using solenoid coil, and the third harmonic components (3 kHz) induced in the solenoid coil when the magnetic field penetrate into the sample is detected. At this time, from the magnetic field strength applied to the sample and the temperature of the sample, the effective H_{c1} of the sample at that temperature (transition temperature) is measured. In addition, by repeating the measurement with various applied magnetic fields, the temperature dependence of H_{c1} is measured.

Sample Stage and Coil Stage

The measurement setup consists of the two copper stages for the sample and the exciting coil. The sample stage has two copper thermal anchors which are equipped with heater for increase sample temperature. The coil stage has also two copper thermal anchors whose bottom ends are immersed in LHe to decrease the sample temperature. By controlling the whole stage position up and down by the vertical mover which movable range is 100 mm, it is possible to control the immersion depth of the copper thermal anchors into the LHe. One of the temperature sensors is directly contact with backside of the sample and the remaining three temperature sensors could monitor the temperature of any part of the stage. The sample put between the two stages. The gap distance of 0.85 mm between sample surface and the coil stage is kept by three small SiN balls embedded in the coil stage (see Figs. 1 and 2).

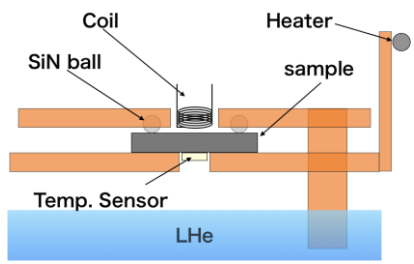


Figure 1: Cross-sectional Schematic of setup.

† hayatoi@post.kek.jp

Content from this work may be used under the terms of the CC BY 3.0 licence (© 2018). Any distribution of this work must maintain attribution to the author(s), title of the work, publisher, and DOI.

ISBN: 978-3-95450-194-6 ISSN: 2226-0366 doi:10.18429/JACoW-LINAC2018-TUPO066

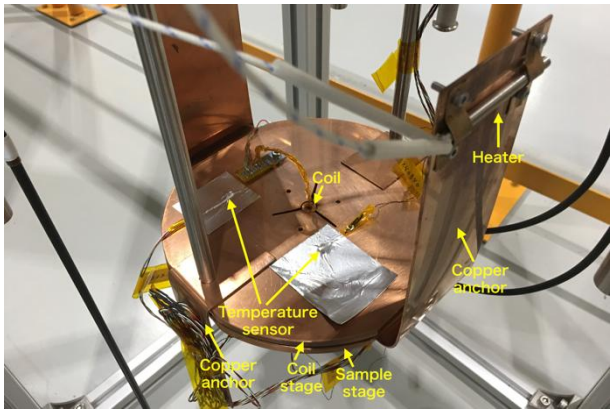


Figure 2: The picture of the copper stage setup for third harmonic measurement.

Circuit

Figure 3 shows the block diagram of the measurement circuit. The signal generator (S.G.) generates 1 kHz sinusoidal waveform with amplitude 1 V_{pp}. The 1 kHz signal passes through 1 kHz band-pass-filter (BPF) with bandwidth of +/- 20 Hz. Another 1 kHz signal passes through the three-multiplier and phase shifter, then fed into the mixer. The amplified 1 kHz signal is applied to the coil in the cryostat to generate magnetic field on the sample. The amplified 1 kHz signal is picked up and fed into 3 kHz BPF with bandwidth of +/- 30 Hz. The detected 3 kHz signal is amplified with gain, 10, 100, and 1000, then fed into the mixer. The mixer detects their phase. The phase signal is fed into the 1 Hz low-pass-filter (LPF). The output of the 1Hz LPF is DC signal and is the third harmonic components in the coil voltage.

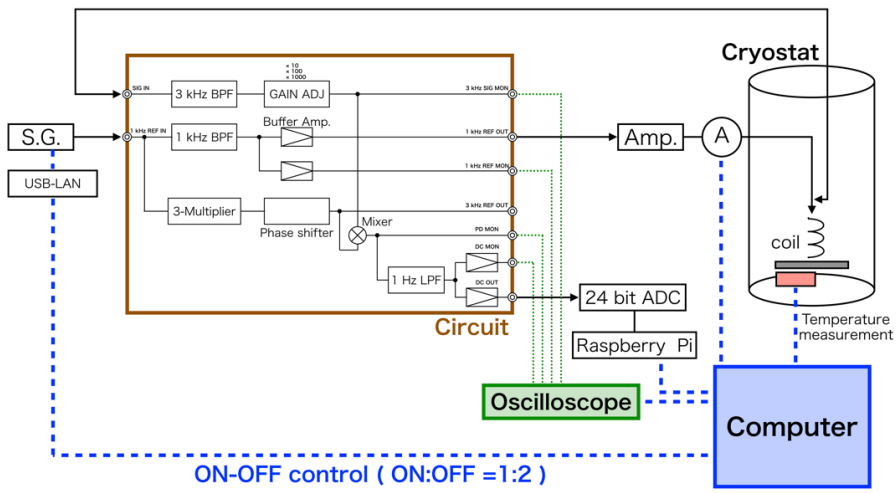


Figure 3: The block diagram of the measurement circuit.

Data Acquisition System

The output of the 1Hz LPF is digitised by the 24 bits ADC and transmitted to the host computer by Raspberry Pi computer. The oscilloscope monitors 3 kHz SIG MON, 1 kHz REF MON, PD MON, and DC MON. Their waveforms are recorded by the host computer. Four temperature sensor and ammeter that monitors the amplified 1 kHz signal are recorded by the host computer.

H_{c1} Definition

The magnetic field strength from the coil at the moment when the third harmonic signal is significantly changed is defined as the H_{c1} and the temperature at that moment is defined as transition temperature. In order to know the applied magnetic field strength on the sample from the coil, calibration was performed using the measurement result of bulk Nb sample assuming that following function $H_{c1}(t)$ is the temperature dependence of H_{c1} of bulk Nb:

$$H_{c1}(t) = 180 \times \left\{1 - (\frac{t}{T_c})^2\right\} \quad (1)$$

where T_c which is the critical temperature of the Nb is free parameter.

MASUREMENT RESULTS

The third harmonic components have the offset proportional to the current in the coil (blue line) (see Fig. 4). Since there is a negative offset of third harmonic components at the point where the current is zero, the offset of third harmonic components was corrected against the negative offset when the magnetic field strength from the coil was calculated (red line).

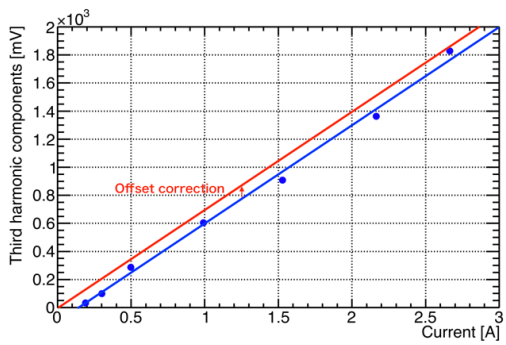


Figure 4: The third harmonic components vs current in the coil at gain 10.

Content from this work may be used under the terms of the CC BY 3.0 licence (© 2018). Any distribution of this work must maintain attribution to the author(s), title of the work, publisher, and DOI.

ISBN: 978-3-95450-194-6 ISSN: 2226-0366 doi:10.18429/JACoW-LINAC2018-TUPO066

Content from this work may be used under the terms of the CC BY 3.0 licence (© 2018). Any distribution of this work must maintain attribution to the author(s), title of the work, publisher, and DOI.

Result of Bulk Nb

Figure 5 shows the typical measurement result of bulk Nb. The vertical axis shows the third harmonic components detected by the 24 bits ADC and the horizontal axis shows the bulk Nb sample temperature. The significant change of the third harmonic components at around T_c of Nb was detected. The intersection point of the two linear fitting curves (red lines) was defined as transition point.

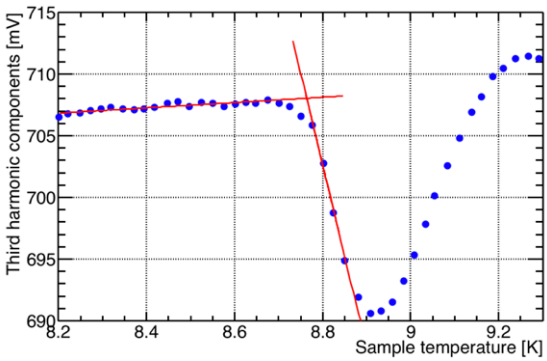


Figure 5: Third harmonic components vs sample temperature at 1 A coil current.

Figure 6 shows the amplitude of the third harmonic component as a function of the transition points obtained in the various applied AC magnetic field. The temperature dependence of H_{c1} of bulk Nb was obtained by relating the amplitude of the third harmonic component of Fig. 6 to the magnetic field using Eq. (1).

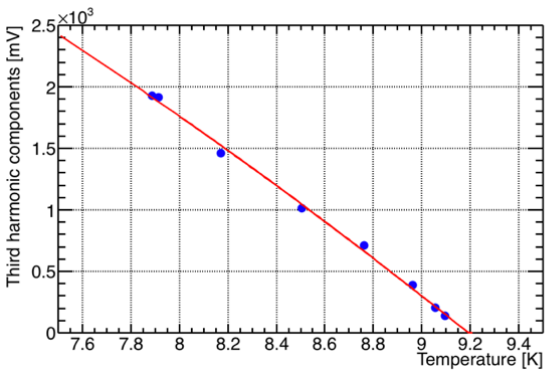


Figure 6: Plot of the transition points in case of the bulk Nb.

Result of NbN-SiO_2 Multilayer Thin Film

Figure 7 shows the measurement result of NbN-SiO_2 multilayer thin film sample. The red line is the Eq. (1) which is used for the calibration of the bulk Nb result. The blue points show calibrated result of bulk Nb. The green dashed line is fitting curve obtained by two triangle points (transition point of NbN-SiO_2 multilayer thin film sample). The third harmonic response of NbN-SiO_2 multilayer thin film sample was detected with only two points at high temperature region at which bulk Nb substrate is normal conducting state (> 9.2 K). At low temperature region at which both bulk Nb substrate and NbN thin film are superconducting state (< 9.2 K), the transition point could not be estimated due to large fluctuation of third harmonic components.

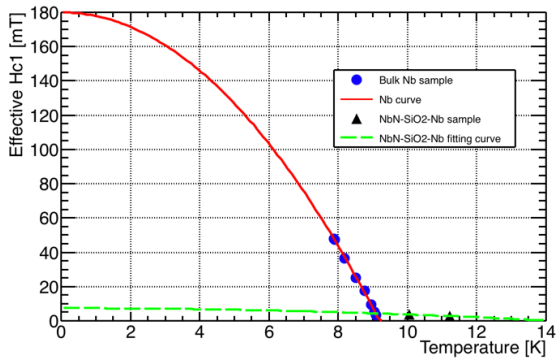


Figure 7: Critical magnetic field vs temperature.

IMPROVEMENTS

After these experiment, we found that the ammeter caused high third harmonic components offset. The offset was suppressed by two orders by replacement of the ammeter. In order to apply strong magnetic field to the sample, the distance between the coil and the sample surface was changed 0.85 mm to 0.45 mm. But fluctuation of third harmonic components became large, distance was restored back.

CONCLUSION

The third harmonic measurement system is constructed and commissioned in KEK. The bulk Nb sample was measured and calibration of magnetic field strength was performed. The measurement of NbN-SiO_2 multilayer thin film sample succeeded in high temperature region. In order to suppress the fluctuation of third harmonic components and make strong magnetic field, the improvements are ongoing.

ACKNOWLEDGEMENT

This work is supported by Japan Society for the Promotion of Science Grant-in-Aid for Young Scientist (A) No.17H04839.

REFERENCES

[1] A. Gurevich, "Enhancement of rf breakdown field of superconductors by multilayer coating", *Appl. Phys. Lett.*, vol. 88, p. 012511, 2006.

[2] T. Kubo *et al.*, "Radio-frequency electromagnetic field and vortex penetration in multi-layered super-conductors", *Appl. Phys. Lett.*, vol. 104, p. 032603, 2014.

[3] C. Z. Antoine, M. Aburas, A. Four *et al.*, "Progress on characterization and optimization of multilayers", in *Proc. 18th Int. Conf. RF Superconductivity (SRF'17)*, Lanzhou, China, Jul. 2017.

ISBN: 978-3-95450-194-6 ISSN: 2226-0366 doi:10.18429/JACoW-LINAC2018-TUPO066

[4] Y. Iwashita, H. Tongu, H. Hayano *et al.*, "Measurement of thin film coating on superconductors", in *Proc. 8th Int. Particle Accelerator Conf. (IPAC'17)*, Copenhagen, Denmark, May 2017.

[5] R. Katayama *et al.*, "Evaluation of superconducting characteristics on the thin- lm structure by NbN and Insulator coatings on pure Nb substrate", in *Proc. 9th Int. Particle Accelerator Conf. (IPAC'18)*, Vancouver, BC, Canada, Apr.-May 2018.

[6] R. Ito, T. Nagata *et al.*, "Development of Coating Technique for Superconducting Multilayered Structure", in *Proc. 9th Int. Particle Accelerator Conf. (IPAC'18)*, Vancouver, BC, Canada, Apr.-May 2018.

Content from this work may be used under the terms of the CC BY 3.0 licence (© 2018). Any distribution of this work must maintain attribution to the author(s), title of the work, publisher, and DOI.

ISBN: 978-3-95450-194-6 ISSN: 2226-0366 doi:10.18429/JACoW-LINAC2018-TUPO067

STUDY ON NEW REMOVAL THICKNESS DISTRIBUTION IMPROVEMENT METHODS FOR NIOBIUM 9-CELL CAVITY VERTICAL ELECTROPOLISHING WITH NINJA CATHODE

K.Nii#, V.Chouhan, Y.Ida, T.Yamaguchi, Marui Galvanizing Co., Ltd., Himeji, Japan
H.Hayano, S.Kato, H.Monjushiro, T.Saeki, M.Sawabe, KEK, Tsukuba, Japan

Abstract

Marui Galvanizing Co., Ltd. has been developing niobium 9-cell cavity vertical electropolishing (VEP) technologies with Ninja cathode in collaboration with KEK. Conventional 9-cell cavity VEP had a serious problem, which was asymmetry of removal thickness distribution. Usually removal thickness of upper side became larger than lower side in case of both in-cell and inter-cell. So far, as one solution, we proposed "bubble diffusion prevention" method and proved it was effective for uniform removal. This time, as other new solution, we tried "cavity flip upside down" and "Ninja cathode masking" VEP methods. In this article we will report the purpose, intention and VEP experiment result of these methods.

INTRODUCTION

Marui Galvanizing Co., Ltd. is working on the development of vertical electropolishing (VEP) technology of niobium SRF cavity using Ninja cathode in collaboration with KEK for mass production and cost reduction. In the 9-cell cavity VEP, there was a problem that the removal thickness distribution became non-uniform (upper side is larger than lower side) because of bubble accumulation so far. We have done a lot of experiments working on solving this problem. Divide the flow path of the EP liquid into the inside and the outside of the Ninja cathode and optimally control the respective flow velocities and providing the power off time, it was shown that bubbles are prevented from accumulating in the cavity, and the removal thickness distribution is greatly improved to be uniform [1,2].

Furthermore, in order to understand the 9 cell cavity VEP and approach it for improvement, we aimed to solve the problem of non-uniform removal thickness in another way this time. One method is to invert the upper and lower sides of the cavity during VEP to make the removal thickness uniform (Cavity flip upside down VEP), and the other is using masked cathode to control the removal thickness of each part to make it uniform (Cathode masking VEP). We conducted VEP experiments using these methods and a 9 cell coupon cavity. The results such as removal thickness distribution are reported in this article.

#keisuke_nii@e-maui.jp

CAVITY FLIP UPSIDE DOWN VEP

Cavity flip upside down VEP was performed using dedicated cavity holder. In this holder, motor – cathode connection side is defined as top and the state where the top is on the upper side is called the forward position. The cathode penetration part of top PVC piece was specially sealed to prevent EP acid leakage in case of reverse position. The setup and inversion procedure are shown in Figure 1.



Figure 1: Cavity flip upside down setup and procedure.

Table 1: Conditions of Cavity Flip Upside Down VEP

Parameters	Cavity flip upside down VEP
Voltage	~14V
Current density	20 – 30 mA/cm^2
Cavity surface temperature	20~25 □C
Cathode rotation speed	20 rpm (forward position) 0rpm (reverse position)
Acid flow rate	5~10 L/min
EP time	5min (F-R)+15min (F-R)+20min (F-R)
Average removal thickness	~30um
Cathode	Ninja-v6 (With metallic wings and mesh cover)

Table 1 shows the conditions of cavity flip upside down VEP experiment. For this experiment, a 9cell coupon cavity [3] and Ninja cathode V6 with metal wings and mesh cover were used. The VEP was performed according to the procedure of 5min (forward position) – 5min (reverse position) – 15min (forward position) – 15min (reverse position) – 20min (forward position) – 20min (reverse position). The cathode rotation was carried out in the forward position, however not in reverse position (concerned about EP acid leakage).

Content from this work may be used under the terms of the CC BY 3.0 licence (© 2018). Any distribution of this work must maintain attribution to the author(s), title of the work, publisher, and DOI.

ISBN: 978-3-95450-194-6 ISSN: 2226-0366 doi:10.18429/JACoW-LINAC2018-TUPO067

Figure 2 shows the average of coupon current on 5min forward and reverse position VEP and the average of them.

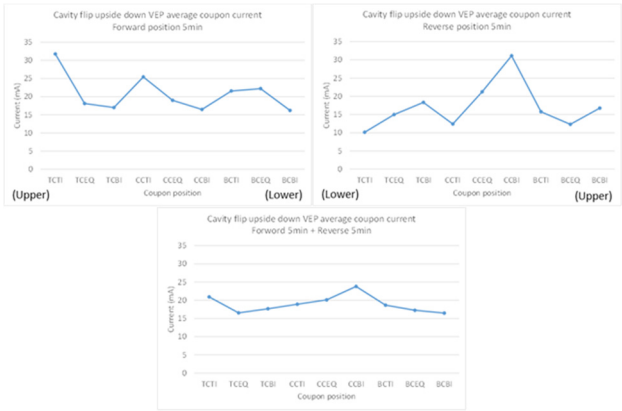


Figure 2: Average of each coupon current, (upper left) 5min forward position VEP, (upper right) 5min reverse position VEP, (lower) the average of them.

It is shown that the upper coupon current is larger than lower one in both forward position and reverse position. This is the same tendency of usual VEP. And taking average of them, coupon current became uniform as a whole. From this it can be seen that the coupon current is made uniform by the effect of cavity flip upside down.

Figure 3 shows the logged data and total average of coupon current during this VEP. Even through all, it is said that the coupon current is averaged and uniform.

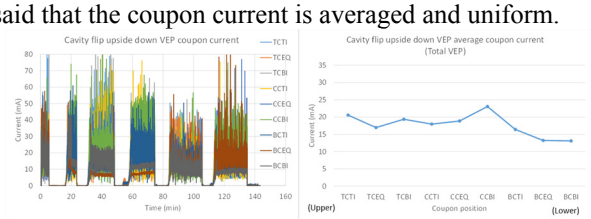


Figure 3: (Left) the logged data of each coupon current, (Right) average of coupon current of total VEP.

Figure 4 shows the removal thickness distribution measurement result after this VEP. The result is compared with that of usual VEP. This measurement was performed using ultrasonic thickness gauge.

On usual VEP, the difference of Max-Min is around 3 times, on the other hand, on flip upside down VEP, that is around within 2 times, it is greatly improved.

Figure 5 shows the coupon surface status and surface roughness.

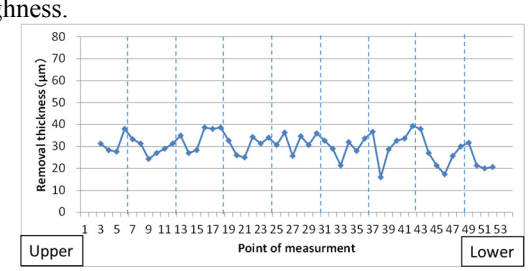


Figure 4: Removal thickness distribution result with cavity flip upside down.

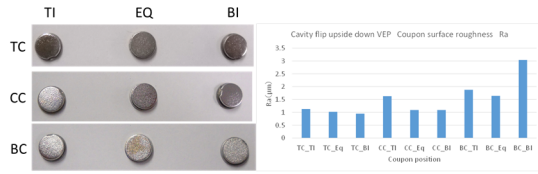


Figure 5: Status and roughness of each coupon after VEP.

The top cell, center cell coupon surface were shiny and low surface roughness, however bottom cell coupon had slightly rough surface. Although the detailed cause is unknown, it is thought that asymmetry of setup is main cause (no rotation in reverse position, different top and bottom PVC piece shape etc.). From now on, we will improve the cathode penetration part seals so that the cathode can be rotated even in the reverse position, adjust the sizes of the top and bottom PVC pieces, and aim for further improvement in removal thickness distribution and polished surface.

CATHODE MASKING VEP

VEP experiments were performed using masked Ninja cathodes with the aim of improving removal thickness uniformity by cathode masking. In order to confirm the effect of cathode masking in the niobium 9-cell cavity VEP, this time we compared the difference between lower 4 cells with no masking and the top 5 cells with masking. Figure 6 shows a schematic view of cathode masking state and Table 2 shows conditions of cathode masking VEP. For this experiment, 9cell coupon cavity and Ninja cathode V6 with metal wings and mesh cover were used.

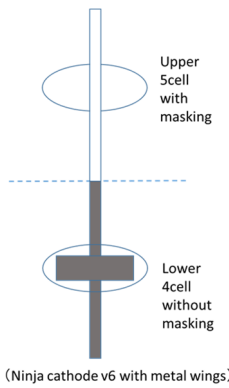


Figure 6: Schematic view of cathode masking state.

Table 2: Conditions of Cathode Masking VEP

Parameters	Cathode masking VEP
Voltage	~15V
Current density	10 – 15 mA/cm^2
Cavity surface temperature	20~25 □C
Cathode rotation speed	20 rpm
Acid flow rate	5~10 L/min
EP time	~60min
Average removal thickness	~20um
Cathode	Ninja-v6 (With metallic wings and mesh cover)

Content from this work may be used under the terms of the CC BY 3.0 licence (© 2018). Any distribution of this work must maintain attribution to the author(s), title of the work, publisher, and DOI.

ISBN: 978-3-95450-194-6 ISSN: 2226-0366 doi:10.18429/JACoW-LINAC2018-TUPO067

Content from this work may be used under the terms of the CC BY 3.0 licence (© 2018). Any distribution of this work must maintain attribution to the author(s), title of the work, publisher, and DOI.

Figure 7 shows IV curves of each coupon and Figure 8 shows logged data of coupon current during VEP. In the top cell and the center cell with masking, the current was suppressed compared to the bottom cell without masking, but it did not become completely 0 and it was somewhat flowed.

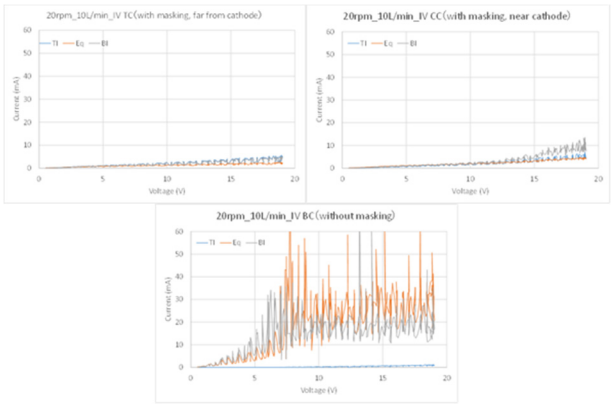


Figure 7: Coupon IV curves of top cell (upper left), center cell (upper right), bottom cell (lower).

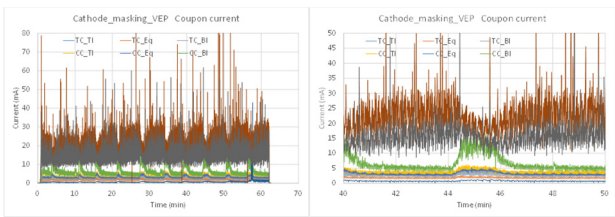


Figure 8: Logged data of coupon current during VEP.

Figure 9 shows the removal thickness distribution measurement result. About no cathode masking part, the distribution tendency was the same as usual VEP, on the other hand cathode masking part, removal thickness became very small, however it was not completely 0 and 5 -10 um removed.

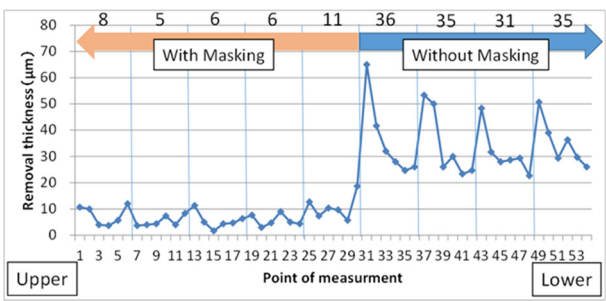


Figure 9: Removal thickness distribution results.

Figure 10 shows the coupon surface status and surface roughness. The top and center cell coupon surface became rough. This seems to be due to the progress of etching under improper conditions in the cathode masking part. Although the effect of masking is seen, it turned out that it is necessary to design the masking shape in consideration of these points in order to realize VEP with uniform removal thickness and shiny surface. We are currently devising a masking shape.

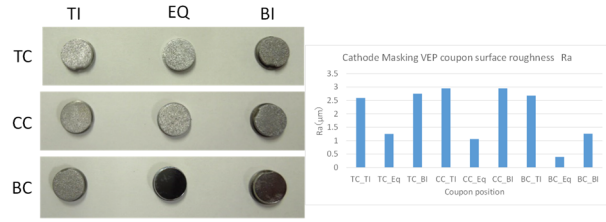


Figure 10: Status and roughness of each coupon after VEP.

SUMMARY

Up to now we have developed EP acid flow separation method to improve the distribution of polishing amount of niobium 9 cell cavity VEP, in addition we have done cavity flip upside down VEP and cathode masking VEP as other methods. On the cavity flip upside down VEP, it was found that the current of each coupon was averaged and the removal thickness distribution greatly improved. The polished surface was almost shiny, but some rough portions were also seen. It seems to be due to the fact that the cathode was not rotated at the time of reverse position and the size of the top and bottom PVC pieces were different. We are making these improvements at the moment and we plan to further advance the VEP experiment. On the cathode masking VEP, although the effect of reducing the polishing amount by masking was observed, there was a problem that the surface was roughened. We plan to proceed with the design and verification experiment of cathode masking VEP considering these in the future.

REFERENCES

[1] V.Chouhan *et al.*, in *Proc. 17th Int. Conf. RF Superconductivity (SRF'15)*, Whistler, Canada, Sep. 2015, paper THPAL030.

[2] V.Chouhan *et al.*, presented at the 29th Linear Accelerator Conf. (LINAC'18), Beijing, China, Sep. 2018, paper TUPO068, this conference.

[3] S.Kato *et al.*, in *Proc. 28th Linear Accelerator Conf. (LINAC'16)*, East Lansing, MI, USA, Sep. 2016, pp. 220--222, doi:10.18429/JACoW-LINAC16- MOPLR038

ISBN: 978-3-95450-194-6 ISSN: 2226-0366 doi:10.18429/JACoW-LINAC2018-TUPO068

VERTICAL ELECTROPOLISHIG OF 1.3 GHz NIOBIUM NINE-CELL SRF CAVITY: BULK REMOVAL AND RF PERFORMANCE

V. Chouhan†, Y. Ida, K. Nii, T. Yamaguchi, Marui Galvanizing Co, Ltd, 672-8022 Himeji, Japan
H. Hayano, S. Kato, H. Monjushiro, T. Saeki, M. Sawabe, H. Ito, KEK, 305-0801 Tsukuba, Japan
H. Oikawa, Utsunomiya University, 321-8505, Utsunomiya, Japan
H. Ito, Sokendai, 240-0193, Hayama, Japan

Abstract

Vertical electropolishing (VEP) technique have been successfully developed for 1.3 GHz niobium (Nb) single cell cavity to achieve a smooth surface with uniform removal and better RF performance as achieved after horizontal EP (HEP) process. VEP parameters for 1.3 GHz Nb nine-cell cavities are being studied using a nine-cell coupon cavity and our unique Ninja cathode. The investigated VEP parameters heretofore were applied on a 1.3 GHz Tesla shape nine-cell superconducting RF cavity for bulk removal of 100 µm followed by fine removal of 20 and 10 µm. The interior surface was found to be smooth and shiny after the VEP process. Our recently developed dual flow technique, in which the EP acid is flown separately in the Ninja cathode housing and cavity, yielded lower asymmetry in removal along the cavity length. The cavity was tested in a vertical cryostat after the final VEP process. The cavity achieved 28.3 MV/m at Q_0 value of 6.7×10^9. The cavity performance was almost the same as in the baseline vertical test performed after the HEP process.

INTRODUCTION

Electropolishing (EP) is now a standard method for surface treatment of niobium accelerating cavities where the EP process is carried out with a horizontal EP (HEP) system. As an alternative way, the cavity can be set vertically to perform electropolishing with a so-called vertical EP (VEP) setup which is comparatively simple and cost-effective. However, the VEP method yielded asymmetric removal and bubble traces on the interior surface of the cavity [1]. In our previous studies, we have shown the major cause of asymmetry is an accumulation of H_2 gas bubbles, generated at the aluminum cathode used for EP process, on the cavity surface [2]. We have successfully resolved the issue of the asymmetric removal and rough surface with our patented Ninja cathode and optimized VEP parameters including cathode rotation speed, operational temperature, applied voltage, and current density [3, 4]. The cathode housing covered with a meshed Teflon sheet guides gas bubbles along the cathode and reduces diffusion of bubbles from the cathode housing to the cavity. However, the removal of bubbles from ~1.2 m long nine-cell cavity is quite difficult and the accumulation of bubbles in the upper cells cannot be avoided with the process and parameters applied on the single cell cavity. We have developed a dual flow technique to remove gas bubbles from the cathode housing quickly so as to reduce bubble diffusion from the housing to the cavity. In this technique, the acid is flown separately in the Ninja cathode housing and cavity while keeping a higher flow rate in the cathode housing [5]. Effect of the technique with adequate flow rates has been presented elsewhere [5]. This paper shows the first bulk VEP of a nine-cell cavity with the Ninja cathode, vertical test result, and future work to further improve the VEP technique.

VEP EXPERIMENTS AND RESULTS

A Tesla shape 1.3 GHz Nb nine-cell superconducting RF cavity (TB9-TSB01), which was surface treated earlier with the HEP process and has a baseline vertical test result, was selected for the VEP process. VEP process was performed with our VEP system (see Fig. 1) which is equipped with auto-controlled valves and programmed acid flow direction. The system is equipped with a water spray facility for cavity cooling and a heat exchanger for acid cooling in the acid reservoir. Pure water is uniformly sprayed at the exterior of the cavity during the EP process. As a cathode for the VEP process, the Ninja cathode having 3 insulating blades in each cell of the cavity was used. The acid inlet line was bifurcated in two lines to flow acid in the Ninja cathode housing and the cavity separately. Two flow meters are set on the two lines to measure the flow rates in the cathode housing and cavity.

Three VEP processes have been carried out for the cavity TB9-TSB01 for bulk removal of 100 µm, fine removal of 20 and 10 µm. The removal thickness was calculated from the measured integrated current with a current hour meter. The cavity was annealed at 750 °C after the bulk VEP and 20 µm removal. After each VEP process, the cavity was rinsed with ultrasonic oscillators and at high pressure water rinsing.



Figure 1: VEP system with auto-valves (left) and cavity set at VEP stand (right) for the VEP process.

†vchouhan@e-marui.jp

Content from this work may be used under the terms of the CC BY 3.0 licence (© 2018). Any distribution of this work must maintain attribution to the author(s), title of the work, publisher, and DOI.

ISBN: 978-3-95450-194-6 ISSN: 2226-0366 doi:10.18429/JACoW-LINAC2018-TUPO068

Content from this work may be used under the terms of the CC BY 3.0 licence (© 2018). Any distribution of this work must maintain attribution to the author(s), title of the work, publisher, and DOI.

VEP parameters studied with the nine-cell coupon cavity were applied for the VEP processes [5]. The cathode was rotated at 20 rpm continuously during the VEP process and the post-EP water rinsing process. The acid was separately flown in the cathode housing and cavity. The flow rates and other VEP parameters are summarized in Table 1.

Table 1: Parameters and Conditions for VEP Process

Conditions	Value
Acid (H_2SO_4:HF)	9:1
Voltage	18.5 V
Cavity temperature	< 15°C
Cathode	Ninja cathode
Cathode rotation	20 rpm
Acid flow condition	Dual
Target flow rate in Ninja cathode	10 L/min
Target flow rate in cavity	5 L/min
Acid flow direction	Bottom to top

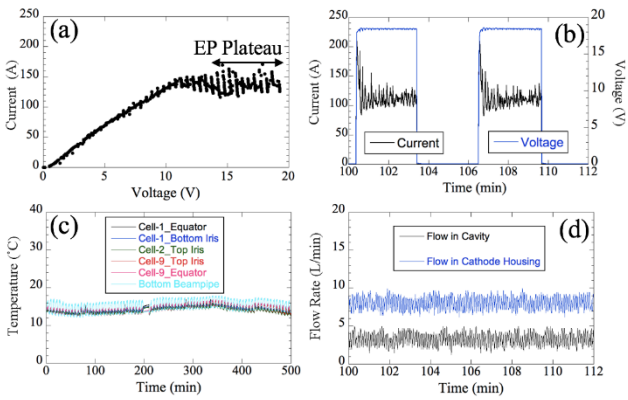


Figure 2: (a) I-V curve, (b) current and voltage cycles, (c) cavity temperature, and (d) acid flow rates in the cathode housing and cavity.

Before the VEP was started, an I-V curve at cathode rotation of 20 rpm was obtained. The I-V curve as in Fig. 1 clearly shows an apparent EP plateau starting from ~13 V. VEP was performed at 18.5 V with on-off voltage cycles. A VEP voltage was selected in the higher side on the EP plateau so that surface etching can be avoided. The on and off times were selected to be 3 min. The off-time was necessary to reduce returning of the bubbles from the acid reservoir to the cavity. Temperatures at totally six positions in the upper and lower sides of the cavity were recorded. Current, voltage, cavity temperatures, and acid flow rates are shown in Fig. 2. The flow rates in the cathode housing and cavity were measured to be around 7 and 3 L/min, respectively. The flow rates were lower than the target values as investigated with VEP experiments of the coupon cavity. The inlet acid pump required maintenance to work with its full capacity. The flow rates in the VEP process done for 20 µm removal were maintained as desired. The bulk VEP was performed totally for around 19 h including the voltage off-time to remove an average thickness of 100 µm.

Removal Thickness

Removal thickness at different positions of the cavity was measured with an ultrasonic thickness gauge. The removal trend (for 100 and 20 µm removal thickness) along the cavity length is shown in Fig. 3. In the bulk VEP, removal asymmetry was found in the cell where the removal at the upper iris was larger than the removal at the bottom iris and equator. However, the asymmetry is significantly less compared to the previous VEP performed with single flow at a flow rate of 5 L/min [5]. The asymmetry might occur due to bubble circulation from the tank, which is only 70 L in the capacity, to the cavity. Although bubbles moved along and inside the cathode, there is a possibility that a fraction of bubble amount diffused from the meshed sheet of the cathode housing and accumulated in the cells. Since the bulk VEP was performed with lower flow rates than the target values, the possibility of bubble diffusion increased. The accumulated bubbles on the upper half cells might impair the viscous layer thickness and enhances the EP rate there [2]. The asymmetry seems to be less in the VEP performed for 20 µm removal since the target acid flow rates were maintained.

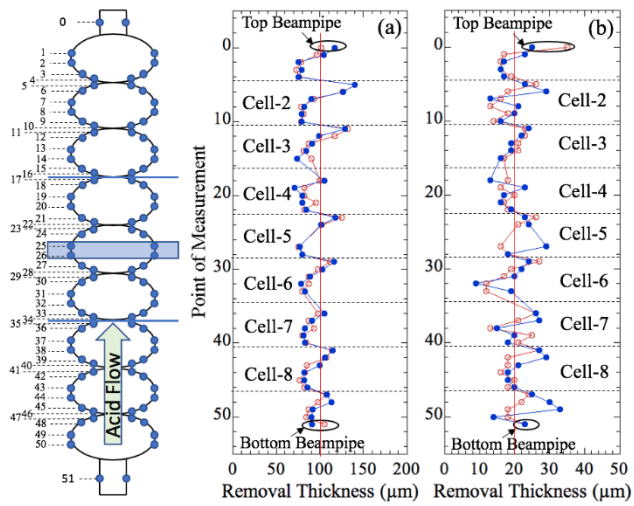


Figure 3: Removal thickness trends along the cavity length in (a) bulk VEP for 100 µm removal and (b) fine VEP for 20 µm removal. The schematic shows positions of thickness measurement. The solid vertical lines show average removal thicknesses.

Cavity Surface

The cavity surface before and after the VEP processes was observed with the Kyoto camera. Figure 4 shows images of the equator surface in the top cell (cell-1), center cell (cell-5), and bottom cell (cell-9) before and after the bulk VEP process. The cavity surface was as smooth as before VEP and no etching sign was seen. The result shows that the applied parameters are adequate to perform EP of the entire surface of the cavity without surface etching. The photograph in Fig. 5 shows the shiny surface of cell-1 and cell-9.

ISBN: 978-3-95450-194-6 ISSN: 2226-0366 doi:10.18429/JACoW-LINAC2018-TUPO068

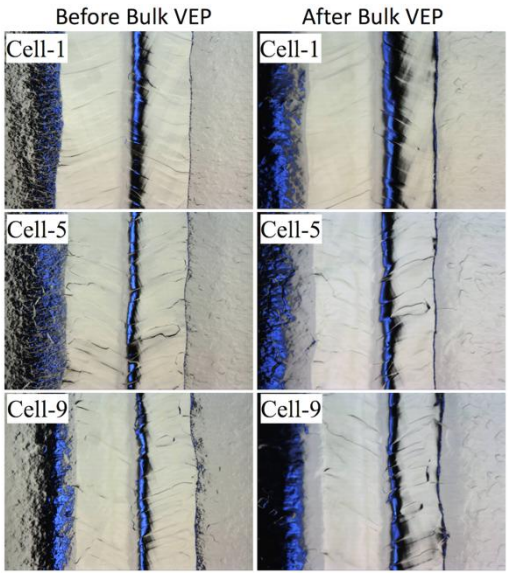


Figure 4: The equator surface in the cell-1, cell-5, and cell-9 of the cavity before (left) and after (right) the bulk VEP for 100 µm removal thickness. The image size is 12x 9 mm.

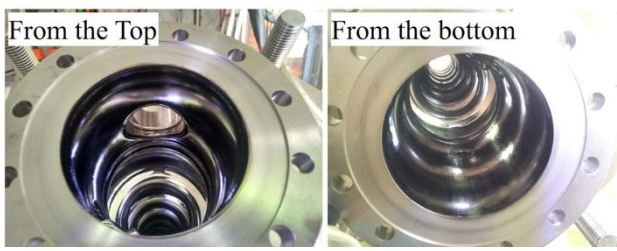


Figure 5: Cavity inner surface after the bulk VEP. Photographs captured from the top and bottom of the cavity.

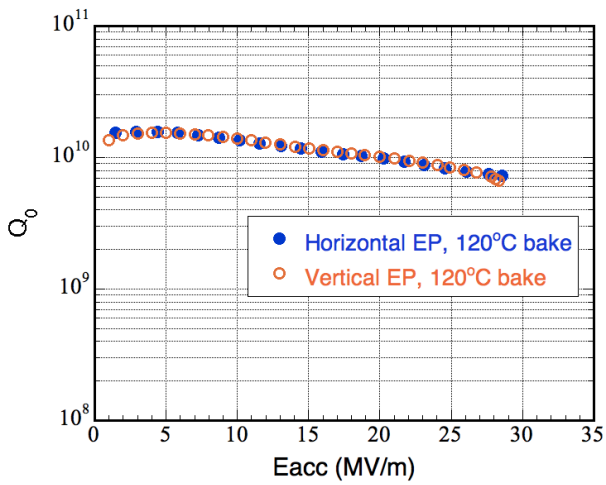


Figure 6: Cavity performance (Q_0 vs Eacc curves) in vertical tests after HEP and VEP processes.

VERTICAL TEST

The first vertical test (VT) as scheduled after the second VEP for 20 µm removal could not be performed because vacuum leak occurred while cooling down the cavity at 2 K. A vertical test was performed at 2 K after the cavity was VEPed for 10 µm removal and baked at 120°C for 48 h. Maximum field gradient (Eacc) of 28.3 MV/m at a quality factor (Q_0) of 6.7×10^9 was achieved in the π-mode. The comparison of Q_0 versus Eacc curves in vertical tests after HEP and VEP processes are shown in Fig. 6. In both the tests, the cavity performance was limited by quench. The cavity showed the similar RF performance after treated with HEP and VEP.

FUTURE WORK

In order to further improve the removal uniformity, the VEP parameters will need to be fine-tuned. The asymmetry might be reduced at higher cathode rotation as observed earlier [6]. The volume of the acid reservoir will be increased to avoid bubble circulation between the acid reservoir and the cavity. The larger tank will make it possible to perform VEP with continuously voltage-ON that will finally enhance the EP rate. Fluid flow simulation will be performed to understand fluid diffusion from the cathode housing to the cavity in dual flow condition and the effect of the acid flow rates.

CONCLUSION

VEP of a nine-cell cavity for bulk removal was successfully performed for the first time with the Ninja cathode and investigated VEP parameters with the nine-cell coupon cavity. The dual acid flow technique was applied to remove the bubbles quickly from the cathode and cavity. The separate flow resulted in less asymmetric removal compared to that with the combined flow. The VEP yielded a smooth and shiny surface and no etching sign was observed in all the cells. RF performance of the cavity was tested in a vertical cryostat at 2 K. The cavity achieved a field gradient of 28.3 MV/m at a Q_0 value of 6.7×10^9 in the vertical test. The RF performance is as good as achieved after the HEP process.

REFERENCES

[1] F. Furuta *et al.*, "Vertical electropolishing studies at Cornell", in *Proc. 17th Int. Conf. on RF Superconductivity (SRF'15)*, Whistler, Canada, Sep. 2015, paper MOPB093, pp. 364-367.

[2] V. Chouhan *et al.*, *Phys. Rev. ST Accel. Beams*, vol. 20, p. 083502, 2017.

[3] V. Chouhan *et al.*, "Study of the Surface and Performance of Single-Cell Nb Cavities After Vertical EP Using Ninja Cathodes", in *Proc. 28th Linear Accelerator Conf. (LINAC'16)*, East Lansing, MI, USA, Sep. 2016, paper MOPLR037, pp. 217-219 .

[4] V. Chouhan *et al.*, "Comparison of Horizontal and Vertical Electropolishing Methods using Niobium Single-Cell Coupon Cavity", in *Proc. IPAC'18*, Vancouver, Canada, April-May 2018, paper THPAL029, pp. 3692-3694.

[5] V. Chouhan *et al.*, "Vertical Electropolishing of 1.3 GHz Niobium 9-Cell Cavity: Parameter Study and Cavity Performance", in *Proc. IPAC'18*, Vancouver, Canada, April-May 2018, paper THPAL030, pp. 3695-3698.

[6] V. Chouhan *et al.*, "Study on Vertical Electropolising of 9-cell Niobium Coupon Cavity", in *Proc. 18th Int. Conf. on RF Superconductivity (SRF'17)*, Lanzhou, China, July 2017, paper TUPB091, pp. 602-606.

Content from this work may be used under the terms of the CC BY 3.0 licence (© 2018). Any distribution of this work must maintain attribution to the author(s), title of the work, publisher, and DOI.

ISBN: 978-3-95450-194-6 ISSN: 2226-0366 doi:10.18429/JACoW-LINAC2018-TUPO069

DEVELOPMENT OF VERTICAL ELECTROPOLISHING FACILITY FOR Nb 9-CELL CAVITY (2)

Y.Ida#, V.Chouhan, K.Nii, Marui Galvanizing, Himeji, Japan
H.Hayano, S.Kato, H.Monjushiro, T.Saeki, M.Sawabe, KEK, Tsukuba, Japan
Takao Akabori, Goh Mitoya, Kenich Miyano, Higashinihon Kidenkaihatsu, Morioka, Japan
Yasunori Anetai, Fukumi Takahashi, WING, Kitakami, Japan

Abstract

In IPAC18 (Vancouver, Canada), we reported our first step of development of niobium 9-cell cavity vertical electropolishing (VEP) facility. In this article, we will report the method, system for uniform polishing for niobium 9-cell cavities and the current situation of our 9-cell cavity VEP facility (the result of polishing uniformity, vertical test will be presented in other posters of this conference). In addition, we will show the movie of experiments of VEP-3 with Ninja cathode. This facility aims not only for test VEP but also for mass production and long-time operation.

INTRODUCTION

In May 2018, at the IPAC-18, we made our first historical report regarding our last 5 years of continuous R&D work on vertical electropolishing (VEP). In the last few months, further improvement has been made targeting good VEP results, system automation, and cost-effective mass production. This second report shows these improvements of the VEP facility. The detailed experimental VEP results are reported by Mr. Nii in TUPO067 [1], and Dr. Chouhan in TUPO068 [2].

DEVELOPMENT OF NINJA-VERTICAL EP SYSTEM

VEP system was designed to use it with our unique Ninja cathode. The system includes acid tank, auto-controlled valves, lower chamber for acid flow bifurcation, Ninja rotary system etc. Figure 1 shows the VEP system photos.



Figure 1: Photos of Ninja-vertical EP system.

#yoshiaki_ida@e-marui.jp

ADVANCED ACID TANK

The acid tank is made of clear PVC material and has a 70L capacity. In order to do EP with the least amount of EP solution, the solution is changed every one or two times of VEP process. Make sure the deterioration of the solution doesn't affect the EP finish. The tank is equipped with a niobium heat exchanger for liquid temperature control. The tank also has mesh filters and an ultrasonic oscillator used to remove hydrogen gas bubbles remaining in EP solution. Figure 2 shows the photos of the acid tank.

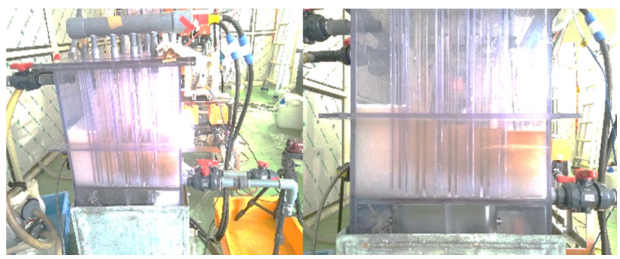


Figure 2: Photos of the acid tank.

AUTOMATIC CONTROLLED VALVES FOR EP SOLUTION CONTROL

For automatic control of EP solution path and direction, electric switching auto valves are used. The operation of valves are controlled with programmed sequences. This allows to select the acid and water flow from bottom to top and vice-versa. The acid and water flow rate can also be remotely controlled with a touch panel screen. Figure 3 shows the touch panel screen and auto valves.

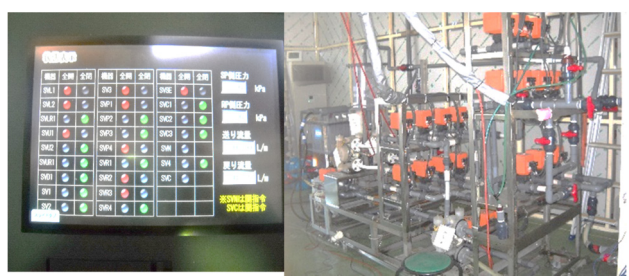


Figure 3: Photos of the touch panel screen and auto valves.

NINJA-VEP SYSTEM

EP solution is inflowed from the lower chamber, and the Ninja cathode is spun. A unique characteristics of the lower chamber is that it can bifurcate the EP solution and allow separate flows in the cathode housing and cavity. This

Content from this work may be used under the terms of the CC BY 3.0 licence (© 2018). Any distribution of this work must maintain attribution to the author(s), title of the work, publisher, and DOI.

ISBN: 978-3-95450-194-6 ISSN: 2226-0366 doi:10.18429/JACoW-LINAC2018-TUPO069

process removes hydrogen gas bubbles quickly from the cathode and cavity. Figure 4 shows the schematic view and the photo of this system.

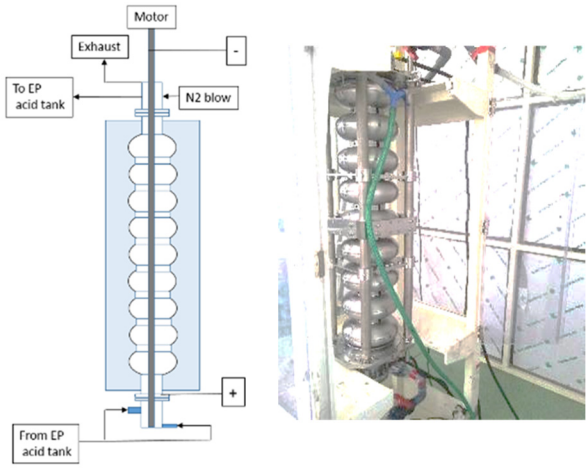


Figure 4: The schematic view and the photo of this system.

POST-EP PROCESS

After EP, the EP solution is drained from the cavity and the interior surface of the cavity is rinsed with pure water. The cavity is then goes to the high pressure water rinsing process. Figure 5 shows ultrasonic rinsing process.



Figure 5: A photo of ultrasonic rinsing process.

SUMMARY

In May 2018 at the IPAC-18 in Vancouver, we made our first report. Following that, we announced our improved version in our second report. The Ninja-type VEP version using manual valves is the basic system, and we are aiming for mass production system that will use auto valves, shorten the VEP time, improve process capacity, achieve uniform polishing, and improve the overall system performance. For the 9C up to the previous process, the inspection is complete, and approved parts are accepted.

REFERENCES

[1] K. Nii *et al.*, "Study on New Removal Thickness Distribution Improvement Methods for Niobium 9-cell Cavity Vertical Electropolishing with Ninja Cathode", presented at LINAC'18, Beijing, China, Sep. 2018, paper TUPO067, this conference.

[2] V. Chouhan *et al.*, "Vertical Electropolishing of 1.3 GHz Niobium Nine-Cell SRF Cavity: Bulk Removal and RF Performance", presented at LINAC'18, Beijing, China, Sep. 2018, paper TUPO068, this conference.

Content from this work may be used under the terms of the CC BY 3.0 licence (© 2018). Any distribution of this work must maintain attribution to the author(s), title of the work, publisher, and DOI.

ISBN: 978-3-95450-194-6 ISSN: 2226-0366 doi:10.18429/JACoW-LINAC2018-TUPO070

DESIGN AND COMMISIONING OF KEK NEW VACUUM FURNACE FOR SRF CAVITY DEVELOPEMENT*

K. Umemori†[1,2], M. Egi[1], E. Kako[1,2], T. Konomi[1,2], S. Michizono[1,2], H. Sakai[1,2]
[1]KEK/[2]SOKENDAI, 305-0801, Tsukuba, Ibaraki, Japan

Abstract

Recently new techniques such as Nitrogen-doping (N-doping) and Nitrogen-infusion (N-infusion) have been developed to improve performance of SRF (Superconducting RF) cavities. We purchased a new vacuum furnace, which is key to realize these techniques. Cleanness of the furnace is most important issue. The furnace has a cryopump and whole of vacuum system is oil-free system. Target vacuum level after cooling down is 1e-6 Pa. Heater, reflectors and support table were made from Molybdenum to avoid contamination during heat treatment. Metal gaskets are used for all vacuum seals, except big doors. Maximum operation temperature is 1150 degrees. Size is around 1 m diameter and 2m long for a 1.3 GHz 9-cell cavity. Entrance of furnace is covered by a clean booth. The furnace was fabricated, assembled at KEK COI building and commissioned. After several burning runs, target vacuum pressure was achieved after cooling down to room temperature (RT). Design and current status of the furnace is presented.

REQUIREMENT FOR FURNACE

N-doping and N-infusion technique are well known to improve SRF cavity performance [1]. KEK also had carried out R&D studies. Throughout our studies, it was realized that cleanness of furnace is very important issue. In the case of N-doping using a diffusion pump, Q-values always decreased even after removing surface by EP [2]. N-infusion studies using J-PARC furnace, with a cryopump, were much better, but still sometimes we were suffered from Q-degradation due to contaminations from the furnace [3].

"Clean" furnace is essential for current SRF development. What "clean" means are excellent available vacuum pressure and less contaminations, especially from carbons. Pumping system of furnace should be oil-free system. Powerful cryopump is desirable. To achieve good vacuum condition and less contaminant circumference, metallic vacuum seals are basically used and usage of SUS at high temperature region is avoided.

Furthermore, furnace should be surrounded by a clean booth to keep cavity handling clean. Operation of furnace is also important to keep cleanness of furnace, including selection of materials to apply heat treatment.

DESIGN AND CONSTRUCTION

Table 1 shows main design parameters for our new furnace. Size of the furnace is fit to install a L-band 9-cell cavity. Molybdenum was used for the heaters, reflectors and a support table. Heating zones are separated to three divisions. Maximum operating temperature is 1150 degrees. Main vacuum pump is a cryopump with 10000 L/sec for Nitrogen.

Table 1: Design Parameters

Parameters	Design values
Inner size of chamber	ϕ950 x L=2080 mm
Effective heating zone	370 x 370 x 1500 mm
Normal operating temperature	~1100 degree
Maximum temperature	1150 degree
Cryopump (CRYO-U20H)	10000 L/sec (N_2)
Drypump (CR300B)	5000 L/min
Heater	Mo heater
Reflector	6 layers of Mo reflector
Target vacuum pressure	RT: 1e-6 Pa 600 degrees: 1e-5 Pa 1000 degrees: 1e-4 Pa



Figure 1: Construction of the furnace.



Figure 2: (top left) Water-cooled baffle, gate-valve and cryopump. (top right) Inside furnace. (bottom) Completed furnace with clean booth.

† kensei.umemori@kek.jp

Content from this work may be used under the terms of the CC BY 3.0 licence (© 2018). Any distribution of this work must maintain attribution to the author(s), title of the work, publisher, and DOI.

ISBN: 978-3-95450-194-6 ISSN: 2226-0366 doi:10.18429/JACoW-LINAC2018-TUPO070

Figure 1 and 2 show construction of the furnace and completed furnace with class-10000 clean booth. The cryopump is located bottom of the furnace. Construction work had performed at FY2017.

COMMISSIONING OF FURNACE

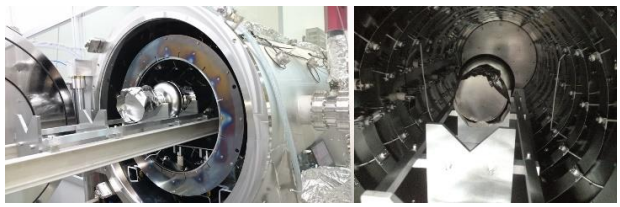


Figure 3: (left) Installing cavity using a lifter. (right) Cavity on a supporting tool inside the furnace.

Several commissioning runs were carried out. Figure 3 shows installation of a single-cell cavity into the furnace using a lifter made of SUS. A cavity supporting tool on the table is also made of Molybdenum.

Figure 4 shows typical 800 degrees x 3 hours commissioning run; log of temperature and vacuum and RGA spectrums. Main components shown in RGA spectrums are H_2, H_2O, N_2/CO, CO_2.

During commissioning runs, reachable vacuum pressures were as following; RT: 1.0e-6 Pa, 600 degrees: 4.4e-6 Pa, 1000 degrees: 7.5e-5 Pa(@955 degree) or 5.4e-6 Pa (with TMP). Target vacuum pressures were almost satisfied.

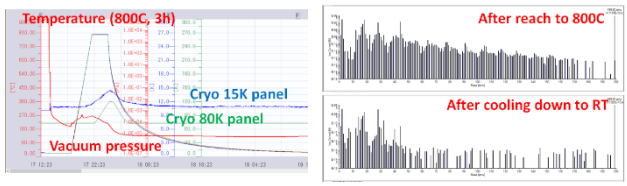


Figure 4: (left) Typical 800 degrees x 3h run. (right) RGA spectrums just after reaching 800 degrees and after cooling down to RT.



Figure 5: (left) TMP used during Nitrogen-injection. (right) Nitrogen-injection system.

Background purity during Nitrogen-injection (N-injection) is also important to realize good performance of SRF cavities. Figure 5 shows N-injection system. A TMP with 700 L/sec pumping speed was used with 90 % rotation speed, while the cryopump is turned off, during N-injection.

G1 grade Nitrogen bombes, 99.9999% purity, are used for Nitrogen treatment. N-injection line is leak-tight and baked. A mass-flow controller is used to precisely control Nitrogen pressure inside the furnace. A capacitance gauge is used to measure the pressure during N-injection.

TEMPERATURE RISE ON CRYOPUMP

Top-left of Fig. 2 is a picture around the cryopump. The cryopump is located bottom of the furnace. An water-cooled baffle is mounted just above a gate-valve to suppress heat input to the cryopump.

Temperature rise on the cryopump, however, became problem during the commissioning runs. We could not even keep 800 degrees. During commissioning runs, sometimes the TMP helped to pump the furnace, instead of the cryopump.

As mentioned above, the water-cooled baffle is used to suppress heat input to the cryopump, but thermal design seemed to be not enough. We decided to add additional reflectors above the cryopump port. Left of Fig. 6 shows 3 layers of SUS plates. They were installed between Mo reflectors and the cryopump port, as shown in right of Fig. 6.

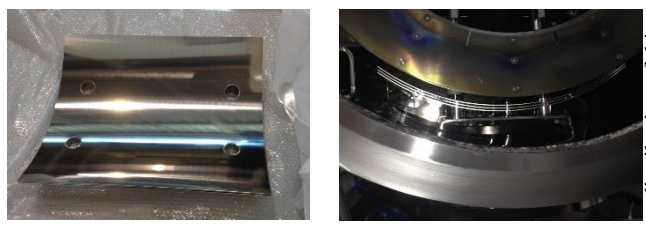


Figure 6: (left) Additional 3 layers of SUS plates. (right) Installed SUS plates between reflectors and a cryopump port.

Figure 7 shows temperature of 15K (left figure) and 80 K (right figure) cryo-panel after installing additional SUS plates. Furnace operation was tested for different temperatures; 800, 850, 900 and 950 degrees. We could keep the furnace at 800 and 850 degrees, 3 hours. But, as shown in Fig. 7, temperature raised up for 900 and 950 degrees operation and it was not possible to continue the cryopump operation.

We are discussing further improvement. One idea is more efficient cooling of the water-cooled baffle using a dedicated chiller. Another possibility is to prepare direct water-cooling line for the added outer SUS plate.

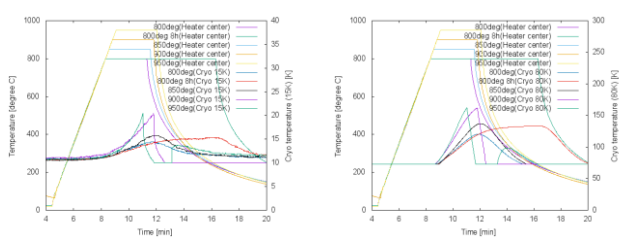


Figure 7: Temperatures of (left) 15K and (right) 80K cryo-panel during operations.

Content from this work may be used under the terms of the CC BY 3.0 licence (© 2018). Any distribution of this work must maintain attribution to the author(s), title of the work, publisher, and DOI.

ISBN: 978-3-95450-194-6 ISSN: 2226-0366 doi:10.18429/JACoW-LINAC2018-TUPO070

Content from this work may be used under the terms of the CC BY 3.0 licence (© 2018). Any distribution of this work must maintain attribution to the author(s), title of the work, publisher, and DOI.

FIRST N-INFUSION TRYAL

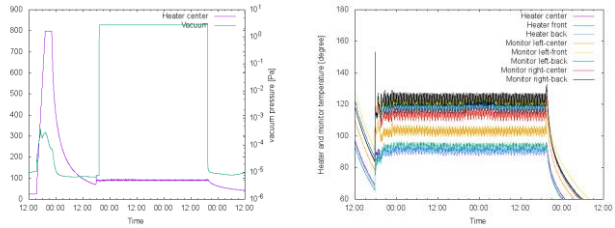


Figure 8: (left) Temperature and vacuum history during N-infusion. (right) Temperatures during N-injection.

First trial of N-infusion at KEK new furnace was applied for an L-band single-cell cavity made from FG material. Before installing into the furnace, HPR was applied to the cavity. Then, the cavity was packed inside clean-room and transferred to the clean booth of the furnace. The cavity was installed into the furnace with Nb caps and foils, as shown in Fig. 3.

Left of Fig. 8 shows temperature and vacuum history of Furnace during N-infusion process. After 800 degrees, 3 hours heat treatment, the furnace was cooled down to 120 degrees, then 3.3 Pa Nitrogen was introduced and the condition of 120 degrees with 3.3 Pa Nitrogen was kept 48 hours. It is noted that temperature adjustment of the furnace was little bit difficult. As shown in right of Fig. 8, measured temperatures were different between the ones for furnace control and the ones for monitoring temperature around cavities.

Again, the cavity was packed inside the clean booth and transferred back to HPR area. After HPR, the cavity was assembled with vertical test flanges.

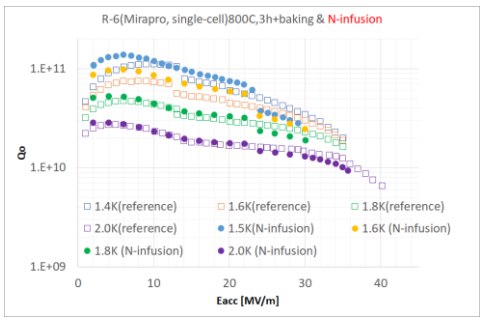


Figure 9: Vertical test results of first N-infusion trial at KEK new furnace, applied for an L-band single-cell cavity. Coloured circles and blank squares are for N-infusion and reference (standard) treatment, respectively.

Vertical test was carried out at KEK-STF. Magnetic field of the vertical test dewar was cancelled by a solenoid coil and remaining magnetic flux was expelled by thermal gradient during cooldown.

Figure 9 shows the results of vertical tests. Coloured circles in the figures are for the data of N-infusion and blank squares are for standard surface treatment, EP + 120 degrees, 48 hours baking. Q-drops around 23 MV/m is known phenomena for this cavity, due to a defect.

First of all, most important message from these results is that no Q-degradation due to contaminations was observed. Cleanness of the furnace was confirmed. Cavity performance was not perfect as a N-infused cavity. There was small improvement of Q-value at low field region, but accelerator gradient decreased.

Systematic study on N-infusion will be carried out and Nitrogen and furnace parameters will be optimized in a future.

SUMMARY

New clean furnace was designed and constructed at KEK. Its pumping system is oil-free system and main pump is a cryopump. Nitrogen injection line is also prepared. Instead of the cryopump, a TMP is used during Nitrogen injection. A mass-flow controller is used to control Nitrogen pressure. Commissioning runs were conducted, and target pressure level was achieved. Temperature rise on cryopump was problem. It was solved partially, not perfect, and normal operation of 800 degrees heat treatment and N-infusion runs were already started. Systematic studies and realization of N-infusion technique is main target for near future studies.

REFERENCES

[1] A. Grassellino *et al.*, "Unprecedented Quality Factors at Accelerating Gradients up to 45 MV/m in Niobium Superconducting Resonators via Low Temperature Nitrogen Infusion", *Supercond. Sci. Technol.* 30 (2017) 094004 (10pp)

[2] K. Umemori et al., "Vertical Test Results of Nitrogen Doped SRF Cavities at KEK", in *Proc. 7th Int. Particle Accelerator Conf. (IPAC'16)*, Busan, Korea, May 2016, paper WEPMB016, pp. 2154-2157. doi:10.18429/JACoW-IPAC2016-WEPMB016

[3] K. Umemori *et al.*, "Study on Nitrogen Infusion for 1.3 GHz SRF Cavities Using J-PARC Furnace", presented at 29th Linear Accelerator Conf. (LINAC'18), Beijing, China. TUPO071, LINAC18, this conference.

ISBN: 978-3-95450-194-6 ISSN: 2226-0366 doi:10.18429/JACoW-LINAC2018-TUPO071

STUDY ON NITROGEN INFUSION FOR 1.3 GHz SRF CAVITIES USING J-PARC FURNACE*

K. Umemori†[1,3], T. Dohmae[1], M. Egi[1], Y. Hori[1,3], E. Kako[1,3], T. Konomi[1,3], S. Michizono[1,3], T. Saeki[1,3], H. Sakai[1,3], Y. Yamamoto[1,3], [1]KEK, 305-0801, Tsukuba, Ibaraki, Japan
S. Kurosawa[2], K. Takeichi[2], J. Kamiya[2], [2]JAEA, 319-1195, Tokai, Naka, Ibaraki, Japan
T. Okada[3], [3]SOKENDAI, 305-0801, Tsukuba, Ibaraki, Japan

Abstract

Nitrogen infusion (N-infusion) is new surface treatment technique for niobium SRF (Superconducting RF) cavities. After cooling down from 800 degrees heat treatment, a vacuum furnace and cavities are kept 120 degrees, 48 hours with about 3 Pa Nitrogen. Improvement of Q-value and accelerating gradient is expected. We used J-PARC furnace, since N-infusion procedure requires clean vacuum furnace. It has a cryo-pump and turbo molecular pumps and its vacuum system is oil-free system. Six times of N-infusion tests were carried out, while changing vacuum condition, N-infusion temperature, Nitrogen pressure, niobium material and so on. Niobium caps were mounted on cavities to avoid contaminations on inner surfaces. Some of trials were successful and vertical test results showed improvement of Q-values and accelerating gradient. However, some of them were not. Most of failed cases showed degradation of Q-values above 5 MV/m. Details of heat treatment procedure including N-infusion and vertical test results are shown in this presentation.

J-PARC FURNACE

N-infusion technique is recently developed to improve SRF cavity performance for both Eacc (accelerating gradient) and Q-values [1]. KEK also had carried out R&D studies to realize high gradient SRF operations.

Throughout N-doping studies we recognized that cleanness of furnace is most important for Nitrogen treatment [2, 3]. Especially, in case of N-infusion, cleanness of furnace could directly affect to cavity performance, since final EP can not apply to the cavity surface.



Figure 1: J-PARC vacuum furnace.

Therefore, we selected J-PARC furnace for N-infusion studies in Japan. Figure 1 shows the J-PARC furnace. This furnace has oil-free and powerful pumping systems. Right and left of Fig. 1 shows a cryopump with 10000 L/sec and three TMPs with 3000 L/sec (x 3), respectively. Vacuum pressure can be reached to around 1e-6 Pa.

One weak point is that this furnace is not dedicated to SRF cavities, but normally used for degassing of beam-duct and components, made of SUS, Cu, ceramic and so on.

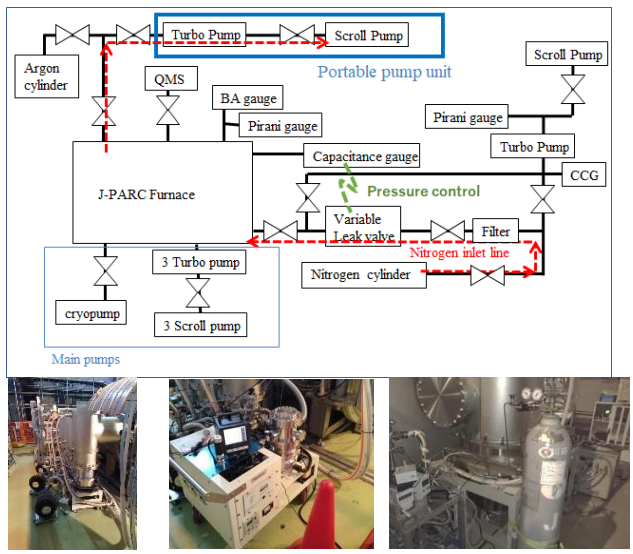


Figure 2: (top) Diagram for N-injection system. (left-bottom) TMPs and scroll pumps. (center-bottom) Portable pumping unit. (right-bottom) N-injection line.

Figure 2 shows Nitrogen-injection (N-injection) system constructed on the J-PARC furnace for the N-infusion study. Nitrogen gas is fed from G1 grade, 99.9999% purity, Nitrogen bombe. Nitrogen pressure in the furnace is controlled by a variable leak valve (right-bottom of Fig. 2). During injection of Nitrogen, the furnace is pumped by pumping system.

At the beginning, a small portable pumping unit (center-bottom of Fig. 2) was used. But we could not maintain clean background condition. Background pressure was estimated to be around 2e-2Pa. After that, we changed to use TMPs with reduced pumping speed. This could improve background pressure to level of 1e-5 Pa.

N-INFUSION PROCEDURE

In order to maintain the furnace as clean as possible, most of case, 950 degrees, 3hours burning runs were carried out, just before N-infusion runs.

Before installing to the furnace, cavities were washed by HPR (High Pressure Rinsing), dried in a cleanroom

† kensei.umemori@kek.jp

Content from this work may be used under the terms of the CC BY 3.0 licence (© 2018). Any distribution of this work must maintain attribution to the author(s), title of the work, publisher, and DOI.

ISBN: 978-3-95450-194-6 ISSN: 2226-0366 doi:10.18429/JACoW-LINAC2018-TUPO071

and packed in a clean bag, at KEK. Then they were transported from KEK to J-PARC furnace. They were unpacked at J-PARC and installed into the J-PARC furnace.

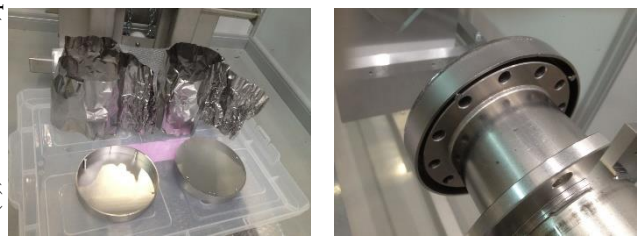


Figure 3: (left) Nb caps and foils to cover flanges. (right) Cavity flange covered with Nb cap.

As shown in Fig. 3, cavity flanges were covered by Nb caps and surrounded by Nb foils. There is enough space, more than several mm, as Nitrogen passage between cavity flanges and Nb caps. These Nb caps and foils are cleaned by CP and ultra-sonic rinsing with detergent, every time. Cavities were supported by Nb jigs and set on Inconel table of the furnace, as shown in top of Fig. 8.

Figure 4 shows typical N-infusion process. (1) The cavity is heat treated at 800 degrees, 3hours, (2) cooled down to 120 degrees, (3) kept at 120 degrees with 3.3 Pa Nitrogen, 48 hours and (4) cooled down to RT. Total of 6 times of N-infusions were applied to total of 8 L-band cavities. It is summarized at Table 1. Right of Fig. 4 shows RGA spectrum of background condition during N-injection. Red (blue) lines are the case using the portable pump unit (TMPs with 50% rotation speed), respectively. These data were taken without Nitrogen. Background condition was clearly improved by using TMPs with reduced speed.

For the 5th and 6th N-infusion runs, two cavities were installed to the furnace at the same time.

After N-infusion, cavities were packed at J-PARC and transferred back to KEK. After HPR, cavities were dried and assembled for vertical tests.

Vertical tests were carried out at KEK-STF. Magnetic field inside dewar was cancelled by a solenoid coil. Typically, remaining field is around 1 mG or less. Thermal gradient on the cavity surface was made by a heater during cool-down for better flux expulsions [4].

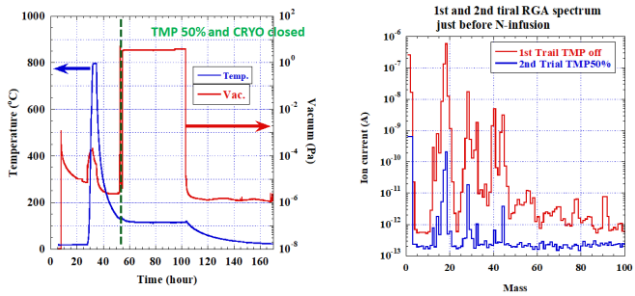


Figure 4: (left) Temperature and vacuum history of typical N-infusion. (right) RGA spectrum of background condition during N-injection. Data was taken without Nitrogen.

VERTICAL TEST RESULTS

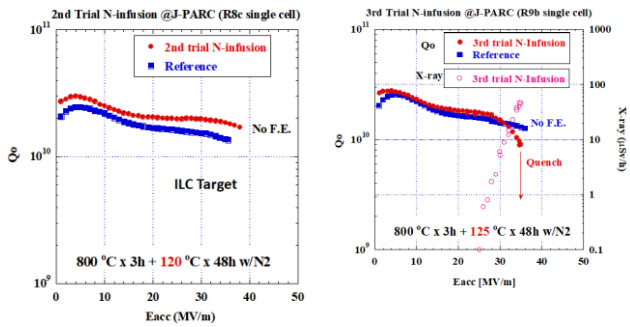


Figure 5: Vertical test results for (left) 2nd N-infusion and (right) 3rd N-infusion.

Figure 5 shows two vertical test results of successful N-infusions. Left and right figure shows results for 2nd and 3rd N-infusion, respectively. In the figures, red and blue points are for N-infusion and reference, which is so called standard treatment; EP + 120 degrees, 48h baking. First of all, Q-degradation or HFQS (High Field Q-Slope) are not observed. In the table 1, "success" of N-infusion is defined as the case for no Q-degradation. Slight improvement of Q-value and Eacc was observed for 2nd N-infusion results. It is noted that N-infusion and reference data were taken at 1.97 K and 2.00 K, respectively. Better Q-values of N-infusion includes temperature effect too. The results for 3rd N-infusion was not so different from reference data. Both data were taken at 1.99 K.

Table 1: Conditions of N-infusion

No.	Date	Cavity name	No. of cells	Nb material	N-infusion process	Pumping system	Results
1	2017.4	R-2	Single	FG (TD)	800C, 3h + 120C, 48h w/ 3.3Pa N_2	Portable	Fail
2	2017.11	R-8c	Single	FG (TD)	800C, 3h + 120C, 48h w/ 3.3Pa N_2	TMP 50%	Success
3	2018.1	R-9b	Single	FG (TD)	800C, 3h + 125C, 48h w/ 3.3Pa N_2	TMP 50%	Success
4	2018.2	R-2	Single	FG (TD)	800C, 3h + 160C, 48h w/ 3.3Pa N_2	TMP 50%	Fail
5	2018.3	R-9	Single	FG (TD)	800C, 3h + 120C, 48h w/ 3.3Pa N_2	TMP 50%	Fail
		R-10b	3-cell	LG (CBMM)			Success
6	2018.4	R-2	Single	FG (TD)	800C, 3h + 120C, 48h w/ 3.3Pa N_2	TMP 50%	Fail
		R-9b	Single	FG (TD)			Fail

Content from this work may be used under the terms of the CC BY 3.0 licence (© 2018). Any distribution of this work must maintain attribution to the author(s), title of the work, publisher, and DOI.

ISBN: 978-3-95450-194-6 ISSN: 2226-0366 doi:10.18429/JACoW-LINAC2018-TUPO071

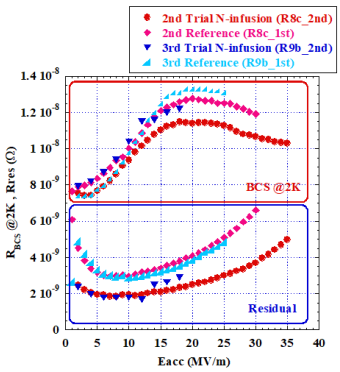


Figure 6: Deconvoluted BCS resistance and residual resistance for 2nd and 3rd N-infusion.

Vertical test results of 2nd and 3rd N-infusion were analysed and deconvoluted to BCS resistance and residual resistance. Figure 6 shows deconvoluted results. Considering temperature effect, mentioned above, BCS resistance for N-infusion and standard treatment does not show clear difference. There is a tendency that residual resistance is smaller for N-infusion case. Up to now, significant improvement of cavity performance can not be observed from N-infusion studies performed using J-PARC furnace.

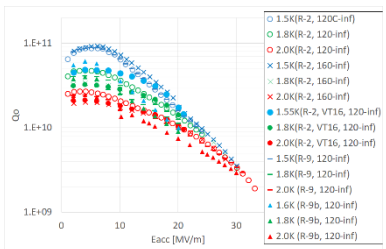


Figure 7: Vertical test results for failed N-infusion. 1st, 4th ,5th (R-9) and 6th (R-2&R-9b) N-infusion results are plotted.

As shown in Table 1, sometimes N-infusion was failed, and Q-degradation was observed. Figure 7 shows vertical test results for failed cases. Results from total of 5 cavities are included; 1st, 4th, 5th (R-9) and 6th(R-2&R-9b). It is interesting that all results show rather similar degradation curves, even the case for different N-infusion conditions. Q-degradation always starts above 5 MV/m and make exponentially degraded Q-slope. It is considered that Q-degradation is caused by contaminations from the furnace. Normal conducting materials might become the source of heating.

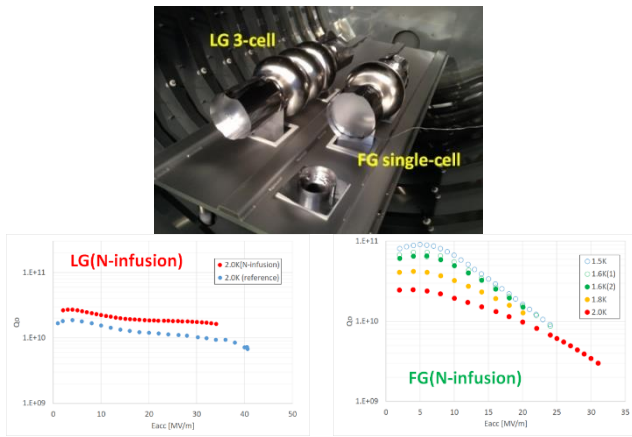


Figure 8: (Top) LG 3-cell and FG single-cell cavities installed to the Furnace. Vertical test results for LG 3-cell (left-bottom) at 2.0K and FG single-cell (right-bottom).

5th N-infusion showed interesting results. LG 3-cell cavity and FG single-cell cavity were installed into the furnace at the same time, as shown in top of Fig. 8. Bottom-left figure shows N-infusion results (red points) compared with standard treatment (blue points) at 2.0K for LG 3-cell cavity. Since magnetic conditions are different between these measurements, Q-values are not compared. Unfortunately, Eacc decreased compared with standard treatment. Bottom-right figure shows N-infusion results for FG single-cell cavity. Q-degradation is clearly observed. These results might indicate dependence on materials.

DISCUSSION

We had carried out series of N-infusion studies using J-PARC furnace. However, we could not reproduce good performance of cavities as expected.

One reason still come from cleanness of furnace. The J-PARC furnace is not dedicated to Nb cavities. Many beamline components have been heat treated. Surface analysis of Nb samples were also investigated to understand the reason of degradations [5]. It is still not clear, but Carbon component might be one of candidate.

Different results for LG and FG cavities are interesting. To understand well, however, more statistics are required.

SUMMARY

KEK had carried out N-infusion study using J-PARC oil-free furnace with the cryopump. The furnace and N-injection line were tried to maintain as clean as possible. TMPs are also used to achieve better background condition during N-injection. There were some successful results, but it was not well reproduced. We often suffered from Q-degradation of cavity caused by furnace contaminations. We will continue N-infusion study to realize high gradient performance using newly constructed KEK furnace [6].

Content from this work may be used under the terms of the CC BY 3.0 licence (© 2018). Any distribution of this work must maintain attribution to the author(s), title of the work, publisher, and DOI.

ISBN: 978-3-95450-194-6 ISSN: 2226-0366 doi:10.18429/JACoW-LINAC2018-TUPO071

Content from this work may be used under the terms of the CC BY 3.0 licence (© 2018). Any distribution of this work must maintain attribution to the author(s), title of the work, publisher, and DOI.

REFERENCES

[1] A. Grassellino *et al.*, "Unprecedented Quality Factors at Accelerating Gradients up to 45 MV/m in Niobium Superconducting Resonators via Low Temperature Nitrogen Infusion", *Supercond. Sci. Technol.* 30 (2017) 094004 (10pp)

[2] K. Umemori et al., "Vertical Test Results of Nitrogen Doped SRF Cavities at KEK", in *Proc. 7th Int. Particle Accelerator Conf. (IPAC'16)*, Busan, Korea, May 2016, paper WEPMB016, pp. 2154-2157. doi:10.18429/JACoW-IPAC2016-WEPMB016

[3] T. Konomi *et al.*, "Trial of Nitrogen Infusion and Nitrogen Doping by Using J-PARC Furnace", in *Proc. 18th Int. Conf. on RF Superconductivity (SRF'17)*, Lanzhou, China, July 2017, paper THPB021, pp. 775-778. doi:10.18429/JACoW-SRF2017-THPB021

[4] K. Umemori *et al.*, "Improvement of Magnetic Condition for KEK-STF Vertical Test Facility Toward High-Q Study", in *Proc. 18th Int. Conf. on RF Superconductivity (SRF'17)*, Lanzhou, China, July 2017, paper TUPB028, pp. 444-447. doi:10.18429/JACoW-SRF2017-TUPB028

[5] T. Konomi *et al*., "Niobium Sample Analysis for Nitrogen Infusion and Doping", presented at 29th Linear Accelerator Conf. (LINAC'18), Beijing, China, Sept. 2018, paper TUPO073, this conference.

[6] K. Umemori *et al*., "Design and Commissioning of KEK New Furnace for SRF Cavity Development", presented at 29th Linear Accelerator Conf. (LINAC'18), Beijing, China, Sept. 2018, paper TUPO070, this conference.

ISBN: 978-3-95450-194-6 ISSN: 2226-0366 doi:10.18429/JACoW-LINAC2018-TUPO072

FIRST TRIAL OF THE IN-SITU NITROGEN INFUSION AT KEK*

T. Konomi†, T. Dohmae, E. Kako, S. Michizono, H. Sakai, K. Umemori, KEK/Sokendai, 305-0801,Tsukuba, Japan
T. Okada, Sokendai, 305-0801, Tsukuba, Japan

Abstract

The nitrogen infusion is the new surface treatment technique for improving the RF loss and the maximum accelerating gradient of superconducting cavity. In this process, it is important to be carried out continuously both the 800 °C annealing in vacuum and 120 °C nitrogen infusion without exposure to the atmosphere. The annealing serves activation process by removing the oxide layer. However, there is a risk of dust particles entrance in to the cavity when the cavity is put in the vacuum furnace. The in-situ nitrogen infusion system was prepared to prevent the dust entrance. The other target is to investigate whether nitrogen infusion effect or something changes happen in the case of applying nitrogen infusion technique without removing the oxide layer. It can only introduce nitrogen into a cavity during 120 °C low temperature baking and transport a cavity to the vertical test system without exposure to the atmosphere. We tried to infuse nitrogen to a single cell by keeping 120 °C and 48 hours with 3 Pa nitrogen. The cavity was annealed in another furnace and applied high pressure rinsing before nitrogen infusion. The vertical test result was same Q as the normal 120 °C baking without nitrogen. It suggests that oxide layer prevents infusion of nitrogen.

NITROGEN TREATMENT

The nitrogen treatment of superconducting niobium cavity is getting a lot of attention as a new technology to improve the performance limit of ILC standard recipe [1]. KEK is studying to apply this technology to ILC. It was applied to 1.3 GHz cavities and confirmed that Q value and accelerating gradient were improved [2,3]. The first step in this procedure at KEK is that the surface is removed by the electropolish to create new niobium surface. The cavity is installed to the vacuum furnace after high pressure rinsing. However, there is a risk of dust particles entrance in to the cavity. We designed the in-situ nitrogen infusion system to prevent the dust particle entrance. The second step is that cavity is annealed at 800 oC for 3 hours, then cooled down to 120 oC and kept in 3.3 Pa nitrogen. It is important not to expose to the atmosphere during heat treatment. The cavity is taken out to the atmosphere and cleaned by high pressure rinsing. Thereafter, cavity is not applied heat treatment such as baking because heat treatment changes the surface condition. The final surface condition is made by 800 oC annealing and 120 oC nitrogen infusion. If additional electropolish is applied to remove defects which limit the maximum field after vertical test, high temperature annealing is required again. We studied whether gradient and Q value change when 120 °C nitrogen infusion applied after exposed the cavity to the atmosphere.

† konomi@post.kek.jp.

IN-SITU NITROGEN INFUSION

The system of the in-situ nitrogen infusion is a modified baking system to control the nitrogen pressure during 120 C baking (Fig. 1). Top and bottom flanges of the cavity each have one vacuum port. The system can be baked before injecting nitrogen into the cavity. Main pump is the turbo molecular pump (HiPace700) which pumping speed is 700 L/min. The pressure reached about 3×10^{-7} Pa after baking. The gas flow can be controlled by the automatic gas regulating valve (RME005) during the nitrogen injecting. The pressure is controlled by monitoring the capacitance gauge mounted at pumping side of the cavity. The purity of the nitrogen cylinder is more than 99.99995 vol.%. This system can keep the same purity of nitrogen gas cylinder in the cavity during nitrogen injection because the base pressure is enough low. The cavity can be transported to the vertical test stand without exposing the inner surface of the cavity to the atmosphere.

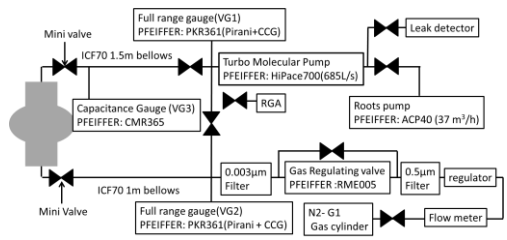


Figure 1: In-situ nitrogen infusion system.

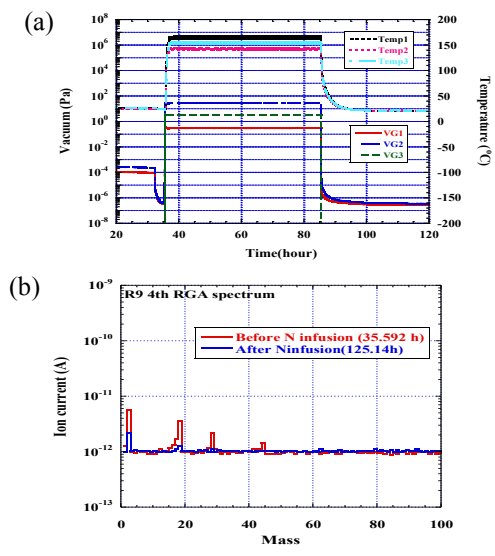


Figure 2: Example of nitrogen infusion. (a) Vacuum and temperature trend. (b) Residual gas spectrum before and after nitrogen infusion.

Content from this work may be used under the terms of the CC BY 3.0 licence (© 2018). Any distribution of this work must maintain attribution to the author(s), title of the work, publisher, and DOI.

ISBN: 978-3-95450-194-6 ISSN: 2226-0366 doi:10.18429/JACoW-LINAC2018-TUPO072

Content from this work may be used under the terms of the CC BY 3.0 licence (© 2018). Any distribution of this work must maintain attribution to the author(s), title of the work, publisher, and DOI.

Figure. 2 shows the example of nitrogen infusion. Nitrogen gas was injected after pumped the system include the cavity. The vacuum gauges are mounted at head of the turbo molecular pump (VG1), just after nitrogen injection port (VG2) and pumping side of the cavity (VG3). These monitored pressure was much differed from each because vacuum pipes are narrow. Since VG3 was kept 3.3 Pa during nitrogen infusion, the cavity pressure would be higher. All temperature monitors were put on the cavity cell. The temperature of each place in the cavity was controlled within ±15 °C. Figure 2(b) shows the residual gas before and after baking with nitrogen. The main residual gas was hydrogen.

CAVITY AND PROCESS

All tests were carried out by using 1.3 GHz single cell cavity (R-9). Nb sheet was fine grain produced by Tokyo Denkai and cavity was fabricated by MiraPro. Table 1 shows the history of the cavity. The study of the in-situ nitrogen infusion started from the 3rd vertical test. The cavity was annealed at 800 °C for 3 hours before 1st Vertical test and applied 20 µm electropolishing before 2nd vertical test. The baking temperature of the in-situ nitrogen infusion was set 120 °C and 160 °C. The cavity was not opened to air between 3rd and 4th VT. Therefore, 160 °C in-situ nitrogen infusion included the 120 °C in-situ nitrogen infusion effect. The standard recipe which baking temperature set to 120 °C and 160 °C, also carried out in 5th and 7th vertical test for comparison. The 6th vertical test was the original nitrogen infusion which continuously applied 120 °C nitrogen infusion after 800 °C annealing in vacuum furnace. However, the Q value was degraded. The reason has not been understood yet. Ref [3] discussed the detail. We focused on the in-situ infusion and standard recipe results.

RESULTS OF VERTICAL TEST

The surface resistance can be divided to the BCS resistance depends on the temperature and residual resistance which is constant term. The residual resistance is mainly increased by the trapped DC magnetic field. The cryostat for vertical test in KEK was modified to decrease the trapped magnetic flux. The magnetic shield and solenoid coil minimize the geomagnetic field around the cavity. And the temperature gradient of the cavity during cool down is controlled by the heater at top beam pipe for the flux expulsion actively [4]. If the cavity is quenched, the magnetic flux is trapped. Figure 3 shows the vertical test results of the in-situ nitrogen infusion and the standard recipe. Unfortunately, the 2K data of 5th and 7th vertical test was measured after quench. The residual resistance is higher than 3rd and 4th. The vertical test data was taken starting from low temperature. In the 5th vertical test, the multipacting was occurred at 15 and 18 MV/m during 1.5 K data taking and the flux was trapped (Fig. 4 (c)). In the 7th vertical test, the cavity was quenched at 26 MV/m in 1.5 K data taking and the flux was trapped. After quenched the cavity, we take the 1.5 K data again (Fig. 4 (d)). The BCS and residual resistance can be separated by using temperature dependence data shown in Fig. 4. The residual resistance can be compared using low temperature data.

It is interesting that there is not field emission in 4th vertical test. The cavity was just applied in-situ nitrogen infusion at 160 C without opening the cavity to the air. High pressure rinsing or other surface treatment were not applied after 3rd vertical test. The nitrogen gas injected to the cavity was as low as 3 Pa, it didn't have force to blow off the field emission source. It is considered that baking suppressed the field emission by changing the surface condition.

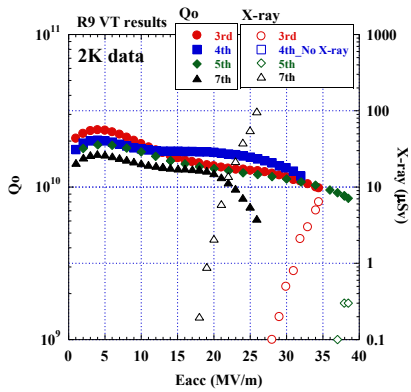


Figure 3: Vertical test results.

Table 1: History of the R-9 Cavity

#	Surface treatment	Detail
1st	800 °C annealing without final EP (EP2)	As received +EP 100 µm +Anneal 800 °C x 3hr +USR 15 min + HPR 3 hr + Baking 120 °C x48 hr, w/o N2
2nd	Standard recipe without baking	+ EP 20 µm + USR 15 min + HPR 3 hr
3rd	120 °C Baking with Nitrogen	+ (without opening to the air) +Baking 120 °C x 48 hr, w/ N2 3Pa
4th	160 °C Baking with Nitrogen	+ (without opening to the air) +Baking 160 °C x 48 hr, w/ N2 3Pa
5th	Standard recipe (120 °C baking without Nitrogen)	+ EP 20 µm + USR 15 min +HPR 3 hr + Baking 120 °C x 48 hr, w/o N2
6th	Nitrogen infusion (120 °C x 48h)	+ N-infusion (800 °C x 3 hr + 120 °C x 48 h, w/N2 3Pa) +USR 15 min + HPR 3 hr
7th	160 °C Baking without Nitrogen	+ EP 20 µm + USR 15 min + HPR 3 hr + Baking 160 °C x 48 hr, w/o N2

ISBN: 978-3-95450-194-6 ISSN: 2226-0366 doi:10.18429/JACoW-LINAC2018-TUPO072

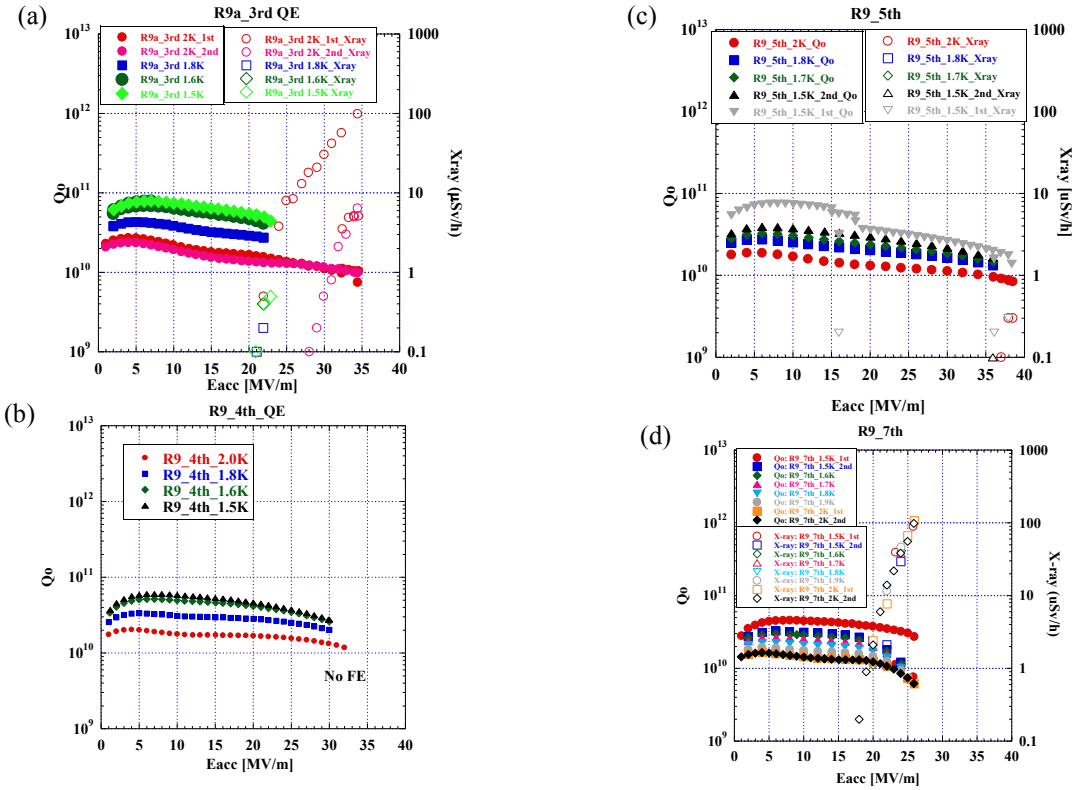


Figure 4: Vertical test results at each temperature. (a) 3rd vertical test; nitrogen infusion at 120 °C, (b) 4th vertical test result; nitrogen infusion at 160 °C, (c) 5th vertical test result; standard recipe at 120 °C, (d)6th vertical test; standard recipe at 160 °C

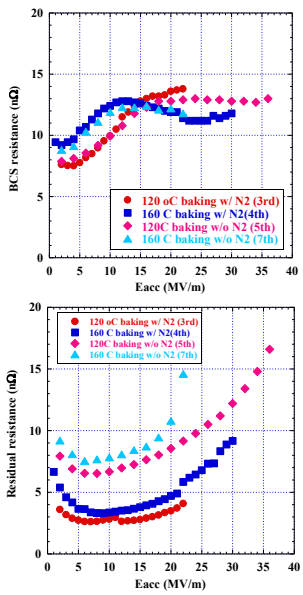


Figure 5: Separated BCS resistance and residual resistance.

Figure 5 shows the BCS resistance part and residual resistance part. The residual resistance is affected by the magnetic flux by the external magnetic field and field emission. It is difficult to discuss the in-situ infusion effect on the residual resistance. The BCS resistance show that the baking temperature is much more influence for the Q value than in-situ nitrogen infusion. These results suggested that high temperature annealing for removing oxidation layer was important for infusing nitrogen into niobium.

SUMMARY

KEK prepared in-situ infusion system that can introduce nitrogen to the cavity during baking and transport to vertical test without exposing to the air. The effect of the in-situ nitrogen infusion was much smaller than baking temperature. It was suggested that the nitrogen was not infused by oxidation layer or nitrogen effect was covered by the other effect. In order to improve the in-situ infusion system, it is necessary to add a system for removing oxidation layer.

REFERENCES

[1] A. Grassellino *et al.*, "Unprecedented quality factors at accelerating gradients up to 45 MV/m in Niobium superconducting resonators via low temperature nitrogen infusion", Supercond. Sci. Technol., vol. 30, p.094004, Aug. 2017, doi:10.1088/1361-6668/aa7afe

[2] T. Okada *et al.*, "Improvement of Cavity Performance by Nitrogen Doping at KEK", presented at the 29th Linear Accelerator Conf. (LINAC18), Beijing, China, Sep. 2018, paper TUPO065, this conference.

[3] K. Umemori *et al.*, "Study on Nitrogen Infusion for 1.3 GHz SRF Cavities Using J-PARC Furnace", presented at the 29th Linear Accelerator Conf. (LINAC18), Beijing, China, Sep. 2018, paper TUPO071, this conference.

[4] K. Umemori *et al.*, "Improvement of magnetic condition for KEK-STF vertical test facility toward high-Q study", in *Proc. SRF'17*, Lanzhou, China, Jul. 2017, pp. 444-447, doi:10.18429/JACoW-SRF2017-TUPB028

Content from this work may be used under the terms of the CC BY 3.0 licence (© 2018). Any distribution of this work must maintain attribution to the author(s), title of the work, publisher, and DOI.

ISBN: 978-3-95450-194-6 ISSN: 2226-0366 doi:10.18429/JACoW-LINAC2018-TUPO073

NIOBIUM SAMPLE ANALYSIS FOR NITROGEN INFUSION AND DOPING

T. Konomi†, E. Kako, S. Michizono, H. Sakai, K. Umemori, KEK 305-0801, Tsukuba, Japan
T. Nojima, Tohoku University, 980-8577, Sendai, Japan
T. Nagata, ULVAC Inc., 289-1226, Sammu, Japan

Abstract

KEK has been investigating the better conditions of the heat treatment in nitrogen, which are called as nitrogen doping and nitrogen infusion. We have tried to understand the high gradient performance of the cavity from the analyses of samples which were prepared in the same conditions for the cavity. The main tools are D-SIMS for the depth profile of the elemental concentration, XPS for composition analysis and SQUID magnetometry for the critical DC magnetic field measurement. The difference in the depth profiles of the nitrogen, car-bon and oxygen between the heat treatment conditions, containing the degree of vacuum and furnace temperature of nitrogen injection, was observed by GD-OES, D-SIMS and XPS. Such a difference correlates with the vortex penetration field measured by SQUID. In particular, that of the nitrogen doping sample was greatly degraded, while that of the nitrogen infusion sample was slightly improved. The tendency is consistent with the RF high gradient test results.

NITROGEN TREATMENT AT KEK

The nitrogen heat treatment can improve the performance of superconducting RF (SRF) cavities. There are two ways for nitrogen treatment. One is the nitrogen doping (N-dope), in which the sample is doped with nitrogen heavily during annealing the cavity at a high temperature in the vacuum furnace and then the heavy doped layer is removed by the electropolishing (EP) [1]. The other way is the nitrogen infusion (N-infusion), in which nitrogen is infused into the sample at a low temperature after annealing the cavity without expose the cavity to the air [2]. In both methods, the oxidized surface layer is removed by high temperature annealing before nitrogen treatment. KEK also succeeded in N-dope and N-infusion using the J-PARC furnace which is equipped with oil free pumps [3, 4]. However, N-infusion decreased the Q value in some cases. In order to investi-gate the cause for the decrease in Q, we installed the niobium reference samples to the furnace together with the cavies and analysed them. First, the samples were cut out of the fine grain niobium sheet produced by the Tokoyo Denkai Co Ltd, which is followed by the EP or chemical polishing (CP) process to remove the surface layer by about 100 µm. Then, the samples were subjected to almost the same heat treatment as the cavity.

DEPTH PROFILE OF N-DOPE

The depth profile of the N-dope sample was measured by the GD-OES (HORIBA, Ltd GD-Profiler 2). The discharge gas was argon. The measured area was 4 mmΦ in the sample with a size of 50×50×3 mm^3. Figure 1 shows the depth profiles of the N-doped and the annealed samples for reference. As shown in Fig. 2 for the temperature and vacuum trend, the N-dope sample was first annealed at 800 °C in a vacuum of 1×10^{-4} Pa for 3 hours and then was doped in 3 Pa nitrogen for 20 minutes, which is followed by the diffusion process of nitrogen to the inner in a vacuum for 30 minutes. No additional EP was applied after heat treatment in both samples. From the data in Fig. 1, it is obvious that the nitrogen doping occurs at least up to 30 µm in depth for the N-dope sample. However, the carbon doping also seems to occur in both samples. We suspected the nitrogen purity in the furnace was poor because a small portable pump was used instead of the main pumps, which were off during nitrogen injection in order to avoid the failure of main pumps. The reached pressure of the small portable pump was 1×10^{-3} Pa. The surface distribution of the carbon can be also seen using the SEM (Hitachi High-Tech Corp., SU6600) in which EDS sensor can be insert from the horizontal axis to the sample surface with the large capture solid angle. Figure 3 shows the reference SEM and EDS image of another N-dope sample prepared in the KEK small furnace which is equipped with an oil diffusion pump. In this case, the carbon distribution is more clearly observed. The carbon seems to be absorbed to the grain boundary. However, the Q-value of the N-doped cavity using J-PARC furnace was improved after EP by several µm. We think that the effect of N-infusion is more sensitive to carbon pollution because the heat treatment affects the final surface.

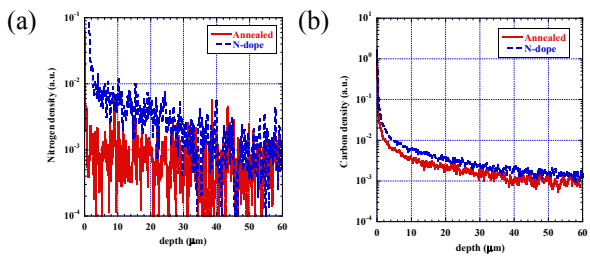


Figure 1: Depth profile of N-dope and annealed samples. (a) nitrogen, (b)carbon.

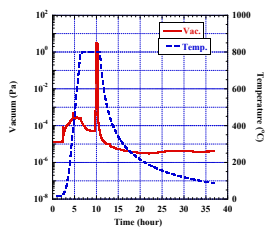


Figure 2: Heat treatment trend of the N-Dope.

† konomi@post.kek.jp.

Content from this work may be used under the terms of the CC BY 3.0 licence (© 2018). Any distribution of this work must maintain attribution to the author(s), title of the work, publisher, and DOI.

ISBN: 978-3-95450-194-6 ISSN: 2226-0366 doi:10.18429/JACoW-LINAC2018-TUPO073

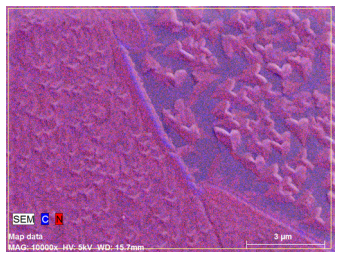


Figure 3: SEM/EDS image of the N-dope sample treated at KEK small furnace using oil diffusion pump. Blue and red show the carbon and nitrogen distribution respectively.

N-INFUSION

The first N-infusion using the J-PARC furnace degraded the *Q* value and gradient. This is due the slow pumping speed during nitrogen injection, resulting in the rather high base pressure of 1×10^{-3} Pa. Hence, the pumping speed was improved for the second N-infusion with a low base pressure of 1×10^{-5} Pa. Figure 4 shows the temperature and vacuum trend of the second N-infusion. In this process, the nitrogen was infused at 120 ºC with the pressure of 3 Pa for 48 hours after the sample was annealed at 800 ºC for 3 hours and cooled down. The difference between the first and second processes of the N-infusion is only the base pressure during nitrogen injection.

The depth profiles of the N-infusion and the annealed samples for reference were measured by dynamic SIMS (ULVAC Phi, Inc.) and XPS (ULVAC Phi, Inc. Versa Probe). The sample size is $7\times7\times3$ mm^3 both for SIMS and XPS. In the SIMS measurements, we used the primary ion beam of Cs^+ with the accelerating voltage of 500 V causing a sputtering rate of 0.015 nm/s. In the XPS measurement, the Al Kα X-ray source with the spot size of 200 μmΦ and the power of 45 W was irradiated with sputtering to take the depth profiles. The sputtering speed was 2.3 nm/min, which was calibrated by using SiO_2 standard sample. Figure 5 shows the comparison of the depth profiles measured by the SIMS for the annealed, first N-infusion and second N-infusion samples, respectively. The nitrogen is obviously infused for the N-infusion samples. The nitrogen infused depth of the first N-infusion is deeper than that of the second N-infusion. The carbon density at 15 nm depth of the first N-infusion sample is higher than other two samples. The oxygen profiles are also much different among three samples. The depth profiles measured by XPS also show the same tendency (Fig. 6). We suspect the large infused depth of oxygen or carbon as the cause of the *Q* degradation in the first N-infusion sample. It is necessary to perform the same measurements using the number of samples with various condition to identify the cause.

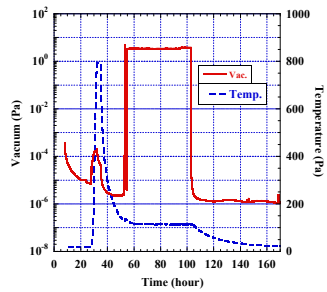


Figure 4: Heat treatment trend of the N-infusion.

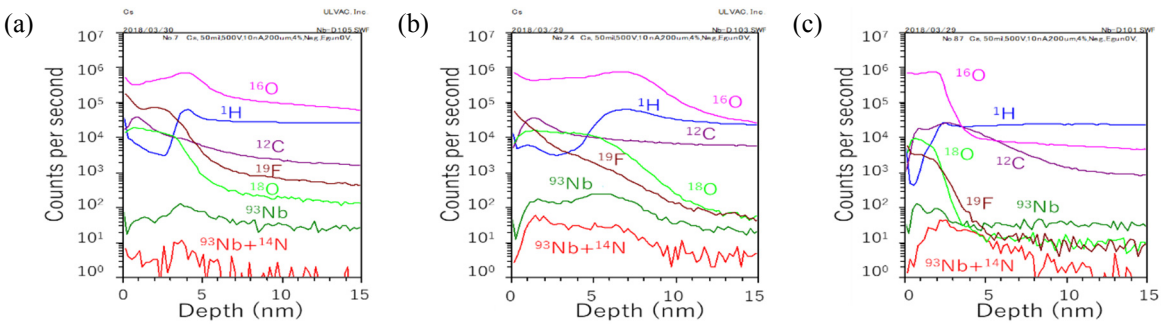


Figure 5: Dynamic SIMS measurement (a)annealed, (b)1st N-infusion, (c) 2nd N-infusion.

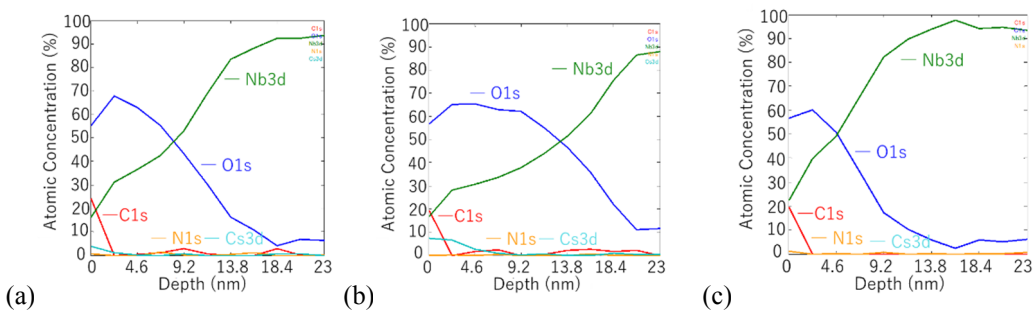


Figure 6: XPS measurements (a) annealed, (b)1st N-infusion, (c) 2nd N-infusion.

Content from this work may be used under the terms of the CC BY 3.0 licence (© 2018). Any distribution of this work must maintain attribution to the author(s), title of the work, publisher, and DOI.

ISBN: 978-3-95450-194-6 ISSN: 2226-0366 doi:10.18429/JACoW-LINAC2018-TUPO073

Content from this work may be used under the terms of the CC BY 3.0 licence (© 2018). Any distribution of this work must maintain attribution to the author(s), title of the work, publisher, and DOI.

DC CRITICAL FIELD MEASUREMENT

The maximum gradient of the cavity is closely related to the vortex penetration field (H_{vp}), which can be measured under a static magnetic field [5]. We compared the H_{vp} values for the annealed (800 °C × 3 hours in vacuum), N-dope and N-infusion samples using the SQUID magnetometer (see Fig. 7) (Quantum Design Inc. MPMS). For the correct comparison, the samples were shaped into a 2 mmΦ sphere. In this case, the demagnetization coefficient of 1/3, leading to the diamagnetic enhanced factor of 150 %. Fabrication error of the sample is 5 μm and the maximum ratio of the vertical and horizontal diameter is 1.005. The enhanced factor is estimated using CST studio (Fig. 8). The error of the enhanced factor is 0.3 %. This value corresponds to 3.6 Oe against the measured H_{vp} of ~1200 Oe, which is small enough as mentioned later. All the samples were polished by 100 μm in terms of CP and heat treated. In addition, the additional 20 μm and 10 μm CP were applied to the annealed and N-dope samples, respectively.

Figure 9 shows the magnetization vs. field (M-H) curves for all the samples measured at 2 K. The measurement range of the magnetic long moment was fixed, because the measurement values became discontinuous at range switching. Therefore, error is large at low field.

In order to distinguish the H_{vp}, $(2M/3\text{-}H))/H$ was calculated from the fact that the demagnetizing magnetization $2M/3$ by the Meissner effect is equal to the external field. Figure 10 shows the $(2M/3\text{-}H)/H$ curves. Edges of H_{vp} are clear in the annealed and N-infusion samples, while H_{vp} of the N-infusion sample is a little higher. On the other hand, it is clearly observed that the vortices penetrate slowly into the N-dope sample, resulting in the difference in H_{vp} of ~200 Oe between the N-infusion and the N-dope samples. The results indicate that the surface barrier of the N-infusion sample is higher than the annealed sample and that of the N-dope one is much lower, which is in the similar tendency to the RF high gradient test results.

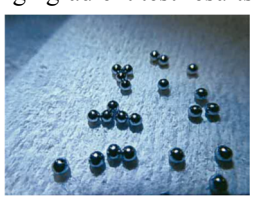


Figure 7: Niobium samples for SQUID.

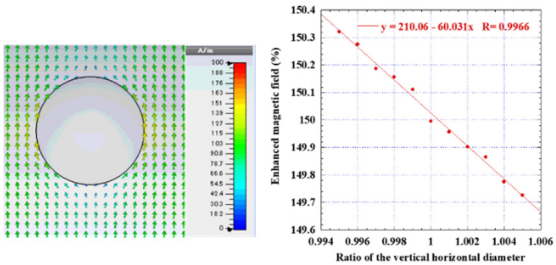


Figure 8: CST simulation of the enhanced factor.

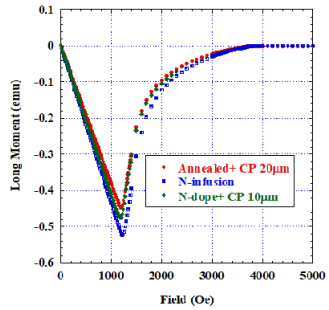


Figure 9: M-H curves of the samples.

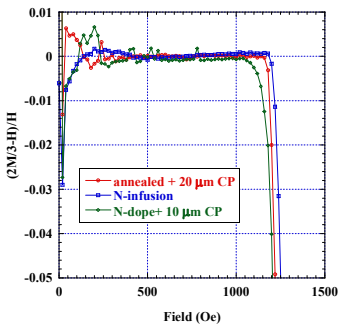


Figure 10: $(M$-$H)/H$ curves.

SUMMARY

KEK has been investigating the better nitrogen treatment conditions. N-infusion degraded the Q-value in some case at KEK. We suspect that the oxygen infused depth or the carbon density is the cause in the examinations by SEM/EDS, SIMS and XPS analysis. In addition, the difference of the H_{vp} value between the N-dope and N-infusion samples derived by the SQUID measurements is consistent with the vertical test results.

ACKNOWLEDGEMENTS

This work was partly supported by Nanotechnology Platform Program (Molecule and Material Synthesis) of the Ministry of Education, Culture, Sports, Science and Technology (MEXT), Japan.

REFERENCES

[1] A. Grassellino et al., "Nitrogen and argon doping of niobium for superconducting radio frequency cavities: a pathway to highly efficient accelerating structures", Supercond. Sci. Technol., vol. 26, 102001, Aug. 2013.
doi:10.1088/0953-2048/26/10/102001

[2] A. Grassellino et al., "Unprecedented quality factors at accelerating gradients up to 45 MV/m in Niobium superconducting resonators via low temperature nitrogen infusion", Supercond. Sci. Technol., vol. 30, 094004, Aug. 2017.
doi:10.1088/1361-6668/aa7afe

[3] T. Okada et al., "Improvement of Cavity Performance by Nitrogen Doping at KEK", presented at the 29th *Linear Accelerator Conf.* (LINAC18), Beijing, China, Sep. 2018, paper TUPO065, this conference.

ISBN: 978-3-95450-194-6 ISSN: 2226-0366 doi:10.18429/JACoW-LINAC2018-TUPO073

[4] K. Umemori et al., "Study on Nitrogen Infusion for 1.3 GHz SRF Cavities Using J-PARC Furnace", presented at the 29th *Linear Accelerator Conf.* (LINAC18), Beijing, China, Sep. 2018, paper TUPO071, this conference.

[5] T. Tan et al., "Magnesium diboride coated bulk niobium: a new approach to higher acceleration gradient", Scientific Reports vol. 6, 35879, 2016, pp. 1-5,
doi: 10.1038/srep35879

Content from this work may be used under the terms of the CC BY 3.0 licence (© 2018). Any distribution of this work must maintain attribution to the author(s), title of the work, publisher, and DOI.

ISBN: 978-3-95450-194-6 ISSN: 2226-0366 doi:10.18429/JACoW-LINAC2018-TUPO074

DESIGN AND FABRICATION OF KEK SUPERCONDUCTING RF GUN #2

T. Konomi†, Y. Honda, E. Kako, Y. Kobayashi, S. Michizono, T. Miyajima, H. Sakai,
K. Umemori, S. Yamaguchi, M. Yamamoto
KEK/Sokendai, Tsukuba, Japan

Abstract

Superconducting RF gun can realize high acceleration voltage and high beam repetition. KEK has been developing the 1.3 GHz elliptical type 1.5 cell superconducting RF gun to investigate fundamental performance. A surface cleaning method and tools are developed by using KEK SRF GUN #1 and high surface peak gradient 75 MV/m was achieved without field emission. SRF GUN #2 equipped with the helium jacket and operable with electron beam was designed based on the SRF GUN #1. It can be operated with transmit type photocathode which include superconducting transparent material. The cathode rod is cooled by thermal conducting from the 2 K helium jacket and photocathode will be kept around 2K to maintain superconductivity. Bulk niobium photocathode rod, and substrate will used for the fundamental performance test. In parallel, the photocathode deposition chamber for multi-alkali photocathode will be prepared.

CAVITY DESIGN

The SRF GUN #2 cavity is 1.5 cell and 1.3 GHz shape designed based on SRF GUN #1. High gradient performance has demonstrated using SRF GUN #1. The maximum surface peak electric field (Esp) reached 75 MV/m [1]. The difference from #1 is that #2 has the helium jacket and the cathode rod size was changed for improving the cathode rod cooling. Figure 1 shows the #2 design. Table 1 shows the RF parameters of KEK SRF GUN#1. Yellow parts are made of niobium and green, blue parts are made of titanium and gray parts are made of stainless steel. Helium jacket can be connected by flanges with indium seal. The choke filter is placed as close to the accelerating cell as possible.

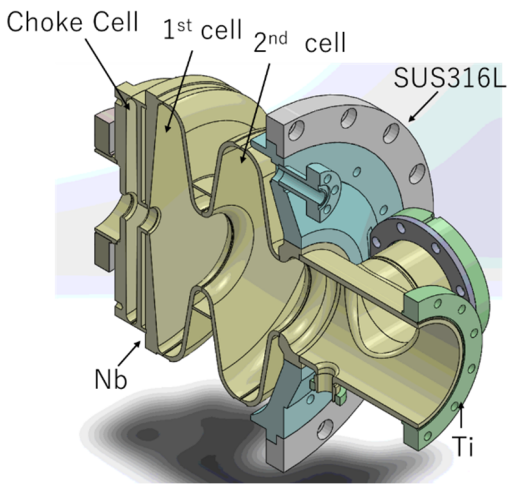


Figure 1: Design of KEK SRF GUN#2.

† konomi@post.kek.jp.

Table 1: RF Parameters of KEK SRF GUN#2

Parameter	Value
Frequency	1300 MHz
Geometrical factor	133.7 Ohm
Hsp/Esp	2.237 mT/(MV/m)
Z factor ($E_{sp} = Z\sqrt{Q_o P_{loss}}$)	234.04

RF leakage from the choke filter is simulated using SUPERFISH because the cathode rod length was shortened. Figure 2 shows the simulation condition. Rod head is made of niobium, niobium surface resistance is set to 10×10^{-9} Ω. Other cathode holder parts are made of oxide free copper (OFC). Electrical resistivity of OFC is set to 1.68×10^{-8} Ω·m. Figure 3 shows the Q value dependence on the choke diameter. When the all surface is made of niobium the Q value is 1.3×10^{10}. The best diameter is 186.6mm. If 1% degradation is tolerated, lose is diameter fabrication tolerance set to ±0.2 mm.

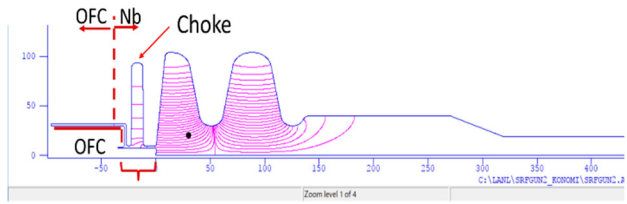


Figure 2: SUPERFISH simulation set up.

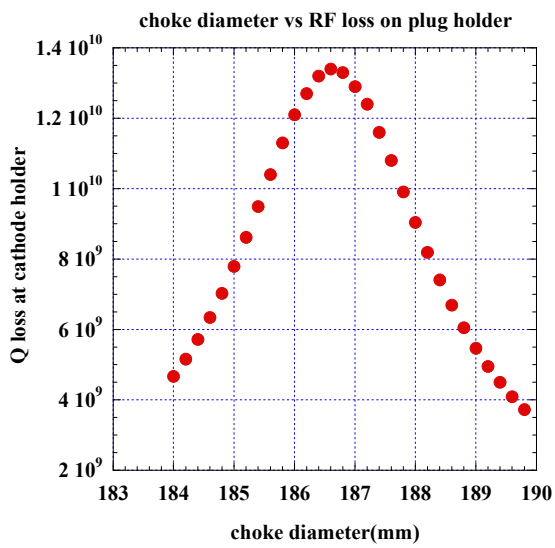


Figure 3: Q value dependence on choke diameter.

Content from this work may be used under the terms of the CC BY 3.0 licence (© 2018). Any distribution of this work must maintain attribution to the author(s), title of the work, publisher, and DOI.

ISBN: 978-3-95450-194-6 ISSN: 2226-0366 doi:10.18429/JACoW-LINAC2018-TUPO074

CAVITY FABRICATION

The cavity fabrication was successfully completed (Figure 4). The three half cells of accelerating cell were press formed with the same die as used for SRF GUN#1. The choke cell and half-cell of 1st cell on cathode rod side were machined from bulk niobium. All parts other than stainless steel flange were connected by the electron beam welding. All parts are welded from the inside except for equator of the 2nd cell.

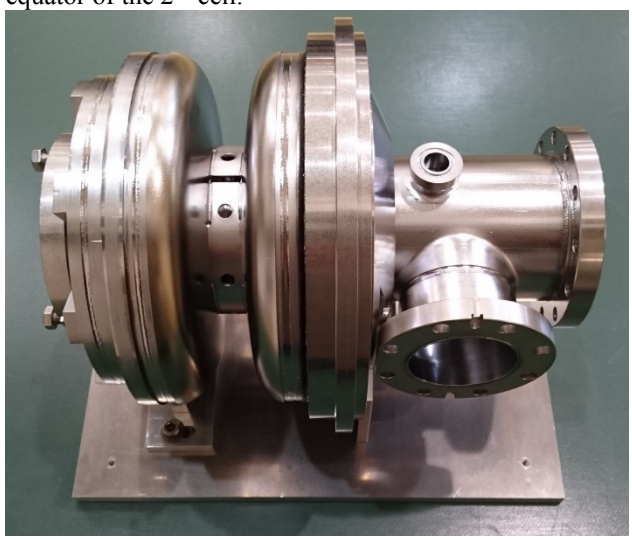


Figure 4: Fabrication completed SRF gun #2.

CATHODE ROD DESIGN

We plan to use a transparent superconductor for the substrate (LiTi2O4) of the photocathode. The transition temperature is 13 K. The cathode rod and holder were designed to cool down to around 2K. The cathode rod holder was designed as a part of the helium vessel. The cathode holder is made of copper block to ensure the thermal conductivity. The cathode rod is connected with flat and smooth surface for easily machining. Spring constant in the cathode rod is 71.21 N/mm. Maximum load is 71.21 N. contact area is about 450 mm^2. Contact pressure is about 158 kN/m^2. According to the solid works database, the thermal resistance is estimated to $1\times10^{-4}\sim10\times10^{-4}$ m^{2}K/W [2]. Figure 5 shows the cooling simulation and thermal pass used CST.

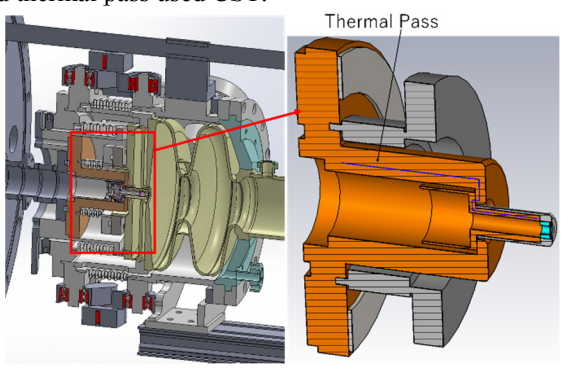


Figure 5: Image of SRF GUN #2 helium jacket (left), cathode rod and cathode rod holder for CST simulation (right)

Figure 6 shows the temperature of the cathode rod head. It can be cooled down to around 2.1 K if the thermal contact resistance is 1×10^{4} m^{2}K/W at connection. However, the thermal contact resistance is difficult to calculate, it is necessary to test using real structure. The machining of the cathode rod holder was completed. These parts will be connected by brazing in hydrogen furnace.

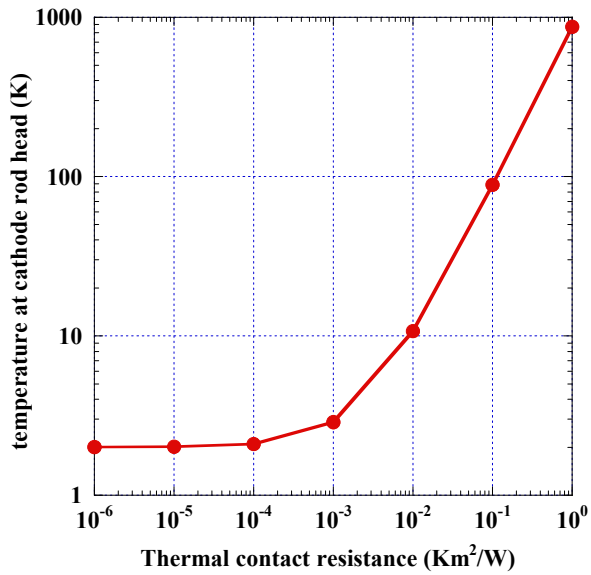


Figure 6: Cathode rod temperature dependence on the thermal contact resistance.

Figure 7 shows the design of the prototype cathode rod. The spring is made of Inconel. Inner parts consist the catching structure for connecting the transfer rod. Copper version of cathode rod was completed. Now we are fabricating the niobium cathode rod after a bit of modification. The K_2CsSb photocathode will be deposited on the head of the cathode rod. We want to use the transparent semiconductor substrate in future. The photocathode mount structure will be designed after proving thermal conductivity and RF performance of this cathode rod.

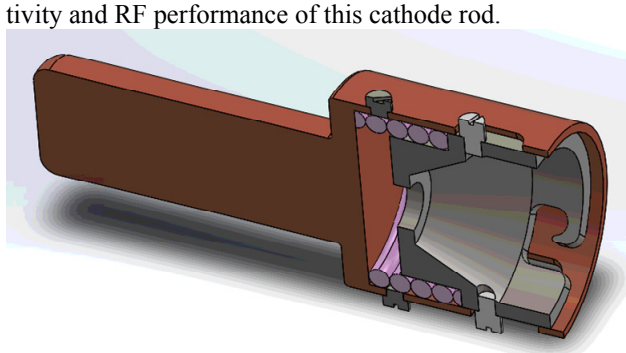


Figure 7: Prototype cathode rod design.

PHOTOCATHODE DEPOSITION CHAMBER

The photocathode deposition chamber was designed for connecting the cavity (Figure 8). The height of the cathode transfer line is aligned to same line of the gun. Deposition sources are SAES caesium dispenser, SAES potassium dispenser and bulk antimony heated by the tantalum

Content from this work may be used under the terms of the CC BY 3.0 licence (© 2018). Any distribution of this work must maintain attribution to the author(s), title of the work, publisher, and DOI.

ISBN: 978-3-95450-194-6 ISSN: 2226-0366 doi:10.18429/JACoW-LINAC2018-TUPO074

Content from this work may be used under the terms of the CC BY 3.0 licence (© 2018). Any distribution of this work must maintain attribution to the author(s), title of the work, publisher, and DOI.

wire. The cathode rod is heated and cleaned at 500 ºC by tantalum wire. The excitation laser can inject from front and back side during deposition. The excitation laser for gun operation will be injected to the photocathode through the deposition chamber during gun operation. The gate valve between gun cavity and the deposition chamber has the view port. The mirror is mounted bottom of the cathode rod holder.

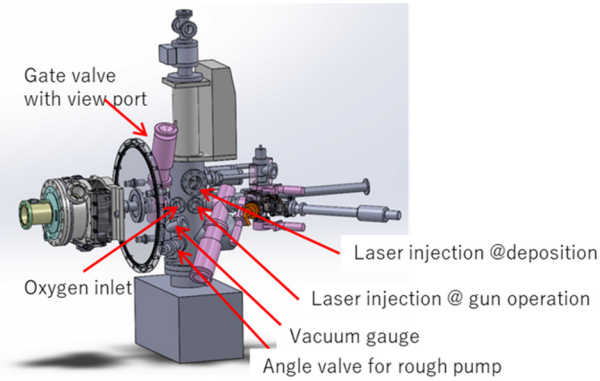


Figure 8: Design of the deposition chamber.

Figure 9 shows the deposition chamber. It should be assembled in clean room. This time, it was assembled for confirmation of assembly procedure and checking the photocathode performance. We plan to clean and reassemble in the clean room as soon as the performance is confirmed in the future. The chamber was vacuumed and baked. The chamber vacuum reached to 4×10^{-8} Pa. The main pump is ion pump which was opened to air several years. It was baked long time. We are now ready for photocathode deposition.

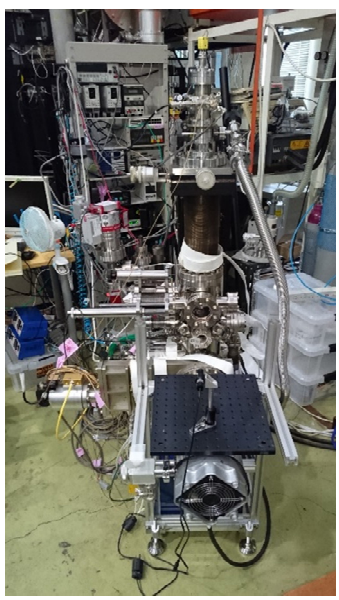


Figure 9: Assembled deposition chamber.

FUTURE PLAN

We are preparing the SRF gun #2 for the beam test using the horizontal cryostat which is operated for various cavities. Figure 10 shows the layout of the SRF GUN #2 in horizontal cryostat. The beam line and gun cavity will be inserted perpendicular to the longitudinal direction of the cryostat. The helium jacket and other parts are now under designing. First vertical test of the SRF GUN #2 will be carried out in this year. The gun cavity and cathode rod were designed focusing on cooling. Temperature of the cathode rod head is difficult to measure in the vertical test system. It is necessary to measure the cathode rod temperature directly in the vacuum using other chamber.

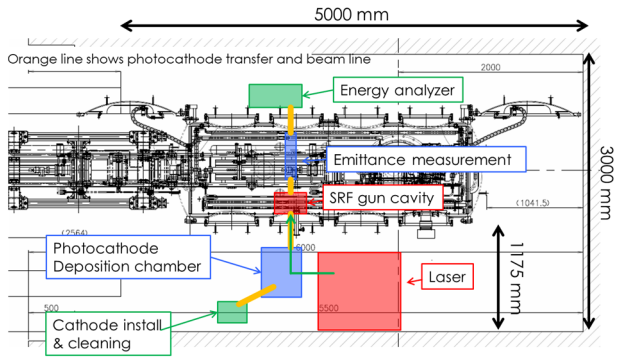


Figure 10: Layout of the SRF GUN #2 in horizontal cryostat.

SUMMARY

KEK has been developing the SRF gun. The fabrication of the KEK SRF gun #2 was successfully completed. Photocathode deposition chamber is also assembled. Vertical test of the gun cavity and photocathode deposition will be carried in this year. Other parts for the beam test is under designing. We are planning to test the beam performance using the horizontal cryostat existing at KEK.

REFERENCES

[1] T. Konomi *et al.*, "Development of SRF Gun Applying New Cathode Idea Using a Transparent Superconducting Layer", 59th ICFA Advanced Beam Dynamics Workshop on Energy Recovery Linacs (ERL2017), Geneva, Switzerland, Sep. 2017, pp.1-3.
doi:10.18429/JACoW-ERL2017-MOIACC002

[2] SOLIDWORKS, http://help.solidworks.com/

ISBN: 978-3-95450-194-6 ISSN: 2226-0366 doi:10.18429/JACoW-LINAC2018-TUPO076

AN INNOVATIVE Nb_3Sn FILM APPROACH AND ITS POTENTIAL FOR SRF APPLICATIONS *

E. Barzi †, C. Ciaccia, S. Falletta, D. Turrioni, FNAL, Batavia, IL, USA
A. Kikuchi, NIMS, Tsukuba, Ibaraki, Japan
H. Hayano, T. Saeki, KEK, Tsukuba, Ibaraki, Japan
H. Ito, SOKENDAI, Hayama, Kanagawa, Japan
G. Eremeev, A.-M. Valente-Feliciano, R. L. Geng, R. Rimmer, JLAB, Newport News, VA, USA

Abstract

A novel electro-chemical technique to produce Nb_3Sn films on Nb substrates was developed and optimized at Fermilab. The Nb_3Sn phase is obtained in a two-electrode cell, by electrodeposition from aqueous solutions of Sn layers and Cu intermediate layers onto Nb substrates. Subsequent thermal treatments in inert atmosphere are realized at a maximum temperature of 700°C to obtain the Nb_3Sn superconducting phase. Several superconducting Nb_3Sn films were obtained on Nb substrates by studying and optimizing most parameters of the electro-plating process. Samples were characterized at Fermilab, NIMS, KEK and JLAB, including EPMA analyses, DC and inductive tests of critical temperature T_{c0}, and lower critical field $H_{c1}(4.2\ K)$ by SQUID. In parallel to sample development and fabrication at FNAL, at JLAB and KEK effort was put into etching and electro-polishing techniques adequate to remove the Cu and bronze phases from the samples' outer surface. This is necessary prior to measurements at JLAB of the surface impedance of flat samples in a setup that make use of an RF host cavity.

INTRODUCTION

The two most important aspects of SRF performance are the accelerating field E_{acc} and the cavity quality factor, Q_0. The accelerating gradient in SRF cavities is proportional to the peak magnetic field on the cavity wall. At RF frequencies the peak magnetic field is limited by the metastable superheating field, H_{sh} [1]. The maximum accelerating gradient expected for Nb cavities in the TESLA shape, for instance, is ~40 MV/m. Nb_3Sn is an attractive alternative because it has a higher T_{c0} of up to 18 K. With a theoretical H_{sh} of 0.42 T, as compared to a T_{c0} of 9 K and H_{sh} of 0.25 T for Nb [2], SRF cavities with a thin layer of Nb_3Sn coated onto their inner surface should produce larger accelerating gradients than Nb. The larger T_{c0} of Nb_3Sn allows for SRF cavities with a Q_0 at 4.2 K about 30 times larger than for Nb. It also has the advantage of allowing the cavities to operate at 4.5 K rather than at ~2 K that is used for Nb cavities to obtain a higher gradient. This means less expensive refrigeration and more cryogenic economy and reliability.

Nb_3Sn coated SRF cavities have been demonstrated to improve the cavity quality factor, but have not produced the theoretically expected gradient. Perhaps the longest standing Nb_3Sn technique for SRF is that of a vapor diffusion process followed by thermal reaction at high temperature to form the Nb_3Sn [3, 4]. It consists of five stages, including degassing at 100° to 200°C to remove moisture; nucleation at intermediate temperature; ramp up to and holding at a coating temperature between 1100°C and 1300°C for Nb_3Sn formation; and finally annealing to diffuse excess tin. This process has not produced so far full cavity assemblies because the scale-up from single cell is challenging. Nb_3Sn coating on 5-cell CEBAF-type cavities was achieved at JLAB [5].

In this paper an alternate process, that of chemical electrodeposition, followed by reaction in inert atmosphere, will be described. The electroplating is performed at near room temperature and at atmospheric pressure. The advantage of electrodeposition is its simplicity, accurate control, and low costs. Also, it can be performed on any 3D surface such as the inner surface of SRF cavities. Electrodeposition should be among the least expensive ways to produce SRF cavities. It should also provide a more uniform Nb_3Sn coating. Improving the quality of the Nb_3Sn could reduce the large gap between the theoretical and measured H_{sh}.

EXPERIMENTAL METHOD

An electro-chemical deposition technique, which had been collaboratively developed with Politecnico di Milano [6, 7] and is under patenting process, to produce superconducting Nb_3Sn films on Nb substrates, was reproduced at Fermilab. In the past year, the equipment and consumables were procured, and the complete electro-chemical system was commissioned.

In electroplating the metallic coating is deposited on another metal surface through an electrolyte solution. The metal to be plated acts as the cathode and when the appropriate current is applied, positively charged ions traveling from the anode into the solution will discharge and get deposited on the cathode until a film of desired thickness is formed. Fig. 1, top shows a schematic with two symmetric anodes for bilateral coating of flat samples. Fig. 1, bottom shows the concept for scale-up to 3D surfaces, such as internal coating of cylinders, as first step to the internal coating of SRF cavities.

Figure 2 shows the sequence of deposited layers. First, using the Nb as cathode and Cu anode, a thin seed layer of

* Work supported by U.S. DOE contract No. DE-AC02-07CH11359
† barzi@fnal.gov

Content from this work may be used under the terms of the CC BY 3.0 licence (© 2018). Any distribution of this work must maintain attribution to the author(s), title of the work, publisher, and DOI.

ISBN: 978-3-95450-194-6 ISSN: 2226-0366 doi:10.18429/JACoW-LINAC2018-TUPO076

Content from this work may be used under the terms of the CC BY 3.0 licence (© 2018). Any distribution of this work must maintain attribution to the author(s), title of the work, publisher, and DOI.

Cu is deposited in an acid solution. The Cu lowers the formation temperature for the A15 compound and suppresses the unwanted $NbSn_2$ and Nb_6Sn_5 phases. In a second electroplating step, the resulting Nb/Cu sample is used as cathode, and a thick layer of Sn is deposited with a Sn anode within a commercial Sn-rich solution. And finally, on the resulting Nb/Cu/Sn sample, a Cu layer is again deposited using a Cu anode. Each electrodeposition step is carried out at near room temperature and at atmospheric pressure. Details are illustrated in [7].

Nb_3Sn is formed through solid diffusion by reacting the multi-layered samples in inert atmosphere (argon) using the temperature profile of Fig. 3, at a maximum temperature of 700°C.

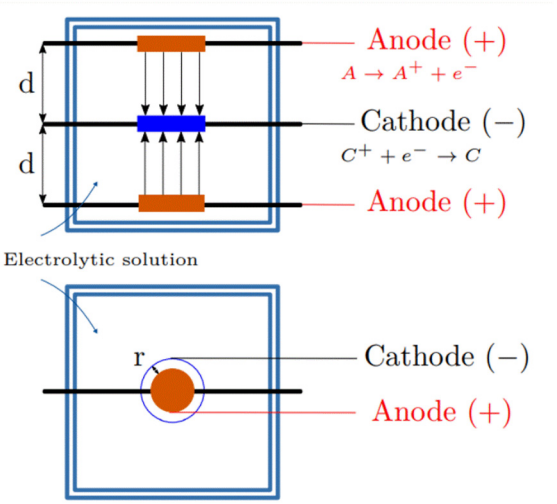


Figure 1: Schematic of electro-chemical cell for bilateral coating of Nb flat samples (top), and internal coating of Nb cylinders (bottom).

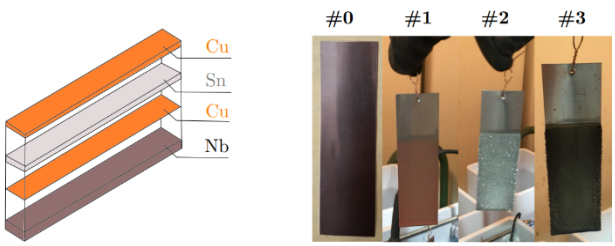


Figure 2: Sequence of deposited layers (left), and pictures of sample at each deposition step (right).

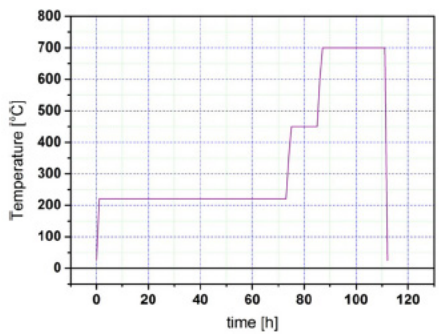


Figure 3: Temperature profile during Nb/Cu/Sn/Cu solid diffusion.

Reacted Nb_3Sn samples were characterized using an Electron Probe Microanalysis (EPMA) for elemental quantitative analysis with Wavelength-Dispersive Spectroscopy (WDS), transport test of critical current I_c *(B)* up to 14 T to determine the upper critical field $\mu_0 H_{c20}$ as a free parameter in the I_c *(B)* data fitting, resistive and inductive critical temperature T_{c0}, as well as SQUID measurements of H_{c1}*(4.2K)*.

Reacted Nb_3Sn film samples were also sent to JLab and to KEK for developing the appropriate etching and/or electropolishing techniques to remove the few micrometres of Cu and bronze phases at the samples' outer surface.

RESULTS

Several superconducting Nb_3Sn films of thickness of up to 12 µm were obtained on Nb substrates of 0.3 mm to 0.5 mm thickness by studying and optimizing most parameters of the electro-plating process, including:

- Bath composition and anode materials for each of the three deposition steps;
- Current densities, deposition times, stirring rates, and cathode and anode relative orientation in DC mode;
- Current densities, deposition times, stirring rates, cathode and anode relative orientation, pulse frequencies, and duty cycles in pulsed mode.

The pulsed mode was eventually chosen for all three deposition steps.

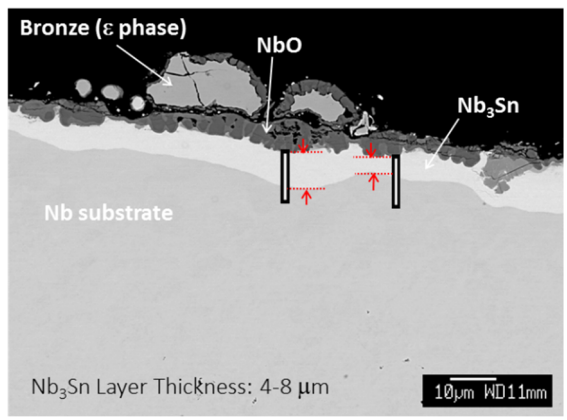


Figure 4: Cross-section of a sample with EPMA results (NIMS).

Figure 4 shows a picture of the longitudinal cross section of a sample (sample No. 23). EPMA was performed and allowed identification of bronze phases as well as Nb oxides on the outer surface of the Nb_3Sn layer. Clearly, for SRF operation these residues must be removed by either etching, electropolishing or mechanically. Fig. 5 shows the T_{c0} result of 17.5 K (defined as in [7]) obtained for the same sample as measured resistively. The same sample was also measured by SQUID (Fig. 6) and the resulting T_{c0} was 17.6 K. The two results are remarkably consistent. Fig. 7 shows

ISBN: 978-3-95450-194-6 ISSN: 2226-0366 doi:10.18429/JACoW-LINAC2018-TUPO076

the *M-H* curve obtained with the SQUID magnetometer. The $H_{c1}(4.2K)$ for this sample was 600 Oe.

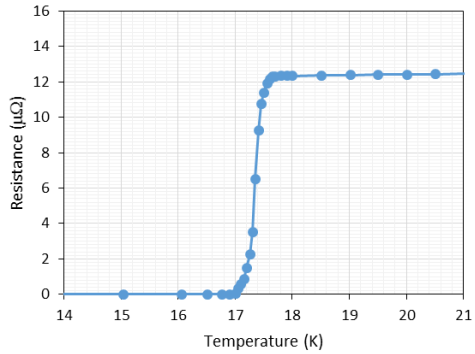


Figure 5: DC test at FNAL of T_{c0} = 17.5 K of a Nb_3Sn film sample.

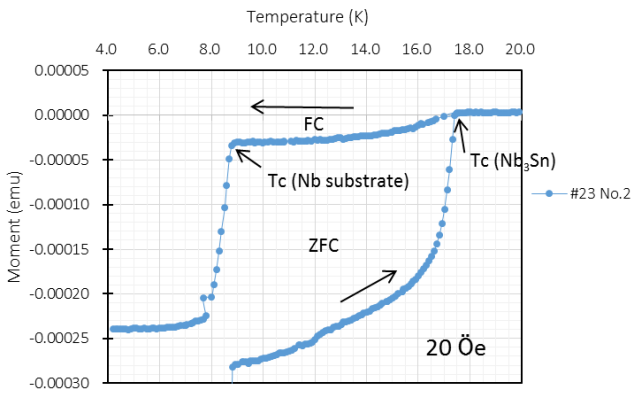


Figure 6: *M-T* curve obtained with SQUID magnetometer at NIMS. The T_{c0} = 17.6 K.

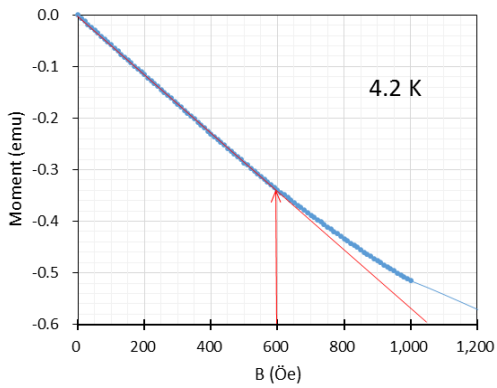


Figure 7: *M-H* curve obtained with SQUID magnetometer at NIMS. The H_{c1}(4.2 K) = 600 Oe.

For this sample, an upper critical magnetic field, $\mu_0 H_{c20}$, of 23.2 T was obtained as a free parameter in the I_c *(B)* data fitting. The measured T_{c0} value of 17.5 K was used as a fixed parameter in the fit.

It is important to know how well these thin film samples would perform in a cavity. A TE011 cavity with a demountable endplate, where a disc sample can be placed, can be used for the measurement of the surface impedance. A cavity test facility of this type exists at JLab [8].

CONCLUSIONS

High gradient, inexpensive superconducting cavities (SRF) will be needed for future accelerators. However, the accelerating field of Nb cavities is limited by the peak magnetic field on the cavity surface. Nb_3Sn SRF cavities should produce larger accelerating gradients and a larger quality factor, Q_0, than Nb cavities. Also, the higher T_{c0} of Nb_3Sn allows cavities to operate at 4.5 K rather than ~2 K that is used for Nb cavities to obtain a higher gradient. This means less expensive refrigeration and more cryogenic reliability.

Nb_3Sn coated SRF cavities, with Nb_3Sn produced by vapor diffusion followed by a thermal reaction at high temperature, have achieved only a fraction of the theoretical predicted gradient. Nb_3Sn plated cavity performance may be improved by using electrochemical deposition. The advantages are its simplicity, accurate control, and low costs. Electrodeposition should be among the least expensive ways to produce SRF cavities, and it should provide a more uniform Nb_3Sn coating. Improving the quality of the Nb_3Sn could reduce the large gap between the theoretical and measured H_{sh}. Electrochemical techniques may also eliminate the problem of a low Sn concentration at the Nb interface, which is a fundamental limit of the current vapor deposition techniques. Lastly, electrodeposition can be performed on any 3D surface such as the inner surface of SRF cavities. Nb_3Sn plating experiments of Nb cylinders are under way.

REFERENCES

[1] K. Saito, "Critical Field Limitation of the Niobium Superconducting RF Cavity," in *Proc. of the 10th Workshop of RF Superconductivity*, Tsukuba (2001), pp 583-587.

[2] D. B. Liarte et al., "Theoretical estimates of maximum fields in superconducting resonant radio frequency cavities: stability theory, disorder, and laminates", *Supercond. Sci. Technol.* 30, 033002 (2017).

[3] M. Liepe and S. Posen, "Advances in the development of Nb_3Sn superconducting radio-frequency cavities", *ST Accel. Beams* **15** 112001 (2014).

[4] G. Eremeev et al., "Development of a Nb_3Sn cavity vapor diffusion deposition system, ", *Proc. SRF 2013*, Whistler (2015).

[5] U. Pudasaini et al., "Nb_3Sn Multicell Cavity Coating at JLAB", in Proc. of IPAC 2018, Apr. – May 2018, paper WEYGBF3, pp. 1798-1803.

[6] U.S. Non-provisional Utility (Patent) Application, "Synthesis of Superconducting Nb-Sn", Attorney Docket No. 9423-94978-02 (2016).

[7] E. Barzi et al., "Synthesis of superconducting Nb_3Sn coatings on Nb substrates," Supercond. Sci. Technol. **29** 015009 (2016).

[8] B. P. Xiao et al., "Radio frequency surface impedance characterization system for superconducting samples at 7.5 GHz", *Review of Scientific Instruments* **82**, 056104 (2011).

Content from this work may be used under the terms of the CC BY 3.0 licence (© 2018). Any distribution of this work must maintain attribution to the author(s), title of the work, publisher, and DOI.

ISBN: 978-3-95450-194-6 ISSN: 2226-0366 doi:10.18429/JACoW-LINAC2018-TUPO078

EXTENSION OF BUSCH'S THEOREM TO PARTICLE BEAMS

L. Groening[1], M. Chung[2], and C. Xiao[1]
[1]Gesellschaft für Schwerionenforschung, Darmstadt, Germany
[2]Ulsan National Institute of Science and Technology, Ulsan 44919, Republic of Korea

Abstract

In 1926, H. Busch formulated a theorem for one single charged particle moving along a region with longitudinal magnetic field. The theorem relates particle angular momentum to the amount of field lines being enclosed by the particle cyclotron motion. It has been extended to accelerated particle beams. This contribution sketches the extension and applies the extended theorem to successfully performed emittance manipulations with electron and ion beams.

BUSCH'S THEOREM FOR SINGLE PARTICLE

In 1926, H. Busch applied the preservation of angular momentum for systems with cylindrical symmetry to a charged particle moving inside a region with magnetic field $\vec{B}$ [1]. Using conjugated momenta, the magnetic field strength is intrinsically included into the equations of motion. In linear systems, the normalized conjugated momenta p_x and p_y are related to the derivatives of the particle position coordinates (x, y) w.r.t. the main longitudinal direction of motion $\vec{s}$ through

$$p_x := x' + \frac{\mathcal{A}_x}{(B\rho)} = x' - \frac{yB_s}{2(B\rho)}, \quad (1)$$

$$p_y := y' + \frac{\mathcal{A}_y}{(B\rho)} = y' + \frac{xB_s}{2(B\rho)}, \quad (2)$$

where $\vec{\mathcal{A}}$ is the magnetic vector potential with $\vec{B} = \vec{\nabla}\times\vec{\mathcal{A}}$, B_s is the longitudinal component of the magnetic field, and $(B\rho)$ is the particle rigidity, i.e., its momentum per charge $p/(qe)$, with p as total momentum, q as charge number, and e as elementary charge. Busch's theorem states that the canonical angular momentum $\tilde{l} = xp_y - yp_x$ is a constant of motion that is written in cylindrical coordinates as

$$m\gamma r^2\dot{\theta} + \frac{eq}{2\pi}\psi = const\,. \quad (3)$$

A general formulation of Eq. (3) has been derived in [2], which is regarded as the generalized Busch theorem

$$\oint_C \vec{v}\cdot d\vec{C} + \frac{eq}{m\gamma}\psi = const\,, \quad (4)$$

i.e., the path integral around a stream of possible particle trajectories along a closed contour C, plus the magnetic flux through the area enclosed by C is an invariant of the motion. Figure 1 illustrates the first part of the left hand side of Eq. (4). Busch's theorem of Eq. (3) is the special case of this generalized form for C being a circle of radius r. It is emphasized that Eq. (4) is only valid for laminar motion.

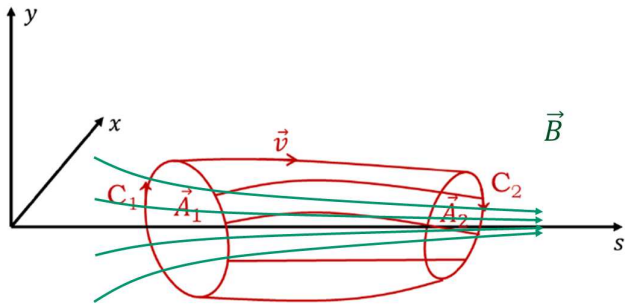


Figure 1: Fig. 3 from [3]: the contour C encloses possible streams of particle trajectories and encloses the area $\vec{A}$.

TRANSVERSE EIGEN EMITTANCES

The transverse eigen emittances were introduced by Dragt in 1992 [4] as the two transverse rms-emittances the beam acquires after all inter-plane correlations have been removed by appropriate linear beam line elements. They are calculated from the 2nd-moments beam matrix

$$\tilde{C} = \begin{bmatrix} \langle x^2\rangle & \langle xp_x\rangle & \langle xy\rangle & \langle xp_y\rangle \\ \langle xp_x\rangle & \langle p_x^2\rangle & \langle yp_x\rangle & \langle p_xp_y\rangle \\ \langle xy\rangle & \langle yp_x\rangle & \langle y^2\rangle & \langle yp_y\rangle \\ \langle xp_y\rangle & \langle p_xp_y\rangle & \langle yp_y\rangle & \langle p_y^2\rangle \end{bmatrix}, \quad (5)$$

together with

$$J = \begin{bmatrix} 0 & 1 & 0 & 0 \\ -1 & 0 & 0 & 0 \\ 0 & 0 & 0 & 1 \\ 0 & 0 & -1 & 0 \end{bmatrix}. \quad (6)$$

as [5]

$$\tilde{\varepsilon}_{1/2} = \frac{1}{2}\sqrt{-tr[(\tilde{C}J)^2] \pm \sqrt{tr^2[(\tilde{C}J)^2] - 16\,det(\tilde{C})}}\,. \quad (7)$$

The product of the two eigen emittances is equal to the 4d rms-emittance $\tilde{\varepsilon}_{4d}$ being in turn equal to the square root of the determinant of $\tilde{C}$. By definition $\tilde{\varepsilon}_{1/2/4d}$ are preserved by linear beam line elements as drifts, quadrupoles, dipoles, and solenoids even if they are tilted.

PRESERVATION OF EIGEN EMITTANCES

Busch's theorem was obtained from expressing preservation of axial angular momentum using conjugate momenta. Its extension to beams is achieved in analogue way by ex-

Content from this work may be used under the terms of the CC BY 3.0 licence (© 2018). Any distribution of this work must maintain attribution to the author(s), title of the work, publisher, and DOI.

ISBN: 978-3-95450-194-6 ISSN: 2226-0366 doi:10.18429/JACoW-LINAC2018-TUPO078

pressing the preservation of the sum

$$\begin{aligned}\tilde{\varepsilon}_1^2 + \tilde{\varepsilon}_2^2 &= -\frac{1}{2}tr[(\tilde{C}J)^2] \\ &= \tilde{\varepsilon}_x^2 + \tilde{\varepsilon}_y^2 + 2(\langle xy\rangle\langle p_x p_y\rangle - \langle yp_x\rangle\langle xp_y\rangle) \\ &= const\end{aligned} \tag{8}$$

using conjugate momenta as shown in detail in [3]. Substitution of the conjugate momenta by Eqs. 1 and 2 leads to the following expression including just laboratory coordinates that can be applied directly to emittance manipulation scenarios

$$\begin{aligned}&(\varepsilon_1 - \varepsilon_2)^2 + \left[\frac{AB_s}{(B\rho)}\right]^2 + \\ &2\frac{B_s}{(B\rho)}\left[\langle y^2\rangle\langle xy'\rangle - \langle x^2\rangle\langle yx'\rangle + \langle xy\rangle(\langle xx'\rangle - \langle yy'\rangle)\right] \\ &= const\,,\end{aligned} \tag{9}$$

where $A := \sqrt{\langle x^2\rangle\langle y^2\rangle - \langle xy\rangle^2}$ is the rms-area of the beam divided by π. The last summand (abbreviated as $2\frac{B_s}{(B\rho)}\mathcal{W}_A$) is invariant under rotation around the beam axis and it vanishes for uncorrelated beams. As shown in [6] Eq. (9) is equivalent to

$$(\varepsilon_1 - \varepsilon_2)^2 + \left[\frac{AB_s}{(B\rho)}\right]^2 + \frac{AB_s}{(B\rho)}\oint_C \vec{r}'d\vec{C} = const\,. \tag{10}$$

Emittance reduction through acceleration can be included by multiplying Eqs. (1) and (2) initially by $p = m\gamma\beta c$, where β is the longitudinal particle velocity normalized to the velocity of light c. The extension of Busch's theorem to beams including acceleration is

$$(\varepsilon_{n1} - \varepsilon_{n2})^2 + \left[\frac{eq\psi}{mc}\right]^2 + \frac{eq\psi\beta\gamma}{mc}\oint_C \vec{r}'\cdot d\vec{C} = const\,, \tag{11}$$

where ψ is the magnetic flux through the beam rms-area A. This expression can be further compressed by using the mechanical canonical momentum $\vec{\mathcal{P}}_c = \vec{\mathcal{P}} + eq\vec{\mathcal{A}}$ with $\vec{\mathcal{P}} := m\gamma\vec{v}$ and the canonical vorticity $\vec{\Omega}_c := \vec{\nabla}\times\vec{\mathcal{P}}_c$ to

$$(\varepsilon_{n1} - \varepsilon_{n2})^2 + \frac{eq\psi}{(mc)^2}\int_A \vec{\Omega}_c d\vec{A} = const\,. \tag{12}$$

FLAT BEAM EXPERIMENT AT FERMILAB

At FERMILAB's NICADD photoinjector, flat electron beams were formed by first producing the beams at the surface of a photo cathode placed inside an rf-gun to which longitudinal magnetic field $B_s = B_0$ was imposed [7]. The schematic beam line is sketched in Fig. 2. Along the subsequent region with $B_s = 0$, the beam was accelerated to

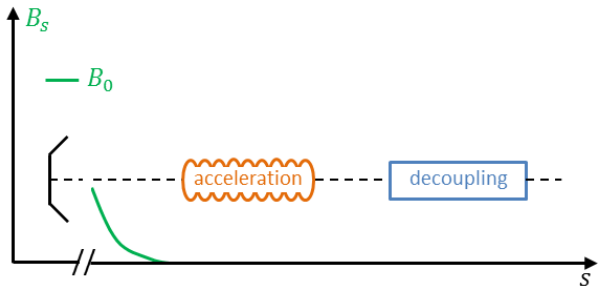


Figure 2: Fig. 6 from [3]: schematic sketch of the beam line of the experiment performed at NICCAD at FERMILAB [7].

16 MeV. Finally, correlations initially imposed by the magnetic exit fringe field of the rf-gun were removed by three skew quadrupole magnets. Equation (11) equalizes the situation at the cathode surface at the left-hand side to the situation of the finally flat beam on the right-hand side ($q = 1$)

$$0 + \left[\frac{eB_0A_0}{mc}\right]^2 + 0 = (\varepsilon_{nf1} - \varepsilon_{nf2})^2 + 0 + 0\,, \tag{13}$$

where A_0 is the beam rms-area at the cathode surface. The authors of [7] used the definitions [8]

$$(\varepsilon_n^u)^2 := \varepsilon_{nf1}\cdot\varepsilon_{nf2} \tag{14}$$

$$\mathcal{L} := (eB_0A_0)/(2m\gamma\beta c) \tag{15}$$

resulting in

$$\varepsilon_{nf1} = \mathcal{L}\beta\gamma \pm \sqrt{(\mathcal{L}\beta\gamma)^2 + (\varepsilon_n^u)^2}\,, \tag{16}$$

of which only the upper sign gives a meaningful positive result. Re-plugging this expression for ε_{nf1} into Eq. (13) leads to

$$\varepsilon_{nf1/2} = \pm\mathcal{L}\beta\gamma + \sqrt{(\mathcal{L}\beta\gamma)^2 + (\varepsilon_n^u)^2}\,, \tag{17}$$

being identical to their original expression (Eq. (1) of [7]).

TRANSVERSE EMITTANCE TRANSFER EXPERIMENT AT GSI

At GSI, the EMittance Transfer EXperiment (EMTEX) transferred emittance from one transverse plane into the other one by passing the beam through a short solenoid [5,9]. The schematic EMTEX beam line is depicted in Fig. 3. In the solenoid center, the ions charge state, i.e., their rigidity was changed by placing a thin carbon foil therein from $^{14}N^{3+}$ to $^{14}N^{7+}$. Charge state stripping is a standard procedure used at several laboratories that deliver heavy or intermediate mass ions [10]. In front of the solenoid, the beam had no inter-plane correlations, and thus, the difference of rms-emittances was equal to the difference of eigen-emittances (mod. sign). Since the solenoid was short, the beam area at the foil $A := A_f$ can be approximated as constant during the beam transit through the solenoid. Table 1 lists the relevant parameters of the experiment. Equation (9)

Content from this work may be used under the terms of the CC BY 3.0 licence (© 2018). Any distribution of this work must maintain attribution to the author(s), title of the work, publisher, and DOI.

ISBN: 978-3-95450-194-6 ISSN: 2226-0366 doi:10.18429/JACoW-LINAC2018-TUPO078

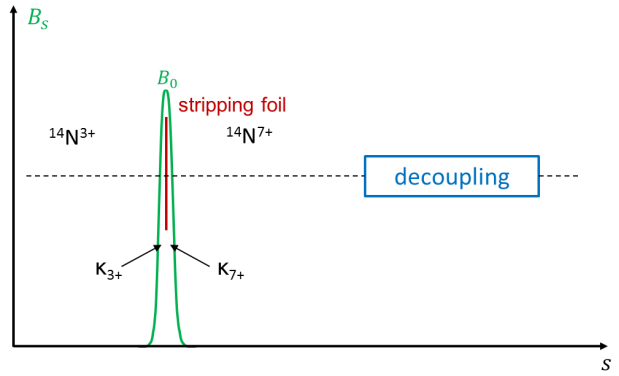


Figure 3: Fig. 7 from [3]: schematic beam line of EMTEX at GSI for transverse emittance transfer [9].

relates the beam parameters in front of the solenoid ($B_s = 0$, no correlations $\rightarrow \mathcal{W}_A = 0$, $\varepsilon_{10} = \varepsilon_{x,3+}$, $\varepsilon_{20} = \varepsilon_{y,3+}$) to those in front of the foil in the center of the short solenoid:

$$(\varepsilon_{x,3+} - \varepsilon_{y,3+})^2 + 0 + 0 = (\varepsilon_{1f} - \varepsilon_{2f})^2 + \left[\frac{A_f B_0}{(B\rho)_{3+}}\right]^2 + \frac{2B_0}{(B\rho)_{3+}}\mathcal{W}_{Af}\,, \quad (18)$$

where the index f refers to the location of the foil. The entrance fringe field of the solenoid causes the rms-vorticity

$$\mathcal{W}_{A_f} = \Delta\mathcal{W}_A = -2\kappa_{3+} \cdot A_f^2 = -2\frac{B_0}{2(B\rho)_{3+}}A_f^2 \quad (19)$$

leading to

$$(\varepsilon_{x,3+} - \varepsilon_{y,3+})^2 + 0 + 0 = (\varepsilon_{1f} - \varepsilon_{2f})^2 - \left[\frac{A_f B_0}{(B\rho)_{3+}}\right]^2 . \quad (20)$$

Using the initial beam parameters of the experiment from Table 1, $A_f = \sqrt{\varepsilon_x \beta_x \varepsilon_y \beta_y} = 4.166\,\text{mm}^2$, and the identity 1 mm mrad = 1 μm gives

$$(\varepsilon_{1f} - \varepsilon_{2f})^2 = (\varepsilon_{x,3+} - \varepsilon_{y,3+})^2 + 2.709\ \mu\text{m}^2 = 2.755\ \mu\text{m}^2\,. \quad (21)$$

Equation (9) is re-used to relate the beam parameters just behind the foil but still at the center of the solenoid to those at the exit of the beam line, where $B_s = 0$ and the beam correlations have been removed again. Angular scattering in the foil is neglected. As the beam changed rigidity in the foil, $(B\rho)_{3+}$ must be properly replaced by $(B\rho)_{7+}$. However, second beam moments are not changed by the foil, i.e., $\mathcal{W}_A = \mathcal{W}_{A_f}$, right in front and right behind the foil. Accordingly,

$$(\varepsilon_{1f} - \varepsilon_{2f})^2 + \left[\frac{A_f B_s}{(B\rho)_{7+}}\right]^2 + \frac{2B_s}{(B\rho)_{7+}}\mathcal{W}_{Af} = (\varepsilon_{x,7+} - \varepsilon_{y,7+})^2 + 0 + 0\,, \quad (22)$$

which by using Eq. (19) and plugging in the values delivers

$$|\varepsilon_{x,7+} - \varepsilon_{y,7+}| = 2.2\ \text{mm mrad} \quad (23)$$

Table 1: EMTEX Beam Parameters

Parameter	Value
kin. energy	11.45 MeV/u
mass number	14
$\varepsilon_{x,3+}$	1.040 mm mrad
$\varepsilon_{y,3+}$	0.825 mm mrad
$\beta_{x,3+}$	3.461 m
$\beta_{y,3+}$	5.845 m
$q_{in/out}$	3+ / 7+
$(B\rho)_{3+/7+}$	2.278 / 0.976 Tm
B_0	0.9 T

fitting well the measured value of 2.0 mm mrad (see Fig. 2 of [9]).

REFERENCES

[1] H. Busch, "Berechnung der Bahn von Kathodenstrahlen im axialsymmetrischen elektromagnetischen Felde", *Annalen der Physik*, vol. 81, pp. 974, (1926).

[2] P. T. Kirstein *et al.*, *Space Charge Flow*. New York, USA: McGraw-Hill Inc., 1967, pp. 14.

[3] L. Groening *et al.*, "Extension of Busch's theorem to particle beams", *Phys. Rev. ST Accel. Beams*, vol. 21, pp. 014201 (2018), doi:10.1103/PhysRevAccelBeams.21.014201

[4] A. J. Dragt, "General moment invariants for linear Hamiltonian systems", *Phys. Rev.* A, vol. 45, no. 4, pp. 2572 (1992), doi:10.1103/PhysRevA.45.2572

[5] C. Xiao *et al.*, "Single-knob beam line for transverse emittance partitioning", *Phys. Rev. ST Accel. Beams*, vol. 16, pp. 044201 (2013), doi:10.1103/PhysRevSTAB.16.044201

[6] L. Groening *et al.*, "Relation between particle beam eigenemittances and canonical vorticity flux", *arXiv*, 1808.01218 (2018).

[7] P. Piot *et al.*, "Photoinjector generation of a flat electron beam with transverse emittance ratio of 100", *Phys. Rev. ST Accel. Beams*, vol. 9, pp. 031001 (2006), doi:10.1103/PhysRevSTAB.9.031001

[8] K.-J. Kim, "Round-to-flat transformation of angular-momentum-dominated beams", *Phys. Rev. ST Accel. Beams*, vol. 6, pp. 104002 (2003), doi:10.1103/PhysRevSTAB.6.104002

[9] L. Groening *et al.*, "Experimental Proof of Adjustable Single-Knob Ion Beam Emittance Partitioning", *Phys. Rev. Lett.*, vol. 113, pp. 264802 (2014), doi:10.1103/PhysRevLett.113.264802

[10] P. Scharrer *et al.*, "Measurements of charge state distributions of 0.74 and 1.4 MeV/u heavy ions passing through dilute gases", *Phys. Rev. Accel. Beams*, vol. 20, pp. 043503 (2017), doi:10.1103/PhysRevAccelBeams.20.043503

Content from this work may be used under the terms of the CC BY 3.0 licence (© 2018). Any distribution of this work must maintain attribution to the author(s), title of the work, publisher, and DOI.

ISBN: 978-3-95450-194-6 ISSN: 2226-0366 doi:10.18429/JACoW-LINAC2018-TUPO079

NUMERICAL AND EXPERIMENTAL STUDY OF H- BEAM DYNAMICS IN J-PARC LEBT

T. Shibata†, K. Ikegami, Y. Liu, A. Miura, F. Naito, K. Nanmo, H. Oguri, K. Ohkoshi, M. Otani, K. Shinto, A. Takagi
J-PARC Center, Tokai, Japan

Abstract

Transport process of negative hydrogen ion (H^-) in LEBT (Low Energy Beam Transport) is investigated by comparison of experimental and numerical results. A three dimensional Particle-In-Cell (PIC) particle transport model has been developed in order to take into account (i) axial magnetic field by two solenoids in J-PARC LEBT and (ii) radial electric field by space charge (SC) effect. Ratio of H^- beam particles inside the RFQ (Radio Frequency Quadrupole) acceptance to the total particles at the RFQ entrance is calculated for different current conditions in LEBT solenoid 1 and 2. The results are compared with RFQ transmission rate measured in the J-PARC linac commissioning. The double peak of RFQ transmission rate to the solenoid applied current seen in the measurement is explained by the calculation results. The results indicate that presence of the LEBT orifice for differential pumping plays a role as a collimator to reduce emittance at RFQ entrance.

LEBT TUNING IN J-PARC LINAC COMMISSIONING

A schematic drawing of J-PARC ion source (IS) and LEBT is shown in Fig.1. In J-PARC Linac commissioning, negative hydrogen ion beam extracted from the IS is focused by two solenoids in LEBT. The focused beam is injected toward the RFQ. The resent commissioning parameter for IS and LEBT are shown in Table 1. In the IS, AMFC (Axial Magnetic Field Correction) coil current, extraction voltage, acceleration voltage and applied currents for horizontal/vertical steering electromagnets (STM) are the adjustment parameters in the commissioning.

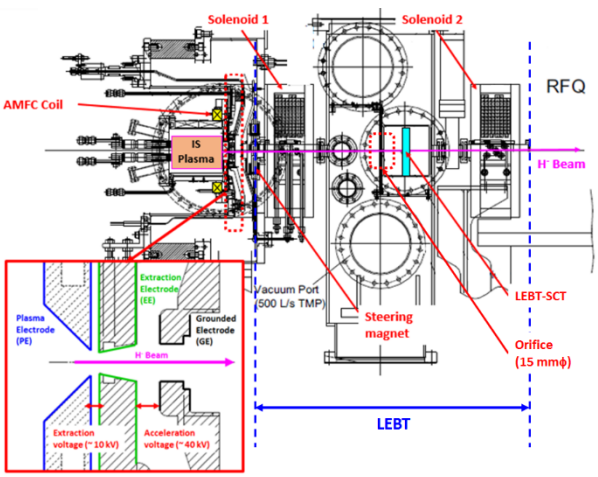


Figure 1: A schematic drawing of J-PARC IS and LEBT.

† email address:takanori.shibata@kek.jp

Table 1: Parameters for LEBT Tuning in J-PARC Linac Commissioning

Commissioning parameters	LI 30mA (2015)	LI 40 mA (2017)
AMFC coil (V)	0.0	2.0
Ext. voltage (kV)	9.9	9.8
Acc. Voltage (kV)	42.0	42.5
Hori. STM (A)	-1.0	-5.0
Vert. STM (A)	-5.5	-4.0
LEBT SOL1 (A)	495	500
LEBT SOL2 (A)	600	620

The AMFC and the extraction/acceleration voltages decide the initial divergence angle and beam energy of the H^- beam extracted from the IS. The beam energy is designed for 50 keV. Therefore, total value of extraction and acceleration voltages is 50 kV. However, recent results show that optimization of RFQ transmission rate is obtained for the total applied voltage up to around 51 – 52 keV while the beam intensity at LEBT increases monotonically with the applied voltage. The steering magnets are located in order to correct H^- beam bent by electron suppression magnets for reduction of co-extracted electron current.

In the LEBT, currents in two solenoid magnets are adjusted to obtain low emittance and Twiss parameter matching at the RFQ entrance. In the commissioning, current applied in the SOL 1 and 2 are set in ranges of 0 – 800 A to produce maximum 1.1 T at the solenoid center on beam axis. Optimization of the SOL currents are also shown in Table 1. At the center of the LEBT chamber, a 15 mm diameter orifice is located for differential pumping to prevent H_2 gas flow from the IS to the RFQ.

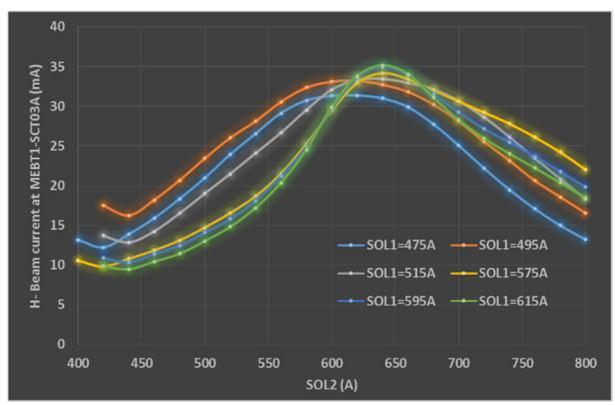


Figure 2: Dependence of H^- beam current measured at MEBT-SCT (just after RFQ exit) to the SOL1 and SOL2 currents in J-PARC Linac 30 mA operation.

Content from this work may be used under the terms of the CC BY 3.0 licence (© 2018). Any distribution of this work must maintain attribution to the author(s), title of the work, publisher, and DOI.

ISBN: 978-3-95450-194-6 ISSN: 2226-0366 doi:10.18429/JACoW-LINAC2018-TUPO079

Content from this work may be used under the terms of the CC BY 3.0 licence (© 2018). Any distribution of this work must maintain attribution to the author(s), title of the work, publisher, and DOI.

The current flow in the LEBT is measured by a current transformer (SCT) located just after the orifice. The beam current transmitted through the RFQ is measured by MEBT-SCT which is located just after RFQ exit. The IS/LEBT parameters in the commissioning are tuned to optimize this MEBT-SCT current or the RFQ transmission rate which is obtained by dividing MEBT-SCT current with LEBT-SCT current.

COMMISSIONING RESULTS

Figure 2 shows dependence of current flow in MEBT-SCT for different SOL 1 and 2 values. The beam current is 33.9 mA in order to extract 30 mA from the Linac. In the figure, two peaks of the current are seen for the SOL current pairs up to (SOL1, SOL2) = (495 A, 600 A) and (615 A, 640 A). The first peak for the lower SOL1 and 2 currents show wider peak while the second peak shows higher and narrower peak. The wider peak means that the beam current supplied from linac is stable for the fluctuation of SOL current due to noise or surge currents. Therefore, we adopted the first peak for the LEBT tuning result. However, reason of these double peak is not clearly understood.

NUMERICAL ANALYSIS

In order to clarify the H^- beam particle transport in the LEBT, a three-dimensional (3D) Particle-In-Cell (PIC) model is developed [1]. Basic equation of H^- particle is 3D Boltzmann equation;

$$m\frac{d\mathbf{v}}{dt} = q\left(\mathbf{E} + \mathbf{v}\times\mathbf{B}\right). \quad (1)$$

The variables $\boldsymbol{v}$, $\boldsymbol{E}$ and $\boldsymbol{B}$ are velocity of H^-, electric field due to SC effect and magnetic field by solenoids. The constants m and q are mass and charge of particles, respectively. For the different beam current and SC neutralization degree, spatial potential ϕ is calculated from Poisson equation;

$$\nabla^2\phi = -\frac{\rho}{\varepsilon_0} \quad (2)$$

where ρ and ε_0 are spatial charge distribution and permittivity in vacuum, respectively. In the present calculation, degrees of SC neutralization are given as parameter in each region. The SC neutralization degree given in different regions are (i) 100 % in the region before the orifice, (ii) 98 % in the region between the orifice and the SOL2 center, and (iii) 97 % between the SOL2 center and the RFQ entrance. In the region before the orifice, gas pressure is relatively high due to the incoming gas flux from the IS. The incoming flux is decreased by the 15 mm diameter orifice. In the actual J-PARC linac, gas pressure in the upper stream of the orifice is around 10^{-3} Pa, while the pressure is in the order of 10^{-4} Pa in LEBT chamber just after the orifice and 10^{-5} Pa near the RFQ entrance. Although it is well known

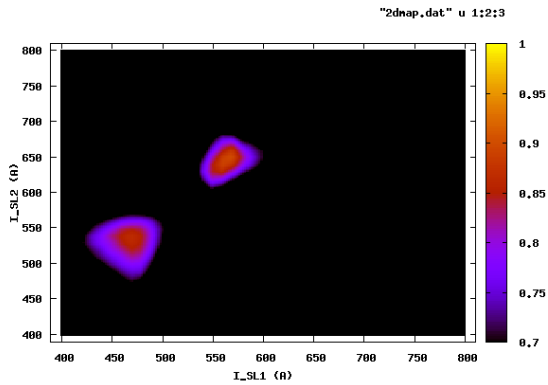
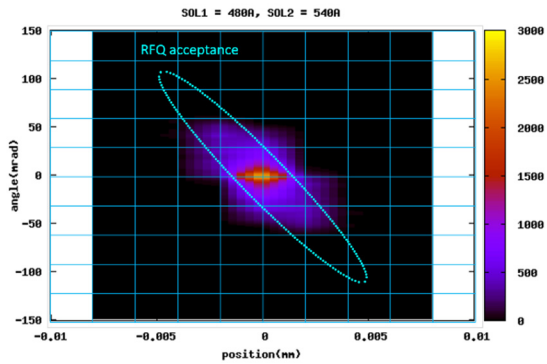
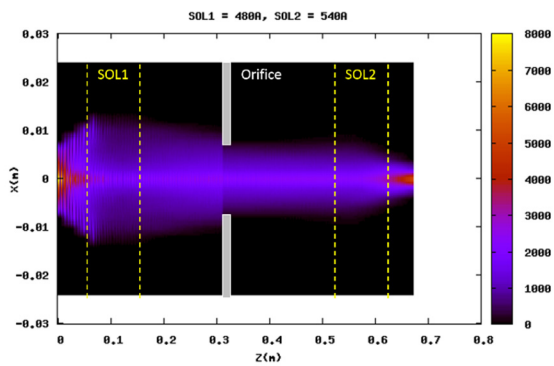


Figure 3: Dependence of RFQ transmission rate (color bar) to the SOL1 (horizontal) and SOL2 (vertical) current setting in the calculation.



(a)



(b)

Figure 4: Calculated phase space (a) and beam profile in XZ plane (b) for condition SOL1 = 480 A and SOL2 = 540 A with RFQ transmission rate 86.8%.

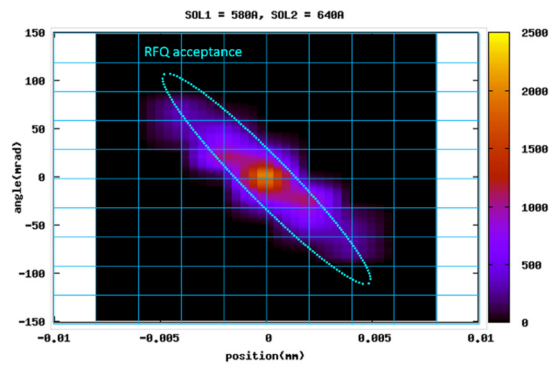
ISBN: 978-3-95450-194-6 ISSN: 2226-0366 doi:10.18429/JACoW-LINAC2018-TUPO079

that the SC neutralization degree is higher for higher gas pressure, the appropriate value of the SC neutralization degree is not studied well. In the present analysis, these values are scan preliminary and decided from the comparison with experimental results. From the SC neutralization degree, spatial charge distribution in a plane perpendicular to the axis is calculated as

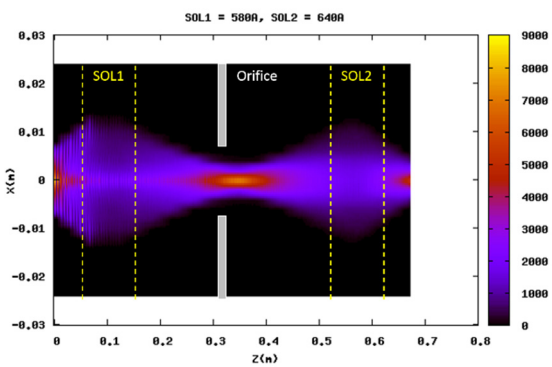
$$\rho(r) = -j_{\mathrm{H}^-} \times \delta(r_{\mathrm{beam}} - r) \times (1 - n_{\mathrm{SC}}) / v_{\mathrm{H}^-} / S_{\mathrm{H}^-}. \quad (3)$$

where j_{H^-} and v_{H^-} are H^- beam current and H^- velocity corresponding to the beam energy. The parameters r_{beam} and S_{H^-} are beam radius and area at certain position on beam axis, respectively. In the present model, charge density distribution in the beam area is given uniformly by step function $\delta(r)$. From the potential distribution solved by Successive-Over-Relaxation (SOR), the electric field in radial direction is given as $E_r = -\partial\phi/\partial r$.

The RFQ transmission rate is calculated by dividing number of particles which are included inside the RFQ acceptance in phase space with total number of particle which reaches to the RFQ entrance.



(a)



(b)

Figure 5: Calculated phase space (a) and beam profile in XZ plane (b) for condition SOL1 = 580 A and SOL2 = 640 A with RFQ transmission rate 90.2%.

NUMERICAL RESULTS AND DISCUSSION

Figure 3 shows dependence of RFQ transmission rate to the SOL1 and 2 currents for the beam current up to 30 mA. It is noticable that double peaks are seen in the RFQ transmission rate for relatively lower SOL current pair (SOL1, SOL2) = (480 A, 540 A) with the calculated rate up to 86.8 % (1st peak) and for higher SOL current pair (SOL1, SOL2) = (580 A, 640 A) with the rate up to 90.2 % (2nd peak). Fixing SOL1 current, the 1st peak shows wide range of high transmissin rate to SOL2 while the 2nd peak shows narrow and higher peak to the SOL2 variation.

A characteristic phase space at the RFQ entrance and beam profile in XZ plane for the 1st peak are shown in Fig.4. As in the figures, the H- beam extracted from the IS exit are focused by the SOL1. For lower magnetic field, the beam component which is not focused enough collides toward the orifice at the center of the LEBT chamber. Since the halo component is collimated at the orifice, focued beam after the SOL2 has low emittance. The low emittance beam at the RFQ entrance leads to high transmission rate.

Phase space and beam profile of the 2nd peak are shown in Fig.5. For the strong SOL1 magnetic field, the beam is well focused and pass through the orifice without injecting the orifice. The SC effect just after the orifice is relatively high which produces strong radial electric field. The expanding beam is focused by the strong SOL2 field. Although the beam emittance at the RFQ entrance is larger thanfor the 1st peak case, the similarity of the phase space to the RFQ acceptance is better in this case. As a result, higher RFQ transmission rate is obtained in the calculation.

CONCLUSION

The beam transport process in the J-PARC LEBT is investigated by comparison between the experimental results in J-PARC commissioning for 30 mA operation and the numerical results by PIC simulation which takes into account the SC effect and the spatial configuration of the beam duct. The both results show high transmission rate in the RFQ for two pairs of SOL1 and SOL2 current settings.

In the case of the 1st peak, low emittance is obtained at the RFQ entrance as the orifice takes a role as collimator of the beam which removes growing halo components. On the other hand, for the strong SOL1 and 2 settings, the beam pass through the orifice. This leads to the relatively larger emittance at the RFQ entrance while the similarity of the beam phase space to the RFQ acceptance is obtained.

The clarifiation of these characteristics observed in the actual commissioning leads to the high reproducability of the beam optics in each RUN. From these results, the transimssion rate is optimized in the Linac commissioning together with LEBT-SCT current which is measured at just after the orifice to avoid beam cut off at the orifice.

REFERENCES

[1] T. Shibata, *et al.*, "LEBT Commissioning of the J-PARC LINAC", in *Proc. LINAC'16*, East Lansing, MI, USA, Sep. 2016, paper MOPLR052, pp. 251-253.

Content from this work may be used under the terms of the CC BY 3.0 licence (© 2018). Any distribution of this work must maintain attribution to the author(s), title of the work, publisher, and DOI.

ISBN: 978-3-95450-194-6 ISSN: 2226-0366 doi:10.18429/JACoW-LINAC2018-TUPO083

BEAM DYNAMICS FOR THE FAIR P-LINAC LADDER RFQ*

M. Syha†, U. Ratzinger, M. Schütt
Institute of Applied Physics of Goethe University, 60438 Frankfurt, Germany

Abstract

After the successful measurements with a 0.8 m prototype the construction of a 3.3 m Ladder-RFQ at IAP, Goethe University Frankfurt, has been finished this summer. It is designed to accelerate protons from 95 keV to 3.0 MeV according to the design parameters of the p-Linac at FAIR. Along the acceleration section the parameters modulation, aperture and synchronous phase are linearly varied with cell number, which differs from former designs from IAP Frankfurt. The ratio of transversal vane curvature radius to mid-cell radial aperture and the vane radius itself are constant to support a flat voltage distribution along the RFQ. This was verified by implantation of the modulated vane geometry into MWS-CST RF field simulations. The development of adequate beam dynamics was done in close collaboration with the IAP resonator design team. The RFQGen-code was used for beam dynamics simulations. Among those were also error studies, that were performed to test the beam dynamic's stability against input Twiss parameter deviations to a degree indicated by the LEBT measurements performed in Q1/2018 at CEA[1] Saclay with participation of GSI's[2] Ion Source Group.

BEAM DYNAMICS DESIGN

The RFQGen-code was used for the beam dynamics calculations [1]. The beam dynamics design determined the mechanical design of the RFQ electrodes and was arrived at in consideration of the source beam as given by the Ion Source and LEBT Group of CEA Saclay and the design parameters of the Proton Linac at FAIR [2] (see Table 1). The current of the entrance cw beam was chosen rather high to 100 mA in order to have a large current margin. It was modeled in RFQGen with 10^5 (macro-)particles arranged in a 4D waterbag distribution. Other than slightly undershooting the final energy, slightly overshooting it poses no problem for the MEBT-section and the CH-DTL. For this reason and to provide a sufficient safety margin the final synchronous energy was set to 3.015 MeV. Figure 1 shows the plots of modulation parameter m, (minimum) radial aperture a and synchronous phase ϕ against the cell number. Their almost linear courses in the acceleration section result in higher acceleration efficiencies along the respective cells [3] and a therefore significantly reduced electrode length (compared to that generated by a more conservative design approach). This design was inspired by the beam dynamics design of CERN's Linac4-RFQ [4, 5].

Table 1: Beam Parameters at the RFQ Entrance and Electrode Design Parameters

Parameter	Value
Entrance Energy	95 keV
Beam Current	100 mA
Transversal $\varepsilon_{in,n,rms}$	0.3 π mm mrad
Twiss Parameter $\alpha_{x/y,in}$	0.7
Twiss Parameter $\beta_{x/y,in}$	0.04 mm/mrad
Frequency	325.224 MHz
Electrode Voltage	88.43 kV
ρ/r_0	0.85
Number of RM Cells	5

Table 2: Beam Parameters at the RFQ Wxit (10 mm behind the end of the electrodes)

Parameter	Value
$\varepsilon_{x,out,rms}$	0.33 π mm mrad
$\varepsilon_{y,out,rms}$	0.32 π mm mrad
$\varepsilon_{z,out,rms}$	0.21 MeV deg
Synchronous Exit Energy W_{syn}	3.015 MeV
Average Exit Energy W_{ave}	3.012 MeV
$W_{syn} - W_{ave}$	3 keV
$\frac{long.losses}{radial losses}$	59 %
Transmission	84.6 %

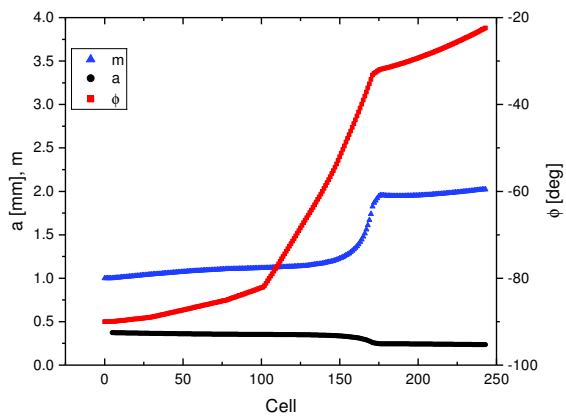


Figure 1: The modulation parameter, m, (minimum) radial aperture a and synchronous phase ϕ against the cell number.

Figure 2 shows the plots of the (macro-)particle losses per cell and the synchronous energy W_{syn} against the cell number as simulated by the RFQGen-Code. Most losses occur at the end of the gentle buncher section, i.e. at $W_{syn} = 0.67$ MeV. Here, the longitudinal losses reduce the longitudinal emittance, which did grow significantly during the earlier

* Work funded by BMBF 05P15RFRBA
† syha@iap.uni-frankfurt.de
[1] French Alternative Energies and Atomic Energy Commission
[2] Society for Heavy Ion Research (Gesellschaft fuer Schwerionenforschung)

Content from this work may be used under the terms of the CC BY 3.0 licence (© 2018). Any distribution of this work must maintain attribution to the author(s), title of the work, publisher, and DOI.

ISBN: 978-3-95450-194-6 ISSN: 2226-0366 doi:10.18429/JACoW-LINAC2018-TUPO083

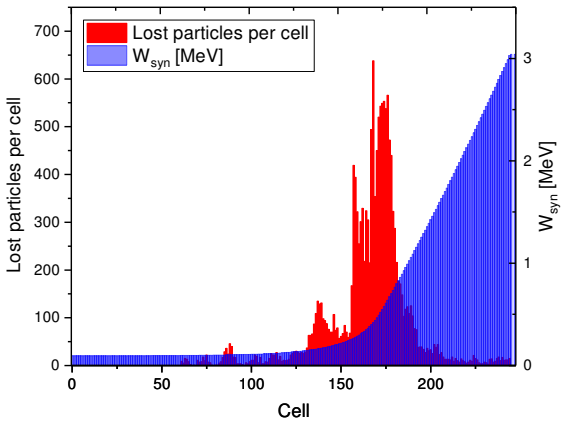


Figure 2: Courses of particle losses per cell (red) and the synchronous energy W_{syn} (purple) against the cell number. The number of entrance (macro-)particles was set 10^5.

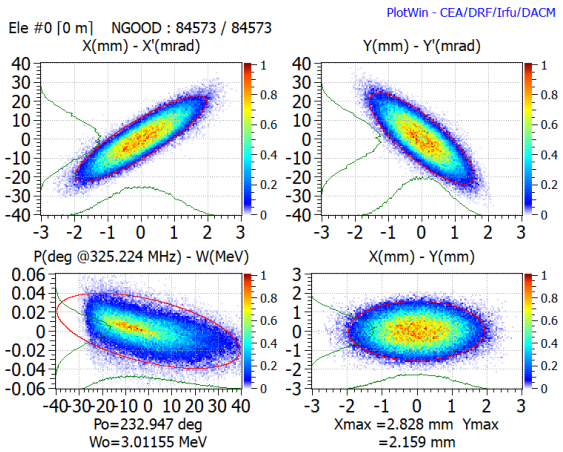


Figure 3: Phase-space plots and distribution projections (green curves) at the RFQ exit (10 mm behind the electrode ends). The entrance current was chosen to 100 mA. The colors of the scatter plots refer to the normalized (macro-) particle density (cf. scales at the right frames of the plots). The red ellipses correspond to the 95 % emittances.

stages of the bunching process, to reach saturation in a value close to that at the end of the shaper section. The losses in cells corresponding to a $W_{syn} > 1.42$ MeV are rather low (< 4.5% of the overall losses). This is important since protons with energies above 2 MeV colliding with the electrodes could lead to cavity activation. The ratio of overall longitudinal to transversal losses along the RFQ is approximately 0.59 (cf. Table 2) with the reduction of beam current due to longitudinally lost particles (i.e. the particles, which's energies differ from W_{syn} more than a sensibly set threshold) amounting to 5.7 mA. The RFQGen-Code does not track how many of the longitudinally lost particles actually still traverse the RFQ. Therefore, the beam current at the RFQ exit might actually be as high as 90.3 mA (= 84.6 mA+5.7 mA) instead of 84.6 mA(cf. Table 2). This was taken into consideration for LORASR-simulations [6] concerning the MEBT-section and the CH-DTL performed at IAP. However, if the allowed difference between a given particle's energy and W_{syn} (i.e. the threshold, that defines if a particle is lost longitudinally) is set unreasonably high (here: almost to the value of the final design energy), transmission is raised to only 86.7 %, i.e. only increased by 2.1 %.

Effects of the Longitudinal Fringe Fields

Because of the unequal potential of adjacent electrodes of 4-ROD RFQs a non-zero longitudinal fringe field exists between the grounded tank and the net potential of the electrodes at the RFQ entrance as well as the exit [7]. If the transient-time factor is taken into account the longitudinal fringe field causes an energy modulation of up to ± 2 keV at the RFQ entrance. The small pre-bunching effect of the longitudinal electric field in the entrance gap of the RFQ on the incoming cw beam will be used to benefit the beam dynamics. At the RFQ exit the ratio between the gap length and the cell length $l = \beta\lambda/2$ is approximately 0.3. Accordingly, the transient time factor approaches one. Depending on the synchronous phase the total effect to the beam energy results to ± 30 keV.

Figure 3 shows the phase-space plots and distribution projections at the RFQ exit in case of the original energy threshold, i.e. one that was chosen reasonably high.

LEBT MEASUREMENTS

In Spring 2018 emittance measurements were performed at CEA Saclay, whereby the Twiss parameters were also determined. They took place after the first solenoid in the LEBT. Theses measurements served as the basis for LEBT-simulations with CEA's TraceWin-Code [8], which led to more realistic values for the Twiss parameters and emittances at the RFQ entrance.

Error Studies

Since the LEBT measurements suggested that the initial Twiss parameters α_{in} and β_{in} might deviate somewhat from their design values (cf. Table 1), error studies were performed with RFQGen. α_{in} was run from 0.1 to 1.5 with a step width of 0.1, whereas β_{in} was varied from 0.01 $\frac{mm}{mrad}$ to 0.14 $\frac{mm}{mrad}$ with a step width of 0.01 $\frac{mm}{mrad}$. This resulted in 210 combinations of α_{in} and β_{in}. Since, unfortunately, the RFQGen-code itself does not include a sweep-function, a short workaround routine was coded with Python to automate the variation of the initial Twiss parameters.

A combination of Twiss parameters α_{in} and β_{in} was considered to lead to an output beam of sufficiently high quality if all of the following criteria were met:

- the transmission was at least 70 %
- each transversal output emittance $\varepsilon_{x/y}$ deviated no more than + 10 % from its assumed value of 0.33 π mm mrad
- the longitudinal output emittance ε_z deviated no more than + 30 % from its assumed value of 0.235 MeV deg.

Content from this work may be used under the terms of the CC BY 3.0 licence (© 2018). Any distribution of this work must maintain attribution to the author(s), title of the work, publisher, and DOI.

ISBN: 978-3-95450-194-6 ISSN: 2226-0366 doi:10.18429/JACoW-LINAC2018-TUPO083

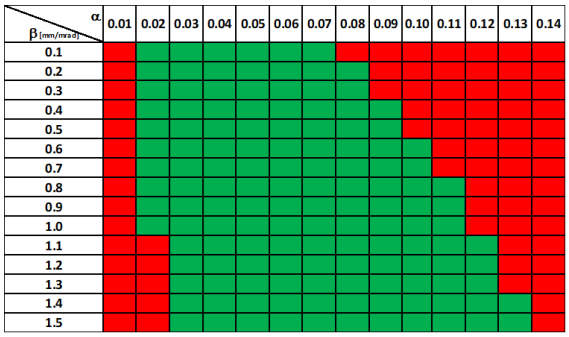


Figure 4: This Matrix provides an overview over the combinations of the initial Twiss parameters α_{in} and β_{in}, that did (green) and did not (red) lead to what were considered to be exit beams of sufficiently high quality.

Figure 4 shows a matrix, in which the results of the error studies are recorded. It can be seen that the RFQ beam dynamics design is able to cope well even with larger deviations from the assumed initial Twiss parameters.

CONCLUSION

The beam dynamics design was developed with the Code RFQGen in accordance with the source beam parameters as given by the Ion Source and LEBT Group of CEA Saclay and the design parameters of the Proton Linac at FAIR. It was inspired by the beam dynamics design of CERN's Linac4-RFQ. Considering the high design current of 100 mA, the desired parameters at the RFQ exit are met remarkably well. Furthermore, the error studies performed on the input Twiss parameters showed that even larger deviations from the design Twiss parameters can be tolerated by the RFQ.

Not only can the effects of the longitudinal fringe fields at the RFQ entrance and exit be coped with well, they even can be used to lead to improved beam dynamics.

In the near future, new TraceWin and RFQGen simulations based on the results of the soon to be conducted measurements behind the second solenoid of the LEBT-line will be performed. In addition, possible effects of mechanical errors and displacements on the beam dynamics will be investigated with CEA Saclay's TOUTATIS-code [9].

ACKNOWLEDGEMENTS

We would like to thank Alessandra Lombardi from CERN for the lively and fruitful exchange on the topic of RFQ beam dynamics and Rustam Berezov from GSI's Ion Source Group for performing the LEBT measurements and for discussing their results with us in great detail. Futhermore, we would like to thank Lloyd Young and James Stovall for their valuable support regarding the RFQGen-code.

REFERENCES

[1] L. M. Young and J. Stoval, "RFQGen User Guide", Los Alamos Scientific Lab., NM, USA, 2017.

[2] FAIR, https://fair-center.eu/index.php?id=1

[3] J. H. Billen, "RFQ Design Codes", Los Alamos Scientific Lab., NM, USA, 2005.

[4] C. Rossi *et al.*, "The Radiofrequency Quadrupole Accelerator for the Linac4", in *Proc. LINAC'08*, Victoria, BC, Canada, Sep.-Oct. 2008, p. 157.

[5] A. Lombardi *et al.*, "End-to-end beam dynamics for CERN Linac4", in *Proc. HB'06*, Tsukuba, Japan, May-Jun. 2006, p. 79.

[6] R. Tiede *et al.*, "LORASR Code Development", in *Proc. EPAC'06*, Edinburgh, Scotland, UK, Jun. 2006, p. 2194.

[7] M. Schuett, U. Ratzinger, and M. Syha, "First RF Measurements of the 325 MHz Ladder RFQ", presented at LINAC'18, Shanghai, China, Aug. 2018, paper THPO060, this conference.

[8] http://irfu.cea.fr/dacm/logiciels/

[9] R. Duperrier, "TOUTATIS: A radio frequency quadrupole code", *Physical Review Special Topics - Accelerators and Beams*, vol. 3, p. 124201, 2000.

Content from this work may be used under the terms of the CC BY 3.0 licence (© 2018). Any distribution of this work must maintain attribution to the author(s), title of the work, publisher, and DOI.

ISBN: 978-3-95450-194-6 ISSN: 2226-0366 doi:10.18429/JACoW-LINAC2018-TUPO084

BEAM DYNAMICS SIMULATIONS FOR THE NEW SUPERCONDUCTING CW HEAVY ION LINAC AT GSI*

M. Schwarz†[1], K. Aulenbacher[2,3], W. Barth[2,4], M. Basten[1], M. Busch[1], F. Dziuba[2], V. Gettmann[2], M. Heilmann[4], T. Kürzeder[2], M. Miski-Oglu[2], H. Podlech[1], A. Rubin[4], A. Schnase[4], S. Yaramyshev[4]
[1]IAP, Goethe University, Frankfurt am Main, Germany, [2]HIM, Mainz, Germany
[3]Johannes Gutenberg University, Mainz, Germany, [4]GSI Helmholtzzentrum, Darmstadt, Germany

Abstract

For future experiments with heavy ions near the coulomb barrier within the super-heavy element (SHE) research project a multi-stage R&D program of GSI/HIM and IAP is currently in progress. It aims at developing a superconducting (sc) continuous wave (CW) LINAC with multiple CH cavities as key components downstream the High Charge State Injector (HLI) at GSI. The LINAC design is challenging due to the requirement of intense beams in CW mode up to a mass-to-charge ratio of 6, while covering a broad output energy range from 3.5 to 7.3 MeV/u with the same minimum energy spread. Testing of the first CH-cavity in 2016 demonstrated a promising maximum accelerating gradient of $E_a = 9.6$ MV/m; the worldwide first beam test with a sc multi-gap CH-cavity in 2017 was a milestone in the R&D work of GSI/HIM and IAP. In the light of experience gained in this research so far, the beam dynamics layout for the entire LINAC has recently been updated and optimized.

INTRODUCTION

In the last decades the periodic table was essentially extended up to the nuclei with proton number $Z = 118$ and neutron number $N = 177$. It turned out, that the most successful methods for the laboratory synthesis of heavy elements are fusion-evaporation reactions using heavy-element targets, recoil-separation techniques and the identification of the nuclei by known daughter decays [1]. For the production of SHE, hot fusion reactions with ^{48}Ca projectiles and targets made of actinide elements ranging from ^{231}Pa to ^{254}Es are considered promising.

To sum it up, all of the experiments have the common challenge of very low cross sections and therefore require the separation of very rare events within weeks of beamtime from intense backgrounds [2]. Fortunately, the yield of SHE and therefore the number of events per unit time depends not only on the cross section but also on the projectile beam intensity, overall beam quality and target thickness. Thus, progress in SHE research is highly driven by technical developments in this fields [3]. Furthermore, the scientific fields of nuclear chemistry and spectroscopy as well as materials research and biology could benefit from these developments.

At GSI a comprehensive upgrade programme is performed. In this context, the UNILAC (Universal Linear Accelerator) is upgraded to the requirements of FAIR (Facility for Antiproton and Ion Research) and will be used as injector [4–9]. The duty factor will be relatively low (below 1 %). Conversely, for SHE experiments a high duty factor is required, which is why the presently available duty cycle of 25 % (5 ms pulse length @50 Hz) will be upgraded to CW-mode [10, 11]. Consequently a superconducting CW-LINAC was proposed [12] and is further investigated and developed [13–18].

BEAM DYNAMICS CONCEPT

Up to now, the reference design for the CW LINAC dates back to the publication of Minaev et al. in 2009 [12]. Meanwhile many experiences have been gained in design, fabrication and operation of superconducting CH-cavities and the associated components. In this context, a revision of the beam dynamics layout was recommended. Optimized cavity layouts resulted in modified voltage distributions. Furthermore, the cryomodule layout and intertank sections were specified in more details. Promising RF- and beam testing with the 15-gap CH0 showed, that higher accelerating gradients can be achieved [19], thus leading to a more efficient design approach. Consequently, extensive beam dynamics studies are carried out to fix the best layout with respect to the beam and all other RF and mechanical requirements. The beam dynamics concept for the CW-LINAC is based on multicell CH-type DTL-cavities operating at 216.816 MHz (f_{HLI} = 108.408 MHz) and focusing by superconducting solenoids. The main requirements and boundary conditions for the LINAC design are summarized in Table 1:

Table 1: Basic CW-LINAC Design Parameters

Parameter	Value
W_{in}	1.4 MeV/u
W_{out}	3.5–7.3 MeV/u
ΔW_{out}	±3 keV/u
I	≤ 1 mA
A/q	≤ 6

With a relatively low beam current, CW-operation and limited longitudinal space, this LINAC is predestined to be operated in the superconducting mode. Further thoughts on

* Work supported by BMBF contr. No. 05P15RFRBA, EU Framework Programme H2020 662186 (MYRTE) and HIC for FAIR
† schwarz@iap.uni-frankfurt.de

Content from this work may be used under the terms of the CC BY 3.0 licence (© 2018). Any distribution of this work must maintain attribution to the author(s), title of the work, publisher, and DOI.

ISBN: 978-3-95450-194-6 ISSN: 2226-0366 doi:10.18429/JACoW-LINAC2018-TUPO084

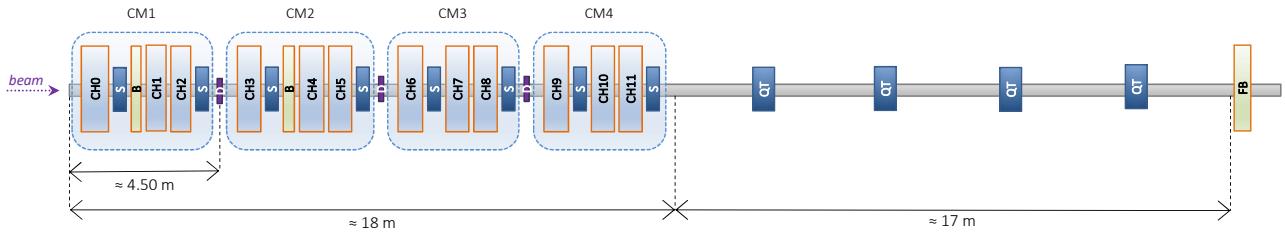


Figure 1: Study for a CW-LINAC layout design with twelve superconducting CH-cavities in four cryomodules. The length of the transport section (here 17 m) has not yet been determined finally and is likely to be shorter. Captions: CM = Cryomodule, S = Solenoid, D = Diagnostics, B = 2-Gap-Buncher, FB = Final 1-Gap-Buncher, QT = Quadrupole magnet triplet.

the choice of technology with regard to superconducting or room-temperature operation can be found at [20].

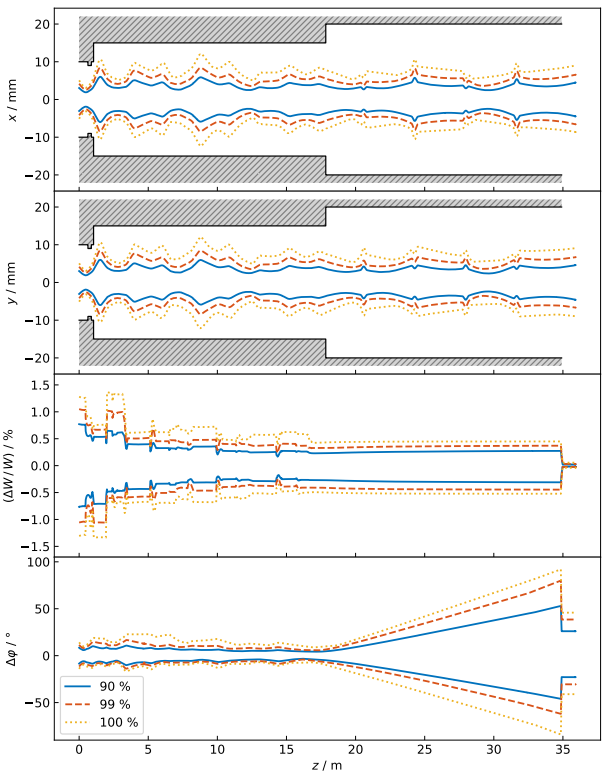


Figure 2: Beam envelopes. From top to bottom: Horizontal *(x)* and vertical *(y)* plane, energy spread in relation to mean energy and longitudinal (phase) envelopes for the studied layout as shown in Fig. 1. Since the final buncher at about $z = 35$ m is operated at 108.408 MHz in this design study, a phase jump is visible.

Recent Beam Dynamics Studies

To optimize the beam dynamics design in terms of acceleration efficiency and therefore relating to total LINAC length, $E_a = 7.1$ MV/m was chosen as design gradient for the upcoming CH-cavities in the nominal case of $A/q = 6$ (see Table 2). This allows to keep the LINAC length comparably short. A revised cryomodule (CM) layout was studied and simulated with LORASR [21] (100,001 particles,

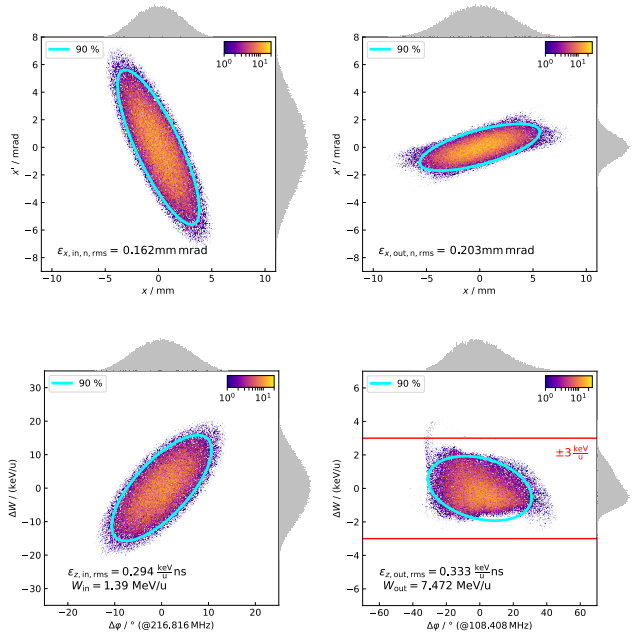


Figure 3: Phase space distributions for the recent beam dynamics layout simulated with LORASR: $x - x'$ *(top)*, $\Delta\varphi - \Delta W$ *(bottom)*, input for first cryomodule *(left)*, output behind the final buncher *(right)*. The particle density is logarithmically color-coded.

$I = 1$ mA, $A/q = 6$). It comprises three CH-DTL cavities and two solenoids per module. Additionally 2-gap Buncher-cavities are foreseen at least in CM1 and CM2 - depending on the outcome of the ongoing simulations for energy variation. This new approach partly reduces the overall drift lengths compared to former considerations and is recently studied in detail. This approach was periodically extended to four cryomodules (see Fig. 1). The beam envelopes for $W_{out} = 7.3$ MeV/u are shown in Fig. 2. The final rms-emittance growth is 13 % for the longitudinal and 26 % for the transverse planes. In this design study, the solenoids provide a magnetic field of up to 7 T for beam focusing. While final transverse matching is not completely optimized and the length of the beam transport line towards the experimental area is not fixed yet, emittance growth and a slight deformation of the beam in transverse phase space is inevitable, mainly due to RF-defocusing in the high ac-

Content from this work may be used under the terms of the CC BY 3.0 licence (© 2018). Any distribution of this work must maintain attribution to the author(s), title of the work, publisher, and DOI.

ISBN: 978-3-95450-194-6 ISSN: 2226-0366 doi:10.18429/JACoW-LINAC2018-TUPO084

celerating gradient cavity fields. The longitudinal phase space distribution stays largely compact through the whole LINAC design, overcoming the challenge of many drifts due to the boundary conditions of a superconducting design. On its way to the experimental area (here roughly initially assumed with 17 m), the bunch length grows to about 175° (@216.816 MHz). The bunch can be easily rotated in phase space by a Rebuncher (here operated @108.408 MHz), resulting in the required energy spread of $\Delta W_{\mathrm{out}} = \pm 3\,\mathrm{keV/u}$ (see Fig. 3).

Table 2: Cavity Specifications Overview

	Gaps	$(\beta\lambda/2)$/mm	E_{a}/(MV/m)
CH0	15	40.8	5.75
B1	2	44.1	5.73
CH1	8	47.7	6.00
CH2	8	47.7	6.50
CH3	8	56.7	7.10
B2	2	57.3	5.50
CH4	8	59.6	7.10
CH5	7	62.4	7.10
CH6	7	70.3	7.10
CH7	6	73.6	7.10
CH8	6	73.9	7.10
CH9	6	80.4	7.10
CH10	6	83.6	7.10
CH11	6	83.9	7.10
FB	1	86.05 / 172.1	TBD

Outlook

A promising new beam dynamics layout was developed, showing a possible design approach for the upcoming CW-LINAC which essentially meets the beam parameter requirements. Beside the presented simulations, extensive beam dynamics studies are ongoing, to finally optimize the current CW-LINAC design. Further simulations for the acceleration of a wide range of different ions (protons to uranium) along the required energy range are in progress. Since maintaining a good beam quality for $3.5\,\mathrm{MeV/u} < W_{\mathrm{out}} < 7.3\,\mathrm{MeV/u}$ is essential, special attention is paid to this and further results will be published soon. In-depth benchmarking the layout with respect to comprehensive error studies for cavity voltage and phase as well as magnet placement and gradient deviations are envisaged as well.

REFERENCES

[1] S. Hofmann, "Super-heavy nuclei", *J. Phys. G: Nucl. Part. Phys.*, vol. 42, no. 11, p. 114001, 2015.

[2] M. Block *et al.*, "Direct mass measurements above uranium bridge the gap to the island of stability", *Nature*, vol. 463, pp. 785–788, Feb. 2010.

[3] G. Münzenberg, "From bohrium to copernicium and beyond SHE research at SHIP", *Nucl. Phys. A*, vol. 944, pp. 5–29, Dec. 2015.

[4] W. Barth *et al.*, "Upgrade program of the high current heavy ion UNILAC as injector for FAIR", *Nucl. Instr. Meth. Phys. Res. Sect. A*, vol. 577, pp. 211–214, 2007.

[5] W. Barth *et al.*, "U^{28+}-intensity record applying a H2-gas stripper cell", *Phys. Rev. ST Accel. Beams*, vol. 18, p. 040101, Apr. 2015.

[6] W. Barth *et al.*, "Heavy ion linac as a high current proton beam injector", *Phys. Rev. ST Accel. Beams*, vol. 18, p. 050102, May 2015.

[7] W. Barth *et al.*, "High brilliance uranium beams for the GSI FAIR", *Phys. Rev. Accel. Beams*, vol. 20, p. 050101, May 2017.

[8] A. Adonin and R. Hollinger, "Beam brilliance investigation of high current ion beams at GSI heavy ion accelerator facility", *Rev. Sci. Instrum.*, vol. 85, p. 02A727, 2014.

[9] L. Groening *et al.*, "Upgrade of the Universal Linear Accelerator UNILAC for FAIR", in *Proc. IPAC'16*, Busan, Korea, May 2016, paper MOPOY017, pp. 880–882.

[10] P. Gerhard *et al.*, "Status and Perspectives of the CW Upgrade of the UNILAC HLI at GSI", in *Proc. HIAT2015*, Yokohama, Japan, Sep. 2015, paper WEA1C03, pp. 1–3.

[11] D. Koser *et al.*, "Prototype Design of a Newly Revised CW RFQ for the High Charge State Injector at GSI", in *Proc. IPAC'17*, Copenhagen, Denmark, May 2017, paper THPIK021, pp. 4142–4144.

[12] S. Minaev *et al.*, "Superconducting, energy variable heavy ion linac with constant beta, multicell cavities of CH-type", *Phys. Rev. ST Accel. Beams*, vol. 12, p. 120101, 2009.

[13] W. Barth *et al.*, "A superconducting CW-LINAC for heavy ion acceleration at GSI", *EPJ Web Conf.*, vol. 138, p. 01026, Mar. 2017.

[14] W. Barth *et al.*, "First heavy ion beam tests with a superconducting multigap CH cavity", *Phys. Rev. Accel. Beams*, vol. 21, p. 020102, 2018.

[15] W. Barth *et al.*, "Superconducting CH-Cavity Heavy Ion Beam Testing at GSI", in *Proc. IPAC'18*, Vancouver, BC, Canada, May 2018, paper TUPAK004, pp. 962–965.

[16] M. Basten *et al.*, "Final factory-side Measurements of the Next SC CH-Cavities for the HELIAC-Project", in *Proc. IPAC'18*, Vancouver, BC, Canada, May 2018, paper TUPAF088, pp. 943–945.

[17] T. Kuerzeder *et al.*, "Infrastructure for Superconducting CH-Cavity Preparation at HIM", in *Proc. IPAC'18*, Vancouver, BC, Canada, May 2018, paper WEPML045, pp. 2796–2799.

[18] S. Yaramyshev *et al.*, "Advanced Approach for Beam Matching along the Multi-Cavity SC CW Linac at GSI", in *Proc. IPAC'18*, Vancouver, BC, Canada, May 2018, paper TUPAK002, pp. 955–958.

[19] F. Dziuba *et al.*, "First Cold Tests of the Superconducting cw Demonstrator at GSI", in *Proc. RuPAC'16*, St. Petersburg, Russia, Nov. 2016, paper WECBMH01.

[20] H. Podlech, "Superconducting versus normal conducting cavities", CERN Yellow Report CERN-2013-001, Mar. 2013.

[21] R. Tiede *et al.*, "LORASR Code Development", in *Proc. EPAC'06*, Edinburgh, Scotland, 2006, paper WEPCH118, pp. 2194–2196.

Content from this work may be used under the terms of the CC BY 3.0 licence (© 2018). Any distribution of this work must maintain attribution to the author(s), title of the work, publisher, and DOI.

ISBN: 978-3-95450-194-6 ISSN: 2226-0366 doi:10.18429/JACoW-LINAC2018-TUPO085

MODELLING OF BEAM PARAMETERS OF RF LINAC FOR GBS-ELI-NP

Piotr Tracz†
for the ELI-NP team
ELI-NP/IFIN-HH, RO-077125 Bucharest-Magurele, Romania

Abstract

The Gamma Beam System at the ELI-NP (Extreme Light Infrastructure – Nuclear Physics) currently being constructed in Magurele/Bucharest, Romania will be a high-brilliance advanced source of gamma rays based on laser Compton back-scattering. For a successful operation of the GBS a high brightness low emittance electron beam is of crucial importance. The warm RF linac is designed in two stages – one with the beam up to 300 MeV, and another one about 720 MeV. The S-band photo-injector is combined with a C-band linac. The beam is transported by transfer lines to the interaction points. In this paper we report the results of computer simulations of the electron beam transport in the low energy linac and transfer line up to the low energy interaction point (IP1). The simulation model makes it possible to predict the beam parameters to be recuperated in case of failure of any magnetic or accelerating elements as well as it enables to determine the optimal parameters of replaced components. It will be used for the development of the Gamma Beam System in the future.

INTRODUCTION

The Gamma Beam System was designed and is being constructed by the EuroGammaS Association – a consortium of European academic and research institutions and industrial partners, and it is hosted by the Horia Hulubei National Institute of Physics and Nuclear Engineering [1]. The technical design of GBS is described with details in [2], and several other publications like e.g. [3-5].

To perform the simulations we used the Elegant [6] code, and SDDS toolkit [7] for processing and graphing of the Elegant output data. The simulations of the beam transport in the injector and calculations of output beam parameters at the injector exit were done with use of the program Parmela [8, 9]. Currently we are studying beam optimization in the injector using the Astra [10] code.

Our study will be extended for the high energy linac. The aim is to provide means to re-optimize the linac settings to new working points in accordance to users' requirements.

S-band Injector

The GBS injector starts at the RF gun with photo-cathode. To suppress the beam loss by transverse spreading there are two focusing solenoid magnets with high gradient field starting very close to the gun exit. They focus the beam to minimum size and make the beam emittance low at the entrance of accelerating structure. The photo-cathode RF gun generates electron beam in the photoemission process. Ultraviolet laser pulses are incident on the copper photo cathode. The charge of the electron bunches depends on the laser power and the conversion efficiency of the photo-cathode material; in case of GBS it is 250pC. The 2D profile of the gun with electric field pattern designed in the electromagnetic code Superfish [11] is shown in Fig. 1. It will operate at π-mode with resonance frequency 2.856GHz with an input power sufficient to achieve 120MeV/m field gradient at cathode.

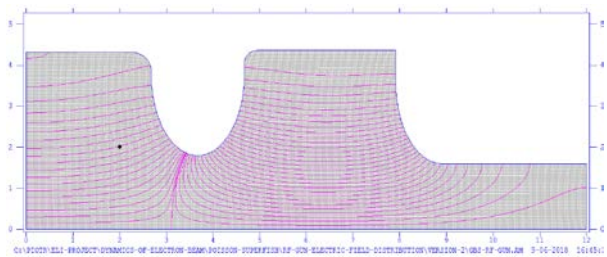


Figure 1: 2D profile of RF gun for GBS with electric field profile.

The RF gun is followed by two TW accelerating structures. These are constant gradient (22MV/m), and will operate in $2\pi/3$ mode. The first structure is surrounded by twelve independent coils. The purpose of them is to keep the radius of the beam from the entrance along the accelerating sections. Additionally the S-band sections will act as a bunch compressor.

Low Energy C-band Linac

The low energy linac that follows the injector is based on four C-band sections operating at 5.712 GHz. The length of each section is 1.78449m and the length of a single cell is 0.017495m. Each section is fed by 52MV RF voltage. The input RF phase of the first two sections is 82.5° and other two 115°. The dogleg type transport line transmits the beam to the interaction point. After the interaction point the beam is transported to the beam dump.

In addition to the accelerating sections the linac modules are completed by magnetic and diagnostic devices. There are two quadrupole triplets in the diagnostic sections. One after the first C-band structure and another one at the end of the low energy linac. They are used for emittance measurement and to provide the desired electron beam focusing. There are several beam profile monitors (screens) located at different positions along the linac to control the transverse profile of the beam. Figure 2 presents the distribution of the quadrupole magnets and the profile monitors in the low energy linac. Two S-band transverse deflecting structures will be used for measuring the longitudinal beam profile.

† email address: piotr.tracz@eli-np.ro

Content from this work may be used under the terms of the CC BY 3.0 licence (© 2018). Any distribution of this work must maintain attribution to the author(s), title of the work, publisher, and DOI.

ISBN: 978-3-95450-194-6 ISSN: 2226-0366 doi:10.18429/JACoW-LINAC2018-TUPO085

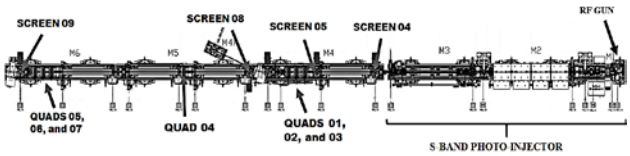


Figure 2: Location of quadrupole magnets and profile monitors in the low energy linac [2].

Transfer Line

The transfer line starts at the dipole magnet. There are two quadrupole triplets. The dispersion of the beam after dipole magnet 01 is corrected by dipole 02. Figure 3 shows the components of the transfer line.

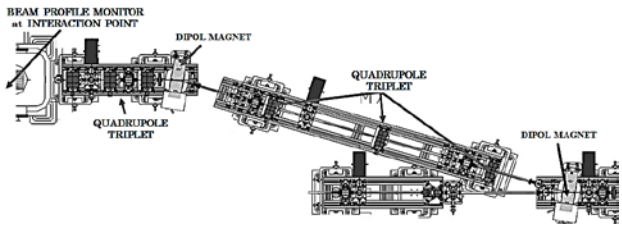


Figure 3: Location of quadrupole magnets and profile monitors in transfer line [2].

RESULTS

Elegant Simulations

For the simulations with the Elegant code 50 000 particles were used. The beam charge $Q = 250pC$, output beam energy at the injector exit $E = 81MeV$, bunch length $\sigma_z \approx 280\mu m$, the transverse normalized emittance (1σ) at the injector exit (screen 04), calculated from the Elegant output data is $\varepsilon_{n\,x,y} \approx 0.43\ [\mu m \cdot rad]$. Input Twiss parameters [9] are: $\beta_x = 31.69$, $\alpha_x = -1.98$, $\eta_x = 0$,
$\beta_y = 31.71$, $\alpha_y = -1.99$, $\eta_y = 0$.

Figure 4 below presents the evolution of the transverse beam profile along the low energy linac, and transfer line.

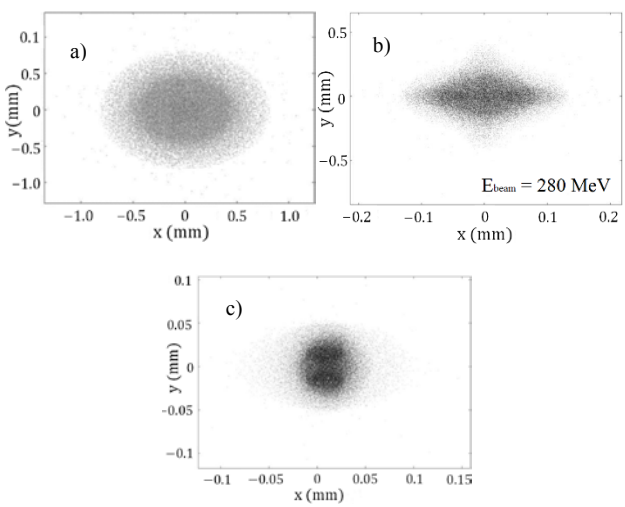


Figure 4: Transverse beam profiles at: injector exit (a), end of low energy linac (b), and interaction point IP1 (c).

The transverse (Figure 5) and longitudinal (Figure 6) beam distributions are the histograms of three coordinates x, y, z. The z coordinate is calculated from the relationship $z = \beta ct$, where βc is the velocity of the particle, and t is time of arrival at the observation point. Figures below include the *rms* sizes of the bunch.

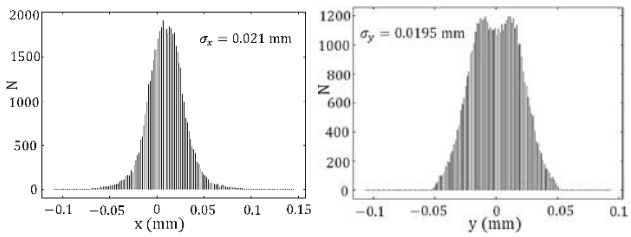


Figure 5: Transverse beam distribution at IP1.

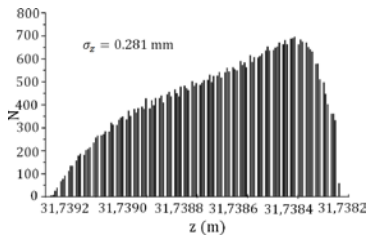


Figure 6: Longitudinal beam distribution at IP1.

A good approximation for the beam shape in phase space is elliptic. An ellipse can be defined by specifying: area, shape, and orientation. The *beta* function $\beta(s)$ is related to the beam shape and size. The beam envelope is determined by the beam emittance and the function $\beta(s)$. The *beta* function is highly dependent on the particular arrangement of the quadrupole magnets. The *alpha* function $\alpha(s)$ is related to the tilt (i.e. orientation) of the beam ellipse. Figures 7 and 8 depict the functions $\beta(s)$ and $\alpha(s)$ along the low energy linac and the transfer line up to IP1. The *gamma* function depends on α- and β-functions in accordance to the relation $\gamma(s) = \frac{1+\alpha^2(s)}{\beta(s)}$.

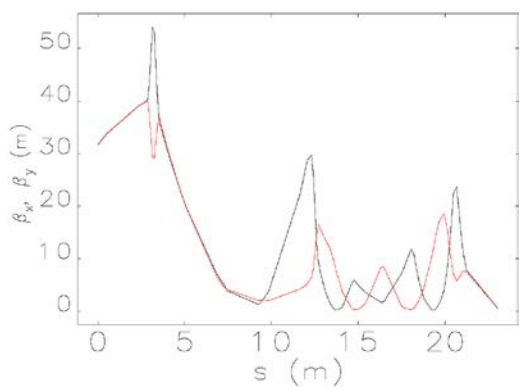


Figure 7: Function *beta* from photo-injector exit down to low energy interaction point IP1 (β_x-black line, β_y-red line).

Content from this work may be used under the terms of the CC BY 3.0 licence (© 2018). Any distribution of this work must maintain attribution to the author(s), title of the work, publisher, and DOI.

ISBN: 978-3-95450-194-6 ISSN: 2226-0366 doi:10.18429/JACoW-LINAC2018-TUPO085

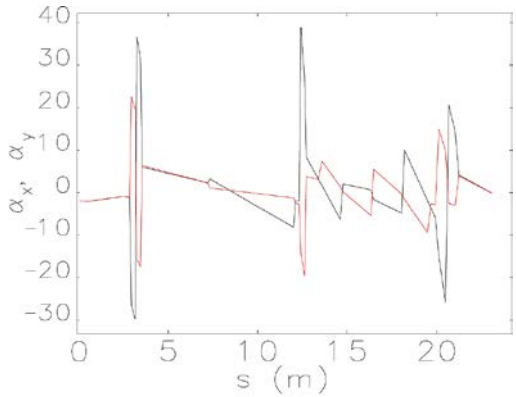


Figure 8: Function *alpha* from photo-injector exit down to low energy interaction point IP1 (α_x-black line, α_y-red line).

The normalized emittance (1σ) at the IP1 calculated from the Elegant output data is $\varepsilon_{n\,x,y} = 0.43\text{-}0.45$ [$\mu m \cdot$ rad].

In Fig. 9 the transverse phase space at IP1 is given.

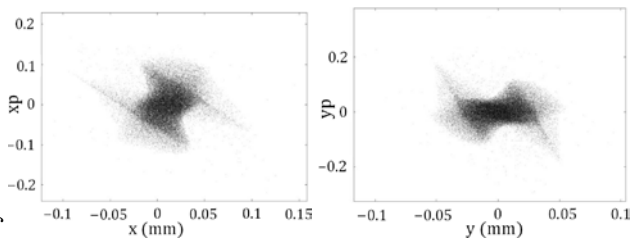


Figure 9: Transverse (horizontal – *left*, vertical - *right*) phase space at IP1.

Figure 10 presents the beam energy spread and beam energy at IP1, and Fig. 11 the energy distribution along the bunch.

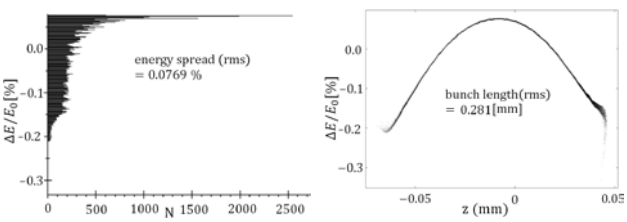


Figure 10: Beam energy spread (*left*) and energy distribution (*right*) at IP1.

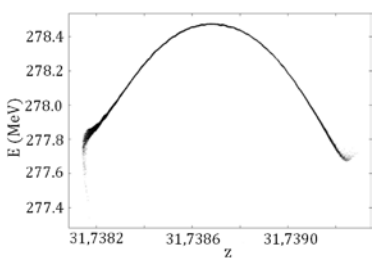


Figure 11: Energy distribution along bunch at IP1.

CONCLUSIONS

We presented the results obtained in simulating the beam transport in the low energy linac and the transfer line for the ELI-NP Gamma Beam System. We used the Elegant code. Our study will be extended for the high energy linac. Calculations of the injector will also be done with use of the Astra code.

ACKNOWLEDGEMENTS

The GBS-ELI-NP project is co-funded by the European Union through the European Regional Development Fund.

REFERENCES

[1] http://www.nipne.ro/ and http://www.eli-np.ro/

[2] O. Adriani et al., "Technical Design Report; EuroGammaS proposal for the ELI-NP Gamma Beam System", arXiv: 1407.3669v1 [physics.acc-ph].

[3] A. Bacci et al., "Electron linac design to drive bright Compton back-scattering gamma-ray sources", J. Appl. Phys. vol. 113, p. 194508, 2013, doi:10.1063/1.4805071

[4] C. Vaccarezza et al., "Optimization studies for the beam dynamic in the RF linac of the ELI-NP gamma beam system", in Proc. IPAC2016, Busan, Korea, May 2016, paper TUPOW041, pp. 1850-1853.

[5] P. Tracz, "ELI-NP gamma beam system – new facility for nuclear physics research", in Proc. PPC2017, Brighton, Great Britain, Jun. 2017, pp. 1-4, doi:10.1109/PPC.2017.8291290

[6] M. Borland, "Elegant: A flexible SDDS-compliant code for accelerator simulation", Advanced Photon Source LS-287, September 2000.

[7] M. Borland, https//ops.aps.anl.gov/SDDSIntroTalk/slides.html

[8] L.M. Young, "PARMELA", Los Alamos National Laboratory Report LA-UR-96-1835 (1996).

[9] C. Vaccarezza, private communication.

[10] ASTRA, K. Floettmann http://www.desy.de/~mpyflo/

[11] laacg.lanl.gov/laacg/services/download_sf.phtml

Content from this work may be used under the terms of the CC BY 3.0 licence (© 2018). Any distribution of this work must maintain attribution to the author(s), title of the work, publisher, and DOI.

ISBN: 978-3-95450-194-6 ISSN: 2226-0366 doi:10.18429/JACoW-LINAC2018-TUPO088

MEASUREMENT OF DIAGNOSTICS RESPONSE BY RF PARAMETERS FOR HARD X-RAY LINE IN PAL-XFEL*

H. Yang†, Pohang Accelerator Laboratory, 37673 Pohang, Korea

Abstract

PAL-XFEL is a hard x-ray (HX) and soft x-ray (SX) FEL machine to generate 2.5 – 15 keV FEL in the HX line and 0.28 – 1.2 keV FEL in the SX line. The HX line consists of an e-gun, a laser heater, S-band accelerators, an X-band linearizer, three bunch compressors (BC), and a dog-leg line. PAL-XFEL maintains the stable operation and FEL delivery with more than 98% availability due to machine stabilities including RF modules. In order to investigate the stable operation, we measure the diagnostics response for bunch charge monitors, energy beam position monitors, bunch length monitors, and a FEL intensity with a photon beam position monitor by RF parameters - RF amplitude and phase for an e-gun, accelerators, and a linearizer. In this paper, we present mainly corresponding RF parameters for e-beam and FEL jitters by this measurement and matrix analysis.

INTRODUCTION

PAL-XFEL is the third XFEL machine in the world using normal conducting linacs for e-beam accelerating. It is combined two lines - a Hard X-ray (HX) line generating 2.5 – 15 keV FEL and a soft x-ray (SX) line generating 0.28 – 1.2 keV FEL [1]. PAL-XFEL has been successfully operating and delivering XFEL since March 2017. The availability is more than 98% and the stability of beam parameters are under 0.02% for the e-beam energy, 7% for the peak current, and 10% for the FEL intensity. Especially, it has under 20 fs timing jitter - the most stable timing among XFEL machines in the world [2].

The HX line of PAL-XFEL consists of an e-gun, a Laser Heater (LH), S-band accelerators, an X-band Linearizer (XL), three Bunch Compressors (BC), and a Dog-Leg (DL) line (Fig. 1). The stable e-beam parameters are caused by the stability of RF devices in the injector and linac section, and magnet devices in bunch compressors and a dog-leg line. The stabilities from the error analysis with the ELEGANT simulation are applied for RF and magnet devices in PAL-XFEL [3]. The required stability of the magnet power supply system is few ten's ppm and it is easy to achieve by the developed technology. However, some stabilities for RF devices are challenging, for example, 0.01° phase jitter for the injector RF device and 0.05° phase jitter for the X-band linearizer. Since we use the RF timing system, there is phase drift in all RF devices by the drift of reference timing.

In order to investigate and quantify effects of jitters, we measured diagnostics responses by RF parameters. Bunch Charge Monitors (BCM), Energy Beam Position Monitors (EBPM), Bunch Length Monitors (BLM), and a Quadratic photon Beam Position Monitor (QBPM) were used in this measurement. The FEL pulse energy can be obtained from the sum value of the QBPM. The RF amplitude and phase of all RF modules were used. The response matrix was obtained from this measurement, and the main RF variables and modes for a FEL jitter were found by the method of Singular Value Decomposition (SVD) for the response matrix [4]

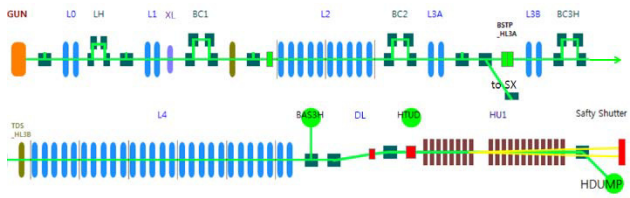


Figure 1: Layout of the HX line in PAL-XFEL.

LATTICE AND INITIAL SETTING

The HX line in PAL-XFEL consists of an injector, the LH, 4 linac sections, 3 BCs, and the DL line. The injector include S-band photo-cathode RF e-gun and 2 linacs with individual RF modules (L0). Electron bunches are generated with the 5-ps bunch length and longitudinally Gaussian distribution in the gun. The e-beam are accelerated to 140 MeV at the end of the injector. The slice energy spread of e-beam are heated in the LH. The linac sections are divided by BCs. We call those as L1, L2, L3, L4, BC1, BC2, and BC3H (Fig. 1). The XL is located between L1 and BC1. 20 undulators and a self-seeding region are in HU1 section. The undulator K-value can be adjusted by moving the undulator gap, but we normally use fixed K-value of 1.87. We set the machine for 9.7 keV FEL generation in this measurement. The detail parameters are in Table 1 and 2.

Table 1: Beam Parameters for Initial Setting

Parameters	Value
Initial charge	248 pC
Final charge	185 pC
Bunch energy at LH	0.14 GeV
Bunch energy at BC1	0.35 GeV
Bunch energy at BC2	2.50 GeV
Bunch energy at BC3H	3.50 GeV
Final bunch energy	8.70 GeV
Initial peak current	20 A
Peak current after BC1	87 A
Peak current after BC2	390 A
Peak current after BC3H	2000 A
FEL energy	9.7 keV
FEL Pulse Energy	1.0 mJ

Content from this work may be used under the terms of the CC BY 3.0 licence (© 2018). Any distribution of this work must maintain attribution to the author(s), title of the work, publisher, and DOI.

ISBN: 978-3-95450-194-6 ISSN: 2226-0366 doi:10.18429/JACoW-LINAC2018-TUPO088

Content from this work may be used under the terms of the CC BY 3.0 licence (© 2018). Any distribution of this work must maintain attribution to the author(s), title of the work, publisher, and DOI.

Table 2: RF and BC Parameters for Initial Setting

Parameters	Value
Gun RF phase	33.7°
L0_01 RF phase	0.00°
L0_02 RF phase	-2.00°
L1 RF phase	-11.05°
L2 RF phase	-20.85°
L3 RF phase	-10.50°
L4 RF phase	-2.00°
BC1 bunching angle	4.97°
BC2 bunching angle	3.00°
BC3H bunching angle	1.60°

The location and kind of diagnostics are in Fig. 2. An initial bunch charge was measured by BCM_INI and a final bunch charge was measured by BCM_FIN. We use collimator in the BC1, the final charge is about 75% of the initial charge. There are EBPMs and BLMs at each BC (EBPM_BC1/BC2/BC3H and BLM_BC1/BC2/BC3H). They are used to measure energies and bunch peak currents at BCs. All BLMs were calibrated by a bunch length measurement system with a transverse deflecting cavity. There are EBPMs at the LH, DL line and HDUMP. EBPM_HDUMP were mainly used for measuring final e-beam energy in this measurement. The FEL pulse energy are measured by the QBPM in a HX beamline. It was calibrated by an energy-loss scanning method. The resolution of these diagnostics are in Table 3.

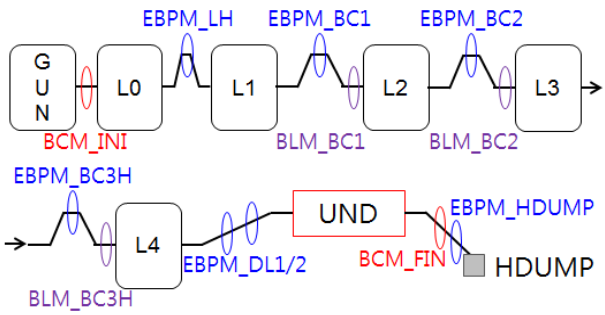


Figure 2: Diagnostics for HX in PAL-XFEL.

Table 3: Resolutions of Diagnostics

Diagnostics	Resolution
BCM_INI/FIN	0.1 pC
EBPM_LH	5.4 keV
EBPM_BC1	8.8 keV
EBPM_BC2	67.1 keV
EBPM_BC3H	168.8 keV
EBPM_HDUMP	85.5 keV
BLM_BC1	0.075 A
BLM_BC2	0.4 A
BLM_BC3H	5.0 A
QBPM (FEL pulse energy)	10 uJ

DIAGNOSTICS RESPONSE

We measured the diagnostics response to refer the reference [4]. During this measurement, we varied the RF variables one by one. All diagnostics and RF variables read out bunch synchronously for each step. The RF variables were varied around initial setting and diagnostics measured over 20 points. We selected linear variation region of responses around initial values of variables and obtained the elements of a response matrix by the linear fitting. The diagnostics responses were divided by their resolutions (Table 3) and RF variations were divided by their sensitivities (Table 4). After measurement, we found that the diagnostics responses by the same kind of RF modules in linac sections are similar. Therefore, we present the response matrix classified by the sections for L1 – L4 in this paper.

Table 4: Resolutions of Diagnostics

RF module	Sensitivity
GUN RF phase	0.020°
S-band linac RF phase (L0 – L4)	0.020°
X-band linearizer RF phase	0.065°
Gun RF amp.	0.02%
S-band linac RF amp. (L0 – L4)	0.02%
X-band linearizer RF amp.	0.12%

Table 5 is the response matrix $\boldsymbol{R}$, where Φ means the RF phase, A means the RF amplitude, C means the bunch charge, I means the peak current, and *FEL_EN* means the FEL pulse energy. The bold numbers indicate the most influential RF variables for each diagnostics. For example, there is large response of the FEL pulse energy by Φ_{XL}, Φ_{L1}, Φ_{GUN}. Since each diagnostics response on each RF variable is linear, this response matrix can be analysed by the method of SVD [5]. The response matrix $\boldsymbol{R}$ is composed into three matrices according to

$$\mathrm{R} = \mathrm{U} \cdot \mathrm{S} \cdot V^{T}, \tag{1}$$

where the matrix $\boldsymbol{S}$ is a diagonal matrix containing the singular values of $\boldsymbol{R}$. $\boldsymbol{S}$ is 11 by 11 matrix, but just 6 by 6 section were analysed here because of their larger singular values. The matrices of $\boldsymbol{S}$, $\boldsymbol{U}$, and $\boldsymbol{V}$ are in Table 6 – 8.

The mode #1 is related the final peak current and e-beam energy. The corresponding variables are mainly Φ_{L1}, Φ_{XL}, A_{L1}, and A_{XL}. The variation of e-beam energy at a BC changes the trajectory into the BC. Since it causes phase and energy gain variation of all RF modules after that BC, there are large response of the final energy and current by the RF modules before the first BC. The mode #2 is related to the final charge and FEL pulse energy. The corresponding variables are mainly Φ_{L1} and Φ_{XL}. Since, we collimate the e-beam at the center of BC1, the x-position, slice energy chirp, and linearization of bunch are related to the final charge. Since EBPM_BC1 is less related to the mode #2, it can be inferred that mode #2 is acting on the linearization and slice energy chirp of bunch. The mode #3 is related to peak currents at BCs and final e-beam energy. The

ISBN: 978-3-95450-194-6 ISSN: 2226-0366 doi:10.18429/JACoW-LINAC2018-TUPO088

main corresponding variables - Φ_{L1}, Φ_{XL}, and A_{XL} - means that RF of L1 and XL affect the phase of the RF modules after BC1. The fourth mode is related to initial charge and the fifth mode is related to the e-beam energy at the injector. The sixth mode is related to the final charge and FEL pulse energy like mode #2, and A_{GUN}, Φ_{L1}, and Φ_{L2} are main corresponding variables. Since the combination of Φ_{L1} and Φ_{L2} adjust the slice energy chirp, it can be concluded that mode #6 is acting on the slice energy spread.

Table 5: Response Matrix (R)

	Φ GUN	Φ L01	Φ L02	Φ L1	Φ XL	Φ L2	Φ L3	Φ L4
C_INI	**1.35**	0.33	0.03	-0.23	0.37	-0.08	-0.03	0.00
C_FIN	-1.05	0.61	0.92	**3.51**	**-2.17**	-0.14	-0.08	-0.01
EBPM_LH	**0.66**	**-0.63**	-0.12	-0.04	-0.01	0.01	0.00	0.01
EBPM_BC1	**0.78**	-0.05	-0.10	**-0.95**	-0.08	0.02	0.00	0.00
EBPM_BC2	-0.06	0.13	0.29	**1.96**	0.26	**-0.52**	0.00	0.02
EBPM_BC3H	0.01	0.07	0.13	**0.87**	0.11	-0.19	-0.10	0.01
I_BC1	-0.35	-0.30	-0.22	**0.82**	**1.56**	-0.03	-0.04	0.01
I_BC2	0.24	-0.51	-0.31	**0.97**	**2.96**	-0.48	0.00	0.03
I_BC3H	0.44	-0.17	0.66	**2.95**	**2.98**	-1.20	-0.03	0.06
EBPM_HD	-0.62	-0.19	-1.02	**-6.58**	**-2.86**	2.13	0.39	-0.17
FEL_EN	**-0.97**	0.33	0.21	**1.12**	**-2.29**	-0.20	-0.01	-0.01
	A GUN	**A L01**	**A L02**	**A L1**	**A XL**	**A L2**	**A L3**	**A L4**
C_INI	-0.06	0.06	-0.03	0.01	-0.62	0.01	0.03	0.02
C_FIN	-0.18	0.48	0.41	0.86	-1.02	-0.01	0.01	0.01
EBPM_LH	0.13	-0.32	-0.24	0.01	-0.05	0.00	0.00	0.00
EBPM_BC1	0.12	-0.15	-0.16	-0.29	0.33	0.00	0.00	0.00
EBPM_BC2	0.06	0.39	0.32	0.70	**-0.84**	-0.09	-0.01	0.00
EBPM_BC3H	0.02	0.17	0.14	**0.31**	**-0.35**	-0.03	-0.04	0.00
I_BC1	-0.07	0.21	0.19	0.43	-0.52	0.00	0.02	0.01
I_BC2	0.06	0.36	0.33	0.65	**-0.83**	-0.02	0.00	0.00
I_BC3H	0.09	0.95	0.87	1.65	**-6.42**	-0.05	-0.04	0.00
EBPM_HD	-0.30	-1.66	-1.47	-3.06	**4.12**	0.08	0.13	0.07
FEL_EN	0.38	0.10	0.16	0.30	0.75	0.00	0.01	0.00

Table 6: Matrix ***S***, Containing the Singular Values of ***R***

	1	2	3	4	5	6	7	8
1	**12.84**	0.00	0.00	0.00	0.00	0.00	0.00	0.00
2	0.00	**5.80**	0.00	0.00	0.00	0.00	0.00	0.00
3	0.00	0.00	**2.99**	0.00	0.00	0.00	0.00	0.00
4	0.00	0.00	0.00	**1.84**	0.00	0.00	0.00	0.00
5	0.00	0.00	0.00	0.00	**0.86**	0.00	0.00	0.00
6	0.00	0.00	0.00	0.00	0.00	**0.77**	0.00	0.00
7	0.00	0.00	0.00	0.00	0.00	0.00	0.25	0.00
8	0.00	0.00	0.00	0.00	0.00	0.00	0.00	0.18

Table 7: Matrix U, Containing the First Six Left Singular Vector of ***R*** as Columns

	1	2	3	4	5	6
C_INI	-0.03	-0.15	-0.14	**-0.63**	-0.31	0.24
C_FIN	-0.19	**0.67**	-0.19	0.12	-0.03	**0.57**
EBPM_LH	0.01	-0.06	-0.01	-0.28	**0.91**	0.24
EBPM_BC1	0.07	-0.11	-0.06	-0.38	0.08	-0.14
EBPM_BC2	-0.17	0.15	0.10	-0.05	0.02	0.05
EBPM_BC3H	-0.08	0.06	0.05	-0.04	0.00	0.06
I_BC1	-0.12	-0.13	**0.26**	0.39	0.06	0.26
I_BC2	-0.19	-0.33	**0.47**	0.23	0.08	0.07
I_BC3H	**-0.59**	-0.32	**-0.68**	0.22	0.09	-0.12
EBPM_HD	**0.72**	-0.16	**-0.42**	0.33	0.06	0.18
FEL_EN	0.03	**0.49**	-0.03	0.07	0.21	**-0.64**

Table 8: Matrix V, Containing the First Six Right Singular Vector of ***R*** as Columns

	1	2	3	4	5	6
Φ_{GUN}	-0.04	-0.27	-0.01	**-0.93**	0.07	0.20
Φ_{L0_01}	0.00	0.15	-0.09	-0.14	**-0.83**	-0.06
Φ_{L0_02}	-0.10	0.15	-0.13	-0.10	-0.16	0.08
Φ_{L1}	**-0.61**	**0.53**	**0.34**	-0.04	0.14	**0.34**
Φ_{XL}	**-0.33**	**-0.73**	**0.48**	0.21	-0.17	0.10
Φ_{L2}	0.19	-0.01	-0.11	0.19	-0.04	**0.62**
Φ_{L3}	0.03	-0.02	-0.05	0.07	0.03	0.01
Φ_{L4}	-0.01	0.00	0.02	-0.02	0.00	-0.04
A_{GUN}	-0.02	0.01	0.03	-0.07	0.26	**-0.54**
A_{L0_01}	-0.16	0.05	0.07	-0.01	-0.33	-0.17
A_{L0_02}	-0.14	0.05	0.06	0.03	-0.20	-0.24
A_{L1}	**-0.29**	0.10	0.16	-0.08	0.08	-0.25
A_{XL}	**0.58**	0.23	**0.76**	-0.11	-0.06	0.00
A_{L2}	0.01	0.00	-0.01	0.01	-0.01	0.01
A_{L3}	0.01	0.00	-0.01	0.01	-0.01	0.06
A_{L4}	0.00	0.00	-0.01	0.01	0.00	0.03

CONCLUSION

We measured diagnostics responses by RF variables - phase and amplitude of all RF modules. The initial and final charge, e-beam energy at LH, BC, and HDUMP, peak current after BCs, and FEL pulse energy read out bunch synchronously for each step of the RF variation in this measurement. The main RF variables for FEL and e-beam jitters were roughly found from the obtained response matrix, it was analysed by the method of SVD. The RF variables - Φ_{L1} and Φ_{XL} are mainly related to the variations of final e-beam energy, peak current, and FEL pulse energy. Also, we could classify the effect for the slice energy spread from XL, and the combination of L1 and L2 by this analysis.

REFERENCES

[1] I. S. Ko, *et al.*, Appl. Sci. **2017**, 7(5), 479.

[2] H. S. Kang, *et al.*, Nature Photonics **11**, 708 (2017).

[3] H. Yang, *et al.*, "Error Analysis for Linac Lattice of Hard X-ray FEL Line in PAL-XFEL," *in Proc. of FEL2014* (Basel, Switzerland, Aug. 25-29, 2014), p. 703.

[4] F. Frei, *et al.*, "Experimental Results of Diagnostics for Longitudinal Phase Space," *in Proc. of FEL2014* (Basel, Switzerland, Aug. 25-29, 2014), p. 657.

[5] D. Kalman, *A Singularly Valuable Decomposition: The SVD of a Matrix*, (The American University, Feb. 13, 2002).

Content from this work may be used under the terms of the CC BY 3.0 licence (© 2018). Any distribution of this work must maintain attribution to the author(s), title of the work, publisher, and DOI.

ISBN: 978-3-95450-194-6 ISSN: 2226-0366 doi:10.18429/JACoW-LINAC2018-TUPO090

ELECTRON-BEAM MATCHING TO SOLENOID MAGNETIC FIELD IN A KLYSTRON*

S. J. Park†, Y. J. Park, Pohang Accelerator Laboratory, POSTECH, 37673 Pohang, Korea
J. H. Hwang, S. G. Shin,
Division of Advanced Nuclear Engineering, POSTECH, 37673 Pohang, Korea
D. H. Yu, S. Y. Hyun, Vitzrotech Co., Ltd., 15603 Ansan City, Korea

Abstract

High-power klystrons for particle accelerators employ high-perveance electron guns which are usually focused by Solenoid magnets. The electron beam should be optically matched to the downstream magnetic field to prevent the beam from scalloping. The task usually requires a series of computer simulations with many design parameters, and therefore requires extensive(sometimes exhaustive) efforts if not aided by a priori experiences. In order to alleviate the difficulties we have developed a matching procedure which is systematic and reliable. In this article we describe the procedure with an example design of a 400 kV, 500 A electron beam with radius 8 - 11 mm.

MATCHING SCHEME

The focusing properties of the electron beam in a klystron is described by the envelope equation [1],

$$\ddot{r} + r\omega_L^2 \left[1 - \left(\frac{B_c}{B}\frac{r_c^2}{r^2}\right)\right]^2 - \frac{\eta I_B}{2\pi r \epsilon_0 u_0} = 0 \qquad (1)$$

where r is the radial position of an electron at a given longitudinal position, the dot denotes derivative with respect to time, $\eta = e/m$ is the charge to mass ratio, $\omega_L = \eta B/2$ is the Larmour frequency, B_c is the magnetic field strength at the cathode center, B is the magnetic field strength at a given longitudinal position, r_c is the cathode radius, I_B is the beam current, and u_0 is the average beam velocity.

Table 1: PAL Klystron Beam Parameters (Fine Tuned for the Beam Matching)

Parameter	Value
Beam Voltage, V_B	400 kV
Beam Current, I_B	500 A
Microperveance, uK	2 upervs
Cathode Radius, r_c	45 mm
Cathode Field, B_c	31 G
Equilibrium Beam Size, b	9.3 mm
Brillouin Field, B_B	735 G
Confinement Factor, m	1.609

Given beam parameters we can solve Eq. (1) numerically to obtain beam envelopes. With example parameters (for the linac klystrons in the Pohang Accelerator Laboratory (PAL)) presented in Table 1 we could obtain the so-called matched condition as shown in Fig. 1.

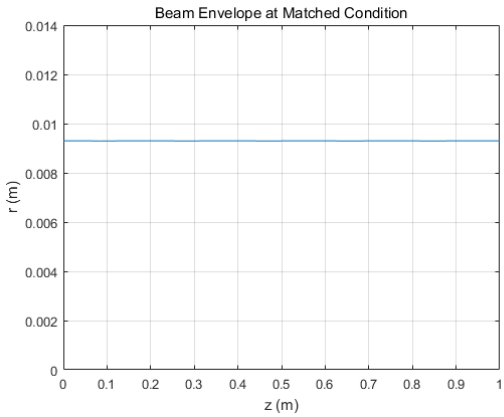


Figure 1: Matched beam envelope with parameters in Table 1.

If we deviate from the matched condition by changing some parameters we can obtain the family of envelopes from which the beam-matching methodology can be inferred. For example changing the B_c results in envelopes as shown in Fig. 2 in which the envelopes for B_c either higher or lower than the matched value (31 G) are quite symmetric. In contrast to this, changing the same parameter for a mismatched beam does not yield symmetric envelope families. Figure 3 is the envelope family for different B_c with a slightly detuned beam-injection angle ($\dot{b_0} = 0.01$) to make the beam mismatched.

From Figs. 2 and 3 it is evident that a scan for a properly chosen parameter for the matched beam results in a symmetric envelope family with its center envelope corresponding to the matched condition. Therefore the parameter scan and the resulting envelope family is a diagnostic tool for checking whether a beam is at the matched condition. It is interesting to see that, unlike the injection-angle detuning (as shown in Fig. 3), detuning the injection beam radius b_0 do not make the beam mismatched but shift the beam to a new matched condition. Figure 4 is the B_c-scanned envelope family for a injection-radius detuned beam. Comparing Figs. 2 and 4 we see that the beam is matched at a new condition of $B_c = 33$ G.

Here we note the importance of scan parameter selection. Figure 5 is the envelope family obtained by scanning the beam voltage V_B. Unlike the B_c-scanning (as shown in Fig. 2) the V_B-scanning does not yield a symmetric envelope

* Work supported by the Ministry of Science and ICT, Korea
† sjpark@postech.ac.kr

Content from this work may be used under the terms of the CC BY 3.0 licence (© 2018). Any distribution of this work must maintain attribution to the author(s), title of the work, publisher, and DOI.

ISBN: 978-3-95450-194-6 ISSN: 2226-0366 doi:10.18429/JACoW-LINAC2018-TUPO090

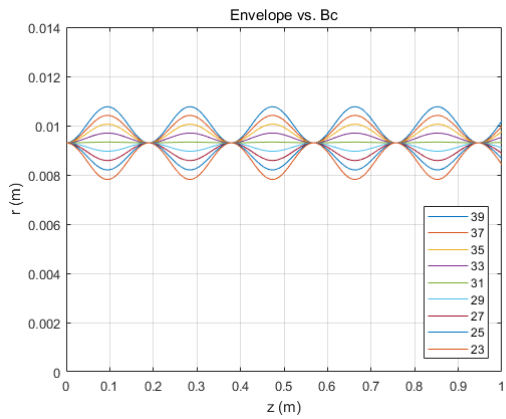


Figure 2: Beam envelopes with different B_c for a matched beam. The unit of the B_c is Gauss. Beam is matched at B_c = 31 G.

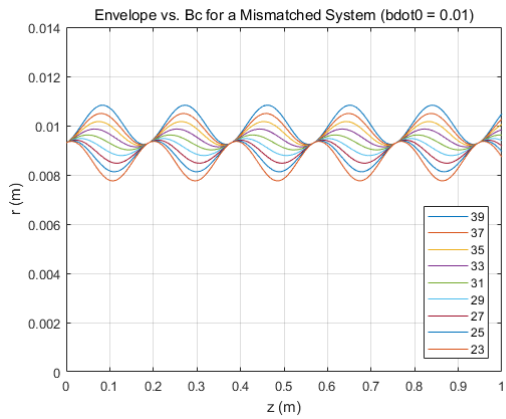


Figure 3: Beam envelopes with different B_c for a mismatched beam. The beam is detuned by making the injection angle ($\dot{b_0}$) = 10 mrad.

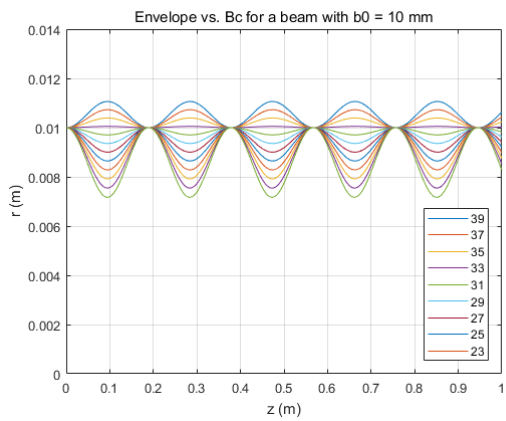


Figure 4: Beam envelopes with different B_c for a mismatched beam. The beam is detuned by making the injection angle ($\dot{b_0}$) = 10 mrad.

family. Furthermore the envelopes decohere for a large z which makes the analysis difficult.

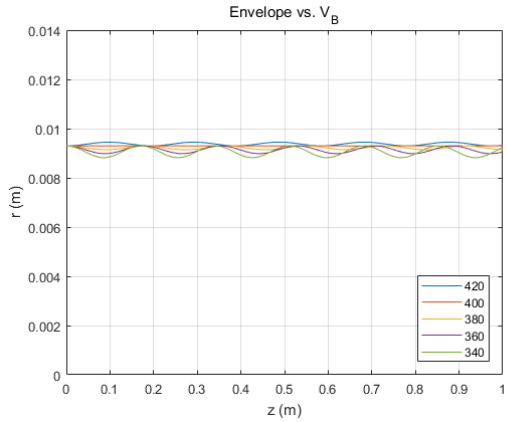


Figure 5: Beam envelopes with different V_B for a matched beam. The unit of V_B is kV

PRACTICAL APPLICATION

We apply the matching scheme outlined in the previous section to the matching designing of PAL klystron. The PAL klystrons are rf sources for the Pohag Light Source II (PLS-II) and PAL X-ray Free Electron Laser (PAL-XFEL). About 70 klystrons are in service and reliable klystron operations with low beam losses have been one of the critical issues for the stable operation of the whole accelerators.

The electron gun of the PAL klystron is the Pierce type and employs a Scandate cathode with the diameter and spherical radius of 90 mm and 73.7 mm respectively. The beam is focused by the electrostatic forces in the gun as well as the magnetic field generated by the Solenoid magnet. Part of magnetic field from the Solenoid reach the cathode and the focusing field strength is 1.6 times the Brillouin field. Electrons emitted from the cathode follow convergent trajectories as they travel in the gun and enter to the cavity section. Magnetic field lines are designed to follow the electron trajectories and, due to this, the basic focusing properties can be described by the envelope equation introduced in the previous section.

Magnetic Field Computation with POISSON

The Solenoid magnet for the PAL klystron consists of 11 main coils, 1 set of bucking coils, and iron yokes & shields. Figure 6 shows the cross section of the magnet overlaid with the magnetic field lines computed by the POISSON code. Field map in the region occupied by the electron beam is obtained by the SF7 code and exported to the EGUN code for trajectory simulation.

Matching Design with EGUN Simulations

In Fig. 7 we show the envelope family for a given gun electrode geometry and Solenoid magnet configuration which were simulated by the EGUN code. Scan parameter is the turn number of the bucking coil (N_B) of the Solenoid magnet, i.e., B_c-scanning. Notice the upper and lower envelopes are not symmetric each other and there is no matched condition. In order to match the beam to the Solenoid field we translate

Content from this work may be used under the terms of the CC BY 3.0 licence (© 2018). Any distribution of this work must maintain attribution to the author(s), title of the work, publisher, and DOI.

ISBN: 978-3-95450-194-6 ISSN: 2226-0366 doi:10.18429/JACoW-LINAC2018-TUPO090

Content from this work may be used under the terms of the CC BY 3.0 licence (© 2018). Any distribution of this work must maintain attribution to the author(s), title of the work, publisher, and DOI.

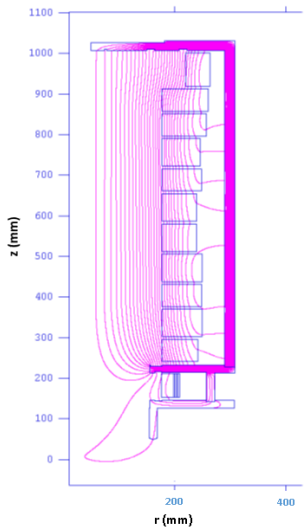


Figure 6: Cross section of Solenoid magnet for the PAL klystron overlaid with POISSON-computed magnetic field lines.

the gun position to the z-direction by z-trans = 5 mm which fine tunes the injection angle ($\dot{b}_0$). This results in Fig. 8 with matched condition established at N_B = 155. Notice symmetric envelopes near the matched one. Further translation (z-trans = 10 mm) detunes the beam and the matched condition disappers (See Fig. 9). It is found that the average beam size for a given N_B increase as the z-trans increases. This is because the B_c increases with the z-trans and the beam size increases with the B_c according to the Busch theorem [2].

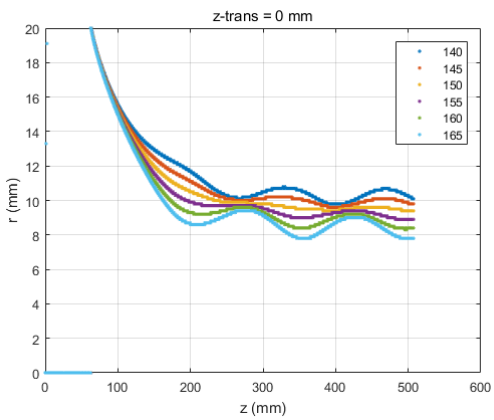


Figure 7: EGUN-simulated beam envelopes for different turn numbers of the bucking coil (N_B).

CONCLUSION

Based on the insights gained from the envelope families obtained by numerically solving the beam envelope equations, we have established a matching procedure for a klystron gun and Solenoid magnet. The procedure is systematic and alleviate extensive optimization work. The procedure has been applied to the PAL klystron and resulted satisfactory results. We expect refined beam matching for the PAL klystron improve the klystron efficiency as well as suppress beam losses and associated radiation generations.

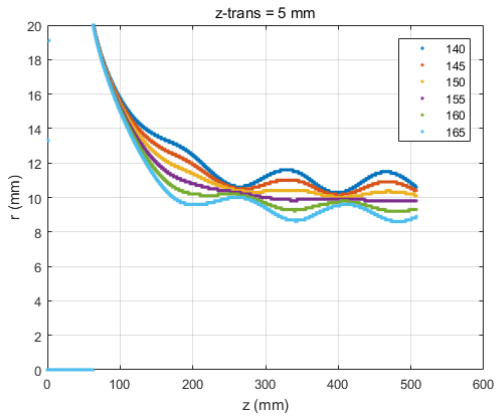


Figure 8: EGUN-simulated beam envelopes for different N_B. Gun is translated to the z-direction by 5 mm to yield matched condition at N_B = 155.

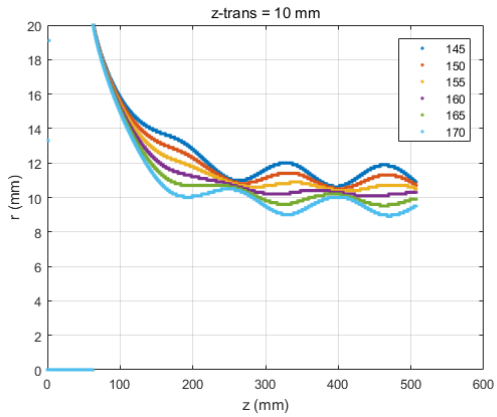


Figure 9: EGUN-simulated beam envelopes for different N_B. Gun is translated to the z-direction by 10 mm and the matching condition obtained in Fig. 8 disappears.

ACKNOWLEDGEMENTS

The work was supported by the National R&D Program (grant number: 2014M1A7A1A02029891, 2016R1A6B2A01016828) through the National Research Foundation of Korea (NRF).

REFERENCES

[1] A. S. Gilmour, *Klystrons, Traveling Wave Tubes, Magnetrons, Crossed-Field Amplifiers, and Gyrotrons*, Boston, MA, USA : Artech House, 2011, p. 142.

[2] J. R. Pierce, *Theory and Design of Electron Beams*, Princeton, NJ, USA: Nostrand, 1954.

ISBN: 978-3-95450-194-6 ISSN: 2226-0366 doi:10.18429/JACoW-LINAC2018-TUPO091

BEAM BREAK UP INSTABILITY ANALYSES FOR CAVITIES, LINACS, AND ENERGY RECOVERY LINACS*

V. Volkov†, V. M. Petrov, BINP SB RAS, Novosibirsk, Russia

Abstract

This analyze argue that *BBU* instability both in separate cavities and in Linacs or *ERLs* is going due to the consequence of fundamental property of dipole modes. "Head-tail" bunch instability has also the same nature. New BBU instability testing methods are described and analytically proved in the article.

INTRODUCTION

Beam Break Up (*BBU*) instability of a beam in a cavity begins to develop when the beam current value becomes higher than some threshold value. Then a transversal beam oscillation appears with avalanche growth that has the frequency of a one of dipole modes in the cavity. The dipole mode amplitude there also becomes to avalanche growth. As a role the process continues up to the beam hit to the channel wall (the tail particles in the first instance) if the beam current source duration is long enough or if the focusing system cannot limit this oscillation. If the growth increment is high enough to have time to pick up BBU instability for a single bunch so this is known as "head-tail" instability.

THRESHOLD CURRENT OF BBU INSTABILITY

The dipole mode growth is attended by transferring of a part of beam kinetic energy to saved dipole mode field energy. Incidentally, some part of this energy disappears in the cavity wall. This energy transferring process is going on due to beam space-modulation (transversal oscillation) appeared with the dipole mode frequency as a result of the beam interaction with the dipole mode. This occurred only for those dipole modes that applies the energy brake to the beam. Only approximately half of all dipole modes in a cavity can do it. Such a ratio of stable and instable dipole modes remind of equal probability of some stochastic process. The reason will be clear then later in the pillbox cavity example.

To be a stable process, the transferred average power (P_{BBU}) must be lower then disappeared power (P_{dis}), i.e. $P_{BBU} \le P_{dis}$. Such an approach has also considered by W.K.H. Panofsky in [1], but we have come to new conclusions.

On Fig.1 the example of the simplest dipole mode TM_{110} is shown in a pillbox cavity. Its resonance frequency (ω) is defined only by the cavity diameter (D) $\omega=0.82c\cdot D$ and is independent on its length (L).

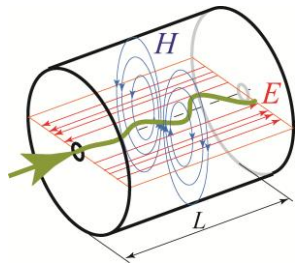


Figure 1: RF field distribution of TM_{110} dipole mode in a pillbox cavity with the view of a beam space-modulated trajectory.

We have to stress, only the average transferred power P_{BBU} plays a role in BBU instability. Each bunch separately hits to different phase of a dipole mode and so it can loss its energy or even to get it. So we can conclude that a bunch repetition frequency does not have an importance if dipole frequency is far enough from any harmonic of repetition frequency. Even any unbunched continuous beam can be instable.

BBU threshold current formula can be given if expressions for powers will be inserted to the above mentioned equation $P_{BBU} \le P_{dis}$: $P_{BBU} = -E_{BBU}\cdot I$, where E_{BBU} is average energy gain of beam particles in the dipole mode in Volts; I is the average beam current. $P_{dis}=\omega\cdot U/Q$, where ω is circular resonance frequency of the dipole mode; U is saved dipole mode energy; Q is loaded quality factor of the dipole mode. After the conversion we get

$$I \cdot Q \le I_Q = -\frac{\omega \cdot U}{E_{BBU}}. \quad (1)$$

The value of threshold current I_Q is the self-sufficing parameter for *BBU* instability as it follows from fundamental properties of dipole modes described further. Instability modes have positive value $I_Q>0$, for stability modes $I_Q<0$. Minus sign in *Eq.1* compensates the sign of energy loss of beam particles $E_{BBU}<0$.

BBU Fundamental Properties of Dipole Modes

One of unique property of dipole modes is the proportionality between values of average particle energy gain and dipole mode saved energy for beams propagating close enough to cavity axis:

$$E_{BBU} = -\frac{1}{I_Q} \cdot \omega U, \quad (2)$$

This proportionality is follows from the fact that rf longitudinal electric field of dipole modes (that caused the particle energy gain) is growth linearly with deviation (x) from

* Work supported by Russian Science Foundation (project N 14-50-00080)
† v.n.volkov@inp.nsk.su.

Content from this work may be used under the terms of the CC BY 3.0 licence (© 2018). Any distribution of this work must maintain attribution to the author(s), title of the work, publisher, and DOI.

ISBN: 978-3-95450-194-6 ISSN: 2226-0366 doi:10.18429/JACoW-LINAC2018-TUPO091

Content from this work may be used under the terms of the CC BY 3.0 licence (© 2018). Any distribution of this work must maintain attribution to the author(s), title of the work, publisher, and DOI.

axis. The proof is followed from the energy build-up equation *Eq.3* and of motion differential equation *Eq.4*. The averaged energy gain E_{BBU} in a longitudinal electric field $E_z(z,x)=x\cdot E'_z(z)$ for the particles moved along some trajectory $x= x(z,\varphi)$ defined by differential equation *Eq.4* is the integral along this trajectory (φ is the phase of the dipole fields at the coordinate $z=0$, then this energy gain is averaged on all φ phases):

$$E_{BBU} = \int_0^{\pi} \int_0^{L} E'_z(z)x(z,\varphi)\frac{\sin(2\pi z/\beta\lambda+\varphi)}{\pi} dz\, d\varphi\,. \quad (3)$$

$$d(\gamma dx/dt)/dt = (e/m)\,\beta cB(z)\cos(\omega t+\varphi), \quad (4)$$

Since the rf field in a cavity are proportional to square root of saved energy and particle deviations are also proportional to the square root of saved energy then the value after the integration is proportional to the saved energy. There can be shown [2, 3] that no initial deviation from the axis no initial inclination of beam do not influence to this conclusion if the trajectory lies close enough to the axis where there are linearity of E_z on x.

Equations *Eq.3* and *Eq.4* can be solved analytically for the simplest case of TM_{110} dipole mode shown in Fig.1. It is easy to show that the value of the threshold current periodically change their sign if the pillbox cavity length is elongated (see Fig.2), though the dipole mode fields there do not change. I.e. the dipole mode becomes periodically instable from stable one and then repeats back

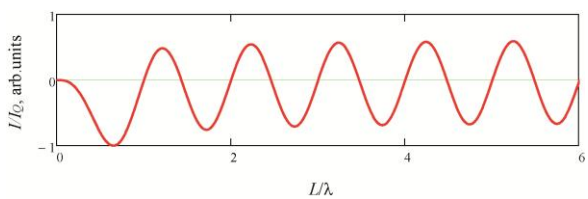


Figure 2: The dependency of backward value of BBU threshold current on the Pillbox cavity length.

The threshold current dependency on the beam energy can be obtained by using *Eq.1*, *Eq.3*, and the expression $U \sim L\lambda^2B^2$, where λ=c/ω: $I_Q \sim (m/e)\omega^2\cdot\gamma/\beta^2$. One can see the low the frequency squared the low threshold current. The threshold current has at least value at the electron energy of *374 keV*. In connection with these we can introduce the new parameter for dipole modes depending only on their properties I_{QD} such that $I_Q = (\gamma/\beta^2)\cdot I_{QD}$. This I_{QD} may be named as Threshold Current of Dipole Modes, that uniquely determine potentially stable modes with $I_{QD}<0$, and instable one with $I_{QD}>0$.

From these we can conclude that BBU effect in cavities is the result of the fundamental property of dipole modes described by the new parameter I_{QD}.

The next unique property of dipole modes is that a space-modulated beam (transversally oscillated) can excite dipole modes independently on temporal distribution of bunches, initial deviation, and initial inclination if its trajectory lies close enough to the axis where longitudinal rf electric field is linear on deviation x. It is natural that this excitation going on due to transferring of kinetic beams energy to the saved dipole field energy.

To operate with polarized dipole modes let introduce the new vector parameter $\boldsymbol{F}$ such that $|\boldsymbol{F}| \equiv U^{1/2}$. The $\boldsymbol{F}$ has the direction of the force acting to the beam, i.e. it is transversally directed to the magnetic field vector $\boldsymbol{B}$ and to the axis.

The space-modulated beam can be described by *Eq.3* if there will be replaced $E_{BBU}\rightarrow E_{MOD}$, where E_{MOD} is the energy gain of space-modulated beam, and $x=r\cdot\sin(2\pi z/\lambda+\varphi+\Phi)$, where Φ is the phase difference between the beam oscillation and the dipole mode B field; r is the amplitude of the beam oscillation. So we can write

$$E_{MOD} = -\sqrt{\omega\,(R_{II}/Q)/4\cdot}\,\cos(\Phi)\cdot(\bar{r}\cdot\bar{F}), \quad (5)$$

where the oscillatory and field polarizations there are taken into account by the scalar product of vectors $\boldsymbol{r}$ and $\boldsymbol{F}$; R_{II}/Q is the conventional coupling impedance of the dipole mode in Ohm/m^2. The specific coupling impedance for a space-modulated beam is less exactly by factor 4 then the conventional one, so in *Eq.5* the conventional coupling impedance is used with the factor of ¼.

On the basis of law of conservation of energy there is true the differential equation: $-E_{BBU}\cdot I - E_{MOD}\cdot I = P_{dis} + \Delta U/\Delta t$. After inserting to this the mentioned expression for P_{dis}, *Eqs.2, 5*, we get:

$$\boldsymbol{F}(t) = \boldsymbol{F}_0\cdot exp\frac{(I/I_Q-1/Q)\omega t}{2} + \frac{\boldsymbol{r_0}}{2}\cos(\Phi)\frac{I\sqrt{(R_{II}/Q)/\omega}}{I/I_Q-1/Q}\times \left(1-exp\frac{(I/I_Q-1/Q)\omega t}{2}\right), \quad (6)$$

where $\boldsymbol{F_o}$, and $\boldsymbol{r_o}$ is the complex values of initial dipole mode field and beam oscillation correspondingly represents the polarization vectors in the complex space.

Let us consider some interesting cases of *Eq.6* applications. Without of the beam ($I=0$) *Eq.6* describes usual process of damped oscillations in a cavity. If the dipole mode is instable ($I_Q>0$), and the beam current there are more than threshold one ($I/I_Q-1/Q>0$) then there begins the avalanche growth of the dipole mode with the increment $\delta=(I/I_Q-1/Q)\omega$, the more the beam current the more the growth rate. Only stable dipole modes with any beam currents gives always damped oscillations

BBU EFFECT IN LINACS

If the cavities are installed one by one like in a Linac ($\Phi=0$), they have the same dipole modes, and the beam current is more than the threshold one $I/I_Q-1/Q>0$ then the growth rate and its increment in each next following cavity is more than it has been in previous one since the initial amplitude r_o becomes more and more. The numerical solving of the differential equation for the case with oscillating growth $r_o\equiv r_o\cdot exp[(I/I_Q-1/Q)\omega t/2]$ in the first cavity have shown the increment growth in the second cavity by the factor 1.34, and in the third cavity by the factor of 1.6, and etc.

The last example demonstrates the importance of a proper beam focusing to suppress the BBU grows rate in

ISBN: 978-3-95450-194-6 ISSN: 2226-0366 doi:10.18429/JACoW-LINAC2018-TUPO091

Linacs – focusing systems must support oscillation r_0 values as less as possible ($r_0 \rightarrow 0$).

BBU EFFECT IN ERLS

In this case, the same beam with different energies comes through each cavity twice. The first passage usually has no space-modulation. The second one can be space-modulated due to BBU instability problems through the passing cavities.

On the basis of law of conservation of energy we can write: $-E_{BBU1}\cdot I - E_{BBU2}\cdot I - E_{MOD2}\cdot I = P_{dis} + \Delta U/\Delta t$, where the index *1* corresponds to the first beam passage, and index *2* – to the second one. After inserting to this the expressions for E_{BBU1}, E_{BBU2} E_{MOD2}, P_{dis} , U, and take into account $I_{Q1}=I_{QD}\cdot\gamma_1$, and $I_{Q2}=I_{QD}\cdot\gamma_2$. After integrating, there can be obtained the same equation of *Eq.6* but only there is the characteristically important replacing:

$$1/I_Q = 1/I_{Q1} + 1/I_{Q2}. \quad (7)$$

So the threshold current for ERLs is less than the least of them among the cavities that occurs in a cavity with the lowest value of beam energy.

The transversal beam oscillation and the dipole mode excited in n-th passage ($t=nT$) acts on the dipole mode in the next passage ($t=(n+1)T$) according to *Eq.6,* where $F_0 \equiv F(nT)\cdot cos(\omega T)$, and $r_o \equiv æF(nT)\cdot cos(\omega T)$. There the phase incursion for a one passage is taken into consideration by the factor of $cos(\omega T)$; $æ = |æ|\, e^{j\theta}$ is the complex coefficient granting the linear relation between the dipole mode and the oscillation; θ is the polarization tern angle of the beam oscillation due to the beam focusing and transportation along the *ERL* ring:

$$\dot{F}\big((n+1)T\big) = F(nT)cos(\omega T)e^{\frac{(I/I_Q - 1/Q)\omega T}{2}} +$$

$$+\frac{æ\cdot F(nT)}{2} cos(\omega T)\frac{I\sqrt{(R_{II}/Q)/\omega}}{I/I_Q - 1/Q}\cdot\left(1 - e^{\frac{(I/I_Q - 1/Q)\omega T}{2}}\right). \quad (8)$$

The stability *BBU* condition in *ERL* is following: $|\boldsymbol{F}((n+1)T)|/|\boldsymbol{F}(nT)| < 1$. To carry out this there don't have enough stability in cavities. Let us find the minimal *ERL* threshold current (I_{QERL}) in the least favorable case when an integer number of oscillations will go into the *ERL* length, i.e. $cos(\omega T)=1$, and the polarization doesn't change, i.e. $\theta=0$. From *Eq.8* it is follows:

$$\frac{-æ}{2}\cdot\frac{I\sqrt{(R_{II}/Q)/\omega}}{I/I_Q - 1/Q} \le 1. \quad (9)$$

If we replace in *Eq.9:* $I\cdot Q = I_{QERL}$, then will get for instable modes ($I_Q>0$) the *ERL* threshold current always less than the cavity one:

$$\frac{I_Q}{1+æ\sqrt{(R_{II}/Q)/\omega}\cdot I_Q} \le I_{QERL} \le I_Q. \quad (10)$$

And for the stable cavity modes ($I_Q<0$):

$$I_{QERL} \le \frac{|I_Q|}{æ\sqrt{(R_{II}/Q)/\omega}\cdot|I_Q|-1}, \quad (11)$$

i.e. even stable cavity modes can be instable in *ERL*. At a sufficiently small æ value the denominator of *Eq.11* becomes negative. So the beam will be absolutely stable at any current if

$$-1/æ\sqrt{(R_{II}/Q)/\omega} < I_Q < 0. \quad (12)$$

At this condition there are enough power transporting from the saved dipole energy to kinetic beam energy to suppress the *BBU* instability in *ERL*.

NEW METHODS OF BBU TESTING

There are new testing methods for detection of instable dipole modes and definition of its threshold currents. If we compare two decrements (δ and δ') of damped oscillations in a cavity, and one of them (δ') is going with any electron beam passing through the cavity then the decrement of stable modes will be grown involving the beam current I but for instable modes it will be fall:

$$\delta'(I) = \delta - I/I_Q. \quad (13)$$

$$I_Q = \frac{I}{\delta - \delta'(I)}. \quad (14)$$

The next method utilizes space-modulated beams. If we compare two fields in a cavity excited by space-modulated beam with different average currents, $F=F(I)$, $F'=F(I')=F(n\cdot I)$, and at the same modulation amplitudes ($r' = r$) then the threshold current can be calculated as

$$I_Q = I\cdot Q\cdot\frac{n(1-F'/F)}{n-F'/F}. \quad (15)$$

This method can be used for testing of trapped dipole modes that cannot be seen by any test probes in the cavity. In this case the F and F' signals in *Eq.15* are the beam oscillation amplitude signals taken from special probes.

Mentioned above methods can be applied both for a special stand and for a Linac itself or ERL. In this case the accelerator beam itself can be the instrument of the testing.

REFERENCES

[1] W. K. H. Panofsky and M. Bander, Asymptotic Theory of Beam Break-Up in Linear Accelerators, Rev. Sci. Instrum. 39, 206 (1968).

[2] V.Volkov, Prediction and suppression of beam breakup instability in multicell superconducting cavities, PRST-AB 12, 011301 (2009).

[3] V.Volkov, J. Knobloch, A. Matveenko. Beam breakup instability suppression in multicell superconducting rf guns, PRST-AB 14, 054202 (2011).

Content from this work may be used under the terms of the CC BY 3.0 licence (© 2018). Any distribution of this work must maintain attribution to the author(s), title of the work, publisher, and DOI.

ISBN: 978-3-95450-194-6 ISSN: 2226-0366 doi:10.18429/JACoW-LINAC2018-TUPO092

BEAM DYNAMICS AND COLLIMATION FOLLOWING MAGIX AT MESA

Ben Ledroit*, Kurt Aulenbacher, Johannes Gutenberg-Universität, 55128 Mainz, Germany

Abstract

The Mainz Energy-recovering Superconducting Accelerator (MESA) will be an electron accelerator allowing operation in energy-recovery linac (ERL) mode, where beam energy is recovered by decelerating the beam in linac cryomodules and transferring kinetic energy to the RF. The ERL mode provides the opportunity to operate experiments at peak energy with thin targets, combining high luminosities typical for storage rings and high beam brightness typical for linacs. The MESA Internal Gas Target Experiment (MAGIX) aims to operate jet targets at high luminosities with different gases up to Xenon. As scattering effects in the beam rise with the atomic number, investigations on the impact of the target on beam dynamics and beam losses are required for machine safety. The goal of this work is to understand target induced halo, track halo particles through downstream sections and protect the machine with a suitable collimation system and shielding from direct and indirect damage through beam losses and radiation. The present status of the investigations is presented.

MESA

An overview of MESA is given in [1]. MESA will supply the P2 experiment in external beam (EB) mode with a beam current of 150 µA at 155 MeV [1, 2]. In EB mode, the whole beam is dumped after interaction with the target. A second beamline is set up for the ERL mode, where the beam passes the MAGIX target and is then phase shifted 180° with respect to the RF and recirculated through the cryomodules for energy recovery. MESA will maintain a 1 mA beam current in the first stage and 10 mA after upgrade at 105 MeV.

MAGIX

ERL operation is possible since MAGIX provides a low density target and only a small fraction of the beam actually interacts with the gas. The target is designed as a gas jet of nearly homogenous density. The jet is of cylindrical shape with 4 mm in height and diameter [3] and is produced by accelerating gas to supersonic speeds in a Laval nozzle perpendicular to the beam axis. A gas catcher is set up opposite to the Laval nozzle to collect the major part of the injected gas in order to keep vacuum conditions at a tolerable level. MAGIX is designed to operate with various gases (H, He, O, Ar, Xe, CH_4) for fundamental physics experiments, e.g. the search for the dark photon as well as investigations on the proton form- and astrophysical S-factor [4]. The setup is shown in Fig. 1.

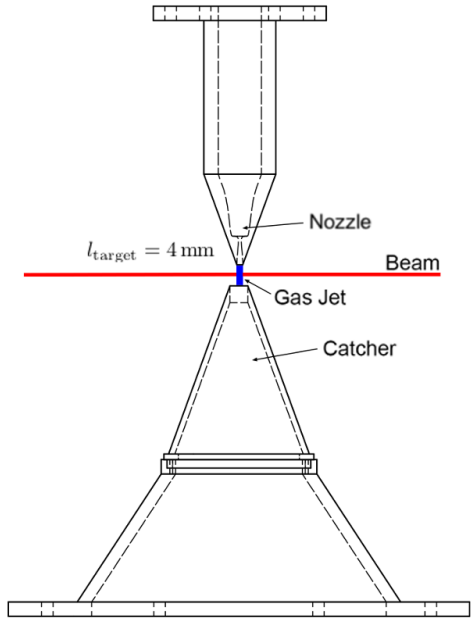


Figure 1: Schematic drawing of the MAGIX gas target [5].

Luminosity Limit Estimation

Target scattering and beam optics limit the luminosity of targets in ERL operation. Luminosity and target density limits for MAGIX can be estimated as presented in [6]. The luminosity limit then depends on beam and target properties. The necessities of radiation protection simultaneously set a limit to beam power losses outside adequately shielded areas. It is therefore important to examine these parameters to ensure reliable ERL operation.

TARGET INDUCED HALO

Scattering on the gas target widens the angle and energy distribution of the electron beam in a way that a halo forms around the original beam cross-sectional area as shown in Fig. 2. The halo is therefore called "Target Induced Halo" (TAIL). TAIL might cause malicious beam dynamical behavior when passing the cryomodules, such as inducing Higher Order Modes (HOMs) in the cavity, or directly damage machine parts when electrons get dumped in the cavities and beam pipes. Radiation produced by dumping electrons may further lead to damage especially to electronic components and generate background noise in the detectors of the experiments reducing measurement precision. It is therefore crucial to carefully investigate on the effects originating from the beam passage of MAGIX and formulate a collimation approach downstream the target to encounter impacts on machine operation safety and reliability.

* bledroi@uni-mainz.de

Content from this work may be used under the terms of the CC BY 3.0 licence (© 2018). Any distribution of this work must maintain attribution to the author(s), title of the work, publisher, and DOI.

ISBN: 978-3-95450-194-6 ISSN: 2226-0366 doi:10.18429/JACoW-LINAC2018-TUPO092

SIMULATION OF TAIL AT MAGIX

Statistical scattering models such as the Moliere distribution in practice quickly get complicated to evaluate owing to the degree of idealization on which these models are based. Simulating the target hence is a key part in understanding the formation of the TAIL. The Open Source simulation toolkit Geant4 is used for this purpose since it offers the greatest flexibility, high precision and high performance in simulating passage of particles through matter. The gas target is modeled with a particle density of 10^{19} cm^{-2} of the above mentioned gases. The beam transverse profile is modeled as an rotationally symmetrical 2-dimensional gaussian. Beam energy and angle distributions are gaussian with $E = 105$ MeV, $\sigma_E = 100$ keV and $\sigma_\theta = 2.5$ mrad respectively. Assuming a beam current of 1 mA as considered for the first stage of MESA, the corresponding luminosity is 6.2×10^{34} cm^{-2} s^{-1}.

Angle Distribution

The impact of target passage on the angle distribution is shown in Fig. 2. The region outside 15 mrad is identified with the TAIL region. A mentionable broadening of the distribution is visible to higher angles. These effects enlarge with higher mass target gases. H, He and CH_4 targets lead to TAIL intensities below 1 W and are therefore assumed to be technical manageable without greater impacts, whereas heavier gas targets greatly increase TAIL power up to 200 W with Xe and therefore have to be handled carefully.

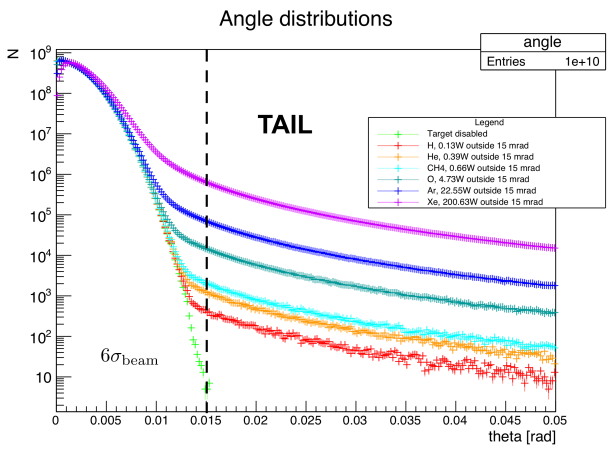


Figure 2: Geant4 simulation of the angle distributions with and without a gas targets as designed for MAGIX. All target gases are modeled with a particle density of 10^{19} cm^{-2} and the beam current is assumed to be 1 mA. TAIL region starts at 15 mrad, corresponding to $6\sigma_{\mathrm{beam}}$.

Energy Distribution

Energy distributions before and after target passage have been extracted to investigate on the effects on the energy distribution. The distributions yield no net widening of energy deviation in the region of the initial beam design energy. The scattering process yet produces low energy electrons as shown in Fig. 3, potentially reaching downstream accelerator sections. These electrons are expected to be dumped after the first dipole magnet, since their energy is much lower than the magnet design value. The amount of low energy halo is again increasing with higher target masses.

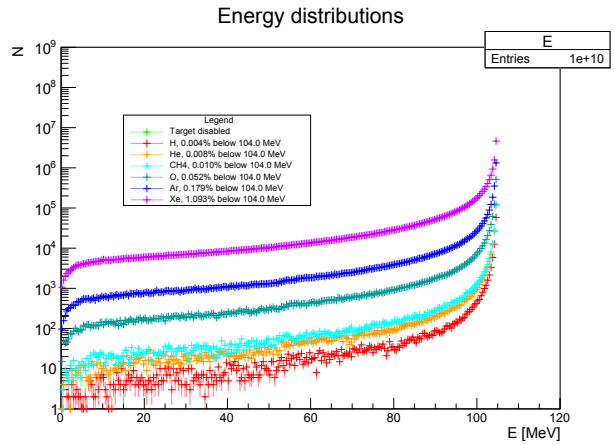


Figure 3: Electron energy spectrum after target passage. Beam mean energy remains virtually untouched, while few low energy particles are produced through scattering.

Bunch Elongation

Scattering processes may result in longer pathlengths of electrons passing the MAGIX target and thus temporal delay of single electrons. An electron bunch may therefore elongate and occupy larger phase intervals when decelerated as for acceleration. However, simulations indicate that this effect is not significant and therefore negligible for the deceleration process.

TAIL TRACKING

The previously generated halo is tracked through the following section to determine where beam losses occur and to estimate their intensity. BDSIM is used for this purpose, as it utilizes Geant4 physics precision and greatly enhances workflow for accelerator design-related simulations [7]. The modelled lattice section is starting at the MAGIX gas jet and ends at the building wall, after which the beam is directed back to the cryomodules. The TAIL resulting from a Xenon target is used as starting distribution for tracking studies, as it reveals the largest angle spread and is therefore considered to be computationally cheapest for beam loss simulations. Working with this worst case scenario, the effects of other mentioned target gases on beam loss are considered to be less severe.

Beam Pipe Material

The accelerator layout uses commercially available beam pipes. These beam pipes consist of aluminium or stainless steel, depending on their desired properties regarding magnetic permeability or their ability to be baked out. The beam pipe is first considered to have the smallest practical aperture

Content from this work may be used under the terms of the CC BY 3.0 licence (© 2018). Any distribution of this work must maintain attribution to the author(s), title of the work, publisher, and DOI.

ISBN: 978-3-95450-194-6 ISSN: 2226-0366 doi:10.18429/JACoW-LINAC2018-TUPO092

Content from this work may be used under the terms of the CC BY 3.0 licence (© 2018). Any distribution of this work must maintain attribution to the author(s), title of the work, publisher, and DOI.

with a diameter of 40 mm to acquire the greatest statistic of beam loss. The wall thickness is chosen to be 3 mm. Two simulations are conducted, one with aluminium and one with stainless steel beam pipes, to estimate radiation safety related advantages. The results are shown in Fig. 4 and indicate that stainless steel stops incident electrons more effective than aluminium due to the higher atomic number and density of iron. Electrons are therefore partly passing aluminium pipe walls and are stopped in the magnet yokes. However, this effect results in reduced energy deposition in aluminium in the drift section directly after the MAGIX target and thus is preferable regarding detector noise. The following considerations therefore use aluminium beam pipes.

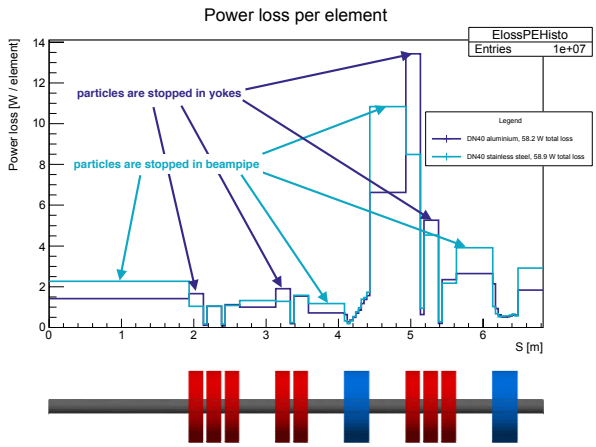


Figure 4: BDSIM halo tracking simulation with DN40 aluminium and stainless steel beam pipes. Drift sections are gray in the lattice plot, quadrupoles red and dipoles blue.

Beam Pipe Aperture

Energy loss is also depending on the aperture size as larger apertures allow more space for the halo to be transported. Figure 5 shows results of energy loss simulations for aluminium pipes with different commercially available DN pipes from 40 mm to 100 mm diameter. Choosing a diameter of 100 mm for the section downstream from MAGIX seems favorable to transport the largest part of TAIL to a collimator, where halo can be lost in a controlled manner.

COLLIMATION STRATEGY

As visible in Fig. 5, the highest loss powers are located following the first dipole magnet, especially in the quadrupole triplet. This is due to low energy electrons in the TAIL, resulting in smaller bending radii compared to design and finally wrong exit angles. Taking this into account, it is convenient to replace the quadrupole triplet with a collimator and surround it with proper shielding to keep energy losses and radiation locally confined.

CONCLUSION

Simulations on TAIL properties were conducted to quantify effects of using an internal gas jet target. The simulations

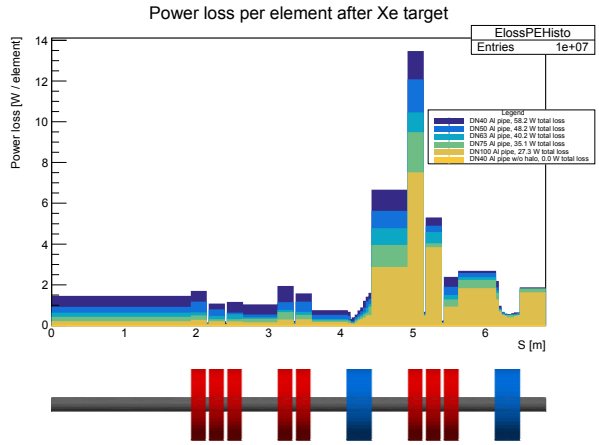


Figure 5: BDSIM halo tracking simulation with aluminium beam pipes of different diameters. The most power is deposited after the first dipole magnet.

show that it is possible to operate such a target in ERL mode, however aiming to operate the target with gases of higher atomic number reduces the maximum reachable luminosity as relative beam loss is rising unavoidably. To counteract uncontrolled beam loss, the losses are now localized and therefore a suitable collimation location found. Current studies are focusing on collimator layout as well as radiation generated by electron losses and its impact on detectors and radiation safety.

ACKNOWLEDGEMENT

We thankfully acknowledge the funding for this project by the DFG through GRK 2128 "AccelencE".

REFERENCES

[1] T. Stengler *et al.*, "Status of the Superconducting Cryomodules and Cryogenic System for the Mainz Energy-recovering Superconducting Accelerator MESA" in *Proc. IPAC'16*, Busan, Korea, May 2016, paper WEPMB009.

[2] D. Simon, "Beamline Design for MESA", Diploma thesis, Institute for Nuclear Physics, Johannes Gutenberg-University, Mainz, Germany, 2014.

[3] S. Aulenbacher, private communication, Sep. 2016.

[4] K. Aulenbacher, "Nuclear Physics Experiments at MESA", presented at the 59th ICFA Advanced Beam Dynamics Workshop on Energy Recovery Linacs, CERN, Geneva, Switzerland, June 2017.

[5] MAGIX, http://wwwa1.kph.uni-mainz.de

[6] G. Hoffstaetter, "Applications for CBETA at Cornell", presented at the 59th ICFA Advanced Beam Dynamics Workshop on Energy Recovery Linacs, CERN, Geneva, Switzerland, June 2017.

[7] BDSIM Manual, http://www.pp.rhul.ac.uk/bdsim/manual/introduction.html

ISBN: 978-3-95450-194-6 ISSN: 2226-0366 doi:10.18429/JACoW-LINAC2018-TUPO093

EXCITATION OF MILLIMETER WAVELENGTH CAVITY STRUCTURE

M. Arsentyeva†[1], A. Barnyakov, A. Levichev[1], D. Nikiforov, BINP, Novosibirsk, Russia
[1]also at Novosibirsk State University, Novosibirsk, Russia

Abstract

In this work excitation of W-band structure is studied. The structure consists of cylindrical cavities with the operating frequency of about 96 GHz. We plan to excite the structure by short bunches from the photocathode RF gun. In order to choose structure geometry and beam duration, we performed estimations and simulations; induced voltage was also estimated. Taking into account feasible parameters of the photocathode RF gun such as beam size and emittance, we studied exciting beam transverse dynamics to define its other characteristics (energy and charge). To lead the beam from the whole structure, focusing is needed. After estimation of required magnetic field, we considered possibility of focusing with help of permanent magnets.

INTRODUCTION

Accelerator facilities on the base of short beams for interdisciplinary research are being developed at research centers [1-3]. Radiofrequency (RF) photocathode gun is usually the source of short beams. Such a facility being developed at Budker Institute of Nuclear Physics (BINP) will provide electron beams of picosecond duration for different experimens that require short beams.

Excitation of W-band accelerating structure could be one of these experiments. Such structures are interesting from the point of view of high gradient [4] due to the higher frequency. Thus, length of the W-band accelerator may be significantly reduced compared to length of the S-band one.

Another motivation to develop W-band accelerating structures is connected with plasma excitation experiments where bunch required length is determined by the Langmuir wavelength

$$\sigma_t \sim c/\omega_p,$$

Here c is the speed of light, $\omega_p = \sqrt{4\pi n_p e^2/m}$, is the plasma frequency, e is the electron charge, n_p is the plasma density, m is the electron mass. With the plasma density of 10^{15} cm^{-3}, required bunch length is about 0.2 mm (0.6 ps). To obtain train of such short bunches, one can excite W-band structure by the "driver" beam from the photocathode gun, and then bunch there the secondary "long" beam. These bunches with spatial period of about mm are suitable for the plasma excitement and for the subsequent wakefield acceleration.

Thus, W-band structures are interesting not only in terms of accelerator fundamental physics but also for the industry where accelerator length may be significantly reduced.

RF PHOTOCATHODE GUN

After the photocathode RF gun (Fig. 1) beam is accelerated in the S-band disk-loaded accelerating structure up to tens MeV. After that it enters the W-band structure to excite it.

RF Photocathode Gun

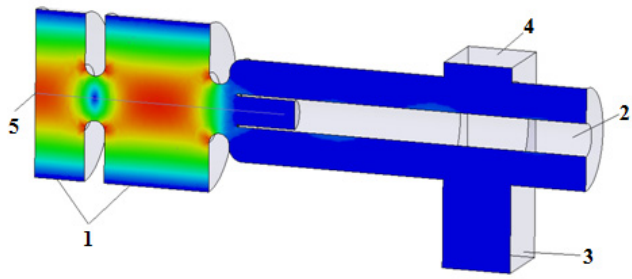


Figure 1: Layout of the photocathode gun with the electric field distribution: 1 — accelerating cavities, 2 — input for the laser beam, 3 — RF power input, 4 — vacuum pumping connection, 5 — photocathode.

Table 1: Photocathode Gun Specifications.

Parameter	Value
Operating frequency	2856 MHz
SWR at the operating mode	1.1
Unloaded quality factor of cavities	12000
Length of the first cavity	24.8 mm
Length of the second cavity	52.3 mm
Cavity diameter	82 mm
Beam duration	1-10 ps
Repetition rate	10 Hz
Beam charge	up to 2 nC
Transverse emittance	10 μm

Substantial feature of the photocathode guns is production of low emittance beams compared to conventional thermionic cathode guns [5]. Emittance evolution for the beam charge of 1nC and 2 nC at the BINP photocathode gun is shown at Fig. 2 (obtained during simulations at ASTRA [6]).

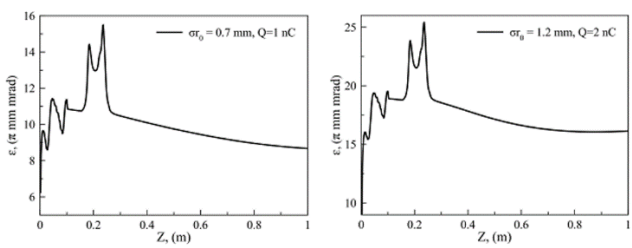


Figure 2: Emittance evolution for the beam from the photocathode gun with the charge of 1 nC (top) and 2 nC (bottom).

For the moment the gun is fabricated, measured and pumped (Fig. 3).

†mariemaltseva@yahoo.fr

Content from this work may be used under the terms of the CC BY 3.0 licence (© 2018). Any distribution of this work must maintain attribution to the author(s), title of the work, publisher, and DOI.

ISBN: 978-3-95450-194-6 ISSN: 2226-0366 doi:10.18429/JACoW-LINAC2018-TUPO093

Content from this work may be used under the terms of the CC BY 3.0 licence (© 2018). Any distribution of this work must maintain attribution to the author(s), title of the work, publisher, and DOI.

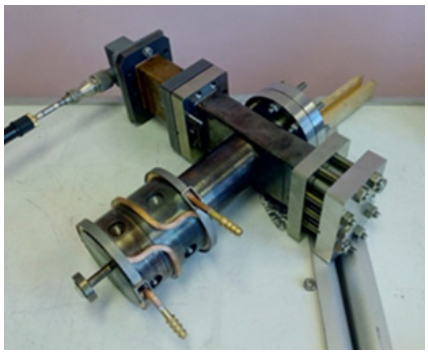


Figure 3: Fabricated photocathode RF gun.

GEOMETRY OF THE W-BAND STRUCTURE

Radius of cavities was defined by the operating frequency close to 96 GHz. Longitudinal parameters of the structure cavities were chosen in such a way that cavities were independent by the electromagnetic field (Fig. 4).

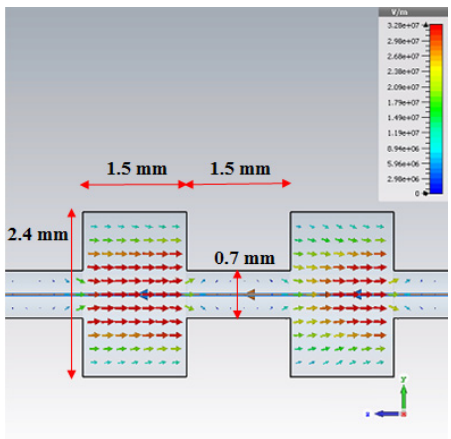


Figure 4: Two cavities of the excited W-band structure by the beam with $\sigma_t = 2$ps, $Q = 2$ nC.

EXCITATION OF THE W-BAND STRUCTURE

Amplitude of the electric field to be excited at the cavity at the mode E_{010} by the beam with gaussian charge distribution is given as

$$E_0 = \frac{q}{\varepsilon_0 \pi R^2 J_1^2(\nu_{01})} \exp\left(-\frac{\omega_0^2 \sigma_t^2}{2}\right),$$

where q is the beam charge, ε_0 is the dielectric constant, R is the cavity radius. J_1 is the 1st order Bessel function, ν_{01} is the 1st zero of the Bessel function $J_0(x)$, $\omega_0 = 2\pi f$, f is the frequency of the excited mode at the cavity, σ_t is the RMS duration of the gaussian beam.That is, in terms of higher accelerating gradient, exciting beam should be as short as possible. However, extremely small beam length is undesirable because of higher mode excitation. Optimal beam duration of 2 ps was chosen as a result of simulations at CST Studio [7]. Figure 5 illustrates spectrum (in logarithmic scale) of the excited electric field at one of the cavities : modes with the frequency higher then 96.2 GHz are several orders of magnitude smaller.

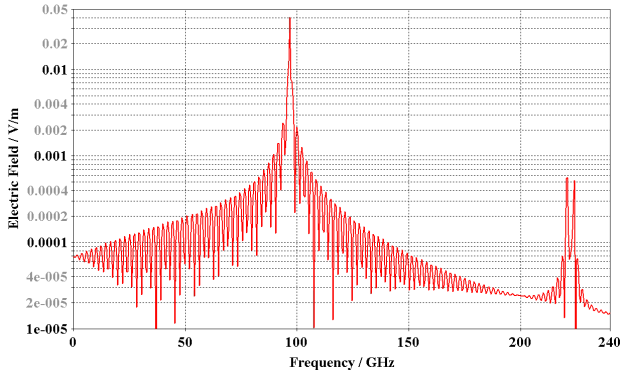


Figure 5: Spectrum of the excited electric field at one of the cavities.

Table 2: Result of Simulations of the W-band Structure Excitation

Parameter	Value
Exciting beam charge	2 nC
Exciting beam RMS duration	2 ps
Frequency of the excited mode E_{010}	96.2 GHz
Amplitude of the excited electric field	50 MV/m
Damping time	60 ns

FOCUSING SYSTEM ON PERMANENT MAGNETS

To lead the beam through the W-band cavity structure, it is necessary to focus it into its small aperture of 2 $a = 0.7$ mm. With Kapchinsky-Vladimirsky beam envelope equation [8] one can estimate required magnetic field B_z for the focusing of the electron beam with given parameters :

$$B_z = \frac{2\beta\gamma mc}{q}\sqrt{\frac{K}{a^2} + \frac{\varepsilon_n^2}{\beta^2\gamma^2 a^4}}.$$

Here β and γ are beam relativistic factors, ε_n is normalized emittance, $K = 2I_b/(I_0\beta^3\gamma^3)$, I_b is the beam current, $I_0 \approx 17$kA. Taking into account beam feasible parameters after the gun (Table 1), one can depict required magnetic field dependence on the beam energy (Fig. 6).

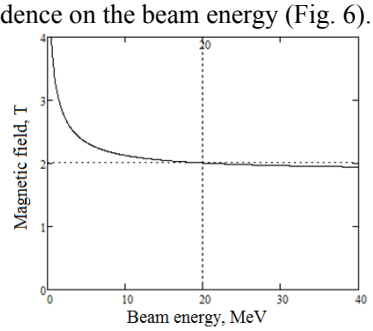


Figure 6: Dependence of focusing magnetic field on the beam energy.

Beam energy of 20 MeV is optimal; focusing magnetic field is about 2 T.

We propose to use permanent magnets producing solenoidal field. This type of magnet has some advantages compared with solenoids, i.e., no need in cooling. Design

ISBN: 978-3-95450-194-6 ISSN: 2226-0366 doi:10.18429/JACoW-LINAC2018-TUPO093

of one magnet module is depicted at Fig. 7; Fig. 8 shows its longitudinal field.

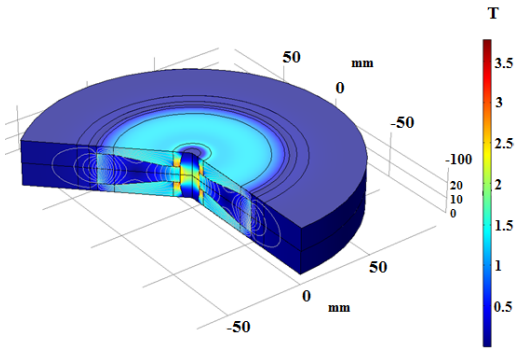


Figure 7: Magnet module with field lines.

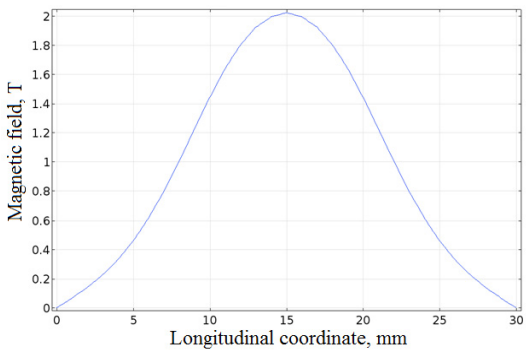


Figure 8: Longitudinal field of the magnet module.

Beam Dynamics Simulations at the Field of Permanent Magnets

Dynamics simulations for the beam with parameters form Table 1 were performed using ASTRA code. Resulting beam envelope is shown at Fig. 9. Many magnet modules (about 20) are used here to form solenoidal field at the whole W-band structure length, field amplitude of a single module of 2 T is enough to maintain beam radius of about 0.27 mm.

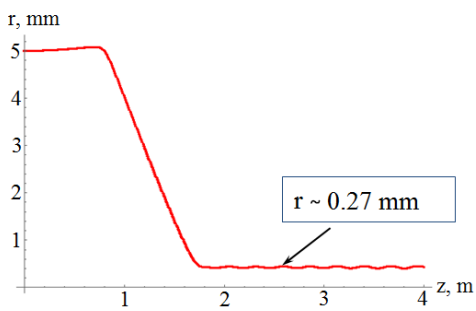


Figure 9: Beam envelope in the field of permanent magnets.

FABRICATION OF THE W-BAND STRUCTURE

Cavities were fabricated (Fig. 10), after that 50 of them were brazed into the structure (Fig. 11).

The structure was checked for tightness; measurements from the outside revealed misalignment of cavities from the structure axis of about 0.02 mm. Future work comprise more precise measurements that will be possible after the structure sawing.

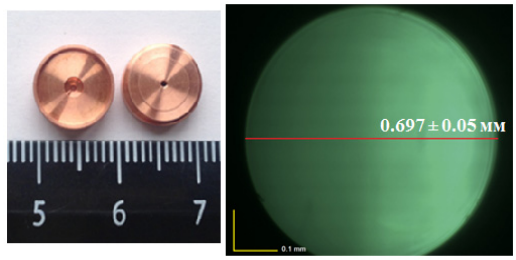


Figure 10: On the left – cavities, on the right – depiction of the aperture obtained with help of microscope.



Figure 11: Brazed W-band structure.

CONCLUSION

We began to develop W-band accelerating structures at BINP. To excite the structure, we plan to use electron beam from the photocathode RF gun.

At result of simulations of the structure excitation, we defined optimal exciting beam parameters. To focus the exciting beam into the small structure aperture, we propose to use permanent magnets; their design is prepared.

W-band cavity structure was successfully manufactured, measurements from the outside showd satisfactory results. The structure precise measurement are in progress.

REFERENCES

[1] R. Assmann, C. Behrens, R. Brinkmann and *et. al.,* in *Proc. 5th Int. Particle Accelerator Conf. (IPAC'14)*, Dresden, Germany, Jun. 2014, paper TUPME047, pp. 1466-1469.

[2] P. A. McIntosh, D. Angal-Kalinin, N. Bliss and *et. al.,* in *Proc. 5th Int. Particle Accelerator Conf. (IPAC'14)*, Dresden, Germany, Jun. 2014, paper WEPME083, pp. 2471-2474.

[3] T. Vardanyan, G. Amatuni, V. Avagyan, *et al.,* in *Proc. 36th Int. Free Electron Laser Conf. (FEL'14)*, Basel, Switzerland, Aug. 2014, paper TUP083, pp. 561-563.

[4] G. A. Loew, J. W. Wang, SLAC-PUB-4647, 1988.

[5] D. Nikiforov, A. Levichev, A. Barnyakov, A. Andrianov, S. Samoylov. Simulation of a Radio-Frequency Photogun for the Generation of Ultrashort Beams, Journal of Technical Physics, vol. 8, №4, p. 12 (in Russian)

[6] ASTRA, http://www.desy.de/~mpyflo/

[7] CST – computer simulation technology, https://www.cst.com

[8] M. Reiser, *Theory and Design of Charged Particle Accelerators*, *Second, Updated and Expanded Edition*, John Wiley and Sons Inc., New York, 2008, p. 187.

Content from this work may be used under the terms of the CC BY 3.0 licence (© 2018). Any distribution of this work must maintain attribution to the author(s), title of the work, publisher, and DOI.

ISBN: 978-3-95450-194-6 ISSN: 2226-0366 doi:10.18429/JACoW-LINAC2018-TUPO095

BEAM LOADING WITH THE FIRST REBUNCHER OF SPIRAL2, FIRST MEASUREMENTS

M. Lechartier, J.F. Leyge, R. Ferdinand, GANIL, Caen, France

Abstract

The SPIRAL2 LINAC acceleration start with an RFQ (Radio Frequency Quadrupole). In the MEBT (Medium Energy Beam Transport) Line, the beam passes through rebunchers. The beam intensity is up to 5 mA. We need to take care of the beam loading as the RF (Radio Frequency) power in the cavity can give energy to the ion beam and also the ion beam can give energy to the cavity. This paper presents the effects of the beam on the rebuncher cavity

REBUNCHER CAVITY

Three identical rebunchers (see Figs. 1 and 2) are located in the MEBT Line. Only the first rebuncher is used today on the diagnostic plate to characterize the different beam parameters [1].

A solid-state amplifier is used with a 10 kW maximal output power. Actually, the power at the cavity entrance is 6-8% lower due to the losses in the circulator and RF transport lines. The maximum nominal voltage is 120 kV. The proton nominal value is 38 kV.

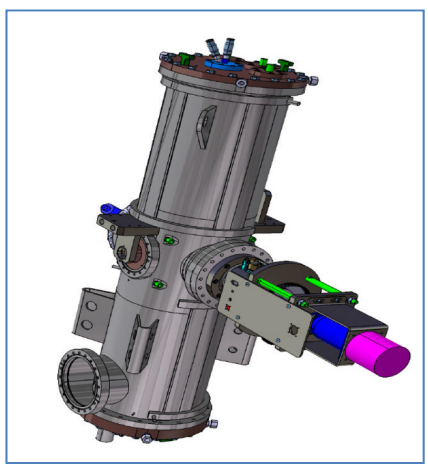


Figure 1: Cavity.

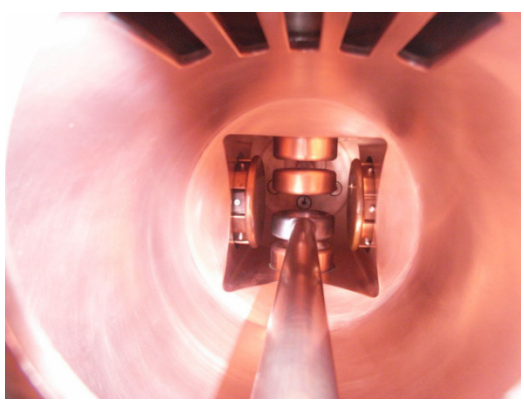


Figure 2: Inside the cavity.

Table 1: Parameters

Parameter	Value	Unit
Design voltage (continuous)	120	kV
Design voltage (50% DC)	190	kV
Beta	0.04	%
TTF	0,38	
Q_L	3335	
Power loss (@120 kV CW)	5.0	kW
Power loss (@190 kV)	12.2	kW
Tuning range	+/-300	kHz/mm
Cavity aperture diameter	60	mm
Gap distances	13 .30 .13	mm
Flange to flange distance	280	mm

RF REGULATION OF THE CAVITY

The RF system is regulated by a general LLRF (Low level radio Frequency) numerical system developed at Saclay. The regulation used in SPIRAL2 is a control feedback loop (see Fig. 3). The frequency choosed for the sample clock is 70.422 MHz (the RF is 88.0525 MHz). The signal reference and the cavity signal are sampled and compared. Then an equation is applied to model the loop filter. The loop filter is a P.I.D. (proportional, integrated, derivated) structure. Actually, we use only the P and I parameters to stabilize the RF voltage. The filtered error is then converted to analog signal and sent to an IQ (In phase and in Quadrature) modulator to correct the error. So, the amplitude and phase compensation cannot be separated.

Others classical systems used are often amplitude and phase separated loops. The goal values for the regulation are : amplitude error < 1% , phase error < 1° for the complete system. It contains a post mortem system which can be used as a precise monitoring system in the ns scale.

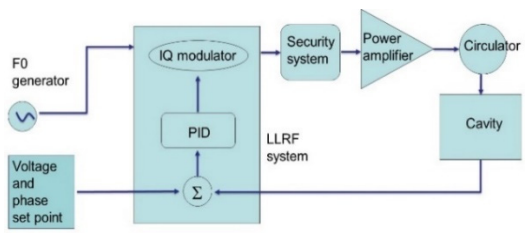


Figure 3: Regulation system.

EXPERIMENTS

The effects of the beam are evaluated when the rebuncher is in open loop regulation and in closed loop. The phase offset between RFQ (reference phase) and rebuncher is tuned from -180 to +180°. We record the phase offset and the voltage offset induced by the beam in both open and close loop regulation. This experience is made for different beam currents.

Content from this work may be used under the terms of the CC BY 3.0 licence (© 2018). Any distribution of this work must maintain attribution to the author(s), title of the work, publisher, and DOI.

ISBN: 978-3-95450-194-6 ISSN: 2226-0366 doi:10.18429/JACoW-LINAC2018-TUPO095

For the experiment, the beam is pulsed during 5 ms 'on', with a repetition rate of 300 ms (see Fig. 4). The transition when the beam passes through the rebuncher can be easily observed.

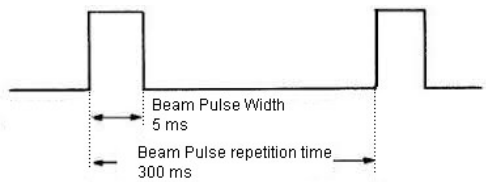


Figure 4: Beam pulsation.

In the following example, the phase timing for the re-buncher is choosed at -60° and the voltage is set to 38 kV

Open Loop

Figures 5 and 6 show the 5 ms beam pulse over a 400 ms observation time for a phase offset of 60°.

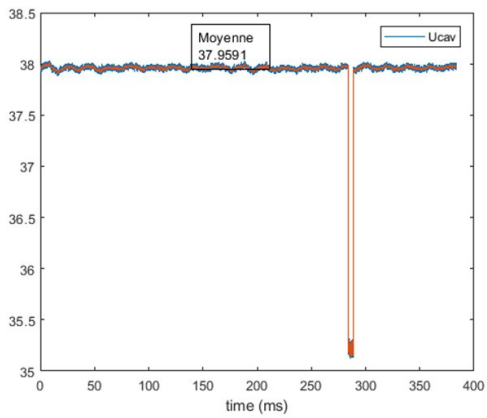


Figure 5: Voltage offset (kV), open loop.

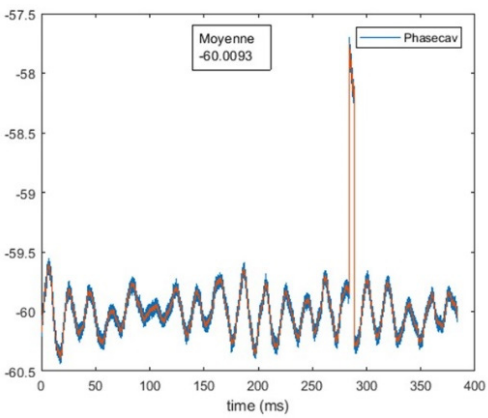


Figure 6: Phase offset (°), open loop.

On these figures, the beam induce a voltage drop of -2.7kV, and a phase increase of +2°.

Closed Loop

Figures 7 and 8 show a temporal zoom of the beam pulse (5 ms) highlighting the beam pulse rise and fall effects.

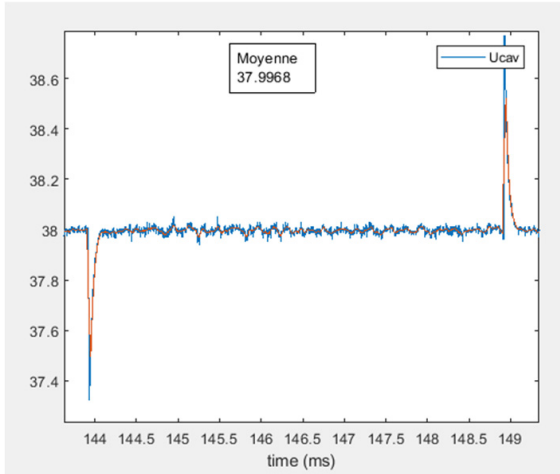


Figure 7: Voltage variation, closed loop.

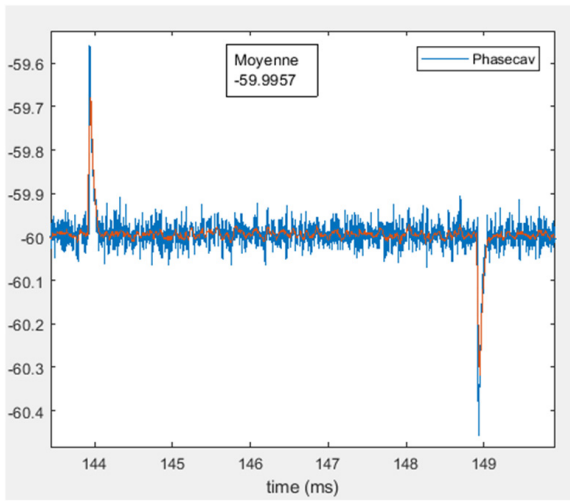


Figure 8: Phase variation, closed loop.

From those figures, the LLRF regulation time is then found to be about 100 µs, a satisfactory value for the LINAC. More important, the remaining voltage error is in this case about +/-1.8%, and far from the 1% acceptable limit when the cavity is phase tuned to the rebuncher mode,

Taking into account the Q_L of the cavity, very little margin should exist to improve the regulation time without introducing instabilities in the amplitude/phase feedback control.

Voltage and Phase Offset with the Rebuncher Phase

Figure 9 shows the measurement for the 2.2 mA beam current. We are varying the RFQ/ rebuncher phase from -180° to +180°. The rebuncher is set in open loop regulation to see the beam influence. The curves indicate the voltage and phase offset induced by the beam during the pulse. The maximum (in absolute value) voltage influence is when the phase offset is zero and the maximum phase influence is when the voltage offset is zero.

Content from this work may be used under the terms of the CC BY 3.0 licence (© 2018). Any distribution of this work must maintain attribution to the author(s), title of the work, publisher, and DOI.

ISBN: 978-3-95450-194-6 ISSN: 2226-0366 doi:10.18429/JACoW-LINAC2018-TUPO095

Content from this work may be used under the terms of the CC BY 3.0 licence (© 2018). Any distribution of this work must maintain attribution to the author(s), title of the work, publisher, and DOI.

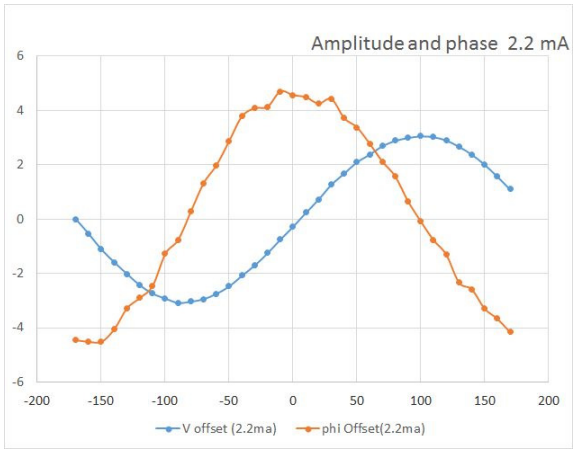


Figure 9: Voltage and phase variations, with the phase setting point of the rebuncher.

Measurements of the Voltage and Phase Offsets with Different Beam Currents

We can observe the proportionality of the voltage and phase deviation (in volts and degrees, see Figs. 10 and 11) with the beam intensity versus the tuning phase of the rebuncher. More the beam intensity is high more the voltage is high but the maximum influence depends on the phase set point. It's the same for the phase.

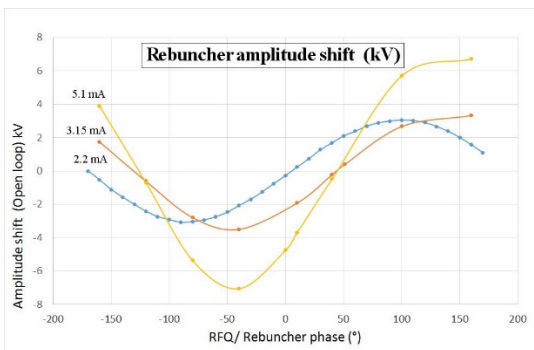


Figure 10: Voltage variations, with the phase setting point of the rebuncher, open loop.

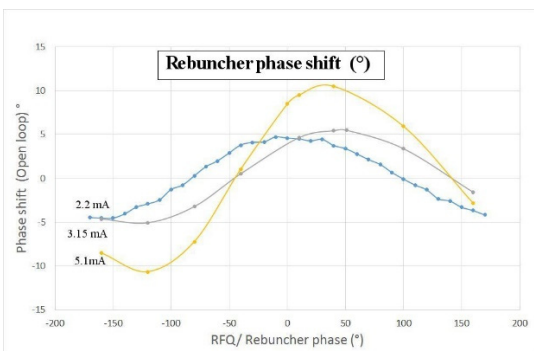


Figure 11: Phase variations, with the phase setting point of the rebuncher, open loop.

SIMULATIONS MATLAB

Many studies have been made on this subject in many laboratories like CEA-Saclay [2] and CERN [3]. The RLC model circuit (Resistance Inductance and Capacitance) of a cavity with a RF generator and Current beam generator describes the system.

The differential equation can be explicated into two differential equations with real and imaginary parts, see Eqs. (1-3):

$$\frac{d^2V}{dt2} + \frac{1}{R_L C}\frac{dV}{dt} + \frac{1}{LC}V(t) = \frac{1}{C}\frac{dI}{dt} \quad (1)$$

$$\frac{dV_{re}}{dt} = -\frac{\omega_0}{2Q_L}V_{re} + (\omega - \omega_0)V_{im} + R_L\frac{\omega_0}{2Q_L}I_{re} \quad (2)$$

$$\frac{dV_{im}}{dt} = -\frac{\omega_0}{2Q_L}V_{im} - (\omega - \omega_0)V_{re} + R_L\frac{\omega_0}{2Q_L}I_{im} \quad (3)$$

Using our rebuncher description we can simulate the beam effect on the cavity RF parameters. As the rebuncher is not a superconducting cavity, we are always in the cavity band pass (Fig. 12).

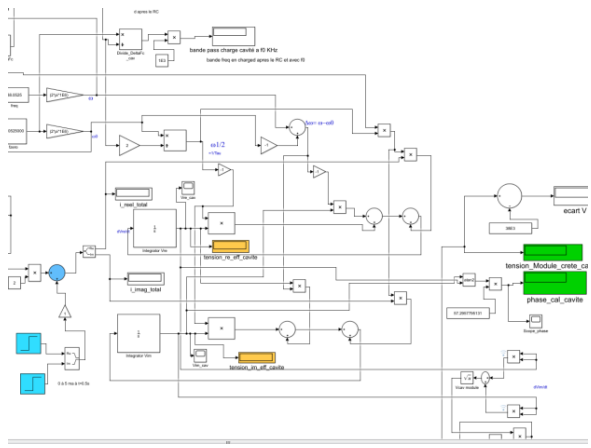


Figure 12: Extract of Matlab Simulink simulation diagram.

Comparing the curves of Fig. 9 (measurement) and Fig. 13 (simulation): The offset seen in voltage is about 5 to 6 kV at his maximum both in measures and simulation and the offset in phase is between 3.8° to 5° at his maximum point.

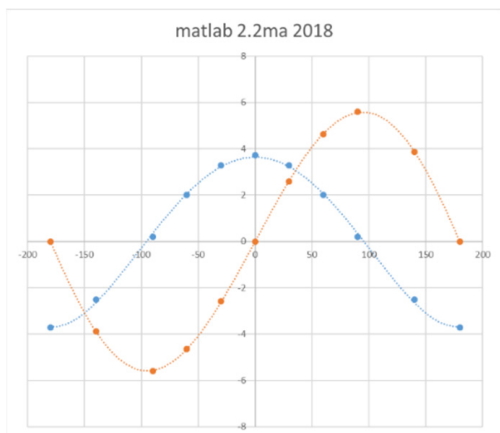


Figure 13: Matlab results.

ISBN: 978-3-95450-194-6 ISSN: 2226-0366 doi:10.18429/JACoW-LINAC2018-TUPO095

CONCLUSION

The comparison between experiments and Matlab calculation are quite in accordance. More precise parameters like the shunt resistance should give better results for the simulation model and find the measured values. An interesting and long work to compare model and measurement is to come.

The next steps are to measure and to take into accounts the effects of the beam, on our cryo-cavities, with control loops, detuning effects and so on, in the aim to tune the beam, up to the experimental areas. The behavior of the phase and voltage in the cavities with the beam will help strongly to find the best solution to apply the right regulation at the good instant, and so to tune the beam in all situations to the end of the Linac.

REFERENCES

[1] R. Ferdinand *et al.*, "SPIRAL2 Injector commissioning", presented at LINAC'18, Beijing, China, Sep 2018, paper THPO047.

[2] O. Piquet, M. Luong, "Modelling and simulation of the RF system for SPIRAL2", in *Proc. PAC'09*, Vancouver, BC, Canada, May 2009, paper WE5PFP070, pp. 2168-2170.

[3] M. Hernande, W. Hofle, CEA team, O. Piquet, J. Tuckmandel, D. Valuch, G. Kotzian, "Progress Report on Simulink Modelling of RF Cavity Control for SPL Extension to LINAC4", Geneva, June 2010.

Content from this work may be used under the terms of the CC BY 3.0 licence (© 2018). Any distribution of this work must maintain attribution to the author(s), title of the work, publisher, and DOI.

ISBN: 978-3-95450-194-6 ISSN: 2226-0366 doi:10.18429/JACoW-LINAC2018-TUPO097

DESIGN OF C-BAND ELECTRON LINEAR ACCELERATOR FOR A COMPLEX OF RADIATION THERAPY*

L. Ovchinnikova†[1], V.I. Shvedunov[1], Skobeltsyn Institute of Nuclear Physics,
Lomonosov Moscow State University (SINP MSU), 119991 Moscow, Russia
[1]also at Laboratory of Electron Accelerators MSU Ltd (LEA MSU), 119234 Moscow, Russia

Abstract

The report presents the design of the linear electron accelerator for a complex of radiation therapy. The three-electrode electron gun and C-band accelerating structure are optimised to produce a therapeutic electron beam with an energy of 6 MeV and a dose rate of 10 Gy/min and a beam with an energy of 2.5 MeV to obtain a portal image. The beam size at the bremsstrahlung target in both modes does not exceed 2 mm. The total length of the accelerating system with the electron gun does not exceed 330 mm. The accelerating structure is fed by RF power from a multibeam klystron at a frequency of 5,712 MHz with a maximum pulsed power of 3.5 MW.

INTRODUCTION

This work describes the results of beam dynamics calculation in the linear accelerator with the maximum energy of 6 MeV, intended for the complex of radiation therapy KLT6 [1].

The following requirements are specified for the linear accelerator KLT6:

- Accelerator length, i.e. distance from the bremsstrahlung target to the radiation shielding exterior part: maximum 350 mm.
- Minimum lateral dimensions of the accelerating structure to reduce the radiation shielding weight.
- Sequential operation at two values of the accelerated electron beam energy: 6 MeV in the therapeutic dose delivery mode and 2.5 MeV in the portal image acquisition mode.
- Maximum dose rate at the axis at the distance of 1 m from the bremsstrahlung target without a flattening filter with the energy of 6 MeV in the therapeutic dose delivery mode: at least 10 Gy/min.
- Electron beam diameter at the bremsstrahlung target: maximum 2 mm at half height of charge distribution.

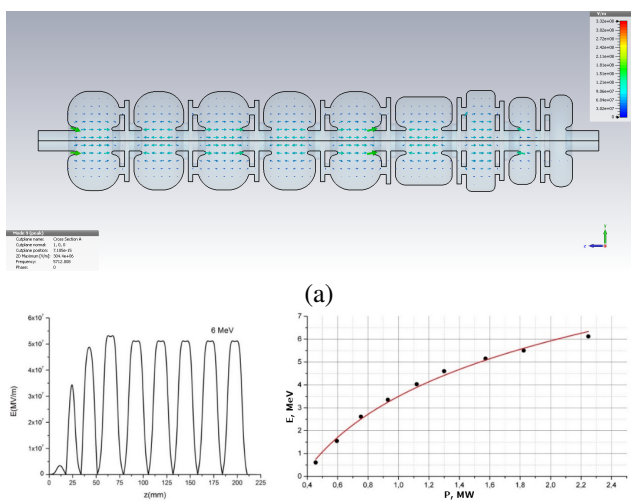
The accelerator, we are developing, differs from those used in similar complexes by a possibility to switch energy of the accelerated electron beam within a broad band, as well as by small longitudinal and lateral dimensions of the accelerating structure.

In order to achieve the declared characteristics of KLT6, we have selected a 5-cm wavelength band of the accelerating field (C-band). As for a combination of a number of characteristic of the accelerating structures (in particular, value of the effective shunt impedance, maximum accelerating field strength, diameter of the beam hole, overall dimensions), the C-band is the most appropriate for the compact electron accelerators with a relatively low average accelerated beam power (no more than several kilowatts).

We plan to use as an RF source the multi-beam klystron KIU-273 with reversed permanent magnet focusing, operating at 5,712 MHz with maximum pulsed power 3.5 MW [2].

PARAMETERS OF THE ACCELERATING STRUCTURE

The basis of the accelerator is a bi-periodic accelerating structure with on-axis coupled cells, operating at the frequency of 5,712 MHz in the standing-wave mode, optimised for operation in a broad band of energies of the accelerating beam. The structure was developed earlier by Laboratory of Electron Accelerators MSU Ltd (LEA MSU) for the accelerator of the mobile cargo inspection system [3]. The distributions of the electric field of operating mode within the structure volume and along its axis are shown in Fig. 1(a) and 1(b), respectively.



(a) (b) (c)

Figure 1: (a) Geometry of the accelerating structure with operating mode electric field distribution. (b) Distribution of the electric field along the axis. (c) Relationship between the output beam energy and the pulsed RF power loss in cavities walls.

* This material is based upon work supported by the Ministry of Education and Science of the Russian Federation, under Grant Agreement No. 14.582.21.0011, Grant Agreement Unique ID RFMEFI58217X0011.
† lub.ovch@yandex.ru

Content from this work may be used under the terms of the CC BY 3.0 licence (© 2018). Any distribution of this work must maintain attribution to the author(s), title of the work, publisher, and DOI.

ISBN: 978-3-95450-194-6 ISSN: 2226-0366 doi:10.18429/JACoW-LINAC2018-TUPO097

The initial part of the accelerating structure was optimised in order to ensure a longitudinal and transverse beam focusing. The accelerated beam energy is regulated by changing the level of RF power delivered to the accelerating structure. With at least a double change in the accelerated beam power, the value of the current capture efficiency of the electron gun is at least 50% and the focal spot size at the bremsstrahlung target does not exceed 2 mm at half height of current distribution. The length of the accelerating structure, including the initial part, is 210 mm. The maximum electric field strength along the axis for the energy of 6 MeV exceeds 50 MV/m and the maximum field strength at the inner surface reaches 170 MV/m. Figure 1(c) shows calculated relationship between the accelerated beam energy and the pulsed RF power loss in the walls. To obtain the energy of 6 MeV, the RF power losses shall be about 2.3 MW; the energy of 2.5 MeV is reached with the RF losses of about 0.8 MW.

The prototype of this accelerator [3] is designed for generation of the maximum dose rate of bremsstrahlung radiation at the axis at the distance of 1 m from the target $D = 0.6$ Gy/min with the duty-off factor $Q = 840$. For the KLT6 project, the dose rate should be increased almost by 20 times with the same duty-off factor.

The pulse current of the accelerated beam required for generation of the specified dose rate may be evaluated based on the empirical formula for the dose rate of bremsstrahlung radiation at an angle of 0° at a distance of 1 m from the bremsstrahlung target [4]:

$$D \approx 0.33 E^3 I_{pulse}/Q \text{ (Gy/min)},$$

where E is an energy of the electron beam at the bremsstrahlung target, MeV; I_{pulse} is a pulse current of the beam, mA. For the values $E = 6$ MeV, $Q = 840$, $D = 10$ Gy/min, we obtain $I_{pulse} \approx 120$ mA. This value of the accelerated beam current can be obtained at the injection current from the electron gun $I_{gun} \approx 250 - 300$ mA.

ELECTRON GUN

To generate the designed dose rate of 10 Gy/min with the energy of 6 MeV and the beam spot size at the bremsstrahlung target of maximum 2 mm, the geometry of the three-electrode electron gun has been optimised. The calculations have been made using the CST code [5].

The design of the electron gun optimised for KLT6 is shown in Fig. 2(a). A cathode having the diameter of 4 mm and the sphere radius of 5 mm and a flat control electrode are used in the gun. Figure 2(b, c) show, respectively, the beam current and the RMS radius at the enterence to the accelerating structure as function of the control electrode voltage. The current value, needed to generate the dose rate of 10 Gy/min, is reached at the control electrode voltage relative to the cathode of less than 3 kV. At the enterence to the accelerating structure, the beam has the RMS radius of no more than 0.6 mm and the moderate divergence, which should ensure its acceleration with low loss in the beam channel of 8 mm in diameter.

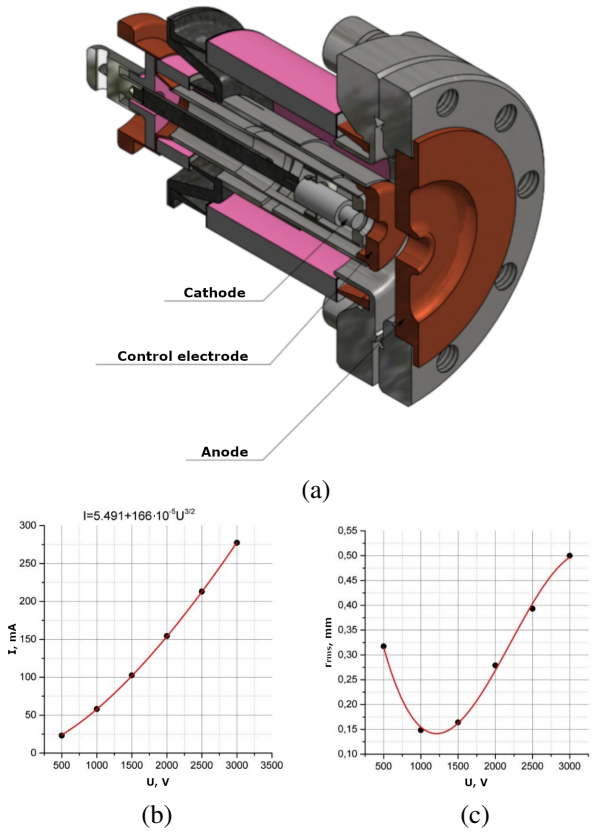


Figure 2: (a) Design of the electron gun of the accelerator for KLT6. (b) Beam current. (c) RMS radius at the enterence to the accelerating structure as function of the control electrode voltage.

BEAM DYNAMICS IN THE ACCELERATING STRUCTURE

The beam dynamics in the accelerating structure with the electron gun described in the previous section has been also calculated using the CST code [5]. Figure 3 shows calculated beam spots, histograms of current transverse distribution, and energy spectra at the bremsstrahlung target for the accelerated beam energies of 6 MeV and 2.5 MeV. The main results of calculations are summarised in Table 1.

Table 1: Main Results of Beam Dynamics Calculation for the Energies of 6 MeV and 2.5 MeV.

Parameter	6 MeV	2.5 MeV
Dose rate, Gy/min	10.5	0.37
Current of the gun, mA	245	245
Accelerated current, mA	150	124
Capture efficiency, %	60	50
RMS radius of the beam, mm	0.7	0.84
RMS divergence, mrad	8.2	29
Energy spectrum width, keV	100	500
RF loss in walls, MW	2.3	0.8
Beam power, MW	0.9	0.25

Content from this work may be used under the terms of the CC BY 3.0 licence (© 2018). Any distribution of this work must maintain attribution to the author(s), title of the work, publisher, and DOI.

ISBN: 978-3-95450-194-6 ISSN: 2226-0366 doi:10.18429/JACoW-LINAC2018-TUPO097

Content from this work may be used under the terms of the CC BY 3.0 licence (© 2018). Any distribution of this work must maintain attribution to the author(s), title of the work, publisher, and DOI.

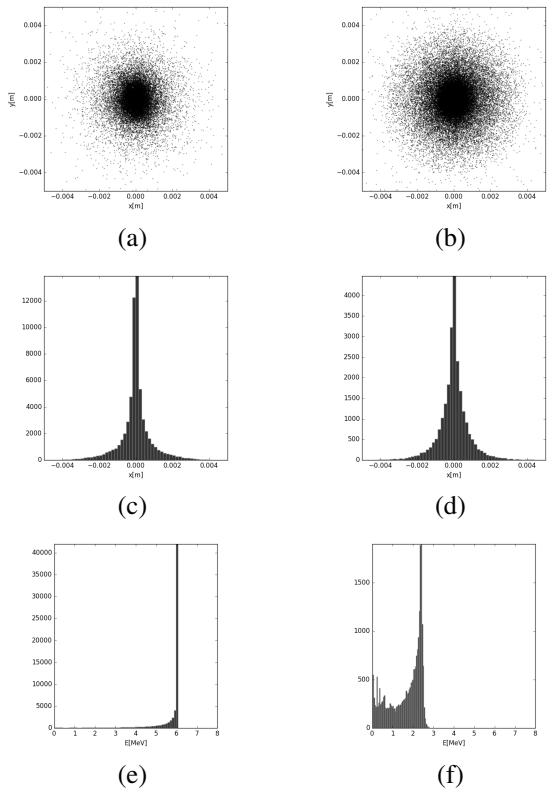


Figure 3: Beam spots (a, b), histograms of current transverse distribution (c, d), energy spectra of the beam (e, f) at the bremsstrahlung target for the energies of 6 MeV (left column) and 2.5 MeV (right column).

As it follows from the calculations, the necessary dose rate for both energies, calculated taking into consideration the energy spectrum of accelerated beam, may be generated with the same voltage at the control electrode of about 3 kV, which ensures the gun current of 245 mA. If necessary, the dose rate may be regulated by changing the duty-off factor by means of regulation of beam current pulse duration or pulse repetition rate.

CONCLUSION

The calculations of beam dynamics in the C-band electron accelerator for the complex of radiation therapy KLT6, intended for the generation of bremsstrahlung radiation with the beam energy switched over between the values of 2.5 MeV and 6 MeV for procedures of stereotactic and 3D conformal radiation therapy, have been made. The calculation data have been used for development of the accelerator design.

ACKNOWLEDGEMENTS

This material is based upon work supported by the Ministry of Education and Science of the Russian Federation, under Grant Agreement No. 14.582.21.0011, Grant Agreement Unique ID RFMEFI58217X0011.

The authors thank N.V. Shvedunov for developing the design of the electron gun and accelerating structure; A.S. Simonov for helpful discussions and advice.

The authors are also grateful professor of the Moscow State University B.S. Ishkhanov and academician of the Russian Academy of Sciences V.P. Smirnov for project support.

REFERENCES

[1] Grant Agreement between the Ministry of Education and Science of the Russian Federation and JSC NIITFA, “Creation and transfer for clinical studies of a sample of an complex of radiation therapy on the base of 6 MeV accelerator and cone-beam tomograph”, Grant Agreement No. 14.582.21.0011, Grant Agreement Unique ID RFMEFI58217X0011, 2017.10.03.

[2] JSC NPP "TORIY", https://www.toriy.ru

[3] “Electron accelerator of the C-band for the mobile inspection complex UELR-6-0,2-D-0,6-1, TU 6912-001-17697883-2017”, Moscow, 2017.

[4] W.P. Swanson, “Radiological Safety Aspects of the Operation of Electron Linear Accelerators”, *IAEA, Technical Reports Series*, N. 188; https://www-pub.iaea.org/MTCD/publications/PDF/trs188_web.pdf, ISBN 92-0-125179-3, 1979

[5] Computer Simulation Technology, https://www.cst.com

ISBN: 978-3-95450-194-6 ISSN: 2226-0366 doi:10.18429/JACoW-LINAC2018-TUPO098

PROOF-OF-PRINCIPLE TESTS FOR SLIT-SCAN-BASED SLICE EMITTANCE MEASUREMENTS AT PITZ

R. Niemczyk*, H. Huck†, P. Boonpornprasert, Y. Chen, J. Good, M. Gross, I. Isaev, D. Kalantaryan, C. Koschitzki, M. Krasilnikov, X. Li, O. Lishilin, G. Loisch, D. Melkumyan, A. Oppelt, H. Qian, Y. Renier, C. Saisa-ard‡, F. Stephan, Q. Zhao§, DESY, 15738 Zeuthen, Germany
W. Hillert, University Hamburg, 22761 Hamburg, Germany

Abstract

Transverse slice emittance is one of the most important properties of high-brightness electron beams for free-electron lasers (FELs). The photo injector test facility at DESY in Zeuthen (PITZ) develops high-brightness electron sources for modern FELs. With a 23 MeV, 1 nC beam at PITZ the experimental slice emittance characterization with the quadrupole scan technique is complicated by strong space charge effects. Combining the slit scan technique with a transverse deflecting cavity (TDS) allows for time-resolved emittance measurements of such a space-charge-dominated beam. The first proof-of-principle results of slice emittance measurements at PITZ based on the 'TDS + slit scan'-technique are presented in this paper.

INTRODUCTION

At the Photo Injector Test facility at DESY in Zeuthen (PITZ) electron guns are developed and optimized for superconducting LINAC-based free-electron lasers (FELs) like FLASH and the European XFEL [1]. Besides gun development, plasma wakefield acceleration (PWFA) [2], accelerator-based THz generation [3] and electron diffraction [4] are also investigated at PITZ.

For FELs, emittance is one of the key parameters for the gain length [5]. Here, the properties of the central slices, i.e., the slices with the highest charges are important, since these slices will rather contribute to lasing than the low-charged head and tail of the bunch [6]. This motivates optimization of the photoinjector not only for projected, but also for slice emittance, especially since simulation results show that the optimum photoinjector setting for both might be different [7]. While a satisfying technique to measure slice emittance at intermediate electron energies exists [6], measurements of the slice emittance at low energies are heavily complicated by space charge forces. These lead to a deviation between the actual beam transport and the beam transport suggested by algorithms [7]. At PITZ, the standard technique to measure the projected emittance is the slit scan [8–10]. The information of the transverse slit position, together with the beamlet size, allows to reconstruct the transverse phase space, so that the normalized emittance can be calculated via

$$\epsilon_{n,x} = \beta\gamma\sqrt{\langle x^2\rangle\langle x'^2\rangle - \langle xx'\rangle^2}, \quad (1)$$

where $\beta = v/c$, with v the electron velocity, c the speed of light, γ the Lorentz factor and $\langle x^2\rangle$, $\langle x'^2\rangle$ and $\langle xx'\rangle$ the second-order beam moments. Employing an rf deflector (TDS) allows the measurement of the slice emittance. High-charge beams with low momenta are observed at photoinjector test facilities and energy recovery LINACs [11, 12], opening the demand for space-charge-resistive slice emittance diagnostics.

MEASUREMENT SET-UP

An overview of the PITZ beamline is given in Fig. 1. The electrons are generated with an UV laser at a Cs_2Te photocathode inside the rf gun, which accelerates the electrons to ~6 MeV. Up to 600 electron bunches are generated with a spacing of 1 µs inside a bunch train and a bunch train repetition rate of 10 Hz [1]. A booster further accelerates the electrons to an energy of ~23 MeV. A normalized emittance of the electron beam down to 0.7 µm for bunches with 1 nC has been obtained [1].

The PITZ beamline is equipped with three emittance measurement system (EMSY) stations, at which a slit mask is located. The mask has slits with 10 µm and 50 µm opening, while only the 10 µm-wide slit is used for measurement of the projected emittance at high charge [13]. During the here presented measurement the 50 µm-wide slit has been used to get a high signal-to-noise ration for the streaked beam. Two EMSY stations are located upstream the TDS, while the third one is upstream the dispersive section HEDA2. For the first slice emittance measurements the second EMSY station has been chosen as slit position to minimize the distance

* raffael.niemczyk@desy.de
† holger.huck@desy.de
‡ On leave from Chiang Mai University, Chiang Mai, Thailand
§ On leave from IMP/CAS, Lanzhou, China

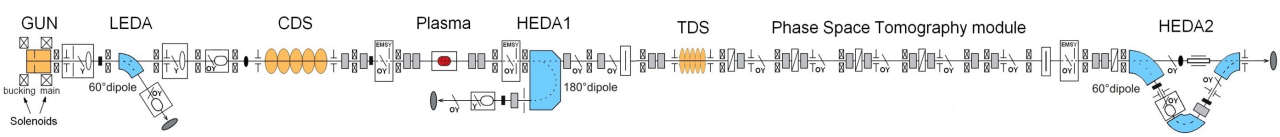


Figure 1: Schematic of the PITZ beamline. The electrons travel from left to right. The plasma cell was not mounted during the slice emittance measurement.

Content from this work may be used under the terms of the CC BY 3.0 licence (© 2018). Any distribution of this work must maintain attribution to the author(s), title of the work, publisher, and DOI.

ISBN: 978-3-95450-194-6 ISSN: 2226-0366 doi:10.18429/JACoW-LINAC2018-TUPO098

Content from this work may be used under the terms of the CC BY 3.0 licence (© 2018). Any distribution of this work must maintain attribution to the author(s), title of the work, publisher, and DOI.

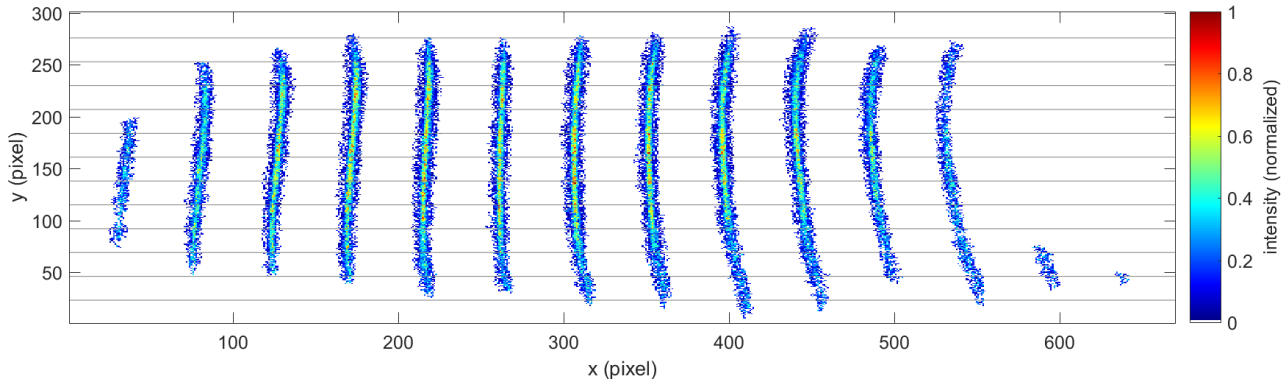


Figure 2: Streaked beamlet images on the observation screen after noise cut. The streak is in the vertical direction y, hence the beamlet images are sliced in the vertical plane. From the horizontal profile of each slice the phase space is reconstructed. The beamlet images have been shifted horizontally to not overlap.

Table 1: Longitudinal Position of Devices at the PITZ Beamline

Element	Long. Position (m)
Cathode surface	0
EMSY1	5.277
EMSY2	7.125
TDS centre	10.985
Observation screen	12.278
EMSY3	16.303

to the TDS where space charge forces act on the beamlet, see Table 1. The TDS streaks the electrons in the vertical plane to measure the slice emittance in the horizontal plane [7]. It has been developed by the Institute for Nuclear Research (INR RAS, Moscow, Russia) in collaboration with DESY [14]. The repetition rate of the TDS is 10 Hz, while the maximum rf pulse length is 3 µs, allowing to streak three consecutive electron bunches from each bunch train, i.e., sum up the signal from three bunches on each image. As observation screen, the first screen downstream the TDS has been chosen, an ytterbium aluminium garnet powder (YAG) screen.

The slice emittance measurement has been carried out with a bunch charge of 500 pC. The laser pulse had ~11 ps FWHM pulse length and a roughly Gaussian time profile. The estimated cathode gradient was 58.2 MV/m, the gun and booster phases were set for maximum acceleration. The FWHM electron bunch length was (14.1 ± 0.5) ps, measured with the TDS with a time resolution of 0.8 ps. For the slice emittance measurement presented here, 14 slit positions with 300 µm spacing have been used. Only a small number of slit positions was used since the data acquisition was not automatised yet.

RESULTS

Images of the streaked beamlets are given in Fig. 2. When projected onto the horizontal axis x, the phase space of the projected beam as well as the projected emittance can be calculated.

Projected Emittance

The phase space of the projected distribution is given in Fig. 3. The beam size obtained from the beamlet images $\sqrt{\langle x^2 \rangle}$ is typically smaller than the beam size σ_x measured with a scintillator screen at the slit position due to lower intensity at the outer slit positions. To account for this fact, at PITZ the scaled emittance

$$\epsilon_{\mathrm{n},x,\mathrm{scaled}} = \frac{\sigma_x}{\sqrt{\langle x^2 \rangle}} \epsilon_{\mathrm{n},x} \tag{2}$$

is used [1]. The unscaled, normalized emittance in the horizontal plane was measured to be 1.3 µm, while the scaled, normalized emittance was 2.3 µm. However, the unscaled projected emittance was measured to be 1.9 µm with the standard software. Besides the switched-off TDS, both methods differ in a different noise cut and the number of slit positions.

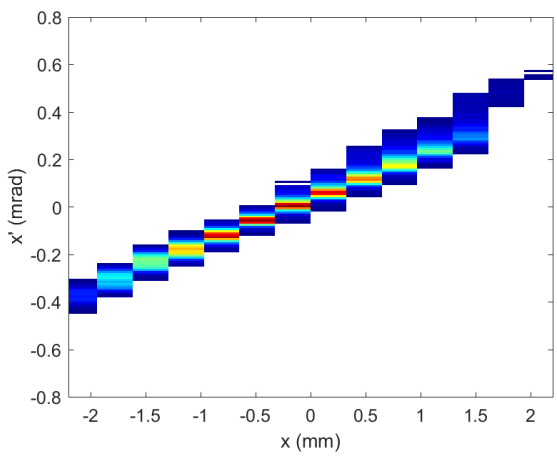


Figure 3: Phase space of the projected electron distribution in the horizontal plane. For the reconstruction of the projected phase space the images of the streaked beamlets have been projected onto the horizontal axis. The scaled, normalized emittance is 2.3 µm.

ISBN: 978-3-95450-194-6 ISSN: 2226-0366 doi:10.18429/JACoW-LINAC2018-TUPO098

For the slice emittance measurement only 14 slit positions have been used due to missing automation, while approx. 130 slit positions have been used for the measurement of the projected emittance. Additionally, the signal-to-noise ratio is smaller during the slice emittance measurements since the charge is distributed on a larger screen area. The low intensity on the observation screen due to the rf streak and the slit mask, especially at the outer slit positions, lead to a big scaling factor. The measured emittance is much higher than the usually achieved values for this charge at PITZ. This is due to the fact that the photoinjector was not optimized for minimal emittance for this proof-of-principle experiments, e.g., the laser shape was Gaussian and too short in time, while a longitudinal flattop laser profile with ~21 ps FWHM yields a smaller emittance. Furthermore, the lowest emittance is measured at EMSY1 [1]. Also, the focussing of the electron beam, as well as the laser beam size on the cathode were not optimized. In addition to the slice emittance, the projected emittance was measured with the standard software while the TDS was off. The measured scaled, projected emittance was 2.3 µm which agrees well with the calculated parameter of the projected emittance from the slice emittance measurement.

Slice Emittance

The scaled and unscaled emittance along the longitudinal bunch axis is given in Fig. 4. The normalized, unscaled emittance for the centre slice, i.e., slice number 0, is 0.76 µm, while the scaled emittance for this slice is 1.3 µm. The scaling of the slice emittance is done similarly to the scaling of the projected emittance via

$$\epsilon_{i,\,\mathrm{scaled}} = \frac{\sigma_{x,i}}{\sqrt{\langle x^2\rangle_i}}\epsilon_{\mathrm{n},x}, \tag{3}$$

where $\sqrt{\langle x^2\rangle_i}$ is the beam size of the slice i, obtained from the beamlet images and $\sigma_{x,i}$ the beam size of the slice i at the slit position. However, this beam size can not be measured. The slice beam size $\sigma_{x,i}$ is approximated with σ_x assuming the same initial beam size for all slices. The emittance is almost flat for most of the slices, just at both ends the unscaled emittance drops to smaller values. This is probably due to the low charge at the ends of the almost Gaussian distribution. The lower-charged slices contribute less to the projected emittance than the bunch centre. Moreover, the mismatch of the slices contributes to a higher projected emittance. At PITZ, no specific design optics exists for slice emittance measurements. Therefore, the slice mismatch, shown in Fig. 4, is calculated via

$$M_i = \frac{1}{2}\left(\beta_i\gamma_\mathrm{P} - 2\alpha_i\alpha_\mathrm{P} + \gamma_i\beta_\mathrm{P}\right), \tag{4}$$

where α_P, β_P and γ_P are the Twiss parameters of the projected distribution and α_i, β_i and γ_i the Twiss parameters of slice i correspondingly. The phase space of the centre slice is given in Fig. 5. In comparison to the phase space of the projected bunch a smaller width was measured.

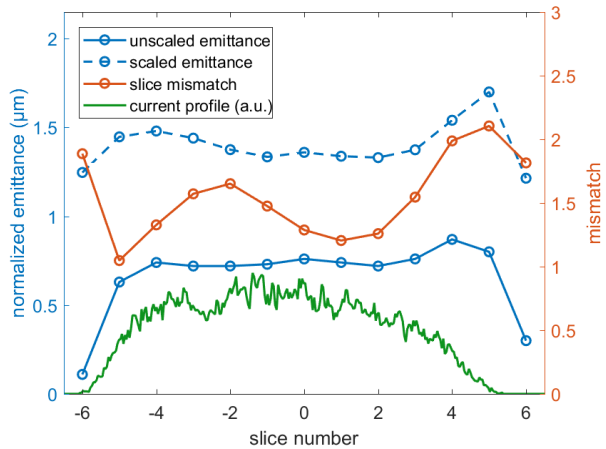


Figure 4: Evolution of the scaled and unscaled emittance along the longitudinal bunch axis, slice mismatch and bunch current profile. The slice emittance is scaled according to Eq. (3), the mismatch is calculated via Eq. (4).

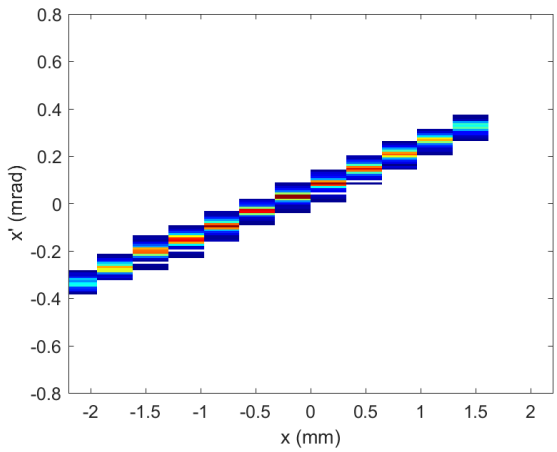


Figure 5: Phase space of the central slice, i.e., slice 0 in Fig. 4, in the horizontal plane. In comparison to the projected phase space, the slice phase space has a smaller width. The scaled, normalized slice emittance is 1.3 µm.

CONCLUSION

This paper shows the first successful proof-of-principle slice emittance measurement done at PITZ, by means of a single-slit scan and usage of a transverse deflecting cavity (TDS). The scaled central slice emittance was measured to be 1.3 µm, while the unscaled value was 0.76 µm. The scaled, projected emittance, calculated from the streaked beamlets is 2.3 µm. The same value was measured with the unstreaked beam and the standard software at PITZ.

High-intensity screens have been installed to solve low-intensity problems when the beam is streaked [15] and the data taking has been automated. Next steps are the comparison of measurements with different number of slit positions, slit widths, EMSY stations, etc. Then the systematic error of the slice emittance measurement has to be determined before the beam dynamics can be investigated.

Content from this work may be used under the terms of the CC BY 3.0 licence (© 2018). Any distribution of this work must maintain attribution to the author(s), title of the work, publisher, and DOI.

ISBN: 978-3-95450-194-6 ISSN: 2226-0366 doi:10.18429/JACoW-LINAC2018-TUPO098

Content from this work may be used under the terms of the CC BY 3.0 licence (© 2018). Any distribution of this work must maintain attribution to the author(s), title of the work, publisher, and DOI.

REFERENCES

[1] M. Krasilnikov *et al.*, "Experimentally minimized beam emittance from an L-band photoinjector", *Phys. Rev. ST Accel. Beams*, vol. 15, p. 100701, 2012.

[2] M. Gross *et al.*, "Observation of the Self-Modulation Instability via Time-Resolved Measurements", *Phys. Rev. Lett.*, vol. 120, p. 144802, 2018.

[3] P. Boonpornprasert *et al.*, "Calculations for a THz SASE FEL based on the measured Electron Beam Parameters at PITZ", in *Proc. FEL'17*, Santa Fe, NM, USA, Aug. 2017, pp. 419–421. https://doi.org/10.18429/JACoW-FEL2017-WEP004

[4] H. Qian *et al.*, "Investigation of High Repetition Rate Femtosecond Electron Diffraction at PITZ", in *Proc. IPAC'17*, Copenhagen, Denmark, May 2017, p. 3727–3729. https://doi.org/10.18429/JACoW-IPAC2017-THPAB017

[5] E. J. Jaeschke *et al.*, "Synchrotron Light Sources and Free-Electron Lasers", Springer Reference, p. 155, 2016.

[6] M. Yan, "Online diagnostics of time-resolved electron beam properties with femtosecond resolution for X-ray FELs", dissertation, Universität Hamburg, Germany, 2015.

[7] H. Huck *et al.*, "Progress on the PITZ TDS", in *Proc. IBIC'16*, Barcelona, Spain, Sep. 2016, pp. 744–747. https://doi.org/10.18429/JACoW-IBIC2016-WEPG47

[8] L. Staykov, "Characterization of the transverse phase space at the photo-injector test facility in DESY, Zeuthen site", dissertation, Universität Hamburg, Germany, 2008.

[9] G. Vashchenko, "Transverse phase space studies with the new CDS booster cavity at PITZ", dissertation, Universität Hamburg, Germany, 2013.

[10] V. Miltchev, "Investigations on the transverse phase space at a photo injector for minimized emittance", dissertation, Humboldt-Universität zu Berlin, Germany, 2006.

[11] J. Baehr, "Low energy high brilliance beam characterization", in *Proc. DIPAC'05*, Lyon, France, Jun. 2005, paper ITWA01, pp. 307-311.

[12] L. Merminga, "Energy Recovery LINACS", in *Proc. PAC'07*, Albuquerque, NM, USA, Jun. 2007, paper MOYKI03, pp. 22–26.

[13] L. Staykov, "Design Optimization of an Emittance Measurement System at PITZ", in *Proc. DIPAC'05*, Lyon, France, Jun. 2005, paper POT032, pp. 220–222.

[14] L. Kravchuk *et al.*, "Layout of the PITZ Transverse Deflecting System for Longitudinal Phase Space and Slice Emittance Measurements", in *Proc. LINAC'10*, Tsukuba, Japan, Sep. 2010, paper TUP011, p. 416.

[15] R. Niemczyk *et al.*, "Comparison of YAG screens and LYSO screens at PITZ", presented at IBIC'18, Shanghai, China, Sep. 2018, paper WEPB04.

ISBN: 978-3-95450-194-6 ISSN: 2226-0366 doi:10.18429/JACoW-LINAC2018-TUPO101

DESIGN OF PRACTICAL HSC TYPE INJECTOR FOR CANCER THERAPY

Chaochao Xing†, Liang Lu, Lei Yang[1], Tao He[1], Chenxing Li, Jia Li[1], Qianxu Xia[1], Zhichao Gao[1],
Institute of Modern Physics, Chinese Academy of Sciences, Lanzhou 730000, China
[1]also at University of Chinese Academy of Sciences, Beijing 100049, China

Abstract

We provided a compact linac injector, HSC (Hybrid single cavity), for cancer therapy. The HSC, operated in TE_{111} mode [1], consists of RFQ section and DTL section. This compact linac injector, running in frequency of 100 MHz, accelerates C^{6+} beams with 20 mA from 20keV/u up to 4 MeV/u [2]. The total length of HSC is designed less than 4 meters. We used RGQGen and PIMLOC to achieve the aims. More details will be given in the next parts.

INTRODUCTION

According to investigations, there are 6 people per minute suffering from cancer in china. Therefore, accelerators in medical applications have a great prospect. Unfortunately, the system of cancer therapy has a complex control system and huge injector. The factor resists the developments of accelerators in medical applications. The new type injector, HSC, has the ability to directly accelerate the high intensity C^{6+} ion beams. Compared with traditional types, HSC adopts DPIS (direct plasma injection scheme), which could easily supply enough C^{6+}ions to the linac. Secondly, RFQ section and DTL section share the operating system and feed system.

BEAM DYNAMICS

RFQ Design and DT Design

The section of RFQ, 4 rod IH type, was designed to accelerate C^{6+}ions to 0.6 MeV/u from 0.02 MeV/u. This RFQ section includes 90 cells. And the total length of RFQ is 1050 mm. The main parameters are listed in Fig. 1 and Table 1. Fig .2 gives the transmission efficiency, which almost over 95%, at last cell.

Table 1: The Main Parameters of the RFQ

Parameters	Value
Voltage	85 kV
B	7.1→9.76
m	1→2.11
ϕ	-90→-26 deg
Input energy	0.02 MeV/u
Output energy	0.6 MeV/u

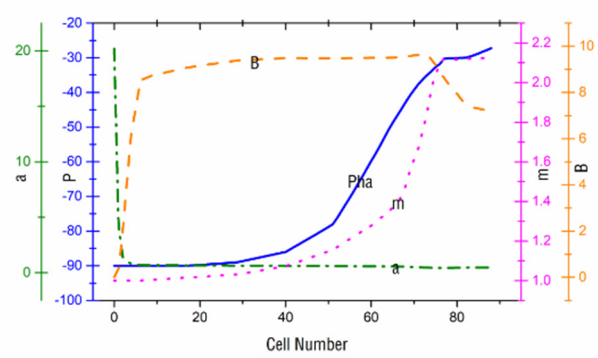


Figure 1: The dynamics parameters of RFQ design.

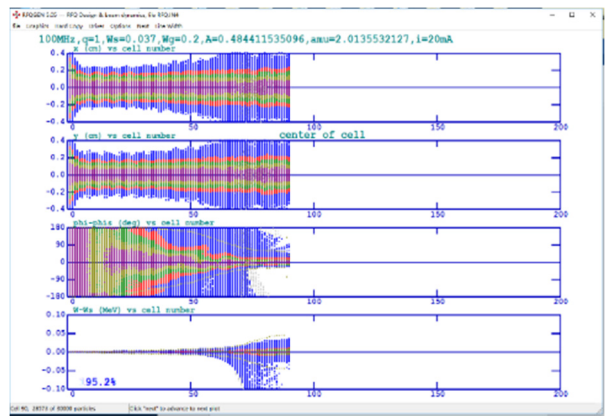


Figure 2: Transmission efficiency at last cell.

The output of RFQ are adopted convergent design for following DT injection. Therefore, the section of DT accelerates C^{6+}ions with 20 mA to 4 MeV/u from 0.6MeV/u. We used the PIMLOC to design the DT section. The most important theory in DT section is APF, Alternative Phase Focus. An APF linac is a modified version of usual drift tube linacs (DTL) and can achieve three-dimensional focusing without the installation of quadrupole lenses into the drift tubes. The phase in each gap was given in Fig. 3.

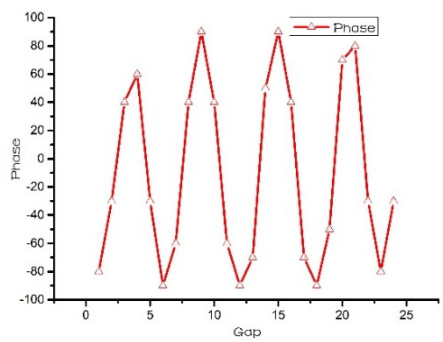


Figure 3: The phase in each gap.

†ccxing@impcas.ac.cn

Content from this work may be used under the terms of the CC BY 3.0 licence (© 2018). Any distribution of this work must maintain attribution to the author(s), title of the work, publisher, and DOI.

ISBN: 978-3-95450-194-6 ISSN: 2226-0366 doi:10.18429/JACoW-LINAC2018-TUPO101

Content from this work may be used under the terms of the CC BY 3.0 licence (© 2018). Any distribution of this work must maintain attribution to the author(s), title of the work, publisher, and DOI.

The more parameters, length of DT and Gap, were showed in Table 2.

Table 2: Main Parameters of DT Design for HSC Linac

Parameters	Value
Voltage	211 kV
Cell number	24
Length	1753 mm
Bore radius	13 mm
DT radius	30 mm
Phase injection	-112 deg
Input energy	0.6 MeV/u
Output energy	4 MeV/u

The number of particles is 10000. Tracing the particles, we could get the results of simulations. Figure 4 gives the transformation of beam envelope. The output at the end was gives in Fig. 5. Transmission efficiency is over 99%. But the acceleration efficiency is only 30%.

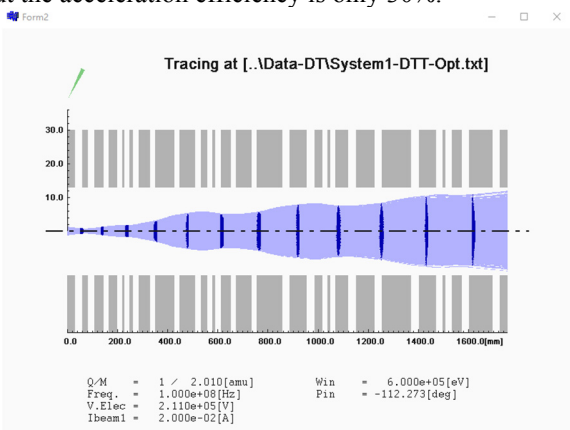


Figure 4: Beam envelope at z axis.

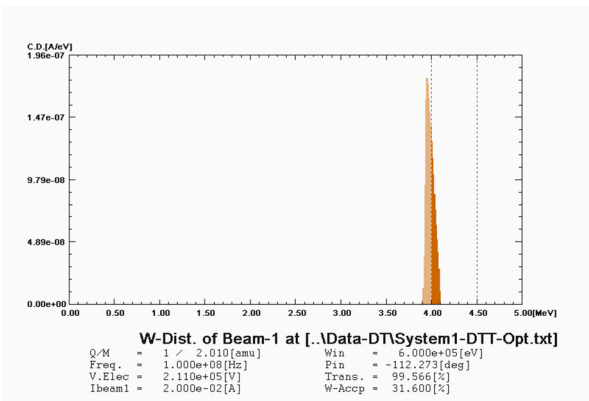


Figure 5: The energy distribution.

HSC Linac Basic Feature

Next, we used the PIMLOC to simulate the whole structure, both RFQ and DTL. The number of particles in HSC is 10000.We can change the length between RFQ and DTL, L RFQ-DTL, to get the results at the end. Table 3 gives the parameters in HSC. And Fig. 6 gives the distribution of electromagnetic fields between RFQ and DTL.

Table 3: The Parameters in HSC

Parameters	Value
Total length	3019 mm
L RFQ-DTL	59 mm
Rcavity(DTL)	280 mm
Rcavity(RFQ)	95 mm

Ordinarily, a MEBT was inserted between RFQ and DTL. On the contrary, the initial HSC model was only combined RFQ structure and DT structure.

According to results, shown as Fig. 6, we can know that the E field is focused in the connection parts of 4-rod and first DT. Beam in gap of rod and 1st DT will be subjected to strong accelerating force, and it should be considered that discharge could be led to high voltage and beam acceleration could be received negative influence by unbalance electric distribution.

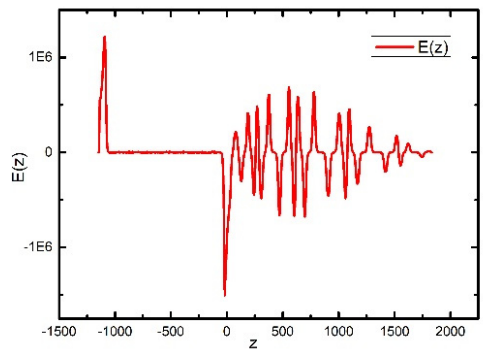


Figure 6: The distribution of E field along the beam direction.

Capacitance in RFQ part is much stronger than DT part. So we could consider that C in whole HSC linac is focused in RFQ section [3]. Therefore, RFQ section shows sensitive in the E field distribution.

For reducing this concentrated E field distribution, interface structure had been designed and discussed. Fig. 7 gives the outline of interface structure and E-field distribution in the different length of interface.

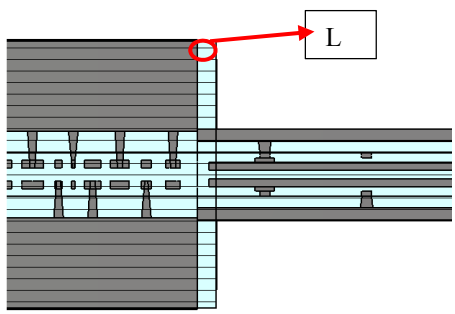
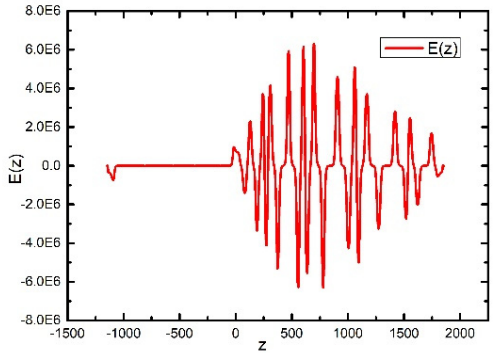


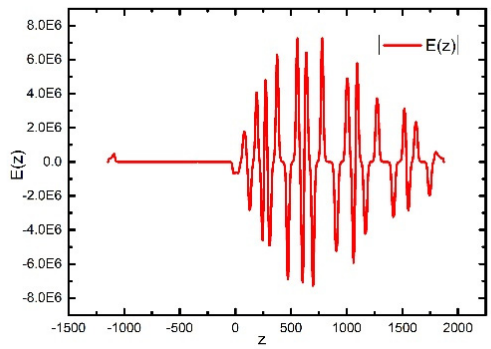
Figure 7: The interface structure and E-field.

When we change the length of L, as the Fig. 8 shown, we can modify the E-field between RFQ and DTL.

ISBN: 978-3-95450-194-6 ISSN: 2226-0366 doi:10.18429/JACoW-LINAC2018-TUPO101



(a)



(b)

Figure 8: (a) L=20, (b) L=40 and the axis E field distributions simulated by MW-S.

SUMMARIES AND FUTURE PLAN

We have studied a new HSC type linac which is a practical and efficient machine to accelerate high intense ion beam. We discussed the E matching designs for reducing the concentrated electric field distribution and investigated relation of meth and power & frequency.

In the next step, we will study multi-physical fields of HSC by ANSYS. The acceleration test will be operated in this November.

REFERENCES

[1] Thomas P Wangler, "RF Acceleration in Linacs", in *RF Accelerators*, pp. 32-52.

[2] L. Lu, T. Hattori, L. Shi, ",*et al.* Low power test of a hybrid single cavity linac", in *Proc. 5th Int. Particle Accelerator Conf. (IPAC'14)*, Dresden, Germany, Jun. 2014, paper THPME025, p. 3274.

[3] L. LU, T. Hattori, *et al.*, "Design and simulation of C^{6+} hybrid single cavity linac for cancer therapy with direct plasma injection scheme", *Nucl Instrum Methods Phys Res A*.

Content from this work may be used under the terms of the CC BY 3.0 licence (© 2018). Any distribution of this work must maintain attribution to the author(s), title of the work, publisher, and DOI.

ISBN: 978-3-95450-194-6 ISSN: 2226-0366 doi:10.18429/JACoW-LINAC2018-TUPO106

MATHEMATICAL PRINCIPLE AND NUMERICAL RECONSTRUCTION IN REAL SPACE MEASUREMENT WITH A ROTATING BPM*

Peiyong Jiang†, Yuan He, Zhijun Wang
Institute of Modern Physics, Chinese Academy of Sciences, Lanzhou, China

Abstract

It is difficult to measure beam profiles and monitor the beam during beam supply for high intensity high power accelerators. Based on the button pick-ups, the mathematical principle of a rotating BPM is proposed. SVD method is used to reconstruct the beam in x-y real space, and the basic parameters used in beam reconstruction are argued. The beam distribution in x-y real space is reconstructed well and compared to the reference beam. The beam reconstruction is sensitive to the electrode radius. The meshing and the grid numbers in the solution window have an import effect on the beam reconstruction.

INTRODUCTION

It is difficult to measure beam profiles for high intensity high power accelerators. The wire scanner system is often used to measure beam profiles [1]. However, the stable operation of wire scanners has much to do with beam power [2]. The beam current has to decrease below a power limit in CIADS project to protect the wire scanners, bringing the difference in x-y real space between the low intensity and the high intensity beams. Besides, the slit and Faraday cup are used to measure beam profiles.

The two methods are invasive diagnostics, which cannot be applied to the high power accelerators with the high requirement of continuity in operation such as CIADS project [3]. Meanwhile, owing to the high requirement of stability and security of CIADS, it is necessary to monitor the beam including the beam profiles dynamically and to adjust the machine parameters properly. Thus, there is a strong need to use a non-invasive beam diagnostic component to measure beam profiles during beam supply, based on which a rotating BPM is proposed mathematically.

BPM PRINCIPLE

BPM is widely used in accelerators to measure the beam orbit, beam phase and beam emittance [4,5,6]. Button pick-ups, shoe box pick-ups and stripline pick-up are the three common kinds of BPM [7]. Figure 1 shows the theory of button pick-ups. There are 4 electrodes in the top, bottom, left and right of the pipe respectively. The electrodes induct the current while a charged beam line pass through the pipe. Considering a beam with current I(r,ϕ) in a straight wire of infinite length in a polar coordinate system, the current density j(a,θ,r, ϕ) on the pipe boundary induced by the straight wire current and its mirror current is

$$j(a,\theta,r,\phi)=\frac{I(r,\phi)}{2\pi a}\frac{a^2-r^2}{a^2+r^2-2\cos(\phi-\theta)} \qquad (1)$$

where (a,θ) is an arbitrary point on the pipe boundary in a polar coordinate system , while a is the pipe radius and θ is the angle pointed to the point. (r,ϕ) is an arbitrary point in the pipe while r is the distance between the beam and the pipe center, and ϕ is the angle pointed to the beam.

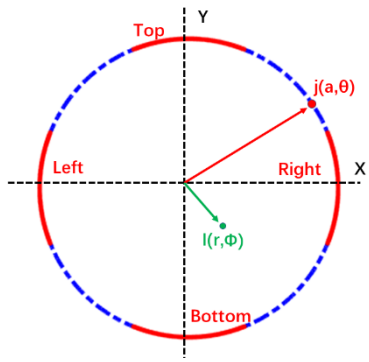


Figure 1: The theory of button pick-ups. The blue dashed circle is the pipe boundary. The red curves at top, bottom, left and right are the BPM electrodes respectively. I(r,ϕ) is the current of a straight wire of infinite length, and j(a,θ,r, ϕ) is the induced current at the point (a,θ) in a polar coordinate system.

As for a beam with a cross section, the total induced current J on the electrode with a flare angle β is an integral as follows:

$$J(a)=\int_{-\beta/2}^{\beta/2}\int\int j(a,\theta,r,\phi)drd\phi d\theta \qquad (2)$$

The integral J changes to be a product while beta is small:

$$J(a)=\beta\int\int j(a,\theta,r,\phi)drd\phi \qquad (3)$$

and the average induced current B is written as:

$$B(a)=\frac{J}{\beta}=\int\int j(a,\theta,r,\phi)drd\phi \qquad (4)$$

By substituting Eq.(1) into Eq.(4), the discrete form of Eq.(4) is obtained:

$$B=M\cdot I \qquad (5)$$

Where I and B are column vectors, and the lengths of I and B are corresponding to the number of straight wires of beam current and the number of BPM electrodes respectively. M is a matrix with

$$M_{b,i}=\frac{1}{2\pi a_b}\frac{{a_b}^2-{r_i}^2}{{a_b}^2+{r_i}^2-2\cos(\phi_i-\theta_b)} \qquad (6)$$

where b is the b[th] electrode, and the i is the i[th] straight wire of beam current.

RECONSTRUCTION

Mathematically, the reconstruction is to solve Eq.(5). However, the matrix is unknown in this equation. Thus during the solving, a solution window has to be assumed,

* Work supported by NSFC (Grant NO. 11605261)
† jiangpeiyong@impcas.ac.cn

Content from this work may be used under the terms of the CC BY 3.0 licence (© 2018). Any distribution of this work must maintain attribution to the author(s), title of the work, publisher, and DOI.

ISBN: 978-3-95450-194-6 ISSN: 2226-0366 doi:10.18429/JACoW-LINAC2018-TUPO106

and it changes during iteration. Figure 2 illustrates the solution window in a rotating BPM.

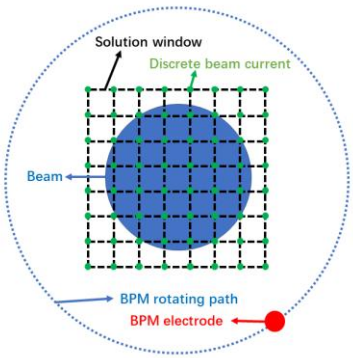


Figure 2: The solution window in a rotating BPM. The red point is the BPM electrode, and the blue dashed circle is the BPM rotating path. The blue disk is the beam which could be solved by being allocated to the green points. The black dashed mesh grids are the solution window, and the green points on the mesh grids are the discrete beam current.

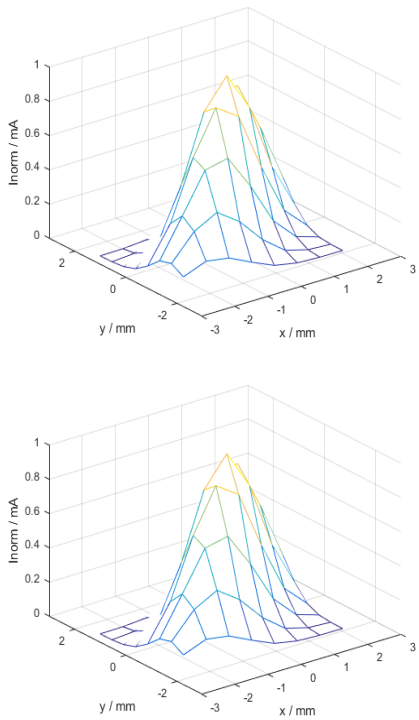


Figure 3: (a): Comparison between the reference beam distribution and the reconstruction beam distribution in X-Y real space. (a): Reference beam; (b): Reconstruction beam.

Given a solution window, M is known, and then the beam distribution on the window grids is solved. If the solved beam is in the solution window, the process finishes; Otherwise the solution window is reset and enters a iterative loop to update M.

The solving process of Eq. (5) is based on 'singular value decomposition' (SVD). The matrix M is decomposed as:

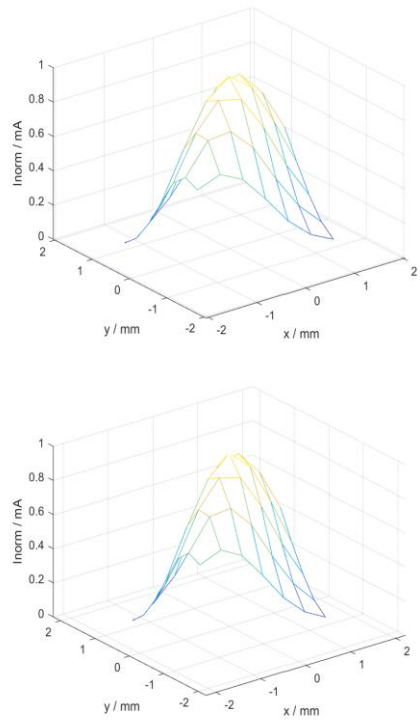
$$M = U \cdot S \cdot V^T \quad (7)$$

The beam current I on the grids is solved as:

$$I = V \cdot S^{-1} \cdot U^T \cdot B \quad (8)$$

The electrode radius has an important impact on the reconstruction. The beam expresses to be an electric monopole if the electrode radius is much larger than the beam size, and to be an electric multipole if the electrode radius is similar to the beam size. If the beam expresses as a monopole, the induced current along rotating path is smooth, and it is difficult to express the details of the beam. Figure 5 shows the reconstruction with the change of the electrode radius. The beam reconstruction makes no change while the electrode radius is restrained, and the beam reconstruction goes worse immediately if the electrode radius is up to a limit. The last plot in Figure 4 shows that the beam core which is further from the electrode goes worse firstly. Since the electrode radius plays an important role in beam reconstruction, the inner layer of BPM expresses more details than the outer layer.

The solution window is important in the reconstruction. Since the values of significance in S which corresponds to the high orders are approximate to 0, the effective rank of determinant M is smaller than the row number of the M. But it is difficult to calculate the effective rank, and to determine how smaller the value in S is that can be ignored in beam reconstruction. The grid numbers of the solution window should be smaller than the effective rank of determinant M. Figure 5 show the experiment on the beam reconstruction with increasing the grid numbers. In this case, the rotating angle is set as 1° .



Content from this work may be used under the terms of the CC BY 3.0 licence (© 2018). Any distribution of this work must maintain attribution to the author(s), title of the work, publisher, and DOI.

ISBN: 978-3-95450-194-6 ISSN: 2226-0366 doi:10.18429/JACoW-LINAC2018-TUPO106

Content from this work may be used under the terms of the CC BY 3.0 licence (© 2018). Any distribution of this work must maintain attribution to the author(s), title of the work, publisher, and DOI.

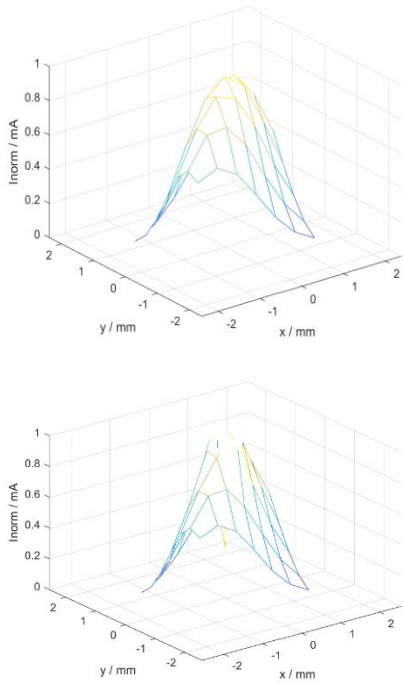
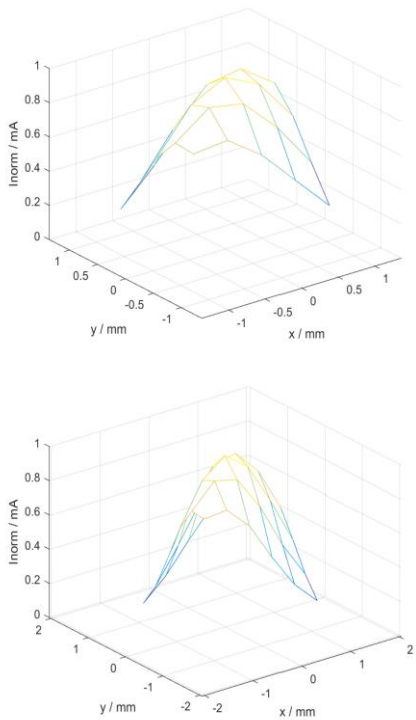


Figure 4: The comparison of the beam reconstruction in X-Y real space with the change of the electrode radius. (a): The electrode radius is 1.2 times the size of the beam; (b): The electrode radius is 1.3 times the size of the beam; (c): The electrode radius is 1.4 times the size of the beam; (d): The electrode radius is 1.5 times the size of the beam.



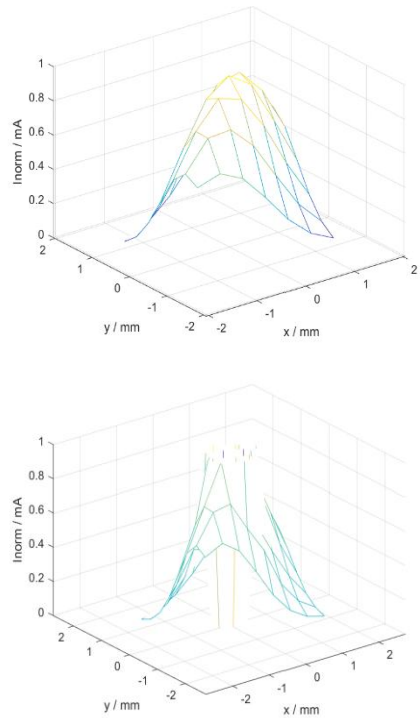


Figure 5: The comparison of the beam reconstruction in X-Y real space with the increase of grid numbers in solution window. (a): The grid numbers in solution window is (5,5); (b): The grid numbers in solution window is (6,6); (c): The grid numbers in solution window is (7,7); (d): The grid numbers in solution window is (8,8).

CONCLUSION

A rotating BPM is proposed while the mathematic principle and numerical solution are shown and the basic parameters are argued in this paper. We hope such idea will be used in X-Y real space beam measurement as a part of conventional beam diagnostic components in high intensity high power accelerators such as CIADS.

REFERENCES

[1] U. Hahn, N. V. Bargen, P. Castro, *et al.*, Wire scanner system for FLASH at DESY, NIMA 592 (2008) 189-196.

[2] T.Yang, S. Fu, T.Xu, *et al.*, Thermal analysis for wire scanners in the CSNS Linac, NIMA 760(2014)10-18.

[3] S.H. Liu, Z.J. Wang, H. Jia, *et al.*, Physics design of the CIADS 25 MeV demo facility, NIMA 843 (2017) 11-17.

[4] M. Month. Lecture notes in physics, frontiers of particle beams: observation, diagnosis and correction. Springer Berlin, 1989, p. 46-64.

[5] P. Strehl. Beam instrumentation and diagnostics. Springer Berlin, 2006.

[6] A. Jansson, Non-invasive measurement of emittance and optical parameters for high-brightness hadron beams in a synchrotron, CERN/PS, 2001-014 (OP).

[7] P. Forck, Lecture notes on beam instrumentation and diagnostics, JUAS, January-March 2011.

ISBN: 978-3-95450-194-6 ISSN: 2226-0366 doi:10.18429/JACoW-LINAC2018-TUPO109

ELECTRON CLOUD ESTIMATES FOR THE JEFFERSON LAB EIC

K. E. Deitrick*, V. S. Morozov, T. Satogata,
Thomas Jefferson National Accelerator Facility, Newport News, VA 23606, USA

Abstract

In this work, we present preliminary estimates for electron cloud build-up and saturation for the ion ring of the Jefferson Laboratory Electron-Ion Collider (JLEIC) currently under development. Using the baseline ion ring design, we study the impact of various operational parameters on the behavior of the electron cloud for a 100 GeV proton beam, including estimated tune shifts.

INTRODUCTION

The Jefferson Lab Electron-Ion Collider (JLEIC) [1], shown in Fig. 1, currently under development anticipates a high luminosity - which requires careful consideration of various collective effects, including electron cloud. The build up of the electron cloud in an ion machines is seeded by primary electrons, which typically originate from three causes - photoelectrons, ionization of residual gas, and electrons produced by collisions between the beam pipe and stray particles. This paper serves as a current evaluation of the severity of electron cloud in the current JLEIC design, using the simulation code PyECLOUD [2].

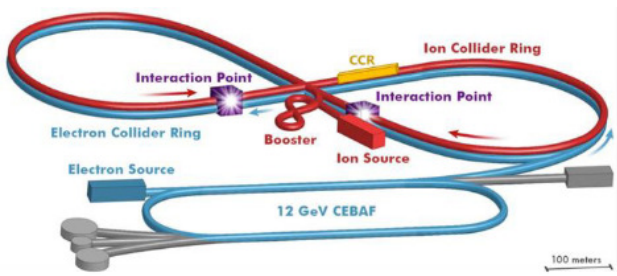


Figure 1: A conceptual layout of JLEIC.

SIMULATION SET UP

Using PyECLOUD, it is possible to observe the density of electrons over time for a given set of proton beam, vacuum, and secondary electron yield (SEY) parameters, which are given in Table 1. The SEY settings assume that the beam pipe is made from stainless steel [4]. These parameters were used to simulate the electron density for a number of cases, including dipoles, drifts, quadrupoles, and sextupoles. These cases are summarized in Table 2. For the quadrupoles and sextupoles, the highest field gradient outside of the interaction region (IR) magnets is used - these are not representative of the average field for these elements.

Table 1: Proton Beam and Vacuum Parameters Used in the simulations

Parameter	Symbol (Unit)	Value
Beam energy	E_b (GeV)	100
Circumference	C (m)	2230
Collision frequency	f_c (MHz)	476
Beam pipe cross-section	-	Circular [3]
Beam pipe radius	r_b (mm)	40 [3]
Number of bunches per train	K_B	1856
Bunch spacing	s_b (ns)	2.1
Bunch population	N_p (10^{10})	0.98
Bunch length	σ_l (cm)	1
Bunch profile	-	Gaussian
Empty bunches between trains	-	126
Normalized emittance	$\epsilon_x^N, \epsilon_y^N$ (μm-rad)	0.5, 0.1
Residual gas pressure	P (nTorr)	5
Temperature	T (K)	4.5
Peak SEY	$\delta_{max} \equiv \delta(E_{max})$	2.25
Ionization cross-section	σ_i (Mbarns)	2
Energy at peak SEY	E_{max} (eV)	300

Table 2: Magnetic Properties for Simulations

Element	Absolute Field Strength	Unit
Drift	-	-
Dipole	3.06	T
Quadrupole	85	T/m
Sextupole	450	T/m^2

RESULTS FOR DIFFERENT ELEMENTS

The electron cloud density for each magnetic element is shown in Fig. 2 over the time span of a single bunch train, which contains 1856 bunches separated by 2.1 ns. Simulations have been performed for multiple bunch trains in dipoles and drifts, separated by 126 empty buckets, and the electron cloud density behavior remains consistent despite the bunch train number - the electron cloud reaches saturation before the end of the bunch train and decreases in the gap between trains. For certain elements, like the sextupole, the preceding bunch train will mean that successive trains reach saturation more quickly. This behavior can be seen

* deitrick@jlab.org

Content from this work may be used under the terms of the CC BY 3.0 licence (© 2018). Any distribution of this work must maintain attribution to the author(s), title of the work, publisher, and DOI.

ISBN: 978-3-95450-194-6 ISSN: 2226-0366 doi:10.18429/JACoW-LINAC2018-TUPO109

Content from this work may be used under the terms of the CC BY 3.0 licence (© 2018). Any distribution of this work must maintain attribution to the author(s), title of the work, publisher, and DOI.

in the electron cloud density within the drift and sextupole over two bunch trains shown in Fig. 3. While the time to saturation in the drift is comparable between the first and second train for the drift, the time to saturation in the second bunch train of the sextupole is quicker than in the first

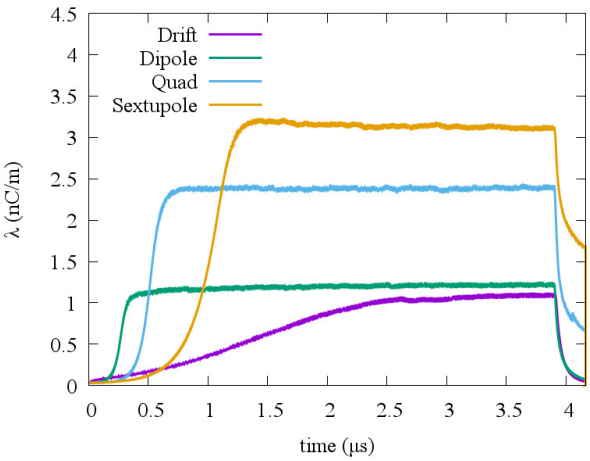


Figure 2: Electron cloud line density over a bunch train (1856 bunches, followed by 126 empty buckets) for various elements and a drift.

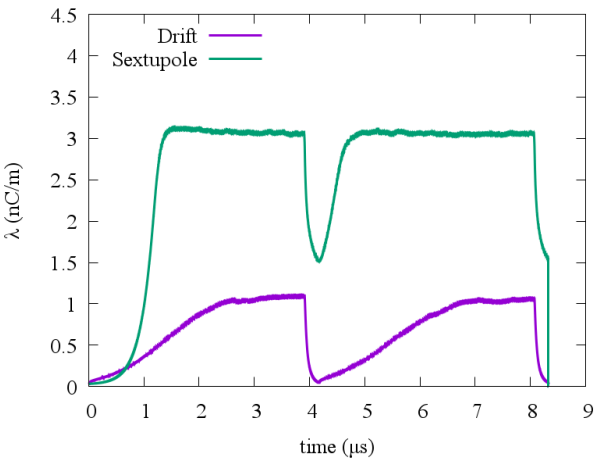


Figure 3: Electron cloud line density over two bunch trains (1856 bunches, followed by 126 empty buckets in each) for a sextupole and a drift.

Using these results, it is possible to calculate the estimated horizontal tune shift per unit length with the formula

$$\Delta\nu_x/L = \frac{r_p\bar{\beta}_x\rho_e}{2\gamma_b} \quad (1)$$

where $r_p = 1.535\times10^{-18}$ m is the classical proton radius, ρ_e is the electron cloud density, $\bar{\beta}_x = 49$ m is the average horizontal beta function, and $\gamma_b = 106.6$ is the typical relativistic factor of the proton beam. The formula for the estimated vertical tune shift per unit length is similar, simply replacing $\bar{\beta}_x$ with $\bar{\beta}_y$, which is 66 m. Taking L to be 2230 m, the circumference of the ion ring, we can estimate the vertical and horizontal tune shift per turn - these results are given in Table 3. All of the estimated tune shifts per turn fall below 4.5×10^{-3}, which does not indicate that electron cloud effects will have a significant impact on the performance of the machine. This is particularly true as taking the highest possible density and assuming it for the entire circumference leads to overestimation.

Table 3: Simulation Results for Different Magnetic Elements

Element	λ_e (nC/m)	ρ_e (m^{-3})	$\Delta\nu_x$ (10^{-3})	$\Delta\nu_y$ (10^{-3})
Drift	1.09	1.36×10^{12}	1.06	1.43
Dipole	1.23	1.53×10^{12}	1.20	1.62
Quadrupole	2.40	2.99×10^{12}	2.34	3.16
Sextupole	3.11	3.87×10^{12}	3.03	4.10

Table 4: SEY Parameters Corresponding to Different Materials

Material	δ_{max}	E_{max} (eV)	σ_i (Mbarns)
Stainless steel [4]	2.25	300	2
Copper [4]	1.90	300	2
Partially scrubbed copper [5]	1.55	125	2

RESULTS FOR DIFFERENT SEY PROPERTIES

Thus far, we have assumed that the beam pipe is made from stainless steel. However, it is suitable to evaluate the electron cloud density for different materials, to evaluate the impact of SEY parameters. The three chosen materials are stainless steel, copper [4], and partially-scrubbed copper [5]. The SEY parameters of the three materials are given in Table 4.

Using these parameters, we have simulated the electron cloud density for two successive bunch trains for the three different materials in the dipoles; the electron cloud density as a function of time for each of the three materials is shown in Fig. 4. Using the same approach as in the previous section, it is possible to estimate the tune shift for the electron cloud density assuming different materials. The results of these calculations are given in Table 5. While it is clear that copper out-performs stainless steel, the saturation density of stainless steel and partially scrubbed copper is comparable. This suggests that improvements in electron cloud performance by using copper only last until the copper gets scrubbed by the proton beam during commissioning or operation.

CONCLUSION

We have presented the current estimate for electron cloud density and its impact for one of the proton beams of the JLEIC design. Though a more detailed estimate remains to

ISBN: 978-3-95450-194-6 ISSN: 2226-0366 doi:10.18429/JACoW-LINAC2018-TUPO109

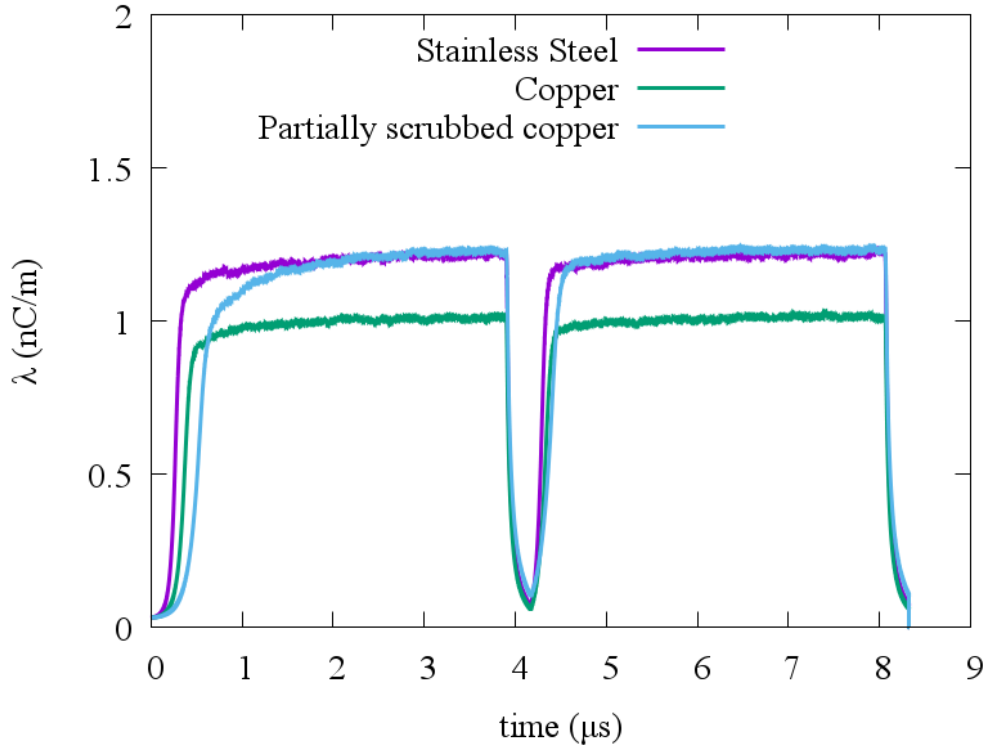


Figure 4: Electron cloud line density in a dipole as a function of time for two successive bunch trains for beam pipes of stainless steel, copper, and partially scrubbed copper.

Table 5: Simulation Results for Different Beam Pipe Materials

Element	λ_e (nC/m)	ρ_e (m^{-3})	$\Delta\nu_x$ (10^{-3})	$\Delta\nu_y$ (10^{-3})
Partially scrubbed copper	1.24	1.54×10^{12}	1.21	1.63
Stainless steel	1.23	1.53×10^{12}	1.20	1.62
Copper	1.02	1.27×10^{12}	0.995	1.34

be done, an upper bound for the beam tune shift has been calculated and found to be reasonable. Future work is the evaluation of the electron cloud in other JLEIC collision schemes, in order to choose the correct material for the machine in all cases.

ACKNOWLEDGEMENT

This material is based upon work supported by the U.S. Department of Energy, Office of Science, Office of Nuclear Physics under contract DE-AC05-06OR23177. K. E. D. would like to thank LINAC'18 for conference support.

REFERENCES

[1] E. Gianfelice-Wendt, *ICFA Beam Dynamics Newsletter* No. 74, p. 92-182 (2018).

[2] G. Iadarola, Electron cloud studies for CERN particle accelerators and simulation code development, Ph.D. thesis, Università degli Studi di Napoli Federico II, 2014.

[3] T. Michalski, R. Fair, R. Rajput-Ghoshal, and P. Ghoshal, "JLEIC SC Magnets: Replace SF and High CM Energy Needs", (2018).

[4] R. Valizadeh, O. B. Malyshev, S. Wang, S. A. Zolotovskaya, W. A. Gillespie, and A. Abdolvand, *Appl. Phys. Lett.* **105**, 231605 (2014).

[5] R. Cimino *et al.*, *Phys. Rev. Lett.* **93**, 014801 (2004).

Content from this work may be used under the terms of the CC BY 3.0 licence (© 2018). Any distribution of this work must maintain attribution to the author(s), title of the work, publisher, and DOI.

ISBN: 978-3-95450-194-6 ISSN: 2226-0366 doi:10.18429/JACoW-LINAC2018-TUPO112

CALCULATION OF ELECTRON BEAM DYNAMICS IN FOUR ACCELERATING STATIONS FOR JINR ELECTRON ACCELERATOR LINAC-200

A. S. Sledneva†, V. S. Aleksandrov, V. V. Kobets,
Joint Institute for Nuclear Research, Dubna, Moscow Region, Russian Federation

Abstract

In the Joint Institute for Nuclear Research a Test Stand with an electron beam generated by the linear accelerator LINAC-200 with the energy up to 200 MeV is being constructed to investigate properties of accelerating and semiconducting structures for advanced detectors, a radiation resistance of detectors based on gallium arsenide semiconductor, to study a free electron laser and to do other applied work. The technical characteristics of the LINAC-200 accelerator make it possible to create an advanced system of test beams for scientific and methodological studies of detectors on its basis.

Four accelerating stations with maximum beam energy up to 200 MeV are put into operation. The work is being carried out for experiments with electron test beams with energy up to 800 MeV

This work presents the calculation results of the magnetic field of the focusing solenoidal system and electron beam dynamics in accelerating stations A00 – A04. In addition, the results on the formation of the electron beam with optimal parameters to be captured in further accelerating sections.

DESCRIPTION OF LINAC-200

Linear electron accelerator LINAC-200 is created on the basis of the accelerator MEA (Medium Energy Accelerator), brought from Dutch National Institute for Subatomic Physics to Dubna in 1999-2000 [1].

Linac-200 consists of 4 accelerating stations A01 – A04 with the maximum energy of about 200 MeV.

Injection station A00 consists of injector, prebuncher and buncher. The buncher is a short acceleration section with the length 1.654 m.

The focusing and transporting systems along the accelerator path includes solenoids, quadruples and beam correction elements. The buncher and short acceleration sections (A0BB, A1AA, B2AA) with the length 3.67 m have a constant solenoidal magnetic field from 100 to 500 Gauss generated by lenses (L1, L2) and solenoidal. After exiting the gun, the beam is picked up by a thin solenoidal magnetic lens 1, which focuses the beam on the chopper collimator. The second thin solenoidal lens focuses the beam on the input to the buncher. The long sections (A3A, B4A, B5A, A6A) with the length 7.35 m have no magnetic field, it contains quadruples Q1 and Q2 (Fig. 1). All quadruple lenses are identical. The internal radius of the channel is 2.5 cm, the field gradient is 7.6 kGauss/m.

† sledneva@jinr.ru

THE RESULTS OF CALCULATIONS ON THE FORMARTION OF THE MAGNETIC FIELD

For calculations on the formation of the magnetic field was used POISSON program [2]. The layout of the magnetic system for accelerating stations A00 – A02 is illustrated In Figure 2. Figure 3 shows a distribution of longitudinal and radial components of the magnetic field in accelerating stations A00 – A02.

Summarizing the calculation results, a Table 1 with the optimum values of the magnetic field was made.

The obtained results are used for further beam dynamics calculations of the electron beam.

Table 1: Optimal magnetic field for different elements of the accelerator

Element	B_{max}, Gauss
Lens 1 (L1)	200
Lens 2 (L2)	100
Buncher	200
A0BB	300
A1AA	400
B2AA	500

THE RESULTS OF ELECTRON BEAM DYNAMICS CALCULATIONS USING PARMELA PROGRAM [3]

The initial distribution of the particles was determined according to the Vladimirsky-Kapchinskii. The number of particles: 10 – 1000.

The goal of a prebuncher and a buncher is to compress the length of the bunch to a value suitable for capturing in the first accelerating section A0BB. Preference was given to variants with phases with a maximum energy of the high-frequency field in the section A0BB. The final choice of the optimal variant was made according to the results of the analysis for the maximum number of particles in the required phase range.

Beam cross-sections along the accelerator are illustrated in Figure 4 (sizes are in cm). Figure 5 shows beam spot (on the left) and energy-phase distribution (on the right). Energy gain along the LINAC-200 is demonstrated in Figure 6.

Content from this work may be used under the terms of the CC BY 3.0 licence (© 2018). Any distribution of this work must maintain attribution to the author(s), title of the work, publisher, and DOI.

ISBN: 978-3-95450-194-6 ISSN: 2226-0366 doi:10.18429/JACoW-LINAC2018-TUPO112

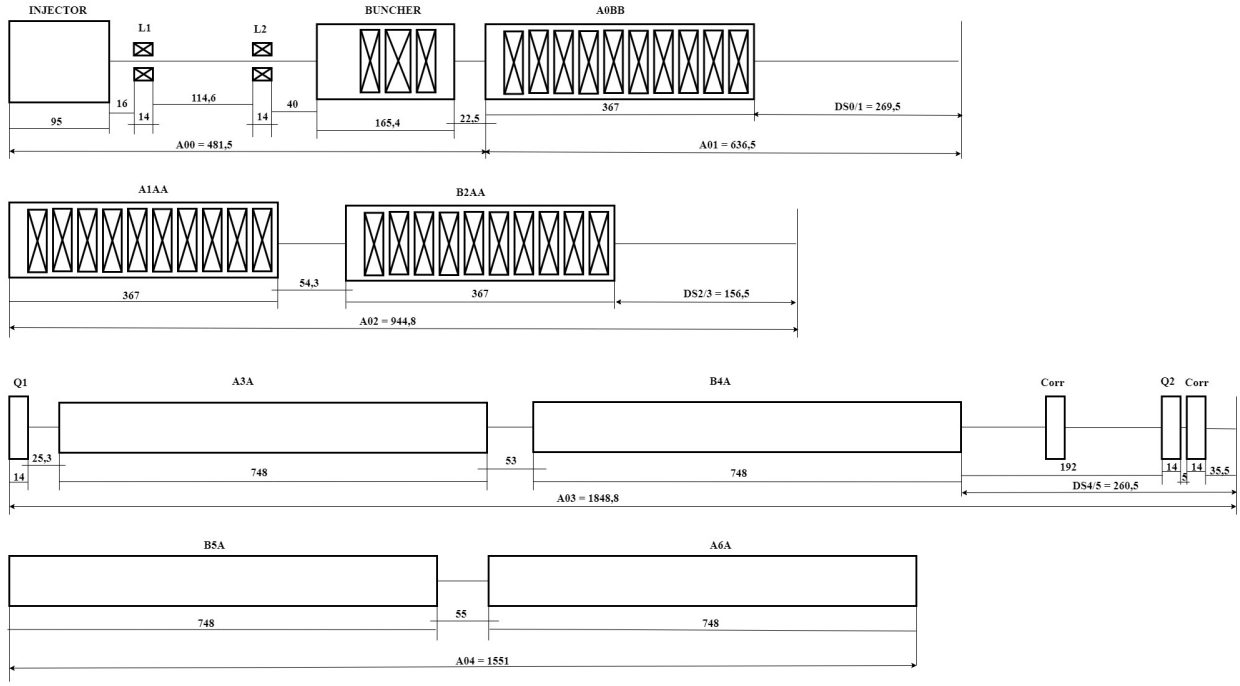


Figure 1: The layout of the magnetic system (sizes are in cm).

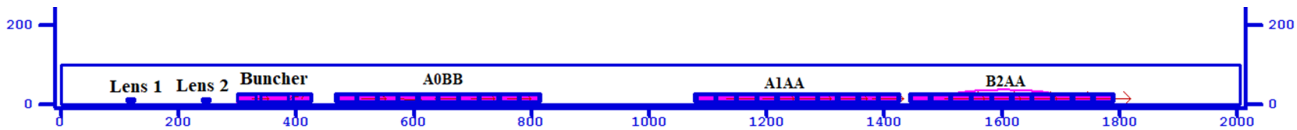


Figure 2: The layout of the magnetic system for accelerating stations A00 – A02 in POISSON program interface (sizes are in cm).

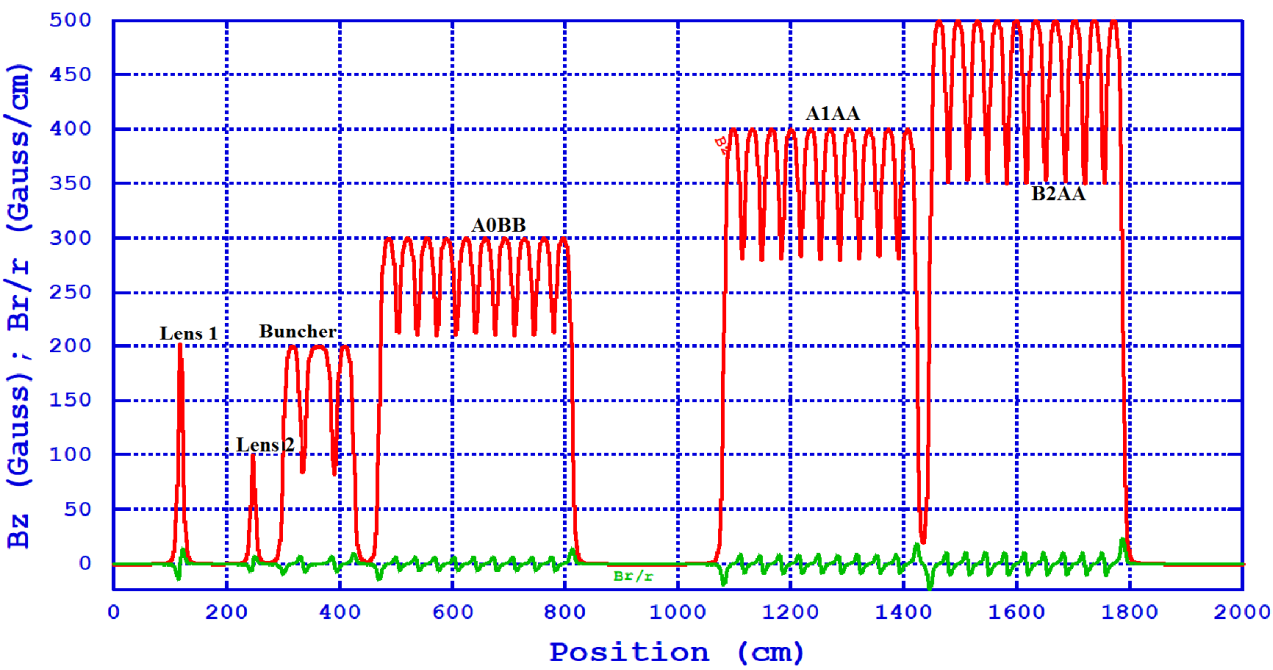


Figure 3: Distribution of longitudinal and radial components of the magnetic field in accelerating stations A00 – A02.

Content from this work may be used under the terms of the CC BY 3.0 licence (© 2018). Any distribution of this work must maintain attribution to the author(s), title of the work, publisher, and DOI.

ISBN: 978-3-95450-194-6 ISSN: 2226-0366 doi:10.18429/JACoW-LINAC2018-TUPO112

Content from this work may be used under the terms of the CC BY 3.0 licence (© 2018). Any distribution of this work must maintain attribution to the author(s), title of the work, publisher, and DOI.

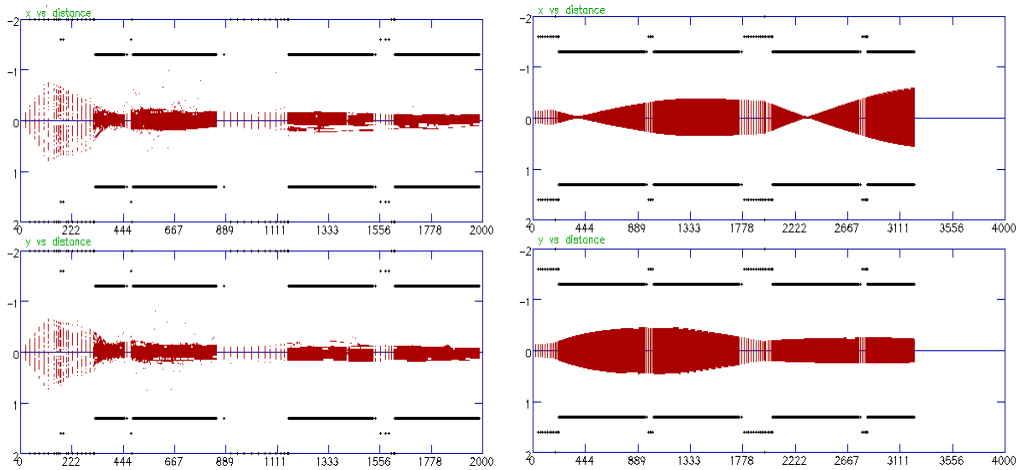


Figure 4: Changes of the transverse dimensions of the beam during acceleration and transport of the beam in accelerating stations A00 – A02 (on the left) and A03 – A04 (on the right).

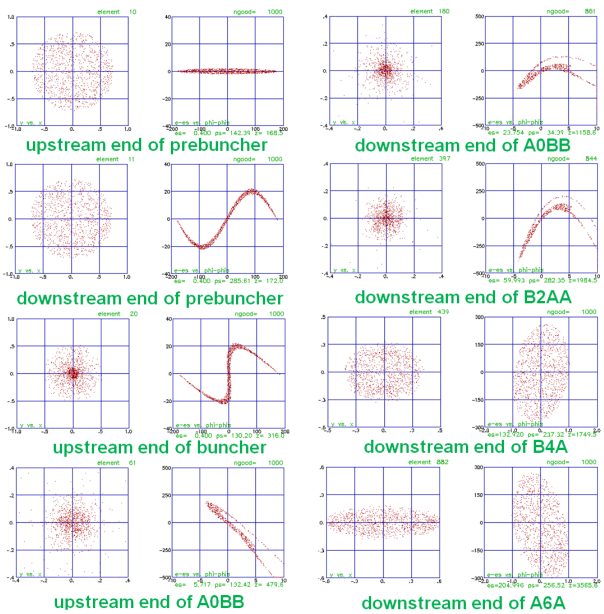


Figure 5: Beam spot (cm), energy-phase distribution (keV, degree).

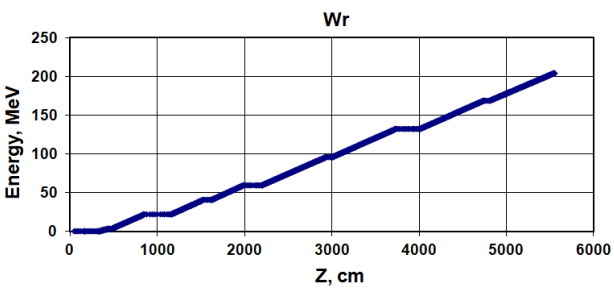


Figure 6: Energy gain along the LINAC-200.

Finally, a Table 2 with energy after each accelerating station was done.

Table 2: Energy after Each Accelerating Section

Accelerating station	Wr downstream end of element, MeV
A00	5.7
A01	23.7
A02	60
A03	133
A04	206

CONCLUSION

The electronic version of A00 - A04 was created. The magnetic field for A00 - A02 was formed. The beam with an X-dimension of about 1mm by a Y-dimension of about 12 mm was obtained behind the station A04. The maximum energy of about 200 MeV was formed behind the station A04.

TODAY'S STATUS/FUTURE

Comparison of data to be obtained with calculation data is to be done. The work is being carried out to measure energy at the exit of the second accelerating station (A02). Modernization by increasing the number of sections to get the energy of 800 MeV and later of 2 GeV is to be done. A free-electron laser is to be constructed.

REFERENCES

[1] V.V. Kobets. et al., Physical Startup of the First Stage of the Electron Linear Accelerator LINAC-800, RuPAC 2012 Conf., S.-Peterburg.
[2] POISSON Program, Los Alamos Acc.Group, LA-UR-87-115, 1987.POISSON Program, Los Alamos Acc.Group, LA-UR-87-115, 1987.
[3] The PARMELA Program, B.Mouton, LAL/SERA 93-455, Orsay, 1993.

ISBN: 978-3-95450-194-6 ISSN: 2226-0366 doi:10.18429/JACoW-LINAC2018-TUPO113

BEAM DYNAMICS STUDIES THROUGH DIELECTRIC THZ ACCELERATING STRUCTURES

R. Apsimon*, G. Burt, , A. Healy, S. Jamison, Lancaster University, Bailrigg, UK
A. Latina, CERN, Geneva, Switzerland
R. B. Appleby, E. Smith, University of Manchester, UK

Abstract

As conventional RF accelerating schemes approach the physical limit of accelerating gradient, the accelerator community is increasingly looking at novel accelerating techniques to overcome these limitations. Moving from the RF to the THz frequency range, higher acceleration gradients of high energy beams can be achieved in compact structures. Beam dynamics studies are crucial as part of the design of novel accelerating structures to maximise the output beam current as well as the accelerating gradient. In this paper we present beam dynamics simulations through dielectric lined waveguide structures using novel techniques to simulate broadband signals for particle tracking studies in RF-Track. The beam parameters through the structure are optimised and we study the dynamics of general broadband accelerating structures.

INTRODUCTION

As conventional RF accelerating schemes approach the physical limit of accelerating gradient, the accelerator community is increasingly looking at novel accelerating techniques in the THz regime to overcome these limitations. Dielectric lined waveguides (DLWs) (Figure 1)are one such accelerating technique, favoured for its ability to produce high field gradients as well as its ease of fabrication.

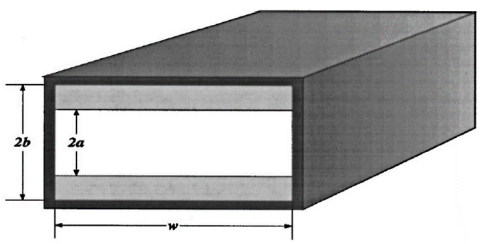


Figure 1: Diagram of a dielectric lined waveguide [1].

Due to the relative simplicity of the physical system for a DLW, a full analytical solution for the electromagnetic fields can be obtained [1]. In this paper, we only consider the LSM_{11} accelerating mode. LSM modes are equivalent to TM modes in a waveguide without any dielectric, but the LSM mode couples to the TM modes in both the vacuum and dielectric regions. If we define a as the half-height of the vacuum region, b as the half-height of the waveguide and w as the full width of the waveguide, as shown in Figure 1, then the dispersion relation for the LSM_{mn} mode is given as

$$k_{mn}^{(1)} \sin\left[k_{mn}^{(1)}(b-a)\right] \sin k_{mn}^{(0)} a - \varepsilon_r k_{mn}^{(1)} \cos\left[k_{mn}^{(1)}(b-a)\right] \cos k_{mn}^{(0)} a = 0 \quad , \tag{1}$$

where

$$k_{mn}^{(0)} = \sqrt{\left(\frac{\omega}{c}\right)^2 - \left(\frac{m\pi}{w}\right)^2 - \beta_{mn}^2}$$
$$k_{mn}^{(1)} = \sqrt{\varepsilon_r \left(\frac{\omega}{c}\right)^2 - \left(\frac{m\pi}{w}\right)^2 - \beta_{mn}^2} \quad . \tag{2}$$

This dispersion relation is a transcendental equation that needs to be evaluated numerically (Figure 2a), but provides a functional relationship between ω and β_{mn}, from which we can obtain the phase velocity, $v_p = \frac{\omega}{\beta_{mn}}$, and group velocity, $v_g = \frac{d\omega}{d\beta_{mn}}$ (Figure 2b). The electric and magnetic fields in the frequency domain within the vacuum region of the DLW respectively are given as

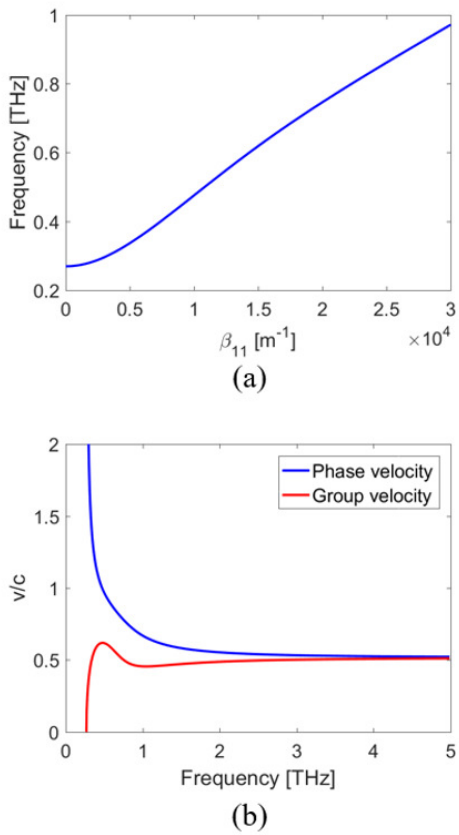


Figure 2: Dispersion relation (a) and phase (blue) and group (red) velocity (b) for a DLW for the LSM_{11} mode with a = 250 µm, b = 300 µm and w = 1200 µm.

* r.apsimon@lancaster.ac.uk

Content from this work may be used under the terms of the CC BY 3.0 licence (© 2018). Any distribution of this work must maintain attribution to the author(s), title of the work, publisher, and DOI.

ISBN: 978-3-95450-194-6 ISSN: 2226-0366 doi:10.18429/JACoW-LINAC2018-TUPO113

Content from this work may be used under the terms of the CC BY 3.0 licence (© 2018). Any distribution of this work must maintain attribution to the author(s), title of the work, publisher, and DOI.

$$\begin{pmatrix}\mathcal{E}_x\\ \mathcal{E}_y\\ \mathcal{E}_z\end{pmatrix} = Ae^{-j\beta_{mn}z}\begin{pmatrix}\frac{m\pi}{w}k_{mn}^{(0)}\cos\left[\frac{m\pi}{w}\left(x+\frac{w}{2}\right)\right]\cos k_{mn}^{(0)}y\\ \left[\left(\frac{m\pi}{w}\right)^2+\beta_{mn}^2\right]\sin\left[\frac{m\pi}{w}\left(x+\frac{w}{2}\right)\right]\sin k_{mn}^{(0)}y\\ -j\beta_{mn}k_{mn}^{(0)}\sin\left[\frac{m\pi}{w}\left(x+\frac{w}{2}\right)\right]\cos k_{mn}^{(0)}y\end{pmatrix}.$$

$$\begin{pmatrix}\mathcal{H}_x\\ \mathcal{H}_y\\ \mathcal{H}_z\end{pmatrix} = Ae^{-j\beta_{mn}z}\begin{pmatrix}-\omega\varepsilon_0\beta_{mn}\sin\left[\frac{m\pi}{w}\left(x+\frac{w}{2}\right)\right]\sin k_{mn}^{(0)}y\\ 0\\ j\omega\varepsilon_0\frac{m\pi}{w}\cos\left[\frac{m\pi}{w}\left(x+\frac{w}{2}\right)\right]\sin k_{mn}^{(0)}y\end{pmatrix} \quad (3)$$

The ratio of field amplitude in the vacuum (A) and dielectric (B) is dependent on the dispersion relation in Eq. 1 and give as

$$\frac{A}{B} = r_{vd} = \frac{\varepsilon_r\cos\left[k_{mn}^{(1)}(b-a)\right]}{\sin k_{mn}^{(0)}a}. \quad (4)$$

In this paper, we will take this analytical description of a DLW and use it to develop a model for the THz fields due to a broadband input pulse. Furthermore we will develop a technique for tracking a particle beam through such a field. Finally we shall show some preliminary results of such a tracking technique.

BROADBAND THZ PULSES

An infinite duration, pure sinusoidal signal has a single frequency component and therefore has zero bandwidth. As the pulse duration decreases, the bandwidth increases. The advantage of using a broadband pulse to accelerate a particle bunch is that all the power is concentrated into a short duration pulse, resulting in higher field gradients seen by the bunch for a constant power. However, due to the dispersive nature of the DLW, only frequency components with a phase velocity close to the beam velocity will remain synchronous with the beam over a long distance. From Figure 2a, one can see that the phase velocity is always higher than the group velocity, thus any beam synchronous beam will eventually overtake the pulse.

As previously mentioned, as the frequency changes, so does the distribution of field in the vacuum and dielectric regions. If we assume the total power in both regions is conserved, and that the normalised amplitudes of the fields in the electric and magnetic regions respectively are A and B, which are both proportional to $\sqrt{P_{in}}$ where P_{in} is the THz power flow into the structure, then $A^2+B^2 \propto P_{in}$, combining this with Eq. 4, we obtain

$$A \propto \left|\sqrt{\frac{r_{vd}^2 P_{in}}{r_{vd}^2+1}}\right|. \quad (5)$$

MODELLING THE FIELD FOR A BROADBAND PULSE

If we assume that an input THz pulse has amplitude $V(t) = \alpha\sqrt{P_{in}(t)}$, where α is a constant to allow us to modify the field amplitudes in the DLW. To obtain the THz amplitude at specific frequencies, we must take a Fourier transform of this input pulse

$$\mathcal{V}(\omega) = FT(V(t)). \quad (6)$$

where $FT(\ldots)$ is the Fourier transform operation. From Eq. 3 we know $\mathcal{E}(\omega,\ \beta_{mn})$ and $\mathcal{H}(\omega,\ \beta_{mn})$, where $\mathcal{E}$ and $\mathcal{H}$ are the E- and H-fields in the frequency domain. From the dispersion relation we can define β_{mn} as a function of ω. To account for the propagation of the pulse along the waveguide, we transform $e^{-j\beta_{mn}z}$ in Eq. 3 to $e^{-j\beta_{mn}(z+v_pt)}$, but $v_p = \omega/\beta_{mn}$, therefore we get $e^{-j(\beta_{mn}z+\omega t)}$. From the dispersion relation, we can again represent this as $e^{-j(\beta_{mn}(\omega)z+\omega t)}$ and when we integrate over all frequencies, this becomes a 'spatio-temporal' inverse Fourier transform [2] and we can now define the E- and H-fields in the time domain for a broadband pulse as

$$\begin{aligned}E(x,y,z,t) &= FT^{-1}\left(\left|\frac{r_{vd}(\omega)}{\sqrt{r_{vd}^2(\omega)+1}}\right|\mathcal{V}(\omega)\mathcal{E}(\omega)\right)\\ H(x,y,z,t) &= FT^{-1}\left(\left|\frac{r_{vd}(\omega)}{\sqrt{r_{vd}^2(\omega)+1}}\right|\mathcal{V}(\omega)\mathcal{H}(\omega)\right).\end{aligned} \quad (7)$$

Figure 3 shows the accelerating gradient on axis for a single-cycle initial pulse [3]. The figure shows the electric field for the pulse after it has propagated 1 mm into the structure and the inset figure shows when the pulse has traveled 1 μm into the structure, to show the pulse dispersion as it propagates through the structure. While we show this method for producing field maps for a broadband pulse in a rectangular DLW, this approach can be used for any broadband pulse, regardless of whether this is an accelerating mode, deflecting or any other mode.

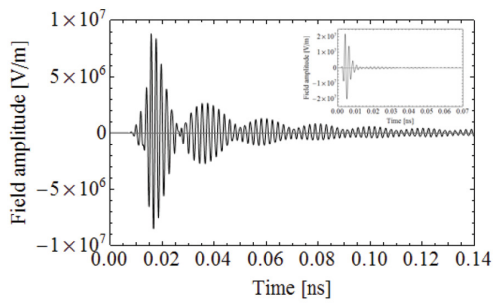


Figure 3: Field amplitude of a single-cycle pulse, 1 mm into the DLW. Inset is the pulse 1 μm into the DLW, showing the broadening due to loss of lower-frequency components [3].

ISBN: 978-3-95450-194-6 ISSN: 2226-0366 doi:10.18429/JACoW-LINAC2018-TUPO113

TRACKING SIMULATIONS

Conventional tracking codes, such as ASTRA, PARMELA, GPT and ELEGANT [4–7], import 1, 2 or 3D field maps, for the 1D case, Maxwell's equations are then used to expand the field map into 3D, and then the codes multiply the field map by $e^{-j\omega t+\phi_{RF}}$ and take the real part as the instantaneous field map. For broadband pulses, this approach does not work. Instead we need a 3D field map for each time step, hence a 4D field map.

Implementation

Initial tracking simulations to study the energy gain vs longitudinal position have been undertaken, looking at different pulse durations (Figure 4). Further details of the studies can be found in [3].

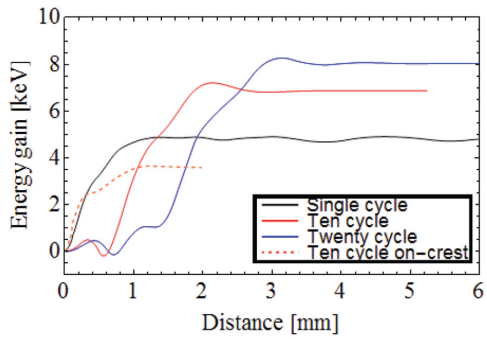


Figure 4: Energy gain vs longitudinal position in the DLW for different pulse durations [3].

Further to this, 6D particle tracking has been simulated using RF-Track [8] and also with a simple 4th-order Runge-Kutta integrator (RK4). The horizontal, vertical and longitudinal phase space distributions are shown respectively in Figures 5-7. The transverse distributions are collimated at ±200 μm, but there is no collimation after the DLW.

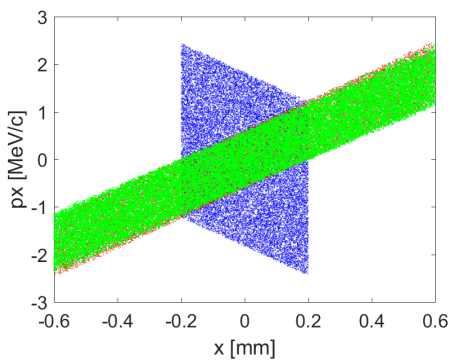


Figure 5: Horizontal phase space distribution before the DLW (blue) and after the DLW, tracked in RF-Track (red) and with an RK4 integrator (green).

The transverse phase space distributions agree well between RF-Track and the RK4 method, however the RK4 integrator exhibits a larger observed momentum spread in the longitudinal phase space distribution; particularly near the extremes of the sinusoidal modulation. Further studies are required to fully understand this.

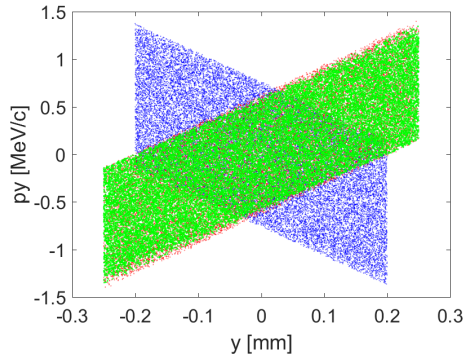


Figure 6: Vertical phase space distribution before the DLW (blue) and after the DLW, tracked in RF-Track (red) and with an RK4 integrator (green).

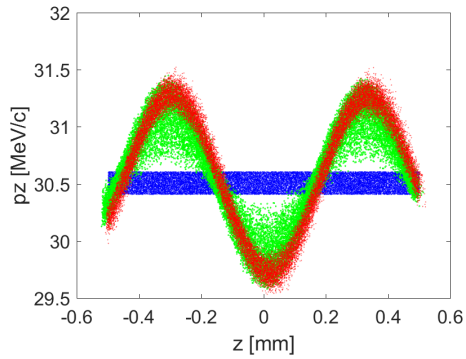


Figure 7: Longitudinal phase space distribution before the DLW (blue) and after the DLW, tracked in RF-Track (red) and with an RK4 integrator (green).

CONCLUSION

Conventional tracking codes assume single frequency fields and are therefore not suitable for modeling broadband pulses. We describe a method for producing field maps for broadband pulses which is completely general and can be applied to any structure and any mode. This method essentially extends the multiplication of a 3D field map by $e^{-j(\omega t+\phi_{RF})}$ to a Fourier transformation. We demonstrate this method for a rectangular dielectric lined waveguide (DLW) and show that the general field maps are 4D rather than 3D as used for single frequency tracking.

1D and 4D tracking simulations of broadband pulses have been presented. We perform 6D tracking simulations with a 4th-order Runge-Kutta (RK4) integrator and compare to RF-Track simulation results. A comparison of these results shows a good qualitative agreement, however there is some disagreement of the energy spread between the two methods. Further studies will be conducted to understand these disparities and to further develop a tracking technique to allow for more general tracking, such as including wakefields directly into the field maps.

Content from this work may be used under the terms of the CC BY 3.0 licence (© 2018). Any distribution of this work must maintain attribution to the author(s), title of the work, publisher, and DOI.

ISBN: 978-3-95450-194-6 ISSN: 2226-0366 doi:10.18429/JACoW-LINAC2018-TUPO113

Content from this work may be used under the terms of the CC BY 3.0 licence (© 2018). Any distribution of this work must maintain attribution to the author(s), title of the work, publisher, and DOI.

REFERENCES

[1] L. Xiao, W. Gai, X. Sun, "Field analysis of a dielectric-loaded rectangular waveguide accelerating structure", DOI: 10.1103/PhysRevE.65.016505.

[2] S. V. Samsonov, A. D. R. Phelps, V. L. Bratman, G. Burt, G. G. Denisov, A. W. Cross, K. Ronald, W. He and H. Yin, "Compression of Frequency-Modulated Pulses using Helically Corrugated Waveguides and its Potential for Generating Multigigawatt RF Radiation," DOI: 10.1103/PhysRevLett.92.118301.

[3] A. L. Healy, G. Burt, S. P. Jamison, "Group velocity matching in dielectric-lined waveguides and its role in electron-terahertz interaction," IPAC'17, Copenhagen, May 2017, WEPVA019, p. 3296

[4] A Space Charge Tracking Algorithm, http://www.desy.de/~mpyflo/

[5] The particle tracking code PARMELA, https://cds.cern.ch/record/749735

[6] General Particle Tracer, http://www.pulsar.nl/gpt/

[7] User manual for elegant, https://ops.aps.anl.gov/manuals/elegant_latest/elegant.html

[8] RF-Track: beam tracking in field maps including space-charge effects. Features and benchmarks, LINAC16, East Lansing, MI, USA, 2016 http://linac2016.vrws.de/papers/moprc016.pdf

ISBN: 978-3-95450-194-6 ISSN: 2226-0366 doi:10.18429/JACoW-LINAC2018-TUPO114

BEAM DYNAMICS STUDIES FOR THE CSNS DTL DUE TO A QUADRUPOLE FAULT

J. Peng†, Y.W. An, M.Y. Huang, L.S. Huang, Y. Li, M.T. Li, Z.P. Li, Y.D. Liu, X.H. Lu, X.B Luo
S.Y. Xu, Y. Yuan, S. Wang, S.N. Fu
Dongguan Campus, Institute of High Energy Physics, Dongguan, 523803 China

Abstract

The China Spallation Neutron Source(CSNS) accelerator systems is designed to deliver a 1.6GeV, 100kW proton beam to a solid metal target for neutron scattering research. It consists of a 50keV H- Ion Source, a 3 MeV Radio Frequency Quadrupole (RFQ), an 80MeV Drift Tube Linac (DTL), and a 1.6 GeV Rapid-cycling Synchrotron (RCS). The DTL consists of four tanks. In 2017, three of four tanks have been commissioned successfully, and beam has been accelerated to 61 MeV with nearly 100% transmission. However, in July 2017, one quadrupole contained in the drift tube was found fault, the beam transmission decreased to 80%. A new lattice has been designed and the 100% transmission has recovered. In January 2018, the last tank of the DTL has been commissioned and accelerated the H- beam to the design energy of 80MeV for the first time. The commissioning progress and the measurement results before and after lattice adjustment will be presented.

INTRODUCTION

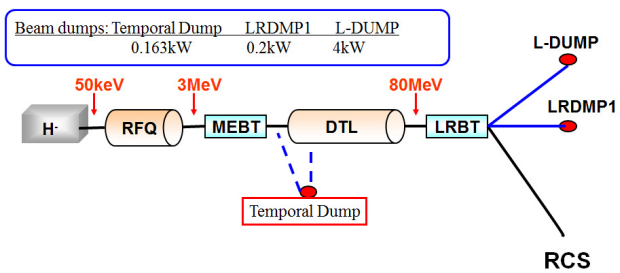


Figure 1: CSNS Linac layout.

The layout of the CSNS Linac is shown in Fig. 1. Details of the Linac design can be found in [1]. The DTL consists of four tanks and accelerates H- beam from 3MeV to 80MeV. Each tank is fed by a 324MHz, 3MW klystron. From 2016 to 2018, the DTL has been commissioned tank by tank. In 2017， since only three klystrons were available, DTL1to3 have been fed and the beam was successfully accelerated to 61 MeV [2]. The last tank has been used as a beam line. Figure 2 shows the CT signals along the Linac. Beam transmission from the DTL to the LRBT (Linac to RCS Beam Transport) was nearly 100%. In May 2017, the vacuum in DTL1 became worse. And one month later, the beam commissioning was interrupted for the DTL vacuum checking. We found that the cooling channel of the EMQ13 in the DTL1 was leaking [3]. So we had to turn off the EMQ13 which made the beam transmission decrease to about 80%. Due to the tough arrangement of the commissioning timetable, beam commissioning has continued. A temporary lattice was used, in which the EMQ13 and EMQ 14 were turned off and the other quadrupoles' setting remained unchangeable. The beam transmission has been fluctuating from 96% to 98% during commissioning. In November 2017, we had two month interval for testing the klystron and RF conditioning of the DTL4. A new lattice for the DTL has been designed. According to this new lattice, every 2 of 4 quadrupoles after the EMQ13 had to exchange the polarities by modifying the cable connection mode. In January 2018, the last tank of the DTL has been commissioned and the H- beam to the design energy of 80MeV for the first time. With the new transverse focusing lattice, the beam transmission has recovered to 100%. Figure3 shows the CT signals along the linac with the new lattice.

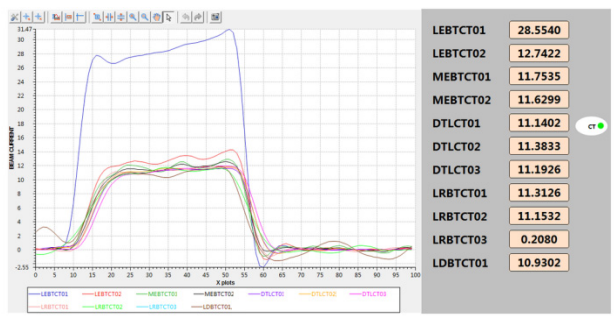


Figure 2: Current transform signals along the Linac with the old lattice.

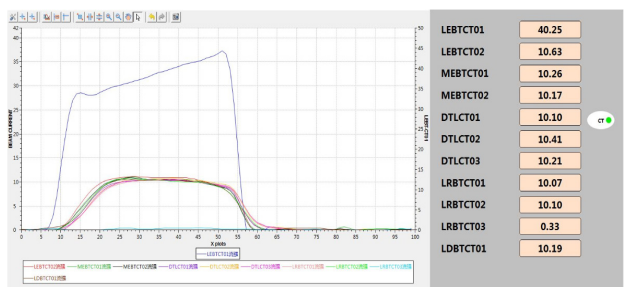


Figure 3: Current Transform signals along the Linac with the new lattice.

Old Lattice

The DTL uses Electrical Magnet Quadrupoles (EMQ) for transverse focusing and the focusing is done in a

*This work is supported by National Natural Science Foundation of China (11505101).
**E-mail:pengjun@ihep.ac.cn

Content from this work may be used under the terms of the CC BY 3.0 licence (© 2018). Any distribution of this work must maintain attribution to the author(s), title of the work, publisher, and DOI.

ISBN: 978-3-95450-194-6 ISSN: 2226-0366 doi:10.18429/JACoW-LINAC2018-TUPO114

Content from this work may be used under the terms of the CC BY 3.0 licence (© 2018). Any distribution of this work must maintain attribution to the author(s), title of the work, publisher, and DOI.

DFFD lattice. The transverse lattice meets the following merits: [4].

1.$\sigma_{0t} \leq 90°/period$

2.$\sigma_{0t} \neq \frac{n\sigma_{0l}}{2}$ for n=1,3…

3. Equipartitioning ratio≈1.0 at full current.

Where σ_{0t} and σ_{0l} are transverse and longitudinal phase advances without space charge. There are total 161 EMQs in the DTL. The gradient of these EMQs are shown in Figure 4.

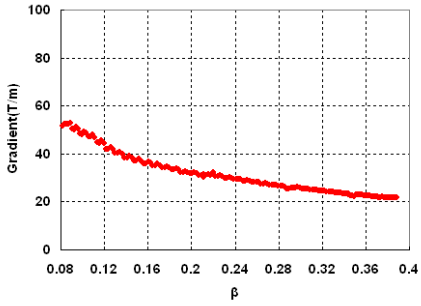
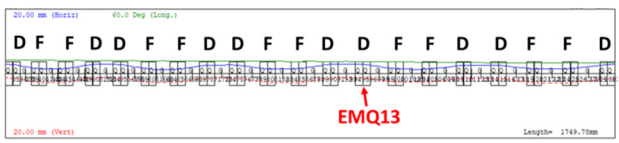
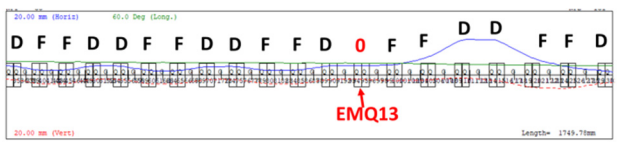


Figure 4: Quadrupole gradient.

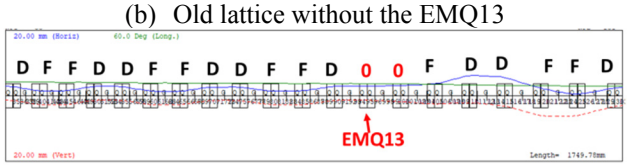
New Lattice



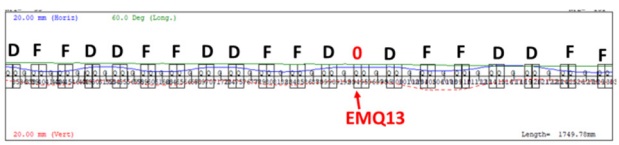
(a) Old lattice with the EMQ13



(b) Old lattice without the EMQ13



(c) Old lattice without the EMQ13、14



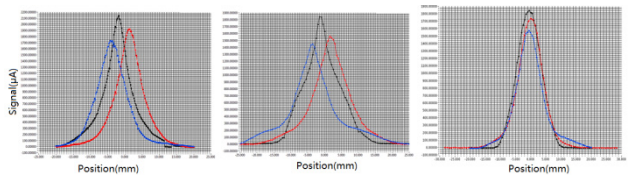
(d) New lattice without the EMQ13

Figure 5: Beam envelope in the DTL1(Blue line represents horizontal envelope, red line represent vertical envelope, green line represent longitudinal phase width).

The EMQ13 is a "D" quadrupole which stands for defocusing proton in the horizontal plane. Because of the fault of the EMQ13, there was a big envelope bump in the DTL1 which made beam lost. Figure 5 shows the beam envelope for the first five transverse periods in the DTL1 by Trace 3D [5].

A temporary lattice was adopted to continue the commissioning progress. As shown in Figure 5, the EMQ13 and EMQ 14 were turned off and the other quadrupoles' setting remained unchangeable. The temporary lattice has supressed the bump. However, there was about 4% beam loss along the linac. And the beam profile measurement showed that significant beam halo formation was observed downstream of the DTL, as shown in Figure 6.

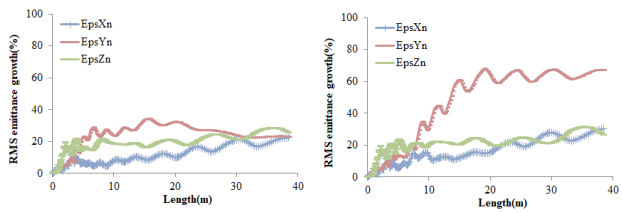
In November 2017, the fourth run of beam commissioning has completed and there was a two month interval to start the fifth beam commissioning. During the interval, a new lattice has been optimized. In the old lattice, the EMQ13 was the first quadrupole for a DFFD focusing period.In the new lattice, we start a DFFD focusing period with the EMQ14. The beam bump was eliminated. And the beam halo from the beam profile measurement was not observed.



(a) Old lattice (b)Temporary lattice (c)New lattice

Figure 6: Beam profiles measured for I_{peak}=10mA at the exit of the DTL.

In January 2018, the fifth beam commissioning has begun. The DTL4 has been fed for the first time. The nominal energy of 80 MeV has reached. The beam transmission along the DTL was nearly 100% with the new lattice. Although the beam transmission recovered, the beam emittance growth raised due to the discontinuity of the transverse focusing. Figure 7 shows the simulated RMS emittance growth for two lattices. At the exit of the DTL, the vertical emittance growth is 23.2% for the old lattice while the value is 67.1% for the new lattice.



(a) Old lattice (b) New lattice

Figure 7: RMS emittance along the DTL.

SUMMARY

Due to the fault of the EMQ13 in the DTL1, the beam transmission through the CSNS DTL decreased from 100% to 80%. With a new lattice, the beam transmission has recovered. No obvious beam halo was observed at the exit of the DTL although a EMQ was turned off.

REFERENCES

[1] J.Peng *et al.* "Design of 132MeV DTL for CSNS", in *Proc. Linac'06*, Knoxville, Tennessee USA, Aug. 2006, paper TUP069.

[2] J.Peng *et al.* "Beam Commissioning Results of the CSNS Linac", in *Proc. IPAC'17*, Copenhagen, Denmark, May 2017, paper TUOBA1.

ISBN: 978-3-95450-194-6 ISSN: 2226-0366 doi:10.18429/JACoW-LINAC2018-TUPO114

[3] H.C.Liu *et al*., "Operation experience of the CSNS DTL", presented at Linac'18, Beijing, China, Sep. 2018, paper THPO030, this conference.

[4] J. Stovall, Quadrupole Law and Steering Options in the Linac4 DTL, CERN LHC-Project-Note-0006, 2009.

[5] K. Crandall and D. Rusthoi, "TRACE 3-D Documentation", LA-UR-97-886.

[6] Harunori T. PARMILA. LA-UR-98-4478, 1998, Revised July 26, 2005.

Content from this work may be used under the terms of the CC BY 3.0 licence (© 2018). Any distribution of this work must maintain attribution to the author(s), title of the work, publisher, and DOI.

ISBN: 978-3-95450-194-6 ISSN: 2226-0366 doi:10.18429/JACoW-LINAC2018-TUPO115

BEAM PARAMETERS MEASUREMENT AND CORRECTION IN CSNS LINAC

Z.P. Li, J. Peng, Y. Li, Dongguan, 523803, China

Abstract

All the beam parameters of China Spallation Neutron Source (CSNS) linac had achieved the acceptance goals in January 2018 after a 2-year commissioning. Parameters of the H- beam were carefully studied and corrected. Beam energy was measured and the energy dispersion are reduced. Transverse emittance are obtained by different tools and methods. Linear optics measurements and corrections were carried out under varied beam energies and peak intensities.

INTRODUCTION

The linear accelerator of CSNS [1] mainly consists of a 50KeV H- ion source, a four-vane radio frequency quadrupole accelerator(RFQ)and a four-tank drift tube linac(DTL) working at RF frequency of 324 MHz. The low energy beam transport line (LEBT) and medium energy beam transport line (MEBT) connect and match the above three accelerating sections. The linac to ring beam transport line (LRBT) which transports the beam from DTL to the Rapid-cycling Synchrotron (RCS) reserves the space for linac upgrading in the further. The total length of the straight section is 200m. The layout of the CSNS linac is shown in Fig. 1.

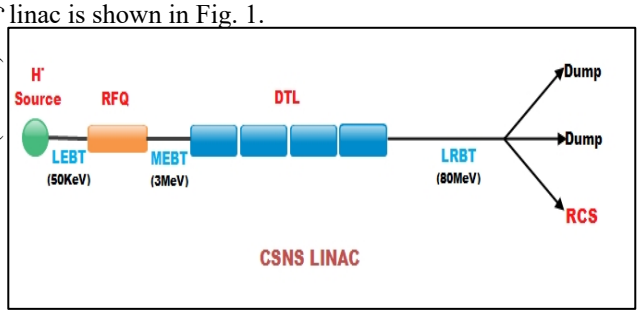


Figure 1: The CSNS Linac Layout.

The beam commissioning of linac started in April 2015 and was separated into 4 runs due to DTL tank installations and klystron failures. By January 2018, the beam peak current intensity reached 15mA and the beam energy achieved the design value of 80 MeV. The overall transport efficiency of DTL reached over 97%.

Beam parameters of CSNS linac were carefully measured and corrected during the commissioning. In this paper, the main beam parameters measurement and correction results will be displayed and discussed. The content includes: beam current intensity measurement and transport efficiency optimization, beam orbit correction, transverse emittance and twiss parameters measuring and matching, beam kinetic energy and momentum spread measurements .

BEAM PARAMETERS MEASUREMENT AND CORRECTION

Beam Current Intensity

The current beam power of CSNS linac is 1 KW with the peak current of 10 to 15 mA, the pulse width of 130 us, and the repetition rate of 25 Hz. Current transformers (CT) in linac beam line monitor the beam intensity and the transport efficiency. Figure 2 shows a set of CT signals along the linac.

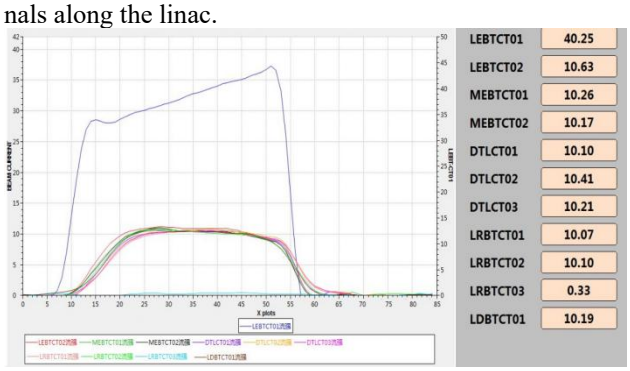


Figure 2: Current Transform Signals of CSNS Linac.

The transport efficiency is one of the most important parameters to be optimized in the linac beam commissioning. By beam orbit correction and operations of beam matching, transport efficiency is greatly improved thus the beam loss satisfies the design standard. The overall transport efficiency of DTL reached over 97%, there is still work to be done for further improvement.

Beam Orbit

Beam orbit is usually the first parameter to measure and correct in beam commissioning. The beam orbit distortion should be as small and as smooth as possible along the beam line, especially for CSNS linac with small aperture. Orbit correction application in XAL was adopted for the case of orbit manipulation in CSNS linac.

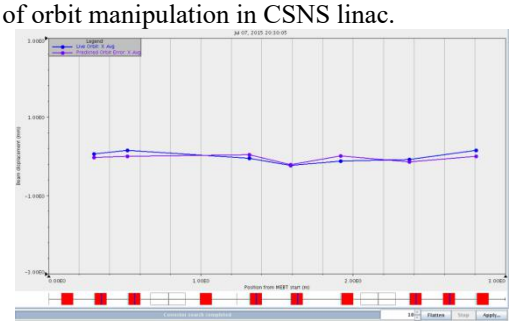


Figure 3: Beam Orbit of MEBT after Orbit Correction.

The Fig. 3 is the result of orbit correction for MEBT. The beam orbit of MEBT can be corrected from 1.5 mm

Content from this work may be used under the terms of the CC BY 3.0 licence (© 2018). Any distribution of this work must maintain attribution to the author(s), title of the work, publisher, and DOI.

ISBN: 978-3-95450-194-6 ISSN: 2226-0366 doi:10.18429/JACoW-LINAC2018-TUPO115

to 0.5 mm. The beam orbit of LRBT can be corrected from 10mm to 2mm. After the corrections, the orbit deviations are suppressed and beam loss is also greatly reduced. However, the orbit correction for DTL is not carried out for no corrector and only one BPM inside.

Transverse Emittance

The transverse emittance of the beam is a key characteristic for high intensity particle accelerator. Measurement and study of emittance is very important for the prediction and control of the beam particle loss. A double scanning slit system and wire-scanners installed in linac are employed for the RMS emittance measurements. Different methods of measurement are introduced and the results are discussed[2].

Double scanning slit system is usually used in the low energy section of beam line. It is developed to get the emittance directly by measure the flux elements f(x, x'). Based on measured particle flux elements f(x, x') passing through a relative position coordinate x with a relative velocity component x', the RMS emittance can be calculated by statistical method. The particle distribution in phase space output by the JAVA code are showed in Figure 4.

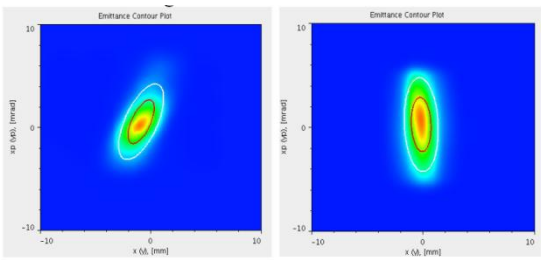


Figure 4: Particle Phase Ellipse by Double slit System: (Left- horizontal, Right-vertical).

Wire-scanner is the other kind of device used for transverse emittance measurement[2]. Two different methods for the wire-scanner measuring are employed. For the muti-changing focusing strength method, one wire-scanner and an upstream quadrupole with multi-changing focusing strength K are employed to perform the measurement. The other method is by scanning the beam parameters and usually 4 or more wire-scanners are needed. Beam transverse emittance measurement results obtained by different methods are presented as below, see Table 1.

Table 1: Emittance Measured by Different Methods

Emittance (MEBT)	Horizontal (mm.mrad)	Vertical (mm.mrad)
Double-Slit	2.28	2.24
Quads-Scanning	2.15	3.04
Multi-wire Scanner	2.02	3.55

Twiss Parameters

Matching of beam parameters is a very important step in the commissioning. The matching between the lattice and the beam parameters will make the beam envelope evolve according to the design value, meet the requirements of DTL transmission and RCS injection, and thus reduce the beam loss.

To get the real transverse twiss parameters of beam, we also use the wire scanners installed on the MEBT and LRBT[3]. By minimizing the discrepancy between the measured values of wire scanners and the simulated values when different upstream twiss parameters initiates, we can get the real twiss parameters of beam.

Figure 5 shows the simulation and measurement results of beam phase ellipse at DTL exit. There is a clear difference between the real beam parameters and the simulation ones. This requires us to perform the corresponding matching adjustments for the actual beam parameters during the commissioning process. The process of beam commissioning shows that the twiss parameter measurement is accurate and effective, and the beam matching meets the design requirements.

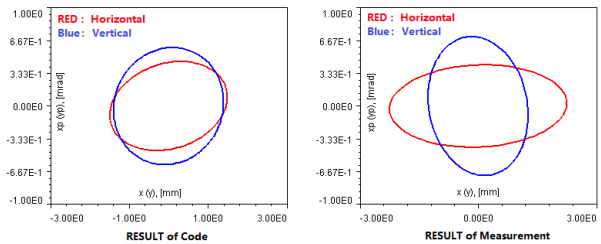


Figure 5: Transverse Phase Ellipse at DTL exit: (Left-simulations, Right-measurement).

Kinetic Energy and Momentum Spread

Beam energy is usually measured with various FCT pairs using the time of flight (TOF) method. The measurement can also be performed by phase scanning method. We scan the phase parameters of the RF cavity to obtain the relationship between the beam energy and the phase of RF cavities. Using the theoretical curves to fit the measured ones, the beam energy and some other parameters can be obtained.

The kinetic energy values of beam at each DTL tank's exit were measured by the two methods above. Deviation of measured beam energy from the design value is less than 1% [4]. The CSNS linac output energy is carefully measured and checked. The results show that the kinetic energy of linac is 80.36 MeV, while the design value is 80.01 MeV, which shows that the design energy of the linac was achieved.

The optimum momentum spread is about 0.1% at the inject point for inducing beam losses during the RCS injection. A debuncher cavity is installed in the LRBT to control the injection momentum spread.

After measuring and matching the beam parameters, we have obtained the actual emittance, alpha, beta, and dispersion functions of the beam. When the beam passes a dipole magnet, the momentum spread of the beam can be obtained by measuring the transverse distribution of the beam downstream the dipole. The momentum spread $\Delta P / P$ of beam at injection point of RCS is about 0.11% after the correction by debuncher.

Content from this work may be used under the terms of the CC BY 3.0 licence (© 2018). Any distribution of this work must maintain attribution to the author(s), title of the work, publisher, and DOI.

ISBN: 978-3-95450-194-6 ISSN: 2226-0366 doi:10.18429/JACoW-LINAC2018-TUPO115

Content from this work may be used under the terms of the CC BY 3.0 licence (© 2018). Any distribution of this work must maintain attribution to the author(s), title of the work, publisher, and DOI.

CONCLUSION

We have presented part of the work in CSNS linac commissioning in this paper. The main parameters of beam in linac, which includes beam current intensity , beam orbit, transverse emittance, twiss parameters, kinetic energy and momentum spread were studied, measured and corrected.

So far, the beam energy, peak current, beam transmission efficiency of the CSNS linac have achieved the engineering acceptance parameters. Our further work is to optimize the parameters of machine and beam, to improve beam power and machine efficiency.

REFERENCES

[1] CSNS Feasibility Study Report, June, 2009, IHEP.

[2] Z. Li *et al.*, "Transverse Emittance measurements in CSNS Linac", *Proc. IPAC'16*, Busan, Korea, paper MOPOY029.

[3] Z. Li *et al.*, "Beam Commissioning of Transport Line LRBT of CSNS", *Proc. IPAC'17*, Copenhagen, Denmark, paper TUPVA098.

[4] J. Peng *et al.*, "Beam Commissioning results of the CSNS lianc", *Proc. IPAC'17*, Copenhagen, Denmark, paper TUOBA1.

ISBN: 978-3-95450-194-6 ISSN: 2226-0366 doi:10.18429/JACoW-LINAC2018-TUPO116

PARTICLE DYNAMICS OPTIMIZATION IN DTL

I. S. Skudnova†, Saint Petersburg University, 198504 Saint Petersburg, Russia

Abstract

The research concerns ion dynamics in linear accelerators with drift tubes (DTL). Permanent quadrupole magnets are placed inside some of the drift tubes. Frequency of the field is 432 MHz. Electromagnetic fields and particle dynamics in the cavity are calculated using Comsol Multiphysics software. The input energy of the beam is 6 MeV, output 10 MeV. Initial beam is assumed to come from Radio Frequency Quadrupole accelerator (RFQ). The considered parameters are drift tubes radii, cavity diameter, gradient of the magnetic field from quadrupoles inside drift tubes and focusing lattice. Effectiveness is estimated by the emittance growth.

INTRODUCTION

The initial part of the injection system of a large ion accelerator often consists of injector, radio-frequency quadrupole (RFQ), drift tube linear accelerator (DTL). This structure is used, for instance, in the Spallation neutron source (SNS) facility in USA [1]. In this study we consider a similar tank with 22 drift tubes mounted inside (Fig.1).

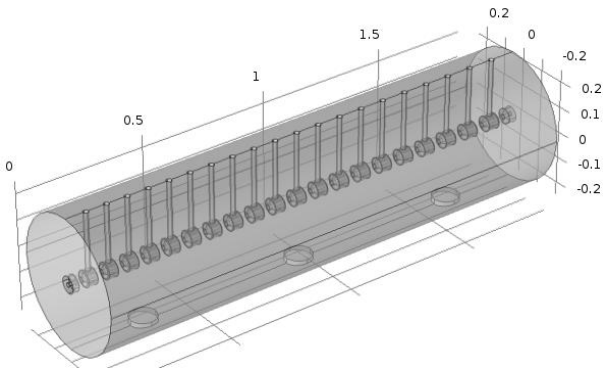


Figure 1: Tank model.

The parameters of the structure are listed in Table 1.

Table 1: DTL Parameters

Parameter	Value
Frequency	432 MHz
Particles	H^-
Input Energy	6 MeV
Output Energy	10 MeV
Cell length	βλ
Gap coefficient (L/L_{gap})	0.25
Drift tube number	22
Tank length	1.863 m
Channel diameter	16 mm

Tube walls are trapeze-shape in section with rounded corners to avoid breakdown. Focusing is provided by permanent magnet quadrupoles, placed inside some drift tubes. Some drift tubes are left empty without magnets. The configuration of the focusing lattice is discussed below. Magnets can be magnetized in two layouts which create focusing and defocusing field. 3 slug tuners are placed inside the cavity to adjust radio frequency.

DESIGN

The model of the tank is created using Comsol Multiphysics - a general-purpose software platform, based on advanced numerical methods, for modeling and simulating physics-based problems [2].

Field Distribution

In the model with preliminary calculated parameters, the first thing to adjust was a resonance frequency of the electric field. The working frequency is 432 MHz. To gain this value the following parameters were altered: cavity diameter, inner and outer diameter of drift tubes, slug tuners.

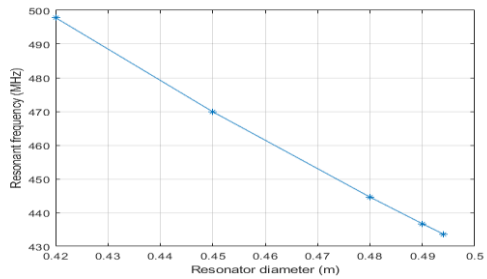


Figure 2: Dependence of the cavity resonant frequency on the cavity diameter.

At first, cavity diameter was estimated (Fig. 2). For the desired value of frequency the appropriate diameter was calculated as 49.6 cm.

To adjust the resonant frequency by means of drift tube diameter at first a constant value of inner and outer diameter was used. But the results were not satisfying. Later the drift tubes were divided into three parts of 11 drift tubes with increasing outer diameter value. Thus, the inner diameter of drift tubes is constant – 16 mm, and outer diameter is 58 mm for first part, 60 mm for second and 62 for third.

The calculation in Comsol Multiphysics of the resonant frequency of the structure uses finite element method. For this purpose the mesh of around 95000 tetrahedral elements was built. While solving eigenfrequency problem Comsol solver provide a number of eigenfrequencies nearest to the specified value. As for the case of desired 432 MHz nearest values were 422.57 MHz and 436 MHz. The gap between these values seems to be tolerable enough.

Three slug tuners are mounted inside, each one of 10 cm diameter. To make the field distribution more uniform slug tuners are set as 1 cm, 1 cm and 3 cm height. After adjusting cavity diameter, drift tubes radii and slug tuners, the

† email address st016313@student.spbu.ru.

Content from this work may be used under the terms of the CC BY 3.0 licence (© 2018). Any distribution of this work must maintain attribution to the author(s), title of the work, publisher, and DOI.

ISBN: 978-3-95450-194-6 ISSN: 2226-0366 doi:10.18429/JACoW-LINAC2018-TUPO116

Content from this work may be used under the terms of the CC BY 3.0 licence (© 2018). Any distribution of this work must maintain attribution to the author(s), title of the work, publisher, and DOI.

final accelerating electrical field normalized distribution along the accelerator axis has the following shape (see Fig. 3):

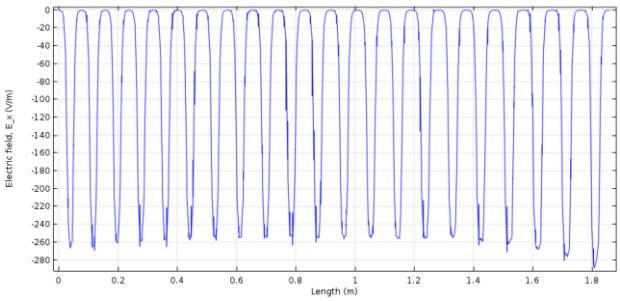


Figure 3: Accelerating electric field distribution along the axis, field frequency is 432.28 MHz.

Permanent Magnet

Permanent quadrupole magnets are placed inside some of drift tubes (Fig.4). All magnets are of the same length 5 cm.

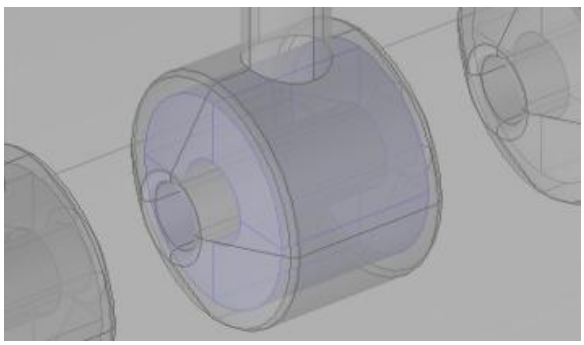


Figure 4: Permanent magnet inside drift tube.

The paper [3] presents the detailed analysis of the permanent quadrupole magnet lenses for the prototype of proton microscope for FAIR (GSI). The results from this work were used for the magnetic field distribution representation, magnetic field is assumed radial in the plane normal to the centre axis:

$$B_r = G(z) r \cos(2\varphi)$$

where $G(z)$ is a field gradient along the centre axis of accelerator and z, r, φ are polar coordinates with z-axis coincide with accelerator axis. Field gradient is approximately a rectangular function with smoothing on both ends. The variation of amplitude of the field gradient as well as magnets placing order were analysed with regard to particle dynamics.

DYNAMICS

Particles are presented as large particles with mass 10000 times bigger than real one. Particle dynamics is calculated using Newtonian 2 order equations. Forces taken into account are accelerating electric force, transverse magnetic force from lenses and Coulomb force for particle interaction. The amplitude of electric force necessary to reach 10 MeV was calculated as 10 kV/m.

The initial beam properties are shown in Table 2.

Table 2: DTL Parameters

Parameter	Value
Maximum transverse displacement	1.6 mm
Maximum relative transverse velocity	0.01
Transverse distribution type	KV
Phase space ellipse rotation angle θ	0.01 rad.
Energy spread	10%
Bunch length	10 mm

Two different types of focusing lattice commonly used were considered: FFDD00 and F0D0 (F – focusing, D – defocusing, 0 – empty drift tube). The variation of amplitude of the magnetic field gradient was studied in the range 2…10 T/m.

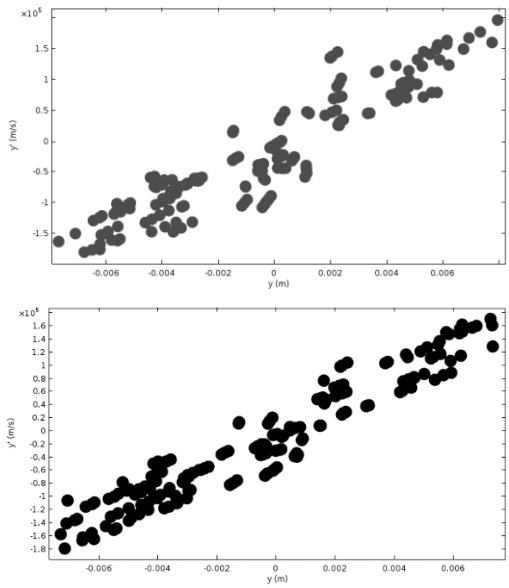


Figure 5: Transverse output beam emittance, magnetic field gradient (top) 4 T/m, (bottom) 2 T/m.

To compare the simulation results for these 2 lattices the output beam transverse emittance was estimated. The difference was negligibly small. The simulation showed than increasing the amplitude of magnetic field gradient over 4 T/m results in decrease of transmission rate. Best transverse emittance values were obtained at 2 T/m field gradient and were 10% better than at 4 T/m (Fig. 5).

REFERENCES

[1] T. Ilg et al., "Mechanical design of the drift-tube linac (DTL) for the Spallation Neutron Source," Proceedings of the 2003 Particle Accelerator Conference, Portland, OR, 2003, vol.5, pp. 2841-2843, doi:10.1109/PAC.2003.1289739

[2] Comsol Multiphysics, http://www.comsol.com

[3] Kantsyrev, A. V., et al., "Quadrupole lenses on the basis of permanent magnets for a PRIOR proton microscope prototype.", Instruments and Experimental Techniques 59.5 (2016): 712-723, doi:10.1134/S0020441216040072

ISBN: 978-3-95450-194-6 ISSN: 2226-0366 doi:10.18429/JACoW-LINAC2018-TUPO119

A DIAGNOSTICS BOX FOR THE LINEAR ACCELERATOR OF INSTITUTE FOR RESEARCH IN FUNDAMENTAL SCIENCES (IPM)

Sh. Sanaye Hajari†, S. Ahmadiannamin, M. Bahrami, H. Behnamian, S. Kasaei, H. Shaker, School of Particles and Accelerators, Institute for Research in Fundamental Sciences (IPM), Tehran, Iran
F. Ghasemi, Nuclear Science and Technology Research Institute (NSTRI), Tehran, Iran

Abstract

The IPM linac is an 8 MeV (up gradable to 11 MeV) electron linear accelerator under development at Institute for Research in Fundamental Sciences, Tehran, Iran. The design and construction of the linac is nearly finished and it is in the commissioning stage. The commissioning is planned in several phase of different energy ranging from 50 keV to 8 MeV. At each phase, appropriate diagnostics is required in order to investigate the linac performance. A diagnostics box including a scintillator view screen, a dipole magnet, and a focusing solenoid is designed to diagnose the beam longitudinal and transverse parameters in wide range of energy. These parameters are the beam transverse profile, size, position, emittance and the energy spectrum.

INTRODUCTION

The IPM linac is an electron linear accelerator with an energy and current up to 8 MeV and 10 mA, respectively. The machine is developed at the Institute for Research in Fundamental Sciences, Tehran, Iran. Labled as Iran's first linear accelerator project, nearly all the components of the linac is designed and constructed within the country, in particular, the RF amplifier system (klystron and its modulator), RF cavities, magnets and beam diagnostics systems. The main aim of this research project is to provide the scientific foundations for the future accelerator projects at IPM.

The linac consists of a thermionic electron gun followed by a pre-buncher, a travelling wave (TW) tapered phase velocity buncher and two constant impedance TW accelerating tube (see Fig.1). The TW tubes are connected together via appropriate flanges and fed with a 2 MW RF power. The tubes are embedded in solenoidal magnetic fields for the focusing. The beam energy at the end of electron gun, TW buncher, first and second tube is 50 keV, 1.4 MeV, 4.8 MeV and 8 MeV, respectively. The design of the different parts of the linac is described in [1-3] and the construction process in [4-6]. The beam parameters at the end of linac are listed in Table 1.

The construction of the linac is nearly finished and it is in the commissioning stage. The commissioning is foreseen in phases of different energies – up to the end of pre-buncher, TW buncher, first and second accelerating tubes. At each phase appropriate beam diagnostics is demanded in order to investigate the linac performance. The parameters to be measured are the beam current, the transverse beam profile, size, divergence, emittance and the energy spectrum. In order to diagnose the mentioned parameter in a relatively large range of energy a flexible diagnostics system is required. For this purpose, according to Fig. 2 a diagnostics box has been designed based on a focusing solenoid and a dipole magnet followed by a movable scintillator view screen. Such an integrated diagnostics box is capable to measure the beam transverse parameters and the energy spectrum of the beam via the beam profile measurement when the dipole magnet is off and on, respectively. At each phase of the commissioning, the diagnostics box will be installed at the end of the structure. In the next sections we first describe the beam profile monitor system then we will present how the beam transverse parameters and its energy spectrum can be extracted from the transverse profile. Special attention has been paid to the resolution of the measurement. For each parameter the resolution of the measurement has been calculated and the corresponding diagnostics system has been designed with the aim of providing the best resolution in the whole range of the energy of interest.

Table 1: Beam Parameters at the End of the Linac

Parameter	Value
Beam energy	8 MeV
Beam current (peak)	10 mA
Rms energy spread	0.23 MeV
Rms bunch length	2.3 mm
Normalised emittance	3.8 mm-mrad

BEAM PROFILE MONITOR SYSTEM

The view screen consists of a 3 cm × 3 cm YAG:Ce scintillator of 30 μm thickness on an aluminium substrate. The substrate ensures the heat and charge transfer. The substrate as well can be connected to an electronics readout system to be used as a Faraday cup for the beam current measurement. The scintillator view screen should be placed at a 45 degree angle and the visible photons are detected with an optical system consists of an aluminium mirror, an achromatic lens and a CCD camera.

† sanayehajari@ipm.ir

Content from this work may be used under the terms of the CC BY 3.0 licence (© 2018). Any distribution of this work must maintain attribution to the author(s), title of the work, publisher, and DOI.

ISBN: 978-3-95450-194-6 ISSN: 2226-0366 doi:10.18429/JACoW-LINAC2018-TUPO119

Content from this work may be used under the terms of the CC BY 3.0 licence (© 2018). Any distribution of this work must maintain attribution to the author(s), title of the work, publisher, and DOI.

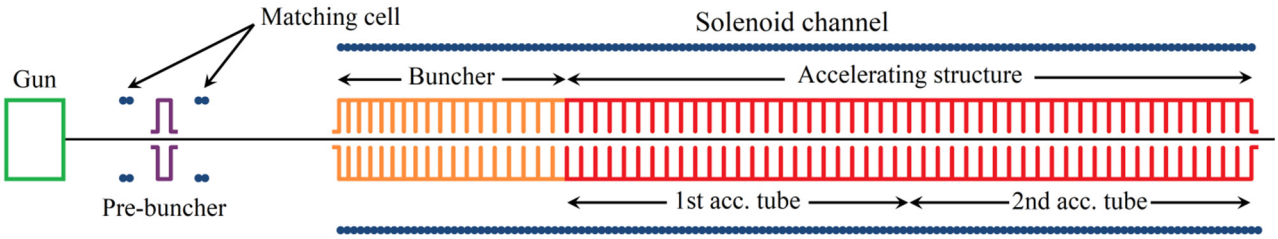


Figure 1: General layout of the ipm linac.

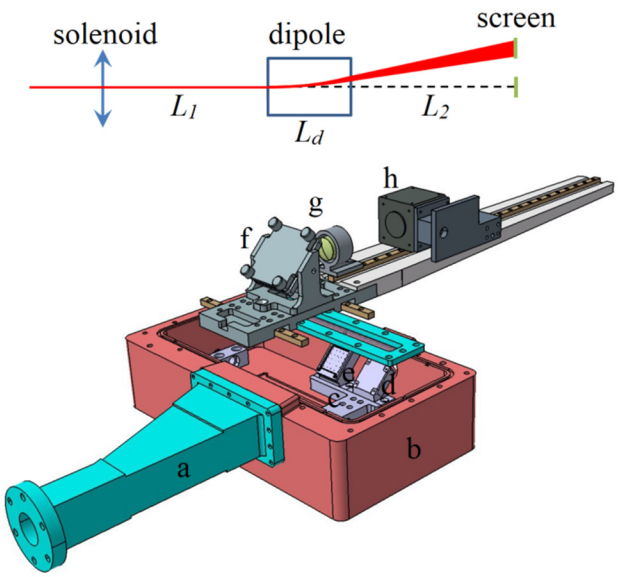


Figure 2: General layout of the diagnostics box (top) and mechanical design of the view screen holder and the optical system (bottom). Details are the dipole magnet position (a), vacuum chamber (b), movable scintillator holder (c), scintillator target (d), calibration target (e), aluminium mirror (f), achromatic lens (g) and the CCD camera (h).

Both the optical system and the scintillator view screen limit the resolution of beam profile measurement. A tilted view screen at 45 degree angle puts a limit on the resolution which can be estimated to be in the order of the illuminated thickness of the scintillator [7]. Multiple scattering of the electrons in the scintillator as well limits the view screen resolution. The resolution limit associated with this effect is estimated by Geant4 simulation [8] of particle trajectories in the scintillator material (see Fig. 3). In each case the question is how large the area of scintillator will be illuminated for an ideal point-like beam. The worst resolution of the scintillator itself in our case will be 30 µm. Several effects limit the optical system resolution. Among these are the camera pixel size and noise, spherical and achromatic aberration of the lens, diffraction and Scheimpflug effect. The optical system has been designed to provide resolution below 100 µm.

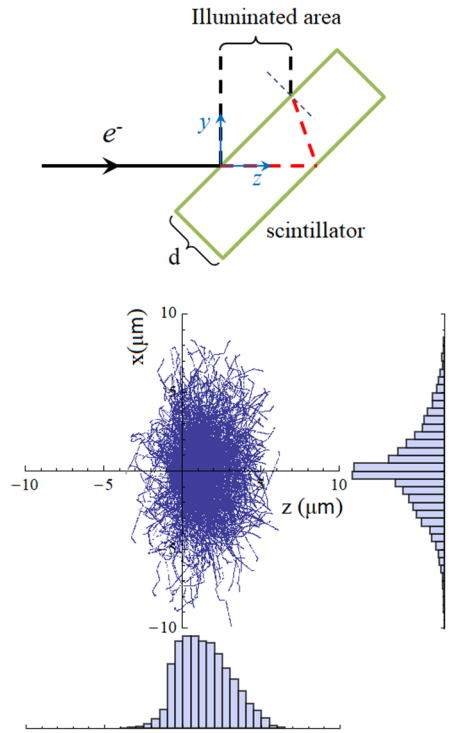


Figure 3: Resolution limiting mechanism due to tilted scintillator (up) and multiple scattering (bottom). The multiple scattering has been simulated by Geant4 for a point like beam of 50 keV energy.

MEASUREMENT OF THE BEAM TRANSVERSE PARAMETERS

The transverse beam parameters – size, divergence and emittance – can be measured using the solenoid scan process [9]. In this method according to Fig. 4, several beam sizes are measured for different solenoid focusing around the minimum beam size at the screen.

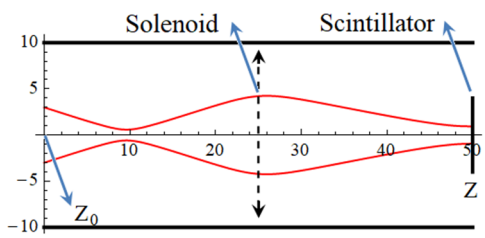


Figure 4: Solenoid scan process experimental setup.

ISBN: 978-3-95450-194-6 ISSN: 2226-0366 doi:10.18429/JACoW-LINAC2018-TUPO119

The transverse beam parameters then can be calculated using the following formula and the least square fit method [10],

$$a^2 = M_{11}{}^2 a_0^2 + 2M_{11}M_{12}a_0a_0' + M_{12}{}^2\left(\frac{\varepsilon^2}{a_0^2} + a_0'^2\right). \quad (1)$$

Here M_{ij} is the transfer matrix elements, a the rms beam size at the screen, ε the geometric emittance, a_0 and a_0' the beam size and its derivative (beam divergence) at an arbitrary origin before the solenoid. In order to determine the three unknown parameters a_0, a_0' and ε at least three measurement is required, however, more measurements provides a better accuracy. The least square fit method in addition to the unknown parameters determined the error propagation as well. Therefore, for a known resolution of beam profile measurement the relative error in other beam transverse parameters can be calculated. In our system in worst case the relative error in the emittance will be less than 20%.

ENERGY SPECTROSCOPY

After measuring the beam transverse parameters the dipole magnet can be turned on to measure the energy spectrum of the beam. Here the view screen will move transversely in order to measure the beam profile. The beam position and its horizontal size will be associated to the beam energy and its spread. Figure 5 shows an example of the beam cross section at the view screen when the dipole is off and on.

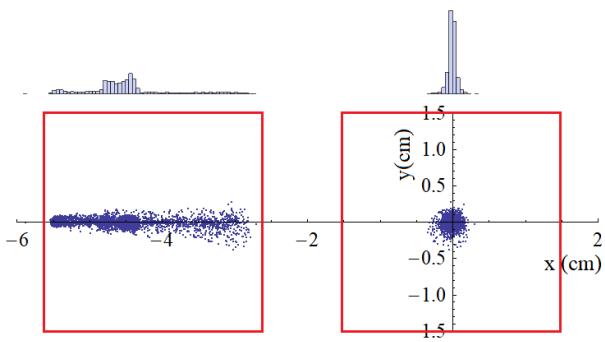


Figure 5: Beam cross section at the view screen when the dipole is off and on.

The main resolution limiting effects here are the betatron motion of the particles. It can be shown that relative error in the relative energy spread, δ, is given as [11]

$$\frac{\sigma_\delta}{\delta} = \frac{a_{off}}{a_{on}} \quad (2)$$

a_{off} and a_{on} are the horizontal beam size when the dipole is off and on, respectively. Therefore, in order to improve the resolution, the beam should be focused well at the screen when the dipole is off. This indicates the role of the focusing solenoid in the spectroscopy.

The movable view screen providing a variable bending angle ensures high resolution energy spectroscopy in a wide range of energy.

CONCLUSION

A diagnostics box has been designed in order to measure the beam parameters in a wide range of energy (from 50 keV to 8 MeV). When the dipole magnet is off the transverse parameters are measured with the solenoid scan process. Then the dipole is turned on in order to perform the energy spectroscopy. The resolution in the measurement of all parameters has been calculated. The diagnostics box provides good resolution in the whole energy range of interest.

ACKNOWLEDGEMENTS

The authors would like to sincerely thank ILSF head and staffs for their support to the IPM Linac project.

REFERENCES

[1] H. Shaker and F. Ghasemi, "Design of a Pi/2 Mode S-Band Low Energy TW Electron Linear Accelerator", in *Proc. IPAC'11*, San Sebastian, Spain, Sep. 2011, paper MOPC009, pp. 80-82.

[2] Sh. Sanaye Hajari, S. Haghtalab, H. Shaker, M. dayyani Kelisani, "RF emittance in a low energy electron linear accelerator", *Nuclear Instruments and Methods in Physics Research* Section A, 888, 250, (2018).

[3] Sh. Sanaye Hajari, H. Shaker and S. Haghtalab, "Low gradient tapered traveling wave buncher and the beam quality", to be published.

[4] F. Ghasemi, *et al.*, "Implementation of Main Waveguide Cavities of Electron Linear Accelerator Using Integrated and Separable Methods and Comparing Their Performance", *International Journal of Electromagnetics and Applications* 2012, 2(6): 163-168.

[5] F. Ghasemi, *et al.*, "Construction of Disk-loaded Buncher for S-Band Low Energy TW Electron Linac", in *Proc. IPAC'12*, New Orleans, LA, USA, May 2012, paper WEPPD063, pp. 2666-2668.

[6] F. Ghasemi, *et al.*, "Design, construction and tuning of S-band coupler for electron linear accelerator of institute for research in fundamental sciences (IPM E-linac)", *Nuclear Instruments and Methods* A, 772 (2015), p. 52.

[7] R. Barday, *et al.*, "Beam Size and Intensity Diagnostics for a SRF Photoelectron Injector in *Proc. IBIC'12*, Tsukuba, Japan, Oct. 2012, paper MOPB73, pp. 241-245.

[8] https://geant4.web.cern.ch/

[9] D. W. Storey, "A View Screen beam profile monitor for the ARIEL e-linac at TRIUMF", Master's thesis, University of Victoria, (2011).

[10] P. H. Richter, "Estimating Errors in Least-Squares Fitting", TDA Progress Report 42-122,(1995).

[11] S. Kasaei, Sh. Sanaye Hajari, M. Bahrami and H. Shaker, "Spectrometer design for diagnostics in a wide range of energy at a linear accelerator", JINST 13 P06021 (2018).

Content from this work may be used under the terms of the CC BY 3.0 licence (© 2018). Any distribution of this work must maintain attribution to the author(s), title of the work, publisher, and DOI.

ISBN: 978-3-95450-194-6 ISSN: 2226-0366 doi:10.18429/JACoW-LINAC2018-TUPO120

THE STUDY OF THE LENGTH AND SHAPE OF BEAM IN A HIGH POWER ELECTRON ACCELERATOR

M. Salehi†, F. A. Davani, B. Ghasemi, Shahid Beheshti University, Tehran, Iran
F. Ghasemi, A. Poursaleh, Nuclear Science and Technology Research, Tehran, Iran

Abstract

The output beam of a high-power linear accelerator, used for industrial purposes, is irradiated on products and scanning them. In order to improve the dosimetry of radiation which products received and to prevent loss of the attacked- beams to the edge of products, the exact evaluation of scanning length is necessary. One of the other challenges of the scanning beam is the lack of uniformity in dosimetry of received radiation. The scanning beam does not collide in parallel to the products, which is also a challenge to accelerator efficiency. To improve dosimetry of received radiation, the use of trajectory correction magnets is suggested. These magnets correct the beams that do not scan in parallel. Also, using the Monte Carlo code, the dosing rate of received radiation to products is simulated and compared in two non-uniform and uniform modes (corrected by trajectory correction magnets).

INTRODUCTION

Various types of industrial accelerators have different applications in the industry by providing an electron beams with energy range of 0.5 to 10 mega electron volts. In these accelerators, the irradiation rate of the products depends on the current and the power of the electron beam. In these accelerators, the irradiation rate to the products depends on the current and the power of the electron beam. At the present, the use of industrial electron accelerators in Iran is restricted to the Yazd radiation monitoring center of the Atomic Energy Organization, which uses TT200 rhodotron accelerators to irradiate their products [1]. At the present, the use of industrial electron accelerators in Iran is restricted to the Yazd radiation monitoring center of the Atomic Energy Organization, which uses industrial accelerators to irradiate their products. In each industrial electron accelerator, the beam enters the extraction beam section after accelerating in the acceleration part. Figure 1 shows the components of the beam extraction system of the industrial accelerator in Yazd. The diameter of output electron beam of industrial accelerators such as linac accelerators is about 1 cm to 2 cm. Therefore, to irradiate it to the product, it is necessary, the beam enters the sweeping magnet. The sweeping magnet is placed at the beginning of the horn and swept the beam into the horn according to the required scan length. Therefore, in a static state the affected cross section has same dimension of beam diameter. Therefore, it is necessary to move the box in front of the beam at the appropriate speed, which is proportional to the amount of doses required. In Fig. 1, the effect of the sweeping magnet on the electron beam is obvious.

The Power supply of the sweeping magnet is such that it starts to sweep the beam linearly from a minimum magnet current and changes with the increase of the current of the scanning angle, so that the minimum and maximum flow rates are in accordance with the angles of the beam in the two corners of the horn. The beam extraction system horn in industrial accelerators is actually a vacuum chamber, which is maintained with a suitable foil of titanium, which is vacuumed relative to room air. Determining the exact length of the scan in Horn and the need to correct the path of the beam in it, are discussed in this article [2].

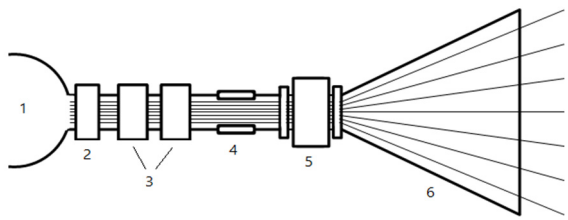


Figure 1: Components of extraction system and transmition of output beam of Linac accelerator. 1) accelerating structure, 2) control magnet, 3) quadrupole doublet, 4) diaphragm, 5) scanning electromagnet, 6) horn.

CHECK THE IMPORTANCE OF DETERMINING PRECISELY AND APPLYING SCAN LENGTH

In industrial accelerator of Yazd radiation center, the output beam of the accelerator at the beginning of the Horn are swept with a frequency of 100 Hz by a sweeper magnet in a way which some of the beams does not collide with the product, and part of the beams does not irradiate products completely and in fact part of power of input beam is wasted. This issue affects the irradiation efficiency.

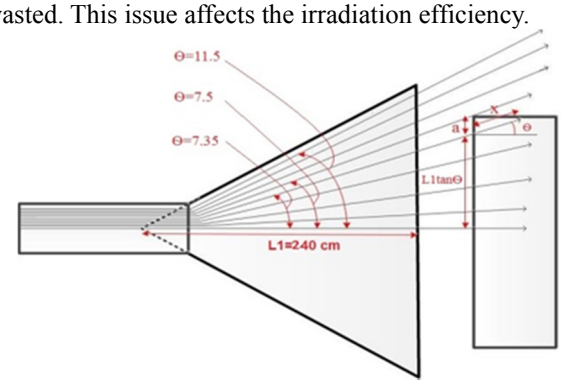


Figure 2: Geometrical parameters at the horn of the beam extraction system.

† Mohammad7salehi@yahoo.com

Content from this work may be used under the terms of the CC BY 3.0 licence (© 2018). Any distribution of this work must maintain attribution to the author(s), title of the work, publisher, and DOI.

ISBN: 978-3-95450-194-6 ISSN: 2226-0366 doi:10.18429/JACoW-LINAC2018-TUPO120

In Fig. 2, a plot of what is happening at the accelerator Horn in Yazd is shown. In this figure, the dimensions are according to reality. As can be seen, according to the dimensions of the horn, including its length and angle, and also the dimensions of the boxes and their distance from the horn, the beam will not hit the product. Studies show that in fact, in the center of irradiation in Yazd, the beam is swept up to 11.5 degrees by the corresponding magnet. This item is used to ensure that the box is properly exposed. Independent of the sweeping frequency, according to (1), the beam does not collide with the product box. Due to the dimensions of the horn of industrial accelerator in the center of Yazd, and the distance between the product box and the Horn, the scan angle is at most 7.5 degree corresponding to the hitted beam to the product box. As a result, product box in not exposed in angle between 7.5 to 11.5 degrees.

ratio of non-collision = (2×(11.5-7.5))/(2×11.5)= 35%

This calculation shows that about 35% of the power of the beam does not hit the product. For example, if the nominal output power of the accelerator is 100 kW, then 35 kilowatts will not reach the product. With an efficiency of 40% for the Rhodotron TT200, 87.5 kW of power consumption will actually be wasted. The results show that an accurate re-examination of the scan length proportional to the dimensions of box is significant, and this issue requires high precision in each irradiation center. The collision of the divergent beam to the box also causes non-uniformity in the curve of percentage of deep dose. In fact, applying a divergent beam change shape of the curve of percentage of deep dose depending on the angle of inclination, α, which is the angle between the central axis of the beam and the perpendicular axis of the product. The larger angle results decreasing in depth of maximum dose and increases the magnitude of the maximum dose. Increasing dose is due to increasing of the electron flux on the central axis of the electron beam [3]. A comparison between these two states of divergent and perpendicular collision, was performed using Monte Carlo simulations in the MCNPX code to examine the power of output beam exits from horn of the industrial electron accelerator. To reduce simulations, one-way radiation is considered. To simulate the divergent collision, assume a source corresponding an electron beam with a diameter of 2 cm above the box with dimensions of 45 cm × 45 cm × 22 cm that containing spice with a density of 0.6 cm3.

For perpendicular collision is also considered to be a source with dimensions of 2 cm × 90 cm above the box. The box is also meshed with a 1 × 0.2 cm square in the transverse plane. The output of these simulations is processed using the MATLAB program, and Fig. 3 shows the distribution of doses in the transverse plane of the beam. In Fig. 4, the difference in the distribution of doses in the box is observed in both the normal and divergent radiation conditions. In the corners of the box, the maximum dose is closer to the surface, indicating the non-uniformity distribution of the dose.

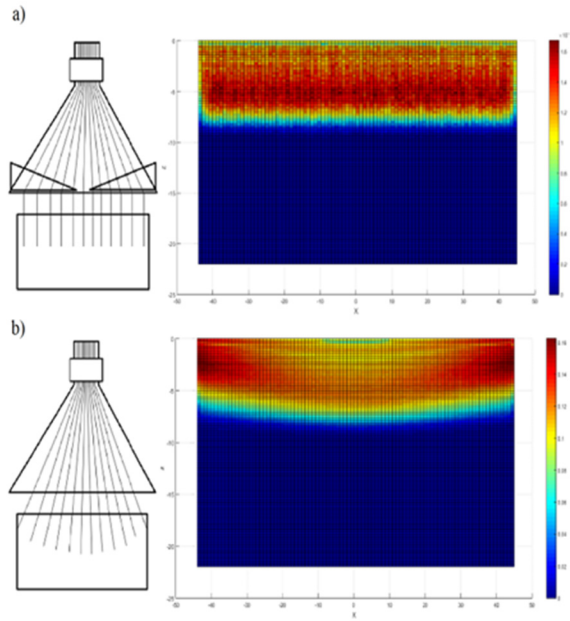


Figure 3: Distribution of doses on the transverse plate. a) perpendicular irradiation. b) divergent irradiation.

As mentioned above,in many radiation center such as in Yazd's center using the scanning angle larger than box length to ensure definite radiation exposure of the products. By this choice, the undesirable effect of moving the box on pallets located on the corresponding conveyors is also eliminated. But this item can be repaired by implementing the proper mechanism for the exact location of the boxes and there is no need to increase the length of the scan for this purpose. . Another solution to fix this problem is the use of suitable magnets on both ends of the horn to direct the beam with larger angles into the product box. In addition to fixing this problem, this magnet can also be effective for perpendicularity the beams which irradiate product, which is discussed in the next section of the paper.

CONCEPTUAL DESIGN OF CORRECTION MAGNET

Before the design of the correction magnets of the electron beam path, for the verification of their designs and simulations, the bending magnets in the Yazd center accelerator were simulated and compared with experimental values. For different energies for the electron beam, the required current in the coils and the magnetic field generated by the magnet, is calculated. These values are compared with the experimental values measured by the magnetic probe. For example, in an energy of 3 MeV, the error of measurements between simulation and experimental values is 13% and 12% for the magnetic field and current, respectively. But magnets used to correct the electron beam path at the end of the horn are of the C-shaped type of bipolar magnets. By applying the current to coils of magnet, the magnetic field is created between the magnet's gap. Magnet's cores are in the form that exposure a larger magnetic field as the beam bends towards the coils. Therefore,

Content from this work may be used under the terms of the CC BY 3.0 licence (© 2018). Any distribution of this work must maintain attribution to the author(s), title of the work, publisher, and DOI.

ISBN: 978-3-95450-194-6 ISSN: 2226-0366 doi:10.18429/JACoW-LINAC2018-TUPO120

Content from this work may be used under the terms of the CC BY 3.0 licence (© 2018). Any distribution of this work must maintain attribution to the author(s), title of the work, publisher, and DOI.

any particle that travels longer in the distance between the gaps will have more magnetic force and a larger deviation.

These magnets were simulated using the CST STUDIO SUITE 2017 software. To simulate an electron beam with energy of 10 MeV, it diverges through the inside of the horn. The maximum magnetic field designed magnets for a beam of 10 MeV and 10 mA, is about 240 Gauss.

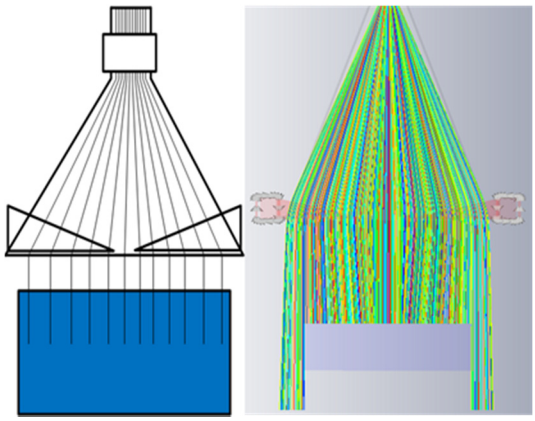


Figure 4: Use of correcting magnets located at the exit window of the horn allows changing the path of the beam.

CONCLUSION

A significant part of the output beam of industrial accelerators that is not exposed to the product due to the lack of optimal collisions it will be lost. With the calculations we found that much of the accelerator power was lost at a scan angle between 7.35 and 11.5 degrees, so that it was determined that the length of the scan should be adjusted to minimize the amount of loss. on the other hand Using magnets that correct the collision path to the product, more efficient systems can be obtained. These magnets are predicted to be about 240 Gauss with a magnetic field.

REFERENCES

[1] Y.Jongen, M.Abs, T. Delvigne, Arnold Herer, “RHodotron Accelerators for Industrial Electron-beam”, Ion Applications, France, 1980.

[2] V. Bezuglov, A. Bryazgin, B. Faktorovich, E. Kokin, V. Radchenko, E. Shtarklev, A. Vlasov., “Beam Extraction System for Industrial Electron Accelerator Ilu-14”, in Proc. RUPAC2012, Saint-Petersburg, Russia.

[3] K. E. Ekstrand and R. L. Dixon. "The Problem of Obliquely Incident Beams in Electron-beam Treatment Planning." Med. Phys. 9, 276-278 (1982).

ISBN: 978-3-95450-194-6 ISSN: 2226-0366 doi:10.18429/JACoW-LINAC2018-TUPO127

ACTIVITIES AT THE LINAC4 TEST STAND

J-B. Lallement†, V. Bencini, S. Bertolo, F. Di Lorenzo, J. Lettry, A. M. Lombardi,
C. Mastrostefano, D. Noll, M. O'Neil,
CERN, Geneva, Switzerland

Abstract

Linac4, the new CERN H- injector to the Proton Synchrotron Booster, has been commissioned and has delivered a beam intensity and quality calculated to be sufficient to produce the standard beams for LHC and the high intensity beams for ISOLDE when connected. The beam current is nevertheless half of what is foreseen and the problem has been identified at the low energy end, between the extraction and the matching to the RFQ. The Linac4 test stand is being used to address this issue by testing different extraction geometries and different plasma generators. A fast method to access the current in the RFQ acceptance has been put in place. This paper reports the results of the measurements obtained so far.

INTRODUCTION

Linac4 is a 160 MeV H- normal conducting linear accelerator that is about to replace the present Linac2 as injector to the whole CERN proton accelerator complex. After a staged commissioning successfully completed in fall 2016, the linac underwent several test runs in 2017 and 2018 during which its performance, reliability and availability were recorded and optimized [1]. Linac4 has met all the required beam quality parameters needed for creating the various beams that the PSB is currently producing from the LHC beams to the fixed-target experiments beams. This is possible with a beam intensity of 25 mA, which represents 60% of the nominal intensity (40 mA). Nevertheless, to open the door to higher intensity in the CERN complex a current of 40 mA is needed. The intensity limitation comes from the pre-injector because the emittance of a 50mA beam from the present source exceeds the RFQ acceptance. For the present source a maximum current of 25 mA falls in the RFQ acceptance. A dedicated test stand, in operation for source development since 2008, is now dedicated to addressing this issue.

THE LINAC4 TEST STAND

The Linac4 pre-injector is made of a RF source, which can provide a 600 µs, 50 mA H- beam at 45 keV with a maximum repetition rate of 2 Hz, and a 352MHz, 3 m long Radio Frequency Quadrupole, bunching and accelerating the beam to 3 MeV. Acceleration is loss-less from 3 MeV onwards and no emittance growth has been observed for peak currents up to 25 mA. The 45 keV beam extracted from the source is matched to the RFQ via a Low Energy Beam Transport line housing 2 magnetic solenoids, an electrostatic pre-chopper, two steerers, a mechanism to inject different gases to influence neutralisation and a beam current transformer and time resolved profile harps for diagnostics.

The Linac4 set-up is not suitable for in-depth studies and source tests. Therefore, a replica of the Low Energy Beam Transport has been assembled at a dedicated test stand, which is equipped with extra diagnostics including a slit-and-grid, time resolved emittance meter, a Faraday cup and profile harps. A very effective procedure to reconstruct a sample beam from emittance measurements has been described in [2] and it has been extensively used to estimate the number of particles falling into the RFQ acceptance and the matching conditions. In parallel a more rapid method has been put in place. This method is based on simulating the RFQ acceptance by a series of four transverse collimators (the mask) and obtaining the current into the RFQ acceptance by measuring the current with a Faraday cup placed downstream. This method, besides being faster, is more suitable for an automatic optimisation of the LEBT parameters (focusing and steering). The layout of the test stand is show in Fig. 1.

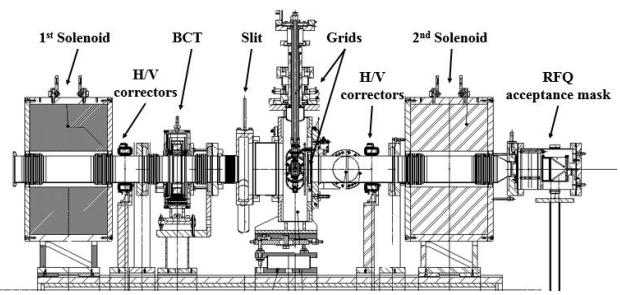


Figure 1: Linac4 test-stand layout.

The RFQ Acceptance Mask

The RFQ acceptance mask device is made of four intercepting plates with squared aperture restrictions. The aperture size and their relative distances are chosen such that only the particles within the RFQ acceptance can pass through all four aperture restrictions. Extensive calculation under different regimes of space charge distribution and intensity have been performed to validate this device.

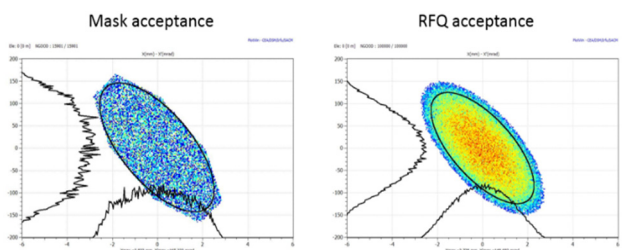


Figure 2: Comparison between the Linac4 RFQ and the mask transverse acceptances at zero current. Mask acceptance on the left, RFQ acceptance on right.

† jean-baptiste.lallement@cern.ch

Content from this work may be used under the terms of the CC BY 3.0 licence (© 2018). Any distribution of this work must maintain attribution to the author(s), title of the work, publisher, and DOI.

ISBN: 978-3-95450-194-6 ISSN: 2226-0366 doi:10.18429/JACoW-LINAC2018-TUPO127

Content from this work may be used under the terms of the CC BY 3.0 licence (© 2018). Any distribution of this work must maintain attribution to the author(s), title of the work, publisher, and DOI.

A comparison between the Linac4 RFQ acceptance as obtained by the code PARMTEQ [3] and the mask acceptances is shown in Fig. 2. The areas and the orientation of the two acceptances ellipses are very similar. As the mask is built with a finite number of aperture restrictions, the edges of the mask acceptance are sharp. The phase advance between the four plates is chosen close to 45° such that the cuts are uniformly distributed around the ellipse.

In order to validate the mask prediction, a variety of beam distributions were simulated through both the Linac4 RFQ and the mask using PARMTEQ [3] and Toutatis [4] for the RFQ simulations and Travel [5] and TraceWin [6] for the mask. In all the tested cases, the mask gives a slightly higher transmission than the RFQ (the highest overestimation is 5%). This discrepancy can be explained as the mask only reproduces the transverse losses, and not the longitudinal losses that occur in the RFQ during the bunching and acceleration processes. It is nevertheless a good guideline for the quality of a source. A sketch of the RFQ acceptance mask is shown in Fig. 3.

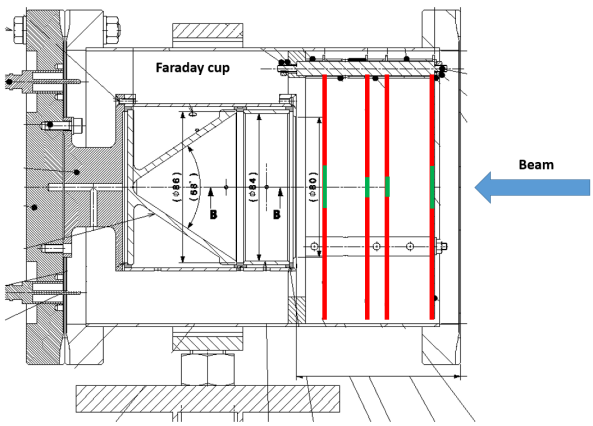


Figure 3: RFQ acceptance mask layout. The intercepting plates in red, with square holes in green (not on scale) are located upstream of a Faraday cup.

IS03 SIMULATION AND MEASUREMENT

The H^- ion source of Linac4 consists of a plasma generator driven by a 2 MHz RF at powers up to 100 kW, and the extraction system shown in Figure 4. Further information on the plasma generator and on the design of the extraction system can be found in [7, 8].

A puller-dump electrode at nominally 10 kV relative to the source, extracts the H- beam along with a significant amount of electrons. Depending on the mode of operation, the ratio between electrons and ions is in the range of 10 to 50 (volume mode). If a small amount caesium is evaporated into the plasma chamber (surface mode), this ratio can be reduced to around one. The puller-dump electrode houses a set of magnets that deflects the electron beam into a cup set into the side of the electrode. Electron currents up to 3 A can be dumped.

After the electrons are dumped, the beam is accelerated to the full energy of 45 keV and additionally focussed by an einzel lens at voltages up to 30 kV.

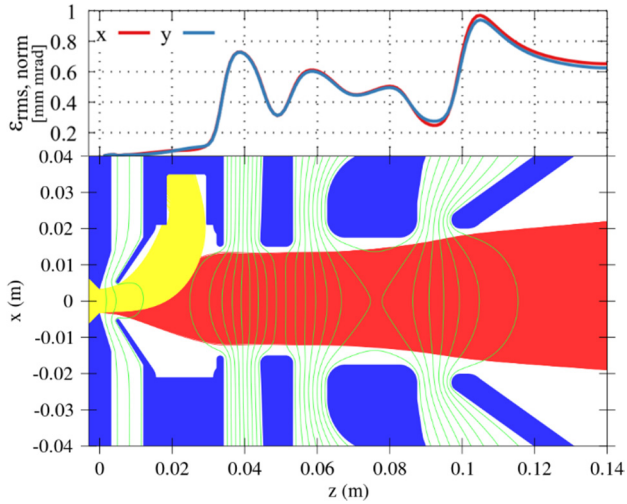


Figure 4: Schematic and emittance evolution of the Linac4's IS03 extraction system at 50 mA beam intensity and an electron to ion ratio of 20.The voltages on the electrodes are (starting from the left) -45kV, -35kV,0,30kV,0.

Predictions from Simulation

The beam emittance depends on two parameters: the current extracted from the source and the puller-dump voltage. The influence of these parameters was studied using IBSIMU [9]. Figure 5 shows a comparison of measured and simulated emittances for the operational range of the puller-dump voltage. During the measurements, the electron to ion ratio was in the range of 1 to 3. For these values, IBSIMU simulation predicts that the emittance remains almost constant in the range from 8-10 kV, while in the simulation there is a dramatic increase towards lower voltages. We observe, however, that for an artificial e/H ratio of 20, the measured emittance are well reproduced. This applies to all rms beam parameters, and when comparing the dependence of the emittance on the beam current.

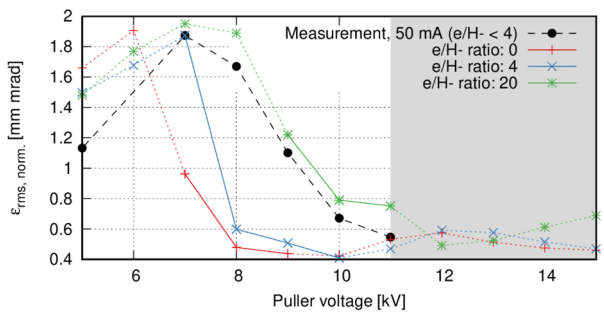


Figure 5: Emittance as a function of puller voltage. Measured data e/H=1-3) and IBSIMU results for different e/H.

Figure 4 shows the evolution of the rms emittance of a 50 mA beam along the system. Since the emittance does not grow significantly until after the electrons are dumped, the differences in emittance for different e/H ratios is not due to aberration caused by the deflected electrons.

However, increasing the current of the co-extracted electrons increases the space charge density in the extraction gap, causing the meniscus to be less and less concave or even convex for higher electron currents. The beam thus

ISBN: 978-3-95450-194-6 ISSN: 2226-0366 doi:10.18429/JACoW-LINAC2018-TUPO127

starts with a higher divergence and passes the rest of the extraction system with a larger size. Due the larger filling degree of the electrodes, the result is aberration and emittance growth further downstream. A large fraction of this growth occurs at the end of the puller-dump electrode, which also acts as a focusing lens.

The higher-than-expected emittance of the beam is thus largely due to aberration caused by a shift in meniscus compared to the assumptions. One possible way to improve the beam quality without a radical redesign is to adapt the extraction gap to the rest of the system.

We simulated a variety of changes to the system:

1. Reducing the distance between plasma electrode and puller electrode causes a higher extraction field and thus a more concave meniscus. Predicted improvement in rms emittance for 1 mm shift around 15% between 40 and 60 mA.

Along with option 1:

2. A larger angle on the plasma electrode causes higher electrostatic focussing and thus a smaller beam in the rest of the system. Predicted improvement in rms emittance at 30° instead of 17°, around 15% between 40 and 60 mA.
3. A larger bore causes the meniscus to be more concave. With a diameter of 7.5 mm instead of 6.5 mm, improvements of up to 50 % in the rms emittance at 60 mA are predicted; however, there is no improvement or even a degradation below 40 mA.

Emittance Results in Volume Mode

All three options were implemented at the test stand and emittances measured in un-caesiated (volume) mode with the idea of testing only the configuration that showed the largest improvement in surface mode.

The control of the emittance meter was automatized using python, making it possible to scan a large number of source settings while recording the beam current and the electron-to-ion ratio.

The emittance measurements contain a signal from particles neutralized in the extraction system. This signal was cut and a noise filter applied, which removes a signal if the sum of the signal in the surrounding area is below a small threshold. The measured rms emittances are plotted in Fig. 6 as a function of beam current.

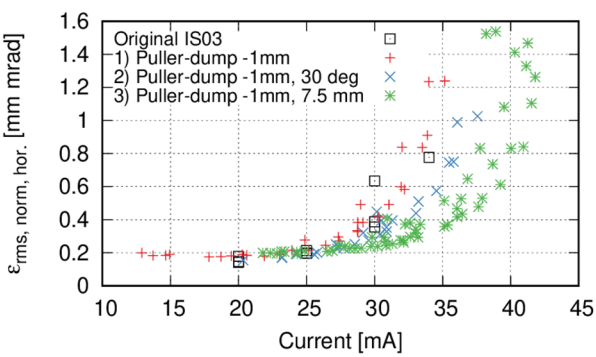


Figure 6: Measured rms emittance for the different electrode configurations. Differences in the electron to ion ratio cause the spread of values at fixed current.

In volume mode, both increasing the angle of the plasma electrode and increasing the plasma bore results in an improvement of the rms emittance and the maximum current, while the movement of the puller-dump electrode shows no clear effect.

Backtracking the measured phase-space distributions of the electrode with 7.5 mm bore diameter and matching these to the acceptance of the RFQ suggests a maximum transmission of up to 32 mA for a source current of 35 mA in volume mode.

MASK MEASUREMENT RESULTS

As for the emittance measurements, transmission through the mask was measured for a wide range of source parameters. Figure 7 shows the maximum current transmitted through the mask as a function of the current provided by the source. As for the emittance measurements, the spread in transmission at fixed currents is caused by differences in electron to ion ratio. Due to venting of the system during installation of the mask, the electron to ion ratio was larger during the mask measurements, also limiting the currents that could be reached.

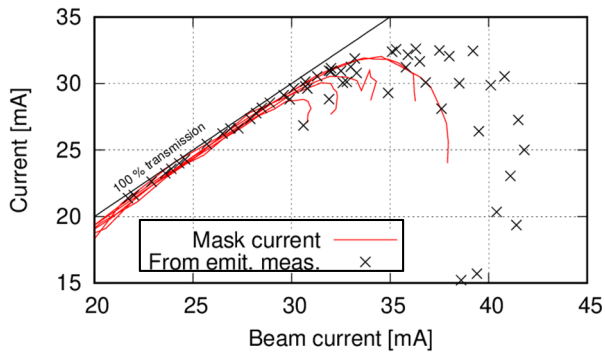


Figure 7: Current through the mask (lines) as a function of the source current in comparison to the current within the RFQ acceptance calculated from emittance measurements.

Both measurement techniques give the same prediction for the RFQ transmission, a maximum of 32 mA for source currents of about 35 mA. In the future, a similar scan will verify the predictions on the Linac4 RFQ.

CONCLUSION AND OUTLOOK

The measurements of different electrode geometries at the Linac4 test stand have given an important insight on how to improve the current through Linac4 RFQ. The technique of measuring a current passing through a system that reproduces the acceptance of the RFQ has been validated. In the future, it will speed up the qualification of a source for the Linac4 RFQ. The slit-and-grid emittance measurement device allows complementing these information with knowledge of the beam distributions and the time structure along the pulse.

Content from this work may be used under the terms of the CC BY 3.0 licence (© 2018). Any distribution of this work must maintain attribution to the author(s), title of the work, publisher, and DOI.

ISBN: 978-3-95450-194-6 ISSN: 2226-0366 doi:10.18429/JACoW-LINAC2018-TUPO127

Content from this work may be used under the terms of the CC BY 3.0 licence (© 2018). Any distribution of this work must maintain attribution to the author(s), title of the work, publisher, and DOI.

REFERENCES

[1] A.Lombardi, "Commissioning of Linac4", these proceedings.

[2] G. Bellodi, V. A. Dimov, L. Hein, J.-B. Lallement, A. M. Lombardi, O. Midttun, R. Scrivens, P. Posocco, "Linac4 45 keV Proton Beam Measurements", in *Proc. Linac'12,* Tel Aviv, Israel*,* Sep 2012, paper THPB011, pp.867-869.

[3] KR. Crandall, TP. Wangler, "PARMTEQ a beam-dynamics code for the RFQ linear accelerator", in Proc. 8th AIP Conference 11/1988; 177(1): 22-28.

[4] R. Duperrier, "Toutatis: A radio frequency quadrupole code", Physical review special topics, Vol. 3, 124201 (2000).

[5] A. Perrin, JF. Armand, "Travel v4.06 user manual", CERN internal note, 2003.

[6] TraceWin
http://irfu.cea.fr/dacm/logiciels/

[7] J. Lettry *et al*., "Linac4 H− ion sources", *Review of Scientific Instruments 87*, 02B139 (2016)

[8] D. Fink *at al*., "H− Extraction Systems for CERN's Linac4 H− Ion Source", Nuclear Inst. and Methods in Physics Research, A Ms. Ref. No.: NIMA-D-18-00635R1

[9] T. Kalvas *et. al*., "IBSIMU: A three-dimensional simulation software for charged particle optics", *Rev. Sci. Instrum*. 81, 02B703, (2010)

ISBN: 978-3-95450-194-6 ISSN: 2226-0366 doi:10.18429/JACoW-LINAC2018-TUPO130

THE DESIGN OF HEPS MAGNET DATABASE AND APPLICATIONS

Y. S. Qiao[1], P. Chu, F. S. Chen[1], Institute of High Energy Physics, 100049 Beijing, China
[1]also at University of Chinese Academy of Sciences, 100049 Beijing, China

Abstract

HEPS (High Energy Photon Source) is a planned ultra-bright and extremely low emittance synchrotron light source which will contain about 2500 magnets. The magnet related data including design, measurements, tests, and operation are typically scattered in various storages which can be hard to access for high-level purposes. For such a large number of magnets, it is very important to have essential magnet information systematically stored in relational databases for efficient management and applications. This paper outlines the conceptual and the functional design for the HEPS magnet database and its associated applications, mainly for design of the database schema and application software architecture. This database is developed with MySQL. To provide a better view and access function of magnet related data, a web-based management platform has been developed for data uploading, querying and data managing.

REQUIREMENTS ANALYSIS

Magnets are among the most important components for a charged particle accelerator. From physics and engineering design to online operation, many kinds of information will be generated. The HEPS magnet related data workflow is shown in Fig. 1. We would like to capture and store all essential data regarding a magnet. For the moment, the Magnet Database is focused on related needs of magnet data management, which includes support for a few particular magnet measurement methods. It should be easy to add more measurement method support at any time. Applications for this database will provide magnet operation curves for the control system [1].

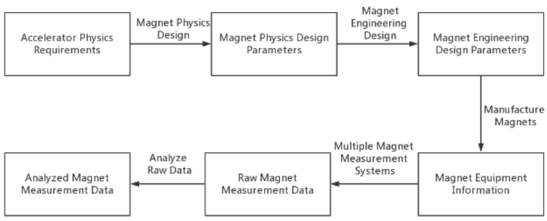


Figure 1: Magnet related data workflow.

Besides the magnet database mentioned here, it is also necessary to establish links for other related data. As magnets being installed and becoming part of the accelerator, the magnet operation data will then be collected and related to this magnet database. Again, the link between the Magnet Database and operation database is through the manufacture equipment ID tag.

DATABASE DESIGN

There are many magnets related data for an accelerator and various applications need to access a combination of these data. With an overall consideration, it is better to store such complicated data in a well-organized relational database like MySQL.

Conceptual Structure Design

The database schema design is implemented to MySQL database systems via MySQL Workbench. The schema holds the following data: magnet design data, magnet measurement data, magnet excitation curve data, and magnet operation or beam-based measurement data in the future. The complete database design schema generated by MySQL Workbench is shown in Fig. 2.

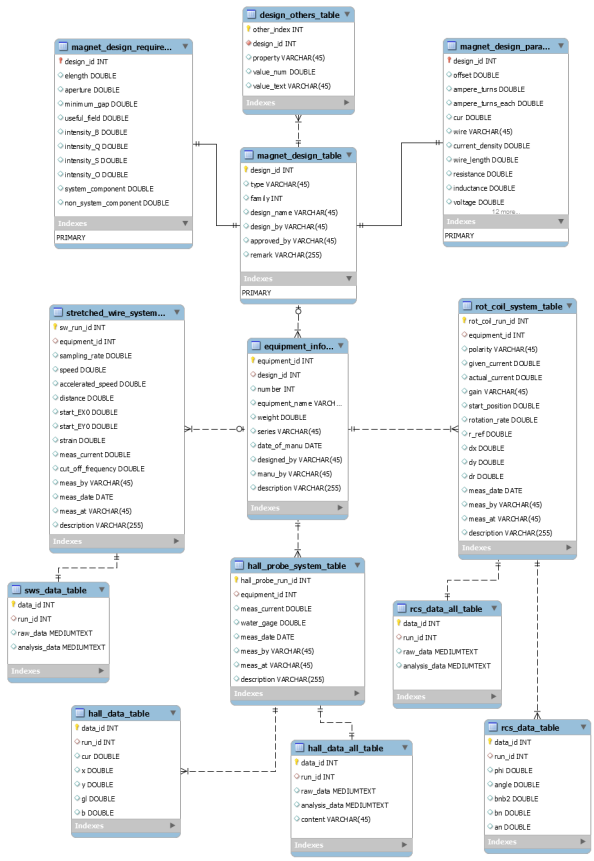


Figure 2: Magnet database schema.

Logical Structure Design

From conceptual design to the logical database design is an important part of the design process. EER (Enhanced entity–relationship) model concept design phase was to reflect the needs of the magnet data model, regardless of the specific DBMS. In order to establish the

Content from this work may be used under the terms of the CC BY 3.0 licence (© 2018). Any distribution of this work must maintain attribution to the author(s), title of the work, publisher, and DOI.

ISBN: 978-3-95450-194-6 ISSN: 2226-0366 doi:10.18429/JACoW-LINAC2018-TUPO130

Content from this work may be used under the terms of the CC BY 3.0 licence (© 2018). Any distribution of this work must maintain attribution to the author(s), title of the work, publisher, and DOI.

required database, conceptual models need to be converted to a specific DBMS support data model. Logical design results based on MySQL are shown in next three sections, including the description of each table and its main fields.

Magnet Design Data

The magnet design section includes the following tables:

- Physics design requirements table
- Engineering design parameters table
- Basic design information table
- User defined parameter table

All the basic parameters such as type and family are stored in design information table, so they can be easily related to other tables and data. The physics design requirement table and engineering design parameter table hold specific magnet design parameters and drawings. The user-defined table was designed to allow different kinds of magnet design with various and flexible parameters. We choose the property name-value pair so the table is general enough for handling most design parameter types.

Magnet Equipment Information Data

The magnet equipment information table is the centre of the whole schema. It connects the data generated before and after the magnet is manufactured by the equipment ID parameter. The table includes the basic information of actual magnets, such as equipment name, weight and series number. Magnet operation data will be stored in Physics database in the future which may provide analysis such as Beam-based Alignment (BBA) results and connect with device information table to add magnet installation and runtime data.

Magnet Measurement Data

The magnet design section contains three measurement systems:

- Stretched wire system
- Rotating coil system
- Hall probe system

All these systems include a measuring condition table and several measured data tables. The measuring condition table stores specific parameters of each system along with the measured date, site performed the measurement and testers' names. Measurement raw data are stored in text format which can be easily exported. For rotating coil and hall probe systems, some formatted raw data can be extracted from the original data files in Excel into MySQL tables and become easier to access and analyse. Users can upload these Excel files through a web-based management platform for now and this function can be plugged into magnet measuring system to upload and extract automatically. Measurement analysis data can be in many different file types, so it is uploaded and saved in the database rather than extracting numbers into MySQL tables. For better query efficiency, the file is saved to a local server machine and the path to the file is stored in the database.

MAGNET MANAGEMENT PLATFORM

The magnet management platform is responsible for providing data upload, access, and display functions through a web browser. People in charge of the magnet design, device registration and measurement can upload the related information separately. All these data sections can be retrieved by several query conditions. Since the tables in MySQL are linked with each other by primary keys and foreign keys, the related data is easily accessible when query specific data.

Key Technologies

The web-based management system provides several data upload and query pages. One can upload magnet data by filling in a simple form or query the wanted information by selecting query conditions.

Data persistence is managed by the Java Persistence API (JPA) which is a standard API for accessing databases from within Java applications [2]. The main advantage of JPA over JDBC (the base Java API for interacting with databases) is that in JPA data is represented by classes and objects rather than by tables and records as in JDBC. Using plain old Java objects (POJO) to represent persistent data can significantly simplify database programming. In this project, every magnet table is represented by an entity object and all the entity objects are stored in MySQL database. Several popular JPA implementations are Hibernate, TopLink, EclipseLink and Open JPA. These implementations are Object Relational Mapping (ORM) tools. The mapping bridges between the data representation in the relational databases (as tables and records) and the representation in the Java applications (as classes and objects). Compared with other ORM tools, EclipseLink is more standard compliant, since it is the reference implementation for JPA 2. Therefore, it is chosen for the implementation of the JPA.

The MVC pattern is applied to the web-based query platform [3], as shown in Fig. 3.

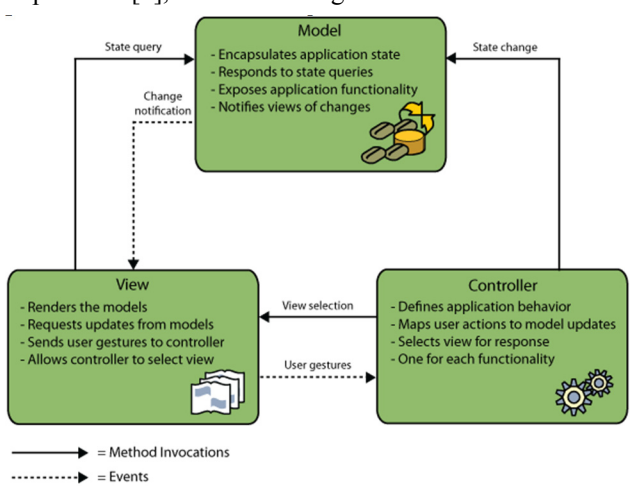


Figure 3: MVC pattern.

ISBN: 978-3-95450-194-6 ISSN: 2226-0366 doi:10.18429/JACoW-LINAC2018-TUPO130

Data Upload

Figure 4 is the design data upload page. Since the magnet design types are limited, all of the magnet design data is required to upload from the uploading form. The form can be divided into four parts: physics design, engineering design, other information and design drawing.

To keep the magnet data uniform, every set of input data is restricted to its own type and format according to its parameters. Users can also add new magnet types, families, and parameters through the GUI buttons.

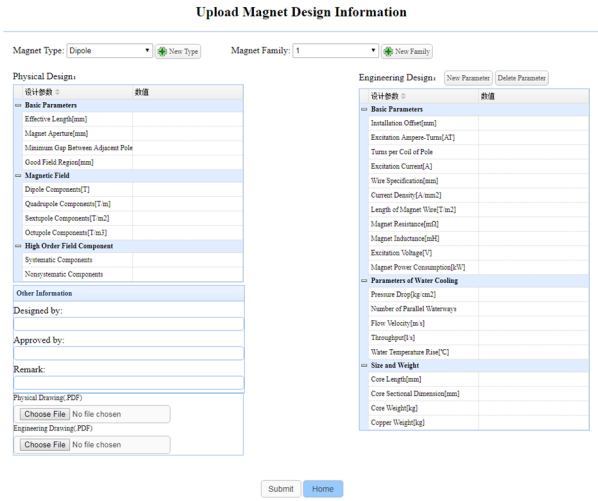


Figure 4: Magnet design upload page.

Every magnet device is linked to one uploaded design, so when uploading the magnet device information, users need to search the design data and select the right design type. Because of the big number of magnets, the magnet device data can be load by batch, and users can upload multiple pieces of device information at one time.

Magnet measurement information page requires users to select the tested device at the very beginning, and then fill in some basic measurement conditions as well as select a raw data file and multiple analysed files to upload.

Data Query

Since the design data, device data and measurement data are all linked by equipment ID tag, users can get all the related data when querying a specific magnet. When queried device information is retrieved, users can simply click the "get the design information" link to open the design data table and get the detail information. The "get the measurement information" button is used to redirect to the measurement data page. After choosing a measurement type, all the measurement conditions will be listed. Clicking the "check measurement files", a file list will then pop out for users to download all the files.

The design information and measurement data can also be queried independently with multiple search terms, such as magnet type, magnet family or magnet intensity.

SUMMARY AND OUTLOOK

The magnet database and its web-based management platform can satisfy the functional needs of users and the data can be processed steadily through the system analysis, system design and system development stages. Through understanding of magnet data and related device operation flow, we put forward some ideas and prospects for future development and software system upgrading:

- Connecting with beamline and naming databases to record the online magnet information and process variables in EPICS (Experimental Physics and Industrial Control System).
- Adding the upload model of the magnet measure system and implement the automatic magnet measurement data upload function.
- By using the Machine Learning Platform [1], the online status and service life of magnet equipment can be monitored and predicted.

REFERENCES

[1] C.P. Chu, Y.S. Qiao, C.H. Wang and H.H. Lv, "HEPS High-Level Software Architecture Plan", in *Proc. 9th Int. Particle Accelerator Conf. (IPAC'18)*, Vancouver, Canada, Apr-May 2018, pp. 1884-1887, doi:10.18429/JACoW-IPAC2018-WEPAF030

[2] JPA, https://www.objectdb.com

[3] MVC Pattern, https://netbeans.org/kb/docs/javaee/ecommerce/design.html#mvcDiagram/

Content from this work may be used under the terms of the CC BY 3.0 licence (© 2018). Any distribution of this work must maintain attribution to the author(s), title of the work, publisher, and DOI.

ISBN: 978-3-95450-194-6 ISSN: 2226-0366 doi:10.18429/JACoW-LINAC2018-TUPO132

IMPLEMENTATION OF THE BEAM LOADING COMPENSATION ALGORITHM IN THE LLRF SYSTEM OF THE EUROPEAN XFEL

L. Butkowski*, Julien Branlard, Mathieu Omet, Radoslaw Rybaniec,
Holger Schlarb, Christian Schmidt,
Deutsches Elektronen-Synchrotron DESY, Hamburg, Germany

Abstract

In the European XFEL, a maximum number of 2700 electron bunches per RF pulse with beam currents up to 4.5 mA can be accelerated. Such large beam currents can cause a significant drop of the accelerating gradients, which results in large energy changes across the macro-pulse. But, the electron bunch energies should not deviate from the nominal energy to guarantee stable and reproducible generation of photon pulses for the European XFEL users. To overcome this issue, the Low Level RF system (LLRF) compensates in real-time the beam perturbation using a Beam Loading Compensation algorithm (BLC) minimizing the transient gradient variations. The algorithm takes the charge information obtained from beam diagnostic systems e.g. Beam Position Monitors (BPM) and information from the timing system. The BLC is a part of the LLRF controller implemented in the FPGA. The article presents the implementation of the algorithm in the FPGA and shows the results achieved with the BLC in the European XFEL.

INTRODUCTION

The European X-Ray Free Electron Laser (XFEL) [1] is coherent light source providing laser pulses of tunable wavelength by the SASE process. It uses an electron beam accelerated to 17.5 GeV in 2 km long superconducting linac, which operates in a pulsed mode. The main superconducting linac in XFEL has been divided into 25 RF stations. Each of the RF stations consist of four cryogenics accelerating modules (CM), one klystron and a dedicated LLRF system that is split into master and slave subsystems [2].

The XFEL general bunch pattern consists of up to 2700 electron bunches with a variable charge distribution at a repetition rate of 4.5 MHz. To ensure highly reproducible and stable photon pulses for users, it is required to regulate precisely the RF filed inside the accelerating cavities, which should be ensured by the Low Level RF (LLRF) system.

The key element of the LLRF system is the digital feedback controller, which is a distributed system that has been implemented in Micro Telecommunications Computing Architecture (MTCA.4) [3]. Its main task is to compensate for field perturbations inside cavities using the feedback information about this field. However, high beam current can cause a significant drop of the accelerating gradient which cannot be compensated using a feedback controller i.a. due to its limited bandwidth. To overcome this issue it is required to use more complex algorithms like Beam Loading Compensation (BLC).

LLRF SYSTEM OVERVIEW

There are two MTCA.4 crates installed at each of the RF stations, one crate in the master and one crate in the slave LLRF subsystems. The simplified block diagram of a RF station is presented in Fig. 1.

One LLRF MTCA.4 crate is filled out with six pairs of down-converter (uDWC) - digitizer (uADC) boards, LLRF controller (uTC), CPU, crate management module (MCH), timing card (x2timer) and a vector modulator placed only in the master crate. Each LLRF subsystem processes RF signals from two cryo-modules while only the master system provides the drive signal to the klystron.

The uTC board in the master subsystem contains the main LLRF controller. It collects all the feedback data which are required to generate proper drive. All the algorithms are implemented in the FPGA chip located on the uTC board. The feedback data are transmitted over optical links or over differential lines within the crate and are received by the main controller using Multi-Gigabit Transceivers (MGTs).

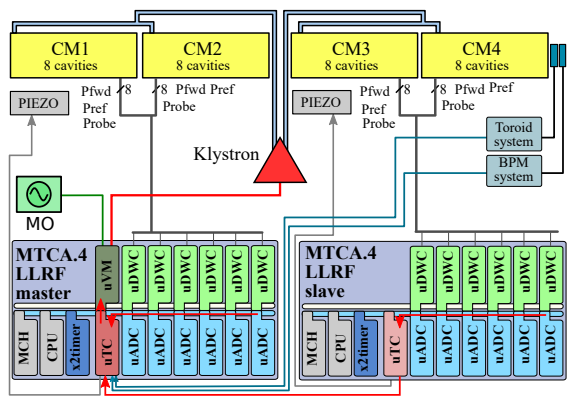


Figure 1: Simplified block diagram of the LLRF system installed at one RF station in XFEL.

BEAM CHARGE INFORMATION

The information about current beam charge can be obtained from the Beam Position Monitor (BPM) and toroid systems. They are located upstream the RF station [4]. Each of these systems sends the data in a real time to the main LLRF controller over a separate optical link working at 3.125 Gbps. A dedicated protocol has been settled, which defines packet of the data transmitted to the LLRF controller. The BPM data packet is presented in Fig. 2.

* lukasz.butkowski@desy.de

Content from this work may be used under the terms of the CC BY 3.0 licence (© 2018). Any distribution of this work must maintain attribution to the author(s), title of the work, publisher, and DOI.

ISBN: 978-3-95450-194-6 ISSN: 2226-0366 doi:10.18429/JACoW-LINAC2018-TUPO132

Additionally to the current beam charge information the timing system provides the expected bunch pattern information. This information is sent from x2timer to the uTC board using the Multipoint-Low Voltage Differential Signaling (M-LVDS) lines located in MTCA.4 crate backplane before the RF pulse starts.

Byte			
3..0	Start of Frame (K27.7 & 0x00)	Intra pulse Bunch Number	header
7..4	Charge [pC] (float)		data0
11..8	Position X (float)		data1
15..12	Position Y (float)		data2
19..16	Status (16 Bit)	Detected Bunch Num	data3
23..20	CRC 32		CRC
28..24	End of Frame (K29.7)		EOF
bit	31 16	15 0	

Figure 2: BPM data packet send to the LLRF system.

BEAM LOADING COMPENSATION ALGORITHM

An electron beam passing through the cavity induces a voltage proportional to the current and the cavity shunt impedance which results in the cavity gradient drop. The feedback loop tries to compensate for this perturbations but due to the limited bandwidth it is not able to do it (Fig. 3a). Solution to this problem is to include scaled beam charge information into the feedforward signal [5]. However, the beam charge information appears in the LLRF system with the delay resulting from the detection of bunches and data transmission. As a result, the first bunches see a different cavity gradient. Also after the last electron bunch there is an overcompensation (Fig. 3b). To overcome this issue a pre-compensation and gating algorithm is used. The principle of its operation consists in insertion of the beam charge information from the previous pulse before the charge information from the current pulse arrives, and then disable BLC when the beam is not awaited (Fig. 3c). The algorithm requires the expected time of the beam. This is ensured by the module that receives the data from the timing system (x2timer). The module can generate indication of the expected beam as well provide coarse values of the expected beam charge.

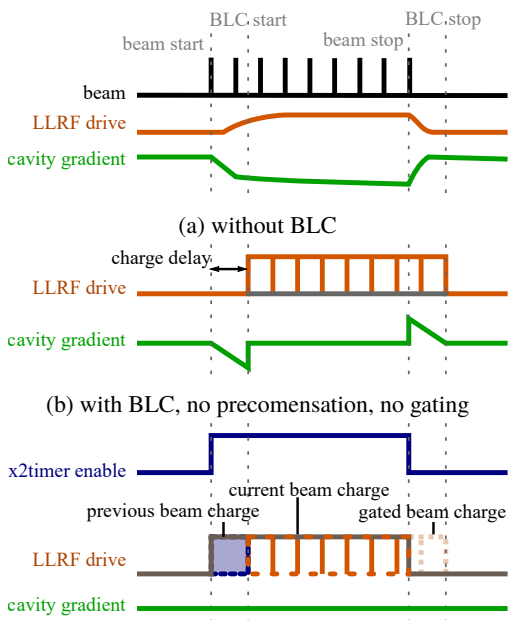


Figure 3: Beam loading compensation and cavity gradient.

At the European XFEL the maximum bunch repetition rate is 4.5 MHz. This is also the frequency of data received by the BLC algorithm. However, the repetition rate of bunches might be lower. In such a case, the algorithms puts zero charge in the place of missing bunches. This gives automatic scaling to the current by controlling of the duty cycle of the compensation signal. It will be shown in the result section.

FPGA IMPLEMENTATION

The main LLRF feedback controller is implemented in FPGA Kintex7 chip located on uTC board (commercial available card DAMC-TCK7). The project was build using the MTCA.4 firmware framework developed in DESY [6].

The block diagram of the firmware including most important components of the main LLRF controller is presented in Fig. 4. The signal flow starts with the calculation of the vector sum, resulting from the contribution of partial vector sums (PVS) of four cryomodules (CM). The controller starts with an error calculation followed by a proportional and a multiple input, multiple output (MIMO) feedback controller. The beam loading compensation (BLC) is placed just after feedforward (FF) and FF correction signals. Finally the klystron linearizion and output correction are applied before the signal is send to the vector modulator for up conversion.

The block diagram of the BLC component is given in Fig. 5. This module implements previously described algorithm. The orange fields in the figure indicate registers that are set by the user during a calibration process. Mainly the scaling of the beam charge and the rotation of the correction vector has to be set. The source of the beam charge infor-

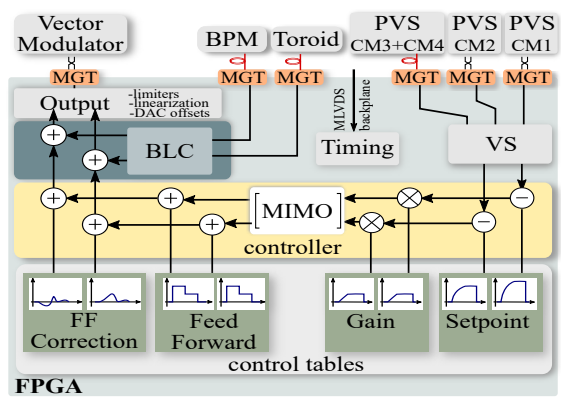


Figure 4: Block diagram of the uTC firmware including the most important components of the LLRF controller.

Content from this work may be used under the terms of the CC BY 3.0 licence (© 2018). Any distribution of this work must maintain attribution to the author(s), title of the work, publisher, and DOI.

ISBN: 978-3-95450-194-6 ISSN: 2226-0366 doi:10.18429/JACoW-LINAC2018-TUPO132

Content from this work may be used under the terms of the CC BY 3.0 licence (© 2018). Any distribution of this work must maintain attribution to the author(s), title of the work, publisher, and DOI.

mation can be selected between BPM and Toroid systems, which gives redundancy and the possibility to select the best source.

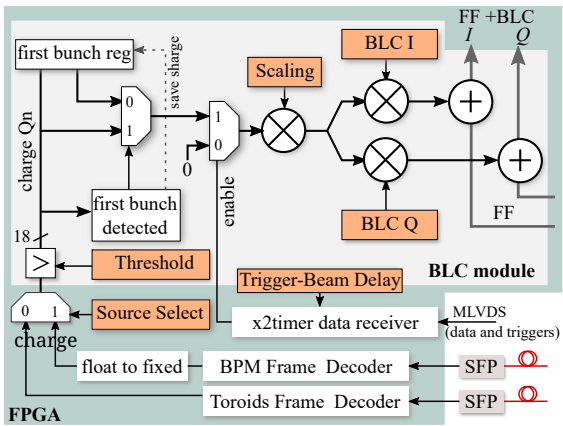


Figure 5: Block diagram of BLC module implementation.

RESULTS

The BLC has been implemented and successfully tested at the European XFEL. Up to now, tests were performed only with the beam charge information provided by BPM system. The results of BLC working for a bunch pattern with 0.25 nC and 1 MHz repetition rate are presented in Figs. 7 and 6. The results of BLC working for a bunch pattern with 0.25 nC and 4.5 MHz repetition rate are presented in Figs. 8 and 9. These figures present the controller output with included BLC signal as well the cavity gradient with enabled and disabled BLC while the feedback loop is closed. We can observe different behavior of the controller output depending on the bunch pattern, as it was described in BLC algorithm section. Presented figures shows that BLC can successfully compensate gradient disturbance caused by passing beam. In Fig. 9 we can see the overcompensation after the beam is off. In this case, it is due th fact the bunch number is shorter then the expected one.

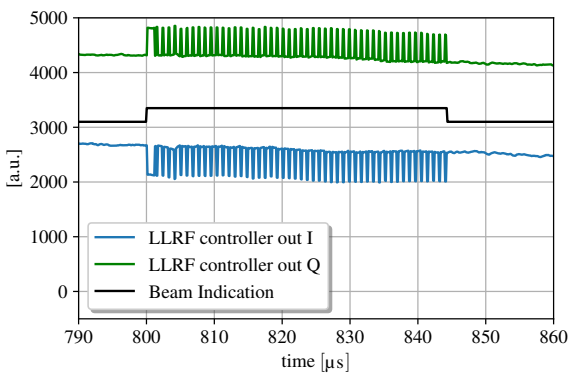


Figure 6: Controller output with the BLC enabled for beam with 50 bunches with 0.25 nC @1 MHz repetition rate.

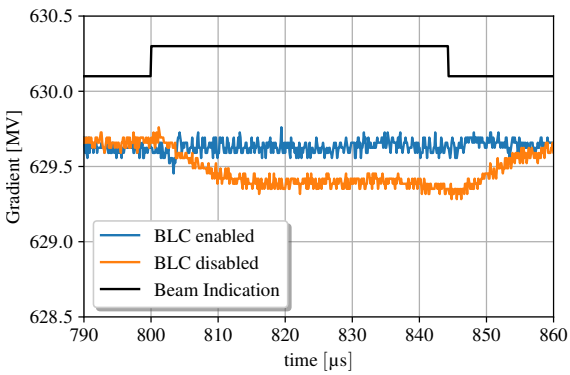


Figure 7: Cavity gradient with BLC enabled and disabled for beam with 50 bunches with 0.25 nC @1 MHz repetition rate.

CONCLUSION AND OUTLOOK

This paper describes a concept of the beam loading compensation method used at the European XFEL. The algorithm as well as its implementation has been described. The presented results show that the addition of the real-time BLC to the LLRF system improves the system response to beam transients.

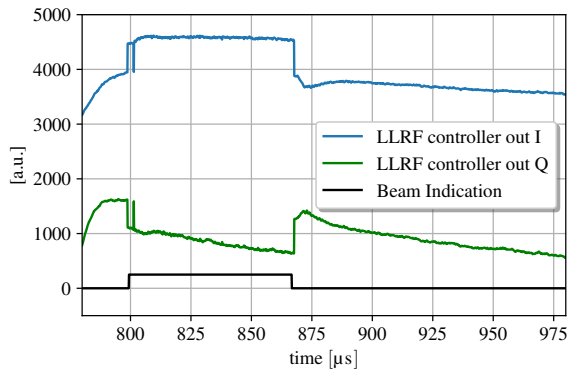


Figure 8: Controller output with the BLC enabled for beam with 300 bunches with 0.25 nC @4.5 MHz repetition rate.

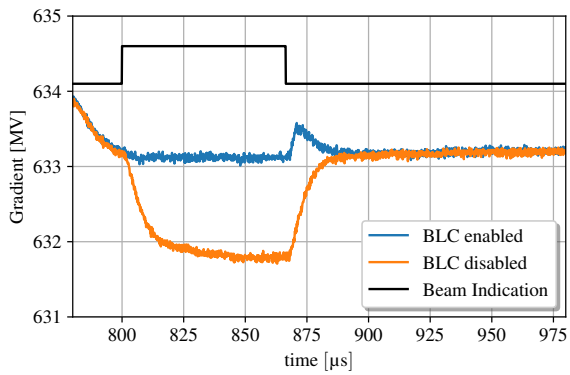


Figure 9: Cavity gradient with BLC enabled and disabled for beam with 300 bunches with 0.25 nC @4.5 MHz repetition rate.

ISBN: 978-3-95450-194-6 ISSN: 2226-0366 doi:10.18429/JACoW-LINAC2018-TUPO132

REFERENCES

[1] R. Abela *et al.*, *The European X-Ray free electron laser technical design report*, M. Altarelli *et al.*, Eds. DESY, Hamburg, Germany, 2007, http://xfel.desy.de

[2] J. Branlard *et al.*, *The European XFEL LLRF system*, in *Proc. IPAC'12*, New Orleans, LA, USA, May 2012, paper MOOAC01, pp. 55-57.

[3] MicroTCA® is a trademark of PICMG, MicroTCA.4 specifications: http://www.picmg.org

[4] D. Lipka, *Very first experience with the standard diagnostics at the European XFEL*, in *Proc. IPAC'17*, Copenhagen, Denmark, May 2017, pp.180-183. doi:10.18429/JACoW-IPAC2017-MOPAB043

[5] E. Vogel *et al.*, *Beam loading compensation using real time bunch charge information from toroid monitor at FLASH*, in *Proc. PAC'07*, Albuquerque, NM, USA, June 2007, paper WEPMN012, pp.2074-2076.

[6] L. Butkowski, T. Kozak, P. Prędki, R. Rybaniec, B. Yang, *FPGA firmware framework for MTCA.4 AMC modules*, in *Proc. ICALEPCS'15*, Melbourne, Australia, October 2015. doi:10.18429/JACoW-ICALEPCS2015-WEPGF074

Content from this work may be used under the terms of the CC BY 3.0 licence (© 2018). Any distribution of this work must maintain attribution to the author(s), title of the work, publisher, and DOI.

ISBN: 978-3-95450-194-6 ISSN: 2226-0366 doi:10.18429/JACoW-LINAC2018-WE1A03

LATEST RESULTS OF CW 100 mA ELECTRON RF GUN FOR NOVOSIBIRSK ERL BASED FEL *

V. N. Volkov †, V. Arbuzov, E. Kenzhebulatov, E. Kolobanov, A. Kondakov, E. Kozyrev, S. Krutikhin, I. Kuptsov, G. Kurkin, S. Motygin, A. Murasev, V. Ovchar, V.M. Petrov, A. Pilan, V. Repkov, M. Scheglov, I. Sedlyarov, S. Serednyakov, O. Shevchenko, S. Tararyshkin, A. Tribendis, N. Vinokurov, BINP SB RAS, Novosibirsk, Russia

Abstract

Continuous wave (CW) 100 mA electron rf gun for injecting the high-quality 300-400 keV electron beam in Novosibirsk Energy Recovery Linac (ERL) and driving Free Electron Laser (FEL) was developed, built, and commissioned at BINP SB RAS. The RF gun consists of normal conducting 90 MHz rf cavity with a gridded thermionic cathode unit. Bench tests of rf gun is confirmed good results in strict accordance with our numerical calculations. The gun was tested up to the design specifications at a test bench that includes a diagnostics beam line. The rf gun stand testing showed reliable work, unpretentious for vacuum conditions and stable in long-term operation. The design features of different components of the rf gun are presented. Preparation and commissioning experience is discussed. The latest beam results are reported.

INTRODUCTION

Recent projects of advanced sources of electromagnetic radiation [1] are based on the new class of electron accelerators where the beam current is not limited by the power of rf system – energy recovery linacs (ERLs). Such accelerators require electron guns operating in continuous wave (cw) mode with high average current. The only solution is an rf gun, where the cathode is installed inside the rf cavity. RF guns have no problem with degradation of the cathode due to absence of back bombardment electrons so the vacuum condition is not important there. The most power Novosibirsk FEL [2] can be more powerful by one order on magnitude with this rf gun [3-5]. Measured rf gun characteristics are presented in Table 1.

RF GUN AND DIAGNOSTIC STAND

The rf gun and diagnostic stand are presented in Fig. 1.

The RF gun cavity is made on the base of standard bimetallic cavity of Novosibirsk ERL Detailed information can be found in [3-5]. Only the insert with the thermionic cathode-grid unit is built into the cavity. The gridded thermionic dispenser cathode is driven by special modulator with GaN rf transistor. The insert focusing electrode executes the strong rf focusing of the beam just near the cathode that ensures the beam emittance compensation at the relatively low electric field at the cathode. Also it ensures the absolute absence of dark currents in the beam.

There are in the stand: 30 kW water cooled beam dump with 5 cm lead radiation shield, wideband Wall Current Monitor (WCM2) inserted into the replaceable target, Transition Radiation Sensor, the pair of standard WCM, three focusing solenoids, and the testing cavity.

Table 1: Measured RF Gun Characteristics

Average beam current, mA	≤100
Cavity Frequency, MHz	90
Bunch energy, keV	100 ÷ 400
Bunch duration (FWHM), ns	0.06 ÷ 0.6
Bunch emittance, mm mrad	10
Bunch charge, nC	0.3 ÷ 1.12
Repetition frequency, MHz	0.01 ÷ 90
Radiation Doze Power, mR/h	100/2m
Operating pressure, Torr	10^{-9}…10^{-7}
Cavity RF loses, kW	20

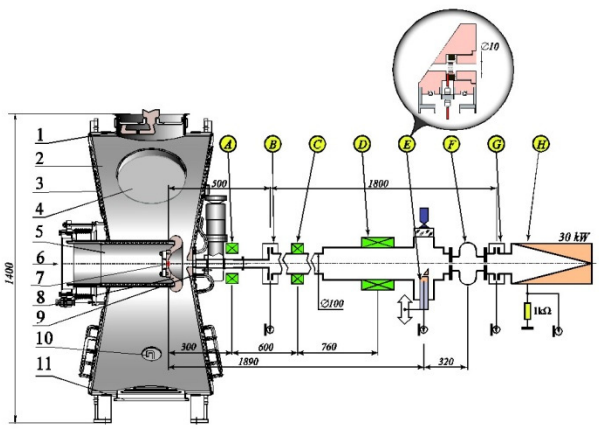


Figure 1: RF gun and stand layout: 1-Power input coupler; 2- Cavity shell; 3-Cavity back wall; 4-Sliding tuner; 5-Insert; 6-Cathode injection/extraction channel; 7-Thermionic cathode-grid unit; 8-Concave focusing electrode; 9-Cone like nose; 10-Loop coupler; 11-Vacuum pumping port; A-Emittance compensation solenoid; B-First Wall Current Monitor (WCM); C, D -Solenoids ; E-Wideband WCM and transition radiation target; F – Test Cavity; G-third WCM; H-Faraday cup and Water-cooled beam dump.

STAND TESTING RESULTS

Beam Current Regulation

There are some methods of beam current increasing: decreasing of the grid bias voltage (V_{bias}), increasing of the modulator pulse voltage (V_{puls}), and increasing of the

* Work supported by Russian Science Foundation (project N 14-50-00080)
† v.n.volkov@inp.nsk.su

Content from this work may be used under the terms of the CC BY 3.0 licence (© 2018). Any distribution of this work must maintain attribution to the author(s), title of the work, publisher, and DOI.

ISBN: 978-3-95450-194-6 ISSN: 2226-0366 doi:10.18429/JACoW-LINAC2018-WE1A03

repetition frequency. Also there must be increased the cathode heating voltage (V_{heat}) to compensate the cathode emission ability derating. The applying of these methods is shown in Fig 2.

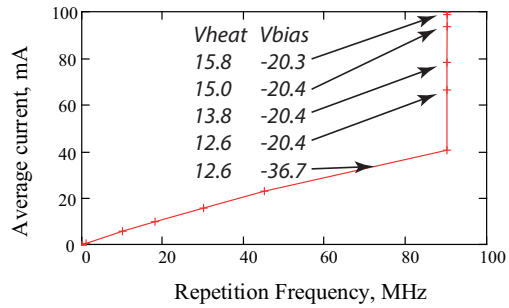


Figure 2: Typical method of current rising.

Calibration of Cavity Voltage Meter

To measure the beam energy there is used the measuring of time delay between two wall current monitors. Since the particle velocities at the relatively low energy are lower than speed of light. It is demonstrated in Fig. 3. This effect was used for the calibration of the cavity voltage meter. The calibration has a high accuracy.

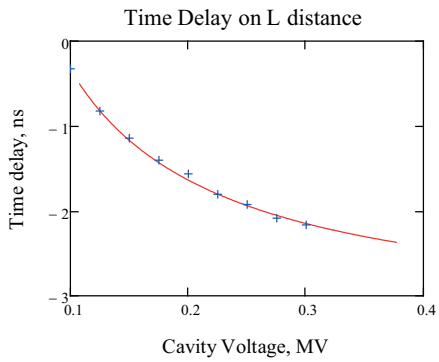


Figure 3: Measured data fitting by theory curve.

Cavity Testing up to 400 kV

The cavity voltage was increased with step by step method. After each step there required 1/2 an hour to normalize the vacuum condition (see Fig. 4).

Maximum beam current at 400 kV was limited by the beam dump permissible power.

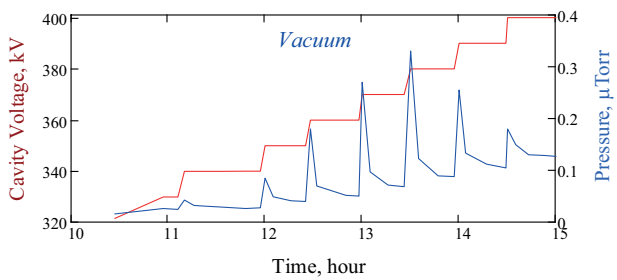


Figure 4: Cavity testing process behavior.

Launch Phase Functions

Energy distribution along the bunch is changed if the launch phase will be changed. The energy of head particles becomes lower at lower launch phases. It is used for velocity bunching at a drift space and the phase instability (jitter) compensation. Also there is changed the bunch energy as it shown in Fig. 5. The maximal bunch particle energy is at 68°, and minimal bunch length at 31°.

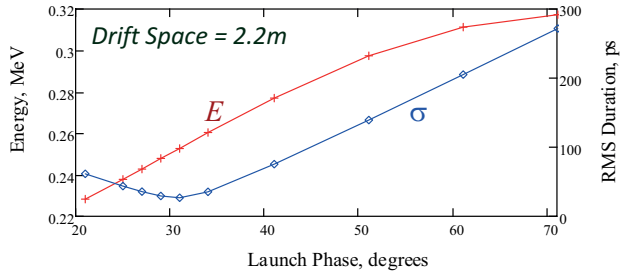


Figure 5: Launch phase functions.

Particle Distribution along the Bunch

There are complex particle distributions along the bunch due to plasma oscillation into a cathode-grid unit. On the drift space this distribution are changed significantly. The example of this at the launch phase of 31° is shown in Fig. 6. Frontal spike is formed into cathode-grid gap. Then it grows and becomes short of about 20 ps FWHM while traveling along the drift space.

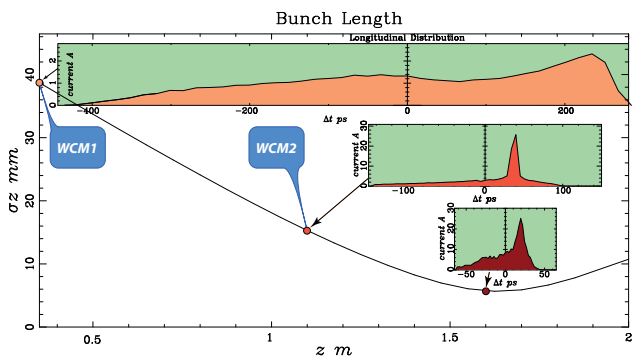


Figure 6: Bunch duration behaviour on the drift space.

Launch Phase Jitter Compensation

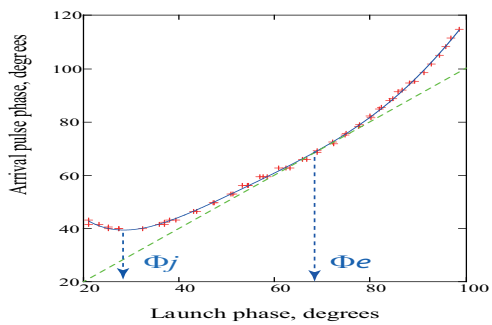


Figure 7: Arrival pulse phase behavior.

The jitter compensation effect has measured between two WCMs with 1.2 m distance between them (see Fig. 7). At the launch phase of 27 degrees the arrival time is independent on launch phase so the jitter is compen-

Content from this work may be used under the terms of the CC BY 3.0 licence (© 2018). Any distribution of this work must maintain attribution to the author(s), title of the work, publisher, and DOI.

ISBN: 978-3-95450-194-6 ISSN: 2226-0366 doi:10.18429/JACoW-LINAC2018-WE1A03

Content from this work may be used under the terms of the CC BY 3.0 licence (© 2018). Any distribution of this work must maintain attribution to the author(s), title of the work, publisher, and DOI.

sated there, I.e. the requirement to the phase stability of the modulator pulses is not high at the launch phase of 27°.

Cathode-Grid Plasma Oscillation Effect

Calculations and experiments have shown the plasma oscillation effect depends on the cathode emission ability. For a low emission ability the bunch at the end of the drift space becomes having two parts. The excitation of a testing cavity by such a bunch will be having anomalous valley due to interfere effect between these parts.

Numerical modeling of the excitation of the test cavity for two HOMs by such bunches is presented in the upper of Fig. 8. And the experiments are at the bottom where the emission ability was regulating by cathode heating voltage.

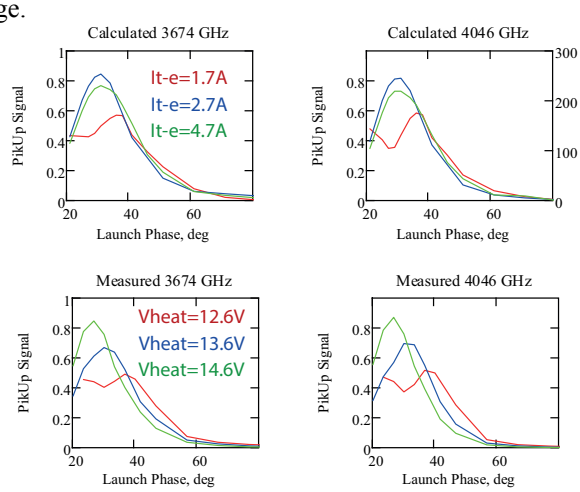


Figure 8: Excitations of test cavity HOMs. Calculations (at the top) and experiment (at the bottom) shows the interference effect for the low cathode emission ability.

Emittance Measurements

Bunch emittance was measured by solenoid focusing method when the spot size of the beam focussed to a target is measured through CCD camera registering the transition radiation.

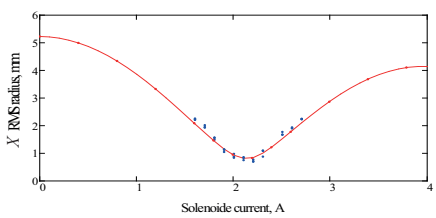


Figure 9: Measured and calculated beam behaviors.

The measured data behaviour on the focusing solenoid strength conforms to ASTRA [6] numerically calculated behaviour (see Fig. 9) with the accuracy of 9%. It corresponds to beam emittance of 15 mm mrad. The emittance can be compensated by proper focusing to 10 mm mrad.

Dark Currents

Two places in the RF gun cavity with peak surface field of 10-14 MV/m are the sources of field emitted dark currents (see Fig. 10). There are no dark currents in the beam absolutely since dark current trajectories are far from the beam.

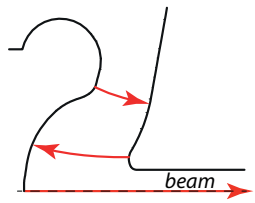


Figure 10: Dark current trajectories in the RF gun cavity.

Radiation Background

The source of bremsstrahlung radiation is the field emission current described by Fouler-Nordheim equation. Radiation background was measured behind the cavity wall with the thickness of 15 mm. The enhancement factor measured is found to be β=628. It was used as the base for calculation of enhancement factors for different thickness (10, 5, 3 mm), for bremsstrahlung power, for field emission particle power, and for field emission current (see Fig. 11). The enhancement factor for emission current is found to be β_I=1250. For the comparison, it large by one order on magnitude than the enhancement factor of superconducting cavities preparing with a perfect modern technology.

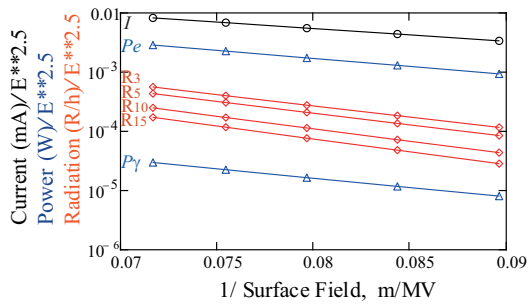


Figure 11: Calculated and measured (R15) field emission process.

REFERENCES

[1] Vinokurov, N. A., Levichev, E. B., 2015. Undulators and wigglers for the production of radiation and other applications, Physics-Uspekhi. 58 850–871.

[2] Volkov V.N., *et al.,* "First test results of RF gun for the Race-Track Microtron Recuperator of BINP SB RAS", in *Proc. RuPAC'12*, Sep. 2012, Saint-Petersburg, Russia, paper TUPPB049.

[3] Volkov V., *et al.,* "Thermionic cathode-grid assembly simulations for rf guns", in *Proc. PAC'09*, Vancouver, Canada, May. 2009, paper MOYRFP087.

[4] V. Volkov, *et al.,* Thermocathode Radio-Frequency Gun for the Budker Institute of Nuclear Physics Free-Electron Laser. ISSN 1547-4771, Physics of Particles and Nuclei Letters, 2016, Vol. 13, No. 7, pp. 827–830.

[5] Kulipanov, *et al.,* Novosibirsk Free Electron Laser—Facility Description and Recent Experiments, IEEE Transactions on Terahertz Science and Technology 5. doi:10.1109/ TTHZ.2015.2453121.

[6] K. Floettmann, ASTRA User`s Manual, http://www.desy.de~mpyflo/Astra_documentation.

ISBN: 978-3-95450-194-6 ISSN: 2226-0366 doi:10.18429/JACoW-LINAC2018-WE1A04

THE HIGH POWER RF SYSTEM FOR THE EUROPEAN XFEL

S. Choroba, Deutsches Elektronen-Synchrotron, DESY, Hamburg, Germany
for the XFEL Work Package High Power RF

Abstract

The RF system for the European XFEL consists of 26 high power RF stations each capable of 10MW RF pulse power. This paper will report on the overall system layout, cover RF system components e.g. klystrons, modulators and high power RF waveguide distribution. It will also cover system modifications during construction phase and report on commissioning results.

DESCENT OF THE EUROPEAN XFEL

The European XFEL descends from the TESLA project, a linear collider with a center-of-mass-energy of 500GeV. In the early 1990s the TESLA collaboration was established and the TESLA Test Facility has been set up at DESY by the TESLA collaboration to develop all components required to construct a linear collider based on superconducting RF technology. A technical design report on the linear collider with integrated free electron laser was published in 2001 [1]. In 2006 it was decided to build the free electron laser as stand-alone facility at DESY. Construction started in 2007 and first X-rays were produced in 2017. The high power RF system components for the European XFEL have been developed to meet the requirements for the TESLA linear collider and have later been modified to meet the European XFEL demands.

The TELSA linear collider proposal served as the basis for the International Linear Collider, ILC, too. Since both, the ILC and the XFEL, descends from the TESLA linear collider, many of the high power RF systems components now in operation for the E-XFEL, might be used for ILC too.

EUROPEAN XFEL

The European XFEL produces X-rays of unprecedented properties in terms of brilliance, average brilliance, coherence, pulse duration and time structure.

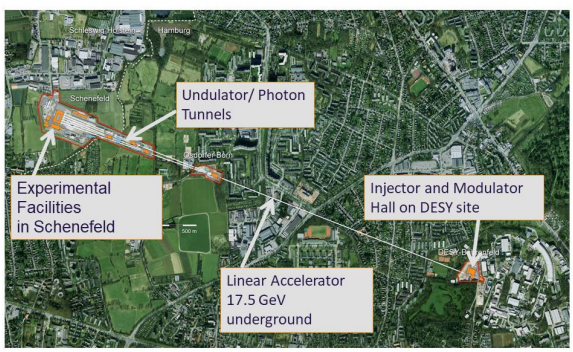


Figure 1: XFEL site.

The E-XFEL is located in Hamburg, with the injector on the DESY site, the experimental facilities in Schenefeld and the main linear accelerator in an underground tunnel in between. The E-XFEL site layout is shown in Figure 1. Electrons generated by a RF gun are accelerated in the superconducting cavities of the linac and are distributed to up to five beam lines for experiments. The total length of the facility is 3.4km. Details can be found in [2].

RF SYSTEM REQUIREMNTS

The linear accelerator of the E-XFEL is based on superconducting RF technology. Electrons are generated in a normal conducting RF gun and are accelerated in the superconducting cavities of the 1.9km long linac. The 2700 electron bunches are accelerated in 600µs long macro-pulses with a repetition rate of 10Hz up to 17.5GeV. The electron beam current is 5mA. The main linac consists of 96 cryogenic modules with 8 superconducting 9-cell Niobium-cavities each. The high power RF system (HPRF) provides RF power at 1.3GHz, at a RF pulse duration of 1.38ms with a repetition rate of 10Hz. The average accelerating gradient is 23.6MV/m.

In order to achieve this gradient 122kW per cavity are required. 32 cavities in 4 cryogenic modules are connected to one RF station. Taking into account losses and a regulation reserve 5.2MW of RF power per station are required in the main linac. The RF station for the RF gun in the injector provides 8MW up to 650µs pulse duration, the station for one single module in the injector up 1.3MW at 1.38ms. Table 1 summarizes the requirements.

Table 1: HPRF Requirements

Number of sc cavities	776
Power per cavity	122kW
Gradient at 17.5GeV	23.6MV/m
Power per 32 cavities (4 cryogenic modules)	3.9MW
Power per RF station main linac/RF gun/injector	5.2MW/8MW/1.3MW
Number of RF stations total/main linac/injector	26/24/2
RF pulse duration main linac/RF gun/injector	1.38ms/0.65ms/1.38ms
Repetition rate	10Hz

Content from this work may be used under the terms of the CC BY 3.0 licence (© 2018). Any distribution of this work must maintain attribution to the author(s), title of the work, publisher, and DOI.

ISBN: 978-3-95450-194-6 ISSN: 2226-0366 doi:10.18429/JACoW-LINAC2018-WE1A04

Content from this work may be used under the terms of the CC BY 3.0 licence (© 2018). Any distribution of this work must maintain attribution to the author(s), title of the work, publisher, and DOI.

RF SYSTEM LAYOUT

Figure 2 shows the layout of one RF station. The high power klystron produces the RF power which is distributed by a RF waveguide distribution system to the superconducting cavities. The HV voltage pulses required by the klystron are generated by a HV pulse modulator which is connected to a pulse transformer by pulse cables. Several racks house additional auxiliary power supplies, interlocks, controls and water cooling. With exception of the modulator, which is installed in a separate hall on the DESY site near the injector, all other components are installed under the cryogenic modules of the main linac which is shown in Figure 3.

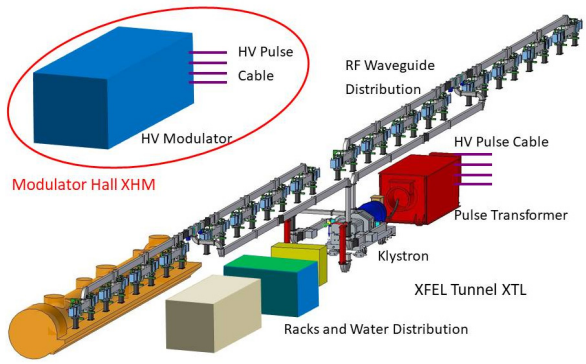


Figure 2: RF station layout.

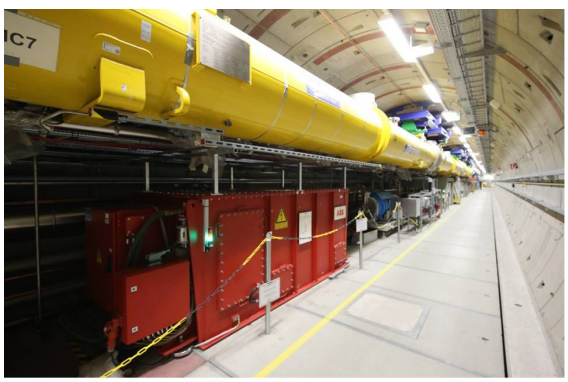


Figure 3: RF station in the E-XFEL tunnel.

The RF stations for the injector are an exception. These are located on the 3rd underground floor in the injector building. Figure 4 shows the RF stations in the injector. The RF power for the RF gun and a one single cryogenic module is transferred by long waveguides in the shafts between the floors to the RF gun and one single module.

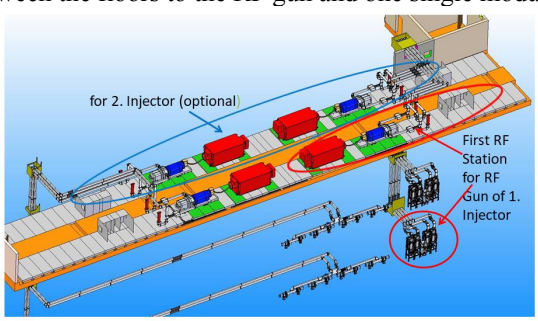


Figure 4: RF stations for injector.

RF SYSTEM COMPONENTS

The main components for the HPRF are klystrons, modulators and RF waveguide distributions, which will be covered in the next subsections. Auxiliary power supplies are standard of the shelves components which are installed under the cryogenic modules in electronic racks which are water-cooled and are covered by concrete blocks for radiation protection. In addition an interlock system based on FPGAs allows for protection of the RF system components, control and monitoring of signals.

Klystrons

Multi beam klystrons (MBK) have been selected as RF power sources. Table 2 shows the requirements of the klystron. The original requirement was for the TESLA linear collider. Therefore 10MW of pulsed RF power was specified. A single beam 10 MW klystron with an efficiency of about 65% would require a cathode high voltage of about 250kV. Reliable operation at this voltage level at long pulse duration of 1.5ms would be difficult to achieve. In addition the high voltage modulators would be expensive.

Table 2: Multi Beam Klystron Requirements

RF Frequency:	1.3GHz
Cathode Voltage:	<120kV
Beam Current:	<140A
µperveance:	<3.5
Max. RF Peak Power:	10MW
RF Pulse Duration:	1.5ms
Repetition Rate:	10Hz
RF Average Power:	150kW
Efficiency	65%
Gain	48dB
Length	ca. 2.5m
Lifetime goal	>40000h



Figure 5: Multi beam klystrons for the E-XFEL.

The use of 6 or 7 beams in one klystron envelope lowers the voltage level to about 120kV. Three vendors developed multi beam klystrons meeting the requirements. Finally two were selected for the European XFEL. Figure 5 shows the multi beam klystrons for the E-XFEL made by THALES and TOSHIBA. Both klystrons are mounted horizontally on girders, which allow easy installation in the accelerator tunnel, have common interface for easy change between klystrons of different vendors and are connected by a connection module with filament transformer, voltage and current measurement

ISBN: 978-3-95450-194-6 ISSN: 2226-0366 doi:10.18429/JACoW-LINAC2018-WE1A04

and for quick HV connection to the pulse transformer. 26 klystrons are installed, 6 klystrons made by TOSHIBA and 20 by THALES. Figure 6 shows the output power generated by the klystrons in the different RF stations. Besides the klystrons for the RF gun and the first injector module, some klystrons produce more power than the expected 5.2MW to achieve the average gradient in the cavities. This is due to the fact that some cryogenic modules are equipped with modules which can be operated at higher gradient. After installation at first operation some klystron showed some klystron gun or cavity arcs. However, the number decreased during operation and is much below specified number. More details can be found in [3].

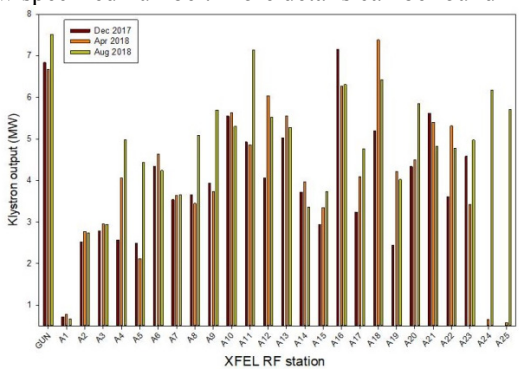


Figure 6: Klystron RF output power for different RF stations at different dates.

Modulators

Pulse step modulators located in a separate hall produce HV pulses at the 10kV level at 1.6kA. The rectangular pulses are transmitted by tri-axial pulse cables to the 1:12 pulse transformers near the klystrons in the tunnel. Each modulator is connected to a pulse transformer by 4 cables of maximum 1.6km length. The modulator is a commercial product made by Ampegon and is shown in Figure 7. It consists of 24 HV modules, which are stacked and which together provide the 10kV HV pulses. The modulator requirements are summarized in table 3. More details can be found in [4].



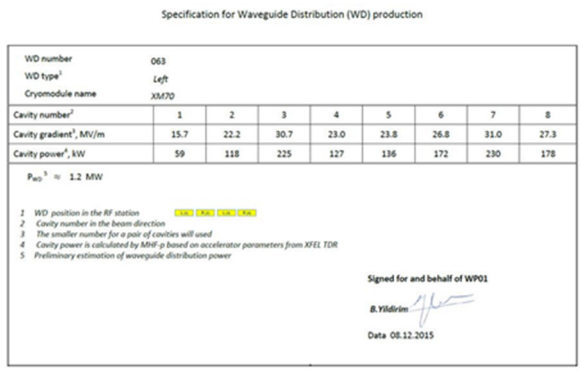
Figure 7: HV modulator.

Table 3: HV Modulator Requirements

	typical	max.
Modulator Pulse Voltage	9.6kV	12kV
Modulator Pulse Current	1.62kA	1.8kA
Klystron Gun Voltage	115kV	132kV
Klystron Gun Current	135A	150A
High Voltage Pulse Duration (70% to 70%)	1.57ms	1.7ms
High Voltage Rise and Fall Time (0 to 99%)	0.15ms	0.2ms
High Voltage Flat Top (99% to 99%)	1.37ms	1.5ms
Pulse Flatness during Flat Top	±0.2%	±0.3%
Pulse-to-Pulse Voltage fluctuation	±0.1%	±0.1%
Energy Deposit in Klystron in Case of Gun Spark	<20J	20J
Pulse Repetition Rate	10Hz	10Hz
Pulse Transformer Ratio	1 :12	1 :12

RF Waveguide Distribution

The RF distribution is made by WR650 waveguide. It distributes the power to the cavities and protects the klystron from reflected power by means of circulators with integrated loads. The first layout was designed to provide equal RF power to the cavities. During production of the cryogenic modules it turned out that cavities had different performance in maximum gradient, some below the average gradient of 23.6MV/m. An example of a test result is shown in Figure 8.


Specification for Waveguide Distribution (WD) production

WD number	063							
WD type[1]	Left							
Cryomodule name	XM70							
Cavity number[2]	1	2	3	4	5	6	7	8
Cavity gradient[3], MV/m	15.7	22.2	30.7	23.0	23.8	26.8	31.0	27.3
Cavity power[4], kW	59	118	225	127	136	172	230	178

P_{WD}[5] ≈ 1.2 MW

1 WD position in the RF station
2 Cavity number in the beam direction
3 The smaller number for a pair of cavities will used
4 Cavity power is calculated by MHF-p based on accelerator parameters from XFEL TDR
5 Preliminary estimation of waveguide distribution power

Signed for and behalf of WP01
B.Yildirim
Data 08.12.2015

Figure 8: Test result of one cryogenic module.

In case of an equal power distribution, the RF station would be limited by the weakest cavity. In order to overcome this problem, the distribution was modified to adjust the power for each cavity. Figure 9 shows the distribution for one module. The adjustment is done by asymmetric

Content from this work may be used under the terms of the CC BY 3.0 licence (© 2018). Any distribution of this work must maintain attribution to the author(s), title of the work, publisher, and DOI.

ISBN: 978-3-95450-194-6 ISSN: 2226-0366 doi:10.18429/JACoW-LINAC2018-WE1A04

Content from this work may be used under the terms of the CC BY 3.0 licence (© 2018). Any distribution of this work must maintain attribution to the author(s), title of the work, publisher, and DOI.

shunt tees, between cavities, a pair of cavities and between modules. All modules have been tested and performance determined before installation. Once the results were available a specific distribution has been tailored and connected to each module. The installation and an installed module distribution can be seen in Figure 10.

After installation in the tunnel waveguide components between modules and to the klystron have been installed. Afterwards modification of power distribution is only possible between modules by change of asymmetric shunt tee between them.

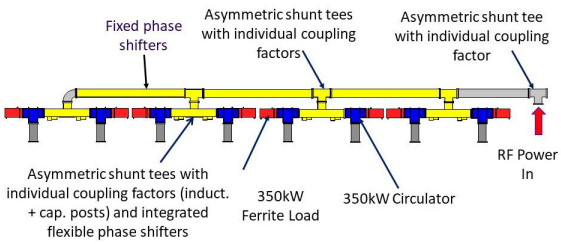


Figure 9: Module waveguide distribution.



Figure 10: Waveguide installation to module.

By this method the potentially achievable energy of the accelerator could be increased beyond 17.5GeV to 19.5GeV, whereas only 15.7GeV would be achieved when limited by the weakest cavity per module. Details can be found in [5].

During commissioning of the accelerator it was difficult to achieve the maximum energy. Some RF stations were limited by different types of commissioning problems, e.g. by waveguide arcs between modules or multipacting in couplers. These problems could be solved by change of waveguide components and RF conditioning. Another reason was that some cavities have changed performance, which caused, that not all distributions fit the new power demand. Since the module waveguide distributions are fixed only the waveguide distribution between modules and to the klystron can be adjusted. The last two RF station were commissioned in spring 2018. The accelerator finally achieved the maximum design energy of 17.5GeV in July 2018. At present it continues user operation at 14GeV.

COMMISSIONING SUMMARY

The high power RF system for the E-XFEL was developed starting in the 1990s for the TESLA linear collider. XFEL construction started in 2007 and was finished in 2016. High power RF systems components have been developed, constructed, tested and installed during this time. Commissioning and first operation of the XFEL showed minor, but up to now no severe problems with the high power RF system. This might be partly due to the fact that an extensive development and test phase has preceded and that several key components have been designed for higher performance at the linear collider. Nevertheless spare components. e. g. klystrons, subsystems for the modulators, electronics, and waveguides have been already ordered. An important modification in the future might be an adjustment of power distribution between modules connected to one RF station.

ACKNOWLEDGEMENT

The author would like to thank all persons who contribute to the XFEL work package HPRF.

REFERENCES

[1] R. Brinkmann *et al.*, "TESLA, Technical Design Report", DESY 2001-011, March 2001.

[2] W. Decking and H. Weise, "Commissioning of the European XFEL accelerator", in *Proc. IPAC2017*, Copenhagen, Denmark, May 2017, pp. 1-6, doi:10.18429/JACoW-IPAC2017-MOXAA1

[3] V. Vogel *et al.*, "Status of the 10MW MBKs during commissioning of the European XFEL in DESY", presented at the 29th Linear Accelerator Conf. (Linac'18), Beijing, China, Sep. 2018, paper MOPO036, this conference.

[4] H.-J. Eckoldt "XFEL Modulators with Pulse Cables", in *Proc. IPAC2018*, Vancouver, Canada, Apr.-May 2018, pp. 2487-2489, doi:10.18429/JACoW-IPAC2018-WEPMF05

[5] B. Yildirim *et al.*, "Series production of the specific waveguide distribution for the European XFEL at DESY", presented at the 29th Linear Accelerator Conf. (Linac'18), Beijing, China, Sep. 2018, paper TUPO027, this conference.

ISBN: 978-3-95450-194-6 ISSN: 2226-0366 doi:10.18429/JACoW-LINAC2018-WE1A05

SwissFEL LINAC COMMISSIONING STATUS, CURRENT PERFORMANCE AND FUTURE PLANS

P. Craievich* on behalf of the SwissFEL team
Paul Scherrer Institut, 5232 Villigen PSI, Switzerland

Abstract

SwissFEL, the hard x-ray free-electron laser facility at PSI, is in an advanced commissioning phase. The commissioning of the 5.8 GeV Linac started in 2016 and the first FEL pilot-experiments were performed at a reduced beam energy in the end of 2017. In 2018, it is foreseen to progressively increase the electron beam energy and photon energy up to the maximum design values, interleaved by several FEL pilot experiments. This paper gives an overview of the commissioning progress including the achieved machine performance and first operational experience.

INTRODUCTION

The newest large research facility at the Paul Scherrer Institute, the hard-X-ray free-electron laser SwissFEL [1] has recently commenced its scientific program with a series of pilot experiments. SwissFEL aims at delivering ultrashort coherent photon pulses through two beam lines called Aramis (hard X-rays, 1-7 Å) and Athos (soft X-rays, 6.5-50 Å). So far only the Aramis beam line has been commissioned with two experimental stations in operation, called Alvra and Bernina. Alvra is a multipurpose pump-probe station focusing on ultrafast biology and chemistry, while Bernina specializes in pump-probe crystallography for the study of ultrafast dynamics in solid matter, in particular strongly correlated systems, as well as structural biology.

The SwissFEL accelerator consists of an electron source, an S-band (3 GHz) booster linac and a C-band (5.7 GHz) main linac (Fig. 1). The electron source is a laser driven 2.5-cell S-band RF photoinjector gun. The electron bunches, with charge ranging between 10 and 200 pC, are longitudinally compressed in two stages at nominal energies of 300 MeV and 2.1 GeV, respectively. A higher-harmonic cavity (X-band, 12 GHz) linearizes the electron phase space before the first compression stage. The accelerated and compressed electron bunches are sent into the Aramis undulator line comprising 13 in-vacuum undulator modules of 4 m length each. A second undulator line, Athos, is currently under construction. It will be driven by 3 GeV electrons extracted in a switchyard halfway along the main linac. Table 1 lists the most important parameters of the SwissFEL facility.

This paper is an updated version of the contribution presented at the IPAC'18 [2] since new important results are been achieved between May and September 2018. SwissFEL linac reached its nominal electron beam energy of 5.8 GeV, first lasing with an photon energy of 9 keV and in the summer period other four pilot experiments were performed.

* paolo.craievich@psi.ch

STATUS OF C-BAND LINAC

The C-band main linac is the centrepiece of the SwissFEL accelerator defining the available electron and hence photon energy. It consists of a total of 26 RF modules, each providing a nominal accelerating voltage of 240 MV with four tuning-free copper structures [3, 4]. Figure 2 shows a part of the tunnel with C-band accelerating structures. The effectively achieved accelerating voltages vary between 200 and 280 MV, depending on the conditioning states of the modules. In each station, an IGBT-switched solid-state modulator manufactured by Ampegon (first half of the linac) or ScandiNova (second half) drives an E37212 Toshiba klystron, which can furnish up to 50 MW for a duration of 3 µs. The RF pulse is compressed in a barrel-open-cavity (BOC) [5] before being delivered to the four structures via a precisely adjusted waveguide network. Currently 25 of the 26 stations are available for beam acceleration. One RF station in Linac 2 is currently used for the upgrade of the software system. In case of failure of one RF station in Linac 1 and/or Linac 3 there is enough RF power reserve in order to guarantee the operations. The delivered power is typically around to 80% of the maximum value.

Table 1: SwissFEL Main Parameters

Parameter	Value
Photon wavelength	0.1-5.0 nm
Photon energy	0.25-12.4 keV
Pulse duration	1-30 fs
Electron energy	5.8 GeV
Electron bunch charge	10-200 pC
Repetition rate	100 Hz

A campaign of measurements on the RF stations has been performed to characterize the actual stability of the klystron voltage. A high performance differential amplifier has been used for this scope. This implements a high stability low-noise voltage generator and a low overdrive recovery time comparator in order to accurately monitor the pulse-to-pulse reproducibility. The results of these measurements showed that pulse-to-pulse stability of the klystron high voltage are better than the specified value of 15 ppm.

After the conditioning periods dedicated for each RF station, typically from 3 to 4 weeks for RF stations, the SwissFEL Linac has reached the nominal electron bunch energy of 5.8 GeV required for Aramis beamline in September 2018. In the present configuration, the linac delivers 5.5 GeV for a total energy of 5.8 GeV (300 MeV from the injector linac). The beam energy is for a compressed bunch with off-crest op-

Content from this work may be used under the terms of the CC BY 3.0 licence (© 2018). Any distribution of this work must maintain attribution to the author(s), title of the work, publisher, and DOI.

ISBN: 978-3-95450-194-6 ISSN: 2226-0366 doi:10.18429/JACoW-LINAC2018-WE1A05

Content from this work may be used under the terms of the CC BY 3.0 licence (© 2018). Any distribution of this work must maintain attribution to the author(s), title of the work, publisher, and DOI.

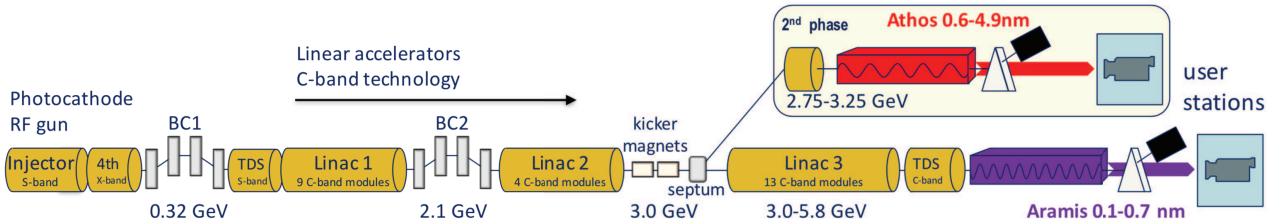


Figure 1: Schematic of SwissFEL accelerator layout (from Ref. [1] and [2]).

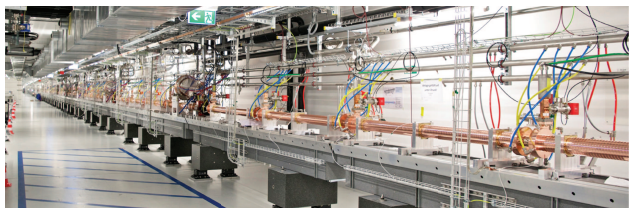


Figure 2: C-band accelerating structures in a part of the Linac 3.

eration in Linac 1. However, the operating energy is usually set according to the requirements for users' experiments and the working point of the single module is fixed to the maximum gradient achievable for a reliable operation. Figure 3 shows a panel with the distribution of the RF amplitudes and phases of the all RF stations including the two RF deflectors, SINDI01and S30CB14, respectively. When less beam energy is required, some of the last structures are set off-line providing the redundancy that is very useful to ensure the operation for the users. The overall objective is to run the facility with a beam energy of 5.8 GeV at a repetition rate of 100 Hz by December of this year. Presently the repetition rate of the electron beam is 25 Hz. All C-band modules are systematically operated at 100 Hz. Recent tests with a low-charge beam at 25, 50 and 100 Hz basically demonstrated beam transport at these rates. After this first year

Station		MV	deg	Station		MV	deg
SINEG01	RF on beam	7.2	90.0	S20CB01	RF on beam	263.0	92.5
SINSB01	RF on beam	68.5	90.0	S20CB02	RF on beam	254.7	90.0
SINSB02	RF on beam	65.4	90.0	S20CB03	RF on beam	235.0	92.8
SINSB03	RF on beam	99.0	67.9	S20CB04	INIT	0.0	
SINSB04	RF on beam	99.0	67.8	S30CB01	RF on beam	207.4	90.0
SINXB01	RF on beam	19.9	264.4	S30CB02	RF on beam	253.5	90.1
SINDI01	RF on delay	4.2	256.9	S30CB03	RF on beam	260.2	90.0
S10CB01	RF on beam	243.8	77.8	S30CB04	RF on beam	249.9	90.0
S10CB02	RF on beam	242.9	77.8	S30CB05	RF on beam	239.6	90.0
S10CB03	RF on beam	249.2	77.8	S30CB06	RF on beam	235.2	90.0
S10CB04	RF on beam	212.7	77.8	S30CB07	RF on beam	235.0	91.8
S10CB05	RF on beam	262.3	77.8	S30CB08	RF on beam	244.1	90.0
S10CB06	RF on beam	253.6	77.8	S30CB09	RF on beam	241.9	90.0
S10CB07	RF on beam	228.5	78.5	S30CB10	RF on beam	265.3	90.0
S10CB08	RF on beam	193.5	77.8	S30CB11	RF on beam	254.0	90.0
S10CB09	RF on beam	237.7	77.8	S30CB12	Conditioning	0.0	196.3
				S30CB14	Conditioning	65.0	2.0

Figure 3: Panel with the status of the RF stations.

of commissioning and operation, an optimization is under study to correct the major down-time sources, increase safety margins and redundancy and extend operating margins of the machine especially in terms of beam energy. The major source of downtime of the S-band and C-band stations is related to klystron arcs. The number has already been reduced by optimizing the the operation point of the klystron. However, a modification of the ramping up procedure is under study to recover the beam operation after an arc. Analysis of the waveform of the anodic voltage and current after an arc are performed to study possible improvement of the recovery procedure.

To control the RF stations a new, in-house developed digital Low Level RF (LLRF) system measures up to 24 RF signals per station and performs a pulse-to-pulse feedback at a repetition rate of 100 Hz. Depending on the location along the machine the LLRF system controls the accelerating fields of up to 4 RF structures. The modular system consists of a common digital processing unit and a frequency dependent RF front-end which converts the differ-ent RF frequencies to a common intermediate frequency (IF). The topology of one C-band RF station includes the reference RF signal that is modulated by a vector modulator, amplified by one klystron and fed into four C- band accelerating structures. The input signal before and after the structure is measured and a vector sum is calculated which is required for a pulse-to-pulse feedback. The LLRF system is introduced to control all the RF stations to provide low noise RF phase and amplitude actuations and precise RF signal detections. Pulse-to-pulse feedbacks are applied on amplitude and phase at up to 100 Hz to achieve the RF stabilities. Drift calibration is required on critical RF signals used for feedback to improve the long-term stability of the system. Automation tools are also required to help the operators to easily setup and operate the RF stations [6, 7].

LINAC STABILITY

The beam stability requirements of the SwissFEL linac result in challenging specifications on the stability of the RF fields that can only be met using reliable and high performance modulators and LLRF systems (mentioned in the previous paragraph). FEL operation requires very high shot-to-shot stability of the electron beam energy, which for the S-band and C-band RF system translates in tight amplitude and phase jitter requirements as listed in Table 2 [8]. The achieved RF amplitudes and phases stabilities are also listed in Table 2. These values include the contribution of all components of the RF station. It is worthwhile noting that the relative beam energy jitter at the Linac end was measured at 4.7 GeV and was resulted approximately 0.01% that is well below the specified value of 0.05%.

ISBN: 978-3-95450-194-6 ISSN: 2226-0366 doi:10.18429/JACoW-LINAC2018-WE1A05

Table 2: Pulse-to-pulse RF Phase and Amplitude Jitters (rms). Stability requirements are also indicated.

RF station	RF phase		RF amplitude	
	Meas. [°]	Spec. [°]	Meas. [%]	Spec. [%]
S-band	0.010-0.04	0.018	0.01-0.02	0.02
X-band	0.05	0.072	0.04	0.02
C-band	0.018-0.04	0.036	0.01-0.02	0.02

SCHEDULE AND PILOT EXPERIMENTS

SwissFEL Aramis has now completed its second phase of pilot experiments, with one more phase to follow. The second phase lasted from June to August of this year and comprises again four pilot experiments, still to be carried out at reduced performance levels with respect to the SwissFEL design values. Figure 4 shows the schedule of the Aramis beamline in details.

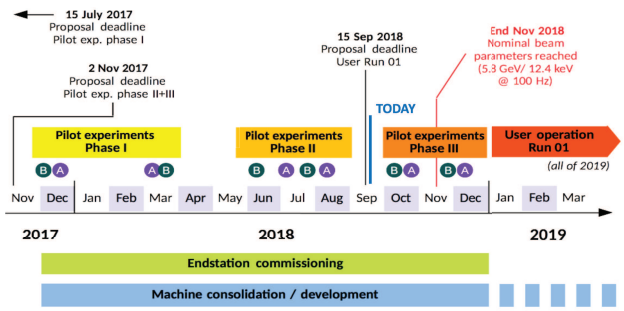


Figure 4: Schedule of the Aramis beamline (more details in [2]).

OUTLOOK

The third phase of the pilot experiments will last from October to December of this year and comprises again four experiments and the full performance level should be available (i.e., photons with up to 12.4 keV energy at 100 Hz pulse rate). This last pilot phase will be utilized to consolidate and characterize the machine performance before starting the first regular user operation run in early 2019 because in spite of the success and important milestones achieved so far, the accelerator and the beamlines are not yet in their final configurations. The commissioning of optical components, photon diagnostics and the experimental stations will proceed throughout 2018, in parallel with the machine development and consolidation program.

During the last shutdown in summer 2018 a pair of planar corrugated structures with orthogonal orientations were installed at the injector before the bunch compressor. For each device, three different corrugations, 1-m long, are mounted on a common support to manipulate and diagnose the bunch by self-inducing longitudinal and transverse wakefield. In one of these corrugations (*linearizer*), the self-induced wakes will partially compensate for the nonlinear energy chirp imprinted by the RF field and the magnetic compression. In particular, we also want to verify that the quadrupole component of the wakefield that increases beam emittance can be effectively canceled with a pair of planar corrugations with orthogonal orientation [9]. However, each device has three different corrugation periods corresponding to as many impedances to carry on several studies as described in [10]. The routine use of such a device at lower energy in a user facility has to still be demonstrated, in particular we want to prove that it can be adjusted to different bunch lengths, charges and that it may be used to provide a more stable FEL beam. Figure 5 shows a drawing of the two passive devices installed on their girder.

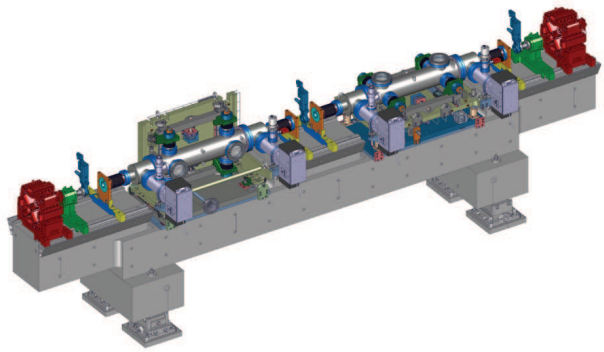


Figure 5: Drawing of the passive devices on their girder.

Athos Soft-X-Ray Line

The extensively redesigned Athos beam line [11] for the generation of soft X-rays in the range 250-1900 eV is currently under construction. Its main features are 16 Apple-X U38 undulators providing full polarization and transverse gradient control, with small magnetic chicanes between them to enable high-performance modes going by names such as "optical klystron", "high brightness" or 'terawatt-attosecond" [12]. In addition, a larger magnetic chicane at the center of the undulator line will allow for two-color operation with controllable delay between the pulses up to 500 fs. A resonant kicker magnet system [13], custom-designed to divert the two bunches separated by 28 ns into the respective beam lines, was installed earlier this year and has recently undergone first tests diverting the second bunch to the Athos dogleg.

As a diagnostic tool, a X-band Transverse Deflection Structure (TDS) will be installed downstream of the undulators of the Athos beamline, which will allow to indirect measurement of the X-Ray pulse length by analysing the induced energy spread on the electron bunch due to the FEL process [14]. Furthermore, thanks to the variable polarization of the TDS [15] it will be possible to perform a complete characterization of the 6D phase space by means of measurements of bunch length, energy and transverse slice emittances (vertical and horizontal) [16]. Since several experiments at DESY (FLASH2, FLASHForward, SINBAD) are also interested in the utilization of such a X-band TDS

Content from this work may be used under the terms of the CC BY 3.0 licence (© 2018). Any distribution of this work must maintain attribution to the author(s), title of the work, publisher, and DOI.

ISBN: 978-3-95450-194-6 ISSN: 2226-0366 doi:10.18429/JACoW-LINAC2018-WE1A05

Content from this work may be used under the terms of the CC BY 3.0 licence (© 2018). Any distribution of this work must maintain attribution to the author(s), title of the work, publisher, and DOI.

systems for high-resolution longitudinal diagnostics, a collaboration between DESY, PSI and CERN has been established to develop and build this advanced modular X-Band TDS system [17]. Figure 6 shows a mechanical drawing of a short version of the TDS constituted by 10 cells (number of cells of the actual prototype is 96).

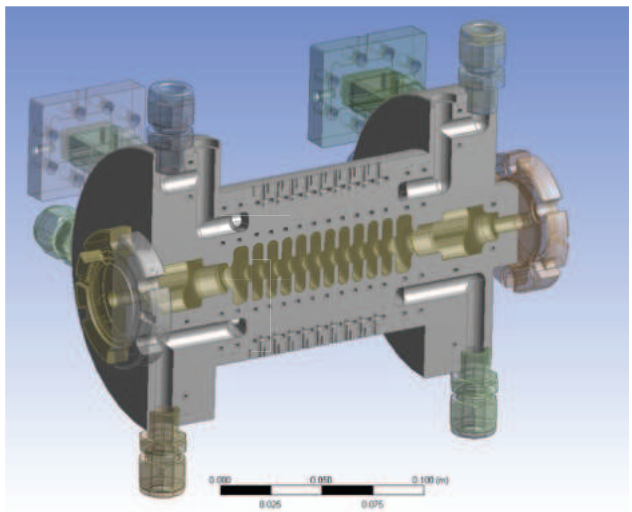


Figure 6: Mechanical drawing of a short version of the TDS constituted by 10 cells.

A first undulator prototype is arrived at PSI in June 2018, the installation of the complete undulator line is scheduled for the period from January 2019 to March 2020. The goal is to carry out a first pilot experiment before the end of 2020, with regular user operation to start in 2021.

CONCLUSION

New important results are been achieved in the SwissFEL between May and September 2018. The linac reached its nominal electron beam energy of 5.8 GeV, first lasing with an photon energy of 9 keV and in the summer period other four pilot experiments were performed. The current system upgrade and beam development program is on track in order to start regular user operation in 2019. In the meantime the installation of the Athos soft-X-ray line is progressing well, aiming at commissioning and first pilot experiments before the end of 2020.

ACKNOWLEDGEMENTS

It is a pleasure to acknowledge the valuable contributions of all the PSI support groups towards the first user operation runs at SwissFEL. To all of them go our acknowledgments. Furthermore, I am personally indebted to Thomas Schietinger for providing me large part of the materials for the talk and manuscript.

REFERENCES

[1] C. J. Milne *et al.*, *Appl. Sci.*, vol. 7, p. 720, 2017.

[2] T. Schietinger, in *Proc. IPAC'18*, Vancouver, BC, Canada, Apr.-May 2018, pp. 24–28. doi:10.18429/JACoW-IPAC2018-MOZGBD1

[3] F. Loehl *et al.*, in *Proc. LINAC'16*, East Lansing, MI, USA, Sep. 2016, pp. 22–26. doi:10.18429/JACoW-LINAC2016-MO3A01

[4] P. Craievich *et al.*, in *Proc. LINAC'18*, Beijing, China, Sep. 2018, paper THPO115, this conference.

[5] R. Zennaro *et al.*, in *Proc. IPAC'13*, Shanghai, China, May 2013, pp. 2827–2829.

[6] Z. Geng *et al.*, in *Proc. LINAC'14*, Geneva, Switzerland, Aug.-Sep. 2014, pp. 1114–1116.

[7] A. Hauff *et al.*, in *Proc. LINAC'14*, Geneva, Switzerland, Aug.-Sep. 2014, pp. 683–685.

[8] R. Ganter (Ed.), "SwissFEL conceptual design report", Paul Scherrer Institut, Villigen, Switzerland, Rep. 10-04, Apr. 2012.

[9] F. Fu *et al.*, *Phys. Rev. Lett.*, vol. 114, p. 114801, 2015.

[10] S. Bettoni *et al.*, in *Proc. IPAC'18*, Vancouver, BC, Canada, Apr.-May 2018, pp. 3401–3404. doi:10.18429/JACoW-IPAC2018-THPAK074

[11] R. Ganter (Ed.), "Athos conceptual design report", Paul Scherrer Institut, Villigen, Switzerland, Rep. 17-02, Sep. 2017.

[12] E. Prat, M. Calvi, R. Ganter, S. Reiche, T. Schietinger, and T. Schmidt, *J. Synchrotron Rad.*, vol. 23, pp. 861–868, 2016.

[13] M. Paraliev, C. Gough, S. Dordevic, and H. Braun, in *Proc. FEL'14*, Basel, Switzerland, Aug. 2014, pp. 103–106.

[14] C. Behrens *et al.*, *Nature Communications*, vol. 5, no. 3762, Apr. 2014.

[15] A.Grudiev, "Design of compact high power rf components at x-band", CERN, Geneva, Switzerland, Rep. CERN-ACC-NOTE-2016-0044, May 2016.

[16] P. Craievich *et al.*, in *Proc. FEL'17*, Santa Fe, NM, USA, Aug. 2017, pp. 491-494. doi:10.18429/JACoW-FEL2017-WEP040

[17] P. Craievich *et al.*, in *Proc. IPAC'18*, Vancouver, BC, Canada, Apr.-May 2018, pp. 3808-3811. doi:10.18429/JACoW-IPAC2018-THPAL068

ISBN: 978-3-95450-194-6 ISSN: 2226-0366 doi:10.18429/JACoW-LINAC2018-WE1A06

PLUSE-TO-PULSE BEAM MODULATION FOR 4 STORAGE RINGS WITH 64 PULSED MAGNETS

Y. Enomoto*, K. Furukawa, T. Kamitani, F. Miyahara, T. Natsui,
M. Satoh, K. Yokoyama, M. Yoshida, KEK, Tsukuba, Japan
S. Ushimoto, Mitsubishi Electric System & Service Co. Ltd. Tsukuba, Japan
H. Saotome, Kanto Information Service Tsukuba, Japan

Abstract

In 2017, sixty-four pulsed magnets (28 quadrupoles and 36 steerings) were installed in the KEK electron positron linac for simultaneous injection to four different rings. Since each ring requires different injection energy, magnetic field in the injector linac has to be changed shot by shot (every 20 ms) according to the destination of the beam. To realize such operation, novel pulsed power supplies and an EVENT timing system compatible PXI based control system were developed. Installation and commissioning of the system were successful and it has been working for one year without severe trouble.

INTRODUCTION

The KEK injector linac [1] has delivered electrons and positrons for particle physics and photon science experiments for more than 30 years. Figure 1 shows electron and positron accelerator complex in the KEK Tsukuba site. There are four storage rings, i.e. two rings for light source, PF and PF-AR, and two rings for electron positron collider, SuperKEKB [2] HER and LER. In addition to them, positron damping ring have been in operation since February 2018. All of the rings require full energy injection, 2.5 GeV for PF, 6.5 GeV for PF-AR, 4 GeV for SuperKEKB LER and 7 GeV for SuperKEKB HER as shown in the Fig. 1. To satisfy the requirement, 64 pulsed magnets were installed in 2017 and 32 more are planned to be installed in 2018. Using these magnets, magnetic field can be changed shot by shot in 20 ms and was optimized for each destination.

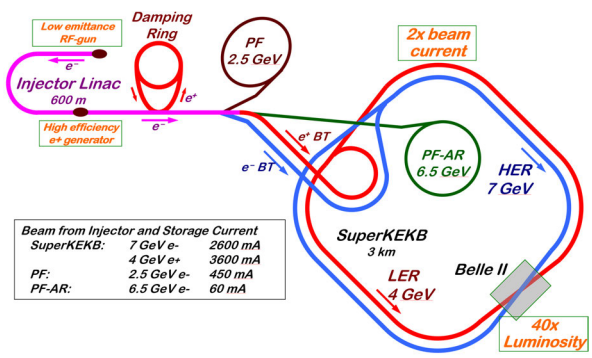


Figure 1: A schematic view of the electron and positron accelerator complex in the KEK.

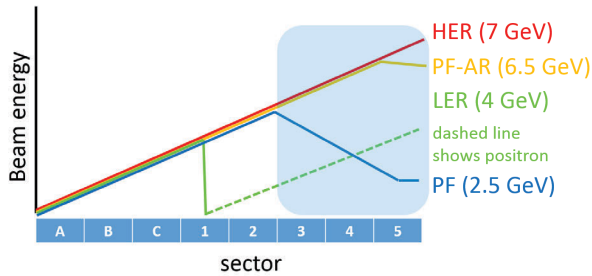


Figure 2: Beam energy along the beam line. Solid line shows electron beam dashed line shows positron beam respectively.

There are 8 (A-C, 1-5) sectors in the linac. Each sector is about 80 m long and the total length of the linac is about 650 m. Figure 2 schematically shows beam energy along the beam line. To minimize the installation of the pulsed magnets, acceleration scheme is carefully adjusted to minimize the length of the beam line where the beam with different energy pass through. The beam for the SuperKEKB HER, it is accelerated all of the sectors. The beam for the PF, it is accelerated in sector A to 2 and decelerated in sector 3 to 5. The beam for the SuperKEKB LER, electrons are accelerated in sector A to 1 and generate positrons at the target located in the middle of the sector 1. Positrons, shown in dashed line, are accelerated rest of the sectors. Since the beam energy is the same in the sector A to C and first half of the sector 1 regardless of the destination, it is not necessary to use pulsed magnets. On the other hand, in sector 3 to 5 shaded by light blue in the Fig. 2, beam with very different energy pass through, magnets in these sectors were completely replaced with pulsed magnets. In sector 2 and a part of sector 1, beam energy of the electron and positron is very different. Magnetic field optimized for the low energy positron beam affect the orbit of the high energy electron beam very little. In these section, DC magnets with compatible setting for both electron and positron beam are used except for several pulsed steering magnets at the moment.

MAGNET AND SUPPORT

Several types of magnets were installed in the beam lines as summarized in the Table 1. Appearance of these magnets are shown in Fig. 3. In sector 3 to 5, a common unit shown in Fig. 4, which consists of two quad magnets (PM_32_4), a horizontal steering magnet (PX_32_4), a vertical steering magnet (PY_32_4) and a beam position monitor located on a motor controlled movable support, was installed at 13 points.

* yoshinori.enomoto@kek.jp

Content from this work may be used under the terms of the CC BY 3.0 licence (© 2018). Any distribution of this work must maintain attribution to the author(s), title of the work, publisher, and DOI.

ISBN: 978-3-95450-194-6 ISSN: 2226-0366 doi:10.18429/JACoW-LINAC2018-WE1A06

Content from this work may be used under the terms of the CC BY 3.0 licence (© 2018). Any distribution of this work must maintain attribution to the author(s), title of the work, publisher, and DOI.

Table 1: Several Parameters of the Installed Pulsed Magnets

Type	L@1 kHz	R	Max current	Magnetic field	Gap	Installed number
PX_16_5	2.4 mH	71 mΩ	40 A	1040 AT	72 mm	1
PY_16_5	2.4 mH	71 mΩ	40 A	1040 AT	72 mm	1
PX_17_2	2.6 mH	127 mΩ	40 A	1440 AT	39 mm	4
PY_17_2	2.6 mH	126 mΩ	40 A	1440 AT	39 mm	4
PX_32_4	2.9 mH	115 mΩ	40 A	1440 AT	20 mm	13
PX_32_4	2.9 mH	115 mΩ	40 A	1440 AT	20 mm	13
PM_32_4	1.0 mH	8 mΩ	330 A	60 T/m	ϕ 20 mm	28

Other types of steering magnets were installed in sector 1 and sector 2. Two quad magnets (PM_32_4) were installed in sector 1 just before the positron production target to focus the electron beam.

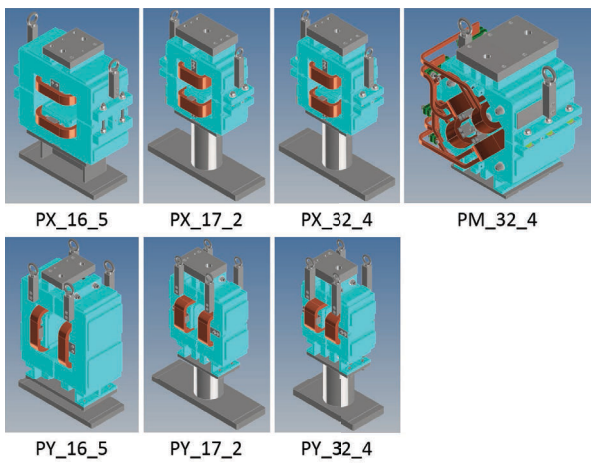


Figure 3: Appearance of installed pulsed magnets.

PULSED POWER SUPPLY

Concept and Overview

There are many requirements for the power supply to truly realize the required flexible operation. In addition, since the required number of the power supply is not a few, unit cost, installation space, energy efficiency are crucially important. Trigger rate of our linac is 50 Hz, but injection pattern is not fixed. The destination of the beam is delivered by the EVENT timing system via optical fiber just after the previous pulse. To interpret the information and change setting within 20 ms, fast and intelligent control system is necessary. To realize these requirements with minimum risks and cost, we decide to develop new power supplies by ourselves following the concepts bellows.

- realize high efficiency with energy recovery
- separate power circuit and control system
- use commercially available components as much as possible
- compatible with existent EVENT timing system
- compatible with existent EPICS control system [3]

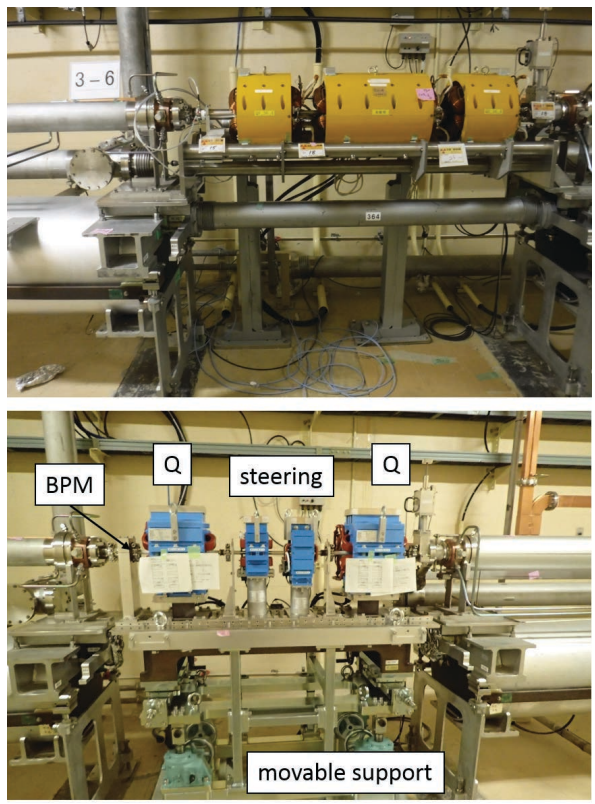


Figure 4: The upper photo shows old DC magnets before replacement. The lower photo shows newly installed unit.

Figure 5 shows a block diagram of the pulsed power supply system [4]. One standard unit which covers 4 quad and 4 steering magnets, shown in Fig. 6, consist of a PXI express unit for fast control, DC power supplies, pulse drivers and NI cRIO unit for interlock and slow data acquisition. There is one computer to control and monitor all of the 64 DC power supplies (DC power supply control server). A CSS archiver and A Network attached storage are used to log various data not only output current of the power supplies but temperature of the IGBT in the pulse driver, status of the DC power supplies and so on. EPCIS channel access protocol is mainly used for the communication among computers. LXI ver 1.3 protocol is used to control the DC power supplies and NI network shared variable is used to send fast waveform data. As for the event timing system, dedicated optical fiber

ISBN: 978-3-95450-194-6 ISSN: 2226-0366 doi:10.18429/JACoW-LINAC2018-WE1A06

is directly connected to the module. Most of the software is written by LabVIEW 2016 (32 bit) with NI DSC module and running on Windows 8.1.

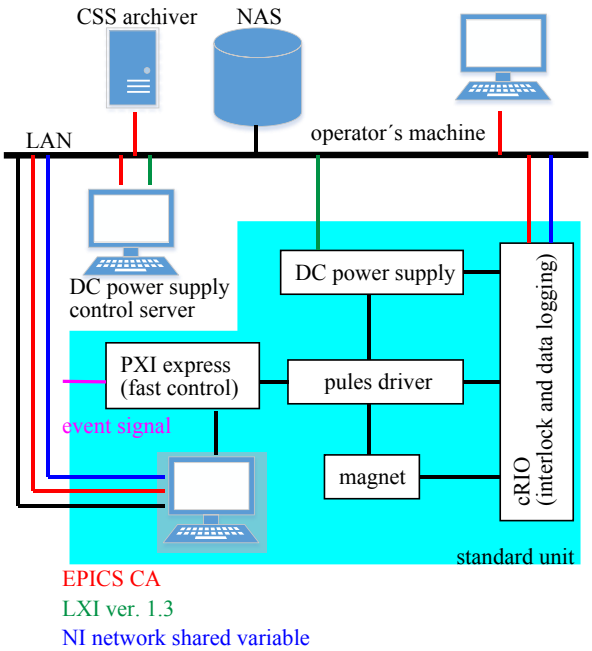


Figure 5: Block diagram of the power supply control and monitor system.



Figure 6: A photo of the standard unit for 4 quad and 4 steering magnets.

Pulse Driver for Quad Magnet

Design parameters of the pulse driver for the Q magnet is summarized in Table 2. To achieve these values, a novel switching power supply with energy recovery circuit was developed

Table 2: Design Parameters of the Pulse Driver for Quad Magnet

Parameter	Value
max current	330 A
max voltage	230 V
stability	0.1%
cooling	water cooled
power consumption	1500 W
repetition	50 Hz

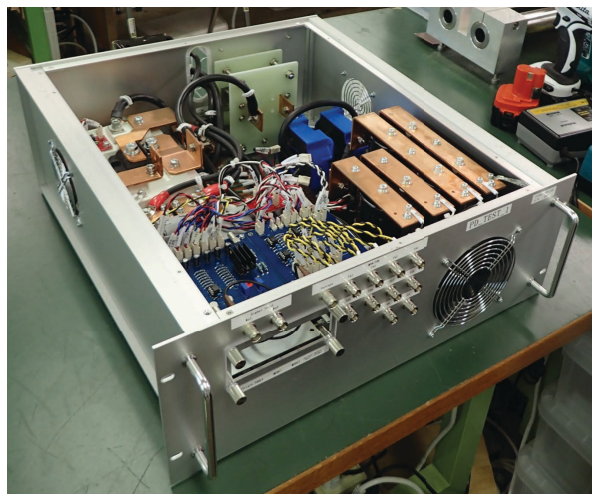


Figure 7: A photo of the pulse driver for quad magnet.

Figures 7 and 8 show an appearance and a conceptual circuit diagram of the pulse driver respectively. The circuit consists of two IGBTs (IGBT 1 and IGBT 2), two capacitors (C_HV and C_LV), two DC power supply (VH and VL) and several diodes. After the trigger signal arrives, first, both of the IGBTs turn on and current provided from both of the capacitors pass the load through red lines shown in the upper figure in Fig. 8. When the current reach the set value, IGBT 1 turn off and the gate voltage of the IGBT 2 is controlled to keep constant output current. Finally, after the beam pass through the magnet, IGBT 2 turn off. Stored energy in the load (magnet) is recovered to the capacitor (C_HV) through the red line shown in the bottom figure Fig. 8.

By combination of such energy recovery mechanism and water cooling system, the outsize dimension of the pulse driver is as small as EIA 3U in height. Output current is monitored and fed back by two independent DCCTs with hall sensor (LEM LF 1005-S) which are calibrated by a more precise external DCCT (Hioki 9709).

Pulse Driver for Steering Magnet

Design parameters of the pulse driver for steering magnet is summarized in Table 3. Compared with the driver for quad magnet, output power is very small but bipolar output is required. To meet with this condition, power operational amplifier (Apex PA12 [5]) was used for the key device. Although such kind of amplifier is low efficiency compared

Content from this work may be used under the terms of the CC BY 3.0 licence (© 2018). Any distribution of this work must maintain attribution to the author(s), title of the work, publisher, and DOI.

ISBN: 978-3-95450-194-6 ISSN: 2226-0366 doi:10.18429/JACoW-LINAC2018-WE1A06

Content from this work may be used under the terms of the CC BY 3.0 licence (© 2018). Any distribution of this work must maintain attribution to the author(s), title of the work, publisher, and DOI.

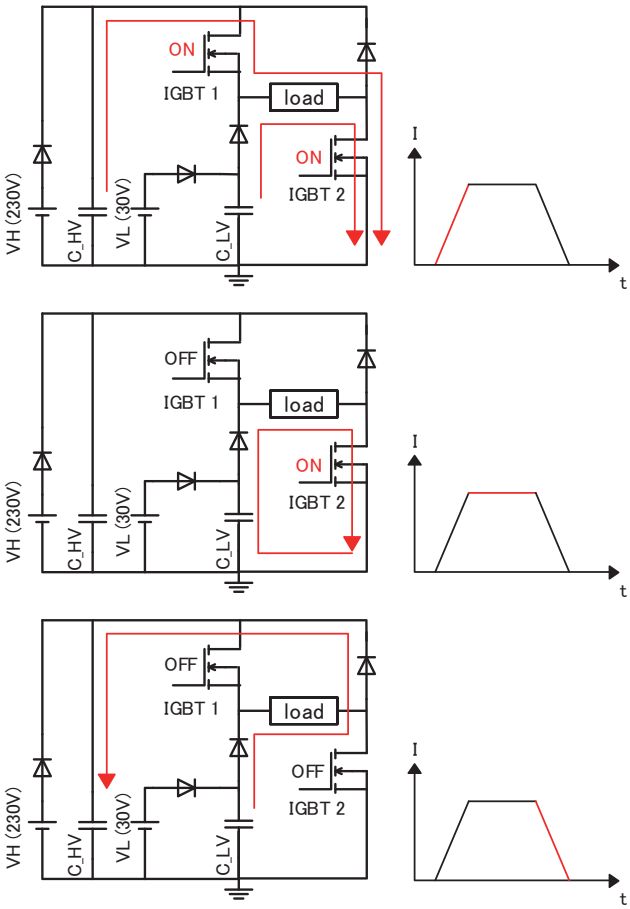


Figure 8: Conceptual circuit diagram of the pulse driver for quad magnet. Red allows shows the current path. Right side figures shows current profiles at corresponding states.

to switching power supply, the output power is very small compared to the quad magnet above and the low efficiency affect the total power consumption very little.

Table 3: Design Parameters of the Pulsed Driver for Steering Magnet

Parameter	Value
max current	± 10 A
max voltage	± 40 V
stability	0.01%
cooling	air cooled
power consumption	750 W
repetition	50 Hz

Figure 9 shows an appearance of the pulse driver for the steering magnet. Air cooling was adopted for the simplicity and cost. Usually steering magnets are used in a pair of horizontal and vertical magnets, there are two circuit in one box of JIS 2U height (99 mm). Output current is monitored and fed back by two independent precision resister of 1 ohm which are calibrated by more precise external DCCT (Hioki 6862).

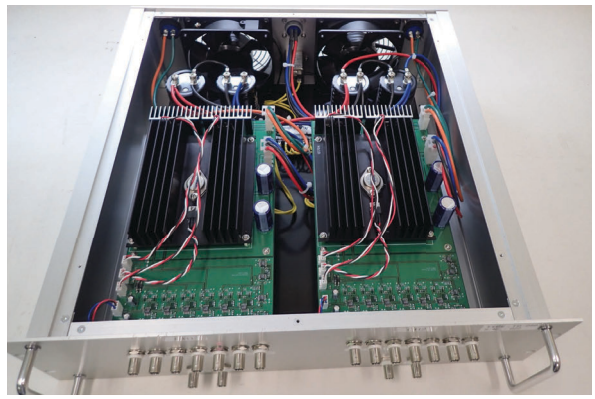


Figure 9: A photo of the pulse driver for steering magnet.

Control and Monitor System

For the fast control, PXI express unit plays major role. The unit shown in Fig. 10 consists of a PC and a PXI express chassis (NI PXIe-1082) with four cards, a controller board (NI PXIe-8381) to connect to the PC, an event receiver board (EVR) (MRF PXI-EVR-230), a DAC board (NI PXI-6733), and a ADC board (NI PXIe-6356), which can set and monitor output current up to 8 pulsed power supply independently in 16 bit resolution with 1 MSa/s sampling or update rate. They are placed in the same rack and connected by a metal cable.

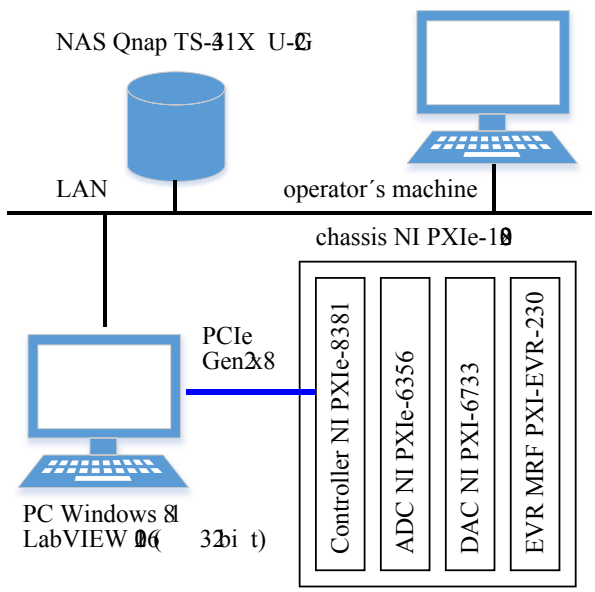


Figure 10: Components of the fast control system.

For the slow data acquisition and interlock system, NI compactRIO (NI cRIO-9063) unit is used. One unit consists of a 32 ch 250 kSa/s/ch ADC module (NI 9205), a 32 ch TTL digital I/O modules (NI 9403) and two 4 ch relay output modules (NI 9482). It covers 4ch of the pulsed power supply, namely for one PXI express unit (8 ch), two cRIO units are needed. To realize robust interlock system, cRIO is working not in a scan engine mode but in a FPGA mode. On the upper

ISBN: 978-3-95450-194-6 ISSN: 2226-0366 doi:10.18429/JACoW-LINAC2018-WE1A06

layer, EPICS CA server is running on the NI RT Linux. Not only the PVs for the ADC and DIO data, but the PVs for the high and low threshold, average number to control data acquisition are also prepared which can be set and read using EPICS CA protocol.

Trigger System

An EVR board in PXI form factor is used to integrate the timing system to the linac timing system. In our linac, event timing system by Micro-Research Finland Oy (MRF) is adopted. The EVR receive not only the timing information but also the mode number and shot ID. The mode number is used to determine the next output setting. The shot ID is used to tag the monitored information. The trigger timing is precisely (8.77 ns step) adjusted 3 ms before the beam arrival. Since the rising and falling time of the magnet current is in the order of ms, pules shape of the power supply does not important as long as the reproducibility is assured.

PERFORMANCE EVALUATION

Efficiency

Power consumption of the pulsed power supply for quad magnet was calculated and measured by a power meter (Hioki, PW3335). Blue bars in Fig. 11 shows calculated power consumption from measured resistance and inductance of the magnet and cables when one magnet was operated at 300 A and 50 Hz without energy recovery. About 15% of energy is lost by ohmic heating of the coil and cable but 85% are stored in the inductance of the coil. It is in principle possible to recover the latter part of the energy to capacitors. Green bar in Fig. 11 shows measured power consumption in total including DC power supply. The red allow corresponds to recovered energy. The energy recovery efficiency compared with stored energy in inductance and total energy are as high as 80.1% and 68.5% respectively.

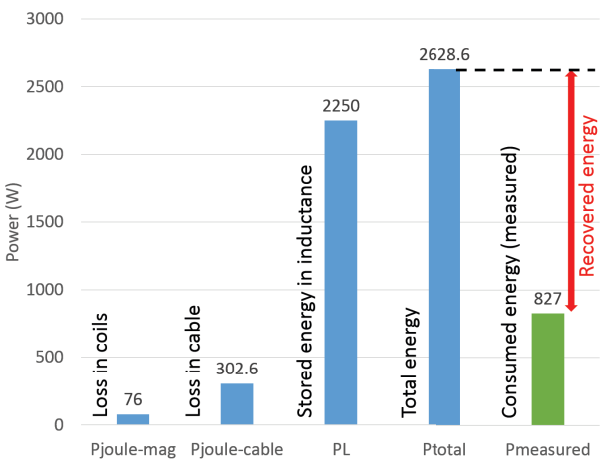


Figure 11: Energy balance of pulsed power supply for Q magnet.

Stability

Figure 12 shows a stability measurement result of pulsed power supply of quad magnet for 24 hours. Horizontal axis shows the measured output current and vertical axis shows the number of entry. Bin width is 0.2 mA Output current was set to alternate between 0 A and 166 A at 50 Hz. Measured mean value and standard deviation of the output current were 165.946 A and 14.578 mA respectively which corresponds to 88 ppm (0.0088%) relative stability at this current. This is much smaller than design value (see Table 2).

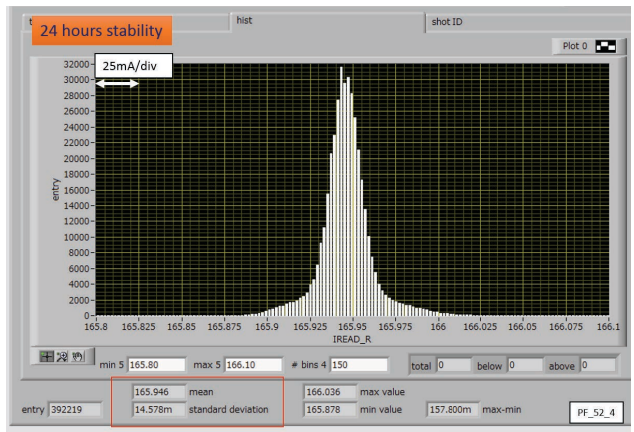


Figure 12: A histogram of the stability measurement of pulsed power supply for quad magnet.

OPERATION

After four months installation work from May, comprehensive test was done for a month in September in 2017. In November, simultaneous injection using the newly installed pulsed magnets were demonstrated successfully. Since the SuperKEKB phase two operation start from March in 2018 and light source rings restart in May, real simultaneous injection operation started in the middle of May and ended July in 2018 for summer shutdown. During entire period, there was no sever problem and the beam was delivered to all of the four rings stably.

CONCLUSION

Large number of DC magnets was replaced with new pulsed magnets in 2017 for the pulse-to-pulse beam modulation for 4 storage rings. Two kinds of pulsed power supplies for quad and steering magnet respectively were developed. Installation and commissioning of the system were successfull and they are now working in the KEK electron positron injector linac without any severe trouble for about 1 year.

REFERENCES

[1] M. Akemoto *et al.*, "The KEKB Injector Linac", *Prog. Theor. Exp. Phys.*, vol. 2013, pp. 03A002, 2013. doi:10.1093/ptep/ptt011

Content from this work may be used under the terms of the CC BY 3.0 licence (© 2018). Any distribution of this work must maintain attribution to the author(s), title of the work, publisher, and DOI.

ISBN: 978-3-95450-194-6 ISSN: 2226-0366 doi:10.18429/JACoW-LINAC2018-WE1A06

[2] Y. Ohnishi *et al.*, "Accelerator design at SuperKEKB", *Prog. Theor. Exp. Phys.*, vol. 2013, pp. 03A011, 2013. doi:10.1093/ptep/pts083

[3] A. Akiyama *et al.*, "Accelerator Control System at KEKB and the Linac", *Prog. Theor. Exp. Phys.*, vol. 2013, pp. 03A008, 2013. doi:10.1093/ptep/pts081

[4] Y. Enomoto *et al.*, "A New Pulse Magnet Control System in the KEK Electron Positron LINAC", in *Proc. IPAC2018*, Vancouver, BC, Canada, pp. 2121-2123, 2018. doi:10.18429/JACoW-IPAC2018-WEPAK014

[5] https://www.apexanalog.com/products/pa12.html

Content from this work may be used under the terms of the CC BY 3.0 licence (© 2018). Any distribution of this work must maintain attribution to the author(s), title of the work, publisher, and DOI.

ISBN: 978-3-95450-194-6 ISSN: 2226-0366 doi:10.18429/JACoW-LINAC2018-WE2A01

FIRST ACCELERATION AT FRIB*

E. Pozdeyev†, H. Ao, J. Brandon, N. Bultman, F. Casagrande, S. Cogan, K. Davidson, E. Daykin, P. Gibson, W. Hartung, L. Hodges, K. Holland, M. Ikegami, D. Jager, S. Kim, M. Konrad, B. Kortum, T. Larter, Z. Li, S. Lidia, S. Lund, G. Machicoane, I. Malloch, H. Maniar, F. Marti, T. Maruta, C. Morton, D. Morris, D. Omitto, P. Ostroumov, A. Plastun, J. Popielarski, H. Ren, K. Saito, J. Stetson, D. Victory, Y. Yamazaki, T. Yoshimoto, J. Wei, J. Wong, M. Xu, T. Xu, S. Zhao, Q. Zhao,
Facility for Rare Isotope Beam, East Lansing, 48824, USA

Abstract

FRIB is now moving to commissioning interleaved with installation. The ECR, low energy transport and RFQ have been commissioned with beam. By the time of the conference the 4K cryogenic system and first three beta 0.041 QWR cryomodules will be commissioned with beam. The talk will focus on hardware and beam performance.

INTRODUCTION

The Facility for Rare Isotope Beams [1] is the premiere DOE-SC national user facility for nuclear physics research built on the campus of Michigan State University. The FRIB driver accelerator will accelerate ions with the mass up to Uranium to energies higher than 200 MeV and beam power on target higher than 400 kW. The main focus of the experimental program is rare isotope beams by fragmentation, gas stopping, and reacceleration.

Project commissioning performance requirements are defined by Key Performance Parameters (KPP) for CD-4:

1. Accelerate Argon beam with the energy larger than 200 Me/u and a beam current larger than 20 pnA
2. Detect 84Se in FRIB separator focal plane. The last KPP requirement for the experimental systems can be translated to the following requirement for the accelerator: accelerate 86Kr beam to produce 84Se by fragmentation.

Phased Beam Commissioning

FRIB has adopted a "paper-clip" design shown in Fig. 1. The FRIB Front End and RFQ are located on the east side of the project site (marked in red). The beam is accelerated in Linac Segment 1 (LS1) through three beta 0.041 (blue) and eleven 0.085 (yellow) 80.5 MHz QWR cryomodules to the energy of approximately 20 MeV/u. A lithium stripper will be installed at the end of LS1. The stripped beam is collimated in first folding segment (FS1) and accelerated by HWRs operating at 325 MHz in linac segments 2 (LS2, green) and 3 (LS3, grey) and sent towards experimental facilities through BDS. Another folding segment FS2 is used between LS2 and LS3 to reduce the footprint of the facility.

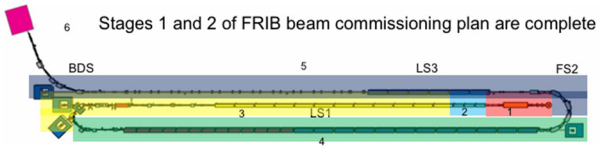


Figure 1: Paper-clip design of the FRIB accelerator. Colors and numbers mark commissioning stages: red - Front End, blue – three beta 0.041 cryomodules, yellow – eleven 0.085 cryomodules and part of FS1, green – LS2, and grey – FS2 and LS3.

FRIB beam commissioning is interleaved with installation and is approached in stages as show in Fig. 1. Commissioning follows installation of linac systems along the beam path starting from the Front End. In this article, we describe commissioning of the Front End, completed earlier in 2018, and the first beam acceleration in the first three beta 0.041 QWR cryomodules demonstrated in July 2018.

HIGHLIGHTS OF TECHNICAL SYSTEMS

Figure 2 shows the layout of the FRIB Front End [2] with the first three beta 0.041 QWR cryomodules and a temporary diagnostics station (D-Station). The front end is located on two levels to allow for maintaining one ion source while the other source is used for the program.

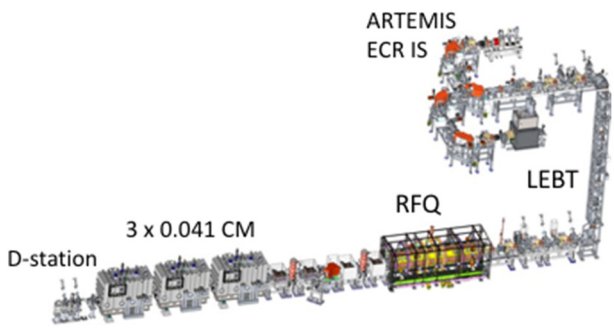


Figure 2: FRIB Front End with the first three 0.041 cryomodules and the temporary diagnostics station.

The front end includes

1. Two ECR sources on High Voltage (HV) platforms. 1) ARTEMIS is a 14 GHz ECR ion source. The source has been installed and commissioned in 2016. 2) The second source is a 28 GHz superconducting (SC) source based on VENUS (LBNL). The superconducting source is under construction, with planned delivery in 2019.

* Work supported by the U.S. Department of Energy Office of Science under Cooperative Agreement DE-SC0000661 and the National Science Foundation under Cooperative Agreement PHY-1102511, the State of Michigan and Michigan State University.
† pozdeyev@frib.msu.edu.

Content from this work may be used under the terms of the CC BY 3.0 licence (© 2018). Any distribution of this work must maintain attribution to the author(s), title of the work, publisher, and DOI.

ISBN: 978-3-95450-194-6 ISSN: 2226-0366 doi:10.18429/JACoW-LINAC2018-WE2A01

Content from this work may be used under the terms of the CC BY 3.0 licence (© 2018). Any distribution of this work must maintain attribution to the author(s), title of the work, publisher, and DOI.

2. LEBT. The beam energy is 12 keV/u. LEBT includes a chopper, electrostatic quads, and solenoids.
3. 4-vane RFQ accelerating ion beams from 12 keV/u to 500 keV/u
4. MEBT, Beam energy is 500 keV. MEBT includes two RF bunchers and quadrupole magnets.
5. Instrumentation and diagnostics
6. Subsystems powering and otherwise enabling front end components: RF, PS, Vacuum, etc.

The commissioned portion of the SRF linac includes

1. Three beta 0.041 cryomodules separated by warm boxes with diagnostics. The design beam energy after the cryomodules is 1.5 m/eV/u.
2. A temporary diagnostic station (D-Station) to characterize the beam accelerated by SRF cavities. D-Station was installed in place of the first beta 0.085 cryomodule, which temporarily was set aside in the tunnel.

Room Temperature Ion Source ARTEMIS B

ARTEMIS B ECR Ion Source is used for FRIB commissioning. ARTEMIS B is a 14 GHz room-temperature ECR ion source built in 2005 as a development source and a spare for Cyclotron operations. The source is based on the design of AECR-U (LBNL) and is easy to operate and maintain. This approach presents a low-risk, low-cost solution for the linac commissioning.

The source performance easily meets intensity requirements for commissioning. The source demonstrated more than 150 eμA of 40Ar9+ beam, corresponding to a beam power of 150 kW on the production target.

RFQ [3]

The FRIB RFQ is a four-vane brazed structure with a variable cross section and voltage profile. Table 1 shows main RFQ parameters while Fig. 3 shows the fully assembled RFQ in the FRIB tunnel. The RFQ engineering design has been developed at FRIB with important contributions from L. Young and J. Stovall. Detailed thermal analysis was performed by the Tsinghua University under a contract from FRIB. An order to procure the RFQ was placed with an industrial vendor. The RFQ 150 kW tube-based amplifier was developed at MSU.

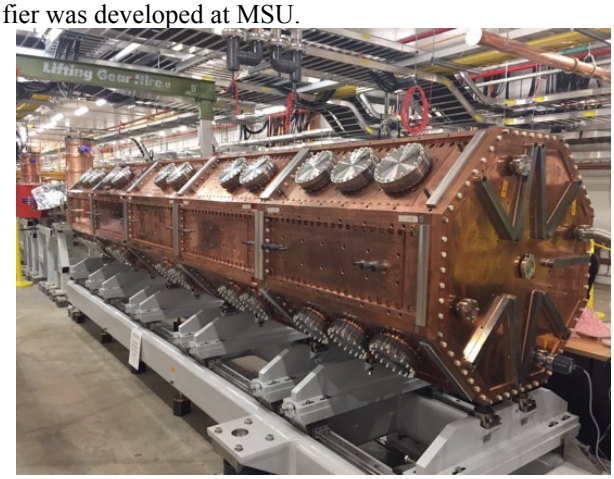


Figure 3: FRIB RFQ in the FRIB tunnel.

Table 1: FRIB RFQ Parameters

Parameter	Value
Frequency, MHz	80.5
Beam energy (Inj/Ext, keV/u)	12/500
Q/A	1/3 – 1/7
Accelerating efficiency	> 80%
CW RF Power (kW, Uranium)	100
Length	5

FRIB RFQ was installed and tuned in the FRIB tunnel in October-November of 2016. Slug tuners were cut to match the required frequency and the voltage profile. The deviation between the measured RFQ field and the target field did not exceed 0.5% after tuning. The frequency correction for the effect of vacuum was implemented, resulting in a frequency error under vacuum of only a few kHz.

The RFQ has been conditioned to 60 kW, sufficient to accelerate KPP beams. At this power, no measurable X-ray radiation above the background level has been detected. The RF amplifier power was limited to 60 kW to allow RFQ operations with personnel present in the tunnel.

Front End Beam Line and Instrumentation

The installation of the beam line was completed in July of 2017. Figure 4 shows LEBT, RFQ, MEBT, and 0.041 cryomodules in the FRIB tunnel.

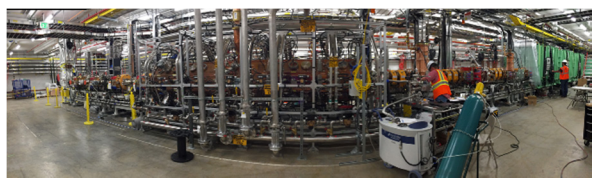


Figure 4: LEBT (left), RFQ (centre), MEBT (right), and 0.041 cryomodules (far right) in the FRIB tunnel.

The front end includes an extensive suite of instrumentation systems, Fig. 5. To start the commissioning, however, only a small subset, consisting of the charge-selection slits, viewers, and Faraday Cups, was used. A 45-degree dipole magnet in MEBT has been used to measure the beam energy of the beam accelerated by the RFQ.

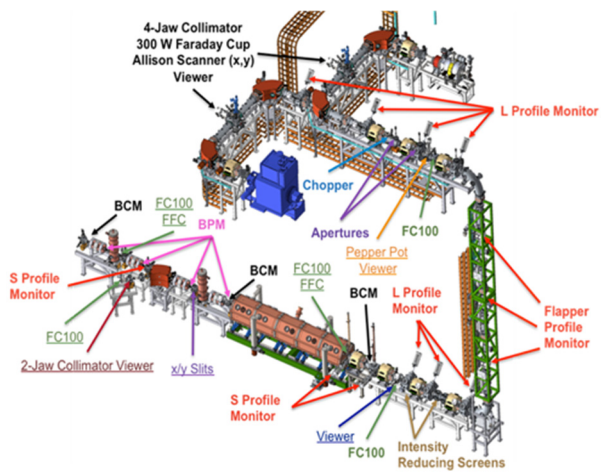


Figure 5: Front End diagnostics.

ISBN: 978-3-95450-194-6 ISSN: 2226-0366 doi:10.18429/JACoW-LINAC2018-WE2A01

Three Beta 0.041 QWR Cryomodules [4, 5]

Linac Segment 1 (LS1) includes three beta 0.041 QWR cryomodules, shown in Fig. 6, and eleven beta 0.085 QWR cryomodules. The 0.041 cryomodules were installed and connected earlier this year. The 0.085 cryomodules with the rest of LS1 will be commissioned in 2019.

Each 0.041 cryomodule includes four QWRs operating at 80.5 MHz and two superconducting solenoids with dipole correctors. The 0.041 resonators were operated in the CW regime at 4K. Eventually, the cavities will be operated at 2K following the staged commissioning of the cryoplant. More details about cryomodule design can be found in [4].

The cryo distribution lines were cooled down in April of 2018 and the cryomodules were cooled down to 4K in the middle of May 2018. All the cavities were conditioned to the nominal field of 5.1 MV/m within a week.



Figure 6: Thee beta 0.041 cryomodules with the D-Station.

D-Station

A temporary diagnostics station (Fig. 7) was installed in place of the first beta 0.085 QWR cryomodule with a goal to fully characterise the beam parameters after the 0.041 cryomodules and before commissioning the rest of the linac. D-Station included the following diagnostics:

- Two BPMs
- Two ACCTs
- Faraday cup
- Profile monitor
- Silicon detector
- Halo monitor Rings with current readout

The components installed in D-Station were temporarily repurposed from other accelerator areas.

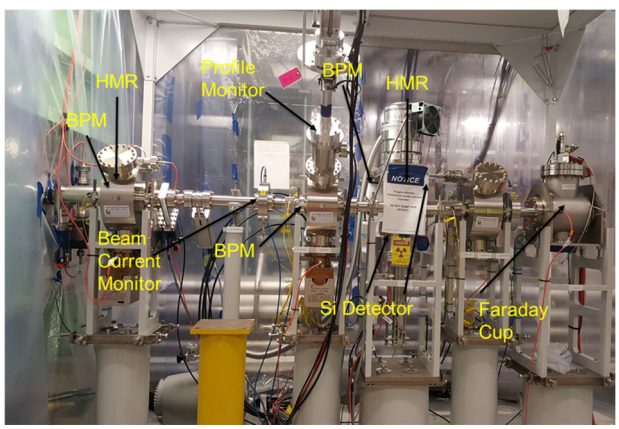


Figure 7: D-Station with its subsystems.

ACCELERATOR READINESS REVIEW PROCESS

FRIB conducts Device Readiness Reviews to assess hardware readiness and authorize a start of integrated testing. The reviews are typically internal unless external expertise is required.

Accelerator Readiness Reviews (ARR) assess readiness of accelerator for beam commissioning. ARRs review system and documentation readiness, people readiness, hardware readiness (see Table 2).

Table 3: ARR Scope, Dates, and Status

Review/ Stage	Scope	Date	Status
ARR1	Front End	7/2017	Complete
ARR2	0.041 CM	5/2018	Complete
ARR3	0.085 CM, LS1	2/2019	Planned
ARR4	FS1, LS2	4/2020	Planned
ARR5	FS2, LS3	9/2020	Planned

COMMISSIONING RESULTS

Front End Commissioning [2]

LEBT was commissioned with the beam in Spring and Summer of 2017 as new sections of LEBT were added. The beam was transported with nearly 100% requiring little tuning. This indicated a good agreement between the machine and its model and good alignment of beam line components.

The beam emittance and Twiss parameters were measured after the ion source using Alison scanners. The measured r.m.s. emittance of the Argon beam was 0.056 mm*mrad and 0.5 mm*mrad in horizontal and vertical planes respectively. This result was in a good agreement with simulations.

The measured Twiss parameters were used to improve beam matching to LEBT. After these adjustments, the measured beam transport agreed well with simulations. Figure 8 shows the beam profile measured by viewers along LEBT (upper row) compared to simulated profile at same locations (lower row). The measured and simulated profiles are in good qualitative and quantitative agreement.

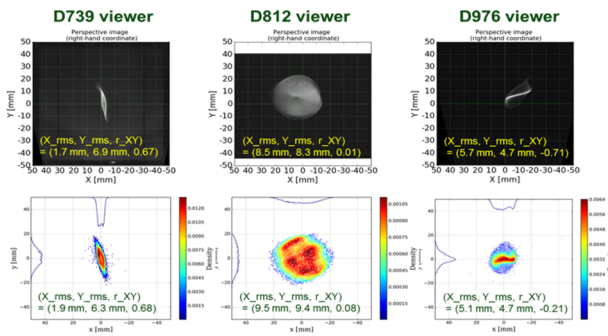


Figure 8: Measured (upper row) and simulated (lower row) beam profiles at LEBT viewers show a good agreement.

Content from this work may be used under the terms of the CC BY 3.0 licence (© 2018). Any distribution of this work must maintain attribution to the author(s), title of the work, publisher, and DOI.

ISBN: 978-3-95450-194-6 ISSN: 2226-0366 doi:10.18429/JACoW-LINAC2018-WE2A01

Content from this work may be used under the terms of the CC BY 3.0 licence (© 2018). Any distribution of this work must maintain attribution to the author(s), title of the work, publisher, and DOI.

In September of 2017, after ARR01, Argon beam was accelerated through RFQ. Initially, the multi-harmonic buncher in front of the RFQ was kept off. The measured acceleration efficiency was 31%. The accelerated current readings measured by the Faraday cup in the straight section and the Faraday cup after the 45-deg. bend were same, confirming that only the accelerated current was measured. The beam energy measured by the dipole magnet was 500 keV/u. The energy spread did not exceed 1%. In several days, the beam line and the RFQ were retuned and Krypton beam was accelerated producing results nearly identical to those with the Argon beam. Figure 9 shows images of the beam spot on the viewer after the MEBT dipole.

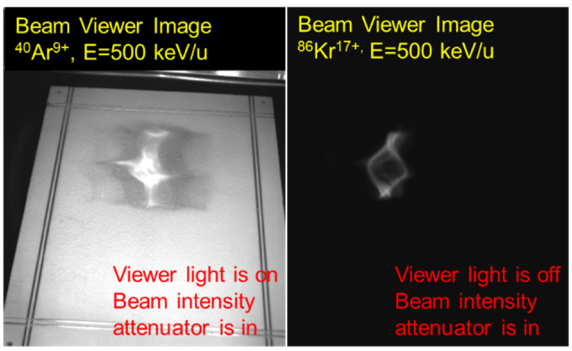


Figure 9: Argon and Krypton beam spots on the viewer situated after the 45-degree bend in MEBT. Beam energy after RFQ is 500 keV/u.

The RFQ acceleration efficiency was measured as a function of the RFQ RF power. Figure 10 shows the measured efficiency and the efficiency simulated by PARMTEQ for 40Ar9+. The two curves nearly overlap. The full transmission efficiency, including non-accelerated current, was measured by two AC current transformers situated on both sides of the RFQ. The measured transmission can reach 100% for good matching. Some degradation of the total transmission efficiency for mismatched beam can be used for beam matching and alignment at the entrance of RFQ.

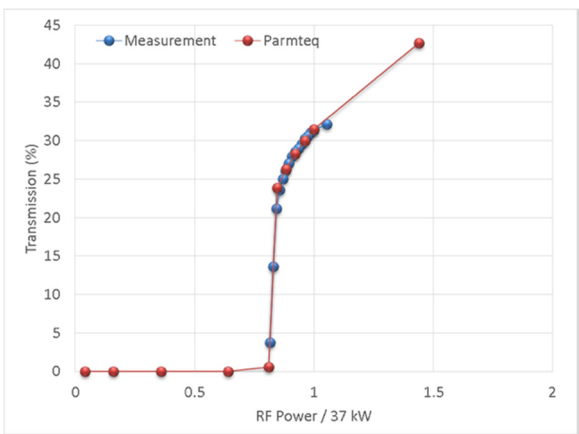


Figure 10: RFQ acceleration efficiency as a function of the RFQ forward power (normalized to 37 kW)

The beam transmission increased to the design value, >80%, with MHB operational. Figure 11 shows the accelerated Ar beam current measured by the FC at the end of MEBT. Krypton beam exhibited very similar behaviour.

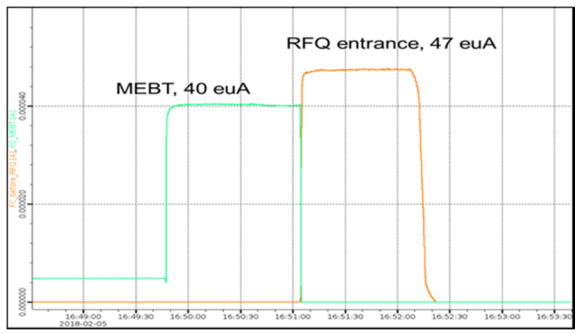


Figure 11: Argon beam current reading from Faraday cups at the entrance of the RFQ and after the RFQ. The transmission efficiency is 86%.

Commissioning of Beta 0.041 Cryomodules

First, the beta 0.041 cryomodules were commissioned with 40Ar9+ beam. Figure 12 shows the measured beam energy as a function of the number of powered cavities. Initially, Cavity 8 exhibited excessive microphonics and was kept off. In this setup, the beam energy reached 2 MeV/u. After the acceleration of Argon, accelerator settings were scaled to accelerate 86Kr17+ beam. The Krypton beam was accelerated to 2 MeV/u with nearly 100% efficiency. After minimal orbit and settings adjustments, the transmission reached 100%. Figure 13 show the beam current measured by ACCTs before the RFQ in LEBT, after RFQ in MEBT, at the exit of MEBT, and in D-Station after the cryomodules. The beam is transported through the RFQ with 100% efficiency but only 80% of the beam is accelerated. The beam accelerated by the RFQ is accelerated further by the cryomodules without losses. Halo monitor rings installed in cryomodules and D-station and sensitive to losses below a nanoamp did not show detectable losses. The lossless transport with minimal tuning and small orbit deviations clearly indicated good alignment of accelerator components and good agreement of between the actual machine and its model.

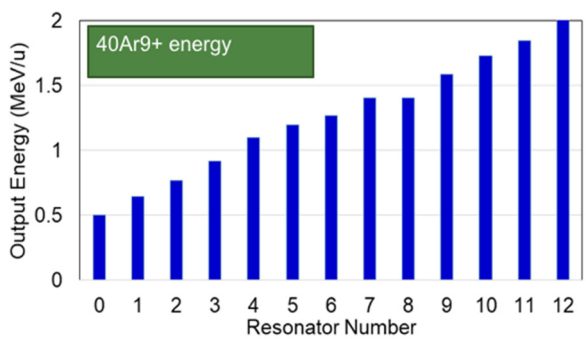


Figure 12: Beam energy after vs the number of energized 0.041 resonators.

ISBN: 978-3-95450-194-6 ISSN: 2226-0366 doi:10.18429/JACoW-LINAC2018-WE2A01

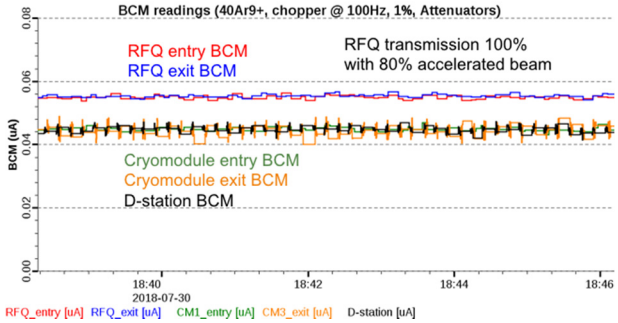


Figure 13: Beam current measured along the accelerator.

The beam emittance was measured in MEBT using the quad scan method and a profile monitor. A similar technique was applied to measure the beam emittance in D-Station but the strength of the last SC solenoid was changed. Both measurements gave very similar number for the beam emittance, showing beam quality preservation (Fig. 14).

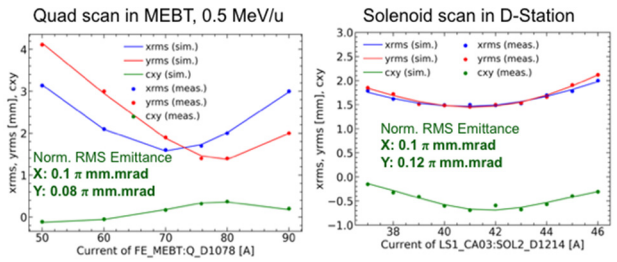


Figure 14: Results of emittance measurements in MEBT and D-Station show beam quality preservation.

The silicon detector installed in D-station was used to measure the absolute energy of the beam, the energy spread, and the longitudinal bunch profile.

The longitudinal emittance in D-Station was measured by scanning the field of the last SRF cavity. Figure 15 shows the bunch length measured by the Si-Detector as a function of the accelerating field in the last cavity. The measurements were done for two settings of the multi-harmonic buncher. The longitudinal emittance can be reduced by changing MHB stings although it is achieved at some loss of beam intensity. The measured emittance numbers were consistent with the expected r.m.s. value of the longitudinal emittance.

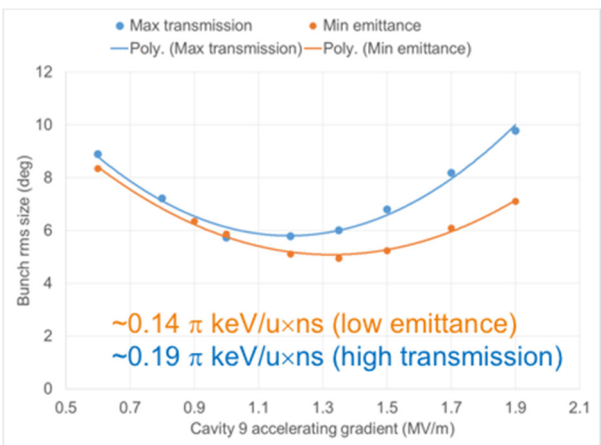


Figure 15: Results of longitudinal emittance measurement.

The maximum energy demonstrated with Argon beam was 2.3 MeV/u. Although even a higher energy was possible, the energy was limited to below 2.4 MeV/u to avoid neutron production at this stage of commissioning.

To test system behaviour under a higher beam power, an attempt to run 35 μA CW beam was made. Unfortunately, extensive outgassing of the D-Station faraday caused us to terminate the test at the duty factor of 30%, corresponding to an average power of ~80W. Other accelerator systems performed reliably and did not exhibit unusual behaviour.

CONCLUSION

FRIB Front End and the three beta 0.041 cryomodules have been successfully commissioned with Argon and Krypton beams. Measured beam properties are consistent with simulations. All commissioned accelerator components operate reliably and as expected. Preparation for commissioning of the rest of LS1 linac systems on track for successful completion.

FRIB commissioning proceeds according to the established plan and schedule.

AKNOWLEDGEMENTS

We would like to our multiple FRIB colleagues for direct and indirect contributions. We would like to thank members of our advisory committees: ASAC, ARR, etc. We thank colleagues, collaborators, and partners from other laboratories for their direct contributions to the project and useful discussions: ANL, Berkeley, BNL, Fermilab, INFN, Legnaro, LANL, SNS, Jefferson Lab, TRIUMF, and Tsinghua University.

REFERENCES

[1] J. Wei *et al.*, "The FRIB Superconducting Linac: Status and Plans", in *Proc. LINAC 2016 Conf.*, East Lansing, MI, USA, Sep. 2016, paper MO1A01, pp. 1.

[2] E. Pozdeyev, "FRIB Front End construction and commissioning", in *Proc. IPAC 2018 Conf.*, Vancouver, Canada, May 2018, paper MOZGBF1, pp. 58.

[3] H. Ren *et al.*, "Commissioning of the FRIB RFQ", in *Proc. IPAC 2018 Conf.*, Vancouver, Canada, May 2018, paper TUPAL039, pp. 1090.

[4] T. Xu *et al.*, "FRIB Cryomodule Design and Production", in *Proc. LINAC 2016 Conf.*, East Lansing, MI, USA, Sep. 2016, paper WE2A02, pp. 673.

[5] C. Compton *et al.*, "The facility for Rare isotope beams (FRIB) cavity and crymodule production", in *Proc. LINAC 2018 Conf.*, Beijing, China, Sep. 2018, paper TU1A04, this conference.

Content from this work may be used under the terms of the CC BY 3.0 licence (© 2018). Any distribution of this work must maintain attribution to the author(s), title of the work, publisher, and DOI.

ISBN: 978-3-95450-194-6 ISSN: 2226-0366 doi:10.18429/JACoW-LINAC2018-WE2A03

CONSTRUCTION STATUS OF THE SUPERCONDUCTING LINAC AT THE RIKEN RADIOACTIVE ISOTOPE BEAM FACILITY

N. Sakamoto*, M. Dantsuka, H. Imao, O. Kamigaito, K. Kusaka, H. Okuno, K. Ozeki, K. Suda, T. Watanabe, Y. Watanabe, K. Yamada, RIKEN Nishina Center, Saitama, Japan
E. Kako, H. Nakai, H. Sakai, K. Umemori, KEK, Ibaraki, Japan
H. Hara, K. Miyamoto, K. Sennyu, T. Yanagisawa,
Mitsubishi Heavy Industries Machinery Systems, Ltd. (MHI-MS), Kobe, Japan

Abstract

The RIKEN Heavy-Ion Linac (RILAC) is undergoing an upgrade to allow it to further investigate super-heavy elements. In this project, a new superconducting (SC) electron cyclotron resonance ion source and SC booster linac are being developed and constructed. The SC Linac consists of 10 TEM quarter-wavelength resonators that are operated at 73 MHz and contained in three cryomodules. The design and construction status of the Superconducting RILAC, including the medium-energy beam transport line, are given in this paper.

INTRODUCTION

The mission of the RIKEN Radioactive Isotope Beam Factory (RIBF) [1, 2] is to improve our understanding of the mechanism of synthesis of elements in the universe via experiments using intense heavy-ion beams. At the RIBF, heavy-ion beams with various energies are available from sub-coulomb energy levels for fusion reactions to intermediate energy levels for radioisotope beam production using fission reactions. Beams of ion species ranging from hydrogen to uranium are accelerated in accordance with experimental requirements.

The most important upgrades are designed to increase the beam intensity and acceleration voltage in order to synthesize super-heavy elements, because its reaction cross section is estimated to be as small as a femtobarn. The original RILAC [3] consists of six drift-tube-linac (DTL) tanks that are frequency-tunable from 17 to 45 MHz, and can accelerate heavy-ions to 2.9 MeV/u at 37.75 MHz. The new element Nh was synthesized by bombarding a ^{209}Bi target with an intense ^{70}Zn^{14+} beam with an energy of 5 MeV/u [4] accelerated by the RILAC, which was upgraded by adding a booster linac [5] comprising six DTLs. The first two DTLs of the booster, A1 and A2, are equipped with short-plate frequency tuning systems to have a frequency range from 36 to 76 MHz, which will expand the energy range of the beam injected to the RIKEN Ring Cyclotron, while the latter four DTLs have a fixed frequency.

The Superconducting RILAC (SRILAC) was proposed [6] in order to allow further experiments on super-heavy element synthesis. To preserve the versatility of the beams that are utilized for coupled operation of the RILAC and RRC, it was decided to upgrade the RILAC by replacing the latter 4 DTLs of the booster linac, which are fixed-frequency cavities, with a SC linac. The goals of the upgrade are listed in Table 1.

Table 1: Specifications of RILAC Before and After Upgrade

Upgrade	Before	After
No. of tanks	12 DTLs	8 DTLs, 3 CMs
Freq. (MHz)	37.75/75.5	36.5*/73.0
Total Acc. V (MV)	25 (A/q = 5)	39 (A/q = 6)

* 36.5 MHz is the fundamental frequency for the RF system of the RIBF accelerators.

The design of the SRILAC is based on the idea of increasing the intensity of the uranium beams and accelerating them to up to 11 MeV/u [7,8]. The original design of the SRILAC consists of 14 cryomodules (CMs), and each CM accommodates four quarter-wavelength resonators QWRs. The QWRs are optimized for a beta of 0.08 and an energy of about 3 MeV/um, which matches the energy of the beams provided by the RILAC. As shown in Fig. 1, the SRILAC consists of three CMs–CM1, CM2, and CM3–with a room-temperature medium-energy beam transport (MEBT) between them. The CMs do not contain superconducting magnets. The design of the CMs is a modification of a prototype CM developed at RIKEN [9–11] as a part of the ImPACT Program [12]. For the MEBT, a newly designed beam energy position monitor will be employed instead of traditional wire scanners. Since the SRILAC will be installed in the existing facility, it is important to have an isolation system to prevent contamination of the SC parts.

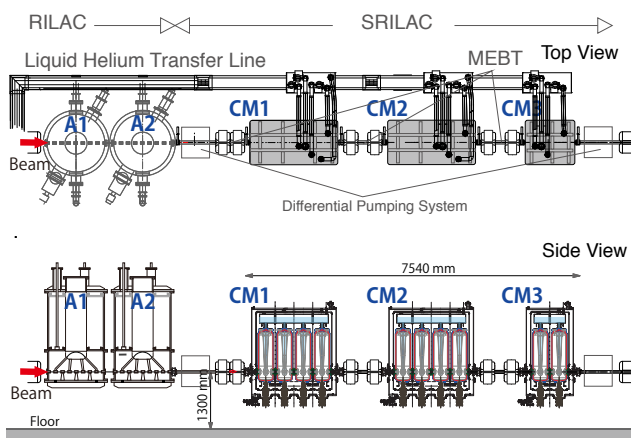


Figure 1: Layout of the Superconducting RILAC.

* nsakamot@ribf.riken.jp

Content from this work may be used under the terms of the CC BY 3.0 licence (© 2018). Any distribution of this work must maintain attribution to the author(s), title of the work, publisher, and DOI.

ISBN: 978-3-95450-194-6 ISSN: 2226-0366 doi:10.18429/JACoW-LINAC2018-WE2A03

SUPERCONDUCTING UPGRADES TO THE RILAC

SC Linac

The SRILAC is designed to operate in continuous wave (c.w.) mode. Operational parameters of the CMs are listed in Table 2. The gap length of the cavity is optimized for β=0.08 particles with a transit time factor (TTF) of 0.9. The gap voltage is 1.2 MV, which corresponds to an acceleration gradient E_{acc} of 6.8 MV/m with a synchronous phase of -25°. The SRILAC is based on 10 superconducting QWRs.

Table 2: Operational Parameters of the SRILAC

Parameter	Value
Frequency (MHz)	73.0 (c.w.)
E_{inj} (MeV/u)	3.6
E_{ext} (MeV/u)	6.5 for A/q = 6
Number of cavities	10
Cavity type	TEM, $\lambda/4$
Max. gap voltage (MV)	1.2
Synchronous phase (°)	–25
Max. acc. gradient (MV/m)	6.8
Target Q_0	1×10^9 @ E_{acc} = 6.8 MV/m
Beam current (μA)	≤100
Q_{ext}	1–4.5 $\times 10^6$
Amplifier output (kW)	7.5

The cavities are made from pure Nb sheets with a residual resistivity ratio of 250, and their inner surfaces are processed by buffered chemical polishing (BCP). Each bulk Nb cavity is contained within a helium vessel made of pure Ti. The operating temperature is 4.5 K and the target Q_0 is 1×10^9 at an E_{acc} of 6.8 MV/m. The maximum current in the heavy-ion beams is 100 μA for the super-heavy element synthesis experiments; therefore, beam loading is negligible. The power coupler is designed with a tunable coupling so that a Q_{ext} range from 1×10^6 to 4.5×10^6 can be achieved by changing the insertion distance of its antenna. Q_{ext} was chosen to be as small as 10^6 due to detuning of the resonance frequency of each QWR. To have an operational bandwidth of ±60 Hz, an output power of 7.5 kW is required for the RF amplifiers.

Due to the vertical asymmetry of the QWR structure, the accelerated beams are kicked downward by the RF magnetic field. To counteract this steering effect, the faces of drift tubes are tilted at an angle of ±2.3° [8,13]. This modification of the drift tube shape produces a vertical component in the electric field to correct the downward steering of the accelerated beams.

SC Cavity

The SC cavity design, as shown in Fig. 2, was modified from the first prototype cavity to reduce the cost. The number of ports was reduced from nine to six, and now there are two rinsing ports, two beam ports, a coupler (vacuum) port, and a pickup antenna port. The geometry of the cavity was optimized using the 3D simulation package CST Microwave Studio [14], as shown in Fig. 2. Characteristics of the optimized QWR are summarized in Table 3. The conical shape of the stem improves RF performance to reduce the peak magnetic field and increase the rigidity against pendulum vibration.

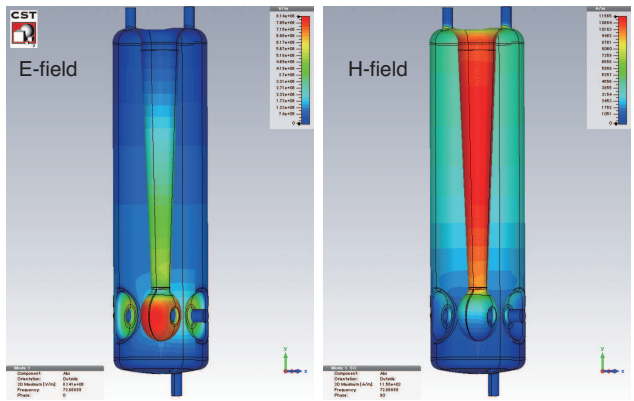


Figure 2: Contour plots of electric (E) and magnetic (H) fields in SC cavity.

Table 3: Characteristics of QWR for SRILAC

Parameter	Value
Frequency at 4.5 K (MHz)	73.0
β_{opt}	0.08
E_{peak}/E_{acc}	6.0
B_{peak}/E_{acc} ($\frac{mT}{MV/m}$)	9.5
R_{sh}/Q_0 for β_{opt} (Ω)	578
G (Ω)	22.6
P_0 (W)	4.0
Inner diameter (mm)	300
Height (mm)	1,100
Beam tube aperture diameter (mm)	40.0

A schematic of the QWR mechanical systems is shown in Fig. 3. Because the operating temperature is 4 K, boiling helium bubbles may induce mechanical vibration in the stem. Thus, a mechanical damper is used to mitigate the effect of microphonics. This damper is a 90 cm cylindrical rod inserted into the stem to attenuate the vibration. Extensive mechanical analysis of the liquid helium pressure was also performed. Dynamic tuning is realized by pressing beam ports. The shift in frequency by the tuner is limited within –20 kHz because the maximum stress on the pure Nb part cannot exceed 90 MPa, as required by regulations for high-pressure safety in Japan.

After validation of prototype cavity, six bulk SC cavities have been fabricated and processed with inner surface treatment to date, and four more are being fabricated. All cavities are carefully inspected after every processing step, including welding, BCP, high-pressure rinsing, annealing,

Content from this work may be used under the terms of the CC BY 3.0 licence (© 2018). Any distribution of this work must maintain attribution to the author(s), title of the work, publisher, and DOI.

ISBN: 978-3-95450-194-6 ISSN: 2226-0366 doi:10.18429/JACoW-LINAC2018-WE2A03

Content from this work may be used under the terms of the CC BY 3.0 licence (© 2018). Any distribution of this work must maintain attribution to the author(s), title of the work, publisher, and DOI.

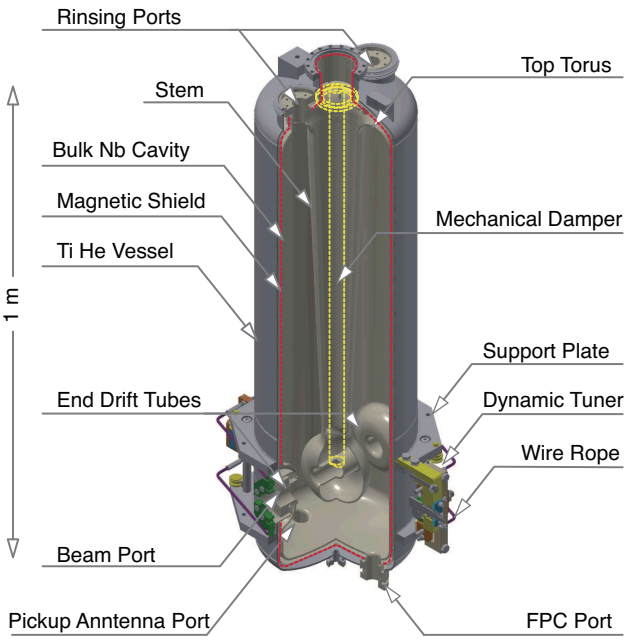


Figure 3: QWR for SRILAC.

venting, and cooling. In addition, during these processing steps, the eigenmode frequency of every cavity is measured and adjusted to maintain this frequency so as to be finally within the range of the dynamic tuner at 4K.

The SRF infrastructure for vertical testing and cleanroom work was constructed at the RIKEN campus [9, 15]. Photographs of the infrastructures are shown in Fig. 4. The constructed horizontal-flow clean room meets International Standards Organization (ISO) class 1 [15] and is equipped with a washing booth with an ultrapure water system. In Fig. 5, Q_0 values are plotted as a function of E_{acc} after cooling down to 4.2 K for the prototype cavity and six delivered cavities. Measurements were performed with a maximum E_{acc} of about 12 MV/m to avoid a degradation of cavity performance due to spark discharge. Note that the maximum value of E_{acc} in the measurement was not limited by field emission or quenching. The Q_0 performance of all cavities shows similar behavior and exceeds the goal of 1×10^9 at E_{acc} of 6.8 MV/m at 4.2 K.

At an E_{acc} of 0.4 and 0.8 MV/m, sudden Q_0 drop due to multipacting phenomena, that is, when RF power is consumed by electron emission, were observed as indicated in Fig. 5. It was found that multipacting at 0.4 MV/m occurred near the surface, where the electric field has a peak value (see Fig. 2), while multipacting at 0.8 MV/m occurred near the top surface of the torus [9]. Occasionally, heavy multipacting at E_{acc} of less than 0.1 MV/m was observed. Empirically, effective conditioning could be performed with c.w. RF power of more than 50 W with an over-coupled input-power antenna position.

The effect of the mechanical damper was also investigated. A power spectrum analysis of the time-series data for frequency during verification testing (VT) was sampled at an interval of 1 ms. The power spectrum with and without a

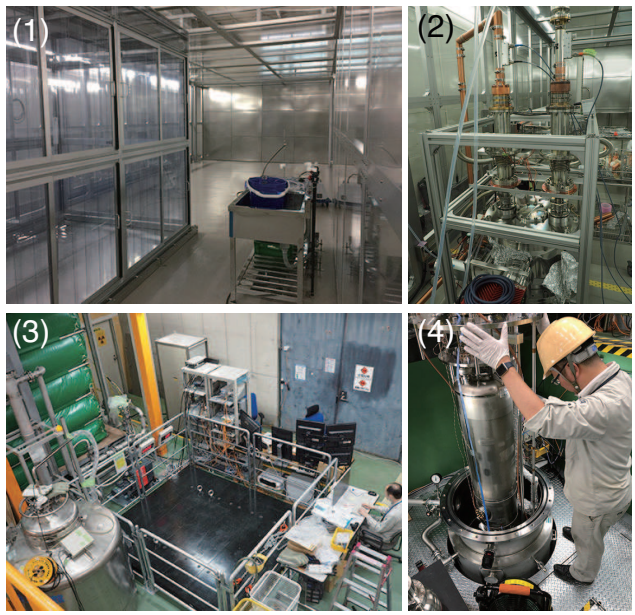


Figure 4: Photos of SRF infrastructure: (1) ISO Class 1 horizontal-flow clean room looking downstream, (2) Coupler test stand in clean room, (3) View of vertical test booth, and (4) Installation of bulk superconducting cavity into the test cryostat for vertical testing (VT).

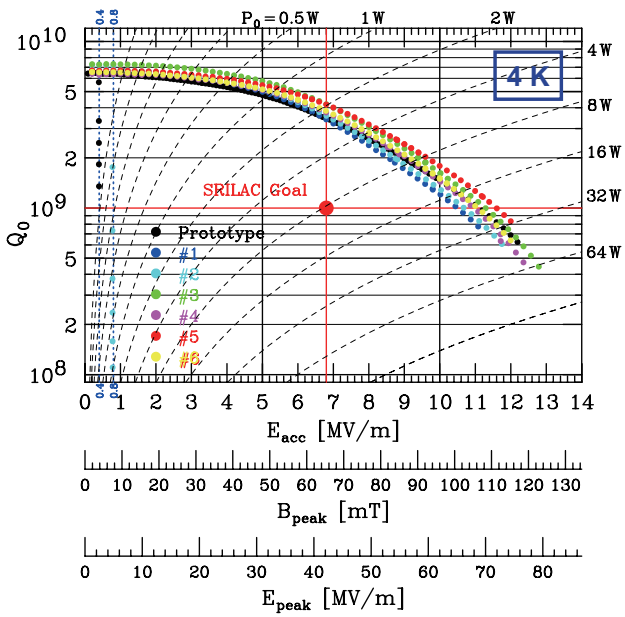


Figure 5: Cavity performance validation. The Q_0 values of bulk cavities measured at 4.2 K are plotted as a function of E_{acc}, E_{peak}, and B_{peak}. Dashed lines indicate lines of constant power dissipation.

damper are plotted in Fig. 6 as green and blue curves, respectively. Three peaks appeared at 24, 50, and 71 Hz for #6 without a damper (green curve in Fig. 6). In contrast, for #5 with a damper, the two peaks at 24 and 71 Hz disappeared and the frequency of the second peak at 50 Hz decreased. The effectiveness of the mechanical damper is still under investigation.

ISBN: 978-3-95450-194-6 ISSN: 2226-0366 doi:10.18429/JACoW-LINAC2018-WE2A03

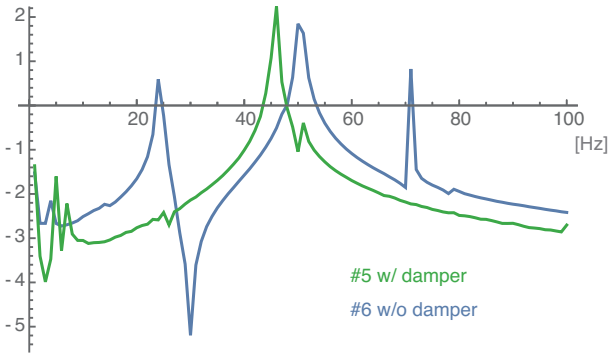


Figure 6: Analysis of time-series data for frequency shift.

After validation of the bulk cavities, helium jackets and magnetic shields made from Mu-Metal sheets will be installed between the cavity and the helium vessel. Before proceeding to cold mass assembly, vertical testing will be performed again to confirm the cavity performance for Q_0, that a no-field-emission condition is maintained, and that the eigenmode frequency does not change. If the eigenmode frequency is not in the tuning range of the dynamic tuner, frequency tuning by differential BCP, for example, will be required.

Meanwhile, the FPCs shown in Fig. 7 with a single-window structure were conditioned using a conditioning resonator [16]. A pair of FPCs were conditioned with 5 kW of c.w. RF power, as shown in Fig. 4(2). The ceramic window is located in the room-temperature part of the coupler. Cleaning of the coupler, assembling the test resonator, and RF conditioning were performed in the ISO class 1 clean room.

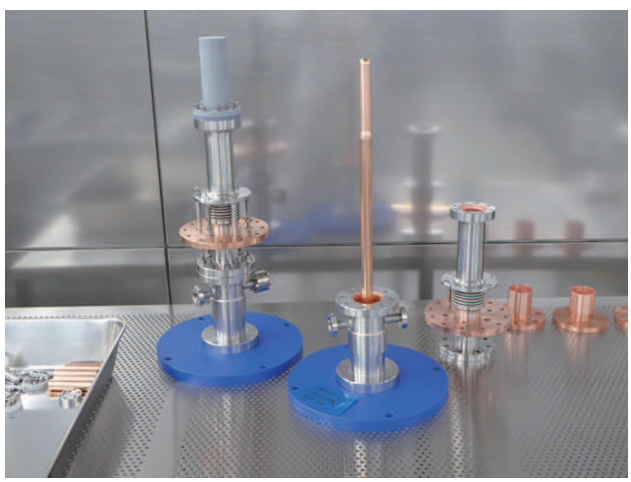


Figure 7: Photo of fundamental power couplers.

The dynamic tuner is attached to the support plates (see Fig. 3), which are welded to the helium vessel. The tuner driven by a stepping motor reduces the frequency in the cavity by tightening the surrounding wires. The driving structure was modified from the original design of the prototype to improve the capability to counteract mechanical losses due to the 4-K temperature.

Cryomodules

The SRILAC CM design is based on the first prototype cryomodules [9]. A schematic of cryomodules CM1 and CM2 is shown in Fig. 8. CM3, which contains two QWRs, is generally based on the same design as CM1 and CM2. The cold mass, which consists of a cavity, magnetic shield, helium vessel, FPC, and dynamic tuner, is supported by pillars made of G10 from the bottom base plate; that is, the CM is not a traditional top-loading type. Each cold mass is connected with beam bellows to separate the cavity vacuum from the insulation vacuum.

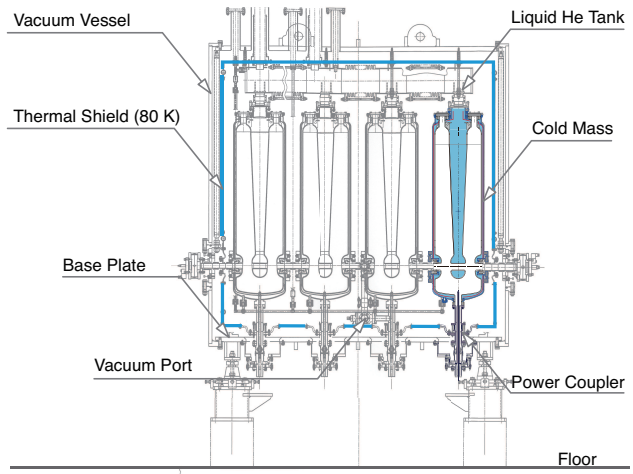


Figure 8: Side views of CM1 and CM2.

The cold mass is cooled by 4-K liquid helium provided by a liquid helium cryogenic system using a HELIAL MF refrigerator (Air Liquide). Thermal anchors connect the support pillars to the 80-K thermal shields, which are cooled by liquid nitrogen. The 80-K thermal shields also provide thermal anchors for the FPCs and beam pipes. No superconducting magnet is installed in the CMs.

Another major modification concerns the magnetic shielding. As mentioned above, the Mu-Metal magnetic shields, indicated by red dashed lines in Fig. 3, are housed inside the helium vessel surrounding the bulk cavity (Fig. 9(1)). This design enables the minimization of the effect of possible magnetization of cold mass components by placing them outside the shields. For example ball bearings are used for the dynamic tuners. Moreover, this arrangement makes it much easier to assemble and handle the cold mass. In addition to the local shielding, the vacuum vessel is made of carbon steel instead of the stainless steel employed to shield the external magnetic field.

Pre-assembly of the CMs is scheduled for October at Mitsubishi Heavy Industries Machinery Systems, Mihara. Full CM assembly will take place in this year at RIKEN, Wako.

OTHER ISSUES

MEBT and Beam Monitor

The MEBT, which connects the CMs, as shown in Fig. 1, has the functions of maintaining the vacuum, transversely

Content from this work may be used under the terms of the CC BY 3.0 licence (© 2018). Any distribution of this work must maintain attribution to the author(s), title of the work, publisher, and DOI.

ISBN: 978-3-95450-194-6 ISSN: 2226-0366 doi:10.18429/JACoW-LINAC2018-WE2A03

Content from this work may be used under the terms of the CC BY 3.0 licence (© 2018). Any distribution of this work must maintain attribution to the author(s), title of the work, publisher, and DOI.



Figure 9: Photos of jacketed cavity: (1) Pre-assembly and (2) Assembly #3 prepared for VT

focusing the beam, and performing beam diagnostics. For beam transport, room-temperature quadrupole magnets, including a function of horizontal and vertical steering, are used. Instead of traditional beam diagnostic devices, such as wire scanners and Faraday cups, beam energy position monitors are employed. These monitors are intended to measure not only the energy and position but also the size of the beam. Since beam measurement is non-destructive, ideally there is neither outgassing nor spattering to produce particulates in the high-vacuum sections. Development of the new beam diagnostics for SRILAC is underway in cooperation with the Beam Diagnostics Group of J-PARC.

Differential Pumping System

One of the most important issues in designing the beam transport line is how to prevent contamination of SC cavities by particulates transported from the room temperature section by gas flow due to the vacuum pressure gradient. While the vacuum pressure level of the SC part reached as high as 10×10^{-8} Pa, the vacuum pressure in the RILAC, designed and built more than 37 years ago (first beam in 1981), is 1×10^{-5} Pa to 1×10^{-6} Pa. To connect the different vacuum level parts and prevent gas flow into the high-vacuum section, a non-evaporable-getter-based differential pumping system was proposed [17]. A schematic of the differential pumping system is shown in Fig. 10. This system reduces pressure from the vacuum of the existing beam line of RILAC to the ultra-high vacuum in the CMs. It has a very compact size of 750 mm. Cleaning and assembly of the parts are underway.

Outlook

To date, six bulk cavities have been tested, and the jacketing process for them is underway. It is planned to have a VT with one more bulk cavity. The other three cavities are going to be jacketed without a VT procedure. Full assembly of the CM will be finished in the first quarter of 2019, and installation in the accelerator building is scheduled for March 2019. After installing the MEBT, including the differential pumping systems, cooling and RF testing will be performed during the second quarter of 2019 with the aim of full beam commissioning in the third quarter of 2019.

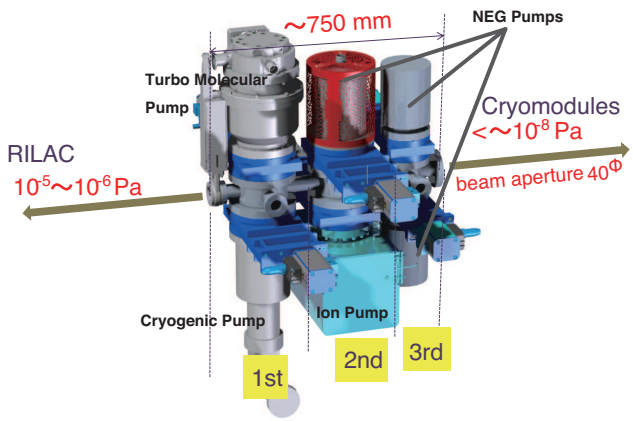


Figure 10: Schematic of compact differential pumping system.

ACKNOWLEDGMENTS

Development of the first prototype QWR and its CM for low-β ions at RIKEN was funded by the ImPACT Program of the Japan Council for Science, Technology, and Innovation (Cabinet Office, Government of Japan). The authors are grateful to Dr. A. Kasugai at QST Rokkasho and Prof. K. Saito at FRIB/MSU for technical discussion on design of the cavity and on assembly work.

REFERENCES

[1] Y. Yano *et al.*, Nucl. Instrum. Methods, vol. B261, p. 1009, 1984.

[2] H. Okuno *et al.*, Prog. Theor. Exp. Phys., vol. 2012, p. 03C002, 2012.

[3] M. Odera *et al.*, Nucl. Instrum. Methods , vol. A227, p. 187(1984).

[4] K. Morita *et al.*, JPSJ, vol. 73, p. 2593, 2004.

[5] O. Kamigaito *et al.*, Rev. Sci. Instrum., vol. 76, p. 013306, 2005.

[6] O. Kamigaito *et al.*, "Present Status and Future Plan of RIKEN RI Beam Factory", in *Proc. IPAC'6*, Busan, Koreas, May 2016, paper, TUPMR022, p. 1281.

[7] K. Yamada *et al.*, "Conceptual Design of SC Linac of RIBF Upgrade Plan", in *Proc. SRF'13*, Paris, France, Sep. 2013, paper MOP021, p. 137.

[8] N. Sakamoto *et al.*, " Design Studies for Quarter-wave Resonators and Cryomodules for the RIKEN SC-Linac", in *Proc. SRF'15*, Whistler, BC, Canada, Sep. 2015, paper WEBA06, p. 976.

[9] N. Sakamoto *et al.*, "Construction and Performance Tests of Prototype Quarter-wave Resonator and its Cryomodule at

ISBN: 978-3-95450-194-6 ISSN: 2226-0366 doi:10.18429/JACoW-LINAC2018-WE2A03

RIKEN", in Proc. SRF'17, Lanzhou, China, Jul. 2015, paper WEYA06, p. 681.

[10] T. Ozeki *et al*. "Cryomodule and power coupler for RIKEN Superconducting QWR", in *Proc. LINAC'16*, East Lansing, MI, USA, Sep. 2016, paper TUPLR061, p. 598.

[11] K. Yamada *et al*., "First Vertical Test of Superconducting QWR Prototype at RIKEN", in *Proc. LINAC'16*, East Lansing, MI, USA, Sep. 2016, paper THPLR040, p. 939.

[12] http://www.jst.go.jp/impact/en/program/08.html

[13] P. N. Ostroumov and K.W. Shepard, *Phys. Rev. ST. Accel. Beams*, vol. 4, p. 110101, 2001.

[14] http://www.cst.com

[15] A. Miyamoto *et al*., "MHI's Production Activities of Superconducting Cavity", in *Proc. SRF'15*, Whistler, BC, Canada, Sep. 2015, paper THPB029, p. 1141.

[16] K. Ozeki *et al*., "Cryomodule and Power Coupler for RIKEN Superconducting QWR", in *Proc. LINAC'16*, East Lansing, MI, USA, Sep. 2016, paper TUPLR061, p. 598.

[17] H. Imao, "NEG-based differential pumping system for SRILAC at RIBF" TTC meeting, Wako, Japan, Jun. 2018, https://indico.desy.de/indico/event/20010/session/21/contribution/106

Content from this work may be used under the terms of the CC BY 3.0 licence (© 2018). Any distribution of this work must maintain attribution to the author(s), title of the work, publisher, and DOI.

ISBN: 978-3-95450-194-6 ISSN: 2226-0366 doi:10.18429/JACoW-LINAC2018-WE2A04

COMISSIONING OF THE NEW SARAF RFQ AND DESIGN OF THE NEW LINAC

A. Perry, D. Berkovits, H. Dafna, B. Kaizer, Y. Luner, J. Rodnizki, A. Shor, I. Silverman, L. Weissman, Soreq Nuclear Research Center, Yavne, Israel
R. Duperrier, G. Ferrand, B. Gastineau, M. Jacquemet, S. Ladegaillerie, C. Madec, N. Pichoff, T. Plaisant, D. Uriot CEA/IRFU, Gif-sur-Yvette, France
A. Bechtold, P. Niewieczerzal Neue Technologien GmbH, Gelnhausen, Germany

Abstract

Soreq Nuclear Research Center (SNRC) and CEA collaborate for the upgrade of the existing Soreq Applied Research Accelerator Facility (SARAF) accelerator up to 5mA Continuous Wave (CW) 40 MeV deuteron and proton beams (Phase 2). SNRC is upgrading the injector: the ion source, the low energy beam transport line and the 4-rods Radio Frequency Quadrupole (RFQ). CEA is in charge of the development and commissioning of the medium energy beam transport line and the superconducting linac. This paper presents the status of the SARAF linac development by CEA and the installation and testing of a new set of rods electrodes in the SARAF RFQ.

INTRODUCTION

Soreq Applied Research Accelerator Facility (SARAF) is based on a high intensity proton/deuteron linac currently in operation at Soreq Nuclear Research Center (SNRC, Israel) [1]. SARAF-Phase 2 project aims to upgrade the existing capabilities and, in particular, increase the available beam energy and current up to 40MeV and 5mA respectively, in both pulsed and Continuous Wave (CW) modes.

Within the frameworks of the Phase 2 project, CEA (France) manages the SARAF-LINAC project [2]. This project includes the design, construction and commissioning of a new Medium Energy Beam Transport (MEBT) line and a new Superconducting Linac (SCL) made of 4 cryomodules (CM1-CM4). These will replace the existing MEBT and Prototype Superconducting Module (PSM) which are now in operation. The SARAF-LINAC project is now approaching the end of its third and final year of detailed design and prototyping, and is about to transition into the production stage. In preparation, several design reviews took place in 2018. The status of the SARAF-LINAC project will be presented in the second part of this paper.

The existing ion source, Low Energy Beam Transport (LEBT) line and Radio Frequency Quadrupole (RFQ) will serve as the injector to the Phase 2 linac. SNRC is modifying these components in order to reach the Phase 2 specifications. In particular, significant efforts have been devoted to improving the RFQ performance. The original SARAF RFQ, designed by the University of Frankfurt [3] and built by NTG GmbH and RI-ACCEL GmbH, has been able to accelerate high intensity (up to 4 mA) proton beams to 1.5 MeV. However, despite numerous conditioning campaigns, acceleration of CW deuteron beams in the RFQ was unachievable for a long time. Over the years a series of major modifications to the RFQ structure have led to a considerable improvement of the RFQ performance and, following the introduction of an additional RF power coupler, record results of high power operation were achieved in April 2016 [4]. Yet, reliable CW operation at the 250 kW power level which was required for CW deuteron acceleration was unachievable. It was therefore decided to re-design the rods modulation in order to enable deuteron acceleration at a slightly lower inter-electrode voltage [5]. Lowering of the applied RFQ voltage, while keeping the RFQ length and the entrance beam properties, has the unavoidable consequence of lowering the inter-rod separation and lowering the outgoing beam energy from 1.5 MeV/u to 1.27 MeV/u. Extensive beam dynamics simulations of the redesigned RFQ were performed using the GPT beam dynamics code [6] and showed that the beam quality in the transverse and longitudinal phase space should improve with the new modulation. Further simulations using the TraceWin code package [7] indicated that the beam emerging from the RFQ can be satisfactorily matched to the SCL. Electromagnetic simulations using CST [8] were performed as well to guarantee proper RF resonance frequency and to estimate the field homogeneity in the structure. Following this work the new rods fabrication was performed at Neue Technologien (NTG).

INSTALLATION OF THE NEW RODS

Installation of the electrodes was accomplished in two sessions utilizing a laser tracking system. The RFQ tank was opened and the old rods and tuning plates were disassembled and stored prior to the first laser tracker session, which focused on measurements of the stems heights. On the basis of these measurements and the metrology of the electrodes a set of precise shims spacers was manufactured to compensate for errors on stems and electrodes. The new electrodes were installed in their positions with the adapted shims during the second installation campaign (June 2017). The top and side positions of all electrode supports were measured. The measuring positions are indicated as red spots in Fig. 1. As seen in Fig. 1 the deviations of the measured and calculated positions are within ±40 and ±10 microns for the top and side surfaces respectively.

Content from this work may be used under the terms of the CC BY 3.0 licence (© 2018). Any distribution of this work must maintain attribution to the author(s), title of the work, publisher, and DOI.

ISBN: 978-3-95450-194-6 ISSN: 2226-0366 doi:10.18429/JACoW-LINAC2018-WE2A04

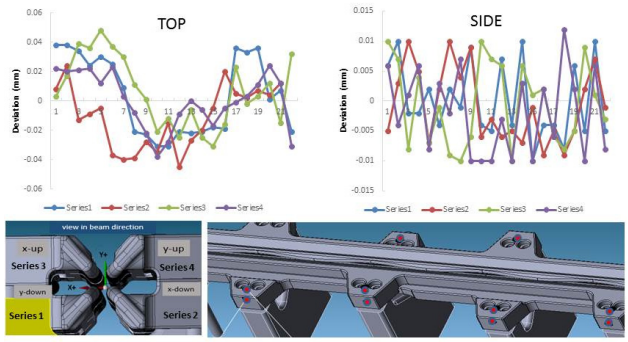


Figure 1: Deviations between the measured and calculated positions of the top and side surfaces of the installed new rods. The red spots indicate the measured positions.

The tuning plates had to be installed after the installation of the electrodes to adjust the resonance frequency and the field homogeneity. At first 15 dummy plates made of aluminium were mounted in between the stems into initial calculated positions. The resonance frequency and the field distribution were brought to the optimum via an iterative procedure (Fig. 2). The field distribution was measured by means of the perturbation method. After determination of the optimum tuning plates positions the dummy tuning blocks were replaced by the newest generation high power tuning plates (made of copper covered by a silver plate). Fine tuning of the plates positions was performed based on additional field measurements. In the final state the resonance frequency, with the RFQ plunger tuners positioned in the middle of their tuning range, was 175.943 MHz in air or 175.986 MHz in vacuum. The final field non homogeneity was around 1.8 % (standard deviation). For comparison the corresponding number for the old structure was 2.7 %, which could only be achieved by a deliberate repositioning of the rods towards the high energy end in order to change the capacitance.

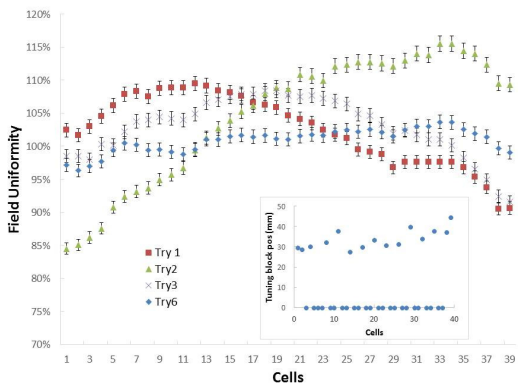


Figure 2: Iterative procedure for tuning the field homogeneity. The final position of the tuning plates is indicated in the inset.

HIGH POWER CONDITIONING

The first tests with proton beams (described in the following section) indicated that the new RFQ structure is performing well within the designed parameters and that the power required for deuteron operation would be 180-190 kW. Hence the goal for the conditioning campaign was set to ~200 kW.

It took five operational days (36 net hours) to reach 180 kW RF power (Fig. 3, left). In the first day only low duty cycle (<1 %) was used to bring the pulsed forward power to the 200 kW level. During the consecutive four days the pseudo CW duty cycle (> 99%) was used and the RF power was gradually increased. Relatively fast progress can be explained by all the recent modifications. In addition a digital reflection protection box was used for the first time instead of a similar analog device. The reflected power measured by the directional coupler was analysed and introduced in an FPGA processor. In case of high reflected power the FPGA processor switched off the input signal to the RF amplifier for a pre-determined period (usually ~60 msec), allowing for a discharge event to decay. Utilization of the protection box is the main reason for performing conditioning in the pulsed pseudo CW mode rather than real CW operation.

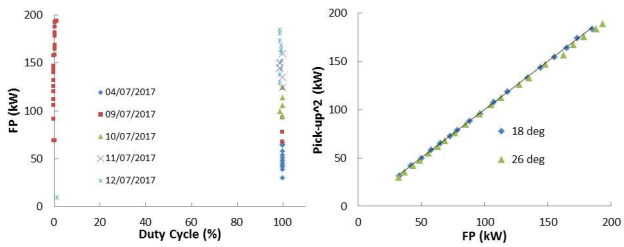


Figure 3: Left. The progress of the first stage of high power conditioning. Right. Dependence of the normalized square of the pick-up amplitude versus the forward power taken for two temperatures of the cooling water.

The final stage of the high power conditioning spanned four days (33 net hours). At the end of this period we were able to keep RFQ: at 195 kW CW for many hours without a single trip and at 205-210 kW CW at the trip rate of one per hour. The dependence of the electrical field (measured using a pick-up antenna) on the forward power is shown in Fig. 3, right. A deviation from linearity may be an indication of 'dark currents' in the RFQ. However, the measurements demonstrate that there is no measurable loss of RF power up to the highest used power values.

BEAM COMISSIONING

The next stage of the RFQ commissioning entailed detailed beam characterization using the SARAF diagnostic plate (D-plate), which is positioned after the SARAF cryomoule. This configuration considerably hindered the measurement of some beam properties at the RFQ exit.
Accurate measurements of the beam energy were done using the Rutherford backscattering (RBS) of beam particles off a thin gold foil introduced into the beam halo [9]. The results of energy measurements for proton and deuteron beams as a function of RF power are displayed in Fig. 4. The obtained beam energy is about 1.275 keV and 2.555 keV for protons and deuterons correspondingly which is very close to the designed values.

Content from this work may be used under the terms of the CC BY 3.0 licence (© 2018). Any distribution of this work must maintain attribution to the author(s), title of the work, publisher, and DOI.

ISBN: 978-3-95450-194-6 ISSN: 2226-0366 doi:10.18429/JACoW-LINAC2018-WE2A04

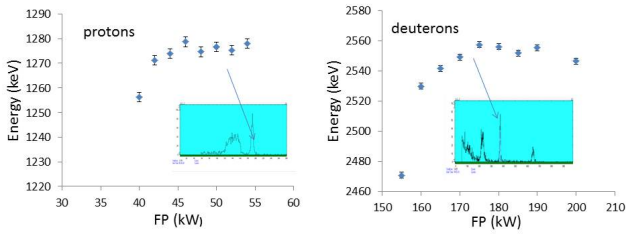


Figure 4: RBS measurement of beam energy as a function of the RF power for protons (Left) and deuterons (Right) are presented. The RBS spectra are shown in the inserts.

Transverse emittance measurements were performed using vertical and horizontal slit-wire sets at the D-plate. The measurements were done with beam pulses of 0.5 ms of protons and deuterons and for various intensities up to 5.5 mA while the RFQ field was operated in CW. The measured values of the normalized rms emittances are within the specifications for both protons and deuterons (~0.2 π·mm·mrad). The measured projections of a 5mA deuteron beam are depicted in Fig. 5. The measured RMS emittance in this case was 0.14/0.23 π mm mrad in the horizontal/ vertical direction respectively.

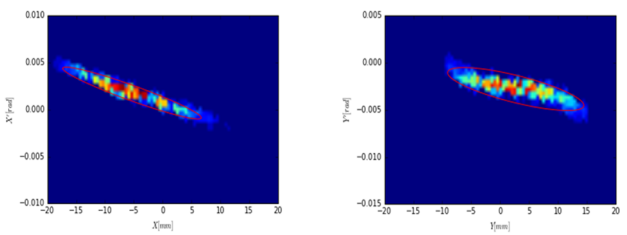


Figure 5: Slit-wire measurements (at the D-plate) of the transverse phase space projections for a 5 mA deuteron beam. The red ellipse is the 4×RMS ellipse.

The RFQ transmission was measured by comparing the current readings at the LEBT and the D-plate Faraday cups. The dependence of the transmission values on the input beam current is compared for the old and new rod structures in Fig. 6. The present and the previous (December 2015) measurements were performed in the same manner - only the ion source magnetron RF power was changed to vary the LEBT current and all the LEBT optical parameters were kept the same, except for fine tuning of the last LEBT solenoid. It is seen in Fig. 6 that the RFQ transmission has improved slightly for the proton beam, although the general trend of the transmission reduction with increase of the current persisted. There is also a modest increase of the transmission for deuterons for the new rod structure. Moderate improvement in RFQ transmission took place in spite of the fact that the physical aperture area between the new rods was reduced effectively by 30 %. The improvement is due, in part, to a smoother gentle bunching section and, in part, to a constant aperture in the accelerating region, as well as due to the improved field homogeneity achieved with the new rod structure.

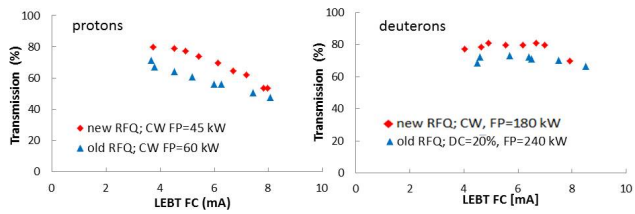


Figure 6: The RFQ transmission as a function of the input current for protons (left) and deuterons (right). Measurements for the new and old rod structures are compared.

Beam dynamics simulations of the phase 2 linac show that the longitudinal emittance of the beam formed by the RFQ is an important parameter. To measure it, the gradient variation technique was invoked in a similar fashion to that described in [10]. During the measurement three superconducting cavities in the PSM were operated. The last cavity was operated as a buncher and its voltage was varied. The beam energy spread was measured using the RBS apparatus for each voltage setting and the RMS emittance was then extracted from the measurements, as shown graphically in Fig. 7. The result, after correcting for an estimated ~20% emittance growth during the transport to the D-plate, is ~1.1 π·keV/u·nsec.

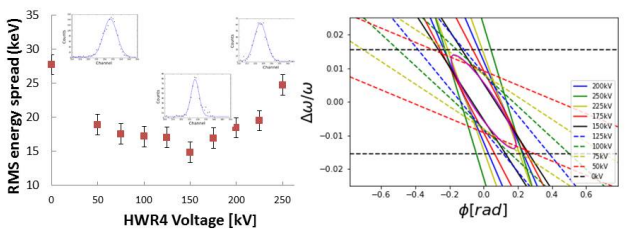


Figure 7: Left - The results of energy distribution measurement are presented. Some examples of spectra are shown in the insets. Right - The phase space ellipse obtained from the RBS measurements.

Finally, demonstration of CW deuteron operation is an important milestone of SARAF Phase I which was overdue for a decade. The test, performed in October 2017, started with acceleration of a low duty cycle beam while the RFQ was working in CW mode at 190 kW. The cryogenic cavities were detuned and the beam was stopped at the beam dump after the D-plate. The pulse intensity was kept at 1.15 mA. The duty cycle was gradually increased using the slow chopper to 99.5 % while monitoring vacuum in the cavities and cryogenics. After reaching the pseudo CW level RFQ was operational for half an hour smoothly until an RFQ trip. Operation of deuteron beam in CW mode is feasible now with the upgraded RFQ structure.

THE SARAF LINAC PROJECT

The components of SARAF-LINAC are planned to be installed and commissioned in 3 phases in: 2020 (MEBT), 2021 (CM1) and 2022 (CM2-4) [2].

Content from this work may be used under the terms of the CC BY 3.0 licence (© 2018). Any distribution of this work must maintain attribution to the author(s), title of the work, publisher, and DOI.

ISBN: 978-3-95450-194-6 ISSN: 2226-0366 doi:10.18429/JACoW-LINAC2018-WE2A04

System

A systematic engineering process is applied to derive and monitor requirements, specifications, solutions and acceptance of each subsystems (from SARAF-LINAC system to small components sub-systems).

The proton or deuteron beam dynamics, from 40 µA to 5 mA, from 1.3 MeV/u to 40 MeV final energy have been calculated (including the error studies) with TraceWin code package [11]. The linac tuning strategy [12] and associated performances [7], mainly focused on beam losses (Fig. 8), have been studied.

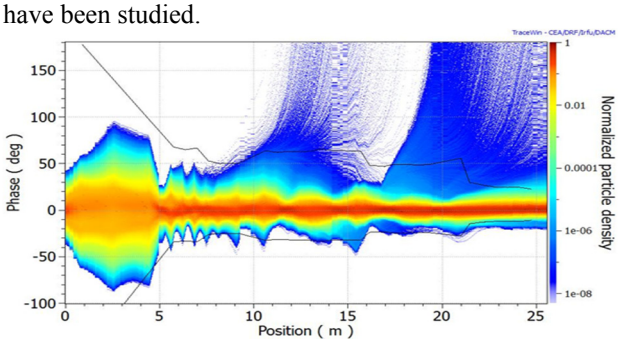


Figure 8: Beam statistical longitudinal distribution with errors. Blue tails represent unhooked particles with very low probability ($<10^{-7}$).

Major Component Status

The major components prototypes or first of series are being built and tested:

- MEBT Rebunchers by SDMS company [13],
- HWR by RI company [14],
- RF Couplers by TETD company [15],
- Solenoid Packages by ELYTT [16] and CRIOTEC [17] companies.

The associated test stands are getting prepared for acceptance tests planned in the second semester of 2018.

In parallel, cryomodules just passed their CDR and enter in call for tender process.

The MEBT Rebuncher



Figure 9: First rebuncher @ SDMS.

The three 105 kV CW, 5 kW, β=0.053 NC rebunchers (RB1-3) are being built by SDMS Company. Acceptance tests of RB1 (vacuum performances, water leaks, frequency tuning (geometry)) before copper coating (Fig. 9) are planned in mid-September @ SDMS. The validation will lead to RB1 copper coating and RB2&3 start of manufacturing. Once copper coated, the RB1 has to be validated (power consumption, cooling performances) at IRFU at early 2019 before copper coating of RB2&3.

The SC HWR

The bare low-beta (0.091) prototype has been built by RI Company. It has been prepared (BCP, HPR) and tested @ 4.5 K by CEA. Multipactor at low and medium fields has been observed and passed through. The measured surface resistance at low field is 15 nOhms (requirement: < 45 nOhm @ 7 MV/m). Maximum accelerating field of 10.6 MV/m has been achieved without X-rays and quench (7 MV/m specified, 6.5 MV/m required). As shown on Fig. 10, a Q-slope is observed leading to a Q0 that is a little bit lower than the specified one (at 7 MV/m).

The high-beta (0.181) prototype is being built by RI. The bare cavity should be delivered to CEA for preparation within one month.

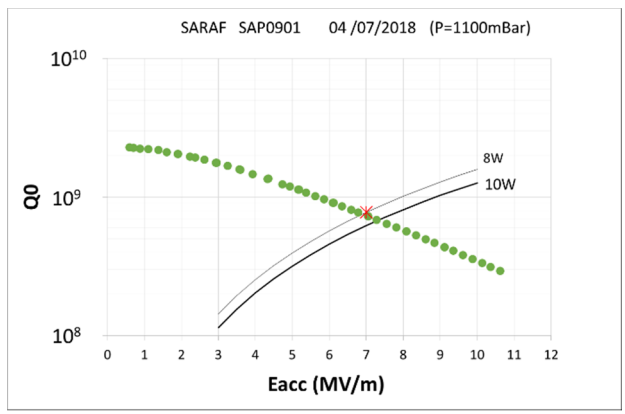


Figure 10: LB HWR prototype results.

The RF couplers

The first 2 RF couplers have just been delivered to IRFU (Fig. 11). They will be conditioned/tested on specific test stand (C2TS) next month.



Figure 11: Coupler 1 prototype (photo by TETD).

Content from this work may be used under the terms of the CC BY 3.0 licence (© 2018). Any distribution of this work must maintain attribution to the author(s), title of the work, publisher, and DOI.

ISBN: 978-3-95450-194-6 ISSN: 2226-0366 doi:10.18429/JACoW-LINAC2018-WE2A04

Content from this work may be used under the terms of the CC BY 3.0 licence (© 2018). Any distribution of this work must maintain attribution to the author(s), title of the work, publisher, and DOI.

The SC Magnet

The Final Design Review of SC magnets has been done at the ELYTT Company's manufacturing site. The prototype is now under construction. The delivery is expected in October

The Current Lead Cluster

The Current Lead Clusters, designed by CEA, are being manufactured by CRIOTEC Company (see Fig. 12).

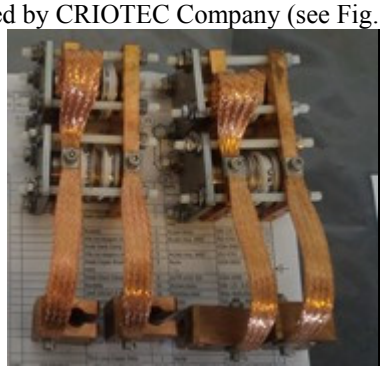


Figure 12: Current lead protection (photo by CRIOTEC).

The Cryomodules

The ~5 m long cryomodules (Fig. 13) of 2 different types (CM1-2, for LB HWR and CM3-4 for HB HWR) passed their CDR in March [18]. The technical specifications for the call for tenders of their components are being written.

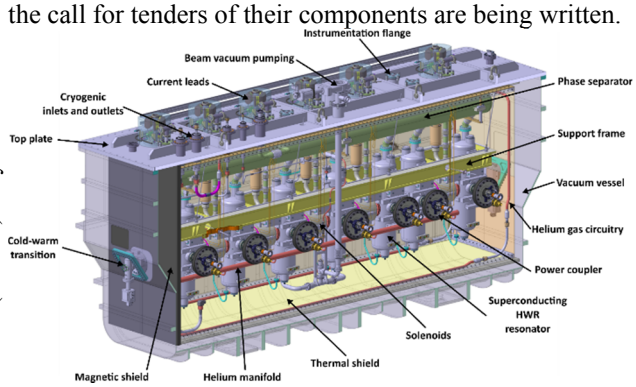


Figure 13: CM2 3D mock-up.

TEST STANDS

The major components will be tested at IRFU in dedicated test stands (TS) all in the same facility (Fig. 14):

- RBTS for Rebunchers.
- VCTS for Vertical Cavities,
- ECTS for Equipped Cavities (with coupler and tuner),
- SPTS for Solenoid Packages and Current Leads,
- CMTS for assembled Cryomodules.

CONCLUSION

A set of new rod electrodes was installed in the SARAF RFQ. Following a short conditioning period acceleration of a 1mA CW deuteron beam has been demonstrated for the first time. All measured beam parameters agree with the design values [19].

The SARAF-LINAC project is approaching the end of the design stage and about to transition into the production stage. All major components prototypes or first of series are being built or already being tested. The cryomodule design passed the CDR and the tendering process for its subcomponents is about to commence.

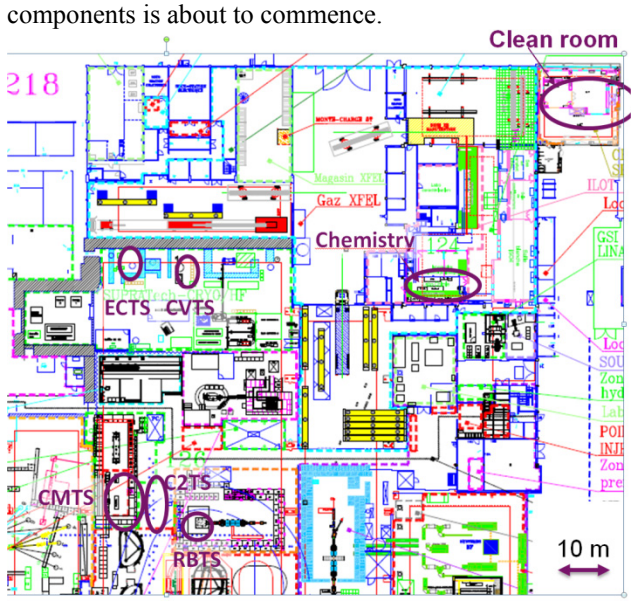


Figure 14: SARAF-LINAC Test Stands @ CEA-Saclay.

REFERENCES

[1] A. Nagler et al., "Status of the SARAF Project", in Proc. LINAC'08, Victoria, Canada, Sep.-Oct. 2008, paper MO203, p. 26.

[2] N. Pichoff et al., "The SARAF-LINAC project 2018 status", in Proc. 9th Int. Particle Accelerator Conf. (IPAC'18), Vancouver, Canada, Apr.-May 2018, p. 994, doi:10.18429/JACoW-IPAC2018-TUPAK015

[3] P. Fischer et al., "Tuning a CW 4-Rod RFQ", in Proc. LINAC'06, Knoxville, Tennessee, USA, August 2006, p. 728.

[4] J. Rodnizki et al., "SARAF 4-rod RFQ RF power Line splitting design and test", in Proc. LINAC'16, East Lansing, Michigan, USA, September 2016, p. 693.

[5] A. Shor and A. Perry , "Redesign of SARAF RFQ Electrode Modulation to Enable CW Deuteron Operation at P=186 kW (HV=56 kV)", Internal SNRC report (2017), available per request.

[6] General Particle Tracer (GPT) code, www.pulsar.nl

[7] J. Dumas et al., "Beam dynamic studies for the SARAF MEBT and SCL", in Proc. IPAC'17, Copenhagen, Denmark, May 2017, p. 655.

[8] CST Microwave Studio, www.cst.com.

[9] L. Weissman et al., "First experience at SARAF with protons beam using Rutherford scattering monitor", in Proc. DIPAC'09, Basel, Switzerland, September 2009, p. 208.

[10] J. Rodnizki et al., "Energy and Energy Spread Measurements using the Rutherford Scattering Technique for Tuning the SARAF Superconducting ", in Proc. LINAC'10, Tsukuba, Japan, September 2010 , p. 620.

[11] D. Uriot et al., "Status of TraceWIN code", in Proc. IPAC'15, Richmond, VA, USA, May 2015, p. 92, doi:10.18429/JACoW-IPAC2015-MOPWA008

ISBN: 978-3-95450-194-6 ISSN: 2226-0366 doi:10.18429/JACoW-LINAC2018-WE2A04

[12] P.A.P. Nghiem et al., "Strategy of Beam tuning implementation for the SARAF MEBT and SC Linac", in Proc. IPAC'17, Copenhagen, Denmark, May 2017, p. 652.

[13] See http://www.sdms.fr

[14] See http://www.research-instruments.de/

[15] See https://etd.canon/

[16] See http://www.elytt.com

[17] See https://www.criotec.com

[18] N. Pichoff et al., "Discussion on SARAF-LINAC Cryomodules", in Proc. HB'18, Daejeon, Korea, June 2018, p. 80, doi:10.18429/JACoW-HB2018-TUA2WC01

[19] L. Weissman et al., "Installation and Commissioning of the Upgraded SARAF 4-rods RFQ", in Proc. HB'18, Daejeon, Korea, June 2018, p. 75, doi:10.18429/JACoW-HB2018-TUA1WC01

Content from this work may be used under the terms of the CC BY 3.0 licence (© 2018). Any distribution of this work must maintain attribution to the author(s), title of the work, publisher, and DOI.

ISBN: 978-3-95450-194-6 ISSN: 2226-0366 doi:10.18429/JACoW-LINAC2018-TH1A01

FIRST EVER IONIZATION COOLING DEMONSTRATION IN MICE

J. Y. Tang*, Institute of High Energy Physics, CAS, 100049 Beijing, China
on behalf of the MICE Collaboration

Abstract

The Muon Ionization Cooling Experiment (MICE) at RAL has studied the ionization cooling of muons. Approximately 350 million of individual particle tracks have been recorded passing through a series of focusing magnets in different configurations with a liquid hydrogen, lithium hydride or polyethylene (wedge) absorber. Measurements of the tracks upstream and downstream of the absorber have shown the expected effects of the 4D emittance reduction as a consequence of ionization cooling. This invited talk presents and discusses these results, and projects the future of ionization cooling.

INTRODUCTION

Muon cooling is one of the basic techniques required for a neutrino factory and muon collider [1]. The international Muon Ionization Cooling Experiment (MICE) at RAL was established to demonstrate the principle and relevant technology [2]. One way of producing high-intensity muons is to collide a high-power proton beam with a target, producing pions that then decay into muons. However, the tertiary muon beam has a very large emittance, typically between 15-20 πmm·rad. In order to optimize the muon yield and fit the beam into cost-effective apertures for further acceleration, one would need to reduce the beam emittance. The desired muon normalized beam emittance at the neutrino factory ranges between 2 and 5 πmm·rad. An initial muon collider needs further cooling with a desired normalized transverse emittance of 0.4 πmm·rad and normalized longitudinal emittance of 1 πmm·rad. Ionization cooling is the only beam cooling technique suitable for reducing the muon beam emittance within the short muon lifetime. MICE successfully demonstrated this technique for the first time.

BEAMLINE

The proton beam used for muon production in MICE is produced by the ISIS proton synchrotron at RAL [3], with a kinetic energy of 800 MeV in a parasitic mode to the operation of the ISIS spallation neutron source and muon source. As shown in Fig. 1, a triplet of quadrupole magnets (Q1, Q2, and Q3), two dipole magnets (D1 and D2), and one decay solenoid (DS) are used for pion transport and proper pion momentum selection, pion decay and muon momentum selection.

Two more triplets prepare the muon beam into the muon cooling channel [4]. As a result, the beam that enters MICE has a small pion content. To ensure further muon beam purity, these pions are tagged and rejected from the cooling measurement using a series of particle identification (PID) detectors (Fig. 2) [5].

* tangjy@ihep.ac.cn

MICE DETECTORS AND ABSORBERS

MICE detectors can be divided into PID and tracking detectors. The primary PID detectors are three Time of Flight (ToF) counters (ToF0, ToF1, and ToF2) made of scintillating slabs. Electrons and pions can be distinguished by their different flight times with the same momentum. In addition, two aerogel Cherenkov detectors help the rejection of pions and electrons. The KLOE-Light (KL) detector is a calorimeter and uses lead layers alternating with scintillating fibers to differentiate between particles based on their energy depositions. Electrons shower in KL and as a result have broader KL distributions compared to muons and pions. The most downstream calorimeter is the Electron Muon Ranger (EMR), made of planes of scintillator extrusions, which makes use of the differing particle track topologies. Electron showers in the EMR typically miss some planes as they travel along their paths (occupancy < 1) in contrast to muon tracks which consistently hit all planes (occupancy ≈ 1) [6].

MICE has two tracking detectors, upstream and downstream of the absorber [7]. Each tracker is composed of five planar scintillating-fiber stations, each with three doublet fiber layers, and is immersed in the solenoidal field of a Spectrometer Solenoid (SS). The upstream and downstream SS consist of five superconducting coils; two match the muon beam into and out of the absorber, and three produce constant fields inside the tracking volumes. For measurement of beam cooling, the input and output beam distributions are compared at the tracker stations immediately upstream and downstream of the absorber (tracker reference planes).

Three kinds of absorbers were used in the cooling experiments, first with lithium hydride (LiH), then liquid hydrogen (LH2) and a wedge type of polyethylene. LiH and LH2 were used to demonstrate the cooling effect in the transverse phase space, and the wedge polyethylene was to demonstrate the emittance exchange between the transverse space and the longitudinal space.

MEASUREMENT OF MUON IONIZATION COOLING

Ionization cooling occurs when muons travel through an absorbing material and undergo a “soft” inelastic collision. With the incoming muon energies significantly larger than the binding energies of the atomic electrons of the material, the atom ionizes, ejecting a valence electron [8]. Concurrent with the ionization energy loss process, elastic collisions with the atomic nuclei of the material can occur. Given the larger mass of the atomic nuclei compared with the incident muons, this process causes very small energy loss [2]. However, it is the driving force behind

Content from this work may be used under the terms of the CC BY 3.0 licence (© 2018). Any distribution of this work must maintain attribution to the author(s), title of the work, publisher, and DOI.

ISBN: 978-3-95450-194-6 ISSN: 2226-0366 doi:10.18429/JACoW-LINAC2018-TH1A01

the scattering of muons by small angles [8]. This process is known as multiple Coulomb scattering and is a source of emittance heating that is a counter effect against the cooling.

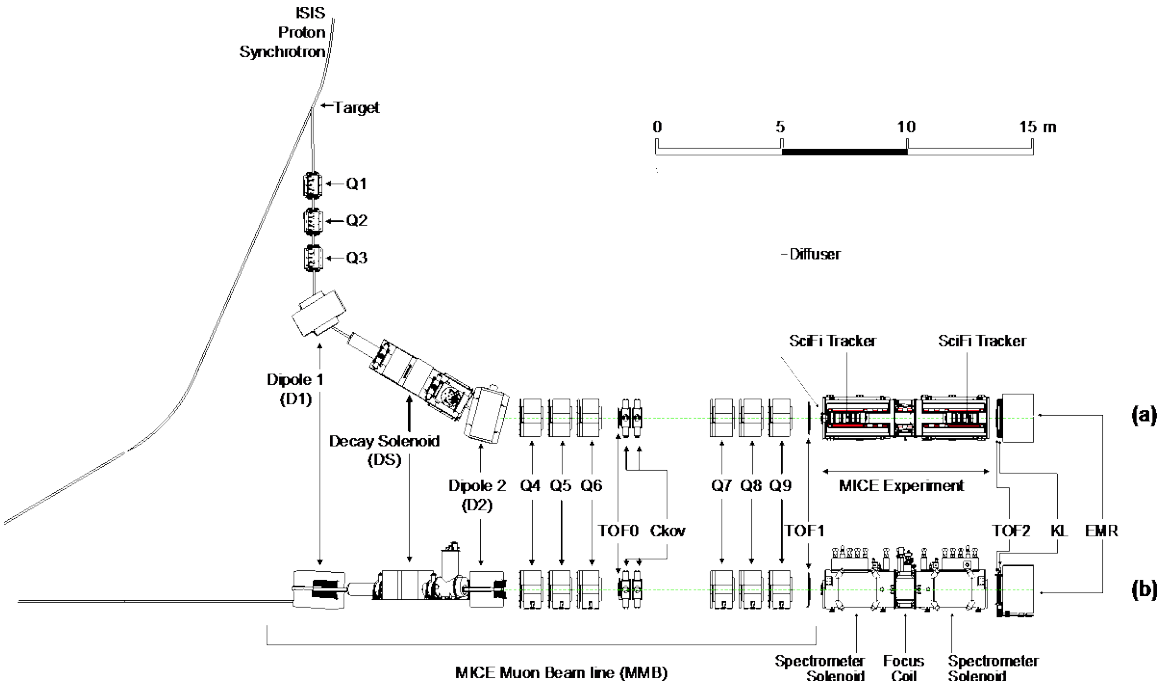


Figure 1: Schematic of the MICE beamline and MICE experiment: (a) and (b) are the top and side views, respectively.

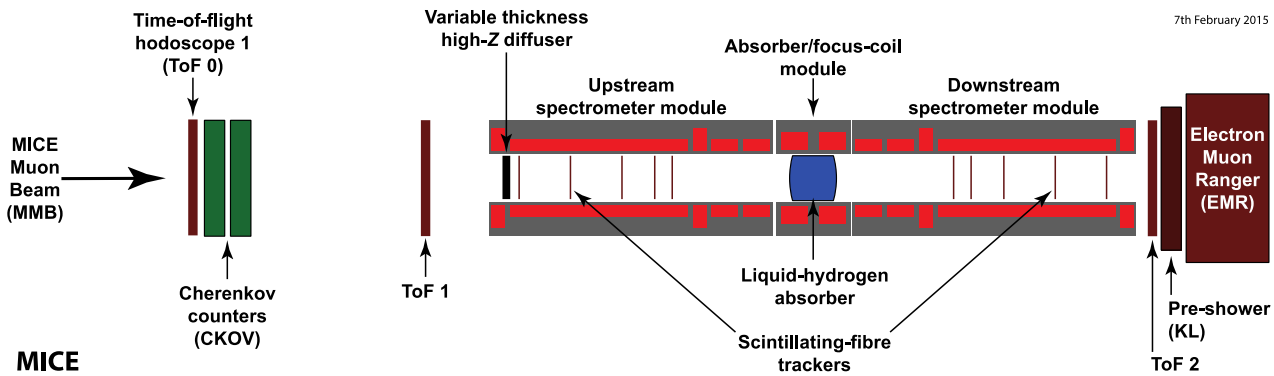


Figure 2: Schematic diagram of MICE in its final configuration.

Content from this work may be used under the terms of the CC BY 3.0 licence (© 2018). Any distribution of this work must maintain attribution to the author(s), title of the work, publisher, and DOI.

ISBN: 978-3-95450-194-6 ISSN: 2226-0366 doi:10.18429/JACoW-LINAC2018-TH1A01

Content from this work may be used under the terms of the CC BY 3.0 licence (© 2018). Any distribution of this work must maintain attribution to the author(s), title of the work, publisher, and DOI.

A good understanding of energy loss and multiple scattering is essential in ionization cooling where the muon momentum is reduced in all directions (both transversely and longitudinally) with a subsequent restoration of the beam longitudinal momentum in RF cavities, suitable for a multi-segment cooling system. The beam cooling equation that describes this process is written in terms of the rate of change of normalized transverse root-mean-square (RMS) emittance [2]:

$$\frac{d\varepsilon_T}{dz} \cong -\frac{\varepsilon_T}{E_\mu \beta^2}\frac{dE_\mu}{dz} + \frac{\beta_\perp}{2mc^2\beta^3}\frac{(13.6\ \mathrm{MeV/c})^2}{E_\mu X_0}, \quad (1)$$

where E_μ is the muon energy, β the muon velocity, dE_μ/dz the magnitude of the ionization energy loss, m the muon mass, X_0 the radiation length, and $\beta_\perp$ the transverse beta function at the absorber.

The first term in the equation represents cooling from ionization energy loss and the second term describes heating from multiple scattering. The minimum achievable emittance, or equilibrium emittance, for a given material and focusing conditions can be described by:

$$\varepsilon_{eq} \cong \frac{\beta_\perp (13.6\ \mathrm{MeV/c})^2}{2X_0(dE/dz)\beta m}, \quad (2)$$

A smaller equilibrium emittance leads to a more effective emittance reduction, which from Eq. (2) occurs when $\beta_\perp$ is minimized and $X_0(dE/dz)$ maximized [2]. Therefore, strong focusing at the absorber and low-Z (low atomic number) absorbing materials such as lithium hydride and liquid hydrogen are needed.

EXPERIMENTAL RESULTS

One figure of merit for muon beam cooling in MICE is the reduction of the normalized transverse RMS emittance. Muon trajectories are recorded by single particles and the phase-space coordinates in (x, p_x, y, p_y) of each muon are reconstructed using the trackers. From the measured phase-space coordinates, the normalized transverse emittance can be calculated. Figure 3 displays the muon beam emittance versus momentum by using the upstream tracker. The emittance is observed to be approximately constant within the momentum range from 180 to 250 MeV/c.

Though multiple Coulomb scattering is a well-understood phenomenon, results from MUSCAT indicate that the effect in low Z materials is not well modelled in simulations such as GEANT4 [9]. MICE therefore measured the multiple Coulomb scattering distribution to validate the scattering model and determine the heating term in Eq. (1), in order to make more realistic predictions of the emittance reduction. Both data with field off and field on in the scintillating fiber tracker are available for a momentum range of 140-240 MeV/c. While the field-on data is still being analyzed, one preliminary analysis result is shown in Fig. 4.

In addition to emittance reduction, the cooling effect can also be expressed by the reduction of the single-particle amplitude that is defined as the weighted distance of each muon from the beam center. It probes the change in density in the core of the beam, where an increase in phase-space density signifies beam cooling. The transverse beam amplitude can be obtained using the measured transverse emittance [10-12], which causes migration of high amplitude muons to low amplitude and indicates beam cooling, i.e. as $R_{Amp} > 1$ in Fig. 5. Two different input emittances of 6 πmm·rad and 10 πmm·rad, and a momentum of 140 MeV/c were used. The ratio in amplitude change R_{Amp} is defined as:

$$R_{Amp} \equiv \sum_{n=1}^{N} A_n^{down} \Big/ \sum_{n=1}^{N} A_n^{up}, \quad (3)$$

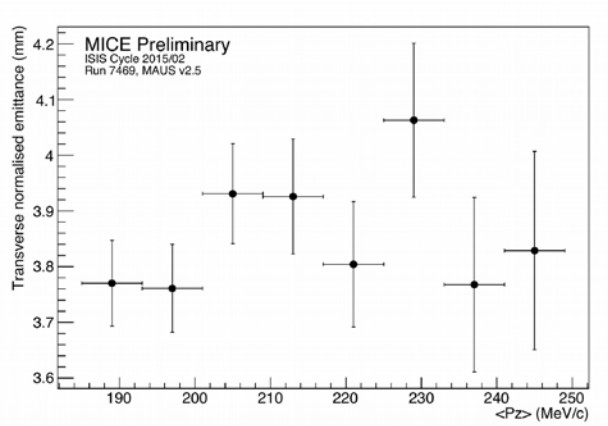


Figure 3: First direct measurement of emittance using the most upstream scintillating fiber tracker station [10].

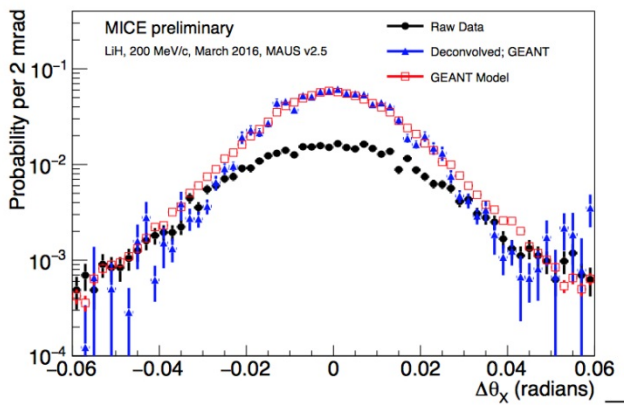


Figure 4: Comparison between experimental multiple Coulomb scattering results and GEANT4 simulations (with LiH, 200 MeV/c).

To express the emittance reduction in 4D-phase space, a fractional emittance that defines the inner phase space volume is used [13-14]. For one RMS emittance in 4D space, which represents about 9% of the total volume, it has a simple relation with the transverse RMS emittance in 2D space:

$$\varepsilon_\alpha = \frac{1}{2}(\pi mc\varepsilon_T)^2 \Rightarrow \frac{\Delta\varepsilon_\alpha}{\varepsilon_\alpha} \approx \frac{2\Delta\varepsilon_T}{\varepsilon_T}. \quad (4)$$

ISBN: 978-3-95450-194-6 ISSN: 2226-0366 doi:10.18429/JACoW-LINAC2018-TH1A01

One experimental result is shown in Fig. 6. One can see the emittance reduction before and after the absorber (LiH).

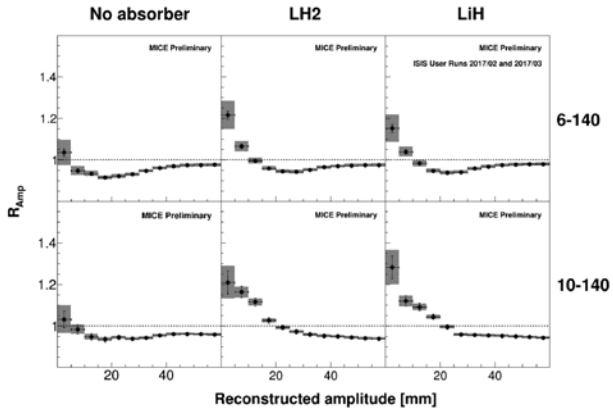


Figure 5: Ratio of cumulative amplitude distributions between upstream and downstream tracker reference plane for the 6-140 (top) and the 10-140 (bottom) nominal beam settings, and three absorber configurations of "no absorber" (empty channel, left), LH2 (middle), and LiH (right).

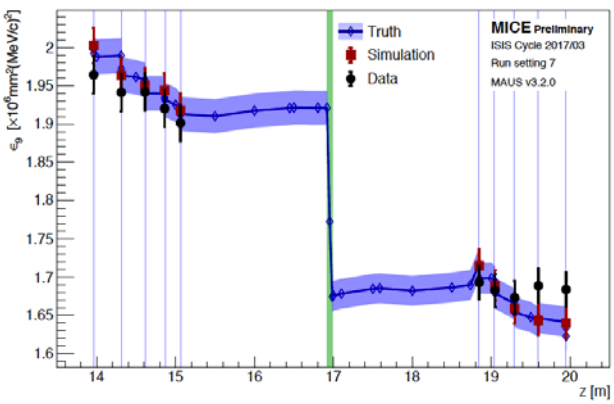


Figure 6: Fractional (9%) emittance evolution (6 πmm·rad, 140 MeV/c, LiH, flip mode)

6D cooling is required by the muon collider, in order to reduce both the transverse and longitudinal emittance for high collision luminosity. One method to produce 6D cooling is to add wedge absorbers in the dispersion location in a cooling section, where the emittance change between the transverse and longitudinal phase spaces happens so the longitudinal emittance cooling is obtained [15]. As there are no magnets producing dispersion in the cooling section, we carried out one experiment by putting a polyethylene wedge in the absorber location (as shown in Fig. 7), and tried to demonstrate reverse emittance change. The reverse emittance exchange is also required by the design of so-called "final cooling" for a multi-TeV muon collider [16]. The data analysis is in progress [17].

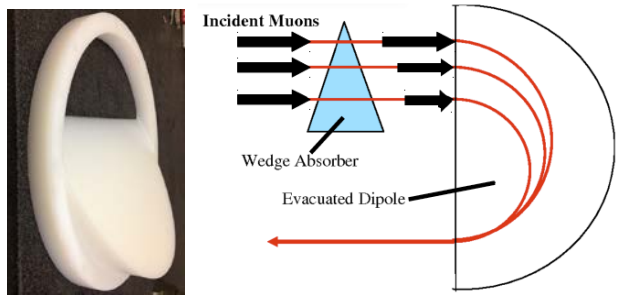


Figure 7: Reverse emittance exchange experiment in MICE: left – polyethylene wedge absorber, right - schematic.

CONCLUSION

The first measurement results of ionization cooling in MICE are presented, and this is an important R&D step towards a future muon collider, neutrino factory, and other cooled muon applications. The measurements of the ratio of the upstream and downstream cumulative amplitude distributions and fractional 4D emittance demonstrate cooling (migration of large transverse amplitude muons to lower amplitudes and emittance reduction after crossing the absorber). MICE has concluded all data taking and is currently in the analysis phase, with several publications in preparation.

ACKNOWLEDGEMENTS

MICE has been made possible by grants from funding agencies from ten participating countries. We acknowledge the support of the staff of the STFC Rutherford Appleton and Daresbury Laboratories, and the use of Grid computing resources deployed and operated by GridPP in the U.K., http://www.gridpp.ac.uk/. The author acknowledges the support from China-US collaboration fund on High-Energy Physics jointly by CAS and IHEP.

REFERENCES

[1] S. Choubey *et al.*, "International Design Study for the Neutrino Factory, Interim Design Report," 2011, arXiv:1112.2853

M. Alsharoa *et al.*, "Recent progress in neutrino factory and muon collider research within the Muon Collaboration," *Phys. Rev. ST Accel. Beams*, vol. 6, p. 081001, 2003.

[2] D. Neuffer, "Principles and applications of muon cooling," *Part. Accel.*, 1983, vol. 14, pp. 75-90, FERMILAB-FN-0378.

[3] C.N. Booth *et al.*, "The design and performance of an improved target for MICE," *JINST*, vol. 11, P05006, 2016.

[4] M. Bonesini *et al.*, "The MICE Muon Beam on ISIS and the beam-line instrumentation of the Muon Ionization Cooling Experiment," *JINST*, vol. 11, P05009, 2012.

[5] P. Soler *et al.*, "Pion Contamination in the MICE Muon Beam," *JINST*, vol. 11, P03001, 2016.

R. Bertoni *et al.*, "The design and commissioning of the MICE upstream time-of-flight system," *Nucl. Instrum. Meth. A*, vol. 615, pp. 14-26, 2010.

Content from this work may be used under the terms of the CC BY 3.0 licence (© 2018). Any distribution of this work must maintain attribution to the author(s), title of the work, publisher, and DOI.

ISBN: 978-3-95450-194-6 ISSN: 2226-0366 doi:10.18429/JACoW-LINAC2018-TH1A01

Content from this work may be used under the terms of the CC BY 3.0 licence (© 2018). Any distribution of this work must maintain attribution to the author(s), title of the work, publisher, and DOI.

L. Cremaldi *et al*., "A Cherenkov Radiation Detector with High Density Aerogels," *IEEE Trans. Nucl. Sci.*, vol. 56, pp. 1475-1478, 2009.

[6] F. Drielsma *et al*., "Electron-Muon Ranger: performance in the MICE Muon Beam," *Journal of Instrumentation,* vol. 10, P12012, 2015.

[7] M. Ellis *et al.*, "The design, construction and performance of the MICE scintillating fibre trackers," *Nucl. Instr. Meth. Phys. Res. A*, vol. 659, p. 136-153, 2011.

[8] C. Patrignani *et al*., (Particle Data Group), *Chin. Phys. C,* vol. 40, p. 100001, (2016, 2017 update).

[9] D. Attwood *et al.*, "The scattering of muons in low Z materials," *Nucl. Instrum. Meth. B*, vol. 251, p. 41, 2006.

MuScat Collaboration, W. J. Murray, "Comparison of MuScat data with GEANT4", *Nucl. Phys. Proc. Suppl.*, vol. 149, p. 99-103, 2005.

[10] V. J. Blackmore, "Emittance Measurement in the Muon Ion- ization Cooling Experiment", *PoS ICHEP2016*, 868 (2016).

[11] C.T. Rogers, "Study of Ionization Cooling with the MICE Experiment," in *Proc. 8th Int. Particle Accelerator Conf. (IPAC'17)*, Copenhagen, Denmark, May 2017, paper WEPAB129.

[12] V. J. Blackmore, "Recent Results from the Study of Emittance Evolution in MICE," in *Proc. 9th Int. Particle Accelerator Conf. (IPAC'18)*, Vancouver, BC, Canada, Apr.-May 2018, paper TUPML067.

[13] T.A. Mohayai, "First demonstration of ionization cooling in MICE", in *Proc. 9th Int. Particle Accelerator Conf. (IPAC'18)*, Vancouver, BC, Canada, Apr.-May 2018, paper FRXGBE3.

[14] D. Rajaram, V. Blackmore, "Phase space density evolution in MICE", in *Proc. 9th Int. Particle Accelerator Conf. (IPAC'18)*, Vancouver, BC, Canada, Apr.-May 2018, paper TUPML065.

[15] D. Kaplan, "Overview of muon cooling", in *Proc.* COOL2015, Newport News, VA, USA, 2015, paper MOWAUD03.

[16] D. Neuffer, "Phase Space Exchange in Thick Wedge Absorbers for Ionization Cooling", *AIP Conference Proceedings,* vol. 441. pp. 270-281. 1998.

[17] T. A. Mohayai *et al*., "A Wedge Test in MICE", in *Proc. 9th Int. Particle Accelerator Conf. (IPAC'18)*, Vancouver, BC, Canada, Apr.-May 2018, arXiv:1806.01824

ISBN: 978-3-95450-194-6 ISSN: 2226-0366 doi:10.18429/JACoW-LINAC2018-TH1A03

HIGH BRIGHTNESS ELECTRON BEAMS FROM PLASMA-BASED ACCELERATION*

A. Marocchino†, E. Brentegani, A. Biagioni, E. Chiadroni, M. Ferrario,
A. Giribono, F. Filippi, R. Pompili, C. Vaccarezza INFN-LNF, Frascati, Italy
A. Cianchi, University of Rome Tor Vergata, Rome, Italy
A. Bacci, A. R. Rossi, INFN MIlano Milano, Italy
V. Petrillo, Università di Milano Milano, Italy

Abstract

Plasma Wakefield acceleration is a promising new acceleration technique that profits by a charged bunch, e.g. an electron bunch, to break the neutrality of a plasma channel to produce a wake where a trailing bunch (or witness) is eventually accelerated. The quest to achieve extreme gradient conserving high brightness has prompted to a variety of new approaches and techniques. Most of the proposed schemes are however limited to the only plasma channel, assuming in the vast majority of cases, ideal scenarios (e.g. ideal bi-gaussian bunches and uniform density plasma channels). Realistic start-to-end simulations, from the photo-cathode to FEL via a high gradient, emittance and energy spread preserving plasma section, are mandatory for paving the way towards plasma-based user facilities.

INTRODUCTION

Plasma-based accelerators (PBAs) represent, today, a new frontier for the development of compact advanced radiation sources and next generation linear colliders. High brightness electron beams are the future goal of such kind of accelerators, a new technology that is envisioned to compete with the RF technology. Since the very first conception [1] great effort (with equivalent progress) has been placed [2–8] to demonstrate the acceleration of electron beams with gradients of the order of several tens of GV/m, produced either by a laser drive (LWFA) or with a particle driven (PWFA). In PWFA the high gradient wakefield is induced by a high-energy charged particle beam (referred to as driver bunch) travelling through a pre-ionised plasma. The background electrons by shielding the charge breakup produced by the driver induce an accelerating field. The second bunch (referred to as trailing bunch or witness) placed on the right phase is so accelerated by the induced electric field [9–11].

The aforementioned publications indicate that either LWFA and PWFA are capable to produce strong accelerating gradients, but do not address the issue of beam acceleration with quality retention. In other words, the capability for a PWFA scheme to accelerate a trailing bunch with an acceptable quality for any scientific applications, such a Free Electron Laser (FEL) or a future particle-particle collider, or even for medical applications is still an open question.

The work presented in this proceeding tries to address the problem of quality bunch transport numerically for a PWFA scheme. The scheme proposed leverages on the well establish RF know-how to produce and manipulate the bunches to match the strict plasma matching requirements, so that, once injected into the plasma the trailing bunch is boosted to the desired energy. The scheme can thus be decoupled into two parts. A first stage aims in generating two electron bunches (the driver and the trailing bunch) with a given time-separation so that once injected into the plasma they will be at right phase to maximize acceleration. The generation, distance positioning and acceleration is achieved using the COMB [12] technique and an RF in the X-band regime, for a final particle energy of 500 MeV. The plasma with a 10^{16} cm^{-3} number density is confined by a millimeter diameter capillary and ionized with plasma discharges, accelerates the particles from 500 MeV to 1 GeV in about 30 cm. The particle extracted from the plasma accelerating section are then injecting into a FEL. The evolution of the beam, from the photo-injector to the FEL via the plasma cell, is performed with a *single* simulation by concatenating several codes used to addressed the different physics occurring in the different accelerating section. We refer to this single simulation as a *start-to-end* simulation. This work is part of EuPRAXIA [13, 14] (European Plasma Research Accelerator with eXcellence In Applications) European project whose final goal is to use PBA to seed a FEL for physical and biological applications. Specifically EuPRAXIA@SPARC_LAB [14] is the envisioned EuPRAXIA European Italian-located facility operating at 1-5 GeV for FEL experiments.

INJECTOR

A comb-like configuration for the electron beam is used to generate simultaneously a 200 pC driver followed by a 30 pC trailing bunch. The comb-like operation foresees the generation of two or more bunches within the same RF accelerating bucket through the so-called laser-comb technique [12, 15] consisting in a train of laser time-spaced pulses illuminating the photocathode. The witness arrives earlier than the driver on the photocathode and then they are reversed in time at the end of the velocity bunching process, during which the longitudinal phase space is rotated. Experimental results have been obtained at SPARC_LAB where the laser-comb technique is routinely used in order to produce trains of multiple electron bunches [16] for narrow-band

* Work supported by European Union Horizon 2020 research and innovation program, Grant Agreement No. 653782 (EuPRAXIA)
† alberto.marocchino@lnf.infn.it

Content from this work may be used under the terms of the CC BY 3.0 licence (© 2018). Any distribution of this work must maintain attribution to the author(s), title of the work, publisher, and DOI.

ISBN: 978-3-95450-194-6 ISSN: 2226-0366 doi:10.18429/JACoW-LINAC2018-TH1A03

Content from this work may be used under the terms of the CC BY 3.0 licence (© 2018). Any distribution of this work must maintain attribution to the author(s), title of the work, publisher, and DOI.

THz generation [17], two-color FEL experiments [18, 19] and resonant particle driven PWFA [20]. Computational studies have been dedicated to provide two bunches separated by 0.55 ps [21], which corresponds to $\lambda_p/2$, being the plasma wavelength $\lambda_p = 330\,\mu$m given $n_p = 10^{16}$ cm^{-3}. Both driver and witness bunches must be compressed down to ~50 fs and 10 fs (FWHM), respectively. The process need some fine tuning to avoid emittance growth, naturally occurring because of the witness-driver overlapping during the velocity bunching regime. The photocathode laser has been shaped in order to provide at the cathode a witness and a driver bunches separated by $\Delta t = 4.8$ ps. With this configuration the beam crossing occurs in the second TW accelerating cavity and a fine-tuning of the RF phases suffices to provide the desired 0.55 ps beam separation corresponding to $\lambda_p/2$. Gaussian longitudinal distribution with $\sigma_z = 120\,\mu$m (RMS) and uniform transverse distribution of radius $r = 0.35$ mm have been assumed for the witness pulse at the cathode. The different intensities between the two pulses permit to generate bunches with different charges: a 30 pC trailing bunch and a 200 pC driver. It is worth to notice by adopting a $\sigma_D = 0.35$ mm, the FWHM witness length does not suffer lengthening, although the minimum RMS witness length is obtained for $\sigma_D = 0.25$ mm. The sliced current at the end of the photo-injector line is plotted in Fig. 1.

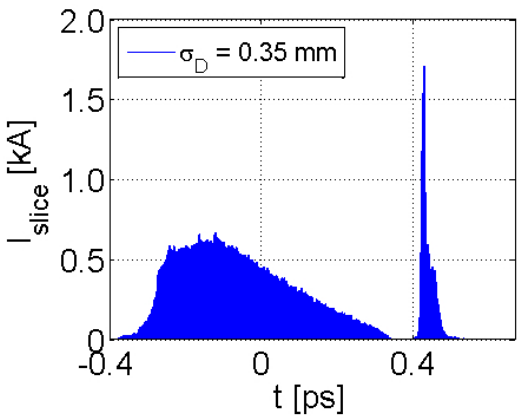


Figure 1: Driver and trailing bunch longitudinal current distribution at the photo-injector exit. The beam is propagating from right to left with the driver arriving earlier than the trailing bunch.

Driver and trailing bunch have been simulated with the TStep code and with 30k and 200k macro-particles respectively. In the described configuration the driver arrives 0.58 ps earlier than the witness at the X-band booster. It is worth to notice that the trailing bunch length is about 3 µm FWHM with a normalized transverse emittance of ~0.7 mm mrad.

LINAC

The X-band RF linac is used to accelerates the entire beam to 500 MeV [22, 23], energy of the beam entering the plasma, specifically the trailing bunch is prepared for plasma injection with a transverse dimension of 1 – 2 µm spot size. The comb-like electron beam undergoes deep over-compression in the photo-injector by means of the velocity bunching scheme. The same accelerating gradient of $E_{acc} \approx 20 - 36$ MV/m is applied in L1 and L2 linac section respectively, and the final electron beam energy is $E_{L2exit} \approx$ 580 MeV, with an energy spread less than 0.1%.The driver and witness bunches are characterized by high charge/low current and low charge/high current, respectively. Moreover, the initial matching conditions for the injection in the X-band linac are quite different for the two bunches, as shown by their transverse phase space at the linac entrance (i.e. injector exit). In this regard, an efficient sharing of the same lattice is achieved by means of a mild transverse focusing that aims to keep the RMS size of the comb beam compatible with the beam stay-clear-aperture through all the X-band accelerator. The same argument applies also to the focusing stage with the permanent quadrupoles at the entrance of the plasma capillary where a residual asymmetry between horizontal and vertical plane for the witness beams is present, see Fig. 2.

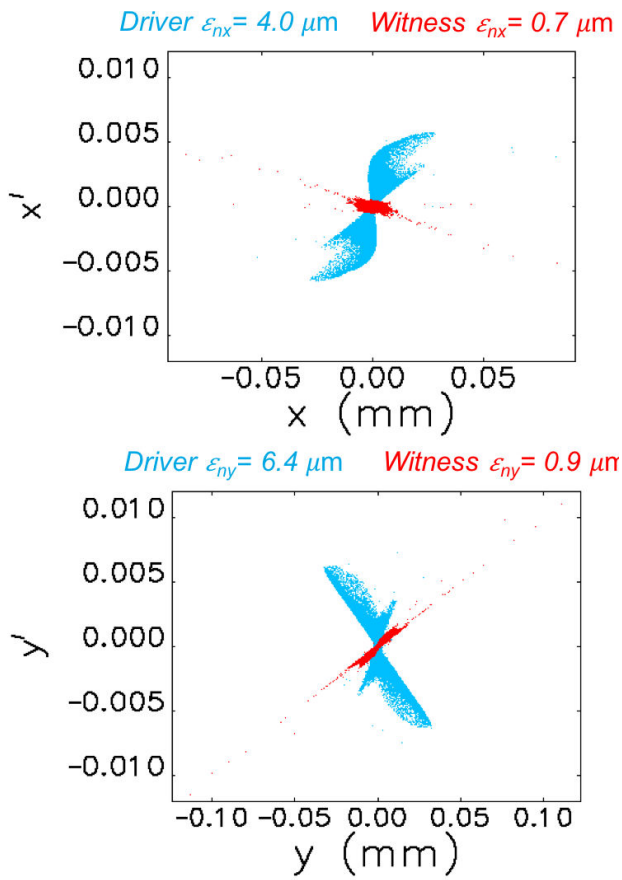


Figure 2: Horizontal and vertical phase space distribution of the PWFA driver (cyan dot) and witness (red dot) beams at the capillary entrance.

ISBN: 978-3-95450-194-6 ISSN: 2226-0366 doi:10.18429/JACoW-LINAC2018-TH1A03

THE PLASMA CELL

Start-to-end simulations use, for the plasma section, the state-of-the-code ARCHITECT [24, 25]. The use of Architect has been dictated by the necessity to run long simulations where a classical particle-in-cell (PIC) approach would have been computationally too expensive. The Architect reduced model, which relies on a fluid background, has been benchmarked numerically against the ALaDyn-PWFA [26] PIC code [25] and versus SPARC_LAB experimental results [27, 28]. Start-to-end simulations are performed by concatenating the use of codes without any phase space manipulation or remapping. Specifically, for the interface RF X-band with plasma The ELEGANT code is used to track particle up to the plasma entrance, the particle phase-space is then imported into the Architect code for the evolution in the plasma section. Simulations described in this section have been run with a longitudinal resolution of 1 µm and a transverse resolution of 0.4 µm, a mesh that allows to resolve the fine structure with a reasonable computational cost. The advancing time step is of 1.1 fs. The number of particle used to discretize the driver is, on average, 30 particles per cell while the witness is discretized with an average of 100 particle per cell. We recall that the goal is to accelerate the trailing bunch retaining as much as possible its original quality. To limit the energy spread growth, the trailing bunch has been designed with a (as much as possible) *triangular* shape. The triangular shape together with a specific value of peak charge represents the optimized longitudinal density profile that limits energy growth spread during propagation. Driver and witness have been designed to perform the best acceleration in terms of quality and in terms of energy transfer (*transformer ratio, R*) [29], parameter that identifies the rate of energy transfer from the driver to the witness. In our case the transformer ratio in estimated in the range 2-3. The foreseen experiment is planned in the so-called weakly-non-linear regime, where despite fields resemble a sawtooth profile linear field sum is still possible. The parameter we used to measure the degree of nonlinearity is the *reduced charge parameter* [30, 31], $Q = \frac{N_b}{n_0}\kappa_p^3$, with N_b the electron bunch number (bunch charge divided by the elementary charge). For this case the driver reduced charge is $Q \sim 0.8 - 0.9$.

Nonetheless, if the upstream application is a FEL application that requires a slice current around 2 kA, combining this requirement with the triangular shape, simulations helps identifying that beam loading compensation occurs for a driver-witness distance 184 µm or $0.55 \times \lambda_p(n_0 = 10^{16})$, where the electric field experienced by the witness is around 1.1 GV/m.

We recall that the accelerating field together with the plasma wavelength depend upon the plasma number density n_0, $\propto n_0^{1/2}$ and $\propto n_0^{-1/2}$ respectively. The capability to control the density would permit some flexibility and adjustments in the bubble profile and accelerating fields, this to compensate -on site- whenever the distance between driver and witness would oscillate or change for experimental unforeseen reasons. The flat density profile, together with the required value is achieved with a capillary tube. The capillary tube, confining the ejected gas, permits a high degree of control to which we can rely on for experimental on site optimization. At present simulations consider some density ramps of the order of 0.5 cm, that are experimentally reasonable and whose length is below the betatron wavelength assuring no bunch oscillations within the ramps to increase acceleration robustness [26]. At plasma entrance, the trailing bunch is delivered with a shape that resemble the triangular required shape, transversally the bunch is fairly symmetric in size and in emittance Table 1. The driver is instead of lower brightness quality, but since the driver will undergo depletion -anyway- we can accept a lower quality since its main purpose is to *only* drive the wake. The setting of the RF line in favor of the witness naturally bring the driver on a less optimized point that is delivered at plasma with a lower quality than the trailing bunch. The driver at plasma entrance has the front part that is highly convergent, convergence that will cause a consequent expansion within the plasma channel producing a unique funnel shape, Fig. 3. The driver is capable to induce a weakly nonlinear wake with an effective maximum field that peaks (at bubble closure) around 2.5-3.0 GV/m, as can been retrieved from Fig. 3. The central part of the driver that mostly contributes to generate the wake looses after 40 cm about 150 MeV, the witness gains about 460 MeV. The slice analysis, reported numerically in Table 1 suggests that the witness head and tail undergo a phase space dilution, while the central slice with very high current retain high quality. The witness, at plasma entrance, has the emittance in both planes as well as the energy spread almost uniform along the entire witness length. After the plasma acceleration section, the bunch has lost this homogeneity exhibiting a different slice quality along its length.

Table 1: PWFA bunch parameters at plasma entrance and at plasma exit. The best slice value is also reported.

Beam	Units	Driver IN	Driver OUT	Tr. B. IN	Tr. B. OUT
Charge	pC	200	200	30	30
σ_x	µm	8	6.4	1.47	1.42
σ_y	µm	3.1	10	3.17	1.4
σ_z	µm	52	50	3.85	3.8
ε_x	µm	2.56	4.1	0.6	0.96
ε_y	µm	4.8	11.4	0.55	1.2
σ_E	%	0.2	20	0.07	1.1
E	MeV	567	420	575	1030
Best Slice					
current	kA			2	2.0
ε_x	µm			0.59	0.57
ε_y	µm			0.58	0.62
σ_E	%			0.011	0.034

The front part and the read part of the witness are characterized by large emittance and energy spread. While ideally

Content from this work may be used under the terms of the CC BY 3.0 licence (© 2018). Any distribution of this work must maintain attribution to the author(s), title of the work, publisher, and DOI.

ISBN: 978-3-95450-194-6 ISSN: 2226-0366 doi:10.18429/JACoW-LINAC2018-TH1A03

Content from this work may be used under the terms of the CC BY 3.0 licence (© 2018). Any distribution of this work must maintain attribution to the author(s), title of the work, publisher, and DOI.

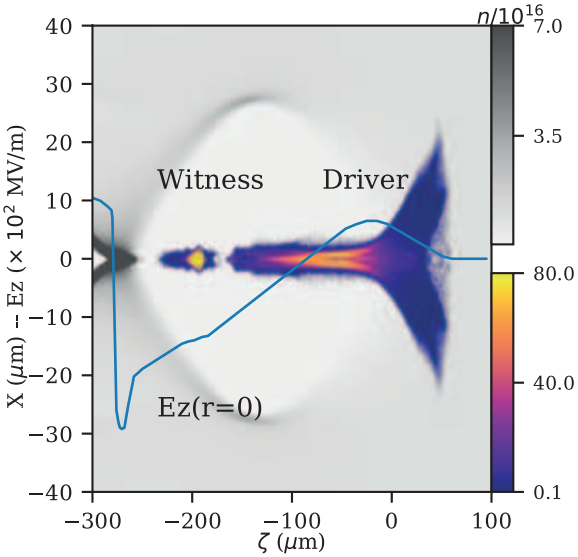


Figure 3: Bunch and background density colormaps after 5 mm within the plasma. The bunch density is plotted with a *plasma* colormap, while the background is plotted with a grey colormap. The longitudinal accelerating electric field, on axis, is over-imposed with a solid blue line. For scale purposes and for sake of clarity the Ez is plotted in hundreds of MV/m.

we wish to conserve quality all along the trailing bunch, the head and tail are characterized by a lower current, condition that allows us some flexibility on these regions since their lasering within the FEL would be negligible. However, and most importantly, the region within the high current bell retains its quality. From Fig. 4, top panel, we notice that under the region of high current the emittance in both plane is almost conserved with little deterioration. The energy spread undergoes some general increase also in the region of maximum current. The slice value, in the region of maximum current, stays below 0.1 %. The peak current value corresponds to the transition from a higher value to the lowest one. The best slice characterized by a 2 kA current, has an energy spread as low as 0.034%, an emittance of 0.57 mm mrad and 0.62 mm mrad in the x and y plane respectively.

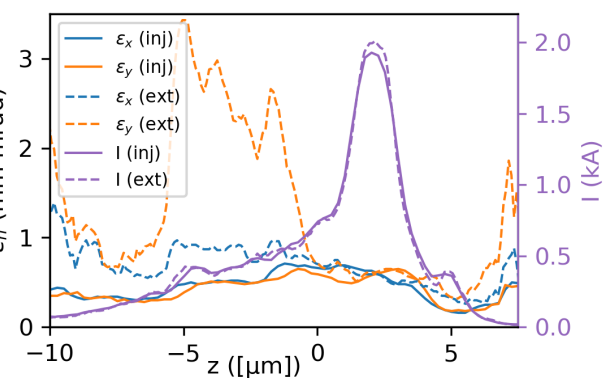


Figure 4: Slice analysis for the witness bunch at plasma input, dashed color, and at plasma exits, solid color.

FEL

The electron beam accelerated by plasma are then transported to an ondulator and photon production is studied with the use of the GENESIS [32] code. Considering a $a_w = 0.8$, the resonant wavelength is $\lambda = 2.987$ nm. The matching to the undulator leads to $\sigma_x = 40.6$ µm and $\sigma_y = 28.6$ µm with the quadrupoles 9 cm long and set at 18 T/m. The FEL parameter results to be $\rho = 2.51 \times 10^{-3}$, its 3D value is $\rho_{3D} = 1.86 \times 10^{-3}$ for $L_{g,3D} = 0.37$ m. Simulations predicts The growth of the radiation, as given by simulations with GENESIS 1.3 [32], is shown in Fig. 5. The saturation length is about 15–25 m with emitted energy 6.5 µJ at 30 m, for a photon flux of 9.76×10^{10} per shot. The minimum bandwidth value, achieved at 20 m is 0.3%, while at 30 m saturation effects have increased it at 0.9%. Finally, the nominal case a1 has been worsened in current, emittance and energy spread by 5% and 10%, we observe a decrease in the emission respectively of 8% and 13%.

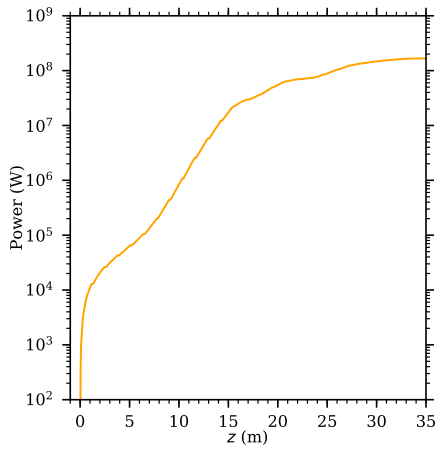


Figure 5: FEL radiation growth along the undulator length.

CONCLUSION

This work focuses on a start-to-end simulations for a FEL machine, driven by a PWFA accelerator whose bunch is generated and accelerated by a RF photo-injector. The RF photo-injector and the subsequent X-band boosting line had been tuned to deliver to the plasma a driver able to accelerated a trailing bunch from 0.5 GeV to 1 GeV by preserving the quality of its core so to well laser inside a FEL machine. The simulation is possible by combining in cascade a series of codes, each devoted to reproduce the relevant physics in the given section.

ACKNOWLEDGEMENTS

This work was supported by the European Unions Horizon 2020 research and innovation programme under grant agreement No. 653782. We acknowledge the CINECA award under the ISCRA initiative, for the availability of high performance computing resources and support.

ISBN: 978-3-95450-194-6 ISSN: 2226-0366 doi:10.18429/JACoW-LINAC2018-TH1A03

REFERENCES

[1] T. Tajima and J. M. Dawson, "Laser electron accelerator," *Physical Review Letters*, vol. 43, no. 4, pp. 267–270, 1979.

[2] S. Corde *et al.*, "Multi-gigaelectronvolt acceleration of positrons in a self-loaded plasma wakefield," *Nature*, 2015.

[3] M. Litos *et al.*, "High-efficiency acceleration of an electron beam in a plasma wakefield accelerator," *Nature*, vol. 515, no. 7525, pp. 92–95, 2014.

[4] W. P. Leemans, B. Nagler, A. J. Gonsalves, and C. Toth, "GeV electron beams from a centimetre-scale accelerator," *Nature*, 2006.

[5] H. Schwoerer, S. Pfotenhauer, O. Jäckel, K. Amthor, *et al.*, "Laser-plasma acceleration of quasi-monoenergetic protons from microstructured targets," *Nature*, 2006.

[6] I. Blumenfeld *et al.*, "Energy doubling of 42 GeV electrons in a metre-scale plasma wakefield accelerator," *Nature*, vol. 445, no. 7129, pp. 741–744, Feb. 2007.

[7] P. Muggli *et al.*, "Generation of Trains of Electron Microbunches with Adjustable Subpicosecond Spacing," *Physical Review Letters*, vol. 101, no. 5, p. 054801, Aug. 2008.

[8] E. Kallos *et al.*, "High-Gradient Plasma-Wakefield Acceleration with Two Subpicosecond Electron Bunches," *Physical Review Letters* vol. 100, no. 7, p. 074802, Feb. 2008.

[9] S. van der Meer, "Improving the power efficiency of the plasma wakefield accelerator," Geneva, Tech. Rep., 1985.

[10] T. Katsouleas, "Physical mechanisms in the plasma wake-field accelerator," *Physical Review A - General Physics*, vol. 33, no. 3, pp. 2056–2064, Mar. 1986.

[11] J. B. Rosenzweig *et al.*, "Acceleration and focusing of electrons in two-dimensional nonlinear plasma wake fields," *Physical Review A (Atomic*, vol. 44, no. 1, pp. R6189–R6192, Nov. 1991.

[12] M. Ferrario *et al.*, "Laser comb with velocity bunching: Preliminary results at sparc," *Nuclear Instruments and Methods in Physics Research Section A: Accelerators, Spectrometers, Detectors and Associated Equipment*, vol. 637, no. 1, pp. S43–S46, 2011.

[13] P. A. Walker *et al.*, "Horizon 2020 EuPRAXIA design study," *Journal of Physics: Conference Series*, vol. 874, p. 012029, Jul. 2017.

[14] M. Ferrario *et al.*, "Eupraxia@sparc_lab design study towards a compact fel facility at lnf," *Nucl. Instrum. Meth.* 2018. [Online]. Available: http://www.sciencedirect.com/science/article/pii/S0168900218301414

[15] F. Villa *et al.*, "Laser pulse shaping for high gradient accelerators," *Nuclear Instruments and Methods in Physics Research Section A: Accelerators, Spectrometers, Detectors and Associated Equipment*, vol. 829, pp. 446–451, 2016.

[16] A. Mostacci *et al.*, "Advanced beam manipulation techniques at sparc," in *IPAC 2011-2nd International Particle Accelerator Conference*, 2011, pp. 2877–2881.

[17] F. Giorgianni *et al.*, "Tailoring of highly intense thz radiation through high brightness electron beams longitudinal manipulation," *Applied Sciences*, vol. 6, no. 2, p. 56, 2016.

[18] V. Petrillo *et al.*, "Observation of time-domain modulation of free-electron-laser pulses by multipeaked electron-energy spectrum," *Physical Review Letters*, vol. 111, no. 11, p. 114802, 2013.

[19] A. Petralia *et al.*, "Two-color radiation generated in a seeded free-electron laser with two electron beams," *Physical review letters*, vol. 115, no. 1, p. 014801, 2015.

[20] E. Chiadroni *et al.*, "Beam manipulation for resonant plasma wakefield acceleration," *Nuclear Instruments and Methods in Physics Research Section A: Accelerators, Spectrometers, Detectors and Associated Equipment*, vol. 865, pp. 139–143, 2017.

[21] A. Giribono *et al.*, "Eupraxia@sparc_lab: the high-brightness rf photo-injector layout proposal," *Accept. Nucl. Instrum. Meth.*, 2018.

[22] C. Vaccarezza *et al.*, "Eupraxia@sparc_lab: Beam dynamics studies for the x-band linac," 2018.

[23] M. Diomede *et al.*, "Rf design of the x-band linac for the eupraxia@sparc_lab project," in *Proceedings IPAC 2018*, 2018.

[24] A. Marocchino *et al.*, "Efficient modeling of plasma wakefield acceleration in quasi-non-linear-regimes with the hybrid code Architect," *Nuclear Instruments and Methods in Physics Research Section A: Accelerators, Spectrometers, Detectors and Associated Equipment*, vol. 829, pp. 386–391, sep 2016.

[25] F. Massimo, S. Atzeni, and A. Marocchino, "Comparisons of time explicit hybrid kinetic-fluid code Architect for Plasma Wakefield Acceleration with a full PIC code," *Journal Of Computational Physics*, vol. 327, pp. 841–850, 2016.

[26] A. Marocchino *et al.*, "Design of high brightness Plasma Wakefield Acceleration experiment at SPARC_LAB test facility with particle-in-cell simulations," *Nucl. Instrum. Meth. A*, 2018.

[27] A. Marocchino *et al.*, "Experimental characterization of the effects induced by passive plasma lens on high brightness electron bunches," *Applied Physics Letters*, vol. 111, no. 18, p. 184101, 2017.

[28] R. Pompili *et al.*, "Experimental characterization of active plasma lensing for electron beams," *Applied Physics Letters*, vol. 110, no. 10, p. 104101, 2017.

[29] F. Massimo *et al.*, "Transformer ratio studies for single bunch plasma wakefield acceleration," *Nuclear Inst. and Methods in Physics Research, A*, vol. 740, no. C, pp. 242–245, mar 2014.

[30] J. Rosenzweig *et al.*, "Energy loss of a high charge bunched electron beam in plasma: Simulations, scaling, and accelerating wakefields," *Physical Review Special Topics-Accelerators and Beams*, vol. 7, no. 6, p. 061302, 2004.

[31] P. Londrillo *et al.*, "Numerical investigation of beam-driven PWFA in quasi-nonlinear regime," *Nuclear Inst. and Methods in Physics Research, A*, vol. 740, pp. 236–241, 2014.

[32] S. Reiche, "Genesis 1.3: a fully 3d time-dependent fel simulation code," *Nuclear Instruments and Methods in Physics Research Section A: Accelerators, Spectrometers, Detectors and Associated Equipment*, vol. 429, no. 1-3, pp. 243–248, 1999.

Content from this work may be used under the terms of the CC BY 3.0 licence (© 2018). Any distribution of this work must maintain attribution to the author(s), title of the work, publisher, and DOI.

ISBN: 978-3-95450-194-6 ISSN: 2226-0366 doi:10.18429/JACoW-LINAC2018-TH1A04

THE PROTON DRIVEN ADVACED WAKE FIELD ACCELERATION EXPERIMENT (AWAKE) AT CERN*

S. Doebert on behalf of the AWAKE collaboration

Abstract

The Advanced Proton Driven Plasma Wakefield Acceleration Experiment (AWAKE) aims at studying plasma wake field generation and electron acceleration driven by proton bunches. It is a proof-of-principle R&D experiment at CERN and the world's first proton driven plasma wake field acceleration experiment. The experiment uses the 400 GeV proton beam from the super proton synchrotron (SPS) which travels through a 10 m long Rb-vapour plasma cell where it gets self-modulated and generates the plasma wake fields. An electron witness beam is injected externally to probe the wake-fields. AWAKE has completed several experimental campaigns, starting in 2016. Results from the initial characterization of the plasma cell and measurements of the seeded self-modulation of the proton beam will be presented. First results on electron witness beam acceleration using the proton driven plasma wake field have been obtained recently and are presented in this paper.

INTRODUCTION

The AWAKE experiment at CERN aims to study and demonstrate for the first time proton driven wakefield acceleration. Laser driven plasma wake field acceleration (LPWA) has been proposed almost 40 years ago [1] and impressive experimental results have been achieved in recent years, demonstrating several GeV electrons from a short plasma cell [2,3]. LPWA provides very high gradients over short, centimetre scale length. To reach particle energies suitable for high-energy physics many acceleration stages have to be coupled and therefore dephasing and energy depletion issues need to be solved.

A second well known and already demonstrated option is electron driven plasma wakefield acceleration, here gradients of the order of 50 GV/m over meter scale plasmas have been demonstrated [4,5]. This scheme suffers from a limited energy transfer from the drive bunch to the witness bunch [6] and therefore requires as well a large number of stages to reach TeV scale energies.

Proton driven wakefield acceleration has in principle the potential to overcome these challenges since high energy proton bunches carry enough energy to accelerate electrons to TeV scale energies in a single stage [7]. Readily available proton beams come from large synchrotrons and have therefore a long, centimetre scale, bunch length, prohibiting high wakefields when used as a driver. The AWAKE experiment therefore uses a seeding laser pulse to trigger a self modulation resulting in a micro-bunching of the long proton bunches [8]. These micro-bunches can then drive the plasma wake fields resonantly up to GV/m gradients. This process will be described below in more detail.

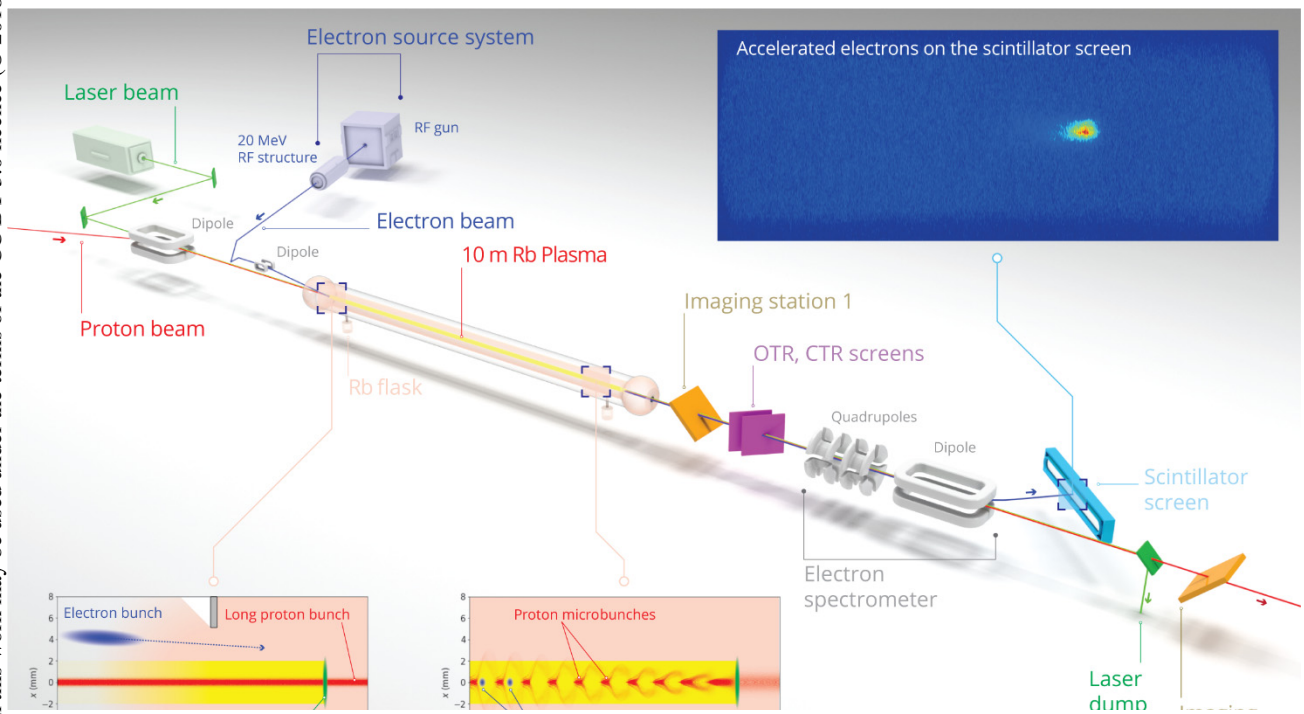


Figure 1: Schematic layout of the AWAKE experiment at CERN. A proton beam from the SPS (left) is focused into a plasma cell. A laser beam and an electron beam are injected synchronized to generate the plasma and probe the wakefileds. A diagnostic section (right) allows to observe the self-modulation process and the accelerated electrons.

Content from this work may be used under the terms of the CC BY 3.0 licence (© 2018). Any distribution of this work must maintain attribution to the author(s), title of the work, publisher, and DOI.

ISBN: 978-3-95450-194-6 ISSN: 2226-0366 doi:10.18429/JACoW-LINAC2018-TH1A04

AWAKE EXPERIMENT

The AWAKE experiment is part of the CERN accelerator complex [9, 10]. It uses a 400 GeV proton beam with an intensity of up to $3 \cdot 10^{11}$ protons/bunch and a bunch length of 12 cm, coming from the SPS. The bunches are extracted from the SPS and focused into a 10 m long plasma cell. A schematic layout of the experiment can be seen in Figure 1. The plasma cell is consisting of a uniformly heated pipe, filled with rubidium vapour at a temperature around 200 ºC corresponding to a nominal plasma density of $7 \cdot 10^{14}$ cm^{-3} [11]. The plasma density can be changed by adjusting the temperature and has a measured uniformity of better than 0.2%. In addition a slight taper of the plasma density can be achieved by adjusting the flow of rubidium from both ends of the plasma cell. The critical parameter of the local plasma density can be measured with a white-light interferometer to a precision of better than 0.2 %. A picture of the installed plasma cell in the AWAKE experiment can be seen in Figure 2.

A high power laser system with a central wavelength of 780 nm delivers short pulses synchronised with the extracted proton beam. The laser ionizes the Rb vapour thus creating the plasma during the passage of the proton beam. The 120 fs long laser pulse with an energy of up to 450 mJ, creates a plasma channel with a radius of about 1 mm collinear with the proton beam trajectory. Secondly the laser pulse is seeding the self-modulation of the proton bunch, transforming it into micro-bunches, which drive the wakefield resonantly. This is indicated in the lower left part of Figure 1.

A fraction of the laser energy tapped off from the laser and frequency tripled, serves to generate the electron beam, using an rf photo injector. The laser and the rf source, used for the electron injector, are synchronised better than 1 ps enabling the witness beam acceleration, while the laser and the proton beam are synchronised to the level of 15 ps which is sufficient given the long bunch length of the proton beam. The electron injector for the witness beam consist of an S-band rf gun and an S-band booster structure powered by a single klystron. The rf gun uses a high quantum efficiency (QE) Cs_2Te cathode which provides a QE of a few percent. The nominal beam parameters are a bunch charge of 200 pC, an energy of 18 MeV and a bunch length of 4 ps (σ). A detailed description of the electron injector can be found in [12].

The entire experiment is equipped with a whole suite of beam diagnostics for all three beams. Cameras and virtual focus lines allow monitoring the alignment and profile of the laser beams in the relevant positions at the photo cathode of the injector and in the plasma cell. Beam position monitors and transverse profile monitors (screens) are installed in both particle beam lines to monitor the trajectory, measure the relevant beam parameters for matching and beam alignment. All three beam have to overlap temporally and spatially in the plasma. The timing can be measured with a streak camera using OTR light from a screen in front of the plasma cell and adjusted with delay lines in the laser setup. Behind the plasma cell, a set of transverse profile monitors allow to observe the transvers proton beam defocusing due to the self-modulation [13]. OTR and CTR radiators are used to characterize the micro bunching of the proton beam, indicating the wake field development. The optical emission is monitored on a second streak camera, delivering time resolved images of the self-modulated proton bunch and the coherent microwave emission can be characterised in the frequency domain with a heterodyne measurement system. The principle diagnostic for acceleration of the witness beam is the spectrometer at the end of the beam line, which deflects the electrons but hardly changes the trajectory of the 400 GeV proton beam. A large high-resolution scintillator screen is used to view the accelerated electron beam.

The AWAKE experiment was divided into two phases. In a first phase mainly in 2017 the seeded self-modulation of the proton beam and the development of the wakefields were studied. The second phase in 2018 is dedicated to demonstrate the proof of principle of proton driven plasma wake field acceleration with an electron witness beam. Finally in a second RUN after the long shutdown at CERN the AWAKE team wants to show acceleration of high quality electron beams [14].

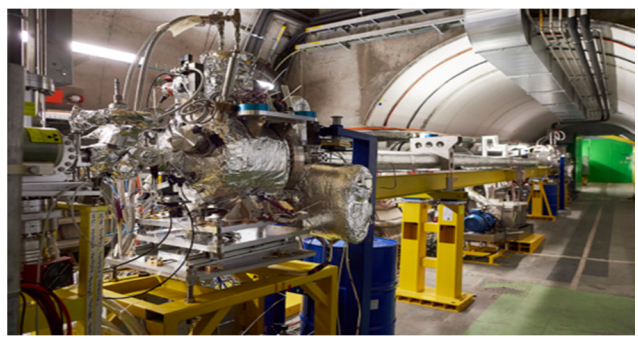


Figure 2: Picture of the 10 m long rubidium vapour plasma cell installed in the AWAKE experiment. One of the endcaps can be seen which includes the RB flask and the flow and temperature regulation.

SEEDED SELF MODULATION (SSM)

The process of self-modulation is essential for the AWAKE experiment because the existing long proton beam would not excite significant wake fields. The plasma frequency $\omega_p = (4\pi n_0 e^2/m_e)^{-1/2}$ depends on the plasma density n_0 with m_e and e being the elementary electron mass and charge. In order to drive a wakefield efficiently the length of the drive bunch ideally needs to be shorter than the plasma wavelength $\lambda_p = 2\pi c/\omega_p$. In AWAKE this problem is solved by converting the long proton bunch into a series of micro bunches, each short enough to drive the wakefield, taking advantage of a self-modulation instability (SMI) [8] seeded by the short laser pulse. Simulations indicated that the instability grows exponentially both along the bunch and along the plasma, resulting in large wakefields suitable for acceleration. The self-modulation

Content from this work may be used under the terms of the CC BY 3.0 licence (© 2018). Any distribution of this work must maintain attribution to the author(s), title of the work, publisher, and DOI.

ISBN: 978-3-95450-194-6 ISSN: 2226-0366 doi:10.18429/JACoW-LINAC2018-TH1A04

Content from this work may be used under the terms of the CC BY 3.0 licence (© 2018). Any distribution of this work must maintain attribution to the author(s), title of the work, publisher, and DOI.

is actually a transverse proton density variation resulting in focused and defocused areas.

This structure of the beam propagates over very long distances in the plasma according to simulations [15]. Figure 3 shows an example of such a simulation of a self-modulated proton beam at different time steps to visualize the process [16]. The modulation starts slowly and consists of alternate transverse focusing and defocusing of the protons resulting in a periodical longitudinal density variation. Finally, a clear micro bunching can be seen which drives the plasma wakefield resonantly.

Phase 1 of the AWAKE experiment was dedicated to verify these predictions and to study the seeded self –modulation of the proton beam extracted from the SPS. The proton beam was aligned collinear with the high power laser in the 10 m long plasma cell. A streak camera could monitor the timing of the laser with respect to the proton bunch after the plasma cell. In the nominal scheme the laser is placed right in the middle of the proton bunch and therefore the modulation should start in the centre of the bunch.

Examples of the original data taken by the streak camera and its analysis can be found in [17] and resemble very much the lower right picture in Figure 3. The self-modulation can be clearly seen in particular that it is a transverse modulation of the proton beam. The plasma cell was set to a density of $2.1 \cdot 10^{14}$ cm^{-3} during the experiment and the distance of the micro-bunches was measured to be 7.6 ps accordingly.

It was found that the spine like structure of the modulated proton bunch is extremely reproducible and consequently produces phase stable wakefields suitable for acceleration. The modulated proton beam can be interpreted therefore as a standing wave accelerating structure with a resonance frequency of 131 GHz. The frequency has been varied in the experiment from 50 GHz to almost 300 GHz by changing the plasma density from $0.5 \cdot 10^{14}$ cm^{-3} to $11 \cdot 10^{14}$ cm^{-3}. The plasma frequency and therefore the frequency of our plasma wakefield accelerator scales with the square root of the plasma density. The modulation frequency has been measured with the streak camera in the time domain using the visible emission from the screen and as well in the frequency domain using microwave detectors at the coherent part of the emission spectrum. Both measurements show excellent agreement with each other and with the theoretical predictions. More in depth insights and analysis of the self-modulation studies can be found in [17, 18]. The transverse defocusing of the proton beam during the self-modulation can be observed indirectly by transverse profile monitoring after the plasma cell [19].

ACCELERATION RESULTS

The first goal of the AWAKE experiment was the study of the seeded self-modulation. It was demonstrated that one can expect a phase-stable wakefield, allowing to inject a probe beam and accelerate particles.

In the second phase the main goal was to demonstrate electron acceleration, using the proton driven wakefields. An electron injector has been added to the experimental facility in 2017, allowing the injection of low energy electron bunches into the wakefield. Ideally, one would use an electron bunch which is short with respect to the plasma wavelength and which can be focused to the transverse size of the useful wakefields. This would require a very sophisticated electron accelerator, which was not available for the first phases of AWAKE.

The injected electron bunches used for the present experiments have an energy of 19 MeV and a bunch charge of 600 pC, the bunch length is about 2-3 ps (σ). They are focused at the entrance of the plasma cell to a spot size with a radius of about 600 µm due to the larger beam emittance compared to the specifications. The electron beam is injected with a delay of approximately 200 ps with respect to the seeding laser. The beam spreads longitudinally over several plasma wavelength and the electron beam focus is larger transversely than the plasma radius defined by the size of the laser beam. The simulations suggest therefore

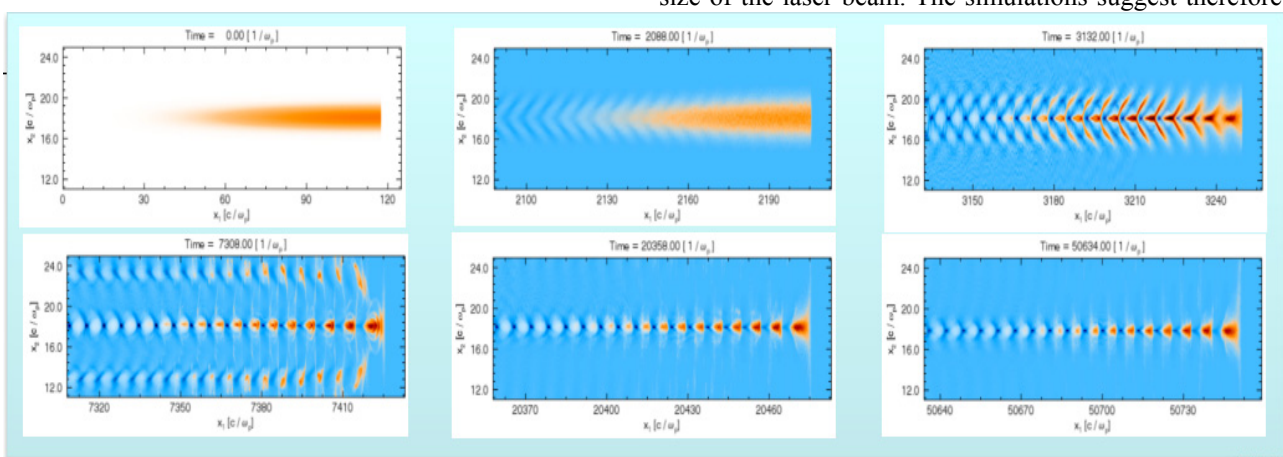


Figure 3: Simulation of the self-modulation process of the proton beam using a short seed-laser in the centre of the proton bunch. From upper left to lower right snapshots at different times during the self-modulation are shown. The first snapshot (upper left) shows no modulation yet, in the third and forth (upper right and lower left) one can clearly see the transverse nature of the modulation resulting in transversely focused and defocused protons. The last picture (lower right) depicts the fully developed modulation. Here the micro-bunches which will drive the wakefield resonantly are clearly visible.

ISBN: 978-3-95450-194-6 ISSN: 2226-0366 doi:10.18429/JACoW-LINAC2018-TH1A04

that some electrons are captured at the right phase and are accelerated in the wakefields up to high energies along the 10 m long plasma cell. Final energies up to 2 GeV with an energy spread of the order of 10-15% are expected [20]. Furthermore, the simulations indicate a better capturing of the electron beam if it is injected with a slight angle with respect to the proton beam. In the experiment a crossing angle between 1-2 mrad with respect to the proton beam was used.

In a first experiment in 2018, electrons have been injected into the plasma and acceleration of electron with energies of up to 2 GeV have been observed [21]. Figure 4 shows an example of such an acceleration event as seen by the spectrometer at the end of the proton beam line. In this example an electron beam with an energy of 800 MeV has been measured, the energy spread is about 17 % FWHM in this case. The captured charge in this first experiment was 0.25 pC.

In this series of measurements a plasma density of $1.8 \cdot 10^{14}$ cm^{-3} has been used with a 5% density taper over the length of the plasma cell. Tapering the plasma density allows to preserve slightly higher wakefields over the length of the plasma cell. During the first acceleration experiments the plasma density and tapering was varied. A summary of the data points obtained can be seen in Figure 5. The acceleration gradient goes up with the plasma density as expected and a density ramp along the cell boosts the wakefields in addition. The uncertainty of the peak energy and energy spread measurements is estimated to 10% because it is dominated by the emittance of the accelerated electrons, which is not measured.

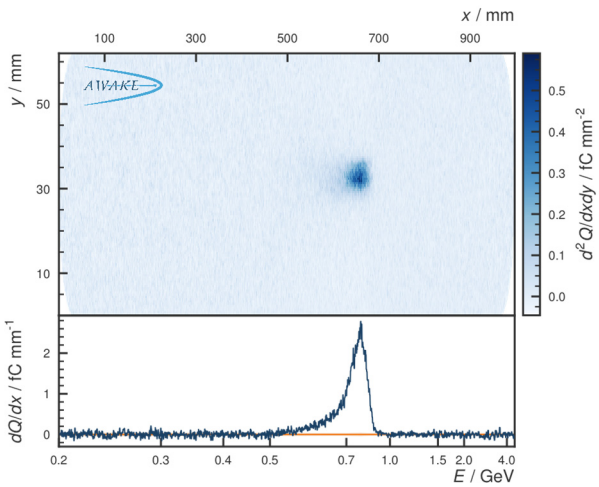


Figure 4: Witness beam acceleration measurement example. The image observed at the spectrometer after background subtraction and its vertical projection below. The charge of the beam is visualized in the colour coding of the image. The red line in the projection graph shows a 1 σ uncertainty band from the background subtraction

In the first proof of principle experiment, the electron beam parameters were not yet optimised. The emittance of the beam is still higher than originally specified and the control of the beam spot and location in the plasma cell not yet fully developed. There is no diagnostic in the plasma cell available were one wants to verify and guaranty the overlap of the three beams. Nevertheless, the acceleration events appeared very consistently and reliably.

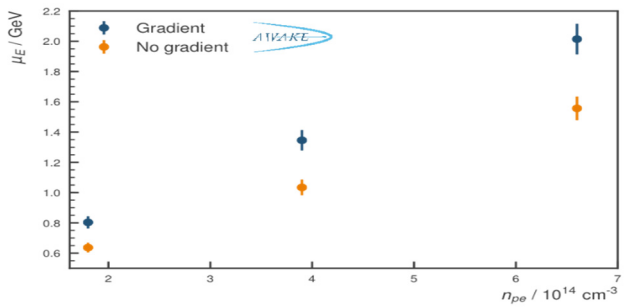


Figure 5: Summary of acceleration results as a function of plasma density. Shown are the highest acceleration results obtained with and without a gradient in the plasma density along the plasma cell.

The next steps are to be able to precisely change the focal point and crossing angle of the electron beam with the plasma, over a wide range of parameters, in order to optimise the acceleration results in terms of captured charge and energy spread. Since reliable 3D simulations of the capturing and acceleration process are very difficult, this is as well the way to systematically study the dependences of the results on these parameters.

CONCLUSION AND OUTLOOK

The AWAKE collaboration managed to observe and study, for the first time, the self-modulation of a proton beam. The seeded self-modulation process provides stable wakefields suitable for high gradient acceleration. This was demonstrated with the first acceleration of electron bunches in a proton driven plasma wakefield. Final energies up to 2 GeV, using a tapered plasma density have been observed. This results present a new milestone in plasma based particle acceleration.

The AWAKE team will continue in 2018 to study and optimise the acceleration process. Afterwards there is a two-year shutdown at CERN with no protons available from the SPS. The next phase of AWAKE called RUN2 will start in 2021 with the goal to accelerate high quality electron beams using the proton driven plasma wakefields. The aim is to demonstrate emittance preservation and low energy spread electron beams to pave the way towards possible high-energy physics application of this scheme. To achieve these goals a new electron injector is probably needed providing electron bunches with a bunch length of the order of 100 fs, a very small emittance and the right intensity to load the wakefields correctly [12]. In addition the electrons have to be injected once the growth of the wakefields during the self-modulation process is saturated and a high accelerating gradient can sustained over a longer distance. Two plasma cells are needed, separating the micro bunching and the pure acceleration, with electron injection in between [14].

Content from this work may be used under the terms of the CC BY 3.0 licence (© 2018). Any distribution of this work must maintain attribution to the author(s), title of the work, publisher, and DOI.

ISBN: 978-3-95450-194-6 ISSN: 2226-0366 doi:10.18429/JACoW-LINAC2018-TH1A04

Content from this work may be used under the terms of the CC BY 3.0 licence (© 2018). Any distribution of this work must maintain attribution to the author(s), title of the work, publisher, and DOI.

Possible applications of such an acceleration scheme are studied by the AWAKE collaboration and as well within the framework of Physics Beyond Collider at CERN [22]. Tens of GeV electron beams could be achievable using the SPS as a driver, for dark matter searches or e-p-collisions while using the LHC as a driver would in principle allow to accelerate electrons to the TeV scale for very high energy e-p collisions [23].

REFERENCES

[1] T. Tajima and J.M. Dawson, "Laser Electron Accelerator", Phys. Rev. Lett,. Vol 43, 1979

[2] W. P. Leemans *et al,* "GeV electron beams from a centimetre scale accelerator", Nature Phys 2, 2006

[3] S. Steinke *et al.,*"Multistage coupling of independent laser plasma accelerators", Nature vol. 530, 2016

[4] P. Muggli *et al.,* "Meter-Scale Plasma-Wakefield Accelerator Driven by a Matched Electron Beam", Phys. Rev. Lett, vol 93, 2004

[5] I. Blumenfeld *et al.,* "Energy doubling of 42 GeV electrons in a metre-scale plasma wakefield accelerator", Nature vol. 445, 2007

[6] P. Chen et al, "On energy transfer in the plasma wakefield accelerator", Phys. Rev. Lett, vol 56, 1986

[7] A. Calswell *et al.*,"Proton driven plasma plasma-wakefield acceleration", Nature Phys., vol. 5, 2009

[8] N. Kumar *et al.,* "Self-Modulation Instability of a Long Proton Bunch in Plasmas", Phys. Rev. Lett., vol 104, 2010

[9] A. Caldwell et al.," Awake Design Report", CERN-SPSC-2013-013

[10] P. Muggli *et al*., "Awake readiness for the study of the seeded self-modulation of a 400 GeV proton bunch", Plasma Physics Conference, Belfast, 2017, arXiv:1708.01087

[11] E. Oz et al., Nucl. Instr. and Meth. Phys. A, vol.740, 2014

[12] K. Pepitone et al., " The electron accelerator for the AWAKE experiment at CERN, Baseline and future Developments", Nucl. Instr. and Meth. Phys. A, 2018

[13] M. Turner et al., Nucl. Instr. and Meth. Phys. A, vol.829, 2016

[14] E. Adli, "Towards Awake Applications: Electron Beam Acceleration in a Proton Driven Plasma Wake", in *Proc. IPAC'16*, Busan, South Korea, May 2016 paper WEPMY008 DOI:10.18429/JACoW-IPAC2016-WEPMY008

[15] J. Viera *et al.,* "Hosing Instability Suppression in Self-Modulated Plasma Wakefields", Phys. Rev. Lett, vol. 112, 2014

[16] Simulation done by J. Vieira using OSIRIS: R. A. Fonseca *et al.,* Lect. Notes Comp. Sci. Vol 2331/2002, (Springer Berlin, (2002).

[17] K. Krieger *et al.,* submitted to Phys. Rev. Lett., arXiv:1809.04478

[18] F. Batsch *et al.,* to be submitted to Phys. Rev. Lett.,

[19] M. Turner *et al.,* submitted to Phys. Rev. Lett., arXiv:1809.01191

[20] A. Caldwell *et al.,* Nucl. Instr. and Meth. Phys. A, vol. 829, 2016

[21] E. Adli *et al.,* "Acceleration of electrons in the plasma wakefield of a proton bunch", Nature, 2018

[22] G. Xia et al., Nucl. Instr. Meth. A ,vol. 740, 2014

[23] A.Caldwell and M. Wing," VHEeP: A very high energy electron-positron collider", Eur. Phys. J.C. 76, No.8, 2016

ISBN: 978-3-95450-194-6 ISSN: 2226-0366 doi:10.18429/JACoW-LINAC2018-TH1A05

JITTER STUDY FOR THE APS LINAC PHOTO-INJECTOR BEAM*

D. Hui[1, †], Y. Sun, M. Borland, J. Byrd
Advanced Photon Source, Argonne National Laboratory, Argonne, Chicago, USA
[1]also at Chinese Academy of Sciences, Beijing, China

Abstract

The APS Linac photo-injector can deliver high brightness electron beams to the Linac Extension Area (LEA) for beam experiments such as TESSA (Tapering Enhanced Stimulated Superradiant Amplification). Beam jitter in the device-under-test (DUT) area of the LEA can adversely affect the quality of data for such experiments. In this paper, a start-to-end simulation of jitter is studied. Sources of jitter include photo-cathode drive-laser arrival time, laser energy, and RF phases and voltages of the photo-cathode gun and accelerating cavities. It is found that at the DUT the relative mean energy jitter is the most significant concern, and that improvements in the Linac RF voltage stability can help to reduce it. RMS energy spread are more sensitive to the laser timing and charge jitter. The laser timing jitter itself can be compressed by the magnetic chicane by a factor of 5.6.

INTRODUCTION

The APS LEA, which is downstream of the APS injector Linac, is designed and being built at Argonne National Laboratory (ANL) to provide high brightness electron beams for advanced beam experiments such as Tapering Enhanced Stimulated Superradiant Amplification (TESSA) and dielectric wakefield accelerator [1-3]. The photo-injector, which is equipped with an upgraded LCLS style Photo-Cathode Gun (PCG), will deliver the high brightness electron beams through the injector Linac down to the LEA.

The high brightness beam in the LEA experiment chamber is dedicated to small aperture apparatuses. Beam jitters in the device-under-test (DUT) area of LEA result in the degradation of the beam quality (such as emittance and energy spread growth, bunch arrival time and bunch length jitters), which will adversely affect the quality of data for the experiments. Characterization of the beam jitter and knowledge about its possible origins are of great importance to compensate or reduce the jitters for future stability improvements of the system. In this paper, *Astra* [4] and *Elegant* [5] codes are combined to study the beam jitter and sensitivity to various jitter sources including photo-cathode drive-laser arrival time and energy (i.e. charge), gun and Linac RF phases and voltages. Beam parameters of particular interest are the relative mean energy, energy spread, bunch arrival time, bunch length etc. Firstly, the beam responses at the DUT to each jitter source are studied, and then the combined effects with jitter in all sources. Jitter correlations between all the studied jitter sources and key beam properties at the DUT are also studied.

APS LINAC AND LEA OVERVIEW

Figure 1 shows a schematic of the APS Linac down to LEA. There are two thermionic RF guns, RG1 and RG2, for usual injector operation (RG1 is a back-up). The PCG, with a maximum field gradient of 120 MV/m, is at the front end of the Linac. And a 3m S-band accelerating structure- “L1”, is equipped downstream of it, delivering the PCG beam to an energy of approximately 40-45 MeV. Then three accelerating sectors known as Linac Two, Linac Four, and Linac Five (“L2”, “L4” and “L5”) is followed. Each sector uses a single SLEDed klystron to drive four S-band accelerating structures, accelerating the beam to a total energy up to 375-500 MeV at the end of L5. A bunch compressor chicane (R56=-65) is set behind the L2 to realize the bunch length compression with a given energy chirp [6], so that provide higher bunch brightness beam into the LEA experiment area. Three fast switching dipole magnets are set downstream of the Linac structure to ensure the interleaving operation for RG beam and PCG beam. During the RG beam operation, the three fast switching dipole magnets are turned on to inject the beam into and extract out of the PAR, and then send into the Booster. These magnets are all turned off during the PCG beam operation, so that the PCG beam will bypass the PAR and Booster, then go straight to the LEA [7]. The RG beam for APS storage ring and the PCG beam for LEA will be operated simultaneously though the Linac in an interleaved fashion. The experiment area in the LEA tunnel is where the DUT will be installed. It is sufficient to accommodate DUTs with up to 2m length. To measure the effect of the DUT on the electron beam, a magnetic spectrometer and several diagnostic YAG screens (not shown here) are also installed downstream of the DUT.

START-TO-END JITTER STUDY

In order to understand the beam properties in the DUT under various jitter sources and provide a guidance for the jitter tolerances of the global Linac, an elaborate beam jitter study using tracking codes has been performed. The simulations apply repeated 6D particle tracking for 150 times with 10k macro-particles per tracked beam pulse while varying machine parameters such as photo-cathode drive-laser arrival time and energy, gun and Linac RF phases and voltages. Also, a beam file with no errors is used as an ideal reference case. The reference bunch is

*Work supported by by the U.S. Department of Energy, Office of Science, under Contract No. DE-AC02-06CH11357.
† dhui@anl.gov

Content from this work may be used under the terms of the CC BY 3.0 licence (© 2018). Any distribution of this work must maintain attribution to the author(s), title of the work, publisher, and DOI.

ISBN: 978-3-95450-194-6 ISSN: 2226-0366 doi:10.18429/JACoW-LINAC2018-TH1A05

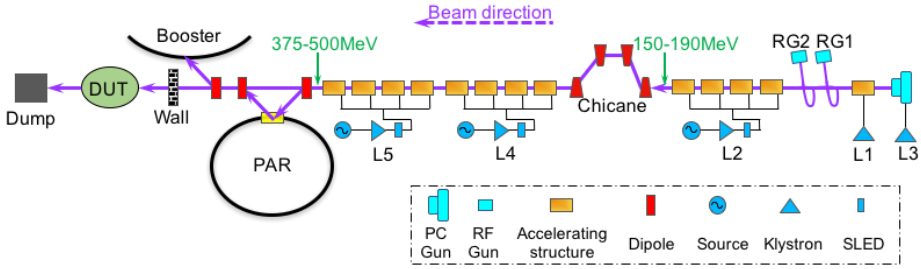


Figure 1: Schematic of the APS Linac down to LEA. Linac rf systems L2, L4, and L5 have a common source, klystron, and SLED configuration.

taken to establish the reference phases and momentum profile. The nominal beam parameters in the simulation are shown in Table 1. In the jitter simulation, *Astra* is employed to simulate the photoinjector (from photo-cathode to the end of L1) with the space charge and Schottky effect taken into consideration. And the *Elegant* is used for the remainder of the Linac and the LEA beamline. The output particle distributions in 6D phase space of 150 seeds from *Astra* are generated and converted into the *Elegant* input format. In the *Elegant* simulation, longitudinal and transverse wakefields of the accelerating structure, coherent synchrotron radiation (CSR) in the dipoles are included.

The jitters are generated using Gaussian distribution with a ±3σ cut-off. Its RMS levels have been considered according to the realistic situation, as shown in first two columns of Table 2. The RMS error of laser timing is assumed to be 0.9 ps, about 1 degree for the 2856 MHz RF of the photo-cathode. The RMS fluctuations in charge per bunch is 5%, corresponding to the laser energy jitter of 5%. All the RF cavities, i.e. the photo-cathode gun and accelerating structure, are taken to have jitter in phase of 0.5 degrees and jitter in peak voltage of 0.5%. The jitters of separate elements are assumed to not have any correlations between different sections. However, the laser timing error will lead to a phase offset not only for the PCG, but with all subsequent accelerator structures, which will have a strong correlation through the entire beamline. The charge fluctuation will also propagate through the beam line via the wakefields in the accelerator structures and the space charge effect when the beam is at low energy level.

Table 1: Nominal Beam Parameters in the Simulation

Parameter	Value	Unit
Bunch charge	0.3	nC
Bunch length	3	ps
Transverse spot size(rms)	0.15	mm
Initial kinetic energy	0.6	eV

Beam Jitter Response at the LEA DUT

The results of start-to-end jitter simulations with 151 random seeds (the reference beam file with nominal parameters is included) using Astra and Elegant are summarized in Table 2. Jitters of key beam parameters including relative mean energy, bunch arrival time, energy spread and bunch length at the LEA DUT are listed. The relative mean energy and bunch arrival time for which statistics shown are averaged over the 10k macro-particles. The energy spread and bunch length are given with RMS spread over the 10k macro-particles. For the jitters response, Table 2 lists mean values and RMS deviations over the 151 simulated pulses. Where meaningful, the RMS deviations are expressed as percentages of the corresponding mean values except for the relative energy and bunch arrival time, of which the mean values are 0 so that only the RMS deviations are shown.

All the beam jitter responses change linearly with each jitter source. From each column of Table 2, we can compare which source is more responsible for each beam jitter. The most significant jitter is highlighted in yellow, and the second significant in light gold. For the relative mean energy, we can see that jitters are dominated by the fluctuations in the laser timing and all the Linac RF voltages. For the bunch arrival time jitter, the accelerating structures right before chicane, i.e. the L2 phase and voltage jitters are more responsible. L2 phase jitter of 0.5 degree induces 0.364 ps arrival time jitter, and L2 voltage jitter of 0.5% corresponds to an arrival time jitter of 0.739 ps, which will adversely affect the experiment in the DUT. Note here that the error in laser timing is compressed by the magnetic chicane, so that a 0.9 ps initial timing jitter yields a timing jitter in the compressed bunch of only 160 fs. For the RMS energy spread and bunch length jitter, the laser timing contributes the most. But luckily, the RMS energy spread jitter is of the order of 10^{-4} level, and the bunch length jitter is less than 200 fs for the given input jitters. Beam sizes and centroids are all in micro-meter level, and their normalized jitters are mostly at the order of 10^{-3} to 10^{-5}. So, jitters in beam size and centroids are not a problem, which are not shown in Table 2.

Overall, seen in column-by-column, we can find that the most serious beam jitters for the experiments in the DUT are the mean energy and bunch arrival time jitter. Considering the effect on the overall beam parameters of each jitter source (observe values row-by-row), one can conclude that jitters in the laser timing, the phase and voltage of the accelerating structures right before chicane are the main contributors to the key beam jitters at the DUT. The beam fluctuations due to the gun, L1, and the accelerating structures after chicane (i.e. L4 and L5) are much smaller.

Content from this work may be used under the terms of the CC BY 3.0 licence (© 2018). Any distribution of this work must maintain attribution to the author(s), title of the work, publisher, and DOI.

ISBN: 978-3-95450-194-6 ISSN: 2226-0366 doi:10.18429/JACoW-LINAC2018-TH1A05

Table 2: Response of Key Beam Parameters at the LEA DUT to the Input Jitters

Quantity	RMS jitter level	Relative mean energy	Bunch arrival time	RMS energy spread		RMS bunch length	
		RMS	RMS/ps	mean	RMS/%	mean/ps	RMS/%
laser timing	0.9ps	1.42×10^{-3}	0.162	6.33×10^{-3}	8.24	1.12	17.76
charge	5.0%	1.61×10^{-4}	0.070	6.04×10^{-3}	3.85	1.20	5.08
gun phase	0.5 deg	2.25×10^{-5}	0.007	6.08×10^{-3}	0.15	1.21	0.18
gun voltage	0.5%	7.78×10^{-5}	0.054	6.08×10^{-3}	0.08	1.22	2.48
L1 phase	0.5 deg	1.10×10^{-5}	0.003	6.07×10^{-3}	1.02	1.21	2.40
L1 voltage	0.5%	4.08×10^{-4}	0.231	6.07×10^{-3}	0.62	1.21	0.39
L2 phase	0.5 deg	6.88×10^{-4}	0.364	6.10×10^{-3}	2.51	1.20	7.47
L2 voltage	0.5%	1.37×10^{-3}	0.739	6.06×10^{-3}	2.22	1.21	0.95
L4 phase	0.5 deg	1.83×10^{-5}	0.000	6.07×10^{-3}	0.56	1.21	0.00
L4 voltage	0.5%	1.45×10^{-3}	0.001	6.07×10^{-3}	0.00	1.21	0.04
L5 phase	0.5 deg	1.83×10^{-5}	0.000	6.07×10^{-3}	0.56	1.21	0.00
L5 voltage	0.5%	1.45×10^{-3}	0.000	6.07×10^{-3}	0.00	1.21	0.04
All	**---**	**3.07×10^{-3}**	**0.986**	**6.39×10^{-3}**	**11.17**	**1.12**	**20.93**

Beam Jitter Development along the Beamline

In order to see the beam jitter development along the whole beamline with various input jitters, the RMS deviations of some key beam parameters over the 151 simulated pulses are calculated at different positions of the beamline. According to Table 2, only those dominant jitter sources (highlighted in yellow or light gold) are taken into account here. Figure 2 shows the jitter evolution of relative mean energy, RMS energy spread, bunch arrival time and RMS bunch length for different dominant jitter sources. Note here that we only show the jitter evolution in the *Elegant*, which means it starts from the L1-output. The compressor chicane is located from s=19.4m to s=22.4m; the L4 starts at about s=26.28mm and ends at s=39.998mm; the L5 is from s=40.56mm to s=54.28mm, shown as asparagus green bars at the bottom of Fig. 2 (a)-(d).

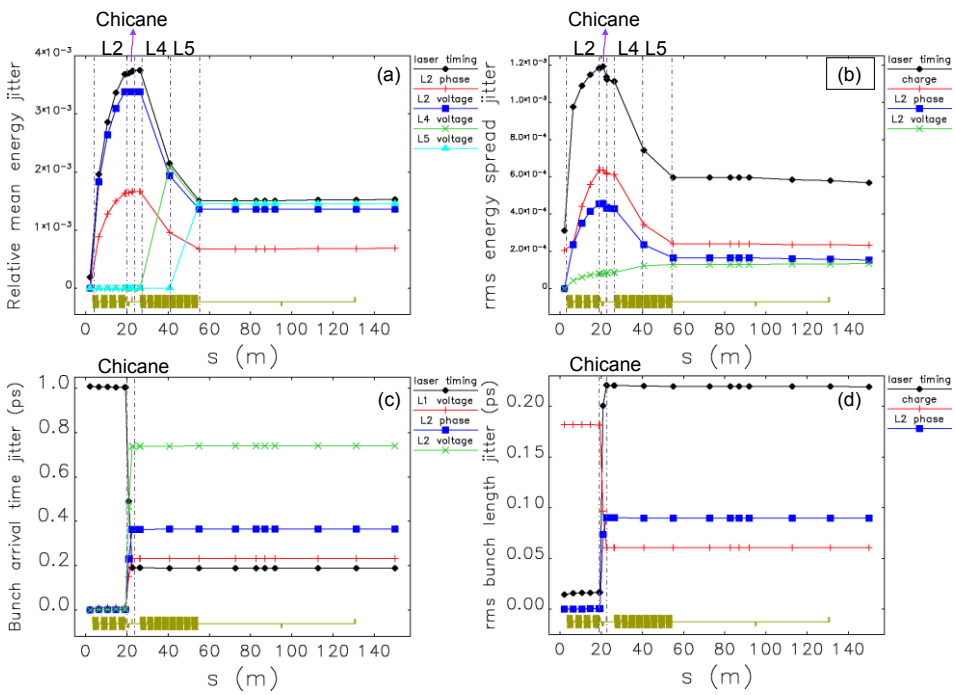


Figure 2: Beam jitter evolution for different dominant jitter sources. (a). the relative mean energy jitter evolution; (b) the RMS energy spread jitter evolution; (c) the bunch arrival time jitter; (d) the RMS bunch length jitter evolution.

Content from this work may be used under the terms of the CC BY 3.0 licence (© 2018). Any distribution of this work must maintain attribution to the author(s), title of the work, publisher, and DOI.

ISBN: 978-3-95450-194-6 ISSN: 2226-0366 doi:10.18429/JACoW-LINAC2018-TH1A05

Content from this work may be used under the terms of the CC BY 3.0 licence (© 2018). Any distribution of this work must maintain attribution to the author(s), title of the work, publisher, and DOI.

According to Fig. 2 (a) we can see the relative mean energy ($_{\Delta}E/E_0$) jitters that induced by laser timing, L2 phase and voltage errors grow gradually until to the L4, after which the jitter decrease. This is because the mean energy(E_0) is being increased by L4 and L5. Figure 2 (b) shows that the RMS energy spread jitters due to laser timing, charge and L2 phase jitters also increase until to the L4, then goes down because of the gradually increased mean energy. The jitter caused by L2 voltage is much smaller, and only has a slight increase before L4. Figure 2 (c) shows the bunch arrival time jitter evolution for several dominant jitter sources. It is worth noting that the arrival time jitter due to the laser timing jitter is compressed by the chicane and the compression factor is about 5.6. Actually, it is demonstrated that it is possible to fully compress the arrival time jitter of the laser timing by properly adjusting the R_{56} of the chicane and keeping a moderate compression of the electron bunch [8]. On the other hand, the phase and voltage jitter of L2, the accelerator structure right before chicane, will be fully converted into the timing jitter downstream as shown in Fig. 2 (c). Figure 2 (d) displays the bunch length jitter evolution for different jitter sources. The bunch length compression of the chicane is realized by introducing an energy chirp via phasing the beam ahead of the crest in L2, thus the compress factor is sensitive to the L2 phase variations. The injector laser timing jitter is also acting like the jitter of L2 phase. Therefore, the L2 phase and laser timing jitter are the dominant jitter sources for the bunch length jitter. Figure 2 (d) shows that the bunch length jitter due to the laser timing and L2 phase suddenly increases in the chicane, but that due to the charge fluctuation drops from 0.18 ps to about 0.06 ps after the chicane. Overall, the chicane is a turning point for most of the beam jitters.

Jitter Correlations at the LEA DUT

Correlation analysis can explain the causes of the beam jitters and help us to focus efforts to optimize the design. From Table 2 in section 3.1, we roughly know that the most dominant jitter sources to the key beam parameters are laser timing, L2 phase and voltage jitters. To obtain a further insight of the correlation between the jitter sources and beam properties, we calculate the corresponding Pearson correlation coefficient C_{xy}:

$$C_{xy} = \frac{cov(x,y)}{\sigma_x \sigma_y}$$

where x and y represent a jitter source and a beam parameter jitter respectively, $cov(x,y)$ is the covariance of the two variables and σ_x, σ_y are the standard deviations of the two variables. "Responsibility" can be defined as the correlation coefficient squared ${C_{xy}}^2$, which gives the proportion of the source error in the beam jitter.

Figure 3 shows the responsibility of all the studied jitter sources for the key beam parameters including relative mean energy, RMS energy spread, bunch arrival time and RMS bunch length. It is shown clearly that the laser timing error is strongly correlated with both the bunch length and RMS energy spread. L2 phase and voltage jitters take more responsibility for the bunch arrival time and relative mean energy jitter, in which the L2 voltage jitter even has a responsibility of more than 60% for the bunch arrival time jitter. Besides, L5 voltage jitter is also a main cause of the relative mean energy jitter. The laser timing, L2 phase and voltage jitters are the most serious sources to the beam jitters at the DUT as concluded in the above sections. Figure 4 displays the scatter plot of the beam properties and the corresponding jitter sources showing strong correlations of the 151 random seeds. The a, b, c, d correspond to the circled point in Fig. 3 respectively.

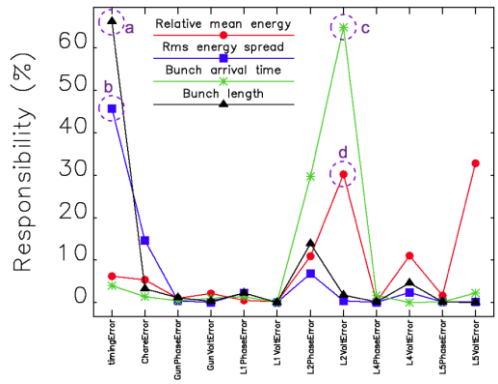


Figure 3: Responsibility of the jitter sources for the key beam parameters jitters.

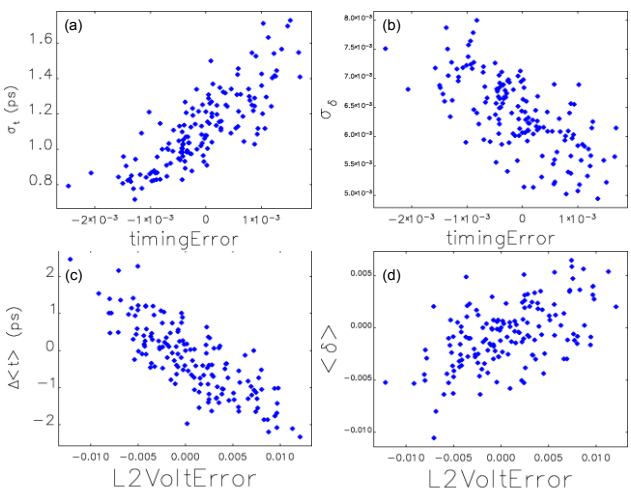


Figure 4: Scatter plots of the beam properties and the jitter sources for the 151 random seeds; (a). jitter correlation between laser timing error and bunch length; (b). jitter correlation between laser timing error and RMS energy spread; (c). jitter correlation between L2 voltage error and bunch arrival time; (d). jitter correlation between L2 voltage error and relative mean energy.

CONCLUSION

In this paper, a start-to-end jitter simulation for the APS Linac is studied on the combined use of *Astra* and *Elegant* codes taking the space charge, Schottky effect, CSR and wakefields into consideration. Beam responses at the

ISBN: 978-3-95450-194-6 ISSN: 2226-0366 doi:10.18429/JACoW-LINAC2018-TH1A05

DUT to the jitter sources, beam jitter development along the beamline and jitter correlations at the DUT are investigated in detail. Jitter analysis reveals that the main origins of the beam jitter are the laser timing and Linac voltage jitter. In particular, requirements on laser timing, and the phase and voltage stability of the accelerator structure right before chicane are very stringent. It is worth pointing out that the arrival time jitter due to the laser timing jitter can be compressed by the the magnetic chicane by a factor of 5.6. On the other hand, the most serious beam jitters for the experiments in the DUT are the mean energy jitter which is mainly caused by voltage jitter of the accelerator structures, and bunch arrival time jitter which is mostly caused by phase and voltage jitter of the accelerator structure right after the chicane. In the future work, the effect of beam jitters on the FEL performance will be evaluated.

ACKNOWLEDGEMENTS

The authors would like to thank A. Zholents for providing helpful information and the many useful discussions. This research was supported by the U.S. Department of Energy, Office of Science, under Contract No. DE-AC02-06CH11357. The authors gratefully acknowledge financial support from University of Chinese Academy of Sciences (UCAS) for studying abroad.

REFERENCES

[1] Y. Park *et al.*, in *Proc. 38th Int. Free Electron Laser Conf. (FEL'17)*, Santa Fe, NM, USA, Aug. 2017, pp.49-52, doi:10.18429/JACoW-FEL2017-MOP011

[2] J. Duris, A. Murokh, and P. Musumeci, "Tapering enhanced stimulated superradiant amplification", *New. J. Phys*., vol. 17, no. 6, p. 063036, 2015, doi:10.1088/1367-2630/17/6/063036

[3] A. Zholents *et al.*, "A preliminary design of the collinear dielectric wakefield accelerator", *Nucl. Instrum. Methods Phys. Res. A*, vol. 829, p. 190, 2016, doi:10.1016/j.nima.2016.02.003

[4] *ASTRA Manual*, K. Floettmann, Mar. 2017, pp. 56-64, http://www.desy.de/~mpyflo/Astra_manual/Astra-Manual_V3.2.pdf

[5] Elegant*: A flexible SDDS-compliant code for accelerator simulation*, M. Borland, 2000, https://www.aps.anl.gov/files/APS-sync/lsn-otes/files/APS_14182K18.pdf

[6] M. Borland, "Design and performance simulations of the bunch compressor for the Advanced Photon Source Low-Energy Undulator Test Line free-electron laser", *Phys. Rev. ST Accel. Beams*, vol. 4, no. 7, p. 074201, 2001, doi:10.1103/PhysRevSTAB.4.074201

[7] S. Shin, Y. Sun, and A. Zholents, "Interleaving lattice for the Argonne Advanced Photon Source linac", *Phys. Rev. Accel. Beams*, vol. 21, no. 6, p. 060101, 2016, doi:10.1103/PhysRevAccelBeams.21.060101

[8] B. Marchetti, R. Assmann, U. Dorda, J. Zhu, "Conceptual and Technical Design Aspects of Accelerators for External Injection in LWFA", *Applied Sciences*, vol. 8, no. 5, p. 757, 2018, doi:10.3390/app8050757

Content from this work may be used under the terms of the CC BY 3.0 licence (© 2018). Any distribution of this work must maintain attribution to the author(s), title of the work, publisher, and DOI.

ISBN: 978-3-95450-194-6 ISSN: 2226-0366 doi:10.18429/JACoW-LINAC2018-TH2A01

NITROGEN INFUSION R&D FOR CW OPERATION AT DESY

M. Wenskat[1*], C. Bate[1,2], T. F. Keller[1], A. Dangwal Pandey[1], B. Foster[1,2,3], D. Reschke[1], J. Schaffran[1], G. Dalla Lana Semione[1,2], S. Sievers[1], A. Stierle[1,2], N. Walker[1], H. Weise[1]
[1] Deutsches Elektronen-Synchrotron, 22607 Hamburg, Germany
[2] University of Hamburg, 20148 Hamburg, Germany
[3] Physics Dept., University of Oxford, Oxford, UK

Abstract

The European XFEL cw upgrade requires cavities with reduced surface resistance (high Q-values) for high duty cycle while maintaining high accelerating gradient for short-pulse operation. To improve on European XFEL performance, a recently discovered treatment is investigated: the so-called *nitrogen infusion*. The recent test results of the cavity-based R&D and the progress of the relevant infrastructure is presented. The aim of this approach is to establish a stable, reproducible recipe and to identify all key parameters for the process. Advanced surface analysis is carried out on cut-outs of cavities and samples treated together with cavities. Techniques used include SEM/EDX, TEM, XPS, XRR, GIXRD and TOF-SIMS. The aim of this approach is to establish a stable, reproducible recipe, to identify key parameters in the process and to understand the underlying processes of the material evolution, that result in the improved performance observed.

THE EUROPEAN XFEL

The successful construction of the 17.5 GeV European X-ray Free Electron Laser (XFEL) [1] represents the culmination of over 20 years of superconducting radio-frequency (SRF) R&D. The core high-gradient 1.3 GHz nine-cell niobium cavity and cryomodule technology was originally developed by an international collaboration coordinated by DESY for the TESLA (TeV-Energy Superconducting Linear Accelerator) project — a 500 GeV center-of-mass electron-positron linear collider and integrated X-ray FEL, proposed in 2003 [2].

A total of 102 cryomodules containing 816 cavities have been produced, of which 97 have been installed in the SRF linacs of the European XFEL, which represents by far the largest deployment of TESLA technology to date [3,4]. The cavities achieved an average usable accelerating field of 29.7 ± 5.1 MV/m and an average quality factor Q_0 of 1.2×10^{10} at the design field of 23.6 MV/m in the vertical acceptance test. The design energy of 17.5 GeV of the superconducting linac was met beginning of August 2018.

The design beam pattern for the user operation of the European XFEL has a duty factor of 1.4% with 2.7k bunches per second accelerated up to the maximum energy. As a future upgrade, more flexible beam patterns are planned, allowing 50k bunches per second and a duty factor of 10-50% up to 10 GeV or a continuous wave (cw) mode with 100k bunches per second up to 8 GeV are planned. In order to achieve these duty factors, higher quality factors of the cavities at medium gradients are necessary.

The current plan for the upgrade is to exchange the first 17 cryomodules (136 cavities) in the tunnel (injector plus section L1 and L2) and possibly lengthen L3 using the cryomodules removed which is otherwise kept unchanged, see Fig. 1. An installation of a SRF gun capable of cw operation, and one Klystrode (IOT) for each rf station of 4 modules is further necessary. This will allow the operation of the European XFEL with short pulses at high energies or with high duty cycles at moderate or low energies [5]. Two R&D topics have been identified to increase the Q_0 of the cavities: *large-grain* (lg) material and *nitrogen infusion* [6,7].

Large-grain niobium material has been studied during the European XFEL preparation phase and is characterized by an average grain size on the order of centimeters, which is several orders of magnitude larger than the standard grain size of $\approx$ 50 μm of the material (fine-grain or fg) for the European XFEL cavity production. Eleven nine-cell and several three- and single-cell cavities have been fabricated and showed on average a 25% higher quality-factor Q_0 compared to fine-grain material with the same surface treatment. Furthermore, a pre-series cryomodule called XM-3, consisting of seven lg and one fg cavities, shows excellent results in cw operation [8]. Recent module tests showed stable operation at 17 MV/m with a Q_0 of 2.3×10^{10} at 2K and long pulse operation with duty factors from 22 - 43% up to 22 MV/m.

The emphasis of this paper will be on the investigation and application of a process called *nitrogen infusion*, which was first presented by Fermilab [7]. Several laboratories including DESY are working on the understanding of the process and its influence on the cavity surface and the relation of the changed surface to the rf performance [9–11]. The current status and plans of DESY's efforts are presented here.

INFUSION R&D AT DESY

The R&D program at DESY has three approaches:

- treating cavities in a large furnace, together with samples as quality control, to reproduce the performance improvements
- treating samples in a UHV mobile chamber with in-situ surface characterization to observe and understand the surface evolution

* marc.wenskat@desy.de

Content from this work may be used under the terms of the CC BY 3.0 licence (© 2018). Any distribution of this work must maintain attribution to the author(s), title of the work, publisher, and DOI.

ISBN: 978-3-95450-194-6 ISSN: 2226-0366 doi:10.18429/JACoW-LINAC2018-TH2A01

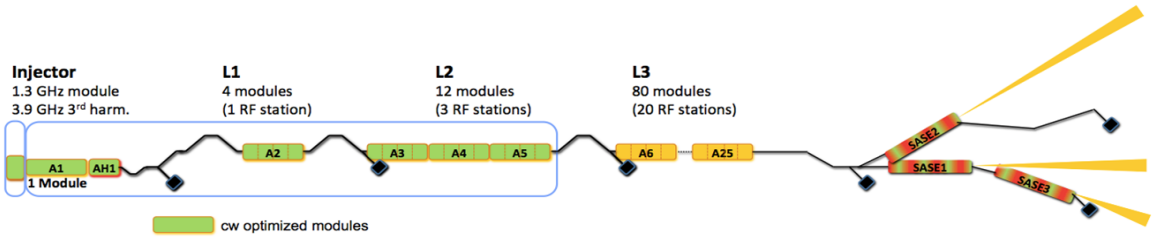


Figure 1: The first 17 modules (136 cavities) of the European XFEL need to be replaced to achieve the desired flexibility for the user operation. An SRF gun based cw injector and one IOT for each rf station is necessary. L3 remains unchanged.

- treating samples in a small furnace to scan the parameter space and optimize the infusion recipe

In addition, a collaboration with other laboratories regarding the exchange of experience, data, cavities and samples has been established or is in the process of being established.

Infusion Recipe

The actual infusion recipe includes a heat treatment of 800°C for 3 hours in a pressure below $5 \cdot 10^{-6}$ mbar. It is widely regarded to be necessary to partially break up the natural surface oxides and create a reactive Nb surface. While still in vacuum, the cavity is cooled down to 120°C and kept there for 48 hours. Nitrogen is injected at a partial pressure of 0.03 mbar which is actively maintained. During this phase, it is assumed that nitrogen enters the material as an interstitial. After 48h, the furnace is evacuated and the cavity is cooled down to room temperature. An additional point is the installation of so-called *caps* onto a cavity before the treatment, see Fig. 2. Initially, they were installed to prevent a Ti contamination in the FNAL furnace from entering the cavity. How these caps affect the inner atmosphere during this procedure, act as a filter or getter material or if they are necessary at all has not yet been clarified.

Cavity and Sample Preparation

Cavities underwent a standard reference test at 2K before any further preparation was done. If a cavity showed a good performance, e.g. similar to the blue data points in Fig. 3, it was prepared for the infusion procedure. This preparation includes the disassembly of all antenna and vacuum components, a high-pressure rinsing of the inner surface to remove any particle contamination from the disassembly, and the installation of the Nb caps onto the flanges. The Nb caps underwent a chemical polishing of ≈ 10 µm before use. Afterwards, the cavity was sealed in a clean-room foil bag and transported to the furnace. The bag was opened under local clean-room conditions and the cavity installed into the furnace.

The samples used are made of standard European XFEL material. Sheets from three different vendors which were still available after the cavity production were cut in a series of standardized sample shapes. The samples underwent the standard European XFEL cavity preparation, including electrochemical surface removal of ≈ 120 – 140 µm, a first outgassing bake at 800°C for 3 h, a second chemical polishing of ≈ 30 µm and another bake of 120°C for 48h. This recipe has been developed over years, see e.g. [12] for details. The samples are placed within an Nb box made from cavity-grade material to simulate the interior of the cavity.

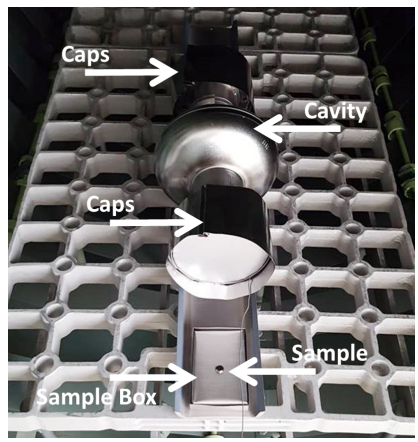


Figure 2: 1DE27 installed in the furnace and the temperature sensor is attached to it. Samples are placed inside a Nb box to simulate the interior of a cavity. One sample for comparison is placed outside the box. The caps cover the flanges of the cavity.

Cavity Furnace

The furnace in use has a volume of 7 m^3, of which an effective volume of $1800 \times 625 \times 660\ mm^3$ has a homogenous temperature during baking, and was produced by the company Ipsen. The maximum achievable, stable temperature is $T_{max} = 1100$°C and the furnace has a temperature stability of ±2°C. The door of the furnace is double sealed by EPDM O-rings with a vacuum in between. Other accessories such as pumps, gauges etc. are sealed by standard EPDM seals. The pre-pumps are rotary vane pumps and a roots pump. The main pumps are two Varian turbo-molecular pumps (TMP) with a pumping speed of 6000 l/s each. The pressure during the baking is monitored with an ionization gauge IKR050 by Pfeiffer Vacuum which is sensitive between $2 \cdot 10^{-9}$ mbar and $5 \cdot 10^{-3}$ mbar. Residual Gas Analysis (RGA) are taken during the 800°C bake and before and after the nitrogen injection at 120°C. Prior to each infusion run, a bake out at $T_{max} = 1100$°C for 3 h is done. The installation in the fur-

Content from this work may be used under the terms of the CC BY 3.0 licence (© 2018). Any distribution of this work must maintain attribution to the author(s), title of the work, publisher, and DOI.

ISBN: 978-3-95450-194-6 ISSN: 2226-0366 doi:10.18429/JACoW-LINAC2018-TH2A01

Content from this work may be used under the terms of the CC BY 3.0 licence (© 2018). Any distribution of this work must maintain attribution to the author(s), title of the work, publisher, and DOI.

nace of a single-cell cavity with niobium caps, the niobium samples in a Nb box can be seen in Fig 2.

RESULTS

Cavity Tests

A total of six cavities have been treated within the R&D program so far. The first cavity, a single-cell cavity, 1DE18 was treated but the rf performance deteriorated after the treatment. During the infusion run, the nitrogen pressure was one to three order of magnitudes lower than the FNAL recipe specified. The reason was that the mass flow was controlled at the nitrogen injection line while the TMP was fully operational, reducing the effective nitrogen pressure in the furnace. As a check of the furnace and to see if a failed nitrogen injection or a pollution of the nitrogen was the cause of the deterioration, a second single-cell cavity 1DE17 was treated similar to 1D18 but without an injection of nitrogen. The cavity deteriorated in the same way. A third cavity, 1DE16 was tested and showed the same characteristics. The key bake parameters and the rf test results before and after the treatment are given in Table 1 and Fig. 3.

Table 1: RF Results and Key Bake Parameters of the First Three Cavities

	1DE18	1DE17	1DE16
Material	Ningxia fine grain	Ningxia fine grain	Plansee fine grain
Reference @ 2K			
$E_{acc,max}[\frac{MV}{m}]$	37.7 - BD	31.2 - BD	32.2 - BD
$Q_0(4\,MV/m)[\times 10^{10}]$	2.8	2.5	2.7
Baking Parameters			
p @ 800°C [mbar]	2×10^{-5}	1.1×10^{-5}	5.5×10^{-6}
P_{N_2} @ 120°C[mbar]	$7-300\times10^{-5}$	w/o	w/o
RF Test @ 2K			
$E_{acc,max}[\frac{MV}{m}]$	20.2 no FE	19.5 no FE	26.3 - BD no FE
$Q_0(4\,MV/m)[\times 10^{10}]$	0.5	1.2	3.2

A detailed analysis of the RGAs obtained during these runs showed rather large contributions from hydrocarbons. Samples from all runs showed C-enriched precipitates on the surface - see e.g. the SEM image in Fig. 4.

Improvements to the pumping systems were carried out with the aim of reducing uncertainties and possible back-flow from the pre-pumps. A subsequent test run of a single-cell cavity, 1DE9, was then carried out. The base pressure at 800°C was 5×10^{-6} mbar. The performance deteriorated again, but showed a different behavior, see Fig. 5.

This behavior was observed before at KEK in their failed infusion runs [11]. A comparison of samples from KEK runs is currently being made, to look for common features. An analysis of all available furnace parameters after the last

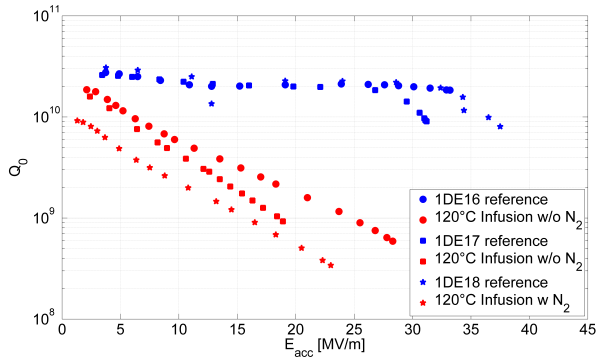


Figure 3: Quality factor versus accelerating field of three cavities. Reference measurements are blue, measurements after the treatments are red data points. 1DE18 (stars), 1DE17 (squares) and 1DE16 (circles) showed the same deterioration, regardless of the injection of nitrogen into the furnace.

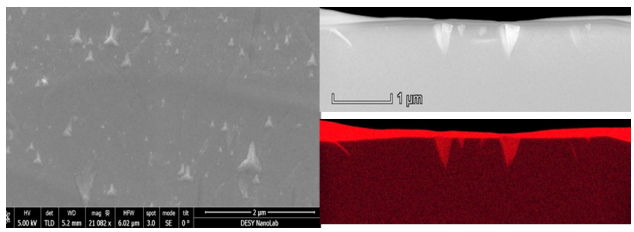


Figure 4: SEM(left) of a sample surface and a bright field TEM and TEM-EDX (top- and bottom-right) of a lamella from the same sample. Star-shaped carbon-enriched precipitates protruding from the surface are observed.

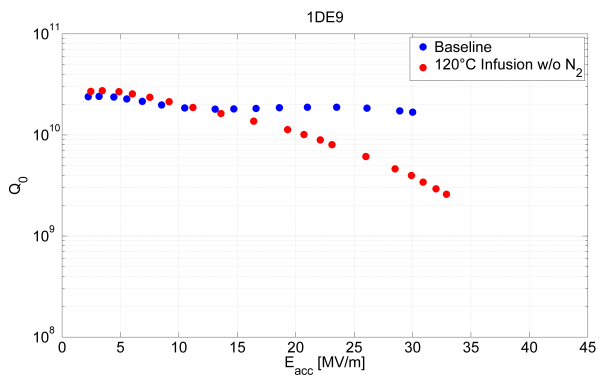


Figure 5: Quality factor versus accelerating field of 1DE9 before (blue) and after the treatment (red).

run showed a saturation in the improvements and that we achieved the best situation with given hardware. The decision for new runs with nitrogen was made. Two cavities, 1DE10 and 1DE27, were infused in two separate runs using a modified infusion recipe: In order to achieve the lowest possible pressure at 800°C and to further reduce high-mass contributions observed in the RGA, a bake at 300°C for 74 h was done in UHV before ramping up the cavity to 800°C. The rationale was to produce a further outgassing of all ma-

ISBN: 978-3-95450-194-6 ISSN: 2226-0366 doi:10.18429/JACoW-LINAC2018-TH2A01

terials without the creation of precipitates. The performance of the cavities is shown in Figs. 6 and 7.

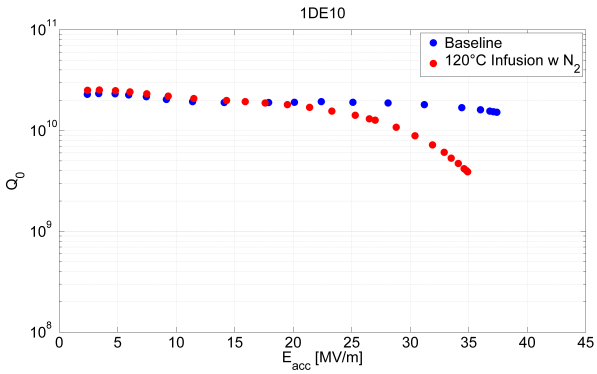


Figure 6: Quality factor versus accelerating field of 1DE10 before (blue) and after the treatment (red).

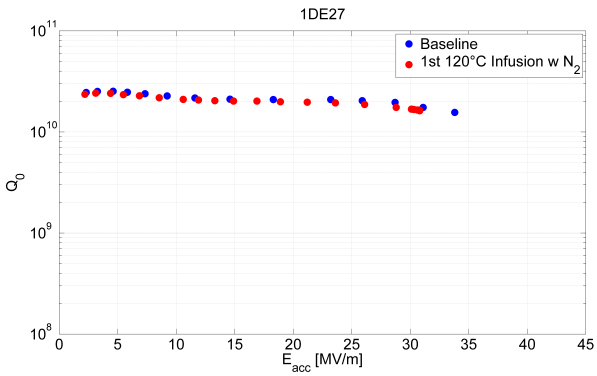


Figure 7: Quality factor versus accelerating field of 1DE27 before (blue) and after the treatment (red).

The rf performance of 1DE10 showed only a deterioration at high fields, but remained unchanged otherwise below 20 MV/m. Possible field emission - due to particle contamination during the assembly - might be the cause of this behavior. The performance of 1DE27 after the treatment is identical to the reference measurement before the treatment. During the cavity-infusion runs, the samples were baked inside the niobium box in an attempt to mimic the interior of the cavity. All samples to date have shown carbon-rich star-shaped precipitates. For the 1DE10 and 1DE27 runs, additional samples were placed on top of the box and were directly exposed to the oven atmosphere. Figure 8 shows the concentration profile obtained by TOF-SIMS of two samples which underwent the same preparation; one was baked inside the box and one was not infused.

Surprisingly, no NbN^- signal is observed, which is usually the key indicator for a successful infusion of nitrogen into niobium. The hydrogen concentration and the thickness of the oxide layer were reduced, which is expected. A strong increase of the carbon signal is in agreement with the precipitates observed with SEM and HR-TEM. Figure 9 shows a further comparison of two samples, identical except that one was placed inside the Nb box, while the other was placed on

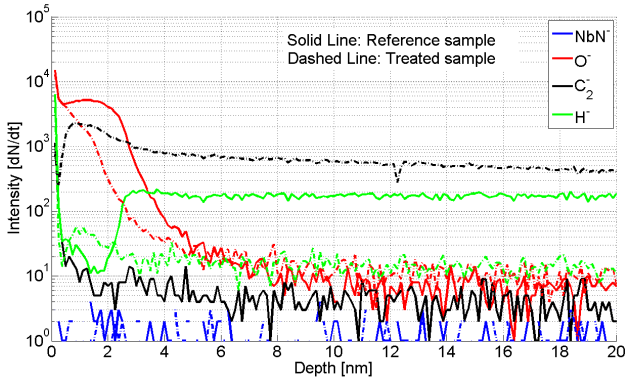


Figure 8: TOF-SIMS data of two samples, counts per second vs. depth are shown. Samples are from the same Nb sheet and were treated identically, except one was infused together with 1DE10. The solid lines are the values for the reference sample, the dashed for the treated sample.

top of it. The sample on top showed no precipitates in the SEM while they were observed on the interior sample.

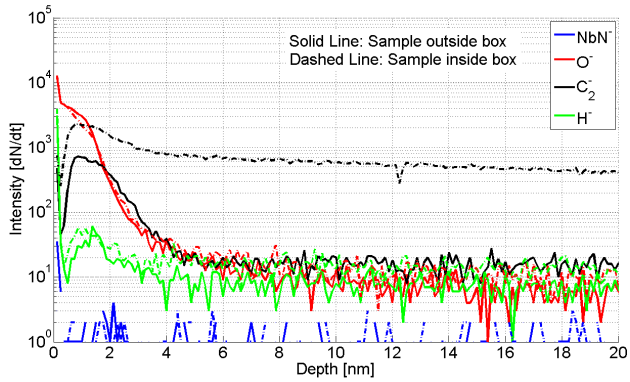


Figure 9: TOF-SIMS data of two samples, counts per second vs. depth are shown. Samples are from the same Nb sheet and were treated identically, and both were infused together with 1DE27. The solid lines are the values for the sample placed outside the box, the dashed lines for the sample placed inside.

Again, no NbN^- signal is observed in either sample. The oxide layer and the hydrogen concentration are identical except that the sample baked inside the Nb box shows a higher C concentration. This suggests that the conditions within the Nb box strongly influence the formation of the precipitates.

Cavity Cut-outs

In order to test the assumption that the samples inside the box mimic the cavity surface, 1DE16 was cut. A thorough investigation was performed to obtain spatial information on rf induced losses and other regions of interests. Eight samples were cut and underwent a dedicated surface characterization program. The first step was an SEM investigation

Content from this work may be used under the terms of the CC BY 3.0 licence (© 2018). Any distribution of this work must maintain attribution to the author(s), title of the work, publisher, and DOI.

ISBN: 978-3-95450-194-6 ISSN: 2226-0366 doi:10.18429/JACoW-LINAC2018-TH2A01

Content from this work may be used under the terms of the CC BY 3.0 licence (© 2018). Any distribution of this work must maintain attribution to the author(s), title of the work, publisher, and DOI.

to check whether the same star-shaped precipitates are observed; the result is shown in Fig. 10. The same kind of

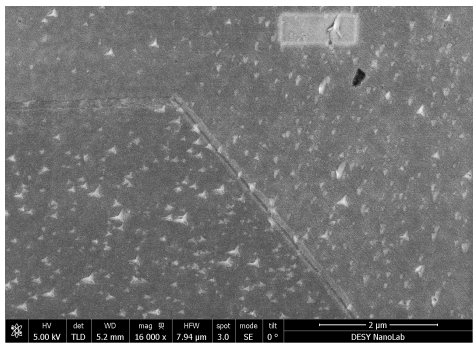


Figure 10: SEM image of a cut out from 1DE16. The same star shaped precipitates are observed as on the sample inside the Nb box.

precipitates are observed, suggesting that the Nb box as well as the caps on the cavity affect the atmosphere the Nb surface is exposed to in comparison to the open furnace volume. It gives some support to the assumption that samples do mimic the inner cavity surface. Further investigation of the cut-outs is ongoing.

In-situ Experiments

Experiments performed at DESY Nanolab [13] showed interesting results [14, 15]. Two single Nb crystals, one heated up to 2000°C for purification, the other from standard large-grain cavity grade Nb, were otherwise treated identically with 800°C for 2 hrs in UHV and then 120°C in 0.03 mbar partial pressure of nitrogen for 48 hrs during the experimental runs in the chamber. Both were investigated with SEM, but the cavity-grade material showed star-shaped precipitates similar to the samples from the cavity furnace, see Fig. 11. In addition, XPS measurements confirm the for-

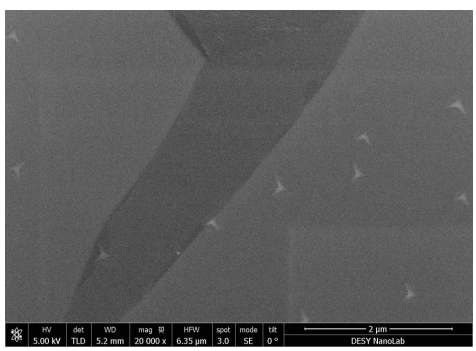


Figure 11: SEM image of a cavity-grade single-crystal sample after baking in an ultra-clean chamber. Similar star-shaped precipitates as on the cavity furnace samples can be seen. No precipitates were observed on the purified sample.

mation of a Nb-C phase present on the surface. This results directly suggest that the sample purity does play a role.

CONCLUSION

The goal of DESY infusion R&D is both reproducing the increased quality factor and high gradients demonstrated elsewhere [7, 9], and also to understand the surface evolution during this process and how this relates to the cavity performance. The three approaches - cavity treatments, in-situ sample investigation, recipe optimization - complement each other but are still in different stages of maturity. First results have suggest that the atmosphere within the cavity during the treatment is somewhat different than the open furnace atmosphere and hence hard to control or monitor. The lack of nitrogen in the TOF-SIMS measurements in all treated samples is not completely understood, but several hypothesis will be tested. A set of caps will be fabricated, to control the pressure within the cavity more accurately and make allow them to be fitted in a more reproducible way. Cavity cut-outs are under investigation to identify the origin of the deterioration of the first three cavities compared to the latter cavities, since the key parameters between all runs were too similar to cause such a difference in the performance. Clearly, not all relevant recipe parameters are yet identified.

ACKNOWLEDGEMENTS

The authors would like to thank all members of the DESY MSL group, J. Koeszegi (HZB), D. Liebertz, A. Ermakov, V. Vonk, S. Kulkarni, A. Jeromin (DESY) and A. Prudnikava for their work. A special thanks to *Research Instruments* for the cap treatment, the BEEM group from the TU Hamburg-Harburg and we acknowledge the use of the FIB dual beam instrument granted by BMBF (5K13WC3, PT-DESY). This work is partially funded from the BMBF project 05H12GU9, and from the Alexander von Humboldt Foundation.

REFERENCES

[1] M. Altarelli *et al.*, DESY, Hamburg, Germany, DESY Report No. 2006-097, 2006

[2] *TESLA The Superconducting Electron Positron Linear Collider with an Integrated X-Ray Laser Laboratory Technical Design Report, Part I Executive Summary*, F. Richard, J. R. Schneider, D. Trines, and A. Wagner, Eds., Hamburg, Germany: DESY, Mar. 2001, arXiv:hep-ph/0106314

[3] W. Singer *et al.*, "Production of superconducting 1.3-GHz cavities for the European X-ray Free Electron Laser", *Phys. Rev. ST Accel. Beams*, vol. 19, p. 092001, 2016.

[4] D. Reschke *et al.*, "Performance in the vertical test of the 832 nine-cell 1.3 GHz cavities for the European X-ray Free Electron Laser", *Phys. Rev. ST Accel. Beams*, vol. 20, p.,042004, 2017.

[5] R. Brinkmann *et al.*, "Prospects for CW and LP operation of the European XFEL in hard X-ray regime", *Nuclear Instruments and Methods in Physics Research Section A: Accelerators, Spectrometers, Detectors and Associated Equipment*, vol. 768, pp. 20–25, 2014.

ISBN: 978-3-95450-194-6 ISSN: 2226-0366 doi:10.18429/JACoW-LINAC2018-TH2A01

[6] W. Singer *et al.*, "Development of large grain cavities", *Phys. Rev. ST Accel. Beams*, vol. 16, p. 12003, 2013.

[7] A. Grassellino *et al.*, 11Unprecedented quality factors at accelerating gradients up to 45 MV/m in niobium superconducting resonators via low temperature nitrogen infusion", *Sup. Sci. Technology*, vol. 30, p. 094004, 2017.

[8] J. Branlard *et al.*, "Highlights of the XM-3 cryomodule tests at DESY", presented at the 29th Linear Accelerator Conf. (LINAC'18), Shanghai, China, Sep. 2018, paper TUPO029, this conference.

[9] P. Dhakal *et al.*, "Effect of low temperature baking in nitrogen on the performance of a niobium superconducting radio frequency cavity", *Phys. Rev. St. Accel. Beams*, vol. 21, p. 032001, 2018.

[10] P. Koufalis *et al.*, "Effects of interstitial oxygen and carbon on niobium superconducting cavities", Jan. 2017, arXiv:1612.08291

[11] K. Umemori *et al.*, "Trial of Nitrogen Infusion and Nitrogen Doping by using J-Parc Furnace", in *Proc. 18th Int. Conf. on RF Superconductivity (SRF'17)*, Lanzhou, China, Jul. 2017, pp. 775–778, http://dx.doi.org/10.18429/JACoW-SRF2017-THPB021

[12] S. Aderhold *et al.*, "Cavity Process", ILC-HiGrade Report-2010-05, 2010

[13] A. Stierle *et al.*, "DESY NanoLab", *J Large-Scale Res Facil JLSRF*, vol. 2, p. A76, 2016. http://dx.doi.org/10.17815/jlsrf-2-140

[14] G. D. L. Semione *et al.*, "Infusion Samples @ DESY Nanolab", presented at the TESLA Technology Collaboration ((TTC) Meeting, INFN, Milan, Italy, 6–9 Feb. 2018.

[15] A. Dangwal-Pandey *et al.*, "Surface study of nitrogen-infused Nb samples", presented at the TESLA Technology Collaboration (TTC) Meeting, RIKEN Nishina Center, Wako, Japan, 26–29 Jun. 2018.

Content from this work may be used under the terms of the CC BY 3.0 licence (© 2018). Any distribution of this work must maintain attribution to the author(s), title of the work, publisher, and DOI.

ISBN: 978-3-95450-194-6 ISSN: 2226-0366 doi:10.18429/JACoW-LINAC2018-TH1P01

LINAC4 COMMISSIONING

A.M. Lombardi for the Linac4 Team, CERN, Geneva, Switzerland

Abstract

This paper reviews the design, construction, and commissioning effort of CERN's new proton linear accelerator, Linac4, which has recently been commissioned and which is presently undergoing a reliability run. Linac4 will be connected to the LHC proton injector chain during the next long LHC shutdown (LS2) and will then replace the ageing Linac2.

MOTIVATION AND BEAM QUALITY REQUIREMENTS

In its June 2007 session the CERN Council approved the White Paper "Scientific Activities and Budget Estimates for 2007 and Provisional Projections for the Years 2008-2010 and Perspectives for Long-Term", which included construction of a 160 MeV H^- linear accelerator called Linac4, and the study of a 5 GeV, high beam power, superconducting proton Linac (SPL).

Since 2011 Linac4 became integrated in the framework of the LHC Injector Upgrade program [1] which includes modification to all CERN's LHC injectors to allow increasing of the beam brightness delivered to LHC and opens the way to the parameters needed for the High Luminosity LHC [2].

During the LHC Long Shutdown 2 (LS2) the Linac4 will be physically connected to the CERN PS Booster (PSB) and will inject via charge-stripping up to 1.3 10^{13} protons per ring at 160 MeV (e.g. an average current of 25 mA along the pulse before chopping, injection over 150 turns of 150 µs). The beam injected into each ring can be tailored to durations from 1 to 150 µsec, and its energy can be dynamically varied by ±0.8 MeV over 40 µs and the rms energy spread varied from 85 to 450 keV rms. The 352 MHz microstructure can be modified by a dedicated beam chopper that can impose patterns between 10 ns and 0.7 µs at the frequency of 1-20 MHz to match the shape of the bucket in the PSB and to further optimise the effect of the longitudinal painting [3]. This flexibility is meant to cover all possible beams needed from the PSB and will require a substantial commissioning and tuning period for the optimum working point once the Linac4 beam is injected into the PSB after LS2.

The Linac4 beam attained the final energy of 160 MeV in October 2016 with a peak current of 18 mA, i.e 70% of the minimum current for the high intensity users. Since then a series of dedicated beam runs lasting typically around three months have been scheduled to further access and optimise the beam quality, to test the injection and stripping mechanism and to access the beam availability and reliability. Before the connection to the PSB, two other beam runs are planned between September and December 2018 and between July and September 2019.

LAYOUT

Linac4 is a normal conducting linear accelerator operating at the frequency of 352 MHz. The first element of Linac4 is a RF ion source which can provide a 600 µsec 50 mA H^- beam at 45 keV with a maximum repetition rate of 2 Hz. The beam is then matched to the first stage of RF acceleration (from 45 keV to 3 MeV) in a 3 m long Radio Frequency Quadrupole. At 3 MeV the beam enters a 3.6 meter long Medium Energy Beam Line (MEBT), consisting of 11 quadrupoles, 3 bunchers and two sets of deflecting plates. The beam is "chopped" by removing selected micro-bunches in the 352 MHz sequence to match the beam to the distribution system (which delivers the beam to the 4 superimposed PSB rings) and to the 1 MHz CERN PSB RF bucket. Presently the preferred scheme envisages to chop 133 bunches out of 352 with a resulting average current reduced by 40%. The part described up to now, where the beam quality for the PSB is determined, goes under the name of pre-injector. After the pre-injector the beam is further accelerated to 50 MeV in a conventional Drift Tube Linac (DTL). The DTL, subdivided in 3 tanks, is 19 meters long in total. Each of the 111 drift tubes is equipped with a Permanent Magnet Quadrupole (PMQ). The acceleration from 50 to 100 MeV is provided by a Cell-Coupled Drift Tube Linac (CCDTL). The CCDTL is made of 21 tanks of 3 cells each for a total length of 25 meters. Three tanks are powered by the same klystron, and constitute a module. The focusing is provided by electromagnetic quadrupoles placed outside each module, with PMQs between coupled tanks. The acceleration from 100 to 160 MeV is done in a PI-Mode structure (PIMS). The PIMS is made of 12 tanks of 7 cells each for a total of 22 m. Focusing is provided by 12 Electromagnetic Quadrupoles (EMQ). A 70 m long transfer line, including 17 electromagnetic quadrupoles, 5 dipole bendings (3 horizontal and 2 vertical) and a PIMS-like debuncher cavity connects the Linac4 high energy end to the present injection line into the PSB. The existing line (110 m in length) will not be modified as it can accommodate and match the beam from Linac4 to the new H^- injection system. It contains 16 electromagnets to transport the beam and match the dispersion, two bending magnets and a distributor to send the beam in the 4 superimposed PSB rings.

A sketch of Linac4 is shown in Fig.1.

Content from this work may be used under the terms of the CC BY 3.0 licence (© 2018). Any distribution of this work must maintain attribution to the author(s), title of the work, publisher, and DOI.

ISBN: 978-3-95450-194-6 ISSN: 2226-0366 doi:10.18429/JACoW-LINAC2018-TH1P01

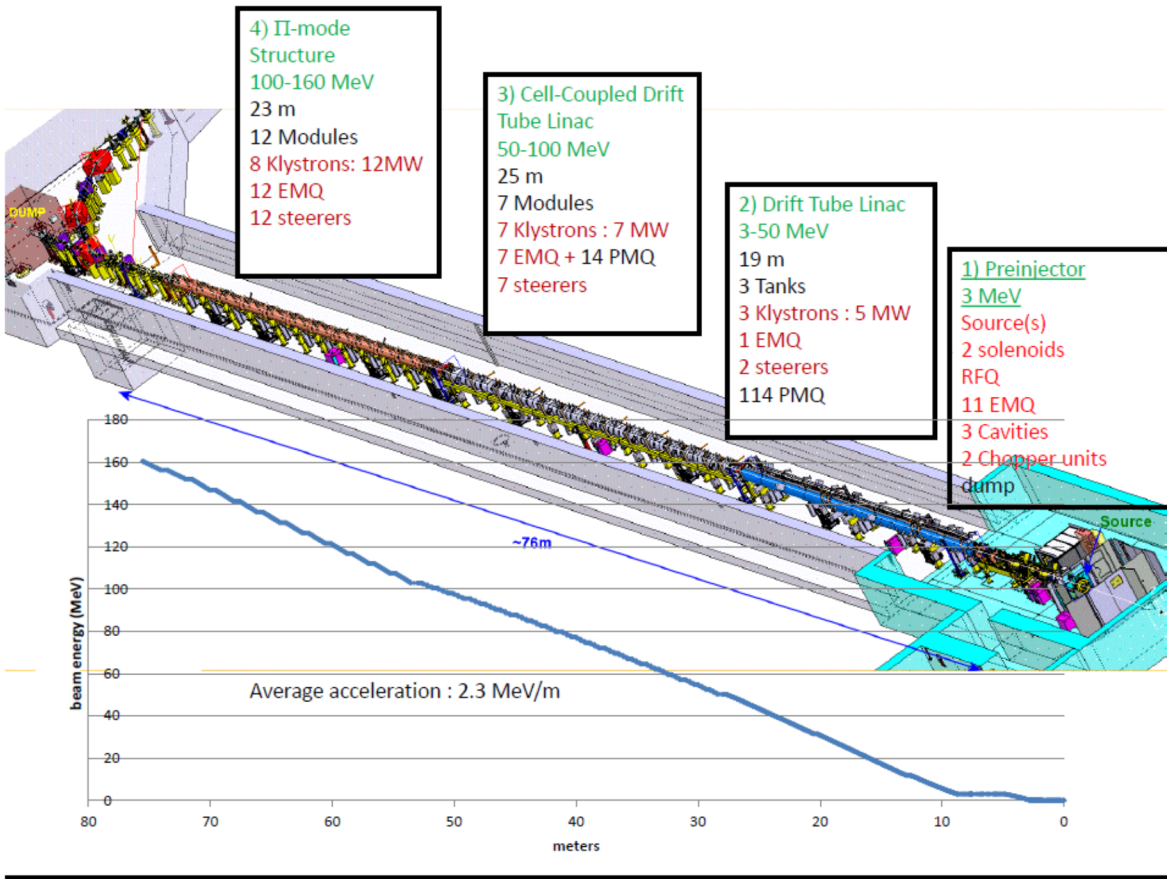


Figure 1: Sketch of Linac4.

All the elements to close the line to the PSB are presently either installed or in-house. The beam can be currently switched between the main dump and a temporary dump in the transfer line. This configuration allows testing of different users on two destinations and especially it allows installing equipment to be tested in one of the parasitic branches. Parasitic test of diagnostics for high intensity linacs but as well for medical application have been performed during beam runs in the line branching off before the main dump that can be seen in Fig. 2. Currently the beam can be disposed of on the main dump or on the temporary dump.

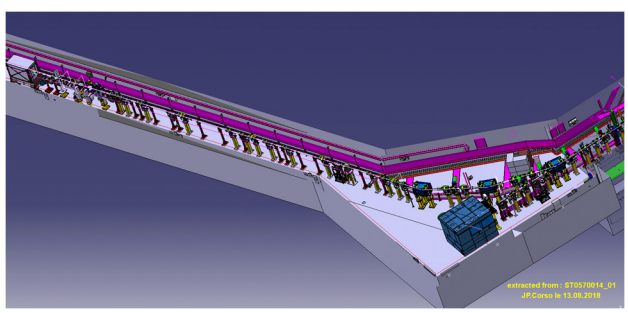


Figure 2: Presently installed hardware in the 160 MeV area. The permanent dump is indicated in blue colour.

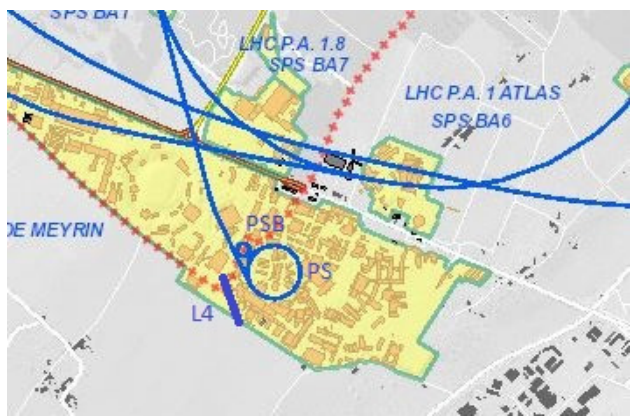


Figure 3: Location of Linac4 on the CERN site.

Figure 3 shows the location of Linac4 on the CERN site. Linac4 lays 2.5 m below the height of the PSB with the consequence of having the beam going through a vertical dogleg. Extensive beam dynamics calculation, also under the influence of errors, have been used to define the best possible arrangement of quadrupoles and dipole bendings to guarantee optimum beam quality, nevertheless a coupling between the horizontal and vertical dispersion is unavoidable and it might pose a limitation for future upgrades.

Content from this work may be used under the terms of the CC BY 3.0 licence (© 2018). Any distribution of this work must maintain attribution to the author(s), title of the work, publisher, and DOI.

ISBN: 978-3-95450-194-6 ISSN: 2226-0366 doi:10.18429/JACoW-LINAC2018-TH1P01

Content from this work may be used under the terms of the CC BY 3.0 licence (© 2018). Any distribution of this work must maintain attribution to the author(s), title of the work, publisher, and DOI.

BEAM QUALITY REQUIREMENTS

The injection into the PSB will be heavily changed from protons at 50 MeV to H- at 160MeV, nevertheless the variety and intensity of the beams that the PSB will have to produce will be the same. Linac4 is equipped with a fast chopper, energy ramping and the possibility of intensity variation pulse to pulse. This unprecedented flexibility should be used to the maximum advantage to produce high quality beam with an intrinsically lower current from the source. In this paper, we focus on two typical extreme beams that the PSB routinely produces: the LHC beam that requires 0.34 10^{13} protons per ring in an rms emittance of 1.7μm and the ISOLDE beam, the most demanding in terms of beam intensity which requires 0.9 10^{13} protons per ring in an emittance of 10 μm [4]. It has been recently simulated that such beams are possible with an intensity after the RFQ of 25 mA peak current so this is the value that was targeted during the 2018 beam quality run. The LHC beam will be obtained by injecting 45 turns (=45 μs) in each of the four PSB rings and the ISOLDE beam by injecting 110 turns in each ring The beam quality required at the injection into the PSB is summarised in Table 1.

Table 1 : Target Beam Quality at the PSB Injection

Parameter	Target value
Intensity flatness along the pulse for pulse lengths < 180 μs	±2%
Intensity flatness along the pulse for pulse lengths >180 μs	±5%
Horizontal/vertical position variations along the pulse	±1 mm
Horizontal/vertical injection angle error along the pulse	±0.4 mrad
Current stability shot-by-shot	±2%
transverse emittances rms norm	<0.4 mm mrad
Beam energy	160MeV
Pulse to pulse energy spread	80-600keV
Nominal chopper operation	65% at 1MHz
Energy painting	±0.8 MeV

Most of the parameters have been achieved during the 2018 run. The flatness along the pulse as well as the stability depends mainly from the source settings and the proper regulation of the Low Level RF that is still in progress. In particular the time it takes to attain a stable neutralisation in the low-energy magnetic beam transport at 45keV makes the first 200-300μsec of the pulse severely out of the stability requirements. Whereas future studies will address the effect of gas injection and the perturbation due to the electrical field of the pre-chopper, a practical approach has been adopted which consists in generating a beam about 50% longer than needed and chop off the unwanted part after the RFQ by means of the chopper. A plot of a typical beam at the source and after the chopper is shown in Figure 4.

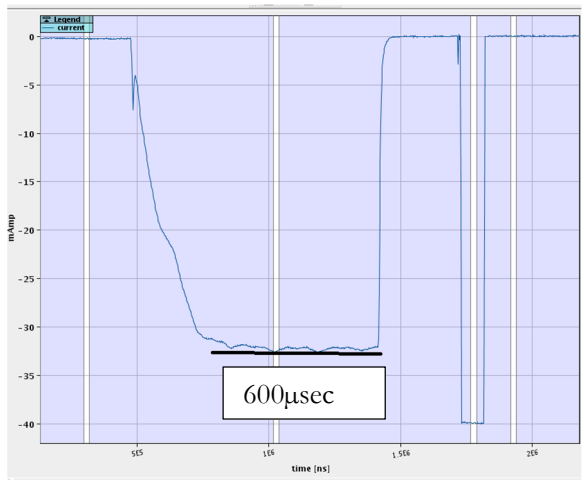


Figure 4: Beam current signal at 45 keV after the source.

The first 350 μs of the pulse the beam is still undergoing time-varying neutralisation effects that result in poor transmission through the RFQ. After 350 μs the beam current (and the beam emittance) is stable. The first 350 μs will be disposed of by the chopper on the inline dump and only the part corresponding to the black line will be transmitted to the PSB.

BEAM COMMISSIONING

The beam commissioning was planned in 6 stages of increasing energies at 45 keV, 3 MeV, 12 MeV, 50 MeV, 100 MeV and finally 160 MeV. At each stage the transverse emittance, the average energy and energy spread have been measured, directly until 12 MeV and by reconstruction from profile measurements from 30 MeV. The commissioning was prepared and accompanied by an extensive series of beam simulations which turned out to be the key for speeding up the time needed to optimise the beam transmission and beam quality at the various energies. On average each commissioning stage took about 3 weeks and never more than few days to get the beam through the new segment of the linac. The key decision was to start the simulation with a particle distribution obtained by measuring the beam in the LEBT under different focusing and back-tracing to the start of the line. Obtaining this representative cloud of macro-particles implied a thorough measurement campaign at the source test stand for as long as 6 months [5]. The global beam quality in terms of energy, energy spread, emittance and transmission have been extensively documented in [6] [7] [8]. In the following a representative measurement for the transverse plane (Fig. 5) is shown, to-gether with the record beam performance at each energy stage (Table 2). Please note that the record peak current measurement were not taken during the same measure-ments campaign.

ISBN: 978-3-95450-194-6 ISSN: 2226-0366 doi:10.18429/JACoW-LINAC2018-TH1P01

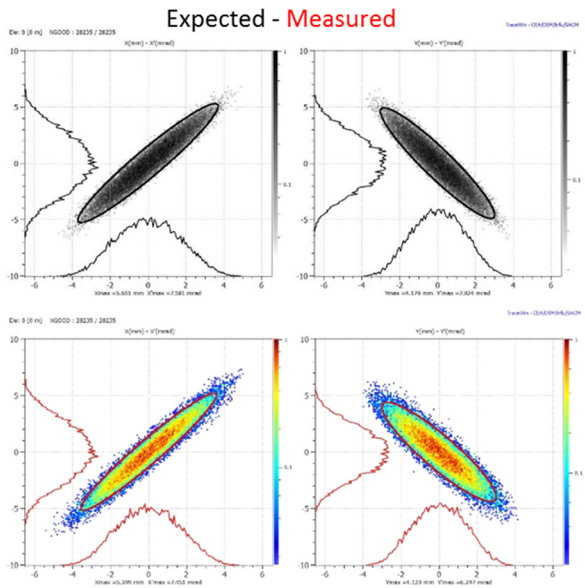


Figure 5: Expected (top) and measured (bottom) transverse emittance at 50MeV

Table 2: Energy and Beam Intensity Milestones

Energy (MeV)	Date	Record peak current (mA)	Emitt rms norm (mmmrad)
0.045	2013	50 mA (Nov15)	0.6
3	Mar 13	30 mA (Oct15)	0.35
12	Aug 14	23 mA (Oct17)	0.3
50	Nov 15	23 mA (Oct17)	0.3
105	June 16	23 mA (Oct17)	0.3
160	Oct 16	23 mA (Oct17)	0.3

BEAM AVAILABILITY

The availability of the beam from Linac is a key parameter in the success of the physics program of CERN, in fact the non-availability of the injectors is the most common cause of down time for the LHC [9]. A demonstrated availability of more than 90% is necessary before connection with the understanding that the more an accelerator is in service the more the availability increases. For example Linac2, that will be serving the PSB until the end of 2018, has in the last year reached an availability of 99%, after 40 years of operation. For Linac4 we have had a first reliability run, from September 2017 to May 2018 articulated in three parts with two technical stops of 3 and 15 weeks respectively for upgrades and repairs. An important effort was made to integrate Linac4 in the CERN Accelerator Fault Tracking system, which keeps tracks of the availability of all accelerators. The results of the availability studies are shown in Figure 6. The average availability over 23 weeks of operation turned out to be 91.5% with main cause of down time the Radio Frequency system followed by the power converters , as expected in the risk analysis reported in [10].

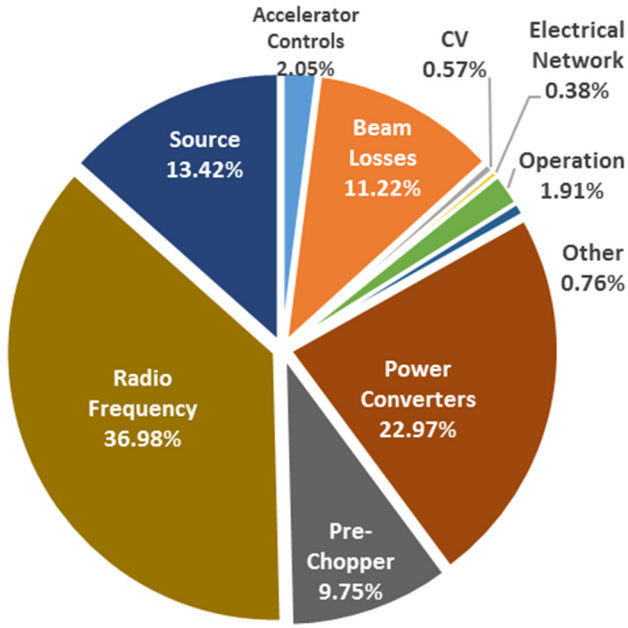


Figure 6: Causes of downtime for the Linac4 during the run 2017-2018. The statistics are taken over 23 weeks of continuous operation.

POTENTIAL AND OUTLOOK

Linac4 will be connected to the PSB during the LS2 and will deliver initially up to 1.25 10^{13} proton per ring. In parallel a program for the upgrade of the emittance/current of the present source will be deployed over the next 3-4 years with the aim of achieving a peak current of 45mA, a value which will allow doubling the intensity of the non-LHC high intensity users (ISOLDE).

ACKNOWLEDGEMENT

Linac4 has been designed, constructed and commissioned thanks to the hard work and the dedication of many people, both at CERN and in collaborating institutes.

REFERENCES

[1] R. Garoby, S. Gilardoni, B. Goddard, K. Hanke, M. Meddahi, M Vretenar, "Plans for the upgrade of the LHC injectors", in *Proc. IPAC'11,* San Sebastian, Spain, Sep 2011, paper WEPS017, pp 2517-2519.

[2] G. Apollinari, I. Bejar Alonso, O. Brüning, M. Lamont, L. Rossi, eds., "High Luminosity Large Hadron collider" CERN, Geneva, Switzerland, Technical Design Rep. V0.1, EDMS n. 1723851.

[3] V. Forte, E. Benedetto, A. M. Lombardi, D. Quartullo, "Longitudinal Injection Schemes for the CERN PS Booster at 160 MeV Including Space Charge Effects", in *Proc.*

Content from this work may be used under the terms of the CC BY 3.0 licence (© 2018). Any distribution of this work must maintain attribution to the author(s), title of the work, publisher, and DOI.

ISBN: 978-3-95450-194-6 ISSN: 2226-0366 doi:10.18429/JACoW-LINAC2018-TH1P01

Content from this work may be used under the terms of the CC BY 3.0 licence (© 2018). Any distribution of this work must maintain attribution to the author(s), title of the work, publisher, and DOI.

IPAC'15, Richmond, VA, USA, May 2015, paper MOPJE042, pp 378-380.

[4] V. Forte, C. Bracco, G.P. Di Giovanni, M. A. Fraser, A. M. Lombardi, B. Mikulec, " Multi-particle simulations of the future CERN PSB injection process with updated Linac4 beam performance ", in *Proc. HB2018*, Daejeon, Korea, 17-22 June, 2018, paper WEP2P007.

[5] G. Bellodi, V. A. Dimov, L. Hein, J.-B. Lallement, A. M. Lombardi, O. Midttun, R. Scrivens, P. Posocco, "Linac4 45 keV Proton Beam Measurements", in *Proc. Linac'12,* Tel Aviv, Israel*,* Sep 2012, paper THPB011, pp.867-869.

[6] J.B. Lallement., "Experience with the construction and commissioning of Linac4", *in Proc. Linac'16*, East-Lansing USA Sept. 2016, paper TU1A03.

[7] A.M. Lombardi., "Commissioning of the Low-Energy Part of Linac4", in *Proc. Linac'14*, Geneva, Switzerland, paper MOIOA02, pp 5-10.

[8] G. Bellodi," Linac4 Commissioning Status and Challenges to Nominal Operation ", in *Proc. HB2018*, Daejeon, Korea, 17-22 June, 2018, paper MOA1PL03.

[9] J. Wenninger," Approaching nominal performance at the LHC ", in *Proc. IPAC'17*, Copenhagen, Denmark, May 2017, paper MOYAA1.

[10] O. Rey Orozco, A. Apollonio, G. Guidoboni, B. Mikulec, S. Schuh-Erhard and J. Uythoven," Performance evaluation of Linac4 during the Reliability Run ", in *Proc. IPAC'18*, Vancouver, Canada, May 2018, paper WEPAF077.

ISBN: 978-3-95450-194-6 ISSN: 2226-0366 doi:10.18429/JACoW-LINAC2018-TH1P02

INJECTION COMPLEX DEVELOPMENT FOR THE NICA PROJECT

A.V. Butenko, A.I. Govorov, B.V. Golovenskiy,D.E. Donets, A.D. Kovalenko, ,K.A. Levterov, D.A. Lyuosev, A.A. Martynov, V.V. Mialkovsky, V.A. Monchinskiy , D.O. Ponkin, K.V. Shevchenko, A.O. Sidorin, I.V. Shirikov, A.V. Smirnov, G.V. Trubnikov
Joint Institute for Nuclear Research, Dubna, Moscow Region, Russia
T.V. Kulevoy
Institute of Theoretical and Experimental Physics NRC "Kurchatov Institute", Moscow, Russia
S.M. Polozov
National Research Nuclear University – Moscow Engineering Physics Institute, Moscow, Russia
H.Höltermann, U.Ratzinger, A.Schempp, H.Podlech
BEVATECH GmbH, Frankfurt, Germany

Abstract

Wide international collaboration is working on construction of NICA collider complex at JINR, Dubna. The main goal of new collider is investigation of the heavy ion collisions with center-of-mass energy up to about √s = 11 GeV/u. Injection complex of the project is under development, it consists of two synchrotron rings with two linear accelerators. Current status of the injection complex development and latest results are presented in this paper.

INTRODUCTION

Nuclotron-based Ion Collider fAcility (NICA) (Fig. 1.) is new accelerator complex developing and constructing at JINR [1] for ion collision and high-density matter study.

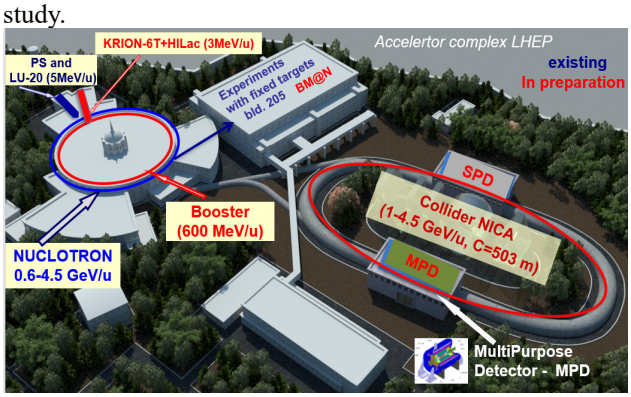


Figure 1: The NICA complex.

For the NICA collider ion beams from p to Au ions with energies from a few hundred MeV/u up to a few GeV/u will be provided by two injection LINACs and two superconducting synchrotrons: the Booster and the Nuclotron. The beams are generated by three new ion sources: SPI (Source of Polarized Ions), LIS (Laser Ion Source) and Krion (ESIS type heavy ion source). The ion sources feed two LINACs: the existing linac LU-20 with a new RFQ as pre-injector and the new heavy ion linac – HILAc. Design and development of RFQ, MEBT and two IH sections of the HILAc was performed by Bevatech GmbH (Frankfurt, Germany) [2] and described in detail in [3]. HILAc commissioning was performed with the C^{3+}, C^{2+} and Fe^{14+} beams from the laser ion source.

HILAC

The main parameters of the HILAc (Fig. 2) are given in the Table 1.

Table 1: HILac Parameters

A/q	6.25
Current	< 10 emA
Pulse length	10 μs – 30 μs
Rep. rate	< 10 Hz
LEBT energy	17 keV/u
RFQ energy	300 keV/u
IH1 energy	1.87 MeV/u
IH2/LINAC max. energy	3.2 MeV/u

The HILac RFQ is a 4-rod structure operating at 100.625 MHz.The RFQ tank is a 3.16 m stainless steel tank of 0.35 m in diameter which is copper-plated inside. The RFQ is powered by a 140 kW solid state amplifier.

The first IH tank contains an internal quadrupole triplet lens. The IH1 and IH2 have 2.42 m and 2.15 m outer length correspondingly. For the design A/q – value of 6.5 the sum voltage gain is 20.8 MV. Both IH cavities are powered by 340 kW solid state amplifiers, one for each cavity.

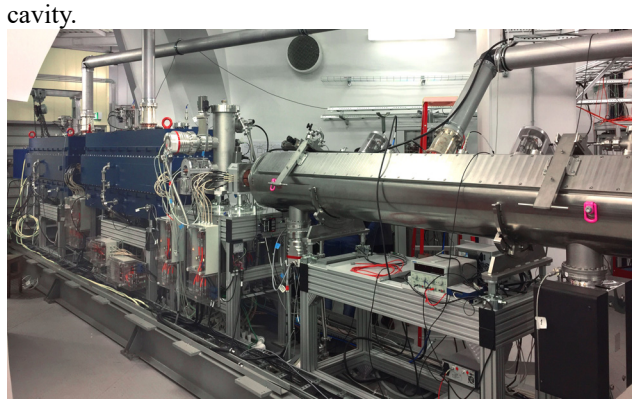


Figure 2: HILAC at JINR.

Before installing the IH cavities the RFQ has been tested with beam. The beam energy was measured with a

Content from this work may be used under the terms of the CC BY 3.0 licence (© 2018). Any distribution of this work must maintain attribution to the author(s), title of the work, publisher, and DOI.

ISBN: 978-3-95450-194-6 ISSN: 2226-0366 doi:10.18429/JACoW-LINAC2018-TH1P02

Content from this work may be used under the terms of the CC BY 3.0 licence (© 2018). Any distribution of this work must maintain attribution to the author(s), title of the work, publisher, and DOI.

magnet spectrometer to be 300 keV/u ± 3%. The beam injected into the RFQ contained a carbon ion species C^{3+} from LIS. The total RFQ beam transmission was up to 90%. Thun the energy measurements was provided by the magnetic spectrometer at the exit of IH2. Spectrums of different beam energies (after RFQ, without acceleration in IH; after IH1 when the IH2 is switched off; and after IH2 with full energy beam 3.2 AMeV) is shown on the Fig. 3. The transmission factor for C^{3+} is about 65% from RFQ exit to IH2 exit at the last stage of running in August 2018.

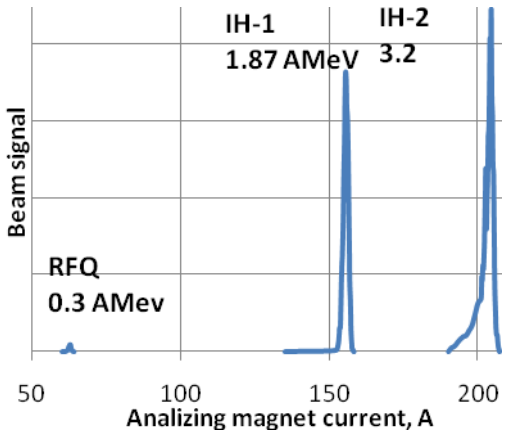


Figure 3: Measurements of the beam energy at the exit of HILac in three steps of acceleration combined in one picture: only RFQ acceleration, RFQ+IH1, and full linac energy.

All accelerating structures, the solid state RF power amplifiers and the digital LLRF system run stable. As one of the next steps the ESIS source will be added providing beam with A/Q = 6.25 using target ions of Au^{31+} for which HILac was designed.

THE BOOSTER & NUCLOTRON

The Nuclotron was built during 1987-92. This accelerator based on the unique technology of superconducting magnetic system [4]. All design, tests and assembling works were carried out at the JINR. 55 runs of the Nuclotron operation were performed since March 1993. During last 7 years all the systems of the ring was completely modernized and prepared for long and stable operation in the NICA complex.

The Booster superconducting ring is under assembling presently. The ring commissioning is planned at the first part of the 2019 year. The main goals of the Booster ring are the following:

-accumulation of $2 \cdot 10^9$ Au^{31+} ions;

-forming of the required beam emittances with electron cooling system;

-acceleration of the heavy ions up to energy required for effective stripping and transferring to the Nuclotron ring.

The magnetic system of the Booster consists of 4 quadrants. The regular period consist of one quadrupole doublet unit and two dipole magnets. The Nuclotron-type design based on a window-frame iron yoke and a saddle-shaped superconducting winding is chosen for the Booster.

The main parameters of both rings are given in Table 2.

Table 2: Booster and Nuclotron Parameters

	Booster	Nuclotron
Magnetic rigidity, T/m	25	45
Circumference, m	211	251
Beam intensity, particles per pulse	2×10^9	1.1×10^9
Max. energy	600 MeV/u	4.5 GeV/u

LINEAR INJECTOR OF LIGHT IONS

Injector of light ions, polarized protons, deuterons and ion ($A/q \leq 3$) beams is based on existing conventional Alvarez-type DTL at the frequency of 145.2 MHz.

The upgrade of this injector includes replacement of the 700-kV DC acceleration tube for the drift-tube linac with an RFQ (Fig. 4). The RFQ designed by ITEP provides 156 keV/u ion beams for following acceleration by the DTL at 2βλ-mode to the energy of 5 MeV/u [5].

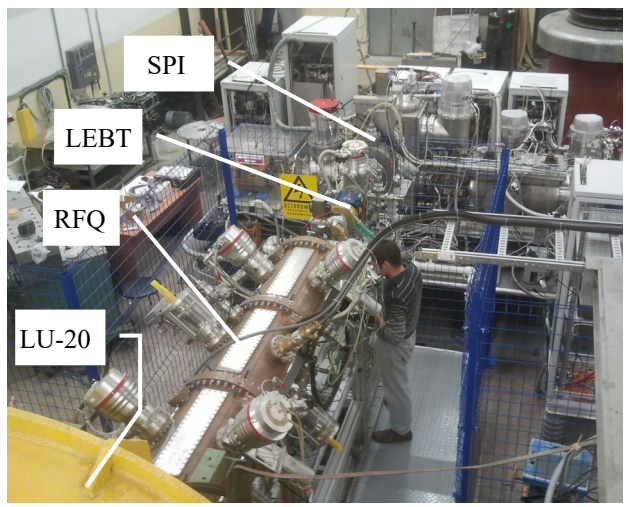


Figure 4: New fore-injector for LU-20.

The 2.2 m of the length the 145.2-MHz RFQ is based on a 4-vane resonator with magnetic coupling windows. The structure provides both reliable dipole-free range and compactness compared to a conventional 4-vane. Higher RF power losses of the structure is not an issue for the RFQ injector since it operates in a pulsed mode at RF pulse width less than 150 μs and repetition rate not higher than 1 Hz.

NUCLOTRON LAST RUNS WITH RFQ

During two last years the new fore-injector of the Lu-20 was operated during three beam runs of the Nuclotron with total duration almost 4000 hours.

Two runs dedicated to experimental investigations in spin physics (with polarized deuterons and protons) was provided in autumn of 2016 and spring 2017. Maximum intensity of the polarized deuteron beam was about

ISBN: 978-3-95450-194-6 ISSN: 2226-0366 doi:10.18429/JACoW-LINAC2018-TH1P02

2 x 10^9 particles per cycle. In this run the acceleration of polarized proton beam from SPI as well as the lithium and carbon beams from the laser source was provided.

During preparation to Run #55 the Krion-6T ion source replaced the SPI at the RFQ injection line. The Run was performed with acceleration of C, Kr and Ar ion beams. Ion source and linac demonstrated stable operation and acceleration with intensity in Nuclotron up to $2 \cdot 10^5$ Kr ions per cycle. Wary good quality of the low intensity extracted beam spill was achieved (Fig 5.).

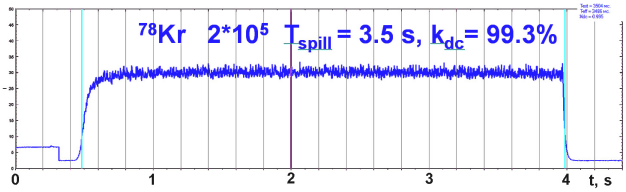


Figure 5: $^{78}Kr^{+36}$ beam spill 2 x 10^5 ppp.

FUTURE DEVELOPMENT

Future development and modernization of NICA injection complex presupposes replacement of the old LU-20 linac (in operation since 1974) with new Light Ion Linear accelerator (LILac, Fig. 6). The first part of new linac for acceleration up to energy of 7 MeV/u, is under design and will be constructed by Bevatech GmbH (Frankfurt, Germany) [6].



Figure 6: LILac project view.

Next step of the LILac project – design of a middle energy section from 7 up to 13 MeV/u. And the third part – additional superconducting RF cavities, which will provide a total energy of the beam up to 50 MeV/u. Increased beam energy of LILac is required for future research with polarized proton beams. SC linac will consist of a number of independently phased cavities and focusing solenoids.

The operating frequency of the linac was chosen equal to 162 MHz for QWRs (Fig. 7) with further increase to 324 MHz for HWR cavities. Detailed QWR design is presented in [7].

The development of the SRF technologies is the key task of new Russian - Belarusian collaboration started on March 2015. Now the JINR, NRNU MEPhI, ITEP of NRC "Kurchatov Institute", INP BSU, PTI NASB, BSUIR and SPMRC NASB are participating in the collaboration.



Figure 7: General view of 162 MHz QWR design model.

CONCLUSION

The injection complex of the NICA project demonstrate good progress. The HILac is ready to provide the first booster run with heavy ion beam. The new RFQ pre-injector was put into operation and well worked during few last runs of the Nuclotron with polarized light ions and heavy ions. Current results of new light ion linac development for the NICA complex showed a good progress.

REFERENCES

[1] G.V. Trubnikov et al., "The NICA Project at JINR", in *Proc. 7th Int. Particle Accelerator Conf. (IPAC'16)*, Busan, Korea, May 2016, paper WEZA02, pp. 2061-2065. doi:10.18429/JACoW-IPAC2016-WEZA02 http://jacow.org/ipac2016/papers/weza02.pdf

[2] G. Trubnikov et al., "Heavy ion collider facility NICA at JINR (Dubna): status and development", in *Proc. 36th International Conference on High Energy Physics (ICHEP'12)*, Melbourne, Australia, July 2012. doi:10.22323/1.174.0554 https://pos.sissa.it/174/554/pdf

[3] Bevatech official website, http://www.bevatech.com/

[4] A.V. Butenko et al, "Development of the NICA injection facility", in *Proc. 4th Int. Particle accelerator conf (IPAC'13)*, Shanghai, China, May 2013, paper HPWO069, pp.3915-3917. doi:10.18429/JACoW-IPAC2013-HPWO069

[5] N. Agapov et al, "Nuclotron at JINR: Operation Experience and Recent Development", in*Proc. of 13th International Conference on Heavy Ion Accelerator Technology (HIAT'2015)*, Yokohama, Japan, paper MOPA19, pp.86-88. doi:10.18429/JACoW-HIAT2015-MOPA19 http://accelconf.web.cern.ch/AccelConf/HIAT2015/papers/mopa19.pdf

[6] A.V. Butenko et al., "Commissioning of New Proton and Light Ion Injector for Nuclotron-Nica", in*Proc. 7th Int. Particle accelerator conf. (IPAC`16)*, Busan, Korea, May 2016, paper MOPOY041, pp. 941-943, ISBN 978-3-95450-147-2. doi:10.18429/JACoW-IPAC2016-MOPOY041 http://accelconf.web.cern.ch/AccelConf/ipac2016/papers/mopoy041.pdf

[7] H. Höltermann et al, "Light Ion Linear accelerator up to 7 AMeV for NICA", presented at 29th Int. Linear accelerator conf. (Linac`18), Beijing, China, September 2018, paper WECAMH02, this conference.

Content from this work may be used under the terms of the CC BY 3.0 licence (© 2018). Any distribution of this work must maintain attribution to the author(s), title of the work, publisher, and DOI.

ISBN: 978-3-95450-194-6 ISSN: 2226-0366 doi:10.18429/JACoW-LINAC2018-TH1P03

NEW TRENDS IN PROTON AND CARBON THERAPY LINACS

S. Benedetti*, CERN, Geneva, Switzerland

Abstract

In the last years, many developments have contributed to make feasible an all linac solution for proton and carbon ion therapy, with typical output energies of about 200 MeV and 400 MeV/u, respectively. The efficient beam matching of the source to the high-energy linacs, operating at 3 GHz, represents one of the major challenges. With the successful test of a 750 MHz RFQ at CERN, this possibility starts to be a reality. At the same time CERN is testing a high-gradient S-band cavity, successfully exceeding the accelerating gradient goal of 50 MV/m - more than twice what has been obtained before - and paving the way to more compact medical facilities. In this paper, some of the most significant projects involving linear accelerators for hadron therapy will be presented.

INTRODUCTION

The energy gain ΔW across a RF cavity is proportional to:

$$\Delta W \propto \sqrt{ZTT \cdot P_d \cdot L} \tag{1}$$

where ZTT is the effective Shunt impedance of the cavity, P_d is the dissipated power on the cavity walls and L the cavity length. Eq. (1) shows that, for a given energy gain and cavity design, one can either increase the power consumption P_d and decrease the cavity length L, or vice versa. At the same time, it can be shown that the cavity design, so its ZTT, is a function of the maximum accelerating gradient achievable, and in particular the higher the accelerating gradient, the lower is the ZTT achievable. Hadron therapy linacs can be thus divided into high-gradient and high-efficiency designs. Though arbitrary, the separation bar between the two approaches can be set at 30 MV/m accelerating gradient; linacs designed for values lower or equal than this threshold can be referred as high-efficiency designs.

Proton therapy linacs have been designed in both high-gradient and high-efficiency solutions. Carbon ions linacs have been predominantly designed in high-efficiency solutions, to limit the RF power consumption [1]. However in recent years a researchers are working on a high-gradient design for carbon ions [2]. The different projects are listed in Table 1.

Two of the most important developments of recent years have been started at CERN. Those are the construction and test of a 750 MHz RFQ [3,4] and of a 50 MV/m accelerating gradient 3 GHz cavity for a relativistic beta of 0.38 [5], corresponding to approximately 70 MeV/u. The 750 MHz RFQ solved the issue of the efficient low energy acceleration and control of the beam, bridging the gap between the ion source and the 3 GHz accelerating cavities. The 3 GHz cavity designed for 50 MV/m accelerating gradient showed that more compact linac designs can be conceived.

LOW ENERGY BEAM ACCELERATION

The low energy beam acceleration is probably the most difficult part in a linac design. Space charge does not affect a medical linac design thanks to the low beam current - average of few nA - needed. However, the need to reduce the footprint as much as possible makes the design challenging in many different ways.

A key aspect in this regard is the choice of the operating frequency f_{RF}. The scaling law $ZTT \propto \sqrt{f_{RF}}$ [6] relates the cavity effective Shunt impedance ZTT with the resonating frequency f_{RF}, and it is valid if the cavity beam aperture is scaled accordingly with the frequency. This is not always possible due to beam dynamics constraints, and in addition different geometries, as the drift tubes in drift tube linacs (DTL) or the septum thickness in coupled cavity linacs (CCL) are bounded in the minimum dimension by mechanical and thermal limitations. For these reasons, while in principle it would be ideal to increase the cavity operating frequency, in reality an optimum has to be found. For hadron therapy linacs it has been historically chosen a frequency of 3 GHz [7], in order to profit of the availability of relatively cost-effective power supplies developed for radiotherapy linacs. In [8] it has been showed that for a proton therapy linac design a 3 GHz solution has to be preferred over a 6 GHz one.

Before 2014, existing RFQs did not have high enough operating frequencies to efficiently inject the beam into the longitudinal acceptance of 3 GHz linacs. In the 2011 TOP-IMPLART project [9, 10] a 425 MHz commercial injector, composed by a 3 MeV RFQ and a 7 MeV DTL, inject into a 3 GHz side coupled DTL (SCDTL), with losses. Researchers proposed the so called cyclinac design [7], where a commercial cyclotron provides the beam acceleration up to 20 to 30 MeV for protons, and around 150 MeV/u for carbon ions, followed by the 3 GHz linac. In this case even higher losses occurred at the injection in the 3 GHz linacs.

The 750 MHz CERN RFQ was explicitly designed to inject into 3 GHz cavities, accepting losses in the RFQ itself but preserving full transmission and a good beam matching in the transition from 750 MHz to 3 GHz, thus maintaining constant the normalized beam emittance. The CERN 750 MHz RFQ is now successfully in operation [11] in the ADAM bunker in the CERN ALICE area.

For low energy beam acceleration, three different type of linear accelerators are usually considered: RFQs, SCDTLs and H-mode DTL cavities. A qualitative assessment of their advantages and disadvantages is proposed in Fig. 1. Each accelerator has been ranked from one to three considering four aspects: the RF efficiency, the maximum accelerating

* stefano.benedetti@cern.ch

Content from this work may be used under the terms of the CC BY 3.0 licence (© 2018). Any distribution of this work must maintain attribution to the author(s), title of the work, publisher, and DOI.

ISBN: 978-3-95450-194-6 ISSN: 2226-0366 doi:10.18429/JACoW-LINAC2018-TH1P03

Table 1: Main Projects of Hadron Therapy Linacs

Linac	E acc [MV/m]	Structures	Status	Where
Proton linacs				
TULIP	40	RFQ, IH, SCDTL, BTW	Design, cavity prototype	CERN, Switzerland
TOP-IMPLART	NA	RFQ, DTL, SCDTL, CCL	Under construction	ENEA, Italy
ADAM Light	16	RFQ, SCDTL, CCL	Under construction	Geneva, Switzerland
Carbon ion linacs				
CABOTO	30	RFQ, IH, SCDTL, CCL	Design	CERN, Switzerland
ACCIL	50	RFQ, DTL, BTW	Design, cavity prototype	ANL & RadiaBeam, USA

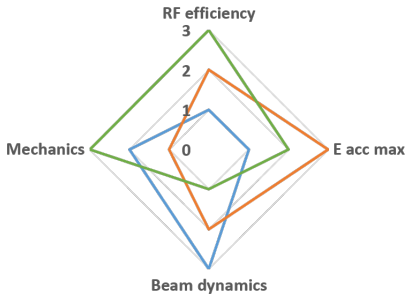


Figure 1: Qualitative assessment between RFQ, DTL and H-type cavities for low energy acceleration. RFQ in blue, DTL in orange, H-type cavities in green.

gradient E_{acc}, the beam dynamics control of the beam and the machinability.

RF Efficiency A simplified geometry, with constant drift tube thickness and stems radius independently on the geometric β, can be considered to preliminary assess the ZTT of different type of cavities using both TE and TM modes. If the structures cell gap is optimized at different geometric β_s, from 5 to 70 MeV/u, one obtains the results shown in Fig. 2.

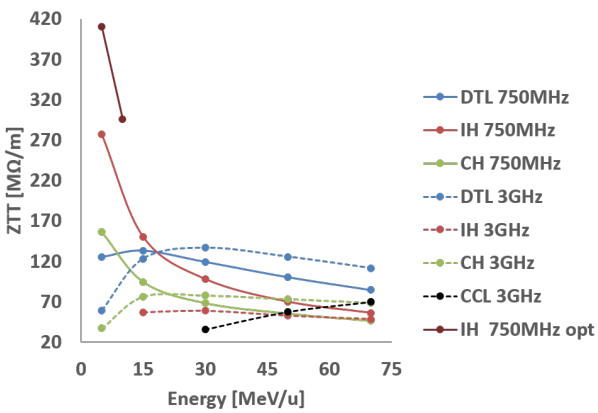


Figure 2: ZTT as a function of the RF cavity energy for different low energy RF cavities [12].

The bore aperture radius chosen is 2.5 mm. Promising cavities at 5 MeV/u are the 750 MHz IH and the 750 MHz CH. The 3 GHz DTL cavity, which is the most efficient choice for higher energies, has a cell length too small at 5 MeV/u, and it is ultimately not as efficient. If one considers only the ZTT, the crossing point between a 750 MHz solution and a 3 GHz solution is around 20 MeV/u.

The results of Fig. 2 hold for the TM mode cavities, as no current flows through the stems. Thus once the optimum gap is found, the thinner the drift tube and the drift stems are, the higher is the ZTT. TE mode DTL cavities have, on the other hand, current flowing through the stems. The induced Ohmic losses can be minimized by increasing the size of drift tubes and stems. However, this reduces the electric field concentration near the z axis. Ultimately, a detailed RF optimization is needed to find the optimum ZTT for a given cell length, taking into consideration machinability and thermal dissipation constraints. A more detailed discussion on the RF optimization of TE cavities can be found in [13]. The design of the optimized 750 MHz IH cavity for medical applications (dark red curve in Fig. 2) is discussed in [14].

The RF efficiency is strictly related with the cost of the facility, which for medical linacs is mostly given by the cost of the RF power sources. Preliminary discussions [15] quantifies in one order of magnitude the cost per peak power of a 750 MHz Inductive Output Tube (IOT) over a 3 GHz Klystron-modulator. This is the main argument to choose a 3 GHz cavity for the low energy acceleration of the beam. For a hadron therapy linac, even considering the cost argument, the crossing point between an high-efficiency 750 MHz H-mode DTL and a 3 GHz structure is at 10 MeV/u [12].

Beam Dynamics DTL cavities use a FODO focusing system to transversally control the beam. When the overall cavity dimension allows it, the focusing quadrupole are inserted in the drift tubes themselves. In the case of high-frequency designs the quadrupoles are placed in drift spaces between accelerating tanks, formed by more than one RF drift tube cell, and DTLs are then called SCDTL. From a beam dynamics point of view, a DTL is a good choice after an RFQ as one can preserve a FODO focusing system, and just needs to rematch the beam to the different transverse phase advance.

H-mode DTL are rather complicated structures from a beam dynamics point of view. In the end-cells takes place a

Content from this work may be used under the terms of the CC BY 3.0 licence (© 2018). Any distribution of this work must maintain attribution to the author(s), title of the work, publisher, and DOI.

ISBN: 978-3-95450-194-6 ISSN: 2226-0366 doi:10.18429/JACoW-LINAC2018-TH1P03

Content from this work may be used under the terms of the CC BY 3.0 licence (© 2018). Any distribution of this work must maintain attribution to the author(s), title of the work, publisher, and DOI.

transition from the TE mode of regular cells to a TM mode, due to the end walls. This decreases significantly the quality factor and thus the ZTT. For this reason, to fully exploit the RF advantages of H-mode DTL, those have to be composed by many RF cells. In this way the detrimental effect of end-cells is minimized. To transversally control the beam, the solution is to accelerate it at a low synchronous phase, either with a KONUS solution [16] or by simply choosing a low synchronous phase and adapting the RF cell with the relativistic β [14]. For this reason, a triplet focusing system is usually adopted, to maximize the acceleration length. The use of PMQs inside the drift tube of H-mode DTL [17] and hybrid RF accelerating-focusing systems were also studied [1]. In addition, in case of cavity designs with a small beam aperture, a dipole kick component is present and this has to be properly controlled [14].

In general, for the same operating frequency, the DTL beam control solution is considered to be simpler to design than for H-type cavities. However, if a 3 GHz SCDTL is compared to a 750 MHz IH, the latter proved to be a better choice. This argument was explicitly studied for a proton solution, where after the 5 MeV 750 MHz RFQ a 3 GHz SCDTL and a 750 MHz IH were compared [12].

It is interesting to discuss the equation of the RF defocusing [18], which is proportional to:

$$\Delta p_r \propto \frac{V_{gap} \cdot f_{RF}}{(\beta\gamma)^2} \tag{2}$$

Eq. 2 shows that, for a gap accelerating voltage V_{gap}, the RF defocusing increases with the RF cavity frequency f_{RF}, while it decreases with the square of the beam momentum $\beta\gamma$. Thus switching to higher frequencies increases the RF defocusing, but this is mitigated by the momentum scaling if done at higher energy. If for instance one chooses to accelerate at 3 GHz at 10 MeV/u instead that at 5 MeV/u, the RF defocusing decreases by 30%.

Maximum E_{acc} The maximum accelerating gradient E_{acc} that can be reached is not limited by breakdown (BD) phenomenon as in high-energy linacs. The two main constraints are instead the thermal RF power dissipation and the need to ensure a good matching with the RFQ output beam. DTL and H-mode DTL are critical in terms of power dissipation due to the bottleneck represented by the drift stems. DTLs were proposed with cooling channel inside the drift tubes, also in the 3 GHz SCDTL design [10]. H-mode DTLs have an advantage in this regard thank to the higher ZTT, however the cavity dimensions are too small and to the author knowledge no one has proposed an IH solution with cooled drift tubes. At the same time, a too high accelerating gradient immediately after the RFQ is unwise due to the longitudinal beam phase space shape at the RFQ output, that requires a smooth acceleration to avoid filamentation [1, 12]. In conclusion, it can be argued that a DTL can be designed with the highest accelerating gradient, as the stems can be made larger and with internal cooling without loosing too much ZTT as in a H-type solutions.

Mechanics Being 0 mode structures, DTLs are very prone to frequency perturbations. For this reason, post couplers are inserted in the geometry, and their resonator band is coupled to the main TM_{01} one [19]. A problem arises when the operating frequency increases: the small dimensions of the tank makes the tuning of the post couplers more difficult. In addition, the bandwidth of the cavity gets smaller at higher frequencies, thus it is more challenging to reach confluence between the post-couplers and the cavity dispersion curves. As a final note, post couplers affect the Q factor of the cavity due to surface currents, thus the ZTT of the DTL cavity is lower than the RF regular cell one. H-mode DTLs are easier to tune and to build. In a preliminary discussion, for the IH 750 MHz medical cavity [14], it was envisaged a similar construction and brazing procedure as for the 750 MHz RFQ [3].

FACILITY SIZE

A major research direction in the field of linear accelerators for hadron therapy is represented by the facility size. In the late 2000s, both researchers and private companies understood that compact, later called single-room, facilities would have been more flexible, patient-friendly, and would have helped in saving infrastructural costs. In 2013 Mevion treated the first patient with its S250 superconducting synchrocyclotron and the first single-room proton linac concept was presented [20]. In the past three years, one half of the 18 proton therapy centres that went into operation were single-room facilities [21].

The TULIP Project

TERA Foundation first proposed a single-room facility based on a cyclinac concept in 2013 [20], called TULIP (TUrning LInac for Proton therapy) [22]. The original idea was to have a commercial cyclotron on the floor, which injects into a linac mounted on a rotating structure around the patient (Fig. 3). As in the original design the linac had an accelerating gradient of 30 MV/m, TERA launched a high gradient research campaign, in collaboration with the CLIC group at CERN, to investigate the high gradient limit of S-Band accelerating structures [8, 23]. Based on the results of these tests, a high gradient (HG) backward travelling wave (BTW) accelerating structure for β=0.38 - approximately 70 MeV/u - with a 50 MV/m design accelerating gradient was built at CERN and is under-going testing [5, 24, 25]. This development allowed to reduce by a factor of two the length of the linac that has to be mounted on the rotating structure, saving size, weight and ultimately costs. The construction of the 750 MHz RFQ permitted to modify the initial cyclinac TULIP design to propose an all-linac high-gradient design (see Fig. 3), reducing the losses and improving the output beam quality.

The TULIP (Fig. 3) all-linac design [12] can be split into a low gradient section, to be placed on the ground, and a high gradient section, to be mounted on a rotating structure, called gantry. The footprint of the facility is driven by the

ISBN: 978-3-95450-194-6 ISSN: 2226-0366 doi:10.18429/JACoW-LINAC2018-TH1P03

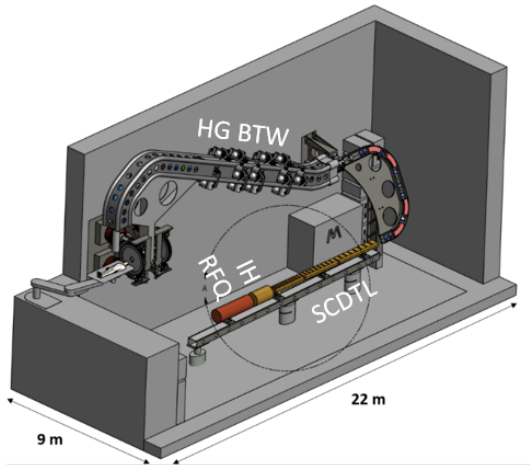


Figure 3: Sketch of TULIP all-linac solution (courtesy of M. Vaziri—TERA Foundation).

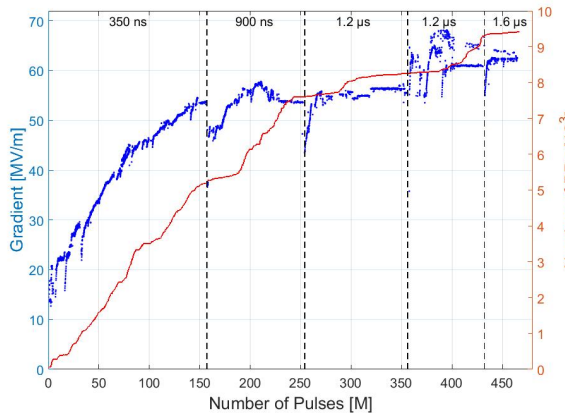


Figure 4: Conditioning history of the first BTW prototype, tested at CERN Sbox [25].

rotating structure, that has to integrate, together with the high gradient linac, also the high energy beam transport (HEBT) line and the beam diagnostic. As a result, about 10 meters are available on the ground to install the linacs that have to boost the particles up to 70 MeV. This length has been fully exploited, in order to minimize the power consumption for a given energy gain according to Eq. (1).

The design is based on a first acceleration up to 10 MeV in 750 MHz structures: the CERN RFQ [3, 4] and the newly designed Inter digital H-mode DTL cavity [14]. Particles are then injected into a 3 GHz linac chain composed of an SCDTL up to 70 MeV, and a HG BTW up to 230 MeV. The beam dynamics linac design downstream of the RFQ features full transmission and minimized emittance growth, and it has been accomplished with full tracking of the particles from the RFQ output up to 230 MeV. Misalignment studies were performed for the first time on a medical linac design validating the beam dynamics studies.

High-gradient S-band BTW Cavity

A HG BTW accelerating structure was designed and built at CERN [5, 24]. The main goal of the project is to define the high gradient limits of S-band cavities in terms of breakdown rate (BDR). In the RF design of the prototype a modified Poynting vector model was used [26]. The prototype cavity is 20 cm long and is designed for β=0.38. The cavity successfully reached accelerating gradients above 60 MV/m, as shown in the conditioning history plot of Fig. 4, thus exceeding the design goal of 50 MV/m. The asymptotic BDR at 60 MV/m is $4 \cdot 10^{-6}$ break-down per pulse (bpp) [25] at 1.2 μs pulse width.

CARBON ION LINACS

The use of carbon ions in radiotherapy oncology is motivated by their higher radio-biological effectiveness - RBE - in treating radio-resistant tumours. The downside is the higher mass per unit charge than protons, so carbon ion linacs are bigger, and more expensive, than proton linacs. Specifically, carbon ions require twice as much kinetic energy per nucleon than protons to travel the same distance through matter, and twice as much voltage, in the most favourable case of fully stripped ions, to reach the same energy per nucleon. Thus, a factor four lies between the overall voltage gain per nucleon of a carbon ion therapy linac over a proton one.

The CABOTO Project

As for the TULIP project, the CABOTO project [27] was initially conceived in a cyclinac design [28], with a cyclotron delivering a beam of fully stripped carbon ions at 150 MeV/u and a 24 m long linac boosting the beam up to 410 MeV/u [29]. In this initial study, the linac was designed with a resonant frequency of 5.7 GHz. In [8] a 3 GHz frequency linac is instead proposed and compared with the 5.7 GHz one, and a 70 MeV/u cyclotron was considered. In CABOTO, the beam losses at the cyclotron to linac injection are more critical than in TULIP due to the higher beam energy, 150 MeV/u with respect to the 24 MeV proposed for TULIP.

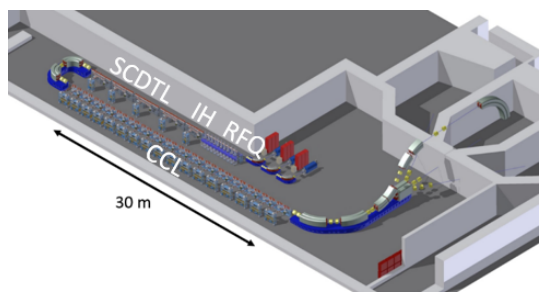


Figure 5: Sketch of CABOTO all-linac solution (courtesy of M. Vaziri—TERA Foundation)

An all-linac solution for fully stripped carbon ions acceleration is proposed in [1], with a final energy of 430 MeV/u (Fig. 5). To reduce the footprint, the linac is split into two branches of equal length. The ion sources, RFQ, IH and SCDTL form one branch, and a CCL the other one. The bottleneck is represented by the CCL section, that has to boost the C^{6+} ions

Content from this work may be used under the terms of the CC BY 3.0 licence (© 2018). Any distribution of this work must maintain attribution to the author(s), title of the work, publisher, and DOI.

ISBN: 978-3-95450-194-6 ISSN: 2226-0366 doi:10.18429/JACoW-LINAC2018-TH1P03

Content from this work may be used under the terms of the CC BY 3.0 licence (© 2018). Any distribution of this work must maintain attribution to the author(s), title of the work, publisher, and DOI.

from 100 MeV/u to 430 MeV/u, therefore a total voltage of 660 MeV. The 100 MeV/u bend was chosen on purpose. In fact, modulation of the beam energy should start at this level, which is equivalent to 70 MeV for protons [30] in terms of penetration in water equivalent tissues. This is convenient, since the beam momentum will change just after the 180 deg bend, thus the dipoles and quadrupoles of the bending can have a static field, and be more cost-effective. For the CCL, an average accelerating gradient of 30 MV/m was chosen, considered an optimum between facility size and power consumption. This choice results in a 30 m long CCL section, which then represents the target for the other branch. Given that ion sources, RFQ and IH cavities are more driven by beam dynamics and power consumption optimization, the length constraint reflects mostly in the accelerating gradient of the DTL linac, resulting in an average value of 15 MV/m.

Thanks to the low RFQ output emittance, in the CABOTO all-linac design it was possible to propose a peculiar beam dynamics design with beam aperture tapered from 2.5 mm to 2 mm in the SCDTL linac, and constant 2 mm in the CCL linac, increasing by 15 % the average ZTT. As a result, the all-linac CABOTO design [1] has the same power consumption of the cyclinac design [8]. As for the TULIP project, a full transmission with a negligible emittance growth is accomplished, with 430 MeV/u output energy, and misalignment studies were performed.

TwinEBIS and the 750 MHz C^{6+} RFQ

TwinEBIS is an Electron Beam Ion Source (EBIS) recently made operational at CERN [31] with a 2 T solenoidal field strength. Goal of the project is to provide a C^{6+} source with 300-400 Hz repetition rate, and 10^8 C^{6+} within 1.5 μs pulse [32]. As such, an ideal injector for high-frequency carbon ion linac as CABOTO, allowing to deliver final beam currents more than ten times larger than state-of-art carbon therapy synchrotron [1]. At the time of writing, beam measurements on the ionising electron beam are under way [33], and beam emittance measurements are being set.

At CERN, the same group that built the 750 MHz proton RFQ is working on a C^{6+} carbon ion RFQ operating at the same RF frequency. Two solutions have been considered, a 2.5 MeV/u design and a 5 MeV/u one with approximately double length and power consumption. For both the two designs, the transmission and output normalized emittances are similar to the already built proton RFQ [34].

The ACCIL Project

The Argonne National Laboratory (ANL), in collaboration with RadiaBeam Technologies, is studying a compact carbon ion linac, named Advanced Compact Carbon Ion Linac (ACCIL) [2]. Two main differences exist with respect to the CABOTO project:

- the use of a commercial ECR ion source, delivering C^{5+}, that are further accelerated by a 476 MHz RFQ until 3 MeV/u and then stripped to C^{6+};
- the choice of a high-gradient solution for the high-energy linac, operating at a 50 MV/m accelerating gradient.

A travelling wave cavity similar to the one developed for the TULIP project [12] has been considered for the high-energy linac - from 45 MeV/u to 450 MeV/u - and is being built [35].

HIGH-ENERGY PROTON THERAPY

With high-energy proton therapy (HEPT) one can treat and at the same time produce a radiography of the patient. A 350 MeV proton beam has a range of more than 60 cm in water equivalent tissue (WET), so it traverses a patient body and can be used for proton radiography. From a treatment point of view, the smaller lateral penumbra of an high-energy beam permits to treat the critical boundaries of the tumour volume, such as the ones near a critical healthy structure.

The IMPULSE project, started at PSI in collaboration with TERA Foundation in 2011 [36] proposed a high-energy cyclotron for this purpose. In [37] it is proposed to couple the PSI proton therapy cyclotron to a 3 GHz linac to accelerate the protons from 250 MeV to 350 MeV.

Similarly, in [38] is proposed a similar approach considering as a starting point the 250 MeV Christie Hospital cyclotron in Manchester, UK.

COMMERCIAL DEVELOPMENTS

The CERN spin-off company ADAM is constructing and testing the first commercial linear accelerator for proton therapy [11, 39], called LIGHT (Linac for Image-Guided Hadron Therapy). Based on the original design presented in [7], LIGHT is composed by an ECR source, followed by the CERN 750 MHz RFQ, a 3 GHz SCDTL and a 3 GHz CCL. At the time of writing, the machine commissioning is ongoing, with reported results of beam acceleration up to 16 MeV, at the output of the second SCDTL module.

SUMMARY

The research on hadron therapy linacs produced significant breakthroughs over the past years. CERN had a leading role in the field, with the test of a high frequency RFQ and of a high-gradient accelerating cavity. These developments solved two of the biggest challenges: the efficient acceleration of low energy beams and the size of the facility. All-linac designs for proton and carbon therapy linacs have been designed, and two projects are currently under construction, the ADAM Light in Geneva and the TOP-IMPLART in Rome. The research effort is now focused on carbon therapy linacs, where the biggest advantages over state-of-art synchrotrons is present.

ACKNOWLEDGEMENTS

The author is sincerely thankful to A. Lombardi and Prof. U. Amaldi for their support on these studies.

ISBN: 978-3-95450-194-6 ISSN: 2226-0366 doi:10.18429/JACoW-LINAC2018-TH1P03

REFERENCES

[1] S. Benedetti, High-gradient and high-efficiency linear accelerators for hadron therapy, PhD Thesis, EPFL, Lausanne, Switzerland 2018.

[2] P.N. Ostroumov *et al*, Compact carbon ion linac, in *Proc. NAPAC'16*, Chicago, IL, Oct. 2016.

[3] M. Vretenar *et al*, A compact high-frequency RFQ for medical applications, in *Proc. LINAC'14*, Geneva, Switzerland, Sep. 2014.

[4] A.M. Lombardi *et al*, Beam Dynamics in a high frequency RFQ, in *Proc. IPAC'15*, Richmond, VA, USA, May 2015.

[5] S. Benedetti *et al*, RF Design of a Novel S-Band Backward Travelling Wave Linac for Proton Therapy, in *Proc. LINAC'14*, Geneva, Switzerland, Sep. 2014.

[6] T.P. Wangler, RF linear accelerators, Wiley-VCH, New York, 2008.

[7] U. Amaldi, S. Braccini and P. Puggioni, High frequency linacs for hadrontherapy, *Reviews of Accelerator Science and Technology*, vol. 02, pp. 111–131, 2009.

[8] A. Degiovanni, High Gradient Proton Linacs for Medical Applications, PhD Thesis, EPFL, Lausanne, Switzerland 2014.

[9] Ronsivalle, C., Carpanese, M., Marino, C. *et al*, The TOP-IMPLART project, *Eur. Phys. J. Plus* (2011) 126: 68.

[10] C. Roncisvalle *et al*, First acceleration of a proton beam in a side coupled drift tube linac, *EPL*, vol. 111, p. 14002, 2015.

[11] V. Dimov *et al*, Beam Commissioning of the 750 MHz Proton RFQ for the LIGHT Prototype, in *Proc. IPAC'18*, Vancouver, Canada, May 2018.

[12] S. Benedetti, A. Grudiev and A. Latina, High gradient linac for proton therapy, *Phys. Rev. ST Accel. Beams*, vol. 20, p. 040101, 2017.

[13] U. Ratzinger, H-type linac structures, CERN Accelerator School: Radio Frequency Engineering, Seeheim, Germany, May 2000.

[14] S. Benedetti, A. Grudiev and A. Latina, Design of a 750 MHz IH structure for medical applications, in *Proc. LINAC'16*, East Lansing, MI, USA, Sep. 2016.

[15] E. Montesinos private communication, 2016.

[16] R. Tiede, KONUS Beam Dynamics Designs Using H-Mode Cavities, in *Proc. HB'08*, Nashville, TN, USA, Aug. 2008.

[17] S. Kurennoy *et al*, H-mode accelerating structures with PMQ beam focusing, *Phys. Rev. ST Accel. Beams*, vol. 15, p. 090101, 2012.

[18] M. Vretenar, Introduction to RF Linear Accelerators, Cern Accelerator School - General Accelerator Physics, Frascati, Italy, 2008.

[19] N. Alharbi, F. Gerigk and M. Vretenar, Field stabilization with post couplers for DTL tank1 of Linac4, CARE-Note-2006-012-HIPPI, 2006.

[20] A. Degiovanni *et al*, Design of a Fast-Cycling High-Gradient Rotating Linac for Protontherapy, in *Proc. IPAC'13*, Shanghai, China, May 2013.

[21] Particle Therapy CoOperative Group, https://www.ptcog.ch/

[22] U. Amaldi *et al*, Ion acceleration system for medical and/or other applications, Patent US 2010/0320403.

[23] A. Degiovanni *et al*, TERA high gradient test program of RF cavities for medical linear accelerators, *Nucl. Instr. Meth.*, vol. 657, pp. 55-58, 2011.

[24] S. Benedetti *et al*, Fabrication and testing of a novel S-Band backward travelling wave accelerating structure for proton therapy linacs, in *Proc. LINAC'16*, East Lansing, MI, USA, Sep. 2016.

[25] A. Vnuchenko *et al*, High gradient performance of an S-band backward traveling wave accelerating structure for medical hadron therapy accelerators, in *Proc. IPAC'18*, Vancouver, Canada, May 2018.

[26] A. Grudiev, S. Calatroni and W. Wuensch, New Local Field Quantity Describing the High Gradient Limit of Accelerating Structures, *Phys. Rev. ST Accel. Beams*, vol. 12, p. 102001, 2009.

[27] U. Amaldi, M. Crescenti, R. Zennaro, Ion acceleration system for hadrontherapy, Patent US 7423278.

[28] S. Verdú-Andrés, U. Amaldi and A. Faus-Golfe, CABOTO, a high-gradient linac for hadrontherapy, *J. Radiat. Res.*, vol. 54, pp. i155-i161, 2013.

[29] A. Garonna, Cyclotron Designs for Ion Beam Therapy with Cyclinacs, PhD Thesis, EPFL, Lausanne, Switzerland 2011.

[30] U. Amaldi, Notes on medical physics - Trento, 1999.

[31] M. Breitenfeldt *et al*, The TwinEBIS setup: Machine description, *Nucl. Instr. Meth.*, vol. 856, pp. 139-146, 2017.

[32] R. Mertzig *et al*, A high-compression electron gun for C6+ production: concept, simulations and mechanical design, *Nucl. Instr. Meth.*, vol. 859, pp. 102-111, 2017.

[33] M. Breitenfeldt *et al*, MEDeGUN Commissioning Results, in *Proc. ICIS'17*, Geneva, Switzerland, Oct. 2017.

[34] V. Bencini *et al* High frequency RFQ design and LEBT matching for the CERN TwinEBIS ions source, this conference.

[35] S.V. Kutsaev *et al*, High-gradient low-β accelerating structure using the first negative spatial harmonic of the fundamental mode, *Phys. Rev. ST Accel. Beams*, vol. 20, p. 120401, 2017.

[36] J. Schippers *et al*, Next step in proton therapy: Boosting to 350 MeV for therapy and radiography applications, in *Proc. PTCOG'51 Conf.*, Seoul, S. Korea, May 2012.

[37] A. Degiovanni, U. Amaldi, Linac booster for high energy proton therapy and imaging, *Phys. Rev. ST Accel. Beams*, vol. 21, p. 064701, 2018.

[38] S. Pitman *et al*, ProBE: Proton boosting extension for imaging and therapy, in *Proc. IPAC'17*, Copenhagen, Denmark, May 2018.

[39] A. Degiovanni *et al*, Status of the Commissioning of the LIGHT Prototype, in *Proc. IPAC'18*, Vancouver, Canada, May 2018.

Content from this work may be used under the terms of the CC BY 3.0 licence (© 2018). Any distribution of this work must maintain attribution to the author(s), title of the work, publisher, and DOI.

ISBN: 978-3-95450-194-6 ISSN: 2226-0366 doi:10.18429/JACoW-LINAC2018-THPO001

DESIGN STUDY ON CEPC POSITRON DAMPING RING SYSTEM*

D. Wang †, C. Meng, J. Gao, D. Gong, J. Zhang, G. Pei, Y. Chi, IHEP, Beijing 100049, China

Abstract

The primary purpose of CEPC damping ring is to reduce the transverse phase spaces of positron beam to suitably small value at the beginning of linac and hence reduce the beam loss in the booster. Before damping ring, an energy spread compression structure is designed to match the RF acceptance of damping ring. A longitudinal bunch length control is also necessary to meet the energy spread requirement in the linac by a bunch compressor system after the damping ring. Both designs for damping ring and energy/bunch compressors are discussed in this paper.

INTRODUCTION

So far, the whole CEPC system is composed of three parts: a linac, a booster, the collider ring [1]. The linac injector system is composed of a 10 GeV S-band linac with electron/positron source and a 1.1 GeV damping ring. The layout of CEPC accelerator chain is shown in Fig. 1.

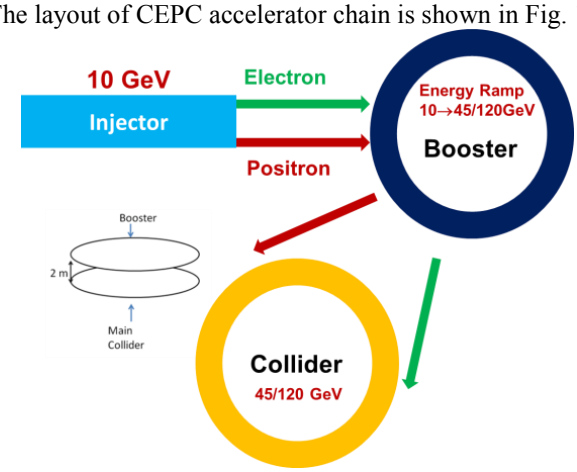


Figure 1: Sketch of CEPC accelerator chain.

The repetition rate of Linac is 100 Hz and one-bunch-per-pulse is considered. To achieve larger than 3 nC positron bunch, a 4 GeV primary electron beam with 10 nC hit tungsten target. The large transverse emittance of the positron beam emerging from the target is transformed to match pre-accelerating section with AMD flux concentrator. The captured positron beam will be pre-accelerated to 200 MeV. Each positron bunch is injected into damping ring every 10 ms and two bunches are stored in the ring so that the storage time for each bunch is 20 ms. The layout of CEPC Linac and damping ring is shown in Fig. 2.

* Work supported by the National Key Programme for S&T Research and Development (Grant NO. 2016YFA0400400) and the National Natural Science Foundation of China (11505198 and 11575218).
† wangd93@ihep.ac.cn

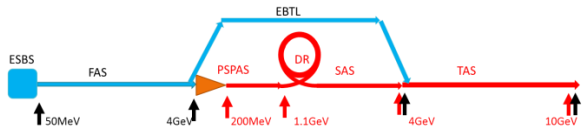


Figure 2: Sketch of CEPC Linac and damping ring.

DAMPING RING DESIGN

The energy of DR is 1.1 GeV and the circumference is 75.4 m. The DR has a racetrack shape and the arcs were designed with 60 degree FODO cell.

The injected emittance (normalized) for DR is 2500 mm·mrad and the injected energy spread is smaller than 0.2%. The positron beam will be stored in DR for 20 ms according to the 100 Hz repetition rate and two-bunch storage scheme. The extracted emittance is better to be smaller than one quarter of the injected emittance. Considering the issue of injection efficiency, the transverse acceptance of DR should be larger than five times of the injection beam size.

DR Parameter Design

The parameters of damping ring are calculated analytically based on the method in reference [2]. The layout of damping ring is shown in Fig. 3 and the main parameters are listed in Table 1.

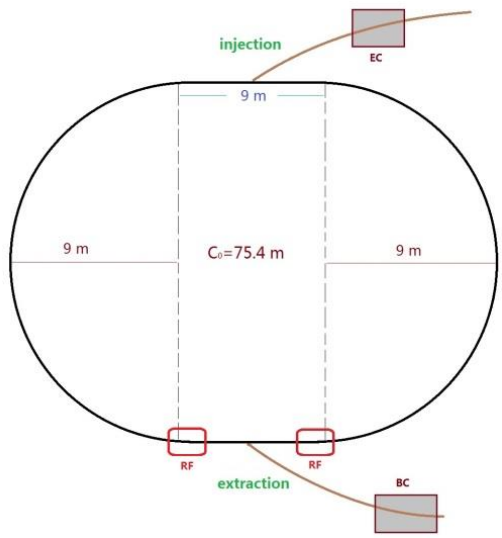


Figure 3: Layout of CEPC damping ring.

Table 1: Main Parameters of Damping Ring

	DR V2.0
Energy (Gev)	1.1
Circumference (m)	75.4
Bending radius (m)	3.6
Dipole strength B_0 (T)	1.03
U_0 (kev/turn)	36.3
Damping time x/y/z (ms)	15.2/15.2/7.6

Content from this work may be used under the terms of the CC BY 3.0 licence (© 2018). Any distribution of this work must maintain attribution to the author(s), title of the work, publisher, and DOI.

ISBN: 978-3-95450-194-6 ISSN: 2226-0366 doi:10.18429/JACoW-LINAC2018-THPO001

δ_0 (%)	0.05
ε_0 (mm.mrad)	376.7
injection σ_z (mm)	5
Extract σ_z (mm)	7.5
ε_{inj} (mm.mrad)	2500
$\varepsilon_{ext\ x/y}$ (mm.mrad)	530/180
$\delta_{inj}/\delta_{ext}$ (%)	0.18 /0.05
Energy acceptance by RF(%)	1.0
f_{RF} (MHz)	650
V_{RF} (MV)	2.0

DR Optics Design

We chose 60°/60° FODO cell and interleave sextupole scheme for the arc. The emittance of the ring is 175 nm. The twiss parameters of DR are shown in Figs. 4-7.

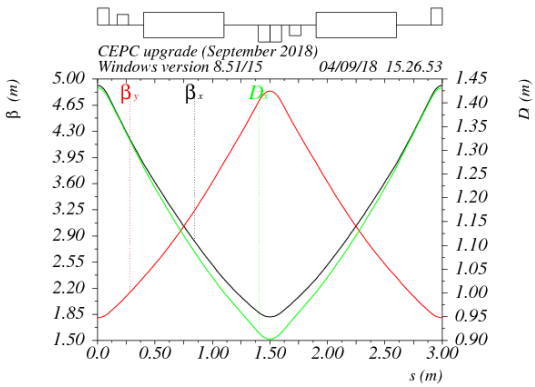


Figure 4: Twiss parameter for the arc FODO cell.

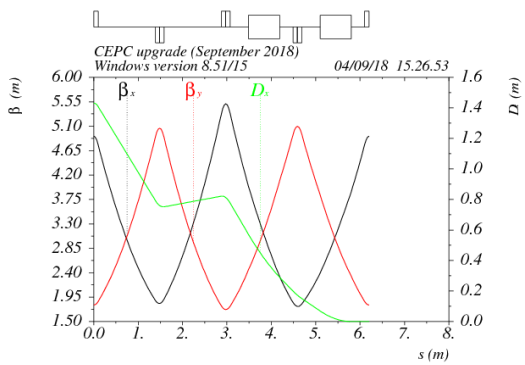


Figure 5: Twiss parameter for the dispersion suppressor.

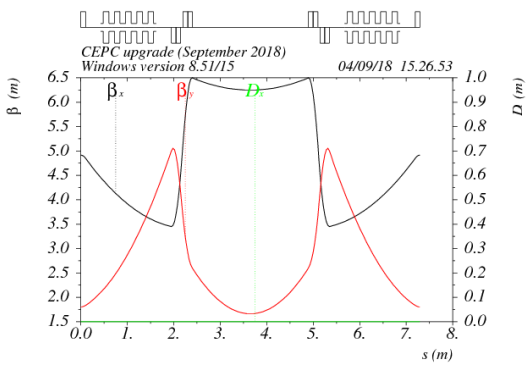


Figure 6: Twiss parameter for injection/extraction section.

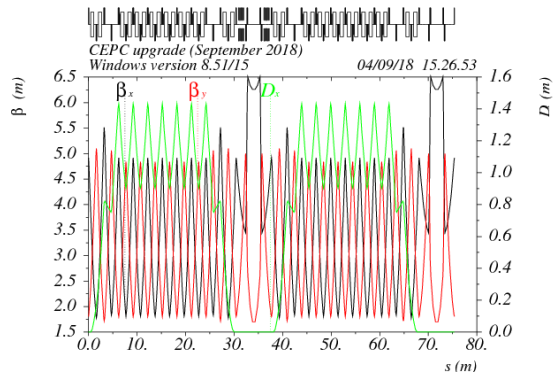


Figure 7: Twiss parameter for the whole ring.

Dynamic Aperture of DR

The chromaticity of the damping ring was corrected by two sextupole families. Then we tracked the DA of damping ring by 240000 turns (4 damping times) using SAD. The DA result is shown in Fig. 8. Since the DA is much larger than 5 times of injection beam size, the injection acceptance for the damping ring should be no problem.

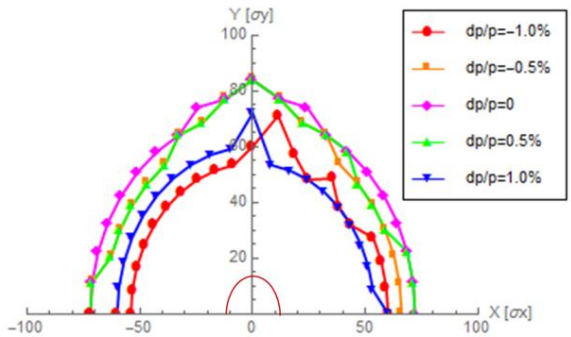


Figure 8: DA of damping ring (red line: 5 times of injection beam size).

ENERGY/BUNCH COMPRESSOR DESIGN

Before damping ring, the energy spread of the positron bunch should be reduced in order to match the RF acceptance of damping ring. After damping ring, longitudinal bunch length control must be provided to minimize energy spread in the linac. Reducing bunch length in the ring to the required value will need very high (~40 MV) RF voltage, so we add a bunch compressor system after the damping ring.

Consideration for EC/BC Design

Our design goal for energy compressor is to get small energy spread (<0.2%) at the entrance of damping ring and get short bunch length (<2mm) before re-injection to the linac. The design principle [2] is same for energy compression and bunch compression due to their inverse relationship. Meanwhile the compression ratio for EC/BC is better to be flexible. The basic structure of BC (EC) in our mind is shown in Fig. 9.

Content from this work may be used under the terms of the CC BY 3.0 licence (© 2018). Any distribution of this work must maintain attribution to the author(s), title of the work, publisher, and DOI.

ISBN: 978-3-95450-194-6 ISSN: 2226-0366 doi:10.18429/JACoW-LINAC2018-THPO001

Content from this work may be used under the terms of the CC BY 3.0 licence (© 2018). Any distribution of this work must maintain attribution to the author(s), title of the work, publisher, and DOI.

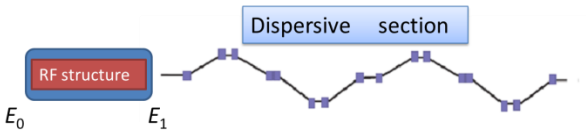


Figure 9: Principle sketch of bunch compressor.

Parameter Design for EC

The injection energy spread for energy compressor is 0.6% and injection bunch length is 1.5 mm. After the energy compressor, the energy spread should be smaller than 0.2% in order to be accepted by the damping ring RF system. The primary parameter designs for EC are listed in table 2. The relationships of injected energy spread and RF voltage with different extracted energy spread are shown in Figs. 10-11.

Table 2: Parameters of CEPC Energy Spread Compressor

	EC
E_0 (GeV)	1.1
δ_0 (%)	0.6
σ_{z0} (mm)	1.5
f_{RF} (MHz)	2860
V_{RF} (MV)	69.2
Length of acc. Structure (m)	3.0
ϕ_{RF} (degree)	89.9
R_{56} (m)	-0.833
E_f (GeV)	1.1
δ_f (%)	0.18
σ_{zf} (mm)	5

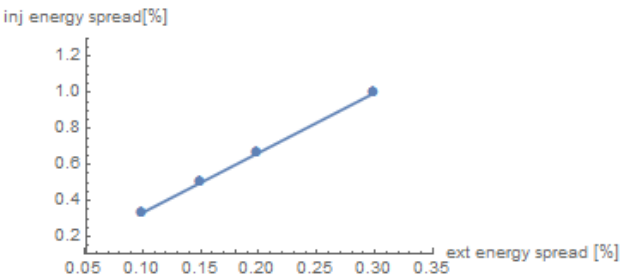


Figure 10: EC inj. energy spread vs. ext. energy spread.

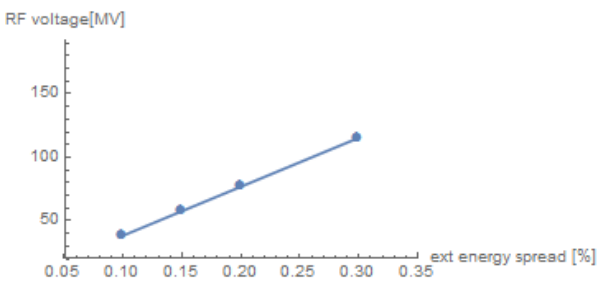


Figure 11: EC RF voltage vs. ext. energy spread.

Parameter Design for BC

The injection bunch length for bunch compressor is 7.5 mm, and the injection energy spread is 0.05%. After the bunch compressor, the beam energy should keep almost 1.1 GeV and the bunch length should be smaller than 2 mm in order to be accelerated in the linac. While the process of bunch compressing is at the cost of enlarging the beam energy spread at the exit of bunch compressor. The primary parameter designs for BC are listed in table 3. The relationships of extracted energy spread and RF voltage with different extracted bunch length are shown in Figs. 12-13.

Table 3: Parameters of CEPC Bunch Compressor

	BC
E_0 (GeV)	1.1
δ_0 (%)	0.05
σ_{z0} (mm)	7.5
f_{RF} (MHz)	2860
V_{RF} (MV)	41.2
Length of acc. Structure (m)	2.0
ϕ_{RF} (degree)	89.9
R_{56} (m)	-1.4
E_f (GeV)	1.1
δ_f (%)	0.54
σ_{zf} (mm)	0.7

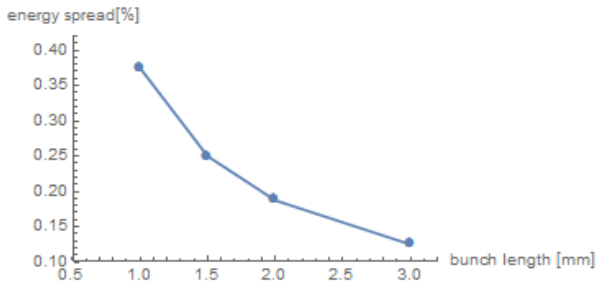


Figure 12: BC ext. energy spread vs. ext. bunch length.

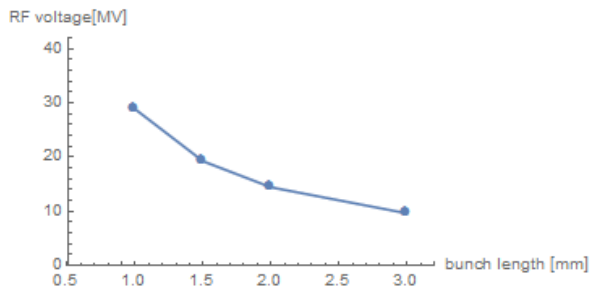


Figure 13: BC RF voltage vs. ext. bunch length.

SUMMARY

The purpose of CEPC damping ring is to reduce the transverse emittance of positron beam. Primary DR design has been finished. DA can fulfil the requirement for injection. Before and after damping ring, an energy compression system and a bunch compression system is needed to adjust energy spread and bunch length. Primary parameter design for EC and BC has been given. The detail optics design and beam dynamics study is underway.

REFERENCES

[1] The CEPC Study Group, "CEPC Conceptual Design Report", Volume I- Accelerator, IHEP-CEPC-DR-2018-01, IHEP-AC-2018-01, August 2018.

ISBN: 978-3-95450-194-6 ISSN: 2226-0366 doi:10.18429/JACoW-LINAC2018-THPO001

[2] D. Wang *et al.*, "Design study on CEPC positron damping ring and bunch compressor", in *Proc. IPAC'17*, Copenhagen, Denmark, May 2017, paper TUPAB009, pp. 1318-1321.

Content from this work may be used under the terms of the CC BY 3.0 licence (© 2018). Any distribution of this work must maintain attribution to the author(s), title of the work, publisher, and DOI.

ISBN: 978-3-95450-194-6 ISSN: 2226-0366 doi:10.18429/JACoW-LINAC2018-THPO002

INVESTIGATION OF SRF ELLIPTICAL CAVITIES MADE BY NEW Nb MATERIALS IN KEK

T. Dohmae†, K. Umemori, Y. Watanabe, M. Yamanaka, KEK, Tsukuba, Japan
M.Okada, SOKENDAI, KEK, Tsukuba, Japan

Abstract

Two kinds of in-house 3-cell superconducting RF cavities were fabricated using two kinds of niobium in KEK. These materials are expected to reduce the cost for the cavity material since some processes in niobium production were skipped. Completed cavities were then RF tested in the vertical cryostat to measure their performance. One of them achieved maximum gradient of 40 MV/m with maximum Q_0 value of 1.87×10^{10}.

INTRODUCTION

The International Linear Collider (ILC) is now under contemplation in Japan. Reducing the cost for cavity fabrication is presently one of the main issue to realize ILC. The Cavity Fabrication Facility (CFF) at KEK which enables the entire process of cavity fabrication approached this issue in terms of cavity materials.

The ratio of tantalum in niobium was first focused on to reduce the material cost. An additional chemical process is generally necessary to remove tantalum from niobium. This process arises niobium production cost. Thus niobium which contains high tantalum is cheaper than one contains low tantalum. The production processes of niobium were also focused on for the cost reduction. Several processes such as melting, forging and rolling are necessary to produce niobium sheets and tubes used for cavity. Skipping some of these process can also reduce material production cost.

The main purpose of this study is evaluation of new niobium for cavity materials which are expected to reduce the cost. Several cavities were fabricated and RF tested using these materials.

FABRICATION

CFF fabricated two types (“type1” and “type2”) of cavities using different materials. The shape of these cavities are all 3-cell Tesla-like [1] shape and designed to be used in 1.3GHz RF operation. Two 3-cell cavities (“cavity1” and “cavity2”) were fabricated for each type respectively.

Type1 Cavity

Figure 1 shows fabricated type1 cavities. Niobium which residual resistance ratio (RRR) is low and containing higher ratio of tantalum was used as start material for type1 cavities. This material was then forged and rolled into niobium sheets and seamless tubes. Niobium sheets were used for stiffener rings and tubes were used for beam tubes. Rest of this material was melted two times by electron beam welding in the vacuum chamber to purify. This melting process is normally done five or more times. Thus, production cost of this material was also reduced. This melted niobium was forged and rolled into niobium sheets and used for cavity cells. RRR of start material was 60~108 (ingot), and it recovered up to 277~298 (ingot). RRR of the sheets (after forge and rolling) used for cells was 293. RRR of ingot varies widely since measured samples were taken from both edges of ingot. RRR are summarised in Table 1. Chemical components of these materials are summarised in Table 2. In Table 2, “Ingot1” represents the value of start materials, “Sheet” represents the value of niobium sheets used for stiffener rings and “Ingot2” represents the value of ingot after two times melting. The start material was supplied by CBMM, and melting, forge and rolling process were done by ULVAC

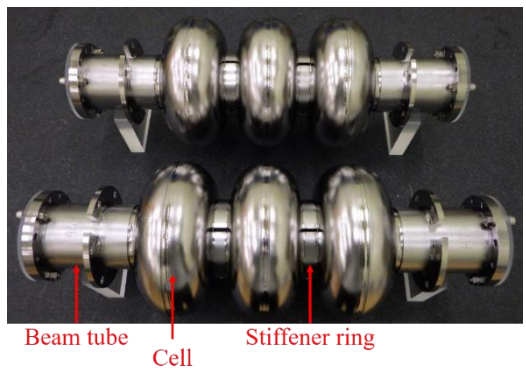


Figure 1: Fabricated type1 cavities and explanation of each parts.

Type2 Cavity

Figure 2 shows fabricated type2 cavities. Niobium sheets directly sliced from niobium ingot which is called large grain (LG) were used for this cavity. Production cost of LG niobium sheet is lower than normal sheet since forge and roll process are skipped. Used niobium sheet for type 2 cavity is shown in Figure 3. LG sheet has strong anisotropy as it has large crystal size which diameter is about 100~150 mm, as shown in Figure 3. This strong anisotropy leads some technical difficulties in fabrication. For example, the roundness of the inside equator is worse than one made of normal sheet due to large deformation after press forming. Hence, a special jig shown in Figure 4 which

Table 1: RRR Values of Materials Used for Each Part of Type1 and Type2 Cavities

	Type1	Type2
Cells	293	242~298
Beam tubes	60~108	60~108
Stiffener rings	60~108	-

Content from this work may be used under the terms of the CC BY 3.0 licence (© 2018). Any distribution of this work must maintain attribution to the author(s), title of the work, publisher, and DOI.

ISBN: 978-3-95450-194-6 ISSN: 2226-0366 doi:10.18429/JACoW-LINAC2018-THPO002

Table 2: Chemical Components of Each Material

Cavity		C	N	O	H	Zr	Ta	Fe	Si	W	Ni	Mo	Hf	Ti	S
Type1	Ingot1	<30	33	26	<2	<1	1194	3	<20	<5	<1	<1	<2	7	<10
	Sheet	<10	30	<10	1	<10	1210	<10	<10	<10	10	<10		<5	
	Ingot2	<10	<10	<10	<1	<10	1430	<10	<10	<10	10	<10		<5	
Type2	ingot	<30	6	5	2		1191	<3		<5		1			<10

forces equator into an exact circle is necessary for electron beam welding (EBW) of an equator. This process is only necessary for LG cavity. Non-uniform thicknesses at the edge of half-cell especially around grain boundaries are observed. This leads an EBW failure such as creation of a hole and not enough penetration. An iris part (constricted part of a cavity) was welded from both outside and inside however it is normally welded only from outside. Such difficulties of fabricating LG cavity is also described in [2].

The chemical components of this material are shown in Table 2. The ratio of tantalum in this niobium is also high.



Figure 2: Fabricated type2 cavities.

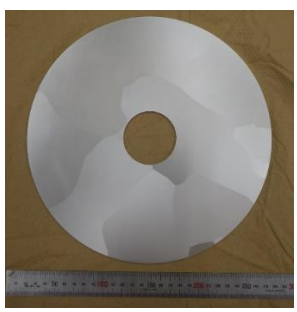


Figure 3: LG niobium sheet used for type2 cavity. The outer diameter is 260 mm.



Figure 4: Special jigs set at equator for EBW.

RRR value varies from 242~298 which is listed in Table 1. LG ingot were supplied by CBMM, and cut by wire saw.

A same material as type1 cavity was used for beam tubes. Recycled niobium from scrapped niobium was used as stiffener rings of type2 cavity.

PERFORMANCE MEASUREMENT

Preparation

Completed cavities were measured its performance in a vertical cryostat. Several surface treatments have been applied to the cavity before measurement in KEK [3]. Brief surface treatment flow is listed below.

1. 100 μm of electropolishing (EP) of inside cavity
2. Ultrasonic rinsing with neutral detergent at 50 ◦C for 15 min and high-Pressure Rinsing (HPR) of the inside cavity with 8 MPa of ultrapure water for 1 h with open flanges
3. Annealing of cavity for 3 hours at 750 □ in a vacuum furnace for hydrogen degassing
4. Frequency tuning
5. 30 μm of EP
6. Ultrasonic rinsing with neutral detergent at 50 ◦C for 15 min and HPR
7. Assembly for the performance measurement in Class 10 clean room
8. Baking for 48 h at 120 ◦C (after assembly)

Measurement

Cavity is cooled down by liquid helium in a vertical cryostat and its performances were measured after surface treatment.

Top two plots in Figure 5 show results of performance measurements of type1 cavities in π-mode. Measurements were done at 1.5 K, 1.8 K and 2 K respectively. Measurement in 1.5 K and 1.8 K were stopped at 15 MV/m intentionally to avoid Q_0 drop due to flux trapping caused by quench. Measurements at 2 K were done twice; first and final. The first 2 K measurement was done after 1.5 K and 1.8 K measurement. The final 2 K measurement was done after other passband mode measurement done after first 2 K measurement. The performance of type1-cavity1 (left top in Figure 5) was limited to 23 MV/m at 2 K due to quench. The performance of type1-cavity2 (right top in Figure 5) was limited 35 MV/m. Q_0 value was dropped over 25 MV/m due to x-ray radiation. Cavities are required to reach accelerator gradients of 35 MV/m and Q_0 value of 0.8×10^{10} at 35 MV/m in ILC technical design report [4]. Both of type1 cavities could not satisfy these requirements.

Content from this work may be used under the terms of the CC BY 3.0 licence (© 2018). Any distribution of this work must maintain attribution to the author(s), title of the work, publisher, and DOI.

ISBN: 978-3-95450-194-6 ISSN: 2226-0366 doi:10.18429/JACoW-LINAC2018-THPO002

Content from this work may be used under the terms of the CC BY 3.0 licence (© 2018). Any distribution of this work must maintain attribution to the author(s), title of the work, publisher, and DOI.

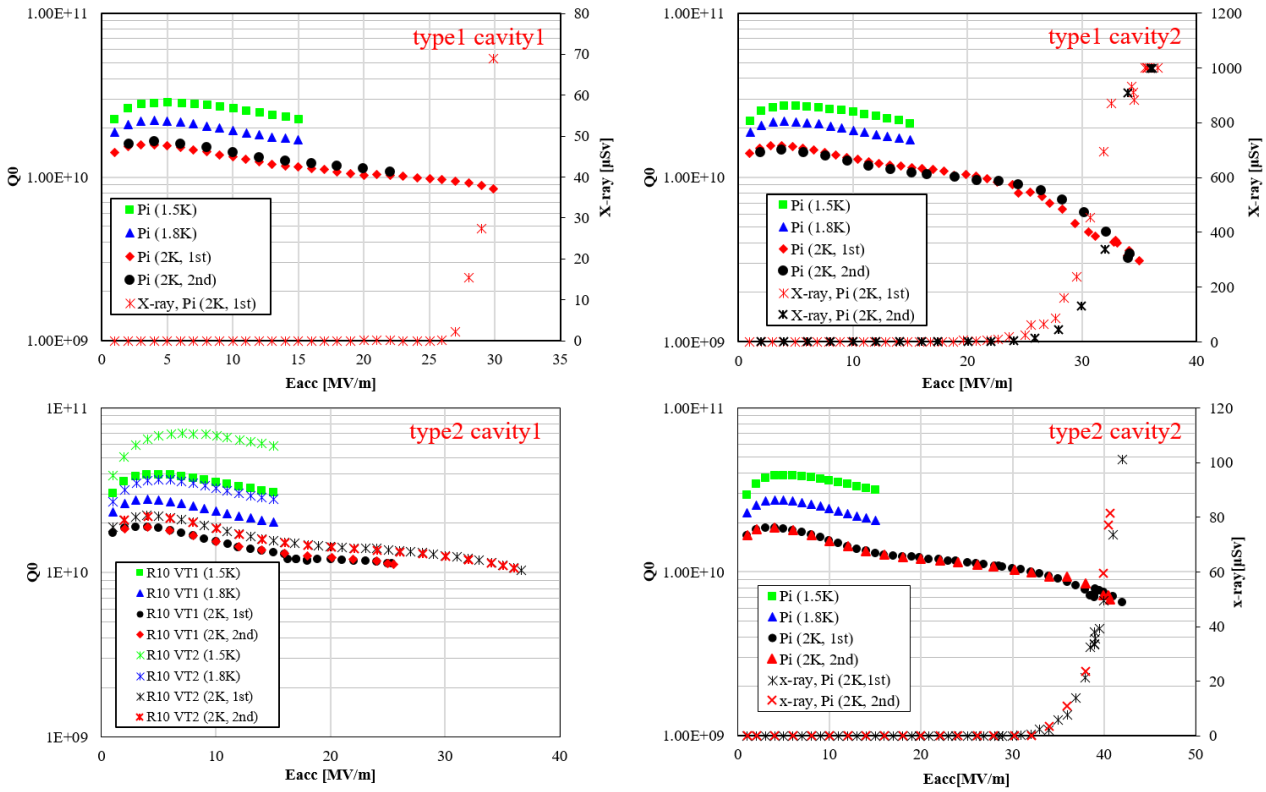


Figure 5: Results of performance measurements.

Bottom two plots in Figure 5 show results of performance measurements of type2 cavities in π-mode. Measurements were done in same sequence as type1 cavities. The performance of type2-cavity1 (left bottom in Figure 5) was limited to 25 MV/m at 2 K due to quench. A suspicious defect was found around quench region by inspection done after performance measurement. This defect was removed, and the cavity was electropolished in 50 μm. The performance of this cavity was then reached to 36 MV/m in the second measurement. The remaining magnetic field around cavity was cancelled by solenoid coil surrounding cavity in the second measurement. Other measurements were done in the remaining magnetic field of 5~10 mG. And, temperature gradient which was made by heater surrounding top beam tube was applied during superconducting transition. The Q_0 value in the second measurement is higher than one from first measurement due to magnetic cancelation and temperature gradient. The performance of type2-cavity2 reached to 40 MV/m in 2K measurement. Both of typ2 cavities satisfied ILC requirements.

CONCLUSION

Two types of niobium were used to fabricate superconducting RF cavities to study cost reduction in terms of cavity materials. Two 3-cell Tesla-like shape cavities were fabricated with each niobium. Completed cavities underwent performance measurement via several surface treatments.

Type1 cavities made of niobium which RRR is around 300 and contains high ratio of tantalum reached 23 MV/m and 35 MV/m respectively.

Type2 cavities made of LG niobium which RRR is around 300 and contains high ratio of tantalum reached 36 MV/m and 40 MV/m which satisfy ILC requirements.

In both cases, beam tubes made of low RRR and high tantalum contained niobium did not affect to cavity performance in the measurement where liquid helium directly cooled down the beam tubes. But further study about an effect from heat conductivity to a beam tubes should be done since the cavity is not directly put into the liquid helium in the practical usage.

LG niobium is expected to achieve more efficient cost reduction. And CFF is fabricating 9-cell cavities using this LG niobium in 2018.

REFERENCE

[1] E. Kako, *et al.*, "Cryomodule tests of four Tesla-like cavities in the Superconducting RF test facility at KEK", *Phys. Rev. ST Accel. Beams* 13, 041002, 2010, doi: 10.1103/PhysRevSTAB.13.041002

[2] T. Dohmae, *et al.*, "Investigation of in-house superconducting radio-frequency 9-cell cavity made of large grain niobium at KEK", *NIM* A, 875, 1-9, doi: 10.1016/j.nima.2017.08.050

[3] E. Kako, *et al.*, "Vertical test results on the STF baseline 9-cell cavities at KEK", in *Proc. SRF'07*, Beijing, China, Oct. 2007, paper WEP10, pp. 453-457.

[4] "The International Linear Collider, Technical Design Report", Volume 3. II : Accelerator Baseline Design.

ISBN: 978-3-95450-194-6 ISSN: 2226-0366 doi:10.18429/JACoW-LINAC2018-THPO003

L-BAND RESONANT RING FOR TESTING RF WINDOWS FOR ILC

B.T. Du†,1, T. Matsumoto1,2, S. Michizono1,2, T. Miura1,2, F. Qiu1,2, N. Liu1
[1] SOKENDAI (The Graduate University for Advanced Studies), 240-0193, Hayama, Japan
[2]High Energy Accelerator Research Organization, 305-0801, Tsukuba, Japan

Abstract

A resonant ring is widely used for the breakdown test of RF components under high power. It can reach power gain of more than 10 dB, which is limited by the attenuation of the ring. An L-band resonant ring is constructed for testing RF components of International Linear Collider (ILC) which is based on an RF frequency of 1.3 GHz. The target of the high power test is 5 MW. We have finished the test of an input power of 500 W using a solid state amplifier, and the principle of the resonant ring is verified. The resonant ring is tuned to an optimal condition, which is preparation for high power operation. This paper details the principle, construction, and test of the L-band resonant ring.

INTRODUCTION

The International Linear Collider (ILC) is a 250 GeV linear electron-positron collider, based on the 1.3 GHz superconducting radio-frequency technology [1]. Figure 1 shows the power distribution system (PDS) for ILC. Every PDS contains one 10 MW multi-beam klystron and that drives 39 cavities. Based on Fig. 1, the power on RF window, which is next to the variable power divider, is 1.1 MW. Considering the maximal standing wave, the power on the RF window may be 4 times to theoretical value, which is 4.4 MW. Therefore, it is necessary to test the RF window under 5 MW using a long operating period.

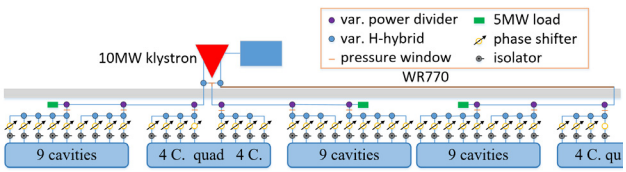


Figure 1: Power distribution system for ILC.

A resonant ring is a closed loop of a waveguide system that can amplify power, and it is widely used for the breakdown test of the RF components under high power [2]. In the superconducting RF test facility (STF), the variable hybrid, the phase shifter and the 500kW circulator have already been developed [3]. Moreover, the 800 kW modulated-anode klystron is developed in the STF, which is employed in the distributed RF system for the ILC [4].

Firstly, we a construct resonant ring with a variable hybrid, a phase shifter and a circulator at a low input power of 500 W from a solid state amplifier. The power gain is compared with one-turn phase of the ring and the coupling factor of the hybrid is tested [5]. The measured result shows that the maximum power gain can reach 10 ~13 dB, and is matched with simulation. A circular power of 5 MW can be achieved by the resonant ring with an input from an 800 kW klystron.

† baiting@post.kek.jp

Secondly, considering the high power test of 5 MW circular power, the ring is expected to be pressurized by SF_6 or N_2 for preventing high power breakdown. The variable hybrid and phase shifter cannot be worked as pressurized due to its construction. Therefore, a fixed 11 dB hybrid is used to replace the variable hybrid and the operating frequency is changed to adjust one-turn phase. Moreover, the 500 kW circulator cannot be used at 5 MW due to the power limit. Even a low reflection generated in the resonant ring will be accumulated in the high reflected power. A 3-stub tuner is inserted in the ring to reduce the reflection in the ring. After adjusting the depth of the stub, the reflection is reduced significantly and the resonant ring worked at an optimal condition with a higher forward power gain.

THEORY AND STRUCTURE

The structure of the resonant ring is shown in Fig. 2. It contains a signal generator, hybrid, dummy load, and certain length of the waveguide system.

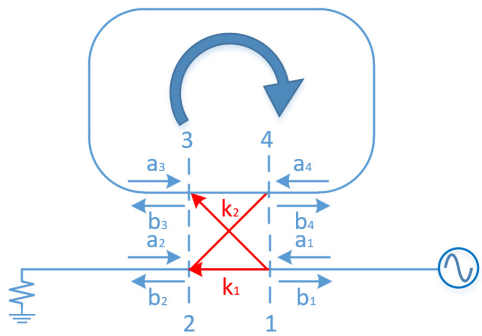


Figure 2: Schematic diagram of the resonant ring.

If the hybrid is assumed to be lossless and symmetrical, with no reflection, then the power gain (G) will be as given in equation (1), where k_1 and k_2 are transmitted and coupling coefficients of the hybrid at voltage respectively; α, β, and L are the attenuation coefficient, phase coefficient, and length of the resonant ring respectively.

$$G = \frac{|b_3|^2}{|a_1|^2} = \frac{k_2^2}{1 + k_1^2 e^{-2\alpha L} - 2k_1 e^{-\alpha L}\cos\beta L} \quad (1)$$

It is obvious that the power gain reaches a maximum when βL=2nπ, where n is an integer. This means that the wave in the ring will be superposed at an optimum condition [6].

$$G_{\max} = \frac{k_2^2}{1 + k_1^2 e^{-2\alpha L} - 2k_1 e^{-\alpha L}} = \frac{1 - k_1^2}{\left(1 - k_1 e^{-\alpha L}\right)^2} \quad (2)$$

Content from this work may be used under the terms of the CC BY 3.0 licence (© 2018). Any distribution of this work must maintain attribution to the author(s), title of the work, publisher, and DOI.

ISBN: 978-3-95450-194-6 ISSN: 2226-0366 doi:10.18429/JACoW-LINAC2018-THPO003

Content from this work may be used under the terms of the CC BY 3.0 licence (© 2018). Any distribution of this work must maintain attribution to the author(s), title of the work, publisher, and DOI.

If the transmitted coefficient k_1 is a variable that corresponds to the variable hybrid, then the eventual maximal power gain is obtained using equation (3) when $k_1=e^{-\alpha L}$.

$$G'_{\max} = \frac{1}{1-e^{-2\alpha L}} \tag{3}$$

SIMULATION AND MEASUREMENT OF THE RESONANT RING

The resonant ring is constructed with a phase shifter, variable hybrid, 500 kW circulator, and an input of 500 W to verify the principle. Figure 3 is the structural diagram of the resonant ring. The maximal power gain relative to k_1 and one-turn phase is measured. Further, the simulation is compared with the measurement.

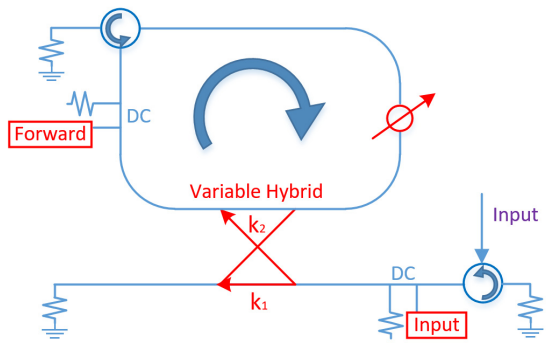


Figure 3: Structure diagram of the resonant ring.

Figure 4 shows the simulated power of the resonant ring compared with time. The parameters for the simulation are obtained from the measurement of the constructed resonant ring, such as one-turn phase, on- turn loss (A) and the transmitted coefficients (k_1^2) of the hybrid are set to 11 times 2π, -0.21 dB and -0.21 dB, respectively. The maximal power gain is 21.18 times (13.26 dB) and the rising time of the forward power from 10% to 90% is 0.89 μs. This showed that the power in the ring is accumulated to a high value by many turns and reaches saturation when the one-turn loss is equal to the coupling input.

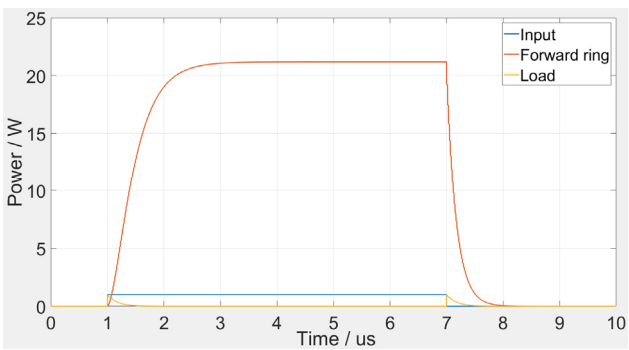


Figure 4: Simulated power with time.

Figure 5 shows the measured and the simulated power gain compared with transmitted coefficient k_1^2. The optimal condition is to make k_1^2 equal to A, and the power gain will decrease faster when k_1^2 is larger than A. Figure 6 shows the measured and simulated power gain compared with one-turn phase drift ($k_1^2 = A$ = -0.21 dB). The delta phase of the x-axis is the phase difference obtained from the optimum condition. The maximal simulated power gain is 13.26 dB with a one-turn loss of -0.21 dB and the maximal measured power gain is 14.12 dB, which corresponds to the one-turn loss of -0.17 dB. This may due to the measuring error of one-turn loss. The 3 dB width is 5.4° for simulation and 4.0° for measurement. If the one-turn phase cannot be adjusted to be an integer times 2π precisely, it is expected to be within the 3 dB width to ensure sufficient power gain.

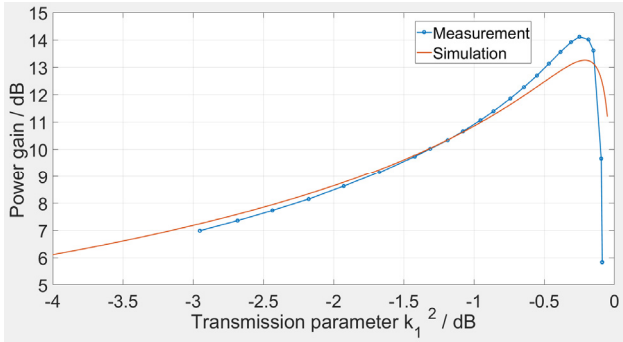


Figure 5: Measured and simulated power gain compared with transmitted coefficient k_1^2.

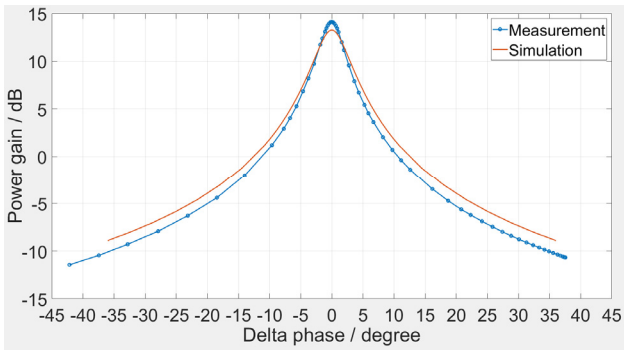


Figure 6: Measured and simulated power gain compared with one-turn phase drift.

PREPARATION FOR HIGH POWER OPERATION

To prevent breakdown at high power, the resonant ring should be pressurized; however, the variable hybrid and phase shifter cannot be used in this condition. The operating frequency is shifted to change the circular phase to adjust the resonant ring to its optimal condition. The fixed hybrid of the coupling coefficient, which is -11.15 dB at 1.3 GHz, replaces the variable hybrid. The reflection due to the hybrid is typically higher than -20 dB around 1.3 GHz.

The circulator cannot be used for the 5 MW case. We find that even small reflections generated in the resonant ring accumulate to cause high reflected power. It is therefore challenging to measure the power of the device under test owing to the serious standing waves generated by the

ISBN: 978-3-95450-194-6 ISSN: 2226-0366 doi:10.18429/JACoW-LINAC2018-THPO003

high reflected power. Thus, it is necessary to suppress or compensate this reflected power in the ring.

A 3-stub tuner is commonly used to match impedance and decrease reflection [7]. Figure 7 is the schematic diagram of the resonant ring with a 3-stub tuner.

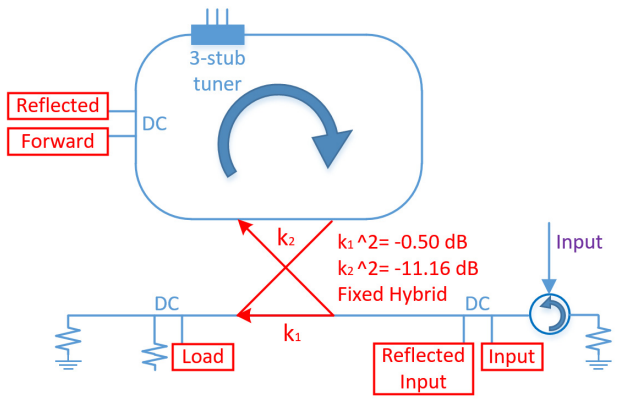


Figure 7: Resonant ring with 3-stub tuner.

For the process of tuning in the preliminary step, a network analyzer is inserted in place of the H-corner near the 3-stub tuner to pre-tune the ring. In the second step, the resonant ring is constructed integrally and an oscilloscope is used to monitor the waveform of the reflected signal in the ring.

Figure 8 shows the measured and simulated response of the fully tuned resonant ring with an input of 500 W. The optimal or peak frequency is found to be 1.3017 GHz. The difference between the forward and reflected power values of the ring is 56.31 dB, as shown in Fig. 9. With the measured one-turn loss of ring *A*, transmitted coefficient k_1^2, and coupling coefficient k_2^2 are -0.04 dB, -0.50 dB, and -11.16 dB, respectively, and the measured and simulated maximal power gain values are 14.80 dB and 13.26 dB, respectively. We consider two possible causes for this difference. First, the measured one-turn loss may be less than the true loss value. Second, if k_1 is not changed and k_2^2 is equal to one subtract k_1^2, the expected *G* will be 14.76 dB, which is close to the measured *G* of 14.80 dB. This means that when the resonant ring is tuned well, all the input power except that delivered to the load will be accumulated as the forward power in the ring. This will make the estimated value of k_2 larger than the measured value, and the hybrid will be operated as the ideal model. For the ideal model of the hybrid, power will only be delivered to the straight and coupling ports but not the isolated port.

Unloaded quality factor Q_{unload} can be calculated using equation (4), where v_g is the group velocity [6]. Measured and simulated Q_{unload} values are 6505 and 3176, respectively. The reason for the difference here is that the measured *G* and power across load are higher than the simulated values.

$$Q_{\text{unload}} = \frac{\pi f}{\alpha v_g} \frac{G(1-A^2)}{1-P_{load}/P_{input}} \tag{4}$$

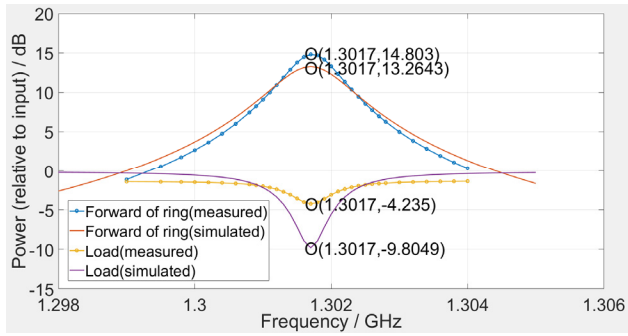


Figure 8: Measured and simulated responses of fully tuned resonant ring with input of 500 W.

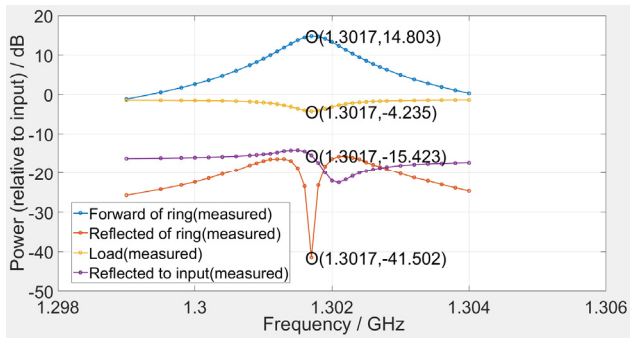


Figure 9: Measured responses of fully tuned resonant ring with input of 500 W.

CONCLUSION

The maximal power gain reached 14.80 dB with an input power of 500 W after the resonant ring was tuned by 3-stub tuner. An 800 kW klystron can satisfy a target of circular power of 5 MW with this power gain. A high power test was conducted after the preparation and a new RF window for PDS of ILC was designed simultaneously.

REFERENCES

[1] ILC, http://www.linearcollider.org/ILC/?pid=1000895

[2] N. Holtkamp, "The S-band Linear Collider Test Facility", in *Proc. 5th European Particle Accelerator Conf. (EPAC'96)*, Barcelona, Spain, 1996, paper TUY05T, pp. 57-61.

[3] S. Kazakov *et al.*, "L-band Waveguide Elements for SRF Application", in *Proc. Particle Accelerator Society Meeting*, Tokai, Japan, 2009, pp. 980-982.

[4] S. Fukuda, "Distributed RF scheme (DRFS)-newly proposed HLRF scheme for ILC", in *Proc. 22nd Linear Accelerator Conf. (LINAC'10)*, Tsukuba, Japan, 2011, paper MOP027, pp. 112-114.

[5] K. Tomiyasu et al., "Attenuation in a Resonant Ring Circuit (Correspondence)". IRE Transactions on Microwave Theory and Techniques, vol. 8, pp. 253-254, 1960, doi: 10.1109/TMTT.1960.1124738

[6] H. Golde et al., "Theory and measurement of Q in resonant ring cir-cuits", IRE Transactions on Microwave Theory and Techniques, vol. 8, pp. 560-564, 1960, doi: 10.1109/TMTT.1960.1124786

[7] D. M. Pozar, Microwave engineering. USA: John Wiley & Sons, 2009.

Content from this work may be used under the terms of the CC BY 3.0 licence (© 2018). Any distribution of this work must maintain attribution to the author(s), title of the work, publisher, and DOI.

ISBN: 978-3-95450-194-6 ISSN: 2226-0366 doi:10.18429/JACoW-LINAC2018-THPO004

PULSED OPERATION OF CEBAF FOR JLEIC INJECTION*

J. Grames, J. Guo#, R. Kazimi, F. Lin, T. Plawski, R. Rimmer, H. Wang,
JLAB, Newport News, VA 23606, USA

Abstract

The JLab Electron-Ion Collider (JLEIC) proposed by Jefferson Lab is planning to use the 12 GeV CEBAF 1497 MHz SRF CW recirculating linac as a full-energy injector for the electron collider ring, which might be the first SRF electron linac to be used as a storage ring injector. The electron collider ring is proposed to reuse the 476MHz PEP-II RF system to achieve high installed voltage and high beam power. The JLEIC electron injection requires 3-10 (or 12) GeV beam in bunch trains <4μs long with low duty factor and high peak current, resulting strong transient beam loading for the CEBAF. In this paper, we present our recent studies on JLEIC electron injection scheme and CEBAF pulsed operation.

JLEIC ELECTRON INJECTION SCHEME

The propose JLEIC, as shown in Fig. 1, is a high luminosity electron-ion collider with 3 to 10 GeV electrons and 20 to 100 GeV protons (or up to 40 GeV per nucleon for heavy ions), with the possibility to upgrade to higher energy [1, 2]. The nominal beam current in the electron ring is 3 A, but the beam current is limited by 10 MW total synchrotron radiation power at energies higher than 7 GeV. The newly upgraded 12 GeV CEBAF linac is chosen as the full energy injector for the electron ring. The preliminary JLEIC injection scheme with CEBAF was initially developed in 2014 as published in [3], and has been evolved since then.

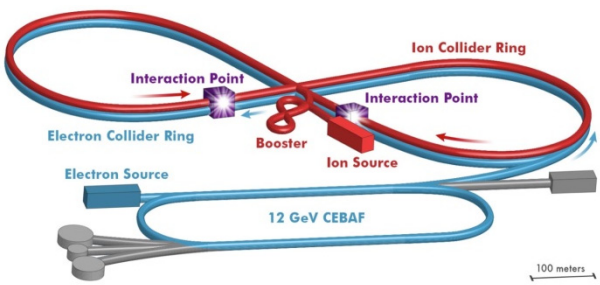


Figure 1: Conceptual layout of JLEIC.

The JLEIC electron injection uses 68.05 MHz bunch repetition rate (and possibly its sub-harmonics in circumstances) , which is 1/22 of the CEBAF RF frequency of 1497 MHz, and 1/7 of the slightly adjusted PEP-II RF system frequency 476.3 MHz. The electron ring has a harmonic number of 3584, with a circumference of around 2256 m and the revolution time of 7.52 μs.

One major capability of JLEIC is colliding polarized electrons with light ions. In this type of runs, the electron rings will provide two bunch trains with opposite spin polarization in the same ring, with two gaps of ~270 ns each in between. The gaps will match the ion ring abort gaps, and serve for the purposes of injection/abort kickers' rise/fall time as well as ion clearing.

The JLEIC electron ring uses transverse phase space injection with damping time τ_d ranges from 6 to 389 ms, depending on the beam energy and the use of damping wigglers. To maximize the total charge injected in one kicker cycle, we can inject a long polarized bunch train into half of the collider ring, with the bunch train length of ~3.5 μs, slightly shorter than the circumference of CEBAF of ~4.38 μs. The kicker cycle has a rise/fall time ~200 ns, and a flat top of 3.5 μs, comparable to the PEP-II abort kickers. At least $2\tau_d$ is needed to damp the injected portion of a bunch before the next kicker bump involving the same bucket; however we can arrange at least two kicker cycles bumping the two halves of the ring during $2\tau_d$. To arrange more than two injections during $2\tau_d$, more gaps might be needed.

CEBAF PULSED OPERATION

The beam in CEBAF can be accelerated during the 6

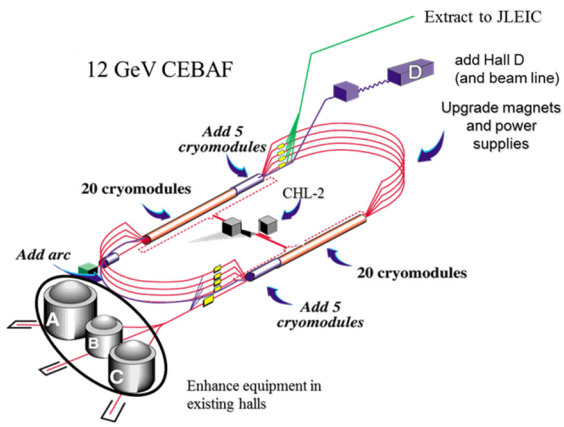


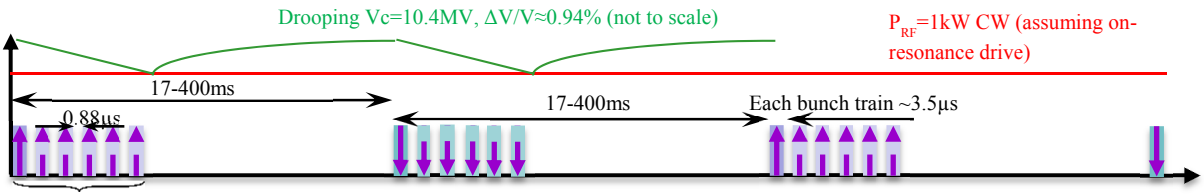
Figure 2: CEBAF after 12 GeV upgrade.

passes in the north linac (NL) and 5 passes in the south linac (SL), before it's extracted to Hall D or JLEIC. If CEBAF RF is operating in the usual CW mode, the major factor limiting the maximum charge in each bunch train is the energy droop along the bunch train caused by the transient beam loading in the SRF cavities. The maximum energy droop is limited by the ±0.2% momentum acceptance of CEBAF arc. If the bunch train is short enough compared to the cavity fill time and the RF feedback delay, and the cavity is operating on-crest on-resonance, the cavity gradient droop under CW RF is

* Authored by Jefferson Science Associates, LLC under U.S. DOE Contract No. DE-AC05-06OR23177
#jguo@jlab.org

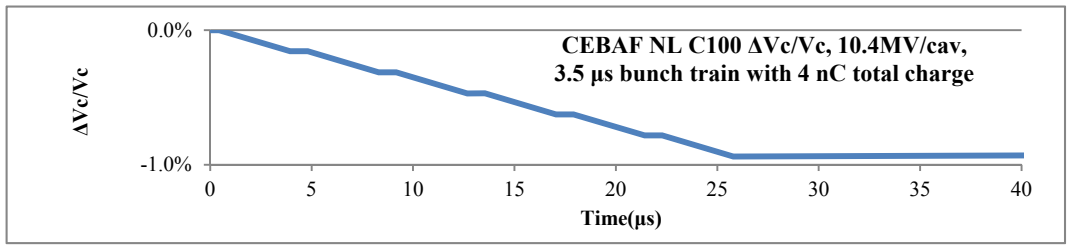
Content from this work may be used under the terms of the CC BY 3.0 licence (© 2018). Any distribution of this work must maintain attribution to the author(s), title of the work, publisher, and DOI.

ISBN: 978-3-95450-194-6 ISSN: 2226-0366 doi:10.18429/JACoW-LINAC2018-THPO004

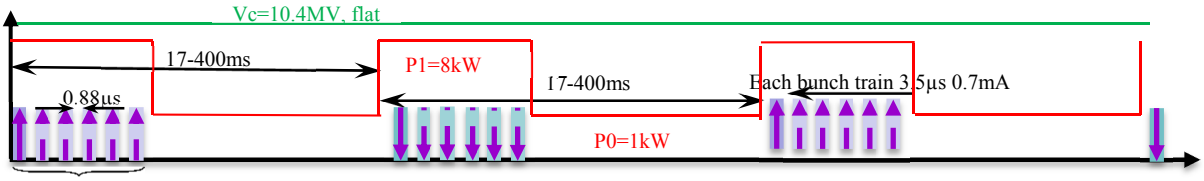


25.4μs, 6 passes-0.88μs in CEBAF NL (~4.38μs per pass), 1.14mA (4 nC per bunch train)

a) Gradient droop in a NL C100 cavity with typical 10.4 MV voltage and 6 passes of bunch train, CW RF



b) Detail of the transient beam loading when a bunch train passes through a C100 cavity 6 passes



25.4μs, 6 turns-0.838μs in CEBAF NL (4.38μs per turn),

c) Correcting transient beam loading in C100 cavities with RF feed-forward

Figure 3: JLEIC injection bunch train time structure in CEBAF and transient beam loading.

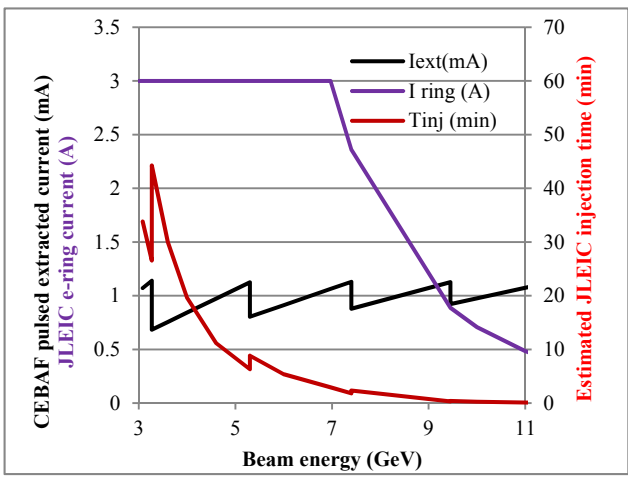


Figure 4. Beam current in the JLEIC e-ring and estimated injection time, no effective RF feed-forward/feedback.

$$\Delta V_c = Q_{train}\frac{\omega}{2}\frac{R}{Q} \quad (1)$$

where Q_{train} is the total charge of a bunch train passing through the cavity, and impedance is defined as $R=V^2/P$. The relative voltage droop is inversely proportional to the cavity voltage, so we can maximize the cavity voltage by minimizing the number of beam passes at lower extraction energies. In this case, we need to add extraction lines in the 2nd to the 6th north linac passes, also shown in Fig. 2.

We can also apply RF feed-forward to compensate the transient beam loading; however the effectiveness is limited by the available RF power and the cavity coupling. A C100 cavity with typical Qext of 3.2×10^7 and 8 kW available klystron power (not including overhead for microphonics etc) will be able to support 0.7mA pulsed extracted current with zero energy droop during the bunch train, as shown in Fig. 3c. The OC style cavities has higher coupling and will be able to support more beam current. If we allow the same 0.2% one pass voltage droop, RF feed-forward may increase the maximum extracted charge per pulse from 4 nC to ~8 nC.

Fig. 4 shows the estimated CEBAF extraction current and the JLEIC injection time at different injection energy, assuming 3.5 μs bunch train, CW RF without feed-forward or fast feedback. The waiting time between two bunch trains will be the larger of transverse radiation damping time and 16.7ms (assuming 60 Hz maximum kicker repetition rate). This estimate did not consider the time needed for the e-ring RF system to adapt to the increasing current, such as adjusting the cavity detuning for the increasing beam loading, usually in a few minutes. According to Fig. 4, the estimated electron injection time is below 30 minutes for most of the energy range, except

Content from this work may be used under the terms of the CC BY 3.0 licence (© 2018). Any distribution of this work must maintain attribution to the author(s), title of the work, publisher, and DOI.

ISBN: 978-3-95450-194-6 ISSN: 2226-0366 doi:10.18429/JACoW-LINAC2018-THPO004

Content from this work may be used under the terms of the CC BY 3.0 licence (© 2018). Any distribution of this work must maintain attribution to the author(s), title of the work, publisher, and DOI.

for 3.3-3.6 GeV, when the energy gain per linac is as low as 0.63 GeV.

CEBAF arc magnets can be adjusted adaptively to the beam energy at the center of the bunch train in each pass. In this case the maximum allowed bunch train head to tail gradient droop for one beam pass is 0.4%. To allow some room for momentum spread caused by other factors, we limit one pass gradient droop to 0.2%.

After 12 GeV upgrade, each of CEBAF's north and south linac has 40 C100 style cavities with R/Q=868.9 Ω and 160 original Cornell (OC) style cavities with R/Q=482.5 Ω. Each linac provides a maximum 1.05-1.09 GeV energy gain per pass. If we have 4.0 nC total bunch charge in the 3.5-4 μs bunch train, the total voltage droop in one linac over one pass will be 2.1 MV, or 0.2% of 1.05 GeV, assuming on-crest on-resonance CW RF without feed-forward or feedback. Fig. 3a shows the gradient droop–recover cycle in a typical C100 cavity with 4 nC total charge in a 6 passes bunch train and under CW RF, while Fig. 3b shows the detail of the droop.

To maximize the CEBAF extracted current to the beam loading limit, the CEBAF gun and capture cavity need to be upgraded to be able to provide about 30 pC per bunch at 68.05 MHz, which is about two order of magnitude higher than CEBAF's current operation, but not beyond state of the art. The 7 sets of 476.3 MHz buckets in the collider ring can be filled in rotation.

CEBAF PULSED BEAM STUDY

A series of CEBAF beam study have been proposed to demonstrate CEBAF's capability to provide the pulsed beam for JLEIC injection. The studies include the measurement of the cavity voltage droop and energy droop due to transient beam loading, sending the long bunch train through CEBAF for multi-passes, and demonstrate the RF feed-forward principle. The demonstration is focused on the transient beam loading and won't involve increasing the charge per bunch for 68.05 MHz operation.

In the beam tests, we run CEBAF hall A/C lasers at 499 MHz in the "viewer limit" mode with 4-10 μs bunch trains and up to 0.4 pC per bunch. These two beams occupy 4 of the 6 CEBAF 249.5 MHz bucket groups. We also use another low current (~1 μA) 249.5 MHz bucket to hold hall B beam in "tune mode", which has a 250 μs bunch train followed by a 4 μs train, and serves as a probe beam for certain BPMs that could not see the 4 μs bunch train.

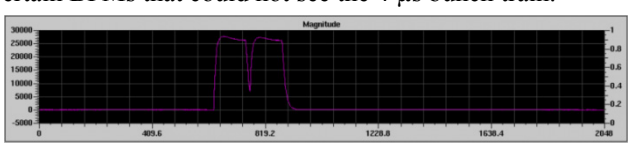


Figure 5. CEBAF NL M56 cavity signal for 100 μA 4μs bunch train accelerated through CEBAF for 1.5 passes.

In one beam study, a 4 μs bunch train with up to 200 μA was sent through CEBAF for 1.5 passes, and the turn by turn beam current was monitored by the NL M56 cavity. There was no beam loss with 100 μA beam current, as Fig. 5 shows. However the M56 cavity probe saturated at 150 μA. A future beam test should have the proper M56 cavity attenuation and 5.5 CEBAF passes, with up to 400 μA pulsed beam current.

We were able to measure the cavity voltage droop in the CEBAF injector cavities. Fig. 6 shows one measurement in the CEBAF cryomodule 0L04 cavity 1, which is a C100 style cavity. The measurement shows a common 60 Hz mode background, but that mode is stable and can be deducted with a measurement without beam. The measured voltage droop for a cavity operating at 7.7 MV/cavity (11 MV/m) was only ~0.05% with 10μs 300μA bunch train, which is about factor of three less than the calculation. Currently we don't yet have a good explanation to this discrepancy; however the experimental results are in favor of faster injection.

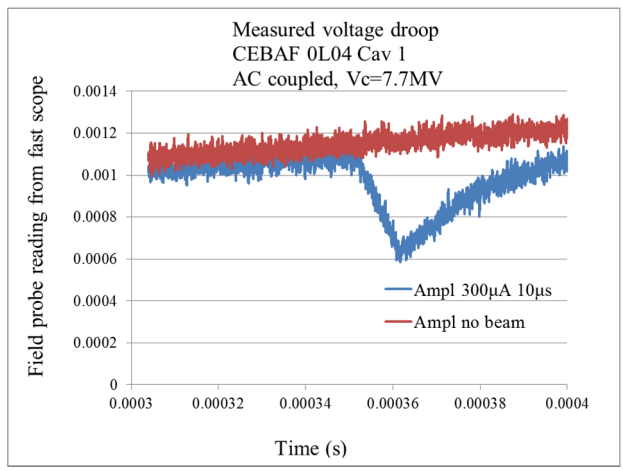


Figure 6. Measured voltage droop in CEBAF 0L04 Cav 1.

SUMMARY

We proposed the JLEIC electron injection scheme using pulsed long bunch trains provided by CEBAF. The main issue of transient beam loading has been studied in CEBAF. Analytical calculation shows that the injection time can be less than 30 minutes for most of the energy range, except for a very small range of beam energy 3.3-3.6 GeV, when we start to use 2.5 passes extraction with the lowest linac energy gain per pass. The injection time can be reduced further with RF feed-forward and/or damping wigglers. The preliminary beam experiments show lower voltage droop than estimated and further study is needed. Energy spread measurements also need to be improved.

REFERENCES

[1] S. Abeyratne, "MEIC Design Summary", arXiv:1504.07961, (2015).

[2] Edited by F. Pilat, "The Jefferson Lab EIC (JLEIC) Design", May 2017 update

[3] J. Guo *et al.*, "Conceptual MEIC Electron Ring Injection Scheme using CEBAF as a Full Energy Injector", in *Proc. IPAC'15*, Richmond, VA, May 2015, paper TUPTY083; pp. 2232-2235.

ISBN: 978-3-95450-194-6 ISSN: 2226-0366 doi:10.18429/JACoW-LINAC2018-THPO005

HIGH ASPECT RATIO BEAM GENERATION WITH THE PHASE-SPACE ROTATION TECHNIQUE FOR LINEAR COLLIDERS

Masao Kuriki*,Hiroshima University, Higashihiroshima, Japan
John Power, Argonne National Laboratory, Argonne, Illinois
Hitoshi Hayano, Xiuguang Jin, Taro Konomi, Yuji Seimiya, Naoto Yamamoto, KEK, Tsukuba, Japan
Philippe Piot,Northern Illinois University, Dekalib, Illinois
Shigeru Kashiwagi, Tohoku University, Sendai, Japan
Kazuyuki Sakaue, Masakazu Washio, Waseda University, Tokyo, Japan

Abstract

Linear colliders is the only way to realize e+ e- collision at higher energy beyond the limit of ring colliders by the huge synchrotron radiation energy loss. In the linear collider, the beam current should be much smaller comparing to the ring collider to save the required electricity. A way to realize an enough luminosity with the small beam current and less energy spread by Beamstrahlung, is collision in flat beam. This high aspect ratio beam can be made by phase-space rotation technique instead of the conventional way with DR (Damping Ring). We present a simulation of this technique and pilot experiments at KEK-STF and ANL WFA.

INTRODUCTION

Electron Positron Collider is the only way to realize annihilation of elementary particles with controlled conditions with the current technology. Because there has been no any significant evidence of Super-symmetry in LHC experiments, the significance of detail studies of Higgs boson and searching inconsistency in the standard model with electron positron collider is maximized. ILC (International Linear Collider) [1] is an e+e- linear collider based on superconducting accelerator with CME from 250 to 1000 GeV. It would be constructed in Iwate, Japan, as the main project of High energy physics.

Luminosity L is the index showing the performance of colliders. It can be expressed as

$$L = \frac{f n_b N^2}{4\pi\sigma_x\sigma_y}, \tag{1}$$

where f is repetition of pulse, n_b is number of bunches in a pulse, N is number of particles in a bunch, $\sigma_{x,y}$ is transverse beam size. In the linear collider, the beam after the collision is dumped. If we employ a large current beam in linear colliders as same as in ring colliders, the required wall plug power is huge and such machine is unrealistic. One way to enhance the luminosity is minimize $\sigma_{x,y}$, but it causes a large energy spread by Beamstrahlung as

$$\Delta E \propto \frac{1}{\sigma_z}\left(\frac{2}{\sigma_x+\sigma_y}\right)^2. \tag{2}$$

A practical way to enhance the luminosity and suppress Beamstrahlung simultaneously is squeezing the beam in one of the transverse direction, e.g. $\sigma_x \gg \sigma_y$. For ILC, The beam size at IP is 640 nm in horizontal direction and 5.7 nm in vertical direction. Emittances are 10 and 0.04 mm.mrad in horizontal and vertical directions, respectively [1]. This asymmetric emittance beam is made by radiation damping in a storage ring in the current design. We propose to generate the flat beam for ILC only with the injector by employing the emittance exchange technique.

* mkuriki@hiroshima-u.ac.jp

PHASE-SPACE ROTATION TECHNIQUES FOR LINEAR COLLIDERS

Emittance exchange technique is change the emittance partitioning among the degree of freedom, i.e. x, y, and z. Any partitioning is possible if 6D phase space volume (emittance) is conserved. There are two methods as the phase-space rotation for the re-partitioning. One is RFBT (Round to Flat Beam Transformation) [2] generating the flat beam from an angular-momentum dominated beam produced by beam emission in a solenoid field. Another is TLEX (Transverse to Longitudinal Exmittance eXchange) exchanging the phase-spaces between longitudinal and transverse directions by dipole mode cavity in a dispersive beam line [3]. These two techniques are experimentally demonstrated by P. Piot et al. [4] for RFBT and Y-E Sun et al. [5] for TLEX. The flat beam generation with RFBT and TLEX are explained in Ref. [6] for more detail.

As explained in the introduction, the flat beam is essential to enhance the beam luminosity for linear colliders. In the ILC current design, the emittance at IP are 10 mm.mrad for horizontal direction, 0.04 mm.mrad for vertical direction, and 8.4×10^5 mm.mrad for longitudinal direction. This beam is made up with radiation damping in 3 km DR in the current design [1]. Figure 1 shows the schematic drawing of the injector with DR.

By employing the emittance exchange techniques (RFBT and TLEX), the ILC compatible beam can be generated only with an injector lilac as shown in Fig. 2. 3.1 km DR can be omitted. The emittance budget is summarized in Table1. The first row is required emittance at IP for ILC. The second row is emittance at Gun when we employ only RFBT. In RFBT, the product of ε_x and ε_y is conserved. To make 10 mm.mrad and 0.04 mm.mrad with RFBT, the emittance from Gun should be 0.6 mm.mrad. This small emittance cause several problems. One is emission density. To make this

Content from this work may be used under the terms of the CC BY 3.0 licence (© 2018). Any distribution of this work must maintain attribution to the author(s), title of the work, publisher, and DOI.

ISBN: 978-3-95450-194-6 ISSN: 2226-0366 doi:10.18429/JACoW-LINAC2018-THPO005

Content from this work may be used under the terms of the CC BY 3.0 licence (© 2018). Any distribution of this work must maintain attribution to the author(s), title of the work, publisher, and DOI.

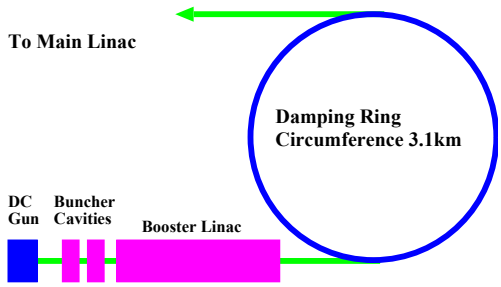


Figure 1: The conventional design of the injector for Linear colliders. The beam is stored in DR to make asymmetric beam emittance in horizontal and vertical directions by radiation damping.

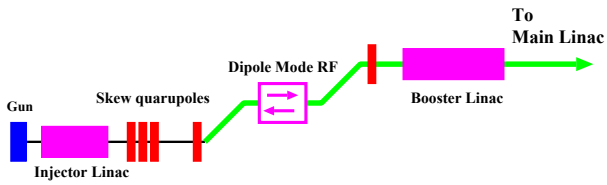


Figure 2: The injector design employing the emittance exchange techniques. The asymmetric emittance beam in horizontal and vertical directions are made by RFBT and TLEX.

small emittance from the gun, the beam spot should be also small, cause a high density beam emission from the cathode surface. Including 50% margin of the bunch charge, 4.8 nC bunch charge should be extracted from the small spot. The bunch length can be large and a careful design for bunching section is required. Another problem is emittance growth by space charge effect. The small beam size cause a strong non-linear space charge increase the beam emittance. If the emittance growth of the space charge is significant, the ILC compatible beam can't be generated with RFBT because the product is not conserved anymore.

The third row shows the emittance at gun when we employ RFBT and TLEX. If we employ RFBT and TLEX, the product of three emittance (x, y, and z) can be conserved and therefore, ε_x and ε_y can be large to avoid the problem at the gun emission and the space charge emittance growth. The fourth row shows the expected emittance with the same parameter at IP. ε_x and ε_y are compatible to the ILC requirement at IP. ε_z is still less than the requirement.

Table 1: Emittance budget for ILC at IP (TDR), case 1 (only RFBT, gun), case 2 (RFBT and TLEX, gun), and case 2 (RFBT and TLEX, IP). Emittance is in mm·mrad.

Design	ε_x	ε_y	ε_z
ILC at IP (TDR)	10	0.04	2.5×10^5
Case 1 (RFBT, gun)	0.6	0.6	2.5×10^5
Case 2 (RFBT+TLEX, gun)	45	45	10
Case 2 (RFBT+TLEX, IP)	10	0.04	5.1×10^4

Table 2: Parameters of the simulation. $G_{1,2,3}$ are field gradient of skew quadrupoles, α is bending angle of dogleg,η and ξ are dispersion and momentum compaction of dogleg. RF voltage of dipole mode cavity is defined at λ from the cavity center.

Parameters	textbfValue	textbfunit
Solenoid field	0.1	T
Initial emittance (x,y)	1.5	mm·mrad
Bunch length	12	ps (full width)
Beam size	1.6	mm (rms)
Lorentz γ after acceleration	49	
G_1	-0.503	T/m
G_2	0.926	T/m
G_3	2.058	T/m
α	0.3	rad
η	0.355	m
ξ	0.106	m
RF voltage	1.29	MV at λ

SIMULATION

A simulation is performed by assuming a beam test at KEK-STF. KEK-STF is a test facility to demonstrate the beam acceleration with super-conducting accelerator. It consists from 1.3 GHz L-band RF Gun which is compatible to XFEL/FLASH, a super-conducting accelerator module with two 1 m Tesla type cavities. The STF is now upgrading to increase number of accelerator module from one to two. The second accelerator module has 12 1 m cavities.

To implement RFBT, solenoid field should be on the cathode surface. Usually, the gun is designed to vanish solenoid field to avoid emittance growth by the angular momentum. The solenoid field can be induced on the cathode by changing the polarity of bucking coil. According to the solenoid design, up to 0.15 Tesla field can be made. In the simulation, 0.1 Tesla field is assumed. The parameters are summarized in Table2. $G_{1,2,3}$ are field gradient of skew quadrupoles, α is bending angle of dogleg,η and ξ are dispersion and momentum compaction of dogleg. RF voltage of dipole mode cavity is defined at λ from the cavity center.

The simulation was performed with GPT. The optimization of skew Q setting was made to minimize the sum of non-diagonal components of Σ matrix, i.e. $< xy >$, $< xy' >$, $< x'y >$, and $< x'y' >$ by steepest descent method. The result of the simulation is shown in Fig. 3. The horizontal axis show the distance from the cathode surface. ε_x, ε_y, and ε_z are drawn with solid line, dashed line, and dotted line, respectively. The emittance evolution is summarized in Table 3. By comparing these numbers with them in Table 1, ILC requirements are almost satisfied.

Please note that the simulation does not include space-charge effect, yet. Next, we perform a simulation with a larger beam emittance at the cathode with space-charge effect to confirm the feasibility of the method.

ISBN: 978-3-95450-194-6 ISSN: 2226-0366 doi:10.18429/JACoW-LINAC2018-THPO005

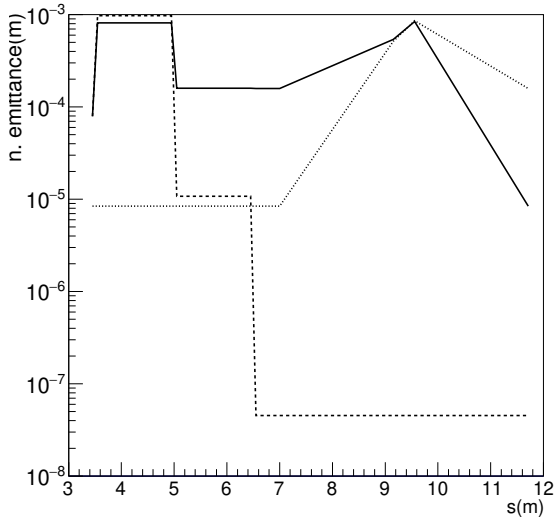


Figure 3: Emittance evolution of the simulation. The horizontal axis shows the distance from the cathode, and the vertical axis shows the normalized emittance in m. ε_x, ε_y, and ε_z are drawn with solid line, dashed line, and dotted line, respectively.

Table 3: Emittance evolution in the simulation. Emittance is in mm·mrad.

Position	ε_x	ε_y	ε_z
Cathode	1.5	1.5	8.5
After RFBT	160	0.045	8.5
After TLEX	8.5	0.045	160

DC GUN OPTION

In the simulation, we assume RF gun to generate the electron beam. For ILC [1], polarized electron beam is required. The strain compensated super-lattice GaAs cathode is employed for high polarization up to 90 % with 1.5 % quantum efficiency. The GaAs cathode is currently not compatible to RF gun, because the operational lifetime of the cathode is limited in RF gun due to the poor vacuum condition. We performed GaAs cathode activation with Cs-Te and Cs-K-Te thin layer according to hetero-junction model [7] [8] and we found significant beam emission in both cases, but quantum efficiency is still low, and the lifetime is also very limited.

In principle, we can use DC gun instead of RF gun for the flat beam generation. In this case, space charge effect could be more significant than that in RF gun case. In addition, we need bunching before the acceleration which is another potential problem.

FUTURE PLAN

We schedule beam test at KEK-STF and ANL(Argonne National Laboratory) WFA(Wake Field Accelerator). In STF, an experiment for RFBT will be performed. In ANL-WFA, RFBT and TLEX will be performed. We will examine the feasibility of the method with these beam tests. If the experiment showed a good performance, a full demonstration should be made by introducing a dipole mode RF cavity in STF as a future plan.

SUMMARY

We propose the flat beam generation for linear colliders by employing the emittance exchange techniques. By using RFBT and TLEX, the flat beam compatible to ILC parameter can be made with a large initial x and y emittance from the cathode. The large emittance from the gun relaxes the condition for the beam emission density and space charge emittance growth. Beam tests will be carried out at KEK-STF and ANL-WFA for further investigations.

ACKNOWLEDGMENT

This work is partly supported by Grant-in-Aid for Scientific Research (B) and US-Japan Science and Technology Cooperation Program in High Energy Physics.

REFERENCES

[1] C. Adolphsen *et al.*, "ILC technical design report", KEK-Report 2013-1, 2013.

[2] R. Brinkmann, Y. Derbenev, and K. Flöttmann, "A low emittance, flat-beam electron source for linear colliders", *Phys. Rev. ST Accel. Beams*, vol. 4, 2001.

[3] M. Cornacchia and P. Emma, "Transverse to longitudinal emittance exchange", *Phys. Rev. ST Accel. Beams*, vol. 5, 2002.

[4] P. Piot, Y.E. Sun, and K.J. Kim, "Photoinjector generation of a flat electron beam with transverse emittance ratio of 100", *Phys. Rev. ST Accel. Beams*, vol. 9, 2006.

[5] Y.E. Sun *et al.*, "Tunable Subpicosecond Electron-Bunch-Train Generation Using a Transverse-To-Longitudinal Phase-Space Exchange Technique", *Phys. Rev. Lett.*, vol. 105, 2010.

[6] M. Kuriki, in *Proc. PASJ'18*, paper THOM07, 2018.

[7] K. Uchida, Master thesis of Hiroshima U., 2015.

[8] K. Masaki *et al.*, in *Proc. PASJ'18*, paper FROM04, 2018.

Content from this work may be used under the terms of the CC BY 3.0 licence (© 2018). Any distribution of this work must maintain attribution to the author(s), title of the work, publisher, and DOI.

ISBN: 978-3-95450-194-6 ISSN: 2226-0366 doi:10.18429/JACoW-LINAC2018-THPO006

STATUS OF 650 MHz SRF CAVITY FOR ERHIC SRF LINAC*

W. C. Xu†, [1], I. Ben-Zvi[1, 2], Y. Gao[1], D. Holmes[1], P. Kolb[1], G. McIntyre[1], R. Porqueddu[1], K. Smith[1], R. Than[1], F. Willeke[1], Q. Wu[1], A. Zaltsman[1],
[1]Collider-Accelerator Department, Brookhaven National Laboratory, Upton, NY, 11790, USA
[2]Physics & Astronomy Department, Stony Brook University, Stony Brook, NY, 11794, USA

Abstract

A 5-cell 650 MHz SRF cavity was design for eRHIC high current SRF linac. One Cu cavity was fabricated for HOM damping study, and one Nb cavity was fabricated for SRF performance study with various post-processing procedures. The SRF performance study includes both high Q-value study (at gradient of 15 ~ 18 MV/m) and high gradient study (> 26 MV/m). This paper reports the HOM measurements results on Cu cavity and first result of vertical test on the Nb cavity.

INTRODUCTION

Collider-Acceletaor Department at Brookhaven National Laboratory (BNL) has been actively working on R&D of an electron-ion collider for more than a decade. This collider, named eRHIC, aims to collide electron beam that is from a new electron accelertor, with proton beams that is provided by existing RHIC [1]. The new electron accelerator will be placed in the RHIC tunnel, and most of components of RHIC will be reused for eRHIC. The layout of eRHIC is shown in Figure 1. To make sure we get the best machine performance with reasonable cost, both ERL-Ring [2] and Ring-Ring eRHIC [3] were studied. However, either design requires high performance SRF cavities.

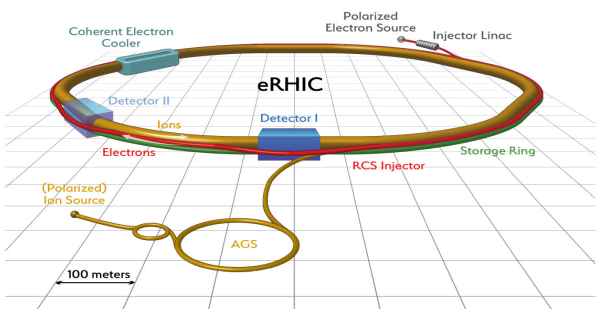


Figure 1: eRHIC layout.

Although the design of 5-cell 647 MHz cavity was aimed for high current ERL-Ring eRHIC[4-5], the cavity will be used for performance study for Ring-Ring SRF as well. A Cu prototype cavity was fabricated for HOM damping study, and an Nb cavity was fabricate for performance study. This paper will report the HOM measurement results, plan of the performance study, and first vertical test result.

* Work supported by LDRD program of Brookhaven Science Associates, LLC under Contract No. DE-AC02-98CH10886 with the U.S. DOE.
† wxu@bnl.gov

HOM MEASUREMENT ON CU CAVITY

The cavity fabrications contract was awarded to RI [6], which we have weekly telephone meeting to discuss the progress and resolve different issue during cavity fabrication. As we expect to have tons of R&D on the cavity, we asked for 4.5 mm cavity wall thickness. However, the geometry deformation tolerance is not allowed to be higher than +/- 0.3mm. To meet the tolerance, RI had to do at least once reshaping of each half cell. The beampipe of the cavity was design to be detachable so that we can study HOM damping in the future, as shown in Figure 2.

The spectrum measured in the Cu cavity matches very well with simulation results, which Figure 3 shows the spectrum comparision of the first HOM passband. This is also benefitted from tight geometry control during cavity fabrication. Due to the large cell-to-cell coupling and tight cavity shape tolerance, the cavity's field flatness is 89% as fabricated, and it required little tuning to reach 98.2% of field flatness.

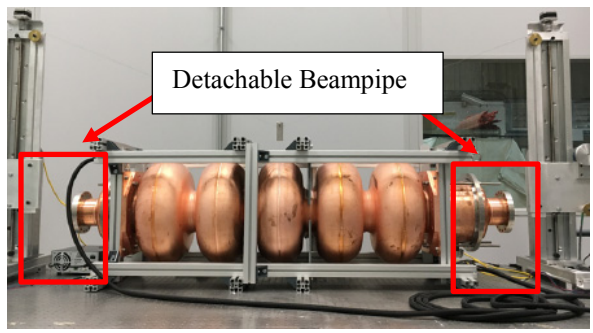


Figure 2: Bare 650 MHz Cu cavity with detachable beampipe.

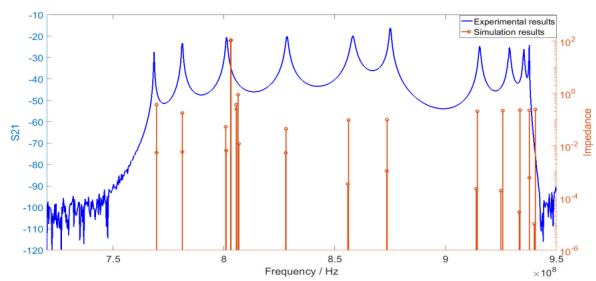


Figure 3: Simulated HOM spectrum and measured HOM spectrum.

NB CAVITY

Cavity fabrication and processing

Cu cavity is kind of a dry-run of the tooling for the Nb cavity fabrication, which made the Nb cavity fabrication much smoothly. However, a lot of dents and scratches were

Content from this work may be used under the terms of the CC BY 3.0 licence (© 2018). Any distribution of this work must maintain attribution to the author(s), title of the work, publisher, and DOI.

ISBN: 978-3-95450-194-6 ISSN: 2226-0366 doi:10.18429/JACoW-LINAC2018-THPO006

discovered in the inspection of the cups and dumb-bells. Cratex was used to grind the local defects found during inspection. Figure 4 shows example of grinded half –cell and beampipe.

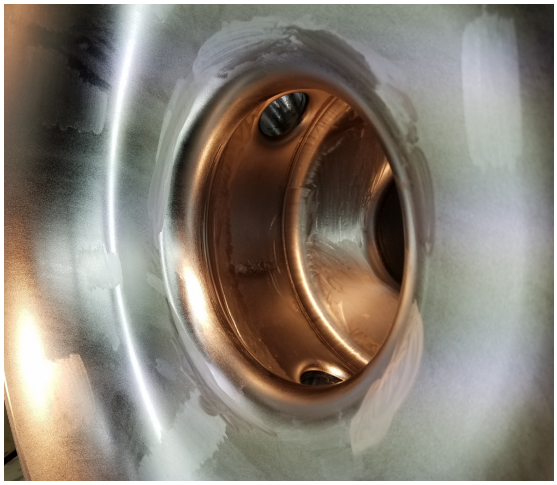


Figure 4: Nb inner surface after ginding with Cratex.

The last weld is done RI's EB-welder vertically because of the cavity is too long for horizontal welding. Following the last welding, the cavity was carried out pressure test up to 26 psia, to satisfy the ASME code.

As shown in Figure 5, the Nb cavity's field was initially tuned up to 99% flatness in the RI, which re-measured as 98 % flatness after shipping to BNL.

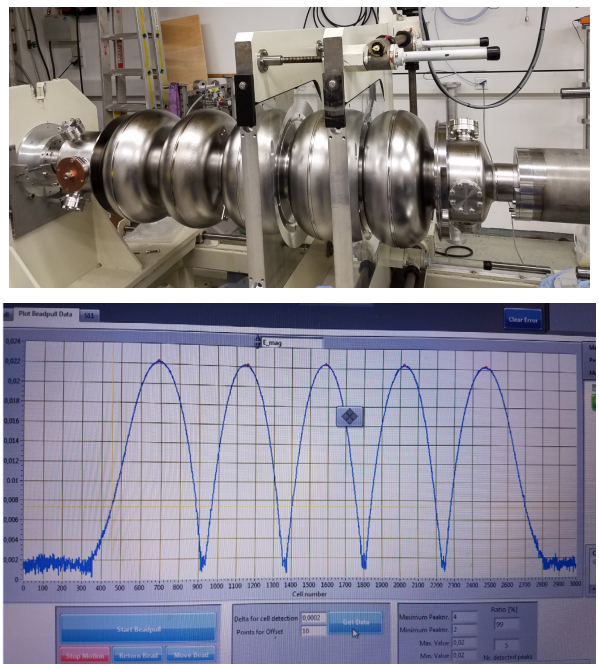


Figure 5: Nb cavity tuned in RI.

The post processing of the 650 MHz cavity is done with combination effort between ANL and BNL. ANL took care of the BCP part, and BNL took care of HPR and 600 C bake. The BCP removed Nb in amount of 115 µm (heavy BCP) and 36 µm (light BCP). Between the heavy and light BCP, the cavity was baked at 600 C for 10 hours. Prior to shipping to ANL for light BCP, the field flatness was measured again, which reduced slightly to 95 %. The field flatness and first passband comparison before and after BCP and bake is shown in Figure 6. One important feature that has to be point out is that the grinding marks from the cavity fabrication were gone after BCP, which can be seen in Figure 7.

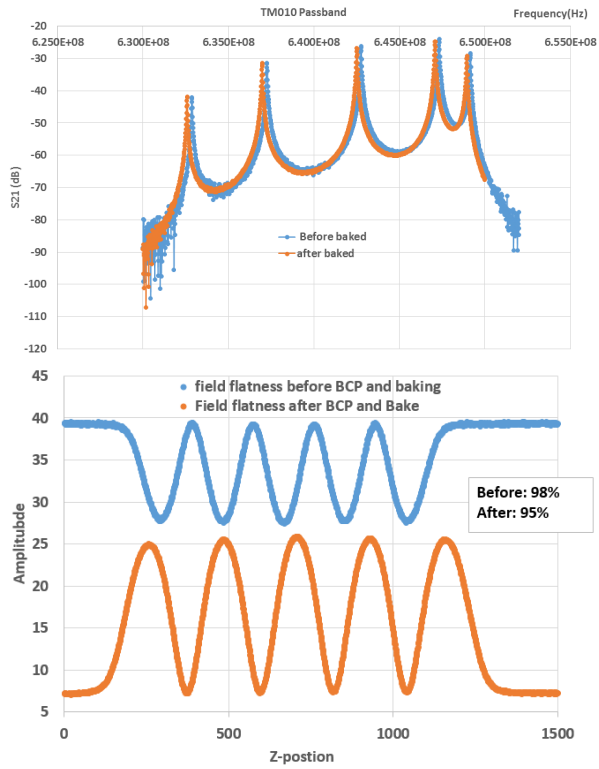


Figure 6: Nb cavity's fundamental sprectrum (Top) and the field flatness (Bottom) before and after heavy BCP and bake.



Figure 7: No grinding marks after BCP.

Preparation for Vertical Test

The vertical test of the 650 MHz cavity is to carry out in the Large Vertical Test Facility (LVTF) at Bldg.912 in BNL. In Figure 8, it shows the 650 MHz cavity in Class 10000 clean room for installation of instrumentations (temperature, helium level and RF) for vertical test. To minimize the RF loss, all HOM ports and beam pipe ports are

Content from this work may be used under the terms of the CC BY 3.0 licence (© 2018). Any distribution of this work must maintain attribution to the author(s), title of the work, publisher, and DOI.

ISBN: 978-3-95450-194-6 ISSN: 2226-0366 doi:10.18429/JACoW-LINAC2018-THPO006

Content from this work may be used under the terms of the CC BY 3.0 licence (© 2018). Any distribution of this work must maintain attribution to the author(s), title of the work, publisher, and DOI.

sealed with Cu disc gaskets, with a venting hole. The estimated total RF loss on the all ports @ 20 MV/m is about 0.2 watt. The liquid helium is provided with a Helium refrigerator. A fixed FPC antenna is used to couple the RF power into the cavity, and Qext of the FPC is 8E9, and a pick up antenna with external Q of 7E10 is used. The maximum available RF power source is 500 W in CW mode.

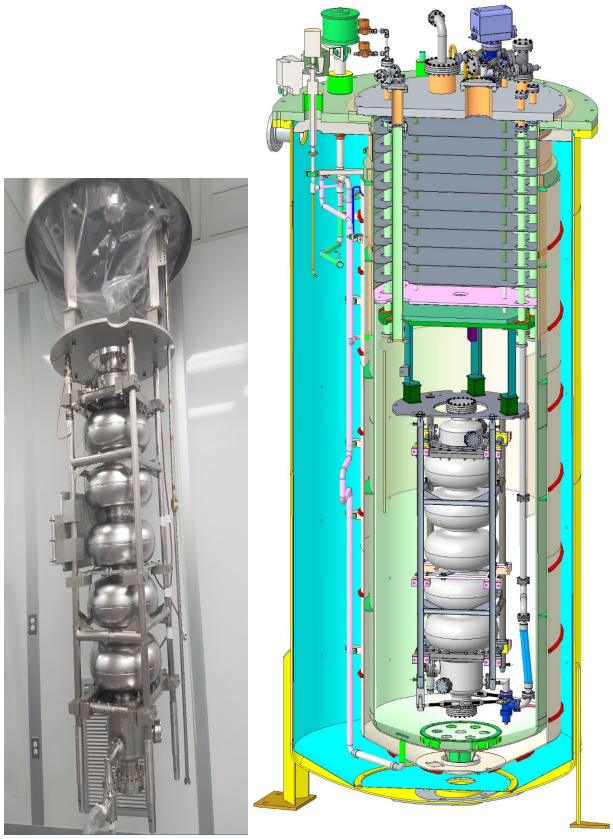


Figure 8: Configuration of the vertical test.

Plan of Study

The SRF performance study includes both high Q-value and high gradient with various post-processing. The first round of post processing (heavy BCP, 600 C bake and light BCP) is to create a baseline for the future reference. Also, it is the first time for using BNL's new-built HPR on an Nb cavity, so commissioning the HPR is a side purpose. The high-Q study goal of the cavity processing is to study various post-processing methods to reach 18 MV/m with Q_0~$2x10^{10}$, which is the goal for the ERL-Ring eRHIC SRF linac. The further processing will be based on the results of the first test. As EP has been proved to be beneficial for cavity gradient, and cavity gradient of 25 MV/m is required for Ring-Ring eRHIC SRF linac, we will try to do EP on the cavity later on.

SUMMARY

A 650 MHz high current SRF cavity has been designed, prototyped, went through first round of post-processing, and ready for vertical test. Various post-processing steps will be carried out for high Q studies for the ERL-Ring SRF linac and for high gradient study for Ring-Ring eRHIC SRF linac.

ACKNOWLEDGEMENGT

The authors would like to thank Michael Pekeler, Aliaksandr Navitski and other experts for useful discussion and resolving the issues that appeared during cavity fabrication.

The authors would like to thank Michael Kelly and Thomas Reid for helping on cavity BCP.

REFERENCES

[1] RHIC, https://www.bnl.gov/rhic/

eRHIC, "eRHIC Design Study: An Electron-Ion Collider at BNL", December 2014, arXiv:1409.1633.

[2] C. Montag *et al.*, "Overview of the eRHIC Ring-Ring Design", in *Proc. 8th Int. Particle Accelerator Conf. (IPAC'17)*, Copenhagen, Denmark, May 2017, paper WEPIK049.

[3] W. Xu *et al*, "Frequency choice of the eRHIC SRF linac", BNL-111776-2016-IR.

[4] W. Xu *et al.*, "RF and Mechanical Design of 647 MHz 5-Cell BNL4 Cavity for eRHIC ERL", in *Proc. 7th Int. Particle Accelerator Conf. (IPAC'16)*, Busan, Korea, May 2016, paper WEPMR041.

[5] W. XU *et al.*, "Progress of 650 MHz SRF cavity for eRHIC SRF linac", in *Proc. 18th Int. Conf. RF Superconductivity (SRF'17)*, Lanzhou, China, Jul. 2017, paper WEPMR041.

[6] RI, http://www.research-instruments.de

ISBN: 978-3-95450-194-6 ISSN: 2226-0366 doi:10.18429/JACoW-LINAC2018-THPO007

MESA - STATUS OF THE IMPLEMENTATION OF THE MicroTCA.4-BASED LLRF CONTROL SYSTEM

J. Bai*, K. Aulenbacher, F. Fichtner, R. Heine, J. Diefenbach
Institut für Kernphysik, Johannes Gutenberg-Universität Mainz, D-55099 Mainz, Germany

Abstract

The Mainz Energy-recovering Superconducting Accelerator (MESA) at the Institut für Kernphysik (KPH) at Johannes Gutenberg-Universität Mainz is a multi-turn Energy-Recovery-Linac (ERL), aiming to serve as user facility for particle physics experiments. The RF-accelerating systems of MESA consist of 12 cavities, four of them are 9-cell TESLA superconducting (SC) cavities. They operate in continuous wave (CW) mode. In order to control the radio frequency (RF) amplitude and phase within the 12 cavities with the required accuracy and stability better than 0.01% and 0.01°, the Micro Telecommunications Computing Architecture (MicroTCA.4) based digital low-level RF (LLRF) control system based on the development at DESY, Hamburg will be adapted for the MESA cavities. A Matlab/Simulink model was created to find the proper control parameters and to predict the system performance. In this paper, the simulation results, the progress of the implementation and the first tests of the LLRF system for MESA are presented.

INTRODUCTION

The MESA accelerator is a multi-turn ERL working at low energy and CW mode for particle physics experiments, which is currently under construction at KPH, Johannes Gutenberg-Universität Mainz. MESA has two different operation modes, the external beam (EB) mode and the energy recovery (ER) mode, which serve for two physics-experiments. The EB mode is mainly to measure the weak mixing angle with the highest accuracy. The polarized electron beam of 150 µA current at 155 MeV energy is dumped after being used with the external fixed target experiment P2. In the ER mode, MESA runs as an ERL, generating an unpolarised beam of 1 mA at 105 MeV. An internal fixed target experiment named MAGIX (MESA Gas Internal target eXperiment) is used in this mode. After a further upgrade of the cryomodules, MESA can achieve a beam current of 10 mA in the ER mode.

MESA CAVITIES

The MESA RF system topology includes four 9-cell TESLA SC cavities working at 1.3 GHz, four normal conducting (NC) pre-accelerator cavities at 1.3 GHz, two chopper cavities at 1.3 GHz, one buncher cavity at 1.3 GHz and the second buncher cavity at 2.6 GHz, which are illustrated in Fig. 1. All cavities will be driven by their own solid state power amplifier (SSPA). Due to the narrow bandwidth of 100 Hz, the SC cavity has tighter requirements for the amplitude and phase stability of the electrical field within the cavities. Tab. 1 shows the main parameters of the MESA SC cavity [1]. MESA requires an amplitude and phase stability better than 0.01% and 0.01°.

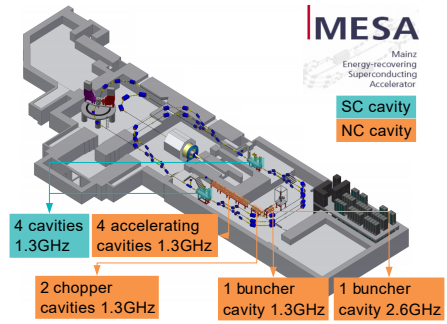


Figure 1: Overview of MESA RF system topology.

Table 1: Main Parameters of the MESA SC Cavity

Max E_{acc}	RF power	Q_L	Bandwidth
12.5 MV/cavity	15 kW	1.4×10^7	100 Hz

LLRF SYSTEM

MESA makes use of the MicroTCA.4 based LLRF system mainly developed by DESY [2]. All cavities are fed by their own RF power source, therefore we are implementing a single cavity LLRF control system [3]. The combination of a SIS8300-L Advanced Mezzanine Card (AMC) digitizer and a DWC8VM1 Rear Transition Module (RTM) analog boards purchased from Struck [4] offers a very compact solution for the single cavity control. The DWC8VM1 consists of 8 channel high frequency down-converters and one channel high frequency up-converter, which is the so-called vector modulator (VM) [5]. In the MESA project, the 1.3 GHz RF input signal picked up by the antenna will be down-converted to a 54 MHz intermediate frequency (IF) signal by means of a 1.354 GHz local oscillator (LO) signal and a low pass filter. The central components of the SIS8300-L are 10 125 MS/s 16-bit analog-digital converters (ADC), a Xilinx Virtex 6 FPGA and two 250 MS/s 16-bit digital-analog converters (DAC) [6]. The polar representation of an RF signal can be decomposed into its Cartesian representation by the so-called inphase (I) and quadrature (Q) components [7]. The advantage of this procedure is that phase and amplitude can be controlled simultaneously using setpoint values in I/Q description. The IF signal is sampled at the 81 MHz by ADCs. On the FPGA, the control deviation is calculated from the

* jibai@uni-mainz.de

Content from this work may be used under the terms of the CC BY 3.0 licence (© 2018). Any distribution of this work must maintain attribution to the author(s), title of the work, publisher, and DOI.

ISBN: 978-3-95450-194-6 ISSN: 2226-0366 doi:10.18429/JACoW-LINAC2018-THPO007

Content from this work may be used under the terms of the CC BY 3.0 licence (© 2018). Any distribution of this work must maintain attribution to the author(s), title of the work, publisher, and DOI.

I/Q components measured by the ADCs and the setpoints given by the central control system. The control of the cavity amplitude and phase within specified requirements are accomplished by two PI (proportional-integral) controllers [8]. The VM is controlled by the I/Q component output signals and generates the RF driving signal for the SSPA based on the 1.3 GHz reference input (REF) signal.

Apart from the phase and amplitude control, the LLRF system is also responsible for the frequency detuning control of the SC cavity. This paper concentrates only on the phase and amplitude control.

LLRF TEST SETUP

The first test setup including of a phase shifter was built to simulate the cavity pick-up signals for the LLRF. Figure 2 is the block diagram of the test setup. The 81 MHz ADC sampling clock, the 1.354 GHz LO signal and the 1.3 GHz REF signal are generated by the synchronization system, which is composed of three synchronized signal generators (a Hewlett Packard 83732B signal generator at 20 dBm in 81 MHz, a Agilent E4432B ESG-D series signal generator at 16 dBm in 1.381 GHz and a Hewlett Packard E4432B ESG-D series signal generator at 16 dBm) in 54 MHz, mixers, filters, amplifiers and power dividers. The 1.3 GHz RF signal is distributed into three paths. One is used as the VM REF signal. Another is the RF input signal of a down converter and a L3 Narda-ATM 360°/GHz phase shifter series P1103D [1] is located in between. An Agilent Technologies MSO9254A mixed signal oscilloscope is used to observe the output reference signal and the VM output signal. As expected the phase difference between the VM output signal and the output reference signal varies when the P1103D shifts phase of the RF input signal. Figure 3 shows the front side view of the test setup.

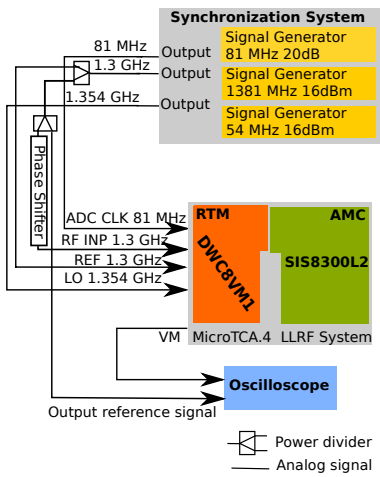


Figure 2: Block diagram of the LLRF test setup.

The RF input signal goes through both the analog and digital processes, which are illustrated in Fig. 4. A detailed

[1] https://www.atmmicrowave.com/coaxial/phase-shifter-line-stretcher/

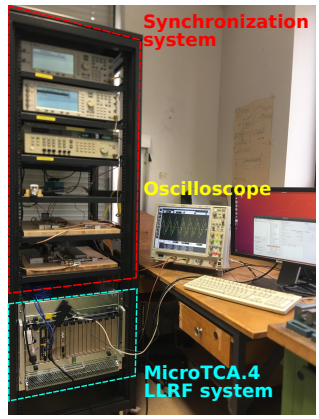


Figure 3: Front side view of the LLRF test setup.

description of the individual processing steps can be found in [9]. In order to maintain the adequate amplitude stability it is necessary to calibrate the DAC offset and gain errors. Then the amplitude stability achieves ±3.5% instead of 16% without the calibration. The PI controller will guarantee the phase and amplitude stability requirements. Figure 5 shows the time difference between the VM output signal and the output reference signal under a certain phase shift.

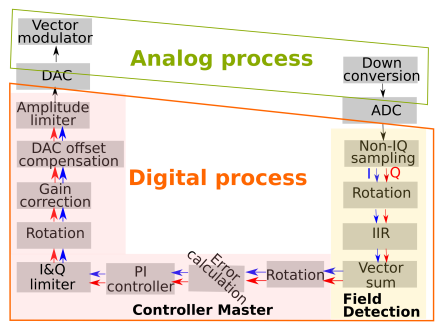


Figure 4: Block diagram of the LLRF firmware.

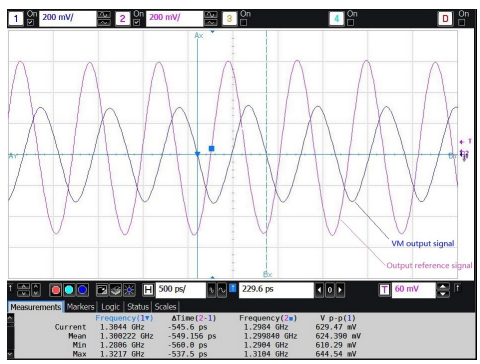


Figure 5: VM output and reference signal and their phase difference observed by the oscilloscope.

MODEL SIMULATION

A Matlab/Simulink model was developed to simulate the system response, perform the stability analysis of the con-

ISBN: 978-3-95450-194-6 ISSN: 2226-0366 doi:10.18429/JACoW-LINAC2018-THPO007

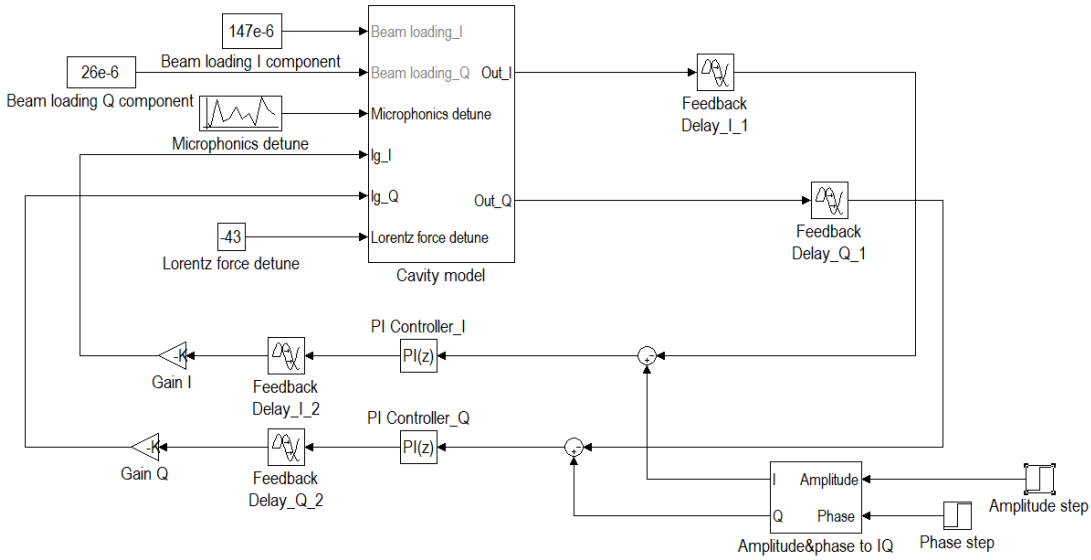


Figure 6: Simulink model of the LLRF control system.

trol system and optimize control parameters. The amplitude and phase control model is shown in Fig. 6. The non-linear dynamics of a single RF cavity can be represented by a state-space equation [10]. Two PI controllers are individually used for I/Q component control. In this paper the EB mode is taken as an example, the amplitude and phase step response were obtained to analyze the stability of the control system. The amplitude setpoint is 12.5 MV and the phase setpoint is 10°. The beam loading I/Q components are calculated for the beam current 150 µA and the synchronous phase 10°. The Lorentz force detune of −43 Hz is estimated by $\Delta f = -k \cdot E_{\mathrm{acc}}^2$, where Δf is the frequency shift, k the Lorentz force coefficient and E_{acc} the accelerating gradient [11]. The microphonics detune is assumed to be an uniform distribution between −50 Hz and 50 Hz. Figure 7 shows the amplitude and phase step responses.

The simulation proved that the I/Q component closed-loops are stable and the cavity field amplitude and phase stability are better than 0.01% and 0.01° after 500 µs. For the practical application, the dead time of the simulation must be corrected according to the LLRF system.

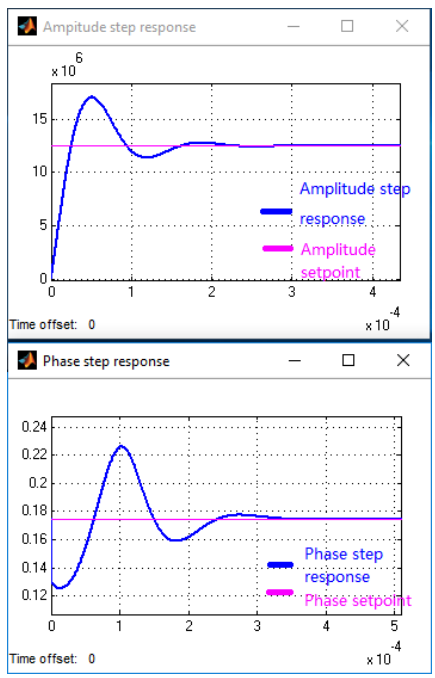


Figure 7: Amplitude and phase step responses of the LLRF control system model. Plot (top) is the amplitude step response with P gain = 400 and I gain = 25000000 and the plot (bottom) is the phase step response with P gain = 300 and I gain = 11000000.

CONCLUSION & OUTLOOK

In summary, as the first functional test, the open-loop phase shift of the MicroTCA.4 based LLRF system was tested. The phase of the VM output signal shifts according to the phase shift of the RF input signal. During this process the amplitude stability reaches ±3.5% with the calibrated VM in the open-loop mode. The Matlab/Simulink model of the LLRF control system was developed to find the P and I gains for the PI controllers. In the coming months, in-depth analysis and tests will be done to assure that the system can fulfill all MESA requirements. The simulation will be used to find the optimum control parameters. Then the frequency detune control will be integrated into the system.

ACKNOWLEDGEMENTS

Authors would like to thank the MicroTCA Technology Lab from DESY for providing the firmware of the MicroTCA.4 based LLRF control system. Further thanks to Pablo Echevarria Fernandez at HZB for his introduction to the firmware.

Content from this work may be used under the terms of the CC BY 3.0 licence (© 2018). Any distribution of this work must maintain attribution to the author(s), title of the work, publisher, and DOI.

ISBN: 978-3-95450-194-6 ISSN: 2226-0366 doi:10.18429/JACoW-LINAC2018-THPO007

Content from this work may be used under the terms of the CC BY 3.0 licence (© 2018). Any distribution of this work must maintain attribution to the author(s), title of the work, publisher, and DOI.

REFERENCES

[1] R. Heine and F. Fichtner, "Concept of the High Power RF Systems for MESA," in *Proceedings, 8th International Particle Accelerator Conference (IPAC 2017), Copenhagen, Denmark, May 14-19, 2017*, pp. 4147–4149, JACOW, Geneva, Switzerland, 2017.

[2] J. Branlard, G. Ayvazyan, V. Ayvazyan, M. Grecki, M. Hoffmann, T. Jeżyński, F. Ludwig, U. Mavrič, S. Pfeiffer, H. Schlarb, *et al.*, "MTCA. 4 LLRF System for the European XFEL," in *Proceedings, 20th International Conference "Mixed Design of Integrated Circuits and Systems"*, pp. 109–112, IEEE, 2013.

[3] K. Przygoda, P. Echevarria, R. Rybaniec, H. Schlarb, and C. Schmidt, "MicroTCA.4 based Single Cavity Regulation including Piezo Controls," in *Proceedings, 7th International Particle Accelerator Conference (IPAC 2016): Busan, Korea, May 8-13, 2016*, p. THOAA03, 2016.

[4] "Struck Innovative Systeme." http://www.struck.de/.

[5] "Datasheet of RTM-DWC8VM1." https://techlab.desy.de/products/rtm/drtm_dwc8vm1/localfsExplorer_read?currentPath=/afs/desy.de/group/msk/www/html/TechLab/DRTM-DWC8VM1/Datasheet\%20DRTM-DWC8VM1.pdf.

[6] "Datasheet of SIS8300-L2." http://www.desy.de/~wwwuser/_publish/sis8300l2-m-x009-1-v101.pdf.

[7] T. Schilcher, "Digital Signal Processing in RF Applications," *Digital Signal Processing CAS*, pp. 249–283, 2007.

[8] K. J. Aström and T. Hägglund, *PID Controllers: Theory, Design, and Tuning*, vol. 2. Instrument society of America Research Triangle Park, NC, 1995.

[9] I. Rutkowski, M. Hoffmann, H. Schlarb, L. Butkowski, and C. Schmidt, "Regae LLRF Control System Overview," in *Proceedings, 4th International Particle Accelerator Conference (IPAC 2013): Shanghai, China, May 12-17, 2013*, pp. 3210–3212, 2013.

[10] M. Hernandez and W. Höfle, "Progress Report on SIMULINK Modelling of RF Cavity Control for SPL Extension to LINAC4," tech. rep., sLHC Project Report 0054, 2011.

[11] Z. Li, C. Adolphsen, M. Ross, L. Xiao, T. Raubenheimer, O. Kononenko, and C. Rivetta, "Multi-physics Analysis of CW Superconducting Cavity for the LCLS-II Using ACE3P," in *Proceedings, 5th International Particle Accelerator Conference (IPAC 2014): Dresden, Germany, June 15-20, 2014* , pp. 2645–2647, 2014.

ISBN: 978-3-95450-194-6 ISSN: 2226-0366 doi:10.18429/JACoW-LINAC2018-THPO008

LONG-TERM OPERATION WITH BEAM AND CAVITY PERFORMANCE DEGRADATION IN COMPACT-ERL MAIN LINAC IN KEK

H. Sakai†, T. Furuya, E. Kako, T. Konomi, T. Miura, F. Qui, K. Umemori, KEK, Ibaraki, Japan

Abstract

We developed ERL main linac cryomodule for Compact ERL (cERL) in KEK. The module consists of two 9-cell 1.3 GHz superconducting cavities. After construction of cERL recirculation loop, beam operation was started in 2013 Dec. First electron beam of 20 MeV successfully passed the main linac cavities [1]. Beam current increased step by step and currently reached to 1 mA (CW) [2]. Energy recovery has successfully achieved. However, field emission was one of the problems for long term operation [3]. Therefore, the performance of the SRF cavities through long term beam operation has been investigated. In this paper, details of SRF beam operation, degradation, applied recovery methods are described.

INTRODUCTION FOR COMPACT ERL

Compact ERL Accelerator

Compact ERL (cERL) [1] is a test facility, which was constructed on the ERL Test Facility in KEK. Its aim was to demonstrate technologies needed for future multi GeV class ERL light source [4]. Recently, the future light source project in KEK was shifted to the high-performance ring accelerator. KEK directorates kept the importance of the R&D for industrial application based on ERL technologies like EUV-lithography [5] and so on. R&D of cERL was shifted to the industrial application from 2017.

cERL consists of 500 kV DC photocathode gun, which made high charge and low emittance electron beam, the injector cavities, the main linac cavity, which made energy recovery, recirculation loop and the beam dump. Detailed design beam parameters are shown in Table 1.

Table 1: Design Parameters of the cERL

Nominal beam energy	35 MeV
Nominal injection energy	5 MeV
Beam current	10 mA (initial goal)
	100 mA (final goal)
Normalized emittance	0.1 – 1 mm-mrad
Bunch length	1-3 ps (usual)
(bunch compressed)	100 fs (short bunch)

Main Linac Cryomodule

The left of Fig. 1 shows a schematic view of the main linac cryomodule [3], which contains two 9-cell KEK ERL model-2 cavities [6] mounted with He jackets. In order to achieve strong HOM damping for high-current ERL, iris diameter is increased to 80 mm. Epeak/Eacc becomes high and to be 3.0. Beampipe-type ferrite HOM absorbers [7] are connected at both sides of cavities, to strongly damp HOMs. The HOM absorbers are placed on 80 K region. Coaxial input couplers [8] with double ceramic windows feed RF power to the cavities. Frequency tuners [9] control cavity resonant frequencies. Cooling pipes of 80K, 5K and 2K are extended throughout the cryomodule. The 80K line was cooled by Nitrogen, and 5K and 2K lines were cooled by Helium. After filling with 4K liquid He, insides of the He jackets were pumped down and the cavities were cooled down to 2K. RF amplitude and phase on the main linac cavities are stabilized by the digital feedback system. RF stability of 0.01% R.M.S. for amplitude and 0.01 degree R.M.S. for phase were achieved [10].

Unfortunately, main linac cavity performance was not so good. Severe field emission was observed from low fields, for both cavities [3]. Operation voltage was limited to 8.6 MV for each cavity, to avoid the problem caused by the heavy radiation. Therefore operation energy of cERL beam was limited to 20 MeV; 2.9 MeV at injector part and 8.6 + 8.6 MeV at main linac part.

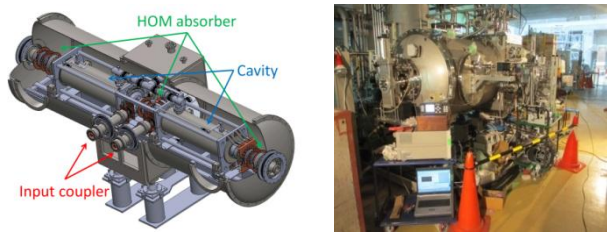


Figure 1: Schematic view of ERL main linac cryomodule (left) and the one placed inside the cERL radiation shielding room (right).

Beam Operation History until 2016

We briefly summarize our beam operation history. After first beam commissioning at December of 2013, we did the energy recovery with 6.5 μA. CW beam in 2nd and 3rd beam operation phase. In this phase, we learned the careful beam tuning without beam loss [11]. We started 100 μA current beam operation at 4th and 5th phase in 2015. During summer shutdown in 2014, we installed Laser Compton Scattering (LCS) beamline to demonstrate the future high-flux gamma-ray source and advanced X-ray imaging technology [12]. By using this high beam current, we successfully obtain clear narrow-band X-ray image come from LCS [13]. During summer shutdown in 2015, we upgraded the DC Gun and added the radiation shield to be operated for 1 mA energy recovery condition. In 2016, we started the 6th phase beam operation for 7 weeks. Finally, energy recovery has successfully achieved with about 1 mA (CW) beam [2].

Q-values of cavities were several times measured until 2016. Results are shown in Fig. 2. Main linac 1 (ML1) and Main linac 2 (ML2) represent the KEK-ERL model-2

† hiroshi.sakai.phys@kek.jp

Content from this work may be used under the terms of the CC BY 3.0 licence (© 2018). Any distribution of this work must maintain attribution to the author(s), title of the work, publisher, and DOI.

ISBN: 978-3-95450-194-6 ISSN: 2226-0366 doi:10.18429/JACoW-LINAC2018-THPO008

Content from this work may be used under the terms of the CC BY 3.0 licence (© 2018). Any distribution of this work must maintain attribution to the author(s), title of the work, publisher, and DOI.

cavity set in main linac cryomodule on the upstream side and downstream side, respectively. Although radiation existed and Q-values were low from the first high power test at 2012, after some period of beam operation, Q-values became further worse. However, we kept cavity performance after degradation from May 2014 to Mar. 2015. The unexpected vacuum burst or discharge event sometimes occurred during beam operation. The cavity performance was kept by using pulse processing method [14]. In 2016, cavity performance of ML1 became worse more. Until 2016, the reason why cavity performances became worse was not clear. Therefore, we continued measuring the cavity performances in 2017 and 2018.

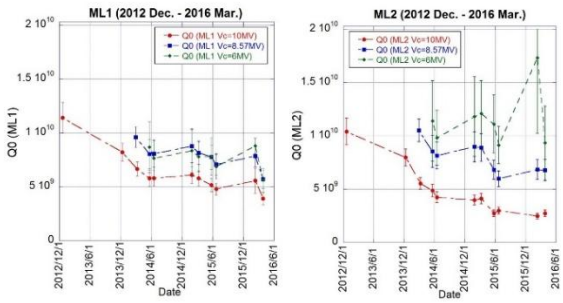


Figure 2: Measurement of the Q-values of 6, 8.57 and 10 MV cavity voltage during long-term beam operation from 2012 to 2016 including high power test of Main linac 1(left) and 2 (right).

MAIN LINAC CAVITY PERFORMANCES DUTING THE LATEST TWO YEARS

Beam Operation from 2017 to 2018

Table 2 shows our beam time during the latest 2 years. R&D of cERL was shifted to the industrial application from 2017. Unfortunately, we did not obtain the sufficient beam time for R&D as shown in Table 2. However, during these short beam operation time, we could many important and interesting R&D for not only industrial application but also the basic beam study for short bunch and high charge beam operation [15-17].

Table 2: cERL Beam Operation from 2017 to 2018

Period (operation time)	Energy [MeV]	Current [mA]	Comment
2017/3 7th phase (3 weeks)	(20→) 17.5	60 pC/ bunch	Degradation of cavity performance. Pulse operation for beam optimization.
2018/3 8th phase (2 weeks)	17.5	60 pC/ bunch	Pulse operation for THz radiation experiment
2018/6 9th phase (4 weeks)	17.5	60 pC/ bunch &1 mA (CW)	Pulse operation for beam optimization & THz radiation experiment & CW beam operation

ML1 Cavity Performance and Processing

We met the severe cavity degradation of ML1 during 7th phase in 2017. Figure 3 shows the time trend of the performance degradation during cavity processing on 8th.Mar.2017 before beam operation. Frist we applied CW field to the ML1 cavity for processing. When the field reached to the 5 MV, the field in the cavity suddenly fell down and cavity vacuum in the ML1 cavity increased. After that, cavity voltage did not increase more than 1 MV.

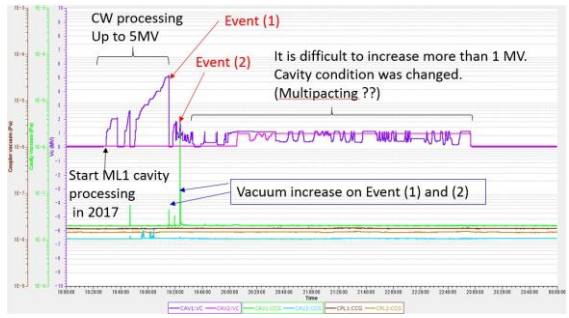


Figure 3: ML1 cavity processing trend on 8th.Mar.2017 before beam operation. Purple (pink) line shows the cavity voltage in ML1 (ML2). Green (line blue) line shows the vacuum inside the cavity of ML1 (ML2). Green (light blue) line shows the vacuum inside the cavity of ML1 (ML2). Brown (Gold) line shows the vacuum in warm side of the input coupler of ML1 (ML2).

Figure 4 show the expanded views of the figure around event (1) and (2) denoted in Fig. 3. The left figure of Fig. 4 shows 2 min. time trend including the first RF down event (event (1)) when the cavity field fell down at first. As the cavity field fell down, ML1 cavity vacuum increased. After event (1), we observed the large vacuum increasing even though the cavity voltage is lower than 5 MV. The right figure of Fig. 4 shows 2 min. time trend including the RF changing event (event (2) after the cavity fell down event (event (1)). The vacuum kept higher pressure than usual for more than 20 sec. after event (2) was occurred at 2 MV cavity field. Discharge event with long time occurred in the ML1 cavity at this time and the cavity condition would be changed drastically. Finally, we did not increase the cavity field after these events; the severe multipacting was observed after these events.

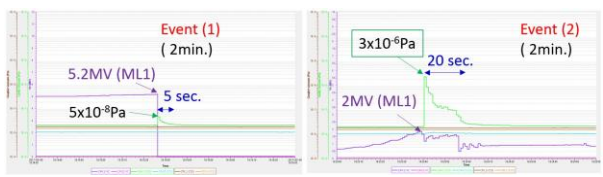


Figure 4: The left (right) figure shows the expanded view around event (1) and (2) denoted in Fig. 3, respectively.

After long processing at a few MV level, we finally processed the cavity again and increased the cavity field up to 6.5 MV. Figure 5 shows the trend of processing after event (1), (2). As the field reached the 6.5 MV field, suddenly field was fell down and we did not increase the cavity field more, even though the field could increase up

ISBN: 978-3-95450-194-6 ISSN: 2226-0366 doi:10.18429/JACoW-LINAC2018-THPO008

to 11 MV before these events were occurred in 2016. We note that we add the pulse processing as shown in Ref. [14] on 7th, 8th and 9th phase to increase the cavity field. Total processing time was about 10 hours. However, we could increase up to only 6.9 MV for ML1 cavity after long term pulse processing. The reason of the limitation of cavity field was not field emission but thermal break down. Some particulates would be made during event (1) or (2) and resulted in the heating the cavity at the lower field.

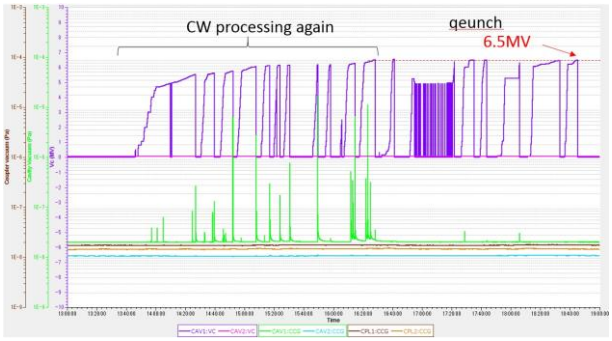


Figure 5: ML1 cavity processing trend again on 10th.Mar.2017 after field decreasing event as shown in Fig. 4.

ML2 Cavity Performance and Processing

Fortunately, event (1) and (2) did not decrease the ML2 cavity performance. However, ML2 cavity met severe field emission. At 8th phase beam operation on Mar.2018. Q-value of ML2 gradually decreased after the beam operation in 7th phase. We applied the pulse processing at 9th phase before beam operation.

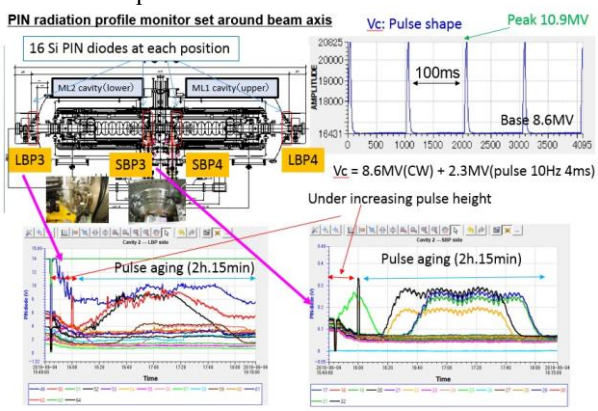


Figure 6: Pulse processing condition for ML2 cavity at 9th phase. Lower figures shows the trend of the PIN diode signals set on the both ends of ML2 cavity under the pulse processing as shown in the upper left figure of this figure.

Figure 6 shows the condition of the pulse processing. We applied the 8.6 MV for the base field and added the pulse peak field up to 10.9 MV to carry out the high power peak processing for this cavity. This pulse repetition is 10 Hz as shown in the right upper figure in Fig. 6. During pulse processing, we saw the PIN diode signals beside the ML2 cavity. After 2 hours pulse processing, all PIN diode signals drastically decreased and we finished the pulse processing.

Measurement of Q-value of Both Cavities

We did not measure the Q-values in 2017 due to the lack of time. After each pulse processing of two cavities, we twice measured the Q-values of both cavities in 2018.

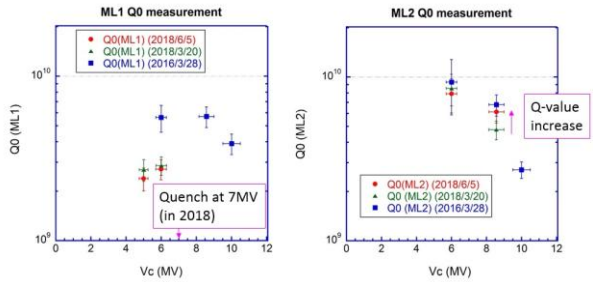


Figure 7: Q-value measurement results of ML1(left) and ML2(right). Horizontal (vertical) axes show the cavity voltage (Vc) and unloaded-Q values of both cavities.

Figure 7 shows the results of the Q-value measurements in 2016 and 2018. After the unexpected event shown in Fig. 3 for ML1, we could not obtain the higher Q-values in 2018 than that in 2016, which already had the lower cavity performance than before. Furthermore, cavity voltage was limited up to 6.9 MV in both 8th and 9th phase beam operation in 2018 even though we tried pulse processing for 10 hours. Pulse processing was not effective for the ML1 cavity after these unexpected events. On the other hand, after the pulse processing for ML2 as shown in Fig. 6, we could recover the ML2 cavity performance. Q-values at 8.6 MV in Jun.2018 increased after the pulse processing and come back to the same value as that in 2016. Field emission was severe problem in ML2. However, cavity performance was recovered by using pulse processing method until now. By keeping this cavity voltages to 6 MV of ML1 and 8.6 MV of ML2, we could start beam operation in Mar. and June. 2018 and could keep 1 mA beam operation again with energy recovery condition.

SUMMARY AND FUTURE PROSPECT

During the latest 2 years operation, cavity performance was degraded. Especially, ML1 cavity was drastically degraded by the unexpected burst event. After this event, we could not recover the cavity performance to the previous values in spite of many pulse processing. For ML2 cavity, we could keep the cavity performance under the severe field emission. Pulse processing worked well to keep the cavity performance for ML2. During the burst event, we observed the long vacuum increasing event. At this event, discharge would occur and some components like HOM absorber, ceramic of the input coupler and/or the other vacuum components near ML1 cavity would break and make some particulates in the ML1 cavity. We plan to increase the beam current up to 10 mA. However, we would like to open the cavity to identify the degradation source by directly seeing the inside of the cavities.

Content from this work may be used under the terms of the CC BY 3.0 licence (© 2018). Any distribution of this work must maintain attribution to the author(s), title of the work, publisher, and DOI.

ISBN: 978-3-95450-194-6 ISSN: 2226-0366 doi:10.18429/JACoW-LINAC2018-THPO008

Content from this work may be used under the terms of the CC BY 3.0 licence (© 2018). Any distribution of this work must maintain attribution to the author(s), title of the work, publisher, and DOI.

REFERENCES

[1] M. Akemoto *et al.*, "Construction and commissioning of the compact energy-recovery linac at KEK", *Nucl. Instr. Meth.*, vol. 877, pp. 197-219, 2018.

[2] T. Obina *et al.*, "Recent Developments and Operational status of the Compact ERL at KEK", in *Proc. 7th Int. Particle Accelerator Conf. (IPAC'16)*, Busan, Korea, May 2016, paper 1835.

[3] H. Sakai *et al.*, "High power CW tests of cERL Main-linac cryomodule", in *Proc. 16th Int. Conf. RF Superconductivity (SRF'13)*, Paris, France, Sep. 2013, paper 855.

[4] "Energy Recovery Linac Conceptual Design Report", KEK Report 2012-4, 2012, http://ccdb5fs.kek.jp/tiff/2012/1224/1224004.pdf

[5] H. Sakai *et al.*, "Superconducting Accelerator for ERL based FEL EUV light source at KEK", in *Proc. 18th Int. Conf. RF Superconductivity (SRF'17)*, Lanzhou, China, Jul. 2017, pp. 13-18.

[6] K. Umemori *et al.*, "Design of L-band superconducting cavity for the energy recovery linacs", in *Proc. of APAC2007*, Indore, India, 2007, p. 570.

[7] M. Sawamura *et al.*, "Cooling properties of HOM absorber model for cERL in Japan", in *Proc. of SRF'2011*, Chicago, U.S.A, 2011, p. 350.

[8] H. Sakai *et al.*, "High power tests of KEK-ERL input coupler for main linac under liquid nitrogen condition", in *Proc. of SRF2011*, Chicago, U.S.A, 2011, p. 356.

[9] K. Enami *et al.*, "Performance evaluation of ERL main linac tuner", in *Proc. of IPAC2014*, Dresden, Germany, 2014, p. 2534.

[10] T. Miura *et al.*, "Performance of RF system for Compact-ERL Main Linac at KEK", in *Proc. IPAC'14*, Dresden, Germany, 2014, p. 2450.

[11] S. Sakanaka *et al.*, "The first beam recirculation and beam tuning in the Compact ERL at KEK", in *Proc. of LINAC'14*, Geneva, Switzerland, 2014, p. 599.

[12] R. Nagai *et al.*, "Construction of a Laser Compton Scattered Photon Source at cERL", in *Proc. of IPAC'14*, Dresden, Germany, 2014, p. 1940.

[13] T. Akagi *et al.*, "Narrow-band photon beam via laser Compton scattering in an energy recovery linac", *Phys. Rev. Accel. Beams*, vol. 19, p. 114701, 2016.

[14] H. Sakai *et al.*, "Measurement of the cavity performances of Compact ERL main linac cryomodule during beam operation", in *Proc. of SRF2015*, Whistler, Canada, 2015, p. 592.

[15] T. Miyajima *et al.*, "60 pC bunch charge operation of the compact ERL at KEK", in *Proc. of IPAC'17*, Copenhagen, Denmark, 2017, p. 890.

[16] Y. Honda *et al.*, arXiv:1807.06195.

[17] Y. Honda *et al.*, "Beam tuning and bunch length measurement in the bunch compression operation at the cERL", *Nucl. Instr. Meth.*, vol. 875, pp. 156-164, 2017.

ISBN: 978-3-95450-194-6 ISSN: 2226-0366 doi:10.18429/JACoW-LINAC2018-THPO009

EVALUATION OF 60 pC BEAM PERFORMANCE AT cERL INJECTOR FOR ERL BASED EUV-FEL

T. Hotei*, SOKENDAI, Tsukuba, Ibaraki, Japan
T. Miyajima, R. Kato, KEK, Tsukuba, Ibaraki, Japan

Abstract

In order to compensate for the emittance which is increased by space charge in the low energy region, it is important to transport the beam as designed. Until now, we did not consider couplers in injector superconducting cavities in optics design. But in this study, to improve optics matching and emittance compensation conditions for space charge dominated beam in cERL at KEK, we introduced a new 3D cavity model. We first investigated the influence of the couplers on electromagnetic field distribution. As a result, it was found that an asymmetric focusing force is generated by the influence of the couplers. It also became clear that the influence of the coupler kick on the optics significantly devastated the emittance compensation condition from the calculating including space charge. Furthermore, it was found that by optimizing the optics in consideration of the coupler kick, it is possible to improve the beam control accuracy and reduce the emittance in beam commissioning.

INTRODUCTION

Energy recovery linac (ERL) is the linear accelerator which can supply high average current beam. ERL based EUV-FEL for semiconductor lithography is designed at KEK [1]. EUV-FEL requires a beam with a bunch charge of 60 pC, kinetic energy of 10 MeV, bunch length of 1 ps and emittance of 1 mm.mrad in the injector.

Since the emittance increases due to space charge in the low energy region, the increased emittance must be compensated. In order to compensate the emittance, it is important to transport the beam as well as the designed optics. But, in beam commissioning at cERL in KEK, we found that the influence on the optics caused by coupler kick of injector cavity can not be ignored [2, 3].

We analyzed numerically and experimentally to study the influence of coupler kick on optics and emittance compensation. In this proceedings, we report on these results.

ELECTROMAGNETIC FIELD ANALYSIS

In order to analyze the influence on the electromagnetic field distribution by the couplers, we created two models of cERL injector cavity [4]; model 1 does not have couplers (Fig. 1 top, 2D model), model 2 has couplers (Fig. 1 bottom, 3D model). The electromagnetic field for 2D model is calculated assuming cylinder symmetry by Poisson/Superfish [5], for 3D model is calculated by CST [6]. 3D model has no cylindrical symmetry.

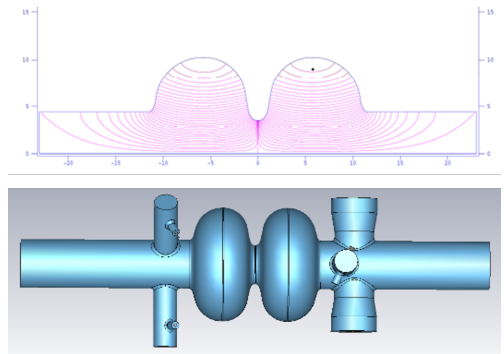


Figure 1: Two models of cERL injector cavity. Top is 2D cavity model and bottom is 3D cavity model.

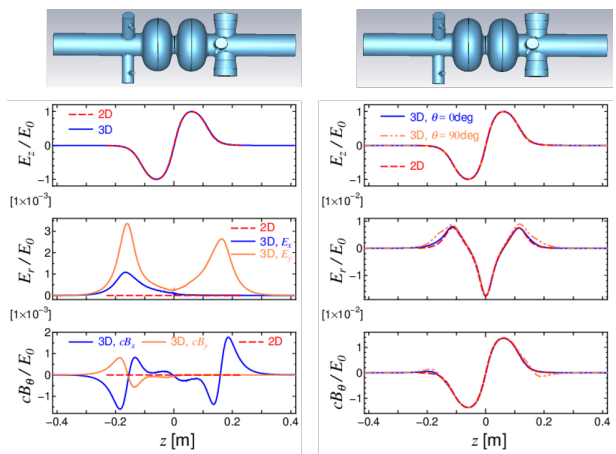


Figure 2: Comparison of electromagnetic field distribution (left: $r = 0$ mm, right: $r = 1$ mm). The red dotted line is the result of 2D model. The blue solid line is the result of 3D model with $\theta = 0$deg. The orange solid line is the result of 3D model with $\theta = 90$deg. The magnitude of the electromagnetic field is normalized by the maximum value of $E_z(r = 0, z)$.

Figure 2 shows the electromagnetic field distribution of $r = 0$ mm (left) and $r = 1$ mm (right) for each model. This indicates that the transverse electromagnetic field is generated on the central axis of the cavity by the couplers. In addition, it can be seen that the transverse electromagnetic field distribution becomes angle dependent by the coupler.

FOCUSING FORCE FROM CAVITY

In order to quantitatively evaluate the influence of coupler on beam dynamics, we tracked the single particle trajectory. The schematic layout is shown in Fig. 3. In this case, the lens whose focusing force is measured is a cavity. The kinetic

* hotei@post.kek.jp

Content from this work may be used under the terms of the CC BY 3.0 licence (© 2018). Any distribution of this work must maintain attribution to the author(s), title of the work, publisher, and DOI.

ISBN: 978-3-95450-194-6 ISSN: 2226-0366 doi:10.18429/JACoW-LINAC2018-THPO009

Content from this work may be used under the terms of the CC BY 3.0 licence (© 2018). Any distribution of this work must maintain attribution to the author(s), title of the work, publisher, and DOI.

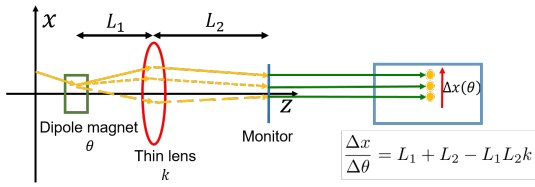


Figure 3: Schematic layout of single particle tracking.

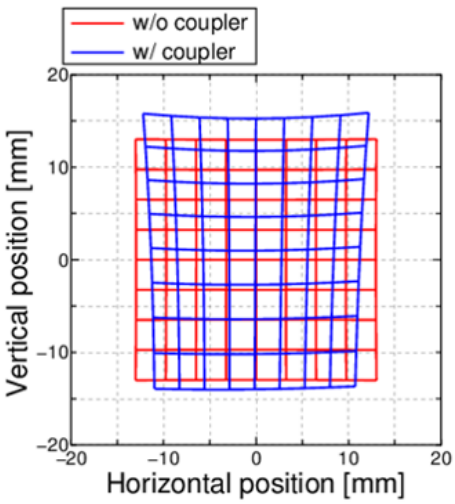


Figure 4: Tracking result. The red line is result of 2D model. The blue line is result of 3D model.

energy of injection particle is 0.5 MeV and after passing through the cavity is 1.7 MeV. The phase of cavity matches the maximum acceleration phase.

We tracked the particle trajectory while changing the dipole kick angle. Figure 4 is a plot of the transverse position of the particle at a certain z position after passing through the cavity. The result of the 2D model shows that the lattice is square. On the other hand, the result of 3D model shows that the lattice is vertically long.

In order to further evaluate quantitatively, the amount of movement of the particle with respect to the dipole kick angle θ were obtained from the linear fit of the scan result in the x-axis direction and y-axis direction. The result of the 2D model is $\Delta x/\Delta\theta = \Delta y/\Delta\theta = 1.16$ m/rad. The result of the 3D model is $\Delta x/\Delta\theta = 1.02$ m/rad, $\Delta y/\Delta\theta = 1.32$ m/rad.

OPTICS AND EMITTANCE MEASUREMENT

In order to evaluate the influence on optics and emittance compensation, we performed multistage calculation including space charge effect. The tracking code is General Particle Tracer (GPT) [7].

The results optimized to minimize the emittance at the final position using the 3D cavity model are shown in Fig. 5. Figure 5 also shows the evolution of beam size and emittance when only the cavity model is changed to 2D model. Since the focusing force from cavity varies depending on the cavity model, the beam size at the downstream is different.

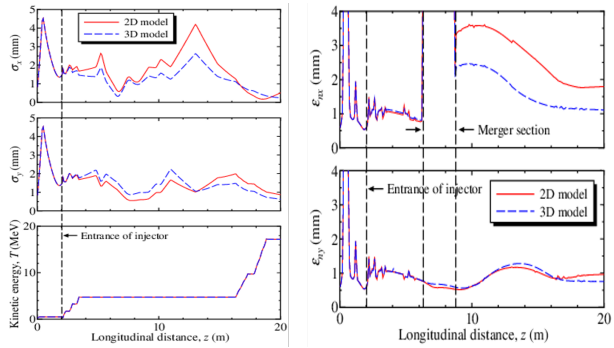


Figure 5: The evolution of RMS beam size (left) and normalized emittance (right). The red solid line is the result of 2D model. The blue dotted line is the result of 3D model.

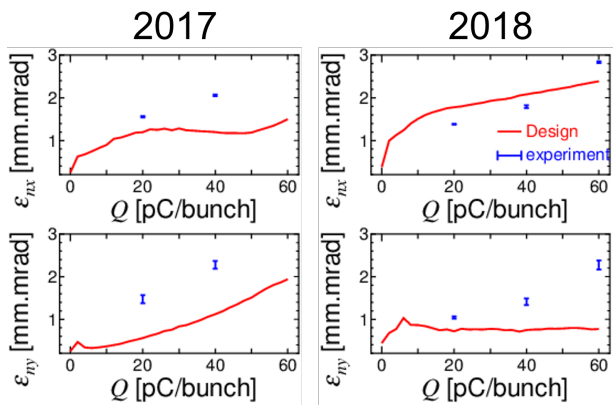


Figure 6: Emittance measurement result (left: 2017, right: 2018). The red line shows designed emittance value.

Although the horizontal emittance up to merger has hardly changed, it turns out that the emittance at the merger exit is greatly changed.

We measured the emittance at the merger exit by Q-scan method in beam commissioning using optics optimized considering coupler kick. To clarify the effect of coupler kick, the results of 2017 measured with optics optimized using 2D model are also shown in Fig. 6. From the comparison of the results it turns out that the emittance is lower in 2018 than in 2017. Moreover, it is understood that the amount of deviation from the designed value is smaller in 2018 than in 2017.

DISCUSSION

From the result of the electromagnetic field analysis, it was found that the influence of the couplers causes a non-zero electromagnetic field in the transverse direction on the central axis of the cavity. The transverse electromagnetic field on the central axis gives a dipole kick to the beam. It was also found that the distribution of the transverse electromagnetic field has circumferential dependence due to the presence of the coupler. This shows that the transverse electromagnetic field gives a beam the focusing force that is asymmetrical in

ISBN: 978-3-95450-194-6 ISSN: 2226-0366 doi:10.18429/JACoW-LINAC2018-THPO009

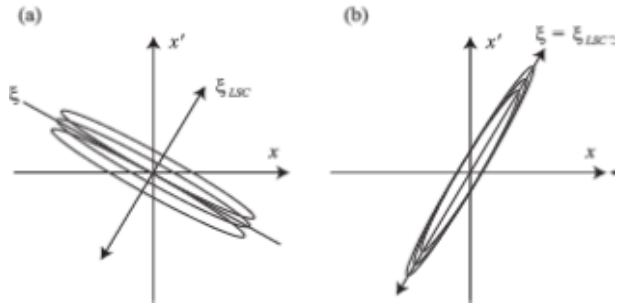


Figure 7: Diagram for compensating the emittance increased in the dispersion region by longitudinal space charge. (a) When the emittance deterioration amount becomes the maximum. (b) When the emittance deterioration amount becomes the minimum.

the horizontal and vertical direction. Therefore, this directly affects beam optics.

The asymmetry of focusing force was quantitatively evaluated from single particle tracking. It was found that the beam movement amount ratio was distorted by 1.3 times, and it was shown that the focusing force in the horizontal direction is stronger than vertical direction. It is consistent with the result of electromagnetic field analysis that the focusing force becomes asymmetric.

In order to investigate the influence on beam transport optics and emittance compensation, multiparticle tracking considering space charge effect was performed. Depending on the model of the cavity, that is, the presence or absence of couplers, it was shown that the downstream beam size is different. This is due to the change in the focusing force from the cavity due to the influence of the couplers. It was also shown that the emittance after passing through the dispersion region (merger) greatly varies depending on the model. This is because compensation of the horizontal emittance increase in the horizontal dispersion region due to the longitudinal space charge effect is determined by the upstream optics [8, 9]. Figure 7 shows a diagram for compensating the emittance increased by longitudinal space charge effect at the dispersion region. Emittance at the merger exit can be reduced by aligning the major axis directions of the ellipses in the direction aligned by the longitudinal space charge effect, that is, matching with the optics of emittance compensation. Therefore, it is considered that the emittance at the merger exit was increased due to the influence of upstream optics change (cavity model change). And we guess that the actual emittance value has been brought close to the designed value since we designed an optics to compensate the emittance using the 3D cavity model.

CONCLUSION

We numerically and experimentally analyzed the influence optics and emittance compensation due to coupler kick. We showed that the electromagnetic field distribution is distorted due to the existence of the couplers, the distorted electromagnetic field distribution gives dipole kick and asymmetric focusing force. An increase in horizontal emittance at the dispersion region by longitudinal space charge is known. Since the change in the focusing force by the couplers directly affects the optics, it can not be ignored against the compensation of the increased emittance. But, by optimizing the optics including the contribution of the coupler kick, the emittance could be brought close to the designed value.

ACKNOWLEDGEMENTS

We acknowledge T. Konomi in KEK who created 3D cERL injector cavity model. We would like to thank members of the cERL commissioning group.

REFERENCES

[1] N. Nakamura *et al.*, "S2E simulation of an ERL-based high-power EUV-FEL source for lithography", in *Proc. IPAC'17*, Copenhagen, Denmark, May 2017, pp. 894-897. doi:10.1088/17426596/874.012013

[2] T. Hotei *et al.*, "Optics design of the compact ERL injector for 60 pC bunch charge operation", in *Proc. IPAC'17*, Copenhagen, Denmark, May 2017, pp. 898-901. doi:10.18429/JACoW-IPAC2017-MOPVA021

[3] T. Miyajima *et al.*, "60 pC bunch charge operation of the compact ERL at KEK", in *Proc. IPAC'17*, Copenhagen, Denmark, May 2017, pp. 890-893. doi:10.18429/JACoW-IPAC2017-MOPVA019

[4] K. Watanabe *et al.*, "Development of the superconducting rf 2-cell cavity for cERL injector at KEK", *Nucl. Instr. Meth. A*, vol. 714, pp. 67-82, 2013. doi:10.1016/j.nima.2013.02.035

[5] Poisson/Superfish, https://laacg.lanl.gov/laacg/services/download_sf.phtml

[6] CST, https://www.cst.com

[7] Pulsar Physics, http://www.pulsar.nl/gpt/index.html

[8] V. N. Litvinenko *et al.*, "Merger designs for ERLs", *Nucl. Instr. and Meth. A*, vol. 557, pp. 165-175, 2006. doi:10.1016/j.nima.2005.10.065

[9] J-G. Hwang *et al.*, "Effects of space charge in a compact superconducting energy recovery linac with a low energy", *Nucl. Instr. and Meth. A*, vol. 684, pp. 16-26, 2012. doi:10.1016/j.nima.2012.03.042

Content from this work may be used under the terms of the CC BY 3.0 licence (© 2018). Any distribution of this work must maintain attribution to the author(s), title of the work, publisher, and DOI.

ISBN: 978-3-95450-194-6 ISSN: 2226-0366 doi:10.18429/JACoW-LINAC2018-THPO010

NOVEL "STRAIGHT" MERGER FOR ENERGY RECOVERY LINACS*

K. E. Deitrick†, A. Hutton‡
Thomas Jefferson National Accelerator Facility, Newport News, VA 23606, USA
S. Overstreet
Center for Accelerator Science, Old Dominion University, Norfolk, VA 23529, USA
A. C. Bartnik, C. M. Gulliford
Cornell Laboratory for Accelerator-Based Sciences and Education,
Cornell University, Ithaca, NY 14853, USA

Abstract

One of the most critical design considerations for an energy recovery linac (ERL) is how to merge the injected bunch onto the linac axis with minimal beam degradation. All merger designs in established and upcoming machines involve significant bending of the injected beam – even using a so-called straight merger bends the injected beam several degrees. We propose a merger which reduces the bending of the injected beam by an order of magnitude. By passing both beams through a septum magnet followed by an rf separator cavity with a superimposed dipole magnetic field, the injected beam bends minimally within the cavity, while the recirculated beam bends to align with the linac axis. Here we describe the concept in detail and present simulation results to demonstrate the advantages of such a design, particularly for magnetized beams or minimal energy separation between the injected and recirculated beams. Measurements from an experiment at CBETA evaluating the beam dynamics of the rf separator are presented and compared with simulation results.

INTRODUCTION

Mergers remain one of the most challenging design aspects of ERLs to date. While significant effort has gone into minimizing the beam degradation due to mergers over the years, all merger designs in established and upcoming machines bend the beam significantly, which is problematic when dealing with beams sensitive to transport asymmetries, such as magnetized beams [1]. As one of the components of the Jefferson Lab Electron Ion Collider (JLEIC) design is a magnetized electron beam to cool the ion beam, driven by an ERL, this is a critical topic in future design work [2]. Additionally, this merger concept works well for ERLs without significant energy separation between injected and recirculated beams, which is traditionally a challenging design prospect.

"STRAIGHT" MERGER

The layout of the "straight" merger concept is shown in Fig. 1. Both the injected and recirculated beams pass through a septum followed by an rf separator with a superimposed magnetic dipole field. The injected beam passes through the zero-field aperture of the septum before passing through the rf separator and magnetic dipole field assembly. When the injected beam passes through this assembly, the separator is on-crest and the dipole field is set to buck, or compensate, for the kick provided by the separator. To first order, the injected bunch is undeflected. The recirculated beam, on the other hand, is deflected by the septum magnet before passing through the cavity and coils assembly. As a consequence of the required 180° phase separation in an ERL between the bunches of the injected and recirculated beams, the separator cavity and dipole field deflect the recirculated beam in the same direction - leading to a deflection twice what either the cavity or magnetic field would provide alone. The combination of the fields in the cavity coil assembly is seen in Fig. 2.

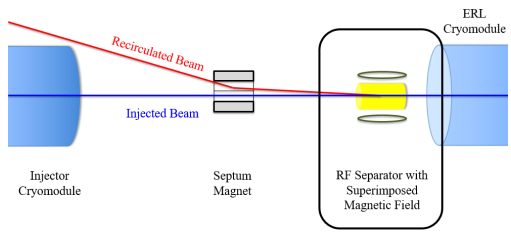


Figure 1: Layout of the "straight" merger concept, Fig. 1 from [3].

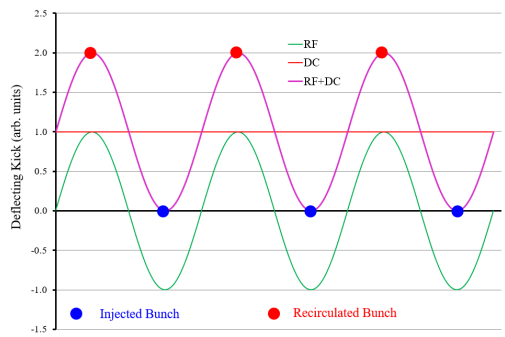


Figure 2: Kick in the rf separator with superimposed magnetic dipole, Fig. 2 from [3].

One of the anticipated higher order effects of this merger design is the "banana" effect. This effect is the deflection

* Authored by Jefferson Science Associates, LLC under U.S. DOE Contract No. DE-AC05-06OR23177.
† deitrick@jlab.org
‡ andrew@jlab.org

Content from this work may be used under the terms of the CC BY 3.0 licence (© 2018). Any distribution of this work must maintain attribution to the author(s), title of the work, publisher, and DOI.

ISBN: 978-3-95450-194-6 ISSN: 2226-0366 doi:10.18429/JACoW-LINAC2018-THPO010

of the head and tail of the injected bunches due to the rf curvature. Fundamentally, different longitudinal slices of the bunch experience different fields from the separator cavity, while experiencing the same fields from the magnetic dipole field. Consequently, the bunch as a whole experiences no net deflection, but the head and tail of the bunch do experience some deflection and a change in energy.

The "banana" effect increases with the rf frequency of the separator cavity, so the 1.3 GHz separator at CBETA allows for this effect to be clearly demonstrated. Ideally, a machine would be designed so that the rf separator cavity has a significantly lower frequency, making this effect relatively negligible [3].

EXPERIMENTAL SETUP

The goal of the first "straight" merger experiment at CBETA was to evaluate the difference between the undisturbed beam, which passes through a drift, and the kicked beam, which passes through the combined rf separator cavity on-crest and coils, with the coil current set so that the centroid of the kicked beam matched the centroid of the undisturbed beam on screens downstream of the separator. In addition, measurements were also taken at phases off-crest, again setting the coil current so that the kicked beam centroid matched the undisturbed beam centroid. This was achieved by setting the CBETA injector to produce a 2.4 MeV electron beam, which traveled through a merger to the diagnostic line. The diagnostic line consists of two pairs of slits, one horizontal and one vertical, and the 1.3 GHz rf separator cavity, followed by a dipole and two screens. Without the dipole, the downstream viewer shows the beam spot. When the dipole is turned on, it is possible to evaluate the longitudinal phase space of the beam [4]. A labeled CAD model of the diagnostic line, with inserts of the cavity and coil assembly and picture of the actual cavity and coil assembly, is shown in Fig. 3.

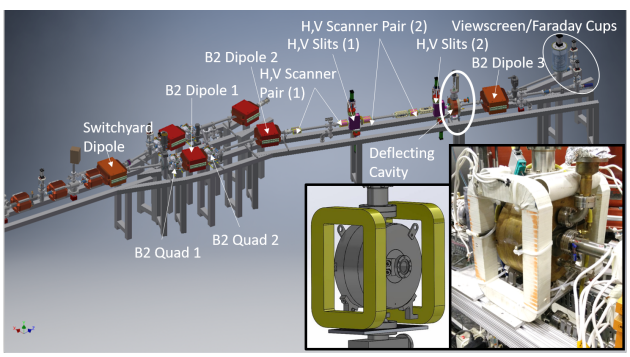


Figure 3: Labeled CAD model of diagnostic line at CBETA, with bottom center insert CAD model of cavity and coil assembly (courtesy of Joe Gubeli), and bottom right insert picture of cavity and coil assembly in the beamline.

While the slits were used during this experiment, this paper focuses primarily on the results obtained using the entire beam, comparing them to simulation results of the experiment, performed by General Particle Tracer (GPT) [5]. One exception to this is the discussion of the banana effect. Unfortunately, there is conflicting calibration data on the deflecting voltage of the cavity - one piece of data indicates 53 kV, while another indicates 113 kV. Fortunately, simulations have shown that the qualitative behavior of the beam, specifically σ_y, the *rms* vertical beam size, as a function of ϕ, the cavity phase, is independent of the deflecting voltage in this regime - this independence breaks down once the deflecting voltage is high enough. Our results show a strong agreement with the simulated qualitative behavior, justifying future experiments of this novel merger concept.

RESULTS

Operating Point

The most "straight"-forward evaluation of the results is the comparison of the undisturbed and kicked beams in terms of beam spot and longitudinal phase space at the operating point, $\phi = 0°$. These four viewscreens are shown in Fig. 4. The top row is the beam spot, while the bottom row is the longitudinal phase space; the undisturbed beam is shown in the left column, while the kicked beam is shown in the right. Looking at these results, it is clear that the kicked beam does not differ significantly from the undisturbed, which matches simulation results and our goal for this concept.

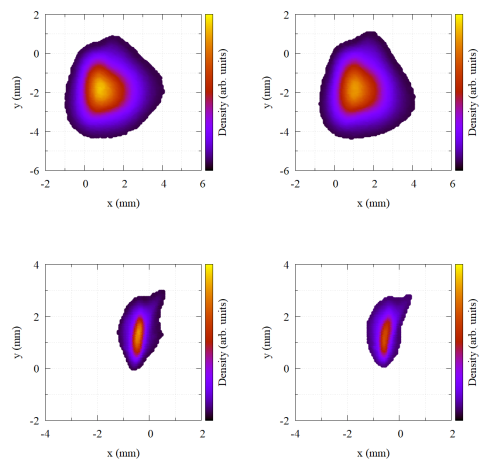


Figure 4: Measurements at the beam spot (top row) and longitudinal (bottom row) screens, for the undisturbed (left column) and kicked (right column) beams.

As a Function of Phase

In order to have more points of comparison than the four measurements shown in Fig. 4, data was also taken while varying the phase of the separator and adjusting the coil current appropriately. The *rms* vertical beam size, being the most impacted, is plotted as a function of phase in Fig. 5 at a number of thresholds for the longitudinal phase space screen. The thresholds applied in the figure are a cleaning

Content from this work may be used under the terms of the CC BY 3.0 licence (© 2018). Any distribution of this work must maintain attribution to the author(s), title of the work, publisher, and DOI.

ISBN: 978-3-95450-194-6 ISSN: 2226-0366 doi:10.18429/JACoW-LINAC2018-THPO010

Content from this work may be used under the terms of the CC BY 3.0 licence (© 2018). Any distribution of this work must maintain attribution to the author(s), title of the work, publisher, and DOI.

mechanism - for a given measurement, beam signal is discarded if it falls below a given percentage of the maximum signal in the measurement. While the measurements shown are given for the longitudinal screen, a similar curve exists for the data taken on the beam spot screen.

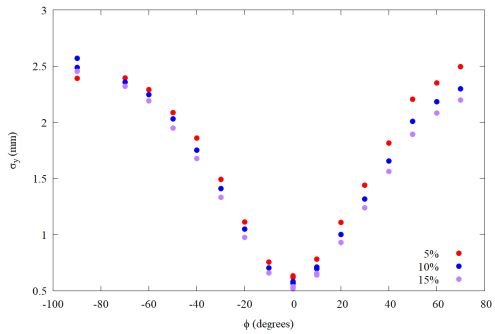


Figure 5: Measured *rms* vertical size, σ_y, on the longitudinal screen plotted as a function of degrees off-crest, ϕ, for different thresholds.

The simulated results of σ_y as a function of ϕ is shown in Fig. 6, for both the longitudinal and beam spot screens. Additional phases have been added to produce a smoother curve. Comparing this to the previous figure, there is significant agreement in the qualitative behavior of the plots. This is emphasized by plotting the longitudinal measurements and simulated curve together in Fig. 7, with the simulated curve scaled and shifted to produce the closest match, showing a strong agreement between the qualitative behavior of measured and simulated results.

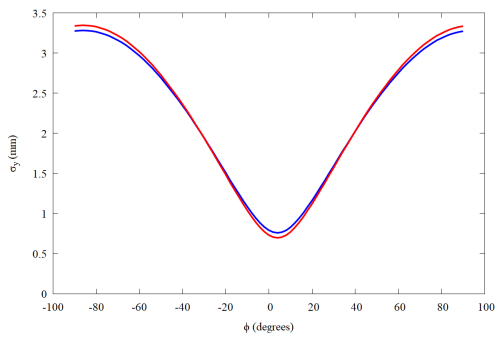


Figure 6: Simulated *rms* vertical size, σ_y, on the longitudinal (red) and beam spot (blue) screens plotted as a function of degrees off-crest.

"Banana" Effect

As mentioned previously, the "banana" effect is the residual kick experienced by the beam at the head and tail of the bunch. While this does occur in the full beam, it is easier and clearer to observe this effect on a beamlet which has passed through horizontal slits prior to passing through the cavity and coils assembly. This effect was observed during the course of our experiment and these measurements are shown in Fig. 8. This figure shows the undisturbed beamlet on the left, while the kicked beamlet on the right has the anticipated banana shape clearly visible.

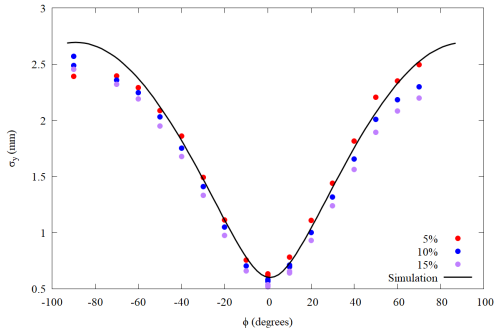


Figure 7: Longitudinal measurements plotted with the simulated curve, which has been shifted and scaled for best agreement.

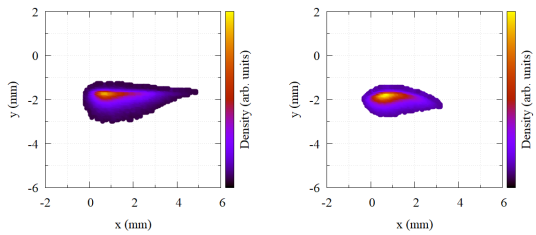


Figure 8: The undisturbed beamlet (left) and kicked beamlet (right), taken at the beam spot screen.

CONCLUSION

Overall, the results of this initial "straight" merger experiment have shown substantial agreement with simulation and provide a strong justification for further exploring this concept as a novel "straight" merger for ERLs.

ACKNOWLEDGEMENTS

This material is based upon work supported by the U.S. Department of Energy, Office of Science, Office of Nuclear Physics under contract DE-AC05-06OR23177. K. E. D. would like to thank LINAC'18 for conference support. S. O. was supported by the National Science Foundation Research Experience for Undergraduates grant number PHY-1659177. A. C. B. and C. M. G. were supported by New York State Energy Research & Development Authority - NYSERDA agreement number 102192. The authors would like to thank everyone at CBETA for their support during this experiment.

REFERENCES

[1] Y. S. Derbenev, "Theory of Electron Cooling", Ph.D. thesis, USSR Academy of Sciences, Siberian Branch, 1978.

[2] T. Satogata and Y. Zhang,"JLEIC–A polarized electron-ion collider at Jefferson Lab", in *ICFA Beam Dynamics Newsletter No. 74*, E. Gianfelice-Wendt, Ed. p. 92-182, 2018.

ISBN: 978-3-95450-194-6 ISSN: 2226-0366 doi:10.18429/JACoW-LINAC2018-THPO010

[3] A. Hutton, " 'Straight" Merger", Jefferson Lab Tech Note, JLab-TN-18-024, 2018.

[4] S. Belomestnykh, I. Bazarov, V. Shemelin, J. Sikora, K. Smolenski, and V. Veshcherevich, "Deflecting cavity for beam diagnostics at Cornell ERL injector", *Nucl. Instrum. Methods Phys. Res., Sect. A*, vol. 614, pp. 179-183, 2010. doi:10.1016/j.nima.2009.12.063

[5] "General Particle Tracer", http://www.pulsar.nl/

Content from this work may be used under the terms of the CC BY 3.0 licence (© 2018). Any distribution of this work must maintain attribution to the author(s), title of the work, publisher, and DOI.

ISBN: 978-3-95450-194-6 ISSN: 2226-0366 doi:10.18429/JACoW-LINAC2018-THPO011

FIRST ENERGY RECOVERY OPERATION AT THE S-DALINAC: RF CONTROL STABILITY MEASUREMENTS*

M. Steinhorst†, M. Arnold, N. Pietralla,
Institut für Kernphysik TU Darmstadt, 64289 Darmstadt, Germany
C. Burandt, Helmholtz-Institut Mainz, 55128 Mainz, Germany

Abstract

Energy recovery linacs (ERL) are used to overcome the rf power limits of rf amplifiers to further increase beam current at particle accelerators. Since the last major upgrade of the electron accelerator S-DALINAC it can be operated in ERL mode. To demonstrate the capability of a stable operation of the current rf control system during ERL operation, measurements regarding the rf control stability and the demand of rf power were done. This contribution is discussing this measurements and possible improvements for future energy recovery beamtimes.

INTRODUCTION

The recirculating superconducting linear accelerator S-DALINAC is one of the main research instruments at the institute for nuclear physics at the TU Darmstadt (see Fig. 1) [1]. Many improvements were implemented at the S-DALINAC since the first recirculated beam in 1991. One of the major enhancements is the upgrade from a twice to a thrice recirculating scheme in 2015/2016 [2]. With this upgrade the S-DALINAC can provide a beam with the same design energy of up to 130 MeV in cw operation at reduced accelerating gradients by using the main accelerator an additional time. Furthermore an rf phaseshift of the beam of up to 360° can be done due to a path length variation of the arcs in the new second recirculation. A phase shift of 180° changes the operation mode of the S-DALINAC between a conventional accelerating and an ERL mode. ERL operation was not possible when the rf control system for the superconducting structures was set up in 2010 [3]. Therefore it is not optimized for this task. The rf control system had to be tested during ERL operation in order to also demonstrate its capability of this mode.

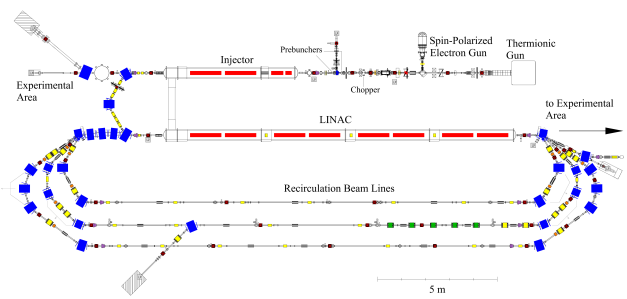


Figure 1: Current layout of the S-DALINAC.

* Supported by DFG (GRK 2128)
† msteinhorst@ikp.tu-darmstadt.de

Table 1: Design Specifications for the 20-cell Superconducting Cavities

Parameter	Design value
Material	Niobium, RRR = 280
R/Q	1995.2 Ω/m
Resonance f_0	2.997 GHz
Unloaded Q_0	3×10^9
Loaded Q_L	variable (typical 3×10^7)
Accelerating E_{acc}	5 MV/m

RF-CONTROL SYSTEM

The current low-level rf (LLRF) control system had to be tested to show its capability in terms of sufficient stability during the new ERL operation. In the following the current setup for LLRF control is briefly described. A design parameter overview of the used superconducting 20-cell structures is given in Table 1.

Hardware

The rf signal proccessing is done analog and digitally by an in-house developed board [3]. The rf signal is analog IQ-demodulated to baseband and for higher precision the amplitude of the rf signal is measured separately by an amplitude detector. Afterwards the analog signals are digitized by 18-bit ADCs with a 1 MS/s sampling rate. The further processing and control is done on an Xilinx Spartan-6 FPGA where a custom digital signal processor is implemented. This digital signal processor executes the control algorithm described in the next section. All data produced during signal processing on the FPGA can be streamed by an USB-2.0 interface at full ADC rate in 8 channels simultaneously. After the digital signal processor the signal is converted back by a DAC and is IQ-modulated to radiofrequency and sent to the cavity.

Control Algorithm

At the S-DALINAC two different control algorithms are used, both controlling the amplitude and phase of the rf signal. The bunching of the continuous beam after the thermionic electron source is done by normal conducting copper cavities with cylindrical geometry. For control of this low Q factor cavities with a resonance bandwidth in the MHz range a generator-driven resonator algorithm is used. The reference master oscillator is used to directly inject the

Content from this work may be used under the terms of the CC BY 3.0 licence (© 2018). Any distribution of this work must maintain attribution to the author(s), title of the work, publisher, and DOI.

ISBN: 978-3-95450-194-6 ISSN: 2226-0366 doi:10.18429/JACoW-LINAC2018-THPO011

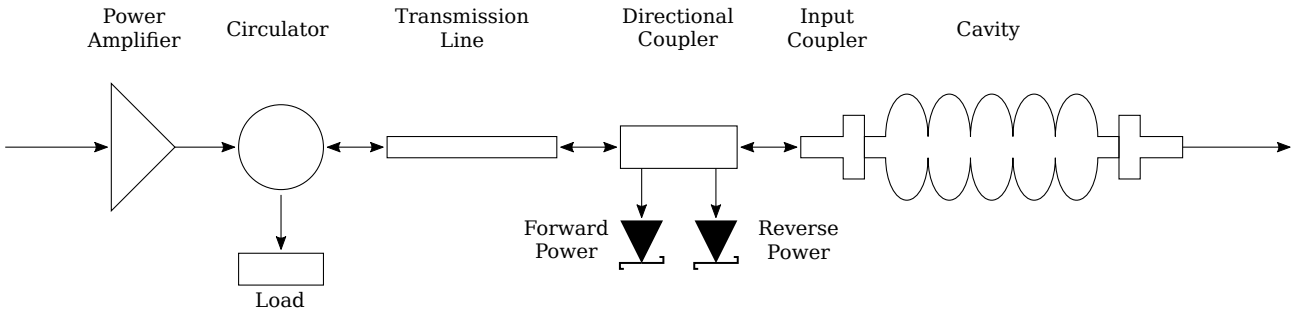


Figure 2: Schematic view of the setup that was used during the ERL operation [4]. By coaxial directional couplers a 40 dB attenuated forward and reverse rf signal was extracted and measured by Schottky diodes. The DC voltage signal after the Schottky diodes was further processed via electronics of the S-DALINAC control system.

signal which is controlled via an electric integral controller to maintain the correct phase and ampltidue setpoints.

The control of the narrow band high Q superconducting cavities used in the injector and main accelerator is done by an algorithm based on a self-excited loop which is phase-locked when phase control is active. To compensate eigen-frequency shifts in the superconducting cavities caused by microphonics, magnetostatic and piezoelectric fine tuner elements are used. The algorithm is using proportional and integral controllers for both amplitude and phase of the signal.

ENERGY RECOVERY LINAC OPERATION

In August 2017 a first once recirculating ERL operation was achieved with a beam current of 1 µA [5]. For comparison of the rf control system stability during ERL operation and commonly used operation modes four different modes were used. During this beamtime several measurements were done regarding rf forward and reverse power and rf control stability. This section covers the rf power measurement at the first main accelerator cavity A1SC01 and rf control stability measurements with A1SC01 as an example.

ERL Introduction

A charged particle beam is accelerated in a rf electric field where the energy gain per cavity pass is given by

$$\Delta W \propto E_0 \cos(\varphi), \tag{1}$$

where E_0 is the amplitude of the electric field and φ is the phase of the particle beam relative to the amplitude. To keep the electric field constant and compensate this energy taken out by the beam from the electric rf field more power has to be sent to the accelerating cavities. This amount of additional power needed is called beam loading. If the particle beam is sent again through the accelerating structure at a 180° shifted phase, the energy gain becomes negative and the beam stores the energy back in the electric field of the cavities. In this case the effective beam loading left is vanishing.

High beam current particle accelerators have a very high beam loading. The beam current itself is limited by the available amount of rf power. One of the ideas using ERL operation is to push the beam current limits because of the very small effective beam loading left.

Power Measurement

The efficiency of an energy recovery operation is a figure of merit for ERLs. It is given by the ratio of the beam loading for a single main accelerator pass to the beam loading during ERL operation. The beam loading can be measured via forward and reverse rf power. The beam loading is in principle given by the difference of both powers. Due to losses in the rf transfer line both powers have an offset without beam loading. This offset is calibrated by measuring both powers without beam where the difference of forward and reverse power is the offset. Considering this offset the beam loading can be measured when beam is on.

During the ERL beamtime the forward and reverse rf power of the first main accelerator cavity A1SC01 was measured. The rest of the cavities could not be measured because no complete power measurement system was existing. For the power measurement 40 dB coaxial directional couplers in the rf transfer line in combination with Schottky diodes (model 423B from Hewlett Packard) were used. The scheme for the setup is shown in Fig. 2. The diodes are transforming the AC signal to a DC signal with a exponential dependence in regard to power. A calibration of the diodes was done beforehand to calculate the power in Watts. The measured forward and reverse powers can be seen in Fig. 3.

RF-Control Stability

The sufficiency of the current LLRF control system had to be demonstrated during ERL operation. Therefore the performance of the control system in conventional operation modes in comparison to ERL operation had to be tested. For better comparability four different operation modes including ERL were used during one run.

During every mode the performance in terms of phase and amplitude stability was measured. Therefore the time series data for phase and amplitude error was measured via datastreaming from the processed signals of the FPGA. This time series were transformed to frequency domain with Fourier transform. The frequency data was additionally

Content from this work may be used under the terms of the CC BY 3.0 licence (© 2018). Any distribution of this work must maintain attribution to the author(s), title of the work, publisher, and DOI.

ISBN: 978-3-95450-194-6 ISSN: 2226-0366 doi:10.18429/JACoW-LINAC2018-THPO011

Content from this work may be used under the terms of the CC BY 3.0 licence (© 2018). Any distribution of this work must maintain attribution to the author(s), title of the work, publisher, and DOI.

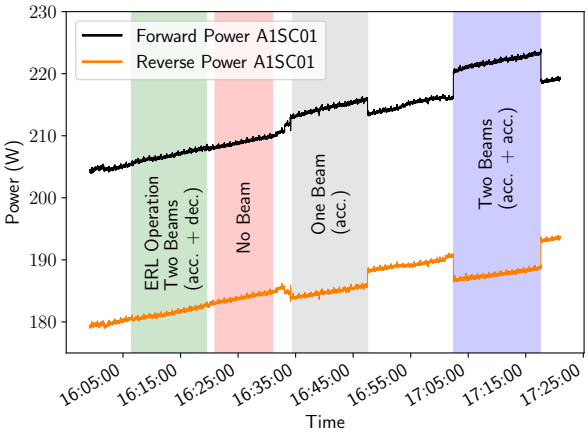


Figure 3: The measured forward and reverse powers of the first main accelerator cavity during the four different operation modes (marked with colored areas) [4]. The beam loading is calculated by the difference of forward and reverse power counting out the offset in the area without beam (red). The increase of both powers over time is dedicated to a heating of the input coupler when the system is not in equilibrium. This powers stay constant when the system is running a certain amount of time.

integrated to better resolve the impact of certain frequencies to rf control. Figure 4 shows the integrated phase and amplitude Fourier spectra of the four different operation modes for the first main accelerator cavity. It can be seen that the performance for all modes is comparable. The errors are dominated by noise. There are two bigger specific disturbance around 50 Hz. One of them is assigned to the beam itself which can be seen especially at the relative amplitude errors during the one beam and two beams mode.

RF POWER MEASUREMENT SYSTEM

During the ERL beamtime the rf power measurement was limited to one cavity because of no dedicated measurement electronics for all cavities. A new rf power measurement system is under development for upcoming beamtimes. The new system will have a wide dynamic range based on the TruPwr™ detector ADL5902 from Analog Devices [6]. A permanent integration to the control system allows to measure and access all cavity powers simulaneously. The beam loading in a cavity depends on the phase of the beam in reference to the accelerating field phase when the beam current is constant according to (1). Therefore via beam loading it is possible to measure the beam phase in reference to the rf phase with the new power measurement system. This can be used to set up the rf phase to on-crest acceleration where the beam loading has its maximum. From on-crest acceleration any other phase can be adjusted. Also rf control schemes based on minimizing the rf forward power could be implemented.

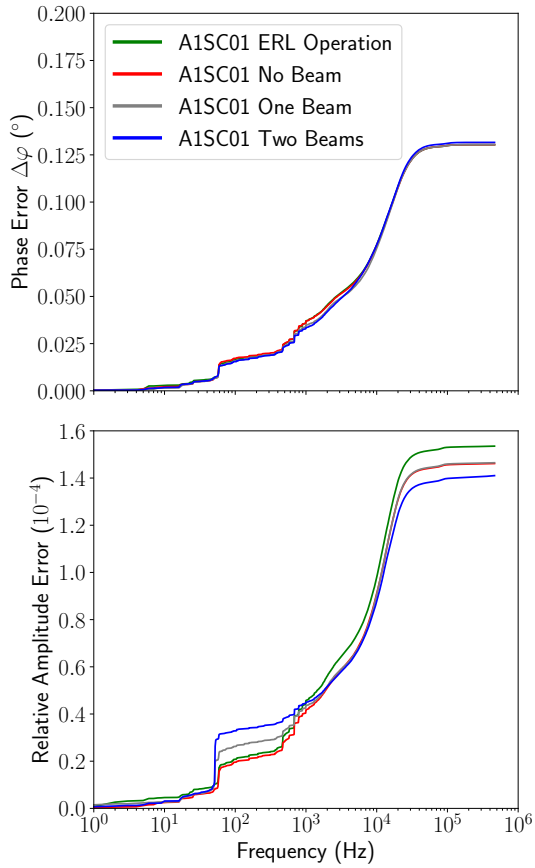


Figure 4: Integrated Fourier spectra of phase and relative amplitude errors of the rf control system during the four different operation modes for the first main accelerator cavity A1SC01 [4]. The total rms errors are corresponding to the maximum values. The similarity of the different spectra curves and maximum values shows that the stability of the rf control system is sufficient to be operated in energy recovery mode at 1 µA beam current.

SUMMARY

In August 2017 the first successful ERL beamtime was achieved. During this beamtime several measurements were done. Investigations regarding rf control stability and rf power consumption were conducted. A sufficient stability of the rf control system was demonstrated with a 1 µA beam current. The behaviour of the rf during ERL mode was comparable to an operation without beam.

An rf power measurement system to measure all cavity powers simultaneously is in development because the power measurement was limited to one cavity during ERL beamtime. Upcoming beamtimes will show the total efficiency of ERL operation.

REFERENCES

[1] Norbert Pietralla, "The Institute of Nuclear Physics at the TU Darmstadt", *Nuclear Physics News*, vol. 28, pp.4-11, 2018. doi:10.1080/10619127.2018.1463013

ISBN: 978-3-95450-194-6 ISSN: 2226-0366 doi:10.18429/JACoW-LINAC2018-THPO011

[2] M. Arnold et al., "Construction and Status of the Thrice Recirculating S-DALINAC", in *Proc. IPAC'17*, Copenhagen, Denmark, May 2017, pp. 1384-1387. doi:10.18429/JACoW-IPAC2017-TUPAB030

[3] M. Konrad et al., "Digital base-band rf control system for the superconducting Darmstadt electron linear accelerator", *Phys. Rev. ST Accel. Beams*, vol. 15, p. 052802, 2012. doi:10.1103/PhysRevSTAB.15.052802

[4] M. Arnold et al., *"First Energy Recovery Linac Operation of S-DALINAC"*, in preparation.

[5] M. Arnold et al., "First ERL operation of S-DALINAC and commissioning of a path length adjustment system", in *Proc. IPAC'18*, Vancouver, British Columbia, Canada, May 2018, pp. 4859-4862. doi:10.18429/JACoW-IPAC2018-THPML087

[6] Analog Devices, TruPwr™ detector ADL5902, http://www.analog.com/en/products/adl5902.html

Content from this work may be used under the terms of the CC BY 3.0 licence (© 2018). Any distribution of this work must maintain attribution to the author(s), title of the work, publisher, and DOI.

ISBN: 978-3-95450-194-6 ISSN: 2226-0366 doi:10.18429/JACoW-LINAC2018-THPO012

ONCE RECIRCULATING ENERGY RECOVERY LINAC OPERATION OF S-DALINAC*

M. Arnold†, J. Birkhan, J. Pforr, N. Pietralla, F. Schließmann, M. Steinhorst
Technische Universität Darmstadt, Darmstadt, Germany
F. Hug, Johannes Gutenberg-Universität Mainz, Mainz, Germany

Abstract

The S-DALINAC is a thrice recirculating superconducting electron accelerator which can be either used in conventional accelerating operation or, since a major upgrade in 2015/2016 was installed, as an energy recovery linac (ERL) alternatively. A once or twice recirculating ERL operation is possible due to the layout of the accelerator. For both setups beam dynamics calculations have been performed or are under investigation at the moment. The once recirculating ERL mode was proven successfully in August 2017, which set the first German ERL into operation. The results will be discussed more in detail in this contribution.

INTRODUCTION

The superconducting linear electron accelerator S-DALINAC is in full operation since 1991 [1]. In the years 2015/2016 a major upgrade modified it to a thrice recirculating machine [2,3]. Featuring the new recirculation beam line, a path length adjustment system was installed which enables a total phase shift of 360°. Thus the change between normal operation and an operation as an ERL is possible [4].

S-DALINAC

Figure 1 shows the floorplan of the thrice recirculating S-DALINAC. It houses two electron sources: A thermionic gun with a pre-acceleration of 250 keV and a spin-polarized source with a pre-acceleration of up to 125 keV. In the normal conducting chopper-prebuncher-section the beam is prepared for an acceleration with 3 GHz in the superconducting RF system. The injector accelerator is able to provide an energy gain of up to 10 MeV (7.6 MeV in case of recirculating operation) with currents of up to 60 µA. For recirculating operation the beam is bent into the main accelerator which then will provide an energy gain of up to 30.4 MeV. The beam can be recirculated up to three times, resulting in four passages through the main accelerator. A total energy of up to 130 MeV with currents of up to 20 µA can be reached.

Energy Recovery Linac Mode

The layout of the S-DALINAC allows a once recirculating or a twice recirculating ERL mode. In case of the once recirculating ERL operation, see Fig. 2, the beam is accelerated in the main linac and then directly bent into the second recirculation beam line. Therefore the ratio of injection energy and main linac energy gain needs to be set to 1:8. A

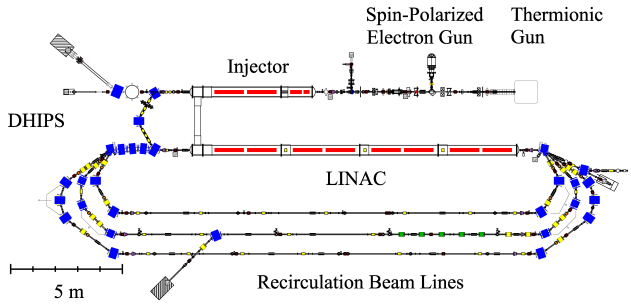


Figure 1: Floorplan of the S-DALINAC.

180° phase shift is done while travelling through the beam line. The beam is re-injected into the main accelerator at a decelerating phase so that it can be dumped at injection energy after leaving the main linac.

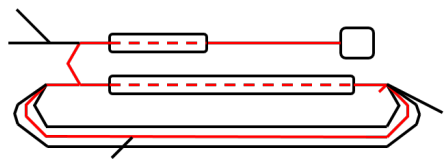


Figure 2: Scheme of the once recirculating ERL operation.

Figure 3 shows the path of the beam in case of the twice recirculating ERL mode. In contrast to the once recirculating mode the beam is first bent into the first recirculation beam line. After a second acceleration in the main linac, a 180° phase shift is performed in the second recirculation beam line. The beam is then guided through the first recirculation beam line a second time. Being twice decelerated in the end, the beam is dumped at injection energy after the last transition through the main linac. In this operation mode the ratio of injection and main linac energy gain is set to 1:4.

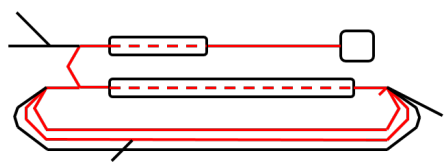


Figure 3: Scheme of the twice recirculating ERL operation.

BEAM DYNAMICS SIMULATION

To ensure the transportation of the beam, it is necessary to conduct dedicated beam dynamics simulations. During the design and installation of the thrice recirculating layout, the lattice was not optimized for ERL mode. Meanwhile

* Work supported by DFG through GRK 2128
† marnold@ikp.tu-darmstadt.de

Content from this work may be used under the terms of the CC BY 3.0 licence (© 2018). Any distribution of this work must maintain attribution to the author(s), title of the work, publisher, and DOI.

ISBN: 978-3-95450-194-6 ISSN: 2226-0366 doi:10.18429/JACoW-LINAC2018-THPO012

the once and twice recirculating ERL operation have been simulated and are still under further investigations. The results of the once recirculating ERL mode are presented (done with *elegant* [5]). Figure 4 shows the beam envelope along the beam path beginning with the acceleration in the main accelerator and ending with the decelerated beam at the position of the beam dump. Figure 5 displays the dispersion curves along the same section. Both plots demonstrate a working setting: the beam envelope stays small and the dispersion curves vanish behind each arc section.

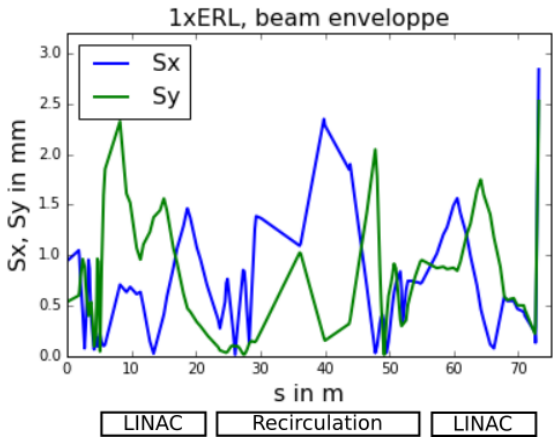


Figure 4: Simulation of horizontal (Sx) and vertical (Sy) beam envelopes for once recirculating ERL mode in x and y along the beam line.

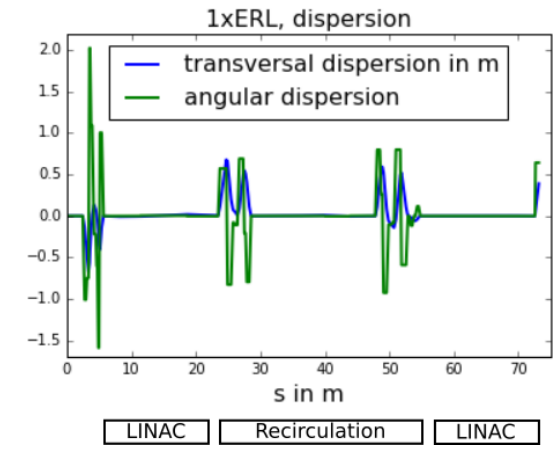


Figure 5: Simulation of dispersion curves for once recirculating ERL mode along the beam line.

ERL OPERATION

In August 2017 the first successful ERL operation took place at the S-DALINAC [6]. The main parameters of this beam setting are summarized in Table 1.

During the run four different beam settings have been investigated and compared:

- No beam in the main accelerator
- Single pass: one beam is accelerated in the main accelerator
- Once recirculating mode: two beams are accelerated in the main accelerator
- ERL mode: one beam is accelerated and decelerated in the main accelerator

Table 1: Overview of parameter settings for the once recirculating ERL operation. The current value refers to a measurement in front of the injector linac.

Parameter	Value
Energy gain injector	2.5 MeV
Energy gain linac	20.0 MeV
Current (before injector)	1.2 µA

The RF power in the first cavity of the main accelerator (A1SC01) as well as the beam currents corresponding to ERL mode (ERL cup) and once recirculating operation (E0F1 cup) have beam measured. Figure 6 gives an overview on the position of these elements and the beam path (marked in red).

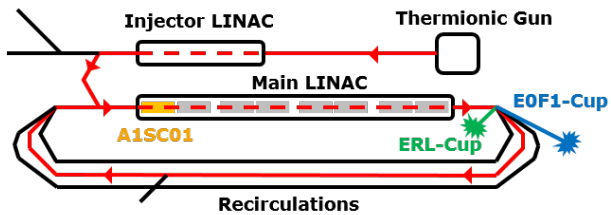


Figure 6: Beam path (red) of the once recirculating ERL mode is shown. The power of the first main linac cavity (A1SC01) as well as the beam currents corresponding to ERL (ERL cup) and once recirculating operation (E0F1) have been measured.

The results are summarized in Fig. 7. The ERL operation was done with a beam current of roughly 1 µA. The phase with no beam in the main linac (red area) defines the steady state of the cavity operation. The change of powers in A1SC01 have been measured in the other operation modes as well. For one accelerated beam a certain amount of RF power is needed for acceleration. If a second beam is accelerated, the power consumption is mainly doubled. During ERL mode the change in powers is very small, they nearly cancel out. The recovery of RF power can be seen clearly. Table 2 gives an overview on the power values measured. The energy recovered in A1SC01 during this ERL operation yields to $88.7^{+9.3}_{-5.1}$ (0.16 and 0.84 quantiles).

RF Stability Measurement

At the time the digital low level RF (LLRF) control system was installed in 2010 [7], the S-DALINAC was not able to be operated as an ERL. Thus, the system was not optimized

Content from this work may be used under the terms of the CC BY 3.0 licence (© 2018). Any distribution of this work must maintain attribution to the author(s), title of the work, publisher, and DOI.

ISBN: 978-3-95450-194-6 ISSN: 2226-0366 doi:10.18429/JACoW-LINAC2018-THPO012

Content from this work may be used under the terms of the CC BY 3.0 licence (© 2018). Any distribution of this work must maintain attribution to the author(s), title of the work, publisher, and DOI.

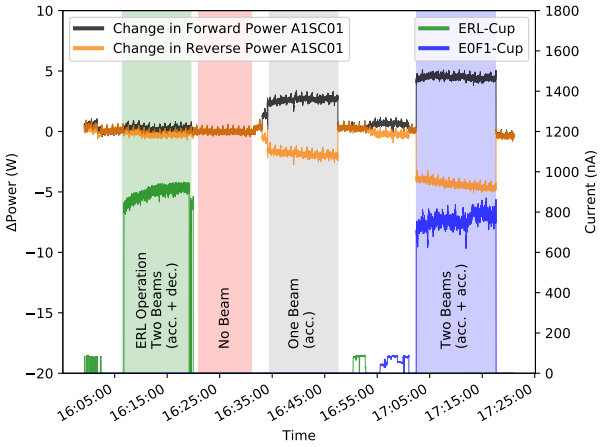


Figure 7: The forward (black curve) and reverse power (orange curve) changes of A1SC01 as well as beam currents for ERL (green curve) and once recirculating operation (blue curve) have been measured during four different beam modes: ERL mode (green area), no beam in the main linac (red area), one accelerated beam (grey area) and two accelerated beams (blue are) in the main linac.

Table 2: Mean values of the beam power with uncertainties (0.16 and 0.84 quantiles) of the distribution at the four S-DALINAC operation modes.

Operation	Mean Beam Power (W)
No Beam	$0.00^{+0.20}_{-0.20}$
ERL (acc. + dec.)	$0.35^{+0.49}_{-0.23}$
One Beam (acc.)	$4.42^{+1.98}_{-0.42}$
Two Beams (acc. + acc.)	$8.62^{+2.26}_{-0.94}$

for this mode. Measurements on the stability are necessary to investigate the capability of the LLRF system during ERL operation. For this reason the phase errors as well as the relative amplitude errors of all main linac cavities have been measured and compared during this four different beam modes. Figure 8 shows the results for A1SC01. The errors measured have been transformed to frequency domain. The Fourier spectra have been integrated to easily compare final values and frequencies where a relevant disturbance occur. The plot for the phase errors shows nearly the same behaviour for all four beam modes. In the measurement of the relative amplitude errors small deviations between the four different modes can be recognized. During the upcoming ERL beam times further investigations will be conducted.

CONCLUSION AND OUTLOOK

The S-DALINAC was operated successfully as first ERL in Germany in August 2017. The layout of the accelerator enables in principle a once and a twice recirculating ERL mode. For both settings beam dynamics simulations have been conducted or are under investigation at the moment.

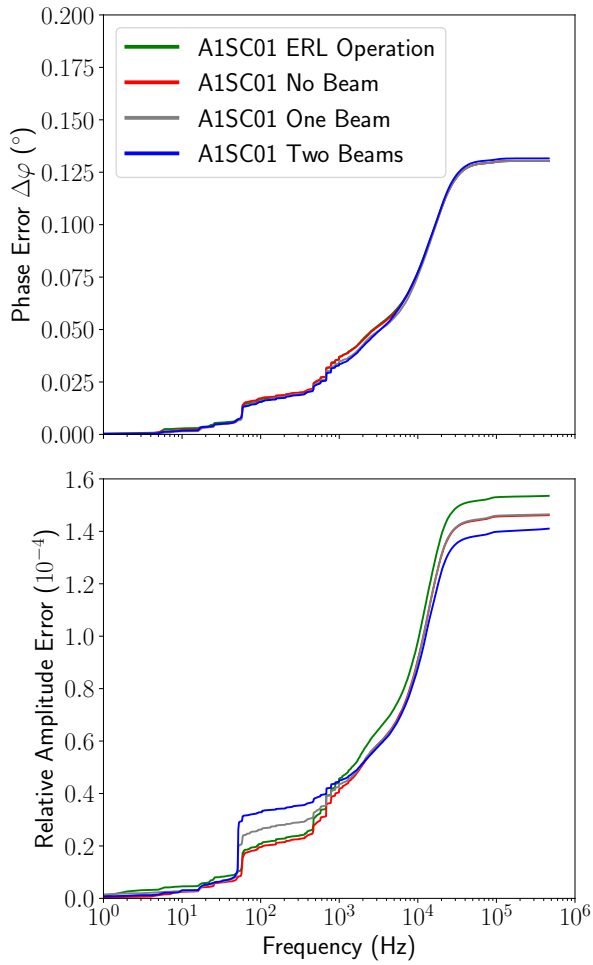


Figure 8: Phase and relative amplitude errors of A1SC01 have been measured during the four different beam modes. The data was transformed to frequency domain and integrated.

During the beam time four different machine settings have been investigated and compared to learn on the different aspects of the ERL operation such as the stability of the RF system or the efficiency of the recovery process.

In the future the twice recirculating ERL mode will be set into operation. To further improve the diagnostics of an ERL mode a system to measure all RF powers simultaneously was installed recently [8]. Further projects will deal with the topic of diagnostics dedicated for ERL usage which means multiple beams of the same energy in the same beam line.

REFERENCES

[1] N. Pietralla, "The Institute of Nuclear Physics at the TU Darmstadt", in *Nuclear Physics News*, vol. 28, no. 2, p. 4-11, 2018.

[2] M. Arnold et al., "Design, Installation and Commissioning of a Third Recirculation Beam Line Featuring an Energy Recovery Linac Mode for the S-DALINAC", in preparation.

ISBN: 978-3-95450-194-6 ISSN: 2226-0366 doi:10.18429/JACoW-LINAC2018-THPO012

[3] M. Arnold et al., "Construction and Status of the Thrice Recirculating S-DALINAC", in *Proc. IPAC 2017*, Copenhagen, Denmark, May 2017, paper TUPAB030 pp. 1384-1387.

[4] M. Arnold et al., "ERL Mode of S-DALINAC: Design and Status", presented at *ERL 2017*, CERN, Geneva, Switzerland, June 2017, paper MOIDCC006, pp. 40-44.

[5] M. Borland, "elegant: A Flexible SDDS-Compliant Code for Accelerator Simulation," Advanced Photon Source LS-287, September 2000.

[6] M. Arnold et al., "First Energy Recovery Linac Operation of S-DALINAC", in preparation.

[7] M. Konrad et al., “Digital base-band rf control system for the superconducting Darmstadt electron linear accelerator”, Phys. Rev. ST Accel. Beams, vol. 15, p. 052802, 2012.

[8] M. Steinhorst et al., “First Energy Recovery Operation at the S-DALINAC: RF Control Stability Measurements”, presented at *LINAC 2018*, Beijing, China, September 2018, paper THPO011, this conference.

Content from this work may be used under the terms of the CC BY 3.0 licence (© 2018). Any distribution of this work must maintain attribution to the author(s), title of the work, publisher, and DOI.

ISBN: 978-3-95450-194-6 ISSN: 2226-0366 doi:10.18429/JACoW-LINAC2018-THPO016

INVESTIGATION OF 2D PBG-WAVEGUIDES FOR THz DRIVEN ACCELERATION

A. Vint and R. Letizia, Cockcroft Institute/Lancaster University, WA4 4AD, Warrington, UK

Abstract

There is significant interest in novel accelerating techniques which can overcome the limitations of conventional radio-frequency (RF) based devices in terms of frequency, gradient, and footprint. Moving from the RF to the terahertz (THz) frequency range, higher accelerating-gradient of high-energy beams can be achieved, as well as structure miniaturisation. Furthermore, in respect to the optical frequency range, THz allows for larger structures and better beam quality. This work has been investigating the use of a 2D photonic-bandgap dielectric waveguide (PBG-W) for THz-driven electron acceleration which could potentially offer a good compromise between dispersion engineering, low losses and ease of parallel illumination. Dispersion characteristics of the accelerating mode are studied to achieve the best compromise between high accelerating field and effective accelerating bandwidth, assuming a ~10% bandwidth of the THz driving pulse.

INTRODUCTION

With current state-of-the-art particle accelerators reaching several kilometres in size, a paradigm shift is required for future technologies to prevent them becoming unattainable. Terahertz (THz) frequencies offer the opportunity to build micron-scale structures, and the use of dielectrics over metal offers the ability to push fields higher due to the increased breakdown resistance—or fluence threshold. Additional benefits over optical frequencies, which similarly exhibit the prior stated benefits of THz, is the larger aperture sizes allowed for the beam and the higher bunch charges THz affords beams to use.

In conventional RF-driven accelerators, sources are typically narrowband—usually on the order of a few percent. In the regime of ultrashort THz pulse, broad bandwidths are generated and require a more careful study of the beam-pulse interaction. Much of the current work investigating THz acceleration has focused on the use of corrugated and dielectric-loaded waveguides (DLWs), of both rectangular and cylindrical geometry. While these devices are effective, they are hindered by the use of metal walls—which at THz frequencies exhibit large ohmic losses. [1] Due to the wavelength scales of THz, employing photonic-crystal (PhC) theory for confinement instead of metal walls can offer low ohmic losses and high fluence threshold. Moreover, the design flexibility offered by PhCs can potentially aid the tailoring of the accelerating mode dispersion for the THz acceleration regime.

For comparison with other designs such as the DLW proposed in [2] and ease of realisation, a rectangular waveguide configuration is chosen. This work focuses on waveguides based on a 2D-PBG slab structure with a triangular lattice of air/vacuum holes, offering a good compromise between design flexibility and ease-of-manufacture.

PBG-WAVEGUIDE DESIGN

Using MPB [3], initial 2D simulations of the PhC unit cell were carried out to optimise the fill factor of the PBG structure for maximum bandgap around the central frequency of 1 THz. The dielectric material used was silicon with relative permittivity $\varepsilon_r \sim 11.6$. The maximum photonic bandgap (PBG) was found to be at a radius of $r = 0.445a$ yielding a bandgap of 50% in the normalised frequency region of 0.29-0.48 $\omega a/2\pi c$, where ω is the angular frequency, a is the PhC period, and c is the speed of light. The schematic of the proposed PBG-waveguide is shown in Fig. 1.

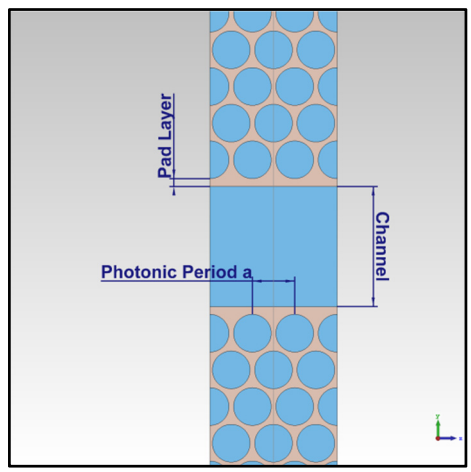


Figure 1: Schematic of three longitudinal unit cells of the PBG-W, with z-axis being direction of propagation.

The PBG-W is then realised by introducing a line defect along the longitudinal direction z across the PhC lattice for confinement of specific electromagnetic states (as propagating modes) within the PBG. In the case of DLWs, the modes can be described as a superposition of both TE and TM modes as the longitudinal-section magnetic (LSM) mode if either x or y components of the magnetic fields is set to 0, likewise longitudinal-section electric (LSE) if one of the transverse electric fields is set to 0 [4].

PBG-Ws such as shown in Fig. 1 are both nonhomogeneous and anisotropic—as such, they cannot support true LSE/LSM modes. At lower wavenumbers however, these modes serve as a good approximation for the PBG-W modes. Higher wavenumbers often exhibit higher levels of coupling to the dielectric over the waveguide channel which modifies the dispersion curve.

Content from this work may be used under the terms of the CC BY 3.0 licence (© 2018). Any distribution of this work must maintain attribution to the author(s), title of the work, publisher, and DOI.

ISBN: 978-3-95450-194-6 ISSN: 2226-0366 doi:10.18429/JACoW-LINAC2018-THPO016

To design the PBG-W, initially 2D models were investigated where the channel width and *pad layer* thickness (Fig. 1) were varied based on the work by Cowan [5]; allowing for a suitable dispersion of the accelerating mode at the point of interaction with $v_p = c$ and f=1 THz to be found at channel width ~ $3a$ and pad-layer ~ $0.1a$. This provided a starting point for the design of the 3D waveguide and its optimisation for highly-relativistic THz acceleration.

A 3D PBG-W was then designed considering a finite thickness of the dielectric slabs bound with metal. It was found that the accelerating mode tends infinitely to zero at the metal walls, so lower losses are expected than in a metal waveguide structure. The thickness of the PBG-W and the channel width were then investigated to study optimisation of the structure-particle beam interaction for broadband pulse excitation by comparing characteristic impedance and accelerating bandwidth.

Characteristic Impedance

One of the main figures of merit (FoM) in conventional RF accelerators is the shunt impedance r_s. The difficulty in applying this to PhCs however is the calculation of the wall dissipation that is not trivial. The characteristic impedance Z_c is typically used in the context of dielectric laser accelerators [1]. This is defined as the product of the accelerating field E_{acc} and wavelength λ with the Poynting vector along the axis of acceleration in the structure S via equation 1.

$$Z_c = \frac{(E_{acc}\lambda)^2}{S} \tag{1}$$

CST Microwave Studio® Eigenmode solver was used to investigate the effects of channel size on the metal bounded PBG-W at the point of beam-wave interaction in structures with a=117 µm, hole radius $0.445a$, and pad layer of 13 µm. Z_c was calculated for PBG-Ws ranging in thickness from 283-425 µm and channel width 266-398 µm. The effects of these two parameters on the characteristic impedance can be seen in Fig. 2, with the centre point taken at the original dimensions chosen. While there exist higher interaction points on the map, these are coupled with a low group velocity which made those points less desirable for THz acceleration due to shorter interaction times between the pulse and bunch.

Dispersion Control

While Z_c can be calculated from a single eigenmode simulation at the point of interaction providing a good FoM for comparison, due to the broadband nature of THz the efficient design of interaction within the PBG-W requires full spectral pulse-beam analysis. One key property to investigate this in the accelerating mode is its dispersion as this conveys information on the acceleration bandwidth, and the phase/group velocities of the EM fields. A comparison of the accelerating mode dispersion of the DLW based on [2] with dielectric layers on the top and bottom at 10% waveguide thickness per layer and the PBG-W with dimensions corresponding to the centre-point of Fig. 2 is shown in Fig. 3.

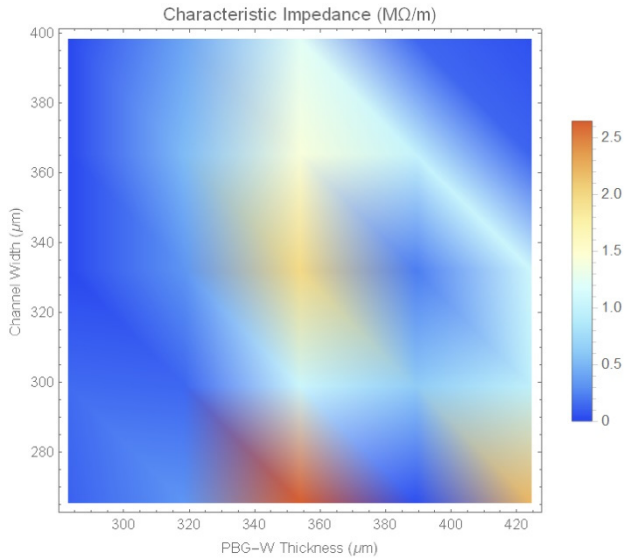


Figure 2: Variation of characteristic impedance with PBG-W thickness and channel width.

Accelerating Bandwidth

When the dispersion of a mode is known, the phase-synchronicity with a particle beam for each frequency is also revealed. In a structure of length L, a certain number of frequencies will propagate with a positive accelerating effect. The Fourier analysis of this acceleration can be calculated via equation 2.

$$VT(\omega) = \int_0^L E_0 \exp\left[iz\left(k_z - \frac{\omega}{c}\right)\right] dz \tag{2}$$

Where E_0 is the electric field at each frequency and k_z is the longitudinal wavenumber. In a structure of 5 mm length, the Fourier series for the PBG-W was calculated.

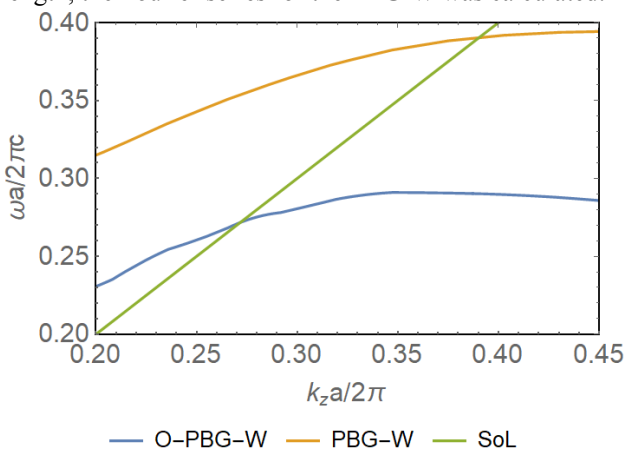


Figure 3: Dispersion of accelerating mode for the PBG-W, the O-PBG-W, and their interaction with the $v_p = c$ line (SoL).

While this information is useful, with the peak showing the likely ideal centre frequency for acceleration, it doesn't give a true picture of what a particle will see

Content from this work may be used under the terms of the CC BY 3.0 licence (© 2018). Any distribution of this work must maintain attribution to the author(s), title of the work, publisher, and DOI.

ISBN: 978-3-95450-194-6 ISSN: 2226-0366 doi:10.18429/JACoW-LINAC2018-THPO016

Content from this work may be used under the terms of the CC BY 3.0 licence (© 2018). Any distribution of this work must maintain attribution to the author(s), title of the work, publisher, and DOI.

when being accelerated. Taking the peak as the centre-frequency and integrating in steps of increasing bandwidth around this point gives a plot of the total voltage seen by a beam when a pulse of a given bandwidth is injected as in equation 3.

$$VT = \int_{\omega_1}^{\omega_2} \frac{VT(\omega)d\omega}{\omega_2 - \omega_1} \quad (3)$$

It can be seen from the blue curve in Fig. 5 that although the accelerating voltage starts high, it rapidly drops off negligible levels by ~13% BW. In broadband pulse driven accelerators, this is not ideal behaviour.

Structure Optimisation for THz Pulses

It can be seen from Fig. 4 that the PBG-W needs to be optimised to better take advantage of the bandwidth of the driving pulses which are typically short at this frequency. Part of this problem is due to matching a broadband pulse with the interaction being near the peak of the dispersion curve thus nearly half of the injected pulse will be wasted and evanescently decay from the injection site or couple to spurious modes. To optimise the structure for this spectral distribution of the driving pulse, the structure was redesigned to operate at a lower point on the dispersion curve. While a hole radius of 0.35a offers a PBG of 41% unlike the 50% PBG available at 0.445a, it still encompassed the dispersion of the accelerating mode at the frequencies of interest. It has the additional benefit of operating in a region with higher group velocity thus contributing positively towards the R/Q of the accelerating structure.

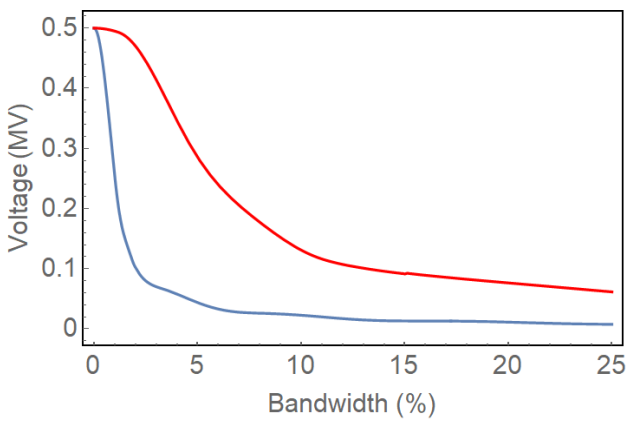


Figure 4: Integrated accelerating voltage for PBG-W (blue), and O-PBG-W (red), both calculated using $E_0 = 100\ MV/m$ across all frequencies.

An optimal geometry was found by introducing the additional parameter of a metal wall dielectric padding layer where both the group velocity and interaction yield better results than the original structure. The parameters for this optimised structure (O-PBG-W) can be seen in Table 1 with dispersion of the accelerating mode compared to the PBG-W and DLW in Fig. 3. Variation of accelerating voltage with pulse bandwidth is shown as the red curve in Fig. 4; it can be noted that a higher total accelerating voltage is realised across the entire bandwidth range.

Table 1: Parameters and FoMs for Optimised PBG-W

Parameter	Value	Unit
PhC Period (a)	82	μm
Hole Radius r/a	0.35	
PBG-W Channel Width	401	μm
PBG-W Thickness	454	μm
PhC Pad Layer	16	μm
Wall Pad Layer	23	μm
Waveguide Length	5.0	mm
Group Velocity	0.24c	
Phase Velocity	1.00c	
Characteristic Impedance	10.51	MΩ/m
R/Q	0.11	MΩ/m

CONCLUSION

The design of a photonic-crystal based waveguide to accelerate highly-relativistic electrons driven by THz radiation has been investigated. It was shown that the photonic bandgap, accelerating mode dispersion and the synchronism point with the beam need to be carefully designed to satisfy the requirements in terms of accelerating bandwidth and characteristic impedance for THz-driven structures. Optimisation of the proposed PBG-W for broad bandwidths has resulted in a 6.5x improvement of accelerating voltage at 10 % bandwidth, and nontrivial accelerating voltages above 13% bandwidth with further optimisation of the structure is expected to improve this figure further. Comparison with other accelerating structures is required to truly quantify the accelerating properties of PBG-W and will be undertaken during further optimisation.

ACKNOWLEDGEMENTS

This work was funded by the Cockcroft Studentship grant. The authors would also like to thank the Institute of Physics and the LINAC Student Grant for their generous contributions towards facilitating attendance at the LINAC 2018 conference.

REFERENCES

[1] England R.J. et al, Dielectric Laser Accelerators, Reviews of Modern Physics, vol 86, pp1338-1389, 2014.

[2] Healy A.L., Burt G., Jamison S.P., Electron-Terahertz Interaction In Dielectric-Lined Waveguide Structures For Electron Manipulation, Nuclear Instruments and Methods A, PREPRINT 2018.

[3] MPB Homepage, https://mpb.readthedocs.io/

[4] Zhang K., Li D., Electromagnetic Theory for Micro-waves and Optoelectronics, 2013.

[5] Cowan B., Photonic Crystal Laser-Driven Accelerator Structures, Thesis SLAC, 2007.

ISBN: 978-3-95450-194-6 ISSN: 2226-0366 doi:10.18429/JACoW-LINAC2018-THPO017

PROGRESS OF THE NOVEL SPIRAL INJECTION TEST EXPERIMENT*

M. A. Rehman†, SOKENDAI (The Graduate University for Advanced Studies), Kanagawa 240-0193, Japan
H. Iinuma, Ibaraki University, Mito, Ibaraki, Japan
S. Ohsawa, H. Nakayama, H. Hisamatsu, K. Furukawa, T. Mibe, High Energy Accelerator Research Organization, 1-1 Oho, Tsukuba, Ibaraki 305-0801, Japan

Abstract

A new muon $g-2$/EDM experiment at J-PARC (E34) is under preparation in order to resolve a 3 σ discrepancy of muon anomalous magnetic dipole moment between the measurement and the standard model prediction. The E34 experiment will employ a unique three-dimensional spiral injection scheme in order to store the muon beam into a small storage orbit. In order to demonstrate the feasibility of this novel injection scheme, the Spiral Injection Test Experiment (SITE) with the electron beam is under construction at KEK Tsukuba campus. The goals of the SITE are divided into two phases. In the first phase of the SITE, 80 keV DC electron beam was injected and detected as a fluorescent light due to the de-excitation of the nitrogen gas into solenoidal storage magnet. In the second phase of the SITE, the pulsed electron beam, and a pulsed magnetic kicker are developed in order to keep the pulsed beam on the very midplane of the solenoidal storage magnet. This paper describes the achievements of the first phase of the SITE and progress towards the second phase.

INTRODUCTION

The muon's anomalous magnetic moment is one of most important measurement in elementary particle physics. The recent measurement of muon $g-2$ results a 3 σ [1] discrepancy with the equally precise standard model prediction. The new J-PARC muon $g-2$/EDM (E34) is under preparation to resolve current discrepancy. The E34 experiment is aiming to measure muon's $g-2$ to the precision of 0.1 ppm and EDM down to the sensitivity of 10^{-21} e.cm [2].

The key idea to measure muon $g-2$ is to store polarized muon beam in a magnetic field and measure the evolution of spin precession vector with respect to time. In E34 a low emittance muon beam of momentum 300 MeV/c from muon accelerator will be injected into a 3-T Magnetic Resonance Imaging(MRI)-type solenoid magnet in order to store the muon beam in 0.66-m diameter orbit. In order to enhance injection efficiency and overcome technical challenges related to small storage orbit, a new three-dimensional spiral injection scheme is under development to inject the muon beam into MRI type storage magnet. Figure 1 shows the basic concept of a three-dimensional spiral injection scheme. The details and recent updates of three-dimensional spiral injection scheme can be found in [3–5].

* Work supported by "Grant in Aid" for Scientific Research, JSPS (KAKENHI#26287055)
† rehman@post.kek.jp

The three-dimensional spiral injection scheme is an unproven idea, therefore, a demonstration experiment to prove the feasibility of this unique scheme is inevitable. A scale down Spiral Injection Test Experiment (SITE) by the use of electron beam is under development at KEK Tsukuba campus. This paper will describe the development of the spiral injection scheme test experiment (SITE).

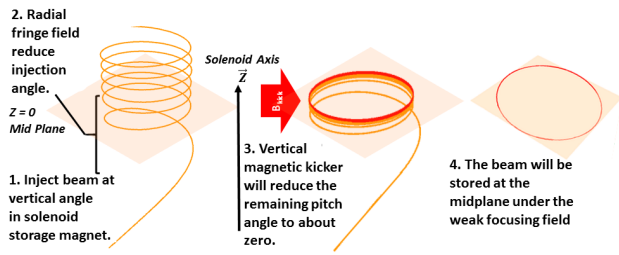


Figure 1: Layout of three-dimensional spiral injection scheme.

SPIRAL INJECTION TEST EXPERIMENT (SITE)

The SITE setup contains a 2 m long straight beamline, a solenoid storage magnet to store the electron beam and forty degrees bend section to guide the electron beam towards the storage magnet. A triode type thermionic electron gun with LaB_6 cathode is used to generate the DC electron beam of 80 keV with current in the range of few μA.

After the electron gun, a magnetic lens is placed to focus the low energy beam. A pair of steering coils also has been placed to control the transverse position of the beam. An electric chopper system has been placed after the electron gun to produce the pulsed beam. Details of the electric chopper can be found in [6]. A collimator of diameter 3 mm and depth 5 mm is placed after the electric chopper. The collimator is served as the beam dump for the chopper system and also used to create the differential vacuum system for the gas monitor in the storage magnet.

A bending magnet (BM1) is placed on the straight beamline to deflect the beam at forty degrees towards the storage magnet. A second bending magnet (BM2) is also placed near the injection point in order to control the injection angle slightly. Air core quadruple magnets have been placed on a bend section to create required beam phase space for the spiral injection.

A pulsed magnetic kicker is also under development in order to keep the beam to the very center of the storage

Content from this work may be used under the terms of the CC BY 3.0 licence (© 2018). Any distribution of this work must maintain attribution to the author(s), title of the work, publisher, and DOI.

ISBN: 978-3-95450-194-6 ISSN: 2226-0366 doi:10.18429/JACoW-LINAC2018-THPO017

Content from this work may be used under the terms of the CC BY 3.0 licence (© 2018). Any distribution of this work must maintain attribution to the author(s), title of the work, publisher, and DOI.

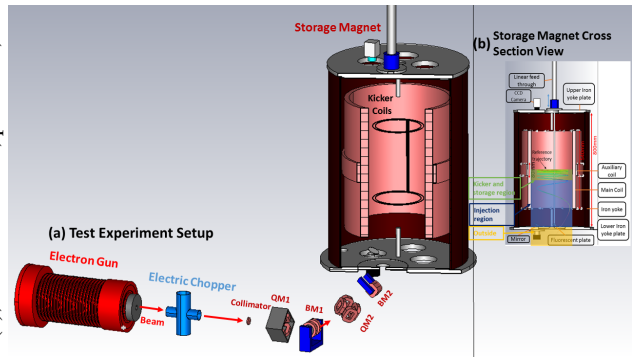


Figure 2: (a) A diagram showing the 3D schematic of spiral injection test experiment. (b) The schematic of the storage magnet with monitors and reference trajectory.

magnet. The kicker system for the SITE will be discussed in the forthcoming sections. The details about each device on the straight beamline of SITE can be found in [7]. The layout of the SITE experimental setup is shown in Fig. 2 (a). The schematic of the storage magnet with a reference trajectory and monitors are shown in Fig. 2 (b). A comparison of parameters between SITE and E34 is given in Table 1.

Table 1: Comparison of Parameters between E34 and SITE

Parameters	E34	SITE
Magnetic field strength	3 T	0.0082 T
Momentum	300 MeV/c	0.296 keV/c
Cyclotron Period	7.4 ns	5 ns
Storage orbit diameter	0.66 m	0.24 m

In the first phase of the SITE, DC electron beam was detected as fluorescent light. In the SITE nitrogen gas monitor was used to detect the DC electron beam spiral track in the storage magnet's vacuum chamber. In the gas monitor, differential vacuum pumping has been employed to detect electron beam as a fluorescent light due to the nitrogen gas de-excitation along the beam path. The details of beam detection in the storage magnet can be found in [7].

BEAM PHASE SPACE FOR SPIRAL INJECTION

The radial fringe of the solenoid storage magnet requires a strongly XY-coupled beam. In Fig. 3 above four plots are showing the beam phase space at the matching point $Z = -500$ mm from the center of the storage magnet. The matching point lies outside of the storage magnet. Black points show the uncoupled beam (ideal parallel beam) and red points show the required coupled beam phase space. The bottom two plots in Fig. 3 shows the beam injection without (black) and with coupled (red) beam. In the Fig. 3 bottom left the beam start diverging vertically after $Z = -100$ mm in the case of non-coupled beam whereas in the case of appropriate coupled beam injection beam do not diverge completely at $Z = -100$ mm.

Air core quadrupole magnets have been mounted on the bend section in order to create required beam phase space. The details calculation of TWISS and coupling parameters can be found in [3].

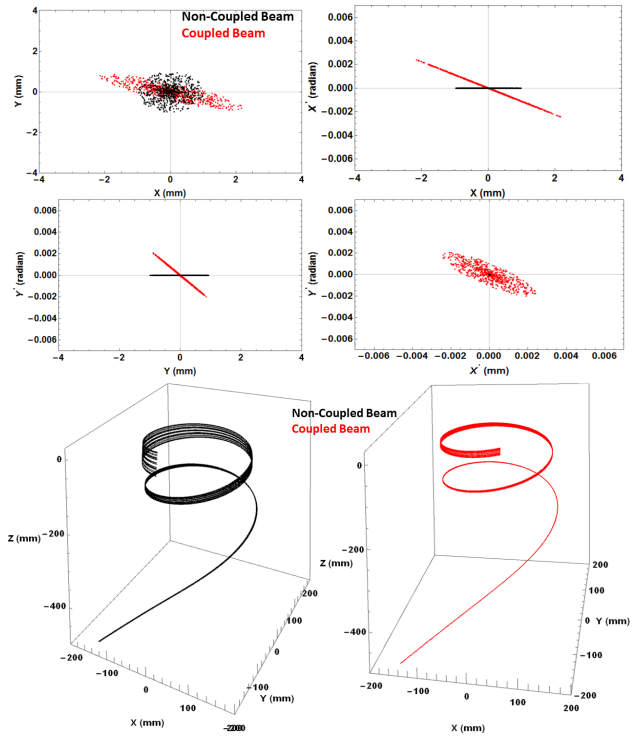


Figure 3: The above four plots are the required phase space at the matching point ($Z = -500$ mm). The black points show the beam phase space without coupling and red points show with coupling. Bottom two plots are showing the beam injection with and without coupled beam.

PULSED MAGNETIC KICKER

The pitch angle of the beam will be reduced to 0.018 rad due to the radial field of storage magnet at $Z = -100$ mm. At the $Z = -100$ mm, the vertical magnetic kicker will apply the kick to guide the beam to the very center of the storage magnet. The kicker field can be defined as follows

$$B_{kick} = B_{peak} Sin\left(\frac{2\pi}{T_{kick}} t\right) \quad (1)$$

where T_{kick} is the duration of the kick and B_{peak} represent the peak kicker field. The half sine shape has been considered for the kick, therefore, $T_{kick} = \frac{T}{2}$ and T is total time period.

After the kick, the beam will be stored under the weak focusing field. In the weak focusing field the beam motion will be oscillatory in the storage volume. The weak focusing magnetic field can be defined as follows

ISBN: 978-3-95450-194-6 ISSN: 2226-0366 doi:10.18429/JACoW-LINAC2018-THPO017

$$B_z = B_0\left(1 - n\frac{\Delta r}{r} + n\frac{z^2}{2r^2}\right) \quad (2)$$

$$B_r = \left(-n\frac{z}{r}\right)B_0 \quad (3)$$

where B_0(= 82.5 Gauss) is the main solenoidal field at r = 12 cm, z = 0 cm and $\Delta r = r - r_0$. Here n is field index $\left(n = -\frac{r_0}{B_0}\frac{\partial B_z}{\partial r}\right)$. The radial and vertical focusing can be achieved if $n < 1$ and $n > 0$ respectively. Figure 4 is showing the magnetic field profile of the SITE storage magnet with the field index value of $n = 1 \times 10^{-3}$.

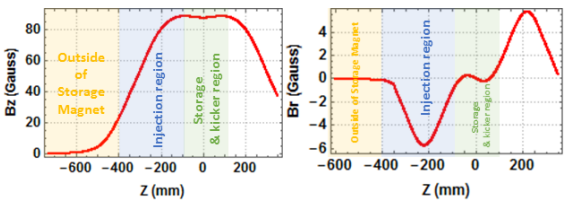


Figure 4: Left: Axial field profile of the storage magnet. Right: Radial field profile of the storage magnet with weak focusing index $n = 10^{-3}$.

Figure 5 (a) shows two kicker coil design for 2π and $\pi/6$ cases. In the 2π configuration of the kicker, the current in upper and lower coils are opposite to each other and they produced cylindrical symmetric radial field. The $\pi/6$ kicker design can be realized by the rectangular dipole coil. In the case of 2π kick shape the required kicker duration is T_{kick} = 95/2 and B_{kick} = 70 mG. In the case of $\pi/6$ kick shape the required kicker duration is T_{kick} = 95/2 and $B_{kick} \cong$ 1 G.

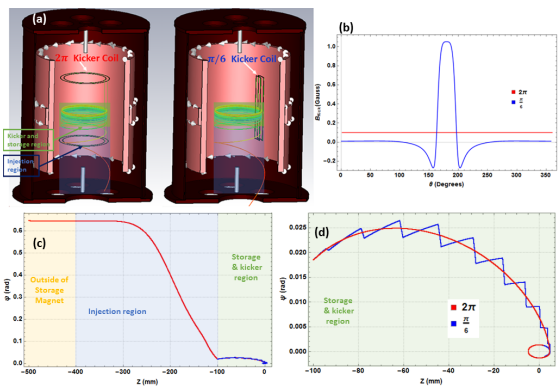


Figure 5: (a) Two models of the magnetic kicker. (b) Magnetic field profile for the 2π and $\pi/6$ kicker model. The required magnitude of magnetic field increase in the case of $\pi/6$ kicker model due to a limited region. (c) The pitch angle starting from the injection point to the storage region as a function of the vertical position (Z). (d) Pitch angle in the kicker and storage region.

Both types of kicker will be tested in SITE in order to find the best shape for the kicker. The bottom two plots in Fig. 5 shows the reduction of the pitch angle due to the kicker field (c) and storage of the beam in midplane (d).

The $\pi/6$ kicker coil shape has been optimized to reduce the inductance of coils. The optimization results in the coils of height 175 mm, width 62 mm and the gap between coils was 35 mm. The total inductance of optimized coils in series has been estimated at 0.8 μH by using CST [8]. Figure 6 left shows the optimized $\pi/6$ coil shape and right shows the magnetic field map in radial and vertical directions. The kicker coil excitation current was set to 10 A for the simulation. The details of the pulsed magnetic kicker can be found in [9].

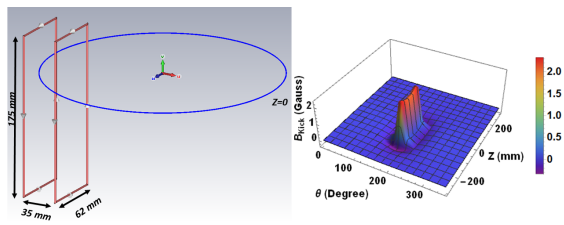


Figure 6: Left:Optimized $\pi/6$ kicker model. Right: Magnetic field map in radial and vertical directions. The exciting current of the coil was set to 10 A.

The pulsed current power supply for the magnetic kicker is also under development. The schematic of an electronic circuit for the current power supply is shown in Fig. 7.

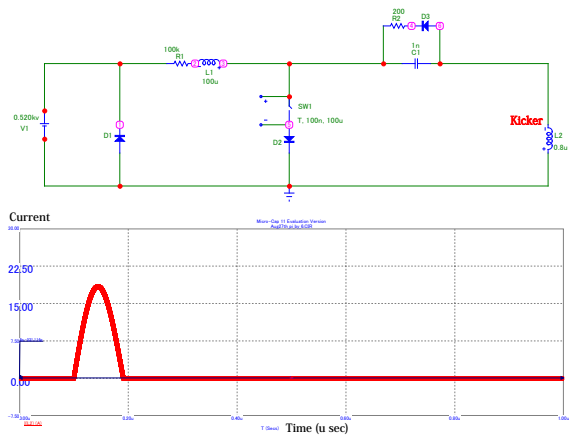


Figure 7: Top: The schematic electronic circuit for the pulsed magnetic kicker. Bottom: The pulsed current through kicker coil.

CONCLUSION

A new three-dimensional spiral injection is under development by using the electron beam in order to realize new J-PARC's muon g – 2/EDM experiment. An electron beamline and storage magnet has been constructed for the SITE. The electron beam in the storage magnet was confirmed as fluorescent light due to the de-excitation of nitrogen gas in the storage magnet. The required beam phase space for the spiral injection has been calculated. A pulsed magnetic

Content from this work may be used under the terms of the CC BY 3.0 licence (© 2018). Any distribution of this work must maintain attribution to the author(s), title of the work, publisher, and DOI.

ISBN: 978-3-95450-194-6 ISSN: 2226-0366 doi:10.18429/JACoW-LINAC2018-THPO017

kicker and the power supply is under development to guide the pulsed beam at the midplane of the storage magnet. Particle tracking studies have been carried out with the different shapes of the kicker in the kicker and weak focusing field in order to find the appropriate magnetic field and time period for a kicker.

REFERENCES

[1] G.W. Bennett *et al.*, "Final Report of the muon E821 anomalous magnetic moment measurement at BNL", *Phy. Rev. D.*, vol. 73, p. 072003, 2006.

[2] M. Aoki *et al.*, "Conceptual Design Report for the Measurement of the Muon Anomalous Moment $g-2$ and Electric Dipole moment at J-PARC (2011)"

[3] H. Iinuma *et al.*, "Three-dimensional spiral injection scheme for the $g-2$/EDM experiment at J-PARC" *Nucl. Instr. Meth.*, vol. A832, pp. 51-62, 2016.

[4] H. Iinuma *et al.*, "Three-dimensional spiral injection for a compact storage ring" in *Proc. IPAC'18*, Vancouver, BC, Canada, 2018. doi:10.18429/JACoW-IPAC2018-TUPML060

[5] H. Iinuma *et al.*, "Development of three-dimensional spiral beam injection scheme with X–Y coupling beam for MRI sized compact storage ring", in *Proc. PASJ'18*, 2018, paper WEOM07.

[6] M.A. Rehman *et al.*, "Development of the three-dimensional injection spiral injection by using electron beam for muon $g-2$ experiment" in*Proc. PASJ'17*, Sapporo, Japan, Aug. 2017, paper WEOM01.

[7] M.A. Rehman *et al.*, "Test experiment of 3-D spiral injection scheme using electron beam for new $g-2$/edm experiment at j-parc," in *Proc. PASJ'16*, Chiba, Japan, Aug. 2016, paper TUP056, pp. 1004–1007.

[8] http://www.cst.com

[9] M.A. Rehman *et al.*, "Development of the pulsed magnetic kicker for the spiral injection test experiment" in *Proc. PASJ'18*, 2018, paper THP006.

Content from this work may be used under the terms of the CC BY 3.0 licence (© 2018). Any distribution of this work must maintain attribution to the author(s), title of the work, publisher, and DOI.

ISBN: 978-3-95450-194-6 ISSN: 2226-0366 doi:10.18429/JACoW-LINAC2018-THPO018

BUILDING A 12 GHz TRAVELING WAVE ACCELERATING STRUCTURE BRAZED THROUGH IRISES

V. A. Dolgashev*, G. B. Bowden, M. Dal Forno, A. Haase, SLAC, Menlo Park, USA
H. Zha, Tsinghua University, Beijing, China
A. Grudiev, CERN, Geneva, Switzerland

Abstract

Accelerating structures are usually manufactured by precision turning of individual cells combined with precision milling for complex parts such as rf power couplers. These multiple parts are staked and brazed into a complete structure. We consider an alternative approach: precision milling of multiple cells and couplers into metal blocks that comprise halves or quadrants of the complete structure. We successfully produced a 12 GHz Compact Linear Collider (CLIC) main linac accelerating structure prototype using this method. A previous prototype was designed as an open structure with a gap between cell irises. Here we describe a different approach, an accelerating structure which is brazed through irises. It is based on a multi-cell traveling wave structure designed at CERN for PSI, so called *T24 PSI 12 GHz*. This brazed-through irises structure was built at SLAC for high power tests at CERN. Here we describe the details of this process.

INTRODUCTION AND MOTIVATION

Accelerating structures of normal conducting linacs are typically built from a multitude of precisely machined cells. Examples are X-band structures of linear colliders [1] or S-band cavities of medical accelerators [2]. The cells are joined using high-temperature brazing or diffusion bonding into a complete structure. An alternative approach has been used for making structures from two halves at W-band [3–6] and X-band [7–10], quadrants [11, 12] or octants [13]. These halves, *etc.* are made by precision milling and then joined together either by clamping [11, 13] or brazing [7, 8, 12]. All these structures were designed with gaps between irises: a small, difficult to control gap [11]; small, controlled gap [12]; and a large gap on the order of a millimeter [3–10, 13]. High power tests of these structures have shown that structures with controlled gaps performed satisfactorily [9, 12].

Here we present an alternative approach to build a constant gradient traveling wave accelerating structure from halves [14]. We braze the halves through irises thus eliminating both rf field enhancement caused by a controlled gap between irises and degradation of high gradient performance attributed to uncontrolled gaps. The geometry of this structure is practically identical to a structure made of discs but with several advantages. In the case of halves, the machined surface area is smaller and number of precision parts to handle is fewer thus reducing fabrication costs.

* dolgash@slac.stanford.edu

More advantages come from the absence of rf current flow through the joints between the halves. This makes pre-brazing rf cold test practical and useful, and reduces risk of arcing or erosion in small, uncontrolled gaps between cells. In cases of structures made from stacked cells rf currents cross these gaps. The gaps could be caused by joints starved for alloy in brazed structures or uneven bonding pressure in diffusion-bonded structures.

DESIGN AND MANUFACTURING

Design

The geometry of our structure is based on the so called *T24 PSI 12 GHz* which was designed at CERN for PSI [15] and was successfully built and high power tested [16]. The rf parameters of this structure are presented in [16] and should be practically identical to our structure. The original structure is made out of symmetric cells with rounded outer diameter. This cells geometry is suitable for manufacturing by milling into halves. Meanwhile the rf couplers (mode launchers) of the *T24 PSI 12 GHz* were brazed of separate milled parts and had to be re-designed both electrically and mechanically. We report this work in [17]. We show a solid model of the mode launcher from [17] in Fig. 1b). With a new coupler the electrical re-design was complete.

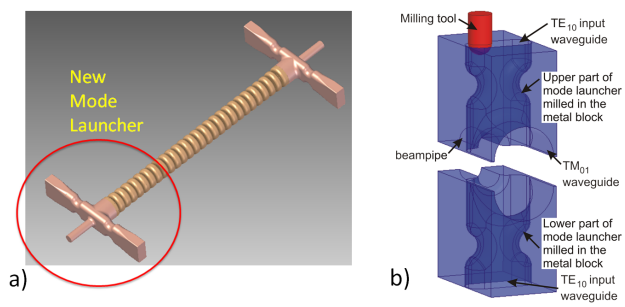


Figure 1: a) Solid model of RF envelope with re-designed mode launcher as imported into Solid Edge from HFSS [18], and b) solid model of the mode launcher, with detail of 8 mm diameter milling tool [17].

Manufacturing

In manufacturing of previous, open structure made of halves [7] we have validated an approach where we built a solid model directly from the electrical model. This electrical model was imported into Solid Edge [19] from HFSS [18]. After mechanical design was finished, the resulting solid model was used to generate the milling machine control program. No interim drawings were utilized for the

Content from this work may be used under the terms of the CC BY 3.0 licence (© 2018). Any distribution of this work must maintain attribution to the author(s), title of the work, publisher, and DOI.

ISBN: 978-3-95450-194-6 ISSN: 2226-0366 doi:10.18429/JACoW-LINAC2018-THPO018

Content from this work may be used under the terms of the CC BY 3.0 licence (© 2018). Any distribution of this work must maintain attribution to the author(s), title of the work, publisher, and DOI.

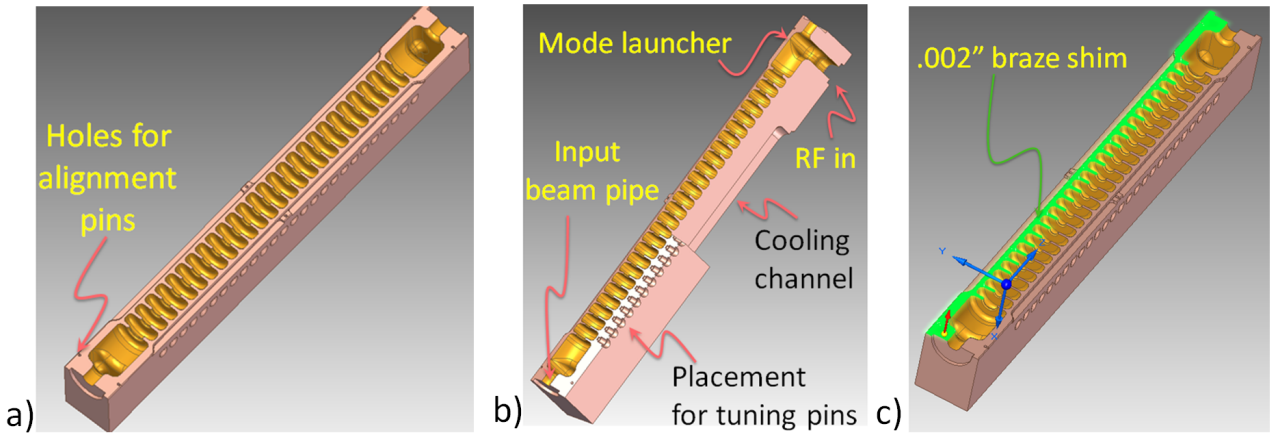


Figure 2: a) Solid model of half cavity. b) Cutaway of the half. c) Braze shim.

mill programming. Here we used the same approach. We show solid model of the imported geometry in Fig. 1a). This model was adapted to be milled out of halves with added cooling, flanges, tuning pins, *etc.* We show solid model of a half in Fig. 2a), cutaway of the half with visible holes for tuning pins and a cooling channel in Fig. 2b), and a design of 0.002 inch braze shim in Fig. 2c).

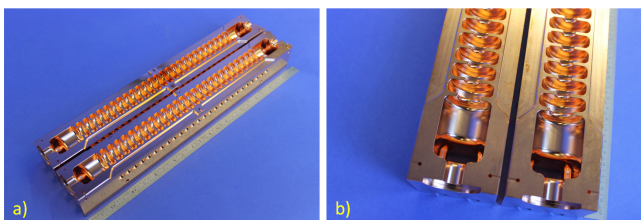


Figure 3: a) Two halves of the accelerating structure after machining. b) Input part of the structure zoomed on integrated milled-mode-launchers.

We planned to fabricate the structure using the following steps: machine halves from imported solid model; then clamp halves with instrument flanges and perform pre-brazing microwave cold measurements on our bead-pull setup; clean then braze; followed by final tuning and vacuum firing. We show milled halves in Fig. 3, and parts prepared for brazing in Fig. 4b).

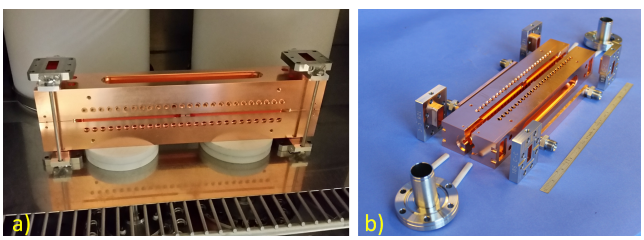


Figure 4: a) Structure clamped for pre-brazing microwave cold-test measurements. b) Structure parts before brazing. Tuning pins are not shown.

Pre-brazing Rf Measurements

We have included per-brazing bead-pull measurement into the fabrication procedure to reduce the risk of finished, brazed structure being outside tuning range. For the measurement of rf phase and amplitude along the structure we use non-resonant perturbation method [20]. We show the structure assembled for the pre-brazing bead-pull test in Fig. 4a). To simulate separation between halves due to melted brazing alloy we have put a 0.0011 inch shim between them. Results of the pre-brazing bead-pull have shown that beam-synchronous frequency is 23 MHz higher than the operating frequency of 11.994 GHz. For our tuning pins this frequency shift is at the limit of the tuning range. The cause of this frequency shift was traced to a machining error. At that point we decided to machine a shallow, 75 µm deep pocket at outside cavity diameter of every cell to drop the frequency by 23 MHz. After the machining we performed dimensional quality control to verify that the sizes of the machined pockets were acceptable and then proceeded to brazing, without additional microwave testing.

Final Tuning

For the tuning of the structure we used a method first published in [21] and refined in [22]. Our bead-pull setup with a tuned structure is shown in Fig. 5. Input reflection of the

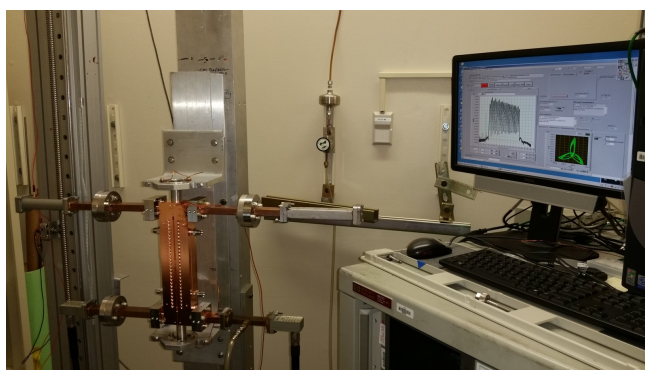


Figure 5: Final bead-pull measurements.

ISBN: 978-3-95450-194-6 ISSN: 2226-0366 doi:10.18429/JACoW-LINAC2018-THPO018

tuned structure is shown in Fig. 6 with -39 dB at operating frequency. Measured amplitude of on-axis field is shown in Fig. 7a). Phase deviation from beam-synchronous 120 deg. per cell is shown in Fig. 7b). Accumulated phase advance between first regular cell and penultimate regular cell is about 1 deg. Phase variations of about +/- 5 deg. for cells 15-25 are caused by a small reflection from output coupler. As brazed the beam-synchronous structure was 15 MHz lower than the operating frequency. This 15 MHz is comfortably within the tuning range. At the moment of publication the cause of this frequency shift is not understood. Possible reasons are miscalculation of the shape of frequency-correcting milled pocket or a manufacturing error.

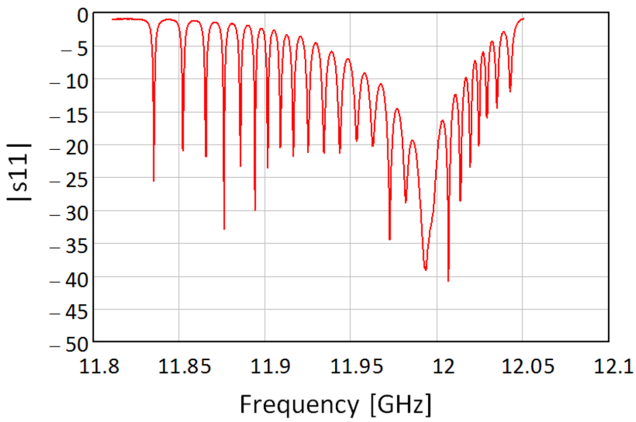


Figure 6: Input S11 of tuned structure with -39 dB at operating frequency.

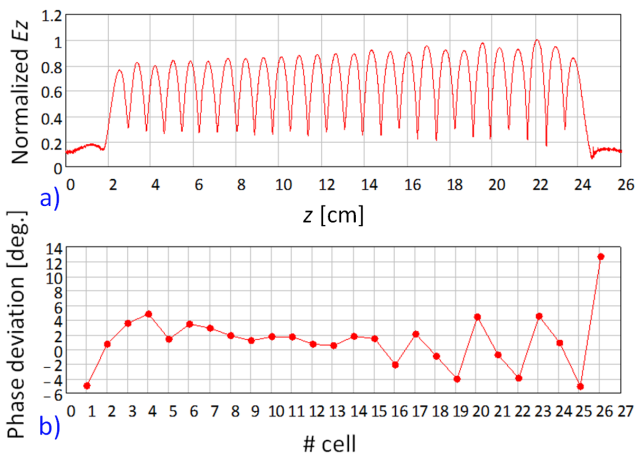


Figure 7: Results of bead-pull measurements made from an input port, input on the left: a) on-axis electric field normalized to peak value; b) deviation of rf phase from nominal 120 deg. per cell.

SUMMARY

We continue developing manufacturing techniques for high gradient accelerating structures. As part of this work, we built a 12 GHz traveling wave structure made of precisely milled halves. At the time of this publication the structure is being shipped to CERN for high power tests. Novelty of this structure is that it is brazed through irises unlike our previous made-of-halves-structures which have an open geometry with a controlled gap between iris halves. Once perfected, this method could reduce cost of linacs for scientific, medical and security applications.

REFERENCES

[1] J. Wang *et al.*, "Fabrication technologies of the high gradient accelerator structures at 100 MV/m range," in *Proc. IPAC'10*, Kyoto, Japan, May 2010, paper WEPD078.

[2] C. J. Karzmark, Craig S. Nunan, and Eiji Tanabe, *Medical Electron Accelerators,* Mcgraw-Hill (Tx) (September 1992).

[3] M. Dal Forno *et al.*, "RF Breakdown Tests of mm-Wave Metallic Accelerating Structures," *Phys. Rev. Accel. Beams*, vol. 19, pp. 011301, Jan. 2016.

[4] M. Dal Forno *et al.*, "Experimental measurements of rf breakdowns and deflecting gradients in mm-wave metallic accelerating structures" *Phys. Rev. Accel. Beams*, vol. 19, pp. 051302, May 2016.

[5] M. Dal Forno *et al.*, "rf breakdown measurements in electron beam driven 200 GHz copper and copper-silver accelerating structures," *Phys. Rev. Accel. Beams*, vol. 19, pp. 111301, 2016.

[6] M. Dal Forno *et al.*, "High gradient tests of metallic mm-wave accelerating structures," *Nuclear Instruments and Methods in Physics Research Section* A: Accelerators, Spectrometers, Detectors and Associated Equipment, vol. 864, pp. 12-28, Aug. 2017.

[7] V. Dolgashev *et al.*, "Building Open Traveling Wave Accelerating Structure," presented at *International Workshop on Breakdown Science and High Gradient Technology (HG2015)*, 2015, Beijing , China. https://indico.cern.ch/event/358352/contributions/1770573/

[8] W. Wuensch *et al.*, "Fabrication and High-gradient Testing of an Accelerating Structure Made from Milled Halves," in *Proc. LINAC'16*, East Lansing, Michigan, USA, Sep. 2016, pp. 237–239. doi:10.18429/JACoW-LINAC2016-MOPLR048

[9] Th. Argyropoulos *et al.*, "Design, fabrication, and high-gradient testing of an X-band, traveling-wave accelerating structure milled from copper halves," *Phys. Rev. Accel. Beams*, vol. 21, pp. 061001, Jun. 2018.

[10] H. Zha, A. Grudiev, and V. Dolgashev, "RF Design of the CLIC structure prototype optimized for manufacturing from two halves," in *Proc. IPAC'15*, Richmond, VA, USA, May 2015, pp. 2147–2149. doi:10.18429/JACoW-IPAC2015-TUPTY054

[11] T. Higo *et al.*, "Fabrication of a Quadrant-type Accelerator Structure for CLIC," in *Proc. EPAC'08*, Genoa, Italy, Jun. 2008, paper WEPP084, pp. 2716-2718.

[12] T. Abe *et al.*, "High-Gradient Test Results on a Quadrant-Type X-Band Single-Cell Structure," presented at the 14th Annual Meeting of Particle Accelerator Society of Japan, 2017, paper WEP039.

Content from this work may be used under the terms of the CC BY 3.0 licence (© 2018). Any distribution of this work must maintain attribution to the author(s), title of the work, publisher, and DOI.

ISBN: 978-3-95450-194-6 ISSN: 2226-0366 doi:10.18429/JACoW-LINAC2018-THPO018

Content from this work may be used under the terms of the CC BY 3.0 licence (© 2018). Any distribution of this work must maintain attribution to the author(s), title of the work, publisher, and DOI.

[13] I. Syratchev and W. Bruns, "Time domain simulations of the CLIC PETS (power extraction and transfer structure) with GdfidL," in *Proc PAC'01*, Chicago, IL, USA, Jun. 2001, paper FPAH047, pp. 3780.

[14] V. Dolgashev *et al.*, "Building Welded and Brazed Accelerating Structures from Halves," presented at CLIC workshop 2017, Mar. 2017, CERN, Geneva, Switzerland. https://indico.cern.ch/event/577810/contributions/2484773/

[15] R. Zennaro and A. Grudiev, "RF Design of T24_PSI 12 GHz Prototype Structure," CERN, 2014.

[16] R. Zennaro *et al.*, "High Power Tests of a Prototype X-Band Accelerating Structure for CLIC," in *Proc. IPAC'17*, Copenhagen, Denmark, May 2017, pp. 4318–4320. doi:10.18429/JACoW-IPAC2017-THPIK097

[17] M. Dal Forno *et al.*, "Design of a high power TM01 mode launcher optimized for manufacturing by milling," SLAC-PUB-16902, 2016.

[18] http://www.ansys.com/

[19] https://solidedge.siemens.com/

[20] C. W. Steele, "A Nonresonant Perturbation Theory," *IEEE Trans. on Microwave Theory and Techniques*, vol. 2, pp. 70-74, Feb. 1966. doi:10.1109/TMTT.1966.1126168

[21] T. Khabiboulline, M. Dohlus, and N. Holtkamp, Internal Report, DESY M-95-02, 1995.

[22] J. Shi *et al.*, "Tuning of X-band traveling-wave accelerating structures," *Nucl. Instrum. Methods Phys. Res.*, Sect. A, vol. 704, pp. 14, 2013.

ISBN: 978-3-95450-194-6 ISSN: 2226-0366 doi:10.18429/JACoW-LINAC2018-THPO020

DYNAMIC BEHAVIOUR OF ELECTRON BEAM UNDER RF FIELD AND STATIC MAGNETIC FIELD IN CYCLOTRON AUTO RESONANCE ACCELERATOR*

Yating Yuan, Kuanjun Fan†, State Key Laboratory of Advanced Electromagnetic and Technology, Huazhong University of Science and Technology, 430074, Wuhan, China
Yong Jiang‡, Yale University, 06520, New Haven, USA

Abstract

The cyclotron auto-resonance accelerator (CARA) is a novel concept of accelerating continuous gyrating charged-particle beams to moderately or highly relativistic energies, which can be used as the high power microwave source and applied in environment improvement area, particularly in the flue gas pollution remediation. In CARA, the continuous-wave (CW) electron beam follows a gyrating trajectory while undergoing the interaction with the rotating TE-mode rf field and tapered static magnetic field. Simulation models are constructed to study the effect of rf field and static magnetic field on electron beam in CARA, where the beam energy, trajectory and velocity component are analysed. The simulation results match reasonably well with theoretical predication, which sets up a solid foundation for future designs of CARA.

INTRODUCTION

The CARA may have application as a compact, low-energy injector for a multimegawatt gyroharmonic converter [1, 2] or for use in a source of radiation that requires low-energy electrons [3, 4]. An alternative technology to combat environmental pollution, electron beam dry scrubbing (EBDS), was introduced in 1970, and subsequently demonstrated in several manifestations [4]. CARA is an efficient process for converting rf energy into electron beam energy [4, 5]. The accelerated beam produced in CARA follows a gyrating trajectory, thus the beam is "self-scanning", requiring no other deflecting device or external field to sweep across a gas stream. So CARA is suitable for environmental applications include sterilization, flue gas and waste water treatment.

BASIC THEORY

When the static magnetic field satisfies a certain resonance condition in CARA, the gyrating electrons are maintained in phase synchronism with a rotating TE_{11} waveguide field, then electron beam can be continuously accelerated [2, 4].

The electron beam will gyrate under guiding magnetic field B_z. The rest electron gyration frequency is

$$\Omega_0 = eB_z / m_0 . \quad (1)$$

where e, m_o are the electron charge and rest mass respectively.

The synchronous axial guiding magnetic field is

$$B_z = m_0 \omega \gamma (1 - n\beta_z) / e . \quad (2)$$

where β_z, γ and ω are normalized axial velocity, relativistic factor and rf field frequency respectively. Refractive index n is expressed by

$$n = k_z c / \omega = c\sqrt{(\frac{2\pi f}{c})^2 - (\frac{1.841}{a})^2} / 2\pi f . \quad (3)$$

The relationship between the β_z and γ can be given

$$\beta_{z1} = \frac{1}{\gamma_1}[n_1(\gamma_1 - \gamma_0) + D^{1/2}] \quad (\gamma_1 > \gamma_0, \beta_{z1} > 0) . \quad (4)$$

where $D = (\gamma_0^2 - 1) - (1 - n_1^2)(\gamma_1 - \gamma_0)^2$, γ_0 is the beam's initial relativistic factor, β_{z1}, γ_1 and n_1 denote the output parameters in CARA.

The maximum acceleration energy [2] in CARA is

$$\gamma_{1\max} = \gamma_0 + \left(\frac{\gamma_0^2 - 1}{1 - n_1^2}\right)^{1/2} . \quad (5)$$

Then the normalized transverse velocity β_T can be expressed by γ and β_z

$$\beta_T = \sqrt{1 - \frac{1}{\gamma^2} - \beta_z^2} . \quad (6)$$

There are many challenges in CARA:

(i) The maximum acceleration energy is related to n according to Eq. (5), so it is important to get a large n (close to 1) in order to achieve high energy electron beam. But n->1 implies large waveguide radius according to Eq. (3).

(ii) In order to achieve an effective acceleration, it is essential to find the appropriate rf field power and axial magnetic field to maintain the resonance condition.

(iii) The rf field strength and the slope of guiding magnetic field always have perturbations in practice, so the effect of the perturbation is of great significance.

SIMULATION MODEL

For simplicity, a cylindrical waveguide is modelled. In order to achieve a high refractive index, the related parameters of this model are showed in Table 1. The simulation indicates that the rf field distribution in the cylindrical waveguide is the $TE_{11\text{-}35}$ mode of standing wave

* Work supported by the National Natural Science Foundation of China
† kjfan@hust.edu.cn
‡ yong.jiang@yale.edu

Content from this work may be used under the terms of the CC BY 3.0 licence (© 2018). Any distribution of this work must maintain attribution to the author(s), title of the work, publisher, and DOI.

ISBN: 978-3-95450-194-6 ISSN: 2226-0366 doi:10.18429/JACoW-LINAC2018-THPO020

Content from this work may be used under the terms of the CC BY 3.0 licence (© 2018). Any distribution of this work must maintain attribution to the author(s), title of the work, publisher, and DOI.

which only has the transverse electric component. Supposing the electron energy γ increases linearly on axial distance z, according to the previous research [2]. Then the related parameters vs axial distance z in CARA are obtained as the following Fig. 1 according to Eq. (2), (4) and (6).

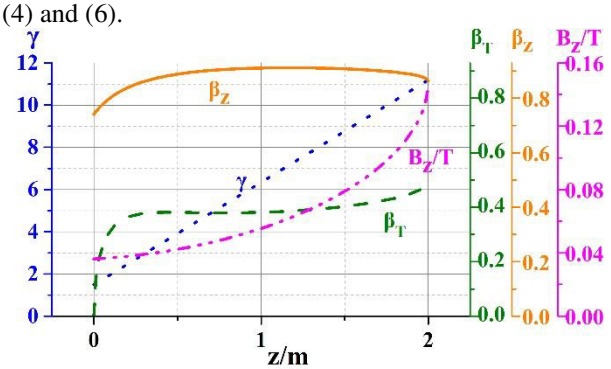


Figure 1: Dependence of initial guiding magnetic field B_z, electron energy γ, transverse velocity β_T and axial velocity β_z on axial distance z in CARA (from z=0 to 2 m).

Table 1: Related Parameter in CARA

Parameter	Value
Length of waveguide	2 m
Radius of waveguide	0.5 m
Refractive index n	0.9935
Initial γ of electron	1.4892
Rf field frequency	2.575 GHz

SIMULATION ANALYSIS

By changing the rf field scaling factor S_{rf} and the slope of the initial magnetic field B_z respectively, the effect of rf field and static magnetic field on electron beam behaviour in CARA.

Dynamic Behaviour under Different RF Field

The rf field strength can be adjusted by changing S_{rf}. Figure 2 shows the projection of the motion of electron on the y-z plane at different S_{rf} value for an initial axial magnetic field showed in Fig. 1. The number of revolutions decreases as the S_{rf} increases, which can be explained by $\Omega = eB_z / m_0\gamma$: the larger S_{rf} means larger acceleration gradient, then the electron can get larger energy γ, resulting in smaller cyclotron frequency. When the S_{rf} is too large to exceed a certain threshold, the electron will not be able to pass through the up-tapered magnetic field and reverse finally because of the Lorenz force caused by the transverse magnetic field component of rf field.

Figure 3 shows the dependence of related parameters on axial distance z at different S_{rf} value in CARA under initial axial magnetic field shown in Fig. 1. From Fig. 3, we can get that when S_{rf}=10, the γ, β_z and β_T curve are closest to the theoretical curve in Fig. 1, indicating the electron is maintained in phase synchronism with a rotating TE_{11-35} waveguide field. And the simulation curves agree well with the theoretical curve. The wiggling in these curves may be related to the non-resonance component in standing wave mode.

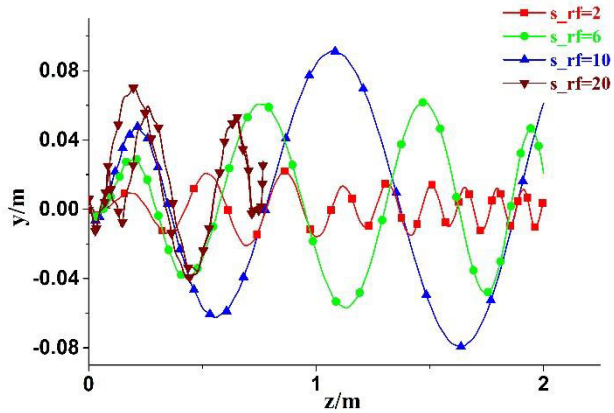


Figure 2: The projection of the motion of electron on the y-z plane under different rf field strength S_{rf}.

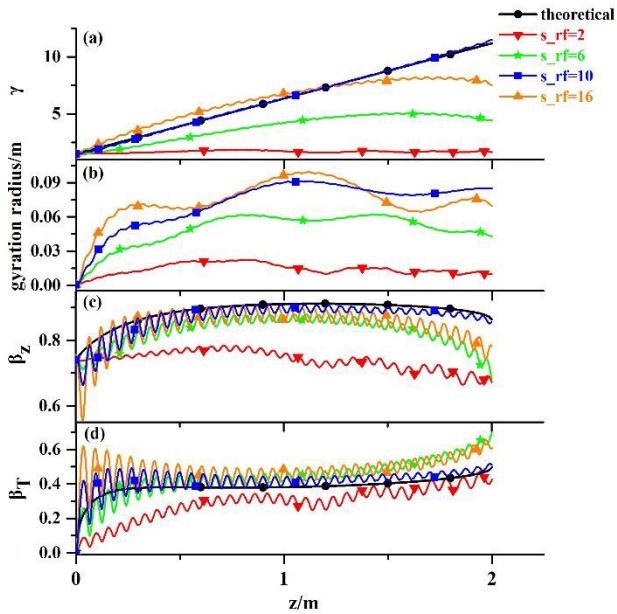


Figure 3: Dependence of (a) electron energy γ, (b) gyration radius ρ, (c) axial velocity β_z and (d) transverse velocity β_T on axial distance z at different S_{rf} value in CARA for a tapered axial magnetic field shown in Fig. 1.

During the movement of electrons, as z increases, β_T increases rapidly at the initial stage, then remains unchanged and finally increases slightly, which indicates that the electron can be accelerated transversely by the transverse electric field of rf field. The larger S_{rf} means the larger the acceleration gradient in CARA, and the slope of β_T curve is larger in the initial stage from z=0 to 0.5 [m]. The β_z does not change very much compared to the β_T. So in general, the γ is increasing almost linearly with z. The ρ also increases along z, which is related to the expression of $\rho = v_T m_0\gamma / eB_z$: the radius is proportional to the β_T and γ.

When rf field deviates from the resonance, the γ and ρ curve increases first and then decreases, which means the electron oscillate during acceleration and deceleration due

ISBN: 978-3-95450-194-6 ISSN: 2226-0366 doi:10.18429/JACoW-LINAC2018-THPO020

to none resonance. The oscillation amplitude increases with the S_{rf} for the β_T and β_z curves, and the curves are unstable compared to the resonant one when rf field is perturbed.

Dynamic Behaviour under Static Magnetic Field

The rf field scaling factor S_{rf} =10 remains a constant in this model. The perturbation magnetic field is set as $B_z^{'} = B_z(z_0) + \alpha \cdot (B_z(z) - B_z(z_0))$, where B_z is the initial magnetic field shown in Fig. 1. By adjusting the parameter α, the perturbation magnetic field with different slope can be obtained.

Figure 4 shows the projection of the motion of electron on the y-z plane at different α value in CARA for a tapered axial magnetic field showed in Fig. 5 (a). The number of revolutions increases as the α increases, which can be explained by $\Omega = eB_z / m_0\gamma$: the larger α means larger magnetic field at each point along z axis, then the larger cyclotron frequency and gyration revolutions. The electron will reverse due to the mirror effect of the high magnetic field.

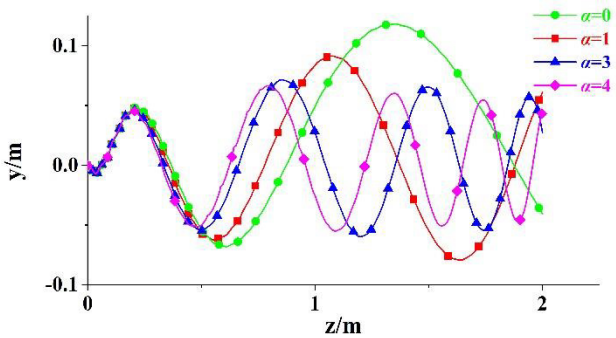


Figure 4: The projection of the motion of electron on the y-z plane under different magnetic field parameter α.

Figure 5 shows the related parameters on axial distance z for a tapered axial magnetic field shown in Fig. 5 (a). During the movement of electrons, the γ, ρ and β_T curves have a clear upward trend while β_z curve almost unchanged after a little growth at the beginning. The axial magnetic field B_z is not perturbed when $\alpha = 1$, and the electron is maintained in phase synchronism condition. When the magnetic field is perturbed, the larger the value of α, the greater the γ and β_T while the smaller the ρ and β_z from Fig. 5. When electron gyrates, the transverse electric field accelerates it, resulting β_T increases. The larger the value of α, the more the revolution numbers. So the electron will get more acceleration from rf field, then the γ and β_T are larger. The larger the axial magnetic field has a larger radial component of magnetic field which causes a reduction in β_z. According to $\rho = v_T m_0\gamma / eB_z$, although the energy increases as α increases, the gyration radius ρ decreases as the increase in magnetic field B_z dominates.

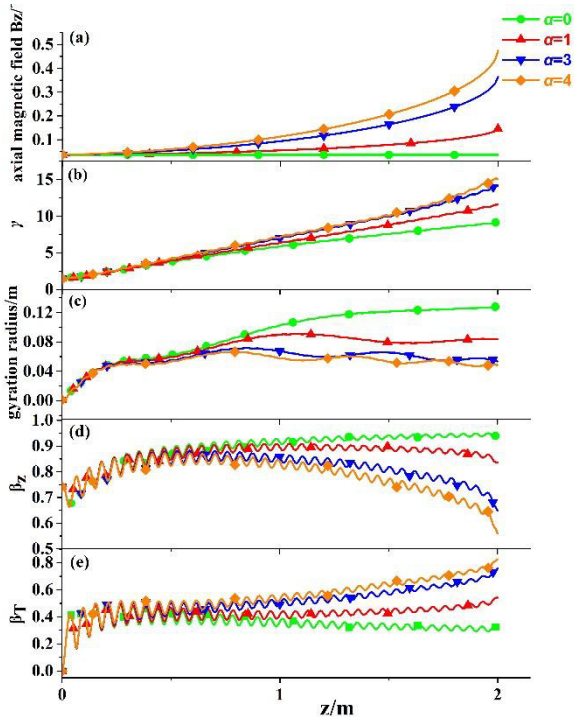


Figure 5: The (a) axial magnetic field B_z distribution along z axis under different α value, dependence of (b) electron energy γ, (c) gyration radius ρ, (d) axial velocity β_z and (e) transverse velocity β_T on axial distance z under a tapered axial magnetic field shown in (a).

SUMMARY

In this paper, we have made an analytical study and simulation of CARA about the effect of rf field and axial magnetic field on electron beam in computer simulation. In summary, we can draw the following conclusions:

(i) When the electron is maintained in phase synchronism with a rotating TE_{11-35} waveguide field using up-tapered axial magnetic field, with axial distance z, γ grows almost linearly, ρ increases and then remains almost unchanged, β_T has a rapidly growth at the beginning and then remains almost a constant, and β_z increases slightly then remains almost unchanged.

(ii) As S_{rf} increases, the revolution number decreases, and the growth rate of γ, ρ and β_T increase obviously while the β_z decreases. The electron will reverse when the S_{rf} is too big. The γ, ρ and β_z at the exist of the waveguide (z=2 m) have the maximum value while the β_T has the minimum value as rf field scaling factor S_{rf} increases.

(iii) As α increases, the revolution number, γ and β_T increase obviously while ρ and β_z decreases. The electron will reverse when the slope exceeds a threshold value.

ACKNOWLEDGEMENT

This work is supported by the National Natural Science Foundation of China.

Content from this work may be used under the terms of the CC BY 3.0 licence (© 2018). Any distribution of this work must maintain attribution to the author(s), title of the work, publisher, and DOI.

ISBN: 978-3-95450-194-6 ISSN: 2226-0366 doi:10.18429/JACoW-LINAC2018-THPO020

Content from this work may be used under the terms of the CC BY 3.0 licence (© 2018). Any distribution of this work must maintain attribution to the author(s), title of the work, publisher, and DOI.

REFERENCES

[1] J. L. Hirshfield, "Coherent radiation from spatiotemporally modulated gyrating electron beams", *Phys. Rev. A.*, vol. 44, pp. 6845-6853, 1991.

[2] Changbiao Wang and J. L. Hirshfield, "Energy limit in cyclotron autoresonance acceleration", *Phys. Rev. E.*, vol. 51, pp. 2456-2464, 1995.

[3] Changbiao Wang and J. L. Hirshfield, in *Proc. IPAC'97*, pp. 3863-3865.

[4] B. Hafizi, P. Sprangle and J. L. Hirshfield, "Electron beam quality in a cyclotron autoresonance accelerator", *Phys. Rev. E.*, vol. 50, pp. 3077-3086, 1994.

[5] M. A. LaPointe *et al*., "Experimental demonstration of high efficiency electron cyclotron autoresonance acceleration", *Phys. Rev. Lett.*, vol. 76, pp. 2718-2721, 1995.

ISBN: 978-3-95450-194-6 ISSN: 2226-0366 doi:10.18429/JACoW-LINAC2018-THPO021

RESEARCH ON X RAY CHARACTERISTICS PRODUCED BY HIGHENERGY PICOSECOND ELECTRON BEAM SHOOTING*

X. D. Zhang†, X. P. Ouyang, X. F.Weng, X. J. Tan, B.Sun
State Key Laboratory of Intense Pulsed Radiation Simulation and Effect (Northwest Institute of Nuclear Technology), Xi'an, China

Abstract

The X ray sources based on electron linac can produce X-rays with high energy, concentrated directions, and strong penetrating power, which have been widely applied in various fields.An electronic linear accelerator which has been built at present can provide an electron beam with energy of 120 MeV and pulse width of picoseconds. The electron beam shooting at the metal targets can produce ultra-fast pulsed X-rays in the order of picoseconds. In this paper, the pulse X ray characteristics are studied through simulating electron beam shooting at four metal targets with different thickness of Au, Ta, U, W and Pb by Monte Carlo methods. The calculation shows that the X-rays can reach about 10^{10} /pulse and the pulse width can reach about picoseconds level, when the pulsed electron beams with energy of 120 MeV, charge of 0.5 nC and pulse width of picoseconds shooting at Ta targets. The yield and time width of pulsed X-rays are related to the diameter and thickness of the target.

INTRODUCTIONS

Since the discovery of X-rays, various types of X-rays generating devices have been developed, among which the most widely used one is the X-ray source devices used in electron linac, such as industrial irradiation electron linac, medical treatment accelerator and so on. These kinds of accelerators produce high energy electron beams，which can produce X-rays with high energy, concentrated direction and strong penetration. They have been widely used in irradiation processing, nondestructive testing, medical and other fields. The generation rate and time characteristic of X-ray are related to the beam energy, beam length, material and thickness of the target. The X-ray produced by this kind of linear accelerator is either DC or pulse, and the pulse width is mostly more than ns.

The electronic linear accelerator currently being built by Northwest Institute of Nuclear Technology can produce energy of 120 MeV and pulse width of 1ps to 3ps and electron beam with diameter of 15 μm. Using this electron beam to shoot target can produce ultrafast X-ray with high intensity and pulse width of picosecond magnitude, which can provide experimental basis for studying nuclear data and ultrafast ray measurement technology. Therefore, it is of great significance to study the target shooting by picosecond electron beam for designing the parameters of electron linac and target. In this paper, Monte Carlo method is used to calculate the X-ray characteristics produced by electron beam shooting, and the relationship between X-ray characteristics and target parameters, beam parameters.

CONVERSION TARGET SELECTION AND BEAM PARAMETERS

According to classical electrodynamics, charged particles accompany electromagnetic radiation when they are accelerated or decelerated. When a high-speed moving charged particle collides with an atom or a nucleus, under the action of the Coulomb potential, it will be deflected and decelerated while emitting x-rays, which is also called bremsstrahlung. In the electromagnetic theory, the intensity of bremsstrahlung is proportional to the square of the target nuclear charge and inversely proportional to the square of the mass of charged particles. Therefore, high-speed electrons are usually used to bombard the target nuclei to obtain high-intensity X-rays, and electrons are radiated in the target material. The energy loss of the electron can be expressed by the following formula [1]:

$$(-\frac{dE}{dx})_r = \frac{z(z+1)e^4 NE}{137 m_0^2 c^4}(4\ln\frac{2E}{m_0c^2} - \frac{4}{3}) \quad (1)$$

Where E is the energy of the incident electron; N is the number density of atoms of the target substance; m_0 is the electron mass; c is the speed of light; and e is the unit charge.

From the electromagnetic theory [2], we can know that bremsstrahlung radiation has the following characteristics: 1) the greater the atomic number, the higher the intensity of X-ray produced by the element; 2) the continuous change of energy; 3) the existence of short-wave limit, short-wave limit $\lambda_{min}=E/(hc)$, in which E is the energy of the incident electron; 4) when the incident electron energy is low, the momentum of the photon is small, the photon is emitted in all directions, and when the incident electron energy is high, the photon tends to emit forward. Therefore, in actual use, an element having a large atomic number and a high energy electron beam are usually selected.

Table 1: Electron Beam Parameters

Parameters	Values	Units
Energy	60～120	MeV
Charges	0.1～0.5	nC
Energy dispersion	0.3%(rms)	
Beam length	1～3(rms)	ps
Beam diameter	~15(rms)	μm
Emittance	<1@0.5nC	mm·mrad

Electron linac is generally used to produce high energy electrons. The electron linac we are currently developing consists of photocathode microwave gun, two acceleration tubes, three microwave power sources, a three-in-one

Content from this work may be used under the terms of the CC BY 3.0 licence (© 2018). Any distribution of this work must maintain attribution to the author(s), title of the work, publisher, and DOI.

ISBN: 978-3-95450-194-6 ISSN: 2226-0366 doi:10.18429/JACoW-LINAC2018-THPO021

Content from this work may be used under the terms of the CC BY 3.0 licence (© 2018). Any distribution of this work must maintain attribution to the author(s), title of the work, publisher, and DOI.

quadrupole lens, deflection magnet and beam measuring devices. The parameters of the electron beam produced by the electron linac are shown in Table 1.

X-RAY CHARACTERISTICS SIMULATION CALCULATION

X-ray Calculations for Different Heavy Nuclei

It is shown from Table 1 that the beam emittance, energy dispersion and beam diameter are small, and the beam emittance and energy dispersion need not be considered in the actual simulation calculation. Therefore, in the simulation process, the conditions are as follows: the electron beam is used to vertically strike the cylindricalheavy target from the axial direction (as shown in Fig. 1), the beam is a 120 MeV single-energy electron source with pulse width of 3 ps (rms), beam diameter of 15 μm (rms), charge of cluster of 0.5 nC, electrons are uniformly sampled in position and the incident direction is consistent with the axial direction of the cylindrical heavy target. Six heavy metal targets, Au, Ta, U, W, Pb and Th, are selected.

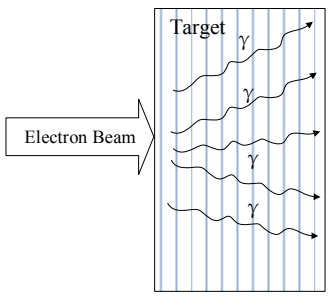


Figure 1: Schematic diagram of response of electron beam to heavy target

Because of the complexity of electron and X-ray motion in target material, it is difficult to calculate X-ray yield, energy spectrum, emission direction and other parameters by formula. Therefore, Monte Carlo method is usually used to simulate and calculate the bremsstrahlung photon characteristics produced by electron beam striking heavy metals. In order to reduce the amount of calculation, the diameter of the target is selected as 1 cm, and the number of X-rays produced by the pulsed electron beam with energy of 120 MeV and charge of 0.5 nC acting on the target with different thickness can be obtained by simulation calculation. The calculation results are shown in Fig. 2. It can be seen from the figure that the X-ray photon number produced in the heavy target can reach 10^{10}/pulse. When the target thickness is less than a certain value, the photon number increases with the increasing of the target thickness. When the target thickness is greater than a certain value, the X-ray photon number remains basically unchanged. That is, it does not change with the thickness of the target.

X-ray Calculation of Ta Target

As can be seen from Fig. 2, the variation of X-ray produced by different nuclides is basically the same. Ta target is the main research object. Monte Carlo method is

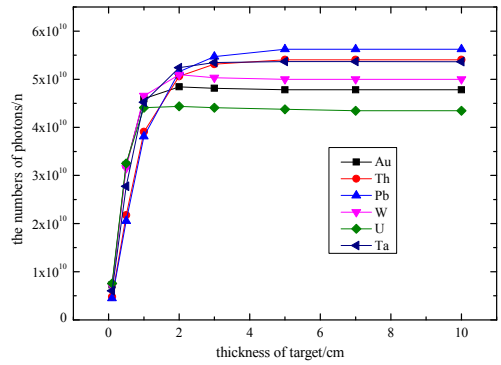


Figure 2: Calculation results of X-ray in heavy targets.

used to simulate the electron beam vertically incident on Ta targets with different diameters and thickness. The results are shown in Fig. 3. As can be seen from Fig. 3, when the diameter of Ta target is less than 2 cm and the thickness of Ta target is more than 4.5 cm, the number of X-ray photons produced by the electron beam in the target increases with the increase of the target thickness; when the diameter of Ta target is less than 2 cm and the thickness of Ta target is more than 4.5 cm, the number of X-ray photons produced by 120 MeV electron beam in the target is almost constant, and does not increase with the target thickness. Additionally, when the diameter of Ta target is above 2 cm and the thickness is below 1.5 cm, the number of X-ray photons produced by 120 MeV electron beam in the target increases with the increase of the target thickness; when the diameter of Ta target is above 2 cm and the thickness is above 1.5 cm, the number of X-ray photons produced by 120 MeV electron beam in the target decreases with the increase of the target thickness.

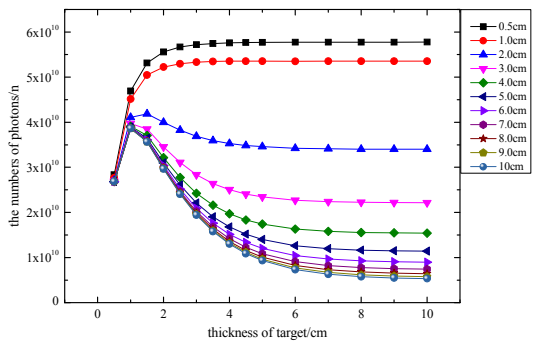


Figure 3: The numbers of X-ray photon produced by electrons in Ta targets.

The energy spectra of X -rayproduced in Ta targets with different diameters and thicknesses is calculated, and the results are shown in Fig. 4. It can be seen that there are four peaks of X-ray photon spectra, which are located near 9 keV, 56 keV, 66 keV and 0.511 MeV respectively. The first three peaks are characteristic X-ray peaks of Ta target, and the last one is positron-negative pair annihilation peak, which is much higher than the first three peaks. The energy spectrum of X ray moves towards low energy with the increase of target thickness and target diameter.

The X-ray time spectrum of Ta targets with different diameters and thicknesses is calculated. The results are

ISBN: 978-3-95450-194-6 ISSN: 2226-0366 doi:10.18429/JACoW-LINAC2018-THPO021

shown in Fig. 5. It can be seen from the figure that the half-width of X-ray produced by Bremsstrahlung of electron beam with pulse width of 3 ps is several ps to tens of ps, and the pulse width increases with the increase of Ta target thickness and diameter.

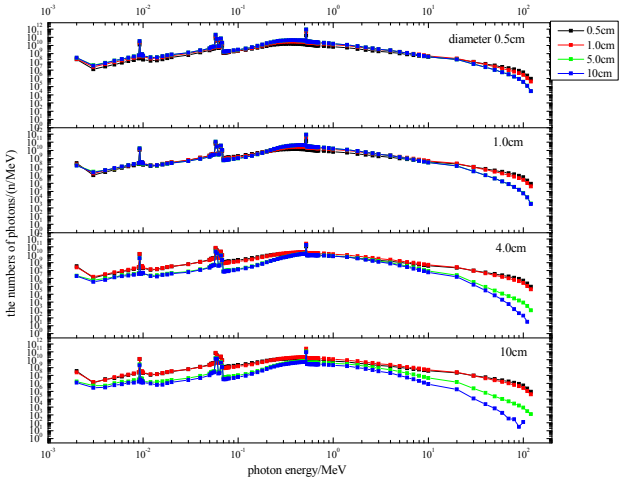


Figure 4: X-ray photon energy spectrum produced by electrons in Ta targets.

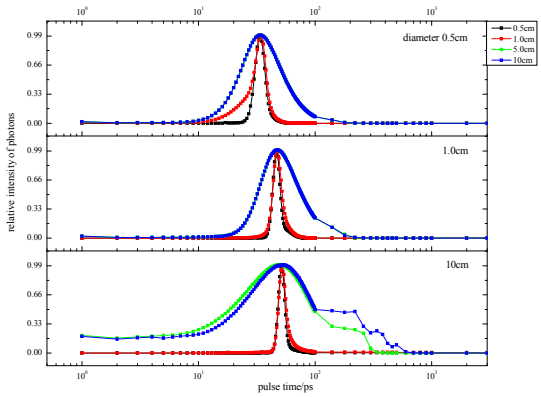


Figure 5: Photon time spectra in Ta targets with different diameters and thicknesses.

The angular distributions of X-ray photons produced by Ta targets with different diameters and thicknesses are calculated. The results are shown in Fig. 6 and Fig. 7. The angles are the angles between the emission direction of photons and neutrons and the incident direction of electron beam. It can be seen from the figure that when the target diameter is below 5 cm, the X-ray emission angle is concentrated in the direction of 0-90 degree; when the target thickness is below 3 cm, the proportion of X-ray photons in the direction of 0-90 degree increases with the increase of the target diameter; when the target thickness is above 3 cm, the proportion of X-ray photons in the direction of 0-90 degree increases with the increase of the target diameter. For the same diameter target, the proportion of X-ray photons in the direction of 0-90 degree decreases with the increase of the target thickness.

CONCLUSION

In this paper, the interaction model of ps electron beam with heavy target is established, and the Monte Carlo

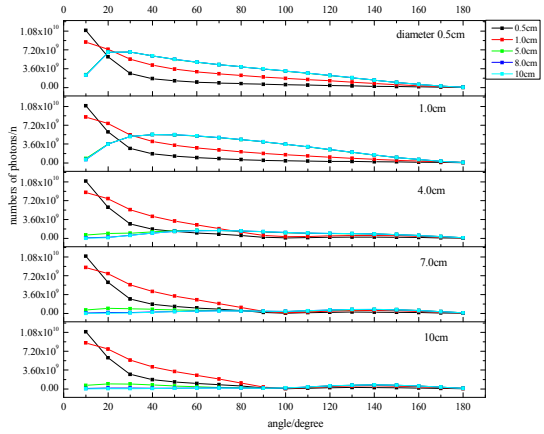


Figure 6: Photon angle spectrum produced in Ta targets with different diameters and thicknesses.

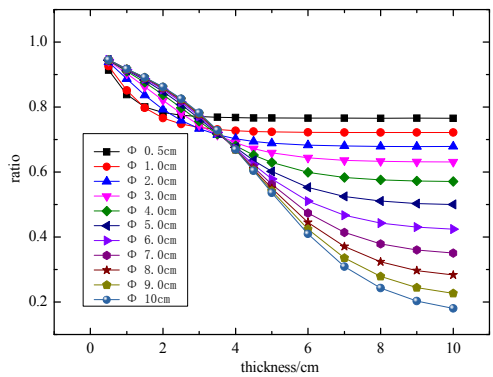


Figure 7: Proportion of photon numbersin the direction of 0-90 degree.

method is used to calculate the interaction between ps electron beam and heavy targets. The results show that the number of X-rays produced by pulsed electron beams with energy of 120 MeV, charge of 0.5 nC and pulse width of 3 ps (rms) in heavy targets with diameter less than 1 cm can reach 10^{10}/pulse. The X-ray characteristics of high-energy electron beam in Ta target are studied. The results show that for 120 MeV electron beam, there are four peaks of X-ray spectrum in Ta target, and the time half-width of X-ray is from several ps to tens of ps. The emission angle distribution of X-ray is related to the diameter and thickness of the target. By studying the X-ray characteristics of ps electron beam incident on heavy target, it can provide important reference value for the ultrafast X-ray application of this type of electron linac.

ACKNOWLEDGEMENTS

Thank you for your help from colleagues from the Northwest Institute of nuclear technology.

REFERENCES

[1] Z.H. Wu, G.Q. Zhao, F.Q. Lu *et al.*, "Experimental Methods of Nuclear Physics", Beijing, China: Atomic Energy Press, 1994: 49.

[2] E. Haug and W. Nakel, "The Elementary Process of Bremsstralung", Beijing, China: Beijing University Press, 2012, pp. 45.

Content from this work may be used under the terms of the CC BY 3.0 licence (© 2018). Any distribution of this work must maintain attribution to the author(s), title of the work, publisher, and DOI.

ISBN: 978-3-95450-194-6 ISSN: 2226-0366 doi:10.18429/JACoW-LINAC2018-THPO022

DEVELOPMENT PROGRESS OF THE H+/H- LINEAR ACCELERATORS AT TSINGHUA UNIVERSITY*

Q.Z. Xing, X.D. Yu, C. Cheng, T.B. Du, X.L. Guan, H.Y. Zhang, S.X. Zheng, Y. Lei, R. Tang, P.F. Ma, S. Wang, C.B. Bi, C.T. Du, Q.K. Guo, X.W. Wang†, Key Laboratory of Particle & Radiation Imaging (Tsinghua University), Ministry of Education, Beijing 100084, China
also at Laboratory for Advanced Radiation Sources and Application, Tsinghua University, Beijing 100084, China
also at Department of Engineering Physics, Tsinghua University, Beijing 100084, China
B.C. Wang, W.L. Liu, M.W. Wang, Y. Yang, C. Zhao, Z.M. Wang, State Key Laboratory of Intense Pulsed Radiation Simulation and Effect (Northwest Institute of Nuclear Technology), Xi'an, 710024, China
W.Q. Guan, Y. He, J. Li, NUCTECH Co. Ltd., Beijing 100084, China

Abstract

We present, in this paper, the development progress of the 13MeV proton linac for the Compact Pulsed Hadron Source (CPHS), and the 7MeV H- linac injector for the synchrotron of the Xi'an 200MeV Proton Application Facility (XiPAF).

INTRODUCTION

One proton and one H- linear accelerators are being constructed. The Compact Pulsed Hadron Source (CPHS) project is aimed at becoming an experimental platform for education, research, and innovative applications at Tsinghua University. The facility will provide the proton beam, together with the neutron beam by delivering the proton beam to bombard the beryllium target. The designed parameters for the proton beam is 13 MeV/50 mA with the pulse length of 500 μs and repetition rate of 50 Hz [1][2]. The Xi'an 200MeV Proton Application Facility (XiPAF) project was launched in the year of 2014 for the research of the single event effect. The facility is mainly composed of one 7 MeV H- linac injector, one 200 MeV six-fold synchrotron and two experimental stations. The designed parameters for the H- beam of the linac injector is 7 MeV/5 mA with the pulse length of 10-40 μs and maximum repetition rate of 0.5 Hz [3].

13 MeV PROTON LINAC FOR CPHS

CPHS project consists of a high-current proton linac (13 MeV, 16 kW, peak current 50 mA, 0.5 ms pulse width at 50 Hz), a neutron target station, a small-angle neutron scattering instrument and a neutron imaging/radiology station. The accelerator system consists of the 50 keV ECR Ion Source (IS), Low Energy Beam Transport line (LEBT), 3MeV four-vane Radio Frequency Quadrupole (RFQ) accelerator, 13 MeV Alvarez-type Drift Tube Linac (DTL), RF power supply and distributor, and High Energy Beam Transport line (HEBT). Figure 1 presents the latest layout of the linac of the compact pulsed hadron source.

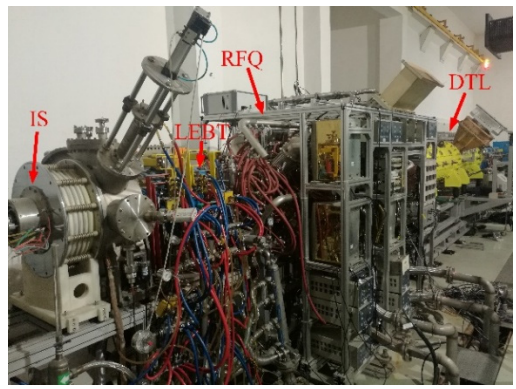


Figure 1: Layout of the linac of the compact pulsed hadron source.

CPHS has provided ~2000 hrs beam time since 2013 to the users with the neutrons produced by the 3 MeV proton beam from the RFQ bombarding on the beryllium target [4]. The application of the neutrons mainly consists of the neutron imaging [5], and the test of the neutron detectors including the B_4C-coated straw-tube [6] and the gadolinium-doped micro-channel plate (MCP) [7].

DTL

The 4.3-meter-long Alvarez-type DTL accelerates the 3 MeV proton beam to 13 MeV. The final tuning of the DTL cavity is completed and it is being installed in the beam line (Fig. 2).

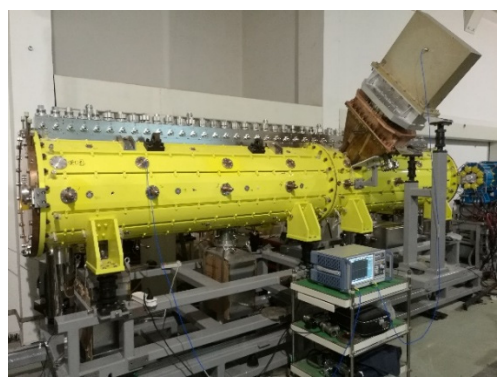


Figure 2: Assembled CPHS DTL for RF measurement.

* Work supported by National Natural Science Foundation of China (Project 11575098 and 11275106).
† wangxuewu@tsinghua.edu.cn

Content from this work may be used under the terms of the CC BY 3.0 licence (© 2018). Any distribution of this work must maintain attribution to the author(s), title of the work, publisher, and DOI.

ISBN: 978-3-95450-194-6 ISSN: 2226-0366 doi:10.18429/JACoW-LINAC2018-THPO022

Figures 3 and 4 illustrate the field distribution of the DTL cavity and the tilt sensitivity after the final tuning, respectively. The relative error of the field between the designed and measured distribution is within 1.6%, and the tilt sensitivity is tuned to be within ±33%/MHz in all cells.

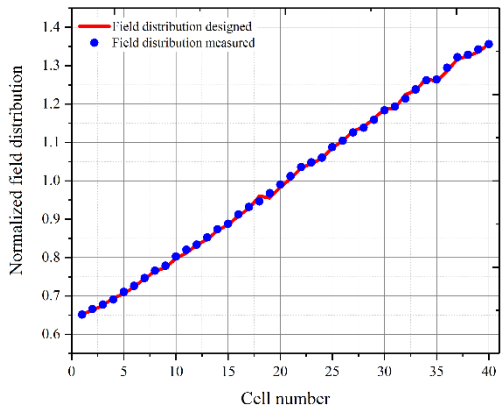


Figure 3: Field distribution of the CPHS DTL after the final tuning.

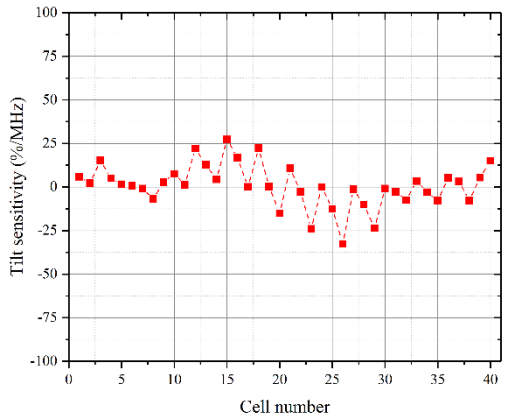


Figure 4: Tilt sensitivity of the CPHS DTL after the final tuning.

RF Power System

The DTL will share with the RFQ the same klystron, which can supply the peak RF power of 3.0 MW with a maximum duty factor of 3.33%. The RF transmission system is being installed, as shown in Fig. 5.



Figure 5: RF power system for the CPHS RFQ and DTL.

7 MeV H⁻ LINAC INJECTOR FOR XiPAF

The 7 MeV H⁻ linac injector for the synchrotron of the XiPAF project is composed of the 50 keV H⁻ ECR source, LEBT, 3 MeV four-vane RFQ accelerator, 7 MeV KONUS-IH-DTL, and the corresponding RF power source system.

ECR Ion Source

The H⁻ source has been assembled as in Fig. 6 and the maximum current of 5.8 mA has been measured by the Faraday cup at the exit of the source (Fig. 7).

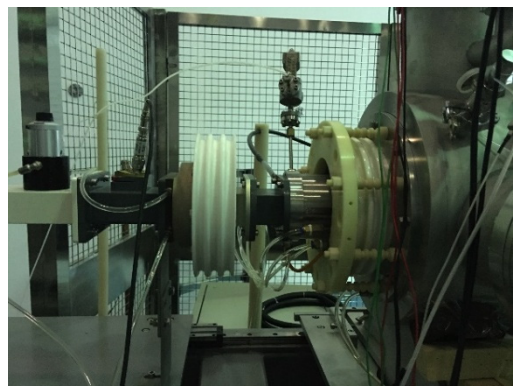


Figure 6: Assembled H⁻ ECR source at site for XiPAF.

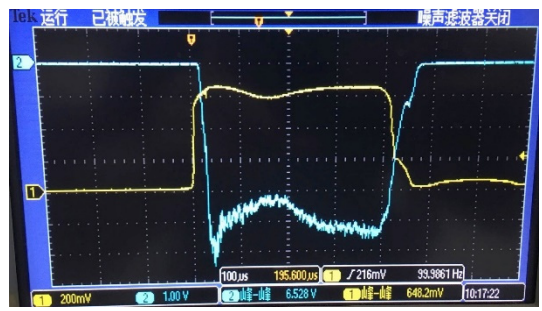


Figure 7: Beam current measured by the Faraday cup at the exit of the H⁻ source.

LEBT

The LEBT will steer and match the beam from the ion source to the RFQ by two solenoids and two steering magnets. The LEBT has been assembled and is under beam conditioning (Fig. 8).

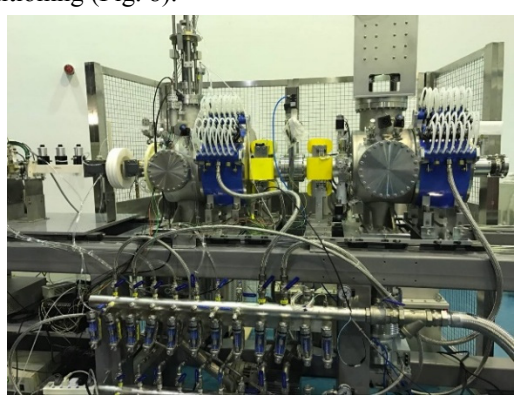


Figure 8: Assembled XiPAF LEBT at site.

Content from this work may be used under the terms of the CC BY 3.0 licence (© 2018). Any distribution of this work must maintain attribution to the author(s), title of the work, publisher, and DOI.

ISBN: 978-3-95450-194-6 ISSN: 2226-0366 doi:10.18429/JACoW-LINAC2018-THPO022

Content from this work may be used under the terms of the CC BY 3.0 licence (© 2018). Any distribution of this work must maintain attribution to the author(s), title of the work, publisher, and DOI.

RFQ

The four-vane RFQ has been assembled (Fig. 9) and tuned. The relative error between the measured field distribution and the designed curve for the operating quadrupole mode is within ±2.7%, and the dipole component is within ±1.9%, as shown in Fig. 10.



Figure 9: Assembled XiPAF RFQ for the tuning.

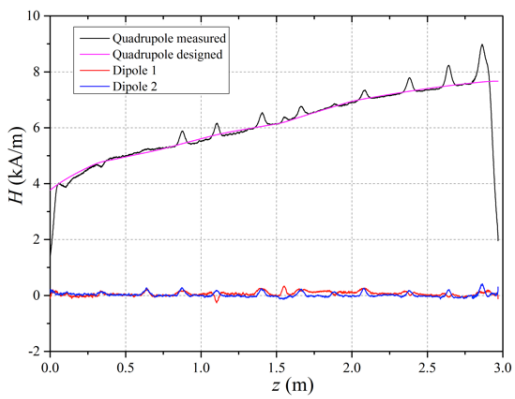


Figure 10: Field distribution of the quadrupole and dipole modes after the tuning.

IH-DTL

The machining of the one-meter-long KONUS-IH-DTL cavity has been completed and the cavity is under tuning. Figure 11 shows the central frame of the cavity.

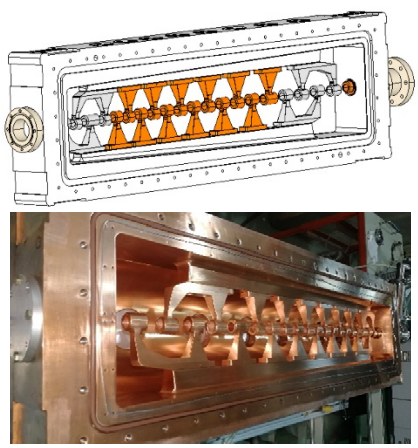


Figure 11: Central frame of the IH-DTL cavity.

RF Power System

The RFQ and DTL will be powered by two 4616V4 tetrode amplifiers. The RF power source has been assembled and successfully produced RF power for 8 hrs at 325 MHz with a peak power up to 500 kW, a repetition rate of 1 Hz, and a pulse width of 150 μs (Fig. 12).



Figure 12: Tetrode-based RF system at site for XiPAF.

CONCLUSION

The assembly of the 13 MeV H^+ linac for CPHS and the 7 MeV H^- linac injector for XiPAF is expected to be completed in this year and the beam conditioning and commissioning are foreseen.

ACKNOWLEDGEMENTS

The authors would like to thank Prof. S.X. Peng for providing the experimental result of the ECR H^- source.

REFERENCES

[1] J. Wei, *et al.*, "The compact pulsed hadron source: a design perspective", *Journal of the Korean Physical Society*, vol. 56, no. 6, pp. 1928-1935, 2010, doi: 10.3938/jkps.56.1928

[2] X.W. Wang, *et al.*, "Delivery of 3-MeV proton and neutron beams at CPHS: a status report on accelerator and neutron activities at Tsinghua University", *Physics Procedia*, vol. 60, pp. 186-192, 2014, doi: 10.1016/j.phpro.2014.11.027

[3] Q.Z. Xing *et al.*, "Design of the 7MeV linac injector for the 200MeV synchrotron of the Xi'an proton application facility", in *Proc. IPAC'16*, Busan, Korea, May 2016, paper MOPMW014, pp. 426-428.

[4] Q.Z. Xing, *et al.*, "Present status of the high current linac at Tsinghua University and its application", in *Proc. HB'16*, Malmo, Sweden, July 2016, paper WEAM3Y01, pp. 413-415.

[5] Z.F. Huang, *et al.*, "Scheme for radiography/tomography with a low-brilliance neutron source at the CPHS", *Nucl. Instr. Meth. Phys. Res., Sect. A*, vol. 651, pp. 32-35, 2011, doi:10.1016/j.nima.2011.01.105

[6] H. Yu, *et al.*, "A multiplex readout method for position sensitive boron coated straw neutron detector", *Nucl. Instr. Meth. Phys. Res., Sect. A*, vol. 797, pp. 324-329, 2015, doi:10.1016/j.nima.2015.05.038

[7] Y.M. Wang, *et al.*, "Readout for a large area neutron sensitive microchannel plate detector", *Nucl. Instr. Meth. Phys. Res., Sect. A*, vol. 784, pp. 226-231, 2015, doi:/10.1016/j.nima.2014.12.058

ISBN: 978-3-95450-194-6 ISSN: 2226-0366 doi:10.18429/JACoW-LINAC2018-THPO026

THE MULTI-PHYSICS ANALYSIS OF DUAL-BEAM DRIFT TUBE LINAC *

Tao He[1,2], Liang Lu[1], Wei Ma[1], Lei Yang[1], Xianbo Xu[1], Liepeng Sun[1], Chaochao Xing[1],
[1]Institute of Modern Physics, Chinese Academy of Science, Lanzhou 730000, China
[2]also at University of Chinese Academy of Sciences, Beijing 100049, China

Abstract

The dual-beam drift tube linac (DB-DTL) prototype has been designed for verification of feasibility of multi-beam accelerator in middle energy region [1] [2]. The DB-DTL will accelerate 1 mA proton from 0.56MeV to 2.5MeV in pulse model. The DB-DTL operates at 81.25MHz, room temperature. The power dissipated on the surface on the DB-DTL internal surface will increase cavity temperature, which cause structure deformation and resonant frequency shifting. It is important to simulate the temperature rise, deformation and frequency shifting of DB-DTL cavity. The detailed three-dimensional multi-physics field analysis of DB-TL will be presented in this paper.

INTRODUCTION

The DB-DTL prototype is proposed to validate the feasibility of multi-beam accelerator in middle energy region. The main parameters are listed in Table. 1. The DB-DTL will operate as pulse injector with the capacity of accelerating proton from 0.56 MeV to 2.5 MeV [3]. The 35.83 kW normalized power dissipation of DB-DTL dissipated on the cavity internal surface will heat the cavity and cause cavity temperature rise and structural deformation, which will lead to resonant frequency shifting. The cooling water takes away the power to resolve this problem. In this paper, detailed multi-physics field simulation of DB-DTL is performed by using ANSYS multi-physics, which is a coupled electromagnetic, thermal and structural analysis.

Table 1: DB-DTL Prototype Main Parameters

Parameters	Value
Particle	H^+
Operation	pulsed
Frequency (MHz)	81.25
Current (mA)	1
Input/output energy (MeV/u)	0.56/2.56
Maximum gap voltage (kV)	387.50
Transmission efficiency (%)	35.0
Power dissipation (MW)	35.83
Kilpatrick factor	2.10
Shunt impedance (MΩ/m)	200.02

MULTI-PHYSICS ANALYSIS

As shown in Fig. 1 [4], the multi-physics analysis is a coupled electromagnetic, thermal, structural and frequency shifting analysis. The ANSYS workbench [5] and CST Microwave Studio (MWS) [6] are employed in the simulation. The total cavity power loss is firstly calculated with the MWS and the distribution of RF thermal loss on the cavity internal surface is simulated with the ANSYS High Frequency Structure Simulator (HFSS), which will be coupled to the next thermal analysis. The thermal solution will generate cavity temperature map based on cavity internal surface heat flux, which is applied to calculate the structural stresses and deformations. The last step is to calculate the resonant frequency shift according to the deformations. Through multi-physics analysis, appropriate parameter of cooling-water is chosen to satisfy the requirement for cavity operation of DB-DTL. The deformation and stress of cavity and corresponding resonant frequency shifting should be within a proper range.

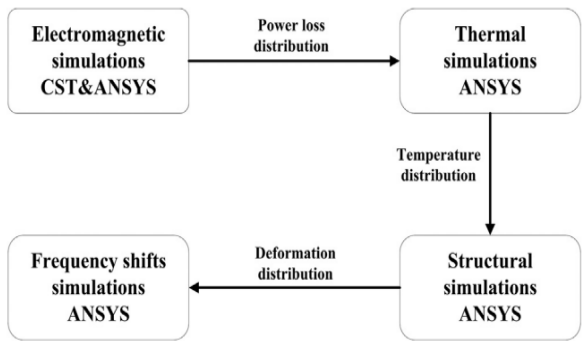


Figure 1: Multi-physics analysis scheme with CST and ANSYS.

The electromagnetic simulation results in MWS show that cavity resonant frequency is 81.24993 MHz. The normalized power dissipation is 35.83 kW and the shunt impedance is 100.01 MΩ/m. Then, verification of electromagnetic calculation by using ANSYS HFSS is performed. Table. 2 gives a comparison of electromagnetic simulation between the MWS and ANSYS, which indicates the difference is enough small to ignore. As shown in Fig. 2, the octahedron cavity shape model is chosen for easily assembling, which includes 8 ridge waterways and 5 wall waterways. The parameter of cooling-water is plotted in Table. 3. Figure 3 shows the distribution of the cavity power dissipation, which will be applied to following thermal simulation. The power dissipated on cavity internal surface will increase temperature rise of DB-DTL cavity. It is important to simulate the temperature distribution of DB-DTL, which is couple to next structural analysis in ANSYS Static Structural code for simulating the deformation and stress distribution of DB-DTL cavity.

The simulation results of multi-physics analysis show that the temperature rise, deformation， stress and resonant frequency are beyond a proper range, which indicate the

* Work supported by NSFC and CAS through Grant Nos. 11475232 and 11535016.
† email address: hetao0216@impcas.ac.cn

Content from this work may be used under the terms of the CC BY 3.0 licence (© 2018). Any distribution of this work must maintain attribution to the author(s), title of the work, publisher, and DOI.

ISBN: 978-3-95450-194-6 ISSN: 2226-0366 doi:10.18429/JACoW-LINAC2018-THPO026

Content from this work may be used under the terms of the CC BY 3.0 licence (© 2018). Any distribution of this work must maintain attribution to the author(s), title of the work, publisher, and DOI.

cooling system is impracticable to CW operation of DB-DTL, as plotted in Table. 4. Actually, the DB-DTL will operate at pulse with 1/1000 duty without cooling-water in future for shorting funds. Therefore, the maximum loadable power test of DB-DTL is studied. The simulation results show that the maximum loadable power of DB-DTL is 18 kW*5/100 with cooling water and 18kW*1/100 without cooling-water, respectively, as illustrated in Fig. 4.

Table 2: DB-DTL Prototype Cavity Parameters

Parameters	MWS	ANSYS
F (MHz)	81.24993	81.9050
Q	13514	12860

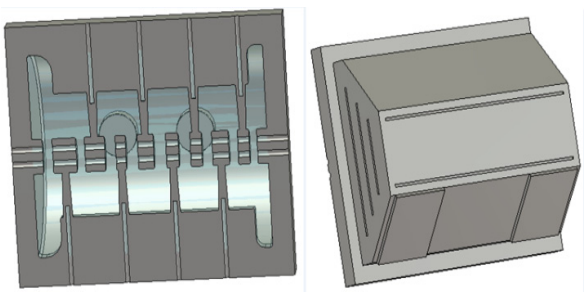


Figure 2: Shape structure model of DB-TL.

Table 3: Main Parameters of Cooling Water

Parameters	Ridge-water	Wall-water
Diameter (mm)	15	15
Velocity (m/s)	2.0	2.0
T.water (^{0}C)	20	20
C.water (W/m2/K)	7860	7860

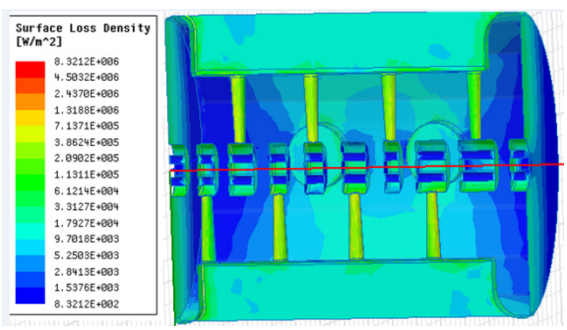


Figure 3: The power loss distribution on the internal surface of DB-DTL cavity.

Table 4: Simulation Results of cw Operation Mode

Parameters	**Value**
Power dissipation	18 kW
Maximum Temperature (^{0}C)	550.22
Maximum Deformation (mm)	1.8114
Maximum Stress (MPa)	230.95
Frequency shifting (kHz)	-685.8

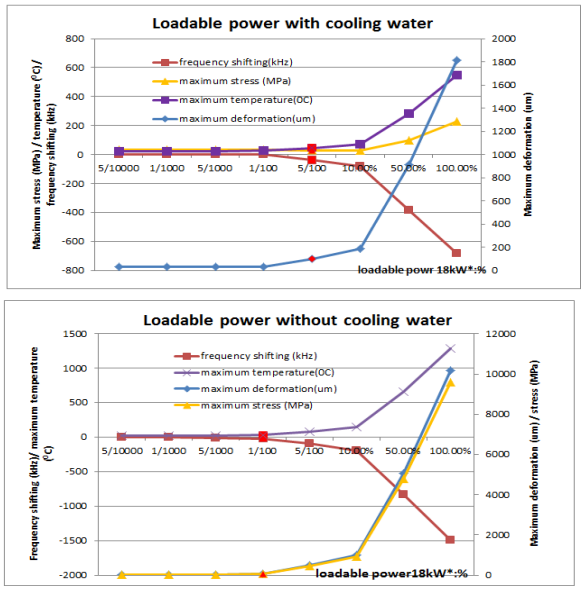


Figure 4: The loadable power dissipation is studied.

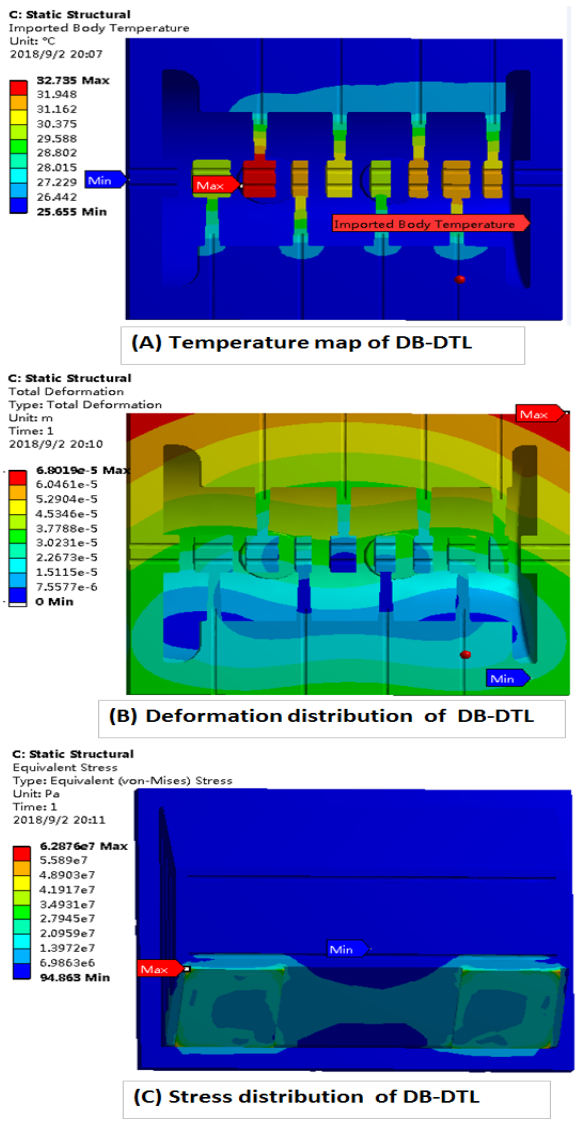


Figure 5: The temperature map, deformation and stress distribution of DB-DTL with 1/100 pulse operation.

ISBN: 978-3-95450-194-6 ISSN: 2226-0366 doi:10.18429/JACoW-LINAC2018-THPO026

Table 5: Simulation Results of (5%) Pulse Operation Mode

Parameters	Value
Power dissipation	18 kW * 5/100
Maximum Temperature (^{0}C)	46.511
Maximum Deformation (um)	99.635
Maximum Stress (MPa)	29.247
Frequency shifting (kHz)	-38.1

Considering 18*1/100 power dissipation, the simulation results of DB-DTL without cooling-water is shown in Fig. 5, which include the distribution of temperature, deformation and stress. The maximum temperature is 32.735 0C located at eighth drift tube and the minimum temperature of drift tube is 29.588 0C. The maximum deformation is 68.018 μm on the external surface and the displacement of drift tubes are between 7.55 μm and 30.231μm. The maximum stress is 62.876 MPa located at fixed supporting flame. The stress distribution of DB-DTL cavity is within a proper range. The deformation of DB-DTL cavity will cause frequency shifting. The frequency shifts were calculated with the HFSS code based on the deformation results. The frequency shift is −16.8 kHz compared with the initial frequency. The resonant frequency shifting for cavity deformation is tuned by tuners with 9.65 kHz/mm frequency tubing ability. The simulation results of 18 kW*5/100 power dissipation with cooling water is plotted in Table. 5. The maximum deformation is located at eighth drift tube. These simulation results indicate that the DB-DTL meets the design goals with 1/1000 pulse operation mode.

FREQUENCY SENSITIVITY STUDYING

The frequency sensitivity of parameters of cooling water is studied for choosing practicable temperature and velocity of cooling water. The DB-DTL frequency sensitivity of cooling water temperature is shown in Fig. 6. The frequency tuning capacities of ridge and wall cooling water temperature are -1.56 kHz/^{0}C and 0.072 kHz/^{0}C, respectively. However, there are some constraints during adjustment of cooling water temperature. As illustrated in Fig. 6, the maximum deformation is varied with the variation of cooling water temperature. Furthermore, the maximum stress is also changed by the change of cooling water temperature. The simulation results indicate that the practical variation range of temperature is between 18^{0}C and 25^{0}C and the adjustment range should be as small as possible for frequency tubing. Otherwise, an everlasting inelastic deformation will occur with long time over-stressed operation and field distribution distortion will be enough big to affect the focusing and accelerating ability of DB-DTL.

CONCLUSION

Three dimensional multi-physics analysis of DB-DTL has been performed, which is a coupled procedure including electromagnetic, thermal, structural and frequency shifting analysis. These simulation results indicate that the DB-DTL without cooling system meet the deign goal of

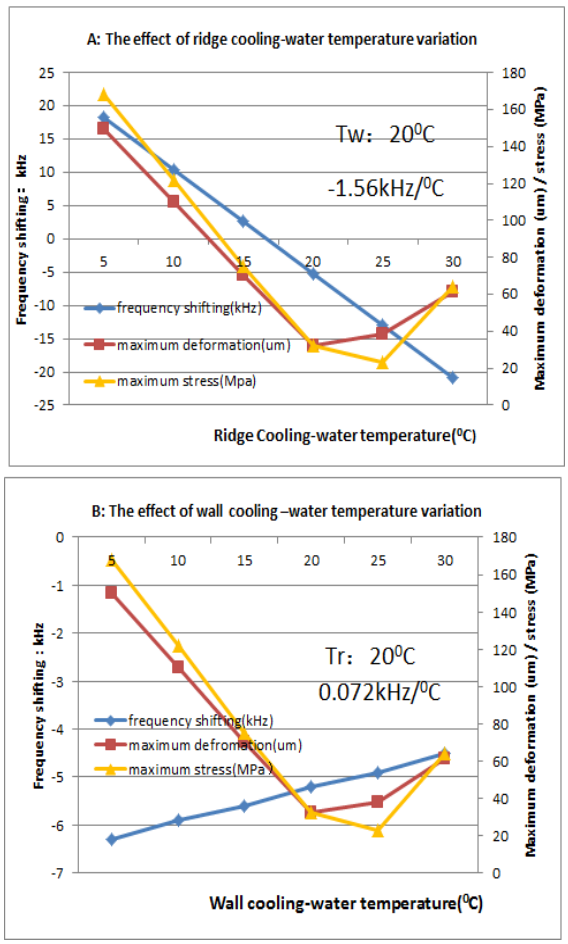


Figure 6: The loadable power test of DB-DTL is studied.

1/1000 pulse operation. The maximum loadable power test has been studied and the maximum pulse operation of DB-DTL without cooling system is 1/100. The simulation results show that the temperature rise, the deformation and stress of DB-DTL cavity are all in the acceptable range. In addition, the maximum pulse operation with cooling water system and the frequency sensitivity of cooling water temperature also have been performed.

REFERENCES

[1] L. Lu, H. Toshiyuki, et al, Study on A Super High Intensity Injector For HIF, the 22nd International symposium on Heavy-ion Fusion and Beam-Driven High Energy Density Science, Daejeon, Korea, HIF2018, 20-24 August 2018.
[2] L. Lu, L. P. Sun, T. He, L. Yang, W. Ma, et al., Research on A Two-Beam Type Drift Tube Linac, in proceeding of LINAC2016, Michigan State University, East Lansing, Michigan, USA, pp989-991.
[3] T. He, L. Lu, W. Ma, L. Yang, et al., Studying A Prototype of Dual-Beam Drift Tube Linac, the 9th International Particle Accelerator Conference IPAC2018, Vancouver, BC, Canada, Apr. 29 – May 4, 2018, TUPAL009, pp1020-1023.
[4] Wei Ma *et al.*, "Three-dimensional multi-physics analysis and commissioning frequency tuning strategy of a radio-frequency quadrupole accelerator", *Nucl. Instr. Meth. A,* vol.866, pp.190-195, Sep.2017.
[5] ANSYS. http://www.ansys.com
[6] CST Simulation packages. http://www.cst.com

Content from this work may be used under the terms of the CC BY 3.0 licence (© 2018). Any distribution of this work must maintain attribution to the author(s), title of the work, publisher, and DOI.

ISBN: 978-3-95450-194-6 ISSN: 2226-0366 doi:10.18429/JACoW-LINAC2018-THPO028

MAGNETIC FIELD MEASUREMENT AND ANALYSIS FOR DRIFT TUBE LINAC OF CSNS*

B. Li[1,†], H. C. Liu[1], Q. Chen[1], X. L. Wu[1], K. Y. Gong, A. H. Li[1], M. X. Fan[1], Y. Wang[1], P. H. Qu[1], J. X. Zhou, W. Kang, China Spallation Neutron Source, Institute of High Energy Physics, China Academy of Sciences, 523803, Dongguan, P. R. China,
[1]also at Dongguan Neutron Science Center, 523808, Dongguan, P. R. China

Abstract

A 324MHz Alvarez-type Drift Tube Linac (DTL) is used to accelerate the H- ion beam from 3 to 80 MeV with peak current 15mA for China Spallation Neutron Source (CSNS). DTL is composed by 36 meters cavity and 161 DTs, the DT magnet coil adopted SAKAE structure with compact, smaller aperture. Magnetic field is measured by self-developed high precision rotating coil measurement system. This paper introduces the rotating coil measurement system simply and presents the 161 DTs magnetic field measurement results comprehensively, include magnetic field center offset, integral magnetic field, higher-order harmonics. In addition, cooling test result of magnet coil is also presented.

INTRODUCTION

Drift Tube Linac of CSNS which accelerating an H- ion beam from 3 MeV to 80 MeV has been designed as 4 tanks with a total length of approximately 36 m [1, 2]. The electromagnetic quadrupoles (EMQs) are used in DTL accelerator for transverse focusing since the magnetic field gradient can be adjusted by varying the current flow in the conductors. The major parameters of the designed DTL quadrupole (DTLQ) are presented in Table 1.

DRIFT TUBE AND ROTATING COIL MEASUREMENT SYSTEM

The structure of Alvarez-type Drift Tube is show in Fig. 1. We adopted an electroformed hollow coil- SAKAE type coil which has no bending radius, for its compact structure. The wire cutting and the Periodic Reverse copper electroforming method are applied to the coil manufacture process. The DT shell and stem are made of oxygen free copper and cooled via the supporting stem. The fabrication process is complex and time consuming accompanied with a series of tests. All joints of the DT and the stem are welded by the electron beam welding (EBW). The space around the magnet in the DT is filled with the epoxy resin by a vacuum impregnation method.

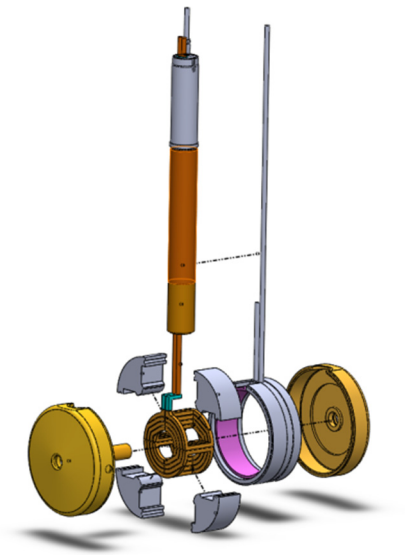


Figure 1: Drift tube structure.

Table 1: Design Parameters of DTL Quadrupole Magnets

Cavity number	Cavity 1		Cavity 2&3	Cavity 4
Magnet type	DTL-QA	DTL-QB	DTL-QC	DTL-QD
Quantity	26	39	69	27
Outer radius(mm)	108	108	108	108
Inner radius(mm)	19	19	23	27
Good field region(mm)	14	14	18	22
Higher-order harmonics(Bn/B2)	$<3.0\times10^{-3}$	$<3.0\times10^{-3}$	$<3.0\times10^{-3}$	$<3.5\times10^{-3}$
Effective length(mm)	40	50	75	70
Field gradient(T/m)$_{max}$	55	55	17	13.5
Integral field(T)	2.2	2.75	1.275	0.945
Field gradient(T/m)$_{min}$	40	25	12	12

† libo0910@ihep.ac.cn

Content from this work may be used under the terms of the CC BY 3.0 licence (© 2018). Any distribution of this work must maintain attribution to the author(s), title of the work, publisher, and DOI.

ISBN: 978-3-95450-194-6 ISSN: 2226-0366 doi:10.18429/JACoW-LINAC2018-THPO028

To verify the DTLQ's design specifications and fabrication quality, a precision harmonic coil magnetic field measurement system was designed for the measurement of the small aperture magnet. Figure 2 shows the overview of the measurement system, the alignment precision of the DTLQ is better than 0.004 mm, and the duplicate measurement errors of the integrated field and harmonics field of this measurement system are better than 4E-3 and 4E-4 respectively [3].

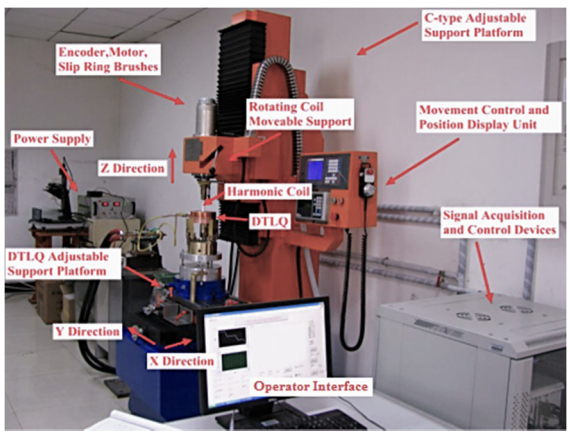


Figure 2: The practicality picture of the measurement system.

MEASUREMENT RESULTS AND ANALYSIS

Magnetic Field Center Offset

Five times at least rotating coil measurement were done during one DT's machining. Figure 3 presents the change trajectory of magnetic field center offset after each machining, finally, the center offset was milled to less than the requirement 0.03 mm.

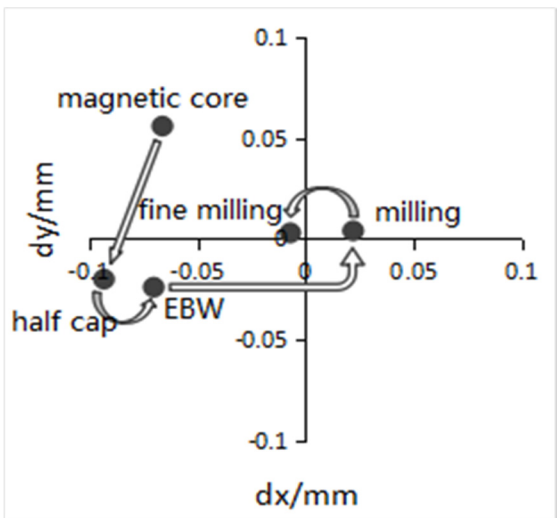


Figure 3: The trajectory of magnetic field center offset after each machining.

Figure 4 shows the measured magnetic field center offset from the mechanical centre defined by the excircle of the DT. It can be found that most of the deviations (dot) less than 0.03 mm, since the DT length increase, the processing precision decline, a few of deviations (circle) fall into [0.03, 0.05]. Appropriate calibrating was made during fabricating to satisfy physical requirements.

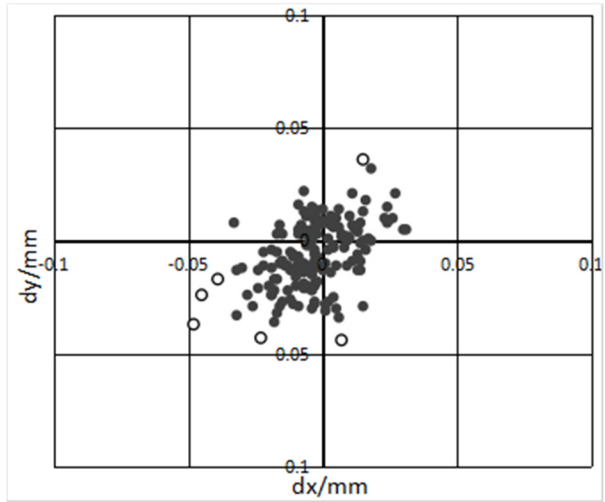


Figure 4: The magnetic field center offset deviation of the 161 DTs.

Integral Field and Higher-Order Harmonics

Four sizes quadrupole magnet were designed for DTL as show in table 1, since less sizes caused easily manufacture. Integral field was continuous through simulation by Trace Win code [4]. The measurement results are shown in Fig. 5 with design values, measurement integral field values that higher 5% corresponding to less than 30 A excitation current are acceptable.

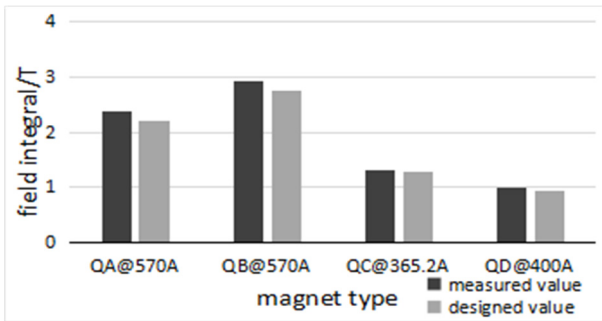


Figure 5: Field integral comparison of measurement value and design value for four sizes magnet.

Higher-Order Harmonics is another important quality index for EMQ. Figure 6 shows the harmonics component of four types magnet. B6/B2 of QA is 2.12E-3, QB is 1.44E-3 and QC is 2.00E-3, less than 3.00E-3, B6/B2 of QD is 3.30E-3, under 3.5E-3. The harmonics of all the 161 quadrupole magnet are low enough for our physical requirement.

Content from this work may be used under the terms of the CC BY 3.0 licence (© 2018). Any distribution of this work must maintain attribution to the author(s), title of the work, publisher, and DOI.

ISBN: 978-3-95450-194-6 ISSN: 2226-0366 doi:10.18429/JACoW-LINAC2018-THPO028

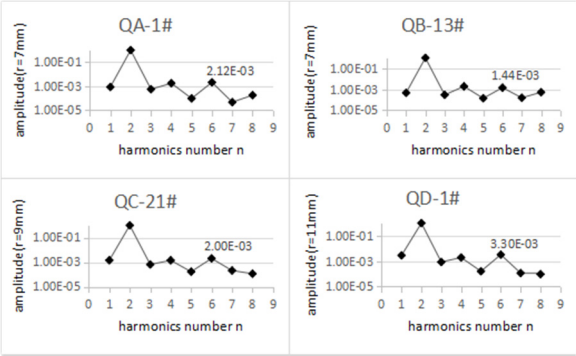


Figure 6: Higher-order harmonics of four types magnet.

COOLING TEST

Attention must be paid to the fever of EMQ, test was done with the maximum rated current 580A, cooling water flow 1.0L/min. The temperature on magnet coil surface is showed in Fig. 7.

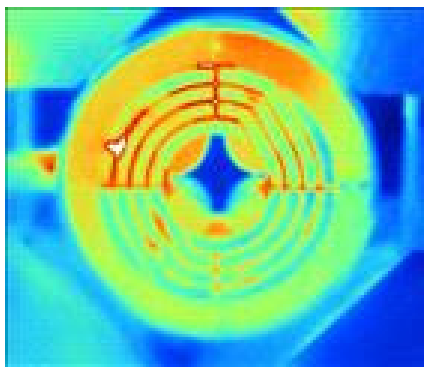


Figure 7: The distribution of temperature on magnet coil surface.

Test result of 9-hours is given in Fig. 8, temperature rise of magnet coil is 11.9° C, coincides very well with the theoretical value 11.5° C, magnet power on well.

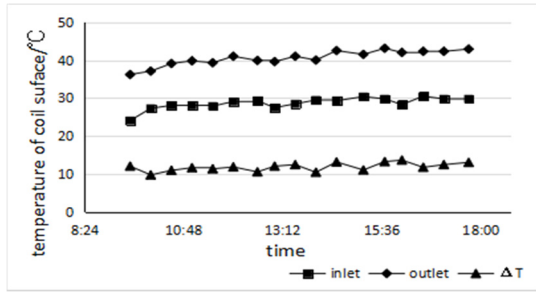


Figure 8: The variation of temperature on magnet coil surface.

CONCLUSION

It took about two and a half years to finish the manufacture of the 161 DTs, and now, the DTL has been running for some time. Although we met some vacuum problems on the working DT, a practical solution is found to overcome it. The DTL is running well and this validate the rightness and feasibility of the DT development technology.

REFERENCES

[1] S. Wang, S.X, Fang, S.N. Fu, *et al.,* "Introduction to the overall physics design of CSNS accelerators" [J]. Chinese Physics C, 2009, 33 (Supp2): 1-3.

[2] J. Wei, S X, Fang, J.Y. Tang, *et al.* "China Spallation Neutron Source: An overview of application prospects" [J]. Chinese Physics C, 2009, 33(11): 1033-1042.

[3] J.X. Zhou, W. Kang, B.G. Yin, *et al.* "The development of magnetic field measurement system for drift-tube linac quadrupole" [J]. Nuclear Instruments and Methods in Physics Research, 2015, 786(A): 142-146.

[4] J. Peng,"Physical design and study of CSNS drift tube linear accelerator" [D]. Beijing: Graduate University of Chinese Academy of Sciences, 2008.

Content from this work may be used under the terms of the CC BY 3.0 licence (© 2018). Any distribution of this work must maintain attribution to the author(s), title of the work, publisher, and DOI.

ISBN: 978-3-95450-194-6 ISSN: 2226-0366 doi:10.18429/JACoW-LINAC2018-THPO029

QUALITY FACTOR AND POWER LOSS OF THE CSNS DTL*

P.H Qu†, H.C Liu, A.H Li, M.X Fan, B. Li , J. Peng, Y. Wang, X.L Wu, Q. Chen, K.Y Gong Institute of High Energy Physics, Chinese Academy of Science, Beijing, China, Dongguan Neutron Science Center, Dongguan, China

Abstract

An Alvarez-type Drift tube linac (DTL) was utilized to accelerate the H^- ion beam of up to 15mA peak current from 3 to 80MeV of China Spallation neutron source (CSNS). For ease of manufacturing and measurement, the CSNS DTL was divided into four independent cavities. The Q factor of four cavities were given, including the measurement results of low-power [1] and high-power [2], and several reasons for the low Q factor of the cavity in the measurement process were analysed. During the operation of the DTL, the frequent alarm of the water flow switch causes the power of the cavity to fall to 0. Estimate the power loss of each component, under the circumstances of ensuring adequate water flow, reduce the alarm threshold of the water flow switch of some components to improve the stability of the system.

INTRODUCTION

Injectors for CSNS include a 50KeV H- ion, a LEBT, a 3MeV Radio Frequency Quadrupole (RFQ), a MEBT and an 80MeV Drift Tube Linac (DTL) as shown in Fig. 1. The Q factor is an important parameter in the DTL cavity design specifications. The Q factor of the hollow cavity reaches more than 89% of the theoretical value, and the cavity copper plating process meets the high-frequency requirement. The hollow cavity does not include stems, drift tubes (DTs), post couplers (PCs) and slug tuners. Each DTL cavity was powered by a 3MW klystron, the Q factor of total cavity which includes stems, DTs, PCs and slug tuners reached more than 75% of the theoretical value, the power loss of each cavity is within the working range of the klystron. In the course of cavity running, the water flow switch warning question becomes prominent day by day. Through two methods of experimental measurement and CST software simulation [3] to estimate the power loss of each component, especially the PCs and slug tuners. Optimized water cooling system, reducing the system failure rate.

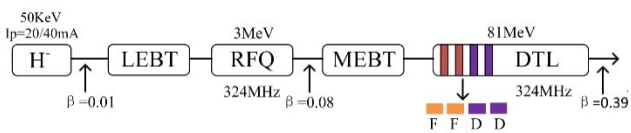


Figure: 1: CSNS Linac injectors.

* Work supported by National Natural Science Foundation of China (11105166), and Youth Innovation Promotion Association of CAS (2015011).
† Email: quph@ihep.ac.cn

Q FACTOR OF HOLLOW CAVITY

The length of first tank DTL1 is 8.5 meters, a total of three units. The first unit DTL1-1 has a length of about 2.8 meters. The unloaded Q factor which called Q_0 of the DTL1-1 hollow cavity which shown in Fig. 2(a) was tested. Hollow cavity of DTL1-1 has no stems, DTs, PCs and slug tuners. The openings of the cavity were sealed with copper plugs as shown in Fig. 2(b) and (c).

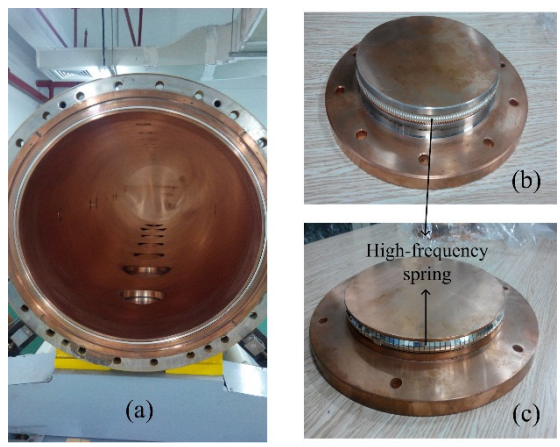


Figure 2: Hollow cavity of DTL1-1 and copper plugs.

Table 1 shows the results of Q_0 of DTL1-1. The final Q_0 was taken as the average of 89.88% of the theoretical value. It shows that the inner wall copper plating process meets the high-frequency requirements. The loaded Q factor Q_L was measured by a vector network analyser using the two-port network method [1]. The Q_0 can be calculated by Q_L, and the formula is shown in Eq. (1).

$$Q_0 = Q_L \cdot (1+\beta_1+\beta_2) = Q_L \cdot \left(1+ {}^{1}\!/\!_{VSR_1} + {}^{1}\!/\!_{VSR_2}\right) \quad (1)$$

The factors that influence the measurement result of Q_0 are as follows. The better the high-frequency spring (shown in Fig. 2) seal of copper plugs, the larger the Q_0 measurement. Partial copper plug diameter is too large to install, milling part of the copper layer, bare iron exposed as shown in Fig. 2 (b), due to a part of the material from copper to iron, which makes a little drop in the measured value of Q_0. During the measurement, the standing wave ratio is reduced, which makes the received signal relatively strong. The three results in table 1 are not much different and the measured Q_0 is more accurate.

Content from this work may be used under the terms of the CC BY 3.0 licence (© 2018). Any distribution of this work must maintain attribution to the author(s), title of the work, publisher, and DOI.

ISBN: 978-3-95450-194-6 ISSN: 2226-0366 doi:10.18429/JACoW-LINAC2018-THPO029

Content from this work may be used under the terms of the CC BY 3.0 licence (© 2018). Any distribution of this work must maintain attribution to the author(s), title of the work, publisher, and DOI.

Table 1: Q Factor of DTL1-1 Hollow Cavity

$VSWR_1$	$VSWR_2$	Q_L	Q_0	Q_0 (design)	Q_0/Q_0 (design)
9.48	13.57	59400	70043	78032	89.77%
9.37	18.68	60500	70195	78032	89.96%
20.28	18.04	63500	70151	78032	89.91%

Q FACTOR OF FOUR DTL CAVITY

The CSNS DTL contains four cavities and the respective Q_0 of them at RF low-power measurements was obtained (see Fig. 3). The specific results are shown in table 2. The results show that the Q_0 are all above 75% of the design value, which ensures that the 3MW klystron can meet the power requirements. The input cavity power of DTL1~4 during operation was 1.53MW, 1.5MW, 1.42MW and 1.35MW respectively.

Table 2: Q_0 of DTL in RF Low-power Measurements

	DTL1	DTL2	DTL3	DTL4
Q_0	44935	46016	45074	49512
Q_0(design)	53828	58313	58894	58936
Q_0/Q_0(design)	83.4%	78.9%	76.5%	84%



Figure 3: RF low-power measurement of DTL cavity.

The Q factor of the four cavity were also tested using the ring-down method [2] when they were loaded with high power. The calculation method of Q_L is shown in Eq. (2) and (3). In formula (3), A(t) represents the amplitude of the electric field at time t in the attenuation curve of the electric field tail.

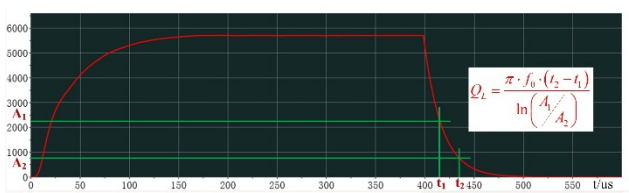


Figure 4: Selecting two A(t) values for calculating Q_L.

As shown in Fig. (4), the Q_L can be calculated by selecting two A(t) values on the attenuation curve tail of the electric field. The ridge waveguides of the DTL cavity are all over-coupled and the calculation method of Q_0 is shown in Eq. (4).

$$Q_L = \pi \cdot f_0 \cdot T \tag{2}$$

$$A(t) = A_0 \cdot \exp(-t/T) \tag{3}$$

$$Q_0 = Q_L \cdot (1+\beta) = Q_L \cdot (1+VSWR) \tag{4}$$

The Q_0 of the four cavity at high-power is shown in Table 3. There are some errors in the high-power measurements in Table 3 and the low-power measurements in Table 2. DTL is such a large cavity that it is indeed difficult to accurately measure its Q_0. However, the measurement results of both methods show that the ratio of the Q_0 of the cavity to the design value exceeds 75%, indicating that the manufacturing process of the cavity meets the engineering requirements.

Table 3: Q_0 of DTL in RF High-power Measurements

	DTL1	DTL2	DTL3	DTL4
VSWR	1.58	1.38	1.49	1.57
Q_L	17888	18756	20105	16725
Q_0	46151	44639	50063	42985
Q_0(design)	53828	58313	58894	58936
Q_0/Q_0(design)	85.7%	76.5%	85%	72.9%

ESTIMATE THE POWER LOSS OF EACH PART OF THE CAVITY AND OPTIMIZE THE WATER COOLING SYSTEM

The drift tube coils of the CSNS DTL and the main heating components such as the drift tube housing, the cavity and the end plate, the slug tuners, the movable tuners, the PCs, the ceramic window, and the ridge waveguide all need to be cooled by circulating water. In order to ensure the normal operation of DTL, the structural layout, mechanical design, manufacture, and stable and reliable operation of its water-cooled distribution system are all very important. Cavity and other components distribution system water supply temperature adjustable 21-28℃, water temperature control accuracy ±0.1℃。 In order to monitor the water flow of each component, in addition to the molecular pump fence and the ion pump fence, all components are equipped with a flow switch.

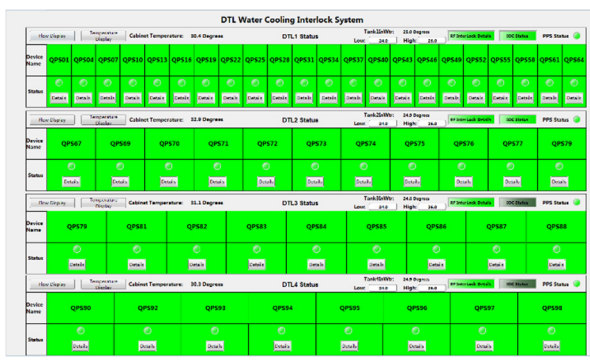


Figure 5: DTL water cooling interlock system.

Each water flow switch is linked to high frequency system. Below the alarm threshold, the power in the cavity

ISBN: 978-3-95450-194-6 ISSN: 2226-0366 doi:10.18429/JACoW-LINAC2018-THPO029

will be reduced to zero. Fig. 5 displays the DTL water cooling interlock system. Because the flow switch alarm threshold is relatively strict, the frequency of the fault is high during the operation of the cavity. The power loss of each part of the cavity was estimated, the temperature rise before and after the drift tube with power was counted, and the alarm threshold of most water flow switches was reduced. The power loss of each part of the cavity was estimated by superfish [4] and the result was displayed in Table 4. There are a few things to note here. First, the bucket does not include the front plate and end plate. Second, the front plate and end plate includes the half DT. Finally, others include post couplers and slug tuners.

Table 4: Power Loss of Each Part of Cavity by Superfish

Power Loss/KW	DTL1	DTL2	DTL3	DTL4
Front plate	13.2	16.0	17.8	19.9
End plate	17.2	23.5	25.7	27.8
Cavity bucket	539.4	567.7	570.7	574.4
Drift tube	349.5	358.6	372.6	391.7
stem	175.4	118.1	101.2	92.8
others	250.4	235.8	234.5	237.6
Total	1345.1	1319.7	1322.6	1344.2

Since superfish cannot estimate the power loss of the post couplers and slug tuners respectively, the CST software simulation and the low-power test data can be used to estimate their values.

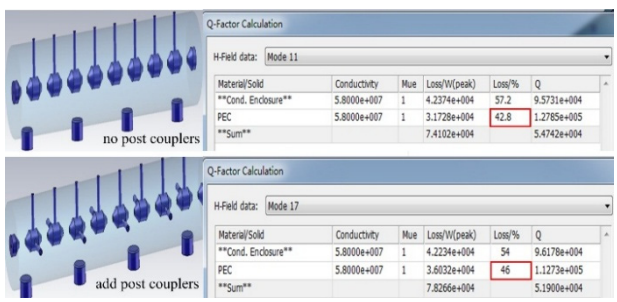


Figure 6: The power loss ratio before and after the PCs were added in the CST.

Figure 6 displays the power loss ratio before and after the PCs were added in the CST. The ratio of Q_0 to its theoretical value before and after adding PCs in low-power test data was shown in Table 5. The simulation and measurement power loss of slug tuners and PCs was shown in Table 6. The measurement value is closer to the actual situation. According to the estimated power loss of each component, some flow switch alarm thresholds are lowered. The specific value are shown in Table 7. Since the drift tube and the internal magnet coil are in a strong electric field region, the alarm threshold does not decrease. After optimizing the water cooling system, the alarm frequency of the water system is greatly reduced when the water supply is stable, and only three alarms occur in about six months.

Table 5: The Ratio of Q_0 to its Theoretical Value before and After Adding PCs in Low-power Test Data

Cavity state (DTL4)	f/MHz	Q_0/Q_0(design)
All slug tuner length is 50mm, no PCs	322.924	79.63%
Average length of slug tuner is 74.4mm, add PCs	323.902	72.03%

Table 6: Power Loss of Slug Tuners and PCs of Simulation and Measurement

Power Loss/KW	simulation	measurement
Slug tuners	191.7	157.9
Post couplers	42	79.6

Table 7: The Water Demand of Each Component and the Switch Alarm Threshold

	Water requirement(L/min)	Flow switch initial alarm threshold(L/min)	Flow switch optimized alarm threshold(L/min)
Drift tube coil	1	0.8	0.8
Cavity bucket	30	25	10(↓)
Front/end plate	6	5	3(↓)
Pcs	2.3	1.5	1(↓)
Ion pump fence	5	/	/
Molecular pump fence	5	/	/
Slug tuners	5	5	2(↓)
Ceramic window	10	10	10
Auto tuners	5	4	4
Ridge waveguide	5	5	5
Drift tube	5	3.5	3.5

CONCLUSIONS

The unloaded Q factor of the DTL1-1 hollow cavity was measured and the final result of Q_0 was taken as 89.88% to its theoretical value. The results of Q_0 of four DTL cavity were given out and the measurement results show that they were all above 75% to its design value. The cavity inner wall copper plating process meets the high-frequency requirement. The power loss of each part of the cavity was estimated and the water cooling system was optimized and the cavity operation failure rate was reduced.

REFERENCES

[1] Z.Y Shen, "Microwave technology," Beijing, National Defense Industry Press, 1980, pp.228.

[2] C.Zhu and Dr. Todd Hubing, "Q-Factor and resonance in the time and frequency domain", Technical Report.

[3] P.H Qu, "3D model analysis of cavity for CSNS DTL", in *Proc. IPAC'17*, Copenhagen, Denmark, May 2017, pp. 4236-4238, doi:10.18429/JACoW-IPAC2017-THPIK061

[4] J Peng, "Physics design and study of the CSNS drift tube linac," Beijing: Institute of high energy physics, Chinese Academy of Sciences, 2008.

Content from this work may be used under the terms of the CC BY 3.0 licence (© 2018). Any distribution of this work must maintain attribution to the author(s), title of the work, publisher, and DOI.

ISBN: 978-3-95450-194-6 ISSN: 2226-0366 doi:10.18429/JACoW-LINAC2018-THPO030

OPERATION EXPERIENCE OF THE CSNS DTL*

Huachang Liu[1,2,3†], Jun Peng[1,2,3], Keyun Gong[1,2],Ahong Li[1,2,3], Bo Li[1,2], Qiang Chen[1,2], Xiaolei Wu[1,2] ,Mengxu Fan[1,2], Yun Wang[1,2] , Peihua Qu[1,2], Shinian Fu[1,2,3]

[1] Institute of High Energy Physics, Chinese Academy of Sciences (CAS), Beijing, China
[2] Dongguan Neutron Science Center, Dongguan 523803, China
[3] University of Chinese Academy of Sciences, Beijing, 100049, China

Abstract

The China Spallation Neutron Source (CSNS) Drift tube linac (DTL) accelerates H- beam from 3 to 80MeV with 4 independent tanks. The 80MeV beam acceleration was achieved in January 2018. The linac is a key to the reliability of the whole CSNS facility since all the beams stop when these upstream facilities fail. Many efforts have been made for DTL reliable operation. This paper presents the operation experience learned in DTL commissioning.

INTRODUCTION

The China Spallation Neutron Source (CSNS) is an accelerator-based multidisciplinary user facility constructed in Dongguan, Guangdong, China [1]. The CSNS complex consists of an H- linear accelerator, a rapid cycling synchrotron (RCS) accelerating the beam to 1.6 GeV, a solid-tungsten target station, and instruments for spallation neutron applications. Construction and commissioning has been completed so far. The facility operates at 25 Hz repetition rate with an initial beam power of approximately 20 kW on target. It can be foreseen that the beam power on target will reach 100kW within 2~3 years. The facility will provide scientists with a world-leading platform for studies in fields such as materials science and technology, life sciences, and new energy, etc.

The 324MHz drift tube linac (DTL) is the main part of CSNS accelerator linac complex (Fig.1). It can provide 15mA peak current beam with energy gain from 3 to 80MeV [2]. It consists of four independent tanks with ~9m in length. Each tank is divided into three short unit sections for ease of fabrication and assembly. A hollow coil based electromagnet is accommodated in each drift tube for its compact structure. The main design parameters of DTL are listed in table 1.

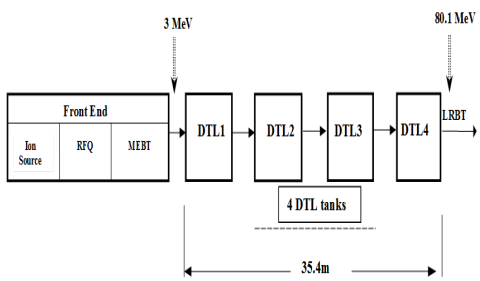


Figure 1: Layout of the CSNS LINAC.

The commissioning of the first DTL tank started in January 2016. The first 20MeV@18mA beam was achieved within ten days. Based on the experience of DTL1 commissioning, the three successive DTL tanks were progressively installed and commissioned. Final 80 MeV acceleration was successfully obtained in January 2018. During the commissioning and operation, the performance of DTL gradually improved owing to a series of prompt action to the troubles.

Table 1: Major Parameters of CSNS DTL

Tank number	1	2	3	4	total
Output energy (MeV)	21.67	41.41	61.07	80.1	80.1
Length (m)	8.51	8.56	8.78	8.8	
Number of cells	64	37	30	26	157
RF driving power (MW)	1.35	1.32	1.32	1.34	5.33
Total RF power (MW)@30mA	1.91	1.92	1.92	1.93	7.68
Accelerating field (MV/m)	2.86	2.96	2.96	3.0	
Synchronous phase (degree)	-35 to -25	-25	-25	-25	
RF frequency(MHz)	324	324	324	324	324
Max. repetition rate(Hz)	25	25	25	25	25
Peak surface field(Kilpatrick)	/	/	/	/	<1.3

BEAM COMMISSIONING

The DTL consists of four accelerating tanks with final output energy 80MeV. The transverse focusing was arranged in a FFDD lattice utilizing electric-magnet quadrupoles. Because no drift tube is empty, diagnostics have to be imbedded between tanks. After each tank, a FCT and a CT were installed to monitor beam phase and current. Between DTL 3 and DTL 4, a Beam Position Monitor (BPM) was added for monitoring beam orbit.

For DTL tanks, it is essential to find the correct tank RF field amplitude and phase to minimize energy spread and mismatch, which are highly required by the following

*Work supported by Youth Innovation Promotion Association of CAS (2015011)
† email address:liuhc@ihep.ac.cn

Content from this work may be used under the terms of the CC BY 3.0 licence (© 2018). Any distribution of this work must maintain attribution to the author(s), title of the work, publisher, and DOI.

ISBN: 978-3-95450-194-6 ISSN: 2226-0366 doi:10.18429/JACoW-LINAC2018-THPO030

RCS. "Phase scan signature matching" method was adopted for determining the RF set points of DTL tanks [3], Time of flight measurement was also performed (Fig.2). For each tank, three FCTs were used to form two short pairs and a long pair. The two short pairs were used to determine the number of integer periods and the long pair was used to calculate beam energy. The beam energy measured by TOF method are summarized in Table 2. The deviation of measured beam energy from the design value is less than 0.5%.

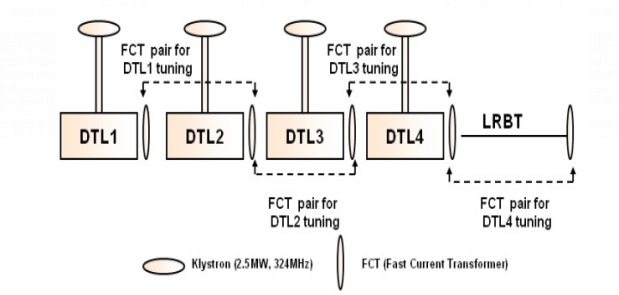


Figure 2: Phase Scan Signature Matching Technique using FCT pairs

Table2: Beam Energy From Time-of-flight Measurements

	Design [MeV]	Measured[MeV]	Deviation (%)
DTL1	21.67	21.73	+0.28
DTL2	41.41	41.54	+0.31
DTL3	61.07	61.36	+0.47
DTL4	80.09	80.34	+0.3

WATER LEAKAGE IN DRIFT TUBE

Each DTL tank is equipped with one 1000Litre/s turbo-molecular pump, and 7~8 1000Litre/s ion pumps, the pressure in operation is in an order of 10^{-6} Pa. In May 2017, the vacuum in DTL1 became worse, and the trip rates of DTL1 increased in the meantime. The beam commissioning was not interrupted by this problem because the speed of vacuum deterioration was relatively slow at the beginning. After nearly one month operation, the poor performance of DTL1 forced us to stop the beam commissioning. External vacuum leak was not found by using a helium leak detector. But the RGA (Residual Gas Analyser) shows an abnormal spectrum (Fig.3) which indicates a great suspicion of water leakage in the drift tube (DT). In order to find the specific location of the leakage area, we shut down the water cooling of DT, heating up the electro-magnetic quadrupole (EMQ) one by one and check the vacuum pressure change in the cavity. An intensive vacuum fluctuation was found while heating the 13th EMQ. This problem was traced to bad e-beam welds.

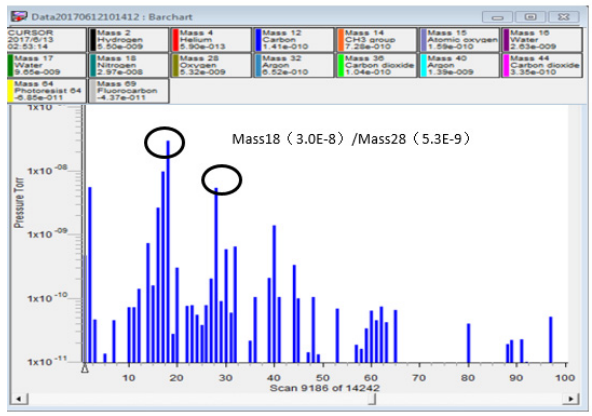


Figure 3: Residual gas spectrum in DTL1.

A spare DT with an EMQ inside was manufactured, new leak testing method was introduced to confirm the electron beam welding (EBW) quality. The water channels are pressurized with He gas while drift tube body is in vacuum chamber. However, to replace a DT inside DTL tank is a very complicated and time consuming engineering subject. The top priority at that time is to restart the beam commissioning as soon as possible, instead we modify the DTL focusing lattice and EMQ's gradient to compensate the malfunctioning DTQ-13.Fig.4 shows the beam envelope without Q13 before and after optimization. The transmission is almost 100% according to the simulation results [4].

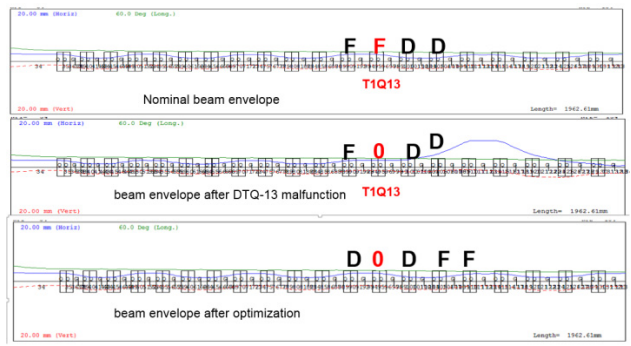


Figure 4: Beam envelope simulation results.

VSWR PROTECTION

The VSWR interlock protection is incorporated into the MPS system in order to protect the high-power components in case of an excessive reflected power. The RF power must be shut off within 2~3 μs if the reflected power is higher than the pre-set threshold. During the initial operation, all RF cavity run stable, no sign of electron activities was observed. The trip rate of DTL2 unexpectedly increased by frequent VSWR protection since January 5th 2018. Experiments have been done to figure out the reason of cavity degradation. It is found based on the machine research that the VSWR interlock protection has behaved erratically, with a response which is not correlated at all with vacuum pressure in the cavity. This false alarm is mainly due to the poor contact of the power plug to the LLRF control circuit board. After replacing the related power plug

Content from this work may be used under the terms of the CC BY 3.0 licence (© 2018). Any distribution of this work must maintain attribution to the author(s), title of the work, publisher, and DOI.

ISBN: 978-3-95450-194-6 ISSN: 2226-0366 doi:10.18429/JACoW-LINAC2018-THPO030

Content from this work may be used under the terms of the CC BY 3.0 licence (© 2018). Any distribution of this work must maintain attribution to the author(s), title of the work, publisher, and DOI.

(Fig.5), the VSWR protection issue was successfully solved.

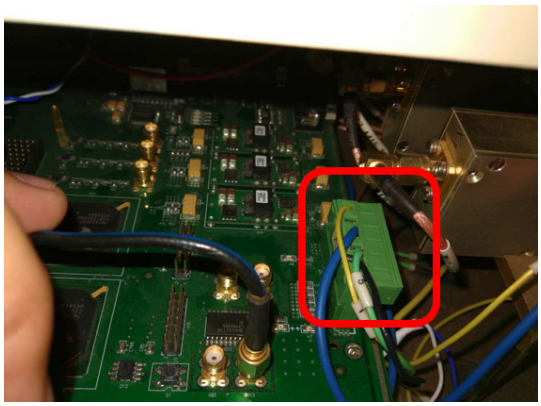


Figure 5: DTL LLRF controller.

COOLING COMPONENTS FAILURE

Under normal operation (beam on), approximately 80% of the RF power is dissipated in the DTL copper structural components. The water cooling system is responsible for removing the undesired RF waste heat. All the RF components include tanks, drift tubes, fixed tuners, movable tuners, post couplers, EMQs, end-plates need sufficient water cooling. In the return of each cooling circuit just prior to the return manifold is a float type flow switch (Fig.6) to detect insufficient flow. The flow switches are monitored by the control system, which annunciates all flow alarms that can provide an MPS signal to shut down the power source and the beam in case of any malfunctions. Flow meters are used on sub manifold return lines. These flow meters will allow operators to detect significant flow blockages.



Figure 6: Flow switch placing on the Drift tube cooling channels.

During the operation, nearly half of flow meters were blocked by the residual scrap in the cooling channel ascribe to the nature of turbine flow meter (Fig.7). These flow meters have advantages of high accuracy, fast response. On the other hand, they are sensitive to the water impurity, and the rotor may easy to get stuck. The water flow in the entire sub manifold line reduced significantly and the related flow switches would trigger the MPS protection. In the maintenance, all the flow meters in the return lines are replaced by straight pipes to improve the reliability of cooling distribution system (Fig.8). All other flow meters in the intake lines are still remained to detect the water flow of each sub manifold.

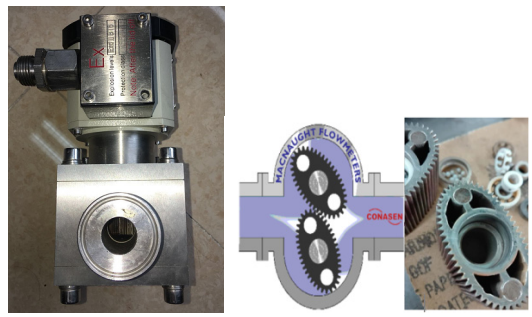


Figure 7: Schematic of flow meter.

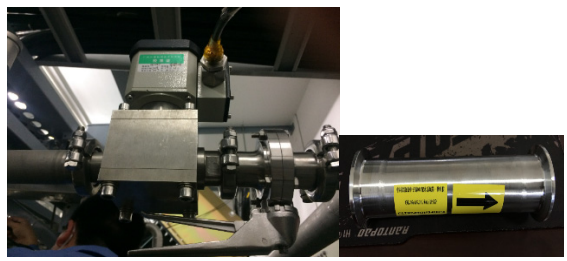


Figure 8: Flow meter and straight pipe.

CONCLUSION

Four DTL tanks were constructed for CSNS facility. The success of DTL beam commissioning verifies the design and manufacturing process. We have experienced many troubles, and all these troubles have been solved. The DTL accelerator shows a stable performance at present, a lot of experience and operation data were learned. We will continue our effort to further increase the beam availability of accelerator facility and to upgrade the system.

REFERENCES

[1] Jie Wei, Hesheng Chen, Yanwei Chen, *et al.*, China Spallation Neutron Source: Design, R&D, and outlook, *Nuclear Instruments and Methods in Physics Research* A 600 (2013) 10-13

[2] X. Yin, J. Peng, K. Gong, H. Liu, Y. Xiao, Z. Sun, A. Li, S. Fu, "Design of the CSNS DTL", in *Proc. LINAC'10*, Tsukuba, Japan, Sep. 2010, paper TUP063, pp. 554-556.

[3] J. Peng, Y.W An, M.Y Huang, *et al.*, "Beam commissioning results for the CSNS MEBT and DTL-1", in *Proc. HB'16*, Malmö, Sweden, Jul. 2016, pp. 329-332, doi:10.18429/JACoW-HB2016-TUPM2Y01D

[4] J. Peng, H.C Liu, *et.al.*, "Beam dynamics studies for the CSNS Linac due to a quadrupole fault", presented at LINAC'18, Beijing China, Sept. 2018, paper TUPO114, this conference.

ISBN: 978-3-95450-194-6 ISSN: 2226-0366 doi:10.18429/JACoW-LINAC2018-THPO031

RF CONDITIONING AND BEAM COMMISSIONING STATUS OF CSNS DTL

Y. Wang[1,†], H. Liu[1], B. Li[1], M. Fan[1], A. Li[1], P. Qu[1], K. Gong[1], X. Wu[1], Q. Chen[1], J.Peng[1]
Institute of High Energy Physics, Chinese Academy of Sciences, 100049 Beijing, China
[1]also at Dongguan Institute of Neutron Science, 523803 Dongguan, China

Abstract

The high power RF conditioning of CSNS DTL was finished in April 2017 with peak input power 1.6 MW, 650 us pulse width, 25 Hz repetition frequency. With careful tuning of RF amplitude and phase, beam was accelerated to 80 MeV successfully with maximum peak beam current 12 mA and about 98% transmission efficiency. DTL operate stably at full power level with several trips per day without beam interruption after six months commissioning. The whole RF conditioning process was presented and some details of beam commissioning were described in this paper.

INTRODUCTION

The CSNS DTL is a Alvarez-type Linac, consists of four cavities, accelerate H^- particle from 3 to 80 MeV [1]. Each cavity is powered by individual klystron with 324 MHz operation resonant frequency. The Lattice structure made up of electromagnets inside every drift tube provide transverse focus force for the beam [2]. The main parameters of the CSNS DTL are listed in Table 1.

Table 1: Main Parameters of the CSNS DTL

Tank number	1	2	3	4	total
Output energy (MeV)	21.67	41.41	61.07	80.09	80.09
Number of cell	64	37	30	26	157
RF driving power (MW)	1.35	1.32	1.32	1.34	5.33
Total RF power (MW) (I=30 mA)	1.91	1.92	1.92	1.93	7.68
Accelerating field (MV/m)	2.86	2.96	2.96	3.0	
Synchronous phase (degree)	-35 to -25	-25	-25	-25	

RF CONDITIONONGING

The high power conditioning started in December 2015, and finished in February 2017. Due to time limitation, the couplers and ceramic windows of all four cavities were not previously conditioned. The actual effective aging time is about 106 days, the DTL-1 cavity took about 61days due to high frequently arcing and poor vacuum condition. After DTL-1 conditioning process, the first beam had been successfully accelerated to design energy 21.6 MeV by deliberately adjusting of input power amplitude and phase. The rest three cavities took about 45 days finishing conditioning process with 700 us, 25 Hz, peak input power 1.6 MW. The RF conditioning parameters are presented as Table 2.

Table 2: RF Conditioning Parameters

Operation Frequency	324 MHz
Repeation Frequency	25 Hz
Power Width	650 us
Input Power	1.5 MW

Figure 1 shows the whole DTL structure. Before conditioning, the interlock protection systems, include temperature sensors mounted on outside wall, vacuum system read from Cold Cathode Gauges, water cooling system which monitors cooling water flow and VSWR protection system used to shut down RF power when severe arc occurs, are rechecked to ensure cavity operation normally.



Figure 1: The CSNS DTL in tunnel.

The high power conditioning process is illustrated as following,

Firstly, 5~10 kW(650 us, 25 Hz) input power is fed in cavity to see whether cavity operation correctly. The ceramic window is sensitive with the increase of input power, which is almost fully reflected back during initial conditioning process. Half of hour later, power is smoothly transferred into cavity, clear signal can be seen in the oscilloscope captured by pickup.

Secondly, as power comes into cavity, the vacuum fluctuation is big due to outgas from internal wall. Input power was increased gradually according vacuum condition changing, which should rebalance to a stable situation after new high power level. If vacuum condition continues to deteriorate because of arcing inside cavity, then input power amplitude should be reduced until vacuum condition getting stable again. Generally, 5~10 kW increasing power per step is reasonable below 1 MW. For keeping high conditioning efficiency, the klystron fre-

* Work supported by Youth Innovation Promotion Association of CAS (2015011)
† wangyun@ihep.ac.cn

Content from this work may be used under the terms of the CC BY 3.0 licence (© 2018). Any distribution of this work must maintain attribution to the author(s), title of the work, publisher, and DOI.

ISBN: 978-3-95450-194-6 ISSN: 2226-0366 doi:10.18429/JACoW-LINAC2018-THPO031

Content from this work may be used under the terms of the CC BY 3.0 licence (© 2018). Any distribution of this work must maintain attribution to the author(s), title of the work, publisher, and DOI.

quency is shifted manually to keep pace with resonant frequency of cavity which drifted away due to ohmic loss by input power.

Thirdly, once input power reached 1 MW, and close to design power level, small power increasing step should be taken, any big arc will do a bad damage to the cavity. Real-time vacuum condition of the cavities should be monitored, interlock systems should be enabled as well. In our case, the VSWR protection threshold is set 20 in one second due to 25 Hz conditioning frequency to protect cavity from arcs, vacuum warning threshold is 5e-5Pa and protection threshold is 1e-4Pa which would trigger interlock system to cut down klystron power. RF power is increased every half hour if no arc was observed. Arcs took place frequently at some power level for CSNS DTL, especially close to 1.5 MW(design value), so we reduce the arc power level a little and make the cavity stay longer at that level until cavity state becoming stable.

During high power level conditioning stage, once a big arc occurred, the cavity state becoming unstable at some power level which is already aged. The cavity should be reconditioned at arcing power level. Sometimes arc took place frequently at high power level close to 1.5 MW, the VSWR protection system frequently cut down input power leading to low conditioning efficiency even after long time aging below that power level. We tried to disable VSWR protection system, and observed cavity vacuum state. As long as cavity vacuum pressure did not exceed 1e-4Pa, then cavity is safe. We believe arcs can eliminate some flaw points inside of cavity.

During DTL-1 conditioning process, several drift tubes were found vacuum leakage, we use Agilent Torr Seal product to block the leak points. Then we repeat the conditioning process for DTL-1. The conditioning process of DTL-2~DTL-4 went smoothly because of better vacuum condition(about 3e-6Pa~1e-5Pa), and the vacuum pressure keep at 3e-6Pa~8e-6Pa while operation at design power level.

The whole conditioning history of CSNS DTL is showed in Fig. 2.

BEAM COMMISSIONING

First beam acceleration had been done after DTL-1finishing conditioning. The H^- ion beam is successfully accelerated to 21.6 MeV measured by two FCT located at temporary beam test line. The transmission was almost 100%, and matches the beam dynamics result very well. Then, after all cavities finishing conditioning, the power amplitude and synchronous phase scan was performed successively cavity by cavity. At last, H^- ion beam was accelerated to 80.1 MeV up to 12 mA with 99% transmission efficiency (Fig. 3), which is also verified the simulation result very well.

In the initial operation, the trip rate of the CSNS DTL is several trips per hour. After six month operation, the operation availability of DTL was improved dramatically. The trip rate of DTL-1 is about 1 trip per hour, and several trips for rest three cavities per day (Fig. 4).

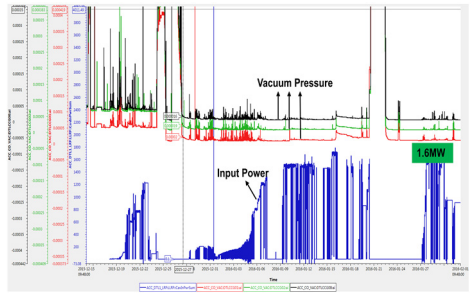


Figure 2a: DTL-1 Conditioning History.

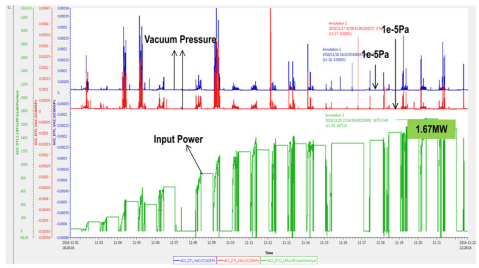


Figure 2b: DTL-2 Conditioning History.

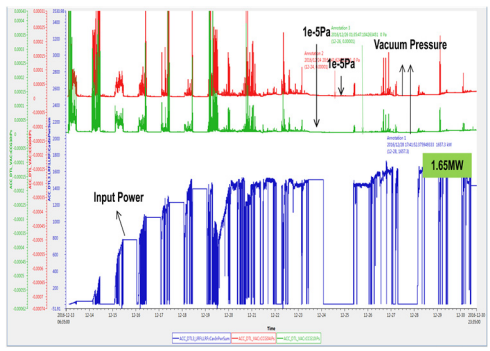


Figure 2c: DTL-3 Conditioning History.

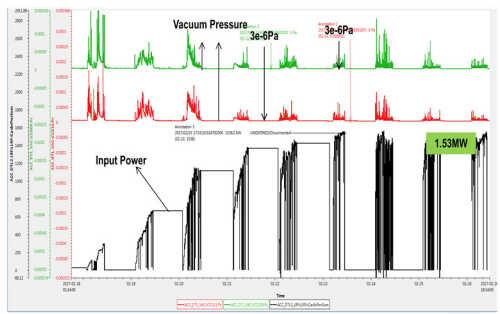


Figure 2d: DTL-4 Conditioning History.



Figure 3: Beam parameters at CT detector.

ISBN: 978-3-95450-194-6 ISSN: 2226-0366 doi:10.18429/JACoW-LINAC2018-THPO031

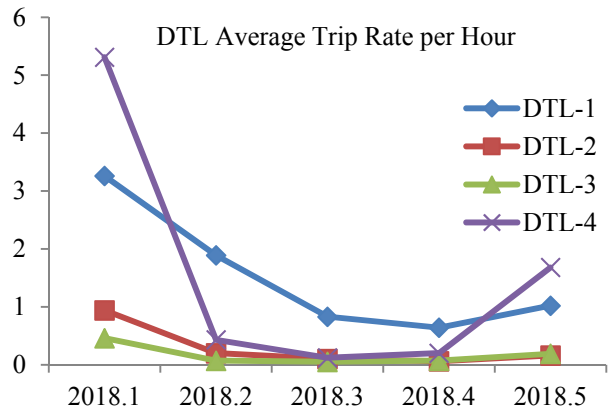


Figure 4: The average trip rate of the CSNS DTL in daily operation (in 5 months).

CONCLUSION

In February 2017, the CSNS DTL finished conditioning (700 us width, 25 repetition frequency, 1.6 MW input power). The scan of power amplitude and synchronous phase of 4 cavities was carried out deliberately. Finally, beam was accelerated to design value (80.1 MeV) with 99% efficiency.

REFERENCES

[1] H. C. Liu, J. Peng, K. Y. Gong, *et al*., DTL Construction Status of China Spallation Neutron Source. Atomic Energy Science and Technology, Vol. 49, Suppl. pp. 556-559, 2015.

[2] X. Yin *et al*., "Design of the CSNS DTL", in *Proc. LINAC'10*, Tsukuba, Japan, Sep. 2010, paper TUP057, pp. 554-566.

Content from this work may be used under the terms of the CC BY 3.0 licence (© 2018). Any distribution of this work must maintain attribution to the author(s), title of the work, publisher, and DOI.

ISBN: 978-3-95450-194-6 ISSN: 2226-0366 doi:10.18429/JACoW-LINAC2018-THPO032

CSNS LINAC BEAM COMMISSIONING TOOLS AND EXPERIENCE

Y. Li, J. Peng, Z.P. Li, S. Wang DINS/IHEP, Dongguan, 523803, China

Abstract

The China Spallation Neutron Source (CSNS) successfully accelerated the H- beam to 80 MeV in January 2018, marking a key progress in the beam commissioning. One of the keys to success is the development and use of software tools. XAL, a Java-based software infrastructure originally developed by SNS was applied for CSNS beam commissioning. We have developed and transplanted many applications based on XAL. Some of the applications for the LINAC are described, and some experiences are shared.

INTRODUCTION

The CSNS [1] accelerator complex consists of an H- injector, a linear accelerator, a RCS ring and associated beam transport lines. The LINAC is 200m with the output energy of 80 MeV in CSNS-I and 250 MeV in CSNS-II. The LINAC commissioning initiated April 2015 and completed in January 2018, was performed in 4 discrete runs with interruption of DTL tank installation and the faults of CPI klystron and DTL vacuum. The beam commissioning for the Front-End to MEBT was form April 2015 to July. The beam transmission of the RFQ is more than 90% and the parameters of MEBT are also accurately measured. DTL-1 beam commissioning was completed in January 2016. The beam transmission is 100% and the peak current is 18 mA, which is higher than the design value of 15 mA. In April 2017, the DTL-2 and DTL-3 beam commissioning was completed, and the beam energy reached 60MeV. In January 2018, the beam commissioning for DTL-4 was finished. The beam energy reached the design value of 80 MeV with the error of $\pm$0.01 MeV, and the overall beam transmission of DTL reached over 97%.

Beam commissioning for LINAC is generally smooth regardless of hardware installation and the major faults. The software tools play an important role for this successful beam commissioning. The XAL [2, 3] and Open XAL were selected as our software development platform. XAL was originally developed and used by SNS for accelerator physics commissioning. It consists of upper applications, physics model of the beam and other toolkit. The XAL was confirmed as our tuning software development platform at the end of 2012, and a large number of physical applications were developed based on the SNS / XAL version between 2014 and 2015 and officially used in April 2015. A lot of useful applications have been developed in subsequent beam commissioning. OPEN XAL is an upgrade of XAL, which is a collaboration among several laboratories, including CSNS. XAL and OPEN-XAL are used simultaneously in our control room now and XAL is used more.

In this paper, the physical applications used in LINAC beam commissioning including longitudinal and transverse were introduced firstly. Then the problems and solutions during the development and use of the software tools will be shown later.

THE APPLICATIONS

Applications for LINAC beam commissioning are mainly divided into three aspects: longitudinal、 transverse and machine management related applications.

RF Phase Scan and Tuning Application

The longitudinal tuning is the first and the most important step for LINAC beam commissioning. To achieve the design value, accurate RF phase and amplitude settings are required. A software application called PASTA [4] in XAL has been written to perform RF phase setting using the signature matching method. The PASTA of CSNS version has been modified in two ways. First, SNS uses Beam Position Monitor (BPM) to measure the phase of the beam, but we use Fast Current Transforms (FCTs), so the corresponding components are replaced. In addition, due to the great difference between CSNS-DTL and SNS-DTL in the relationship between the transition time factor and Beta, we also revised the underlying energy calculation code to make it consistent with the CSNS-DTL acceleration characteristics. Figure 1 is the analysis panel of the PASTA application with the result of DTL-4 tank. It shows the error is very small in the range of 70 degrees and the calculated energy is very close to the design energy. The energy of LINAC is also measured using the Time-of-Flight (TOF) method, which is also close to the design value and the maximum difference is less than 0.5%.

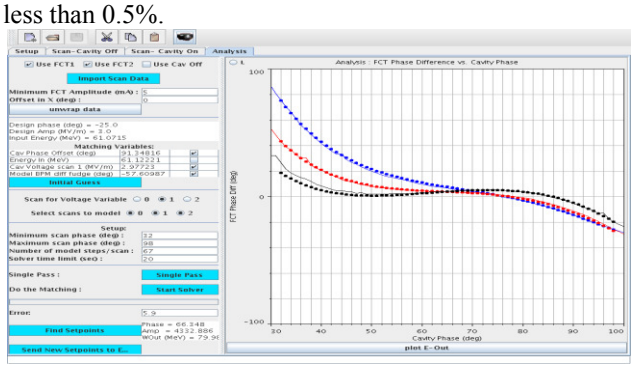


Figure 1: The analysis panel of the PASTA application.

Orbit Correction

Due to the small aperture of the vacuum beam pipe in LINAC, the beam orbit distortion should be small and smooth. The “orbit correction” application in XAL can realize orbit distortion measurement and correction [5]. Based on the response matrix of BPM to corrector (theoretical or measurement response matrix), the Solver calculation module was used to fit the measured orbit and predicted orbit. After repeated iterations, the correspond-

Content from this work may be used under the terms of the CC BY 3.0 licence (© 2018). Any distribution of this work must maintain attribution to the author(s), title of the work, publisher, and DOI.

ISBN: 978-3-95450-194-6 ISSN: 2226-0366 doi:10.18429/JACoW-LINAC2018-THPO032

ing corrector values and orbits are found. In the beginning of beam commissioning, the measured response is usually used firstly.

The figure 2 is the result of orbit correction for LINAC. The left is for MEBT and the orbit can be corrected from ±1.5mm to ±0.5mm. LRBT is on the right and the orbit can be adjusted from ± 13mm to near 1mm. After the corrections, the orbit deviations are suppressed and beam loss is also greatly reduced. The orbit correction for DTL is not carried out due to no corrector and only one BPM inside.

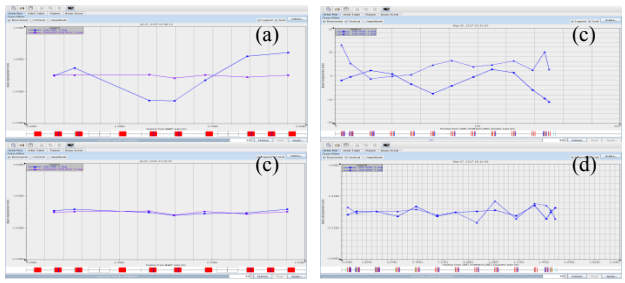


Figure 2: Orbit correction of LINAC (The left is the orbit of MEBT. The right is LRBT).

Emittance and Twiss Parameters Measurements

The emittance of LINAC can be given in two ways. One method is to use the slit-slit scanning to get the beam position and angle distribution in phase space directly. The other is indirect method which measure the transverse beam size with more than three wire scanners and give the emittance, that is, the three-grid method.

Two slit-slit instruments are installed in the middle of the MEBT to measure the horizontal and vertical emittance respectively. The application for processing the original measurement data is developed. Figure 3 is the interface of the application. The beam RMS emittance ε and Twiss α, β parameters were calculated by statistical and Gaussian fitting methods. In addition, the relationship between the threshold value and emittance and Twiss parameters can be given, from which the threshold value can be inferred. Figure 3 shows the MEBT emittance obtained with slit-slit scan.

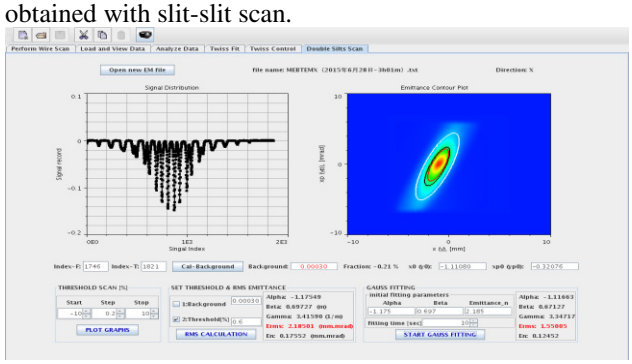


Figure 3: MEBT emittance obtained with slit-slit scan.

The three-grid method can be used to calculate the emittance and Twiss parameters. Four wire scanners were installed in MEBT and 6 were installed in LRBT straight line. There is a "wire analysis" application in the original XAL, which can be used to fit the raw data of wire scanners in various ways. Then the emittance and the Twiss parameters at entrance are given by iteration with the algorithm package of XAL. Figure 4 shows the beam envelope of LRBT before and after matching with 6 wire scanners. The beam envelope oscillation is large before matching, and the beam loss is large too. According to the calculated entrance parameters, we can rematch the beam and make a new lattice. As can be seen from the following figure, after matching, the envelope of the measured beam is close to the design value, the oscillation is small, the beam loss were greatly reduced too.

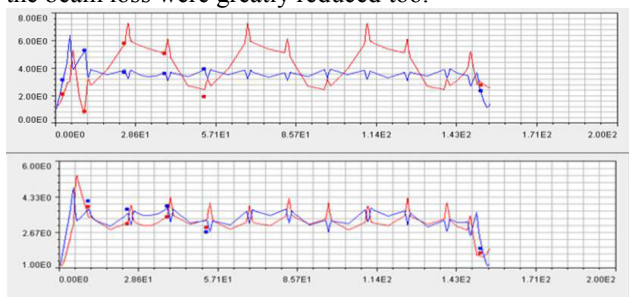


Figure 4: Beam envelope of LRBT before and after matching.

Machine Parameters Management

The energy span for LINAC beam commissioning is large, involving 3 MeV, 20 MeV, 40 MeV, 60 MeV and 80 MeV. The magnets settings are not exactly the same for different energy, especially the magnets for matching function. To master the state of the machine and restore the machine quickly, we need save the magnetic field, cavity parameters, even the beam parameters, timing and other important parameters.

"Model management" and "SCORE" applications can realize the management of machine parameters with a little difference in function. The former application only stores magnetic field and cavity parameters, but it can do lattice calculation and give the Twiss parameters in the form of graphs. Figure 5 is the interface of management application developed by ourselves. This program plays a great role in the early beam commissioning and remote control operation for power supply.

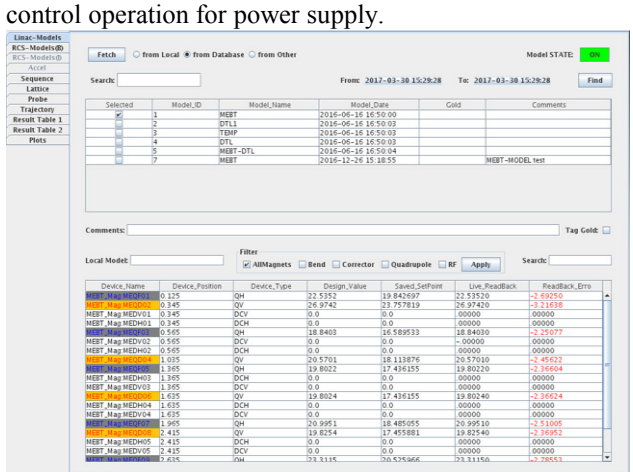


Figure 5: The interface of the Model Management application.

Content from this work may be used under the terms of the CC BY 3.0 licence (© 2018). Any distribution of this work must maintain attribution to the author(s), title of the work, publisher, and DOI.

ISBN: 978-3-95450-194-6 ISSN: 2226-0366 doi:10.18429/JACoW-LINAC2018-THPO032

Content from this work may be used under the terms of the CC BY 3.0 licence (© 2018). Any distribution of this work must maintain attribution to the author(s), title of the work, publisher, and DOI.

The SCORE (Save-Compare and Restore) [5] application was developed by SNS, which really realized machine parameter management. Figure 6 is the interface of SCORE application that stores a large number of parameters to database by PV (Process Variables) key-value pairs which is composed of any two PVs. Usually, we give the set and read back signals, for example, the setting value and the read back value of current of power supply. With the great advance of beam commissioning, more and more important signals are stored in the database. The program can not only record the signal related to the current model, but also make on-line comparison and machine recovery. Each model also provides annotations with 250 words.

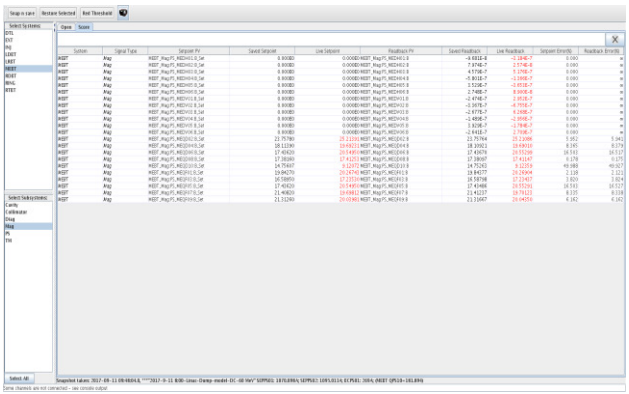


Figure 6: The interface of the SCORE application.

PROBLEMS AND EXPERIENCE

Since the selection of XAL as the CSNS accelerator physical tuning software in 2012, a large number of physical applications have developed and tested on the basis of XAL, which played a key role during beam commissioning. However, there are many problems encountered in the development and use of application programs. Many important applications in the XAL / SNS version contain the SNS specific parameters, some of which are hidden at the bottom, requiring a lot of patience and repetition to adapt to the needs of CSNS. For example, our RF frequency is 324MHZ, and SNS is 402.5MHZ, so this parameter needs to be changed. Other problems happened when transplanting the applications to CSNS. For example, SNS uses Oracle database, and we use the free MySQL database, so SCORE and PV Logger applications can not directly used, which need to modify the relevant interface functions. Some applications were normal with the use of virtual accelerator debugging, but were in trouble in beam commissioning. For example, the "orbit correction" application could not display the track normally at first. It was found that the BPM timestamp was not synchronized. The BPMs in LRBT are distributed in two sub-stations and two different electronic systems were selected, which resulting the BPM timestamp asynchrony. After the synchronization, orbit correction can work normally. So we need test the key applications repeatedly and be familiar with the underlying algorithm and its suitable conditions for direct transplantation applications before the beam commissioning.

CONCLUSION

From April 2015 to January 2018, CSNS completed the beam commissioning for LINAC with energy of 80 MeV. As a physical software tool, XAL plays a key role in the beam commissioning. We have accumulated a lot of experience to learn from during the development and employment of these applications. With the increasing beam power, there are still many physical problems to be studied in LINAC, and more and more convenient applications need to be developed in the next several years.

REFERENCES

[1] CSNS Feasibility Study Report, June, 2009, IHEP.

[2] T. Pelaia, *et al.*, "XAL Status", in *Proc. ICALEPCS'07*, Oak Ridge, TN, USA, Oct. 2007, paper MOPB02, pp. 34-36.

[3] J. Galambos, *et al.*, "XAL Application Programming Framework" in *Proc. ICALEPCS'03*, Gyeongju, Korea, Oct. 2003, paper WE204, pp. 332-33.

[4] J. Galambos, *et al.*, "PASTA – An RF Phase and Amplitude Scan and Tuning Application", *in Proc.* PAC'05, Knoxville, TN, USA, May 2005, paper FPAT016, pp. 1491-1493.

[5] T. Pelaia, *et al.*, "Beam Trajectory Correction for SNS", *in Proc.* PAC'05, Knoxville, TN, USA, May 2005, paper FPAT015, pp. 1425-1427.

ISBN: 978-3-95450-194-6 ISSN: 2226-0366 doi:10.18429/JACoW-LINAC2018-THPO033

THE DEVELOPMENT OF PERMANENT MAGNET QUADRUPOLES FOR XiPAF DTL

B. C. Wang, Z. M. Wang, M. T. Qiu, C. Y. Wei, State Key Laboratory of Intense Pulsed Radiation Simulation and Effect (Northwest Institute of Nuclear Technology), 710024 Xi'an, China
S. X. Zheng[1], Q. Z. Xing[1], Q. K. Guo[1], C. T. Du[1], X. W. Wang[1], Department of Engineering Physics, Tsinghua University, 100084 Beijing, China
[1]also at Key Laboratory of Particle & Radiation Imaging (Tsinghua University), Ministry of Education, 100084 Beijing, China; Laboratory for Advanced Radiation Sources and Application, Tsinghua University, 100084 Beijing, China

Abstract

Permanent magnet quadrupoles (PMQs) are developed for the DTL of Xi'an 200 MeV Proton Application Facility (XiPAF). In this paper, we describe the fabrication and measurements for the Halbach-type PMQs. The main procedure of the PMQ manufacture is presented. And the magnetic measurements of PMQs are carried out with the help of vibrating wire, Hall probe and rotating coil respectively. The results show the PMQs are able to meet the requirements of XiPAF DTL.

INTRODUCTION

The Alvarez-type DTL is being built to accelerate the H- beam from 3 MeV to 7 MeV for Xi'an 200 MeV Proton Application Facility (XiPAF). The permanent magnet quadrupoles (PMQs) are adopted for focusing the beam. The Halbach-type PMQ is developed by our team to meet the requirements obtained by beam dynamics calculations. All the PMQs are fabricated and measured.

The main parameters and requirements of the PMQs are listed in Table 1 and Table 2. The gradient of the PMQ is about 80 ~ 90 T/m. It is worth noting that the integrated gradient *Gl* makes more sense in accelerators. Therefore, *Gl* is listed in the requirements rather than the gradient.

Table 1: Main Parameters of the PMQs

Parameter	Symbol	Values
Inner diameter	*DI*	22 mm
Outer diameter	*DO*	60 mm
Length	*l*	40 mm
Integradient gradient deviation	Δ*Gl*/*Gl*	1.5%

Table 2: Integrated Gradient Requirements of the PMQs

Type	Integrated Gradient *Gl* (T)	Quantity
A	3.293	1
B	3.540	1
C	3.570	1
D	3.587	1
E	3.336	19

PMQ DEVELOPMENT

The 16-segment type PMQ is adopted in our facility. Figure 1 illustrates the cross section of a PMQ consisting 16 SmCo segments wherein the arrows indicate the easy axis orientation of each segment.

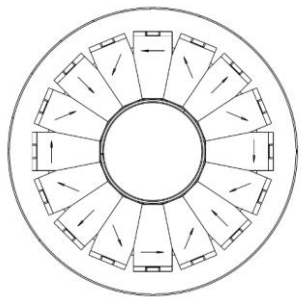


Figure 1: Cross section of the PMQ.

The fabrication procedure of the PMQs can be summarized as follows. Firstly, a number of SmCo segment blocks, which are shown in Figure 2, are produced in order to achieve enough qualified PMQs. Secondly, all the blocks are aged for 12 hours at 180 degrees Celsius. Thirdly, the magnetic field direction and strength of each blocks are measured and screened. Fourthly, the qualified blocks are then sorted by the strength and direction. Lastly, the blocks are assembled together with specified accuracy. Figure 3 and Figure 4 show one PMQ being assembled and after assembling respectively.

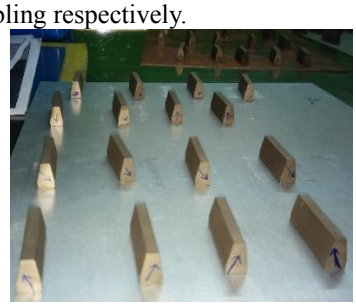


Figure 2: The aged blocks.



Figure 3: One PMQ being assembled.

Content from this work may be used under the terms of the CC BY 3.0 licence (© 2018). Any distribution of this work must maintain attribution to the author(s), title of the work, publisher, and DOI.

ISBN: 978-3-95450-194-6 ISSN: 2226-0366 doi:10.18429/JACoW-LINAC2018-THPO033

Content from this work may be used under the terms of the CC BY 3.0 licence (© 2018). Any distribution of this work must maintain attribution to the author(s), title of the work, publisher, and DOI.



Figure 4: One completed PMQ.

PMQ MEASUREMENTS

The magnetic measurements are very important for the PMQ development. The magnetic measurements are dedicated not only to verifying that the PMQs meet the requirements, but also to guiding us for better designs. The magnetic center, integrated gradient and multipole contents are measured separately.

Magnetic Center Measurements

The magnetic center is measured and related to the mechanical center with the help of the vibrating wire. Our team have developed one vibrating wire setup. The study of the improved vibrating wire method has been detailed in ref [1] and [2].

Typically, the magnetic center of the PMQ is not exactly coincides with the mechanical center at the beginning. It is because of the assembling errors and the imperfections of the blocks. After the measurement, the mechanical center is reprocessed to coincide with the magnetic center according to the measurement result. For our PMQ, the mechanical center is the symmetric axis of the cylindrical surface. And the position of the mechanical center can be changed by reprocess the cylindrical surface. At the beginning, the outer diameter of the PMQ is 61 mm. After the reprocessing, the deviation between the mechanical center and the magnetic center is smaller than 0.02 mm. Meanwhile, the final diameter of the PMQ is reduced to 60 mm.

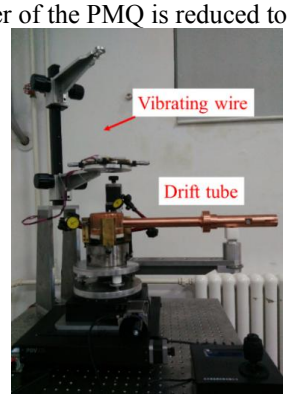


Figure 5: Vibrating wire measurement for the drift tube.

As shown in Figure 5, this vibrating wire setup is also suitable for measuring the magnetic center of the drift tube. The magnetic center measurements were kept going after the PMQs were installed into the drift tubes. These measurements are dedicated to ensuring the magnetic center coincides the mechanical center of the drift tube during the following process.

Integrated Gradient Measurements

The integrated gradient value indicates the strength of a quadrupole. The measurements of integrated gradient are especially important for PMQs. Because it is very hard to adjust it after one PMQ is installed into the drift tube. The integrated gradient should be precisely measured and screened before the installation.

The Hall probe method is adopted and improved for measuring PMQs. It is different from the electromagnet that the Halbach-type PMQ has a circularly symmetrical shape. Accordingly, the roll angle alignment for the magnet, the Hall probe and the motor stage is very difficult for the PMQs. Our team have proposed a roll angle alignment method based on the field distribution. And a setup has been built.

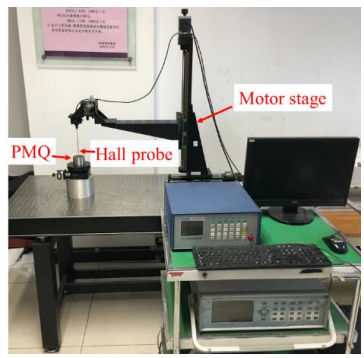


Figure 6: Hall probe measurement.

The setup is shown in Figure 6. The PMQ to be measured is placed on a rotary table. The symmetric axis of the PMQ is adjusted along vertical z axis. The PMQ can be rotated around its symmetric axis with the help of the rotary table. The Hall probe is mounted on the motor stage. A computer controls the motion of the motor stage and records the magnetic field data.

The measurement results for the 5 types of PMQs are shown in Figs. 7 to 11. They show enough quantity of PMQs to meet the requirements listed in Tables 1 and 2.

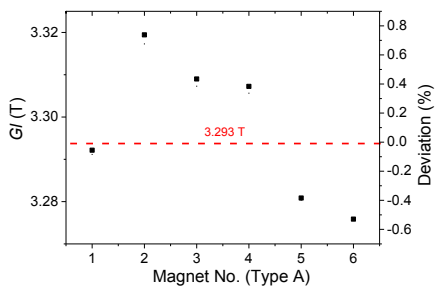


Figure 7: Measured integrated gradient and deviation of Type A PMQs.

ISBN: 978-3-95450-194-6 ISSN: 2226-0366 doi:10.18429/JACoW-LINAC2018-THPO033

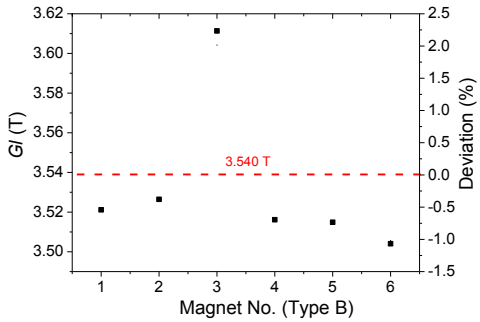


Figure 8: Measured integrated gradient and deviation of Type B PMQs.

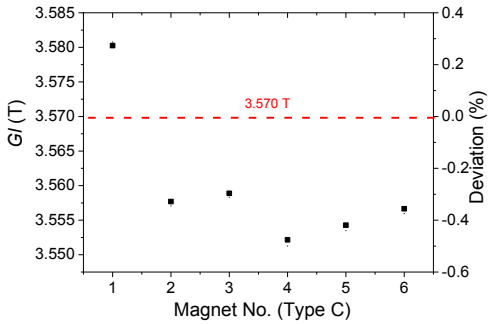


Figure 9: Measured integrated gradient and deviation of Type C PMQs.

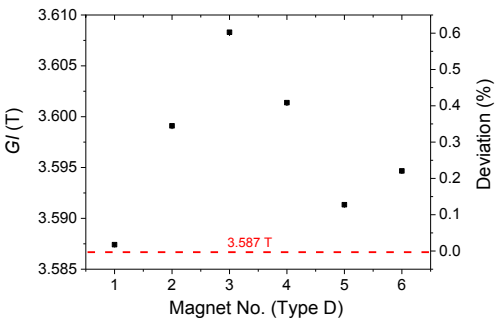


Figure 10: Measured integrated gradient and deviation of Type D PMQs.

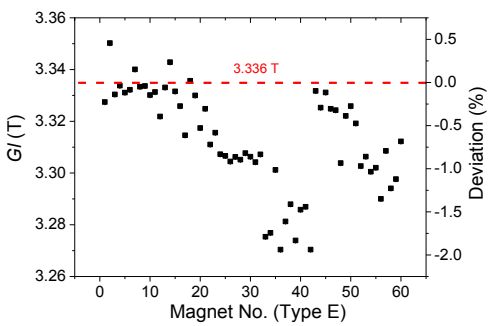


Figure 11: Measured integrated gradient and deviation of Type E PMQs.

Multipole Measurements

The multipole contents indicate the quality of the quadrupole field. They are measured by the rotating coil provided by IHEP. As shown in Figure 12, the PMQ to be measured is placed on a platform. The 8 mm-diameter coil penetrates the PMQ. The rotating axis is along the vertical *z* axis.



Figure 12: Rotating coil measurement.

The measurements show 85% of PMQs can meet the multipole requirements. The PMQs with larger multipole contents may be due to the imperfections of blocks and assemblings. Figure 13 presents a typical measurement result of one PMQ E-4. It shows that the multipole contents of orders less than 15 are smaller than 1% individually.

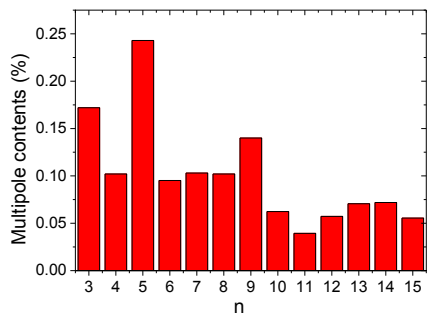


Figure 13: Multipole measurement result of PMQ E-4

CONCLUSIONS

The PMQs with the inner diameter of 22 mm and outer diameter of 60 mm are developed successfully. Magnetic measurements including vibrating wire, Hall probe and rotating coil are carried out. And results confirm enough quantity of PMQs meet the requirements.

ACKNOWLEDGEMENTS

All the authors would like to thank IHEP for the help in rotating coil measurements.

REFERENCES

[1] Wang, B., *et al.*, "Fiducialization of the small-aperture quadrupoles based on the vibrating wire method", *Nuclear Instruments and Methods in Physics Research* Section A: Accelerators, Spectrometers, Detectors and Associated Equipment, 2016. 812: p. 37 - 42.

[2] Wang, B.C., *et al.*, "Vibrating wire measurements for the XiPAF permanent magnet quadrupoles", in *Proc. IPAC'16*, Busan, Korea, May 2016, pp. 1124-1126, doi:10.18429/JACoW-IPAC2016-TUPMB009

Content from this work may be used under the terms of the CC BY 3.0 licence (© 2018). Any distribution of this work must maintain attribution to the author(s), title of the work, publisher, and DOI.

ISBN: 978-3-95450-194-6 ISSN: 2226-0366 doi:10.18429/JACoW-LINAC2018-THPO034

EXPERIMENTAL STUDY OF TUNING METHOD ON A MODEL ALVAREZ DTL CAVITY FOR CPHS PROJECT

Y. Lei[1,2], S. X. Zheng[1,2], Q. Z. Xing[1,2†], R. Tang[1,2], X. L. Guan[1,2], X. W. Wang[1,2], Key Laboratory of Particle & Radiation Imaging (Tsinghua University), Ministry of Education, Beijing 100084, China
[1]also at Laboratory for Advanced Radiation Sources and Application, Tsinghua University, Beijing 100084, China
[2]also at Department of Engineering Physics, Tsinghua University, Beijing 100084, China

Abstract

This article is devoted to the experimental study of tuning method for an Alvarez-type drift tube linac (DTL) of the Compact Pulse Hadron Source (CPHS) project at Tsinghua University. The biperiodic structure based on the post couplers are introduced to overcome the instability of the Alvarez DTL tank which is used to operate in 0 (or 2π) mode. The experimental method and results are presented, and the tuning scheme for the formal CPHS DTL is summarized from the tuning experiment.

INTRODUCTION

The effective shunt impedance of the Alvarez-type DTL is typically high when it operates in a typical 0 (or 2π) mode with the group velocity of 0. But the structure is very susceptible to perturbation such as the beam loading, mechanical and installation error, because of the narrow space near the adjacent modes on the TM dispersion curve. The post couplers, which are the resonant-coupling elements constitutionally, are mounted on the wall of the DTL cavity oppositely and alternatively to introduce a new PCs (post couplers) dispersion curve. When the stopband between the two passbands of the dispersion curves disappears by adjusting the slugging length of the post couplers, the lowest frequency of the TM passband will be moved to the π/2 mode point of the new dispersion curve. Therefore the new stable biperiodic structure of the DTL will be achieved [1].

To verify the tuning method, one model cavity has been machined and the turning experiment is carried out based on the cavity. The cavity is designed and manufactured for verifying the mechanical design and undertaking some low-power experiment. The model cavity consists of ten full drift tubes, two half drift tubes mounted on the end flanges, three post couplers and two tuners [2]. The end of the post couplers is designed to be eccentric to facilitate the tuning of the local field distribution by rotating the post.

TUNING EXPERIMENTAL CONFIGURATION

On the experimental stand as shown in Fig. 1, the measurement based on the bead-pull method is executed. According to the perturbation theory, when the bead is pulled into the field between the two adjacent drift tubes, the resonant frequency changes. Then the corresponding phase shift can be detected by a vector network analyzer (VNA) and the electric field along the beam-axis can be deduced [3].

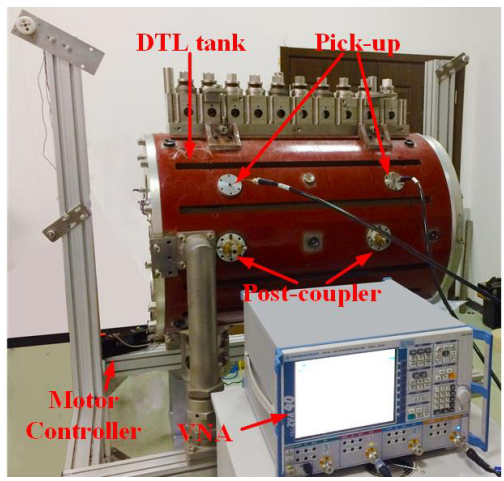


Figure: 1 Tuning experimental stand.

A stepping motor is adopted to pull a fine nylon line on which the small perturbation bead is fixed. The size of the bead shall be rather appropriate, so that the responsive signal caused by the bead is big enough compared with the background noise and at the same time within the linear range of the phase around the resonant frequency. It depends on the Q factor of the cavity. The Q factor of this model cavity is measured as 17796 which is about 44% of the designed value. It is because that the surfaces of the interior copper-plated cavity wall and the aluminous end flanges are oxidic. With the value of the Q factor, the radius of the bead is determined as 0.7 mm by estimation.

To ensure the accuracy of the measurement, the peak field is employed to represent the field distribution instead of the integral one due to its further advantages [4]. Before the measurement, the reproducibility is checked. The reproducibility R_{ij} is defined by Eq. (1).

$$R_{ij} = \frac{E_{ij}}{\left(\sum_{j=1}^{n} E_{ij}\right)/n} . \quad (1)$$

where E_{ij} is the measured electric field strength of the i^{th} cell for the j^{th} time, and n is the number of times of the measurements. Ten sequential measurement is analyzed by this definition, and the reproducibility is better than ±0.15% as shown in Fig. 2.

† xqz@tsinghua.edu.cn

Content from this work may be used under the terms of the CC BY 3.0 licence (© 2018). Any distribution of this work must maintain attribution to the author(s), title of the work, publisher, and DOI.

ISBN: 978-3-95450-194-6 ISSN: 2226-0366 doi:10.18429/JACoW-LINAC2018-THPO034

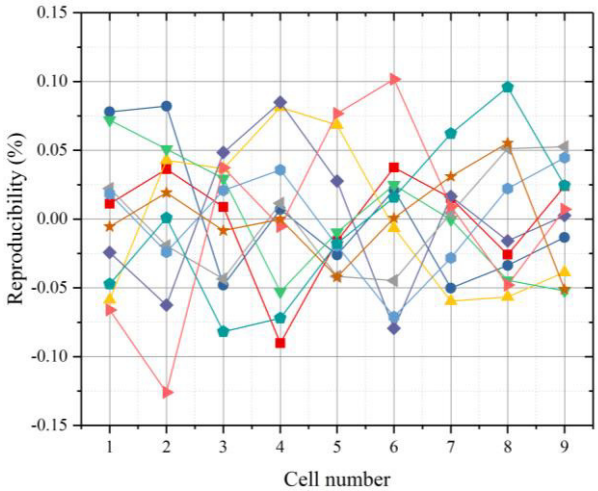


Figure 2: The measured reproducibility of the peak field on the model cavity for CPHS.

For predicting the performance of the tuners, the tuning effect by adjusting the slugging length of tuners is checked. The motioning range of tuners is from 0 mm to 100 mm corresponsive to slugging length of them. The tuning gradient of the tuners is about 0.02 MHz/mm in the condition of slugging the same length of all the tuners at the same time. Satisfactory linearity can help predict the adjusting value of tuners during the tuning process.
Considering the different status of the cavity with or without vacuum condition and under the different temperatures, the tuning resonant frequency shall be set as 324.9 MHz according to the following estimate:

Temperature Effect

Coefficient of the thermal expansion of the carbon steel DTL tank α is 1.2×10^{-5}/ºC. Compared with the operating temperature 25 ºC with the resonant frequency f_0 of 325 MHz, the experimental temperature is 7 ºC (ΔT=-7 ºC). So, the frequency shift Δf_T by the temperature effect can be calculated by Eq. (2):

$$\Delta f_T = \alpha f_0 \Delta T \ . \tag{2}$$

Atmospheric Effect

It is assumed that the scantly differences are the permittivity ε and permeability μ. The relative permittivity in air $\varepsilon_{\lambda\alpha}$ =1.000585, and the relative permeability in air $\mu_{\lambda\alpha}$ =1.00000004. The new resonant frequency in the air f_α can be calculated by Eq. (3):

$$f_\alpha = \frac{1}{2\pi\sqrt{(\varepsilon_0\varepsilon_{\lambda\alpha}A_C)(\mu_0\mu_{\lambda\alpha}A_L)}} \ . \tag{3}$$

where ε_0 the is the permittivity in vacuum, μ_0 is the permeability in vacuum, A_C and A_L are the capacitive calculating factor and inductive calculating factor which are relevant to the geometry of the DTL cavity respectively. Therefore, the frequency shift by the atmospheric effect can be calculated by Eq. (4):

$$\Delta f_A = f_\alpha - f_0 \ . \tag{4}$$

TUNING EXPERIMENT AND RESULTS

At the beginning of the tuning experiment, the error of field distribution is tuned to be better than ±2% as required at about 324.8 MHz with tuners but without post couplers. Because the frequency of the DTL without post couplers will introduce a frequency shift about 0.1 MHz, and the local tuning capacity of the post couplers is finite. The tuning rules are identical with the perturbation theory: when the inserted length of the tuner located at the bottom of the cavity rose, the frequency increase and the electric field decrease, and vice versa.

The tilt sensitivity can be tuned when all the three couplers are inserted into the cavity. The tilt sensitivity is an important criterion of the cavity stability. The tilt sensitivity of the i^{th} cell TS_i is defined by Eq. (5):

$$TS_i = \frac{\left(E_i^p - E_i\right)/E_i}{\Delta f}\times 100\% \ . \tag{5}$$

where E_i is the electric field before the perturbation, E_i^p is the electric field after the perturbation, and Δf is the frequency shift caused by a hollow metallic pipe slide into the cavity at the beam aperture of the high energy end flange. E_i shall be measured before the perturbation. E_i^p shall be measured after the Δf being compensated by tuner close to the low energy end. To obtain the lowest TS which the slope of the TS is closed to 0, the slopes of TS parameters are recorded every time the gap between the drift tube and post-coupler changed. The relationship between the TS parameters and the gaps is shown in Fig. 3.

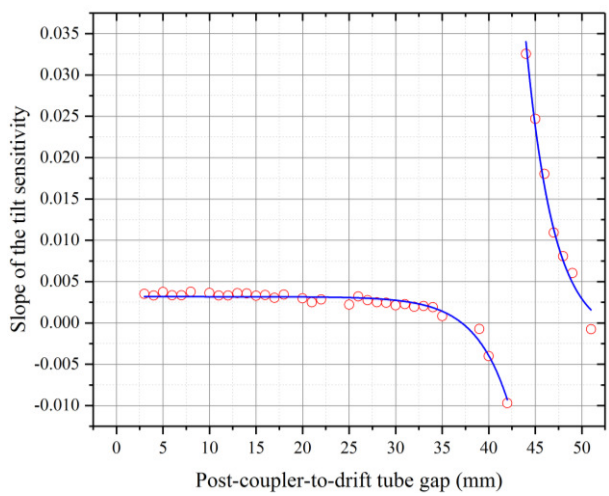


Figure 3: TS parameters vs. the gap between the drift tube and post-couplers.

The lowest TS slope corresponds to the 39 mm gap, and the gaps are set to be 39 mm uniformly. The TS_i distribution

Content from this work may be used under the terms of the CC BY 3.0 licence (© 2018). Any distribution of this work must maintain attribution to the author(s), title of the work, publisher, and DOI.

ISBN: 978-3-95450-194-6 ISSN: 2226-0366 doi:10.18429/JACoW-LINAC2018-THPO034

Content from this work may be used under the terms of the CC BY 3.0 licence (© 2018). Any distribution of this work must maintain attribution to the author(s), title of the work, publisher, and DOI.

is shown as Fig. 4 which corresponds to the electric field distribution shown as Fig. 5.

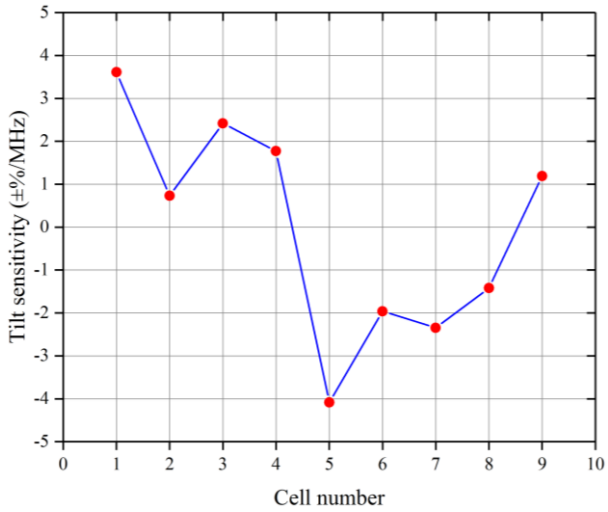


Figure 4: TS_i distribution per 0.15 MHz when the gaps between the drift tubes and the post-couplers are 39 mm.

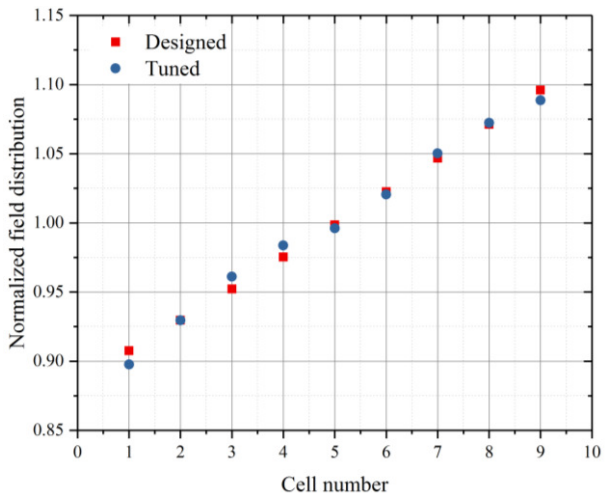


Figure 5: Electric field distribution when the gaps between the drift tubes and the post-couplers are 39 mm.

The local distribution can be tuned to the required range by rotating the post couplers. However, there is coupling relationship between the *TS* and the field distribution because of the eccentric structure of the post coupler. With several iterations, the field flatness is better the ±1.2% and *TS* is less than ±4.2%/MHz.

TUNING SCHEME FOR THE FORMAL DTL CAVITY

There are 39 drift tubes, 13 post-couplers and 9 tuners in the formal DTL cavity for CPHS. The size of each tuning element should be determined and installed permanently. For getting an accurate tuning result finally, the elements cannot be changed in one time, there should be an elements-replacing scheme as following:

1)According the first tuning result, manufacture a half of the elements including post couplers and tuners (except the first and last ones).

For 13 post couplers，No.3, 4, 7, 8, 11 and 12 will be replaced；

For 7 tuners, No.2, 4, 6 and 8 will be replaced.

2)Tuning the field again with the remaining aluminium elements.

3)According the second results, manufacture a half of the remaining elements (except the first and last tuners).

For the 7 post couplers, No.5, 9 and 13 will be replaced；

For the 3 tuners，No.2 and 6 will be replaced.

4)Tuning the field again with the remaining aluminium elements.

5)According the third results, manufacture and replaced the remaining elements.

6)Check the field distribution and tilt sensitivity, tuning the filed with the first and last tuners if necessary.

7)If everything is OK, tuning process is completed.

CONCLUSION

The tuning experiment on the model cavity of the CPHS project is accomplished at Tsinghua University. With the tuning experience, the tuning scheme for the formal DTL cavity is determinated. The gap between the drift tube and the post-couplers will not be coincident because of the different geometries of 40 cells, but the gap can be predicted through the theoretical analyzation and experimental results of this article.

ACKNOWLEDGEMENTS

The authors would like to express their special thanks to James Stovall and Lloyd Young for helpful discussions.

REFERENCES

[1] D.A. Swenson, *et al.*, “Stabilization of the drift tube linac by operation in the π/2 cavity mode”, in *Proc. 6th International Conference on High-Energy Accelerators*, Cambridge, Massachusetts, U.S.A., 1967, 167-173.

[2] S.X. Zheng, *et al.*, “Research on drift tube linac model cavity for CPHS”, in *Proc. LINAC’10*, Tsukuba, Japan, Sep. 2010, paper TUP071, pp. 575-577.

[3] L.C. Maier, *et al.*, “Field strength measurements in resonant cavities”, *J. Appl. Phys.* vol. 23, no. 68, pp. 68-77, 1952

[4] M.R. Khalvati, *et al.*, “Tuning and field stabilization of the CERN LINAC4 drift tube linac”, in *Proc. LINAC’14*, Geneva, Switzerland, Aug.-Sep. 2014, paper TUPP089, pp. 631-633.

ISBN: 978-3-95450-194-6 ISSN: 2226-0366 doi:10.18429/JACoW-LINAC2018-THPO035

TUNING AND LOW POWER TEST OF THE 325 MHz IH-DTL AT TSINGHUA UNIVERSITY

R. Tang[1,2], W.B. Ye[1,2], P.F. Ma[1,2], Y. Lei[1,2], S. X. Zheng[1,2†], Q. Z. Xing[1,2], H.Y. Zhang[1,2], C. T. Du[1,2], K. D. Man[1,2], X. L. Guan[1,2], X. W. Wang[1,2],
C. X. Tang[1,2], Key Laboratory of Particle & Radiation Imaging (Tsinghua University), Ministry of Education, Beijing 100084, China
[1]also at Laboratory for Advanced Radiation Sources and Application, Tsinghua University, Beijing 100084, China
[2]also at Department of Engineering Physics, Tsinghua University, Beijing 100084, China
J. Li, NUTECH Co.Ltd, Beijing 100084,China

Abstract

An interdigital H-mode drift tube linac (IH-DTL), which accelerates proton beam from 3 MeV to 7 MeV has been designed and assembled at Tsinghua University. There are 8 plungers in the 1 m tank and one coaxial coupler is used to feed the power. The frequency is tuned to 325 MHz. The field distribution is measured by the bead perturbation method. Finally, the gap voltage error has been tuned to be within ±3.0%, which satisfies the design requirement. The Q factor of the tank is 7000 while the power dissipation is 244 kW. Details of the low power test is presented.

INTRODUCTION

Since 1950s, IH DTL was firstly proposed by J.P. Blewett, it has been carefully studied and been adopted as the heavy ion accelerators. Because of its high shunt impedance and high accelerating field, IH DTL is adopted widely for the injection of the synchrotron-based medical facilities [1-3]. A 325 MHz IH DTL has been designed, fabricated and assembled at Tsinghua University for the medical purpose [4,5]. The length of the IH DTL is about 1 m and the 3 MeV proton from the RFQ can be accelerated to 7 MeV. A modified KONUS beam dynamics has been adopted in the design [5]. There are no magnets in the tank. The RF characteristics has been studied with the 3D microwave studio. The Q_0 factor is 11300 and the power dissipation is 151 kW. The designed parameters of the IH DTL are listed in Table. 1.

The tuning method of the IH DTL has been carefully studied. Several kinds of the IH tank has been tuned and reported [2,3,6]. The relative error between the measurement and the design is within ±3% mostly. For the 325 MHz IH DTL, 8 symmetric plungers are adopted for the tuning. The tuning range of the frequency is about 10 MHz. After the error analysis of the beam dynamics, the requirement of the error between the measurement and the design is≤±3.0%, which is consistent with the other IH DTLs. Details of the low power test and the tuning will be presented.

Table 1: Parameters of the IH-DTL

Parameters	Value
Particle species	Proton
Frequency	325 MHz
Injection energy	3 MeV
Output energy	7 MeV
Tank length	1.14 m
Number of cells	21
Frequency	325 MHz
Q_0	11300
Power	151 kW
Z [MΩ/m]	193 MΩ/m
$ZTT\times\cos^2(\phi)$ [MΩ/m]	107 MΩ/m
E_{peak}	2.3 Kp

LOW POWER TEST PLATFORM

The low power test plat form is composed of a stepped motor with the controller, a vector network analyser, and a co-axial coupler. The electric field is much smaller at the both ends of the tank while the magnetic field is much bigger. Thus, an insulated bead is adopted for the bead perturbation measurement [7]. The bead is pulled by the stepped motor with constant velocity and S21 signal of the VNA is used to measure the phase variation.

The low power test has been divided into two stages. The first stage of low power test is performed at Tsinghua University before the paint. The frequency is tuned to 325 MHz and the relative gap voltage error is within ±3.0% with the adjustable aluminium plungers. The high power operation will be performed at site where is one thousand kilometres far from Tsinghua University. The performance of the tank is worried after the long-distance transportation, therefore the second low power test is performed. Figure 1 shows the platform at both sites. There is no difference between the two measurement. Thus, the result shows that the long-distance transportation causes little influence on the tank.

Content from this work may be used under the terms of the CC BY 3.0 licence (© 2018). Any distribution of this work must maintain attribution to the author(s), title of the work, publisher, and DOI.

ISBN: 978-3-95450-194-6 ISSN: 2226-0366 doi:10.18429/JACoW-LINAC2018-THPO035

Content from this work may be used under the terms of the CC BY 3.0 licence (© 2018). Any distribution of this work must maintain attribution to the author(s), title of the work, publisher, and DOI.



Figure 1: The low power test platform of the IH DTL (up: Tsinghua University, down: NIST).

TUNING WITH THE ALUMINIUM PLUNGER TUNERS

There are two kinds of tuners for the IH DTL tuning: the movable aluminium plunger tuners and the fixed-length copper tuners, shown in Fig. 2. The tank of the IH DTL is tapered to adjust the electric field on the axis. The depth of the tuners is defined as the distance from the tuner to the axis. At the beginning, the aluminium tuners are inserted to the design position. Due to the fabrication and assembly error, the resonant frequency is 321.8 MHz while the simulation result is 324.9 MHz. There is a 3.1 MHz offset between the real tank and the simulation model. From the design position, all the tuners are moved the same distance. Then, the measured frequency is consistent with the simulation result if the offset is considered, exhibited in Fig. 3. Thus, the tuning range of the eight tuners is about 10 MHz. After changing the depth of each tuner, the frequency of the tank is tuned to 324.9 MHz under atmospheric pressure, which is corresponding to the 325 MHz under the working situation. Meanwhile, the electric field is tuned to the design.



Figure 2: Two kinds of tuners (left: aluminium plunger tuner, right: copper tuner).

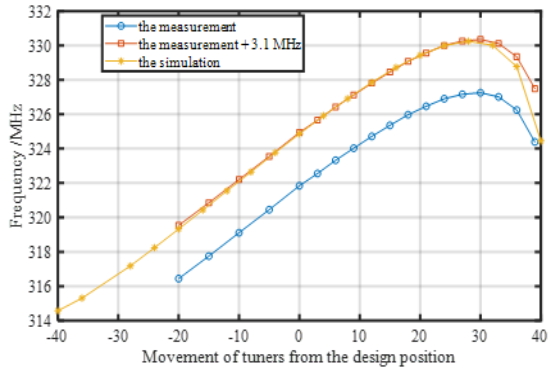


Figure 3: The tuning range of the tuners.

The stepped motor is not triggered by the VNA trigger signal. Thus, the start and end of the measured phase data of S21 are not related to the movement of the insulated bead. There is some random noise of the phase in the measurement as well. A detailed data processing is necessary. The flowchart of the data processing is shown in Fig. 4. Firstly, the peak points of the measured phase for different cells is found. A parabolic fitting of the data near peaks is used to get the more accurate position of the peaks. Then the measured peak points are fitted to the simulated peak points to get the relationship between the measured data and the simulated data. Next, a low pass filter is adopted to decrease the random noise. The baseline of the measurement is varying during the measurement. The baseline error is decreased by minus the broken line composed by the zero points (the zero points is the minimum points between the neighbouring two cells). Then, the square root of the phase shift is proportional to the electric field on the axis. The voltage of each cell is the integral of the electric field. Fig. 5 shows the electric field distribution and the cell voltage distribution. The depth of each aluminium tuner is changed to tune the frequency as well as the field distribution of the tank. The final error of the field distribution and voltage is $\leqslant \pm 3.0\%$. The quality factor of the tank is 5600 with the aluminium tuners.

ISBN: 978-3-95450-194-6 ISSN: 2226-0366 doi:10.18429/JACoW-LINAC2018-THPO035

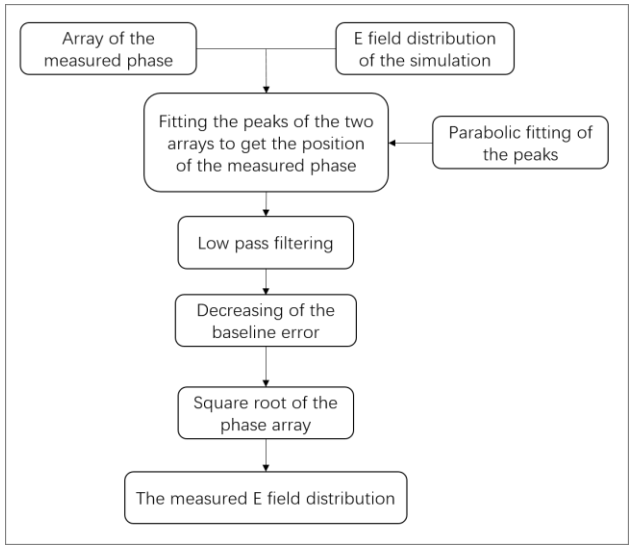


Figure 4: Flowchart of the data processing.

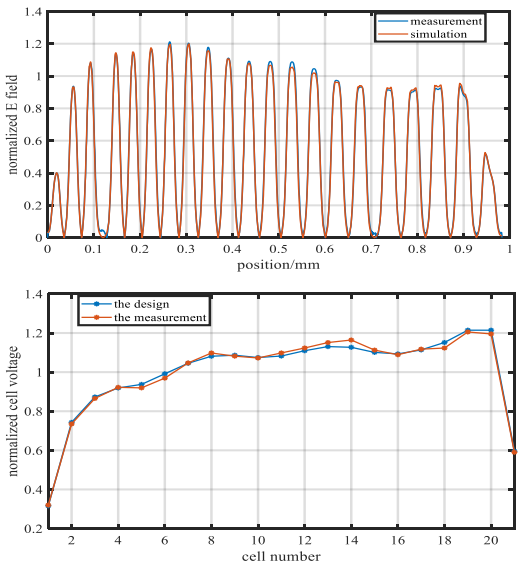


Figure 5: The electric field distribution and cell voltage of the IH DTL tank.

RESULTS WITH COPPER TUNERS

After tuning the IH DTL, the aluminium tuners are replaced by the copper tuners. Thus, the tank can be operated with the high power in the future. The C rings and O rings are adopted to seal the RF and the vacuum separately. Finally, the quality factor of the tank is about 7000 and the frequency remains to be 324.9 MHz. Ten times of the bead perturbation method are adopted to estimate the random noise of the measurement. The results are exhibited in Fig. 6. The random error of the measurement is bigger at the first cell and the last cell where the electric field is much smaller than the others. The random error of all cells is $\leq \pm 0.5\%$ and $\leq \pm 2.0\%$ for the peaks and the cell voltage separately, exhibited in Fig. 7. The difference of the measured electric field and the design is $\leq \pm 3.0\%$, which satisfies the design requirement.

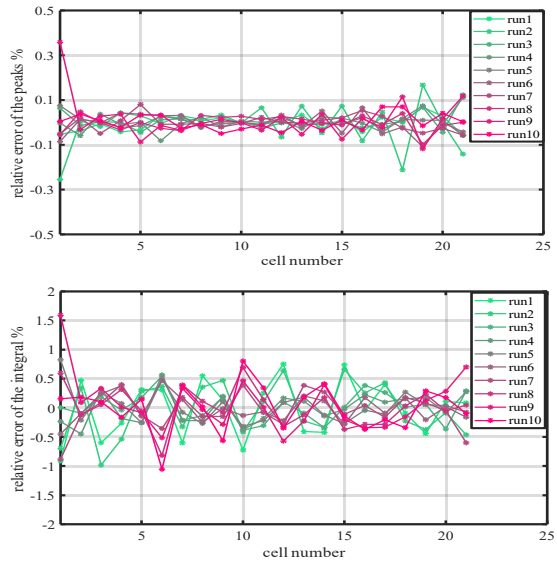


Figure 6: Repeatability of the measurement (up: peaks, down: cell voltage).

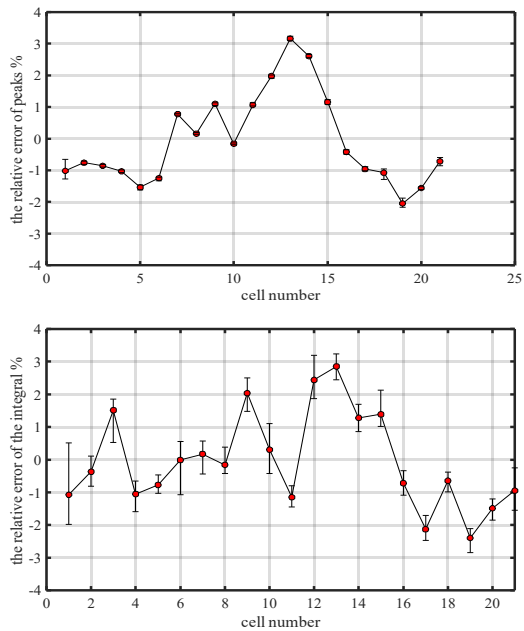


Figure 7: Relative error of the measurement with copper tuners and the design.

CONCLUSION

The fabrication and assembly of the 325 MHz IH DTL have been done at Tsinghua University. The tuning and low power test have been finished. A bead perturbation method is adopted to measure the electric field distribution on the axis. The relative error between the measurement and the design is smaller than ±3.0% in most of the cells which satisfies the design requirement. The Q_0 of the tank is 7000 and the corresponding power dissipation is 244 kW.

Content from this work may be used under the terms of the CC BY 3.0 licence (© 2018). Any distribution of this work must maintain attribution to the author(s), title of the work, publisher, and DOI.

ISBN: 978-3-95450-194-6 ISSN: 2226-0366 doi:10.18429/JACoW-LINAC2018-THPO035

Content from this work may be used under the terms of the CC BY 3.0 licence (© 2018). Any distribution of this work must maintain attribution to the author(s), title of the work, publisher, and DOI.

REFERENCES

[1] U. Ratzinger, "H-Type Linac Structures", in CERN Accelerator School 2000, CERN Yellow Report 2005003, Geneva, Switzerland, 2005, pp. 351-380.

[2] Y. Lu, "Development of an IH-DTL Injector for the Heidelberg Cancer Therapy Project", (Ph.D. thesis), Physics Department, Frankfurt University, Frankfurt, Germany, 2005.

[3] Y. Iwata *et al*., "Model cavity of an alternating-phase-focused IH-DTL", *Nuclear Instruments and Methods in Physics Research Section A: Accelerators, Spectrometers, Detectors and Associated Equipment,* 566.2 (2006): 256-263.

[4] R. Tang *et al*., "Beam Dynamics of a 325 MHz IH-DTL with KONUS", in *Proc. SAP2017*, Jishou, Hunan, China, 2017. doi:10.18429/JACoW-SAP2017-MOPH12

[5] R. Tang *et al*., "Mechanical Design and Error Analysis of a 325 MHz IH-DTL Test Cavity", in *Proc. IPAC2018*, Vancouver, Canada, 2018. doi:10.18429/JACoW-IPAC2018-TUPAL075

[6] K. Yamamoto, H. Tanaka, H. Harada *et al*., "Experimental verification of an APF Linac for a Proton Therapy Facility[J]", *Nuclear Instruments and Methods in Physics Research Section B: Beam Interactions with Materials and Atoms*, vol. 269(24), pp. 2875-2878, 2011.

[7] L.C. Maier, J.C. Slater. Field strength measurements in resonant cavities, J. Appl. Phys. 23, 68 (1952) 68-77.

ISBN: 978-3-95450-194-6 ISSN: 2226-0366 doi:10.18429/JACoW-LINAC2018-THPO036

ERROR STUDY OF CPHS DTL AFTER ASSEMBLY

P.F. Ma[1,2], Q.Z. Xing*[,1,2], R. Tang[1,2], Y. Lei[1,2], Q.K. Guo[1,2], C.T. Du[1,2], S.X. Zheng[1,2], X.L. Guan[1,2], X.W. Wang[1,2], Key Laboratory of Particle and Radiation Imaging, Tsinghua University, Ministry of Education, Beijing 100084, China
B.C. Wang, State Key Laboratory of Intense Pulsed Radiation Simulation and Effect, Northwest Institute of Nuclear Technology, Xi'an, 710024, China
[1]also at Laboratory for Advanced Radiation Sources and Application, Tsinghua University, Beijing 100084, China
[2]also at Department of Engineering Physics, Tsinghua University, Beijing 100084, China

Abstract

The Compact Pulsed Hadron Source (CPHS) at Tsinghua University is one multi-purpose pulsed neutron source. The injector of the CPHS is a linac, which mainly consists of a source, a low-energy beam transport line (LEBT), a radio frequency quadrupole (RFQ) and a drift tube linac (DTL). The error study of the DTL for CPHS is presented in this paper. The error study can provide the field tolerances in the DTL cavity and the alignment tolerance between the RFQ and DTL.

INTRODUCTION

Compact Pulsed Hadron Source (CPHS) at Tsinghua University is a pulsed hadron-source scientific facility based on one high-intensity proton linac. The linac mainly consists of an electron cyclotron resonance (ECR) source, a low-energy beam transport line (LEBT), a radio frequency quadrupole (RFQ) and a drift tube linac (DTL). The construction was launched in 2009 [1]. In July 2013, the 3 MeV RFQ was built, the proton beam was accelerated to 3 MeV [2, 3] and the neutron beam was produced [4]. So far, the 13 MeV DTL cavity is assembled [5]. The DTL will be commissioned and the neutron beam will be produced by the 13 MeV proton beam bombarding the Beryllium target.

PARAMETERS OF DTL

The DTL will accelerate 50 mA proton beams from 3 MeV to 13 MeV to bombard the target [6,7]. The permanent magnet quadrupoles (PMQs) are used to focus the beam downstream of the RFQ. The PMQs are mounted in the drift tubes with an FD lattice. Besides, no MEBT is used to match the beam between the RFQ and the DTL as the phase advance in the RFQ and DTL are optimized to be continuous.

The total length of the DTL is 4.4 m. The bore radius is 10 mm. The DTL cavity is presented in Fig. 1 [8].

The main design parameters of the DTL are listed in Table 1 [7].

BEAM DYNAMICS

The alignment of the drift tubes has been finished [5]. The alignment results of the DTL, including the displacements and the rotation around the z-axis of the PMQs, are presented in Fig. 2. The RMS value of the displacements of the PMQs is 0.13 mm (x)/ 0.10 mm (y), which is slightly larger than the required value (0.1 mm) [7].

The emittance measured is different from the designed value. According to the result of the emittance meter at the downstream of the RFQ, the normalized RMS emittance is 0.34 π mm·mrad (x)/ 0.35 π mm·mrad (y) [9], which is much larger than the designed value. We can assume that the normalized RMS emittance at the entrance of the DTL is the same on the basis of Liouville's theorem.

As the PMQs are difficult to rectify in the drift tubes, it is necessary to figure out the tolerances of other parameters after the alignment.

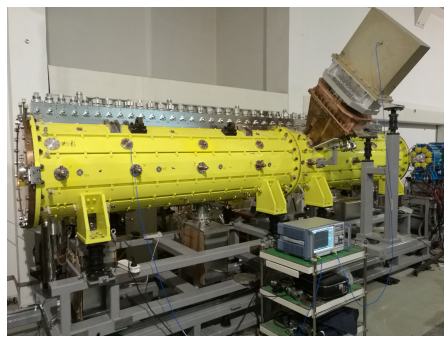


Figure 1: CPHS DTL cavity.

Table 1: DTL Design Parameters

Parameter	Value
Ion type	Proton
Input beam energy	3 MeV
Output beam energy	13 MeV
Input Norm. RMS emit.	0.25 π mm·mrad
Peak current	50 mA
RF frequency	325 MHz
Pulse length	0.2 ms
Pulse repetition rate	50 Hz
Cell number	40
Accelerating field	2.2 to 3.8 MV/m
Total RF peak power	1.2 MW
Total length	4.4 m

* xqz@tsinghua.edu.cn

Content from this work may be used under the terms of the CC BY 3.0 licence (© 2018). Any distribution of this work must maintain attribution to the author(s), title of the work, publisher, and DOI.

ISBN: 978-3-95450-194-6 ISSN: 2226-0366 doi:10.18429/JACoW-LINAC2018-THPO036

Content from this work may be used under the terms of the CC BY 3.0 licence (© 2018). Any distribution of this work must maintain attribution to the author(s), title of the work, publisher, and DOI.

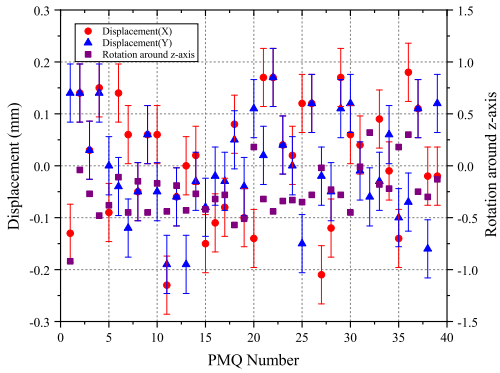


Figure 2: The alignment result of the DTL.

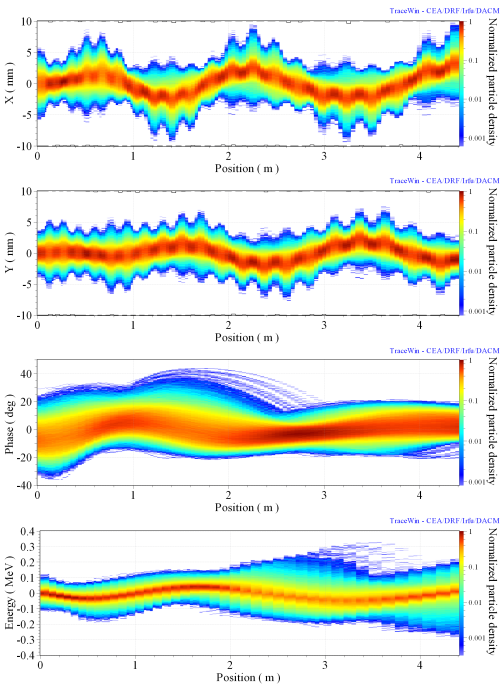


Figure 3: Beam dynamics in the DTL after assembly.

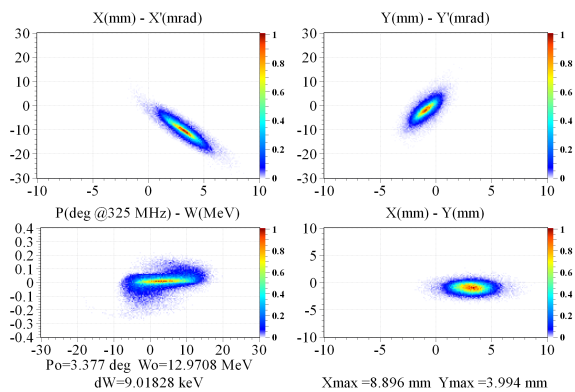


Figure 4: Phase space at the exit of the DTL.

The beam simulation with the alignment results is performed by the TraceWin code [10]. The displacements of the PMQs strongly affect the beam envelope of the DTL, which is shown in Fig. 3. The transmission rate of the DTL given by TraceWin is 99.9%. The phase space at the exit of the DTL is given in Fig. 4.

ERROR ANALYSIS

As the alignment of the drift tubes has been finished, error analysis is now to give a guide to the tuning of the DTL and the alignment between the RFQ and DTL. The process of error analysis is as follows [11, 12]. First, the acceptance will give the allowable range of the input beam. Second, the undetermined errors are checked with error sensitivities. Then the error sensitivities and the practical abilities are used to determine the undetermined error. At last, with all the errors, simulations are carried out to check whether the tolerances need to be modified or not.

Acceptance

The acceptance of the DTL can give a reference to the input beam tolerances. With the displacements of the PMQs, the acceptance of the DTL can be obtained. We also find that the beam center of the acceptance is not in the center of the pipe. The normalized RMS acceptance (see Fig. 5) is 2.19 π mm·mrad (x)/ 2.78 π mm·mrad (y). The center of the acceptance is (1.15 mm, 6.29 mrad) and (-0.53 mm, 3.06 mrad) in x-x' plane and y-y' plane separately. The acceptance is large enough even though the PMQs are misaligned and the real emittance is larger.

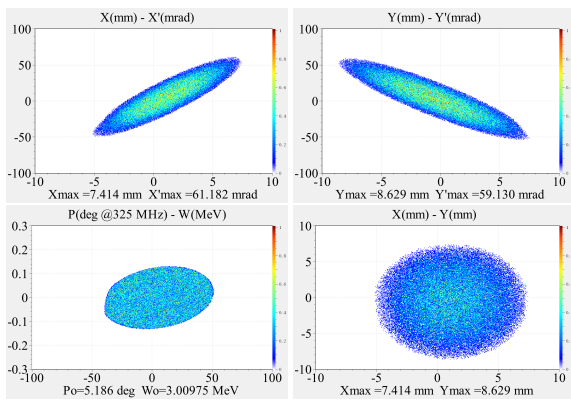


Figure 5: Acceptance of the DTL.

Undetermined Errors

Undetermined errors consist of 1) input beam errors: position and divergence of the beam center, emittance change of the beam, phase and energy jitter, mismatching of the Twiss parameters, current jitter; 2) quadrupole errors: rotation and gradient and 3) RF field errors: field distribution and phase, field and phase of the RF source, field amplitude tilt. Tilt error is introduced in the tuning process as the slope error of the accelerating field [13]. A tilt error of 3% means $0.97E_{0,low}$ at low energy end, $1.03E_{0,high}$ at high energy end, where $E_{0,low}$ and $E_{0,high}$ are the designed values of accelerating field at low and high energy ends.

ISBN: 978-3-95450-194-6 ISSN: 2226-0366 doi:10.18429/JACoW-LINAC2018-THPO036

As the beam center out from the RFQ is measured by the emittance meter, with an accuracy of ±0.2 mm, the beam position tolerances should be larger.

The error sensitivities of the undetermined errors are studied and the main error tolerances of the DTL are listed in Table 2. "Coupled" and "uncoupled" values in Table 2 correspond to the tolerances of the field of the RF source and field distribution.

Table 2: The Main Error Tolerances of the DTL

Input beam tolerances		**RF field tolerances**	
Position	±0.55 mm	Amplitude (uncoupled)	±3%
Divergence	±5.5 mrad		
Mismatch	15 %	Phase (uncoupled)	±3°
Energy	±0.04 MeV		
Phase	±2°	Amplitude (coupled)	±2%
PMQ tolerances			
Gradient	±3%	Phase (coupled)	±2°
Rotation around *x*,*y*	±3°	Amplitude tilt	±3%

Combined Errors

After the error tolerances are given, the comprehensive error study of the beam transmission rate is performed with combinations of all the undetermined errors listed above, including the input beam errors, the quadrupole errors and the RF field errors. The displacement values of the PMQs are the alignment results with an error bar of ±0.056mm. The measured value of emittance is used as the emittance at the entrance of the DTL. The beam center is in the center of the pipe.

The simulation is performed for 1500 times with 50000 macro-particles in each run. The errors are uniformly random distributed within the tolerances. The simulation results are shown in Fig. 6. Beam transmission rate is larger than 98% with the probability of 99%. The beam center is within the range of ±6 mm and ±20 mrad.

FIELD AND BEAM REQUIREMENTS

The field tolerances are guidelines for the tuning, the field distribution error should be smaller than ±3%, the tilt error should be smaller than ±3%. With 20 kHz perturbation, the required tilt sensitivity is less than 150%/MHz.

Also, the proton beams which come out from the DTL probably are not in the center (see Fig. 6), steerers are needed in the HEBT. If the input beam center is the required value, (1.15 mm, 6.29 mrad)(*x*)/(-0.53 mm, 3.06 mrad)(*y*), the simulation result with the same tolerances in Table 2 is shown in Fig. 7. Beam transmission rate is larger than 99% with the probability of 99%. Fewer particles are lost in the DTL, which is beneficial for the radiation protection.

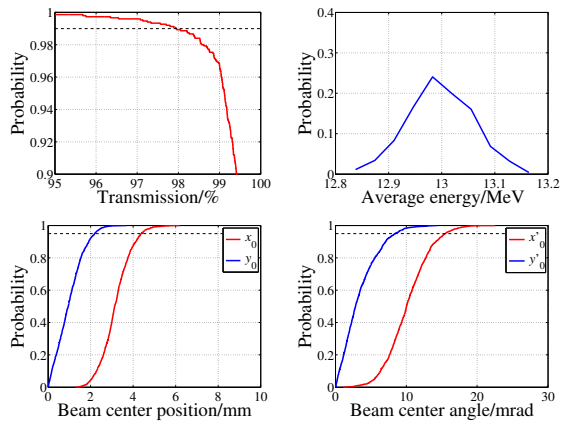


Figure 6: Probability of the transmission rate (top-left), the average energy (top-right), beam center position (bottom-left), beam center angle (bottom-right) at the end of the DTL.

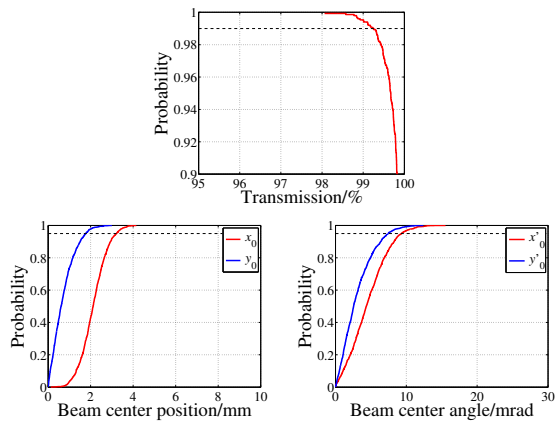


Figure 7: Probability of the transmission rate of the DTL (top), beam center position (bottom-left), beam center angle (bottom-right) at the end of the DTL after changing the input beam.

CONCLUSION AND FUTURE WORK

The error study of the CPHS DTL after collimating has been presented. The error study provides the field tolerances in the DTL cavity and the alignment tolerance between the RFQ and DTL, which guides the tuning and aligning work. Under varies of the errors, the DTL can still perform well, with low particle losses.

The tuning of the DTL has been finished, which meets the demand of the above field tolerances. The DTL will be aligned downstream the RFQ and the beam test of the DTL is expected.

REFERENCES

[1] J. Wei *et al.*, "Compact Pulsed Hadron Source-A university-based accelerator platform for multidisciplinary neutron and proton applications", in *Proc. PAC'09*, Vancouver, BC, Canada, 2009, paper TU6PFP035, pp. 1360-1362.

Content from this work may be used under the terms of the CC BY 3.0 licence (© 2018). Any distribution of this work must maintain attribution to the author(s), title of the work, publisher, and DOI.

ISBN: 978-3-95450-194-6 ISSN: 2226-0366 doi:10.18429/JACoW-LINAC2018-THPO036

Content from this work may be used under the terms of the CC BY 3.0 licence (© 2018). Any distribution of this work must maintain attribution to the author(s), title of the work, publisher, and DOI.

[2] Q.Z. Xing *et al.*, "High power test and beam commissioning of the CPHS RFQ accelerator", in *Proc. IPAC'13*, Shanghai, China, 2013, paper THPWO050, pp. 3884-3886.

[3] Q.Z. Xing *et al.*, "CPHS Linac status at Tsinghua University", in *Proc. IPAC'14*, Dresden, Germany, 2014, paper THPME032, pp. 3268-3270.

[4] X. Wang *et al.*, "Delivery of 3-MeV proton and neutron beams at CPHS: A status report on accelerator and neutron activities at Tsinghua University", *Physics Procedia* 60 (2014): 186-192.

[5] Q.K. Guo *et al.*, "The alignment of the drift tube of the DTL for the Compact Pulsed Hadron Source", in *The Fifth National Conference on alignment and mechanical design of particle accelerators*, Suzhou, China, 2017 [in Chinese].

[6] J. Stovall, J. Billen, and L. Young, "CPHS DTL design", in *CPHS mini-workshop*, Santa Fe. 2010.

[7] S.X. Zheng *et al.*, "Primary design of DTL for CPHS", in *Proc. IPAC'10*, Kyoto, Japan, 2010, paper MOPD048, pp. 795-797.

[8] Q.Z. Xing *et al.*, "Development progress of the H+/H- linear accelerators at Tsinghua University", presented at LINAC'18, Beijing, China, 2018, paper THPO022, this conference.

[9] M.W. Wang *et al.*, "Design and test results of a double-slit emittance meter at XiPAF", presented at IBIC'18, Shanghai, China, 2018, unpublished.

[10] *Tracewin documentation*, D. Uriot and N. Pichoff, CEA Saclay, July 2017.

[11] R. De Prisco *et al.*, "Error study on the normal conducting ESS linac", in *Proc. LINAC'14*, Geneva, Switzerland, Sep. 2014, paper THPP042, pp. 942-944.

[12] P.F. Ma *et al.*, "Conceptual design of a drift tube LINAC for proton therapy", in *Proc. IPAC'18*, Vancouver, BC, Canada, 2018, paper TUPAL073, pp. 1182-1185.

[13] X.J. Yin *et al.*, "Preliminary study on the RF tuning of CSNS DTL", *Chinese Physics C* 38.2 (2014): 027002.

ISBN: 978-3-95450-194-6 ISSN: 2226-0366 doi:10.18429/JACoW-LINAC2018-THPO038

STATUS OF THE POWER COUPLERS FOR THE CSNS DTL*

M. X. Fan†, H. C. Liu, K. Y. Gong, P. H. Qu, B. Li, X. L. Wu, Y. Wang, A. H. Li, Q. Chen
Institute of High Energy Physics, Chinese Academy of Sciences (CAS), Beijing, China
also at Dongguan Neutron Science Center, Dongguan, China

Abstract

There are four Drift Tube Linac (DTL) tanks in China Spallation Neutron Source (CSNS) Project. Each DTL tank requires a power coupler with a peak power of 2 MW and a duty cycle of 1.5% for beam operation. After approximately two years machining, all four couplers were already installed in the tunnel before year 2017. Up to now, the first phase of beam tuning has been completed, the maximum transmission power of the coupler exceeds 1.7 MW with a pulse width of 650 μs and a repetition rate of 25 Hz, meanwhile, the vacuum is maintained on the order of 10^{-6} Pa during the operation and no breakdown was observed. This paper describes the architecture, the fabrication, the low power test results and the high power conditioning process of the coupler. Some problems encountered are also presented.

INTRODUCTION

The Accelerator system of China Spallation Neutron Source (CSNS) Project contains a 50 keV H^- Ion Source, a 3 MeV Radio Frequency Quadrupole (RFQ), a 80 MeV Drift Tube Linac (DTL) and a 1.6 GeV Rapid-cycling Synchrotron (RCS) successfully passed the technology acceptance test with a beam power over 10 kW in March 2018. The DTL section is 34.67 m long and is divided into 4 physical tanks. Each DTL tank has a similar design and is equipped with the same size power coupler in the center position. The type of half-height WR2300 ridge waveguide power coupler is chosen for DTL, design parameters of the coupler are shown in Table 1. Preliminary design of the coupler was quite early before 2012, and a cold model was manufactured to determine the dimension

Table 1: Parameters of the Coupler

Type	Waveguide
Frequency	324 MHz
Peak RF power	2 MW
Average RF power	30.2 kW
Pulse width	650 μs
Repetition rate	25 Hz
Maximum duty factor	1.625%
Coupling coefficient	1.3±0.1

of the coupler. Measurement of the cold model was made in 2015, and some dimensions were modified to optimize the coupling coefficient. Finish machining, installation and high power conditioning of the power couplers were executed between December 2015 and March 2017. The coupler has been in operation for most of the time since April 2017.

DESIGN AND SIMULATION OF THE COUPLER

Preliminary design of the power coupler draws on the successful experience of America Spallation Neutron Source (SNS) and Korea Proton Engineering Frontier Project (PEFP). It uses a dog-bone shaped coupler iris to connect the tapered ridge waveguide with a constant ridge width and the DTL cavity. The size near the side of the ceramic window is designed to be the size of half-height WR2300 waveguide, the size close to the cavity side is given by optimizing the return loss (s11). To improve the simulation efficiency, a simplified model-a pillbox loaded with two symmetrical dog-bone shaped couplers is used. According to the simulation, the size of the hole diameter is determined to be 25.5 mm [1].

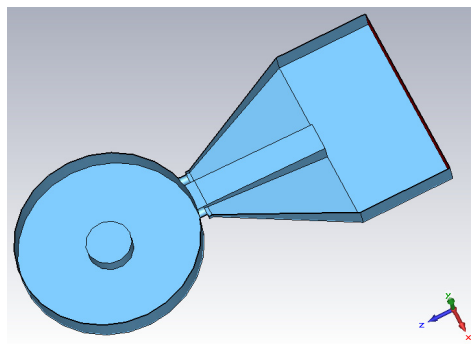


Figure 1: A cutplane of the new simulation model.

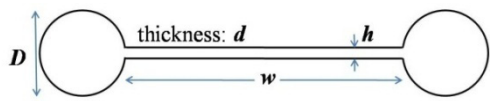


Figure 2a: Geometry of the dog-bone shaped aperture.

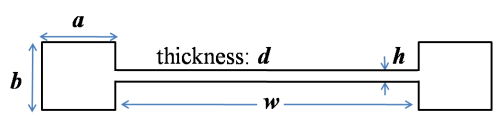


Figure 2b: Geometry of the modified dog-bone shaped aperture.

On the basis of preliminary design, a cold model is manufactured. Measurement of the cold model was taken in August 2015, and the results were far from the simulation. Considering that the dimensions of the hole diameter and ridge waveguide have an impact on matching, a new simulation model closer to the real situation is proposed,

* This work was supported by Youth Innovation Promotion Association of CAS (2015011)
† fanmx@ihep.ac.cn

Content from this work may be used under the terms of the CC BY 3.0 licence (© 2018). Any distribution of this work must maintain attribution to the author(s), title of the work, publisher, and DOI.

ISBN: 978-3-95450-194-6 ISSN: 2226-0366 doi:10.18429/JACoW-LINAC2018-THPO038

Content from this work may be used under the terms of the CC BY 3.0 licence (© 2018). Any distribution of this work must maintain attribution to the author(s), title of the work, publisher, and DOI.

as shown in Figure 1. First, the simulation results using ensure the applicability, and a scaling factor of 0.8 is used here to correct the difference between the simulation (lossless) and measurement (loss). Secondly, the influence of main parameters on the coupling coefficient is analyzed. Finally, limited by the size of the coupler, the dog-bone shaped iris consist of a narrow slot with two cylindrical holes is modified to a narrow slot with two rectangular holes, as can be seen in Figure 2. Meanwhile, the angle between the two ridges is increased by increasing the distance between the two ridges near the ceramic window. The coupling coefficient of DTL1 is optimized to 1.35 at last, and all four couplers will use this design size [2].

MANUFACTURE OF THE COUPLER

Manufacture of the coupler is very complicated, it needs dozens of process and the accuracy requirements are relatively high. A cold model is required to determine the size of the iris and four formal ridge waveguides are required for operation. There is no need to consider the effect of vacuum in cold model manufacturing, so it eliminates the process of welding, leak detection and ultimate vacuum test. However, iris size of the cold model should be easy to change, so a split design is used. The cold model is made of aluminum, it consists of half waveguide A, half waveguide B and a transition part, as shown in Figure 3. This structure allows us to install and disassemble the transition part easily, thus facilitating the efficiency of measurement.

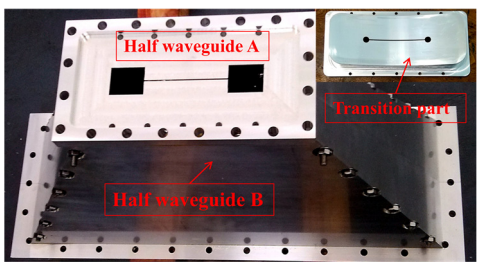


Figure 3: Split design of the cold model.

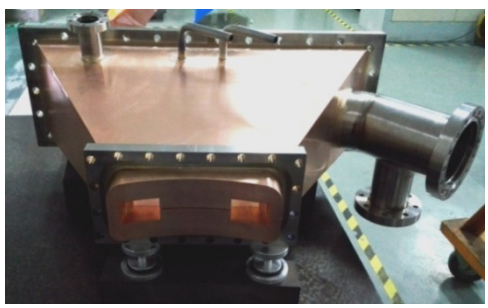


Figure 4: The formal model that has been welded.

The formal model (Figure 4) is mainly made of oxygen-free copper material, considering the high vacuum requirements, every model needs two vacuum brazing processes, one is to weld two copper halves, the other is this model are compared to the measurement results to to weld the copper body with different flanges and cooled pipes, and vacuum leak detection is taken after each brazing process to ensure the welding quality. After all of this, a 5×24 hours vacuum baking is also performed, and the vacuum of the ionic pump port of all four formal models is better than 1e-6 pa.

RF TEST RESULTS

Low power measurement of the cold model is taken as soon as the end of DTL1 field tuning in the tunnel. Detailed results can be found in Ref [2]. Each formal model is also measured on the corresponding DTL cavity in the tunnel. Figure 5 shows the setup of the measurement, it consist of the DTL cavity, the power coupler, the ceramic window, the WR2300 to N transformer and the N5221A Network analyzer. The low power test of the power coupler must be made after each DTL cavity field tuning, because the field distribution will greatly influence the measurement results. Measurement results of the couplers

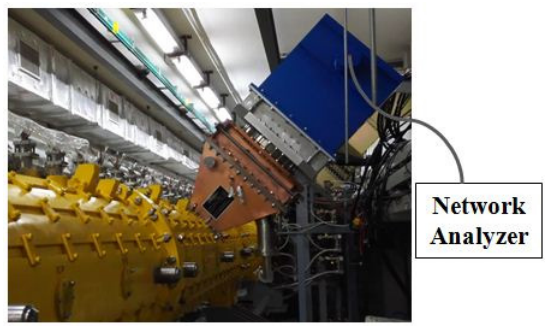


Figure 5: Setup of the measurement.

are listed in Table 2. Results of the DTL1 power coupler are the results of re-measurement after high power conditioning, and the coupling coefficient of the DTL1 coupler is almost the same to the simulation value 1.35. Frequency shift is also observed, the resonant frequency in atmosphere is shifted by 0.00197% after evacuation to vacuum. This value is quite consistent with the humidity-effect nomograph given in Ref [3] with a measurement temperature of 25 ºC and relative humidity of 50% [4]. The measurement results of the other three couplers are the results of non-conditioning.

Table 2: Low Power Test Results of the Couplers

Coupler	Coupling coefficient	Resonant frequency/MHz
DTL1(atmosphere)	1.32	323.99285
DTL1(vacuum)	1.33	323.99932
DTL2	1.33	323.89277
DTL3	1.27	323.88747
DTL4	1.20	323.89248

A direction coupler is placed between the ceramic window and the circulator to measure the positive and reflected power before ceramic window. Thus the coupling

ISBN: 978-3-95450-194-6 ISSN: 2226-0366 doi:10.18429/JACoW-LINAC2018-THPO038

coefficient can be calculated by the data obtained by it. Table 3 lists the coupling coefficient of each coupler when the beam with a peak current of 5.5 mA, a repetition rate of 25 Hz and a pulse width of 115 μs is accelerated, accordingly, the peak power through the coupler is 1.7 MW and the pulse width of it is 400 μs. These data are samples at a particular monument and the actually coupling coefficients fluctuate over time in a small range depend on the state of the cavity. The resonant frequency of all DTL tanks is 324MHz. Comparing the coupling coefficient in beam range (β_{beam}) and the coupling coefficient in non-beam range ($\beta_{non\text{-}beam}$), shifts are observed due to the beam loading, different shift values may be caused by the system error and different power loss of each cavity. Comparing the low power test results of the coupling coefficient and the operation status of the coupling coefficient, we found that the coupling coefficient of all couplers have different degrees of increase. Reasons can be considered as follows: (1) Measurement error of the direction coupler. (2) The state of DTL cavities has changed. There are two movable tuners for each DTL cavity and the initial insertion depth of them is 50 mm during the low power RF test. However, the insertion depth of all movable tuners is changed during the operation for frequency compensation. This will change the field distribution in DTL cavity and affect the coupling coefficient. In addition, the temperature rise of cavities and drift tubes also have some influence on the coupling coefficient when high power is fed. (3) Non-conditioning of the coupler, ceramic window and DTL cavity. Although the coupling coefficient has some increase, the power transmission efficiency of the coupler at current beam is greater than 97.2%. It fully meets the operational requirements.

Table 3: Coupling Coefficient of the Couplers when Beam is Accelerated

Coupler	β_{beam}	$\beta_{non\text{-}beam}$	$\beta_{non\text{-}beam}$-β_{beam}
DTL1	1.40	1.52	0.12
DTL2	1.33	1.43	0.10
DTL3	1.36	1.46	0.10
DTL4	1.24	1.32	0.08

HIGH POWER CONDITIONING AND OPERATION

High power conditioning of the coupler and ceramic window are together with the conditioning of DTL cavity due to the progress of CSNS. Figure 6 shows the power transmitted by the coupler, the vacuum of the coupler and the vacuum of the DTL2 cavity as a function of time. At first, the input power with a max duty factor was less than 15 kW and was almost fully reflected due to the non-conditioning of the ceramic window and power coupler. At the same time, vacuum of the coupler fluctuated significantly. 15-20 hours later, most of the input power was fed into DTL cavity and we gradually increased the power level to 1MW. In this stage, violent outgassing occurred in both the cavity and the coupler and window, but the outgassing of the coupler and window was more frequent. After the power exceeded 1 MW, the main outgassing position was transferred from coupler to DTL2 cavity. But due to the short time of power conditioning, obvious degassing in the coupler and window could still be seen during each power increase. After more than one year of operation, the coupler can work stable with little degassing, as shown in Figure 7. The conditioning process of the other three couplers is similar to that of DTL2 coupler, and all four couplers are conditioned to the max power of 1.7 MW with a pulse width of 650 μs and a repetition rate of 25 Hz. In addition, the vacuum of the coupler is better than that of DTL cavity for most of the time during the operation.

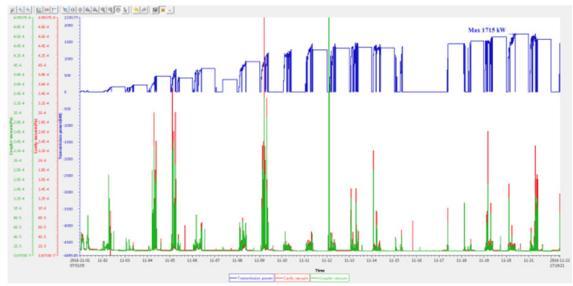


Figure 6: High power conditioning process.

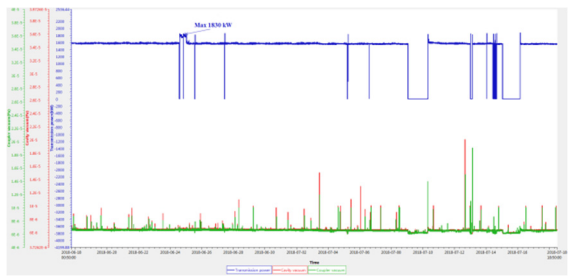


Figure 7: Operation status.

CONCLUSION

The whole process of design, manufacture, low power RF test and high power conditioning of the power couplers for the CSNS DTL is described in this paper. All four couplers have entirely gone through the RF conditioning and beam commissioning process with no breakdown. Now, they are operating steadily with a pulse width of 400 μs and a repetition rate of 25 Hz when a beam with pulse width of 115μs and repetition rate of 25 Hz is accelerated. As the current beam power is relatively low, more observation would be taken on the couplers with the increase of beam power.

REFERENCES

[1] H. C. Liu *et al.*, "RF power coupling for the CSNS DTL", *Chinese Physics C,* vol. 35, pp. 92-*95*, 2011.

[2] M. X. Fan *et al.*, "Low power RF test and analysis of China Spallation Neutron Source Drift Tube Linac RF power coupler", *High Power Laser and Particle Beams*, vol. 29, no. 06, p. 29065105-, 2017.

Content from this work may be used under the terms of the CC BY 3.0 licence (© 2018). Any distribution of this work must maintain attribution to the author(s), title of the work, publisher, and DOI.

ISBN: 978-3-95450-194-6 ISSN: 2226-0366 doi:10.18429/JACoW-LINAC2018-THPO038

[3] C.G. Montgomery, *Technique of Microwave Measurement*. New York and London McGraw-Hill Book Company Inc., 1947.

[4] Y. Taira *et al*., "Fabrication and low-power RF test of C-band RF gun", *Nuclear Instruments and Methods in Physics Research Section B: Beam Interactions with Materials and Atoms*, vol. 331, pp. 27-*30*, 2014.

Content from this work may be used under the terms of the CC BY 3.0 licence (© 2018). Any distribution of this work must maintain attribution to the author(s), title of the work, publisher, and DOI.

ISBN: 978-3-95450-194-6 ISSN: 2226-0366 doi:10.18429/JACoW-LINAC2018-THPO039

THE STATUS OF CSNS FRONT END*

H. Li, H. F. Ouyang†, X. Cao, W. Chen, S. Fu, T. Huang, S. Liu, Y. J. Lv, Y. C. Xiao, K. Xue, China Spallation Neutron Source (CSNS), Institute of High Energy Physics (IHEP), Chinese Academy of Sciences (CAS), 523803 Dongguan, China

Abstract

The commissioning and improvement of front end as well as the laboratory construction are summarized. The improvement as well as its effects mainly focuses on a low energy beam transport line (LEBT) and a 3.0MeV four-vane type radio frequency quadrupole (RFQ). In addition, the constitution, significance and construction of laboratory are mentioned.

INTRODUCTION

The China Spallation Neutron Source (CSNS) is an accelerator-based high power project with multipurpose currently under commissioning. The accelerator complex consists of an 81MeV H- linear accelerator as the injector and a 1.6GeV rapid cycling proton synchrotron (RCS). The linear accelerator consists of a 50keV H- penning surface plasma ion source (IS), a low energy beam transport line (LEBT), a 3.0MeV four-vane type radio frequency quadrupole (RFQ) accelerator, a medium energy beam transport line (MEBT), a 81MeV drift tube linear accelerator (DTL) and a high energy beam transport line (HEBT).

As shown in Figure 1, the front end means the front part of linac that includes IS, LEBT, RFQ and MEBT. As the start point of CSNS, the condition of front end is one of key factors which influence the stable operation of CSNS. Based on the beam requirement of CSNS phase I, the front end should provide a stable H- beam with energy of 3.0MeV, a maximum pulsed peak current up to 15mA, a beam duty factor 1.0% at a repetition of 25Hz and beam pulse width of 400us before chopping. The installation of CSNS front end was completed in 2015. Although the front end satisfies the beam requirement of CSNS phase I, the stability of the front end is not satisfactory during beam commissioning. The instability mainly comes from the ion source and RFQ sparking. After last 3 years commissioning and improvements, now the stability of CSNS front end was improved a lot.

PENNING IS

The main design parameters of penning IS for CSNS phase I are listed in Table 1.

Table 1: Main Design Parameters of IS for CSNS Phase I

Parameter	Value
Ion source	H-
Output Energy (keV)	50
Output Current (mA)	>20
Emittance $\varepsilon_{n,rms}$ (π mm · mrad)	<0.20
Repetition Rate (Hz)	25
Beam Duty Factor (%)	1.3
Lifetime (month)	>1

During the last 3 years commissioning and operation of CSNS, there are in total used about 20 sets of ion source discharge chamber. In general, for each set of discharge chamber, the ion source can produce up to 50mA H- ion beam with a beam duty factor about 1.25% (500us & 25Hz) and a normalized rms. emittance about 0.8π mm·mrad. Although the emittance is much larger than the acceptance of RFQ (0.2π mm·mrad), the H- ion beam current is still larger than 20mA within the acceptance of RFQ, which satisfies the current requirement of CSNS phase I. The average expected lifetime of CSNS IS, mainly limited by the discharge chamber, is about 1 month, which satisfies the requirement of CSNS phase I. The longest operation time for one of the 20 discharge chambers is near to 50 days.

Since the ion source was installed in CSNS tunnel in Oct. 2014, many improvements have been made for the ion source. Firstly, the electric penning magnet, which was integrated with the bending magnet before, was replaced by an independent permanent magnet that has the same electric potential as the discharge chamber; Sec ondly, the extraction power supply was moved into tunnel where was much closer to the source to decrease the induced voltage by the cable; Thirdly, the post acceleration

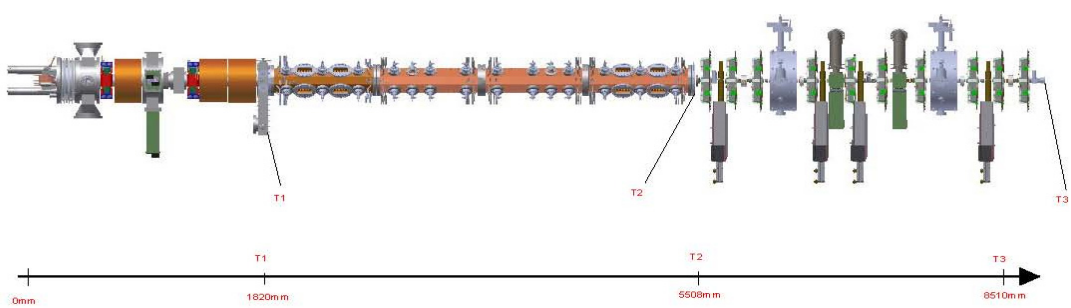


Figure 1: The beam line of CSNS Front End.

Content from this work may be used under the terms of the CC BY 3.0 licence (© 2018). Any distribution of this work must maintain attribution to the author(s), title of the work, publisher, and DOI.

ISBN: 978-3-95450-194-6 ISSN: 2226-0366 doi:10.18429/JACoW-LINAC2018-THPO039

Content from this work may be used under the terms of the CC BY 3.0 licence (© 2018). Any distribution of this work must maintain attribution to the author(s), title of the work, publisher, and DOI.

ceramic insulator was replaced by a new insulator with an additive 45mm high collar to increase the creepage distance; Lastly, the post acceleration power supply with 55kV and 10mA is replaced by the one with 65kV and 80mA. After these improvements, the stability and reliability of the ion source is highly enhanced [1]. Now, the only factor leading to the instability of ion source comes from the extraction sparking at very low beam duty factor.

This instability could be also well controlled through strictly limiting the consumption of cesium. In addition, a new extraction power supply with double voltage-output pulses is also developed to solve the extraction sparking. With this new power supply, the extracting beam by one pulse with lower voltage output (<8kV) is used to clean out the cesium deposited on the extractor. The beam functioning as cleaning out cesium on extractor is lost in LEBT, and only the beam extracted by another pulse with normal voltage output (15kV-18kV) can transport through LEBT and into RFQ. The new extraction power supply is now commissioning in ion source laboratory and works well as expected.

LEBT

As shown in Figure 1, a double slit type emittance monitor (EM) is installed downstream the first solenoid. Results of emittance and beam current measurement are shown in Figure 2. At the beam current of 53mA, the rms. emittance is 0.892π mm·mrad in x-x' phase plane and 0.742π mm·mrad in y-y' phase plane, respectively; Within the beam rms. emittance of 0.2π mm·mrad, the beam current is 15mA in x-x' phase plane and 25mA in y-y' phase plane, respectively.

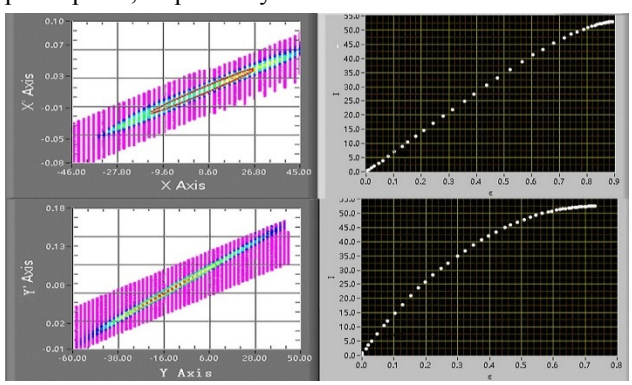


Figure 2: Results of emittance and current measurement: The left two plots show the emittance in x-x' and y-y' phase plane at the beam current of 53 mA. In the right two plots the beam current is shown as a function of the emittance in x-x' and y-y' phase plane, respectively.

To deal with the asymmetrical emittance of the beam from ion source, three solenoids are adopted in LEBT. It is proved theoretically and experimentally that, with three solenoids, the asymmetrical emittance can switch to symmetrical emittance and match the acceptance of RFQ.

As shown in Figure 3 (left), because the normalized rms. emittance of the beam from ion source is about 0.8π mm·mrad, larger than the acceptance of RFQ (rms. 0.2π mm·mrad), the beam transmission efficiency of RFQ in the beam commissioning of front end is often among 75-88.5% (86.5% here), but the maximum current at exit of RFQ could be largeur than 30mA. Considering this beam current is much larger than the requirement current of CSNS phase I, in order to raise the beam transmission efficiency of RFQ and reduce the risk of damage on RFQ done by the beam losses, a moveable aperture plate (in the second vacuum chamber) and a collimator (in the third vacuum chamber) are designed and installed in LEBT.

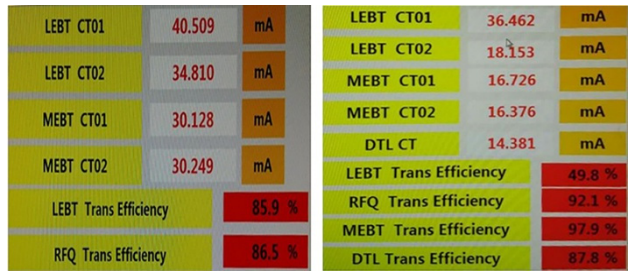


Figure 3: The beam transmission efficiency of RFQ without a beam collimator in LEBT (left) and with a beam collimator in LEBT (right).

With both of the aperture and the collimator, the RFQ transmission could be high up to 98.5% while the current is usually 4 to 5 mA at the exit of RFQ, and this beam intensity just satisfies the requirement for the DTL beam commissioning. With the collimator but without the aperture, the RFQ transmission ranges from 90% to 96% in the light of the beam current from 10mA to 18mA at the exit of RFQ. As shown in Figure 3 (right), the beam transmission of RFQ is about 92.1% when the beam current is 16.726mA at the exit of RFQ.

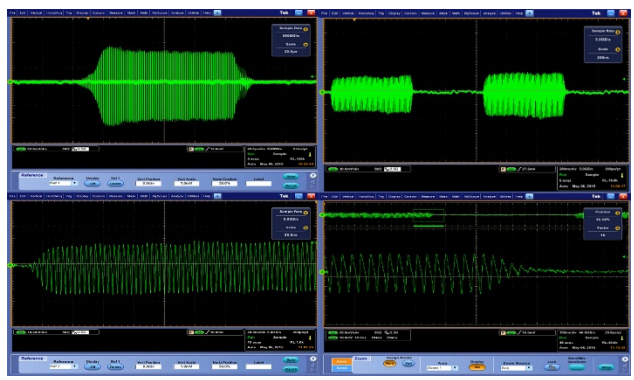


Figure 4: Beam signal of BPM after chopping. The upper plots: (left) the macro pulse of beam: 20μs/div; (right) the micro pulse of beam: 200 ns/div. The lower plots: (left) the rising edge of beam signal; (right) the falling edge of beam signal.

For CSNS, only one electrostatic pre-chopper is employed in LEBT to chop beam to the required beam structure asked for RCS, which is installed at entrance of RFQ. In the chopping experiment shown as in Figure 4, the macro pulse beam with a width 100μs and a repetition rate 1Hz is chopped to the micro pulse beam with a width of 500 ns and a repetition rate 1MHz. The chopping ratio shown here is 50%, but it is adjustable from 50% to 75% in beam commissioning. The results shown in Figure 4

ISBN: 978-3-95450-194-6 ISSN: 2226-0366 doi:10.18429/JACoW-LINAC2018-THPO039

are got from the beam position monitor (BPM) at the exit of RFQ. It can be seen that both the rise and fall time for the chopped beam are about 3 to 4 periods of the working RF (1 period time=3.086ns), i.e. both the rise and fall time are less than 15ns. With a higher applied chopping voltage, the minimum rise/fall time is about 10ns.

RFQ

A four-vane type RFQ with energy 3.0MeV is the first accelerating structure of CSNS accelerator complex. The design current of 40mA for RFQ is aimed to satisfy the future upgrading of CSNS [2].

As mentioned above, the chopped beam is designed to lose in RFQ for a small load capacitance of pre-chopper. For this chopping design, RFQ sparking problem is not sharp in the initial beam commissioning when the beam duty factor is low. However, when the proton beam power on the target is near to 20kW, RFQ sparking problem becomes very seriously. At last, the operation of CSNS has even to be suspended to wait for the RF conditioning of RFQ due to the sparking from May to June, 2018. After a series of analyses and experiments, the sparking reason is focused on the chopped beam.

Based on the injection beam parameters of RFQ, thermal analysis shows the chopped beam cannot melt the vane. The main damage of the lost beam on the vane top of RFQ is due to sputtering, which will cause the increase of surface roughness of vane. For the initial installation angle of the pre-chopper, most of the chopped beam lost in RFQ will hit on the same vane-top area. In order to solve the sparking problem caused by sputtering, the pre-chopper is rotated clockwise 45 degrees about the beam center. In addition, the envelope size of the beam into RFQ is also restricted by the smaller beam bore on the entrance plate of RFQ. The beam bore on the entrance plate now has the same size as the beam envelope. After improvements, the chopped beam almost does not bombard on the vanes but goes through the gap between vanes and then hits on the wall of RFQ.

Other improvements of RFQ include the development of a RF auto-conditioning program and the renovation of RF conditioning strategy. The program can automatically and quickly reduce the RF power feeding into the cavity to interrupt the sparking when sparking occurs, and then restore and increase the RF power feeding according to the settings after a period without sparking.

Two RF conditioning strategies are adopted in taking use of the RF auto-conditioning program. The main difference of the two strategies is the step value of power reduction when sparking occurs. Comparing to the second strategy, the first strategy limits the sparking number to a very small value by setting a larger step of power reduction. In this case, for most of the time, the power keeps on a lower value when sparking occurs. To reach the same operating power and duty factor, the time taken for RF conditioning of RFQ was 14 days from May 10 to May 23, 2018 by using the first strategy, while the taken time was only 9 days from Jun 12 to Jun 20 by using the second strategy. In addition, the RF conditioning of RFQ from May 31 to Jun 11 had no effect by using the first strategy.

After all above improvements have been done, the failure time of RFQ is dramatically reduced. For example, the total failure time of RFQ was about 477mins during subsequent operation period of CSNS from June 21, 2018 to July 13, 2018, the average failure time is about 22mins a day.

MEBT

All diagnostics instruments, the two bunchers and the 10 quadrupole magnets in MEBT work normally since the beam commissioning started in 2015. The normalized rms beam emittance measured at MEBT is about 0.22 π mm·mrad for both horizontal and vertical plane which is the same as the simulation result while the beam transmission keeps near to 100% during all the operation time.

THE LABORATORY OF ION SOURCE

There are three sets of ion source test stands in lab. The first one is the hot spare stand which aims to check the discharge chamber, create plasma discharge and produce pulsed arc (without beam extraction). This stand makes the time needed for exchanging the discharge chamber and putting ion source into operation again reduce to 3-4 hours. The second one, named on-line test stand of IS, consists of an ion source and a LEBT which are both the same with these in tunnel of CSNS. It is used to make IS improvements and beam diagnosis. The new developed extraction power supply with double voltage-output pulses is now experimented on this stand. The last one is RF ion source R&D stand [3]. Its purpose is to provide an RF ion source for the future upgrading of CSNS.

SUMMARY

The performance of CSNS front end was stable until May 2018. As to the beam characteristics of Penning IS, three solenoids and one beam collimator are used in LEBT to produce an appropriate beam and raise the beam transmission of RFQ. The beam damage to RFQ is also avoided through changing the installation angle of pre-chopper and reducing the beam bore on the entrance plate of RFQ. The conditioning strategy with higher efficiency is chosen for RFQ conditioning but needs to verify in the following operation of front end.

REFERENCES

[1] S. Liu *et al.*, "The modification at CSNS ion source," in *Fifth International Symposium on Negative Ions, Beams and Sources*, vol. 1869, D. Faircloth, Ed. AIP Conference Proceedings, 2017.

[2] Y. Xiao *et al.*, "Development of CSNS RFQ," *Nuclear Techniques,* vol. 38, no. 12, pp. 120201-1-120201-7, 2015 2015, Art. no. 0253-3219(2015)38:12<120201:zgslzz>2.0.tx;2-4.

[3] W. Chen *et al.*, "RF H-Minus Ion Source Development in China Spallation Neutron Source," in *Fifth International Symposium on Negative Ions, Beams and Sources*, vol. 1869, D. Faircloth, Ed. (AIP Conference Proceedings, 2017.

Content from this work may be used under the terms of the CC BY 3.0 licence (© 2018). Any distribution of this work must maintain attribution to the author(s), title of the work, publisher, and DOI.

ISBN: 978-3-95450-194-6 ISSN: 2226-0366 doi:10.18429/JACoW-LINAC2018-THPO040

OPERATION EXPERIENCES OF THE J-PARC LINAC

Kazuo Hasegawa*, for the J-PARC Linac group, J-PARC, JAEA/KEK, Tokai-mura, Japan

Abstract

The J-PARC linac has delivered beam to users since 2008. As of 2018, the linac provides a 40 mA beam at an energy of 400 MeV to the following Rapid Cycling Synchrotron. We have had many issues that impede high availability during the operation. One of them was troubles of high voltage power supply of klystrons. The other category is related to vacuum property in accelerating cavities. The cleaning of the inside surface of some acceleration cavities were performed after the big earthquake in 2011. The cooling water flow rate drop had been a long-time issue. We modified a cooling system to take better flow balances. As a result of these improvements, the availability is approximately 93% or more in these days. The operation experiences and availability improvement at the J-PARC linac are presented.

INTRODUCTION

The J-PARC facility consists of a linac, a 3-GeV Rapid Cycling Synchrotron (RCS), a 30-GeV Main Ring synchrotron (MR) and three experimental facilities[1]. The linac consists of a negative hydrogen ion source, a 3-MeV RFQ, a 50-MeV DTL (Drift Tube Linac), a 191-MeV SDTL (Separated-type DTL) and a 400-MeV ACS (after the upgrade) as shown in Fig. 1. RF frequencies are 324 MHz and 972 MHz for the low energy section (RFQ, DTL and SDTL) and for the high energy section (ACS), respectively. A proton beam from the RCS is injected to the Materials and Life Science Experimental Facility (MLF) for neutron and muon experiments. The MR has two beam extraction modes; a fast extraction (FX) for the neutrino beam line (NU) for the Tokai-to-Kamioka (T2K) experiment, and a slow extraction (SX) for the Hadron Experimental Facility (HD).

The goal of the J-PARC project is to deliver a 1-MW beam from the RCS and a 0.75-MW beam from the MR-FX. To achieve the goal, the linac have had big upgrade work such as peak current and energy upgrade[2]. On the way of the beam operation, we have had many issues that impede high availability and also have taken countermeasures.

BEAM HISTORY

The history of the beam power from the RCS to the MLF is shown in Fig. 2. User operation was started in 2008. At that time, trip rate of the RFQ was high and operation days and power ramp-up were limited. The beam current was low at 5 mA, and the RCS beam power was 20 kW. This was mostly settled by the vacuum improvement work during the summer shutdown of 2009 [3]. The progress of beam power of the J-PARC linac by 2015 is described in Ref[4].

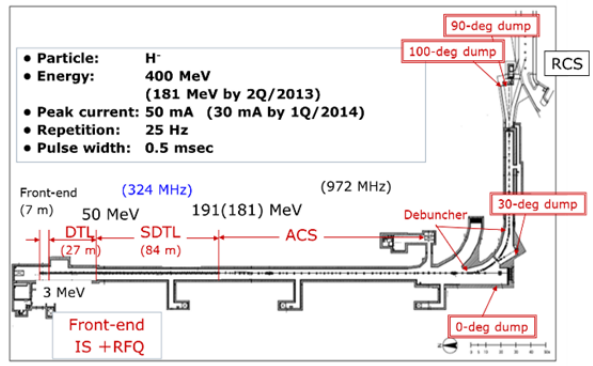


Figure 1: Configuration and main parameters of the J-PARC Linac

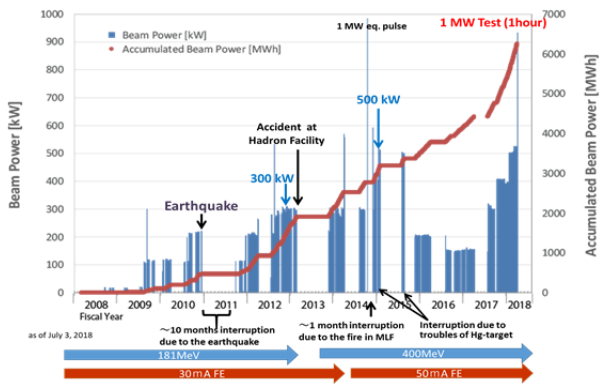


Figure 2: Beam power history for the MLF. (by courtesy of the MLF group, modified).

We had a crisis of the Great Earthquake in March 2011 and the J-PARC facilities were severely damaged. We resumed beam operation in December and user operation in January 2012[5]. We started beam operation sooner, but several aftereffects were left. The number of trips in the RFQ and some of the SDTL cavities was serious. As conditioning and operation days continued for half a year, the number of trips decreased as vacuum conditions went better. As described later, the SDTL remained issues.

We have steadily increased a beam power after the energy upgrade (from 181 to 400 MeV) in 2013 and beam current upgrade (ion source and RFQ replacement, from 30 to 50 mA) in 2014. As a result of these upgrade, we demonstrated a 1-MW-equivalent single shot beam from the RCS successfully. For continuous operation, we need to mitigate beam losses and to consolidate some power supplies, but this was a great milestone to perform the potential of accelerators.

We have steadily increased the beam power up to 500 kW at the MLF. But we had two neutron production target failures in April and November 2015[6]. After that, we used a spare target and the power was limited to 200-150 kW. During the maintenance period of summer 2017, we exchanged for a target with a new design[7]. Then we have gradually increased the power from 300 kW, 400

* hasegawa.kazuo@jaea.go.jp

Content from this work may be used under the terms of the CC BY 3.0 licence (© 2018). Any distribution of this work must maintain attribution to the author(s), title of the work, publisher, and DOI.

ISBN: 978-3-95450-194-6 ISSN: 2226-0366 doi:10.18429/JACoW-LINAC2018-THPO040

kW and 500 kW successfully, while checking target conditions.

OPERATION EXPERIENCE

The performance of accelerators is not only shown as a beam power but availability. Table 1 shows operation statistics in FY2017 (April 2017 to March 2018). Operation hours, which is defined by the shift-leader assigned time including RF conditioning, was 6,448 hours. The availability of 93% for MLF shows that the linac, the RCS and the MLF operated favorably.

Table 1: Availability for J-PARC facilities in Japanese Fiscal Year of 2017 (April 2017 – March 2018)

Facility	User time (hours)	Trouble, Acc. only (hours)	Trouble, Fac. only (hours)	Net time, (hours)	Availability, Total (%)
MLF	4,555	270 (5.9%)	35 (0.8%)	4,249	93.3
Neutrino (FX)	1,978	185 (9.4%)	35 (1.8%)	1,757	88.8
Hadron (SX)	1,601	506 (31.6%)	39 (2.4%)	1,055	65.9

Figure 3 shows downtime by major subsystems in FY2017. The "SlowExt" in the MR is due to nearly one month downtime by an electric static septum trouble. It was an exception in the year and the reason of the low availability of 66% for the MR-SX in Table 1. The linac (and the RCS also) is generally a key of the availability of the whole J-PARC facility because all the beams stop when these upstream facilities down. The RCS is rather stable, and the linac contributes most of the downtime, which makes beam stops and degrade availability.

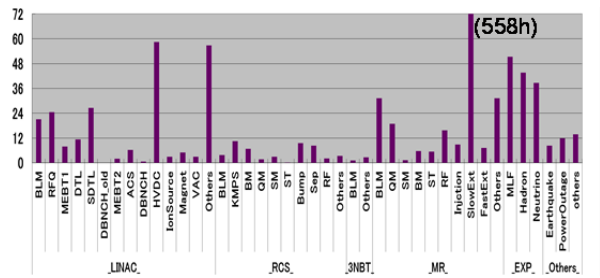


Figure 3: Downtime statistics in hours by components in FY 2017.

The categories "HVDC (high voltage power supply for klystrons", "Others", and "DTL and SDTL" are dominant causes in these years. These downtime variation from 2011 is shown in Fig. 4. We have had many countermeasures against troubles to improve availability.

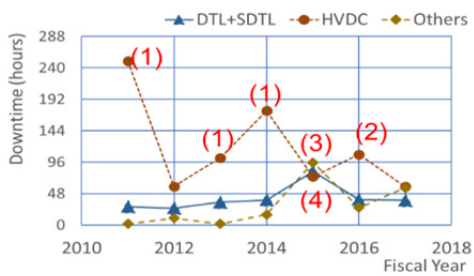


Figure 4: Downtime history for major causes.

Downtime in "HVPS"

Figure 5 shows a circuit diagram of the HVDC. The rectifier diodes at the 110 kV high voltage terminal were broken after the operation of 30,000 hours FY11, FY13 and FY14 as shown (1) in Fig.4. The reason was not clear at the beginning, but it was found out. Many steps of diodes are connected in series to rectify the high voltage. Capacitors are connected in parallel to the diode in order to reduce the influence of variations of the capacitance of the diode for the revers voltage. But due to the temperature difference in the insulation oil as well as aging effects, changing of the capacitance enhanced the voltage imbalance and the diodes were broken-down. As a measure, we have increased the series number of elements from 66 to 84 stages and better temperature characteristics capacitors. After that, we haven't had the same troubles, although not all the diode modules haven't replaced yet.

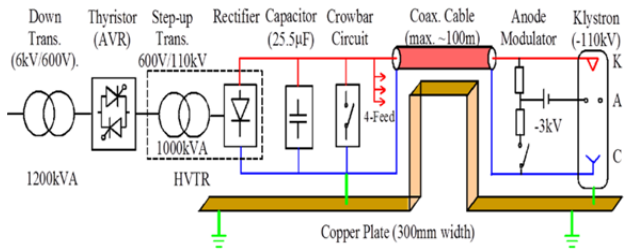


Figure 5: Circuit diagram of the HVDC.

We expected better downtime in 2015, but we faced another issues. Anode modulators, which consists of a bias power supply and a semiconductor switch as shown in Fig. 5, broken occasionally in FY16 as shown (2) in Fig. 4 and partly in FY15. The main reason is an aging of these parts. We replaced with new power supplies and switches, then the downtime reduces from 2017. But it was a mid-term measure and we should consider against root causes: cooling consolidation of the insulation oil and the circuits to take longer lifetime.

The "HVDC" is not limited to the power supply but covers high power RF components. Several defects comprised of a klystron failures and insulation breakdown of high voltage cables. We are using 20 324-MHz klystrons and most of the operation hour is roughly 50,000. When klystrons approach the end of life, number of discharges increases and availability goes down. We have 11 replaced klystrons as of summer 2018 and average operation time of these is 41,870 hours. It is important to take systematic procurement to keep operation availability.

Downtime in "Others"

The category of "Others" in 2015 as shown (3) in Fig. 4 is higher than usual. It consists of several utility related downtime. The cooling tower failure stopped for 19 hours, then we added a new cooling tower to be a redundant system. Cooling water valve failure stopped for 11 hours, Ventilation system was stopped for 32 hours due to grounding. We took leak current sensors but the grounding hasn't occurred again and the reason has not clear yet.

Content from this work may be used under the terms of the CC BY 3.0 licence (© 2018). Any distribution of this work must maintain attribution to the author(s), title of the work, publisher, and DOI.

ISBN: 978-3-95450-194-6 ISSN: 2226-0366 doi:10.18429/JACoW-LINAC2018-THPO040

Content from this work may be used under the terms of the CC BY 3.0 licence (© 2018). Any distribution of this work must maintain attribution to the author(s), title of the work, publisher, and DOI.

Another cause in "Others" is related to network and control devices as a baseline of FY16 and FY17. Some of these components are 15 years old or more and it's a timing to replace new ones. Some of the components' faults are not easy to define the caused devices. It takes long time to identify and restart a beam.

Downtime by Cooling Water Flow Drop

Some other linac downtimes were groups in "DTL" and "SDTL". The condition of the cavities is not poor except for some SDTL cavities with multipacting. As an issue at the linac in these years, some cooling water flow rates gradually decreased with the operation over several days to several weeks. When it drops below the preset flow rate, the beam stops to protect components. Then we have to enter the accelerator tunnel and re-adjust the flow rate. It stopped at least for several hours.

In the "DTL+SDTL" category in FY15 as shown (4) in Fig. 4, cooling water flow decrease stopped beam operation several times. We adjusted cooling water flow rates in the weekly scheduled maintenance day, but some of the flow rates dropped unexpectedly.

One of the reasons was that the flow of one cooling water pump was largely branched to the north (4,000L/min) and the south (1,200L/min), and the balance of the system was lost due to the many branches. In order to solve it, a pump for the south was added and separated from the north path[8]. Furthermore, in particular the flow balance in a narrow channel is more sensitive, the inner surfaces of the coil of the Q magnets were cleaned using compressed air and water to remove the accumulated sludge.

Figure 6 shows the flow rate before and after these measures for two months. The flow rate is stabilized after the measures.

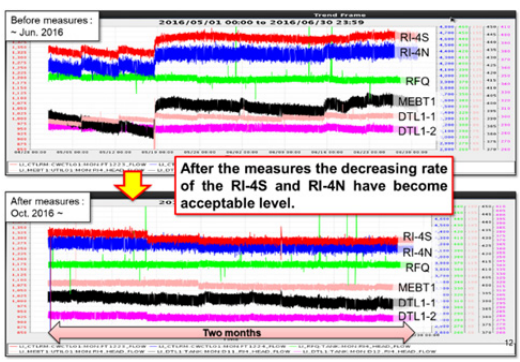


Figure 6: Cooling water flow rates for several cavity systems before (top) and after (bottom) the measure.

Multipacting at SDTL Cavities

Since the earthquake in 2011, several SDTL cavities became unstable (the reflection increased in the vicinity of the designed RF power), and since 2015 we have had an internal cleaning (wiping by acetone dipped cloth)[9]. As a result, good results have been obtained that the RF reflection decreases. Figure 7 shows the VSWR of the SDTL #5 cavities (it consists of two cavities of tank-A and B). The tank-B is stable by the cleaning in the previous year, but the tank-A has a high reflection area. As a result of cleaning, the unstable area disappeared. By that time, in order to avoid the unstable area, we had to operate at higher power level than the design value, but it is possible to operate with the design value. The discharge frequency of the cavities was also suppressed and stable operation can be performed.

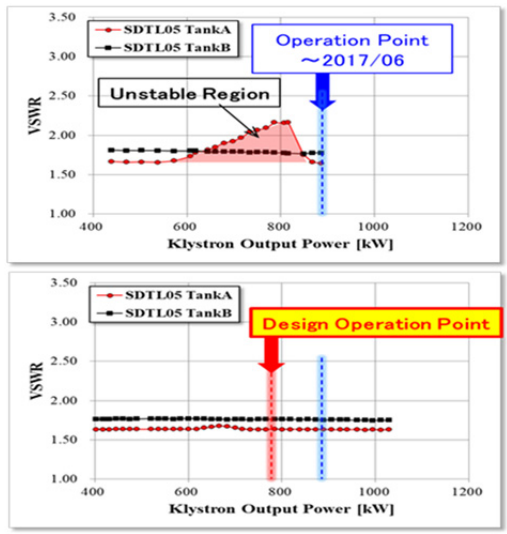


Figure 7: Voltage standing wave ratio for the SDTL#5 (Tank-A and B) cavities before (top) and after (bottom) the clean-up of the SDTL#05-tank-A cavity.

SUMMARY

The linac shows good performance to deliver beam to fulfil the J-PARC goal. We have had many hardware upgrades, modifications and beam commissioning to improve the performance. The linac and the RCS provide beams to the MLF and the MR. After the replacement with the new designed neutron production target at MLF, we increased a power step by step up to 500 kW for user operation. High power beam at 1 MW 1-hour was successfully demonstrated on July 3 before the summer shutdown 2018.

There are several sources of downtimes. Some of them come from aged components after 10 years of user operation. To obtain better availability in the limited resources, risk analysis like procedure and prioritization are to be processed.

ACKNOWLEDGEMENT

The authors would like to acknowledge the linac group members to perform the operation and upgrade work. We would like to give special thanks to Drs. H. Oguri, T. Ito, E. Chishiro and F. Naito for useful discussion and help of materials.

REFERENCES

[1] J-PARC, http://www.j-parc.jp

ISBN: 978-3-95450-194-6 ISSN: 2226-0366 doi:10.18429/JACoW-LINAC2018-THPO040

[2] H. Oguri, "Approaches to High Power Operation of J-PARC Accelerator", presented at LINAC18, Beijing, China, paper MO1P02, this conference.
[3] K. Hasegawa *et al.*, "Status of the J-PARC RFQ", *in Proc. IPAC'10*, pp. 621-623.
[4] K. Hasegawa, "Progress and Operation Experiences of the J-PARC Linac", in *Proc. LINAC2016*, pp. 257-260.
[5] K. Hasegawa, "Recovery of the J-PARC Linac from the Earthquake", in *Proc. LINAC2012*, pp. 1069-1073.
[6] K. Haga *et al.*, "Technical Investigation on Small Water Leakage Incident Occurrence in Mercury Target of J-PARC", in *J. Nucl. Sci. Tech.*, 55, pp.160-168 (2018).
[7] T. Wakui *et al.*, "Recent Study for Structural Integrity Evaluation and Defect Inspection of the J-PARC Spallation Neutron Target Vessel", in *J. Nucl.Mater.*, 506 pp. 3-11 (2018).
[8] K. Suganuma *et al.*, "Present Status of Water Cooling System at J-PARC Linac 2018", in *Proc. of PASJ2018*, Nagaoka, Niigata, Japan, paper WEP012, to be published (2018).
[9] T. Ito *et al.*, "Multipactor Problem of J-PARC SDTL", in *Proc. IPAC2017*, pp. 4184-4186.

Content from this work may be used under the terms of the CC BY 3.0 licence (© 2018). Any distribution of this work must maintain attribution to the author(s), title of the work, publisher, and DOI.

ISBN: 978-3-95450-194-6 ISSN: 2226-0366 doi:10.18429/JACoW-LINAC2018-THPO042

AN OPTIMIZATION METHOD OF THE NOSE-CONE BUNCHER CAVITY

W. L. Liu, P. T. Cong, Z. M. Wang, State Key Laboratory of Intense Pulsed Radiation Simulation and Effect (Northwest Institute of Nuclear Technology), Xi'an 710024, China
S. X. Zheng[1,2], H. P. Jiang[3], Department of Engineering Physics, Tsinghua University, Beijing 100084, China
[1]also at Key Laboratory of Particle & Radiation Imaging (Tsinghua University), Ministry of Education, Beijing 100084, China
[2]also at Laboratory for Advanced Radiation Sources and Application, Tsinghua University, Beijing 100084, China
[3]also at Space Environment Simulation Research Infrastructure, Harbin Institute of Technology, Harbin 150001, China

Abstract

The nose-cone buncher cavity is widely used on proton accelerators. It's important to properly optimize the cavity geometry for fine RF performance. However, currently the optimization is usually carried out manually and the criteria are not objective enough. In this paper, an optimization method using the multi-objective, multi-variable optimization approach is presented. The geometry and RF parameters are considered as the variables and objectives respectively. The goal function is defined as the weighted sum of multiple RF parameters. The multi-variable functions are approximately derived from the single-variable functions based on electromagnetic simulation. And an optimization code is developed accordingly which has been applied to the XiPAF debuncher optimization.

INTRODUCTION

The Xi'an proton application facility (XiPAF) is a synchrotron proton accelerator built for radiation effects research. There's a debuncher on the medium energy transport line (MEBT) to reduce the beam energy spread. The nose-cone buncher cavity is adopted, which has been widely used on proton accelerators as bunchers or debunchers [1, 2]. Since the RF performance depends on the cavity geometry, the optimization of the cavity geometry is a vital procedure of debuncher design. The optimization aims for optimized RF performance like low probability of RF breakdown and high shunt impedance and Q factor while keeps the resonance frequency exactly equal to the RF frequency, which is 325 MHz in the case of XiPAF.

A lot of optimization work of nose-cone buncher cavities has been carried out, in which, the manual way that determining the geometry parameters by evaluating their effects on the RF parameters based on electromagnetic (EM) simulation is adopted accordantly [1-4]. However, since multiple RF parameters should be optimized synchronously while their values are decided by multiple geometry parameters, the criteria of the manual optimization approach are not objective enough and the results mostly rely on experience. Therefore, a common optimization method which could automatically accomplish the nose-cone buncher cavity optimization under specific demands is in need.

An optimization method using the multi-objective, multi-variable optimization approach is presented in this paper. By treating geometry parameters and RF parameters as the variables and objectives respectively, the optimized cavity geometry would be obtained mathematically via optimization algorithm.

APPROXIMATE FUNCTION

Relation Between RF and Geometry Parameters

The function between variables and objectives are the footstone of multi-objective, multi-variable optimization. The RF and geometry parameters considered as the variables, objectives and constraint in the optimization are shown in Table 1. Three geometry parameters that affect the cavity geometry most intensely are adopted as the optimization variables primarily.

Using EM simulation software CST a parametric model of the nose-cone cavity is established as shown in Fig. 1, based on which the relation between the RF and geometry parameters is studied by parameter sweep. The effective cavity voltage VT is 160 kV and the beam energy E_{beam} is 7 MeV while calculating the bravery factor b and the transient time factor T.

Applying polynomial fit to the simulation data, one-dimensional approximate functions between RF and geometry parameters are acquired.

Table 1: Variables, Objectives and Constraint

roles	parameters	symbol
objective	effective shunt impedance	R
	Q factor	Q
	bravery factor	b
variable	cavity radium	r
	gap length	g
	nose cone angle	t
constraint	resonance frequency	f

Approximate Function between RF and Geometry Parameters

The multidimensional functions that contain all variables for each objective are in need to accomplish the optimization. It can be approximately derived from the one dimension functions acquired via EM simulation.

Content from this work may be used under the terms of the CC BY 3.0 licence (© 2018). Any distribution of this work must maintain attribution to the author(s), title of the work, publisher, and DOI.

ISBN: 978-3-95450-194-6 ISSN: 2226-0366 doi:10.18429/JACoW-LINAC2018-THPO042

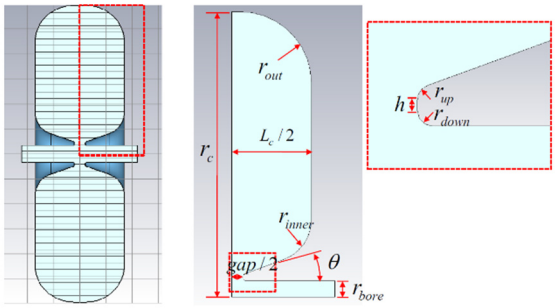


Figure 1: The parametric EM model of the nose-cone cavity.

Assuming that the wanted approximate functions of RF parameters are in the form of polynomial as follows:

$$F(x,y,z) = F_1(x) + F_2(y) + F_3(z) + A \tag{1}$$

where A is an unknown constant and F_j is a one-dimensional polynomial function:

$$F_j(t) = \sum_{i=1}^{n} p_{ji} t^i \quad t = x, y, z; \quad j = 1,2,3; \quad n = 1,2,..... \tag{2}$$

where p_{ji} is the polynomial coefficient. According to the EM simulation result, F as one-dimensional functions near the anchor point of the 3-dimensional domain (x_0, y_0, z_0) are acquired. Then F_j can be derived from the following equations:

$$F(x,y,z)|_{y=y_0,z=z_0} = F_1(x) + A_1 \tag{3}$$

$$F(x,y,z)|_{z=z_0,x=x_0} = F_2(y) + A_2 \tag{4}$$

$$F(x,y,z)|_{x=x_0,y=y_0} = F_3(z) + A_3 \tag{5}$$

where A_1, A_2, A_3 are unknown constants. Name the value of $F(x, y, z)$ at (x_0, y_0, z_0) as F_0.

$$F_0 = F(x_0,y_0,z_0) = F_1(x_0) + F_2(y_0) + F_3(z_0) + A \tag{6}$$

Then $F(x, y, z)$ can be expressed with F_0 and F_j.

$$\begin{aligned} F(x,y,z) &= F_0 + (F - F_0) \\ &= F_0 + [F_1(x) - F_1(x_0)] + [F_2(y) - F_2(y_0)] + [F_3(z) - F_3(z_0)] \\ &= \sum_{i=1}^{n} p_{1i}(x^i - x_0^i) + \sum_{i=1}^{n} p_{2i}(y^i - y_0^i) + \sum_{i=1}^{n} p_{3i}(z^i - z_0^i) + F_0 \end{aligned} \tag{7}$$

By this means the approximate function of the objectives can be expressed as follows:

$$Q(r,g,t) = \sum_{i=1}^{n} p_{ri}(r^i - r_0^i) + \sum_{i=1}^{n} p_{gi}(g^i - g_0^i) + \sum_{i=1}^{n} p_{ti}(t^i - t_0^i) + Q_0 \tag{8}$$

$$R(r,g,t) = \sum_{i=1}^{n} p_{ri}(r^i - r_0^i) + \sum_{i=1}^{n} p_{gi}(g^i - g_0^i) + \sum_{i=1}^{n} p_{ti}(t^i - t_0^i) + R_0 \tag{9}$$

$$E(r,g,t) = \sum_{i=1}^{n} p_{ri}(r^i - r_0^i) + \sum_{i=1}^{n} p_{gi}(g^i - g_0^i) + \sum_{i=1}^{n} p_{ti}(t^i - t_0^i) + E_0 \tag{10}$$

as well as the approximate constraint function:

$$f(r,g,t) = \sum_{i=1}^{n} p_{ri}(r^i - r_0^i) + \sum_{i=1}^{n} p_{gi}(g^i - g_0^i) + \sum_{i=1}^{n} p_{ti}(t^i - t_0^i) + f_0 \tag{11}$$

The range of parameters are shown in Table 2 which covers the existing application of buncher cavities reported [1-4]. In order to get fine accuracy the whole range is separated into three parts and the frequency at three anchor points are 310 MHz, 330 MHz, 350 MHz.

Table 2: Range of Parameters

parameters	range	anchor point
f/MHz	300~360	310,330,350
g/mm	10~25	17.5
t/°	10~45	27.5
r/mm	236.9~313.8	298.9，271.6，247.6

OPTIMIZATION ALGORITHM

Goal Function

To solve the optimization mathematically a goal function is in need firstly. Knowing the aim of optimization is to get larger Q and R as well as lower b, the goal function is defined as the weighted sum of those RF parameters where the weight of b is minus. Then considering the approximate functions of the RF and geometry parameters the goal function can be expressed as

$$P(g,t,r) = k_Q Q(g,t,r) + k_R R(g,t,r) - k_b b(g,t,r) \tag{12}$$

Where k_F is the weight value of each objective, initially set as 1. Note that Q, R, b are parameters with different dimensions. In order to add them up the non-dimensional values are adopted as shown in Table 3. The bigger the P is, the more the corresponding result is preferred under the given weight values.

Table 3: Units for the Non-Dimensional Values

objectives	unit
Q	10^4
R	MΩ
b	1

For the expected RF frequency f_{RF}, the constraint condition is as follows:

$$f(g,t,r) = f_{RF} \tag{13}$$

Optimization Code

An optimization code is developed with MATLAB accordingly. It could automatically output a set of optimized geometry parameters g, t, r corresponding to the given frequency and weights. The run time of the code is only a few seconds since the calculation is as complex as the second order polynomial. The algorithm of the code is as follows:

- Set the optimization conditions including f_{RF} and weights k_Q, k_R, k_b.
- Sweep the variables g, t while calculate the corresponding r using the constraint condition. The step widths are Δg =0.5 mm, Δt =2.5 ° . The ranges of g, t are shown in Table 2.

Content from this work may be used under the terms of the CC BY 3.0 licence (© 2018). Any distribution of this work must maintain attribution to the author(s), title of the work, publisher, and DOI.

ISBN: 978-3-95450-194-6 ISSN: 2226-0366 doi:10.18429/JACoW-LINAC2018-THPO042

Content from this work may be used under the terms of the CC BY 3.0 licence (© 2018). Any distribution of this work must maintain attribution to the author(s), title of the work, publisher, and DOI.

- Calculate the goal function P with current variables at each step.
- Select the optimized variables g_{best}, t_{best}, r_{best} corresponding to the biggest P, *i.e.*, P_{best} as the optimization solution.

Figure 2 is the flow chart of the optimization code.

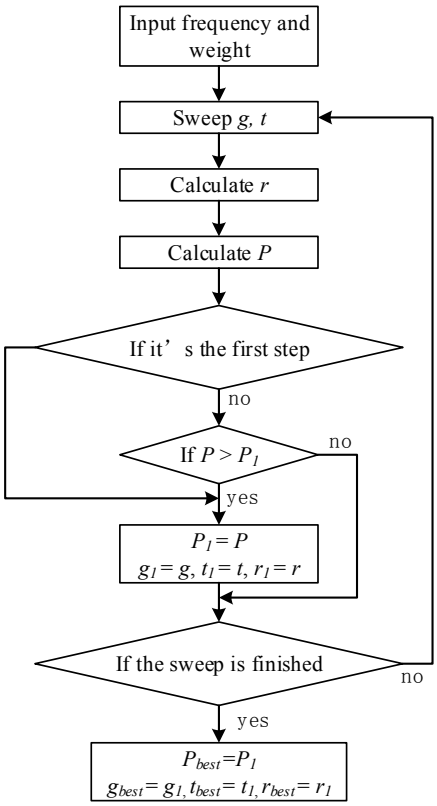


Figure 2: The flow chart of the code.

Performance of Optimization Code

Test the performance of optimization code by comparing the optimization results with the anchor point where f is 330 MHz. Calculate the corresponding RF parameters by CST and the results and conditions are shown in Table 4.

Table 4: Conditions and Results of the Test Run

parameters		initial	optimized
constraint	f / MHz	330.0	329.8
objectives	Q	28486	30065
	R / MΩ	3.69	3.81
	b	1.13	0.99
variables	r / mm	271.6	299.5
	g / mm	17.5	25
	t / °	27.5	10
conditions	VT/ kV	160	160
	E_{beam} / MeV	7	7
	f_{RF} / MHz	330	330
	k_Q, k_R, k_b	-	1

It's obvious that all the RF parameters are optimized while the constraint is satisfied within the accuracy of 1 MHz.

OPTIMIZATION OF THE XIPAF DEBUNCHER

Utilize the code to optimize the XiPAF debuncher cavity. In the initial run all the weights are set as 1 while Q and b are optimized compared to the original design that accomplished by manual optimization approach. In order to get better R, adjust the weights in the following run. When kQ, kR, kb are set as 4, 4, 1 respectively, all three RF parameters are optimized as shown in Table 5. The eventual optimized result (optimized 2 in Table 5) is adopted for the XiPAF debuncher manufacture.

Table 5: Optimization of the XiPAF Debuncher

parameters		original	optimized 1	optimized 2
constraint	f / MHz	324.9	324.8	325.7
objectives	Q	27155	30166	28973
	R / MΩ	3.86	3.84	4.09
	b	1.32	0.99	1.11
variables	r / mm	261.2	305.5	291.1
	g / mm	13	25	20
	t / °	20	10	10
conditions	VT / kV	160	160	160
	E_{beam} / MeV	7	7	7
	f_{RF} / MHz	325	325	325
	k_Q	-	1	4
	k_R	-	1	4
	k_b	-	1	1

CONCLUSION

By applying the multi-objective, multi-variable approach to the nose-cone cavity optimization, the optimization code could output the optimized geometry parameters corresponding to the given weights and frequency. It would be a sufficient supplement to the manual optimization work. The optimization result of the XiPAF debuncher via the code has been adopted for manufacture. Currently only three of the geometry parameters are considered as variables while all of them affect the RF performance of the cavity. Besides the suitable beam energy for utilizing the code is 7 MeV only. These should be improved in the further work.

REFERENCES

[1] S. Pei, H. Ouyang, J. Zhang, X. Li, "325 MHz CW room temperature high power bunching cavity for the China ADS MEBT1". in *Proc. LINAC'12*, Tel-Aviv, Israel, 2012, paper THPB025, pp.903-905.

[2] M. Larrañaga, R. Enparantza, C. Plostinar, "Design optimisation of the re-bunching cavities for the Front End Test Stand at RAL", in *Proc. LINAC'10*, Tsukuba, Japan, 2010, paper MOP080, pp.238-240.

[3] Oscar González, Juan Luis Muñoz, Ibon Bustinduy, "Preliminary Electromagnetic Design of the Re-bunching RF Cavities for the ESS MEBT", ESS Bilbao, Spain, Rep. ESS/AD/0036, March 2012.

[4] Liu Hua-Chang, Ouyang Hua-Fu, "Thermal analysis and water-cooling design of the CSNS MEBT 324 MHz buncher cavity", *Chinese Physics C*, vol. 32, no. 4, pp.280-284, Apr. 2008.

ISBN: 978-3-95450-194-6 ISSN: 2226-0366 doi:10.18429/JACoW-LINAC2018-THPO043

ESS NORMAL CONDUCTING LINAC STATUS AND PLANS

E. Sargsyan†, H. Danared, F. Hellström, G. Hulla, Ø. Midttun, J. S. Schmidt, European Spallation Source ERIC, Lund, Sweden
L. Celona, S. Gammino, L. Neri, INFN-LNS, Catania, Italy
A-C. Chauveau, B. Pottin, CEA/IRFU, Gif-sur-Yvette, France
I. Bustinduy, N. Garmendia, J. L. Muñoz, ESS-Bilbao, Bilbao, Spain
F. Grespan, A. Pisent, INFN-LNL, Legnaro, Italy
P. Mereu, INFN-Torino, Torino, Italy

Abstract

The European Spallation Source (ESS) uses a linear accelerator to deliver the high intensity proton beam to the target station for producing intense beams of neutrons. The average beam power is 5 MW with a peak beam power at the target of 125 MW. The normal conducting linear accelerator (linac) operating at 352.21 MHz accelerates a proton beam of 62.5 mA from 0.075 to 90 MeV. It consists of an ion source, Low Energy Beam Transport (LEBT), Radio Frequency Quadrupole (RFQ), Medium Energy Beam Transport (MEBT), and Drift Tube Linac (DTL). The design, construction and testing of those structures is done by European partner labs as an in-kind contribution to the ESS project. This paper presents the status and plans for the ESS normal conducting linac.

INTRODUCTION

The ESS linear accelerator (linac) generates and accelerates protons to 2 GeV energy, delivering them onto a rotating tungsten target to create neutrons, via the spallation process, for use by research instruments [1]. The linac is composed of normal conducting structures followed by superconducting spoke and elliptical cavities. The layout of the ESS linac is shown in Fig. 1. The normal conducting linac (NCL) consists of an ion source, Low Energy Beam transport (LEBT), Radio Frequency Quadrupole (RFQ), Medium Energy Beam Transport (MEBT) and Drift Tube Linac (DTL). The NCL operates at 352.21 MHz frequency, 14 Hz repetition rate, with 62.5 mA peak beam current and 2.86 ms beam pulse length.

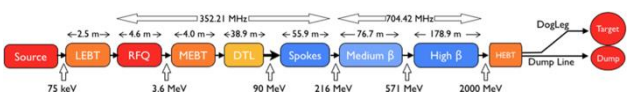


Figure 1: Layout of the ESS linac.

STATUS AND PLANS

The ESS facility is currently under construction, with the start of the user programme planned for 2023. The installation of the utilities and accelerator components in the accelerator tunnel and the klystron gallery is ongoing at ESS. All sections of the ESS NCL are presently under construction, while the ion source and LEBT are already delivered and installed at ESS. A brief description, status and plans for the ESS NCL are presented below.

† edgar.sargsyan@esss.se

Ion Source and LEBT

The ion source and LEBT are in-kind contribution from INFN-LNS, Catania, Italy. The source is a 2.45 GHz microwave discharge ion source with a flexible magnetic system [2]. The requirements include proton beam current of 74 mA, normalised rms emittance of 0.25 π.mm.mrad at the RFQ entrance, proton fraction of >75%, intra-pulse beam current stability of ±2%, pulse to pulse stability of ±3.5%, repetition rate of 14 Hz, beam pulse length of 6 ms from the source and 2.86 ms in the LEBT. The LEBT consists of two solenoid magnets with embedded steerers, and beam diagnostics to measure the beam current, emittance, position, and fraction. It also contains a fast electrostatic chopper to remove the first part of the beam pulse during which the plasma needs to stabilise. An iris with six movable blades reduces the beam current for running the linac in low-power mode.

The ion source and LEBT were installed and commissioned in Catania prior to the delivery to ESS. The range of possible extracted beam currents and stability were measured during the spring 2017 [3]. The current range with stable beam was 40-120 mA. With the nominal ion source settings, the fractions of the different ion species were 85%, 12% and 3% for protons, H_2^+ and H_3^+ respectively. With this proton fraction, the proton beam current was 85 mA. The measured stability was ±1.5% inside the beam flat top, and ±3% among pulses as shown in Fig. 2.

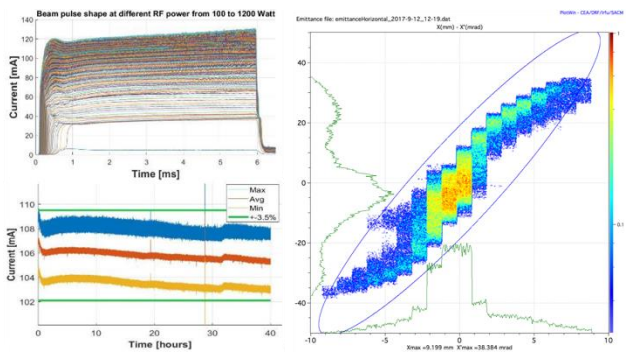


Figure 2: Ion source intra-pulse beam stability (top left), pulse-to-pulse stability (bottom left), and emittance at the RFQ entrance (right).

The ion source produced the nominal time structure of 6 ms pulse length and 14 Hz repetition rate, with the first 3 ms removed by the chopper. Beams with flat top pulse

Content from this work may be used under the terms of the CC BY 3.0 licence (© 2018). Any distribution of this work must maintain attribution to the author(s), title of the work, publisher, and DOI.

ISBN: 978-3-95450-194-6 ISSN: 2226-0366 doi:10.18429/JACoW-LINAC2018-THPO043

Content from this work may be used under the terms of the CC BY 3.0 licence (© 2018). Any distribution of this work must maintain attribution to the author(s), title of the work, publisher, and DOI.

length in the range of 1-3 ms have been produced, without significant changes in the beam current.

The emittance was measured 150 mm downstream the LEBT-RFQ lattice interface. The measured emittance containing 99% of the beam current was 2.26 π.mm.mrad (see Fig. 2), which is within the required value. Further optimisations will be done during the beam commissioning phase at ESS.

The ion source and LEBT were delivered to ESS in Dec. 2017 and installed in Jan-Feb 2018 by INFN-LNS. A safety fence with lead shielding and access control is installed around the ion source to protect personnel from the high voltage and X-rays. This enables commissioning and operation of the ion source and LEBT while allowing access to the tunnel for installation. Figure 3 shows the ion source, safety fence and LEBT installed at ESS.



Figure 3: Ion source (left), safety fence and LEBT (right) installed at ESS.

A Safety Readiness Review with an external committee was successfully held at ESS in July 2018. The systems are now ready for the beam commissioning starting in Sep. 2018. The first plasma was obtained on Sep. 11, 2018 and is currently being conditioned. The commissioning and long-term tests of the ion source and LEBT will continue up to the delivery of the RFQ to ESS.

RFQ

The design, construction, installation and RF conditioning of the ESS RFQ is done by CEA/IRFU, France. It is a 4.6-meter long, four-vane accelerating structure designed to bunch and accelerate the proton beam from 75 keV to 3.62 MeV energy at a frequency of 352.21 MHz [4, 5]. The design is based on a sinusoidal evolution of the inter-vane voltage, which is increasing from 80 to 120 kV over the length of the RFQ. The RFQ is made of pure copper in five sections of 0.9 m each. The vanes are machined with 20 μm precision, then positioned and brazed with 30 μm precision. Two power couplers transfer the RF power to the cavity. The total required peak RF power is 1.6 MW. Each coupler is able to handle a maximum peak RF power of 1 MW.

A test stand, shown in Figure 4, has been built at CEA for testing and validation of various components of the RFQ [6]. A test cavity was used for the conditioning of the power couplers and validation of interfaces. The two power couplers and a spare have been successfully conditioned on the test cavity in March 2018, reaching 1 MW peak power, 14 Hz repetition rate and 3.6 ms pulse length.

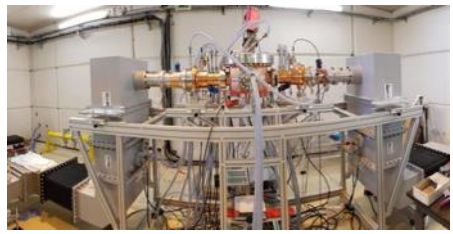


Figure 4: RFQ coupler conditioning test stand at CEA.

The prototypes of adjustable tuners are machined, brazed, and successfully tested. The water-cooling skid of the RFQ has been delivered to ESS in May 2018. It was installed and successfully tested in June 2018 (see Fig. 5).



Figure 5: RFQ water-cooling skid installed at ESS.

The machining of the RFQ vanes is ongoing. Each machining stage is first performed and validated on an aluminium mock-up before repeating it on the actual copper vane. Bead-pull measurements are done before and after the brazing of the vanes together for each section in order to verify the voltage law. A brazing mock-up has been prepared and successfully tested, including vacuum leak test, to validate the brazing process.

The RFQ will be first assembled and tested, excluding high-power RF, at CEA. The delivery to ESS is expected in Dec. 2018. The assembly and tuning in the tunnel is planned during Q1 2019. Once the RF system is available, the conditioning of the RFQ can start in Q3 2019. A temporary shielding wall will be installed across the tunnel at the location of the last DTL tank, to allow for installation of the superconducting linac downstream while the RFQ, MEBT and DTL are being commissioned.

MEBT

The design, construction, testing and installation of the MEBT is done by ESS-Bilbao, Spain. The 3.81-meter long MEBT [7] transports and matches the RFQ output beam to the DTL both transversally and longitudinally. The transverse focusing is done by 11 quadrupoles with embedded steerers, and the longitudinal matching is done by three buncher cavities resonating at 352.21 MHz and providing an effective gap voltage of 150 kV. A strip-line fast chopper removes longitudinal edges of the 3.62 MeV beam with a rise time of <10 ns, acting together with the slow LEBT chopper. The deflected beam is intercepted by an adjustable beam dump, which is designed to absorb a maximum peak beam power of 240 kW and 40 μs pulse length. A comprehensive set of beam diagnostics includes 8 Beam Position Monitors (BPM), 3 Beam Current Transformers (BCM), 2 Non-invasive Profile Monitors (NPM), 3 Wire Scanners (WS), a Longitudinal Beam Profile Monitor (LBPM), Slit-Grid emittance measurement unit, and a

ISBN: 978-3-95450-194-6 ISSN: 2226-0366 doi:10.18429/JACoW-LINAC2018-THPO043

Faraday Cup (FC). A set of collimators along the MEBT are designed to scrape particles at large beam radii.

The first magnet [8] has been successfully tested and delivered to Bilbao in May 2018 (see Fig. 6). The remaining magnets will be delivered in Oct. 2018. All three bunchers [9] have been manufactured in stainless steel and copper plated (see Fig. 6). Vacuum, low-power RF and bead-pull measurements have been successfully done.

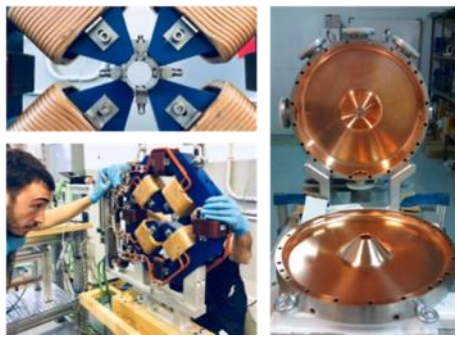


Figure 6: MEBT quadrupole with and without embedded BPM (top left, bottom left) and buncher (right).

The chopper and its vacuum vessel have been manufactured, and high voltage vertical integration tests have been successfully done in Bilbao achieving 5.4 kV with 6.3 ns rise time. The three WSs, the first set of collimators and their vacuum vessels have been received and tested in Bilbao. The BPMs have successfully passed vacuum tests and are currently being RF tested in Bilbao. The FC has been tested and integrated, including tests with 45 keV, 40 mA beam from the Bilbao ECR ion source.

Prior to the delivery and installation at ESS, the MEBT will be fully assembled in Bilbao in Q4 2018. This will allow verification of mechanical interfaces and validation of the assembly and alignment procedure. The installation in the ESS accelerator tunnel is planned for Q1 2019.

DTL

The design, constructions, testing, installation and RF conditioning of the DTL is done by INFN-LNL, Italy. The 39-meter long DTL is designed to accelerate the proton beam from 3.6 to 90 MeV and operates at a frequency of 352.21 MHz [10, 11]. Each of the five DTL tanks consists of 4 modules of ~2 m length and a diameter of 521 mm. The tanks are made of stainless steel with copper plated internal surface. The drift tubes contain a total of 89 permanent magnet quadrupoles (PMQ) and 30 steerers. Each tank is equipped with two power couplers to feed the required 2.2 MW peak RF power into the DTL tanks. A total of 123 post couplers have been integrated for field stabilisation during the tuning process. Active tuners control the resonance frequency during operation and tune the field distribution locally. DTL tanks contain 17 BPMs and the inter-tanks sections contain 5 BCMs and 2 FCs.

The machining of the DTL tanks and girders is ongoing. All four sections of the DTL tank #4 (first to be assembled and installed) are completed. One of the sections has been copper plated (see Fig. 7). The machining of the drift tubes is done at INFN in Legnaro and Torino. The PMQs and steerers are delivered to INFN-LNL and are being assembled into the drift tubes. The first batch of eight drift tubes have been brazed at INFN-LNL.

An aluminium mock-up model of the DTL has been produced by INFN-LNL in order to optimise the tuning procedure and to train the personnel. The tuning of the mock-up has been successfully accomplished (see Fig. 8).



Figure 7: First copper plated DTL section at GSI (left) and aluminium mock-up model of the DTL (right).

The assembly of the DTL tanks will be done in a dedicated workshop at ESS. The workshop is currently being installed in the klystron gallery technical area. The assembly of the first tank is planned to start in Nov. 2018 and the installation in the tunnel in Q2 2019.

REFERENCES

[1] R. Garoby *et al.*, "The European Sapllation Source design", *Physica Scripta*, vol. 93, p. 014001, Dec 2017.

[2] L. Celona *et al.*, "A high intensity proton source for the European Spallation Source facility", in *Proc. IPAC'15,* Richmond, VA, USA, paper WEPWA010.

[3] L. Neri *et al.*, "Beam commissioning of the high intensity proton source developed at INFN-LNS for the European Spallation Source", in *Proc. IPAC'17*, Copenhagen, Denmark, May 2017, paper WEOBB2, pp. 2530-2532.

[4] A. Ponton, "Note on the ESS RFQ design update", ESS, Lund, Sweden, Rep. ESS-0036077, 2013.

[5] A. France, M. Desmons, O. Piquet, "ESS RFQ radiofrequency design", CEA, Saclay, France, Rep. CEA-ESS-RFQ-RP0002A, 2015.

[6] N. Misiara *et al.*, "The Saclay test stand for conditioning the ESS RFQ power couplers at high RF power", in *Proc. IPAC'18*, Vancouver, BC, Canada, May 2018, paper WEPMF004, pp. 2375-2377.

[7] I. Bustinduy *et al.*, "Progress on ESS medium energy beam transport", in *Proc. LINAC'14*, Geneva, Switzerland, Sep. 2014, paper TUPP025.

[8] D. Fernández *et al.,* "Quadrupole magnet design for the ESS MEBT", in *Proc. IPAC'17*, Copenhagen, Denmark, May 2017, paper THPIK082.

[9] O. González *et al.*, "RF design and low power measurements of a nose cone single gap buncher cavity", in *Proc. LINAC'14*, Geneva, Switzerland, Sep. 2014, paper THPP025.

[10] F. Grespan *et al.*, "ESS DTL design and drift tube prototypes" in *Proc. LINAC'14*, Geneva, Switzerland, Sep. 2014, paper THPP087.

[11] P. Mereu *et al.*, "ESS DTL mechanical design and prototyping", in *Proc. IPAC'16*, Busan, Korea, May 2016, paper WEPMB008.

Content from this work may be used under the terms of the CC BY 3.0 licence (© 2018). Any distribution of this work must maintain attribution to the author(s), title of the work, publisher, and DOI.

ISBN: 978-3-95450-194-6 ISSN: 2226-0366 doi:10.18429/JACoW-LINAC2018-THPO045

TUNING ESPERIENCE ON THE ESS DTL COLD MODEL

F. Grespan, A. Baldo, P. Bottin, G. S. Mauro, A. Palmieri, A. Pisent INFN-LNL, Legnaro (PD), Italy
P. Mereu, M. Mezzano, INFN-Turin, Turin, Italy

Abstract

An aluminum mock-up of the ESS DTL tank 2 was produced to INFN-LNL in December 2017. The tank is 7.1 m long, equipped with movable tuners and movable post couplers. The purpose of this DTL model is to verify the RF design choices (in particular on the first 2 tanks where the Post coupler distribution is irregular) as well as to implement and to debug algorithms and procedure for stabilization and tuning. The preparatory simulation work and the results of measurements campaign are presented here.

INTRODUCTION

The 5 tanks of the ESS DTL are equipped with post couplers (PCs) for field stabilization [1]. The number of post couplers of each DTL tank was fixed following the criterion of the minimum number of PCs per unit length which guarantees to keep the accelerating field E_0 within specifications (±2%) in case of perturbation [2]. The distribution must be compliant with the increasing cell length as well as with the 2 m tank modulation. As a consequence of these boundaries, the distribution of post couplers per number of cells changes along Tank 1 and Tank 2, while it is regular in Tank 3, 4 and 5, as listed in Table 1.

Table 1: PCs Distribution of ESS DTL Tanks

	T1	T2	T3	T4	T5
N Cells	61	34	29	26	23
N DTs	60	33	28	25	22
N.PCs	24	23	28	25	22
PCs/DT	-up to DT 14th: 1/4 -up to DT 32nd: 1/3 -up to end: 1/2	-up to DT 21st: 1/2 -up to end: 1/1	1/1	1/1	1/1

The distance between post couplers is then gradually increasing as βλ in the last three tanks, while is jumping from 4 βλ to 3 βλ to 2 βλ in Tank 1 and from 2 βλ to 1 βλ in Tank 2.

In particular, in Tank 2, looking to the PCs as the second chain of resonators, this is equivalent to say that the period of the PC chain is suddenly changing from 43 cm to 21.5 cm. For this reason – along with the opportunity to test and define hardware and procedures for DTL tuning - it was decided to produce an aluminium model of DTL tank 2, to demonstrate the proper stabilization of a DTL with such irregular post coupler distribution (Fig. 1).

ALUMINUM DTL AND BEAD-PULL APPARATUS

The purpose of the aluminum mock-up is to provide a valid test bench for the bead pulling activities, without duplicating a real DTL tank, for cost and time optimization. The mock-up is geometrically identical to the actual DTL Tank 2; thus the cavity internal diameter, the modularity (i.e. the length of each module), distribution and positioning of the ports for the corresponding components (Drift Tubes, Pick-Ups, Tuners and Post Couplers) are the same as in the real DTL Tank; the vacuum ports and the RF coupler ports were not realized, as they are irrelevant for bead pulling purposes.

The structure is made of a 2-mm-thick aluminum skin bended with 521 mm internal diameter. The proper form of the aluminum skin is given by four ribs, evenly placed along each module. Each rib is machined by milling from a 20 mm-thick solid aluminum sheet. The flexural stiffness of the module is provided by 5 struts made of structural steel beams with rectangular hollow section. The struts provide also the housing for the interfaces of the ports. The module is supported at each rib by a welded structure, which is coupled to a corresponding carriage with longitudinal skid. An isostatic alignment system is provided between the welded structure and the carriage for the proper relative positioning of the modules. The pair of rails for the longitudinal movement during the coupling of the modules is fixed to a substructure made of four aluminum profile beam support, fixed to the ground. The tank is terminated by two covers, which integrate the corresponding half Drift Tube, with a central hole for the passage of the bead. In Fig. 2 an internal view of the DTL mock-up is shown

The alignment of the dummy Drift Tube is reached using a Laser Tracker and is made with an isostatic regulation on top of the upper strut, which permit a complete spatial regulation (6 DOF) of each Drift Tube. The final alignment reached has been with a spatial error from the nominal position less than 0,1 mm.

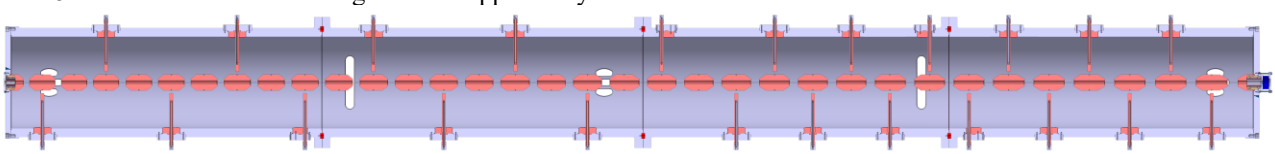


Figure 1: The ESS DTL Tank 2: it is possible to notice the tank subdivision as well as the PC distribution change.

Content from this work may be used under the terms of the CC BY 3.0 licence (© 2018). Any distribution of this work must maintain attribution to the author(s), title of the work, publisher, and DOI.

ISBN: 978-3-95450-194-6 ISSN: 2226-0366 doi:10.18429/JACoW-LINAC2018-THPO045

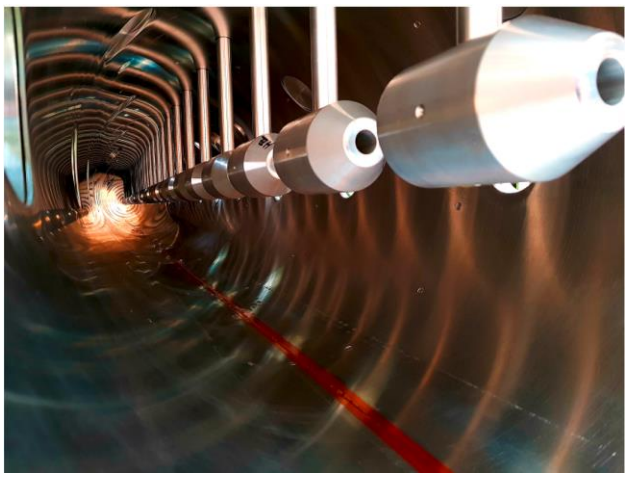


Figure 2: Internal view of the aluminum DTL.

The interfaces of the ports are the same as in the real DTL Tank, duplicating the actual geometry (i.e. diameter of the port, distance of the interfaces surfaces from the tank geometrical axis, position of the screw holes and sealing housing). This was done in order to carry out the bead pulling on the mock-up with the same movable tuner which will be used in the bead pulling of the DTL Tank in the DTL assembly workshop before the transfer and integration of the assembled and tested tank to the ESS accelerator.

The system for bead-pulling mainly consists of 2 aluminum plates directly fixed to the end plates of the DTL tank and supported to the ground by 2 adjustable aluminum bar. A step motor controlled by LABVIEW moves the dielectric thread through a system of pulleys, pulling a metallic bead along the beam axis line of the cavity. The same routine launches the Network Analyzer acquisition. The plates are qualified in CMM, and the precise positioning of the bead wire in the DTL geometrical center is provided by laser tracker references located on each plate. The tension of the thread can be varied by acting on a screw and it is monitored during the measurement by a load cell. The interfaces of this measurements apparatus were studied to be compatible with the real DTL tank geometry (Fig. 3).



Figure 3: Aluminum DTL with bead pull system, movable tuners and post couplers (courtesy of CERN-Linac4) and VNA.

RF MEASUREMENTS : STABILIZATION AND TUNING PROCEDURES

The stabilization procedures for the DTL foresee the consolidated method of the on-purpose perturbation of the cavity at one end of the structure and then to the other one; this provokes a frequency shift Δf and a field perturbation at each DTL cell. Therefore, it makes sense to introduce a Tilt Sensitivity parameter

$$TS_i = \frac{E_{0i}^{(he)} - E_{0i}^{(le)}}{\Delta f}$$

Where $E_{0i}^{(he)}$ and $E_{0i}^{(le)}$ refer to axial field values of the i-th cell in the case of perturbation at the high and low energy end respectively. This parameter is an index of the response of the cavity to perturbations and therefore the stabilization procedure consists of the determination of the set of PC lengths that minimize such parameter. In this case, the perturbing object is a hollow cylinder of 11 mm diameter, whose axis coincides with the beam axis and which is inserted in such a way to have the same Δf at both cavity ends (typically in the order of about -120 kHz). In the initial measurements, all the PCs were set at the length of 190 mm and with all the tuners set at 55 mm insertion. In this configuration, the TM and the PC mode bands are well separated (about 30 MHz) and therefore the TM modes only contribute to perturb the operational one. The TM_{010} frequency is equal to 352.1 MHz and the loaded Q is equal to about 2700, while the 1st upper mode is about 700 kHz higher than the TM_{010} one. The related TS is shown in Fig. 4. As one can expect, the TS is rather large (about ± 50 MHz^{-1}) and it is dominated by the 1st upper TM_{011} mode, moreover the E_0 varies in a range of ±11% about its mean value.

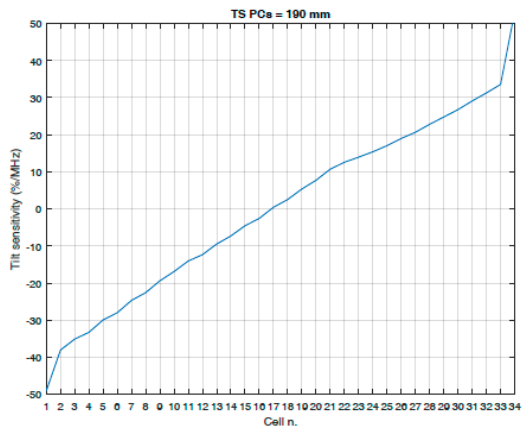


Figure 4: Tilt sensitivity for the initial PC setting.

At first, the optimum PC lengths were sought looking at the $TS_i' = TS_i - TS_{i-1}$, according to [3]: this procedure requires the determination of the resonance length of each PC looking to the discontinuity of resonance TM_{010} frequency. Nonetheless, in our case, the cavity 3dB bandwidth of about 240 kHz is too high to reliably distinguish such resonance. Therefore, it was decided to directly vary the PC lengths in order to reduce the TS, by trials and errors. This step took about 30 successive iterations. The

Content from this work may be used under the terms of the CC BY 3.0 licence (© 2018). Any distribution of this work must maintain attribution to the author(s), title of the work, publisher, and DOI.

ISBN: 978-3-95450-194-6 ISSN: 2226-0366 doi:10.18429/JACoW-LINAC2018-THPO045

best PC settings allowed the tilt sensitivity to reach the minimum value of ± 5 MHz^{-1} (Fig. 5).

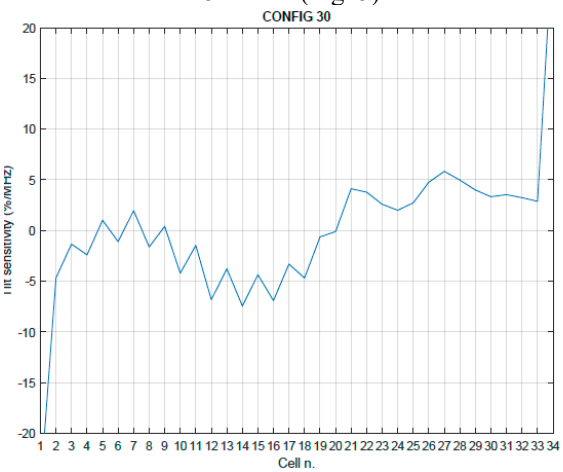


Figure 5: Tilt sensitivity for the final PC setting.

In correspondence to this result, the mode-free zone about the accelerating mode is such that f0-fPC1=2.4 MHz and f0-f1=-2.4 MHz. The PC lengths vs the PC number are shown in Fig. 6.

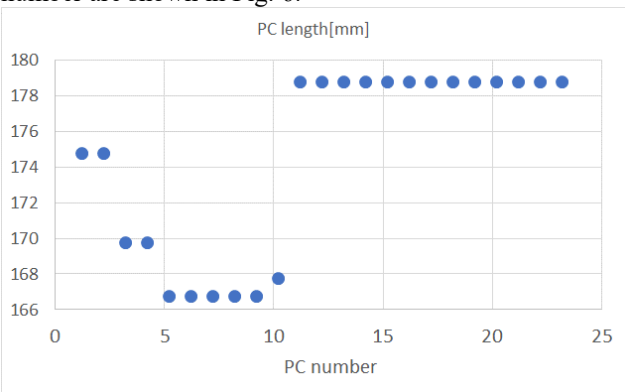


Figure 6: PC lengths vs PC number corresponding to the minimum TS.

The next step was the tuning of the DTL field by moving the 20 slug tuners of 50 mm diameter. The algorithm followed for such procedure is the same of [3], with an eventual correction of the first three tuners in the low energy part of the DTL. In the following Fig. 7 the field distribution after tuning procedure is shown, in which the field uniformity is ±3%. It should be noticed that the large field dip at Cell 27th corresponds to the interface between module 3 and 4 of the tank, and it adds a 2 % error to the field flatness.

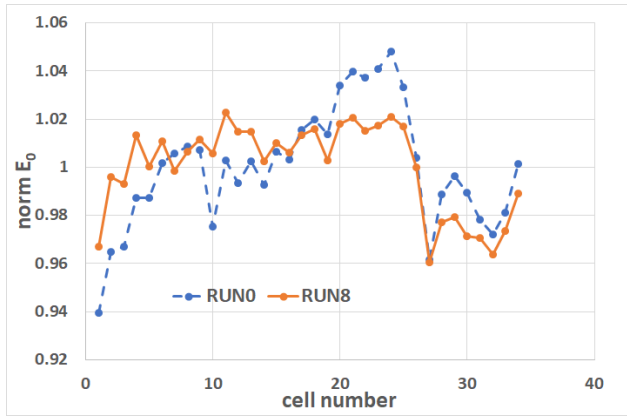


Figure 7: Axial Field distribution before (RUN0) and after (RUN 8) tuning.

The frequency obtained after this tuning operation is 352.196 MHz. In the following Fig. 8, the tuner corresponding tuner height distribution is shown.

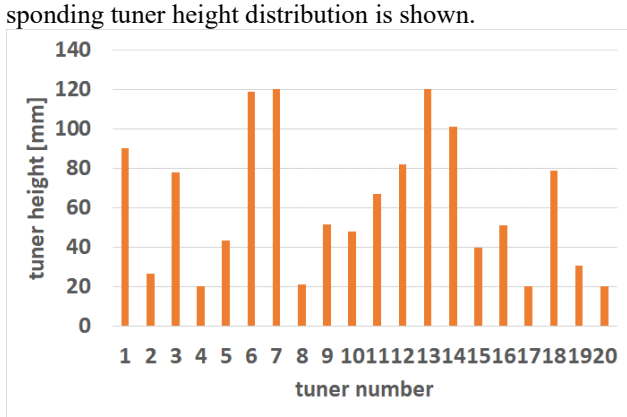


Figure 8: The actual tuner height distribution.

CONCLUSION

The experience on the DTL Tank 2 aluminum model has demonstrated the stabilization and tuning of a tank with PCs irregular distribution, even if the RF discontinuity between module did not allow to reach the goal of ±2% field flatness and to apply the stabilization by resonance PC length. Moreover the hardware and procedures for DTL bead pulling has been debugged and the personnel trained to measurements.

REFERENCES

[1] F. Grespan, et al. *Physical Review Accelerators and Beams* **15**, 010401 (2012).

[2] F. Grespan et al., "ESS DTL Design and Drift Tube Prototypes", in *Proc. LINAC'14*, Geneva, Switzerland, Aug.-Sep. 2014, paper THPP087, p1050. doi:10.18429/JACoW-LINAC2014-THPP087

[3] M. R. Khalvati et al. *Physical Review Accelerators and Beams* **19**, 042001 (2016).

Content from this work may be used under the terms of the CC BY 3.0 licence (© 2018). Any distribution of this work must maintain attribution to the author(s), title of the work, publisher, and DOI.

ISBN: 978-3-95450-194-6 ISSN: 2226-0366 doi:10.18429/JACoW-LINAC2018-THPO046

STATUS OF THE FAIR PROTON LINAC

C. Kleffner, S. Appel, R. Berezov, J. Fils, P. Forck, M. Kaiser, K. Knie, C. Muehle, S. Puetz, A. Schnase,G. Schreiber, A. Seibel, T. Sieber, V. Srinivasan, J. Trueller, W. Vinzenz, C. Will, GSI, Darmstadt
A. M. Almomani, H. Hähnel, U. Ratzinger, M. Schuett, M. Syha, IAP, Frankfurt am Main, Germany

Abstract

As part of the accelerator chain for antiproton production of the FAIR facility, a special high-intensity short pulsed 325 MHz Proton Linac is being developed [1], [2]. The Proton Linac is designed to deliver a beam current of 70 mA with an energy of 68 MeV. A 2.45 GHz ECR source designed for the generation of 100 mA beams with an energy of 95 keV is currently being tested at CEA/Saclay. The production of the structure of the IAP ladder RFQ is nearly completed. All parts of the RFQ vacuum chambers have been successfully copperplated at the GSI. Seven Thales Klystrons have been delivered to GSI at the beginning of 2018 and are nearly ready for use. The completion of the setup of the HV modulator is expected mid of the year 2019. The state of procurement and development of further accelerator components will be presented.

OVERVIEW

Figure. 1 and Table 1. shows main properties and the structure of the Proton Linac. A 2.45 GHz ECR source generating 100 mA of 95 keV protons is followed by a Low-Energy Beam Transport line (LEBT) based on two sole-noid magnetic lenses enclosing a diagnostics chamber. A ladder 4-Rod RFQ will be built behind the LEBT, which is followed by a chopper and a beam conus in front of the RFQ entrance. Six normal conducting crossbar cavities of CCH and CH type arranged in two sections accelerate the beam to the final energy of 68 MeV.

The construction work on the Proton Linac beam dump and the eight meter thick radiation safety wall as seen in fig. 2 has been build up alongside the existing TK tunnel. This work has been executed as part of the GAF project in the first quarter of 2018.

PROTON LINAC BUILDING

After submission of the building application for the Proton Linac building in October 2017 the execution planning of the technical infrastructure started.



Figure 2: Proton Linac Interface Wall with the construction area for the Proton Linac in front.

ION SOURCE AND LEBT

The commissioning of the Proton source takes place at CEA, Saclay [3]. The 100 kV/150 mA high voltage power supply of the source has been commissioned successfully. By means of AC current transformer, fast current transformer FC, Wien filter (beam proportion) and Alison Scanner (emittance measurements) the extracted Proton beam has been characterized, see fig.3.

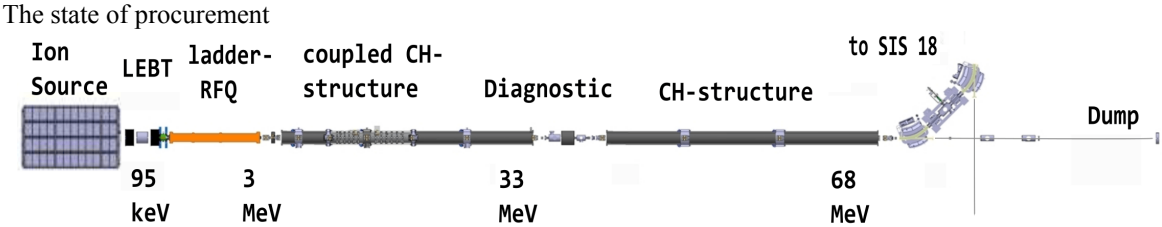


Figure 1: Layout of the FAIR Proton Linac.

Table 1: Proton Linac Main Parameters

Particle	Proton (H^{+})
Ion source	95 keV
MEBT energy	3 MeV
CCH section	33 MeV
Final energy	68 MeV
Pulse current	70 mA
RF-frequency	325.224 MHz
Rep. rate	2,7 Hz

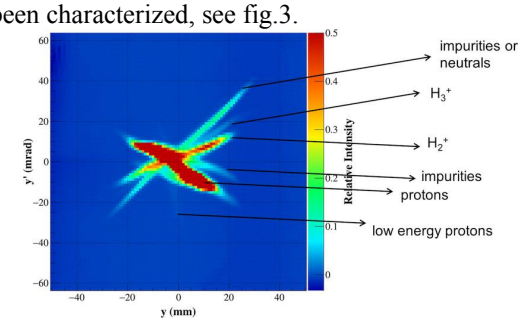


Figure 3: Typical emittance measurement taken at the diagnostic section within the LEBT.

Content from this work may be used under the terms of the CC BY 3.0 licence (© 2018). Any distribution of this work must maintain attribution to the author(s), title of the work, publisher, and DOI.

ISBN: 978-3-95450-194-6 ISSN: 2226-0366 doi:10.18429/JACoW-LINAC2018-THPO046

Content from this work may be used under the terms of the CC BY 3.0 licence (© 2018). Any distribution of this work must maintain attribution to the author(s), title of the work, publisher, and DOI.

A current of 92 mA (80 mA H^+) with a RMS emittance of 0.3 π mm mrad behind the first solenoid has been produced.

LADDER RFQ

The ladder RFQ is under construction and will be delivered by IAP Frankfurt [4]. The production of the vacuum chambers as well as the ladder structure and the RFQ electrodes has been completed. All parts of the vacuum chambers have been successfully copperplated at the GSI galvanic workshop (fig. 4). After the first assembly of the RFQ first low level measurements show excellent consistency with the RF-simulations. This as well as well as details of the beam dynamic calculations are presented at this conference [6] [7].

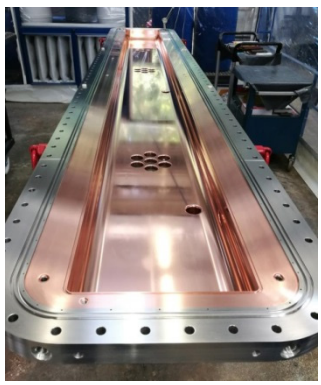


Figure 4: Copperplated RFQ half shelve at the GSI galvanic workshop.

CH-DTL LAYOUT

The final design for the entire CH-DTL was completed by IAP [5] at the beginning of the year. The current focus of the work is on the mechanical integration of all components.

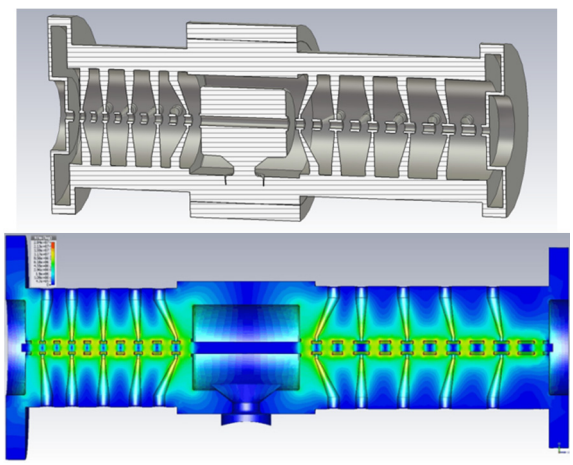


Figure 5: Layout of the first CCH-type cavity CCH1 and corresponding CST Microwave Studio calculations.

Another CH dummy prototype (fig. 6) with realistic stem geometries will be produced and copper-plated in the near future. For the first time the new additive planned for the GSI galvanic workshop will be used for this purpose.

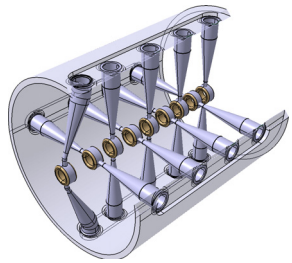


Figure 6: Model of the CCH1 dummy segment for welding and galvanic testing purposes.

In order to decrease welding and postprocessing time and to increase the welding quality all joints will be designed to be compatible with orbital electron beam welding. Extensive tests for the welding procedure are planned within this year.

RF & POWER SUPPLIES

Seven klystrons have been delivered beginning of this year and are stored on-site, see fig. 7. The eight klystron was ordered by the collaboration partner CNRS and will be availble mid of next year. With some interlock modifications the klystrons are ready for use.



Figure 7: Three of the delivered klystrons stored on-site.

The construction of a HV modulator is indispesible for further rf tests on site. The work on the HV modulators are ongoing. Two sets of racks as well as full set of capacitors were delivered. The tender process on the HV switches and the purchase of the transformers and charger power supply are ongoing.

ERROR STUDIES CH-DTL

After creation of a cooperation of GSI with IAP concering beam dynamics calculations an advanced error analysis study was initiated for the CH-DTL section with the LORASR code [8], [9] and has been redone this year with the final CH-DTL design. Parameters that enter into beam dynamics simulations are subject to errors following a Gaussian distribution. Many runs were made with different assumptions on errors in quadrupole alignments (±0.1 mm) as well as in RF-amplitudes & -phases (±1%, ±1°). A resulting beam loss scenario is plotted in fig. 8 including beam envelopes along the CH-DTL section. In blue the beam envelope in vertical as well as in horizonal of the nominal run is shown together with the overlap of all envelopes in red. The studies include corrections by steerers,

ISBN: 978-3-95450-194-6 ISSN: 2226-0366 doi:10.18429/JACoW-LINAC2018-THPO046

marked with the black arrows. It turned out as in the previous studies that the losses are dominated by quadrupole translations.

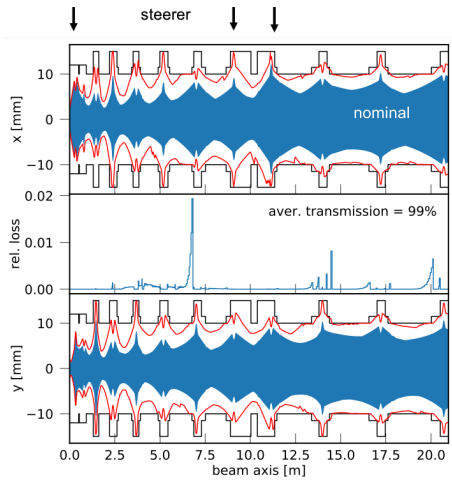


Figure 8: Simulated horizontal (upper) and vertical (lower) beam envelopes along the whole DTL section for a simulated current of 70 mA. In blue the nominal case, in red the overlap of all envelopes form all errors runs. Related loss (middle) along the DTL resulting from systematic error studies.

OPTIMIZATION OF THE MULTI-TURN INJECTION

For the multiturn injection (MTI) into the SIS18 synchroton emittance should be in a reachable value frame for the injector linac. On the other hand, if the available horizontal SIS18 acceptance is almost occupied, increasing of the so called multiplication factor lead to an increasing of injection loss. The MTI performance depends on various machine parameters and strongly on the injector beam parameters since a smaller emittance translates directly into better MTI performance [10].

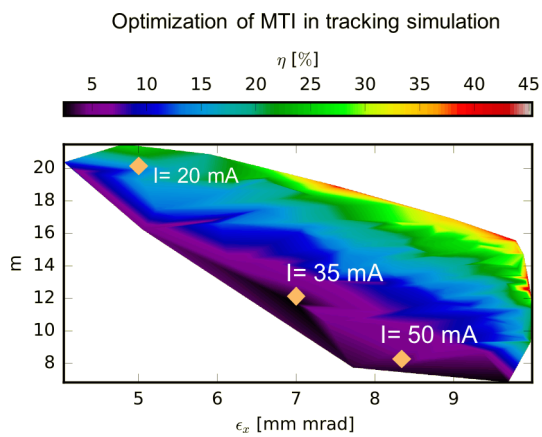


Figure 9: Proton linac MTI performance plot for the SIS18 synchrotron.

A new approach to solve such difficult but realistic problems is the use of genetic algorithms (GA) [11]. The outcome of GA optimization of simulation of injection loss, multiplication factor and beam emittance of injector is shown in fig. 9.

Three case with brilliance of 4, 5 and 6 mA/(mm mrad) has been marked in the figure. The simulations and heuristic optimization of the MTI demonstrate, that a low-loss injection to fill SIS18 up to the space charge limit for several emittance over many turns could be achieved for various proton puls currents. The optimal settings of the proton pulse current is expected to between 35 and 50 mA.

CONCLUSION AND OUTLOOK

The overview of the current status of the pLinac project shows the progress of the project. The design of all major components has been finished by now. One of the most important tasks in the near future will be the the creation of specifications for the CH-DTL cavity tanks.

REFERENCES

[1] U. Ratzinger, *et al.,* "A 70 MeV Proton Linac for the FAIR Facility Based on CH Cavities", in *Proc. LINAC 06,* paper TH1004, 2006.

[2] Technical Design Report (2008), Proton Linac, www.edms.cern.ch/document/994418/1.

[3] R. Berezov *et. al.,* "High intensity proton injector for the FAIR P-LINAC", *ICIS 2017*, CERN – CICG, Geneva.

[4] M. Schuett, U. Ratzinger, R. Brodhage, Development of a 325MHz Ladder-RFQ of the 4-ROD Type, *Proc. of IPAC'15*, Richmond, USA, p. 3745. (2015)

[5] U. Ratzinger, "Calculations of the CH- and CCH-Cavities for the FAIR proton linac", 2018, IAP Frankfurt, Final Report

[6] M. Schuett *et al.,* "First RF Measurements of the 325 MHz Ladder RFQ", presented at LINAC'18, Beijing, China, Sep. 2018, paper THPO060, unpublished.

[7] M. Syha *et al.*, "Beam Dynamics for the FAIR-p-linac-rfq", presented at LINAC'18, Beijing, China, Sep. 2018, paper TUPO083, unpublished.

[8] G. Clement, "Beam Dynamics Layout of the FAIR Proton Injector", in Proc. of the ICFA HB2008 Workshop, Nashville, U.S.A., 2008.

[9] R. Tiede, A. Almomani, M. Busch, F. Dziuba und U. Ratzinger, "Improved Beam Dynamics and Cavity RF Design for the FAIR Proton Injector", in *Proc. LINAC'16*, East Lansing, MI, USA, Sep. 2016, pp. 111-113, doi:10.18429/JACoW-LINAC16-MOPRC018

[10] S. Appel, Y. E. Hayek, M. Maier, C. Xiao und L. Groening, "Injection optimization through generation of flat ion beams", *Nucl. Instr. Meth.* A 866, 2017.

[11] S. Appel, O. Boine-Frankenheim und F. Petrov, "Injection optimization in a heavy-ion synchrotron using genetic algorithms", NIM A 852, 2017.

Content from this work may be used under the terms of the CC BY 3.0 licence (© 2018). Any distribution of this work must maintain attribution to the author(s), title of the work, publisher, and DOI.

ISBN: 978-3-95450-194-6 ISSN: 2226-0366 doi:10.18429/JACoW-LINAC2018-THPO047

SPIRAL2 INJECTOR COMMISSIONING

R. Ferdinand†, M. Di Giacomo Marco, H. Franberg, O. Kamalou, J-M. Lagniel, G. Normand, A. Savalle, F. Varenne GANIL, Caen, France
D. Uriot, DRF/IRFU/DACM, Saclay, France

Abstract

The SPIRAL2 injector is composed of two ion sources (p/d and heavy ions up to A/Q=3) followed by a 730 keV/u RFQ. Beam commissioning has started in 2014 in parallel with the superconducting linac and HEBT installations. The RFQ beam commissioning started soon after the first RF conditioning done in October 2015. This paper describes the RFQ beam measurements done on the diagnostic plate for the reference particles (H^+, $^4He^{2+}$ and recently $^{18}O^{6+}$) and the difficulties encountered for the RFQ commissioning at the A/Q=3 field level.

INTRODUCTION

The layout of the SPIRAL2 driver takes into account a wide variety of beams to fulfill the physics requests [1]. It is a high power CW superconducting linac delivering up to 5 mA proton or deuteron beams or 1 mA ion beams for Q/A > 1/3 (Table 1). Our major challenges are to handle the large variety of different beams due to their different characteristics (in terms of particle type, beam currents – from a few µA to a few mA - and/or beam energy), a high beam power (200 kW, CW) and to answer correctly to the safety issues, especially with the deuteron beam.

Table 1: Beam Specifications

Particles	H^+	D^+	ions	option
A/Q	1	2	3	6
Max I (mA)	5	5	1	1
Max energy (MeV/A)	33	20	15	8.5
Max beam power (kW)	165	200	45	51

We do not have yet the authorization to accelerate deuteron beams or to inject in the LINAC. A test bench, the Diagnostic-plate (D-plate), is used after the RFQ to validate the RFQ performances, to tests various diagnostics and to measure the beam characteristics for the future Linac injection.

BEAMS FOR COMMISSIONING

Three beams have been selected to demonstrate the injector performances.

The 5 mA proton beam requires only 40 kV on the RFQ vane voltage. It is the easiest to produce, requires little RF in the RFQ cavity but is the most difficult to transport in the LEBT because of space charge forces.

The $^4He^{2+}$ was selected in order to mimic the future deuteron beam. It allows to test the A/Q=3 ECR source and LEBT and requires a little higher RFQ vane voltage (80 kV).

The ultimate injector performances require an A/Q=3 beam up to 1 mA. The $^{18}O^{6+}$ has been selected. The RFQ vane voltage rise to 114 kV (1.65 Kilpatrick). We were not able to achieve stable operation of the RFQ and associated RF system at such set point until recently. 105 kV was easier to achieve and $^{16}O^{6+}$ beam (A/Q=2.67) was used as backup for performance measurement. Recent improvement in the cavity conditioning and LLRF tuning allow a much better cavity operation, leading to an availability of about 75% at nominal voltage (114 kV). The merit of this is that the measurement results for both oxygen beams can be compared, and $^{18}O^{6+}$ can be measured à 105 and 114 kV.

D-PLATE DESCRIPTION

The D-Plate is installed in the Medium Energy Beam Transport Line (MEBT, Fig. 1). It allows to measure:

- Intensity with Faraday cups, ACCT and DCCT
- Transverse profiles with classical multi wire profilers and ionisation gas monitor (MIGR in the text)
- H and V transverse emittance with Allison type scanners
- Energy with a Time of Flight (TOF) monitor
- Phase with the TOF and the 2 BPMs
- Longitudinal profile with a Fast Faraday Cup (FFC), and a Beam Extension Monitor (BEM)
- Beam position and ellipticity ($\sigma_x^2 - \sigma_y^2$), with the BPMs.

The diagnostics performances are given in [2,3,4]

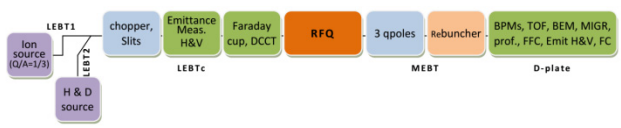


Figure 1: Injector scheme up to Diagnostic Plate.

RFQ RF CONDITIONING

The RFQ RF conditioning improved during the past few months with a better control of the RF chains and better conditioning methods. At first, the RF conditioning was managed in pulse mode with a Duty Cycle (DC) low enough to avoid copper heating. It allows to burn the dusts and spikes. We were quickly able to reach 125 kV (240 kW), 500 µs/100 ms, ending with operation without sparks. The LLRF is then switched in CW mode, integrating a PLL. In both cases (pulsed, CW with PLL), the cavity frequency tuning is manual using the temperature control. In CW mode, the cavity starts to spark at 105 kV, much lower than the level achieved just before in pulse mode. The copper heating in CW mode increases an outgassing inducing sparks at lower voltage. The RF conditioning is greatly improved increasing the copper temperature up to 55°C with RF for few weeks. Coming back to the normal LLRF operation, unfortunately without PLL during the

Content from this work may be used under the terms of the CC BY 3.0 licence (© 2018). Any distribution of this work must maintain attribution to the author(s), title of the work, publisher, and DOI.

ISBN: 978-3-95450-194-6 ISSN: 2226-0366 doi:10.18429/JACoW-LINAC2018-THPO047

power ramp-up, the cavity can now hold the designed voltage (114 kV vane voltage for the A/Q=3 particles) during a few hours, and the reduce 105 kV without sparks. Nevertheless, at design voltage, most of the sparks still create difficulties in the RF chains resulting in long period of beam shut down (30 min to 2 hours). LLRF (Low Level RF) improvement is ongoing, integrating a PLL operation mode. Progresses are expected soon.

RESULTS

Longitudinal Emittances

The longitudinal emittance has been measured (Fig. 2), monitoring the bunch length versus the rebuncher voltage on two different diagnostics: the FFC (σ_{rms}= 320–330 ps) and the BEM (σ_{rms}= 47 ps). The BEM results are equal to the calculated value for our reference beams (Table 2).

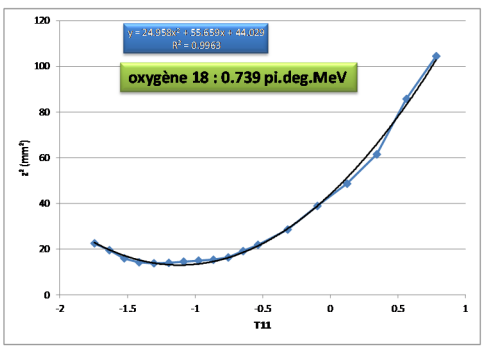


Figure 2: Analyze of Beam Extension Monitor measurements in view of longitudinal emittance calculation.

Table 2: Longitudinal Emittance Measurements

Particle	Expected (π.deg.MeV)	Measured (π.deg.MeV)	difference
Proton	0.034	0.039	+15%
Helium	0.19	0.13	-32%
$^{16}O^{6+}$	0.72	0.64	-11%
$^{18}O^{6+}$	0.78	0.81	+4%

Transverse Emittances

The transverse emittances measured for the reference particles in both planes before and after the RFQ are all within the expected values. More important, the MEBT transport can be remarkably well simulated using the TraceWin code (Fig. 3, 4 and 5). This is unfortunately not the case for the LEBT comparison. We suspect that the solenoid strong focusing into the RFQ cavity generates transverse emittance growth. Variations of the space charge compensation do not allow us to get satisfying simulations.

A 6-slit collimator in the LEBT allows to define the emittance injected in the RFQ. It will be use to generate the pencil beam required for Linac commissioning. Defining an emittance of 0.06 π.mm.mrad with the slits, we were able to measure this value before the LEBT last solenoid, but the measured emittances in the MEBT was ×3 time bigger.

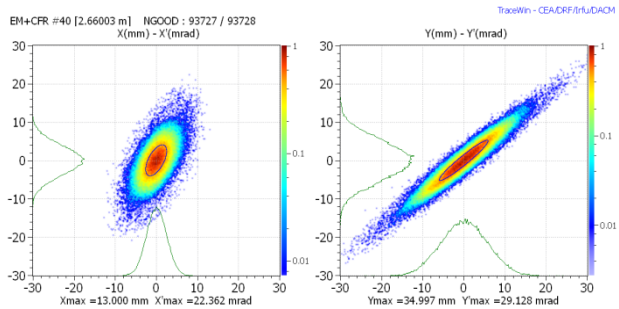


Figure 3: Calculated MEBT emittance – $^{18}O^{6+}$.

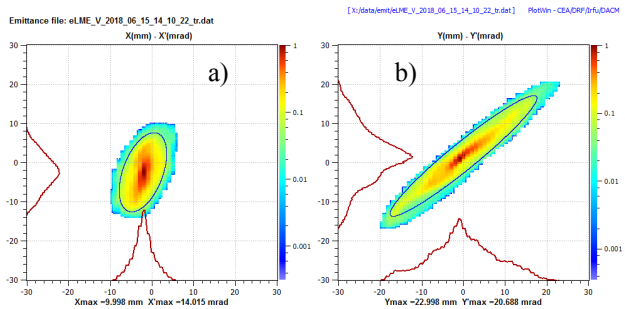


Figure 4: Measured MEBT Emittance – $^{18}O^{6+}$.

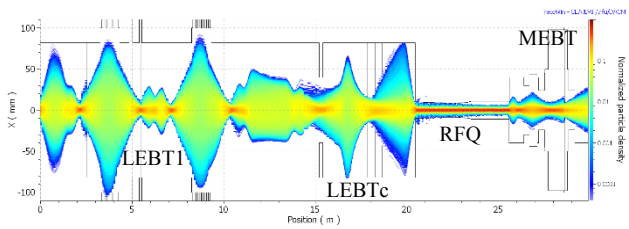


Figure 5: Density plot simulation of the $^{18}O^{6+}$.

RFQ Transmission

The 100% RFQ transmission has been validated for an A/Q=3 beam in CW mode, at the nominal 114 kV (Fig. 6 in CW beam measurement and fig. 7 in pulse mode). The CW $^{18}O^{6+}$ beam was accelerated with success at the reduced voltage of 105 kV with 93% transmission.

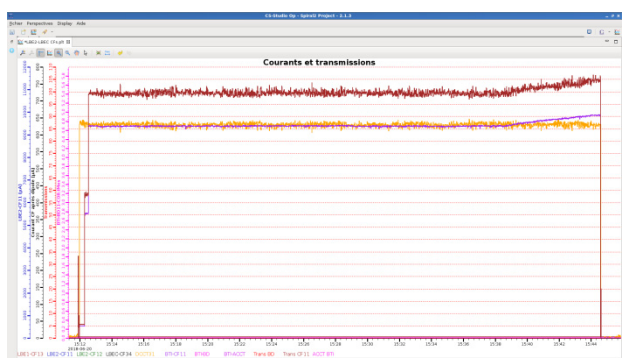


Figure 6: CW operation of the 650µA $^{18}O^{6+}$ beam. At first at reduce 105 kV then at 113 kV. Red is the RFQ transmission, orange the beam current before RFQ, violet beam current after the RFQ.

Content from this work may be used under the terms of the CC BY 3.0 licence (© 2018). Any distribution of this work must maintain attribution to the author(s), title of the work, publisher, and DOI.

ISBN: 978-3-95450-194-6 ISSN: 2226-0366 doi:10.18429/JACoW-LINAC2018-THPO047

Content from this work may be used under the terms of the CC BY 3.0 licence (© 2018). Any distribution of this work must maintain attribution to the author(s), title of the work, publisher, and DOI.

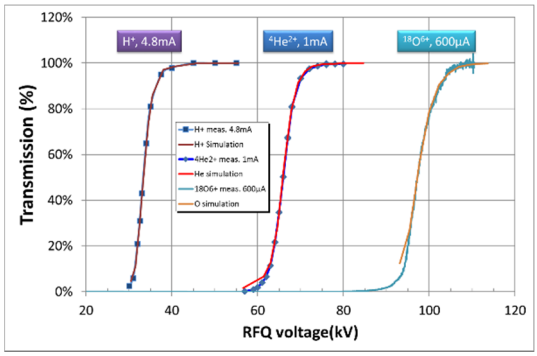


Figure 7: Transmission of the 3 references particles.

Cavity Tuning

The diagnostic plate (D-Plate) serves also as a development platform for the accelerator diagnostics and also presently for the test of the procedure which will be used to tune the SC linac cavities. The rebuncher is used with two longitudinal phase measurements among the 2 BPMs and 3 TOF pick-ups. The tests are done using the well known Signature Matching procedure [5].

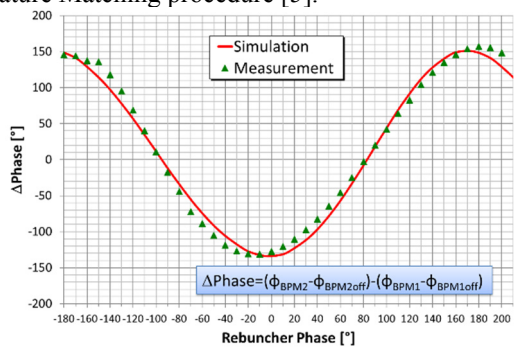


Figure 8: Discrepancy between the phase scan measurements (green dots) and the simulation (red line).

Figure 8 is a typical plot showing the large differences observed between the measurements and the result of the fit done to compute the cavity phase and amplitude tunings. Multiparticles simulations are used to understand the difficulty.

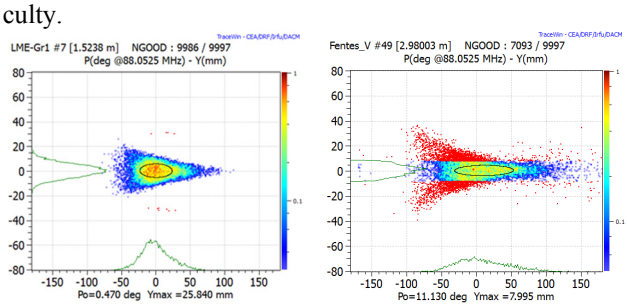


Figure 9: Left, phase – vertical position (ϕ-Y plane) correlation created in the rebuncher. Right, same representation after the MEBT slits. Red particles are lost in the slits.

When the second phase is measured after the MEBT slits, it has been demonstrated that a phase–y plane coupling occurring in the rebuncher induces part of the error. As shown by Fig. 9, the slits located between the 2 BPMs induce a phase shift of more than 10° by cutting dedicated phase in the y-plane.

However, error of several degrees remain using a second phase PU located upstream the slits.

Other Results

Various results were already reported for proton and helium beams [6,7]. They can be resumed as following:

- Ability to extract 11 mA CW from the light ion source resulting in more than 6 mA proton beam at the RFQ entrance and exit.
- Ability to control the beam intensity and radial emittances using the 6 H and 6 V slit system.
- Ability to limit the LEBT emittance growth with pressure increase at the end of the LEBT. Nevertheless, we are not able to have simulations reproducing the observed beams.
- RFQ transmissions are measured to be between 98% to 100% depending on the RFQ injection quality.

CONCLUSION

The great successes of the proton, helium and oxygen beams are promising for the next Linac injection.

Depending on the Nuclear Safety authorization, the D-plate is expected to be removed before the end of the year. Linac RF test should start in April next year and a first beam injection to follow.

ACKNOWLEDGEMENT

The authors wish to thank all the GANIL and partner labs staff for their deep involvement in the SPIRAL2 project. The presented results are a great reward after so many years of their involvement.

REFERENCES

[1] J-M. Lagniel, "Advances of the SPIRAL2 project", HIAT'15, in *Proc. HIAT15*, Yokohama, Japan, Sept. 2015, TUA2I01, p.148-152.

[2] C. Jamet, W. Le Coz, G. Ledu, S. Loret, C. Potier de Courcy, "Energy and Longitudinal Bunch Measurements at the SPIRAL2 RFQ Exit", in *Proc. IBIC'16*, Barcelona, Spain, Sept. 2016, pp. 723-727, DOI:10.18429/JACoW-IBIC2016-WEPG42

[3] P. Ausset, M. B. Abdillah, G. Joshi, P. D. Motiwala, S. K. Bharade, G. Randale, R. Ferdinand, D. Touchard, "Operation of the Beam Position Monitor for the Spiral 2 Linac on the Test Bench of the RFQ", in *Proc. IBIC'16*, Barcelona, Spain, Sept 2016, pp. 642-645, DOI:10.18429/JACoW-IBIC2016-WEPG11

[4] R. Revenko and JL Vignet, "Bunch Extension Monitor for LINAC of SPIRAL2 Project", in *Proc. IBIC 2016*, Barcelona, Spain, Sept 2016, pp.486-490, DOI:10.18429/JACoW-IBIC2016-TUPG59

[5] T.L. Owens, M. Popovic, K. Junck, T Kroc, E. Mccrory, "Phase scan signature matching for LINAC tuning », in *Proc. LINAC 94*, Tsukuba, Japan, August 1994, pp. 893-895, TH-80

[6] R. Ferdinand, P. Bertrand, M. Di Giacomo, H. Franberg, O. Kamalou, J. M. Lagniel, G. Normand, A. Savalle, F. Varenne, D. Uriot, J. L. Biarrotte, "Status of SPIRAL2 and RFQ beam commissioning", in *Proc. LINAC'16*, East

ISBN: 978-3-95450-194-6 ISSN: 2226-0366 doi:10.18429/JACoW-LINAC2018-THPO047

Lansing, USA, Sept. 2016, pp. 668-672. DOI: 10.18429/JACoW-LINAC2016-WE1A06

[7] R. Ferdinand et all "Commissioning of SPIRAL2 CW RFQ and LINAC", in *Proc. IPAC2017*, Copenhagen, Denmark, May 2017, pp. 2462-2465, DOI: 10.18429/JACoW-IPAC2017-WEOAA1.

Content from this work may be used under the terms of the CC BY 3.0 licence (© 2018). Any distribution of this work must maintain attribution to the author(s), title of the work, publisher, and DOI.

ISBN: 978-3-95450-194-6 ISSN: 2226-0366 doi:10.18429/JACoW-LINAC2018-THPO048

LOW POWER MEASUREMENT OF A 1300-MHz RFQ COLD MODEL

Y. Kondo*, T. Morishita, J. Tamura, JAEA, 319-1195, Tokai, Japan
M. Otani, KEK, 305-0801, Tsukuba, Japan

Abstract

A muon linac development for a new muon g-2 experiment is now going on at J-PARC. Muons from the muon beam line (H line) at the J-PARC muon science facility are once stopped in a silica-aerogel target, and room temperature muoniums are evaporated from the aerogel. They are dissociated with lasers, then accelerated up to 212 MeV using a linear accelerator. In the current reference design, a 324-MHz radio frequency quadrupole (RFQ) and an interdigital H-mode drift tube linac (IH-DTL) are used for the low beta acceleration. We propose a 1300 MHz (L band) RFQ instead of the 324 MHz RFQ and IH-DTL as an alternative to simplify the configuration of the muon linac. In this paper, the present status of the design and the measurement of a cold model of this world first 1300-MHz RFQ is described.

INTRODUCTION

The muon anomalous magnetic moment $(g-2)_\mu$ is one of the most promising probe to explore the elementary particle physics beyond the standard model (SM). Currently, the most precise $(g-2)_\mu$ experiment is E821 of Brookhaven national laboratory [1]. The precision is 0.54 ppm and the measured value indicates approximately three standard deviations from the SM prediction. The J-PARC E34 experiment aims to measure the $(g-2)_\mu$ with a precision of 0.1 ppm. In addition, the electric dipole moment (EDM) also can be measured with a precision of $1 \times 10^{-21}\, e\cdot$cm [2]. The experimental method of E34 is completely different from that of the previous experiments. The previous experiments directory used decay muons from the secondary pions generated on the production target. The emittance of such muon beam is very large (typically, 1000π mm mrad); this is a major source of uncertainty of the measurement. On the other hand, E34 will use a low emittance muon beam to improve the precision. The required beam divergence $\Delta p_t/p$ is less than 10^{-5}, and assumed transverse emittance is 1.5π mm mrad. To satisfy this requirement, we are planning to use ultra-slow muons (USMs) generated by laser-dissociation of thermal muoniums (Mu: μ^+e^-) form a silica-aerogel target [3]. The room temperature USMs (25 meV) should be accelerated to 212 MeV to obtain the required $\Delta p_t/p$. A linac realizes rapid acceleration required to accelerate muons, whose lifetime is very short (2.2 µs). Figure 1 shows the configuration of the muon linac [4].

The muon linac will be constructed at the H line [5] of the J-PARC muon science facility. The USMs are bunched and accelerated to 340 MeV by a radio frequency quadrupole linac (RFQ). Following the RFQ, an interdigital H-mode drift tube linac (IH-DTL) [6] is used to accelerate to 4.5 MeV.

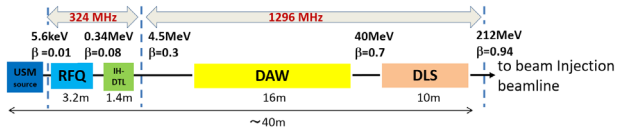


Figure 1: Configuration of the muon linac.

Then, muons are accelerated to 40 MeV through a disk and washer (DAW) coupled cavity linac section, and finally, accelerated to 212 MeV using disk loaded traveling wave structures (DLS) [7].

To reduce the development costs, a spare RFQ for the J-PARC linac will be used, therefore, the resonant frequency is 324 MHz. Removing the restriction to use the J-PARC RFQ, if the same frequency of the following linac, which is 1.3 GHz (L-band), can be used, is becomes reasonable because only one type of the RF source should be prepared. In case of the proton acceleration, the cell length for 50 keV, which is typical injection energy to the RFQ, is $\beta\lambda/2 =$ 1.2 mm: this is too short to fabricate. On the other hand, for muon acceleration it becomes a feasible length of 3.5 mm. Therefore, we propose to replace the 324-MHz RFQ and IH-DTL by an 1300-MHz RFQ shown in Table 1bl:requirement as an alternative of the muon linac baseline design. In this paper, the present status of the design of the 1300-MHz RFQ and low-power measurement of a cold model.

Table 1: Requirements for the 1300-MHz RFQ

Parameter	Value
Beam species	μ^+
Resonant frequency	1296 MHz
Injection energy	30 keV
Extraction energy	5.2 MeV
Peak beam intensity	1×10^6
Transverse emittance (normalized rms)	$< 0.25\pi$ mm mrad
Repetition rate	25 Hz
RF pulse length	20 µs
RF duty factor	0.05%

DESIGN OF THE 1300-MHz RFQ

The beamdynamics design of the 1300-MHz RFQ has been done using RFQGEN [8]. Figure 2 shows the cell parameters, and the obtained design parameters are listed in Table 2. In this design, the average bore radius r_0 is kept same as that of the 324 MHz RFQ to be acceptable the present injection muon beam. Due to this design concept, the power dissipation is rather high. The matching between the RFQ and injection design is an issue from now on.

* yasuhiro.kondo@j-parc.jp

Content from this work may be used under the terms of the CC BY 3.0 licence (© 2018). Any distribution of this work must maintain attribution to the author(s), title of the work, publisher, and DOI.

ISBN: 978-3-95450-194-6 ISSN: 2226-0366 doi:10.18429/JACoW-LINAC2018-THPO048

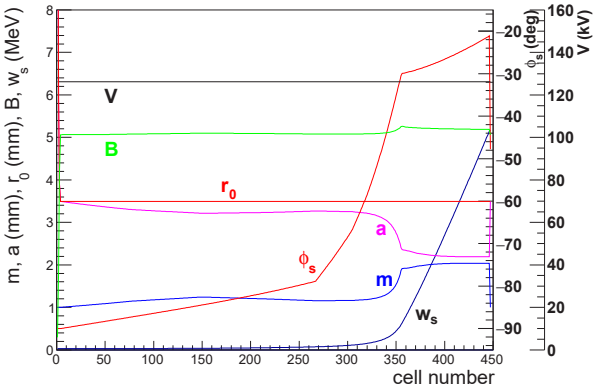


Figure 2: Cell parameters of the 1300-MHz RFQ.

Table 2: Design Parameters of the 1300-MHz RFQ Obtained with RFQGEN

Parameter	Value
Vane length	3.7 m
Number of cells	448
Inter-vane voltage	126 kV
Maximum surface field	53.0 MV/m (1.65 Kilpatrick)
Average bore radius (r_0)	3.50 mm
ρ_t/r_0 ratio	0.75 (ρ_t = 2.62 mm)
a_{min}	2.23 mm
m_{max}	2.19
$\phi_{s,max}$	-21.1 deg

Figure 3 shows the result of the particle simulation. The transmission is 100% for the injection beam with a normalized rms emittance of 0.2π mm mrad, and the normalized rms transverse and longitudinal emittances at the RFQ exit are 0.26π mm mrad and 0.095π MeV deg, respectively. The decay loss of the muon for this RFQ length is 8%.

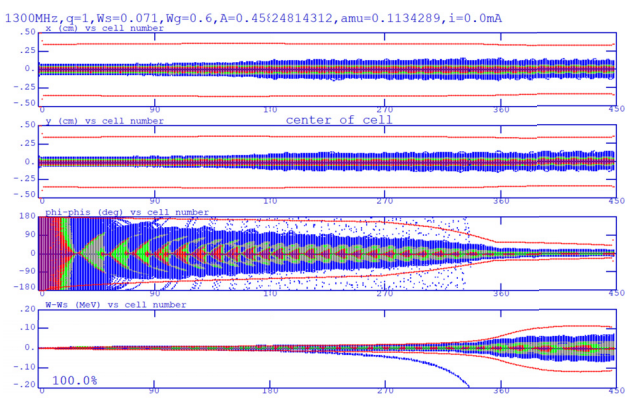


Figure 3: Phase-space evolution of the 1300-MHz RFQ.

Based on this beamdynamics design, the cross-sectional shape of the cavity was designed using RFQFISH [9], as shown in Fig. 4. Calculated Q value is 6554 and power dissipation is 3 MW. The dimensions of the vane endcuts

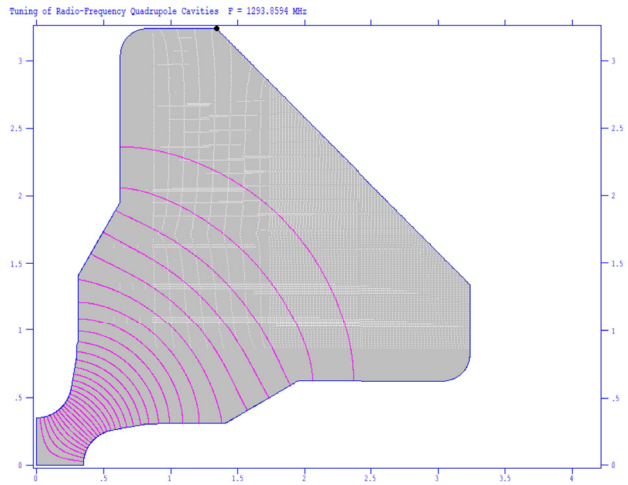


Figure 4: Cross-sectional view of the 1300-MHz RFQ.

were determined by tree-dimensional calculation using CST Micro Wave Studio (MWS) [10]. The resonant frequency of the half-length model with the endcuts was tuned to be same as the infinite-length model without endcuts.

COLD MODEL OF THE 1300-MHz RFQ

Based on the obtained design in the previous section, a cold model with a length of 450 mm was fabricated. Figure 5 show this cold model together with a 324-MHz RFQ as a reference.

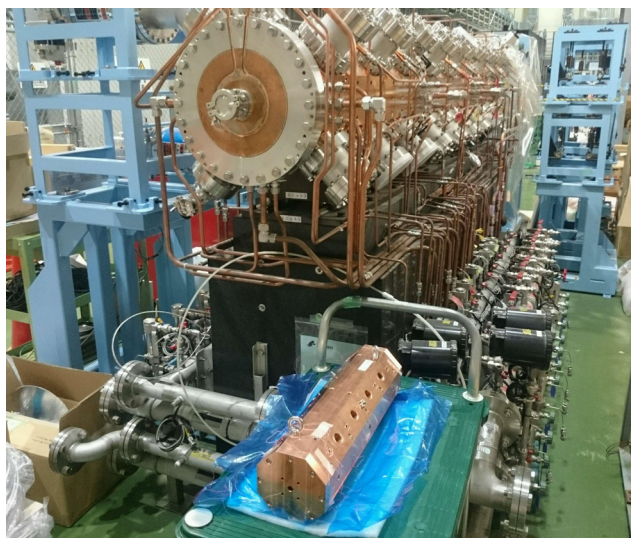


Figure 5: The 1300-MHz RFQ cold model together with a 324-MHz RFQ.

To confirm the RF property, an aluminum model is enough, however, this cold model is made of oxygen free copper (OFC) to confirm also the machining accuracy. Figure 6 shows the result of the coordinate measurement of the vane tips. Except for the downstream side of the major vane 1, the discrepancy from the design value is within ±15 µm. Although the machining accuracy of major vane 1 itself is also within ±15 µm, the overall accuracy is worsen due to a warp of the vane; it is an issue from now on.

Content from this work may be used under the terms of the CC BY 3.0 licence (© 2018). Any distribution of this work must maintain attribution to the author(s), title of the work, publisher, and DOI.

ISBN: 978-3-95450-194-6 ISSN: 2226-0366 doi:10.18429/JACoW-LINAC2018-THPO048

Content from this work may be used under the terms of the CC BY 3.0 licence (© 2018). Any distribution of this work must maintain attribution to the author(s), title of the work, publisher, and DOI.

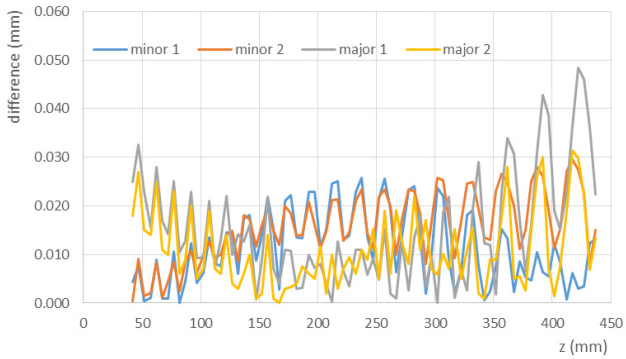


Figure 6: Coordinate measurement of the vane tips.

Figure 7 shows the interior view of the cold model. The outer diameter of the cavity is 135 mm. It is equipped with four tuners and five pickup ports per one quadrant. The tuners are threaded plugs made of OFC.

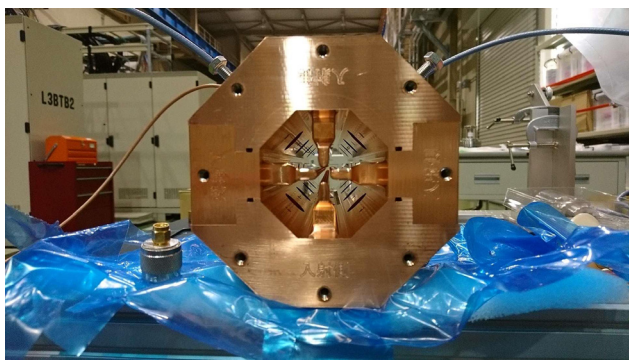


Figure 7: Interior view of the 1300-MHz RFQ cold model.

Figure 8 shows the eigenmode frequencies of the cold model. This measurement was done without tuners. The 1284 MHz peak is consistent with the calculated TE210-mode frequency of the MWS model without tuners.

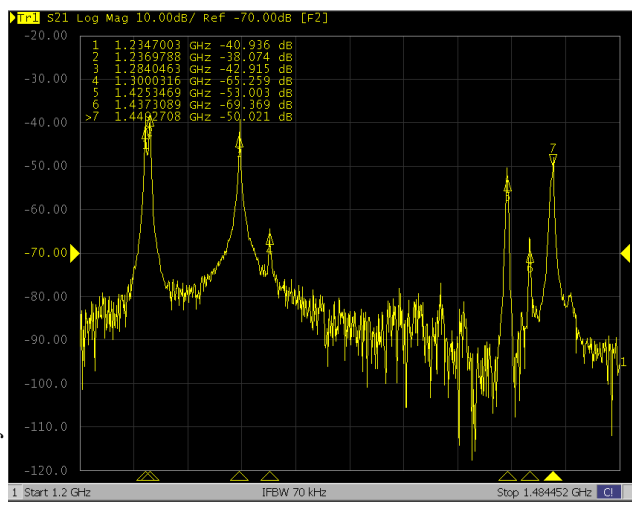


Figure 8: Eigenmode frequencies of the 1300-MHz RFQ cold model.

A bead drive system for this cold model is now under preparation, but preliminary measurement was conducted to confirm this mode to be a fundamental quadrupole mode. Figure 9 represents the result. The S_{21} parameter was measured by connecting the port 1 of the network analyzer to a pickup of the quadrant 1 and the port 2 to quadrant 4. A bead is inserted in the quadrants 2 and 3, and the phase difference at 1284 MHz was plotted in Fig. 9. Four dents correspond to sinks of the field due to the tuner ports. The measured field strength of the quadrants 2 and 3 are almost same and the distribution is flat. Therefore this eigenmode frequency is identified as TE210 mode.

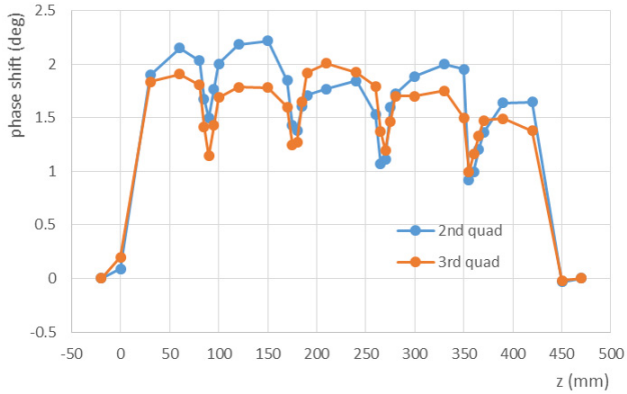


Figure 9: Preliminary bead-pull measurement.

SUMMARY

We proposed a 1300-MHz RFQ as an alternative of the low energy section of the muon linac. RFQs with this frequency have not been realistic due to the very short cell length even for proton acceleration. However, for muon acceleration, the cell length becomes fabricable length. For feasibility studies, a cold model of the 1300-MHz RFQ was fabricated and frequency and preliminary bead-pull measurement have been conducted. The bead-pull system for this RFQ is now under preparation, and after the system is ready, we will tune the frequency and fields.

ACKNOWLEDGEMENTS

This work is supported by JSPS KAKENHI Number JP17K18784.

REFERENCES

[1] G. W. Bennett *et al.*, "Final report of the E821 muon anomalous magnetic moment measurement at BNL," *Phys. Rev.* D, vol. 73, p. 072 003, 2006.

[2] T. Mibe and edit., "J-PARC E34 conceptual design report," KEK, Tech. Rep., 2011.

[3] G. A. Beer *et al.*, "Enhancement of muonium emission rate from silica aerogel with a laser-ablated surface," *Prog. Theor. Exp. Phys.*, vol. 2014, no. 91C01, 2014.

[4] M. Otani *et al.*, "Development of muon linac for the g-2/EDM experiment at J-PARC," in *Proc. LINAC2016*, East Lansing, MI, USA, Sep. 2016, pp. 1037–1041. doi:10.18429/JACoW-LINAC2016-FR1A05

ISBN: 978-3-95450-194-6 ISSN: 2226-0366 doi:10.18429/JACoW-LINAC2018-THPO048

[5] N. Kawamura *et al.*, "H line; A beamline for fundamental physics in J-PARC," *JPS Conf. Proc.*, vol. 2, p. 010 112, 2014.

[6] M. Otani *et al.*, "Interdigital H-mode drift-tube linac design with alternative phase focusing for muon linac," *Phys. Rev. Accel. Beams*, vol. 19, p. 040 101, 2016.

[7] Y. Kondo, K. Hasegawa, M. Otani, T. Mibe, M. Yoshida, and R. Kitamura, "Beam dynamics design of the muon linac high-beta section," *Journal of Physics:* Conference Series, vol. 874, no. 1, p. 012 054, 2017. doi:10.1088/1742-6596/874/1/012054

[8] *Linear Accelerators LLC*, RFQGEN.

[9] J. H. Billen and L. M. Young, "Poisson Superfish," LA-UR-96-1834, 1996.

[10] CST MICROWAVE STUDIO, CST, http://www.cst.com/

Content from this work may be used under the terms of the CC BY 3.0 licence (© 2018). Any distribution of this work must maintain attribution to the author(s), title of the work, publisher, and DOI.

ISBN: 978-3-95450-194-6 ISSN: 2226-0366 doi:10.18429/JACoW-LINAC2018-THPO049

FIELD TUNING OF A RADIO-FREQUENCY QUADRUPOLE USING FULL 3D MODELING

T. Morishita†, Y. Kondo, H. Oguri, K. Hasegawa, JAEA, 319-1195, Tokai, Japan
M. Otani, KEK, 305-0801, Tsukuba, Japan

Abstract

The radio-frequency quadrupole (RFQ) is operating in the frontend of the J-PARC linac to accelerates 50-mA negative hydrogen beams from 0.05 MeV to 3 MeV. As a backup, the spare RFQ has been fabricated in 2018. The vane-voltage ramping is adopted to improve the acceleration efficiency so that the cross-sectional shape is adjusted longitudinally to produce the designed voltage distribution. Then, the three-dimensional cavity models including modulations and cutbacks were created in CST Micro-Wave Studio. The vane-base widths and cutback depths were optimized to produce the desired vane-voltage distribution. In the final tuning, the insertion depths of the stub turners were also determined based on the tuner responses obtained from the full 3D models.

INTRODUCTION

The J-PARC (Japan Proton Accelerator Research Complex) is a complex research facility consisting of high-intensity proton accelerators and experimental facilities. The accelerator comprises an injector linac, a 3-GeV Rapid-Cycling Synchrotron and a Main Ring. The front end of the linac consists of a negative hydrogen ion source and an RFQ with an output energy of 3 MeV. For the beam current upgrade, the new frontend (RF ion source, RFQ, chopping system) is installed in summer 2014. Since then, the beam current was increased to 30 mA, and to 40 mA from January 2016. We continued operation without major trouble, however, the spare RFQ was fabricated in 2018 in preparation for unexpected trouble. In this paper, the detailed design process of the cavity dimensions and the result of the low-power measurements are described.

RFQ PARAMETERS

The major parameters of the spare RFQ are shown in Table 1. The vane voltage distribution of the operating RFQ in J-PARC is taken to be uniform in the longitudinal direction [1], but in the new RFQ, the vane voltage distribution is designed to make the ramping on the downstream side of the cavity to improve the acceleration efficiency. Figure 1 show the longitudinal variation of the vane voltage, the average bore radius, and the maximum surface field. The average bore radius increases smoothly toward the downstream so that the maximum surface field is almost constant. Figure 2 shows the test pieces of a vane tip. From left to right, the modulations for the longitudinally centre, entrance, and exit of the vane, respectively. Prior to the fabrication, the machining conditions of the vane-tip modulations using the ball-end mill were confirmed based on this prototype.

Table 1: Major Parameters

Frequency [MHz]	324
Cavity type	Four vane
Vane length [m]	3.1
Inter-vane voltage[kV]	61.3 ~ 143
Max. surface field [MV/m]	29.8(1.67 Kilpatrick)
Average bore radius [mm]	2.6 ~ 6.2
Vane-tip curvature [mm]	$0.75r_0$

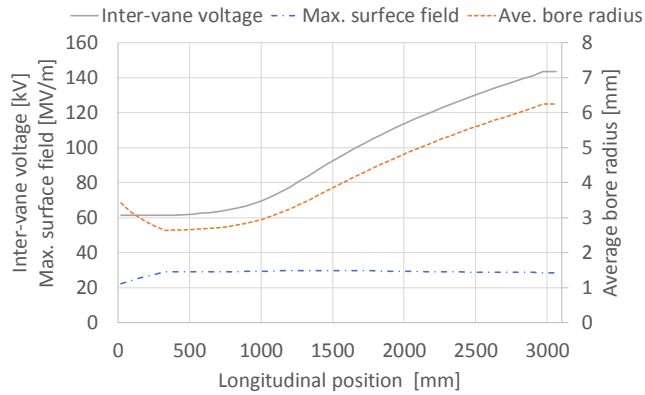


Figure 1: Longitudinal variation of the vane voltage and the average bore radius.

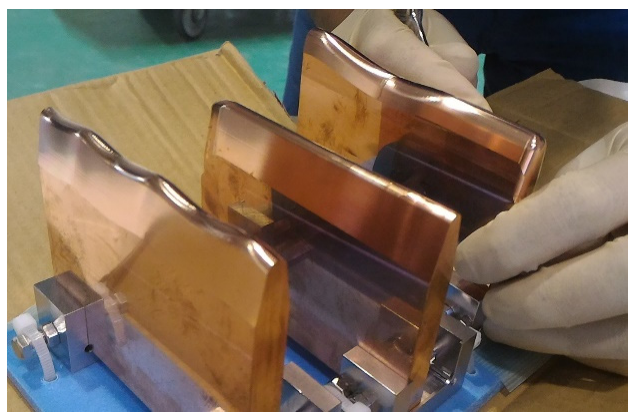


Figure 2: Test piece of the vane tip for checking the surface roughness with the machining conditions.

RF DESIGN

To make the vane-voltage distribution in the longitudinal direction, the vane-base width was adjusted. Cross sectional shape of the cavity is shown in Fig. 3.

† takatoshi.morishita@j-parc.jp

Content from this work may be used under the terms of the CC BY 3.0 licence (© 2018). Any distribution of this work must maintain attribution to the author(s), title of the work, publisher, and DOI.

ISBN: 978-3-95450-194-6 ISSN: 2226-0366 doi:10.18429/JACoW-LINAC2018-THPO049

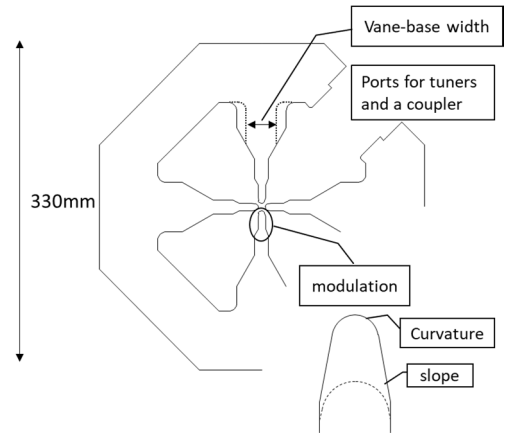


Figure 3: Cross-sectional shape of the RFQ cavity. The cavity radius is 110 mm.

The three-dimensional model for the RF simulation was created by the following procedure using SUPERFISH [2] and CST microwave studio [3].

- The cross-sectional shape of the cavity is determined using SUPERFISH.
- Initially, the vane-base width with the average radius is calculated using RFQFISH along the longitudinal position.
- Based on the obtained vane-base width and the average radius, a three-dimensional CAD model is constructed. Here, the vane-base widths are parameterized to connect with 18 faces in the longitudinal direction (Fig. 4). The end-cut depths are parameterized as well.

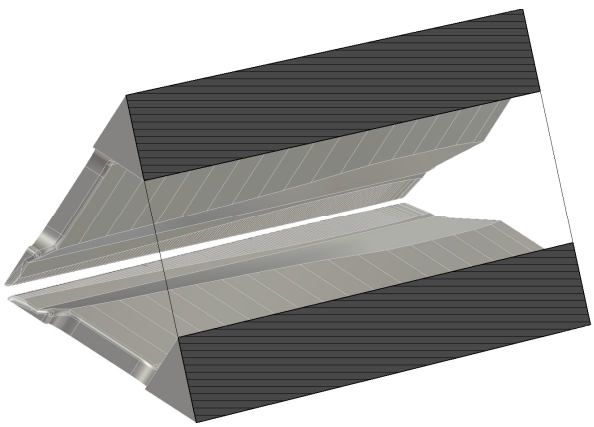


Figure 4: 1/4 model for tuning the vane-base widths and the depths for end cut.

From the three-dimensional simulation result for the electric field distribution, the voltage distribution at the vane tip is obtained by integrating the electric field. Although it is possible to fabricate a cavity with the dimensions calculated by RFQFISH and adjust the electromagnetic distribution using tuners, the voltage distribution was adjusted by optimizing the vane-base width to avoid increasing the stroke necessary for the tuners. Then, the tuners will adjust the errors for manufacturing and the RF calculations. Optimization of the above dimension parameters were carried out in the following procedure.

- The electromagnetic fields are calculated with changing the value of parameterized 19 points of vane-base width and end-cut depths by 1 mm, independently.
- To evaluate the variation of the vane-tip voltage distribution per unit length of these parameters, the vane-tip voltage is sampled at intervals of 20 mm, and created the matrix $\boldsymbol{X}$ with elements normalized by the average voltage for all parameters.
- The difference between the vane voltage for the case of the initial parameters and the designed voltage distribution is a column vector $\boldsymbol{B}$.
- The correction for all parameters (vector $\boldsymbol{A}$) is obtained by $\boldsymbol{A} = (\boldsymbol{X}^T\boldsymbol{X})^{-1}\boldsymbol{X}^T\boldsymbol{B}$,where $\boldsymbol{X}\boldsymbol{A} = \boldsymbol{B}$.

If the three-dimensional model is complicated, the calculation time per case becomes long, therefore, the modulation was not implemented in the model for the matrix X calculation. The radial matching section and the fringe field section were connected with the average bore radius.

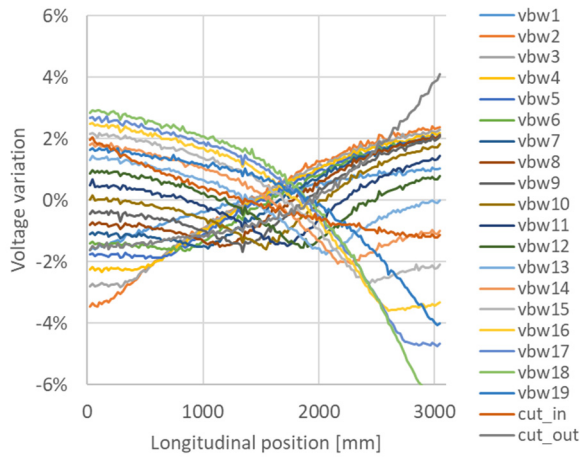


Figure 5: Voltage variations of the vane voltage for each cavity shape parameter.

The variation of the vane-tip voltage distribution per unit length (elements of the matrix X) of the parameters are shown in Fig 5. The curves are not smooth due to the roughness of the calculation mesh, but it is enough to adjust the voltage distribution within a certain (less than 1%) accuracy. After the designed voltage distribution is obtained with several iterations, the magnetic field distribution at the bead measurement position is calculated. Then, the modulations are implemented in the three-dimensional model and the optimization procedure carried out again to be equal to the target magnetic field distribution. At the low power measurement, this calculated magnetic field distribution is also a target value for tuner adjustment.

LOW-LEVEL TUNING

For the low-level tuning, the magnetic field distribution of each quadrant was measured using a bead-pull measurement method. The bead position is outside the dipole rod, where the magnetic field dominates. As shown in Fig. 6, the beads are passed through the hole outside the DSR. To

Content from this work may be used under the terms of the CC BY 3.0 licence (© 2018). Any distribution of this work must maintain attribution to the author(s), title of the work, publisher, and DOI.

ISBN: 978-3-95450-194-6 ISSN: 2226-0366 doi:10.18429/JACoW-LINAC2018-THPO049

Content from this work may be used under the terms of the CC BY 3.0 licence (© 2018). Any distribution of this work must maintain attribution to the author(s), title of the work, publisher, and DOI.

evaluate the magnetic field strength, the phase fluctuation is measured by a network analyzer.

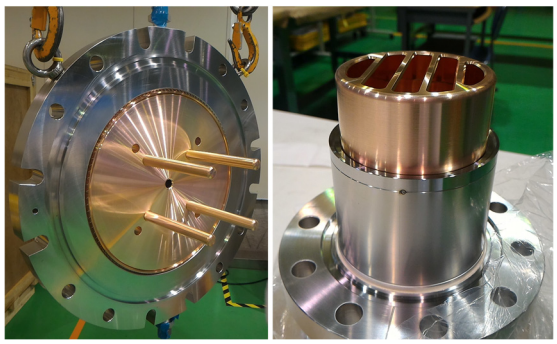


Figure 6: End plate and tuner.

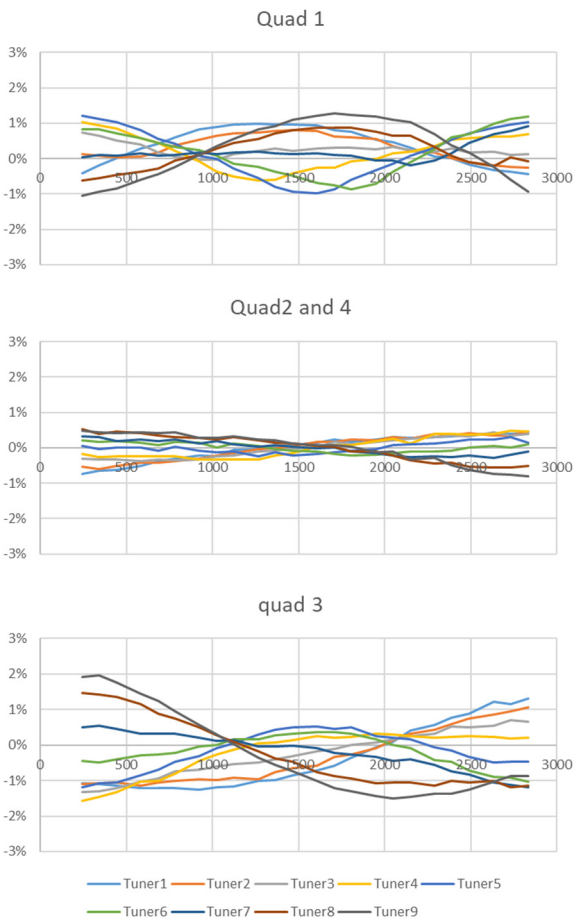


Figure 7: Magnetic field variations with tuner insertion.

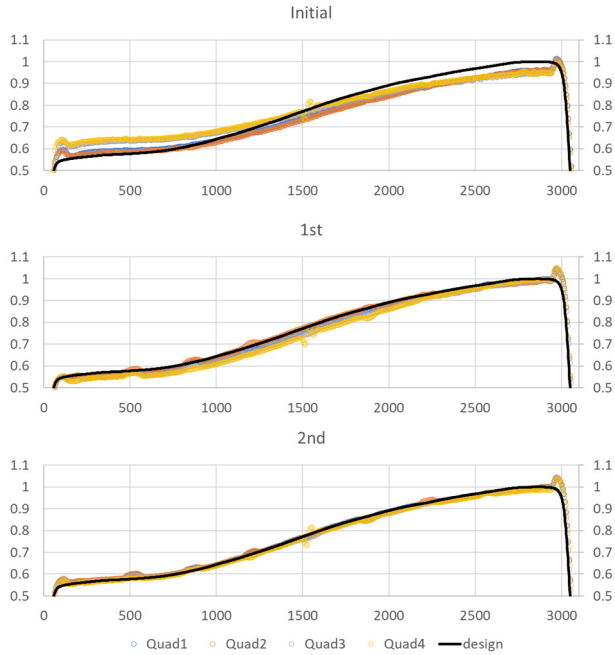


Figure 8: Bead-pull measurement result.

Although it is possible to create a response matrix by measuring the variation of the magnetic field distribution with changing the tuner insertion depth, to shorten the tuning period, the response matrix for the tuners is created by the RF simulation as the same procedure as the above-mentioned optimization for the dimension parameters. To evaluate the field variation by a tuner, it is necessary to use a full model including all quadrants. The calculated variation of the magnetic field distribution when inserting the tuners of the first quadrant by 1 mm is shown in Fig. 7. Only the tuner responses of the first quadrant was calculated, and all matrix elements were given by the quadrant symmetry. The insertion depths are given by summation of the inverse matrix results and the frequency offset length (all tuners equalized).

The bead measurement results before and after the tuning are shown in Fig. 8. After two iterations, the field error from the designed distribution was ± 1.5%. The local bumps in the first and second iterations are due to the disturbance by the tuner. Finally, the range of the insertion depth for all tuners were from -0.7 mm to +1.9 mm.

CONCLUSION

The RF design of the RFQ has been done based on the three-dimensional cavity models including modulations and cutbacks. The vane-base widths and cutback depths were optimized using the pseud-inverse matrix method to produce the desired vane-voltage distribution. In the low-level tuning, the insertion depths of the stub turners were also determined based on the tuner responses obtained from the full 3D model.

ISBN: 978-3-95450-194-6 ISSN: 2226-0366 doi:10.18429/JACoW-LINAC2018-THPO049

REFERENCES

[1] Y. Kondo *et al.*, Phys. Rev. ST Accel. Beams **15**, 080101 (2012).

[2] J. H. Billen, L. M. Young, Poisson Superfish, Tech.rep., LAUR-96-1834 (1996).

[3] CST Micro Wave Studio, www.cst.com.

Content from this work may be used under the terms of the CC BY 3.0 licence (© 2018). Any distribution of this work must maintain attribution to the author(s), title of the work, publisher, and DOI.

ISBN: 978-3-95450-194-6 ISSN: 2226-0366 doi:10.18429/JACoW-LINAC2018-THPO050

RESEARCH ON THE NEW CAVITY STRUCTURE OF RFQ ACCELERATOR WITH BENT VANES AT IMP *

Lei Yang † [1], Liang Lu, Zhouli Zhang,
Liepeng Sun, Chenxing Li, Tao He[1], ChaoChao Xing[1], Yaun He
Institute of Modern Physics, Chinese Academy of Sciences, Lanzhou 730000, China
[1]also at University of Chinese Academy of Sciences, Beijing 100049, China

Abstract

A new cavity structure of RFQ accelerator with bent vanes has been proposed at IMP. The new structure can reduce the lateral dimension of the cavity and possesses simple cooling structure in the low frequency field. In this paper, the dynamics of an 81.25 MHz bent-vane RFQ has been designed as a prototype device of the bent-vane RFQ. The 2D EM simulation of the bent-vane RFQ has been performed. Detailed description is presented in this paper.

INTRODUCTION

Four-vane type and four-rod type are commonly used in radio frequency quadrupole (RFQ) linac structure. Four-vane type RFQ is mainly used in the high frequency field and four-rod type RFQ applies to the low frequency field prevailingly [1]. In continuous wave (CW) operating mode, it is necessary that RFQ structure should have a complete cooling structure so that it can fully cool the RFQ cavity to ensure stable operation with a large amount of heat generated by the cavity during CW mode. The CW four-rod type RFQ cooling structure is quite complicated, which makes it difficult to design and machine the cavity, which limits the application and development of four-rod type RFQ in CW condition. Although the four-vane type RFQ is suitable for working in CW condition with single cooling structure and sufficient cooling efficiency，in the low frequency field, its lateral dimension is large, and the lower the frequency, the larger the lateral dimension, which increases machining difficulty and cost.

In order to overcome the disadvantages of four-rod and four-vane RFQ in the CW condition and the low frequency band, we put forward a kind of new RFQ accelerator structure called bent-vane type RFQ at Institute of Modern Physics (IMP),Chinese Academy of Sciences. The bent-vane type RFQ combines the advantages of four-rod type RFQ and four-vane type RFQ. It significantly reduces the lateral dimension of the cavity in the low frequency field and has a water-cooled system with a simple structure and sufficient cooling efficiency. In this paper, we present an 81.25 MHz bent-vane RFQ beam dynamics design and two-dimensional electromagnetic field (2D EM) simulation.

RFQ BEAM DYNAMICS DESIGN

The beam dynamics design of the bent-vane RFQ is simulated by the code RFQGen [2]. Taking into account research requirements and cost, the design parameters of the bent-vane RFQ are listed in Table 1.

The bent-vane RFQ accelerates He^+ (q/A=1/4) from 4 keV/u to 42.5 keV/u. In order to decrease the cavity length, the maximum peak surface electric field is 18.23 MV/m, which is 1.73 times higher than the Kilpatrick limit. The transverse focusing strength (B) keeps constant to decrease the cavity machining difficulty. The simulation results of beam transmission are shown in Fig. 1. The transmission efficiency is 96.9 % at 5 mA.

Table 1: The Design Parameters of the Bent-vane RFQ

Parameter	Value
Particle	He^+(q/A=1/4)
Frequency(MHz)	81.25
Beam current(mA)	5
Input energy(keV/u)	4
Output energy(keV/u)	42.5
Vane voltage(kV)	70
Vane length(mm)	533.76
Kilpatrick factor	1.73
Transmission efficiency(%)	96.9

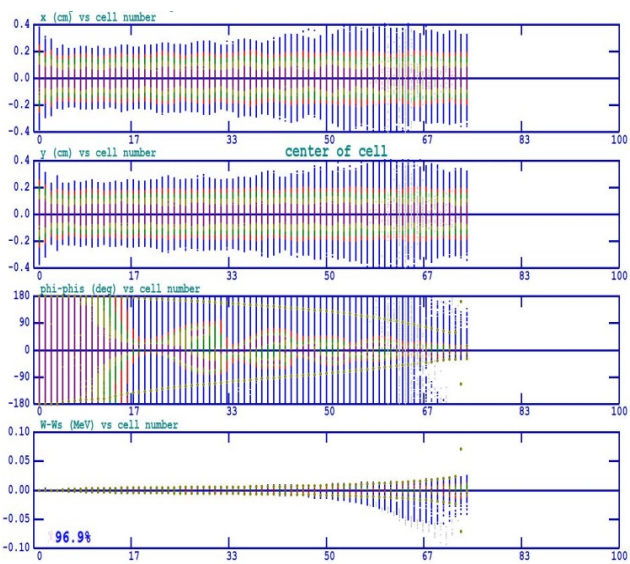


Figure 1: Beam dynamics simulation of the bent-vane RFQ (RFQGen).

2D EM SIMULATION

The cross-section profile is important in the bent-vane RFQ EM design, which is shown in Fig. 2. The cross-

* Work supported by Natural Science Foundation of China (Grant No. 11675236, 11475232 and 11535016)
† email address: yanglei@impcas.ac.cn

Content from this work may be used under the terms of the CC BY 3.0 licence (© 2018). Any distribution of this work must maintain attribution to the author(s), title of the work, publisher, and DOI.

ISBN: 978-3-95450-194-6 ISSN: 2226-0366 doi:10.18429/JACoW-LINAC2018-THPO050

section geometry of the bent-vane RFQ is defined with 13 independent variables. Their Preliminary optimization values are listed in Table 2.

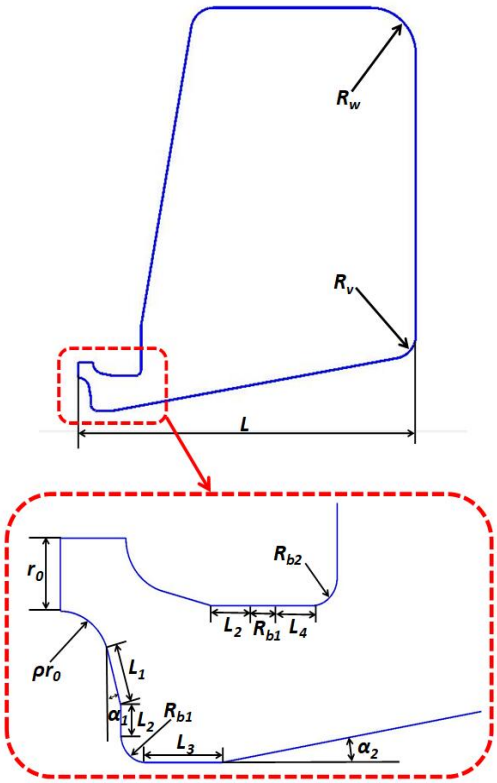


Figure 2: The cross-section profile of the bent-vane RFQ.

Table 2: The Parameters of the Bent-Vane RFQ Cross-section

Parameter	Value	Parameter	Value
r_0	5.347 mm	L	275 mm
ρ	0.75	R_v	20 mm
α_1	10 Deg.	α_2	5 Deg.
L_1	10 mm	R_w	40 mm
L_2	5 mm	L_4	10 mm
R_{b1}	5 mm	R_{b2}	5 mm
L_3	10 mm		

Verifying TE210 Mode of the Bent-Vane RFQ

RFQ can accelerate particle beam because the EM field mode of its electrode tip is TE210. Particle beam can be accelerated, focused and bunched in TE210 mode. In the bent-vane RFQ, TE210 mode is found in electrode tip, shown in Fig. 3.

Parameters Optimization

The main parameters of RFQ are obtained from the 2D EM simulation. The parameters of cross-section profile can be achieved and optimized by using the CST MWS [3]. The slice model of the bent-vane RFQ is effectively used to verify the parameters of the cross-section profile. The slice model is shown in Fig. 4.

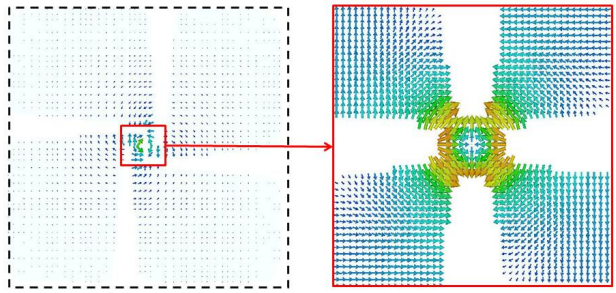


Figure 3: The electric field distribution of the bent-vane RFQ.

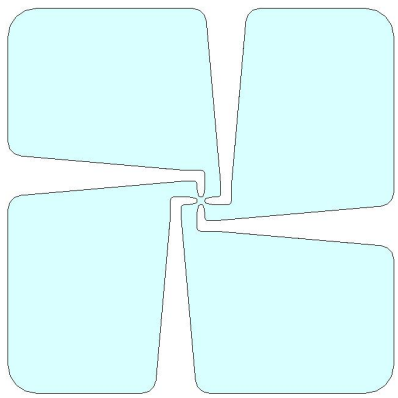


Figure 4: The slice model of the bent-vane RFQ.

The parameters of the cross-section profile can directly influence physical properties of the bent-vane RFQ. In RFQ accelerator, the lateral dimension (L), quality factor and shunt impedance are one of the most important physical quantities. In the thirteen parameters, the values of r_0, ρ and α_1 are defined in the code RFQGen. Hence, keeping the frequency (81.25 MHz) constant, the effects of the other nine parameters are shown in Fig. 5 on the lateral dimension, quality factor and shunt impedance of the bent-vane RFQ (Only presenting two parameters).

The final RF parameters of the slice model of the bent-vane RFQ are listed in Table 3.

Table 3: The RF Parameters of the Slice Model

Parameter	Value
Frequency	81.246 MHz
Nearest dipole mode frequency	79.569 MHz
Quality factor	18446
Peak electric field	16.06 MV/m
Power loss	11.59 W/mm
L	279.11 mm

CONCLUSION AND FUTURE PLAN

A new cavity structure of RFQ accelerator is proposed called the bent-vane RFQ at IMP. The dynamics of an 81.25 MHz bent-vane RFQ has been designed as a prototype device of the bent-vane RFQ. The 2D EM simulation of the bent-vane RFQ has been performed. The cross-section geometry of the new structure is defined with 13

Content from this work may be used under the terms of the CC BY 3.0 licence (© 2018). Any distribution of this work must maintain attribution to the author(s), title of the work, publisher, and DOI.

ISBN: 978-3-95450-194-6 ISSN: 2226-0366 doi:10.18429/JACoW-LINAC2018-THPO050

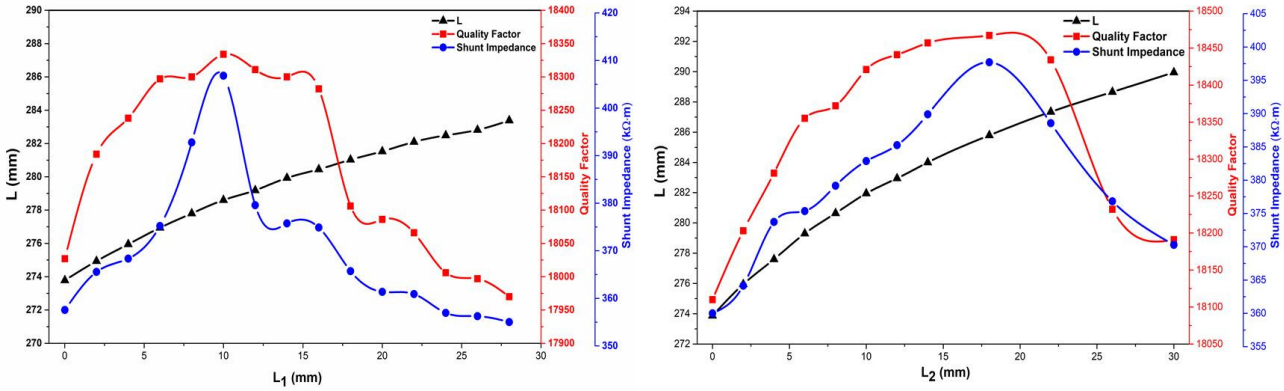


Figure 5: The variation of the lateral dimension (L), quality factor and shunt impedance of the bent-vane RFQ as the functions of the parameters of the cross-section profile (Only presenting two parameters).

independent variables. The TE210 mode is verified in the bent-vane RFQ. The slice model RF parameters are simulated and achieved. 3D simulation and Multi-physics study will be performed in the near future.

ACKNOWLEDGEMENTS

This work is supported by the National Natural Science Foundation of China (Grant No. 11675236, 11475232 and 11535016).

REFERENCES

[1] T.P. Wangler, *RF Linear Accelerators*, John Wiley & Sons, New York, 2008.

[2] K. R. Crandall *et al.*, *RFQ Design Codes*, LA-UR-96-1836, 1998.

[3] CST Simulation Packages, https://www.cst.com/

Content from this work may be used under the terms of the CC BY 3.0 licence (© 2018). Any distribution of this work must maintain attribution to the author(s), title of the work, publisher, and DOI.

ISBN: 978-3-95450-194-6 ISSN: 2226-0366 doi:10.18429/JACoW-LINAC2018-THPO051

THE MULTI-PHYSICS ANALYSIS OF LEAF RFQ

X. Xu, L. Lu, W. Ma, L. Sun, C. Li, L. Shi, T. He, L. Yang, C. Xing, A. Shi, Y. He, H. Zhao,
Institute of Modern Physics, CAS, Lanzhou, China

Abstract

The 81.25 MHz CW RFQ is designed to accelerate heavy ions with Q/A from 1/7 to 1/2 at 0.5 MeV/u for the Low Energy Accelerator Facility (LEAF) at the Institute of Modern Physics (IMP) of the Chinese Academy of Science (CAS). The four-vane RFQ consists of six modules with a total length of 5.95 meters, For the CW operating mode, thermal management will be a very important issue, Therefore a multi-physics analysis is necessary to ensure that the cavity can stably operate at the high RF power . The multi-physics analysis process includes RF electromagnetic analysis, thermal analysis, mechanical analysis, and the frequency shift, the cooling water system is used for frequency tunning by the temperature adjustment, and also analyze RFQ undercuts, fixed tuners, and pi-mode rods, the results show that the thermal and structural design of this RFQ is reasonable.

INTRODUCTION

The LEAF project is being developed at the Institute of Modern Physics(IMP), composed of superconducting ECR ion source, low energy beam transport line (LEBT), CW radio frequency quadrupole accelerator (RFQ), medium energy beam transport line(MEBT) and an experimental platform [1], the layout of the LEAF project is shown in Fig. 1.

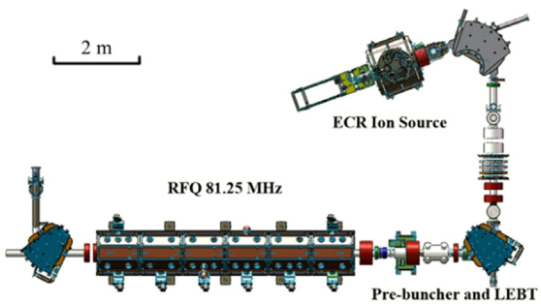


Figure 1: The layout of the LEAF project.

The four-vane RFQ will accelerate heavy ions beams from from 14 keV/u up to 500 keV/u. The operating frequency is 81.25 MHz. The PI-mode rods are used for frequency separation. The cavity will be divided into six segments about 5.95m long. The oxygen-free high-conductivity copper (OFHC) is adopted because of its good heat conduction performance and. An octagon cavity structure is chosen for its structural stability to avoid cavity deformation and convenient design of water cooling system [2].

For high power CW RFQ, the thermal issue will cause structure deformation, frequency shift, and other harmonics. So it's very important to calculate the deformation and evaluate its influence to the electromagnetic field in theory. The thermal and structural distortion of the cavity is calculated by ANSYS code [3], both the temperature rise and the frequency shift can be controlled in an acceptable level according to the optimization of the cooling water design.

The main parameters of the RFQ are listed in Table 1.

Table 1: The Main Parameters of the RFQ

Parameters	Value
Frequency (MHz)	81.25
Injection/Output energy (keV/u)	14/500
Design charge-to-mass ratio	1/7-1/2
Inter-vane voltage (kV)	70
Kilpatrick factor	1.55
Peak current (emA)	2
Transmission efficiency (%)	97.2
Length of the vane (mm)	5946.92
Average radius of the aperture (mm)	5.805

THIN SLICE MODEL SIMULATION

The multi-physics analysis procedure include RF electromagnetic, thermal and mechanical analysis [4], A 1/4 part of the cross section is used for simulation due to symmetry, thin slice model with water cooling channels are shown in Fig. 2.

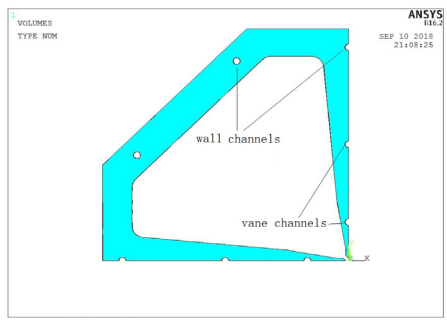


Figure 2: Thin slice model with water cooling channels.

The RF analysis has been carried out with ANSYS code, the result gives RF power losses in cavity in order to obtain a temperature map.

Content from this work may be used under the terms of the CC BY 3.0 licence (© 2018). Any distribution of this work must maintain attribution to the author(s), title of the work, publisher, and DOI.

ISBN: 978-3-95450-194-6 ISSN: 2226-0366 doi:10.18429/JACoW-LINAC2018-THPO051

Content from this work may be used under the terms of the CC BY 3.0 licence (© 2018). Any distribution of this work must maintain attribution to the author(s), title of the work, publisher, and DOI.

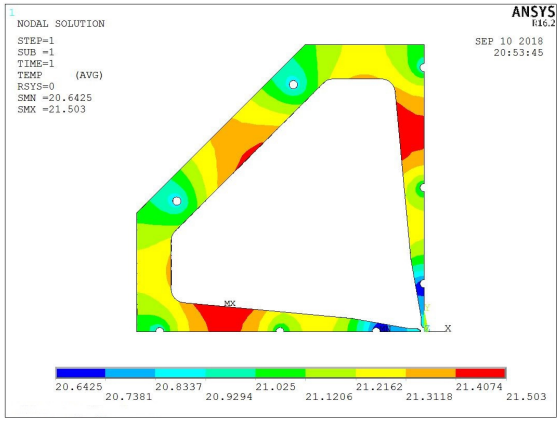


Figure 3: The temperature distribution of the RFQ.

The tempreture distribution from the thermal analysis is shown in Fig. 3, the heat load is produced by the RF power losses which is applied to the inner cavity wall surfaces, according to the optimization for channel position, channel diameter, fluid and velocity temperature，the maximum temperature is 21.5℃ and is located at the vanetips, the RFQ cavity temperature only rises 2℃ above initial water temperature. This temperature rise causes deformation and resonant frequency shift of the cavity.

The water cooling channels parameters are listed in Table 2.

Table 2: The Water Cooling Channels Parameters

	vane/wall
Diameter (mm)	12
Flow speed (m/s)	2.29
Number of Channels (/unit)	4/4
Heat transfer coefficient (W/m2.K)	9723

The final heat flux is coupled to a mechanics structrue to estimates the stress and deformation due to thermal expansion. The frequency shift is obtained through a new RF simulate of the deformed structure.

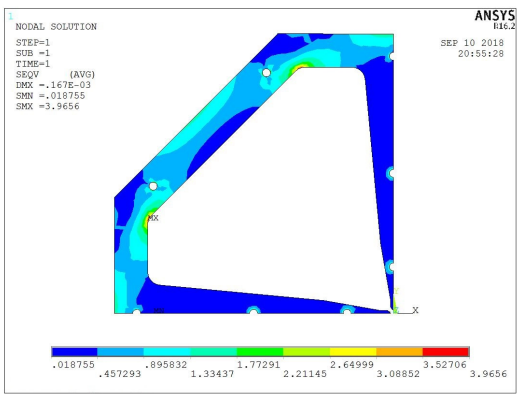


Figure 4: The von-Mises stress distribution of the RFQ.

The von-Mises stress distribution is shown in Fig. 4, the maximum stress is 3.9656 MPa at the corners of cavity, the displacement distribution is given in Fig. 5, the maximum displacement is 0.167mm around the external wall.

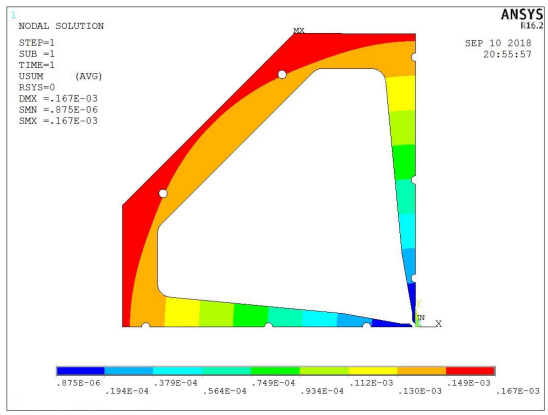


Figure 5: The displacement distribution of the RFQ.

The displacement of the cavity will cause the frequency shift. The final frequency were calculated with the ANSYS code according to the new cavity geometry which represents the steady-state operating condition, The frequency shift is -26.3 kHz compared with the initial frequency.

RFQ UNDERCUTS SIMULATION

The RFQ undercuts are simulated by a similar mean as the thin slice model with the ANSYS code, the tempreture result is shown in Fig. 6. The maximum temperature occurs at the tips of the cutbacks, where the water cooling channels can't distribution.

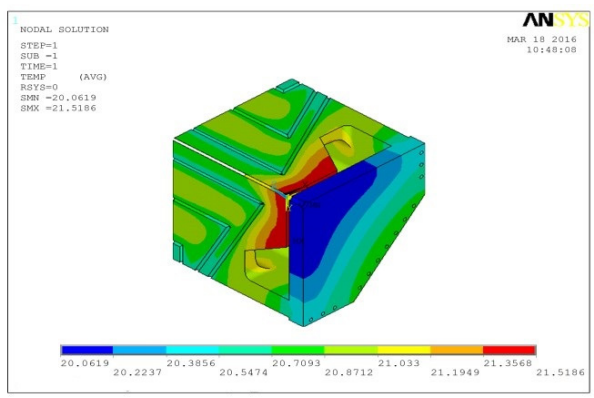


Figure 6: The temperature distributions of the RFQ undercuts.

ISBN: 978-3-95450-194-6 ISSN: 2226-0366 doi:10.18429/JACoW-LINAC2018-THPO051

RFQ TUNERS AND PI-MODE RODS SIMULATION

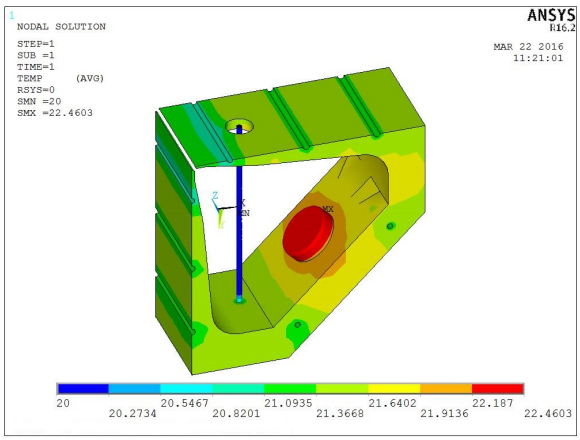


Figure 7: The temperature distributions of the tuners and Pi-mode rods.

There are totally twenty water cooling channels distributed over of the RFQ and one water cooling channel per Pi-rod. The temperature distributions of the RFQ tuners and Pi-mode rods is shown in Fig. 7, the maximum temperature of the RFQ is 22.46℃ which is located in the tuners. The tuners will work safely without water cooling.

CONCLUSIONS

The multi-physics analysis of the LEAF RFQ has been accomplished including the RF, thermal and structural simulations using thin slide model, undercuts model, tuners and Pi-mode rods model. The results show that the cooling water system can meet the requirements of RFQ operating at CW full power. The multi-physics results provide the data for RFQ frequency tuning strategy.

REFERENCES

[1] W. Ma, L. Lu, T. Liu *et al.*, "Three-dimensional multi-physics analysis and commissioning frequency tuning strategy of a radio-frequency quadrupole accelerator", *Nucl. Instrum. Methods Phys. Res.*, vol. 866, pp. 190–195, 2017.

[2] W. Jing, H. Long, H. Yuan *et al.*, "Multi- Physics analysis of the RFQ for the injector scheme II of CADS driver linac", *Chinese Physics C*, vol. 38 , pp. 97-101, 2014.

[3] ANSYS, http://www.ansys.com

[4] A.K. Orduz, C. Bontoiu, A. Berjillos *et al.*, "Thermal and structural analysis of the 72.75 MHz lince RFQ", in *Proc. 6th Int. Particle Accelerator Conf. (IPAC'15)*, Richmond, VA, USA, May 2015, pp. 3857-3860.

Content from this work may be used under the terms of the CC BY 3.0 licence (© 2018). Any distribution of this work must maintain attribution to the author(s), title of the work, publisher, and DOI.

ISBN: 978-3-95450-194-6 ISSN: 2226-0366 doi:10.18429/JACoW-LINAC2018-THPO052

HIGH POWER TEST OF THE LEAF-RFQ*

L. LU†, W. MA, Y. H. ZHAI, Y. YANG, L.P. Sun, L. B. Shi, L.T. Sun, Y. He, H.W. Zhao
Institute of Modern Physics (IMP), CAS
509 Nanchang Rd., Lanzhou, Gansu, China

Abstract

An 81.25 MHz continuous wave (CW) radio frequency quadrupole (RFQ) accelerator has been designed and fabricated for the Low Energy Accelerator Facility (LEAF) by the Institute of Modern Physics (IMP) of the Chinese Academy of Science (CAS). The operation frequency is 81.25 MHz and the inter-vane voltage is a constant of 70 kV. It took about 44 hours continuous conditioning to reach RF power of 75 kW which is 1.1 time of the maximum designed operation power, and the successful CW acceleration of 150 eμA He^+ beam to the designed energy of 0.5 MeV/u. Both the results of the high power test and the beam test will be reported in this paper.

INTRODUCTION

The LEAF project was launched as a pre-research facility for the high intensity Heavy Ion Accelerator Facility (HIAF) project and a heavy ion irradiation facility for material research at IMP [1, 2]. The LEAF will consist of a 2 mA U^{34+} electron cyclotron resonance ion source, a low energy beam transport line, a CW 81.25MHz RFQ accelerator [3], a medium energy beam transport and an experimental platform for nuclear physics. The layout of the LEAF project is shown in Fig. 1. The LEAF-RFQ shown in Fig. 2 will operate as a CW injector with the capability of accelerating all ion species from proton to uranium from 14 keV/u up to 500 keV/u. The design goal is to design a compact type cavity with lower power loss and high operation stability. Considering the LEAF-RFQ will operate in CW mode, a four-vane structure is a better choice than four-rod type, because the four-vane structure is a more stable structure for water cooling. The PISLs structure is adopted to suppress the dipole effect. In addition, tuners and undercuts are used for frequency tuning and field flatness. The main parameters of the LEAF-RFQ are listed in the Table 1. In this paper, we report the results of the low power test and the high power test.

Table 1: Main Parameters of the LEAF-RFQ

Parameters	Value
A/q	7
Operation	CW/pulsed
Vane type	Four vane
Frequency (MHz)	81.25
Input energy (keV/u)	14
Output energy (MeV/u)	0.5
Inter-vane voltage (kV)	70
Kilpatrick factor	1.55
Peak current (emA)	2
Transmission efficiency (%)	97.2
Acceleration efficiency (%)	81.7
Length of vane (mm)	5946.92
Average radius of aperture (mm)	5.805

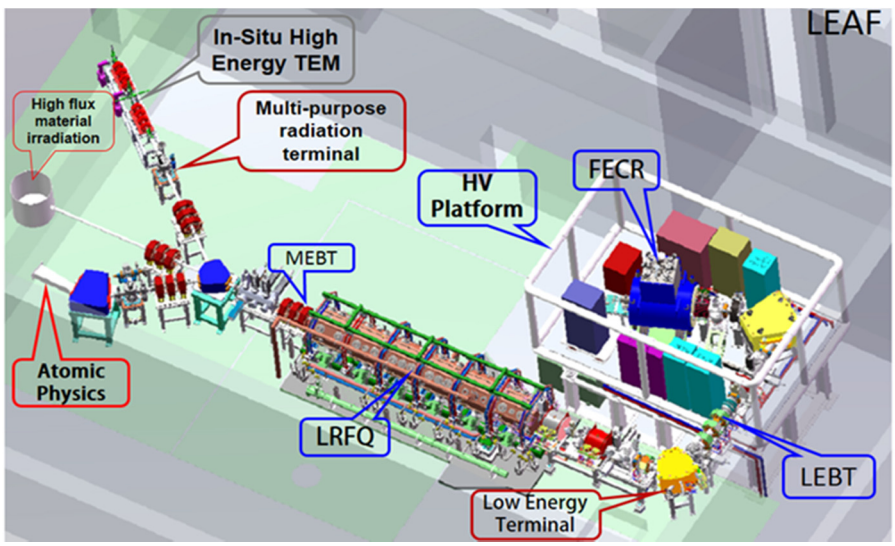


Figure 1: Layout of LEAF facility.

*Work supported by the NSFC under Grant No. 11427904, No. 11475232 and No. 11535016.
†luliang@impcas.ac.cn

Content from this work may be used under the terms of the CC BY 3.0 licence (© 2018). Any distribution of this work must maintain attribution to the author(s), title of the work, publisher, and DOI.

ISBN: 978-3-95450-194-6 ISSN: 2226-0366 doi:10.18429/JACoW-LINAC2018-THPO052

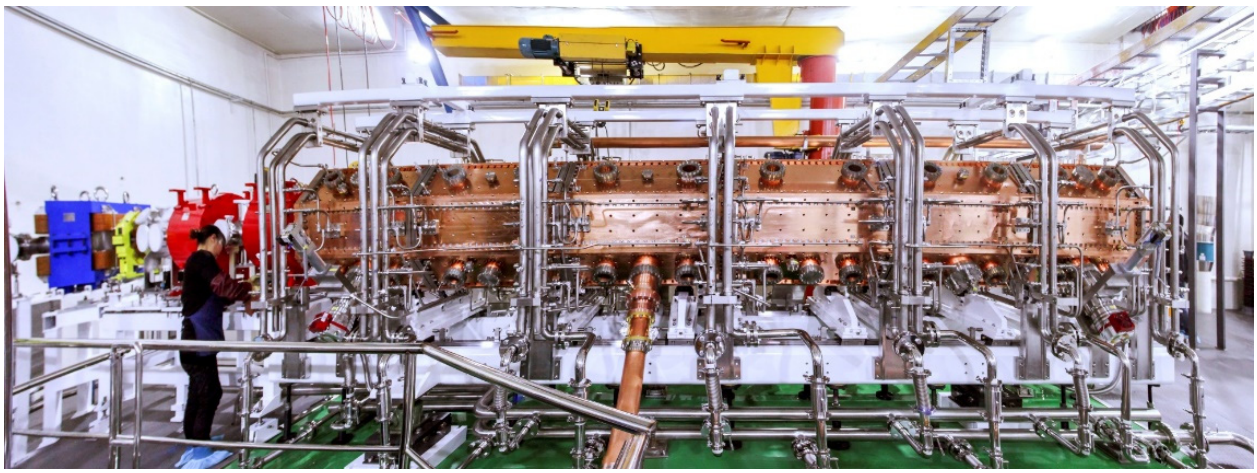


Figure 2: Side view of installed RFQ after full assembly on site.

LOW POEWR TEST

The LEAF-RFQ was assembled in the end of December of 2017, and the low power test was started in the early January of 2018. The low power tests and tuning of the whole cavity were carried out through three steps. Firstly, frequencies, Q factor and fields were measured in the cavity with aluminum end-plates and aluminum tuners inserted into the cavity 26 mm, the same situation as the simulation. Secondly, through the tuning code LRFQtuning (a code developed for LEAF RFQ tuning based on the Matlab), the depths of the tuners were adjusted to meet the requirements of frequency and fields. After a few iterations, a satisfactory resonant frequency and field distribution will be achieved. Lastly, the copper tuners with the final insertion and copper end-plates replaced aluminum those. This step was to check the resonant frequency and field distribution, meanwhile, the Q factor was measured.

The LEAF-RFQ low power test consists of each section test and the whole cavity test. The low power tests of single section were carried out to check the machining and brazing quality. The average frequency difference between the simulated and the measured after brazed is 10.15 kHz. The average frequency difference between the measured before brazed and after brazed is 23.35 kHz. Shown in Table 2, the low power test of the full length RFQ showed that the final quadrupole mode frequency is 81.253 MHz which meets well with the design value of 81.25 MHz, the measured Q factor is 16230 which is 90.3% of the simulated value and the measured frequency separation was 5.54 MHz which is enough for safe operation. Figure 3 shows the measured longitudinal field distributions of the quadrupole, two dipole fields in the cavity with two aluminum end-plates and copper tuners with the tuned tuners [4]. The relative error of the quadrupole field is less than 1% and the admixtures of the two dipole modes are within 1.5% of the quadrupole field. Therefore, the frequency and field distribution meet the operation requirement.

Table 2: Main Parameters of the LEAF-RFQ

Measured results	Value
Quadrupole frequency (MHz)	81.253
Q factor	16230 (90.3%)
Q field relative error (%)	0.8
Admixture of dipole field (%)	1.5
Separated Δf (MHz)	5.587

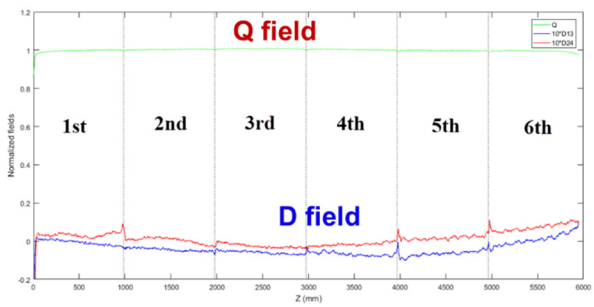


Figure 3: Measured Q and D field of the LEAF-RFQ.

RF CONDITIONING AND BEAM COMMISSIONING

After installing the equipments of vacuum, couplers, cooling routers, ARC detectors and pick-ups, and connecting with two 60kW solid state type RF source, the RF commissioning was started from Feb. 3rd 2018 aiming to 75 kW (1.12 times of necessary power). With a base vacuum condition of ~1×10^{-5} Pa, it took about 44 hours continuous conditioning to reach goal of 75 kW.

The LEAF-RFQ was designed for $2 \leq A/q \leq 7$ ion acceleration, and the designed Kilpatrick factor was 1.54. the He^+ beam was adopted for beam commissioning. The first pulse beam using 100 μA He^+ ions passed the RFQ in Feb. 9th 2018. Under the condition of pulse beam, the beam energy was measured as 0.5 MeV which meet the designed value. And two hours late, the first CW He^+ beam passed the RFQ. The current of the CW beam was measured as 150 μA. With supplying of correction magnet, the beam conditioning was restarted in June 1st 2018, the beam

Content from this work may be used under the terms of the CC BY 3.0 licence (© 2018). Any distribution of this work must maintain attribution to the author(s), title of the work, publisher, and DOI.

ISBN: 978-3-95450-194-6 ISSN: 2226-0366 doi:10.18429/JACoW-LINAC2018-THPO052

Content from this work may be used under the terms of the CC BY 3.0 licence (© 2018). Any distribution of this work must maintain attribution to the author(s), title of the work, publisher, and DOI.

transmission and acceleration efficiency was measured as 97.21% and 50.11%, respectively. The measured transmission agreed with the design, the acceleration efficiency is lower than the design because an upstream multi-harmonic buncher is not installed yet.

Shown in Fig. 4 and Fig. 5, in Sep. 5th 2018, the first N^{2+} beam was successfully accelerated 110 μA up to the designed 500 keV/u with 97.97% transmission and 56.45% acceleration efficiency measured in pulse mode (5μs), and, the CW 110μA N^{2+} beam pass 15 minutes. The high current N^{2+} beam will be operated in one month when the multi-harmonic buncher is installed.

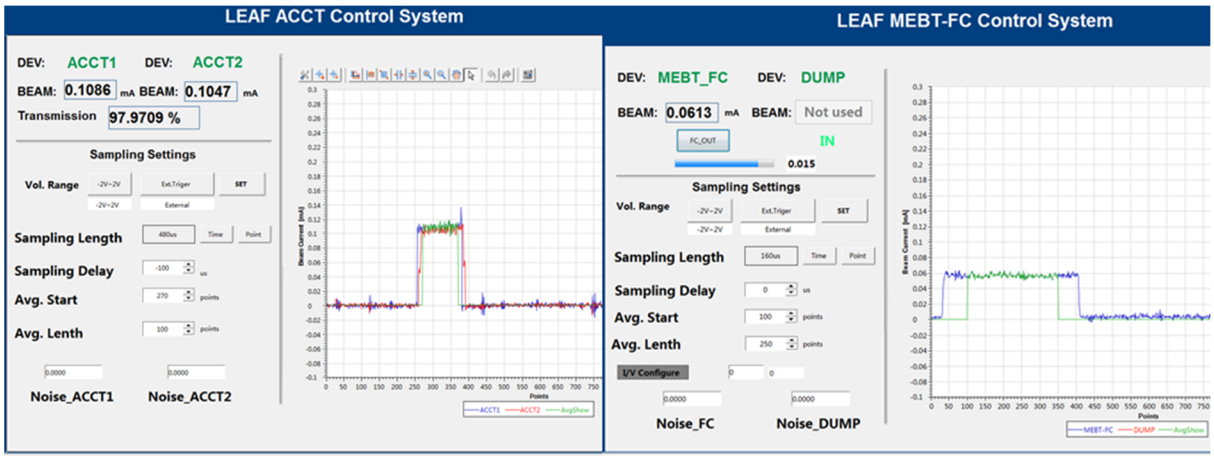


Figure 4: Measured signals of N^{2+} beam current form ACCTs and a Faraday Cup.

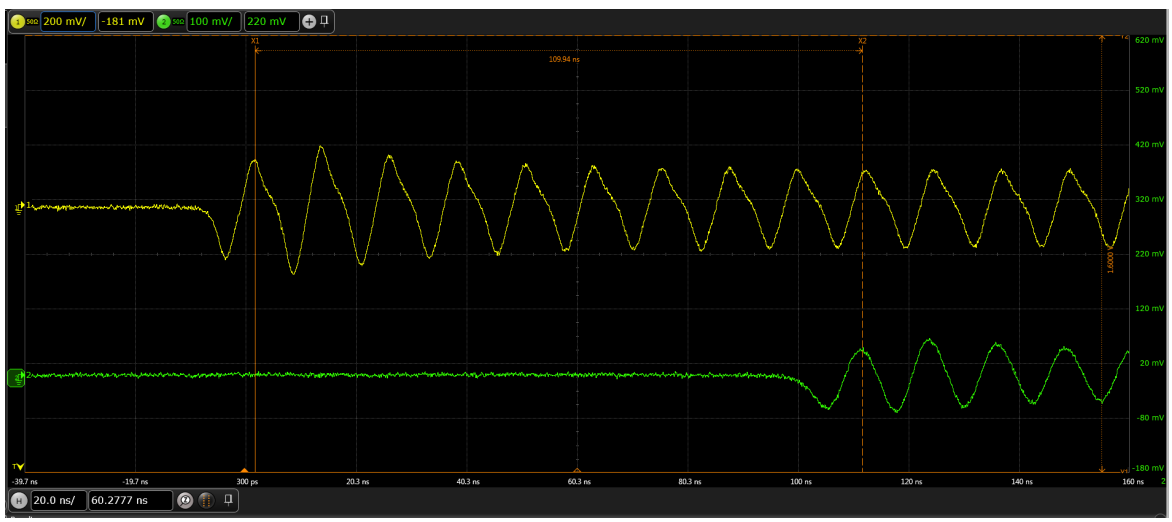


Figure 5: Measured signals of N^{2+} beam current form two BPMs.

CONCLUSION AND FUTURE PLAN

The LEAF-RFQ has been designed and simulated and the beam test was performed. The RFQ is an octagon four-vane type with 48 tuners and 12 pairs PISLs. It is about 6 m long with a good mode separation and a flat field distribution between inter-vanes. According to the high power test, several milestone goals have been achieved, such as the successful RF commissioning of LRFQ to its maximum designed power, and the successful CW acceleration of 150 eμA He^{+} beam to the designed energy of 0.5 MeV/u with 97.21% transmission. For the next, as N^{2+} has the A/q=7 close to U^{34+}, it will be used to test the performance of the RFQ.

REFERENCES

[1] Yang J, Xia J, Xiao G, Xu H, Zhao H *et al.*, *Nucl. Instr. Meth.*, vol. 317, pp. 263-5, 2013.

[2] Li C, Sun LP, He Y *et al.*, *Nucl. Instr. Meth.*, vol. 729, pp. 426-33, 2013.

[3] Wei Ma, L. Lu, Xianbo Xu, Liepeng Sun *et al.*, *Nucl. Instr. Meth.*, vol. 847, pp. 130-135, 2017.

[4] Wei Ma, L. Lu, Ting Liu, Longbo Shi *et al.*, *Nucl. Instr. Meth.*, vol. 901, pp. 180-188, 2018.

ISBN: 978-3-95450-194-6 ISSN: 2226-0366 doi:10.18429/JACoW-LINAC2018-THPO053

STATUS OF THE CHINA MATERIAL IRRADIATION FACILITY RFQ*

Chenxing Li †, Weiping Dou[1], Weilong Chen[1], Zheng Gao, Yuan He, Guirong Huang, Chunlong Li, Liang Lu, Aimin Shi, Longbo Shi, Liepeng Sun, Fengfeng Wang, Wenbin Wang, Zhijun Wang, Qi Wu, Xianbo Xu, Lei Yang[1], Peiyan Yu[1], Bin Zhang, Junhui Zhang, Peng Zhang, Tieming Zhu
Institute of Modern Physics, CAS, Lanzhou, China
[1]also at University of Chinese Academy of Sciences, Beijing, China

Abstract

The pulsed high power test and beam test of the China Material Irradiation Facility RFQ have been implemented. Before this, the radio frequency measurements and tuning are performed. In this paper, the processes and results of the radio frequency measurements, tuning, pulsed high power test and beam test will be presented. The results of tests are in good agreement with the design.

INTRODUCTION

Material study is important for the fusion energy utilization. It is important to construct accelerator-based neutron sources for verification of materials candidate to fusion reactor. The IFMIF project is a part of ITER project for this purpose. As counterpart to CFTER, the CMIF project is proposed. As a key equipment of CMIF, the RFQ is designed to accelerate 10 mA CW deuteron beam from 20 keV/u to 1.5 MeV/u. The design procedure is expatiated in references [1] and [2]. The key parameters are listed in Table1.

Table 1: Parameters of CMIF RFQ

Parameters	Values
Particle	D+
Frequency (MHz)	162.5
Energy (I/O, MeV/u)	0.02/1.55
Beam current (mA)	10
Cavity length (m)	5.34
Inter-vane Voltage(kV)	65
Kilpatrick factor	1.4
Transmission efficiency (%)	98.9

TUNING OF CMIF RFQ

Fabrications of single modules were completed May 2017. And assembly of whole length cavity is completed during July 2017. Rf measurements and tuning of the RFQ was carried out during July and August. The tuning process was expatiated in references [3]. The tuning was implemented by utilizing 100 slug tuners. Owe to the utilization of PISLs, the dipole perturbative components are below 1% during tuning, so there is no need for tuning of dipole perturbative components. Therefore, the lengths of tuners with same longitudinal position will be set to the same length. The evolution of the lengths of tuners is plot in Fig. 1. The quadrupole perturbative component during tuning is measured and plot in Fig. 2.

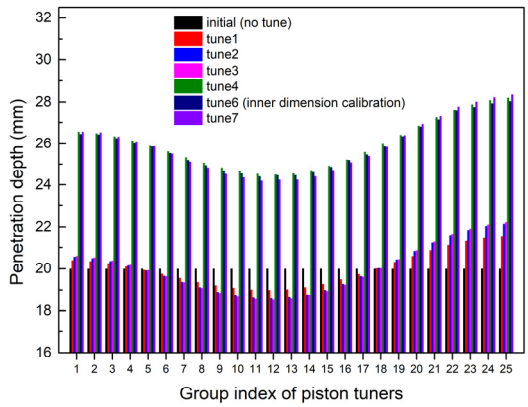


Figure 1: Evolution of lengths of slug tuner groups.

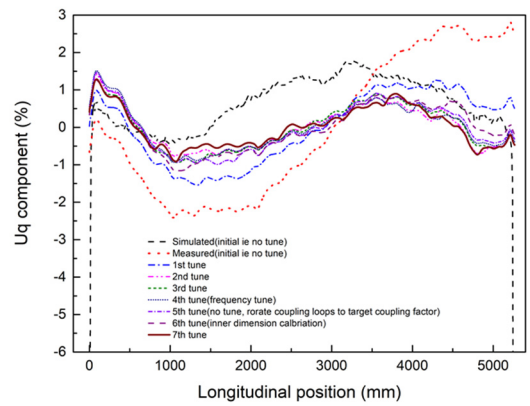


Figure 2: Evolution of the quadrupole perturbative component during tuning.

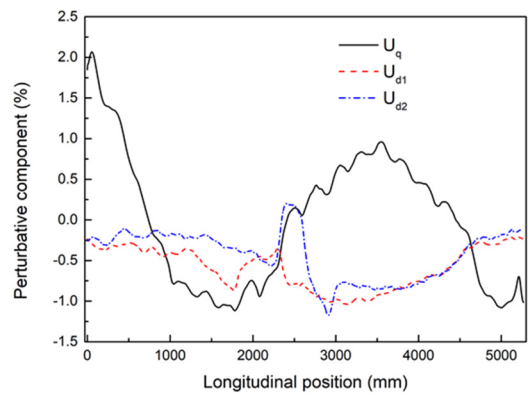


Figure 3: The measured perturbative components after the assembly of copper slug tuners.

* Work supported by the National Magnetic Confinement Fusion Science Program of China (Grant No. 2014GB104001) and the National Natural Science Foundation of China (Grant No. 91426303).
† email address: lichenxing@impcas.ac.cn

Content from this work may be used under the terms of the CC BY 3.0 licence (© 2018). Any distribution of this work must maintain attribution to the author(s), title of the work, publisher, and DOI.

ISBN: 978-3-95450-194-6 ISSN: 2226-0366 doi:10.18429/JACoW-LINAC2018-THPO053

Content from this work may be used under the terms of the CC BY 3.0 licence (© 2018). Any distribution of this work must maintain attribution to the author(s), title of the work, publisher, and DOI.

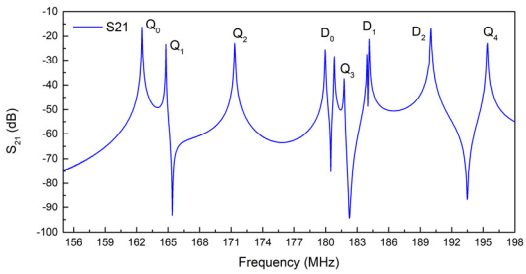


Figure 4: Frequency spectrum of the cavity after tuning.

The perturbative components after the assembly of copper slug tuners are plot in Fig. 3. After tuning, the frequency spectrum is measured and plot in Fig. 4. The Q_0 of cavity is derived by using the Smith circle fitting method [4], which is less vulnerable to coupling factor of pick up. The results of rf measurements and tuning is list in Table 2.

Table 2: Results of RF Measurements and Tuning

Parameters	Values
Frequency (MHz)	162.630
Q_0	12560
U_q	$<2\%$
U_d	$<1.5\%$

PULSED CONDITIONING OF CMIF RFQ

Due to the lack of cooling water, the condition is limited to the pulse low than 0.1 ‰ while the repetition keeps 1 Hz. The TH781 Tetrode Amplifier [5] is used for pulsed conditioning of CMIF RFQ. There is a splitter and phase shifter in the rf power transmission system. In order to lower the trip rate due to reflected power, critical coupling is obtained through adjustment of phase shifter. This is verified by the measured Smith Chart of S11 form the input of main transmission coaxial tube. The requisition of Q_0 value form Smith Circle fitting is plot in Fig. 5. The measured Q_0 value is in coincidence with that measured from couplers. Through evaluation using the measured Q_0 value, the nominal power should be 123 kW for reach the nominal intervane voltage. After 71 hours conditioning, this value is reached. The cavity power and vacuum during conditioning are recorded and plot in Fig. 6 and Fig. 7. The deterioration of vacuum at the late of test is contributed to breakdown of some of the cryo-pumps.

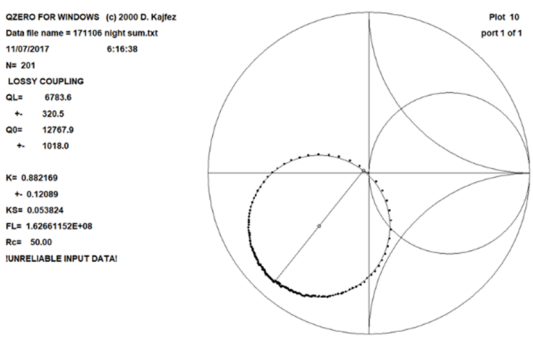


Figure 5: Smith Chart of S11 to the direction of cavity measured from the the main coaxial waveguide.

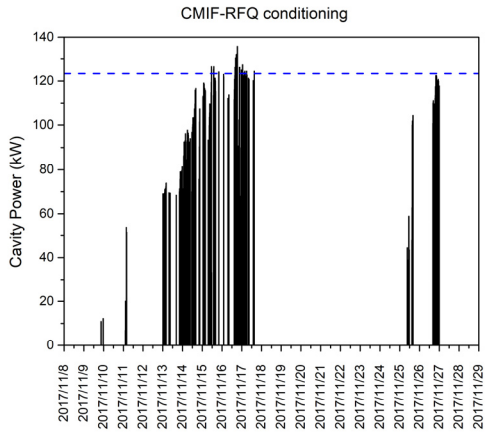


Figure 6: Cavity power records during pulsed conditioning(nominal power level is represented by blue dash line).

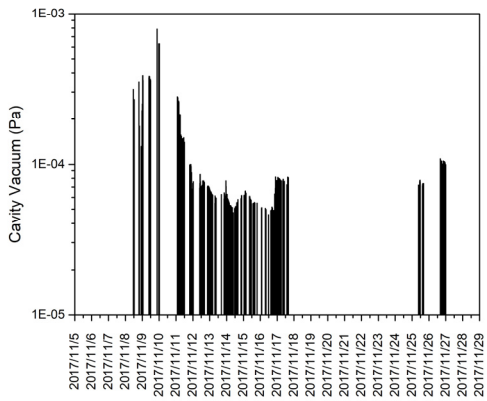


Figure 7: Cavity vacuum records during pulsed conditioning of CMIF RFQ.

PULSED BEAM TEST OF CMIF RFQ

The beam test system as shown in Fig. 8 was built which consists of ECR ion source, LEBT, RFQ and diagnostic plate. The diagnostic instruments include a Faraday cup (FC) in LEBT, a fast current transformer (FCT), a beam position monitor (BPM), and a beam dump in D-plate. In order to decrease difficulty of shielding, H_2^+ is selected as the test beam instead of deuteron.

After the power of cavity could sustain at the nominal level, the beam test was performed. Due to the lack of instruments of beam diagnostic, an FCT and a BPM were assembled on the diagnostic plate to measure the time of flight of the accelerated beam bunch (Fig. 9). It is worth noting that for our circumstance, the signal amplitude of beam bunch at the BPM is 0 while peak at the FCT (Fig. 10). The measured beam energy is 3.11±0.01 MeV.

ISBN: 978-3-95450-194-6 ISSN: 2226-0366 doi:10.18429/JACoW-LINAC2018-THPO053



Figure 8: View of RFQ test area.

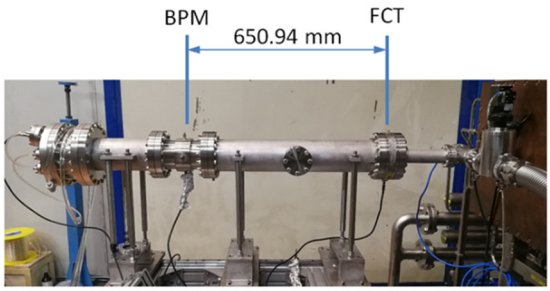


Figure 9: configuration of FCT and BPM on D-plate.

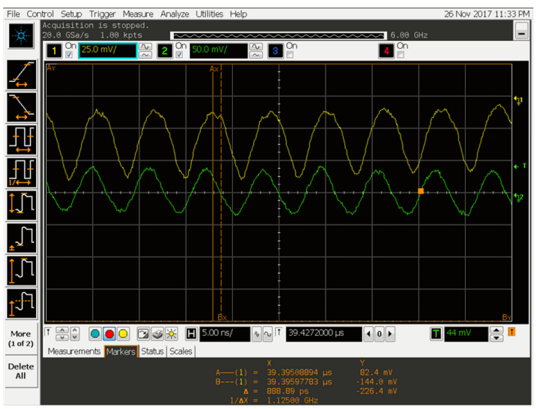


Figure 10: Signals of beam bunches on FCT(yellow) and BPM(green).

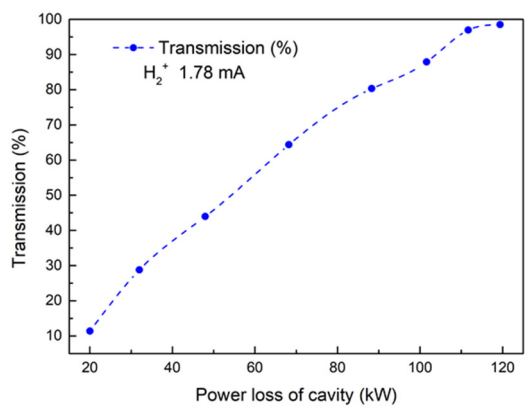


Figure 11: Measured Beam Transmission as a function of RF Power.

The beam current is measured using FC and beam dump in D-plate. The measured current in the FC was 8.04 mA, and the current at the beam dump was 7.85 mA. The transmission efficiency from FC to beam dump is 97.6 %. An experiment was also performed to explore the variation of the beam transmission corresponding to the change of cavity power, and the results are plot in Fig. 11.

CONDITIONING OF CMIF RFQ ON LINE

An upgrade plan has been performed on the 25 MeV proton Linac in Institute of Modern Physics, CAS. One main change is replacement of the origin ADS-RFQ [6] by CMIF-RFQ. Then the accelerator can accelerate Helium ion to do some material irradiation research. In 27 April, 2018, the CMIF RFQ was hoisted into tunnel of the 25 MeV proton Linac. The conditioning on beam line was started on 26 May, 2018. The RF power is provided by two solid-state amplifiers [7]. In order to protect RFQ, spark rate is recorded as a criterium for evaluating the state of the conditioning process. The conditioning level will not be increased until there is no spark in several hours. Due to the occupation of the power source for 973 RFQ test [8], the conditioning is suspended and will continue next week.

CONCLUSION

The tuning, rf measurements, conditioning and beam test of CMIF RFQ had been implemented in 2017. As a part of the upgrade 25 MeV Linac, the CW condition of CMIF RFQ should be completed in 2018. And CW beam test will be also performed after the nominal power level reached.

REFERENCES

[1] Dou, Wei-Ping, et al. "Beam dynamics and commissioning of CW RFQ for a compact deuteron–beryllium neutron source." *Nuclear Inst. And Methods in Physics Research*, A 903 (2018): 85-90.

[2] Li, Chenxing, et al. "RF Structure Design of the China Material Irradiation Facility RFQ." *Nuclear Inst. And Methods in Physics Research*, A 869 (2017): 38-45.

[3] Li, Chenxing, et al. "Radio Frequency Measurements and Tuning of the China Material Irradiation Facility RFQ", *Nuclear Inst. And Methods in Physics Research,* A 890 (2018): 43-50.

[4] D. Kajfez, Q Factor, Vector Forum, Oxford, MS (1994).

[5] Sun L.P., et al. “Overview of RF system for C-ADS injector II radio frequency quadrupole High Power Laser Part”, Beams, 29 (6) (2017), p. 065107.

[6] Z.L. Zhang, et al., Development of the injector II RFQ for China ADS project, in *Proc. of IPAC2014*, Dresden, Germany, 2014, pp. 3280-3282.

[7] Sun, Liepeng, et al. "OPERATING STATUS OF INJECTOR II FOR C-ADS PROJECT." in *Proc. of LINAC2016*, pp. 254-256.

[8] Fu, Qi, et al. "Progress Work on a CW Deuteron RFQ with Magnetic Coupling Windows." in *Proc. of IPAC2018*, Vancouver, BC, Canada, 2018, pp. 1123-1125.

Content from this work may be used under the terms of the CC BY 3.0 licence (© 2018). Any distribution of this work must maintain attribution to the author(s), title of the work, publisher, and DOI.

ISBN: 978-3-95450-194-6 ISSN: 2226-0366 doi:10.18429/JACoW-LINAC2018-THPO054

RECENT PROGRESS OF A CW 4-ROD RFQ FOR THE SSC-LINAC*

Z. S. Li[1], J. W. Xia[1], Y. J. Yuan, J. C. Yang, Y. He, Y. Q. Yang, Z. Xu, Y. Cong, J. Meng, L. Jing, H. Du[1], Z. J. Wang, Y. Zhang, X. N. Li[1], K. D. Wang[1], W. J. Xie, Y. Wei, H. M. Xie[1], G. D. Shen[1], Q. Y. Kong[1], X. J. Yin[1, †], J. X. Wu[1, ‡],
Institute of Modern Physics of Chinese Academy of Sciences, 730000 Lanzhou, China
Y. R. Lu[§],
State Key Lab of Nuclear Physics and Technology, Peking University, 100871 Beijing, China
[1]also at Huizhou Research Center of Ion Sciences, 516003 Huizhou, China

Abstract

The SSC-LINAC is under design and construction as a linear injector for the Separated-Sector Cyclotron (SSC) of the Heavy Ion Research Facility at Lanzhou (HIRFL). The continuous-wave (CW) 4-rod radio-frequency quadrupole (RFQ) of the SSC-LINAC has important progress in past years. In the autumn of 2016, the cavity has been operated with 35 kW on CW mode in automatic RF controlled mode during RF power commissioning, which is needed to accelerate $^{238}U^{34+}$ beams. The beam transmission efficiency, transverse emittance and energy spread has been obtained in beam commissioning. In this paper, the results of experiments will be presented and discussed in detail.

INTRODUCTION

To achieve excellent performance in nuclear and atomic physics, the Heavy Ion Research Facility in Lanzhou (HIRFL) was upgraded with a multifunctional Cooler Storage Ring (CSR) at the end of 2007 [1]. As the only injector of the HIRFL, the Sector Focusing Cyclotron (SFC) is needed to provide ion beams for the Separated Sector Cyclotron (SSC) and the CSR. The SSC has to be shut down when the SFC provides the beams to the CSR, which results in the low utilization of the HIRFL. Furthermore, several new experiment such as the Super Heavy Elements (SHE) and precise mass measurement experiments have a higher beam current requirement, which cannot be satisfied by the SFC. To solve these problems, a room-temperature heavy ion linac called SSC-LINAC was proposed as a new injector of the SSC to replace the SFC [2], as shown in Fig. 1. The SSC-LINAC mainly consists of a superconducting high-charge-state electron cyclotron resonance (ECR) ion source, a low energy beam transport (LEBT) system, a CW 4-rod RFQ, a medium energy beam transport (MEBT) system, three IH-DTLs and a high energy beam transport (HEBT) section [3].

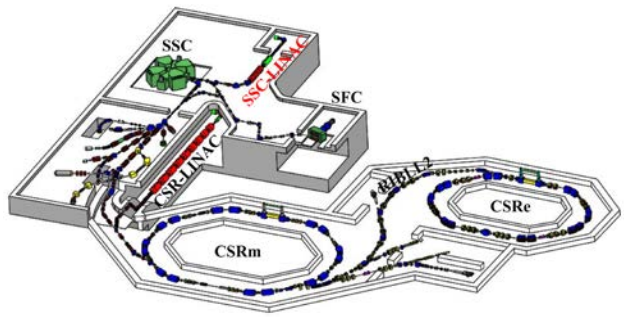


Figure 1: Layout of the HIRFL with the SSC-LINAC.

As a critical component of the SSC-LINAC, the RFQ is required to accelerate intense beams and operate in CW mode, which was the greatest challenge. In beam dynamics, a quasi-equipartitioning design strategy was applied to control the emittance growth and beam losses caused by intense beams [4]. The main parameters of the RFQ are listed in Table 1. The thermal analysis and cooling design have been done carefully by the CST [5] code. A bottom plate, 12 stems and 4 mini-vanes are all cooled by deionized water to ensure security and reliability of the CW mode operation [6].

Table 1: Main Parameters of the SSC-LINAC RFQ [4]

Parameters	US Letter Paper
Frequency	53.667 MHz
Ratio of Charge to Mass	1/3~1/7
Beam Current	0.5 pmA
Duty Factor	100%
Input Energy	3.728 keV/u
Output Energy	143 keV/u
Inter-Vane Voltage	70 kV
Vane Length	2.508
Transmission efficiency	94.1%

The SSC-LINAC has important progress in past years. The cavity was delivered to the Institute of Modern Physics (IMP) in the first season of 2013. The RF performance measurement, including the frequency, quality factor Q_0 and the electric field distribution, was finished in 2014. Then, the commissioning with high RF power and ion beams has been finished. In this paper, the RF power and beam commissioning are reported. The experimental setup for the RFQ test is depicted in Fig. 2.

* This work was supported by the National Natural Science Foundation of China (Nos. 11375243, 11405237, and 11475235) and the Guangdong Innovative and Entrepreneurial Research Team Program (No. 2016ZT06G373).
† yinxj@impcas.ac.cn
‡ wujx@impcas.ac.cn
§ yrlu@pku.edu.cn

Content from this work may be used under the terms of the CC BY 3.0 licence (© 2018). Any distribution of this work must maintain attribution to the author(s), title of the work, publisher, and DOI.

ISBN: 978-3-95450-194-6 ISSN: 2226-0366 doi:10.18429/JACoW-LINAC2018-THPO054

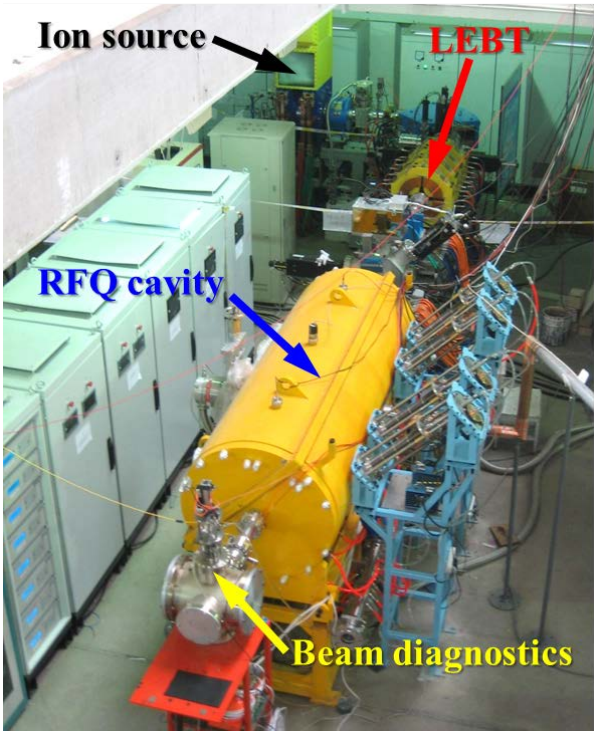


Figure 2: Overview of the RFQ test area.

RF POWER COMMISSIONING

The main goal of the SSC-LINAC RFQ high power commissioning is the demonstration of RF features and stable operation of the 4-rod RFQ in automatic RF controlled mode.

The commissioning began from pulse mode with a 5%. duty factor. The amplitude of the pulse power of the cavity and the pulse length rise gradually without any serious sparking and vacuum troubles. In the first season of 2015, the cavity has been operated with 35 kW on CW mode with the vacuum under 5.0×10^{-5} Pa. According to the experimental results of the bremsstrahlung spectrum [7] emitted from the electrodes, a 35-kW power is needed to generate a 70-kV inter-vane voltage for accelerating beams with the ratio of charge to mass of 1/7 such as $^{238}U^{34+}$.

The frequency shift and water temperature are monitored during the high-power test on CW mode. As shown in Fig. 3, the temperature of the output cooling water raised gradually when the RF power increased. The RFQ cavity operated on 35-kW CW mode with the maximum temperature increment of 7.0℃. The temperature of the inlet water had a temperature fluctuation as shown in the blue curve of Fig. 3, because the cooling water comes from an air-cooling system. Figure 4 shows that the resonance frequency decreased linearly with the RF power of the cavity during the CW mode operation. A linear fitting method was used to analyse the relationship between the resonance frequency and RF power. The fitted rate of the frequency shift is -2.58 kHz/kW. The shift will be tuned by automatic RF controlling system with four plungers, so that the RFQ can operate with a stable resonance frequency.

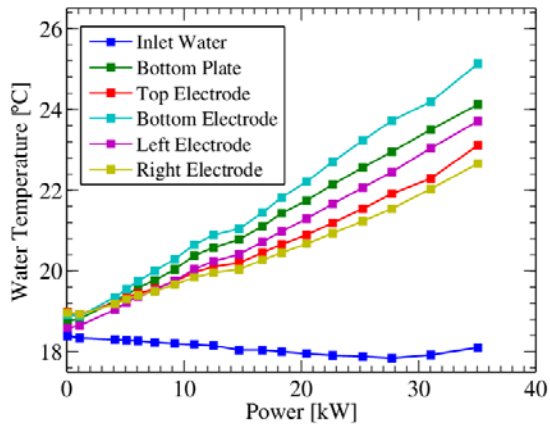


Figure 3: Temperature of the deionized water at the water outlet port except the inlet water.

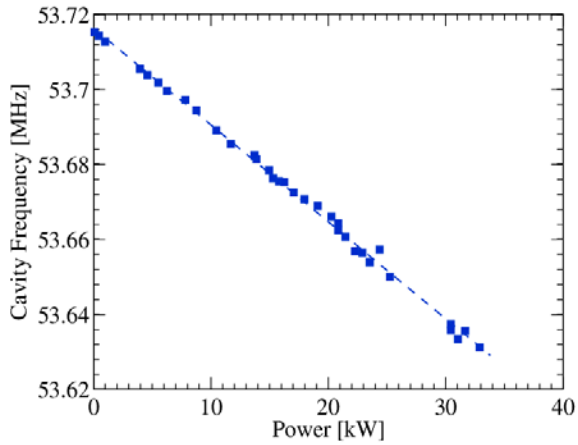


Figure 4: Frequency shift caused by the increasement of the RF power without tuning during CW operation.

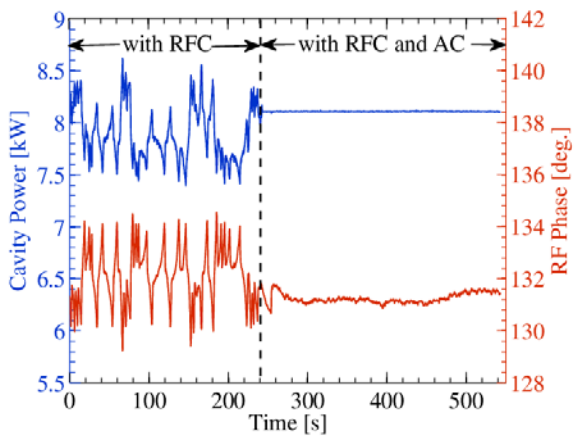


Figure 5: RF power of the cavity and RF phase during CW operation in automatic RF controlled mode.

The automatic RF controlling system consists of an automatic resonant frequency controlling (RFC) system and an automatic RF amplitude controlling (AC) system. The operation in automatic RF controlled mode was begun in 2014. The 4-rod RFQ was operated successfully with the

Content from this work may be used under the terms of the CC BY 3.0 licence (© 2018). Any distribution of this work must maintain attribution to the author(s), title of the work, publisher, and DOI.

ISBN: 978-3-95450-194-6 ISSN: 2226-0366 doi:10.18429/JACoW-LINAC2018-THPO054

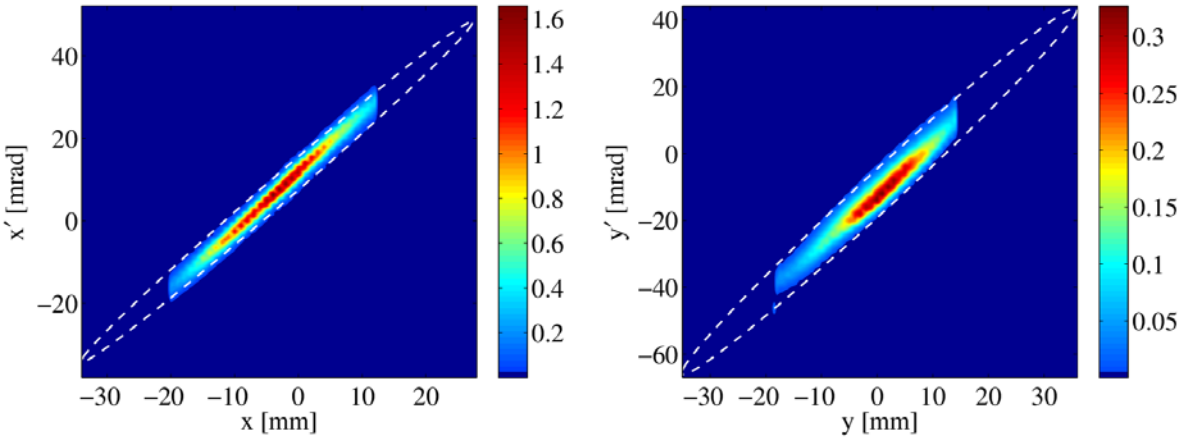


Figure 6: The horizontal (left) and vertical (right) phase space projection measured at the exit of RFQ. The color temperature map is the measured projection, and the white dashed line is the theoretical ellipse.

automatic RF controlling system in March 2016.Then, a 35-kW CW commissioning was finished in the autumn of 2016. Figure 5 represents the variation of RF power and phase with an 8-kW power. The power shift range of ±0.6 kW was achieved with the operation of the RFC system only. When the RFC and AC system were all operated, the RFQ operated stably with a power fluctuation of ± 4.2 W.

BEAM COMMISSIONING

After the RF power commissioning, the beam commissioning with the beam transmission efficiency, transverse emittance and energy spread measurement was performed on CW mode.

The transmission efficiency of 94% was measured by two faraday cups at the upstream and downstream of the RFQ, respectively. The beam energy of 142.78 keV/u was obtained by the time of flight (TOF) method. Both the transmission and beam energy satisfy the injection requirement of the downstream DTL.

The output transverse phase space projection for $^{16}O^{5+}$ beams were measured by two slit-wire type emittance scanners at the diagnostics station downstream of the RFQ. Figure 6 shows a preliminary measurement result. The measured normalized RMS emittance in the horizontal and vertical plane after RFQ are 0.23 πmm·mrad and 0.35 πmm·mrad, respectively. Because of large beam transverse envelopes due to have no quadrupoles at the RFQ exit, some beams cannot be accepted by emittance scanners, as shown in the color temperature map of Fig. 6. While, compared with the theoretical ellipse (see the dashed line in Fig. 6) there is still a good coincidence.

In the measurement of energy spread, combined beams with $^{12}C^{3+}$ and $^{16}O^{4+}$ ions were used for the reason of the calibration of the energy spread detector. Figure 7 represents the energy spectrum of $^{12}C^{3+}$ and $^{16}O^{4+}$. The measured full width at half maximum (FWHM) of the energy spread is approximately 7.5%.

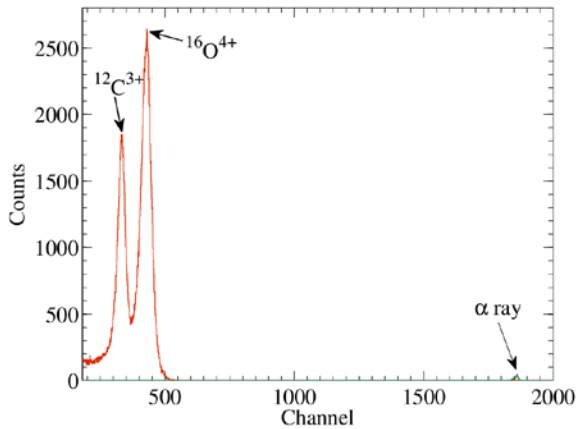


Figure 7: The energy spectrum of combined beams.

CONCLUSION

The RF power and beam commissioning of the SSC-LINAC have been finished at the IMP. The RF power commissioning demonstrated that the 4-rod RFQ for SSC-LINAC operated stably in automatic RF controlled mode with a 35-kW CW power. In the beam commissioning, the normalized RMS horizontal emittance of 0.23 πmm·mrad, vertical emittance of 0.35 πmm·mrad and FWHM value of the energy spread of 7.5% were obtained at exit of the RFQ. The results of commissioning can meet the requirement of the SSC-LINAC project.

In the near future, the accurate measurement of the emittance will be performed with a triplet at the RFQ exit, and the beam tests with a higher charge-to-mass ratio such as $^{238}U^{34+}$ are desired.

REFERENCES

[1] J.W. Xia *et al.*, "The heavy ion cooler-storage-ring project (HIRFL-CSR) at Lanzhou", *Nucl. Instrum. Meth. A*, vol. 488, no. 1-2, p. 11, Aug. 2002. doi: 10.1016/S0168-9002(02)00475-8

Content from this work may be used under the terms of the CC BY 3.0 licence (© 2018). Any distribution of this work must maintain attribution to the author(s), title of the work, publisher, and DOI.

ISBN: 978-3-95450-194-6 ISSN: 2226-0366 doi:10.18429/JACoW-LINAC2018-THPO054

[2] Y. He *et al.*, "Conceptual Design of Linear Injector for SSC of HIRFL", in *Proc. LINAC'10*, Tsukuba, Japan, Sep. 2010, pp. 482-484.

[3] X. Yin *et al.*, "The R&D Status of SSC-LINAC", in *Proc. IPAC'14*, Dresden, Germany, Jul. 2014, pp. 3277-3279. doi.org/10.18429/JACoW-IPAC2014-THPME026

[4] G. Liu *et al.*, "Design of a CW high charge state heavy ion RFQ for SSC-LINAC", *Nucl. Instrum. Meth. A*, vol. 701, p. 186, Feb. 2013. doi: 10.1016/j.nima.2012.11.017

[5] CST, https://www.cst.com/

[6] Y. R. Lu *et al.*, "A CW High Charge State Heavy Ion RFQ for SSC-LINAC", in *Proc. IPAC'13*, Shanghai, China, May 2013, pp. 3878-3880.

[7] X.J. Yin *et al.*, "Design, Fabrication, and Beam Commissioning of a Continuous-wave Four-rod RF Quadrupole". *Phys. Rev. ST Accel. Beams*, vol. 19, p. 010402, Jan. 2016. doi: 10.1103/PhysRevAccelBeams.19.010402

Content from this work may be used under the terms of the CC BY 3.0 licence (© 2018). Any distribution of this work must maintain attribution to the author(s), title of the work, publisher, and DOI.

ISBN: 978-3-95450-194-6 ISSN: 2226-0366 doi:10.18429/JACoW-LINAC2018-THPO057

REDESIGN OF CERN LINAC3 RFQ FOR LEAD 29+

S. Benedetti *, A.M. Lombardi, G. Bellodi, J.B. Lallement, CERN, Geneva, Switzerland

Abstract

CERN Linac3 is at the heart of the CERN Heavy Ion Facility, providing 4.2 MeV/u ion beams to the Low Energy Ion Ring (LEIR). It mostly accelerates $^{208}Pb^{29+}$, though in recent years runs were performed with $^{40}Ar^{11+}$ and $^{129}Xe^{22+}$, in view of the raising interest of the physics community towards lighter ions experiments. In the framework of the LHC Injectors Upgrade (LIU) project, measurements and beam dynamics simulations showed that a transmission bottleneck of Linac3 is represented by the RFQ. As this accelerator was originally designed for $^{208}Pb^{25+}$, the lower beam rigidity of the heavy ions currently in used – and planned to be used – permits a redesign of the RFQ aimed at increasing its transverse acceptance, and thus the transmitted beam current. The methodology adopted and the results of this study are presented.

INTRODUCTION

Linac3 [1] is composed by an Electron Cyclotron Resonance (ECR) source producing heavy ion beams at 2.5 keV/u. The desired charge state is filtered by a Low Energy Beam Transport (LEBT) line and further accelerated by a 101.28 MHz RFQ to 250 keV/u. A Medium Energy Beam Transport (MEBT) line matches the beam, both longitudinally and transversally to an Interdigital H-type (IH) linac, which boosts the beam to 4.2 MeV/u. After the IH linac, the beam is stripped to a higher charge state and transported to LEIR. The layout of Linac3 is shown in Fig. 1.

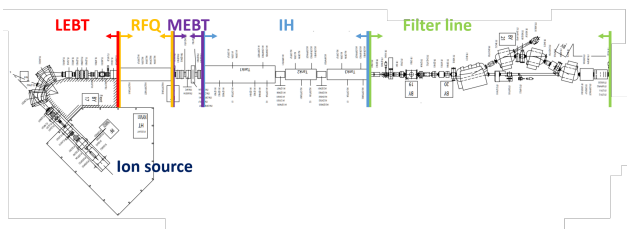


Figure 1: Linac3 layout, with the different sections marked.

In 2005, the original Linac3 ion source was replaced by a higher intensity 14.5 GHz room temperature ECR ion source (GTS-LHC) [2]. This source operates mostly in afterglow mode to produce $^{208}Pb^{29+}$, and in recent years, $^{40}Ar^{11+}$ and $^{129}Xe^{22+}$. This change called for a new study of the beam dynamics in Linac3 [3]. A major result is that the RFQ represents a bottleneck of the line, with transmission of 70 % or lower, depending on the accelerated ion species, while originally the transmission was higher than 90 %. The phase space orientation of the beam emittance appears to be reasonably well matched at the RFQ input, with the losses due to the input emittance larger than the acceptance (Fig. 2).

* stefano.benedetti@cern.ch

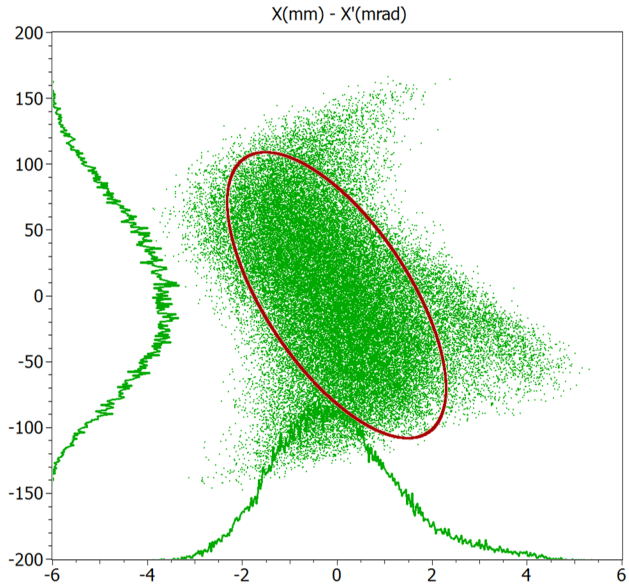


Figure 2: RFQ acceptance in red (0.45 mm.mrad 95 % beam) and simulated beam in green dots (0.97 mm.mrad 95 % beam) at the RFQ input for the the x-x' plane.

The lower beam rigidity of the currently accelerated ions with respect to the originally considered $^{208}Pb^{25+}$ permits to redesign the RFQ increasing its transverse acceptance. The redesign shall meet the constraints discussed in the following section.

CONSTRAINTS OF THE REDESIGN

The RFQ redesign had to meet three constraints: to maintain the same cavity length – 2.5 m – and operating frequency – 101.28 MHz, to maintain the same vane voltage V_0 – 71 kV – and maximum surface electric field – 23.9 MV/m, to maintain or decrease the output longitudinal emittance, 39 π.deg.keV/u for 95 % of the particles.

The first constraint guarantees a minimal change of the line, as only the rod modulation and aperture will change, while the outer tank and power supply would not be replaced. The second point ensures that the redesigned has the same Break-Down (BD) rate of the current one. Operating at 101.28 MHz, with a maximum surface electric field of nearly 24 MV/m, the cavity Kilpatrick factor is 2.1.

The last constraint – to maintain or decrease the output longitudinal emittance – is a consequence of the small longitudinal acceptance of the IH linac that follows the RFQ.

The transmission through the IH cavities was measured as a function of the phase of the input beam. This was achieved by changing the RFQ RF phase, which accepts a continuous input beam and it is thus unaffected by this modification. The phase of the buncher cavities between the RFQ and the IH were also changed accordingly, in order to guarantee

Content from this work may be used under the terms of the CC BY 3.0 licence (© 2018). Any distribution of this work must maintain attribution to the author(s), title of the work, publisher, and DOI.

ISBN: 978-3-95450-194-6 ISSN: 2226-0366 doi:10.18429/JACoW-LINAC2018-THPO057

that the same longitudinally matched beam reaches the IH input, though with the different RF phases. The result of the measurement is a very sharp drop in the transmission as soon as the RF phase of the beam changes (Fig. 3). The beam dynamics simulations agree with this measurement, as the beam phase space in the longitudinal plane at the IH input is just contained by the IH acceptance (Fig. 4). In conclusion, the longitudinal output emittance from the RFQ has to be preserved, if not reduced, to guarantee a good transmission through the IH linac.

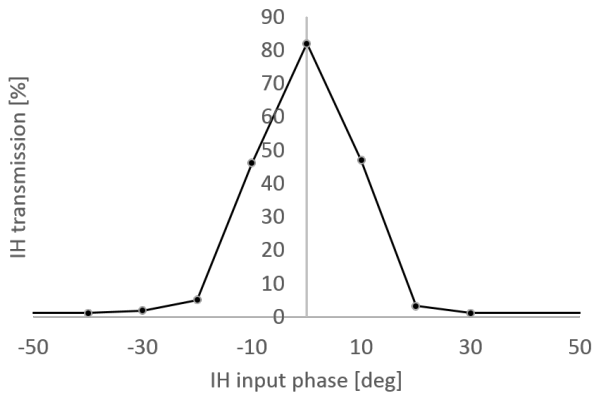


Figure 3: Measured transmission through the IH linac as a function of the IH input phase.

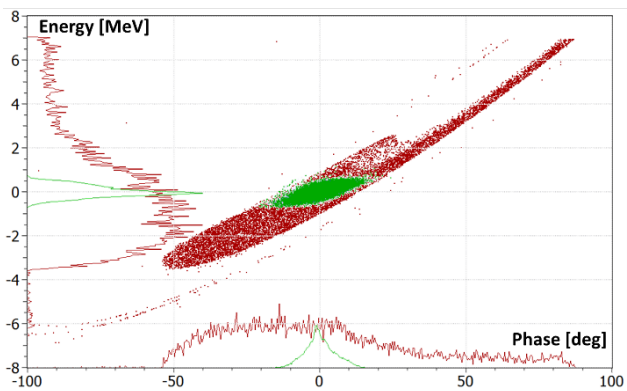


Figure 4: Simulated IH cavities longitudinal acceptance (red dots) and comparison with the simulated beam at the IH input (green dots).

The redesign specification parameters are summarized in Table 1.

CURRENT DESIGN

Linac3 RFQ became operational in 1994. It has been originally commissioned for a $^{208}Pb^{25+}$ beam, with 2.5 keV/u input energy and 250 keV/u output energy. This four-rod RFQ is characterized by a bunching section where the modulation m and the synchronous phase are quickly increased shortly after the RFQ input. The bunching section itself is relatively short with respect to a standard design. Therefore, the transverse acceptance is lower than that of a more standard RFQ. This peculiar design approach [4] is observable in Fig. 5 top.

Table 1: Main Design Specifications for The Linac3 RFQ Redesign

Parameters	Value
Input/Output energy	2.5/250 keV/u
Operating frequency	101.28 MHz
Length	2.5 m
Input transverse acceptance (95%)	> 0.5 mm.mrad
Output longitudinal emittance (95%)	< 40 deg.keV/u
Max surface electric field	24 MV/m

BEAM DYNAMICS REDESIGN

A standard RFQ design with the Los Alamos National Laboratory (LANL) codes [5] was adopted at the first stage of this study. Even with optimization of the gentle buncher, it was not possible to reach the required small longitudinal output emittance that represents the main peculiarity of the actual RFQ design. The main parameters that have been varied were the gentle buncher length - by setting the desired phase and energy at the end of this section - the average focusing strength B, the ratio between the rods transverse radius of curvature ρ and the average aperture r_0, and the vane voltage V_0.

As a second approach, it was decided to consider four reference designs, considering 71 kV vane voltage and a 0.95 ρ/r_0 as the reference design, and focusing strength B of 4.5, 5, 5.5 and 6, respectively. As a remark, the reference Linac3 RFQ has a focusing strength B=4. Considering the 16 % increase in q/m, this would translate in B=4.6 for the new redesign. In the redesigns, B<4.5 did not permit to have an RFQ length of 2.5 m, while B>6 had a too high maximum surface electric field E_s.

As a final step, the modulation and the phase of the buncher section were modified with the aim of reducing the longitudinal output emittance to the goal value. Designs exceeding Es of 24.0 MV/m were discarded. A lower modulation in the bunching section decreases the longitudinal output emittance, as well as the surface electric field Es and the transverse acceptance. The same behaviour is obtained by decreasing the synchronous phase. Goal of this redesign was to exploit the surface electric field limit – around 24 MV/m – throughout the whole cavity. The best result was achieved considering as a starting point a design with B factor 5.2, with a lower modulation in the bunching section and a slower increase of the synchronous phase (Fig. 5 bottom).

The main beam dynamics parameters of the two designs are summarized in Table 2.

Content from this work may be used under the terms of the CC BY 3.0 licence (© 2018). Any distribution of this work must maintain attribution to the author(s), title of the work, publisher, and DOI.

ISBN: 978-3-95450-194-6 ISSN: 2226-0366 doi:10.18429/JACoW-LINAC2018-THPO057

Content from this work may be used under the terms of the CC BY 3.0 licence (© 2018). Any distribution of this work must maintain attribution to the author(s), title of the work, publisher, and DOI.

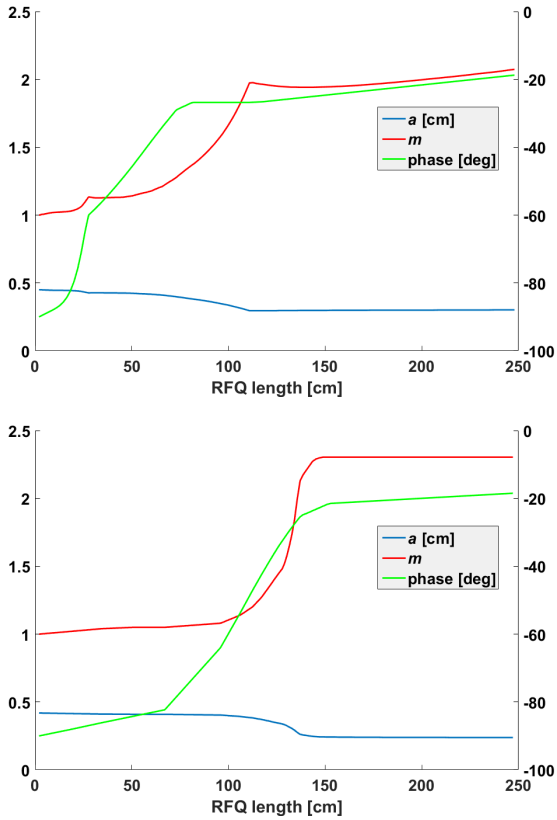


Figure 5: Minimum aperture a, modulation factor m and synchronous phase for the current Linac3 RFQ (top) and for the redesign proposed in this paper (bottom).

Table 2: Comparison Between the Main Beam Dynamics Parameters for the Two RFQ Designs

	$^{208}Pb^{25+}$ design	$^{208}Pb^{29+}$ design
Vane voltage	71 kV	
ρ / r_0	0.95	
Final synch. phase	18.5 deg	
Min aperture radius	3.0 mm	2.4 mm
Max modulation m	2.1	2.3
Number of cells	253	357
Output phase spread	± 12 deg	± 11 deg
Output energy spread	± 1.3 %	± 1.2 %
Input transv. accept. (95%)	0.45 mm.mrad	1.02 mm.mrad
Output long. emit. (95%)	39 deg.keV/u	34 deg.keV/u
Max surface E field	23.9 MV/m	

BEAM CURRENT INCREASE AT LINAC3 OUTPUT AND DISCUSSION

Parmteq [5] and Toutatis [6] were used to validate the new design of the Linac3 RFQ with multi-particle simulations. The beam phase space was reconstructed from beam profile measurements before the RFQ, and tracked through it until the MEBT Faraday cup (FC). With the current design, the simulated beam transmission is 68 %, in agreement with the measurements taken during the 2017 Xe run [3]. If the same beam is tracked considering the $^{208}Pb^{29+}$ redesigned RFQ, it shows a simulated transmission of nearly 100 %. As the redesign RFQ is nearly loss-free, the normalized transverse emittance is preserved, and thus the $^{208}Pb^{29+}$ redesigned RFQ has a larger output emittance than the current one. Thus this output beam has to be further simulated through the IH linac to obtain a complete comparison of the two scenarios. After the RFQ, the beam is transversally and longitudinally matched to the IH cavities by the MEBT line. Uncertainty in the quadrupoles calibration makes the beam dynamics simulations in this part of the line challenging [3]. For this part of the line the multi-particle code TRAVEL was used [7]. For all the simulations a complete beam aperture model is considered.

Adopting a conservative approach, the simulated transmission from the RFQ output to the IH output is 70 %. Thus the losses would increase in the MEBT line with respect to the current design, where the simulated transmission is 80 %. Overall, the simulated beam transmission from the LEBT to the IH linac output would however increase, thanks to the higher transmission through the RFQ, as summarized in Table 3

Table 3: Total Simulated Transmission from the LEBT Triplet to the IH Linac Output With the Current RFQ $^{208}Pb^{25+}$ Design and the $^{208}Pb^{29+}$ Redesign

$^{208}Pb^{25+}$ design	56 %
$^{208}Pb^{29+}$ design	69 %
Relative current increase at Linac3 output	23 %

The Linac3 diagnostic in the MEBT line has been recently improved. This should permit to estimate with more precision the final beam current increase to be expected.

SUMMARY AND OUTLOOK

A redesign study of the CERN Linac3 RFQ has been made profiting of the lower rigidity of the heavy ions nowadays accelerated with respect to the first conservative assumption, $^{208}Pb^{25+}$. The main RFQ parameters, cavity length, vane voltage and Kilpatrick limit, have been kept equal to the original design. The redesign was carried out only by modifying the rods shapes. From simulations, the RFQ transmission would increase from 68 % to nearly 100 %, and the current at the end of Linac3 would increase by 20 %.

REFERENCES

[1] D. Warner (ed), "CERN heavy-ion Facility Design Report", Rep. CERN-93-01, April 1993.

[2] C.E. Hill *et al.* GTS-LHC: A New Source For The LHC Ion Injector Chain, in *Proc. AIP Conf.*, vol. 749, pp. 127, 2005.

[3] S. Benedetti *et al.*, "Xe measurements and beam dynamics simulations at CERN", submitted for publication.

ISBN: 978-3-95450-194-6 ISSN: 2226-0366 doi:10.18429/JACoW-LINAC2018-THPO057

[4] G. Bezzon *et al.*, "Construction and Commissioning of the RFQ for the CERN Lead Ion Facility", in *Proc. LINAC'94 Conf.* Tsukuba, Japan, Aug. 1994, paper TH-12, pp. 722.

[5] K.R. Crandall *et al.*, "RFQ Design Codes", Rep. LA-UR-96-1836, Los Alamos, Revised Dec. 2005.

[6] R. Duperrier, "TOUTATIS, a radio frequency quadrupole code", *Phys. Rev. ST Accel. Beams*, vol. 3, pp. 124201, 2000.

[7] A. Perrin *et al.*, "Travel user manual", CERN Manual, Revised Apr. 2007.

Content from this work may be used under the terms of the CC BY 3.0 licence (© 2018). Any distribution of this work must maintain attribution to the author(s), title of the work, publisher, and DOI.

ISBN: 978-3-95450-194-6 ISSN: 2226-0366 doi:10.18429/JACoW-LINAC2018-THPO058

RF DESIGN OF A HIGH-FREQUENCY RFQ LINAC FOR PIXE ANALYSIS*

H. W. Pommerenke†,1,2, A. Bilton[1], A. Grudiev[1], A. M. Lombardi[1], S. Mathot[1], E. Montesinos[1], M. Timmins[1], M. Vretenar[1], U. van Rienen[2]
[1] CERN, Geneva, Switzerland
[2] University of Rostock, Germany

Abstract

Protons with an energy of few MeV are commonly used for Ion Beam Analysis of materials, in particular with the Proton Induced X-ray Emission technique (PIXE). Because of its non-damaging character, PIXE is used in a variety of fields, in particular for the diagnosis of cultural heritage artwork. A compact accelerator based on a high frequency RFQ (Radio Frequency Quadrupole) linac has been designed and is being built at CERN. The length of the RFQ is only one meter and it allows the acceleration of a proton beam up to an energy of 2 MeV. The complete system is conceived to be transportable, allowing PIXE analysis almost anywhere. This paper covers the RF design of the compact RFQ operating at 750 MHz. We present general accelerator parameters and the current state of the RF design, which includes RFQ geometry and coupler design, thermal simulation and first particle tracking results.

INTRODUCTION

The Proton Induced X-Ray Emission (PIXE) [1] is a widely used method for cultural heritage material characterization (among others). It allows for a non-damaging and highly sensitive quantitative analysis by stimulating specimen atoms using 2 to 4 MeV proton beams and measuring the emitted X-ray spectrum.

Conventional electrostatic PIXE accelerators require significant space and infrastructure and are thus installed in dedicated centres. Contrarily, an RFQ operating at 750 MHz is able to provide 2 MeV protons over the length of just one meter, as proposed in [2]. The PIXE RFQ is developed within the context of the MACHINA project [3], whose aim is to build the first transportable system for *in situ* ion beam analysis. The RFQ design is based on the high-frequency RFQ for medical applications [2, 4, 5], adapted to the requirements of PIXE analysis. A selection of design parameters is presented in Table 1.

RF DESIGN

In general, all geometries are optimised to a resonant frequency of $f_0 = 749.48$ MHz, as well as minimum surface losses expressed by a maximum Q_0 factor. While a circular shape of the four quadrants would be the optimum in this regard, a planar back side surface is used to simplify the machining (Fig. 1). The cavity geometries of the two RFQ modules are slightly different to account for the changing vane modulation.

Table 1: Design Parameters of the PIXE RFQ

Input energy	$\mathcal{E}_{in}$	20	keV
Output energy	$\mathcal{E}_{out}$	2	MeV
RF frequency	f_0	749.48	MHz
RFQ length		1072.938	mm
Vane voltage	V	35	kV
Min. aperture		0.7	mm
Vane tip radius		1.439	mm
Peak current		200	nA
Transmission	T	30	%
Max. duty cycle	d_{max}	2.5	%

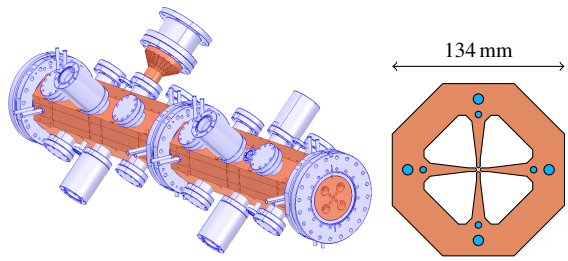


Figure 1: CAD model of the PIXE RFQ. (a) Accelerator with equipped tuners, pumping ports, and coupler. (b) 2D cavity cross section with water cooling channels.

The RFQ is terminated by two end plates with holes in each quadrant that allow for bead-pull measurement access. Further, four dipole stabilization rods on each end plate are used to give the maximum possible spectral margin of ±12 MHz from the quadrupole operating mode (TE_{210}) to the next closest higher order modes (TE_{211} and TE_{111}).

Figure 2 shows the surface electric field E_s at the vane tip. The overall maximum $E_s = 39.1$ MV/m occurs at the gap between the two RFQ modules (Fig. 2b). Excluding this effect, the maximum surface field is located in the bunching section of the RFQ with $E_s = 36.5$ MV/m (Fig. 2a).

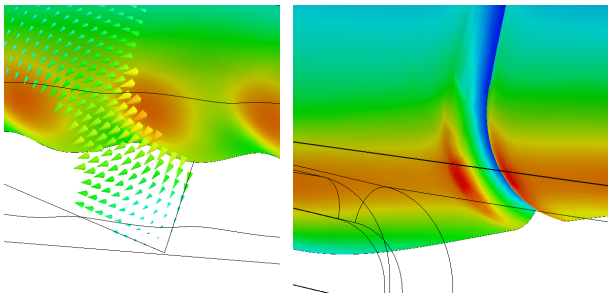
The shapes of tuners and pumping ports are similarly optimised for minimum losses. The tuners are copper slugs with a conic tip (Fig. 3a). The pumping ports end with crossbars that help conducting the surface currents (Fig. 3b).

The total RF power P_0 dissipated through surface losses can be estimated by longitudinally decomposing the RFQ

* This work has been sponsored by the Wolfgang Gentner Programme of the German Federal Ministry of Education and Research (grant no. 05E15CHA).
† hermann.winrich.pommerenke@cern.ch

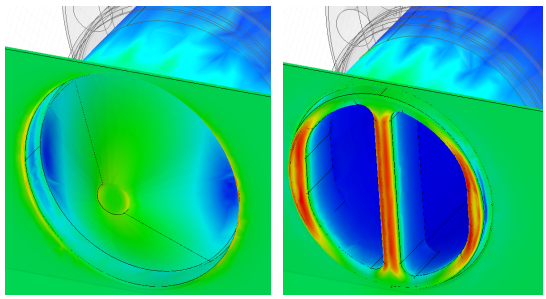
Content from this work may be used under the terms of the CC BY 3.0 licence (© 2018). Any distribution of this work must maintain attribution to the author(s), title of the work, publisher, and DOI.

ISBN: 978-3-95450-194-6 ISSN: 2226-0366 doi:10.18429/JACoW-LINAC2018-THPO058



(a) (b)

Figure 2: Surface and transverse electric field (a) at the vane and (b) at the module gap with a maximum of $E_s = 39.1\,\mathrm{MV/m}$.



(a) (b)

Figure 3: Conical copper slug tuner (a) and vacuum pumping port (b) with surface current distribution.

into segments assuming that the stored energy over length W/L is constant along the RFQ. By individual simulation of the segments we obtain the loss factor $Q_{0,s}$ of each segment s. The capacitance over length $C'(z) = \mathrm{d}C/\mathrm{d}z$ changes along the accelerator due to the vane modulation and is interpolated by computing specific isolated cells. Using $P_0 = \omega_0 W/Q_0$ with $\omega_0 = 2\pi f_0$ and $W = CV^2/2$ for each segment we arrive at

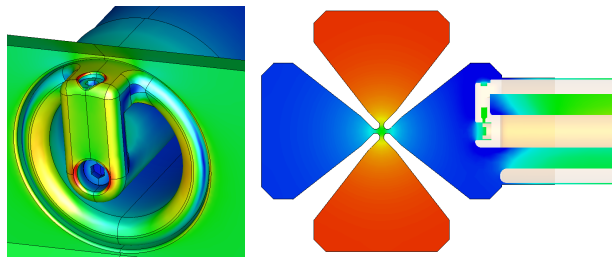
$$P_0 = \frac{\omega_0 V^2}{2} \sum_s \frac{1}{Q_{0,s}} \int_{\text{Seg. } s} C'(z)\mathrm{d}z, \qquad (1)$$

which gives 64.1 kW for the nominal voltage $V = 35\,\mathrm{kV}$. The approach allows to compute capacitance and power loss of the entire accelerator without having to simulate the full model. For verification, we nevertheless conducted simulations of the full RFQ, from which we obtain 64.5 kW. The quantities are summarised in Table 2.

Table 2: Computed RF Quantities for 35 kV Nom. Voltage

Loss factor	Q_0	6000	
Capacitance	C'	125	pF/m
Stored energy	W	82	mJ
RF power loss	P_0	64.5	kW
Max. surface field	E_s	39.1	MV/m

The PIXE RFQ features one single input power coupler (Fig. 4), which replaces one of the pumping ports in the second module. It is a coaxial magnetic loop coupler, which is over-coupled by design with the coupling coefficient of $Q_0/Q_E = 1.25$ as safety margin. The coupler will be mounted on a rotatable flange which allows for reducing the external Q_E to achieve reflection-free coupling after assembly.



(a) (b)

Figure 4: Input power coupler with coaxial loop geometry: (a) surface current distribution and (b) transverse section with z-component of magnetic field.

THERMAL SIMULATION

Due to the RF power loss at the inner surface of the RFQ, the temperature of the structure increases and it is deformed by thermal expansion, which shifts the resonant frequency of the cavity. Thermal simulations are conducted to study the dependence of the shift Δf on duty cycle d and cooling water temperature θ_w, utilising software [6–8].

The heat transfer coefficients depend on the water speed v_w: For $v_w = 2\,\mathrm{m/s}$, values of 7500 and 7310 $\mathrm{W/m^2/K}$ are assumed for the ∅5 and ∅8 cooling channels respectively, while for $v_w = 1\,\mathrm{m/s}$ both channels have 3900 $\mathrm{W/m^2/K}$. Additionally, the copper-to-air convection is estimated with 10 $\mathrm{W/m^2/K}$.

Distributions of heat load, temperature and deformation are shown in Fig. 5. Figure 5c demonstrates that if the RFQ is heated, the tank size and thus the inductance L increases. Due to the temperature difference between vane and tank however, the vane tips move closer towards the beam axis, increasing capacitance C. Both effects reduce the resonance frequency, since $\partial f/f = -(\partial C/C + \partial L/L)/2$ holds for a resonant LC circuit. The frequency shift within the considered domain is linear with respect to duty cycle and water temperature (Fig. 6). The sensitivities are $\partial f/\partial\theta_w = -13.3\,\mathrm{kHz/K}$ and $\partial f/\partial d = -67.3\,\mathrm{kHz/\%}$ for a 2 m/s water flow speed. The latter changes only slightly when choosing a smaller (average) water flow speed, however it significantly reduces the requirements on the chiller in the cooling circuit. Therefore, a flow speed of 1 m/s is chosen.

Since the 3 dB bandwidth of the RFQ is only ±125 kHz, the RF source has to follow the shifting resonance frequency of the cavity to minimise reflected power. For the proposed range of operation (up to 2.5 % duty cycle), the effect on the particle transmission is minimal, as is shown at the end of the following section.

Content from this work may be used under the terms of the CC BY 3.0 licence (© 2018). Any distribution of this work must maintain attribution to the author(s), title of the work, publisher, and DOI.

ISBN: 978-3-95450-194-6 ISSN: 2226-0366 doi:10.18429/JACoW-LINAC2018-THPO058

Content from this work may be used under the terms of the CC BY 3.0 licence (© 2018). Any distribution of this work must maintain attribution to the author(s), title of the work, publisher, and DOI.

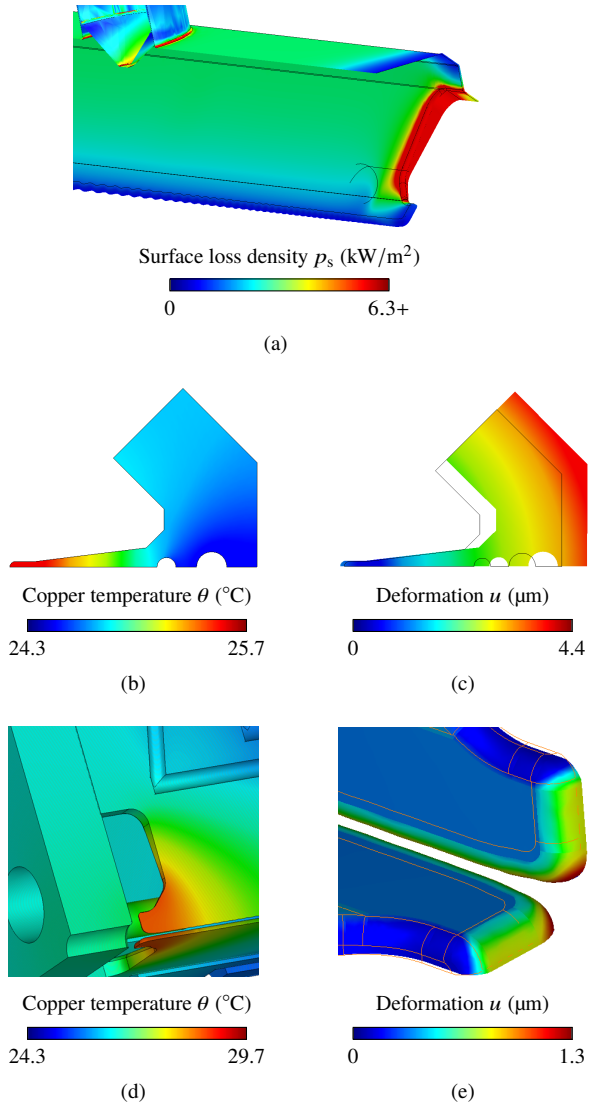


Figure 5: Thermal simulation results for nominal parameters (2.5 % duty cycle, $\theta_w = 22$ °C, $v_w = 1$ m/s). (a) Power loss p_s on cavity surface. (b) temperature θ and (c) deformation u of the octant-symmetric cross section; (d), (e) respective results around the vane nose.

1D PARTICLE TRACKING

To validate computed RF fields, particle tracking is performed to simulate the effect of these fields on the longitudinal beam dynamics. Phase and energy of the particles are calculated in the RF field. The particles are moving with $x = y = 0$ along the z-axis of the RFQ. The initial phase spreads from 0 to 2π and the initial energy is 20 keV.

Figure 7 shows the computed phase and energy along the beam axis. As the particle velocity changes significantly over the length of the RFQ, we define the phase from the vane modulation:

$$\Delta\phi_p(t) = \phi_{0,p} + \omega_0 t - \pi \int_{z_0}^{z_p(t)} \frac{\mathrm{d}z}{\mathcal{L}(z)}, \qquad (2)$$

where $z_p(t)$ is the computed trajectory of particle p and $\mathcal{L}(z)$ is a continuous function interpolated from the lengths of the

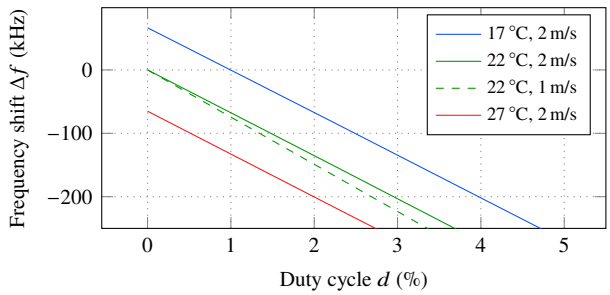


Figure 6: Dependence of the frequency shift of the RFQ cavity subject to RF losses in on the duty cycle.

RFQ cells. The transmission T is defined as the percentage of input particles that are bunched and accelerated to 2 MeV. Because of the peculiar setup solely considering longitudinal beam dynamics, $T = 23$ % of particles are captured within the first 10 cm of the RFQ. As mentioned in the previous section, the effect of a shifting RF frequency within the limits of Fig. 6 is minimal, which is demonstrated in Fig. 8.

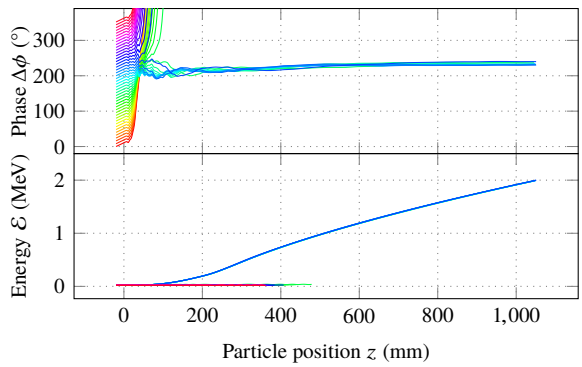


Figure 7: Phase and energy of the tracked particles along the RFQ. The color indicates the start phase of the particle relative to the RF field.

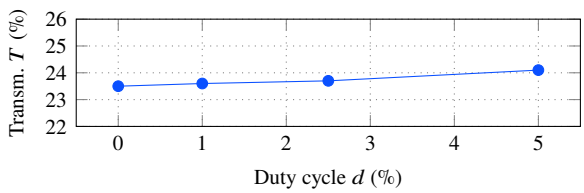


Figure 8: Transmission of a beam through the RFQ as a function of the duty cycle.

CONCLUSION

The RF design of the PIXE RFQ linac has been conducted including cavity geometry, tuners, pumping ports, and power coupler. The thermal expansion and resulting resonant frequency shift due to RF power dissipation has been studied to yield the requirements on the cooling circuit. Further, first results of particle tracking through the RF field have been presented. It has been shown, that the frequency shift due thermal expansion has little effect on the beam dynamics.

ISBN: 978-3-95450-194-6 ISSN: 2226-0366 doi:10.18429/JACoW-LINAC2018-THPO058

REFERENCES

[1] S. A. E. Johansson *et al.*, *Particle-induced X-ray emission spectrometry (PIXE)*, vol. 133, John Wiley & Sons, 1995

[2] M. Vretenar *et al.*, "High-frequency compact RFQs for medical and industrial applications," in *Proc. 28th Linear Accelerator Conf. (LINAC'16)*, East Lansing, MI, USA, 2016. doi:10.18429/JACoW-LINAC2016-TH1A06

[3] L. Giuntini *et al.*, "MACHINA: movable accelerator for cultural heritage in-situ non-destructive analysis," in *Proc. 16th International Conference on Nuclear Microprobe Technology and Applications (ICNMTA'18)*, Guilford, Surrey, England, 2018

[4] A. Lombardi *et al.*, "Beam dynamics in a high frequency RFQ," in *Proc. 6th Int. Particle Accelerator Conf. (IPAC'15)*, Richmond, VA, USA, 2015. doi:10.18429/JACoW-IPAC2015-MOPJE042

[5] B. Koubek *et al.*, "Tuning of the CERN 750 MHz RFQ for medical applications," in *Proc. 28th Linear Accelerator Conf. (LINAC'16)*, East Lansing, MI, USA, 2016. doi:10.18429/JACoW-LINAC2016-THOP09

[6] Computer Simulation Technology, *CST Studio Suite 2018*

[7] ANSYS. Electromagnetics Suite, *Release 17.2*

[8] ANSYS. Mechanical, *Release 17.2*

Content from this work may be used under the terms of the CC BY 3.0 licence (© 2018). Any distribution of this work must maintain attribution to the author(s), title of the work, publisher, and DOI.

ISBN: 978-3-95450-194-6 ISSN: 2226-0366 doi:10.18429/JACoW-LINAC2018-THPO060

FIRST RF MEASUREMENTS OF THE 325 MHz LADDER-RFQ

M. Schuett*, U. Ratzinger and M. Syha
Institute for Applied Physics, Goethe University, Frankfurt, Germany

Abstract

Based on the positive results of the 0.63 m unmodulated 325 MHz Ladder-RFQ prototype from 2013 to 2016 [1], a modulated 3.3 m Ladder-RFQ (see Fig. 1) has been designed and built. In this paper, we will show the results of manufacturing as well as first low level RF measurements of the Ladder-RFQ.

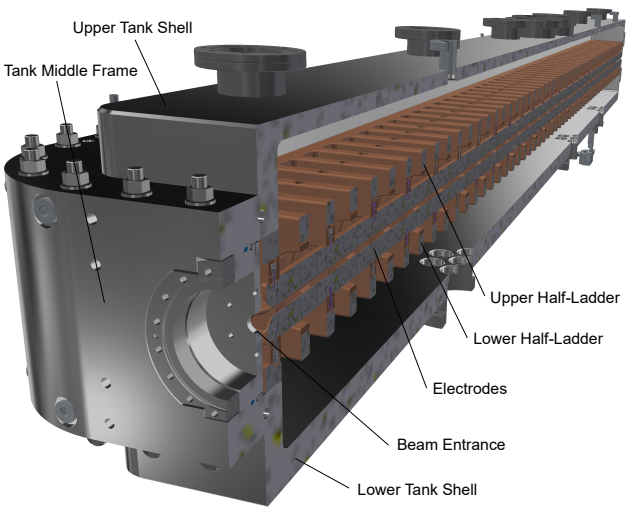


Figure 1: Isometric view of the 3.3 m modulated Ladder-RFQ. Copper carrier-rings guarantee the electrode positioning as well as the RF contact. The ladder structure consists of bulk copper components. Any brazing or welding processes were avoided for the assembly of the main components.

INTRODUCTION

The idea of the Ladder type RFQ firstly came up in the late eighties [2, 3] and was realized successfully for the CERN Linac3 operating at 101 MHz [4] and for the CERN antiproton decelerator ASACUSA at 202 MHz [5].

Due to its high symmetry, this Ladder-RFQ features a very constant voltage along the axis. The Ladder-RFQ prototype was high power tested at the GSI test stand. It accepted 3 times the RF power level needed in operation [6]. That level corresponds to a Kilpatrick factor of 3.1 with a pulse length of 200 µs. The 325 MHz RFQ is designed to accelerate protons from 95 keV to 3.0 MeV according to the design parameters of the proton linac within the FAIR project. This particular high frequency creates difficulties for a 4-ROD type RFQ, which triggered the development of a Ladder-RFQ with its higher symmetry. The results of the unmodulated prototype have shown, that the Ladder-RFQ is a suitable candidate for that frequency. For the present design duty cycles are feasible up to 5%. The basic design and tendering of the RFQ has been successfully completed in 2016 [7]. Manufacturing of the large components has been completed in September 2018.

Table 1: Main RF and Geometric Parameters of the Modulated Ladder-RFQ

Parameter	Value
No. of RF cells	55
Q-Value (simulated)	6800
Loss (with sim. Q)	675 kW
Shunt Impedance (sim.)	45 kΩm
Vane-Vane Voltage	88.43 kV
Frequency	325.224 MHz
Repetition Rate	4 Hz
Pulse Duration	200 µs
Total Length	3410 mm
Cell Length	40 mm
Spoke Height	280 mm
Spoke Width	150 mm
Electrode Length	3327 mm

DESIGN AND MANUFACTURING

The mechanical design consists of an inner copper ladder structure mounted into an outer stainless steel tank. The tank is divided into three parts - the lower and upper shells and a middle frame.

The lower shell of the tank carries and fixes the position of the inner resonating ladder structure. Due to manufacturing reasons, the ladder structure is divided into two lower and two upper half-ladder elements, which are precisely aligned via guide pins. The half-ladders themselves are machined from solid copper blocks. Between the half-ladder elements, the electrodes are precisely fixed via carrier-rings [8]. Those carrier-rings furthermore guarantee a seamless RF connection between the electrodes and the ladder structure.

The RF features are mainly determined by the resonating structure, while the dimensions of the tank have no significant influence on the frequency. Based on the successful high power tests of the unmodulated prototype, we decided to develop a new beam dynamics for a vane-vane voltage of 88.4 kV [9]. For details of the final beam dynamics see [10]. The basic physical and mechanical parameters of the Ladder-RFQ results are shown in Table 1. Furthermore, the thickness of the tank walls inside the entrance and exit flange of the RFQ have been reduced to 10 mm within the flange diameter of 100 mm (CF100). That allows an integration of preceding and following components like a cone or steerer to reduce an emittance growth caused by an additional drift. The next step, beginning in 2019, is the development of

* schuett@iap.uni-frankfurt.de

Content from this work may be used under the terms of the CC BY 3.0 licence (© 2018). Any distribution of this work must maintain attribution to the author(s), title of the work, publisher, and DOI.

ISBN: 978-3-95450-194-6 ISSN: 2226-0366 doi:10.18429/JACoW-LINAC2018-THPO060

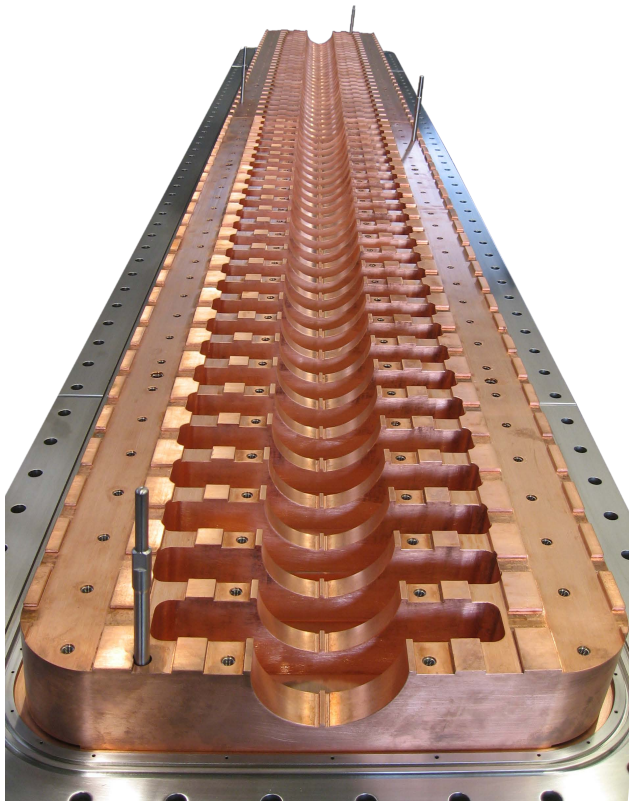


Figure 2: Lower half-ladder structure after finalization of surface treatment and assembly on the lower tank shell.

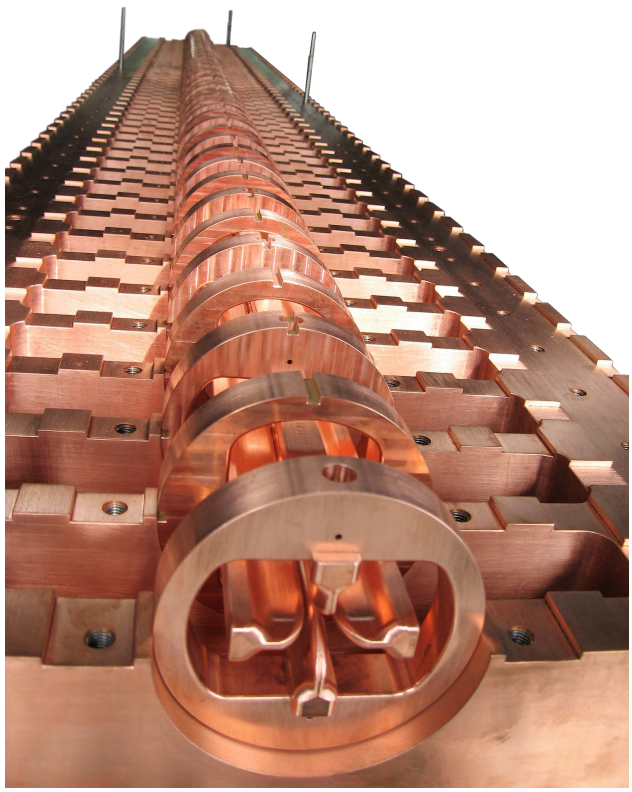


Figure 3: Assembly of the electrodes and carrier rings.

a new loss cone for the chopped beam integrated into the entrance flange of the RFQ.

Manufacturing of the tank components, consisting of an upper tank shell, middle frame and lower tank shell started in September 2017. The middle frame had been completed in November 2017 and was copper-plated by GSI in December 2017. The upper and lower tank shell followed in March and April 2018, respectively. Copper-plating of all components has been finished within Q2/2018. The copper structure has been machined in parallel from 02-04/2018 (see Fig. 2) and finalized in 08/2018. The electrodes have been completed in September 2018. The whole assembly was accomplished within two day. Figure 3 depicts the Ladder-RFQ during assembly after installation of the electrodes and rings prior to closing the tank.

MEASUREMENTS

As manufacturing and first assembly of the RFQ has finished on 10.09.2018, the frequency and first bead pull measurements could be performed prior to LINAC conference. The measured resonance frequency is 338.04 MHz which is 0.1% above simulation. The Q-Value reached up to 4600 which is 65% of the simulated value. During the measurements, tank parts were not screwed on tightly. The screws between the half ladders as well as rings and electrodes have not been silver-plated yet. No RF sealing has been used. Therefore, an increase of the quality factor is expected as conductivity increases. The flatness prior to any tuning process is shown in Fig. 4. The relative deviation of the electric field along the beam axis is $< \pm 3\%$.

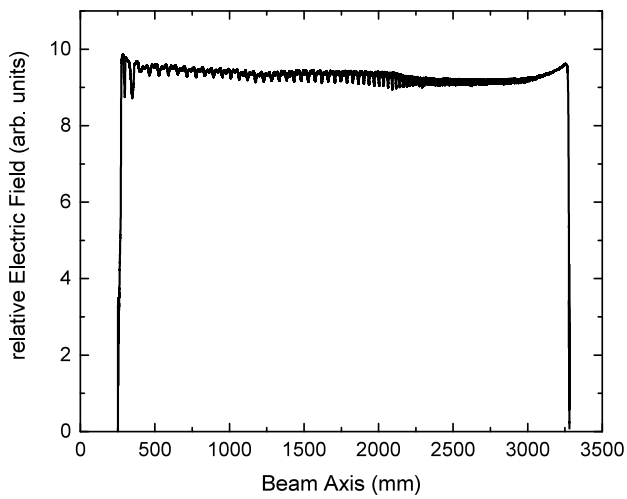


Figure 4: Field flatness of the Ladder-RFQ along the beam axis before tuning procedures.

BEAMMATCHING BETWEEN LEBT AND RFQ

As adjacent electrodes of 4-ROD RFQ's do have a floating potential along the beam axis, there will be a non distinguishable longitudinal fringe field between the

Content from this work may be used under the terms of the CC BY 3.0 licence (© 2018). Any distribution of this work must maintain attribution to the author(s), title of the work, publisher, and DOI.

ISBN: 978-3-95450-194-6 ISSN: 2226-0366 doi:10.18429/JACoW-LINAC2018-THPO060

Content from this work may be used under the terms of the CC BY 3.0 licence (© 2018). Any distribution of this work must maintain attribution to the author(s), title of the work, publisher, and DOI.

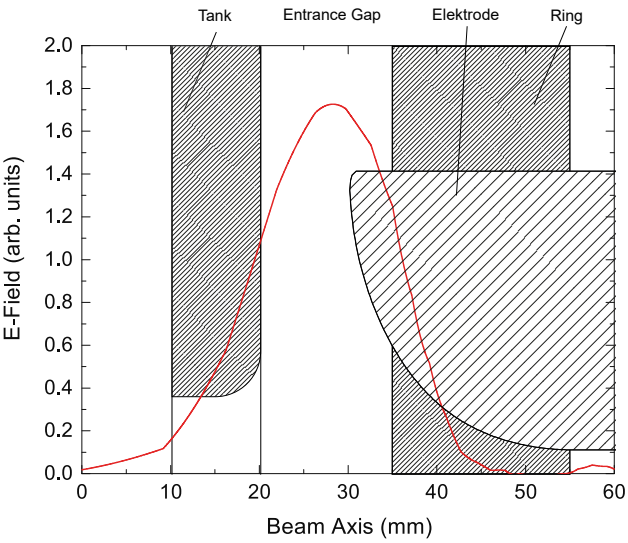


Figure 5: Longitudinal fringe field in the entrance gap/radial matching section of the RFQ.

grounded tank and the net potential of the electrodes at the RFQ entrance and exit gap (see Fig. 5). Depending on the distance between the walls and the electrodes as well as on the actual electrode potential the field may reach up to 50% of the incoming particle energy. In case of the Ladder-RFQ and regarding the time-transient factor, this field causes an energy modulation of up to ±2 eV.

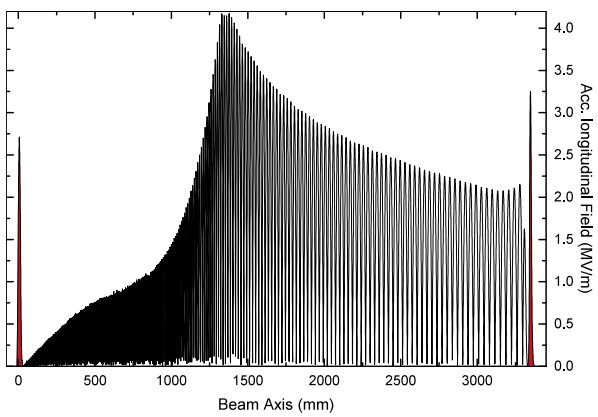


Figure 6: Longitudinal electric field on the beam axis. Simulation result of a complete 3D EM eigenmode simulation considering the entire final modulation of the electrodes. The entrance and exit fields are colored in red.

That longitudinal electric field in the entrance gap of the RFQ (see Fig. 6) will now be beneficially used to pre-bunch the incoming cw beam. According to simulations, the bunching effect is comparable to that within the first five RFQ cells after the radial matcher. Therefore, the phase of the incoming synchronous particle, which is the zero-crossing on the rising edge of the energy modulated cw beam, has to pass the center of the first RFQ cell after the radial matcher at a phase of $\varphi_s = -90°$. By adding a focusing quadrupole drift channel, i.e. a non modulated extension of the electrodes with a constant mean aperture between the end of the radial matcher and the first modulated RFQ cell, the relative phase of the synchronous particle referred to the RF is shifted. After that additional drift, the synchronous particle is centered within the phase space of ±180°.

OUTLOOK

The next steps within 2018 are further bead pull measurements with different methods and beads. Afterwards, the measurements will be compared to the simulations to define the individual ladder cell height needed for the final machining and tuning procedure. Furthermore, the inductive coupling strength will be measured to define the final coupling loop. Beginning late 2019, conditioning and high power tests are envisaged. Additionally, in 2019, a new cone after the chopper, which shall be integrated into the RFQ flange to avoid any additional drift length, will be designed and build.

ACKNOWLEDGEMENT

We acknowledge the efficient cooperation with the GSI p-Linac team, especially Klaus Knie and Carl Kleffner. Many thanks to Kress Maschinenbau GmbH for successfully manufacturing the Ladder-RFQ. The authors would also like to thank the galvanic workshop of GSI, Darmstadt, for copper plating the tank.

REFERENCES

[1] M. Schuett, U. Ratzinger, C. Zhang, "Development of a 325 MHz Ladder-RFQ of the 4-Rod-Type", in *Proc. IPAC'16*, Busan, Korea, May 2016, pp. 899-901. doi:10.18429/JACoW-IPAC2016-MOPOY024

[2] A. Fabris, A. Massarotti, M. Vretenar, "A model of four rods RFQ ", in *Seminar on New Techniques for Future Accelerators*, Erice, Sicily, 1866, pp. 265-269.

[3] M.J. Browman, G. Spalek, P.B. Friedrichs and T.C. Barts, "Studies of the four-rod RFQ using the MAFIA codes", in *Proc. LINAC'88*, Los Alamos, NM, USA, paper MO3-33, 1988, pp. 119-121.

[4] G. Bezzon, A. Lombardi, G. Parisi, A. Pisent, M. Weiss, "Construction and commissioning of the RFQ for the CERN Lead-Ion Facility", in *Proc. LINAC'94*, Tsukuba, Japan, 1994, paper TH-12, pp. 722-724.

[5] Y. Bylinsky, A.M. Lombardi, W. Pirkl, "RFQD - A decelerating radio frequency quadrupole for the CERN Antiproton Facility", in *Proc. LINAC2000*, Monterrey, CA, USA, paper TUD05, pp. 554-556.

[6] M. Schuett, M. Obermayer, U. Ratzinger, "Development and measurements of a 325 MHz RFQ", in *Proc. LINAC'16*, Lansing, MI, USA, 2016, pp. 578-580. doi:10.18429/JACoW-LINAC2016-TUPLR053

[7] M. Schuett, U. Ratzinger, A. Schnase, M. Syha, M. Obermayer, "Status of the modulated 3 MeV 325 MHz Ladder-RFQ", *J. Phys.: Conf. Ser.*, vol. 874, p.012048, 2017. doi:10.1088/1742-6596/874/1/012048

ISBN: 978-3-95450-194-6 ISSN: 2226-0366 doi:10.18429/JACoW-LINAC2018-THPO060

[8] U. Ratzinger, K. Kaspar, E. Malwitz, S. Minaev, R. Tiede, "The GSI 36 MHz high-current IH-type RFQ and HIIF-relevant extensions", in *Nucl. Instrum. Meth. A*, vol. 415, pp. 281-286, 1998.

[9] M. Syha, M. Obermayer, U. Ratzinger, M. Schuett, in *Proc. IPAC'17*, pp. 2252-2254.

[10] M. Syha, U. Ratzinger, M. Schuett, "Beam dynamics for the FAIR p-Linac Ladder RFQ", presented at LINAC'18, Beijing, China, September 2018, paper TUPO083, this conference.

Content from this work may be used under the terms of the CC BY 3.0 licence (© 2018). Any distribution of this work must maintain attribution to the author(s), title of the work, publisher, and DOI.

ISBN: 978-3-95450-194-6 ISSN: 2226-0366 doi:10.18429/JACoW-LINAC2018-THPO061

BEAM CHARACTERIZATION OF THE MYRRHA-RFQ*

P. P. Schneider†, Martin Droba, Oliver Meusel, Holger Podlech, Alwin Schempp
Institute for Applied Physics (IAP), Goethe-University, Frankfurt am Main, Germany
D. Noll, European Organization for Nuclear Research (CERN), Geneva, Switzerland

Abstract

The Linear Accelerator for the MYRRHA project [1] is under construction. In a first step, the linac up to 100 MeV will be realized. The LEBT section has been set into operation in Belgium and the RFQ is installed in summer 2018. A system to analyze the ion beam consisting of a slit-grid emittance scanner, a beam dump and a momentum spectrometer, called diagnostic train descripted in [2], will be set on the rails to characterize the beam at the RFQ injection point. The results will be used to adjust the optimal matching for the RFQ. After the measurements downstream the LEBT, the diagnostic train begins its journey along the beam line and at the first station the RFQ is installed. The accelerated beam of the RFQ is then analyzed and optimized. In addition to optimization of transmission the artificial production of beam offsets in the LEBT is of special interest. These will be measured at the injection point to estimate the range of possible offsets. In the following measurements these offsets will be used to study the influence of the offsets on the RFQ performance. Furthermore, the RFQ parameters are varied to see their influence on the beam transport, transmission and beam quality.

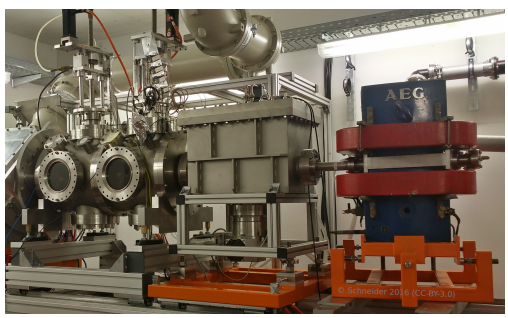


Figure 1: The diagnostic train in operation (left to right): emittance meter – beam dump – momentum spectrometer.

INTRODUCTION

In order to optimize the transport of an ion beam in an accelerator, it is important that each component is tested and optimized as independently as possible after its installation. For this purpose, the installation of the MYRRHA injector includes a measurement of the ion beam after the installation of each individual acceleration component. A flexible diagnostic train was developed to measure the ion beam at different stations along the accelerator chain using the same components for comparable results.

Based on the experiences in [2] numerical evaluations were performed to prepare and optimize the beam and its measurements.

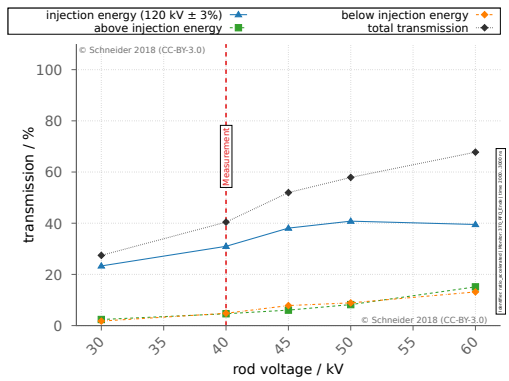


Figure 2: Influence of the rod voltage on the transmission of a Helium beam (120 keV, 1 mA) at rod voltages of $U_{\mathrm{Rod}} = 30\,\mathrm{kV}...60\,\mathrm{kV}$, operating the RFQ in transport mode. The beam remains unaccelerated. The measurements of [2] were performed at $U_{\mathrm{Rod}} \approx 40\,\mathrm{kV}$.

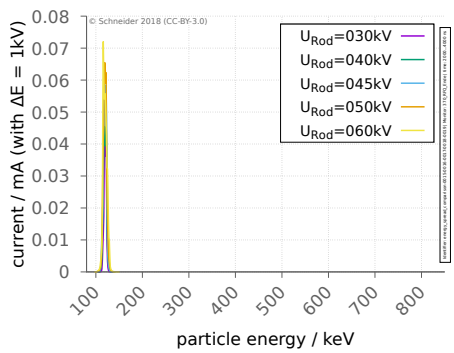


Figure 3: Energy histogram for a Helium beam (120 keV, 1 mA) at various rod voltages of the RFQ in transport mode. The beam remains unaccelerated and the energy spread is very narrow. This makes it perfect for the calibration of a momentum spectrometer.

Diagnostic Train

The diagnostic train as seen in Fig. 1 consists of an emittance meter followed by a beam dump with an 1 mm aperture and a trailing momentum spectrometer.

It was set up for measurements at the Frankfurt Neutron Source and is now calibrated for the upcoming measurements at the MYRRHA injector in Louvain-la-Neuve, Belgium.

* This work is supported by the German Federal Ministry of Education and Research (BMBF) #05P15RFRBA and HORIZON 2020 for the MYRRHA project #662186 and HIC for FAIR.
† schneider@iap.uni-frankfurt.de

Content from this work may be used under the terms of the CC BY 3.0 licence (© 2018). Any distribution of this work must maintain attribution to the author(s), title of the work, publisher, and DOI.

ISBN: 978-3-95450-194-6 ISSN: 2226-0366 doi:10.18429/JACoW-LINAC2018-THPO061

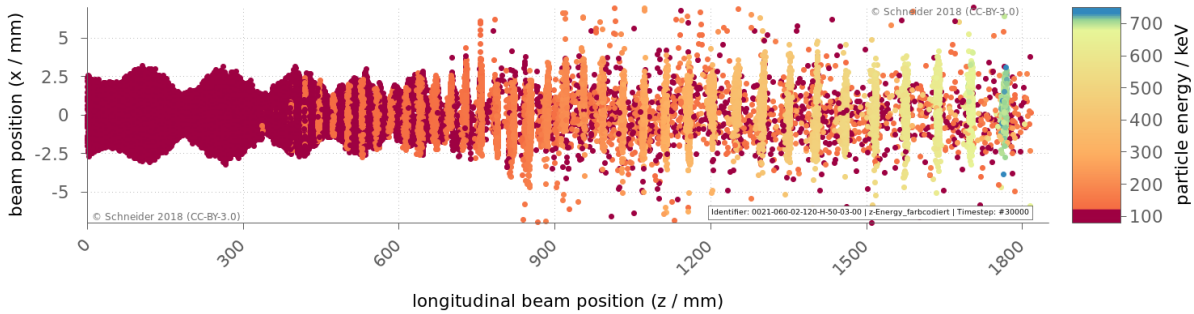


Figure 4: z-x-plane of the RFQ in acceleration mode, the energy of the individual particles is color-coded. The final energy is 700 keV (green), which is reached in the last cell. Parameters are: U_{Rod} = 60 kV, I_{Beam} = 50 mA, $W_{\mathrm{B,in}}$ = 120 keV.

NUMERICAL EVALUATION

To evaluate the measurements made so far, the ion beam was simulated with the 3D particle-in-cell-code bender [3]. In these measurements, a He^+-beam was adjusted for a transport through the RFQ. Helium gives some advantages over protons for this experiments: as it has only one (practical reachable) charge state, one can establish a controlled environment and exclude multiple peaks due to different molecular forms of Hydrogen (H_2^+, H_3^+). Though a He^+-beam can be matched transversally into the RFQ acceptance, the longitudinal acceptance is unreachable in case the extraction potential (120 keV) is equal to the one of the design ion (H^+). Figure 2 shows the possible transmission for a He^+-beam matching the transversal acceptance of the RFQ for different rod voltages.

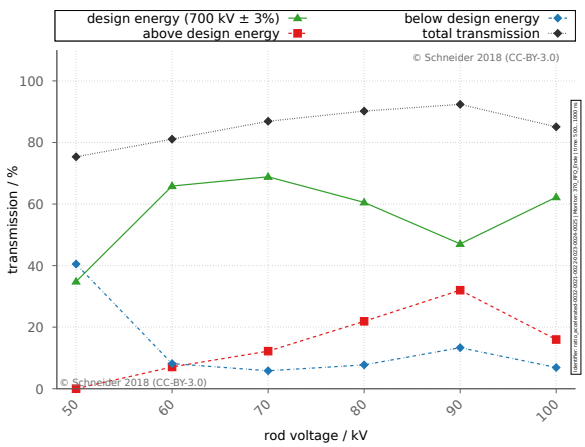


Figure 5: Influence of the rod voltage on the transmission of a proton beam (120 keV, 50 mA) at rod voltages of U_{Rod} = 50 kV...100 kV operating the RFQ in acceleration mode. It can be seen that the optimal transmission does not necessarily coincide with the largest proportion of accelerated particles.

Transport Mode

As seen in Fig. 2, the transmission depends on the rod voltage, increasing rod voltage results in an increased transmission rate. Of interest is the energy spread of the Helium beam downstream the RFQ because it is crucial for the calibration of the momentum spectrometer.

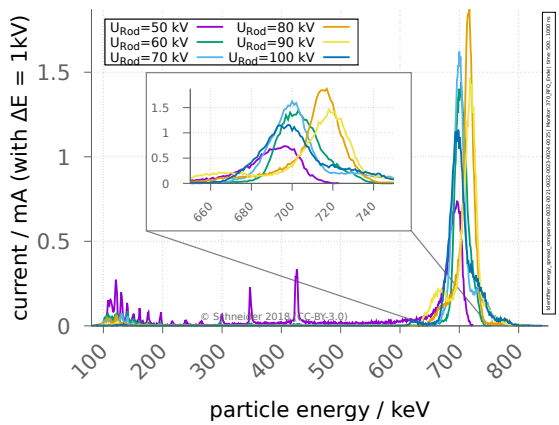


Figure 6: Energy histogram of a 120 keV, 50 mA proton beam downstrem the RFQ in acceleration mode at rod voltages of U_{Rod} = 50 kV...100 kV.

Figure 3 shows the energy histogram of an Helium beam (120 keV, 1 mA) downstream the RFQ. The energy spread is very narrow and exactly at the injection energy of 120 keV. Therefore it is perfect to calibrate the momentum spectrometer of the diagnostic train. The simulations confirmed that the ions are transported by the RFQ but not accelerated. This mode is called the *transport mode* in which the RFQ operates only as a focussing transport element and does not accelerate the beam. The *transport mode* is well suited for calibrating a momentum spectrometer and the support of RFQ conditioning with the ion beam scrubbing technique, similar to [4].

RFQ Beam Optimization

Simulations for the later acceleration of protons have been carried out to optimize the RFQ transport. First results of the impact of various rod voltages on the transmission and energy spread are shown in Figures 4–6, 8 and 9. The rod voltage was choosen for variation in the range of U_{Rod} = 50 kV...100 kV. An example for U_{Rod} = 60 kV is shown in Fig. 4

Content from this work may be used under the terms of the CC BY 3.0 licence (© 2018). Any distribution of this work must maintain attribution to the author(s), title of the work, publisher, and DOI.

ISBN: 978-3-95450-194-6 ISSN: 2226-0366 doi:10.18429/JACoW-LINAC2018-THPO061

Content from this work may be used under the terms of the CC BY 3.0 licence (© 2018). Any distribution of this work must maintain attribution to the author(s), title of the work, publisher, and DOI.

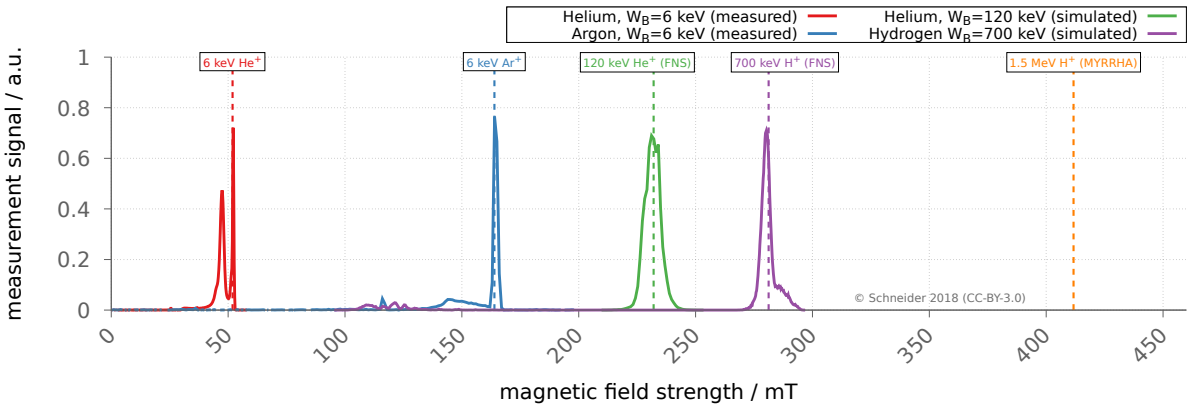


Figure 7: Momentum spectra of the several cases discussed in this paper. While Helium and Argon at $W_B = 6$ keV are measured, Helium at $W_B = 120$ keV and protons at $W_B = 700$ keV (both downstream the RFQ) are simulated with the PIC-code bender.

The simulations show that the rod voltage has an influence on the total transmission and especially on the energy distribution of the particles. This allows to determine the optimal working point of the RFQ. The largest transmission of particles with a small $\frac{\Delta E}{E}$ ratio does not coincide with the optimum of the total transmission, as seen in Fig. 5.

In addition, the H^+-case can be used to crosscheck the simulation with the later measurements by the momentum spectrometer. The predicted spectra can be found in Fig. 6.

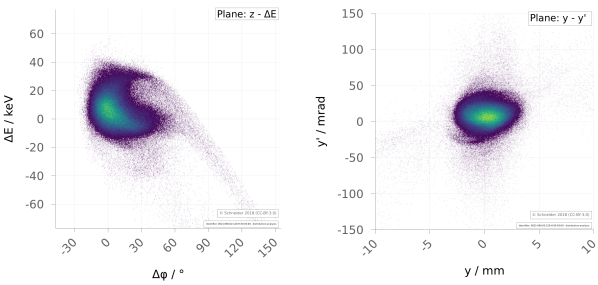


Figure 8: Particle distributions for the simulation of 50 mA protons with $W_B = 700$ keV at a rod voltage of 60 kV.

EXPERIMENTAL TESTS

In order to perform the calibration of the diagnostic train, a test stand with low beam energies was set up where a helium and an argon beam are measured with a beam energy of 6 keV. Figure 7 shows the momentum spectra for the experimental results (red: He^+, blue: Ar^+) as well as the expected spectra from the PIC-simulations for 120 keV Helium downstream the RFQ in transport mode and 700 keV protons downstream the RFQ in acceleration mode.

EMITTANCE MEASUREMENTS

The expected phase-space distributions were evaluated to be able to compare them with the later emittance measurements. The longitudinal and transversal distribution is shown in Fig. 8. Due to the possibilities offered by the Bender code, it was possible to transport all particles independent of their longitudinal energy to the end of the RFQ. Their distribution within the phase space is seen in Fig. 9.

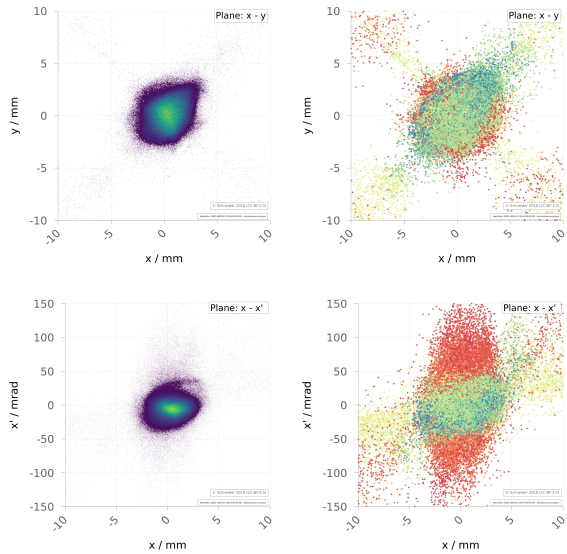


Figure 9: Particle distributions of the simulation of 50 mA protons with $W_B = 700$ keV at a rod voltage of 60 kV.

OUTLOOK

Simulations show promising results and form the basis for further investigations of the effects of offsets at the RFQ injection plane. After the tests with the emittance measuring system, the diagnostic train is ready for operation. Once the diagnostic train has been calibrated at low energies, it is quickly ready for use to enable future measurements with high accuracy and low lead time. After the measurements at Frankfurt University are completed, the following up measurements will take place at the MYRRHA injector in Leuwen la Neuwe, Belgium.

ISBN: 978-3-95450-194-6 ISSN: 2226-0366 doi:10.18429/JACoW-LINAC2018-THPO061

REFERENCES

[1] H. Abderrahim *et al.*, "Myrrha: A multipurpose accelerator driven system for research and development," *Nuclear Instruments and Methods in Physics Research Section A: Accelerators, Spectrometers, Detectors and Associated Equipment*, vol. 463, no. 3, pp. 487–494, 2001, Accelerator driven systems, ISSN: 0168-9002. DOI: https://doi.org/10.1016/S0168-9002(01)00164-4. http://www.sciencedirect.com/science/article/pii/S0168900201001644

[2] P. P. Schneider *et al.*, "First experiments at the cw-operated rfq for intense proton beams," *Proceedings of LINAC'16, East Lansing, MI, USA*, no. TUOP05, 2001. DOI: https://doi.org/10.18429/JACoW-LINAC2016-TUOP05. http://accelconf.web.cern.ch/AccelConf/linac2016/papers/tuop05.pdf

[3] D. Noll, C. Wiesner, O. Meusel, K. Schulte, U. Ratzinger, and M. Droba, "The particle-in-cell code bender and its application to non-relativistic beam transport," *Proceedings of HB2014, East-Lansing, MI, USA*, no. WEO4LR02, 2015. http://accelconf.web.cern.ch/AccelConf/HB2014/papers/weo4lr02.pdf

[4] E. Mahner, J. Hansen, J.-M. Laurent, and N. Madsen, "Molecular desorption of stainless steel vacuum chambers irradiated with 4.2 mev/u lead ions," *Physical Review Special Topics-Accelerators and Beams*, vol. 6, no. 1, p. 013 201, 2003.

Content from this work may be used under the terms of the CC BY 3.0 licence (© 2018). Any distribution of this work must maintain attribution to the author(s), title of the work, publisher, and DOI.

ISBN: 978-3-95450-194-6 ISSN: 2226-0366 doi:10.18429/JACoW-LINAC2018-THPO062

IFMIF/EVEDA RFQ PRELIMINARY BEAM CHARACTERIZATION

E. Fagotti, L. Antoniazzi, L. Bellan, M. Comunian, F. Grespan†, M. Montis, A. Palmieri, A. Pisent, F. Scantamburlo, INFN-LNL, 35020 Legnaro, Italy
T. Akagi, K. Kondo, T. Shinya, M. Sugimoto, K. Sakamoto, QST, Aomori, Japan
P. Cara, IFMIF/EVEDA Project Team, Aomori, Japan
H. Dzitko, R. Heidinger, A. Marqueta, I Moya, F4E, Garching, Germany
I. Podadera, CIEMAT, Madrid, Spain

Abstract

The IFMIF/EVEDA RFQ is the longest and powerful operated. Therefore, it requires a careful characterization from several aspects: beam dynamics, RF, mechanics, installation and commissioning. Due to the very large power handling, the preliminary beam operation was decided to be performed with a low proton beam current at one half of the voltage needed for deuteron acceleration, i.e. from 8 mA to 30 mA at 2.5 MeV in pulsed mode, with respect to the nominal 130-mA deuteron beam at 5 MeV in CW. In this framework, it will be presented the characterization of the RFQ in terms of simulation and measurements.

INTRODUCTION

The Linear IFMIF Prototype Accelerator (LIPAc) is composed of an ion source, a LEBT, a RFQ, a MEBT and a SC linac and HEBT, with a final energy of 9 MeV [1].

This paper is mainly focalized on Normal Conducting linac performance. In particular RFQ is a CW linac capable of delivering 125 mA of D^+ beam at 5 MeV. The 10-m-long, 175-MHz RFQ structure is designed to accelerate the DC 100 keV, 130 mA D^+ beam from the injector with more than 90% transmission [2].

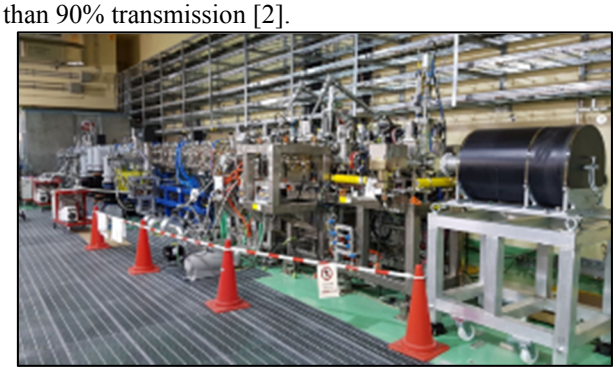


Figure 1: IFMIF/EVEDA LIPAc in Rokkasho (Japan).

RFQ is installed in IFMIF site in Rokkasho (Fig. 1) since April 2016. The low power RF characterization (bead pulling and tuning) was concluded in September 2016. We installed the 8 power couplers in December 2016, checking the field by pick-up reading. After baking and connection to the cooling system and to the 8 RF systems, RF conditioning started in July 2017. Some problems slowed down hardware conditioning and integration: the 132 kV max nominal voltage for D^+ beam was reached on January 2018 with very short RF pulses (20 μs/125 ms). Maximum power reached in CW was 60 kW. Until now the RFQ did not show any problem in terms of RF performances [3].

These partial results were nevertheless enough to start RFQ beam commissioning phase B1, consisting in the acceleration of a pulsed proton beam up to 2.5 MeV. On June 13th first proton beam was successfully accelerated through the RFQ. Beam operation continued until August 10th despite some trouble in one RF power supply which was then bypassed by operating with 7 over 8 RF chains only.

LIPAC CONFIGURATION

The accelerator configuration for beam commissioning of LIPAc RFQ is shown in Fig. 2. LEBT optics includes two solenoids (Sol#) with integrated steering magnet pairs (ST#). Diagnostics include Doppler-Shift Spectroscopy, a 4 grid analyser, an Allison-Scanner, a beam stop, two CCD beam profile monitors. Three cm before RFQ matching point, there is LEBT-ACCT. RFQ input plate includes an electron repeller (-3 kV). Cavity is maintained at 10^{-8} mbar vacuum level by 10 cryo-pumps. For RFQ beam characterization, MEBT is equipped with an ACCT just after the gate valve separating it from the RFQ, a Fast Current Transformer (FCT) and 4 BPM's. Diagnostic-Plate next to MEBT includes 3 BPM's, 2 Slits combined with SEM-Grids for profile and emittance measurement, an ACCT-DCCT, a Residual Gas Bunch Length Monitor (RGBLM), a Fluorescence Profile Monitor (FPM) and an Ionization Profile Monitor (IPM). Lastly, a Low Power Beam Dump (LPBD) is used as Faraday Cup.

In this first beam commissioning period, profile diagnostics and Doppler-Shift diagnostic were not operational yet. Hence, results presented in the following are based on the ACCTs, LPBD and BPMs diagnostics.

COMMISSIONING PLAN AND SIMULATIONS

Beam operation represents the first integrated test of LIPAc systems. In the followed approach, beam intensity was gradually increased while verifying and debugging each sub-system and their interfaces. This constitutes a safe operation mode with respect to starting directly at nominal proton current (65 mA). Low current and so low power beam operation allows using interceptive diagnostics while increasing RFQ acceptance with respect to the input mismatch.

For a better extraction conditions at low currents, injector was equipped with a 3 mm radius extraction hole instead of the original 6 mm.

* The views and opinions expressed herein do not necessarily reflect those of the author's home institutions or research funders.

† francesco.grespan@lnl.infn.it

Content from this work may be used under the terms of the CC BY 3.0 licence (© 2018). Any distribution of this work must maintain attribution to the author(s), title of the work, publisher, and DOI.

ISBN: 978-3-95450-194-6 ISSN: 2226-0366 doi:10.18429/JACoW-LINAC2018-THPO062

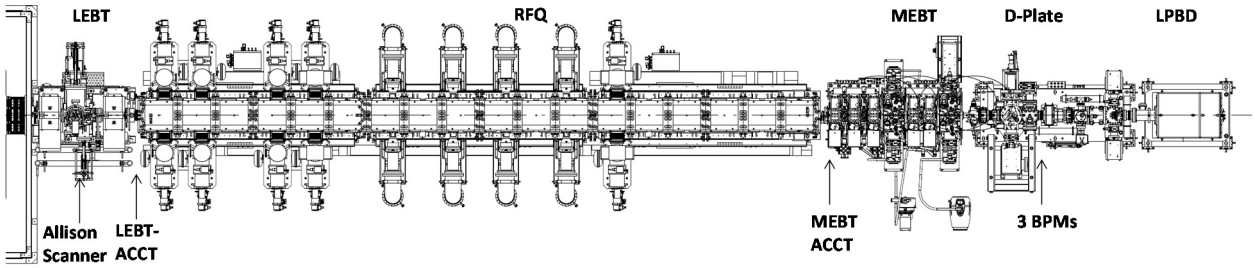


Figure 2: LIPAc configuration showing main systems and diagnostics mentioned in this paper.

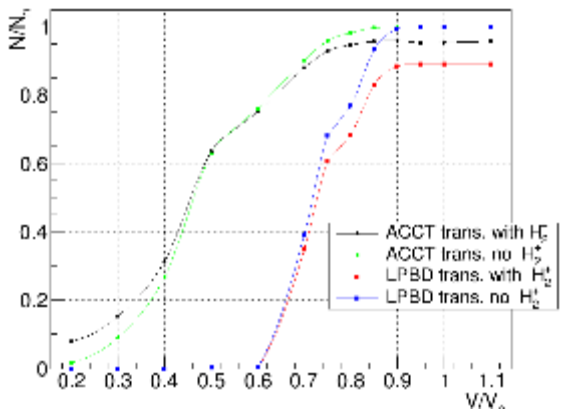


Figure 3: simulated transmission trough RFQ with/without contaminants for 8 mA input current [4].

Commissioning began in a pulsed low–power mode defined by: repetition rate = 1 Hz, injector RF pulse = 1.3 ms, RFQ RF pulse = 500 µs, beam chopper pulse = 300 µs, and injected beam current = 7 mA.

The MEBT quadrupoles (one triplet and one doublet) were set as for the matched beam, and as further protection for equipment, two scrapers at the MEBT input are both placed to a square of 20 mm side seen by the beam.

Performances of the RFQ were reproduced with an advanced simulation model of the system [4], which contains the measured geometry of the cavity and the voltage profile obtained from bead-pull measurements. Simulations were particularly useful in order to interpret effects of the input conditions and effects of contaminants on RFQ transmission (Fig. 3).

Once performances of subsystems were verified, commissioning was focused on beam current increase up to the maximum current obtainable with the 3 mm hole extraction electrode (I_{extr}=40 mA), without changing pulse length or period.

EXPERIMENTAL RESULTS

Transmission Optimization

For the very first injection, on June 13th, the RFQ was in amplitude open-loop, with voltage oscillating between 70-75 kV. Source total extracted current was 13 mA with a large H_2^+ contamination. With LEBT magnets at nominal values, no beam was extracted from RFQ.

After some manual LEBT adjustment, the following results were obtained: LEBT-ACCT = 5.3 mA, MEBT-ACCT = 1.7 mA (30% transmission), LPBD = 1.2 mA (20% transmission). LEBT magnets were set as: Sol1 = 90A (nominal), Sol2 = 155A (nominal=186A), ST1Hor = 0, ST1Ver = 40A, ST2Ho r= 0, ST2Ver = 0.

This was the first clue of a strong misalignment of the accelerator column and LEBT with respect to the RFQ input. Weaker Sol2 value allows filling the RFQ acceptance compensating misalignment effects, taking advantage of the increased RFQ acceptance for low current beam.

Operations were then stopped and a script for automatic scan of the 6 LEBT magnets was prepared to allow the systematic study of RFQ transmission towards LPBD, in function of input parameters.

We restarted operation on June 15th with RFQ in amplitude close-loop at voltage 70 kV. After running the scan routine only on LEBT ST1 and ST2, (solenoids set at nominal values, we obtainined the following transmission results: LEBT-ACCT = 7.4 mA, MEBT-ACCT = 6.3 mA (85%), LPBD = 5.4 mA (72%), with LEBT magnets: Sol1 = 90A (nominal), Sol2 = 186A (nominal), ST1Hor = -20A (saturated), ST1Ver = 80A, ST2Hor = -20A, ST2Ver = 20A (saturated).

Photon radiation measurements confirmed that protons with energy larger than 2.4 MeV impinged on copper.

The same procedure was repeated for different current values. Results are reported in Table 1.

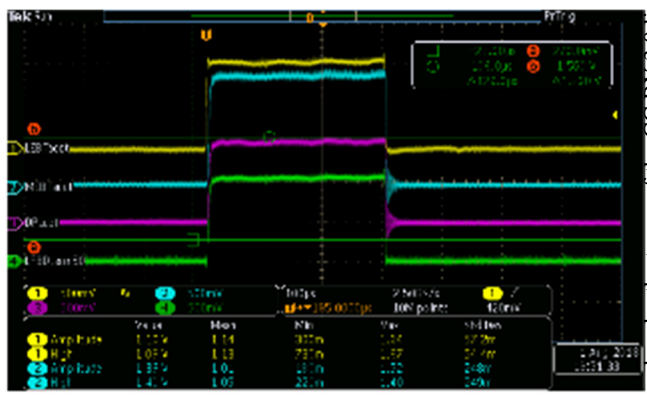


Figure 4: current signals at different points of the LIPAC for I_{extr}=30 mA. (V_{scope}~50 Ω·I_{beam}; only for the MEBT-ACCT V_{scope}~67 Ω·I_{beam})

We observed that:

- The proton fraction at the RFQ input was unknown and the RFQ itself could transmit some contaminants that could not reach LPBD (Fig. 3). So we tried to maximize the transmission to LPBD.

Content from this work may be used under the terms of the CC BY 3.0 licence (© 2018). Any distribution of this work must maintain attribution to the author(s), title of the work, publisher, and DOI.

ISBN: 978-3-95450-194-6 ISSN: 2226-0366 doi:10.18429/JACoW-LINAC2018-THPO062

Content from this work may be used under the terms of the CC BY 3.0 licence (© 2018). Any distribution of this work must maintain attribution to the author(s), title of the work, publisher, and DOI.

Table 1: Transmission values at different extracted currents. Marked magnets are saturated* or temporarily out of order†. Some inconsistency of current measurements. (i.e. MEBT < LPBD).

I_{extr} (mA)	ε (π mm.mrad)	LEBT (mA)	MEBT (mA)	LPBD (mA)	Sol1 (A) Exp/Sim	Sol2 (A) Exp/Sim	Steerers
13	0.09	6.6	6.3 (95%)	5.8 (87%)	130/90	180/186	H1*=-20A, V1=107A, H2†=0A, V2*=20A
20	0.10	9.8	N.A.	9.4 (96%)	130/140	177/153	H1*=-20A, V1=105A, H2†=0A, V2=0A
30	0.14	21.7	20.6 (95%)	20.9 (96%)	135/137	160/145	H1*=-20A, V1=75A, H2†=0A, V2*=-20A
35	0.12	27.0	25.0 (93%)	25.7 (95%)	140/137	148/145	H1*=-20A, V1=65A, H2=-8A, V2=-10A
40	0.20	29.3	25.8 (88%)	26.1 (89%)	137/N.A.	151/N.A.	H1*=-20A, V1=63A, H2=-10A, V2=-10A

- The experimental reference emittance measured between two solenoids in order to match RFQ input should be ε ≤ 0.15 π mm*mrad. The point at I_{extr}=40 mA has a larger emittance and may have a consequent lower transmission due to emittance growth at the RFQ injection point [5].
- At very low current the fraction of H_2^+ extracted is larger as well as the acceptance of the RFQ for H_2^+. This explains the losses in the MEBT at I_{extr}=13mA, consistently with simulations (Fig. 3).
- The misalignment effects (Sol1 and STV1&2) decreases with increasing current, due to the different value of the source intermediate electrode.

Voltage and Transmission

We measured the RFQ transmission as a function of the RFQ Field Amplitude for different input currents listed in Table 1 and we compared them to the simulated RFQ transmission for 24 mA input current (Fig. 5).

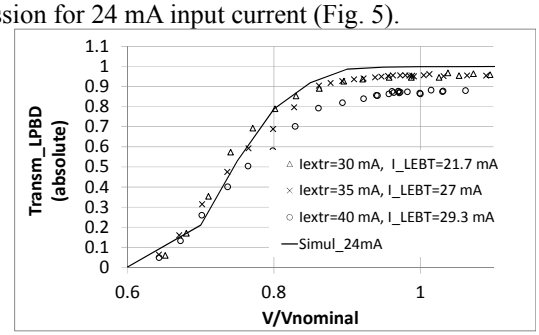


Figure 5: Absolute LPBD transmission vs RFQ voltage.

According to simulations [6], RFQ and MEBT transmission should be 100%, for proton currents up to 30 mA. Our hypothesis to explain the discrepancies shown in Fig.5 is the combination of:

- Presence of contaminants at LEBT-ACCT (Fig. 3);
- Residual misalignment at RFQ input (due to steerer saturation);
- Emittance at RFQ input (see Table 1, I_{extr}=40 mA).

By rescaling transmission data to maximum value, superimposition to simulation results is possible. This comparison, shown in Fig.6, confirms the expected trend.

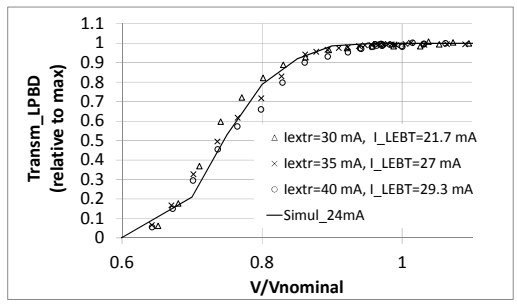


Figure 6: Relative transmission to LPBD vs RFQ voltage.

Output Energy Measurements

The Time of Flight measurement between the three D-Plate BPMs was performed with oscilloscope. The signals are two shifted sine waves at 175 MHz. We measured the time δt_{kj} between two adjacent peaks. Since the pulse rising edge is not sharp, we cannot determine the correspondence between bunch and signal peak. Nevertheless considering two measurements with cables swapped (δt_{kj} and δt_{jk}), the cable delay contribution is removed [7].
Table 2 shows that the 2.5 MeV output energy protons is confirmed with an error of 1%.

Table 2: Result of ToF Measurements.

	Distance (mm)	δt_{kj} [ns]	δt_{jk} [ns]	Energy [MeV]
BPM1-2	155.8	4.07	4.39	2.52
BPM1-3	1265.3	3.13	4.71	2.48

CONCLUSIONS AND PERSPECTIVES

This first month of RFQ beam commissioning confirmed the expected performances of the RFQ in terms of beam transmission and energy and this is an encouraging result. After the maintenance and realignment of the injector as well as the recovering of the profile diagnostics we should be able to have more significant comparisons with simulations after resuming the operation by the end of this year. In the meantime RF conditioning should continue up to 132 kV-CW to demonstrate the full characteristics of the cavity.

ISBN: 978-3-95450-194-6 ISSN: 2226-0366 doi:10.18429/JACoW-LINAC2018-THPO062

REFERENCES

[1] M. Sugimoto, *et al.,* "Progress Report on LIPAC", presented at LINAC'18, Beijing, China, Sep. 2018, paper TU2A04, this conference.

[2] J. Knaster *et al.,* "Challenges of the high current prototype accelerator of IFMIF/EVEDA", in *Proc. IPAC'16*, Busan, Korea, May 2016. doi:10.18429/JACoW-IPAC2016-MOZB02

[3] E. Fagotti *et al.* "Beam Commissioning of the IFMIF EVEDA Very High Power RFQ" in *Proc. IPAC'18*, Vancouver, BC, Canada, Apr.-May 2018. doi:10.18429/JACoW-IPAC2018-THXGBF2.

[4] L. Bellan *et al.,* "Beam Dynamics of the First Beams for IFMIF-EVEDA RFQ Commissioning", in *Proc. IPAC'18*, Vancouver, BC, Canada, Apr.-May 2018 doi: 10.18429/JACoW-IPAC2018-THPAK019

[5] M. Comunian *et al.,* "Beam Dynamics Redesign of IFMIF-EVEDA RFQ for a Larger Input Beam Acceptance", in *Proc. IPAC'11*, San Sebastian, Spain, Sep. 2011, paper MOPS031.

[6] M. Comunian *et al.,* "The IFMIF-EVEDA RFQ: Beam Dynamics Design", in *Proc. EPAC'08*, Genova, Italy, Jun. 2008, paper THPP075.

[7] F. Grespan, A. Palmieri, "First RFQ H+ output energy estimation by TOF measurements between DPlate BPMs", https://users.jt60sa.org, internal note.

Content from this work may be used under the terms of the CC BY 3.0 licence (© 2018). Any distribution of this work must maintain attribution to the author(s), title of the work, publisher, and DOI.

ISBN: 978-3-95450-194-6 ISSN: 2226-0366 doi:10.18429/JACoW-LINAC2018-THPO064

TUNING OF A FOUR-VANE RFQ FOR XI'AN 200 MeV PROTON APPLICATION FACILITY

X.D. Yu†, Q.Z. Xing, Q.K. Guo, P.F. Ma, Y. Lei, S.X. Zheng, Y. Li, S. Wang, K. Liu, X.L. Guan, X.W. Wang, Key Laboratory of Particle & Radiation Imaging (Tsinghua University), Ministry of Education, 100084 Beijing, China
also at Laboratory for Advanced Radiation Sources and Application, Tsinghua University, 100084 Beijing, China
also at Department of Engineering Physics, Tsinghua University, 100084 Beijing, China
B.C. Wang, C. Zhao, Z.M. Wang, State Key Laboratory of Intense Pulsed Radiation Simulation and Effect (Northwest Institute of Nuclear Technology), 710024 Xi'an, China

Abstract

This paper mainly describes the procedures and results of tuning a four-vane Radio Frequency Quadrupole (RFQ) accelerator for the Xi'an 200 MeV Proton Application Facility (XiPAF) project. The 3-meter-long RFQ will accelerate a 50 keV H^- beam from the ECR source to 3 MeV, and deliver it to the downstream drift tube linac (DTL) with a peak current of 5 mA, pulse length of 10-40 μs and maximum repetition rate of 0.5. The machining, assembly, and RF tuning of the RFQ cavity has been completed successfully. After tuning, the relative error of the operating quadrupole mode field is within ±2.7%, and the dipole mode component is within ±1.9% of the quadrupole mode. The RFQ now is ready for high-power RF conditioning.

INTRODUCTION

The four-vane Radio Frequency Quadrupole (RFQ) accelerator will be used as a component of the linac injector for the Xi'an 200 MeV Proton Application Facility (XiPAF) project, a facility capable of providing single-event effect test of semiconductor devices in spacecraft electronic systems. The main function of this RFQ is to bunch, focus and accelerate low-speed H^- beam and finally match the beam to the DTL. To make this RFQ compact, the inter-vane voltage of XiPAF RFQ rises from the low-energy end to high-energy end.

Tuning plays an important role for the operation of an RFQ. Due to the deviation of undercut design and machining error, the actual field distribution of RFQ is always different from the designed one. The relatively large error of the field distribution can lead to changes in the synchronous energy, twiss parameters, and transmission efficiency of the beam at the RFQ exit. In order to adjust the field distribution, 48 tuners are equipped on this RFQ.

The main objectives of tuning the XiPAF RFQ are as follows: 1) Reduce the field distribution difference between the measured and designed quadrupole field; 2) decrease the dipole mode field component; 3) tune the frequency to the desired value; 4) adjust the coupling coefficient of the power coupler to the desired value; 5) enlarge the frequency separation between the operating quadrupole mode and the nearest dipole modes to enhance the field stability. In order to ensure that the final field distribution can meet the requirements, the RFQ has been tuned twice, including the pre-braze tuning and final tuning.

†yxd17@mails.tsinghua.edu.cn

XIPAF RFQ

Main parameters of the XiPAF RFQ are shown in Table 1 [1].

Table 1: Main Design Parameters of XiPAF RFQ

Parameters	Value	Unit
Particle	H^-	
Input energy	50	keV
Output energy	3	MeV
Frequency	325	MHz
Peak current intensity	5	mA
Maximum reputation rate	0.5	Hz
Beam pulse length	10-40	μs
Peak wall power	388	kW
Q_0	8600	

Assembled XiPAF RFQ is shown in Fig. 1. This RFQ consists of three segments. A total of 48 tuners are equipped in the four quadrants of the cavity. Each segment is about 1 meter long and contains 16 tuners. Four dipole-mode stabilizer rods [2] are mounted on each of the two flanges in order to adjust the frequency separation between the quadrupole mode and adjacent dipole modes. Undercuts [3] are separately designed for each end of the RFQ in order to help achieve the field distribution close to the designed one. The RFQ is fed by only one power coupler and the coupler is located in the first quadrant in the middle of the RFQ. Power is fed into the cavity by loop coupling [4] and the coupling coefficient can be adjusted by rotating the coaxial coupler.

EXPERIMENTAL SETUP

The magnetic field distribution near the outer wall is obtained by the bead-pull method. Main measuring device is a vector network analyser. One port of the network analyser is connected to power coupler and the other port is connected to a field probe. The probe is inserted into the cavity through a vacuum port to measure the S12 signal. A hollow metal bead with a diameter of 11.5 mm is used for a perturbation. The bead passes through the four quadrants under the drive of a stepper motor.

Content from this work may be used under the terms of the CC BY 3.0 licence (© 2018). Any distribution of this work must maintain attribution to the author(s), title of the work, publisher, and DOI.

ISBN: 978-3-95450-194-6 ISSN: 2226-0366 doi:10.18429/JACoW-LINAC2018-THPO064

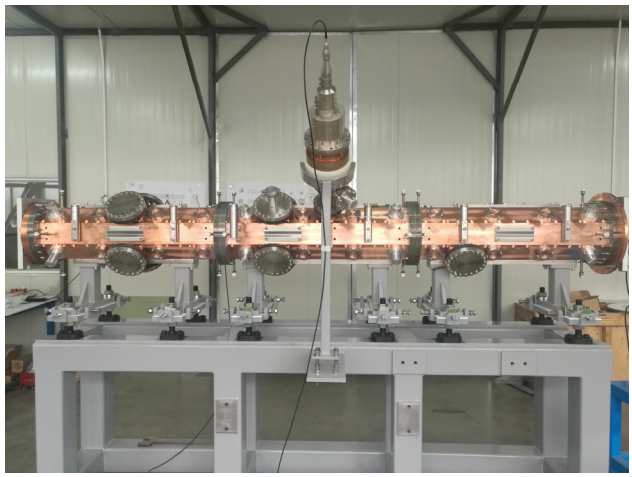


Figure 1: Assembled XiPAF RFQ.

Field distribution is obtained by measuring the phase change of the S12 signal. Figure 2 shows the linear relationship between the S12 phase and frequency. It can be seen that there is a good linearity in the range of ±5 kHz near the centre frequency. The disturbance slightly exceeds +5 kHz near the last tuner in Fig. 2(b). However, the data near tuners are not actually used in the tuning program. Therefore, the method for such measurement is reasonable.

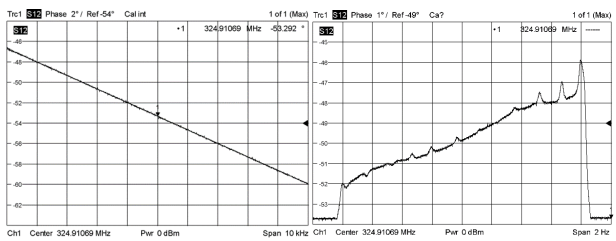


Figure 2: Assessment of the linear relationship between the S12 phase and frequency (a) and phase shift of signal S12 with the bead position (b) in one measurement.

PRE-BRAZE TUNING

Before the pre-braze tuning, the four vanes of the XiPAF RFQ are assembled, but not brazed together. The dipole-mode stabilizer rods are not brazed on the flanges and the lengths can still be adjusted. A dummy coupler is mounted on the cavity to imitate a real coupler. The main objectives for the pre-braze tuning are: 1) verify that both the field distribution and resonance frequency can be tuned to meet requirements; 2) determine the length of dipole-mode stabilizer rods to ensure a large frequency separation between the operating quadrupole mode and the nearest dipole modes.

The pre-braze tuning begins with all the aluminium tuners flush with the inner surface of the cavity wall. Before pre-braze tuning, the relative error of the operating quadrupole mode field is within ±25.0%, and the dipole mode component is within ±12.8% of the quadrupole mode. With the field distribution measured, the tuning program THURT [5] can calculate new insertion depth of tuners.

After several iterations, the relative error of the operating quadrupole mode field drops below ±2.0% while the dipole mode component is about ±16%. The dipole component is rather large, because we finally find that a wrong normalization method for the dipole field has been adopted during the pre-braze tuning. Figure 3 shows the corrected normalized field distribution of the quadrupole and dipole modes after pre-braze tuning.

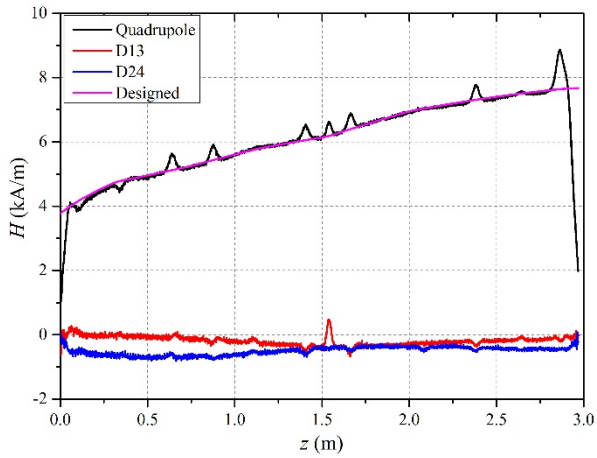


Figure 3: Normalized field distribution of the quadrupole and dipole modes after pre-braze tuning (22 °C, and 42% humidity).

After the field distribution and frequency are tuned, the frequency separation of the operating mode and adjacent dipole modes is adjusted by adjusting the length of the dipole-mode stabilizer rods. Figure 4 shows Measured frequency of operating mode and adjacent modes with the rod length. As the length increases, the frequency separation of the operating mode and adjacent dipole modes first increases and then decreases. The length of the dipole mode stabilizer rod is finally set to 150 mm, and the frequencies of the nearest dipole mode are separated from the operating mode by at least 5.25 MHz.

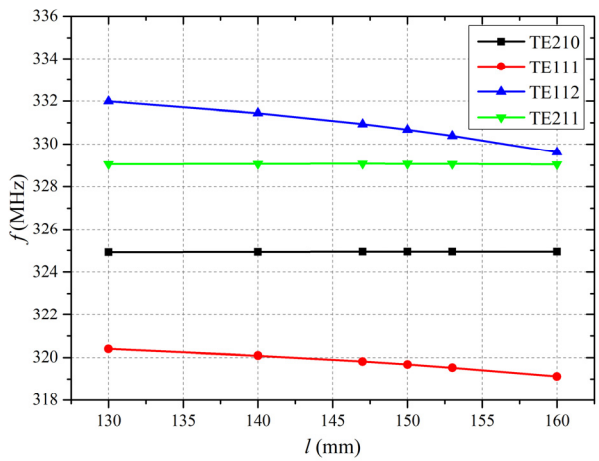


Figure 4: Measured frequency of operating mode and adjacent modes with the rod length.

Content from this work may be used under the terms of the CC BY 3.0 licence (© 2018). Any distribution of this work must maintain attribution to the author(s), title of the work, publisher, and DOI.

ISBN: 978-3-95450-194-6 ISSN: 2226-0366 doi:10.18429/JACoW-LINAC2018-THPO064

Content from this work may be used under the terms of the CC BY 3.0 licence (© 2018). Any distribution of this work must maintain attribution to the author(s), title of the work, publisher, and DOI.

FINAL TUNING

The final tuning is carried out after the vanes of the RFQ are brazed together. Main objectives of the final tuning are: 1) determine the length of the copper tuners so that both field distribution and resonance frequency meet requirements; 2) determine the size and angle of the coupling loop in order to adjust the coupling coefficient to the target value.

The final field distribution is shown in Fig. 5. It can be seen that after the final tuning, the relative error of the operating quadrupole mode field is within ±2.7%, and the dipole mode component is within ±1.9% of the quadrupole mode. Quadrupole field error exceeds ±2% only in a small part of the bunching section.

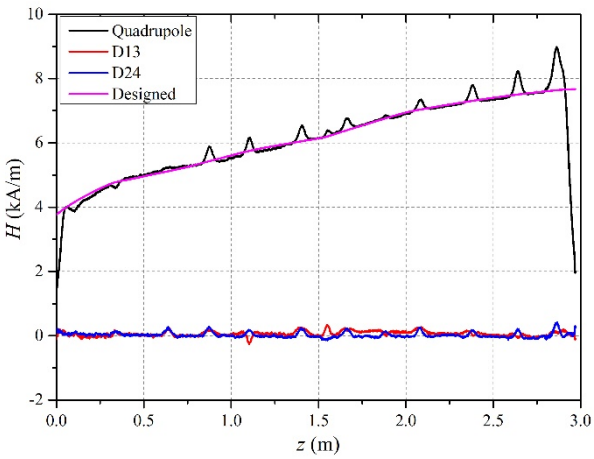


Figure 5: Normalized field distribution of the quadrupole and dipole modes after final tuning (23.7°C, with nitrogen fed into the cavity).

The resonance frequency of the operating mode is 324.89 MHz in the environment of 22°C and 10% humidity. The frequency spectrum is shown in Fig. 6. It can be seen that the frequency difference between the operating quadrupole mode and the nearest dipole mode is 4.85 MHz. And we have measured the resonance frequency of operating mode in the environment of 23°C and 0.25 Pa inside the cavity later. It shows that the frequency rises to 325.02 MHz, and the frequency becomes 325.01MHz when the environment is converted to 25°C, vacuum. The difference between the frequency converted and target value is only 10 kHz.

The final coupling coefficient measured is 1.03 while the quality factor Q_0 is 7300. Peak cavity power with this Q_0 should be 457 kW and peak beam power is 18 kW. The desired coupling coefficient should be $\beta = 1 + P_{\mathrm{beam}}/P_{\mathrm{cavity}} = 1.04$. The attenuation of all pickups falls in -59.5 dB~ -60.5 dB area after adjusting.

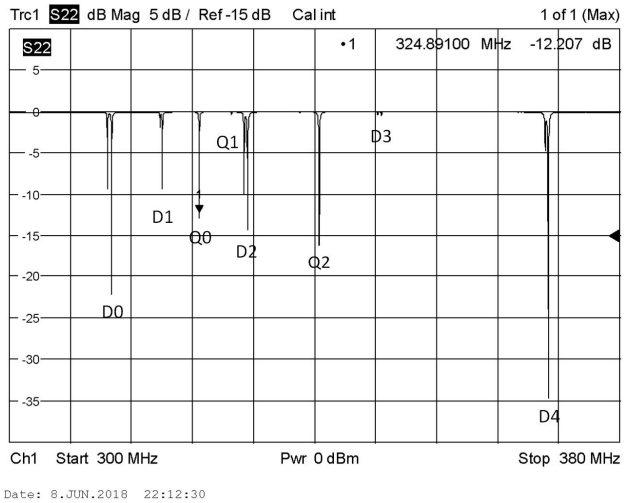


Figure 6: Frequency spectrum of XiPAF RFQ after final tuning (22 °C, 10% humidity).

CONCLUSIONS

One 325 MHz four-vane RFQ accelerator with ramped inter-vane voltage has been manufactured for the 7 MeV linac injector of the XiPAF project. The machining, assembly, and RF tuning of the RFQ cavity has been completed successfully. The magnetic field distribution near the outer wall is obtained by the bead-pull method. The RFQ is tuned twice to meet the requirements, pre-braze tuning and final tuning. The relative error of the operating quadrupole mode field is within ±2.7%, and the dipole mode component is within ±1.9% of the quadrupole mode. The final measured coupling coefficient of the RF power coupler equals 1.03, with the desired value of 1.04.

REFERENCES

[1] Q. Z. Xing et al., "Delopement Progress of the 7 MeV Linac Injector for the 200 MeV Synchrotron of Xi'an Proton Application Facility, in *Proc. 8th Int. Particle Accelerator Conf. (IPAC'17)*, Copenhagen, Denmark, May 2017, p. 426, doi:10.18429/JACoW -IPAC2017-TUPVA104

[2] L. M. Young, "An 8-meter-long coupled cavity RFQ linac", in Proc. 1994 International Linac Conference, Tsukuba, Japan, Aug 21-26, 1994, Paper MO52, pp. 178.

[3] M. Browman, G. Spalek, and T. Barts, "Studying the end regions of RFQs using the MAFIA codes", in Proc. 1988 Linac Conference, Virginia, USA, Oct. 3-7,1988, Paper MO3-11, pp. 64.

[4] Y. Lei et al., "Power-conditioning cavity design and measurement of the coaxial coupler for the injector of XIPAF project", in *Proc. 8th Int. Particle Accelerator Conf. (IPAC'17)*, Copenhagen, Denmark, May 2017, p. 4218, doi:10.18429/JACoW -IPAC2017-THPIK055

[5] L. Du et al., "A fast tuning method for a RFQ accelerator with ramped inter-vane voltage", Nucl. Instrum. Methods Phys. Res., Sect. A 726, 91, 2013.

ISBN: 978-3-95450-194-6 ISSN: 2226-0366 doi:10.18429/JACoW-LINAC2018-THPO066

FIRST HIGH POWER TEST OF THE ESS HIGH BETA ELLIPTICAL CAVITY

H. Li, M. Jobs, R. Santiago Kern, L. Hermansson, R. Ruber
FREIA Lab, Uppsala University, Sweden,
G. Devanz, T. Hamelin, CEA, France

Abstract

ESS, the European Spallation Source, will adopt elliptical multi-cell superconducting cavities with a beta value of 0.86 to accelerate the proton beam up to 2 GeV at the last section of the linac. A 5-cell high-beta cavity for ESS project was tested with high power at FREIA Laboratory. A pulse mode test stand based on a self-excited loop was used in this test. The qualification of the cavity package involved a 5-cell elliptical cavity, a fundamental power coupler, a cold tuning system, LLRF system and a RF station. These tests represented an important verification before the series production. This paper presents the test configuration, RF conditioning history, first high power performance and experience of this cavity package.

INTRODUCTION

The ESS elliptical SRF linac section is composed of two types of state-of-the-art 704.42 MHz cavities, medium-beta (MB) of 0.67 and high-beta (HB) of 0.86, to accelerate the proton beam from the spoke superconducting linac up to full energy [1]. A total of 84 5-cell HB elliptical cavities are designed at CEA and will be grouped by 4 in 21 cryomodules [2]. Figure 1 shows the layout of the ESS accelerator.

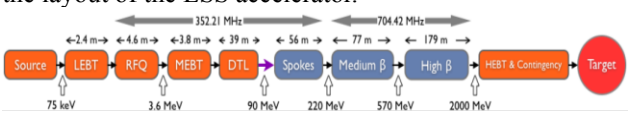


Figure 1: The layout of the ESS accelerator.

The nominal operation parameters of HB section are shown in Table 1 [3].

Table 1: Main Parameters of 5-cell HB Cavities

Frequency [MHz]	704.42
Beta_optimum	0.86
Operating gradient [MV/m]	19.9
Temperature [K]	2
G [Ohm]	241
R/Q [Ohm]	435
Lacc [m]	0.915
Bpk/Eacc [mT/MV/m]	4.3
Epk/Eacc	2.2
Qext	7.6×10^5
π and 4π/5 mode separation [MHz]	1.2

FREIA, at Uppsala University, was established in order to support the development of instrumentation and accelerator technology and started high power test of ESS double spoke cavity tests in 2015 [4, 5]. In 2018, FREIA laboratory also implemented the first high power test of overall HB elliptical cavity package. A power conditioning stand for klystron and a RF test system were commissioned in this test. An optimal procedure for both klystron and power coupler conditioning was used to reduce the time and effort of overall power conditioning. The object of this test thus became the validation of the complete chain as used in ESS: klystron, high power circulator, RF load, high power RF distribution, fundamental power coupler (FPC), HB elliptical cavity, cold tuning system (CTS) and low level RF system (LLRF).

RF CONDITIONING

The warm coupler conditioning was completed with an effective conditioning time of 20 hours and finally achieved 1 MW peak power with a standing wave regime at 14 Hz repetition rate @ 500 μs and 300 kW peak power with 14 Hz repetition rate @ 2600 μs. Lots of outgassing happened at low power with short pulses, as shown in Fig. 2 (a). At the first phase of 50 μs @ 1Hz, the first arcing occurred in the FPC at about 600 kW, afterward it was very hard to increase the RF power without severe outgassing. Half of the total warm conditioning time (10 hours) was taken to reach 1 MW and completed the first phase. Figure 2 (b) shows all following phases which went smoothly through. The conditioning procedure was finally finished by 2 hours power sweeping from 15 kW to 300 kW with 2.6 ms and 14 Hz repetition rate. The choice of pulse duration is limited by the capacity of the modulator prototype. In order to condition and sweep as much area as possible in the FPC, the cold conditioning of the FPC was carried out by the same system but at two different frequencies, with one slightly higher and one slightly lower than the cavity resonant frequency. Each frequency was about 100 kHz away from the cavity resonant frequency of 704.08 MHz at 2K (with free end), in order to make sure there was no RF coupled in to build a field in the cavity.

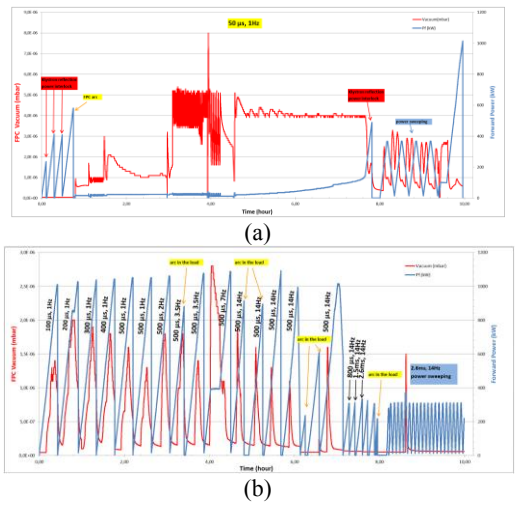
Compared to the FPC conditioning, the RF conditioning of the cavity with its power coupler, so-called cavity package, is done by a self-excited loop (SEl) at resonant frequency. Since the tuner feedback controller is still under development, SEL naturally becomes a substitute for following the cavity resonant frequency without feedback. In order to produce pulses in the SEL, a RF switch controlled by a programmable trigger signal is introduced. In the vertical test, this cavity showed high performance but unfortunately quenched at 18 MV/m,

Content from this work may be used under the terms of the CC BY 3.0 licence (© 2018). Any distribution of this work must maintain attribution to the author(s), title of the work, publisher, and DOI.

ISBN: 978-3-95450-194-6 ISSN: 2226-0366 doi:10.18429/JACoW-LINAC2018-THPO066

Content from this work may be used under the terms of the CC BY 3.0 licence (© 2018). Any distribution of this work must maintain attribution to the author(s), title of the work, publisher, and DOI.

therefore the test range at high power was first limited up to 15 MV/m [6]. A soft multipacting barrier from 9 to 12 MV/m was encountered and successfully processed. After about 3 hours of conditioning, the cavity package reached and was stably kept at 15 MV/m flattop accelerating gradient.



(a)

(b)

Figure 2: (a) HB cavity RF conditioning history with 50 μs and 1 Hz repetition rate; (b) HB cavity RF conditioning history with longer pulse duration at different repetition rate, where the blue curve represents the RF power and the red one represents the coupler vacuum.

HIGH POWER PERFORMANCE

The Q factor measurement of the cavity package is based on the self-exited loop at FREIA. The cavity was operated at a pulse mode of 2.55 ms duration and 14 Hz repetition rate. With a peak power less than 200 kW, a field with a flattop gradient up to 16 MV/m was successfully reached. The preliminary result of the quality factor of the cavity package vs. gradient is shown in Fig. 3.

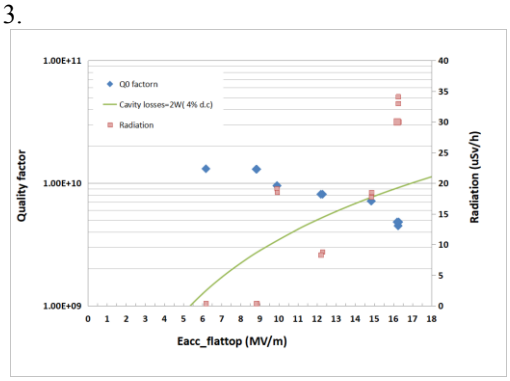


Figure 3: HB cavity package performance as a function of accelerating gradient.

The HB cavity package gives a Q factor of 1.3×10^{10} at low field and 7.1×10^{9} at 15 MV/m. X-ray radiation was start from 10 MV/m, which implied field emission in the cavity package. After 30 minutes conditioning, the cavity performance has unfortunately no significant improved.

The average cavity package dissipated power at 15 MV/m is about 2 W with 2.55 ms pulse. To assured the measurement accuracy, the dynamic heat load was recorded from 0.2 W and above. Two different methods of dynamic heat load measurements have been used in order to cross check the system performance. For the first method, the helium inlet to the 2K tank was kept closed when applying RF power to the cavity. An absolute heat load of the whole cavity package was calculated from the helium gas flow at atmospheric pressure and room temperature. The second method comprises a higher accuracy heat load measurement based on pressure rise. The helium level in the 2K tank was kept between 76% and 78% during the whole test. A known amount of resistive heat was applied to the helium bath. Once the system was stabilized both inlet and outlet valves of the cryostat were closed and the pressure rise as a function of time was recorded for 1 minute. These values were then part of the heat load calibration curve. Finally, RF power was loaded in the cavity and the dynamic load was calculated by comparing with the calibration curve.

Nonpropagating Longitudinal Modes

For a multi-cell cavity, monitoring the longitudinal modes of the first passband is usually adopted as an effective way of checking the cavity condition during transportation and cool down procedures. Longitudinal modes of the first passband of the ESS HB cavity were studied at different temperatures and the characteristics of 5 modes are listed in Table 2. The measurement result shows that the relative frequency distance between different modes has been kept the same, which implies that no unexpected issue has happened during cool down. On the other hand, the frequency distance between π mode and 4π/5 mode is bigger than1.2 MHz, which fulfills the ESS requirement.

Table 2: The Characteristics of 5 Modes of First Passband

Parameters	T emperature		
	300 K	4 K	2 K
π mode	702.991	704.120	704.081
4π/5 mode	701.761	702.889	702.848
3π/5mode	698.464	699.592	699.551
2π/5 mode	694.370	695.494	695.454
π/5 mode	691.104	692.22	692.187

Lorentz Force Detuning

For a pulsed accelerator such as ESS, the dynamic Lorentz force detuning (LFD) caused by the deformation of the cavity wall with an accelerating electromagnetic field leads to beam instability. By monitoring and manipulating the complex signal from the cavity during the pulse, LFD at different accelerating gradients have been studied by using a FPGA-based LabView program at FREIA. The forward pulses with step pulse profile were used, as shown in the top graph of Fig. 4, RF power 6 dB higher than the flattop was applied during the filling time.

ISBN: 978-3-95450-194-6 ISSN: 2226-0366 doi:10.18429/JACoW-LINAC2018-THPO066

The LFD experimental result of 15 MV/m, shown in the bottom picture of Fig. 4, suggests that there is around 220 Hz frequency shift with 2.55 ms pulse length. Please note that the cavity was restricted by the stepper motor during the test. The LFD coefficient is therefore about -1 Hz/(MV/m)^2 with tuner contacted condition , which is in agreement with the simulation [3]. For a nominal accelerating gradient of 19.9 MV/m, the shift will be 1/3 of the cavity bandwidth. The fast frequency compensation with piezo tuners has been successfully tried with the above pulse settings and an optimal piezo operation is under study.

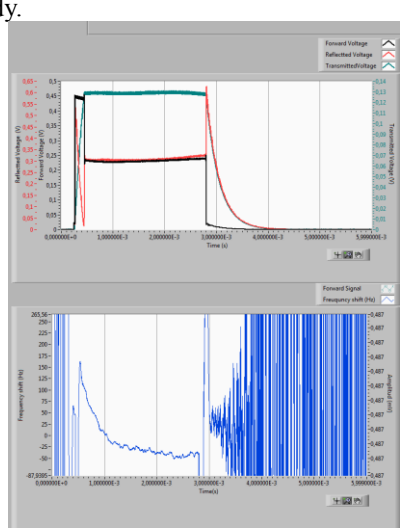


Figure 4: Top: Forward (black), reflected (red) and transmitted (green) signal during 2.55 ms pulses. Bottom:Dynamic Lorentz detuning of ESS HB elliptical cavity at 15 MV/m.

Pressure Sensitivity

Helium pressure fluctuations inside the tank detune the cavity resonance frequency. During cool down from 4 K to 2 K, the frequency sensitivity as a function of the helium pressure has been carried out from 50 to 800 mbar. As shown in Fig. 5, a pressure sensitivity of +37 Hz/mbar is measured.

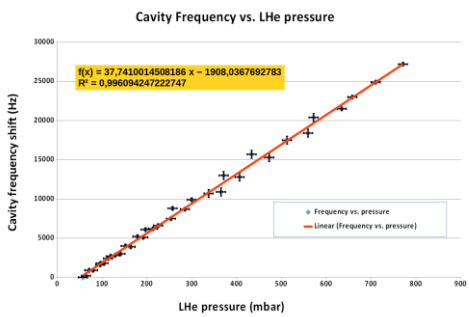


Figure 5: Cavity frequency shift as a function of helium pressure from 50 to 800 mbar.

Tuning Sensitivity

The cold tuning system is attached to the HB cavity to adjust its resonant frequency in order to counteract the frequency detuning. The HB CTS integrates two different functions: a slow tuning capability over a wide frequency range by using a stepper motor and a fast tuning system by means of piezoelectric actuators inserted in the mechanical system of the CTS. The behavior of the slow tuning system was studied at 2 K at FREIA, as shown in Fig. 6. A tuning sensitivity of 17.3 KHz/motor turn, corresponding to 173 kHz/mm, was found. Here the distance is defined as the longitudinal deformation of the cavity.

Several tuning runs were repeated back and forth around the resonant frequency in order to check the linearity of the CTS and a well agreement of tuning sensitivity was determined.

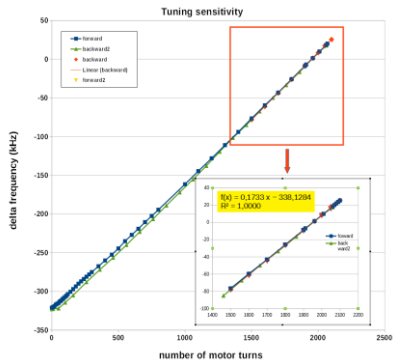


Figure 6: Tuning sensitivity of ESS HB elliptical cavity.

CONCLUSION

The first ESS HB elliptical cavity assembled with all ancillary components was installed in the HNOSS cryostat and successfully completed the high power test based on self-exited loop at FREIA. This qualification of the cavity package represents a milestone before the module assembly.

The longitudinal modes of the first passband were monitored at different temperature. Same frequency difference with neighboring modes confirmed that this cavity was well kept during installation and test procedure. This cavity was operated at the pulse mode of 2.55 ms duration and 14 Hz repetition rate. A Q factor of 1.3×10^{10} at low field and 7.1×10^{9} at 15 MV/m was determined. The dynamic Lorentz detuning was studied by a signal generator driven system with step forward pulse, LFD coefficient of -1 Hz/(MV/m)^2 is measured. The study of fast detuning compensation is undergoing. Furthermore, this cavity was found to have a pressure sensitivity of +37 Hz/mbar and a tuning sensitivity of 173 kHz/mm.

ACKNOWLEDGMENT

This project has received funding from the European Union's Horizon 2020 Research and Innovation programme under Grant Agreement No 730871. The authors wish to thank our collaborators from CEA who help us with the installation and testing and helpful discussions with ESS experts. Also many thanks to all colleagues of FREIA for their hard work on the cavity tests.

Content from this work may be used under the terms of the CC BY 3.0 licence (© 2018). Any distribution of this work must maintain attribution to the author(s), title of the work, publisher, and DOI.

ISBN: 978-3-95450-194-6 ISSN: 2226-0366 doi:10.18429/JACoW-LINAC2018-THPO066

Content from this work may be used under the terms of the CC BY 3.0 licence (© 2018). Any distribution of this work must maintain attribution to the author(s), title of the work, publisher, and DOI.

REFERENCES

[1] ESS Technical Design Report, (2013); https://europeanspallationsource.se/accelerator-documents

[2] G. Devanz *et al.*, "ESS Elliptical Cavities and Cryomodules", in *Proc. SRF'13*, Paris, France, Sep. 2013, paper FRIOC02.

[3] G. Devanz *et al.*, "Conceptual Design of the beta = 0.86 cavities for the superconducting Linac of ESS", in *Proc. 15th Int. Conf. RF Superconductivity (SRF'11)*, Chicago, IL, USA, Jul. 2011, paper MOPO041.

[4] M. Olvegård et al., "Progress at the FREIA Laboratory", in *Proc. 6th Int. Particle Accelerator Conf. (IPAC'15)*, Richmond, VA, USA, May 2015, pp. 3072-3075, doi:10.18429/JACoW-IPAC2015-WEPMN065

[5] H. Li, A.K. Bhattacharyya, L. Hermansson, M. Jobs, R.J.M.Y. Ruber, and R. Santiago Kern, "High Power Testing of the First ESS SPOKE Cavity Package", in *Proc. 18th Int. Conf. on RF Superconductivity (SRF'17)*, Lanzhou, China, July 2017, pp. 817-820. doi:10.18429/JACoW-SRF2017-THPB035

[6] F. Peauger, C. Arcambal, S. Berry, N. Berton, P. Bosland, E. Cenni, *et al.*, "Progress in the Elliptical Cavities and Cryomodule Demonstrators for the ESS LINAC", in *Proc. 17th International Conference on RF Superconductivity*, Whistler, BC, Canada, 13-18, 2015, paper TUPB007, pp. 544-548. doi:10.18429/JACoW-SRF2015-TUPB007

ISBN: 978-3-95450-194-6 ISSN: 2226-0366 doi:10.18429/JACoW-LINAC2018-THPO067

CONTROL SYSTEM AND EXPERIMENT FOR RAON HWR CRYOMODULES*

Heetae Kim†, Moo Sang Kim, Min Ki Lee, Yong Woo Jo, Jong Wan Choi, Youngkwon Kim, Juwan Kim, Sangbeen Lee, Yoochul Jung, Kitaek Son, Doyoon Lee, Ohryong Choi, Kyungtae Seol, Hyojae Jang and Hoechun Jung
Rare Isotope Science Project, Institute for Basic Science, Daejeon 34047, Republic of Korea

Abstract

A prototype of half-wave resonator (HWR) cryomodules is fabricated and tested. Cables and tray are installed for horizontal test. The design and the piping and instrumentation diagram (P&ID) of the HWR cryomodule are presented. The HWR cryomodule is tested with developed programmable logic controller (PLC) and experimental physics and industrial control system (EPICS) control systems. The heat loads of the HWR cryomodule for static and dynamic are measured.

INTRODUCTION

Cryogenic system is required to construct a linear accelerator when superconducting cavities are used to accelerate ion beams. The coolants of cryogenic systems are liquid helium, supercritical helium, liquid nitrogen, etc.

The Stefan-Boltzmann constant for n-dimensional blackbody radiation [1] and the size effect of thermal radiation were studied [2]. The effective temperature was investigated for non-uniform temperature distribution [3, 4]. RAON accelerator system was designed [5], QWR and HWR cryomodules were developed [6] and superconducting radio frequency (SRF) test facility was constructed [7]. The SRF test facility consists of cleanroom, cryogenic system, vertical test site and horizontal test site. Cavity processes and cavity assembles are performed in the cleanroom. Temperature measurement techniques was introduced for RAON cryomodules [8] and RF power couplers for half wave resonator (HWR) were designed [9]. In this research we design, fabricate and test a HWR cryomodule with developed PLC control system. Tray and cable information are shown for horizontal test. Design, feedthrough and radio frequency (RF) amplifier information are presented for the HWR cryomodule. The HWR cryomodule is tested, so static and the dynamic heat loads of the cryomodule are measured.

TRAY AND CABLE INSTALLATION

In order to perform the horizontal test, we develop the programmable logic controller (PLC) for cryomodules. To operate the PLC, tray and cables are installed in the horizontal test site. Figure 1 shows the pictures of tray and cables for the horizontal test. The PLC racks are located outside of the horizontal test bunker. All of the cables are connected with the PLC and the cables come to the local box as shown in Figure 1(c). Cables come out of the local box and are connected to the feedthroughs of cryomodules with connectors. The bunker consists of tray, local box, cables with connectors, compressed air distributors, RF power lines and helium transfer lines.

The cable of 1.5SQ is used for the power line of turbo pumps, dry pumps and heaters. Solenoid valves are used with 20AWG shielded pair cable. 22AWG shielded pair cable is used for gate valves, vacuum gauges, turbo pumps, dry pumps, control valves, temperature sensors and liquid helium level sensors. The connectors of 32 PIN are used for temperature sensors and the connectors of 10 PIN are used for heaters, pressure gauges and level sensors. Specific plastic connectors are used for pumps, display control units (DCUs), gate valves, vacuum valves, vacuum gauges, heaters, etc. The display control unit (DCU) is a universal operating unit for the monitoring and control the Pfeiffer turbo pumps.

Tray sizes are 300X100 (mm^2) and 500X100 (mm^2) which depend on the number of cables.

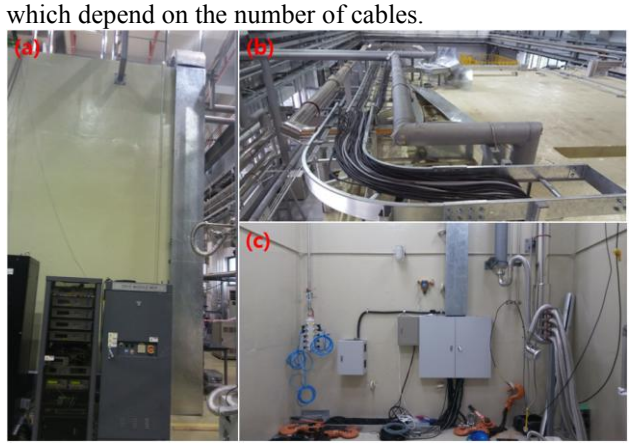


Figure 1: Pictures of tray and cables for horizontal test. (a) PLC rack and tray, (b) cables in tray on the roof of the horizontal test bunkers and (c) cables with connectors, tray, local box, compressed air distributors, RF power lines and helium transfer lines inside of the bunker.

HWR CRYOMODULE

A prototype of a HWR cryomodule is designed. Figure 2 represents the design of the HWR cryomodule. The HWR cryomodule consists of two liquid helium reservoirs, two cavities, two couplers, two tuners, thermal shield, magnetic shield, etc. The operation frequency and temperature of the HWR cryomodule at RAON accelerator

* Work supported by by the Rare Isotope Science Project of Institute for Basic Science funded by the Ministry of Science, ICT and Future Planning (MSIP) and by the National Research Foundation (NRF) of the Republic of Korea under Contract 2013M7A1A1075764. …
† kimht7@ibs.re.kr

Content from this work may be used under the terms of the CC BY 3.0 licence (© 2018). Any distribution of this work must maintain attribution to the author(s), title of the work, publisher, and DOI.

ISBN: 978-3-95450-194-6 ISSN: 2226-0366 doi:10.18429/JACoW-LINAC2018-THPO067

Content from this work may be used under the terms of the CC BY 3.0 licence (© 2018). Any distribution of this work must maintain attribution to the author(s), title of the work, publisher, and DOI.

site are 162.5 MHz and 2.05 K, respectively. Temperature sensors such as Cernox-1050 are calibrated in the temperature range between 1.9 K and 325 K with physical property measurement system (PPMS) [8]. The calibration

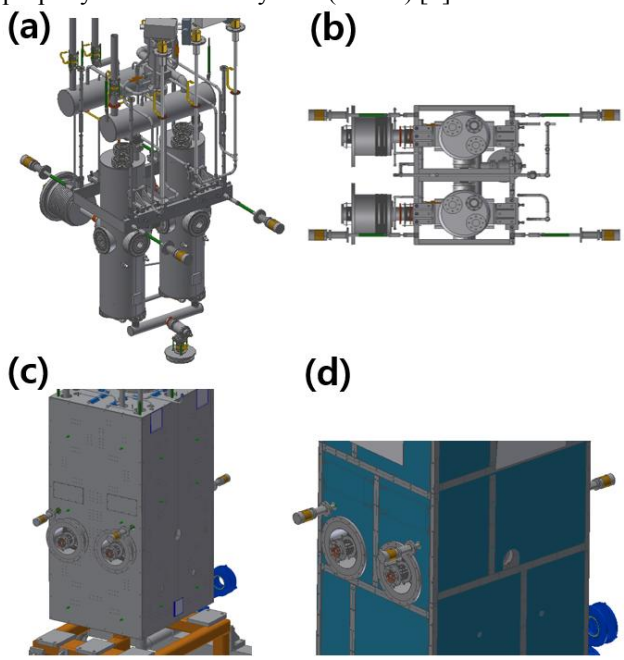


Figure 2: Design of a HWR cryomodule. (a) Liquid helium reservoirs, cavities and couplers, (b) top view of cavities, (c) thermal shield and (d) magnetic shield.

data which represents resistance as a function of temperature is saved as 340 files for each temperature sensor. The calibrated data of the 340 files are uploaded to Lake Shore Model 224 temperature monitors using Lake Shore Curve Handler. The calibrated cernox sensors and Pt100 temperature sensors are attached on the cryomodule to monitor temperature.

Feedthrough connectors of 32 Pin are used for temperature sensors and tuners. Feedthrough connectors of 10 Pin are used for liquid helium level monitors, heaters, pressure gauges and solenoid valves. Special connectors are used for cryogenic valves, turbo pumps, dry pumps, gate valves, vacuum valves and vacuum gauges.

HORIZONTAL TEST

The PLC program for HWR cryomodules are developed with compact logix PLC and studio 5000 software of rockwell automation. Allen bradley PLC controls pumps, heaters and valves. The PLC communicates with temperature monitors through Ethernet cable. The EPICS is developed from the PV lists of the PLC program. The PLC and EPICS control or monitor pumps, heaters, cryogenic valves, solenoid valves, liquid helium levels, temperature sensors, the vacuum pressures of cavity and vessel and the vapor pressures of helium reservoirs through switching hub.

The HWR cryomodule is installed at the bunker after the fabrication of the cryomodule and the cavities are assembled to the cryomodule in cleanroom with top-down assembly. Magnetic field strength inside of the cryomodule is measured to be below 15 mG. Figure 3 represents the HWR cryomodule installed in the horizontal test facility and the P&ID for the HWR cryomodule. The P&ID of the

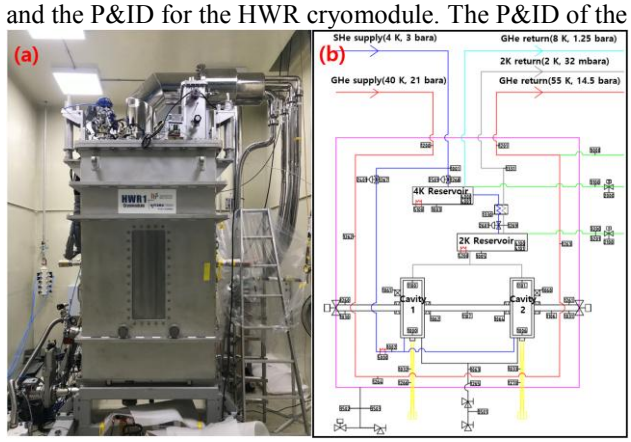


Figure 3: Picture of (a) the HWR cryomodule in horizontal test facility and (b) the P&ID for the HWR cryomodule.

HWR cryomodule is for RAON linear accelerator site. The prototype of the HWR cryomodule is tested at SRF test facility, so liquid nitrogen is used instead of helium gas and liquid helium is used instead of supercritical helium. The cables from the local box in the bunker are connected to the feedthroughs and special plastic connectors of the cryomodule. Compressed air pressure which keeps up to 7 bars in the bunker are needed to control gate valves, vacuum valves and cryogenic valves. The gate valves and vacuum valves work around 7 bars and the cryogenic valves work around 4 bars. Cylindrical type of compressed nitrogen gas is used to control vacuum valves when the compressed air pressure is lower than about 6 bars. Vacuum valves are not closed completely when the compressed air pressure is lower than the recommended pressure. The helium transfer line adaptor of the HWR cryomodule is connected with transfer lines which include helium inlet, helium outlet, nitrogen inlet, nitrogen outlet and 2K outlet.

The solid state power amplifier (SSPA) for the HWR cryomodule and the connection of a coaxial line to a power coupler are shown in Figure 4. The solid state power amplifier (SSPA) has the drive frequency of 162.5 MHz, continuous-wave (CW) operating mode and the maximum power of 7 kW. The efficiency of the SSPA is higher than 50%. Radio frequency (RF) power is transferred to the power coupler of the HWR cavity through the coaxial line. The power coupler can be biased up to 1 KV.

The cavities and vessel of the cryomodule are evacuated by using dry pumps and turbo pumps. Leak test is performed for cavity, vessel, helium transfer lines and thermal shield lines in the cryomodule. To do leak test for the helium transfer line, the helium leak rate is monitored from the vessel while helium gas is supplied to the helium transfer lines while three cryogenic valves are opened. To do leak test for the thermal shield, the helium leak rate is monitored from the vessel while helium gas is supplied to the thermal shield transfer lines.

ISBN: 978-3-95450-194-6 ISSN: 2226-0366 doi:10.18429/JACoW-LINAC2018-THPO067

Coupler radio frequency (RF) conditioning is performed for about 8 hours with 400 V DC bias at room temperature. In order to cool down the cryomodule, liquid nitrogen is supplied to the thermal shield and then liquid helium is supplied to the helium reservoirs. The initial liquid helium path to cool down the cryomodule is from helium inlet to 4 K reservoir, 2 K reservoir and then helium outlet. By

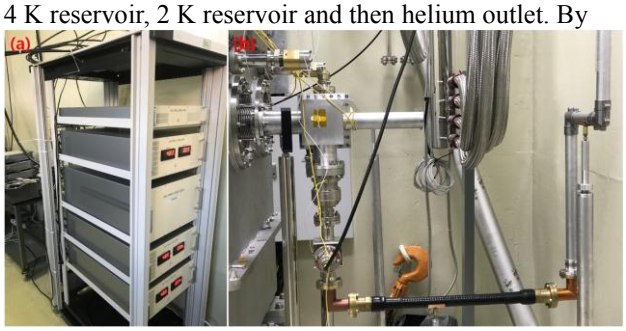


Figure 4: RF test of a HWR cryomodule. (a) SSPA and (b) the connection of a coaxial line to a power coupler in the cryomodule.

opening fast cooldown cryogenic valve, we can supply liquid helium to the bottom of cavities and then the liquid helium goes to 2 K reservoir, after that, the liquid helium goes out to 2 K outlet. Best superconducting niobium cavity requires the clean surface which does not have damages, dust particles and hydrides. Chemical etching and high pressure rising are performed for the cavities before cavities are installed to the cryomodule. Fast

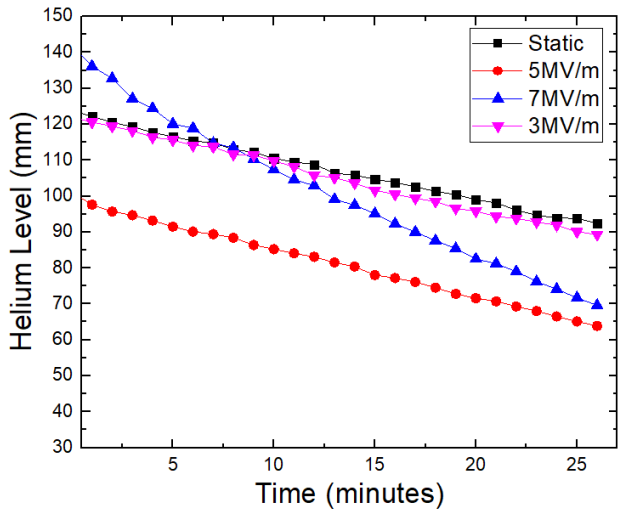


Figure 5: Static and dynamic heat load measurement for a HWR cryomodule at 2.1 K. The static heat load is 6.6 W. The total heat loads for 3 MV/m, 5 MV/m and 7 MV/m are 7.0 W, 8.7 W and 14.5 W, respectively.

cooldown is known to help to prevent Q disease coming from hydrides formation, so we perform fast cooldown. We supply liquid helium with high flow rate to cavities when the temperature of the cavities is decreased from 150 K to 50 K. The fast cooldown time is below 40 minutes in the temperature range between 150 K and 50 K. Cavity RF conditioning is performed for about 24 hours at 4.3 K once liquid helium level is increased at two helium reservoirs.

After finishing RF conditioning for two cavities, the cryomodule is cooled down to 2.1 K. In order to measure dynamic heat loads, we let the level of 4 K reservoir and 2 K reservoirs rise while RF power is supplied to one of the cavities. The cryogenic valve for the 2 K reservoir is closed and the liquid helium level of the 2 K reservoir is decreased as times goes. Here, the liquid helium level of the 2 K reservoir is measured as a function of time. The temperature of the cavity is kept by controlling the valve of 2 K pumps. The temperature of the cavity corresponds to the vapor pressure of 2 K reservoir. The dynamic heat loads are measured by considering the evaporation rate of the liquid helium in 2 K reservoir. The static heat load is measured without RF power. Figure 5 shows the static and dynamic heat load measurement for the HWR cryomodule at 2.1 K. The measurement time for each experiment is about 30 minutes. The static heat load is 6.6 W. The total heat loads for 3 MV/m, 5 MV/m and 7 MV/m are 7.0 W, 8.7 W and 14.5 W, respectively.

After finishing experiment, warm-up process is started. We close the valve of 2 K pump and stop liquid helium and liquid nitrogen supply. Pumps to make 2 K are stopped. During warm-up process, the liquid helium in reservoirs and cavities evaporates rapidly above 4.5 K. Therefore, we make the evaporated helium go out to either helium outlet or 2 K outlet while the cryogenic valves are opened.

SUMMARY

We have designed, fabricated and tested the prototype of the HWR cryomodule. Tray and cables are installed for horizontal test. The 3D drawing and P&ID of the HWR cryomodule are shown and the utility information for the horizontal test at the bunker is also shown. Feedthrough information are shown for temperature sensors, tuners, level monitors, heaters, pressure gauges and solenoid valves. The PLC and EPICS for the cryomodule are developed to operate the cryomodule. The experimental procedure for the horizontal test is introduced. The static and dynamic heat loads of the HWR cryomodule are measured.

REFERENCES

[1] P.T. Landsberg and A. De Vos, “The Stefan-Boltzmann constant in n-dimensional space”, *Journal of Physics A: Mathematical and General*, vol. 22, p.1073, 1989.

[2] Soon-Jae Yu, Suk Joo Youn, and Heetae Kim, “Size effect of thermal radiation”, *Physica B*, vol. 405, p.638, 2010.

[3] Heetae Kim, Myung-Soo Han, David Perello, and Minhee Yun, “Effective temperature of thermal radiation from non-uniform temperature distributions and nanoparticles”, *Infrared Physics & Technology*, vol. 60, p. 7, 2013.

[4] Heetae Kim, Chang-Soo Park, and Myung-Soo Han, “Effective temperature of two-dimensional material for non-uniform temperature distribution”, *Optics Communications*, vol. 325, p. 68, 2014.

[5] D. Jeon *et al.*, “Design of the RAON accelerator systems”, *Journal of the Korean Physical Society*, vol. 65, p. 1010, 2014.

Content from this work may be used under the terms of the CC BY 3.0 licence (© 2018). Any distribution of this work must maintain attribution to the author(s), title of the work, publisher, and DOI.

ISBN: 978-3-95450-194-6 ISSN: 2226-0366 doi:10.18429/JACoW-LINAC2018-THPO067

[6] Woo Kang Kim, Heetae Kim, Hyung Jin Kim, Youngkwon Kim, Min Ki Lee, and Gunn-Tae Park, "Design and Assembly of the QWR and the HWR Cryomodules", *Journal of the Korean Physical Society*, vol. 67, p. 1287, 2015.

[7] Wookang Kim, Mijoung Joung, Yoochul Jung, Heetae Kim, Jongwon Kim, Youngkwon Kim, and Ilkyoung Shin, "Fabrication and Low Temperature Test Plan for Rare Isotope Science Project", in *Proc. LINAC'16*, East Lansing, MI, USA, Sep. 2016, pp. 585-587, doi:10.18429/JACoW-LINAC16- TUPLR072

[8] Heetae Kim, Yoochul Jung, Yong Woo Jo, Min Ki Lee, Jong Wan Choi, Youngkwon Kim, Juwan Kim, Won-Gi Paeng, Moo Sang Kim, Hoechun Jung, and Young Kwan Kwon, "Temperature Measurement Techniques for RAON Cryomodule", *Applied Science and Convergence Technology*, vol. 27, p. 30, 2018.

[9] Sangbeen Lee, Eun-San Kim, and Ilkyoung Shin, "Design of RF Power Coupler for RISP Half Wave Resonator", in *Proc. IPAC'16*, Busan, Korea, May 2016, pp. 2208-2210, doi:10.18429/JACoW-IPAC2016- WEPMB041

Content from this work may be used under the terms of the CC BY 3.0 licence (© 2018). Any distribution of this work must maintain attribution to the author(s), title of the work, publisher, and DOI.

ISBN: 978-3-95450-194-6 ISSN: 2226-0366 doi:10.18429/JACoW-LINAC2018-THPO068

AN EFFECT OF FIELD EMISSION ON LOW BETA SUPERCONDUCTING CAVITIES*

Xinmeng Liu†, Yuan He , Guirong Huang,Zheng Gao
Institute of Modern Physics, Chinese Academy of Sciences 730000, Lanzhou, China

Abstract

Superconducting RF (SRF) technology is widely applied in particle accelerators to shorten the accelerator length and lower the construction price due to its high acceleration gradients with low rf losses. Field emission is the chief limitation associated with the surface electric field which will finally determine the cavity performance during the operation. The pickup-drop signal caused by field emission seriously affect the stable operation of the superconducting linac in the Chinese initiative Accelerator-Driven Sub-critical System (CiADS) demon facility. Simulations of the field emission effect and experimental measurements of the pickup-drop signal have been performed on the half wavelength resonator (HWR) cavity. And a modified design of the pickup antenna will be discussed to solve the pickup-drop problem.

INTRODUCTION

The Chinese initiative Accelerator Driven Sub-critical System (CiADS) project is based on a 10 mA, 1.5 GeV CW proton linac for nuclear waste transmutation. CiADS project needs a high stability linac to demonstrate the technology of 10 mA CW beam of superconducting front-end linac for ADS technology. The first cryo-module of this demon SRF linac includes six 162.5 MHz HWR010 cavities working at 4K with optimum beta equal to 0.1.

In one of coulping ports of the cavity, a power transmission antenna rooted in a RF ceramic window to pick up the RF field power. We measured the pickup-drop signal of HWR010 PT and showed in Fig. 1. The frequently deviant signal result to the irregular responses of LLRF control system and limit the stable operation of the SRF linac.

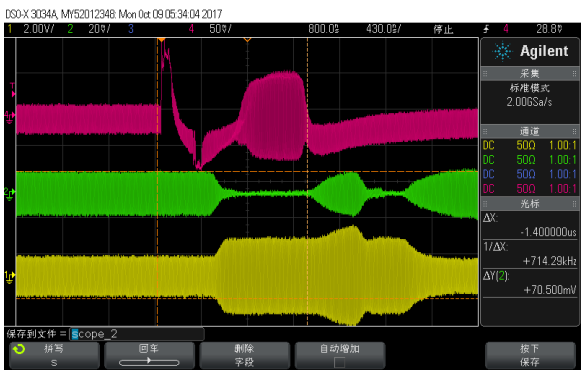


Figure 1: The signal with pickup-drop on oscilloscope.

In Fig. 1, the pink signal is pick up power (Pt) from cavity, the green one is forward RF power (Pf) and the yellow one is reflected RF power (Pr). The pick up signal shows that there is discharge happened on the surface of RF ceramic window , which is called flashover[1]. What's behind it is should be the effect of continuous field emission electron beam hit on the surface of ceramic window[2].

SIMULATION OF FE PARTICAL

This simulation was performed in CST Microwave Studio. The simulation results of electromagnetic field of the cavity is showed in Fig. 2 and Fig. 3.

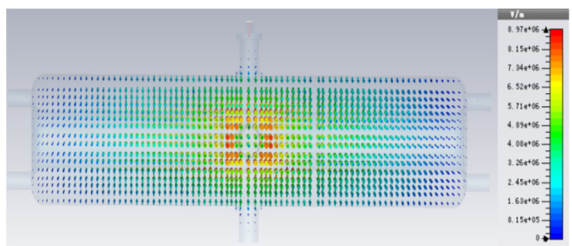


Figure 2: The electric field in HWR010 SRF cavities.

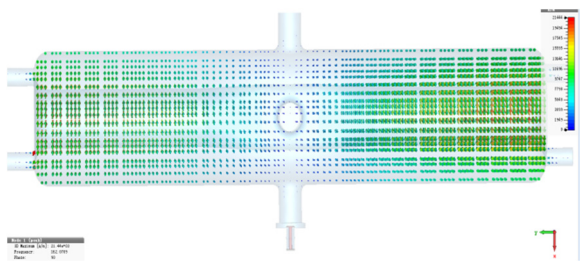


Figure 3: The magnetic field in HWR010 SRF cavities.

The electric field is strongest in the middle of the cavity and is weakest at the ends. The magnetic field is weakest in the middle and strongest at the ends. FE particles were attached to the cavity surface with the high electric field area.

The particles movement in electromagnetic field shows in Fig. 4. From Fig. 4, The particles movements straightly alone the electric field line for the movements were dominated by the electric field, and the weak magnetic field has little effect on their direction of motions. These particles will finally hit on the PT antenna and ceramic window, as shown in Fig. 4 (d). Electrons constantly accumulated on the surface of ceramic window due to the electric property of ceramics, flashover happened when the accumulation to the limit.

* This work was supported by National Natural Science Foundation for Young Scientists of China (Grant NO. 11505255)
† liuinmeng@impcas.ac.cn

Content from this work may be used under the terms of the CC BY 3.0 licence (© 2018). Any distribution of this work must maintain attribution to the author(s), title of the work, publisher, and DOI.

ISBN: 978-3-95450-194-6 ISSN: 2226-0366 doi:10.18429/JACoW-LINAC2018-THPO068

Content from this work may be used under the terms of the CC BY 3.0 licence (© 2018). Any distribution of this work must maintain attribution to the author(s), title of the work, publisher, and DOI.

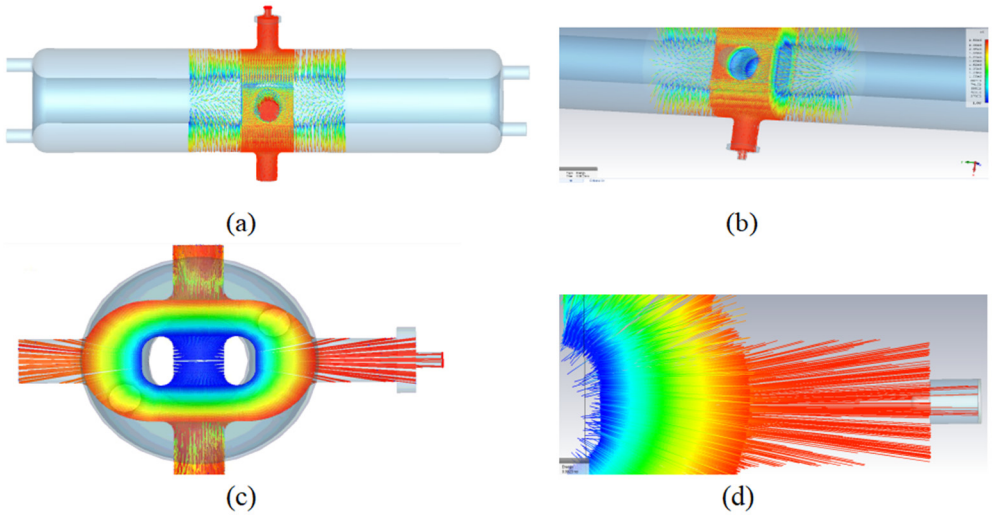


Figure 4: The FE particles trajectory simulation of HWR.

EXPERIMENT IN SRF ACCELERATOR

As mentioned above, one of the reasons affect the operation stability of our linac is the pick-up-drop signal of the HWR010 cavities. In order to further understand the physics between the phenomena, therefore, we set up a 162.5M digital LLRF control system to monitor the pick-up-drop signal by the apparatus as shown in Fig. 5. Figure 6 shows the frequency of the pickup-drop signal at different accelerating gradient, the interval of each pickup-drop decreases as the increase in accelerating gradient. Figure 6 also displays the radiation dose caused by bremsstrahlung effect increases exponentially with the accelerating gradient, which indicates that the field emission effect inside the cavity is much stronger at high accelerating gradient, and it agrees with the F-N theory [3]. Therefore, the frequency of pickup-drop is proportional to field emission.

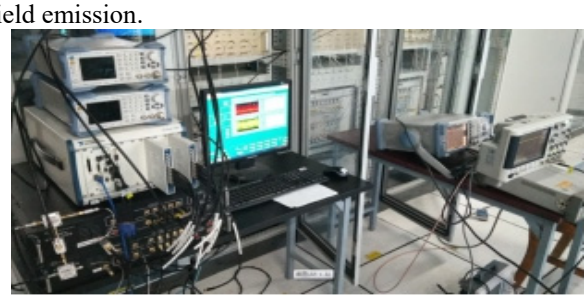


Figure 5: Monitoring system.

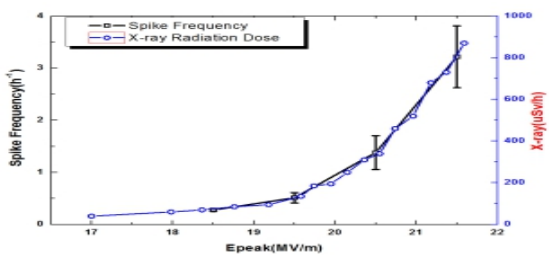


Figure 6: The frequency of pickup-drop and radiation dose are proportional to gradient.

SOLUTIONS

In light of above analyses, in order to solve the problem, it is essential to avoid the FE electron impact the ceramic window of pick-up coupler. Two types of pick-up coupler were designed with the Qe of about 5E11. One is an electrical coupler, whose antenna was designed with a cap on its top to absorb the FE electrons and guide them away through cable, at the same time the cap of the antenna covers the ceramic window at the bottom to avoid the impact of FE electrons (see Fig. 7).



Figure 7: A modified design of electrically coupled antenna.

The other type of the pick-up coupler will be set at the end of the cavity with strong magnetic field and weak electric field. The electric field in this region is too weak to support FE effect act. As the magnetic field is strong in this region, the pickup antenna is designed a magnetic coupled loop made by niobium (see Fig. 8).

ISBN: 978-3-95450-194-6 ISSN: 2226-0366 doi:10.18429/JACoW-LINAC2018-THPO068

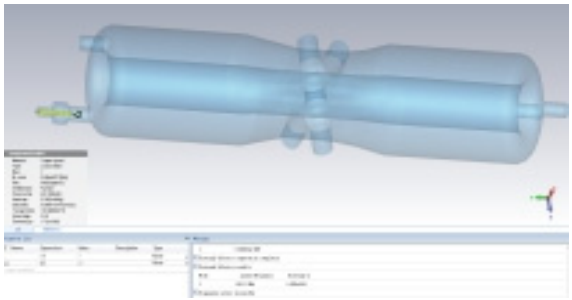


Figure 8: A modified design of magnetic coupled antenna.

CONCLUSION

The frequently pickup-drop on PT signal is one of the rea-sons to interfere the LLRF control system and the stable operation of the SRF Linac. From all the results, it can be con cluded that the pickup-drop signal are caused by the flashover on ceramic window and field emission (FE) should be the source of origin. To solve this problem, two modified designs of transmitted power had be presented, and they will be validate in our following experiments.

ACKNOWLEDGMENT

This work was supported by the SRF group and the LLRF group of Linear Accelerator Center at IMP.

REFERENCES

[1] G. Blaise, C. Le Gressus, Charging and flashover induced by surface polarization relaxation process, *Journal of Applied Physics* 69, 6334 (1991); doi: 10.1063/1.348832,

[2] R. L. Geng, "Field emission in SRF accelerators: instrumented measurements for its understanding and mitigation", *in Proc. IBIC2017*, Grand Rapids, USA,2017, pp.470-477.

[3] H. Padamsee, J. Knobloch, T. Hays, "RF Superconductivity for Accelerators", JohnWiley & Sons, New York, 1998, pp. 3–4.

Content from this work may be used under the terms of the CC BY 3.0 licence (© 2018). Any distribution of this work must maintain attribution to the author(s), title of the work, publisher, and DOI.

ISBN: 978-3-95450-194-6 ISSN: 2226-0366 doi:10.18429/JACoW-LINAC2018-THPO069

THE DEVELOPMENT OF TE-SAMPLE HOST CAVITY AT IMP*

Shichun Huang†, Yuan He, T. Tan, shengxue Zhang, Institute of Modern Physics, Chinese Academy of Sciences, 73000 Lanzhou, China

Abstract

As a part of the research and development work of thin-film materials for superconducting radio frequency(SRF) application in future accelerator projects at Institute of Modern Physics, CAS, such as Heavy Ion Accelerator Facility(HIAF) and the SRF proton Linac for Chinese Accelerator Driven System etc., a 3.9GHz sample host cavity is being developed for the purpose of characterizing the RF property and the loss mechanism of the superconducting thin-film materials (e.g., Nb/Cu, Nb3Sn and MgB2 etc.). The cavity operates in the TE011 mode and accommodates disk sample with 110mm diameter, theoretically, the maximum magnetic field on sample surface can go up to 100mT, the resolution of surface resistance on sample can reach nOhm scale by using thermometry technique(T-Mapping). In this paper, the electromagnetic optimization result of TE-sample host cavity will be presented, and the design consideration of coupler and T-mapping system are also discussed.

INTRODUCTION

SRF technology has long been adopted in many particle accelerators world-wide in the past, such as Continuous Electron Beam Accelerator Facility(CEBAF) at Jefferson Lab and Spallation Neutron Source(SNS) at Oak Ridge National Lab, will be also used in future accelerator projects, such as FRIB at MSU, LCLS-II at SLAC, ESS and XFEL in Europe, Heavy Ion Accelerator Facility (HIAF) and the proton Linac for Chinese Accelerator Driven System at IMP, CAS, Light Source at IHEP, CAS, FEL at SINAP, CAS etc.. The key components in SRF accelerators are SRF cavities, which have been routinely fabricated by Niobium material. The performance of SRF cavity made out of niobium is mainly determined by the superheating magnetic field Hsh of niobium material (Hsh~=240mT (T=0K)). After more than half a century development in SRF science and technology (the optimization of cavity structure and the advance in cavity surface processing techniques etc.) [1]. For the high beta cavities (beta=v/c, v: the velocity of beam, c: the speed of light), its performance is approaching its material limit (Corresponding accelerating gradient Eacc~=60MV/m) [2]. However, the performance of low beta (0.01-0.3) cavities is still below its material limit, which is mainly determined by electron-loading effect inside the cavities (e.g., field emission effect and multipacting effect etc.) [1], and the cost of niobium bulk technique is still expensive.

* Work supported by National Natural Science Foundation for Young Scientists of China (Grant NO. 11505255).
†huangshichun@impcas.ac.cn.

In order to further reduce the total cost of the SRF cavities system in accelerator (i.e., the cost of SRF cavities and the cryogenic plant) and/or improve the accelerating field of the SRF cavities. One of the solutions is to use superconducting materials thin film technology for the fabrication of the cavity. Niobium thin film on copper substrate technology is attractive due to the high thermal conductivity of copper substrate. Other materials such as MgB2 and Nb3Sn etc. have great potential because of their higher critical temperature and superheating field (i.e. for MgB2: Tc=40K, Hsh=430mT (T=0K); for Nb3Sn: Tc=18.3K, Hsh=540mT (T=0K)) [3,4]. Many laboratory around the world are developing thin film technology for accelerator application.

At IMP, Our accelerator projects, HIAF and CiADS proton Linac both will use SRF technology as mentioned above. Therefore, we started our thin film study two year ago. Both niobium thin film on copper substrate and Nb3Sn on niobium substrate technology are being developed. Normally, the RF properties of thin film can be obtained by low temperature testing of the cavity coated with material thin film. But the results are averaged over the whole cavity surface, local loss mechanism cannot be precisely characterized. And coating the cavity with material thin film is complex and time-consuming. Another way to measure the RF properties of material thin film is to test the thin film sample, where the sample is set as part of the host cavity. To date, there are two methods to characterize the sample, i, end-plate replacement method; ii, RF-DC calorimetric method; the details of above methods are described in reference [5,6]. The measurement apparatus of method two is much complex in comparison with that of method one, because it needs to thermal decouple between host cavity and sample. In order to make host cavity structure simpler and easy to attach sample, reduce the testing period of each sample. Therefore we adopted the end-plate replacement method for the characterization of sample, the sample host cavity will operating in TE011 mode, For perfect TE011 mode, there will be no electric field perpendicular to cavity surface, to ease the electric related effect, such as mulptipacting and field emission effect. And no RF current cross the joints between host cavity and sample disk, to obtain high resolution of RF surface resistance.

In this paper, the electromagnetic optimization of the TE- sample host cavity will be presented, and the design consideration of coupler and T-mapping system will also be discussed.

CAVITY DESIGN

In the end-plate replacement methods, the host cavity resonates in the TE0mn mode, where the sample is one of the end-plates of the host cavity. By measuring the un-

Content from this work may be used under the terms of the CC BY 3.0 licence (© 2018). Any distribution of this work must maintain attribution to the author(s), title of the work, publisher, and DOI.

ISBN: 978-3-95450-194-6 ISSN: 2226-0366 doi:10.18429/JACoW-LINAC2018-THPO069

loaded quality factor Q0 of the sample host cavity with reference sample and with the sample under investigation respectively. The RF surface resistance of the sample can be deduced from the difference in Q0.

Since the diameter of the sample is inversely proportional to the frequency of the host cavity. The surface resistance is proportional to square of the frequency. The thermal feedback analysis from Cornell university shows that the breakdown magnetic field of niobium cavity with thickness of 3mm are 60mT at frequency of 6GHz, and above 120mT at a frequency of 4GHz [5,7].

The optimization goal of our host cavity is as following:

1) TE011 mode operation, the frequency is less than 4GHz;
2) Sample size: the diameter is 110mm, with about 86mm diameter area of sample exposed to magnetic field;
3) Maximize the ratio of peak surface magnetic field on sample (Hpk,sample) over peak surface magnetic field on the host cavity wall (Hpk,wall).
4) Maximize Gsample/Gcavity, Gsample is the geometric factor of the sample plate and Gcavity is the geometric factor of the host cavity.

The electromagnetic optimization of the sample host cavity was performed by CST Microwave Studio. We started our optimization from the two geometric structures shown in Fig.1, one with cone part and the other one with Sphere part. Each structure parameterized by corresponding geometric parameters. All the parameters were swept in CST Microwave Studio, the optimal geometric parameters were obtained to meet our optimization goal of the host cavity.

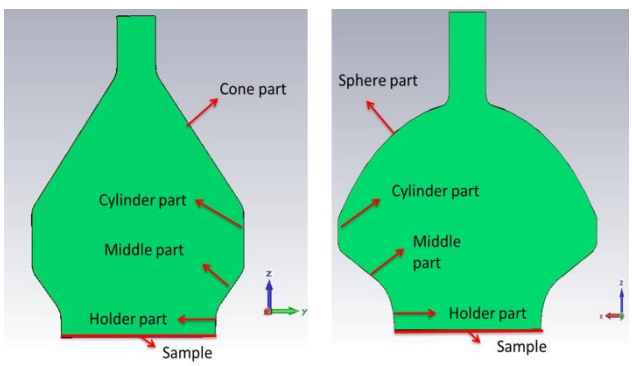


Figure 1: The geometric structures where we started our EM optimization. With cone part (left) and with sphere part (right).

Table 1 gives the optimization result of the sample host cavity. The ratio of peak surface magnetic field on sample surface over the peak surface on the host cavity is 0.85. According to the thermal feedback analysis [5,7], the maximum magnetic field on the sample surface can reach above 100mT. Fig.2 displays the distribution of the absolute value of electric field (top) and magnetic field (bottom) on the symmetric plane. As one can see, the electric field on cavity surface does go to zero, and the magnetic field at the joints between sample disk and host cavity is approaching to zero. Therefore, the electron-loading effects can be avoided inside the cavity theoretically. The surface preparation will be much easier compared to that of the SRF cavity used in accelerators.

Table 1: The Optimization Result of the Sample Host Cavity

Parameters	Value
Frequency[GHz]	3.9
Sample Diameter(mm)	110
Hpk,sample/Hpk,wall	0.906

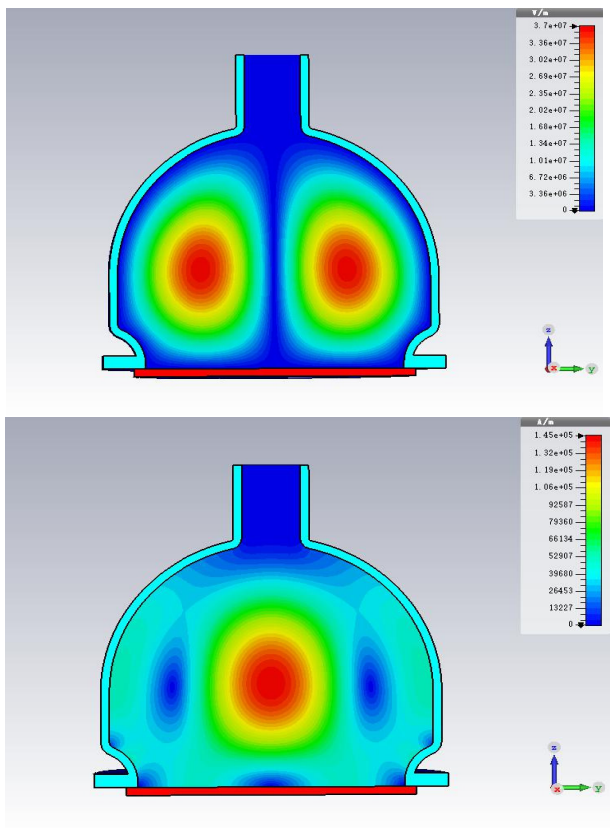


Figure 2: The distribution of absolute value of electric field (top) and magnetic field (bottom) on the symmetric plane.

COUPLER DESIGN CONSIDERATION

As mentioned before, our sample host cavity will used to characterize both niobium thin film coated on copper substrate and Nb3Sn thin film coated on niobium substrate. Therefore the variable coupler should be design to test different sample with different RF surface resistance. The external quality factor of the coupler should be in the range of 1E7 to 1E10. The off-center hook coupler described in reference [5] will be considered for our sample host cavity.

T-MAPPING SYSTEM

The back-side of sample surface will be attached with high resolution temperature sensors. As a first step, ten five silicon diode sensors were procured and will be set on two

Content from this work may be used under the terms of the CC BY 3.0 licence (© 2018). Any distribution of this work must maintain attribution to the author(s), title of the work, publisher, and DOI.

ISBN: 978-3-95450-194-6 ISSN: 2226-0366 doi:10.18429/JACoW-LINAC2018-THPO069

concentric rings, and the corresponding Labview program is being developed.

CONCLUSION

Presently, both the niobium thin film coated on copper substrate and Nb3Sn thin film coated on niobium substrate techniques is being developed at Institue of Modern Physics, CAS. As a part of the development of above techniques, we started to develop a sample host cavity operating in TE011 mode and by using end-plate replacement methods combined with the thermometry system. To date, the electromagnetic optimization has been performed. The sample host cavity has a frequency of 3.9 GHz and characterize the sample disk with a diameter of 110mm. Theoretically, the peak magnetic field on sample surface can reach above 100mT.The sample will attached with high resolution temperature sensors, and the variable coupler will be further optimized.

ACKNOWLEDGEMENTS

This work was supported by National Natural Science Foundation for Young Scientists of China (Grant NO. 11505255).

REFERENCES

[1] Hasan Padamsee, Jens Knobloch, and Tom Hays, RF Superconductivity for Accelerators.

[2] R. L. Geng, G. V. Eremeev, H. Padamsee, "High Gradient Studies for ILC with Single Cell Re-entrant Shape and Elliptical Shape Cavities made of Fine-grain and Large-grain Niobium", in *Proc. PAC'07*, Albuquerque, New Mexico, USA, paper WEPMS006, pp. 2337-2339.

[3] S. Posen, "Understanding and overcoming limitation mechanisms in Nb3Sn superconducting RF cavities", PhD thesis, Cornell University, 2015.

[4] T. Tajima *et al.*, "Studies on superconducting thin films for SRF applications", in *Proc. LINAC'10*, Tsukuba, Japan, Sep. 2010, paper THP042, pp. 854-856.

[5] Yi Xie，"Development of Superconducting RF Sample Host Cavities and Study of Pit-Induced Cavity Quench", PhD thesis, Cornell University, 2013.

[6] Tobias Junginger, "Investigations of the surface resistance of superconducting materials", PhD thesis, the Ruperto-Carola University of Heidelberg, 2012.

[7] D.L. Hall , M. Liepe, I. Madjarov, Y. K. McDermott, N. Valles, "Development and Performance of a High Field TE-mode Sample Host Cavity", in *Proc. SRF'13*, Paris, France, paper THP038, pp. 985-987.

Content from this work may be used under the terms of the CC BY 3.0 licence (© 2018). Any distribution of this work must maintain attribution to the author(s), title of the work, publisher, and DOI.

ISBN: 978-3-95450-194-6 ISSN: 2226-0366 doi:10.18429/JACoW-LINAC2018-THPO072

CRYOGENIC TESTS OF THE SUPERCONDUCTING BETA=0.069 CH-CAVITIES FOR THE HELIAC-PROJECT*

M. Basten[1,†], K. Aulenbacher[3,4], W. Barth[2,3], M. Busch[1], F. Dziuba[3], V. Gettmann[3], M. Heilmann[2], T. Kürzeder[3], M. Miski-Oglu[3], H. Podlech[1], M. Schwarz[1], S. Yaramyshev[2]

[1]IAP University of Frankfurt, 60438 Frankfurt am Main, Germany
[2]GSI Helmholtz-Centre, 64291 Darmstadt, Germany
[3]HIM Helmholtz-Institute Mainz, 55099 Mainz, Germany
[4]KPH Mainz University, 55128 Mainz, Germany

Abstract

In the future the existing UNILAC (UNIversal Linear Accelerator) at GSI will be most exclusively used as an injector for FAIR to provide short pulse high intensity heavy ion beams at low repetition rates [1]. A new superconducting (sc) continuous wave (cw) high intensity heavy ion Linac should provide ion beams with max. duty factor above the coulomb barrier for the Super Heavy Element (SHE) program at GSI. The fundamental Linac design comprises a low energy beam transport (LEBT)-section followed by a sc Drift Tube Linac (DTL) consisting of sc Crossbar-H-mode (CH) structures for acceleration up to 7.3 MeV/u [2, 3]. After the successful test and commissioning of the first demonstrator section with heavy ion beam from the HLI in 2017 [4], the next two sc CH-structures have been constructed and the first one has been extensively tested at cryogenic temperatures at the Institute for Applied Physics (IAP) at Goethe University Frankfurt (GUF). The results of the final cold test of the first CH-structure as well as the next steps realizing a new sc cw heavy ion LINAC at GSI will be presented.

INTRODUCTION

The construction of two sc 217 MHz CH-cavities (CH 1 and CH 2) for the new advanced demonstrator started in December 2016 and was finished in March (CH1) and September 2018 (CH2). During the construction phase several factory side measurements have been performed to monitor crucial parameters like frequency and the tuning concept [5, 6]. Both cavities have the same geometry and the same constant beta profile. Compared to recent sc CH-cavities both cavities are designed without girders and with stiffening brackets on each inclined end cap (see Fig. 1) aiming for increased mechanical stiffness and reduced pressure sensitivity. Each cavity is equipped with two dynamic bellow tuners to adjust the frequency accordingly during operation. The design gradient is 5.5 MV/m, which has to be achieved by eight accelerating cells. In Table 1 the main parameters of the first two 217 MHz CH-cavities are depicted.

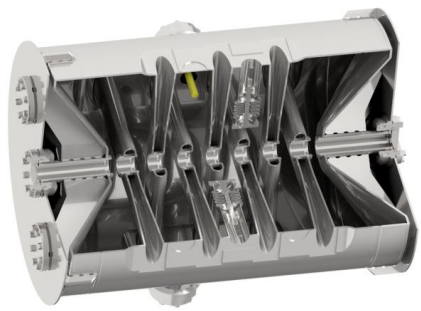


Figure 1: Layout of the sc 217 MHz CH-cavity CH1/CH2.

Table 1: Main Parameters of CH-cavity CH1/CH2

Parameter	Unit	Value
β		0.069
Frequency	MHz	216.816
Accelerating cells		8
Length ($\beta\lambda$-definition)	mm	381.6
Cavity diameter (inner)	mm	400
Cell length	mm	47.7
Aperture diameter	mm	30
Static tuner		3
Dynamic bellow tuner		2
Wall thickness	mm	3-4
Design Accelerating gradient	MV/m	5.5
E_p/E_a		6
B_p/E_a	mT/(MV/m)	<10
G	Ω	50
R_a/Q_0	Ω	1070

EXPERIMENTAL SETUP

After the delivery of CH1 to GUF in March 2018, cavity preparations have been started for the first test at 4.2 K in a vertical cryostat at IAP. The cavity has been equipped with eight temperature probes, 60 Thermo-Luminescence-Dosimeters (TLD's) and two piezo elements (see Fig. 2). The TLD's around the cavity surface record the x-ray-spectra generated inside the cavity during high field levels to observe possible sources of field emission. The piezo elements can be used as actuator and sensor to analyze the mechanical eigenfrequencies of the cavity. The RF measurement setup

* Work supported by BMBF Contr. No. 05P15RFRBA and the EU Framework Programme H2020 662186 (MYRTE)
† Basten@iap.uni-frankfurt.de

Content from this work may be used under the terms of the CC BY 3.0 licence (© 2018). Any distribution of this work must maintain attribution to the author(s), title of the work, publisher, and DOI.

ISBN: 978-3-95450-194-6 ISSN: 2226-0366 doi:10.18429/JACoW-LINAC2018-THPO072

Content from this work may be used under the terms of the CC BY 3.0 licence (© 2018). Any distribution of this work must maintain attribution to the author(s), title of the work, publisher, and DOI.

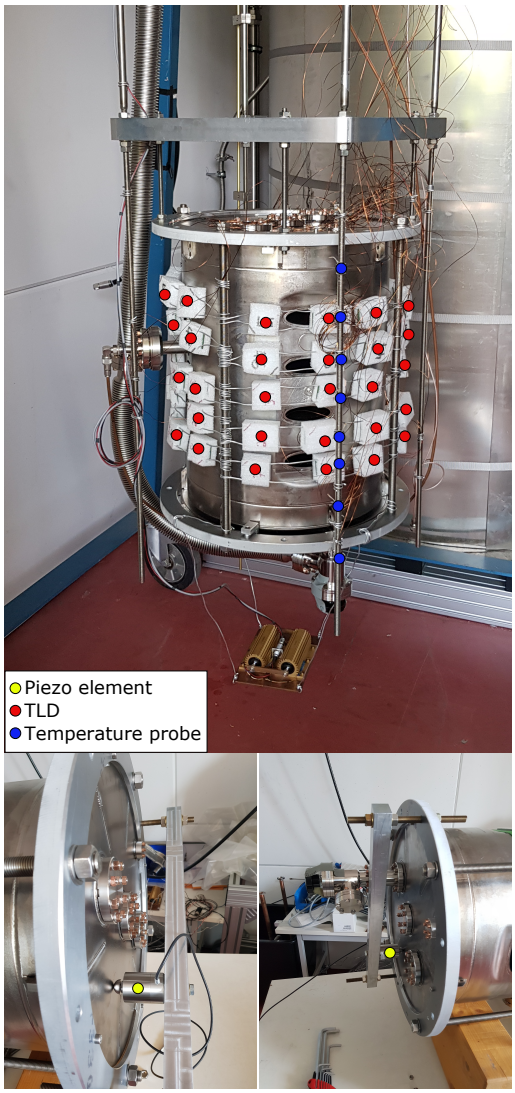


Figure 2: Vertical string with cavity in a support frame equipped with TLD's, temperature probes and piezo elements.

comprises of an RF generator, a 50 W broadband amplifier, an RF control system, several power meters, scopes, network analyzers and a piezo amplifier.

MEASUREMENT RESULTS

After the assembly of the cavity string into the vertical cryostat the liquid nitrogen shield was partially filled to precool the cavity, directly followed by a rapid cooldown with liquid helium down to 4.2 K. Avoiding hydrogen related Q-disease the temperature change was in the range of 1.8 K/min. After cooldown to 4.2 K the mean residual pressure inside the cavity came down to 5×10^{-10} mbar by using a turbomolecular and an ion getter pump. After several days of RF conditioning at various power levels and sweep times, all multipacting barriers could permanently be surmounted and the RF performance of the cavity could be determined. Figure 3 shows the resulting Q_0 vs. E_a curve of the vertical (test

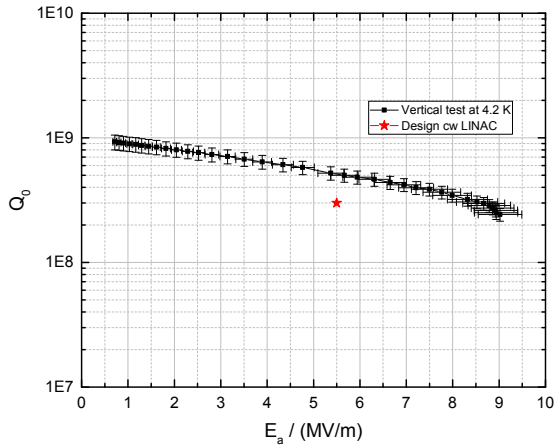


Figure 3: Q_0 vs. E_a curve at 4.2 K.

without helium vessel). The maximum Q-value at low field levels (Q_0^{low}) was approx. 1.02×10^9 and a maximum gradient of 9 MV/m corresponding to 3.32 MV voltage could be reached. The unloaded Q-value Q_0 dropped down to 2.43×10^8 at this field level which is near to the external Q_e-value of the input power coupler of 1.68×10^8. The design Q-value of 3×10^8 is reached at an gradient of 8.52 MV/m, which is 55% more than the design gradient of 5.5 MV/m. The main measurement results of the first RF test at 4.2 K are summarized in Table 2.

Table 2: Main Results of the First RF Test of CH1 at 4.2 K

Parameter	Unit	Value
Q_0^{low}		$1.02 \cdot 10^9$
Q_e^{low}		$1.68 \cdot 10^8$
R_s	nΩ	48.4
R_{BCS}	nΩ	12.6
R_{mag}	nΩ	9.78
R_0	nΩ	26.02
E_a	MV/m	9
U_{eff}	MV	3.32
Q_0^{high}		$2.43 \cdot 10^8$
Q_e^{low}		$1.68 \cdot 10^8$

FIELD EMISSION

Due to technical limitations, High Pressure Rinsing (HPR) could be performed only along the beam axis of the cavity. A new HPR installation in the new laboratories at the Helmholtz-Institute in Mainz will allow rinsing of each quadrant of the cavity in the next future. To determine if there are still impurities on the inner surface it is necessary to evaluate the power consumption inside the cavity P_c^{total} depending on the accelerating gradient E_a. The total power loss P_c^{total} comprises of ohmic losses P_c^{ohmic}, expected with a constant

ISBN: 978-3-95450-194-6 ISSN: 2226-0366 doi:10.18429/JACoW-LINAC2018-THPO072

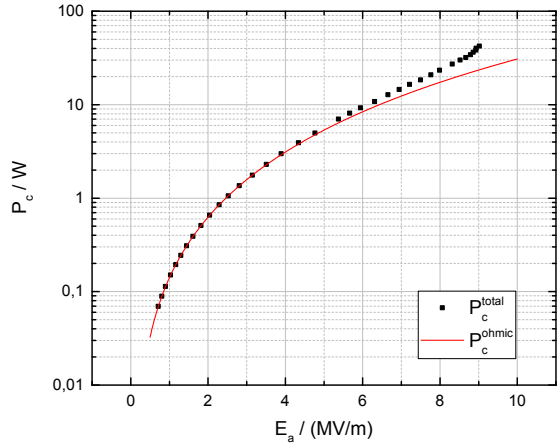


Figure 4: Total losses P_c^{total} as well as pure ohmic losses P_c^{ohmic} inside the cavity depending on E_a.

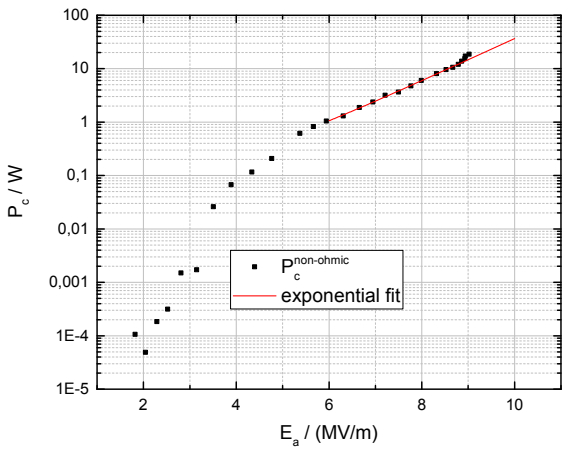


Figure 5: Non-ohmic losses $P_c^{non-ohmic}$ inside the cavity depending on E_a.

Q-value, and non-ohmic losses $P_c^{non-ohmic}$ e.g. field emission. Figure 4 shows P_c^{total} as well as P_c^{ohmic} while Fig. 5 shows $P_c^{non-ohmic}$, depending on E_a. Both figures show increased non-ohmic losses from $E_a = 5\,\mathrm{MV/m}$ which indicates the activation of a field emitter. But even at high field gradients the additional losses induced by the field emission are still low considering the fact that the HPR treatment could only be performed along the beam axis. This can also be seen in the corresponding Fowler-Nordheim plot shown in Fig. 6. It illustrates the enhancement factor $\beta_{FN} = 84.3$ of the electric fields on the surface of the field emitter an indicates how pointed it's geometry is. The corresponding maximum electric field E_p is in the range of 4.6 GV/m at the maximum accelerating gradient of $E_a = 9\,\mathrm{MV/m}$.

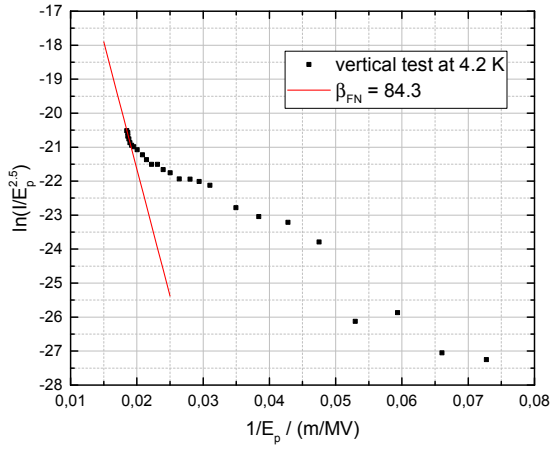


Figure 6: Fowler-Nordheim plot for the first RF test at 4.2 K.

SUMMARY & OUTLOOK

The first test with low level RF power of CH1 at 4.2 K at IAP was successful and has shown a very promising gradient of 9 MV/m. Although the surface preparation could only be done along the beam axis, field emission started at high gradients above 5 MV/m and the field enhancement factor was in the range of $\beta_{FN} = 84.3$ only. The next step is the first cryogenic test with CH 2, to compare the results with CH 1 as well as a possible test at 2 K with both cavities. Additionally an improved surface preparation to be performed at the Helmholtz-Institute in Mainz on both cavities is foreseen when the construction of the laboratories is finished to improve the surface conditions even further.

ACKNOWLEDGEMENT

This work has been supported by Helmholtz-Institute Main (HIM), Gesellschaft für Schwerionenforschung (GSI) and HIC for FAIR. This work was financially supported by BMBF Contr. No. 05P15RFRBA and the EU Framework Programme H2020 662186 (MYRTE).

REFERENCES

[1] W. Barth *et al.*, "High brilliance uranium beams for the GSI FAIR", *Phys. Rev. ST Accel. Beams*, vol. 20, 050101, 2017.

[2] W. Barth *et al.*, "Further investigations for a superconducting cw-Linac at GSI", in *Proc. IPAC'17*, Copenhagen, Denmark, May 2017, pp. 2197-2200. doi:10.18429/JACoW-IPAC2017-TUPVA055

[3] H. Podlech *et al.*, "Superconducting CH structure", *Phys. Rev. ST Accel. Beams*, vol. 10, 080101, Aug. 2007.

[4] W. Barth *et al.*, "First high intensity heavy ion beam tests with a superconducting multi gap CH-cavity", *Phys. Rev. ST Accel. Beams*, vol. 21, 020102, 2018.

[5] M. Basten *et al.*, "First measurements of the next sc CH-cavities for the new superconducting cw heavy ion LINAC@GSI", in *Proc. SRF'17*, Lanzhou, China, July. 2017, paper TUPB022, pp. 433-436.

Content from this work may be used under the terms of the CC BY 3.0 licence (© 2018). Any distribution of this work must maintain attribution to the author(s), title of the work, publisher, and DOI.

ISBN: 978-3-95450-194-6 ISSN: 2226-0366 doi:10.18429/JACoW-LINAC2018-THPO072

[6] M. Basten *et al.*, "Final factory-side measurements of the next sc CH-cavities for the HELIAC-Project", in *Proc. IPAC'18*, Vancouver, Canada, April 2018, pp. 943-945. doi:10.18429/JACoW-IPAC2018-TUPAF088

Content from this work may be used under the terms of the CC BY 3.0 licence (© 2018). Any distribution of this work must maintain attribution to the author(s), title of the work, publisher, and DOI.

ISBN: 978-3-95450-194-6 ISSN: 2226-0366 doi:10.18429/JACoW-LINAC2018-THPO073

RF COMMISSIONING OF THE SUPERCONDUCTING 217 MHz CH CAVITY FOR HEAVY IONS AND FIRST BEAM OPERATION

F. Dziuba[1,*], K. Aulenbacher[1,4], W. Barth[1,2], M. Basten[3], M. Busch[3], V. Gettmann[1], M. Heilmann[2], J. Salvatore[2], T. Kürzeder[1], M. Miski-Oglu[1], H. Podlech[3], A. Schnase[2], M. Schwarz[3], S. Yaramyshev[2]

[1]HIM Helmholtz Institute Mainz, 55099 Mainz, Germany
[2]GSI Helmholtzzentrum für Schwerionenforschung GmbH, 64291 Darmstadt, Germany
[3]IAP Goethe University Frankfurt, 60438 Frankfurt am Main, Germany
[4]KPH Johannes Gutenberg University Mainz, 55128 Mainz, Germany

Abstract

Future research programs at GSI in the field of super heavy element (SHE) synthesis require high intense heavy ion beams above the coulomb barrier and high average particle currents. The upcoming demands exceed the technical opportunities of the existing UNIversal Linear ACcelerator (UNILAC). Furthermore, the existing machine will be exclusively used as an injector for FAIR (Facility for Antiproton and Ion Research) providing high power heavy ion beams at a low repetition rate. Consequently, a new dedicated superconducting (sc) continuous wave (cw) linac is crucial to keep the SHE research program at GSI competitive on a high level. Recently the first linac section, serving as a prototype to demonstrate the reliable operability of 217 MHz multi gap crossbar-H-mode (CH) cavities under a realistic accelerator environment, has been extensively tested with heavy ion beams delivered from the GSI High Charge State Injector (HLI). Fulfilling its role as a key component of the whole demonstrator setup, the first sc 217 MHz CH cavity (CH-0) successfully accelerated heavy ions up to the design beam energy and even beyond at high beam intensities and full transmission. In this contribution the RF commissioning and the first beam operation of the cavity is presented.

INTRODUCTION

Regarding the future construction of a sc cw linac at GSI an R&D program has been initiated in collaboration with the Institute of Applied Physics (IAP) of Goethe University Frankfurt. In a first step realizing the proposed HElmholtz LInear ACcelerator (HELIAC) it was intended to build and test the first linac section with beam as a demonstrator at the GSI High Charge State injector (HLI) [1, 2]. The demonstrator setup is directly located behind the HLI as shown in Fig. 1. As a key component it contains a 850 mm long 15 gap sc CH cavity (CH-0) [3] operated at 217 MHz (see Fig. 2). Three dynamic bellow tuners inside the cavity allow slow and fast frequency adjustment during operation [4]. The beam dynamics concept of the cavity is based on the EQUidistant mUlti-gap Structure (EQUUS) layout [5, 6]. For beam tests with strong input coupling a 2 kW cw coaxial power coupler is available. Furthermore, the cavity is embedded by two sc 9.3 T solenoids providing the required transverse beam focusing. All components are mounted on a common support frame suspended inside a horizontal cryomodule. After final surface preparation steps and assembly of the helium jacket, the cavity has been extensively tested with low level RF power at 4.2 K followed by a successful full performance test with heavy ion beams.

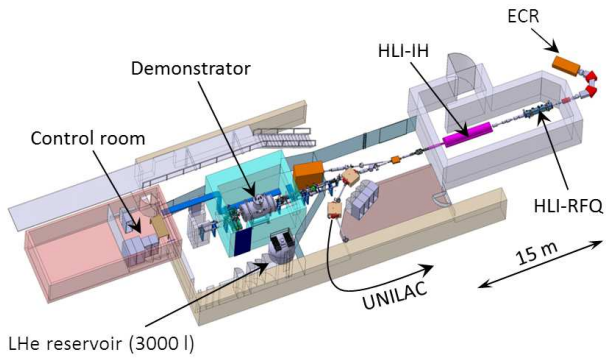


Figure 1: Demonstrator test environment at GSI.



Figure 2: 3D model of the sc 217 MHz CH cavity [7].

RF COMMISSIONING

A first cold test of the CH-0 cavity with low level RF power has been performed in a vertical bath cryostat without helium jacket at IAP beginning of 2016 [7]. During this test the cavity performance was strongly limited by field emission due to an insufficient surface preparation. Nevertheless,

* f.dziuba@gsi.de

Content from this work may be used under the terms of the CC BY 3.0 licence (© 2018). Any distribution of this work must maintain attribution to the author(s), title of the work, publisher, and DOI.

ISBN: 978-3-95450-194-6 ISSN: 2226-0366 doi:10.18429/JACoW-LINAC2018-THPO073

a maximum accelerating gradient of $E_a = 6.9$ MV/m at $Q_0 = 2.19 \times 10^8$ has been reached.

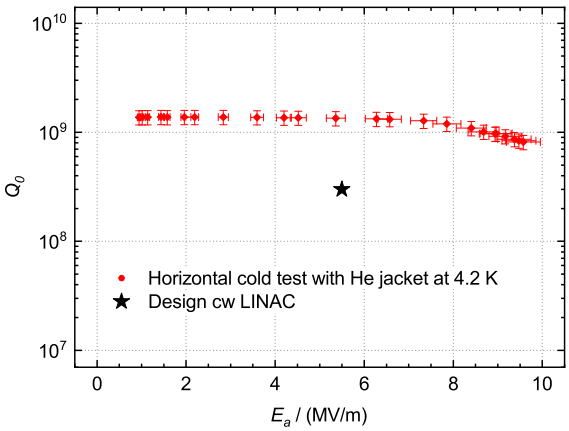


Figure 3: Measured Q_0 vs. E_a curve at 4.2 K [8].

After final assembly of the helium vessel and further High Pressure Rinsing (HPR) the cavity was delivered to GSI and prepared for a second RF test in the horizontal cryomodule. To determine Q_0 during the test and especially for RF conditioning, a slightly over coupled input probe was used. Therefore, a coupling strength of $\beta_e \approx 7$ leading to an external quality factor of $Q_e = 1.9 \times 10^8$ has been chosen. A 50 W broadband amplifier was used to deliver the required RF power. The cavity was operated within a phase locked loop (PLL). Subsequently, after cool down of the cavity to 4.2 K, RF conditioning has been performed. For conditioning with low field levels a network analyzer (VNA) was used sweeping over the resonance frequency of the cavity while varying the forward power. A strong multipacting band remaining for 6 hours occurred at accelerating gradients between 0.2 – 0.33 MV/m which corresponds to a transmitted power (P_t) in the range of 110 – 290 µW. All multipacting barriers up to 3.6 MV/m (340 μW) could permanently be surmounted within 24 hours. Afterwards, the RF performance of the cavity was reviewed. Figure 3 shows the related Q_0 vs. E_a curve measured in the horizontal cryomodule. The maximum Q-value at a low field level (Q_0^{low}) was measured for 1.37×10^9. Recently, the cavity showed an improved performance due to an advanced HPR treatment. The initial design quality factor at 5.5 MV/m has been exceeded by a factor of four. Furthermore, a maximum accelerating gradient of $E_a = 9.6$ MV/m at $Q_0 = 8.14 \times 10^8$ was reached, which is an excellent performance result considering the complex multigap structure of the cavity. The maximum gradient was limited by thermal cavity quenches.

SETUP OF THE RF SYSTEM

After the final RF test the whole demonstrator setup was modified and prepared for beam commissioning. In this context the cavity was demounted from the cryomodule and brought into the clean room at GSI for cold string assembly. Thereby, the input coupling probe has been replaced by a 2 kW high power coupler. Previously, coupler conditioning up to 2.5 kW in cw and 5 kW in pulsed mode has been performed [9–11]. To optimize the power delivery to the beam as well as to provide stable frequency operation during the beam test, the cavity was strongly over coupled to reach a sufficient bandwidth of 300 Hz. Therefore, Q_e was adjusted accordingly to 7.1×10^5. In a next step three tuning devices were mounted to the cavity for controlling the resonance frequency. Each tuning device consists of a stepper motor connected in series with a piezo actuator to drive one of the bellow tuners with a maximum force <800 N. This leads to a maximum mechanical displacement of ±1 mm which corresponds to a total tuning range of ±60 kHz per tuner. After reassembling the string to the cryomodule and cool down to 4.2 K a short RF conditioning phase has been performed. The high power coupler was cooled by the LN_2 shield of the cryostat. This was necessary to keep the heat load into the liquid helium bath as low as possible. In addition, the bellow tuning system has been tested for the first time. Tuner #3 did not respond during the test due to a short at the limit switch. Nevertheless, tuner #1 and #2 showed the desired behavior under cold conditions. Moving each stepper motor 1000 steps in forward (pushing) and backward (pulling) direction caused a bellow displacement of respectively ±50 µm. The related frequency shift per tuner was measured for ±1.4 kHz.

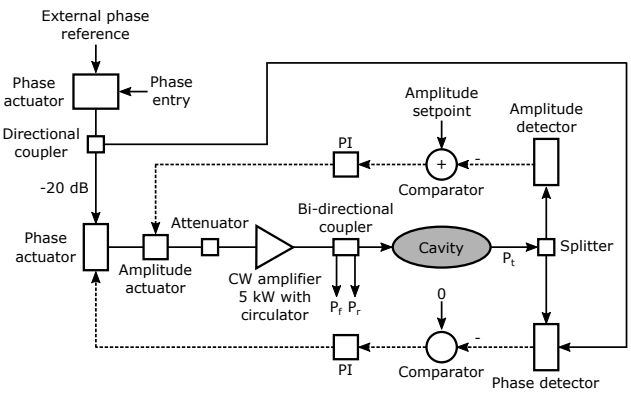


Figure 4: Schematic view of the RF feedback loop. The straight lines represent the RF path while the dashed lines indicate the low frequency part.

In beam acceleration mode the cavity was operated within an analog feedback loop (see Fig. 4). In this system the control units for RF phase and amplitude can be activated independently. The required RF power was provided by an 217 MHz, 5 kW solid state cw amplifier connected to a 1-5/8" coaxial transmission line. Resonance frequency tuning of the cavity during operation was accomplished within a separate feedback loop driving bellow tuner #1, while tuner #2 was kept in standby mode. The piezo actuators have not been used at this time. A maximum frequency shift of 700 Hz during the whole commissioning phase could be observed. This corresponds to a step width of 500 and a bellow displacement of 25 µm, respectively. The average movement of the stepper motor over the complete test range was about 1 step/min due to helium level changes inside the

Content from this work may be used under the terms of the CC BY 3.0 licence (© 2018). Any distribution of this work must maintain attribution to the author(s), title of the work, publisher, and DOI.

ISBN: 978-3-95450-194-6 ISSN: 2226-0366 doi:10.18429/JACoW-LINAC2018-THPO073

cryomodule. Within the chosen resonance bandwidth the bellow tuning system allowed stable frequency operation of the cavity during the complete test period. Due to a broken resistive heater it was not possible to determine Q_0 during this test in presence of the heavily coupled input antenna. In other words, the helium gas flow-meter could not be calibrated to measure the cryogenic losses and to deduce the related power losses. Recently, this was fixed and the measurement will be repeated during the next cold test at the end of this year. Nevertheless, a maximum accelerating gradient of 6.4 MV/m at a forward power of 1.5 kW could be reached.

BEAM COMMISSIONING

After the sc 217 MHz CH cavity was tested with low level RF power at 4.2 K, a full performance test with beam has been performed at GSI [12–14]. Therefore, argon and helium ion beams with different charge states ($^{40}Ar^{11+}$, $^{40}Ar^{9+}$, $^{40}Ar^{6+}$, $^{4}He^{2+}$) have been provided by the ECR source of the HLI. The maximum achieved average beam intensity of 1.5 pμA was limited by the pulse intensity of the HLI and its duty factor of 25% (50 Hz, 5 ms). Initially, the cavity accelerated successfully $^{40}Ar^{11+}$ ions with 95% of beam transmission up to the design energy of 1.86 MeV/u, which corresponds to a total energy gain of 0.5 MeV/u. Considering the forward and the reflected RF power by neglecting the losses inside the cavity walls, the cavity was powered with 10 W (net RF power) providing an accelerating gradient of more than 2.6 MV/m ($\beta\lambda$-definition). During the whole beam test the cavity was operated in cw mode. A minimum bunch length of 0.25 ns (FWHM) or 20° could be detected by means bunch shape monitor (BSM) [15] behind the demonstrator setup while, the beam emittance growth is less than 15% in transversal and 10% in longitudinal plane. For determining the beam emittance a slit grid scanner was used. Meanwhile the design gradient could be verified by accelerating heavy ions with $A/q = 6.7$. Figure 5 shows a full measured 3D-scan for $^{40}Ar^{9+}$ of beam energy and transmission depending on different accelerating fields and RF phases. By ramping up the accelerating gradient a linear increase of beam energy could be observed for different RF phases, while beam transmission was kept above 90%. These measurements confirm nicely the feature of energy variation between 1.2 – and 2.2 MeV/u by changing the RF phase and amplitude without particle losses and significant beam quality degradation referable to the EQUUS beam dynamics.

SUMMARY & OUTLOOK

The sc 217 MHz CH cavity has been tested at GSI with low level RF power at 4.2 K. A very promising gradient of 9.6 MV/m could be reached after an advanced surface preparation. Afterwards the cavity was prepared for beam operation. Therefore, the 2 kW high power coupler and the new RF control system in combination with slowly driven bellow tuners have been successfully commissioned for the

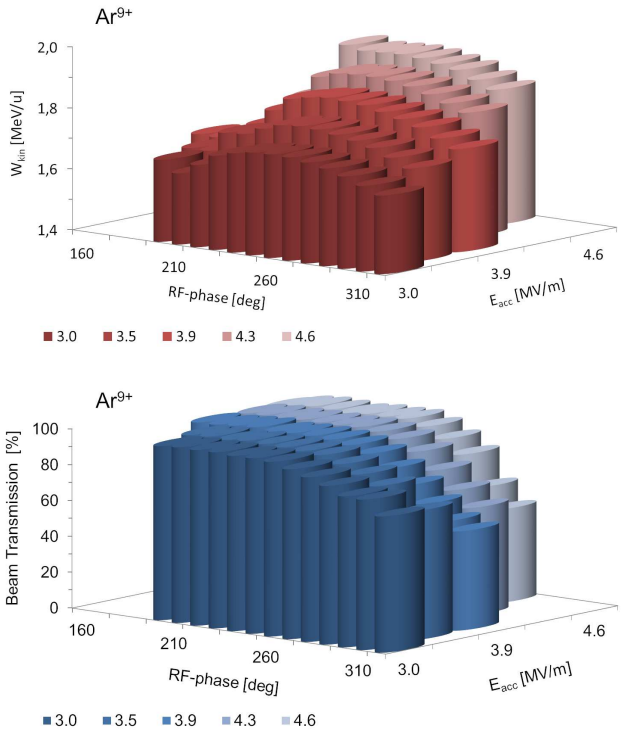


Figure 5: Measured 3D-scan of an $^{40}Ar^{9+}$ beam showing beam energy (top) and beam transmission (bottom) versus accelerating gradient and RF phase [12].

first time. Recently a full performance test of the cavity with heavy ion beam was accomplished. The demonstrator cavity reached acceleration of heavy ions up to the design beam energy. Furthermore, the design accelerating gradient was achieved even above the design mass to charge ratio ($A/q = 6.7$) at high beam intensities. At full beam transmission the beam quality was measured as excellent. The worldwide first successful beam test of the sc CH cavity was an important step on the way realizing the proposed cw HELIAC. Additionally, the first short sc 217 MHz CH cavity (CH-1) with a simplified geometry for the advanced demonstrator [16, 17] has been already successfully tested with low level RF power at 4.2 K in a vertical cryomodule [18, 19]. The cavity reached a very nice gradient of 9 MV/m at $Q_0 = 2.4 \times 10^8$ reproducing the excellent results made so far with the demonstrator cavity (CH-0). Furthermore, the fabrication of a second short sc 217 MHz CH cavity (CH-2) is almost finished. It is planned to test this cavity with low level RF power at the end of this year.

ACKNOWLEDGEMENT

The full performance test of the demonstrator especially successful beam commissioning could only be accomplished by the strong support of highly motivated people from different GSI departments. The first beam operation of a sc CH cavity is an important milestone of the R&D work of HIM and GSI in collaboration with IAP, Goethe University Frankfurt.

Content from this work may be used under the terms of the CC BY 3.0 licence (© 2018). Any distribution of this work must maintain attribution to the author(s), title of the work, publisher, and DOI.

ISBN: 978-3-95450-194-6 ISSN: 2226-0366 doi:10.18429/JACoW-LINAC2018-THPO073

Content from this work may be used under the terms of the CC BY 3.0 licence (© 2018). Any distribution of this work must maintain attribution to the author(s), title of the work, publisher, and DOI.

REFERENCES

[1] S. Mickat *et al.*, "The sc cw-linac-demonstrator -– SRF technology finds the way to GSI", in *Proc. SRF'11*, Chicago, USA, July 2011, paper THIOA05, pp. 646-649.

[2] V. Gettmann *et al.*,"The sc CW-linac demonstrator -– first section of a sc CW-linac", in *Proc. SRF'11*, Chicago, USA, July 2011, paper MOPO030, pp. 144-146.

[3] F. Dziuba *et al.*, "Development of superconducting crossbar-H-mode cavities for proton and ion accelerators", *Phys. Rev. ST Accel. Beams*, vol. 13, p. 041302, 2010.

[4] M. Amberg *et al.*, "The fast piezo-based frequency tuner for sc CH-cavities", in *Proc. LINAC'14*, Geneva, Switzerland, Sep. 2014, paper MOPP068, pp. 214-216.

[5] S. Minaev *et al.*, "Superconducting, energy variable heavy ion linac with constant β, multicell cavities of CH-type", *Phys. Rev. ST Accel. Beams*, vol. 12, p. 120101, 2009.

[6] M. Schwarz *et al.*, "Beam dynamics simulations for the new superconducting cw heavy ion linac at GSI", presented at LINAC'18, Beijing, China, Sep. 2018, paper TUPO084, this conference.

[7] F. Dziuba *et al.*, "First performance test on the superconducting 217 MHz CH cavity at 4.2 K", in *Proc. LINAC'16*, East Lansing, USA, Sep. 2016, pp. 953-955. doi:10.18429/JACoW-LINAC2016-THPLR044

[8] F. Dziuba *et al.*, "First cold tests of the superconducting CW demonstrator at GSI", in *Proc. RuPac'16*, St. Petersburg, Russia, Nov. 2016, paper WECBMH01, pp. 83-85.

[9] F. Dziuba *et al.*, "Performance tests of the of the superconducting 217 MHz CH cavity for the CW demonstrator", in *Proc. SRF'17*, Lanzhou, China, July 2017, pp. 440-443. doi:10.18429/JACoW-SRF2017-TUPB024

[10] J. List, "Untersuchungen an den 217 MHz Leistungskopplern für das cw-Linac/Demonstrator-Projekt an der GSI", Master thesis, Institute for Applied Physics, Goethe-University Frankfurt, Germany, 2018.

[11] J. List *et al.*, "High power coupler R&D for superconducting CH-cavities", presented at LINAC'18, Beijing, China, Sep. 2018, paper THPO107, this conference.

[12] W. Barth *et al.*, "First heavy ion beam tests with a superconducting multigap CH cavity", *Phys. Rev. ST Accel. Beams*, vol. 21, p. 020102, 2018.

[13] W. Barth *et al.*, "First acceleration of heavy ion beams with a superconducting continuous wave HIM/GSI cw-linac", presented at LINAC'18, Beijing, China, Sep. 2018, paper TU2A01, this conference.

[14] M. Miski-Oglu *et al.*, "Steps towards superconducting CW-linac for heavy ions at GSI", in *Proc. SRF'17*, Lanzhou, China, July 2017, pp. 112-114. doi:10.18429/JACoW-SRF2017-MOPB024

[15] A. V. Feschenko, "Technique and instrumentation for bunch shape measurement", in *Proc. RuPac'12*, St. Petersburg, Russia, Sep. 2012, paper FRXOR01, pp. 181-185.

[16] W. Barth *et al.*, "Further R&D for a new superconducting CW heavy ion linac@GSI", in *Proc. IPAC'14*, Dresden, Germany, June 2014, paper THPME004, pp. 3211-3213.

[17] W. Barth *et al.*, in *Proc. Baldin ISHEPP XXIII*, Dubna, Russia, Sep. 2016, EPJ Web of Conferences, 138, 01026 (2017).

[18] M. Basten *et al.*, "First measurements of the next sc CH-cavities for the new superconducting cw heavy ion linac@GSI", in *Proc. SRF'17*, Lanzhou, China, July 2017, pp. 433-436. doi:10.18429/JACoW-SRF2017-TUPB022

[19] M. Basten *et al.*, "Cryogenic tests of the superconducting beta=0.069 CH-cavities for the HELIAC-Project", presented at LINAC'18, Beijing, China, Sep. 2018, paper THPO072, this conference.

ISBN: 978-3-95450-194-6 ISSN: 2226-0366 doi:10.18429/JACoW-LINAC2018-THPO076

MULTI-PHYSCIS DESIGN STUDIES OF A SUPERCONDUCTING QUARTER-WAVE RESONATOR AT PEKING UNIVERSITY*

Meng Chen, Feng Zhu†, Shengwen Quan‡, Jiankui Hao, Wei Cheng, Shu Chen, Anqi Cheng
Institute of Heavy Ion Physics & State Key Laboratory of Nuclear Physics and Technology, Peking University, Beijing, 100871, China

Abstract

A 81.25MHz, geometric beta=0.046 quarter-wave resonator has been designed and analysed at Peking University. This paper mainly presents the multi-physics studies of this cavity, include electromagnetic design, mechanical analysis and multipacting simulation, to predict its behaviour under practical operating process. Various transverse vibration modes of inner conductor were found under different fixed conditions and an asymmetric shorting plate was adopted to avoid high possibility of multipacting.

INTRODUCTION

There's presently a growing amount of CW high current heavy-ion linear accelerator facilities based on superconducting technology to better support various field of science [1]. Based on that, we designed a quarter-wave resonator for the demand of low beta high current cavity. Structural design is an important aspect overall cavity and cryomodule implementation. Because of the asymmetric geometry of the cavity and usually a long pendulous inner conductor, the thin-wall structure of QWR cavity can be easily deformed by the impact of various fluctuations, causing resonant frequency shift. Excessive frequency shift require additional RF power to control the RF amplitude and phase [2]. Thus a stable resonant frequency is required. We did a sequential coupled field simulations to predict the behaviour of the naked cavity under practical operation, several coupled field analysis were carried out. For the issue of multipacting, an asymmetric shorting plate was adopted to lower the possibility of multipacting.

RF DESIGN

The model of 81.25 MHz QWR is shown in Fig. 1, it is designed and optimized in CST MWS [3]. Taper-shape inner and outer conductors can improve the RF performance relative to using straight cylinders [4]. The top and bottom four ports are used for rinse and the bottom two are also used for power coupler and pick up. All ports are located at a proper position that the water pipes can go deep into the cavity, at the meanwhile they won't influence the surface peak electromagnetic field as shown in Fig. 1. In addition, donut-shaped drift tube was adopted to reduce the magnetic field in the gap [5]. Additional methods to supress the beam steering effect have been studied.

The main geometry and RF parameters of this cavity are summarized in Table 1.

* supported by National Basic Research Project (2014CB845504)
† zhufeng7726@pku.edu.cn
‡ qsw@pku.edu.cn

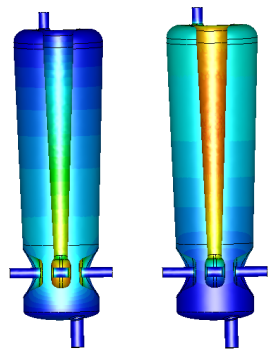


Figure 1: Magnetic field distribution (left) and electric field distribution (right) for the 81.25 MHz mode.

Table 1: The Main Parameters of 81.25 MHz QWR. Surface Resistance was Assumed to be 25nΩ @4.5K in the Calculation

Frequency[MHz]	81.25
β_g	0.046
G[Ω]	21
R_{sh}/Q[Ω]	592
Q_0	8.4e8
Epk/Eacc	4.9
Bpk/Eacc[mT/(MV/m)]	6.4
Beam aperture[mm]	34
Cavity height[mm]	980
Cavity diameter[mm]	270

MECHANICAL SIMULATION

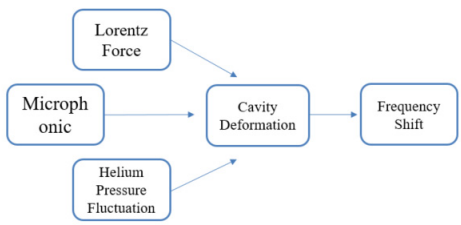


Figure 2: Multi-physics field coupling with cavity.

As shown in Fig. 2, cavity deformations from cooling down, Lorentz force, Helium Pressure Fluctuations (HPF) and microphonics can lead to resonant frequency change, the prediction of the resonant frequency change depends on the accuracy of the calculated electromagnetic fields as well as the calculated mechanical deformation. Due to the asymmetric structure with four ports, we used the whole structure to do the simulation.

Content from this work may be used under the terms of the CC BY 3.0 licence (© 2018). Any distribution of this work must maintain attribution to the author(s), title of the work, publisher, and DOI.

ISBN: 978-3-95450-194-6 ISSN: 2226-0366 doi:10.18429/JACoW-LINAC2018-THPO076

Content from this work may be used under the terms of the CC BY 3.0 licence (© 2018). Any distribution of this work must maintain attribution to the author(s), title of the work, publisher, and DOI.

To predict the frequency change, in general, we need two models: high frequency vacuum model to calculate the frequency before and after the cavity deformed, and a shell structure model to evaluate the displacement field distribution after applying loads. Thus corresponding two solvers are needed, Eigenmode Solver and Mechanical Solver. Actually, the displacement is very small compared to the scale of cavity, so we used sensitive analysis in Eigenmode Solver to evaluate the frequency change with more efficiency. In this way, we don't have to establish a totally new deformed structure but by importing the displacement field distribution to the original model in Eigenmode Solver, the frequency change due to the displacement field can be evaluated by using derivative information and no real deformation is applied to the structure or the mesh.

LORENTZ FORCE DETUNING

Using the vacuum model of QWR cavity we simulated the RF field distribution at 81.25 MHz for the accelerating mode-see Fig. 1

The distribution of Lorentz force density applied to the walls of cavity can be calculated as follows:

$$\vec{F} = \frac{1}{4}(\mu|\vec{H}|^2 - \varepsilon|\vec{E}|^2) \cdot \vec{n}$$

and the Lorentz force detuning coefficient is:

$$K_L = -\frac{\Delta f}{{E_{acc}}^2}$$

K_L is a constant. We calculated the frequency change in a range of accelerating gradients, result shows that the LFD coefficient, $K_L = -5.296\text{Hz}/(\text{MV/m})^2$.

HELIUM PRESSURE FLUCTUATION AND MICROPHONICS

Superconducting cavities operate at a low temperature by immersed in liquid helium, thus pressure fluctuations in the liquid helium will be transmitted to cavity wall, leading to cavity deformation and resonant frequency shift. We use df/dp to characterize the frequency sensitivity to the helium pressure fluctuation. In our simulation, a constant pressure P=0.1MPa was applied to the outside of cavity wall. We studied the effects of various fixed condition to df/dp. See Table. 2

Table 2: df/dp Under Various Fixed Condition

	Port1	Port2	Beam pipe	df/dp(Hz/mbar)
1	DOF	Free	Free	-18
2	Free	DOF	Free	-27
3	Free	Free	DOF	-15
4	DOF	DOF	Free	-4.8
5	DOF	Free	DOF	-4.97
6	Free	DOF	DOF	-15
7	DOF	DOF	DOF	-4.1

In practical operation, the constraints fall in between all ports fixed and totally free, so the value of df/dp is between -27~-4.1.

Because of the long pendulous inner conductor and the thin-wall structure, quarter-wave cavities have a pair of degenerate mechanical eigenmodes, with relatively low frequency ~30-60 Hz [6], which may be excited by the low frequency helium pressure fluctuation. This can be simulated in ANSYS WORKBENCH Modal and Harmonic Response systems [7]. We set the helium pressure fluctuation amplitude at ±10mbar [8], the results of frequency response spectrum caused by the HPF under various constraints are as follows (Fig. 3). Static helium pressure cause inner conductor sink in vertical direction, and dynamic helium pressure fluctuation may cause inner conductor vibration in transverse dimension. Without any port fixed, the lowest mechanical vibration mode frequency is about 31 Hz with a wide bandwidth, and when some ports are fixed,

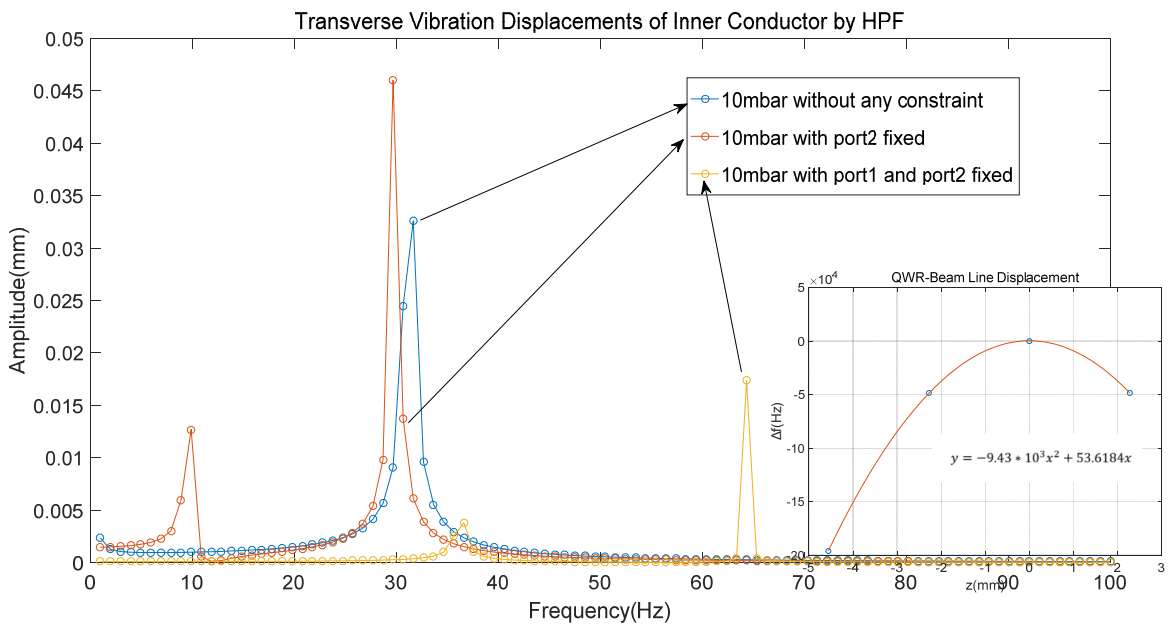


Figure 3: Transverse frequency response of drift tube to HPF.

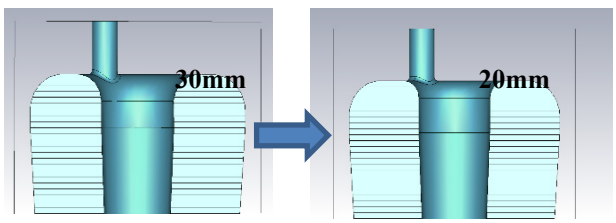
ISBN: 978-3-95450-194-6 ISSN: 2226-0366 doi:10.18429/JACoW-LINAC2018-THPO076

the vibration mode will degenerate to 2 modes with relative narrow bandwidth, the values of 2 mechanical resonant frequencies may get larger or smaller than 31 Hz depend on the cavity constraint condition. Thus it is necessary to be careful with possible external low frequencies resonant sources even with a stiffening rib.The frequency shift Δf is a quadric function of the transverse displacement Δz of inner conductor, which is shown in Fig. 3.

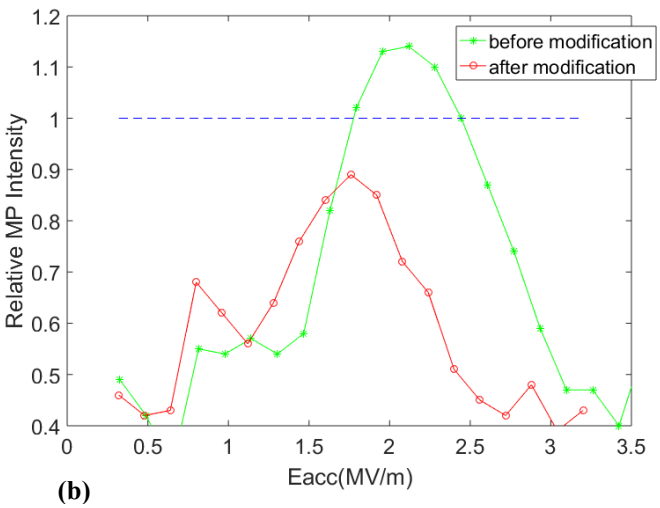
MULTIPACTING SIMULATION

For the QWR cavities, multipacting effect is another issue to consider in the cavity design stage. Large number of electrons build a stable resonant process, absorbing RF power so that it becomes impossible to increase the cavity fields by raising the incident power. The electrons collide with the structure walls leading to temperature rise and eventually may cause cavity thermal breakdown [9]. Generally in QWR, the most serious multipacting regions are top shorting plate, power coupler port and beam pipe in certain accelerating gradient. We firstly simulated the MP effect of shorting plate, which was finished in CST Particle Tracking Solver.

A first-order two-points multipactor barrier occured in the region of top shorting plate, the relative MP intensity is above 1 in the accelerating gradient range of 1.8MV/m~2.4MV/m, the number of electrons grows exponentially over time, that represents a high possibility that multipacting effect may occur. To avoid possible multipacting effect, we modified the inner fillet radius of top shorting plate-see Fig. 4 (a), from 30mm to 20mm, then we recalculated the multipacting effect, as we can see in Fig. 4 (b), the relative MP intensity in the calculated accelerating gradient range is below 1. This is a traditional way to lower the possibility of multipacitng effect in the design stage, the effect of the asymmetric shorting plate to the mechanical properties will be further studied. Multipacting on rinse port and power coupler port will also be studied next.



(a)



(b)

Figure 4: Top shorting plate modification (a) relative MP Intensity before and after modification (b).

CONCLUSION

Peking University has designed an 81.25 MHz QWR cavity for low beta high current ion beams. Simulations and analysis of electromagnetic and mechanical properties were performed in this paper. The coefficient of Lorentz Force Detuning of naked cavity is about -5.296 Hz/(MV/m)^2, a vibration mode differentiation of inner conductor occurred under various ports constraints. For multipacting effect, an asymmetric top shorting plate is adopted to lower the possibility of multipacting.

REFERENCES

[1] H.T.X Zhong *et al.,* "Study on high order modes in a beta=0.09 SRF HWR cavity for 100 mA proton acceleration", High Power Laser And Particle Beams. vol. 29, no. 8, p. 085102, Aug, 2017

[2] E. Zaplatin *et al.* "Structural analyses of MSU Quarter-Wave Resonators", in *Proc. SRF'09*, Berlin-Dresden, Germany, Sep. 2009, paper THPPO013.

[3] CST, http://www.cst.com

[4] Zachary A.Conway, "Superconducting cavity cryomodules for Heavy-Ion Accelerators @ Argonne", in *Proc. 13th International Conference on Heavy Ion Accelerator Technology (HIAT'15)*, Yokohama, Japan, Sep. 2015. doi:10.18429/JACoW-HIAT2015-WEM1I01

[5] C.Zhang *et al.* "Design of the Superconducting Quarter Wave Resonators for HIAF", in *Proc. SRF'17*, Lanzhou, China, Jul. 2017. doi:10.18429/JACoW-SRF2017-MOPB007.

[6] Mike Kelly, "TEM-class Cavity Design", presented in SRF'13 Tutorial Program, Ganil, Caen, Sep. 2013, unpublished.

[7] ANSYS, Inc., Canonsburg, Pennsylvania, USA. www.ansys.com

[8] J. Rodnizki *et al.*, "Superconducting accelerating cavity pressure sensitivity analysis and stiffening", in *Proc. 27th Linear Accelerator Conf. (LINAC'14)*, Geneva, Switzerland, Sep. 2014, paper MOPP134.

[9] Hasan Padamsee *et al.*, "RF Superconductivity for Accelerators", Cornell University, Ithaca, New York, USA: Wiley, 1994, pp.179.

Content from this work may be used under the terms of the CC BY 3.0 licence (© 2018). Any distribution of this work must maintain attribution to the author(s), title of the work, publisher, and DOI.

ISBN: 978-3-95450-194-6 ISSN: 2226-0366 doi:10.18429/JACoW-LINAC2018-THPO079

RF TEST OF STANDING WAVE DEFLECTING CAVITY WITH MINIMIZED LEVEL OF ABERRATIONS

V. Paramonov*, INR of the RAS, Moscow, Russia
K. Floettmann, DESY, Hamburg, Germany

Abstract

For diagnostics of longitudinal distribution of electrons in the unique REGAE bunches a specially developed deflecting structure with a minimized level of aberrations in the field distribution and improved RF efficiency is applied. A short deflecting cavity has been constructed and installed on the REGAE beam line. The cavity is tested at the operational level of RF power. The main distinctive features of the cavity are mentioned and the obtained results are reported.

INTRODUCTION

The periodical Deflecting Structures (DSs) were introduced for charged particle deflection and separation. The bunch crosses the DS synchronously with the deflecting field Ed, which corresponds to the phase $\phi = 0$ in the DS and all the particles get the similar increment in the transverse momentum p_t.

Now DSs find new applications in bunch rotation for the purpose of diagnostics of the longitudinal distribution, the emittance exchange and the luminosity improvements in colliders. For these applications a DS operates in another mode - the central particle of the bunch crosses the DS at a zero E_d value, $\phi = 90^o$. Downstream and upstream particles get opposite increments in p_t. In applications for bunch rotation a DS should produce the minimum possible own distortions in the original distributions of particles in the 6D phase space.

METHODOLOGICAL AND PHYSICAL BASIS

The concept of DSs with a minimized level of own aberrations in E_d distribution, preferred for bunch rotation, was introduced in [1]. The equivalent deflecting field E_d is defined by transverse components of RF field as:

$$E_d = E_x - \beta Z_0 H_y, \quad Z_0 = \sqrt{\frac{\mu_0}{\epsilon_0}}, \tag{1}$$

where β is the relative velocity of particles. The reasons for the transverse emittance growth during bunch rotation are the aberrations - the nonlinear additives in the E_d distribution, which take place due to non relativistic energy of particles, additions from higher multipole modes and the higher spatial harmonics in the distribution of the dipole deflecting field. The analysis of the deflecting field distributionwas performed [2] using the basis of hybrid waves HE and HM [3].

Both for travelling wave and standing wave DS operations, the deflecting field distribution can be represented [2] as an equivalent travelling wave. The main attention should be drawn to the higher spatial harmonics in E_d distribution [2, 4].

To estimate the level of higher spatial harmonics in E_d distribution and as a criterion for DS shape optimization parameters $\delta\psi_j(z)$ and Ψ_j at the DS axis are introduced:

$$\delta\psi_d(z) = \psi_d(z) + \frac{\Theta_0 z}{d}, \quad \Psi_d = max(|\delta\psi_d(z)|), \tag{2}$$

in the physical sense as the deviation and the maximal deviation in phase of the equivalent travelling wave E_d distribution from the synchronous harmonic. Here Θ_0 is the operating phase advance, d is the DS period length and $\psi_d(z)$ is the phase distribution for the equivalent travelling E_d wave. During bunch deflection or bunch rotation, the central particle in the bunch sees the field:

$$E_{def}(z) = E_{d0} cos(\psi_d(z)) \sim E_{d0}(1 - \frac{\Psi_d^2}{2}), \tag{3}$$
$$E_{rot}(z) = E_{d0} sin(\psi_d(z)) \sim E_{d0}\Psi_d,$$

where E_{d0} is the deflecting field amplitude. With DS shape optimization we can change the ratio $\frac{E_x}{Z_0 H_y}$ in E_d distribution, Eq. 1. Minimizing Ψ_d we keep the bunch close to the DS axis, where the nonlinear field of higher spatial harmonics is not large. Simultaneously the level of higher spatial harmonics in E_d will be reduced - the spatial harmonics in E_x compensate the spatial harmonics in $Z_0 H_y$. As a result, we have in orders smaller transverse emittance growth during bunch rotation [4].

For conventional DSs [3] Ψ_d minimization is an additional limitation and can be achieved only at the expense of reduction in the effective shunt impedance value Z_e. To combine the requirements for high RF efficiency and high field quality we need more freedom in the structure design. Based on promising parameters of the DS with a 'TE-like' operating mode [5] a decoupled DS was proposed with separated control on the RF efficiency and on the field quality. Possible solutions with decoupled DS are introduced in [6]. Later on the decoupled DS was investigated and optimized more thoroughly, showing very high rates in RF efficiency together with high field quality. A variety of possible attractive combinations in parameters of the developed DSs is described in [7].

CAVITY DESIGN PARAMETERS

For implementation in the deflecting cavity for diagnostics of longitudinal particles distribution in the REGAE (Rela-

* paramono@inr.ru

Content from this work may be used under the terms of the CC BY 3.0 licence (© 2018). Any distribution of this work must maintain attribution to the author(s), title of the work, publisher, and DOI.

ISBN: 978-3-95450-194-6 ISSN: 2226-0366 doi:10.18429/JACoW-LINAC2018-THPO079

tivistic Electron Gun for Atomic Exploration) [8] a decoupled DSs option was selected as a compromise between RF parameters, low energy and other extreme beam parameters, reasonability in construction and a space available. The geometry of the decoupled DS, selected for implementations, is shown in Fig. 1. Operating in the standing wave mode, a

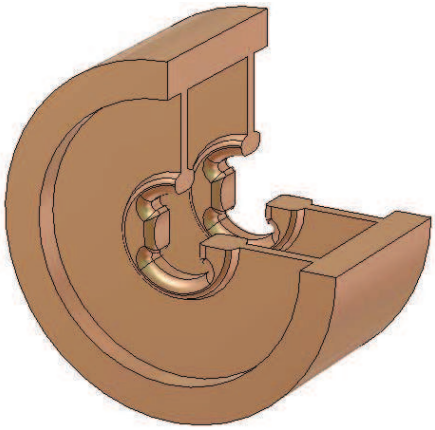


Figure 1: Geometry of the a decoupled structure, selected for deflecting cavity in the REGAE facility.

short cavity has three regular cells and two half cells at ends. The procedure for the end half cells formation is described, for example, in [6]. The main design parameters of the cavity are listed in Table 1. Figure 2 shows the distribution of

Table 1: Cavity Design Parameters

Parameter	Unit	Value
Operating frequency	MHz	2997.925
Energy of electrons	MeV	5
Operating phase advance	radian	π
Active cavity length	mm	≈ 210
Total cavity length	mm	270
Calculated quality factor		12550
Maximal phase deviation	radian	0.033
Separation with nearest mode	MHz	13.68
Effective shunt impedance, DS	$\frac{MOm}{m}$	43.2
Effective shunt impedance, cavity	MOm	7.58
Input RF power	kW	5
Expected deflecting voltage	kV	190

the effective deflecting field along the cavity axis, see Eq. 4, for bunch deflection (blue curve) and bunch rotation (red curve). As one can estimate from the red curve in Fig. 2, THE reduced oscillations of the bunch are expected for the bunch as a whole. The rms radius of the REGAE beam iN the place of deflecting cavity is expected to be ≈ 0.5 mm. Figure 3a depicts the surface for distribution of effective deflecting voltage $\frac{V_d(x,y)}{V_d(0,0)}$ in the region -4 mm $\leq x, y \leq 4$ mm near the cavity axis. From the corresponding contour maps in Fig. 3b for deviation $|\frac{V_d(x,y)-V_d(0,0)}{V_d(0,0)}|$ one can estimate V_d deviations as $\leq \pm 0.5\%$ for the region -2 mm $\leq x, y \leq 2$ mm

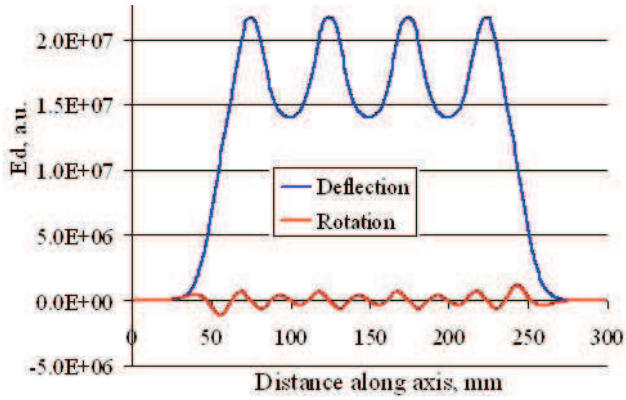


Figure 2: Distribution of the deflecting field E_d along the cavity axis for bunch deflection (blue curve) and bunch rotation (red curve).

and $\leq \pm 1.0\%$ for the region -3 mm $\leq x, y \leq$ 3mm. The total beam is expected to be in a very linear deflecting field.

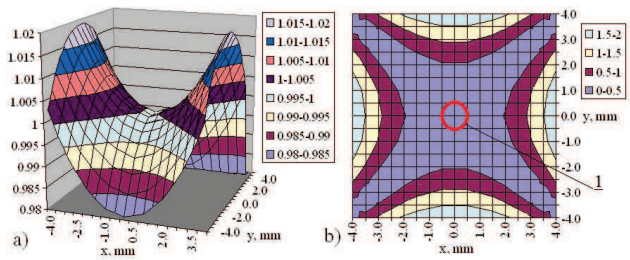


Figure 3: The surface of normalized value $\frac{V_d(x,y)}{V_d(0,0)}$ (a) and contour map for normalized deviation $|\frac{V_d(x,y)-V_d(0,0)}{V_d(0,0)}|$ near the cavity axis, 1 - rms diameter for the REGAE beam.

CONSTRUCTION AND RF TUNING



Figure 4: Parts of the cavity after machining, CANDLE SRI.

Technical design of the cavity was developed and cavity parts with high precision and high quality of surface treatment, Fig. 4, were manufactured in CANDLE SRI, Yerevan, Armenia. After high temperature brazing with silver alloys in DESY the cavity was tuned to a frequency of 2997.91 MHz assuming vacuum conditions and operating temperature of 35 C^o [9]. The bead pull measurements showed

Content from this work may be used under the terms of the CC BY 3.0 licence (© 2018). Any distribution of this work must maintain attribution to the author(s), title of the work, publisher, and DOI.

ISBN: 978-3-95450-194-6 ISSN: 2226-0366 doi:10.18429/JACoW-LINAC2018-THPO079

Content from this work may be used under the terms of the CC BY 3.0 licence (© 2018). Any distribution of this work must maintain attribution to the author(s), title of the work, publisher, and DOI.

following values of the transverse electric field component E_x 100/100.08/100.04/99.86 in the middle points of irises. It indicates a very narrow spread in the cell frequencies and confirms high precision in cells dimensions.

CAVITY AT THE REGAE BEAMLINE

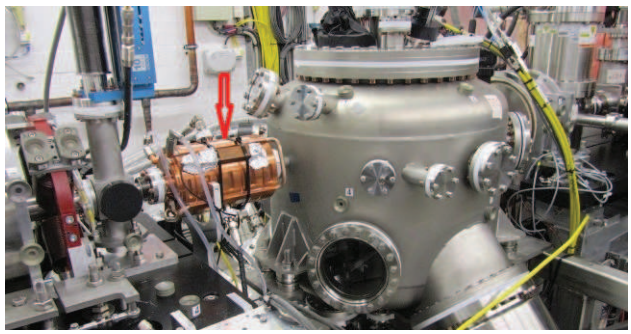


Figure 5: Cavity mounted at the REGAE beam line.

After RF tuning and vacuum test the inner cavity surface was cleaned according to cleaning procedure [10] and mounted at the REGAE beam-line, Fig. 5. The control over the operating frequency is carried out by the temperature of the water in the channels, adhered to the cavity body by heat conducting paste. The source of RF power supply is a solid-state amplifier with a nominal RF power of 5 kW. The input RF coupler is a loop, due to small dimensions produced by 3D printing and coated with a thin film of gold. By rotation a driving RF loop was matched to the reflection coefficient $S_{11} = -31.6$ dB. The loaded quality factor Q_l, estimated from S_{11} measurements as $Q_l = 4570$, corresponds to the own quality factor $Q_0 \approx 9150$. The reasons for a moderate result in the obtained quality factor are under consideration. The transmission coefficient from driving to signal loops was adjusted to $S_{12} = -37.1$ dB, ensuring sufficient power for RF diagnostics. RF power up to 5.5 kW was achieved in the cavity without any problem, Fig. 6. The cavity operates

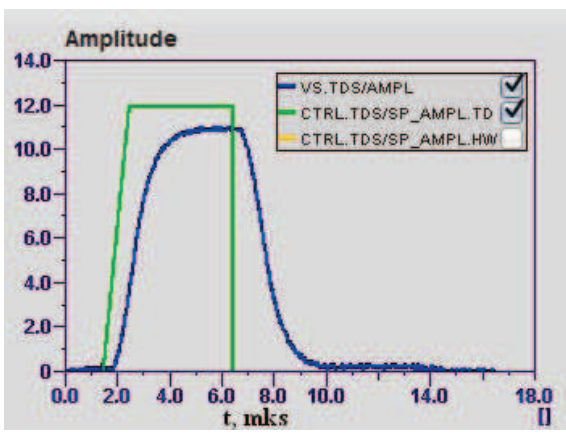


Figure 6: Envelopes of an output RF signal from the amplifier (green curve) and from RF probe in the cavity (blue curve).

with a very moderate value of deflecting field $E_d \approx 0.9 \frac{MV}{m}$ and, correspondingly, rather low RF power. There were no indications or proofs for multipacting discharge during operation with nominal RF power.

SUMMARY

For the first time a deflecting cavity specially optimized for minimal transverse emittance perturbation during rotation of a bunch was realized and RF tested. As compared to conventional deflecting structures, such z cavity provides physical benefits in applications for transformation of particle distributions in the bunch. These performances are requested in the facilities with unique bunch parameters. The successful test of the cavity at the nominal RF power was carried out. The cavity is ready for operation by purpose.

ACKNOWLEDGEMENT

The authors are deeply grateful to the CANDLE SRI group for careful, accurate and high-quality manufacturing of cavity parts.

REFERENCES

[1] V. Paramonov, " Deflecting Structures with Minimized Level of Aberrations", in *Proc. Linac 2012*, Tel Aviv, Israel, September 2012, p. 445.

[2] V. Paramonov, "Field distribution analysis in deflecting structures", DESY 18-13, DESY, arXiv:1302.5306v1, 2013.

[3] H. Hahn, "Deflecting Mode in Circular Iris-Loaded Waveguides", *Rev. Sci. Inst.*, v. 34, n. 10, p. 1095, 1963.

[4] K. Floettmann and V. Paramonov, "Beam dynamics in transverse deflecting rf structures", *Phys. Rev. ST Accel. Beams*, vol. 17, p. 024001, 2014.

[5] V. Paramonov, L. Kravchuk and K. Floettmann, "RF Parameters of the TE - Type Deflecting Structure", in *Proc. Linac 2012*, Tel Aviv, Israel, September 2012, p. 366.

[6] V. Paramonov, L. Kravchuk and K. Floettmann, "Standing Wave RF Deflectors with Reduced Aberrations", in *Proc. RuPAC 2012*, St. Peterburg, Russia, October 2012, p. 590.

[7] V. Paramonov, "Effective RF deflecting structures for bunch rotation and deflection", in *Proc. RuPAC 2016*, St. Peterburg, Russia, Novemver 2016, p. 201.

[8] S. Manz et. al., "Mapping atomic motion with ultrabright electrons: towards fundamental limit in space time resolution", in *Faraday Discussion*, 177, p. 467-491, 2015, http://dx/doi/org/10.1039/C4FD00204K

[9] V. Danielyan, K. Floettmann, V. Paramonov, A. Simonyan, V. Tsakanov, "Design, construction and tuning of an RF deflecting cavity for the REGAE facility", in *Journal of Physics: Conference Series*, to be published.

[10] A. Brinkmann, J. Ziegler, "Dry-ice cleaning of RF-structures at DESY", in *Proc. Linac 2016*, East Lansing, September 2016, p. 52. doi:10.18429/JACoW-LINAC2016-MOOP05

ISBN: 978-3-95450-194-6 ISSN: 2226-0366 doi:10.18429/JACoW-LINAC2018-THPO080

DESIGN VALIDATION OF A CHOPPING AND DEFLECTING SYSTEM FOR THE HIGH CURRENT INJECTOR AT IUAC

Sanjay Kumar Kedia[1, 2*], Rajeev Mehta[1], Rajesh Kumar[1], Rajeev Ahuja[1]
[1]Inter-University Accelerator Centre, Aruna Asaf Ali Marg, New Delhi-110067
[2]Department of Physics, Indian Institute of Technology Delhi, New Delhi-110016

Abstract

A chopping and deflecting system (CDS) has been designed and developed to provide the chopped beam with various repetition rates to the experimental facilities at the Inter-University Accelerator Centre (IUAC). The CDS consists of four pairs of deflecting plates with increasing gap from 15 mm to 21 mm to provide the maximum effective electric field and to achieve the maximum current within the same voltage conditions. The design of CDS has been validated with various simulation codes including CST MWS, Solid Works, Python and TRACE 3D etc. The deflecting plates, bushes and spacer have been fabricated and assembled within the accuracy of 100 microns. The mechanical measurements were carried out using a slip gauge and Coordinate Measuring Machine. A high vacuum chamber has been designed and developed to incorporate the entire inner assembly. The whole assembly has been installed in the high vacuum chamber and aligned using theodolite. The assembly has been leak tested using helium leak detector in the range of $1x10^{-9}$ mbar.liter/sec. The electrical design of CDS has been validated by installing and testing in the Low Energy Ion Beam Facility (LEIBF) at IUAC. A slit has been introduced to cut the undesired particles, and a beam profile monitor and Faraday cup has been installed to measure the amount of deflection and beam current respectively. The DC voltage has been applied across the four pairs of deflecting plates and amount of deflection was measured accordingly. The design, development, and DC beam test will be discussed in the article.

INTRODUCTION

The accelerator-based experimental facilities at the Inter-University Accelerator Centre (IUAC) depend on the 15 UD Pelletron [1] accelerator and the niobium superconducting quarter wave resonator based superconducting linear accelerator operating (SC-LINAC) at 97 MHz [2]. The ion beams delivered by Pelletron accelerator can be used directly for the experiments or injected into the superconducting linear accelerator for further energy gain. An alternative injector was felt to be necessary due to the limitation of the existing Pelletron accelerator. The High Current Injector (HCI) [3] accelerator has been designed to overcome the limitation of the existing Pelletron accelerator and to provide the high current with varieties of the ion species including inert gases etc. which are not feasible with the existing 15 UD Pelletron accelerator. The HCI was proposed as an alternative injector to the SC-LINAC, and the current Pelletron accelerator will serve as a standalone facility.

The HCI consists of various normal conducting RF cavities including Radio Frequency Quadrupole [4], Six IH type Drift Tube Linear Accelerator [5], Spiral Buncher [6] and low beta cavity. The nuclear physics experimental facilities at IUAC require a clean pulsed beam without dark current at various repetition rates. A requirement of a chopper and deflector was found to be necessary to provide a chopped beam with multiple repetition rates to the IUAC experimental facilities. The LEBT section was found to be the most suitable section for CDS since it needs lower voltage to deflect the undesired charged particles. Due to space constraint, both chopper and travelling wave deflector (TWD) has to combine, and a single device has been designed called chopping and deflecting system [7]. The CDS has been designed within 220 mm space along the beam direction (see Fig. 1).

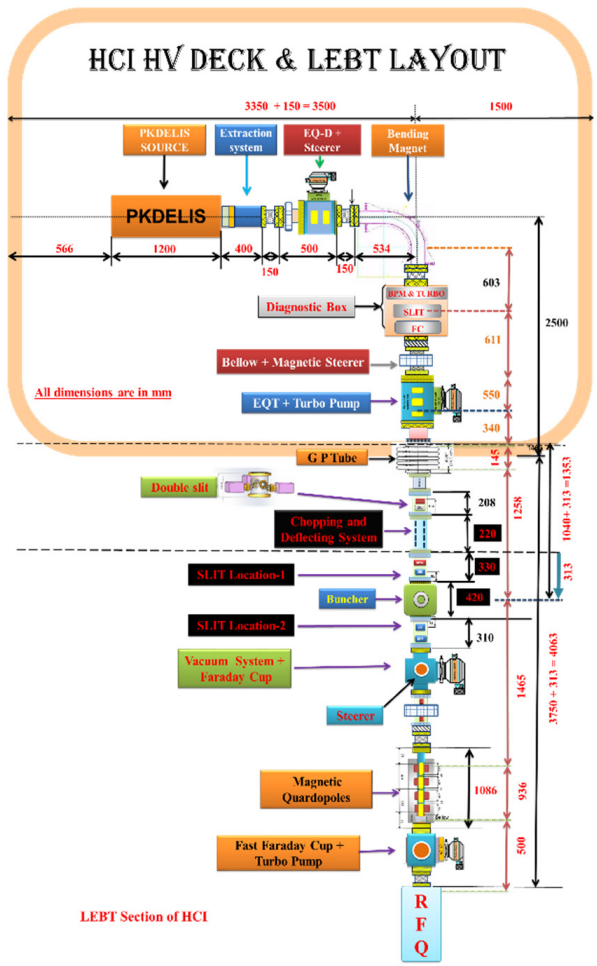


Figure 1: The location of CDS has been depicted in the layout of the LEBT section of the High Current Injector.

Content from this work may be used under the terms of the CC BY 3.0 licence (© 2018). Any distribution of this work must maintain attribution to the author(s), title of the work, publisher, and DOI.

ISBN: 978-3-95450-194-6 ISSN: 2226-0366 doi:10.18429/JACoW-LINAC2018-THPO080

Content from this work may be used under the terms of the CC BY 3.0 licence (© 2018). Any distribution of this work must maintain attribution to the author(s), title of the work, publisher, and DOI.

DESIGN AND SIMULATIONS

Electrical Design

The CDS incorporates the four pairs of deflecting plates with varying gaps between the deflecting plates, and the separation between the pairs of deflecting has been kept constant as shown in Fig. 2.

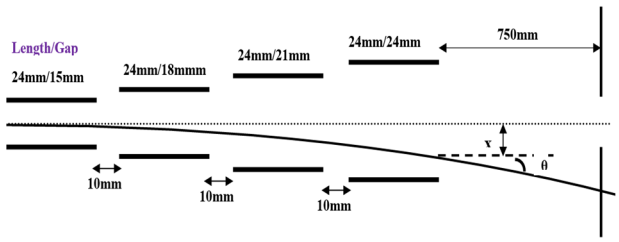


Figure 2: The 2D design of chopping cum deflecting system for HCI.

The length of the deflecting plate has been optimised to achieve the maximum current in the bunch of 60 ns. The gap between the deflectors has been chosen to increase the effective electric field within the same voltage conditions. The centre to centre spacing between the pair of deflectors has been kept constant which is equivalents to 28.3 ns transit time period. A delay will be fixed to provide the synchronisation. The semi-cylindrical contour has been incorporated in the deflector plates to improve the linearity and effective voltage as shown in Fig. 3. Two slit locations have been traced out to cut the undesired charged particles. It was simulated that the second slit location which is located at 750 mm is capable of providing more no of charged particles comparatively.

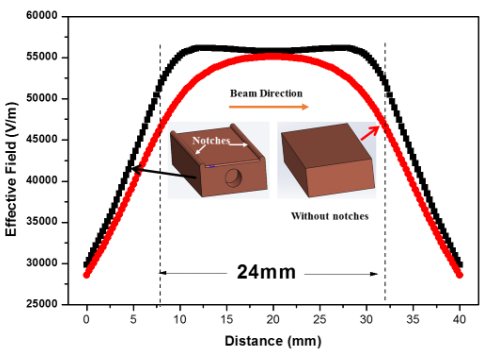


Figure 3: The plate design modification to improve the linearity and effective electric field.

By the incorporation of the contour, the linearity has been increased by a multiplication factor of two and effective field seen by the charged particle has been increased by 10% [7]. The various simulation codes have been used to validate the electric design.

Mechanical Fabrication and Installation

The mechanical fabrication has been divided into two steps inner assembly and outer assembly (see Fig. 4). The inner assembly consists of deflector plates, bushes, spacers, top plate and bottom plate etc. The OFHC copper has been used to fabricate the deflector plates. The inner assembly has been built, cleaned using an ultra-sonic coater and assembled within the accuracy of 100 microns. The outer housing consists of a vacuum chamber. The outer chamber has been fabricated, and leak tested in the range of $1x10^{-9}$ mbar.liter/sec. The outer chamber has two 8 inches CFF flange to install the chamber in the beam line. The inner assembly has been mounted in the vacuum chamber and aligned using theodolite. The mechanical measurements were carried out using a slip gauge and Coordinate Measuring Machine within the error of 3%.

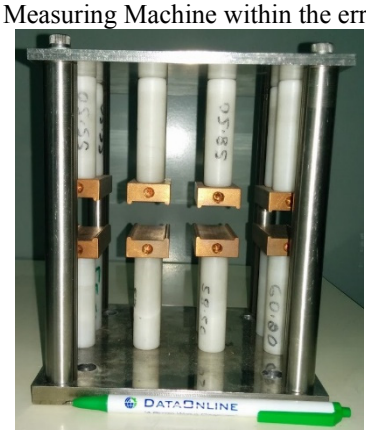


Figure 4: The complete inner assembly with its four pairs of deflecting plates.

The complete CDS system with its accessories has been installed in the LEIBF to validate the electric design. A compact diagnostic box [8] including a slit, Faraday cup and slit scanner has been installed at 750 mm far away from the CDS system as shown in Fig. 5. The deflector plates have been provided with a DC bias voltage using four feed-throughs as shown in Fig. 6. The SHV connectors and high voltage power supplies have been used to produce the DC voltage to deflectors. All the deflectors are electrically isolated to each other. The field of opposite polarity has been provided to the pair of deflectors to minimise the fringing field.

RESULTS AND DISCUSSIONS

The chamber has been installed in the LEIBF facility and aligned using theodolite. The high vacuum has been achieved within ~5 hours. The deflectors have been connected to the high voltage power supplies. Due to unavailability of the beam time in the LEIBF facility, the beam test has been postponed. A python code has been developed to validate the design parameters. The design parameters closely match with the simulated value. The beam test will be presented separately.

CONCLUSION

The design, development of CDS have been completed. We are in the process to purchase and development of a 4 MHz RF pulsers in collaboration with BHELKE company. The RF pulsers has been designed to provide the 60 ns off time at various frequencies including 4, 2, 1, 0.5, 0.125. The beam test will be discussed separately after procuring the RF pulsers.

ISBN: 978-3-95450-194-6 ISSN: 2226-0366 doi:10.18429/JACoW-LINAC2018-THPO080

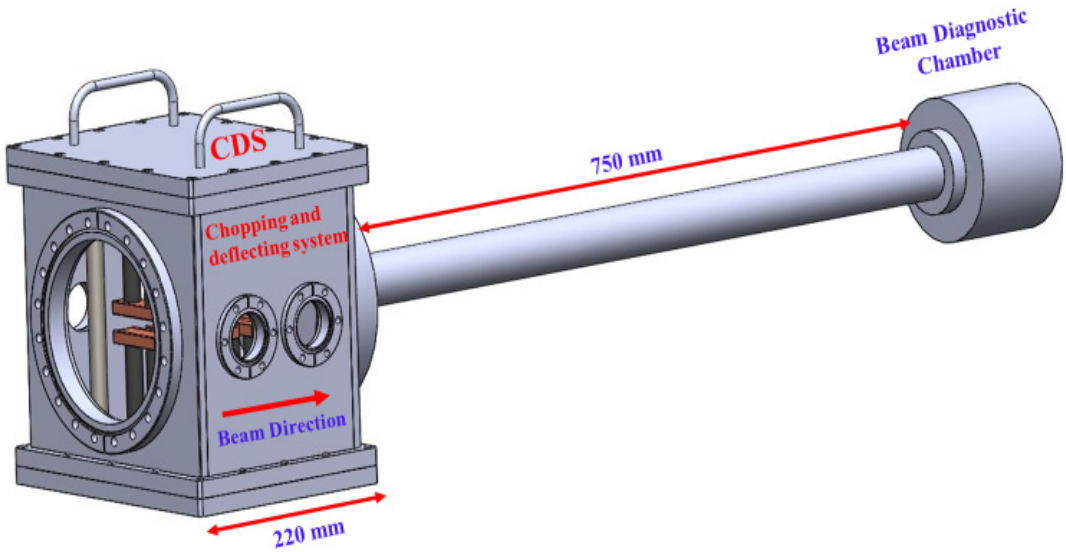


Figure 5: The CDS system including inner assembly, an outer chamber, the drift of length 750 mm, and a diagnostic box.

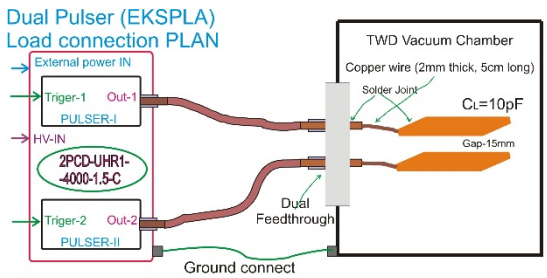


Figure 6: The deflector plates are connected to the power supply using feedthroughs.Results and Discussions.

REFERENCES

[1] D Kanjilal *et al.*, "Testing and operation of 15 UD Pelletron at NSC", *Nucl. Instrum. Methods* A, 328 (1993) 97.

[2] Amit Roy, "Accelerator development at Nuclear Science Centre", *Current Science*, 76 (1999) 149.

[3] D Kanjilal, *et al.*, "High Current Injector at Nuclear Science Centre", in: Proc. APAC Korea (2004) 73.

[4] R Ahuja, *et al.*, "Design & fabrication of Radio Frequency Quadrupole (RFQ) accelerator at IUAC", New Delhi, in: Proc. InPAC'09, RRCAT Indore, February 2009.

[5] B P Ajith Kumar *et al.*, "Beam optics and resonator design for the 97 MHz DTL at IUAC", in: Proc. InPAC2009, RRCAT Indore, India.

[6] Rajeev Mehta *et al.*, "Development of spiral buncher and diagnostic systems for the high current injector at IUAC", in: Proc. InPAC2018, RRCAT Indore, India.

[7] S K Kedia, Rajeev Mehta, "Design and development of a chopping and deflecting system for the high current injector at IUAC", *Nucl. Instrum. Methods* A, 889 (2018) 22.

[8] R V Hariwal *et al.*, "Compact and complete beam diagnostic system for HCI at IUAC", in *Proc. IBIC'15*, Melbourne, Australia, Sep. 2015, pp. 351-353, doi:10.18429/JACoW-IBIC15-TUPB018

Content from this work may be used under the terms of the CC BY 3.0 licence (© 2018). Any distribution of this work must maintain attribution to the author(s), title of the work, publisher, and DOI.

ISBN: 978-3-95450-194-6 ISSN: 2226-0366 doi:10.18429/JACoW-LINAC2018-THPO082

PHYSICAL DESIGN OF A RECTANGULAR RF-DEFLECTOR FOR ULTRA-SHORT BUNCH LENGTH MEASUREMENT*

J. Bai, Q. Chen, K. Fan†, State Key Laboratory of Advanced Electromagnetic and Technology, Huazhong University of Science and Technology (HUST), [430074] Wuhan, China

Abstract

Cylindrical deflectors which are now widely used for bunch length measurement suffer from the degeneration of polarization, while rectangular deflectors can separate polarization mode easily. This paper is focused on the study of a one-cell rectangular deflector, which is considerably different from cylindrical structure or multi-cell structure. A one-cell structure is free of π mode restriction and can achieve higher deflection efficiency per unit length. The proposed scheme is expected to achieve time resolution better than 200fs with the driving power less than 1MW. Cavity optimization and beam dynamic simulation are introduced in this paper.

INTRODUCTION

The linac-based terahertz free-electron laser (THz-FEL) facility with an independent tunable cavity (ITC) RF gun built in Huazhong University of Science and Technology (HUST) has undergone a long term beam commissioning [1]. One important reason is that there is no adequate beam diagnostic instruments due to the ultra-compact structure. In FEL, bunch length that defines the peak current is a critical parameter for the amplification process, but we still have not had an effective method to measure it accurately. Using RF deflector is an attractive method to measure bunch length in sub-picosecond level, while conventional cylindrical cavities suffer from degeneration of polarization due to their axial symmetry [2]. So we propose to use a rectangular structure with an aspect ratio not equal to 1. For 10 MeV electron beams and 1 MW driving power, the rectangular RF deflector system is targeted to be shorter than 1 m and is supposed to achieve time resolution better than 200 fs.

THEORY OF RF-DEFLECTOR SYSTEM

An RF-deflector imparts a transverse momentum on the bunch and directly relates the longitudinal bunch distribution into transverse one. The bunch length can then be inferred after measuring the downstream beam profile. According to the Panofsky-Wenzel theorem [3], the deflecting voltage is:

$$V_d = \int_h [E_\perp + (v \times B)_\perp] dz \,. \qquad (1)$$

Where h is cavity length along the beam direction (z-axis).

Considering a simple case in which there is only a drift between the deflector and the downstream screen, the bunch length can be computed as:

$$\sigma_t = \frac{p_z c}{q V_d L \omega} \sqrt{\sigma_{ys}^2 - \sigma_{yso}^2} \,. \qquad (2)$$

Where p_z is the longitudinal momentum of the electron bunch, L is the drift distance from the center of the RF-deflector to the downstream screen, c is the velocity of the light, σ_{ys} and σ_{yso} are the beam size on the screen with the deflector on and off, respectively. Temporal resolution σ_{t_res} is defined as:

$$\sigma_{t_res} = \frac{p_z c}{q V_d L \omega} \sigma_{ys0} \,. \qquad (3)$$

For a specific electron beam and power source, higher deflecting voltage will result in better time resolution [4] The goal of the cavity design optimization is to find a cell geometry to maximize the deflecting voltage.

OPTIMIZATION OF THE CELL GEOMETRY

For the TM_{120} mode, there is no transverse electric field. According to Eq. (1), the analytical form of V_d can be expressed by,

$$V_d = \sqrt{\frac{2PQ\omega\varepsilon}{a^3 b h}} \frac{8\pi\mu_0 c}{k_c^3} \sin(\frac{\omega h}{2v_z}) \,. \qquad (4)$$

Where a and b are the horizontal and vertical dimensions of the cavity, P is the power loss on the inner wall, Q is the quality factor of the cavity in TM_{120} mode, ε is the dielectric constant, k_c is the wave number, v_z is the particle velocity along the z axis. Eq. (4) is assumed as the basis for optimizing the cavity in this paper.

As for a rectangular cavity operated in the TM_{120} mode, the quality factor is determined by its geometry:

$$Q = \frac{2}{\delta} \frac{\int_v |H^2| dv}{\oint_s |H_\tau^2| ds} = \frac{1}{\delta} \frac{abh(a^2 + 4b^2)}{a^3(b+2h) + 4b^3(a+2h)} \,. \qquad (5)$$

Where δ is the skin depth, H_τ is the tangential magnetic field of the cavity surface.

According to Eq. (5), Eq. (4) can be re-written as:

$$V_d = A \sqrt{\frac{(a^2 + 4b^2)}{a^5(b+2h) + 4a^2 b^3 (a+2h)}} \sin(\frac{\omega h}{2v_z}) \,. \qquad (6)$$

* Work supported by the National Natural Science Foundation of China (No. 11705062) and the China Postdoctoral Science Foundation (No. 2018T110763).
† Email address: kjfan@hust.edu.cn

Content from this work may be used under the terms of the CC BY 3.0 licence (© 2018). Any distribution of this work must maintain attribution to the author(s), title of the work, publisher, and DOI.

ISBN: 978-3-95450-194-6 ISSN: 2226-0366 doi:10.18429/JACoW-LINAC2018-THPO082

Where $A = \frac{8\pi\mu_0 c}{k_c^3}\sqrt{\frac{2P\omega\varepsilon}{\delta}}$.

What is more, there is a constraint of a and b because this cavity operates at 2856 MHz. Thus giving,

$$a = \frac{4}{\sqrt{(\frac{2f}{c})^2 - (\frac{1}{b})^2}} . \quad (7)$$

As mentioned in the previous section, our aim is to maximize the deflecting voltage. We use MATLAB for numerical optimization. Fig.1 shows the optimal a and the corresponding deflecting voltage Vd as a function of h. Based on the curve of the deflecting voltage, it can be simply thought that the value of h corresponding to the extreme point is the optimal solution. Then, the optimal solution of the value of a could be determined and the optimal solution of the value of b could be obtained by inverting Eq. (7). Finally, we conclude that for an ideal and closed rectangular cavity operated in TM120 mode, the optimal dimension to generate maximum deflecting efficiency is 120.59 mm × 106.64 mm × 46.96 mm (x×y×z).

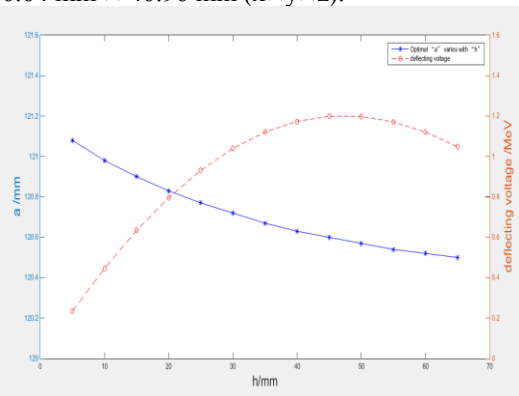


Figure 1: Optimal a and the deflecting voltage as a function of h, the power loss P is assumed as 1 MW.

CST SIMULATION

In practical applications, round corners, beam pipes, and couplers all affect the field distribution and the resonant frequencies of the cavity. In this section, the 3-D simulation software CST is used to adjust the parameters of the RF-deflector cavity and calculate the distribution of electromagnetic field and S-parameter. The left panel of Fig.2 shows the model of the RF-deflector.

The design of the coupler directly affects the efficiency of the feed power. The right panel of Fig. 2 shows a partial enlarged view of the coupling hole. Having consider the effect of a beam current of 0.2 A on the coupling coefficient in this standing-wave cavity, we find it makes better use of feed power when the reflection coefficient reaches -20.66 dB. For this reason, we changed the parameters of coupling hole to gain a suitable reflection coefficient and the optimal dimensions of the coupler is found to be 10.47 mm × 1.00 mm × 34.04 mm (x×y×z).

The magnitude and polar plot of S-parameter of RF-deflector cavity are shown in Fig. 3 and Fig. 4, respectively.

Finally, we simulated a practical open cavity operated in TM_{120} mode, the optimal dimension to generate maximum deflecting efficiency is 120.80 mm × 104.20 mm × 46.96 mm (x×y×z).

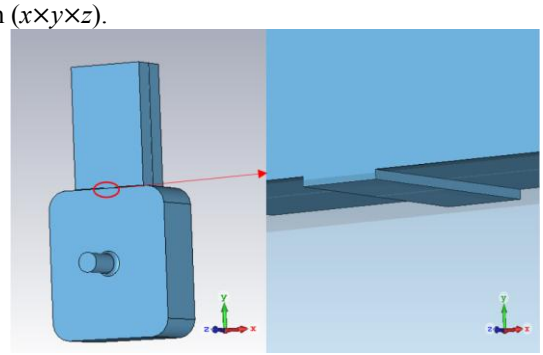


Figure 2: Structure of the RF-deflector cavity.

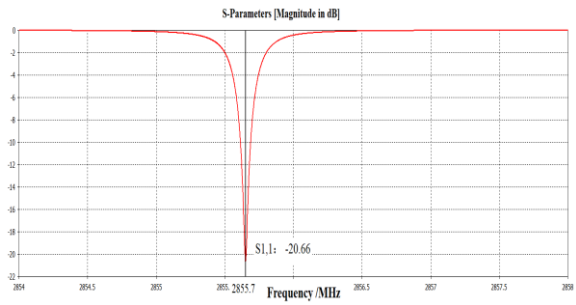


Figure 3: The magnitude of S-parameter of rf-deflector.

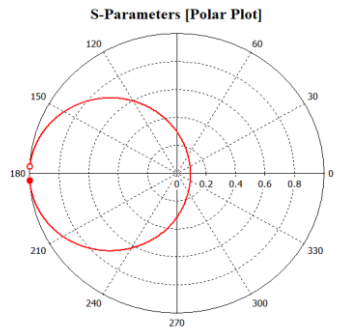


Figure 4: The polar plot of S-parameter of rf-deflector.

BEAM DYNAMICS SIMULATION AND ANALYSIS

Having imported the resonant field data produced by CST, we use Parmela to simulate the beam dynamics.

As mentioned above, when the beam energy is 10 MeV and the RF-deflector system is shorter than 1 m, our target is to achieve time resolution better than 200 fs with the driving power less than 1MW. The parameters of bunch are shown in Table 1.

According to Eq. (3), the calculated time resolution is 174.15 fs and meets our requirements. We used Parmela for particle tracking and for evaluation of the performance of the cavity. This electron beam is focused to a vertical beam size of 0.3 mm (RMS), and it will enlarge to 0.884 mm (RMS) when the RF-deflector is on. Figure 5 shows the transverse profile of the electron beam with the RF-deflec-

Content from this work may be used under the terms of the CC BY 3.0 licence (© 2018). Any distribution of this work must maintain attribution to the author(s), title of the work, publisher, and DOI.

ISBN: 978-3-95450-194-6 ISSN: 2226-0366 doi:10.18429/JACoW-LINAC2018-THPO082

tor off and on, respectively. The parameters of RF-deflector are shown in Table 2. According to Eq. (2), the RMS bunch length is about 482.70 fs. There is a 0.70% deviation between our calculations and theoretical results (486.11 fs). Overall the RF-deflector system in principle meets the design requirements.

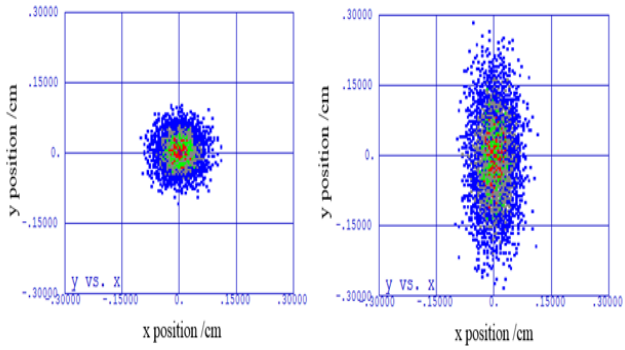


Figure 5: Transverse profile of the electron beam with the RF-deflector off (left) and RF-deflector on (right).

Table 1: Parameters of Bunch

Parameter	Value
Beam energy E [MeV]	10
Bunch length (RMS) [fs]	486.11
Change [pC/bunch]	100
Beam size σ_{yso} [mm]	0.3

Table 2: Parameters of RF-Deflector Design

Parameter	Value
Input rf-power Pin [MW]	1
Operation frequency f [MHz]	2856
Drift length L [m]	0.8
Deflecting Voltage V[MV]	1.20
Temporal resolution σ_{t_res} [fs]	174.15

CONCLUSIONS

In this paper, we introduced the basics of RF-deflector for sub-picosecond bunch measurement and obtained an optimal solution for the cavity size. We built a model of this cavity by 3-D simulation software CST, and calculated the distribution of electromagnetic field. For 10 MeV electron beams, the designed RF-deflector system, which is shorter than 1 m, achieves the time resolution better than 200 fs. Theoretical calculations have been verified by Parmela. In the future, we will install the RF-deflector system in the THz-FEL facility in HUST.

REFERENCES

[1] Q. Chen, et al., "Design of RF chopper system for improving beam quality in FEL injector with thermionic gun", *Nuclear Inst. and Methods in Physics Research*, no. 755, pp. 78-84, 2014.

[2] Y. Nishimura, et al., "Design of a two-cell RF-deflector cavity for ultra-short electron bunch measurement", *Nuclear Inst. and Methods in Physics Research, A*, no. 764, pp. 291-298, 2014.

[3] W. K. H. Panofsky and W. A. Wenzel, "Some considerations concerning the transverse deflection of charged particles in radio-frequency fields", *Review of Scientific Instruments,* no.72, p.967, 1956.

[4] Y. Nishimura, et al., "Study on two-cell RF-deflector cavity for ultra-short electron bunch measurement", in *Proc. IPAC'13*, Shanghai, China, May 2013, paper WEPFI023, pp. 2753-2755.

Content from this work may be used under the terms of the CC BY 3.0 licence (© 2018). Any distribution of this work must maintain attribution to the author(s), title of the work, publisher, and DOI.

ISBN: 978-3-95450-194-6 ISSN: 2226-0366 doi:10.18429/JACoW-LINAC2018-THPO083

TRANSVERSE DEFLECTING CAVITY FOR LONGITUDINAL BEAM DIAGNOSTICS AT bERLinPro

G. Kourkafas*, T. Kamps, A. Neumann, Helmholtz-Zentrum Berlin, Berlin, Germany
B. Keune, RI Research Instruments GmbH, Bergisch Gladbach, Germany

Abstract

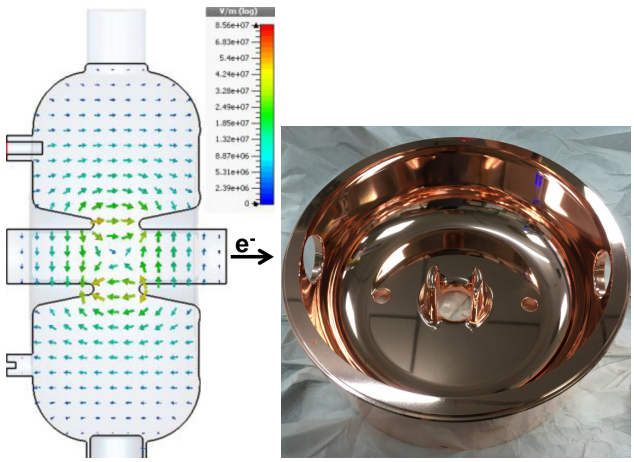
The Berlin Energy Recovery Linac Prototype (bERLinPro) at Helmholtz Zentrum Berlin (HZB) aims to deliver a continuous-wave electron beam of high average current (100 mA) and brilliance (normalized emittance below 1 mm·mrad). The achievement of these ambitious goals necessitates a thorough determination of the bunch parameters after the first acceleration stages, namely the photoinjector and the succeeding booster module. For the measurement of primarily the bunch duration and subsequently the longitudinal phase space and transverse slice emittance, a single-cell 1.3-GHz TM110-like mode vertically deflecting cavity was manufactured by RI Research Instruments GmbH, following the respective design developed for the Cornell ERL injector. This article summarizes the design parameters, manufacturing procedure and testing of this pulsed RF resonator, together with the expected temporal measurement resolution for the nominal beam energies at the initial acceleration stages of bERLinPro.

MOTIVATION AND DESIGN

A new Energy Recovery Linac (ERL) is being constructed at Helmholtz Zentrum Berlin (HZB) under the name Berlin Energy Recovery Linac Prototype (bERLinPro). The goal of this project is to develop the ERL operation principle towards user-oriented applications. The design of bERLinPro is that of a single-pass electron ERL which utilizes superconducting radiofrequency (SRF) technology to deliver a continuous-wave operation of high average current (100 mA) and brilliance (normalized emittance below 1 mm·mrad) [1]. The longitudinal beam properties at the initial acceleration stages (up to 6.5 MeV kinetic energy) will be diagnosed by a transverse deflecting cavity (TCAV).

A TCAV offers a straightforward way of measuring the electron bunch duration, or even the complete longitudinal phase space when combined with a spectrometer dipole, as well as the transverse slice emittance with the help of a quadrupole magnet [2]. It consists of an RF resonator operated in the TM_{110} mode (Fig. 1a), which when phased properly, transversely deflects the head and tail of the bunch in opposite directions. As a result, the longitudinal plane is projected into the transverse after some drift. Due to the damage threshold of the projection viewscreens, TCAV will be operated only in a special diagnostics mode of bERLinPro with reduced repetition rate which allows up to 0.5 μA average current. When passive, the cavity will not interfere with high beam currents as long as it is detuned from its resonant frequency (up to 75 mA demonstrated at Cornell ERL [3]).

The design of the cavity followed closely the one developed for the Cornell ERL injector, due to the resemblance of requirements for both applications [4]. In short, this design features a single-cell copper RF resonator with a transverse impedance of more than 5 MΩ and a resonance frequency of 1.3 GHz, tunable by a motorized plunger. Necessary adjustments were made to accommodate the available interfaces of HZB (Fig. 2): a) coaxial power feedthrough with 50 Ω matched impedance, 100 W average power rating and 2.7 kV_{rms} tolerance, b) coaxial 50 Ω RF pickup coupled at -51 dB to the input power, providing a mW signal level after cable attenuation (-13dB) at nominal operation, c) UHV-compatible linear stage for the adjustment of the plunger position up to ±25 mm, positioned at the bottom of the structure for improved particulate-free conditions, d) ion getter pump at the top of the structure.



(a) Electric field map. (b) Pot of TCAV after machining.

Figure 1: Inner contour of TCAV. Protrusion cones improve the vertical impedance and orientation of the dipole mode.

Two cavities were manufactured by RI Research Instruments GmbH according to these specifications. The manufacturing procedure, the results of the RF and vacuum testing and conditioning as well as the estimated resolution of the e-beam measurements at bERLinPro are described below.

CAVITY MANUFACTURING

The most significant adjustment from the original Cornell configuration was building the cavity out of two pieces, namely pot and lid, instead of two lids and a center ring. This increased the manufacturing precision, while minimizing the process time and risk. Each cavity part was milled from

* georgios.kourkafas@helmholtz-berlin.de

Content from this work may be used under the terms of the CC BY 3.0 licence (© 2018). Any distribution of this work must maintain attribution to the author(s), title of the work, publisher, and DOI.

ISBN: 978-3-95450-194-6 ISSN: 2226-0366 doi:10.18429/JACoW-LINAC2018-THPO083

Content from this work may be used under the terms of the CC BY 3.0 licence (© 2018). Any distribution of this work must maintain attribution to the author(s), title of the work, publisher, and DOI.

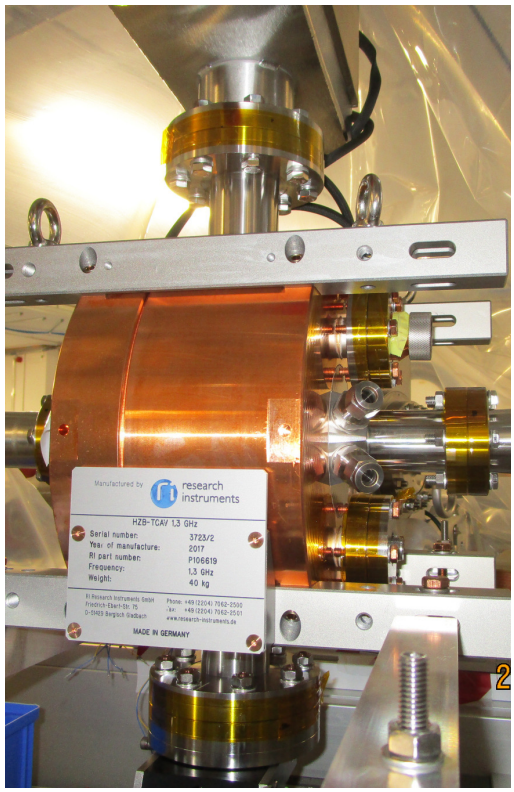


Figure 2: TCAV installed at bERLinPro. The ion getter pump can be seen on top, the ports of the input-power coupler, water cooling and RF pickup on the right side, and the frequency-tuning system on bottom.

OFHC copper on a 5-axis CNC milling machine. The surface roughness was better than R_a=0.2 µm, leaving a mirror like finish on the RF surfaces (Fig. 1b). Each individual part was equipped with the cooling channel lids, the CF ports for vacuum and RF equipment in a high temperature brazing step.

A new tuning concept was introduced to finally match the resonant frequency of the cavity before the last brazing step. A collar surrounding the noses was left on the lid of the cavity. The height of this collar was iteratively reduced by machining based on the results of clamped RF measurements until the resonance was matched. Then the final high temperature vacuum brazing was conducted. During the final RF testing also the field profile was recorded with an uncalibrated bead-pull measurement, showing a very symmetric distribution.

The cavity was assembled on a transport frame in a class ISO4 cleanroom together with the RF power coupler, the RF pickup, the ion getter pump and the motorized tuner. As part of the factory acceptance test (FAT), an integral leak test, a bake out at 130°C, a residual gas analysis (RGA) and pressure rise measurements have been performed (Table 1).

TESTING AND CONDITIONING

Before installing TCAV-2 in the bERLinPro beamline the following tests and procedures were performed at HZB:

Table 1: Resonance frequency f at 28°C, tuning range Δf for ±10 mm plunger movement, unloaded quality factor Q_0 and input coupling β_c from specification and FAT measurements

Parameter	Specs	TCAV-1	TCAV-2	Unit
f (28°C)	1300±0.2	1299.96	1300.02	MHz
Δf (±10mm)	~2	1.3	2.5	MHz
Q_0	>11000	12930	12460	-
β_c	1±0.1	0.9	0.97	-

- A leak test at a vacuum level of 10^{-9} mbar, measuring a leak rate in the order of 10^{-10} mbar·l/min.
- RGA showed low particulate concentrations, with peaks at H_2, H_2O, N_2 and CO_2.
- The resonant RF frequency, input coupling and quality factor were measured with respect to the plunger position at room temperature under vacuum. A 4 MHz tuning range has been demonstrated (Fig. 3), with the coupling ranging between 1.08-1.34 and the unloaded quality factor between 14200-12750 (6850-5550 loaded).
- RF conditioning was performed by feeding up to 12 kW peak power in the cavity with pulses of up to 40 μs at a repetition rate up to 200 Hz. Stable vacuum conditions were reached easily and no heating was observed with a 3.2 l/min flow of 28°C cooling water.

The results of the above tests met all specifications, while the design value of 5.3 MΩ for the transverse shunt impedance will be verified with beam measurements during operation.

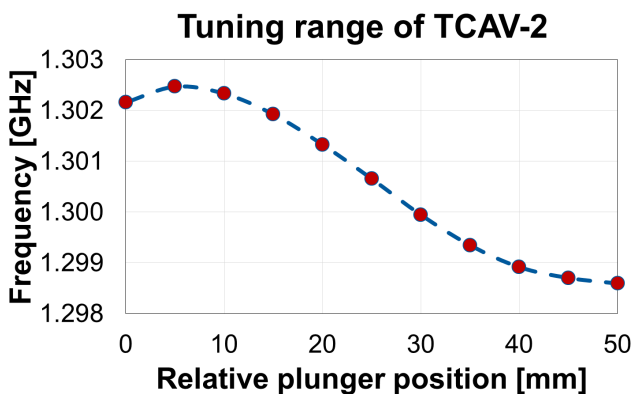


Figure 3: Measured range of the resonant frequency with respect to the relative position of its plunger. The nominal frequency is reached around 30 mm, which corresponds to a penetration of the plunger 10 mm inside the cavity.

TEMPORAL RESOLUTION

The vertical rms size of the deflected beam at the measurement screen downstream the TCAV is given by [5, 6]:

$$\sigma_s = \sqrt{\sigma_0^2 + \sigma_z S}, \quad (1)$$

ISBN: 978-3-95450-194-6 ISSN: 2226-0366 doi:10.18429/JACoW-LINAC2018-THPO083

where σ_0 is the corresponding size at the screen in the absence of RF deflection, σ_z the rms bunch length and S the shear parameter, defined as S=e$V_T kl/pc$, where p is the longitudinal momentum, l the drift length between cavity and measurement screen, k is the wave number for 1.3 GHz and $V_T = \sqrt{2PR_T}$ the peak deflecting voltage, with P being the peak RF power and R_T the vertical shunt impedance.

The most widely-used definition for the temporal resolution, which is relevant for the longitudinal phase-space measurements and slice emittance measurements is mentioned here as *slice resolution*. This corresponds to the minimum longitudinal distance between adjacent slices (or alternatively the minimal slice length δ_z), so that their transverse distance after deflection ($\delta_z S$) is bigger than the non-deflected vertical beam size (regarded as $2\sigma_0$), namely $\delta_z \geq 2\sigma_0/S$.

On the other hand, the shortest bunch duration which can be measured is the one whose transverse deflected size is bigger than its non-deflected vertical size by the amount of the optical resolution ρ of the readout system. In terms of rms values, this criterion can be written as $\sigma_s - \sigma_0 \geq \rho/2$, so that 2 sigma of the beam's transverse size will occupy an additional pixel on the camera of the projection screen. In combination with Eq. 1, this results in: $\sigma_z \geq \frac{\sqrt{(\rho/2+\sigma_0)^2 - \sigma_0^2}}{S}$, which is going to be referred as *bunch-length resolution* or *accuracy*.

For a given optical resolution, drift length, beam momentum, RF frequency and power, both definitions of the longitudinal resolution depend on the non-deflected vertical beam size at the projection screen σ_0. In order to reach the lower limit, a quadrupole magnet which is positioned 0.7 m upstream the TCAV can be used. The best focus (σ^*) which can be achieved in a drift section l can be calculated by the known beta-star optics relationship: $\beta(l) = \beta^* + l^2/\beta^*$, with $\beta^* = \sigma^*/\epsilon$ being the minimum achievable corresponding Courant-Snyder parameter for a geometrical emittance ϵ. After some calculations we get to $\sigma^* = \sqrt{\frac{\sigma^2 - \sqrt{\sigma^4 - 4l^2\epsilon^2}}{2}}$ under the condition that the beam size at the beginning of the drift is $\sigma \leq \sqrt{2l\epsilon}$. In this case the phase advance between quadrupole and projection screen approaches 90° and the measurement resolution is optimized [6].

Using all of the above, both resolution definitions are plotted in Fig. 4 versus RF peak power for the design kinetic energies of bERLinPro after the photoinjector (2.7 MeV) and the subsequent booster (6.5 MeV). For this calculation, the estimated optical resolution of 30 μm and a drift of 1.8 m were used, together with the expected beam parameters of 2 mm rms vertical beam size and 1 mm·mrad normalized emittance at the location of TCAV [7], assuming maximum focusing at the measurement screen. A 7.5 kW solid-state amplifier is planned to be used at bERLinPro, delivering 5 kW peak power into the cavity. This results to a bunch-length resolution of 70 fs and 100 fs for the photoinjector and booster regimes respectively and a 0.3 ps slice resolution, which will resolve more than 20 longitudinal slices according to the expected bunch parameters. When using realistic non-nominal beam parameters, a 35% variation of the bunch resolution and a 65% variation of the slice resolution in logarithmic terms is expected, according to a draft estimation. Simulations of the bunch-length measurement have been presented in [8].

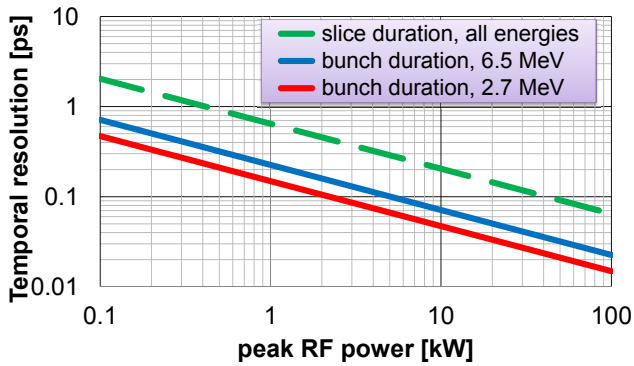


Figure 4: Temporal resolution of TCAV versus RF peak power for the nominal beam parameters at bERLinPro after the photoinjector (2.7 MeV) and the booster (6.5 MeV).

According to RF simulations, the cavity could receive up to 100 kW peak power without reaching the 2 Kilpatrick limit. However the existing feedthrough tolerance allows less than 40 kW when taking into account the doubling of the peak voltage due to the superposition of the incoming and reflected power during the filling time, plus a 30% safety margin. For this power level, the repetition rate should not exceed 200 Hz with RF pulses of 10 μs at minimum, according to the loaded quality factor and average power rating.

CONCLUSION

A transverse deflecting cavity for longitudinal electron beam diagnostics has been manufactured by RI Research Instruments GmbH by adapting a corresponding design developed at Cornell. The cavity has been installed at the straight diagnostics beamline of the bERLinPro facility at Helmholtz Zentrum Berlin after being tested and conditioned. The first beam measurements are expected to take place in 2019 and deliver a sub-ps temporal resolution.

ACKNOWLEDGEMENT

The authors would like to thank W. Anders, J. Hwang, F. Pfloksch, M. Schuster, H. Stein and J. Voelker from HZB for their technical support and useful discussions, as well as B. Dunham, F. Sannibale, V. Veshcherevich, D. Mallroy, T. Weis and M. Yan for sharing their work and experience on TCAV and the corresponding components.

REFERENCES

[1] M. Abo-Bakr et al., "Status Report of the Berlin Energy Recovery Linac Project BERLinPro", *Proc. IPAC2018*, Vancouver, Canada, paper THPMF034, pp. 4127-4130.

Content from this work may be used under the terms of the CC BY 3.0 licence (© 2018). Any distribution of this work must maintain attribution to the author(s), title of the work, publisher, and DOI.

ISBN: 978-3-95450-194-6 ISSN: 2226-0366 doi:10.18429/JACoW-LINAC2018-THPO083

Content from this work may be used under the terms of the CC BY 3.0 licence (© 2018). Any distribution of this work must maintain attribution to the author(s), title of the work, publisher, and DOI.

[2] P. Emma et al., "A Transverse RF deflecting structure for bunch length and phase space diagnostics", *Proc. PAC2001*, Chicago, USA, paper WPAH116, pp. 2353-2355.

[3] A. Bartnik, private communication, Jun. 2017.

[4] S. Belomestnykh et al., "Deflecting cavity for beam diagnostics at Cornell ERL injector", *Nucl. Instr. Meth. Phys. Res. A*, vol. 614, pp. 179–183, 2010.

[5] D. Alesini, "RF deflector based sub-ps beam diagnostics: Application to FEL and advanced accelerators", *Int. J. Mod. Phys. A*, vol. 22, p. 3693, 2007.

[6] K. Floettmann and V. Paramonov, "Beam dynamics in transverse deflecting rf structures", *Phys. Rev. ST Accel. Beams*, vol. 17, p. 024001, 2014.

[7] B. Kuske and M. Abo-Bakr, "Optics development and trajectory tuning of bERLinPro at low energies", *Proc. IPAC2017*, Copenhagen, Denmark, paper MOPAB033, pp. 153-155.

[8] M. McAteer et. al., "Simulations for beam-based measurements in bERLinPro", *Proc. IPAC2017*, Copenhagen, Denmark, paper MOPVA007, pp. 859-861.

ISBN: 978-3-95450-194-6 ISSN: 2226-0366 doi:10.18429/JACoW-LINAC2018-THPO084

BPM TIME OF FLIGHT MEASUREMENTS FOR SETTING-UP THE RF CAVITIES OF THE CERN LINAC4

M. Bozzolan†, CERN, 1211 Geneva 23, Switzerland

Abstract

The newly constructed H- LINAC4 at CERN has recently completed its first extended reliability run. It is equipped with Beam Position Monitors (BPMs) based on shorted-stripline pick-up electrodes to measure both position and Time of Flight (ToF). The ToF, in turn used to calculate the kinetic energy of the beam, is determined through signal phase shift measurements between pairs of BPMs. ToF measurements are performed by scanning of the phase of the RF injected into the cavities to find the nominal RF settings for optimal beam acceleration. This paper focuses on the technical aspects of the ToF measurement as well as on the results obtained during beam commissioning and their comparison with beam dynamics simulations.

INTRODUCTION

At the restart of the CERN accelerator complex in 2020, following a long shutdown (LS2), the CERN LINAC4 will be the first stage in the LHC injector chain for protons, replacing the ageing LINAC2. It is a normal conducting 80 m long H- LINAC which will supply beam pulses up to 600 μs long with an initial peak current of 25 mA, later to be increased to 40 mA [1].

The nominal output energy of 160 MeV is reached after a sequence of RF cavities, which include a Radio Frequency Quadrupole (RFQ), 3 Drift Tube Linac Tanks (DTL), 7 Cell Coupled DTL modules (CCDTL) and 12 Pi-mode Structures (PIMS) operating at f_{RF}=352.2 MHz

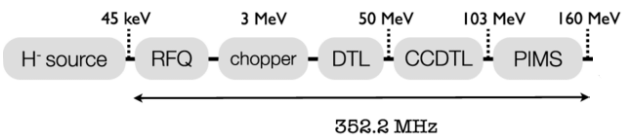


Figure 1: LINAC 4 accelerating structure – not to scale.

There are 15 BPMs installed inside the LINAC between the DTL (12 MeV) and the last PIMS module (see Fig. 1) and another 27 in the transfer line which connects LINAC4 with the PS booster [2].

Each BPM stripline electrode is directly connected to a 50—Ω cable, with lengths of the order of 100 m. These feeds the first analog stage of the acquisition system located in the instrumentation rack outside the tunnel, where the signals are amplified, downconverted to an intermediate frequency (IF) of 22.0125 MHz, filtered and digitized individually.

A ToF-based beam energy measurement is performed by measuring the time delay of the beam between two BPMs in a drift space (Fig. 2). As the distance between BPMs *L* is known the kinetic energy of the beam can be calculated by mean of the relativistic formulas

$$\beta = \frac{L}{TOF \cdot c}$$

$$E_{KIN} = \frac{m_0 \cdot c^2}{\sqrt{1-\beta^2}} - m_0 \cdot c^2$$

The electrode output signal, bandpass filtered at the LINAC bunching frequency f_{RF}, for the two BPM locations can be written as

$$y_{BPM1}(t) = A_1(t) * \sin(\omega_{RF} * t + \varphi_1)$$

$$y_{BPM2}(t) = A_2(t) * \sin(\omega_{RF} * t + \varphi_2)$$

Bunch shape, and therefore the amplitude modulation *A(t)* is not conserved, so a calculation of the time delay by cross correlation is not an option and only phase shift Δφ is used.

Since the phase wrap around every 360 °, we know only the fractional part **δ** of the ToF

$$TOF = NT + \delta = \frac{1}{f_{RF}}\left(N + \frac{\Delta\varphi}{360°}\right)$$

while the integer number *N* of RF periods (i.e. the number of bunches between the two BPMs) cannot be measured.

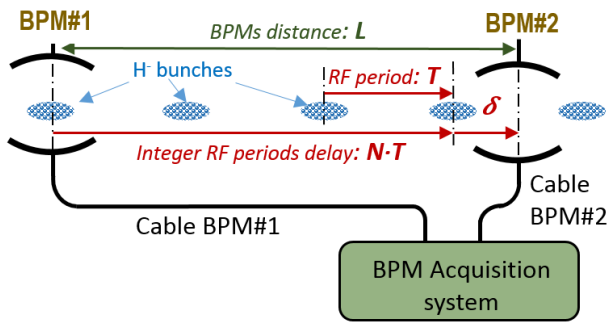


Figure 2: ToF principle.

PHASE MEASUREMENT & CALIBRATION

The sampling clocks at 4 times the IF frequency are phase locked to the linac RF, so that amplitude and phase of the signals can be recovered as

$$A = \sqrt{I^2 + Q^2}$$

$$\varphi = arctg\left(\frac{Q}{I}\right)$$

where I and Q are two consecutive samples.

For an operational system a precise phase (and amplitude for position measurement) calibration is needed

† michele.bozzolan@cern.ch

Content from this work may be used under the terms of the CC BY 3.0 licence (© 2018). Any distribution of this work must maintain attribution to the author(s), title of the work, publisher, and DOI.

ISBN: 978-3-95450-194-6 ISSN: 2226-0366 doi:10.18429/JACoW-LINAC2018-THPO084

Content from this work may be used under the terms of the CC BY 3.0 licence (© 2018). Any distribution of this work must maintain attribution to the author(s), title of the work, publisher, and DOI.

in order to distinguish the different contributions of cable and acquisition electronic.

In the LINAC4 BPM system this is performed by injecting a short, 352.2 MHz pulse into the cable coming from the electrode. Half the power of that signal (direct pulse) appears at the analog input, the other half travels down the cable, where it is fully reflected at the shorted end of the stripline electrode, and travels back to the electronics (reflected pulse) (Fig. 3).

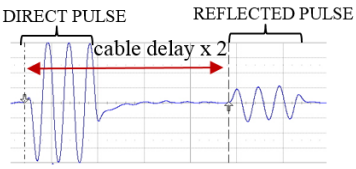


Figure 3: Calibration signals.

Since the calibration signal carries the reference phase for all the BPMs, it is distributed in such a way that it arrives at all the input channels with the same phase. Active components have been avoided in the calibration path because of the amplitude and phase shifts that occur due to temperature variation and aging.

TIME OF FLIGHT CALCULATION

The phase delay α between two BPMs is measured as the difference in phase of the signal from a given electrode (e.g. upper BPM electrode: H+)

$$\alpha = \Delta\varphi_{H+} = \varphi_{H+(BPM2)} - \varphi_{H+(BPM1)}$$

The measured delay has three contributions, the first is due to the beam, what we are looking for, the second is related to the cable delay difference and the third is related to the acquisition delay difference

$$\alpha = \Delta\varphi_{BEAM} + \Delta\varphi_{CABLES} + \Delta\varphi_{ELEC}$$

Since the calibration pulses are phase synchronous for all the channels, the phase shift due to the acquisition electronics is

$$\Delta\varphi_{ELEC} = \varphi_{DIRECT_PULSE(BPM2)} - \varphi_{DIRECT_PULSE(BPM1)}$$

Here no multiple integer parts of RF period are present because all the paths are virtually identical, with differences much less than one RF period.

The cable contribution $\Delta\varphi_{CABLES}$ is calculated from the individual phase shift of the cables

$$\Delta\varphi_{CABLES} = \varphi_{CABLE(BPM2)} - \varphi_{CABLE(BPM1)}$$

However what we actually measure for each BPM is

$$2 * \varphi_{CABLE} = \varphi_{DIR,MEAS} - \varphi_{REFL,MEAS} + M * 360° + 180°$$

where the 180° contribution is due to the shorted end of the BPM and *M* is an integer number of RF periods.

The Time of Flight can be written as

$$TOF = \frac{1}{f_{RF}} \cdot \frac{\Delta\varphi_{BEAM} + K * 180°}{360°}$$

with K=2N+M an integer number.

The periodicity becomes half an RF period as for the cable phase shift, since we can only measure the round trip of the signal.

K needs to be known in order to calculate the ToF and depends on the distance of the BPMs and the relativistic β of the beam. Putting an upper limit on the BPM distance ensures the value of *K* remains constant throughout the RF phase scan of the cavity, and it's value is known from simulations or from previous measurements. If this is not the case, the ToF is ambiguous as two or more values are possible.

However, reducing the distance between BPMs limits the precision, since a given error in the measured phase translates in a larger energy error for more closely spaced BPMs.

BEAM MEASUREMENTS

For the ToF we always have to ensure that there is no acceleration occurring between the involved BPMs. Therefore, in LINAC4, the cavities downstream of the first BPM used are switched off and detuned.

Moreover, the choice of BPMs that can be used for the RF scan of the cavities often have a distance that results in multiple possible values of K.

To overcome this it is possible to use two or more BPM pairs, calculate the energy as a function of K and then select the energy value that provides the smallest variance for all the pairs used. This method works well at the end of the LINAC4, for the scan of the last PIMS cavities where the absolute energy can be directly found with this method.

Figure 4 shows a graphical explanation of the method for a single energy using two BPMs pairs. The different calculated energy values as a function of K are plotted for each pair, with an energy of 160 MeV fittings precisely a particular K for both pairs.

Unfortunately this method does not work well for lower beam energies, providing inconsistent results. While the actual reason is not yet fully understood, a possible explanation is related to beam losses, which results in charged particles hitting the BPM electrodes and then altering the measurements. More beam studies are foreseen during the next run of the LINAC4 to improve the ToF algorithm for lower energies.

For the ToF measurement early in the linac at low β (DTLs and CCDTLs), a different approach is used to overcome the limitations encountered before.

Instead of individually correlating pairs of BPMs at a given phase, only the first BPMs pair after the scanned cavity is used and multiple values of K are considered.

Figure 5 shows a RF phase scan of CCDTL1 with only one BPMs pair. To extract the correct beam energy, the measurement is compared with a simulated RF phase scan (Fig. 6).

Even though this method does not provide a direct measurement of the beam energy for a single RF phase setting, it allows the exact behaviour of the cavities to be recovered through a complete phase scan.

ISBN: 978-3-95450-194-6 ISSN: 2226-0366 doi:10.18429/JACoW-LINAC2018-THPO084

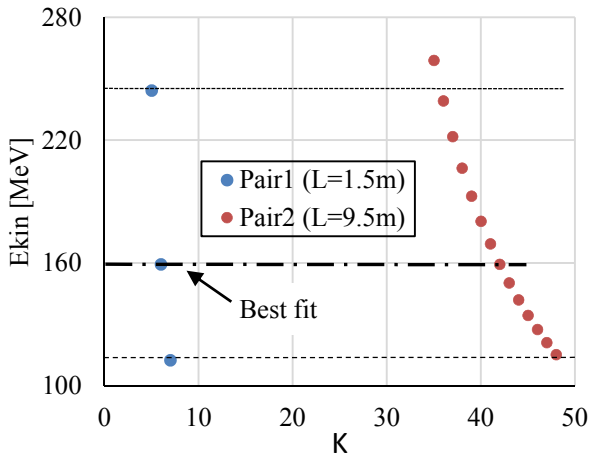


Figure 4: Single energy ToF measurement using 2 BPM pairs.
K=8 and 42 for PAIRS 1 and 2 give the same energy.

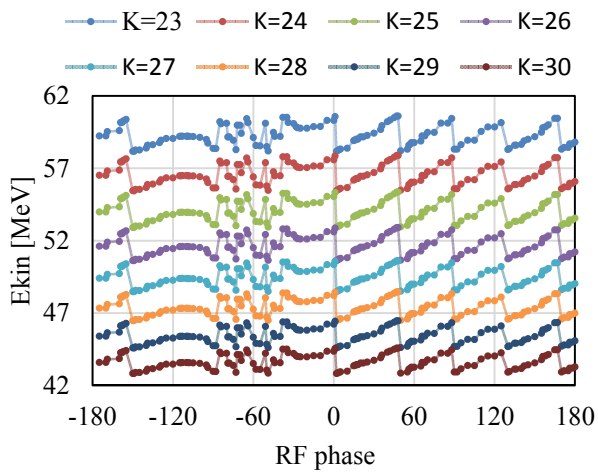


Figure 5: CCDTL1 phase scan: single BPM pair with different K values.

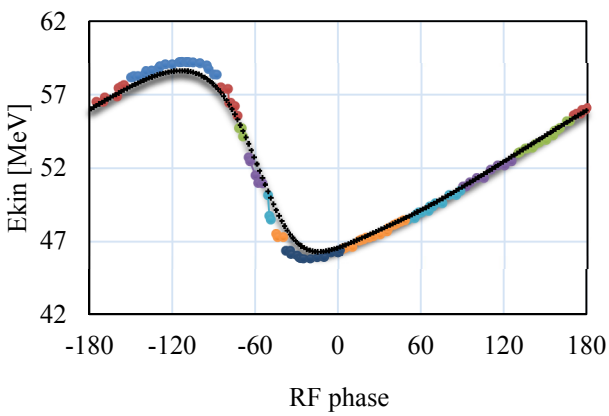


Figure 6: CCDTL1 RF phase scan cleaned after fitting. Simulated data as black crosses.

This procedure is still an expert task since the output beam energy depends not only on the RF phase but also on it's amplitude and on the energy of the beam entering the cavity.

The beam dynamics simulations provided so far show, for most part, a very good agreement with the measurements. Performing different phase scans for different amplitudes of the RF power has also been used as a crosscheck to validate the results.

CONCLUSIONS

The time of flight method for beam energy measurement in LINAC4 is now an operational tool for the RF phase adjustment of the cavities. While the high energy measurements are fairly simple, measurements for the DTL cavities, operating at low kinetic energy is still an expert task. The ToF algorithm is therefore being further refined, possibly to include changing the settings of the focusing elements during the RF phase scan, to provide a more automated measurement.

ACKNOWLEDGEMENTS

I would like to acknowledge the LINAC4 supervisor team for their help in performing the beam measurements.

REFERENCES

[1] .Lombardi, "LINAC4 Commissioning", presented at the 29th Linear Accelerator Conference (LINAC'18), Beijing, China, Sep. 2018, paper TH1P01, this conference.

[2] J.Tan, M.Sordet, L.Soby, "Beam Position Monitor for the CERN LINAC4", in Proceedings of DIPAC2011, Hamburg, Germany, May 2011, paper MOPD97, pp. 272-274

Content from this work may be used under the terms of the CC BY 3.0 licence (© 2018). Any distribution of this work must maintain attribution to the author(s), title of the work, publisher, and DOI.

ISBN: 978-3-95450-194-6 ISSN: 2226-0366 doi:10.18429/JACoW-LINAC2018-THPO086

BEAM LOSS AND AVERAGE BEAM CURRENT MEASUREMENTS USING A CWCT

F. Stulle*, H. Bayle, J. Bergoz, T. Delaviere, L. Dupuy
Bergoz Instrumentation, Saint Genis Pouilly, France
P. Forck, M. Witthaus, GSI Helmholtzzentrum für Schwerionenforschung, Darmstadt, Germany
D. Vandeplassche, Belgian Nuclear Research Centre SCK-CEN, Mol, Belgium
J. Wu, Institute of Modern Physics, Chinese Academy of Sciences, Lanzhou, China

Abstract

The CWCT is a novel instrument adapted to an accurate average current determination of bunched CW beams or macro pulses. By combining a high-droop current transformer with novel electronics for signal analysis, an output signal bandwidth of DC to about 500 kHz and a current resolution down to the micro-ampere level are achieved. Beam current fluctuations are followed within microseconds, permitting fast detection of beam loss. These characteristics render the CWCT an ideal instrument for HPPAs, for example ADS linacs, and other proton or ion accelerators. We present the CWCT principle and the CWCT performance achieved in beam experiments at UNILAC, GSI.

INTRODUCTION

New trends in accelerators are driven by the society to better and faster serve its needs in medicine, energy and materials studies:

- Accelerators for proton-hadron therapy and medical isotopes production,
- High-power proton accelerators (HPPA) for accelerator driven systems (ADS), e.g. nuclear waste transmutation or subcritical reactors, and spallation neutron sources (SNS),
- Accelerators for materials studies.

Additional background information can be found in [1].

These accelerators, initially developed to produce macropulses at low repetition rate, began to evolve towards CW beam accelerators, which hinders the use of ACCTs and introduces beam instrumentation challenges interfering with the use of DCCTs:

- Beam power damages equipment, rendering fast loss detection mandatory.
- Temperature variations are large.
- In low to medium energy sections, magnetic stray-fields are high due to compact designs.
- Space for instrumentation is scarce.

Moreover, longitudinal bunch profiles vary during the energy ramp further complicating average current measurements and accurate beam loss detection.

In response, Bergoz Instrumentation developed a novel system for average beam current measurements. It consists of a current transformer (CWCT) and analog electronics (BCM-CW-E) to process the CWCT's output signal. CWCT and BCM-CW-E are an alternative to ACCTs and DCCTs, well suited in many cases where those cannot be used.

Their characteristics were optimized for CW proton and ion accelerators, e.g. the injectors of the China ADS project [2] or the MYRRHA ADS project [3]. Though they can be used for macropulse measurements and in other types of accelerators. Table 1 summarizes CWCT and BCM-CW-E design specifications. Fig. 1 shows photographs.

Table 1: CWCT and BCM-RF-E Design Specifications

Bunch repetition rate	50 MHz … 500 MHz
Current measurement range	10 µA ... 200 mA
Reaction time (full bandwidth)	1 µs (10% ... 90%)
Output noise (10 kHz bandwidth)	1 µArms
Output noise (100 Hz bandwidth)	0.5 µArms
Output voltage (in 1 MΩ)	–4 V ... +4 V
Controlled via TTL or USB	

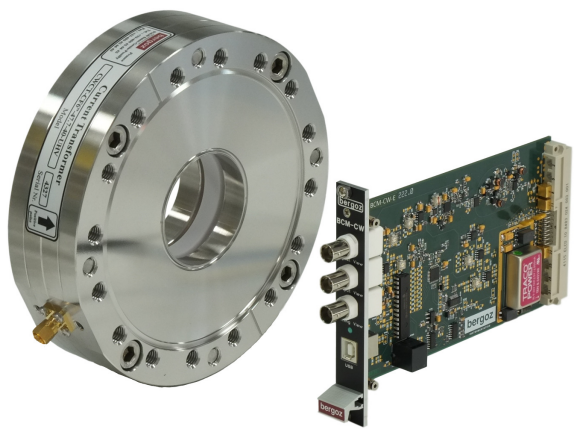


Figure 1: CWCT and BCM-CW-E.

CWCT and BCM-CW-E electronics were installed at UNILAC, GSI [4] for beam measurements. UNILAC can accelerate a wide variety of ions at different charge states up to several MeV/u kinetic energy. It is capable of fast switching between two different ion sources and sets of accelerator parameters. Like this, changing the macropulse current and its position as well as changing length and width of the individual pulses could be done with little impact on other beam users.

CWCT / BCM-CW-E PRINCIPLE

Passive current transformers (CT) are only capable of measuring AC currents down to a certain minimum

* stulle@bergoz.com

Content from this work may be used under the terms of the CC BY 3.0 licence (© 2018). Any distribution of this work must maintain attribution to the author(s), title of the work, publisher, and DOI.

ISBN: 978-3-95450-194-6 ISSN: 2226-0366 doi:10.18429/JACoW-LINAC2018-THPO086

frequency $f_{\mathrm{CT,min}}$, depending on CT characteristics like number of turns and relative permeability of the transformer core. In time-domain, the loss of low frequency spectral contributions manifests itself by the droop $D_{\mathrm{CT}} = 2\pi f_{\mathrm{CT,min}}$, which describes the CT signal's tendency towards zero for long input signals.

An example of a steady-state CT response, i.e. after several time constants $\tau_{\mathrm{CT}} = 1/D_{\mathrm{CT}}$, to a CW stream of pulses is shown in Fig. 2. The average of such a signal is zero.

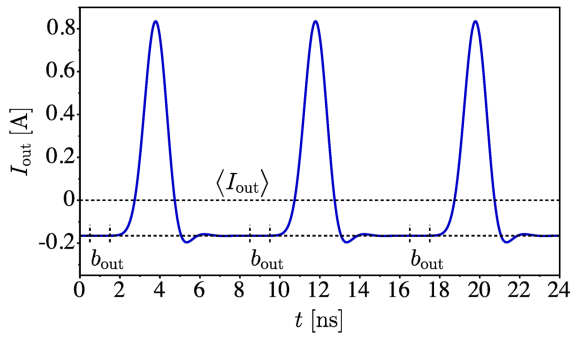


Figure 2: Drooped CT output signal for a CW input beam.

In between consecutive pulses, the CT output signal I_{out} drops to a certain value b_{out}, which is its baseline value. The following constraints must be fulfilled to allow its use for the determination of the average input current:

- The beam pulses including tails must be shorter than the pulse repetition period t_{rep}.
- For non-relativistic beams, the electromagnetic field lines detected by the CT are longitudinally deformed [5]. On the vacuum chamber wall, the EM field pulses must remain shorter than t_{rep}. In other words, the CT input signal I_{in} must drop to zero after each pulse.
- The CT pulse response must be sufficiently well behaving to allow I_{out} falling to a constant baseline after each pulse. That means, the CT output pulses must be shorter than t_{rep} and all ringing must have vanished.
- τ_{CT} must be considerably longer than t_{rep} to avoid a notable impact of the CT droop on I_{out} in between two pulses.

Under these assumptions, b_{out} is a direct measure of the average input current:

$$\langle I_{\mathrm{in}} \rangle = -b_{\mathrm{out}}/g_{\mathrm{CT}},$$

where g_{CT} is the CT gain.

This can be understood by considering that the CT droop induces a DC offset but does not noticeably deform the output signal if $\tau_{\mathrm{CT}} \gg t_{\mathrm{rep}}$, thus preserving the distance between average signal and baseline. The CT's high-frequency response may deform the signal but has no impact on average signal or baseline.

Already in [6] it had been recognized that the baseline of some beam diagnostics signals could be directly used to determine a beam's average current. Interestingly, it seems this idea has not been widely adopted.

The baseline can be accurately reconstructed from I_{out} by applying fast sample-and-hold techniques. After each pulse I_{out} is sampled over short time intervals and the value is held until the next sample is taken, leading to a piecewise constant signal I_{base}.

Since the CT's reaction time to pulse-to-pulse charge fluctuations, i.e. average beam current fluctuations, is limited to τ_{CT}, any beam induced variation of I_{base} must be equal to or longer than τ_{CT}. Hence, I_{base} is a good measure of the baseline at any point in time if $\tau_{\mathrm{CT}} \gg t_{\mathrm{rep}}$.

Prior to sampling, low-frequency noise is removed from I_{out} by high-pass filtering at a frequency $f_{\mathrm{in,max}} \geq f_{\mathrm{CT,min}}$. After sampling, high-frequency noise and the possible sampling steps are removed from I_{base} by low-pass filtering a little above $f_{\mathrm{in,max}}$. Almost no beam information is lost due to such a low-pass filter. This is possible because the sampling is a non-linear transformation. The high-pass filter prior to sampling acts on a different spectrum than the low-pass filter after sampling.

An additional low-pass filter prior to sampling is added to avoid that contributions at unnecessarily high frequencies deteriorate the sampling accuracy. It reduces noise and avoids that strong but short signal spikes drive the electronics into saturation.

The CWCT and BCM-RF-E working principle is outlined in Fig. 3.

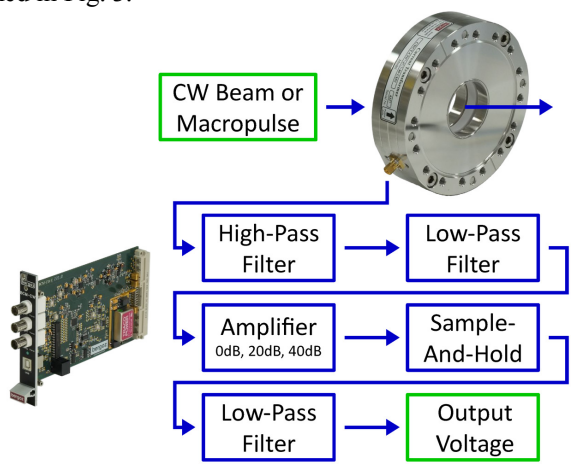


Figure 3: CWCT and BCM-CW-E principle.

In general, I_{base} can be considered the signal of a low-pass filter of upper cut-off frequency $f_{\mathrm{base,max}} = f_{\mathrm{CT,min}}$. The corresponding response time $t_{\mathrm{r,base}}$ (10% - 90%) is:

$$t_{\mathrm{r,base}} \approx 0.35/f_{\mathrm{CT,min}}.$$

MEASUREMENTS

CWCT and BCM-CW-E were installed at the end of UNILAC's X2 beamline at GSI, Darmstadt. Their performance was tested with 100 µs long macropulses of Argon ions. The pulse repetition rate within a macropulse was 36 MHz as given by UNILAC's first acceleration stage. The second acceleration stage is operated at 108 MHz, fixing the pulse length to the nanosecond level. The rather low pulse repetition rate combined with short pulses render the UNILAC beam well-adapted for first tests. The previously mentioned constraints on beam and CWCT / BCM-RF-E characteristics are fulfilled.

Content from this work may be used under the terms of the CC BY 3.0 licence (© 2018). Any distribution of this work must maintain attribution to the author(s), title of the work, publisher, and DOI.

ISBN: 978-3-95450-194-6 ISSN: 2226-0366 doi:10.18429/JACoW-LINAC2018-THPO086

Content from this work may be used under the terms of the CC BY 3.0 licence (© 2018). Any distribution of this work must maintain attribution to the author(s), title of the work, publisher, and DOI.

A further advantage was that the beam current could also be measured using a close-by ACCT manufactured by GSI [7]. The ACCT accuracy was about 1% of the full-scale value as determined by a test pulse from a current source. This allowed a comparison of the CWCT to a well-established reference. CWCT and ACCT signals were recorded using a 12bit oscilloscope. The trace data was saved for offline analysis.

Since the ACCT signal had a lower bandwidth than the CWCT signal, the CWCT data was mathematically low-pass filtered at 90 kHz to achieve a similar rise-time. Still, ACCT and CWCT signals remained slightly different.

Current Scan

The average current was varied from 10 µA up to 4500 µA. In some data sets strong current fluctuations were observed along the macropulses. Rapidly changing parts of the output signals were not considered for ACCT and CWCT comparison because of above-mentioned bandwidth differences. An example for the macropulse current measured by the two systems is shown in Fig. 4.

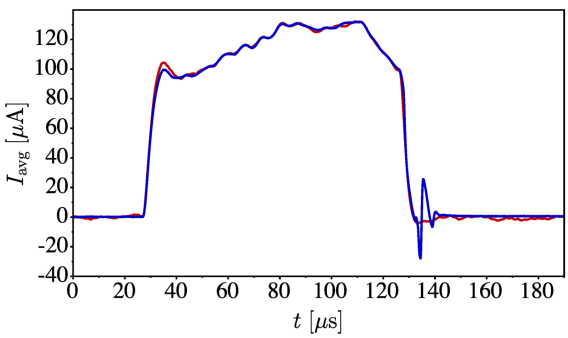


Figure 4: Currents measured by ACCT (blue) and CWCT filtered at 90 kHz (red). The trailing wiggle in the ACCT data is an irrelevant artefact of signal clamping.

For each CWCT gain setting, the measured CWCT output voltages U_{CWCT} were fitted to the corresponding currents I_{ACCT} as measured by the ACCT. Using the obtained scaling factors and offsets, the CWCT voltages were transformed into currents I_{CWCT}. The resulting transfer functions were:

$$I_{\mathrm{CWCT,0dB}} = 48547.3\,\frac{\mu\mathrm{A}}{\mathrm{V}}\,(U_{\mathrm{CWCT}} - 0.0373\ \mathrm{V})$$

$$I_{\mathrm{CWCT,20dB}} = 4469.7\,\frac{\mu\mathrm{A}}{\mathrm{V}}\,(U_{\mathrm{CWCT}} - 0.0435\ \mathrm{V})$$

$$I_{\mathrm{CWCT,40dB}} = 390.7\,\frac{\mu\mathrm{A}}{\mathrm{V}}\,(U_{\mathrm{CWCT}} - 0.0498\ \mathrm{V})$$

The resulting I_{CWCT} is compared to I_{ACCT} in Fig. 5. The relative deviation of I_{CWCT} from I_{ACCT} is shown in Fig. 6.

Very good linear correlation of CWCT and ACCT was achieved for all three CWCT gain settings. At 0 dB gain, some CWCT noise was present. However, all CWCT values stayed within ±7% of the ACCT values. At 20 dB gain, the CWCT values stayed within ±1% for currents above 1 mA. At 40 dB gain, from 90 µA to 250 µA the CWCT values remained within ±2%. Above 250 µA, amplifier saturation started to become important.

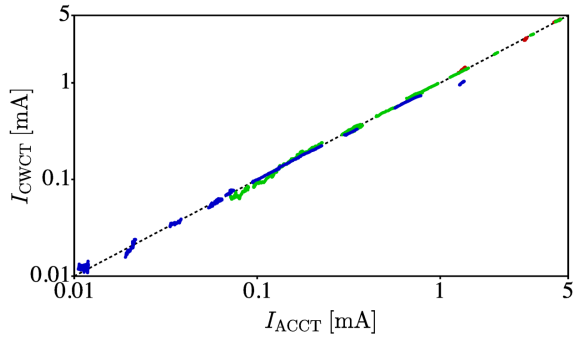


Figure 5: I_{CWCT} versus I_{ACCT}. CWCT 0 dB gain (red), CWCT 20 dB gain (green) and CWCT 40 dB gain (blue). The black dotted line marks equal currents.

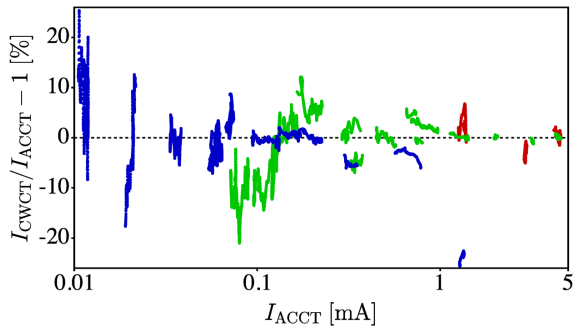


Figure 6: Relative deviation of I_{CWCT} from I_{ACCT}. CWCT 0 dB gain (red), CWCT 20 dB gain (green) and CWCT 40 dB gain (blue). For 40 dB gain, amplifier saturation is visible above 250 µA.

The observed variations may be partially caused by systematic effects, e.g. oscilloscope vertical scale switching.

Nevertheless, by choosing an appropriate CWCT gain an agreement between ACCT and CWCT better than ±5% could be achieved for currents of 90 µA and above.

Pulse Length, Width and Position Scans

Further to the current scan also the length of the pulses, their width and position were changed to determine possible dependences on these parameters. During these tests, ACCT and CWCT showed both no signs of measurement quality degradation until beam loss started.

CONCLUSION

The CWCT and BCM-CW-E were developed for average current measurements of CW beams and macropulses. Their properties are ideal for proton and ion accelerators.

Performance was examined with beam at UNILAC, GSI. Very good agreement was found with a close-by ACCT.

The macropulse current was varied from 10 µA to 4500 µA. ACCT and CWCT showed a linear correlation for all three CWCT gain settings. The CWCT noise floor was at a few microamperes.

Tests varying pulse length, pulse width and pulse position revealed no dependencies on such beam properties.

ACKNOWLEDGEMENTS

We would like to thank H. Reeg (GSI) for valuable discussions and support during the experiments.

ISBN: 978-3-95450-194-6 ISSN: 2226-0366 doi:10.18429/JACoW-LINAC2018-THPO086

REFERENCES

[1] Accelerators for Society initiative of the TIARA project, http://www.accelerators-for-society.org, http://www.eu-tiara.eu

[2] Z. Li *et al.*, "Physics design of an accelerator for an accelerator-driven subcritical system", *Phys. Rev. ST Accel. Beams*, vol. 16, p. 080101, Aug. 2013 doi:10.1103/PhysRevSTAB.16.080101

[3] D. De Bruyn, H. Aït Abderrahim, P. Baeten, C. Angulo, "The Belgian MYRRHA ADS Programme. Part 1: The new phased implementation plan", in *Proc. ICAPP'18*, Charlotte, NC, USA, Apr. 2018, paper 23786, pp. 1066-1073

[4] W. Barth *et al.*, "Development of the UNILAC towards a Megawatt Beam Injector", *in Proc. LINAC'04*, Lübeck, Germany, Aug. 2004, paper TU103, pp. 246-250

[5] A. Hofmann, T. Risselada, "Measuring the ISR impedance at very high frequencies by observing the energy loss of a coasting beam", in *Proc. PAC'83*, Santa Fe, NM, USA, Mar. 1983, pp. 2400-2402

[6] H. Koziol, "Beam Diagnostics", in *Proc. CERN Accelerator School: 3rd General Accelerator Physics Course*, Salamanca, Spain, Sep. 1988, pp. 63-101, doi:10.5170/CERN-1989-005

[7] H. Reeg, N. Schneider, "Current Transformers for GSI's keV/u to GeV/u Ion Beams - An Overview", in *Proc. DIPAC'01*, Grenoble, France, May 2001, paper PS08, pp. 120-122

Content from this work may be used under the terms of the CC BY 3.0 licence (© 2018). Any distribution of this work must maintain attribution to the author(s), title of the work, publisher, and DOI.

ISBN: 978-3-95450-194-6 ISSN: 2226-0366 doi:10.18429/JACoW-LINAC2018-THPO090

THE ANALYSIS OF MODULES FAILURE IN SOLID-STATE AMPLIFIER FOR HIGH CURRENT RFQ

Liepeng Sun#, Longbo Shi, Guirong Huang, Xianbo Xu,
Chenxing Li, Liang Lu, Aimin Shi, Yuan He, Hongwei Zhao
Institute of Modern Physics, Chinese Academy of Sciences, Lanzhou 730000, China

Abstract

The new RF system of Radio Frequency Quadrupole accelerator (RFQ) in ADS project at IMP was upgraded in the beginning of 2017, the original tetrode amplifier was replaced by two new solid-state amplifiers (SSA) for proton acceleration, they are the same 80kW rated power to combine at least 120kW inside the cavity through two uniform couplers. But for SSA, since too many power modules were set on the amplitude and phase for power combination, one or some damaged circulator (including sink loads) may lead to high risk of whole RF system fail. Especially, according to experiments and simulation, when the transmission line between two different level combiners meets a specific condition, the scattering parameter of system would have a great fluctuation, even cut-off, if some problems happen in circulators or sink loads. In this paper, the simulated methods aiming at simulating the multi-level synthetic amplifying were introduced in detail, the failure analysis and related experiments focusing on amplifying links of SSA under the special circumstances was also presented simultaneously.

INTRODUCTION

Since the old 200kW tetrode amplifier was operated in high current beam without a circulator, two new SSAs was considered to replace it on site due to their specialties of stable, sustainable and reliable, whose cavity operates in 162.5MHz, the dissipated power reaches up to approximate 90kW, and especially, the beam power has also 21kW while 10mA beam current was applied [1]. thus, some special technologies of new generation SSA were developed for this kind of high intensity accelerator in BBEF, such as two types of reflection power experiments on module including long-term continuous wave power and four times pulsed power. Due to too high power, the design of power module and combiner need to be considered the scattering parameters in the situation of mismatch resulting from the multi-port balance [2].



Figure 1: The four-vane RFQ cavity with two couplers.

sunlp@impcas.ac.cn

SSA MODULES FAILURE

In our case, over 120 power modules are integrated through several level synthesizers for full power output, which shows in Fig. 1, and every module can provide maximum 850W RF power for 80kW power output even when one pre-amplifier fails. Last June, 19 power modules were burned at the same time, within them, almost all power transistors, circulators and sink loads (connected directly with the circulators) were damaged on the same time only to be replaced. When failure happened, the power values was recorded from many directional couplers in the screen of control system, the specific values were presented in Fig. 2.

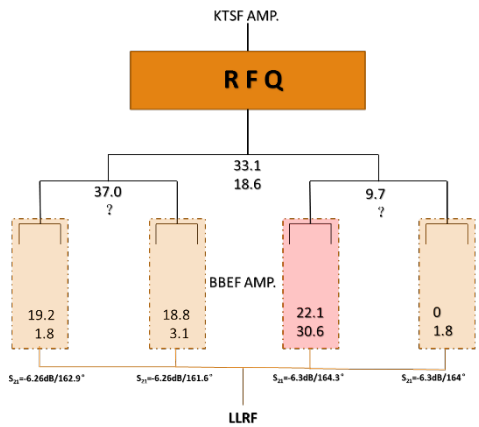


Figure 2: The screenshot of failure situation.

From it, our SSA was consisted of four 20kW sections to integrate gradually for providing 50 or 60kW RF power (without beam or 10mA beam) for separate coupler simultaneously. And after basic analysis and check on the machine, one most possible reason for accident should be too sensitive of driving signal interlock in 3# section comparing other three sections, the input signal of 3# section was shut down suddenly because of abnormal interlock during the operation, other three sections were influenced to increase rapidly power at that time due to LLRF close loop on the amplitude modulation. Furthermore, the weird location of all injured modules indicate that some inappropriate RF configuration need to be removed and optimized.

In this dangerous situation, more than half transistors, circulators and sink loads in 3# section were burnt severely. However, it is very difficult to explain clearly the phenomenon which the broken modules are all belong to 3# section, especially on the left side.

Content from this work may be used under the terms of the CC BY 3.0 licence (© 2018). Any distribution of this work must maintain attribution to the author(s), title of the work, publisher, and DOI.

ISBN: 978-3-95450-194-6 ISSN: 2226-0366 doi:10.18429/JACoW-LINAC2018-THPO090

ANALYSIS FROM SIMULATION

For the convenience of analysis, a simple model of multi-port power combiner was created in simulation software Microwave Studio to figure out the variation regularities of the scattering parameter. According to the simulated results, if any one port was open or short, the parameter S_{21} along transmission line on this port have a very great fluctuation along 360^0 phase, even when the wavelength equal to a certain value, the scattering parameter take dramatic turn to block the RF signal, the sweep results in CST while the wavelength was changed gradually, which indicates there be some reflected power points to block the power through combiners when λ meet certain demand.

Generally, the most advantage of SSA is stable output while one or some modules fails, except for the decreasing of output power. For instance, n modules fail in a 7kW combiner with 9 modules, the output power was degraded $(9\text{-}n)^2/9^2*100\%$. However, the situation would be much complicated while the circulators inside the module fail rather than field-effect transistors, the same as some phase shift and short circuit resulted in high reflected power, n ports network was gained through the matrix analysis [3], Sm=SII+SIIIΓ(1-SIIII)-1SIII [4] is degraded matrix of n ports network with the arbitrary load, m ports in them with no loads (full reflection), and according to symmetry and lossless of nine ports combiner, the scattering matrix of 8-1 power synthesizer is:

$$S=\begin{bmatrix} -\frac{7}{8} & \frac{1}{8} & \cdots & \frac{1}{8} & \sqrt{\frac{1}{8}} \\ \frac{1}{8} & \ddots & \cdots & \frac{1}{8} & \vdots \\ \vdots & \vdots & \ddots & \frac{1}{8} & \vdots \\ \frac{1}{8} & \frac{1}{8} & \frac{1}{8} & -\frac{7}{8} & \sqrt{\frac{1}{8}} \\ \sqrt{\frac{1}{8}} & \cdots & \cdots & \sqrt{\frac{1}{8}} & 0 \end{bmatrix}_{(9*9)}$$

the degraded matrix was gain easily,

$$S=\begin{bmatrix} \frac{1}{64e^{2\sigma t}+56}-\frac{7}{8} & \frac{1}{64e^{2\sigma t}+56}+\frac{7}{8} & \cdots & \frac{1}{64e^{2\sigma t}+56}+\frac{7}{8} & \frac{\sqrt{2}}{32e^{2\sigma t}+28}+\frac{\sqrt{2}}{4} \\ \frac{1}{64e^{2\sigma t}+56}+\frac{7}{8} & \ddots & \cdots & \vdots & \vdots \\ \vdots & \vdots & \ddots & \vdots & \vdots \\ \frac{1}{64e^{2\sigma t}+56}+\frac{7}{8} & \cdots & \cdots & \ddots & \frac{\sqrt{2}}{32e^{2\sigma t}+28}+\frac{\sqrt{2}}{4} \\ \frac{\sqrt{2}}{32e^{2\sigma t}+28}+\frac{\sqrt{2}}{4} & \cdots & \cdots & \frac{\sqrt{2}}{32e^{2\sigma t}+28}+\frac{\sqrt{2}}{4} & \frac{1}{8e^{2\sigma t}+7} \end{bmatrix}_{(8*8)}$$

When one output port in them was short, the degenerate matrix [5] can be deduced as above. So, when the phase of short port was 0 or π, the minimum S_{11} of 0.0667 and reflected power of input port would be gained simultaneously. and when phase was 900, S_{11} get the maximum value of -1 to mean the full power reflection [6]. The S_{11} and Sn1 were plotted according to the formula in Fig. 3.

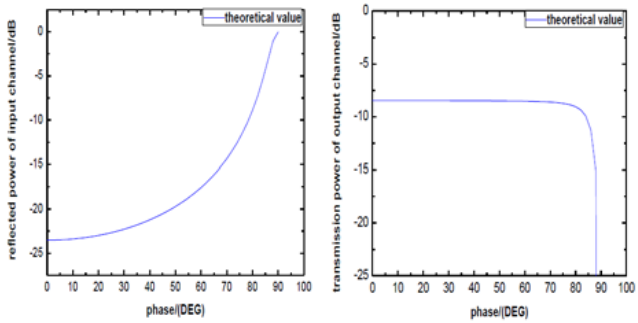


Figure 3: The simulation of wavelength influence.

EXPERIMENTS FOR SIMULATION

Obviously, the results from formula had a good agreement with the CST simulated ones. then a targeted experiment was prepared for this situation, which takes advantage of a three-level combiner/ divider to measure the scattering parameter while any one port mismatches (short or open circuit). A 1-8 combiner/ divider was re-fabricated into three-level components for changing the wavelength between the different levels in Fig. 4.

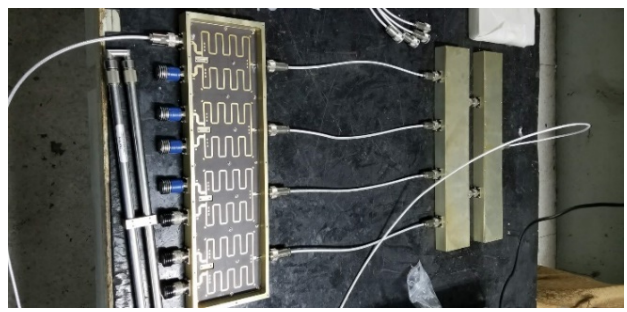


Figure 4: A special test stand with three-staged combiner.

For these three-level combiners [7], the failure of one port would lead to change greatly, even block completely RF signal. And according to the rule of scattering parameter, S_{11} along the transmission line of full reflection point will fluctuate severely, which shows in Fig. 5.

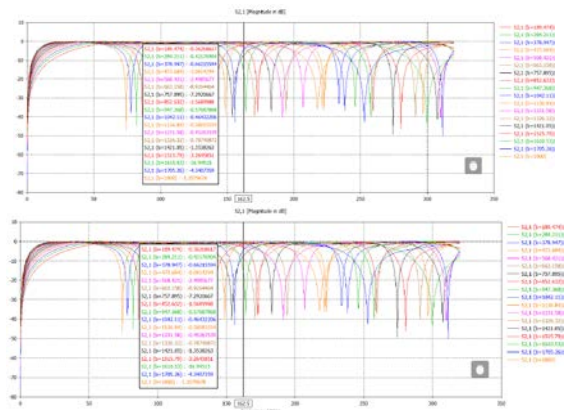


Figure 5: The S_{11} plot along the different transmission line while one port short or open circuit.

The measured results indicate the simulation of one port failure be right in this three-stage combiner testbench

Content from this work may be used under the terms of the CC BY 3.0 licence (© 2018). Any distribution of this work must maintain attribution to the author(s), title of the work, publisher, and DOI.

ISBN: 978-3-95450-194-6 ISSN: 2226-0366 doi:10.18429/JACoW-LINAC2018-THPO090

shown in Fig. 6, the VNA can gain precisely scattering parameters and phase when certain one port was connected with the phase shifter and open/short components.

The measured S_{11} were displayed in Fig. 6 when all ports matched except one port mismatched, the S_{11} close to -20dB indicates a very good matching from left figure. And in the right figure, the Max. S_{11} would reach up to -5dB which means serious mismatching when one port fails. As a result, the scattering parameter was analysed to find out the specific regularities while the length of the phase shifter was changed gradually.



Figure 6: The S_{11} results when all match and one port fail.

According to the measurements, the electrical length of one phase shifter was about 118^0 on 162.5MHz. Three phase shifters can measure the S parameter of whole range while the one port failure, the worst matching (that is the block point) was shown in Fig. 7.

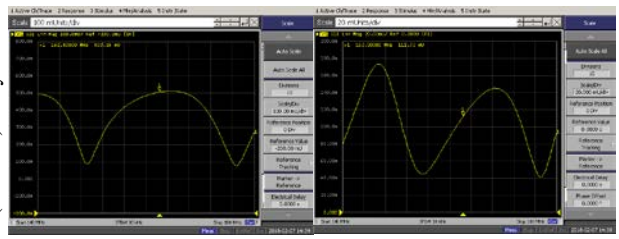


Figure 7: The worst S_{11} and S_{21} results along the full length while one port fails.

CONCLUSION

From the simulations and related experiments as above, it is impossible that the power modules with circulator were damaged or burned down due to the severe power reflection, one reason was unreasonable electrical length between the different two level of combiners when uncertain one or several ports mismatch, while the phase meets the particular demand, the power transmission may be attenuated extremely between the modules, even block power completely. The simulation focused on it and measurements on related experiments agree well each other. New SSA design should consider phase relationship while one port fails according to its operating frequency, which can improve greatly reliability and reduce the risk of failure and its cost.

REFERENCES

[1] Sun Liepeng, Shi Aimin, Zhang Zhouli *et al.*, "Engineering Design of the RF Input Couplers for C-ADS RFQ", in *Proc. 5th Int. Particle Accelerator Conf. (IPAC'14)*, Dresden, Germany, Jun. 2014, paper THPRI049.

[2] Thomas P, Wangler. Principles of RF Linear Accelerators, a Wiley-Interscience Publication, 1998.

[3] Single-Ended and Differential. S-Parameters, Maxim Integrated Products, MAXIM High- Frequency/Fiber Communications Group[S]. Application Note HFAN-5.1.0(Rev.0, 03/01), 2001- 3.

[4] K Kurokawa, Powerwaves and the scattering matrix[J]. IEEE Trans.Microwave Theory Tech,1965.3, MTT- 13:194-202.

[5] Xiong Zhengfeng, Ning Hui, Chen Huaibi *et al.*, "Design of compact power combiner in rectangular wafeguide", *High power laser and particle beams*, 2014 26 (06): 26063013-1-26063013-4.

[6] D E Bockelman, W R Eisenstadt. Combined Differential and Common-Mode Scattering Parameters: Theory and Simulation [J]. IEEE Trans. Microwave Theory Tech, 1995, 7: MTT-43, 1530- 1539.

[7] Zhao Min, Zhou Xing, Wang Qingguo *et al.*, "Design and analysis on power synthesis of all-solid-state pulse source with fast-edge", *High power laser and particle beams*, 2015 27 (10): 27103232-1-27103232-4.

Content from this work may be used under the terms of the CC BY 3.0 licence (© 2018). Any distribution of this work must maintain attribution to the author(s), title of the work, publisher, and DOI.

ISBN: 978-3-95450-194-6 ISSN: 2226-0366 doi:10.18429/JACoW-LINAC2018-THPO091

90 kW SOLID-STATE RF AMPLIFIER WITH A TE011-MODE CAVITY POWER-COMBINER AT 476 MHz

Yuji Otake†, Takao Asaka and Takahiro Inagaki, RIKEN SPring-8 Center, RIKEN, 1-1-1 Kouto, Sayo-cho, Sayo-gun, Hyogo, Japan
Hiroto Yamada, Tsuneyuki Okuyama, Kenji Nagatsuka, Shuichi Aizawa, Kazuyuki Sato, Nihon koshuha Co., Ltd, 1119 Nakayama-cho, Midori-ku, Yokohama, Japan

Abstract

Solid-state rf amplifiers, which have long lifetimes and small failures, are the recent trend as reliable and stable high-power rf sources for particle accelerators. Hence, we designed a 90kW solid-state amplifier with an extreme low-loss TE011 mode cavity (Q0=100,000) power-combiner operated at 476 MHz and a 50 us pulse width. Developing this amplifier is for replacement of an IOT rf amplifier, at the X-ray free-electron laser, SACLA. In SACLA, highly RF phase and amplitude stabilities of less than 0.02 deg and 10^{-4} in rms are necessary in order to obtain stable lasing within a 10 % intensity fluctuation. The amplifier comprises a drive amplifier, a reentrant cavity rf power divider, 100 final amplifiers with a 1 kW output each and a TE011 mode cavity combiner. Water-cooling with precise temperature regulation at 10 mK and a DC power supply with a noise of less than -100 dBV at 10 Hz for the amplifier are necessary in order to realize the previously mentioned stabilities. Based on the test results of the amplifier, the above-mentioned specifications with the extreme low-loss are confirmed. The amplifier also allows us to operate in pulsed and CW rfs for linacs and ring accelerators.

INTRODUCTION

Medium-power rf sources comprising vacuum tubes, such as triodes, tetrodes [1] and an induction output tube (IOT, klystrodes) [2] based on the traditional rf technology, usually drive acceleration cavities for proton and injectors. These medium rf-output powers are form 10 kW to 100 kW, if it is compared with the output power of a high-power klystron over mega-watts. In the case of an X-ray free-electron laser (XFEL), SACLA [3], a 476 MHz IOT having a 100 kW rf-output power with a 50 μs pulse width is unexceptionally used to drive a booster cavity, which accelerates an electron beam up to 1 MeV [4]. We recently decided to replace from our IOT to a solid-state amplifier, since the IOT had some troubles, such as the end of its lifetime, shortage of its supply.The reference [5], which mentions the design of this amplifier, describes the detail reason of the replacement.

Based on the design concept described in the reference [5], we developed a 90 kW, 476MHz rf solid-state amplifier with a pulse width of 50 μs using a field effect transistor (FET) with a 1 kW output each [6]. Therefore, this amplifier used these 100 FETs in order to generate 90 kW. Furthermore, because of this FET could work in a continuous wave (CW) mode, we also aimed for diverting this amplifier to ring accelerator rf sources. This CW operation mode is one of the development concepts [5]. Concerning use of this amplifier as the CW rf source, an extreme low-loss rf cavity combiner using a TE011 resonant mode (Q0=100,000) was employed. Since the rf combing loss exactly corresponded to many of the output power of the FETs, in order to reduce the costs of the solid-state amplifier, reducing loss by an rf-combining method is important. The intended combing loss of the rf power combiner including the loses of rf connectors and cables is 0.1 dB [5]. On the other hand, since SACLA is going to use this amplifier, ultra-stable rf-output is also indispensable feature in order to realize stable XFEL intensity [3]. Highly rf phase and amplitude stabilities of less than 10^{-4} and 0.02 deg. in rms are necessary for stable lasing within a 10 % intensity fluctuation. An ultra-low noise DC power supply technique for realizing the rf stability already established in SACLA [7] is also needed. Realization of the 90 KW, 476 MHz amplifier had great possibility in the design stage in order to obtain the demanded XFEL intensity stability, since, in the design stage, we already obtained a 1kW rf output of the final amplifier module [5]. Furthermore, because of environmental temperature change largely affected the rf phase and amplitude changes of the amplifier, counter measures in order to reduce the temperature change are crucial. Hence, to employ a precise temperature controller originally developed for SACLA [8] having a temperature regulation within 10 mK is a big candidate. In addition to the above-mentioned requirements, because the SACLA building did not have a sufficient-big space for installing the amplifier instead of the IOT, the compactness of the amplifier was also important.

We have finally built a 90 kW, 476 MHz pulse solid-state amplifier with an extreme low-loss rf-power combining method using a TE011 mode rf-cavity. In this paper, we describe the test results and the final characteristics of the amplifier.

CONFIGURATION OF AMPLIFIER

In this summer, we finished to build the 100 kW, 476 MHz pulse solid-state amplifier. Table 1 tablets the specifications of the amplifier. Figure 1 shows electrical configuration of the amplifier using the FET described in Table 2. The amplifier comprises a 20 W amplifier in order to drive the final stage amplifier modules through a re-entrant type cavity power divider. Following the driving amplifier, there are 100 final stage amplifier modules

† email address otake@spring8.or.jp

Content from this work may be used under the terms of the CC BY 3.0 licence (© 2018). Any distribution of this work must maintain attribution to the author(s), title of the work, publisher, and DOI.

ISBN: 978-3-95450-194-6 ISSN: 2226-0366 doi:10.18429/JACoW-LINAC2018-THPO091

Content from this work may be used under the terms of the CC BY 3.0 licence (© 2018). Any distribution of this work must maintain attribution to the author(s), title of the work, publisher, and DOI.

including 2 FETs of a push-pull configuration in one package, which can handle a 1 kW rf output power. After the final amplifiers, a TE011 mode cavity rf power combiner is connected to the final amplifier modules. On the other hand, the amplifier equips auxiliary instruments, such as extreme low-noise DC power supplies and a control module using a programable langrage controller (PLC). To obtain the rf stability of the amplifier output demanded for the XFEL, we can use a method of the ultra-stable (~$2x10^{-5}$) and low-noise (-100 dBV@10 Hz) power supply technique employed for SACLA [7]. Because the technique almost determines the rf stability and already achieve the rf stabilities of of less than 0.01 deg. in phase and 10^{-4} in amplitude in rms at SACLA [7]. The extreme low-noise DC power supply for this amplifier uses the technique. Installation of the precise temperature control system having control performance within +/- 10mK is planned, when this amplifier is going to be placed in the SACLA's klystron gallery. This control system greatly helps in order to achieve the demanded rf amplitude and phase stabilities. However, we do not presently and unfortunately install the control system yet.

Table 1: Specifications of the 476 MHz Amplifier

Frequency	476 MHz
Output Power	90 ~ 100 kW
Pulse Width	50 μs
Repetition	60 pps
Amplification Class	AB

Table 2: Specifications of the LDMOS FET (MRFE6VP61K25H, NXP)

Frequencies	1.8 ~ 600 MHz
Handing Power	1250 W (CW or Pulse)
Gain	27 dB at Maximum
Efficiency	58 % at 500 MHz, at maximum

Figure 2 describes the actual fabrication condition of the amplifier. Since the amplifier should fit an installation space (2 m x 2 m) at the SACLA injector, the rf power combiner is used as a support structure for the amplifier modules, as shown in Fig. 2. Hence, the extra support for the components of the amplifier is eliminated. On the other hand, we devised the following items for easy maintenance (quick replacement of the modules), because of the many final amplifier modules. The top plate of the combiner has roles of cooling water ducts and a cooling water distribution header. The water-cooled 100 final-amplifier modules attach on the top plate through quickly-detachable water joints [9], which realize ease replacement of the module. Furthermore, the top plate has another role as an rf power transmission lines using striplines with air insulator (Air line) in order to connect among the final amplifier modules and the input ports of the rf combiner on it. These air lines are to reduce the rf loss. These air lines through the inside of the top plate structure are connected with quickly-detachable rf connectors [10] for easy replacements of the module.

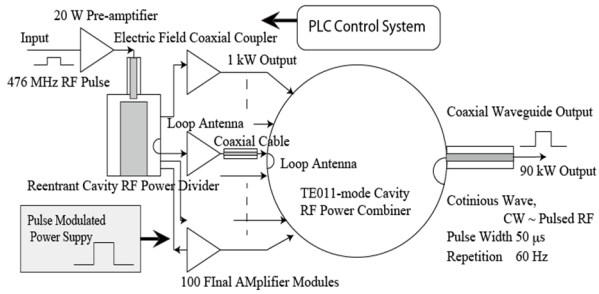


Figure 1: Block-diagram of the amplifier.

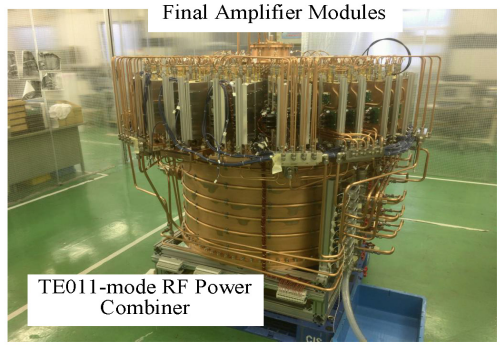


Figure 2: Actual fabrication condition of the amplifier.

TEST AND PERFORMNCE

We built the 90 kW, 476 MHz pulse solid-state amplifier in this summer and tested it. The performances of the amplifier, such as the 90 kW peak output rf power, the low loss, the rf phase and amplitude stability, were checked. Figure 3 shows an rf output power change of the amplifier of up to 109 kW, as a function of an input rf power. Rf phase and amplitude measurement apparatus are also connected through rf couplers for monitoring at the rf input and output ports. Figure 4 describes the rf output power trend for 8 hours. The amplifier rf output in the figure is 90 kW at peak with a pulse width of 50 μs and a pulse repetition rate of 20 pps. In this experiment, a cooling water temperature for the amplifier was controlled within +/- 0.5 K. From the trend data, an rf phase stability is +/- 0.4 deg. and an rf amplitude stability is 1 %, respectively. Rf amplitude and phase jitters are 0.036 %/min. and 0.044 deg./min. in rms, respectively. An oscilloscope takes these jitter data for 1 minute. Because of a cooling water temperature change is +/- 1 K, the previously mentioned rf amplitude and phase drifts are reasonable values, which correlated to the temperature change. If the temperature is controlled within ~ 10 mK, like SACLA's case, the rf phase and amplitude drifts could be ~0.004 deg. and ~10^{-4}, respectively. The reflection loss distribution of the 108 input ports of the combiner are shown in Fig. 5. The average reflection loss and its standard deviation (STD) value are -20.469 dB and 0.105 dB, respectively. The total average insertion loss in rms of the

ISBN: 978-3-95450-194-6 ISSN: 2226-0366 doi:10.18429/JACoW-LINAC2018-THPO091

combiner is -0.135 dB. Phase displacement values distribution at the 108 output ports of the combiner is shown in Fig. 6. The rms phase deviation is 2.71 deg.. These representative rf-loss related data and some experimental results of the amplifier are tabulated in Table 3.

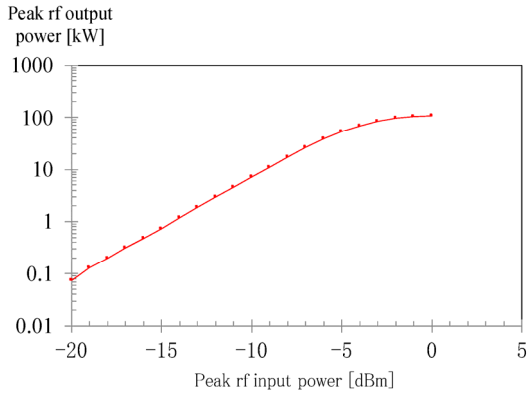


Figure 3: Rf output power as a function of the input rf power. The rf output power reaches 109 kW at peak.

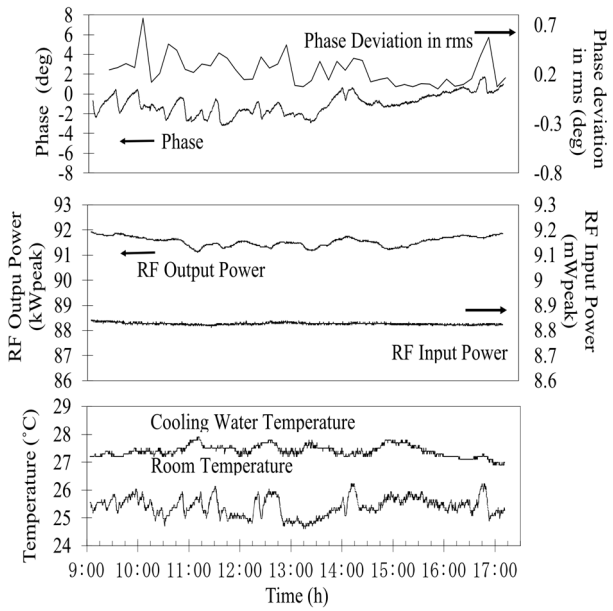


Figure 4: Rf power trend of the phase and amplitude of the amplifier output for 8 hours. Each point data are 10 minutes average of each 1 second data. The phase deviation of the most upper graph shows the rms phase jitters taken from the phase measurement points data for each 10 minutes.

CONCLUSION

We successfully built a 90 kW, 476 MHz rf pulse amplifier. The amplifier was tested to confirm its performances. The idea in order to reduce rf loss for adapting CW operation of the amplifier by using a TE011 mode cavity type rf combiner was evaluated with fruitful results. The rf power combining loss is -0.135 dB in total, which is almost our requirement. Furthermore, this our development technically established elaborated stabilities of the output rf phase and amplitude of the amplifier for driving stable XFEL intensity. The phase and amplitude stabilities are +/- 0.4 deg./1K and +/- $5x10^{-3}$ /1K, respectively. These could correspond to about +/- 0.004 deg./10mK and about +/- $5x10^{-5}$/10 mK, respectively. On the other hand, in order to reduce installation space for the amplifier, the large size of the combiner works well as a support structure for many final amplifier modules, as which we originally intended. From the above-mentioned results, we think this development successfully finished. The amplifier will be installed in SACLA's building for user operation.

Table 3: Summary of the Measured Parameters of the Amplifier

Rf output power	109 kW
Rf amplitude stability in rms for 8 hours	+/- 0.5 % /K
Rf phase Stability in rms for 8 hours	+/- 0.4 deg./K
Total insertion loss of the combiner	- 0.135 dB
Standard deviation of the losses (combiner input)	0.105 dB
Rms deviation of the phases (combiner input)	2.71 deg.

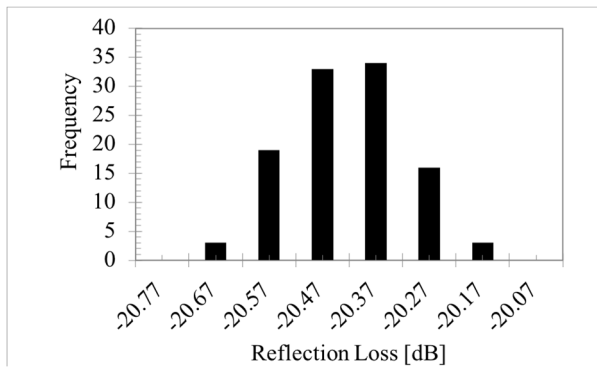


Figure 5: Reflection-loss values distribution of the 108 input ports of the rf power combiner. These values were measured by S21. The average reflection loss and its STD value are -20.469 dB and 0.105 dB, respectively.

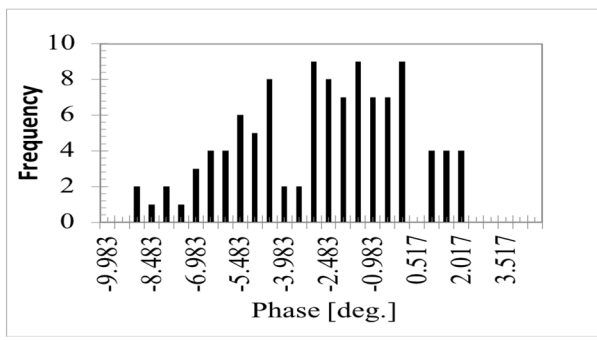


Figure 6: The phase deviation values distribution from the ideal at the 108 input ports of the rf power combiner. These values were measured by S21.

ACKNOWLEDGEMENT

We thank to Dr. Tanaka and Director Ishikawa for their support to this development and members of the XFEL

Content from this work may be used under the terms of the CC BY 3.0 licence (© 2018). Any distribution of this work must maintain attribution to the author(s), title of the work, publisher, and DOI.

ISBN: 978-3-95450-194-6 ISSN: 2226-0366 doi:10.18429/JACoW-LINAC2018-THPO091

research and development division for their help. We also appreciate members of Nihon Koshuha Co., Ltd. for their support to build this amplifier.

REFERENCES

[1] A. S. Gilmour, Jr, Microwave Tubes, Chap. 8, 191 (1986).

[2] A. S. Gilmour, Jr, Microwave Tubes, Chap. 8, 196 (1986).

[3] T. Ishikawa. et. al., *Nature Photonics* 6, 540 (2012).

[4] T. Asaka et al., *PRAB*, 20, 080702-1-080702-12 (2017).

[5] Y. Otake et al., Design of a 100 kW Solid-state rf Amplifier with a TE011 Mode rf Combiner at 476 MHz, in *Proc. of IPAC2017*, THPIK038, 4180-4183 (2017).

[6] http://www.nxp.com/products/rf/rf-power-transistors/rf-broadcast-and-ism/1.8-600-mhz-1250-w-cw-50-v-wideband-rf-power-ldmos-transistors: MRFE6VP61K25H

[7] Y. Otake et al., PRAB, 19, 022001-1-22001-20 (2016).

[8] T. Hasegawa et. al., Status of a Precise Temperature-regulation System for the C-band Accelerator at XFEL/Spring-8, Proc. of IPAC10, 1488-1490 (2010).

[9] http://www.sanwa-et.co.jp: in Japanese

[10] https://www.pasternack.com

Content from this work may be used under the terms of the CC BY 3.0 licence (© 2018). Any distribution of this work must maintain attribution to the author(s), title of the work, publisher, and DOI.

ISBN: 978-3-95450-194-6 ISSN: 2226-0366 doi:10.18429/JACoW-LINAC2018-THPO092

LCLS II FUNDAMENTAL POWER COUPLER MANUFACTURING STATUS AND LESSONS LEARNED

S. Sierra†, C. Lievin, I. Yao Leclerc, THALES, Vélizy, France
G. Garcin, G. Vignette, THALES, Thonon les Bains, France
M. Knaak, M. Pekeler, R.I. Research Instruments Gmbh, Bergisch Gladbach, Germany

Abstract

Thales and RI Research Instrument have manufactured and assembled half of the Power Couplers for the LCLSII Project,. This paper remains main characteristics of these couplers, main challenges overcomed and among them thickness of copper coating on Warm Internal Conductor (WIC) at 150 µm. It also proposes some possible optimization for a future mass production and parameters which could be relevant for a better understanding link to statistic results obtained from this production and the one from XFEL production.

MAIN CHARACTERISTICS AND COUPLERS DESCRIPTION

The design of these couplers (Fig. 1) is an adaptation of the TTF3/XFEL Fundamental Power Coupler (FPC) [1].

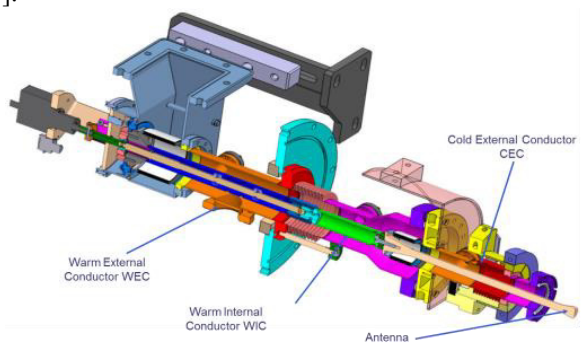


Figure 1: General Layout of the Coupler.

Main parameters of the coupler are:
- RF frequency: 1.3 GHz
- Power up to 7 kW CW
- Tuning: ± 10 mm
- Two ceramics windows

Main modifications in respect to the XFEL/TTF3 design are:
- Antenna profile in order to be adapted to the cavities performances
- Copper coating thickness of the WIC defined at a thickness of 150 µm, compared to 30 µm for E-XFEL, in order to avoid too large temperature heating when operating at full power of 7 kW.
- Residual Gas Analysis (RGA) is made during baking operation at 150°C.

† serge.sierra@thalesgroup.com

MANUFACTURING

Main metallic sub-assemblies: Warm External Conductor (WEC), Warm Internal Conductor (WIC), Cold External Conductor (CEC) and antenna (Fig. 2) were manufactured and copper coated at Thonon factory then sent to RI factory. Ceramics are TiN coated and then the coupler is assembled by Electron Beam Welding (EBW) at RI factory.

After cleaning and assembly on the test stand, they are sent to JLAB/Fermilab for integration on cryomodules.



Figure 2: CEC, Antenna and WEC.

Overview on Manufacturing Difficulties:

Due to the XFEL manufacturing experience [2] (where more than 670 couplers were manufactured at a rate up to more than 10 couplers a week) there were not a lot of difficulties for the manufacturing of LCLSII FPC.

The copper plating process is the trickiest step for the coupler manufacturing which also have been developed during XFEL production except for the WIC where the thickness of 150 µm had been obtained. During the manufacturing of all couplers, check of coating thickness (Fig. 3) and Residual Resistivity Ratio (RRR) have been done

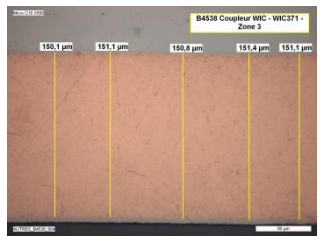


Figure 3: Example on Copper Coating Measurement

This was done also statistically on parts of main components (Figs. 4 and 5).

Content from this work may be used under the terms of the CC BY 3.0 licence (© 2018). Any distribution of this work must maintain attribution to the author(s), title of the work, publisher, and DOI.

ISBN: 978-3-95450-194-6 ISSN: 2226-0366 doi:10.18429/JACoW-LINAC2018-THPO092

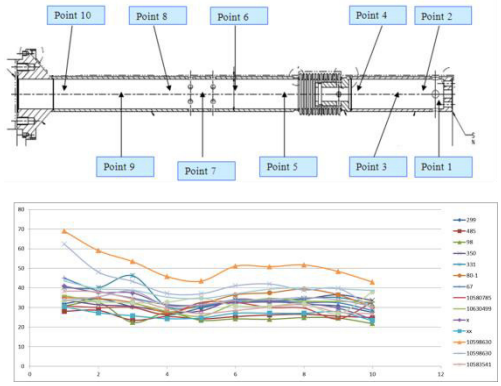


Figure 4: Measured Position for WIC at 30 µm.

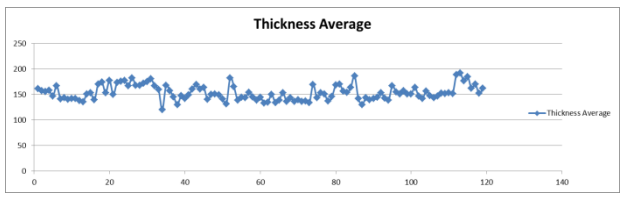


Figure 5: WIC Thickness Measurement at 150µm.

LESSONS LEARNED AND POSSIBLE OPTIMIZATION

Manufacturing improvements and possible ways to increase rate of production could be considered [3], [4].

Technical:

In order to improve manufacturing for a FPC mass production, studies could be done in order to avoid processes which are operator dependent like remaining welding steps which could be replaced by brazing. This will allow for manufacturing by batches in furnaces.

It is also necessary to clearly define objective and shared visual acceptation criteria of what is acceptable and what is not [4].

Due to the XFEL and LCLSII experience in manufacturing couplers it appears that statistically some parameters must be more clearly understood.

Among them, two parameters need to be better understood: RRR dispersion and Tinted ceramics.

Concerning RRR dispersion (Fig.6), it appears that statistically, RRR value could vary on parts (sample or part of coupler) in the same bath when coated at the same time.

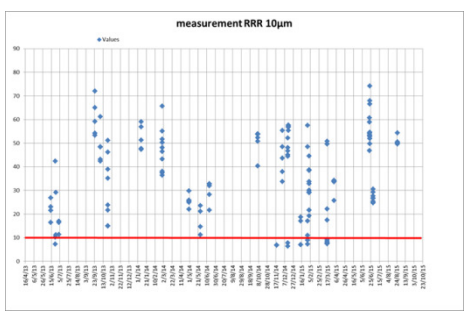


Figure 6: RRR dispersion for 10 µm coating.

Tinted ceramics occurred (Fig.7) (a few tens on a few hundred pieces manufactured)

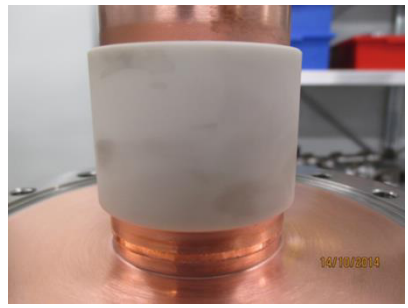


Figure 7: Example of Tinted Ceramic.

This tinted ceramics appears during RF conditioning, the only impact on conditioning being a small longer processioning time due to vacuum behavior.

Scheduling and Program:

Ramp up and ramp down on manufacturing must be strongly considered. Ramp-up is mandatory for assuring that all processes are under control and operators fully operational.

Ramp-down is also mandatory. During manufacturing, couplers are assembled by pair, and some sub-assemblies could be rejected just because their behavior is not well understood or correlated to the other coupler of the same pair. **B**ut at the end of the program, it becomes necessary to reconsider what is acceptable and what is definitely not acceptable.

STATUS

The 150 couplers for LCLSII have been delivered in due time at a rate of 4 couplers/weeks.

With E-XFEL experience, a production rate of more than 10 couplers a week and a total production of more than 820 couplers have been demonstrated, and 670 of them are on an operative accelerator.

.

REFERENCES

[1] W.Kaabi, et al., "Power couplers for XFEL", in Proc. IPAC'13, Shanghai, China(2013).

[2] S.Sierra et al., "Status of the Fundamental Power Coupler Production for the European XFEL Accelerator" Proceedings of the SRF 2015, Whistler, Canada.

[3] S.Sierra et al. "Lesson learned on the manufacturing of Fundamental Power Couplers for the European XFEL Accelerator", SRF 2015, Whistler, Canada.

[4] S.Sierra et al. "Experience on FPC mass production for a future project", TTC Meeting December 2015, SLAC, USA

Content from this work may be used under the terms of the CC BY 3.0 licence (© 2018). Any distribution of this work must maintain attribution to the author(s), title of the work, publisher, and DOI.

ISBN: 978-3-95450-194-6 ISSN: 2226-0366 doi:10.18429/JACoW-LINAC2018-THPO093

STATUS AND RESULTS OBTAINED ON A RF CONDITIONING TEST BENCH FOR 704 MHz COUPLERS IN THE FRAME OF ESS PROJECT

S. Sierra†, Y. Amal, C. Lievin, I. Yao Leclerc, THALES, Vélizy, France
M. Chahbazian, J.De Oliviera, A. Goeury, L. Nenning, S. Petitjean,
GERAC Thales, Le Barp, France

Abstract

Thales and GERAC are developing a test bench able to make the RF conditioning of the Fundamental Power Couplers at 704 MHz in the frame of the ESS project for CEA. The status of the development of the test bench is described, including the modulator, klystron and all relative equipment. We describe also the results obtained at this date.

OVERVIEW OF THE TEST BENCH

The RF test bench consists of a fully integrated power station including:

- RF power station,
- High power modulator,
- A 1.5 MW klystron TH2182A at 704 MHz,
- Interlocks and acquisition system
- RF power network including High power circulator.

KLYSTRON

The TH2182A klystron has been designed to comply with ESS specification [1]. Main characteristics of the klystron are:

- Built-in electromagnet (water cooled)
- Built-in X-ray shielding (easily removable)
- Built-in oil tank with heater transformer
- Diode gun
- 6 cavities with 3rd one on second harmonic
- Coaxial window and cross-bar coax to waveguide transition
- Low cathode loading
- Low DC gradient on beam forming electrode

The 3D model (Fig. 1) shows the disposition of klystrons sub-assemblies, from the diode gun to the collector.

This Klystron has been design with a low beam perveance of 0.6 $\mu A/V^{1.5}$ generated by a diode gun, at an operating point of 108 kV and 21.4 A. In order to have a safe value at the operating point, the electrical gradient on the beam forming electrode remains below 4.7 kV/mm. Due to the large cathode size, the cathode loading is low (< 2A/mm²), with low temperature cathode for a long lifetime, more than 100.000 hours and low Barium evaporation rate.

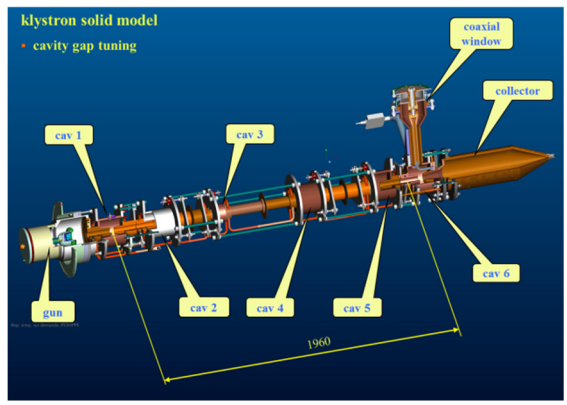


Figure 1: klystron.

The klystron is mounted in a built-in electromagnet water cooled (Fig. 2) composed of 14 independent coils on a supporting frame which allow to install X-ray shielding which could be easily removed.



Figure 2: assembly of the Klystron.

MODULATOR

Modulator is composed of an AC/DC power supply charging the capacitor bank up to 2 kV. Then RF converters at 25 kHz allow setting the pulse shape at the primary of pulse transformers. At the secondary of these pulse transformers, addition of redressed voltages allows to give the desired voltage and current to the Klystron (Fig. 3).

† serge.sierra@thalesgroup.com

Content from this work may be used under the terms of the CC BY 3.0 licence (© 2018). Any distribution of this work must maintain attribution to the author(s), title of the work, publisher, and DOI.

ISBN: 978-3-95450-194-6 ISSN: 2226-0366 doi:10.18429/JACoW-LINAC2018-THPO093

Content from this work may be used under the terms of the CC BY 3.0 licence (© 2018). Any distribution of this work must maintain attribution to the author(s), title of the work, publisher, and DOI.

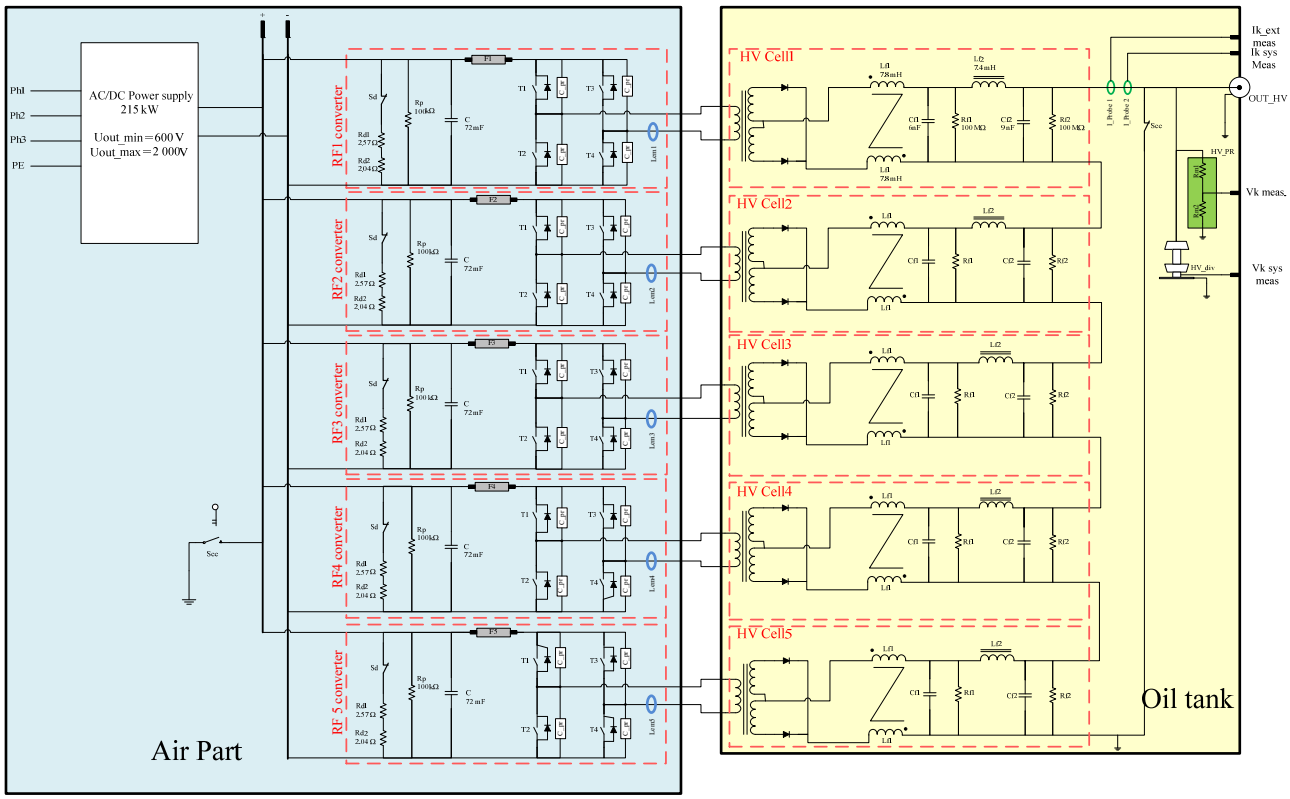


Figure 3: Electrical Diagram Of The Modulator.

In order to minimize oil volume and make maintenance easier, the modulator is composed of two separate parts. All primary circuits up to 2kV are in air. Pulse transformers (Fig. 4) and secondary circuits are in an oil tank

Five "independent" identical circuits are used for managing High Voltage from low voltage. Each individual RF converter is based on 4 IGBTs working at 25 kHz and allowing to set the pulse to the desire value and transmit the voltage at the primary of the pulse transformer. Transformers with a ratio of 13 have been fully simulated and designed internally by the Gerac.

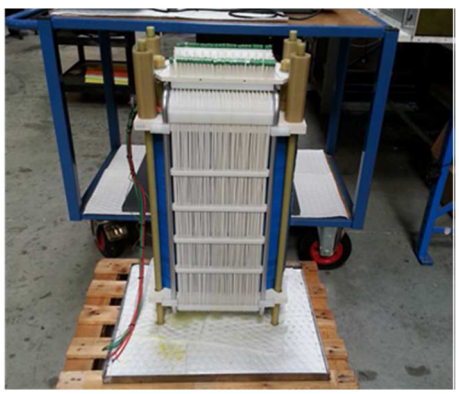


Figure 4: Pulse Transformer.

The modulator has been assembled and is under high power test at Gerac site on a dummy load (Fig. 5) in order to set parameters and verify performances.



Figure 5: Modulator Under Tests.

High voltage pulse have been measured (Fig. 6) at 100 kW and 1300 V dc at the primary of pulse transformer. The output pulse flatness is of 1.17 %. Due to the difference between the impedance of dummy load and the klystron one, this will be improved in the future and after having achieved full power.

ISBN: 978-3-95450-194-6 ISSN: 2226-0366 doi:10.18429/JACoW-LINAC2018-THPO093

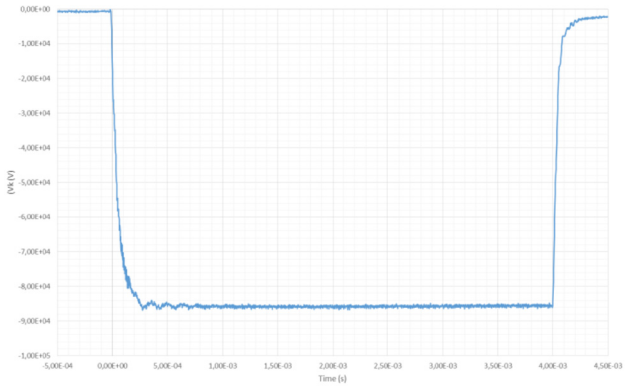


Figure 6: High Voltage Pulse Measured at 100 kW.

CONTROL COMMAND SYSTEM

In order to achieve all command needed for running the test bench a control command system has been developed.

On the General User Interface (Fig. 7) operator can change parameters of the test bench like pulse repetition rate, high voltage applied to the Klystron. It can also have all status for parameters from faults to current status.

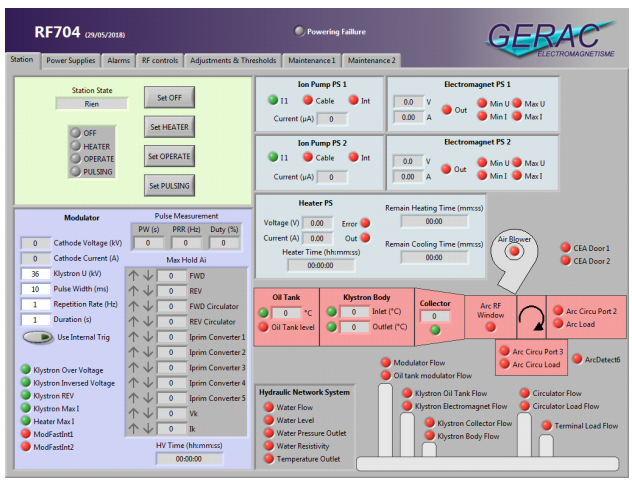


Figure 7: Example of GUI of the Test Bench.

GENERAL STATUS

The Modulator is under test at the GERAC factory on a dummy load. An output higher than 100 kW has been achieved. Klystron has been accepted at the Thales factory. With ancillaries and RF chain, it is installed at CEA site and ready for tests (Fig. 8).

RF power tests on RF loads, including the one for the circulator have been achieved independently



Figure 8: Klystron and Ancillaries distribution.

A dedicated cooling system (Fig. 9) is also installed in order to be independent of the overall installation at the exception of a primary cooling.



Figure 9: Dedicated Cooling System.

Tests are ongoing at the Gerac factory, up to 200 kW. After completion, the modulator will be sent to the final site and connected to the klystron in order to achieve the commissioning and final tests of the overall test bench.

REFERENCES

[1] A. Beunas, Y. Rozier, R. Marchesin, C. Poirot, J.L. Piquet "A High Efficiency UHF Klystron for Proton linac", in *Proc. 16th International Vacuum Electronics Conference (IVEC 2015)*, Beijing, China, April 2015.

Content from this work may be used under the terms of the CC BY 3.0 licence (© 2018). Any distribution of this work must maintain attribution to the author(s), title of the work, publisher, and DOI.

ISBN: 978-3-95450-194-6 ISSN: 2226-0366 doi:10.18429/JACoW-LINAC2018-THPO095

PRESENT STATUS OF CAPACITOR-CHARGING POWER SUPPLIES FOR KLYSTRON MODULATORS IN SuperKEKB INJECTOR LINAC

M. Kawamura†, M. Akemoto, H. Nakajima, T. Natsui, T. Shidara, S. Fukuda, H. Honma,
S Michizono, KEK, 305-0801 Tsukuba, Japan
O. Endo, H. Akikawa, K. Sato, Nihon Koshuha Co., Ltd., 226-0011 Yokohama, Japan

Abstract

Capacitor charging power supplies (CCPSs) have been used in compact klystron modulators. Two main types of CCPSs, the normal model and highly precise model, have been developed by Nihon Koshuha Co. in collaboration with KEK since JFY2012. In the KEK, regarding the output voltage stability of normal model, almost the same characteristic as the specification 0.2 %p-p was measured. After some repairs for the discharge problems, the CCPSs in the SuperKEKB injector linac were operated without important breakdown for about 6,000 h from autumn in 2017 to summer in 2018.

INTRODUCTION

The SuperKEKB injector linac has delivered electrons and positrons for particle physics and photon science experiments since 1982 [1]. At present, 59 S-band (2856 MHz) klystrons are used as RF sources in the injector.

One klystron modulator supplies pulsed high-power to one klystron. All klystron modulators have pulse-forming networks (PFNs). Thirteen compact klystron modulators [2-5] and 46 conventional klystron modulators [6] are now used. Regarding the charging method of PFN capacitors, compact modulator is a switching charging type using a capacitor-charging power supply (CCPS) [2-5,7-11], and conventional modulator is the resonant charging type. Further, the former is almost 1/3 the size of the latter.

Compact modulators and CCPSs have been developed since JFY2002 [3-5]. At first, the CCPSs were developed by Toshiba Electro-Wave Products Co. [3-5,7], and since JFY2012, they have been mainly developed by Nihon Koshuha Co. (NIKOHA) [8-11], in collaboration with KEK.

This article describes the present status of the CCPSs developed by NIKOHA. It includes the specifications, the difference between the normal model and the highly precise one, the measured results, and operation conditions in KEK.

OUTLINE OF NIKOHA CCPS

At present, 18 normal model CCPSs, two highly precise models and one exclusive model for the flux concentrator modulator [12] have been developed [11].

Figure 1 shows the outward appearances of the normal model and highly precise model, and Table 1 shows their specifications [8-11].

† masato.kawamura@kek.jp



Figure 1: Outward appearances of the normal model (left) and highly precise model (right) of Nikoha CCPSs [11].

Figure 2 shows the schematic diagram of the 30 kJ/s normal model [8]. The normal model consists of three sections; the rectifier section,

Table 1: Specifications of the normal model and highly precise model of Nikoha CCPSs (for 0.62 μF load)

	Normal [8]	Highly Precise [9]
Input voltage	AC 420V±5% (3-phase)	
Charging power	30 kJ/s	35 kJ/s (Main: 30 kJ/s, Sub: 5kJ/s)
Output voltage	43 kV	
Average output current	1.6 A	1.8 A (Main:1.6 A, Sub:0.2 A)
Repetition rate	50 pps	50 pps
Output voltage stability	0.2 %p-p (at 43 kV)	0.03 %p-p (at 43 kV)
Efficiency	More than 80%	
Cooling	Water 5 L/min.	Water 5 L/min. (Main) Air (Sub)
Size (mm^3)	480×760×680	480×760×980

inverter section, and HV section.

The rectifier section converts 3-phase 420 V AC input to 600 V DC output. The inverter section is an IGBT-switched 20 kHz inverter, and it is constructed by two se-

Content from this work may be used under the terms of the CC BY 3.0 licence (© 2018). Any distribution of this work must maintain attribution to the author(s), title of the work, publisher, and DOI.

ISBN: 978-3-95450-194-6 ISSN: 2226-0366 doi:10.18429/JACoW-LINAC2018-THPO095

ries resonant circuits in parallel. The HV section is constructed by a high-frequency transformer and diode bridge circuits. The

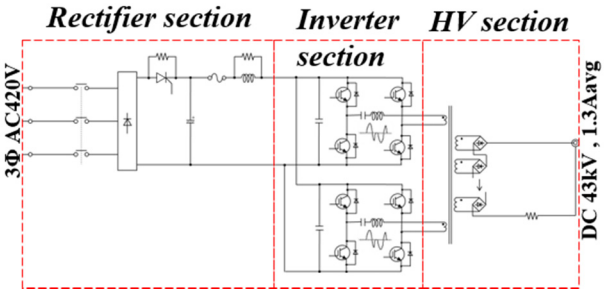


Figure 2: Schematic diagram of the normal model CCPS.

voltage ratio of transformer is more than one hundred times, and diode bridge circuit is constructed by ten full-wave rectifier devices in series. The HV section supplies at most 43 kV to the PFN capacitors.

This model controls two stages in the charging period. At the beginning of capacitor-charging, the two series resonant circuits operate in parallel to facilitate reduction in charging time (1st stage). When the capacitor voltage is close to the setting value, one series resonant circuit charges, to facilitate improvement of the peak voltage stability (2nd stage). The exclusive model for the flux concentrator modulator has a specification of 20 kV output voltage [10-11].

The highly precise model [9] is the CCPS where two power supplies (PSs) are combined as shown in Table 1; a 5 kJ/s PS (the sub PS) and a 30 kJ/s normal model (the main PS). The inverter section of the sub PS is constructed by one series resonant circuit, and the switching frequency is changed from 35 kHz to 17.5 kHz. The sub PS can be controlled by an optical signal for noise reduction.

In the highly precise model, the sub PS is connected to both loads (PFN capacitors) by a HV cable and upper dominance control equipment by control cables. The output HV cable from the main PS passes inside the sub PS. The sub PS generates control signals of the main PS. The highly precise model controls five stages in the charging period, using on-off operation of the three series resonant circuits and changing the switching frequency of the sub PS.

At the test in NIKOHA, the result of output voltage stabilities, namely 0.2%p-p of the normal model [8] and 0.022%p-p of the highly precise model [9], were observed.

All models of NIKOHA CCPSs are equipped with a function named “abnormal charge pulse set function”. When a few incomplete charges being unrelated to important breakdown happen accidentally, the HV-off interlock doesn’t function until the above situation counts successively to the established number of times. This function contributes the continuous operation.

PRESENT STATUS OF NIKOHA CCPS

At present, in the SuperKEKB injector linac, most compact klystron modulators use NIKOHA CCPSs at present. Since last summer, 12 NIKOHA CCPSs (and 1 Toshiba Electro-Wave Products Co. CCPS) have been operating [13].

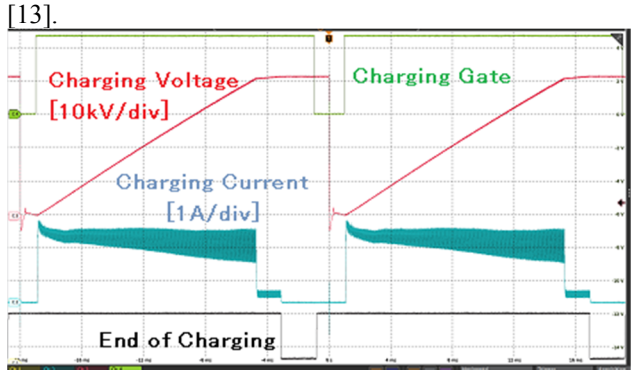


Figure 3: Waveforms of input-output signals of the normal model CCPS. The horizontal scale is 4 ms/div.

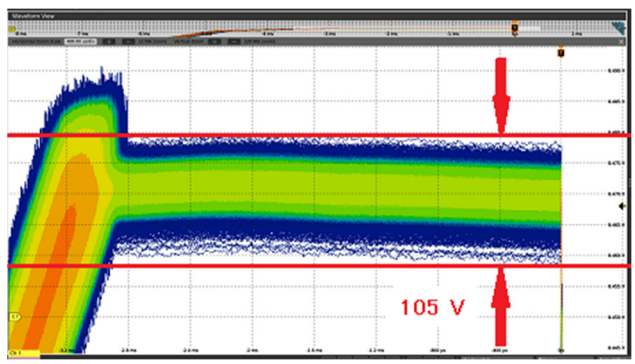


Figure 4: Collected flat-top zoomed-in signals of charging output voltage of normal model CCPS for 10 min. The horizontal scale is 200 μs/div.; the vertical scale is 25 V/div.

Characteristics of NIKOHA CCPS Measured in KEK

Figure 3 and 4 are the waveforms obtained at a KEK test station. The setting output voltage is 43 kV and the repetition rate is 50 pps. The waveforms of Fig. 3 are always indicated in all compact klystron modulators for confirming the state of CCPSs. The charging gate signal is input from the upper dominance control. The waveform of the charging gate signal shows that the ordered charging period is 18 ms. The charging voltage, current signals, and the end of charging signal are outputs from the CCPS. The waveforms of the charging voltage and current shows that the observed charging period is 16 ms and two stage control is accomplished.

The waveforms of Fig. 4 were measured to confirm the output voltage stability. There was a 105 V maximum unsteadiness at the flat-top for 10 min. Since the measured output voltage was 42.4 kV, the output voltage stability was calculated as 0.248%, which is very close to the specification. At the same time, using the histogram calculation function of the oscilloscope, a datum with the standard deviation σ of 26.6 V was obtained. Therefore, the error calculated as the absolute value of $\pm 2\sigma$ is 106 V, which is also very close to the above unsteadiness 105 V.

Content from this work may be used under the terms of the CC BY 3.0 licence (© 2018). Any distribution of this work must maintain attribution to the author(s), title of the work, publisher, and DOI.

ISBN: 978-3-95450-194-6 ISSN: 2226-0366 doi:10.18429/JACoW-LINAC2018-THPO095

Content from this work may be used under the terms of the CC BY 3.0 licence (© 2018). Any distribution of this work must maintain attribution to the author(s), title of the work, publisher, and DOI.

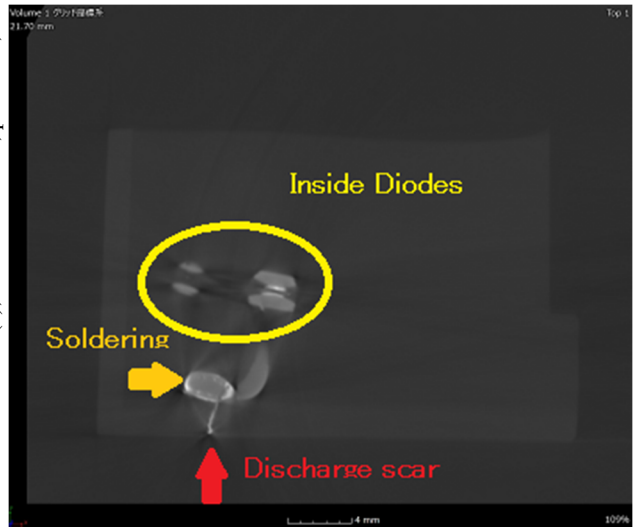


Figure 5: X-ray CT picture of a broken device [11].

Operation Conditions of CCPSs in SuperKEKB Injector Linac

The operating hours were greater than 5,000 h from autumn in 2015 to summer in 2016 [10], were about 3,600 h from autumn in 2016 to summer in 2017 [11] and were about 6,000 h from autumn in 2017 to summer in 2018 [13].

In October, 2015, two CCPSs broke down successively. The full-wave rectifier devices short-circuited. It seemed that the cause of the short was trash in the oil tank, which is built into the HV section of the CCPS. The check and cleaning of all CCPSs were performed in a clean room (a thermostat tank) [10].

In November, 2016, one CCPS broke down, but there was no trash in the oil tank. Non-destructive tests with X-ray computed tomography (X-ray CT) were commissioned to an outside agency (Tokyo Metropolitan Industrial Technology Research Institute, TIRI [14]) to confirm the situation inside the broken parts of the devices. Figure 5 is one of image data obtained by X-ray CT. Some discharge scars were observed from the soldering points. To avoid the discharge, both spacings for insulation of metal parts and shapes of the parts in the oil tank were reconsidered and changed in the broken CCPS [11].

After the repairs described above were performed, 12 CCPSs in the SuperKEKB injector linac were operated without breakdown from autumn in 2017 to summer in 2018 [13].

CONCLUSION

The NIKOHA CCPSs have been used by most compact klystron modulators, and after some repairs, their reliability is confirmed gradually by recent operation. In the future, longer operation will be performed, and the characteristics of the highly precise model will have to be measured in KEK.

REFERENCES

[1] K. Furukawa *et al.*, "Rejuvenation of 7-GeV SuperKEKB Injector Linac", in *Proc. 9th Int. Particle Accelerator Conf. (IPAC'18)*, Vancouver, BC, Canada, May 2018, paper MOPMF073, pp. 300-303, doi:10.18429/JACoW-IPAC2018-MOPMF073

[2] M. Akemoto *et al.*, "Present Status of the Klystron Modulator for SuperKEKB Injector Linac", presented at LINAC'18, Beijing China, Sep. 2018, this conference.

[3] M. Akemoto *et al.*, "The KEKB injector linac", *Prog. Theor. Exp. Phys.*, vol. 2013, p. 03A002, 2013, doi:10.1093/ptep/ptt01

[4] H. Nakajima *et al.*, "Characteristic and Future's Problem of Compact Klystron Modulator", in *Proc. of the 28th Linear Accelerator Meeting in Japan,* Tokai, Japan, Jul. 2003, pp. 48-50 (in Japanese).

[5] M. Akemoto *et al.*, "Present Status of Klystron Modulators for the KEK Electron-Positron injector Linac", in *Proc. of the 5th Annual Meeting of Particle Accelerator Society of Japan and the 33rd Linear Accelerator Meeting in Japan,* Higashihiroshima, Japan, Aug. 2008, pp. 892-894 (in Japanese).

[6] H. Honma *et al.*, "Upgrade of the PF 2.5-GeV Linac Klystron Modulator for the KEKB", in *Proc. of the 1994 Int. Linac Conf. (LINAC'94)*, Tsukuba, Japan, Aug. 1994, paper TU-30, pp. 436-438.

[7] K. Iida *et al.*, "Capacitor-Charging Inverter Power Supply", in *Proc. of the 27th Linear Accelerator Meeting in Japan,* Kyoto, Japan, Aug. 2002, pp. 252-254 (in Japanese).

[8] O. Endo *et al.*, "Development of High-Power Switching Power Supply", in *Proc. of the 10th Annual Meeting of Particle Accelerator Society of Japan,* Nagoya, Japan, Aug. 2013, pp. 621-623 (in Japanese).

[9] H. Akikawa *et al.*, "Development of High-Precision Capacitor-Charging Power Supply for Pulse Modulators", in *Proc. of the 12th Annual Meeting of Particle Accelerator Society of Japan,* Tsuruga, Japan, Aug. 2015, pp. 1143-1145 (in Japanese).

[10] M. Kawamura *et al.*, "Present Status of Inverter Power Supplies for Modulators in KEK Electron-Postron Linac", in *Proc. of the 13th Annual Meeting of Particle Accelerator Society of Japan,* Chiba, Japan, Aug. 2016, pp. 412-415 (in Japanese).

[11] M. Kawamura *et al.*, "Present Status of Inverter Power Supplies for Modulators in KEK Electron-Postron Linac (2)", in *Proc. of the 14th Annual Meeting of Particle Accelerator Society of Japan,* Sapporo, Japan, Aug. 2017, pp. 481-485 (in Japanese).

[12] M. Akemoto *et al.*, "Present Status of Flux Concentrator Modulator for SuperKEK", in *Proc. of the 14th Annual Meeting of Particle Accelerator Society of Japan,* Sapporo, Japan, Aug. 2017, pp. 504-506 (in Japanese).

[13] M. Kawamura *et al.*, "Present Status of Inverter Power Supplies for Modulators in KEK Electron-Postron Linac (3)", in *Proc. of the 15th Annual Meeting of Particle Accelerator Society of Japan,* Nagaoka, Japan, Aug. 2018, paper WEP062, to be published.

[14] TIRI, https://www.iri-tokyo.jp/site/english/

ISBN: 978-3-95450-194-6 ISSN: 2226-0366 doi:10.18429/JACoW-LINAC2018-THPO096

DESIGN STUDY OF A HIGH EFFICIENCY KLYSTRON FOR SuperKEKB LINAC

F. Qiu, S. Fukuda, S. Matsumoto, T. Matsumoto, T. Miura, T. Natsui
Accelerator Laboratory, KEK, Tsukuba, Japan

Abstract

The injector linear accelerator (linac) for the SuperKEKB particle accelerator requires a higher efficiency klystron than the currently used 50 MW, S-band, pulsed unit (PV3050/E3730), which operates at the same voltage, to increase the power redundancy. The efficiency is expected to improve from the currently observed 45% to more than 60%. We propose a type of high efficiency klystron using novel bunching mechanisms. The 1-D disk model based code is used for preliminary optimization of the tube parameters; these parameters are further checked by 2-D codes known as field charge interaction (FCI) and MAGIC. In this paper, the design consideration of the high efficiency klystron is presented.

INTRODUCTION

The KEKB electron–positron (e-/e+) collider is being upgraded to the SuperKEKB to achieve a 40-times higher luminosity [1]. As shown in Fig. 1, the linac consists of eight sectors (A–C and 1–5). The black squares in each sector represent the accelerating units that provide an energy gain of approximately 160 MeV each [1-2]. A total of 60 accelerating units are mounted in the SuperKEKB injector.

The klystron drive line for each unit is shown in Figure 2 (left). The low-level radio frequency (LLRF) system generates 4 μs RF pulses at first, and the phase of the RF pulse is reversed by 180° during the last 1 μs. The RF pulse is then amplified by the 600 W solid state amplifier (SSA). In the next step, the output of the SSA drives an S-band 50 MW klystron (PV3050/E3730A). A SLAC energy doubler (SLED) compresses the 4 μs pulse from the klystron output and generates a shorter 1 μs pulse with high peak power, thus powering four 2-m accelerating structures with an accelerating field of 21 MV/m. The picture and specifications of the klystron PV3050 are shown in Figure 2 (right) and Table 1, respectively [3].

High efficiency klystrons have become popular in recent years owing to their benefits of reducing the operating costs of the accelerators as well as increasing the operating margins. In cooperation with MELCO (Mitsubishi Electric Corporation), KEK has a plan to develop a type of high efficiency klystron (PV3064) to replace the current PV3050 tubes [4]. Several methods have been proposed to increase the efficiency of a klystron. These methods can be divided into two main categories: The first kind is a multi-beam klystron (MBK) which has several low perveance beam-lets because lower perveance usually corresponding to higher efficiency [5]. Each beamlet carries a small amount of current, but the total current can be large. The other kind focuses on novel bunching mechanisms. Based on this idea, the core oscillation method (COM) [6], bunching-alignment-collection (BAC) [7], and core stabilization method (CSM) [8] are proposed. It would be useful if we can develop a compatible tube of the existing PV3050 with minor modifications by following the recent trends in efficiency improvement. These techniques can also be extended to other projects such as the international linear collider (ILC). In this paper, based on the existing PV3050, we present a compatible BAC-based tube. To achieve higher efficiency, the cavity parameters are first optimized, and the focusing magnet and tube length are modified slightly. The RF window would need to be redesigned because of the increment in the output power; however, this is not considered in the current work.

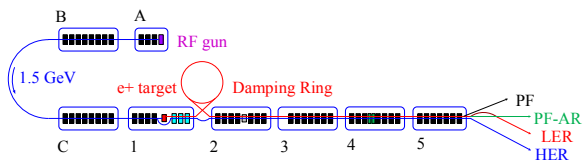


Figure 1: Layout of SuperKEKB injector linac.

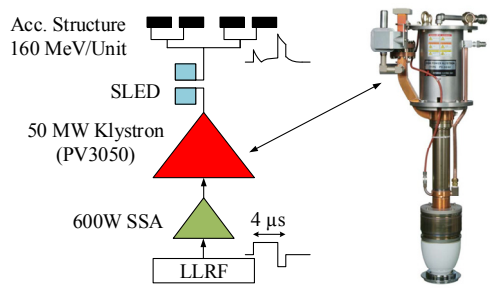


Figure 2: Klystron drive line (left), and the 50 MV klystron PV3050 (right).

Table 1: Specifications of PV3050

	Value	Unit
Frequency	2856	MHz
Peak RF power	50	MW
Repetition rate	50	Hz
Efficiency	45	%
RF pulse duration	4	μs
Beam voltage	310	kV
Gain	50	dB

Content from this work may be used under the terms of the CC BY 3.0 licence (© 2018). Any distribution of this work must maintain attribution to the author(s), title of the work, publisher, and DOI.

ISBN: 978-3-95450-194-6 ISSN: 2226-0366 doi:10.18429/JACoW-LINAC2018-THPO096

Content from this work may be used under the terms of the CC BY 3.0 licence (© 2018). Any distribution of this work must maintain attribution to the author(s), title of the work, publisher, and DOI.

BAC METHOD

The existing PV3050 klystron has the potential to provide increased efficiency from the present 45% to a higher value owing to introduction of the BAC section. We have tentatively applied four additional BAC cavities, including two second harmonic cavities, to the drift tube. Various codes, such as AJDISK [9], FCI [10], MAGIC, and CST, can be used for klystron design. The one-dimensional (1-D) code AJDISK is used for preliminary optimization of the tube parameters (e.g., cavity detuning and external Q of the output cavity), and the effect of the magnetic field and beam profile are subsequently checked with the two-dimensional (2-D) code (e.g., FCI). Finally, the tube is simulated using a PIC code such as MAGIC or CST.

Figure 3 compares the 1-D AJDISK simulation of the original PV3050 tube and the proposed BAC-based klystron. As mentioned above, we have added four cavities between the 3rd cavity and the penultimate cavity of the PV3050 tube (indicated by the green box). Compared with the original PV3050 tube, more outside bunches are collected by the BAC tubes at output cavity. The predicted efficiency is improved from the original 45% to approximately 69%.

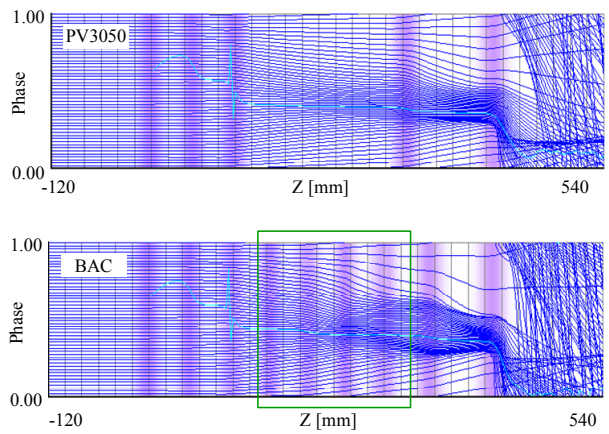


Figure 3: Phase diagrams of PV3050 (top) and proposed BAC-based klystron (bottom) in the AJDSIK simulation. The BAC cavities are indicated by the green box.

SIMULATION RESULT OF 2-D CODE

Because of the limitations posed by the 1-D code (e.g., distribution of the magnetic field and current density), we have to check the parameters obtained from AJDISK with the 2-D code (and the 3-D code as well). The FCI and MAGIC are used to verify the BAC-based design [10]. For the 2-D codes, the electron gun parameters and magnetic field need to be considered first.

Gun and Solenoid

The prototype of the particle gun for the planned BAC klystron is mostly derived from the gun of the PV3050. The trajectories of the gun with an applied voltage of 310 kV are simulated using MAGIC and DGUN code as shown in Figure 4. The simulation results for the current density obtained from MAGIC together with that of DGUN are shown in Fig. 5. Furthermore, the perveances of the gun obtained using these two codes are compared in Table 2. For further confirmation, the simulation results from CST are also presented in the table.

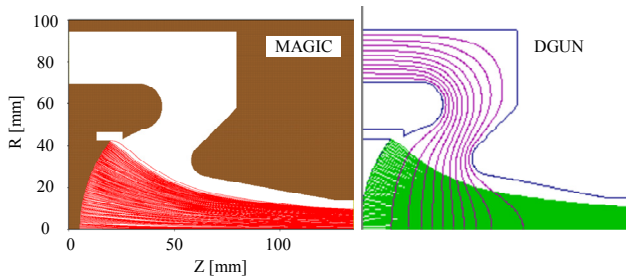


Figure 4: Simulation result of electron gun. Left: Magic, right: DGUN.

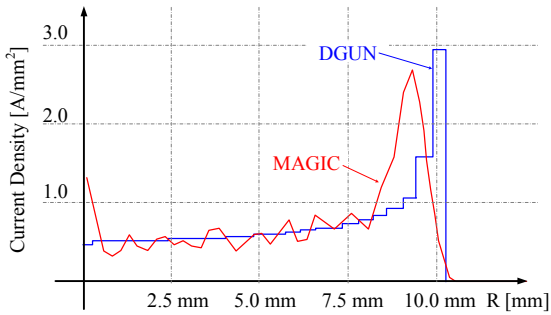


Figure 5: Current-density distribution of the electron gun 120 mm away from the cathode.

Table 2: Performance of the GUN Simulation

	DGUN	MAGIC	CST
μPerveance	1.86	1.88	1.87
Mesh size[mm]	0.25	0.25	0.25

The solenoids in the BAC are primarily based on the PV3050 klystron as well. A total of eight solenoids is used in the klystron PV3050. The focusing magnet is then simulated using POISSON SUPERFISH code [11]. We have compared the simulated magnetic field with the measured value of the PV3050 (indicated by the blue and red lines in Fig.5). The results show that the simulated field is in good agreement with the measured field.

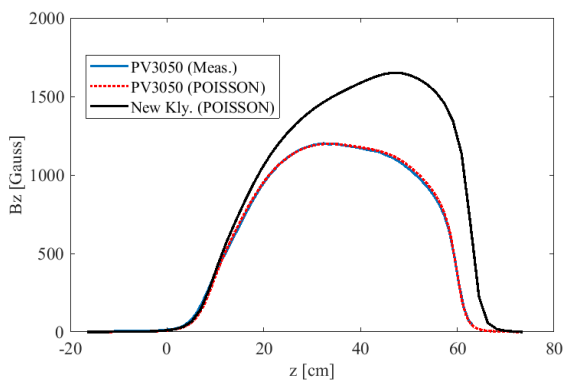


Figure 6: Comparison of the magnetic field on axis.

ISBN: 978-3-95450-194-6 ISSN: 2226-0366 doi:10.18429/JACoW-LINAC2018-THPO096

For the BAC klystron, because we have extended the length of the klystron tube to obtain a higher efficiency (see Figure 7), it is necessary to have a longer magnet that has a stronger field at the output cavity to suppress the scalloping effect. The new magnetic field obtained is thus shown as the black line in Figure 6.

Tube Simulation

The electron gun parameters shown in Figure 4 and the corresponding magnetic field are used in the 2-D code. The FCI code is applied first because it is faster compared to the MAGIC code. Figure 7 shows the comparisons of the FCI simulations of PV3050 and proposed BAC tube. It should be noted that the distances of the penultimate cavity and output cavity were increased by approximately 5-cm because it was found that the efficiency could be further improved under this condition. As seen from the beam profile of these two cases, compared with PV3050, more particles are bunched by the BAC tube at the output cavity. The FCI code predicted the maximum efficiencies of PV3050 and BAC klystron as 44% and 68%, respectively. The efficiency of the BAC tube predicted by FCI is shown in Figure 8.

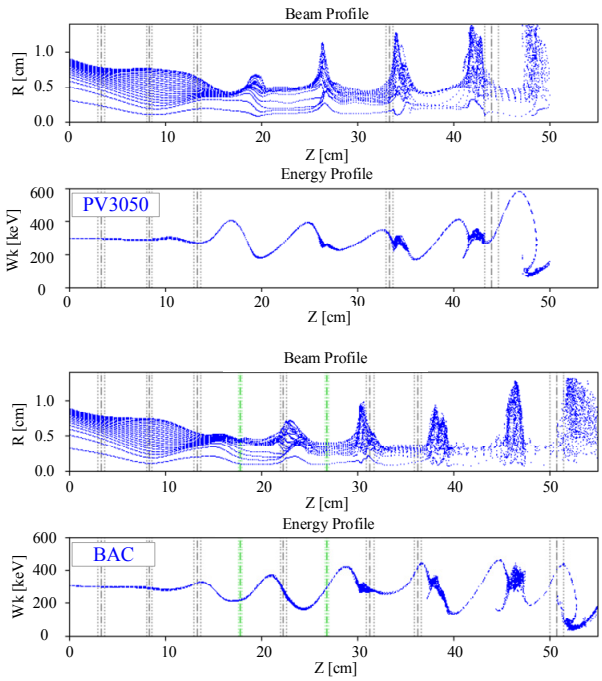


Figure 7: Beam and energy profiles from FCI simulation. Top: PV3050, bottom: BAC tube.

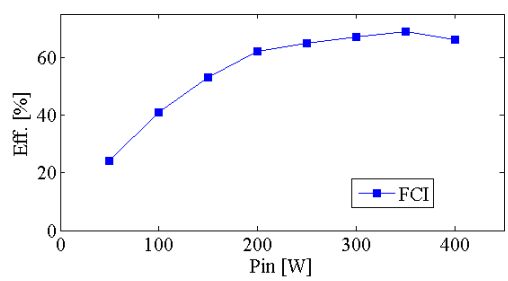


Figure 8: Predicted efficiency curve of the BAC tube.

It is possible to realize an all-in-one simulation with the MAGIC code, which means the gun, focusing magnetic field, and cavity tubes can be simulated at the same time. However, in our simulation, owing to limited time, we record the beam information of the GUN outlet region first and then import this beam information from the inlet of the klystron tubes. We expect that we can achieve a high efficiency as according to FCI predictions. However, for MAGIC, the predicted efficiency at the saturation point is approximately 52% (~15% lower than those of FCI and AJDISK). As shown in Figure 9, the currents of MAGIC and FCI were not in good agreement. Noted that we have modified the position of the output cavity for the MAGIC code to achieve the highest efficiency. It can be seen that the two codes are in agreement before the second 2nd harmonic cavity. However, the currents show disagreement after the pre-penultimate cavity. We attempted to reduce the mesh size of the MAGIC code, but the result did not improve significantly. Furthermore, we attempted to change the detuning of the 2nd harmonic and penultimate cavities by some extent, but we could not achieve high efficiency as expected. The reason for this is not understood thus far, and further simulations with other codes may be required in future studies.

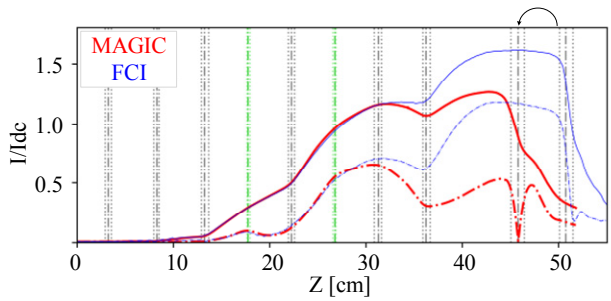


Figure 9: Current comparison of MAGIC and FCI code.

CONCLUSION

Recently, interesting methods based on the novel bunching mechanism are proposed for the high efficiency klystron. KEK is planning to develop a high efficiency klystron to improve the operating margin of the SuperKEKB project. We present our work at developing a compatible tube for the existing PV3050. By adding four BAC cavities, the efficiencies predicted by the AJDISK and FCI codes are improved by more than 20% at the saturation point. However, disagreements are observed for simulations with the MAGIC code, and the reason for this is not well understood thus far. Further simulations are required to address this in the future.

REFERENCES

[1] K. Furukawa *et al.*, "Rejuvenation of 7-GeV SuperKEKB injector linac", in *Proc. IPAC'18*, Vancouver, BC, Canada, May 2018. pp. 300-303.

[2] T. Miura *et al.*, "LLRF control unit for SuperKEKB injector linac", in *Proc. IPAC'18*, Vancouver, BC, Canada, May 2018. pp. 2134-2136.

Content from this work may be used under the terms of the CC BY 3.0 licence (© 2018). Any distribution of this work must maintain attribution to the author(s), title of the work, publisher, and DOI.

ISBN: 978-3-95450-194-6 ISSN: 2226-0366 doi:10.18429/JACoW-LINAC2018-THPO096

Content from this work may be used under the terms of the CC BY 3.0 licence (© 2018). Any distribution of this work must maintain attribution to the author(s), title of the work, publisher, and DOI.

[3] S. Fukuda *et al*., "Development of the B-factory linac 50-MW pulse Klystron", in Proc. Int. Linac Conference, Tsukuba, Japan, 1994. pp.427-429.

[4] S. Fukuda, "Project Oriented Klystron Developments in Japan, China and India", *Journal of the Korea Physical Society*, vol. 71, no. 11, pp. 769-774, Dec. 2017.

[5] A. larionov *et al*., "Design of Multi-Beam Klystron in X-Band", in *Proc. 27th Linear Accelerator Meeting in Japan*, Kyoto, Japan, Aug. 2002.

[6] A. Yu. Baikov, C. Marrelli, I. Syratchev, "Toward high power klystrons with RF power conversion efficiencies on the order of 90%", *IEEE. Trans. Elec. Dev.,* vol. 62, no. 10, pp. 3406-3412, Oct. 2015.

[7] I. A. Guzilov, "BAC method of increasing the efficiency in klystrons", in *Proc. 10th Int. Vacuum Elec. Sources Conf. (IVESC '14)*, Saint Petersburg, Russia, July 2014.

[8] G. Burt *et al*., "Particle-in-cell simulation of a core stabilization method klystron", in *Proc. of IEEE International Vacuum Electronics Conference. (IVEC 2017)*, London, UK, April, 2017.

[9] T. Shintake, "FCI-Field Charge Interaction Program for High Power Klystron Simulation", in Proc. *IEEE Particle Accelerator Conf. (PAC'89)*, Chicago, IL, USA, pp. 94-96, Mar 1989.

[10] A. J. Jensen *et al*., "Developing sheet beam klystron simulation capability in AJDISK", *IEEE Trans. Elec. Dev*., vol. 61, no. 6, pp. 1666-1671, June 2014.

[11] K. Halbach, R. F. HOLSINGER, "SUPERFISH –A computer Program for Evaluation of RF cavities with Cylindrical Symmetry", *Particle Accelerators*, vol. 7, pp. 213-222, 1976.

ISBN: 978-3-95450-194-6 ISSN: 2226-0366 doi:10.18429/JACoW-LINAC2018-THPO097

RECENT RESULTS FOR STUDY OF CERAMIC AND COPPER PLATING FOR POWER COUPLERS

Y. Yamamoto†, E. Kako, S. Michizono, KEK, Tsukuba, Japan
Y. Okii, Nomura plating Co., Ltd., Osaka, Japan
E. Cenni, F. Aurelien, IRFU/CEA, Gif-sur-Yvette Cedex, France

Abstract

KEK has conducted a survey to select an optimum ceramic after withdrawal by a domestic manufacturing company two years ago. For this selection, there are four important items on the properties of ceramic; that is, relative permittivity, dielectric loss tangent, surface and volume resistance, and secondary electron emission coefficient. For measurements of these parameters, ten kinds of ceramic samples supplied from five companies were measured using three kinds of measurement systems. For measurement of secondary electron emission, scanning electron microscope (SEM) with beam blanking system was used. On the other hand, residual resistivity ratio (RRR) for copper plating, which is the most important item for quality control, has also been carried out by collaboration with KEK-CEA. In this report, the recent results for these studies will be presented in detailed.

INTRODUCTION

In the E-XFEL, ESS, LCLS-II, etc. which have been constructed (or under construction) in recent years, several hundred superconducting cavities are used, and the quality control of the power coupler has become important. In particular, the manufacturing cost of copper plating covering the inner surface of the power coupler, ceramics used for RF windows, and titanium nitride coating (TiN coating) deposited on the surface of ceramic is also a large proportion of cost, which are the main items for this R&D. R&D for power coupler is also included in the framework of cost reduction R&D for the International Linear Collider (ILC) concluded between KEK and the US Fermi National Laboratory (FNAL) in 2017. Currently, various investigations and studies under the cooperation with affiliated companies, are being advanced at KEK [1].

SURVEY AND RESEARCH ON COPPER PLATING

The quality control of copper plating is an item which became a problem frequently also in E-XFEL [2], which is still an important matter in the other projects under construction. The quality control is generally evaluated by RRR measurement. RRR measurement has been carried out in KEK/COI by using small refrigerator with conduction cooling method. Figure 1 shows the measurement system (upper) including the small cryostat in the COI building in KEK, and the stage (lower) for placing the sample. Four samples can be mounted at the same time and can be measured with different electric current values (for example, three stages such as 1 mA, 10 mA, 100 mA). The electric current is bi-directionally loaded and the average resistance value is calculated. After the preliminary tests, the optimum electric current value was found to be 1 to 10 mA. And, the optimum sample size is fixed to 150 mm x 5 mm x 0.5 mm, because this system uses the conduction cooling method, and too large sample cannot be cooled.

As a way of evaluating the RRR of the copper plating, after measuring the resistance to a copper plating sample, the copper plating is peeled off and returned to the base material SUS316L, and resistance measurement is performed again. As the final step, by estimating with the ratio of the two measured values of room temperature and low temperature, the net RRR for copper plating is obtained. With respect to the SUS316L material, it is not necessary to peel off for all the copper plating samples in order to take almost the same resistance values.

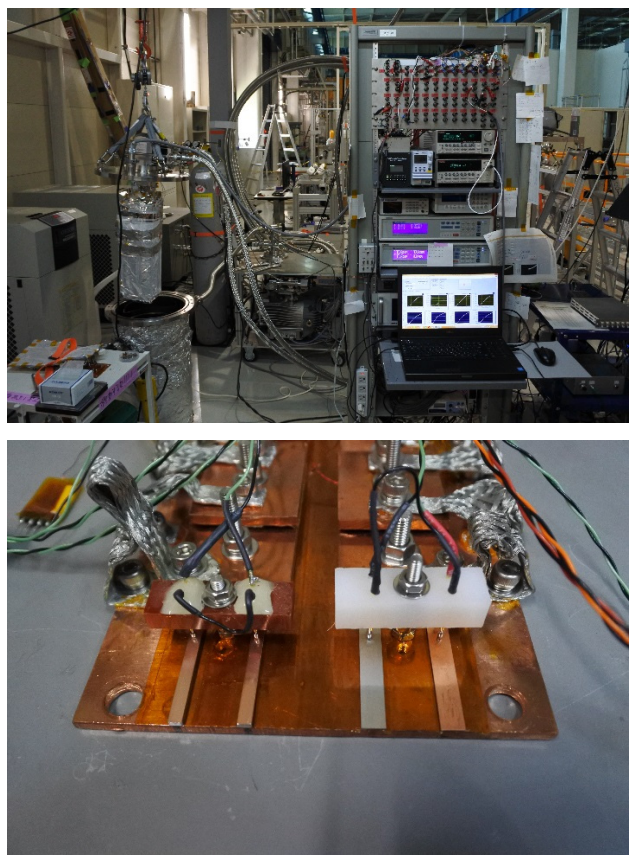


Figure 1: Residual Resistivity Ratio (RRR) measurement system (top) and four samples on the stage (bottom) in KEK/COI.

† yasuchika.yamamoto@kek.jp

Content from this work may be used under the terms of the CC BY 3.0 licence (© 2018). Any distribution of this work must maintain attribution to the author(s), title of the work, publisher, and DOI.

ISBN: 978-3-95450-194-6 ISSN: 2226-0366 doi:10.18429/JACoW-LINAC2018-THPO097

Content from this work may be used under the terms of the CC BY 3.0 licence (© 2018). Any distribution of this work must maintain attribution to the author(s), title of the work, publisher, and DOI.

After several commissioning tests, four copper plating samples were made and RRR measurements were made. As for two of these, it was found that the RRR changed remarkably from 15 to 75 as a result of measuring several times with the time being shifted. Since there was a possibility that a malfunctioning occurred in the measurement system, two samples were sent to IRFU/CEA in France and similar RRR measurements were carried out there, and the same result was obtained, therefore this phenomenon is not related to the measurement system. This result is still under investigation. Figure 2 shows the correlation plot between temperature and resistance of copper plating and SUS316L samples. Blue point shows the first result, and green one the second (three months later) for the same copper plating sample. Between two measurements, this sample was in desiccator with low humidity. SUS316L sample has the same result for every sample in every measurement.

Recently, new copper plating samples, fabricated by electroforming method, are ready for RRR measurement. It is possible to obtain the resistivity for copper plating directly. As a next step for this R&D, the temperature dependence and the impurity dependence on copper plating will be investigated in detailed.

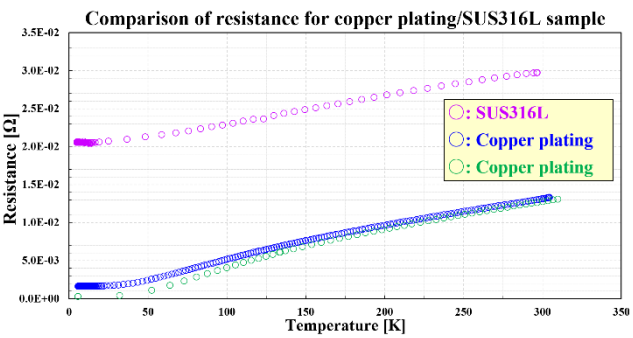


Figure 2: Correlation plot between resistance and temperature for copper plating and SUS316L samples. There are two data for one copper plating sample between different measurement periods.

SURVEY AND RESEARCH ON CERAMIC

Surveys and research on ceramics are carried out on the following four items.

- Surface/volume resistance (ρ)
- Relative permittivity (ε)
- Dielectric loss tangent (tanδ)
- Secondary electron emission coefficient (δ_{SEE})

Measurement of secondary electron emission coefficient is under progress and 10 types of samples were offered from 5 companies. For the measurement of δ_{SEE}, it is common to use a scanning electron microscope (SEM). Moreover, it is essential to use a pulse beam, because ceramic is an insulator. For the generation of a pulse beam, beam blanking system (like a kicker magnet) was installed into SEM in KEK/COI. The following items show the specification for measurement system.

- Scanning electron microscope SU3500 (HITACHI)
- Cathode voltage: 0.6 to 30 kV (measured 4 times for each voltage)
- Use of beam blanker (for pulse beam generation)
- Use of pulse beam with pulse width of 1 msec
- Use of bias voltage (primary current: +50V, absorption current: −50V)
- Measuring with one pulse per point (avoidance of charge-up)
- Carbon target used for primary beam current measurement
- Area injection (avoidance of charge-up) for ceramics and point injection for a carbon target
- Current amplifier (KEITHLEY)

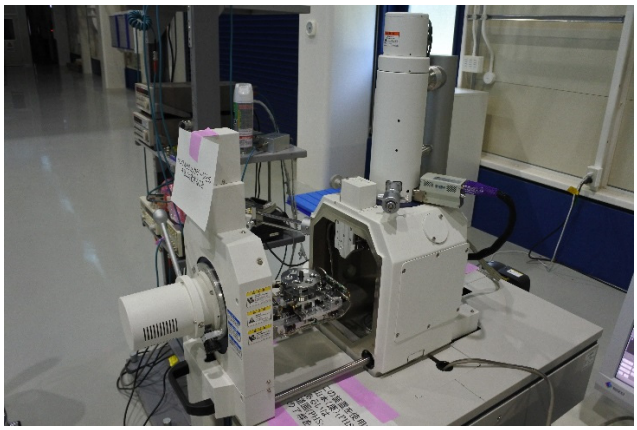
Figures 3 (a) and (b) show the SEM, and the sample holder where the sample is placed. On the stage, in addition to ceramic samples, carbon target for primary beam current measurement are placed together. In addition, the carbon target is provided with a non-penetrating hole with a diameter of 1 mm, and the beam is incident by the point injection. Figure 3 (c) shows the schematic view of measurement system including SEM, and observed signals for primary beam current on carbon and absorption current on ceramic. From the difference between the primary beam current and the absorption current, a reflected current including secondary electrons is obtained, and the δ_{SEE} can be obtained by taking the ratio to the primary beam current. Figure 3 (d) shows the δ_{SEE} of a ceramic sample. For ceramics, measurements are made four times at the same cathode voltage, and the average value is obtained, as shown by red line in Figure 3 (d). This result is in well-agreement with the previous result, therefore this means that the preliminary measurement for secondary electron emission coefficient was successfully done. At present, several ceramic samples were already measured. In near future, the comparison among 10 types of ceramic, the comparison between with and without TiN coating, the comparison among various rinsing methods including ultrapure water, ethanol, ultrasonic, and ozonized (O_3) water will be done.

With regard to the other properties of ceramic, for one part of many samples, relative permittivity and dielectric loss tangent was measured by a common measurement device. Moreover, surface/volume resistivity was also measured by using two measurement devices. Finally, it turned out that one of two is more reliable. In this fiscal year, these tests will be completed.

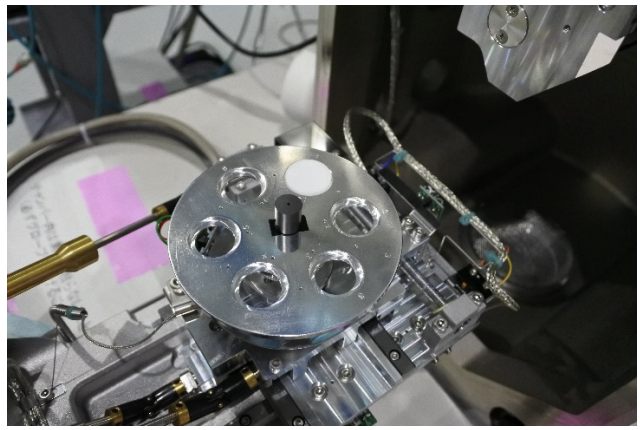
CONCLUSION

For the cost reduction R&D for power coupler in ILC, the survey and the research for copper plating and ceramic property have been continued from 2017. As for copper plating, RRR measurement is under progress with collaboration among KEK, Nomura plating and IRFU/CEA. In KEK/COI, SEM with beam blanking system for the measurement of secondary electron emission coefficient was commissioned successfully, and several ceramic samples were already measured. New results will be presented in IPAC19 or SRF19.

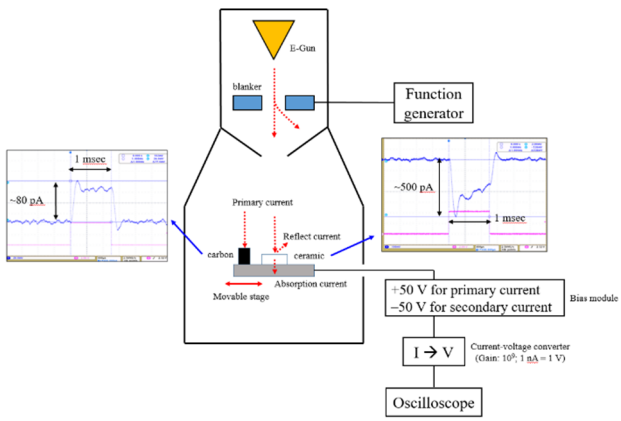
ISBN: 978-3-95450-194-6 ISSN: 2226-0366 doi:10.18429/JACoW-LINAC2018-THPO097



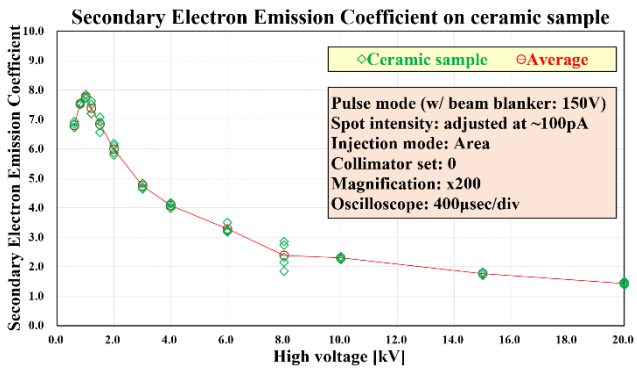
(a) Scanning electron microscope



(b) Sample holder



(c) Schematic view of measurement system



(d) Secondary electron emission coefficient for ceramic

Figure 3: (a) Scanning electron microscope (SEM) (b) Sample holder (c) Schematic view of measurement system (d) Secondary electron emission coefficient for ceramic.

ACKNOWLEDGEMENT

The authors would like to thank J. Taguchi (Nomura plating), T. Sudo (HITACHI High-Technologies Corporation), T. Okada and M. Iitake (K-VAC), M. Asano and H. Yamada (NAT).

REFERENCES

[1] Y. Yamamoto *et al.*, "Fundamental Studies for the STF-type Power Coupler for ILC", *in Proc. of SRF2017*, Lanzhou, China, Jul. 2017, pp. 194-198, doi:10.18429/JACoW-SRF2017-MOPB063

[2] W. Kaabi *et al.*, "Main RF power coupler for European-XFEL", *LCWS2017*, Strasbourg, France. https://agenda.linearcollider.org/event/7645/

Content from this work may be used under the terms of the CC BY 3.0 licence (© 2018). Any distribution of this work must maintain attribution to the author(s), title of the work, publisher, and DOI.

ISBN: 978-3-95450-194-6 ISSN: 2226-0366 doi:10.18429/JACoW-LINAC2018-THPO100

DEVELOPMENT OF A 1.5GHz HIGH-POWER CW MAGNETRON FOR SRF ACCELERATOR

Li Wenliang[1], Liu Youchun[2], Sun Lingbin[2], Zhou Bowen[1], Zhang Pengjiao[1], Ke Yijing[1], Zhao Lei[3], Hou Rui[3], Li Junzhou[3], Zhang Liping[3], Sun An[1,3]
[1]PLAI, Nanjing University, Nanjing 210046, China
[2]Nanjing Sanle Electronic Information Industry Group Co., Ltd., Nanjing 211899, China
[3]Andesun Technology Group Co., Ltd., Nanjing 210046, China

Abstract

An 1.5 GHz, 13.5 KW CW high-power magnetron for a superconducting RF accelerator has been developed by Andesun Technology Group Co., Ltd. with Nanjing Sanle Electronic Information Industry Group Co., Ltd., in order to replace the klystron, that could reduce the power source cost to about one-third. The cavity, output power antenna and coupling door-nob have been optimized by using CST Studio. Testing results have shown that the resonance frequency and output power have met the requirements, and the efficiency of the magnetron is higher that 78.45%.

INTRODUCTION

At present, the microwave energy of the RF superconducting accelerator is mainly provided by the klystron internationally. However, the klystron as a microwave source is characterized by low efficiency and high cost, which increases operating costs of the entire accelerator system. So the magnetron with a cost of one-third of the klystron is the best choice for the replacement of the original SRF accelerator microwave source. In order to meet the urgent need of microwave sources for SRF accelerator, a 1.5 GHz、13.5 kW CW magnetron for SRF accelerator is researched and developed by Andesun Technology Group Co., Ltd. with Nanjing Sanle Electronic Information Industry Group Co., Ltd.

The development of this magnetron is based on the 2450 MHz magnetron. First, the frequency of magnetron is reduced from 2450 MHz to 1500 MHz by increasing the radius of the cavity and so on. The CST Studio is used to optimize the coupling output part of the magnetron and gets the best parameter of the coupled antenna [1]. The electronic simulation of the magnetron is completed by the Particle-in-cell solver, which gains a general understanding of the performance of the magnetron [2]. The prototype measurement shows that the output power of the magnetron reached the requirement, the whole tube efficiency is 78.45%, and the tuning range is 10 MHz.

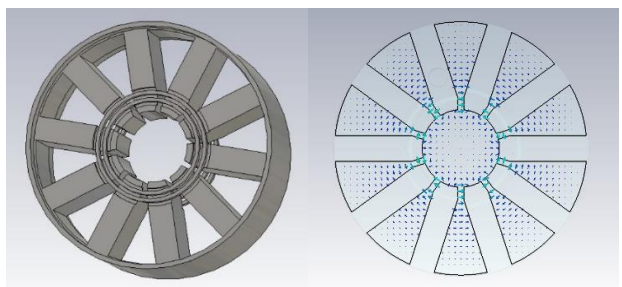
DESIGN OF THE MAGNETRON

According to the working parameters of the SRF accelerator, the performance parameters of this magnetron are as follows:

(1) Working frequency: 1.5 GHz
(2) Average output power: 13.5 kW
(3) Peak power: 17 kW
(4) Efficiency: ≥70%
(5) VSWR: ＜1.4
(6) Way of working: CW

Cavity Design

The anode cavity of the magnetron adopts a fan-slot type co-cavity resonance system with a diaphragm belt. A total of 10 cavities were used and the blade-to-slot ratio is 3.01. Figure 1 shows the simulation model and the electric field distribution of the π mode which is the magnetron operating mode. Cavity simulation with strips gains that the mode separation is 84.6%.



(a) (b)

Figure 1: (a) The simulation model. (b) The electric field distribution of the π mode.

Output Structure Design

The magnetron uses an axial energy extraction device. The design of the excitation cavity is based on the WR-650 standard waveguide. The semi-cylindrical short-circuit surface is used, and the output part of the antenna is designed as a bullet type. The parameters of the bullet antenna are decided by simulation with the excitation cavity. The simulation result shows that the S_{11} curve is lower than -70 dB at 1.5 GHz and lower than -40 dB within 20 MHz bandwidth. Figure 2 shows the simulation curve of S_{11}. Figures 3 shows the finished excitation chamber and output coupling antenna.

Content from this work may be used under the terms of the CC BY 3.0 licence (© 2018). Any distribution of this work must maintain attribution to the author(s), title of the work, publisher, and DOI.

ISBN: 978-3-95450-194-6 ISSN: 2226-0366 doi:10.18429/JACoW-LINAC2018-THPO100

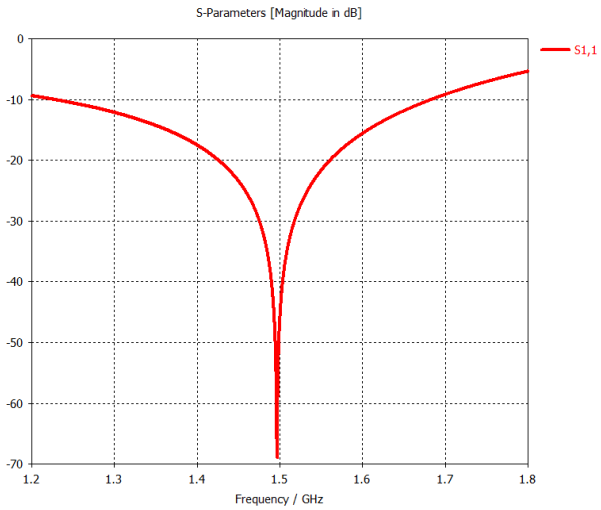


Figure 2: S_{11} of output structure.



(a) (b)

Figure 3: (a)The finished excitation chamber. (b)The finished output coupling antenna.

Whole Magnetron Simulation

After completing the design of each size of the magnetron, the magnetron is thermally simulated by Particle-in-cell solver. When we apply a voltage of 12,100 V and magnetic field of 2100 Gs, the simulation achieves optimal output performance. Figure 4 is a distribution image of electrons, which can clearly see the five electron spokes in the interaction space of magnetron. Figure 5 shows the output signal of the magnetron. The output power is obtained from the Fig. 5 according to the formula $P = {280^2}/{2}339200$ W [3]. Through the Fourier transform of the output signal, we get the output frequency of 1.527 GHz, and we can accept the difference of 30 MHz within the error range of the simulation.

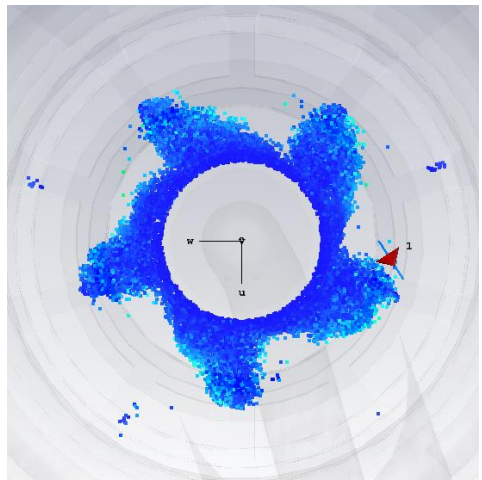


Figure 4: The electron distribution in the interaction space.

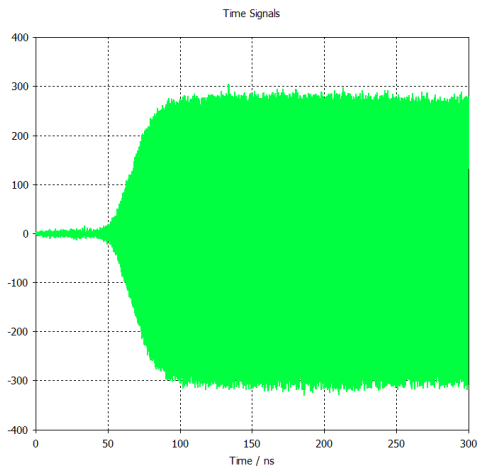


Figure 5: The output signal of the magnetron.

TESTING SYSTEM

The finished magnetron is shown in Fig. 6. The permanent magnet is used to generate an applied magnetic field, and the cavity is cooled by water.



(a) (b)

Figure 6: (a)The finished cavity. (b)The protype of 1.5 GHz CW magnetron.

Content from this work may be used under the terms of the CC BY 3.0 licence (© 2018). Any distribution of this work must maintain attribution to the author(s), title of the work, publisher, and DOI.

ISBN: 978-3-95450-194-6 ISSN: 2226-0366 doi:10.18429/JACoW-LINAC2018-THPO100

Content from this work may be used under the terms of the CC BY 3.0 licence (© 2018). Any distribution of this work must maintain attribution to the author(s), title of the work, publisher, and DOI.

The schematic diagram of the power test of the magnetron is shown in the Fig. 7. The black frame circle represents the main test system, and the orange and yellow colors represent the power test section and the water cooling system, respectively. The microwave generator controls the voltage and current applied to the magnetron, then the microwave energy generated by the magnetron is coupled into the excitation chamber, and the output energy from the magnetron and the reflected energy of testing system are measured through the coupler. After passing through a three-port circulator, the power is eventually absorbed by the water load. The isolation of the three-port circulator is 20 dB. The actual test platform is completed as shown in Fig. 8.

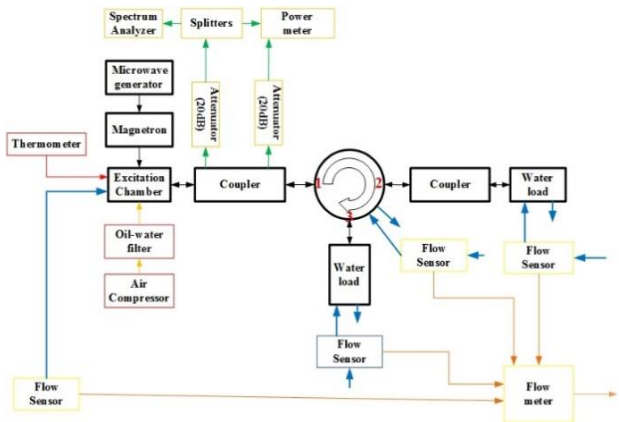


Figure 7: The schematic diagram of the power test of the magnetron.

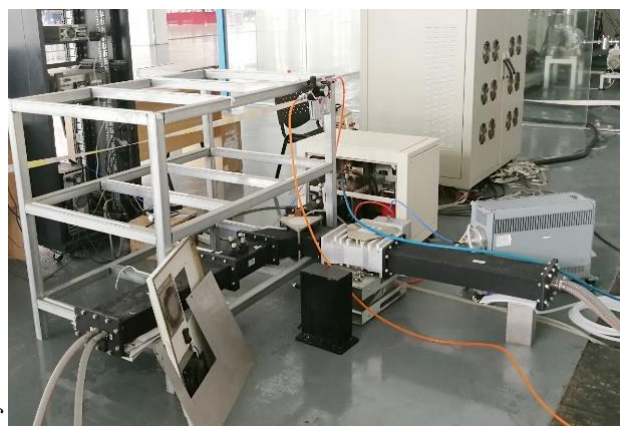


Figure 8: The test platform of magnetron.

TESTING RESULT

After preheating the cathode for 30s under the voltage and current of 3.5 V, 28 A, the voltage and current of cathode are gradually reduced to 0.2 V, 6 A to keep the magnetron working normally, and the working power of cathode is 1.2W. Figure 9 shows the curves that the applied anode voltage and current as the function of time. The final test results are shown in the Fig. 10. When the magnetron is operated at 1.49779 GHz, the output power reaches 14.23 kW, which exceeds the expected power of 13.5 kW, and the voltage applied at this time is 10,670 V, the magnetic field is 2100 Gs. The overall working efficiency exceeds 78.45%.

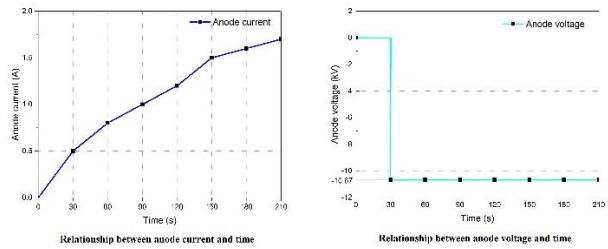


Figure 9: Curves of applied anode voltage and current as the function of time.



Figure 10: Testing results of 1.5 GHz CW magnetron.

CONCLUSIONS

A 1.5GHz high-power CW magnetron for SRF accelerator is successfully developed by Andesun Technology Group Co., Ltd. with Nanjing Sanle Electronic Information Industry Group Co., Ltd. The test results show that the 1.5GHz magnetron meets the design requirements and can meet the application requirements of SRF accelerator.

REFERENCES

[1] CST Particle Studio, CST Studio Suite, Computer Simulation Technology, CST, GmbH, Darmstadt, Germany, 2006.

[2] Türker ˙Isenlik and Korkut Ye˘gin, "Tutorial on the Design of Hole-Slot-Type Cavity Magnetron Using CST Particle Studio", *IEEE Transactions on Plasma Science*, vol. 41, NO. 2, February 2013.

[3] MC Balk, "3D magnetron simulation by means of graphical processing units with CST STUDIO SUITE™", in V*acuum Electronics Conference*, Monterey, CA, USA, 2012, pp. 25-26.

ISBN: 978-3-95450-194-6 ISSN: 2226-0366 doi:10.18429/JACoW-LINAC2018-THPO102

DESIGN STUDIES OF OUTPUT WINDOW FOR CEPC KLYSTRON

Z. J. Lu[1,2,4], S. Fukuda[1,3],Z. S. Zhou[1,4], S. C. Wang[1,4], O. Z. Xiao[1,4], Zaib-un-Nisa[1,4], G. X. Pei[1,4], Y.L.Chi[1,4]

[1]Institute of High Energy Physics, Chinese Academy of Sciences, Beijing 100049, China
[2]University of Chinese Academy of Sciences, Beijing 100049, China
[3]High Energy Accelerator Research Organization (KEK), Tsukuba 305-0801, Japan
[4]Key Laboratory of Particle Acceleration Physics and Technology, Institute of High Energy Physics, Chinese Academy of Sciences, Beijing 100049, China

Abstract

A high power and high efficiency klystron for the Circular Electron Positron Collider (CEPC) is developed at IHEP. This paper presents the design and simulation for a high-power coaxial window of the 650MHz, 800kW CW klystron, and the coupler design for high power test of window are also included. CST, ANSYS and Multipac 2.1 are used for design of window microwave performance, thermal analysis and multipacting effect. The simulation results of the coaxial window S-parameter analysis, shows a low reflection at the desire frequency of 650 MHz after optimized. The E-field and thermal simulation shown a good temperature distribution and maximum temperature has been found to be 36 Celsius degree at ceramic with water cooling in the inner and outer conductor. And the multipacting simulation for the window shows that multipacting has less chance to occur on the surface of ceramic.

INTRODUCTION

The Institute of High Energy Physics (IHEP), Chinese Academy of Sciences (CAS), has proposed a future plan of Circular Electron-Positron Collider (CEPC), which will be the biggest electron-positron collider in the world. Klystron is a critical component for an operation of accelerator. As RF power sources, more than 200 high efficiency klystrons with a frequency of 650 MHz and CW 800 kW output power are required. Those klystrons are designed at IHEP and the first prototype klystron is going to manufacture in China. The specifications of CEPC klystron are listed at Table 1 [1], we aim at more than 65 percent of the efficiency for the first klystron and more than 80 percent for the future plan to reduce the operation cost.

Table 1: CEPC Klystron Design Parameters

Frequency(MHz)	650
Output Power(kW)	800
Beam Voltage(kV)	81.5
Beam Current(A)	15.1
Efficiency (%)	>65

For successful operation of CEPC, the stable operation of klystrons is crucial, and an output window used in the klystron is one of the key components. Output window is a critical part of transmitting high RF power from klystron vacuum side to the external atmosphere, therefore a low power dissipation and no breakdown is important for window.

We had made a strategy to manufacture a reusable klystron with two steps or more as shown in Fig. 1. Before build the tube, the window itself must be manufactured and evaluated by using the existing RF power source to ensure the power handling capability.

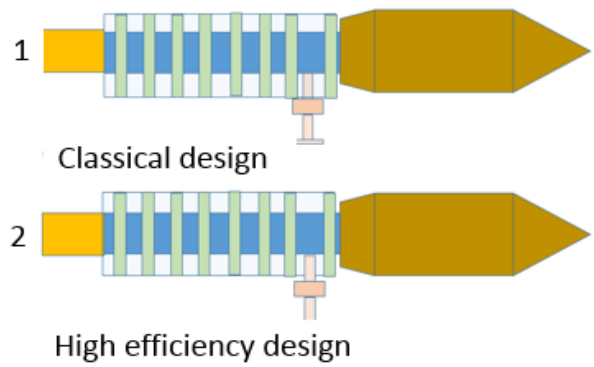


Figure 1: Klystron development strategy.

WINDOW DESIGN

WR1500 (381 mm×190.5 mm) waveguide is used to transmit 650 MHz RF power from klystron to accelerator, but it is difficult to use the pill-box window with rectangular waveguide to the klystron output cavity because of its big size. The pill-box window has a difficulty in cooling the center of ceramic so the high temperature may cause a high thermal stress that possibly may cause ceramic window breakdown.

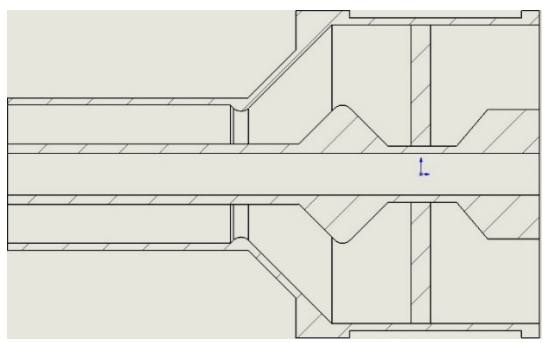


Figure 2: Schematic drawing of CEPC klystron output window.

Content from this work may be used under the terms of the CC BY 3.0 licence (© 2018). Any distribution of this work must maintain attribution to the author(s), title of the work, publisher, and DOI.

ISBN: 978-3-95450-194-6 ISSN: 2226-0366 doi:10.18429/JACoW-LINAC2018-THPO102

Content from this work may be used under the terms of the CC BY 3.0 licence (© 2018). Any distribution of this work must maintain attribution to the author(s), title of the work, publisher, and DOI.

Therefore, we use the coaxial structure coupling to the output cavity and then transfer the power to WR1500 waveguide. Schematic drawing of CEPC 650 MHz klystron window is shown in Fig. 2 [2]. The microwave design of window was carried out by CST Microwave Studio [3]. The thickness of ceramic is about 11 mm. With high purity alumina (99.7%) we obtained -85 dB of return loss at the 650 MHz and less than -30 dB at 50 MHz bandwidths as shown in Fig. 3. At actual operation, the required VSWR of the window is less 1.05 (-32.3 dB), so S-parameter in our design satisfies this requirement.

Figure 4 shows the electromagnetic field (E-field) calculated by CST CODE. The maximum of E-field is around 9×10^5 V/m, and the maximum of H-field is about 2000 A/m at 800 kW operate condition. We obtained the similar results for ANSYS CODE. The E-field in this type of RF window shows small concentration on ceramic surface.

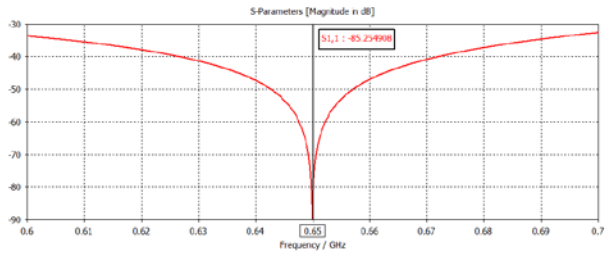


Figure 3: Return loss (S11) and insert loss (S21).

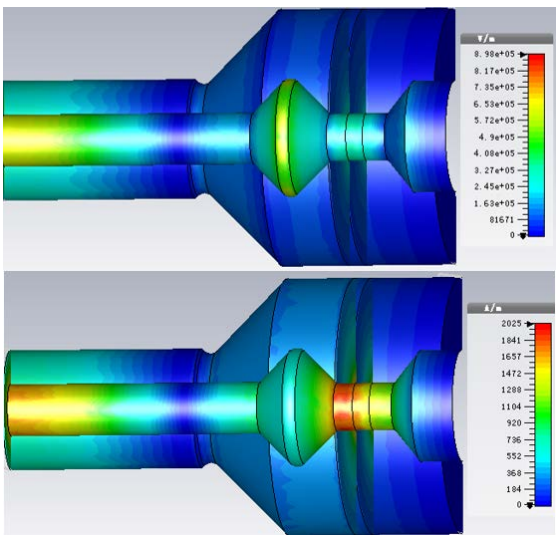


Figure 4: Electromagnetic field simulation by CST. Upper is electric, lower is magnetic field.

THERMAL ANALYSIS

Water cooling was prior to be considered because of its cooling power capability for 800 kW operation. The thermal loss of the window was evaluated to be about 800 W. Most of the loss are mainly generated on the inner conductor, and these losses resulted in several hundred degree Celsius. So only the forced air cooling might not be enough.

Water cooling of the inner conductor is important but since it is difficult to make a water channel from the output cavity of the klystron, the water is introduced from waveguide transition side (air side). In order to obtain better cooling, double piping structure is adopted after negotiated with TETD (Toshiba Electron-Tube Division), so the water directly flow by the ceramic inner thin copper surface to obtain the good cooling for the humps and inner conductor. The outer conductor of ceramic window part is also cooled by water.

Thermal simulations in ANSYS CODE [4] are carried out by calculating the convective heat transfer coefficient and radiation coefficient, but since the radiation effect was too small to consider in this temperature range which was enough to consider the thermal convection.

The thermal simulation results are simulated under the normal steady-state condition. Figure 5 shows the simulation results when water cooling is supplied in inner conductor and outer conductor. As shown in Fig. 6, the difference between the maximum and the minimum temperature in ceramic plate is about 10 ℃ and the maximum thermal stress caused by temperature difference is about 25 MPa, which much less than 99.7% purity alumina stress capacity of 320 MPa. And the structure deformation by temperature difference is in negligible. Since the conductivity of copper is enough to transfer the heat from conductor to the cooling water, the cooling of overall window is sufficient even in the case of the maximum temperature on the surface of ceramic which is about 36℃.

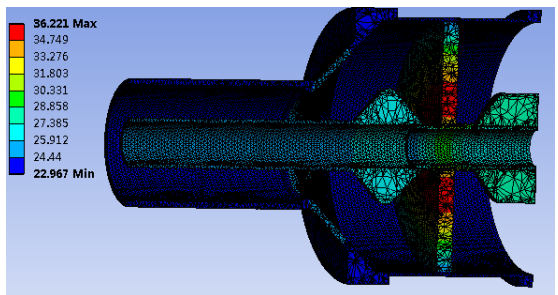


Figure 5: Thermal Simulation in ANSYS.

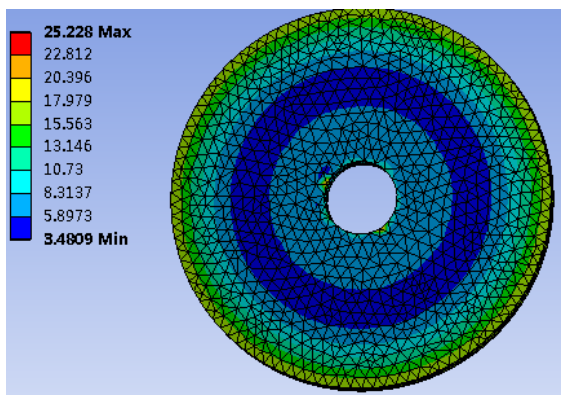


Figure 6: Thermal stress on the ceramic surface.

MULTIPACTING

Destruction of klystron output ceramic windows were

ISBN: 978-3-95450-194-6 ISSN: 2226-0366 doi:10.18429/JACoW-LINAC2018-THPO102

often caused by multipacting [5]. Multipacting directly results in surface local overheating of alumina ceramic and ceramic cracking or melting, the vacuum leak of the tube subsequently. In this chapter, multipacting phenomena is studied.

Multipacting is a common phenomenon in the high-power operating ceramic window, in some cases it causes serious damages. Therefore, avoid serious multipacting was achieved by not only the designing of structure but also by choosing a low SEY (Secondary Electron Yield) ceramic surface.

The ceramic coating with thin coating of low SEY characteristic materials such as TiN is a common way to suppress secondary emission. The SEY can be as high as 6 in maximum value for high purity alumina ceramic if has no coating on the surface of ceramic. Since TiN is resistive material and thick film increases loss, there is an optimum thickness to suppress the secondary electrons and with low loss. TiN coating thickness is about 5 nm from the past experience as described in Ref. [6]. With so many high-power klystrons employ TiN coating on the ceramic, therefore this process is simulated to confirm if the TiN coating effect.

The multipacting simulation is performed using the code Multipac [7] as shown in Fig. 7. In this code, initial electron source is automatically distributed along the setting boundary of window. The c_0 is initial free electron number in the boundary and c_{20} is the free electron number after 20 impacts. Ef_{20} is the average impact energy of the last impact in eV, e_{20} is secondary electron number after 20 impacts. The simulation results are shown in Fig. 7 when the ceramic surface in vacuum side is coated with TiN. In this figure, horizontal axis shows average incident power in kW. If Ef_{20} is in the range of high SEY area, multipacting may be serious. In the case of TiN coating of 5nm, though the impact energy is also between 100 eV and 1000 eV where SEY is larger than 2, the secondary electrons number is quite low and hard for multipacting or electron avalanche to continue.

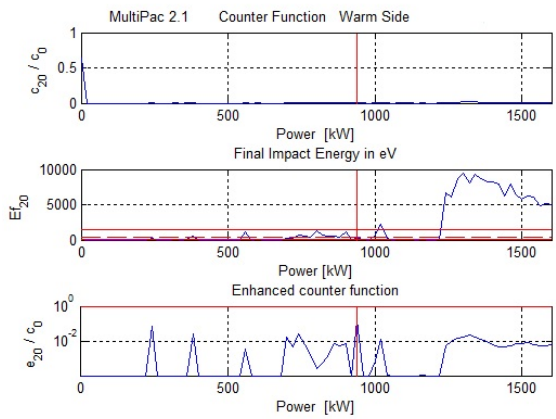


Figure 7: Secondary electron emission on the ceramic with 5 nm TiN coating simulation result in multipacting.

From this result, it is concluded that secondary electron may even exist with coating, but multipacting has less chance to be happened on the surface of ceramic

HIGH POWER TEST PLAN

Since this window is going to be used in the klystron, so one side of the window is evacuated. Therefore, in vacuum two windows which are connected by the waveguide structure required to be evaluated its performance similar with the window of the klystron. To achieve the water cooling for inner conductor, doorknob coupler has designed. The inside pressure should be as low as that of klystron pressure, which is about 10^{-7} Pa. Before testing, the window and coupler will be baked.

Proper cooling system with inlet and outlet of water supplied from the doorknob side through double piping structure is necessary for the hot test including high power capability of ceramic window.

Power will be increased step by step same as in klystron high power test. A solid-state amplifier (SSA) with CW 150 kW is available for this test at IHEP. Firstly, the power transmission test with load is planned and then by changing the phase full reflection test is followed. We can evaluate the power capability of 600 kW equivalently with this test.

The ceramic coating is very important, so the windows manufactured by TETD having coated with 5nm TiN (O) film on the surface of ceramic. In order to detect the multipacting or arcing problems, the viewport and arc-detector are used.

CONCLUSION

We have finished simulation of RF coaxial output window to be used in the CEPC 650 MHz, 800 kW, CW klystron. RF design is fulfilled, and the S-parameter have been optimized. The thermal loss and multipacting in ceramic have also been considered at the high-power operation. Good window cooling was successfully introduced after the thermal analysis. After the simulation using MultiPac, it was successfully shown that suppression of the multipacting with 5nm TiN coating is achieved. We have finished the mechanical design and started to manufacture it. The high-power test plan is also described.

REFERENCES

[1] Zhou Z S, Fukuda S *et al.*, "CEPC 650 MHz Klystron Development", in *Proc. 7th Int. Particle Accelerator Conf. (IPAC'16)*, Busan, Korea, May 2016, p. 3891.

[2] Naito F, Yoshimoto S *et al.*, "The input coupler for the KEKB ARES cavity", KEK, 1998, preprint 98-44.

[3] http://www.cst.com

[4] http://www.ansys.com/Products/Platform

[5] Saito Y, "Breakdown of Alumina rf Windows", *Review of Scientific Instruments*, 60, 1736 (1989).

[6] Saito Y, "Surface Breakdown Phenomena in Alumina RF Windows", *IEEE Trans. Electr. Insul.*, vol. 2, pp. 243-250, 1995.

[7] Yl¨a-Oijala P, Lukkarinen J, J¨arvenp¨a¨a S, Ukkola M, "MultiPac 2.1 Multipacting Simulation Toolbox with 2D FEM Field Solver and MATLAB Graphical User Interface", Rolf Nevanlinna Institute, Helsinki, 2001.

Content from this work may be used under the terms of the CC BY 3.0 licence (© 2018). Any distribution of this work must maintain attribution to the author(s), title of the work, publisher, and DOI.

ISBN: 978-3-95450-194-6 ISSN: 2226-0366 doi:10.18429/JACoW-LINAC2018-THPO103

APPLICATION OF SOLID STATE AMPLIFIERS IN ADS PROJECT AT IHEP*

O. Z. Xiao†, 1,2), Z. S. Zhou1,2), X. P. Ma1,2), N. Gan1,2), Y. L. Chi1,2)
1) Institute of High Energy Physics, Chinese Academy of Sciences, Beijing 100049, China
2) Key Laboratory of Particle Acceleration Physics and Technology, Institute of High Energy Physics, Chinese Academy of Sciences, Beijing 100049, China

Abstract

The solid state amplifier is an important part of the RF power source system of ADS project at IHEP. Three kinds of solid state amplifier with different power and frequency have been applied. In this paper, the specifications of solid state amplifier are presented. In addition, the principle of breakdown of power modules during the high power test of coupler are analyzed.

INTRODUCTION

With the progress of transistor technology, the output power and efficiency of a single transistor has been greatly improved. The high power can be obtained by combination of numerous transistors. Recently the power capability of solid state amplifier (SSA) can extend from a few kW to several hundred kW, and the operating frequency from less than 100 MHz to above several GHz[1 - 4]. Compared with vacuum tube, there are many advantages for SSA such as high reliability for redundancy design, high flexibility for module design, high stability, absence of warm-up time and reasonable efficiency [5]. So the SSA is a priority RF power source for injector I of accelerator driven subcritical transmutation system (ADS). Three kinds of solid state amplifier with different power and frequency have been used to feed the cavities or test high power coupler in injector I of ADS at institute of high energy and physics (IHEP), whose performance and detailed parameters are presented in this paper.

325 MHz/10 kW SSA

The 325 MHz/10 kW SSA is used to feed bunchers and spoke cavities of injector I of ADS. The one cavity per source is chosen to simplify the LLRF control and RF distribution system. The bandwidth of SSA needs more than 2 MHz for LLRF control requirement. The nominal maximum power of 10 kW is achieved with less than 1 dB compression, and the harmonic output power is less than -30 dBc. The AC to RF efficiency goal for the SSA at the rated power is at least 50%. The single power module must include circulator and absorbing load to ensure isolation between modules and withstand the full reflection power. Each SSA must monitor the status data of every power module such as voltage, current and temperature. Ethernet port is required to communicate with control system. Also, interlock is necessary for external faults like water leaks. The mean time between failures (MTBF) should be larger than 20,000 hours, and less than 5% of the power modules fail per year. The failure of one power module can still run. The output port is 3-1/8 inch rigid coaxial line. The 325 MHz/10 kW SSA specifications are shown in Table 1.

In July 2012, the first 325 MHz/10 kW SSA was delivered to IHEP by BBEF, which was used to build a workbench for the high power test of the coupler of spoke cavity. In September 2013, another one was delivered for the horizontal test of spoke cavity. In April 2014, 14 SSAs were installed and commissioned in power supply hall. In 2015, 9 SSAs were put into operation. In March 2016, another two SSAs were delivered by the 38th institute of CETC. In the end of 2016, 16 325 MHz/10 kW SSAs were used in injector I, as shown in Fig. 1.

Table 1: 325 MHz/10 kW SSA Specifications

Parameters	Value
Frequency(MHz)	325
Output Power(kW)	10
Gain(dB)	≥65
Bandwidth(MHz)	≥ 2
Amplitude stability	≤1%
Phase stability	≤1°
Harmonic(dBc)	< -30
Spurious(dBc)	< -65
MTBF(h)	20000
Efficiency at 10 kW	≥50%



Figure 1: 325 MHz/10 kW SSA.

* Work supported by ADS Injector I solid state RF power system
† email address xiaooz@ihep.ac.cn

Content from this work may be used under the terms of the CC BY 3.0 licence (© 2018). Any distribution of this work must maintain attribution to the author(s), title of the work, publisher, and DOI.

ISBN: 978-3-95450-194-6 ISSN: 2226-0366 doi:10.18429/JACoW-LINAC2018-THPO103

325 MHz/25 kW SSA

The 325 MHz/25 kW SSA was used to feed spoke cavities of CM4. In order to facilitate maintenance, the power module and power supply should adopt fast plug and pull technology. The power module must include self-protection for overheating. The output port is 4-1/2 inch rigid coaxial line. The performance requirements are similar to the previous 10 kW SSA. The 325 MHz/25 kW SSA specifications are shown in Table 2.

In the end of 2014, the contract of the prototype of 325 MHz/25 kW SSA was signed with Chengdu Kaiteng Sifang Quartet Digital Broadcasting & TV Equipment Co. Ltd (KTSF). In April 2016, the acceptance test of the prototype was completed at IHEP. In May 2017, 6 325 MHz/25 kW SSAs were installed and commissioned for CM4 in Lanzhou city, as shown in Fig. 2.

Table 2: 325 MHz/25 kW SSA Specifications

Parameters	Value
Frequency(MHz)	325
Output Power(kW)	25
Gain(dB)	≥70
Bandwidth(MHz)	≥ 2
Amplitude stability	≤1%
Phase stability	≤1°
Harmonic(dBc)	< -35
Spurious(dBc)	< -70
MTBF(h)	20000
Efficiency at 25 kW	≥50%



Figure 2: 325 MHz/25 kW SSA.

650 MHz/150 kW SSA

The 650 MHz/150 kW SSA is the key equipment of the ADS power source system, which is the highest output power SSA in China. The 650 MHz/150 kW SSA was designed and manufactured by KTSF. The output port is WR1500 waveguide. The failure of 4 power modules can still run. The AC to RF efficiency goal for the SSA at the rated power is at least 45%, which reaches 51.3% for acceptance test. The performance requirements are similar to the previous 25 kW SSA. The 650 MHz/150 kW SSA specifications are shown in Table 3.

In September 2016, a 650 MHz/150 kW SSA was completed factory acceptance test in KTSF. At the end of 2016, the 650MHz/150kW SSA was delivered to IHEP and completed installation. In March 2017, the acceptance test of the prototype of 650 MHz/150 kW SSA was completed, as shown in Fig. 3.

Table 3: 650 MHz/150 kW SSA Specifications

Parameters	Value
Frequency(MHz)	650
Output Power(kW)	150
Gain(dB)	≥75
Bandwidth(MHz)	≥ 2
Amplitude stability	≤1%
Phase stability	≤1°
Harmonic(dBc)	< -35
Spurious(dBc)	< -70
MTBF(h)	20000
Efficiency at 150 kW	≥50%



Figure 3: 650 MHz/150 kW SSA.

POWER MODULE BREAKDOWN

In August 2014, several power modules failed when the coupler was carried out high power test in standing wave mode. The ceramic absorbing load was seriously breakdown, as shown in Fig. 4. It indicated that the reflected power exceeded the load rated value of 800W .The principle can be expressed as follows: The reflected power due to the mismatch of output port of SSA will be equally distributed to each port of combiner. To simplify the design of the power combiner, all ports are not isolated from each other. When one of the power modules fails, the wave from the other port will combine at this port in phase. So the total reflected wave of the module failed is the sum of the reflected wave from the mismatched load and the combined wave from the other port. In the worst case,

Content from this work may be used under the terms of the CC BY 3.0 licence (© 2018). Any distribution of this work must maintain attribution to the author(s), title of the work, publisher, and DOI.

ISBN: 978-3-95450-194-6 ISSN: 2226-0366 doi:10.18429/JACoW-LINAC2018-THPO103

Content from this work may be used under the terms of the CC BY 3.0 licence (© 2018). Any distribution of this work must maintain attribution to the author(s), title of the work, publisher, and DOI.

these two wave will combine in phase. Then the total reflected power can be expressed as follows:

$$P_{total} = (\frac{N-1}{N} + \Gamma)^2 P \qquad (1)$$

Where P_{total} is the total reflected power, P is the output power of a single power module, N is the port number of combiner, and Γ is the reflection coefficient of the output port of SSA. When P is 550W, N is 10 and Γ is 1, the maximum reflected power is 1985.5W which is far in excess of load capacity. In order to avoid the load breakdown, a high power circulator can be used at the output port of SSA when the coupler was tested in standing wave mode.



Figure 4: Power module Breakdown.

CONCLUSION

The solid state amplifier has been widely used in accelerator due to high reliability and easy maintenance, which has become an important part of power source system of injector I of ADS. During the process of application, some useful suggestions were fed back to companies to improve the design. The application of solid state power source in large-scale scientific projects has greatly promoted the domestic solid state power source industry and R&D capability.

ACKNOWLEDGEMENT

We would like to acknowledge the companies cooperate with us. We are thankful to R. Liu for his useful discussion and suggestions.

REFERENCES

[1] P. Marchand, R. Lopes, F. Ribeiro, et al., "Development of high RF power solid state amplifiers at SOLEIL, *Proceedings of IPAC2011*, Spain, 2011.

[2] F. Wang, et al., "Using a 1.3 GHz 20 kW solid state amplifier as RF power supply for DC-SRF Photo-Injector", *Proceedings of ERL2015*, Stony Brook, NY, USA, 2015.

[3] A. Smirnov, A. Krasnov, I. Rezanov, et al., "The layout of 352 MHz 400 kW RF power amplifier, *Proceedings of PAC2013*, Pasadena, CA USA, 2013.

[4] G. Wang, et al., "Microwave Power Amplifier Design based on ADS", Nuclear Electronics & Detection Technology, VOL. 28, NO. 2, March, 2008.

[5] R. G. Carter, Review of RF power sources for particle accelerator, Lancaster University, Lancaster, UK.

ISBN: 978-3-95450-194-6 ISSN: 2226-0366 doi:10.18429/JACoW-LINAC2018-THPO104

DEVELOPMENT OF 150.4MHz CW SOLID-STATE AMPLIFIER

Zhao Lei [1], Sun An[2,3], Zhou Bowen[2], Li Wenliang[2], Zhang Pengjiao[2], Ke Yijing[2]
[1]School of Materials Science and Technology, Nanjing University of Aeronautics and Astronautics, Nanjing 211146, China
[2]PLAI, Nanjing University, Nanjing 210046, China
[3]Andesun Technology Group Co., Ltd., Nanjing 210046, China

Abstract

A 150.4MHz to 155.4MHz, 300W continuous wave solid-state amplifier as an accelerator power source has been developed by us. In order to increase the lifetime of MOSFET and meet the requirements of every parameters, Drain voltage and quiescent current is set at a better point with a well-designed heat dissipation structure, we make the solid state amplifier stable in performance. Taking the microwave leakage into account, the chassis structure is optimized and designed, and the microwave absorption device is adopted to make the structure compact, protect other parts not affected by the microwave leakage. After the assembly is completed, the working parameters meet the design requirements very well. The MOSFET flange temperature and output parameters meet the design requirements.

INTRODUCTION

RF power amplifier is a traditional key component in the field of microwave technology. It is an important part of the microwave system and is still in the process of continuous development. Currently solid-state amplifiers are the most active part of microwave power sources. With the development of semiconductors, the development of solid-state amplifiers has entered a new climax [1].

Many years ago, electric vacuum tubes as the microwave source in the accelerator system. They output different energies. We can see in the Table 1 [2].

Table 1: Different Power Device in Common use in Accelerator

Device	Frequent	Mode	Power
Electric vacuum tubes	30~300 MHz	CW and pulse	~2.5 MW
IOT	500~1500 Mhz	CW and pulse	100 kW
Klystron	300~10 GHz	CW and pulse	2 MW
FET		CW and pulse	1250 W

In recent years, solid-state amplifiers are used more and more in accelerator system. Some of them as exciting source to provide incentives to the klystron, some of them as RF sources to the excitation cavity.

In this paper, a high power CW solid-state amplifier is designed for superconducting cavity power source. MOSFET has many advantages such as small size, voltage control, low heat generation and so on, therefore, NXP's MOSFET - MRFE6VP61K25H is selected by us as the core to design the final amplifier module. The 10W small power amplifier module with the gain is 35 dB is used as the boosting stage, combine with the power supply system, the power monitoring system, the cooling system, and the control system, we completed the solid-state amplifier.

CIRCUIT DESIGN

The Overall Circuit Design

The overall principle is shown in Figure 1. The low-power RF signal enters the push-level amplifier module through the input coupler and the RF switch. The push-level module inputs the amplified RF signal to the final amplifier module, and the final output high-power signal is output through the output coupler. The coupler coupling ends are connected to the corresponding power detection module to detect input, output, and reflected power in real time. The signal of detection modules are input to the control system to protect the amplifier modules and display power on the screen. Table 2 shows insertion loss.

Table 2: Insertion Loss in the RF Circuit

Item	Insertion Loss
The coaxial cables of input	0.6 dB;
RF switch	0.4 dB
The coaxial cable between pusher amplifier and final amplifier	0.2 dB
The coaxial cables of output	0.4 dB
Isolator of output	0.4 dB

Considering that the maximum input power is 0dBm, we could calculate and get:

P(the input power of pusher amplifier)≤-1 dBm;
P(the output power of pusher amplifier)≤34 dBm;
P(the input power of final amplifier)≤33.8 dBm.

Content from this work may be used under the terms of the CC BY 3.0 licence (© 2018). Any distribution of this work must maintain attribution to the author(s), title of the work, publisher, and DOI.

ISBN: 978-3-95450-194-6 ISSN: 2226-0366 doi:10.18429/JACoW-LINAC2018-THPO104

Content from this work may be used under the terms of the CC BY 3.0 licence (© 2018). Any distribution of this work must maintain attribution to the author(s), title of the work, publisher, and DOI.

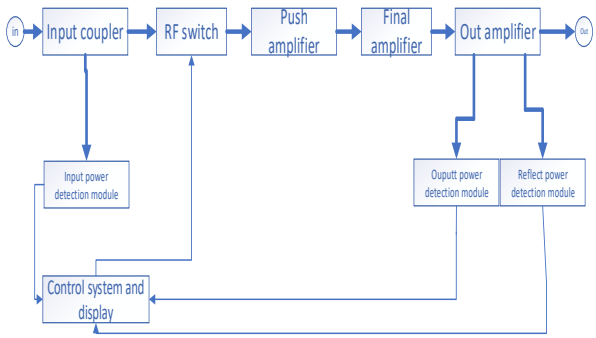


Figure 1: Basic block diagram.

The Final Amplifier Module

The relationship of the drain voltage, gain and power could be obtained as are shown in Figure 2 and Figure 3. Because the gain of pusher amplifier module we design is 35dB and the final output power is 300 W(54.8 dBm) [calculate by Eq. (1)], the gain of final amplifier module should more than 21.8 dB. From Fig. 2 we could get that the efficiency decreases with increasing drain voltage. So low drain voltage is prefered. But the MOSFET may get saturation when in high power output condition. This cause us bother more heart dissipation. Therefore, comprehensive consideration, the drain voltage is set to 42 V, I_{Dq} is set to 100 mA, then we get the gate voltage -2.36 V.

$$P = 10 \bullet \log_{10}\left(\frac{p}{p_0}\right) \tag{1}$$

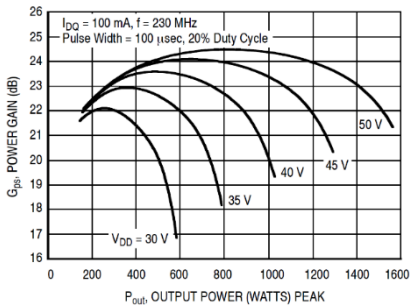


Figure 2: Power Gain versus Output Power Peak.

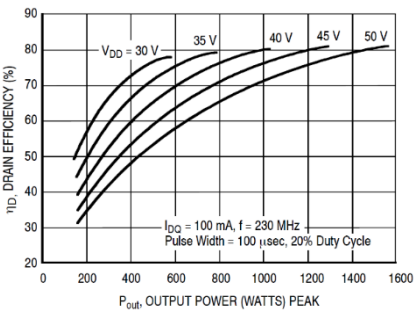


Figure 3: Drain Efficiency versus Output Power.

According to the data sheet [3], reference the Reference Circuit Schematic (Fig. 5) and the Reference Circuit Component Layout (Fig. 6), we make some modifications, adjustments and design matching input and output circuits and a power supply circuit, then finally get the final amplifier module circuit component layout (Fig. 7) .

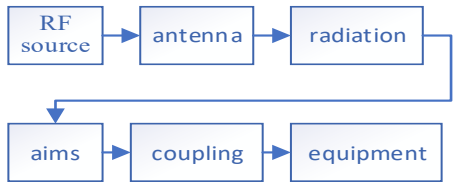


Figure 4: Microwave emission and mechanism of action.

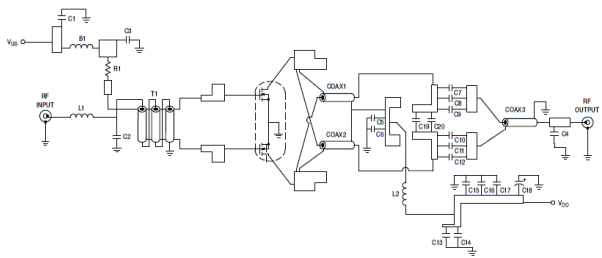


Figure 5: Reference circuit schematic.

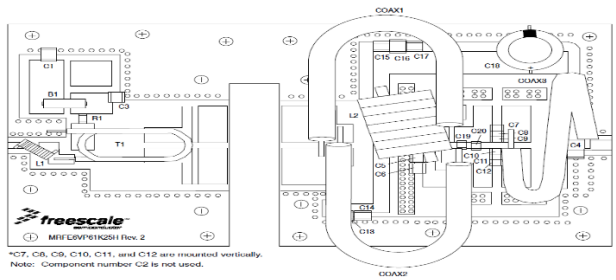


Figure 6: Reference circuit component layout.

The Microwave Leakage

There are many ways to cause microwave leakage microwave radiation leakage. Such as from the RF coaxial, the circuit board, power supply line.

Microwave emission and mechanism of action are shown in Fig. 4.

Leakage through the power supply line is the most direct way. It would though the power supply line feed in the control system, monitor system.

Power line coupling is a way of microwave interface that can't be avoided. Power line coupling is similar to transmission cable coupling. The power line is often exposed to microwave field, so it is easy to introduce microwave interference [4]. According to the equation Eq. (2), a thin aluminium could shield the microwave in the space. And we use electrolytic capacitors between the end of positive electrode and ground which provide power to amplifiers. This will absorb the microwave leakage from power line.

$$A = 131.43\sqrt{f \mu_t \delta_t} \tag{2}$$

ISBN: 978-3-95450-194-6 ISSN: 2226-0366 doi:10.18429/JACoW-LINAC2018-THPO104

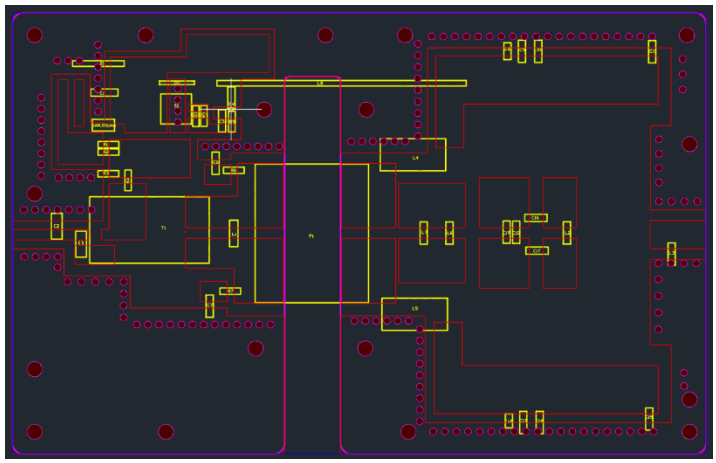


Figure 7: Amplifier module circuit component layout.

TEST RESULT

Maximum Power

The power of the signal source is set to 0 dBm, change the frequency from 150.4 MHz to 155.4 MHz by 1 MHz and measuring the power of output simultaneously, then we get the curve of frequency versus output power (Figure 8). We can see that the maximum power require has been met over the entire bandwidth and the flatness is 0.75 dB, which is better than the require (1dB).

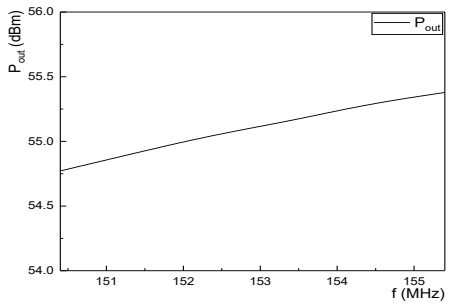


Figure 8: Frequency versus Output power.

Linearity

Second the frequency is set to 153 Mhz. Then we can get the curve of the power of input versus output (Figure 9).It is show in the curve that the amplifier is working at a far position from the P1 dB compression point. This proves that the output matching circuit is well designed.

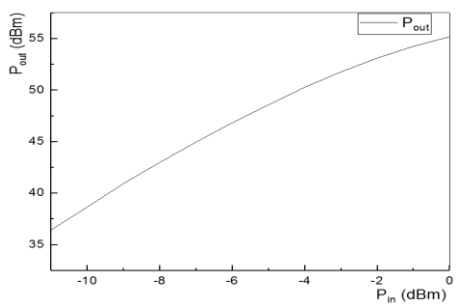


Figure 9: Power of input versus output.

CONCLUSION

This paper presents a solid-state amplifier which is service for cyclotron system. By adjusting the MOSFET drain voltage and quiescent current of the final amplifier properly, it is set to a good operating mode. Heat dissipation, protection, microwave radiation shielding etc. are took into account, the amplifier systems are designed rationally to make the solid-state amplifier work normally. The output power in the entire band from 150.4 MHz to 155.4 MHz is more than 300 W. The flatness is better than 1dB. It could be utilized in the cyclotron system and driving the conducting cavities.

ACKNOWLEDGEMENTS

Thanks to out teacher, the professor Sun give us many help in every aspect.

Thank to my friends in our office, they give me lots of good advice in the study.

REFERENCES

[1] Zuo Xiuquan, “L-band solid-state power amplifier design and amplification technology research” M.S. thesis; mach. Chang’ an University, Xi’ an, China, 2017.

[2] YUAN zhen-yu” application research of SSA for accelerator field” *nucl, vol*, 49, suppl. Oct. 2015.

[3] *Freescale Semiconductor, Inc,* High Tech Campus 605656 AG Eindhoven, The Netherlands, 2010-2014, pp. 12-14. https://www.nxp.com/docs/en/datasheet/MRFE6VP61K25H.pdf

[4] Diao Zhenhe, “The Research on the Defense against High power Microwave” M.S. thesis, phy.. National University of Defense Teehnology, Changsha, Hunan, China, 2016.

Content from this work may be used under the terms of the CC BY 3.0 licence (© 2018). Any distribution of this work must maintain attribution to the author(s), title of the work, publisher, and DOI.

ISBN: 978-3-95450-194-6 ISSN: 2226-0366 doi:10.18429/JACoW-LINAC2018-THPO107

HIGH POWER COUPLER R&D FOR SUPERCONDUCTING CH-CAVITIES

J. List*[1], K. Aulenbacher[1,4], W. Barth[1,2], M. Basten[3], M. Busch[3], F. Dziuba[1], V. Gettmann[1], M. Heilmann[2], T. Kürzeder[1], M. Miski-Oglu[1], H. Podlech[3], J. Salvatore[2], A. Schnase[2], M. Schwarz[3], and S. Yaramyshev[2]

[1]HIM, Helmholtzinstitute Mainz, 55099 Mainz, Germany
[2]GSI Helmholtzzentrum, 64291 Darmstadt, Germany
[3]IAP, Goethe-University Frankfurt, 60438 Frankfurt am Main, Germany
[4]IKP, Johannes Gutenberg-University Mainz, 55128 Mainz, Germany

Abstract

The upcoming demands of the future research programs at GSI exceed the technical opportunities of the existing GSI UNIversal Linear ACcelerator (UNILAC). Besides, the existing machine will be exclusively used as an injector for FAIR (Facility for Antiproton and Ion Research) providing high power heavy ion beams at a low repetition rate for injection into a heavy ion synchrotron. A new dedicated superconducting (sc) continuous wave (cw) linac is crucial to keep the GSI research program competitive. The first part of the cw-linac, comprising a 217 MHz multi gap Crossbar-H-mode (CH) cavity surrounded by two sc solenoids inside a cryostat, already served as a prototype demonstrating reliable operability in a realistic accelerator environment. A sufficient high power RF-coupling concept is needed to feed this newly developed cw-RF cavity with up to 5 kW of RF-power in cw-mode. A high power coupler test stand was recently built to provide for a testing environment; further upgrade measures of this test area are foreseen in the next future. This contribution deals with the recent coupler R&D for the demonstrator set up. Besides that simulations of thermal losses at the coupler (inside the RF-cavity) will be shown as well.

INTRODUCTION

The 13 m superconducting continuous wave linac proposed to be built at the GSI, comprises Crossbars-H-mode (CH) RF-cavities, to accelerate heavy ions up to 7.3 MeV/u [1]. The first part of the accelerator, called 'Demonstrator', comprises one CH-cavity and two 9.3 T solenoids in a cryostat. This structure was already successfully tested with beam in summer 2017 [2–4]. It was the first sc CH-cavity in the world running with beam. In the next stage an advanced module consisting of three CH-cavities [5], a rebuncher and two solenoids will be set up for further testing. This module will be the prototype for three following similar modules (Fig. 1) to complete the entire cw-LINAC. Recent beam dynamics studies indicate, that only 2 of the modules need a rebuncher [6]. The heavy ion beam is provided by the GSI - High Charge State injector (HLI).

* j.list@gsi.de

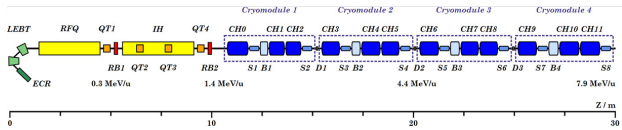


Figure 1: Recent desing of the cw-LINAC at GSI made with four standard cryo modules [7].

HIGH POWER COUPLER FOR CH-CAVITIES

For suitable coupling the RF-cavities are equipped with a capacitive, coaxial power coupler [8]. The design is a modification of an existing Fermilab power coupler [9]. Noteworthy is a diameter jump from a $3\frac{1}{8}''$ rigid line to a CF-40 line since the space at the cavities coupler port is strongly limited. The reflection caused by a parasitic capacitance due to the changing diameters is canceled out by a shift between the diameter jump the of inner and outer conductor, called "gap" (see Fig. 2). The two RF-windows of the coupler are coated with TiN for a lower secondary electron yield.

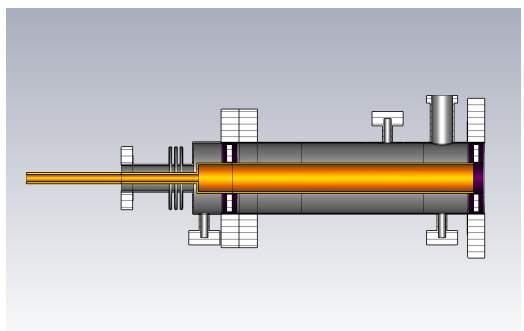


Figure 2: Cross section of the CST Microwave Studio [10] - coupler model.

COUPLER TEST STAND

A coupler test stand was established at GSI, where two couplers can be tested and conditioned in paralell. It features a quarter wave resonator (QWR)-type cavity (see Fig. 3) with an extended center-tube, presented in [11]. It has a broadband RF-transmission of ± 10 MHz. A 5 kW cw solid

Content from this work may be used under the terms of the CC BY 3.0 licence (© 2018). Any distribution of this work must maintain attribution to the author(s), title of the work, publisher, and DOI.

ISBN: 978-3-95450-194-6 ISSN: 2226-0366 doi:10.18429/JACoW-LINAC2018-THPO107

state amplifier is used to power the test stand. Each coupler is equipped with a pressure sensor and two Langmuir probes to detect multipacting. A temperature sensor is attached to each RF-window. The test configuration also includes two directional couplers, with connected power meters.

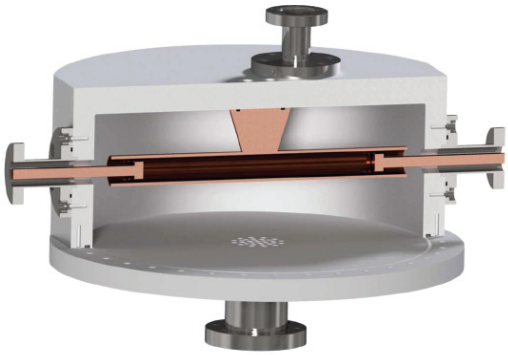


Figure 3: Cross section of the QWR-type test cavity [11].

COUPLER TESTS

Two couplers have been tested and conditioned in April 2017. Initially the conditioning was performed in pulsed power mode with a duty factor of 1%. During the conditioning campaign the duty cycle was continuously increased up to cw-mode. The power was boosted up to 5 kW in pulsed mode and 2.5 kW in cw-mode.

Figure 4 shows the pressure changes in the couplers during an early conditioning campaign. During that degassing could be observed, that subsides over time.

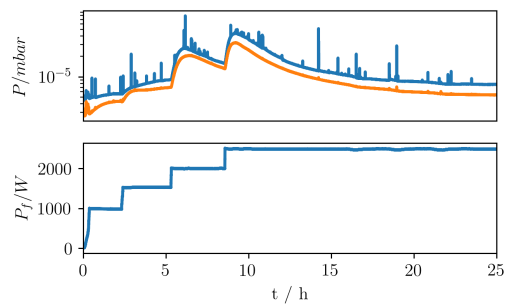


Figure 4: Degassing events in the input coupler (blue curve) and the output coupler (orange curve) during conditioning.

In a final step the forwarded power was changed randomly as shown in Fig. 5. After changes in power affected the multipacting current and the pressure only marginally, the coupler was considered as conditioned.

During cw-power conditioning the couplers showed major heating at the RF-windows. In Fig 6 the temperature measured at the windows are depicted. The input coupler's cold window reached 91.1 °C. This is of course to high for a usage in a cryogenic environment. The forward power was not increased further, because thermal stress could potentially destroy the windows.

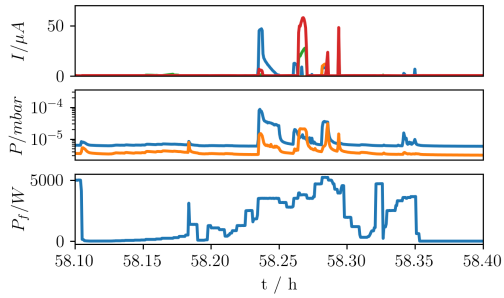


Figure 5: Changing the power randomly in the final conditioning phase.

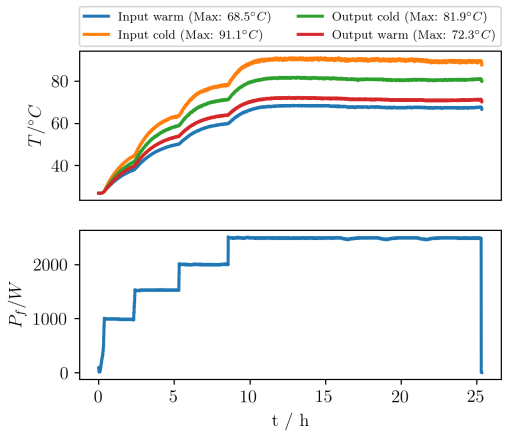


Figure 6: Temperatures of the coupler windows during conditioning with cw-power. Orange (cold window) and blue (warm window) represent the the temperatures of the input coupler. Green (cold window) and red (warm window) represent the the temperatures of the output coupler.

Despite the heating, one coupler was used successfully in the beamtest two months later.

THERMAL SIMULATION

To estimate the heat flow from the coupler to the cryostat, simulations with CST Microwave Studios were performed.

An RF and a thermal simulation were coupled, reconstructing the temperature profile of the coupler test. With this the heat losses of the coupler could be calculated.

For this a detailed model of the coupler was developed. This included the heat transfer to the environment. To size the heat transfer an experiment was done. A coupler was equipped with nine temperature sensors and heated in an oven. After taking the coupler out of the oven, the cooling process was recorded. Besides that the cooling process was simulated. The heat transfer coefficients and other parameters of the simulation were adjusted, that the curves of the experiment and the simulation were overlapping (shown in Fig. 7).

After setting the right parameters the main simulations could be started. In the first step an RF- simulation was

Content from this work may be used under the terms of the CC BY 3.0 licence (© 2018). Any distribution of this work must maintain attribution to the author(s), title of the work, publisher, and DOI.

ISBN: 978-3-95450-194-6 ISSN: 2226-0366 doi:10.18429/JACoW-LINAC2018-THPO107

Content from this work may be used under the terms of the CC BY 3.0 licence (© 2018). Any distribution of this work must maintain attribution to the author(s), title of the work, publisher, and DOI.

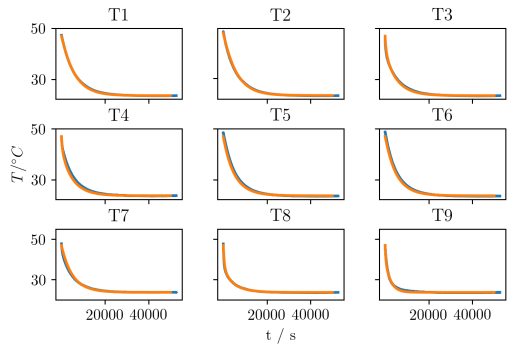


Figure 7: Cooling process of the coupler after heating in an oven for simulation (orange) and experiment (blue) with nine different temperature sensors attached to coupler (T_1 - T_9).

performed, to evaluate dielectric losses and losses caused by surface currents. These losses were imported to a thermal simulation acting as a heat source. The outer flanges was set to room temperature. With their relatively high mass the adjoining cavity and RF-line could be considered as heat a sink.

Due to the TiN coating of the coupler windows, the loss factor $tan(\delta)$ was significantly higher than for standard Al_2O_3 ($tan(\delta) \approx 10^{-4}$).

As the losses caused by surface currents were fixed, the loss factor was increased, trying to reconstruct the temperature profile of the coupler test. Figure 8 shows the temperature determined by the simulation with changing $tan(\delta)$. The yellow diamonds mark the loss factor $tan(\delta) = 0.0492$ to reconstruct the temperatures rise during the coupler test.

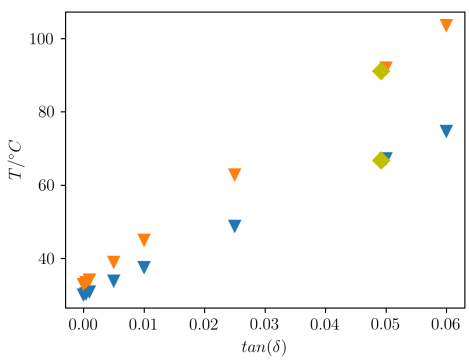


Figure 8: Temperature of the coupler windows with increasing loss factor. The yellow diamonds mark the $tan(\delta)$ reconstructing the temperatures during the coupler test.

Under these conditions a total heat loss of 70 W was calculated, when using a forward power of 2500 W (for more details see Table 1).

The static heat load was calculated to 2.73 W. The total calculated heat load is 72.81 W. It is obvious that the heat loss is caused mainly by the coating of the windows. The windows have a TiN coating of 25 nm. This increases the loss factor significantly [12]. A new advanced coupler is going to be designed without any window coating. Changes to the window distance and the *gap* will be made for improved RF-performance. The improved design could be the first of series for the cw-linac.

Table 1: Heat Losses Calculated by CST Microwave Studio for Three Different Forward Power Levels

P_f	1 W	2500 W	5000 W
Warm window	0.013 W	31.75 W	63.50 W
Cold window	0.014 W	34.08 W	68.16 W
Surface current	1.7×10^{-3} W	4.25 W	8.5 W
Total	0.028 W	70.08 W	140.16 W

FUTURE COUPLER-TEST-STAND

Several other couplers have to be tested and conditioned during the cw-linac commissioning. Therefore the test stand has to be extended and further improved. The design of a movable reflector already successfully used at Fermilab, [13] was adapted to the coupler's frequency of 217 MHz recently and is manufactured right now (shown in Fig. 9).Located in front of the input coupler along the RF-line, it allows to operate the test stand in a resonance mode for increased power.

A movable ring on the inner conductor is applied as a semitransparent mirror analog to an optical resonator. It can be moved more than half the wavelength. At the other side of the coupler test stand are shorted wave guides of variable length, acting like a full mirror.

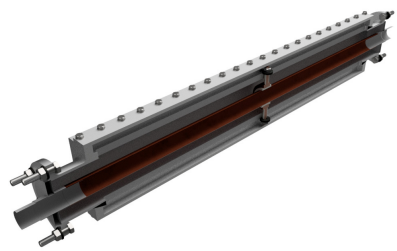


Figure 9: Model of the movable reflector.

To ease the process it is intended to automate the conditioning process in the future.

SUMMARY AND OUTLOOK

Two 217 MHz coaxial power coupler were tested and conditioned at GSI. Simulations were performed to estimate the heat losses of the coupler. The results of the testing and the simulations will be used to further improve the design. An improved coupler could be the first of a series for future cw-linac cavities. A movable reflector is manufactured at the moment to extend the existing coupler test stand at GSI.

ISBN: 978-3-95450-194-6 ISSN: 2226-0366 doi:10.18429/JACoW-LINAC2018-THPO107

REFERENCES

[1] W. Barth *et al.*, "Further layout investigations for a superconducting cw-linac for heavy ions at GSI," in *Proceedings of SRF 2017, Lanzhou, China*, JACoW Publishing, 2017. DOI: 10.18429/JACoW-SRF2017-MOPB023.

[2] W. Barth *et al.*, "First heavy ion beam tests with a superconducting multigap CH cavity," *PHYSICAL REVIEW ACCELERATORS AND BEAMS 21, 020102*, Mar. 1, 2018.

[3] W. Barth *et al.*, "First Acceleration of Heavy Ion Beams with a Superconducting Continuous Wave HIM/GSI CW-linac," presented at LINAC'18 , Bejing, China, paper TU2A01, this conference, 2018.

[4] F. Dziuba *et al.*, "RF Commissioning of the Superconducting 217 MHz CH Cavity for Heavy Ions and First Beam Operation," presented at LINAC'18 , Bejing, China, paper THPO073 , this conference, 2018.

[5] M. Basten *et al.*, "Cryogenic Tests of the Superconducting Beta=0.069 CH-cavities for the HELIAC-Project," presented at LINAC'18 , Bejing, China, paper THPO072 , this conference, 2018.

[6] M. Schwarz *et al.*, "Beam Dynamics Simulations for the New Superconducting CW Heavy Ion LINAC at GSI," presented at LINAC'18 , Bejing, China, paper TUPO084, this conference, 2018.

[7] S. Yaramyshev *et al.*, "Advanced approach for beam matching along the multi-cavity sc cw linac at gsi," in *Proceedings of IPAC2018, Vancouver, BC, Canada*, JACoW Publishing, 2018. DOI: 10.18429/JACoW-IPAC2018-TUPAK002.

[8] R. Blank, "Entwicklung eines 217 MHz Hochleistungskopplers für das cw-LINAC-Demonstrator Projekt," Master's thesis, Johann Wolfgang von Goethe Universität Frankfurt, 2015.

[9] S. Kazakov *et al.*, "Main couplers for project X*," in *Proceedings of IPAC2012, New Orleans, Louisiana, USA*, paper WEPPC050, 2012, pp. 2324–2326.

[10] CST-Computer Simulation Technology AG. (Sep. 7, 2018), https://www.cst.com/products/cstmws

[11] M. Busch *et al.*, "Further tests on the final state of the sc 325 MHz CH-cavity and coupler test bench update," in *Proceedings of IPAC2018, Vancouver, BC, Canada*, JACoW Publishing, 2018. DOI: 10.18429/JACoW-IPAC2018-WEPML040.

[12] J. Lokiewicz *et al.*, "Characteristics of TiN anti-multipactor layers reached by titanium vapor deposition on alumina coupler windows," in *Proceedings of the 11th Workshop on RF Superconductivity, Lübeck/Travemünde, Germany*, paper THP31, 2003, pp. 697–699.

[13] S. Kazakov *et al.*, "Testing of 325 MHz couplers at test stand in resonance mode," in *Proceedings of SRF2015, Whistler, BC, Canada*, paper THPB098, 2015, pp. 1376–1378.

Content from this work may be used under the terms of the CC BY 3.0 licence (© 2018). Any distribution of this work must maintain attribution to the author(s), title of the work, publisher, and DOI.

ISBN: 978-3-95450-194-6 ISSN: 2226-0366 doi:10.18429/JACoW-LINAC2018-THPO108

DEVELOPMENT OF AN HIGH GRADIENT SIDE COUPLED CAVITY FOR PROBE

S. Pitman, R. Apsimon, G. Burt, Cockcroft Institute/Lancaster University, Lancaster, UK
W. Wuensch, N. Catalan-Lasheras, A. Grudiev, CERN, Geneva, Switzerland
H. Owen, Cockcroft Institute/University of Manchester, Manchester, UK

The PROBE project aims to develop a high gradient proton accelerator for protons with energies from 250-350 MeV for proton radiography. Detailed studies have shown that the optimum design is a side-coupled cavity at S-band. With an aperture of 8 mm a gradient of 54 MV/m can be obtained with 13 MW of RF power in a 30 cm structure. A prototype cavity has been machined by VDL and will be diffusion bonded by Bodycote. We present initial measurements of the prototype.

INTRODUCTION

The use of proton therapy is increasing with the expected number of centres offering protons reaching over 50 worldwide [1]. The advantage of protons compared to photons is the precision to which the dose can be delivered, providing lower doses to healthy tissue and organs. However to make full use of this precision we need to ensure that we can target the dose with sufficient accuracy, which requires knowledge of the proton stopping power of the imaged patient. Currently patients are imaged using CT scans and the Hounsfield units are converted to proton stopping power, but this method employs approximations limiting the accuracy of the dose placement. Recent studies have shown that using proton CT (pCT) scans can provide better estimates of proton stopping power. The limitation in pCT is that the protons should not be stopped in the patient but rather in the detector, hence this technique is only useful for children or head imaging using a 250 MeV beam. In order to do full-body scanning of adults higher energy protons are required, up to perhaps 330-350 MeV. The PRoton BOosting Extension (PROBE) project aims to provide a linac that can be retrofitted to an existing proton therapy cyclotron, in order to boost the proton energy for pCT. The linac should fit in a 3 meter space based on available space at the Christie Proton Therapy centre.

BEAM TRANSPORT

While the beam current required for pCT is small (~3 pA) compared to treatment, the linac will have a minimum duty cycle meaning the beam losses may still be a concern. For example, one requires 2% beam transmission for a 50 Hz repetition rate and a 5 μs pulse; however, lower transmission or a shorter RF pulse only results in a longer imaging time so is not a strict limit. As the protons will be delivered from a cyclotron the longitudinal and transverse phase space of the input beam is relatively large hence focussing is required to keep the beam losses to 2%. The project specification was to achieve 100 MV in 3 meters of linac length, however as we require focussing between the cavities this implies a higher gradient than 33.3 MV/m. We believe the minimum feasible drift length between two cavities will be around 135 mm, so having a larger number of shorter cavities will have more drift spaces and hence a higher gradient would be required, while with longer cavities it may be difficult to keep the losses on the aperture within limits. In addition we expect losses both on the aperture and on the energy selection system due to the cyclotron proton bunch being significantly longer than the RF period. Hence we set the energy selection system to collimate particles outside ±1% of the desired beam energy. After the first cavity we can select the synchronous phase of subsequent cavities to either provide more gradient or more capture. In this study we choose a synchronous phase of -20 degrees as this gives only a 6% drop in gradient from the peak while capturing almost 14% of the beam.

A study was performed of the maximum gradient reach of a re-entrant standing wave cavity as a function of beam aperture; in reality the requirement for coupling between cells will reduce this but it is a useful starting point. For a given cavity length we reduce the aperture (using an analytical estimate) until we reach 2% transmission; we increase the aperture by a factor 1.3 as a safety factor. We then in CST optimise a single-cell S-band cavity without side coupling for that cavity length and aperture to see the maximum gradient, and compare this to the required gradient using a 10% safety margin. In this study we limit the peak surface electric field to 200 MV/m, the modified Poynting vector to 2 W/sq-μm [2] and the input power to 100 MW for the 3 meter linac, based on scaling results obtained by other groups [3,4].

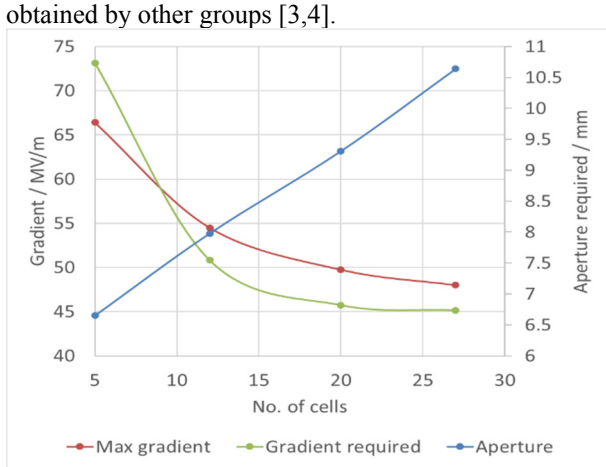


Figure 1: Required and achievable gradients as a function of number of cells per cavity, and the aperture required to meet transmission targets.

Content from this work may be used under the terms of the CC BY 3.0 licence (© 2018). Any distribution of this work must maintain attribution to the author(s), title of the work, publisher, and DOI.

ISBN: 978-3-95450-194-6 ISSN: 2226-0366 doi:10.18429/JACoW-LINAC2018-THPO108

As can be seen in Fig. 1, the largest gradient overhead is obtained for cavities between 11 and 27 cells in length. However, this is not a smooth curve as we can only have an integer number of cavities. As the increased coupling to the side-coupled cells - required for longer structures - will reduce the gradient, we choose the shortest cavity length of 11 cells as the optimum length, thus requiring an 8 mm aperture.

ASTRA was used to further study the beam losses through the PROBE linac as a function of cavity length for an 8 mm aperture [5]. The 2% transmission target is met for an 11-cell cavity requiring a gradient of 55 MV/m, as can be seen in Fig 2. The final beams phase space can be seen in Fig 3.

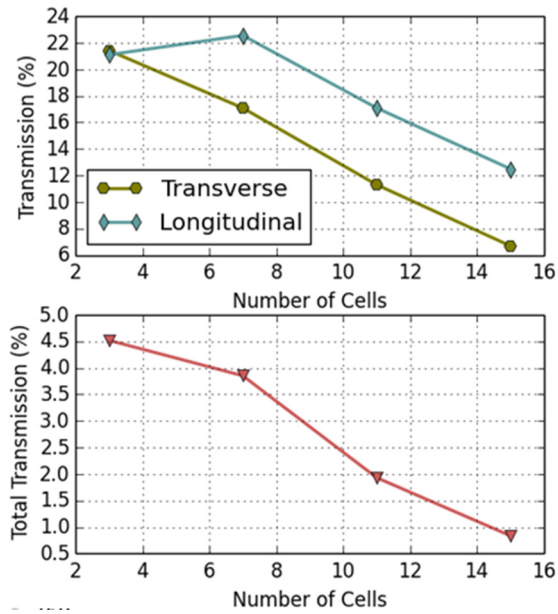


Figure 2: Transmission as a function of number of cells per cavity for an 8-mm aperture structure from ASTRA.

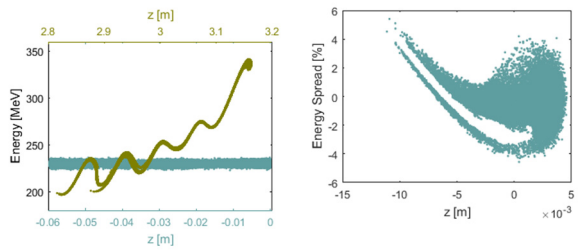


Figure 3: Longitudinal phase space at the linac entrance and exit obtained from ASTRA (left) and the acceptance of the linac (right).

CAVITY DESIGN

We have compared four different structures - backwards travelling wave (bTW) [6] and side-coupled standing wave (SW) cavities, at both S-band and C-band frequencies. In this study we limit the Epk to 200 MV/m, Hpk to 300 kA/m, the modified Poynting vector to 1.75 W/sq-um, and the input power to 12 MW. The structure is required to reach 50 MV/m with a length of 30 cm. As it's difficult to optimise a TWS to exactly match the maximum gradient limited by each parameter, we decided to always be on the side of the higher shunt impedance such that higher gradients could be obtained at higher breakdown rates if the structure performed better than expected. In each case we optimise the nose-cone geometry, and also any coupling slots or cavities in order to maximise the achievable gradient.

The gradient achievable in each structure is roughly similar, as shown in Table I, but the S-band side-coupled structure has a much lower modified Poynting vector. Some studies at CERN suggest structures may operate with higher peak electric field for a given breakdown probability if Sc is low [2], hence this S-band structure was chosen. We slightly modified the number of cells in the final design to 11 cells, which allowed the gradient to increase to 54 MV/m.

Table 1: Comparison of Different Cavity Options

	Parameter	S-band bTW	C-band bTW	C-band SW	S-band SW	Units
f	Frequency	3	5.7	5.7	3	GHz
L	Cell Length	24.8	13.1	15.7	29.8	mm
N	Number of cells	15	22	19	10	a.u
v_g/c	Group Velocity	-0.2	-0.5	4.2	2.3	%
k	k-factor	-0.04	-0.0			
Z	Shunt Impedance	85.4	65.6	61.2	75.3	$M\Omega/m$
P_{in}	Input Power	10	10	11.4	11.6	MW
E_{acc}	Gradient	48.6	47.5	46.8	51.1	MV/m
E_{pk}	Peak Surface E-field	204	200	200	200	a.u.
H_{pk}	Peak Surface H-field	153	256	302	267	kA/m
S_c	Peak Modified Poynting Vector	1.6	1.53	1.74	0.8	$W/\mu m^2$

Based on an S-band, 11 cell side-coupled structure we completed a full RF design of the structure. The final design is shown in Fig 4.

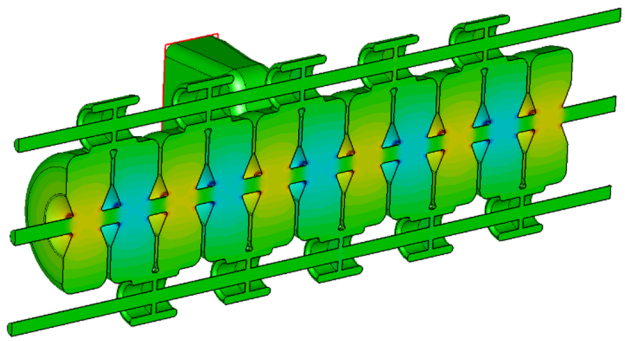


Figure 4: Final PROBE cavity design, with electric field amplitude shown in arbitrary units.

In order to work out the maximum duty cycle for operation, we performed thermal analysis of the cavity assuming water at 32 C inlet temperature. CST was then used to work out the frequency shift due to the deformation of the cavity, allowing us to plot frequency shift versus average power. While we can tune out long-term frequency deviations by altering water temperature, cell-to-cell frequency variations cannot be corrected in this way. The

Content from this work may be used under the terms of the CC BY 3.0 licence (© 2018). Any distribution of this work must maintain attribution to the author(s), title of the work, publisher, and DOI.

ISBN: 978-3-95450-194-6 ISSN: 2226-0366 doi:10.18429/JACoW-LINAC2018-THPO108

Content from this work may be used under the terms of the CC BY 3.0 licence (© 2018). Any distribution of this work must maintain attribution to the author(s), title of the work, publisher, and DOI.

cavity's 3dB bandwidth is 230 kHz hence we chose this as a suitable maximum allowable frequency shift. This gives us a maximum average power of 3 kW, (see Fig. 5), but we are likely to only require 2.4 kW based on our RF design. If we allow a water temperature rise of 2 K this will require a chiller with a 16.6 litres per minute capacity.

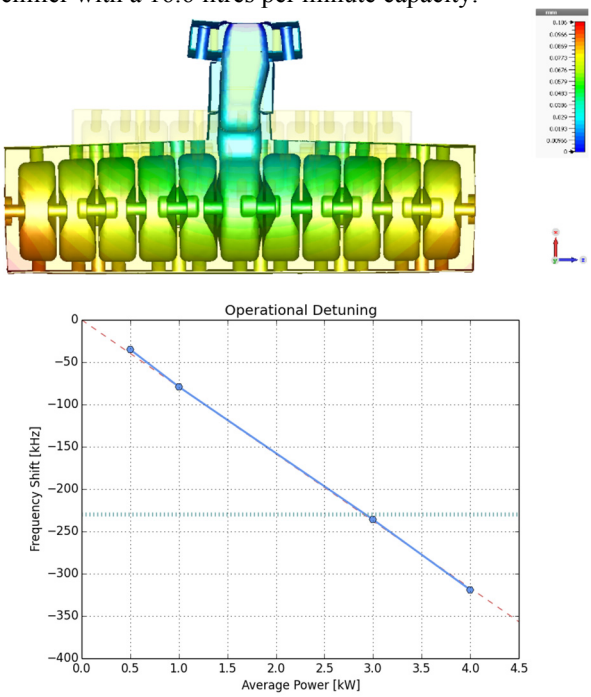


Figure 5: Deformation of the cavity due to RF heating (top) and frequency shift versus average power (bottom).

CAVITY MEASUREMENTS

A prototype cavity is currently being manufactured; the cells have been machined at VDL [7] and have been clamped together to check the cell frequencies. In order to reduce the peak magnetic field on the coupling cell slot we have rounded the edges. However it is difficult to manufacture this part to high precision by stacking disks, when each disk is exactly one cell long. Instead we manufacture each cell in two parts, one including the iris of the accelerating cell and the other containing the nose cones in the coupling cell, such that the slot coupling the accelerating cell and the coupling cell are bisected, as shown in Fig. 6. This provides better access for each slot allowing low peak fields and more accurate machining [8].

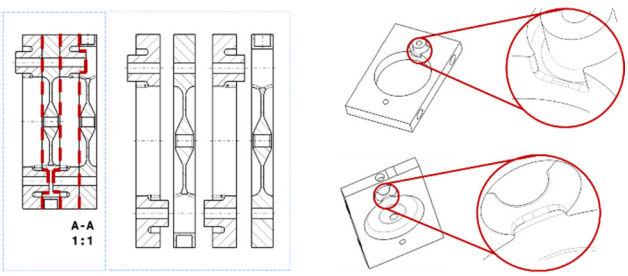


Figure 6: Drawing of the cavity cells to allow improved manufacturing tolerances.

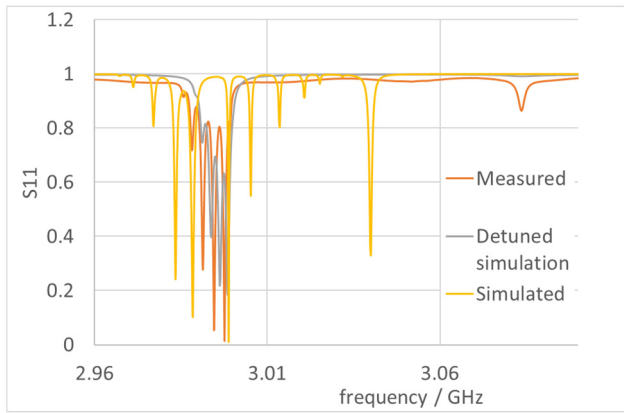


Figure 7: Measure reflections from the clamped structure and simulated results.

The final structure has been manufactured (Fig. 8) and has been clamp-tested as shown in Fig. 7. Unfortunately, the clamped measurements do not correspond well to the simulated cavity; however the π/2 mode has the correct frequency and coupling plus we see an additional mode 80 MHz away from the centre frequency. This suggests that the side-coupled cells are off tune by 80 MHz. A CST simulation was performed with detuned side-coupled cells and agrees well with the measured results. This is likely due to the large capacitance in those cells making them very sensitive to the gap.

After bonding the cavity will be transported to CERN for high gradient testing at CLEAR to validate the high gradient performance of side-coupled linacs.

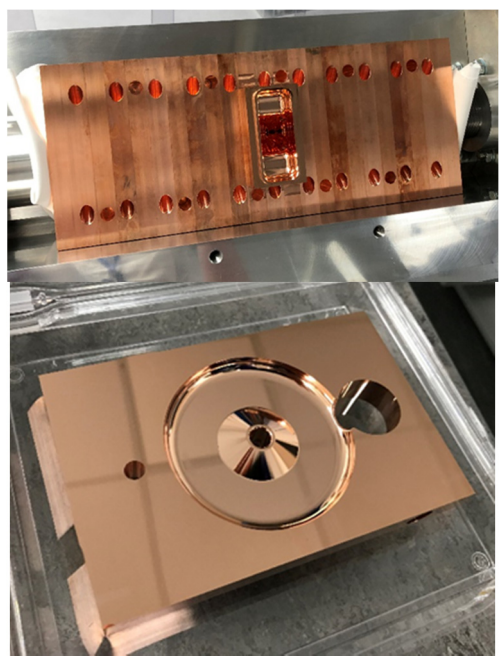


Figure 8: Manufactured cavity cell from VDL.

ACKNOWLEDGEMENTS

This work has been supported by STFC via the Cockcroft Institute core grant and an IPS grant.

ISBN: 978-3-95450-194-6 ISSN: 2226-0366 doi:10.18429/JACoW-LINAC2018-THPO108

REFERENCES

[1] Particle Therapy Co-Operative Group (PTCOG), www.ptcog.ch

[2] A. Grudiev, S. Calatroni and W.Wuensch, "A New Local Field Quantity Describing the High Gradient Limit of Accelerating Structures", *Phys. Rev. ST Accel. Beams* 12/10 (2009) 102001.

[3] A. Degiovanni *et al.*, *Nucl. Instr. and Meth.* A (2011). doi:10.1016/j.nima.2011.05.014.

[4] S. Verdú-Andrés *et al.*, "High Gradient Test of a 3GHz Single Cell Cavity", *Proc. LINAC'10*, Tsukuba, Japan, Sep. 2010, paper THP037, pp. 839-841.

[5] R. Apsimon *et al.*, "Coupled Longitudinal and Transverse Beam Dynamics Studies for Hadron Therapy Linacs," in *Proc. IPAC'17*, Copenhagen, Denmark, May 2017, pp. 4772-4775. doi:10.18429/JACoW-IPAC2017-THPVA134.

[6] S. Benedetti, PhD thesis (2018).

[7] VDL, http://www.vtl-group.com/

[8] S. Pitman *et al.*, International Patent Application No. PCT/GB2018/051343.

Content from this work may be used under the terms of the CC BY 3.0 licence (© 2018). Any distribution of this work must maintain attribution to the author(s), title of the work, publisher, and DOI.

ISBN: 978-3-95450-194-6 ISSN: 2226-0366 doi:10.18429/JACoW-LINAC2018-THPO109

A NEW SPHERICAL PULSE COMPRESSOR WORKING WITH DEGENERATED "WHISPERING GALLERY" MODE*

Z. Li[1], W. Fang[#], Q. Gu, Z. Zhao[†], SINAP, CAS, Shanghai, China
A. Grudiev, CERN, Geneva, Switzerland
[1]also at UCAS, Beijing, China

Abstract

This paper introduces a new design concept of spherical pulse compressor. The main characteristics of this new design can be described as: spherical storage cavity, degenerated "Whispering Gallery" mode and a compact mode launcher.

INTRODUCTION

CLIC is focusing on the Compact Linear Collider. To obtain a relatively high accelerating gradient, CLIC utilizes Pulse Compressors to increase the input power of accelerators. This work is to make an alternative design for CLIC pulse compression scheme. There are several kinds of pulse compressor: SLED, BOC, SLED-II, spherical pulse compressor and so on. Usually, a spherical cavity, including BOC, can offer a higher Q factor compared with a cylindrical cavity. This design utilizes a spherical cavity working with degenerated "Whispering Gallery" mode.

THEORY OF BOC

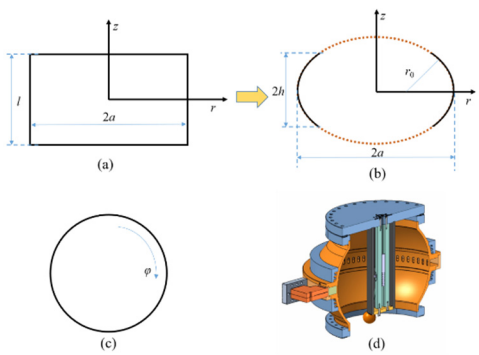


Figure 1: Cylindrical cavity (a), BOC (b), Top-view of BOC (c) and 3D-view of BOC (d).

BOC [1,2] is short for *Barrel-shaped Open Cavity*. This cavity and its theory can be derived from a cylindrical cavity by removing the two ends of a CC (cylindrical cavity) and bending the boundary inside like shown in Fig. 1(a) and Fig. 1(b). The definitions of TE and TM mode in BOC are the same as in CC: z is the longitudinal direction, and φ [Fig. 2(c)] and r are the transverse directions. The definitions of mode indexes m, n, p are also the same as in CC respectively. Fig. 1(d) shows a typical BOC.

The cavity profile of BOC is an ellipse. But it is not a perfect cavity. There's no cavity wall where the red dotted line shows in Fig. 1(b), which indicates the name "Open Cavity". The analytical formula of the ellipse is:

$$\frac{z^2}{ar_0}+\frac{r^2}{a^2}=1, \tag{1}$$

where a is the major axis of the ellipse, and r_0 is the curvature radius.

This kind of cavity shape allows the existence of the modes only those who have large number of azimuthal variations (so called "Whispering Gallery" modes), while the other modes that have weak azimuthal dependence cannot be formed. Because of the reflection of the cavity walls, the electromagnetic field of "Whispering Gallery" mode is concentrated in a relatively small area close to the cavity surface around the equator plane, like shown in Fig. 2.

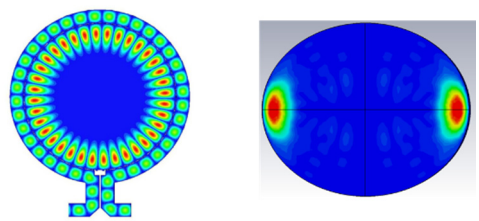


Figure 2: Top-view and side-view of "Whispering Gallery" mode.

According to its field distribution, the "Whispering Gallery" mode is a TM mode. The resonant frequency of a TM mode in BOC is:

$$ka=\upsilon_{mn}+\frac{(p-1/2)\alpha}{\sin\theta}, \tag{2}$$

where k is the wavenumber in the free space, m and p are the azimuthal and longitudinal indexes of the mode, respectively. For TM modes, υ_{mn} is the n-th positive root of Bessel function of order m and its derivative for TE modes. Angle α is defined as: $\sin\alpha=(a/r_0)^{1/2}\sin\theta$, where θ can be calculated from $\cos\theta=m/\upsilon_{mn}$.

For "Whispering Gallery" mode, the indexes n=1, p=1, and m is determined by the required Q factor and the working frequency. The Q factor is:

* Work supported by the National Natural Science Foundation of China (No. 11675249)
# fangwencheng@sinap.ac.cn
† zhaozt@sinap.ac.cn

Content from this work may be used under the terms of the CC BY 3.0 licence (© 2018). Any distribution of this work must maintain attribution to the author(s), title of the work, publisher, and DOI.

ISBN: 978-3-95450-194-6 ISSN: 2226-0366 doi:10.18429/JACoW-LINAC2018-THPO109

$$Q_0 = \frac{a}{\sigma}. \quad (3)$$

where σ is the skin depth.

The expression of Q factor for WG mode in BOC is the same as the TE mode in SLAC spherical cavity [3, 4]. It is because that the two modes in the two different cavities are actually the same one, but with different definitions. Or, in some ways, spherical cavity is a special kind of BOC. In this design, we utilize a spherical cavity. But for convenience, the definitions in BOC will be used.

A traditional BOC-type pulse compressor is consist of a BOC and a circle of rectangular waveguide surrounding the cavity. Power can be coupled through a lot of coupling apertures between cavity and waveguide, shown in Fig. 3(a). In this new design, we plan to use a coupling slot instead of these apertures, which can be machined more precisely. Moreover, the cavity and mode launcher can be designed separately [5].

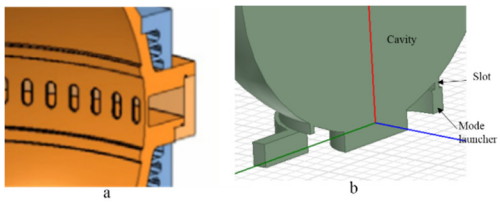


Figure 3: Illustrations of a traditional BOC (a) and the new design (b).

ANALYZE AND RF DESIGN

As a pre-research, the goals of design are set to Q_0=2×10^6 and coupling coefficient β=10.

TM$_{24,1,1}$ Mode

According to Eq. 3, the Q factor is proportional to the cavity radius. We need the Q factor as high as 2×10^6, so the cavity radius should be no less than 120 mm. For WG mode, both the theory of BOC and SC (spherical cavity) can be used, and two theories give the same result:

- For BOC, according to Eq. 2, when m=24, n=1, and p=1, the resonant frequency of a cavity with radius a=120.3 mm is 12 GHz, and the Q factor is 2×10^6.
- For SC, according to $f=u_{np}/[(2\pi a(\varepsilon\mu)^{1/2})]$, when n=24 and p=1, we have the same result of a=120.3 mm and Q_0=2×10^6.

The simulation results of a SC with radius 120.3 mm are shown in Table 1.

Table 1: Simulation Results of Spherical Cavity

Parameter	Value
Radius	120.3 mm
Mode	TM$_{24,1,1}$
Frequency	11995.8 MHz
Q_0	199,374

The field distribution is shown in Fig. 4.

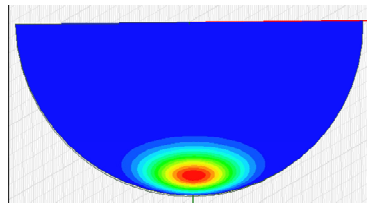


Figure 4: Field distribution of TM$_{24,1,1}$.

As shown in Fig. 3 (b), we would like to couple power from the bottom, which makes the mode launcher relatively large and complicated to design.

TM$_{9,1,16}$ Mode

The size and the mode coupling make the design of mode launcher difficult. To reduce the size, we move to TM$_{9,1,16}$, a degenerated mode of TM$_{24,1,1}$.

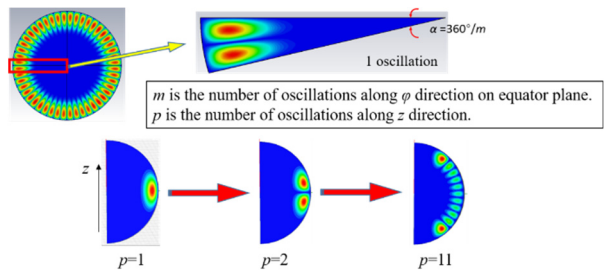


Figure 5: Illustrations of index m and p.

As illustrated in Fig. 5, if we reduce the index m, but increase the index p and keep m+p=25 as well as n=1, all these modes have the same resonant frequency. They are so called degenerated modes.

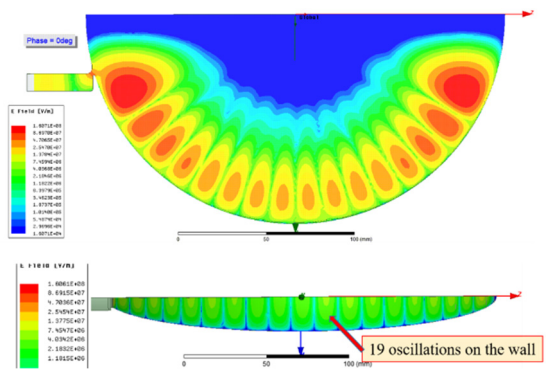


Figure 6: Field distribution inside the cavity and on the wall for TM$_{9,1,16}$ mode.

Figure 6 shows the field distribution of the cavity. Due to the coupling of the neighboring modes, there is some mixture between modes, which makes the Q factor lower than a perfect cavity.

Simulation result shows that the Q factor is reduced by about 2.5% like shown in Fig. 7, which is acceptable.

Content from this work may be used under the terms of the CC BY 3.0 licence (© 2018). Any distribution of this work must maintain attribution to the author(s), title of the work, publisher, and DOI.

ISBN: 978-3-95450-194-6 ISSN: 2226-0366 doi:10.18429/JACoW-LINAC2018-THPO109

Content from this work may be used under the terms of the CC BY 3.0 licence (© 2018). Any distribution of this work must maintain attribution to the author(s), title of the work, publisher, and DOI.

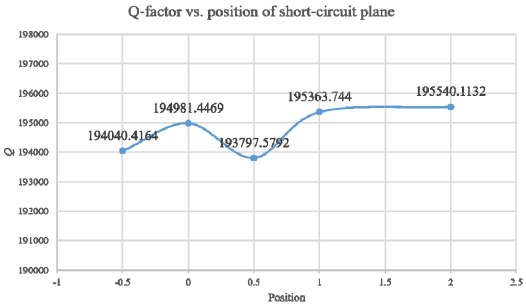


Figure 7: Q factor of $TM_{9,1,16}$.

Mode Launcher

The use of a smaller index *m* makes the mode launcher more compact. Figure 8 shows the new mode launcher for $TM_{9,1,16}$ mode. The red arrows indicate the power flow. Power input from a standard rectangular waveguide will be converted to two degenerated $TE_{9,1}$ modes and extracted from the coaxial waveguide to storage cavity.

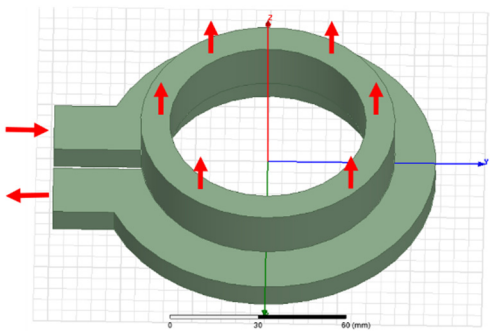


Figure 8: Mode launcher of $TM_{9,1,16}$.

The best results for now are shown in Fig. 9. S_{11}(reflection) is about -41 dB and S_{21}(transmission) is -23 dB, while $S_{3(18)1(1)}$ and $S_{3(19)1(1)}$ are -3.66 dB and -3.45 dB, respectively. The goal of mode launcher optimization is that the two degenerated coaxial $TE_{9,1}$ modes take half of the input power separately, which is -3.01 dB, and phase difference between these two modes is 90°. The optimizer is still running now.

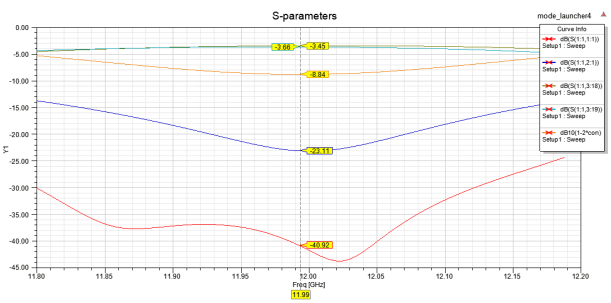


Figure 9: Best results of mode launcher for now.

Figure 10 shows a comparison of the size of three mode launchers: $TM_{24,1,1}$, $TM_{14,1,11}$ and $TM_{9,1,16}$. The use of degenerated WG mode makes the mode launcher much more compact.

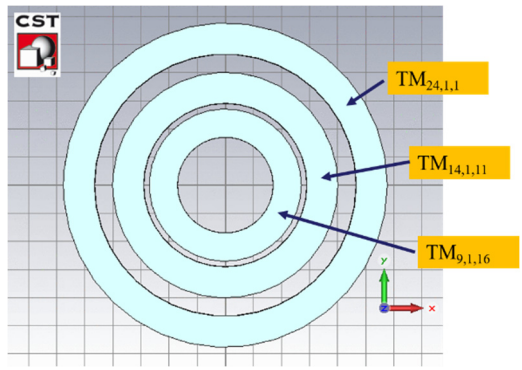


Figure 10: Comparison of three mode launchers.

CONCLUSION

A new design concept of spherical pulse compressor is made for CLIC. The use of a spherical storage cavity makes the Q factor high enough while keeping the pulse compressor small in size. To improve the machining accuracy, the coupling apertures of BOC are replaced by a coupling slot. What's more, the degenerated "Whispering Gallery" mode is utilized instead of the traditional working mode, which reduces the size of mode launcher significantly.

REFERENCES

[1] I. Syratchev, "The Progress of X-band 'Open' Cavity RF Pulse Compression Systems", in *Proc. EPAC'94*, London, England, May 1994, pp 375-379.

[2] I. Syratchev, "Barrel Open Cavity RF Pulse Compression System", 2013.

[3] J. W. Wang, S. G. Tantawi, X. Chen, "New SLED 3 System for Multi-mega Watt RF Compressor", arXiv preprint arXiv: 1408.4851(2014).

[4] Z. Li, W. Fang, Q. Gu, and Z. Zhao, "RF Design of a C-band Compact Spherical RF Pulse Compressor for SXFEL", Nucl. Instrum. Methods Physic Res., Sect A (Accel., Spectrometers, Detect. Assoc. Equip.): v863, p7-14, Aug. 11, 2017.

[5] J. Hirshfield, S. V. Kuzikov, M. I. Petelin and V. G. Pavelyev, "Whispering Gallery Pulse Compressor", 2014.

ISBN: 978-3-95450-194-6 ISSN: 2226-0366 doi:10.18429/JACoW-LINAC2018-THPO111

THE TEST OF RF BREAKDOWNS OF CPHS RFQ

W.B.Ye, S.X.Zheng†, J.R.Shi, C.Cheng, Q.Z.Xing, X.L.Guan, X.W.Wang, Key Laboratory of Particle & Radiation Imaging (Tsinghua University), Ministry of Education, Beijing 100084, China
also at Laboratory for Advanced Radiation Sources and Application, Tsinghua University, Beijing 100084, China
also at Department of Engineering Physics, Tsinghua University, Beijing 100084, China
M.C.Wang, State Key Laboratory of Intense Pulsed Radiation Simulation and Effect (Northwest Institute of Nuclear Technology), Xi'an, 710024, China

Abstract

The high accelerating gradient is significant for a compact linear accelerator, and RF breakdowns is a limitation for the high gradient. This work aims to research RF breakdowns of a 325 MHz proton Radio Frequency Quadrupole (RFQ) accelerator of the Compact Pulsed Hadron Source（CPHS）. The breakdown rate (BDR) of the RFQ has been measured. Breakdown waveforms have been recorded, which have been used for counting breakdown time distribution and analyzing the location of RF breakdowns.

INTRODUCTION

Linear accelerator (linac) is an important component of the wide family of accelerators. Since charged particles pass accelerating structures only once in a linac, high accelerating gradient is significant for a compact linac to achieve high energy. The accelerating gradient of a linac is mainly limited by RF breakdown. Up to now, numerous studies have been conducted to research the mechanism of RF breakdown. However, most of them concern about electron linacs whose frequency is usually GHz [1,2]. There has been very little research on RF breakdown of proton linac with much lower frequency. The purpose of this study is to research RF breakdown of a 325 MHz proton Radio Frequency Quadrupole (RFQ) accelerator.

The Compact Pulsed Hadron Source（CPHS）project at Tsinghua University is a university-based proton accelerator platform for multidisciplinary and proton application. The CPHS accelerator consists of an ECR proton source, a low-energy beam transport line (LEBT), a radio frequency quadrupole (RFQ) and a drift tube linac (DTL). The breakdown test was conducted on RFQ of the CPHS project. The main design parameters of the CPHS RFQ are listed in Table 1 [3].

EXPERIMENTAL SETUP

Figure 1 shows the experimental setup. There have three pickups on RFQ cavity so that we can get the RFQ cavity field signal from these pickups. From the directional coupler, we can get the reflected wave. An oscilloscope is used to record these waveforms. Control system help us record some other parameters, like RF power, pulses width, repetition rate, number of breakdowns, and vacuum of RFQ. During the conditioning and beam commissioning of the RFQ, when an RF breakdown happened, the reflected wave amplitude increased and then the breakdown would be detected and the waveforms would be recorded by the oscilloscope.

Table 1: Main Design Parameters of CPHS RFQ

Parameters	Value
Species	Proton
Type	Four-vane
Frequency	325 MHz
Input beam energy	50 keV
Output beam energy	3.0 MeV
Peak beam current	50 mA
Emittance (norm. rms)	0.2 π mm mrad
Maximum surface field	32.1 MV/m
Pulse length	0.5 ms
Pulse repetition rate	50 Hz
RF peak power	537 kW
Beam duty factor	2.5%

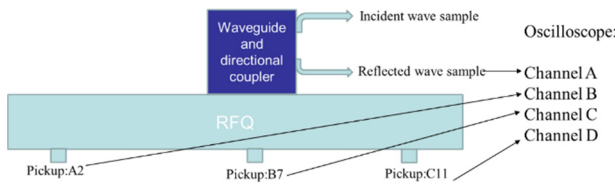


Figure 1: Experimental setup layout.

DATA AND ANALYSIS

Figure 2 is the operation history of CPHS RFQ. The left part and the right of Fig. 2 are corresponding to the conditioning and beam commissioning history of CPHS RFQ respectively. This figure shows the power loss of RFQ and accumulated number of breakdowns with respect to the accumulated number of pulses.

In previous work, CERN has proposed a scaling law to describe the relationship of breakdown rate, accelerating gradient and pulse length for the accelerating structures with very high frequency (usually several GHz) [1]:

$$\frac{E_0^{30}\tau^5}{BDR} = const \quad (1)$$

where E_0 indicates the accelerating gradient (depend on power loss of the structure) and τ the rf pulse length.

† zhengsx@tsinghua.edu.cn

Content from this work may be used under the terms of the CC BY 3.0 licence (© 2018). Any distribution of this work must maintain attribution to the author(s), title of the work, publisher, and DOI.

ISBN: 978-3-95450-194-6 ISSN: 2226-0366 doi:10.18429/JACoW-LINAC2018-THPO111

Content from this work may be used under the terms of the CC BY 3.0 licence (© 2018). Any distribution of this work must maintain attribution to the author(s), title of the work, publisher, and DOI.

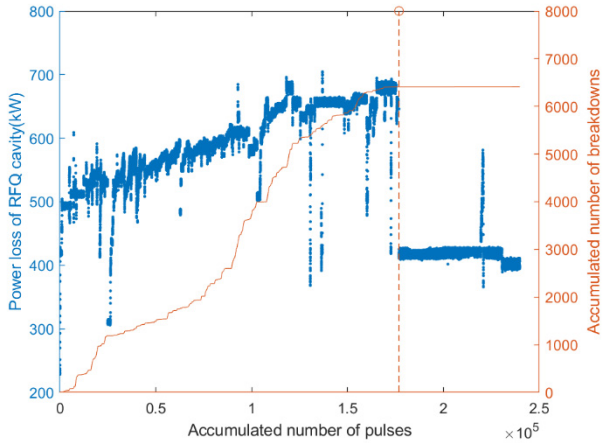


Figure 2: The blue dots represent power loss of RFQ, the red line represents accumulated number of breakdowns.

Based on the scaling law, the "scaling gradient" was defined and has been applied to process conditioning data [2]:

$$E_0^* = \frac{E_0 \tau^{\frac{1}{6}}}{BDR^{\frac{1}{30}}} \quad (2)$$

We want to find the scaling law which is suitable for our RFQ, that is one reason why we conducted this experiment. If we want to find the scaling law, we should measure the BDR of the RFQ under the different pulse length and accelerating gradient after the conditioning finished, since the BDR under a certain pulse length and gradient will decrease during the conditioning. However, we do not finish the whole conditioning at present so that we cannot get the scaling law directly. So, we use the scaling law and the scaling gradient proposed by CERN to process data, Fig. 3 shows the result after applying the scaling gradient to data. After the process, the scaling gradient curve is smoother than before, which indicate that the scaling law proposed by CERN is perhaps suitable for the RFQ with much lower frequency.

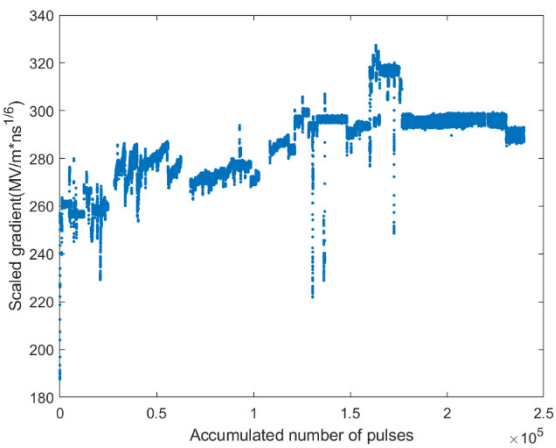


Figure 3: Scaled gradient vs number of accumulated pulses.

BREAKDOWN TIME DISTRIBUTION

The left plot of Fig. 4 is the normal waveforms, the right is the waveforms when a breakdown happened. The blue waveform is the reflected wave, the other three are the pickups' signal. When a breakdown happened, the reflected wave amplitude increased and would be recorded. Fig. 5 shows the breakdown happened time distribution (pulse length is 50 us). Most of breakdowns happened in the range of 10 us to 14 us, which is closed to the filling time of RFQ. That indicates when the build-up of the field just finished, RF breakdown has a bigger probability to happen.

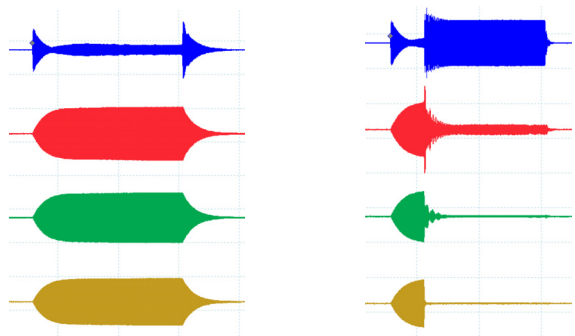


Figure 4: Left: normal waveforms; right: breakdown waveforms.

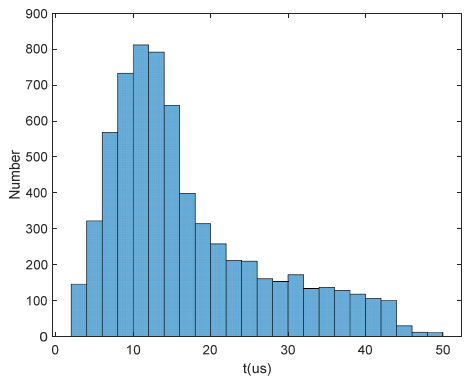


Figure 5: Breakdowns time distribution.

BREAKDOWN LOCATION ANALYSIS

Fig. 6 is an example of breakdown waveforms. Fast Fourier Transform(FFT) has been used to analyze the breakdown waveforms. As shown in Fig. 7, many frequency peaks different from original resonance frequency appeared in breakdown waveforms' frequency spectrum. 3 mainly component frequencies of breakdown waveforms have been listed in Table 2. The signal of pickup B7, pickup C11, and the reflected wave have the same main component, which indicates that the breakdown probably happened between pickup A2 and pickup B7 as shown in Fig. 8.

ISBN: 978-3-95450-194-6 ISSN: 2226-0366 doi:10.18429/JACoW-LINAC2018-THPO111

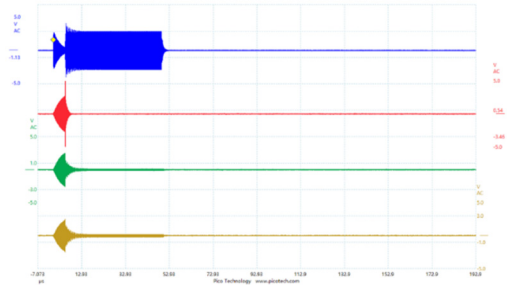


Figure 6: A breakdown waveforms.

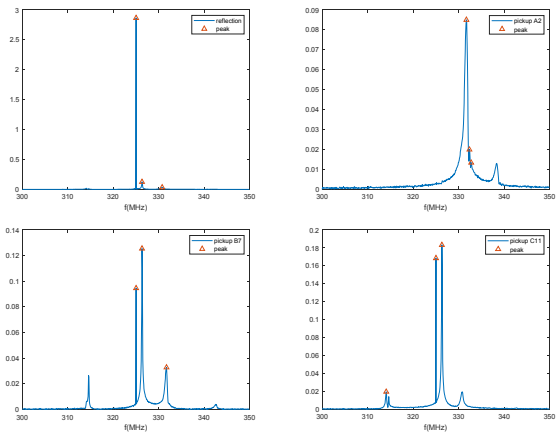


Figure 7: FFT result.

Table 2: Frequency Spectrum

Frequency (MHz)	Peak1	Peak2	Peak3
Reflected wave	325.00	326.31	330.75
Pickup A2	331.69	332.37	332.75
Pickup B7	326.31	325.00	331.69
Pickup C11	326.31	325.00	324.06

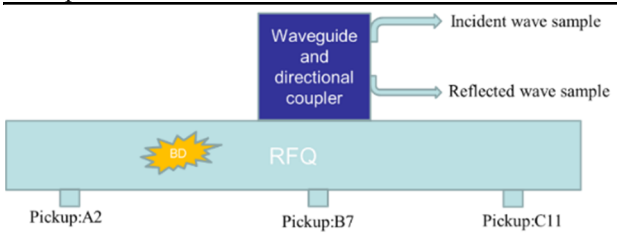


Figure 8: Breakdown location.

In order to explain the frequency spectrum, we have done the CST simulation. Breakdown is accompanied by the formation of a metal ion plasma just above the surface of the breakdown site. When a breakdown occurred, the plasma formed and expanded [4]. The electrodes of RFQ was short-circuited by plasma. The cavity seemed to be divided into two segments, and then each segment has new resonance frequencies. In CST simulation, we use a thin metal cylinder to replace the plasma, as shown in Fig. 9. The simulation results are shown in Fig. 10. Many new modes occur and the field of these modes concentrate on only one side, the cavity seems to be two segments. Pickup on the left side and pickup on the right side will see the different modes, so the frequency spectrum of these two pickups will be different.

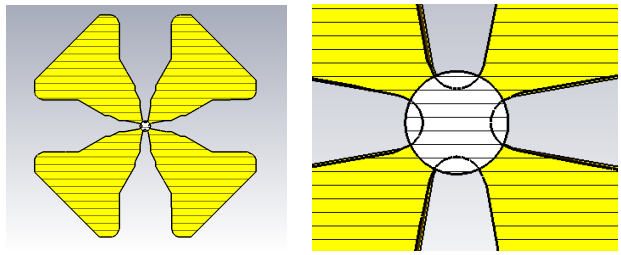


Figure 9: RFQ electrodes model.

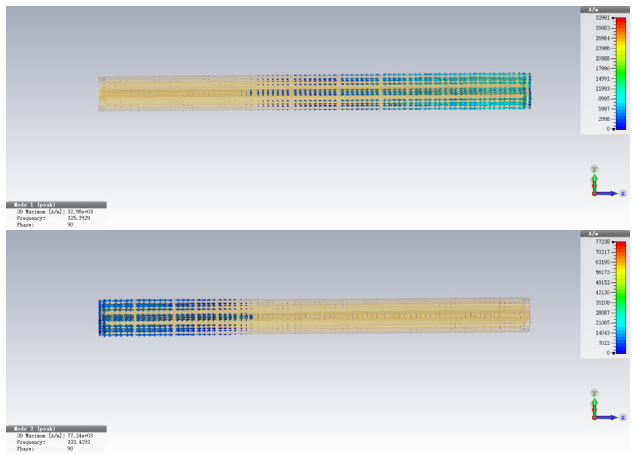


Figure 10: CST simulation results.

CONCLUSION

This work has researched the RF breakdown of CPHS RFQ preliminary. The scaling law proposed by CERN is probably also suitable for RFQ, however it still need more data to validate. RF breakdowns have a great probability to happened when the bulid-up of field just finished .The breakdown location can be determined by analyzing the breakdown waveforms and CST simulation.

ACKNOWLEDGEMENTS

The authors would like to thank to Alessandra Lombard and Walter Wuensch advise us to conduct high power test on RFQ and give us a lot of advice.

REFERENCES

[1] A. Grudiev, S. Calatroni, and W. Wuensch, "New local field quantity describing the high gradient limit of accelerating structures," *Physical Review Special Topics-Accelerators and Beams*, vol. 12, no. 10, p. 102001, 2009.

[2] A. Degiovanni, W. Wuensch, and J. Giner Navarro, "Comparison of the conditioning of high gradient accelerating structures," *Physical Review Special Topics Accelerators & Beams,* vol. 19, no. 3, 2015.

[3] Q. Z. Xing *et al.*, "A 3-MeV RFQ accelerator for the Compact Pulsed Hadron Source at Tsinghua University," *Physics Procedia,* vol. 26, pp. 36-43, 2012.

[4] F. Wang and C. Adolphsen, "Localization of RF Breakdowns in a Standing Wave Cavity," *Physical Review Special Topics - Accelerators and Beams,* vol. 12, no. 12, p. 042001, 2009.

Content from this work may be used under the terms of the CC BY 3.0 licence (© 2018). Any distribution of this work must maintain attribution to the author(s), title of the work, publisher, and DOI.

ISBN: 978-3-95450-194-6 ISSN: 2226-0366 doi:10.18429/JACoW-LINAC2018-THPO113

DESIGN OF 4 AMPERE S-BAND LINAC USING SLOTTED IRIS STRUCTURE FOR HOM DAMPING*

J. Pang†, X. He, S. Chen, Institute of Fluid Physics, CAEP, Mianyang, China
S. Pei, J. Zhang, H. Shi, Institute of High Energy Physics, CAS, Beijing, China

Abstract

An S-band LINAC with the operating frequency of 2856 MHz and beam current of 4 A was designed for flash X-ray radiography for hydrodynamic test. The optimization of the parameters of the LINAC was processed to obtain the minimum beam radius and the maximum energy efficiency. For the purpose of reducing the beam orbits offset at the exit of LINAC, a slotted iris accelerating structure would be employed to suppress the transverse Higher Order Modes (HOMs) by cutting four radial slots in the iris to couple the HOMs to SiC loads. In this paper, we present the design of the LINAC and the results of beam dynamic analysis.

INTRODUCTION

Linear induction accelerators were used in large-size or full-size radiographic hydrodynamic test with dose of hundreds of Rad by accelerating several-kA electron beam to tens of MeV. In addition, small machine, such as pulsed X-ray machine with several hundred kV and anode-pinch diode, was used in small-size hydrodynamic subdivision experiments for dynamic material characteristic study, micro jetting diagnosis, et al. Figure 1 shows a typical layout of flash X-ray radiography system.

In the past twenty years, intense-beam normal conducting RF accelerator has been developed with great achievement due to the development of large collider technology. The CLIC Test Facility, CTF3, has accelerated the beam with current of up to 5A to150MeV with full beam loading [1-2]. The HOM was damped by using slotted iris constant aperture (SICA) accelerating structures. The 100 MeV/100 kW LINAC, constructed by IHEP and used as a driver of a neutron source in KIPT, Ukraine, has accelerated a beam of 2 A to 100 MeV by using detuning accelerating tubes [3-5].

The great progress in intense-beam linac motivates the compact radiographic facility driven by a 4 A 30 MeV linac, which might be utilized for multi-pulse radiographic with the material planar density of several to tens g/cm2. The most considered parameter, FWHM of transverse distribution of electron beam, should be limited less than 1 mm. A radiographic system has been discussed in [6]. Simulation results showed that the exposure dose 1 m away from the target right ahead was about 9.1 R and the X-ray spot sizes were not increased with the increment of the thickness of target material. The results also showed that pulse number was limited up to 8 when using a fixed target

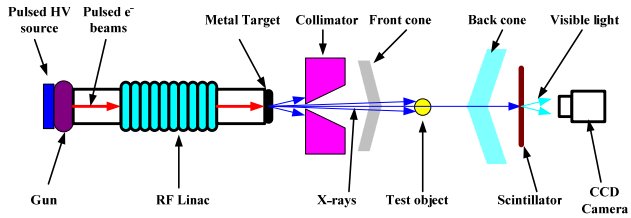


Figure 1: Layout of a typical flash X-ray radiography system using RF accelerator.

when FWHM of transverse size was about 1 mm with bunch charge of 400 nC.

In this paper, the design of accelerator was described. A beam dynamic analysis was carried out with the primary design of the accelerating structure. BBU effect calculation was also carried out.

GENERAL DESCRIPTION OF THE ACCELERATOR

Layout of the accelerator, which consists of a DC gun, 3 accelerating tube, a chicane and matching beam line, was shown in Fig. 2. The total length is about 14 m and could be reduced by farther optimization. Table 1 lists main parameters.

Table 1: Main Linac Parameters

Parameter	Value	Unit
RF frequency	2856	MHz
Energy	>30	MeV
Beam current (max)	4	A
Energy spread (FWHM)	<0.01	
Emittance (RMS)	<50	mm mrad
Beam pulse length	100	ns
Number of pulses in a train	4-8	
RF pulse duration	10	μs
Pulse repetition rate	10	Hz
Number of ACC. structure	3	
Gun voltage	~120	kV

ACCELERATING STRUCTURE

General Design

The goal of the design of accelerating structure is to achieve a high RF-beam power efficiency with short length as much as possible. Two type of structure was considered: the conventional disk-load structure and constant-aperture structure. Both of them should be slotted on the iris to suppress the HOM modes, which would be introduced by

* Work supported by Key Laboratory of Pulsed Power, CAEP (Contract NO. PPLF2014PZ05) and Key Laboratory of Particle Acceleration Physics &Technology, IHEP, CAS (Contract NO. Y5294109TD)
† jpang@caep.cn

Content from this work may be used under the terms of the CC BY 3.0 licence (© 2018). Any distribution of this work must maintain attribution to the author(s), title of the work, publisher, and DOI.

ISBN: 978-3-95450-194-6 ISSN: 2226-0366 doi:10.18429/JACoW-LINAC2018-THPO113

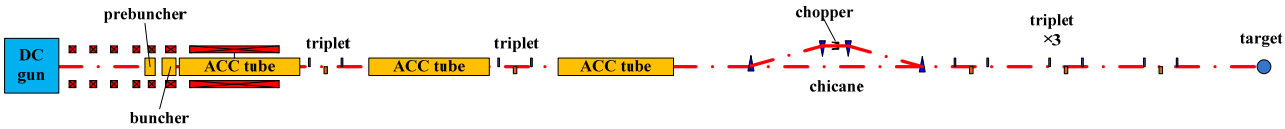


Figure 2: Layout of the accelerator.

the beam. The input power, limited by klystron power and transmission efficiency, was determined as 45 MW. There were 3 rules to determine cell arrangements for constant gradient along the axis when there is no beamloading. These rules were described in Ref. [7]

The arrangement of disk-load structure has only a unique solution in the case of certain input power and average unload gradient. Some results with unloaded gradient of 12 MV/m with the different input power calculation are shown in Fig. 3. With a certain beam load and unloaded gradient, the number of cells required to achieve specific microwave-beam efficiency (90% in evaluation) increased linearly with input power, and the loaded gradient satisfying the above requirements did not change.

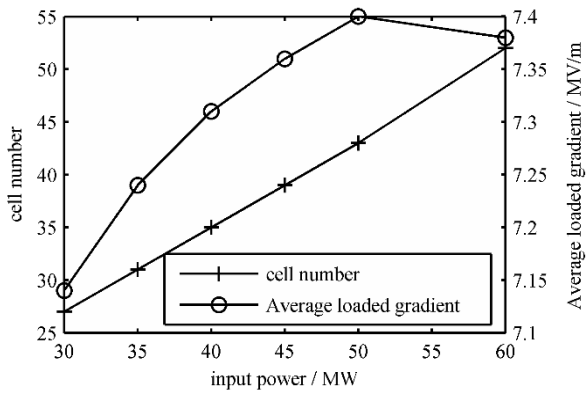


Figure 3: Calculation results of disk-load structure with a certain unloaded gradient of 12 MV/m with various input power.

With the employee of nose cone to achieve constant-aperture, the arrangement is also determined by the iris diameter. With a certain input power, there will be an appropriate value of iris diameter resulting maximum surface electric field as shown in Fig. 4.

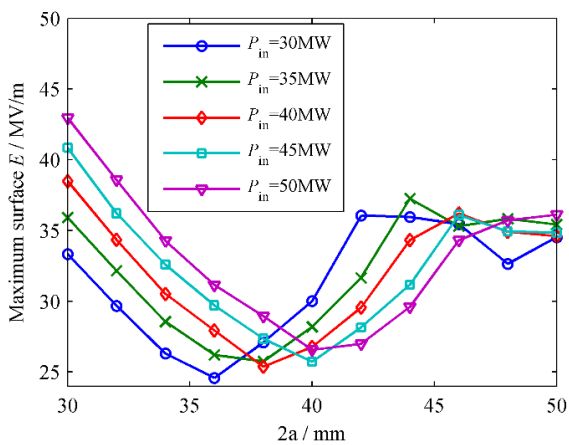


Figure 4: Maximum surface electric field of different structure design.

The designs of two types of structure for 45 MW input power, which are quite similar, are listed in Table 2. The average loaded gradient is larger to CTF3 2998 MHz structure (6.5 MV/m for beam current of 3.5 A [1]), but more critical to the RF breakdown threshold with about 6 times larger RF pulse length. The uniform un-loaded gradient design will bring a lower surface electric field of whole accelerating structure. We chose the disk-load type for our further design.

Table 2: Design of Two Type Accelerating Structures

Parameter	Unit	Disk-load	Constant-aperture
Input power	MW	45	45
E_{acc} (no beamloading)	MV/m	12.0	12.1
E_{acc} (max beamloading)	MV/m	7.36	7.38
E_{max} on surface	MV/m	27.66	29.70
Phase advance per cell		2π/3 - mode	
RF-beam effeciency		0.893	0.895
Number of cells		39	39
Iris diameter ($2a$)	mm	36.010-35.051	36.000
Length of nose cones	mm	-	0.031-0.706
Ratio of v_g to c		0.0558-0.0515	0.0550-0.0504
Energy gain	MeV	9.95	9.98

HOM Damping Design

Four radial slots were cut in the iris to couple HOMs to outer waveguides, where the HOMs would be dissipated in SiC loads. Simulation results shown the frequency and Q_0 of fundamental mode would not be affected by cutting slots with width less than 5 mm.

After cutting slots, the number of dipole modes with frequency below 10GHz of 1st cell has increased from about 10 to about 60. Most modes are trapped in ridge waveguides. Important modes have been inherited with large kick factors. Those modes could be considerably damped by using SiC loads, with dielectric constant and tangent delta as 23 and 0.2, relatively, which are quite feasible. The slot width was chosen carefully to minimize BBU effect. The final decision was 3 mm. Beam obits dispersion simulation was described later in this paper.

The slotted iris would bring a considerable enhancement of surface electric field of fundamental mode in the area near the slot and the center of iris. With a blending radius as 0.3 mm, the enhancement factor would be reduced to about 1.6. When the blending radius was less than 0.2, the calculation of enhancement factor became non-convergent.

Content from this work may be used under the terms of the CC BY 3.0 licence (© 2018). Any distribution of this work must maintain attribution to the author(s), title of the work, publisher, and DOI.

ISBN: 978-3-95450-194-6 ISSN: 2226-0366 doi:10.18429/JACoW-LINAC2018-THPO113

Content from this work may be used under the terms of the CC BY 3.0 licence (© 2018). Any distribution of this work must maintain attribution to the author(s), title of the work, publisher, and DOI.

Test Prototype Tube

A 6-cell prototype tube has been manufactured to test the SiC-copper connecting technique. Six cells were stacked and brazed together without input and output couplers. No crack or detachment of SiC had been found. We are planning to manufacture another prototype tube, which consist of 6 cells and two power couplers, to test our design by high-power conditioning. The double-coupling design would be used to minimum the dipole kick at the entrance of the tube.

BEAM DYNAMIC

Beam dynamic analysis was carried out using PARMELA code without consideration of BBU. The FWHM of beam horizontal distribution at the end of the accelerator can be controlled less than 1 mm in the case of the 4 A beam load. Figure 5 shows the beam envelop along z axis. Figure 6 shows beam transverse distribution.

If the BBU effect was taken into account, the beam lateral size jitter will be in the order of mm without HOM damping. +200 μm/+200 μrad initial beam offset and angle were assumed at the exit of the buncher and orbit correction were considered.

Calculation results shown that the beam position jitter can be controlled quite well with HOM damping. Figure 7 shows beam obits dispersion along the accelerating axis with shot width as 1 mm (left) and 3 mm (right). With a 3-mm slot width, the acc. structure shows a better performance of BBU inhibiting, which was shown more clearly in Figure 8. At the exit of accelerator, there were 98% of bunches limited in ±0.02 mm beam position jitter when slot width is 3 mm, comparatively, 94% of bunches in ±0.1 mm range when slot width is 1 mm.

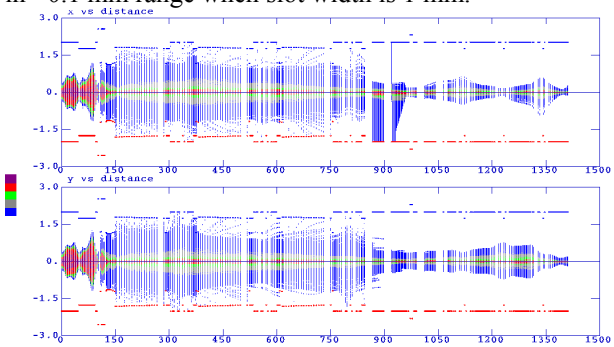


Figure 5: Beam envelope calculation result.

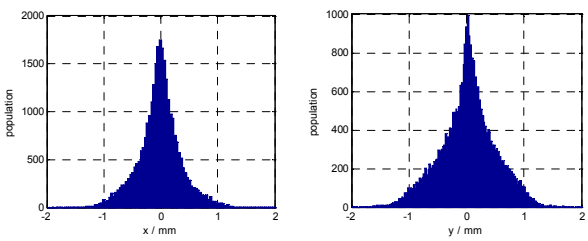


Figure 6: Beam transverse distribution at the exit.

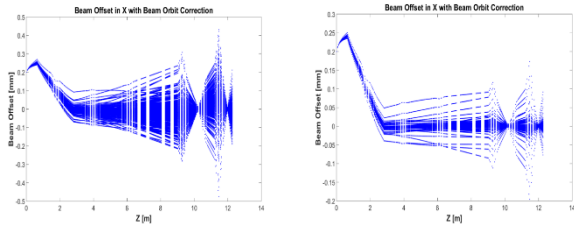


Figure 7: Simulation results of horizontal beam obits dispersion along the accelerating axis with a 200ns RF duration (including RF fill-up time) considering long-range wakefield with shot width of accelerator structures as 1 mm (left) and 3 mm (right).

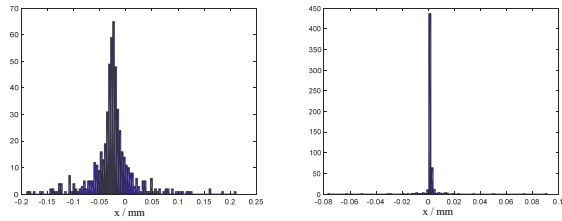


Figure 8: Horizontal distribution of beam obits dispersion at the exit with shot width of accelerator structures as 1 mm (left) and 3 mm (right).

REFERENCES

[1] P. Urschütz *et al.,* "Efficient long-pulse fully loaded CTF3 LINAC operation", in *Proc. LINAC'2006*, Knoxville, Tennessee, USA, 2006, paper MOP002, pp. 31-33.

[2] M. Aicheler *et al.,* "A Multi-TeV linear collider based on CLIC technology: CLIC Conceptual Design Report", CERN, Geneva, Switzerland, Rep. CERN-2012-007, Oct. 2012.

[3] Y. Chi *et al.*, "Design studies on 100MeV/100kW electron linac for NSC KIPT neutron source on the base of subcritical assembly driven by LINAC", in *Proc. 2nd Int. Particle Accelerator Conf. (IPAC'11)*, San Sebastián, Spain, 2011, paper TUPC034, pp. 1075-1077.

[4] M. Aizatskiy *et al.,* "100 MeV/100 kW electron linear accelerator driver of the NSC KIPT neutron source", in *Proc. 4th Int. Particle Accelerator Conf. (IPAC'13)*, Shanghai, China, 2013, paper THOAB203, pp. 3121-3123.

[5] S. Pei, private communication, May. 2017.

[6] J. Pang *et al.*, "Analysis of bremsstrahlung characteristic by 30 MeV multi-pulse beams bombarding rotated tantalum-based target", *High power* laser *and particle beams*, vol. 29, no. 6, p. 065101, Jun. 2017.

[7] J. Pang *et al.*, "Primary Design of 4 A S-band LINAC using slotted iris structure for HOM damping", in *Proc. The 13th Symposium on Accelerator Physics (SAP'2017)*, Jishou, China, 2017, paper MOPH22, pp.76-78.

ISBN: 978-3-95450-194-6 ISSN: 2226-0366 doi:10.18429/JACoW-LINAC2018-THPO115

CONSOLIDATION AND EXTENSION OF THE HIGH-GRADIENT LINAC RF TECHNOLOGY AT PSI

P. Craievich*, M. Bopp, H. Braun, A. Citterio, H. Fitze, T. Garvey, T. Kleeb,
F. Loehl, F. Marcellini, M. Pedrozzi, J.-Y. Raguin, L. Rivkin, K. Rolli, R. Zennaro
Paul Scherrer Institut, 5232 Villigen PSI, Switzerland

Abstract

For SwissFEL a novel production process for high-gradient, high-precision C-band accelerating structures had been developed at PSI and was implemented for series production in collaboration with industry. The copper parts of the structures are machined and brazed relying on a ultra-high precision manufacturing process and tight mechanical tolerances; no RF tuning methods are applied during or after production. So far none of the structures of the series production failed during RF power conditioning and operation in the SwissFEL facility. After completing the series production for SwissFEL PSI started collaborations with CERN, ELETTRA and DESY for applying the production process and related know-how to other frequencies, namely S-band (3 GHz) and X-band (12 GHz). This paper gives an overview on the ongoing and planned R&D activities and results obtained so far.

INTRODUCTION

The SwissFEL project [1], presently under commissioning at the Paul Scherrer Institut (PSI), produces FEL radiation for hard X-rays with pulse durations ranging from a few to several tens of femtoseconds. The SwissFEL accelerator consists of an electron source, an S-band (3 GHz) booster Linac and a C-band (5.7 GHz) main Linac. A total of 26 C-band modules are installed in the C-band Linac and each module consists of four 2-m long C-band structures that are mounted onto two granite girders (see [2] for a schematic and [3] for further information). The C-band structures [4] are stacked and brazed at PSI out of copper cells that were produced at VDL ETG (J-couplers) and VDL ETG Switzerland (regular cells) with micrometer precision using ultra-precision diamond milling and turning. These structures do not undergo any tuning steps from cup production to installation into the bunker. The target precision of a single copper cup is less than ±2 µm with a surface finish Ra of 25 nm and concentricity of less than 50 µm before and after brazing of a stack of 111 copper regular cells and two couplers. Bead pull measurements have confirmed the high precision machining of the cups and couplers and thus validated the choice to produce the structures without implementing mechanical tuning on the cups, i.e., any push-pull technique. Furthermore, the measurement of the Q-factor was within 1% of the simulated one and the rms phase advance error was less than 2° over the whole structure which has a negligible effect on the energy gain. The manufacturing process of the individual cup was developed and tested at PSI before transferring the technology to the industry for the series production. It consists of an initial raw-cut and then pre-turned on a conventional and numerical lathe to a precision of about 10 µm while the finishing of the cups is performed on a sturdy and pneumatically stabilized slanted bed lathe using poly and mono-crystalline diamond (PCD, MCD) tools in a temperature and humidity controlled machining compartment of the lathe itself. Metrology measurements on the copper cells have shown a turning precision better than ±0.5 µm. The copper is oxygen free, high-conductivity and forged in three dimensions to have a homogeneous distribution of the small pores, a stress-free and intrinsically stable material. In order to assure the required concentricity, a robot with an action radius of 2 m and a tridimensional accuracy of 5 µm is used for the stacking of the cups before brazing [5]. This production process allows one to avoid any tuning steps while still achieving excellent field flatness and phase advance errors. In addition to the four structures, each Linac module also comprises a barrel open cavity (BOC) pulse compressor [6], and these were machined and brazed at PSI [7]. A picture of the C-band module is shown in Figure 1. A module is fed by a single RF source with up to 50 MW. The achieved straightness of the structures is excellent, the maximum measured deviations from a straight line are typically below 25 µm. The RF properties of the C-band structures have been measured using the bead-pull technique and an example result is shown in Fig. 2. All structures achieved an excellent electric field profile along the longitudinal coordinate of the

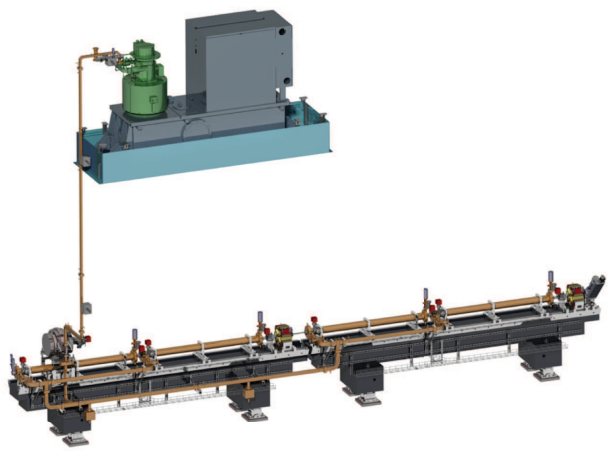


Figure 1: C-band module composed from four C-band accelerating structures, a pulse compressor and 50 MW Toshiba klystron.

* paolo.craievch@psi.ch

Content from this work may be used under the terms of the CC BY 3.0 licence (© 2018). Any distribution of this work must maintain attribution to the author(s), title of the work, publisher, and DOI.

ISBN: 978-3-95450-194-6 ISSN: 2226-0366 doi:10.18429/JACoW-LINAC2018-THPO115

Content from this work may be used under the terms of the CC BY 3.0 licence (© 2018). Any distribution of this work must maintain attribution to the author(s), title of the work, publisher, and DOI.

structures. The RF conditioning of the first C-band module was mainly performed without issue and Fig. 3 shows the progress. The maximum power from the klystron, 50 MW, was reached, yielding beyond 300 MW of power after the pulse compressor. Counting the number of arcs produced by the extraction of electrons from the metallic surface, the breakdown rate (BDR) can be estimated as a function of the accelerating gradient. Figure 4 shows an example of a BDR measurement where an accelerating gradient of approximately 52 MV/m was reached on the C-band prototype [8].

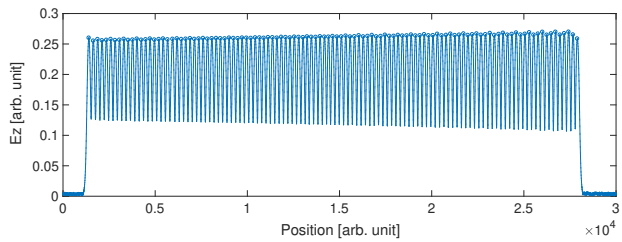


Figure 2: Example of the bead-pull measurements. Measured on-axis electric field along the longitudinal coordinate of the 2-m long C-band structure.

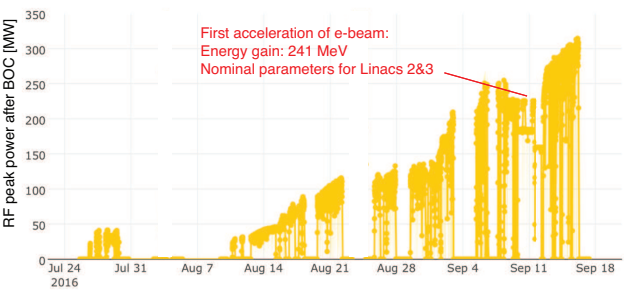


Figure 3: Conditioning progress for first C-band RF module.

PSI is interested in extending, consolidating and broadening its know-how to other frequency ranges, as for instance in the S-band (3 GHz) and X-band (12 GHz) range. Our research group is presently involved in the following projects:

- development of an X-Band tune-free T24 prototype for CLIC [9];
- development of a high-gradient S-Band tuning-free prototype for the FERMI Linac at ELETTRA [10];
- development, in collaboration with DESY and CERN, of POLARIX, an X-band tune-free deflector with variable polarization [11].

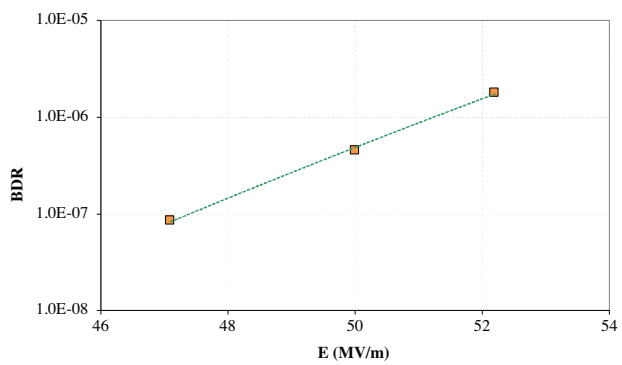


Figure 4: Example of the breakdown rate (BDR) as a function of the accelerating gradient for the C-band structure.

X-BAND T24 PROTOTYPES FOR CLIC

The mechanical topology is very similar to that of the SwissFEL C-band structure with the main difference being the input/output couplers which are of the mode launcher type as for many CLIC test prototypes. All cups and the two couplers were produced by the company VDL. The inner profiles of the cups are all well within the specified tolerances (±2 µm) and the average surface roughness (Ra) is below 20 nm. The cups have been vacuum fired at 400 °C for two hours before brazing to remove residual oxidation. The final straightness after brazing is better than 10 µm. The classical RF design had to be slightly modified to adapt it to the PSI mechanical design which is based on double rounded copper disks with one half cell machined on each side in order to have the brazing plane in the middle of the cell [9]. As an example of the excellent high power performances, Figure 5 demonstrates the second PSI structure conditioning history to date. The extrapolated BDR at the nominal gradient (100 MV/m) is $2 \cdot 10^{-7}$. It is worthwhile noting that the results are only provisional and that the test is not completed yet.

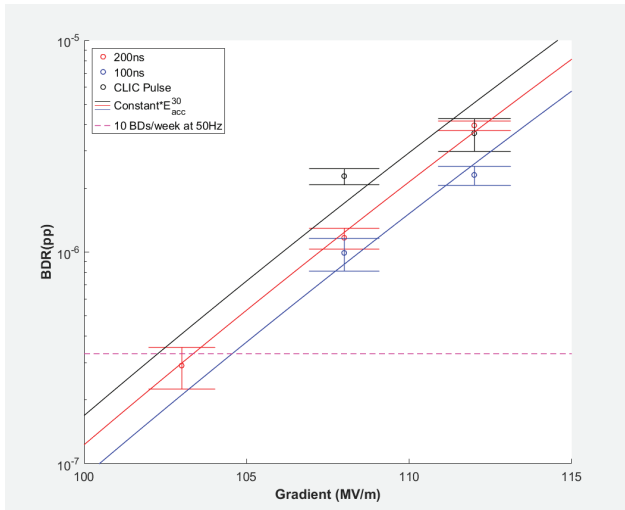


Figure 5: BDR for the second PSI structure manufactured for CERN (courtesy of CERN).

S-BAND HIGH GRADIENT STRUCTURES FOR FERMI

An upgrade of the FERMI Linac is currently under study and it foresees that each 6-m long Backward Travelling Wave structure equipping the high energy section of the Linac would be replaced by two, 3-m long, high gradient structures fed by the same power source. This upgrade would ensure a reliable accelerating gradient of 30 MV/m at 50 Hz and increase in beam energy from 1.5 GeV to 1.8 GeV [10].

ISBN: 978-3-95450-194-6 ISSN: 2226-0366 doi:10.18429/JACoW-LINAC2018-THPO115

The technology applied to the present prototype of S band cavity is also very similar to that of the SwissFEL C-Band structures. A first step is the production at PSI of a short test structure that should confirm the validity of the PSI technology also at S band. The cold measurements of this prototype, i.e., bead pulling and S-parameter confirmed the possibility to produce without tuning. The operating temperature is 36.4 °C, only 1.4 °C higher than the design value (35 °C). This deviation may be reduced during the production of the series. The field along the structure, as shown in Fig. 6 is perfectly flat and the mismatch is below −30 dB at both couplers [10]. The structure is under high power test at ELETTRA Trieste. Preliminary results are very encouraging, reaching the nominal operating condition of 30 MV/m with a pulse length of 600 ns after only 295 breakdown events.

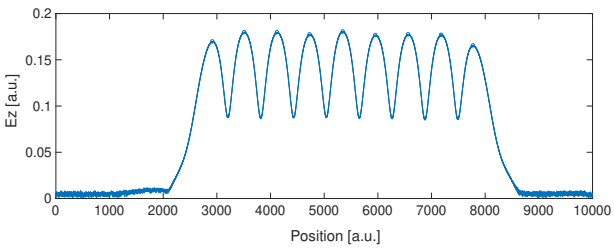


Figure 6: Results of a bead pull test at PSI.

POLARIX TDS

A collaboration between DESY, PSI and CERN has been established to develop and build an advanced modular X-band transverse deflection structure (TDS) system with the new feature of providing variable polarization of the deflecting force [12]. This innovative CERN design requires very high manufacturing precision to guarantee the highest azimuthal symmetry of the structure for avoiding accidental rotations of the polarization of the streaking field along the cavity. Therefore, the high-precision tune-free production process developed at PSI for the C-band and X-band accelerating structures will be used for the manufacturing. Several experiments at DESY (FLASH2, FLASHForward, SINBAD) and PSI (ATHOS at SwissFEL) are interested in the utilization of such high-gradient X-band TDS systems for high resolution longitudinal diagnostics [13]. The prototype of this novel X-band TDS [11], the Polarizable X-band (PolariX) TDS, is under production at PSI and bead-pull RF measurements will be performed in October. Figure 7 shows the detail of the input and output couplers (left), the whole TDS prototype (middle) and the basic disk geometry (right).

CONCLUSION

Developments in Ultra Precision (UP) turning and innovative vacuum brazing procedures at PSI for SwissFEL have led to a production technique for new structures. The strong motivation to improve the cavity technology at PSI was that the fabrication of traveling-wave accelerating structures had

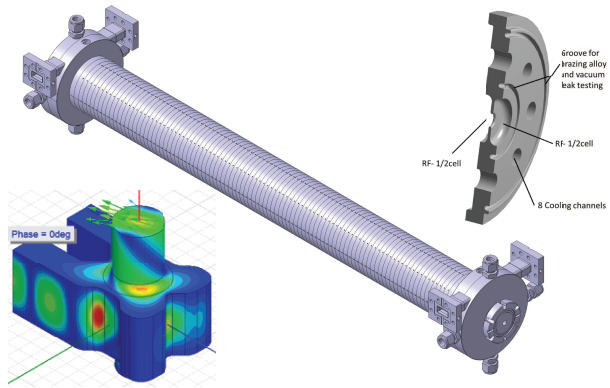


Figure 7: Left: detail of the input/output coupler. Middle: whole TDS prototype. Right: basic disk.

to meet the stringent RF requirement while minimizing the cost and achieving a stable process for an economical industrial series production. In that case the mass production foresaw the construction of 120 structures. PSI is now interested in extending, consolidating and broadening its know-how to other frequency ranges, obtaining already encouraging results at S- and X-Band frequencies.

ACKNOWLEDGEMENTS

The work presented in this paper is the results of collaborations involving four institutes: CERN, DESY, ELETTRA and PSI. These results benefited from the large and efficient support of colleagues from these organisations. To all of them go our acknowledgments. The X-band T24 prototype was partially funded by an SNF FLARE grant 20FL20_147463.

REFERENCES

[1] C. J. Milne *et al.*, *Appl. Sci.*, vol. 7, p. 720, 2017.

[2] F. Loehl *et al.*, in *Proc. FEL'13*, New York, USA, 2013, pp. 317-321.

[3] F. Loehl *et al.*, in *Proc. FEL'14*, Basel, Switzerland, 2014, pp. 322-326.

[4] J.-Y. Raguin and M. Bopp, in *Proc. LINAC'12*, Tel-Aviv, Israel, 2012, pp. 501-503.

[5] U. Ellenberger *et al.*, in *Proc. FEL'13*, New York, USA, 2013, pp. 245-249.

[6] R. Zennaro *et al.*, in *Proc. IPAC'13*, Shanghai, China., 2013, pp. 2827-2829.

[7] U. Ellenberger *et al.*, in *Proc. FEL'14*, Basel, Switzerland, Aug 2014, pp. 859-863.

[8] R. Zennaro *et al.*, in *Proc. LINAC'14*, Geneva, Switzerland, 2014, pp. 333-335.

[9] R. Zennaro *et al.*, in *Proc. IPAC'17*, Kopenhagen, Danmark, 2017, pp. 4318-4320.

[10] C. Serpico *et al.*, in *Proc. IPAC'18*, Vancouver, BC, Canada, 2018, WEPMF067.

[11] P. Craievich *et al.*, in *Proc. IPAC'18*, Vancouver, Canada, 2018, pp. 3808-3811.

Content from this work may be used under the terms of the CC BY 3.0 licence (© 2018). Any distribution of this work must maintain attribution to the author(s), title of the work, publisher, and DOI.

ISBN: 978-3-95450-194-6 ISSN: 2226-0366 doi:10.18429/JACoW-LINAC2018-THPO115

[12] A. Grudiev, CLIC-Note -1067, CERN, Geneva, Switzerland, May 2016.

[13] B. Marchetti *et al.*, in *Proc. IPAC'17*, Copenhagen, Denmark, 2017, pp. 184-187.

Content from this work may be used under the terms of the CC BY 3.0 licence (© 2018). Any distribution of this work must maintain attribution to the author(s), title of the work, publisher, and DOI.

ISBN: 978-3-95450-194-6 ISSN: 2226-0366 doi:10.18429/JACoW-LINAC2018-THPO116

SPACE-CHARGE DOMINATED PHOTOEMISSION IN HIGH GRADIENT PHOTOCATHODE RF GUNS

Y. Chen*[a], P. Boonpornprasert[a], H. Chen[b], H. De Gersem[c], M. Dohlus[d], Y. C. Du†[b], E. Gjonaj[c], J. D. Good[a], M. Gross[a], W. H. Huang[b], H. Huck[a], I. Isaev[a], D. Kalantaryan[a], C. Koschitzki[a], M. Krasilnikov‡[a], O. Lishilin[a], G. Loisch[a], D. Melkumyan[a], R. Niemczyk[a], A. Oppelt[a], H. J. Qian§[a], Y. Renier[a], S. Schmid[c], F. Stephan[a], C. X. Tang[b], Q. L. Tian[b], L. X. Yan[b]
[a]DESY, 15738 Zeuthen, Germany; [b]Tsinghua University, 100084 Beijing, China
[c]TEMF, 64289 Darmstadt, Germany; [d]DESY, 22607 Hamburg, Germany

Abstract

The cathode emission physics plays a crucial role in the overall beam dynamics in an RF gun. Interplays between intricate emission mechanisms in the cathode vicinity strongly influence the cathode quantum efficiency (QE) and the intrinsic emittance. The presence of strong space-charge effects in high gradient RF guns further complicates the emission process. A proper modeling of photoemission and a careful treatment of the space-charge contribution is thus of great necessity to understanding the formation of the beam slice emittance. In this article, emission measurements are carried out using the L-band cesium-telluride photocathode RF gun at the Photo Injector Test Facility at DESY in Zeuthen (PITZ) and the S-band copper photocathode RF gun at Tsinghua University. Following the Dowell model a simple so-called space-charge iteration approach is developed and used to determine the QE through temporal- and spatial-dependent electromagnetic fields. An impact of the space-charge cooling on the intrinsic emittance is presented. Measurement data are shown and discussed in comparisons to preliminary simulation results.

INTRODUCTION

High gradient photocathode RF guns provide high brightness electron beams for coherent light sources [1–3]. Such applications require rather high bunch charge and very small transverse normalized emittance from the injector. Optimization of the injector performance to fulfill the beam requirements is essentially a trade-off between multiple machine operation parameters. Experimental results at PITZ [2, 4, 5] have revealed optimum injector parameters from which the space-charge dominated photoemission at the cathode is identified. A detailed understanding of the contribution of the strong space-charge effects present in the cathode vicinity onto the emission process is, therefore, a prerequisite to characterize crucial beam properties at extraction, such as the thermal emittance which occupies a major part of the overall emittance budget [6].

In this article, the photoemission characterization is performed at two gun facilities, the L-band cesium-telluride photocathode RF gun at PITZ whose copies are in use at the European XFEL and FLASH, and the S-band copper photocathode RF gun at Tsinghua University [3, 7] which has been used, for example, as the electron source for the compact Tsinghua Thomson Scattering X-ray Source [8] and many other research programs [9].

BEAM DYNAMICS

Figure 1 shows the extracted bunch charge (Q) from a cesium-telluride photocathode in the PITZ gun scanned over the full range of the emission phase (ϕ) and the applied cathode drive UV laser pulse energy (E_{las}). An 11 ps (FWHM) temporal Gaussian laser pulse with a transverse spot size of 1.2 mm in diameter is used for these measurements. The gun is operated at a maximum electric field gradient of 60 MV/m. The zero-crossing phase is at about 45°. The maximum mean momentum gain (MMMG) phase is at 6°. The charge is collected with a Faraday cup which is 0.78 m downstream of the cathode. The so-called Schottky scans (Q vs. ϕ) using different laser pulse energies and the emission curves (Q vs. E_{las}) at various RF phases are also shown in the 2D projections. In the Schottky scans, the increase of the bunch charge around 45° essentially relates to the pulse shape of the drive laser and the sharpness of the rising edge is limited by the space-charge effects as the laser pulse energy is increased. The slow increase of the charge in the middle of these curves reveals the Schottky-like effect. For the emission phases far away from the MMMG, a major part of the emitted electrons gets lost during beam transportation due to strong RF phase slippage (see [5, 10] for more details).

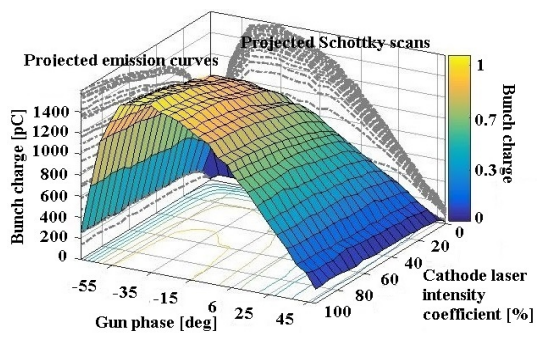


Figure 1: 3D reconstruction of a characterized photoemission distribution obtained from the experiments at PITZ. Note that the laser pulse energy is represented by the laser intensity coefficient following a linear correlation.

* ye.lining.chen@desy.de
† dych@mail.tsinghua.edu.cn
‡ mikhail.krasilnikov@desy.de
§ houjun.qian@desy.de

Content from this work may be used under the terms of the CC BY 3.0 licence (© 2018). Any distribution of this work must maintain attribution to the author(s), title of the work, publisher, and DOI.

ISBN: 978-3-95450-194-6 ISSN: 2226-0366 doi:10.18429/JACoW-LINAC2018-THPO116

Content from this work may be used under the terms of the CC BY 3.0 licence (© 2018). Any distribution of this work must maintain attribution to the author(s), title of the work, publisher, and DOI.

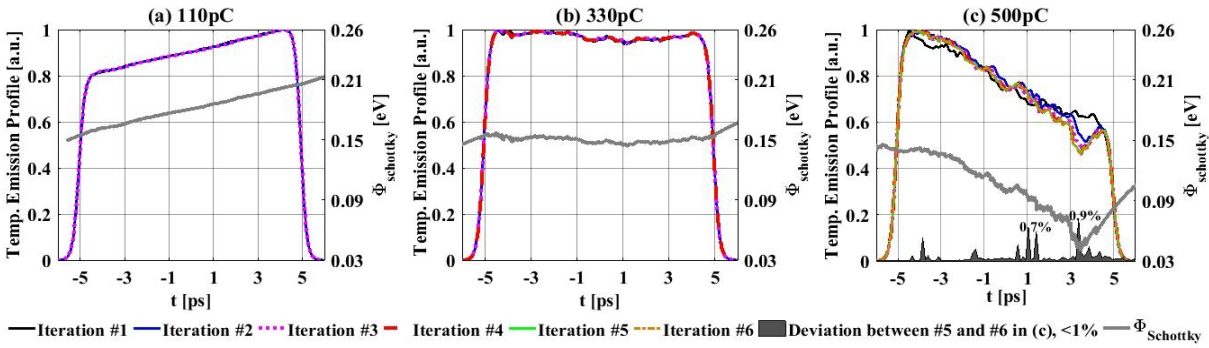


Figure 2: Demonstration of temporal emission profile correction due to a space-charge dependent cathode work function in numerical simulations.

PHOTOEMISSION MODEL

A dispersive QE formulism is developed by David H. Dowell and John F. Schmerge [11] for metal cathodes using the Fermi-Dirac model, which reads

$$QE(\omega) = \frac{\alpha(\hbar\omega - \Phi_{\text{eff}})^2}{8\Phi_{\text{eff}}(E_{\text{F}} + \Phi_{\text{eff}})} \tag{1}$$

with Φ_{eff}, $\hbar\omega$, E_{F} and α denote the effective cathode work function, the photon energy, the Fermi energy and the form factor for characterizing the material properties, respectively. The effective work function can be written as $\Phi_{\text{eff}} = \Phi_0 \pm \Phi_{\text{schottky}} + \Phi_{\text{p}}$, where Φ_0 represents the intrinsic cathode work function, the terms Φ_{schottky} and Φ_{p} refer to the modifications of Φ_0 due to the Schottky effect and the so-called plasma layer shielding effect [12], respectively. The term Φ_{p} is resulted from the formation of an effective charge layer in close to cathode vicinity at very high laser intensities which shields the electrons from further emission. This results in an effective increase of the cathode work function. We model these nonlinear effects by introducing $\Phi_{\text{p}}(r_\perp, t) = kI^m(r_\perp, t)$ and $\Phi_{\text{schottky}}(r_\perp, t) = e\sqrt{e[E_{\text{rf}}(r_\perp, t, z=0) + E_{\text{sc}}(r_\perp, t, z=0)]/4\pi\epsilon_0}$. The symbols I, E_{rf} and E_{sc} stand for the spatial and temporal dependent parameters: the cathode drive laser intensity, the RF and space-charge fields at the cathode position, respectively. The terms k and m are fitting parameters to the experimental data. The symbol "±" in Φ_{eff} marks the moment when the full field changes its sign at $z = 0$ which refers to the cathode position.

SPACE-CHARGE DEPENDENT CATHODE WORK FUNCTION

Accurate modeling of strong space-charge effects puts a big challenge to numerical convergence of the existing space-charge tracking algorithms. To take into account the space-charge contribution to the cathode work function more properly, and therefore, to the QE, a treatment of this issue is proposed by introducing a simple "space-charge iteration approach" based on Eq. (1). The algorithm takes the emitted bunch charge produced by the drive laser following a linear run of the measured emission curve, and iteratively injects the bunch at the cathode for particle dynamics simulations from which the full fields at the cathode position are obtained. Given the fields and the prior known cathode drive laser distribution, a temporal- and spatial-dependent QE profile can be consistently determined in the iterative approach until the relative change of the temporal emission profiles between two subsequent iterations is below numerical tolerance (e.g., roughly 1% in Fig. 2 (c)). Note also that the realistic transverse emission map (see next section) is used for the modification of the transverse beam distribution while the temporal emission profile is being modulated. An in-house developed MATLAB code is used for the simulation.

In Fig. 2, simulation results of normalized temporal emission profiles and the Schottky work functions are shown for three bunch charges. The symbol "#" in the bottom legend of Fig. 2 gives the sequential number of the iteration. Note, in addition, that the smoothness of the temporal emission profiles shown here can be improved by refining the numerical parameters (e.g., number of macro-particles), and that only the longitudinal fields are considered for these simulations at the moment. Figure 4 shows the improved agreements of simulation predictions (orange and blue curves) with the measurement data (black curves) in comparison to the conventional beam dynamics simulations (dashed and dotted gray curves). The deviations in bunch charge are below 50 pC for both cases.

CHARACTERISTIC EMISSION CURVES

The space-charge iteration approach is applied to simulate the characteristic emission curves measured with a copper photocathode at Tsinghua University. The experimental conditions are summarized in Table 1. The measured transverse laser intensity distribution is shown in Fig. 3. The transverse emission map is the convolution of the QE map with the transverse distribution of the laser intensity. In our simulations, the measured laser intensity distribution is used to produce the emission map assuming a transverse homogeneous QE. All machine parameters used in the experiments are then directly plugged into the simulations for the comparison with the measurement data.

ISBN: 978-3-95450-194-6 ISSN: 2226-0366 doi:10.18429/JACoW-LINAC2018-THPO116

Table 1: Machine Parameters

Parameters	Values
Diameter of emission area	1.8 mm
Trans. cathode laser distri.	shown in Figure 3
Cathode laser pulse energy	18 – 131 μJ
Temp. cathode laser distri.	flattop, 0.5/10\0.5 ps
Max. RF E-field gradient	108 MV/m
RF phase w.r.t. zero crossing	30 ^{o} and 22 ^{o}

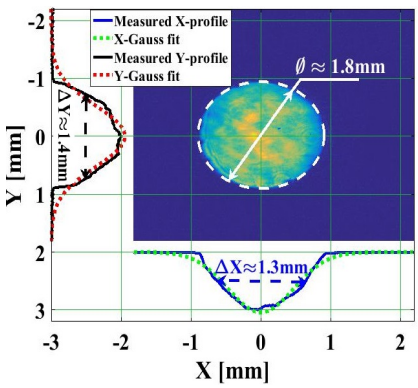


Figure 3: Measured transverse intensity distribution of the cathode drive laser spot.

The saturation charge level is of interest for determining the maximum cathode beam brightness. In the cases presented in this section, the length that the electron beam extends into the vacuum by the end of the laser pulse is estimated using a cathode-anode gap model as $\Delta z \approx \frac{eE_0}{2m}\Delta t^2$ [13], where E_0 refers to the gun field applied at the cathode and Δt denotes the laser pulse duration. Compared to the radius of the transverse emission area, the length Δz is much shorter. A pancake aspect ratio of the beam is thus defined. This leads to the appliance of the "pancake emission model" in which the maximum extractable charge is simply predicted according to the maximum allowed surface charge density as $Q_{\mathrm{sat}} \approx \epsilon_0 E_0 \pi R^2$. As shown in Fig. 4, the predicted saturation charge levels (green lines) are in good agreements with the simulated and measured ones.

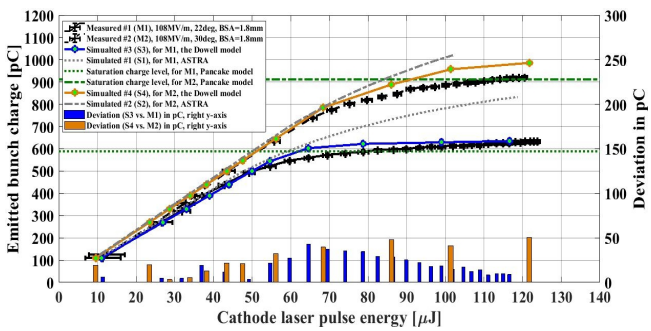


Figure 4: Characteristic emission curves: measurement vs. simulation. The terms k and m for determining Φ_{p} in the overall work function are estimated as 0.1 and 0.35, respectively. The ASTRA code is used for particle tracking [14].

where σ_x represents the rms beam size while the square root stands for the rms of the dimensionless transverse momentum. As discussed in earlier sections, the effective cathode work function is time- and space-dependent according to the spatial and temporal dependent fields formulated in Eq. (1). This effect results in a transient correlation of the sliced intrinsic emittance on the cathode surface with the emission time clock. Figure 5 shows this (surface) thermal emittance evolution during emission for variable bunch charges. The inset gives the averaged emittance as a function of the bunch charge. Higher extracted bunch charge corresponds to lower averaged beam intrinsic emittance on the cathode surface and vise versa (dotted lines). This is due to the fact that higher space-charge fields cancel out more applied acceleration fields at the cathode leading to an increased cathode work function, and therefore, a lower thermal emittance. This means, the space-charge cools down the thermal emittance, which, in fact, may partially explain why the optimum operation condition for the overall minimized transverse emittance at PITZ always results in a space-charge dominated emission at beam extraction, since the thermal emittance is one of the major parts of the optimized transverse beam emittance.

INTRINSIC EMITTANCE

The intrinsic emittance for metals is derived in [11] as

$$\epsilon_n = \sigma_x \sqrt{\frac{\hbar\omega - \Phi_{\mathrm{eff}}}{3mc^2}}, \qquad (2)$$

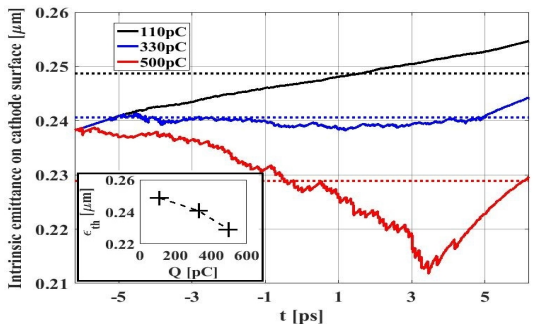


Figure 5: Space-charge influenced transient thermal emittance on the cathode surface for different bunch charges.

SUMMARY

The photoemission mechanism and the associated beam dynamics are discussed with a focus on the space-charge dominated regime. Space-charge contributions to the cathode work function are modeled through the Schottky-effect. A photoemission model is then used to link the modified cathode work function to the modulated QE. Based on a proposed space-charge iteration approach, a time- and space-dependent QE results and a transient beam intrinsic emittance on the cathode surface is obtained. A space-charge cooling effect is presented which can be potentially used for improving the overall beam emittance by reducing the thermal emittance through the extraction of multiple bunch charges. Beam dynamics simulation results show good agreements with the characteristic emission measurement data with a copper cathode at Tsinghua University. More

Content from this work may be used under the terms of the CC BY 3.0 licence (© 2018). Any distribution of this work must maintain attribution to the author(s), title of the work, publisher, and DOI.

ISBN: 978-3-95450-194-6 ISSN: 2226-0366 doi:10.18429/JACoW-LINAC2018-THPO116

Content from this work may be used under the terms of the CC BY 3.0 licence (© 2018). Any distribution of this work must maintain attribution to the author(s), title of the work, publisher, and DOI.

detailed analysis and modeling work will be presented in the near future.

REFERENCES

[1] F. Stephan and M. Krasilnikov, "High Brightness Photo Injectors for Brilliant Light Sources", in *Chapter of the book "Synchrotron Light Sources and Free-Electron Lasers"*, editors E. Jaeschke, S. Khan, J.R. Schneider, J.B. Hastings, Springer International Publishing Switzerland, ISBN 978-3-319-04507-8, 2016.

[2] M. Krasilnikov *et al.*, "Experimentally minimized beam emittance from an L-band photoinjector", *Phys. Rev. ST Accel. Beams*, vol. 15, 100701, 2012.

[3] C. X. Tang *et al.*, "Low Emittance and High Current Electron Linac Development at Tsinghua University", in *Proc. LINAC'16*, East Lansing, MI, USA, Sep. 2016, pp. 17–21. doi:10.18429/JACoW-LINAC2016-MO2A04

[4] Y. Chen *et al.*, "Modeling and simulation of RF photoinjectors for coherent light sources", *NIM A*, vol. 889, pp. 129–137, 2018.

[5] Y. Chen *et al.*, "Investigations of the Space-Charge-Limited Emission in the L-Band E-XFEL Photoinjector at DESY-PITZ", in *Proc. IPAC'15*, Richmond, VA, USA, May 2015, pp. 162–164. doi:10.18429/JACoW-IPAC2015-MOPWA029

[6] V. Miltchev *et al.*, "Transverse Emittance Measurements at the Photo Injector Test Facility at DESY Zeuthen in *Proc. FEL'04*, Trieste, Italy, Sep. 2004, paper TUPOS09, pp. 399.

[7] H. J. Qian *et al.*, "Rf Design and High Power Tests of a New Tsinghua Photocathode Rf Gun", in *Proc. FEL'12*, Nara, Japan, Aug. 2012, paper MOPD55, pp. 165–167.

[8] Y. C. Du *et al.*, "Generation of first hard X-ray pulse at Tsinghua Thomson Scattering X-ray Source", *Rev. Sci. Instrum.*, vol. 84, p. 053301, 2013.

[9] H. J. Qian *et al.*, "Experimental investigation of thermal emittance components of copper photocathode", *Phys. Rev. ST Accel. Beams*, vol. 15, p. 040102, 2012.

[10] Y. Chen *et al.*, "3d Full Electromagnetic Beam Dynamics Simulations of the PITZ Photoinjector", in *Proc. IPAC'14*, Dresden, Germany, June 2014, pp. 391–393. doi:10.18429/JACoW-IPAC2014-MOPME008

[11] David H. Dowell *et al.*, "Quantum efficiency and thermal emittance of metal photocathodes", *Phys. Rev. ST Accel. Beams*, vol. 12, p. 074201, 2009.

[12] Max Zolotorev, "Nonlinear effects in photocathodes", Tech. Rep., SLAC-PUB-5896, 1992.

[13] D. Filippetto *et al.*, "Maximum current density and beam brightness achievable by laser-driven electron sources", *Phys. Rev. ST Accel. Beams*, vol. 17, p. 024201, 2014.

[14] K. Floettmann, A Space Charge Tracking Algorithm (ASTRA), http://www.desy.de/ mpyflo/.

ISBN: 978-3-95450-194-6 ISSN: 2226-0366 doi:10.18429/JACoW-LINAC2018-THPO118

BEAM TRANSVERSE COUPLING AND 4D EMITTANCE MEASUREMENT SIMULATION STUDIES FOR PITZ

Q. Zhao†, [1], M. Krasilnikov, H. Qian, F. Stephan, DESY, Zeuthen, Germany
[1]now at Institute of Modern Physics, Chinese Academy of Sciences, Lanzhou, China

Abstract

The Photo Injector Test Facility at DESY, Zeuthen site (PITZ) was built to test and optimize high brightness electron sources for Free Electron Lasers (FELs) like FLASH and the European XFEL. Although the beam emittance has been optimized and experimentally demonstrated to meet the requirements of FLASH and XFEL, transverse beam asymmetries were observed during operation of the RF guns. Based on previous studies [1], the beam asymmetries most probably stem from beam transverse coupling by quadrupole field errors in the gun section. A pair of normal and skew gun quadrupoles was successfully used for reducing the beam asymmetries in experiment. In this paper, we discuss the beam transverse coupling between X and Y planes due to quadrupole field errors and its impact onto horizontal and vertical rms emittance. Multi-quads scan and two quads with rotated slits scan were proposed to measure the 4D beam matrix for PITZ and tested by simulation, which will give the residual beam coupling after gun quadrupoles compensation and would be helpful for minimizing the 2D rms emittance experimentally.

INTRODUCTION

During several years of operation with different generations of guns, the transverse beam asymmetry was always observed from experiments in PITZ [1-3]. From previous studies [4-5], a PITZ gun RF coupler kick was found from RF field simulations. In the transition region from the coupler to the gun, the RF field distribution is not circularly symmetric. The RF coupler kick optics can be modelled as a rotated quadrupole and a rotated quadrupole near the coupler is effective at compensating for the coupler kicks, cancelling both the coupling emittance and the astigmatic focusing [6-7]. Another source of the beam asymmetries may come from solenoid field imperfections [8]. The feature of the beam transverse coupling from rotated quadrupoles can be observed from beam transverse distributions in experiment. These effects will result in an increase of the 2D rms emittances. For FELs this would imply a deterioration of the laser performance. Linear coupling can be compensated in principle by additional rotated quadrupoles [9-10].

† zhaoquantang@impcas.ac.cn

QUADRUPOLE FIELD ERRORS EFFECT ON THE 4D EMITTANCE AND COUPLING TERMS SIMULATION STUDIES

4D Emittance and Coupling Factor

In order to know the compensation quadrupoles strength and how much the coupling is decoupled, a full four-dimensional (4D) beam matrix measurement becomes necessary to measure precisely and possibly further correct the transverse coupling.

The 4D beam matrix, shown in formula (1) describes the transverse statistical properties of the beam:

$$\sigma^{4D} = \begin{bmatrix} <xx> & <xx'> & <xy> & <xy'> \\ <x'x> & <x'x'> & <x'y> & <x'y'> \\ <yx> & <yx'> & <yy> & <yy'> \\ <y'x> & <y'x'> & <y'y> & <y'y'> \end{bmatrix} = \begin{bmatrix} \sigma_{xx} & \sigma_{xy} \\ \sigma_{xy}^{T} & \sigma_{yy} \end{bmatrix} \quad (1)$$

And the 4D emittance is determined by (2):

$$\varepsilon_{4D} = \varepsilon_1 \varepsilon_2 = \sqrt{\det(\sigma^{4D})} \quad (2)$$

where x and y are the horizontal and vertical coordinates, respectively, x' and y' are their derivatives with respect to the longitudinal coordinate, and the ε_1, ε_2.are intrinsic emittance [11-12]. The matrices σ_{xx} and σ_{yy} describe the 2D horizontal and vertical motions, and σ_{xy} describes the cross-plane coupling. If one or more elements of σ_{xy} are nonzero, the beam is x-y coupled and the projections onto the x and y planes exhibit an increase of the observed emittance values. The transverse coupling contribution to the 2D rms emittances can be quantified by the coupling factor (3),

$$t = \frac{\varepsilon_x \varepsilon_y}{\varepsilon_1 \varepsilon_2} - 1 \geq 0 \quad (3)$$

Where ε_x, ε_y are the x and y plane 2D rms emittance. For t = 0 the beam is decoupled and for t > 0 the beam is transversely coupled.

Quadrupole Field Errors Effect on the Coupling Simulation Studies

Based on quadrupole field errors model [3], it is possible to study these kinds of field errors effect on the coupling factor t and to show how the 2D rms emittance increases by the quadrupole field errors. The simulation was done by ASTRA [13] and the machine settings are as follows: gun gradient is 51.36 MV/m, solenoid current is 350 A (arbitrary one, not the optimized current), bunch charge is 500 pC, and laser rms size is 0.3 mm with longitudinal Gaussian distribution. Beam momentum after gun is 5.8 MeV/c and after the booster is 20.8 MeV/c. A pair of normal and skew quadrupole field errors are modelled and added in the simulation and placed in the correspond-

Content from this work may be used under the terms of the CC BY 3.0 licence (© 2018). Any distribution of this work must maintain attribution to the author(s), title of the work, publisher, and DOI.

ISBN: 978-3-95450-194-6 ISSN: 2226-0366 doi:10.18429/JACoW-LINAC2018-THPO118

Content from this work may be used under the terms of the CC BY 3.0 licence (© 2018). Any distribution of this work must maintain attribution to the author(s), title of the work, publisher, and DOI.

ing positions: Qs (skew) at z = 0.18 m (the distance from cathode); Qn (normal) at z = 0.36 m, and the effective length of both are 1 cm. By scanning the Qs and Qn strengths, range from -0.1 T/m to 0.1 T/m, one can get the influence on the beam distribution at High1.Scr1. From the simulated beam distribution, the beam matrix correlation terms and coupling factor t can be calculated for each pair of quadrupole field errors settings. The coupling factor as a function of Qs and Qn is shown in Fig. 1, and in the red square, it's the normal case for PITZ operation (Qs is negative polarity and Qn is positive polarity). When the Qs becomes from 0 to -0.05 T/m and Qn increases from 0 to 0.05 T/m, the coupling factor increased from 0.000479 to 0.322 (shown in white squares), and the coupling contribution to the 2D rms emittance is about 15% increase.

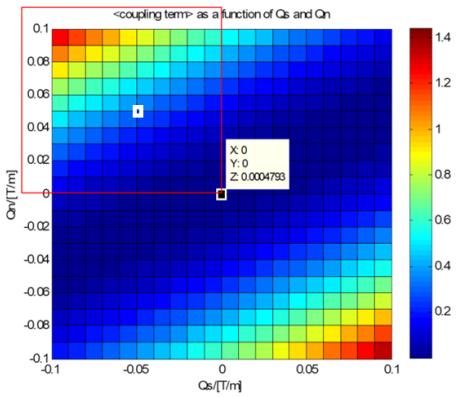


Figure 1: Simulation results for the coupling factor (colour code) as a function of Qs and Qn.

4D EMITTANCE MEASUREMENT METHOD SIMULATION STUDIES

Multi-quads Scan Method

First method to measure the 4D beam parameters is based on the multiple-optics/single-location approach: the beam parameters (<xx>, <yy> and <xy>) are measured at a single position and quadrupole strengths are changed to generate the required optics for the 4D measurement. Here we propose using the multiple-quadrupole scan technique to optimize the optics for the 4D measurement, which results in a minimization of the error of the reconstructed parameters. The reconstruction algorithm and detailed information are referred in [11, 14].

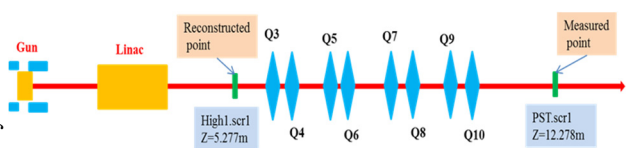


Figure 2: layout of the PITZ beam line for simulation studies of the multi-quads scan method for 4D emittance measurements.

The PITZ beam line used for this measurement is shown in Fig. 2. The reconstruction point is at High1.Scr1, the measured point is at PST.Scr1, and eight quadrupoles (Q3-Q10) are used for scanning. The machine settings are the same as before and Qs and Qn are chosen as -0.01 T/m and 0.01 T/m, respectively, which give a beam coupling and with the calculated coupling factor t = 0.014. The reconstruction point is chosen at EMSY1, because normally the 2D beam emittance and Twiss parameters are measured at this position by slits scan. It is convenient to match the beam optics by multi-quads for experiment. The basic requirements on the multi-quads scan for these measurements is to scan the phase advance between the optics reconstruction position and the measurement screen in one plane over 180 degree (if possible) and keep it constant in the second plane and the beam size at the measurement position has to be big enough for measurement. For described above set up, the phase advance scan can be from 10 to 120 degree. The designed multi-quads scan settings with MAD-X [15] are shown in Fig. 3: first 7 scans for x plane measurement and second 7 scans for y plane measurement. The total 14 scans are used for correlation terms reconstruction.

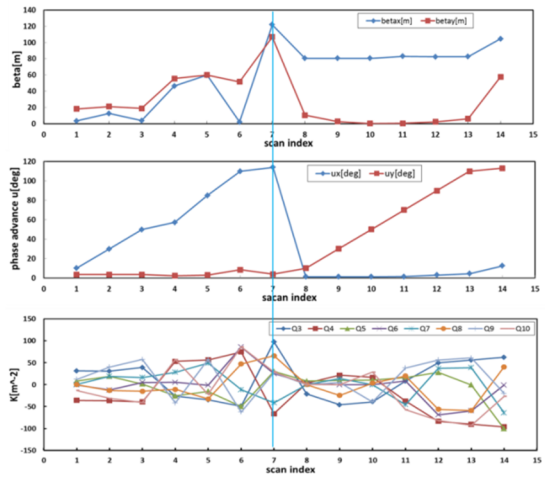


Figure 3: Beam matching for multi-quads scan method for simulation studies: beam size (β_x, β_y) at measured point, phase advance (μ_x, μ_y) between reconstructed point and measured point, and eight quads (Q3-Q10) settings for each scan.

Due to the low beam energy in PITZ, for 500 pC bunch charge, the space charge effect cannot be neglected. Therefore, the simulation studies are done for three cases, 500 pC bunch charge without space charge, 500 pC bunch charge with space charge and 100 pC bunch charge with space charge. The multi-quads settings are the same for the three cases. The reconstructed correlations terms in 4D beam matrix for the three cases are shown in Fig. 4. Compared with the initial values of the correlation terms, the 500 pC without space charge and 100 pC with space charge can be precisely measured with this method, but for 500 pC with space charge, this method has some errors and the correlation terms are over estimated. For the coupling factor, the initial beam has 0.0140, for the 500 pC without space charge case, it is 0.0142, for the 500 pC with space charge, it is 0.0075 and for 100 pC with space charge, it is 0.0113.

ISBN: 978-3-95450-194-6 ISSN: 2226-0366 doi:10.18429/JACoW-LINAC2018-THPO118

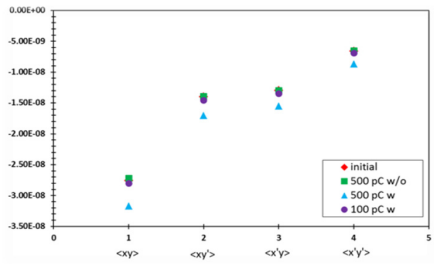


Figure 4: Reconstructed 4D emittance correlation terms from simulation studies with multi-quads scan method and compared with the initial ones.

Rotated Slits Plus Two Quads Scan Method

Another 4D emittance measurement method, rotated slits plus two quads scan is also investigated for the PITZ beam line by simulation. The detailed algorithm of this method is referred in [12]. For this method, three slits, 0 degree, 90 degree and one more rotated slit(not 0 or 90 degree) and two quadrupoles are needed. For the PITZ beam line, the experimental layout is shown in Fig. 5. The reconstruction position is chosen at EMSY1, same as previous method and only two quadrupoles Q3-Q4 are used, the slits are at EMSY2 position, and the beamlet measurement position is at High1.Scr5. For the current PITZ set up, this method only needs one more slit install at EMSY2 with 45 degree (in this study) rotation angle, which is easy to implement in PITZ set up and also the Fastscan software for slits scan emittance measurement can be used directly. For the simulation studies, the machine settings are the same as before. The reconstruction position and the coupled beam distribution (to be reconstructed) induced with Qs = -0.1 T/m and Qn = 0.1 T/m are also same with previous method used in simulation.

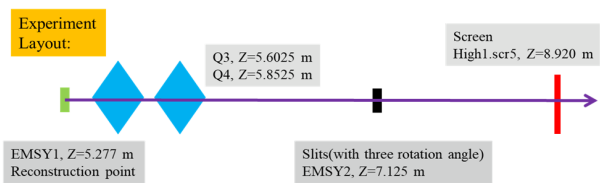


Figure 5: Layout of PITZ beam line used for the simulation study of the 4D emittance measurement with rotated slits plus two quads.

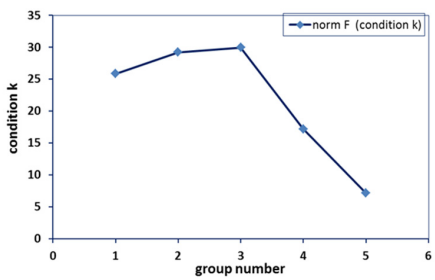


Figure 6: Condition k value for each group of two quads settings in simulations.

A pair of quadrupoles with two different settings ($Q3^a$&$Q4^a$ and $Q3^b$&$Q4^b$) is used for the scan. We can do the three slits scan respectively both for a and b settings. From described above six measurements, the 4D beam matrix at reconstruction point can be reconstructed completely and reliably. Minimum measurements is four, 0, 90 and 45 degree slits scan with a settings and 45 degree slits scan with b settings.

For this method, the most important is the determination of the two quads settings, which is determined by condition number k [12]. Well-conditioned matrices have condition numbers which are close to 1.0. Two different quadrupoles settings are selected by varying in brute force search method and from which we need to get 100% beam transmission from reconstruction point to the measurement screen and reasonable beam size at slit and screen. From simulation we tried five groups settings of the two quadrupoles, which meet the above requirement, and the condition number k for each group is shown in Fig. 6. For group 5 settings, the condition number k is the smallest.

The reconstructed correlation terms of the 4D beam matrix are shown in Fig. 7 for each group of two quadrupoles settings. Compared with the initial correlation terms value, for group 5 settings, the reconstructed values are most close to the initial value. Furthermore, the simulation was done with and without space charge for 500 pC bunch charge. It is clearly shown that the space charge has less effect for the 4D beam matrix correlation terms measurement.

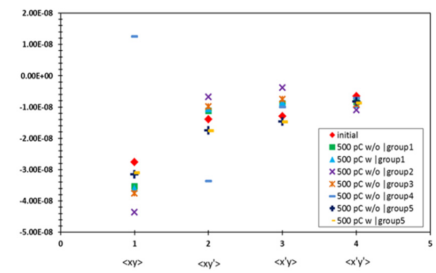


Figure 7: Reconstructed 4D beam matrix correlation terms from simulation studies with rotated slits plus two quads method and compared with the initial ones.

CONCLUSION

The beam transverse coupling due to RF coupler kick and solenoid field imperfection for PITZ was studied by simulation with quadrupole field errors model. These quadrupole field errors would increase the 2D rms emittance. Two methods for measuring the 4D beam matrix are proposed for the PITZ beam line and tested by simulation. For multi-quads scan method, it is still affected by the space charge effect, thus good for low bunch charge measurement at PITZ. But it is valid for European-XFEL injector 4D emittance measurement with high beam energy. The second method is rotated slits with two quads scan, the simulation results show it is possible to get approximate results with good quads settings and the space charge has less effect on the 4D emittance measurement. This method is easy to implement for the PITZ accelerator. Beam transverse coupling and 4D emittance measurement simulation studies are helpful for PITZ to fully experimentally optimize the 2D rms emittance with gun compensation quadrupoles [10].

Content from this work may be used under the terms of the CC BY 3.0 licence (© 2018). Any distribution of this work must maintain attribution to the author(s), title of the work, publisher, and DOI.

ISBN: 978-3-95450-194-6 ISSN: 2226-0366 doi:10.18429/JACoW-LINAC2018-THPO118

Content from this work may be used under the terms of the CC BY 3.0 licence (© 2018). Any distribution of this work must maintain attribution to the author(s), title of the work, publisher, and DOI.

REFERENCES

[1] Q. Zhao *et al*., "Beam asymmetry studies with quadrupole field errors in the PITZ gun section", in *Proc. FEL'17*, WEP010.

[2] M. Krasilnikov *et al*., "Experimentally minimized beam emittance from an L-band photoinjector", *PRST-AB*, vol. 15, 100701, 2012.

[3] M. Krasilnikov, Q. Zhao *et al*., "Investigations on electron beam imperfections at PITZ", Proc. of LINAC'16, MOPLR013.

[4] I. Isaev, "RF field asymmetry simulations for the PITZ RF Photo Gun", DPG-Frühjahrstagung Wuppertal, 9 March 2015.

[5] Y. Chen *et al*., "Coaxial Coupler RF Kick in the PITZ RF Gun", in *Proc. FEL'17*, WEP005.

[6] M. Dohlus et al., "Coupler kick for very short bunches and its compensation", in *Proc. EPAC'08*, pp. 580-582, Genoa, Italy.

[7] D. Dowell, "Analysis and cancellation of RF coupler-induced emittance due to astigmatism". Report no. LCLS-2 TN-15-05, SLAC, 2015.

[8] J. Schmerge, "LCLS gun solenoid design considerations", Report no. SLAC-TN-10-084, SLAC, 2010.

[9] H. Wiedemann, *Particle Accelerator Physics*, Third Edition, pp 605-620.

[10] M. Krasilnikov *et al*., "Electron beam asymmetry compensation with gun quadrupoles at PITZ", in *Proc. of FEL'17,* WEP007.

[11] Eduard Prat and Masamitsu Aiba. Four-dimensional transverse beam matrix measurement using the multiple-quadrupole scan technique. PRST-AB 17, 052801, 2014.

[12] C. Xiao, M. Maier, X. N. Du, P. Gerhard, L. Groening, S. Mickat, and H. Vormann. Rotating system for four-dimensional transverse rms-emittance measurements, *PRAB 19*, 072802, 2016.

[13] K. Floettmann, ASTRA particle tracking code, `http://www.desy.de/~mpyflo/.`

[14] Florian L¨ohl, Measurements of the Transverse Emittance at the VUV-FEL, Diploma thesis, 2005.

[15] MAD-X, `http://madx.web.cern.ch/madx/.`

ISBN: 978-3-95450-194-6 ISSN: 2226-0366 doi:10.18429/JACoW-LINAC2018-THPO124

DESIGN OF PULSED HV AND RF COMBINED GUN SYSTEM USING GRIDDED THERMIONIC-CATHODE

T. Asaka†, H. Tanaka, RIKEN SPring-8 Center, Hyogo 679-5148, Japan
T. Taniuchi, Y. Otake, JASRI/SPring-8, Hyogo 679-5198, Japan

Abstract

We propose a simple and compact electron gun system with a control grid, which can provide a low emittance of a few mm mrad. The system is composed of a 50-kV thermionic-gun with a gridded cathode and a 238-MHz rf cavity, each of which is manufactured by extending the well-established technology. The rf cavity accelerates the extracted electrons from the thermionic-gun up to 500 keV to preserve the low emittance. Using the CST and PARMELA particle tracking simulation codes, the proposed system can generate a beam with a low emittance of 2 mm mrad by an extraction charge of 0.6 nC by optimizing voltage parameters of the 50-keV thermionic-gun and the 238-MHz rf cavity.

INTRODUCTION

As a low emittance electron source, a photocathode rf gun [1], or a 500-kV thermionic-gun with a single crystal cathode [2] are usually used. Each electron gun system has own strong and weak points. The rf gun system is rather compact but it requires a large and complicated laser system to obtain highly stable beam. On the other hand, the 500-kV thermionic-gun is almost maintenance-free. However, the weak point of the thermionic-gun is to prepare the large and difficult high voltage system.

In order to remove the above-mentioned weak point, one of the authors (Otake) proposed a robust, compact and low-cost electron gun system, while keeping the low emittance and an electron energy above 500 keV. The system comprises of a thermionic-gun with a charging voltage of 50-kV and a 238-MHz rf cavity in order to increase beam energy up to 500 keV. This system adopts a commercially available gridded cathode. An electron pulse length of less than 1 ns extracted from the cathode is sufficiently short to be captured by the phase space of the following acceleration rf. These combining instruments can eliminate the laser system.

Concern in the above-mentioned idea is an emittance growth by the distorted electric field (lens effect) in the grid [3]. It is well-known effect depends on the electric potential shape and strength on the grid wire and the space-charge field strength of the beam [4]. There is the cancelling point of both electric field strengths between the lens effect and the space charge effect. In order to improve this emittance deterioration, we have investigated the optimum condition of this cancellation by using computer simulation. In this paper, we describe basic design of the gun system and the optimized parameters of a beam transport to keep the low emittance.

† asaka@spring8.or.jp

DESIGN OF PULSED HV AND RF COMBINED GUN SYSTEM

The low-emittance pulsed HV and rf combined gun system just consists of extension of the established technology. To generate the pulsed beam without the laser system, the 50-kV thermionic-gun with a gridded cathode is employed. The gridded cathode is Y845, which is manufactured by CPI Corporation. To extract beam with a pulse length of 600 ps from the Y845, a fast pulser drives a voltage between a cathode and a grid mesh. Furthermore, the 238-MHz rf cavity is placed as close as possible to its acceleration gap and just behind of the 50-kV thermionic-gun for obtaining a relativistic beam energy of over 500 keV. This positioning is indispensable to reduce the emittance growth by the space charge effect, as which means quickly accelerating to a high β the electron. Furthermore, we consider rf leakage from the rf cavity to the grid and the cathode surface. The acceleration phase space of the 238-MHz rf cavity can capture the pulsed beam, which is beam acceleration scheme similar to a rf gun. In this case, nonlinearity of a rf voltage curvature is one of cause of the emittance growth. When the energy spread of the beam caused by the rf nonlinearity is less than a few percent, there is slight the emittance growth. It is acceptable for our design.

In the 50-kV thermionic-gun, a high-voltage instruments can operate in the atmosphere without insulation oil. Furthermore, a solid-state device can be handle this voltage for a pulser and a power supply. On the other hand, the device installed in a rf amplifier, which has long lifetime and lower failure, and can also drive the 238-MHz for the rf cavity. These are advantage of the gun system. This advantage is not only cost saving, but also improving maintainability.

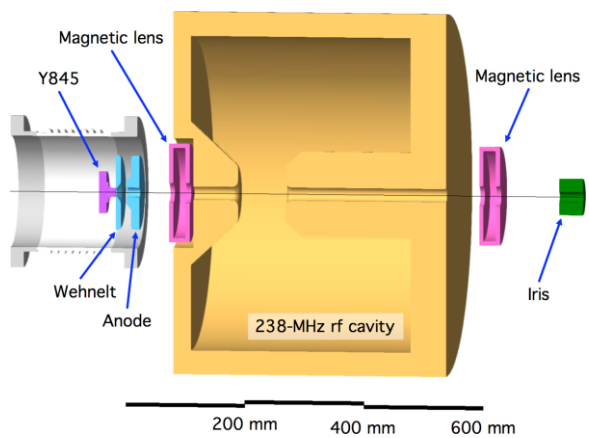


Figure 1: Schematic drawing of the low-emittance pulsed HV and rf combined gun system.

Content from this work may be used under the terms of the CC BY 3.0 licence (© 2018). Any distribution of this work must maintain attribution to the author(s), title of the work, publisher, and DOI.

ISBN: 978-3-95450-194-6 ISSN: 2226-0366 doi:10.18429/JACoW-LINAC2018-THPO124

Content from this work may be used under the terms of the CC BY 3.0 licence (© 2018). Any distribution of this work must maintain attribution to the author(s), title of the work, publisher, and DOI.

Based on the design, we finally decide the configuration of the low-emittance pulsed HV and rf combined gun system, as shown in Fig. 1. In this system, there is still a problem, which is the emittance deterioration by the lens effect in the grid. This point is crucial for deciding the feasibility of this system. In the next section, we mainly concentrate this discussion.

LOW-EMITTANCE BEAM GENERATION

Cancellation of Lens Effect

In order to improve the emittance deterioration, the electric field and electron trajectories near the grid are simulated using the CST code. Figure 2 illustrates the electric field strength and the electron trajectories near the grid. Individual drawings in the figure correspond to the grid voltage conditions of 35 V, 45 V and 55 V, respectively. When the grid voltage is 35 V, the electric field distortion gives a transverse kick to the electron passing through the grid mesh, as shown in Fig. 2 (a). Increasing the grid voltage, the transverse kick decreases, as shown in Fig. 2 (b) and (c). There is the optimum voltage so as to balance the space charge force of the beam and the focusing force, which is generated by the lens effect, as shown in Fig. 2 (c).

Based on the above results of the lens effect, the relation between emittances and beam charges, and the dependence on the grid voltages are simulated in order to find the minimum emittance. In the cases of the anode voltages of 50 kV, 60 kV and 70 kV, Fig. 3 shows the emittances and beam charges at the exit of the thermionic-gun, as functions of the grid voltage. The normalized emittance reaches 1 mm mrad with the beam charge of 1 nC (1.7 A / 0.6 ns) in the grid voltage of around 70 V. It is turned out that a normalized emittance of less than 1 mm mrad is obtained, even though the beam charge is increased. It means that this is the emittance is insensitive to the region of this anode voltage change.

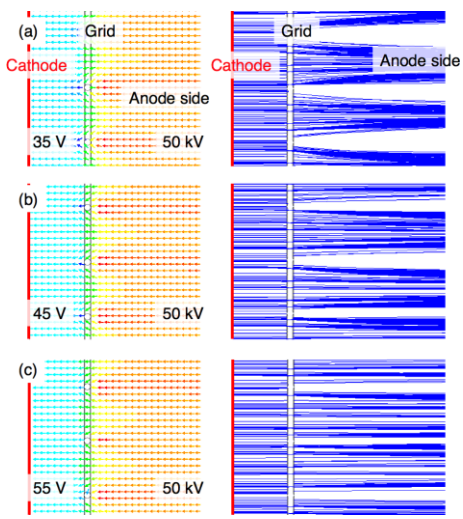


Figure 2: Electric field strength (left) and beam trajectory near grid of Y845 (right) simulated using CST code. (a), (b) and (c) correspond to the grid voltage conditions of 35 V, 45 V and 55V, respectively.

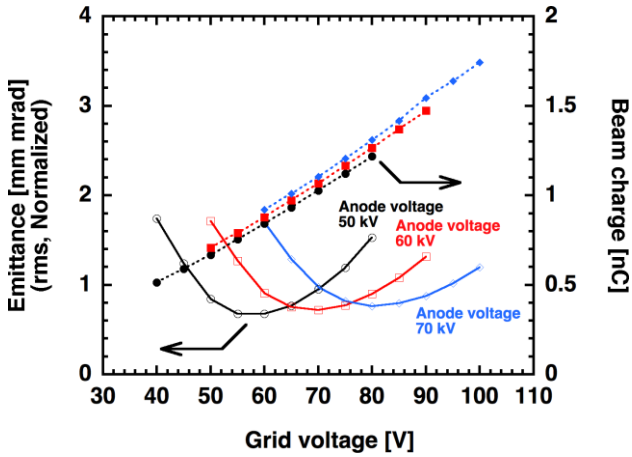


Figure 3: Emittance (solid lines) and beam charge (dashed lines) at the exit of the thermionic-gun as functions of grid voltage simulated using CST code.

50-kV Thermionic-gun

In the design of the 50-kV thermionic-gun, the arrangement and shape of each electrode is optimized by the CST simulation so as to be a collimated beam at the exit of the thermionic-gun. Figure 4 shows the electron trajectories emitted from Y845 to the anode. Figure 5 shows a particle distribution in the horizontal phase space at the exit of the thermionic-gun. Table 1 summarizes the parameters of the gridded cathode and beam characteristics at the exit of the thermionic-gun. As the result, the designed the thermionic-gun satisfy the required specification of the normalized emittance of 1 mm mrad with the beam charge of 1nC.

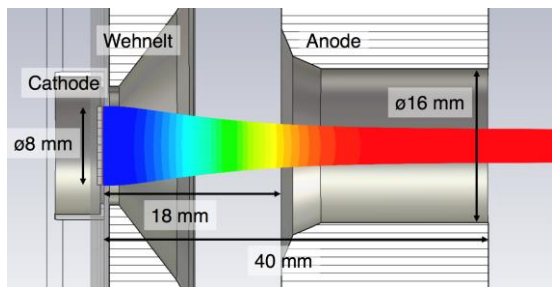


Figure 4: Electron trajectories from Y845 to the anode simulated by CST code. The colormap shows a beam energy change (from the blue: 10 eV to the red: 50 keV).

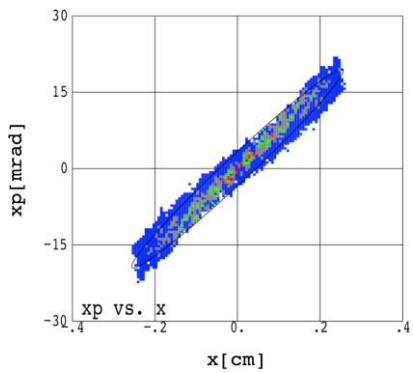


Figure 5: Particle distribution in horizontal phase space at the exit of the 50-kV thermionic-gun.

ISBN: 978-3-95450-194-6 ISSN: 2226-0366 doi:10.18429/JACoW-LINAC2018-THPO124

Table 1: Main Parameters of the 50-kV Thermionic-gun

Physical parameter of thermionic-cathode (Y845)	
Cathode diameter	8 mm
Distance between cathode and grid	180 μm
Grid spacing	180 μm
Wire diameter of grid	20 μm
Temperature	1000 ˚C
Work function	1.68 eV
Anode voltage / Grid voltage	-50 kV / 70 V
Beam characteristics of 50-kV thermionic-gun	
Charge (current / pulse width)	1 nC (1.7 A / 0.6 ns)
Normalized emittance	1 mm mrad

Beam Transport, Acceleration and Collimation

The distance between the 50-kV thermionic-gun and the 238-MHz rf cavity is shorten as much as possible in order to minimize the emittance growth due to the space charge effect. In order to control the beam envelope, a magnetic lens is located between the 50-kV thermionic-gun and the 238-MHz rf cavity, as shown in Fig. 1. The 50-keV beam is accelerated up to 500 keV on the crest phase of the 238-MHz rf cavity.

The beam transport and the acceleration in the 238-MHz rf cavity is simulated using PARMELA code. An energy spread by the rf nonlinearity is 2.7% without the space charge effect. An emittance due to the energy spread increases by a factor of 1.1. The simulation results with the space charge effect are shown in Fig. 6. A normalized emittance after the 238-MHz rf cavity is 3 mm mrad with a beam charge of 1 nC. The beam before an iris, which is located after the 238-MHz rf cavity, has a uniform distribution, as shown in Fig. 7. In order to extract the beam core, the iris removes the halo of the 500-keV beam. The extracted beam has a normalized emittance of 2 mm mrad with a beam charge of 0.6 nC, as shown in Fig. 6. Emittances and beam charges can be adjusted by the aperture size of the iris, as shown in Fig. 8.

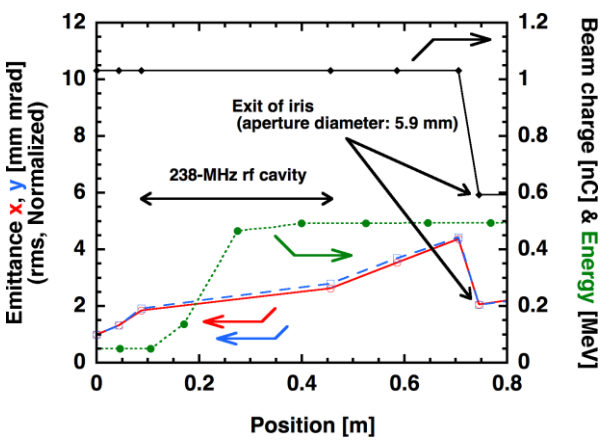


Figure 6: Emittances and beam charges in acceleration process of the gun system simulated by PARMELA code. The origin point is the exit of the 50-kV thermionic-gun.

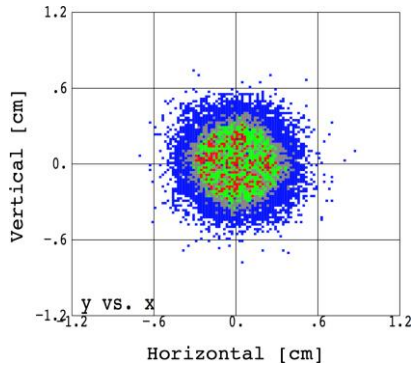


Figure 7: 500-keV beam profile before the iris simulated by PARMELA code.

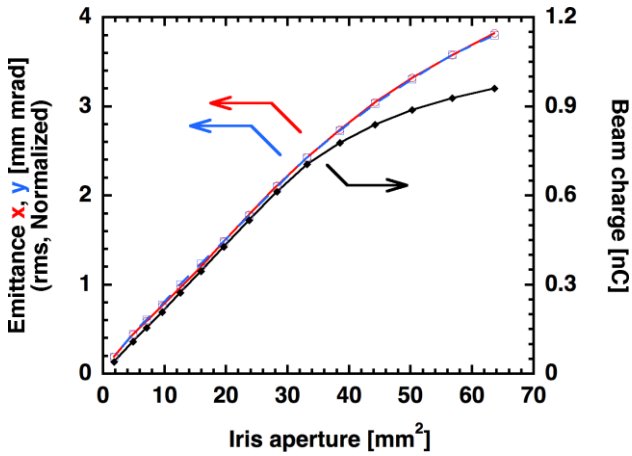


Figure 8: Emittances and beam charges as functions of the aperture sizes of the iris simulated using PARMELA code.

CONCLUSION

We proposed a low-emittance pulsed HV and rf combined gun system composed of a 50-kV thermionic-gun and a 238-MHz rf cavity. The main causes of the emittance deterioration in this system are the lens effect in the gridded cathode, the space charge effect between the thermionic-gun and the rf cavity, and the energy spread by the rf nonlinearity. To improve the emittance deterioration, each component was optimized by the particle tracking simulation. The simulation result shows that an emittance of less than 2 mm mrad is achievable in a beam charge smaller than 0.6 nC/pulse. Currently, the test bench has been constructed to confirm the beam performance including the low emittance predicted by the simulation.

REFERENCES

[1] M. Ferrario and T. Shintake, High performance electron injectors, Rev. Accel. Sci. Technol. **03**, 221 (2010).

[2] K. Togawa *et al.*, CeB_6 electron gun for low-emittance injector, Phys. Rev. ST Accel. Beams **10**, 020703 (2007).

[3] C. Bourat, Beam dynamics for FEL injection of the linac preinjector of ELETTRA, Nucl. Instr. and Meth. A304 (1991) 317-321.

[4] M. Yamada *et al.*, Beam simulations for a mesh gridded electron gun, *Proceedings of the 23rd Linear Accelerator Meeting in Japan* (Tsukuba, 1998), p. 148, in Japanese.

Content from this work may be used under the terms of the CC BY 3.0 licence (© 2018). Any distribution of this work must maintain attribution to the author(s), title of the work, publisher, and DOI.

ISBN: 978-3-95450-194-6 ISSN: 2226-0366 doi:10.18429/JACoW-LINAC2018-THPO125

RUNNING STATUS OF SRF GUN-II AT ELBE CENTER*

R. Xiang†[1], A. Arnold[1], P. Lu[1,2], P. Murcek[1], J. Schaber[1], J. Teichert[1], H. Vennekate[1,3], P. Zwartek[1]
[1]Helmholtz-Zentrum Dresden-Rossendorf, 01328 Dresden, Germany

Abstract

As a new electron source with higher brilliance, the second version of the superconducting RF photoinjector (SRF Gun-II) has been successfully commissioned at the ELBE Center for high power radiation sources since 2014. SRF Gun-II features an improved 3.5-cell niobium cavity as well as a superconducting solenoid in the same cryomodule. With Mg photocathode SRF Gun-II can provide high current beam with bunch charge up to 300 pC at 100 kHz repetition rate. For user operation the SRF Gun-II successfully generated stable beam with 200 pC in CW mode and sub-ps bunch length. In this presentation the gun's status and beam parameters will be presented.

INTRODUCTION

The unique feature of the ELBE accelerator is its ability to operate in continuous wave (CW) mode for high average power output. Hence, a flexible CW electron source is required. An rf photoinjector based on superconducting technology represents the ideal solution for this task. It produces high field gradients causing enhanced beam parameters and large beam currents due to increased repetition rates.

The ELBE SRF Gun project is the R&D effort to provide such an injector. Commissioning with further improvements and optimization of components as well as our operational experience has increased the performance and reliability so that the SRF Gun-II is now applied for user operation.

SRF GUN-II

SRF Gun-II has been installed in the accelerator hall since May 2014 [1]. The main design is based on the first SRF Gun [2] with a modified 1.3 GHz Nb cavity and a superconducting solenoid at about 70 cm from the cathode [3]. The combination of 258nm laser and Mg cathode allows to provide beam with bunch charge up to 300 pC, which is limited by the space charge effect in the gun with an acceleration gradient of 8 MV/m (20.5 MV/m peak field on axis).

SRF Cavity and RF Performance

The 1.3 GHz Nb cavity was built, treated and tested at JLab [4]. It consists of three TESLA like cells, a specially designed half-cell and a choke filter. This filter is surrounding the cathode, preventing RF leakage into the cathode support system (see Fig. 1).

The performance of cavity has been measured regularly in the gun cryomodule without or with cathodes. Compared to the last vertical test at Jlab the cavity lost about 30% of its performance. A serious contamination was caused by particles sputtered from cathode surface onto the first iris of the cavity. Nevertheless, the remaining gradient is still higher than that of SRF gun-I. The safe gradient for the routine operation is 7 MV/m, with field on cathode 10.7 MV/m, and the main drawback is the field emission under higher field.

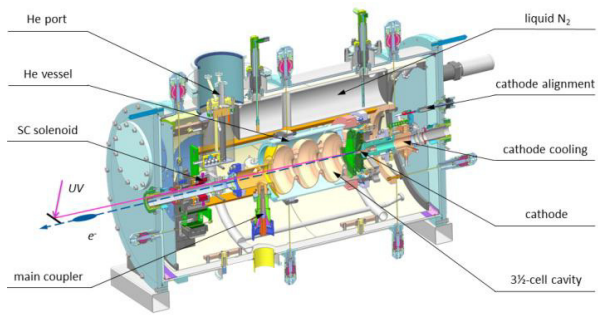


Figure 1: Cross section of the ELBE SRF gun II cryomodule, holding a 3.5 cell gun cavity and a superconducting solenoid at about 70 cm from the cathode.

Photocathode and Laser

In the first SRF gun at ELBE operating until 2014, the main problem caused by Cs_2Te photocathodes was multipacting in the gap of cathode hole, but the lifetime was not a problem [5]. In SRF Gun-II, the life time of Cs_2Te photocathodes was only two weeks. The possible reason of its degradation is the overheating of the cathode plugs during the operation. Further detailed studies and technical modifications are going on.

Mg cathodes made of bulk magnesium and cleaned with focused UV laser beam are working for the regular ELBE user operation with the SRF gun. Magnesium has a low work function of 3.6 eV. Illuminating with UV laser light at 258 nm, the expected quantum efficiency (QE) of Mg can be as good as 0.6 %, which is the best QE ever reported in rf guns. The UV drive laser can deliver pulses with up to 3 μJ at 100 kHz repetition rate, which is enough to produce bunches up to 300 pC with a Mg photocathode. The laser spot size on photocathode is about ϕ 4 mm. The temporal profile is Gaussian with an rms pulse length of about 2 ps.

Figure 2 shows the measured Faraday cup current (and bunch charge) versus drive laser phase for different laser power. The laser phase of the SRF gun in operation is indicated by the vertical zone between 40° to 60°. One

† email address: r.xiang@hzdr.de
2 present address: RI Research Instruments GmbH, Bergisch Gladbach
3 present address: KLA-Tencor, Shanghai

Content from this work may be used under the terms of the CC BY 3.0 licence (© 2018). Any distribution of this work must maintain attribution to the author(s), title of the work, publisher, and DOI.

ISBN: 978-3-95450-194-6 ISSN: 2226-0366 doi:10.18429/JACoW-LINAC2018-THPO125

can observe a strong space charge effect at the low rf phase and Schottky effect at the rf phase higher than 50°.

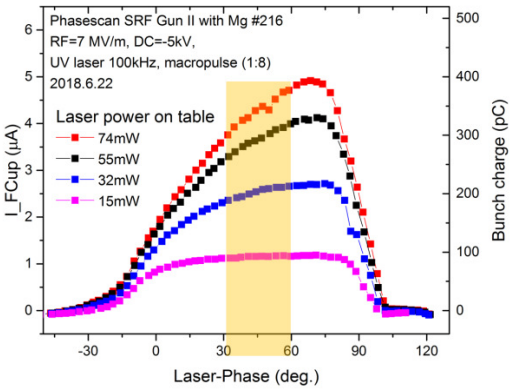


Figure 2: Measured Faraday cup current (and bunch charge) vs. drive laser phase. The working laser phase of the SRF gun is indicated by the vertical zone (40° to 60°).

Diagnostics Beamline

A separate diagnostics beamline lies directly behind the SRF gun at ELBE. An insertable Faraday cup after the solenoid is to measure the total current. Three quadrupoles focus the beam for further transport, followed by five screen-stations for beam observation, plus moving slit for transverse phase space distribution and emittance measurement. The rms transverse emittance is showed in Fig. 3 with an error less than 15% [6].

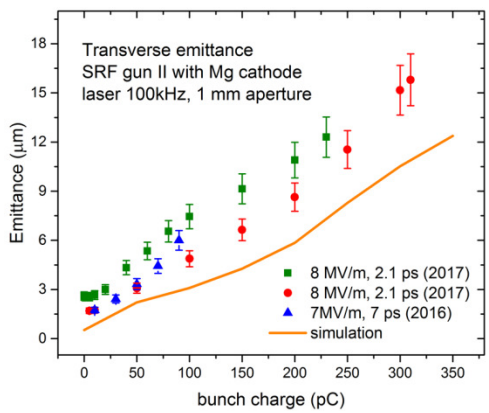


Figure 3: Measured transverse emittance vs. bunch charge, compared with the ASTRA simulation result.

A 180° horizontal dipole (C-bend) is for energy and energy spread measurement. Figure 4 presents the energy and energy spread versus the laser phase, with gradient of 8 MV/m. In the gun operation, laser phase is set as 40° to 60°, and the energy spread is 5 - 25 keV.

To do the measurement of the longitudinal distribution and bunch length, ELBE Linac is used by applying the zero phase chirping method [6].

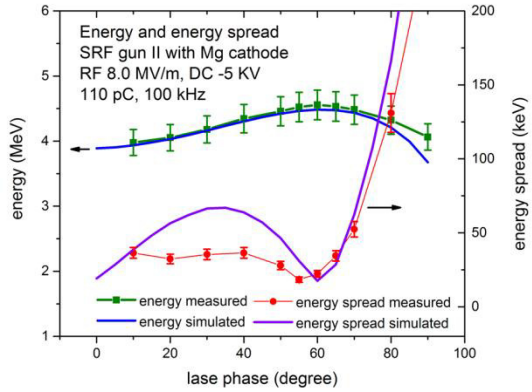


Figure 4: Energy and energy spread versus the laser phase, here with gradient 8 MV/m. The working phase for SRF Gun II is between 40° to 60°.

BEAM PARAMETERS

Table 1 lists the main beam parameters of SRF gun-II with Mg cathode. For the injector of a user facility, the stability is one of the most important characters. Figure 5 shows the beam current measured from cathode and collected by the Faraday cup. The difference between the two curves came from about 5% beam loss and also due to some calibration issue. The small fluctuation on cathode current in the first houses was induced by the treating effect of a DC gun nearby. In more than 24 hours of continuous operation the current kept high stability of 1%.

Table 1: Main beam parameters of SRF gun with Mg cathode (with gun gradient 8 MV/m).

Parameter	Measured
energy	4.5 MeV
bunch charge	0 – 300 pC
transverse emittance	2 – 15 µm
energy spread	5 – 25 keV
micro pulse rate	100 – 500 kHz
beam current (CW)	30 µA
dark current	50 nA

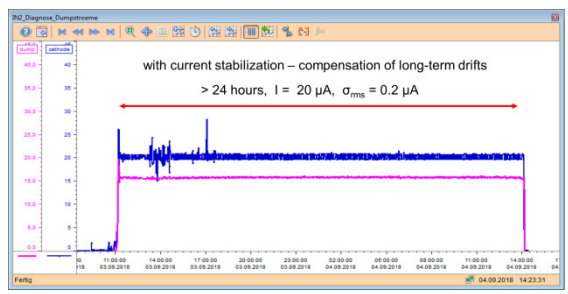


Figure 5: Beam current measured from cathode and collected by the Faraday cup. The beam loss from cathode to FC is 5%. The rest difference in between is due to some calibration issue. A high stability of 1% is kept in 24 hours of continuous operation.

Content from this work may be used under the terms of the CC BY 3.0 licence (© 2018). Any distribution of this work must maintain attribution to the author(s), title of the work, publisher, and DOI.

ISBN: 978-3-95450-194-6 ISSN: 2226-0366 doi:10.18429/JACoW-LINAC2018-THPO125

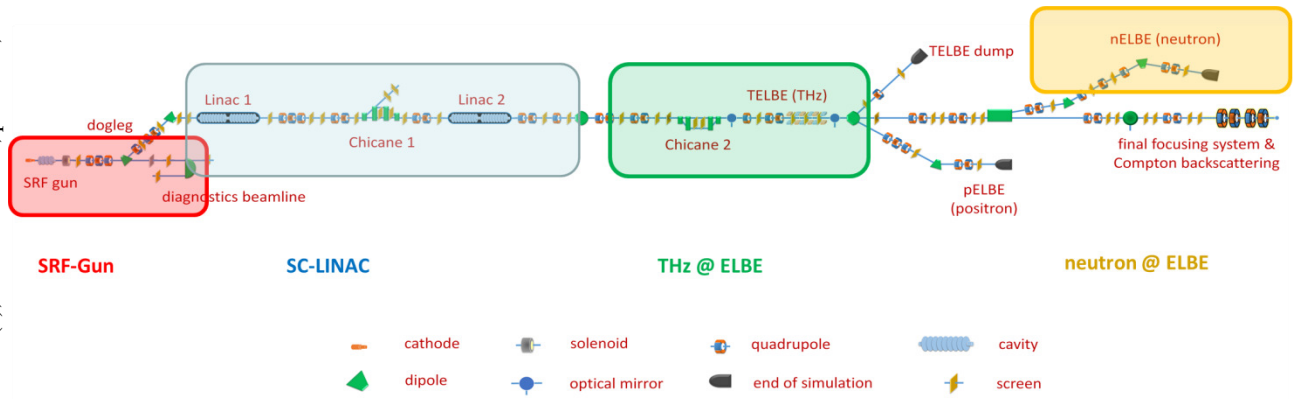


Figure 6: Layout of the SRF gun and SRF linac followed by THz beam line (TELBE) and neutron beam line (nELBE).

USER APPLICATION

Figure 6 shows the beamline layout at ELBE hall for the THz radiation production with the SRF gun injection into ELBE SRF Linac. The beam leaves the SRF gun, passes through a matching quadrupole triplet and the achromatic dogleg structure and enters into the ELBE Linac beam line. There the relativistic beam is further accelerated on-crest in the SRF Linac 1 and off-crest in the Linac2 in order to produce the required energy chirp for bunch compression. The final beam energy is 26.5 MeV in the latest experiment. In the magnetic bunch compressor (chicane 2) the bunch is compressed to sub-ps length. The electron beam passes through the undulator U300. In this electromagnetic undulator with 8 periods and a period length of 300 mm the super-radiant undulator radiation is produced with a designated range between 0.1 and 3 THz [7].

The SRF gun operated stably for a number of subsequent shifts without any shutoffs. Applying the SRF gun with a bunch charge of 200 pC, convincing results for THz production has been obtained. The output power was four times higher compared to that with the thermionic injector (80 pC/bunch), reaching more than 300 mW at 1 THz. Consequently, higher THz power together with better stability could be delivered to user experiments.

CONCLUSION AND OUTLOOK

Although SRF Gun-II doesn't reach the designed parameters due to cavity pollution, it has successfully provided electron beams for ELBE user operation. The SRF gun operated stably for a number of subsequent shifts without any shutoffs in 2018. Applying the beam with high bunch charge of 200 pC and sub-ps pulses with the bunching concept in ELBE, the convincing results for THz production has been obtained.

A new gun lab consisting of an SRF gun and a diagnostics beamline has been planned at ELBE centre to support the research and development of SRF gun since 2018. It will be separated from the ELBE accelerator hall in order to offer more time for the gun experiments.

ACKNOWLEDGEMENTS

We would like to thank the whole ELBE team for their help with this project. The work was partly supported by the German Federal Ministry of Education and Research (BMBF) grant 05K12CR1 and Deutsche Forschungsgemeinschaft (DFG) project (XI 106/2-1).

REFERENCES

[1] J. Teichert *et al.*, ''Commissioning of an Improved Superconducting RF Photo Injector at ELBE" in *Proc. FEL'14*, Basel, Switzerland, Aug. 2014, paper THP061, p. 881.

[2] A. Arnold, et al. "Development of a superconducting radio frequency photoelectron injector", *Nuclear Instruments and Methods A 577 (2007) 440*.

[3] H. Vennekate et al., "ELBE SRF Gun II - Emittance Compensation Schemes", in *Proc. 17th Int. Conf. RF Superconductivity (SRF'15)*, Whistler, Canada, Sep. 2015, paper THPB057, p.1235-1237.

[4] A. Arnold, et al., "RF Performance Results of the 2nd ELBE SRF Gun", in *Proc. 17th Int. Conf. RF Superconductivity (SRF'15)*, Whistler, Canada, Sep. 2015, paper THPB055, p. 1227-1229.

[5] R. Xiang et al., *Physical Review Special Topics - Accelerators and Beams 13(2010)4, 043501*

[6] P. Lu et al.,"Diagnostics of ELBE SRF Gun - Status and Future Design", in *Proc. IBIC2017*, Grand Rapids, MI, USA. ISBN 978-3-95450-192-2.

[7] B. Green, *et al.*, "High-Field High-Repetition-Rate Sources for the Coherent THz Control of Matter", *Scientific Reports 6, 22256 (2016).*

Content from this work may be used under the terms of the CC BY 3.0 licence (© 2018). Any distribution of this work must maintain attribution to the author(s), title of the work, publisher, and DOI.

ISBN: 978-3-95450-194-6 ISSN: 2226-0366 doi:10.18429/JACoW-LINAC2018-THPO126

COMPACT H+ ECR ION SOURCE WITH PULSE GAS VALVE

Y. Takeuchi*, H. Tongu, Y. Iwashita, Kyoto University, Uji, Kyoto 611-0011 Japan

Abstract

We are developing a compact ECR H+ ion source with a fast pulse gas valve. In the case of high current ion linac, the distance between the ion source and the first accelerating tube such as RFQ must be as short as possible to reduce the space charge effect, while operation in a high electric field a good vacuum condition is desirable. Since hydrogen gas always flows out from ion sources when the plasma chamber is filled with the gas, vacuum pumping systems have to evacuate the gas enough before the first accelerating tube. The quick pulse gas injection system achieved by a fast piezoelectric gas valve can reduce the gas load to the vacuum evacuation system and is suitable for installing the ion source close to RFQ. In order to optimize the operating parameter of the ion source, a multi-collector mass analyzing system is developed. The current status is reported together with the preliminary measurement data of the quick mass analysis and spectroscopy of the emitted lights from the plasma.

INTRODUCTION

In an ion source using gas discharge, not only ion beam but also neutral gas flows out from extraction hole. Most of the neutral gas is pumped out by the vacuum pumping system in the Low Energy Beam Transport (LEBT), and a part of the gas diffuses to the accelerating tube. Conventionally, even in the case of a pulsed ion source, neutral gas is constantly supplied and ion beam is extracted from the ion source during the pulse period, while neutral gas continues to flow out of the plasma chamber. In a high-intensity ion accelerator, it is desirable that the length of the LEBT is as short as possible in order to reduce the adverse effect of the space charge effect. However, if the LEBT is short, the effect of the inflow neutral gas to the acceleration tube increases. Then, frequent discharges in the accelerating tube may happen, which may interrupt operation. Chopping the supply of the gas into the plasma can reduce the gas flow. Therefore, we have developed ECR ion source with less gas load [1].

COMPACT H+ ECR ION SOURCE WITH PULSE GAS VALVE

Currently, we have developed a compact ECR H+ ion source with pulse gas valve and test its performance. Since it is assumed to be used for small neutron sources based on proton linac, H+ was chosen as the ion species. In order to achieve high H+ ratio in the extracted beam, the ECR method was adopted. The pulse gas injection system achieved by a fast piezoelectric gas valve can reduce the gas load to the vacuum evacuation system and is suitable for a close installation of the ion source to RFQ.

* takeuchi.yusuke.64z@st.kyoto-u.ac.jp

Desgin

The source is build on a ICF203 flange. There are two radial permanent magnet rings at the upstream and downstream of the chamber. Each magnet ring consists of twelve trapezoidal pieces and their magnetic holder. The extraction system consists of a plasma electrode and a set of three electrodes with a negative potential inserted between the two grounded electrodes, and up to 25 kV can be applied to the plasma electrode. The high voltage assembly is insulated and supported from ground potential by polyethylene insulators. The ion source unit is covered by an iron magnetic return yoke that reduces the stray magnetic field around the ion source. The structure of the ion source is shown in Fig. 1.

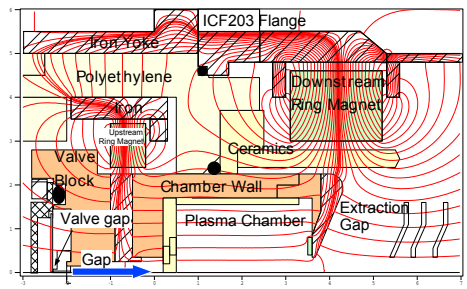


Figure 1: Schematic drawing of the ion source structure. Red lines indicate magnetic flux.

Gas Valve

We developed a fast pulse gas valve using a piezoelectric element KBS-27DA-5A to chop gas supply to ion source [2]. If positive voltage is applied to the piezoelectric element, the gas entrance into the chamber is blocked by the piezoelectric element, so that the gas does not flow into the chamber. However, when negative voltage is applied to the piezoelectric element, the piezoelectric element curves oppositely to open the flow path, and the gas flows into the chamber. By applying a quick pulse voltage to the piezoelectric element, it is possible to inject and chop gas quickly. Figure 2 shows a schematic diagram of the operating principle of the pulse gas valve using the piezoelectric element.

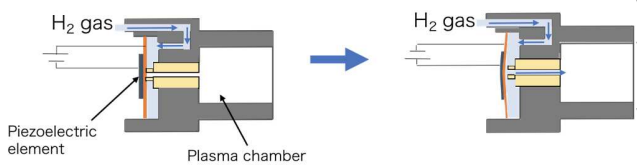


Figure 2: Operating principle of the pulse gas valve.

Magnetic Field

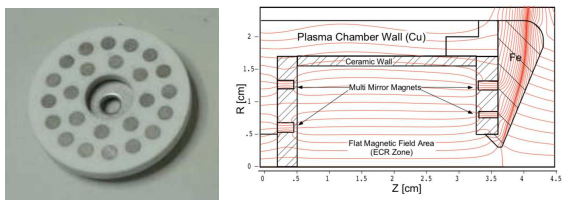
The magnetic field strength satisfying the ECR condition at 6 GHz is about 220 mT. For the generation of the magnetic

Content from this work may be used under the terms of the CC BY 3.0 licence (© 2018). Any distribution of this work must maintain attribution to the author(s), title of the work, publisher, and DOI.

ISBN: 978-3-95450-194-6 ISSN: 2226-0366 doi:10.18429/JACoW-LINAC2018-THPO126

Content from this work may be used under the terms of the CC BY 3.0 licence (© 2018). Any distribution of this work must maintain attribution to the author(s), title of the work, publisher, and DOI.

field, the miniaturization is aimed at by using a permanent magnet. In addition, a multi-mirror magnetic field scheme is adopted for the purpose of flattening the magnetic field strength distribution on the beam axis and widening the ECR region [3]. Figure 3 shows a photograph of a disk-shaped ceramic with small magnets embedded in it, and the magnetic field distribution when it is loaded in the chamber. Figure 4 shows the measurement result of the axial magnetic field strength on the beam axis. While there is a room to improve the magnetic field distribution by adjusting the shape of the magnet, the magnetic field is well flat on the axis of the chamber position.



(a) (b)

Figure 3: (a) downstream cylindrical magnet columns embedded in a ceramic disc with the diameter of 34 mm. The diameter of each magnet column is 3 mm. (b) schematic flux plot with multi-mirror field.

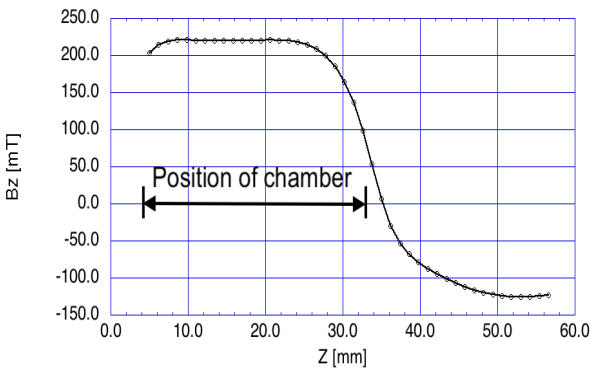


Figure 4: Magnetic field distribution on the beam axis.

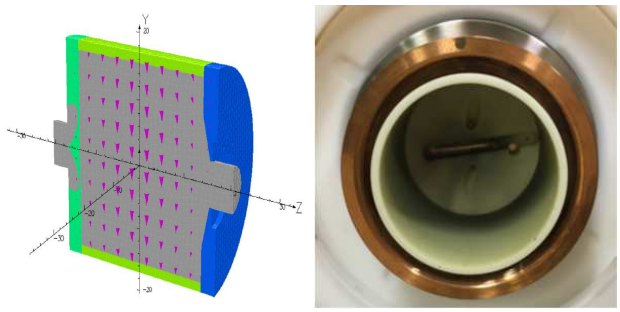
Plasma Chamber

Because the plasma chamber volume should not exceed 50 cc to keep the time constant of the gas stay in the chamber small enough, 34 mm inner diameter 28 mm length cavity was fabricated and the operating frequency is at around 6 GHz. Due to the small volume allowed, the cavity is operated at single mode. Because of the small space available for RF feeding, an antennae coupling through a coaxial line is used instead a waveguide (Fig. 5).

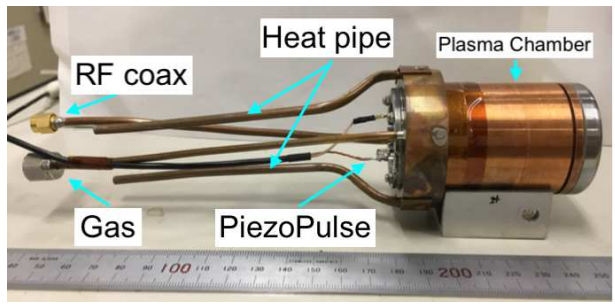
PERFORMANCE TEST

Experimental Setup

A test bench has been constructed to evaluate the beam generation performance of the ECR ion source. The 6 GHz RF power of up to 200 W can be supplied by amplifying the



(a) (b)



(c)

Figure 5: (a) Calculated RF mode of TE111 in a cavity. (b) Picture of the inside of the plasma chamber viewed from the downstream side. All the inner cavity walls are covered with ceramics, and an antenna coupling through the coaxial line is seen in the center back. (c) The plasma chamber and the piezoelectric valve assembly.

RF power generated by a signal generator with a solid state amplifier. The amplified RF power is fed to a waveguide with a coaxial-waveguide conversion adapter at both the ends of the waveguide. A DC blocker inserted in the waveguide blocks the HV. Hydrogen gas is generated by a hydrogen gas generator for gas chromatography. The generated gas is stored in a gas buffer tank, and the gas flow rate to the plasma chamber can be adjusted by changing the gas supply pressure to the pulse gas valve. The gas flow rate is measured by a mass flow meter.

In order to know the ratio of ion species in the extraction beam, we installed a mass analyzer with an analysis magnet and multiple collector electrodes [4] just after the ion source. The feature of this mass analyzer is that it can analyze multiple kinds of ions in the extraction beam simultaneously and almost in real time. This greatly improves the efficiency of examining the properties of the beam generated by the ECR ion source, which is determined by complex involvement of many parameters such as magnetic field distribution, gas pressure, and RF power and frequency. The signals from multiple electrodes are scanned by a fast multiplexer and the multiplexed signal is sent to the outside and then digitized by a PC based oscilloscope. In addition, a lens for a spectrometer was installed at downstream position of the beam line for spectroscopy of light emitted from the plasma in the ion source. Schematic diagram of experimental setup is shown in Fig. 6.

ISBN: 978-3-95450-194-6 ISSN: 2226-0366 doi:10.18429/JACoW-LINAC2018-THPO126

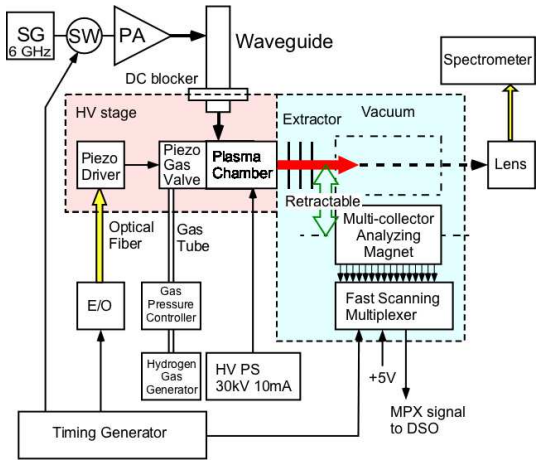


Figure 6: Schematic diagram of experimental setup. The mass analyzer can be retractable from the beam line and can switch between mass analysis and spectroscopy configuration.

Preliminary Results

Mass analysis Figure 7 shows a measurement result of extracted beam current using the mass analyzer (with 0.6 % gas pulse duty; 2 ms pulse duration with 3 pps , RF power; 6.16 GHz, 67 W, 2ms). Pressure in the plasma chamber estimated from ϕ6 mm extraction hole conductance and average mass flow was 32 mTorr. Total extracted beam current at peak was about 8 mA, and H^+ current was about 1 mA. The highest was H_2^+ current, in addition, heavy ions considered to be not hydrogen-derived were also detected more than H^+ in this trial case.

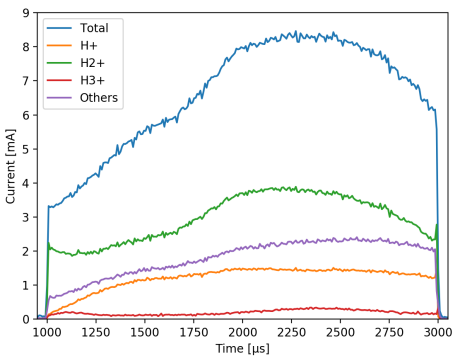


Figure 7: The horizontal axis is time, and the vertical axis is current. RF power is fed from 1000 to 3000 μs and the gas valve is open from 0 to 2000 μs.

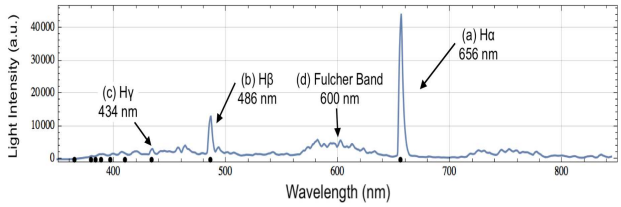


Figure 8: Typical spectrum obtained by a spectrometer where Balmer series and Fulcher band are shown.

Spectroscopy Figure 8 shows a typical visible light spectrum obtained by spectroscopy of a plasma generated by the ion source. The Balmer series H-alpha (a) at 656 nm, H-beta (b) at 486 nm, H-gamma (c) at 434 nm lines and Fulcher band (d) are shown. It is expected that we can grasp the details of the plasma generated by the ion source by investigating the data obtained by spectroscopy in detail.

CONCLUSION

We are developing a compact ECR H^+ ion source with pulse gas valve and testing its performance. Fast pulse gas valve reduces gas load to evacuation system. The real-time mass analysis of the extracted beam enables us to optimize the parameters. The less amount of proton beam current for now may be requiring us to make some modification to the structure in addition to the parameter optimizations. A fast shutter before the spectrometer may enable us to investigate the time structure of the pulse plasma.

REFERENCES

[1] Y. Iwashita, H. Tongu, Y. Fuwa, and M. Ichikawa, *Rev. Sci. Instrum.*, vol. 87, pp. 02A718, 2016.

[2] M. Ichikawa *et al.*, "Development of Piezoelectric Pulse Gas Valve", in *Proceedings of 4th Annual Meeting of Particle Accelerator Society of Japan* and *32nd Linear Accelerator Meeting in Japan*, August 2007, pp. 103–105 .

[3] Y. Iwashita *et al.*, "Compact H^+ ECR Ion Source with Pulse Gas Valve", presented at ICIS 2017, Geneva, Switzerland, will appear in *RSI Special Topics Section*.

[4] Y. Takeuchi *et al.*, "Development of Real-Time Mass Analysis System with Permanent Magnet for Ion Beam", in *Proc. IPAC'18*, Vancouver, BC, Canada, Apr. 29-May 4 2018, pp. 2236–2238. doi:10.18429/JACoW-IPAC2018-WEPAL033

Content from this work may be used under the terms of the CC BY 3.0 licence (© 2018). Any distribution of this work must maintain attribution to the author(s), title of the work, publisher, and DOI.

ISBN: 978-3-95450-194-6 ISSN: 2226-0366 doi:10.18429/JACoW-LINAC2018-THPO127

THE EFFECT OF ENERGY FLUCTUATION ON THE MULTI-BUNCH ACCELERATION IN E-DRIVEN ILC POSITRON SOURCE

Masao Kuriki,* Hisayasu Nagoshi, Tohru Tahakashi, Hiroshima University, Higashihiroshima, Japan
Kentaro Negishi, Iwate University, Morioka, Japan
Toshiyuki Okugi, Tsunehiko Omori, KEK, Tsukuba, Japan
Masashi Satoh, Yuji Seimiya, Junji Urakawa, Kaoru Yokoya, Shigeru Kashiwagi,
Tohoku University, Sendai, Japan

Abstract

E-Driven method is a technical backup for positron source for ILC. In the positron source, the positron is generated and accelerated in a multi-bunch format with gaps in a macro-pulse. We employ AM (Amplitude Modulation) to suppress the transient beam-loading, but a small fluctuation is still expected, depending on the compensation accuracy. In this article, the positron yield which is ratio of numbers of positrons over electrons, is evaluated as a function of the compensation accuracy. With this result and the detail investigation of the beam loading compensation accuracy by AM, the positron yield of E-Driven Positron source for ILC is evaluated.

INTRODUCTION

ILC (International Linear Collider) [1] is an e+e- linear collider with CME from 250 to 1000 GeV. It would be constructed in Iwate, Japan, as the main project of High energy physics. In the E-driven ILC positron source, the positron is generated in a macro-pulse with 6.15 ns bunch spacing [2]. Schematic drawing of the E-Driven ILC positron source is shown in Fig. 1 3.0 GeV electrons hit W-Re(26) alloy target to generate positrons through pair creation process. At the downstream of the target, AMD (Adiabatic Matching Device) is placed [3] to suppress the transverse momentum. Thereafter, it is accelerated up to 250 MeV by 36 of 11-cell normal conducting L-Band Standing Wave (SW) cavities [4] surrounded by 0.5 T solenoid field. After a chicane removing electrons from the bunch, the positron booster composed from L-Band and S-Band Traveling Wave (TW) cavities accelerates the positron up to 5 GeV. After the booster, the positrons are injected to DR (Damping Ring) for radiation damping through ECS (Energy Compressor Section) for better phase-space matching. In ILC, positrons of 3.2 nC per bunch are required at the collision point. In the DR, the required bunch charge is 4.8 nC including 50% margin. The design criteria for the E-driven ILC positron source is to obtain a sufficient amount of positron in DR acceptance defined in a phase space [3]. The condition in the longitudinal phase-space is 70 mm in z and 1.5% in energy (full width).

Because the macro pulse is a copy of a part of DR (Damping Ring) fill pattern, there is a gap as shown in Fig. 2. This is an example and number of gaps depends on DR fill pattern. Seimiya performed a start-to-end simulation of the E-Driven ILC positron source without the beam loading effect [3].

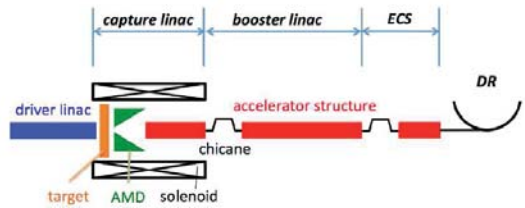


Figure 1: Schematic view of ILC E-driven Positron source.

Kuriki perform the simulation with the beam loading effect, but it is only for the injector part (up to 250 MeV) [4]. To accelerate the beam in such format, the transient beam loading effect which varies the accelerating field at the macro pulse and every mini-train heads, has to be compensated.

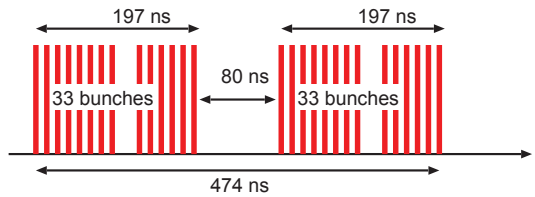


Figure 2: An example of macro-pulse structure in E-Driven ILC positron source. The macro pulse is composed from two mini-trains of 33 bunches with 6.15 ns bunch spacing. There is a gap of 80 ns.

M. Kuriki [5] shows that the energy variation by the beam loading with this beam format can be compensated by controlling timing and RF envelope in standing wave accelerator. H. Nagoshi et al. [6] shows that amplitude modulation [5] is effective to compensate the beam loading in travelling wave accelerator. The compensation can be perfect, but it requires a high peak RF input. The compensation have some imperfection if we limit the peak RF power [6] and an energy variation in pulse due to this imperfection is expected. In this article, we evaluate the yield variation of the positron source by the energy variation in pulse.

RESULT AND DISCUSSION

The transient beam loading effect should be compensated in the macro-pulse acceleration for ILC E-Driven positron source. Otherwise, we will have a large variation on the positron bunch intensity in DR. The large fluctuation causes a difficulty on the acceleration in the main linac, because the beam loading in a macro-pulse will be varied and we will

* mkuriki@hiroshima-u.ac.jp

Content from this work may be used under the terms of the CC BY 3.0 licence (© 2018). Any distribution of this work must maintain attribution to the author(s), title of the work, publisher, and DOI.

ISBN: 978-3-95450-194-6 ISSN: 2226-0366 doi:10.18429/JACoW-LINAC2018-THPO127

Table 1: L-Band and S-Band TW Cavity Parameters

Parameter	L-Band	S-Band	Unit
Frequency	1300	2600	MHz
Shunt Impedance	47.2	57.8	MΩ/m
Aperture (2a)	34	20	mm
Filling time	1.28	0.554	μs
Q Value	20000	13600	none
Attenuation	0.261	0.333	none
Length	2.0	1.956	m
RF power	22.5	36	MW

have a large energy spread. With such beam, the luminosity is much spoiled. Here, we consider the beam loading compensation with an Amplitude Modulation (AM) of the input RF. The detail of the method is described in Ref. [5]. In this study, acceleration voltage and its variation of TW cavities by assuming the ILC macro-pulse format is evaluated. Table 1 shows the parameters of the TW cavities.

According to Ref. [6], if we apply a square RF pulse to the S-band structure, the average accelerating voltage for positron bunches is 37.65 ± 5.54 MV. This voltage (energy) variation by the transient beam loading can be compensated perfectly by AM on the input RF [5] in an ideal case. The input RF power is increased discontinuously when we start the acceleration at $t = t_f$ to suppress the transient beam loading. The input power has to be low in the train gap to keep the accelerator voltage. The linear modulation on the mini-train is necessary [5]. In this case, the transient beam loading is suppressed perfectly, i.e. there is no energy variation in the macro pulse. The acceleration voltage is 23.05 ± 0.00 MV. The input RF power is peaked at $t = t_f$ and the value is adjusted to 36 MW which is the maximum RF power provided by the source. In the L-Band case, that was 14.42 ± 0.00 MV.

Under this perfect correction condition, the accelerating voltage becomes less than that in the square RF pulse case, 37.65 ± 5.54 MV, because the high peak power is required at $t = t_f$. To recover the accelerating voltage, we consider omitting the high peak power part at $t = t_f$. We call this compensation method as quasi-perfect compensation. In such case, the compensation is imperfect and we will have the variation again with a higher voltage. The accelerating voltage and the variation are in trade-off. Figures 3 and 4 are examples of L-band and S-band cavities, respectively.

In Fig. 3, AM has only constant components and no linear component. The voltage is not flat in the mini-train part (solid line) , but the variation is not so large. The peak power is adjusted to 22.5 MW. The average acceleration voltage was 16.60 ± 0.14 MV (peak-to-peak). The spread of the acceleration voltage is about 2% in full width. In S-band case, the input RF power is flattened as shown in Fig. 6 around t = tf. The peak RF power is adjusted at 36 MW. The results are shown in Fig. 4 with the same manner in Fig. 3. The average acceleration voltage was 25.76 ± 0.19

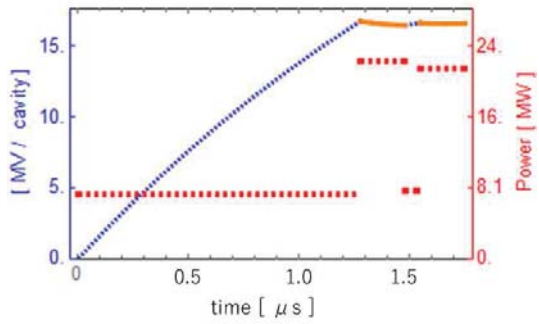


Figure 3: Accelerating voltage and RF power evolution of the L-Band TW accelerator by the quasi-perfect compensation are shown with the same manner in Fig. 3. The average acceleration voltage was 16.60 ± 0.14 MV (peak-to-peak).

MV (peak-to-peak), and the spread of acceleration voltage for each bunch was 1.5% in full width.

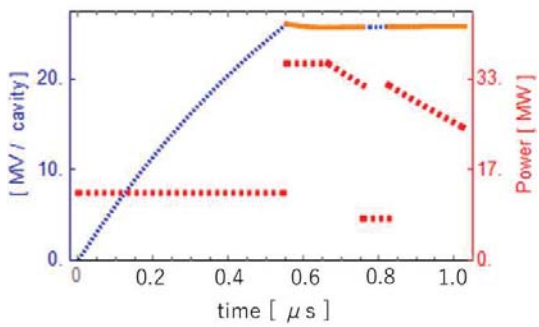


Figure 4: Accelerating voltage and RF power evolution of the S-Band TW accelerator by the quasi-perfect compensation are shown with the same manner in Fig. 3. The average acceleration voltage was 25.76 ± 0.19 MV, (peak-to-peak).

The difference between the optimum solution for L-band and S-band comes from the filling time. Because the L-band cavity has a long filling time, 1.28 us, AM with the constant components is very effective. In contrast, the filling time of the S-band cavity is 0.554 us and the variation becomes too large if we employ only the constant components. Based on the accelerator performance evaluated with the quasi-perfect compensation for the transient beam loading effect, we designed the booster section. The beam optics has been designed by Seimiya based on a basic FODO lattice [3]. The number of lattice is adjusted for each section giving a same (or close) acceleration energy. Table 2 shows the result. 4Q+1L means that a lattice is composed from 4 quadrupoles and 1 L-band TW cavity and so on. In total, there are 144 TW L-Band cavities and 104 TW S-band cavities.

The bunch energy after the booster is evaluated based on the accelerating voltage calculated in Figures 3 and 4. The results are shown in Fig. 5. The horizontal axis is time in the macro-pulse, corresponding to the bunch order. The energy

Content from this work may be used under the terms of the CC BY 3.0 licence (© 2018). Any distribution of this work must maintain attribution to the author(s), title of the work, publisher, and DOI.

ISBN: 978-3-95450-194-6 ISSN: 2226-0366 doi:10.18429/JACoW-LINAC2018-THPO127

Content from this work may be used under the terms of the CC BY 3.0 licence (© 2018). Any distribution of this work must maintain attribution to the author(s), title of the work, publisher, and DOI.

Table 2: The lattice configuration and the number of cells for each section. 4Q+1L means that a lattice is composed from 4 quadrupoles and 1 L-band TW cavity and so on.

Lattice	No. Cells
4Q + 1L	14
4Q + 2L	29
4Q + 4L	18
4Q + 4S	26

of the first bunch is the highest and that at the last bunch of the first mini-train is the least. The average is 5.31 ± 0.04 GeV (peak-to-peak) which corresponds to 1.4% (full width). This enery variation is larger than the energy acceptance (dynamic aperture) of DR, but it should not be compared directly to the acceptance. ECS suppress the energy spread greatly down to 0.1 %.

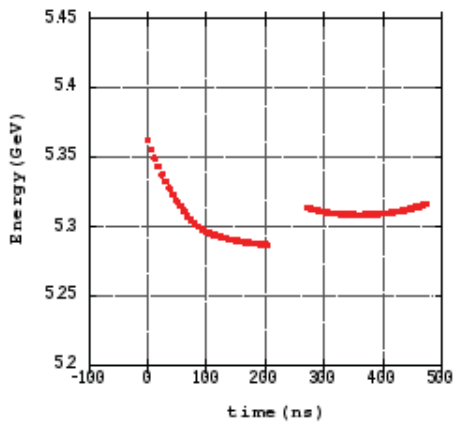


Figure 5: Expected energy after the booster for the macro-pulse. The horizontal axis is time in the macro-pulse.

Figure 6 shows the positron yield variation in a pulse. t = 0 corresponds to the pulse head, and the area between t = 205ns and t = 270ns corresponds to the train gap. The variation is larger for the first train, because of the larger energy variation. For the whole pulse, the positron yield variation is 1.91 - 2.03, which corresponds to 6% in full width.

This intensity variation is not large, but the effect should be carefully investigated. Potential problem is acceleration in main linac. In the main linac, super-conducting accelerator is employed. In the super-conducting accelerator, accelerating voltage variation is caused by the beam current variations. In fact, the variation is suppressed by a feed-back control to the input RF power. The highest intensity variation capable by the RF feed-back depends on the reserve capacity.

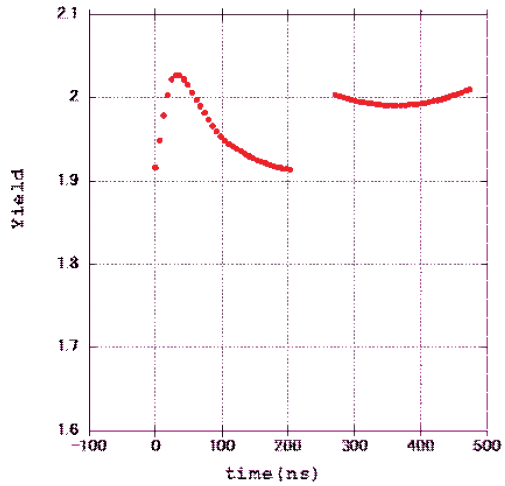


Figure 6: Positron yield variation in a pulse.

SUMMARY

As a design study of E-Driven ILC positron source, we examined the beam loading compensation for the multi-bunch acceleration in the positron booster. By AM technique, the energy variation of the positron bunches in the booster can be compensated perfectly. In the perfect compensation, a high peak power is required at t = tf. and a relatively low acceleration field has to be accepted. With the quasi-perfect compensation, the accelerating field is recovered paying an energy variation. The results were 16.60 ± 0.14 MV (peak-to-peak) for L-band 2m cavity driven by 22.5 MW power and 25.76 ± 0.19 MV (peak-to-peak) for S-band 2m accelerator driven by 36 MW power with 0.78 A beam loading. We are designed the booster based on the accelerator performance. The energy after the booster is expected to be 5.31 ± 0.04 GeV (peak-to-peak) for the macro-pulse, 1.4 % in full width. It cause the variation of the positron yield 1.91 -2.03, 6% in full width. This intensity variation determine the reserve capacity of the RF feed-back in the main linac.

ACKNOWLEDGMENT

This work is partly supported by Grant-in-Aid for Scientific Research (B) and US-Japan Science and Technology Cooperation Program in High Energy Physics.

REFERENCES

[1] *ILC Technical Design Report (TDR)*, KEK, Tsukuba, Japan, KEK-Rep. 2013-1, 12 Jun. 2013.

[2] T. Omori, *et al.*, *Nucl. Instr. Meth. A*, vol. 672, p. 52, 2012.

[3] Y. Seimiya *et al.*, "Positron capture simulation for the ILC electron-driven positron source", *Progress of Theoretical and Experimental Physics*, vol. 2015, no. 10, p. 103G1, Oct. 2015. doi:10.1093/ptep/ptv136

[4] M. Kuriki *et al.*, "A Simulation Study of E-driven ILC Positron Source", presented at the Int. Workshop on Future Linear Colliders (LCWS'17), Strasbourg, France, Oct. 2017.

ISBN: 978-3-95450-194-6 ISSN: 2226-0366 doi:10.18429/JACoW-LINAC2018-THPO127

[5] M. Kuriki, "Energy Spread Compensation in Arbitrary Format Multi-Bunch Acceleration With Standing Wave and Traveling Wave Accelerators", in *Proc. IPAC'18*, Vancouver, BC, Canada, Apr.-May 2018, pp. 307-310. doi:10.18429/JACoW-IPAC2018-MOPMF076

[6] H. Nagoshi *et al.*, "A Design Study of the Electron-driven ILC Positron Source Including Beam Loading Effect", in *Proc. IPAC'18*, Vancouver, BC, Canada, Apr.-May 2018, pp. 311-314. doi:10.18429/JACoW-IPAC2018-MOPMF077

Content from this work may be used under the terms of the CC BY 3.0 licence (© 2018). Any distribution of this work must maintain attribution to the author(s), title of the work, publisher, and DOI.

ISBN: 978-3-95450-194-6 ISSN: 2226-0366 doi:10.18429/JACoW-LINAC2018-THPO132

STUDY OF THE ELECTRON BEAM TRANSFER LINE FOR THE AWAKE RUN II EXPERIMENT AT CERN*

Seong-Yeol Kim[1], Moses Chung[1†], UNIST, 44919 Ulsan, Republic of Korea
Mohsen Dayyani[2], Institute For Research in Fundamental Sciences, 19395-5531, Tehran, Iran
Steffen Doebert[3‡], CERN, CH-1211, Geneva, Switzerland

Abstract

Proton Beam-Driven Plasma Wakefield Accelerator (PBD-PWFA) has been actively investigated at CERN within the AWAKE experiments to study the electron beam acceleration using plasma wake fields of the order of GV/m. In the AWAKE RUN 1 experiments an electron beam with an energy of 19 MeV and a bunch length of 2.2 ps rms has been used for the first demonstration of electron beam acceleration in the plasma wake fields. It has been observed that the energy gain of the electron beam is up to 2 GeV, and electron capture efficiency is few percent. Higher capturing efficiency and emittance preservation could be achieved by making the electron beam short enough to be injected only into the acceleration and focusing phase of the plasma wake fields. The electron accelerator needs to be upgraded for AWAKE RUN 2 experiments to obtain a bunch length less than 100 fs which corresponds to a quarter of the plasma wavelength. Planned electron beam parameters for the AWAKE RUN 2 are a beam charge of 100 pC, and a beam energy larger than 50 MeV. In this paper, we show the electron beam parameters for RUN 2, and the parameters of the transfer line such as Twiss parameters, beam envelope, and emittance.

INTRODUCTION

In the first run of the AWAKE to demonstrate the acceleration of 19 MeV electron beam through the PBD-PWFA, it has been observed that the energy gain of the electron beam is in the order of GeV [1]. Furthermore, a new experimental setup is now under study for the next run of AWAKE starting from 2021 to study electron acceleration with high energy and emittance preservation. For the RUN 2 experiments, target parameters have been determined from the simulation [2]. The beam size and length are less than 50 μm and 100 fs, respectively to increase capturing efficiency to more than 90 %. In addition, while a single Rb-Vapor plasma cell has been used for both Seeded Self-Modulation (SSM) and accelerating of the electron beam In RUN 1, it is considered for RUN 2 experiment that an additionally introduced 4 m plasma cell is used only for SSM to generate the micro-bunches of the proton beam. Then, the modulated proton beam propagates to another 10 m of plasma to generate the plasma wake fields, which are going to be used to accelerate the electron beam. The electron beam has to be injected in between the two plasma cells.

* Work supported by NRF
† mchung@unist.ac.kr
‡ steffen.doebert@cern.ch

In this paper, studies on electron beamline optimization using RUN 2 beam parameters are shown, and a new beamline is briefly proposed. For the beamline simulation, ASTRA [3], MAD-X [4] and ELEGANT [5] codes are used to simulate the beam, and for the optimization of the beam parameters along the beamline.

ELECTRON BEAMLINE AND OPTIMIZATION

The beam parameters considered for RUN 2 are obtained from a new injector combining S- and X-band electron accelerator [6]. Apart from a S-band RF gun, it consists of X-band buncher and a traveling wave structure to reduce the bunch length out of the linac section. Beam parameters at the end of the injector are shown in Table 1.

Table 1: Beam Parameters Out of the Linac Section

Parameters	Values
E_k	85 MeV
σ_E	0.33 %
σ_r	0.14 mm
σ_z	82.57 fs
$\epsilon_{nx,ny}$	0.5 mm mrad

Conventional Electron Beamline Optics

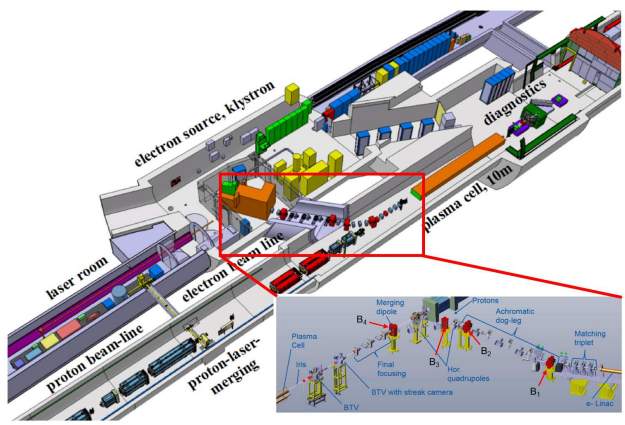


Figure 1: AWAKE tunnel and current electron beamline.

First, it has been studied whether the existing electron beamline for RUN 1 can be used also for the RUN 2 experiments with the initial beam parameters described in Table 1. The current electron beamline is depicted in Fig. 1 [7, 8].

Content from this work may be used under the terms of the CC BY 3.0 licence (© 2018). Any distribution of this work must maintain attribution to the author(s), title of the work, publisher, and DOI.

ISBN: 978-3-95450-194-6 ISSN: 2226-0366 doi:10.18429/JACoW-LINAC2018-THPO132

The beamline has been built following the constraints of the existing tunnels. The beam propagates through the matching triplet, and achromatic dog-leg for zero-dispersion. Then, it goes to the merging point with the proton beam. Since the tunnel has a slope, the final dipole magnet B_4 has a tilt angle to match the beam trajectory to the slope of the tunnel.

Optimization process for β function in Twiss parameters and dispersion (η) function have been done using MAD-X simulation code. At the plasma merging point, β and dispersion are matched to 0.6 m, 0 m, respectively. Figure 2 shows β and dispersion functions along the beamline. Due to the tilt angle of B_4 magnet, derivative of dispersion value exists on the vertical plane at the plasma merge.

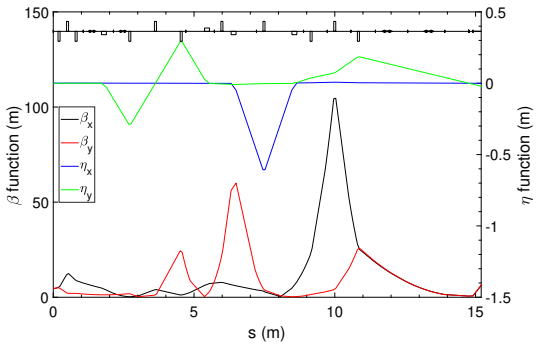


Figure 2: β and dispersion functions along the beamline.

Particle tracking has been done using ELEGANT code with given quadrupole strength obtained from MAD-X simulation. In this simulation study, space charge calculation has been ignored. In Fig. 3, beam size and normalized emittance are shown. Solid line indicates the value with considering higher order terms (chromatic effects), while dashed line is the value with consideration of both higher order terms, and coherent synchrotron radiation (CSR). The beam size $\sigma_{x,y}$, and the normalized emittance $\epsilon_{nx,ny}$ values at the plasma merge are described in Table 2.

Table 2: $\sigma_{x,y}$ and Normalized $\epsilon_{x,y}$ at the Plasma Merge

Parameters	Higher order terms included	Higher order terms and CSR included
σ_x	71.41 μm	377.01 μm
σ_y	82.31 μm	277.07 μm
ϵ_{nx}	1.03 mm mrad	6.36 mm mrad
ϵ_{nx}	2.35 mm mrad	8.98 mm mrad

When higher order terms and CSR effects are included in the simulation, the emittance value, and beam size of the merging point are rapidly increased at due to large β, η values along the beamline (e.g., β_x at 10 m), and the tilt angle at the final dipole magnet.

Moreover, the bunch length σ_z at the plasma merge is about 300 fs in the conventional beamline. When the beam passes through the B_3 magnet, its length increases sharply. In the longitudinal phase space before passing through the magnet (Fig. 4), particles (red dot; hot particles) that have

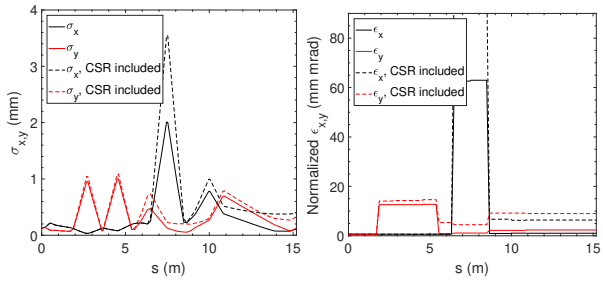


Figure 3: Beam envelope and normalized emittance.

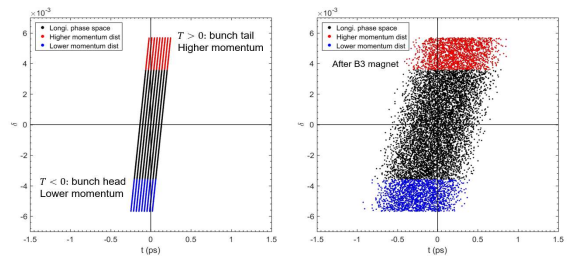


Figure 4: Longitudinal phase space before B_3 (left), and after B_3 (right).

momentum larger than the reference momentum are mainly in the bunch tail ($t > 0$), while the cold particles (blue dot) are in the bunch head ($t < 0$). According to the transport matrix, bunch length can be calculated from Eq. (1) where R is transport matrix of the B_3 dipole magnet.

$$s_1 = R_{55}s_0 + R_{56}\delta_0 \quad (1)$$

Since the hot and cold particles are randomly distributed in the transverse phase space, we can ignore corresponding terms on calculating of the bunch length. On the bunch tail, s_1 is balanced by $s_0 + R_{56}\delta$ while on the bunch head, $s_1 = -s_0 - R_{56}\delta$. It means that the bunch head and tail have longer path length compared to the particles before entering the dipole magnet. In order to reduce the bunch length, it is needed to control R_{56}. However, since the dipole magnets are used for the tunnel constraints, we cannot modify a configuration of the dipole magnet.

New Electron Beamline Optics

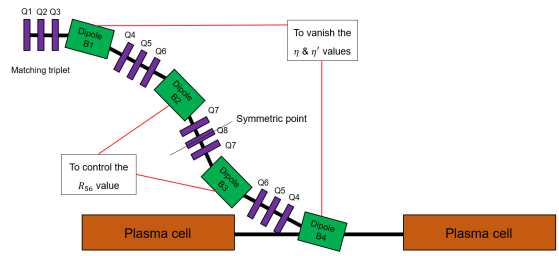


Figure 5: Schematic view of the parallel electron beamline.

In order to overcome the bunch lengthening, another type of electron beamline has been studied. In this case, a four-bend chicane [9] has been considered to control the R_{56}

Content from this work may be used under the terms of the CC BY 3.0 licence (© 2018). Any distribution of this work must maintain attribution to the author(s), title of the work, publisher, and DOI.

ISBN: 978-3-95450-194-6 ISSN: 2226-0366 doi:10.18429/JACoW-LINAC2018-THPO132

Content from this work may be used under the terms of the CC BY 3.0 licence (© 2018). Any distribution of this work must maintain attribution to the author(s), title of the work, publisher, and DOI.

component. Figure 5 shows the layout of the parallel electron beamline. Proton beamline and plasma cell for SSM are located next to the electron beamline. The bending magnets, B_1 and B_4 with respect to the central quadrupole Q_8 are placed to compensate the η and η'. In the middle of the beamline, B_2 and B_3 are for controlling the R_{56} component. In fact, such a chicane can receive a positive and negative R_{56}. The bending angle of the dipole magnets is 16°, and they bend the beam only in the horizontal plane. In addition, concerning the technical issue of the beamline, distance between two plasma cells should not exceed 1 m for the vacuum-plasma transition of the proton beam. Therefore, the distances between B_1 and Q_4, and Q_4 and B_4 are set to be 1.1 m to avoid space conflicts, and for the symmetry of the beamline.

The matched beamline optics including dispersion function are described in Fig. 6. β at the plasma entrance is 0.5 m, and η is 0 m.

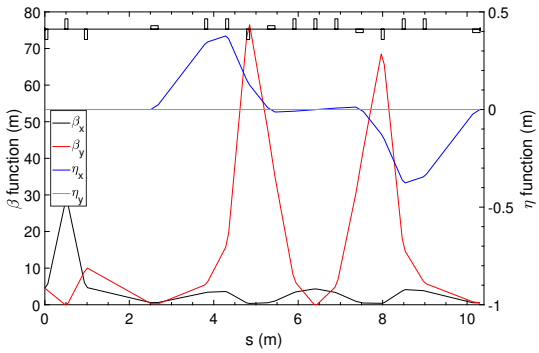


Figure 6: β and η functions along parallel beamline.

The beam envelope, emittance, and bunch length obtained including higher order terms and CSR from the ELEGANT simulations are shown in Fig. 7, and Fig. 8. The beam size and bunch length at the end are about 50 μm and 92 fs with chromatic effects only. However, when the CSR effects is included, σ_x and σ_z at the plasma entrance become 246 μm, and 120 fs, while σ_y maintains its target parameter. The large increases of the σ_x is caused by the CSR effects which is only in the horizontal plane by using only the horizontal bending dipole magnets.

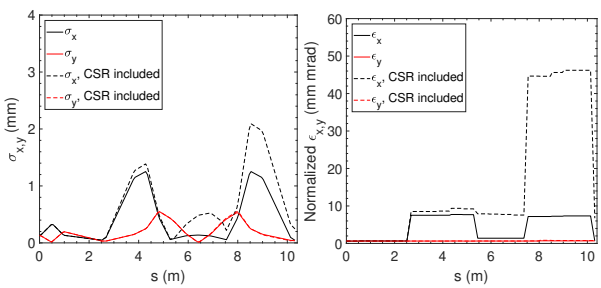


Figure 7: Beam envelope and normalized emittance.

However, we confirmed from the simulation that a higher beam energy can minimize the CSR effects on the σ_x. In this case, 164 MeV electron beam has been used. We also

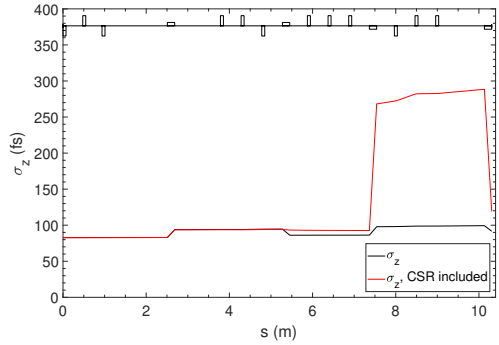


Figure 8: Bunch length along the beamline.

considered the space charge forces on the transfer line using PARMELA [10]. It has been checked that the beam parameters at the end of the beamline are close to the target parameters using the optimized quadrupole strength under the space charge forces. From the PARMELA simulation, σ_x and σ_y at the end of the line are 54 μm, 65 μm, and the bunch length is 79 fs. When the optimized quadrupole strength is used for the ELEGANT simulation for the CSR effects, obtained beam size and bunch length are about 40 μm, and 81.40 fs.

SUMMARY AND FUTURE WORK

The newly introduced transfer line is completely flexible from the bunch length controlling point of view, and it can provide any desired value for the bunch length. However, since the space charge forces and the CSR effects has not been considered simultaneously, studies on the beamline optimization will be done with both effects for the target parameters.

ACKNOWLEDGEMENT

This work was supported by NRF (National Research Foundation of Korea) Grant funded by the Korean Government (NRF-2016-Fostering Core Leaders of the Future Basic Science Program/Global Ph.D. Fellowship Program)

REFERENCES

[1] E. Adli *et al.*, "Acceleration of electrons in the plasma wakefield of a proton bunch," *Nature*, Aug. 2018.

[2] E. Adli, "Towards AWAKE applications: Electron beam acceleration in a proton driven plasma wake," in *Proc. IPAC'16*, Busan, Korea, 2016. doi:10.18429/JACoW-IPAC2016-WEPMY008

[3] "A Space Charge Tracking Algorithm", http://www.desy.de/~mpyflo/

[4] "Methodical Accelerator Design", http://mad.web.cern.ch/mad/

[5] M. Borland, "elegant: A Flexible SDDS-Compliant Code for Accelerator Simulation," Advanced Photon Source LS-287, September 2000.

[6] K. Pepitone *et al.*, "The electron accelerators for the AWAKE experiment at CERN—Baseline and Future Developments," *Nucl. Instrum. Meth. A*, Feb. 2018.

ISBN: 978-3-95450-194-6 ISSN: 2226-0366 doi:10.18429/JACoW-LINAC2018-THPO132

[7] J. S. Schmidt *et al.*, "Status of the proton and electron transfer lines for the AWAKE Experiment at CERN," *Nucl. Instrum. Meth. A*, Jan. 2016.

[8] E. Gschwendtner, "AWAKE, A Particle-driven Plasma Wakefield Acceleration Experiment," *arXiv preprint arXiv:1705.10573*.

[9] A. Sharma, A.D. Ghodke, G. Singh, Abdurrahim, "OPTICS DESIGN OF TRANSFER LINE-2 FOR CTF3," CTF3-Note-091, 2008.

[10] L. M. Young, "PARMELA," Los Alamos National Laboratory report LA-UR-96-1835 (Revised April 22, 2003).

Content from this work may be used under the terms of the CC BY 3.0 licence (© 2018). Any distribution of this work must maintain attribution to the author(s), title of the work, publisher, and DOI.

ISBN: 978-3-95450-194-6 ISSN: 2226-0366 doi:10.18429/JACoW-LINAC2018-FR1A01

RESULTS FROM THE 6D DIAGNOSTICS TEST BENCH AT SNS

B. Cathey, A. Aleksandrov, S. Cousineau, A. Zhukov
Oak Ridge National Laboratory, Oak Ridge, TN, USA

Abstract

This paper presents the method and results for measuring the full six-dimensional phase space of a low energy, high intensity hadron beam. This was done by combining four-dimensional emittance measurement techniques along with dispersion measurement and a beam shape monitor to provide the energy and arrival time components. The measurements were performed on the new Beam Test Facility (BTF) at the Spallation Neutron Source (SNS), a 2.5 MeV functional duplicate of the SNS accelerator front end. The results include a correlation the had not previously been observed.

INTRODUCTION

For high power, high intensity accelerators, beam loss is one of the limiting factors for performance and achievable beam power [1]. Today's state-of-the-art simulation codes provide accurate tracking for the RMS values of the beam through the beam line for many cases, and in principle should also be able to accurately track the beam halo formation and beam loss through the accelerator. However, successful simulation of beam halo and beam loss have yet to be accomplished. As the capabilities of the simulations should be sufficient, the problem may then lie in an incorrect initial assumption, and the most likely candidate is the initial particle distribution, as it is generally approximated [2].

In order to determine the initial particle distribution, the beam must be measured over all six independent spatial and momentum parameters in such a way that correlations between parameters can be seen. The Beam Test Facility at SNS is a small-scale accelerator that can accomplish this task [3].

EMITTANCE MEASUREMENT

Typically, three separate two dimensional phase space measurements are combined to create a six dimensional distribution. However, because the un-measured cross-terms are assumed to be zero in this reconstruction, this distribution may not be identical the actual six dimensional distribution. In order to determine true six dimensional distributions, all six degrees of freedom must be directly measured together. The technique used here is a generalization of the two-dimensional phase space measurement method using slits and a charge collector for the complete six-dimensional phase space.

The particles go through a series of five apertures and a Beam Shape Monitor (BSM). Each aperture allows particles through at the coordinate being measured. By combining two pairs of apertures, one pair being horizontal slits and the other pair vertical slits, the four-dimensional transverse phase space is measured.

To select the longitudinal momentum, we use a 90-degree bending magnet. During the turn, the beam spreads as higher momentum and lower momentum particles separate horizontally due to dispersion. This creates a correlation between the horizontal position and the longitudinal momentum of a particle allowing the selection of particles with certain momentum based on their horizontal position. This selection is executed using a third movable vertical slit.

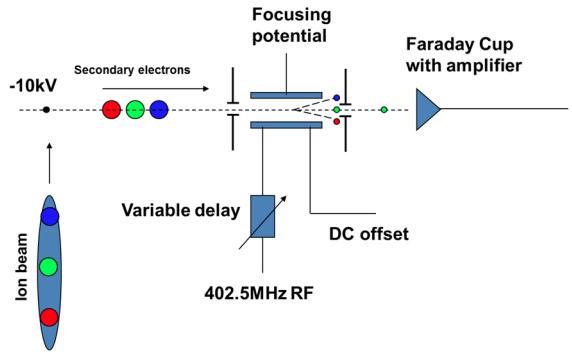


Figure 1: A diagram of the basic concept behind the BSM for measuring the longitudinal phase distribution in the beam.

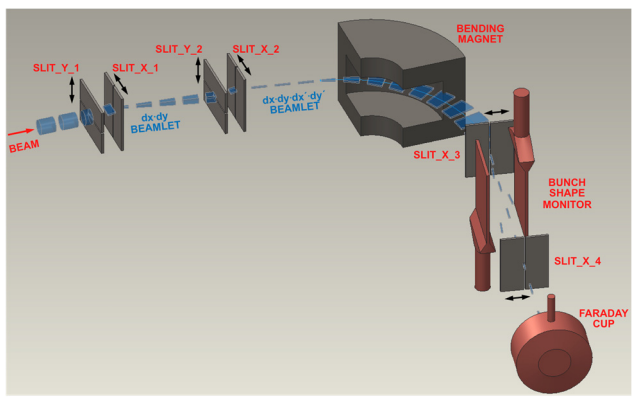


Figure 2: A diagram showing the concept of a full six-dimensional emittance scan.

The longitudinal measurement is conducted with a Beam Shape Monitor (BSM). The BSM contains a suspended wire with a potential in the beam pipe. When the hadron beam hits the wire, electrons are emitted which travel through a RF field and final aperture. See Fig. 1 and [3] for more details. These electrons then hit a detector and are measured as current. This final current measurement reflects the number of particles in the beam with the six measurements described above, particles with a specific horizontal, vertical, and longitudinal position and momentum. Figure 2 shows the full conceptual schematic for the six-dimensional measurement. After a measurement is made for a specified arrangement of apertures, one aperture is moved to the next position. This

Content from this work may be used under the terms of the CC BY 3.0 licence (© 2018). Any distribution of this work must maintain attribution to the author(s), title of the work, publisher, and DOI.

ISBN: 978-3-95450-194-6 ISSN: 2226-0366 doi:10.18429/JACoW-LINAC2018-FR1A01

continues until all the wanted coordinates had been measured.

A modification to the above plan is the use of scintillating screens. A screen can measure an entire dimension at once to greatly reduce scan time. Two screens were installed in the BTF. The first is the energy slit, which can be seen in Fig. 3. The second replaces the aperture and Faraday cup after the deflector inside the BSM. Because using a screen blocks the beam, the energy screen cannot be used for a full six-dimensional scan as the beam cannot reach the BSM. As the beam travels through slits for select coordinates, a large fraction of particles is lost. By the end, approximately 10^{-7} of the particles from the original beam core reach the detector. This is sufficient for five-dimensional scans but not for six-dimensional scans using the BSM screen. As such, a micro-channel plate (MCP) is used to increase the signal strength for the BSM screen.

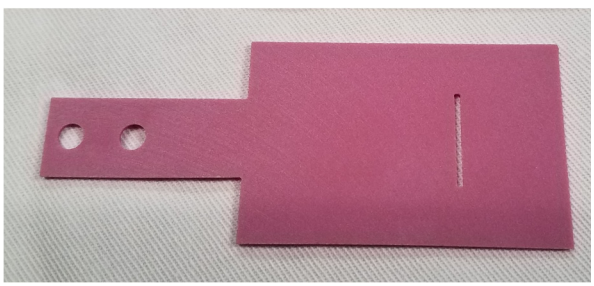


Figure 3: The Energy (fifth) slit that also doubled as a scintillating screen.

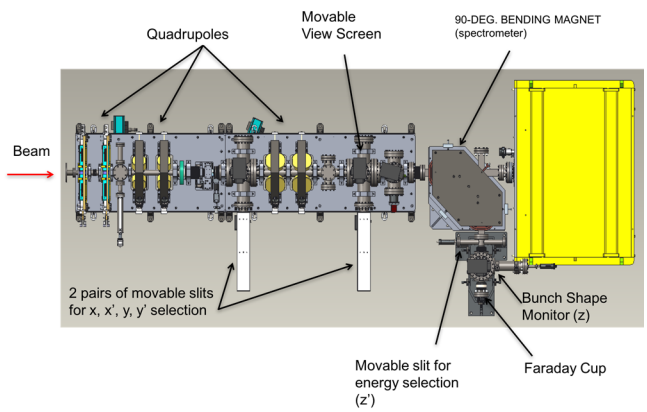


Figure 4: A schematic view of the BTF section where the diagnostics for the six-dimensional scan occur.

The Beam Test Facility (BTF) at the Spallation Neutron Source (SNS) houses the experiment [4]. Figure 4 shows the beam line downstream of the RFQ where the diagnostics are located. After the RFQ, there are four quadrupole magnets for focusing followed by two moveable slits, one aligned on the horizontal and the other on the vertical. The third pair of quadrupoles is followed by the second pair of identical slits. These slits all have an aperture width of 200 μm. Next is the 90^0 bend using a dipole magnet, followed by a final moveable aperture aligned vertically. The beam line ends at the Beam Shape Monitor. Specialized scripts based on an Open XAL framework were developed and are used to perform the multidimensional scans [5].

DATA ANALYSIS

After a scan is made, it is necessary to interpolate the raw data because it is rarified and not on a regular grid. Interpolating to a regular grid allows for quick integration over dimensions to view subsets of the data and helps generate more realistic distributions for simulations. However, interpolating so many points in six dimensions is complicated.

Custom codes were written to take advantage of how the data is saved. A linear interpolation method is shown in Fig. 5 for a six-dimensional scan. The logic is to interpolate one dimension at a time in the order the measurements are made, starting by interpolating over the set of x points for each different set of (y, x', y', w). This is done by interpolating the phase plots point by point linearly to determine the phase plot at new regular x points. The result is a regular 2D grid for each set of (y, x', y', w) of x and phase. This technique continues for each dimension, interpolating point by point for increasing dimensionalities, using the same order as the scan until a regular 6D space is built. Once the data has been interpolated, correlations can be found quicker and distributions can be generated for simulations.

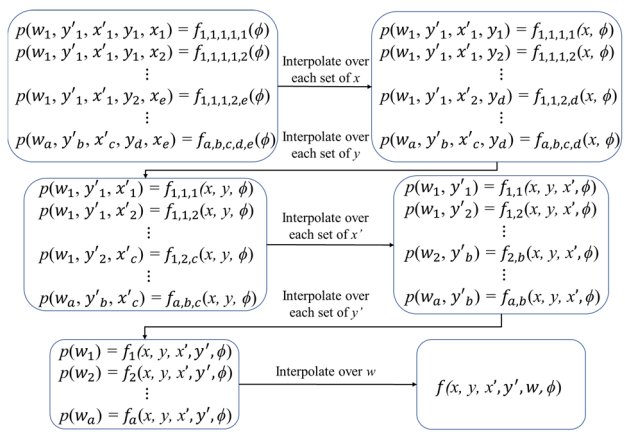


Figure 5: Scheme for 6D interpolations.

Many measurements, including the first full six-dimensional scan, were completed using the technique described above. The six-dimensional scan took 32 hours and resulted in 5,675,740 points on a near-regular grid in the 6D phase space. Figure 6 shows that the beam current during the 6D scan, measured upstream of the slits, remained constant for the duration except for a few dropouts. The experimental data provide an opportunity to explore the internal structure of the full phase space distribution, and specifically to check for correlations between coordinates in all six degrees of freedom. There is no proven technique for finding arbitrary correlations in high dimensional spaces. The linear correlation coefficients can be calculated for all combinations of the six degrees of freedom, but even zero values for the correlation coefficients do not guarantee the absence of

Content from this work may be used under the terms of the CC BY 3.0 licence (© 2018). Any distribution of this work must maintain attribution to the author(s), title of the work, publisher, and DOI.

ISBN: 978-3-95450-194-6 ISSN: 2226-0366 doi:10.18429/JACoW-LINAC2018-FR1A01

Content from this work may be used under the terms of the CC BY 3.0 licence (© 2018). Any distribution of this work must maintain attribution to the author(s), title of the work, publisher, and DOI.

higher order correlations, and a correlation of any order invalidates the common assumptions for the 6D phase space. Full exploration of this problem remains to be done.

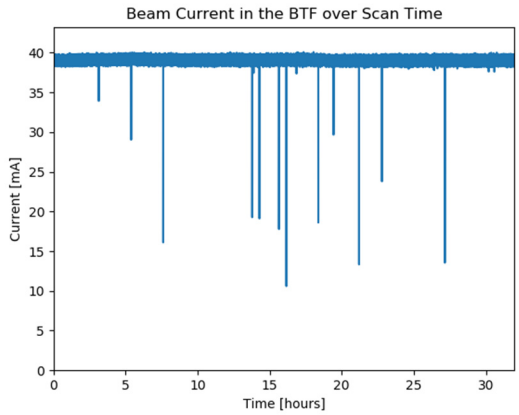


Figure 6: The beam current upstream of the slits measured during the 6D scan.

In order to visually show possible correlations within the distributions, a method of displaying the 6D results in 2D is needed. This is done through various 1D and 2D projections and partial projections of the higher dimension distributions. The key advantage of using the partial projections is that they avoid integration over all dimensions, which can mask important details of the high dimensionality distribution. The following definitions are used in the data analysis discussion below. Full projections are reduced dimensionality distribution functions obtained by integrating over all unused coordinates:

1D: $$f(a) = \int_{-\infty}^{\infty} f_6(a,\vec{x})\, d\vec{x},$$

2D: $$f(a,b) = \int_{-\infty}^{\infty} f_6(a,b,\vec{x})\, d\vec{x}.$$

On the other hand, partial projections are reduced dimensionality distribution functions obtained by fixing some coordinates to constant values and integrating over others:

1D: $$p(a) = \int_{-\infty}^{\infty} f_6(a,\vec{v}=\overrightarrow{v_0},\vec{x})\, d\vec{x},$$

2D: $$p(a,b) = \int_{-\infty}^{\infty} f_6(a,b,\vec{v}=\overrightarrow{v_0},\vec{x})\, d\vec{x}.$$

In the formulas above a, b are any coordinate from (x,x',y,y',w,φ) set; $\vec{v}$ is a vector of coordinates remaining in (x,x',y,y',w,φ) set after a, b are removed; $\vec{x}$ is the vector of coordinates remaining in (x,x',y,y',w,φ) set after a, b and $\vec{v}$ are removed. Vector $\vec{v}$ is equal to the vector $\vec{v}_0$, which is the fixed coordinate of interest for the partial projection. A partial projection can be measured directly by leaving the selectors responsible for the fixed coordinate $\vec{v}_0$ at fixed positions during a scan. These scans are much faster than full 6D scans and allow exploring spaces of interest with higher resolution. Multiple scans with different beam parameters can also be done this way in reasonable time durations.

RESULTS

Below are some results from past scans. Figure 7 shows a one-dimensional scan that used a single slit to measure the horizontal beam distribution and the one-dimensional horizontal axis projection from a four-dimensional scan. Note the agreement is very good. Figure 8 is the two-dimensional horizontal phase space component of a five-dimensional scan measurement. And Figure 9 shows the two-dimensional distribution of vertical momentum against horizontal position projected from the same five-dimensional scan.

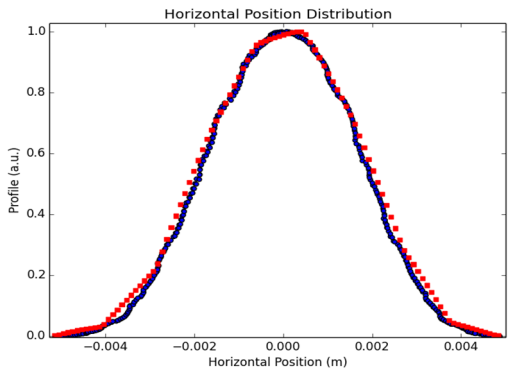


Figure 7: The horizontal beam distribution. Blue is directly measured with a single slit. Red is the projection from a 4D measurement.

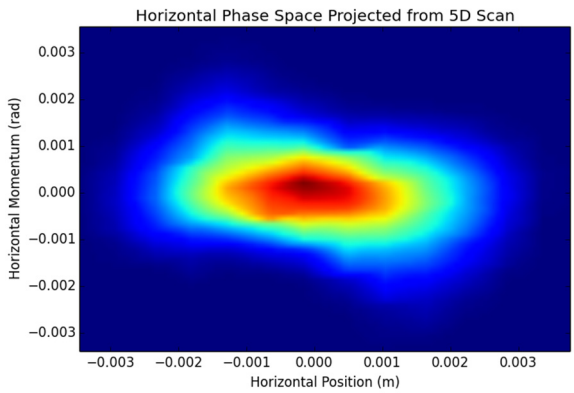


Figure 8: The horizontal phase space from a 5D measurement.

An interesting result was found using five-dimensional scans. Figure 10 shows a 2D color map of the $p(x',w)$ partial projection with $x = y = y' = 0$ (these slits were fixed in the beam center while the x' slit was allowed to move) and integrated over φ (the energy screen was used). A dependence of the w distribution upon the coordinate value x' is obvious in the plot. The w distribution showed similar dependence with x, y, and y' as well. Figure 11 is a graph of the energy spread for an entire 5D scan projected to a single dimension, showing the expected distribution peaking at the target energy.

ISBN: 978-3-95450-194-6 ISSN: 2226-0366 doi:10.18429/JACoW-LINAC2018-FR1A01

Figure 12, in turn, shows the graph of selected energy spreads measured near the beam core. These are individual measurements with the transverse position and vertical momentum all located at the beam center, but with three different horizontal momenta. The blue curve is where the horizontal momentum is zero. Two peaks with a dip at the reference energy are observed. This result was only found at the beam core; the measured distribution was Gaussian as expected farther away from the center. Figure 13 shows a partial projection of the longitudinal phase space where the transverse slits were all arranged to allow the center of the beam through, $x = y = x' = y' = 0$. This measurement represents a single part of a full 6D measurement. The distribution shows the expected linear correlation between energy and phase with the two peaks seen in the previous figures.

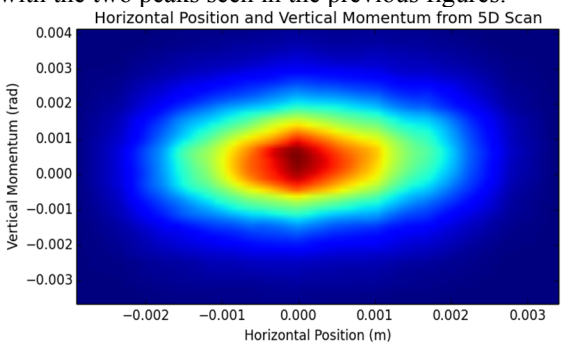


Figure 9: Vertical momentum versus horizontal position distribution from a 5D measurement.

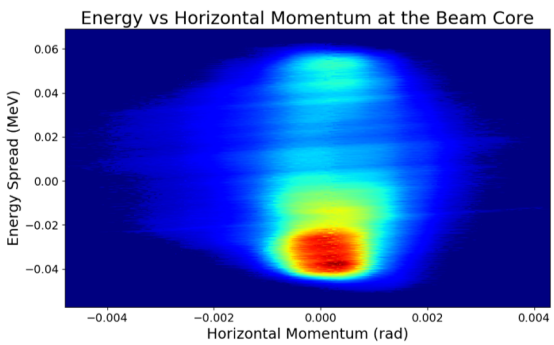


Figure 10: The energy spread from a 5D scan

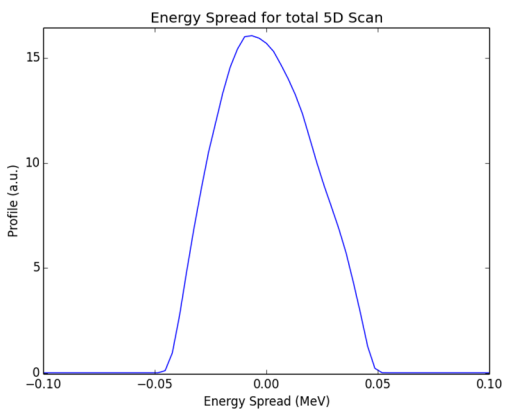


Figure 11: The energy spread from a 5D scan.

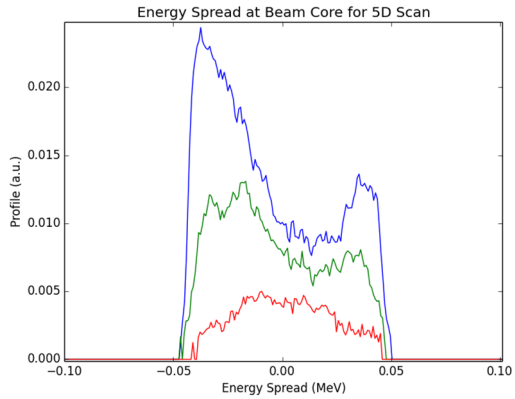


Figure 12: Energy spread from beam core in 5D scan. Blue is with no horizontal momentum. Green and red have horizontal momenta progressively further from zero.

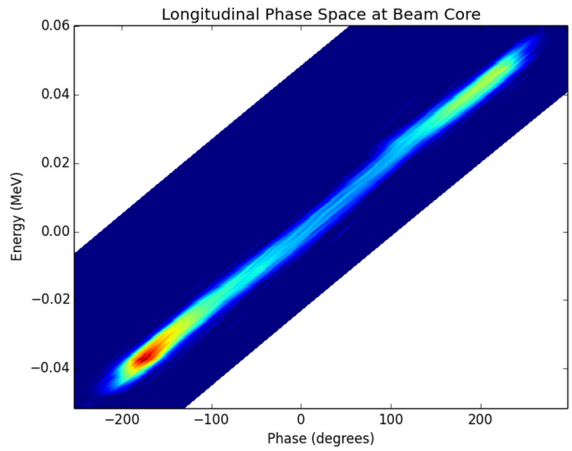


Figure 13: The longitudinal phase space measured at the beam core.

The plots in Fig. 14 show 1D partial projection energy spectrums with different numbers of fixed coordinates: the green line shows the energy spectrum measured with $x = x' = 0$ and integrated over y, y'; the red line shows the energy spectrum measured with $x = x' = y = 0$, integrated over y'; and the blue line shows the energy spectrum measured with $x = x' = y = y' = 0$. All three measurements are integrated over φ. The plots demonstrate the necessity of performing the scan in at least 4D for the correlation to become visible, and in 5D for resolving the details. The plots in Fig. 15 show 1D partial projections with four fixed coordinates $x = x' = y = y' = 0$ (all slits fixed at the beam center) measured for beam currents of 40, 30, and 20 mA. The correlation is well pronounced at 40 mA, becomes less visible with a smaller beam current of 30 mA, and completely disappears at 20 mA. This measurement convincingly demonstrates that the observed correlation is created by the Coulomb forces within the distribution.

Content from this work may be used under the terms of the CC BY 3.0 licence (© 2018). Any distribution of this work must maintain attribution to the author(s), title of the work, publisher, and DOI.

ISBN: 978-3-95450-194-6 ISSN: 2226-0366 doi:10.18429/JACoW-LINAC2018-FR1A01

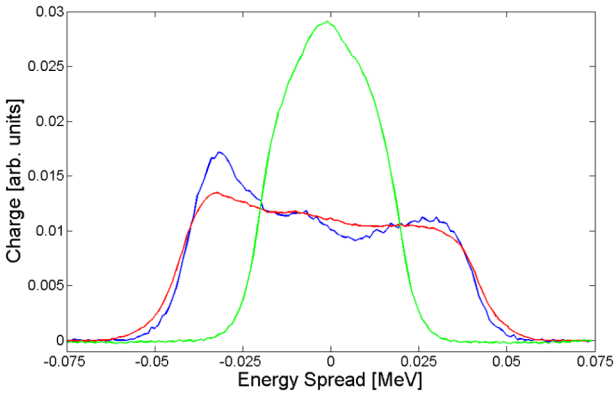


Figure 14: Plots of three different 1D partial projections on energy. Each plot has a different number of fixed slits near the center of the beam. The green curve fixes two slits, the red curve fixes three, and the blue curve fixes four. The curves are normalized by area.

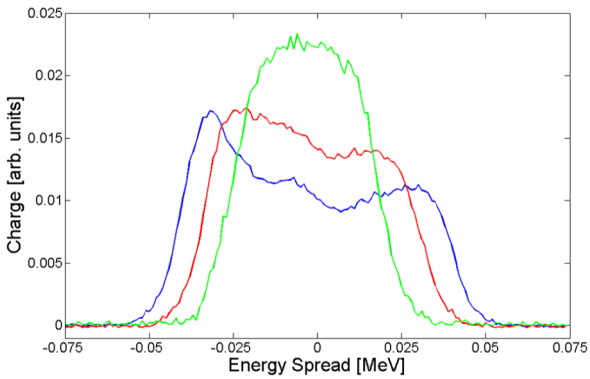


Figure 15: Plots of partial projections on energy with three different beam currents. The green curve is from 20 mA, the red curve is from 30 mA, and the blue curve is from 40 mA. The correlation is more pronounced with increasing current, which indicates Coulomb forces cause the correlation. The curves are normalized by area.

While a precise simulation using the measured distribution is left for future work, a simple computer simulation is sufficient to elucidate the beam physics. A 1 m long transport line consisting of drifts and four quadrupole magnets arranged similarly to the first 1 m of the BTF beam line was simulated using PARMILA particle-in-cell code [6]. An ideal 6D Gaussian function was used to generate the initial particle coordinates. Partial projections on the *w-y'* plane of the distribution function at the beam line exit are shown in Fig. 16 for two cases: a 10 mA and a 100 mA beam current. A pattern similar to the measurement in Fig. 10 is clearly visible only on the projection for high beam current, confirming that Coulomb forces are responsible for creating this correlation in the 6D phase space distribution. Furthermore, it is interesting to note that reproducing the correlation in simulation does not require any novel or complex beam physics. In parallel with the experiment, the key is knowing to look at the partial rather than the integrated 2D projection (e.g., to maintain a high dimensional approach when viewing the lower dimensional subspaces). This reinforces the notion that the full 6D distribution is required for a complete understanding of the beam physics.

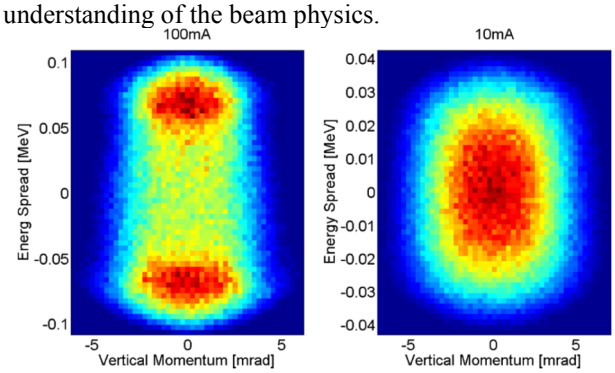


Figure 16: Two plots of the partial projection of the energy spread w against the vertical momentum y for a 100 mA (left) and a 10 mA (right) simulated beam transport.

The time required to complete a scan is the largest limiting factor for higher dimensionality scans. This limitation was partially diminished with the use of luminescent screens to measure the energy or the phase. Figure 17 shows a plan to significantly decrease scan time by removing the energy slit so that the two longitudinal dimensions can be completely measured simultaneously. In the future, we plan to add a FODO line to the end of the BTF with matching and mismatching quadrupoles to study beam halo development and benchmark simulations against the new measured distributions [7].

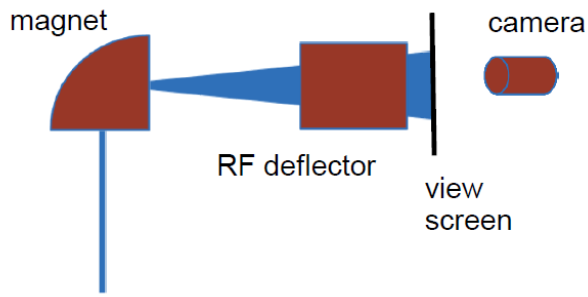


Figure 17: Proposed plan to measure the entire 2D longitudinal phase space simultaneously.

ACKNOWLEDGEMENT

This work has been partially supported by NSF Accelerator Science grant 1535312.

This manuscript has been authored by UT-Battelle, LLC, under Contract No. DE-AC0500OR22725 with the U.S. Department of Energy. The United States Government retains and the publisher, by accepting the article for publication, acknowledges that the United States Government retains a non-exclusive, paid-up, irrevocable, world-wide license to publish or reproduce the published form of this manuscript, or allow others to do so, for the United States Government purposes. The Department of Energy will provide public access to these results of federally sponsored research in accordance with the DOE Public Access Plan (http://energy.gov/downloads/doe-public-access-plan).

Content from this work may be used under the terms of the CC BY 3.0 licence (© 2018). Any distribution of this work must maintain attribution to the author(s), title of the work, publisher, and DOI.

ISBN: 978-3-95450-194-6 ISSN: 2226-0366 doi:10.18429/JACoW-LINAC2018-FR1A01

REFERENCES

[1] S. Machida and R.D. Ryne, "Summary of session C: Space charge simulation and experiment," in *Proc. ICFA HB'04*, Bensheim, 2004, p. 454.

[2] J. Qiang, P.L. Colestock, D. Gilpatrick, H.V. Smith, T.P. Wangler, and M.E. Schulze, "Macroparticle simulation studies of a proton beam halo experiment," *PRSTAB*, vol. 5, no. 124201, 2002.

[3] A.V. Feschenko, "Methods and Instrumentation for Bunch Shape Measurements", in *Proc. PAC'01*, Chicago, IL, USA, Jun. 2001, pp. 517-519.

[4] A. Aleksandrov, M. Champion, M. Crofford, K. Ewald, Y. Kang, A. Menshov, M. Middendorf, S. Murry, R. Saethre, M. Stockli, A. Webster, R. Welton, A. Zhukov, "Status of the New 2.5 MeV Test Facility at SNS," in *Proc. LINAC'14*, Geneva, Switzerland, 2014, p. 1105.

[5] A. Zhukov et al., "Open XAL Status Report 2018," in *Proc. IPAC'18*, Vancouver, B.C., Canada, Apr.-May 2018, doi:10.18429/JACoW-IPAC2018-THPAK069

[6] J.H. Billen and H. Takeda, "PARMILA Manual", Los Alamos, NM. USA, 1998 Technical Report No. LAUR-98-4478 (revised 2004).

[7] Z. Zhang et al., "FODO Lattice Design for Beam Halo Research at SNS", presented at IPAC17, Copenhagen, Denmark, May 2017. doi.org/10.18429/JACoW-IPAC2017-TUPVA148

Content from this work may be used under the terms of the CC BY 3.0 licence (© 2018). Any distribution of this work must maintain attribution to the author(s), title of the work, publisher, and DOI.

ISBN: 978-3-95450-194-6 ISSN: 2226-0366 doi:10.18429/JACoW-LINAC2018-FR1A02

BUNCH LENGTH MEASUREMENTS USING TRANSVERSE DEFLECTING SYSTEMS

M. Hüning†, DESY, Hamburg, Germany

Abstract

Shorter and shorter bunch lengths (some 10 fs) require sophisticated bunch length measurement devices. Free electron lasers - but not only - use transverse deflecting systems. Employing suitable diagnostic tools measurements are not limited to bunch lengths but can be extended to longitudinal profiles and phase-space distributions, and slice emittances. Not only do successfully operated systems aid the commissioning and operation of FELs but they allow control over more sophisticated phase-space manipulations. The design and construction of such systems, actually operated at different RF frequencies, includes cavity design and fabrication, powerful RF systems, low level RF control, beam lines, diagnostics, and data analysis.

INTRODUCTION

Many applications for electron beams require very short bunchlengths in the order of a few 10 fs and below. These applications range from FEL and electron diffraction to experiments towards novel accelerator schemes. Often the electron bunches are created with a considerably longer pulse length and only later they are compressed to their ultimate length. During the acceleration and compression process several non-linear effects can occur. Also coherent effects excited by the short intense bunches may occur. For a well-controlled operation of such accelerators longitudinal beam diagnostics with sufficiently low time resolution is required. Streak cameras which are used for diagnosing bunch lengths in the picosecond range are limited at resolutions of approximately 100 fs [1, 2]. Other diagnostic methods have been developed like spectroscopy of coherent radiation from the beam [3, 4, 5] or electro-optic sampling of the self-field of the beam [6]. Often these measurement techniques suffer from frequency cut-off, resonances or loss of phase information. Furthermore they are limited to diagnosing the current profile only. Another possibility is longitudinal phase space tomography by energy-modulating the bunches, which suffers from an uncomplete rotation in phase-space [7].

A much more straightforward method for measuring the longitudinal phase space is by streaking the original bunches with a transverse deflecting structure [8].

LAYOUT OF TDS BEAM DIAGNOSTICS

The most basic layout of a TDS beam diagnostics system is the combination of a high frequency deflector with a viewscreen after a short drift. By injecting the beam into the deflector at the zerocrossing of the RF the electrons in receive a transverse kick depending on their relative position within the bunch. The beam size on the viewscreen is given by the square sum of the streaked and un-streaked beam size [9]:

$$\sigma_y = \sqrt{\sigma_{y0}^2 + \sigma_{ys}^2},$$

with

$$\sigma_{ys} = \omega\sigma_t \frac{eV_0}{E} \cos\varphi \sqrt{\beta_d \beta_s} \sin\Delta\psi, \quad (1)$$

with ω the angular frequency and V_0 the effective deflecting voltage of the RF and E the beam energy, β_d, β_s the beta function at the deflector and screen, respectively, and $\Delta\psi$ the betatron phase advance between deflector and screen. The RF phase φ is zero at the zerocrossing of the field. The lower limit for the resolution may be defined as the point when the streak equals the natural beam size on the screen. This condition results in the following expression for the minimum achievable resolution [10]

$$\frac{1}{\sigma_{t0}} = \omega \frac{eV_0}{E} \cos\varphi \sqrt{\beta_d/\varepsilon} \sin\Delta\psi. \quad (2)$$

It is interesting to note that the resolution does not depend on the beta function at the location of the screen.

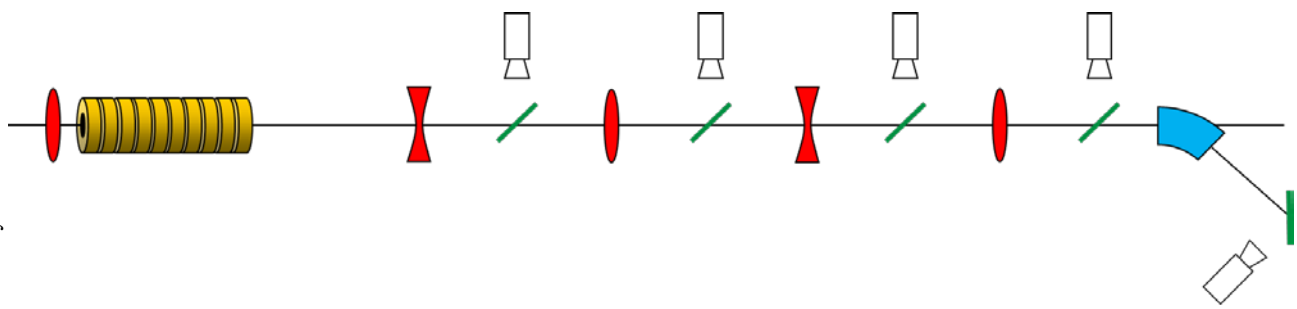


Figure 1: Typical setup of a TDS beam diagnostic system. The minimal system consists of a structure and a viewscreen. A spectrometer magnet allows to image the longitudinal phase-space. A series of screens along a FODO structure serves to measure slice emittances easily.

† markus.huening@desy.de

Content from this work may be used under the terms of the CC BY 3.0 licence (© 2018). Any distribution of this work must maintain attribution to the author(s), title of the work, publisher, and DOI.

ISBN: 978-3-95450-194-6 ISSN: 2226-0366 doi:10.18429/JACoW-LINAC2018-FR1A02

The physics of the deflecting mode in first order result in the following relation between transverse kick and off-axis acceleration (Panofsky-Wenzel [11])

$$V_z(y) = kyV_0. \quad (3)$$

The above basic setup was used in the first applications of this measurement scheme [9, 12]. The full potential of a TDS system is achieved with an extended setup. For this a spectrometer dipole and an additional screen is required. This allows for direct imaging of the longitudinal phase space [13]. The above relations (2) and (3) however imply a conflict between the achievable longitudinal $\sigma_z=c\sigma_t$ and relative energy resolution $\delta_E=\sigma_E/E$

$$\delta_E\sigma_z = \varepsilon. \quad (4)$$

Figure 1 shows one further extension of the setup. Here 4 screens positioned with suitable phase advance within a FODO lattice are used to quickly measure the transverse emittance of slices of the bunch [14]. Due to the need to space the screens appropriately for the emittance measurement one has to find a compromise between this and the optimal phase advance for the TDS streak [15]. Unimpeded measurement of the slice emittance is only possible in the plane perpendicular to the deflection of the TDS. In the direction of the streak the longitudinal and transverse distribution are intermixed. One might attempt to de-convolute the two with tomographic methods. However, even when an algorithm suitable for the limited rotation data [16] is applied, the resolution of the beam size measurement will suffer [7].

In the case of the superconducting linacs FLASH and the European XFEL the evolution was advanced another step by placing the viewscreens away from the beam axis. The bunches to be measured are deflected onto the screens by fast kicker magnets [17]. That way it is possible to perform the diagnostics for selected bunches within the bunch train only.

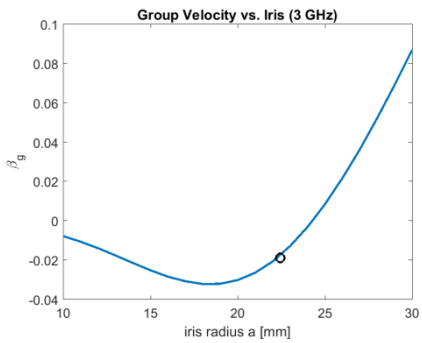


Figure 2: Group velocity of the deflecting mode versus radius of the iris at 3 GHz.

BASIC PROPERTIES OF THE DEFLECTING MODE

In the literature the deflecting mode is referred to as hybrid EM mode HEM_{11} [17]. It shows a strong resemblance of the TM_{11} mode but latter waveguide mode does not provide any deflection at a phase velocity equal *c*. In a cylindrically symmetric structure the two polarizations of the mode are degenerate and can mix. To prevent this, the symmetry of the structure is broken on purpose. Usually holes are placed into the iris walls for this.

For analysis of the deflecting mode numerical studies with CST MICROWAVE STUDIO [18] have been performed and some general scaling behaviour studied.

Figure 2 shows the group velocity as a function of iris radius for a mode frequency of 2.856 GHz and a phase shift of 120° per cell. At small iris sizes the coupling between the cells is dominantly magnetic and hence the group velocity negative. The circle indicates properties of LOLA IV [19]. The slight deviation from the curve is caused by the simplified model. The corresponding effective average deflecting field is shown in Fig. 3. At the crossover point of the group velocity the calculation diverges and becomes unreliable. Apparently the deflection becomes very strong for small apertures.

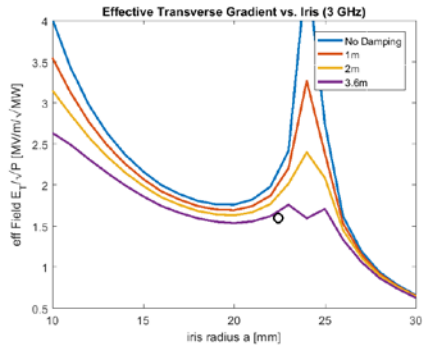


Figure 3: Effective average deflecting field.

When the iris radius is kept constant to a certain degree this counteracts the increase of field with frequency that normally would be expected (see Fig. 4). This is due to the fact that the group velocity increases at the same time. Note however that according to Eq. (2) the higher frequency is still advantageous for time resolution. But for other applications this might be interesting.

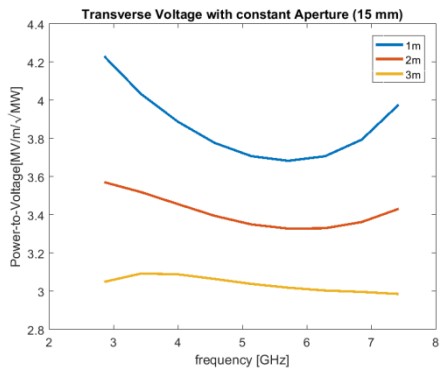


Figure 4: Deflecting field versus frequency while keeping the aperture constant.

Figure 5 shows the expected behaviour of increasing voltage when the cell is scaled as a whole. For longer structures this effect is limited by the increase of damping with frequency. Here the usual optimizations of structure length apply. For comparison the plot also shows the total voltage with the power split into two shorter structures.

Content from this work may be used under the terms of the CC BY 3.0 licence (© 2018). Any distribution of this work must maintain attribution to the author(s), title of the work, publisher, and DOI.

ISBN: 978-3-95450-194-6 ISSN: 2226-0366 doi:10.18429/JACoW-LINAC2018-FR1A02

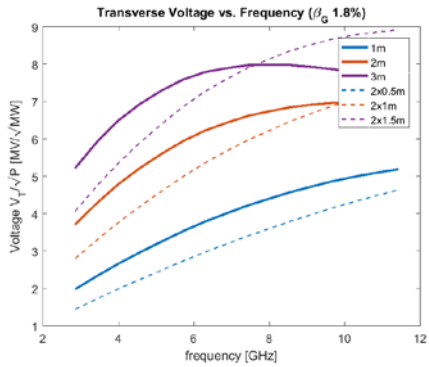


Figure 5: Deflecting field versus frequency with constant group velocity. The dashed curves are calculated for two structures with the input power split between the two.

EXAMPLE TDS SYSTEMS

Depending on the intended application there is a wide range of design parameters to choose from. Table 1 gives a summary of a few examples of transverse deflecting structures for beam diagnostics. The most important boundary conditions are of course the intended streak, the beam energy and the available space. Given the considerable cost involved with building and maintaining a high power RF station the availability of a suitable RF source plays an important role, too.

Consequently the first implementations [9, 11] relied on the structure LOLA IV that was available in storage at SLAC and klystrons from the SLAC linac. The systems allowed for time resolution in the order of 10 fs. Currently they are used in the bunch compressor of the LCLS [20] and in the first undulator beamline of FLASH [11].

At the Shanghai DUV-FEL facility a TDS was installed directly at the RF gun [21, 22]. Because of the low beam energy and availability of excess RF power from the gun klystron a shortened version of LOLA IV was the most straightforward solution.

At the SPARC facility a standing wave TDS was developed [23] to be used at beam energy of 150 MeV. The design results in a very high power to voltage ratio. For mode stabilization longitudinal rods are placed into the cells. The design was so successful that it was adopted for FERMI@Elettra [24, 25] and the SwissFEL injector test facility [26].

At the high energy end of the FERMI@Elettra facility a system of two TDS is installed [25, 27]. One of the two deflects horizontally the other vertically. The nominal input power of 15 MW is provided by one output arm of a high power klystron that can be switched between the two deflectors. The other arm of the klystron serves to power an accelerating structure [28].

For the European XFEL a deflector with an active length of 1.5 m was developed [29]. A shortened version of 0.5 m is used in the injector at 150 MeV, a single TDS is foreseen for the first bunch compressor at 700 MeV and a combination of two structures is installed in the second bunch compressor at 2.4 GeV. The latter two are connected in series to effectively form a 3 m structure. The fill-time of the structure was chosen such, that it can be filled and emptied between two consecutive bunches in 4.5 MHz operation of the FEL.

The drive linac for the FEL facility SACLA operates in C-Band. It was therefore logical to also design a C-Band TDS [30]. The change in frequency not only boosts power to voltage ration but also with the factor ω in Eq. (2) increases the speed of the streak. The overall improvement in temporal resolution over an otherwise comparable S-Band deflector is approximately a factor of 3.

Table 1: Specifications of Selected TDS Structures

	LOLA IV	Shanghai DUV-FEL IHEP	SPARC FERMI SwissFEL	FERMI	European XFEL INR	RAIDEN SACLA SwissFEL	LCLS	PolariX
Active length [m]	3.64	0.35	0.25	2.466	2×1.5	2×1.7	2×1	1
Frequency [GHz]	2.856	2.856	2.998	2.998	2.998	5.712	11.424	11.995
Fill-Time [ns]	645	62	800	500	2×333	2×269	2×106	130
Group Velocity/c	-0.0189	-0.0189	SW	-0.0157	-0.0152	-0.0214	-0.0315	-0.0266
Iris Diameter [mm]	44.88	44.88	36	25	43.4	12×20	10	8
typ. Vltg, Pwr [MV, MW]	26, 20	0.56, 1	4.9, 5	23, 15	25.9, 20	60, 40	85, 160	12.8, 6
Pwr-to-Vltg [MV/m/√MW]	1.6	1.6	8.8	2.4	1.9	4	5.46	6.12
Beam Energy [MeV]	1100	5	150	1200	1500	1450	15000	1100

Content from this work may be used under the terms of the CC BY 3.0 licence (© 2018). Any distribution of this work must maintain attribution to the author(s), title of the work, publisher, and DOI.

ISBN: 978-3-95450-194-6 ISSN: 2226-0366 doi:10.18429/JACoW-LINAC2018-FR1A02

Another noteworthy design feature is the phase advance per cell of $5\pi/6$ in contrast to $2\pi/3$ used elsewhere. This reduces the number of irises per length and hence the manufacturing cost [31]. The iris has a racetrack shape for mode stabilization. To highlight this, the inventors dubbed the structure RAIDEN.

At the SwissFEL it was decided to obtain structures of this kind at their first undulator (Aramis) [32]. Two commercially available structures were installed and are routinely operated at 80 MV deflecting voltage [33].

The availability of equipment and yearlong experience in X-Band enabled SLAC to develop and install an X-Band TDS for LCLS [34]. The large deflecting voltage and high frequency allow for time resolution of a few femtoseconds at the full beam energy of 15 GeV [35]. The structure is located behind the undulator and allows to indirectly measure the length of the X-ray pulse [36].

NEW DEVELOPMENTS

As mentioned above slice emittance measurements are only possible perpendicular to the streaking direction. Therefore it is desirable that the streaking direction may be changed. This is of course possible with a second deflector but a deflector with adjustable polarization would be superior.

A design has been proposed at CERN for X-Band TDS with variable polarization. A collaboration has been formed between CERN, PSI and DESY to design, build and test such structures [38]. The input coupler with two arms is built such that the phase relation between the two arms determines the orientation of the mode that is fed into the structure. The structure itself is strictly axially symmetric to avoid any cause for deterioration of the mode polarization. There is no cell tuning or RF pickup. Meanwhile the design is well advanced and the prototype underway [39]. High power RF tests are foreseen for early 2019 and first beam tests in the following summer. Referring to the main features of the structure it is called PolariX.

At INR an RF deflector has been proposed [40] with a field configuration that more closely resembles a TE_{11} mode. It promises better RF efficiency than the conventional structures and the design was optimized to reduce higher order aberrations of the field. This will be advantageous for high precision measurements or in cases where the TDS is used for beam manipulations. A prototype has been built and soon will be tested with beam in the REGAE facility [41] at DESY.

RF CONTROL

The streak applied in the most powerful TDS systems is so fast that the requirements for RF phase stability are governed by limits to beam position jitter. These limits are either given by the size of the beam image on the screen or even by particle loss. In the case of LCLS the limit was derived to be smaller than 0.1° at X-Band [35]. This corresponds to 20 fs and is 10 times the resolution of the measurement. For the PolariX TDS in FLASH the requirement for phase stability was determined to be 0.25°. This corresponds to a temperature stability of 35 mK in the structure and 10 mK in the pulse compressor.

RF feedback loops acting from pulse to pulse can relax the temperature requirements assuming that temperature changes develop over the time span of several RF pulses. Given the short duration of the RF pulses a fast feedback within the pulse is often next to impossible. This means that fast jitters are often passed on undamped.

The biggest source for fast phase jitter is the klystron modulator. For a 6 MW X-Band klystron as it is used at FLASH the translation is 3 fs phase jitter per 10 ppm voltage jitter. This stability can indeed be achieved with the most modern semiconductor switched modulators. The voltage stability of more conventional modulators however lies in the range of several 100 ppm, which can pose a limit to the maximum available streak [37].

APPLICATIONS

The first and most obvious application of TDS was for pure bunch length and longitudinal bunch profile measurements [9, 11]. A whole new domain is the extension to measuring the longitudinal phase space. This allows for example to adjust RF phases and bunch compression in real-time [13]. Measurements of the slice emittance and matching [14, 42] offer a much better handle on adjusting the beam optics than measuring the pure projected emittance ever could. For the commissioning and operation of two color [43] or seeding schemes [44] TDS are practically indispensable.

Moving the TDS behind the undulator opened up more diagnostics possibilities and enables continuous monitoring [35]. This way it is possible to not only measure the longitudinal profile of the electron bunch but indirectly also the length of the X-ray pulse [36]. This is very useful when the beam is manipulated to achieve X-ray pulses even shorter than the electron bunches [45].

CONCLUSION

Transverse deflecting structures provide very powerful means for time resolved beam diagnostics in the femtosecond range. Their full potential is still being explored and expanded. The only limit to their widespread application seems to be the cost involved for building and maintaining such systems.

The overview presented here is by nature subjective and limited. By no means are topics or devices not mentioned here considered unimportant.

ACKNOWLEDGEMENTS

The author wishes to thank the colleagues B. Beutner, P. Craievich, J.P. Dai, Y. Ding, H. Ego, P. Krejcik and V. Paramonov for providing material and input for the presentation at the conference.

REFERENCES

[1] https://www.hamamatsu.com

Content from this work may be used under the terms of the CC BY 3.0 licence (© 2018). Any distribution of this work must maintain attribution to the author(s), title of the work, publisher, and DOI.

ISBN: 978-3-95450-194-6 ISSN: 2226-0366 doi:10.18429/JACoW-LINAC2018-FR1A02

Content from this work may be used under the terms of the CC BY 3.0 licence (© 2018). Any distribution of this work must maintain attribution to the author(s), title of the work, publisher, and DOI.

[2] https://optronis.com

[3] A. Azima *et al.*, "Comparative study of bunch length and arrival time measurements at FLASH", Proc. of EPAC2006, Edinburgh, UK, 2006.

[4] T. Maxwell *et al.*, "Middle-infrared prism spectrometer for single-shot bunch length diagnostics at the LCLS", *Proc. of IBIC2012*, Tsukuba, Japan, 2012.

[5] S. Wesch *et al.*, "Fast bunch profile monitoring with THz spectroscopy of coherent radiation at FLASH", *Proc. of BIW2012*, Newport News, USA, 2012.

[6] G. Knippels *et al.*, "Single Shot Electron-Beam Bunch Length Measurements", *Proc. of DIPAC 2003*, Mainz, Germany, 2003.

[7] M. Hüning, "Analysis of Surface Roughness Wake Fields and Longitudinal Phase Space in a Linear Electron Accelerator", DESY-THESIS-2002-029, Hamburg, Germany, 2002.

[8] X.J. Wang, "Producing and Measuring Small Electron Bunches", *Proc. of PAC99*, New York, USA, 1999.

[9] R. Akre, L. Bentson, P. Emma, P. Krejcik, "A Transverse RF Deflecting Structure for Bunch Length and Phase Space Diagnostics", *Proc. of PAC01*, Chicago, IL, USA, 2001.

[10] C. Behrens, C. Gerth, "On the limitations of longitudinal phase space measurements using a transverse deflecting structure", *Proc. of DIPAC09*, Basel, Switzerland. 2009.

[11] W.K.H. Panofsky, W.A. Wenzel, Rev. of. Sci. Instr. 27, 967, 1956.

[12] M. Hüning *et al.*, "Observation of femtosecond bunch length using a transverse deflecting structure", *Proc. of FEL2005*, Palo Alto,USA, 2005.

[13] E. Vogel *et al.*, "Test and Commissioning of the Third Harmonic RF System for FLASH", *Proc. of IPAC10*, Kyoto, Japan, 2010.

[14] M. Yan *et al.*, "Comparison of quadrupole scan and multi-screen method for the measurement of projected and slice emittance at the SwissFEL injector test facility", *Proc. of FEL2014*, Basel, Switzerland, 2014.

[15] M. Röhrs, C. Gerth, "Electron beam diagnostics with transverse deflecting structures at the European X-ray free electron laser", *Proc. of FEL08*, Gyeongju, Korea, 2008.

[16] G. Minerbo, "MENT: A Maximum Entropy Algorithm for Reconstructing a Source from Projection Data", *Computer Graphics and Image Processing*, 1979.

[17] C. Gerth *et al.*, "Online longitudinal bunch profile and slice emittance diagnostics at the European XFEL", *Proc. of IBIC2017*, Grand Rapids, USA, 2017.

[18] CST MICROWAVE STUDIO, http://www.cst.com

[19] R. Helm, G. Loew, R. Miller, R. Neal, "Recent Developments at SLAC", SLAC-PUB-420, Palo Alto, USA, 1968.

[20] P. Krejcik *et al.*, "Ultra-Short Electron Bunch and X-Ray Temporal Diagnostics with an X-Band Transverse Deflecting Cavity", *Proc. of IBIC2012*, Tsukuba, Japan, 2012.

[21] J.P. Dai *et al.*, "Bunch length measurement using a traveling wave RF deflector", *Chinese Physics C*, 34, p138-142, 2010.

[22] J.R. Zhang, J.P. Dai, G.X. Pei, M. Hou, "Bunch Length Measurement using a Travelling Wave RF Deflector", *Proc. of PAC09*, Vancouver, Canada, 2009.

[23] D. Alesini *et al.*, "RF deflector design and measurements for the longitudinal and transvere phase space characterization at SPARC", *NIM A* 568, 488-502, 2006.

[24] P. Craievich *et al.*, "A low energy RF deflector for the FERMI@Elettra project", *Proc. of FEL2010*, Malmö, Sweden, 2010.

[25] M. Veronese *et al.*, "Longitudinal electron beam diagnostics for the FERMI@Elettra FEL", *Proc. of BIW2012*, Newport News, USA, 2012.

[26] Rasmus Ischebeck *et al.*, "Instrumentation Activities at the SwissFEL Injector Test Facility", *Proc. of IBIC2013*, Oxford, UK, 2013.

[27] P. Craievich *et al.*, "A transverse RF deflecting cavity for the FERMI@Elettra project", *Proc. of DIPAC2007*, Venice, Italy, 2007.

[28] M. dal Forno, "High Energy RF Deflectors for the FERMI@elettra Project", *Proc. of IPAC 2013*, Shanghai, China, 2013.

[29] D. Denisenko, V. Paramonov, "Transverse deflecting structure parameters study", *Proc. of RuPAC2008*, Zvenigorod, Russia, 2008.

[30] H. Ego, H. Maesaka, Y. Otake, T. Sakurai, "Transverse C-Band Deflecting Structure for Longitudinal Phase Space Diagnostics in the XFEL/SPRING-8 SACLA", *Proc. of IPAC2011*, San Sebastián, Spain, 2011.

[31] H. Ego, Y Otake, "Design of the transverse C-Band deflecting structure for measurement of bunch length in X-FEL", *Proc. of EPAC08*, Genoa, Italy, 2008.

[32] P. Craievich *et al.*, "Transverse Deflecting Structures for Bunch Length and Slice Emittance Measurements on SwissFEL", *Proc. of FEL 2013*, New York, USA, 2013.

[33] P. Craievich, *private communication.*

[34] P. Krejcik *et al.*, "Engineering Design of the new LCLS X-Band Transverse Deflecting Cavity", *Proc. of IBIC2013*, Oxford, UK, 2013.

[35] Y. Ding *et al.*, "Commissioning of the X-Band Transverse Deflector for Femtosecond Electron/X-Ray Pulse Length Measurements at LCLS", *Proc. of IPAC2013*, Shanghai, China, 2013.

[36] C. Behrens *et al.*, "Few-femtosecond time-resolved measurements of X-ray free-electron lasers", *Nat. Comm.* 5, 3762/4762, 2014.

[37] P. Krejcik, *private communication.*

[38] B. Marchetti et al., "X-Band TDS Project", *Proc. of IPAC2017*, Copenhagen, Denmark, 2017

[39] P. Craievich *et al.*, "Status of the PolariX-TDS project", *Proc. of IPAC2018*, Vancouver, Canada, 2018.

[40] V. Paramonov, L. Kravchuk, K. Flöttmann, "RF Parameters of a TE-Type Deflecting Structure for the S-Band Frequency Range", *Proc. of LINAC2012*, Tel Aviv, Israel, 2012.

[41] M. Hachmann, K. Flöttmann, "Transverse Emittance Measurement at REGAE", *Proc. of IPAC 2015*, Richmond, USA, 2015.

[42] M. Röhrs *et al.*, "Measurement of Slice-Emittance using Transverse Deflecting Structure", *Proc. of FEL2005*, Palo Alto, USA, 2005.

[43] A. Marinelli *et al.*, *Nat Comm.* 6, 6369, 2015.

[44] G De Ninno *et al.*, *Nat. Comm.* 6, 8075, 2015.

[45] Y. Ding et al., APL 107, 191104, 2015.

ISBN: 978-3-95450-194-6 ISSN: 2226-0366 doi:10.18429/JACoW-LINAC2018-FR1A03

FRONTIERS OF BEAM DIAGNOSTICS IN PLASMA ACCELERATORS*

A. Cianchi†, University of Rome Tor Vergata, 00133 Rome, Italy
D. Alesini, M. P. Anania, M. Bellaveglia, F. Bisesto, M. Castellano, E. Chiadroni
G. Costa, M. Ferrario, F. Filippi, A. Giribono, A. Marocchino, R. Pompili, V. Shpakov,
C. Vaccarezza, F. Villa, INFN-LNF, 00044 Frascati, Italy
A. Mostacci, Sapienza University of Rome, 00185 Rome, Italy

Abstract

Advanced diagnostics tools are crucial in the development of plasma-based accelerators. Accurate measurements of the beam quality at the exit of the plasma channel are mandatory for the optimization of the plasma accelerator. 6D electron beam diagnostics will be reviewed with emphasis on emittance measurement, which is particularly complex due to the peculiarity of the emerging beams.

INTRODUCTION

High energy particles physics has driven for a long time the accelerators to reach higher energy or intensity. However, nowadays accelerators are also widely used in very different fields, covering a huge range of applications, including light sources for medical and industrial applications. Compared to other novel scheme, like high-frequency W-band metallic RF structures [1], dielectric wakefield structures [2] or direct laser acceleration [3], the plasma acceleration offers the highest gradient and compactness. It paves the way to use compact and cost affordable accelerators in universities, medical centers and small laboratories, with a lot of possible applications.

Laser beams (laser wakefield accelerator, LWFA) or charged particle beams (particle wakefield accelerator, PWFA) may be used to excite space-charge oscillations in plasma. They produce both accelerating and focusing fields.

The EuPRAXIA [4] (European Plasma Research Accelerator with eXcellence In Applications) project is expected to be the first Research Infrastructure devoted to establish the scientific and technological basis required to build a compact and cost effective high energy (up to 5 GeV) machine based on plasma accelerator technology.

While there is not yet a final decision about the acceleration scheme to be used, we noticed that in term of beam diagnostics there is not so much difference between different solutions. In all cases the driver must be removed, being a high power laser or an electron beam, because it prevents to put diagnostics downstream of the plasma interaction. In all cases the high beam divergence and large energy spread will force to capture the beam as soon as possible after the plasma stage. So, it is difficult to put diagnostics between the plasma and the capture optics.

In addition to the complications inherent to the plasma acceleration, as driver removal, shot by shot pointing or timing instabilities, large energy spread, there are specific issues about the resolution in measuring the 6D phase space. Time resolution must be in order of few fs, transverse emittance resolution better than 1 mm-mrad, the charge must be discriminate at the level of pC and the trajectory must be known at μm level. Sometimes it is forgiven that if the accelerator must be compact, the diagnostics have to be compact as well, resulting in a complete redesign of even conventional diagnostics.

At the same time in INFN-LNF Frascati a satellite project has been started [5] showing about the same problems in term of beam diagnostics.

This paper, starting from the state of the art, wants to emphasize the peculiarity of the plasma acceleration, and the challenges in measuring such kind of beams, giving also information about our developments still in progress. Longitudinal diagnostics will be the argument of Section I, while we will focus on transverse diagnostics in Section II, giving also more details about our work.

SECTION I:LONGITUDINAL DIAGNOSTICS

In a compact machine a longitudinal compressor is more appealing that a magnetic chicane, due to the shorter path required for its implementation. However, to set the correct compression phase in the velocity bunching and to recover the correlated energy spread induced in this way, a longitudinal diagnostics is mandatory. Longitudinal phase space measurement can be performed with a X-band RF deflector (RFD), i.e a RF cavity with a transverse deflecting mode, combined with a magnetic dipole. While the fs resolution is state-of-the-art for these devices, so far only one X-band RFD is operating, at SLAC [6], for an energy one order of magnitude greater than our case. It means that the design must be reconsidered and particular attention must be put in several details that usually are neglected. For instance the reduced iris aperture and the possibility that the beam goes inside out of the center must be evaluated with simulations. Particular attention must be put also in RF time jitter and the structure temperature stability, tailoring this requirements to the beam energy and the available beam line. As a rule of thumb, for GeV level beam, a temperature stability in the order of tens of mK and time stability in the order of tens of femtoseconds are required.

In a plasma accelerator, especially during the commission phase, a one to one correlation between the longitudinal properties of the beam sent into the plasma and the beam

* Work supported by European Union Horizon 2020 research and innovation program, Grant Agreement No. 653782 (EuPRAXIA)
† alessandro.cianchi@uniroma2.it

Content from this work may be used under the terms of the CC BY 3.0 licence (© 2018). Any distribution of this work must maintain attribution to the author(s), title of the work, publisher, and DOI.

ISBN: 978-3-95450-194-6 ISSN: 2226-0366 doi:10.18429/JACoW-LINAC2018-FR1A03

Content from this work may be used under the terms of the CC BY 3.0 licence (© 2018). Any distribution of this work must maintain attribution to the author(s), title of the work, publisher, and DOI.

emerged from it is mandatory. Non-intercepting single shot longitudinal profile measurement is needed.

Diffraction radiation [7] is emitted when a charged particle passes through a hole with transverse dimension smaller with respect to the radial extension of the electromagnetic field traveling with the charge. Coherent emission arises when the observed wavelength is longer with respect to the bunch length [8]. In our case the bunch length can be few ps (on-crest acceleration) down to few fs (compression regime). It reflects in the use of different detector to cover wavelength from far infrared to visible light.

To measure the spectrum in a single shot is needed the dispersion of the radiation by several grating or even several spectrometers. The complete analysis of the spectrum leads to the reconstruction of the longitudinal bunch shape.

Different approaches have been used to this end. A single KRS-5 (thallium bromoiodide) prism [9], dispersing the radiation on a linear detector et al..lowing the measuring of a wide spectrum, or a series of separate spectrometer working in different wavelength scales [10] have been already succesfully tested. Using really a small space in the beamline they can be consider excellent candidate to work also in a plasma machine.

Other single shot devices can be based on EOS (Electro Optical Sampling). The electric field co-propagating with the bunch can rotate the polarization of a laser impinging on a non linear crystal such as GaP or ZnTe.

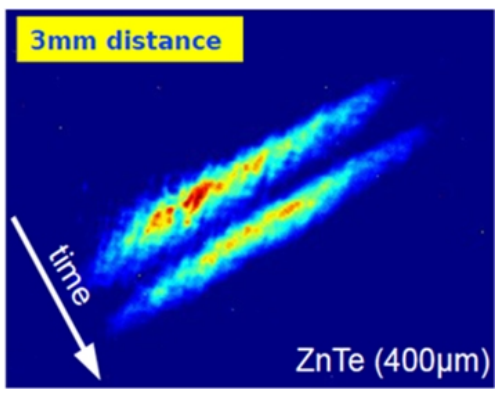


Figure 1: Image EOS of a bunch train of two bunches, 80 pC on each bunch, pulse lenght 160 fs and 200 fs respectively. Their distance was 800 fs.

Using *spatial decoding* scheme [11], realized with an angle of incidence between the probe laser and the crystal, it is possible to retrieve the longitudinal beam profile in one shot. In Fig. 1 is shown the signal retrieved by a ZnTe crystal, placed at 3 mm from the beam line. The train of the two pulses, with a distance of 800 fs is clearly resolved. However, the temporal resolution, limited or by the crystal bandwidth or by the length of the laser probe is in the order of 40-50 fs [12].

Also EOS can be often used as bunch of arrival monitor, that it is very important in some plasma acceleration schemes, as for instance external injection [13].

SECTION II:TRANSVERSE DIAGNOSTICS

For the beam produced by a RF linac, the emittance measurement can be performed with very well-known techniques, like quadrupole scan and multiple screens [14]. However, in a plasma accelerator single shot measurements are highly desirable. Also, the diagnostics is narrowed between two competitive effects: the driver-witness separation prevents to have any diagnostics just after the plasma channel, while the large energy spread (usually above % level) produce an unwanted increase of the emittance even during a drift [15], making urgent the measurement as soon as possible.

Recentely it was introduced the concept of chromatic lenght [16], defined as the distance where the emittance grows of a factor $\sqrt{2}$ as

$$L_C = \frac{\sigma_x}{\sigma_x' \sigma_E} \tag{1}$$

where σ_x is the rms beam size, σ_x' is the rms beam divergence and σ_E is the relative rms energy spread at plasma extraction. In a conventional accelerator L_C is usually longer than the whole machine, while in plasma accelerators, depending on the value of the energy spread, could be in a range between few centimeters and few meters. To overcome this problem the only solution is a fast capture of this beam and a mitigation of the energy spread, even at cost of some charge reduction.

For all of these reasons we decide to separate the measurements of the properties of the beam inside the plasma channel from the measurements after the capture optics. Being not possible to place anything after the plasma, the only source of information for the beam inside is the radiation emitted during the process of the acceleration.

Betatron Radiation Based Techniques

The diagnostics based on betatron radiation [17] has been developed in recent years in several laboratories, relying on the measurement of the spectrum, (for instance among the other see [18])or on the diffraction from a knife edge [19]. However, these systems were able to measure just the beam profile and divergence, neglecting the correlation term. Only recently a new algorithm to retrieve the correlation term [20] has been developed.

A simultaneous measurement of the electron and radiation energy spectrum and the plasma density allows the reconstruction of the whole phase space. However, being this measurement made on a self-injected beam, some approximation on the initial beam phase space were needed, while if the beam is externally injected inside the plasma, the knowledge of the initial 6D phase space removes this ambiguity.

In Fig. 2 is reported a reconstructed phase space with this technique.

While this algorithm is based on the reconstruction of the beam 1D profile, the full 2D beam profile characterization

ISBN: 978-3-95450-194-6 ISSN: 2226-0366 doi:10.18429/JACoW-LINAC2018-FR1A03

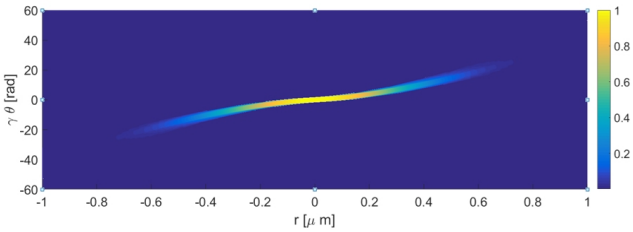


Figure 2: Reconstructed phase space with betatron radiation from self-injected electron beam. [20]. Laser parameters: energy 1J, pulse duration 30 fs (FWHM), 10 µm diameter focus, $a_0 \approx 4.4$; plasma density $=(8\pm1)10^{18}$ cm^{-3}.

has also been shown to be possible to be measured using the correlation between spectrum and angle [21]. This particular technique could allow to resolve beam size in the order of 50 nm.

The overlap between synchrotron radiation, eventually produced by a downstream magnet to separate beam and radiation, is negligible with respect to betatron radiation. However, an open problem is related to the separation between the betatron radiation coming from the witness and from the driver in the beam driven scheme. The driver contains much more charge with respect to the witness and so only a clear energy separation of the two spectra can solve the problem. Obviously in the case of external injection (i.e. a laser driven case) this problem disappears.

A betatron radiation based measurement can allow to properly tune the plasma source. However, to match the beam with an undulator, for instance, a single shot emittance measurement is needed. The solution of this problem is still unclear, even if a lot of work is ongoing.

Single Shot Emittance

Two papers about a single shot emittance measurement has been recently published [22, 23], relying on a method developed some years ago [24]. An electron beam produced by means of ionization injection is then focused in a triplet of permanent quadrupoles before entering in a dipole. The measurement is performed after the dipole. Due to the large energy spread, common in beams produced with this method and in the level of several %, different energy beam parts are focused in different transverse dimensions. The method is basically the same that conventional quadrupole-scan [14], but in this case the quadrupoles are permanent magnets. It is very remarkable also the calculation of the possible resolution of this method, in the order of 0.1 mm-mrad reported in [25] where the technique is fully described systematically. Of course there is an inherent approximation: different beam parts, belonging to different energies, must have the same emittance. This methods works very well for self-injected beams and it is for sure the solution that we were looking for. However, the reduction on the energy spread, highly desirable for beam that have to drive a FEL, reduces as well also the resolution of the measurement.

Pepper pot like techniques [26] are not easy to be implemented at high energy, because a very tick target is needed to increase the signal to noise ratio in the beamlets. But increasing the thickness reduces the angular acceptance of the beam, resulting in a likely cut of the phase space. However, the pepper pot suffers also for a problem related to the sampling nature of this measurement, as already discussed in [27].

A more careful analysis of the sampling limitation reveals that part of the reduction in the sensitivity of this technique comes from the use of a double sampling, one on the target that selects beamlets, and one on the screen to image them. We have proposed and we are testing a new device [28], a sort of optical pepper pot, where there is only one sampling at the source level. It makes use of Optical Transition Radiation (OTR) produced when a charge passes through a metallic foil. In Fig. 3 there is a sketch of the system

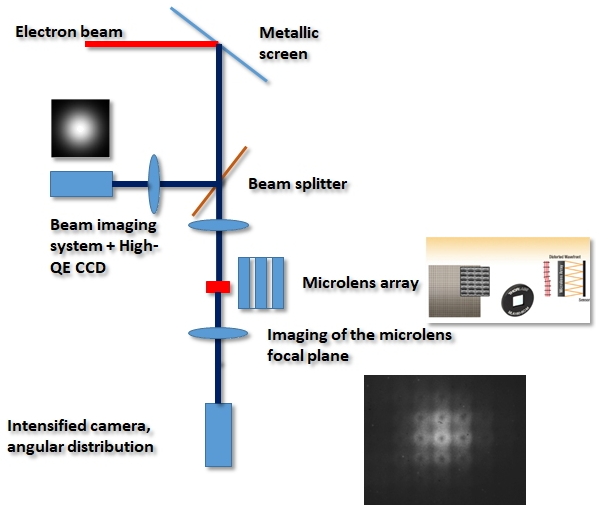


Figure 3: OTR generated by the beam in the interaction with a metallic foil is split in two arms. In the first arm a CCD camera measures the beam size. in the second ones a replica of the source radiation field is propagated on a microlens array. The back focal plane of the array is then imaged on an intensified camera. In the right corner there is a picture of a real image. The OTR angular distribution is reproduced by every single microlens.

The experiment has been performed at SPARC_LAB photoinjector at 125 MeV The angular distribution of the emerging radiation contains information about the angular divergence of the beam. Using an optical system to reproduce outside the vacuum chamber the source radiation field, and sampling by means of a microlens array, it is possible to measure the angular distribution and so the value of the beam divergence, in different transverse positions. It allows the retrievement of the correlation term. Acquiring at the same time also the beam spot allows, in principle, the measurement of the emittance in single shot. While we have already performed a test of this device we were not able so far to retrieve the value of the emittance. The resolution is too poor at actual SPARC_LAB [29] energy value.

Content from this work may be used under the terms of the CC BY 3.0 licence (© 2018). Any distribution of this work must maintain attribution to the author(s), title of the work, publisher, and DOI.

ISBN: 978-3-95450-194-6 ISSN: 2226-0366 doi:10.18429/JACoW-LINAC2018-FR1A03

Content from this work may be used under the terms of the CC BY 3.0 licence (© 2018). Any distribution of this work must maintain attribution to the author(s), title of the work, publisher, and DOI.

The resolution of the measurement is strictly correlated with the beam energy, due to the narrowing of the angular distribution at higher energy. Using the Fig. 3 of the paper [28] is visible that the resolution change dramatically in the range of the energies below 200 MeV showing an increment, while is flattening for energies above 500 MeV. We are studying this system both for low energy (in any case >200 MeV) than for 1 GeV. The increase in the energy reflects also in the enlargement of the field transverse dimensions. It effects the diffraction of the microlenses. This effect is shown in Fig. 4.

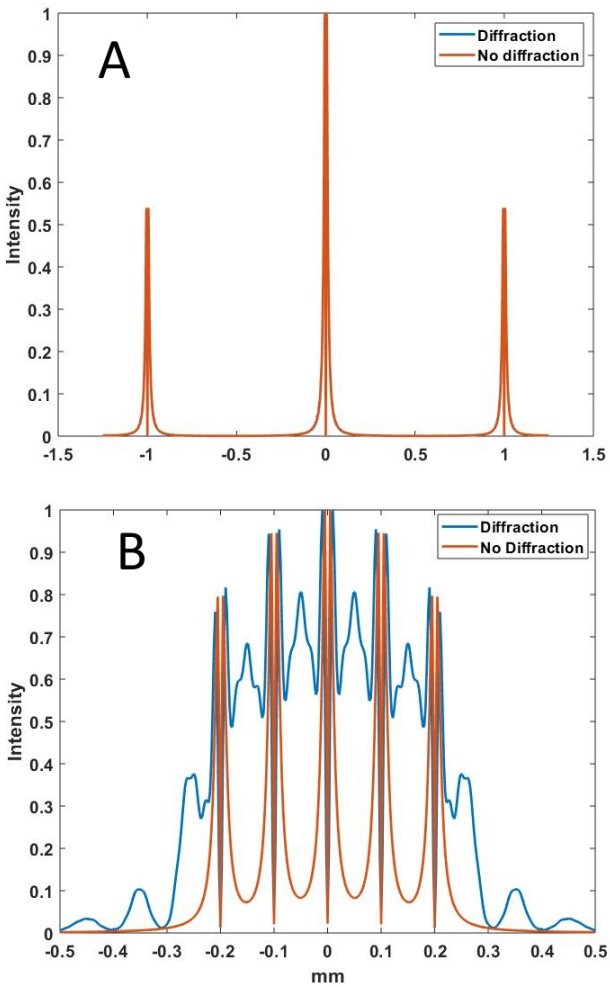


Figure 4: A:lens focal length f=10 mm, diameter D=1mm, beam energy=1 GeV; B: lens focal length f=10 mm, diameter D=.1mm, beam energy=1 GeV

While for energy up to few hundreds of MeV diffraction effects are not relevant, at GeV they impact the choice of the microlens array size. Enlarging the lens dimensions solves the problem, but it impacts on the sampling rate of the measurement. So a fine tuning between energy and array size, taking into the account the possibility to play with moderate magnification with the optics, must be found.

Use of Plasma Lenses

Some years ago a paper [30] showed the possibility to measure the emittance in a single shot, recording at the same time the OTR produced by several very tiny screens. The method is the multiple-screen, a variation of the quadrupole scan method. There are indeed accelerators that have a dedicated space to host multiple screens for such a measurement. For instance at FLASH2 in Desy the space is roughly about 10 meters. Such a long path is not compatible with a plasma accelerator, where the dimensions must be very compact. Also, as pointed out in [31], this system really works only if there is a significant phase advance between every screen. It means that a magnetic optics is mandatory. But again it costs space, and it cannot be the case for a compact machine. Recently several papers have been published about plasma lenses [32–34], a new and compact device, only few cm length. These devices not only show a magnetic field at least one order of magnitude larger than permanent quadrupoles, but they focus also on both planes at the same time, they show much smaller chromaticity with respect to conventional magnets, they can be tuned and they have very short (few cm) focal length.

It is possible to foresee that the use of plasma lenses together with multiple OTR screens will allow the realization of a real compact multiple screens system, maybe less than 1 meter long. Such a device could be installed in every machine, especially in a plasma accelerator.

CONCLUSION

The plasma acceleration promises to change the field of particle accelerators, not only for high energy physics, but more likely for light source, industrial and medical applications. Compact, single shot, high resolution devices must be foreseen to properly monitor the machine. Working on the project of a future plasma accelerator we found that while there are already several diagnostics for longitudinal parameters, that can be adapted to our case, there is a lack of techniques for single shot emittance. Intrinsic difficulties related to plasma acceleration make difficult to have diagnostics just after the acceleration stage. To overcome this problem we propose a widely use of the betatron radiation, to monitor the beam properties inside the plasma channel, and to test some new ideas outside the plasma, but only after a capture optics, to measure the properties of the beam that will be used for applications.

ACKNOWLEDGEMENTS

This work was supported by the European Unions Horizon 2020 research and innovation programme under grant agreement No. 653782.

REFERENCES

[1] D. Wang *et al.*, Physical Review Letters 116, 054801 (2016)

[2] G. Andonian *et al.*, Physical Review Letters 108, 244801 (2012)

ISBN: 978-3-95450-194-6 ISSN: 2226-0366 doi:10.18429/JACoW-LINAC2018-FR1A03

[3] C Gahn *et al.*, Physical Review Letters 83, 4772 (1999)

[4] P. Walker *et al.*, Journal of Physics: Conference Series 874,1, 012029 (2017)

[5] M. Ferrario *et al.*, EuPRAXIA@ SPARC_LAB Design study towards a compact FEL facility at LNF, Nuclear Instruments and Methods in Physics Research Section A: Accelerators, Spectrometers, Detectors and Associated Equipment (2018).

[6] V. Dolgashev, AIP Conference Proceedings, 1507, 682 (2012)

[7] Ter-Mikaelian, High energy electromagnetic processes in condensed media, Wiley (1972)

[8] M. Castellano *et al.*, Physical Review E 63, 56501 (2001)

[9] T. J. Maxwell *et al.*, Physical Review Letters 111, 184801 (2013)

[10] , M. Heigoldt, Physical Review Special Topics-Accelerators and Beams 18, 121302 (2015)

[11] R. Pompili *et al.*, Nuclear Instruments and Methods in Physics Research Section A: Accelerators, Spectrometers, Detectors and Associated Equipment 740, 216 (2014)

[12] B. Steffen *et al.*, Physical Review Special Topics-Accelerators and Beams 3,32802 (2009)

[13] C. E. Clayton *et al.*, IEEE Transactions on Plasma Science 24, 400 (1996)

[14] F. Lohl *et al.*, Physical Review Special Topics-Accelerators and Beams 9, 92802 (2016)

[15] M. Migliorati *et al.*, Physical Review Special Topics-Accelerators and Beams 16, 11302 (2016)

[16] M. Rossetti Conte *et al.*, Nuclear Instruments and Methods in Physics Research Section A: Accelerators, Spectrometers, Detectors and Associated Equipment (2018).

[17] A. Rousse *et al.*, Physical Review Letters 93, 135005 (2004)

[18] G. R. Plateu *et al.*, Physical Review Letters 109, 64802 (2012)

[19] S. Kneip *et al.*, Physical Review Special Topics-Accelerators and Beams 15, 21302 (2012)

[20] A. Curcio *et al.*, Physical Review Accelerators and Beams 20, 12801 (2017)

[21] A. Curcio *et al.*, Applied Physics Letters 111, 133105 (2017)

[22] S. Barber *et al.*, Physical Review Letters 119, 104801 (2017)

[23] F. Li *et al.*, Plasma Physics and Controlled Fusion 60, 044007 (2018)

[24] R. Weingartner *et al.*, Physical Review Special Topics-Accelerators and Beams 15, 111302 (2012)

[25] F Li *et al.*, and Controlled Fusion 60, 014029 (2018)

[26] C. Lejeune and J. Aubert, Applied Charged Particle Optics supp 13 (1980)

[27] A. Cianchi *et al.*, Nuclear Instruments and Methods in Physics Research Section A: Accelerators, Spectrometers, Detectors and Associated Equipment 720, 153 (2016)

[28] A. Cianchi *et al.*, Nuclear Instruments and Methods in Physics Research Section A: Accelerators, Spectrometers, Detectors and Associated Equipment 865, 63 (2017)

[29] M. Ferrario *et al.*, Nuclear Instruments and Methods in Physics Research Section B: Beam Interactions with Materials and Atoms 39, 183 (2013)

[30] C. Thomas *et al.*, Journal of Instrumentation 6, 7004 (2011)

[31] P. Castro, DESY-Technical-note-2003-03. CM-P00042419, 2003.

[32] J. van Tilborg *et al.*. PRL 115, 184802 (2015)

[33] R. Pompili *et al.*. Applied Physics Letters 110 104101 (2017)

[34] A. Marocchino *et al.*. Applied Physics Letters 111 184101 (2017)

Content from this work may be used under the terms of the CC BY 3.0 licence (© 2018). Any distribution of this work must maintain attribution to the author(s), title of the work, publisher, and DOI.

ISBN: 978-3-95450-194-6 ISSN: 2226-0366 doi:10.18429/JACoW-LINAC2018-FR1A05

DEVELOPMENT OF PULSED GAS STRIPPERS FOR INTENSE BEAMS OF HEAVY AND INTERMEDIATE MASS IONS

P. Gerhard*[1], W. Barth[1,2], M. Bevcic[1], Ch. E. Düllmann[1,2,3], L. Groening[1], K. P. Horn[1], E. Jäger[1], J. Khuyagbaatar[1,2], J. Krier[1], M. Maier[1], P. Scharrer[1], A. Yakushev[1]
[1]GSI Helmholtzzentrum für Schwerionenforschung GmbH, 64291 Darmstadt, Germany
[2]Helmholtz-Institut Mainz, 55099 Mainz, Germany
[3]Johannes Gutenberg-Universität Mainz, 55099 Mainz, Germany

Abstract

The GSI UNILAC together with SIS18 will serve as a high current, heavy ion injector for the future FAIR. It has to deliver high beam brilliance at a low duty factor. A modified 1.4 MeV/u gas stripper setup has been developed, aiming at an increased yield into the particular desired charge state. The setup delivers short pulses of high gas density in synchronization with the beam pulse. This provides a higher gas density and at the same time reduces the gas load for the differential pumping system. Different gases as stripping targets were tested for optimum stripping results under operational conditions. Measurements with various isotopes and gas densities were conducted to investigate the stripping properties. High intensity beams of $^{238}U^{4+}$ were successfully stripped and separated using hydrogen as stripping gas. The stripping efficiency into the desired 28+ charge state was significantly increased by up to 60% while the beam quality remained suitable. The new stripper setup and major results achieved during the development are presented, including a comparison to the present gas stripper based on a N_2-gas jet.

During the last tests in 2016 problems with the fast valves arose while they were used at high back pressures for a longer duration for the first time. This triggered another revision of the setup and led to an exchange of the valves. In parallel, the installation of the required infrastructure for regular operation of the gas stripper using hydrogen was planned. These recent developments are reported in the last part.

INTRODUCTION

The UNIversal Linear ACcelerator (UNILAC) will serve as part of the heavy ion injector chain for the Facility for Antiproton and Ion Research (FAIR), currently under construction at GSI, Darmstadt, Germany. The reference projectile for FAIR is the heavy ion ^{238}U [1]. To meet the beam requirements for FAIR, an upgrade program of the UNILAC has been started to increase the delivered beam intensities especially for U. The task is to deliver $\approx 3 \cdot 10^{11}$ U^{28+} ions within 100 µs pulse length and adequate emittance at repetition rates of up to 2.7 Hz to the subsequent heavy ion synchrotron SIS18.

All ion beams for the UNILAC are delivered by three different ion sources in a time sharing mode. For the production of heavy ions like ^{238}U, a Vacuum ARc Ion Source [2] is used, which is one of the two sources located at the high current injector (HSI). The HSI comprises of a Radio Frequency Quadrupole (RFQ) structure and an Interdigital H-(IH-)structure Drift Tube Linac (DTL) [3]. After charge state and isotope separation in the LEBT ions with $A/q \leq 65$ are accelerated to 1.4 MeV/u by the HSI before they enter the gas stripper section (Fig. 1).

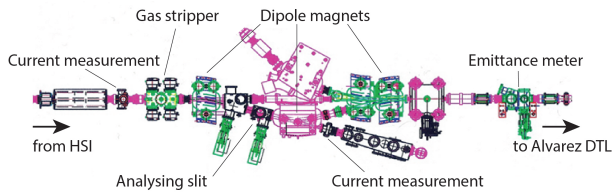


Figure 1: The UNILAC gas stripper section between the high current injector and the Alvarez DTL.

HEAVY ION STRIPPER

After the HSI, a gas stripper is used to increase the charge state of the ions. At this stage, the ions are stripped at an energy of 1.4 MeV/u, so far by a supersonic N_2-jet as a target, created by a Laval nozzle with a back pressure of up to 0.45 MPa [4]. In the gas stripper, the charge state of the ions is increased by charge changing processes occurring in the collisions between beam ions and neutral gas particles. After passing through the gas target, the ion beam is deflected by a fast switchable dipole magnet with a nominal deflection angle of 15°. Thereby the ions are separated according to their charge state, forming multiple beamlets. These are focused onto a charge analysing slit, which only ions having the desired charge state can pass. The remaining beam is then transported by two more fast switchable dipole magnets, matched and injected into the subsequent Alvarez DTL.

To reach the target beam parameters for FAIR injection, a development program for the gas stripper was conducted, aiming at increasing the stripping efficiency, e. g. into the 28+ charge state for uranium. Improving the performance of the gas stripper has proved difficult in the past especially for uranium operation. The main reason was the high gas load for the differential pumping system due to the continuous gas flow of the jet type stripper used [5]. With the existing N_2-jet stripper, the stripping efficiency into the U^{28+} charge state is about 12.7%, and the average charge state of the corresponding distribution is about 26.8 [6].

* p.gerhard@gsi.de

Content from this work may be used under the terms of the CC BY 3.0 licence (© 2018). Any distribution of this work must maintain attribution to the author(s), title of the work, publisher, and DOI.

ISBN: 978-3-95450-194-6 ISSN: 2226-0366 doi:10.18429/JACoW-LINAC2018-FR1A05

In an attempt to use carbon foils instead of the N_2-jet, stripping efficiencies around 20% for U^{39+} and U^{40+} were achieved, depending on the foil thickness [7]. However, the lifetime of the foils was limited to a few hours due to thermal stress and irradiation effects. The use of stripper foils proved to be not feasible for uranium beam operation at FAIR intensity, pulse length and rate requirements. Another approach was taken to enhance the performance of the jet stripper by using gases other than nitrogen. Especially for hydrogen, applying sufficient gas densities in the interaction zone was hindered by the limitations of the pumping system. The equilibrium charge state distribution could not be reached using the continuous gas jet stripper [5].

PULSED GAS STRIPPER

The basic idea to overcome the limitation of the pumping speed is to exploit the low duty factor f of the ion beam. For synchrotron operation, which is the reference for FAIR, $f \ll 1\%$. Due to the low duty factor, most of the time there is no beam in the gas stripper, and the continuous operation of the jet is not required. If gas would only be injected while a beam pulse passes the gas stripper, the gas load on the vacuum pumps could be reduced by about two orders of magnitude. To accomplish this, a fast valve is needed. Additionally, higher gas densities for the stripping process could be attained by enabling a significantly increased back pressure on the gas inlet.

The pulsed gas injection was realized by implementing a fast gasoline valve normally used in automotive applications. Its operation is synchronized with the accelerator timing. Shortly (≈0.4 ms) before the beam pulse passes the gas stripper, the valve opens to build up the gas density in the interaction zone, and closes immediately afterwards. This was tested using a newly developed setup replacing the Laval nozzle. A schematic model of the main stripper setup is shown in Fig. 2. The flange on top of the main stripper chamber carries the actual stripper setup. It was exchanged with a newly developed flange incorporating the pulsed gas valve, as shown in the figure. The valve is placed directly above the beam line without a Laval nozzle, so no gas jet is formed. To prevent the gas from instantaneous exhaustion and to increase the gas density in the interaction zone, a T-fitting with 44 mm length in direction of the beam was added below the valve. This fitting matches the aperture of 22 mm of the beam line through the stripper. The surrounding setup was not changed, it uses the same pumping system as the gas jet stripper [8]. It consists of a roots vacuum pump (8000 m^3/h) directly below the main stripper chamber and four turbo pumps (1200 m^3/h each) in the four adjacent differential pumping sections. They are separated by diaphragms to minimize the molecular conductance between the sections.

A first setup of the pulsed gas injection was tested in 2014 [9]. The reduction of the gas load allowed increased densities even for gases like hydrogen as stripper targets, which are difficult to pump, in comparison to the N_2-jet. At the end of 2014, measurements were conducted using a wide range of different gases to test the stripping performance for uranium beams and to increase the stripping efficiency into U^{28+} [6,8]. During this series, a limitation of the achievable average charge state was noticed, caused by the limited gas back pressure on the inlet. Therefore, the setup was modified to enable higher back pressures as well as shorter opening times [10–12].

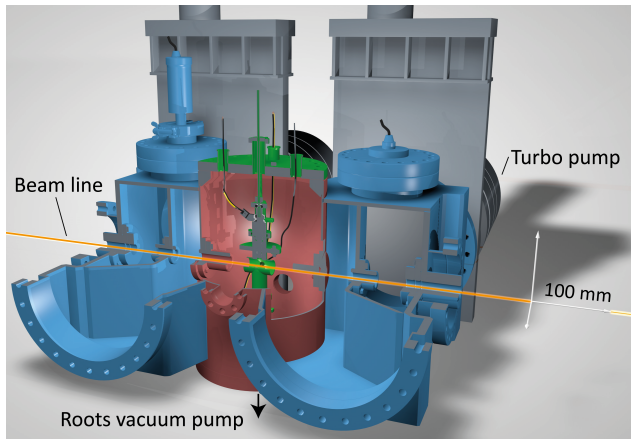


Figure 2: Main setup of the gas stripper (schematic). The pulsed gas injection is mounted on the top flange (green) of the main chamber (red). Together with the adjacent sections (blue) this constitutes a four stage differential pumping system [8].

MEASUREMENTS AND RESULTS

Target Investigations

To evaluate the quality as a stripper target, the stripping efficiency into each populated charge state and the beam quality, namely the energy loss and the horizontal and vertical beam emittance, were measured for various gases.

The stripping efficiency into a specific charge state i, $q_i = \frac{n_i}{n_{\text{total}}}$, is the ratio of the number of ions n_i going into this charge state and the total number of ions n_{total} in front of the stripper. To obtain n_i and n_{total}, the electrical beam current is measured and divided by the charge state of the ions. The energy loss due to the collisions between the beam ions and the stripper gas is determined by the difference of the beam energies behind the stripper with and without gas applied. The energy of the beam ions is measured by time-of-flight measurements using phase probes along the beam line. The beam emittance is measured using a slit grid measurement system behind the charge separation [13].

At a certain target thickness, the cross sections for the electron capture and electron loss processes reach an equilibrium. At this point, the charge state distribution does not change anymore with increasing target thickness.

The stripping properties of H_2, He, Ne, N_2, O_2, Ar, and CO_2 were investigated. Back pressures in the range of 2–12 MPa were applied for each type of gas. U^{4+} ions with a beam pulse length of 100 µs were used as stripping probes

Content from this work may be used under the terms of the CC BY 3.0 licence (© 2018). Any distribution of this work must maintain attribution to the author(s), title of the work, publisher, and DOI.

ISBN: 978-3-95450-194-6 ISSN: 2226-0366 doi:10.18429/JACoW-LINAC2018-FR1A05

Content from this work may be used under the terms of the CC BY 3.0 licence (© 2018). Any distribution of this work must maintain attribution to the author(s), title of the work, publisher, and DOI.

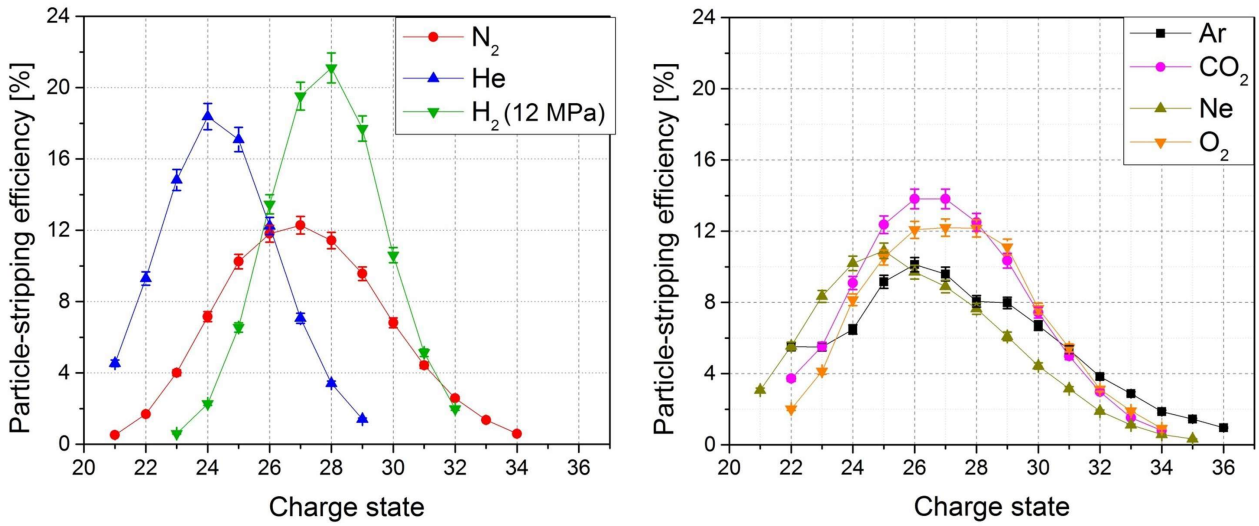


Figure 3: Charge state distributions for U stripped by N_2, He and H_2 (left), Ar, CO_2, Ne and O_2 (right), measured with the pulsed gas stripper at 1.4 MeV/u beam energy. The graphs show the equilibrated stripping efficiencies q_i as functions of the charge state i except for H_2, where the distribution was still not equilibrated at 12 MPa back pressure with the setup used [6].

at a repetition rate of 1 Hz. The opening time of the valve was set to 0.5 ms to achieve a maximum gas density during the beam transit.

The corresponding charge state distributions are shown in Fig. 3. For all gases except hydrogen equilibrium was reached within the measured back pressure range. The heavier gases generate relatively broad charge state distributions at average charge states between 25 and 27. For the light gases H_2 and He the charge state distributions are more narrow. This leads to increased stripping efficiencies for the populated charge states. For H_2 compared to He, the average charge state of the distribution is increased [14].

For different target thicknesses, the charge state distributions for U passing through H_2 are shown in Fig. 4. For increasing target thickness, the average charge state rises from about 23+ to 29+, while the width of the distributions as well as the maximum efficiency stays constant above $\approx 7\,\mu g/cm^2$ within the error range. These data were taken with the improved gas supply providing higher back pressures, therefore equilibrium could be achieved at $\approx 19\,\mu m/cm^2$.

By applying H_2 as a stripper gas at sufficient back pressure, the efficiency into U^{28+} could be increased from 13% for the N_2-jet stripper to 21% [6, 8, 10, 12]. Finally, hydrogen turned out to be the most preferable stripping target and was therefore chosen for further investigations.

Projectile Investigations

^{238}U is the reference ion for FAIR, nevertheless the UNILAC will also deliver other heavy ions in the future. To investigate the stripping properties of H_2 as target for different heavy ions, the equlibrated charge state distributions of ^{238}U, ^{209}Bi, ^{50}Ti, and ^{40}Ar after passing the pulsed gas stripper were measured under similar conditions [11]. In

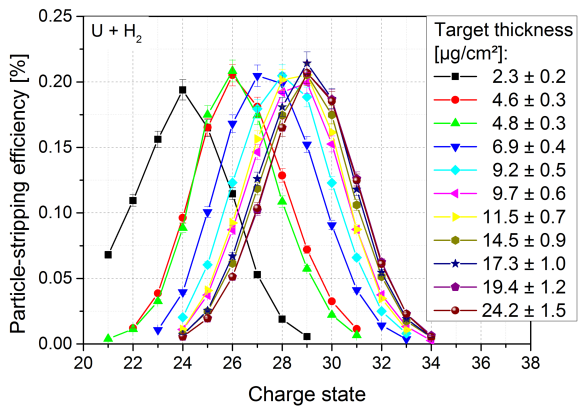


Figure 4: Charge state distributions for U on H_2 for different target thickness, measured at 1.4 MeV/u beam energy. The solid curves are fitted to the data using a gaussian fit with a skewness correction. Target thickness is estimated from energy loss measurements using SRIM2013 [10, 15].

Fig. 5, the results are shown and compared to the distributions measured with the N_2-jet gas stripper[1].

For all measured isotopes, stripping with H_2 leads to an increase of the average charge state compared to N_2. Moreover, for the heavier ions, ^{238}U and ^{209}Bi, the distributions are more narrow for H_2 than for N_2, while there is no difference in the width for the lighter ions. This results in increased stripping efficiencies for the populated charge states for the heaviest isotopes. The Beam quality remains well acceptable, even though generally the transverse emittances

[1] The sum $Q = \sum_i q_i = 1$ of the stripping efficiencies of all populated charge states is the total transmission through the stripper, which should be 100%. However, optimal accelerator settings could not be achieved for all shown measurements. Therefore, the total stripping efficiencies shown is normalized to 1, showing the charge fractions of the ion beam behind the gas stripper.

ISBN: 978-3-95450-194-6 ISSN: 2226-0366 doi:10.18429/JACoW-LINAC2018-FR1A05

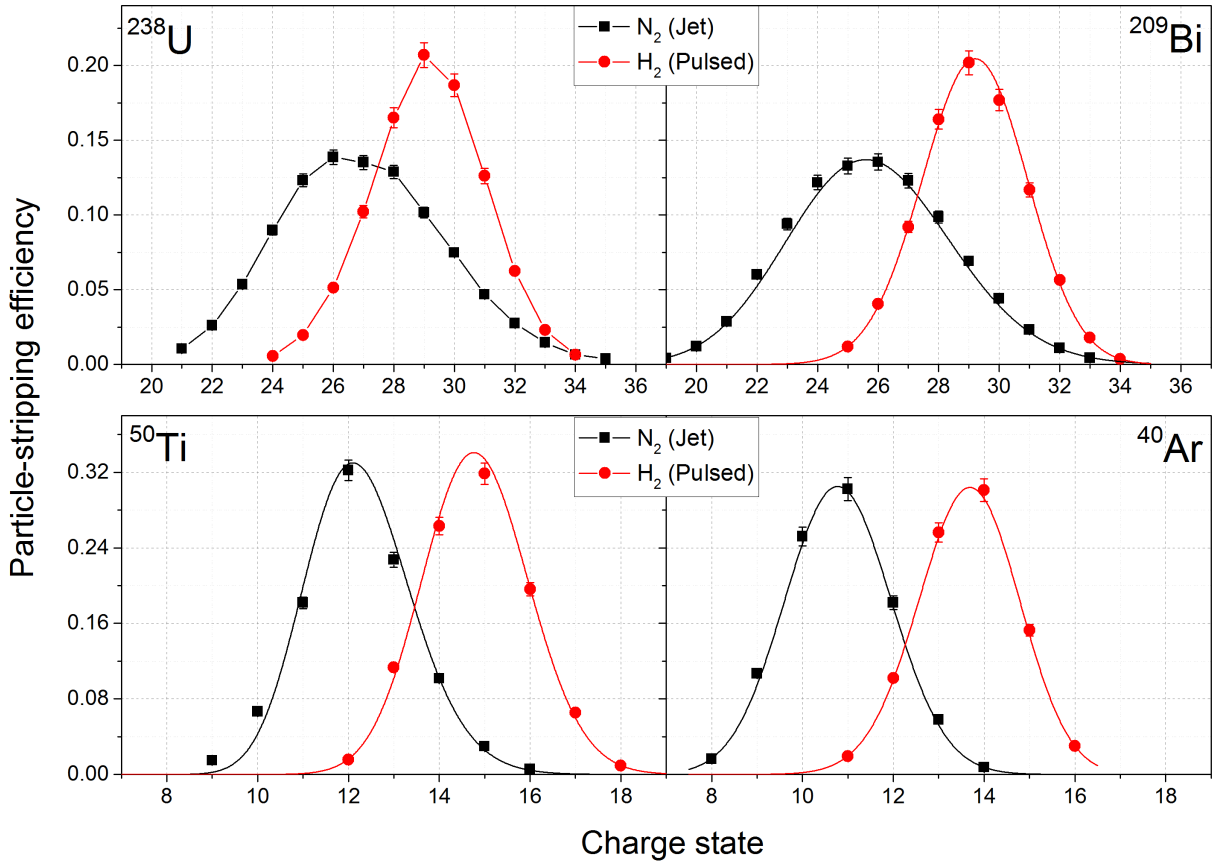


Figure 5: Equlibrated charge state distributions for ^{238}U, ^{209}Bi, ^{50}Ti, and ^{40}Ar ions after passing the N_2-jet gas stripper (black) and the pulsed gas stripper using H_2 as target (red) [11]. See text for details.

as well es the beam energy loss are higher with the pulsed gas stripper using hydrogen. This is due to the increased target thicknesses. More details can be found in [11]. A detailed description of the complete experimental data set and a discussion of the relevant effects can be found in [14].

LATEST REVISION

The measurements of the different stripping properties were complemented by a test run of three weeks with the pulsed gas stripper setup in 2016. During this period, a uranium beam stripped with H_2 was delivered to the SIS18 and different users. At the end of the test, the fast valves showed significant leakage problems. It turned out that this type of valves, which is originally designed for gasoline injection, can not be used with gaseous media for long term operation. The reason is the design of the valve seating, which relies on the damping by a liquid fuel when it is closing. Therefore another type of injection valves, which are also originally used for automotive applications, but designed for gaseous fuels, was chosen (Fig. 6). A new stripper setup was designed to accomodate two of the new, mechanically different valves (Fig. 7). These valves are slower compared to the gasoline valves, but still fast enough for the application in the UNILAC stripper, and they require a completely different, much lower range of back pressure. Therefore, the gas supply was modified to allow for proper gas supply to the valve at the much lower pressures. The properties regarding opening, closing and flow rates are also different. For evaluation of the new type of valves without beam, a test stand was built. A new valve controller was also commissioned.



Figure 6: Fast valve for gasoline operation (left) and for gaseous media (right).

Content from this work may be used under the terms of the CC BY 3.0 licence (© 2018). Any distribution of this work must maintain attribution to the author(s), title of the work, publisher, and DOI.

ISBN: 978-3-95450-194-6 ISSN: 2226-0366 doi:10.18429/JACoW-LINAC2018-FR1A05

Content from this work may be used under the terms of the CC BY 3.0 licence (© 2018). Any distribution of this work must maintain attribution to the author(s), title of the work, publisher, and DOI.

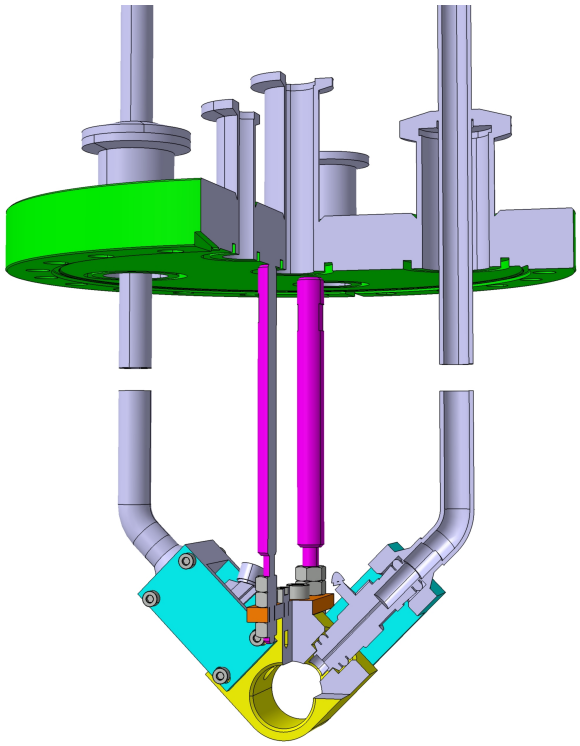


Figure 7: Latest stripper setup accomodating two fast valves for gaseous media.

All tests were successfully accomplished beginning of 2018. The setup with the new valves is now being prepared for evaluation with beam.

CONCLUSION AND OUTLOOK

The original continuous flow jet gas stripper was replaced by a pulsed gas stripper. This reduced the average gas load on the pumping system, which limits the effective performance of the stripper. Various gases were tested regarding their performance as stripping targets. H_2 could be applied as stripping target at increased target thickness, enabled by the pulsed valves and an improved gas supply. Equilibrium charge state distributions could be achieved and the distributions are more narrow with H_2 compared to N_2, resulting in an overall increase of the particle stripping efficiency of about 60% for ^{238}U.

H_2 turned out to be the most preferable stripper gas. Further investigations with different ions stripped by H_2 were conducted. For all ions, a higher average charge state was found. Only for heavy ions the width of the distribution is reduced, leading to an increase in stripping efficiency. This results in higher beam intensities for the heavy ions, which is important for the future operation of the UNILAC and FAIR. Due to the increased target thickness, the energy loss and the beam emittance is generally increased, which affects the beam quality and the matching to the subsequent Alvarez DTL.

A first long term test showed that the fast valves used so far are not suitable for operation with gases. Different valves, designed for gaseous fuels, are adopted and enable higher gas flow at reduced back pressures due to an enlarged orifice. Evaluation at a test stand was successful, measurements with beam for the newly revised setup are anticipated for end of 2018.

The planning of the infrastructure necessary for regular operation of the gas stripper with hydrogen is in progress. This includes

- a gas supply station capable of continuous operation at a maximum flow rate of 200 l/min H_2,
- an explosion protected and radiation safe exhaust gas system able to dispose of the same amount of H_2 from the vacuum pumps exhaust safely to the outside,
- a comprehensive explosion protection upgrade for the vacuum system in the gas stripper area, and
- incorporation of the pulsing functionality of the new gas stripper into the accelerator control system.

Realization is planned for 2019, first regular operation of the pulsed stripper for 2020.

REFERENCES

[1] FAIR Baseline Technical Report, vol. 2, GSI Darmstadt, pp. 335ff, 2006

[2] R. Hollinger *et al.*, "Status of vacuum arc ion source development for injection of high current uranium ion beams into the GSI accelerator facility", *Nucl. Instr. Methods* B 239, 2005. doi:10.1016/j.nimb.2005.04.062

[3] U. Ratzinger *et al.*, "The New GSI Prestripper Linac for High Current Heavy Ion Beams", in *Proc. LINAC'96*, Geneva, Switzerland, Aug. 1996, paper TU202, pp. 288-292

[4] W. Barth and P. Forck, "The New Gas Stripper and Charge State Separator of the GSI High Current Injector", in *Proc. LINAC'00*, Monterey, USA, Aug. 2000, paper MOD13, pp. 235-237

[5] B. Schlitt *et al.*, "Charge Stripping Tests of High Current Uranium Ion Beams with Methane and Hydrogen Gas Strippers and Carbon Foils at the GSI UNILAC", in *Proc. IPAC'13*, Shanghai, China, May 2013, paper THPWO010. p. 3779-3781

[6] P. Scharrer *et al.*, "A Pulsed Gas Stripper for Stripping of High-Intensity, Heavy-Ion Beams at 1.4 MeV/u at the GSI UNILAC", in *Proc. HIAT'15*, Yokohama, Japan, Sep. 2015. doi:10.18429/JACoW-HIAT2015-TUA1C01

[7] W. Barth *et al.*, "High Current U^{40+} operation in the GSI-UNILAC", in *Proc. LINAC'10*, Tsukuba, Japan, Sep. 2010, paper MOP044, pp. 154-156

[8] P. Scharrer *et al.*, "Stripping of High Intensity Heavy-Ion Beams in a Pulsed Gas Stripper Device at 1.4 MeV/u", in *Proc. IPAC'15*, Richmond, VA, USA, May 2015, doi:10.18429/JACoW-IPAC2015-THPF035

[9] P. Scharrer *et al.*, "Electron stripping of Bi ions using a modified 1.4 MeV/u gas stripper with pulsed gas injection", *J. Radioanal. Nucl. Chem.*, vol. 305, no. 3, pp. 837–842, 2015. doi:10.1007/s10967-015-4036-2

[10] P. Scharrer *et al.*, "An Upgrade for the 1.4 MeV/u Gas Stripper at the GSI UNILAC", in *Proc. IPAC'16*, Busan, Korea, May 2016. doi:10.18429/JACoW-IPAC2016-TUPMR058

ISBN: 978-3-95450-194-6 ISSN: 2226-0366 doi:10.18429/JACoW-LINAC2018-FR1A05

[11] P. Scharrer *et al.*, "Developments on the 1.4 MeV/u Pulsed Gas Stripper Cell", in *Proc. LINAC'16*, East Lansing, MI, USA, Sep. 2016. https://doi.org/10.18429/JACoW-LINAC2016-TUOP03

[12] W. Barth *et al.*, "U^{28+}-intensity record applying a H_2-gas stripper cell", *Phys. Rev. ST Accel. Beams*, vol. 18, pp. 040101, 2015. doi:10.1103/PhysRevSTAB.18.040101

[13] G. Riehl *et al.*, "Investigation of Beam Aberrations and Beam Halo by 3-Dimensional Emittance Measurements", in *Proc. EPAC'90*, Nice, France, Jun. 1990, paper TH459, p. 756-758

[14] P. Scharrer *et al.*, "Measurements of charge state distributions of 0.74 and 1.4 MeV/u heavy ions passing through dilute gases", *Phys. Rev. Accel. Beams*, vol. 20, pp. 043503, 2017. doi:10.1103/PhysRevAccelBeams.20.043503

[15] J.F. Ziegler *et al.*, *The Stopping and Range of Ions in Solids*, Vol. 1, Pergamon Press, New York, 1985

Content from this work may be used under the terms of the CC BY 3.0 licence (© 2018). Any distribution of this work must maintain attribution to the author(s), title of the work, publisher, and DOI.

ISBN: 978-3-95450-194-6 ISSN: 2226-0366 doi:10.18429/JACoW-LINAC2018-FR1A06

PULSE-BY-PULSE BEAM PARAMETER SWITCHING OF HIGH-QUALITY BEAMS FOR MULTI-BEAMLINE OPERATION AT SACLA

H. Maesaka†, T. Fukui, T. Hara, RIKEN SPring-8 Center, 679-5148 Sayo, Hyogo, Japan
N. Hosoda, C. Kondo[1], S. Matsubara, T. Ohshima[1], M. Yamaga, Y. Otake,
Japan Synchrotron Radiation Research Institute 679-5198 Sayo, Hyogo, Japan
T. Hasegawa, O. Morimoto, Y. Tajiri, S. Tanaka, M. Yoshioka,
SPring-8 Service Co., Ltd. 679-5165 Tatsuno, Hyogo, Japan
[1]also at RIKEN SPring-8 Center, 679-5148 Sayo, Hyogo, Japan

Abstract

Since the number of beamlines in a linac-based X-ray free-electron laser (XFEL) facility is limited, it is quite important to increase the machine time for user experiments. In the XFEL facility, SACLA, a new XFEL beamline, BL2, was constructed in addition to the existing beamline, BL3, and a kicker magnet was installed into the beam switchyard to distribute a 60 Hz electron beam to both beamlines one after another. Since a beam energy and an optimum bunch length are usually different for each beamline, we developed a beam route and parameter switching software to change beam parameters pulse-by-pulse. The switching system successfully distributed high quality electron beams to both beamlines and XFEL performance for each beamline was individually optimized. When a high-quality electron beam having less than 1 mm mrad normalized emittance, 10 fs FWHM bunch length, 10 kA peak current, etc. was injected into BL2, however, the XFEL intensity of BL2 was significantly smaller than BL3 due to the growth of the emittance and pointing jitter coming from coherent synchrotron radiation (CSR). Therefore, we rearranged the optics of the transport line to mitigate the CSR effect and the XFEL intensity comparable to BL3 was achieved. We are also developing an on-demand beam route and parameter switching system needed for the beam injection from SACLA to the SPring-8 storage ring. The on-demand system also showed a sufficient performance and it will be used for the user operation in the near future.

INTRODUCTION

Linac-based X-ray free-electron laser (XFEL) facilities were constructed for the past decade or so and they have contributed for various breakthroughs about microscopic phenomena. However, the number beamlines of an XFEL facility is much smaller than a ring-based light source. Therefore, increasing opportunities to use XFEL is quite important to maximize scientific outcomes.

The XFEL facility, SACLA, has been providing brilliant X-ray laser pulses since 2011 in a photon energy region from 4 keV to 20 keV [1]. SACLA mainly consists of a low-emittance thermionic electron gun [2] followed by sub-harmonic accelerators [3], C-band main accelerators up to 8 GeV [4] and XFEL beamlines with in-vacuum undulators, as shown in Fig. 1. The user operation of SACLA started with one XFEL beamline, BL3, with a maximum repetition rate of 60 Hz. An additional XFEL beamline, BL2, was constructed in 2014 to double the user time effectively and a kicker magnet was also installed into the switchyard to switch the beam route pulse-by-pulse [5]. In addition, the SCSS test accelerator [6] was moved to SACLA-BL1 in 2014, the maximum beam energy was upgraded to 0.8 GeV in 2016, and it has been providing soft-XFEL in the photon energy region around 0.1 keV [7]. Thus, SACLA is now providing three XFELs in parallel and the experimental opportunity of SACLA is increased substantially.

Furthermore, SACLA has a beam transport line to the SPring-8 storage ring (XSBT) and the beam injection from SACLA to SPring-8 is planned in the near future. This is because the low-emittance upgrade of the SPring-8 storage ring was proposed [8] and the upgraded ring requires a low-emittance injection beam from SACLA. Therefore, a flexible beam route switching system is necessary to provide electron beams to both XFEL beamlines and the SPring-8 storage ring in parallel.

Since the XFEL photon energy is different for each experimental user, the electron beam energy for each beamline must be changed pulse-by-pulse. In addition, the optimum bunch length is different for each beamline [5], since the optics of each electron beam transport line is significantly different. Therefore, we are developing a flexible rf parameter switching system of each accelerator unit to change the beam parameter pulse-by-pulse.

In fact, we encountered an instability problem that the horizontal emittance and the horizontal pointing stability deteriorated after the dogleg beam transport line of BL2 [5]. Since this instability was suppressed for a longer bunch beam with a lower peak current, the cause of the instability was considered to be a coherent synchrotron radiation (CSR) effect. The rf parameter switching system helped the suppression of the CSR effect by stretching the bunch length for BL2. However, the XFEL intensity of BL2 was significantly smaller than BL3 in case of a longer bunch length. Therefore, an improvement of the optics of the BL2 dogleg part was necessary for the mitigation of the CSR effect to generate XFEL comparable to BL3.

In this article, we describe the design and operation status of the pulse-by-pulse beam route and parameter control system of SACLA. We also discuss the mitigation of the instability due to the CSR effect in the dogleg part of BL2.

† maesaka@spring8.or.jp

Content from this work may be used under the terms of the CC BY 3.0 licence (© 2018). Any distribution of this work must maintain attribution to the author(s), title of the work, publisher, and DOI.

ISBN: 978-3-95450-194-6 ISSN: 2226-0366 doi:10.18429/JACoW-LINAC2018-FR1A06

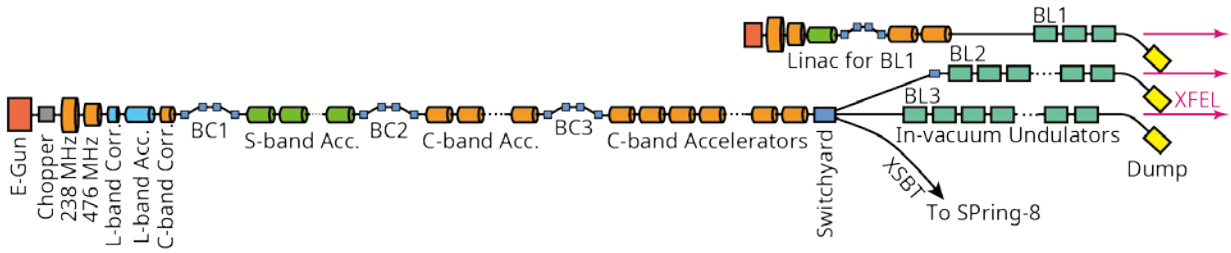


Figure 1: Schematic layout of SACLA.

STRATEGY AND EQUIPMENTS FOR BEAM ROUTE AND PARAMETER CONTROL

The control items of the beam route and parameter control system are the beam route, the beam energy and the bunch length for each pulse. The beam route is switched by the kicker magnet in the switchyard. The beam energy is changed by turning on and off the triggers for accelerator units after the third bunch compressor, BC3. The bunch length is adjusted by changing the phases of accelerator units before BC3.

In this section, we introduce the development strategy of the pulse-by-pulse beam route and parameter control system. We then describe the beam switchyard for the beam route control including the transport line of BL2 and the timing and low-level rf (LLRF) system for each accelerator unit to change the beam energy and bunch length pulse-by-pulse.

Development Strategy

The pulse-by-pulse beam parameter control system has been developed in two steps. The first step is to deliver electron beams to each beamline with an equal rate one after another. Since XFEL users prefer a constant interval between XFEL pulses, the condition of the first step is sufficient for the machine operation only for the XFEL beamlines. The second step is to switch the beam route and parameter in on-demand basis. Since the frequency of the beam injection to the SPring-8 storage ring during the top-up operation is 0.1 Hz or less, the beam route should be switched to XSBT only at an injection request. Therefore, on-demand switching of the beam route and parameter control is necessary for the beam injection from SACLA to SPring-8. We focus on the first step of the switching system in this section and we describe the second step in the later section.

Beam Switchyard

The electron beam is distributed to each of BL2, BL3 and XSBT in the switchyard. The bending angles are +3° for BL2, 0° for BL3 and –3° for XSBT. The switchyard was initially equipped with a single DC bending magnet having the bending angle of ±3°. We replaced the DC magnet with a combination of a kicker magnet and a twin-septum magnet in accordance with the construction of BL2 so as to switch the beam routes for individual 60 Hz bunches pulse-by-pulse [5]. The bending angle of the kicker and septum magnets are ±0.53° and 2.47°, respectively. Magnet arrangements and beam optics around the dogleg of BL2 is shown in Fig. 2. The optics of the dogleg was designed to be achromatic and it could also be made isochronous by using two small dipoles in the middle of the dogleg.

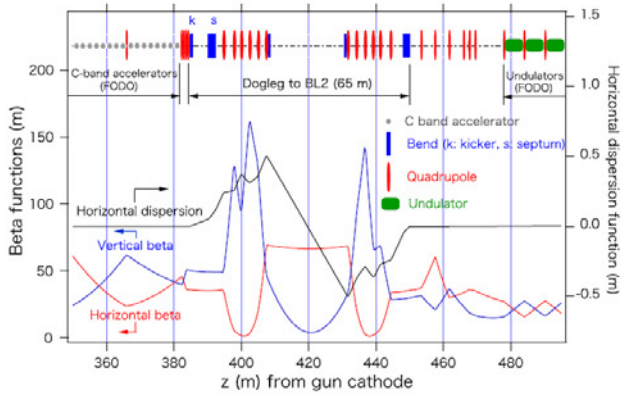


Figure 2: Magnet arrangements and beam optics around the BL2 dogleg in 2014. Dipole and quadrupole magnets are indicated by the blue and red symbols, respectively. Horizontal and vertical beta functions and a horizontal dispersion are plotted by red, blue and black lines, respectively.

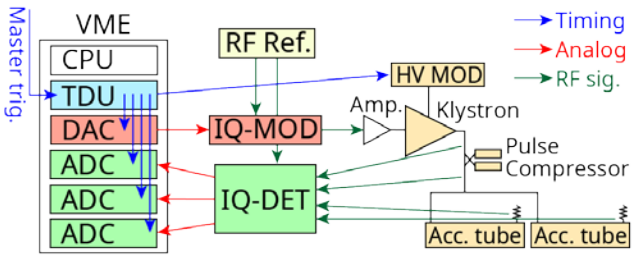


Figure 3: Schematic diagram of the timing and low-level rf system for each accelerator unit.

Timing and Low-Level RF Control System

A schematic diagram of the timing and low-level rf system for each accelerator unit [9] is shown in Fig. 3. The rf signal for each accelerator is synthesized by an in-phase and quadrature modulator (IQ-MOD). The IQ baseband waveform is generated by a 238 MSPS VME-DAC module. The rf signal from each high power rf component is detected by an IQ detector (IQ-DET). The IQ baseband waveforms are digitized by 238 MSPS VME-ADC modules.

Trigger signals for a klystron high-voltage pulse modulator (HV MOD), VMA-DAC, ADC, etc. are generated by VME trigger delay unit (TDU). The TDU receives a

Content from this work may be used under the terms of the CC BY 3.0 licence (© 2018). Any distribution of this work must maintain attribution to the author(s), title of the work, publisher, and DOI.

ISBN: 978-3-95450-194-6 ISSN: 2226-0366 doi:10.18429/JACoW-LINAC2018-FR1A06

Content from this work may be used under the terms of the CC BY 3.0 licence (© 2018). Any distribution of this work must maintain attribution to the author(s), title of the work, publisher, and DOI.

60 Hz master trigger signal and outputs the trigger signal for each component at an appropriate timing.

Beam Energy Control

The beam energy is changed pulse-by-pulse by turning on or off the trigger signals for some of the accelerator units [10]. The example of the energy control scheme is illustrated in Fig. 4. Since the VME-TDU has a frequency division function of the master trigger input, the trigger rate of each accelerator unit can be set individually. In case of Fig. 4, high and low energy beams are generated one after another with a total repetition rate of 60 Hz (30 Hz each). Since the acceleration voltage of each C-band unit is approximately 120 MeV, the beam energy can be changed in this energy step. Of course, the energy can be adjusted by changing the output rf power of the klystron. Although the quadrupole strength in the accelerator is the same for both high and low energy beams, the beam envelop can be matched by quadrupoles after the switchyard. We confirmed that two beams with the energy ratio of 1:2 could be appropriately accelerated and transported by the same quadrupole setting [10].

Bunch Length Control

The bunch length is shortened by three bunch compressors in SACLA. Since the bunch compression ratio depends on the energy chirp generated by upstream accelerator units, the bunch length can be varied by adjusting the phase of the accelerator units. In contrast to the TDU utilized for beam energy control, the VME-DAC and ADC do not have the function to change behavior one after another. Therefore, we developed software to change the rf phase pulse-by-pulse, as shown in Fig. 5.

The MADOCA control system [11] used in SACLA controls the VME modules by the equipment manager (EM) on the VME-CPU. MADOCA can run some EM agent (EMA) processes for real-time control. The pulse-by-pulse rf parameter control is implemented to the EMA processes, EMA-SW, EMA-PID1 and EMA-PID2. EMA-SW accesses the IQ data to the DAC and from the ADC. EMA-PID1 and -PID2 regulate the phase of each beam route by proportional-integrate-differential (PID) control. The ADC data taken by EMA-SW is sorted to each of EMA-PID1 and -PID2 according to the trigger number from the TDU. The set values calculated by EMA-PID1 and -PID2 are sent to EMA-SW and written to DAC.

DEMONSTRATION OF BUNCH LENGTH CONTROL

We tested the bunch length control software with an actual beam. The phase of one the C-band accelerator units in the upstream of BC3 was changed between bunching (–50° from the crest) and debunching phases (+50° from the crest) pulse-by-pulse. The bunch length was measured by a transverse rf deflector system after BC3 [12]. As shown in Fig. 6, the bunch length was compressed to 20 fs FWHM for the bunching phase and the 100 fs FWHM for the debunching phase. Thus, the bunch length was appropriately controlled pulse-by-pulse.

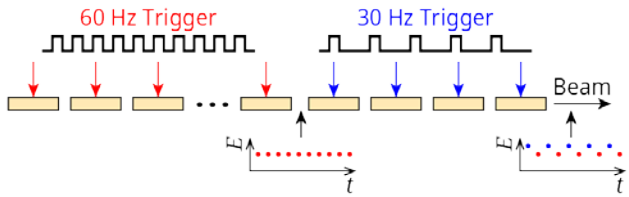


Figure 4: Pulse-by-pulse beam energy control scheme.

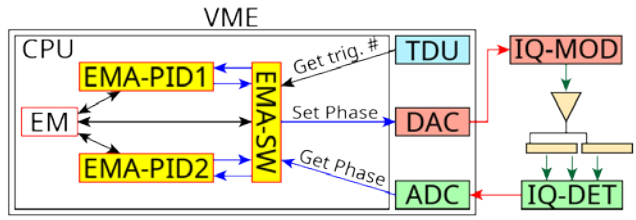


Figure 5: Schematic diagram of the rf parameter switching system.

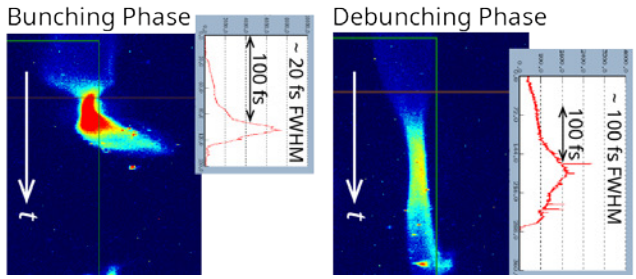


Figure 6: Bunch length measurement results with the rf deflector system. The left image shows a temporal profile for the bunching phase and the right one shows that for the debunching phase.

In this experiment, we found a large orbit distortion for the debunching phase, even though the orbit distortion was small enough for the bunching phase. The kick source of the orbit distortion was the accelerator used for the rf phase switching. Therefore, this orbit distortion was considered to be due to the phase-dependent focusing effect of the accelerator tube [13]. This kick indicates the displacement of the beam from the axis of the accelerator. Thus, the accelerator tubes should be precisely aligned, when the bunch length is largely changed pulse-by-pulse.

MITIGATION OF THE CSR EFFECT IN THE BL2 DOGLEG PART

When the electron beam optimized for BL3 was transported to BL2, the XFEL intensity of BL2 did not exceed 30 μJ per pulse, corresponding to less than 1/10 of BL3 [5], due to the emittance growth and the pointing jitter degradation coming from the CSR effect. Even if we stretched the bunch length to reduce the CSR, the maximum XFEL intensity was still 150 μJ per pulse at most.

We found that the phase space distortion due to CSR at the upstream bend of the dogleg can be canceled out by the downstream one and the emittance growth can be diminished [14]. The new beam optics of the BL2 dogleg is shown in Fig. 7. The cancellation condition can be satisfied by using the double-bend achromat (DBA) lattice for both bends of the dogleg and by setting the beta-

ISBN: 978-3-95450-194-6 ISSN: 2226-0366 doi:10.18429/JACoW-LINAC2018-FR1A06

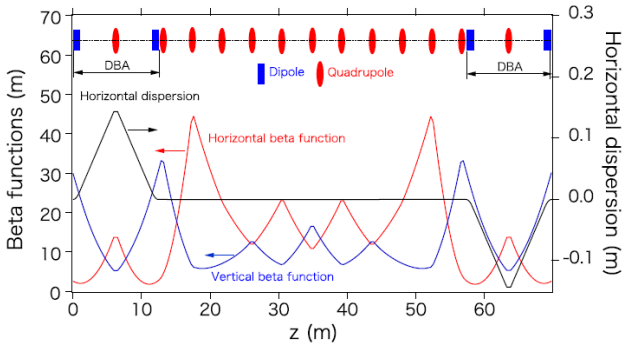


Figure 7: Magnet arrangement and beam optics of the new BL2 dogleg. The legend is the same as Fig. 2.

tron phase advance between the two DBAs to π. The quality of the electron beam, such as a 0.8 mm mrad emittance, a 10 kA peak current and a 10 fs FWHM bunch length, was almost conserved in the new dogleg, although the emittance deteriorated about one order of magnitude in the old dogleg case. We replaced the magnets of the BL2 dogleg in 2017 to mitigate the CSR effect. The deflection angle of the new kicker magnet is ±1.5°, which is three times larger than the old one. Therefore, we developed a new kicker magnet power supply driven by SiC MOS-FETs [15].

To confirm the cancellation of the CSR effect after the replacement of the dogleg, we measured an electron beam pointing jitter with two rf cavity beam position monitors (BPM) [16]. The phase space distributions of the pointing jitter are plotted in Fig. 8. While the volumes of the vertical phase space distributions were almost same, the horizontal pointing jitter was significantly improved for the new optics.

Typical trend graphs of the XFEL intensities of BL2 and BL3 are plotted in Fig. 9. A beam energy, a photon energy and an undulator K-value were 7.8 GeV, 10 keV and 2.1, respectively, for both beamlines. The 60 Hz electron beam was equally distributed to the two beamlines (30 Hz eachThe acceleration rf parameters for each beam-

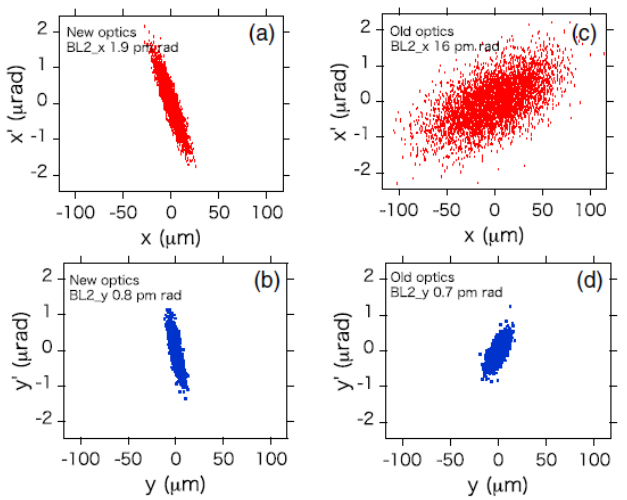


Figure 8: Horizontal (a, c) and vertical (b, d) phase space distributions of the electron beam pointing jitter after the BL2 dogleg for new (a, b) and old (c, d) optics.

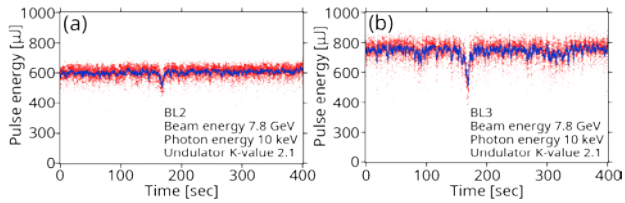


Figure 9: XFEL intensity trend graphs of BL2 and BL3 with pulse-by-pulse switching of the beam route and parameter.

line was individually optimized to maximize the XFEL intensity by using the rf parameter switching software described in the previous section. These graphs show that the XFEL intensities are comparable each other.

The rf phase for each beamline was slightly different, since the optimum bunch length depends on the optics of the transport line. The phase difference of the 238 MHz sub-harmonic buncher cavity, for example, was 0.1°. Thus, the rf parameter switching system has sufficient precision to adjust the bunch length of the electron beam for each beamline.

DEVELOPMENT OF THE ON-DEMAND BEAM ROUTE AND PARAMETER SWITCHING SYSTEM

Toward the injection to the SPring-8 storage ring in parallel with the XFEL operation, we are developing an on-demand beam route and parameter switching system as the second step. A schematic diagram of this system is shown in Fig. 10. The beam route information is distributed pulse-by-pulse by using a reflective memory network. The interface to this network is realized by a mezzanine card mounted on the VME-CPU. The route information consists of the previous, current and next route numbers and the current master trigger number. The rf parameter for each accelerator unit, the current of the kicker magnet etc. are switched according to the route information. The route number, the rf parameters and the master trigger number are recorded by an event-synchronized data-acquisition (DAQ) system [17] pulse-by-pulse in order to check whether the beam parameter was switched appropriately or not.

The sequence of the on-demand switching system is summarized below:

1. DAQ takes the data related to the route and rf parameter switching (SW-DAQ) 16 ms after the previous master trigger.
2. DAQ starts taking the other data (All-DAQ) just after the end of SW-DAQ.
3. EMA-SW gets the route information just after the master trigger and sets the trigger and rf parameter 5 ms after the master trigger (SW-Set).

We tested the on-demand parameter switching system in a VME test bench in a laboratory and a linac for BL1. The beam route was switched by a given pattern of three or four beam routes. Some waveforms of the ADC modules were also acquired once a second to impose a certain load to the VME bus.

Content from this work may be used under the terms of the CC BY 3.0 licence (© 2018). Any distribution of this work must maintain attribution to the author(s), title of the work, publisher, and DOI.

ISBN: 978-3-95450-194-6 ISSN: 2226-0366 doi:10.18429/JACoW-LINAC2018-FR1A06

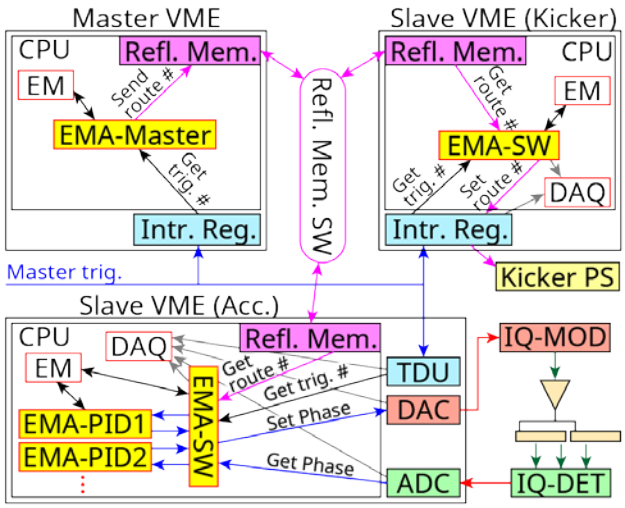


Figure 10: Schematic diagram of the on-demand beam route and parameter switching system.

The test setup in the test bench consists of two VMEs, one master VME and one slave VME. We executed an on-demand parameter switching software for more than 100 hours. The analysis of obtained data showed only one delay of parameter switching. This error rate is smaller than the other failures, such as a trip of the klystron high-voltage power supply.

For the evaluation in the linac for BL1, we used one master VME and four slave VMEs. The test data were taken for more than 40 hours and failure in the parameter switching was not found. Even though the only one inconsistency in the data was found, it was confirmed to be a delay of SW-DAQ and not to be the delay of EMA-SW itself. Figure 11 shows the histograms of the time stamp of SW-Set, SW-DAQ and All-DAQ. Although SW-DAQ must be done before the start of SW-Set, only one event (indicated by the red circle in the figure) was not in time with SW-Set. Since the parameter switching system is implemented by software, this kind of DAQ delay is unavoidable. However, the error rate is only 1×10^{-7} per pulse, which is smaller than the other failures. Thus, the parameter switching system can be used for the user operation of SACLA.

SUMMARY

We installed a new XFEL beamline, BL2, in addition to BL3 and replaced the DC bending magnet with a kicker magnet in order to increase opportunities for user experiments by switching a beam route pulse-by-pulse. We also developed a beam route and rf parameter switching system to provide the optimized electron beam to each beamline. Although the XFEL performance of the initial version of the BL2 dogleg was not sufficient due to the CSR effect in the bending magnets, we modified the optics of the dogleg and the XFEL intensity comparable to BL3 was obtained in BL2. This result was achieved in combination with the rf parameter switching system, since the optimum beam parameters were slightly different even after the optics improvement. We are developing an on-demand beam route and parameter switching system

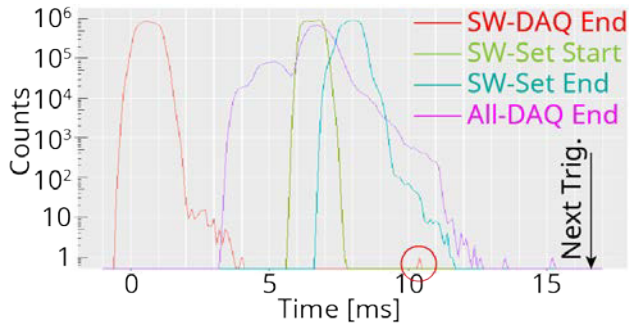


Figure 11: Histogram of the time stamp of the parameter switching and DAQ processes. Red, green, cyan and magenta lines show the end of DAQ for parameter switching, the start of parameter setting, the end of parameter setting and the end of all the DAQ. Horizontal axis is the delay time from the master trigger.

needed for beam injection to the SPring-8 storage ring. This system was tested in the test bench and the linac for BL1 and it worked well with sufficiently small failure rate of 1×10^{-7} per pulse. This new switching system will be in use in the next year.

REFERENCES

[1] T. Ishikawa *et al.*, "A compact X-ray free-electron laser emitting in the sub-ångström region", *Nature Photonics*, vol. 6, pp. 540–544, 2012, doi:10.1038/NPHOTON.2012.141

[2] K. Togawa *et al.*, "CeB_6 electron gun for low-emittance injector", *Phys. Rev. ST Accel. Beams*, vol. 10, p. 020703, 2007, doi:10.1103/PhysRevSTAB.10.020703

[3] T. Asaka *et al.*, "Low-emittance thermionic-gun-based injector for a compact free-electron laser", *Phys. Rev. Accel. Beams*, vol. 20, p. 080702, 2017, doi:10.1103/PhysRevAccelBeams.20.080702

[4] T. Inagaki *et al.*, "High-gradient C-band linac for a compact x-ray free-electron laser facility", *Phys. Rev. ST Accel. Beams*, vol. 17, p. 080702, 2014, doi:10.1103/PhysRevSTAB.17.080702

[5] T. Hara *et al.*, "Pulse-by-pulse multi-beamline operation for x-ray free-electron lasers", *Phys. Rev. Accel. Beams*, vol. 19, p. 020703, 2016, doi:10.1103/PhysRevAccelBeams.19.020703

[6] T. Shintake *et al.*, "A compact free-electron laser for generating coherent radiation in the extreme ultraviolet region", *Nature Photonics*, vol. 2, pp. 555–559, 2008, doi:10.1038/NPHOTON.2008.134

[7] K. Togawa *et al.*, "A Soft X-ray Free-Electron Laser Beamline of SACLA", in *Proc. 8th Int. Particle Accelerator Conf. (IPAC'17)*, Copenhagen, Denmark, May 2017, pp. 1209–1212, doi:10.18429/JACoW-IPAC2017-TUOAA2

[8] SPring-8-II Conceptual Design Report, Nov. 2014, http://rsc.riken.jp/pdf/SPring-8-II.pdf

[9] Y. Otake *et al.*, "Timing and low-level rf system for an x-ray laser", *Phys. Rev. Accel. Beams*, vol. 19, p. 022001, 2016, doi:10.1103/PhysRevAccelBeams.19.022001

[10] T. Hara *et al.*, "Time-interleaved multienergy acceleration for an x-ray free-electron laser facility", *Phys. Rev. ST Accel. Beams*, vol. 16, p. 080701, 2013, doi:10.1103/PhysRevSTAB.16.080701

Content from this work may be used under the terms of the CC BY 3.0 licence (© 2018). Any distribution of this work must maintain attribution to the author(s), title of the work, publisher, and DOI.

ISBN: 978-3-95450-194-6 ISSN: 2226-0366 doi:10.18429/JACoW-LINAC2018-FR1A06

[11] T. Fukui *et al.*, "Status of the Control System for the SACLA/SPring-8 Accelerator Complex", in *Proc. 16th Int. Conf. on Accelerator and Large Experimental Control System (ICALEPCS'17)*, Barcelona, Spain, Oct. 2017, pp. 1995–1999, doi:10.18429/JACoW-ICALEPCS2017-FRAPL03

[12] Y. Otake *et al.*, "Beam monitor system for an x-ray free electron laser and compact laser", *Phys. Rev. ST Accel. Beams*, vol. 16, p. 042802, 2013, doi:10.1103/PhysRevSTAB.16.042802

[13] H. Maesaka *et al.*, "Analysis and Measurement of Focusing Effects in a Traveling Wave Linear Accelerator", in *Proc. 35th Int. Free-Electron Laser Conf. (FEL'13)*, New York, USA, Aug. 2013, paper TUPSO46, pp. 329–333.

[14] T. Hara *et al.*, "High peak current operation of x-ray free-electron laser multiple beam lines by suppressing coherent synchrotron radiation effects", *Phys. Rev. Accel. Beams*, vol. 21, p. 040701, 2018, doi:10.1103/PhysRevAccelBeams.21.040701

[15] C. Kondo *et al.*, "A stable pulsed power supply for multi-beamline XFEL operations", *Rev. Sci. Instrum.*, vol. 89, p. 064704, 2018, doi:10.1063/1.5025109

[16] H. Maesaka *et al.*, "Sub-micron resolution rf cavity beam position monitor system at the SACLA XFEL facility", *Nucl. Instr. Meth.*, sec. A, vol. 696, pp. 66–74, 2012, doi:10.1016/j.nima.2012.08.088

[17] M. Yamaga *et al.*, "Event-Synchronized Data-Acquisition System for SPring-8 XFEL", In *Proc. 12th Int. Conf. on Accelerator and Large Experimental Control System (ICALEPCS'09)*, Kobe, Japan, Oct. 2009, paper TUB003, pp.69–71.

Content from this work may be used under the terms of the CC BY 3.0 licence (© 2018). Any distribution of this work must maintain attribution to the author(s), title of the work, publisher, and DOI.

ISBN: 978-3-95450-194-6 ISSN: 2226-0366 doi:10.18429/JACoW-LINAC2018-FR2A02

COMMISSIONING OF THE EUROPEAN XFEL*

D. Nölle†, Deutsches Elektronen-Synchrotron DESY, Hamburg, Germany
on behalf of the European XFEL Commissioning Team

Abstract

The European X-ray Free-Electron Laser (EUROPEAN XFEL) in Hamburg, Northern Germany, was built to produce X-rays in the range from 0.25 up to 25 keV out of three undulators that can be operated simultaneously with up to 27,000 pulses per second. The EUROPEAN XFEL is driven by a 17.5 GeV superconducting linac. This linac is the worldwide largest installation based on superconducting radio-frequency acceleration, using the so-called TESLA technology which was developed for the superconducting version of an international electron positron linear collider. The construction of the European XFEL has been finished at the end of 2016 and commissioning has been started. Meanwhile the entire facility, driving 3 Free-Electron-Lasers in the hard and soft X-ray regime, is in operation. This contribution will report on commissioning and the transition to user operation.

INTRODUCTION

The European XFEL aims at delivering X-rays from 0.25 to up to 25 keV out of three SASE undulators [1, 2]. The FELs are driven by a superconducting linear accelerator based on TESLA technology [3]. The accelerator operates in 10 Hz pulsed mode and can deliver up to 2,700 bunches per RF-pulse. Electron beams can be distributed to three different beamlines within a RF-pulse allowing for simultaneous operation of three FELs.

Construction of the European XFEL started in early 2009. The beam commissioning of the facility began end of 2015 with a ½ year long operation of the injector [4]. End of 2016 the installation of the main linac was ready, and commissioning started with the cool-down of the superconducting accelerator. Now, 23 months after the first beam was injected in the beginning of 2017, the accelerator is operational, all three FELs are lasing and the experimental program has started for one hard X-ray beamline with the experimental stations FXE and SPB [5, 6]. The other two photon beamlines are in the commissioning process, and will start operation within a few months.

FACILITY LAYOUT

The complete facility is constructed underground, in a 5.2 m diameter tunnel about 25 to 6 m below the surface level and fully immersed in the ground water. The 50 m long injector is installed at the lowest level of a 7 stories underground building whose downstream end also serves as the entry shaft to the main linac tunnel. Next access to the tunnel is only about 2 km downstream, at the bifurcation point into the beam distribution lines. The beam distribution provides space for in total 5 undulators - 3 being initially installed. Each undulator is feeding a separate beamline so that a fan of 5 almost parallel tunnels, separated each by about 17 m, enters the experimental hall located 3.3 km away from the electron source. The schematic layout of the accelerator is shown in Fig. 1.

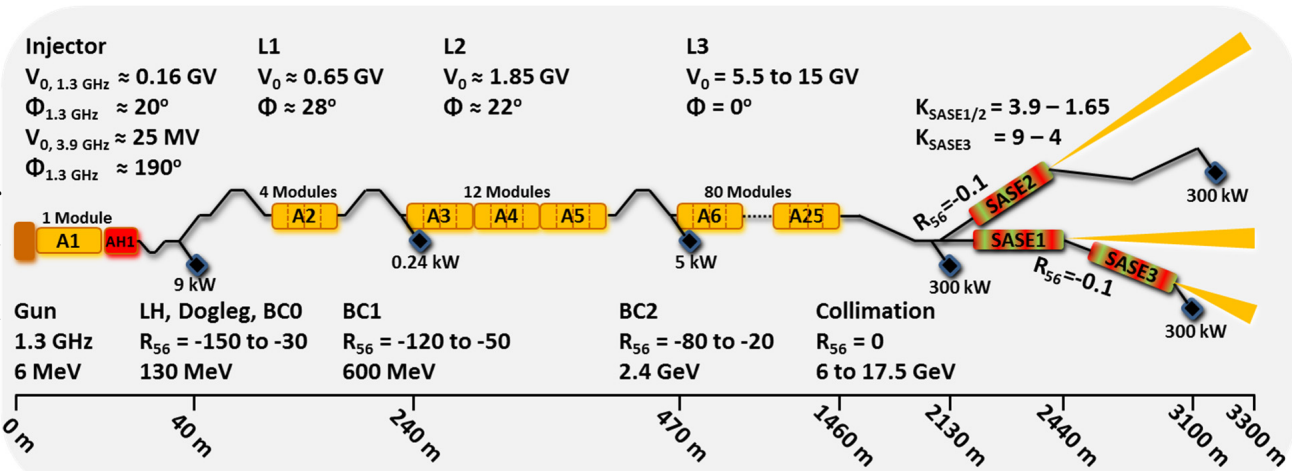


Figure 1: Schematic overview of the European XFEL accelerator. Single RF stations are named A*n* and feed either one module (A1) or 4 modules (A2-A25). R_{56} ranges for the bunch compressors are given in mm, and the phases of the different linac sections refer to typical compression set-ups. The maximum allowed beam power of the three commissioning dumps after the injector and the 2nd and 3rd bunch compressor (BC1 and BC2) as well as of the main dumps after the linac and each beam distribution line is given.

* Work supported by the respective funding agencies of the contributing institutes; for details please see http:\\www.xfel.eu
† dirk.noelle@desy.de

Content from this work may be used under the terms of the CC BY 3.0 licence (© 2018). Any distribution of this work must maintain attribution to the author(s), title of the work, publisher, and DOI.

ISBN: 978-3-95450-194-6 ISSN: 2226-0366 doi:10.18429/JACoW-LINAC2018-FR2A02

The injector consists of the normal conducting gun, one TESLA type accelerating module and a 3.9 GHz module [7] for phase space linearization, a laser heater system [8], followed by a diagnostic section [9]. This installation was completed and commissioned one year before the main LINAC, so that most essential parts of almost all systems could be commissioned during this time [4, 10].

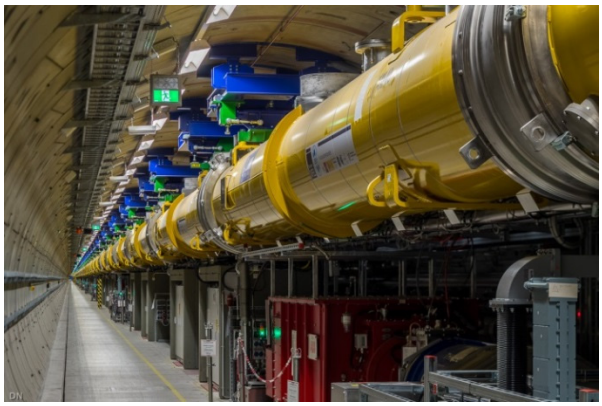


Figure 2: View into the linac tunnel with the accelerator modules suspended from the ceiling and the RF infrastructure placed below, on the floor.

From the injector the beam is fed to the main accelerator tunnel. The superconducting linear accelerator consists of 96 TESLA type accelerator modules [11]. The accelerator is grouped into 3 sections, intercepted by the 3 stage bunch compression. The first L1, consisting of 4 modules, the second L2 with 12 modules and the main linac L3 with 80 modules. The cryogenic installation is built as one continuous cryostat. Always 4 modules are fed by one 10 MW multi-beam klystron providing sufficient RF power for high gradients and regulation reserve. The accelerator modules are suspended from the ceiling (see Fig. 2), while the complete RF infrastructure (klystron, pulse transformer, LLRF electronics), except the modulator is installed below the modules. The modulators are placed in one single hall above ground, and the high-voltage pulse is fed to the pulse transformer by up to 2 km long cables.



Figure 3: First bunch compression chicane.

The bunch compressor B0 is located in front of L1 at 130 MeV and B1 before L2 at 700 MeV (Fig. 3). The final stage B2 at 2.4 GeV is located between L2 and the main linac. All magnetic chicanes are tuneable within a wide range of R_{56} allowing for flexible compression scenarios. Diagnostic stations are placed after the second and third compression stage, the later is equipped with a transverse deflecting system (TDS) for longitudinal phase space diagnostics [12].

After bunch compression to a few 10 fs, the beam is accelerated in the main linac to energies up to 17.5 GeV. The main linac is followed by a collimation section providing collimation of transverse phase space to about 60 σ and energy collimation for particles exceeding 2% relative energy deviation [13]. Between collimation and beam distribution section the Intra-Bunch-Train-Feedback System (IBFB) [14] for fast trajectory feedback within the bunch train is located. The beam distribution system is built from two switchyards [15] based on a combination of kicker and DC Lambertson septum. A fast kicker system allows to kick single bunches out of the train into the 300 kW dump line (TLD) at the end of the accelerator tunnel. The bandwidth of the kicker system allows removing single bunches out of the train, even at 4.5 MHz bunch repetition rate.

The second switchyard is based on a high precision kicker with a rise time of the order of 20 μs and a precise flat top. With this system the bunch train is split into two parts, one going straight to the SASE1/3 branch, and the other being kicked into the SASE2 branch. The beam dumps at the end of these beam lines are capable for another 300 kW electron beam power. In the SASE1/3 branch, the electron beam first passes the hard X-ray FEL SASE1 followed by the soft X-ray FEL SASE3.The other branch currently contains the hard X-ray FEL SASE2 only, but the tunnel system has space for up to 2 more FELs. The beam distribution system allows providing beam to all FELs within the same RF pulse, thus serving experiments for real parallel operation.

The fully commissioned facility will operate electron bunch charges from 20 pC to 1000 pC, with resulting bunch length after compression ranging from 3 fs to 150 fs FWHM [16]. With three different linac energies (8.5, 14, and 17.5), and the variable gap undulators, photon energies from 0.25 keV to 25 keV will be covered.

COMMISSIONING RESULTS

Injector Commissioning

The injector is operated in a separate radiation enclosure, well separated from remaining tunnel installations. The beam dump at the end of the injector allows injector operation up to full beam power.

The superconducting accelerator of the injector was cooled down in December 2015 and first electrons were accelerated to 130 MeV on Dec. 18th. Also at that early stage the 3rd harmonic linearliser was commissioned and from then on operated at the design gradient throughout

Content from this work may be used under the terms of the CC BY 3.0 licence (© 2018). Any distribution of this work must maintain attribution to the author(s), title of the work, publisher, and DOI.

ISBN: 978-3-95450-194-6 ISSN: 2226-0366 doi:10.18429/JACoW-LINAC2018-FR2A02

Content from this work may be used under the terms of the CC BY 3.0 licence (© 2018). Any distribution of this work must maintain attribution to the author(s), title of the work, publisher, and DOI.

the complete run [7]. The injector commissioning ended in July 2016, to connect the cryogenic distribution boxes of the main accelerator to the cryo-infrastructure.

Within this commissioning most of the design parameters of the European XFEL injector could be reached or even exceeded [4]. Long bunch trains were produced and the measured slice emittance at 500 pC was between 0.4 and 0.6 mm mrad, depending on the measurement technique. Extensive emittance studies were made possible by a 4-off-axis-screen measurement stage. This enabled fast parameter scans and the study of the emittance evolution along long bunch trains [9]. Combined with a transverse deflecting structure, slice properties along the bunch train were measured.

Main Accelerator System

The commissioning of the XFEL accelerator started mid of January 2017, immediately after successful cool down of the superconducting accelerator [17]. The effort was planned such, that beam transport to subsequent sections can be achieved as early as possible.

Two tasks were performed in parallel; commissioning of the RF stations and establishing beam transport. Due to a feature of the timing system [18], the RF pulse of individual RF stations can be shifted in timing away from the beam arrival. This allows working on these stations without any influence of the beam.

While the RF commissioning team was working on the first linac section L1, consisting of only 1 RF station, the beam operation team was establishing the beam transport, using the 130 MeV beam from the injector without further acceleration. As soon as the RF station was operational, the timing shift was removed, and the beam was accelerated. With moderate bunch number of 30 bunches, the initial phasing of the RF system was optimized. After one week of operation, 600 MeV beam was available up to the dump before L2.

This strategy was continued with L2 and its 3 RF stations, so that on Feb. 22nd 2.4 GeV could be transported to the BC2 dump in front of the main linac L3. Using this 2.4 GeV beam the electron beamline up to the TLD dump was commissioned. First beam up to about 1950 m could be achieved on even on Feb. 22nd, full transmission to the TLD dump was demonstrated on Feb. 25th. Using the principle of shifting RF stations of the beam, the RF commissioning was continued parallel to beam operation.

The RF commissioning went extremely smooth. Multipacting was observed at almost all RF stations at an accelerating gradient of 17-18 MV/m but could be conditioned in all cases with an effort of a couple of hours per station. The phase and amplitude stability was measured inner loop to be better than 0.01° and 0.01%. Preliminary beam energy jitter measurements give an upper limit for the RMS relative energy jitter of 3e-4 after BC1 and 1e-4 after BC2.

As soon as new RF stations got available for operation, they were shifted to the beam to do the commissioning steps with beam. In the way the beam energy was raised step by step allowing for 12 GeV beam energy on April 8th.

In the shadow of the beam being send further and further down the accelerator, also the diagnostic systems have been taken into operation. Due to careful technical preparation, the availability of a self-trigger mode all charge monitors [19] and BPMs [20] were able to provide data for the initial steering. Due to the high sensitivity of these devices, even almost lost bunches on a pC level could be detected and used. All screens and the full beam loss monitor system have also been available from the very beginning [21].

The efficient commissioning work was well supported by the DOOCS control system. The newly developed MTCA.4 standard for the control crates provided stable and reliable access to all devices [22, 23]. A vast suite of high-level control software integrates and automates more complex tasks like emittance measurement and optics matching. The readiness of the control software upon start-up was one of the key preconditions for the fast success of the commissioning.

While the accelerator was reaching reasonable beam energies, the SASE1/3 branch was completed, and operation permission was given by the authorities on April 27th. Immediately operation was extended up to the undulators. Nevertheless the commissioning work on the main accelerator continues. Meanwhile all RF stations are available, advanced commissioning work was increasing the performance. The maximum beam energy achieved up to now is 17.6 GeV, with still some potential to increase [24]. Long bunch train operation with bunch spacings of 222 ns and 888 ns has been demonstrated. The intra-train feedbacks of the RF system as well as the fast intra-bunch-train orbit feedback IBFB [14] work well, and provide stable beam conditions. Even if standard operation is only up to 120 bunches per RF pulse due to safety restrictions of the photon beam lines, bunch trains up to 500 bunches have been operated without any problems. The demonstration of 2700 bunches per RF pulse is planned at the end of 2018.

SASE1/3 Branch Commissioning

Immediately after the permission of the authorities the beam was for the first time injected to the SASE1/3 beamline on April 27th. As in case of the main linac the diagnostics worked in self-triggered mode, so that steering to the main dump of this section and full transmission could be accomplished within one shift. Shortly after establishing first beam, the SASE1 undulator was closed and first SASE operation was demonstrated in the night from May 2nd to 3rd with a 6.4 GeV beam at 9 Å [25]. After this successful but rather empirical first lasing attempt, a systematic program for photon beamline and diagnostics commissioning started. Beam based alignment (BBA) of SASE1 was resulting in significant position corrections of the movable quadrupoles of the undulator intersections.

ISBN: 978-3-95450-194-6 ISSN: 2226-0366 doi:10.18429/JACoW-LINAC2018-FR2A02

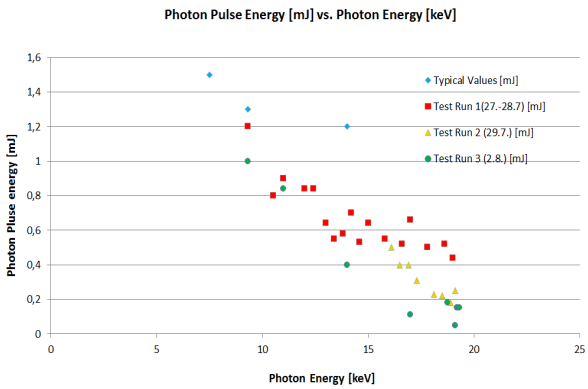


Figure 4: Photon pulse energy versus photon energy for dedicated test runs of the SASE1 FEL.

With these new settings and some basic photon diagnostics available, lasing at 2 Å or 6.2 keV with a 10.4 GeV beam was demonstrated on May 24th. Due to optimization of machine and undulator settings the SASE power could be increased to the mJ level within the next days. With ongoing commissioning work beam energy was further increased up to 14 GeV and a first standard working point at 9.3 keV was established with SASE levels of more than 500 µJ and up to 30 bunches/train. This working point was used for the commissioning of the photon beamlines, the initial commissioning of the two experimental stations of SASE1 and during the first user period, which was scheduled just 9 month after start of beam commissioning. The number of bunches per RF pulse is steadily increasing. For the first user period up to 30 bunches were provided. Currently up to 120 pulses with up to 1.5 mJ/pulse and photon energy ranging from 7.5 to 14 keV are provided during user operation. With the shutters of the experiments closed the machine was running 500 bunches at a repetition rate of 4.5 MHz with an average SASE pulse energy of 1.3 mJ, thus more than 6 W of average power. During development times the photon energy of SASE1 was varied over a wider range. Only with tuning the undulator gap and small adjustments of orbit and launch condition, the photon energy could be increased to 19.4 keV. After some tuning the pulse energy was still on the order of 150 µJ/pulse, so that with 30 bunches per pulse train mJ power levels could easily be produced at these photon energies. Figure 4 shows the photon pulse energy versus the photon energy during these test runs.

Parallel to the ongoing user program of SASE1, commissioning work of the soft X-Ray FEL SASE3 and the corresponding beamline has been done. As shown on the facility layout picture (Fig. 1) SASE3 is using the same beam as SASE1. As soon as the initial photon commissioning of the SASE3 beamline was ready, first lasing of SASE3 at 13 Å or 900 keV was possible on February 8th 2018, immediately reaching mJ pulse energies.

First operation was done with the spend beam from SASE1. As expected SASE1 and SASE3 photon pulse energies show a strong coupling. As expected [26] bunches lasing in SASE1 almost at saturation were producing a rather weak intensity in SASE3. But as soon as SASE in the hard X-ray gets disturbed, the intensity in SASE3 strongly increases.

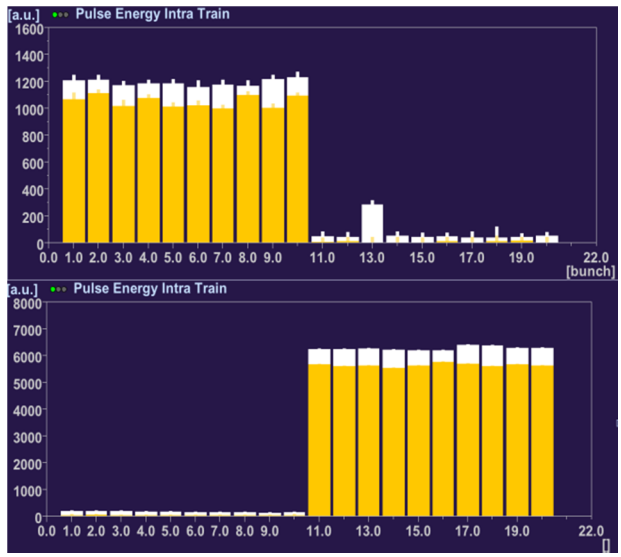


Figure 5: Fresh bunch operation of SASE1 (top) and SASE3 (bottom). Bunches foreseen to lase in SASE3 are kicked by a fast kicker in the switchyard, and put to SASE3 lasing orbit by a DC corrector. The y-axis is cross-calibrated with the XGM pulse energy measurement [27, 28], and thus gives the pulse energy in µJ.

In order to provide a sufficient decoupling of the two FEL sources fast kickers of the dump switchyard are used to send individual bunches to different trajectories in SASE1 and SASE 3. This scheme, called “soft kick” or “fresh bunch technique” [29], allows to suppress lasing of bunches foreseen to lase in SASE3 in SASE1, while bunches having lased in SASE1 produce much lower intensity in SASE3. Making further use of the different angle these bunches emit some FEL radiation in SASE3, their intensity can be further suppressed by apertures along the photon beam line. The decoupling of both lasers with SASE1 bunches delivering hard X-rays, while “SASE3 bunches” produce up to 7 mJ pulse energy in the soft X-ray regime has already been demonstrated. A picture showing the photon pulse energies during such an operation is shown in Fig. 5.

SASE2 Branch Commissioning

On March 13th the beam was send to the SASE2 branch for the first time. 100% transmission and stable beam conditions in the about 1 km beamline could be established within a single shift. Due to user program and shutdown work, the first lasing attempts for SASE2 had to be delayed. After some initial BBA first lasing of SASE2 was achieved on May 1st 2018, less than one year after SASE1. Meanwhile photon pulse energies of up to 900 µJ have been achieved at a photon energy of 7.5 keV with a 14 GeV beam.

The BBA results and also photon position data in the beamline indicate an issue with the initial alignment of

Content from this work may be used under the terms of the CC BY 3.0 licence (© 2018). Any distribution of this work must maintain attribution to the author(s), title of the work, publisher, and DOI.

ISBN: 978-3-95450-194-6 ISSN: 2226-0366 doi:10.18429/JACoW-LINAC2018-FR2A02

Content from this work may be used under the terms of the CC BY 3.0 licence (© 2018). Any distribution of this work must maintain attribution to the author(s), title of the work, publisher, and DOI.

the FEL and photon beamline, which is currently under investigation.

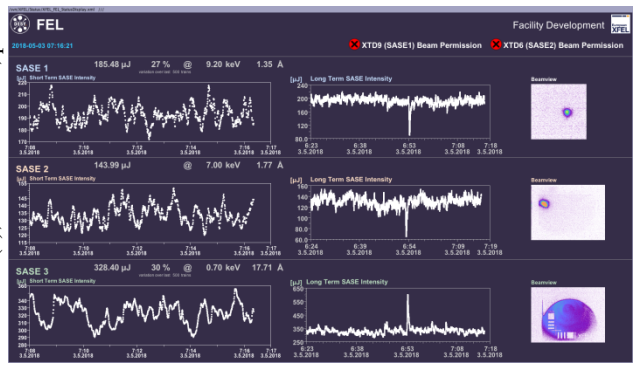


Figure 6: Screenshot of the SASE level display of EUROPEAN XFEL with all 3 SASE lines in operation. On the right hand side an image of a screen in photon beam line can be seen.

Simultaneous Operation of 3 FELs

Shortly after first lasing in SASE2, simultaneous lasing three FELs was demonstrated (Fig. 6), making use of the flexible distribution system. Even if this test was done under poor lasing conditions, it proofs the flexibility of EUROPEAN XFEL to operate the corresponding beamlines in parallel.

Operation Parameters

The current operation parameters of EUROPEAN XFEL as well as the design parameters and the parameters planned to be archived still in 2018 are summarized in Table 1.

Table 1: Parameter set of EUROPEAN XFEL, Comparing Project Goals, with Current Status Perspective for 2019

Quantity	Unit	Project Goal	Achieved	Routine
Beam energy	GeV	8-17.5	6 - 17.6	14
Rep Rate (intra train)	MHz	4.5	.58 – 4.5	0.58-4.5
Charge	pC	10-1000	10-500	250
Bunch length (FWHM)	fs	2-180	20, 50	20
Beam power	kW	500	18	1,8
Pulses/s	1/s	27000	5000	600
SASE1				
Photon Energy	keV	3-25	7.5-19.4	7.5-14
Pulse Energy	mJ		1.5	1.2
SASE2				
Photon Energy	keV	3-25	7.5	-
Pulse Energy	mJ		0.9	-
SASE3				
Photon Energy	keV	0.25 - 3	0.65–0.9	-
Pulse Power	mJ		7	

CONCLUSION AND OUTLOOK

The European XFEL accelerator has been put into operation. All major commissioning targets were achieved. The initial accelerator operation is smooth, the performance of the chosen superconducting technology is convincing. All 3 FEL sources had first lasing within 1 year and have been operated on mJ levels with up to 5000 pulses/s. The user program aiming to host highest quality user experiments with major impact on science has already started, 9 month after beginning of beam commissioning [5, 6].

The user program is going to be extended from hard to also soft X-ray experiments. First experiments at SASE3 are scheduled for November 2018. The second hard X-ray line served by SASE2 will start user operation in spring 2019. In parallel the accelerator will be further developed towards longer bunchtrains and higher beam power and flexible bunch patterns. After 840 hours of user operation in 2017 and 2000 hours in 2018, full operation with 4,000 user hours per year is foreseen in 2019.

ACKNOWLEDGEMENT

The European XFEL is a joint achievement of many colleagues from the participating labs working in different parts of the project. The Author wishes to thank all of them for their long lasting devotion and enthusiasm. In addition the author would like to acknowledge the strong commitment of the DESY and European XFEL staff for the effective commissioning phase of the facility. Special thanks go to the colleagues from CANDLE, ELETTRA, PSI, and SLAC for their supporting actions during the commissioning. Collaboration is the key to success!

REFERENCES

[1] M. Altarelli *et al.* Ed., "The European X-Ray Free-Electron Laser–Technical Design Report", DESY, Hamburg, Germany, Rep. DESY 2006-097, July 2007.

[2] R. Brinkmann *et al.* Ed., "TESLA XFEL Technical Design Report Supplement", DESY, Hamburg, Germany, Rep. DESY 2002-167, March 2002.

[3] R. Brinkmann *et al.* Ed., "TESLA Technical Design Report – Part II: The Accelerator", DESY, Hamburg, Germany, Rep. DESY 2001-011, March 2001.

[4] F. Brinker for the European XFEL Commissioning Team, "Commissioning of the European XFEL Injector", in *Proc. IPAC'16*, Busan, Korea, May 2016, paper TUOCA03, pp. 1044-1047.

[5] M. Wiedorn *et al.*, "Megahertz serial crystallography", Nature Communications, accepted.

[6] M. Grünbein *et al.*, "Megahertz data collection from protein microcrystals at an X-ray free-electron laser", Nature Communications, accepted.

[7] C. Maiano *et al.*, "Commissioning and Operation Experience of the 3.9 GHz System in the EUROPEAN XFEL Linac", presented at IPAC'17, Copenhagen, Denmark, MOPVA059, pp. 999-1002.

ISBN: 978-3-95450-194-6 ISSN: 2226-0366 doi:10.18429/JACoW-LINAC2018-FR2A02

[8] M. Hamberg *et al.*," Electron Beam Heating with the European XFEL Laser Heater", presented at FEL 2017, Santa Fe, USA, WEP018, pp 450-451.

[9] C. Gerth *et al.*, "Online Longitudinal Buch Profile and Slice Emittace Diagnostics at the European XFEL", presented at IBIC 2017, Grand Rapids, USA, TUPCC03, pp. 153-156.

[10] D. Lipka *et al.*, "First Experience with the Standard Diagnostics at the European XFEL Injector", presented at IBIC'2016, Barcelona, Spain, MOBL02, pp. 14-19.

[11] H. Weise, "How to Produce 100 Superconducting Modules for the European XFEL in Collaboration and with Industry", presented at IPAC'14, Dresden, Germany, WEIB03, pp. 1923-1928.

[12] M. Hüning, "Bunch Length Measurements using transverse Deflecting Systems", presented at LINAC'2018, Beijing, China, to be published.

[13] V. Balandin, R. Brinkmann, W. Decking, and N. Golubeva, "Post-linac collimation system for the European XFEL", presented at PAC'09, Vancouver, Canada, May 2009, paper TH6PFP030, pp. 3763-3765.

[14] B. Keil *et al.*, "Status of the European XFEL Transverse Intra Bunch Train Feedback System", presented at IBIC'15, Melbourne, Australia, TUPN064, pp. 492-496.

[15] W. Decking, F. Obier, "Layout of the Beam Switchyard at the European XFEL", presented at EPAC'08, Genoa, Italy, WEPC073, pp. 2163-2165.

[16] G. Feng *et al.*, "Beam dynamics simulations for European XFEL", DESY, Hamburg, Germany, Rep. TESLA-FEL 2013-04, 2013.

[17] T. Schnautz *et al.*, „First operation of the XFEL LINAC with the 2K cryogenic system", presented at CEC-ICMC 2017, Madison, USA.

[18] A. Aghababyan *et al.*, "XFEL Timing System Specifications", Conceptual Design Report - Version 2.2, Hamburg, Germany, May 2013, http://ttfinfo2.desy.de/doocs/Timing/CDRv2.2short.pdf

[19] M.Werner *et al.*, "A Toroid Based Bunch Charge Monitor System with Machine Protection Features for FLASH and XFEL", presented at IBIC'2014, Monterey, USA WEPF02, pp. 521-524.

[20] B. Keil *et al.*, "The European XFEL Beam Position Monitoring System", presented at IPAC'2010, Kyoto, Japan, MOPE064, pp. 1125-1127.

[21] D. Nölle, "The Diagnostic System at the European XFEL; Commissioning and First User", presented at IBIC'2018, Shanghai, China, TUAB01, to be published.

[22] H. Schlarb, T. Walter, K. Rehlich, and F. Ludwig, "Novel crate standard MTCA.4 for industry and research", presented at IPAC2013, Shanghai, China, May 2013, paper THPWA003, pp. 3633-3635.

[23] T. Walter, M. Fenner, K. Kull, and H. Schlarb, "MicroTCA Technology Lab at DESY: Start-Up Phase Summary", presented at IPAC'17, Copenhagen, Denmark, May 2017, paper THOAB2, to be published.

[24] J. Branlard *et al.*, RF Operation Experience at the European XFEL, presented at LINAC 2018, Beijing, China, 2018, this conference.

[25] W. Decking, H. Weise, "Commissioning of the European XFEL Accelerator", presented at IPAC'17, Copenhagen, Denmark, MOXAA1, pp. 1-6.

[26] E. A. Schneidmiller and M.V.Yurkov, "Baseline Parameters of the European XFEL", presented at FEL 2017, Santa Fe, USA, MOP033, pp. 109-112.

[27] K. Tiedtke *et al.*, "Gas-detector for X-ray lasers", *J. Appl. Phys.*, vol. 103, p. 094511, 2008.

[28] T. Tschentscher *et al.*, "Photon Beam Transport and Scientific Instruments at the European XFEL", *Appl. Sci.* 2017, *7*, 592.

[29] R. Brinkmann *et al., Nucl. Instr. Meth.,* vol. 429, pp. 233, 1999.

Content from this work may be used under the terms of the CC BY 3.0 licence (© 2018). Any distribution of this work must maintain attribution to the author(s), title of the work, publisher, and DOI.

ISBN: 978-3-95450-194-6 ISSN: 2226-0366

ISBN: 978-3-95450-194-6 ISSN: 2226-0366

List of Authors

Bold papercodes indicate primary authors; ~~crossed out~~ papercodes indicate 'no submission'

— A —

Abbasi Davani, F. MOPO026, TUPO120
Abbasi, F. MOPO070
Abbon, P. TU2A04
Abe, M. MOPO125
Adam, J. TUPO013
Aguilera Murciano, D. TUPO013
Agustsson, R.B. ~~MOOP11~~, MOPO077
Ahmadiannamin, S. MOPO026, TUPO119
Ahuja, R. THPO080
Aizawa, S. ~~THOP07~~, THPO091
Akabori, T. TUPO069
Akagi, T. TU2A04, THPO062
Akemoto, M. THPO095
Akikawa, H. THPO095
Aksoy, A.A. MOPO102
Alcorta, M. TU1A03
Aleksandrov, A.V. FR1A01
Aleksandrov, V. ~~SPWR032~~, TUPO112
Alekseev, P.N. TUPO011
Alesini, D. MO2A03, FR1A03
Alexeev, N.N. **TUPO011**
Alimov, A.S. MOPO060, MOPO061, MOPO062
Almomani, A. THPO046
Amal, Y. THPO093
Ames, F. TU1A03
An, S. THPO100, THPO104
An, Y.W. TUPO114
Anania, M.P. FR1A03
Andersson, J. MOPO027
Andreev, V. TUPO011
Anetai, Y. TUPO069
Ang, Z.T. ~~MOOP01~~, MOPO092, **TUPO014**
Angal-Kalinin, D. ~~**MOOP03**~~, **MOPO035**, ~~WE1A01~~
Antoine, C.Z. ~~TUOP03~~, TUPO030, TUPO066
Antoniazzi, L. TU2A04, THPO062
Apostolov, E.M. TUPO027
Appel, S. THPO046
Appleby, R.B. TUPO113
Apsimon, R. **TUPO113**, ~~THOP08~~, THPO108
Arakawa, D.A. ~~SPWR027~~, MOPO107
Arbuzov, V.S. WE1A03
Arduini, G. ~~WE1A01~~
Arias, T. TUPO055
Arnold, A. THPO125
Arnold, M. MOPO018, THPO011, **THPO012**
Arnold, P. MO1P03
Arsentyeva, M.V. ~~**SPWR030**~~, **TUPO093**
Aryshev, A. ~~TU1P03~~
Asaka, T. ~~THOP07~~, THPO091, **THPO124**
Atieh, S. TUPO022
Atoian, G. MOPO100
Au, T. ~~MOOP01~~, MOPO092, TUPO014
Aulenbacher, K. ~~SPWR010~~, ~~SPWR025~~, ~~SPWR034~~, TU2A01, TUPO084, THPO072, THPO073, THPO107, TUPO092, THPO007
Aydin, A. MOPO102
Ayvazyan, V. ~~SPWR026~~, ~~MOOP09~~, MOPO038, MOPO104, TUPO029

— B —

Bacci, A. **TU1P01**, TH1A03
Bachimanchi, R. MOPO115
Bade, D. MOPO101
Bae, S. ~~SPWR015~~, TUPO010
Bahrami, M. MOPO070, TUPO119
Bai, J. ~~**SPWR028**~~, **THPO082**
Bai, J.N. **THPO007**
Balalykin, N. MOPO010
Baldo, A. THPO045
Banerjee, N. ~~WE1A02~~
Barbanotti, S. ~~MOOP07~~, MOPO037
Barcikowski, A. ~~MOOP11~~, MOPO077
Bardorfer, A. MOPO081
Baricevic, B.B. **MOPO081**
Barkley, W.C. ~~**MOOP12**~~, **MOPO095**
Barley, J. ~~WE1A02~~
Barnyakov, A.M. ~~SPWR030~~, TUPO001, TUPO093
Barth, W.A. ~~SPWR010~~, ~~SPWR025~~, ~~SPWR034~~, **TU2A01**, TUPO084, THPO072, THPO073, THPO107, FR1A05
Bartnik, A.C. ~~WE1A02~~, THPO010
Barzi, E.Z. **TUPO076**
Basten, M. TUPO017, ~~**SPWR010**~~, ~~SPWR025~~, ~~SPWR034~~, TU2A01, TUPO084, **THPO072**, THPO073, THPO107
Bate, C. TH2A01
Battistello, A. MOPO124
Battisti, A. MO2A03
Bayle, H. THPO086
Bazarov, I.V. ~~WE1A02~~
Bazin, N. TU2A04
Bazyl, D.B. MOPO018
Beaugerard, N. MO2A03
Beauvais, P.-Y. TU2A04
Bechtold, A. WE2A04
Beebe, E.N. ~~THOP12~~, ~~THPO117~~
Behnamian, H. TUPO119
Bellan, L. TU2A04, THPO062
Bellandi, A. ~~**SPWR026**~~, **MOPO104**, TUPO029
Bellaveglia, M. MO2A03, FR1A03
Bellodi, G. THPO057
Ben-Zvi, I. THPO006
Bencini, V. ~~**SPWR013**~~, **TUPO016**, TUPO127

Content from this work may be used under the terms of the CC BY 3.0 licence (© 2018). Any distribution of this work must maintain attribution to the author(s), title of the work, publisher, and DOI.

ISBN: 978-3-95450-194-6 ISSN: 2226-0366

Content from this work may be used under the terms of the CC BY 3.0 licence (© 2018). Any distribution of this work must maintain attribution to the author(s), title of the work, publisher, and DOI.

Benedetti, S. **TH1P03**, **THPO057**
Benot-Morell, A. TUPO013
Berezov, R. THPO046
Berg, J.S. ~~WE1A02~~
Bergamaschi, M. ~~MOOP08~~, MOPO020
Bergoz, J.F. THPO086
Berkovits, D. WE2A04
Bernaudin, P.-E. TUPO019
Bertolo, S.B. TUPO127
Bettoni, S. ~~MOOP06~~, MOPO034
Bevcic, M. FR1A05
Bezditko, O. ~~**SPWR006**~~, ~~SPWR008~~, **MOPO028**, TUPO002
Bhang, J.B. TUPO052
Bi, C.B. ~~THOP06~~, THPO022
Biagioni, A. TH1A03
Bilton, A. ~~SPWR016~~, ~~THOP04~~, THPO058
Bini, S. MO2A03
Birch, S.L. MO1P03
Birkhan, J. THPO012
Bisesto, F.G. FR1A03
Björklund Svensson, J. MOPO027
Blackmore, V. MOPO129
Bogacz, S.A. ~~WE1A01~~
Bolzon, B. TU2A04
Bonnay, P. TUPO019
Bonne, F. TUPO019
Bonomi, R. TUPO013
Boonpornprasert, P. TUPO098, ~~THOP11~~, THPO116
Bopp, M. THPO115
Borden, M.J. ~~MOOP12~~, MOPO095
Borland, M. TH1A05
Borotto Dalla Vecchia, F. MOPO124
Bortolato, D. TU2A04
Bottin, P. MOPO124, THPO045
Bousson, S. ~~WE1A01~~
Bowden, G.B. THPO018
Bozzolan, M. **THPO084**
Brandin, M. MOPO027
Branlard, J. ~~SPWR026~~, ~~**MOOP09**~~, **MOPO038**, MOPO039, MOPO104, **TUPO029**, TUPO132
Braun, H.-H. THPO115
Breitenfeldt, M. ~~SPWR013~~, TUPO013, TUPO016
Brentegani, E. TH1A03
Brooks, S.J. ~~WE1A02~~
Bruni, C. ~~MOOP08~~, MOPO020
Brynes, A.D. ~~MOOP03~~, MOPO035
Brüning, O.S. ~~WE1A01~~
Buckley, S.R. ~~MOOP03~~, MOPO035
Bukai, M. MOPO093
Bulygin, A.M. ~~SPWR022~~, TUPO045
Burandt, C. THPO011
Burke, D.C. ~~WE1A02~~
Bursali, H. TUPO023
Burt, G. TUPO113, ~~THOP08~~, THPO108
Burton, M.C. **TUPO042**
Busch, M. ~~SPWR010~~, ~~SPWR025~~, ~~SPWR034~~, TU2A01, TUPO084, THPO072, THPO073, THPO107
Bustinduy, I. THPO043
Butenko, A.V. TUPO017, **TH1P02**
Butkowski, Ł. ~~MOOP04~~, ~~MOOP09~~, MOPO036, MOPO038, MOPO039, **TUPO132**
Bylinskii, Y. TUPO014
Byrd, J.M. TH1A05

— C —

Cabaleiro Magallanes, F. TUPO013
Calaga, R. ~~WE1A01~~
Caldara, M. TUPO013
Candolfi, C. TUPO013
Cao, J.S. ~~FR1A04~~
Cao, X. THPO039
Cara, P. TU2A04, THPO062
Cardelli, F. MO2A03
Carroll, J. TUPO043
Cash, R.J. ~~MOOP03~~, MOPO035
Cassou, K. MO2A03
Castellano, M. FR1A03
Castorina, G. TUPO013
Catalán Lasheras, N. TUPO022, TUPO023, ~~THOP08~~, THPO108
Cathey, B.L. **FR1A01**
Celona, L. THPO043
Cenni, E. THPO097
Cerne, R. MOPO081
Cerv, M. TUPO013
Cha, H.J. **TUPO051**, TUPO052
Chabot, D. ~~TUOP02~~, TUPO007
Chahbazian, M.E. THPO093
Chaikovska, I. ~~WE1A01~~
Champion, M.S. MO1P01
Chapman, E. TU1A03
Chauveau, A.C. THPO043
Chauvin, N. TU2A04
Chel, S. TU2A04
Chen, F.S. TUPO130
Chen, H. ~~THOP11~~, THPO116
Chen, J.E. ~~TUOP08~~, TUPO003
Chen, M. TUPO049, **THPO076**
Chen, Q. THPO028, THPO029, THPO030, THPO031, THPO038
Chen, Q.S. ~~SPWR028~~, THPO082
Chen, S. THPO113
Chen, S. **TUPO049**, THPO076
Chen, T. **MOPO029**
Chen, W. THPO039
Chen, W.L. THPO053
Chen, Y. TUPO098, ~~**THOP11**~~, **THPO116**
Cheng, A.Q. THPO076
Cheng, C. ~~THOP06~~, THPO022, THPO111

ISBN: 978-3-95450-194-6 ISSN: 2226-0366

Cheng, W. THPO076
Cherepenko, A. ~~MOOP04~~, MOPO036
Chi, Y.L. THPO001, THPO102, THPO103
Chiadroni, E. TH1A03, FR1A03
Choi, B.H. MOPO094, TUPO009
Choi, C.O. MOPO094, THPO067
Choi, J.W. THPO067
Choi, S. ~~SPWR015~~, TUPO010
Choi, Y.W. MOPO063, MOPO064
Choroba, S. ~~MOOP04~~, MOPO036, TUPO027, **WE1A04**
Chouhan, V. TUPO067, **TUPO068**, TUPO069
Chu, C.P. TUPO130
Chung, M. ~~SPWR036~~, ~~TUOP09~~, TUPO078, THPO132
Ciaccia, C. TUPO076
Cianchi, A. TH1A03, **FR1A03**
Cibinetto, G. MOPO089
Cichalewski, W. ~~SPWR026~~, MOPO104, TUPO029
Citterio, A. THPO115
Clarke, R.F. ~~MOOP03~~, MOPO035
Cogan, S. ~~TUOP02~~, TUPO007
Colombo, A.G. MOPO124
Compton, C. **~~TU1A04~~**
Comunian, M. TU2A04, THPO062
Cong, P.T. THPO042
Cong, Y. THPO054
Connell, M. S. MO1P01
Conventi, D. MOPO124
Corbet, J. MOPO101
Corlett, P.A. ~~MOOP03~~, MOPO035
Corsini, R. ~~MOOP08~~, MOPO020
Costa, G. FR1A03
Cousineau, S.M. FR1A01
Cowie, L.S. ~~MOOP03~~, MOPO035
Cox, G. ~~MOOP03~~, MOPO035
Craievich, P. **WE1A05**, **THPO115**
Crittenden, J.A. ~~WE1A02~~
Cueva, P. TUPO055
Cultrera, L. ~~WE1A02~~
Curbis, F. MOPO027
Curcio, A. ~~MOOP08~~, MOPO020

— D —

D'Auria, G. TUPO013
Dafna, H. WE2A04
Dai, J. TUPO064
Dal Forno, M. THPO018
Daly, E. MOPO019
Danared, H. THPO043
Dangwal Pandey, A.D. TH2A01
Dassa, L. ~~WE1A01~~
Davis, G.K. MOPO019
Dayyani, M. ~~SPWR036~~, THPO132
De Gersem, H. MOPO018, ~~THOP11~~, THPO116
De Michele, G. **TUPO013**, MOPO081
De Silva, S.U. ~~TUOP04~~, **~~TUOP05~~**, ~~TUOP12~~, TUPO031, TUPO032, **TUPO033**, TUPO035
Degiovanni, A. TUPO013
Dehler, M.M. ~~MOOP06~~, MOPO034
Deitrick, K.E. **TUPO109**, **THPO010**, **MO2A04**
Delaviere, T. THPO086
Delayen, J.R. MO2A04, ~~TUOP04~~, ~~TUOP05~~, **~~TUOP12~~**, TUPO031, TUPO032, TUPO033, **TUPO035**
Deng, H.X. ~~SPWR003~~, MOPO042
Devanz, G. ~~THOP05~~, THPO066
De$_O$liveira, J.G. THPO093
Di Giacomo, M. ~~THOP01~~, THPO047
Di Lorenzo, F.D.L. TUPO127
Di Raddo, R.D. MO2A03
Diaz, M. MOPO115
Diefenbach, J. THPO007
Dimov, V.A. TUPO013
Dobbins, J. ~~WE1A02~~
Döbert, S. ~~SPWR036~~, ~~MOOP08~~, MOPO020, **TH1A04**, THPO132
Dohlus, M. ~~THOP11~~, THPO116
Dohmae, T. ~~SPWR019~~, TUPO065, TUPO071, TUPO072, **THPO002**
Dolgashev, V.A. **THPO018**
Donets, D.E. TUPO017, TH1P02
Dong, C. TUPO064
Dong, L. MOPO080
Dou, W.P. TUPO005, THPO053
Douglas, D. ~~WE1A01~~
Douillet, D. MO2A03
Droba, M. ~~SPWR017~~, THPO061
Du, B. **~~SPWR005~~**, ~~SPWR027~~, MOPO107, **THPO003**
Du, C.T. ~~SPWR014~~, ~~THOP06~~, THPO022, THPO033, THPO035, THPO036
Du, H. ~~TUOP08~~, TUPO003, **TUPO004**, THPO054
Du, T.B. ~~THOP06~~, THPO022
Du, X. TU2A03
Du, Y. C. **~~MO2A02~~**, ~~THOP11~~, THPO116
Düllmann, Ch.E. FR1A05
Dumbell, K.D. ~~MOOP03~~, MOPO035
Dunning, D.J. ~~MOOP03~~, MOPO035
Duperrier, R.D. WE2A04
Dupraz, K. MO2A03
Dupuy, L. THPO086
Dyunin, E. MOPO093
Dzitko, H. THPO062, TU2A04
Dziuba, F.D. ~~SPWR010~~, ~~SPWR025~~, ~~SPWR034~~, TU2A01, TUPO084, THPO072, **THPO073**, THPO107

— E —

Ebisawa, T. TU2A04

Content from this work may be used under the terms of the CC BY 3.0 licence (© 2018). Any distribution of this work must maintain attribution to the author(s), title of the work, publisher, and DOI.

ISBN: 978-3-95450-194-6 ISSN: 2226-0366

Echevarria, P. THPO007
Egi, M. TUPO070, TUPO071
Elcim, O.F. MOPO102
Enami, K. TUPO053
Enders, J. MOPO018
Endo, O. THPO095
Enomoto, Y. **WE1A06**
Eremeev, G.V. MOPO019, TUPO076
Ermakov, A.N. **MOPO060**, MOPO061, MOPO062
Eschke, J. TUPO029
Esposito, M. TUPO013

— F —

Fagotti, E. TU2A04, **THPO062**
Faillace, L. TU1P01
Fakhari, M. MOPO039
Falletta, S. TUPO076
Falone, A. MO2A03
Fan, K. THPO020, ~~SPWR028~~, THPO082
Fan, M.X. THPO028, THPO029, THPO030, THPO031, **THPO038**
Fanella, S. TUPO013
Fang, W. ~~SPWR023~~, ~~THOP09~~, THPO109
Fang, X. TUPO005
Fang, Z. MOPO082, MOPO111
Farabolini, W. ~~MOOP08~~, MOPO020
Fatkullin, R. TUPO012
Fazio, D. TUPO013
Fedotov, A.V. MOPO004
Feisi, H.F.S. TUPO064, ~~TH2A02~~
Felber, M. MOPO121
Feldmeier, E. **MOPO106**
Feng, G. ~~SPWR029~~, MOPO118, MOPO119
Feng, L.W. TUPO049
Ferdinand, R. TUPO095, ~~THOP01~~, **THPO047**
Ferrand, G. WE2A04
Ferrari, E. ~~MOOP06~~, MOPO034
Ferrari, L. MOPO124
Ferrario, M. TH1A03, FR1A03
Ficcadenti, L. MO2A03
Fichtner, F. THPO007
Filippi, F. TH1A03, FR1A03
Fils, J. THPO046
Fink, D.A. TUPO013
Fischer, R.L. ~~MOOP11~~, MOPO077
Fitze, H. THPO115
Flöttmann, K. ~~THOP10~~, THPO079
Fong, K. TU1A03, TUPO014, TUPO020
Forck, P. THPO046, THPO086
Forehand, D. TUPO041
Foster, B. TH2A01
Four, A. ~~TUOP03~~, TUPO030, TUPO066, THPO097
Franberg, H. ~~THOP01~~, THPO047
Fu, S. **MO1A01**, TUPO114, THPO030, THPO039
Fujiwara, T. ~~MOOP10~~, ~~MOPO053~~
Fukao, Y. ~~SPWR015~~, TUPO010
Fukuda, M.K. MOPO082
Fukuda, S. THPO102, THPO095, THPO096
Fukui, T. FR1A06
Fukui, Y. MOPO082, MOPO111
Furukawa, K. ~~SPWR009~~, WE1A06, THPO017
Furuta, F. TUPO059, ~~WE1A02~~
Furuya, T. THPO008
Fusco, Y. TUPO013
Futatsukawa, K. ~~SPWR015~~, MOPO082, **MOPO111**, TUPO010
Fuwa, Y. MOPO125

— G —

Gacheva, E. MOPO010
Galambos, J. **MO1P01**
Gallagher, R.E. ~~WE1A02~~
Gallas, M.T. TUPO013
Gallo, A. MO2A03
Gamba, D. ~~MOOP08~~, MOPO020
Gammino, S. THPO043
Gan, N. THPO103
Gao, J. THPO001
Gao, S.L. ~~TUOP08~~, TUPO003
Gao, Y. THPO006
Gao, Z. ~~SPWR011~~, MOPO120, THPO053, THPO068
Garcin, G. THPO092
Garmendia, N. THPO043
Garnett, R.W. ~~MOOP12~~, MOPO095
Garoby, R. MO1P03
Garolfi, L. ~~**MOOP08**~~, **MOPO020**
Garvey, T. THPO115
Gastineau, B. WE2A04
Gavela, D. TU2A04
Ge, M. **TUPO057**, **TUPO058**, **TUPO059**, ~~WE1A02~~
Geng, R.L. **MOPO130**, TUPO076
Gerhard, P. TU2A03, **FR1A05**
Gerigk, F. ~~WE1A01~~
Gettmann, V. ~~SPWR010~~, ~~SPWR025~~, ~~SPWR034~~, TU2A01, TUPO084, THPO072, THPO073, THPO107
Gex, D. TU2A04
Ghasemi, B.G. TUPO120
Ghasemi, F. MOPO026, MOPO069, MOPO070, TUPO119, TUPO120
Ghribi, A. TUPO019
Gibson, S. TUPO013
Giribono, A. TH1A03, FR1A03
Gjonaj, E. ~~THOP11~~, THPO116
Gobin, R. TU2A04
Goeury, A.G. THPO093
Golovenskiy, B.V. TUPO017, TH1P02
Gong, D.J. THPO001

Content from this work may be used under the terms of the CC BY 3.0 licence (© 2018). Any distribution of this work must maintain attribution to the author(s), title of the work, publisher, and DOI.

ISBN: 978-3-95450-194-6 ISSN: 2226-0366

Gong, K.Y. MOPO080, THPO028, THPO029, THPO030, THPO031, THPO038
Gonnella, D. TUPO058
Gonzalez, A. S. TUPO013
Gonzalez, M. TUPO013
Good, J.D. TUPO098, ~~THOP11~~, THPO116
Gorgisyan, I. ~~MOOP08~~, MOPO020
Govorov, A. TUPO017, TH1P02
Gradassi, P. TUPO013
Grames, J.M. THPO004
Grecki, M.K. ~~MOOP09~~, MOPO038
Grespan, F. MOPO089, MOPO124, TU2A04, THPO043, **THPO045**, THPO062
Groening, L. TU2A03, ~~**TUOP09**~~, **TUPO078**, FR1A05
Groß, M. TUPO098, ~~THOP11~~, THPO116
Gruber, T. TUPO059
Grudiev, A. ~~SPWR016~~, ~~SPWR023~~, TUPO023, ~~THOP04~~, ~~THOP08~~, ~~THOP09~~, THPO018, THPO058, THPO108, THPO109
Gu, Q. ~~SPWR023~~, ~~THOP09~~, THPO109
Guan, W.Q. ~~THOP06~~, THPO022
Guan, X. ~~SPWR014~~, ~~THOP06~~, THPO022, THPO034, THPO035, THPO036, THPO064, THPO111
Gulley, M.S. ~~MOOP12~~, MOPO095
Gulliford, C.M. ~~WE1A02~~, THPO010
Gumus, C. ~~SPWR026~~, **MOPO102**, MOPO104, TUPO029
Guo, H. ~~TUOP06~~, TUPO036
Guo, J. **THPO004**
Guo, Q.K. ~~SPWR014~~, ~~THOP06~~, THPO022, THPO033, THPO036, THPO064
Guo, Y.H. TUPO005
Gusarova, M. ~~SPWR022~~, TUPO045

— H —

Haase, A.A. THPO018
Haba, H. ~~THOP12~~, ~~THPO117~~
Haberer, Th. MOPO106
Hähnel, H. THPO046
Hall, D.L. TUPO055
Hall, T.D. TUPO043, TUPO059
Hama, H. ~~SPWR004~~, MOPO076
Hamelin, T. ~~THOP05~~, THPO066
Han, G. MOPO084
Han, J.H. MOPO041
Hannon, F.E. ~~WE1A01~~
Hao, J.K. TUPO049, TUPO064, THPO076
Hara, H. WE2A03
Hara, T. FR1A06
Hartl, I. ~~MOOP07~~, MOPO037
Hartung, J. ~~MOOP04~~, MOPO036
Hasegawa, K. MOPO082, ~~SPWR015~~, MOPO085, TUPO010, **THPO040**, THPO049
Hasegawa, T. FR1A06
Hayakawa, K. MOPO024, MOPO073
Hayakawa, Y. MOPO024, MOPO073
Hayano, H. ~~TUOP03~~, TUPO030, TUPO050, TUPO053, TUPO066, TUPO067, TUPO068, TUPO069, TUPO076, THPO005
Hayashizaki, N. ~~MOOP10~~, ~~MOPO053~~, MOPO085
Hayes, T. MOPO004
He, T. MOPO088, TUPO101, ~~THOP03~~, **THPO026**, THPO050, THPO051
He, X. THPO113
He, Y. ~~SPWR011~~, ~~SPWR012~~, MOPO087, ~~TUOP06~~, ~~TUOP08~~, TUPO003, TUPO036, TUPO038, TUPO106, ~~THOP03~~, THPO050, THPO051, THPO052, THPO053, THPO054, THPO068, THPO069, THPO090
He, Y. ~~THOP06~~, THPO022
Healy, A.L. TUPO113
Heidinger, R. TU2A04, THPO062
Heilmann, M. ~~SPWR010~~, ~~SPWR025~~, ~~SPWR034~~, TU2A01, TU2A03, TUPO084, THPO072, THPO073, THPO107
Heine, R.G. THPO007
Hellström, F. THPO043
Heltsley, B.K. ~~WE1A02~~
Hermann, B. ~~MOOP06~~, MOPO034
Hermansson, L. ~~THOP05~~, THPO066
Hierholzer, M. ~~MOOP09~~, MOPO038, MOPO039, MOPO102
Higashiguchi, T. TUPO053
Higgins, H. MOPO115
Hillert, W. TUPO098
Hinode, F. ~~SPWR004~~, MOPO076
Hirata, Y. TU2A04
Hisamatsu, H. ~~SPWR009~~, THPO017
Hodgkinson, C. ~~MOOP03~~, MOPO035
Höltermann, H. TUPO017, TH1P02
Hoffmann, M. ~~MOOP09~~, MOPO038, MOPO039
Hoffmann, M.G. ~~MOOP09~~, MOPO038
Hoffstaetter, G.H. ~~**WE1A02**~~
Holmes, D. MOPO004, THPO006
Holzer, B.J. ~~WE1A01~~
Honda, Y. MOPO082, ~~**TU1P03**~~, TUPO074
Honkavaara, K. MOPO039
Honma, H. THPO095
Hori, Y. ~~SPWR019~~, TUPO065, TUPO071
Horn, K.P. FR1A05
Hornickel, P.C. ~~MOOP03~~, MOPO035
Hosoda, N. FR1A06
Hotei, T. ~~**SPWR001**~~, ~~TU1P03~~, **THPO009**
Hounsell, B. ~~WE1A01~~
Hovater, C. MOPO115
Howell, M.P. MO1P01
Hu, C.F. ~~TUOP06~~, TUPO036

Content from this work may be used under the terms of the CC BY 3.0 licence (© 2018). Any distribution of this work must maintain attribution to the author(s), title of the work, publisher, and DOI.

ISBN: 978-3-95450-194-6 ISSN: 2226-0366

Content from this work may be used under the terms of the CC BY 3.0 licence (© 2018). Any distribution of this work must maintain attribution to the author(s), title of the work, publisher, and DOI.

Hu, T. ~~SPWR029~~, MOPO118, MOPO119
Huang, G. ~~SPWR011~~, THPO053, THPO068, THPO090
Huang, L. TUPO114
Huang, M.Y. TUPO114
Huang, S.C. MOPO130, ~~TUOP06~~, TUPO036, **THPO069**
Huang, T. THPO039
Huang, W.-H. ~~THOP11~~, THPO116
Huck, H. TUPO098, ~~THOP11~~, THPO116
Hüning, M. **FR1A02**
Hug, F. THPO012
Hui, D. **TH1A05**
Hulla, G. THPO043
Humphries, B. TU1A03
Hunt, C. MOPO129
Huran, J. MOPO010
Hutton, A. TUPO032, ~~WE1A01~~, THPO010
Hwang, J.H. TUPO090
Hwang, J.H. MOPO063, MOPO064
Hyun, S.Y. TUPO090

— I —

Ichimiya, R. TU2A04
Ida, Y.I. TUPO067, TUPO068, **TUPO069**
Iijima, T. ~~SPWR015~~, TUPO010
Iinuma, H. ~~SPWR009~~, ~~SPWR015~~, MOPO085, TUPO010, THPO017
Ikeda, S. ~~THOP12~~, ~~THPO117~~
Ikegami, K. ~~TUOP10~~, TUPO079, MOPO082
Imao, H. WE2A03
Inagaki, T. ~~THOP07~~, THPO091
Inman, M.E. TUPO043
Inoue, H. TUPO053
Isaev, I.I. TUPO098, ~~THOP11~~, THPO116
Isaksson, L. MOPO027
Ischebeck, R. ~~MOOP06~~, MOPO034
Ishida, K. ~~SPWR015~~, TUPO010
Ito, H. ~~TUOP03~~, TUPO030, TUPO050, **TUPO066**, TUPO068, TUPO076
Ito, R. ~~TUOP03~~, TUPO030, **TUPO050**, TUPO066
Ivanisenko, Ye. MOPO081, TUPO013
Iwashita, Y. ~~SPWR037~~, MOPO085, **MOPO125**, ~~TUOP03~~, TUPO030, TUPO050, TUPO066, THPO126
Iwata, Y. MOPO085

— J —

Jackson, F. ~~MOOP03~~, MOPO035
Jacquemet, M. WE2A04
Jäger, E. FR1A05
Jamison, S.P. TUPO113, ~~**TH1A06**~~
Jang, H. MOPO094, THPO067
Jang, S.W. TUPO051, TUPO052
Jeff, A. TUPO013
Jensch, K. ~~MOOP07~~, MOPO037
Jensen, E. ~~WE1A01~~
Jensen, J.-P. **MOPO122**
Jensen, M. MO1P03
Jeong, S.-H. MOPO041
Jia, H. TUPO005
Jiang, H. THPO042
Jiang, J. ~~**SPWR029**~~, **MOPO118**, MOPO119
Jiang, P. **TUPO106**
Jiang, Y. THPO020
Jiménez-Rey, D. TU2A04
Jin, S. TUPO064
Jin, X.J. THPO005
Jing, L. TUPO005, THPO054
Jo, Y.W. THPO067
Jobs, M. ~~THOP05~~, THPO066
Jokinen, A. TU2A04
Jones, J.K. ~~MOOP03~~, MOPO035
Joo, J. TUPO009
Jung, H.C. MOPO094, TUPO009, THPO067
Jung, Y. **TUPO009**, THPO067
Jung, Y.G. MOPO041
Jusic, D. ~~WE1A02~~

— K —

Kaabi, W. ~~**WE1A01**~~
Kaiser, M. TU2A03, THPO046
Kaizer, B. WE2A04
Kako, E. ~~SPWR019~~, TUPO052, TUPO065, TUPO070, TUPO071, TUPO072, TUPO073, TUPO074, WE2A03, THPO008, THPO097
Kalantaryan, D.K. TUPO098, ~~THOP11~~, THPO116
Kamalou, O. ~~THOP01~~, THPO047
Kamanin, A.N. MOPO060, MOPO062
Kamigaito, O. WE2A03
Kaminskiy, V.I. MOPO066
Kamitani, T. WE1A06
Kamiya, J. ~~SPWR019~~, TUPO065, TUPO071
Kampmeyer, C. K. TUPO017
Kamps, T. THPO083
Kanesue, T. ~~THOP12~~, ~~THPO117~~
Kang, H.-S. ~~SPWR002~~, ~~MOOP05~~, MOPO040
Kang, W. THPO028
Kang, Y.N. MOPO063, MOPO064
Kanomata, K. ~~SPWR004~~, MOPO076
Kaplan, R.P.K. ~~WE1A02~~
Karnaukhov, I.I. ~~SPWR006~~, MOPO028
Kasaei, S. TUPO119
Kashiwagi, S. ~~SPWR004~~, MOPO076, THPO005, THPO127
Kasugai, A. TU2A04
Katagiri, H. ~~SPWR027~~, MOPO107
Katalev, V.V. TUPO027
Katayama, R. ~~**TUOP03**~~, **TUPO030**, TUPO050, TUPO066

ISBN: 978-3-95450-194-6 ISSN: 2226-0366

Kato, R. ~~SPWR001~~, ~~TU1P03~~, THPO009
Kato, S. TUPO067, TUPO068, TUPO069
Kaufman, J.J. TUPO059
Kawamura, M. **THPO095**
Kawamura, N. ~~SPWR015~~, MOPO085, TUPO010
Kaya, Ç. MOPO102
Kazimi, R. THPO004
Ke, Y.J. THPO100, THPO104
Kedia, S. **THPO080**
Keikha, M. TUPO020
Keir, J.J. ~~TUOP07~~, TUPO014, TUPO020, TUPO039, TUPO040
Keller, T.F. TH2A01
Kenzhebulatov, E. WE1A03
Kerstiens, E.L. ~~MOOP12~~, MOPO095
Kester, O.K. TU1A03
Keune, B. THPO083
Khabiboulline, T.N. TUPO041
Khalafi, H. MOPO069
Khan, V. F. TUPO013
Khankin, V.V. MOPO060, MOPO061, **MOPO062**
Khuyagbaatar, J. FR1A05
Kikuchi, A. TUPO076
Killenberg, M. ~~MOOP09~~, MOPO038
Kim, A.R. MOPO063, MOPO064
Kim, B. ~~SPWR015~~, TUPO010
Kim, C. ~~SPWR002~~, ~~MOOP05~~, MOPO040
Kim, D.E. MOPO041
Kim, D.Y. TUPO052
Kim, E.-S. TUPO051, TUPO052
Kim, G. ~~SPWR002~~, ~~MOOP05~~, MOPO040
Kim, G.J. MOPO063, MOPO064
Kim, H. TUPO009, **THPO067**
Kim, I.S. MOPO063, MOPO064
Kim, J.I. MOPO063, MOPO064
Kim, J.N. MOPO063, MOPO064
Kim, J.W. TUPO009, THPO067
Kim, K.R. TUPO051, TUPO052
Kim, M.J. MOPO041
Kim, M.S. THPO067
Kim, S. MOPO063, **MOPO064**
Kim, S.-H. MO1P01
Kim, S.Y. **~~SPWR036~~**, **THPO132**
Kim, Y. TUPO009, THPO067
Kino, K. ~~MOOP10~~, ~~MOPO053~~
Kirpitchev, I. TU2A04
Kishi, D. TU1A03, ~~TUOP07~~, TUPO020, TUPO039
Kitamura, R. **~~SPWR015~~**, MOPO085, **TUPO010**
Kiy, S. ~~MOOP01~~, MOPO092
Kleeb, T. THPO115
Kleffner, C.M. **THPO046**
Klein, M. ~~WE1A01~~
Klein, U.K. ~~WE1A01~~
Klinke, D. ~~MOOP07~~, MOPO037
Knaak, M. THPO092
Knaster, J. TU2A04
Knie, K. THPO046
Ko, I.S. ~~SPWR002~~, ~~MOOP05~~, MOPO040
Ko, J.H. **~~SPWR002~~**, **~~MOOP05~~**, **MOPO040**
Kobayashi, H. MOPO082
Kobayashi, Y. TUPO074
Kobets, V.V. ~~SPWR032~~, TUPO112
Kobzeva, L. TUPO013
Kolb, P. THPO006, TUPO040
Kolobanov, E.I. WE1A03
Kondakov, A.A. WE1A03
Kondo, C. FR1A06
Kondo, K. TU2A04, THPO062
Kondo, Y. ~~SPWR015~~, MOPO085, TUPO010, **~~THOP02~~**, **THPO048**, THPO049
Kong, A. TUPO040
Kong, Q.Y. ~~TUOP08~~, TUPO003, TUPO004, THPO054
Konomi, T. ~~SPWR019~~, TUPO065, TUPO070, TUPO071, **TUPO072**, **TUPO073**, **TUPO074**, THPO005, THPO008
Konoplev, I.V. ~~SPWR022~~, TUPO045
Koschitzki, C. TUPO098, ~~THOP11~~, THPO116
Koscielniak, S.R. **TU1A03**, TUPO020
Kostin, D. ~~MOOP07~~, ~~MOOP09~~, MOPO037, MOPO038, TUPO029
Kostka, P. ~~WE1A01~~
Kostroun, V.O. ~~WE1A02~~
Kotur, M. **MOPO027**
Koubek, B. **TUPO017**
Koufalis, P.N. ~~SPWR018~~, ~~TUOP01~~, TUPO054, TUPO057
Kourkafas, G. **THPO083**
Kovalenko, A.D. TH1P02
Kozak, T. MOPO121
Kozlov, A.V. TUPO012
Kozyrev, E.V. WE1A03
Krafft, G.A. MO2A04
Krasilnikov, M. TUPO098, ~~THOP11~~, THPO116, THPO118
Krier, J. FR1A05
Kropachev, G. TUPO012
Krupka, N. TUPO028
Krutikhin, S.A. WE1A03
Kubo, T. ~~TUOP03~~, TUPO030, TUPO050, TUPO066
Kubota, C. MOPO082
Kürzeder, T. ~~SPWR010~~, ~~SPWR025~~, ~~SPWR034~~, TU2A01, TUPO084, THPO072, THPO073, THPO107
Kulevoy, T. TUPO011, **TUPO012**, TH1P02
Kulina, G. TUPO057
Kumada, H. MOPO082
Kumar, R. THPO080
Kuptsov, I.V. WE1A03
Kurennoy, S.S. **MOPO096**

Content from this work may be used under the terms of the CC BY 3.0 licence (© 2018). Any distribution of this work must maintain attribution to the author(s), title of the work, publisher, and DOI.

ISBN: 978-3-95450-194-6 ISSN: 2226-0366

Kurihara, T. MOPO082
Kuriki, M. **THPO005**, **THPO127**
Kurilik, A. MOPO062
Kurkin, G.Y. WE1A03
Kuroda, R. ~~MOOP10~~, ~~MOPO053~~
Kurosawa, S. ~~SPWR019~~, TUPO065, TUPO071
Kusaka, K. WE2A03
Kutsaev, S.V. ~~**MOOP11**~~, **MOPO077**
Kümpel, K. **MOPO090**

— L —

Ladegaillerie, S. WE2A04
Lagniel, J.-M. ~~THOP01~~, THPO047
Lallement, J.-B. ~~SPWR013~~, TUPO016, **TUPO127**, THPO057
Lamb, T. ~~MOOP09~~, MOPO038, MOPO121
Lamehi, M. MOPO070
Lamprecht, S. MOPO090
Lang, D. ~~TUOP07~~, TUPO014, TUPO020, TUPO039
Latina, A. TUPO113
Laxdal, R.E. **MO1A02**, ~~**MOOP01**~~, **MOPO092**, TU1A03, ~~TUOP07~~, TUPO014, TUPO020, TUPO039, TUPO040
Le Barillec, T. MO2A03
Lebet, S. TUPO023
Lechartier, M. **TUPO095**
Ledroit, B. **TUPO092**
Lee, D.Y. **MOPO094**, THPO067
Lee, H.-G. MOPO041
Lee, J. TUPO009
Lee, J. TUPO052
Lee, J.H. MOPO063, MOPO064
Lee, M. THPO067
Lee, S. TUPO009, THPO067
Lee, S.B. MOPO041
Lee, Y.S. **MOPO063**, MOPO064
Leewe, R. TUPO014
Lehn, T. MOPO100
Lei, Y. ~~SPWR014~~, ~~THOP06~~, THPO022, **THPO034**, THPO035, THPO036, THPO064
Lepercq, P. ~~MOOP08~~, MOPO020
Letizia, R. ~~SPWR007~~, THPO016
Lettry, J. TUPO127
Levichev, A.E. ~~SPWR030~~, TUPO001, TUPO093
Levichev, E.B. ~~WE1A01~~
Levterov, K.A. TUPO017, TH1P02
Levy, G. TUPO013
Leyge, J.F. TUPO095
Li, A.H. THPO028, THPO029, THPO030, THPO031, THPO038
Li, B. **THPO028**, THPO029, THPO030, THPO031, THPO038
Li, B.T. ~~SPWR021~~, TUPO048
Li, C.G. MOPO084
Li, C.L. ~~TUOP06~~, TUPO036, THPO053
Li, C.X. ~~SPWR012~~, MOPO087, TUPO101, ~~THOP03~~, THPO050, THPO051, **THPO053**, THPO090
Li, D.M. ~~MOOP02~~, MOPO132
Li, H. ~~**THOP05**~~, **THPO066**
Li, H. **THPO039**
Li, J. ~~THOP06~~, THPO022, THPO035
Li, J. MO1A01
Li, J. TUPO101
Li, J.H. **MOPO084**
Li, J.Z. THPO100
Li, M.T. TUPO114
Li, S. ~~SPWR015~~, TUPO010
Li, W. MOPO029
Li, X. ~~MOOP02~~, **MOPO079**, MOPO132
Li, X. TUPO098
Li, X.N. ~~TUOP08~~, TUPO003, THPO054
Li, Y. ~~WE1A02~~
Li, Y. TUPO114, TUPO115, **THPO032**
Li, Y.M. ~~TUOP06~~, TUPO036
Li, Z. ~~TUOP05~~, TUPO033
Li, Z. MOPO084
Li, Z. ~~**TUOP02**~~, **TUPO007**
Li, Z.B. ~~**SPWR023**~~, ~~**THOP09**~~, **THPO109**
Li, Z.P. TUPO114, **TUPO115**, THPO032
Li, Z.Q. TUPO064
Li, Z.S. ~~TUOP08~~, TUPO003, TUPO004, **THPO054**
Lidia, S.M. ~~TUOP02~~, TUPO007
Liepe, M. ~~SPWR018~~, ~~TUOP01~~, TUPO054, TUPO055, TUPO057, TUPO058, TUPO059, ~~WE1A02~~
Lievin, Ch.L. THPO092, THPO093
Lilje, L. ~~MOOP09~~, MOPO038, TUPO020
Lin, F. THPO004
Lin, L. TUPO049
Lindau, F. MOPO027
Lindroos, M. MO1P03
Lindvall, R. MOPO027
Lingbin, S. THPO100
Lishilin, O. TUPO098, ~~THOP11~~, THPO116
List, J. ~~**SPWR025**~~, **THPO107**
Liu, B.Q. TUPO064
Liu, C. ~~WE1A02~~
Liu, G. ~~TUOP08~~, TUPO003
Liu, H. ~~TUOP07~~, TUPO039
Liu, H.C. MO1A01, MOPO080, THPO028, THPO029, **THPO030**, THPO031, THPO038
Liu, K.X. TUPO049
Liu, L.B. MOPO120
Liu, N. ~~SPWR005~~, ~~**SPWR027**~~, **MOPO107**, THPO003
Liu, S. THPO039
Liu, S.M. MOPO080

Content from this work may be used under the terms of the CC BY 3.0 licence (© 2018). Any distribution of this work must maintain attribution to the author(s), title of the work, publisher, and DOI.

ISBN: 978-3-95450-194-6 ISSN: 2226-0366

Liu, W.B. **MOPO129**
Liu, W.L. ~~THOP06~~, THPO022, **THPO042**
Liu, X. ~~**SPWR011**~~, ~~TUOP06~~, TUPO036, **THPO068**
Liu, X.J. TUPO005
Liu, Y. ~~TUOP10~~, TUPO079
Liu, Y.D. TUPO114
LoDestro, V. MOPO100
Löhl, F. THPO115
Loisch, G. TUPO098, ~~THOP11~~, THPO116
Lollo, V.L. MO2A03
Lombardi, A.M. ~~SPWR013~~, ~~SPWR016~~, TUPO016, TUPO127, **TH1P01**, ~~THOP04~~, THPO057, THPO058
Long, F. MOPO116
Longuevergne, D. ~~WE1A01~~
Lorkiewicz, J.A. ~~MOOP07~~, MOPO037
Lou, W. ~~WE1A02~~
Lu, L. **MOPO088**, TUPO005, TUPO101, ~~THOP03~~, THPO026, THPO050, THPO051, **THPO052**, THPO053, THPO090
Lu, P.N. THPO125
Lu, W. TUPO005
Lu, X.H. TUPO114
Lu, X.Y. ~~SPWR021~~, TUPO048
Lu, Y. ~~SPWR029~~, MOPO118, **MOPO119**
Lu, Y.R. ~~TUOP08~~, TUPO003, THPO054
Lu, Z.J. **THPO102**
Lukaszew, R.A. TUPO042
Luner, J. WE2A04
Luo, T. MOPO080
Luo, X.B. TUPO114
Lv, Y.J. THPO039
Lyuosev, D.A. TUPO017, TH1P02

— M —

Ma, L.Z. ~~TUOP08~~, TUPO003
Ma, P.F. ~~**SPWR014**~~, ~~THOP06~~, THPO022, THPO035, **THPO036**, THPO064
Ma, W. MOPO088, TUPO005, THPO026, THPO051, THPO052, THPO053
Ma, X. THPO103
Ma, Y. TU1A03, ~~TUOP07~~, **TUPO020**, TUPO039
Madec, C. **TU1A01**, WE2A04
Maebara, S. TU2A04
Maesaka, H. **FR1A06**
Magnoni, S. TUPO013
Magrin, G. TUPO013
Mahler, G.J. ~~WE1A02~~
Maier, M.T. FR1A05
Man, K.D. THPO035
Maniscalco, J.T. ~~**SPWR018**~~, ~~**TUOP01**~~, **TUPO054**, TUPO055, TUPO057
Mansten, E. MOPO027
Mapes, M. MOPO100
Marcellini, F. ~~MOOP06~~, MOPO034, THPO115
Marhauser, F. ~~SPWR022~~, TUPO032, TUPO045, ~~WE1A01~~
Marocchino, A. **TH1A03**, FR1A03
Marqueta, A. THPO062
Marraffa, A. TUPO013
Marroncle, J. TU2A04
Martens, A. MO2A03
Martins, C.A. MO1P03
Martynov, A.A. TUPO017, TH1P02
Mastrostefano, C.M. TUPO127
Matheson, B. ~~TUOP07~~, TUPO039, TUPO040
Mathot, S.J. ~~SPWR016~~, ~~THOP04~~, THPO058
Matsievskiy, S.V. **MOPO066**
Matsubara, S. FR1A06
Matsumoto, S. THPO096
Matsumoto, T. ~~SPWR005~~, ~~SPWR027~~, MOPO107, THPO003, THPO096
Matsumoto, Y. MOPO082
Mauro, G.S. THPO045
Mavrič, U. ~~MOOP09~~, MOPO038
Mazor, O. **MOPO093**
McIntyre, G.T. MOPO004, THPO006
McKenzie, J.W. ~~MOOP03~~, MOPO035, ~~WE1A01~~
McNerney, A. MOPO100
Mehta, R. THPO080
Melkumyan, D. TUPO098, ~~THOP11~~, THPO116
Méndez, P. TU2A04
Meng, C. THPO001
Meng, J. ~~TUOP08~~, TUPO003, THPO054
Méot, F. ~~WE1A02~~
Mereu, P. **MOPO089**, **MOPO124**, THPO043, THPO045
Mernick, K. MOPO004, MOPO005, MOPO006
Meusel, O. ~~SPWR017~~, THPO061
Mezzano, M. MOPO089, THPO045
Mi, Z.H. TUPO064
Mialkovskiy, V.V. TH1P02
Mibe, T. ~~SPWR009~~, ~~SPWR015~~, MOPO085, TUPO010, THPO017
Michishio, K. ~~MOOP10~~, ~~MOPO053~~
Michizono, S. ~~SPWR005~~, ~~SPWR027~~, MOPO107, TUPO070, TUPO071, TUPO072, TUPO073, TUPO074, THPO003, THPO095, THPO097
Michnoff, R.J. ~~WE1A02~~
Mickat, S. **TU2A03**
Midttun, Ø. THPO043
Migliorati, M. MO2A03
Milanese, A. ~~WE1A01~~
Militsyn, B.L. ~~MOOP03~~, MOPO035, ~~WE1A01~~
Milla, A. TUPO013
Millet, F. TUPO019
Milyachenko, A.D. TUPO011
Minashkin, V.F. MOPO010

Content from this work may be used under the terms of the CC BY 3.0 licence (© 2018). Any distribution of this work must maintain attribution to the author(s), title of the work, publisher, and DOI.

ISBN: 978-3-95450-194-6 ISSN: 2226-0366

Content from this work may be used under the terms of the CC BY 3.0 licence (© 2018). Any distribution of this work must maintain attribution to the author(s), title of the work, publisher, and DOI.

Mingioni, C. MOPO089, MOPO124
Minty, M.G. ~~WE1A02~~
Miski-Oglu, M. ~~SPWR010~~, ~~SPWR025~~, ~~SPWR034~~, TU2A01, TUPO084, THPO072, THPO073, THPO107
Mitoya, G.M. TUPO069
Mittelbach, A.K. ~~MOOP06~~, MOPO034
Miura, A. ~~TUOP10~~, TUPO079
Miura, S. ~~SPWR004~~, MOPO076
Miura, T. ~~SPWR005~~, ~~SPWR027~~, MOPO107, THPO003, THPO008, THPO096
Miura, T. MOPO082
Miyahara, F. WE1A06
Miyajima, T. ~~SPWR001~~, MOPO082, ~~TU1P03~~, TUPO074, THPO009
Miyake, Y. ~~SPWR015~~, TUPO010
Miyamoto, A. WE2A03
Miyano, K. TUPO069
Miyazaki, A. TU1A05
Möller, W.-D. ~~MOOP07~~, MOPO037
Mohseni Kejani, M. **MOPO026**, MOPO069
Moisieienko, M. ~~**SPWR008**~~, **TUPO002**
Mollá, J. TU2A04
Monchinsky, V.A. TUPO017, TH1P02
Monjushiro, H. TUPO067, TUPO068, TUPO069
Montesinos, E. ~~SPWR016~~, ~~WE1A01~~, ~~THOP04~~, THPO058
Montis, M. TU2A04, THPO062
Mori, S. **MOPO008**
Morimoto, O. FR1A06
Morishita, T. ~~SPWR015~~, MOPO085, TUPO010, ~~THOP02~~, THPO048, **THPO049**
Morozov, P. TUPO027
Morozov, V.S. TUPO109
Moser, R. TUPO013
Moss, A.J. ~~MOOP03~~, MOPO035
Moss, J. MO1P01
Mostacci, A. MO2A03, FR1A03
Motygin, S.V. WE1A03
Mounts, C.I. MOPO115
Moya, I. TU2A04
Moya, I.M. THPO062
Mühle, C. THPO046
Müller, J.M. **MOPO121**
Müller, P. MOPO090
Muller, D.A. TUPO055
Muñoz, J.L. THPO043
Murasev, A.A. WE1A03
Murcek, P. THPO125
Muroga, T. ~~MOOP10~~, ~~MOPO053~~
Mustapha, B. ~~MOOP11~~, MOPO077
Muto, T. ~~SPWR004~~, MOPO076
Mytsykov, A. ~~SPWR008~~, TUPO002
Müller, W.F.O. MOPO018

— N —

Nachtigal, Y. TUPO027
Nadig, P. TUPO013
Nagasawa, I. ~~SPWR004~~, MOPO076
Nagata, T. ~~TUOP03~~, TUPO030, TUPO050, TUPO066, TUPO073
Nagatsuka, K. ~~THOP07~~, THPO091
Nagimov, R.R. TUPO020
Nagoshi, H. THPO127
Nagura, N. MOPO082
Naito, F. MOPO082, ~~TUOP10~~, TUPO079
Nakai, H. WE2A03
Nakajima, H. THPO095
Nakayama, H. ~~SPWR009~~, THPO017
Nakazawa, Y. ~~SPWR015~~, **MOPO085**, TUPO010
Nanbu, K. ~~SPWR004~~, MOPO076
Nanmo, K. MOPO082, ~~TUOP10~~, TUPO079
Natsui, T. WE1A06, THPO095, THPO096
Navarro Quirante, J.L. TUPO013
Ndiaye, C.F. MO2A03
Negishi, K. THPO127
Nenni, M. MOPO089, MOPO124
Nennig, L.J. THPO093
Neri, L. THPO043
Neumann, A. THPO083
Niemczyk, R. **TUPO098**, ~~THOP11~~, THPO116
Nietubyć, R. ~~MOOP07~~, MOPO037
Niewieczerzal, P. WE2A04
Nii, K.N. **TUPO067**, TUPO068, TUPO069
Nikiforov, D.A. ~~SPWR030~~, TUPO093
Nikolaev, V.I. TUPO011
Ninomiya, S. ~~SPWR004~~, MOPO076
Noakes, T.C.Q. ~~MOOP03~~, MOPO035
Nölle, D. **FR2A02**
Nogami, K. MOPO024, MOPO073
Nojima, T. TUPO073
Noll, D. ~~SPWR017~~, TUPO127, THPO061
Nordt, A. MO1P03
Normand, G. ~~THOP01~~, THPO047
Nozdrin, M.A. **MOPO010**
Nuessle, G. TUPO013
Nugent, J.C. MOPO127
Nusbaum, D. MOPO093

— O —

O'Neil, M. TUPO127
O'Rourke, B.E. ~~**MOOP10**~~, ~~**MOPO053**~~
Obina, T. MOPO082, ~~TU1P03~~
Ogawa, H. ~~MOOP10~~, MOPO024, ~~MOPO053~~, MOPO073
Ogawa, Y. MOPO007
Oguri, H. **MO1P02**, ~~TUOP10~~, TUPO079, THPO049
Oh, B.G. MOPO041
Oh, T.G. MOPO063, MOPO064
Oh, Y.A. MOPO063, MOPO064

ISBN: 978-3-95450-194-6 ISSN: 2226-0366

Ohba, T. MOPO082
Ohgaki, H. MOPO073
Ohkoshi, K. ~~TUOP10~~, TUPO079
Ohsawa, S. ~~SPWR009~~, THPO017
Ohshima, T. FR1A06
Oikawa, H. ~~TUOP03~~, TUPO030, TUPO050, **TUPO053**, TUPO066, TUPO068
Okada, T. ~~**SPWR019**~~, **TUPO065**, TUPO071, TUPO072, THPO002
Okamura, M. ~~**THOP12**~~, ~~**THPO117**~~
Okii, Y. THPO097
Okugi, T. THPO127
Okuno, H. WE2A03
Okuyama, T. ~~THOP07~~, THPO091
Olivier, G. ~~WE1A01~~
Olry, G. ~~WE1A01~~
Omet, M. ~~MOOP09~~, MOPO038, TUPO132
Omori, T. THPO127
Onishi, T. MOPO082
Oppelt, A. TUPO098, ~~THOP11~~, THPO116
Oshima, N. ~~MOOP10~~, ~~MOPO053~~
Ostroumov, P.N. ~~**TU2A02**~~
Otake, Y. THPO124, ~~**THOP07**~~, **THPO091**, FR1A06
Otani, M. ~~SPWR015~~, ~~TUOP10~~, TUPO010, TUPO079, MOPO085, ~~THOP02~~, THPO048, THPO049
Ouchi, T. MOPO082
Ouyang, H.F. MO1A01, THPO039
Ouyang, X.P. THPO021
Ovchar, V.K. WE1A03
Ovchinnikova, L. MOPO061, **MOPO059**, MOPO060, **TUPO097**
Overstreet, S.A. THPO010
Owen, H.L. ~~THOP08~~, THPO108
Ozeki, K. WE2A03

— P —

Pahl, H. ~~SPWR013~~, TUPO016
Pakhomov, N.I. MOPO060, MOPO062
Palczewski, A.D. TUPO041, TUPO042
Palmer, D.T. MO2A03
Palmieri, A. TU2A04, THPO045, THPO062
Palumbo, L. MO2A03
Pan, F. ~~TUOP06~~, TUPO036, TUPO038
Pan, W.M. ~~TH2A02~~, ~~FR2A01~~
Panero, R. MOPO124
Pang, J. **THPO113**
Paramonov, V.V. ~~**THOP10**~~, **THPO079**
Park, C.S. TUPO052
Park, H. ~~TUOP05~~, **TUPO032**, TUPO033, ~~**TUOP04**~~, ~~TUOP12~~, **TUPO031**, TUPO035
Park, K.-H. **MOPO041**
Park, S. H. TUPO051, TUPO052
Park, S.J. **TUPO090**
Park, Y.J. TUPO090
Patino-Revuelta, A. TUPO013
Patterson, J.R. ~~WE1A02~~
Pavetits, H. TUPO013
Paz Neira, P. TUPO013
Pedrozzi, M. THPO115
Peggs, S. ~~WE1A02~~
Pei, G. THPO001, THPO102
Pei, S. THPO102, THPO113
Pei, Y.J. ~~SPWR029~~, MOPO029, MOPO118
Peinaud, Y. MO2A03
Pekeler, M. THPO092
Pellegrini, D. ~~WE1A01~~
Pellegrino, L. MO2A03
Peng, J. MO1A01, **TUPO114**, TUPO115, THPO029, THPO030, THPO031, THPO032
Peng, S.X. ~~**TH2A03**~~
Pengjiao, Z. THPO100, THPO104
Perry, A. **WE2A04**
Peters, A. MOPO106
Petitjean, S.P. THPO093
Petrillo, V. TH1A03
Petrov, V.M. TUPO091, WE1A03
Petry, N.F. MOPO090
Pettinacci, V. MO2A03
Pfeiffer, S. ~~SPWR026~~, ~~MOOP09~~, MOPO038, **MOPO039**, MOPO104
Pforr, J. THPO012
Phillips, G. TU2A04
Phillips, H.L. TUPO042
Pichoff, N. WE2A04
Pieck, M. ~~MOOP12~~, MOPO095, ~~**WE2A02**~~
Piersanti, L. **MO2A03**
Pietralla, N. MOPO018, THPO011, THPO012
Pikin, A.I. ~~SPWR013~~, TUPO016
Pilan, A.M. WE1A03
Pioli, S. MO2A03
Piot, P. THPO005
Pisent, A. MOPO089, MOPO124, TU2A04, THPO043, THPO045, THPO062
Pitman, S. ~~**THOP08**~~, **THPO108**
Pitters, J. ~~SPWR013~~, TUPO016
Plaisant, Th. WE2A04
Planche, T. TU1A03
Plawski, T. E. **MOPO115**, THPO004
Plum, M.A. MO1P01
Podadera, I. TU2A04, THPO062
Podlech, H. TUPO017, TH1P02, ~~SPWR010~~, ~~SPWR017~~, ~~SPWR025~~, ~~SPWR034~~, MOPO090, MOPO101, TU2A01, TUPO084, THPO061, THPO072, THPO073, THPO107
Polozov, S.M. TH1P02
Pommerenke, H.W. ~~**SPWR016**~~, ~~**THOP04**~~, **THPO058**
Pompili, R. TH1A03, FR1A03

Content from this work may be used under the terms of the CC BY 3.0 licence (© 2018). Any distribution of this work must maintain attribution to the author(s), title of the work, publisher, and DOI.

ISBN: 978-3-95450-194-6 ISSN: 2226-0366

Content from this work may be used under the terms of the CC BY 3.0 licence (© 2018). Any distribution of this work must maintain attribution to the author(s), title of the work, publisher, and DOI.

Ponkin, D.O. TUPO017, TH1P02
Porqueddu, R. THPO006
Porter, R.D. **TUPO055**, TUPO059
Poteomkin, A. MOPO010
Pottin, B. THPO043
Poursaleh, A.P. TUPO120
Power, J.G. THPO005
Pozdeyev, G. **WE2A01**
Pruneri, G. TU2A04
Przygoda, K.P. ~~SPWR026~~, MOPO104, TUPO029
Ptitsyn, V. ~~WE1A02~~
Pu, Y.H. ~~MOOP02~~, MOPO132, MOPO079
Puetz, S. THPO046
Pupkov, Yu.A. ~~WE1A01~~
Purwar, H. ~~MOOP08~~, MOPO020

— Q —

Qian, C. ~~TUOP08~~, TUPO003
Qian, H.J. TUPO098, ~~THOP11~~, THPO116, THPO118
Qiao, J. ~~MOOP02~~, MOPO132
Qiao, Y.S. **TUPO130**
Qiu, F. ~~SPWR005~~, ~~SPWR027~~, MOPO107, THPO003, THPO008, **THPO096**
Qiu, M.T. THPO033
Qu, P.H. THPO028, **THPO029**, THPO030, THPO031, THPO038
Quan, S.W. TUPO049, THPO076
Quigley, P. ~~WE1A02~~

— R —

Radhakrishnan, R. TUPO043, TUPO059
Rädel, S.D. ~~MOOP01~~, MOPO092, TU1A03
Raguin, J.-Y. THPO115
Rahmani, F. MOPO069
Raparia, D. **MOPO100**, ~~THOP12~~, ~~THPO117~~
Ratzinger, U. TUPO017, TH1P02, ~~SPWR033~~, TUPO083, THPO046, THPO060
Razuvaev, G.P. ~~SPWR015~~, TUPO010
Reece, C.E. TUPO042, TUPO043
Rees, D. ~~MOOP12~~, MOPO095
Regidor, D. TU2A04
Rehman, M.R. ~~**SPWR009**~~, **THPO017**
Reiche, S. ~~MOOP06~~, MOPO034
Reilly, A.V. MOPO019
Renard, B. TU2A04
Renier, Y. TUPO098, ~~THOP11~~, THPO116
Repkov, V.V. WE1A03
Reschke, D. TUPO028, TH2A01
Riemer, B.W. MO1P01
Rimmer, R.A. TUPO076, ~~WE1A01~~, THPO004
Ritter, J. MOPO100
Rivkin, L. THPO115
Roblin, Y. ~~WE1A01~~
Rocipon, H. MO2A03
Rodnizki, J. MOPO093, WE2A04
Rodriguez-Castro, E. TUPO023
Rolli, K. THPO115
Roper, M.D. ~~MOOP03~~, MOPO035
Roser, T. ~~WE1A02~~
Rossetti Conti, M. TU1P01
Rossi, A.R. TH1A03
Rowe, M. TU1A03
Ruber, R.J.M.Y. ~~THOP05~~, THPO066
Rubin, A. ~~SPWR034~~, TU2A01, TU2A03, TUPO084
Rui, Hou,R. THPO100
Rutter, T. TUPO013
Ryabov, A. MOPO059
Rybaniec, R. ~~SPWR026~~, ~~MOOP09~~, MOPO038, MOPO104, TUPO132

— S —

Sabol, D.M. ~~WE1A02~~
Saegebarth, S. TUPO028
Saeki, T. ~~SPWR019~~, ~~TUOP03~~, TUPO030, TUPO050, TUPO065, TUPO066, TUPO067, TUPO068, TUPO069, TUPO071, TUPO076
Sagan, D. ~~WE1A02~~
Saisa-ard, C. TUPO098
Saito, H. ~~**SPWR004**~~, **MOPO076**
Saito, N. ~~SPWR015~~, MOPO085, TUPO010
Sakai, H. ~~SPWR019~~, TUPO065, TUPO070, TUPO071, TUPO072, TUPO073, TUPO074, **THPO008**
Sakai, H. WE2A03
Sakai, T. **MOPO024**, MOPO073
Sakamoto, K. TU2A04, THPO062
Sakamoto, N. **WE2A03**
Sakaue, K. THPO005
Sakurayama, H. MOPO082
Salehi, M. **TUPO120**
Salvatore, J. ~~SPWR025~~, THPO073, THPO107
Salveter, F. TUPO013
Samoshkin, A. TUPO013
Sanaye Hajari, S. **TUPO119**
Santiago Kern, R. ~~THOP05~~, THPO066
Saotome, H.S. WE1A06
Sargsyan, E. **THPO043**
Sato, D. ~~MOOP10~~, ~~MOPO053~~
Sato, K. ~~THOP07~~, THPO091, THPO095
Sato, M. **MOPO082**
Sato, Y. MOPO111
Satogata, T. TUPO109
Satoh, D. MOPO008
Satoh, M. WE1A06, THPO127
Satov, Yu.A. TUPO011
Sauza-Bedolla, J. **TUPO022**, **TUPO023**
Savalle, A. ~~THOP01~~, THPO047
Sawabe, M. TUPO067, TUPO068, TUPO069
Scantamburlo, F. TU2A04, THPO062

ISBN: 978-3-95450-194-6 ISSN: 2226-0366

Schaber, J.S. THP0125
Schaffran, J. TUP0028, TH2A01
Schalwat, M. TUP0028
Scharrer, P. FR1A05
Scheglov, M.A. WE1A03
Schempp, A. TUP0017, TH1P02, ~~SPWR017~~, THP0061
Schilling, P. TUP0028
Schlarb, H. ~~SPWR026~~, ~~M0OP09~~, MOP0038, MOP0039, MOP0102, MOP0104, MOP0121, TUP0017, TUP0029, TUP0132
Schließmann, F. THP0012
Schmid, S. A. ~~TH0P11~~, THP0116
Schmidt, Ch. ~~SPWR026~~, ~~M0OP09~~, MOP0038, MOP0039, MOP0102, MOP0104, TUP0132
Schmidt, J.S. THP0043
Schmökel, M. ~~M0OP07~~, MOP0037, TUP0028
Schnase, A. ~~SPWR025~~, ~~SPWR034~~, TU2A01, TUP0084, THP0046, THP0073, THP0107
Schneider, P.P. **~~SPWR017~~**, **THP0061**
Schreiber, G. THP0046
Schreiber, S. MOP0039
Schuett, M. ~~SPWR033~~, TUP0083, THP0046, **THP0060**
Schulte, D. ~~WE1A01~~
Schulz, S. MOP0121
Schwarz, M. ~~SPWR010~~, ~~SPWR025~~, **~~SPWR034~~**, **MOP0101**, TU2A01, **TUP0084**, THP0072, THP0073, THP0107
Scott, D.J. ~~M0OP03~~, MOP0035
Sears, J. TUP0058, ~~WE1A02~~
Seberg, S.K. MOP0004
Sedlyarov, I.K. WE1A03
Sei, N. ~~M0OP10~~, MOP0024, ~~M0P0053~~, **MOP0073**
Seibel, A. THP0046
Seidman, D.J. MOP0115
Seimiya, Y. THP0005, THP0127
Sekutowicz, J.K. ~~SPWR026~~, ~~M0OP07~~, MOP0037, MOP0104, TUP0029
Selesnev, D.N. TUP0012
Semennikov, A.I. TUP0012
Semione, G.D.L. TH2A01
Sennyu, K. WE2A03
Seol, K.T. THP0067
Seol, Y. J. MOP0063, MOP0064
Serafini, L. MO2A03
Serednyakov, S.S. WE1A03
Seryi, A. ~~SPWR022~~, TUP0045
Severino, F. MOP0004, MOP0005, MOP0006
Sha, P. **TUP0064**
Shaker, H. TUP0119
Shashkov, Ya.V. **~~SPWR022~~**, MOP0066, **TUP0045**
Shea, T.J. MO1P03
Shehzad, N. ~~M0OP09~~, MOP0038
Shelbaya, O. ~~M0OP01~~, MOP0092
Shelley, F.E. ~~M0OP12~~, MOP0095
Shen, G.D. THP0054
Shepherd, B.J.A. ~~M0OP03~~, MOP0035
Shevchenko, K.V. TUP0017, TH1P02
Shevchenko, O.A. WE1A03
Shi, A. THP0051, THP0053, THP0090
Shi, H. THP0113
Shi, J. **~~TU1A02~~**, THP0111
Shi, L. **~~M0OP06~~**, **MOP0034**
Shi, L.B. THP0051, THP0052, THP0053, THP0090
Shibata, T. **~~TU0P10~~**, **TUP0079**, MOP0082
Shidara, T. THP0095
Shimada, M. ~~TU1P03~~
Shin, I. TUP0052
Shin, J.S. MOP0063, MOP0064
Shin, S.-G. TUP0090
Shinozaki, S. MOP0111
Shinto, K. ~~TU0P10~~, TUP0079
Shinya, T. TU2A04, THP0062
Shirikov, I.V. TUP0017, TH1P02
Shirkov, G. MOP0010
Shishido, T. ~~M0OP10~~, ~~M0P0053~~
Shor, A. WE2A04
Shore, C.H. ~~WE1A02~~
Shpakov, V. FR1A03
Shuai, S. ~~TH0P06~~, THP0022
Shumshurov, A. TUP0011
Shvedunov, I.V. MOP0060, MOP0062
Shvedunov, N.V. MOP0060, MOP0061, MOP0062
Shvedunov, V.I. MOP0059, MOP0060, TUP0097, MOP0061, MOP0062
Sidorin, A.O. TH1P02
Sieber, T. THP0046
Sierra, S. **THP0092**, **THP0093**
Sievers, S. ~~M0OP07~~, MOP0037, **TUP0028**, TH2A01
Silverman, I. WE2A04
Simonov, A.S. MOP0062, MOP0060, MOP0061
Sitaraman, N. TUP0055
Sitnikov, A. TUP0012
Skudnova, I. **~~SPWR031~~**, **TUP0116**
Sledneva, A. **~~SPWR032~~**, **TUP0112**
Smedley, J. ~~M0OP07~~, MOP0037
Smirnov, A.V. TH1P02
Smirnov, A.Yu. ~~M0OP11~~, MOP0077
Smith, B.G. ~~M0OP12~~, MOP0095
Smith, E.J.H. TUP0113
Smith, E.N. ~~WE1A02~~
Smith, K.S. MOP0004, MOP0005, MOP0006, THP0006
Smith, R.J. ~~M0OP03~~, MOP0035
Smolenski, K.W. ~~WE1A02~~

Content from this work may be used under the terms of the CC BY 3.0 licence (© 2018). Any distribution of this work must maintain attribution to the author(s), title of the work, publisher, and DOI.

ISBN: 978-3-95450-194-6 ISSN: 2226-0366

Content from this work may be used under the terms of the CC BY 3.0 licence (© 2018). Any distribution of this work must maintain attribution to the author(s), title of the work, publisher, and DOI.

Snedden, E.W. ~~MOOP03~~, MOPO035
Snyder, S.T. TUPO059
Sobrino-Mompean, P. TUPO023
Solodko, A. TUPO023
Solopova, A.D. **TUPO041**
Son, K.T. MOPO094, THPO067
Song, H. MOPO080
Song, Y.K. ~~TUOP06~~, TUPO036
Soriano, S.G. TUPO013
Srinivasan, V. TU2A03, THPO046
Stabile, P. TUPO013
Stachyra, K. TUPO013
Steffey, R. W. MO1P01
Steinhau-Kühl, N. ~~MOOP07~~, MOPO037, TUPO028
Steinhorst, M. **THPO011**, THPO012
Stephan, F. TUPO098, ~~THOP11~~, THPO116, THPO118
Stierle, A. TH2A01
Stocchi, A. ~~WE1A01~~
Straka, B. TUPO043
Stulle, F. **THPO086**
Sturm, W. TU2A03
Suda, K. WE2A03
Sue, Y. ~~SPWR015~~, MOPO085, TUPO010
Sugimoto, M. **TU2A04**, THPO062
Sugimura, T. MOPO082
Suh, H.S. MOPO041
Sulimov, A.A. ~~MOOP07~~, MOPO037
Sumbaev, A.P. **TUPO001**
Sumitomo, Y. MOPO024, MOPO073, THPO127
Sun, B. THPO021
Sun, L.P. TUPO005, ~~THOP03~~, THPO026, THPO050, THPO051, THPO052, THPO053, **THPO090**
Sun, L.T. ~~TUOP08~~, TUPO003, TUPO005, THPO052
Sun, Y. TH1A05
Sunesson, A. **MO1P03**
Suzuki, R. ~~MOOP10~~, ~~MOPO053~~
Svärd, R. MOPO027
Sydlo, C. MOPO121
Syha, M. **~~SPWR033~~**, **TUPO083**, THPO046, THPO060
Syresin, E. TUPO017
Szypula, K. T. TUPO023

— T —

Taghibi Khotbeh-Sara, A. **MOPO069**
Tajiri, Y. FR1A06
Takagi, A. MOPO082, ~~TUOP10~~, TUPO079
Takahashi, F. TUPO069
Takahashi, K. ~~SPWR004~~, MOPO076
Takahashi, T. THPO127
Takahashi, Y. MOPO024
Takai, R. ~~TU1P03~~
Takasaki, E. MOPO082
Takeishi, K. ~~SPWR019~~, TUPO065, TUPO071
Takeuchi, Y. **~~SPWR037~~**, **THPO126**
Tamura, J. ~~THOP02~~, THPO048
Tan, T. THPO069
Tan, W.W. ~~SPWR021~~, TUPO048
Tan, X.J. THPO021
Tanaka, H. THPO124
Tanaka, M. ~~MOOP10~~, ~~MOPO053~~
Tanaka, S. FR1A06
Tanaka, Su. MOPO082
Tanaka, T. MOPO024, MOPO073
Tang, C.-X. ~~THOP11~~, THPO035, THPO116
Tang, J.Y. **MOPO127**, **TH1A01**
Tang, R. ~~THOP06~~, THPO022
Tang, R. ~~SPWR014~~, THPO034, **THPO035**, THPO036
Tang, Zh. X. MOPO029
Taniuchi, T. THPO124
Tararyshkin, S.V. WE1A03
Taylor, E.J. TUPO043, TUPO059
Teichert, J. ~~MOOP07~~, MOPO037, THPO125
Tennant, C. ~~WE1A01~~
Terunuma, N. MOPO125
Terzić, B. MO2A04
Than, R. MOPO004
Thie, J.H. ~~MOOP07~~, MOPO037
Thieberger, P. ~~WE1A02~~
Thoeng, E. TUPO040
Thominet, V.G. ~~MOOP06~~, MOPO034
Thompson, N. ~~MOOP03~~, MOPO035
Thonet, P.A. ~~WE1A01~~
Thorin, S. MOPO027
Tian, H. **TUPO043**
Tian, Q.L. ~~THOP11~~, THPO116
Tiede, R. TUPO017
Timmins, M.A. ~~SPWR016~~, ~~THOP04~~, THPO058
Titberidze, M. MOPO121
Tollervey, C. ~~MOOP03~~, MOPO035
Tomassini, S. MO2A03
Tongu, H. ~~SPWR037~~, ~~TUOP03~~, TUPO030, TUPO066, THPO126
Toyokawa, H. ~~MOOP10~~, ~~MOPO053~~
Tracz, P.S. **MOPO009**, **TUPO085**
Trbojevic, D. ~~WE1A02~~
Tribendis, A.G. WE1A03
Trubnikov, G.V. TH1P02
Trüller, J. THPO046
Tsoupas, N. ~~WE1A02~~
Tu, X.D. ~~SPWR029~~, MOPO118, MOPO119
Tuozzolo, J.E. ~~WE1A02~~
Turrioni, D. TUPO076

— U —

Uchiyama, T. ~~TU1P03~~
Umemori, K. ~~SPWR019~~, TUPO065, **TUPO070**, **TUPO071**, TUPO072, TUPO073,

ISBN: 978-3-95450-194-6 ISSN: 2226-0366

TUPO074, WE2A03, THPO002, THPO008
Urakawa, J. THPO127
Uriot, D. ~~THOP01~~, THPO047, WE2A04
Ushimoto, S. WE1A06

— V —

Vaccarezza, C. FR1A03
Valente-Feliciano, A-M. MOPO019, TUPO042, TUPO076
Vallerand, C. ~~MOOP08~~, MOPO020, ~~WE1A01~~
Valloni, A. TUPO013, ~~WE1A01~~
van der Horst, B. ~~MOOP07~~, MOPO037, TUPO028
van Rienen, U. ~~SPWR016~~, ~~THOP04~~, THPO058
Vandeplassche, D. THPO086
Varela, R. TU2A04
Varenne, F. ~~THOP01~~, THPO047
Variola, A. MO2A03
Vassal, A.V. **TUPO019**
Vennekate, H. THPO125
Venturini Delsolaro, W. **TU1A05**
Verma, A. ~~MOOP11~~, MOPO077
Verzilov, V.A. TU1A03
Veshcherevich, V. ~~WE1A02~~
Vignette, G. THPO092
Villa, F. FR1A03
Vinokurov, N.A. WE1A03
Vint, A. ~~**SPWR007**~~, **THPO016**
Vinzenz, W. THPO046
Vogel (Fogel), V. ~~**MOOP04**~~, **MOPO036**
Vogel, E. ~~**MOOP07**~~, **MOPO037**, TUPO028
Vogel, V. ~~MOOP09~~, MOPO038
Vogt, M. MOPO039
Volkov, V. **TUPO091**, **WE1A03**
Vretenar, M. ~~SPWR016~~, ~~THOP04~~, THPO058

— W —

Walker, N. ~~MOOP09~~, MOPO038, TH2A01
Wallet, L. TUPO013
Walsh, D.A. ~~MOOP03~~, MOPO035
Wang, B.C. ~~SPWR014~~, ~~THOP06~~, THPO022, **THPO033**, THPO036, THPO064
Wang, D. ~~MO2A01~~
Wang, D. **THPO001**
Wang, D. **MOPO016**, ~~**TU1P02**~~
Wang, F. TUPO049, TUPO064
Wang, F.F. ~~SPWR012~~, MOPO087, MOPO120, THPO053
Wang, H. THPO004
Wang, K.D. ~~TUOP08~~, TUPO003, TUPO004, THPO054
Wang, M.C. THPO111
Wang, S. MO1A01, TUPO114, THPO032
Wang, S.C. THPO102
Wang, W.B. THPO053
Wang, X. **MOPO116**
Wang, X.W. ~~SPWR014~~, ~~THOP06~~, THPO022, THPO033, THPO034, THPO035, THPO036, THPO064, THPO111
Wang, Y. THPO028, THPO029, THPO030, **THPO031**, THPO038
Wang, Z. ~~TUOP08~~, TUPO003
Wang, Z.J. ~~SPWR012~~, MOPO087, TUPO106, THPO053, THPO054
Wang, Z.M. ~~THOP06~~, THPO022, THPO033, THPO042, THPO064
Waraich, B.S. ~~TUOP07~~, TUPO014, TUPO039, TUPO040
Washio, M. THPO005
Watanabe, T. WE2A03
Watanabe, Y. THPO002
Watanabe, Y. WE2A03
Watazu, A. ~~MOOP10~~, ~~MOPO053~~
Webber, R.C. ~~TUOP02~~, TUPO007
Weber, M. TU2A04
Wei, C.Y. THPO033
Wei, W. TUPO005, THPO054
Weih, S. **MOPO018**
Weise, H. ~~MOOP07~~, MOPO037, TUPO028, TH2A01
Weisend, J.G. MO1P03
Weissman, L. WE2A04
Welsch, C.P. ~~WE1A01~~
Wenander, F.J.C. ~~SPWR013~~, TUPO016
Weng, X.F. THPO021
Wenliang, L. **THPO100**, THPO104
Wenskat, M. **TH2A01**
Werin, S. MOPO027
Weston, T.M. ~~MOOP03~~, MOPO035
Wheelhouse, A.E. ~~MOOP03~~, MOPO035
White, K.S. MO1P01
Widger, D. ~~WE1A02~~
Wiencek, M. ~~MOOP07~~, MOPO037, TUPO028
Will, C. THPO046
Willeke, F.J. ~~WE1A02~~, THPO006
Williams, P.H. ~~WE1A01~~
Wilson, J.T.G. ~~MOOP03~~, MOPO035
Wilson, K.M. MOPO019
Winkelmann, L. ~~MOOP07~~, MOPO037
Witte, H. ~~WE1A02~~
Witthaus, M. THPO086
Wu, A.D. ~~**TUOP06**~~, **TUPO036**
Wu, J.X. ~~TUOP08~~, TUPO003, THPO054, THPO086, ~~**FR1A04**~~
Wu, Q. MOPO004, THPO006
Wu, Q. THPO053
Wu, X.L. **MOPO080**, THPO028, THPO029, THPO030, THPO031, THPO038
Wuensch, W. ~~THOP08~~, THPO108

— X —

Xia, J.W. ~~TUOP08~~, TUPO003, THPO054
Xiang, R. **THPO125**

Content from this work may be used under the terms of the CC BY 3.0 licence (© 2018). Any distribution of this work must maintain attribution to the author(s), title of the work, publisher, and DOI.

ISBN: 978-3-95450-194-6 ISSN: 2226-0366

Content from this work may be used under the terms of the CC BY 3.0 licence (© 2018). Any distribution of this work must maintain attribution to the author(s), title of the work, publisher, and DOI.

Xiao, B. P. MOPO004, **MOPO005**, **MOPO006**
Xiao, C. ~~TUOP09~~, TUPO078
Xiao, L. ~~SPWR021~~, TUPO048
Xiao, O. THPO102, **THPO103**
Xiao, Y.C. THPO039
Xie, D. ~~SPWR021~~, TUPO048
Xie, H.M. THPO054
Xie, W.J. ~~TUOP08~~, TUPO003, THPO054
Xie, X.C. ~~**MOOP02**~~, **MOPO132**, MOPO079
Xin, T. MOPO004, MOPO005, MOPO006
Xing, C.C. MOPO088, **TUPO101**, ~~THOP03~~, THPO026, THPO050, THPO051
Xing, Q.Z. ~~SPWR014~~, ~~**THOP06**~~, **THPO022**, THPO033, THPO034, THPO035, THPO036, THPO064, THPO111
Xiong, P.R. ~~TUOP06~~, TUPO036
Xiong, Y.Q. ~~SPWR029~~, MOPO118, MOPO119
Xu, S.Y. TUPO114
Xu, W. **MOPO004**, MOPO006, **THPO006**
Xu, X.B. THPO026, **THPO051**, THPO053, THPO090
Xu, Z. ~~TUOP08~~, TUPO003, THPO054
Xudong, X.D. ~~THOP06~~, THPO022
Xue, K. THPO039

— Y —

Yako, T. MOPO125
Yakushev, A. FR1A05
Yamada, H. ~~THOP07~~, THPO091
Yamada, K. WE2A03
Yamaga, M. FR1A06
Yamaguchi, S. TUPO074
Yamaguchi, T.Y. TUPO067, TUPO068
Yamamoto, M. TUPO074
Yamamoto, N. ~~TU1P03~~, THPO005
Yamamoto, Y. ~~SPWR019~~, TUPO065, TUPO071, **THPO097**
Yamanaka, M. THPO002
Yamazaki, T. ~~SPWR015~~, MOPO085, TUPO010
Yan, J.W. ~~**SPWR003**~~, **MOPO042**
Yan, L.X. ~~MO2A02~~, ~~THOP11~~, THPO116
Yan, X.Q. ~~TUOP08~~, TUPO003, ~~**TH1A02**~~
Yanagisawa, T. WE2A03
Yang, D.Y. ~~SPWR021~~, TUPO048
Yang, F. ~~MOOP02~~, MOPO079, MOPO132
Yang, H. **TUPO088**
Yang, J.C. THPO054
Yang, J.H. **MOPO058**
Yang, L. MOPO088, ~~TUOP06~~, TUPO036, TUPO101, ~~**THOP03**~~, THPO026, **THPO050**, THPO051, THPO052, THPO053
Yang, Y. **TUPO005**, THPO052
Yang, Y. ~~**SPWR021**~~, **TUPO048**
Yang, Y. ~~THOP06~~, THPO022
Yang, Y. MOPO058
Yang, Y.Q. ~~TUOP08~~, TUPO003, THPO054
Yang, Z.Q. **TUPO038**
Yano, Y. ~~SPWR027~~, MOPO107
Yao Leclerc, I. THPO092, THPO093
Yao, Q.G. ~~TUOP08~~, TUPO003
Yao, Z.Y. TU1A03, ~~**TUOP07**~~, TUPO014, TUPO020, **TUPO039**, **TUPO040**
Yaramyshev, S. ~~SPWR010~~, ~~SPWR025~~, ~~SPWR034~~, TU2A01, TUPO084, THPO072, THPO073, THPO107
Yasuda, H.Y. MOPO085
Ye, W.B. THPO035, **THPO111**
Yildirim, B. **TUPO027**
Yin, X. ~~**TUOP08**~~, **TUPO003**, TUPO004, THPO054
Yokoya, K. THPO127
Yokoyama, K. WE1A06
Yoon, J.Y. TUPO051, **TUPO052**
Yoshida, M. MOPO007, MOPO008, MOPO085, WE1A06
Yoshioka, M. FR1A06
Youchun, L. THPO100
Yu, D.H. TUPO090
Yu, G. MOPO058
Yu, P.Y. ~~**SPWR012**~~, **MOPO087**, THPO053
Yu, X.D. **THPO064**
Yuan, Y. TUPO114
Yuan, Y.J. ~~TUOP08~~, TUPO003, THPO054
Yuan, Y.T. **THPO020**
Yue, W.M. ~~TUOP06~~, TUPO036
Yurov, D.S. MOPO060, **MOPO061**, MOPO062

— Z —

Zaib, U. N. THPO102
Zaltsman, A. MOPO004, MOPO005, MOPO006, THPO006
Zannini, C. TUPO013
Zarei, S. MOPO026, **MOPO070**
Zarubin, A. TUPO011
Zelenogorsky, V. MOPO010
Zelenski, A. MOPO100
Zelinsky, A.Y. ~~SPWR006~~, ~~SPWR008~~, MOPO028, TUPO002
Zemella, J. MOPO039
Zen, H. MOPO073
Zeng, Z.Q. MOPO058
Zennaro, R. THPO115
Zha, H. THPO018
Zhai, J.Y. TUPO064
Zhai, Y.H. TUPO005
Zhang, B. ~~SPWR012~~, MOPO087, MOPO120, THPO053
Zhang, C. ~~TUOP06~~, TUPO036
Zhang, H.Y. ~~THOP06~~, THPO022, THPO035
Zhang, J.H. THPO053
Zhang, J.R. THPO001, THPO113

ISBN: 978-3-95450-194-6 ISSN: 2226-0366

Zhang, L. **MOPO120**
Zhang, L.P. THPO100
Zhang, P. THPO053
Zhang, R. MOPO007
Zhang, S.H. ~~TUOP06~~, TUPO036
Zhang, S.X. THPO069
Zhang, W. ~~TUOP08~~, TUPO003
Zhang, X.D. **THPO021**
Zhang, X.Y. TUPO064
Zhang, X.Z. ~~TUOP08~~, TUPO003
Zhang, Y. ~~TUOP08~~, TUPO003, THPO054
Zhao, C. ~~THOP06~~, THPO022, THPO064
Zhao, H.W. ~~TUOP06~~, ~~TUOP08~~, TUPO003, TUPO005, TUPO036, THPO005, THPO051, THPO052, THPO090, ~~**FR2A01**~~
Zhao, L. **MOPO019**
Zhao, L. **THPO104**, THPO100
Zhao, M.H. ~~MOOP02~~, MOPO079, MOPO132
Zhao, Q.T. TUPO098, **THPO118**
Zhao, Z.T. ~~SPWR023~~, ~~**MO2A01**~~, ~~MOOP02~~, MOPO132, ~~THOP09~~, THPO109
Zheng, H.J. TUPO064
Zheng, Q. ~~TUOP07~~, TUPO014, TUPO020, TUPO039, TUPO040
Zheng, S.X. ~~SPWR014~~, ~~THOP06~~, THPO022, THPO033, THPO034, THPO035, THPO036, THPO042, THPO064, THPO111
Zhou, B.Z. THPO100, THPO104
Zhou, J.X. THPO028
Zhou, X. **MOPO007**
Zhou, Z.S. THPO102, THPO103
Zhou, Z.Z. ~~TUOP08~~, TUPO003
Zhu, F. TUPO049, THPO076
Zhu, K. ~~TUOP08~~, ~~**TUOP11**~~, TUPO003, ~~**TUPO015**~~
Zhu, T.M. THPO053
Zhu, Z.B. MOPO058
Zhukov, A.P. FR1A01
Zimmermann, S. MOPO090
Ziskind, G. MOPO093
Zomer, Z.F. MO2A03
Zummack, F. MOPO121
Zvyagintsev, V. ~~MOOP01~~, MOPO092, ~~TUOP07~~, TUPO014, TUPO020, TUPO039, TUPO040
Zwartek, P.Z. THPO125

Content from this work may be used under the terms of the CC BY 3.0 licence (© 2018). Any distribution of this work must maintain attribution to the author(s), title of the work, publisher, and DOI.

ISBN: 978-3-95450-194-6 ISSN: 2226-0366

ISBN: 978-3-95450-194-6 ISSN: 2226-0366

Institutes List

A.D.A.M. SA
Meyrin, Switzerland
- Adam, J.
- Aguilera Murciano, D.
- Benot-Morell, A.
- Bonomi, R.
- Cabaleiro Magallanes, F.
- Caldara, M.
- D'Auria, G.
- De Michele, G.
- Degiovanni, A.
- Esposito, M.
- Fanella, S.
- Fazio, D.
- Fink, D.A.
- Fusco, Y.
- Gonzalez, M.
- Gradassi, P.
- Kobzeva, L.
- Levy, G.
- Magrin, G.
- Marraffa, A.
- Milla, A.
- Moser, R.
- Nadig, P.
- Nuessle, G.
- Patino-Revuelta, A.
- Rutter, T.
- Salveter, F.
- Samoshkin, A.
- Wallet, L.

ADS
Jiangsu Province, People's Republic of China
- Li, J.Z.
- Rui, Hou,R.
- Zhang, L.P.

AEOI
Tehran, Iran
- Khalafi, H.

AIST
Tsukuba, Ibaraki, Japan
- Fujiwara, T.
- Kino, K.
- Kuroda, R.
- Michishio, K.
- O'Rourke, B.E.
- Ogawa, H.
- Oshima, N.
- Sato, D.
- Sei, N.
- Suzuki, R.
- Tanaka, M.
- Toyokawa, H.
- Watazu, A.

ALSYOM
Argebteuil, France
- Rocipon, H.

Ankara University Institute of Accelerator Technologies
Golbasi, Turkey
- Elcim, O.F.

Ankara University, Accelerator Technologies Institute
Golbasi / Ankara, Turkey
- Aksoy, A.A.
- Aydin, A.
- Kaya, Ç.

ANL
Argonne, Illinois, USA
- Barcikowski, A.
- Borland, M.
- Byrd, J.M.
- Fischer, R.L.
- Hui, D.
- Mustapha, B.
- Power, J.G.
- Sun, Y.

Ariel University
Ariel, Israel
- Dyunin, E.

ATOX
Ibaraki, Japan
- Ouchi, T.
- Sakurayama, H.

AVO-ADAM
Meyrin, Switzerland
- Breitenfeldt, M.
- Candolfi, C.
- Castorina, G.
- Cerv, M.
- De Michele, G.
- Dimov, V.A.
- Gallas, M.T.
- Gibson, S.
- Gonzalez, A. S.
- Ivanisenko, Ye.
- Jeff, A.
- Khan, V. F.
- Magnoni, S.
- Navarro Quirante, J.L.
- Pavetits, H.
- Paz Neira, P.
- Soriano, S.G.
- Stabile, P.

Content from this work may be used under the terms of the CC BY 3.0 licence (© 2018). Any distribution of this work must maintain attribution to the author(s), title of the work, publisher, and DOI.

ISBN: 978-3-95450-194-6 ISSN: 2226-0366

Content from this work may be used under the terms of the CC BY 3.0 licence (© 2018). Any distribution of this work must maintain attribution to the author(s), title of the work, publisher, and DOI.

- Stachyra, K.
- Valloni, A.
- Zannini, C.

Ben-Gurion University in the Negev
Beer Sheva, Israel
- Ziskind, G.

BERGOZ Instrumentation
Saint Genis Pouilly, France
- Bayle, H.
- Bergoz, J.F.
- Delaviere, T.
- Dupuy, L.
- Stulle, F.

BEVATECH
Frankfurt, Germany
- Basten, M.
- Höltermann, H.
- Koubek, B.
- Podlech, H.
- Ratzinger, U.
- Schempp, A.
- Tiede, R.

BINP SB RAS
Novosibirsk, Russia
- Arbuzov, V.S.
- Barnyakov, A.M.
- Kenzhebulatov, E.
- Kolobanov, E.I.
- Kondakov, A.A.
- Kozyrev, E.V.
- Krutikhin, S.A.
- Kuptsov, I.V.
- Kurkin, G.Y.
- Levichev, A.E.
- Levichev, E.B.
- Motygin, S.V.
- Murasev, A.A.
- Nikiforov, D.A.
- Ovchar, V.K.
- Petrov, V.M.
- Pilan, A.M.
- Pupkov, Yu.A.
- Repkov, V.V.
- Scheglov, M.A.
- Sedlyarov, I.K.
- Serednyakov, S.S.
- Shevchenko, O.A.
- Tararyshkin, S.V.
- Tribendis, A.G.
- Vinokurov, N.A.
- Volkov, V.

BNL
Upton, Long Island, New York, USA
- Atoian, G.
- Beebe, E.N.
- Ben-Zvi, I.
- Berg, J.S.
- Brooks, S.J.
- Fedotov, A.V.
- Gao, Y.
- Hayes, T.
- Holmes, D.
- Ikeda, S.
- Kanesue, T.
- Kolb, P.
- Lehn, T.
- Liu, C.
- LoDestro, V.
- Mahler, G.J.
- Mapes, M.
- McIntyre, G.T.
- McNerney, A.
- Méot, F.
- Mernick, K.
- Michnoff, R.J.
- Minty, M.G.
- Okamura, M.
- Peggs, S.
- Pikin, A.I.
- Porqueddu, R.
- Ptitsyn, V.
- Raparia, D.
- Ritter, J.
- Roser, T.
- Seberg, S.K.
- Severino, F.
- Smedley, J.
- Smith, K.S.
- Than, R.
- Thieberger, P.
- Trbojevic, D.
- Tsoupas, N.
- Tuozzolo, J.E.
- Willeke, F.J.
- Witte, H.
- Wu, Q.
- Xiao, B. P.
- Xin, T.
- Xu, W.
- Zaltsman, A.
- Zelenski, A.

Budker INP & NSU
Novosibirsk, Russia
- Razuvaev, G.P.

CAEP/IFP
Mainyang, Sichuan, People's Republic of China
- Chen, S.
- He, X.
- Pang, J.

ISBN: 978-3-95450-194-6 ISSN: 2226-0366

CEA
Grenoble, France
- Millet, F.

CEA/DRF/IRFU
Gif-sur-Yvette, France
- Four, A.
- Uriot, D.

CEA/DSM/IRFU
France
- Bernaudin, P.-E.
- Devanz, G.
- Farabolini, W.
- Hamelin, T.
- Madec, C.

CEA/INAC
Grenoble Cedex 9, France
- Bonnay, P.
- Bonne, F.

CEA/IRFU
Gif-sur-Yvette, France
- Abbon, P.
- Antoine, C.Z.
- Bazin, N.
- Bolzon, B.
- Cenni, E.
- Chauveau, A.C.
- Chauvin, N.
- Chel, S.
- Duperrier, R.D.
- Ferrand, G.
- Gastineau, B.
- Gobin, R.
- Jacquemet, M.
- Madec, C.
- Marroncle, J.
- Pichoff, N.
- Pottin, B.
- Renard, B.
- Uriot, D.

Center for Optical Research and Education, Utsunomiya University
Utsunomiya, Japan
- Higashiguchi, T.

CERN
Geneva, Switzerland
- Arduini, G.
- Atieh, S.
- Bellodi, G.
- Bencini, V.
- Benedetti, S.
- Bergamaschi, M.
- Bertolo, S.B.
- Bilton, A.
- Bozzolan, M.
- Brüning, O.S.
- Calaga, R.
- Catalán Lasheras, N.
- Corsini, R.
- Curcio, A.
- Dassa, L.
- Di Lorenzo, F.D.L.
- Döbert, S.
- Farabolini, W.
- Gamba, D.
- Garolfi, L.
- Gerigk, F.
- Gorgisyan, I.
- Grudiev, A.
- Holzer, B.J.
- Jensen, E.
- Lallement, J.-B.
- Latina, A.
- Lebet, S.
- Lettry, J.
- Lombardi, A.M.
- Mastrostefano, C.M.
- Mathot, S.J.
- Milanese, A.
- Miyazaki, A.
- Montesinos, E.
- Noll, D.
- O'Neil, M.
- Pahl, H.
- Pellegrini, D.
- Pitters, J.
- Pommerenke, H.W.
- Rodriguez-Castro, E.
- Sauza-Bedolla, J.
- Schulte, D.
- Sobrino-Mompean, P.
- Solodko, A.
- Szypula, K. T.
- Thonet, P.A.
- Timmins, M.A.
- Valloni, A.
- Venturini Delsolaro, W.
- Vretenar, M.
- Wenander, F.J.C.
- Wuensch, W.

CFEL
Hamburg, Germany
- Fakhari, M.

China Institute of Atomic Energy
Beijing, People's Republic of China
- Han, G.
- Li, J.H.
- Zhu, Z.B.

Content from this work may be used under the terms of the CC BY 3.0 licence (© 2018). Any distribution of this work must maintain attribution to the author(s), title of the work, publisher, and DOI.

ISBN: 978-3-95450-194-6 ISSN: 2226-0366

Content from this work may be used under the terms of the CC BY 3.0 licence (© 2018). Any distribution of this work must maintain attribution to the author(s), title of the work, publisher, and DOI.

CIAE
Beijing, People's Republic of China
- Li, C.G.
- Yang, J.H.
- Yang, Y.
- Yu, G.
- Zeng, Z.Q.

CIEMAT
Madrid, Spain
- Gavela, D.
- Jiménez-Rey, D.
- Kirpitchev, I.
- Mollá, J.
- Méndez, P.
- Podadera, I.
- Regidor, D.
- Varela, R.
- Weber, M.

Cockcroft Institute
Warrington, Cheshire, United Kingdom
- Dumbell, K.D.
- Shepherd, B.J.A.

Cockcroft Institute, Lancaster University
Lancaster, United Kingdom
- Apsimon, R.
- Burt, G.
- Healy, A.L.
- Jamison, S.P.
- Letizia, R.
- Pitman, S.
- Vint, A.

College of Engineering and Applied Sciences for Nanjing University
Nanjing, People's Republic of China
- Wenliang, L.

Consorzio RFX, Associazione Euratom-ENEA sulla Fusione
Padova, Italy
- Pruneri, G.

Cornell University
Ithaca, New York, USA
- Arias, T.
- Cueva, P.
- Jusic, D.
- Muller, D.A.
- Sears, J.
- Sitaraman, N.

Cornell University (CLASSE), Cornell Laboratory for Accelerator-Based Sciences and Education
Ithaca, New York, USA
- Banerjee, N.
- Barley, J.
- Bartnik, A.C.
- Bazarov, I.V.
- Burke, D.C.
- Crittenden, J.A.
- Cultrera, L.
- Dobbins, J.
- Furuta, F.
- Gallagher, R.E.
- Ge, M.
- Gruber, T.
- Gulliford, C.M.
- Hall, D.L.
- Heltsley, B.K.
- Hoffstaetter, G.H.
- Kaplan, R.P.K.
- Kaufman, J.J.
- Kostroun, V.O.
- Koufalis, P.N.
- Kulina, G.
- Li, Y.
- Liepe, M.
- Lou, W.
- Maniscalco, J.T.
- Patterson, J.R.
- Porter, R.D.
- Quigley, P.
- Sabol, D.M.
- Sagan, D.
- Sears, J.
- Shore, C.H.
- Smith, E.N.
- Smolenski, K.W.
- Veshcherevich, V.
- Widger, D.

CSNS
Guangdong Province, People's Republic of China
- Cao, X.
- Chen, W.
- Fan, M.X.
- Huang, T.
- Li, A.H.
- Li, B.
- Li, H.
- Li, J.
- Li, M.T.
- Liu, S.
- Liu, Y.D.
- Lu, X.H.
- Luo, T.
- Luo, X.B.
- Peng, J.
- Qu, P.H.
- Wang, Y.
- Wu, X.L.
- Xue, K.

DESY
Hamburg, Germany
- Ayvazyan, V.

ISBN: 978-3-95450-194-6 ISSN: 2226-0366

- Barbanotti, S.
- Bellandi, A.
- Branlard, J.
- Butkowski, Ł.
- Cherepenko, A.
- Choroba, S.
- Dangwal Pandey, A.D.
- Dohlus, M.
- Eschke, J.
- Felber, M.
- Flöttmann, K.
- Foster, B.
- Grecki, M.K.
- Gumus, C.
- Hartl, I.
- Hartung, J.
- Hierholzer, M.
- Hoffmann, M.G.
- Hoffmann, M.
- Honkavaara, K.
- Hüning, M.
- Jensch, K.
- Jensen, J.-P.
- Kampmeyer, C. K.
- Katalev, V.V.
- Keller, T.F.
- Killenberg, M.
- Klinke, D.
- Kostin, D.
- Kozak, T.
- Krupka, N.
- Lamb, T.
- Lilje, L.
- Mavrič, U.
- Möller, W.-D.
- Morozov, P.
- Müller, J.M.
- Nachtigal, Y.
- Nölle, D.
- Omet, M.
- Pfeiffer, S.
- Przygoda, K.P.
- Reschke, D.
- Rybaniec, R.
- Saegebarth, S.
- Schaffran, J.
- Schalwat, M.
- Schilling, P.
- Schlarb, H.
- Schmidt, Ch.
- Schmökel, M.
- Schreiber, S.
- Schulz, S.
- Sekutowicz, J.K.
- Shehzad, N.
- Sievers, S.
- Steinhau-Kühl, N.
- Sulimov, A.A.
- Sydlo, C.
- Thie, J.H.
- Titberidze, M.
- van der Horst, B.
- Vogel (Fogel), V.
- Vogel, E.
- Vogel, V.
- Vogt, M.
- Walker, N.
- Weise, H.
- Wenskat, M.
- Winkelmann, L.
- Yildirim, B.
- Zemella, J.
- Zummack, F.

DESY Zeuthen
Zeuthen, Germany
- Boonpornprasert, P.
- Chen, Y.
- Good, J.D.
- Groß, M.
- Huck, H.
- Isaev, I.I.
- Kalantaryan, D.K.
- Koschitzki, C.
- Krasilnikov, M.
- Li, X.
- Lishilin, O.
- Loisch, G.
- Melkumyan, D.
- Niemczyk, R.
- Oppelt, A.
- Qian, H.J.
- Renier, Y.
- Saisa-ard, C.
- Stephan, F.
- Zhao, Q.T.

DNSC
Dongguan, People's Republic of China
- Liu, S.M.

Elettra-Sincrotrone Trieste S.C.p.A.
Basovizza, Italy
- D'Auria, G.

ESS
Lund, Sweden
- Arnold, P.
- Birch, S.L.
- Danared, H.
- Garoby, R.
- Hellström, F.
- Hulla, G.
- Jensen, M.
- Lindroos, M.
- Martins, C.A.
- Midttun, Ø.
- Nordt, A.
- Sargsyan, E.

Content from this work may be used under the terms of the CC BY 3.0 licence (© 2018). Any distribution of this work must maintain attribution to the author(s), title of the work, publisher, and DOI.

ISBN: 978-3-95450-194-6 ISSN: 2226-0366

Content from this work may be used under the terms of the CC BY 3.0 licence (© 2018). Any distribution of this work must maintain attribution to the author(s), title of the work, publisher, and DOI.

- Schmidt, J.S.
- Shea, T.J.
- Sunesson, A.
- Weisend, J.G.

ESS Bilbao
Zamudio, Spain
- Bustinduy, I.
- Garmendia, N.
- Muñoz, J.L.

F4E
Germany
- Dzitko, H.
- Knaster, J.
- Moya, I.M.

Faraday Technology, Inc.
Clayton, Ohio, USA
- Hall, T.D.
- Inman, M.E.
- Radhakrishnan, R.
- Snyder, S.T.
- Taylor, E.J.

Federal State Unitary Enterprise, Laboratory of Electron Accelerators MSU, Ltd
Moscow, Russia
- Shvedunov, I.V.
- Simonov, A.S.

Fermilab
Batavia, Illinois, USA
- Barzi, E.Z.
- Ciaccia, C.
- Khabiboulline, T.N.
- Turrioni, D.

FRIB
East Lansing, USA
- Chabot, D.
- Cogan, S.
- Compton, C.
- Li, Z.
- Lidia, S.M.
- Ostroumov, P.N.
- Pozdeyev, G.
- Webber, R.C.

Friedrich-Alexander Universität Erlangen-Nuernberg, University Erlangen-Nuernberg LFTE
Erlangen, Germany
- Mittelbach, A.K.

Fusion for Energy
Garching, Germany
- Beauvais, P.-Y.
- Dzitko, H.
- Gex, D.
- Heidinger, R.
- Jokinen, A.
- Marqueta, A.
- Moya, I.
- Phillips, G.

GANIL
Caen, France
- Bernaudin, P.-E.
- Di Giacomo, M.
- Ferdinand, R.
- Franberg, H.
- Ghribi, A.
- Kamalou, O.
- Lagniel, J.-M.
- Lechartier, M.
- Leyge, J.F.
- Normand, G.
- Savalle, A.
- Varenne, F.
- Vassal, A.V.

GERAC Thales
Le Barp, France
- Chahbazian, M.E.
- De Oliveira, J.G.
- Goeury, A.G.
- Nennig, L.J.
- Petitjean, S.P.

GSI
Darmstadt, Germany
- Appel, S.
- Barth, W.A.
- Berezov, R.
- Bevcic, M.
- Du, X.
- Düllmann, Ch.E.
- Fils, J.
- Forck, P.
- Gerhard, P.
- Groening, L.
- Heilmann, M.
- Horn, K.P.
- Jäger, E.
- Kaiser, M.
- Khuyagbaatar, J.
- Kleffner, C.M.
- Knie, K.
- Krier, J.
- Maier, M.T.
- Mickat, S.
- Mühle, C.
- Puetz, S.

ISBN: 978-3-95450-194-6 ISSN: 2226-0366

- Rubin, A.
- Salvatore, J.
- Scharrer, P.
- Schnase, A.
- Schreiber, G.
- Seibel, A.
- Sieber, T.
- Srinivasan, V.
- Sturm, W.
- Trüller, J.
- Vinzenz, W.
- Will, C.
- Witthaus, M.
- Xiao, C.
- Yakushev, A.
- Yaramyshev, S.

HIM
Mainz, Germany
- Aulenbacher, K.
- Barth, W.A.
- Burandt, C.
- Düllmann, Ch.E.
- Dziuba, F.D.
- Gettmann, V.
- Khuyagbaatar, J.
- Kürzeder, T.
- List, J.
- Miski-Oglu, M.

Hiroshima University, Graduate School of Science
Higashi-Hiroshima, Japan
- Takahashi, T.

HIT
Heidelberg, Germany
- Feldmeier, E.
- Haberer, Th.
- Peters, A.

HKK
Morioka, Japan
- Akabori, T.
- Mitoya, G.M.
- Miyano, K.

HU/AdSM
Higashi-Hiroshima, Japan
- Kuriki, M.
- Nagoshi, H.

Huazhong University of Science and Technology, State Key Laboratory of Advanced Electromagnetic Engineering and Technology,
Hubei, People's Republic of China
- Fan, K.

HUST
Wuhan, People's Republic of China
- Bai, J.
- Chen, Q.S.
- Fan, K.
- Feng, G.
- Hu, T.
- Jiang, J.
- Lu, Y.
- Tu, X.D.
- Xiong, Y.Q.
- Yuan, Y.T.

HZB
Berlin, Germany
- Echevarria, P.
- Kamps, T.
- Kourkafas, G.
- Neumann, A.

HZDR
Dresden, Germany
- Arnold, A.
- Lu, P.N.
- Murcek, P.
- Schaber, J.S.
- Teichert, J.
- Vennekate, H.
- Xiang, R.
- Zwartek, P.Z.

I-Tech
Solkan, Slovenia
- Bardorfer, A.
- Baricevic, B.B.
- Cerne, R.

IAP
Frankfurt am Main, Germany
- Almomani, A.
- Bade, D.
- Basten, M.
- Busch, M.
- Corbet, J.
- Droba, M.
- Hähnel, H.
- Kümpel, K.
- Lamprecht, S.
- Meusel, O.
- Müller, P.
- Petry, N.F.
- Podlech, H.
- Ratzinger, U.
- Schempp, A.
- Schneider, P.P.
- Schuett, M.
- Schwarz, M.
- Syha, M.
- Zimmermann, S.

Content from this work may be used under the terms of the CC BY 3.0 licence (© 2018). Any distribution of this work must maintain attribution to the author(s), title of the work, publisher, and DOI.

ISBN: 978-3-95450-194-6 ISSN: 2226-0366

Content from this work may be used under the terms of the CC BY 3.0 licence (© 2018). Any distribution of this work must maintain attribution to the author(s), title of the work, publisher, and DOI.

IAP/RAS
Nizhny Novgorod, Russia
- Gacheva, E.
- Poteomkin, A.
- Zelenogorsky, V.

Ibaraki University
Hitachi, Ibaraki, Japan
- Iinuma, H.
- Nakazawa, Y.

IBS
Daejeon, Republic of Korea
- Choi, B.H.
- Choi, C.O.
- Choi, J.W.
- Jang, H.
- Jo, Y.W.
- Joo, J.
- Jung, H.C.
- Jung, Y.
- Kim, H.
- Kim, J.W.
- Kim, M.S.
- Kim, Y.
- Lee, D.Y.
- Lee, J.
- Lee, M.
- Lee, S.
- Seol, K.T.
- Shin, I.
- Son, K.T.

IFIN-HH
Bucharest - Magurele, Romania
- Tracz, P.S.

IFJ-PAN
Kraków, Poland
- Wiencek, M.

IFMIF/EVEDA
Rokkasho, Japan
- Cara, P.

IHEP
Beijing, People's Republic of China
- An, Y.W.
- Cao, J.S.
- Chen, F.S.
- Chen, Q.
- Chi, Y.L.
- Chu, C.P.
- Dai, J.
- Dong, C.
- Dong, L.
- Feisi, H.F.S.
- Fu, S.
- Fukuda, S.
- Gan, N.
- Gao, J.
- Gong, D.J.
- Gong, K.Y.
- Huang, L.
- Huang, M.Y.
- Jin, S.
- Kang, W.
- Li, Y.
- Li, Z.P.
- Li, Z.Q.
- Liu, B.Q.
- Liu, H.C.
- Liu, W.B.
- Long, F.
- Lu, Z.J.
- Lv, Y.J.
- Ma, X.
- Meng, C.
- Mi, Z.H.
- Ouyang, H.F.
- Pan, W.M.
- Pei, G.
- Pei, S.
- Qiao, Y.S.
- Ryabov, A.
- Shi, H.
- Song, H.
- Tang, J.Y.
- Wang, D.
- Wang, S.C.
- Wang, S.
- Wang, X.
- Xiao, O.
- Xiao, Y.C.
- Xu, S.Y.
- Yuan, Y.
- Zaib, U. N.
- Zhai, J.Y.
- Zhang, J.R.
- Zhang, X.Y.
- Zheng, H.J.
- Zhou, J.X.
- Zhou, Z.S.

IKP
Mainz, Germany
- Aulenbacher, K.
- Bai, J.N.
- Diefenbach, J.
- Fichtner, F.
- Ledroit, B.

ILSF
Tehran, Iran
- Ahmadiannamin, S.

ISBN: 978-3-95450-194-6 ISSN: 2226-0366

IMP/CAS
Lanzhou, People's Republic of China
- Chen, W.L.
- Cong, Y.
- Dou, W.P.
- Du, H.
- Fang, X.
- Gao, Z.
- Guo, H.
- Guo, Y.H.
- He, T.
- He, Y.
- Hu, C.F.
- Huang, G.
- Huang, S.C.
- Jia, H.
- Jiang, P.
- Jing, L.
- Kong, Q.Y.
- Li, C.L.
- Li, C.X.
- Li, J.
- Li, X.N.
- Li, Y.M.
- Li, Z.S.
- Liu, L.B.
- Liu, X.J.
- Liu, X.
- Lu, L.
- Lu, W.
- Ma, L.Z.
- Ma, W.
- Meng, J.
- Pan, F.
- Qian, C.
- Shen, G.D.
- Shi, A.
- Shi, L.B.
- Song, Y.K.
- Sun, L.P.
- Sun, L.T.
- Tan, T.
- Wang, F.F.
- Wang, K.D.
- Wang, W.B.
- Wang, Z.J.
- Wei, W.
- Wu, A.D.
- Wu, J.X.
- Wu, Q.
- Xia, J.W.
- Xie, H.M.
- Xie, W.J.
- Xing, C.C.
- Xiong, P.R.
- Xu, X.B.
- Xu, Z.
- Yang, J.C.
- Yang, L.
- Yang, Y.Q.
- Yang, Y.
- Yang, Z.Q.
- Yao, Q.G.
- Yin, X.
- Yu, P.Y.
- Yuan, Y.J.
- Yue, W.M.
- Zhai, Y.H.
- Zhang, B.
- Zhang, C.
- Zhang, J.H.
- Zhang, L.
- Zhang, P.
- Zhang, S.H.
- Zhang, S.X.
- Zhang, W.
- Zhang, X.Z.
- Zhang, Y.
- Zhao, H.W.
- Zhao, Q.T.
- Zhou, Z.Z.
- Zhu, T.M.

Imperial College of Science and Technology, Department of Physics
London, United Kingdom
- Blackmore, V.
- Hunt, C.

INFN- Sez. di Padova
Padova, Italy
- Colombo, A.G.

INFN-Ferrara
Ferrara, Italy
- Cibinetto, G.

INFN-Roma
Roma, Italy
- Ficcadenti, L.
- Mostacci, A.
- Palumbo, L.
- Pettinacci, V.

INFN-Roma1
Rome, Italy
- Migliorati, M.

INFN-Torino
Torino, Italy
- Borotto Dalla Vecchia, F.
- Mereu, P.
- Mezzano, M.
- Mingioni, C.
- Nenni, M.
- Panero, R.

Content from this work may be used under the terms of the CC BY 3.0 licence (© 2018). Any distribution of this work must maintain attribution to the author(s), title of the work, publisher, and DOI.

ISBN: 978-3-95450-194-6 ISSN: 2226-0366

Content from this work may be used under the terms of the CC BY 3.0 licence (© 2018). Any distribution of this work must maintain attribution to the author(s), title of the work, publisher, and DOI.

INFN/LNF
Frascati (Roma), Italy
- Alesini, D.
- Anania, M.P.
- Battisti, A.
- Bellaveglia, M.
- Biagioni, A.
- Bini, S.
- Bisesto, F.G.
- Brentegani, E.
- Cardelli, F.
- Castellano, M.
- Chiadroni, E.
- Costa, G.
- Di Raddo, R.D.
- Falone, A.
- Ferrario, M.
- Filippi, F.
- Gallo, A.
- Giribono, A.
- Lollo, V.L.
- Marocchino, A.
- Mostacci, A.
- Pellegrino, L.
- Piersanti, L.
- Pioli, S.
- Pompili, R.
- Rossi, A.R.
- Shpakov, V.
- Tomassini, S.
- Vaccarezza, C.
- Variola, A.
- Villa, F.

INFN/LNL
Legnaro (PD), Italy
- Antoniazzi, L.
- Baldo, A.
- Battistello, A.
- Bellan, L.
- Bortolato, D.
- Bottin, P.
- Comunian, M.
- Conventi, D.
- Fagotti, E.
- Ferrari, L.
- Grespan, F.
- Mauro, G.S.
- Montis, M.
- Palmieri, A.
- Pisent, A.
- Scantamburlo, F.

INFN/LNS
Catania, Italy
- Celona, L.
- Gammino, S.
- Neri, L.

Institut Theorie Elektromagnetischer Felder, TU Darmstadt
Darmstadt, Germany
- Schmid, S. A.

Institute of High Energy Physics (IHEP)
People's Republic of China
- Xiao, O.

Institute of High Energy Physics (IHEP), Chinese Academy of Sciences
Beijing, People's Republic of China
- Sha, P.

IPM
Tehran, Iran
- Bahrami, M.
- Behnamian, H.
- Dayyani, M.
- Kasaei, S.
- Lamehi, M.
- Sanaye Hajari, S.
- Shaker, H.

IPN
Orsay, France
- Bousson, S.
- Longuevergne, D.
- Olivier, G.
- Olry, G.

IRFU, CEA, University Paris-Saclay
Gif-sur-Yvette, France
- Ladegaillerie, S.
- Plaisant, Th.

ISMA
Ibaraki, Japan
- Muroga, T.
- Shishido, T.

Istituto Nazionale di Fisica Nucleare
Milano, Italy
- Bacci, A.
- Palmer, D.T.
- Serafini, L.

ITEP
Moscow, Russia
- Alekseev, P.N.
- Alexeev, N.N.
- Andreev, V.
- Fatkullin, R.
- Kozlov, A.V.
- Kropachev, G.
- Kulevoy, T.
- Milyachenko, A.D.
- Nikolaev, V.I.

ISBN: 978-3-95450-194-6 ISSN: 2226-0366

- Satov, Yu.A.
- Selesnev, D.N.
- Semennikov, A.I.
- Shumshurov, A.
- Sitnikov, A.
- Zarubin, A.

IUAC
New Delhi, India
- Ahuja, R.
- Kedia, S.
- Kumar, R.
- Mehta, R.

Iwate University
Morioka, Iwate, Japan
- Negishi, K.

IZTECH
Izmir, Turkey
- Bursali, H.

J-PARC, KEK & JAEA
Ibaraki-ken, Japan
- Ikegami, K.
- Liu, Y.
- Ohkoshi, K.
- Otani, M.
- Saito, N.
- Shibata, T.

JAEA
Ibaraki-ken, Japan
- Hasegawa, K.
- Kurosawa, S.
- Takeishi, K.

JAEA/J-PARC
Tokai-mura, Japan
- Hasegawa, K.
- Kamiya, J.
- Kondo, Y.
- Miura, A.
- Morishita, T.
- Oguri, H.
- Shinozaki, S.
- Shinto, K.
- Tamura, J.

JAI
Oxford, United Kingdom
- Konoplev, I.V.

JASRI
Hyogo, Japan
- Kondo, C.
- Otake, Y.
- Yamaga, M.

JASRI/SPring-8
Hyogo-ken, Japan
- Hosoda, N.
- Matsubara, S.
- Ohshima, T.
- Taniuchi, T.

JINR
Dubna, Moscow Region, Russia
- Aleksandrov, V.
- Balalykin, N.
- Butenko, A.V.
- Donets, D.E.
- Golovenskiy, B.V.
- Govorov, A.
- Huran, J.
- Kobets, V.V.
- Kovalenko, A.D.
- Levterov, K.A.
- Lyuosev, D.A.
- Martynov, A.A.
- Minashkin, V.F.
- Monchinsky, V.A.
- Nozdrin, M.A.
- Ponkin, D.O.
- Shevchenko, K.V.
- Shirikov, I.V.
- Shirkov, G.
- Sledneva, A.
- Smirnov, A.V.
- Sumbaev, A.P.
- Syresin, E.
- Trubnikov, G.V.

JINR/VBLHEP
Dubna, Moscow region, Russia
- Donets, D.E.
- Levterov, K.A.
- Lyuosev, D.A.
- Martynov, A.A.
- Mialkovskiy, V.V.
- Ponkin, D.O.
- Shevchenko, K.V.
- Shirikov, I.V.
- Sidorin, A.O.

JLab
Newport News, Virginia, USA
- Bachimanchi, R.
- Bogacz, S.A.
- Burton, M.C.
- Carroll, J.
- Daly, E.
- Davis, G.K.
- Deitrick, K.E.
- Delayen, J.R.

Content from this work may be used under the terms of the CC BY 3.0 licence (© 2018). Any distribution of this work must maintain attribution to the author(s), title of the work, publisher, and DOI.

ISBN: 978-3-95450-194-6 ISSN: 2226-0366

Content from this work may be used under the terms of the CC BY 3.0 licence (© 2018). Any distribution of this work must maintain attribution to the author(s), title of the work, publisher, and DOI.

- Diaz, M.
- Douglas, D.
- Eremeev, G.V.
- Forehand, D.
- Geng, R.L.
- Grames, J.M.
- Guo, J.
- Hannon, F.E.
- Higgins, H.
- Hovater, C.
- Hutton, A.
- Kazimi, R.
- Krafft, G.A.
- Lin, F.
- Marhauser, F.
- Morozov, V.S.
- Mounts, C.I.
- Palczewski, A.D.
- Park, H.
- Phillips, H.L.
- Plawski, T. E.
- Reece, C.E.
- Reilly, A.V.
- Rimmer, R.A.
- Roblin, Y.
- Satogata, T.
- Seidman, D.J.
- Solopova, A.D.
- Straka, B.
- Tennant, C.
- Tian, H.
- Valente-Feliciano, A-M.
- Wang, H.
- Wilson, K.M.
- Zhao, L.

Johannes Gutenberg University Mainz, Institut of Nuclear Chemistry
Mainz, Germany
- Düllmann, Ch.E.

Kanto Information Service (KIS), Accelerator Group
Ibaraki, Japan
- Saotome, H.S.

KEK
Ibaraki, Japan
- Akemoto, M.
- Arakawa, D.A.
- Aryshev, A.
- Dohmae, T.
- Egi, M.
- Enami, K.
- Enomoto, Y.
- Fang, Z.
- Fukao, Y.
- Fukuda, M.K.
- Fukuda, S.
- Fukui, Y.
- Furukawa, K.
- Furuya, T.
- Futatsukawa, K.
- Hayano, H.
- Hisamatsu, H.
- Honda, Y.
- Honma, H.
- Hori, Y.
- Ikegami, K.
- Inoue, H.
- Jin, X.J.
- Kako, E.
- Kamitani, T.
- Katagiri, H.
- Kato, R.
- Kato, S.
- Kawamura, M.
- Kawamura, N.
- Kobayashi, H.
- Kobayashi, Y.
- Konomi, T.
- Kubo, T.
- Kubota, C.
- Kurihara, T.
- Matsumoto, S.
- Matsumoto, T.
- Mibe, T.
- Michizono, S.
- Miura, T.
- Miyahara, F.
- Miyajima, T.
- Miyake, Y.
- Monjushiro, H.
- Mori, S.
- Naito, F.
- Nakai, H.
- Nakajima, H.
- Nakayama, H.
- Nanmo, K.
- Natsui, T.
- Obina, T.
- Ogawa, Y.
- Ohsawa, S.
- Okugi, T.
- Omori, T.
- Otani, M.
- Qiu, F.
- Saeki, T.
- Sakai, H.
- Sato, M.
- Satoh, D.
- Satoh, M.
- Sawabe, M.
- Seimiya, Y.
- Shibata, T.
- Shidara, T.
- Shimada, M.
- Sugimura, T.
- Takagi, A.
- Takai, R.
- Takasaki, E.

ISBN: 978-3-95450-194-6 ISSN: 2226-0366

- Terunuma, N.
- Uchiyama, T.
- Umemori, K.
- Urakawa, J.
- Watanabe, Y.
- Yamaguchi, S.
- Yamamoto, M.
- Yamamoto, N.
- Yamamoto, Y.
- Yamanaka, M.
- Yamazaki, T.
- Yano, Y.
- Yokoya, K.
- Yokoyama, K.
- Yoshida, M.
- Zhang, R.
- Zhou, X.

KERI
Changwon, Republic of Korea
- Choi, Y.W.
- Kim, G.J.
- Kim, I.S.
- Kim, J.I.
- Kim, S.
- Lee, J.H.
- Lee, Y.S.

KNTU
Tehran, Iran
- Rahmani, F.
- Taghibi Khotbeh-Sara, A.

Korea University Sejong Campus
Sejong, Republic of Korea
- Bhang, J.B.
- Cha, H.J.
- Jang, S.W.
- Kim, E.-S.
- Kim, K.R.
- Park, C.S.
- Park, S. H.
- Yoon, J.Y.

KPH
Mainz, Germany
- Heine, R.G.
- Hug, F.

Kyoto ICR
Uji, Kyoto, Japan
- Abe, M.
- Iwashita, Y.
- Katayama, R.
- Takeuchi, Y.
- Tongu, H.
- Yako, T.

Kyoto University
Kyoto, Japan
- Ohgaki, H.
- Zen, H.

Kyoto University, Research Reactor Institute
Osaka, Japan
- Fuwa, Y.

Laboratory of Electron Accelerators MSU, Ltd, Physics Department, Lomonosov Moscow State University
Moscow, Russia
- Ovchinnikova, L.

LAL
Orsay, France
- Bruni, C.
- Cassou, K.
- Chaikovska, I.
- Douillet, D.
- Dupraz, K.
- Kaabi, W.
- Le Barillec, T.
- Lepercq, P.
- Martens, A.
- Ndiaye, C.F.
- Peinaud, Y.
- Purwar, H.
- Stocchi, A.
- Vallerand, C.
- Zomer, Z.F.

Lancaster University
Lancaster, United Kingdom
- Letizia, R.

LANL
Los Alamos, New Mexico, USA
- Barkley, W.C.
- Borden, M.J.
- Garnett, R.W.
- Gulley, M.S.
- Kerstiens, E.L.
- Kurennoy, S.S.
- Pieck, M.
- Rees, D.
- Shelley, F.E.
- Smith, B.G.

LEA MSU
Moscow, Russia
- Alimov, A.S.
- Ermakov, A.N.
- Khankin, V.V.
- Kurilik, A.
- Ovchinnikova, L.
- Pakhomov, N.I.

Content from this work may be used under the terms of the CC BY 3.0 licence (© 2018). Any distribution of this work must maintain attribution to the author(s), title of the work, publisher, and DOI.

ISBN: 978-3-95450-194-6 ISSN: 2226-0366

Content from this work may be used under the terms of the CC BY 3.0 licence (© 2018). Any distribution of this work must maintain attribution to the author(s), title of the work, publisher, and DOI.

- Shvedunov, N.V.
- Shvedunov, V.I.
- Simonov, A.S.

LEBRA
Funabashi, Japan
- Hayakawa, K.
- Hayakawa, Y.
- Nogami, K.
- Sakai, T.
- Sumitomo, Y.
- Takahashi, Y.
- Tanaka, T.

MAX IV Laboratory, Lund University
Lund, Sweden
- Andersson, J.
- Björklund Svensson, J.
- Brandin, M.
- Curbis, F.
- Isaksson, L.
- Kotur, M.
- Lindau, F.
- Lindvall, R.
- Mansten, E.
- Svärd, R.
- Thorin, S.
- Werin, S.

MEPhI
Moscow, Russia
- Bulygin, A.M.
- Gusarova, M.
- Kaminskiy, V.I.
- Kulevoy, T.
- Matsievskiy, S.V.
- Polozov, S.M.
- Shashkov, Ya.V.

MGH
Hyogo-ken, Japan
- Chouhan, V.
- Ida, Y.I.
- Nii, K.N.
- Yamaguchi, T.Y.

MHI
Hiroshima, Japan
- Hara, H.
- Yanagisawa, T.

MHI-MS
Kobe, Japan
- Miyamoto, A.
- Sennyu, K.

Mitsubishi Electric System & Service Co., Ltd
Tsukuba, Japan
- Ushimoto, S.

Nagoya University, Graduate School of Science
Chikusa-ku, Nagoya, Japan
- Iijima, T.
- Sue, Y.

Nanjing University of Aeronautics and Astronautics
Jiangning, People's Republic of China
- Zhao, L.

NCBJ
Świerk/Otwock, Poland
- Lorkiewicz, J.A.
- Nietubyć, R.

Nihon Koshuha Co. Ltd
Yokohama, Japan
- Aizawa, S.
- Akikawa, H.
- Endo, O.
- Nagatsuka, K.
- Okuyama, T.
- Sato, K.
- Yamada, H.

NIMS
Tsukuba, Ibaraki, Japan
- Kikuchi, A.

NINT
Shannxi, People's Republic of China
- Cong, P.T.
- Liu, W.L.
- Ouyang, X.P.
- Qiu, M.T.
- Sun, B.
- Tan, X.J.
- Wang, B.C.
- Wang, M.C.
- Wang, Z.M.
- Wei, C.Y.
- Weng, X.F.
- Yang, Y.
- Zhang, X.D.
- Zhao, C.

Nippon Advanced Technology Co., Ltd.
Tokai, Japan
- Nagura, N.
- Ohba, T.
- Sato, Y.

ISBN: 978-3-95450-194-6 ISSN: 2226-0366

NIRS
Chiba-shi, Japan
- Iwata, Y.

Nomura Plating Co, Ltd.
Osaka, Japan
- Okii, Y.

Northern Illinois University
DeKalb, Illinois, USA
- Piot, P.

NRC
Moscow, Russia
- Kulevoy, T.

NSC/KIPT
Kharkov, Ukraine
- Bezditko, O.
- Karnaukhov, I.I.
- Moisieienko, M.
- Mytsykov, A.
- Zelinsky, A.Y.

NSTRI
Tehran, Iran
- Ghasemi, F.
- Poursaleh, A.P.

NSU
Novosibirsk, Russia
- Arsentyeva, M.V.

NTG Neue Technologien GmbH & Co KG
Gelnhausen, Germany
- Bechtold, A.
- Niewieczerzal, P.

Nuclear Science and Technology Research, InstituteRadiation Application School
Tehran, Iran
- Zarei, S.

NUCTECH
Beijing, People's Republic of China
- Guan, W.Q.
- He, Y.
- Li, J.

ODU
Norfolk, Virginia, USA
- De Silva, S.U.
- Deitrick, K.E.
- Delayen, J.R.
- Krafft, G.A.
- Overstreet, S.A.
- Park, H.
- Terzić, B.

ORNL
Oak Ridge, Tennessee, USA
- Aleksandrov, A.V.
- Champion, M.S.
- Cousineau, S.M.
- Galambos, J.
- Howell, M.P.
- Kim, S.-H.
- Moss, J.
- Plum, M.A.
- Riemer, B.W.
- White, K.S.
- Zhukov, A.P.

ORNL RAD
Oak Ridge, Tennessee, USA
- Cathey, B.L.
- Connell, M. S.
- Steffey, R. W.

Oxford University, Physics Department
Oxford, Oxon, United Kingdom
- Foster, B.

PAL
Pohang, Kyungbuk, Republic of Korea
- Han, J.H.
- Jeong, S.-H.
- Jung, Y.G.
- Kang, H.-S.
- Kim, C.
- Kim, D.E.
- Kim, G.
- Kim, M.J.
- Lee, H.-G.
- Lee, S.B.
- Oh, B.G.
- Park, K.-H.
- Park, S.J.
- Park, Y.J.
- Suh, H.S.
- Yang, H.

PKU
Beijing, People's Republic of China
- Chen, J.E.
- Chen, M.
- Chen, S.
- Cheng, A.Q.
- Cheng, W.
- Feng, L.W.

Content from this work may be used under the terms of the CC BY 3.0 licence (© 2018). Any distribution of this work must maintain attribution to the author(s), title of the work, publisher, and DOI.

ISBN: 978-3-95450-194-6 ISSN: 2226-0366

Content from this work may be used under the terms of the CC BY 3.0 licence (© 2018). Any distribution of this work must maintain attribution to the author(s), title of the work, publisher, and DOI.

- Gao, S.L.
- Hao, J.K.
- Li, B.T.
- Lin, L.
- Liu, G.
- Liu, K.X.
- Lu, X.Y.
- Lu, Y.R.
- Peng, S.X.
- Quan, S.W.
- Tan, W.W.
- Wang, F.
- Wang, Z.
- Xiao, L.
- Xie, D.
- Yan, X.Q.
- Yang, D.Y.
- Yang, Y.
- Zhu, F.
- Zhu, K.

PLAI
Nanjing, People's Republic of China
- An, S.
- Ke, Y.J.
- Lingbin, S.
- Pengjiao, Z.
- Wenliang, L.
- Youchun, L.
- Zhao, L.
- Zhou, B.Z.

Politecnico di Torino
Torino, Italy
- Falletta, S.

POSTECH
Pohang, Kyungbuk, Republic of Korea
- Hwang, J.H.
- Ko, I.S.
- Ko, J.H.
- Shin, S.-G.

PSI
Villigen PSI, Switzerland
- Bettoni, S.
- Bopp, M.
- Braun, H.-H.
- Citterio, A.
- Craievich, P.
- Dehler, M.M.
- Ferrari, E.
- Fitze, H.
- Garvey, T.
- Hermann, B.
- Ischebeck, R.
- Kleeb, T.
- Löhl, F.
- Marcellini, F.
- Pedrozzi, M.
- Raguin, J.-Y.
- Reiche, S.
- Rivkin, L.
- Rolli, K.
- Shi, L.
- Thominet, V.G.
- Zennaro, R.

QST
Aomori, Japan
- Akagi, T.
- Ebisawa, T.
- Hirata, Y.
- Ichimiya, R.
- Kasugai, A.
- Kondo, K.
- Maebara, S.
- Sakamoto, K.
- Shinya, T.
- Sugimoto, M.

RadiaBeam
Santa Monica, California, USA
- Agustsson, R.B.
- Kutsaev, S.V.
- Smirnov, A.Yu.
- Verma, A.

RAS/INR
Moscow, Russia
- Paramonov, V.V.

RI Research Instruments GmbH
Bergisch Gladbach, Germany
- Keune, B.
- Knaak, M.
- Pekeler, M.

RIKEN Nishina Center
Wako, Japan
- Haba, H.
- Imao, H.
- Ishida, K.
- Kamigaito, O.
- Kusaka, K.
- Okuno, H.
- Ozeki, K.
- Sakamoto, N.
- Suda, K.
- Watanabe, T.
- Watanabe, Y.
- Yamada, K.

RIKEN SPring-8 Center
Sayo-cho, Sayo-gun, Hyogo, Japan
- Asaka, T.
- Fukui, T.

ISBN: 978-3-95450-194-6 ISSN: 2226-0366

- Hara, T.
- Inagaki, T.
- Maesaka, H.
- Otake, Y.
- Tanaka, H.

RISE
Tokyo, Japan
- Washio, M.

RLNR
Tokyo, Japan
- Hayashizaki, N.

Rostock University, Faculty of Computer Science and Electrical Engineering
Rostock, Germany
- Pommerenke, H.W.
- van Rienen, U.

Saint Petersburg State University
Saint Petersburg, Russia
- Skudnova, I.

SCK•CEN
Mol, Belgium
- Vandeplassche, D.

SCU
Chengdu, People's Republic of China
- Li, Z.

SEIV
Mérignac, France
- Beaugerard, N.

SES
Hyogo-pref., Japan
- Hasegawa, T.
- Morimoto, O.
- Tajiri, Y.
- Tanaka, S.
- Yoshioka, M.

Shahid Beheshti University
Tehran, Iran
- Abbasi Davani, F.
- Abbasi, F.
- Ghasemi, B.G.
- Mohseni Kejani, M.
- Salehi, M.

Shanghai APACTRON Particle Equipment Company Limited
Shanghai, People's Republic of China
- Pu, Y.H.
- Xie, X.C.
- Yang, F.

SINAP
Shanghai, People's Republic of China
- Deng, H.X.
- Fang, W.
- Gu, Q.
- Li, D.M.
- Li, X.
- Li, Z.B.
- Pu, Y.H.
- Qiao, J.
- Wang, D.
- Xie, X.C.
- Yan, J.W.
- Zhao, M.H.
- Zhao, Z.T.

SINP MSU
Moscow, Russia
- Alimov, A.S.
- Ermakov, A.N.
- Kamanin, A.N.
- Khankin, V.V.
- Kurilik, A.
- Ovchinnikova, L.
- Pakhomov, N.I.
- Shvedunov, N.V.
- Shvedunov, V.I.
- Yurov, D.S.

SLAC
Menlo Park, California, USA
- Bowden, G.B.
- Dal Forno, M.
- Dolgashev, V.A.
- Gonnella, D.
- Haase, A.A.
- Li, Z.
- Seryi, A.

Slovak Academy of Sciences, Institute of Electrical Engineering
Bratislava, Slovak Republic
- Huran, J.

SNU
Seoul, Republic of Korea
- Bae, S.
- Choi, S.
- Kim, B.

Content from this work may be used under the terms of the CC BY 3.0 licence (© 2018). Any distribution of this work must maintain attribution to the author(s), title of the work, publisher, and DOI.

ISBN: 978-3-95450-194-6 ISSN: 2226-0366

Content from this work may be used under the terms of the CC BY 3.0 licence (© 2018). Any distribution of this work must maintain attribution to the author(s), title of the work, publisher, and DOI.

Sokendai
Ibaraki, Japan
- Hori, Y.
- Hotei, T.
- Ito, H.
- Kako, E.
- Konomi, T.
- Matsumoto, T.
- Miura, T.
- Okada, T.
- Qiu, F.
- Rehman, M.R.
- Sakai, H.
- Umemori, K.
- Yamamoto, Y.

Sokendai - Hayama
Hayama, Japan
- Du, B.
- Liu, N.

Soreq NRC
Yavne, Israel
- Berkovits, D.
- Bukai, M.
- Dafna, H.
- Kaizer, B.
- Luner, J.
- Mazor, O.
- Nusbaum, D.
- Perry, A.
- Rodnizki, J.
- Shor, A.
- Silverman, I.
- Weissman, L.

STFC/DL
Daresbury, Warrington, Cheshire, United Kingdom
- Cash, R.J.
- Clarke, R.F.
- Cox, G.
- Hodgkinson, C.
- Smith, R.J.
- Wilson, J.T.G.

STFC/DL/ASTeC
Daresbury, Warrington, Cheshire, United Kingdom
- Angal-Kalinin, D.
- Brynes, A.D.
- Buckley, S.R.
- Corlett, P.A.
- Cowie, L.S.
- Dumbell, K.D.
- Dunning, D.J.
- Hornickel, P.C.
- Jackson, F.
- Jamison, S.P.
- Jones, J.K.
- McKenzie, J.W.
- Militsyn, B.L.
- Moss, A.J.
- Noakes, T.C.Q.
- Roper, M.D.
- Scott, D.J.
- Shepherd, B.J.A.
- Snedden, E.W.
- Thompson, N.
- Tollervey, C.
- Walsh, D.A.
- Weston, T.M.
- Wheelhouse, A.E.
- Williams, P.H.

Technical University of Sofia
Sofia, Bulgaria
- Apostolov, E.M.

TED
Velizy-Villacoublay, France
- Amal, Y.
- Garcin, G.
- Lievin, Ch.L.
- Sierra, S.
- Vignette, G.
- Yao Leclerc, I.

TEMF, TU Darmstadt
Darmstadt, Germany
- Bazyl, D.B.
- De Gersem, H.
- Gjonaj, E.
- Müller, W.F.O.

The Catholic University of Korea
Seoul, Republic of Korea
- Hwang, J.H.
- Kang, Y.N.
- Kim, A.R.
- Kim, J.N.
- Oh, T.G.
- Oh, Y.A.
- Seol, Y. J.
- Shin, J.S.

The College of William and Mary
Williamsburg, Virginia, USA
- Lukaszew, R.A.

The University of Liverpool
Liverpool, United Kingdom
- Hounsell, B.
- Klein, M.
- Klein, U.K.
- Kostka, P.
- Welsch, C.P.

ISBN: 978-3-95450-194-6 ISSN: 2226-0366

The University of Tokyo, Graduate School of Science
Tokyo, Japan
- Li, S.

Tohoku University
Sendai, Japan
- Nojima, T.

Tohoku University, Research Center for Electron Photon Science
Sendai, Japan
- Hama, H.
- Hinode, F.
- Kanomata, K.
- Kashiwagi, S.
- Miura, S.
- Muto, T.
- Nagasawa, I.
- Nanbu, K.
- Ninomiya, S.
- Saito, H.
- Takahashi, K.

TRIUMF
Vancouver, Canada
- Alcorta, M.
- Ames, F.
- Ang, Z.T.
- Au, T.
- Bylinskii, Y.
- Chapman, E.
- Fong, K.
- Humphries, B.
- Keikha, M.
- Keir, J.J.
- Kester, O.K.
- Kishi, D.
- Kiy, S.
- Kolb, P.
- Kong, A.
- Koscielniak, S.R.
- Lang, D.
- Laxdal, R.E.
- Leewe, R.
- Liu, H.
- Ma, Y.
- Matheson, B.
- Nagimov, R.R.
- Planche, T.
- Rowe, M.
- Rädel, S.D.
- Shelbaya, O.
- Thoeng, E.
- Verzilov, V.A.
- Waraich, B.S.
- Yao, Z.Y.
- Zheng, Q.
- Zvyagintsev, V.

Tsukuba University
Ibaraki, Japan
- Onishi, T.

Tsukuba University, Graduate School of Comprehensive Human Sciences
Ibaraki, Japan
- Kumada, H.
- Matsumoto, Y.
- Tanaka, Su.

TU Darmstadt
Darmstadt, Germany
- Arnold, M.
- Birkhan, J.
- Enders, J.
- Pforr, J.
- Pietralla, N.
- Schließmann, F.
- Steinhorst, M.
- Weih, S.

TUB
Beijing, People's Republic of China
- Bi, C.B.
- Chen, H.
- Cheng, C.
- Du, C.T.
- Du, T.B.
- Du, Y. C.
- Guan, X.
- Guo, Q.K.
- Huang, W.-H.
- Jiang, H.
- Lei, Y.
- Ma, P.F.
- Man, K.D.
- Shi, J.
- Shuai, S.
- Tang, C.-X.
- Tang, R.
- Tian, Q.L.
- Wang, D.
- Wang, X.W.
- Xing, Q.Z.
- Xudong, X.D.
- Yan, L.X.
- Ye, W.B.
- Yu, X.D.
- Zha, H.
- Zhang, H.Y.
- Zheng, S.X.

TUL-DMCS
Łódź, Poland
- Cichalewski, W.

Content from this work may be used under the terms of the CC BY 3.0 licence (© 2018). Any distribution of this work must maintain attribution to the author(s), title of the work, publisher, and DOI.

ISBN: 978-3-95450-194-6 ISSN: 2226-0366

Content from this work may be used under the terms of the CC BY 3.0 licence (© 2018). Any distribution of this work must maintain attribution to the author(s), title of the work, publisher, and DOI.

ULVAC, Inc
Chiba, Japan
- Ito, R.
- Nagata, T.

ULVAC, Inc.
Tsukuba, Japan
- Nagata, T.

UMAN
Manchester, United Kingdom
- Appleby, R.B.
- Owen, H.L.
- Smith, E.J.H.

UNIST
Ulsan, Republic of Korea
- Chung, M.
- Kim, S.Y.

Universita' degli Studi di Milano
Milano, Italy
- Petrillo, V.

Universita' degli Studi di Milano & INFN
Milano, Italy
- Faillace, L.
- Rossetti Conti, M.

University of Chinese Academy of Sciences
Beijing, People's Republic of China
- Li, X.
- Yang, L.

University of Glasgow
Glasgow, United Kingdom
- Nugent, J.C.

University of Hamburg
Hamburg, Germany
- Bate, C.
- Semione, G.D.L.
- Stierle, A.

University of Hamburg, Institut für Experimentalphysik
Hamburg, Germany
- Foster, B.
- Hillert, W.

University of Tokyo
Tokyo, Japan
- Kitamura, R.
- Yasuda, H.Y.

Università di Roma II Tor Vergata
Roma, Italy
- Cianchi, A.

Uppsala University
Uppsala, Sweden
- Hermansson, L.
- Jobs, M.
- Li, H.
- Ruber, R.J.M.Y.
- Santiago Kern, R.

USTC/NSRL
Hefei, Anhui, People's Republic of China
- Chen, T.
- Li, W.
- Pei, Y.J.
- Tang, Zh. X.

Utsunomiya University
Utsunomiya, Japan
- Oikawa, H.

Vitzrotech Co., Ltd.
Ansan City, Kyunggi-Do, Republic of Korea
- Hyun, S.Y.
- Kim, D.Y.
- Lee, J.
- Yu, D.H.

Waseda University, Waseda Institute for Advanced Study
Tokyo, Japan
- Sakaue, K.

WING. Co.Ltd
Iwate-ken, Japan
- Anetai, Y.
- Takahashi, F.

Yale University, Beam Physics Laboratory
New Haven, Connecticut, USA
- Jiang, Y.

ISBN: 978-3-95450-194-6 ISSN: 2226-0366

Participants List

— A —

Akemoto, Mitsuo
KEK, Japan

Anetai, Yasunori
WING. LTD, Japan

Ang, Zhengting
TRIUMF, Canada

Ao, Dante
Pfeiffer, Germany

Apsimon, Robert
Lancaster, UK

Arai, Yuta
Miyoshi Gokin Kogyo, Japan

Arnold, Michaela
IKP, TU Darmstadt, Germany

Arsentyeva, Mariya
BINP, Russia

Asaka, Takao
RIKEN, Japan

— B —

Bacci, Alberto
INFN, Italy

Bai, Bowen
IHEP, China

Bai, Jiaoni
JGU, Germany

Bai, Jin
IAEE/HUST, China

Bai, Yu
IHEP, China

Baricevic, Borut
Instrumentation, Slovenia

Barth, Winfried
GSI, Germany

Basten, Markus
IAP Frankfurt, Germany

Bellandi, Andrea
DESY, Germany

Bencini, Vittorio
CERN, Switzerland

Berner, Thomas
WIENER, Germany

Bezditko, Oleksandr
NSC KIPT, Ukraine

Bian, Lin
IHEP, China

Bozzolan, Michele
CERN, Switzerland

Branlard, Julien
DESY, Germany

Brynes, Alexander
STFC, UK

Burt, Graeme
Lancaster, UK

Button, David
ANSTO, Australia

Byrd, John
ANL, USA

— C —

Cabaleiro, Francisco
AVO-ADAM, Switzerland

Cao, Shuchun
IMP-CAS, China

Cathey, Brandon
Tennessee, USA

Cha, Hyuk Jin
Korea Univ., Korea

Chen, Jinfang
SINAP-CAS, China

Chen, Meng
PKU, China

Chen, Nelson
Lake Shore, USA

Chen, Shu
PKU, China

Chen, Ye
DESY, Germany

Cheng, Anqi
PKU, China

Cheng, Sinong
IHEP, China

Chi, Yunlong
IHEP, China

Chin, Yong Ho
KEK, Japan

Choroba, Stefan
DESY, Germany

Chouhan, Vijay
Marui, Japan

Chrin, Jan
PSI, Switzerland

Chu, Chungming
IHEP, China

Cianchi, Alessandro
Univ. of Rome, Italy

Clark, Jamie
Microwave Amps, UK

Compton, Chris
FRIB, USA

Conde, Manoel
ANL, USA

Craievich, Paolo
PSI, Switzerland

— D —

De Michele, Giovanni
AVO-ADAM, Switzerland

Deitrick, Kirsten
JLab, USA

Delaviere, Tom
Bergoz, France

Di Giacomo, Marco
GANIL-SPIRAL2, France

Ding, Hongli
DICP-CAS, China

Doebert, Steffen
CERN, Switzerland

Dohmae, Takeshi
KEK, Japan

Du, Baiting
KEK, Japan

Du, Yingchao
Tsinghua, China

Dunkel, Kai
RI Research, Germany

Dziuba, Florian Dirk
HIM, Germany

Content from this work may be used under the terms of the CC BY 3.0 licence (© 2018). Any distribution of this work must maintain attribution to the author(s), title of the work, publisher, and DOI.

ISBN: 978-3-95450-194-6 ISSN: 2226-0366

Content from this work may be used under the terms of the CC BY 3.0 licence (© 2018). Any distribution of this work must maintain attribution to the author(s), title of the work, publisher, and DOI.

— E —

Easton, Matt
PKU, China

Eaton, Douglas
ScandiNova, USA

Einarson, Stephen
CPI, USA

Elkamchi, noureddine
CNRS-LAL, France

Enomoto, yoshinori
KEK, Japan

Ermakov, Andrei
SINP MSU, Russia

— F —

Fabris, Alessandro
Elettra, Italy

Facco, Alberto
INFN, Italy

Faia, DANIEL A.
Lake Shore, USA

Fan, Mengxu
IHEP, China

Feldmeier, Eike
HIT, Germany

Ferdinand, Robin
GANIL, France

Feschenko, Alexander
INR RAS, Russia

Fu, Shinian
IHEP, China

— G —

Galambos, John
ORNL, USA

Gao, ZhangFeng
SINAP-CAS, China

Garolfi, Luca
CERN, Switzerland

Ge, Mingqi
Cornell Univ., USA

Gerhard, Peter
GSI, Germany

Ghaderi Beromi, Rouhollah
SUT, Iran

Ghasemi, Farshad
NSTRI, Iran

Gresele, Ambra Alessia
Ettore Zanon, Italy

Grespan, Francesco
INFN-LNL, Italy

Groening, Lars
GSI, Germany

Gumus, Cagil
DESY, Germany

Guo, Jiquan
JLab, USA

Guo, Lei
IMS, Japan

— H —

Hasegawa, Kazuo
JAEA, Japan

Hayano, Hitoshi
KEK, Japan

He, Yuan
IMP-CAS, China

Hillenberg, Jakob Spencer
Allied Metals, USA

Höltermann, Holger
BEVATECH, Germany

Holen, Paul
Stangenes Industries, USA

Honda, Yosuke
KEK, Japan

Hotei, Takahiro
KEK, Japan

Hou, Xueying
IHEP, China

Hrovatin, Rok
Cosylab , Slovenia

Hu, Xing
Nuclear , China

Huening, Markus
DESY, Germany

Hwang, Jihyun
PAL, Korea

— I —

Ida, Yoshiaki
Marui, Japan

Irikura, Masao
Toshiba, Japan

Ito, Hayato
KEK, Japan

Ito, Ryohei
ULVAC, Japan

Iwashita, Yoshihisa
Kyoto Univ., Japan

— J —

Jamison, Steven
Lancaster, UK

Janezic, Elvis
Instrumentation, Slovenia

Jensen, Jens-Peter
DESY, Germany

Ji, Daheng
IHEP, China

Ji, Hongfei
IHEP, China

Jia, Huan
IMP-CAS, China

Jiang, Jiao
HUST, China

Jolly, Simon
UCL, UK

ISBN: 978-3-95450-194-6 ISSN: 2226-0366

— K —

Kaabi, Walid
LAL-CNRS, France

Kako, Eiji
KEK, Japan

Kang, Heung-Sik
PAL, Korea

Katayama, Ryo
Kyoto Univ., Japan

Kawamura, Masato
KEK, Japan

Kedia, Sanjay Kumar
IUAC, India

Khankin, Vadim
SINP MSU, Russia

Kim, Sanghoon
KERI, Korea

Kim, Seongyeol
UNIST, Korea

Kitamura, Ryo
Tokyo Univ., Japan

Kleffner, Carl
GSI, Germany

Ko, Jun Ho
POSTECH, Korea

Kon, Kenichi
Iwate, Japan

Kondo, Yasuhiro
JAEA, Japan

Konomi, Taro
KEK, Japan

Koscielniak, Shane
TRIUMF, Canada

Kourkafas, Georgios
HZB, Germany

Kulevoy, Timur
ITEP, Russia

Kurennoy, Sergey
LANL, USA

Kutsaev, Sergey
RadiaBeam, USA

— L —

Lagniel, Jean-Michel
GANIL, France

Lallement, Jean-Baptiste
CERN, Switzerland

Laxdal, Robert
TRIUMF, Canada

Lechartier, Michel
GANIL, France

Ledroit, Ben
JGU, Germany

Lee, Jongman
VITZROTECH, Korea

Lee, Yongseok
KERI, Korea

Leopoldes, David
Sigmaphi, France

Li, AHong
IHEP, China

Li, Han
Uppsala, Sweden

Li, Jingyi
IHEP, China

Li, Lu
IMP-CAS, China

Li, Wenliang
Nanjing Univ., China

Li, Yunhai
HeFei LeiKe, China

Li, ZhiYong
FRIB, USA

Li, Zijia
Bergoz , China

Li, Zongbin
SINAP-CAS, China

List, Julian
HIM, Germany

Liu, Jiaji
IHEP, China

Liu, Bo
SINAP-CAS, China

Liu, Huachang
IHEP, China

Liu, Jie
IHEP, China

Liu, NA
KEK, Japan

Liu, Wolong
NINT, China

Liu, Xing
IHEP, China

Liu, Xinmeng
IMP-CAS, China

Liu, Yiyong
SINAP-CAS, China

Liu, Yuefeng
SINAP-CAS, China

Loïc, Amoudry
LAL, France

Lorenzo, Peli Mario
UCVAC,

Lu, Zhijun
IHEP, China

Lu, Liang
IMP-CAS, China

Lu, Yao
HUST, China

Lyu, Hongqing
Wuxi Creative, China

Content from this work may be used under the terms of the CC BY 3.0 licence (© 2018). Any distribution of this work must maintain attribution to the author(s), title of the work, publisher, and DOI.

ISBN: 978-3-95450-194-6 ISSN: 2226-0366

Content from this work may be used under the terms of the CC BY 3.0 licence (© 2018). Any distribution of this work must maintain attribution to the author(s), title of the work, publisher, and DOI.

— M —

Ma, Pengfei
Tsinghua, China

Ma, Yongsheng
IHEP, China

Madec, Catherine
CEA, France

Maesaka, Hirokazu
RIKEN, Japan

Manini, Paolo
SAES, Italy

Maniscalco, James
Cornell Univ., USA

Marocchino, Alberto
INFN, Italy

Martin, Beatrice
DB, Italy

Martynov, Andrei
JINR, Russia

Massarelli, Emanuele
EEI, Italy

Masui, Hiroaki
ULVAC, Japan

McAteer, Meghan
HZB, Germany

McCausey, Amy
MSU, USA

McIntosh, Peter
STFC, UK

Meng, Xianghua
SAES, China

Mereu, Paolo
INFN, Italy

Mickat, Sascha
GSI, Germany

Mingioni, Carlo
INFN, Italy

Mitoya, Goh
Higashi-Nihon Kidenkaihatsu, Japan

Moisieienko, Maxym
NSC KIPT, Ukraine

Mori, Shingo
KEK, Japan

Morishita, Takatoshi
JAEA, Japan

— N —

Nagata, Tomohiro
ULVAC, Japan

Naito, Fujio
KEK, Japan

NamkunG, Won
PAL, Korea

Neil, George
Neil, USA

Niemczyk, Raffael
DESY, Germany

Nii, Keisuke
Marui, Japan

Nikbakht, Mohsen
AUT, Iran

Nisa, Zaib Un
IHEP, China

Nölle, Dirk
DESY, Germany

Nozdrin, Mikhail
JINR, Russia

— O —

Ogasawara, Yoshihito
Miyoshi Gokin, Japan

Oguri, Hidetomo
JAEA, Japan

Oh, Nak-kyun
VITZROTECH, Korea

Oikawa, Hiroki
Utsunomiya Univ., Japan

Okada, Takafumi
KEK, Japan

Okubo, Yoshihisa
Toshiba, Japan

O'Rourke, Brian
AIST, Japan

Ostroumov, Peter
MSU, USA

Otake, Yuji
JASRI, Japan

Ouyang, Huafu
IHEP, China

Ovchinnikova, Liubov
SINP MSU, Russia

— P —

Pagani, Carlo
INFN, Italy

Pan, Feng
IMP-CAS, China

Pan, Qian
IHEP, China

Pang, Jian
IFP, CAEP

Paramonov, Valentin
INR RAS, Russia

Park, HyeKyoung
ODU, USA

Park, Kihyeon
PAL, Korea

Pattalwar, Shrikant
STFC, UK

Pei, Guoxi
IHEP, China

Peng, Maomao
Tsinghua, China

Peng, Shixiang
PKU, China

Peng, Jun
IHEP, China

PERRY, Amichay
Soreq NRC, Israel

Petit-Jean-Genaz, Christine
CERN, Switzerland

Pichoff, Nicolas
CEA, France

Pieck, Martin
LANL, USA

Piersanti, Luca
INFN, Italy

Plawski, Tomasz
JLab, USA

Plückthun, Mark
Allied Metals, USA

Podlech, Holger
IAP Frankfurt, Germany

PommerenkE, Hermann Winrich
CERN, Switzerland

Pozdeyev, Eduard
FRIB/MSU, USA

ISBN: 978-3-95450-194-6 ISSN: 2226-0366

— Q —

Qi, Mengyao
IHEP, China

Qiao, Jian
SINAP-CAS, China

Qiao, Yusi
IHEP, China

Qin, Chuan
IHEP, China

Qin, Qing
IHEP, China

Qin, Wenwen
Mitsubishi, China

Qiu, Feng
KEK, Japan

Qiu, Zhi
Cosylab, China

— R —

Raparia, Deepak
BNL, USA

Ratzinger, Ulrich
Goethe Univ., Germany

Reece, Charles
JLab, USA

Rehman, Muhammad Abdul
KEK, Japan

Rodnizki, Jacob
Soreq NRC, Israel

Roh, Sung-Joo
VITZROTECH, Korea

Rossi, Massimo
DB , Italy

Ruan, Yufang
IHEP, China

Ruelas, Marcos
RadiaBeam, USA

— S —

Saeki, Takayuki
KEK, Japan

Saito, Hirotoshi
Tohoku Univ., Japan

Sakai, Hiroshi
KEK, Japan

Sakai, Takeshi
Nihon Univ., Japan

Sakakibara, Mitsuru
Ohtama, Japan

Sakamoto, Naruhiko
RIKEN, Japan

Sato, Masaharu
KEK, Japan

Sauza-Bedolla, Joel
CERN, Switzerland

Schaa, Volker RW
GSI, Germany

Schlarb, Holger
DESY, Germany

Schneider, Philipp
IAP Frankfurt, Germany

Schuett, Maximilian
IAP Frankfurt, Germany

Schwarz, Malte
IAP Frankfurt, Germany

Sekutowicz, Jacek
DESY, Germany

Sha, Peng
IHEP, China

Shashkov, Yaroslav
NRNU MEPhI, Russia

Shen, Xiaokang
IMP-CAS, China

Shi, Jiaru
Tsinghua, China

Shi, liangliang
PSI, Switzerland

Shi, Rongjian
IHEP, China

Shibata, Takanori
KEK, Japan

Sierra, Serge
Thales, France

Sievers, Sven
DESY, Germany

Skudnova, Irina
SPbU, Russia

Sledneva, Anna
JINR, Russia

Solopova, Anna
JLab, USA

Song, Naibin
HE-Racing, China

Steinhorst, Manuel
IKP, TU Darmstadt, Germany

Stulle, Frank
Bergoz, France

Sugimoto, Masayoshi
QST, Japan

Sumbaev, Anatoly
JINR, Russia

Sun, Anjun
Ohtama, Japan

Sun, Liepeng
IMP-CAS, China

Sunesson, Anders
ESS ERIC, Sweden

Syha, Marc
IAP Frankfurt, Germany

— T —

Takahashi, Fukumi
WING. LTD, Japan

Takeuchi, Yusuke
Kyoto Univ., Japan

Tang, Jingyu
IHEP, China

Telyari, Mohammad
SUT, Iran

Tetsuka, Katsuhiko
Toshiba, Japan

Thomson, Jana
TRIUMF, Canada

Tracz, Piotr Stanislaw
IFIN-HH, Romania

— U —

Umemori, Kensei
KEK, Japan

Content from this work may be used under the terms of the CC BY 3.0 licence (© 2018). Any distribution of this work must maintain attribution to the author(s), title of the work, publisher, and DOI.

ISBN: 978-3-95450-194-6 ISSN: 2226-0366

Content from this work may be used under the terms of the CC BY 3.0 licence (© 2018). Any distribution of this work must maintain attribution to the author(s), title of the work, publisher, and DOI.

— V —

Valeriy, Kobets
JINR, Russia

Vassal, Adrien
GANIL, France

Venturini Delsolaro, Walter
CERN, Switzerland

Vint, Andrew
Cockcroft , UK

Vogel, Elmar
DESY, Germany

Vogel, Hanspeter
RI Research, Germany

Vogel, Vladimir
DESY, Germany

Volkov, Vladimir
BINP, Russia

Vretenar, Maurizio
CERN, Switzerland

— W —

WAN, Jinyu
IHEP, China

Wang, Baichuan
NINT, China

Wang, CHAO
IMP-CAS, China

Wang, Dong
SINAP-CAS, China

Wang, lei
Wuxi Creative, China

Wang, Shan
IHEP, China

Wang, Wangsheng
IMP-CAS, China

Wang, Xu
IHEP, China

Wei, Tao
IFP, CAEP

Weih, Simon
IKP, TU Darmstadt, Germany

Weise, Hans
DESY, Germany

Wenskat, Marc
DESY, Germany

Wu, Andong
IMP-CAS, China

Wu, Junxia
IMP-CAS, China

— X —

Xiang, Rong
HZDR, Germany

Xiao, Binping
BNL, USA

Xiao, Dengjie
IHEP, China

Xie, Xiucui
SINAP-CAS, China

Xing, Chaochao
IMP-CAS, China

Xing, Qingzi
Tsinghua, China

Xu, Hang
IHEP, China

Xu, Jiankun
Ophir, Asia-Pacific

Xu, Wencan
BNL, USA

— Y —

Yamamoto, Yasuchika
KEK, Japan

Yamasaki, Toshifumi
ULVAC, Japan

Yan, Jiawei
SINAP-CAS, China

Yan, Xueqing
PKU, China

Yang, Haeryong
PAL, Korea

Yang, Jinghe
CIAE, China

Yang, Lei
IMP-CAS, China

Yang, Na
IHEP, China

Yang, Yujia
PKU, China

Yang, Yao
IMP-CAS, China

Yao, Zhongyuan
TRIUMF, Canada

Ye, Jian
Cosylab, China

Ye, Wenbo
Tsinghua, China

Yeckel, Christopher
Stangenes, USA

Yildirim, Burcu
DESY, Germany

Yin, Xuejun
IMP-CAS, China

Yin, Zhe
Signalmicrowave, China

Yu, Peiyan
IMP-CAS, China

Yu, Xudong
TSU, China

Yu, Yong
DICP-CAS, China

Yuan, jiandong
IMP-CAS, China

Yuan, Yating
IAEE/HUST, China

Yurov, Dmitry
SINP MSU, Russia

Yushiro, Osamu
ScandiNova, Japan

— Z —

Zahir Joozdani, Mohsen
IUST, Iran

Zhai, Jiyuan
IHEP, China

Zhang, Shipeng
IHEP, China

Zhang, Lei
IMP-CAS, China

Zhang, PengJiao
Andesun , China

Zhang, Xiaodong
NINT, China

Zhang, Yaqian
IHEP, China

Zhang, Yong
IMP-CAS, China

ISBN: 978-3-95450-194-6 ISSN: 2226-0366

Zhang, Zuofu
Marui , Japan

Zhao, Hongwei
IMP-CAS, China

Zhao, Liang
JLab, USA

Zhao, Ning
IHEP, China

Zhao, Quantang
IMP-CAS, China

Zhao, Zhentang
SINAP-CAS, China

Zheng, Qiwen
TRIUMF, Canada

Zheng, shuxin
Tsinghua, China

Zhou, Bowen
Nanjing Univ., China

Zhou, Jie
IHEP, China

Zhou, Xiangyu
KEK, Japan

Zhou, Youwei
IMP-CAS, China

Zhou, Zusheng
IHEP, China

Zhu, Yunliang
IMP-CAS, China

Zong, Yang
IMP-CAS, China

Zukeyama, Suehiro
Ohtama, Japan

Content from this work may be used under the terms of the CC BY 3.0 licence (© 2018). Any distribution of this work must maintain attribution to the author(s), title of the work, publisher, and DOI.